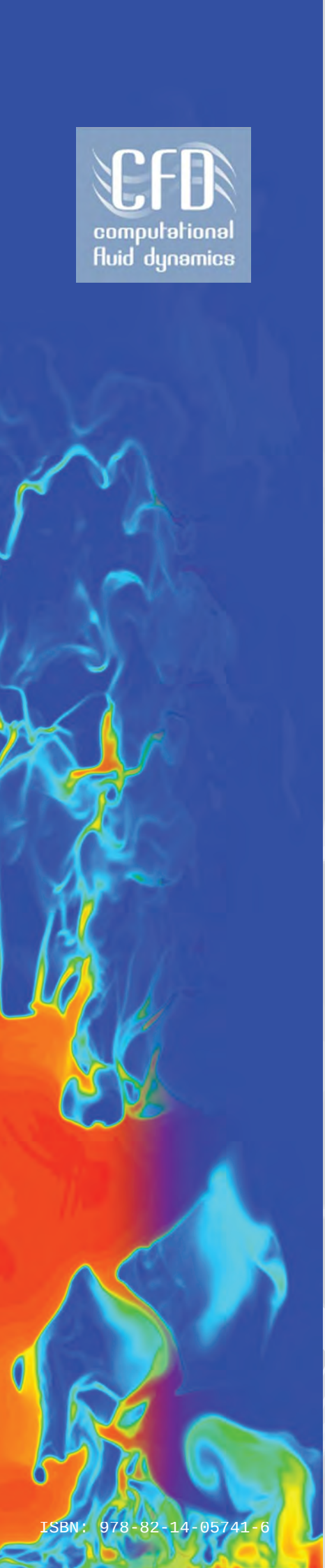

June 17- 19, Trondheim, Norway

CFD 2014

10th International Conference on

Computational Fluid Dynamics
in the Oil & Gas, Metallurgical and Process Industries

PROCEEDINGS

Organized by:

SINTEF

Main sponsors:

ANSYS

TOTAL

ISBN: 978-82-14-05741-6

PROCEEDINGS

of the 10th International Conference on Computational Fluid Dynamics in the Oil & Gas, Metallurgical and Process Industries

SINTEF is pleased to host the 10th international conference in this series. The conference series was initiated by CSIRO and Phil Schwarz in 1997. So far the conference has been alternating between CSIRO in Melbourne and SINTEF in Trondheim. The conferences focuses on the application of CFD in the oil and gas industries, metal production, mineral processing, power generation, chemicals and other process industries. The conference is also known as CFD2014 for short.

This document contains all approved papers for the conference. These have been reviewed by SINTEF and other conference participants. These constitute the official proceedings of the conference. A few authors have chosen to present without submitting a full paper. These are not part of the official proceedings.

The organizing committee would like to thank everyone who has helped with paper review, those who promoted the conference and all authors who have submitted scientific contributions. We are also grateful for the support from the conference sponsors: FACE (the multiphase flow assurance centre), Total, ANSYS, CD-Adapco, Ascomp, Statoil and Elkem.

Stein Tore Johansen & Jan Erik Olsen

The following pages contain the papers of the proceedings. Note that the preceding list of papers is linked to the respective papers and can thus be used for navigation.

Trondheim, June 2014

ISBN: 978-82-14-05741-6

Pragmatic Modelling
On pragmatism in industrial modeling, K.E. Trætli-Einarsrud, A. Solheim, S.T. Johansen & J. Zoric
A six chemical species CFD model of alumina reduction in a Hall-Héroult cell, P.J.Witt, Y.Q.Feng, G.A.Snook, I.Eick & M.Cooksey
A pragmatic approach to CFD modelling of separation processes, K.E.Trætli-Einarsrud, B.Panjwani & V.Pauchard
Multi-scale process models to enable the embedding of CFD derived functions: Curtain drag in flighted rotary dryers, A. Lee, M. Sheehan & P.A. Schneider
CFD in problem analysis and optimization – the importance of correct boundary conditions, E.Manger
A combined multifluid-PBE model for a slurry bubble column reactor: application to the Fischer-Tropsch synthesis, C.B.Vik, J.Solsvik & H.A.Jakobsen
Packed Beds
A two-fluid model coupled with porous medium description to predict liquid spreading in trickle-bed reactors, Z.Solomenko, M.Fourati, Y.Haroun, F.Larachi, C.Boyer & F.Augier
Local simulation of the effect of void fraction on the overall reaction rate in packed beds reactors, M. Rolland
Transport of the moments of the age distr. by CFD in fixed bed operation units, L.Fangueiro Gomes, F.Augier, D.Leinekugel-le-Cocq, I.Vinkovic & S.Simoëns
A multi-scale model for oxygen carrier selection and reactor design applied to packed bed CLC, M.Tabib, J.Morud, S.T.Johansen & S.Amini
Casting & Solidification
Prediction of mass transfer between liquid steel and slag at continuous casting mold, P.Gardin, S.Gauthier & S.Vincent
Structure effect of turbo-swirl in an uphill teeming ingot casting process, H. Bai, M. Ersson & P. Jönsson
Modelling of tracer mixing in continuous casting tundishes, C.Chen, A. Tilliander, L.T.I. Jonsson, G. Cheng & P. Jönsson
Num. investigation of the immersion quenching process for heat treated parts using an eulerian multi-fluid approach, R.Kopun, D.Greif, Z.Kovacic & M.Suffa
Particles & DEM
DEM-CFD simulations and imaging experiments on charging of pneumatically conveyed powders, M.W.Korevaar, J.T.Padding, J.Wang, M. De Wit, M.A.I.Schutyser, M.A.van der Hoef & J.A.M.Kuipers
Establishing predictive capability of DEM simulations: sliding and rolling friction coefficient of non-spherical particles, L. Benvenuti, A. Aigner, D. Queteschiner, M. Combarros, S. Pirker & C. Kloss
Understanding segregation in granular media, G.G.Pereira, M.Sooriyabandara & P.W.Cleary
Hard-sphere modelling of liquid bridge agglomeration, B.V.Balakin, G.Shamsutdinova & P.Kosinksi
High Temperature Processes
Multi-scale modeling of hydrocarbon injection into the blast furnace raceway, C.Maier, C.Jordan, C.Feilmayr, C.Thaler & M.Harasek
CFD modelling of a rotating arc plasma reactor, S.G.Johnsen & A.J.Simonsen
Numerical investigation of syngas combustion in a HITAG system using CFD techniques, M.Saffari Pour, P.Mellin, W.Yang & W. Blasiak
CFD Simulation of a burner head in a secondary reformer for ammonia synthesis, J.Bujalski & J.Dauparas
Fluidized Beds
Numerical investigation of the vertical plunging force of a spherical intruder into a prefluidized granular bed, Y.Xu , J.T.Padding, M.A.van der Hoef & J.A.M.Kuiper
Operating experience with a high-temperature pseudo-2D fluidized bed reactor designed especially for detailed local data collection, A.Zaabout, S.Cloete, S.T.Johansen, S.Amini
Heat transfer in gas-solid fluidized bed through an integrated DIA/PIV/IR technique, A.Patil, E.A.J.F.Peters & J.A.M.Kuipers
Hybrid Eulerian-Lagrangian modelling of bi-disperse fluidized beds, S.Schneiderbauer, S.Puttinger & S.Pirker
The parametric sensitivity of fluidized bed reactor simulations carried out in different flow regimes, S.Cloete, J.H.Cloete, S.T.Johansen & S.Amini
Bed expansion and pressure drop in a bubbling fluidized bed, K.J.Mandich & R. J.Cattolica
Validation of a CFD model for 3d cylindrical gas-solid fluidized beds, V.Verma, J.T. Padding, N.G. Deen & J.A.M.Kuipers
Procedural method for simulating an industrial urea granulation process, P. Lau & M. Kind
DEM development of heat and mass transfer in a spout fluidized bed with liquid injection, V.S. Sutkar, S.Taalman, N.G. Deen, V.Salikov, S.Antonyuk, S.Heinrich & J.A.M.Kuipers
Simulation of rectangular fluidized bed with Geldart D particles, M.P.Tandon & A.Karnik
Hydrodynamic investigation into a novel IC-CLC reactor concept for power production with integrated CO2 capture, A.Zaabout, S.Cloete & S.Amini
CFD modelling of heat supply in fluidized bed fast pyrolysis of biomass, P.Mellin, Y. Wu, E.Kantarelis & W.Yang

Euler-Lagrangian Models
Comparing Euler-Euler and Euler-Lagrange based modelling approaches for gas-particle flows, M.Braun, M.Lambert, S.Ozarkar & J.Sanyal
Agglomeration study in the inlet section of a large scale spray dryer using stochastic Euler-Lagrange modelling, S.K.Pawar, J.T.Padding, N.G.Deen, A.Jongsma, F.Innings & J.A.M.Kuipers
State of the art in mapping schemes for dilute and dense Euler-Lagrange simulations, S.Radl, B.Capa Gonzales, C.Goniva & S.Pirker
Numerical simulation of ice accretion on vessels and structures due to sea spray, M.Popescu & S.T.Johansen
Combustion & Turbulence
Multi-scale modelling of turbulent flows by embedded lattice-Boltzmann co-simulation, S.Pirker, S.Puttinger, P.Seil, S.Schneiderbauer
Modeling of post combustion inside the off-gas duct system of the Ovako electric arc furnace, N.Arzpeyma, M.Ersson & P.Jönsson
Modelling of the Ferrosilicon furnace: effect of boundary conditions and burst, B.Panjwani & J.E.Olsen
Population Balance Methods
A study of breakage by single drop experiments, J. Solsvik & H.A. Jakobsen
Modelling of bubble size distr. by using homogeneous and inhomogeneous population balance approaches, L.Deju, S. C. P.Cheung, G. H.Yeoh & J.Y.Tu
Simulation of polydisperse gas-liquid systems with QBMM, A.Buffo, D.L.Marchisio, M.Vanni, J.Hofinger & P.Renze
Rotating Machinery
CFD simulations of a Wankel pump with moving and static grids, J. Y. C Leong, T. Ba, S. Y. M. Wan, Y. Zhao, C. W. Kang, W. L. Loh & A. T. B. Lim
CFD study of the Influence of pre-rotation of multiphase flow on pump performance, M.P.Strongin
Pipe Flow
Forecasting turbulent drag reduction in a pipeline flow on the basis of Taylor-Couette device experimental data, D.Eskin
CFD modelling of gas entrainment at a propagating slug front, J.Hua, J.Nordbø & M.Foss
Computational modelling of subsea hydrates formation and associated risks and impact on flow assurance, M.Labois, N.Pagan, D.Lakehal & C.Narayanan
CFD modelling of the two-phase flow of different mixtures in a closed system flow wheel, J.F. Roca R, J.N.E. Carneiro, J.E.S. Oliveira, S. Mo, M. Fossen & S.T.Johansen
Modelling of particle transport and bed-formation in pipelines, C. Narayanan, S. Gupta & D. Lakehal
Quasi-3D modelling of two-phase flows in pipes, A. Vichansky
Simulation of two-phase viscous oil flow, S.T.Johansen, S.Mo, J.Kjølaas, C.Brekken & I.Eskerud Smith
Packed Beds & Permeability
CFD simulations of flow in random packed beds of spheres and cylinders: analysis of the velocity field, F.Dorai, M.Rolland, A.Wachs, M.Marcoux & E.Climent
Pore-scale simulation of fluid flow in packed-bed reactors via rigid-body simulations and CFD, G. Boccardo, L. Del Plato, D. Marchisio, F. Augier, Y. Haroun, D. Ferre & M. Icardi
Automated workflow for spatially resolved fixed bed reactors with spherical and non-spherical particles, T.Eppinger, N.Jurtz & R.Aglave
Numerical model for flow in rocks composed of materials of different permeability, R Li, S. Yang, J.Pan, G.G. Pereira, J. Taylor, B. Clennell & C. Zou
Modeling of bubbly flows with free surface using a hybrid volume of fluid and discrete bubble model approach, D.Jain, J.A.M.Kuipers & N.G.Deen
Metallurgy & Leaching
Modelling thermal effects in the molten iron bath of the HIsmelt reduction vessel, P. Witt, Y.Q.Feng & M. P. Davis
Design optimization of a metal tapping room for minimized dust emission, B.Panjwani, B.Wittgens, S.T.Johansen & B.Ravary
Heap leaching simulation: beyond shrinking core models, L.Cai, R.Ferrier, Q.Lin, P, Mostaghimi, J.G.Gorman & S.Neethling
Design and improvement of an industrial airlift reactor using computational fluid dynamics, T.Song, K.Jiang, J.Zhou, D.Wang, N.Xu & Y.Feng
Bubble & Droplet Dynamics
A critical comparison of surface tension models for the volume of fluid method, M.W. Baltussen, J.A.M. Kuipers & N.G. Deen
Numerical simulation of the influence of bubble bursting on a molten iron surface, Y.G.Xu, M.Ersson & P.G.Jönsson
An enhanced front tracking method featuring volume conservative remeshing and mass transfer, I.Roghair, M.van Sint Annaland & J.A.M.Kuipers
Drop breakup modelling in turbulent flows, B. Lalanne, S. Tanguy, J. Vejrazka, O. Masbernat & F. Risso

Oil & Gas Applications
Cool down simulations of subsea equipment, A. Jensen & S. Grafsrønningen
Predicting emulsion pressure drop in pipes through CFD multiphase rheology models, N. J. Inkson, J. Plasencia & S. Lo
Transient modelling of relief lines for surface testing application, B.Zielinska, F.Allouche, L.Fraser & N.Zafar
Methods & Fundamentals
Towards a mechanistic model for subcooled flow boiling at low-pressure, S.Vahaji , S.C.P.Cheung, G.H.Yeoh & J.Y.Tu
Enabling CFD codes to perform systematic parameter continuation and stability analysis for realistic applications, N.Cheimarios, E.D.Koronaki, H.Laux & A.G.Boudouvis
Extending a serial 3D two-phase CFD code to parallel execution over MPI by using the PETSc library for domain decomposition, Å.Ervik, S.T.Munkejord & B.Müller
Space-time hp-adaptive DG-FEM scheme for one-dimensional multiphase flow models, J.S.B.van Zwieten, R.A.W.M.Henkes, D.R. van der Heul, P.I. Rosen Esquivel, B. Sanderse & C.Vuik
Fluid Interfaces
Lattice Boltzmann simulations applied to understanding stability of multiphase interfaces, G.G.Pereira
Orr-Sommerfeld stability analysis of two-fluid Couette flow with surfactant using Chebyshev collocation method, V.Bojja & M.Fernandino
Effect of compressibility in CFD simulations of an oscillating water column device, A.Kamath, H.Bihs, J.E.Olsen, Ø.A.Arntsen
CFD multiphase simulation of two-fluid sloshing with free surface motion using the level set method, H.Bihs, A.Kamath & Ø.Arntsen
Discrete Particle Modelling (DPM/DBM)
Adding argon injection through the DPM+VOF technique to an advanced multi-physics and multiscale model for continuous casting of steel, P.E.Ramirez Lopez, P.Jalali, U.Sjöström & C.Nilsson
Governing physics of shallow and deep subsea gas release, J.E.Olsen & P.Skjetne
Modeling of bubbly flows with free surface using a hybrid volume of fluid and discrete bubble model approach, D.Jain, J.A.M.Kuipers & N.G.Deen
Particles & Deposition
Analysis of particle deposition from turbulent liquid-flow onto smooth channel walls, M.Dupuy, A.Xayasenh, E.Waz, P.Le Brun & H.Duval
Modelling of pulverised fuel transport for industrial applications, A.I.J.Love, D.Giddings & H.Power
Numerical Study of the gas-particle flow in a conveying line: accounting for wall-friction and wall-roughness, A.Soleimani, S.Schneiderbauer & S.Pirker
A study of simulation and experiment on airborne wear particles from wheel-rail contacts, H.Liu, L.Jonsson & P.Jönsson
Industrial Applications
Fully coupled multiphase simulation of a bottom-spray wurster coater using a hybrid cpu/GPU CFD/DEM approach, E. Siegmann, C. Radeke & J.G. Khinast
Benchmark of multi-component diffusion models for simulation of MOVPE reactors, J.Bassen & H.Laux
Effect of the wind turbine wake in large offshore wind farms, M. Popescu, B.Panjwani, J.Samseth & E.Meese
A modeling strategy for large-scale mechanical draught air-cooled systems,C.J. Meyer & A. Zapke
Bubbly Flows
A Baseline model for monodisperse bubbly flows, R. Rzehak , E. Krepper, Th. Ziegenhein & D. Lucas
Monodisperse bubbly flows with ANSYS CFX and OpenFOAM: a comparison, S.H.L. Kriebitzsch, R. Rzehak & D. Lucas
Experimental studies of bubbly flow in a micro-structured bubble column reactor using digital image analysis, K. Thiruvalluvan Sujatha, J.A.M. Kuipers & N.G. Deen
Two dimensional numerical simulation of bubble dynamics in a vertical Hele-Shaw cell, X.Wang, B.Klaasen, B.Blanpain & F.Verhasghe
Separation
CFD modeling of oil-water separation efficiency in three-phase separators, L. Oshinowo, E. Elsaadawy and R. Vilagines
Towards simulating flotation with OpenFOAM, G.Holzinger, G.Wierink & S.Pirker
Lagrangian and Eulerian simulations of inclusion behaviour in liquid metal processing, J.P. Bellot, V. Descotes & A. Jardy

ON PRAGMATISM IN INDUSTRIAL MODELING

Josip Zoric, Stein Tore Johansen, Kristian Trætli-Etienne Einarsrud, Asbjørn Solheim
SINTEF Materials and Chemistry, Trondheim, Norway
(Josip.Zoric; Stein.T.Johansen; Kristian.Etienne.Einarsrud; Asbjorn.Solheim @sintef.no)

ABSTRACT

Many natural or industrial processes are of extreme complexity, and where the time- and length scales range from atomistic level to years and kilometers. Often the processes or phenomena consist of multiple sub processes in which each comprises its own length and time scales. An example can be production of aluminum by the Hall-Heroult process, where process streams or raw materials, flow dynamics and segregation in silos, with time varying quality, the feeding and operational routines, the reduction cells with numerous sub processes, and the tapping process, all make up a complete process. To optimize such type of production with respect to economic and environmental parameters we will have to develop models which can give the overall picture and at the same time be accurate enough to support the optimization process. As there are many dynamic aspects of an industrial production, the ultimate need will be a model which can compute much faster than real time and which can be used to support operation and to develop new processes.
In this paper we discuss how this type of pragmatic industrial models can be developed. We will identify and discuss the tools needed for such an analyses, including the analyses process itself and the frameworks needed for such analyses. Key elements in our pragmatic modeling concepts are human knowledge, including capabilities to understand complex phenomena and how these can be modeled simplified but "good enough", systematic use of existing information, systematic analyses of what information (model results) is needed and at with which accuracy and speed the results must be produced. Another key element is the selection and collection of experiment data and the exploitation of data, organized and made accessible in the optimal manner to support the predictiveness of the pragmatism based model. The organization of all types of data is organized by a "bridge" (modeling middleware) between complex scientific (aspect/phenomenon oriented) physical models, simplified models and process data. We believe that this type of pragmatic industrial models will enable a step change in both operation, operator training and process optimization, as well as design of new processes. Finally, in a case study, we apply our pragmatic modeling concept to the aluminum production process and discuss the implications of our proposed concept.

Keywords: Modeling, framework, pragmatism, industry, process.

1. INTRODUCTION

Position and Motivation

Many natural or industrial processes are of extreme complexity, and where the time and length scales range from atomistic level to years and kilometers. Often the processes or phenomena consist of multiple sub processes in which each comprises its own length and time scales. An example can be production of aluminum by the Hall-Heroult process [1] where process streams or raw materials, flow dynamics and segregation in silos, with time varying quality, the feeding and operational routines, the reduction cells with numerous sub processes, and the tapping process, all make up a complete process. To optimize such type of production with respect to economic and environmental parameters we will have to develop models which can give the overall picture and at the same time be accurate enough to support the optimization process. As there are many dynamic aspects of an industrial production, the ultimate need will be a model which can compute much faster than real time and which can be used both to support operation and to develop new processes.
It has been stated at a previous CFD conference in Melbourne that no metallurgical process has hitherto been designed based on CFD. At the same time significant CFD work has been done on metallurgical processes. Keeping in mind the extreme complexity in a full process we realize that CFD, applied to optimize a single process step without seeing this as element in a larger system, would not be capable of driving technological-economical step changes. We will therefore have to investigate ways to model a process; ways which are simplified, but fast and sufficiently accurate to serve its purpose. These models should be based on

physics, which is critical to ensure predictive power. However, if this type of pragmatic industrial models can be developed, they will enable a step change in both operation, operator training and process optimization, as well as design of new processes.
Over many years SINTEF has been involved into research projects where the costumer's needs have been in focus and scientific excellence may conflict with the need to give the user something which can be applied immediately. Examples of this type of work are illustrated by following two applications:

1) To advice mitigation of large HF emissions in aluminum plants CFD was performed. To to run a larger parametric study the complex 3D problems were extremely simplified to smaller 2D problems. In this manner it was possible to complete the study and the results could give clear and, as later observed, successful advices.
2) In the second case [2] melt refining of liquid aluminum was predicted and optimized with a simulation tool, which was based on a combination of 1D and 0D transient models, and where sub-scale information (closures) were obtained from experimental studies and 3D CFD simulations. With this approach it was possible to make sufficiently accurate predictions much faster than real time, allowing this to become an operational tool.

In general we have experienced that use of interpolation inside pre-calculated (by CFD or similar) tables is a powerful approach, to be used as part of a model or application. As an example we have made a complete application, which is based on interpolation within data obtained from CFD calculations. However, for design of the "experimental matrix" we see clear needs for scientific experiment planning methods, including high/low analyses and factorial designs, as crucial tools for generating such tables. These observations indicated the need for a more systematic and scientific approach in development of industrial models, and we need to start out from where the scientific community currently stands on these issues.

From scientific to pragmatic

The great efforts of the natural science community ensured that many phenomena can be understood to a high level of details. Of course, in many cases the existing techniques may have to be improved or new techniques developed, for obtaining the needed information. However, these detailed and accurate studies (numerical or experimental) usually require significant time. In many cases long-time work with detailed phenomena has resulted in engineering correlations such as wall friction in pipe flow. Hence, these correlations can be used to make very fast calculations of pressure drops and flow capacities. If we move to the more complex multiphase pipeline flows, development of accurate correlations becomes much more demanding. E.g. may gas flow as bubbles or continuous liquid, while liquid flows as droplets and continuous liquid. At the same time the droplets and bubbles are in continuous evolution due to coalescence, breakup, deposition and entrainment. Currently, we have direct simulation techniques that enable simulation of detailed bubbly flows [3]. Such simulations can be performed on volumes containing at most a few liters of fluid, and where the simulations over some seconds of real time may take several days on a high performance computer cluster. In an extreme industrial case like the potential Russian Shtokman pipeline, the volume of the flow line is around 10^{11} liters, and the flow time scales are of the order of weeks (10^6 sec). Accordingly, it is for now impossible to simulate the transient flow in such a pipeline with a multidimensional approach. Our best hope is to develop simplified 1D model, which by learning from fundamental simulations, such as in Lu & Tryggvason [3] and experiments, may be made accurate enough to be industrially useful. In the past, this has been done using different pragmatic approaches, and also with varying success.

From pragmatic to scientific

As discussed above, we will in many situations need a pragmatic approach to obtain industrially relevant information. For the industrial user the model result must be available within a given time span. If not, the results may have no value. At the same time, the accuracy of the model should be quantified (probably a collaborative effort of the industrial user (case owner) and solution architects (see Figure 1 and Figure 2), such that the user knows the significance of the prediction result and resulting recommendations. The industrial model will have to be built on different building blocks, which will have to be put into system (orchestrated) by a well-defined framework (our view on the elements of the pragmatic analysis and its analytical framework are illustrated in Figure 1). What emerges from this is a need to put all these critical elements into a scientifically founded framework. As has been learned from the past, not every pragmatic approach has been successful, urging that we need to put science into the pragmatism itself.

Structure of this work

This work is organized in the following way. *Introductory section* of this paper gives our position and motivation for pragmatism in industrial modeling. We continue by discussing how to move from scientific analysis to its industrial counterpart, and vice versa. Both are important for effective and pragmatic contribution to the industry activities.
Section 2 takes a process view on pragmatic industrial analysis, including in addition to the modeling (a primary focus of our work) experimental activity,

various theoretical analyses and organizational and management activities. Before focusing on modeling, it is important to enlighten its contribution to the total analytical process, and its interplay with other, equally important parts of the pragmatic analysis. This interplay of practical, holistically organized and orchestrated methods is the property that makes the pragmatic analysis so important for the industry and different from other scientific and research approaches.

Section 3 narrows our analysis on its modeling part. Our system view on modeling is inspired by software (SW) engineering. We start by discussing modeling frameworks (an effective way to organize modeling functionality and its SW realizations), existing research body and modeling industry trends. We continue by summarizing the research and scientific requirements for a modeling framework, and map them to SW engineering requirements. We suggest the necessary evolution of modeling frameworks, for their more effective industrial use. Thereafter we treat analysis and modeling as workflows, and give a simplified example of interacting models that are orchestrated and give solution/answer on an industry-relevant problem. This introduces the section 4, which illustrates the modeling workflow on the example of industrial Al electrolysis.

Section 4 follows the analysis workflow logic suggested above on the example of industrial Al electrolysis (the Hall-Héroult process [1]). In this practical case the questions to be answered are:

- How does the heat loss from the process vary with the anode-cathode distance for the case when interfacial waves are neglected?
- What is the thickness of the frozen bath crust (side-ledge) as function of the anode-cathode distance?

Section 5 discusses our experiences with this theoretical and practical exercise and suggests future steps and improvements. We try to motivate the reader for future systematic treatment of the field "pragmatic industrial modeling", because the standardization and consolidation in industry and research, as well as SW technology, might lead to much more effective use and reuse of modeling, analyses and results.

For the reader's convenience we offer a list of terms and definitions at the end of the paper, because this multi-disciplinary paper uses many terms coming from SW engineering, system sciences and other research disciplines. We have tried to take over as much standard definitions as possible (from common Web definition sources [4-9]), and just slightly adjust them for our use. In such a way we want to contribute to the spirit of standardization of the research praxis, which this paper strongly advocates.

2. PROCESS VIEW ON PRAGMATIC INDUSTRIAL ANALYSIS

Pragmatic industrial analyses should be carefully organized, planned and executed. They require a structure not just in models, simulations, experiments, information and data, but also in analytical processes, concluding by well-structured communication of the results and the analytical context in which the results are valid. We see these important elements as parts of the analytical framework (FW), illustrated in Figure 1. Let us shortly discuss some of the important phases, and the results they produce:

1. ***Problem and Context Identification*** - this analytical phase requires discussions between the actors and stakeholders involved in industrial analysis. It includes clarifications of the use case, specification of the industrial/analytical context, agreement on needed accuracy of the solution, specification of necessary input and output information (its data formats etc.), as well as required interaction with other information systems and processes. Explicit simulations and experiments are agreed to answer given, posed questions. There are many available SW Engineering tools, standards and methodologies that can help structuring these important specifications (e.g. requirement analysis, use case specifications, pilot and demo exercises etc.). These analyses we group in ***step 1*** in Figure 1.
2. ***Analytical Strategy and Plan*** – Many industrial cases are complex and resource/time demanding. They require a good analytical strategy and planning. (This may even be in contrast with the systems that will use their results (e.g. Decision Support Systems), because they might require information, which will be provided in real-time or nearly real-time conditions.). Thus, in some cases, it will not be possible to give the answer with sufficient speed and accuracy. In such cases we need to carefully plan the experimental work or numerical experiments. Correct analytical strategy and planning (e.g. including metamodeling techniques) is critical for obtaining the results, which can be properly analyzed and qualified (illustrated as ***step 2*** in Figure 1). Several statistical methods, such as Analysis of variance (ANOVA), are available to analyze how combinations of input parameters may impact the results. Example tools that support executing such analyses are DAKOTA [10] and Mode Frontier [11].
3. ***Architecture of the Analytical Framework*** - The agreed analytical questions will often need models at many different levels to give acceptable answers. As the complexity of a model increases the organization of the model will need some framework for systemizing and orchestrating it's

sub models. Such an analytical framework must be well structured, applying an organized set of models, simulations, experiments and related information/data structures (***step 3*** in Figure 1). An example of such a framework is the volume-averaging technique [12,13]. The volume-averaging technique allows the derivation of continuum based conservation equations, based on a continuum model for the underlying materials and fluids. The approach allows multiple layers of averaging, which allows treatment of very complex systems. Such a procedure is also known as multi-scale or multi-level modeling [14].

4. ***Execution (Orchestration of Analyses, Simulations and Experiments)*** – by completing the first 3 steps illustrated in Figure 1, we have prepared the necessary set of models, simulations, experiments and other analytical procedures, and can proceed with the ***step 4***, - orchestrating them as a holistic analysis. Such an orchestration might include various modeling and analytical techniques, varying in complexity and heterogeneity. E.g. meta-modeling becomes increasingly important as the complexity of models increases. In the case of multilevel modeling the volume averaging techniques are critical in analyzing, constructing and developing part of the model framework. The volume averaging technique, when applied to a class of problems, will allow reuse of models, rules and constraints. When analysis of the problem tells that the time needed to answer a request from a higher level in the model hierarchy is too long, we have to resort to pre-calculation or experiments. This is fully possible if we have developed a solid procedure for this.

5. ***Evaluation of the Solution*** - When we are doing experiments or simulations to answer posed questions, it is critical to understand the consequence of modeling results. It is tempting to make one prediction and give a fast feedback. However, we need to have a systematic approach to assessing the results (***step 5*** in Figure 1 – solution analysis). From experience, it is well known that simulation models have many weaknesses, as well as the human limited knowledge. This imperfection is illustrated by giving 10 different, but qualified people, an industrial problem and asking for the solution based on a given CFD code (common to them all). This will in most cases give 10 different answers, where probably one answer will be close to the truth! Such challenges illustrate that our systematic approach must try to reduce the uncertainty in predictions and for now primarily by quantifying it. Then we have obvious reasons to apply ANOVA methods on both numerical and experimental data, as well as their combinations. Hence, it will be possible to quantify the accuracy of a given answer to a given question. The knowledge extraction process will often require handling of large data sets or streams. In these cases the productivity will be increased by using script based analyses tools such as MatLab [15] or Octave [16].

6. ***Conclusion and Communication*** – it is very important to conclude pragmatic analysis by a communication of the analytical results (step 6 in Figure 1). Usefulness of produced and published modeling and analytical results is often limited, because it is not well related to the analytical context. It is important to relate the analysis to its context, containing among others: (a) important analytical parameters, (b) information about modeling scale, (c) accuracy of the proposed solution, (d) estimates of representability, (e) predictive power, (f) computing and experimental resource consumption, etc.

   Information about analytical context is needed not just for the evaluation of existing models/analyses/experiments, but also for their future use and reuse. One could even require that such information gets standardized, and in such a way facilitate efficient and standard interworking (and possibility to combine existing and new analyses in solution of industrial problems).

If we succeed in standardizing, we might even manage to "decouple" the analyses from their context and reuse them in new applicable analytical situations (context). One of the reasons why models are not used widely might be that they suffer from lack of analytical transparency.

In the engineering literature there are no clear strategies for how a complex model should be designed, assembled and qualified. Most typical is to build the model based on some specification, or let the model develop organically. However, industrial models very often have clear specification of the needed time response, accuracy, formats for information flow, as well as the rules and the framework for building the entire model system (frequently specified by requirements and/or use cases). To give one example:

The accurate prediction of liquid holdup and pressure drop in multiphase pipelines is of significant industrial value. A 3D model takes typically two orders longer time than a 2D/Q3D model, which takes typically two orders longer time than a 1D flow model. These models are extremely time-consuming compared to a multiphase point model (steady state) which typically gives results in 1 ms or faster. Still such a superfast model has around 15 input parameters (properties, geometry, and velocities). If we want to cover a full matrix with 10 values for each input parameter, simulation of the matrix once will need more than 18 years of CPU time. This illustrates

that we need a scientific approach to all phases of pragmatic industrial modelling, and standardization and systematization of its phases.

3. SYSTEM VIEW ON INDUSTRIAL ANALYSIS - MODELING FRAMEWORKS

This section focuses on the modeling part of pragmatic industrial analysis (phase 3 and 4 in Figure 1). Our system view on modeling is inspired by SW engineering. We start by discussing requirements for modeling frameworks, comment on existing engineering efforts, research and industry trends. We suggest standardization and development actions for modeling frameworks, which will enhance their effective scientific and industry use. We also analyze the modeling with help of scenario and workflow techniques and give a simplified example that will be used in the practical example in section 4.

3.1 Existing research and engineering work

Based on observations from industrially related development work over many years (some referenced below), we see that there is a need for a well-structured, scientifically founded, and highly standardized framework for developing industrial models. Such a framework should be well defined in several perspectives: e.g. domain knowledge (e.g. physics, chemistry, structural mechanics…), mathematical/numerical aspects, and SW engineering perspective.

In this section we discuss the SW engineering perspective, which focus on the modeling frameworks (often called modeling platforms), their modeling elements/modules, and their architecture, topology and implementation technology.

The main purpose of so-called "pragmatic modeling" is to adjust the research models to the realism/world of industrial processes, their scope, perspective and challenges. So-called industrial models have requirements as: (a) industrial scope and perspective, (b) usefulness, (c) required accuracy and predictive-ness, (d) simplicity of use, (e) response time and speed, (f) compatibility with other (industrial) models, etc.

To meet the above-mentioned requirements, the number of the "practical" system and SW engineering requirements have to be realized, e.g.:

- Interactivity with well-established industrial standards,
- Modularity,
- Clear interfaces / API with other models and modeling tool-boxes,
- Compliancy with industrial and SW engineering standards,
- Well-defined "insertion procedures" and interaction rules in calculations (meshing interactions, initial and boundary condition inclusion, libraries of user-defined functions, procedures for solver algorithms changes etc.),
- Inter-model interworking and interoperability,
- Well-structured and standardized raw data and metadata,
- Documentation.

There is currently extensive work on modeling technology, showing variety of approaches, modelling architectures, modeling strategies, modeling technologies, e.g. expert systems based on qualitative reasoning engines and elements of AI [17], hybrid multi-zonal CFD models [18], coupling modeling and decision tools [19], model-centric support for manufacturing operations [20], and optimizations by reduced CFD models [21].

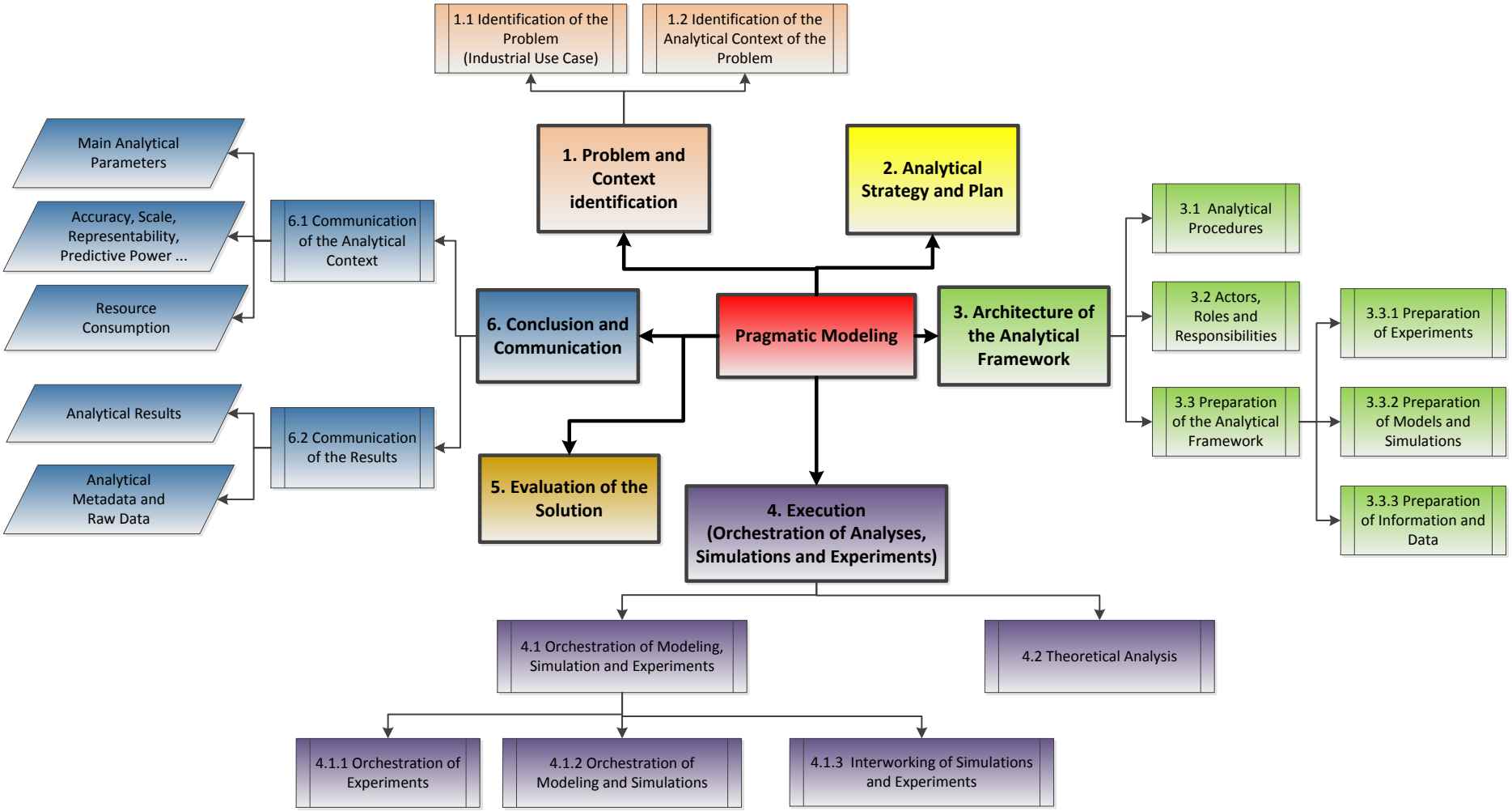

Figure 1. Some of the important phases, processes and results in a typical pragmatic analysis (terms and definitions are given in section 7).

Various model types are being combined in solutions of industrial problems, e.g.: [20,22-25]. CFD models are used for different purposes. Ref. [24] discusses embedded quantitative models in Decision Support Systems. Authors emphasize that the nature of interconnected models can vary from algebraic, decision analytic, financial, simulation, optimization and many other types. Ref. [24] stresses the need for standardization of data structures (XML), protocols and other involved ICT technologies. Lang et al. [20] discusses the need for standardization of industrial models, with example of computer-aided process engineering (CAPE). Authors emphasize two particular advances the industry can benefit from: (1) general-purpose custom-modeling platforms and (2) standardization of interface specification for component-based process simulations.

Rolandi & Romagnoli [20], as well as Urban et al. [25] stress the lack of development of both high-level frameworks and low-level mechanisms to assist the formulation of "models" of process engineering problems for support of process operations.

Rolandi & Romagnoli [20] divides the framework models in several categories: (a) first-principles process models, (b) high-fidelity process models, (c) plant-wide process models, (d) large-scale process models. They also discusses different modeling framework components, used in various phases of the modeling/analytical process: the data pre-processing environment, the estimation / reconciliation environment, the consistent data etc. They give a schema for typical modeling activities included in a typical framework for integrated model-centric support of process operations.

Lang et al. [21] describes a use of reduced order CFD models in optimization of IGCC processes. The procedure for development of reduced order models (ROM) is explained in [21,26]. They "wrap" the ROM to fit the modular framework of the simulator. Lang et al. [21] expects that the future work will continue the improvement of methods to develop accurate and efficient ROMs from CFD models, along with their integration and validation within process optimization environments.

This implementation will also be extended to the CAPE-OPEN software standard [28] and to integration within the APECS system.

Several industrial initiatives [29] and open standards / approaches, such as in [28], are getting momentum; however, at the current time, generic, standardized frameworks for scientific computing are not wide-spread. Several software vendors are instead progressing towards product-centric multiphysics frameworks, such as ANSYS workbench [30] and COMSOL Multiphysics [31]. However, a two way connectivity of such software platforms, such as recently realized between MATLAB [15] and MAPLE [32], has still not been fully realized.

Industry makes efforts towards proprietary customizable workbench solutions, which enable connecting external tools to their solutions. Workbench solutions include a combination of standard scripting languages, e.g. Python [30], data standards and interfaces, standardized modeling techniques, with well-defined protocols [30,33]. Such tools combine technologies as: bidirectional CAD connectivity, powerful highly-automated meshing, project-level update mechanisms, pervasive parameter management and various integrated optimization tools. Examples of these customizable modelling technologies include references [10,11,28,34-36].

Several strategies (both centralized and decentralized modeling approaches) to "bridging" scientific and industrial models are used in praxis:

- **Direct inclusion** of new scientific models (or their approximations / simplifications) into industrial models – enrichment of industrial models, (e.g. via libraries of user-defined functions, modification in calculation procedures / algorithms, new modeling modules, new solvers etc.)
- **Building completely new industrial models** – from scratch, based on the newest achievements of scientific models and equation solver strategies.
- **Orchestration** of various model types (e.g. script-based orchestration of models with well-arranged information exchange between models). A combination of extra-model orchestration (middleware-based) and intra-model interventions (by changing user-defined functions (UDFs), boundary conditions etc.), exchange of input/output files etc.

We expect that the future evolution of modeling frameworks for pragmatic modeling will (with respect to the topology) head in two directions:

(1) *Centralized architectures* (main modeling tool controls the modeling/simulation process, including underlying tools and modeling elements) and

(2) *Decentralized architecture*s (middleware for model orchestration: script-based or middleware-based orchestration of various models and modeling tools).

We would like to motivate further development and standardization of the SW engineering related to modeling frameworks, e.g.:

- **Standardization of the modelling middleware including standardization of:**
  - Application Programming Interfaces (APIs) and protocols, and their module-like implementations,
  - Scripts for orchestration of models, and related workflow like data exchange,
  - Monitoring, logging and control routines and mechanisms.

- **Standardization of data exchange formats (e.g. XML-based)...**
- **Standardization of modelling metadata:**
  - Specifying the analytical context in which industrial problem will be solved.
  - Specifying the accuracy, sensitivity and quality of models and simulations (this can be organized as a part of the analytical context).
  - Ensuring the description of the data entities, models, their modules and processes.

3.2 Modeling workflow – a scenario perspective

Pragmatic modeling is often a part of a complex analytical and/or design process (Figure 1). It is a team work, as illustrated by Figure 2, driven by analytical workflows (often structured by usage/analytical scenarios (Figure 2- Figure 4)). It employs a modeling framework / architecture and a set of modeling technologies. The system architects specify a set of data/information exchange standards, protocols and interfaces (to mention just a few SW design artefacts), a number of design tools (e.g. [10,11]) and modeling tools ([37,15]). Designers and analytics verify often the results by various model analyses and fine-tuning techniques (e.g. sensitivity analyses – evaluated against physical elements).

Figure 2 gives a high-level over-simplified illustration of an abstract analysis/design process, which will include modeling support in its decision-making. It illustrates pragmatic modeling roles and scenarios, modelled in unified modeling language [38].

Figure 3 shows the main analysis process as a Sequence Diagram [38]. Main Analysis triggers the Analysis 1, the algorithm of which relies upon the Analyses 2 and 3. The interaction of various analyses and their respective models is shown as sequence diagram interactions. One interaction can involve several data/information exchange processes and respective algorithms.

Figure 4 details the interaction between the Analysis 1 and the Analysis 2 (illustrated in Figure 3). In this figure we see the details of the algorithm of the Analysis 2 and the data/information exchanged among its model elements.

These high level diagrams (Figure 2- Figure 4) illustrate the SW engineering view on modeling. We will illustrate it by concrete examples offered in Section 4. We use SW-focused view to discuss the requirements and SW Engineering issues related to model interaction, data/information exchange, interfacing, standardization and other important elements for design of pragmatic models.

4. PRACTICAL EXAMPLE

4.1 Analysis 1 – Aluminum electrolysis

Primary aluminum is manufactured exclusively by the Hall-Héroult process [1]. The process is based on electrolytic decomposition of alumina dissolved in a fluoride mixture serving as electrolyte at 960 ^{o}C, using consumable carbon anodes and horizontal anode configuration. A cross-sectional view through a typical electrolysis cell is shown in Figure 5).

Owing to the high temperature, highly corrosive and opaque environment, the interior of the cell has limited access for inspection and measurement, and the processes taking place are strongly coupled. It is, therefore, necessary to apply models for predicting how the entire system will react on changes in construction or operation. For instance, to optimize the energy consumption in the cell, such changes could be related to the anode topology,

In the Hall-Héroult process, several questions may be asked, which need to be answered by models and modeling frameworks. In the present example the main question to be answered is:

- How does the heat loss from the process vary with the anode-cathode distance for the case when interfacial waves are neglected?
- Additional response requested: What is the thickness of the frozen bath crust (side-ledge) as function of the anode-cathode distance.
- Answering such questions requires some mathematical model, as direct empiric is insufficient for such an extremely complex process. As a result of the complexity and requirements to get fast and at least qualitatively correct answers, a large number of partial process models have been developed in Microsoft Excel [39]. Such models are for instance used for predicting the current efficiency, the cell voltage, the energy balances taking into account the enthalpies for the main chemical and electrochemical reactions as well as the distribution of the heat losses, and finally the temperature, pressure, and gas composition inside the cell superstructure and the flue gas scrubbing system. All partial models are based on first principles wherever possible and include fitted experimental and numerical data.
- Considering our posed question above on the overall heat loss, we simplify the heat loss from the central part of the cell bottom by regarding this as a 1D problem, and calculating the heat loss by standard engineering formulas for a layered structure. The heat loss from the sides and ends are calculated by subdivision of these regions into a number of 2D elements connected by thermal

resistances depending on the cell geometry and the thermal conductivities of the materials used. The heat loss through the different parts of the top of the cell (crust, anode, anode stubs) is computed by analytical expressions derived from numerical calculations and real measurements. The cell voltage is based on similar approaches, ranging from standard engineering formulas (ohmic resistances) via thermodynamic and electrochemical data (reversible cell voltage) to fitted laboratory and numerical data (overvoltages).

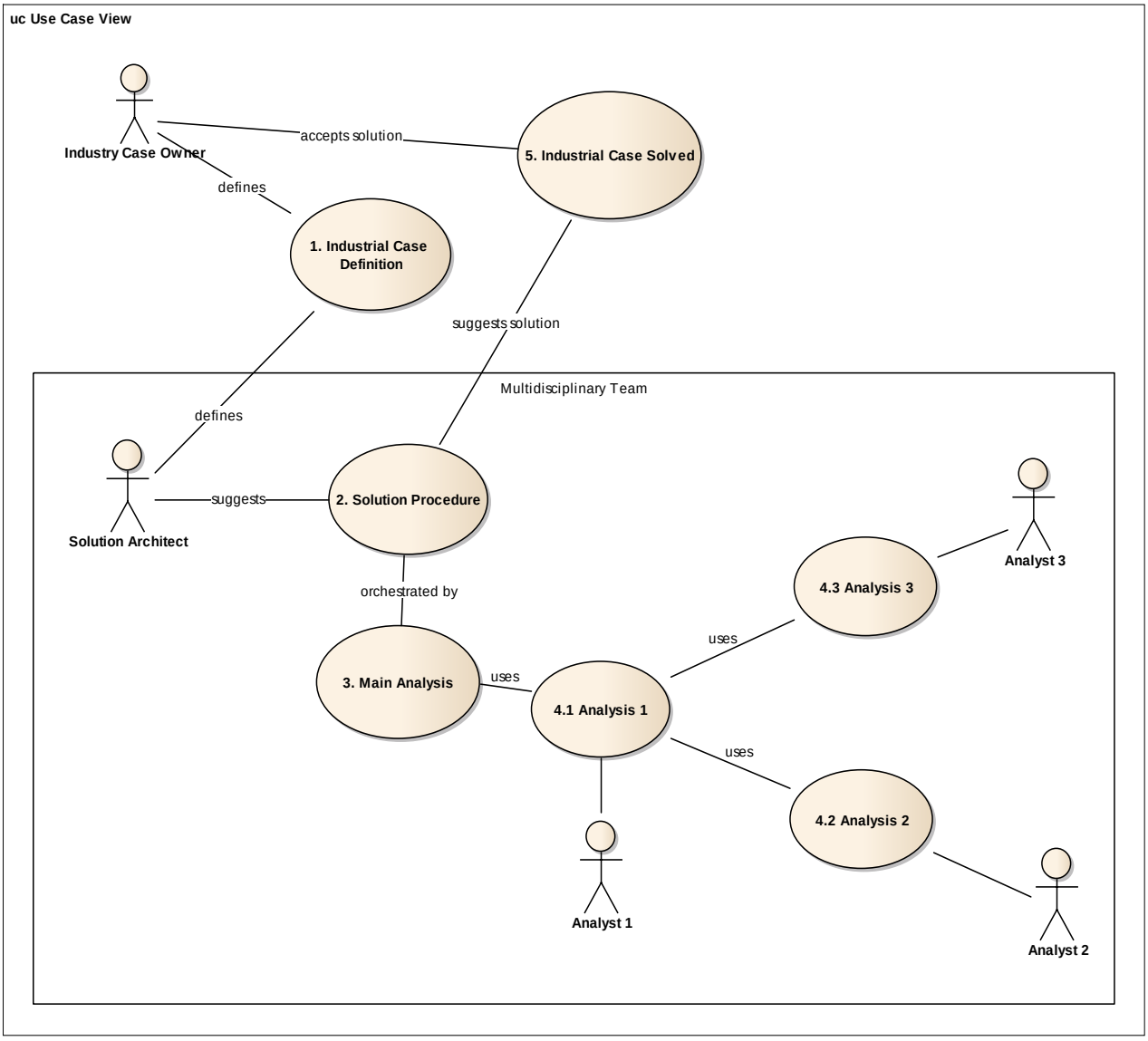

Figure 2. Use case diagram (modelled in Unified Modeling Language [38]) illustrating a simplified collaboration among actors (with their roles and responsibilities) in a pragmatic industrial modeling process.

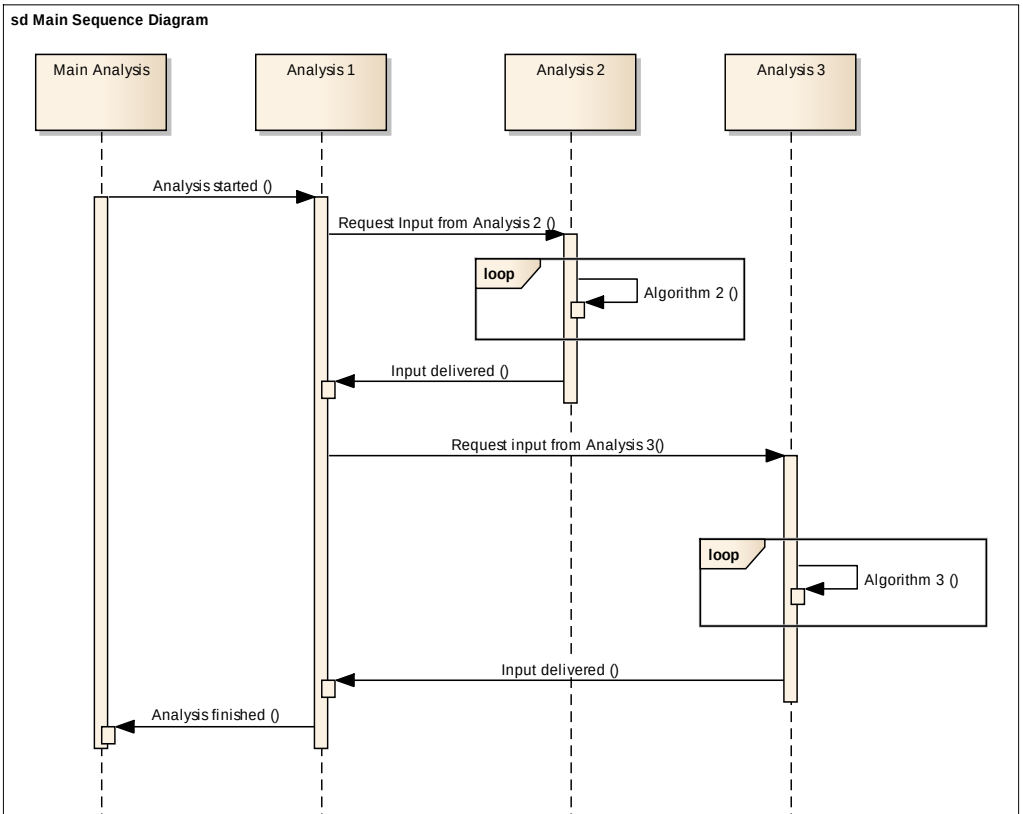

Figure 3. Sequence diagram (in Unified Modeling Language [38]) illustrating the partial realization of the use cases for the Main Analysis (shown in Figure 2).

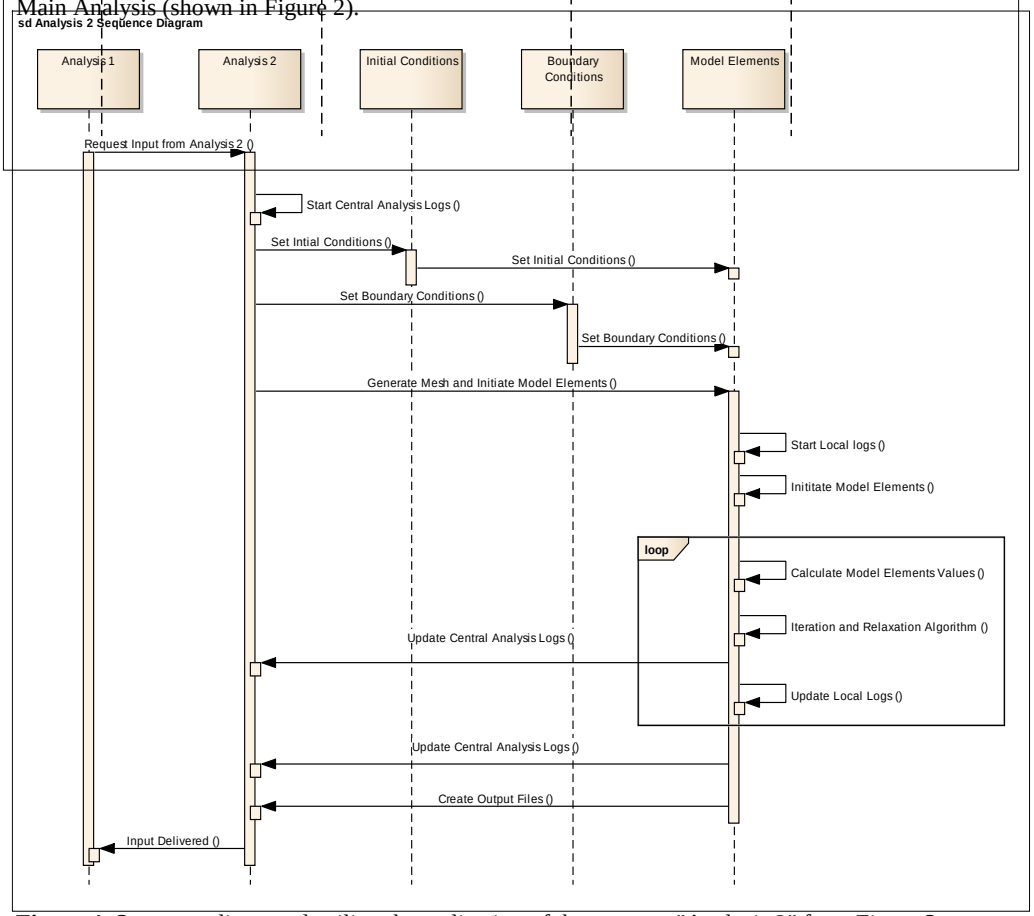

Figure 4. Sequence diagram detailing the realization of the use case "Analysis 2" from Figure 3.

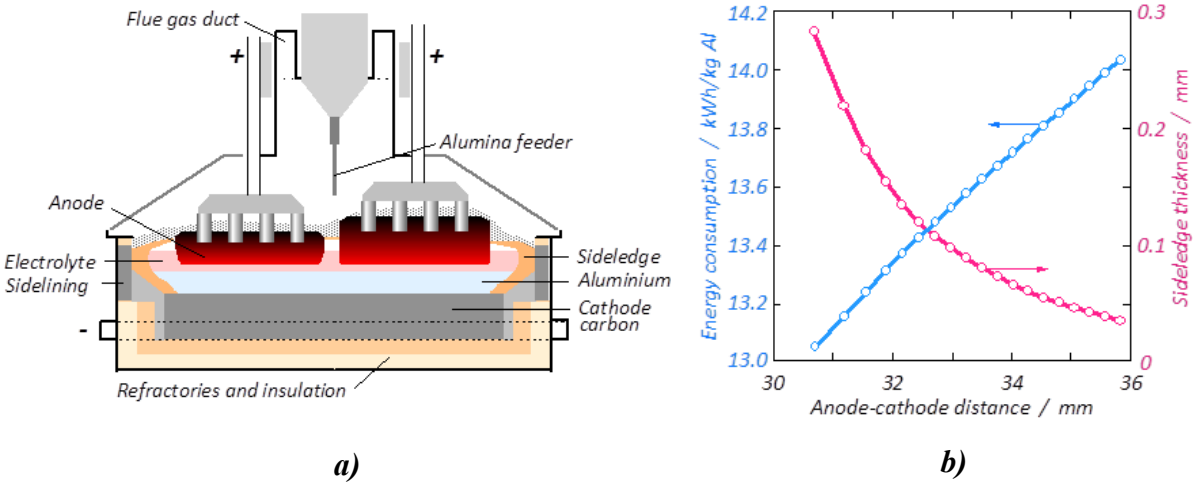

Figure 5. ***a)*** Schematic cross-section through an aluminum electrolysis cell, ***b)*** Predicted energy consumption and side ledge thickness versus anode-cathode distance.

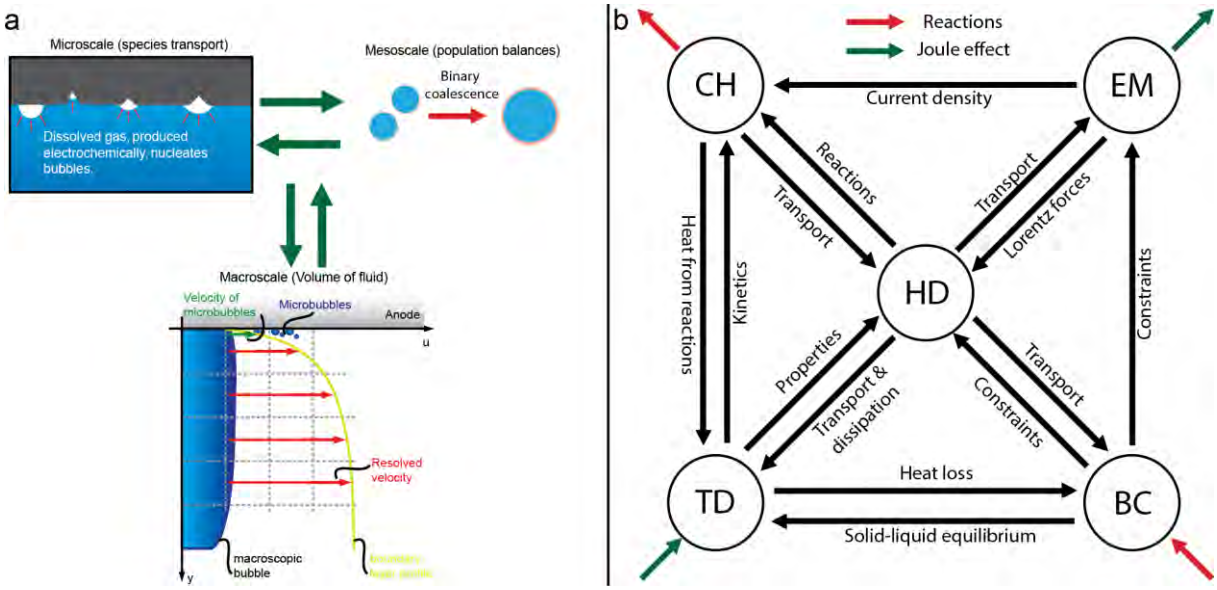

Figure 6. Schematic of multiscale approach a), and principal coupling diagram b), indicating the coupling between different phenomena in an electrolysis cell; chemical reactions (CH), electromagnetism (EM), boundary conditions (BC), thermodynamics (TD) and hydrodynamics (HD).

Some of the partial models can be used as stand-alone models, but they are all included in a total electrolysis cell modelling framework, allowing for coupled calculations and thus a holistic understanding of the overall heat balance of the cell.

The main numerical task in the framework is related to adjusting the anode-cathode distance of each individual anode until the cell voltage and the total current equal the pre-determined values, and the thickness of the side-ledge is varied until the total heat loss exactly balances the difference between the total energy input and the change in enthalpy in the process. Unfortunately, there is no way of measuring the anode-cathode distance accurately, and this parameter must be calculated from the bath voltage. The bath voltage is the difference between the total cell voltage and the remaining voltage terms, which can be either measured or modelled. The electrochemical overvoltages and the extra voltage drop due to the shielding effect of the gas bubbles ("bubble overvoltage"), which both are significant, are however difficult to measure. Presently, the calculation of the "bubble overvoltage" is based on a water model. Today, it is within reach to use CFD modelling to obtain better data on the extra resistance due to bubble shielding resulting from

different complicated anode geometries , and being a function of the gas evolution rate and flow conditions. As response to the questions posed above, a typical answer (prediction) from the model is seen in Figure 5b).
If the required correlations for bubble overvoltage are not available for the current configuration, for instance due to a novel anode design, the current analysis will ask for specific input (for instance a correlation between bubble overvoltage, anode topology and current density) from an analysis performed by a separate model framework. The calculation of such a correlation is exemplified in the following section.

4.2 Analysis 2 – Gas Evolution in Al Electrolysis

A simulation framework allowing for the description of bubble evolution on a single anode has recently been developed [40], based on a multiscale coupled population balance / Volume of Fluid approach, as sketched in Figure 6 a): On a (micro) species level, gas is produced electrochemically by the presence of an electrical current. Following saturation, mesoscale bubbles are formed, treated by population balance modeling. As small bubbles evolve due to coalescence and mass transfer, macro-scale bubbles are formed, treated by the Volume of Fluid method. Owing to low electrical conductivity, the presence of bubbles alters the current density, consequently altering the distribution of gas on the microlevel, and thus also future nucleation events. Evidently, such a framework involves coupled phenomena spanning several disciplines, as indicated in Figure 6 b).

The *simulation* framework is fully orchestrated within the user-defined-function (UDF) functionality available in ANSYS FLUENT [37], allowing a user to add and couple additional models to the solver, based on specific macros supplied by the solver. The execution order of the conservation equations (i.e. mass, momentum, turbulence and scalar fields) is fixed by the solver, while the additional required UDFs can be executed either following each iteration or each time step. Currently, resulting source terms, for instance Lorentz forces, are calculated based on converged values of the fields at the previous time step, i.e. a time-splitting scheme is adopted. As the UDFs can be used to specify only specific terms used (although choices are vast) and that the overall execution order is dictated by the solver, this is an example of a product specific orchestration.
Considering the calculation of bubble induced voltage drop, several values must be given initially, for instance the nominal current density, system temperature, fluid properties and sought anode position in the cell, all of which can be supplied from the main analysis described above. Moreover, the anode shape and surface structure (i.e. porosity distribution) are required for realistic simulations. These properties can be obtained by other modelling approaches or material databases. The conditions supplied from other models and databases serve as initial and boundary conditions for the bubble flow simulation, as sketched in Figure 6 for a general analysis.
Following meshing, on a coarse or fine level, depending upon sought accuracy and time constraints set by Analysis 1, and initialization, the bubble simulation loop is initiated and run following a specific order, based on source terms and material properties obtained at the previous time step:

1) Flow, mass and turbulence equations are solved.
2) Electrical potential is solved, and current densities are determined.
3) Additional scalar fields are solved, representing chemical species and bubble number densities (population balance model)
4) New source terms are calculated based on converged fields, initiating the next time step.

After reaching a statistically steady state, the bubble induced voltage component is monitored and averaged for a given amount of time, finally yielding the output sought by Analysis 1, which in this specific example is a correlation between bubble overvoltage, anode topology, current density and electrolyte composition. This correlation can now be returned to the model in Chapter 4.1, yielding the required output, using the requested data format.

Our experiences with this practical modeling exercise (where we have tried to follow the modeling and analytical framework mindset (section 3)) show that significant energy has been used to establish a common view on the problem, understanding of the analytical context, the common knowledge base and the common problem dictionary. When those obstacles have been removed, the orchestration of various analyses towards the final solution was reduced to a manageable problem.

With respect to SW engineering technology, our modeling FW was based on a combination of "in-house" developed models (MsExcel [39] – based macro development (Analysis 1), with a customized workbench solution – based on ANSYS FLUENT product portfolio [37, 30]. We preferred to work as close as possible to industry standards, and the closest available approach was the customization of the widely-accepted SW products.

With respect to standardized processes for pragmatic industrial analyzes we have not found available and wide-spread methodologies. Therefore we have proposed the approach illustrated in Figure 1 and described in sections 2 and 3.

5. DISCUSSION AND CONCLUSION

In many situations a pragmatic analytical and modeling approach is needed to obtain industrially relevant information. For the industrial user the model result should be available within a given time span. If not, the results may have no value. At the same time, the accuracy of the model should be quantified, such that the user knows the significance of the prediction result and resulting recommendations. The industrial model will have to be built on different building blocks, which will have to be put into system (orchestrated) by a well-defined analytical and modeling framework.

Our view on the elements of the pragmatic analysis and its analytical framework is illustrated in Figure 1. What emerges from this is a need to put all these critical elements into a scientifically founded framework. As has been learned from the past, not every pragmatic approach has been successful, urging that we need to put science into the pragmatism itself.

We believe that almost all the six phases in a typical industrial (pragmatic) analytical process illustrated in Figure 1 can be to some extent standardized, e.g.: (1) problem and context identification, (3) architecture of the analytical framework, (5) standard ways and criteria to evaluate the solution, and (6) standards for communicating the results and analytical context (for which they are valid, and usable). We can standardize the structure of the processes, the tools that are used, the quality assurance methods, as well as establish standards for how the results and analytical context are presented and described.

We would like to motivate the establishment of a scientific discipline that will focus on pragmatic industrial analyses and modeling frameworks. The effort of transforming the scientific results to industrial praxis is not just a methodological approach, but also a strategic activity. We hope that this paper and our technical opinion will contribute to establishing such a knowledge body.

6. REFERENCES

1. Thonstad, Fellner, Haarberg, Hives, Kvande and Sterten, Aluminium Electrolysis – Fundamentals of the Hall-Héroult process, 3rd Ed., Aluminium Verlag, 2001.
2. S.T. Johansen, S. Graadahl, P. Tetlie, B. Rasch, and E. Myrbostad, “Can Rotor-Based Refining Units Be Developed and Optimised Based on Water Model Experiments?”, Light Metals, Edited by Barry Welch , TMS, 1998, pp. 805-810.
3. Lu, J. and G. Tryggvason (2007). "Effect of bubble size in turbulent bubbly downflow in a vertical channel." Chemical Engineering Science 62(11): 3008-3018.
4. http://www.dictionary.reference.com
5. http://www.thefreedictionary.com
6. http://whatis.techtarget.com/definition/
7. http://wikipedia.org
8. http://searchsoa.techtarget.com/definition/
9. http://www.businessdictionary.com/definition/
10. Dakota, http://www.dakota.sandia.gov/about.html
11. Model Frontier, http://www.esteco.com/modefrontier.
12. Whitaker S., Advances in Theory of Fluid Motion in Porous Media, Ind. Eng. Chem.,Vol 61:12, pp 14-28, 1969.
13. Soo, S.L., Particulates and continuum: Multiphase Fluid Dynamics, Hemisphere Publishing, New York, 1989.
14. Ghosh, S. , Micromechanical Analysis and Multi-Scale Modeling Using the Voronoi Cell Finite Element Method, CRC Press, 2011.
15. Matlab, http://www.mathworks.se/products/matlab/.
16. Octave, http://wiki.octave.org/
17. R. Enemark-Rasmussen et.al. A simulation based engineering method to support HAZOP studies, Education of Chemical Engineers 7 (2012) e153-e162.
18. F. Bezzo, S. Macchietto, C. C. Pantelides, A general methodology for hybrid multizonal/CFD models, Part I. Theoretical Framework, Computers and Chemical Engineering 28 (2004) 501-511.
19. N. L. Rossing et. al., A functional HAZOP methodology, Computer and Chemical Engineering 34 (2010), 244-253.
20. P. A. Rolandi and J. A. Romagnoli, Integrated model-centric framework for support of manufacturing operations. Part I: The framework, Computers and Chemical Engineering 34 (2010) 17-35.
21. Y. Lang, S. E. Zitney and L.T. Biegler, Optimization of IGCC processes with reduced order CFD models, Computers and Chemical Engineering 35 (2011) 1705-1717.
22. A predictive system for blast furnaces by integrating a neural network with qualitative analysis, J. Chen, Engineering Applications of Artificial Intelligence 14 (2001) 77-85.
23. A. M. Malkawi et.al. Decision support and design evolution: integrating genetic algorithms, CFD and visualization, Automation in Construction 14 (2005) 33-44.
24. D. J. Power, R. Sharda, Model-driven decision support systems: Concepts and research directions, Decision Support Systems 43 (2007) 1044-1061.
25. Urban Z, Cheng Y-S, Pantelides CC, 2009, High-fidelity modelling and detailed design of PEM fuel cell stacks,Conference Proceedings - 2009 AIChE Annual Meeting, 09AIChE
26. Lang, Y.-D., Malacina, A., Biegler, L. T., Munteanu, S., Madsen, J. I., & Zitney, S. E. (2009). Reduced order model based on principal component analysis for process simulation and optimization, Energy and Fuels, 23, 1695–1706.
27. Aspen Custom Modeler, https://www.aspentech.com/products/aspen-custom-modeler.aspx
28. The CAPE-OPEN Laboratories Network, www.colan.org.
29. IMS, Intelligent Manufacturing Systems, www.ims.org.
30. ANSYS Workbench Integrated Environment, http://www.ansys.com/Products/Workflow+Technology/ANSYS+Workbench+Platform.
31. COMSOL Mulitiphysics, http://www.comsol.com
32. Maple, http://www.maplesoft.com/products/Maple/professional/
33. ANSYS DesignXplorer®, http://www.ansys.com/Products/Workflow+Technology/ANSYS+Workbench+Platform/ANSYS+DesignXplorer
34. Dymola, Dynamic Modeling Laboratory, http://www.3ds.com/products-services/catia/capabilities/systems-engineering/modelica-systems-simulation/dymola

35. SIMULIA V6 Overview, http://www.3ds.com/products-services/simulia/portfolio/simulia-v6/overview.
36. Open Modelica, https://www.openmodelica.org/
37. Ansys, Fluent, http://www.ansys.com/Products/Simulation+Technology/Fluid+Dynamics/Fluid+Dynamics+Products/ANSYS+Fluent
38. Unified Modeling Language, www.uml.org
39. http://office.microsoft.com/en-us/excel/
40. Einarsrud, A Treatise on Interpolar Transport Phenomena, Ph.D. Thesis 2012:201, Norwegian University of Science and Technology (NTNU), 2012.

7. TERMS AND DEFINITIONS

Table 1. List of terms and definitions.

(To offer as standard approach as possible (with respect to industry, SW engineering and usual modeling and simulation praxis), all the definitions in the paper are taken over from the common Web definition sources [4-9] and sometimes slightly adjusted for the use in this paper.)

Term	**Definition** (Definitions are taken over from the following Web definition sources - references [4-9], and sometimes slightly adjusted for the use in this paper.)
Analytical Process	• A method of studying the nature of something or of determining its essential features and their relations [4]. • In this work – a chosen method for studying an industrial problem, containing a number of well-defined steps, and results, with clear roles and responsibilities for participating actors (see also FIGURE 2).
Framework (FW)	• A skeletal structure designed to support or enclose something [4]. A frame or structure composed of parts fitted together [5], the manner of construction of something and the arrangement of its parts [5]. The underlying structure; "providing a factual framework for future research" [5]. • In general, a framework is a real or conceptual structure intended to serve as a support or guide for the building of something that expands the structure into something useful [6]. • In computer systems, (definition used in [6]) a framework is often a layered structure indicating what kind of programs can or should be built and how they would interrelate. Some computer system frameworks also include actual programs, specify programming interfaces, or offer programming tools for using the frameworks. A framework may be for a set of functions within a system and how they interrelate; the layers of an operating system; the layers of an application subsystem; how communication should be standardized at some level of a network; and so forth. A framework is generally more comprehensive than a protocol and more prescriptive than a structure [6]. • In this work – we will mostly use the definition taken from computer system sciences [6].
Analytical FW	• In this work – a conceptual structure of various analytical methods (experiments, modeling, simulations, theoretical analyses), incorporated and orchestrated in an analytical process.
Modeling FW	• In this work – we take over the definition taken from computer system sciences [6], and use it in modeling, simulations and related SW engineering activities.
Orchestration	• Orchestration describes the automated arrangement, coordination, and management of complex computer systems, middleware, and services [7]. • In this work we discuss orchestration of modeling, simulation and analytical processes in general.
Unified Modeling Language (UML)	• The Unified Modeling Language (UML) is a general-purpose modeling language in the field of software engineering. The basic level provides a set of graphic notation techniques to create visual models of object-oriented software-intensive systems. Higher levels cover process-oriented views of a system [7,38].
Use Case	• In software and systems engineering, a use case is a list of steps, typically defining interactions between a role (known in UML as an "actor") and a system, to achieve a goal. The actor can be a human or an external system. In systems engineering, use cases are used at a higher level than within software engineering, often representing missions or stakeholder goals [7,38].
Scenario	• A predicted or postulated sequence of possible events [5], an outline of the plot of dramatic work, giving particulars of the scenes, characters etc. [5].

	(We can talk of modeling scenarios, simulation scenarios, usage scenarios, analytical scenarios etc.)
Workflow	• The set of relationships between all the activities in a project, from start to finish. Activities are related by different types of trigger relation. Activities may be triggered by external events or by other activities [4].
Sequence Diagram	• A sequence diagram is an interaction diagram that shows how processes operate with one another and in what order. A sequence diagram shows object interactions arranged in time sequence. It depicts the objects and classes involved in the scenario and the sequence of messages exchanged between the objects needed to carry out the functionality of the scenario. Sequence diagrams are typically associated with use case realizations in the Logical View of the system under development [7,38].
Interface	• In computer science, an interface is the point of interaction with software, or computer hardware. Some computer interfaces can send and receive data, while others can only send data [7]. The types of access that interfaces provide between software components can include: constants, data types, types of procedures, exception specifications and method signatures [7]. The interface of a software module is deliberately kept separate from the implementation of that module. The latter contains the actual code of the procedures and methods described in the interface, as well as other "private" variables, procedures, etc. [7].
Application Programing Interface (API)	• In computer programming, an application programming interface (API) specifies how some software components should interact with each other [7]. An API specification can take many forms, including an International Standard such as POSIX, vendor documentation such as the Microsoft Windows API, the libraries of a programming language, e.g., Standard Template Library in C++ or Java API. Web APIs are also a vital component of today's web fabric. An API differs from an application binary interface (ABI) in that an API is source code based while an ABI is a binary interface [7].
Middleware	• In the computer industry, middleware is a general term for any programming that serves to "glue together" or mediate between two separate and often already existing programs. A common application of middleware is to allow programs written for access to a particular database to access other databases. Typically, middleware programs provide messaging services so that different applications can communicate. The systematic tying together of disparate applications, often through the use of middleware, is known as enterprise application integration (EAI) [8].
Raw data	• Raw data (also known as primary data) is a term for data collected from a source. Raw data has not been subjected to processing or any other manipulation, and are also referred to as primary data. Raw data is a relative term (see data). Raw data can be input to a computer program or used in manual procedures such as analyzing statistics from a survey. The term can refer to the binary data on electronic storage devices such as hard disk drives (also referred to as low-level data) [7].
Metadata	• Metadata is "data about data". Structural metadata is about the design and specification of data structures and is more properly called "data about the containers of data"; descriptive metadata, on the other hand, is about individual instances of application data, the data content [7]. As information has become increasingly digital, metadata are also used to describe digital data using metadata standards specific to a particular discipline. By describing the contents and context of data files, the quality of the original data/files is greatly increased [7].
Context	• Background, environment, framework, setting, or situation surrounding an event or occurrence [9]. • In computer science, a task context (process, thread ...) is the minimal set of data used by this task that must be saved to allow a task interruption at a given date, and a continuation of this task at the point it has been interrupted and at an arbitrary future date [7].
Analytical Context	• In this work the analytical context is a minimal set of data and metadata, needed to describe, define the analytical procedure (and if necessary reproduce it).

A SIX CHEMICAL SPECIES CFD MODEL OF ALUMINA REDUCTION IN A HALL-HÉROULT CELL

Peter J. WITT[1*], Yuqing FENG[1], Graeme A. SNOOK[2], Ingo EICK[3] and Mark COOKSEY[2]
[1] CSIRO Computational Informatics, Melbourne 3169, AUSTRALIA
[2] CSIRO Process Science and Engineering, Melbourne 3169, AUSTRALIA
[3] Hydro Aluminium Deutschland GmbH, Neuss, GERMANY
* E-mail: peter.witt@csiro.au

ABSTRACT

The industrial process for producing primary aluminium metal is the reduction of powdered alumina in a Hall-Héroult reduction cell. These cells operate at temperatures above 940 °C with a highly corrosive electrolyte making physical measurement of the process difficult or nearly impossible. Computational models of the electro-magnetic fields and heat transfer are widely used in industry to design cells. Only recently (Feng et al., 2010b, Witt et al., 2012) have detailed computational models of the molten liquid-gas bath become available. Alumina distribution within the cells is important for cell efficiency and preventing anode effects. Using the bath flow information and an assumption of uniform reduction, a single scalar transport equation has been used to track the time variation of alumina within cells (Feng et al., 2011).

In this work the previous single species model is extended to include six chemical species and four chemical reactions. The reaction pathway developed for the model is that solid alumina particles are fed to the bath surface, where they mix and submerge into the liquid bath, and then undergo dissolution from solid particles to the liquid species $Na_2Al_2O_2F_4$. Within the bath $Na_2Al_2O_2F_4$ converts to $Na_2Al_2OF_6$, which is involved in an oxidation reaction with carbon to produce carbon dioxide and AlF_3 at the anode surface. At the metal pad a cathodic reaction occurs with AlF_3 converting to aluminium metal. Species solubility rates are based on the work of Solheim et al. (1995).

A CFD model of a single anode in a bubbly cryolite bath was built based on a corner anode from an industrial cell. Steady state bath flows were calculated and used to transport the six chemical species in the new bath chemistry model. Results were obtained for 20,000 seconds of real time for species distributions in the anode to cathode distance (ACD), change in mass of species in the bath with time, rates for the four reactions at locations in the bath and change in the species mass fraction with time at various locations during a feeding cycle.

Keywords: CFD, Process metallurgy, Alumina reduction chemistry, Hall-Héroult aluminium cell, Multiphase chemistry.

NOMENCLATURE

Symbols

A_{Anode} Anode surface area, [m^2].
$A_{Cathode}$ Cathode surface area, [m^2].
F Faradays constant = 96 485 [A s mol^{-1}]
J_{Anode} Current density at anode, [A m^{-2}].
$J_{Cathode}$ Current density at cathode, [A m^{-2}].
k_1 Reaction rate equation (1), [mol s^{-1}].
k_2 Reaction rate equation (2), [mol s^{-1}].
k_3 Reaction rate equation (3), [mol s^{-1}].
k_4 Reaction rate equation (4), [mol s^{-1}].
r Cryolite ratio (molar ratio of NaF and AlF_3)
x_1 Molar fraction of $Na_2Al_2OF_6$
x_2 Molar fraction of $Na_2Al_2O_2F_4$
Y_i Mass fraction for species *i*.

Sub/superscripts

a Anode
c Cathode
i Index *i.*

INTRODUCTION

The Hall-Héroult process is the dominant industrial scale technology for reducing alumina powder to primary aluminium metal. Reduction cell performance is dependent on a mix of complex physical processes that occur in the cell and includes electrochemical, electro-magnetic, heat transfer and hydrodynamic processes.

Alumina particles are periodically feed on to the top of this molten cryolite bath; these particles then dissolve into the bath. Electrical current is supplied to the cell through anodes that are partially immersed into the top of the bath. Through an electrochemical reaction this

electrical current reduces alumina in the presence of carbon anode to aluminium metal and carbon dioxide. Evolved carbon dioxide gas forms bubbles under the anodes where buoyancy forces cause these bubbles to travel along the anode's base, before they rise to the surface beside the anode. A strong internal flow of liquid bath is established by the bubble motion and this acts to transport alumina and heat through the bath. Aluminium metal, reduced by the reaction, forms a layer of molten metal in the bottom of the cell.

Aluminium reduction cells operate in a harsh environment as the bath is molten cryolite, known to dissolve most engineering materials, and at a temperature of approximately 940°C. Electrical currents in the range of 100 to 450 kA are typical in reduction cells. Such currents induce strong magnetic fields, which act on conducting liquid metal and the molten bath, inducing secondary flows by Lorentz forces. These conditions along with restricted access make measurements on operating cells very difficult and greatly limit the amount of information that can be obtained.

To develop new cells and to improve the economic and environmental performance of existing cells, new tools are needed. Moxnes et al. (2009) described how optimised alumina feeding through experimentation can improve performance. However, experimentation is very costly and time consuming. Mathematical models can provide a tool to understand and explore how changes to cell geometry and operation affect performance (Gusberti et al. 2012). Thus validated mathematical models can provide a more efficient means of achieving improved cell performance than through experimentation.

The above description of the alumina reduction process is vastly simplified but has been successfully used previously to develop a computational fluid dynamics (CFD) model of alumina distribution in these cells. Feng *et al.* (2010a) and Feng *et al.* (2011) tracked an alumina species using a predicted bath flow field and assumed that uniform reduction occurred throughout the anode to cathode distance (ACD) under the anodes. Alumina distribution within the cell and feeding policies were able to be investigated; such an investigation was reported by Feng et al. (2010a).

In practice the bath consists of a number of ionic species that undergo a series of complex reactions. Work such as those by Gagnon *et al.* (2011), Kvande (1986) Mandin *et al.* (2009) and Solheim (2012) among others have proposed reaction models and bath species. All have assumed species transport by diffusion or simple hydrodynamic models.

In this work we extend the earlier alumina distribution model of Feng *et al.* (2011) to include six chemical species so as to more accurately represent the underlying electro-chemistry occurring in Hall-Héroult cells.

MODEL DESCRIPTION

The CFD modelling approach used in this work is to solve a steady-state model for the bath and bubble flow within a cell. Then by holding the bath flow fixed a transient model of the alumina transport, feeding and consumption is used to predict the time varying alumina concentration in the cell.

Details of the CFD model physics, approach and implementation in ANSYS/Fluent (ANSYS, 2013) have been previously documented in previous works Feng *et al.* (2010a, 2010b, 2011) and Witt *et al.* (2012). For brevity only an overview of the bath flow model is presented here.

The bath flow model describes the steady state flow of both gas and liquid phases based on a time averaged method. Key features of the bath flow model are:

- Gas and liquid flow are modelled using the Eulerian-Eulerian or two-fluid approach,
- Small-scale structures such as bubbles and turbulent structures are averaged in time and space,
- Drag from the bubbles is modelled using the Ishii and Zuber (1979) drag law,
- Turbulent effects are modelled using the *k-ε* turbulence model with modifications for multiphase flow to include, turbulent dispersion Lopez de Bertodano (1991), bubble induced turbulence (Smith, 1998 and Olmos *et al.*, 2003) and enhanced turbulent viscosity.
- Electro-magnetic effects are included through the Lorentz force, which is calculated from magnetic and electric fields for a typical pot line.

The alumina distribution model describes the transient distribution of alumina and other chemical species within the liquid bath. Transport of alumina and other chemical species is based on the steady state bath flow model.

The key stages in reduction of alumina to aluminium metal are:

- **Feeding** of alumina to the bath surface, this can occur at various times and at a number of locations,
- **Initial breakup, mixing** and submersion of particles from the surface into the liquid bath, assumed to occur over 10 seconds, this is used to set boundary condition for the alumina such that the mass from a feed event is averaged over a 10 second period,
- **Dissolution** of alumina particles into the bath through the reaction:

$$Al_2O_{3(sol)} + 3\ NaF + AlF_3 \overset{k1}{\Rightarrow} \frac{3}{2}\ Na_2Al_2O_2F_4 \qquad (1)$$

- **Equilibrium** bath reaction:

$$Na_2Al_2O_2F_4 + 2\ NaF + 2\ AlF_3 \overset{k2}{\Leftrightarrow} 2\ Na_2Al_2OF_6 \qquad (2)$$

- **Anode** boundary layer reaction:

$$2\ Na_2Al_2OF_6 + C \overset{k3}{\Rightarrow} 4e^- + 4\ AlF_3 + 4\ Na^+ + CO_2 \qquad (3)$$

- **Cathode** or metal pad boundary layer reaction:

$$AlF_3 + 3\,Na^+ + 3e^- \overset{k4}{\Rightarrow} Al + 3\,NaF \qquad (4)$$

Reactions rates are required for equations (1) to (4).

The rate for alumina dissolution into the bath is based on the work of Frovolov *et al.* (2007) who observed alumina dissolution in both an industrial bath and a modified bath with fast dissolution properties. By fitting two straight lines to their data for the industrial cell, as shown in Figure 1, the following rate equation can be obtained:

$$k_1 = \max\left(0, 0.35 - \frac{0.35}{0.03} Y_{Al2O3dis}, 0.164 - \frac{0.164}{0.07} Y_{Al2O3dis}\right) \qquad (5)$$

To limit the reaction in areas of low undissolved alumina the equation is modified to:

$$k_1 = (1.0 - e^{-500 Y_{Al2O3Und}}) \max\left(0, 0.35 - \frac{0.35}{0.03} Y_{Al2O3dis}, 0.164 - \frac{0.164}{0.07} Y_{Al2O3dis}\right) \qquad (6)$$

Where $Y_{Al2O3dis}$ is the mass fraction of dissolved alumina in the bath and $Y_{Al2O3Und}$ the undissolved alumina in the bath. In this work the dissolved alumina species are $Na_2Al_2O_2F_4$ and $Na_2Al_2OF_6$.

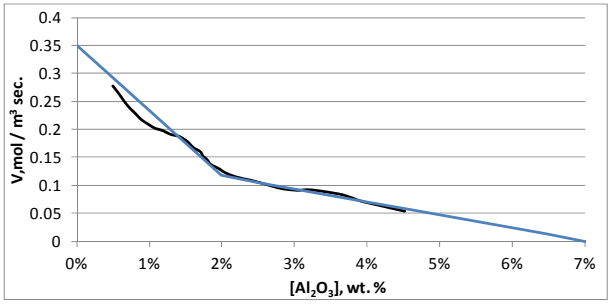

Figure 1: Dissolution rate of alumina in industrial baths at temperature 960 °C from Frovolov *et al.* (2007) –black line and the model of equation (5) – blue line.

For equation (2), data from Solheim and Sterten (1999) was used to derive the equilibrium condition that was reported in Solheim (2013) as:

$$\frac{x_1^2}{x_2} = 11.3e^{-2.63r} \qquad (7)$$

where x_1 and x_2 are the molar fractions of $Na_2Al_2OF_6$ and $Na_2Al_2O_2F_4$ respectively, and r is the molar ratio (Cryolite Ratio) of NaF and AlF_3. From the equilibrium condition in equation (7), the reaction rate, k_2, needed to bring the two species into equilibrium in that time step is determined.

Reaction rates for the anode and cathode reactions (equations (3) and (4)) are based on the current density such that:

$$k_3 = \frac{J_{Anode} dA_a}{4F} \qquad (8)$$

and

$$k_4 = \frac{J_{Cathode} dA_c}{3F} \qquad (9)$$

where J_{Anode} is the current density at the anode, $J_{Cathode}$ is the current density at the cathode, F is Faradays constant and dA_a.is surface area of the anode and cathode.

Since the current density is not solved in the model, a fixed value at the anode of 0.9 [A cm^{-2}] is used and then, assuming conservation of charge, the cathode current density is $J_{Cathode} = J_{Anode} \frac{A_{anode}}{A_{cathode}}$.

GEOMETRY AND BOUNDARY CONDITIONS

Geometry for the single anode model was based on a Hydro Aluminium HAL300 cell and is shown in Figure 2. The full industrial cell has 30 anodes, to simplify the model for this work a corner anode from the full cell was built including a typical ledge profile and meshed using ANSYS/ICEM to give 124,000 hexahedral cells. The anode had two slots; the centreline of the full cell is treated using a symmetry plane while the inter-anode gap is considered to be a vertical wall.

Details of the physics and boundary conditions used are as per the full cell model reported in Witt *et al.* (2012). Gas enters the model through the anode base coloured red in Figure 2. Gas leaves the domain through the free surface coloured green via a degassing boundary condition. Alumina feeding could be varied to different positions in the cell and in this work was to the top of the side channel of the cell through the purple region shown in Figure 2. Each feed was chosen to be 0.15 kg of alumina uniformly added over a 10 second period and was added every 80 seconds.

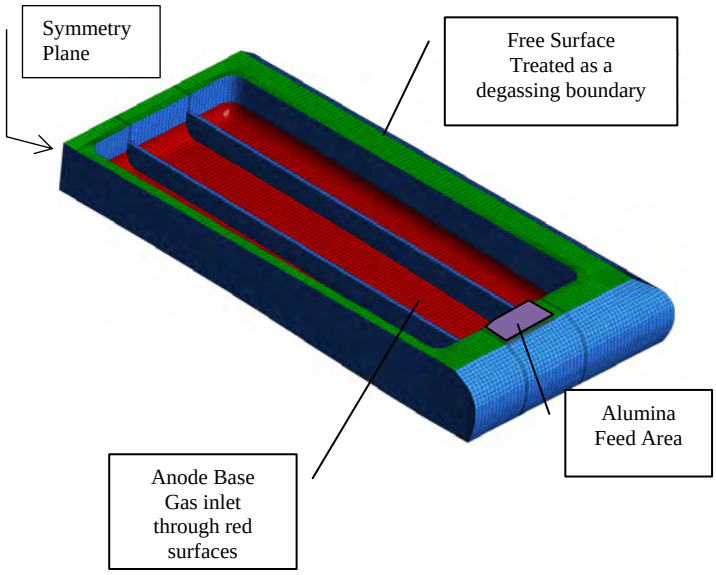

Figure 2: Single Anode Model Geometry.

Initial concentrations for the mass fractions are given in Table 1, which gives a cryolite ratio of 2.2, from which the equilibrium condition for $Na_2Al_2OF_6$ and $Na_2Al_2O_2F_4$ can be determined. The model was run for a time of 20,000 seconds with 1 second time steps.

Table 1: Initial Species mass fraction in the Single Anode Model.

Al_2O_3	$Na_2Al_2O_2F_4$	$Na_2Al_2OF_6$	Na	NaF	AlF_3
0.025[1]	0.044[2]	0.084[2]	0.070[2]	0.420[2]	0.382[2]

[1] Mass fraction of total liquid phase
[2] Mass fractions of dissolved species

RESULTS

For the anode model the steady state bath flow model was first run to calculate the bath flow field. Results for the bath flow are shown by the streamlines plotted in Figure 3, velocity vectors in the ACD plotted in Figure 4 and the gas volume fraction plotted on two vertical slices near the centre of the anode in Figure 5. These plots show that the model predicts a thin gas layer under the anode that drives a strong bath flow under the anode towards the centre channel. Liquid bath then flows to the end channel, along the end channel and back to the side channel.

Using PIV measurements the bath flow model formulation used in this work was validated for a three anode water model by Feng *et al.* (2010b), thus we expect that the current model should also predict reasonable results. Geometry used by Feng *et al.* (2010b) differs from the current geometry in a number of keys areas: a single anode rather than three anodes, a narrower centre channel, shaped external cell walls due to ledge formation rather than vertical walls, slotted rather than unslotted anodes and an anode slope of nearly 2° upward at the centre channel compared to the flat anodes in the earlier work. These changes prevent direct comparison and have an effect on the flow field. Measurements reported by Feng *et al.* (2010b) show the velocity in the ACD can exceed 0.12 m s^{-1} with a complex flow field. Due to the sloping base of the current anode, which will create stronger and more directional buoyancy forces, flow is directed along the anode length to the centre channel and velocity in the ACD is higher with predicated values up to 0.2 m s^{-1}.

Analysis of streamlines indicates that the travel time for the bath from the side channel under the anode to the centre channel and back along the end channel is approximately 50 seconds.

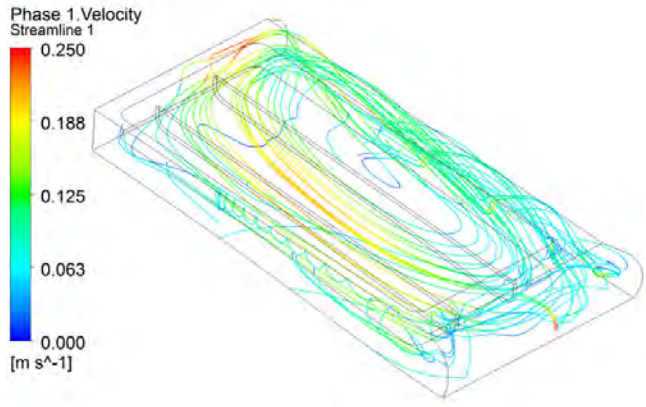

Figure 3: Streamlines showing the bath flow in the Single Anode Model.

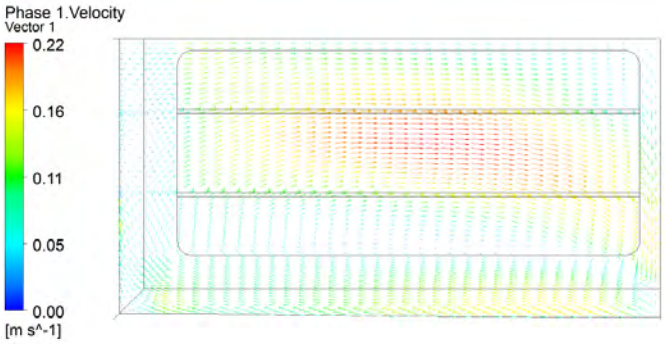

Figure 4: Liquid velocity vectors on a plane through the ACD showing the bath flow in the Single Anode Model.

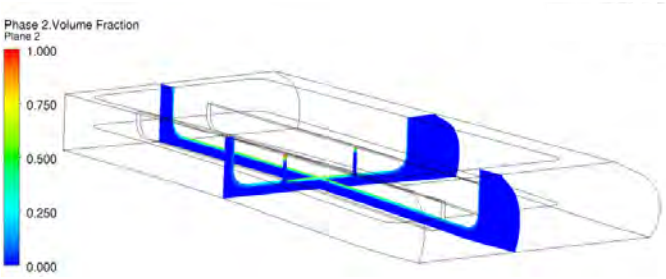

Figure 5: Gas volume fraction on two vertical planes in the Single Anode Model.

Mass fractions for the undissolved and dissolved alumina species considered in the single anode model are plotted on two vertical planes in Figures 6 to 8 after 20,000 seconds (5 hrs 33 minutes). This time instant was selected as it is just before a feed of alumina is about to occur and thus is likely to be close to the point of minimum alumina concentration under the anode. Low alumina concentration in the ACD is one potential cause of anode effects. As alumina is fed to the top of the side channel, undissolved alumina mass fraction is highest in the side channel but lowest in the inter-anode gap and centre channel. The dissolved alumina species in Figures 7 and 8 have a similar concentration distribution to the alumina but note that the plot range is very narrow to highlight the distribution within the cell.

The reaction rate for the dissolution reaction is shown in Figure 9 and indicates that the rate is constant through the cell. The equilibrium reaction rate is plotted in Figure 10 and shows that the reaction proceeds strongly under the anode and reverses in parts of the side and end channels. Figure 11 plots the reaction rate for the anode reaction, and shows the reaction has a slightly lower rate in the centre of the anode due to the gas holdup. The cathode reaction rate is not shown as it is uniform across the metal pad surface.

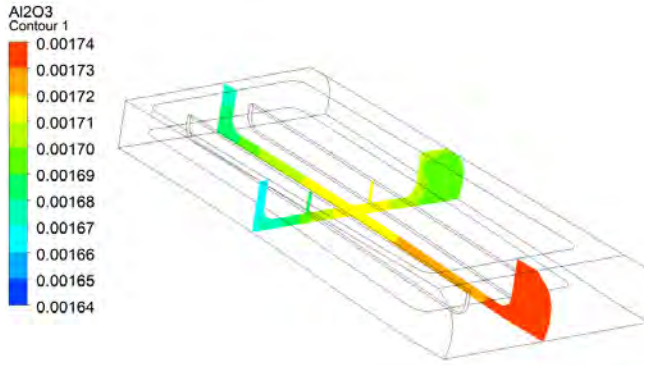

Figure 6: Undissolved alumina mass fraction on two vertical planes in the Single Anode Model at 20,000 [s].

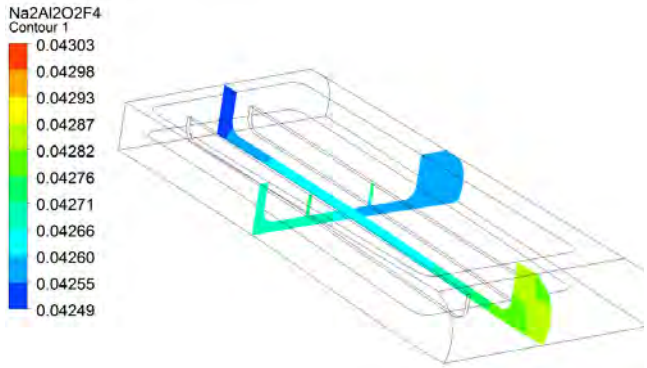

Figure 7: $Na_2Al_2O_2F_4$ mass fraction on two vertical planes in the Single Anode Model at 20,000 [s].

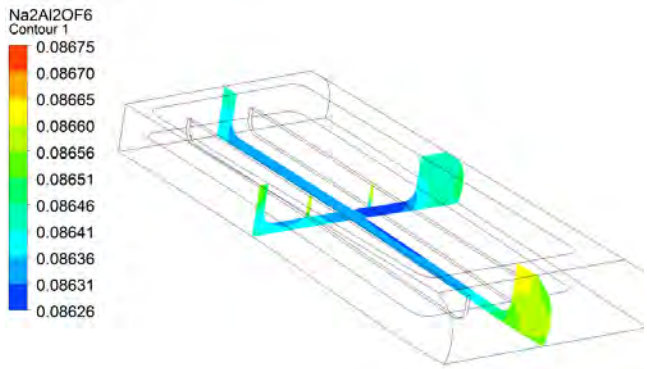

Figure 8: $Na_2Al_2OF_6$ mass fraction on two vertical planes in the Single Anode Model at 20,000 [s].

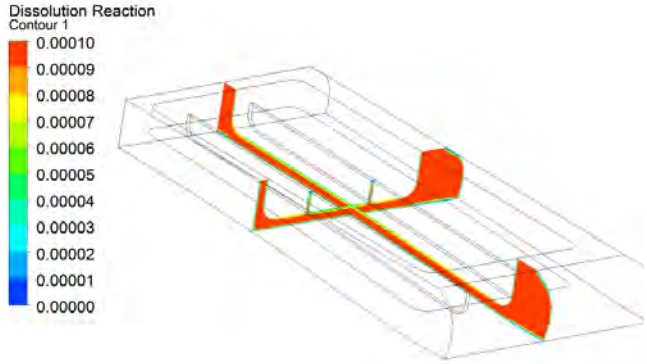

Figure 9: Dissolution reaction rate on two vertical planes in the Single Anode Model at 20,000 [s].

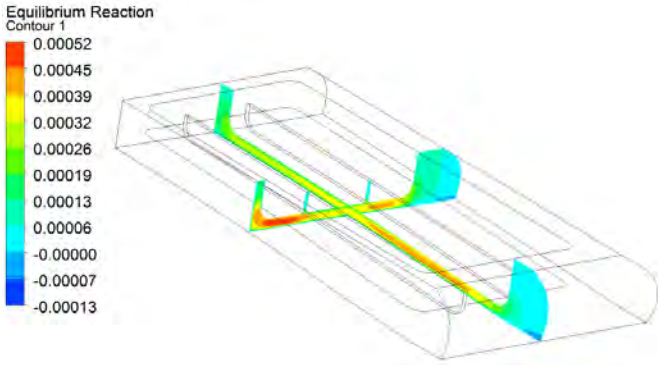

Figure 10: Equilibrium reaction rate on two vertical planes in the Single Anode Model at 20,000 [s].

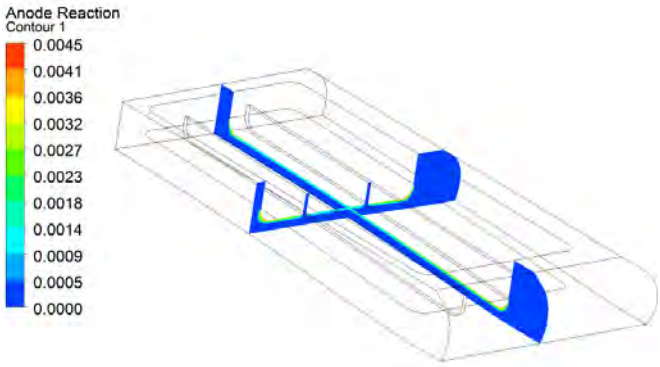

Figure 11: Anode reduction reaction rate on two vertical planes in the Single Anode Model at 20,000 [s].

Figure 12 shows the variation in undissolved alumina on a plane through the centre of the ACD at 20,000 seconds. The magnitude of the variation in species mass fraction is not great but results indicate regions of higher and lower concentrations. Figure 13 plots the equilibrium reaction rate on a plane through the ACD. The equilibrium reaction rate is the fastest under the one-third of the anode near the inter-anode gap and the reaction is predicted to reverse in the side and end channels.

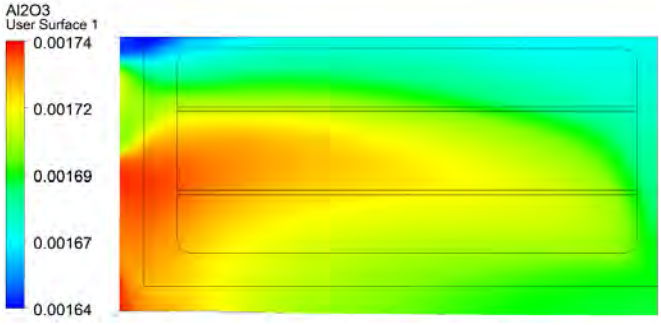

Figure 12: Undissolved alumina mass fraction on a plane through the ACD in the Single Anode Model at 20,000 [s].

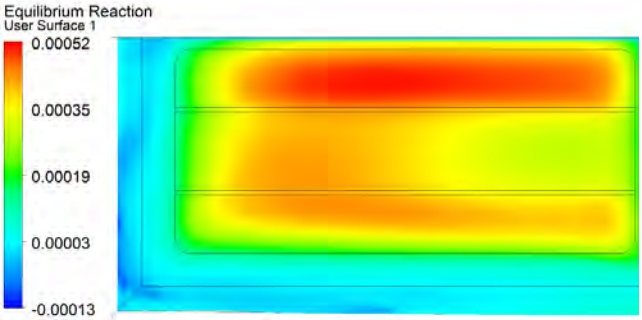

Figure 13: Equilibrium reaction rate on a plane through the ACD in the Single Anode Model at 20,000 [s].

The total mass of the chemical species in the bath and how they change with time is plotted in Figures 14 to 16. In Figure 14 the mass of alumina in the bath varies due to periodic feeding, as shown by the inset; this results in what appears as a wide band for the alumina mass at any time instant. The initial condition for this run was an undissolved alumina mass of 0.984 kg; this reduced rapidly to between 0.7 and 0.8 kg after about 5,000 seconds. After this time the mass is reducing slightly indicating the bath has not completely reached a steady operating condition, but is close to a steady condition. Two other preliminary calculations were run; one with a zero initial undissolved alumina concentration and one with the initial mass set to 4 kg. Both of these showed significant changes in the mass of alumina but would require significantly more than 20,000 seconds before reaching a steady condition. From these preliminary calculations the initial value of 0.984 kg was identified as being close to the steady condition. Mass of the other bath species are plotted in Figures 15 and 16 and show slight changes in their mass with time.

Based on the above results it was concluded that the model was at close to stable operating species concentrations and conditions at 20,000 seconds. To assess the magnitude of the change in bath chemistry between feed additions the results at 20,000 seconds were used to restart the model, from which time it was run for a further 100 seconds. During this short run species mass fractions at nine monitoring points were stored at each time step. The locations of the points are shown in Figure 17. Points 1 to 4 are located on the top of the bath with point 1 being at the feed location. The remaining 5 points are located in the ACD with point 6 being near the centre of the anode and the other four located near the anode edge.

Figure 18 plots the change in undissolved alumina at these locations. The mass fraction at the feeding location, Point 1, initially increases from 0.002 to 0.007 during feeding and the initial 10 second immersion. After feeding it drops rapidly back to the steady state condition, indicating that convective transport rapidly disperses the alumina particles. Points 2 and 8 show nearly a 50% rise in concentration approximately 20 seconds after feeding commences. The streamline in Figure 3 and velocity vectors in Figure 4 show the bath flows from the feed location towards the inter-anode gap and then along the anode to the centre channel, which transports the alumina through the cell and results in the increase in alumina concentration at points 2 and 8.

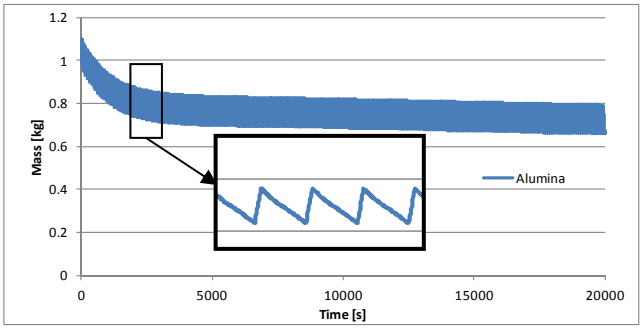

Figure 14: Change in Undissolved Alumina Mass with time for the Single Anode Model.

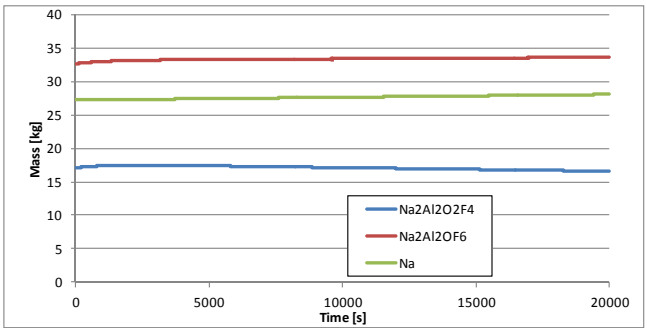

Figure 15: Change in species mass with time for the Single Anode Model.

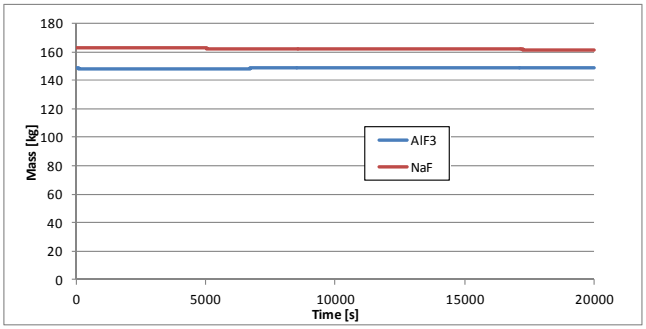

Figure 16: Change in AlF_3 and NaF mass with time for the Single Anode Model.

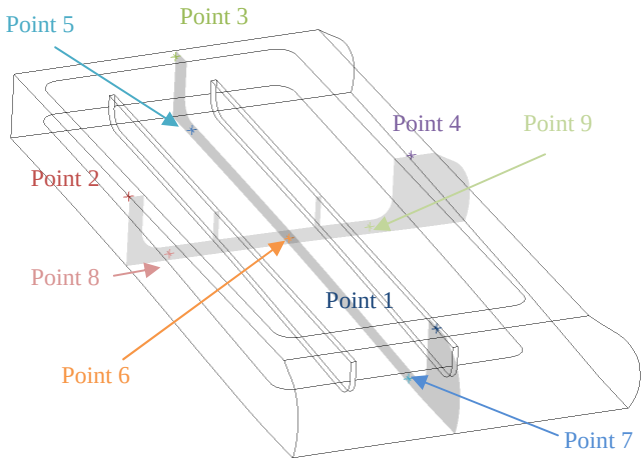

Figure 17: Location of monitoring points in the Single Anode Model.

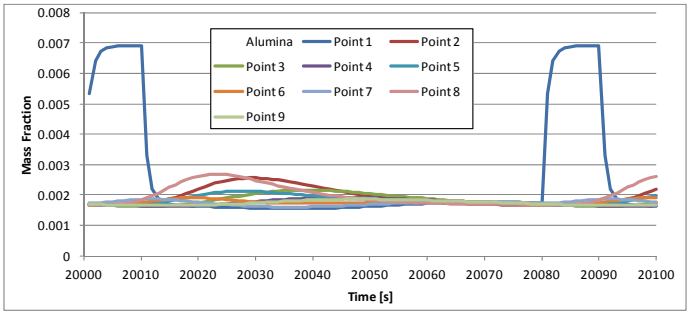

Figure 18: Change in undissolved Alumina mass fraction with time at various locations in the Single Anode Model.

DISCUSSION

The complex reactions, high temperature and harsh chemical environment make direct validation of the single anode model extremely difficult. Based on our past work (Feng *et al.*, 2010a, 2010b and Witt *et al.* 2012) we have a reasonable level of confidence in the bath flow and alumina distribution predictions. Further work using a water model with tracers could be used to improve confidence in the model. Moxnes *et al.* (2009) have used AlF_3 addition to change bath conductivity and measure changes in anode currents. In future work it may be possible to apply this approach to validate the model on a full cell.

For simplicity at the present stage of model development we assume a uniform current distribution across the anode base. This leads to uniform gas generation rate and uniform anode and cathode reaction rates. Clearly this is a simplification as current distribution is non-uniform and a function of gas generated through the anodic reaction. Our plan in future work is to include current distribution in the model and to link the anode and cathode reactions to the local current density. A further complication is our present use of a steady-state bath flow. We propose to iterate between the bath flow and transient chemical reaction models to couple the effects of anode reaction, gas generation, bubble flow and species distribution to overcome limitations in the present approach.

CONCLUSION

We have proposed a new alumina reduction model for the Hall-Héroult process that consists of six chemical species and four reactions. The reaction pathway developed for the model is that solid alumina particles are feed to the bath surface; they take a short time to mix and submerge into the liquid bath, where they undergo dissolution from solid particles to the liquid species $Na_2Al_2O_2F_4$. Within the bath a reaction reduces $Na_2Al_2O_2F_4$ to $Na_2Al_2OF_6$, which is further reduced to carbon dioxide and AlF_3 at the anode surface. At the metal pad a cathodic reaction reacts AlF_3 to form aluminium metal.

A previously published CFD model is used to transport chemical species within the bath based on bubble and MHD driven flow. Reaction for the new bath chemistry model were included in the CFD and tested on the geometry for a single anode that was run for 20,000 seconds of real time.

Key findings from the model are:

- Preliminary calculations show that if the initial undissolved alumina mass fraction is significantly different from the steady operating state then real times of over 20,000 seconds maybe be required to reach steady conditions.
- Alumina was fed to the top of the side channel and because of this the highest concentration of undissolved alumina was found in the side channel. This location was also where the undissolved alumina mass fraction increased from 0.002 to 0.007 during feeding.
- At a location near the inter-anode gap and midway along the anode the undissolved alumina mass fraction increased by approximately 50% about 20 seconds after feeding commenced.
- Other species showed only a small variation in mass fraction both across the cell and with time.
- Reaction rate for the dissolution reaction was found to be reasonably constant throughout the cell.
- The equilibrium reaction rate was high in the ACD under the anode and highest for the part of the anode near the inter-anode gap. In some parts of the side and end channels the equilibrium reaction was predicted to go in the reverse direction.

ACKNOWLEDGMENTS

The present work was supported by the project “Gas and Alumina Distribution and Transport” (GADT), financed by the Research Council of Norway and Hydro Primary Metal Technology. Permission to publish the results is gratefully acknowledged.

The authors wish to acknowledge the valuable discussions and advice provided by Asbjorn Solheim on the electro-chemical reactions, rates and processes in aluminium reductions cells.

REFERENCES

ANSYS Workbench / Fluent 14.5, ANSYS Inc., USA. 2013.

FENG, Y.Q., COOKSEY, M. and SCHWARZ, M.P., (2010a), “CFD Modelling of alumina mixing in aluminium reduction cells”, *Light Metals 2010*, 455-460.

FENG, Y.Q., YANG, W., COOKSEY, M. and SCHWARZ, M.P., (2010b), “Development of Bubble Driven Flow CFD Model Applied for Aluminium Smelting Cells”, J. Comp. Multiphase Flows, 2(3), 179-188.

FENG, Y.Q., COOKSEY, M. and SCHWARZ, M.P., (2011), “CFD Modelling of alumina mixing in aluminium reduction cells”, *Light Metals 2011*, 543-548.

FROLOV, A.V., GUSEV, A.O., ZAIKOV, Y.P., KHRAMOV, A.P., SHUROV, N.I., TKACHEVA, O.Y., APISAROV, A.P. and KOVROV, V.A. (2007), “Modified alumina-cryolite bath with high electrical conductivity and dissolution rate of alumina”, *Light Metals 2007*, 571-576.

GAGNON, F., ZIEGLER, D. and FAFARD, M., (2011), "A preliminary finite element electrochemical model for modelling ionic species transport in the cathode block of a Hall-Héroult cell"**,** *Light Metals*, 537-542.

GUSBERTI, V., SEVERO, D.S., WELCH, B.J., and SKYLLAS-KAZACOS, M., (2012), "Modeling the mass and energy balance of different aluminium smelting cell technologies", *Light Metals 2012*, 929-934.

ISHII, M. and ZUBER, N., (1979), *AIChE J.*, **25**, 843-855.

LOPEZ DE BERTODANO, M., (1991), *Turbulent bubbly flow in a triangular duct*, Ph.D. Thesis, Rensselaer Polytechnic Institute, New York.

KVANDE, H. (1986), "The structure of alumina dissolved in cryolite melts", *Light Metals*, 451-459.

MANDIN, P., WATHRICH, R. and ROUSTAN, H. (2009) "Industrial Aluminium Production: the Hall-Heroult Process Modelling" in *ECS Transactions*, p. 1, Industrial Electrochemistry and Electrochemical Engineering General Session - 215th ECS Meeting, San Francisco, CA.

MOXNES, B., SOLHEIM, A., LIANE, M., SVINSÅS, E. and HALKJELSVIK, A., (2009), *Light Metal*, 461-466.

OLMOS, E., GENTRIC, C. and MIDOUX, N., (2003) "Numerical description of flow regime transitions in bubble column reactors by a multiple gas phase model", Chemical Engineering Science, **58**, 2113-2121.

SMITH, B.L., (1998) "On the modelling of bubble plumes in a liquid pool", *Applied Mathematical Modelling*, **22**, 773-797.

SOLHEIM, A. (2012), "Concentration gradients of individual anion species in the cathode boundary layer of aluminium reduction cells", *Light Metals*, 665-670.

SOLHEIM, A., (2013), Personal Correspondence.

SOLHEIM, A. and STERTEN, A., (1999) "Activity of Alumina in the System NaF-AlF_3-Al_2O_3 at NaF/AlF_3 Molar rations ranging from 1.4 to 3", *Light Metals 1999*, 445-452.

SOLHEIM, A. ROLSETH, S., SKYBAKMOEN, E. STØEN, L. STERTEN Å. and STØRE, T. (1995) "Liquidus Temperature and Alumina Solubility in the System Na_3AlF_6-AlF_3-LiF-CaF_2-MgF_2", Light Metals 1995, 451-460.

WITT, P.J., FENG, Y.Q., EICK, I. and SCHWARZ, M.P., (2012), "Modelling bubble flow with CFX and Fluent for aluminium reductions cells", *9th Int. Conference on CFD in the Mineral and Process Industries*, CSIRO, Melbourne, Australia, 10-12 Dec.

A PRAGMATIC APPROACH TO CFD MODELLING OF SEPARATION PROCESSES

Kristian Etienne TRÆTLI-EINARSRUD[1]*, **Balram PANJWANI**[1], **Vincent PAUCHARD**[1]

[1]SINTEF Materials and Chemistry, 7465 Trondheim, NORWAY

* E-mail: kee@sintef.no

ABSTRACT

In the separation process of an emulsion, smaller droplets grow in size due to binary coalescence and simultaneously sediment/cream due to gravity. Finally, droplets coalesce at a homogeneous interface due to interfacial coalescence. Even the above simplified description of separation introduces several requirements for the modelling of such processes:

- Relative motion between phases of different properties.
- Free settling of droplets, with possibility of stratification owing to different sedimentation velocities.
- Formation and behavior of a dense packed layer (DPL), ultimately leading to the release of water.
- Droplet-droplet interactions (e.g. coalescence) within the free settling zone and DPL.
- Influence and interaction of surfactants on the above phenomena.

This paper presents recent advancement in the development of a simulation framework for separation processes, aiming to aid the community increase their knowledge of relevant phenomena (binary and interfacial coalescence, surfactants, phase inversion etc.) and to allow for use of this knowledge to improve engineering tools, in particular CFD simulations of gravity separation. The proposed framework is based on the Eulerian framework for multiphase flows with population balance modelling in order to capture the dynamical evolution of the droplets by coalescence. Separation is enabled through phase inversion, allowing free water to be formed from the emulsion. In addition, the current framework allows for the treatment of surfactants and thus opens for detailed simulations of for instance batch separation.

Keywords: Pragmatic industrial modelling, Oil & Gas processing, Oil/water separation, Surfactants and interfaces .

NOMENCLATURE

Greek Symbols

α_k	Volume fraction of phase k, $[-]$
ρ_k	Mass density of phase k, $[kg/m^3]$
τ_k	Stress acting on phase k, $[Pa]$
Γ	Surface concentration, $[kg/m^2]$
Γ_{crit}	Critical surface concentration, $[kg/m^2]$
Γ_∞	Surface excess concentration, $[kg/m^2]$
Ψ	Water release rate, $[m/s]$
ϕ	General custom field, $[-/-]$

Latin Symbols

p	Pressure, $[Pa]$.
$\mathbf{u}_k$	Velocity of phase k, $[m/s]$.
$\mathbf{g}$	Gravitational acceleration, $[m/s^2]$.
$\mathbf{f}_{kj}$	Momentum exchange term, $[kg/m^2s^2]$.
$n_{i,kd}$	Number density of droplets, $[\#/m^3]$.
d_i	Mean diameter of droplet in bin i , $[m]$.
d_{32}	Sauter mean diameter, $[m]$.
$\tilde{a}$	Droplet area density, $[1/m]$.
c	Intrinsic volumetric concentration, $[kg/m^3]$.
C	Extensive volumetric concentration, $[kg/m^3]$.
S	Surfactant source term, $[kg/m^3s]$.
D_{sc}	Diffusion coefficient of surfactants, $[m^2/s]$.
K	Partitioning constant, $[m^3/kg]$.
m	Mass, $[kg]$.
K^∞_{kj}	Momentum exchange coefficient, $[kg/m^3s]$.
h	Hindrance factor, $[-]$.

Sub/superscripts

k	Phase index.
i	PBM bin index.
kd	Dispersed phase index.
w	Water.
o	Oil.
$surf$	Droplet surface.
$bulk$	Continous bulk.
tot	Total.
inv	Inversion.
DPL	Dense packed layer.
PBM	Population balance model.
int	Interface.

INTRODUCTION

Although separation processes are used in many industrial applications, the approach to separator design is still often based on phenomenological models. Phenomenological models can only be considered to simulate bulk water removal in cases dominated by coalescence effects and not by hydrodynamic effects. Such models are obviously of interest to avoid the overflow of the dense packed layer (DPL) past the weir. They do however not tell much about the fate of the smaller droplets that do not sediment during the residence time in the gravity separator nor about the influence of the inlet geometry (plate, vane, cyclonic, etc.). Moreover, coalescence and separation are much impacted by the presence of surfactants, both stabilizers (such as asphaltenes) and

demulsifiers. Emulsions are of particular importance to the Oil and Gas industry, where oil and water typically are produced together and thus need to be separated. This is primarily achieved by means of gravity separators. Optimization of such processes is critical for offshore developments in particular when subsea separation is considered. With that respect CFD should play a major role as it is by nature the tool for capturing the complex flow within such vessels (effect of inlet geometry, effect of flow rates, sedimentation profiles, coalescence etc.). On the other hand CFD simulations traditionally do not account explicitly for the effect of surfactants on coalescence events. Furthermore, CFD doesn't account explicitly for the detailed sedimentation profiles as a function of the flow conditions, water release rate and height of the DPL.

Let us consider a consolidated DPL, i.e. the maximum compaction reached at any vertical position. When a droplet coalesces towards the continuous water; the volume fraction of dispersed phase decreases locally. This has two consequences. First, the driving force for water release (the water release rate depends on the diameter of droplets and dispersed water volume fraction) decreases and following droplet-homophase coalescence events are delayed. Second, a downward osmotic pressure gradient appears throughout the DPL and causes the downward motion of a droplet from the inside of the DPL to the free water surface (Princen and Kiss (1989), Princen (1986)). Consequently the macroscopic water release rate can be seen as a dynamic combination of coalescence kinetics and motion kinetics. Phenomenological models such as those proposed by Hartland and Vohra (1978) and Jeelani and Hartland (1985) do however not account for motion kinetics. As a consequence, these models do not provide fundamental insight on separator design.

One solution to the problem is to develop a model for water release rate and DPL height which can be easily coupled with CFD, as CFD inherently calculates the velocity of droplets at any location of the separator from classical equations (mass and momentum conservation). Accurate prediction of the water release rate then requires the accurate calculation of the sum of the motion and coalescence times. Ideally this should be based upon explicit description of both motion (from compressive settling equation) and coalescence (from film drainage equations) in the DPL. For compressive settling of stable emulsions, data and models are scarce (Watson *et al.*, 2005). For film drainage, multiple and evolving contacts between droplets make simulations extremely complex and mostly qualitative so far (Lobo *et al.*, 1993). It is therefore unlikely that the coupling of those two complex phenomena is implemented into a generic CFD code in the foreseeable future.

Optionally, the problem can be reversed and have the motion of droplets in the DPL control the water release rate. The present research work is mainly oriented towards this option, where the velocity of the droplet is controlled in sedimentation and DPL zone through an ad-hoc hindrance factor, thus predicting the evolution of the volume fraction of the dispersed phase at any axial position and time in the separator, from mass and momentum conservation laws.

With respect to surfactants, the most that is done so far is to account for interfacial mobility in coalescence kernels (cf. for instance (Chesters, 1991), (Liao and Lucas, 2010)). Such kernels are however very qualitative (mobile, immobile, partially mobile interfaces) and although such an approach is viable for a steady state situation in which you can select an appropriate mobility type, it cannot account for several important features due to surfactants. For example, as coalescence occurs in a separator the distribution/partition of surfactant changes which could lead to a change in interfacial mobility, thus rendering such simulations hazardous. Furthermore coalescence times, e.g. droplet stability in an emulsion, seem to depend strongly on coverage of water droplets by surfactants, as indicated by the pioneering work of Fischer and Harkins (1932). To the extreme coalescence seems even to be blocked above a certain critical surface coverage, as observed for particles (Pawar *et al.*, 2011), asphaltenes (Yarranton *et al.* (2007), Pauchard and Roy (2014))) and proteins (Wierenga *et al.* (2006), Tcholakova *et al.* (2003)).

When considering advection of droplets in an emulsion (Figure 1a), it is evident that this can result in an accumulation of surfactants close to the free water surface (Figure 1b). The surfactants present in the proximity of the free water surface will rely upon diffusion for redistribution (Figure 1c), which necessarily results in elevated separation times, as observed by Grimes *et al.* (2010).

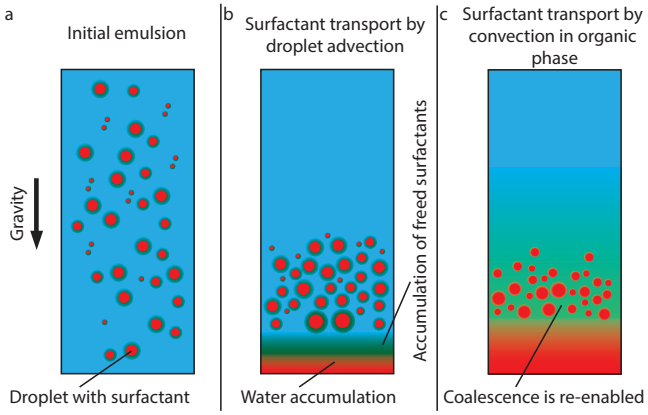

Figure 1: Evolution of emulsion with surfactants. Gravity drives droplets (with surfactants) towards bottom of system (a) where coalescence and separation free surfactants (due to reduced specific area) resulting in surfactant accumulation and temporary blockage of further coalescence (b). Accumulated surfactants redistribute in the bulk and allow for coalescence and separation to continue (c).

The need for process optimization/intensification not only requires adapted physical sub-models but also a CFD framework able to account for both detailed flow and surfactant simulations. The aim of the current activities has been to work out such a preliminary CFD framework, which can treat:

- Dynamic dispersed phases by means of population balance modelling, with possibilities for both homogeneous and inhomogeneous droplet populations.
- Coupled adsorption/desorption of surfactants on droplet interfaces.
- Anisotropic convection of surfactants.
- Surfactant dependent coalescence kinetics.
- Formation of free water by means of phase inversion.
- Controlling the motion of droplets inside the DPL and free sedimentation zone through a hindrance factor.

To start with the necessary developments some simplifications must be made. The current work will focus mainly on

the equilibrium size and surfactant concentrations of droplets within a population which initially is unstable (i.e. initial surface coverage below the critical value). Kinetics will not be considered, in particular related to adsorption and desorption, implying that surface coverage will be in instantaneous equilibrium with surrounding solution. In a real situation desorption (if any) will take some time, thus transiently limiting coalescence but not altering the final state. Moreover, details regarding coalescence will not be considered. Instead, a hypothetical coalescence kernel which fully blocks coalescence above the critical coverage will be used.

Experiments (with asphaltenes as surfactants) corresponding to the above simplifications exist as of Pauchard and Roy (2014) and Yarranton *et al.* (2007) in which droplet sizes were measured in stirred emulsions. Upon a decrease in agitation, droplets coalesce until a critical coverage is reached. The value of this coverage is independent from history (adsorption time, initial droplet size). For very aliphatic mixtures, asphaltenes are almost irreversibly adsorbed and surface coverage is inversely proportional to diameter, leading to a proportional dependency of equilibrium droplet size over the ratio mass of water to mass of asphaltenes (equation of limited coalescence in Pickering emulsions). The simplifying assumption of an irreversible adsorption does not hold anymore with more aromatic solvents (like a crude oil). Upon coalescence, partial desorption has to occur in order to restore the equilibrium between surface coverage and bulk concentration. Nevertheless, the limited coalescence equations can be coupled to an adsorption isotherm to account for partitioning.

Given the overall objective to generate engineering tools, detailed simulations at individual droplet scales are beyond the current scope. Instead, activities have focused on a global treatment of the droplets, i.e. a population balance model approach.

MODEL DESCRIPTION

General fluid flow

Consider an N-phase Eulerian model coupled with the discrete population balance model for treatment of the dispersed phases. The discrete population balance is chosen over the other available models (Standard Method of Moments and Quadrature Method of Moments) as it allows for a direct computation of the droplet size distribution. The Eulerian model is adopted due to the (mainly) dispersed nature of the flow.

In the Eulerian framework, transport equations are solved for each phase. In the current context, assuming isothermal conditions without phase transition, the relevant transport equations for each of the k phases are conservation of mass:

$$\frac{\partial}{\partial t}\left(\alpha_k \rho_k\right) + \nabla \cdot \left(\alpha_k \rho_k \mathbf{u}_k\right) = 0 \tag{1}$$

where α_k is the volume fraction of the phase with density ρ_k moving with velocity $\mathbf{u}_k$ and conservation of momentum:

$$\frac{\partial}{\partial t}\left(\alpha_k \rho_k \mathbf{u}_k\right) + \nabla \cdot \left(\alpha_k \rho_k \mathbf{u}_k \mathbf{u}_k\right) = -\alpha_k \nabla p + \nabla \cdot \tau_k + \alpha_k \rho_k \mathbf{g} + \mathbf{f}_{kj} \tag{2}$$

where $\mathbf{f}_{kj}$ is a momentum exchange term between phases k and j, i.e. drag, lift and virtual mass forces, typically taken to be a function of the Sauter diameter of the dispersed phase. It should be noted that the Eulerian formulation is limited by fact that interaction between phases is, by default, only through the momentum exchange term, meaning that for instance observed increased pressure losses in horizontal flow must be treated by means of additional force terms or by adopting adequate formulations for a mixture viscosity.

The discrete population balance model (PBM) deals with the evolution of the number density $n_{i,kd}(\phi_i, t)$ of droplets belonging to (dispersed) phase kd, where ϕ_i is a set of internal variables representing a prescribed class of droplets. For instance, if the internal variable is the droplet volume, all droplets with volume v_i on the interval Δv_i would belong to the i-th droplet bin. The droplet volume in a neighbouring bin is in the discrete PBM given by a discretization factor q, i.e.

$$v_{i+1} = 2^q v_i. \tag{3}$$

The population evolves as

$$\frac{\partial}{\partial t}\left(n_{i,kd}\right) + \nabla \cdot \left(\mathbf{u}_{kd} n_{i,kd}\right) = B_i - D_i, \tag{4}$$

where $\mathbf{u}_{kd}$ is the velocity of the k-th dispersed phase and B_i and D_i respectively represent birth and death rates of the i-th particle bin, typically due to coalescence and breakup, where applicable.

Two different formulations are possible for a discrete PBM, denoted the homogeneous and inhomogeneous formulations. In the homogeneous formulation, the entire population belongs to a single dispersed phase and all droplets are consequently advected with a velocity determined by the (local) Sauter diameter, meaning that local segregation due to different particle sizes is not possible with this formulation. In the inhomogeneous formulation, however, the droplet population is allowed to span several phases (within the same material). The benefit of this formulation is obvious, as polydispersity can be treated in a far more realistic manner, as indicated in Figure 2. The schematic of the droplet motion for both homogeneous and inhomogeneous formulation inside the CFD cell is shown in Figure 2. In the homogeneous formulation all the droplets are assumed to be moving with a same velocity in the CFD cell (see Figure 2a). But in reality the droplets of different sizes will have different velocity and to capture this phenomena inhomogeneous formulation is required (see Figure 2b). The drawback, however, is that the simulations become significantly more CPU-intensive, as mass and momentum conservation equations must be solved for each of the additional phases introduced. As polydispersity is believed to be of essence for several separation-related applications, the current framework is developed based on this formulation, as the homogeneous case is easily obtained as a special case of the general formulation.

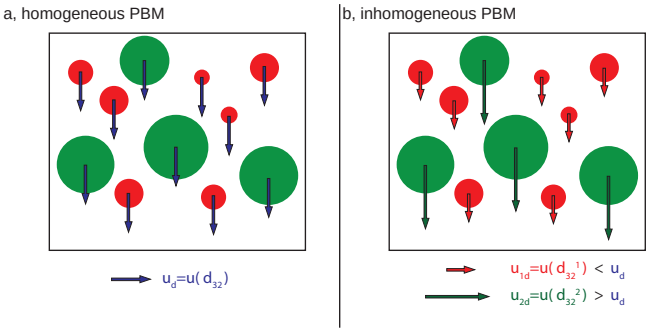

Figure 2: Homogeneous (a) and inhomogeneous (b) formulations of PBM.

The number density of droplets, together with the (mean)

droplet diameter, d_i, of the corresponding bin is used to determine two important properties in the current framework: the total Sauter mean diameter

$$d_{32} = \frac{\sum_{kd} \sum_{i \in kd} n_{i,kd} d_i^3}{\sum_{kd} \sum_{i \in kd} n_{i,kd} d_i^2} \tag{5}$$

and the area density of droplets

$$\tilde{a} = \pi \sum_{kd} \sum_{i \in kd} n_{i,kd} d_i^2 = \sum_{kd} \tilde{a}_{kd} \tag{6}$$

In the above two definitions, the inner sum is taken over all bins present in dispersed phase kd, while the outer sum is taken over all dispersed phases. Evidently, in the case of a homogeneous formulation, the outer is not present, and the standard form of the Sauter-diameter is obtained.
It should be stressed that in the inhomogeneous formulation, the velocities of the dispersed phases are determined from the Sauter-diameter of that particular phase, i.e.

$$d_{32}^{kd} = \frac{\sum_{i \in kd} n_{i,kd} d_i^3}{\sum_{i \in kd} n_{i,kd} d_i^2} \tag{7}$$

and that

$$d_{32} \neq \sum_{kd} d_{32}^{kd}. \tag{8}$$

Surfactants

As indicated in the introduction, surfactants are present in two states in the system, namely in the bulk fluid and on the surface of droplets. Consequently, surfactants present in each state can move relatively to each other and redistribute according to the global fluid flow. For surfactants adhering to droplets, the redistribution of the volumetric concentration of surfactants adhering to the droplet surface in the k-th dispersed phase, c_{surf}^{kd}, is governed by

$$\frac{\partial c_{surf}^{kd}}{\partial t} + \nabla \cdot \left(\mathbf{u}_{kd} c_{surf}^{kd} \right) = S_{surf}^{kd} - S_{bulk}^{kd}, \tag{9}$$

with $\mathbf{u}_{kd}$ being the velocity of the k-th dispersed phase, that is, surface adhering surfactants are advected with the dispersed phase and source terms S_{surf}^{kd} and S_{bulk}^{kd} respectively representing sources due to adsorption and desorption, inherently linked to adsorption kinetics and local breakup/coalescence dynamics of the droplet population.
The volumetric concentration of surface adhering surfactants is determined by the area density of droplets and the surface concentration of surfactants, Γ_{kd}:

$$c_{surf}^{kd} = \tilde{a}_{kd} \Gamma_{kd}. \tag{10}$$

Correspondingly, the extensive bulk concentration $C_{bulk} = m_{bulk}/\Delta V$, ΔV being the volume of a computational cell containing a mass m_{bulk} of surfactants, is governed by the advection-diffusion equation

$$\frac{\partial C_{bulk}}{\partial t} + \nabla \cdot (\mathbf{u}_c C_{bulk} - D_{sc} \nabla C_{bulk}) = \sum_{kd} \left(S_{bulk}^{kd} - S_{surf}^{kd} \right), \tag{11}$$

where D_{sc} the diffusion coefficient of the surfactants in the (continuous) bulk and $\mathbf{u}_c$ is the velocity of the continuous phase. The extensive bulk concentration is related to the intrinsic bulk concentration, which will be used for actual calculations, by $C_{bulk} = \alpha_c c_{bulk}$, where α_c is the volume fraction of the continuous phase. It should be noted that volume fraction effects are treated implicitly for the surface concentrations, as $\tilde{a}_{kd} \propto \alpha_{kd}$.

Assumptions

Two important assumptions are made with respect to surfactants at the current stage:

- Surfactant distributions are homogeneous within a *computational* cell.
- Local equilibrium between surface coverage and surfactant concentration in the bulk is instantaneous.

The first assumption (homogeneity within a computational cell) is a limitation arising from the current finite volume-PBM formulation in which only a single concentration (the average) is known in each computational cell. Although droplets with different adsorption history in principle could be treated by means of a multidimensional population balance (cf. Ali *et al.* (2012)), such an approach is not yet developed in the current framework.
The second assumption (immediate adsorption) is only true up to a certain surface coverage (i.e. the diffusion limited adsorption kinetics in pendant droplet experiments). In many cases, however, the primary objective is to simulate equilibrium droplet sizes, in which case this simplification should not impact the results. It should be noted that the lack of a multidimensional PBM formulation also implies that surfactants adhering to droplets belonging to different phases k are in equilibrium with each other, in addition to being in equilibrium with the bulk.
In addition to the above simplifications, a hypothetical coalescence kernel of the form

$$\gamma_{ij} = \Omega_{ij} P_{ij}^c f_s(\Gamma) \tag{12}$$

is adopted, where Ω_{ij} is the collision frequency (based on some applicable model, such as for instance inertial subrange turbulence (cf. Luo (1993)) or Stokes flow in combination with Brownian motion as proposed by Grimes (2012)), P_{ij}^c is the corresponding coalescence probability and $f_s(\Gamma)$ is function depending upon surface concentration, defined as

$$f_s(\Gamma) = 1 - H(\Gamma - \Gamma_{crit}), \tag{13}$$

Where $H(\Gamma - \Gamma_{crit})$ is a Heaviside step function which ensures that coalescence does not occur if $\Gamma > \Gamma_{crit}$, i.e. if the surface coverage is greater than the critical value, in accordance with experiments (Pauchard and Roy (2014)).
It should be noted that the choice of collision frequency and coalescence probability in the current formulation does not influence the equilibrium state of droplets, only the time required to reach it.

Modelling of surfactants: Adsorption equilibrium

Assuming immediate adsorption, the surface coverage can be calculated at any time as the value in equilibrium with the surrounding solution (so-called sub-surface layer). Assuming a Langmuir type equation of state (as shown by Rane *et al.* (2012)), an adsorption isotherm of the same type is chosen to describe equilibrium adsorption:

$$\Gamma = \frac{Kc\Gamma_\infty}{1 + Kc}, \tag{14}$$

where Γ_∞ is the surface excess coverage, K is a partitioning constant (depending upon chemical potential of surfactant in the bulk solution and hence related to solubility), Γ is the total surface concentration and c is the concentration

of surfactants in the sub-surface layer. Assuming homogenous distribution of surfactants in each computational cell, the concentration in sub-surface layer is equal to the concentration in the cell, i.e. $c = c_{bulk}$, which is the only information known to the CFD code with the current modelling approach. For a single droplet in a large volume of surfactant solution, adsorption at the interface only marginally decreases the initial bulk concentration. Upon completion of adsorption, equilibrium surface coverage will then be solely a function of the initial bulk concentration in the system (c^0_{bulk}) and the adsorption isotherm. For an emulsion, the ratio of the interfacial area to the available amount of surfactant is high. Adsorption progressively leads to depletion of the surfactant solution and stops when surface coverage is in equilibrium with the depleted concentration. This requires coupling the adsorption isotherm to a surfactant mass conservation equation:

$$m_{bulk} + m_{surf} = m_{tot} \tag{15}$$

where the individual terms respectively represent the bulk, surface and total mass of surfactants and holds for the total volume of fluids. In the case of a homogenous volume of fluids (no mass exchange between phases), the above equation can be written as a local balance in concentrations:

$$\alpha_c c_{bulk} + \tilde{a}\Gamma = \alpha_c c_{tot}, \tag{16}$$

where α_c is the volume fraction of the continious phase. Substituting the surface concentration in the above equation with that given by the adsorption isotherm leads to a second order equation for the equilibrium bulk concentration, for which only the positive root is physical. The solution is:

$$c_{bulk} = \frac{-\alpha_c - \tilde{a}K\Gamma_\infty + c_{tot}\alpha_c K + \beta}{2\alpha_c K}, \tag{17}$$

where

$$\beta = \sqrt{\left(Kc_{tot}+1\right)^2 \alpha_c^2 - 2K\tilde{a}\Gamma_\infty \alpha_c \left(Kc_{tot}-1\right) + \tilde{a}^2 K^2 \Gamma_\infty^2}, \tag{18}$$

which upon substitution in the adsorption isotherm yields the (local) equilibrium surface coverage.

Evidently, the above set of equations yields a coverage depending upon the partitioning constant K, and the droplet size at which coalescence blockage occurs will depend upon the choice of this parameter.

The formalism is necessarily simplified in the case of insoluble surfactants, as the equilibrium concentration in the bulk equals to zero. The surface concentration can in this case be obtained directly from equation 16, with $c_{tot} = c^0_{bulk}$, i.e. the initial concentration of surfactants (prior to adsorption).

The above set of equations yields the (local) total surface concentration. However, as seen from equation 9, the phase specific surface concentration should be the transported property. Owing to the equilibrium assumption between droplets belonging to different phases, one can write

$$\Gamma_{kd} = \frac{\alpha_{kd}}{\sum_{kd}\alpha_{kd}} \frac{\tilde{a}}{\tilde{a}_{kd}} \Gamma, \tag{19}$$

which fulfils the requirements

$$\tilde{a}\Gamma = \sum_{kd} \tilde{a}_{kd}\Gamma_{kd} \tag{20}$$

and

$$\lim_{\alpha_{kd}\to 0} \Gamma_{kd} = 0. \tag{21}$$

Modelling of dispersed phase motion and release

The system at hand consists of four distinct zones, as shown schematically in Figure 3; The aforementioned dense packed layer (DPL) governs the water release rate, forming a free water layer upon which the DPL rests. Above the DPL a sedimentation zone is present, feeding droplets to the DPL. Finally, above the sedimentation zone, pure oil is present.

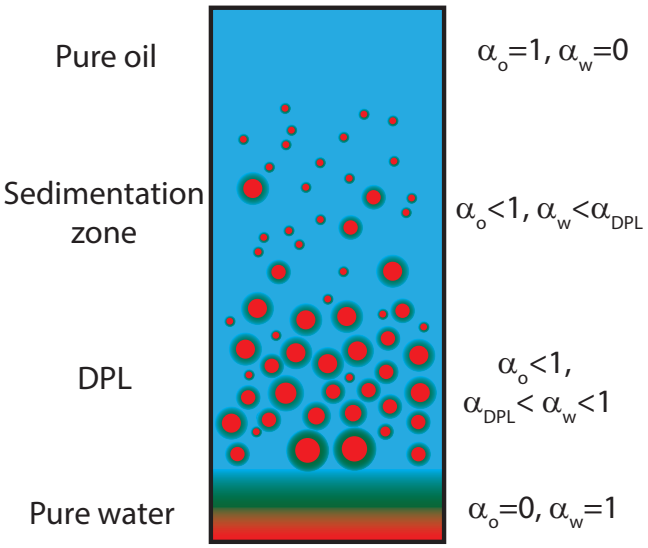

Figure 3: Zones of interest in a separator, defined by pure phase volume fractions α_k, assuming water (w) and oil (o) phases. The DPL is defined as the region with $\alpha_{DPL} < \alpha_w < 1$

Evidently, a predictive modelling framework for separation must, in addition to the treatment of surfactants, correctly describe the formation of free water, the flux of droplets arriving at the top of the DPL and the motion within the DPL itself, i.e. all the zones indicated in Figure 3 must be consistently coupled by adequate closure laws. While the sedimentation zone can be adequately described by existing closure laws for such flows, the DPL and inherent coupling to free water formation is somewhat more challenging. In the current framework, this will be realized by means of a hindrance factor coupled with an inversion type conversion of dispersed water into bulk water. The required elements of such a modelling approach are described in the following.

Phase inversion

With the phase inversion concept, the release of the dispersed phase is intermittent: Dispersed water is immediately converted into continuous water when the volume fraction of dispersed water in oil exceeds a predefined value ($\alpha_{wd} > \alpha_{inv}$). α_{inv} is a model constant supplied by the user, but needs to be higher than the mean volume fraction in the DPL α_{DPL}.

Since the droplet velocity is finite, the corresponding time required for a computational cell to fill up to the inversion point must be also, resulting in an average water release rate

$$\Psi = \frac{V^{inv}}{\Delta A t_{inv}} = u_{wd}\alpha_{wd}, \tag{22}$$

where V^{inv} is the volume of inverted water, ΔA is cross section of the computational cell though which a volume fraction α_{wd} of dispersed water passes with velocity u_{wd} and t_{inv} is the time required to reach the inversion criteria.

Modelling the sedimentation zone

A model for hindrance factor in the free sedimentation zone is required, in order to obtain physically reasonable sedimentation velocities for the droplets. In the current formulation, the hindrance factor enters through the momentum exchange term between phases k and j, $\mathbf{f}_{kj}$. Assuming that the only source of momentum exhange is drag, this term can be written as

$$\mathbf{f}_{kj} = \frac{K_{kj}^{\infty}(\mathbf{u}_k - \mathbf{u}_j)}{h}, \tag{23}$$

where h is the hindrance factor and

$$K_{kj}^{\infty} = \frac{\alpha_k \alpha_j \rho_k F(Re)}{\tau_k} \tag{24}$$

is the momentum exhange coefficient, depending upon the droplet diameter through the Reynolds number (entering the friction factor $F(Re)$) and the particle relaxation time τ_k.
Many correlations for the hindrance factor as a function of the volume fraction of dispersed phase are reported in the literature. The most widely used is the Richardson-Zaki correlation (Richardson and Zaki, 1954):

$$h(\alpha_{kd}) = (1-\alpha_{kd})^m, \tag{25}$$

with m values ranging from -2.5 to -5. However, this correlation tends to over-predict the hindrance factor for droplets. The problem is particularly critical for the simulation of separation since the volume fraction of the dispersed phase is to increase continuously at the bottom of the separator (up to values close to packing, for which shear thinning is expected). Frising *et al.* (2008) performed two experimental studies; the first experiment was meant to achieve pure sedimentation without coalescence and the objective of the second experiment was to obtain sedimentation and coalescence. The sedimentation velocities from both the experiments were compared with the Richardson-Zaki correlation. The sedimentation velocity was reasonably predicted with the Richardson-Zaki correlation in the pure sedimentation case, but measurements were poorly reproduced for combined sedimentation and coalescence cases, owing to growing droplets.

Modelling the DPL

In the dense packed layer (the DPL), the motion of droplet is very restricted and generally, a free sedimentation drag law will not be applicable. Unfortunately no correlation could be found in the literature that accounts explicitly for the deformability of droplets through their size, interfacial tension, buoyancy etc.
Movement of droplets inside the DPL is due to binary coalescence, interfacial coalescence and gravitational forces. In the present study a model which implicitly depends on these phenomena is proposed, explicitly dependent on a predefined water release rate, for instance a Hartland type model. The sought hindrance factor is derived from the 1D version of the *two phase* conservation of mass (dispersed water in oil and continiuous oil) *in the DPL*:

$$\alpha_{wd} u_{wd} + (1-\alpha_{wd}) u_o = 0 \tag{26}$$

and momentum, assuming that all terms except gravity and drag are negligible,

$$\frac{K_{wd,o}^{\infty}}{h}(u_o - u_{wd}) + \alpha_{wd} g \Delta\rho = 0. \tag{27}$$

Combining the above two equations, the velocity of the dispersed phase is given as

$$u_{wd} = h \frac{\alpha_{wd}(1-\alpha_{wd}) g \Delta\rho}{K_{wd,o}^{\infty}}. \tag{28}$$

Substitution with the water release rate, equation 22, yields

$$h = \frac{\Psi K_{wd,o}^{\infty}}{\alpha_{wd}^2 (1-\alpha_{wd}) g \Delta\rho} \tag{29}$$

for the hindrance factor in the DPL. The water release rate can be a function of any type, for instance depending upon droplet size, osmotic pressure etc. As an example, the Ψ can be described by a Hartland-type function:

$$\Psi = \alpha_{DPL} C_{DPL} \left(\frac{\Delta h_{DPL}}{d_0} \right)^n, \tag{30}$$

where α_{DPL} is the mean volume fraction of the dispersed phase with diameter d_0 in the DPL with instantaneous height Δh_{DPL}, with C_{DPL} and n as model constants determined from experiments.
For inhomogeneous population balance modelling, the above formulation must be altered in order to take into account the different dispersed phases present. Assuming that all droplets move with the same velocity in the DPL, i.e.

$$u_{wd,k} = u_{wd}, \tag{31}$$

the corresponding *oil* velocity in the DPL can be determined from the mass conservation equation:

$$u_o = \frac{u_{wd} \sum_k \alpha_{wd,k}}{1 - \sum_k \alpha_{wd,k}} \tag{32}$$

Correspondingly, the water release rate is written as

$$\Psi = u_{wd} \sum_k \alpha_{wd,k}. \tag{33}$$

In the inhomogenous formulation, separate momentum equations are dolved for each dispersed phase. Consequently, a separate hindrance factor is needed for each of these phases. Following the above analysis, the *phase specific* hindrance factor is given as

$$h_k = \frac{\Psi K_{wd,o}^{\infty}}{\alpha_{wd,k} \sum_k \alpha_{wd,k} \left(1 - \sum_k \alpha_{wd,k}\right) g \Delta\rho}. \tag{34}$$

The homogeneous formulation (equation 29) can be obtained from the above hindrance factor by noting that

$$\alpha_{wd} = \sum_k \alpha_{wd,k} \tag{35}$$

in this case.

Water release and surfactants

The formation of free water is due to interfacial coalescence between droplets in the lower region of the DPL and the free water interface. Corresponding to the binary coalescence present in the sedimentation zone and DPL, interfacial coalescence events can be blocked due to the presence of surfactants. In order to simulate such events, the water release is written as

$$\Psi^* = \Psi f_s(\Gamma_{int}), \tag{36}$$

where $f_s(\Gamma_{int})$ is the function introduced in equation 12 and Γ_{int} is the surface concentration of surfactants on *the free water interface*.

Proposed solution procedure

The proposed set of extensions to a traditional CFD code will rely upon adequate customization of the code, for instance through custom field functions, ϕ, representing surfactant concentrations. In order to ensure stability and consistency, a time-splitting strategy is proposed for future CFD simulations of separation processes, as shown schematically in Figure 4.

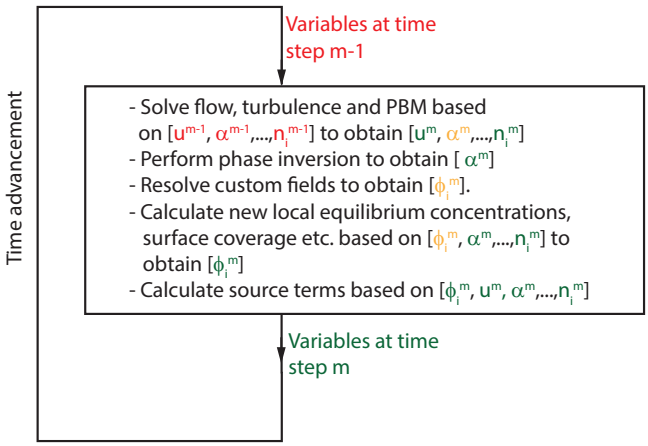

Figure 4: Proposed solution strategy for separation processes. Red variables denote state at previous time step, orange denotes variables which are re-initialized and green variables denote an updated state which is passed to the next time step.

DISCUSSION AND CONCLUSIONS

A generic modelling framework intended for CFD simulations of separation processes has been presented, showing how essential parts of such processes can be treated. Applying the proposed framework to CFD tool can in principle allow for treatment of:

- Dynamic dispersed phases by means of population balance modelling, with possibilities for both homogeneous and inhomogeneous droplet populations.
- Coupled adsorption/desorption of surfactants on droplet interfaces.
- Anisotropic convection of surfactants.
- Surfactant dependent coalescence kinetics.
- Formation of free water by means of phase inversion.
- Droplet motion control inside the DPL and free sedimentation zone through a hindrance factor.

Owing to the lack of generic closure laws, for instance related to coalescence kernels in the DPL, the framework as presented here cannot by itself be used as a general predictive tool *at the current time*. However, it does allow for pinpointing which elements are required for future predictive simulations, for instance coalescence rates within the DPL, water release models, adsorption/desorption kinetics of surfactants etc. Moreover, the proposed framework allows for testing and development of new closure laws within a coupled environment, thus allowing users to for instance study the influence of flow features in the sedimentation zone upon the water release rate. This feature is necessarily also useful when designing experiments.

ACKNOWLEDGEMENTS

The authors acknowledge the financial support from The Multiphase Flow Assurance Innovation Centre (FACE). FACE is a research cooperation between IFE, NTNU and SINTEF. The centre is funded by The Research Council of Norway and by the following industrial partners: Statoil ASA, GE Oil & Gas, SPT Group, FMC Technologies, CD-adapco, Shell Technology Norway.

REFERENCES

ALI *et al.* (2012). "Mathematical modeling for the activation of t-lymphocytes: Population balance modeling with non-conventional growth law". *5th Asian Particle Technology Symposium*.

CHESTERS (1991). "The modelling of coalescence processes in fluid-liquid dispersion". *Chemical Engineering Research and Design*, **69**, 259–270.

FISCHER and HARKINS (1932). "Monomolecular films. the liquid-liquid interface and the stability of emulsions." *Journal of Physical Chemistry*, **36**, 98–110.

FRISING *et al.* (2008). "Contribution of the sedimentation and coalescence mechanisms to the separation of concentrated water in-oil emulsions". *Journal of Dispersion Science and Technology*, **29**, 827–834.

GRIMES (2012). "Population balance model for batch gravity separation of crude oil and water emulsions. part i: Model formulation". *Journal of Dispersion Science and Technology*, **33**, 578–590.

GRIMES *et al.* (2010). "Analysis of dynamic surfactant mass transfer and its relationship to the transient stabilization of coalescing liquid-liquid dispersions". *J. Colloid and Interface Sci.*, **348**, 479–490.

HARTLAND and VOHRA (1978). "Shape of a vertical column of drops approaching and interface". *AIChe Journal*, **24**, 811–817.

JEELANI and HARTLAND (1985). "Prediction of steady state dispersion height from batch settling data". *AIChe Journal*, **31**, 711–720.

LIAO and LUCAS (2010). "A literature review on mechanisms and models for the coalescence process of fluid particles". *Chem. Eng. Sci.*, **65**, 2851–2664.

LOBO *et al.* (1993). "Dispersion coalescence: Kinetic stability of creamed dispersions". *AIChe Journal*, **39**, 322–334.

LUO (1993). "Breakup and liquid circulation in bubble column reactors". *PhD Thesis 105, Norwegian Institute of Technology (NTH)*.

PAUCHARD and ROY (2014). "Blockage of coalescence of water droplets in asphaltenes solutions: a jamming perspective". *Colloids and Surfaces A: Physicochemical and Engineering Aspects*, **443**, 410–417.

PAWAR *et al.* (2011). "Arrested coalescence in pickering emulsions". *Soft Matter*, **7**, 7710–7716.

PRINCEN (1986). "Osmotic pressure of foams and highly concentrated emulsions: I. theoretical considerations". *Langmuir*, **2**, 519–524.

PRINCEN and KISS (1989). "Rheology of foams and highly concentrated emulsions: Iv. an experimental study of the shear viscosity and yield stress of concentrated emulsions". *Journal of Colloid and Interface Science*, **128**, 176–187.

RANE *et al.* (2012). "Adsorption kinetics of asphaltenes at the oil-water interface and nano-aggregation in the bulk". *Langmuir*, **28**, 9986–9995.

RICHARDSON and ZAKI (1954). "The sedimentation of

a suspension of uniform spheres under condition of viscous flow". *Chem. Eng. Sci.*, **8**, 65–73.

TCHOLAKOVA *et al.* (2003). "Interrelation between drop size and protein adsorption at various emulsification conditions". *Langmuir*, **19**, 5640–5649.

WATSON *et al.* (2005). "Sedimentation in bidisperse and polydisperse colloids". *Journal of Colloid and Interface Science*, **1**, 176–186.

WIERENGA *et al.* (2006). "Importance of physical vs. chemical interactions in surface shear rheology". *J. Colloid and Interface Sci.*, **119**, 131–139.

YARRANTON *et al.* (2007). "Effect of interfacial rheology on model emulsion coalescence ii: Emulsion coalescence". *J. Colloid and Interface Sci.*, **310**, 253–259.

10th International Conference on CFD in Oil & Gas, Metallurgical and Process Industries
SINTEF, Trondheim, Norway *CFD 2014*
17-19 June 2014

MULTI-SCALE PROCESS MODELS TO ENABLE THE EMBEDDING OF CFD DERIVED FUNCTIONS: CURTAIN DRAG IN FLIGHTED ROTARY DRYERS

Andrew LEE[2], Madoc SHEEHAN[1] , Phil SCHNEIDER[1]
[1] James Cook University, 4812 Townsville, AUSTRALIA
[2] University of Melbourne, 3010 Melbourne, AUSTRALIA

Email: madoc.sheehan@jcu.edu.au

ABSTRACT

Flighted rotary dryers are large industrial devices which are commonly used to dry mineral ores and mineral concentrates, as well as other valuable commodity products. They are high capital cost units as well as large consumers of energy. Solids movement and energy exchanges within these devices occurs via a range of complex mechanisms that involve rolling and bouncing in a dense bed of solids, as well as the falling through a cross-flowing gas stream in lean particle curtains. Although a fundamental approach is attractive, full CFD simulations of such devices would be prohibitively expensive. The complexity of such a model would preclude its use for design and control applications, which are the most prevalent concerns to industry. Pseudo-physical compartment modelling is a powerful alternative technique that can be used to reproduce, in a physically meaningful way, the important characteristics of dryers such as residence time distributions and loading states. This scalable modelling approach also provides a convenient multi-scale structure that facilitates the representation of a system (in this case a flighted rotary dryer) as a series of smaller, distinctive, interacting phases. It is these smaller phase structures, such as the air-borne phase, that are suitable for modelling with either CFD or DEM type approaches. In this paper CFD modelling of single particle curtains and multiple side-by-side particle curtains is presented, with particular emphasis on quantifying gas induced drag and gas penetration into the curtain phase. The results are discussed in terms of their suitability to integrate CFD derived phase information within the broad process model. The simulations described in this paper provide valuable insights into the dryer design considerations such as flight serrations and axial flight staggering. The methodology presented in this paper provides an example that could be adapted to enable the evaporation, convection and radiation heat transfer in curtains to be accounted for.

Keywords: CFD, compartment model, particle curtain, drag, multi-scale, dryers

INTRODUCTION

Flighted rotary dryers (FRD's) are used extensively in a range of industries for control of the temperature and moisture content of free flowing, particulate solids, such as grains, sugar, and mineral ores as shown in Fig.1. FRDs range from small bench scale apparatus in pharmaceutical manufacturing, to 30m long, 6m diameter, industrial ore dryers. FRDs offer simplicity, low operating costs, and handle a wide range of throughputs and feed-stocks. Due to their size, rotary dryers often represent a significant capital expense. Thus it is necessary to have a good understanding of dryer operations and design features to ensure that the unit meets desired operational requirements.

Many different types of flighted rotary dryers exist, including multi-pass units and units with centre fills. However the simplest and most common flighted rotary dryers consist of a rotating, inclined drum with lifters or flights fitted to the internal walls. Moist solids are fed into the dryer at one end where they are collected in the flights. The flights carry the solids into the upper half of the drum, where they are released in a series of continuous curtains across the width of the dryer (see Figure 1). These particles fall under the influence of gravity and return to the floor of the dryer where they are collected once again by the flights. Axial transport of solids within the dryer is caused by the slope of the drum and occurs via both the cascading off flights and rolling/kilning motion. Drying gasses, commonly air or combustion gasses, are fed through the dryer either co- or counter-currently. These interact with the falling curtains of solids, removing heat and moisture and creating drag forces that will influence the curtains of

falling particles, causing dispersion of the solids within the dryer. The rolling solids also interact with the drying gasses, but to a lesser extent.

Whilst flighted rotary dryers are widely used and have been widely studied, their complex solids transport behaviour and the difficulty in integrating solids transport and heat and mass transfer phenomena have proved to be significant stumbling blocks. As a rotary dryer and the behaviour of its contents are three-dimensional, a comprehensive model of a dryer would need to be three-dimensional in order to capture the full detail of the solids transport. Furthermore, both granular flow (flight and kilning solids) and pneumatic flow (curtaining solids) occur within these devices and particle numbers in a full scale unit are enormous. Clearly, a rigorous fluid dynamic or discrete element model of the entire dryer is not feasible. Unfortunately, simple empirical models have been shown to be unable to predict the full behaviour of the system (Cao and Langrish (1999), Lee *et al*. (2009)).

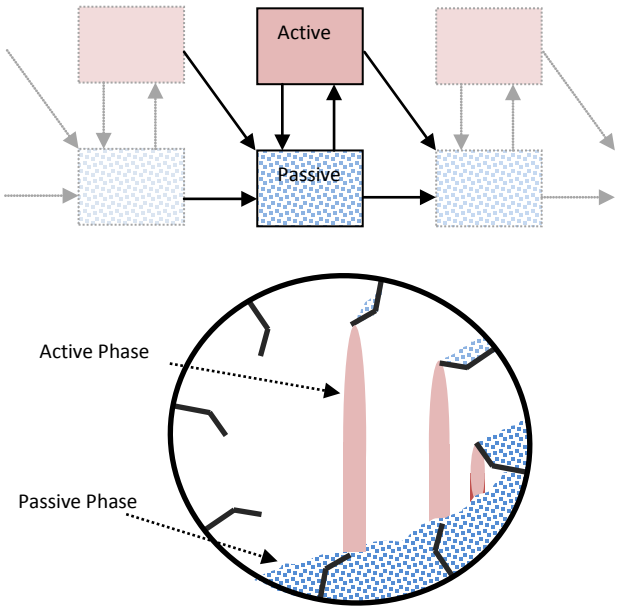

Figure 1. Cross section of an operating flighted rotary dryer (below) and the corresponding pseudo-physical compartment model (above). The light-shaded solids are the airborne solids (curtains) and the patterned solids are the flight and drum borne solids.

Early semi-empirical applications of compartment modelling of FRD's by both Matchett and Baker (1987) and Duchesne *et al* (1996) led to the development of more realistic representations of dryers. The model structures were capable of reproducing typical dryer experimental observations such as residence time distributions. The important model features developed in these works were the use of a twin tanks in series model structure, where one tank represented the flight and drum borne solids and the other tank represented the airborne solids (see Figure 1). Sheehan *et al.* (2005) and Britton *et al.* (2006) extended this work by developing a multi-scale flighted rotary dryer model, integrating physically-derived model parameters into the compartment model structure, in an approach they called pseudo-physical compartment modelling (PPCM). In this approach, scalable dynamic models were derived and the effects of internal geometry, operating conditions and solids flow properties on dryer performance could be accurately predicted. Each well-mixed tank was defined by its corresponding dynamic mass and energy conservation equations, as well as geometric capacity constraints. A separate unloading flight geometry model was used to generate model parameters controlling the flows in and out of each tank or phase. The PPCM is an adaptable model framework, and it has been successfully used to model a full-scale zinc concentrate dryer with both flighted and unflighted sections (Ajayi, 2011) and a fluidised drum granulator (Rojas *et al.*, 2010).

In the discussion that follows, we describe aspects of the process model in sufficient detail as to make obvious the potential to utilise CFD simulation to generate model parameters within the PPCM. In particular, we emphasise model parameters (such as the airborne solids residence time) that are responsible for moderating the flow and quantity of solids that enter the airborne phase.

The movement of solids between different phases is primarily due to the action of the flights lifting and discharging solids within the dryer. Cascading solids will be transported axially to the neighbouring dryer elements (i.e. tank) due to dryer inclination as well as gas-drag. Solids also roll or kiln along the drum base due to dryer inclination. Lee and Sheehan (2010) showed that for a free flowing material which discharges continuously from the flights, the discharging behaviour of a flight as it travels around the circumference of the dryer can be calculated solely from the geometry of the flight and drum, the amount of solids present in the flight, and the solids dynamic angle of repose. Thus, an unloading profile of the flight (mass flow versus time) can be calculated.

In previous examples of the PPCM, the geometric unloading profile was linked to a single particle model (SPM), which is used as an approximation for bulk curtain behaviour. Using the trajectory of an average particle, Newtons equations of motion are solved to obtain average properties that are then used to approximate the curtain behaviour. In particular, approximate air-borne and flight-borne residence times are used directly as the inter-phase transport

coefficients. For example, the solids flow rates out of each compartment in the model are calculated using the form $F_i = m_i / \overline{t}_i$ where F_i is the flow rate of solids leaving compartment i and m_i and $\overline{t}_i$ are the solids holdup and residence time in compartment i, respectively. We propose that CFD simulation of particle curtains could be used instead of the SPM to determine more realistic values for $\overline{t}_i$. Additionally, the SPM is used to calculate the axial advance for the average particle experiencing drag from cross flowing gas. Which is used within the PPCM to constrain tank lengths and to apportion flows to the surrounding tanks (Britton et al., 2006). CFD could be utilised in this context as well. Referring back to the broad PPCM framework, because smaller distinctive zones are defined within the larger unit model, it facilitates the integration of more sophisticated modelling (using CFD or DEM for example) of the individual phases.

In this paper we use the case study of a flighted rotary dryer as context for describing new CFD modelling of drag within particle curtains. We describe the CFD modelling of a single cascading curtain as well as multiple cascading curtains and also discuss the potential for embedding CFD derived information within multi-scale process compartment models.

CFD curtain modelling

A number of researchers have studied the effects of the gas-solids interactions in the active phase on the solids transport operations within a rotary dryer. Obviously, the moving stream of drying gasses will result in a displacement of the falling solids due to drag effects. Previous research has demonstrated that the gas-solids interactions within a rotary dryer are complicated. Simplifications of the system, such as the extremes of assuming isolated spherical particles (maximum drag) or flat-plate behaviour (minimum drag) (Baker, 1992), are generally insufficient. However, modelling the gas-solids interactions within a single curtain of falling solids is well within the capabilities of current CFD packages.

In order to model the gas-solids interactions influencing the active phase, a multi-phase CFD approach was implemented in Ansys CFX® 5.7.1. Due to the large number of solid particles present a Lagrangian method was not feasible, whilst the solid curtain was not considered dense enough to warrant the use of a granular model for the solids. Thus an Eulerian-Eulerian approach was used with a full buoyancy model and a k-ε model for turbulence. Although the k-ε model remains the industry standard, and has been widely used to model gas-solid systems (Du *et al*. (2006) for example), it's accuracy has been noted to depend on the use of sufficiently fine mesh and time step (Fletcher *et al*. (2006)). Uncertainty in the choice of turbulence modelling emphasizes the importance of experimental data to validate model predictions. In this work we draw confidence in our model choices and the resulting simulation results, from prior studies comparing experimental (isothermal) curtain profiles to the simulated curtain profiles that were determined using the same model approach, but for a scaled-down system. In those wind tunnel studies (Wardjiman *et al*. (2008, 2009)), both free falling curtains in still air and free falling curtains exposed to cross flowing gas were examined. Good agreement between the experimental and simulated results was obtained under both scenarios. Wardjiman *et al*. (2008, 2009) found that a cutoff solids volume fraction of 5.6×10^{-4} corresponded well with the experimentally observed curtain boundaries, and a similar threshold of 4.3×10^{-4} has been used in this work. However, to ensure complete confidence in the results presented in this paper, a comprehensive set of experimental data for curtain profiles would be required.

Gas-solids interactions occurring within a full rotary dryer are complex, with multiple flights unloading solids at different locations. Each of these individual curtains will have different mass flow rates, particle velocities and solids volume fractions, and the presence of the curtains will affect the flow of gas through the dryer. In this work, two series of simulations were conducted. The first studied a single curtain of solids falling perpendicular to a moving gas stream (i.e. a single curtain in isolation) and the second examined multiple parallel curtains to determine whether the presence of multiple curtains affected the displacement of solids and extent of gas penetration.

Single Curtain Studies

In order to achieve meaningful results from the single curtain simulations, it was necessary to determine a set of initial conditions that would represent the average gas-solids interactions for the falling curtain in a typical industrial dryer. The curtain conditions for the average fall path of a particle were used, based on the predictions of the geometric unloading model of Lee and Sheehan (2010) and experimental observations (Lee, 2008). These gave an initial curtain width of 18 mm with an initial vertical particle velocity of 1 m/s and a mass flow rate per metre of flight length of 5.18 kg/m·s. The single curtain studies were simulated in a tunnel 0.8 m long, 0.52 m wide and 2 m tall. Solids were introduced through an 18 mm wide variable length inlet along the centreline of the tunnel, allowing a 0.1m entry

zone for the gas stream. Turbulence was modelled using the k-ε model and a full buoyancy model was used. Drag forces were modelled using the Schiller-Naumann (Schiller and Naumann, 1935) equation assuming a particle size of 850 µm.

The numerical domain was discretised with a 9 mm tetrahedral mesh applied to the region occupied by the particle curtain and extended for a minimum of 50 mm beyond the expected curtain boundaries. The remainder of the tunnel was discretised using a maximum mesh size of 35mm, resulting in a total mesh of 136,000 nodes. The system was solved using the inbuilt Automatic Timescale calculator in CFX 5.7.1 (Ansys CFX (2006)) until all residuals were less than 10^{-4}, or 100 iterations had been performed. The gas velocity at the inlet to the duct was specified at the experimental conditions and at the solids inlet, the mass flow rate, velocity and initial solids volume fraction were specified. The inlet solids volume fraction of solids, r_{p0} , was calculated based on experimental data using the following equation $r_{p0} = \frac{\dot{M}_p}{\rho_p U_0 A}$, where $\dot{M}_p$ is the mass flow rate of solids entering the system, U_0 is the initial velocity of the solids entering the duct, and A is the cross-sectional area of the solids inlet. At the downstream end of the duct, the boundary was defined as an outlet boundary, such that material can only exit the system through this boundary. In the absence of experimental data, the gas and solids inlets were given a turbulence intensity of 5% (Ansys CFX (2006)). The remaining boundary conditions were governed by the no-slip condition.

In order to test the influence of gas velocity on the curtain displacement, simulations were conducted with a curtain length of 0.5m, and gas velocities of 0.5 m/s (slow), 1 m/s (normal gas velocity for rotary dryers) and 2 m/s (fast). Although not presented here, simulations were also conducted with 5 different curtain lengths (i.e. axial distances) to study how far the moving gas stream penetrated the falling curtain, and how solids displacement varied with curtain length.

Figure shows the simulated results for the curtain profile measured at the centreline of the tunnel, for a 0.5 m long curtain at different gas velocities. It can be clearly seen that the gas velocity has a significant effect on the leading edge of the curtain, with increasing gas velocities causing greater displacement of the solids. At the trailing edge however, the profile is very similar at both 0.5 m/s and 1 m/s, with the solids falling almost vertically under these conditions. It is only with a gas velocity of 2 m/s that the gas is able to fully penetrate and the trailing edge of the curtain is displaced.

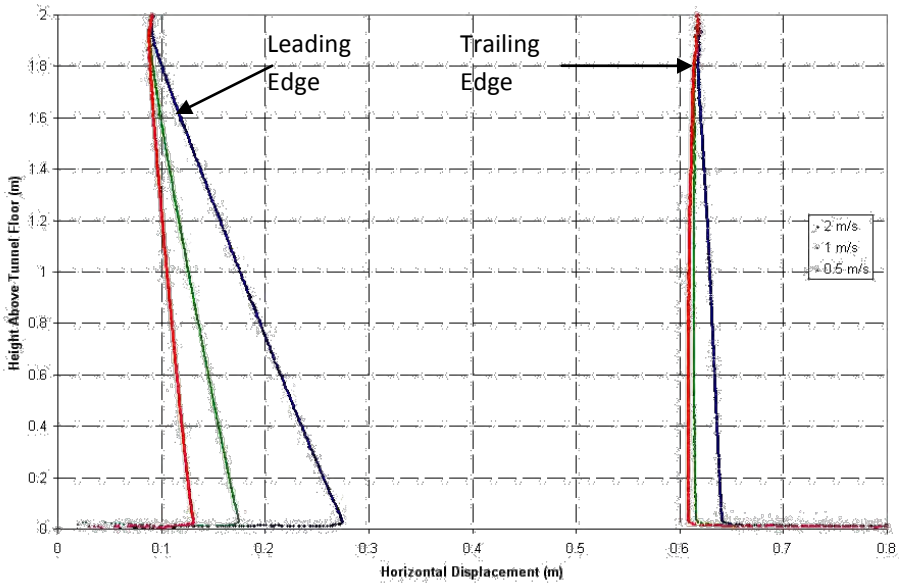

Figure 2. Solids curtain profile at different gas velocities (0.5 - 2m/s).

Figure shows a colour map of the horizontal component of the gas velocity for the 1 m/s simulation. These measurements were taken in the horizontal plane at a height of 1 m above the tunnel floor (arbitrarily chosen to illustrate the behaviour of the system), with the gas being introduced from the

bottom of the figure. The black line indicates the edge of the particle curtain (defined as a solids volume fraction of 0.43×10^{-3}). Figure clearly shows the gas being channelled around the solids curtain, with increases of up to 25% in the gas velocity being observed around the curtain. It can also be seen that the moving gas only penetrates a short distance into the solid curtain, producing an area of negligible horizontal velocity throughout large portions of the curtain. Figure shows the same measurement as Figure for an initial gas velocity of 2 m/s, and again gas velocities up to 25% greater than the initial velocity can be observed. Clearly, the increased gas velocity has a significant impact on the leading edge of the curtain, causing appreciable curtain displacement and compression. It can also be seen that the moving gas penetrates deeper into the curtain than in the 1 m/s simulation, however there is still an area of negligible horizontal gas velocity throughout large portions of the curtain. Given that flights are often staggered to maximise gas-solid interactions, these results provide useful guides to appropriate spacing. In industry flights are typically staggered at around 1-2 m intervals, yet this study suggests that staggering of between 10 and 20 cm would be more effective in promoting gas penetration.

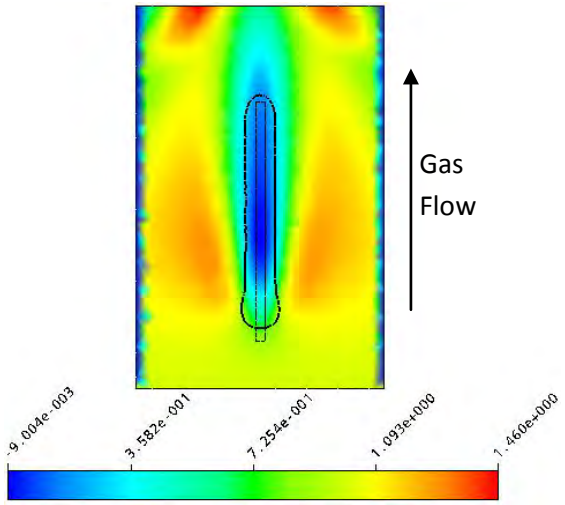

Figure 3. Horizontal gas velocity colour map at 1 m above tunnel floor (1 m/s initial gas velocity, 0.5 m inlet, 5.18 kg/m.s solids flow rate). Units are m/s.

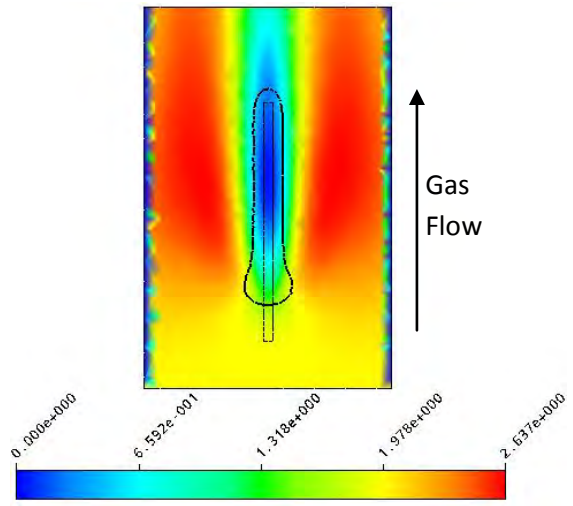

Figure 4. Horizontal gas velocity colour map at 1 m above tunnel floor (2 m/s initial gas velocity, 0.5 m inlet, 5.18 kg/m.s solids flow rate). Units are m/s.

From the results of these simulations, it is possible to assess curtain displacement resulting from changes in gas velocity. Figure shows the trend in the displacement of the curtains leading edge over a fall of 2 metres at the gas velocities studied. The curtain displacement is well represented by a second order polynomial, which reconciles with fact that drag is proportional to velocity squared.

Simulations such as this provide an example whereby CFD can be used to generate correlations to use in up-scaled process models such as an industrial FRD, modelled using the PPCM framework. In this case, PPCM parameters (e.g. curtain displacement) could be derived as functions of operating variables such as gas velocity. Extensions would include the effects of variations in solids flow rates and particle size into these CFD derived correlations. Furthermore, using averaged CFD curtain properties such as the fall time (i.e. mean residence times in the active phase), can be used to replace SPM predictions. This would be advantageous because it is well known that drag in curtains is different to that experienced by isolated single particles (Hurby *et al.* (1988)).

The predicted displacement of the solids due to gas-solids interactions appears small in comparison to those reported by Baker (1992), which is likely due to and different initial conditions of the curtain. In these simulations, the initial conditions were taken using experimental data from a flight unloading apparatus with an un-serrated flight (Lee and Sheehan, 2010). However, most industrial dryer use serrated flights, which create a broader, less dense curtain. This reduced density allows greater gas-solids interaction and thus greater displacement of solids. Another possible factor affecting the results is the interactions between curtains. In a system with

multiple curtains there will not be as much space available for channelling around the curtains, which may cause greater interactions between the gas and solids.

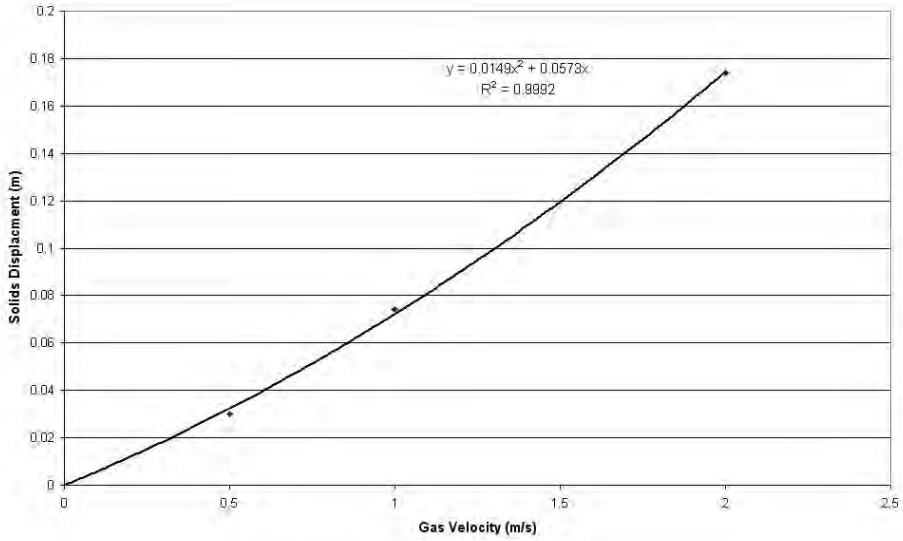

Figure 5. Simulated single curtain displacement over 2 metres at different gas velocities.

Multiple Curtain Studies

The phenomenon of channelling of the gas flow around the falling curtains in a rotary dryer was first considered by Baker (1992) as part of his studies into the gas-solids interactions. In a system with multiple curtains, the gas flow should channel between curtains, resulting in channels of high gas velocity that may influence solid particles at the curtain edges. In order to understand channelling behaviour, a series of simulations were conducted using multiple curtains with different spacing between curtains.

CFD simulations were conducted using the average particle curtain properties used for the single curtain simulations for all curtains, which is a reasonable approximation for the middle of the unloading profile where the unloading rate is reasonably constant. The simulations were conducted using a tunnel 500 mm high, 340 mm across and 800 mm long. A smaller system geometry (compared to the single curtain simulations) was used due to the greater mesh requirements to resolve the gas-solids interactions for the multiple curtains. Solids were introduced along the top of the tunnel starting 100 mm from the gas inlet, and allowing 200 mm between the end of the inlet and the end of the tunnel. The tunnel was discretised with an 8.4 mm tetrahedral mesh across the entire tunnel, resulting in 368,780 nodes. Four simulations were run with curtain spacing varying between 50 mm and 80mm. Curtains were equally spaced across the tunnel, with the two outermost curtains extended to reach the wall to prevent gas for being channelled along the wall without affecting the curtain. Due to the fixed size of the tunnel, the constant curtain spacing meant that the number of curtains present in the simulations also varied with curtain spacing, making extrapolations based on total curtain numbers difficult.

Figures 6 to 7 show the simulated solids volume fraction at a horizontal cross-section 0.25 m above the floor of the tunnel (halfway through the fall) for the different curtain spacing, with gas entering from the right hand side at 1m/s. The black boxes show the location of the solid inlets. As can be seen, with a curtain spacing of 50 mm, the curtains have merged to form a single broad curtain, but as the curtain spacing increases to 80mm, individual curtains begin to become apparent. This agrees well with the results reported by Wardjiman *et al.* (2009). In these experiments, it was observed that falling curtains of solids with high solids volume fractions tended to expand until a stable state was reached. They proposed that this was due to the difference in pressure inside the curtain compared to outside, causing the curtain to expand until the pressures equalised. This explains the expansion of the curtains observed in the multiple curtain simulations, resulting in the merging of the curtains into a uniform phase when the curtain spacing is small enough.

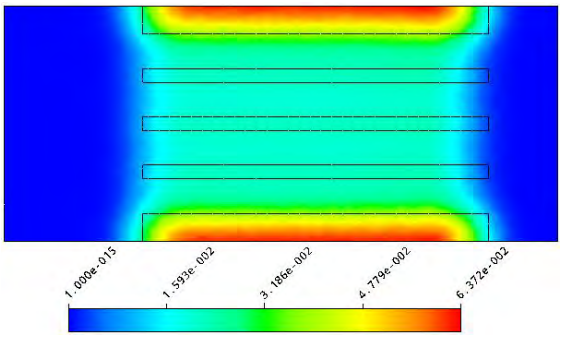

Figure 6. Solids volume fraction colour map at 0.25 m above tunnel floor with 50 mm curtain spacing.

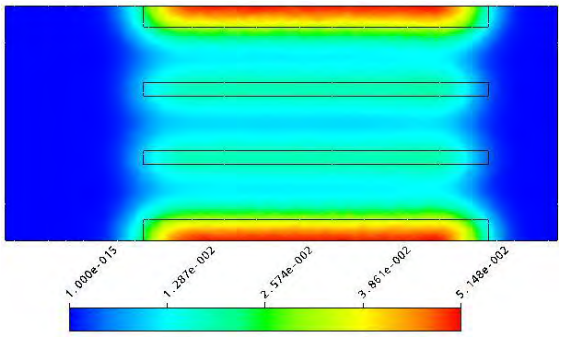

Figure 7. Solids volume fraction colour map at 0.25 m above tunnel floor with 80 mm curtain spacing.

This means that at low curtain spacing, where the curtains have merged into a single uniform phase, the gas flow through the curtain should also be uniform, as there are no regions of reduced solids volume fraction through which the gas will channel. As the curtain spacing increases, and individual curtains become distinct, and the regions of lower solids volume fraction between the curtains will allow for the gas to be channelled. This effect is seen in Figures 8 and 9, which show the gas velocity profile through the same cross-section of the tunnel. The thick black line indicates the contour of a solids volume fraction of $4.3x10^{-3}$.

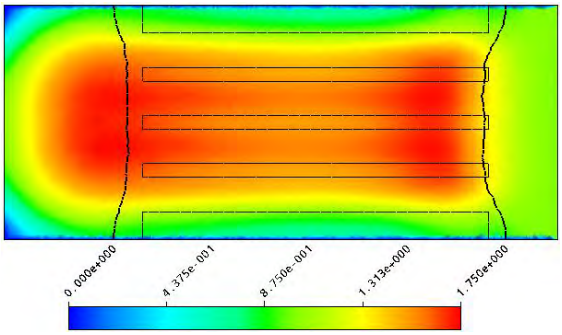

Figure 8. Horizontal gas velocity colour map at 0.25 m above tunnel floor with 50 mm curtain spacing. Units are m/s and the inlet gas velocity is 1m/s.

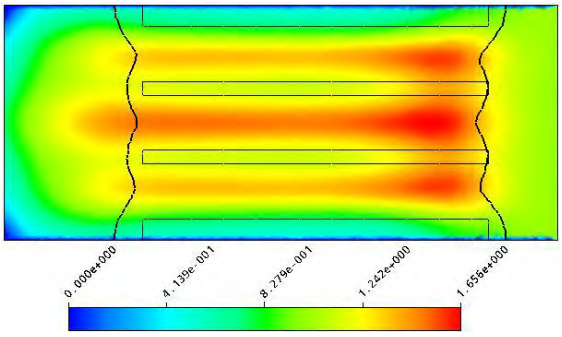

Figure 9. Horizontal gas velocity colour map at 0.25 m above tunnel floor with 80 mm curtain spacing. Units are m/s and the inlet gas velocity is 1m/s.

As can be seen, the channelling of gas flow between the curtains increases with increasing curtain spacing. At a curtain spacing of 50 mm and a fall height of 0.25 m, the gas velocity through the combined curtains is close to uniform, whilst at a curtain spacing of 80 mm significant channelling of the gas flow can be seen. Larger velocity differences between the cross-flowing gas and falling solids within the curtains would lead to enhanced heat and mass transfer. Clearly CFD simulations involving heat and/or mass transfer would be an important step defining these potential enhancements and would have significant repercussions for flight design. Particularly selecting the appropriate number of flights/curtains. In these simulations, it can be seen that there is significant gas velocity within the curtains, unlike the single curtain experiments where the gas velocity within the curtain could be considered negligible in comparison. This increased gas velocity within the falling curtain of solids would result in an increased displacement of the solids compared to the single curtain simulations, as was shown in Figure 10. Figure 10 shows the profile of the falling curtain, defined by a solids volume fraction of $4.3x10^{-3}$, for the different simulations compared to the single curtain simulation with the same initial conditions. The curtain profile was measured along the centreline of one of the solid inlets.

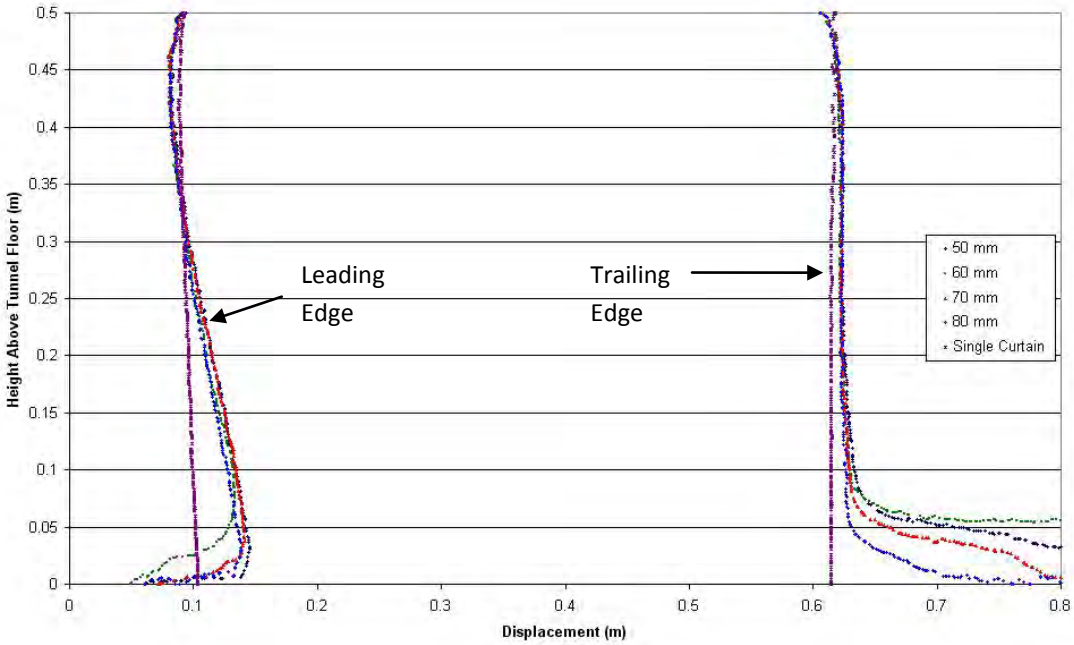

Figure 10. Curtain profiles for different curtain spacing and cross flowing gas at 1m/s.

It can be clearly seen that the single curtain simulation predicts less displacement of the solids curtain, due to the channelling of the gas around the curtain. It can be seen that the effects of the gas-solids interactions occur primarily at the leading edge of the curtain, with a significant displacement of solids being observed.

CONCLUSIONS

The pseudo-physical compartment model is presented as a convenient structure to reduce the size and scale of modelled phenomena whist maintaining physical realism. In this case, a flighted rotary dryer is modelled in such a way that the behaviour of falling curtains of particles is isolated and emphasised. Eularian-Eularian CFD simulations of gas induced drag on the curtain phase within a flighted rotary dryer are described. Both single curtain simulations and multiple curtain simulations are presented. Examples illustrating the use of CFD results to develop correlations suitable for use within the PPCM are described.

Single curtain simulations show substantial channelling of gas around the sides of the particle curtain, leading to reduced particle drag (except at the leading edge) and low levels of gas penetration (20cm or less at 2m/s gas velocity). However, simulation of multiple curtains lead to more significant gas penetration that is dependent on the curtain to curtain spacing distances. In terms of particle drag, the displacements of solids in the single curtain simulations with 850 µm particles are less than expected. The simulations conducted in this study used data measured from unserrated flights, resulting in thinner, denser curtains, that potentially under-predict solids displacement that would be observed when using serrated flights. An experimental study of the unloading behaviour of serrated flights is necessary in order to develop a better model for the gas-solids interactions in flighted rotary dryers.

REFERENCES

Ajayi OO (2011) Multiscale modelling of industrial flighted rotary dryers. PhD thesis, School of Engineering and Physical Sciences, James Cook University, Townsville.

Ansys CFX Solver Modelling Guide, (2006), Ansys Inc., Canonsburg

Baker, C.G.J., (1992), "Air-Solids Drag in Cascading Rotary Dryers", *Drying Technology*, **10**, 365-393

Britton P.F., Sheehan M.E. and Schneider P.A., (2006) A physical description of solids transport in flighted rotary dryers. *Powder Technology* **165**, 153-160.

Cao, W.F. and Langrish, T.A.G., (1999) Comparison of residence time models for cascading rotary dryers. *Drying Technology*, **17** (4&5), 825-836.

Du, W., Bao, X., Xu, J. and Wei, W., (2006) "Computational fluid dynamics modelling of spouted bed: assessment of drag coefficient correlations", *Chem. Eng. Science*, **61**, 1401-1420

Duchesne, C., Thibault, J. and Bazin, C., (1996) "Modelling of the Solids Transportation within an

Industrial Rotary Dryer: A Simple Model", *Ind. Eng. Chem. Research*, **35**, 2334-2341

Fletcher, D.F., Guo, B., Harvie, D., Langrish, T.A.G., Nijdam, J.J. and Williams, J., (2006) "What is important in the simulation of spray dryer performance and how do current CFD models perform? ", *App. Math. Modelling*, **30**, 1281-1292

Hurby, J., Steeper, R. Evans, G. and Crowe, C., (1988) An experimental and numerical study of flow and convective heat transfer in freely falling curtain of particles. *Journal of Fluid Engineering - Trans ASME*, **110**, 172-181.

Lee A (2009) Modelling the solids transport phenomena within flighted rotary dryers. PhD thesis, School of Engineering and Physical Sciences, James Cook University, Townsville.

Lee, A. and Sheehan, M.E., (2010), "Development of a Geometric Flight Unloading Model for Flighted Rotary Dryers", *Powder Technology*, **198**, 395-403

Matchett, A.J. and Baker, C.G.J. (1987) Particle residence times in cascading rotary dryers Part 1 - Derivation of the two-stream model. *Journal of Separation Process Technology*, **8**, 11-17.

Rojas, R., Piña, J., Bucala, V., (2010), "Solids transport modeling in a fluidised drum granulator", *Ind. Eng. Chem. Res.*, **49**, 6986-6997

Schiller, L. and Naumann, Z., (1935), "A Drag Coefficient Correlation", *Zeitschrift des Vereines Deutscher Ingenieure*, **77**, 318-320

Sheehan, M.E., Britton, P. and Schneider, P.A., (2005), "A Model for Solids Transport in Flighted Rotary Dryers Based on Physical Considerations", *Chem. Eng. Science*, **60**, 4171-4182

Wardjiman, C., Lee, A., Sheehan, M. and Rhodes, M., (2008), "Behaviour of a Curtain of Particles Falling Through a Horizontal Gas Stream", *Powder Technology*, **188(2)**, 110-118

Wardjiman, C., Lee, A., Sheehan, M. and Rhodes, M., (2009), "Shape of a Particle Curtain Falling in Stagnant Air", *Powder Technology*, **192(3)**, 384-388

A TWO-FLUID MODEL COUPLED WITH POROUS MEDIUM DESCRIPTION TO PREDICT LIQUID SPREADING IN TRICKLE-BED REACTORS

Zlatko SOLOMENKO[1] , Manel FOURATI[1]*, Yacine HAROUN[1], Faïçal LARACHI[2], Christophe BOYER[1], Frédéric AUGIER[1]

[1] IFP Energies nouvelles, Rond-point de l'échangeur de Solaize, BP 3, 69360 Solaize, France

[2] Department of Chemical Engineering, Laval University, Québec, QC, Canada, G1V 0A6

* manel.fourati@ifpen.fr

ABSTRACT

CFD is used to study liquid spreading in gas-liquid co-current trickle-bed reactors using two-fluid approach. In order to propose a model that describes exhaustively all interaction forces acting on each fluid phase as well as dispersion mechanisms, a discussion of closure laws available in literature is proposed. Liquid dispersion is recognized to result from two main mechanisms: capillary and mechanical. The proposed model is then implemented in two trickle-bed configurations matching with two experimental set ups (Boyer et al., 2005 and Marcandelli et al., 2000). In the first configuration, simulations on a 2D axisymmetric geometry are considered and the model is validated upon a new set of experimental data. Liquid distribution obtained from γ–ray tomography is provided for different geometrical and operating conditions.

In the second configuration, a 3D simulation is considered and the model is validated upon experimental liquid flux patterns at the bed outlet. A sensitivity analysis of liquid spreading to bed geometrical characteristics in terms of particles diameter as well as to gas and liquid flow rates is proposed. The model is shown to be in good agreement with experimental data and to predict, accurately, tendencies of liquid spreading for various geometrical bed characteristics and phases flow-rates.

Keywords: trickle-bed reactors, liquid spreading, capillary dispersion, mechanical dispersion, CFD, two-fluid model.

NOMENCLATURE

Greek Symbols

$\alpha_k = \frac{V_k}{\sum_{k=l,g} V_k}$	Saturation of phase k [-]
$\varepsilon_k = \frac{V_k}{V}$	Volume fraction of phase k [-]
ε	Bed void-fraction [-]
μ_k	Dynamic viscosity of phase k, [kg/m.s]
ρ_k	Density of phase k, [kg/m^3]
σ	Surface tension, [N/m]

Latin Symbols

$\overline{\overline{C}}_k$	Inertial resistance tensor [m^{-1}]
$\overline{\overline{D}}_k$	Viscous resistance tensor [m^{-2}]
d_p	Particle diameter, [m]
E_1, E_2	Ergun constants, [-].
$\vec{F}_{gs}, \vec{F}_{ls}$	Gas-solid and liquid-solid interaction forces, [Nm^{-3}].
$\vec{F}_{lk}$	Gas-liquid interaction force, [Nm^{-3}].
$\vec{F}_{D,k}$	Total dispersion force exerted on phase k, [Nm^{-3}].
$\vec{F}_{D,mech,k}$	Mechanical dispersion force exerted on phase k, [Nm^{-3}]
$\vec{F}_{D,cap,l}$	Capillary dispersion force exerted on liquid phase, [Nm^{-3}]
$\vec{g}$	Gravity vector, [m/s^2]
M_f	Maldistribution index, [-]
N	Number of liquid collectors, [-]
p	Pressure in gas phase, [Pa]
p_c	Capillary pressure, [Pa]
Q_i	Liquid flow rate on collector of index i, [m^3/s]
Q_{mean}	Mean liquid flow rate, [m^3/s]
Q_G	Gas flow-rate, [m^3/s]
Q_L	Liquid flow-rate, [m^3/s]
R_{jet}	Liquid jet width [m]
s_m	Spread factor [m]
$\vec{u}_k$	Velocity vector of phase k, [m/s]
$\vec{u}_{D,k}$	Drift velocity vector of phase k, [m/s]
V_k	Volume of phase k [m^3]
V_{SL}	Superficial liquid velocity, [m/s]
V_{SG}	Superficial gas velocity, [m/s]
V	Elementary volume [m^3]

Sub/superscripts

k=g, l Gas and Liquid.
i collector index

INTRODUCTION

Trickle-bed reactors are widely used in refining industry, particularly in hydro-treatment processes, and continue to mobilize R&D efforts, especially with the growing constraints on sulphur level in diesel and gasoline (Boyer et al., 2005; Martinez et al., 2012). In these reactors catalyst particles are packed to form a fixed bed where, most commonly, liquid and gas reactants flow downwards in cocurrent mode of operation (Wang et al., 2013).

Liquid distribution in trickle bed reactors is a key hydrodynamic criterion for the reactor performance. A poor liquid distribution can basically result in poor utilization or precocious deactivation of the catalyst and may induce local hot spots and low reactor efficiency (Atta et al., 2007; Martinez et al., 2012). It is therefore crucial to investigate liquid spreading in trickle-bed reactors and, ideally, develop predictive models to solve for liquid distribution based on fundamental understanding of hydrodynamic phenomena in such systems. Since pilot-scale experiments are usually time-consuming and costly, their deployment could not cover large range of operating, geometrical and physical conditions (Lappalainen et al., 2011). Numerical modelling has then a growing attractiveness in studying hydrodynamics in trickle-bed reactors and should help assess proper design of such systems.

Many numerical approaches have been considered so far to solve for the two-phase gas-liquid flow in trickle-bed reactors. Wang et al. (2013) made a literature survey of trickle-bed reactors modelling and pointed out two main methods based on Eulerian description, where gas and liquid are treated as interpenetrating continua: volume of fluid method and two-fluid (or Euler-Euler) method. In the first, a surface tracking technique is used to solve for gas-liquid interface requiring an adapted refined mesh which makes the method applicable for relatively small bed scales (Raynal et al., 2007; Augier et al., 2010; Haroun et al., 2014). The second is based on averaging method of local mass and momentum conservation equations where the trickle-bed is represented through an "effective porous medium" (Wang et al., 2013). Since these models do not simulate directly the flow over the real physical geometry, one should deal with a closure problem where interactions with the solid surface of particles, as well as fluid-fluid interactions should be accounted for through specific closure laws.

In this work, CFD is used to investigate liquid spreading in gas-liquid flow in trickle-bed reactors using two-fluid approach. Closure laws as regards fluid-solid interactions, gas-liquid interaction, and exhaustive dispersion mechanisms are discussed based on literature survey. The retained models were then implemented as body source terms in momentum conservation equations within ANSYS Fluent 14.5 environment.

Simulations were carried out for different bed geometrical characteristics in terms of particle diameter and void-fraction. The impact of gas and liquid flow-rates has been investigated as well. Simulation results are then validated upon experimental data of liquid distribution obtained from literature (Marcandelli et al., 2000 and Boyer et al., 2005). Moreover, a new extensive set of data regarding different bed geometries and operating conditions is presented based on γ-ray tomography technique already validated in Boyer et al., (2005).

In light of the simulations, a discussion of predominant dispersion mechanisms depending on bed geometrical characteristics as well as operating flow rates is proposed. Therefore, the ability of the model presented in this work to assess accurate prediction of liquid spreading in trickle-bed reactors is highlighted.

TWO-FLUID MODEL DESCRIPTION

In order to solve for hydrodynamics at the macro-scale of a gas-liquid trickle-bed reactor, a two-fluid approach has been retained. Derivation of conservation equations at macro-scale results from averaging pore-scale Navier-Stokes equations over representative volumes that contain significant number of pores but remain small when compared to trickle-bed size. Derivation of the generic two-fluid model equations for porous media using averaging procedure has been described in several works (Whitaker, 1986; Whitaker, 1999).

Averaging procedure gives rise to several terms containing pore-scale information such as local pressure and velocity deviations. These terms require closure laws in order to solve for the macro-scale problem (Whitaker, 1986; Mewes et al., 1999; Liu, 1999; Lappalainen et al., 2008).

Mass and momentum balances are written considering the following average quantities for each phase denoted k (k refers to gas or liquid) over a representative volume V:

- Volume fraction of phase q: $\varepsilon_k = \frac{V_k}{V}$ where V_k is the volume of phase k within the representative volume which results in the following geometric relation: $\sum_{k=g,l} \varepsilon_k = \varepsilon$
- Intrinsic Average velocity of phase k: $\vec{u}_k = \frac{1}{V_k}\int_{V_k} \vec{u}_{pk} dV$ where $\vec{u}_{pk}$ is the interstitial pore-scale velocity of phase k.

The continuity equation for phase k writes:

$$\frac{\partial}{\partial t}\left(\varepsilon_k \rho_k\right) + \vec{\nabla}.\left(\varepsilon_k \rho_k \vec{u}_k\right) = 0 \quad (1)$$

The macro-scale momentum balances for gas and liquid phases resulting from averaging procedure over pore-scale Navier-Stokes could be written as follows (Boyer et al., 2005; Lappalainen et al., 2009-a, b; Fourati et al., 2013) :

$$\frac{\partial}{\partial t}\left(\varepsilon_g \rho_g \vec{u}_g\right) + \vec{\nabla}.\left(\varepsilon_g \rho_g \vec{u}_g \vec{u}_g\right) = -\varepsilon_g \vec{\nabla} p + \varepsilon \mu_g \nabla^2 \vec{u}_g + \varepsilon_g \rho_g \vec{g} - \vec{F}_{gs} + \vec{F}_{Il} + \vec{F}_{D,g} \quad (2)$$

$$\frac{\partial}{\partial t}\left(\varepsilon_l \rho_l \vec{u}_l\right) + \vec{\nabla}.\left(\varepsilon_l \rho_l \vec{u}_l \vec{u}_l\right) = -\varepsilon_l \vec{\nabla} p + \varepsilon \mu_l \nabla^2 \vec{u}_l + \varepsilon_l \rho_l \vec{g} - \vec{F}_{ls} + \vec{F}_{Ig} + \vec{F}_{D,l} \quad (3)$$

In equations (2) and (3), $\vec{F}_{gs}$ and $\vec{F}_{ls}$ refer respectively to gas-solid and liquid-solid interaction forces due to porous resistances (Fourati et al., 2013). Gas-liquid interactions are accounted for using the shear term $\vec{F}_{Ik}$ analogous to drag force in dispersed gas-liquid flows. $\vec{F}_{D,g}$ and $\vec{F}_{D,l}$ are dispersion forces in the porous medium that apply, respectively, to gas and liquid and include capillary as well as mechanical contributions (Lappalainen, 2009 a, b).
Finally, the momentum balance at gas-liquid interface writes: $\vec{F}_{Il} + \vec{F}_{Ig} = \vec{0}$.

- **Porous resistances and gas-liquid interaction**

Proposals to model gas-solid and liquid-solid interactions in porous media are mostly inspired from Darcy-Forchheimer formalism (Whitaker, 1996) that allows modeling the resistance induced by the medium geometry in a given phase. With respect to this formalism, gas-solid and liquid-solid interactions include viscous and inertial forces that could be written for the three flow directions owing to viscous and inertial resistance tensors : $\overline{\overline{D}}_k$ and $\overline{\overline{C}}_k$ (Fourati et al., 2013).

$$\vec{F}_{kS} = -\left(\mu_k \overline{\overline{D}}_k \vec{u}_k + \frac{1}{2}\rho_k \|\vec{u}_k\| \overline{\overline{C}}_k \vec{u}_k \right) \quad (4)$$

where k accounts for gas or liquid.
Attou et al. (1999) built a phenomenological hydrodynamic model in trickle-bed reactors based on the balance of forces exerted on both phases at a particle scale. Within this formalism, the suggested porous resistance that applies to liquid is weighted by the medium tortuosity, itself estimated as the reciprocal of the liquid saturation. Boyer et al. (2007) conjectured that tortuosity in liquid phase depends, via liquid film curvature (and thus surface tension), on gas inertia. Based on experimental data for aqueous and organic liquids, the authors suggested tortuosity to write as $\alpha_l^{\,n}$ where $\alpha_l = \varepsilon \times \varepsilon_k$ is the liquid saturation and n values are respectively -0.53 and -0.02.
The hydrodynamic model of Boyer et al. (2007) is examined in this work. In addition to porous resistances, the latter model includes gas liquid interaction force based on a mechanistic approach. The resulting macroscopic model allows prediction of liquid saturations and over-all pressure drop with relative errors as low as 8% and 16%, respectively. It has been thus retained to model porous resistances as well as gas-liquid interactions in the present study. By viewing trickle-bed reactors as isotropic media, porous resistances described in equation (4) on both phases write as follows (Boyer et al., 2007): $\vec{F}_{kS} = -K_{kS}\,\vec{u}_k$ (5)
Where K_{kS} write respectively for gas and liquid as follow:

$$K_{gs} = E_1 \mu_g \frac{(1-\varepsilon_g)^2}{\varepsilon_g d_p^2}\left(\frac{1-\varepsilon}{1-\varepsilon_g}\right)^{\frac{2}{3}} + E_2 \rho_g \frac{1-\varepsilon_g}{d_p}\left(\frac{1-\varepsilon}{1-\varepsilon_g}\right)^{\frac{1}{3}} \|\vec{u}_g\| \quad (6)$$

$$K_{ls} = \alpha_l^n \left(E_1 \mu_l \frac{(1-\varepsilon)^2}{\varepsilon_l d_p^2} + E_2 \rho_l \frac{1-\varepsilon}{d_p} \|\vec{u}_l\| \right) \quad (7)$$

In closure laws expressed in equations (6) and (7), viscous and inertial Ergun constants E_1 and E_2 are taken equal to 150 and 1.75. These have been validated upon pressure drop measurements in single-phase upward liquid flow on 5 different liquid-solid systems (Boyer et al., 2007).
Gas-liquid interaction force contains viscous and inertial contributions as well and writes as follows:

$$\vec{F}_{Ig} = K_{gl}\left(\vec{u}_g - \vec{u}_l\right) \quad (8)$$

Where K_{gl} is a gas-liquid interaction coefficient that writes as follows:

$$K_{gl} = E_1 \mu_g \frac{(1-\varepsilon_g)^2}{\varepsilon_g d_p^2}\left(\frac{1-\varepsilon}{1-\varepsilon_g}\right)^{\frac{2}{3}} + E_2 \rho_g \frac{1-\varepsilon_g}{d_p}\left(\frac{1-\varepsilon}{1-\varepsilon_g}\right)^{\frac{1}{3}} \|\vec{u}_g - \vec{u}_l\| \quad (9)$$

- **Capillary dispersion force**

The Euler-Euler model described in equations (2) and (3) allows solving for a single averaged pressure field that equals gas pressure. Therefore a capillary pressure model is needed to account for the pressure jump, p_g - p_l, across gas-liquid interface due to local film curvature. The gradient of capillary pressure induces "capillary dispersion" that applies for the liquid by choosing gas-phase pressure as the dependent pressure variable in the model formulation (Lappalainen et al., 2008; Fourati et al., 2013).
Attou and Ferschneider (2000) phenomenological model, validated upon a large range of experimental data, has been retained in this work to account for capillary dispersion.

$$\vec{F}_{D,cap,l} = \varepsilon_l \times \vec{\nabla} p_c = -\frac{2\sigma}{3}\left(\frac{\varepsilon}{1-\varepsilon}\right)\left(\frac{1}{d_p} + \frac{1}{d_{\min}}\right) F\left(\frac{\rho_g}{\rho_l}\right)\left(\frac{1-\varepsilon}{1-\varepsilon+\varepsilon\alpha_l}\right)^{\frac{4}{3}} \times \vec{\nabla}\alpha_l \quad (10)$$

In equation (10) the characteristic diameter d_{min} is defined as the minimum equivalent diameter of the area delimited between three contacting spheres and is expressed as follows:

$$d_{\min} = \left(\frac{\sqrt{3}}{2} - \frac{1}{2}\right)^{\frac{1}{2}} \times d_p$$

- **Mechanical dispersion force**

Mechanical dispersion is a phenomenon that occurs in packed bed reactors in general due to the particular geometry of the porous medium in which the fluids are allowed to evolve. A few closure laws for mechanical dispersion are suggested in the literature (Mewes et al., 1999; Liu and Long, 2000; Lappalainen et al., 2008). Lappalainen et al. (2009-b) introduced a closure law for mechanical dispersion based on analogy with diffusion

of passive tracers. Authors suggested that mechanical dispersion is essential to predict liquid spreading and has increasing effect as particle size goes up. Fourati et al. (2013) discussed the mechanistic origin as well as the theoretical foundation of mechanical dispersion forces in packed beds. These authors interpreted dispersion as a phenomenon due to local spatial fluctuations of liquid velocity at pore scale. It is indeed the macroscopic velocity deviation from the volume-averaged velocity which per se causes dispersion.

Mechanical dispersion forces in liquid and gas write respectively as follows (Lappalainen et al., 2009-b, Lappalainen et al., 2011, Fourati et al., 2013):

$$\vec{F}_{D,mech,l} = \alpha_l K_{ls} \vec{u}_{D,l} + \varepsilon K_{gl} \left(\vec{u}_{D,l} - \vec{u}_{D,g} \right) \quad (10)$$

$$\vec{F}_{D,mech,g} = \alpha_g K_{gs} \vec{u}_{D,g} + \varepsilon K_{gl} \left(\vec{u}_{D,g} - \vec{u}_{D,l} \right) \quad (11)$$

In these equations, K_{ks} (k=g,l) and K_{gl} are respectively momentum exchange coefficients and gas-liquid interaction coefficients previously expressed in equations (6), (7) and (9).

Drift velocities for liquid and gas are functions of fluid saturation gradient and write as follows (Lappalainen et al., 2009-b):

$$\vec{u}_{D,k} = -\frac{S_m}{\alpha_k} \left(\left\| \vec{u}_k \right\| \vec{\nabla} \alpha_k - (\vec{u}_k \cdot \vec{\nabla} \alpha_k) \frac{\vec{u}_k}{\left\| \vec{u}_k \right\|} \right) \text{(k=g,l)} \quad (12)$$

In equation (13), S_m is a spread factor that represents a characteristic length of liquid dispersion in a given trickle-bed geometry. For a given particles diameter, S_m is given by correlation of Baldi and Specchia (1976) validated upon experimental data of tracer dispersion over particles of different shapes and sizes (Lappalainen et al., 2009-b): $S_m = 0.015 \times \sqrt{d_p}$ (13)

SIMULATION CASES

1- Liquid spreading from a source point : Boyer et al. (2005)

Boyer et al. (2005) measured liquid distribution in a 0.4 m diameter and 1.8 m high packed-bed filled with spherical glass beads using γ-ray tomography technique. They considered an air/water system and a diameter of particles of 1.99 mm. Liquid was fed from a central nozzle located at top of the column at a volumetric flow rate of 35.6E-6 m^3/s. Gas was injected from a lateral nozzle for two volumetric flow rates: 12.5E-3 and 25E-3 m3/s. The experimental apparatus used by authors is described on Figure 1.

In addition to these measurements, a new set of data based on Boyer et al. (2005) experiments is added including various particles diameters as well as liquid and gas flow-rates (see Table 1).

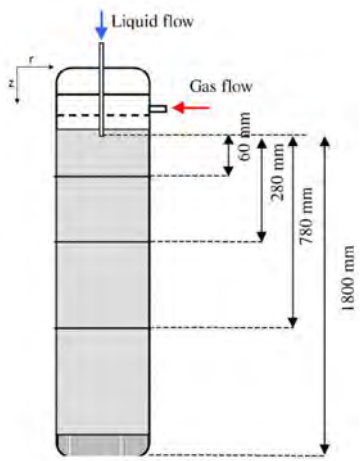

Figure 1: Boyer et al. (2005) experimental apparatus

Table 1: experimental conditions of simulated cases

Case	1	2	3	4	5	6
	Boyer et al. (2005)	Boyer et al. (2005)	New	New	New	New
d_p (mm)	1.99	1.99	1.99	6	6	6
ε (%)	37	37	37	41	41	41
Q_L (10^{-6} m^3/s)	35.6	35.6	125.8	35.6	35.6	125.8
Q_G (10^{-3} m^3/s)	12.5	25	12.5	12.5	25	12.5

γ–ray tomography was used to build liquid saturation profiles at different column sections located respectively at 60, 280 and 780 mm from liquid inlet (Figure 1). This technique as well as the reconstruction algorithm used to acquire liquid saturation maps have been extensively described and validated in Boyer and Fanget (2002). The uncertainty on liquid saturation has been shown to be less than ± 3%.

In order to simulate liquid spreading experiments described in this section, a two-dimensional axisymmetric computational grid has been considered. Bed void-fractions are assumed constant across the trickle-bed for both considered particles sizes, namely, 1.99 mm and 6 mm (Table **1**). The corresponding void-fractions used in the simulations are respectively, 37% and 41%.

2- Liquid spreading from off-center inlet distribution : Marcandelli et al. (2000)

Marcandelli et al. (2000) investigated liquid distribution in a 0.3 diameter and 1.3 high column packed with 2 mm glass beads and using air/water system. These authors considered different liquid and gas feeding configurations and measured liquid flow rate using 9 collectors of constant surface at the bottom of the column. In this study, we chose only off-center liquid feeding configuration where gas was fed through four 25 mm ID chimneys while liquid is injected through two 2.5mm ID orifices as illustrated in Figure 2 in the co-current mode.

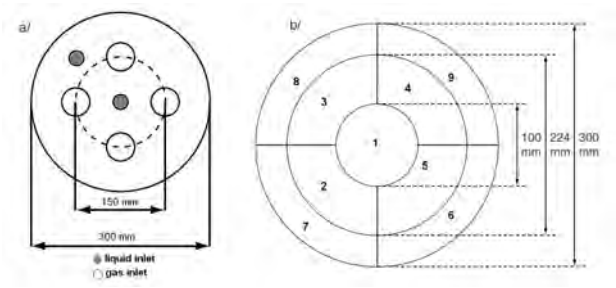

Figure 2:a/ feeding geometry at top of the bed ; b/ collectors geometry at bottom of the bed from Marcandelli et al. (2000).

In order to quantify liquid distribution at the bed outlet, Marcandelli et al. (2000) defined a "maldistribution index" ranging from 0 to 1 and calculated as follows:

$$M_f = \sqrt{\frac{1}{N(N-1)}\sum_i \left(\frac{Q_i - Q_{mean}}{Q_{mean}}\right)^2}$$ where N accounts for the number of collectors (9 in this case), Q_i for the liquid flow rate through a given collector referenced by i and Q_{mean} for the mean flow rate defined as an arithmetic average of flow rates (equal area sampling domains) collected at bottom of the packed bed.

Experimental data have been provided in terms of liquid distribution profiles by means of percentage of total liquid flow rate in each collector as well as maldistribution index. These authors indicated relative errors on measured liquid flow rates in collectors ranging from 8 to 10%.

Simulations have been carried out considering 3D grid that represents half of the column. Void-fraction is set equal to 39% (Llamas, 2009).

RESULTS AND DISCUSSION

Simulations were carried out within Ansys 14.5 CFD environment. The basic Euler-Euler formalism available within this software has been extended with User defined Functions to account for the specific closure laws described above. Simulations have been carried out using unsteady solver with implicit temporal discretization scheme of order 2. Upwind scheme of order 2 has been considered for spatial discretization.

1- Liquid spreading from a source point

In Figure 3, liquid saturation fields as well as liquid jet widths in simulation and experimental cases described in Table 1 are reported at different longitudinal distances from liquid inlet: respectively at 60, 280 and 780 mm as defined in Boyer et al. (2005).

Liquid jet width (R_{jet}) is defined as the radial coordinate r that indicates liquid flow extent.

Experimentally, liquid jet width is determined via the reconstruction algorithm described in Boyer et al. (2005). The liquid jet extent is supposed to be reached when a sharp density gradient is detected in the radial direction, indicating the interface between a liquid-rich and a gas-rich region.

Numerically, determination of the extent of liquid jet for given conditions requires a criterion on liquid saturation or derivative thereof. In the first case, a threshold of saturation at the liquid jet limit is to be considered making liquid jet contours dependent on that specific value. In this study, liquid jet width is defined as the radial coordinate r at which a discontinuity is observed on liquid saturation gradient in the radial direction: $\frac{\partial \alpha_l}{\partial r}$. This criterion is deemed more objective than the first one.

Different criteria for determination of liquid jet extent may induce artificial discrepancies between experimental and numerical data in terms of liquid spreading for the same conditions. Therefore, one should keep this in mind and focus on order of magnitude of the results when comparing liquid jet widths obtained experimentally and numerically.

On Figure 3, liquid jet contours obtained from CFD are compared to experimental data. The results show that the model allows predicting accurately the order of magnitude of liquid jet width for all simulated cases. Relatively highest discrepancies are obtained for particles of diameter 1.99 mm as will be discussed further.

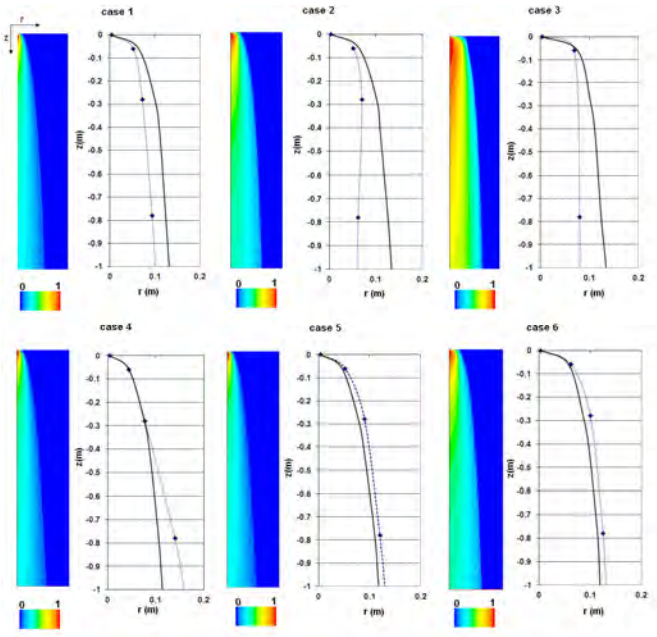

Figure 3: Liquid saturation fields and liquid jet contours in simulation cases described in Table 1, continuous curve: simulations, discrete points: experiments

- Effect of particles diameter on liquid spreading

Experimental data in terms of R_{jet} (Figure 3) show more important liquid jet spreading for particles of diameter 6mm as compared to 1.99 mm ones at intermediate and lower longitudinal positions (z=280mm and z=780mm). However, for upper longitudinal position (z=60mm), R_{jet} remains globally slimmer for 6 mm particles than for 1.99 mm ones. As far as simulations are concerned, globally less subsequent liquid jet spreading across the bed is predicted for 6mm particles. Liquid spreading shortage for coarser particles is essentially due to the decrease of capillary dispersion forces with particle

diameter. On the other hand, mechanical dispersion forces become more important when particle diameter increases as pointed out in Eq.13. However such increase is insufficient to compensate for the loss due to capillary forces thus generating less jet spreading for 6 mm particles.
Moreover Figure 3 shows very good agreement between experimental and predicted profiles of liquid jet for larger particle diameter. Relatively higher relative errors are observed for smaller particle. This implies, in all likelihood, that mechanical dispersion, though more accurately described in the present model, is not sufficient considering that current capillary dispersion force tends to inflate liquid spreading for particles of small diameter.
More experimental studies are still needed to confirm liquid dispersion dependence on particle sizes. From a numerical point of view, accuracy of the two-fluid model for a large range of particle diameters should be enhanced. Future modeling work should address both dispersion mechanisms, namely, capillary and mechanical. The two latter mechanisms are in competition but both keep having significant order of magnitude over the tested range of particles diameter.

- Effect of liquid flow-rate on liquid spreading

Experimental data show that an increase in liquid flow-rate leads liquid jet to widen at upper and intermediate elevations of the trickle-bed (~35% wider) then to tighten for lower longitudinal positions (~12% tighter). Such observations are persistent for both particle sizes examined in this work.
Simulations predict basically liquid jet widening at top of the trickle-bed (~18% wider) when liquid flow rate increases but liquid jet extent remains almost unchangeable at deeper downstream bed locations. Increase of liquid jet width near the trickle-bed top for higher liquid flow rates is explained by important liquid velocity at the bed entrance in single-point injection conditions. This results in higher mechanical dispersion force (Eq. 11, 12 and 13) and consequently wider liquid jet at top of trickle-bed.
For lower positions, experimental impact on liquid jet extent is more moderate. Discrepancy with numerical results at this position could be partly attributed to the difference between the CFD and experimental criteria used for determination of liquid jet extent as explained earlier.

- Effect of gas flow-rate on liquid spreading

Experimentally, increasing gas flow rate does not influence liquid spreading near the bed inlet but causes jet confinement for downstream positions (~15% tighter liquid jet). This is basically observed for both particle sizes examined in this work. Figure 4 presents evolution of constant liquid saturation lines obtained from simulations in cases 1 and 2 (Table 1). Liquid jet confinement is well reproduced by simulations since constant liquid saturation lines are translated towards smaller radial coordinates when gas flow rate increases. Based on Figure 4, liquid jet width reduction is only ~7%. More important liquid jet confinement is obtained in experiments.

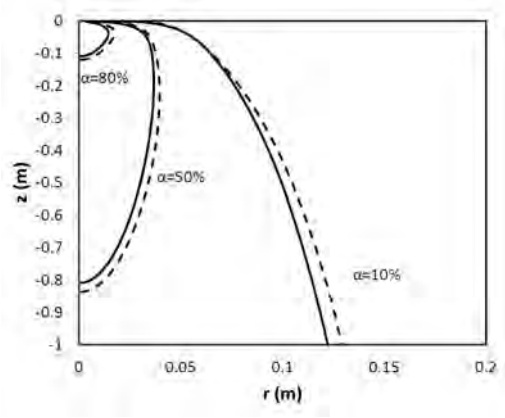

Figure 4: Liquid iso-saturation contours for d_p=1.99 mm, discontinuous line: Q_g=12.5E-03m^3/s, continuous line: Q_g=25E-03m^3/s

2- Liquid spreading from off-center inlet distribution

Figure 5 shows liquid saturation contours in the simulated trickle-bed in the particular configuration of two liquid injection points (Figure 2-a) considered in Marcandelli et al. (2000) experiments. One could notice liquid spreading along the column. Dissymmetry of liquid patterns is kept but still attenuated at lower positions of the trickle-bed.
In order to characterize liquid distribution at the bed outlet, ratio of liquid flow rate in each virtual collector (Figure 2-b) to total liquid flow rate is calculated. Figure 6 shows good agreement between experimental and numerical data bearing in mind relative errors on measured liquid flow rates that range between 8 and 10% (Marcandelli et al., 2000).
Moreover simulation predicts a global maldistribution factor of 27% which is quite close to this reported by Marcandelli et al. (2000): 23%.
Atta et al. (2007) attempted to simulate Marcandelli et al. (2000) experiments as well. The model proposed by the authors predicts well liquid distribution in homogeneous inlet conditions but failed in predicting the flow in the case of decentred liquid injection. This is in all likelihood due to the absence of dispersion forces in the k-fluid model considered by the authors. In fact, simulations carried out in this study without taking into account capillary and mechanical dispersion forces showed negligible spreading of liquid in the trickle-bed.

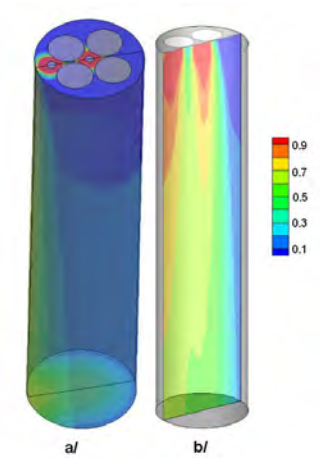

Figure 5: contours of liquid saturation obtained by simulation in the case of Marcandelli et al., (2000) experiment. a/ on the entire domain, b/ on the symmetry plane

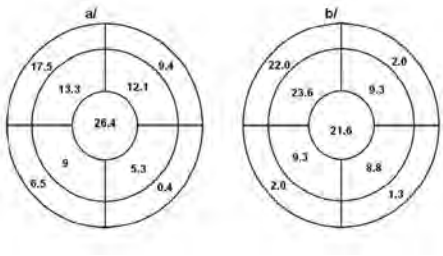

Figure 6: liquid distribution at bottom of the trickle-bed in terms if % of total liquid flow rate. a/ experimental results (Marcandelli et al., 2000), b/simulation results

CONCLUSION

In this work, a two-fluid model is proposed and validated to simulate hydrodynamics in trickle-bed reactors in terms of liquid spreading. Closure laws are discussed in order to account for fluid-solid interactions, fluid-fluid interactions as well as dispersion forces induced by the medium geometry and phasic inertia. The model includes exhaustive description of dispersion mechanisms that contribute to liquid dispersion, namely, capillary (Attou and Ferschneider, 2000) and mechanical (lappalainen et al., 2009-b). In order to validate the model, simulations have been conducted in experimental conditions described in the studies of Boyer et al. (2005) and Marcandelli et al. (2000). In the first configuration, liquid is injected in the trickle bed from a centered single feeding point located at top of the bed. The second configuration corresponds to an off-center injection resulting in 3D flow patterns.

Calculations in the first feeding conditions show satisfactory agreement with experimental data in terms of liquid jet extent at different bed positions. A sensitivity analysis to bed geometry in terms of void-fraction and particle sizes has been assessed. It has been shown that mechanical dispersion is predominant over capillary dispersion for growing particle diameter. Accuracy of k-fluid model has been pointed out based on a good concordance with experimental data, mainly for big particles for which mechanical dispersion mechanism is predominant. Gas and Liquid flow rates impact on liquid spreading has been also investigated. Liquid flow rate is shown to enhance liquid spreading near the bed inlet but not to engender subsequent over-all spreading across the bed. Gas flow rate increase is shown to engender a moderate liquid jet confinement across the trickle-bed. Simulation data inherent in this liquid feeding configuration are compared to data of Boyer et al. (2005) as well as to a new set of data based on the same method. Finally, a simulation is made in the off-center liquid injection conditions described in Marcandelli et al. (2000). The developed 3D model allows predicting accurately liquid flow patterns in this case.

Provided it is used in conjunction with pilot-scale experimental studies, CFD is shown to be a powerful and complementary asset to predict flow-structure hydrodynamic phenomena in trickle-bed reactors. In order to enhance the model prediction for different geometrical and operating conditions, extensive experimental data are still required in order to confirm liquid spreading tendencies for significant range of particles diameter and phases flow rates. Improvement of capillary and mechanical dispersion models for trickle-bed reactors at different operating regimes is also required.

REFERENCES

Atta A., Roy S., Nigam K.D.P., (2007), "Investigation of liquid maldistribution in trickle-bed reactors using porous media concept in CFD", *Chem. Eng. Sci*, **62, 7033-7044**.

Attou A., Boyer C., Ferschneider G., 1999, "Modelling of the hydrodynamics of the cocurrent gas-liquid trickle flow through a trickle-bed reactor", *Chem. Eng. Sci*, **54**, **785-802**.

Attou A., Ferschneider G., 2000, "A two-fluid hydrodynamic model for the transition between trickle an pulse flow in a cocurrent gas-liquid packed-bed reactor", *Chem. Eng. Sci*, **55**, **491-511**.

Augier F., Koudil A., Royon-Lebeaud A., Muszynski L.,Yanouri Q., 2010, "Numerical approach to predict wetting and catalyst efficiencies inside trickle bed reactors", *Chem. Eng. Sci*, **65**, **255-260.**

Baldi, G., Specchia, V., 1976, "Distribution and radial spread of liquid in packed towers with two-phase cocurrent flow: effect of packing shape and size", *Quaderni dell'Ingegnere Chimico Italiano*, **12**, **107-111**.

Boyer C., Koudil A., Chen P., Dudukovic MP., 2005, " Study of liquid spreading from a point source in a trickle-bed via γ-ray tomography and CFD simulation", Chem. Eng. Sci, **60**, **6279-6288**.

Boyer C., Volpi C., Ferschneider G., 2007, "Hydrodynamics of trickle bed reactors at high pressure: Two-phase flow model for pressure drop and liquid holdup, formulation and experimental validation", Chem. Eng. Sci, **62**, **7026-7032.**

Fourati, M., Roig V., Raynal L., 2013, "Liquid dispersion in packed columns: Experiments and numerical modelling", Chem. Eng. Sci, **100**, **266-278**.

Haroun Y., raynal L., Alix P., 2014, "Prediction of effective area and liquid hold-up instructured packings by CFD", Chem. Eng. Res. Des, doi.org/10.1016/j.cherd.2013.12.029.

Holub R. A., Dudukovic M.P., Ramachandran P.A., 1992, "A phenomenological model for pressure drop, liquid holdup, and flow regime transition in gas-liquid trickle flow", Chem. Eng. Sci, **47**, **2343-2348**.

Lappalainen K., Alopaeus V., Manninen M., Aittamaa J., 2008, "Improved hydrodynamic model for wetting efficiency, pressure drop, and liquid holdup in trickle bed reactors", *Industrial & Engineering Chemistry Research*, **47**, **8436-8444**.

Lappalainen K., Manninen M., Alopeus V., Aittamaa J., Dodds J., 2009-a, "An analytical model for capillary pressure-saturation relation for gas-liquid system in a packed-bed of spherical particles", *Transport in Porous Media*, **77**, **17-40**.

Lappalainen K., Manninen M., Alopaeus V., 2009-b, "CFD modeling of radial spreading of flow in trickle-bed reactors due to mechanical and capillary dispersion", *Chem. Eng. Sci*, **64**, **207-218**.

Lappalainen K., 2009-c, "Modelling gas liquid flow in trickle-bed reactors", Doctoral thesis, Helsinki University of Technology.

Lappalainen K., Gorshkova E., Manninen M., Alopeus V., 2011, "Characteristics of liquid and tracer dispersion in trickle-bed reactors: effect on CFD modeling and experimental analyses", *Computers and Chemical Engineering*, **35**, **41-49**.

Llamas JD., 2009, "Etude expérimentale de la maldistribution des fluides dans un réacteur à lit fixe en écoulement co-courant descendant de gaz et de liquide », Doctoral thesis, Institut National Polytechnique de Lorraine.

Liu S., 1999, "A continuum approach to multiphase flows in porous media", *Journal of Porous Media*, **2**, **295-308**.

Marcandelli C., Lamine A.S., Bernard J.R., Wild G., 2000, "Liquid distribution in trickle-bed reactor", *Oil & Gas Science and Technology*, **55**, **407-415**.

Martinez M., Pallares J., Lopez J., Lopez A., Albertos F., Garcia MA., Cuesta I., Grau FX., 2012, "Numerical simulation of the liquid distribution in a trickle-bed reactor", *Chem. Eng. Sci*, **76**, **49-57**.

Mewes D., Loser T., Millies M., 1999, "Modelling of two-phase flow in packings and monolith's", *Chem. Eng. Sci*, **54**, **4729-4747**.

Raynal, L., Royon-Lebeaud, A., 2007. A multi-scale approach for CFD calculations of gas–liquid flow within large size columnequipped with structured packing. Chem. Eng. Sci., vol. 62, pp. 7196–7204.

Wang Y., Jinwen C., Larachi F., 2013, "Modelling and simulation of trickle-bed reactors using computational fluid dynamics: a state-of-the-art review", *The Canadian Journal of Chemical Engineering*, **91**, **136-180**.

Whitaker S., 1999, "The Method of Volume Averaging", Kluwer Academic Publishers, Dordrecht.

Whitaker S., 1986, "Flows in porous media II: The governing equations for immiscible two-phase flow, *Transport in Porous Media*, **1**, **105-125**.

LOCAL SIMULATION OF THE EFFECT OF VOID FRACTION ON THE OVERALL REACTION RATE IN PACKED BED REACTORS

Matthieu ROLLAND[1]*

[1] IFPEN, Process Intensification, 69390, France

* E-mail: matthieu.rolland @ifpen.fr

ABSTRACT

In lab-scale fixed bed reactors, void fraction is dependent on the solid loading procedure. In this work we are interested in determining whether void fraction has an impact of the reactor apparent performance using direct numerical simulation of the reactive flow in structured (periodic) arrays of spheres (simple cubic, body centred cubic and face centred cubic). The apparent conversion has been simulated varying the following parameters: fluid velocity, kinetic constant, molecular diffusion, lattice spacing has been performed.

Reactor apparent conversion in structured periodic arrays of spheres depends mostly on sphere arrangement and to a lower extent on sphere spacing. In structured periodic arrays, void fraction is not a good predictor of overall reactor performance.

Sensitivity to void fraction increases in presence of mass transfer limitations.

Tortuosity, that is the amount of interaction between flow channels, favours transverse dispersion and thus lowers mass transfer limitations (or equivalently favours higher conversions). We therefore expect better transverse dispersion and mass transfer coefficient in random packed-beds than in structured ones.

For all packing, effect of void fraction can be significant when the ratio u/k is lower than 0.1: is when reaction is relatively fast compared to convection. This is coherent with the classical knowledge that mass transfer coefficients increase with velocity. When operating at constant contact time, this favours design of unstructured, long and narrow reactors.

Keywords: Chemical Reactors, Packed beds, Multiphase mass transfer.

NOMENCLATURE

Greek Symbols

ρ	Mass density, [kg/m^3].
μ	Dynamic viscosity, [kg/m.s]

Latin Symbols

bcc	body centred cubic structure
c	concentration [mol/m^3]
d_p	particle diameter [m]
fcc	face centred cubic structure
k	surface kinetic constant [m/s]
sc	simple cubic structure
u	inlet velocity [m/s]
z	vertical coordinate [m]
D_m	molecular diffusion [m^2/s]
L	lattice expansion factor compared to compact case
L_0	lattice expansion used as reference, L_0 = 1.01
RD_L	Relative Difference to the L= L_0 case

$$RD_L = \frac{C_{out,L} - C_{out,L_0}}{C_{out,L_0}}$$

Dimensionless numbers

Bi	Biot	$Bi = \frac{k.d_p}{D_m}$
Da	Damköhler	$Da = \frac{k}{u}$
Pe	Peclet	$Pe = \frac{u.d_p}{D_m}$

INTRODUCTION

In lab-scale fixed bed reactors, void fraction is dependent on the solid loading procedure. Despite all precautions, it can never be exactly equal when repeating loading. The only practical criteria available to ensure that a reactor is correctly loaded is the repeatability of the packed bed height, and hence is based on the average void fraction. To our knowledge, no experimental results support this approach and we are interested in investigating the effect of void fraction on reactor overall reaction rate.

Direct numerical simulation of flow in fixed bed reactors for single phase flow has been performed for many years with various computations methods such as Finite Volume (Wachs, 2010), lattice-Boltzmann (Maier, 1998) in structured or random packed beds. Recent trends are about improving numerical methods, dealing with packing of complex shaped objects (non-convex), or larger systems (parallel computing). Freund (2003) demonstrated simulating reactive transport in a random packing. Gunjal (2005) simulated heat transfer as function of Reynolds number in structured array of spheres and not as function of void fraction. Recently Rong (2013) simulated the effect of void fraction on pressure drop. So far, the link between void fraction and reactivity has not been studied.

In this work, we will use DNS to simulate laminar flow and reactive transport in regular structures. We use Comsol Multiphysics, a commercial software package based on finite elements. We take for granted that it has been validated on the basic fluid dynamics problems that are laminar single phase flow and scalar transport.

MODEL DESCRIPTION

Geometry

Three structured packing of identical spheres have been studied (Figure 1, Figure 2): simple cubic (sc), body centred cubic (bcc), and face centred cubic (fcc). Spherical particle diameter is set to 3 mm.

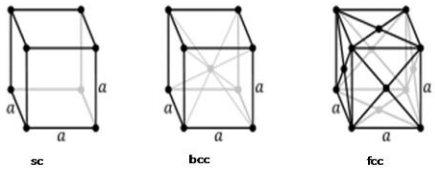

Figure 1: Structures of (sc), (bcc) and (fcc) lattices, (from http://nano-physics.pbworks.com).

An empty space of at least one particle diameter has been inserted before and after the spheres so as to level out any side effects induced by the inlet and outlet boundary conditions (Figure 2).

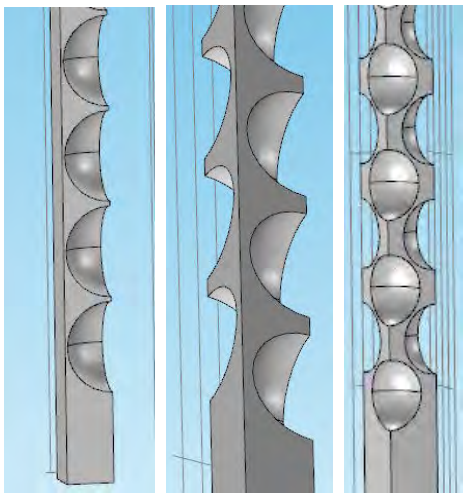

Figure 2: Close-ups of geometry for (sc), (bcc) and (fcc) cases.

To study the effect of void fraction, the lattice size was varied from 1.01 to 1.05 times the compact lattice size while keeping the spheres diameter constant. Consequently, there is no contact point between the spheres.

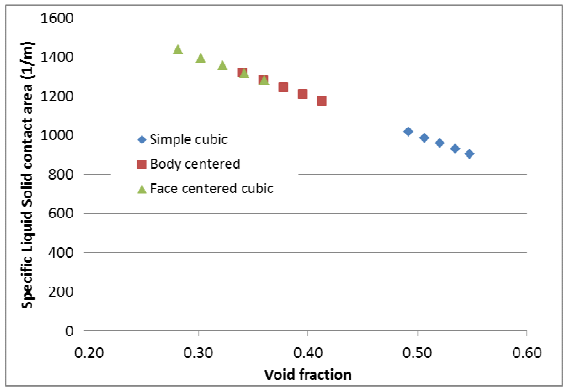

Figure 3: Specific liquid solid contact area for all 3 geometries x 5 lattice spacing.

CFD model

Navier-Stokes equations (Re < 60) for a single phase fluid are solved to compute the velocity field in described geometries. Boundary conditions are uniform pressure at outlet, uniform velocity at inlet, no-slip conditions at the spheres surface. On the sides, we use natural symmetry of each structure to reduce the size of the problem.

Reactor chemical performance is computed by solving the convection – diffusion equation with a source term representing reaction of the particles surface. Boundary conditions are: uniform concentration c=1 at inlet, first order surface reaction at spheres surface and convective flow at the outlet. The surface reaction rate is expressed as '– k.c' where k is a kinetic constant with the unit of a velocity. It is assumed that the concentration variations have no effect on the physical properties of the fluid, allowing solving separately and sequentially the flow and the concentration solution.

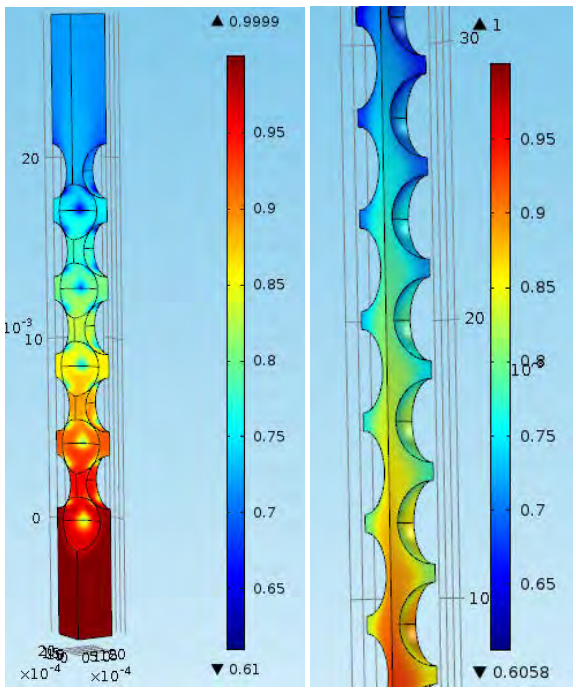

Figure 4: Examples of concentration field in (fcc) case (left) and (bcc) case (right). Flow is upward.

Results presented hereafter are the mixing cup concentration integrated over the outlet surface, and

called "outlet concentration". Examples of concentration solutions are presented in Figure 4.

Parametric study

Physical properties and parameters required to run the model are density, viscosity, molecular diffusion, inlet velocity and surface kinetic constant. In all simulations, density is set to 800 kg/m^3 and viscosity to 4.10^{-4} Pa.s which would correspond to a light hydrocarbon liquid such as heptane.

A parametric study has been performed on molecular diffusion (D_m: 10^{-10} to 10^{-5} m^2/s), inlet velocity (u: 10^{-5} to 10^{-2} m/s) and surface kinetic constant (k: 10^{-8} to 10^{-3} m/s). One should not forget at this stage that the lattice spacing parameter L is also varied from 1.01 to 1.05 to vary the void fraction.

Grid independence

In Comsol Multiphysics, meshing is an automated process based on the physics involved. The meshing was performed using hexahedral elements to capture boundary layers and tetrahedral elements in the fluid bulk. Grid dependence was assessed using 3 levels of mesh refinement (Coarse, Normal and Fine) that correspond in a (sc) structure with 20 periodic cells to 160, 300 and 650 thousands unknown variables to be solved.

As can be observed in Figure 5, mesh independence is not reached with the selected mesh refinement for the convection - reaction problem. Our analysis of the results (not presented here) tends to show that the grid dependence is due to significant numerical diffusion induced by the numerical schemes. There is little that can be done about it. For this reason, we are unsure that further grid refinement would lead to grid convergence.

Effect of lattice spacing are however grid independent with a normal of fine meshing strategy. As we are interested in investigating the effect of lattice spacing, we conducted all simulations with the "normal" mesh refinement. Our results should not be used as "stand alone" nor be considered as predictive.

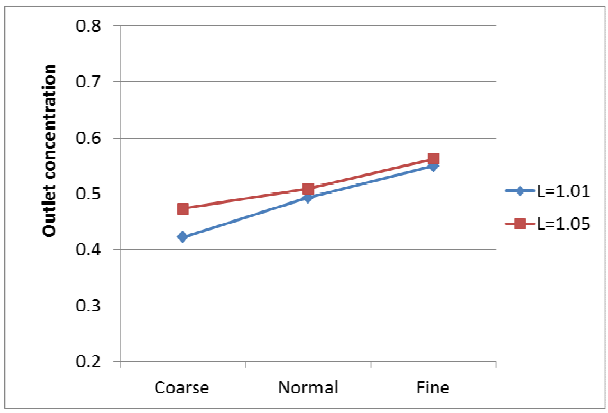

Figure 5 : Effect of mesh refinement (Coarse, Normal, Fine) on outlet concentration for the (sc) structure (20 periodic cells).

RESULTS

Effect of lattice spacing for a given structure

In this part, all periodic structures are made of 20 periodic cells, meaning that bed height and number of catalyst particles depend on the lattice structures (sc, bcc and fcc). Therefore, in this part, results are not comparable between structures.

Data analysis

In all structures (sc, bcc, fcc), the general trend is that increasing the lattice spacing leads to a lower overall conversion: increasing the average flow path diameter slows the transverse transport from the main flow line to the catalyst surface. Thus results are best presented in comparison to the most compact cases, the L=1.01case (Figure 6). For this purpose we introduce the relative difference RD_L defined as the relative difference of solution with lattice spacing L to the solution with lattice spacing L_0 = 1.01 for identical physical parameters and structure:

$$RD_L = \frac{C_{out,L} - C_{out,L_0}}{C_{out,L_0}}$$

RD_L is a measure of the effect of void fraction for a given structure. It is maximum for high conversion (low outlet concentration), and decreases in an exponential manner to 0 for very low conversion cases.

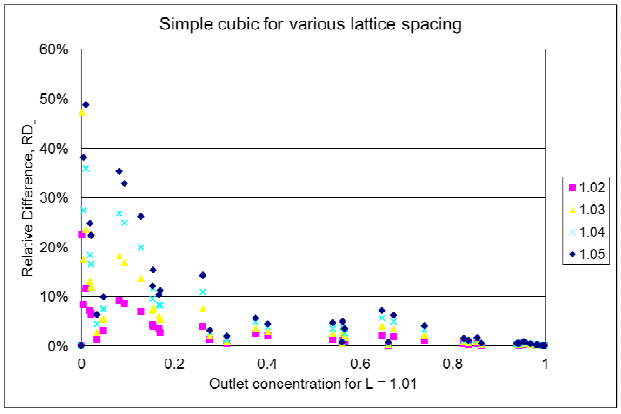

Figure 6: Relative Difference RD_L for the simple cubic (sc) structure for L = 1.02 to 1.05, all results represented.

Results

For all structures, the magnitude of the effect of void fraction on outlet concentration is strongly dependant on the relative values of parameters (u, k, D_m). It appears that the most influential parameter is the ratio of the inlet velocity to kinetic constant u/k (inverse of the Damköhler number). See Figure 7. For ratio u/k larger than 10^3, the spacing, hence void fraction, has negligible effect (less than 1% difference on mean outlet concentration). On the other hand, mean outlet concentration could differ by up to 30 - 50% (log RD > -0.5) for u/k ratio smaller than a threshold that depends on the parameters and is always larger than 0.1 (in the case of the parameters presented in Figure 7, the threshold is 10). This corresponds to "fast" reactions.

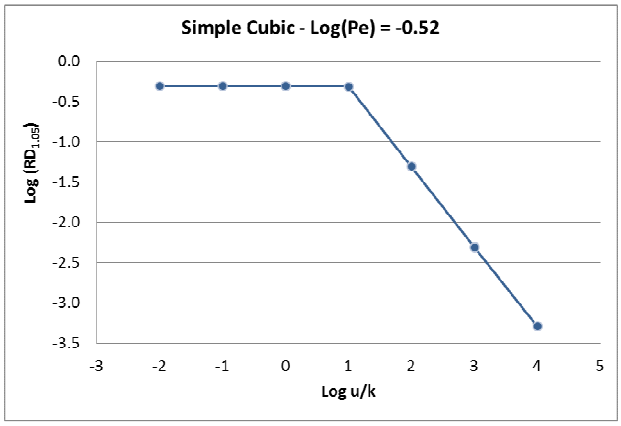

Figure 7: $RD_{1.05}$ as a function of u/k for the simple cubic (sc) structure and a constant Pe.

In the simple cubic lattice, a Peclet number (Pe) in the range 10^{-2} to 10^{2} maximizes the effect of void fraction (Figure 8). At very low Pe, diffusion is fast and concentration uniform transverse to the flow regardless of the geometry. At very high Pe, convection is fastest and the reaction is mass transfer limited. In the simple cubic lattice, effect of void spacing is maximal when diffusion and convection are competing.

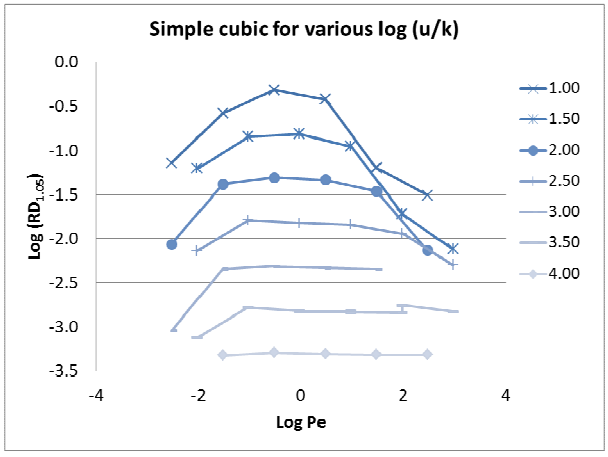

Figure 8: $RD_{1.05}$ as a function of Pe for (sc) structure and various values of log(u/k).

In the other lattices (bcc and fcc), the effect of local Peclet number was not significant. As the (sc) lattice is the least tortuous, we propose that flow meandering improves effective cross-flow dispersion and limits the effect of flow path diameter increase.

Comparison between packing structure

The comparison between packing structures is only meaningful if it is done with a similar flow-rate to catalyst particle number ratio. In this part, the catalyst particle number is set to 20 spheres. This translates into a different height depending on the structure (fcc packing are shorter). All simulations are run with the same flow rate so as to keep the ratio flow to catalyst mass constant. As the horizontal lattice period differs according to the lattice structure, the superficial velocity depends on the structure and lattice spacing. Table 1 summarizes the geometrical information.

Table 1: Geometric parameters when comparing at same ratio of flow-rate to catalyst amount (20 spheres).

	Simple cubic	Body centered cubic	Face centered cubic
Horizontal Period (a)	L.R	$2.L.R/\sqrt{3}$	$\sqrt{2}$ L.R
Packing height	40 LR	$40.L.R/\sqrt{3}$	$10\sqrt{2}$ L.R

Computation are presented for 2 sets of parameters (Table 2) corresponding to medium (~ 0.35) and high conversion (~ 0.8) level. For each set of parameters, simulations have been run all 3 structures and 5 values of void fraction corresponding to lattice parameter L ranging from 1.01 to 1.05. Results are presented in term of reactor conversion, based on the mixing cup outlet concentration.

Table 2: Physical parameters for medium and high conversion cases.

Conversion level	Medium	High
u (m/s)	10^{-5}	10^{-4}
D_m (m^2/s)	10^{-9}	10^{-9}
k (m/s)	10^{-9}	10^{-5}
Pe	30	300
Bi	0.3	30

In the medium and high conversion cases (Figure 9 and Figure 10), lattice structure has a much larger impact than void fraction on reactor performance. As fcc and bcc void fraction overlap, we conclude that void fraction is not a predictor of packing performance. Structures are ranked in the same order as their tortuosity.

A larger lattice spacing improves conversion. Keeping the ratio of flow-rate to catalyst mass constant results in a velocity that depends on void fraction. So the results are not in contradiction with the previous section where comparison was performed at constant velocity.

In the medium conversion case, conversion remains in a narrow range (0.43 - 0.5) and is therefore weakly dependent on the lattice structure and spacing.

DISCUSSION

Link between effects of structure with mass transfer limitations?

A closer look at the concentration fields (Figure 11) makes it possible to offer a physical explanation for effect of structure. In the high conversion case, concentration is very low (actually near 0) near the spheres, whereas fluid with high concentration of tracer flows in the largest spaces between spheres. This high conversion case is clearly marked with mass transfer limitations. In the middle conversion case, concentration is much more uniform in cross-flow planes. Mass transfer limitations are weak. We conclude that effect of structure and void fraction is higher in presence of mass transfer limitations. We reached a similar conclusion

when studying the reactive flow around 8 cylindrical catalyst pellets (Rolland, 2013).

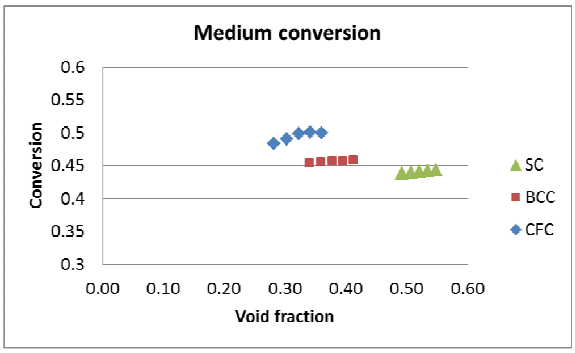

Figure 9: Medium conversion case: effect of void fraction and structure.

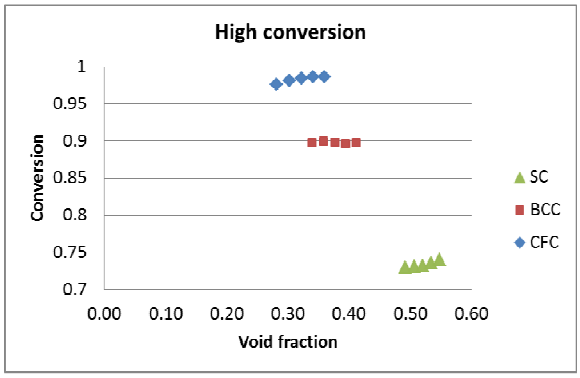

Figure 10: High conversion case: effect of void fraction and structure.

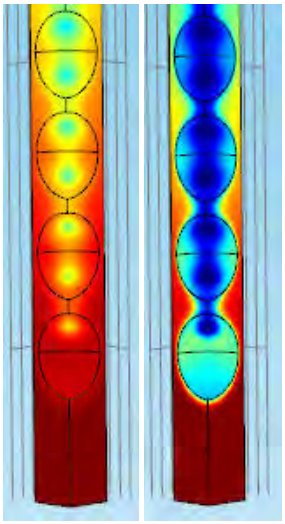

Figure 11: Concentration field in the bcc structure (L=1.01) for medium (left) and high (right) conversion. (Scale is different in each case. Dark red = 1 = inlet)

In the mass transfer limitation regime, conversion is limited by the ability to bring reactant to the catalyst surface. Effect of lattice structure can be explained by the "tortuosity" that forces parallel flow channels to interact (fcc and bcc cases), whereas, in sc lattice, flow channels are straight and parallel and do not interact with each other. This implies that a significant part of transverse dispersion is due to interaction between flow channels. We therefore expect better transverse dispersion and thus overall performance in random packed beds than in structured ones.

Correlating the results?

As aforementioned, outlet concentration is not independent of mesh refinement. For this reason, we do not present any correlations aiming at predicting either mass transfer coefficient or apparent conversion. Although not accurate, we believe the curve presenting the average outlet concentration as a function of (u/k) and Pe (Figure 12) is worth presenting as it shows a quite a complex shape.

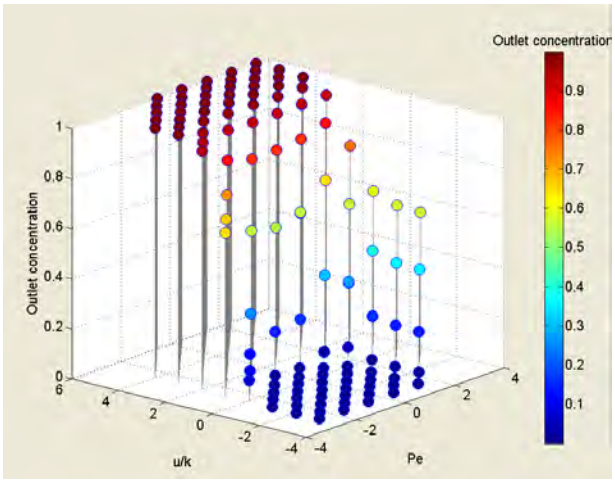

Figure 12 : 3D plot of outlet concentration vs. Pe and u/k for (sc) structure.

CONCLUSION

Reactor apparent conversion in structured periodic arrays of spheres depends mostly on sphere arrangement and to a lower extent on sphere spacing. In structured periodic arrays, void fraction is not a good predictor of overall reactor performance.

Sensitivity to void fraction increases in presence of mass transfer limitations.

Tortuosity, that is the amount of interaction between flow channels, favours transverse dispersion and thus lowers mass transfer limitations (or equivalently favours higher conversions). We therefore expect better transverse dispersion and mass transfer coefficient in random packed beds than in structured ones.

For all packing, effect of void fraction can be significant when the ratio u/k is lower than 0.1: when reaction is relatively fast compared to convection. This is coherent with the classical knowledge that mass transfer coefficients increase with velocity. When operating at constant contact time, this favours design of unstructured, long and narrow reactors.

Perspective of the work is to continue this study in large random packed beds, using more accurate numerical solvers, which requires massively parallel simulation tools.

REFERENCES

FREUND, H., ZEISER, T., HUBERA, F., KLEMMA, E., BRENNER, G., EMIG, F. D. G., (2003), "Numerical simulations of single phase reacting flows in randomly packed fixed-bed reactors and experimental validation", *Chemical Engineering Science*, **58**, 903-910.

GUNJAL P.R., RANADE V.V., CHADHARI R.V., (2005), "Computational Study of a Single-Phase Flow in Packed Beds of Spheres", *AICHE Journal*, **51** (2), 365-378.

MAIER, R.S., KTOLL D.M., KUTSOVSKY Y.E., DAVIS, H.T. BERNARD R.S., (1998), "Simulation of flow through bead packs using the lattice Boltzmann method", *Phys. Fluids*, **10** (1), 60-74.

ROLLAND, M., (2013), "Significant Effect of Catalyst Position and Orientation in Fixed-bed Reactors", World Congress of Chemical Engineering, Seoul, Korea.

RONG, L.W., DONG, K.J., YU, A.B., (2013), "Lattice Boltzmann simulation of fluid flow through packed beds of uniform spheres: Effect of porosity", *Chemical Engineering Science*, **99**, 44-58.

WACHS A., (2010), "PeliGRIFF, a parallel DEM-DLM/FD direct numerical simulation tool for 3D particulate flows", *Journal of Engineering Mathematics*, **71**, 131-155.

TRANSPORT OF THE MOMENTS OF THE AGE DISTRIBUTION BY CFD IN FIXED BED OPERATION UNITS

Leonel Fangueiro Gomes[1,2], Frédéric Augier[1*], Damien Leinekugel-Le-Cocq[1], Ivana Vinkovic[2], Serge Simoëns[2]

[1] IFP Energies Nouvelles, BP3, 69360 Solaize, FRANCE

[2] Laboratory of Fluid Mechanics and Acoustics, CNRS UMR 5509, Ecole Centrale de Lyon, Ecully, FRANCE

* E-mail: frederic.augier@ifpen.fr

ABSTRACT

In fixed bed operations as catalytic reactors or adsorption columns, any deviation from the perfect plug flow may impact the conversion or the separation performances. In the case of interest of the Simulated Moving Bed (SMB), multiple dispersive agents are present, such as macroscale obstacles within the porous media, the porous media itself and free media chambers between the beds. In order to dissociate the dispersion induced by the different agents, it is needed to simulate hydrodynamics of the bed taking into account the free media chambers between beds where the flow is turbulent.

In this work, a specific geometry, representative of the SMB hydrodynamics, is investigated. A pseudo-2D experimental mock-up comprising a packed bed of glass spheres between two turbulent flow regions is used to validate a CFD model involving the k-ε turbulence model for free liquid volumes and the Brinkmann-Forchheimer formulation for the porous media. Hydrodynamics modelling is coupled with transport of moments of the age distribution, a recent approach developed by Liu (2012) to characterize the degree of mixing. The quality of the CFD simulations and results concerning the degree of mixing are discussed and compared with the classic Dispersive Plug Flow (DPF) or Cascade of Continuous Stirred-tank Reactors (nCSTR) hydrodynamics models.

Keywords: fixed bed, hydrodynamics, age distribution, separation.

NOMENCLATURE

Greek Symbols

β Non-Darcy coefficient, [m^{-1}]
ε Bed porosity, [-]
ε_T Turbulent kinetic energy dissipation rate, [m^2/s^3]
μ Dynamic viscosity, [Pa.s]
μ_e Effective dynamic viscosity, [Pa.s]
μ_n Central moment of order n, [s^n]
μ_T Turbulent dynamic viscosity, [Pa.s]
ρ Density, [kg/m^3]
σ^2 Variance, [s^2]
σ_k k-ε model parameter, [-]
σ_ε k-ε model parameter, [-]
τ Residence time, [s]

Latin Symbols

C Concentration, [mol/m^3]
$C_{\varepsilon 1}$ k-ε model parameter, [-]
$C_{\varepsilon 2}$ k-ε model parameter, [-]
C_μ k-ε model parameter, [-]
D_M Molecular diffusion [m^2/s]
D_P Mechanical dispersion, [m^2/s]
d_p Particle diameter, [m]
D_T Turbulent diffusivity, [m^2/s]
E Exit age, [1/s]
J Degree of mixing, [-]
K Bed permeability, [m^2]
k Turbulent kinetic energy, [m^2/s^2]
L Outlet length, [m]
m_n Raw moment of order n, [s^n]
n Order of the moment, [-]
N_{CSTR} Number of CSTR, [-]
p Pressure, [Pa]
Pe_{ax} $v.d_p/D_{ax}$: Granular axial Peclet number, [-]
Pe_{rad} $v.d_p/D_{rad}$: Granular radial Peclet number, [-]
P_k k-ε model parameter, [-]
Re_p $d_p.u.\rho/\mu$: particular Reynolds number, [-]
Sc_T $\mu_T/\rho.D_T$: Turbulent Schmidt number, [-]
t Time, [s]

u Fluid superficial velocity, [m/s]
v Fluid interstitial velocity, [m/s]

Sub/superscripts
e Exit
V Volume average

INTRODUCTION

Inside industrial fixed beds, as adsorption columns or catalytic reactors, the flow can deviate from the desired plug flow for different reasons. Depending on the operation units, flow discrepancies can be induced by macro scale objects within the packing such as pipes or beams, the packing itself or non-ideal injection and collecting devices. For instance, Simulated Moving Bed (SMB) adsorption processes cumulate the difficulties listed above as their performances are very sensitive to axial dispersion, and their complex geometry perturbs the streamlines, resulting in strong deviations from ideal plug flow. The classic approach for chemical engineers consists in characterizing the Residence Time Distribution (RTD) and to estimate the global axial dispersion resulting from internal flow patterns. The axial dispersion may then be used in a Dispersive Plug Flow (DPF) model to take into account the effect of hydrodynamics on the simulations of reaction or separation operations (Minceva and Rodrigues, 2002). This approach may be useful when the effect of hydrodynamics does not play a major role on the operation performance. However if its impact is of first relevance, DPF models are not sufficiently accurate and a faithful description of real hydrodynamics is required. For that, the degree of mixing is known as an important parameter (Danckwerts, 1958 and Zwietering, 1959), in addition to RTD characterization. Still, until recent developments it was not possible to calculate it accurately.
By measuring the resulting variance, Augier et al. (2008) estimated the impact of obstacles within porous media on the dispersion of concentration fronts.
The objective of this study is to evaluate how relevant the use of CFD is to characterize the degree of mixing inside porous media as fixed bed reactors or adsorption columns. For this purpose, the transport of the moments of the age distribution of molecules, a new calculation method recently developed by Liu and Tilton (2010) and Liu (2012), has been applied to characterize a simple fixed bed device and to illustrate this promising numerical approach. In this work, the dispersive effect of different sources was studied through tracer tests in an experimental setup representative of a slice of a bed of the SMB and compared to the results obtained through CFD simulations. The experimental setup comprises a packed bed of glass spheres with a free media chamber above the bed and another one below it (see Fig. 1).
The study is divided in three steps:

- Residence Time Distribution (RTD) experiments in a given porous media geometry of an adsorption SMB process
- CFD calculations, simulation of RTD and comparison with experiments
- Calculation with CFD of the different moments of the age distribution and of the degree of mixing. A discussion is also proposed on the results and the observed deviation from a perfect plug flow.

MODEL DESCRIPTION

Free media hydrodynamics

In the free media volumes surrounding the porous media, the flow is described using the standard k-ε turbulence model for a steady and incompressible fluid (Wilcox, 1998) where the turbulent dynamic viscosity is modelled by:

Turbulent dynamic viscosity equation

$$\mu_T = \rho \cdot C_\mu \frac{k^2}{\varepsilon_T} \quad (1)$$

The turbulent kinetic energy k and its dissipation rate ε_T are transported according to:

Turbulent kinetic energy (TKE) equation

$$\rho \cdot \vec{u} \cdot \nabla k = \nabla \cdot \left(\left(\mu + \frac{\mu_T}{\sigma_k} \right) \cdot \nabla k \right) + P_k - \rho \cdot \varepsilon_T \quad (2)$$

TKE dissipation rate equation

$$\rho \cdot \vec{u} \cdot \nabla \varepsilon_T = \nabla \cdot \left(\left(\mu + \frac{\mu_T}{\sigma_\varepsilon} \right) \cdot \nabla \varepsilon_T \right) + C_{\varepsilon 1} \frac{\varepsilon_T}{k} P_k - C_{\varepsilon 2} \cdot \rho \frac{\varepsilon_T^2}{k} \quad (3)$$

C_μ, σ_k, σ_e, $C_{\varepsilon 1}$ and $C_{\varepsilon 2}$ are k-ε model constants determined from experimental data (Wilcox, 1998).
The production term P_k is calculated by:

Production term equation

$$P_k = \mu_T \cdot \left(\nabla \vec{u} : \left(\nabla \vec{u} + (\nabla \vec{u})^T \right) - \frac{2}{3} \cdot (\nabla \cdot \vec{u})^2 \right) - \frac{2}{3} \rho \cdot k \nabla \cdot \vec{u} \quad (4)$$

In order to describe the mixing of a scalar due to eddy motion, a turbulent diffusivity coefficient must be calculated through the turbulent viscosity and by imposing a constant turbulent Schmidt number. Such diffusivity coefficient must be added to the molecular diffusion, in the free media volumes, to describe appropriately the mixing in the turbulent regions. Koeltzsch (2000) reviewed several experimental investigations and concluded that most authors use a constant turbulent Schmidt number that ranges between 0.5 and 0.9 for wind tunnel experiments. Flesch et al. (2002) stated turbulent Schmidt numbers ranging between 0.18 and 1.34 in field observations under different atmospheric stability and wind conditions. For this work, the turbulent Schmidt number is firstly assumed as 0.7 which is the average of the values stated above.
This model relies on several assumptions. The most important is that the Reynolds number is sufficiently high. Otherwise the accuracy of the solution given by the model is dubious.

The tracer molecules are transported by diffusion and convection, and the transport equation in the free media is:

Free media transport equation

$$\frac{\partial C}{\partial t} = \nabla \cdot \left[\left(D_M + D_T \right) \cdot \nabla C - \vec{u} C \right] \quad (5)$$

The global dispersion coefficient results from the sum of the molecular diffusion (D_M) and the turbulent diffusivity (D_T), both isotropic.

Porous media hydrodynamics

The model developed describes hydrodynamics and scalar transport at a scale larger than the packing particles but much smaller than the experimental setup. This is acceptable due to the high ratio between the bed dimensions and the particle diameter. The contact between the fluid and the particles is not simulated in the CFD model, but modelled through a diffusive term in the momentum and transport balance equations. To do this, the Brinkman-Forchheimer model (Vafai and Tien, 1982) is used:

Brinkman-Forchheimer model equation

$$\rho\left(\vec{v} \cdot \nabla \vec{v}\right) = -\nabla p - \vec{v} \frac{\mu}{K} + \mu_e \cdot \nabla^2 \vec{v} - \rho \cdot \beta \cdot |\vec{v}| \cdot \vec{v} \quad (6)$$

Here $\vec{v}$ is the interstitial velocity vector, i.e. the superficial velocity $\vec{u}$ divided by the bed porosity. This model results from a modification of the laminar Navier-Stokes equations and takes into account the diffusion of the momentum due to viscosity effects through the Brinkman term ($\mu_e \cdot \nabla^2 \vec{v}$) and the inertial effects caused by friction between the fluid and the particles with the use of the Forchheimer term ($\rho \cdot \beta \cdot |\vec{v}| \cdot \vec{v}$). The validity of this model has been discussed by Nield (1991), Vafai and Kim (1995) and Augier et al. (2008) and it has been rather successfully compared to experimental results by Benyahia (2004) and Chan et al. (2000), although its applicability to interfaces between turbulent and porous media regions was not verified. The effective dynamic viscosity μ_e has been widely discussed. Some authors propose its calculation as the turbulent dynamic viscosity as a function of the particle Reynolds number, $\mu_e = \mu_T\left(\mathrm{Re}_p\right)$, (Guo et al., 2006) while others defend that for low particle Reynolds numbers it can be assumed equal to the molecular viscosity, $\mu_e = \mu$, (Chan et al., 2000).

For a fixed bed of spheres, the bed permeability K and the non-Darcy coefficient β can be calculated through Ergun's law (1952):

Ergun's law

$$K = \frac{\varepsilon^3 d_p^2}{150(1-\varepsilon)^2} \quad (7)$$

$$\beta = 1.75 \frac{1-\varepsilon}{\varepsilon^3 d_p} \quad (8)$$

This law was developed for one-dimensional flows within isotropic media, but Zeng and Grigg (2006) showed that its application is acceptable when the permeability term of equation 6 is more important than the Forchheimer term, which is fulfilled in this case.

The tracer molecules are transported throughout the inter-particle void volume:

Porous media transport equation

$$\varepsilon \frac{\partial C}{\partial t} = \nabla \cdot \left[\varepsilon \left(D_M + D_P \right) \cdot \nabla C - \varepsilon \vec{v} C \right] \quad (9)$$

Within the porous media the global dispersion coefficient results from the sum of the molecular diffusion and the mechanical dispersion (D_P). While the molecular diffusion is isotropic, the mechanical dispersion is described by a diagonal tensor comprising the radial (D_{rad}) and axial dispersion (D_{ax}) coefficients, relatively to the flow direction. These two coefficients are calculated by imposing two constant granular Peclet numbers, one radial and one axial, that quantify the ratio between convective and diffusive transport. The radial and axial Peclet numbers are firstly assumed to be 11 and 2 respectively, following the results obtained by Foumeny et al. (1992). Delgado (2006) showed that these values are considered to be asymptotic for liquid flows with particular Reynolds numbers greater than 20.

FLOW CHARACTERIZATION

Residence Time Distribution

The RTD is widely used to describe the macromixing and hydrodynamics of industrial equipment (Nauman, 2008). This method consists in the measurement of the outlet concentration over time, after a tracer injection. The exit age distribution can be obtained through the velocity weighted concentration in the outlet of the vessel:

Exit age distribution

$$E(t) = \frac{\int_0^L C_e(x,t) \cdot u_e(x) dx}{\overline{u_e} \int_0^L \int_0^\infty C_e(x,t) dt dx} \quad (10)$$

where the subscript "e" indicates that the concentration and the fluid velocity are measured in the exit, and L is the outlet length. This function gives the probability of a particle to leave the vessel, at a given time. Its integral is equal to unity. The average fluid velocity in the exit is given by:

Average exit fluid velocity

$$\overline{u_e} = \frac{1}{L} \int_0^L u_e(x) dx \quad (11)$$

To perform a quantitative analysis of probability density functions (PDF), it is usual to rely on the moments of these functions. The raw and the central moments can be calculated according to:

Raw moment of order n of a PDF

$$m_n = \int_0^\infty t^n \cdot E(t)dt \tag{12}$$

Central moment of order n of a PDF

$$\mu_n = \int_0^\infty (t - m_1)^n \cdot E(t)dt \tag{13}$$

The first moment is the mean of the distribution, which is equal to the average residence time of a vessel, given by the ratio between the volume of the vessel and the inlet volumetric flow.
The second central moment is the variance (σ^2) and its positive square root is the standard deviation. In the case of an ideal plug flow, σ^2 is equal to 0. All the molecules that entered together in the vessel will all exit at the same time.
The third central moment is the skewness. It measures the asymmetry of a PDF.
By measuring the first two moments of the concentration curves it is possible to obtain the mean age and the dispersion in the outlet of the studied vessel. This is sufficient to fit a simple flow model as DPF or nCSTR.

Degree of Mixing

The RTD is useful to characterize the macromixing of a given system, although the system internal information remains inaccessible. If we consider a system of two consecutive reactors, for example one Continuous Stirred-Tank Reactor (CSTR) and one Plug Flow Reactor (PFR), the resulting RTD is the same regardless the order that the two reactors are placed. However, in the presence of non-linear phenomena, as a second order kinetics, the two systems (CSTR+PFR and PFR+CSTR) will produce different results. To explain this Danckwerts (1958) and Zwietering (1959) formulated a criterion: the degree of mixing that quantifies the quality of the mixing of a given vessel. The degree of mixing can vary between 0 (perfectly mixed system, such as a perfect CSTR) and 1 (completely segregated system, PFR). The degree of mixing is defined as the variance of the mean age of the molecules averaged over all the points of a vessel, divided by the variance of the ages of all the molecules within a vessel. For about 50 years the degree of mixing couldn't be quantified, but Liu (2012) showed that it can be calculated through the volume average of the first two raw moments:

Degree of mixing (Liu, 2012)

$$J = \frac{\overline{m_{1,V}^2} - \overline{m}_{1,V}^2}{\overline{m}_{2,V} - \overline{m}_{1,V}^2} \tag{14}$$

Liu and Tilton (2010) showed that the raw moments of the age distribution were transported by diffusion and convection and could be obtained through steady state CFD simulations:

Transport equation of the raw moments of the age distribution (Liu and Tilton, 2010)

$$\nabla \cdot (D \cdot \nabla m_n - \vec{u} \cdot m_n) = n \cdot m_{n-1} \tag{15}$$

The coefficient D comprises all the dispersive phenomena present in the vessel (such as turbulent or mechanical dispersion). The source term on the right-hand side is the product between the order of the moment (n) and the moment of order $n-1$ (m_{n-1}), i.e. the source term is equal to 1 when transporting the first moment, and equal to $2m_1$ when transporting the second raw moment. With this, it is possible to obtain the first two moments of the age distribution, in every point of a vessel, through steady state simulations that are much cheaper in terms of computation time than dynamic simulations of tracer injections.
For a system that comprises an enchainment of CSTR that share the same residence time, the degree of mixing of the system can be obtained through the number of enchained CSTR (appendix A):

Degree of mixing for an enchainment of CSTR

$$J = \frac{N_{CSTR} - 1}{N_{CSTR} + 5} \tag{16}$$

This criterion may be useful to develop simple hydrodynamic models. A classic approach based on 2 or 3 first moments of RTD experiments may lead to several candidate models. Among them, the closest degree of mixing may be a guarantee of accurate hydrodynamic representation, in the presence of non-linear phenomena.

EXPERIMENTAL SETUP DESCRIPTION

The dispersion caused by the different factors introduced above was studied using a cold mock-up representative of a slice of a SMB bed, whose dimensions are shown in Figure 1.

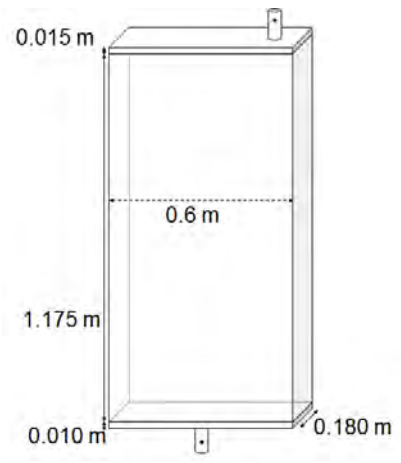

Figure 1: Schematic view of the experimental setup and respective dimensions.

The experimental setup comprises 1.175 m of a packed bed of glass spheres with a diameter of 1 mm, between two free media chambers: one above the bed with 0.015 m and one below it with 0.010 m. Tracer experiments were performed by injecting a solution of salt in the inlet water stream and by measuring the conductivity in the inlet and in the outlet of the mock-up with the aid of 2 sensors (with a frequency of 8 Hz).
These tests were performed with a volumetric flow of 6 m^3/h which corresponds to a fluid superficial velocity of 0.0154 m/s, close to the SMB operating conditions. Afterwards a square-shaped obstacle (250x250x180 mm) was introduced within the packed bed, and the tests were repeated so that the dispersion provoked by the obstacle could be measured. The experimental results were then compared to those obtained through CFD, in order to validate this software for the simulation of hydrodynamics including turbulent and porous media regions.

RESULTS

The RTD obtained experimentally exhibits long tails and some residual noise associated to the conductivity sensors, as shown in Figure 2.

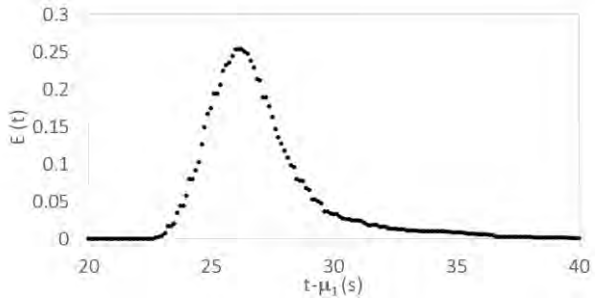

Figure 2: RTD obtained experimentally in the absence of obstacles within the porous media.

The signal noise in the tail of the RTD induces considerable errors in the measurement of the moments of order higher than one. Any signal post treatment or arbitrary choice of final measuring time may strongly influence high order moments. Thus, the validity of the model will be studied through the visual comparison between the experimental and CFD RTD curves, rather than comparing its moments. For this reason, only indicative ranges of experimental σ^2 are reported.
The parameters used in the 2D CFD simulations are shown in Table 1.

Table 1: Simulation parameters.

Parameter	Value	Units
ε	0.357	-
μ	0.001138	Pa.s
D_M	1.00×10^{-9}	m^2/s
d_p	1.00×10^{-3}	m
Pe_{ax}	2	-
Pe_{rad}	11	-
Sc_T	0.7	-
u_{in}	1.132	m/s

The normalized numbers used were chosen from the bibliography described above, and no parameter fitting was performed.
Through the transport of the raw moments of the age distribution, it is possible to obtain a mapping of the moments, as shown in Figure 3.

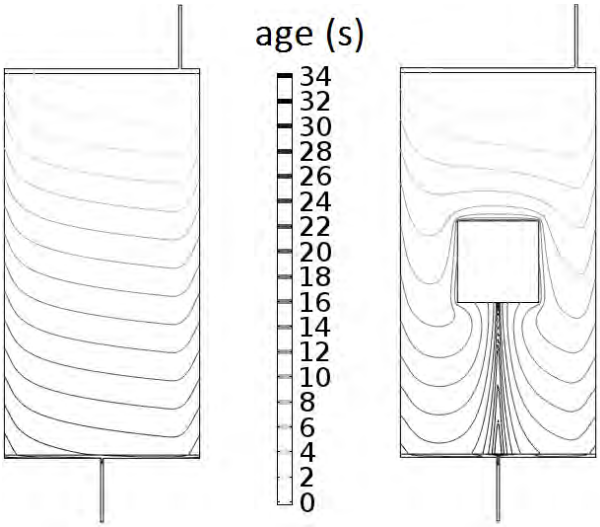

Figure 3: Ages of the particles obtained locally without (left) or with (right) a square obstacle.

From the left figure, the front of ages (and consequently the front of concentration, when simulating the tracer injection) advances obliquely since the inlet is positioned on the right side of the mock-up. This explains the tails on the RTD curves. In the presence of a square obstacle within the porous media, the front of ages is severely disturbed. A delay region is created below the obstacle. Also, the injected molecules arrive quicker on the right-hand side of the obstacle (closer to the inlet) creating a by-pass effect.
The mean age, the variance and the skewness obtained at the outlet of the setup and the degree of mixing are shown in Table 2. The experimental and numerical RTD are compared in Figure 4. All the curves are centered on their first moment.

Table 2: Three first central moments and degree of mixing for the two geometrical configurations.

	μ_1 (s)	σ^2 (s^2)	μ_3 (s^3)	J (-)
Exp. without obst.	28.6	2-7	-	-
CFD without obst.	28.6	1.8	10.8	0.990
Exp with obst.	28.2	15-20	-	-
CFD with obst.	28.2	18.8	127.2	0.978

The results show that the first moments are well predicted by CFD and that the variances are in the range of the experiments. Good agreement between the CFD and experimental RTD curves is found for the chosen conditions. The CFD model is capable of simulating the dispersion and the skewness of the experimental setup in the absence and in the presence of the square obstacle.
From the CFD results it can be concluded that the addition of the obstacle increases the variance by a factor about ten, and the skewness by more than that.

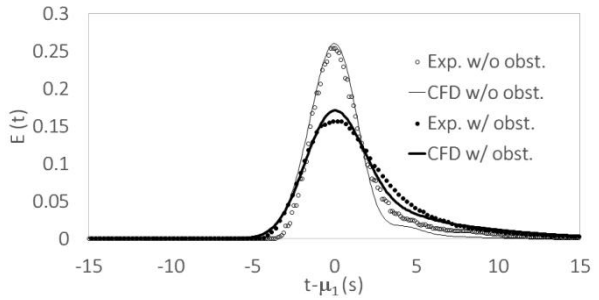

Figure 4: Experimental and CFD RTD curves obtained in the absence (w/o obst.) and in the presence (w/ obst.) of a square obstacle**.**

Good agreement between CFD and the experimental values is also found when the RTD curves are centered relatively to their mean values. As before, the CFD model is capable of simulating the dispersion and the skewness of the experimental setup in the absence and in the presence of a square obstacle.
The values of the degree of mixing obtained for the two configurations are close to an ideal PFR, despite all the internal dispersion due to the free media chambers, the obstacle and the packing. The degrees of mixing of an enchainment of CSTR of equal residence time and variance ($N_{CSTR}=\mu_1^2/\sigma^2$) in the absence and in the presence of the obstacle, given by equation 16 are 0.987 and 0.872, respectively. In the absence of the square obstacle, an enchainment of CSTR may be able to reproduce the impact of hydrodynamics on non-linear phenomena since both degrees of mixing are similar (0.990 from CFD and 0.987 from equation 16), although the skewness of such enchainment ($\mu_3=2N_{CSTR}\tau^3$, where τ is the residence time of one CSTR) will be way smaller than the one obtained from CFD (0.2 s^3 much smaller than the 10.8 s^3 obtained through CFD). This will result in a RTD close to perfect symmetry. Regarding the case where the obstacle is placed within the porous media, the degree of mixing obtained from equation 16, 0.872, is much smaller than the one obtained through CFD, 0.978. This can induce severe discrepancies in the impact of hydrodynamics on non-linear phenomena in each model. Also, the skewness of the enchainment, 25.5 s^3, remains smaller than the one obtained through CFD, 127.2 s^3, resulting in a smaller tail leaning to the right.
A more refined method must be used when performing the 1D modelling of the setup with the obstacle, such as the multiple side exits DPF described by Zwietering (1959).

CONCLUSIONS

The CFD model is capable of reproducing the RTD of the experimental setup without any fitting of the adimensional numbers (such as the Peclet or the Schmidt number). The Brinkman-Forchheimer model reproduces the hydrodynamics at the interfaces between a turbulent region and the porous media, with a satisfactory accuracy. The dispersion and skewness are well reproduced when comparing the RTD obtained, despite the discrepancies found between the RTD moments obtained experimentally and through CFD. These discrepancies are due to noise associated to the conductivity sensors, resulting in long tails that induced errors when integrating the RTD.
The degree of mixing can only be obtained through CFD simulations, and shows that the flow is close to a completely segregated system, despite the internal dispersion of the experimental setup, due to the free media chambers, the packing and the obstacle. The impact of the setup hydrodynamics, which is representative of an SMB bed, on non-linear phenomena may not be fairly reproduced by a simple enchainment of CSTR (equivalent to a DPF for high N_{CSTR}). In the absence of the obstacle, the discrepancies between the enchainment of CSTR and the setup will be due to the low skewness of the enchainment, while in the presence of the obstacle, the skewness and the degree of mixing will both induce errors in the coupling between hydrodynamics and non-linear phenomena, such as adsorption in the case of the SMB, or nonlinear kinetics in the case of fixed bed reactors.

REFERENCES

AUGIER, F., LAROCHE, C. and BREHON, E., (2008), "Application of computational fluid dynamics to fixed bed adsorption calculations: effect of hydrodynamics at laboratory and industrial scale", *Separation and Purification Technology* 63.2, 466-474.
BENYAHIA, F., (2004), "On the modeling of flow in packed bed systems", *Particulate science and technology*, *22*(4), 367-378.
CHAN, E.C., FUE-SANG, L. and YOVANOVICH, M.M., (2010), "Numerical study of forced flow in a back-step channel through porous layer", *2000 National Heat Transfer Conference, Pittsburgh, PA*.
DANCKWERTS, P.V., (1958), "The effect of incomplete mixing on homogeneous reactions", *Chemical Engineering Science* 8.1, 93-102.
DELGADO, J. M. P. Q., (2006), "A critical review of dispersion in packed beds", *Heat and mass transfer* 42.4, 279-310.

ERGUN, S., (1952), "Fluid flow through packed columns", *Chem. Eng. Prog.* 48.
FLESCH, T.K., PRUEGER, J.H. and HATFIELD, J.L., (2002), "Turbulent Schmidt number from a tracer experiment", *Agricultural and Forest Meteorology* 111.4, 299-307.
FOUMENY, E.A., et al., (1992), "Estimation of dispersion coefficients in packed beds", *Chemical engineering & technology* 15.3, 168-181.
GUO, B., et al., (2006), "Simulation of turbulent flow in a packed bed", *Chemical engineering & technology* 29.5, 596-603.
KOELTZSCH, K., (2000), "The height dependence of the turbulent Schmidt number within the boundary layer", *Atmospheric Environment* 34.7, 1147-1151.
LIU, M., and TILTON, J.N., (2010), "Spatial distributions of mean age and higher moments in steady continuous flows", *AIChE journal* 56.10, 2561-2572.
LIU, M., (2012), "Age distribution and the degree of mixing in continuous flow stirred tank reactors", *Chemical Engineering Science* 69.1, 382-393.
MINCEVA, M. and RODRIGUES, A.E., (2002), "Modeling and simulation of a simulated moving bed for the separation of p-xylene", *Industrial & engineering chemistry research* 41.14, 3454-3461.
NAUMAN, E.B., (2008), "Residence time theory." *Industrial & Engineering Chemistry Research* 47.10, 3752-3766.
NIELD, D.A., (1991), "The limitations of the Brinkman-Forchheimer equation in modeling flow in a saturated porous medium and at an interface", *International Journal of Heat and Fluid Flow* 12.3, 269-272.
VAFAI, K. and KIM, S.J., (1995), "On the limitations of the Brinkman-Forchheimer-extended Darcy equation", *International Journal of Heat and Fluid Flow* 16.1, 11-15.
VAFAI, K. and TIEN, C.L., (1982), "Boundary and inertia effects on convective mass transfer in porous media", *International Journal of Heat and Mass Transfer* 25.8, 1183-1190.
VILLERMAUX, J., (1993), "Génie de la réaction chimique", *Lavoisier, Paris*.
WARNECKE, H.J., PRÜSS, J. and LANGEMANN, H., (1985), "On a mathematical model for loop reactors—I. Residence time distribution, moments and eigenvalues", *Chemical engineering science* 40.12, 2321-2326.
WILCOX, D.C., (1998), *Turbulence modeling for CFD*, Vol. 2. La Canada, CA, DCW industries.
ZENG, Z. and GRIGG, R., (2006), "A criterion for non-Darcy flow in porous media", *Transport in Porous Media* 63.1, 57-69.
ZWIETERING, Th.N., (1959), "The degree of mixing in continuous flow systems", *Chemical Engineering Science* 11.1, 1-15.

APPENDIX A

Deduction of the degree of mixing of an enchainment of CSTR

The mean and the variance of an enchainment of CSTR can be obtained as a function of the residence time of one CSTR, τ, and the number of enchained CSTR (Warnecke et al., 1985):

$$\mu_1 = \tau \cdot N_{CSTR} \tag{17}$$

$$\sigma^2 = \tau^2 \cdot N_{CSTR} \tag{18}$$

Thus, through the definition of variance:

$$\begin{aligned} &\sigma^2 = m_2 - m_1^2 \\ &\Leftrightarrow m_2 = \tau^2 \left(N_{CSTR}+1\right) N_{CSTR} \end{aligned} \tag{19}$$

With this it is possible to obtain the first two raw moments in every enchained CSTR, by replacing N_{CSTR} by the position of the CSTR in the chain, in equations 17 and 19. The volume average of these two raw moments is equal to their sum over all the reactors and divided by N_{CSTR}:

$$\overline{\mu}_{1,V} = \overline{m}_{1,V} = \frac{\sum_{i=1}^{N_{CSTR}} i\tau}{N_{CSTR}} = \frac{\tau}{2}\left(N_{CSTR}+1\right) \tag{20}$$

$$\overline{m}_{2,V} = \frac{\sum_{i=1}^{N_{CSTR}} i(i+1)\tau^2}{N_{CSTR}} = \frac{\tau^2}{3}\left(N_{CSTR}+1\right)\left(N_{CSTR}+2\right) \tag{21}$$

The volume average of the squared first moment, can equally be obtained:

$$\overline{m_{1,V}^2} = \frac{\sum_{i=1}^{N_{CSTR}} (i\tau)^2}{N_{CSTR}} = \frac{\tau^2}{6}\left(N_{CSTR}+1\right)\left(2N_{CSTR}+1\right) \tag{22}$$

Replacing equations 20, 21 and 22 in equation 14:

$$J = \frac{\frac{\tau^2}{6}\left(N_{CSTR}+1\right)\left(2N_{CSTR}+1\right) - \left[\frac{\tau}{2}\left(N_{CSTR}+1\right)\right]^2}{\frac{\tau^2}{3}\left(N_{CSTR}+1\right)\left(N_{CSTR}+2\right) - \left[\frac{\tau}{2}\left(N_{CSTR}+1\right)\right]^2} \tag{23}$$

$$\Leftrightarrow J = \frac{N_{CSTR}-1}{N_{CSTR}+5}$$

For high N_{CSTR}, the enchainment of CSTR behaves similarly to a DPF with a Peclet number equal to $2N_{CSTR}$ (Villermaux, 1993), and the degree of a DPF is given by:

$$J = \frac{Pe-2}{Pe+10} \tag{24}$$

A MULTI-SCALE MODEL FOR OXYGEN CARRIER SELECTION AND REACTOR DESIGN APPLIED TO PACKED BED CHEMICAL LOOPING COMBUSTION

Mandar TABIB[1], John MORUD[2], Stein Tore JOHANSEN[1], Shahriar AMINI[1*]

[1] Flow Technology Department, SINTEF Materials and Chemistry, Trondheim, Norway.
[2]Chemical Engineering Department, SINTEF Materials and Chemistry, Trondheim, Norway

* E-mail: Shahriar.Amini@sintef.no

ABSTRACT

Proper selection of a catalyst shape (or a particle shape) can improve the performance of a gas-solid packed bed reactor. The particle shape affects the packing structure and the transport phenomena within the packed bed. This information is not available for many non-spherical particle shapes which limit reactor design options. To enable catalyst and reactor design, a validated 3D Computational Fluid Dynamics (CFD)-Discrete Element Method (DEM) model has been developed to resolve the flow around these particles and to obtain information on the transport phenomena (pressure drop correlation and heat/mass transfer coefficient). The DEM is used to obtain realistic packing structures for different particle shapes, and the CFD is conducted on these DEM generated packing structure. However, the 3D CFD-DEM model cannot be applied on the whole reactor as it is computationally prohibitive. Hence, a multi-scale modelling approach is developed, wherein correlations obtained by the 3D CFD-DEM model from a representative 3D volume of the packed bed are used as closures in a 1D model for reactor design. The validations for all the models have been done. The multi-domain 1D particle-reactor model developed here is a combination of (1) a particle model for radial distribution of chemical species and temperature within a catalyst particle and (2) a 1D reactor model for mass and energy balance along the reactor. This 1D model is able to account for both intra-particle and inter-particle heat and mass transfer phenomena. The proposed multi-scale modelling approach has been applied to select an appropriate oxygen carrier shape for a Chemical Looping Combustion (CLC) packed bed reactor. This work compares the performance of different oxygen carrier shapes (fluted ring shape, cylindrical pellet shape and spherical shape) in terms of reactor operation. The simulations are used to recommend a pellet shape that offers least pressure drop, highest conversion and no early fuel slip for efficient CO_2 capture.

Keywords: Chemical looping combustion, Catalyst design, Packed bed reactor, Multi-scale modelling, CO_2 capture, Discrete Element Modelling, CFD.

NOMENCLATURE

Latin

A	Blake–Kozeny–Carman constant	[ ]
a	Particle surface area per volume of bed	[m^2/m^3]
B	Burke-Plummer constant	[ ]
C	Concentration	[$kmol/m^3$]
Cp	Heat capacity	[J/kg.K]
D_{eff}	Effective diffusivity	[m^2/s]
d_p	Particle diameter	[m]
F_h	Flux of enthalpy	[$J/m^2.s$]
F	Flux	$kmol/m^2.s$
G	Mass flux of gas	[$kg/m^2.s$]
h	Heat transfer coefficient	[$W/m^2.K$]
H	Enthalpy	[J/kmol]
k_g	Mass transfer coefficient	[m/s]
M	Molecular Weight	[Kg/kmol]
P	Pressure	[bar]
R	Particle radius	[m]
Rg	Gas constant	[J/kmol.K]
T	Temperature	[K]
t	Time	[s]
U	Internal energy	[J/m^3]
X_k	Mass fraction of species "k"	[-]
X_j	Conversion of species j	[-]
v_g	Superficial gas velocity	[m/s]
w_f	Fluid mass flow rate	[Kg/s]
w	Weight fraction	[-]
z	Axial position	[m]
r	radial position	[m]
c_∞	Concentration in bulk phase	
r_l	Reaction rate of species "*l*"	[kmol/Kgs]

Greek

$-\Delta H_{rx}$	Heat of reaction	[J/kmol]
ε	Void fraction	[-]
ξ	Ratio of moles of gas to solid needed for the reaction	
Γ_k	Source term for species "k"	[kmol/m3.s]
Γ_u	Source term for enthalpy	[J/m3.s]
λ	Particle thermal conductivity	[W/m.K]
λ_{ax}	Effective bed thermal conductivity	[W/m.K]
μ	Gas viscosity	[kg/m.s]
ρ	Gas density	[kg/m3]
ρ_s	Oxygen carrier density	[kg/m3]
τ	Oxygen carrier tortuosity	[-]

Sub/superscripts

k	*Species "k"*
tot	*Total*
g	*Gas phase*
s	*Solid particle*
l	*Number of Reactions*
kg	*Gas species in gas phase*
ks	*Gas species in particle pores*
j	*Active solid species j*

INTRODUCTION

Significant performance improvements can be obtained in a packed bed reactor by understanding the role of the particle in influencing the intra-particle and inter-particle transport phenomena. The particle can be a catalyst or an oxygen carrier (as in CLC based applications). The physical feature of a particle influences the overall packing structure, pressure drop, heat-transfer, mass-transfer and overall reaction rate in the reactor. Hence, researchers experimentally study different particle shapes (spheres, cylinder, fluted rings, tri-lobe, quadrulobe, monoliths, wagon wheels, hollow extrudates, discs, etc) to identify the most suitable shape/size for a given process. Selecting a suitable particle shape and size involves making compromises between reactivity and pressure drop.

In this regard, development of an accurate modelling approach for enabling catalyst (pellet) shape selection and reactor design will be useful. The packed-bed reactor offers an ideal platform to develop a multi-scale model that can account for the multi-scale phenomena in the packed bed, like: (a) at the pore level within the particle, the reactant gas species diffuses and reacts at the internal pore surface. For processes with high intrapellet Damkohler number (like, for the CLC process under study, it is two orders of magnitude high), the diffusional resistances will play an important role as the species diffusivity is low and intrinsic rate kinetics is fast, (b) at the microscopic boundary layer level formed at external surface of the particles may offer viscous resistance to the flow, and offer external resistance to the transport of gaseous species and heat from bulk gas phase to the particle surface, (c) at the meso-scale (interstitial regions between particles): the wakes behind the particles results in additional form drag and will influence the heat and mass transfer, (d) at the reactor level, the movement of thermal and reaction fronts in the entire bed needs to be captured. The influence of reactor geometry on packing structure and the near wall effects (which is dependent on ratio of particle diameter to reactor diameter) needs to be accounted.

These multi-scale effects can be resolved by accounting and simulating the actual particles in a 3D simulation. But, simulating the whole reactor with particles is prohibitive owing to high mesh grid requirements and computational time. Few multi-scale models have been proposed in literature to overcome this difficulty. Ingram (2004) has showed how three different multi-scale strategies (Multi-domain, Parallel and Embedded) can be applied to simulate a packed bed reactor. From application point of view, the use of simultaneous multi-scale (CFD only) or Parallel multi-scale approach (CFD+1D) are also prohibitive. Here, we propose a novel multi-scale modelling approach that can enable catalyst shape selection and reactor design in an efficient and effective way using a validated 3D-CFD-DEM modelling tool in-conjunction with a validated multi-domain 1D particle-reactor model. The methodology is explained in the next section.

MULTI-SCALE METHODOLOGY

A multi-domain 1D particle-reactor model is an efficient tool for large industrial-scale reactor design, as advanced modelling tools like 3D CFD-DEM will be computationally prohibitive to apply on larger scales. However, the 1D model will need accurate closure information to arrive at precise results. The required closure information involves information on packing structure (porosity, particle surface area per unit reactor volume) and information on transport phenomena (pressure drop correlation, external heat transfer and mass transfer correlation). For many non-spherical particles, such closure information is not available.

In the proposed multi-scale methodology, 3D CFD is applied on a representative volume of a DEM generated packed-bed to obtain the closure information for the 1D model. The use of a representative volume makes the simulations computationally tractable. The Discrete Element Method (DEM) is used to generate a realistic packing structure for spherical/non-spherical particles. In an earlier work (Tabib et. al., 2013), a validated 3D CFD-DEM methodology has been developed to select the dimensions (size) of the bed-segment which can serve as a good representative for the whole packed bed. The 1D model uses the accurate closures derived by the 3D CFD-DEM model to design the large-scale reactor and to study the effect of particle shape/size on the reactor performance. Figure 1 illustrates this multi-scale concept. This form of multi-scale modelling can be termed as a 'Serial by Simplification' multi-scale approach.

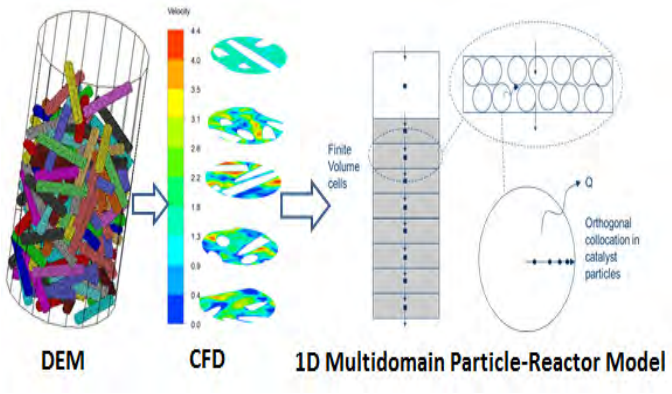

Figure 1 shows schematic representation of Multi-scale formalism. The 3D DEM generates a packed-bed structure, and then 3D CFD is applied on the DEM generated bed-segment to obtain closures for the multi-domain 1D Particle-Reactor model. The 1D model comprises of Finite Volume method on axially discretised reactor space and orthogonal collocation technique on radially discretised particle model.

The devised multi-scale methodology can be described step-wise as:

1. 1. Model the shape of the non-spherical particle using multiple spheres (called multi-sphere approach). For this work, the Fluted ring shape and cylindrical pellet shapes with Aspect ratio 1 (AR1), Aspect ratio 2 (AR2) pellet and Aspect ratio 7 (AR7) pellet have been created. Figure 2 shows the cylindrical pellet (AR7) and the Fluted Ring particle. These shapes are selected to evaluate them for application in a gas-solid non-catalytic Chemical looping combustion unit for power generation integrated with CO_2 capture.

2. Fill a volume (or reactor vessel) with the new catalyst/oxygen carrier shape using Discrete Element

Method. Figure 2 shows the packing structure generated for different particle shapes.

3. Obtain information on bed voidage (or solid porosity profile) and overall particle surface area per unit reactor volume from the DEM generated packing structure. Figure 3 shows the porosity profile obtained for each DEM generated packing and Table 1 shows the particle surface area per unit reactor volume. This information is to be used as closure for the 1D model.

4. Identify the minimum size of the DEM-generated bed-segment that can be a representative of the whole packed bed. The validated methodology to select the cut-segment size is described in Tabib et. al. (2013). The methodology relies on examining the sensitivity of CFD results to varying sample volume size (or to varying dimensions of the cut-segments).

5. The selected cut-segment size is used to simulate flow for wide-range of Reynolds numbers using CFD. Figure 4 shows the 3D CFD-DEM applied on fluted ring and cylindrical pellet. The pressure drop and particle heat transfer coefficient results at different Reynolds number are used to develop an engineering correlation for each of the particle shape.

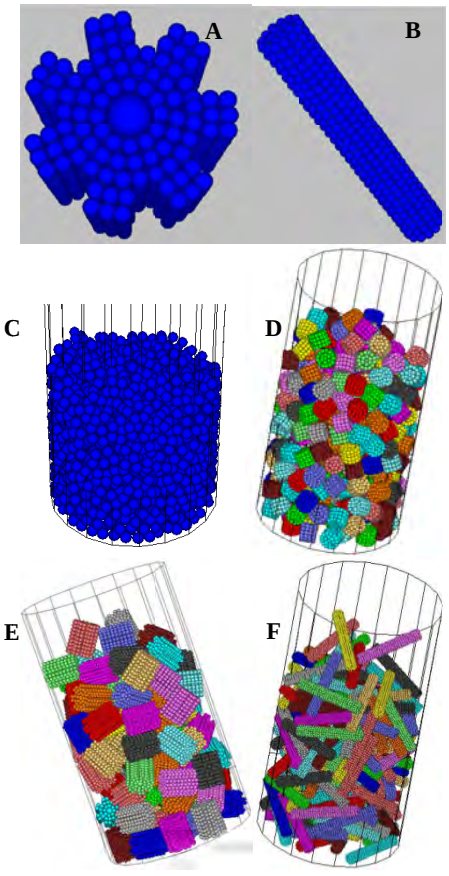

Figure 2 shows (A) Fluted ring particle and (B) cylindrical pellet with aspect ratio 7 generated using multi-sphere approach and the DEM generated packing structure for (C) spherical particle, (D) Aspect ratio 1 particle, (E) Aspect ratio 7 and (F) Fluted Ring.

6. Use the transport phenomena and packing structure information obtained for each packing as closure for the 1D model. The 1D model provides information on conversion profiles, temperature profiles, fuel slip and pressure drop for large scale industrial reactor.

7. Select the catalyst/oxygen carrier shape that provides the lowest pressure and higher reactivity with no fuel slip, and decide the reactor cycle time.

VALIDATION OF MODELS USED IN MULTI-SCALE METHODOLOGY

The 3D DEM-CFD and 1D model developed to implement the proposed multi-scale approach must be validated. The section covers the validation of 3D DEM-CFD model for predicting accurate closures and the validation of 1D model in accurately simulating a CLC operation.

Validation of DEM generated packing and porosity information

Bed voidage and total particle surface area within a reactor volume are important parameters that affect reactivity, pressure drop and cycle-time. Hence, voidage predicted by DEM has been validated with well-established correlations and with the values reported in literature. Figure 2C-2F shows the DEM generated packing for a spherical packing, two cylindrical pellets packing with pellets of aspect ratio 1 and 7, and a fluted ring packing.

The DEM predicted radial variation of bed-voidage (or porosity) for the spherical packing is similar to that predicted by De Klerk (2003) correlation (as seen in Figure 3). Both predict the voidage oscillations to exist up-to a distance of 5 particle-diameters from the wall (see Figure 3A), after which the oscillations settle down to a constant uniform bulk voidage. The constant bulk voidage (bulk porosity) of DEM generated spherical bed packing is around 0.404, which is same as that predicted by Dixon's correlation (1988) and by De Klerk correlation (2003). The amplitude of oscillations predicted by DEM is lower than the De-Klerk prediction. However, the current 1D model requires the constant bulk voidage as an input and not the radial profile. The bulk voidage predictions in DEM are affected by the particle-particle friction coefficient and particle-wall friction coefficient parameters (value of 0.3 used in this work). If the friction coefficient is high, then the particle will get balanced on each other and counteract the gravity. So, a higher friction coefficient would cause a loose packing (leading to higher porosity). Since, the bulk porosity prediction is accurate, so the current DEM parameters can be considered for further studies. The PFC3D software has been used to conduct these DEM simulations and uses the Hertz-Mindlin model to simulate particle collisions and motion.
Figure 3 shows the radial profiles of voidage (porosity) for the spherical particle (Figure 3A), cylindrical pellets with aspect ratio 1 (Figure 3B), aspect ratio 2 (Figure 3C) and aspect ratio 7 (Figure 3D). DEM predicts that as the aspect ratio of pellet increases (or as the non-sphericity increases), the amplitude and frequency of the near-wall radial bed-voidage oscillations decreases and

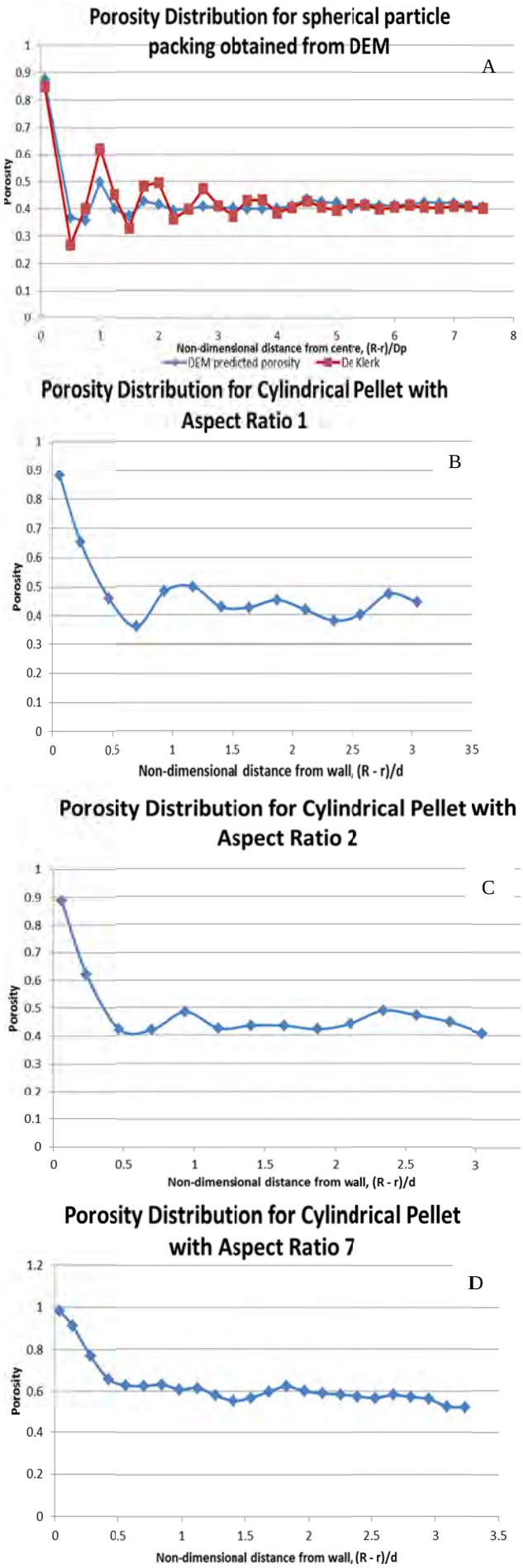

Figure 3 Porosity distribution obtained from DEM generated packing for (A) sphere, (B) AR1, (C) AR2 and (D) AR7.

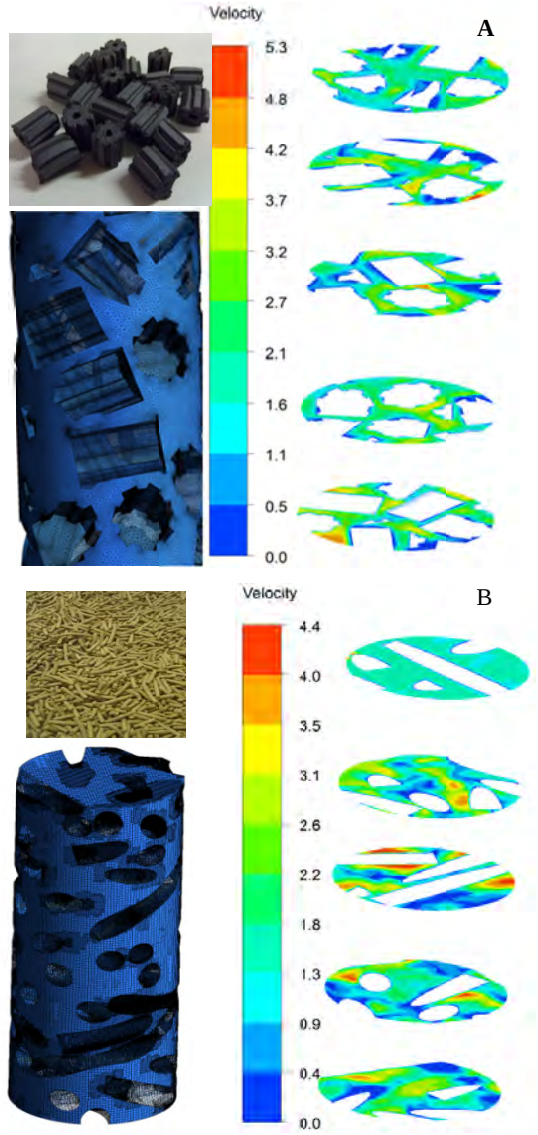

Figure 4 shows 3D CFD-DEM applied on (A) fluted ring and (B) cylindrical pellet.

the wall effect is confined to lesser distance from wall (Figure 3). As seen in Figure 3, there are more oscillations in radial voidage profile for aspect ratio 1 pellet than for aspect ratio 2 pellet. The Aspect ratio 7 pellet shows the least oscillatory behaviour. Comparatively, amongst the three pellets, the radial voidage profile of aspect ratio pellet 1 packing is nearer in behaviour to the spherical packing. The near wall region in Aspect ratio 1 and spherical extends upto five particle-diameters from wall, while for aspect ratio 7 and aspect ratio 2, the near-wall region is limited to two particle diameters from wall. These DEM predictions are quite similar to the observations made by various researchers regarding the variation of bed-voidage with variation of non-sphericity (Roblee (1958), Bey and Eigenberger (1997), Giese et. al. (1998), Caulkin et. al. (2012)). The work done by Nemec and Levec (2005) suggests that with increasing aspect ratio, the bed voidage increases. DEM is also predicting a higher voidage as the aspect ratio of the pellet increases. Thus, DEM predictions for bulk porosity have been validated with well-established correlations for spherical particle and match the observed trends for non-spherical particles.

Validation of 3D CFD-DEM methodology for obtaining closure information

The validation of CFD-DEM methodology to determine the cut-segment size and to obtain the correlations has been presented in Tabib et. al. (2013). Tabib et. al. (2013) conducted CFD simulations on the DEM generated packing segments for a wide particle Reynolds number range (from laminar to turbulent regime) for both the spherical and non-spherical particles. For the spherical particles, the validation was done by comparing the results with well-established correlations, like: Ergun equation (1952) for pressure drop, Wakao correlation (1979) and multi-particle Ranz-Marshal correlation (1952) for particle heat transfer coefficient and Dixon-Lubua (1985) and Colledge-Paterson (1984) correlation for wall heat transfer coefficient. For the non-spherical particles, the correlations obtained for the long cylindrical pellet (aspect ratio 7) packed bed has been compared with the correlation provided by Nemec and Levec (2005) for cylindrical pellet with aspect ratio of 5.77. These comparisons had shown good agreements. This validation gave us the confidence that the proposed CFD-DEM methodology can be used for obtaining useful information on transport phenomena within the bed, which can be used for designing and comparison of performance of large-scale packed bed reactor composed of unique particle shapes. The correlations developed for Aspect ratio 7 pellet and Fluted Ring using this methodology has been used in this work. Table 1 cites the input to be provided to 1D model as closure using the results from 3D CFD – DEM approach.

Validation of 1D model for a chemical looping combustion process (gas-solid non-catalytic reactions)

The 1D model is validated with analytical results for a packed-bed chemical looping combustion (CLC) reactor, which involves cyclic gas-solid non-catalytic reactions. The next section describes the 1D model.

1D model

A software application based on a 1D particle-reactor model has been developed to simulate a packed bed reactor operation. The developed 1D particle-reactor model is a combination of (1) a particle model for simulating radial distribution of chemical species and temperature within a catalyst/oxygen carrier particle and (2) a 1D reactor model for solving mass and energy balance along the reactor. The model accounts for the effect of intra-particle and inter-particle heat and mass transfer on the reactor performance. The reactor model and particle model are coupled together using mass and heat source terms computed at the particle surface. The 1D particle-reactor model can simulate for several different particle shapes (cylindrical pellet, slab and sphere) and offers flexibility in choice of closures (pressure drop correlations, heat-transfer/mass-transfer correlations, voidage and total particle surface area per unit reactor volume). The solution methodology involves a Finite Volume discretization technique for solving gas-phase equations along the reactor and an orthogonal collocation technique for solving the reaction-diffusion equations within the particle. This code is written in Fortran-90, and is easy to use as Microsoft Excel interface has been created. The fortan-90 code has been compiled into a direct link library (dll) form and is linked to the excel sheet using Visual Basic for Application (VBA) programming language. The coded 1D model solves the following equations. All the variables are explained in notation.

Ideal gas equation of state

$$P = C_{tot} R_g T_g \qquad (1)$$

Ergun pressure drop equation

$$\frac{\partial P}{\partial z} = -\frac{G}{\rho d_p}\left(\frac{1-\epsilon_g}{{\epsilon_g}^3}\right)\left(\frac{A(1-\epsilon_g)\mu}{d_p} + BG\right) \qquad (2)$$

Material balance for species "k" in gas phase

$$\varepsilon_g \frac{\partial C_k}{\partial t} + \frac{\partial F_k}{\partial z} = \Gamma_k$$

$$where,\ F_k = F_{tot} X_k - C_{tot} D_{eff,kg} \frac{\partial X_k}{\partial z} \qquad (3)$$

Energy balance for gas phase

$$\varepsilon_g \frac{\partial U}{\partial t} + \frac{\partial F_h}{\partial z} = \Gamma_U$$

$$where,\ F_h = F_{tot} H - \lambda_{ax} \frac{\partial T}{\partial z} \qquad (4)$$

Boundary conditions for gas phase

z=0: mass and energy inlet flux

z=L: $\frac{\partial C_k}{\partial z} = 0, \quad \frac{\partial T}{\partial z} = 0$ (5)

Source terms for gas phase mass- and energy balance arising due to mass and heat transfer at the gas-particle interface.

$$\Gamma_k = k_g \ a \ \left(C^s_{k,r=R} - C_k\right)$$

$$\Gamma_U = h \ a \ \left(T^s_{r=R} - T\right) \qquad (6)$$

$$for\ computing\ h\ ,\ \frac{h d_p}{k} = 2.0 + A_c Re_p{}^x Pr^y$$

where, the heat transfer coefficient (*h*) is computed using the Ranz-Marshall equation shown above and k_g is the mass transfer coefficient. The constant A_c for fluted ring and AR7 packed bed system has been obtained by fitting the CFD-DEM heat transfer results to the above Ranz-Marshall correlation (1952) (as described in Tabib. et. al. (2013)).

Solid particle (oxygen carrier or catalyst) model

Mass balance for species "k" inside a catalyst particle volume

$$\varepsilon_s \frac{\partial C^s_k}{\partial t} = \frac{\varepsilon_s D_{eff,ks}}{\tau} \nabla^2 C^s_k + \rho_s r_k \qquad (7)$$

Where, ε_s is the porosity in the particle, $m^3_{pore}/m^3_{particle}$ and C^s_k is Kmol/ m^3_{pore}. $D_{eff,ks}$ is diffusivity of gas species k.

Energy balance for a catalyst particle volume

$$\rho_s C_{ps} \frac{\partial T^s}{\partial t} = \lambda \nabla^2 T^s + \rho_s \sum_l r_l \left(-\Delta H_{rx,l}\right) \quad 8$$

Boundary conditions for catalyst particles
Symmetry at r=0:

$$\frac{\partial C_k^s}{\partial r} = 0 \ \text{ and } \ \frac{\partial T^s}{\partial r} = 0 \quad 9$$

Catalyst surface, r=R:

$$-\frac{\varepsilon_s D_{eff,k}}{\tau}\frac{\partial C_k^s}{\partial r} = k_g\left(C^s_{k,r=R} - C_k\right)$$
$$-\lambda\frac{\partial T^s}{\partial r} = h\left(T^s - T\right) \quad 10$$

For each particle configuration, the 3D CFD-DEM and DEM helps to determine the values of voidage (ε), the Blake–Kozeny–Carman constant (A) and Burke–Plummer constant (B) in Ergun Equation (2) , the heat transfer coefficient *h* and surface area per unit reactor volume *a* in Equation 6 (see Table 1). The current 1D model uses the reaction kinetics proposed by Abad et. al. (2011) for ilmenite in all the simulations. The 1D model is able to solve for this stiff reactions scheme as it uses an implicit backward differentiation formula for temporal discretization. The upwind scheme is used for the convective terms. The next section provides a brief description of the packed bed reactive CLC process and the validation result.

Chemical looping combustion and validation

The chemical looping combustion packed bed reactors involves cyclic gas-solid non-catalytic reactions, wherein the fixed packing (made of metal/metal oxide particles) is alternatively exposed to fuel gas stream (reduction cycle) and air stream (oxidation cycle). When exposed to the fuel gas stream (syngas), the metal oxide reduces. This reduction cycle results in production of hot stream of carbon dioxide and super-heated steam, which can be used for energy generation. The CO_2 is isolated by condensing steam. The reduced metal oxide bed is then exposed to the air stream, which re-oxidizes it. This exothermic oxidation cycle produces a stream of hot gas that can also be used for energy production. The reduction-oxidation cycle is then repeated continuously leading to power generation and CO_2 capture. The reaction system studied here is :

$4FeO + O_2 \rightarrow 2Fe_2O_3$ (Oxidation with air)
$Fe_2O_3 + CO \rightarrow 2FeO + CO_2$ (Reduction with syngas)
$Fe_2O_3 + H_2 \rightarrow 2FeO + H_2O$ (Reduction with syngas)

In the present validation study, ilmenite (FeO-Fe_2O_3-TiO_2) is used as an oxygen carrier. Initially, it is in a fully reduced state (i.e. only FeO-TiO_2 is present and no Fe_2O_3 is present). The system is fed with air at inlet temperature of 650 C and the initial bed is considered to be at the same temperature. As the oxygen is exposed to the solid ilmenite particle, the exothermic oxidation reaction takes place. The oxidation reaction continues till the particle is completely oxidized. A reaction front exists as a result of this process. These CLC processes are characterized by the presence of both the reaction front and the thermal front. Both these fronts are identifiable by temperature profile and concentration profile along the reactive bed. The movement of these fronts and the maximum temperature rise predicted by the 1D model is compared to that predicted by an analytical model (Noorman et. al., 2010). The maximum temperature that can be reached in the bed due to the heat liberated by the reaction front and due to the cooling down by incoming gas at the thermal front is obtained using an energy balance, which results in Equation 11. The analytical model provides equation 12 for computing reaction front velocity and Equation 13 for computing thermal front velocity.

$$\Delta T = \frac{\left(-\Delta H_{Rxn,l}\right)}{\frac{C_{p,s}M_s}{w_{sj}X_j\tau} - \frac{C_{p,g}M_g}{w^{in}_{g,k}}} \quad 11$$

$$w_r = \frac{\rho_g w^{in}_{g,k} v_g M_{si}}{\varepsilon_s \rho_s w_{s,j} X_j M_{g,k} \xi} \quad 12$$

$$w_h = \frac{\rho_g v_g C_{p,g}}{\varepsilon_s \rho_s C_{p,s}} \quad 13$$

As per the analytical model, the reaction front velocity is 1.12 x 10^{-2} m/s and the thermal front velocity is 1.43 x 10^{-3} m/s. The reaction front moves about an order of magnitude faster than the thermal front. Figure 5 shows that the 1D model is able to capture the movement of the reaction front and the thermal front quite accurately. The 1D model shows dispersion in reaction and thermal front as compared to the steep front predicted by analytical model. This dispersion is expected owing to the finite heat transfer rate and finite reaction rate in the actual operation (as is considered in the 1D model). The analytical solution assumes infinite reaction rate and infinite heat transfer rate, which is not a realistic condition. Analytically, predicted maximum temperature rise (equation 11) for the oxidation reaction is about 470 °C. So, the maximum temperature that can be reached in the reactor is about 1120 °C (Maximum temperature = Inlet air temperature + Max. temperature rise = 650 °C + 470 °C).

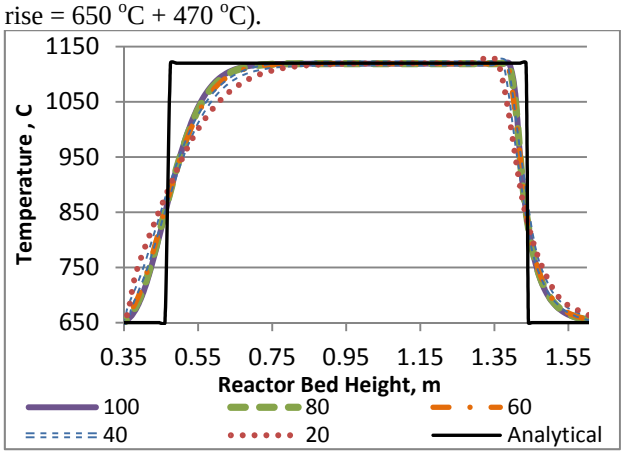

Figure 5 compares 1D model prediction of thermal front movement, reaction front movement and the maximum temperature rise with the analytical result. The results for 1D model are presented at several grid points (20,40,60,80 and 100) to check for grid independence.

Figure 5 shows that the 1D model predicts a maximum temperature of 1120 ^{o}C and the bed region between the thermal and reaction front is at this maximum temperature. Thus, the 1D model is able to capture the movement of the thermal and reaction fronts as well as the maximum temperature rise. This validates the use of the 1D model for the non-catalytic gas-solid operations like chemical looping combustion. The validated models have now been used in conjunction to implement the multi-scale approach for reactor design

APPLICATION OF MULTI-SCALE METHODOLOGY FOR OXYGEN CARRIER SELECTION AND CLC REACTOR DESIGN

Figure 6 and 7 compares the performance of seven different particle shape/size configurations for a 500KW fixed bed CLC reactor operation (height 1.5m and diameter 0.3 m) with air fed at 0.81 Kg/s for oxidation and syn-gas fed at for 0.078 Kg/s (corresponding to 500KW inlet heat) for reduction cycle. The comparisons are made for bed conversion, fuel-slip, pressure drop and cycle-time. The closures obtained for different particle configurations by 3D CFD-DEM has been used (See Table 1) by the 1D model. All the 1D simulations have been done using 80 grid points as the solution becomes grid-independent (see Figure 5). The packing configuration that can provide: (a) lower pressure drop, (b) higher reactivity, (c) Zero or minimal fuel- slip, and (c) lower cycle-time operation should be selected for the chemical looping combustion operation.

Table 1 show that some of the particles being studied have the same particle volume (same effective diameter of 7.5mm) but different shapes (sphere-7.5mm, cylindrical pellet with Aspect ratio (AR) of 1, pellet with Aspect ratio of 2 and pellet with Aspect ratio of 7). This will help to understand the effect of shape for a given size.

Particle Shape and size (effective diameter, actual diameter and height)	**For Ergun Equation (constants A and B in Equation 2).**		**For Ranz-Marshal for *h* in Eqn 6.**	**Voidage and Surface Area per unit Reactor Volume, m^{-1}**
	A	**B**	**A_c**	
Sphere (3mm, 5mm and 7.5mm)	**150**	**1.75**	**1.8**	**0.4 voidage & 1200 m^{-1} (for 3mm), 780 m^{-1} (for 5mm) and 486 m^{-1} (for 7.5mm).**
AR 1 d_{eff} =7.5mm & d_{actual}=6.4mm, h_{actual}= 6.4mm	**310**	**4.56**	**1.8**	**0.42 & 538 m^{-1}**
AR 2 d_{eff} =7.5mm & d_{actual}=10.26mm, h_{actual}= 5.12mm	**180**	**2**	**1.8**	**0.44 & 545 m^{-1}**
AR 7 d_{eff} =7.5mm & d_{actual}=3.4mm, h_{actual}= 23mm	**210**	**2.5**	**1.65**	**0.545 & 577 m^{-1}**
Fluted Ring, AR = 1.4 d_{eff} =14mm & d_{actual}=12.4mm, h_{actual}= 17.3mm	**253**	**2.21**	**1.68**	**0.53 & 560 m^{-1}**

Table 1. Closures for 1D model from DEM & 3D CFD-DEM.

We also study the effect of size by varying the size for a given spherical shape (3mm, 5mm size and 7.5mm) and a fluted ring with 14 mm effective diameter. All the particles are composed of ilmenite and the reaction kinetics proposed by Abad et. al. (2011) has been used in all the cases. Some of these ilmenite based particle shapes/sizes are being considered for the demonstration scale chemical looping combustion operation at Puertollano, Spain under the EU DemoCLOCK project. This scenario offers an ideal platform for developing and implementing the proposed multi-scale approach using validated models. The results are described below.

For reduction cycle, Figure 6A compares the Fe_2O_3 conversion profile along the length of bed after 60 s of reduction cycle operation for 7 different packing, while Figure 6B shows the overall Fe_2O_3 conversion as a function of time. The reaction front moves the fastest for Aspect ratio 7 packing (Figure 6A) and the whole bed is reduced within 74 s (as seen in Figure 6B). In terms of fastest bed conversion (or fastest reaction front), Aspect ratio 7 is followed by Aspect ratio 2, then the spherical pellets, the Aspect ratio 1 pellet and the Fluted ring. Similar trends are observed for oxidation cycle as well (Figure 7A). These trends are because the voidage of the packing structure increases as pellet aspect ratio increases (as predicted by DEM). Higher voidage results in lower amount of solid mass to be converted in the reactor bed. Figure 3 and Table 1 shows that the DEM predicted voidage for Aspect ratio 7 pellet packing is the highest followed by Aspect ratio 2, followed by spherical particles and Aspect ratio 1. The spherical particle and Aspect ratio 1 pellet shape have more compact packing (less voidage and more mass in the reactor) than the high aspect ratio pellets as a result they need more reactor operation time for complete bed conversion (as seen in Figure 6B-7B and Figure 6A-7A for both the oxidation and reduction). Figure 6A-7A shows that reaction fronts of Aspect ratio 1 and spheres (3mm, 5mm and 7.5mm) move with similar velocity, but have varied dispersions along the similar 'mean' front locations. The dispersion in reaction front increases as the size of sphere increases. The slower the effective reaction rate, higher is the dispersion of the reaction front around the mean location. The reason for this dispersion is the mass-transfer limitations accounted by the particle model of 1D particle-reactor model. As the diameter of sphere increases from 3mm to 7.5mm, the mass-transfer diffusional limitations increases and the effective overall rate of reaction decreases, leading to a more dispersed reaction front for higher diameter spheres. Similarly, the Aspect ratio 1 pellet shows more dispersion in reaction front than Aspect ratio 2 and Aspect ratio 7 pellet. This is because for the same particle volume, the actual diameter of pellets increases with decreasing aspect ratio ($diameter_{AR1}$ > $diameter_{AR2}$ >$diameter_{AR7}$). Thus, the Aspect ratio 1 offers higher mass-transfer diffusional resistance to the reactant gaseous species than Aspect ratio 2 and Aspect ratio 7 pellet.

Now, the Fluted Ring packing also has a higher voidage and very less mass within the reactor (equivalent to Aspect ratio 7 pellet), and even the total particle surface area available is comparable to Aspect ratio 7, so one would expect a quick complete bed conversion

(similar to Aspect ratio 7 case). However, as Figures 6B and 7B reveal that at any given time, the Fluted Ring bed is the least converted amongst all and the bed is not completely converted even after 150 s of reactor operation (only 91% conversion). Figure 6A and 7A reveals that Fluted Ring has the most diffused reaction front amongst all the particles (suggesting a very slow effective rate of reaction). The Fluted Ring has the largest particle diameter amongst all the particles and the mass transfer resistances encountered by the gaseous species would reduce the overall effectiveness. The 1D model is able to capture the mass-transfer limitation within the particle. The mass-transfer limitation dominates the faster intrinsic rate kinetics leading to slower conversion of the fluted ring particle.

Thus, a study of conversion profiles reveal that the Aspect ratio 7 pellet and 3 mm sphere particles offer high reaction rates (owing to lower mass-transfer limitations), while Aspect ratio 7 and Aspect ratio 2 packing results in a faster moving reaction front (owing to higher voidages and lower mass). A study of fuel-slip and pressure drop will enable us to make proper choice.

Figure 6C shows the fuel-slip time for the reduction operation. An early fuel-slip of reactant CO and H_2 will disallow any efficient isolation and capture of CO_2 from the exit-gas stream, thus leading to an unsuccessful operation. An early fuel-slip can occur owing to slower effective reaction rate (i.e. diffused reaction front) caused by mass-transfer limitations. The CO fuel-slip is known to occur earlier than hydrogen fuel slip in all the cases (owing to slow effective rate of reaction of CO). Hence we analyze the CO-slip results to compare the different packed beds. A good packing configuration is where the onset of fuel-slip occurs when nearly most of the bed is converted (i.e. when the reaction front reaches the end). Figure 6C and 6B indicate that the onset time of fuel-slip is better for 3mm sphere (75% bed reduced), followed by Aspect ratio 7 (60% bed reduced), 5mm and 7.5mm spherical particles (nearly 60% reduced), Aspect ratio 2 pellet (40% bed reduced) and Aspect ratio 1 pellet (30% bed reduced). This is expected as the reaction rate is higher for 3mm sphere and the Aspect ratio 7 pellet (as indicated by the sharpness of reaction front) than others. Their high reactivity can be explained on the basis of low diffusional resistances (owing to lower particle diameter) and high particle surface area per unit reactor volume.

Amongst the particle of same volume (i.e. same effective diameter of 7.4 mm but different shape, as shown in Table 1), Aspect ratio 7 provides the highest surface area per unit reactor volume (577 m^{-1}) and the lowest diffusional resistance. For both 3mm sphere and Aspect ratio 7 packed bed, by the time the CO exit gas concentration reaches 5%, almost the entire bed is converted.

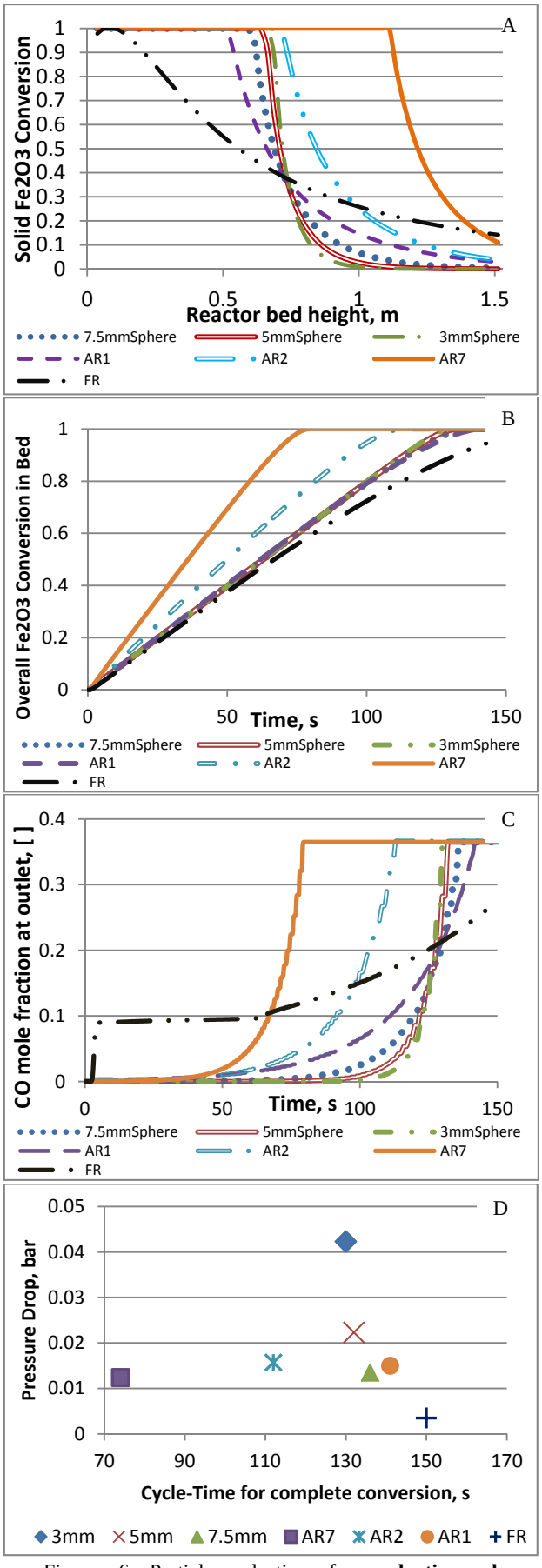

Figure 6 Particle selection for **reduction phase**: comparison of seven different particle configurations : (A) Conversion (Reaction front movement) after 60 s of reactor operation, (B) Overall conversion at a given time, (C) Fuel-slip at reactor exit and (D) Pressure drop and Cycle-time for each particle shape.

With regards to the process, the 14mm Fluted ring can be safely rejected for this CLC application due to a substantial early fuel-slip. This is owing to high mass-transfer limitation that causes a highly diffused reaction front.

Figure 6C and 6B shows that for fluted ring, the fuel slip occurs within first 10 s of reactor start-up and the outlet CO concentration suddenly reaches 10% even though the overall bed is only 5% reduced. Thus, based on the fuel-slip and bed-conversion (reactor bed-utilization) criteria, the Aspect ratio 7 and spherical pellets seem to be good possible choices. However, one needs to look at the pressure drop as well. A higher pressure drop can lower the reaction rate and increase the operating cost. A pressure drop high enough to overcome the weight of the bed can fluidize it or blow it. So, pressure drop is an important criterion.

Figure 6D and 7D shows the pressure drop and cycle-time for packing of each packing configuration for reduction and oxidation, respectively. The figure reveals that the pressure drop is highest for the 3mm sphere followed by 5mm sphere, and is the lowest for the Aspect ratio 7 pellet and fluted ring. The higher particle surface area and lower voidage offered by the 3mm sphere packing ensures that fluid experiences high viscous or skin friction resistance, which results in a higher pressure drop. The pressure drop reduces with increasing sphere size, as is expected. Amongst the particle of same volume, the high voidage in the Aspect ratio 7 packing ensures a lower pressure drop. Though, the pressure drop could have been higher for Aspect ratio 7 and Fluted Ring owing to their higher non-sphericity (which results in higher values of Blake–Kozeny–Carman constant value and the Burke–Plummer constant in the modified Ergun equation, See Table 1) and a higher surface area per unit volume (that can cause higher viscous resistances), but the effect of loose packing (higher voidage) offsets these factors.

From the results of both the oxidation and reduction cycle, it seems that Aspect ratio 7 pellet packed bed can be a good choice as it offers the least pressure drop, high reactivity and a fast moving reaction front that ensures lower cycle-time. The Aspect ratio 7 pellet performs better than Aspect ratio 2, Aspect ratio 1 and spherical particle of the same particle volume. The alternative can be the 3mm sphere, for which the operating costs could be higher owing to higher pressure drop and higher cycle time (as more mass of catalyst fits in the reactor bed due to low voidage) than the Aspect ratio 7 pellet. However, before finalizing any particle, the ability of the particles to withstand the thermal, chemical and mechanical stress owing to a high temperature-high pressure cyclic operation must be experimentally tested.

Thus, this work has demonstrated the use of a novel multi-scale model in selecting an oxygen carrier for a packed bed chemical looping combustion operation. This methodology can also be applied to create a new catalyst shape and analyze its performance for a catalytic gas-solid reaction.

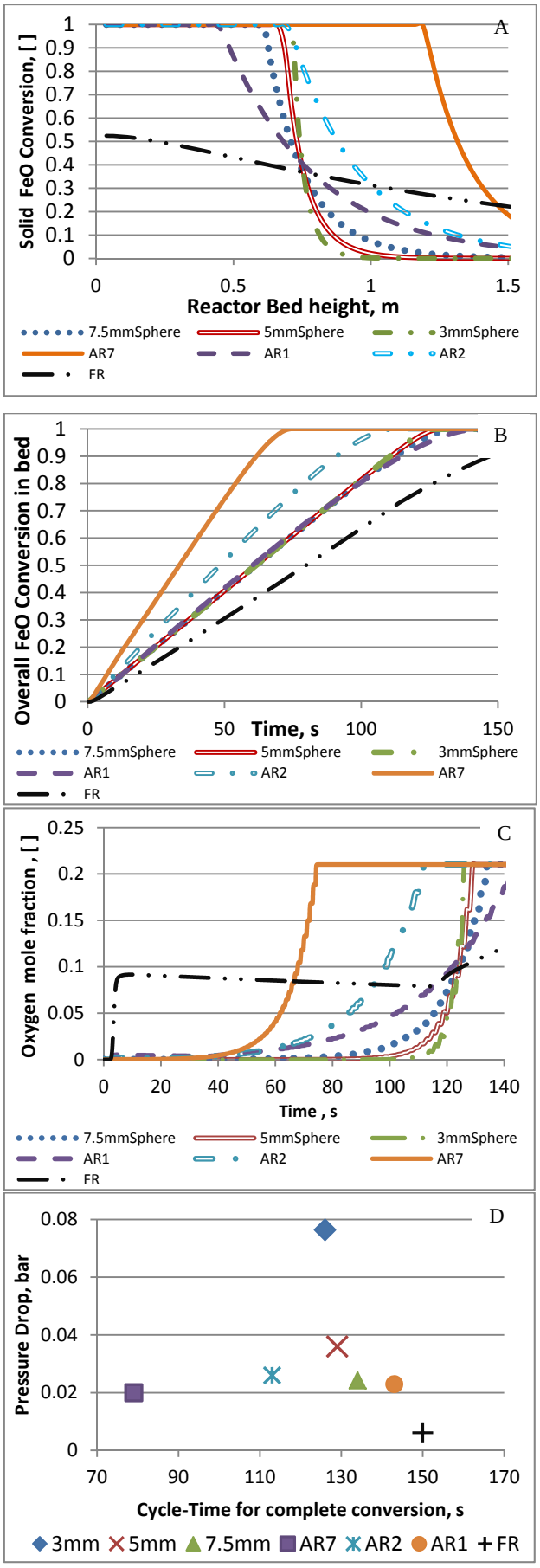

Figure 7 Particle selection for **oxidation phase**: comparison of seven different particle configurations : (A) Conversion (Reaction front movement) after 60 s of reactor operation, (B) Overall conversion at a given time, (C) Fuel-slip comparison and (D) Pressure drop and Cycle-time for each particle shape.

CONCLUSION

A multi-scale modelling approach is developed for enabling oxygen carrier selection and reactor design. The approach can potentially be used for catalyst design. The multi-scale approach involves a 3D CFD-DEM (Computational Fluid Dynamics and Discrete Element Method) simulation in-combination with a multi-domain 1D particle-reactor model. In this multi-scale approach, a representative segment of the packed bed (generated by DEM) is simulated using CFD to obtain correlation for pressure drop and heat transfer coefficient. These correlations along with the information on packing structure (i.e. porosity and surface area per unit reactor volume obtained from the DEM generated packing) have been used by the 1D particle-reactor model. The 1D model, which includes the inter-particle and intra-particle limitations, is used for simulating the large scale packed bed reactor. The multi-scale approach provides a faster and reasonably accurate means of comparing the effect of oxygen carrier (or catalyst or pellet shape) on reactor performance.

The multi-scale model has been applied to compare performance of different particle configurations (spherical, Aspect ratio 7 pellet, Aspect ratio 2 pellet, Aspect ratio 1 pellet and fluted ring) for a gas-solid non-catalytic chemical looping combustion packed bed reactor. For particles of same equivalent diameter (volume), the Aspect ratio 7 pellet filled reactor offers the least pressure drop, highest reactivity and provides a lower cycle-time operation as compared to spherical pellets and other low aspect ratio cylindrical pellets. The higher voidage created by the aspect ratio 7 packing is the reason for the lower pressure drop. Further, the high surface area per unit reactor volume and lower actual pellet diameter (low diffusional resistance) of aspect ratio 7 packing leads to high catalyst effectiveness, faster reaction rates and avoids early fuel-slip. The 14mm fluted ring offers higher diffusional limitations that results in slower reaction rates and early CO fuel slip is rejected as it will prohibit the isolation and capture of CO_2.

Thus, the work has successfully demonstrated a novel multi-scale modeling approach involving 3D-DEM-CFD-1D model for selecting optimum size/shape of pellets for a packed bed reactor operation. This methodology can be applied to create new particle shapes and analyze their performance (for catalyst design) and for studying pre-existing shapes (like tri-lobe quadrulobe, monoliths, wagon wheels, hollow extrudates, discs etc.).

ACKNOWLEDGEMENT

A POP-SEP funding from SINTEF has been used for the 1D particle-reactor model software development. The multi-scale model development has been carried out as a part of the DemoCLOCK project, which is an EU FP7 funded project under the ENERGY.2010.6.1-1 programme.

REFERENCES

ABAD, A., ADÁNEZ, J., CUADRAT, A., GARCÍA-LABIANO, F., GAYÁN, P., AND DE DIEGO, L. F. (2011), "Kinetics of redox reactions of ilmenite for chemical-looping combustion", *Chemical Engineering Science*, **66**, 92-97.

BEY, O., AND EIGENBERGER, G., (1997) , "Fluid flow through catalyst filled tubes", *Chem Eng Sci*, **52,** 1365-1376.

CAULKIN, R., JIA, X., FAIRWEATHER, AND M.. WILLIAMS, R.A, (2012), "Predictions of porosity and fluid distribution through nonspherical-packed columns", *AIChE Journ*al, **58**, 1503-1512.

COLLEDGE, R.A.P. AND PATTERSON, W. R., (1984) , "Heat Transfer at the Wall of a Packed Bed: A j-Factor Analogy established", *11th Annual Research Meeting; Institution of Chemical Engineers: Bath*, 6 .

DIXON, A.G. AND LABUA, L.A., (1985), Wall-to-fluid coefficients for fixed bed heat and mass transfer, *International Journal of Heat and Mass Transfer*, **28,** 879-881.

DIXON, A.G., (1988), Correlations for wall and particle shape effects on fixed bed bulk voidage, *Canadian Journal of Chemical Engineering*, **66,** 705-708.

DEKLERK, (2003) "Voidage variation in packed beds at small column to particle diameter ratio", *AIChE Journal*, **49,** 2022-2029.

ERGUN, S., Fluid Flow through Packed Columns, *Chem. Eng. Prog*, **48** (1952) 89.

GIESE, M., ROTTSCHÄFER, K., AND VORTMEYER, D., (1998), "Measured and Modeled Superficial Flow Profiles in Packed Beds with Liquid Flow", *AIChE Journal*, **44** , 484-490.

INGRAM, G.D., CAMERON, I.T., AND HANGOS K.M., (2004), "Classification and analysis of integrating frameworks in multiscale modelling", *Chem Eng Sci*, **59** 2171-2187.

NEMEC, D. AND LEVEC, J., (2005), "Flow through packed bed reactors: 1. Single-phase flow", *Chem Eng Sci*, **60** , 6947-6957.

NOORMAN, S., VAN SINT ANNALAND, M., AND KUIPERS, J. A. M, (2010), "Experimental validation of packed bed chemical-looping combustion", *Chemical Engineering Science*, **50**, 1968-1980.

RANZ, W.E. AND MARSHALL, (1952), W.R. "Evaporation from Drops, Part II.", *Chem. Eng. Prog.* , **48,** 173.

ROBLEE, L.H.S., BAIRD, R. M. AND TIERNEY, J. W., (1958) , "Radial porosity variations in packed beds", *A.I.Ch.E.J*., 460-464.

TABIB, M.V., JOHANSEN, S.T., AND SHAHRIAR, A., (2013), "A 3D CFD-DEM methodology for simulating industrial scale packed bed Chemical Looping Combustion reactors", *Industrial and Engineering Chemistry Research*, **52** (34) 12041–12058.

WAKAO, N., KAGUEI, S., AND FUNAZKRI, T. (1979), "Effect of fluid dispersion coefficients on particle-to-fluid heat transfer coefficients in packed beds: Correlation of nusselt numbers", *Chem. Eng. Sci*., **34**, 325−336.

PREDICTION OF MASS TRANSFER BETWEEN LIQUID STEEL AND SLAG AT CONTINUOUS CASTING MOLD

Pascal GARDIN[1*], Ségolène GAUTHIER[1], Stéphane VINCENT[2]
[1] ArcelorMittal Global R&D, 57283 Maizières-lès-Metz, FRANCE
[2] I2M, Trèfle department, 33607 Pessac, FRANCE

* E-mail: pascal.gardin@arcelormittal.com

ABSTRACT

For the prediction of steel desulphurization and dephosphorization or the evolution of slag composition at continuous casting mould, mass transfer between two immiscible fluids in a turbulent situation should be calculated.
For this purpose, two possibilities are offered for the simulation. The first one consists in the calculation of the local chemical equilibrium with the simultaneous prediction of the species transport, but the cost is that very fine mesh should be used. The second is based on the assessment of the mass transfer coefficient from hydrodynamic calculations and further use of thermodynamic code fed with interface area and transfer coefficients. On a computing time point of view, this second method is more affordable for 3D configurations than the first one, but it is less accurate. Literature survey indicates that it is possible to obtain a realistic evaluation of the mass transfer coefficient from hydrodynamic calculations, under the condition of very precise description of the flow near the interface.
The paper explains the reasons for the different simplifications which were made to predict the mass transfer between liquid steel and slag, gives indication on interest and limitation of the coupling between fluid dynamics and thermodynamics to get the local and time dependent evolution of chemical composition in the two phases. The modelling to predict the mass transfer coefficient is also described and compared to correlation proposed in the literature. Finally, a correlation is proposed to get mass transfer coefficient up to Schmidt number = 1000.

Keywords: *CFD, Pragmatic industrial modelling, Multiphase Heat and Mass transfer, Casting, Slag.*

NOMENCLATURE

Greek Symbols
Λ Integral length scale of turbulence, [m].
δ_s Thickness of species boundary layer, [m].
δ_m Thickness of momentum boundary layer, [m].
μ Dynamic viscosity, [kg/m.s].
β Mass transfer coefficient, [m/s].
Δz Cell thickness near interface, [m].

Latin Symbols
C Non-dimensional concentration.
D Mass diffusivity, [m^2/s].
H Half height of the channel, [m].
Sc Schmidt number.
u* Friction velocity at interface, [m/s].
u_{max} Maximum velocity in the phase, [m/s].

Sub/superscripts
G Gas phase.
i Interface.
ls Liquid steel.
sl Slag.
∞ Far from interface.

.

INTRODUCTION

All along the steel refining route and casting, the liquid steel is rarely exposed to the ambient atmosphere. It is often covered with a thermal insulation: the slag. This is the case in a continuous casting mould, which is the reactor largely used to solidify steel. Figure 1 gives a schematic diagram of the operation and the various phases present in a mould:
▪ the liquid steel, also carrying argon bubbles and micro-particles coming from an endogenous precipitation in the liquid steel, is introduced through a nozzle into the mould (typical section of 1800 * 220 mm^2), the value of the Reynolds number at the outlet nozzle is in the order of 70000, which produces a high degree of turbulence in the mould and at the interface between liquid metal-slag; the argon bubbles limit the clogging phenomena inside the nozzle and strongly disturb the liquid steel / slag interface when crossing.

▪ the flux powder is deposited continuously on the upper surface and at about 1000 °C, it liquefies over a thickness of a few millimetres to form the liquid slag.

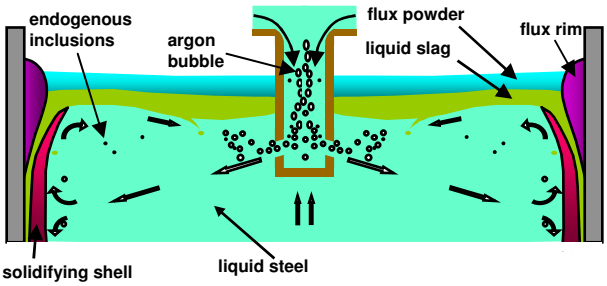

Figure 1: Different phases in a continuous casting mould, Pericleous (2008).

In a mould, the liquid slag has another specific function: it is entrained between the mould and the solidifying skin and facilitates lubrication. In the latter case, it is important to control the composition of the slag, to guarantee its good viscosity and its ability to lubricate.
Another characteristic is that the slag should not be fragmented; if slag droplets are suspended in the liquid steel, they can be entrapped by the solidifying shell and produce surface defects on the final product. It is currently one of the major defects in our steel plants.

New steels grades (such as Advanced High-Strength Steel) contain alloying elements that can affect the slag behaviour; for example, depending on the aluminium mass fraction inside the liquid steel, Al_2O_3 content of the slag can vary between 3-4 % and 30-35 %, which deeply affects its viscosity (multiplied by 5), Shahbazian et al. (2002), and its thermal conductivity, modifying the extraction of the heat flux through the mould. Robustness issues of the process are then encountered; if the viscosity increases, the quality of the lubrication is degraded, which leads to a rupture of the slag film and a direct contact of the molten steel with the mould: if a sticking takes place, it may be impossible to extract continuously the steel from the mould and the process should be stopped and the mould replaced.

Process control means that mass transfer should be controlled to have insight into the chemical evolution of the slag. In this context, we have to control the dynamic behaviour of the interface between liquid steel and slag and detect if interface fragmentation will occur or not, since it will affect interfacial area for mass transfer and steel quality if slag droplets are entrapped by the solidifying shell. Several mechanisms are involved in the fragmentation, which is already the subject of dedicated studies, Hagemann (2013), Real-Ramirez (2011). Figure 2 shows a typical interface behaviour observed in a water model. Part of the flow coming from the nozzle is deviated towards the interface and, above a critical water velocity, the interface is strongly distorted and can be fragmented. Another mechanism can be observed: the creation of a drainage cone which can produce small droplets of the upper phase in the lower one when it breaks.

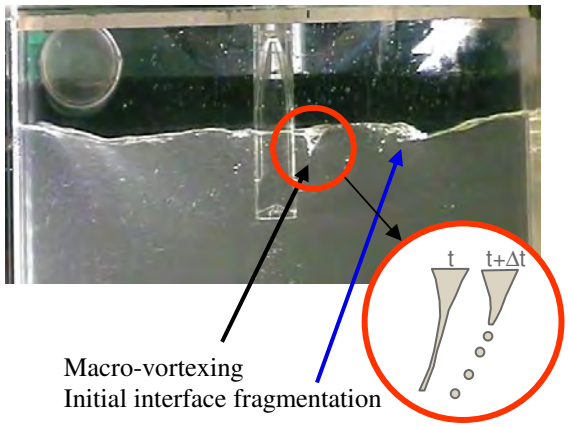

Figure 2: Typical behaviour of interface.

Mass transfer across a turbulent interface has already been investigated. In the steelmaking community, KTH teams have published some papers showing the evolution of slag compositions interacting with the liquid metal, Jonsson (1998), Andersson (2002), Doostmohammadi (2010).
However, as soon as CFD and thermodynamics are coupled, it is difficult to understand in details the numerical procedure for the coupling and there is a too brief discussion on different topics: dependence of the result to the mesh size and treatment of the interfacial turbulence (on the basis of RANS turbulence models). Although the method is qualitatively interesting, further investigations are necessary.

To get the mass transfer coefficient, different teams proposed interesting papers based on CFD calculations. In the case of a plane interface between water and liquid Calmet (1998) has shown the relevance of using a LES turbulence model to describe the interface with and without shear stress, and to identify the coefficient of mass transfer up to Schmidt number 200. More recently, Figueroa-Espinoza (2010) extended the method to predict the mass transfer between a bubble with a variable shape, using a mesh conforming to the shape of the bubble, for values of the Schmidt number up to 500.

Banerjee (2004) also took into account the deformation of the interface and made calculations for Schmidt numbers up to 10-20; he proposed the promising "surface divergence" model for deriving the mass transfer coefficient.

EVOLUTION OF CHEMICAL COMPOSITION

The objective is to get the time evolution of the steel and slag compositions. We have to calculate the flow, the local composition and advection/diffusion of the different chemical species, but also the chemical reactions between steel and slag. Ansys-Fluent™ predicts the flow of liquid steel and slag phases with the Volume Of Fluid model, each phase being constituted of a mix of several species. An in-house code is used for the thermodynamics calculations. Because precipitation and chemical compositions in liquid or solid steel are very specific, ArcelorMittal R&D developed its own

code, called CEQCSI, for Chemical EQuilibrium Calculation for the Steel Industry. It allows the calculation of local compositions and precipitations of different oxides (SiO_2 -TiO_2 - Ti_2O_3 - Cr_2O_3 - Al_2O_3 - Fe_2O_3-CrO - FeO -MgO - MnO - CaO…) and slag-metal reactions, Lehmann (2008).

By means of User Defined Functions that can be addressed in Ansys-Fluent ™, we can detect the cells where slag and steel are both present; mass fraction of the different species at time t are sent to Ceqcsi which makes the calculations for the new equilibrium composition in each phase and then gives the resulting source terms for each specie to Ansys-Fluent™. Advection/diffusion takes place during Δt and new composition is calculated in the entire domain at t+Δt by Ceqcsi. With this iterative procedure, it is possible to have the time evolution of the chemical composition in each phase.

We initiated calculations in 2D. The geometry of the top region is displayed on Figure 3. The height is 1500 mm and width is 800 mm. Initial slag thickness is 50 mm. The number of cells, for the initial calculations is 21600. VOF-PLIC method is used to predict the interface and realisable k-ε is selected for turbulence modelling. Turbulence damping at interface is considered by means of a source term in the ε transport equation, Gardin (2011). Because slag is consumed to lubricate the mould, we impose slag inlet along the horizontal top line (Velocity inlet (1)) and slag is extracted by the two vertical segments (Velocity inlet (2)) with the composition of adjacent cells and negative velocity to get outlet conditions. Slag can be consumed or created due to the composition adjustment calculated by Ceqcsi; it means that slag volume, and by consequence steel volume, can change with time according to the chemical equilibrium with steel. The consequence is also that thermodynamics should be coupled with fluid flow calculations at each time step: unfortunately, freezing the steel/slag interface for further thermodynamics calculations is not possible and transient calculations should be performed.

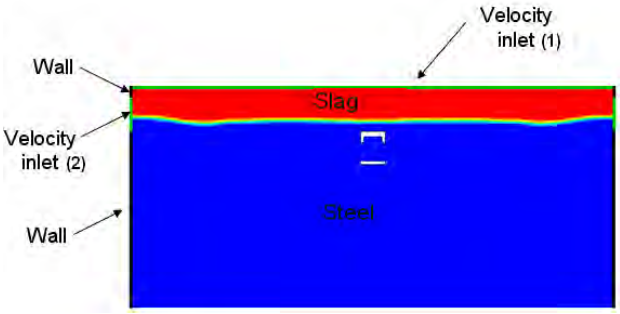

Figure 3: Top region of the calculation domain with boundary conditions.

Figure 4 illustrates the 2D velocity field that we obtained. The slag movement is mainly due to momentum transfer from liquid steel to slag at interface. The impact of slag injection by the top on slag movement is very small.

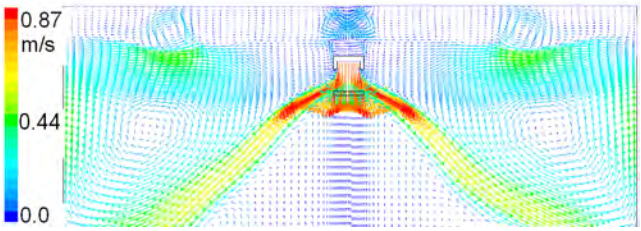

Figure 4: Typical velocity field in steel and slag.

The coupling between Ansys-Fluent™ and Ceqcsi was applied with the composition of steel and slag as it is expressed in Table 1 at t=0 s.

Table 1: Initial steel and slag compositions.

species	Steel %wt	Slag %wt
Fe	98.8273	
Al	0.031	
Mn	/	
Si	/	
Ca	/	
S	/	
O	0.0005	
SiO_2		38
Al_2O_3		9
Fe_2O_3		/
FeO		/
MnO		/
MgO		/
CaO		27
CaF_2		/

As we can see on Figure 5, Al distribution in the mould is heterogeneous after 113 s of calculation, especially near the interface. Al is transported towards the interface and there is a progressive Al consumption to form Al_2O_3 in the slag; in consequence, there is a progressive decrease of Al concentration as the flow transports Al along the interface towards the centre of the mould

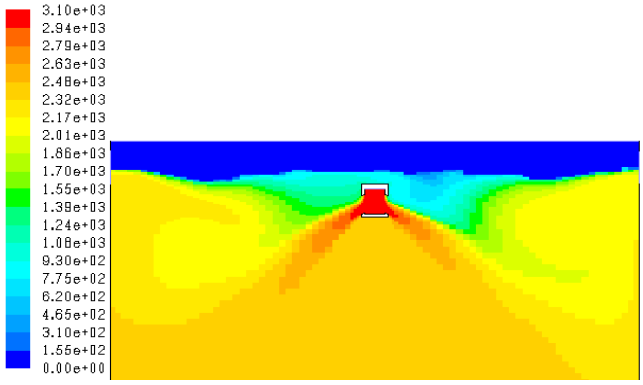

Figure 5: Mass fraction of Al (ppm) at t=113 s – time step for CEQCSI call: 0.05 s.

The Al distribution in liquid steel should be related to the alumina distribution in the slag (Figure 6) which also displays important variations; it is observed low Al_2O_3 concentration in low velocity regions: mixing by advection/diffusion is too slow with the consequence of slag viscosity heterogeneously distributed.

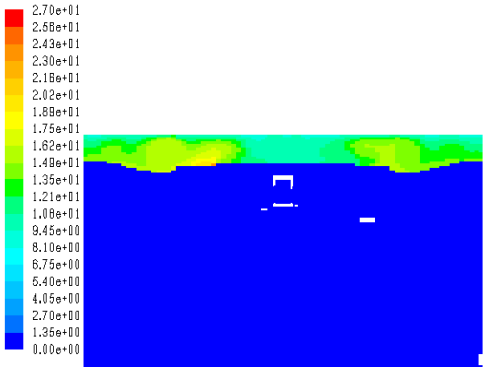

Figure 6: Mass fraction of Al_2O_3 (ppm) at t=113 s – time step for CEQCSI call: 0.05 s.

Analysis of the influence of the mesh size near the interface was realized. Initial mesh which was used for the previous results is displayed on Figure 7. Then, cells are successively divided by 2 and 4 in the region containing the interface. Cell thickness is respectively 4, 2 and 1 mm.

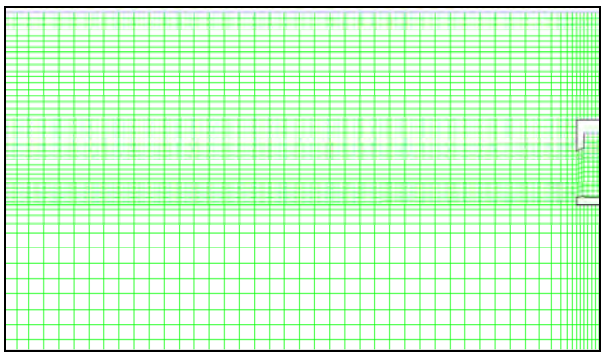

Figure 7: Initial mesh – half geometry is considered

The time step between two successive Ceqcsi calls is maintained constant to 0.05s and mean Al_2O_3 content in the slag is drawn for the three cases. Figure 8 clearly shows that results are strongly mesh dependant and that stationary concentration is more rapidly obtained for large mesh. If time step to call Ceqcsi is decreased, other calculations show that Al_2O_3 evolution is quicker than with 0.05s. At this stage, we conclude that results are mesh and time-step dependant.

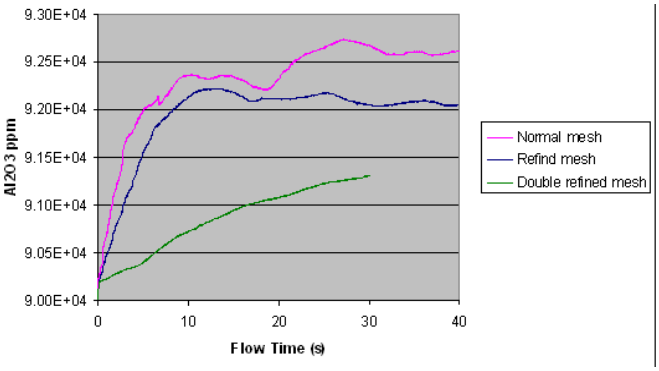

Figure 8: Mean Al_2O_3 content in slag – time step for CEQCSI call: 0.05 s.

The main idea to determine the adequate Ceqcsi time step call consists in adjusting it with the species renewal time of the cell. If we keep in mind that the species renewal in a cell is limited by the vertical diffusion, then we should have:

$(\Delta z)^2/\Delta t=D$ and Δt is the renewal time.

Δt can be identified to the Ceqcsi time step call. Table 2 gives the Δt values when diffusion length is imposed to be the cell thickness.

Table 2: Adaptation of time step to call the thermodynamics model.

Cell thickness (mm)	4	2	1
Diffusivity (m^2/s)	$4\ 10^{-5}$	$2\ 10^{-5}$	10^{-5}
Time step for Ceqcsi call (s)	0.4	0.2	0.1
Diffusion length $(D\Delta t)^{0.5}$ (mm)	4	2	1

Figure 9 shows that the superimposition of the curves is much better than previously. But, if we consider a realistic species diffusivity D ~ $3.0\ 10^{-9} m^2/s$, the Ceqcsi time step should be 1h30 when Δz is 4 mm: it is not possible to have calculations for such long time and the numerical diffusions should overcome the molecular one. If cell thickness is 100 µm, then Δt is 3 s, which is a realistic value on the CFD point of view, with the insurmountable drawback of huge number of cells for an industrial application.

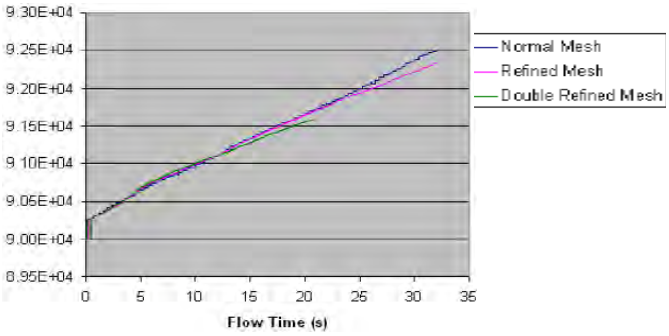

Figure 9: Mean Al_2O_3 content in slag **-** results independent of mesh size.

At this moment, these calculations are possible on a qualitative point of view, using much larger species diffusivity than real ones, with cell thickness larger than 1 mm. Some trends will be obtained but the time evolution will be much quicker than what it should be. Nevertheless, the information we get is sufficient to classify the mutual influence of steel grades and initial slag composition on the slag viscosity. On an engineering point of view, the coupling between CFD and thermodynamics can be fruitfully used.

To get more realistic values of the time evolution of slag composition, another method should be used, which will be explained now.

CAN WE USE CORRELATIONS BASED ON FLOW AND FLUID PROPERTIES TO EXTRACT THE MASS TRANSFER CEFFCIENT?

As it was already investigated by Calmet (1998) or Banerjee (2004), CFD can provide some valuable correlations to get the mass transfer coefficient β. For instance, the following relation can be considered (valid for Sc < 100):

$$\beta\, Sc^{0.5} / u^* \sim 0.108 - 0.158$$

$$u^* = \sqrt{\frac{\tau_i}{\rho}} \quad \text{is the friction velocity} \qquad (1)$$

where $\tau_i = \mu\left(\frac{\partial \bar{u}}{\partial n}\right)_i$ is the interface shear stress

or this one which was proposed by Banerjee, known as "surface-divergence" correlation:

$$\beta \approx Sc^{-1/2} u^* \mathrm{Re}_t^{-1/2} \left[\left(\frac{\partial u}{\partial x} + \frac{\partial v}{\partial y}\right)^2\right]_i^{1/4} \qquad (2)$$

where $Re_t = \Lambda u_{max}/\nu$ (the integral length scale of turbulence Λ is assimilated here to the height of liquid steel phase H or slag when slag is considered) and (x, y) plane is the interface plane.

When β and the interfacial area are known, Ceqcsi can calculate the time evolution of the slag composition. Interfacial area can be determined by VOF-PLIC method, see Figure 10, as soon as interface deformation is not too complex.

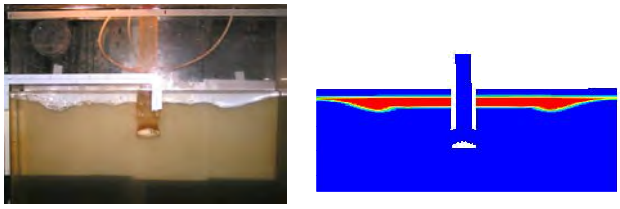

Visualisation of the interface shape

3D calculations with Ansys-Fluent

Figure 10: Schematic diagram of geometry.

But equation (1) or (2) cannot be used directly in our case since species Sc is around 1000 (value depending on species) and out of the validity range. A specific study should be carried out to extend the correlation up to Sc~1000-2000. The method consists in performing two kinds of calculations:

1- a scalar value is imposed at the interface and scalar profile is drawn at different positions and times; the profile is then used to identify the mass transfer coefficient, as it was explained by Haroun (2008).

2- based on a sufficient number of previous calculations, scaling laws are built: for instance $\beta_L \sim Sc^{-n}$ or $\beta_L \sim u^{*m}$ (n=-1/2 and m=1 for equation (1)).

Preliminary calculations were realised with Ansys-Fluent™ but, unfortunately, we did not manage to respect the interfacial shear stress continuity across a flat interface, even for very thin cells around 10 µm thickness. It was the reason why we decided to switch to another CFD code: Thetis.

Thetis is developed at Institut de Mécanique et d'Ingénierie de Bordeaux, Trèfle department. It is devoted to the prediction of multiphase flow in laminar or turbulent situation and special emphasis is given to accurate description of interface tracking based on VOF method, see Vincent (2010).

A first set of calculations was realised in the case of a channel flow with two counter-current stratified fluids: liquid in the bottom and gas at the top. The momentum source is a pressure gradient in both fluids. Intensive CFD work was already realised by Fulgosi (2003) and Adjoua (2010): their work is considered as reference to test Thetis reliability. In Thetis, mesh refinement in the interface region is adapted to get at minimum 3 cells in the viscous sub-region. Dynamic LES turbulence model is used, without adaptation of the subgrid scale model at the interface. A very good agreement with results published by Adjoua was obtained (Figure 11) and interface shear stress continuity was respected.

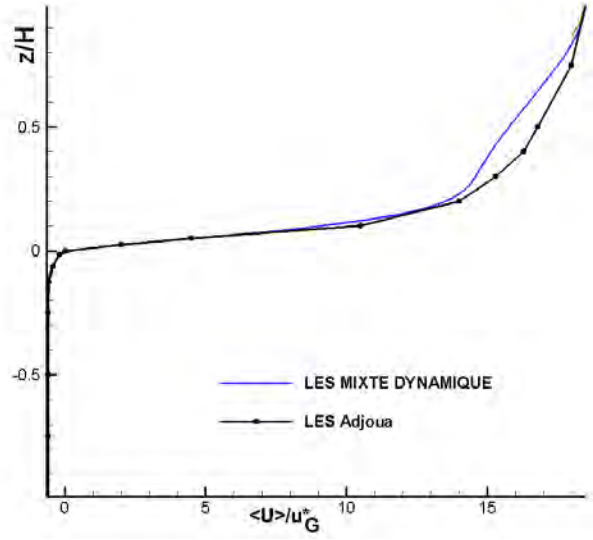

Figure 11: Dimensionless vertical coordinate according to mean velocity - comparison between LES model of Thetis and LES of Adjoua.

Since the good behaviour of Thetis was established, a second configuration was studied. It is still a channel flow but with liquid steel at the bottom and slag at the top.

The momentum source is a pressure gradient in the liquid steel phase and slag is entrained by the shear stress exerted at the interface (as it is in a real mould). The fluid properties are given in Table 3.

Table 3: Fluid properties.

	Steel	Slag
Density – kg/m^3	7000	2500
Viscosity – Pa.s	0.00539	0.0539
Interface tension	1.2 N/m	

The boundary conditions are periodic in the streamwise and spanwise directions whereas symmetry conditions are imposed in the direction normal to the interface. The initial velocity guess is chosen as a fluctuating instantaneous field coming from the simulations of Adjoua after the turbulence was developed. The maximum liquid steel velocity is selected to be 0.3 m/s (close to what is measured in real continuous casting mould near the interface) and the height of the channel filled with liquid steel is 0.009576 m. Reynolds number is then 3730.

The mesh in the interface region is depending on Schmidt number, according to $\delta_s \approx \delta_m Sc^{-1/3}$. If Sc=1000, species boundary layer is 10 times lower than momentum one and much more cells are necessary to describe the species behaviour.

It is important to control that we have shear stress continuity across interface (see Table 4, transient calculations), which makes possible the calculation of the friction velocity on both sides of the interface.

Table 4: Shear stress and friction velocity at interface at different times.

	$\tau_{i,ls}$ (Pa)	$\tau_{i,sl}$ (Pa)	u^*_{ls} (m/s)	u^*_{sl} (m/s)
t=1.4s	0.46	0.48	0.0081	0.014
t=4s	0.23	0.26	0.0057	0.01
t=6s	0.22	0.22	0.0055	0.0092

Figure 11 displays the concentration field at time t=4 s, when the concentration at the interface is imposed to be 1, and makes explicit the need to refine the mesh depending on Schmidt number.

The interface is totally flat and aligned with the cells, which is very important to have negligible numerical diffusion. We checked that, in the case of laminar flow with very large Sc (>10^7), the species diffusion in the vertical direction is totally negligible.

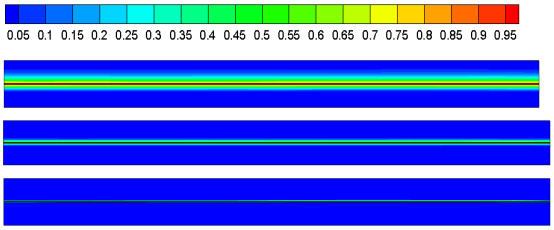

Figure 11: Mean species concentration at t=4 s, for Sc=10 (top), 100 (middle), 1000 (bottom).

Vertical concentration profiles are extracted, Figure 12. Z=0 corresponds to interface position, z < 0 is steel and z > 0 is slag. Due to the fluid properties, diffusion is not symmetrical, with deeper diffusion when species diffusivity is higher, as it is the case for slag compared to steel.

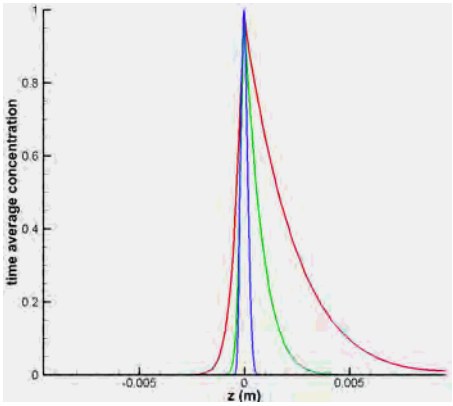

Figure 12: Vertical concentration profile at t=4 s, for Sc=10 (red), Sc=100 (green), Sc=1000 (blue).

The curves can be used to get the mass transfer coefficient, according to equation (3):

$$\beta = \frac{D\left(\frac{\partial C}{\partial z}\right)_i}{(C_i - C_\infty)} \qquad (3)$$

Table 5 summarises the results. Higher mass transfer coefficient is confirmed at the slag side. Those values are referenced as “Steel-simulation” on Figure 13.

Table 5: Mass transfer coefficients, t=4 s.

	Mass transfer coefficient, steel side ($m.s^{-1}$)	Mass transfer coefficient, slag side, ($m.s^{-1}$)
Sc=10	4.94E-05	4.23E-04
Sc=100	1.16E-05	1.33E-04
Sc=1000	1.37E-06	2.81E-05

Then, mass transfers obtained with species diffusion were compared to the ones obtained using correlation, for instance equation (2) proposed by Banerjee.

Mass transfer coefficients obtained with (2) are referenced as “Steel-SD” in Figure 13.

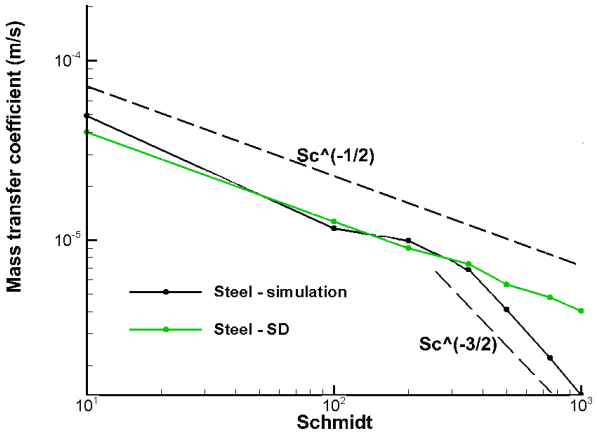

Figure 13: Dependence of mass transfer on Schmidt number, liquid steel side.

The main conclusions when we compare the two methods are:

▪up to Sc 200-300, the two methods give similar results; it is very encouraging to note that the species diffusion method also provides the $Sc^{-1/2}$ scaling law.
▪for large Sc (> 400), which is our situation for steelmaking systems, we deviate from $Sc^{-1/2}$ scaling law and have $Sc^{-3/2}$; this new result needs to be investigated in more details to understand why the scaling law is depending on Sc with a rupture around Sc=350; there are significant effects on a practical point of view, since low mass transfer coefficient is very detrimental for our process productivity.
▪standard correlations cannot be used but should be adapted for high Sc number; the species diffusion method proposed here is probably the good method to enlarge the validity range of the correlations, since the numerical diffusion is negligible; but we have to keep in mind that LES results should be compared to DNS to better assess the LES reliability near interface when typical length scales for species diffusion are much smaller than the viscous sublayer.

Further calculations were realised, with different interface frictions and Schmidt numbers. Then, a fitting function was built for both liquid steel and slag. Comparison is drawn on Figure 14 (u^*_{ls}=0.0057 m/s, u^*_{sl}=0.0103 m/s).

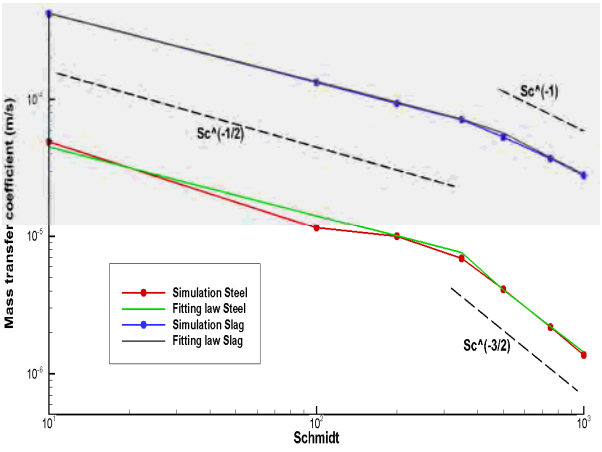

Figure 14: Dependence of mass transfer on Schmidt number, liquid steel and slag sides.

Below are the expressions of the fitting functions:

$$\beta_{ls} = u^*_{ls}\left(B_{ls}Sc^{-1/2} + E_{ls}Sc^{-3/2}\right)$$

$$\beta_{sl} = u^*_{sl}\left(B_{sl}Sc^{-1/2} + E_{sl}Sc^{-1}\right)$$

With :

$$B_{ls} = 0.025 I_{0\text{–}350}$$

$$E_{ls} = 8 I_{350\text{–}1000}$$

$$B_{sl} = 0.13 I_{0\text{–}350}$$

$$E_{sl} = 5 I_{350\text{–}1000}$$

$I_{0\text{-}350}$, $I_{350\text{-}1000}$ are the characteristic Heavyside functions being equal to 1 on the interval and 0 elsewhere.

In the near future, we will have to consolidate those correlations and understand why they are slightly different in liquid steel and slag.

When the correlations are applied in the case of continuous casting mold, the shear stress between liquid steel and slag can be approximated using the assumption of flat free surface with no-slip boundary condition. Then the shear stress is in the range 1-10 Pa and mass transfer in the liquid steel side is approximately 10^{-5} m/s (much smaller than in the slag side), which is coherent with values taken by Chaubal (1992).

CONCLUSIONS

Coupling between fluid dynamics and thermodynamics was realised to predict chemical composition of both liquid steel and slag. To get rid of mesh size dependence, it was proposed to align the time step call to thermodynamic software with the typical diffusion time across the cell near the interface. This coupling can provide qualitative information on chemical evolution but is not suitable for quantitative prediction.

Improvement of the modelling is based on the prediction of the mass transfer coefficient β. Scalar diffusion method was used to calculate β for different Schmidt numbers. Classical dependence β / u^* ~ $Sc^{-1/2}$ was predicted, but the scaling law was changed when Sc > 350. A correlation was proposed for both liquid steel and slag, to be applied in the range 10 < Sc < 1000. Further work will be necessary to test the correlations but the order of magnitude is compatible with values already published.

REFERENCES

ADJOUA, S., (2010), “Développement d'une méthode de simulation de films cisaillés par un courant gazeux”, *Thesis report, Toulouse University*.

ANDERSSON, M., HALLBERG, M., JONSSON, L., JÖNSSON, P., (2002), “Slag-metal reactions during ladle treatment with focus on desulphurisation”, *Ironmaking & Steelmaking*, **29(3)**, 224-232.

BANERJEE, S., LAKEHAL, D., M. FULGOSI, M., (2004), “Surface divergence models for scalar exchange between turbulent streams”, *International Journal of Multiphase Flow*, **30**, 963-977.

CALMET, I., MAGNAUDET, J., (1998), “High-Schmidt number mass transfer through turbulent gas-liquid interfaces”, *International Journal of Heat and Fluid Flow,* **19**, 522-532.

CHAUBAL, P., BOMMARAJU, R., (1992), “Development and use of a model to predict in-mold slag composition during the continuous casting of steel”, *Steelmaking Conference Proceedings,* 665-675.

DOOSTMOHAMMADI, H., ANDERSSON, M., KARASEV, A., JÖNSSON, P.G., (2010), “Use of Computational Thermodynamic Calculations in Studying the Slag/Steel Equilibrium during Vacuum Degassing”, *steel research international*, **81(1)**, 31-39.

FIGUEROA-ESPINOZA, B., LEGENDRE, D., (2010), “Mass or heat transfer from spheroidal gas bubbles rising through a stationary liquid”, *Chemical Engineering Science*, **65**, 6296-6309.

FULGOSI, M., LAKEHAL, D., BANERJEE, S., DE ANGELIS, V., (2003), "Direct numerical simulation of turbulence in a sheared air–water flow with a deformable interface", *J. Fluid. Mech.*, **282**, 319-345.

GARDIN, P., SIMONNET, M., GAUTHIER, S., (2011), "Inclusion elimination in steelmaking ladle", *8th International Conference on CFD in Oil & Gas, Metallurgical and Process Industries, Trondheim.*

HAGEMANN, R., SCHWARZE, R., HELLERAND, H.P., SCHELLER, P.R., (2013), "Model Investigations on the Stability of the Steel-Slag Interface in Continuous-Casting Process", *Metallurgical and Materials Transactions B*, **44B**, 80-90.

HAROUN, Y., (2008), "Etude du transfert de masse réactif Gaz-Liquide le long de plans corrugués par simulation numérique avec suivi d'interface", *Thesis, University of Toulouse*.

JONSSON, L., SICHEN, D., JONSSON, P., (1998), "A New Approach to Model Sulphur Refining in a Gas-stirred Ladle- A Coupled CFD and Thermodynamic Model", *ISIJ International*, **38(3)**, 260-267.

LEHMANN, J., (2008), "Application of ArcelorMittal Maizières thermodynamic models to liquid steel elaboration", *Revue de Métallurgie*, **105 (11)**, 539-550.

PERICLEOUS, K., DJAMBAZOV, G., DOMGIN, J.F., GARDIN, P., (2008), "Dynamic modelling and validation of the metal/flux interface in continuous casting", *6th European Conference on Continuous Casting 2008, Riccione.*

REAL-RAMIREZ, C.A., GONZALEZ-TREJO, J.I., (2011), "Analysis of three-dimensional vortexes below the free surface in a continuous casting mold", *International Journal of Minerals, Metallurgy, and Materials*, 2011, **18(4)**, 397-407.

VINCENT, S., BALMIGÈRE, G., CALTAGIRONE, J.P., MEILLOT, E., (2010), "Eulerian-Lagrangian multiscale methods for solving scalar equations – Application to incompressible two-phase flows", *J. Comput. Phys.*, **229**, 73-106.

STRUCTURE EFFECT OF TURBOSWIRL IN AN UPHILL TEEMING INGOT CASTING PROCESS

Haitong BAI[1*] , Mikael ERSSON[1], Pär G. JÖNSSON[1]

[1] Division of Applied Process Metallurgy, KTH Royal Institute of Technology, SE-100 44 Stockholm, Sweden

* E-mail: haitong@kth.se

ABSTRACT

It would be possible to produce a steel with a better surface quality in the uphill teeming process if a much more stable flow pattern could be obtained in the runners. Several technics have been utilized in the industry to try to obtain a stable flow of liquid steel. For instance, a swirl blade inserted in the horizontal or vertical runners could generate a swirling flow in order to make a lower hump height to avoid mold flux entrapment and to improve the quality of the ingot products. In this research, a new novel swirling flow generation component, TurboSwirl, was introduced to improve the flow pattern. It has recently been demonstrated that the TurboSwirl method could effectively decrease the risk of mold flux entrapment, lower the maximum wall shear stress, and decrease velocity fluctuations. The TurboSwirl is built at the elbow of the runners as a connection between the horizontal and vertical runners. It is located near the mold and it generates a tangential flow that can be used with an expanding nozzle in order to decrease the axial velocity of a vertical flow. This would enable a stable flow before the fluid enters the mold. However, high wall shear stresses appear on the walls due to a fierce rotation in the TurboSwirl. In order to gain a calmer flow and to protect the refractory wall, some structural improvements were applied. It was found that by changing the flaring angle of the outlet nozzle, it was possible to get a lower axial velocity and wall shear stress. Moreover, when the vertical runner was not placed on the centre of the TurboSwirl, a much more beneficial flow pattern was obtained. In addition, the swirling numbers of all the situations above were calculated to ensure that the swirling flow was strong enough to generate a swirling flow of the steel in the TurboSwirl.

Keywords: ingot casting; TurboSwirl; swirling flow; turbulence modeling; flaring angle.

NOMENCLATURE

A complete list of symbols used, with dimensions, is required.

Greek Symbols

α Rotation angle, [°].
ρ Mass density, [kg/m^3].
μ Dynamic viscosity, [Pa·s].
ε Dissipation rate of turbulence energy, [m^2/s^3].

Latin Symbols

G_θ Axial flux of the angular momentum, [m^5/s^2]
G_z Axial flux of the axial momentum, [m^4/s^2]
I Turbulence intensity.
l Turbulence length, [m].
k turbulent kinetic energy, [m^2/s^2]
P Pressure, [Pa]
r enlarged radius, [mm].
R Radius, [m].
S Swirl number.
u Inlet velocity, [m/s].
U Axial velocity, [m/s].
$\boldsymbol{u'}$ Fluctuating velocity vector, [m/s].
$\boldsymbol{U}$ Mean velocity vector, [m/s]
W Tangential velocity, [m/s].

INTRODUCTION

Although the amount of steel production by ingot casting is smaller compared with that cast by continuous casting, it is still highly used by manufacturers of special steel, such as forgings, low-alloyed steel. In addition, to produce a final steel compared with a huge geometry up to several hundred tons, ingot casting is suitable. Two methods are widely used to pour the molten steel from the ladle into the ingot mold, top pouring and bottom pouring (Hurtuk, 2008). The choice of pouring method is of great importance and serious which is determined by final use of the steel ingots. Instead of pouring the molten steel into the ingot directly by top pouring, the bottom pouring (uphill teeming) could result in an ingot steel with a better surface quality. More specifically, it is more stably cast due to the lower turbulence in the pouring process.

During the uphill teeming process, the flow pattern plays a very important role, since an inappropriate flow pattern may induce a high velocity of the liquid steel before pouring into the mold where mold flux entrapment might appear. Therefore, a large consideration of controlling the flow pattern should be taken in advance. Several improvements have been investigated by previous researchers. First, a flaring angle was designed at the entrance of mold, which could reduce the velocity of liquid steel entering the mold and result in a more stable surface to avoid mold flux entrapment (Eriksson et al., 2004). Another way to control flow pattern was to generate a swirling flow, which had been used in numerical simulations and water modelling experiments

of the continuous casting nozzle (Yokoya et al., 1998). Moreover, a twist-tape swirl blade was placed in the SEN to let the liquid steel rotate, which could reduce the uneven flow in continuous casting mold. Then the swirl blade was inserted into either the horizontal or the vertical runner of the ingot casting system for computational fluid analysis indicated that a much more uniform flow pattern were obtained with a calmer filling process (Hallgren et al., 2006, 2010; Tan, et al., 2012). A swirl blade inserted in the runner has a potential risk to be clogged, which may bring in new inclusion to the liquid steel before solidification. Therefore, a new swirling flow generator was introduced, TurboSwirl, which uses the tangential velocity to generate the swirling flow at the intersection of the runners of ingot casting. Studies have been done to demonstrate that a much calmer filling condition was observed during the initial filling stage, which result in a lower hump height and a lower maximum wall shear stress (Tan et al., 2013).

In this work, based on Tan's research (Tan et al., 2013), some structural modifications were made to optimize the flow pattern in order to obtain a more even swirling flow generated by the TurboSwirl device. The flow field in the TurboSwirl was significantly influenced by the outlet of the TurboSwirl. Therefore, the first attempt of the optimization was to change the degree of flaring angle of the outlet nozzle to minimize the axial velocity and the maximum wall shear stress. Furthermore, the swirl number is calculated to make sure that the rotation of liquid steel was strong enough to generate a swirling flow. Further, the position of the outlet nozzle was moved to the off-centre position of the TurboSwirl with different radius and angles. Finally, a prediction of the optimization of the structural design on the outlet nozzle of TurboSwirl or similar structures was carried out.

MATHEMATICAL MODELING

A general Schematic diagram of ingot casting of Tan's research is shown in **Figure 1**. This two-mold gating system was originally used without the TurboSwirl in the industry and can produce 6.2 tons ingots each time (Tan et al., 2013). This new component, TurboSwirl with a flaring angle, was located at the elbow of the horizontal and vertical runner, which is shown with a dashed line in **Figure 1**. Since more attention was paid to the part of the TurboSwirl, a reduced model was built in this research. A specific scheme of the computational domain is shown in **Figure 2** with its original design. The TurboSwirl has a diameter of 150 mm and a height of 50 mm with an outlet nozzle with a 49º flaring angle and 20 mm length. Additionally, a part of the horizontal runner with diameter of 45mm and length of 120mm and vertical runner diameter of 45mm and length of 145mm were also included in the simulations.

The modification of this research involved two parts: first, the flaring angle of the outlet nozzle was altered from 30º to 90º with a series of cases to find trends of the axial velocity and wall shear stress; then, the outlet nozzle together with the vertical runner were placed on several estimated positions around the centre of the TurboSwirl.

The density ρ of the steel in this simulation was 6900 kg/m^3, and the dynamic viscosity μ was 0.006Pa.

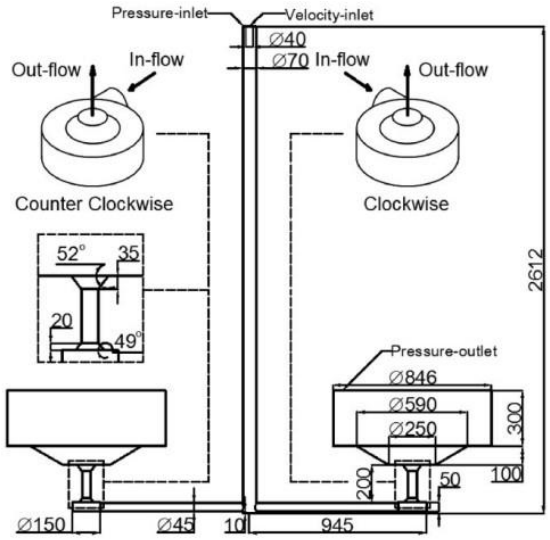

Figure 1: Schematic diagram of ingot casting (Tan et al., 2013).

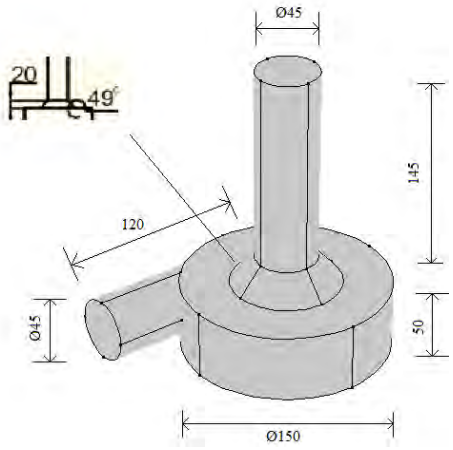

Figure 2: Dimension of computational domain (Original design, unit: mm).

All the simulation were based on the following assumptions: 1) the TurboSwirl is completely filled with molten steel (single phase); 2) the liquid steel is incompressible Newtonian fluid; 3) chemical reaction, heat transfer and solidification are not considered; 4) all the physical properties are constant. These numerical simulations were done by COMSOL Multiphysics® 4.4, and the standard k-ε turbulence model was used to simulate turbulence. Reynolds-averaged Navier-Stokes (RANS) equations were used as transport equations as below (COMSOL, 2012):

$$\rho\frac{\partial \mathbf{U}}{\partial t}+\rho\mathbf{U}\cdot\nabla\mathbf{U}+\nabla\cdot\overline{(\rho\boldsymbol{u}'\otimes\boldsymbol{u}')}=-\nabla \mathrm{P} +\nabla\cdot\mu(\nabla\mathbf{U}+(\nabla\mathbf{U})^{T})+F \quad (1)$$

$$\rho\nabla\cdot\mathbf{U}=0 \quad (2)$$

The transport equations for the turbulent kinetic energy, k, and the dissipation rate of turbulence energy, ε, were (Launder et al., 1974):

$$\rho\frac{\partial \mathrm{k}}{\partial t}+\rho\mathbf{u}\cdot\nabla \mathrm{k}=\nabla\cdot\left(\left(\mu+\frac{\mu_T}{\sigma_k}\right)^T\nabla \mathrm{k}\right)+P_k-\rho\varepsilon \quad (3)$$

$$\rho\frac{\partial \varepsilon}{\partial t}+\rho\mathbf{u}\cdot\nabla\varepsilon=\nabla\cdot\left(\left(\mu+\frac{\mu_T}{\sigma_\varepsilon}\right)^T\nabla\varepsilon\right)+C_{\varepsilon 1}\frac{\varepsilon}{k}P_k+C_{\varepsilon 2}\rho\frac{\varepsilon^2}{k} \quad (4)$$

Where,

$$\mu_T=\rho C_\mu\frac{\mathrm{k}^2}{\varepsilon} \quad (5)$$

$$P_k=\mu_T\left(\nabla\mathbf{u}:(\nabla\mathbf{u}+(\nabla\mathbf{u})^T)-\frac{2}{3}(\nabla\cdot\mathbf{u})^2\right)-\frac{2}{3}\rho k\nabla\cdot\mathbf{u} \quad (6)$$

The model constants in **Equation (3)** - **(6)** were determined from previous work (Launder et al., 1974) and the values are listed in **Table1**.

Table 1: model constants.

C_μ	$C_{\varepsilon 1}$	$C_{\varepsilon 2}$	σ_k	σ_ε
0.09	1.44	1.92	1.0	1.3

The velocity inlet boundary conditions are shown in **Table 2** (Tan et al., 2011). The numbers of cells were different from 80000 to 90000 according to the different flaring angle or outlet nozzle positions.

Table 2: Velocity inlet boundary condition.

u (m/s)	I	l (m)	k (m^2/s^2)	ε (m^2/s^3)
1.0479	0.04096	0.00315	2.763E-3	7.577E-3

RESULTS AND DISCUSSION

The flow pattern has a great influence on the exogenous inclusion generation and mold flux entrapment during uphill teeming, so it is of great importance to improve the flow pattern of the TurboSwirl as part of the whole ingot casting equipment. The fluid field is mainly affected by the dimension of the structure, and the outlet affects most due to the generated swirling flow in the TurboSwirl device. Generally, there is limitation on the height of the vertical runner part, so the height of the outlet nozzle must be fixed. Therefore, the flaring angle was chosen to be altered to change the flow pattern. In this research, the following flaring angles were studied: 30º, 41º, 45º, 49º, 53º, 57º, 63º, 68º, 72º, 80º, 90º, respectively. This series of degrees was determined by several simulations which could represent the physical phenomenon of the scope around every single degree. Examples of TurboSwirl with different degrees of flaring angle are shown in **Figure 3**.

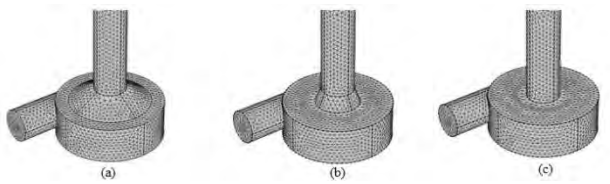

Figure 3: Examples of different degrees: (a): 30º; (b): 68º; (c): 90º.

The molten steel was poured from the horizontal runner into the TurboSwirl, where the steel was forced to begin to rotate around the TurboSwirl device. In this study, the TurboSwirl was assumed under the processing of casting, which means there was nothing but liquid steel in the simulated domain. Due to the effect of the pouring velocity, the liquid steel was pushed to rotate and rise up in the mold for the final solidification. Liquid steel moved along the refractory material where frictions help the steel to slow down the velocity and obtain a calmer flow in the mold. From **Figure 4**, it is clear that the axial velocity increases with an increase of the degree of the flaring angle from 30º to 53º. Then, it fluctuates up to 90º with the highest maximum axial velocity of around 2.2 m/s. If the flaring angle is decreased to a lower degree, which means an enlarging of the outlet nozzle to the edge of the TurboSwirl, a much lower maximum axial velocity could be gained. However, **Figure 4** still shows that the lower degree of flaring angle causes a high maximum wall shear stress, which could result in serious erosion of the refractory surface and a supply of additional inclusions to the liquid steel. Similarly, when the degree comes to 90º, a much higher maximum wall shear stress appears. Furthermore, a 90º angle means that there is no outlet nozzle located on the top of the TurboSwirl. This proves the effect of an outlet nozzle to alleviate the severe fluctuation of the flow field.

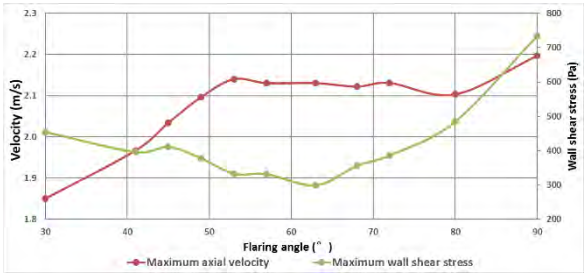

Figure 4: Maximum axial velocity and maximum wall shear stress of different flaring angles.

In order to judge whether the swirling flow was strong enough for achieving a calmer flow or not, the swirl number was calculated from the simulations. The swirl number is a commonly used parameter used to characterise the intensity of swirl in enclosed and fully separated flows, and is defined by the ratio of the axial flux of the angular momentum to the axial flux of the axial momentum (Sheen et al., 1996):

$$S=\frac{G_\theta}{RG_Z}=\frac{\int_0^R UWr^2dr}{R\int_0^R U^2rdr} \quad (7)$$

In this simulation, the bottom area of the outlet nozzle was changed gradually with different flaring angles, so that the swirl number on the bottom of outlet nozzle more precisely can reflect how fierce the rotation flow with a different flaring angle was. Four positions of bottom of outlet nozzle were selected based on the directions where a high wall shear stress usually appeared and they are shown in **Figure 5**. According to **Equation (7)**, the swirl numbers on the four positions of different flaring angles

were plotted in **Figure 6** together with maximum wall shear stress.

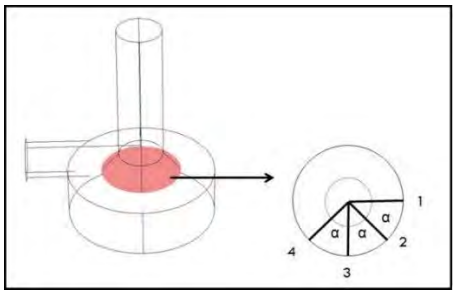

Figure 5: Positions and directions selected for calculating swirl number (α=45º).

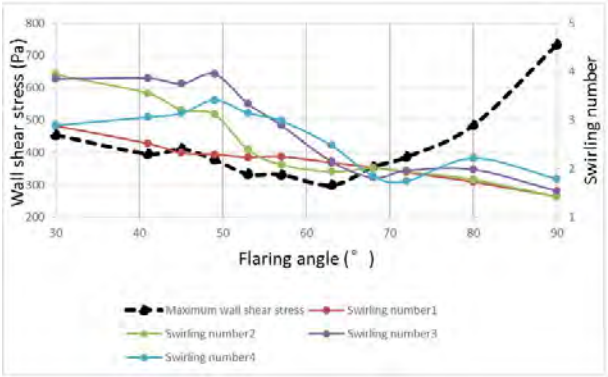

Figure 6: Swirl numbers and maximum wall shear stress of different flaring angles.

High swirl number reflects a fierce rotation, which means the most energy of the fluid is consumed for generating the swirling flow, and in contrast less energy will be carried to the mold leading to a calmer flow. The phenomenon is really expected for the teeming process to supply a lower inlet velocity of the mold and to lower the hump height (Tan et al., 2011). In **Figure 6**, the swirl number is over 2 when the flaring angle is smaller than 60º. This means that, strong rotation happened and that less energy was used to pull up the liquid steel to the mold which results in opposite trend for the maximum axial velocity on **Figure 4**. The swirling flow always has a great dependence on the wall shear stress. A stronger rotation of a fluid induces a high wall shear stress, as seen from the curves of maximum wall shear stress in **Figure 6**. However, when the flaring angle increases to higher values, a lower swirl number induce even higher maximum wall shear stress. This is because the intensity of a swirling flow is not only related to the maximum wall shear stress, but also related to the constraint of the structure. A lower flaring angle value at the bottom of the nozzle outlet has a weak constraint of the swirling flow. However, this is not the major constraint when the value is lower than 60º. Also, the maximum wall shear stress appears at the top part of the outlet nozzle (**Figure7a**). Conversely, a higher flaring angle value (**Figure7c**) makes the whole fluid domain approximately close to the domain without an outlet nozzle (**Figure7d**). Also, a strong constraint was applied to fluid flow, so the maximum wall shear stress appeared at the bottom part of nozzle outlet. As the flaring angles is increased from 30º to 80º, the location of the maximum wall sear stress begin to move down from the top to bottom part (**Figure7b**).

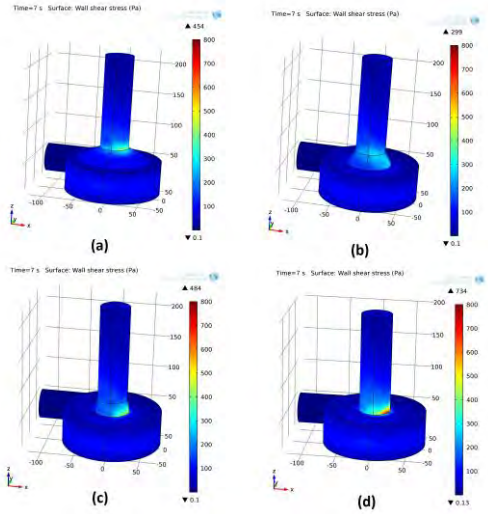

Figure 7: Wall shear stress distribution of different degrees: (a): 30º; (b): 63º; (c): 80º; (d): 90º.

From the discussion above, it is clear that a decreased flaring angle value could generally result in a lower maximum axial velocity and a higher swirl number. Furthermore, a relative high maximum wall shear stress also appeared at the same time. Therefore, a further modification was made to optimize the swirling flow pattern. The aim was to get a lower maximum wall shear stress. The basic principle was to try to avoid the original position of maximum wall shear stress. If the position of the vertical runner together with the outlet nozzle could be moved a little farther from the inlet of the TurboSwirl (horizontal runner), the maximum velocity gradient may not appear on the wall. Instead, a lower maximum wall shear stress may be obtained. In this research, the vertical runner together with the outlet nozzle was moved to an off-centred location with a series of radius and angles, as shown in **Figure 8**. The radius was enlarged from 2.5mm, 5mm, 10mm to 28.65mm (golden ratio to the radius of the radius of TurboSwirl). Furthermore, and the rotation angle α was changed from 90º to -90º based on the cross section of the TurboSwirl. Zone I (0º<α<90º) and zone II (-90º<α<0º) were divided to indicate the approximated area of modifications. The flaring angle of outlet nozzle was still 49º for the original design to enable comparison of the results and to determine if there was any improvement of these modifications.

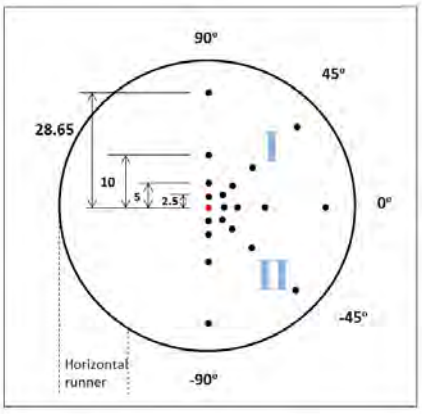

Figure 8: Selected position (black points) with enlarged radius and rotation angles for off-centre calculation (unit: mm).

Since the location of the vertical runner and outlet nozzle were changed, the flow pattern in the TurboSwirl was affected, which can be seen from **Figure 9**. The maximum axial velocity distributes from 1.6 m/s to 2.7 m/s compared to 2.1 m/s of original design (centre located). Generally, the maximum axial velocity in zone II is less than that of in zone I. This is because the liquid steel flowed longer distance and time before entering the outlet nozzle and suffered more constraint from the wall due to the clockwise flow in the TurboSwirl. Specifically, when the enlarged radius is smaller, the minimum values of maximum axial velocity that take place at a rotation angle of -45º, are around 1.6 to 1.8 m/s. However, when the radius is further enlarged, the maximum axial velocity changes slightly according to different rotation angle.

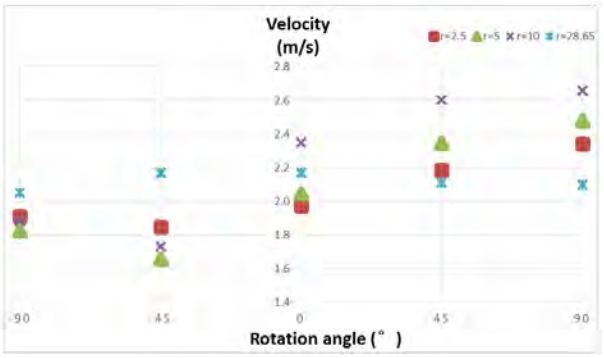

Figure 9: Maximum axial velocity of different positions.

For the maximum wall shear stress, similar trends for the maximum axial velocity are found in **Figure 10**. The maximum wall shear stress with a smaller enlarged radius in zone II are smaller than the values in zone I. Also the values are less than 350 Pa, which shows a great improvement compared to the original design. Although an even lower maximum wall shear stress is found when the radius is enlarged to 28.65 mm, especially in zone I, the swirl numbers in **Figure 11** are nearly 50% smaller than for other smaller enlarged radius. That is because the new position of the outlet nozzle is too far away from the inlet of the TurboSwirl. Thus much more energy is consumed during the swirling flow. Therefore, an excessive off-centre location of the outlet nozzle can reduce the maximum wall shear stress. Meanwhile intensity of swirling flow decreases as well, and relative higher maximum axial velocity appears in **Figure 9**.

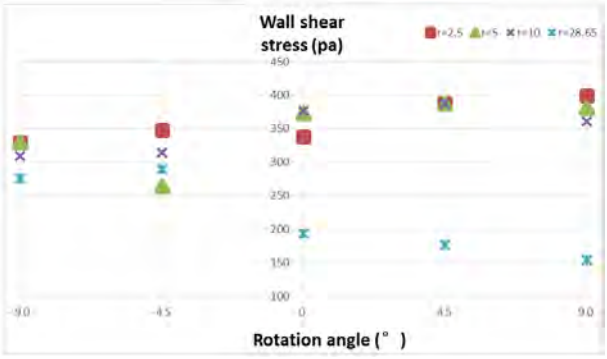

Figure 10: Maximum wall shear stress of different positions.

The swirl numbers in **Figure 11a-11d** show consistent trends compared with **Figure 6**: the swirl numbers increase from swirl number 1 to swirl number 4 gradually. The swirling flow into the outlet nozzle passing the line 1 in **Figure 5** first and passing line 2-4 afterwards, then the intensity increase step by step correspondingly. Except swirl number 4, all the other swirl numbers of same enlarged radius show little dependent by the changing of the rotation angle. Generally, the closer to the centre of the TurboSwirl the location is, the higher swirl number is obtained.

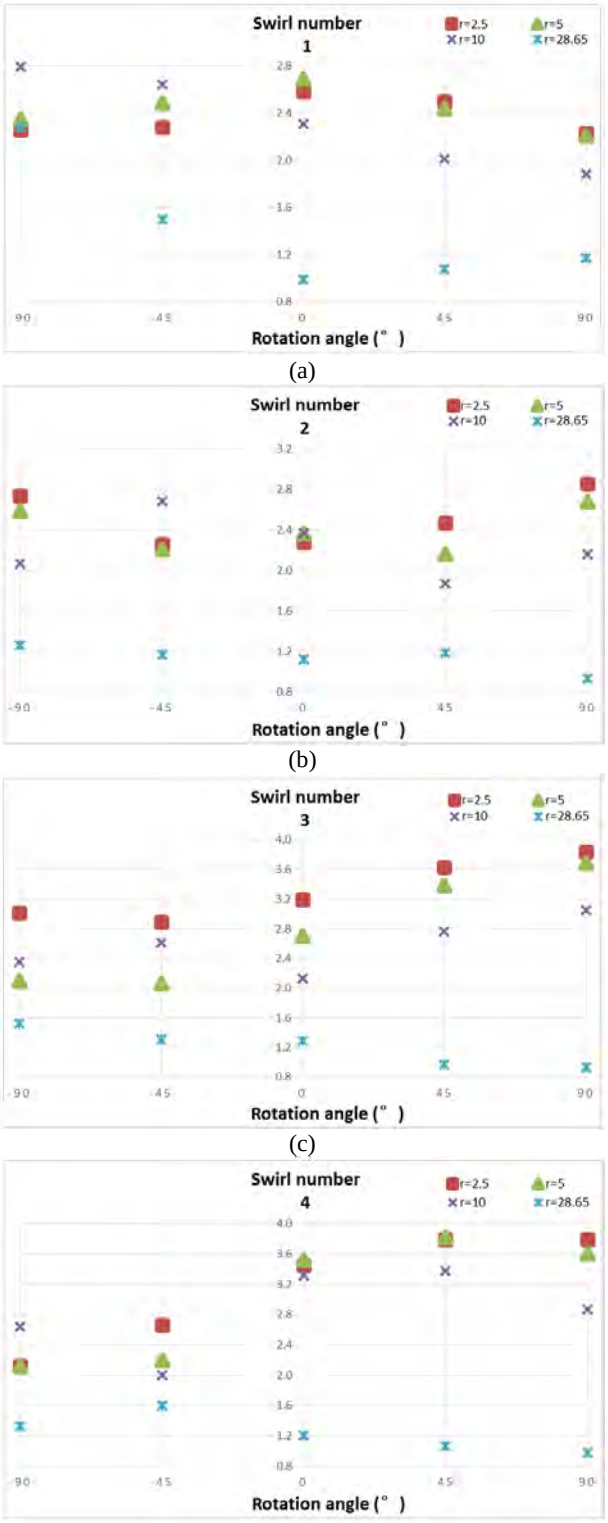

(a)

(b)

(c)

(d)

Figure 11: Swirl number of different positions;
(a): swirl number 1; (b): swirl number 2;
(c): swirl number 3; (d): swirl number 4.

CONCLUSION

This work aims to investigate the structural effect on the flow pattern of an uphill teeming ingot casting process. From the results and analysis above, the conclusion could be gained below:

(1) The flow pattern is influenced much by the structure design with different flaring angle and location of outlet nozzle;
(2) Enlarging the flaring angle of outlet nozzle can result in a lower maximum axial velocity; lower or higher degree of flaring angle causes high maximum wall shear stress;
(3) Swirl numbers on the bottom area of the outlet nozzle were calculated. Swirl numbers of flaring angle less than 60º are dependent of the maximum wall shear stress, and the intensity of swirling flow with higher degree of flaring angle is influenced more by the structural constraint of the TurboSwirl;
(4) The outlet nozzle on zone II could gain a lower maximum wall shear stress to protect refractory wall and a lower maximum axial velocity to lead to a calmer flow in the mold;
(5) When the radius of location of outlet nozzle is enlarged to higher, the maximum axial velocity is independent of the rotation angle. Although a much lower maximum wall shear stress appeared at the same time, but the swirling flow generates lower intensity as well;
(6) The swirl numbers of same enlarged radius changes little on the zone I and II with different rotation angle, higher intensity of swirling flow takes place when the outlet nozzle is placed closer to the centre of the TurboSwirl;
(7) In order to optimize the flow pattern of liquid steel in the TurboSwirl, lower degree of flaring angle could decrease the maximum axial velocity and intensity of swirling flow. The problem of potential high maximum wall shear stress can be solved by moving the location of TurboSwirl with smaller enlarged radius on zone II.

ACKNOWLEDGMENT

The author would like to acknowledge the finical support of China Scholarship Council (CSC).

REFERENCES

D. J. Hurtuk, (2008), "Steel ingot casting", *ASM International*, **15**, 911-917.

R. Eriksson, L. Jonsson, and P.G. Jönsson, (2004), "Effect of entrance nozzle design on the fluid flow in an ingot mold during filling", *ISIJ international*, **44**, 1358-1365.

S. Yokoya, S. Takagi, M. Iguchi, Y. Asako, R. Westof and S. Hara, (1998), "Swirling effect in immersion nozzle on flow and heat transport in billet continuous casting mold" , *ISIJ international*, **38**, 827-833.

L. Hallgren, S. Takagi, R. Eriksson, S. Yokoya and P.G. Jönsson, (2006), "Effect of nozzle swirl blade on flow pattern in runner during uphill teeming", *ISIJ international*, **46**, 1645-1651.

L. Hallgren, A. Tilliander, S. Yokoya, P.G. Jonsson and S. Hagman, (2010), "A first attempt to implement a swirl blade in production of ingots", *ISIJ international*, **50**, 1763-1769.

Z. Tan, M. Ersson and P.G. Jönsson, (2011), "Mathematical modelling of initial filing moment of uphill teeming process considering a trumpet", *ISIJ international*, **51**, 1461-1467.

Z. Tan, M. Ersson and P.G. Jönsson, (2012), "Modeling of initial mold filling with utilization of swirl blades", *ISIJ international*, **52**, 1066-1071.

Z. Tan, M. Ersson, P. Lidegran and P.G. Jönsson, (2013), "Uphill teeming utilizing TurboSwirl to control flow pattern in mold", *Steel research international*, **84**, 837-844.

COMSOL Multiphysics® 4.4, http://www.comsol.se/.

COMSOL, CFD Module User's Guide, (2012), 161-166.

B.E. LAUNDER and D.B. SPALDING, (1974), "THE NUMERICAL COMPUTATION OF TURBULENT FLOWS", *Computer method in applied mechanics and engineering*, **3**, 269-289.

H. J. Sheen, W. J. Chen, S. Y. Jeng and T.L. Huang, (1996), "Correlation of swirl number for a radial-type swirl generator", *Experimental Thermal and Fluid Science*, **12**, 444-451.

Modelling of Tracer Mixing in Continuous Casting Tundishes

Chao CHEN[1,2*] , Anders TILLIANDER[1], Lage T.I. JONSSON[1], Guoguang CHENG[2], and Pär G. JÖNSSON[1]

[1] Division of Applied Process Metallurgy, Department of Materials Science and Engineering, KTH-Royal Institute of Technology, SE-100 44 Stockholm, SWEDEN

[2] State Key Laboratory of Advanced Metallurgy, University of Science and Technology Beijing, 100083 Beijing, P.R.CHINA

* E-mail: cchao@kth.se

ABSTRACT

A mathematical model of a tundish was developed based on water modelling experiment to study the two categories of tracer mixing in tundishes. The mixed composition fluid model was reliable to simulate the tracer and water two phase flow. The measured and predicted black ink propagation contours agree well. Besides, a close similarity between experimental and predicted Residence Time Distribution (RTD) curves was observed in KCl tracer experiment. The two kind of tracers with different densities lead to a different flow behaviour, i.e. the lighter black ink flow up to the top surface. The heavier KCl solution's flow sink to the bottom and form a stagnant region between the tundish walls and the turbo stopper.

Keywords: Mixing, Process Metallurgy, Tundish, Tracer mixing, Alloy mixing.

NOMENCLATURE

Greek Symbols

ρ Mass density, [kg/m^3].

ρ_T Tracer density, [kg/m^3].

ρ_W Water density, [kg/m^3].

μ_{eff} Effective viscosity, [kg/m.s].

μ_l Laminar viscosity, [kg/m.s].

μ_t Turbulence viscosity, [kg/m.s].

k Turbulence kinetic energy, [m^2/s^2].

ε Turbulence kinetic energy dissipation rate, [m^2/s^3].

P_k Turbulence kinetic energy production rate, [m^2/s^3].

δ_{ij} Kronecker delta operator.

Latin Symbols

a Characteristic length, [m].

c_T Local value of the mass concentration for tracer.

c_W Local value of the mass concentration for water.

c_1 Local value of the mass concentration for the scalar in scalar transport equation.

C_μ $C_{1\varepsilon}$ $C_{2\varepsilon}$ $C_{3\varepsilon}$ σ_k σ_ε Constants in turbulence model

D_{eff} Effective diffusion coefficient, [m^2/s].

D_l Laminar diffusion coefficient, [m^2/s].

D_t Turbulence diffusion coefficient, [m^2/s].

p Pressure, [Pa].

Sc_t Turbulence Schmidt number.

$\mathbf{u}$ Velocity vector, [m/s].

Sub/superscripts

i Index *i*.

j Index *j*.

k Index for turbulence kinetic energy.

ε Index for turbulence kinetic energy dissipation rate.

INTRODUCTION

Alloy injections can successful be carried out during the taping of EAF or injection in ladle (ASEA-SKF), CAS, RH degasser etc. in metallurgical industry. On the other hand, a tundish, as a continuous reactor, is also an alternative reactor for alloy mixing. The earliest patent regarding alloying additions in a tundish can be dated back to 1975. (Nemoto et al., 1975). Early attempts were made by Cu addition in tundishes in late 1980s in order to study the fluid flow characteristics and to verify the water modelling and mathematical modelling results. (Szekely, Ilegbusi, 1989), (Vassilicos, Sinha, 1992). Meanwhile, nozzle clogging for the steel containing rare earth element emerged (Zhao et al., 1982). Therefore, a debate against the alloy injection methods (such as wire injection in continuous casting mould, injection of REM alloy in tundish, and ladle) has lasted more than 20 years. Andersson et al. (2006) pointed out that the tundish is the most appropriate reactor to add alloys from a homogenous mixing perspective.

To simulate the alloy dispersion and distribution in metallurgical reactors, there are two aspects to be considered: a) "alloy melting" which considers the alloy melting enthalpy release in the heat transfer process as

well as the alloy shell melting kinetics (Ehrich et al., 1978); b) "alloy mixing" i.e. semi-liquid or liquid alloy melt flow phenomenon and alloy elements diffusion process, can be found in review by Jönsson and Jonsson, (2001).

Regarding the alloy mixing, a number of research works have been focused on alloy mixing during tapping of EAF and in a ladle using CFD method. (Tanaka et al., 1993), (Mazumdar, Guthrie, 1993), (Berg et al., 1999), (Jauhiainen et al., 2001).

The flow pattern of an alloy melt or an inlet stream in a tundish is strongly affected by the thermal buoyancy force and the buoyancy force due to the density difference. Sheng and Jonsson (2000) developed a two fluid mathematical model and investigated the thermal buoyancy effect by introducing the inlet stream with a temperature variation as the second fluid while maintaining the original liquid in the bath as the first fluid. Based on a tundish water model, Damle and Sahai (1995) studied the buoyancy force using the density difference of KCl solution tracer and water. The single phase fluid density was set as a linear function of KCl solute concentration. Chen et al. (2012 a) summarized their water modelling results and addressed that larger amount of denser salt tracer will influence on the fluid flow behaviour significantly.

Before establishing a thoroughly mathematical model to study the alloy mixing phenomenon in a steel tundish, a mathematical model based on Chen et al.'s (2012 a) 0.4-scaled water model tundish was developed to study the tracer mixing in water model tundish. A mixed composition fluid model was used to describe the water and tracer phase. Two categories of tracer flow behaviours in the water model tundish were studied. The simulations were validated with the experimental results, i.e. the mixing of less denser black ink in water; the mixing of denser KCl salt solution in water.

MODEL DESCRIPTION

Model Assumption

The three dimensional mathematical model is based on the following assumptions:
1) This current model is a full size tundish based on the water modelling geometry as shown in **Figure 1**.
2) Chen-Kim *k-ε* turbulence model is used to describe the turbulence phenomenon in the tundish.
3) Water and tracers are assumed as the liquid phase. The dissolution of the tracer solute, which corresponds to the alloy shell melting process, is not involved.
3) The top surface is flat and frictionless.
4) The heat transfer process is not studied.
5) The chemical reactions are not accounted for.

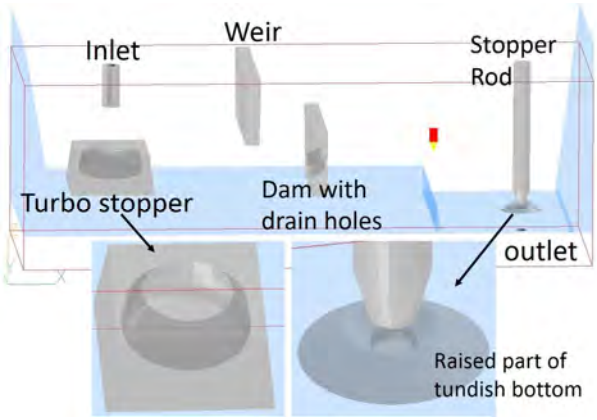

Figure 1: Schematic diagram of tundish geometry.

Governing Equations

Continuity equation

$$\frac{\partial \rho}{\partial t}+\frac{\partial}{\partial x_i}(\rho \mathbf{u}_i)=0 \qquad (1)$$

Momentum equation

$$\frac{\partial(\rho \mathbf{u}_i)}{\partial t}+\frac{\partial(\rho \mathbf{u}_j \mathbf{u}_i)}{\partial x_j}=-\frac{\partial p}{\partial x_j}+\frac{\partial}{\partial x_j}\left[\mu_{eff}\left(\frac{\partial \mathbf{u}_i}{\partial x_j}+\frac{\partial \mathbf{u}_j}{\partial x_i}\right)\right]-\rho g \delta_{3j} \qquad (2)$$

where effective viscosity is the sum of laminar viscosity and turbulence viscosity $\mu_{eff}=\mu_l+\mu_t$. The gravity is active in negative z direction as the Kronecker delta operator δ_{3j} indicates.

Turbulence Model

The turbulence viscosity is given as follows:

$$\mu_t=\rho C_\mu \frac{k^2}{\varepsilon} \qquad (3)$$

where C_μ =0.09. (Launder, Spalding, 1974). k and ε are turbulence kinetic energy and turbulence kinetic energy dissipation rate, respectively.
Chen-Kim *k-ε* turbulence model (Chen and Kim, 1987) assumes spectral non-equilibrium and existence of both turbulence production rate time scale k/P_k and turbulence dissipation rate time scale k/ε, where P_k is the production rate of turbulence kinetic energy. In eq. (5), as the third term at the RHS, an extra source term represents the turbulence energy transfer rate from large-scale to small-scale turbulence controlled by the production-range timescale. This turbulence model has shown advantages in simulations applied for metallurgical industry (Ni et al., 2013). The equations of kinetic energy and dissipation rate in Chen-Kim *k-ε* turbulence model are as follows:

$$\rho\frac{\partial k}{\partial t}+\frac{\partial}{\partial x_i}\left[\rho k \mathbf{u}_i-\frac{\mu_t}{\sigma_k}\frac{\partial k}{\partial x_i}\right]=\rho(P_k-\varepsilon) \qquad (4)$$

$$\rho\frac{\partial \varepsilon}{\partial t}+\frac{\partial}{\partial x_i}\left[\rho \varepsilon \mathbf{u}_i-\frac{\mu_t}{\sigma_\varepsilon}\frac{\partial \varepsilon}{\partial x_i}\right]=\rho\frac{\varepsilon}{k}(C_{1\varepsilon}P_k-C_{2\varepsilon}\varepsilon)+\rho C_{3\varepsilon}\frac{P_k{}^2}{k} \qquad (5)$$

where $C_{1\varepsilon}$ =1.15, $C_{2\varepsilon}$ =1.9, $C_{3\varepsilon}$ =0.25, σ_k =0.75, σ_ε =1.15, are the constants in the model. The production rate of turbulence kinetic energy P_k is related to the mean strain of the velocity field as follows:

$$P_k = \frac{\mu_t}{\rho}\left[\begin{array}{l}\left(\frac{\partial \mathbf{u}_i}{\partial x_j}+\frac{\partial \mathbf{u}_j}{\partial x_i}\right)^2 + \\ 2\left(\left(\frac{\partial \mathbf{u}_i}{\partial x_i}\right)^2+\left(\frac{\partial \mathbf{u}_j}{\partial x_j}\right)^2\right)\end{array}\right] \quad (6)$$

Treatment of tracer

The mixed composition fluid model

The mixed composition fluid model is used to predict the tracer flow within the water as follows:

$$\frac{\partial}{\partial t}(\rho_W c_W)+\frac{\partial}{\partial x_i}(\rho_W \mathbf{u}_i c_W)=\frac{\partial}{\partial x_i}\left(\rho_W D_{eff}\frac{\partial c_W}{\partial x_i}\right) \quad (7)$$

$$\frac{\partial}{\partial t}(\rho_T c_T)+\frac{\partial}{\partial x_i}(\rho_T \mathbf{u}_i c_T)=\frac{\partial}{\partial x_i}\left(\rho_T D_{eff}\frac{\partial c_T}{\partial x_i}\right) \quad (8)$$

where the local value of the mass concentration for water c_W initially has value 1 in the regions where there is only water and has the value 0 in the regions where initially only contained tracer. Similarly, c_T has values of 0 and 1 in the regions where the tundish initially contains only water and tracer. This method was also used by Grip et al., (1997).

The effective diffusion coefficient is the sum of laminar diffusion coefficient and turbulence diffusion coefficient $D_{eff} = D_l + D_t$. In this study, the laminar diffusion coefficient of tracer was not considered. The turbulence diffusion coefficient can be derived as follows:

$$D_t = \frac{\mu_t}{\rho Sc_t} \quad (9)$$

where Sc_t is the turbulence Schmidt number, which is set 1.0 in the model.

The density of the fluid in all the continuity, momentum, and turbulence equations is calculated as follows:

$$\frac{1}{\rho}=\frac{c_W}{c_W+c_T}\frac{1}{\rho_W}+\frac{c_T}{c_W+c_T}\frac{1}{\rho_T} \quad (10)$$

where ρ_W and ρ_T are the density of water and tracer, respectively.

Solving the scalar transport equations only

Apart from the mixed composition fluid model, a simple one phase scalar transport model without considering the tracer density difference was used to describe the "tracer" concentration distribution and variation with the incoming stream in tundish. Rigidly, this tracer was not the physical tracer as discussed before, and this tracer could be a flow tracing scalar. In this case, the following equation is solved.

$$\frac{\partial}{\partial t}(\rho_W c_1)+\frac{\partial}{\partial x_i}(\rho_W \mathbf{u}_i c_1)=\frac{\partial}{\partial x_i}\left(\rho_W D_{eff}\frac{\partial c_1}{\partial x_i}\right) \quad (11)$$

where c_1 has values 0 and 1 in the regions where the tundish initially contains only water and this flow tracing scalar. The density of the "tracer" was the same with the water. The laminar diffusion coefficient of the scalar was not considered. The velocity field $\mathbf{u}_i$ was already known from a steady state simulation and remained constant during the calculation. This method is the same as Andersson et al. (2013) did.

Boundary Conditions

1) The inlet velocity in z direction is set as a constant value -0.905875 m/s determined by the experiment values.
2) The turbulence intensity is assumed to be 1% in the inlet.
3) The pressure is set to a constant and is equal to the atmosphere at the outlet.
4) The top surface is flat and frictionless.
5) The x-z plane at the middle of the y direction of tundish is set as symmetry plane where the velocity in y direction is set as zero.
6) The roughness of the inlet shroud, turbo stopper, stopper rod and the raised part of the tundish bottom near the stopper rod are set to 1×10^{-5} m, the roughness in other solid walls are set to 2×10^{-6} m. A log-law wall function is employed for all solid walls.

Initial Conditions

The tracer injection is a pulse process.
1) During the tracer injection time steps, c_W = 1.0 and c_T =0 in the whole region cells except the tracer injection cells, while in the tracer injection cells, c_W = 0 and c_T =1.0.
2) After the injection time steps, c_W = 1.0 and c_T =0 in the tracer injection cells.

In this study, the tracer injection cells are 6 cells (height 0.056m) beneath the inlet in the pipe. The time step for black ink tracer is 0.12s corresponding to 50mL in water model experiment. The time step for KCl saturated salt solution tracer is 0.6s corresponding to 250mL in water model experiment.

Properties

The density of water is 998.2kg/m^3. The tracer density is 1163.2kg/m^3 for the saturated KCl solution and 950kg/m^3 for the black Ink study, respectively.

Numerical Procedure

The solution of the governing equations with boundary conditions and initial conditions are obtained using the commercial software package PHOENICS (2012) which is based on Finite Volume Method. The geometry and the coordinate system are shown in **Figure 1**, the domain in the Cartesian coordinate system is discretized into 168×71×70 cut-cell girds as illustrated in **Figure 2**. The red box in the figure is the monitor probe.

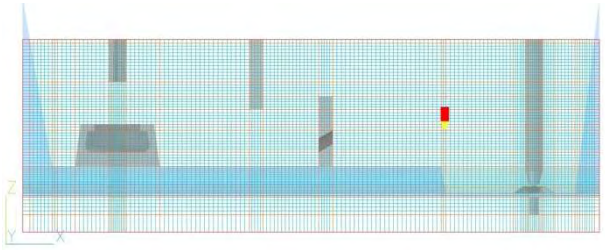

Figure 2: Grid used in the mathematical model.

The discretisation of all terms are using SMART scheme, which will reduce the numerical diffusion errors. (Gaskell and Lau, 1998). The solution algorithms for velocity and pressure are using the Semi-Implicit Method for Pressure-Linked Equations ShorTened, abbreviated as SIMPLEST method (Spalding, 1980), which is a modified version of well-known SIMPLE method (Patankar and Spalding, 1972).

The initialization of transient simulation case was based on a steady state simulation result. The steady state calculation needed 19000 iterations to reach the cut off error of 1×10^{-5}. For the transient simulation, the time step was gradually increased e.g. 0.06s, 0.075s, 0.09375s, 0.1125s, 0.135s, 0.1575s, 0.18s, and 0.225s with 30 to 80 iterations in each time step. A typical calculation for a 552s transient simulation took about 280h on a pc Intel core i7 with a 3.4 GHz processor and 32GB RAM.

In the one phase scalar transport model, the time step was 0.04s with 30 iterations, and it took 100h for a 80s transient simulation.

RESULTS

Steady state velocity field

The steady state flow field is shown in **Figure 3, 4, 5**. As shown in **Figure 3**, the inlet stream hits the turbo stopper and rebound to the surface. Furthermore, the rebound fluid flow up to the tundish left wall corner and forms a small vortex. Similarly, the rebound flow form a recirculation flow at the right side near the weir. There is a strong trend that the fluid flows above the dam towards the surface. From **Figure 4**, the fluid also flows through the dam holes, which were designed for tundish drainage (Chen et al., 2012 b). Near the outlet, the fluid flow into the tundish outlet-nozzle follows the sudden contraction shape as shown in **Figure 5**.

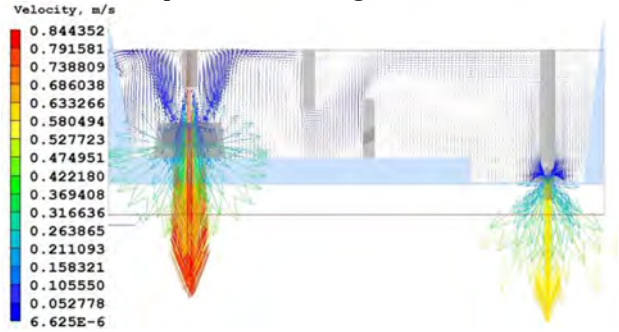

Figure 3: Velocity vectors from a steady state simulation at x-z plane in the center of y direction.

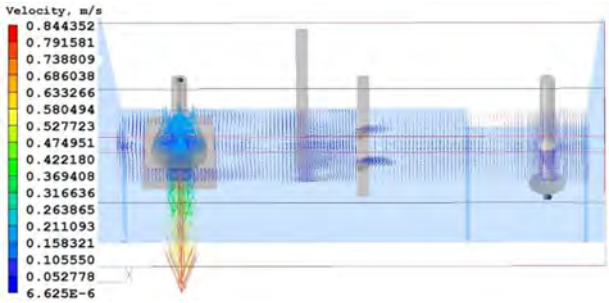

Figure 4: Velocity vectors from a steady state simulation at the x-y plane.

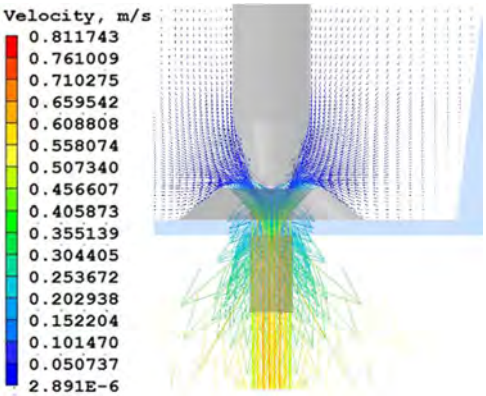

Figure 5: Velocity vectors near the tundish nozzle from a steady state simulation at x-z plane in the center of y direction.

Validation with black ink experiment

The black ink is recorded by photographs in the water modelling experiments. These photos consisted as overlapped x-z planes. The ink concentration iso-surfaces are used for the validation instead of the concentration contours. The iso-surface of the minimum concentration value in the current time step is chosen because this value represents the black ink propagation edge. A comparison of the results are shown in **Figure 6-Figure 9** for 1s, 6s, 70s, 110s, respectively. As can be seen in **Figures 6** to **9**, the agreement of the dispersion profiles between the black ink water model and the mathematical model simulation is fairly good.

Figure 6: Black ink dispersion photo in the water model compared to simulated tracer concentration iso-surface of mathematical model at time 1s.

Figure 7: Black ink dispersion photo in the water model compared to simulated tracer concentration iso-surface of mathematical model at time 6s.

In **Figure 6** and **Figure 7,** the black ink flows towards to top surface at 1s and 6s. There is small difference between the experimental and mathematical modelling results for the 6s. In the mathematical modelling, the ink concentration dispersed to the weir but it does not reach the weir as in water modelling result shows, this can be attributed to the strong molecule diffusion of the ink material itself, which is not considered in the mathematical modelling.

On the other hand, the wave motion occurs at the free surface near the tundish inlet as was stressed by Szekely and Ilegbusi (1989). In the water model experiments, the presence of a surface wave fluctuation in the inlet area was observed which may promote the black ink dispersion. Furthermore, the weir which was located near the inlet also supports the wave motion by reducing the free surface space for the wave propagation.

While in the mathematical modelling a flat and frictionless top surface is assumed and therefore cannot describe the wave behavior.

Figure 8: Black ink dispersion photo in the water model compared to tracer concentration iso-surface of mathematical model at time 70s.

In **Figure 8,** the mathematical model can predict the mixing of the stream flow above the dam and the stream flow throughout the holes fairly well. These two streams start to mix at time 70s.

Figure 9: Black ink dispersion photo in the water model compared to tracer concentration iso-surface of mathematical model at time 110s.

The result at time 110s in shown in **Figure 9**. The black ink is diluted and opaque in the water modelling photos, but the propagation shape is very similar between the simulations and the experiments.

Besides, the black ink in the water modelling experiment is viscous than water. The different viscosities of ink and water may also cause a difference while this difference was not considered in this investigation.

Validation with KCl tracer RTD curve

The KCl solution concentration was measured by a conductivity probe located in the outlet as described in Chen et al.'s (2012a). If an instantaneous concentration is plotted as a function of time, that's Residence Time Distribution (abbreviated as RTD) curve which is widely used for the flow analysis in continuous reactors in metallurgical and chemical engineering industry.

From the point of view of mathematical modelling, most of the studies predict the RTD curve by stop solving all the other equations and by solving only the scalar transport equation. In the current study, the density as a function of the mass concentration of tracer is coupled in all the continuity, momentum, turbulence equations which can describe the density effect. A comparison of the experiment and the mathematical RTD curve is shown in **Figure 10**.

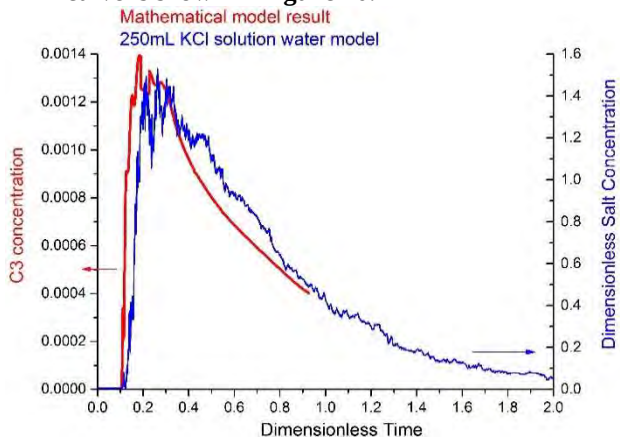

Figure 10: KCl tracer RTD curve in the water model experiments and a comparison with mathematical model prediction results.

The current mathematical model only simulates 552s (dimensionless time 0.927). Besides, the concentration is not transformed to the dimensionless value, since this

analysis requires the ensemble average of the whole RTD curve.

The start period of the RTD curve is magnified as shown in **Figure 11**. The dimensionless breakthrough time 0.108 in mathematical model. That value is acceptable compared with the value 0.125 from the water modelling. Different from smooth RTD curve in the scalar transport equation solving method results (Chen et al. 2012a), the concentration fluctuations occurred in the current mathematical model RTD curves which can be attributed to the unstable flow of the tracer throughout the outlet. Essentially, this type of flow is often observed in the water modelling results as well.

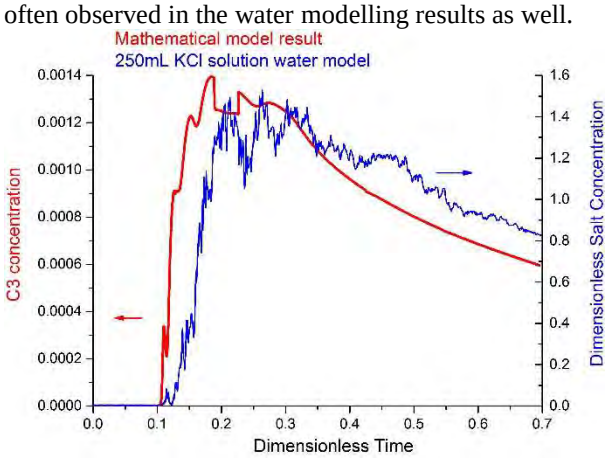

Figure 11: KCl tracer RTD curve in the water model experiments and a comparison with mathematical model prediction results (dimensionless time from 0 to 0.69).

The discrepancies as shown in **Figure 10** and **Figure 11** may be improved by adding the laminar diffusion coefficient for KCl something that was not considered in the current study.

Tracer density discussion

The tracer concentration contours of ink and KCl solution and the scalar transport equation result are shown in **Figure 12**. The variable C1 in **Figure 12 a)** is the concentration of the scalar c_1 in equation (11), similarly the variable C3 in **Figure 12 b),c)** and **Figure 13** are c_T in equation (8).

The black ink density is 4.8% less than that of water, and the concentration contour shows a small difference. On the contrary, the density of the KCl saturated solution is 16.4% heavier than that of water. Therefore, the flow will sink to the bottom against the rebounded flow in the turbo stopper.

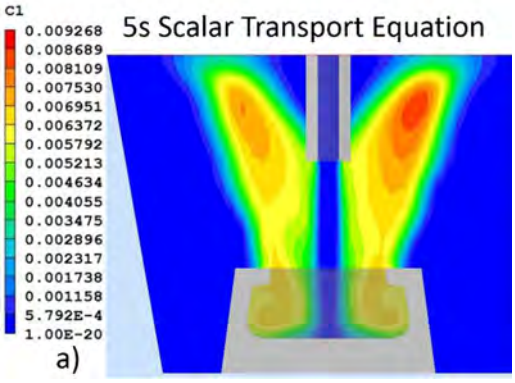

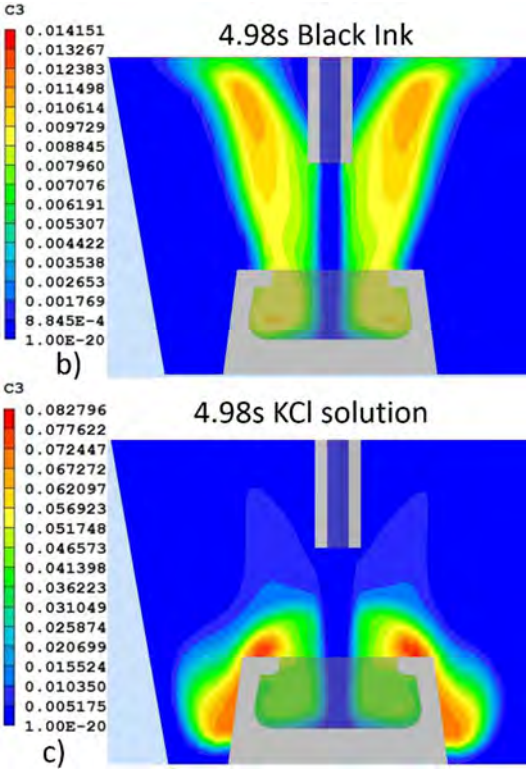

Figure 12: Mathematical model results of a) the scalar transport equation, b) black ink, c) KCl solution tracer contours at 5s at x-z plane in the center of y direction.

The concentration contours at 19.98s are compared, as shown in **Figure 13.** It's clear to see that the heavier KCl salt tracer sinks to the bottom. However, the lighter black ink tracer flow up to the top surface.

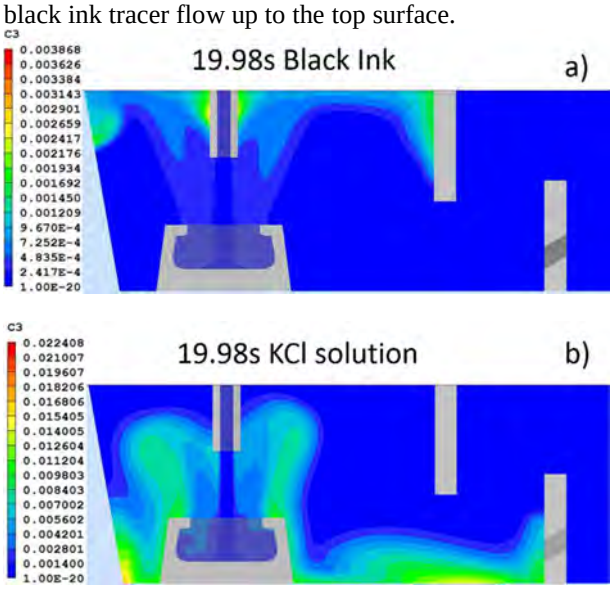

Figure 13: Mathematical model results of a) black ink, b) KCl solution tracer contours at 19.98s at x-z plane in the center of y direction.

From **Figure 13 b)**, the KCl concentration is big at the region between the turbo stopper and tundish left wall. To further compare the sinking of the KCl tracer to the bottom, the iso-surfaces with a fixed KCl concentration value of 0.006 at time 30s, 75s, 150s, 200s are compared in **Figure 14**. Since the tundish is a continuous reactor and the tracer was injected for a time period instead of continuously input, the concentration of KCl tracer will decrease with time. The 30s result in **Figure 14** shows that the tracer flows throughout the

holes in the dam. The 75s result indicates that there is a large area below the holes with this concentration 0.006. Even at 150s and 200s, the tracer with this concentration level 0.006 can be found around the turbo stopper and the walls. For the 200s result, there is a "blank" near the tundish left wall in the iso-surface figure; this could be explained as the strong turbulent flow and mixing at the center of y direction.

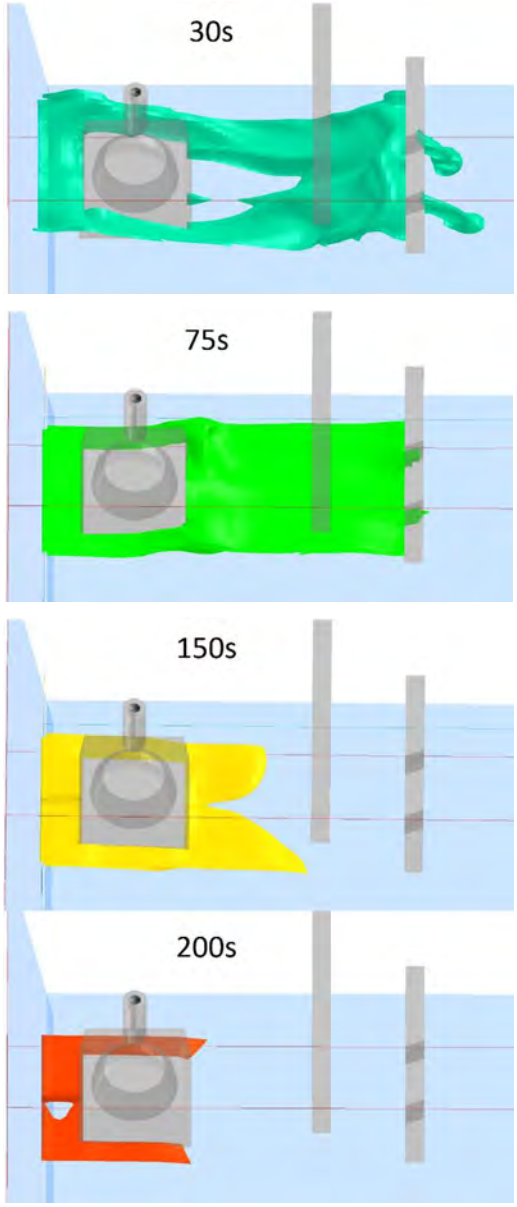

Figure 14: KCl solution iso-surfaces with the concentration value 0.006 at different time, 30s, 75s, 150s, 200s.

It's clear that the KCl tracer sink in the region between the walls of tundish and the turbo stopper. This stagnant region will influence the homogenization of tracer concentration in the whole tundis. This suggests it's important to consider the stagnant region for heavier alloys mixing in a real steel tundish.

CONCLUSION

The two categories of tracer flow in tundish water modelling were simulated using a 3D mathematical model. The following conclusions were obtained:

1. The mixed composition fluid model was reliable to simulate the tracer and water two phase flow. The measured and predicted black ink propagation contours agree well. Besides, a close similarity between experimental and predicted RTD curves was observed in KCl tracer experiment.
2. The two kind of tracers with different densities lead to different flow behaviour in tundish, i.e. the lighter black ink flows up to the top surface, and the heavier KCl solution flow sinks to the bottom.
3. Since the density of KCl saturated solution is 16.4% heavier than water, the KCl solute will sink to the tundish bottom. This results in a stagnant region between the left walls of tundish and the turbo stopper.

FURTHER WORK

1. The molecule diffusion coefficient of KCl solute could be involved in a further model.
2. The fluid viscosity as a function of the mass concentration of tracer could be involved to check the effect of viscosity on fluid flow and mixing.
3. This model can be applied to simulate the molten alloy mixing in a steel tundish. Both with respect to a smaller amount of alloy mixing as a stimulus input and for a continuous feeding. Based on these, the model can be extended to combine the alloy particles with a solid shell melting kinetics. Moreover to couple thermodynamics to involve the alloy dissolution process.

REFERENCES

ANDERSSON, M., APPELBERG, J., TILLIANDER, A., NAKAJIMA, K., SHIBATA, H., KITAMURA, S., JONSSON, L. And JÖNSSON, P., (2006), "Some Aspects on Grain Refining Additions with Focus on Clogging during Casting", *ISIJ Int.*, **46,** 814-823.

ANDERSSON, N.Å.I., TILLIANDER, A., JONSSON, L. and JÖNSSON, P., (2013), "Fundamental Decarburization Model of AOD Process", *Ironmak. Steelmak.*, **40,** 390-397.

BERG, H., LAUX, H., JOHANSEN, S.T. and KLEVAN, O.S., (1999), "Flow pattern and alloy dissolution during tapping of steel furnaces", *Ironmak. Steelmak.*, **26,** 127-139.

CHEN, C., CHENG, G., SUN, H., HOU, Z., WANG, X. and ZHANG, J., (2012a), "Effects of Salt Tracer Amount, Concentration and Kind on the Fluid Flow Behaviour in a Hydrodynamic Model of Continuous Casting Tundish", *Steel Res. Int.*, **83,** 1141-1151.

CHEN, C., CHENG, G., SUN, H., WANG, X. and ZHANG, J., (2012b), "Optimization of Flow Control Devices in a Stainless Steel Tundish", *Adv. Mater. Res.*, **476-478,** 156-163.

CHEN, Y.S. and KIM, S.W., (1987), "Computation of Turbulent Flows using an extended k-ε Turbulence Closure Model", *NASA Report*, NASA CR-179204.

DAMLE, C. and SAHAI, Y., (1995), "The Effect of Tracer Density on Melt Flow Characterization in Continuous Casting Tundishes- A Modeling Study", *ISIJ Int.*, **35,** 163-169.

EHRICH, O., CHUANG, Y.K. and SCHWERDTFEGER, K., (1978), "The Melting of Metal Spheres Involving the Initially Frozen Shells with Different Material Properties", *Int. J. Heat. Transfer*, **21,** 341-349.

GASKELL, P.H. and LAU, A.K.C., (1988), "Curvature-compensated Convective Transport: SMART, a New Boundedness-preserving Transport Algorithm", *Int. J. Num. Meth. Fluids*, **8,** 617.

GRIP, C.E., JONSSON, L. and JÖNSSON, P.G., (1997), "Prediction of Emptying Flows in Ladles and Verification with Data from Trace Element Plant Trails", *ISIJ Int.*, **37,** 1081-1090.

JAUHIAINEN, A., JONSSON, L. and SHENG, D.Y., (2001), "Modelling of alloy mixing into steel- Influence of porous plug placement in the ladle bottom on the mixing of alloys into steel in a gas-stirred ladle", *Scand. J. Metall.*, **30,** 242-253.

JÖNSSON, P.G. and JONSSON, L.T.I., (2001), "The Use of Fundamental Process Models in Studying Ladle Refining Operations", *ISIJ Int.*, **41,** 1289-1302.

LAUNDER, B.E. and SPALDING, D.B., (1974), "The Numerical Computation of Turbulent Flows", *Comp. Meth. In Appl. Mech. & Eng.*, **3,** 269.

MAZUMDAR, D. and GUTHRIE, R.I.L., (1993), "Motions of Alloying Additions in the CAS Steelmaking Operations", *Metall. Trans. B*, **24B,** 649-655.

NEMOTO, H., KAWAWA, T., SATO, H., SAKAMOTO, E., KOYANO, T. and ANZAI, T., (1975), "Method of Adding Rare Earth Metals or Their Alloys into Liquid Steel", *US Patent*, US3871870.

NI, P., JONSSON, L.T.I., ERSSON, M., and JÖNSSON, P., (2013), "Turbulent Flow Phenomena and Ce_2O_3 Behavior during a Steel Teeming Process", *ISIJ Int.*, **53,** 792-801.

PATANKAR, S.V. and SPALDING, D.B., (1972), "A Calculation Procedure for Heat, Mass and Momentum Transfer in Three-Dimensional Parabolic Flows", *Int. J. Heat Mass Transfer*, **15,** 1787-1806.

PHOENICS, 2012. PHOENICS-VR Reference Guide, in CHAM TR 326, CHAM, London.

SHENG, D.Y. and JONSSON, L., (2000), "Two-Fluid Simulation on the Mixed Convection Flow Pattern in a Non isothermal Water Model of Continuous Casting Tundish", *Metall. Mater. Trans. B*, **31B,** 867-875.

SPALDING, D.B., (1980), "Mathematical Modeling of Fluid Mechanics, Heat Transfer and Mass Transfer Processes", *Report HTS/80/1*, Mechanical Engineering Department, Imperial College of Science, Technology and Medicine, London.

SZEKELY, J. and ILEGBUSI, O.J., (1989), "The Physical and Mathematical Modeling of Tundish Operations", Springer-Verlag, Berlin, 49.

TANAKA, M. MAZUMDAR, D. and GUTHRIE, R.I.L., (1993), "Motions of Alloying Additions during Furnace Tapping in Steelmaking Processing Operations", *Metall. Tran. B*, **24B,** 639-648.

VASSILICOS, A. and SINHA, A.K., (1992), "Tracer property effects on computed and measured response in continuous casting tundishes", *Proc. 10th Process Tech. Conf.*, I&S Society, Toronto, April, 187.

ZHAO, S., SHEN, F., HAN, Q. And SHAO, G., (1982), "Study on the Nozzle blockage Mechanism of Steel Containing Rare Earth Metals during Casting", *Iron and Steel*, **17,** 24-31. (In Chinese).

ACKNOLEDGEMENT

One of the authors, Chao Chen wants to thank CSC (Chinese Scholarship Council) for the financial support of his study at KTH, Sweden.

Chao Chen would also express his appreciation to:

i) Mr. Hailong Liu, Tech. Lic. Peiyuan Ni and Dr. Nils Å.I. Andersson in Division of Applied Process Metallurgy, KTH for their fruitful discussion regarding the PHOENICS software settings;

ii) Prof. Jiaquan Zhang, Dr. Haibo Sun in Department of Ferrous Metallurgy, University of Science and Technology Beijing (USTB) for fruitful discussions on mathematical modelling of tundish during March to July 2011;

iii) Dr. Fang Jiang, Dr. Zhe Qin, Dr. Qixuan Rui in State Key Laboratory of Advanced Metallurgy, University of Science and Technology Beijing (USTB) for fruitful discussions on modelling of alloy injection during May 2010 to September 2012.

Numerical Investigation of the Immersion Quenching Process for Heat Treated Parts Using an Eulerian Multi-Fluid Approach

R. KOPUN[1] , D. GREIF[1], Z. KOVACIC[1], M. SUFFA[2*]

[1] AVL AST doo, Maribor, SLOVENIA

[2] AVL List GmbH, Graz, AUSTRIA

Corresponding author's e-mail: maik.suffa@avl.com

ABSTRACT

This paper summarizes a computational methodology to predict by simulation the heat transfer between a heat-treated casted part and a quenchant (e.g. water). The numerical model implemented in the commercial Computational Fluid Dynamics (CFD) code AVL FIRE® v2013.1 accounts for the phase change within the quenchant due to the heat released from a heated casted part when submerged into the sub-cooled liquid by using an Eulerian multi-fluid modeling approach. Simulation results are presented and compared with measured data. Different solid part orientations were studied on a step-plate, a test piece with segments of varying thickness along its height, in respect to resulting solid temperatures and stresses. With the applied methodology the predicted temperature gradients in the solid material correlate very well with the provided experimental data. The paper will also provide examples for the industrialization of the method.

Keywords: CFD, hydrodynamics, chemical reactors.

NOMENCLATURE

Greek Symbols

α	Volume fraction	[-]
ρ	Density	[kg/m^3]

Latin Symbols

C	Constant	[-]
d	Diameter	[m]
Eo	Eötvös number	[-]
F	Force	[N]
n	Normal vector	[-]
p	Pressure	[N/m^2]
Re	Reynolds number	[-]
T	Temperature	[K]
v	Velocity	[m/s]
y	Distance	[m]
z	Height	[m]

Sub/superscripts

b	bubble
c	continuous
d	dispersed
h	maximum vertical dimension of a bubble
l	liquid
L	lift
max	maximum
min	minimum
v	vapor
w	wall
WL	wall lubrication

INTRODUCTION

Modern powertrain development is driven in direction of weight reduction by replacing heavier metals with low-cost alloys for industries such as automotive, aerospace and process engineering. Accurate prediction and optimization of the heat treatment process of cast parts is important in order to achieve low residual stress levels resulting from even temperature distribution during the cooling process and thereby prevent component failure during operation. Among all other heat treatment techniques, immersion quenching process has long been identified as one of the most important ways how to fulfil the aforementioned requirements. In order to achieve the desirable microstructure and mechanical properties of the metal piece, solid is heated to a very high temperature and then immediately submerged into a sub-cooled liquid [1, 2].

The paper outlines the recently improved Eulerian multi-fluid modeling approach implemented within the commercial CFD code AVL FIRE®, where the combination of the additional interfacial forces and variable Leidenfrost temperature is used. Simulation results of a real-time quenching process featuring different thicknesses along the height of the test piece are compared and discussed with the available measurement data. The temperature gradients predicted by the presented model correlate very well with the provided measurement data and represent a reliable spatially resolved temperature input for later Finite Element Analysis (FEA) of thermal stresses.

MODEL DESCRIPTION

Eulerian multi-fluid model considers each phase as interpenetrating continua coexisting in the flow domain, with inter-phase transfer terms accounting for phase interactions where conservation laws apply [3]. The averaged continuity, momentum, energy and boiling models equations are well described in the work of Srinivasan *et al*. [4] and Greif *et al*. [5].

Many researchers reported that drag force is the most important force affecting the vapour bubbles, Srinivasan *et al*. [4], although there are some other forces as well. Ustinenko *et al.* [6] found that the lift and wall lubrication forces are important in obtaining correct two-phase radial distribution and flow characteristics. The wall lubrication force is

introduced in order to push the bubbles away from the wall and to assure the experimentally found zero void condition near vertical walls [7]. It is described by

$$F_{WL} = \alpha_g \rho_l C_{WL} \left\{ \left(\vec{v}_g - \vec{v}_l \right) - \left[\left(\vec{v}_g - \vec{v}_l \right) \cdot \vec{n}_w \right] \vec{n}_w \right\}^2 \vec{n}_w \quad (1)$$

where $\vec{n}_w$ is the unit wall normal vector (pointing from the wall into the fluid) and C_{WL} stands for wall lubrication coefficient. Based on Tomiyama`s work, Frank *et al.* [7] proposed an extended and generalized wall lubrication force model

$$C_{WL} = C_W(Eo)\, max\left[0, \frac{1}{C_{W,D}} \frac{1 - \frac{y_w}{C_{W,C} d_b}}{y_w \left(\frac{y_w}{C_{W,C} d_b} \right)^{p-1}} \right], \quad (2)$$

with

$$C_W(Eo) = \begin{Bmatrix} e^{-0.933Eo+0.179} & 1 \le Eo \le 5 \\ 0.007Eo + 0.04 & 5 \le Eo \le 33 \\ 0.179 & 33 < Eo \end{Bmatrix} \quad (3)$$

where $p = 1.7$, $C_{W,c} = 10$ and $C_{W,d} = 6.8$ are tuning coefficients according to Tomiyama [8].

When the continuous phase field is non-uniform or rotational, the bubbles experience the lift force perpendicular to the relative velocity. This force F_L is derived by:

$$F_L = -\alpha_g \rho_l C_l \left(\vec{u}_g - \vec{u}_l \right) \times \left(\nabla \times \vec{u}_l \right) \quad (4)$$

Tomiyama's lift model is employed to determine the lift coefficient as described in reference [8]:

$$C_L = \begin{Bmatrix} \min[0.28 \tanh(0.12 \cdot \mathrm{Re}_g), f(Eo_d)] & Eo_d < 4 \\ f(Eo_d) & 4 \le Eo_d \le 10 \\ -0.27 & Eo_d > 10 \end{Bmatrix} \quad (5)$$

Where the function of the bubble Eötvös number is expressed as

$$f(Eo_d) = 0.00105 Eo_d^3 - 0.0159 Eo_d^2 - 0.0204 Eo_d + 0.474 \quad (6)$$

The primary criterion for determination of the boiling regime is Leidenfrost temperature limit. Film boiling is activated and the associated heat transfer coefficient is computed, when the quenched surface temperature is above the Leidenfrost threshold. After the wall temperature has dropped below the Leidenfrost temperature, the transition model is activated. In the present paper the modification of the constant Leidenfrost temperature was introduced into the code in order to achieve better agreement with the available measurement data. Higher vapor concentration will appears at the top of the quenched piece, therefore transition to nucleate boiling will be occur at lower temperature due to vapor arriving from the bottom areas and accumulating at the top, thereby slowing down heat removal.

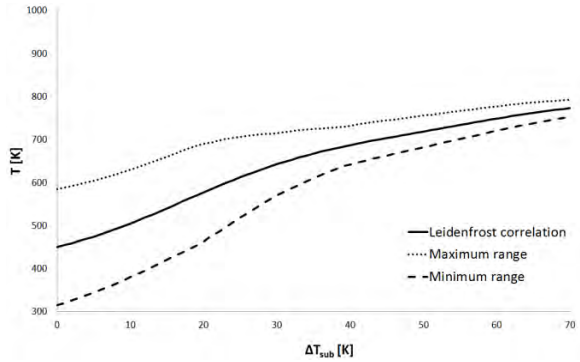

Figure 1: Leidenfrost temperature correlation

Presented correlation shown in Fig. 1 assumes that the Leidenfrost temperature is a function of pool temperature (sub cooled liquid effect), interpolated form existing correlations from Drucker & Dhir [9] and Cheng *et al.* [10]. The Leidenfrost limits are indicated in the Fig. 1 and are varied based on the sub cooled temperature, where can be seen that higher the pool temperature result in a higher Leidenfrost temperature range. Linear interpolation of Leidenfrost temperature as a function of height has been tested and can be written as

$$T_{Leiden,\max} = T_{Leiden,mean} + \frac{\Delta T_{Leiden,range}}{z_{\max} - z_{\min}} (z - z_{mean}) \quad (6)$$

and

$$T_{Leiden,\min} = T_{Leiden,mean} - \frac{\Delta T_{Leiden,range}}{z_{\max} - z_{\min}} (z - z_{mean}) \quad (7)$$

where detailed information concerning the variable Leidenfrost temperature treatment is provided by Kopun et al. [11].

Temperature measurements have been performed at monitoring locations of the step-plate shown in Fig. 2, right. The data has been used for validation of predicted temperatures within the solid. Spatial temperatures thereafter served as input for the FEA analysis of stresses/strains. The computational grid and the applied boundary conditions are depicted in Fig. 2, left.

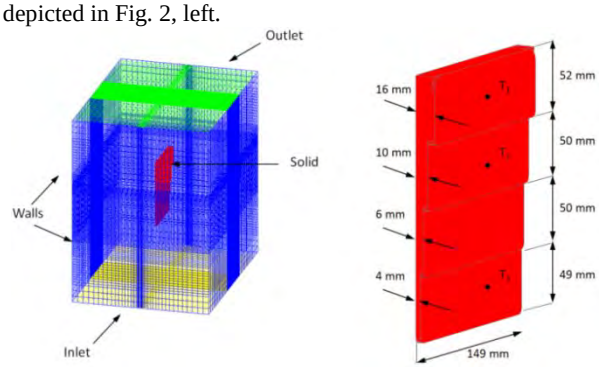

Figure 2: Computational domain and step plate test piece dimensions

Fixed atmospheric pressure was prescribed at the outlet boundary (green surface at the top), whereas the inlet section was treated with the velocity boundary condition (yellow part at the bottom). The dipping velocity was set to a constant value of 0.14 m/s until the final submerging depth has been reached. Temperature measurements on the step plate test piece featuring different thickness were performed in the middle of the piece width-wise, at three different heights and are referred to as T_1, T_2 and T_3 respectively (Fig. 1 right). The fluid flow was assumed to be laminar, as proposed by other authors [12].

RESULTS

The comparison of measured temperatures and numerically predicted results, immersed into the pool temperature of 353 K is presented in Fig. 3. Monitoring point temperatures are compared with fastest and slowest measured cooling curves, as indicated in Fig. 3a-c. Overall good agreement has been achieved at all three monitoring points. Based on the assumption of a variable Leidenfrost temperature presented in this paper, Leidenfrost temperature varies between 650 K for point T_3 up to 560 K for the monitoring location T_1. With this assumption the maximum deviation of less than 2 seconds has been found for all monitoring points, when comparing predicted temperatures with the mean measurement values.

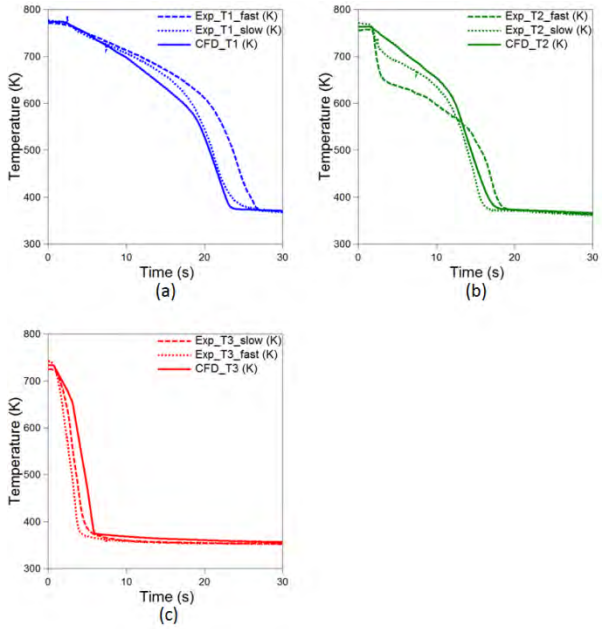

Figure 3: Comparison of numerically predicted and measured solid part temperature with fastest and slowest cooling trends for water temperature of 353 K at monitoring points T_1 (a), T_2 (b) and T_3(c).

The phase distribution results are presented on the Fig. 4. It can be seen that the vapor film covers the entire test piece even after 10 seconds (Fig. 4b), whereas after 20 seconds vapor is present only at the upper part, Fig. 4c). At the time of 30 seconds, as shown in Fig. 4d), aluminum test piece is completely cooled to the temperature of the liquid pool.

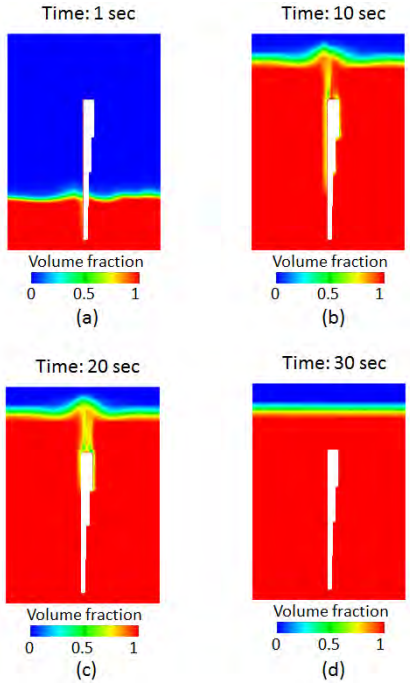

Figure 4: Liquid volume fraction at different time steps for water temperature of 353 K.

Fig. 5 shows the development of temperatures (results of CFD part) and deformations (result of FEA part) during water quenching. Deformation of the tested component depends on stiffness of the component (geometry and material properties) and temperature gradients. The principal mechanism of deformation development is contraction at the side which is immersed first, accompanied by a mostly tensile stress state at warm conditions and ductile response of the material (Fig. 5, 10 seconds). When water front reaches the far side and begins to cool it down and, consequently, to contract as well, the previously tensile reaction begins to turn, because the initially cooled material has to follow the contraction of the still warmer side (Fig. 5, between 20 seconds and 30 seconds). This causes a global deformation effect, which reaches its peak during the beginning of quenching and is then subsequently reduced. The highest global deformations due to temperatures are evident in the time period between 5s and 15s after the start of quenching.

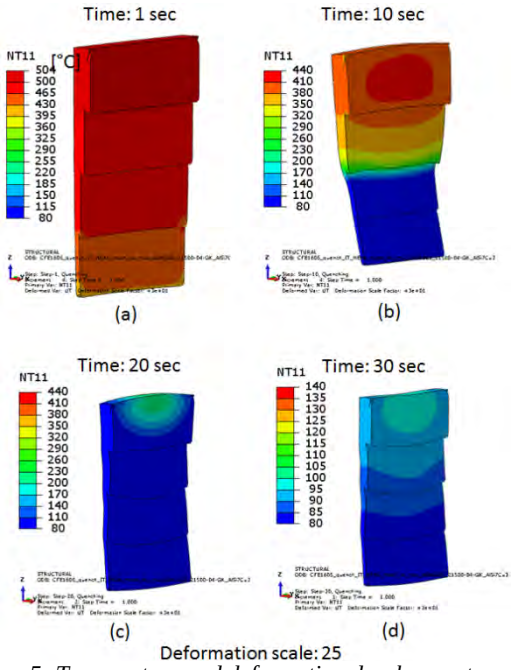

Figure 5: Temperature and deformation development scale of 25 during the water quenching

CONCLUSION

The applied CFD code AVL FIRE® in combination with a variable Leidenfrost model and additional interfacial forces is capable of predicting real time quenching effects for different solid configurations. The influence of film and transition boiling regime is well described and predicted, where the variable Leidenfrost temperature approximation has a significant effect on the solid temperature histories. Very good agreement between the numerical and available measured data has been achieved and it can therefore be concluded that the improved CFD model represents a solid basis for future research in the field of real-time cylinder head immersion quenching application and FEA stress and deformation analysis.

ACKNOWLEDGEMENTS

This research work was partly funded by the European Union, European Social Fund and SPIRIT Slovenia, Slovenian Public Agency for Entrepreneurship, Innovation, Development, Investment and Tourism. Parts of the results presented in this paper were obtained within the FFG funded project QUENCH-IT, project number 828697.

REFERENCES

[1] N.A.F. Campbell, S.J. Charlton, L. Wong, Designing towards nucleate boiling in combustion engines, IMechE C496/092, pp. 587-595, (1995).

[2] R. Kopun, D. Greif, D.Zhang, B. Stauder, L. Škerget, M. Hriberšek; Advances in Numerical Investigation of immersion

Quenching at Different Pool temperatures, SAE Brasil under revision.
[3] AVL LIST GmbH, FIRE CFD Solver, Eulerian Multi-fluid model. Solver Theory Guide. 2013, Graz, Austria.
[4] V. Srinivasan, D. Greif, B. Basara, On the heat and mass transfer modeling to simulate quenching heat treatment process, 6th International Quenching and Control of Distortion Conference, Chicago, USA, (2012).
[5] D. Greif, Z. Kovacic, V. Srinivasan, D.M. Wang, M. Suffa, Coupled numerical analysis of quenching process of internal combustion engine cylinder head, BHM Journal,Vol.154, (2009).
[6] V. Ustinenko, M. Samigulin, A. Loilev, S. Lo, A. Tentner A, A. Lychagin, A. Razin, V. Girin, Ye. Vanyukov, Validation of CFD-BWR, a new two-phase computational fluid dynamics model for boiling water reactor analysis, Nucleate Engineering and Design Vol. 238, (2008), pp. 660-670.
[7] T. Frank, J.M. Shi, A.D. Burns, Validation of Eulerian Multiphase Flow Models for Nuclear Safety Applications, 3rd International Symposium on Two-Phase Flow Modelling and Experimentation, Pisa, Italy, 2004.
[8] A. Tomiyama, Struggle with computational bubble dynamics, ICMF'98, 3rd Int.Conf.Mph Flow, pp. 1-18V, (1998).
[9] Dhir, V.K., Purohit, G.P., "Subcooled film boiling heat transfer from spheres", Nuclear Engineering and Design, Vol. 47, No.1, pp. 49-66, 1978.
[10] Drucker, M., Dhir, V.K., "Effects of high temperature and flow blockage on the reflood behavior of a 4-rod bundle", EPRI Report, pp. 2122, 1981.
[11] R. Kopun, L. Škerget, M. Hriberšek, D.Zhang, B. Stauder, D. Greif; Numerical simulation of immersion quenching process for cast aluminium part at different pool temperatures, Appl. Thermal Eng, under revision.
[12] K. Meduri Phani, R. Warrier Gopinath, Vijay K. Dhir, Wall heat flux partitioning during subcooled forced flow film boiling of water on a vertical surface, International Journal of Heat and Mass Transfer, 52, pp. 3534-3546, (2009).

CFD IN PROBLEM ANALYSIS AND OPTIMISATION – THE IMPORTANCE OF CORRECT BOUNDARY CONDITIONS

Eirik MANGER[1]*

[1] Acona Flow Technology, Uniongata 18, 3732 Skien, NORWAY

* E-mail: eirik.manger@acona.com

ABSTRACT

This paper demonstrates the importance of having correct boundary conditions as input to simulations. Two specific applications are studied. The model predictions are compared against measurements and findings in the real systems, and the validity of the models is discussed.

In the first application, gas mixing upstream two ammonia burners was investigated. A CFD simulation confirmed the mixing problem, and indicated that an extra static mixer would improve this. After rebuilding the situation did not improve, but was in some strange manner reversed and worsened. Different models were tested, without finding the cause of this change. Finally the response seen in the plant was traced back to a possible faulty mixer element upstream the newly installed static mixer. When rebuilding this, the mixing became sufficient – as predicted by the CFD simulation.

In the second application, local recirculation in a shell/tube gas condenser was studied. It was suspected that this phenomenon could be the reason for inlet corrosion. Local analysis using CFD indicated however that recirculation at the inlet did not extend into the condensing zone, ruling out this as a possible cause. Taking the investigation one step further revealed that the inlet recirculation zone will be significantly longer if the flow is angled in towards the tube inlets. By extending the calculation domain further upstream, the CFD results showed that such conditions did occur, corresponding well with the region in which material wear was observed. The CFD model could then be used to establish a new design which now seems to work well.

The two examples chosen illustrate clearly the importance of applying correct boundary conditions. Inappropriate input will lead to wrong conclusions – no matter how accurate the models are.

Keywords: CFD, Mixing, Process Industry.

INTRODUCTION

CFD has during the last decades developed and matured significantly, and is today an accepted tool within problem analysis and optimisation. There are lots of efforts spent in developing new and more accurate models handling e.g. turbulence and other complex physical phenomena. Still, superior models will only predict reliable estimates as long as the input provided by the user has equally good quality. In the authors opinion this might be an even larger source for erroneous simulation results than model accuracy.

This paper aims at demonstrating the importance of having correct boundary conditions as input to simulations. Two specific applications, a gas mixing problem before two parallel ammonia burners and local recirculation in a shell/tube condenser are used as examples. The model predictions are compared against measurements and findings in the real systems, and the validity of the models is discussed.

A GAS MIXING PROBLEM

In nitric acid plants there are often multiple ammonia burners to increase the production. It is also common to share piping and other equipment as much as possible thereby saving investment and maintenance costs.

For parallel burners gas mixing before the burners is crucial to obtain correct operating conditions. Gauze temperatures are directly proportional to the ammonia content in the gas, and a poorly mixed gas could lead to temperature differences between parallel burners as well as hotspots on the gauzes.

For the plant of interest, an average temperature difference of around 12°C was observed between the burners. This corresponds to ammonia mole fractions of around 10.4 and 10.2 percent into the warmest and coldest burner, respectively. These figures were also confirmed with gas composition measurements. The problem was to be investigated through CFD modelling, and suggestions for improvements should be made.

Model Description

The work reported on here was done back in 1999/2000 with significantly less computer resources and facilities that exist today. Thus both mesh characteristics and model selection might not be according to present best practice, but the intentions were the best.

Figure 1 shows the calculation domain. Cold air enters at the bottom of the domain, and the ammonia injection point is located in the lower part of the first vertical pipe section. This is then followed by two static mixers; the first one in the vertical section downstream the injection point, and the second mixer in the top horizontal pipe section. The pipe diameter is 1.4 m, and the height of the vertical pipe section is approximately 12 m.

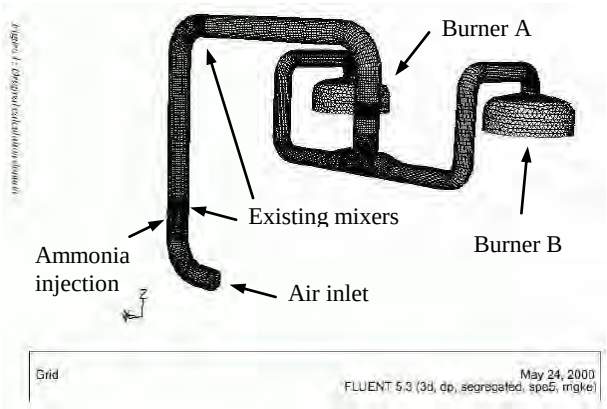

Figure 1: Calculation domain.

The static mixers used in the system are traditional plate mixers from Sultzer. A generic model, visualised in Figure 2, was established so that the mixers readily could be inserted replacing parts of the original pipe section. In this manner the effects of additional mixers at different positions could be investigated.

The reader should note that the chosen mixers have a preferred mixing direction. Since the design consists of folded plates directed ±45° against the stream-wise direction and covering the entire cross section, mixing will only occur in the parallel plane to the plates. Normal to this plane there will be little or no mixing. This means that the directions of the mixers are important.

The CFD modelling work was done using Fluent v. 5.3. The original CFD model had approximately 1 million cells, and consisted of a combination of hexahedrons and tetrahedrons. Chemical species were tracked, and the RNG k-ε turbulence model was initially used.

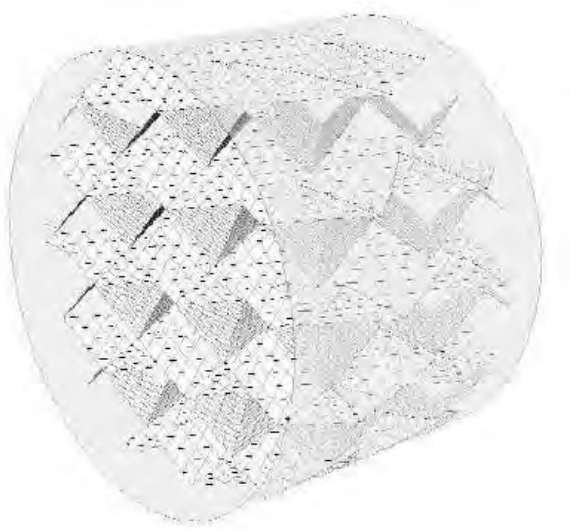

Figure 2: A generic mixer element.

First Results

The first calculations were done using the given design of the system, i.e. with two mixer elements as described in the previous section. Figure 3 shows the predicted ammonia mole fractions along parts of the feed pipe, whereas Figure 4 depicts the local mole fractions in the main pipe and in the individual branches leading to each ammonia burner. Note that the scales are different to emphasize the differences and gradients.

Averaging mole fractions of ammonia in each branch, as seen in Figure 4, indicated that the current design with two mixers gave different levels onto each of the burners. With the current conditions, a level of 10.4% ammonia was predicted into burner A, whereas only 10.2% was estimated entering burner B. These figures corresponded very well with plant observations, and the model established was believed to capture the relevant physics.

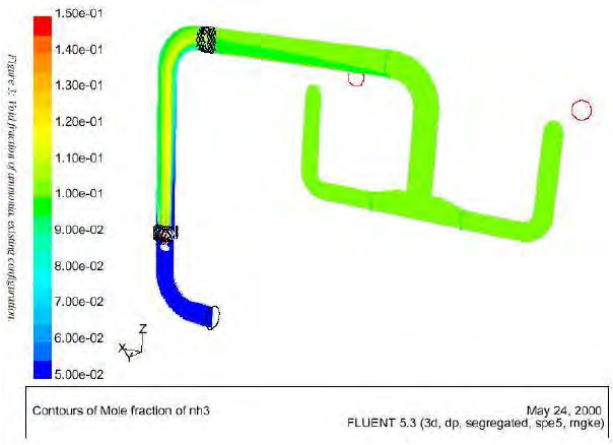

Figure 3: Gas mixing along the feed pipe for the original configuration with two mixer elements.

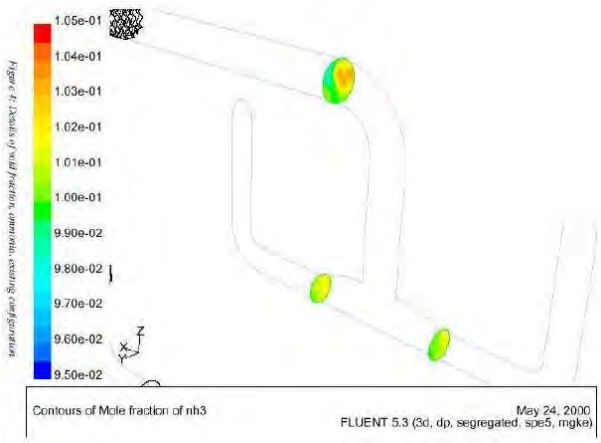

Figure 4: Details of gas mixing in the separate feed pipes for the original configuration with two mixer elements.

With good confidence in the model, the work proceeded looking at possible remedies. An obvious solution seemed to add a mixer just before the split. Since the task for the new mixer element would be to ensure equal mole fractions between the two parallel burners, it was decided that the new element should have a preferred mixing direction parallel to the T-split. The proposed solution design is shown in Figure 5, with the additional mixer element located just above the T-split.

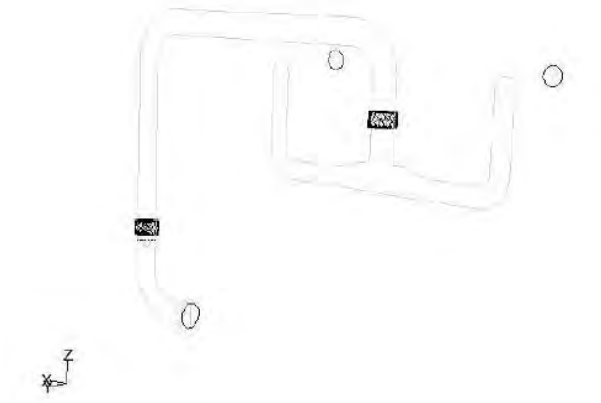

Figure 5: Proposed modification with a new mixer element close to the T-split.

Calculations with the new geometric layout indicated significantly better performance than the original design. The difference between the burners was now reduced to 0.04 mole percent; 10.32% to burner A and 10.28% to burner B. The results were considered to be within the model accuracy, and it was recommended to move on with the installation.

After Installation

The new mixer element was prefabricated and installed according to recommendations late 2001. Pictures from the work are shown in Figure 6. The effect of the design change was however not as expected. Not only had the installation reverted the situation – burner A was now colder than burner B – but the situation was actually worsened. Estimated ammonia mole fractions were 10.1% into burner A and 10.5% into burner B, with a temperature difference of more than 20°C between the burners. Upon rather devastating results, the search for explanations on what had gone wrong commenced.

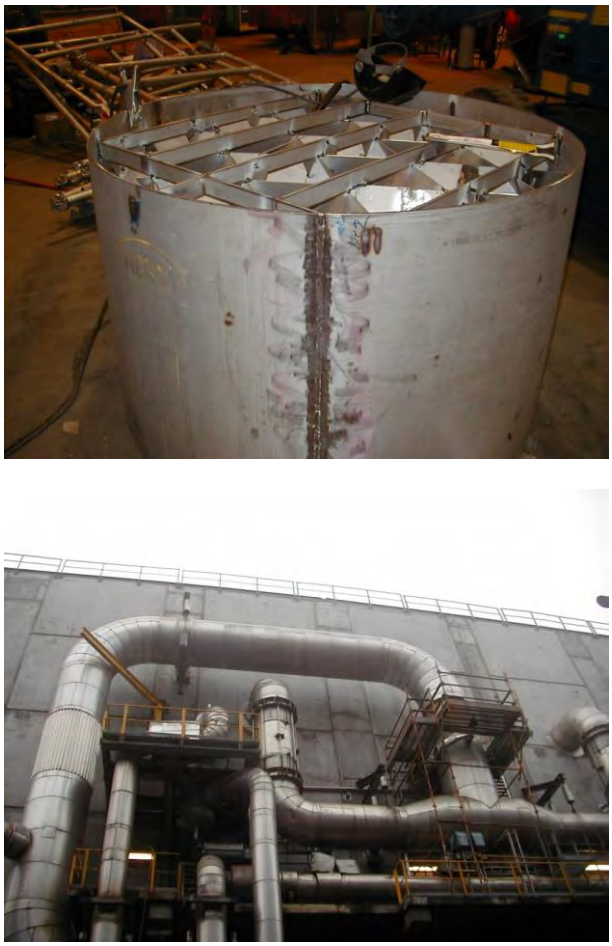

Figure 6: New prefabricated mixer element (top) and installation on site (bottom).

Several ideas and initiatives were launched to explain the observed changes at the plant. Different turbulence models were tested, higher order discretisation schemes were introduced and the mesh was refined and improved. All the modelling tests indicated that the implemented design should be superior compared against the old layout.

After spending quite some time ruling out direct modelling errors, it was finally realised that the largest remaining uncertainty was actually related to the geometric description of the system, more specifically questioning the conditions of the existing mixers. Interviewing the maintenance and operation personnel at the plant indicated that the existing mixers might not be fully intact. This again led to questions on the form "what if …", and it was time to establish a new and smaller model.

A New and Simplified Model

Since the original CFD model of the system was (at those times) quite large and rigid, it was considered advantageous to establish a new model for the "What if"-analysis. Besides being lighter and faster to run, the model should also have the option to specify inlet conditions onto the third mixer, so that the effect of the implemented design change could be explicitly investigated.

Figure 7 shows the new, simplified model of the system. The burner tops have been left out, and the inlet to the calculation domain is now positioned just after where the second mixer element is assumed to be. The inlet is constructed so that different ammonia profiles can be prescribed and fed into the system.

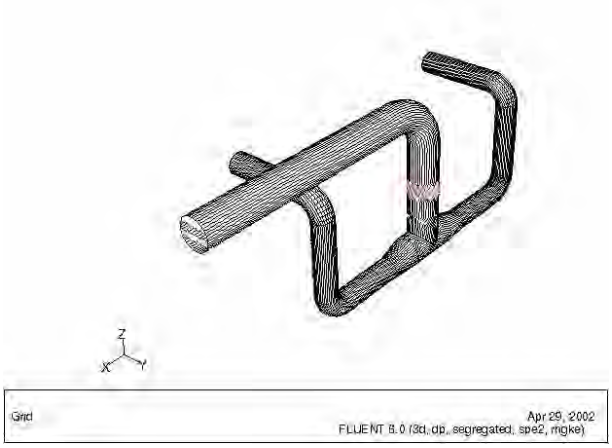

Figure 7: Simplified model with optional new mixer element.

Results with the New Model

Several different cases were studied with the new model, but only two of them will be reported on here. Only the boundary conditions were varied, more specifically the ammonia inlet profile.

The rationale for the first case studied with the simplified model was an assumption that the first two mixers worked as they should and were mostly intact. This resembles the situation modelled earlier, and would provide a check of the simplified model. A higher temperature in burner A suggested somewhat higher ammonia mole fractions at the bottom of the pipe, since this naturally will flow towards the A side. A slightly skewed distribution was chosen, having 9.3 mole percent of ammonia in the upper part and 11.3 in the lower part of the pipe. The results with and without the new mixer is shown in Figure 8. Moreover, the quantitative findings compares very well with the values from the complete model, i.e. 10.4% and 10.2% are predicted changing to 10.32% and 10.28% after insertion of the new mixer element.

Figure 8: Effect of an additional mixer on a skewed ammonia inlet distribution.

In the second case a centred ammonia profile was selected. The ammonia inlet further upstream the test section is centred, and since ruined mixers will not affect the distribution significantly, such a profile seemed plausible. An extreme situation was prescribed, with 0% ammonia at the top, 20% in the centre and 1% in the bottom. The results of this inlet condition were astonishing. First of all, the model indicated that even with the poor mixing leading into the T-split, the distribution between the burners was not that horrible – in fact, the same distribution as earlier was predicted, with 10.4% to burner A and 10.2% to burner B. This means that the prescribed ammonia profile into the test section could very well have been present before installing the new mixer element – which corresponded to the plant observation.

Moreover, when calculating with the new mixer installed, the ammonia distribution between the burners actually reverted and got worse. In this case the model predicted 10.1% ammonia on burner A and 10.5% on burner B – exactly the behaviour that had been observed at the plant. The impact of the new mixer element is shown in Figure 9. Based on the results it was concluded that the two old mixers did not perform a proper mixing job, and it was recommended to inspect and repair the existing mixers.

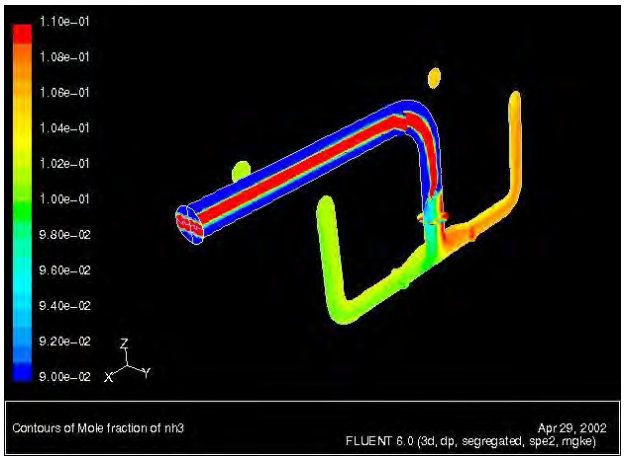

Figure 9: Effect of an additional mixer on a centred ammonia inlet distribution.

The Second Installation and Final Remarks

The company operating the ammonia plant still had some faith in the modelling, and the recommendations were followed. Upon inspection of the second mixer, it was found that this was very open and far from the condition that had been assumed. A picture of the mixer is shown in Figure 10. After replacing the second mixer, the temperature difference between the burners reduced to less than 5°C, which is within the error margin of the measurements.

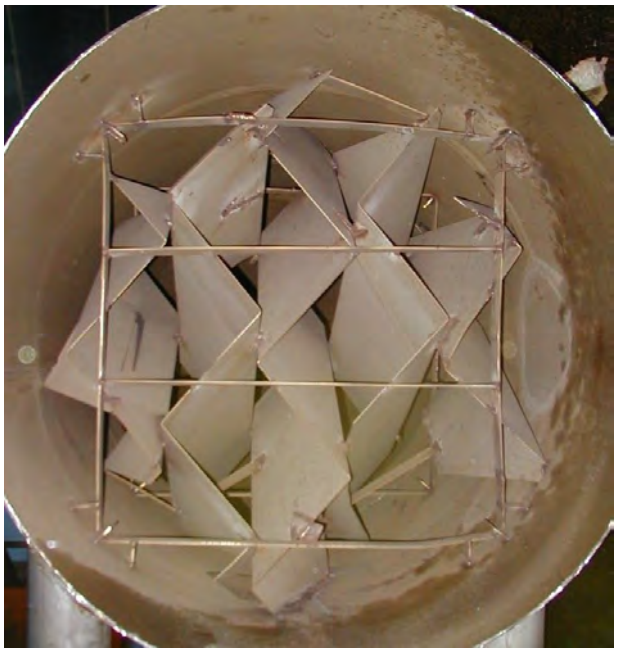

Figure 10: The ruined mixer with large open holes.

A few important lessons should be learnt from these cases. First of all, the boundary conditions must be appropriate and correct if a model should have predictive properties. The boundary conditions more or less determine the solution, and errors here will lead to wrong conclusions. Secondly, all the models seem to perform quite well (if the boundary conditions are correct …), relatively independent on choice of turbulence model, discretisation schemes and other settings.

A RECIRCULATION PROBLEM

The second case study relates to corrosion problems in a tube/shell condenser situated at an ammonia plant. The material wear was positioned around 40 mm into the tube sheet.

The company operating the plant initially had an opinion about the origin of the phenomenon, and asked Acona Flow Technology (AFT) to verify their hypothesis. A recirculation zone described as a *vena contracta* could bring condensate from the pipe back towards the inlet, where water evaporates in the hot zone forming strong acid. This could then cause the corrosion.

Based on the hypothesis above, simulation models for analysing the inlet part of the condenser should be established. The models should then be used for studying both the flow and the heat transfer in the system, in particular near the entrance region of the condenser tube sheet. Based on the calculations, AFT should determine a probable cause for the problems and later propose and investigate means for improving the situation.

2D Simulation Model

To test the initial hypothesis associated with the *vena contracta*, a CFD model of the inlet to the condenser was established using the commercial CFD code ANSYS FLUENT v14.0. An axisymmetric calculation domain was constructed from drawings provided by the plant operator, see illustration in Figure 11.

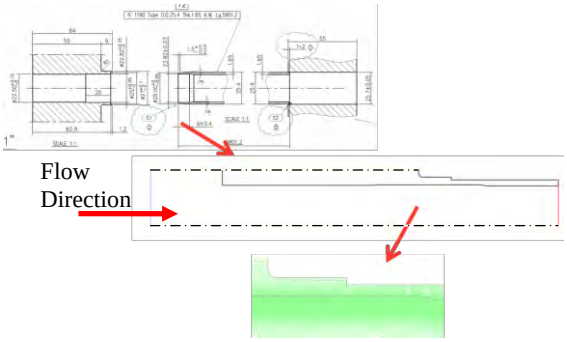

Figure 11: Details of the 2D calculation domain.

The cooling water on the shell side was assumed to have a temperature around 25°C. The heat transfer coefficient will depend somewhat on the flow conditions, but estimates based on empirical relationships suggest values between 7 000 W/m^{2}K and 12 000 W/m^{2}K.

First Results

The 2D calculations indicate that the *vena contracta* extends 1-2 cm into the tube sheet. This can be seen from Figure 12 where the axial velocity near the tube sheet and pipe walls is plotted vs. distance. Note the large impact of the relative small variations in wall y-coordinate. The length of the recirculation zone is found where the axial velocity changes sign. There are also some signs of a small recirculation a little bit further downstream, but this is not regarded as sufficient for transporting condensate backwards.

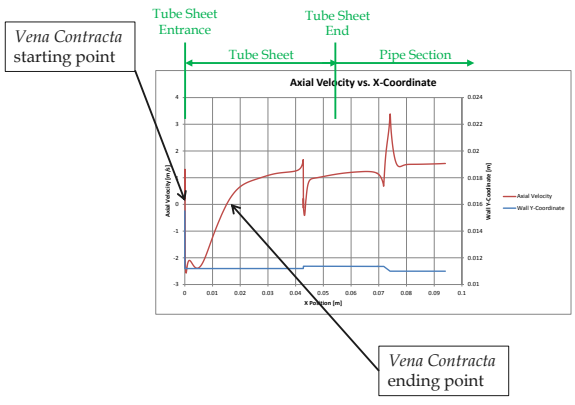

Figure 12: Flow though the tubes, here represented by axial velocity.

The length of the *vena contracta* must now be held together with temperature profiles to determine if there is overlap with the condensation zone. Figure 13 shows the axial temperature profiles along the walls for two different heat transfer coefficients. The profiles indicate that condensation starts some 5-6 cm inside the tube sheet.

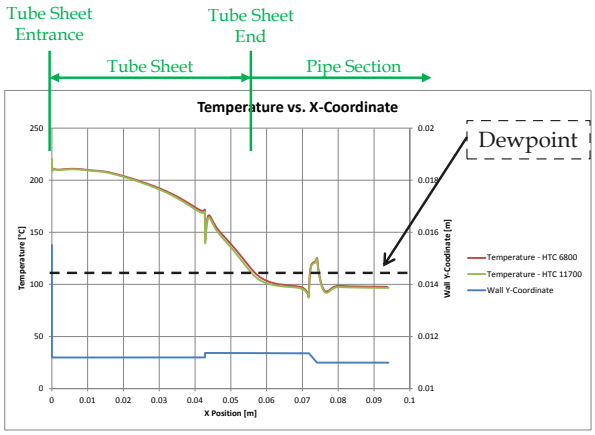

Figure 13: Gas temperature profiles shown for the two different heat transfer coefficients.

This means that the 2D results show no direct connection between the condensation zone and the recirculation zone due to the *vena contracta*, and the initial hypothesis is not supported. Thus, more work is needed to find a possible and plausible explanation for the observed material corrosion.

More Comprehensive Analyses

Realizing that the flow is not 2D, it could be interesting to consider the length of the *vena contracta* if the flow enters the holes in the tube sheet with an angle. Since the inlet to the condenser is a central pipe, the gas must redistribute before entering the pipes, see illustration in Figure 14. This means that the gas will enter the tube sheet with an angle, which again could affect the *vena contracta*. Thus, a slightly revised hypothesis is investigated through some simplified simulations: could the angle of attack cause overlap between the condensation zone and the *vena contracta* in certain areas?

A Simplified Model

To study the effect of flow attack angle, a small 3D simulation model considering just half a hole in the tube sheet was established. The calculations were set up so that the mass flow through this hole is approximately correct, i.e. assuming perfect distribution between the heat exchanger pipes. Four different geometries, varying the flow attach angles from 15 to 60 degrees were calculated, assuming symmetry along a centre plane. Figure 15 shows the geometry used for this test, whereas some results are depicted in Figure 16. From this figure it is seen that the maximum length of the recirculation zone and the shape of the zone have changed significantly compared against the 2D simulations.

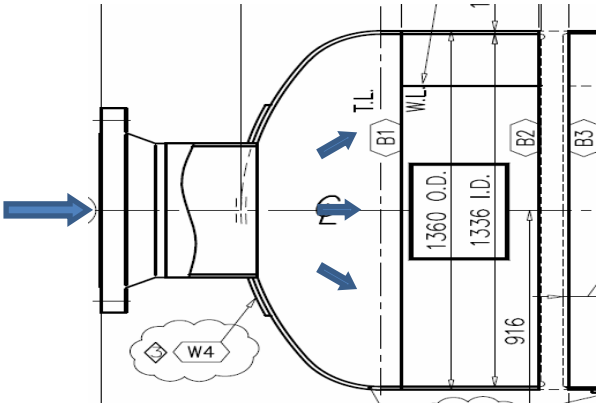

Figure 14: Illustration of how the flow approaches the tube sheet.

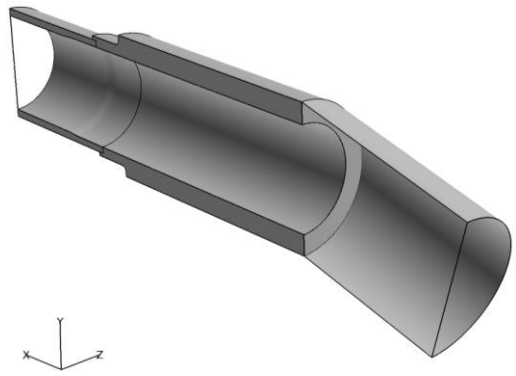

Figure 15: Computational domain for analysing flow with an attack angle.

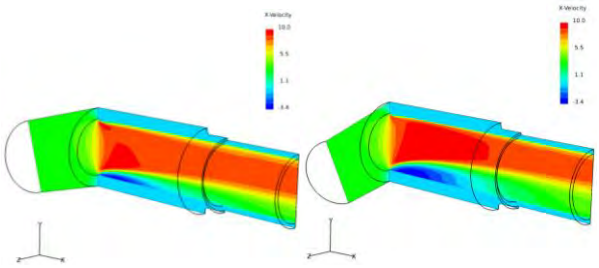

Figure 16: Predicted horizontal velocities for 15° (left) and 30° attack angle (right).

The 3D simulations strongly indicate that the flow attack angle influences the length and the shape of *vena contracta* significantly, further illustrated in Figure 17. The maximum length of *vena contracta* stretches from approximately 15 mm at 0° flow attack angle, up to more than 70 mm at a 60° flow attack angle into the tubes. This more or less confirms the revised hypothesis.

Even though an angled flow into the tube sheet can result in a larger recirculation zone, the hypothesis should be further strengthened by looking at the actual flow angles that hits the tube sheet. If successful, the pattern of the damage locations in the condenser should even correspond somewhat to the recirculation, depending on the attack angle and gravity.

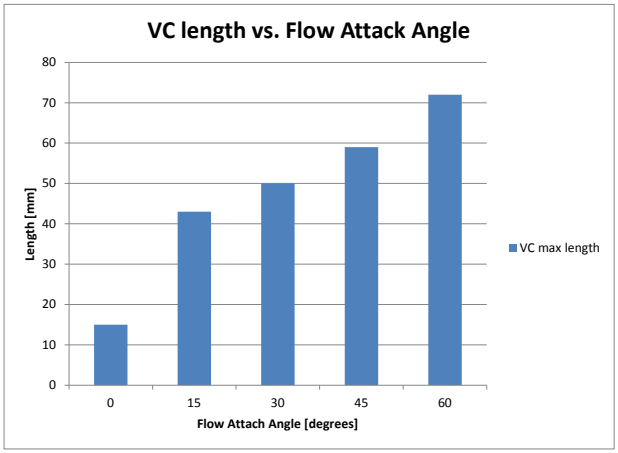

Figure 17: Estimated length of the *vena contracta* (VC) vs. flow attack angle.

A More Comprehensive Model

After finding indications that recirculation could be caused by flow attack angle, an additional and more comprehensive model was established. The purpose with this was to further strengthen the hypothesis on the mechanism, and secondly to explore possible remedies. The porous jumps indicated in Figure 18 represent the frictional resistance through the tubes (which are approximately 4 metres long), so that an approximately correct flow distribution could be maintained.

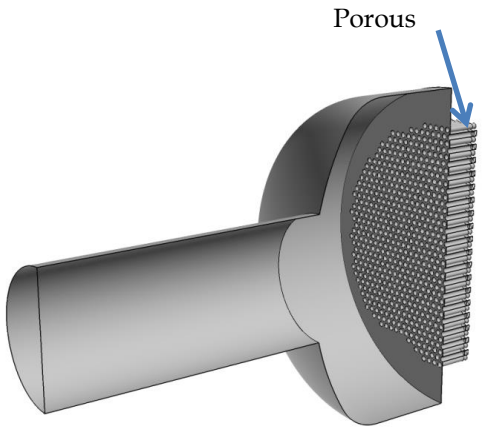

Figure 18: Calculation domain for the detailer 3D model.

Results from the More Comprehensive Model

Figure 19 shows the velocity vectors for the detailed model. There is a clear indication that there is angled flow into the tube sheet in some areas, with the arrows being almost normal to the tube direction in some regions. To further show how the flow attack angle is distributed on the tube sheet entrance this is plotted in Figure 20. Note that only the angle against the axial coordinate is considered. Besides a small area in the centre of the tube sheet the angle of attack is in general larger than 45°.

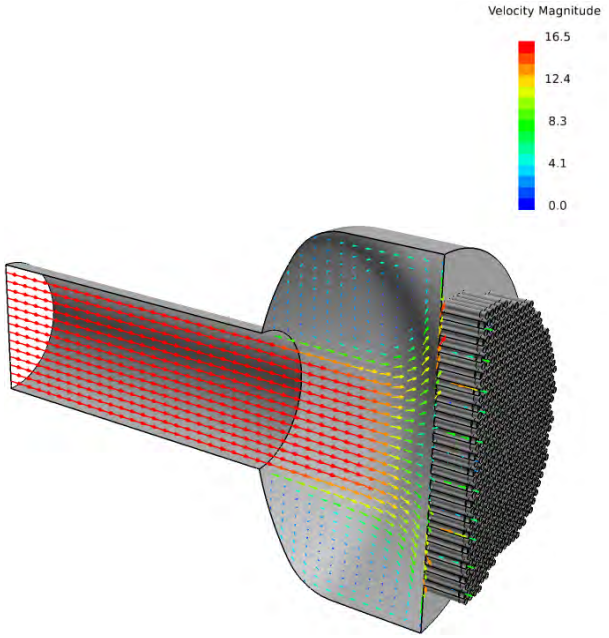

Figure 19: Predicted velocity vectors leading in towards the tube sheet.

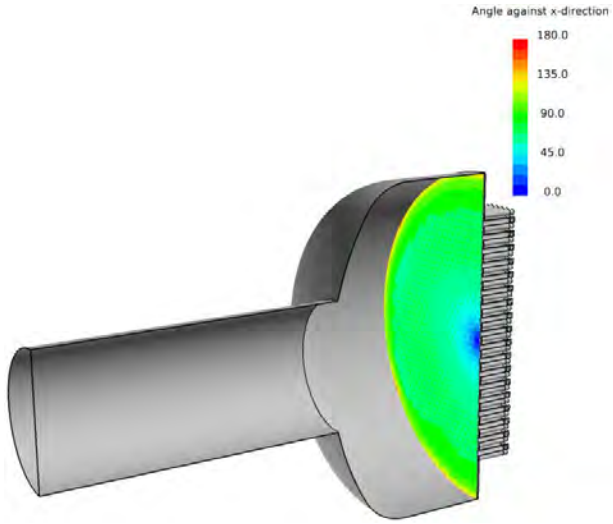

Figure 20: Predicted flow attack angle towards the tube sheet.

At this point a note should be made on the damages found in the condenser. When discussing the findings with the plant, it was revealed that a vast majority of the wear was located in a region between 10 and 2 o'clock, and from one third to two third the distance between the centre and the wall. The latter corresponds nicely to the wall/centre distance for which maximum attack angle is predicted. Moreover, when holding observations against calculation results, the wear seems to occur in a region where the stretched *vena contracta* is located at the bottom of the tubes. This is also crucial, since the condensed phase then can recirculate in a relatively calm zone here.

Improving the Situation

Several possible enhancements to improve the situation were suggested and tested, but one of the simplest changes proposals ended up as the best – a porous plate for straightening the flow upstream the tubes.

A solution with two porous plates was investigated, but simulations indicated that two porous plates actually do a too good job. Straightening the flow completely means that the gas in the outermost part, where there are no tubes, must make a 90° inward turn to enter the holes in the tube sheet. This could again lead to problems with the *vena contracta* length in this area. Due to this reason it was recommended to install only one, rather coarse porous plate.

With an optimum placement, one porous plate efficiently redistributes the flow, and the result is plotted in Figure 21. The redistribution changes the picture completely, and from having large areas with recirculation in the original design, there seems to be only short recirculation zones with this new design. Moreover, the velocity plot shows the porous plate's property in diverting the flow, but still not setting up a too straight flow towards the tube sheet.

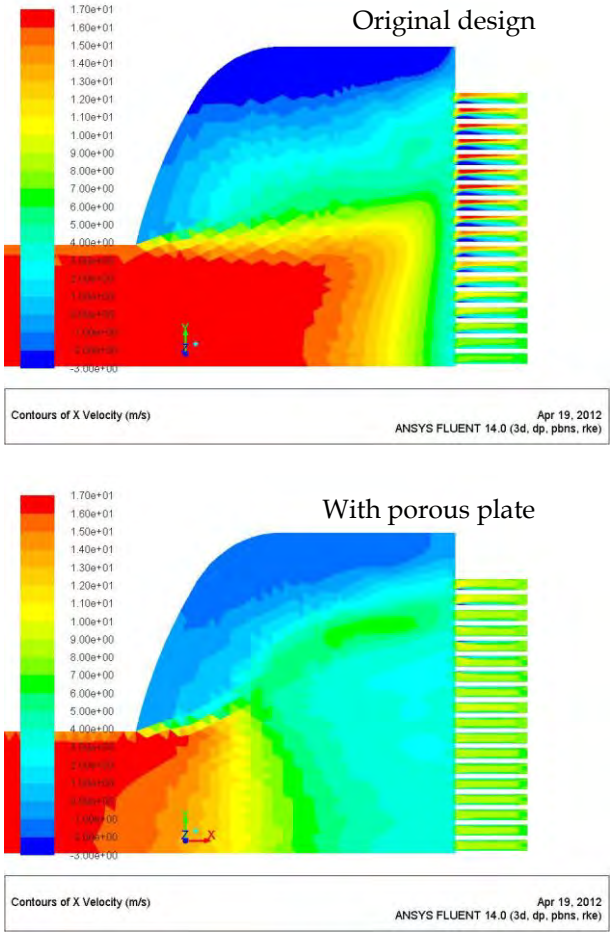

Figure 21: Contours of axial velocity [m/s] for the detailed geometry, original design (upper) and porous plate (lower).

Further exploring the effect of the proposed modification, details of the axial velocity is shown in Figure 22. Here the axial velocity is plotted against the axial position, for all the holes in the tube sheet continuing into the heat exchanger pipes. The original design is shown in black, and the modified design with porous plate is drawn in red. The line drawn at zero velocity indicates the limit for backflow. From this figure, it is clear that the modified design reduces the length of the recirculating zone significantly.

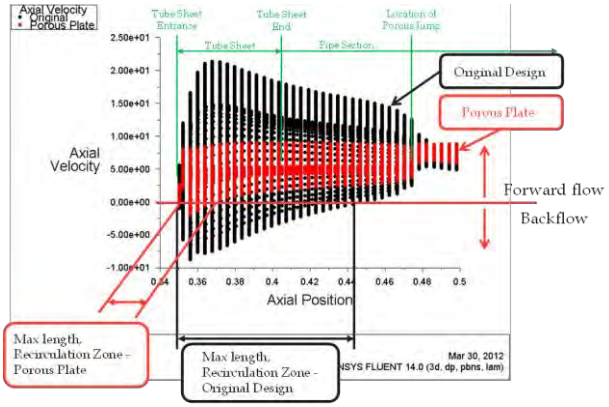

Figure 22: Details of axial velocity shown for the original design (black) and the modified design (red).

The prediction of recirculation zones is known to be a classical challenge within CFD, hard to predict. Higher order numerical schemes should be applied to increase the accuracy of the calculations. Unfortunately, the length of the recirculating zone increases when applying a 2nd order numerical scheme, from approximately 20 mm to some 40 mm. This is still well outside the area at which condensation is predicted to start – around 55 mm inside the tube sheet. The safety margin has however decreased.

Installation of such a porous plate has only minor impact on the total pressure drop across the unit. The pressure drop for the original design is 106 mmWC, which is predicted to increase to 133 mmWC for the modified design. The recommended solution was implemented and has now been running for more than a year with no significant material wear.

CONCLUSIONS

The importance of boundary conditions in CFD has been demonstrated through two practical examples.

In the first case, insufficient geometric descriptions were used when studying gas mixing in a nitric acid plant. This again led to non-optimal decisions which did not improve the situation. A simpler model was later used as a fault localiser, strongly suggesting that the geometry applied in the first study had been wrong. Inspection revealed destroyed mixer elements, and after fixing these the model and plant observations matched.

A second example studied local recirculation in a shell/tube condenser. The *vena contracta* forming at the tube entrances was believed to cause corrosion problems due to strong acid concentrations. A simple 2D axisymmetric approach however indicated that the recirculation zone was not long enough for this phenomenon to occur. Again looking at the boundary conditions for the problem, it was realised that the flow might enter the tube sheet with an angle. Simple 3D simulations showed that for such conditions the *vena contracta* could become significantly longer compared against the axisymmetric case. A simulation of the entire inlet geometry showed that the flow is indeed angled towards the tube sheet, and the mechanism was confirmed. This complete model also showed that the recirculation zone lengths could be significantly reduced if straightening the inlet flow by e.g. installation of a porous plate, recommended to the plat operator.

The cases discussed showed that care must be taken when defining geometries and boundaries for the problems. Incorrect boundary conditions will inevitably lead to non-optimal or wrong decisions – no matter how accurate the models are. In many industrial applications obtaining and using the right boundary conditions can be even harder than finding the appropriate physical models and numerical schemes.

A COMBINED MULTIFLUID-PBE MODEL FOR A SLURRY BUBBLE COLUMN REACTOR: APPLICATION TO THE FISCHER-TROPSCH SYNTHESIS

Camilla Berge VIK[1*], **Jannike SOLSVIK**[1†], **Hugo Atle JAKOBSEN**[1‡]

[1]NTNU Department of Chemical Engineering, 7491 Trondheim, NORWAY

[*] E-mail: camilla.berge.vik@ntnu.no
[†] E-mail: jannike.solsvik@ntnu.no
[‡] E-mail: hugo.a.jakobsen@ntnu.no

ABSTRACT

A two-dimensional steady-state isothermal combined multifluid-population balance equation (PBE) model for a slurry bubble column (SBC) was implemented for the Fischer-Tropsch synthesis (FTS). The model consists of a set of mass, species mass and momentum balance equations for the liquid-phase, and the corresponding PBE (mass), species mass and momentum balance equations for the gas phase. The flow variable profiles predicted by the model are reasonable for both phases as compared to literature experimental data. Moreover, the chemical part of the model predicts results giving a chemical conversion of the reactants in good agreement with literature experimental data.

Keywords: Clean energy, industrial reactive flows, population balance equation, Fischer-Tropsch synthesis, slurry bubble column, orthogonal collocation.

NOMENCLATURE

Greek Symbols

α	Volume fraction, $[-]$
α_{ASF}	Parameter in the Anderson-Schultz-Flory distribution, $[-]$
Γ	Mass transfer term, $[kg/m^3\ s]$
ζ	Daughter bubble diameter, $[m]$
μ	Dynamic viscosity, $[kg/ms]$
ν	Stochiometric coefficient, $[-]$
ξ	Bubble diameter, $[m]$
Ξ	Microscopical velocity in property space, $[m/s]$
ρ	Mass density, $[kg/m^3]$
ρ_{cat}	Catalyst density in reactor, $[kgcat/m^3]$
σ	Surface tension, $[N/m]$
τ	Microscopical temperature, $[K]$
Υ	Microscopical mass, $[kg]$
ψ	Generic conserved quantity, units dependent on quantity
ω	Weight fraction, $[-]$
Ω	Microscopical weight fraction, $[-]$

Latin Symbols

a	Kinetic parameter, $[kmol/kgcat\ s\ Pa^2]$.
a_L	Gas-liquid interfacial area per unit liquid volume, $[m^2/m^3]$
b	Kinetic parameter, $[1/Pa]$.
C_s	Mass concentration of solids in slurry, $[kg/m^3]$
C_D	Drag coefficient, $[-]$
d_s	Sauter mean diameter, $[m]$
D	Diameter of column, $[m]$
$D_{\text{eff,z}}$	Eff. axial dispersion coefficient, $[m^2/s]$
E_0	Eötvös number, $[-]$
f_{drag}	Drag force, $[N/m^3]$
$\boldsymbol{F}$	Force, $[N]$
g	Standard acceleration of gravity, $[m/s^2]$
j	Flux, $[kg/m^2\ s]$
J	Source term, $[kg/m^3\ s]$
k_L	Liquid side mass transfer coefficient, $[m/s]$
K	Equilibrium constant describing the relationship y_i^*/x_i^* at given conditions, $[-]$
m	Mass, $[kg]$
M_w	Molecular weight, $[kg/kmol]$
$\overline{M}$	Average molar mass, $[kg/kmol]$
p	Density function, $[\#/(m^3[m/s\ m\ K\ kg])]$.
p	Pressure, $[Pa]$.
r_{CO}	Reaction rate in terms of CO conversion, $[kmol\ s/kgcat]$
R	Reaction term, $[kg/m^3\ s]$
Re_p	Particle Reynolds number, $[-]$
t	Time, $[s]$.
v	Velocity, $[m/s]$
T	Temperature, $[K]$
x	Liquid phase mole fraction, $[-]$
y	Gas phase mole fraction, $[-]$
z	Dispersion height, $[m]$

Sub/superscripts

$B-D$	Birth and death terms.
$coll$	Collisions.
d	(mass) density function.
G	Gas.
i	Component i or direction i.
L	Liquid.
r	Physical space.
s	Superficial (superscript).
s	Solid (subscript).
ξ	Property space.

INTRODUCTION

Forecasts about decreasing fossil liquid fuel sources have induced increasing interest in synthesized liquid fuels, among them second generation biofuels. Such a liquid fuel may be produced through the Fischer-Tropsch synthesis (FTS). A particular reactor choice for this heterogeneously

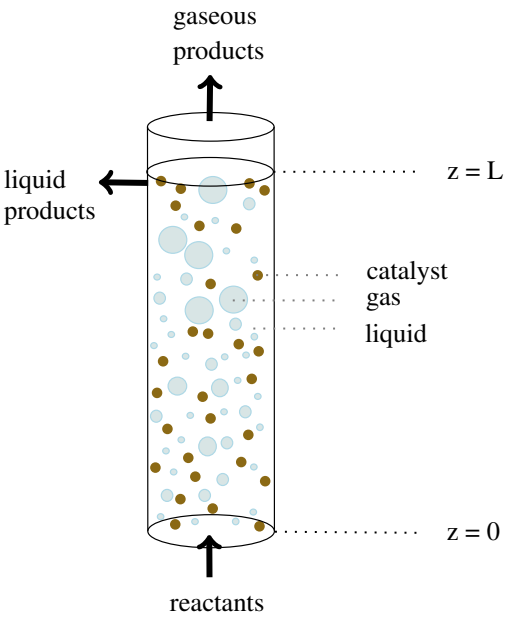

Figure 1: Simplified sketch of a slurry bubble column, with gas bubbles (light blue), liquid (white) and dispersed catalyst particles (brown).

catalyzed liquid reaction is the slurry bubble column (SBC) (Figure 1), with reactants injected in the gas phase and the solid catalyst present along with the liquid products in the slurry.

The Fischer-Tropsch synthesis

The basis FTS reaction can be described as the formation of paraffinic or olefinic chains and water from carbon monoxide and hydrogen (Guttel, 2009), where the main product is paraffins. The chemical reaction is given as:

$$\mathrm{nCO} + (2\mathrm{n}+1)\mathrm{H_2} \rightarrow \mathrm{C_nH_{2n+2}} + \mathrm{nH_2O} \qquad (1)$$

Transport and kinetic resistances
A number of resistances limit the gaseous reactants in being converted to products (Kohler, 1986) (Figure 2): (1) Transport of reactants from bulk gas phase to gas-liquid interface, (2) transport of reactants from gas-liquid interface to the bulk liquid, (3) transport of reactants from bulk liquid to the catalyst surface, (4) intraparticle diffusion of reactants in the pores of the catalyst, (5) adsorption of reactants on the active sites of the catalyst and (6) surface reaction of reactants to yield products. The products are transported from the catalyst partly to liquid and gas phases. Step (1) is usually much smaller than step (2), as the diffusion coefficients are smaller in liquids than in gases. Inga and Morsi (1996) found steps (2) and (5+6) to be rate determining for typical Fischer-Tropsch conditions. Wang *et al.* (2007) and Sehabiague and Morsi (2013) state that the gas-liquid mass transfer limitation may cause a decrease in the reaction conversion, especially at high solid concentrations and superficial gas velocities in slurry reactors. The interfacial mass transfer fluxes are thus important for the Fischer-Tropsch reaction. The interfacial heat transfer is also important, as the reaction is highly exothermic.

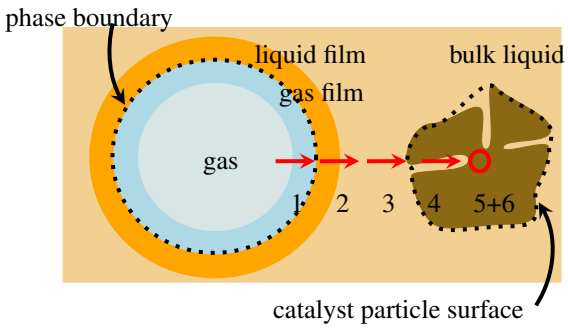

Figure 2: Simplified sketch of resistances seen by the reactants on their way to become products. Steps 2 and 5+6 are claimed to be rate determining.

Kinetic model
Many kinetic models have been developed for FTS, particularly for iron and cobalt catalysts (see e.g. Sehabiague and Morsi (2013) for a summary). In this work, the kinetic model by Yates and Satterfield (1991) for a cobalt catalyst is applied:

$$r_{CO} = \frac{a p_{CO} p_{H_2}}{(1 + b p_{CO})^2} \qquad (2)$$

The kinetic rate expression is given in terms of partial pressures of the two reactants in Equation 1; CO and H_2.

Interfacial transfer fluxes

The interfacial mass, momentum and heat transfer fluxes are given by the product of the transfer coefficients, the contact area per unit volume and the driving force. The contact area is determined by the bubble size distribution. Along the reactor length, bubble-bubble interactions and fluid-bubble interactions will give rise to bubble breakage and coalescence phenomena, affecting the bubble size distribution in the reactor (Figure 3). This size distribution will influence the reaction rate as larger bubbles have a smaller contact area per volume, and the contrary for smaller bubbles. The bubble size distribution can be modeled through the population balance equation (PBE).

The Population Balance Equation

The PBE describes a population and has its roots in the Boltzmann equation. In particular, it is a statement of *continuity* in *particle phase space*. The particle phase space is the number of independent coordinates required to describe the state of a particle. The population in this work is the dispersed gas bubbles. One may distinguish between two types of processes or events that can alter the population; *continous* and *discontinous* processes. Continous processes may result from convective motion in particle phase space and cause no change in the number of particles in the system (except from entering / leaving at the boundary). In contrast, *discontinous processes* change the number of particles in the system in a discontinous manner and are generally modelled by source / sink terms. The population balance equation includes both continous and discontinous terms. Examples of discontinous phenomena for the Fischer-Tropsch synthesis in a slurry bubble column is birth and death of particles due to bubble breakage and bubble coalescence.

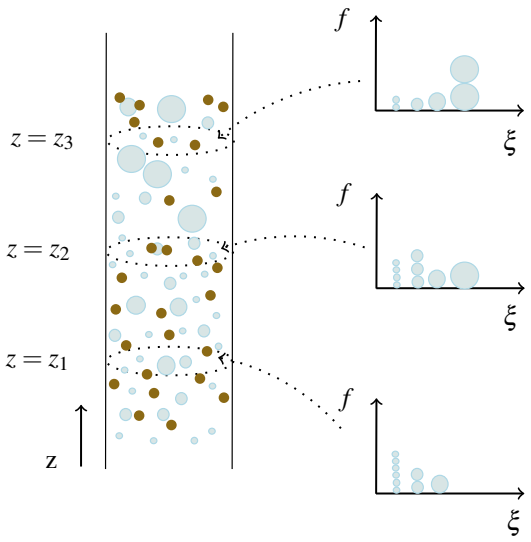

Figure 3: The gas phase particles (bubbles) have a density function f, denoting the number of entities per volume and per size ξ along the dispersion length.

The Multifluid-PBE model

Single-phase fluid flow systems can be described using continuum equations for the (one) fluid in question, two-phase systems require two sets of equations, three-phase require three and so on. Multi-fluid models describe a single phase, but allow for variations within the phase (e.g. in size), i.e. allowing for multiple fluids within one fluid. Multifluid-PBE utilise the population balance framework in modeling the fluid. Multifluid-models applied on dispersed flows describe multiple fluids within the dispersed phase, e.g. gas bubbles with different size. We will here use a multifluid-PBE model for the dispersed phase and conventional cross-sectionally averaged equations for the slurry phase. The population in question is a number (mass) density of particles in the particle phase space.

A novel modeling framework has been developed formulating a combined multifluid-PBE model explicitly in terms of a mass density function and solved by weighted residual methods. A high order least squares method was developed for the solution of the PBE containing convection and breakage terms by Dorao (2006) and Dorao and Jakobsen (2006). Zhu (2009) and Zhu *et al.* (2008) extended the constant density model to a steady-state 1D combined multifluid-PBE model with coalescence, including a dispersed phase momentum balance and the corresponding continuity and momentum balances for the liquid phase. Nayak *et al.* (2011) followed up by allowing variable dispersed phase velocity along the reactor length and as a function of particle size, hence $v_r = v_r(z,\xi)$. Sporleder *et al.* (2011) evaluated different inner coordinates, using a similar modelling approach as of Nayak *et al.* (2011). Borka and Jakobsen (2012) modified the coalescence terms in the model proposed by Nayak et al. In terms of numerical solution of PBE problems, the members of the methods of weighted residuals family have been evaluated by Solsvik *et al.* (2014) and Solsvik and Jakobsen (2013b). The potential of the least squares method in particular has been evaluated against the quadrature method of moments (Dorao and Jakobsen, 2006) and the finite difference methods (Zhu *et al.*, 2008).

MODEL DESCRIPTION

Previous work on combined multifluid-PBE models for bubble columns has been reported for cold flow. In this work, the modelling framework is extended to include a chemically reactive process. The model is applied to the Fischer-Tropsch synthesis and solved using the orthogonal collocation method. This section describes the model equations.

Model Assumptions

The slurry bubble column consists of three phases; (i) a gas phase containing reactants and the gaseous products (H_2O and lighter hydrocarbons) (ii) a liquid phase containing dissolved reactants and liquid products (heavier hydrocarbons) and (iii) the solid catalyst particles. The homogeneous pseudo-phase consisting of (ii) and (iii) is referred to as slurry phase. The slurry phase is assumed to consist of liquid with suspended catalyst particles. The suspended catalyst particles are assumed stationary in space over time, and perfectly distributed within the fluid (i.e. no settling of particles). A constant volume fraction of solids per volume of reactor is applied. The pressure is assumed equal in the gas and liquid phases, but varies along the dispersion height. Ideal gas law is assumed valid for the gas phase. A constant liquid density is applied, however, the average molar mass of the liquid is allowed to change along the dispersion height. The reactor is modelled steady-state and isothermal and only the z-direction is considered in external space. The particle phase space consists of z and ξ; particle diameter.

Gas Phase Equations

The model employed in this study represents an extension of the cold flow model by Nayak *et al.* (2011) to reactive systems. A density function describing discrete particles can be defined as

$$p = p(t, \boldsymbol{r}, \xi, \boldsymbol{c}, \tau, \Upsilon, \Omega_i) \tag{3}$$

where t denotes time, $\boldsymbol{r}$ denotes coordinate in physical space, ξ denotes coordinate in property space, $\boldsymbol{c}$ denotes microscopical velocity, τ microscopical temperature, Υ microscopical mass and Ω_i microscopical weight fraction of component i. The term microscopical denotes a property of a single particle, in contrast to a macroscopical property which is the average property for a collection of particles. A Boltzmann-like equation describing the change in the density function in case of particle collisions, birth and death can then be stated as:

$$\frac{Dp}{Dt} = \frac{\partial p}{\partial t}|_{\text{coll}} + \frac{\partial p}{\partial t}|_{\text{B-D}} \tag{4}$$

Writing out the terms gives

$$\frac{\partial p}{\partial t} + \frac{\partial p}{\partial \boldsymbol{r}} \cdot \frac{\partial \boldsymbol{r}}{\partial t} + \frac{\partial p}{\partial \xi}\frac{\partial \xi}{\partial t} + \frac{\partial p}{\partial \boldsymbol{c}} \cdot \frac{\partial \boldsymbol{c}}{\partial t} + \frac{\partial p}{\partial \tau}\frac{\partial \tau}{\partial t} + \frac{\partial p}{\partial \Upsilon}\frac{\partial \Upsilon}{\partial t} + \frac{\partial p}{\partial \Omega_i}\frac{\partial \Omega_i}{\partial t} = \frac{\partial p}{\partial t}|_{\text{coll}} + \frac{\partial p}{\partial t}|_{\text{B-D}} \tag{5}$$

In order to obtain a density function describing an *average* of particles (macroscopical) rather than a single particle (microscopical), the density function is integrated over the desired variables. Further, it is distinguished between a *number* and a *mass* average property. The number average is the amount

of property per number of particles, whilst the mass average is the amount of property per mass of particles. As the goal (for this work) is a density function on the form $f(\boldsymbol{r},\xi,t)$, the averaging procedure must also integrate over the remaining microscopical properties τ, Υ and Ω_i. The integrated density function $f(\boldsymbol{r},\xi,t)$ describing the number of particles per unit phase volume is defined in Equation 6.

$$f(\boldsymbol{r},\xi,t)=\int_{-\infty}^{\infty}p(t,\boldsymbol{r},\xi,\boldsymbol{c},\tau,\Upsilon,\Omega_i)d\boldsymbol{c}d\tau d\Upsilon d\Omega_i\,. \tag{6}$$

The *number average* of a generic property ψ, denoted $\overline{\psi}$, is thus defined as:

$$\overline{\psi}=\frac{1}{f(\boldsymbol{r},\xi,t)}\int_{-\infty}^{\infty}\psi p(t,\boldsymbol{r},\xi,\boldsymbol{c},\tau,\Upsilon,\Omega_i)d\boldsymbol{c}d\tau d\Upsilon d\Omega_i \tag{7}$$

The *mass average* of a generic property ψ, denoted $\langle\psi\rangle$, is given by:

$$\langle\psi\rangle=\frac{1}{\overline{m}f(\boldsymbol{r},\xi,t)}\int_{-\infty}^{\infty}m\psi p(t,\boldsymbol{r},\xi,\boldsymbol{c},\tau,\Upsilon,\Omega_i)d\boldsymbol{c}d\tau d\Upsilon d\Omega_i \tag{8}$$

where $\overline{m}$ is the number average for m obtained inserting for $\psi=m$ in Equation 7. In line with the framework of Chao (2012) and Lindborg (2008), i.e. extending the framework of Nayak *et al.* (2011) to include chemical reaction, the resultant govering equation of change for an average property ψ is thus found from an equivalent to Equation 5 to be:

$$\begin{aligned}&\frac{\partial}{\partial t}(\overline{m}f\langle\psi\rangle)+\nabla_{\boldsymbol{r}}\cdot(\overline{m}f\langle\boldsymbol{c}\psi\rangle)+\frac{\partial}{\partial\xi}(\overline{m}f\langle\Xi\psi\rangle)=\\&\overline{m}f\left\langle\frac{\boldsymbol{F}}{\Upsilon}\cdot\frac{\partial\psi}{\partial\boldsymbol{c}}\right\rangle+\overline{m}f\left\langle\frac{\partial\psi}{\partial\tau}\frac{\partial\tau}{\partial t}\right\rangle+\overline{m}f\left\langle\frac{\partial\Upsilon}{\partial t}\left(\frac{\partial\psi}{\partial\Upsilon}+\frac{\psi}{\Upsilon}\right)\right\rangle\\&+\sum_i\overline{m}f\left\langle\frac{\partial\Omega_i}{\partial t}\frac{\partial\psi}{\partial\Omega_i}\right\rangle\\&+\int_{-\infty}^{\infty}m\frac{\partial p}{\partial t}|_{\text{coll}}\psi d\boldsymbol{c}d\tau d\Upsilon d\Omega_i+\int_{-\infty}^{\infty}m\frac{\partial p}{\partial t}|_{\text{B-D}}\psi d\boldsymbol{c}d\tau d\Upsilon d\Omega_i\end{aligned} \tag{9}$$

where the two latter terms are the source terms describing changes in ψ due to collisions and birth and death processes, respectively. For simplicity, the change in ψ due to birth and death processes is renamed:

$$\int_{-\infty}^{\infty}m\frac{\partial p}{\partial t}|_{\text{B-D}}\psi d\boldsymbol{c}d\tau d\Upsilon d\Omega_i=J(\boldsymbol{r},\xi,t) \tag{10}$$

The change in ψ due to collisions is neglected;

$$\int_{-\infty}^{\infty}m\frac{\partial p}{\partial t}|_{\text{coll}}\psi d\boldsymbol{c}d\tau d\Upsilon d\Omega_i\approx 0 \tag{11}$$

By inserting for the appropriate quantity ψ, the equations for mass ($\psi=1$), species mass ($\psi=\Omega_i$) and momentum ($\psi=c_i$) can be found as:

Mass Conservation

$$\begin{aligned}&\frac{\partial}{\partial t}(m(\boldsymbol{r},\xi,t)f(\boldsymbol{r},\xi,t))+\nabla_{\boldsymbol{r}}\cdot(\boldsymbol{v}_{\boldsymbol{r}}(\boldsymbol{r},\xi,t)m(\boldsymbol{r},\xi,t)f(\boldsymbol{r},\xi,t))\\&+\frac{\partial}{\partial\xi}(v_\xi(\boldsymbol{r},\xi,t)m(\boldsymbol{r},\xi,t)f(\boldsymbol{r},\xi,t))=\Gamma+J(\boldsymbol{r},\xi,t)\end{aligned} \tag{12}$$

Species Mass Conservation

$$\begin{aligned}&\frac{\partial}{\partial t}(\omega_{i,G}(z)m(\boldsymbol{r},\xi,t)f(\boldsymbol{r},\xi,t))+\nabla_{\boldsymbol{r}}\cdot(\langle c\Omega_i\rangle m(\boldsymbol{r},\xi,t)f(\boldsymbol{r},\xi,t))\\&+\frac{\partial}{\partial\xi}(\langle\Xi\Omega_i\rangle m(\boldsymbol{r},\xi,t)f(\boldsymbol{r},\xi,t))=\Gamma_i+J(\Omega_i,\boldsymbol{r},\xi,t)\end{aligned} \tag{13}$$

Momentum Conservation

$$\begin{aligned}&\frac{\partial}{\partial t}(m(\boldsymbol{r},\xi,t)v_{r,i}(\boldsymbol{r},\xi,t)f(\boldsymbol{r},\xi,t))\\&+\nabla_{\boldsymbol{r}}\cdot(\langle\boldsymbol{c}c_i\rangle m(\boldsymbol{r},\xi,t)f(\boldsymbol{r},\xi,t))+\frac{\partial}{\partial\xi}(\langle\Xi c_i\rangle m(\boldsymbol{r},\xi,t)f(\boldsymbol{r},\xi,t))\\&=f(\boldsymbol{r},\xi,t)[v_{r,i}(\boldsymbol{r},\xi,t)\frac{\partial m(\boldsymbol{r},\xi,t)}{\partial t}+\langle\boldsymbol{c}c_i\rangle\cdot\nabla_{\boldsymbol{r}}\,m(\boldsymbol{r},\xi,t)\\&+\langle\Xi c_i\rangle\frac{\partial m(\boldsymbol{r},\xi,t)}{\partial\xi}+\boldsymbol{F}_{\boldsymbol{r}}(\boldsymbol{r},\xi,t)m(\boldsymbol{r},\xi,t)]+J(c_i,\boldsymbol{r},\xi,t)\end{aligned} \tag{14}$$

where it is noted that

$$\begin{aligned}\overline{m}f\left\langle\frac{\partial\Upsilon}{\partial t}\left(\frac{\partial 1}{\partial\Upsilon}+\frac{1}{\Upsilon}\right)\right\rangle=\Gamma\\\overline{m}f\left\langle\frac{\partial\Upsilon}{\partial t}\left(\frac{\partial\Omega_i}{\partial\Upsilon}+\frac{\Omega_i}{\Upsilon}\right)\right\rangle=\Gamma_i\end{aligned} \tag{15}$$

The *mass* average (as opposed to the *number* average) of the microscopical velocities have been inserted; $\langle c_i\rangle=v_{r,i}$ and $\langle\Xi\rangle=v_\xi$. In other words, the individual velocity for each particle multiplied with the individual mass is integrated using the framework given in Equation 8:

$$\begin{aligned}\langle c_i\rangle&=\frac{1}{\overline{m}f(\boldsymbol{r},\xi,t)}\int_{-\infty}^{\infty}mc_ip(t,\boldsymbol{r},\xi,\boldsymbol{c},\tau,\Upsilon,\Omega_i)d\boldsymbol{c}d\tau d\Upsilon d\Omega_i\\&=v_{r,i}(\boldsymbol{r},\xi,t)\end{aligned} \tag{16}$$

$$\begin{aligned}\langle\Xi\rangle&=\frac{1}{\overline{m}f(\boldsymbol{r},\xi,t)}\int_{-\infty}^{\infty}m\Xi p(t,\boldsymbol{r},\xi,\boldsymbol{c},\tau,\Upsilon,\Omega_i)d\boldsymbol{c}d\tau d\Upsilon d\Omega_i\\&=v_\xi(\boldsymbol{r},\xi,t)\end{aligned} \tag{17}$$

The sum (integral) of all particle velocity-times-mass products is divided by the total mass of particles, yielding a mass averaged macroscopical velocity. For the mass averages of the product terms i.e. $\langle\Omega_ic\rangle$ an analogy of the Reynolds decomposition is applied; decomposing the products into an average and a fluctuating term:

$$\langle\Omega_ic\rangle\approx\langle\Omega_i\rangle\langle c\rangle+\langle\Omega_i'c'\rangle \tag{18}$$

The product terms appear in the species mass momentum balances. For the species mass balance, the fluctuating term is modelled analogous to the Boussinesq hypothesis, yielding a diffusion term:

$$\langle\Omega_i'c'\rangle\propto-D_{\text{eff,z,G}}\frac{\partial\omega_{i,G}}{\partial z} \tag{19}$$

For the momentum equation, the fluctuating term is neglected (i.e. neglecting diffusive momentum transport). Further introducing the assumptions of steady-state and z-direction only, along with re-writing the number density function into a mass density function $m(z,\xi)f(z,\xi)=\rho_G(z)V(\xi)f(z,\xi)=f_d(z,\xi)$ gives the

following set of model equations:
Mass Conservation

$$\frac{\partial}{\partial z}(v_r(z,\xi)f_d(z,\xi)) + \frac{\partial}{\partial \xi}(v_\xi(z,\xi)f_d(z,\xi)) = \frac{\partial}{\partial \xi}\Gamma + J(m(z,\xi)) \tag{20}$$

where the source term $J(m(z,\xi))$ is given as (Solsvik and Jakobsen, 2013a):

$$J(m(z,\xi)) = -b(\xi)f_d(z,\xi) + V(\xi)\int_{\xi}^{\xi_{max}} h_b(\xi,\zeta)b(\zeta)\frac{f_d(z,\zeta)}{V(\zeta)}d\zeta - f_d(z,\xi)\int_{\xi_{min}}^{(\xi^3_{max}-\xi^3)^{1/3}} c(\xi,\zeta)\frac{f_d(z,\xi)}{\rho_d(z)V(\zeta)}d\zeta + \frac{\xi^2}{2}\int_{\xi_{min}}^{(\xi^3-\xi^3_{min})^{1/3}} \frac{c([\xi^3-\zeta^3]^{1/3},\zeta)f_d(z,[\xi^3-\zeta^3]^{1/3})f_d(z,\zeta)}{[\xi^3-\zeta^3]^{2/3}V([\xi^3-\zeta^3]^{1/3})\rho_d(z))V(\zeta)}d\zeta \tag{21}$$

Species Mass Conservation

$$\frac{\partial}{\partial z}(v_r(z,\xi)f_d(z,\xi)\omega_{i,G}(z)) + \frac{\partial}{\partial \xi}(v_\xi(z,\xi)f_d(z,\xi)\omega_{i,G}(z)) = \frac{\partial}{\partial z}\left(f_d(z,\xi)D_{\text{eff,z,G}}\frac{\partial \omega_{i,G}}{\partial z}\right) + \frac{\partial}{\partial \xi}\Gamma_i + J(\omega_{i,G}(z)m(z,\xi)) \tag{22}$$

Subtracting continuity (Equation 20) from the species mass balance (Equation 22) gives

$$v_r(z,\xi)f_d(z,\xi)\frac{\partial \omega_{i,G}(z)}{\partial z} = \frac{\partial}{\partial z}\left(f_d(z,\xi)D_{\text{eff,z,G}}\frac{\partial \omega_{i,G}}{\partial z}\right) + \frac{\partial}{\partial \xi}\Gamma_i - \omega_{i,G}(z)\frac{\partial}{\partial \xi}\sum_i \Gamma_i + J(\omega_{i,G}(z)m(z,\xi)) - \omega_{i,G}(z)J(m(z,\xi)) \tag{23}$$

Since ω_i is independent of ξ, Equation 23 can be averaged over ξ - resulting in the conventional axial dispersion model defined as:

$$\rho_G(z)v_G(z)\alpha_G(z)\frac{d\omega_{i,G}(z)}{dz} = -\omega_{i,G}(z)\sum_i \Gamma_i(z) - \frac{dj_{i,G}(z)}{dz} + \Gamma_i(z) \tag{24}$$

where the effective dispersion flux $j_{i,G}$ is defined as

$$j_{i,G}(z) = -\int_{\Omega_\xi} f_d(z,\xi)d\xi D_{\text{eff,z,G}}\frac{d\omega_{i,G}(z)}{dz} = -\alpha_G(z)\rho_G(z)D_{\text{eff,z,G}}\frac{d\omega_{i,G}(z)}{dz} \tag{25}$$

and the mass tranfer term is given as

$$\Gamma_i = -k_{L,i}(z)a_L(z)\rho_l\left(\frac{1}{K_i}\frac{\overline{M_G}(z)}{\overline{M_L}(z)}\omega_{i,G}(z) - \omega_{i,L}(z)\right) \tag{26}$$

Momentum Conservation

$$\frac{\partial}{\partial z}(f_d(z,\xi)v_r(z,\xi)v_r(z,\xi)) + \frac{\partial}{\partial \xi}(f_d(z,\xi)v_\xi(z,\xi)v_r(z,\xi)) = +J(z,xi,c_i) - \frac{f_d(z,\xi)}{\rho_G(z)}\frac{\partial p(z)}{\partial z} + f_d(z,\xi)g + f_{\text{drag}}(z,\xi) \tag{27}$$

The relative size of the drag force term is very large compared to the convective and diffusion terms. Therefore, the latter terms are neglected. The term $J(z,\xi,c_i)$, denoting momentum transfer due to bubble interactions is also neglected. The drag force is defined as (Patruno *et al.*, 2009)

$$f_{\text{drag}}(z,\xi) = -\frac{3}{4}\rho_L\frac{C_D}{\xi}\frac{f_d(z,\xi)}{\rho_G(z)}|v_r(z,\xi)-v_L(z)|(v_r(z,\xi)-v_L(z)) \tag{28}$$

The drag coefficient C_D for clean water by Tomiyama (1998) (see Table 4) is applied. A correction factor for the drag coefficient C_D relative to gas volume was implemented. The correction factor p (see Table 4) introduced by Ishii and Zuber (1979) and later discussed by Rampure *et al.* (2007) was set to $p = 2$.

Liquid Phase Equations

For the liquid phase, the standard cross-sectionally averaged equations are applied. The continuity equation for the liquid phase is given as:
Mass Conservation

$$\frac{\partial}{\partial z}(\rho_L v_L(z)\alpha_L(z)) = -\sum_i \Gamma_i(z) \tag{29}$$

For the species mass balance in the liquid phase, the axial dispersion model subtracting continuity (equation 29) is used:
Species Mass Conservation

$$\rho_L v_L(z)\alpha_L(z)\frac{d\omega_{i,L}(z)}{dz} = \omega_{i,L}(z)\sum_i \Gamma_i(z) - \frac{dj_{i,L}(z)}{dz} - \Gamma_i(z) + R_i(z) \tag{30}$$

$$j_{i,L}(z) + \alpha_L(z)\rho_L D_{\text{eff,z,L}}\frac{d\omega_{i,L}(z)}{dz} = 0 \tag{31}$$

were Γ_i is defined as in equation 26 and R_i is defined as

$$R_i(z) = \nu_i r_{CO}(z)M_{w,i}\rho_{cat} \tag{32}$$

It is desired to express the reaction rate in terms of liquid concentrations. Hence the expression is re-written based on the simplified relation:

$$K_i x_i = y_i = p_i/p \tag{33}$$

where y_i and x_i are the gas and liquid mole fractions of species i. Values for K_i have been found using the process simulation software Aspen HYSYS®. The kinetic rate expression then yields

$$r_{CO}(z) = \frac{aK_{CO}x_{CO}(z)K_{H_2}x_{H_2}(z)p(z)^2}{(1+bK_{CO}x_{CO}(z)p(z))^2} \tag{34}$$

The product distribution was described using the well-known Anderson-Schlulz-Flory distribution

$$x_{\text{n}} = (1-\alpha_{ASF})\alpha_{ASF}^{\text{n}-1} \tag{35}$$

The reaction products were lumped into four groups; C_1-C_{10}, C_{11}-C_{20}, C_{21}-C_{30}, and C_{31+}.
Momentum Conservation
The liquid phase momentum equation is given by

$$\alpha_L(z)\rho_L v_L(z)\frac{\partial v_L(z)}{\partial z} = -\alpha_L(z)\frac{\partial p(z)}{\partial z} - \int_0^\infty f_{\text{drag}}(z,\xi)d\xi + \alpha_L(z)\rho_L g \tag{36}$$

Additional Equations

In addition to the equations given above, the sum of the volume fractions must be unity:

$$\alpha_L(z) + \alpha_s + \alpha_G(z) = 1 \tag{37}$$

The volume fraction α_G is computed as

$$\alpha_G(z) = \int_0^\infty \frac{f_d(z,\xi)}{\rho_G(z)} d\xi \tag{38}$$

The gas phase density is calculated from the ideal gas law:

$$\rho_G(z) = \frac{p(z)\overline{M_G}(z)}{RT} \tag{39}$$

The particle Reynolds number, Re_p and the Eötvös number, E_0, are defined as:

$$Re_p(z,\xi) = \frac{\rho_L |v_r(z,\xi) - v_L(z)|\xi}{\mu_L(z)} \tag{40}$$

$$E_0(z,\xi) = \frac{g(\rho_L - \rho_G(z))\xi^2}{\sigma_L(z)} \tag{41}$$

Initial and Boundary Conditions

Both inlet superficial velocities were set:

$$\begin{aligned} v_G^s|_{z=0} &= v_G^{s,0} \\ v_L^s|_{z=0} &= v_L^{s,0} \end{aligned} \tag{42}$$

The species mass balances were written as a set of two equations; Equation 30 (solving for flux j_i) and Equation 31 (solving for ω_i) for each phase. For Equations 24, 30 the derivative of the flux at the outlet was set to zero:

$$\begin{aligned} \frac{dj_{i,G}}{dz}|_{z=L} &= 0 \\ \frac{dj_{i,L}}{dz}|_{z=L} &= 0 \end{aligned} \tag{43}$$

For Equations 25, 31 the weight fractions were specified at the inlet for each component:

$$\begin{aligned} \omega_{i,G}|_{z=0} &= \omega_{i,G,0} \\ \omega_{i,L}|_{z=0} &= \omega_{i,L,0} \end{aligned} \tag{44}$$

For the momentum balance in the gas phase, used to calculate the gas phase velocity, no initial condition is required as this is an algebraic equation with the simplifications presented (diffusion, source/sink and convection terms neglected). For the momentum balance in the liquid phase (Equation 36), the outlet pressure was specified:

$$p_{|z=L} = p_0 \tag{45}$$

The initial bubble size distribution $f_d(z_0,\xi)$ was chosen as a Gaussian curve with the following parameters:

$$f_d(z_0,\xi) = \frac{k_1}{k_2\sqrt{\pi}} exp\left[-\frac{(\xi-\overline{\xi})^2}{2k_2^2}\right] \tag{46}$$

where $k_1 = 4$, $k_2 = 0.0009$, $\overline{\xi} = 12$ mm. Further,

$$f_d(z,\xi = \xi_{min}) = 0 \tag{47}$$

for all values of z.

SIMULATION SETUP

The model above and boundary conditions were implemented by use of the programming language MATLAB®. Correlations used for the parameters in the model are given in Table 4. Operating conditions are given in Table 1. Physical properties of the gases and liquids are given in Table 2, other parameters in Table 3. The breakage frequency function $b(\xi)$ by Coulaloglou and Tavlarides (1977) was used along with the daughter redistribution function $h_b(\zeta)$ of Diemer and Olson (2002). The coalescence efficiency function $c(\xi,\zeta)$ of Prince and Blanch (1990) was utilised.

Table 1: Operating conditions.

Reactor temperature	T	220 °C
Reactor outlet pressure	p_0	3 MPa
Inlet superficial gas velocity	$v_G^{s,0}$	0.26 m/s
Inlet superficial liquid velocity	$v_L^{s,0}$	0.01 m/s
Dispersion (reactor) height	H	50 m
Reactor diameter	D	9 m
Catalyst volume fraction in reactor	α_s	0.05
Product distribution parameter	α_{ASF}	0.9
Inlet gas wt. fraction, CO	$\omega_{CO,G,0}$	0.8698
Inlet gas wt. fraction, H_2	$\omega_{H_2,G,0}$	0.1243
Inlet gas wt. fraction, H_2O	$\omega_{H_2O,G,0}$	0.002
Inlet gas wt. fraction, C_1-C_{10}	$\omega_{C_1-C_{10},G,0}$	0.003
Inlet gas wt. fraction, C_{11}-C_{20}	$\omega_{C_{11}-C_{20},G,0}$	0.002
Inlet gas wt. fraction, C_{21}-C_{30}	$\omega_{C_{21}-C_{30},G,0}$	0.003
Inlet gas wt. fraction, C_{31}+	$\omega_{C_{31+},G,0}$	0.0049
Inlet liquid wt. fraction, CO	$\omega_{CO,L,0}$	0.0012
Inlet liquid wt. fraction, H_2	$\omega_{H_2,L,0}$	0.0001
Inlet liquid wt. fraction, H_2O	$\omega_{H_2O,L,0}$	0.0000
Inlet liquid wt. fraction, C_1-C_{10}	$\omega_{C_1-C_{10},L,0}$	0.0000
Inlet liquid wt. fraction, C_{11}-C_{20}	$\omega_{C_{11}-C_{20},L,0}$	0.0001
Inlet liquid wt. fraction, C_{21}-C_{30}	$\omega_{C_{21}-C_{30},L,0}$	0.0025
Inlet liquid wt. fraction, C_{31}+	$\omega_{C_{31+},L,0}$	0.9960
H_2/CO feed (mole based) ratio	-	2

Table 2: Gas and liquid properties.

Liquid density	ρ_L	651 kg/m^3
Catalyst density	ρ_s	3154 kg/m^3
Liquid surface tension	σ_L	0.017 N/m

Table 3: Parameter values.

Breakage kernel pre-factor	K_B	2×10^{-3}
Coalescence kernel pre-factor	K_C	3×10^{-5}

RESULTS AND DISCUSSION

Conversion

The overall conversion of CO in the reactor was 45%. For $T = 220°$ C, 3 MPa, superficial gas velocity of 0.26 m/s, H_2/CO-ratio of 2 and $C_S = 550 kg/m^3$, Sehabiague and Morsi (2013) found a syngas conversion of 45-50 %. Maretto and Krishna (1999) found a conversion of 0.45 for $\alpha_S = 0.2$ (lowest simulated) for a 7m diameter, 30m high reactor. The simulated results are in the same range. The weight fractions for gas and liquid phase are shown in 4 and 5. The concentration of CO and H_2 are decreasing, but the reactor is far from 100

Table 4: Correlations for the parameters in the model, taken from (in order of appearance): Deckwer *et al.* (1980), Yang and Fan (2003), Tomiyama (1998), Ishii and Zuber (1979), Calderbank and Moo-Young (1961) .

$D_{\text{eff,z}} = 0.68 D^{n_D} v_G^{s,0.3}$ (SI units)
$n_D = n_{D,0}(1 - 0.11 ln\left(\frac{\rho_G}{\rho_{G,0}}\right))$; $n_{D,0} = 1.34$
$C_D^0 = \max\left\{\min\left[\frac{16}{Re_p(1+0.15Re_p^{0.687})}, \frac{48}{Re_p}\right], \frac{8}{3}\frac{E_0}{E_0+4}\right\}$
$C_D = C_D^0(1-\alpha_G)^p$
$k_L = 0.42(N_{Sc})^{-1/2}\left(\frac{\Delta\rho\mu_L g}{\rho_L^2}\right)^{1/3}$

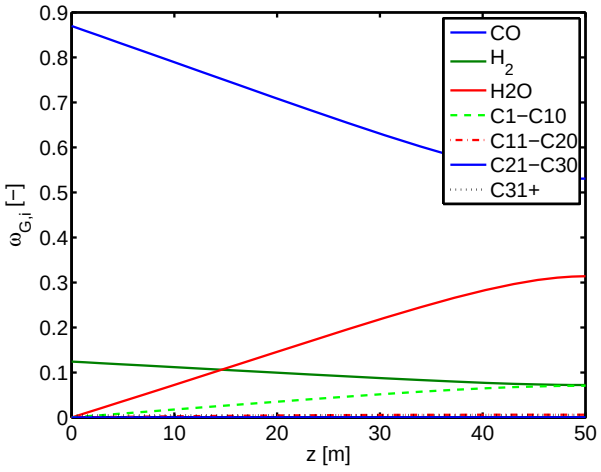

Figure 4: Gas weight fractions.

% conversion. The gaseous reaction products, H_2O being the largest, are shown to increase throughout the reactor. The liquid phase gas fractions do not change much, as the reactor is initially charged with a weight fraction of heavy product (C_{31+}) close to 1.

Pressure

Figure 6 shows the pressure profile in the column. As expected, the profile is close to linear, indicating a hydrostatic pressure profile. The pressure difference from bottom to top corresponds to the weight of the 50 m high liquid column with a gas holdup α_G of approximately 0.5.

Gas Density

Figure 7 shows the gas density. The gas density is increasing throughout the reactor due to the formation of heavier products than the reactants. This effect is more important than the effect of a decreasing pressure. Close to the outlet of the reactor, the boundary conditions imply a flat concentration profile and hence a relatively flat density profile.

Gas Velocity

The velocity of the gas phase calculated from the momentum equation is shown in figures 8 and 9, where the latter is integrated over the bubble size ξ. The drop in the velocity at the inlet of the reactor is due to the decrease in bubble rise velocity caused by the drag force.

Gas Holdup

The drag force also affects the gas volume fraction, as seen in Figure 10. A steep increase due to the decrease in bubble rise velocity is seen at the inlet. The gas volume fraction overall

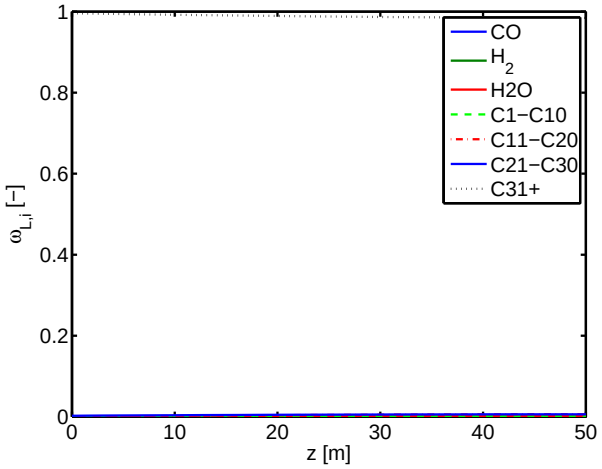

Figure 5: Liquid weight fractions.

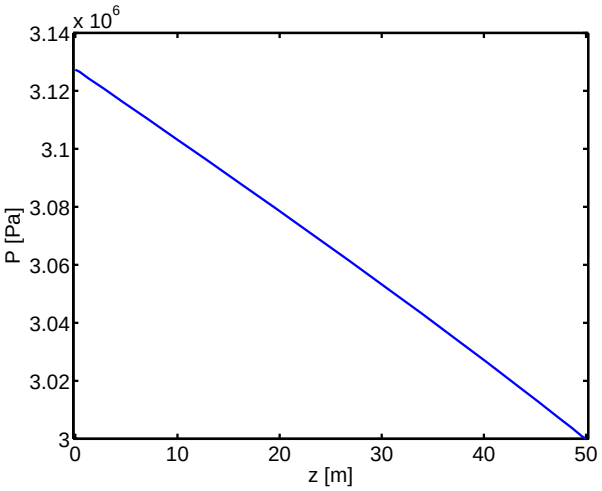

Figure 6: Pressure profile.

decreases throughout the reactor due to the net formation of fewer gas molecules by the chemical reaction. Sehabiague (2012) measured the gas holdup in a system with N_2 and He in Sasol wax, obtaining $\alpha_G = 0.4$ at $3MPa$, 450 K, 0.24 m/s gas superficial velocity and 10 vol% Al_2O_3. Behkish *et al.* (2007) measured the total gas holdup in N_2-Isopar-M and H_2-Isopar-M at different pressures and with solids concentrations of 0, 10 and 20 vol%. For 10 % solids concentration and 30MPa, the value for α_G was 0.45 for N_2-Isopar-M and slighly above 0.3 for H_2-Isopar-M. For both systems, the gas holdup decreased with increased solids concentration. In the case of no solids, the volume fraction was $\alpha_G = 0.6$ and $\alpha_G = 0.4$ respectively. The gas holdup was found to increase with higher pressure. By distinguishing between the total holdup and the holdup of large bubbles only, Behkish *et al.* (2007) found that the holdup of large gas bubbles remained constant when the pressure increased, whilst the total holdup increased. This indicated that higher pressure increases the holdup of smaller bubbles. This finding was also supported by Jordan *et al.* (2003). Fan *et al.* (1999) found that the rise velocity of single bubbles in liquids and liquid-solid suspensions decreased with an increase in pressure. This decrease, along with the pressure effect of reducing the bubble size, contributes to high gas holdups observed at high pressures.

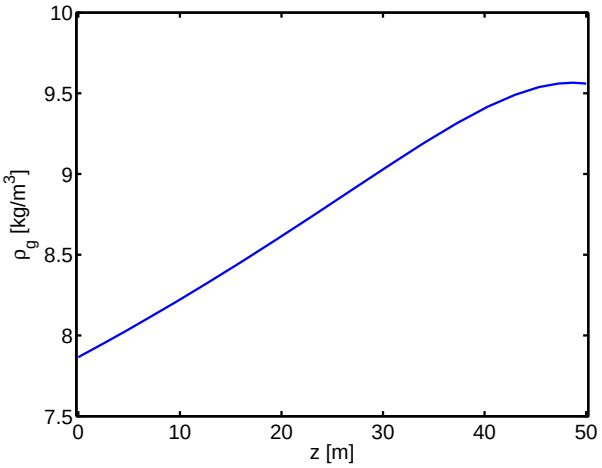

Figure 7: Gas density.

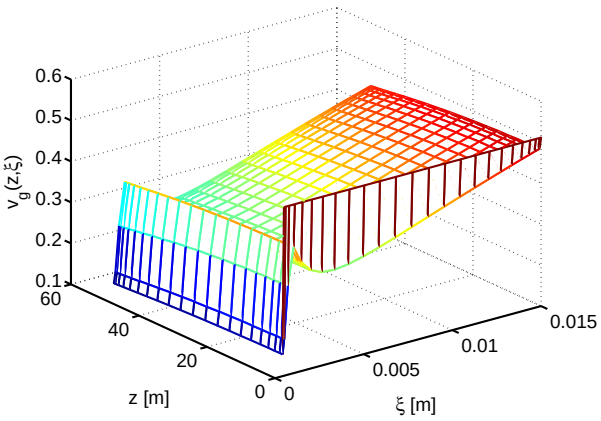

Figure 8: Gas phase velocity.

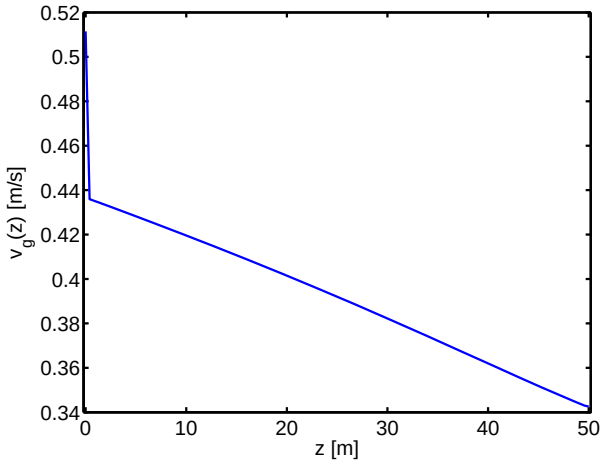

Figure 9: Cross-sectionally averaged gas phase velocity.

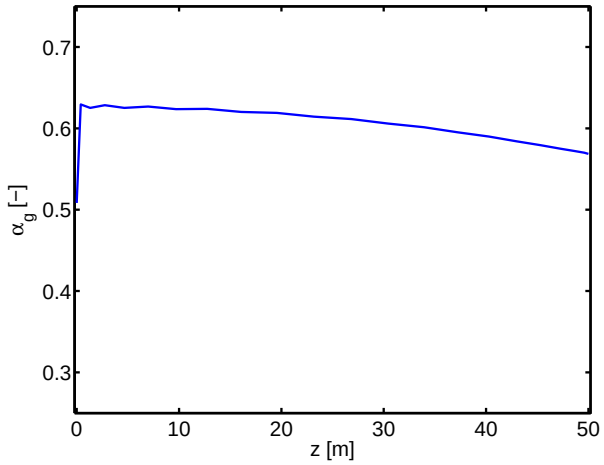

Figure 10: Gas volume fraction.

The authors also found a significant decrease in the rise velocity for high solids holdups, especially for high viscosity. High pressure and high gas density are related and give rise to similar effects on the gas holdup when the concentration increase is due to increased pressures. However, as is the case for chemical reaction, when the gas density is altered due to change in composition, the gas holdup increases with higher density (Sehabiague, 2012). This is the opposite of what is seen in Figure 10. As there is a net decrease in the number of moles of gaseous molecules during the Fischer-Tropsch reaction, the volume of gas is decreasing along the reactor height, even though the density increases.

Liquid Velocity

The velocity of the continous phase calculated from the liquid phase continuum equation shows an increase due to the change in the volume fraction at the inlet. Towards the top of the reactor the liquid velocity is slightly decreasing, as the liquid volume fraction is increasing.

Bubble size

The bubble size, represented by the Sauter mean diameter (Figure 12) is decreasing throughout the reactor. Behkish *et al.* (2007) measured the bubble size distribution in N_2/Isopar-M/Alumina and H_2/Isopar-M/Alumina at 12.31 bar and 0.176m/s superficial gas velocity. For N_2 the Sauter mean diameter increased from below 1 mm to 10 mm for values from 0 to 15 vol% alumina. For 10 % the value was approximately 6 mm. For H_2 the Sauter mean diameter incresed from 2 to 8 mm, with a value of about 6 mm at 10 vol% alumina. The Sauter mean diameter was found to decrease with increasing pressure. In the study by Behkish *et al.* (2007) the increase in solids concentration appeared more important than that of increasing pressure. Increasing the pressure caused an increase in volume fraction of small bubbles, whereas increasing the solids content decreased the volume fraction of small bubbles. In the same study, the total gas holdup was found to increase with temperature due to the decrease of liquid viscosity and surface tension. Sehabiague (2012) found that the Sauter mean diameter decreased with increasing gas concentration. The effect of gas-liquid surface tension is accounted for through the breakage and coalescence functions. The predicted bubble sizes lie in the upper range of the mean bubble sizes found in the literature.

Validity of assumptions

In particular, the assumptions of uniform solids distribution and uniform temperature need to be addressed. The solids distribution affects the concentration profile as the reaction rate is a function of the amount of catalyst present. de Swart and Krishna (2002) found a rather flat catalyst profile over the reactor using a liquid velocity of 0.01 m/s. The temper-

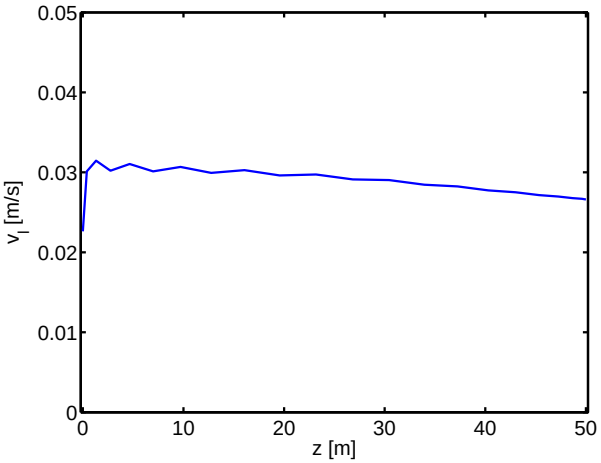

Figure 11: Continous phase velocity.

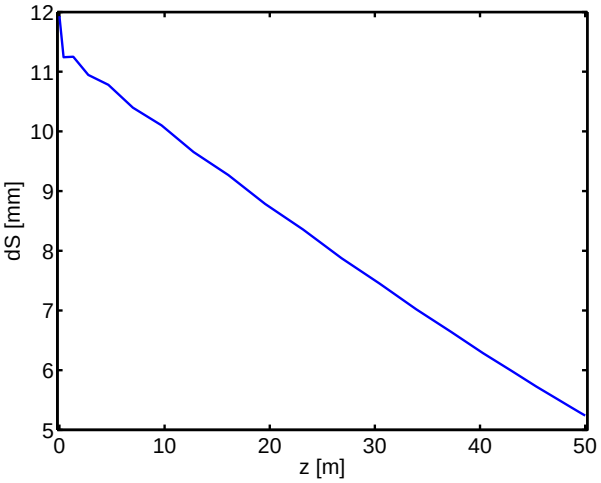

Figure 12: Sauter mean diameter.

ature also affects conversion, as the reaction rate is largely dependent on temperature. Increasing temperature gives increased reaction rate. de Swart and Krishna (2002) simulated FTS dynamically in a SBC with diameter 7.5 m and a dispersion height of 30 m and found a temperature difference between inlet and outlet of between 2 and 20 K dependent on the axial dispersion. This indicates that the deviations using an isothermal temperature profile is not significant for high backmixing levels, but may be important for low levels of backmixing.

CONCLUSION

A two-dimensional steady-state isothermal combined multifluid-population balance equation (PBE) model for a slurry bubble column was implemented for the Fischer-Tropsch synthesis (FTS). The flow variable profiles are considered reasonable although no experimental data for direct validation of the velocity profiles are available. Moreover, the chemical part of the model predicts results giving a chemical conversion of the reactants in good agreement with literature experimental data. The model can be used to study the influence of bubble size on flow profile and conversion for the FTS in a SBC. Further improvements of the model may include temperature dependency and a non-uniform

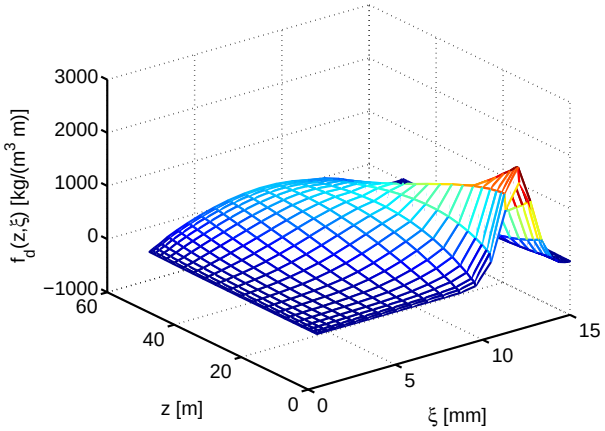

Figure 13: Bubble size distribution.

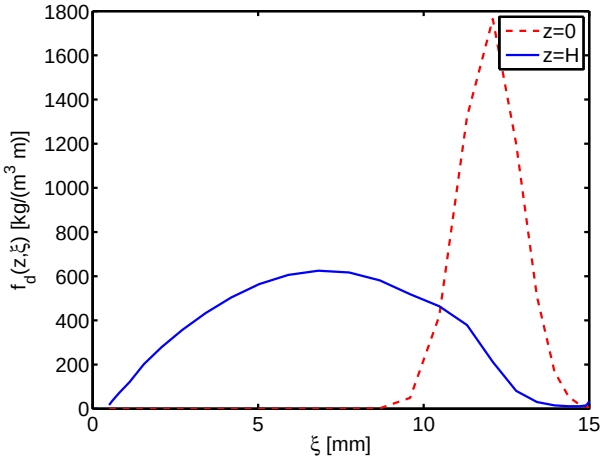

Figure 14: Inlet and outlet bubble size distribution.

catalyst profile throughout the reactor.

REFERENCES

BEHKISH, A. *et al.* (2007). "Gas holdup and bubble size behavior in a large-scale slurry bubble column reactor operating with an organic liquid under elevated pressures and temperatures". *Chemical Engineering Journal*, **128**, 69–84.

BORKA, Z. and JAKOBSEN, H.A. (2012). "Least squares higher order method for the solution of a combined multifluid-population balance model: Modeling and implementation issues". *Procedia Engineering*, **42**, 1121–1132.

CALDERBANK, P.H. and MOO-YOUNG, M.B. (1961). "The continous phase heat and mass-transfer properties of dispersions". *Chemical Engineering Science*, **16**, 39–54.

CHAO, Z. (2012). *Modeling and Simulatino of Reactive Three-phase FLows in Fluidized Bed Reactors: Application to the SE-SMR Process*. Ph.D. thesis, Norwegian University of Science and Technology (NTNU).

COULALOGLOU, C. and TAVLARIDES, L. (1977). "Description of interaction processes in agitated liquid-liquid dispersions". *Chem. Eng. Sci.*, **(30)**, 1289–1297.

DE SWART, J. and KRISHNA, R. (2002). *Chemical Engineering and Processing*, **41**, 35–47.

DECKWER, W.D. *et al.* (1980). "Hydrodynamic properties of the fischer-tropsch slurry process". *Industrial and Engineering Chemistry Process Design and Development*, **19(4)**, 699–708.

DIEMER, R.B. and OLSON, H.J. (2002). *Chemical Engineering Science*, **57**, 4187–4198.

DORAO, C.A. (2006). *High Order Methods for the Solution of the Population Balance Equation with Applications to Bubbly Flows*. Ph.D. thesis, Norwegian University of Science and Technology (NTNU).

DORAO, C.A. and JAKOBSEN, H.A. (2006). "The quadrature method of moments and its relationship with the method of weighted residuals". *Chemical Engineering Science*, **61**, 7795–7804.

FAN, L.S. *et al.* (1999). *Chemical Engineering Science*, **54**, 4681–4709.

GUTTEL, R. (2009). Ph.D. thesis, Clausthal University of Technology.

INGA, J.R. and MORSI, B.I. (1996). "A novel approach for the assessment of the rate-limiting step in fischerâĽŠtropsch slurry process". *Energy & Fuels*, **10(3)**, 566–572.

ISHII, M. and ZUBER, N. (1979). "Drag coefficient and relative velocity in bubbly, droplet or particulate flows". *AIChE Journal*, **25**, 843–855.

JORDAN, U. *et al.* (2003). "Dynamic gas disengagement in a high-pressure bubble column". *The Canadian Journal of Chemical Engineering*, **81**, 491–498.

KOHLER, M.A. (1986). "Comparison of mechanically agitated and bubble column slurry reactors". *Applied Catalysis*, **22**, 21–53.

LINDBORG, H. (2008). *Modeling and Simulations of Reactive Two-Phase Flows in Fluidized Beds*. Ph.D. thesis, Norwegian University of Science and Technology (NTNU).

MARETTO, C. and KRISHNA, R. (1999). "Modelling of a bubble column slurry reactor for fischer-tropsch synthesis". *Catalysis Today*, **52(2-3)**, 279–289.

NAYAK, A. *et al.* (2011). "A combined multifluid-population balance model for vertical gas-liquid bubble-driven flows considering bubble column operating conditions". *Ind. Eng. Chem. Res.*, **50(3)**, 1786–1798.

PATRUNO, L.E. *et al.* (2009). "Identification of droplet breakage kernel for population balance modelling". *Chemical Engineering Science*, **64**, 638–645.

PRINCE, M.J. and BLANCH, H.W. (1990). *AIChE*, **36**, 1485–1499.

RAMPURE, M.R. *et al.* (2007). "Hydrodynamics of bubble column reactors at high gas velocity: Experiments and computational fluid dynamics (cfd) simulations". *Industrial & Engineering Chemical Research*, 8431–8447.

SEHABIAGUE, L. (2012). *Modeling, Scaleup and optimisation of slurry bubble column reactors for Fischer-Tropsch synthesis*. Ph.D. thesis, University of Pittsburgh.

SEHABIAGUE, L. and MORSI, B.I. (2013). "Modeling and simulation of a fischerâĂŞtropsch slurry bubble column reactor using different kinetic rate expressions for iron and cobalt catalysts". *International Journal of Chemical Reactor Engineering*, **11(1)**, 1–22.

SOLSVIK, J. and JAKOBSEN, H. (2013a). "On the solution of the population balance equation for bubbly flows using the high-order least squares method: implementation issues". *Rev. Chem. Eng.*, **29(2)**, 63–98.

SOLSVIK, J. and JAKOBSEN, H.A. (2013b). "Evaluation of weighted residual methods for the solution of a population balance model describing bubbly flows: The least-squares, galerkin, tau, and orthogonal collocation methods". *Industrial & Engineering Chemistry Research*, **52(45)**, 15988–16013.

SOLSVIK, J. *et al.* (2014). "On the solution fo the dynamic population balance model describing emulsification: evaluation of weighted residual methods". *The Canadian Journal of Chemical Engineering*, **92**, 250–265.

SPORLEDER, F. *et al.* (2011). "Model based on population balance for the simulation of bubble columns using methods of the least-square type". *Chemical Engineering Science*, **66**, 3133–3144.

TOMIYAMA, A. (1998). "Struggle with computational bubble dynamics". *Multiphase Science and Technology*, **10(4)**, 369–405.

WANG, T. *et al.* (2007). "Slurry reactors for gas-to-liquid processes:âĂŹ a review". *Industrial & Engineering Chemistry Research*, **46(18)**, 5824–5847.

YANG, G. and FAN, L. (2003). *AIChE*, **49**, 1995–2008.

YATES, I.C. and SATTERFIELD, C.N. (1991). "Intrinsic kinetics of the fischer-tropsch synthesis on a cobalt catalyst". *Energy & Fuels*, **5(1)**, 168–173.

ZHU, Z. (2009). *The Least-Squares Spectral Element Method Solution of the Gas-Liquid Multi-fluid Model Coupled with the Population Balance Equation*. Ph.D. thesis, Norwegian University of Science and Technology (NTNU).

ZHU, Z. *et al.* (2008). "A least-squares method with direct minimization for the solution of the breakage-coalescence population balance equation". *Math. Comput. Simul.*, **79(3)**, 716–727.

DEM-CFD SIMULATIONS AND IMAGING EXPERIMENTS ON CHARGING OF PNEUMATICALLY CONVEYED POWDERS

Martin W. KOREVAAR[1*], **Johan T. PADDING**[1†], **Jue WANG**[2], **Martin DE WIT**[2], **Maarten A.I. SCHUTYSER**[2], **Martin A. VAN DER HOEF**[3], **Hans (J.A.M.) KUIPERS**[1]

[1]Eindhoven University of Technology, Department of Chemical Engineering and Chemistry, P.O. box 513, 5600 MB Eindhoven, THE NETHERLANDS

[2]Wageningen University, Department of Food Process Engineering, P.O. box 17, 6700 AA Wageningen, THE NETHERLANDS

[3]Twente University, Department of Physics, P.O. box 217, 7500 AE Enschede, THE NETHERLANDS

[*] E-mail: m.w.korevaar@tue.nl
[†] E-mail: j.t.padding@tue.nl

ABSTRACT

As the world population increases, the demand for food increases as well. This urges the production of (enriched) food to become more energy efficient in order to have a sustainable situation. A possible approach is to switch to separation techniques that do not require water. One such a method is tribo-electric separation where the driving force for separation is the different polarity and/or magnitude acquired by different fractions due to contact charging (also known as tribo-electric charging or tribo-electrification). Contact charging occurs always when objects of different material touch; the magnitude and polarity is a property of the combination of the two touching materials. Consequently, the method is suitable to separate mixtures in which the components have sufficiently different charging characteristics. Many configurations are possible to utilize contact charging to charge powders. Here we investigate pneumatic conveying of powder through a metal duct; while traveling through the duct, particles will hit the walls and acquire charge. As the experimental set-up is such that optical access is possible, Digital Image Analysis is performed on the duct. From this, the particles' spatial distribution in the duct can be determined. The results show the same trend as predicted by our simulations.

Keywords: Tribo-electrification (contact charging), powders, pneumatically conveyed, particle distribution, DEM-CFD, Digital Image Analysis (DIA) .

NOMENCLATURE

Greek Symbols

α	Charging efficiency, $[-]$.
β	Coefficient of tangential restitution, $[-]$.
Δt_{DEM}	Time step size of DEM. $[s]$.
Δt_{CFD}	Time step size of flow solver. $[s]$.
Δq	Charge acquired in one collision, $[C]$.
δ	Overlap of colliding particles, $[m]$.
ε	Porosity, $[-]$.
ε_0	Permittivity of vacuum, $[Fa\,m^{-1}]$.
η	Dynamic viscosity, $[kg\,m^{-1}s^{-1}]$
ζ	Damping coefficient , $[s\,kg^{-1}]$.
μ	Coefficient of friction, $[-]$.
ρ	Mass density, $[kg\,m^{-3}]$.
σ_{sat}	Saturation charge density, $[C\,m^{-2}]$.
Φ	Electric potential, $[J\,C^{-1}]$.
ω	Angular velocity, $[s^{-1}]$

Latin Symbols

A^*	Effective area, $[m^2]$.
A	Area, $[m^2]$.
D	Diameter, $[m]$.
e	Coefficient of normal restitution, $[-]$.
$\mathbf{e}$	Unit vector, $[-]$.
$\mathbf{F}$	Force, $[N]$.
I	Moment of inertia, $[kg\,m^2]$.
k	Spring stiffness, $[N\,m^{-1}]$.
L_x, L_y, L_z	Length of duct in depth, width and axial direction, $[m]$.
m	Mass, $[kg]$.
$\dot{m}$	Mass rate, $[kg\,s^{-1}]$.
N	Number of subscript, $[-]$.
N_x, N_y, N_z	Number of flow cells in depth, width and axial direction, $[-]$.
p	Pressure, $[Pa]$.
R	Radius, $[m]$.
$\mathbf{r}$	Interparticle distance vector, $[m]$.
$\mathbf{T}$	Torque, $[N\,m]$.
t	Time, $[s]$.
q	Charge, $[C]$.
$\mathbf{v}$	Velocity, $[m\,s^{-1}]$.
x, y, z	Position in depth, width and axial direction, $[m]$.

Sub/superscripts

∇p	Pressure gradient.
bg	Background.
c	Contact.
D	Drag.
el	Electrostatic.
g	Gas.
i	Index i.
im	Regarding image charges.
j	Index j.
n	Normal direction.
p	Particle.
$p \rightarrow p$	Particle-to-particle.
$p \rightarrow w$	Particle-to-wall.
t	Tangential direction.

INTRODUCTION

Contact charging or triboelectrification is the ubiquitous phenomenon of material acquiring charge when they make contact with another material; this is often enhanced by rubbing. For example, when you get charged when walking on

a carpet which manifests itself by the shock you get when touching the door knob. Or when your hair becomes electrostatically charged due to the combing, resulting in a bad hair day. But contact charging is not just the cause these annoying daily life problems, it also gives rise to major industrial scale issues. For example, the triboelectrification of particles in fluidized beds when used for polyethylene production causes sheeting of the walls which leads to costly reactor shut down(Giffin and Mehrani, 2013) or the risks of dust explosions ones the particles get charged (Bailey, 1993). On the other hand, triboelectrification can also be applied beneficially , as is done in electrostatic coating (Mayr and Barringer, 2006) or electrostatic separation. The latter is generally referred to as tribo(electric) separation. The driving force of this separation procedure is the different polarity and/or magnitude that different materials acquire when making contact (Higashiyama and Asano, 1998; Dascalescu *et al.*, 1999; Wu *et al.*, 2013).

Although the charging of materials on contact was already observed in ancient Greece, its mechanism is still obscure. It is for example still unknown whether the charging occurs due to transfer of electrons or ions, the exchange of material or maybe a combination of them all. A very small overview of previous work is given in the following; for a comprehensive review on this matter, the reader is referred to the excellent paper of (Matsusaka *et al.*, 2010).

The literature shows a great deal of experiments performed on many configurations with respect to contact charging. Charging during continuous contact (Harper, 1951; Greason, 2000; Peterson, 1954) or due to impact (Matsuyama and Yamamoto, 1995b,a) , on single particles (Watanabe *et al.*, 2006) or on an ensemble of particles (Watano, 2006). All these methods try to determine the charge on the particle, or in case of many particles, the average charge on the particles. As a different approach, (Murtomaa *et al.*, 2002) investigated the covering of the wall due to the sticking of the charged particles and how it influenced charge on the particles. With a microscope the wall was imaged and they found that the smaller particles stick to the wall which hampered the charging of the bigger glucose particles (Watano, 2006). Another way of examining the influence of charge on particle distribution is to investigate the sheeting after the experiments stopped by opening the duct, as is done in (Sowinski *et al.*, 2012).

The novelty in this work is that we show that the particles' spatial distribution can be measured *in situ*. This is been achieved using a high speed, high resolution camera in combination with Digital Image Analysis (DIA) which is possible because the duct though which the particles are blown through is optical accessible. The distributions are compared to those retrieved from similar DEM-CFD simulations which incorporate electrostatic interaction and contact charging. Both experiments and simulation show the same trend.

METHODS

Model description

In this work a CFD-DEM model is applied; the gas phase is solved using Computational Fluid Dynamics while the particle dynamics are determined by solving Newton's second law. The dynamics of the two phases are solved in a coupled fashion by the interphase drag and the porosity; an overview of the interactions is given in Fig. 1. This has been implemented in an in-house code which has been extensively described in previous work (Van der Hoef *et al.*, 2006, 2008). This code is extended with particle-particle and particle-wall electrostatic interaction as well as a particle charging model to account for triboelectrification; this is elaborately described in (Korevaar *et al.*, 2014). For completeness, the main equations of this framework are here repeated. The values of the most important parameters of the simulation are listed in Table 1.

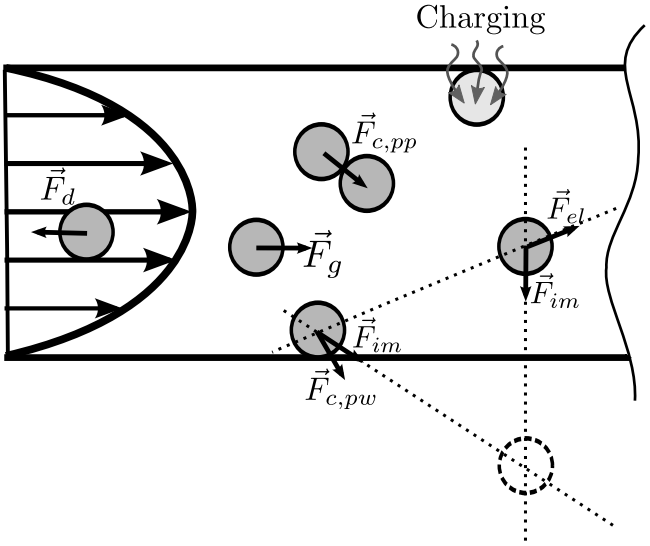

Figure 1: A side view of the charging duct with a graphical overview of the physics accounted for in the model. $\mathbf{F_d}$ is the two-way coupled drag force between gas and particle, $\mathbf{F}_{c,pp}$ and $\mathbf{F}_{c,pw}$ are the contact forces with other particles and walls respectively, $\mathbf{F}_{el}$ is the electrostatic force caused by direct interaction with other charged particles. Finally, $\mathbf{F}_{im}$ is the electrostatic force caused by the charge induced in the metal wall, which is modeled using image charges. Note that the actual experiments and simulations are performed on a vertical duct.

CFD-DEM

In order to solve the dynamics of the gas in this gas-solid system, the modified continuity and Navier-Stokes equations (Anderson and Jackson, 1967) are solved on rectangular, regular grid. These equations are given respectively as

$$\frac{\partial(\varepsilon\rho_g)}{\partial t}+\nabla\cdot(\varepsilon\rho_g\mathbf{v}_g)=0 \tag{1}$$

and

$$\frac{\partial(\varepsilon\rho_g\mathbf{v}_g)}{\partial t}+\nabla\cdot(\varepsilon\rho_g\mathbf{v}_g\mathbf{v}_g)=-\varepsilon\nabla p + \nabla\cdot\left(\varepsilon\eta_g\left((\nabla\mathbf{v}_g)+(\nabla\mathbf{v}_g)^T\right)\right)-\mathbf{S}_{f\to p}+\varepsilon\rho_g\mathbf{g}. \tag{2}$$

Here ε is the porosity, ρ the density, $\mathbf{v}$ the velocity vector, t time, p, pressure, μ viscosity, $\mathbf{S}_{f\to p}$ the drag from fluid on particles, and $\mathbf{g}$ the gravity. The subscript $_g$ indicates that the quantities relate to the gas. The boundary conditions at the walls are no slip, at the outlet prescribed pressure and at the inlet a prescribed flow profile of a developed flow in a squared duct.

The particle dynamics are solved by solving Newtons second law of motion where the gravity, $\mathbf{F}_g$, the pressure gradient force, $\mathbf{F}_{\nabla p}$, drag of gas on particle, $\mathbf{F}_D$, the particle-particle and particle-wall contact force, $\mathbf{F}_c$, and the electrostatic force

$\mathbf{F}_{el}$ are taken into account, i.e.

$$\begin{aligned} m_p \frac{\mathrm{d}\mathbf{v}_p}{\mathrm{d}t} &= \mathbf{F}_g + \mathbf{F}_{\nabla p} + \mathbf{F}_D + \mathbf{F}_c + \mathbf{F}_{el} \\ I \frac{\mathrm{d}\omega_p}{\mathrm{d}t} &= \mathbf{T}. \end{aligned} \tag{3}$$

Here m_p is the mass of the particle, $\mathbf{v}_p$ the velocity of the particle, I the particle's moment of inertia and ω_p the angular velocity of the particle. The expressions for the forces $\mathbf{F}$ and the torque $\mathbf{T}$ are given in Table 3. For the drag force we use the well established, empirical drag relation of Wen and Yu (Wen and Yu, 1966) because the porosity in this work is always higher than 0.9. For the contact forces a linear spring dashpot model is used.

Electrostatic interaction

For the interparticle electrostatic interaction, Coulomb's law is used

$$\mathbf{F}_{el,i} = \sum_{j \neq i} \mathbf{F}_{el,ij} = \sum_{j \neq i} \frac{q_i q_j}{4\pi\varepsilon_0 r_{ij}^2} \frac{\mathbf{r}_{ij}}{\|\mathbf{r}_{ij}\|}. \tag{4}$$

Because the walls are conducting and grounded, charged particles induce a charge of opposite sign on the walls. The interaction with these induced charges is taken into account using the method of images. Because the image charge in one wall, also has an image in the opposite (parallel) wall, an infinite sum of images needs to be calculated Fig. 2. This is achieved by calculating the first two images explicitly; the remainder of the sum is approximated using the solution of the integral representation of the sum. For distances further away than two wall-to-wall distances L_y, Pumplin derived an analytical solution for the infinite series Eq. (20)b; note how the electrostatic force decreases exponentially with the interparticle distance (Pumplin, 1969). It can be derived that the electrostatic interaction between two particles is less than 1% of the gravitational force on a particle when their distance is three wall-to-wall distances. Therefore, all interaction between particles further away than this distance are neglected. Note that in this work we consider only two out of the four wall conducting, because simplicity and numerical efficiency. Only the walls at $y = 0$ and $y = L_y$ are conducting and give charge during contact charging, the walls at $x = 0$ and $x = L_x$ are inert in both electrostatic interaction as well as in contact charging.

Charging model

Due to triboelectrification, particles attain charge as soon as they hit the wall. It is assumed that no charge is transferred when two particles collide because they are made from the

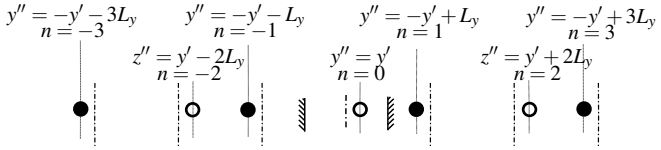

Figure 2: Illustration of the mirror images needed to have an exact description of the force between a charged particle and two parallel and conducting walls. The filled circles are of opposite sign of the open ones. The actual particle is indicated with $n = 0$, its image $n = \pm 1$, their image $n = \pm 2$ etc. y' is the y-position (between the walls) of the particle, y'' the position of the images. This pattern should be repeated infinitely. L_y is the wall-to-wall distance.

Table 1: Overview of simulation parameters. The symbols are defined in the nomenclature.

quantity	value	dim	quantity	value	dim
D_p	60	μm	$\bar{v}_{bg}$	10	$m\,s^{-1}$
ρ_p	1050	$kg\,m^{-3}$	ρ_g	1.29	$kg\,m^{-3}$
N_p	10^4	-	η_g	18	$\mu Pa\,s$
L_x, L_y	2	mm	L_z	200	mm
N_x, N_y	10	-	N_z	500	-
Δt_{DEM}	0.1	μs	t_{sim}	0.2	s
Δt_{CFD}	15	μs	σ_{sat}	27	$\mu C\,m^{-2}$
$e_{p\to p}$	0.97	-	$e_{p\to w}$	0.85	-
$\beta_{p\to p}$	0.46	-	$\beta_{p\to w}$	0.55	-
$\mu_{p\to p}$	0.189	-	$\mu_{p\to w}$	0.189	-

same material *and* because the flow is dilute and thus interparticle collisions are less frequent than particle-wall collisions. For the charging model it is assumed that the whole effective contact area, A_c^* receives some saturation charge density, σ_{sat}. The acquired charge of a collision can than be written as

$$\Delta q = \sigma_{sat} A_c^*. \tag{5}$$

This model is supported by the experimental observation that the acquired charge scales linearly with the contact surface and the charge density is equal for all impacts (Watanabe *et al.*, 2006). In this work we choose $\sigma_{sat} = 27\,\mu C\,m^{-2}$ based on the break-down strength of air. It is reported however that values of $100\,\mu C\,m^{-2}$ (Watanabe *et al.*, 2006) or $200\,\mu C\,m^{-2}$ (Watano, 2006) can also be used, depending on the material. Furthermore, it is assumed that the particle is a perfect insulator, consequently, the charge is fixed on the surface. Because a charged part of the surface cannot attain more charge, only that part of the contact surface that makes contact for the first time should acquire charge. We account for this using the first order estimation for A_c^*

$$A_c^* = \alpha A_c \left(1 - \frac{A_{charged}}{A_p}\right), \tag{6}$$

with A_c the actual contact surface which is calculated using Hertz contact theory and the normal component of the impact velocity. Furthermore, $A_{charged}$ is the contact area charged in (a) previous collision(s) and A_p the contact surface of the whole particle. Rolling and sliding of the particle increases its cumulative contact area of a collision. However, in this model this is neglected because only the normal component of the velocity component is used to determine A_c. To still be able to account for the influence of the tangential velocity, we multiplied the contact surface with a constant α; α may be interpreted loosely as a charging efficiency. Because this value is not known before hand we first investigated the sensitivity to this parameter by using the range $\alpha = 0, 10, 30, 100, 300$. These values follow from a first order estimation of the order of magnitude of α. Assuming that the particle is perfectly rolling during the particle-wall collision, the extra contact area is given by

$$A_{c,rolling} = v_t t_c 2R_c \tag{7}$$

with v_t the tangential impact velocity, t_c the contact time, and R_c the radius of the contact area of the normal impact velocity. The contact time can be obtained from Hertz contact theory.

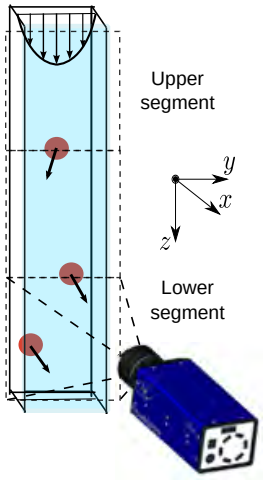

Figure 3: A schematic of the experimental set-up as used for the experiments described in this paper. Particles and gas are introduced at the top, particles hit the walls while traveling through the duct and exit at the bottom. Three segments can be distinguished from which the results of the upper and lower are used in this paper. The cover is transparent which enables the camera to capture the particles. The depth, width and length of the duct are its dimensions in the x, y and z direction as indicated in the figure.

Experimental set-up description

An experimental set-up has been built to enable investigation of the charging behavior of materials as well as their separation potential. In this paper we focus on the charging duct, which is schematically represented in Fig. 3. The setup is able to dose the powder accurately between 35 to 208 mg/s. In this work it is chosen to work within these limits; between 35 and 174 $mg/$. The particles are fed at the top and will attain charge while traveling through the duct as they hit the walls; the particles enter the duct together with the gas which is fed cocurrently. The gas flow rate can be set independently of the mass rate. In this work it has been set such that the average flow in the duct is 2.5 m/s. The walls are made out of alumina, except for the cover which is made of transparent poly(methyl methacrylate) (PMMA). Consequently, the charging slit is non-invasively but optically accessible enabling high speed and high resolution images acquisition from which particle velocity and positions can be determined. In order to be able to detect the particles using Digital Image Analysis (DIA), the particles should cover sufficient pixels on the camera's CCD. The camera used in this work is LaVision Imager pro HS 4M in combination with their software Davis. In order to have about 14 pixels per diameter, a 200mm macro lens was applied and positioned at about 55cm from the duct. Drawback of the macro lens is its limited focus depth, however, it turned out that the whole depth of the duct could be sufficiently captured in the field of focus. As this was the case even with a fully opened aperture it was set maximally open for all measurements. In order to capture the particles without motion blur, a sufficiently short exposure time needs to be set. It was found that for the chosen velocity of 2.5 m/s an exposure time of 50 μs suffices. With such small particles and such a short exposure time, lighting can be a problem. This was covered by pointing some strong LED lights at the duct. The draw back is that this yields strong reflections at the walls (Figs. 6 and 7) making it hard to distinguish the exact position of the wall.

Table 2: Overview of experimental parameters. The symbols are defined in the nomenclature.

quantity	value	dim	quantity	value	dim
$\bar{v}_{bg}$	2.5	m/s			
L_x	2.6	mm	L_y	3	mm
L_z	210	mm	$\dot{m}$	35 and 174	mg/s
Polystyrene particles					
ρ_p	1050	$kg\,m^{-3}$	D_p	400	μm

Furthermore, it hampers the segmentation of the particles using the DIA algorithm. From the results it appears however, that this can be overcome sufficiently, when the lights are positioned correctly.
The image processing is done in MATLAB by making use of the *imfindcircle* function from MATLAB's Image Processing toolbox to segment the particles. In this function an edge filter is applied, on which results the Hough transfer for circles is applied. The Hough transfer basically matches for every pixel how well the surrounding of the image looks like a circle of certain radius. If it matches well enough it is considered a circle. The interested reader is referred to (Atherton and Kerbyson, 1999; Yuen *et al.*, 1990) or MATLAB's (online) help for more details on the algorithm. Whether and when a part of the image is considered to match a circle sufficiently well, is determined by the 'sensitivity' parameter. Because this varies between different measurements it is determined each one separately.
The charge of the particles will probably make them attract to the wall, this will be visible in a PDF (Probability Density Function) of the particle position; there will be a higher probability for the particle to be near the wall compared to the center. This may also change throughout the duct. At the inlet, the position PDF is determined by the inlet conditions. At the outlet the position PDF is determined by the image-charge interactions because these have acted on the particles for a longer time in one direction (to the wall). Therefore, we have recorded the duct at the inlet (top) and exit (bottom) and use the aforementioned image analysis to measure the particles' position from which the PDF of their spatial distribution can be derived. This is done for different mass rates (35 and 174 mg/s) to determine the influence of particle loading on the process. The parameters of the experiments are summarized in Table 2. Note that the particle diameter and gas velocity are different from those used in the simulations. Therefore, care should be taken when comparing experiments and simulations.

RESULTS

Model

The results of the model are shown in Fig. 4. The upper figure shows how the distribution of the acquired charge per particle changes with changing charging efficiencyα: the higher α the higher the acquired charge. The width of the distribution changes from very narrow to very wide to increasingly narrow again with increasing α. The middle figure shows how the particles tend to reside more and more near the wall for increasing α (and thus increasing charge). From the bottom figure it is clear that near the walls, mostly the particles with the higher charge reside. Data similar to the second figure can also be measured using the experimental set-up described above and thus compared.

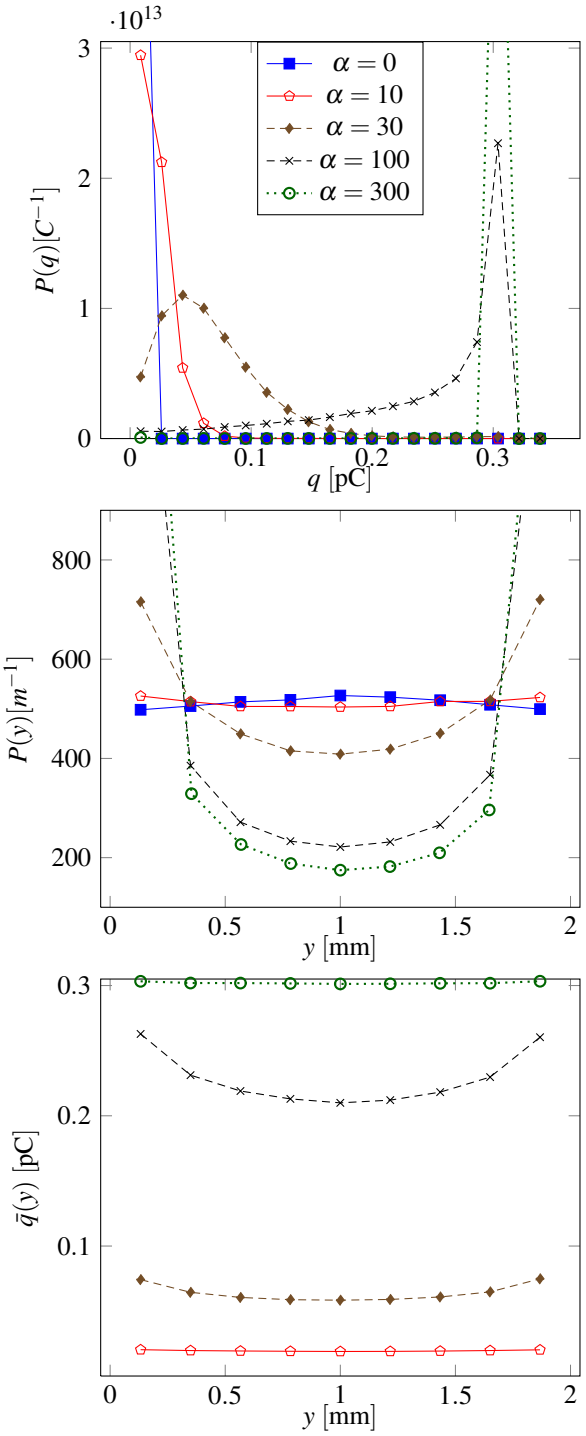

Figure 4: Results of simulations: PDF of charge per particle (upper) and particle's y position (middle). The lowest figure shows the average charge per particle on a certain y-position. Note that the saturation charge of the particles lies at $q = 0.305\,pC$ and that the walls of the duct lie at $y = 0$ and $y = 2\,mm$. The different lines indicate different charging efficiencies, α. The mass rate is 100 mg/s.

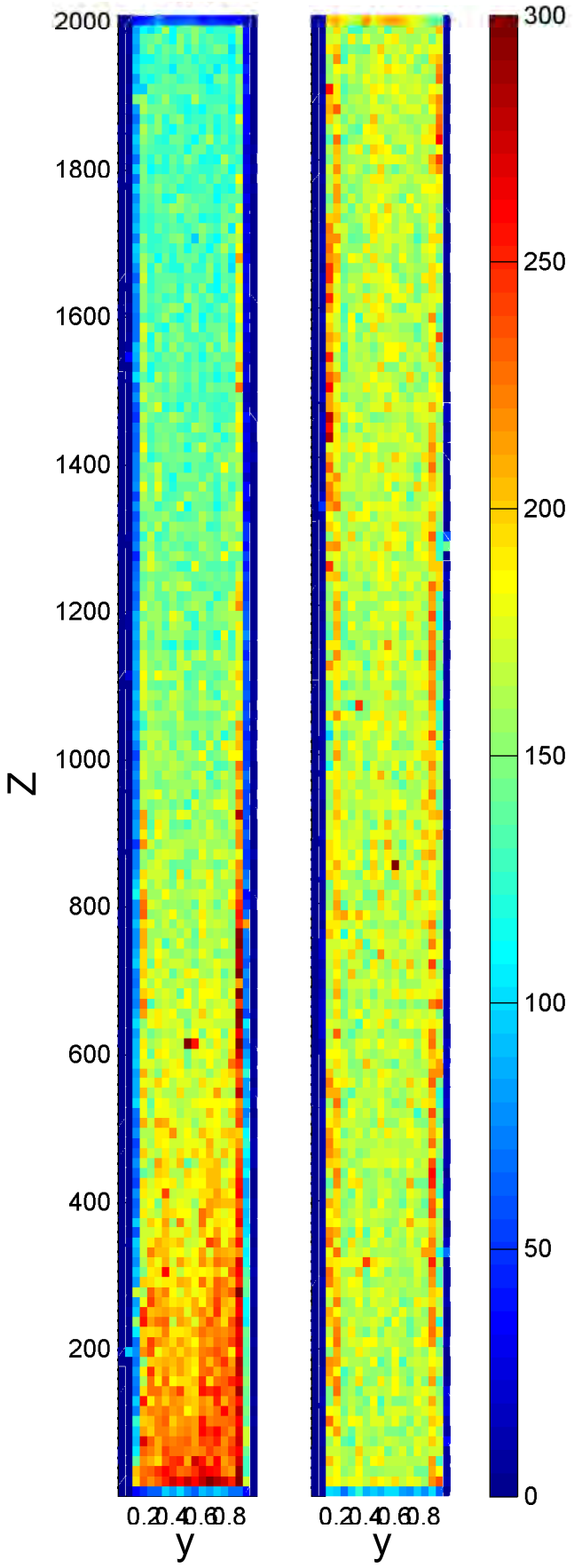

Figure 5: 2D histograms of the occurence of a particle at a certain z,y-position in the top (left) and bottom (right) segment. For these experiments, $\dot{m} = 174\,mg/s$, $\bar{v}_{bg} = 2.5\,m/s$. Note that the entrance is at the bottom, which is the opposite position compared to Figs. 6 and 7

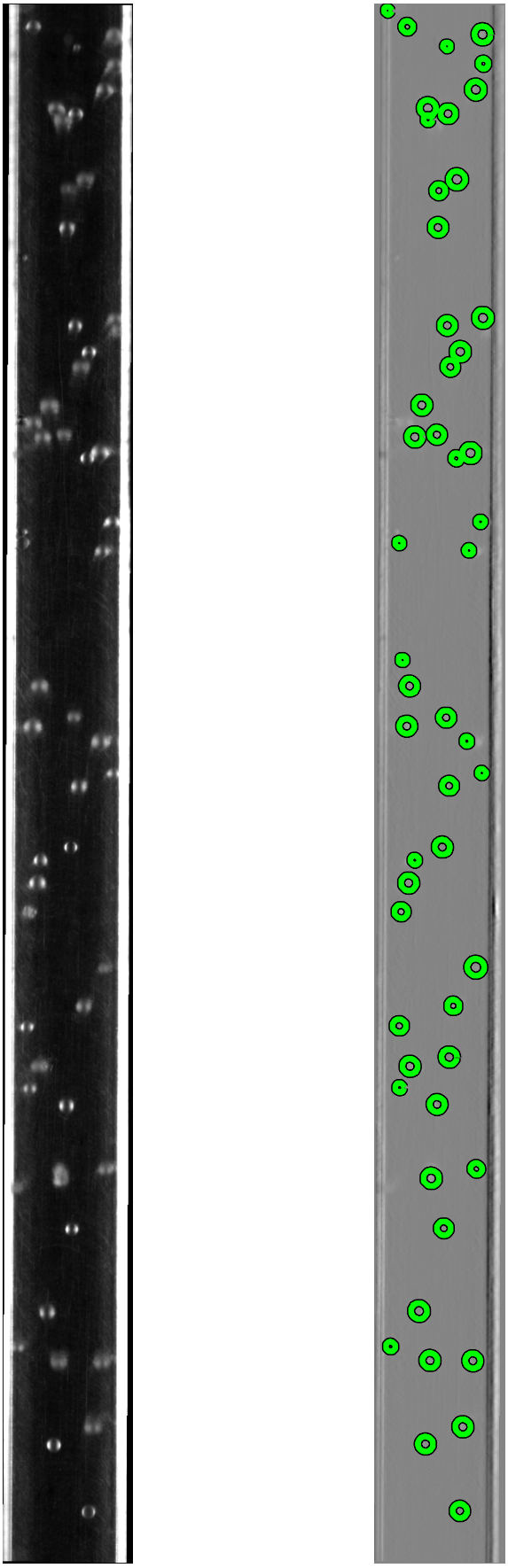

Figure 6: In this figure the images used for DIA are shown. Left the raw image, right the raw image with an overlay of the segmentation results. ($\dot{m} = 35\,mg/s$, $\bar{v}_{bg} = 2.5\,m/s$). Note in the raw image the thick, white, vertical lines; these are the reflections of the wall.

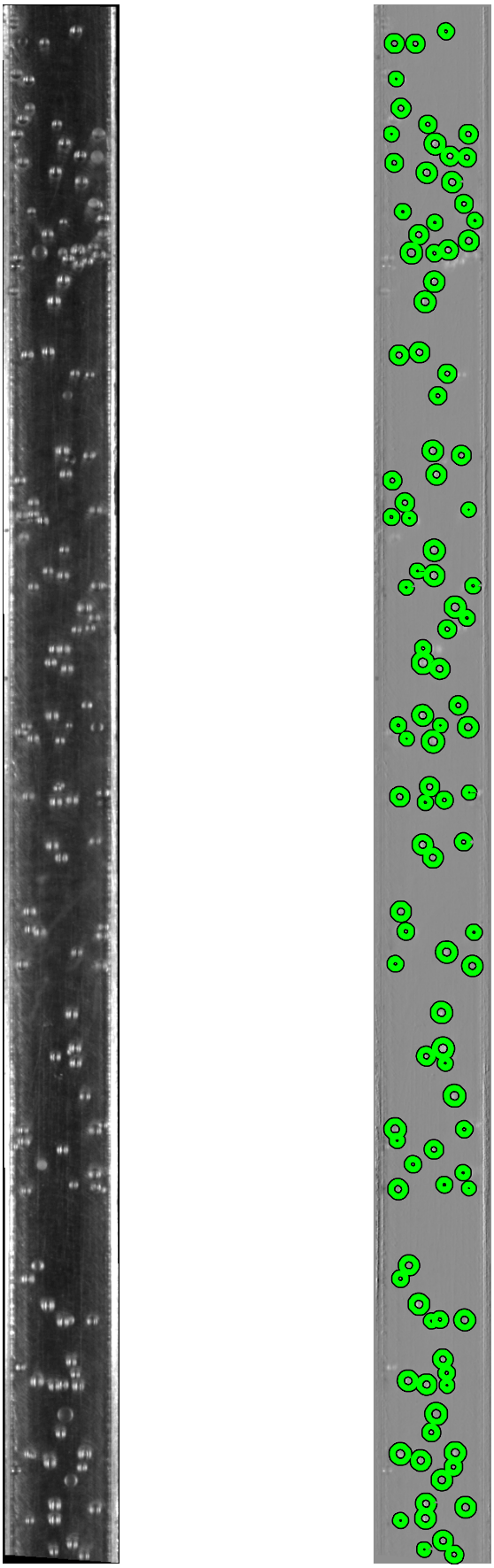

Figure 7: Same as Fig. 6, but here $\dot{m} = 174\,mg/s$.

Experiments

The images as captured by the camera are shown in Figs. 6 and 7 together with the results of the segmentations. The images show that the segmentation is very good for both high and low particle loading. In Fig. 5 the histogram of the particles position in the z, y plane are shown for the top segment (left) and bottom segment (right). The histogram at the entrance (left figure) is mainly determined by the inlet condition; the high count near the wall at the beginning is probably caused by fact that the particles do not enter the tube uniform and straight, but with a certain skewness in position and/or velocity. (Note that in these figures the entrance is at the bottom!). However a little bit further downstream, the particles are already distributed in a more symmetric fashion. In the bottom segment (right figure), clearly a higher number of occurrences near the wall than in the center is observed.

To be able to compare better between different mass rates, a projection of the images in Fig. 5 has been made in the longitudinal direction. The same experiments have been repeated several times to be able to give an estimate of the repeatability. In Fig. 9 the positions of all particles have been collected; from that collection one PDF is calculated. The result from Fig. 10 is calculated by determining the PDF of each experiment separately; from those PDF the average PDF is determined by assigning equal weight to each experiment. The number of experiments used for each average is 4 to 5. Despite the two different methods for averaging, more or less the same result is achieved. In all the cases, the particles are more likely to be near the wall compared to the center. For the higher mass rate there is only little influence of the segment. For the lower mass rate, the particles tend to be more near the wall for the lower segment compared to the upper. So it seems an 'equilibrium distribution' is faster achieved with a higher particle loading. This is expected because the increase in particle-particle interactions tends to have this effect.

In Fig. 8 the average and 95% confidence interval (plus/minus two times the standard deviation) are shown when the same averaging as for Fig. 9 is applied. The higher mass rate yields smaller confidence intervals because more particles are processed. Those images also show that especially near the walls, the difference between experiments is large, while the likelihood in the center is similar. This is caused by a high sensitivity to the lighting of the duct when filming. The lights cannot be set in the exact same position, while a small change in the position of the lights does have a difference in the lighting (especially) near the walls. This makes it hard to reproduce the results because suboptimal lighting settings introduce a negative bias to one or both of the walls. Therefore, an assessment on the accuracy of measurements and a possible bias to either wall would be desirable. This is however, very hard to achieve. Nevertheless, the results clearly show that the particles tend to reside near the walls rather than in the center.

It was also observed in the simulations that particles reside more near the walls than the center (Fig. 4 middle), but only if the particles had sufficient charge. This learns us that the electrostatic particle-wall interaction is indeed important and should be taking into account when considering such systems. Finally, this illustrates that the spatial distribution can be used as an extra parameter besides the average charge per particle, to validate such models on triboelectrification of pneumatically conveyed powders. Note however, that the results from these experiments and simulations cannot be

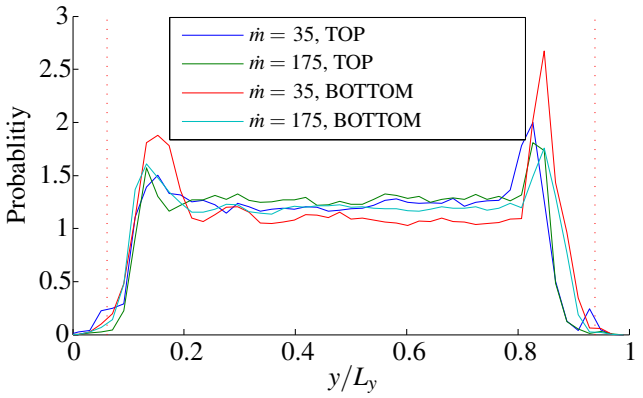

Figure 9: The PDF of the lateral position of the particles in the given segment in the duct are shown. The red, dashed lines indicate one particle radius distance from the wall; no particle should be detected there. For these experiments, $\bar{v}_{bg} = 2.5\,m/s$. The PDF has been created for the top and bottom segment of the duct as indicated in the legend. The mass rate is given in mg/s .

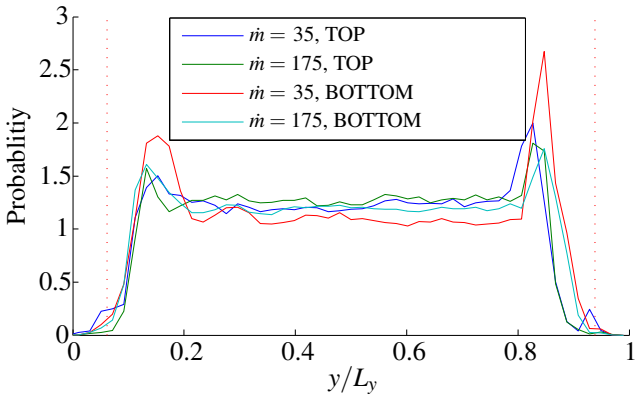

Figure 10: Same as Fig. 9 but averaged over all datasets instead of taken together.

compared one to one, because the both the particle size and the gas velocity differ. Furthermore, in the experiment three walls are conducting and one insulating while in the simulation only two (opposite) walls were conducting and the other two electrostatically 'inert'. Nevertheless, the similar trends observed between experiments and simulations show that modeling is a viable route to understanding and improving such charging systems. We are now working on a more detailed charging model; this model will be applied to a system that can be compared one-to-one with the experiments.

CONCLUSION AND OUTLOOK

In this work we have shown that it is possible to segment particles in a charging duct using a Digital Image Analysis. From these segmented particles a PDF of the spatial distribution between two walls was derived which is consistent between different experiments. The PDF showed a higher likelihood for the particles to be near the wall compared to the center. This segregation was stronger in the lower section of the duct compared to the upper section for the lower mass rate. This dependence on axial position vanished when using a higher mass rate. The same segregation between wall and center was also observed in the simulations if the charge was sufficiently high. This illustrates the particles in the duct are charged and that the spatial distribution can be used as an

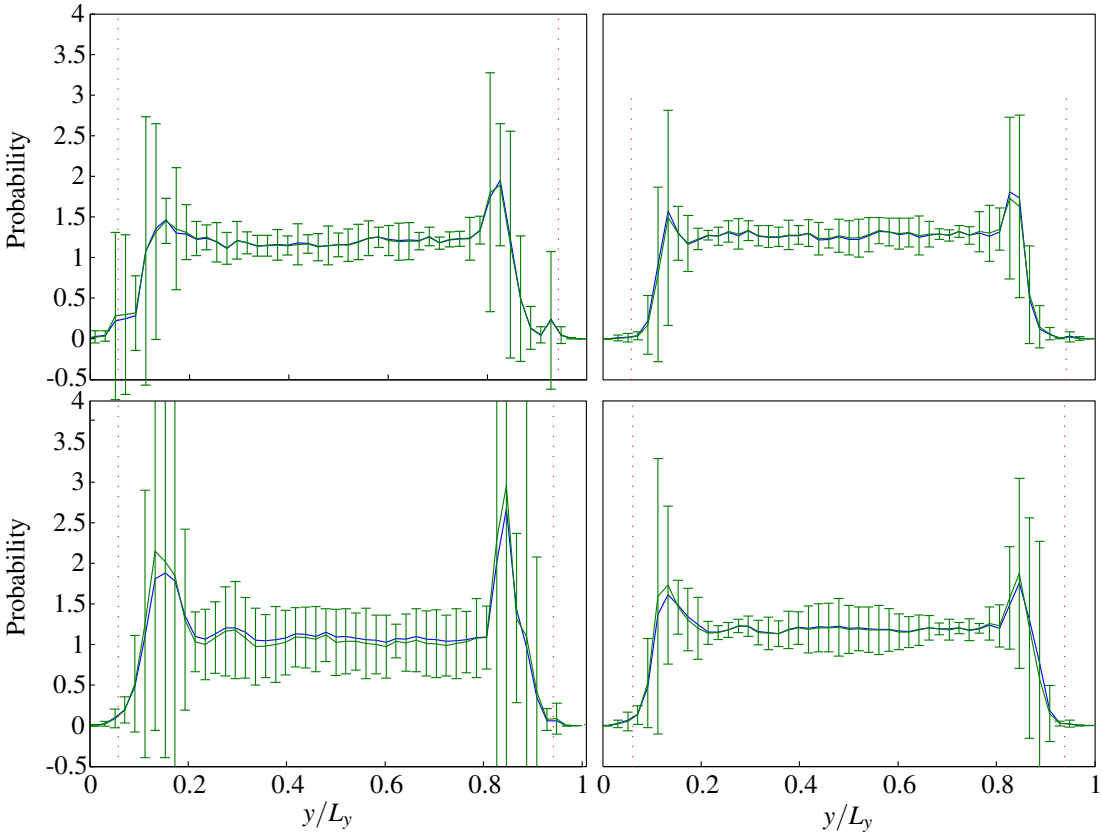

Figure 8: Averaged PDF of different measurements at same simulation conditions. Left column: $\bar{v}_{bg} = 2.5 m/s$, $\dot{m} = 35 mg/s$ at the top (top row) and bottom (bottom row) of the duct. Right column: $\bar{v}_{bg} = 2.5 m/s$, $\dot{m} = 175 mg/s$ at the top (top row) and bottom (bottom row) of the duct. The green line is the average (Fig. 10), the error bars indicate $\pm 2\sigma$, thus 95% confidence interval. The blue line is the PDF when all measurements are taken together (Fig. 9)

extra parameter to validate the simulations to experiments. In future work we will not only extract the positions of the particles in the duct, but also their velocities. This can be added to the validation parameters. Furthermore, we will improve our model in order to be able to make a one to one comparison to the experiments. We will do simulations with 3 conducting and 1 isolating wall, we will improve our charging model by taking explicitly into account the rolling and sliding during particle-wall collision and we will change our particle size and gas velocity.

ACKNOWLEDGMENTS

This research is supported by the Dutch Technology Foundation STW, which is part of the Netherlands Organization for Scientific Research (NWO), and which is partly funded by the Ministry of Economic Affairs. Additional support is obtained from the Institute for Sustainable Process Technology, ISPT. The authors would like to thank the members of the user committee for the stimulating discussions on dry separation.

REFERENCES

ANDERSON, T.B. and JACKSON, R. (1967). "Fluid Mechanical Description of Fluidized Beds. Equations of Motion". *Industrial & Engineering Chemistry Fundamentals*, **6(4)**, 527–539. http://pubs.acs.org/doi/pdf/10.1021/i160024a007, URL http://pubs.acs.org/doi/abs/10.1021/i160024a007.

ATHERTON, T.J. and KERBYSON, D.J. (1999). "Size invariant circle detection ". *Image and Vision Computing* , **17(11)**, 795–803. URL http://www.sciencedirect.com/science/article/pii/S0262885698001607.

BAILEY, A.G. (1993). "Charging of Solids and Powders ". *Journal of Electrostatics* , **30(0)**, 167–180. URL http://www.sciencedirect.com/science/article/pii/030438869390072F.

DASCALESCU, L. *et al.* (1999). "Electrostatic Technologies for the Recycling of Non-Ferrous Metals and Plastics from Wastes". I. Inculet, F. Tanasescu and R. Cramariuc (eds.), *The Modern Problems of Electrostatics with Applications in Environment Protection*, vol. 63, chap. NATO Science Series, 77–87. Springer Netherlands. URL http://dx.doi.org/10.1007/978-94-011-4447-6_8.

GIFFIN, A. and MEHRANI, P. (2013). "Effect of gas relative humidity on reactor wall fouling generated due to bed electrification in gas-solid fluidized beds ". *Powder Technology* , **235(0)**, 368–375. URL http://www.sciencedirect.com/science/article/pii/S0032591012007140.

GREASON, W.D. (2000). "Investigation of a test methodology for triboelectrification". *Journal of Electrostatics*, **49(3–4)**, 245–256. URL http://www.sciencedirect.com/science/article/pii/S0304388600000139.

HARPER, W.R. (1951). "The Volta Effect as a Cause of Static Electrification". *Proceedings of the Royal Society of London. Series A, Mathematical and Physical Sciences*, **205(1080)**, –83. URL http://www.jstor.org/stable/98725.

HIGASHIYAMA, Y. and ASANO, K. (1998). "Recent progress in electrostatic separation technology". *Particulate*

science and technology, **16(1)**, 77–90.

KOREVAAR, M.W. *et al.* (2014). "Integrated DEM–CFD modeling of the contact charging of pneumatically conveyed powders ". *Powder Technology* , **258(0)**, 144–156. URL http://www.sciencedirect.com/science/article/pii/S0032591014002204.

MATSUSAKA, S. *et al.* (2010). "Triboelectric charging of powders: A review". *Chemical Engineering Science*, **65(22)**, 5781–5807. URL http://www.sciencedirect.com/science/article/pii/S0009250910004239.

MATSUYAMA, T. and YAMAMOTO, H. (1995a). "Characterizing the electrostatic charging of polymer particles by impact charging experiments". *Advanced Powder Technology*, **6(3)**, 211–220.

MATSUYAMA, T. and YAMAMOTO, H. (1995b). "Charge relaxation process dominates contact charging of a particle in atmospheric conditions". *Journal of Physics D: Applied Physics*, **28**, 2418.

MAYR, M. and BARRINGER, S. (2006). "Corona Compared with Triboelectric Charging for Electrostatic Powder Coating". *Journal of Food Science*, **71(4)**, E171–E177.

MURTOMAA, M. *et al.* (2002). "Effect of surface coverage of a glass pipe by small particles on the triboelectrification of glucose powder ". *Journal of Electrostatics* , **54(3–4)**, 311–320. Selected Papers from the 28th Annual Conference of the Electrosta tics Society of America , URL http://www.sciencedirect.com/science/article/pii/S0304388601001589.

PETERSON, J.W. (1954). "Contact charging between nonconductors and metal". *Journal of Applied Physics*, **25(7)**, 907–915.

PUMPLIN, J. (1969). "Application of Sommerfeld-Watson transformation to an electrostatics problem". *American Journal of Physics*, **37**, 737.

SOWINSKI, A. *et al.* (2012). "Effect of fluidizing particle size on electrostatic charge generation and reactor wall fouling in gas–solid fluidized beds ". *Chemical Engineering Science* , **71(0)**, 552–563. URL http://www.sciencedirect.com/science/article/pii/S000925091100830X.

VAN DER HOEF, M.A. *et al.* (2008). "Numerical simulation of dense gas-solid fluidized beds: A multiscale modeling strategy". *Annu. Rev. Fluid Mech.*, **40**, 47–70.

VAN DER HOEF, M. *et al.* (2006). "Multiscale Modeling of Gas-Fluidized Beds". *Advances in chemical engineering*, **31**, 65–149.

WATANABE, H. *et al.* (2006). "Measurement of charge transfer due to single particle impact". *Particle & Particle Systems Characterization*, **23(2)**, 133–137.

WATANO, S. (2006). "Mechanism and control of electrification in pneumatic conveying of powders". *Chemical Engineering Science*, **61(7)**, 2271–2278. URL http://www.sciencedirect.com/science/article/pii/S0009250905003945.

WEN, C. and YU, Y. (1966). "Mechanics of fluidization". *Chem. Eng. Prog. Symp. Ser.*, vol. 62.

WU, G. *et al.* (2013). "Triboelectrostatic separation for granular plastic waste recycling: A review". *Waste Management*, **33(3)**, 585–597. URL http://www.sciencedirect.com/science/article/pii/S0956053X1200476X.

YUEN, H.K. *et al.* (1990). "Comparative study of Hough Transform methods for circle finding ". *Image and Vision Computing* , **8(1)**, 71–77. URL http://www.sciencedirect.com/science/article/pii/026288569090059E.

Table 3: Overview of implemented forces. The symbols are defined in the nomenclature above.

Gravity

$$\mathbf{F}_g = m_p\, g \mathbf{e}_z \tag{8}$$

Pressure force

$$\mathbf{F}_{\nabla p} = -V_p \nabla p \tag{9}$$

Drag force

$$\mathbf{F}_D = V_p\, \beta\, (\mathbf{v}_g - \mathbf{v}_p) \tag{10}$$

$$\beta = \tfrac{3}{4} C_D \frac{\rho_g}{D_p} \|\mathbf{v}_g - \mathbf{v}_p\| \varepsilon^{-1.65} \quad \text{for} \quad \varepsilon > 0.80 \tag{11}$$

with

$$C_D = \begin{cases} \dfrac{24}{Re_p}\left(1 + 0.15\, Re_p^{0.687}\right) & \text{for} \quad Re_p < 1000 \\ 0.44 & \text{for} \quad Re_p \leq 1000 \end{cases} \tag{12}$$

$$Re_p = \frac{\varepsilon\, \rho_g \|\mathbf{v}_g - \mathbf{v}_p\| D_p}{\eta_g} \tag{13}$$

Contact forces

$$\mathbf{F}_{c,i} = \sum_{j=1}^{N_c} \left(\mathbf{F}_{n,ij} + \mathbf{F}_{t,ij} \right) \tag{14}$$

$$\mathbf{F}_{n,ij} = -k_n \delta_n \mathbf{e}_n - \zeta_n (\mathbf{v}_{p,i} - \mathbf{v}_{p,j}) \cdot \mathbf{e}_n \tag{15}$$

$$\mathbf{F}_{t,ij} = \begin{cases} -k_t \delta_t \mathbf{e}_t - \zeta_t (\mathbf{v}_{p,i} - \mathbf{v}_{p,j}) \cdot \mathbf{e}_t & \text{if} \quad \|\mathbf{F}_{t,ij}\| \leq \mu \|\mathbf{F}_{n,ij}\| \\ -\mu \|\mathbf{F}_{n,ij}\| \mathbf{e}_t & \text{if} \quad \|\mathbf{F}_{t,ij}\| > \mu \|\mathbf{F}_{n,ij}\| \end{cases} \tag{16}$$

$$\zeta_n = \frac{-2 \ln e \sqrt{m_{eff} k_n}}{\sqrt{\pi^2 + \ln^2 e}}, \quad \zeta_t = \frac{-2 \ln \beta \sqrt{2/7 m_{eff} k_t}}{\sqrt{\pi^2 + \ln^2 \beta}} \tag{17}$$

$$\mathbf{T}_i = \sum_{j=1}^{N_c} \left(\tfrac{D_i}{2} \mathbf{e}_n \times \mathbf{F}_{t,ij} \right), \quad 1/m_{eff} = 1/m_i + 1/m_j \tag{18}$$

Electric forces

$$\mathbf{F}_{el,i} = -q_i \nabla_i \Phi_i \tag{19}$$

$$\Phi_i = \sum_{j=1}^{N_p} \frac{q_j}{4\pi\varepsilon_0} \times \begin{cases} \displaystyle\sum_{n=-N_{im}}^{N_{im}\prime} \left(A_{ij,n} - B_{ij,n} \right) + \xi_{ij,N_{im}} & \text{for} \quad z_{ij} \leq z_{ff} \\ \dfrac{2}{L_y} \sqrt{\dfrac{8}{\rho_{ij} L_y}} \cos\left(\dfrac{\pi y_i}{L_y}\right) \cos\left(\dfrac{\pi y_j}{L_y}\right) e^{-\dfrac{\pi \rho_{ij}}{L_y}} & \text{for} \quad z_{ff} < z_{ij} \leq z_c \\ 0 & \text{for} \quad z_{ij} > z_c \end{cases} \tag{20}$$

where $\sum'$ indicates that the term $n = 0$ is omitted if $i = j$,

$$A_{ij,n} = \left({\rho_{ij}}^2 + (y_i - y_j + 2n L_y)^2 \right)^{-1/2}, \quad B_{ij,n} = \left({\rho_{ij}}^2 + (y_i + y_j + (2n+1) L_y)^2 \right)^{-1/2} \tag{21}$$

$$\xi_{ij,N_{im}} = \tfrac{1}{2} \left(\int_{N_{im}}^{\infty} (A_{ij,n} + A_{ij,-n} - B_{ij,n} - B_{ij,-n})\, \mathrm{d}n + \int_{N_{im}+1}^{\infty} (A_{ij,n} + A_{ij,-n} - B_{ij,n} - B_{ij,-n})\, \mathrm{d}n \right) \tag{22}$$

$$\rho_{ij} = \sqrt{(x_i - x_j)^2 + (z_i - z_j)^2} \tag{23}$$

ESTABLISHING THE PREDICTIVE CAPABILITIES OF DEM SIMULATIONS: SLIDING AND ROLLING FRICTION COEFFICIENTS OF NON-SPHERICAL PARTICLES

Luca BENVENUTI[1]*, **Andreas AIGNER**[1], **Daniel QUETESCHINER**[1], **Mar COMBARROS**[2], **Stefan PIRKER**[1], **Christoph KLOSS**[1]

[1]JKU Department of Particulate Flow Modelling, 4040 Linz, Austria

[2]TUBS Institut fur Partikeltechnik, 38104 Braunschweig, Germany

* E-mail: luca.benvenuti@jku.at

ABSTRACT

Discrete Element Method (*DEM*) simulations are widely used to understand particle behavior. Among the key parameters, defining the inter-particle friction parameters is very relevant to perform simulations of granular flows. To model non-spherical particles with spherical elements, we used an elasto-plastic rolling friction model in combination with Coulomb's law in the *DEM* code LIGGGHTS. The bulk solids were characterized using Schulze ring shear cell and simplified Jenike shear cell testers. The sliding and rolling friction coefficients were obtained by fitting numerical simulations of the shear cells to experimental data. The calculated DEM coefficients of friction of iron ore, limestone and silibeads accord well with published data and in-house experiments. Further, we validated the DEM parameters by means of angle-of-repose experiments and simulations and conclude that the described setup successfully defined the DEM parameters for the materials tested.

Keywords: Meshless methods (DEM), Rheology, experimental validation studies, process industries, process metallurgy, LIGGGHTS, Material characterization .

NOMENCLATURE

Greek Symbols

β	restitution parameter, $[-]$
γ	viscoelastic damping constant for contact, $[kg/s]$
$\Delta\theta_r$	incremental rotation between two particles, $[-]$
Δti	time step, $[s]$
δ_n	$= d - r =$ overlap distance of 2 particles, $[m]$
δ_t	tangential displacement vector between 2 spherical particles which is truncated to satisfy a frictional yield criterion, $[m]$
ι	maximum angle of a slope on which the rolling resistance torque counterbalances the torque produced by gravity acting on the body
μ	coefficient of friction, $[-]$
μ_e	coefficient of internal friction, $[-]$
ν	Poisson ratio, $[-]$
ρ	mass density, $[kg/m^3]$
σ	stress, $[Pa]$
τ	shear stress, $[Pa]$
ϕ_e	angle of internal friction, $[^\circ]$

Latin Symbols

AOR	angle of repose, $[^\circ]$.
C	check parameter, $[-]$.
c	damping, $[kg/s]$.
d	$= R_i + R_j =$ contact distance, $[m]$
e	coefficient of restitution, $[-]$
E	Young's modulus, $[N/m^2]$
F	force, $[N]$
f	friction, $[-]$
G	shear modulus, $[N/m^2]$
k	elastic constant stiffness for contact, $[kg/s^2]$
M_r	total rolling resistance torque, $[kNm]$
M_r^k	spring rolling resistance torque, $[kNm]$
M_r^m	torque at a full mobilisation rolling angle, $[kNm]$
m	mass of the particle, $[kg]$
R	radius of the particle, $[m]$
r	distance between two particles of radii R_i and R_j, $[m]$
S	damping parameter, $[kg/s^2]$
SC	sum of the checks, $[-]$.
v	relative velocity of the 2 particles, $[m/s]$
x	displacement, $[m]$
ti	time, $[s]$

Sub/superscripts

b	bulk
eq	equivalent
exp	experimental
i	particle i
j	particle j
k	normal load during pre-shear k
k	% of the normal load during shear l
n	normal
p	particle
psh	pre-shear
r	rolling
sim	simulation
s	sliding
sh	shear
t	tangential

INTRODUCTION

Particles in various forms - ranging from raw materials to food grains and pharmaceutical powders - play a major role in a variety of industries, including process industry and metallurgy. In his book, Holdich (2002) stated that "between 1 and 10% of all the energy is used in comminution, i.e. the processes of crushing, grinding, milling, micronising". However, a univocal method to characterize these particles has

so far not been established. From the experimental point of view, the main issues are the difficult setups and the general reliability and reproducibility of the tests. From the numerical point of view, no general procedure is available, and the existence of a mathematically unique solution describing macro/micro particle contact has yet to be proved. Moreover, in a recent study, Krantz *et al.* (2009) implied "that the dynamic properties of a powder cannot be applied to universally predict the static properties of a powder, and, likewise, the static properties cannot be used to predict dynamic properties".

Discrete Element Method (DEM) simulations are widely used to understand particle behavior. Mishra and Rajamani (1992) defined the *DEM* as "a special class of numerical schemes for simulating the behavior of discrete, interacting bodies". The force that particle i exerts on particle j is defined as:

$$m\ddot{x}_{ij} + c\dot{x}_{ij} + kx_{ij} = F_{ij}. \tag{1}$$

Further details on the method can be found in Pöschel and Schwager (2004). *LIGGGHTS* (LAMMPS improved for general granular and granular heat transfer simulations) is one of the most powerful open source *DEM* simulation software packages available. The models it can analyze are described in detail in the literature (Kloss *et al.*, 2012). In combination with shear cell tester simulation (Aigner *et al.*, 2013), *LIGGGHTS* has correctly defined the coefficient of sliding friction for coarse round particles - a critical parameter describing inter-particle friction in medium to dense granular flows simulations.

Since the bulk solid is represented by perfect spheres, the only parameter the software uses to describe its shape is the radius of the particle (R). However, since the shape is one of the most relevant aspects defining particle behavior, we consider the coefficient of rolling friction (μ_r) as an additional *DEM* shape parameter. It is proportional to the torque counteracting the rotation of the particle and defined as (Eq. 2):

$$\mu_r = \tan(\iota). \tag{2}$$

DEM simulations have recently been used to reduce the bias of the experiments, and more precise devices such as the Schulze ring shear cell tester (SRSCT)(see Schulze *et al.* (2001)) have been built. A dedicated workflow that combines experiments and simulations must now be devised following the Design of Experiments method, as illustrated by Grossman and Vecchio (2008).

The main goal of this new procedure should be the characterization of non-spherical particles, especially the *DEM* coefficients of friction, following standardizable steps. With this objective in mind, we profited from the shear cell experimental and numerical setup in combination with *LIGGGHTS* simulation to improve the accuracy and the range of applicability of particle characterization. Since this study was supported by the metallurgical industry, the materials examined were: silibeads (2 mm), coke, iron ore, limestone (all 0-3.15 mm).

MODEL DESCRIPTION

For the raw materials used in this work di Renzo and di Maio (2004) suggested using the non-linear Hertzian model without cohesion for the particle-particle and particle-wall contacts.

This granular model uses the following formula for the force between two granular particles (Eq. 3):

$$F_{ij} = \begin{cases} F_{n,ij} + F_{t,ij} = \left(k_n \delta_{n,ij} + \gamma_n v_{n,ij}\right) + \left(k_t \delta_{t,ij} + \gamma_t v_{t,ij}\right) & \text{if } r < d, \\ 0 & \text{if } r > d, \end{cases} \tag{3}$$

while the tangential force component is truncated to fulfill

$$F_{t,ij} \leq \mu_s F_{n,ij}. \tag{4}$$

Both the normal and the tangential force comprise two terms, a spring force and a damping force. The shear force is a "history" effect that accounts for the tangential displacement ("tangential overlap") between the particles for the duration of contact.

The k_n, k_t, γ_n, and γ_t coefficients are calculated from the material properties as follows:

$$\begin{aligned} k_n &= \frac{4}{3} E_{eq} \sqrt{R_{eq} \delta_n}, \\ \gamma_n &= 2\sqrt{\frac{5}{6}} \beta \sqrt{S_n m_{eq}}, \\ k_t &= 8 G_{eq} \sqrt{R_{eq} \delta_n}, \\ \gamma_t &= 2\sqrt{\frac{5}{6}} \beta \sqrt{S_t m_{eq}}. \end{aligned} \tag{5}$$

In addition to the equations 5 the following relations (Eqns. 6) are required:

$$\begin{aligned} \frac{1}{E_{eq}} &= \frac{1-\nu_i^2}{E_i} + \frac{1-\nu_j^2}{E_j}, \\ \frac{1}{G_{eq}} &= \frac{2(2+\nu_i)(1-\nu_i)}{E_i} + \frac{2(2+\nu_j)(1-\nu_j)}{E_j}, \\ \frac{1}{R_{eq}} &= \frac{1}{R_i} + \frac{1}{R_j}, \\ \frac{1}{m_{eq}} &= \frac{1}{m_i} + \frac{1}{m_j}, \\ \beta &= \frac{\ln(e)}{\sqrt{ln^2(e) + \pi^2}}, \\ S_n &= 2 E_{eq} \sqrt{R_{eq} \delta_n}, \\ S_t &= 8 G_{eq} \sqrt{R_{eq} \delta_n}, \\ k_r &= k_t R_{eq}^2. \end{aligned} \tag{6}$$

The μ_r parameter enters the equations according to the elasto-rolling resistance model presented by Wensrich and Katterfeld (2012) and Ai *et al.* (2011), also used by Goniva *et al.* (2012), based on the work of Jiang *et al.* (2005)(and in contrast to Iwashita and Oda (1998)). The model is called EPSD2 in LIGGGHTS. This is appropriate for the one way rolling cases as well as the cycling rolling ones. The total rolling resistance torque is (Eq. 7):

$$\begin{aligned} M_r &= M_r^k, \\ M_{r,ti+\Delta ti}^k &= M_{r,ti}^k - k_r \Delta\theta_r, \\ |M_{r,ti+\Delta ti}^k| &\leq M_r^m = \mu_r R_{eq} F_n. \end{aligned} \tag{7}$$

Given these equations, completely defining a dry material for DEM simulations requires these data:

- the radius of the particles (R);

- the Young's modulus (E) and the Poisson's coefficient (ν);
- the particle density (ρ_p) and the coefficient of restitution (e);
- the coefficients of sliding (μ_s) and rolling (μ_r) friction.

EXPERIMENTAL SETUP

The first step of the procedure was using shear testers - a simplified Jenike shear cell tester (*JSCT*, see ASTM (2013a)) and a SRSCT (see ASTM (2013b)) to characterize particle flow properties, especially the complete yield locus. Each experiment was performed on a fresh material sample.
In the tests with the simplified *JSCT*, a representative sample of bulk solid was placed in a shear cell of 104 mm diameter. This specimen was pre-consolidated by twisting the shear cell cover while applying a compressive load (from 0.488 to 1.379 kg) normal to it. Since this was a simplified tester, the specimen was then sheared with the same normal load at a constant velocity. In fact, the *shear to failure* phase was missing in these *simplified* tests, and the *consolidation* phase was not completely serialized. The steady-state flow horizontal stress (Fig. 2) is called pre-shear stress (τ_{psh}). Knowing the normal stress, it gives (Eq. 8) the angle of internal friction of the pre-shear phase (ϕ_{e-psh}), our first flowability value (Schulze, 2008):

$$\begin{aligned} \phi_{e-psh} &= \arctan\left(\frac{\tau_{psh}}{\sigma_{n,psh}}\right), \\ \mu_{psh} &= \tan(\phi_{e-psh}). \end{aligned} \tag{8}$$

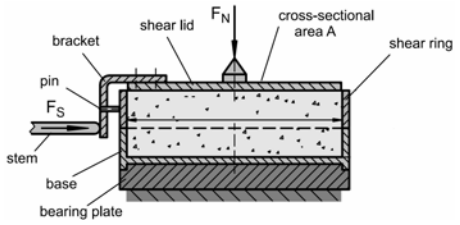

Figure 1: Jenike shear cell tester (Schulze, 2008)

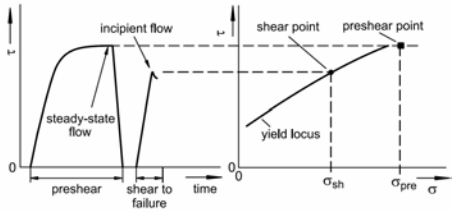

Figure 2: Jenike shear cell tester diagram (Schulze, 2008)

Analogously, in the *SRSCT* tests a representative sample of bulk solid was placed in a shear cell of specified dimensions ($external\ radius = 100\ mm$, $internal\ radius = 50\ mm$). A normal load was applied to the cover, and the specimen was pre-sheared until a steady-state shear value was reached, again obtaining ϕ_{e-psh}. The normal stress and the angular velocity were then immediately reduced to zero. Subsequently, the specimen was sheared under a fraction of the first normal load until the shear force reached a maximum and began to decrease. Both the pre-shear and shear phases were executed at constant velocity. We define the horizontal stress during the shear force peak as maximum shear stress, thus obtaining (Eq. 9)(Schulze, 2008):

$$\begin{aligned} \phi_{e-sh} &= \arctan\left(\frac{\tau_{sh}}{\sigma_{n,sh}}\right), \\ \mu_{sh} &= \tan(\phi_{e-sh}). \end{aligned} \tag{9}$$

From three to four different pre-shear normal loads were applied in the experiment. For each we used a proportional shear increasing from stage one (40%) to stage four (100%) with two escalating intermediate stages (60% and 80%). The ϕ_{e-psh} values for the limestone obtained with the *SRSCT* and the simplified *JSCT* were in good accordance (less than 1% difference), therefore we were able to validate the latter experimental device for this material.

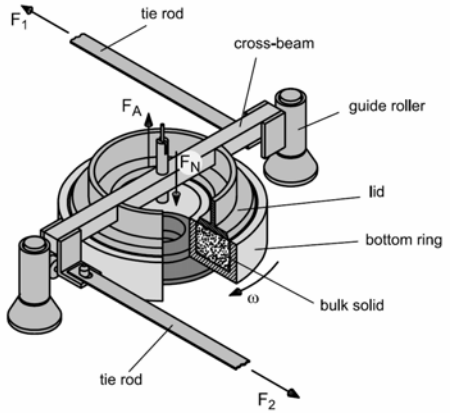

Figure 3: Schulze ring shear cell tester (Schulze, 2008)

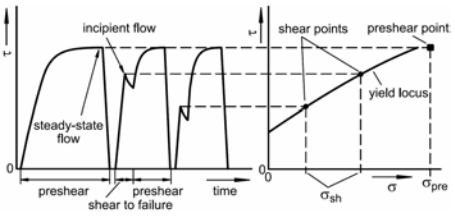

Figure 4: Schulze ring shear cell tester diagram (Schulze, 2008)

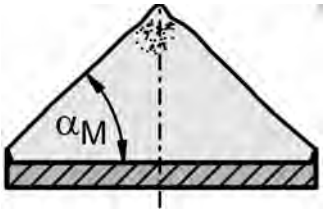

Figure 5: Angle of repose tester (Schulze, 2008)

Furthermore, in order to recreate the repose angle observed in a pile of the real material, a sample was deposited on a 20 cm diameter plate with liftable boundary, called static angle of repose (*AOR*) tester (Fig. 5). Once the particles were in position, the boundary was lifted, allowing some particles to drop. Once stabilized, the *AOR* was measured eight times using a digital protractor at different positions of the heap. The result is given as the average of the measurements (Tab. 3).

SIMULATIONS

LIGGGHTS, the simulation toolbox we used, meets most of the requirements of modelling the shear tester described above. First, it is capable of importing triangulated meshes of the two rings and a top lid. Since the real set-up had a wall thickness, both rings have additional horizontal walls that prevent the particles from falling out of the shear cell. Further, all particle-wall contact forces acting on a mesh are summed and can be saved, and thus shear force calculation is available out of the box. Moreover, the code can move a mesh with constant velocity as required for the measurement. To determine the shear stresses, the bulk solid had to be stressed with user-defined normal stresses. Therefore, a stress-controlled wall (*servo − wall* in *LIGGGHTS*) was applied to the lid.

Table 1: Material properties and final simulation parameters

name	average particle radius	average particle density	DEM Young's modulus	DEM Poisson's ratio
unit	[mm]	[kg/m3]	[Gpa]	[-]
coke	0.7	1500	5	0.40
iron ore	0.7	4000	10	0.40
limestone	0.7	3000	5	0.40
silibeads	1.0	2500	10	0.45
name	DEM sliding friction	DEM rolling friction	DEM coefficient restitution	constant ring velocity
unit	[-]	[-]	[-]	[mm/s]
coke	0.80	0.40	0.50	2.1
iron ore	0.40	0.80	0.40	2.1
limestone	0.90	0.80	0.50	2.1
silibeads	0.08	0.06	0.75	3.0

Although the geometry differs, the *SRSCT* was designed to obtain the same values for the shear stresses as the *JSCT*, but with improved automation and reliability (Schulze, 2008). For this reason, the simulation setup realized included only the *JSCT*, and it had been used to compare both experimental testers. As suggested by Aigner *et al.* (2013), the diameter and the height of the rings operated in the simulations were respectively 50 and 13 times the diameter of the particles involved. The layout of the simulation geometry can be seen in Figure 6.

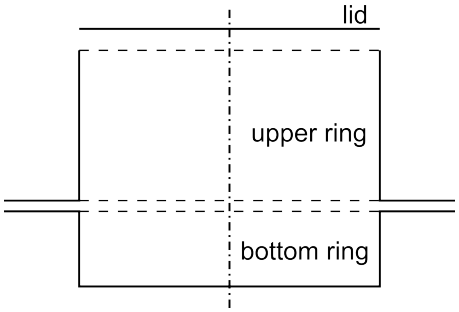

Figure 6: shear cell simulation layout

To reduce the computational effort in the simulation, only one average value was used for each parameter indicated in the *model description* section, except for the coefficients of friction. A simulation run comprised four phases. First,

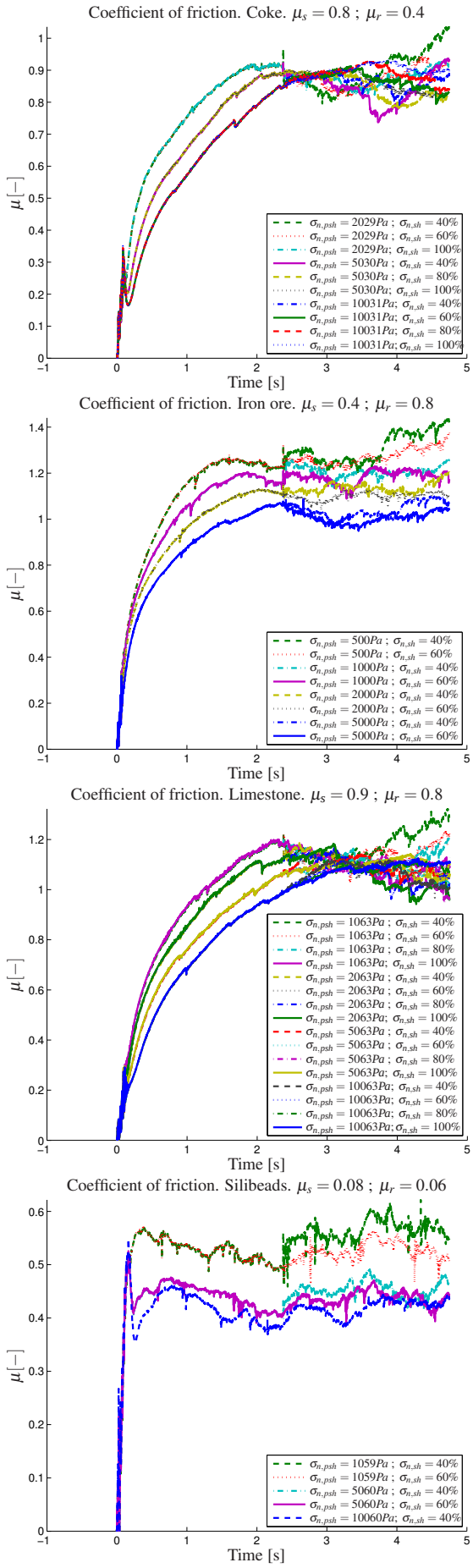

Figure 7: JSCT simulation with different materials

the shear cell was filled with the granulate material, and it was allowed to settle. Then, the top lid was lowered and applied the first normal stress to the bulk solid. Next, the ring moved for a distance $l = 0.1875 \cdot radius\ of\ the\ ring$, and the required pre-shear force was measured. Finally, the normal load was reduced to a fraction of the initial load, the ring was moved again by a distance l, and the shear force was recorded. Unlike in the original experiment, the bottom ring was moved to facilitate the numerical simulation.
The normal stresses (pre-shear and shear phases) applied in each simulation were the same as in the experiments. The corresponding τ_{psh} and τ_{sh} were calculated - as in the experiments - from the mean of the plateau (Fig. 7). Thus, we obtained the μ_{psh} and the μ_{sh} values to be compared with the experimental values. The *DEM* μ_s and μ_r were calibrated via trial-and-error to match these values.
Further, we also performed *AOR* simulations. Here we tried to replicate meticulously the experimental setup, considering both the plate and the liftable boundary, respectively 50 and 20 times the diameter of the particles involved. The particles had the same properties as in the shear cell simulation, and featured the calibrated μ_s and μ_r. The first phase was identical to that of the shear cell simulation. After lifting the boundary, the particles formed a heap (Fig. 8). An image post-processing software was used to obtain the average slope. The whole *AOR* simulation setup was handled using a beta graphical user interface for *LIGGGHTS*.
Furthermore, in both simulation setups the E value was not realistic, but reduced to increase the time step. This led to a reduction in computational time, resulting in 22 minutes with 32 cores for each shear cell simulation and 6 hours for each *AOR* simulation.

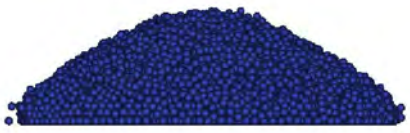

Figure 8: AOR simulation, heap of particles

RESULTS

The numerical results for μ_{psh} and μ_{sh} were compared with the experimental results from the *SRSCT*. For each material, each simulation was performed with a different pair of μ_s and μ_r values and different normal load k and fraction of normal load l for the second phase. This gives 16 simulations for each pair, as shown in Table 2. First, we tried a widely spaced range of μ_s and μ_r parameters (0.2, 0.4, 0.6, 0.8, 1.0) ($16 \cdot 5 \cdot 5 = 400$ *simulations* for the first run for each material). We then compared for each normal load and fraction of normal load the μ_{psh} and μ_{sh} experimental and simulated, respectively $\mu_{psh,exp}$ and $\mu_{sh,exp}$, and $\mu_{psh,sim}$ and $\mu_{sh,sim}$ by determining the check parameter C_{kl} according to Equation 10:

$$C_{kl} = \begin{cases} 1 & \text{if } (|1 - \frac{\mu_{psh,sim}}{\mu_{psh,exp}}| < 5\% \text{ and } |1 - \frac{\mu_{sh,sim}}{\mu_{sh,exp}}| < 5\%), \\ 0 & \text{else.} \end{cases} \quad (10)$$

Subsequently, we applied Equation 11

$$SC = \sum_{k=1}^{4} \sum_{l=1}^{4} C_{kl}. \quad (11)$$

Table 2: Comparison between experimental and numerical results in limestone for the given parameters

normal load $[kPa]$ Pre-shear	normal load $[\%]$ shear	μ_{e-psh} exp	μ_{e-psh} sim	μ_{e-psh} Δ %	k;l
1	40	1.472	1.085	0.263	1;1
1	60	1.310	1.087	0.170	1;2
1	80	1.082	1.089	-0.006	1;3
1	100	0.975	1.090	-0.119	1;4
2	40	1.204	1.031	0.143	2;1
2	60	1.038	1.033	0.005	2;2
2	80	0.990	1.034	-0.044	2;3
2	100	0.892	1.035	-0.160	2;4
5	40	1.263	0.930	0.263	3;1
5	60	1.042	0.931	0.106	3;2
5	80	0.720	0.932	-0.295	3;3
5	100	0.879	0.933	-0.062	3;4
10	40	1.179	0.863	0.269	4;1
10	60	0.989	0.864	0.127	4;2
10	80	0.924	0.864	0.065	4;3
10	100	0.856	0.865	-0.011	4;4

normal load $[kPa]$ Pre-shear	normal load $[\%]$ shear	μ_{e-sh} exp	μ_{e-sh} sim	μ_{e-sh} Δ %	C_{kl}
1	40	1.457	1.205	0.173	0
1	60	1.290	1.146	0.112	0
1	80	1.111	1.097	0.013	1
1	100	0.975	1.055	-0.082	0
2	40	1.160	1.081	0.068	0
2	60	1.049	1.065	-0.015	1
2	80	1.019	1.033	-0.014	1
2	100	0.892	1.009	-0.131	0
5	40	1.214	1.073	0.116	0
5	60	1.053	1.085	-0.031	0
5	80	0.997	1.098	-0.102	0
5	100	0.879	1.113	-0.266	0
10	40	1.155	1.068	0.075	0
10	60	0.986	1.099	-0.115	0
10	80	0.947	1.093	-0.154	0
10	100	0.856	1.100	-0.285	0

For each material we selected the μ_s and μ_r pairs with the maximum *SC* sum. If $SC < 2$, we restarted from the first step with more closely spaced series of values (down to 0.02 spacing). For validation purposes, the chosen μ_s and μ_r pairs were used to run *AOR* simulations, and then compared with the experimental values. If the results differed by less than $\pm 5\%$, we deemed the pair to be reliable *DEM* parameters.

Since the consolidation phase is not completely reliable, the simplified *JSCT* produced different μ_{psh} results than the *SRSCT*. Although we compared these results with the numerical values, they cannot be considered valid before the unconsolidated state is accurately defined for all materials. For coke, the chosen parameters were not validated by the *AOR* simulation. Instead of using values from the literature, we decided to focus on our experimental and numerical systematic routine in order to establish a comprehensive workflow for the characterization. We believe that the deviation from the *AOR* values could be reduced by improved calibration of the particle density.
The final *DEM* parameters selected on the basis of over 7000 simulations can be found in Table 1, and the comparison be-

Table 3: Comparison between experimental and numerical results, for the given parameters

coeff.	μ_{e-psh}	μ_{e-sh}	μ_{e-psh}	μ_{e-sh}
tester	SRSCT	SRSCT	SRSCT	SRSCT
normload	1 kPa	1 kPa	2 kPa	2 kPa
coke	0.895	0.898	0.897	0.897
iron ore	1.217	1.170	1.125	1.132
limestone	1.111	1.082	1.049	1.038
silibeads	0.616	0.603	0.560	0.552
coeff.	μ_{e-psh}	μ_{e-sh}	μ_{e-psh}	μ_{e-sh}
tester	DEM	DEM	DEM	DEM
normload	1 kPa	1 kPa	2 kPa	2 kPa
coke	0.909	0.908	0.875	0.876
iron ore	1.166	1.201	1.085	1.104
limestone	1.089	1.097	1.034	1.049
silibeads	0.596	0.578	0.443	0.531
coeff.	μ_{e-psh}	μ_{e-sh}	μ_{e-psh}	μ_{e-sh}
tester	SRSCT	SRSCT	SRSCT	SRSCT
normload	5 kPa	5 kPa	10 kPa	10 kPa
coke	0.808	0.808	0.917	0.890
iron ore	1.066	1.057	0.889	0.917
limestone	1.035	0.976	0.987	0.986
silibeads	0.435	0.437	0.424	0.411
coeff.	μ_{e-psh}	μ_{e-sh}	μ_{e-psh}	μ_{e-sh}
tester	DEM	DEM	DEM	DEM
normload	5 kPa	5 kPa	10 kPa	10 kPa
coke	0.811	0.842	0.872	0.893
iron ore	0.903	0.972	0.870	0.974
limestone	0.932	1.092	0.864	1.090
silibeads	0.435	0.446	0.405	0.430
coeff.	μ_{e-psh}	μ_{e-psh}	μ_{e-psh}	*AOR*
tester	SJSCT	SJSCT	SJSCT	exp
normload	0.561kPa	1.026kPa	1.588kPa	[°]
coke	0.853	0.794	0.748	42.11
iron ore	1.870	1.484	1.307	43.01
limestone	1.236	1.098	0.916	44.85
silibeads	0.378	0.339	0.302	21.09
coeff.	μ_{e-psh}	μ_{e-psh}	μ_{e-psh}	*AOR*
tester	DEM	DEM	DEM	DEM
normload	0.561kPa	1.026kPa	1.588kPa	[°]
coke	0.978	0.912	0.900	33.64
iron ore	1.055	1.132	0.973	42.07
limestone	1.155	1.058	1.051	45.42
silibeads	0.540	0.488	0.462	21.80

tween the experimental and numerical values is presented in Table 3.

CONCLUSION

We have discussed the determination of *DEM* inter-particle friction parameters that are critical in medium to dense granular flow simulation. In particular, we have characterized the materials more commonly used in steel-making, with special regard to their non-sphericity. We used a *SRSCT*, a *simplified JSCT* and an *AOR* tester to acquire experimental data. Then we employed a numerical shear cell tester and a numerical *AOR* tester for the simulations. We could not collect valid data from the *simplified JSCT*, since the consolidation phase was not completely reliable. Since our results for iron ore, limestone and glass silibeads are in very good agreement with published data and in-house experiments, we can conclude that the described experimental and simulation setup successfully defined the *DEM* parameters for these materials. Furthermore, the effectiveness of *LIGGGHTS* as simulation software has again been demonstrated.

Improved calibration of the particle density could be obtained by modifying the shear cell simulation. We could thus assess the variation of the bulk density ρ_b, and then compare it with the experimental ρ_b from the *SRSCT*. We are planning to follow this path to obtain solid *DEM* parameters for coke fines.

Both the shear cell and the *AOR* experiments will be part of a series of procedures that should enable the complete characterization of particle properties within a 1% range of difference in the validation experiments.

AKNOWLEDGEMENTS

This study was funded by Christian Doppler Forschungsgesellschaft, Siemens VAI Metals Technologies and Voestalpine Stahl. The authors gratefully aknowledge their support.

REFERENCES

AI, J. *et al.* (2011). "Assessment of rolling resistance models in discrete element simulations". *Powder Technology*, **206(3)**, 269–282.

AIGNER, A. *et al.* (2013). "Determining the coefficient of friction by shear tester simulation". 335–342.

ASTM, I. (2013a). "Astm d6128 - 06 - standard test method for shear testing of bulk solids using the jenike shear cell".

ASTM, I. (2013b). "Astm d6773 - 02 - standard shear test method for bulk solids using the schulze ring shear tester".

DI RENZO, A. and DI MAIO, F.P. (2004). "Comparison of contactforce models for the simulation of collisions in dembased granular flow codes". *Chemical Engineering Science*, **59(3)**, 525–541.

GONIVA, C. *et al.* (2012). "Influence of rolling friction on single spout fluidized bed simulation". *Particuology*, **10(5)**, 582–591.

GROSSMAN, R.F. and VECCHIO, R.J.D. (2008). *Chapter 22 : Design of Experiments*, 515. Handbook of Vinyl Formulating. Wiley - Interscience.

HOLDICH, R.G. (2002). *Fundamentals of Particle Technology*. Midland Information and Technology and Publishing.

IWASHITA, K. and ODA, M. (1998). "Rolling resistance at contacts in simulation of shear band development by dem". *Journal of Engineering Mechanics*, **124(3)**, 285–292.

JIANG, M.J. *et al.* (2005). "A novel discrete model for granular material incorporating rolling resistance". *Computers and Geotechnics*, **32(5)**, 340–357.

KLOSS, C. *et al.* (2012). "Models, algorithms and validation for opensource dem and cfddem". *Progress in Computational Fluid Dynamics, an International Journal*, **12(2)**, 140–152. URL `http://dx.doi.org/10.1504/PCFD.2012.047457`.

KRANTZ, M. *et al.* (2009). "Characterization of powder flow: Static and dynamic testing". *Powder Technology*, **194(3)**, 239–245.

MISHRA, B.K. and RAJAMANI, R.K. (1992). "The discrete element method for the simulation of ball mills". *Applied Mathematical Modelling*, **16(11)**, 598–604.

PÖSCHEL, T. and SCHWAGER, T. (2004). *Computational Granular Dynamics*. Springer.

SCHULZE, D. (2008). *Powders and bulk solids: behavior, characterization, storage and flow*. Springer.

SCHULZE, D. *et al.* (2001). "The ring shear tester as a valuable tool for silo design and powder characterization". *Powder Handling and Processing*, **13(19-26)**.

WENSRICH, C.M. and KATTERFELD, A. (2012). "Rolling friction as a technique for modelling particle shape in dem". *Powder Technology*, **217(0)**, 409–417.

UNDERSTANDING SEGREGATION IN GRANULAR MEDIA

Gerald G. PEREIRA[1*], **Mahasen SOORIYABANDARA**[1], **Paul W. CLEARY**[1†]

[1]CSIRO Computational Informatics, Clayton 3169, AUSTRALIA

[*] E-mail: gerald.pereira@csiro.au
[†] E-mail: paul.cleary@csiro.au

ABSTRACT

Segregation and mixing in granular media is significantly important in a variety of industries ranging from pharmaceuticals and food processing to mining and metallurgy. Segregation of granular media occurs when discrete particles of different size, shape, density, or some other fundamental particle property are forced to flow together. Various fundamental physical mechanisms such as percolation cause one particle type (for example in percolation it is the smaller particles) to segregate from the remainder of the particles. As yet, this is not clearly understood and a fundamental device for studying segregation is a rotating tumbler roughly half filled with a granular material. In this study we investigate segregation in granular mixtures in a rotating tumbler where the mixtures particles differ in size, density and/or some other fundamental property. We use Discrete Element Method (DEM) as well as fundamental, continuum type models to explain the variety of segregation patterns which evolve. We particularly focus on the dynamics of segregation and its relationship to the underlying segregation mechanisms.

Keywords: Granular flows, meshless methods, mixing segregation .

NOMENCLATURE

Greek Symbols

μ	coefficient of sliding friction, [dimensionless]
ω	angular speed, [rad/s]

Latin Symbols

F	Force, $[N]$.
k	spring constant, $[N/m]$.
C	damping coefficient, $[Ns/m]$.
Δx	spatial increment, $[m]$.
v	speed, $[m/s]$.
g	gravity, [m/s^2]
S	smoothed concentration, [dimensionless]
R	cylinder radius, [m]
f	volume fraction, [dimensionless]

Sub/superscripts

n	Normal component.
t	Tangential component.
A	component A.
B	component B.

INTRODUCTION

Granular materials abound around us with applications in the minerals industry to food processing and pharmeceuticals industry. Yet they still remain scientifically challenging (Duran, 2000; Jaeger and Nagel, 1992). Segregation in granular materials occurs when moving particles differ in some fundamental property such as size, density, shape or even friction. This commonly occurs in any sheared flow situation such as flow down a chute (S. Wiederseiner and Ancey, 2011; Felix and Thomas, 2004) or on the surface of a deep granular particle bed (G. Metcalfe and Ottino, 1995) or in vibrated systems (A. Rosato and Swendsen, 1988). On the other side of the same coin, in many industrial processes it is required to mix different granular particles together to form a homogenous mixture. In this case, the flow of the granular mixture can induce unwanted segregation into the mixture.

In this paper we are concerned with segregation which occurs in a rotating cylinder (or tumbler) (Ottino and Khakhar, 2000; D.V. Khakhar and Ottino, 1997; G.G. Pereira and Sutalo, 2011) which consists of a cylindrical drum roughly half-filled with the granular media. The drum is placed with its cylindrical axis perpendicular to the gravitational field and then rotated slowly about this axis (one revolution per minute is a typical speed). After a few revolutions, particles tend to segregate. For example, in a binary granular medium (i.e., the media consists of two different particle types) the smaller and/or the denser particles segregate to the center, while larger and/or less dense particles segregate to the periphery. Note, in granular media literature (Ottino and Khakhar, 2000) the physical mechanism underlying segregation of different size particles is commonly referred to as *percolation* or *kinetic sieving*. In this case, the smaller particles fall through the voids created by larger particles. On the other hand the mechanism underlying segregation due to density effects is commonly referred to as *buoyancy*. In this case, denser particles sink into a bed of less dense particles (or conversely the less dense particles float on the bed of denser particles). Clearly, depending on the particle properties these two mechanisms can be either made to oppose each other or enhance each other. Following the terminology used in a previous experimental study on these mixtures by Jain *et al* (N. Jain and Lueptow, 2005) we denote mixtures where the two mechanisms oppose each other as S-D (size minus density).

In this paper we consider the complex scenario where the particle sizes and densities cause the segregation mechanisms to oppose each other. For example, if we have a mixture of

small, less dense particles and large, denser particles will the smaller particles segregate to an inner core, or will the larger ones or will the mixture remain mixed? Under what conditions does mixing occur and under what conditions does segregation occur?

Most studies on segregation in rotating tumblers have focused either on segregation for mixtures composed of particles which differ only in their diameter or mixtures composed of particles which only differ in their density. Fewer studies, to the best of our knowledge, have considered the question of segregation in mixtures composed of particles which differ both in diameter and density. Alonso *et al* (M. Alonso and Miyanami, 1991) used experimental methods in pseudo 2D drums to study the segregation of binary granular mixtures (whose particles differed in both size and density). From this they developed a parameter which could be used to describe whether mixing or segregation would occur. Metcalfe and Shattuck (Metcalfe and Shattuck, 1996) and Metcalfe *et al* (G. Metcalfe and Liffman, 1999) used a combination of pseudo-2D and 3D drums (with a ratio of length to diameter of about 3) to study these binary mixtures (composed of spherical glass beads and brown mustard seeds). They attempted to find a mixture of large, dense particles and small, less dense particles for which only mixing would occur during rotation of the tumbler. Jain *et al* (N. Jain and Lueptow, 2005) appear to have carried out the most in depth experimental study for binary granular mixtures whose particles differ in both size and density. They considered two different particle densities and four different particle sizes and were able to determine a phase diagram for the presence or absence of segregation.

It is important to note that the previous experimental studies on segregation in binary granular media (where percolation and buoyancy effects oppose each other) have relied on qualitative observations to decide whether a particular pattern is mixed or segregated. This is probably because it is quite difficult to quantitatively measure segregation in a particle bed experimentally. Computational methods have the advantage that they can easily quantify the state of a particle bed and measure important quantities which can aid us in determining whether a mixture is segregated or not. In this study we will use both qualitative particle distributions and two quantitative measures (described in Section 2.3) to decide whether a particle bed is mixed or segregated. Hence we can be more certain about our classifications and this is important when trying to differentiate between various patterns.

In this paper we use Discrete Element Method (DEM) simulations in an attempt to understand the physics of segregation in binary mixtures whose particles differ both in size and density. The fundamental question we address is can the percolation and buoyancy mechanisms be tuned so that they cancel each other out and hence result in a mixed particles bed? We believe this question is best answered at the particle-scale and DEM is a useful tool for such investigations. Such a numerical study has not been carried out for systems where particle size and density vary together, to the best of our knowledge. It is clearly an important question, since many practical systems fall in this category.

MODEL DESCRIPTION

DEM is a simulation method that models particulate systems whose motions are dominated by collisions. This involves following the motion of every particle or object in the flow and modeling each collision between the particles and between the particles and their environment (stationary and moving objects such as mills and crushers). The discrete element algorithm has three main stages:

1. A search grid is used to periodically build a near-neighbor interaction list that contains all the particle pairs and object-particle pairs that are likely to experience collisions in the short term. Using only pairs in this list reduces the force calculation to an $O(M)$ operation, where M is the total number of particles. Industrial simulations with 50 million particles are now possible in reasonable times on current desktop workstations.

2. The forces on each pair of colliding particles and/or boundary objects are evaluated in their local reference frame using a suitable contact force model, and then transformed into the simulation frame of reference.

3. All the forces and torques on each particle and object are summed and the resulting equations of motion are integrated to give the resulting motion of these bodies. Time integration is performed using a second-order predictor-corrector scheme and typically uses between 15 and 25 time steps to integrate accurately each collision. This leads to small time steps (typically 10^{-4} to 10^{-6} seconds depending on the controlling length and time scales for each application).

Collision model

The general DEM methodology and its variants are well established and are described in review articles (Campbell, 1990; Barker, 1994; Walton, 1994). The implementation used here is described in more detail in (Cleary, 2009). Briefly, the grains (which we model as either spherical or super-quadric shaped particles) are allowed to overlap and the amount of overlap Δx and normal v_n and tangential v_t relative velocities determine the collisional forces via a contact force law. We use the linear spring-dashpot model for this work because of its simplicity and robustness. This is shown diagrammatically in Fig. 1. The normal force

$$F_n = -k_n \Delta x + C_n v_n, \tag{1}$$

consists of a linear spring to provide the repulsive force and a dashpot to dissipate a proportion of the relative kinetic energy. As particles separate the dashpot component (which is then negative) can exceed the elastic component so F_n is restricted to be positive since we are modelling non-adhesive materials. The maximum overlap between particles is determined by the stiffness k_n of the spring in the normal direction. The normal damping coefficient C_n is chosen to give the required coefficient of restitution (defined as the ratio of the post-collisional to pre-collisional normal component of the relative velocity), and is given in Schwager and Pőschel (Schwager and Pőschel, 2007).

The tangential force is given by:

$$F_t = \min \left\{ \mu F_n, k_t \int v_t dt + C_t v_t \right\}, \tag{2}$$

where the vector force F_t and velocity v_t are defined in the plane tangent to the surface at the contact point. Here k_t is the tangential spring for which we use $k_t = k_n/2$. C_t is the tangential dashpot and is taken to be the same value as for the normal dashpot. μ is the coefficient of sliding friction. The integral term represents an incremental spring that stores energy from the relative tangential motion and models the elastic tangential deformation of the contacting surfaces,

while the dashpot dissipates energy from the tangential motion and models the tangential plastic deformation of the contact. Depending on the history of the contact, it is possible for the spring to be loading in one direction and simultaneously unloading in the orthogonal direction. The total tangential force F_t is limited by the Coulomb frictional limit μF_n, at which point the surface contact shears and the particles begin to slide over each other.

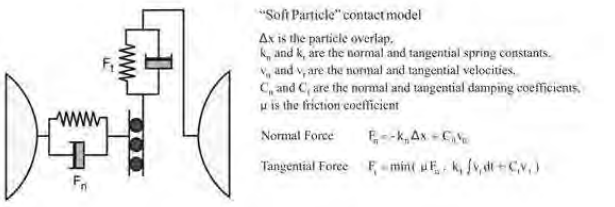

Figure 1: Linear spring and dashpot model.

Simulation set-up and Physical Parameters

To begin we specify some parameters for our simulation model. We model our simulations on typical experiments which use combinations of glass (density 2595 kg/m^3), aluminium-iron metal composites (density 5200 kg/m^3), steel (density 7707 kg/m^3), lead (density 11370 kg/m^3) and platinum (density 15570 kg/m^3) spherical balls of varying diameter (1 mm, 1.2 mm, 1.5 mm, 2 mm and 3 mm). We shall also see that particle shape is important for the streak patterns. Thus in some simulations we shall also use non-spherical, blocky-type particles. We will clearly define these simulations and the precise shape of these particles. In most experiments the cylinder walls are covered with sand-paper which introduces a degree of roughness as well as larger friction. In our initial work on numerical modeling of segregation in rotating tumblers ((G.G. Pereira and Sutalo, 2011)) we made an in-depth study on tuning the frictional coefficients and normal coefficient of restitution between the various components to experiments. We use similar values for frictional coefficients and normal coefficient of restitution in this study. (As examples we use $\mu = 0.4$ for the pair of lead and glass and 1.0 for the pair of sandpaper (wall) and lead and for the coefficient of restitution we use 0.9 for a pair of lead balls.) In fact we have varied these frictional coefficients slightly and found the results do not vary appreciably thus the major contributions to the granular flow are the cylinder rotation and collisions between particles and/or cylinder walls. We use cylindrical drums which are 10 cm in diameter (so R=5 cm) and 2 cm in length and which are periodic boundaries in the axial direction to simulate a long cylinder (see later). The rotational (angular) speed (ω) used is approximately 1 rev/min. The Froude number for these parameters is $Fr \equiv \omega^2 R/g = 5 \times 10^{-5}$ which puts the flow on the border of the avalanche and continuous flow or rolling regimes (Ottino and Khakhar, 2000). (g is gravity.) The fill level used corresponds to a volume fraction of 0.5, which is the optimal fill level for segregation because the active layer is as large as possible (both in terms of surface area and depth). The initial condition for these simulations is a random distribution of the different particles.

It is convenient from now on to define an axis system for our cylinder. We orient the z-axis along the cylinder axis and the y-axis in the opposite direction to gravity. Hence the x-axis is oriented orthogonal to these two directions with the origin of our co-ordinate system being the center of the cylinder. In this study our focus is the radial segregation that occurs in the rotating cylinder. In most practical cases the length of the cylinder is larger than the diameter. As has previously been shown ((G.G. Pereira and Sutalo, 2011)), both axial and radial segregation occur in the cylinder. However, the axial segregation is limited to a region of about 10-15 particle diameters from each wall. In the middle region the axial segregation does not vary (when the duration of the rotation is of the order of 5-10 cycles). The periodic length is about 10 particle diameters (2 cm). Particles exiting on one side the slice then re-enter on the opposite side.

DEM segregation measures

We have previously studied binary mixtures of particles which differ only in their density in quite some detail and made comparisons with experiments (Pereira *et al* (G.G. Pereira and Sutalo, 2011)). Besides the qualitative pictures of the segregation patterns, we also give two other quantitative measures to evaluate the amount of segregation.

The first measure is the volume fraction of each particle type, (f_A or f_B) as a function of the distance from the center of the cylinder (averaged over the axial direction). To obtain this we divide the cylindrical cross-section into 15 equally spaced annuli and calculate the volume of each type of particle within each annulus (i.e., has its center located within the annulus). This volume is normalized by the total volume of particles within each annulus, yielding a value between zero and one. Thus we get a volume fraction for each particle type which is a function of the scaled distance from the center of the cylinder (scaled with the cylinder radius).

The second measure is a smoothed concentration of the particle distribution as follows. If a particle is located at (x_0, y_0) at time t we then associated a two-dimensional Gaussian function with it as follows,

$$\phi(x,y) = A \exp\left(-\frac{(x-x_0)^2}{2R} - \frac{(y-y_0)^2}{2R} \right). \qquad (3)$$

Note, that the z position of the particle is disregarded in this calculation since we are focussing on radial segregation. Then summing this function over all particles from either the A component or B component yields the smoothed field

$$S(x,y,t) = \sum_{i \in A} \phi(x_i(t), y_i(t)) - \sum_{j \in B} \phi(x_j(t), y_j(t)). \qquad (4)$$

The smoothed distribution S can either be positive or negative. We normalize it so that its values range from -1 to +1. This value is then mapped to a colour scale and represented as a smoothed colour map indicating regions of high A-component concentration (red) to high B-component concentration (blue). Both of our measures are calculated throughout the segregation so that we can obtain a dynamic evolution of the segregation patterns.

RADIAL SEGREGATION IN S-D SYSTEMS

Initially, we would like to determine when a particular segregation pattern appears, for given particles size ratios and density ratios. To do this we use a number of density and size ratios to map out a "*phase diagram*" for the S-D system. We denote the ratio of diameters of the two particle types in a particular simulation by r_s and the ratio of densities of the two particle types by r_d. Given these previous results, we shall therefore limit our study to the following ranges of size and density ratios: $1 \leq r_s \leq 3$ and $2 \leq r_d \leq 6$.

Since we have previously presented the simulations to obtain this phase diagram in detail (G.G. Pereira and Cleary, 2014; Pereira and Cleary) here we briefly present the results and then get onto the more interesting question of whether the two mechanisms (percolation and buoyancy) can be made to cancel each other resulting in an unmixed bed and dynamics of segregation.

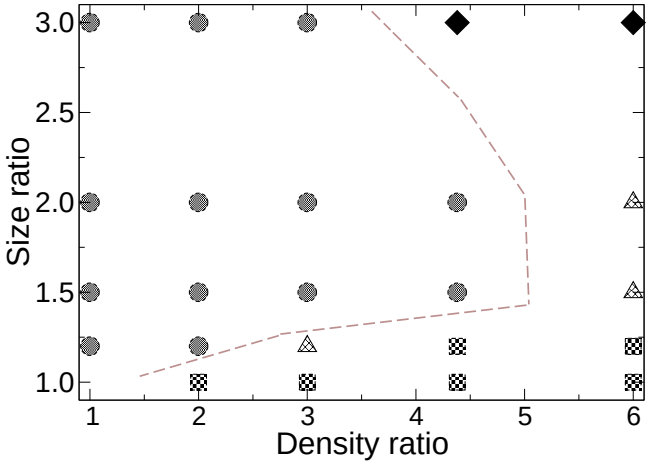

Figure 2: Phase diagram for segregation and mixing with grey filled circles corresponding to S-Core pattern, checkerboard squares to D-Core, hash-filled triangles to Core-and-band pattern and black diamonds to a transitional pattern. The dashed grey line corresponds to the boundary between S-Core and other patterns (S-Core to the left of dashed line).

Figure 2 shows a phase diagram from our simulations. There are four distinct regions that have been identified. Firstly, the region where a core of small particles (called S-core) is formed (grey circles), which extends to the the left of the dashed grey line. One can see that S-Core dominates in the size ratios between 1.5 to 3 and tapers away out of this range. Hence this is the range in which the domination of the percolation mechanism leads to significant segregation. Typical radial volume fractions and smoothed concentrations are shown in Figs. 3 and 4. Between (and below) the dashed grey line and the horizontal axis lies the region where a core of the denser particles (called D-core) is formed (checkerboard squares). It appears the buoyancy mechanism, which is a consequence of a density contrast between particles is weaker in comparison to the percolation mechanism since the D-core region only extends a small distance from the horizontal axis. Typical radial volume fractions, smoothed concentrations and discrete particles distribution are shown in Figs. 5 and 6. A noticeable difference between the S-Core and D-Core patterns is that the S-Core results in a much more high purity core region. This would indicate the percolation mechanism is a stronger mechanism than the buoyancy mechanism. In addition, the S-core region occupies a much larger region of the phase diagram (Fig. 2) than the D-Core region.

If we increase the particle size ratio (for relatively large densities) we get into a region which we denote as Core-and-Band (hash filled triangles). In this region, we obtain a core with a higher concentration of small particles and also a thin band with a very high concentration of small particles close to the cylinder walls (see Figs. 7 and 8) Between these two regions is a thicker band consisting of higher concentration of large particles (red). The radial distribution plots for the Core-and-Band case are distinct from the S-Core and D-Core cases since they have two maxima for smaller particles. One maxima is closer to the centre and is of lower magnitude and the second maxima is at the container wall (and is of high magnitude). This indicates three distinct segregation regions have formed in contrast to the S-Core and D-Core patterns, where only two segregation regions appear.

Finally, for large size and density ratio we find a region which we denote as "transitional. In this region it is difficult to classify whether the pattern is Core-and-band or mixed as

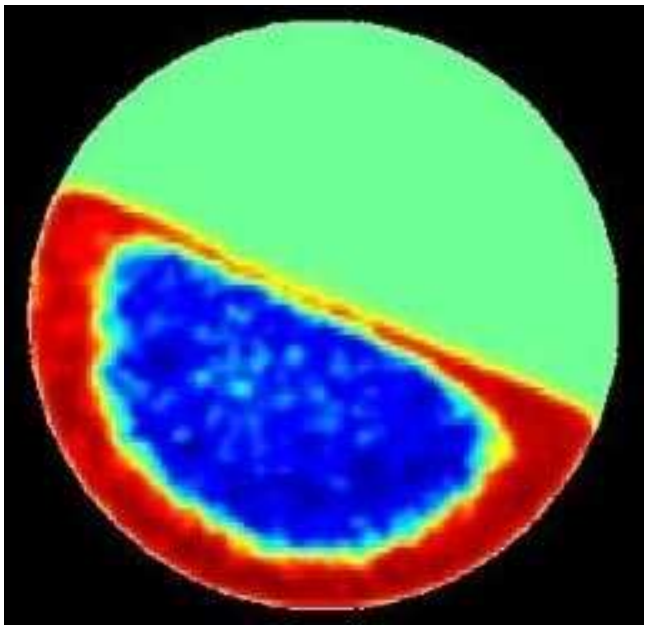

Figure 3: Smoothed concentration map for an S-Core pattern. A high concentration/volume fraction of the small (blue) particles are found in the core.

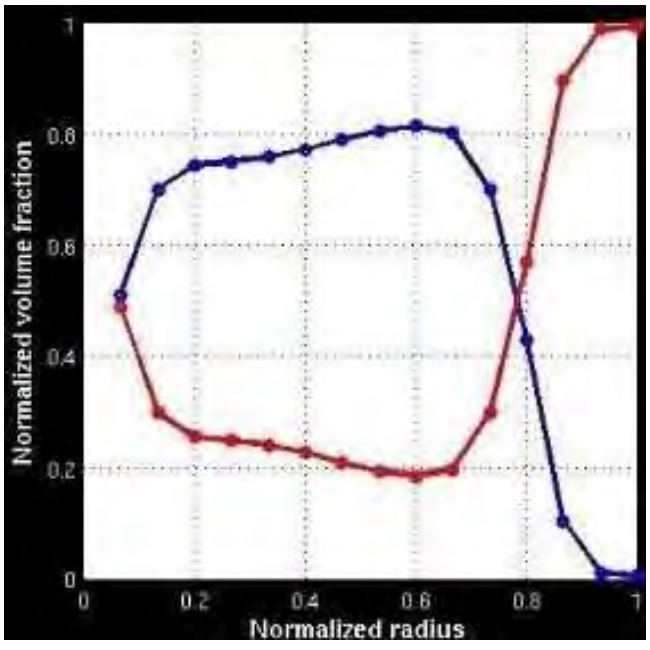

Figure 4: Radial distribution of the S-Core pattern corresponding to Fig. 3. The blue (red) curve corresponds to small (large) particles.

our different measures point to one or the other. For very large size ratio ($r_s > 4$) the big particles tended to become more immobile as they began to form a contact network with other big particles. In addition, the voids between the big particles were so large that the smaller particles would flow through them rather easily (almost like a fluid through a porous medium). This in turn resulted in the small particles coexisting in regions with bigger particles. In a sense the two segregation mechanisms cease to operate at large size ratios, since although small particles flow downwards, there is not the accompanying upward flux of large particles. Generally

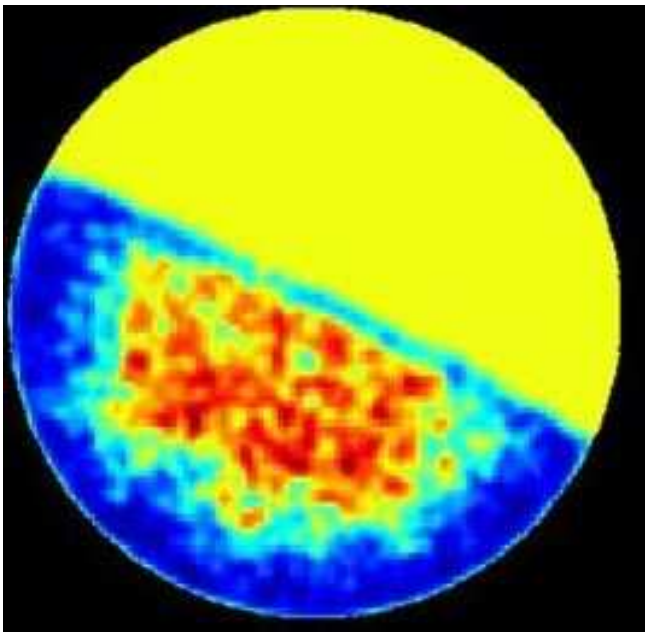

Figure 5: Smoothed concentration map for a D-Core pattern. A high concentration/volume fraction of the larger and denser (red) particles are found in the core while smaller and less dense particles are in the periphery.

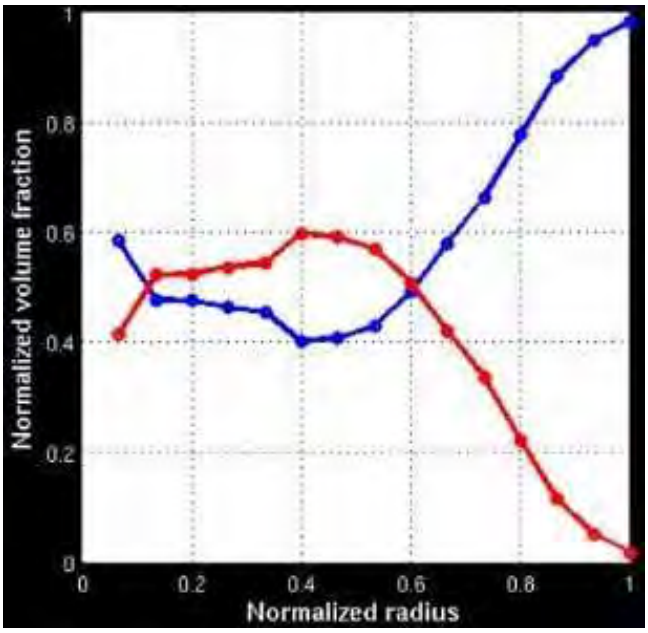

Figure 6: Radial distribution corresponding to the case in Fig. 5. The blue (red) curve corresponds to the less dense (denser) particles.

the dynamics of segregation can also give a clue as to the type of segregation pattern that evolves. Size and density segregation are quite rapid, with segregation occuring within half a revolution. On the other hand the Core-and-band pattern is much slower, evovling over a number of revolutions.

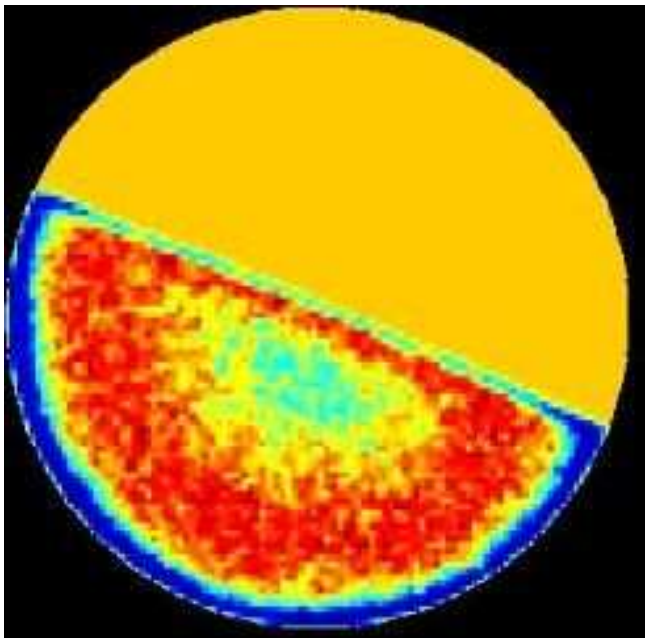

Figure 7: Smoothed concentration map for a Core-and-Band pattern. A high concentration/volume fraction of the smaller (blue) particles are found near the periphery with a lower concentration of small particles in the core. Meanwhile larger particles are located between these two regions.

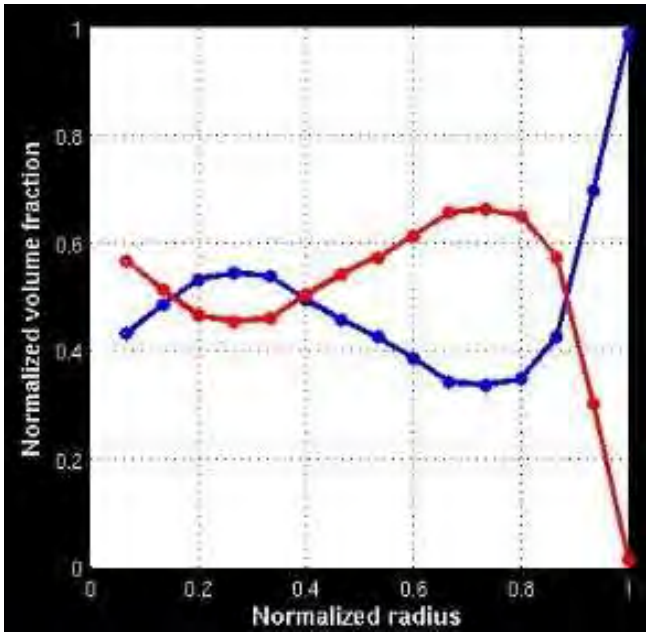

Figure 8: Radial distribution corresponding to the case in Fig. 7. The blue (red) curve corresponds to the smaller (larger) particles.

CORE-AND-BAND PATTERN

We have identified the Core-and-Band pattern which occurs between the S-core and D-core on increasing size ratio. Since

this pattern occurs between the S-core and D-core we hypothesize it represents where the percolation and buoyancy mechanisms tend to cancel each other out. However, if these two mechanisms are cancelling each other out, should'nt the bed remain mixed? To answer this question we now consider this case in much greater detail.

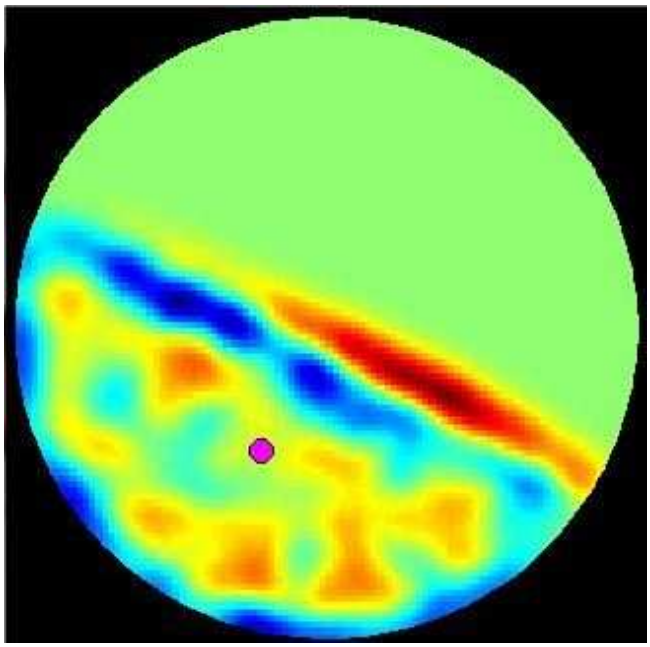

Figure 9: Initial evolution of segregation in the S-Core case. A noticeable jet of smaller (blue) particles emenate from the head of the flowing layer.

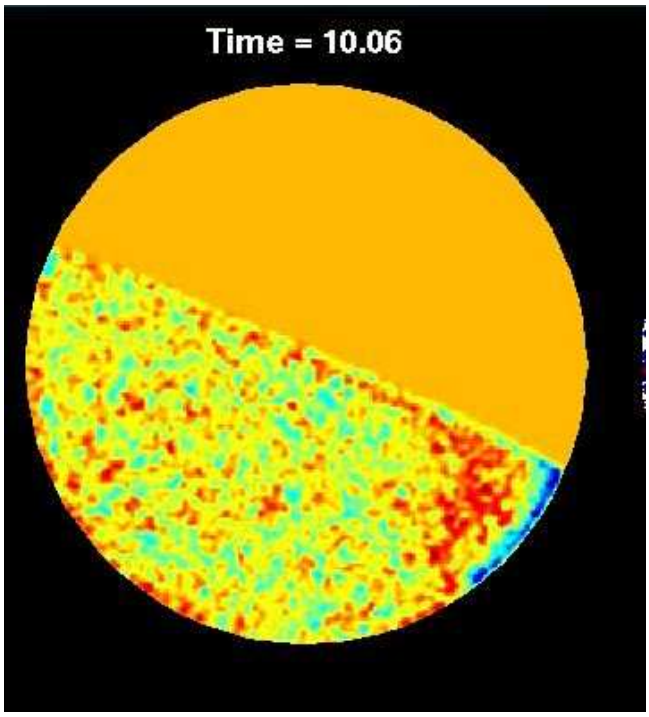

Figure 10: Initial evolution of segregation in the Core-and-Band case. Initially segregation occurs at the bottom end of the flowing layer (toe) where a small region of blue (small) particles appear.

In the rotating tumbler it is well known that segregation occurs in the top-most flowing or *active layer*. This is the layer of thickness around 5-10 particle diameters at the top of the particle bed. (For a schematic of this layer see Figure 18 of reference (G.G. Pereira and Sutalo, 2011).) In the rest of the particle bed the particles are essentially static (with respect to each other and also the rotating cylinder) and as such segregation only occurs in the active layer. When segregation occurs due to percolation (S-Core) or buoyancy (D-core) this initially occurs at the top of the flowing layer, adjacent to the cylinder wall (called the head). As the bed rotates, a mixture of particles are transported to the head of the flowing layer. Now particles become free to move and they avalanche down the flowing layer. Segregation begins rapidly at the head, with the smaller (percolation dominates) or denser (buoyancy dominates) moving into the lower regions of the flowing layer and the other particles flowing along the top of the active layer. Hence a core of the smaller or denser particles rapidly form (G.G. Pereira and Sutalo, 2011; Pereira and Cleary).

In the case of a Core-and-Band pattern a different scenario evolves. As before, particles are transported the head of the flowing layer by the cylinder rotation but now the percolation and buoyancy mechanisms are roughly equal but in an opposing sense. Hence segregation does not occur at the head of the bed. So a core does not form immediately. As evidence for this we compare the early stage of segregation between the Core-and-Band case and the S-Core case (see Figs. 9 and 10). The smoothed shows a jet of blue and above this a layer of red which emanate from the head. However, the Core-and-band case shows no segregation near the head of the bed. There is only the beginnings of thin layers of small (blue) particles and larger particles (red) near the toe of the bed. In the Core-and-Band case, segregation initially occurs close to the toe of the flowing layer.

Given that the percolation and buoyancy mechanisms are effectively cancelling each other out (and we know this because otherwise a core of the smaller or denser particles would form) why is there still segregation occuring near the toe? Peroclation and buoyancy are the primary or first order segregation mechanisms. Since these have cancelled each other out, second order segregation mechanisms must become important in the system. The two most reasonable candidates for these second order mechanims are (i) Different frictional characteristics of the particles and (ii) the larger particles (due to their greater surface area) undergo more random collisions with other particles and hence experience a larger drag which slows them to a greater extent than the smaller particles when traversing the flowing layer. The proximity of the segregation near the bottom wall might indicate the influence of the wall on segregation, which will also need to be investigated closely.

One can determine the effect of different friction on different particle types by using a binary mixtures of particles drawn from the same size distribution and same density but only differing in their frictional properties. We have tried the following sets of parameters (i) Same friction as we have used in the cases above (ii) slightly larger frictional difference and (iii) exactly the same frictional properties. When running these DEM simulations we used particle densities which were the same as glass (ie. 2700 kg/m^3) and a mean diameter of 2mm. The result of these simulations were that the particles with larger friction segregate to the core while the lower friction particles segregate to the periphery. The dynamics of segregation and final segregation pattern appear quite similar to the S-Core and D-Core cases. So although frictional differences can cause segregation of particles, we do not believe

it is the driving mechanism for segregation in the Core-and-Band case.

To investigate the second scenario, where the large particles may experience a large effective drag than the smaller particles is more difficult with DEM. A better tool could well be a Cellular Automata type model (Baxter and Behringer, 1990) where we can vary mechanisms as we desire and see the resulting segregation pattern. This will be the focus of our future work. However, it is clear from this study the Core-and-Band pattern involves a different mechanism, compared to the S-Core and D-Core patterns.

CONCLUSION

The rotating tumbler is a fundamental device to investigate segregation in granular media made up of particles which differ in size, density, shape or frictional properties. In the avalanching/rolling regimes of flow, a core of one type of particle (either smaller or denser) segregates from the other type of particles (found near the cylinder walls). In the past, the segregation patterns leading to cores of smaller or denser particles have been investigated intensively and underlying physical mechanisms are now quite well understood. However, in this study we have focussed on a much less understood segregation pattern called the Core-and-Band pattern. This segregation pattern is quite different to the S-Core and D-Core patterns with three segregation regions appearing - (i) a band with a higher concentration of small particles near the cylinder walls, (ii) a core with a lower concentration of small particles and (iii) a higher concentration of large particles in the region between these two.

We postulate that the Core-and-Band patterns represent a cancelling of the two fundamental mechanisms of percolation and buoyancy. Then a second order mechanism comes to the fore to induce segregation. We have hypothesised these mechanisms could either be different frictional properties or a higher effective drag on larger particles (due to their larger surface area). While we have put forward a possible mechanism for the Core-and-Band pattern, this still has to be validated. Hence, our future work will focus on this issue using Cellular Automata models.

REFERENCES

A. ROSATO, K.J. STRANDBOURG, F.P. and SWENDSEN, R. (1988). "Why the brazil nuts are on top: size segregation of particulate matter by shaking". *Phys. Rev. Lett.*, **58**, 1038–1040.

BARKER, G. (1994). "Computer simulations of granular materials". *Granular Matter: An interdisciplinary approach*. Springer-Verlag, New York.

BAXTER, G. and BEHRINGER, R. (1990). "Cellular automata models of granular flow". *Phys. Rev. A*, **42**, 1017–1020.

CAMPBELL, C. (1990). "Rapid granular flows". *Ann. Rev. Fluid Mech*, **22**, 57–92.

CLEARY, P. (2009). "Industrial particle flow modelling using dem". *Eng. Computat.*, **26**, 698–743.

DURAN, J. (2000). *Powders and Grains. An introduction to the physics of granular matter*. Springer-Verlag, New York.

D.V. KHAKHAR, J.M. and OTTINO, J. (1997). "Radial segregation of granular mixtures in rotating cylinders". *Phys. Fluids*, **9**, 3600–3614.

FELIX, G. and THOMAS, N. (2004). "Evidence of two effects in the size segregation process in dry granular media". *Phys. Rev. E*, **70**, 051307 1–16.

G. METCALFE, L. GRAHAM, J.Z. and LIFFMAN, K. (1999). "Measurement of particles motions within tumbling granular flows". *Chaos*, **9**, 581–593.

G. METCALFE, T. SHINBROT, J.M. and OTTINO, J. (1995). "Avalanche mixing of granular solids". *Nature*, **374**, 39–41.

G.G. PEREIRA, N.T. and CLEARY, P. (2014). "Segregation of combined size and density varying binary granular mixtures in a slowly rotating tumbler". *Granul. Matter*, **0**, 00–00.

G.G. PEREIRA, M.D. SINNOTT, P.C.K.L.G.M. and SUTALO, I. (2011). "Insights from simulations into mechanisms for density segregation of granular mixtures in rotating cylinders". *Granul. Matter*, **13**, 53–74.

JAEGER, H. and NAGEL, S. (1992). "Physics of the granular state". *Science*, **255**, 1523–1531.

M. ALONSO, M.S. and MIYANAMI, K. (1991). "Optimum combination of size ratio, density ratio and concentration to minimize free surface segregation". *Powder Technol.*, **68**, 145–152.

METCALFE, G. and SHATTUCK, M. (1996). "Pattern formation during mixing and segregation of flowing granular materials". *Physica A*, **233**, 709–717.

N. JAIN, J.O. and LUEPTOW, R. (2005). "Regimes of segregation and mixing in combined size and density granular systems: an experimental study". *Granul. Matter*, **7**, 69–81.

OTTINO, J. and KHAKHAR, D. (2000). "Mixing and segregation of granular materials". *Ann. Rev. Fluid Mech*, **32**, 55–91.

PEREIRA, G. and CLEARY, P. (). "Radial segregation of multi-component granular matter in a rotating tumbler".

S. WIEDERSEINER, N. ANDREINI, G.E.C.G.M.M.M.J.G. and ANCEY, C. (2011). "Experimental investigation into segregating granular flows down chutes". *Phys. Fluids*, **23**, 013301 1–10.

SCHWAGER, T. and PőSCHEL, T. (2007). "Coefficient of restitution and linear daspot model revisited". *Granul. Matter*, **9**, 465–469.

WALTON, O. (1994). "Numerical simulation of inelastic frictional particle-particle interaction". *Particulate two-phase flow*. Springer-Verlag, New York.

HARD-SPHERE MODELLING OF LIQUID BRIDGE AGGLOMERATION

Boris V. BALAKIN[1]*, **Guzel SHAMSUTDINOVA**[2†], **Pawel KOSINSKI**[3‡]

[1]Bergen University College, 5020 Bergen, NORWAY

[2]Far Eastern Federal University, Vladivostok, RUSSIA

[3]University of Bergen, Department of Physics and Technology, 5020 Bergen, NORWAY

* E-mail: boris.balakin@hib.no
† E-mail: guzel.sh13@gmail.com
‡ E-mail: pawel.kosinski@ift.uib.no

ABSTRACT

The present paper describes a novel approach for CFD-modelling of liquid bridge agglomeration in multiphase flows. The model is based on the Lagrangian technique for the dispersed phase treatment where the bridge-dominated in-phase interactions are modelled with the use of analytic functions that come out from precursive theoretical solutions of inter-particle contact mechanics. In contrast with the distinct element method (DEM) based on direct numerical treatment of every particle interaction, our model avoids computationally expensive sub-stepping. The model was implemented into an in-house code and validated against analytic models from literature. In addition, the computational cost when compared with the DEM package available in the commercial CFD software STAR-CCM+ was reduced by a factor of five.

Keywords: DEM, CFD, pragmatic modelling, Lagrangian methods, multiphase pipeline transport, STAR-CCM+ .

NOMENCLATURE

Greek symbols

α	collision efficiency	
$\bar{\alpha}$	average filling angle of the bridge	
γ	shear rate	[1/s]
ε	coefficient of restitution	
ϕ	dimensionless auxiliary parameter	
$\bar{\phi}$	volume fraction	
σ	surface tension	[N/m^2]
μ	dynamic viscosity	[Pa·s]
ν	dimensionless relative velocity	
ρ	density	[kg/m^3]
θ	wetting angle	
Θ	granular temperature	[m^2/s^2]
ξ	dimensionless interparticle separation	

Latin symbols

A, B, C	dimensionless auxiliary parameters	
Ca	Capillary number of the bridge	
C_D	drag coefficient	
d	diameter	[m]
e	relative volume fraction	
F, f	force	[N]
f_0, f_1, f_2	dimensionless auxiliary parameters	
g_0	distribution function	
m	mass	[kg]
n	number density	[1/m^3]
p	pressure	[Pa]
R	radius	[m]
Re	Reynolds number	
t	time	[s]
u	velocity of the continuous phase	[m/s]
v	particle/interparticle velocity	[m/s]
V	liquid bridge volume	[m^3]
$\hat{V}$	dimensionless volume of the bridge	
X	interparticle separation	[m]

Sub/superscripts

0	initial
1, 2	particle number
A	approach
b	bridge
C	continuous
e	equivalent radius $R_e = \frac{R_1 R_2}{R_1+R_2}$ or mass $m_e = \frac{m_1 m_2}{m_1+m_2}$
eq	equilibrium
f	final
i	particle index
max	maximum
min	minimum
p	particle
Σ	total
S	separation

INTRODUCTION

Agglomeration of particles by liquid flocculants is often met in petroleum industry and therefore the importance of its numerical reproduction is indubitable. The most accurate approach to multiphase flow modelling is of the Euler-Lagrange type (Crowe *et al.*, 1998) where the motion of a separate particle or a droplet is resolved individually. Nevertheless, an industrial scale system contains billions of dispersed objects and it often requires extensive computational costs to be investigated numerically. The situation is even more complicated by the need to account for inter-particle interactions, which, in case of liquid bridge agglomeration, involve capillary and lubrication forces. These forces are the drivers of agglomeration that act within nano- or micro-layer of flocculant. The so-called distinct element approach (DEM) (Cundall and Strack, 1979) is capable for the precise integration of the aforementioned forces during the entire collision, that is, the dynamics of interparticle motion

is resolved for each pair of colliding particles. The spatial and temporal resolution required by DEM models is, however, high. The technique thus is hardly applicable to industrial scales. The present research proposes an alternative and pragmatic way to model interparticle collisions using the Eulerian-Lagrangian approach. The model implies an analytic pre-solution of the dynamics of collision in a way that it is capable for prediction of either the velocities of particles after collision in presence of the liquid bridge or particle agglomeration. This strategy is generally inspired by the well-known hard-sphere technique (Crowe *et al.*, 1998). The technique is based on the estimation of the particle velocity after collision using solely analytic relations. The hard-sphere model was further updated in this research: we took into account the amount of relative momentum conserved by the bridge applying the expressions derived in our recent work (Balakin *et al.*, 2013). Similar to our (Balakin *et al.*, 2013) two-body systems were previously considered by, for example, Drabi et al. (Darabi *et al.*, 2009) and Davis et al. (Davis *et al.*, 2002). However it is presently unknown whether those analytics have been incorporated into the multiphase CFD-code. In the present paper we report results of the modelling of liquid bridge agglomeration of 200-μm solid spheres in a Couette flow of viscous oil. The simulation results focus on spatial positions and granulometry of resulting agglomerates.

MODEL DESCRIPTION

Eulerian-Lagrangian model

The flow of the carrier phase is modelled with the set of standard Navier-Stokes equations for the viscous incompressible flow and the continuity equation:

$$\nabla \vec{u} = 0, \tag{1}$$

$$\rho_c \left[\frac{\partial \vec{u}}{\partial t} + \vec{u} \nabla \vec{u} \right] = -\nabla p + \mu_c \nabla^2 \vec{u} - \vec{f}_{p,\Sigma}. \tag{2}$$

The latter is coupled with the flow of the dispersed phase via the total drag force, applied to the carrier phase from all the particles located within the computational cell $\vec{f}_{p,\Sigma}$. The present model assumes isothermal flow of both phases thus the conservation of energy is accounted for via the conservation of the momentum.

In the Lagrangian reference frame the particles are considered to behave as separate objects. Each of them follows the Newtonian dynamics:

$$m_i \frac{d\vec{v}_i}{dt} = \vec{f}_{p,i}, \tag{3}$$

where the drag force is calculated as:

$$\vec{f}_{p,i} = \frac{\pi}{64} R_i^3 C_{D,i} \rho_c \left(\vec{u} - \vec{v}_i\right) |\vec{u} - \vec{v}_i|. \tag{4}$$

The expression for the drag coefficient is taken from (Schiller and Naumann., 1935):

$$C_{D,i} = \frac{24}{Re_{p,i}} \left(1.00 + 0.15 Re_{p,i}^{0.687}\right), \tag{5}$$

where $Re_{p,i} = 2\rho_c R_i |\vec{u} - \vec{v}_i| / \mu_c$.

The total drag force from Eq. (2) is calculated with respect to the amount of particles within the computational cell N:

$$\vec{f}_{p,\Sigma} = \sum_{i=1,N} \vec{f}_{p,i}. \tag{6}$$

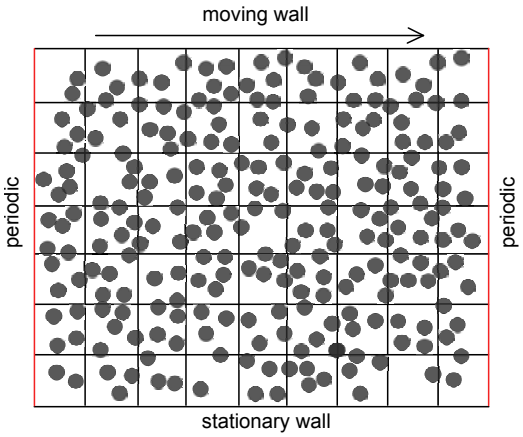

Figure 1: Schematic representation of the computational domain.

The study considers the flow of Couette type thus the torque from the continuous phase is assumed to be negligible.

The rectangular computational domain with the dimensions 0.15350 x 0.0768 x 1.0000 m is presented in Fig. 1. The periodic boundary conditions are applied on the left and right sides of the domain while the upper wall moves at the velocity of 4.5 m/s. The lower wall is stationary and the symmetry boundary conditions are applied to the frontal edges of the domain. Thus the configuration of boundary conditions simulates, for instance, a two-dimensional recirculative flow in a part of a rheometer.

The model is spatially discretized into 4096 regular control volumes and temporary with the use of Euler implicit technique (Kosinski *et al.*, 2009) (with the CFL coefficient equal to 0.25). Eqs. (1-2) are numerically solved using the Chorin-Temam technique (Griebel *et al.*, 1997). The initial condition for the model is the prescribed linear velocity profile of the carrier phase and zero reference pressure. Heavy oil with the density ρ=1000 kg/m^3 and dynamic viscosity μ_c=0.176 Pas was assumed for the carrier phase. 10 000 spherical particles with radius R=100 μm were injected with zero velocity into the carrier fluid upon the establishment of the fully developed velocity profile. The density of the particles ρ_p was set to 4000 kg/m^3.

Interparticle collisions

The interparticle collision is modelled via a theoretical expression for the relative momentum lost in the collision which is derived in the present subsection. This is done in order to avoid direct numerical treatment of every interparticle collision as in DEM. Instead of doing so, the study is aimed at the analysis of pre-collisional interparticle motion for the prediction of their relative after-collisional behaviour. The process of the collision is therefore assumed to go in three stages:

1. the mutual approach of two rough particles within the bridge;
2. the physical contact of particles;
3. the mutual separation of particles until the break-up of the bridge.

Those stages are illustrated in Fig. 2 in terms of the particle relative velocity v scaled with its pre-collisional value $v_0^A < 0$. The scheme at the bottom of Fig. 2 presents relative positions of the particles at each stage of the collision

and forces applied to them. The present study assumes only the normal component of the relative velocity to be affected by the bridge due to its negligible thickness in the tangential direction (Balakin *et al.*, 2013).

The forces applied to the particle at the approach stage are the capillary force $F_c < 0$ which attracts the particles, and the lubrication dissipative force $F_d > 0$ hindering the particle relative motion. The amount of the relative momentum spent at the first stage is $\varepsilon_A = v_f^A / v_0^A$, where $v_f^A < 0$ is the velocity before the physical contact between the particles, that is, $v_f^A = v(X_{\min})$.

For the second stage it is assumed that the particles are rough and they experience physical contact at the minimum separation distance $X_{\min}$=0.5 μm. The standard hard-sphere model described in, for instance, Crowe et al (Crowe *et al.*, 1998) is used at this stage. The hard-sphere model parameters: the restitution coefficient ε=0.8 and the friction coefficient f=0.15 define the velocity $v_0^S > 0$ after the physical contact. It has to be noted that the particle tangential velocity is modified at this stage due to Coulombian friction.

During the third stage the particles move in the opposite direction where the capillary force $F_c < 0$ acts towards the centres of the particles. The dissipative force $F_d < 0$ is again directed oppositely to the particle motion. The particles leave the bridge with velocity v_f^S.

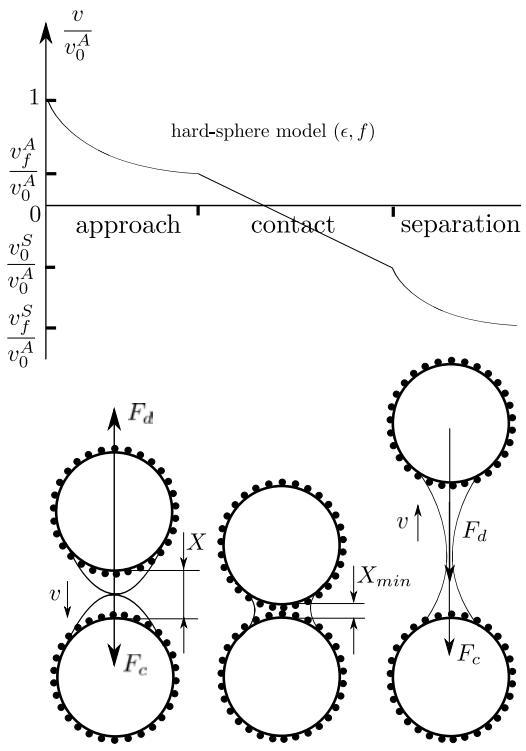

Figure 2: Bridge-dominated collision. Particle velocity scaled with its initial value v_0^A for different stages of process. It has to be noted that the forces are applied to both particles symmetrically while drawn only for one particle.

The equation of the particle motion within the bridge is given according to (Balakin *et al.*, 2013):

$$m_e v \frac{dv}{dX} = -\frac{2\sigma V cos(\theta)}{X^2} - 3\pi\mu_b R_e^2 \frac{v}{X}, \tag{7}$$

where the first term in the right-hand-side of the Eq. (7) represents the capillary force acting in bridge and the second term is the dissipative lubrication force.

The equation of motion is further made dimensionless substituting dimensionless separation distance $\xi = X/R_e$, bridge volume $\hat{V} = V/(\pi R_e^3)$, velocity $\nu = v\left(\pi R_e^2 \sigma / m_e\right)^{-1/2}$ and the capillary number of the bridge $Ca = \frac{3\mu_b}{\sigma}\sqrt{\frac{\pi R_e^2 \sigma}{m_e}}$:

$$\nu \frac{d\nu}{d\xi} = -\frac{2\hat{V}\cos\theta}{\xi^2} - Ca\frac{\nu}{\xi}. \tag{8}$$

The boundary conditions for Eq. (8) are:

1. $\nu(\xi_{\max})$=ν_0^A, $\nu(\xi_{\min})$=ν_f^A for the approach stage,
2. $\nu(\xi_{\min})$=ν_0^S, $\nu(\xi_{\max})$=ν_f^S for the separation stage.

The maximum separation distance is given by (Balakin *et al.*, 2013), (Pitois *et al.*, 2001):

$$\xi_{\max} = (1+0.5\theta)\left(1+\sqrt{\frac{Ca\nu_0^A}{3}}\right)\hat{V}^{\frac{1}{3}}. \tag{9}$$

Eq. (8) is analytically solved with respect to ν assuming that the shape of the bridge could be represented by a cone (Balakin *et al.*, 2013):

$$\nu = \frac{-B - \sqrt{B^2 - 4AC}}{2A}, \tag{10}$$

$$A = 0.5\phi f_2, \tag{11}$$

$$B = \phi f_1 - \nu_0^k \phi f_2 - Ca, \tag{12}$$

$$C = \phi f_0 - \phi f_1 \nu_0^k + 0.5\phi f_2 \nu_0^{k2} + Ca^2\left(\ln\left(\frac{1}{\xi}\right) - K_k\right), \tag{13}$$

$$f_0 = \ln\left(Ca\nu_0^k + \phi\right), \tag{14}$$

$$f_1 = \frac{Ca}{Ca\nu_0^k + \phi}, \tag{15}$$

$$f_2 = -f_1^2, \tag{16}$$

$$\phi = \frac{2}{3}\bar{\alpha}^2\cos\theta, \tag{17}$$

$$\bar{\alpha} = \frac{\sqrt{3\hat{V}}}{2}\left(\sqrt{\frac{1}{\xi_{\max}}} + \sqrt{\frac{1}{\xi_{\min}}}\right), \tag{18}$$

$$K_k = \ln\left(\frac{1}{\xi_{\max/\min}}\right) - \frac{Ca\nu_0^k - \phi f_0}{Ca^2}, \tag{19}$$

where index k stays either for approach A or separation S.

The momentum distribution coefficients in the normal direction are therefore given as $\varepsilon^A = \nu_f^A/\nu_0^A$ and $\varepsilon^S = \nu_f^S/\nu_0^S$ for the approach and separation respectively. Then the normal component of interparticle relative velocity after the collision is given by $v_f^S = -v_0^A \varepsilon^A \varepsilon\varepsilon^S$. The agglomeration of particles takes place when $\varepsilon^S \leq 0$.

The post-collisional linear and angular velocity of agglomerate are calculated as in (Kosinski and Hoffmann, 2010) accounting for the conservation of linear and angular momentum. The radius of the agglomerate is calculated based on the equivalent-circle approach (two-dimensional problem), i.e. $R = \sqrt{R_1^2 + R_2^2}$.

In the present model the particles were set to be covered by liquid flocculant with the following parameters: V=5.0·10^{-19} m^3, σ=2.0·10^{-2} N/m, θ=0.7 and μ_b=0.001 Pa·s.

RESULTS AND VALIDATION

The simulation results are shown in Fig. 3 in terms of the positions of agglomerated particles in the computational domain at 10, 50 and 150 seconds from the start of injection. The particles are coloured by the value of their diameter.

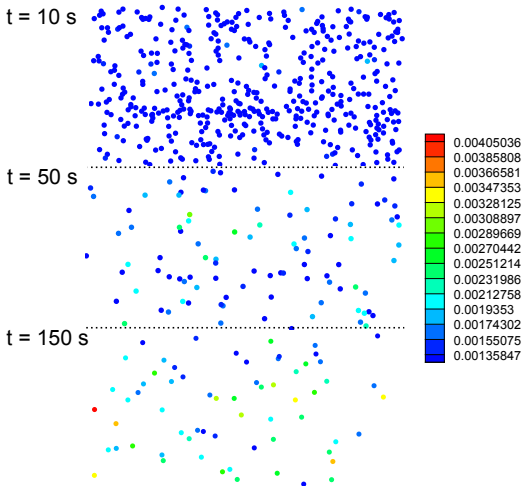

Figure 3: Agglomerate positions in space after 10, 50 and 150 s of the process. The colour scale illustrates their diameter in [m].

It follows from the figure that the amount of agglomerated particles and the mean particle size increase with time. The total amount of treated objects reduces in the process since agglomerates consume free particles. On the early stages of the process the agglomeration starts in the vicinity of the moving wall as the most intensive agitation of the granular phase takes place there. The maximum particle size is further shifted to the centre of computational domain due to higher compactioning of particles there which takes place during multiple interactions with the moving wall.

The temporal evolution of the system-average particle size is given in Fig. 4. It follows from the figure that the early stages of the process are characterized by the steep diameter increase. Nevertheless, after 320 s of the process the diameter gets into the equilibrium statistical steady-state condition.

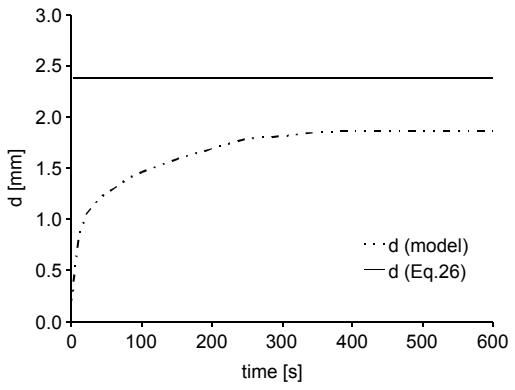

Figure 4: Mean particle size as a function of time. Simulation results are compared with analytical expression from Eq. (26).

The model does not account for the destruction of agglomerates due to mechanical collisions or the carrier phase shear stresses induced on the particle surface. The existence of the equilibrium particle size is therefore not explained by the balance of the rates of agglomeration and fragmentation as it is often done in the flocculation studies (Chimmili *et al.*, 1998). However, the temporal decrease of amount of agglomerates in the system is responsible for the significant increase of the mean free path of the particles above the values of theoretical interparticle distance. In the terminology proposed by (Crowe *et al.*, 1998), the flow becomes *dilute* when the particle size follows the expression:

$$d_{eq} = \frac{3\mu_c}{\bar{\phi}\rho_p \bar{v}}, \tag{20}$$

where $\bar{v}$ is the mean interparticle relative velocity (an unknown parameter). The interparticle collision rate depends on $\bar{v}$ as follows from e.g. the model shown in (Crowe *et al.*, 1998):

$$N = \pi d_{eq}^2 n^2 \bar{v}. \tag{21}$$

According to (Gidaspow, 1994), the collision rate is dependent on the granular temperature, Θ:

$$N = 4 d_{eq}^2 n^2 g_0 \sqrt{\pi\Theta}, \tag{22}$$

where g_0 is the distribution function (Gidaspow, 1994):

$$g_0 = \left(1 - \left(\frac{\bar{\phi}}{\bar{\phi}_{\max}}\right)^{\frac{1}{3}}\right)^{-1}, \tag{23}$$

where $\bar{\phi}_{\max}$=0.7405. Θ is described for a shear flow by following expression (Gidaspow, 1994):

$$\Theta = \frac{\left(\frac{5\pi}{96}\right)\gamma^2 d_{eq}^2}{12\bar{\phi}^2(1-e^2)}, \tag{24}$$

where $e = \bar{\phi}/(1-\bar{\phi})$. It is possible to suggest the equivalence of Eqs. (21-22), which results in the expression for the mean relative velocity:

$$\bar{v} = 0.26 \frac{g_0 \gamma d_{eq}}{\bar{\phi}\sqrt{1-e^2}}. \tag{25}$$

The steady-state particle size could therefore be found by the substitution of Eq. (25) into Eq. (20):

$$d_{eq} = 3.39 \left(\frac{\mu_c \sqrt{1-e^2}}{\rho_p g_0 \gamma}\right)^{\frac{1}{2}}. \tag{26}$$

Figure 4 shows the results of validation of our model with Eq. (26). The equilibrium steady particle size predicted by model agrees to a certain degree with the theoretical value. The discrepancy of 28% could be addressed to the difference between the three-dimensional theory (Eq. 26) and the two-dimensional modelling.

The model allows determination of the collision efficiency of agglomeration process. Following (Agarwal, 2002) the parameter could be extracted from the model as:

$$\alpha = -\frac{\pi \ln \frac{n}{n_0}}{4\bar{\phi}\gamma t}., \tag{27}$$

where n_o is the initial number density of particles.

Figure 5 shows the temporal evolution of model-predicted collision efficiency. As it follows from the figure, the efficiency of the doublet formation for the liquid-bridging agglomeration of 200-μm spheres is approximately 0.14. The significant reduction of α is further observed within 100 s of the process due to increase of the mean particle size.

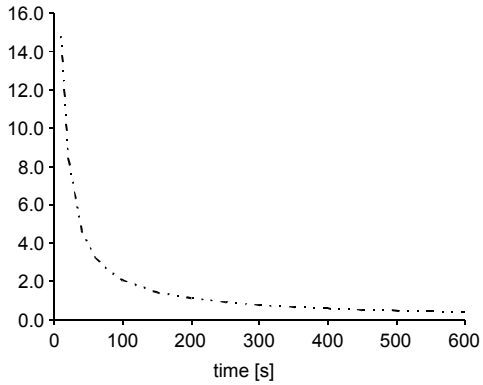

Figure 5: Collision efficiency as a function of time

The model was further compared with the commercial software STAR-CCM+ from cd-Adapco. DEM-simulation was performed in STAR-CCM+ v.8 with equivalent mesh, time step, particle size, boundary conditions, and properties of the carrier and dispersed phases. The amount of particles in DEM was, however different (11 000) due to specifics of particle injection definition. van-der-Waals force was considered to be the driver of agglomeration for the DEM case because STAR-CCM+ does not incorporate the physics of the liquid bridge flocculation. Taking into account these differences, we scale the machine time consumed by each model with the respective total amount of particles and do not provide quantitative comparison on the evolution of mean particle size. Following average machine times are obtained for the simulation of one-second of the physical time of the process per one Lagrangian particle: 1.43 s for the present model and 7.25 s for STAR-CCM+. It has to be, however, noted that STAR-CCM+ does not reduce the amount of particles in the system upon agglomeration and resolves force balance for the particles inside agglomerates. Moreover, this comparison is done in order to quantify the difference even so it is evident that the hard-sphere approach is faster than DEM.

CONCLUSIONS

The paper describes the hard-sphere approach to simulate the liquid bridge agglomeration using the Eulerian-Lagrangian approach. Following assumptions were made:

- although the model is generally applicable for 3D applications, the present results are produced in two dimensions for the conservation of computational costs. It is also necessary to note that 3D results could quantitatively differ from our data as it was demonstrated by Liu and Schwarz (Liu and Schwarz, 2009);
- laminar isothermal flow while standard turbulence model could be utilized in the model with no account for the bridge turbulisation;
- negligible thickness of the liquid bridge neck;
- rough particle;
- infinite strength of formed agglomerates, that is, as soon as they form, they do no break.

The general description of the agglomeration process is highlighted in terms of the history of the mean particle size and collision efficiency. The simulation results are in satisfactory agreement with the theoretical expression for the equilibrium steady particle size in the dilute flow.

Further work is required to make the model applicable for a broad range of industrial applications. Right now the model is capable for the prediction of liquid bridge agglomeration in case the binder solidifies upon agglomeration. Moreover, the model could be incorporated to a commercial or open-source CFD software with a set of already given turbulence models. The computational time spent for our simulations is approximately five times lower than for the equivalent DEM-simulation performed by the CFD commercial software STAR-CCM+ provided by cd-Adapco. This illustrates the efficiency of the technique used in this research.

REFERENCES

AGARWAL, S. (2002). *Efficiency of shear-induced agglomeration of particulate suspensions subjected to bridging flocculation*. West Virginia University, the USA.

BALAKIN, B. *et al.* (2013). "Micromechanics of agglomeration forced by the capillary bridge: The restitution of momentum". *AICHE Journal*, **59**, 4045–4057.

CHIMMILI, S. *et al.* (1998). "Shear-induced agglomeration of particulate suspensions". *Industrial & Engineering Chemistry Research*, **37**, 2073–2077.

CROWE, C. *et al.* (1998). *Multiphase flows with droplets and particles*. CRC Press, Boca Raton.

CUNDALL, P.A. and STRACK, O. (1979). "A discrete numerical model for granular assemblies". *Geotechnique*, **29**, 47–65.

DARABI, P. *et al.* (2009). "A novel coalescence model for binary collision of identical wet particles". *Chemical Engineering Science*, **64**, 1868–1876.

DAVIS, R.H. *et al.* (2002). "Elastohydrodynamic rebound of spheres from coated surfaces". *Journal of Fluid Mechanics*, **468**, 107–119.

GIDASPOW, D. (1994). *Multiphase flow and Fluidization: Continuum and Kinetic Theory Descriptions*. Academic Press, Boston.

GRIEBEL, M. *et al.* (1997). *Numerical simulation in fluid dynamics*. Society for Industrial and Applied Mathematics.

KOSINSKI, P. and HOFFMANN, A.C. (2010). "An extension of the hard-sphere particle-particle collision model to study agglomeration". *Chemical Engineering Science*, **65**, 3231–3239.

KOSINSKI, P. *et al.* (2009). "Simulation of solid particles behaviour in a driven cavity flow". *Powder Technology*, **191**, 327–339.

LIU, T.Y. and SCHWARZ, M.P. (2009). "Cfd-based multiscale modelling of bubble-particle collision efficiency in a turbulent flotation cell". *Chemical Engineering Science*, **64**, 5287–5301.

PITOIS, O. *et al.* (2001). "Rupture energy of a pendular liquid bridge". *The European Physics Journal B*, **23**, 79–86.

SCHILLER, L. and NAUMANN., Z. (1935). "A drag coefficient correlation". *Ver. Deutsch. Ing.*, **77**, 318–325.

MULTI-SCALE MODELING OF HYDROCARBON INJECTION INTO THE BLAST FURNACE RACEWAY

C. MAIER[1]*, **C. JORDAN**[1], **C. FEILMAYR**[2], **C. THALER**[2], **M. HARASEK**[1]

[1]Vienna University of Technology, 1060 Vienna, AUSTRIA

[2]voestalpine Stahl GmbH, 4020 Linz, Austria

* E-mail: christian.maier@tuwien.ac.at

ABSTRACT

Injection of alternative reducing agents via lances in the tuyères of blast furnaces is widely applied to reduce the consumption of metallurgical coke. Besides liquid hydrocarbons and pulverized coal the injection of recycled waste plastics is possible, offering the opportunity to chemically reuse waste material and also utilize the energy contained in such remnants.

In this work CFD models were developed and implemented that capture the multiphase nature of reducing agent injections, accounting for homogenoeus and heterogeneous reactions of materials in charge. The model is applied to the raceway zone of the blast furnace. Various geometry setups are investigated and discussed aiming at increasing the knowledge on impact of these parameters on the conditions in the blast furnace.

Keywords: CFD, multiphase heat and mass transfer, multiscale, blast furnace, direct injection.

INTRODUCTION

The majority of liquid raw iron is produced via the blast furnace route, traditionally utilizing metallurgical coke as the main reducing agent. Aiming at a reduction of primary resources, using alternative reducing agents such as liquid hydrocarbons, natural gas and waste plastics contributes to the reduction of coke rates. In the blast furnace these agents also deliver the heat necessary for melting processes as well as endothermic reduction reactions.

To optimize the utilization of the input materials, thorough examination of the impact of fuel injection is necessary. However, due to the extreme conditions in the blast furnace, the application of experimental techniques is very limited. A promising alternative is to conduct numerical experiments applying the methods of computational fluid dynamics. In this work, models are developed to study the process that takes place on multiple scales and aspects, e.g. in terms of (Pirker, 2014):

- length scales: wide range from microscopic length scales where heterogeneous chemical reactions take place on defects in the atomic structure towards global flow phenomena in the blast furnace shaft
- time scales: variation from very fast processes and high velocities in the zone of hot blast injection to comparatively low velocities of coke bed movement
- multiple phases: appearance of solid, liquid and gas phases and intense interactions

The blast furnace studied is operated by voestalpine Stahl GmbH in Linz, Austria. This furnace is arranged with equipment allowing for the utilization of a wide range of alternative reducing agents including natural gas, processed waste plastics, heavy fuel oil and tar etc. Currently, a facility for the injection of pulverized coals is installed. A schematic illustration of this blast furnace is given in figure 1.

To successfully model the utilization of feed materials in the blast furnace it is necessary to apply considerable simplifications in order to limit the computational effort to affordable levels. An important aspect is also the definition of sound boundary conditions to properly describe the conditions at the edges of the simulation domain and reliably compute thermophysical properties of involved material streams.

MODEL DESCRIPTION

CFD-simulations were carried out using the framework of the multi-purpose solver ANSYS FLUENT® v6.3.23 (FLUENT, 2007). The modeling capabilities of the solver were extended by compiling user-defined subroutines into the code to implement the functionality necessary to describe processes in the raceway of blast furnaces.

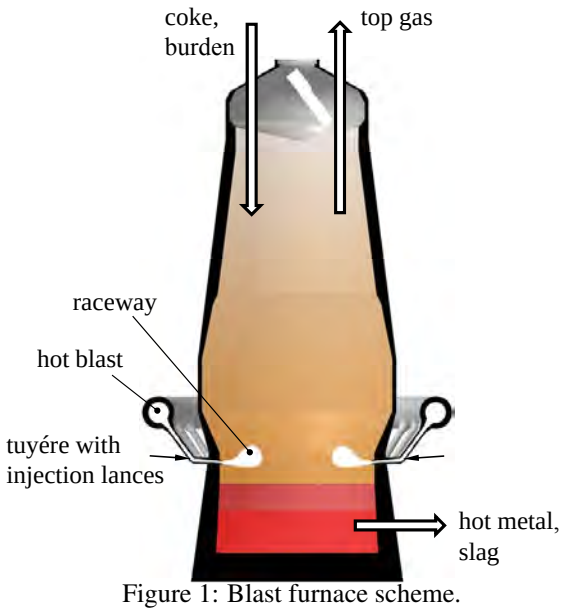

Figure 1: Blast furnace scheme.

The final model setup includes the description of multiple phases such as solid coke, gases, injected liquid hydrocarbons and plastic particles, accounting for heterogeneous heat and mass transfer phenomena. Non-equilibrium between the slowly descending bed of metallurgical coke and countercurrently ascending gases is considered by solving separate sets of conservation equations applying a multi-grid method (Maier *et al.*, 2012b, 2013b).

Simulation of coke bed movement

The flow of solids charged to the blast furnace has considerable influence on the operating characteristics as the loading of iron ore and coke on top of the bed and the bulk flow in shaft, raceway and hearth zone determine the operational stability to a great extent (Dong *et al.*, 2007; Zaïmi *et al.*, 2000). While the burden move further downwards coke is partially gasified and iron ores are reduced. The ore is molten in the cohesive zone. Below this region coke remains as the only solid material, allowing for liquid raw iron and slag to move downwards, countercurrent to hot blast moving towards the top of the furnace. The flow of solids in a blast furnace is mainly driven by melting of iron ore and conversion of coke in the raceway zone.

For the simulation of the flow of solid matter several approaches of problem formulations are available, including e.g. discrete elments methods (DEM), Euler-granular models or viscous flow models (Dong *et al.*, 2007). The latter accounts for the characteristic behaviour of moving beds of particles based on the representation of the bed as a continuous, single-phase fluid with modified viscosity (Nogami and Yagi, 2004; Zhang *et al.*, 1998). Therein, friction between particles is described by introducing a fictive solids viscosity that can be used in the Navier-Stokes equations. This approach offers the big advantage that the flow field of solid matter can be calculated using a finite volume solver. Furthermore, computational demands are decreased considerably as compared to calculation of solids movement from first principles applying e.g. DEM methods: Computations can be performed applying steady-state solvers, avoiding computationally very demanding time-discretization of the conservation equations. The currently implemented model treats the bed of coke applying continuum fluid mechanics, including the ability to describe the driving forces for coke movement (i.e. coke utilization by oxidation and gasification reactions, momentum transfer from hot blast). Various authors state the possibility to model the movement of a bed of solids as a viscous fluid with properties of *Bingham media* (Nogami and Yagi, 2004; Schatz, 2000; Chen *et al.*, 1993).

In this model viscous properties are described by two parameters: yield viscosity μ_0 and yield stress τ_0. These parameters were determined experimentally for various solid matters (Nogami and Yagi, 2004). Parameters for coal particles were used in the present study ($\mu_0 = 1230\,\mathrm{Pas}$, $\tau_0 = 1.14\,\mathrm{Pa}$).

As coke particles are usually larger than the length scale of roughness of the furnace refractory lining, the typically applied no-slip boundary condition for solid velocities is not valid (Zhang *et al.*, 1998). Actually, partial slip of solids at the furnace insulation material is possible. Consequently, in the simulation of coke flow a slip boundary is applied at rigid walls.

Hot blast injection, raceway cavity

In the lower region of the blast furnace oxygen-enriched air, preheated to high temperatures is injected at velocities of up to $200\,\mathrm{m/s}$ via tuyères. Due to the high momentum of the gas jet and consumption of coke via heterogeneous reactions, a cavity is formed adjacent to each tuyère. In the core of this structure the void fraction of the coke bed approaches unity, leaving space for alternative reducing agents injected via lances in the tuyère. The size and shape of the cavity strongly influences the utilization of injected materials as it determines the travelling distances and therefore the time available for gasification and combustion reactions prior to the impact on the coke bed at the boundary of the raceway zone.

In the current model framework, to limit computational efforts to reasonable levels, the formation of the raceway zone is not computed explicitly during the solution process but given as a boundary condition. The cavity is implemented by defining a porosity profile in the coke bed, its shape is taken from from literature sources (Zhou, 2008). The size of the raceway cavity is calculated depending on the actual blast furnace operating conditions considering rates and properties of injected hot blast as well as geometry issues (i.e. tuyère diameter, height of the coke bed in the furnace shaft etc.) applying a one-dimensional model (Gupta and Rudolph, 2006). This model accounts for the impact of blast momentum, hearth diameter, coke particle properties as well as height and void fraction of the coke bed in the blast furnace on raceway formation. Particle friction was identified as an important factor. For the blast furnace the decreasing part of the hysteresis curve of the raceway formation process was reported to be the determining step. The parameters used to compute the raceway size are summarized in table 1.

Table 1: Properties of blast furnace coke particles, applied for the computation of raceway size using the model of Gupta and Rudolph (2006).

property	value	
coke particle density	1100	$\mathrm{kg/m^3}$
particle size	25	mm
particle shape factor	0.7	–
angle of particle-particle friction	43.3	°
coke bed porosity	0.5	–
upward facing fraction of raceway	0.8	–
coke bed height (max. fill level)	26	m
hearth diameter	12	m

The impact of hot blast momentum on the raceway size at typical operating conditions as calculated applying this model is shown in figure 2. In the case of a constant blast rate, blast momentum increases with decreasing tuyère diameter, therefore the penetration depth of hot blast is enhanced and cavity volume is estimated to increase by a factor of approx. 2.8 as the tuyère diameter is decreased from 160 to 130 mm.

Measurements of the coke bed voidage at stopped blast furnaces and hot model experiments showed that the porosity varied between approx. 0.3 near the boundary of the raceway cavity and 0.5 further away (Gupta and Rudolph, 2006). Therefore, the porosity in far-field of the raceway was implemented as $\varepsilon = 0.5$. The resulting porosity distribution in the computational domain, highlighting the raceway cavity, is shown in figure 3.

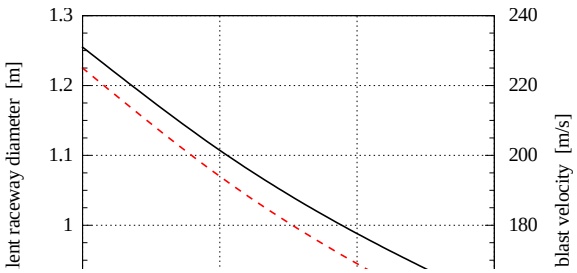

Fi
di
pr

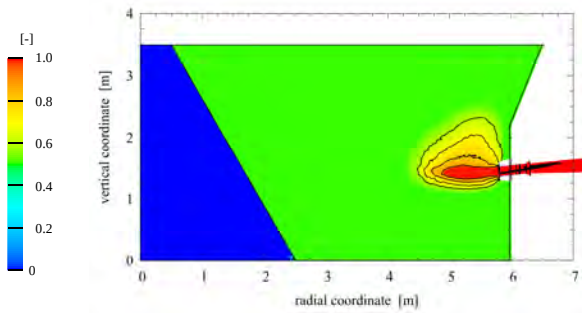

Figure 3: Porosity field in the blast furnace.

Injection of alternative reducing agents

The injection of liquid hydrocarbons and plastic particles is modeled applying tracking schemes in a Lagrangian frame of reference. Heating rates are computed accounting for contributions from laminar and turbulent convective transfer as well as radiation. The release of mass from the liquid fuel to the gas phase is computed applying a multicomponent evaporation model based on temperature dependent saturation pressures of mixture components.

Homogeneous reactions

Rates of homogeneous gas-phase reactions are calculated considering educt species mixing on finest scales of turbulent eddies. The considered reactions are (for detailed discussion of reaction rates please refer to (Jordan *et al.*, 2008a,b)):

$$CH_4 + 2O_2 \longrightarrow CO_2 + 2H_2O \quad (R\,1)$$

$$2CO + O_2 \longleftrightarrow 2CO_2 \quad (R\,2)$$

$$2H_2 + O_2 \longrightarrow 2H_2O \quad (R\,3)$$

$$CO + H_2O \longleftrightarrow CO_2 + H_2 \quad (R\,4)$$

$$CH_4 \longleftrightarrow C_s + 2H_2 \quad (R\,5)$$

Cracking of hydrocarbon vapor to form smaller gaseous constituents as well as combustion is modeled in the gaseous regime:

$$C_{19}H_{30} + 17O_2 \longrightarrow 19CO + 15H_2O \quad (R\,6)$$

$$C_{19}H_{30} + 6O_2 \longrightarrow H_2 + 7CH_4 + 12CO \quad (R\,7)$$

$$C_{19}H_{30} \longrightarrow C_s + 3H_2 + 6CH_4 \quad (R\,8)$$

Heterogeneous reactions

Heterogeneous reactions of coke with gas mixture components are evaluated considering major reaction routes such as oxidation, steam and CO_2 gasification and methanation (reactions R 9-R 12; kinetic expressions for reaction rates are given in table 2):

$$CH_xO_y(s) + (\frac{x}{4} - \frac{y}{2})O_2 \xrightarrow{k_{O_2}} CO_2 + \frac{x}{2}H_2O \quad (R\,9)$$

$$CH_xO_y(s) + CO_2 \xrightarrow{k_{CO_2}} 2CO + yH_2 + (\frac{x}{2} - y)H_2O \quad (R\,10)$$

$$CH_xO_y(s) + (1-y)H_2O \xrightarrow{k_{H_2O}} CO + (1 + \frac{x}{2} - y)H_2 \quad (R\,11)$$

$$CH_xO_y(s) + (2 + y - \frac{x}{2})H_2 \xrightarrow{k_{H_2}} CH_4 + yH_2O \quad (R\,12)$$

Table 2: Kinetic rate expressions for heterogeneous reactions.

	rate expression	reference
R 9	$k_{O_2} = 3.8 \cdot 10^7 \cdot e^{-\frac{150500}{R \cdot T_{coke}}}$	(Rumpel, 2000)
R 10	$k_{CO_2} = 2.7 \cdot 10^5 \cdot e^{-\frac{185200}{R \cdot T_{coke}}}$	(Rumpel, 2000)
R 11	$k_{H_2O} = 3.42 \cdot T_{coke} \cdot e^{-\frac{129700}{R \cdot T_{coke}}}$	(Tepper, 2005)
R 12	$k_{H_2} = 0.00342 \cdot T_{coke} \cdot e^{-\frac{129700}{R \cdot T_{coke}}}$	(Tepper, 2005)

Rates of reactions are computed resolving educt species transport on a particulate scale, accounting for boundary layer diffusion, diffusion in the porous coke structure and intrinsic reaction kinetics (see fig. 4). The thickness of the particle boundary layer strongly depends on local gas flow conditions, particle properties and coke bed voidage and is calculated with respect to local turbulence and gas phase properties. The diffusive transport processes are considered as a series of resistances to the actual chemical reaction. This approach allows for the computation of effective reaction kinetics for wide temperature ranges.

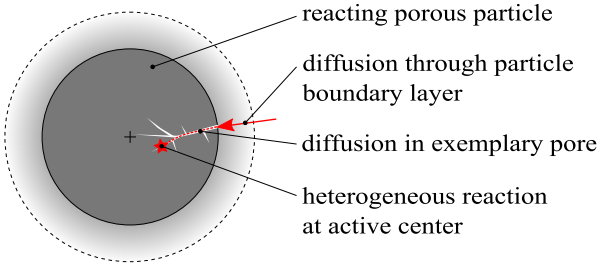

Figure 4: Schematic illustration of educt species diffusion from gas bulk flow towards the actual reaction site.

Rates of CO_2-gasification of metallurgical coke as a function of temperature at various gas-solid relative velocities are shown in figure 5. In this chart, pressure and species concentrations are similar to conditions at the boundary of a blast furnace raceway.

The heat of reactions are computed from standard state enthalpy differences at local temperatures using polynomial expressions available for thermophysical properties (Lemmon *et al.*, 2014). The standard enthalpy of formation of solid coke was estimated from the tabulated values of gas species involved in the combustion reaction using the lower heat of combustion of coke given from experimental examination.

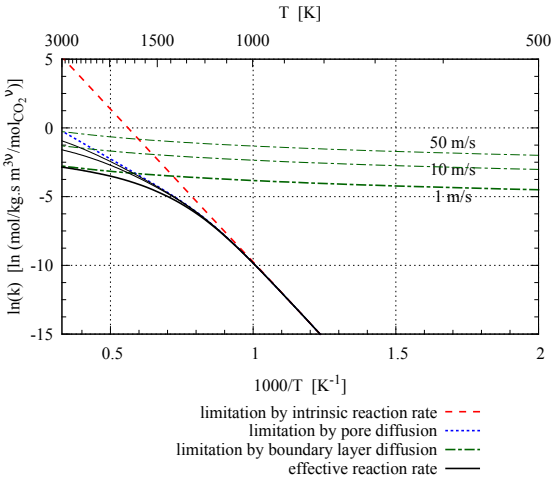

Figure 5: Heterogeneous CO_2 gasification of metallurgical coke. Conditions: gas velocities 1 m/s, 10 m/s and 50 m/s, $p =$ 5.1 bar, coke particle size 21 mm, coke bed voidage $= 0.8$, gas mixture: 10 %$_{v/v}$ H_2O, 16.8 %$_{v/v}$ CO_2, 5.7 %$_{v/v}$ O_2, balance N_2.

The model was implemented stepwise towards full model complexity, each module was validated by comparison of simulation results with experimental data, starting from simple processes involving heterogeneous heat transfer towards cases with homogeneous reactions and finally arriving at setups with heterogenous coke utilization (Maier *et al.*, 2012a,b, 2013a,b).

G

Th
th
Pe
tir
eit

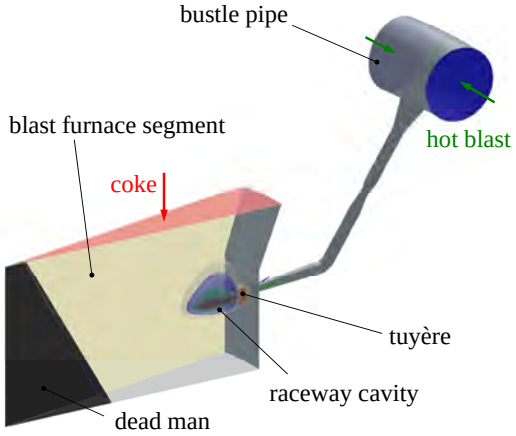

Figure 6: Overview of the simulation domain.

The geometry includes a detailed description of the tuyère and lances for injection of alternative reducing agents (fig. 7).

RESULTS

In the next sections simulation results for the full blast furnace geometry are discussed. Basic operating conditions of the furnace are summarized in table 3. In the parametric study conditions are varied, these are explained in the according subsections. The strategy is set up such that the effect of one specific parameter is studied at a time by variation, while keeping the remaining variables at base conditions.

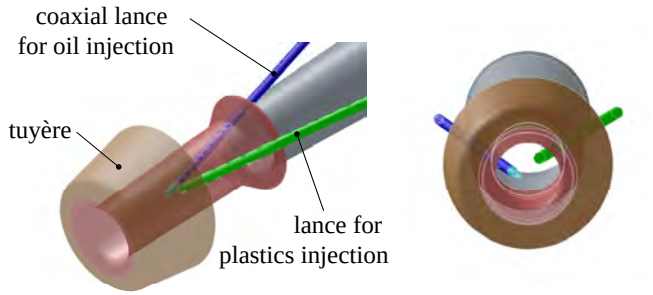

Figure 7: Geometry of simulation domain, detail: Tuyère and lances for injection. Left: isometric, right: front view.

Table 3: Blast furnace baseline operating conditions.

hot metal production rate	360 t_{hm}/h
number of tuyères	32
tuyère diameter	140 mm
hot blast rate	316000 Nm^3/h
hot blast temperature	1220 °C
hot blast O_2 concentration	27.4 %$_{v/v}$
operating pressure	4.2 bar

Base

In the
First t
the bc
the co
exerte
chang
leave

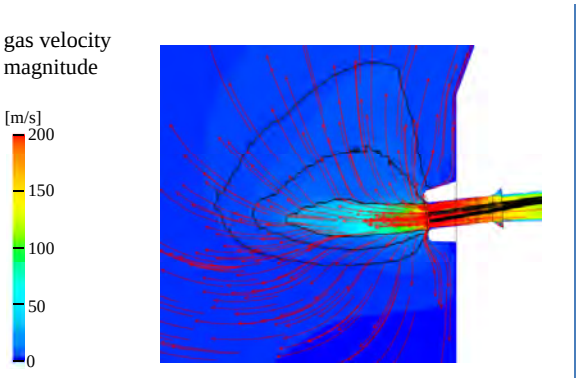

Figure 8: Gas flow field near the tuyère opening: Path-lines of gas flow and contours of velocity magnitude.

Due to inter-phase momentum transfer, coke particles are accelerated towards the center of the blast furnace. This is especially the case for material that enters the raceway cavity from top, falling into the gas jet. During the short time of flight these particles are not fully consumed by heterogeneous reactions, resulting in a circulating movement of coke particles in the zone near the tuyère opening (fig. 9). This behavior was also reported from experimental observation of operating blast furnaces using optical techniques (Kase *et al.*, 1982).

Liquid hydrocarbons that are utilized in the blast furnace under consideration consist of a mixture of heavy fuel oil and crude tar from coke production. Due to fierce conditions

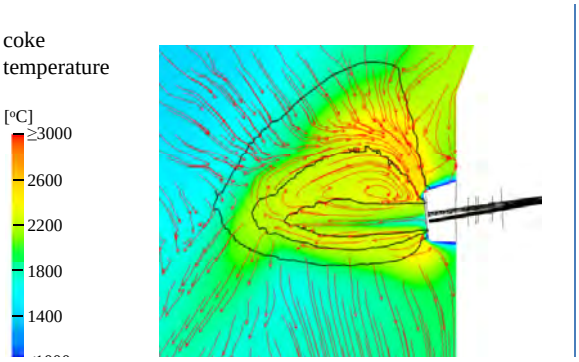

Figure
openi
peratu

at flui
mean
is des
the ga
spray
ter res
in figu

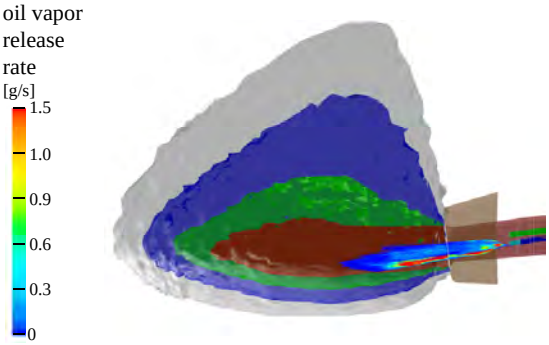

Figure 10: Trajectories of injected liquid hydrocarbons, colored by evaporation rate.

Waste plastics for injection are fed at much larger size classes (average particle diameter: 7 mm, see also fig. 11). Naturally this leads to longer residence times in the range of several seconds. This means that during time of flight particles pass the raceway zone and reach the boundary of the raceway cavity. In the simulations plastic particles are modeled to mechanically interact with the coke bed (note particle tracks in fig. 12). This behavior was also found in operating blast furnaces by investigation using high-speed imaging of the tuyère zone.

Figure 11: Processed waste plastics for injection into the furnace.

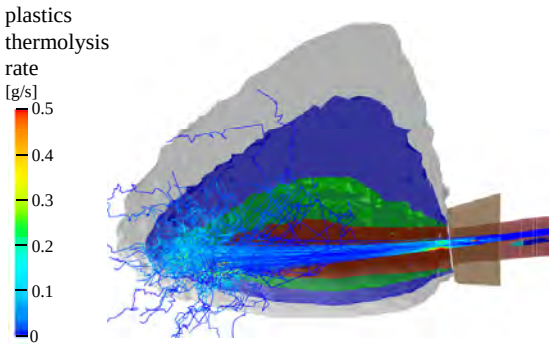

Figure 12: Trajectories of injected waste plastics, colored by thermolysis rate.

Right in front of the tuyère high temperatures as well as good mixing due to high turbulence intensity contribute to the rate of heterogeneous coke reactions as well as homogeneous reactions consuming pyrolysis products from gasification of injected alternative reducing agents. Oxygen contained in the hot blast is consumed fast, accordingly combustion products as well as heat of reactions are released in this zone. Consequently, in this zone coke temperatures reach maximal values to be expected in the blast furnace. Figure 13 shows the profile of gas species concentrations and temperature on a radial coordinate on tuyère level, also highlighting tuyère opening and shape of the raceway cavity.
At the conditions present in a blast furnace, equilibria of Boudouard as well as water-gas reaction (reactions R 10 and R 11) are shifted to the right side, accordingly CO_2 and H_2O react with coke, releasing CO and H_2. These gases are utilized in the furnace for indirect reduction of iron oxides to raw iron. The heat required for these endothermic reactions is delivered by the reaction of injected materials and coke with oxygen introduced with the hot blast.

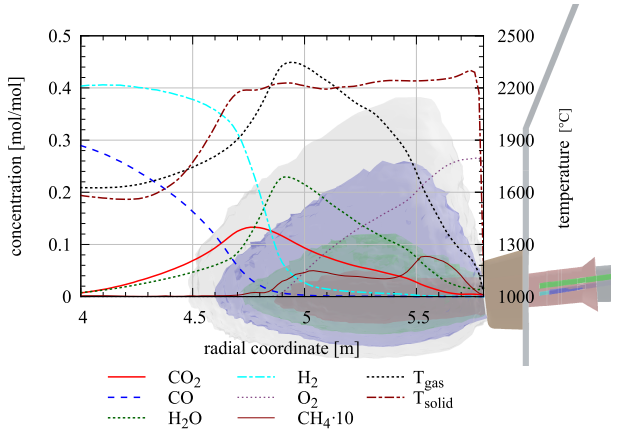

Figure 13: Radial species concentration and temperature profiles in the blast furnace on tuyère level.

The hurtling movement of coke particles in the raceway cavity also contributes to fuel utilization as heat is transferred convectively from zones with elevated temperatures (e.g. raceway boundary) towards the raceway core.

Tuyère diameter variation

To obtain stable furnace operation and successful feed utilization, deep penetration of hot blast into the coke bed is desired. As mentioned above, the diameter of the tuyères directly correlates to the hot blast momentum and consequently to the size of the raceway cavity. The effect of the inner diameter of the tuyères on heterogeneous coke reactions and utilization of injected alternative reducing agents was studied by conducting simulation runs with varying tuyère geometry while the hot blast rate was kept constant at the value given in table 3.

Table 4: Tuyère diameter variation.

case ID	tuyère diameter	raceway volume
case 1	140 mm	0.71 m^3
case 2	150 mm	0.51 m^3
case 3	160 mm	0.37 m^3

As summarized in table 4, in the range of parameter variation the volume of the raceway cavity increases by a factor of approx. 1.9. Accordingly, the residence time of hot blast and therefore the time available for combustion of injected fuels increases, resulting in a shift of gas-phase species concentration profiles. In terms of coke bed void fraction, oxygen is consumed in regions further away from the raceway core, the

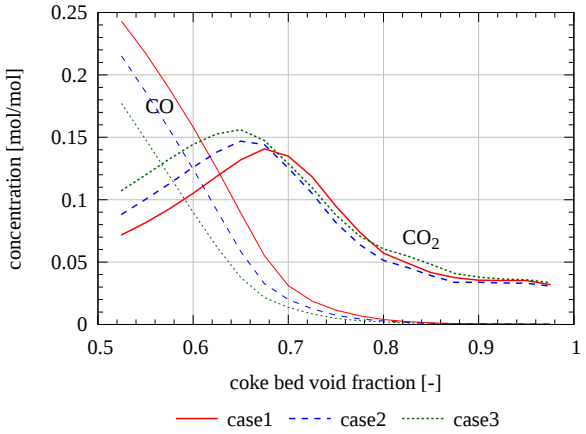

Figure 14: Tuyère diameter variation: CO and CO_2 concentration vs. coke bed void fraction.

The situation for the conversion of steam to H_2 via heterogeneous reactions is quite similar, as shown in figure 15. However, in the case with smallest raceway zone, case3, the boundary of the raceway is located closest to the tuyère opening. In this setup a part of the injected fuel oil spray is evaporated near the raceway boundary, causing a shift of the location of steam release with respect to the coke bed void fraction.

The volume of the raceway cavity is larger if a smaller tuyère is installed, as expected a deeper penetration of hot blast into coke bed is achieved, see e.g. coke utilization by heterogeneous water-gas shift reaction in figure 16.

Lance tip position

The position of release of alternative reducing agents is determined by the position of lance tips. In the baseline setup, the lances for injection do not overlap each other (see fig. 7). Two additional geometry setups with deeper inserted lances as outlined in figure 17 were studied.

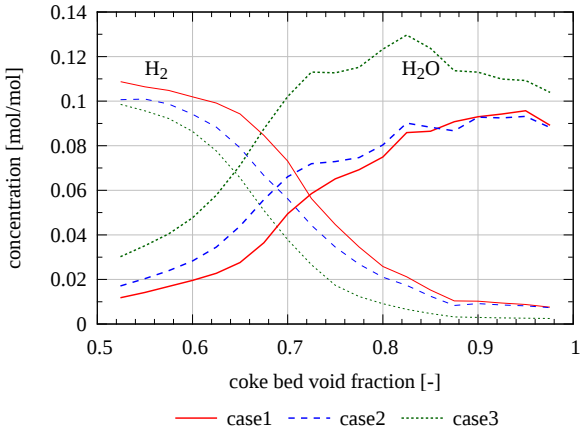

Figure 15: Tuyère diameter variation: H_2/H_2O concentration

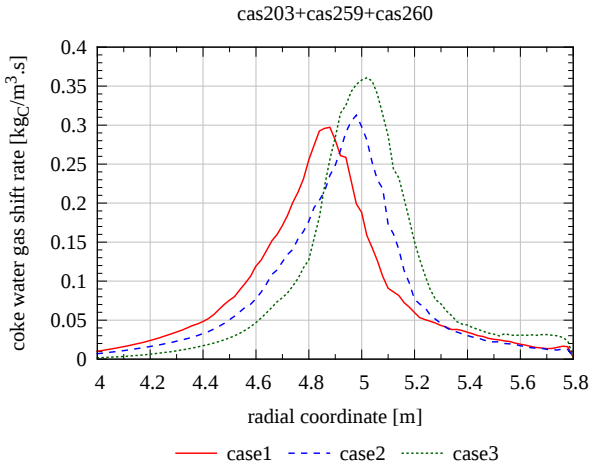

Figure 16: Tuyère diameter variation: Radial profile of coke consumption by steam gasification on tuyère level.

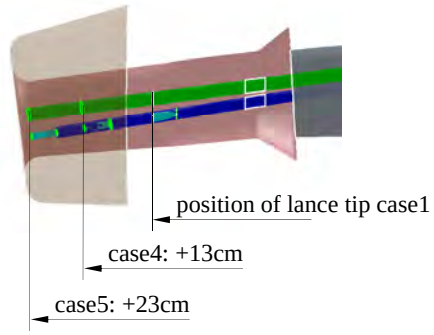

Figure 17: Sideview of tuyère and lances, highlighting range of lance tip position variation.

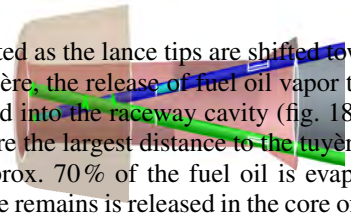

As expected as the lance tips are shifted towards the opening of the tuyère, the release of fuel oil vapor to the gas phase is transferred into the raceway cavity (fig. 18). In case 1 lance tips feature the largest distance to the tuyère opening. In this setup approx. 70 % of the fuel oil is evaporated within the tuyère, the remains is released in the core of the raceway cavity. In case 4 oil vapor release is already moved towards the coke bed but still gasification is completed in the region with void fractions of 90 – 100 %, while for case 5 already some oil gasification takes place in the boundary of the raceway zone.

Energy necessary to evaporate the fuel droplets is provided by radiation (far-field energy transfer) as well as locally from the gas phase by convective and conductive heat transfer. Therefore, at the point of fuel oil release a cooling impact is

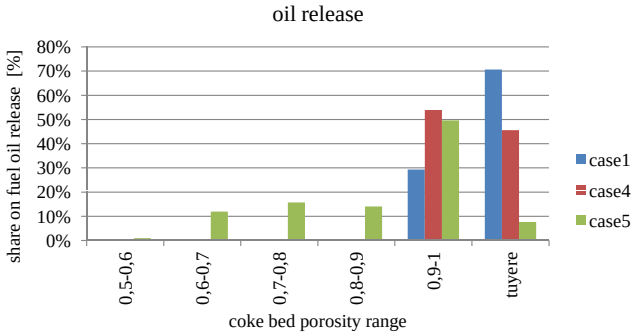

Figure 18: Location of fuel oil release, lance length variation.

exerted on the gas flow until the combustion of volatiles overbalances this effect and temperature levels increase. In the blast furnace tuyères are installed with water-cooling systems to prevent materials from damage due to overheating. The cooling effect from oil pyrolysis influences the heat transferred via the inner surface of the tuyère and therefore the cooling duty, as summarized in table 5.

The location of the release of the oil spray also has an impact on the mean droplet residence times as the gas-temperatures in the surroundings of the spray vary. In case 5 the evaporating spray reaches very hot regions located near the boundary of the raceway cavity, therefore computed mean residence times are reduced significantly (table 5).

Table 5: Variation of lance tip position: Heat transfer via inner wall of tuyère, oil droplet and plastics residence times.

case ID	heat transfer rate	time to oil evaporation	time to plastics gasification
case 1	203 kW	4.36 ms	1.54 s
case 4	206 kW	3.20 ms	1.50 s
case 5	210 kW	2.10 ms	1.42 s

Due to the large particle sizes of injected waste plastics, lance length has only a minor impact on the position of plastics pyrolysis as compared to fuel oil release (fig. 19). However, due to variation in gas-particle temperature differences plastics residence times vary in the range of 8 %.

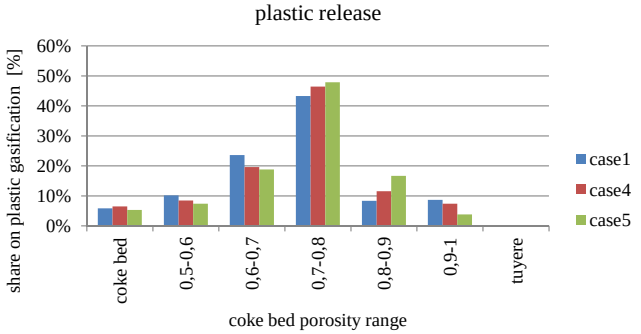

Figure 19: Location of plastics thermolysis, lance length variation.

CONCLUSIONS

A steady-state CFD model for alternative reducing agents injection into the raceway of ironmaking blast furnaces focussing on the utilization of feed materials by homogeneous and heterogeneous reactions was developed. In a parametric study the tuyère geometry was varied in terms of inner diameter and length of lances for injection. A smaller tuyère diameter contributes to increased penetration depth of hot blast into the coke bed, however at the cost of increased pressure drop of hot blast introduction. The position of the lance tip for injection of liquid hydrocarbons strongly influences estimated droplet residence times as well as the zone where oil evaporation takes place, also affecting the cooling duty of the tuyères.

The model will be applied to further operating conditions including e.g. oxygen enrichment levels, hot blast temperature and hot metal production rates. Future work will also include the extension of the model setup by a module for simulation of pulverized coal injection.

REFERENCES

CHEN, J. *et al.* (1993). "Modeling of solid flow in moving beds". *ISIJ International*, **33(6)**, 664–671.

DONG, X. *et al.* (2007). "Modelling of multiphase flow in a blast furnace: Recent developments and future work". *ISIJ International*, **47(11)**, 1553–1570.

FLUENT (2007). *http://www.fluent.com/*. FLUENT Inc.

GUPTA, G.S. and RUDOLPH, V. (2006). "Comparison of blast furnace raceway size with theory". *ISIJ International*, **46(2)**, 195–201.

JORDAN, C. *et al.* (2008a). "CFD simulation of heat transfer and high temperature conversion of plastic particles after injection into blast furnace raceway". *Proceedings of CHT-08, ICHMT International Symposium on advances in computational heat transfer*, ISBN: 978-1-56700-253-9. Marrakech, Morocco.

JORDAN, C. *et al.* (2008b). "Die Bildung von H_2 und CO durch Eindüsung von gasförmigen, flüssigen und festen Einsatzstoffen in den Hochofen". Tech. Rep. TU-ThVT-1662-2008011, Technische Universität Wien.

KASE, M. *et al.* (1982). "Analysis of coke behaviour in raceway using endoscope and high-speed camera". *Transactions of the Iron and Steel Institute of Japan*, **22(10)**, 811–819.

LEMMON, E. *et al.* (2014). *Thermophysical Properties of Fluid Systems in NIST Chemistry WebBook*. 69. National Institute of Standards and Technology.

MAIER, C. *et al.* (2012a). "Development and validation of a CFD-model for heterogeneous transfer phenomena in blast furnace processes". *5th International Conference from Scientific Computing to Computational Engineering IC-SCCE*, ISBN: 978-960-98941-9-7, 162–169. Athens, Greece.

MAIER, C. *et al.* (2012b). "Implementation and validation of a three-dimensional multiphase-CFD-model for blast furnace processes". *Chemical Engineering Transactions*, **29**, 925–930.

MAIER, C. *et al.* (2013a). "CFD-simulation of the blast furnace process: Injection of heavy oil and plastic particles into the raceway". *AISTech, The Iron and Steel Technology Conference and Exposition*, ISBN: 978-1-935117-32-2, 595–607. AIST, Pittsburgh, PA, USA. Session ID: 4041.

MAIER, C. *et al.* (2013b). "Investigation of alternative reducing agent injection into the raceway of blast furnaces using CFD". *Chemical Engineering Transactions*, **35**, 1345–1350.

NOGAMI, H. and YAGI, J.I. (2004). "An application of Bingham model to viscous fluid modeling of solid flow in moving bed". *ISIJ International*, **44(11)**, 1826–1834.

PIRKER, S. (2014). "Simulation - a corporate research topic in K1-Met". *K1-MET Scientific Exchange Day 2014*. Leoben, Austria. www.k1-met.at; 10.03.2014.

RUMPEL, S. (2000). *Die autotherme Wirbelschichtpyrolyse zur Erzeugung heizwertreicher Stützbrennstoffe*. Ph.D. thesis, Institut für Technische Chemie, Universität Karlsruhe.

SCHATZ, A. (2000). *Lump Ore, Pellets and Dead Men*. Ph.D. thesis, Johannes Kepler Universität Linz, A-4040 Linz.

TEPPER, H. (2005). *Zur Vergasung von Rest- und Abfallholz in Wirbelschichtreaktoren für dezentrale Energieversorgungsanlagen*. Ph.D. thesis, Otto-von-Guericke-Universität Magdeburg.

ZAÏMI, S.A. *et al.* (2000). "Validation of a blast furnace solid flow model using reliable 3-d experimental results". *ISIJ International*, **40(4)**, 332–341.

ZHANG, S.J. *et al.* (1998). "Modelling of the solids flow in a blast furnace". *ISIJ International*, **38**, 1311–1319.

ZHOU, C.Q. (2008). "CFD modeling for high rate pulverized coal injection (PCI) into the blast furnace". Tech. Rep. DE-FC36-97ID13554, Purdue University - Calumet, Dept. of Mechanical Engineering, Hammond, Indiana 46321, USA.

CFD MODELING OF A ROTATING ARC PLASMA REACTOR

Sverre G. JOHNSEN[1]*, **Are J. SIMONSEN**[1]†
[1]SINTEF Materials and Chemistry, 7465 Trondheim, NORWAY

* E-mail: sverre.g.johnsen@sintef.no
† E-mail: are.simonsen@sintef.no

ABSTRACT

The Plasma Production of Materials reactor developed at SINTEF, has previously been utilized for production of e.g. carbon nano-tubes. The reactor is presented in several publications, most recently in a PhD thesis by A. Westermoen. Due to novel employment of the plasma reactor to produce new materials, a CFD study was undertaken to assess the reactor temperature field with special focus on optimizing substrate surface temperature, and for designing the substrate holder.

The reactor geometry was approximated by a 2-dimensional axisymmetric model. The CFD model employed a Source Domain model for the plasma arc, assuming a steady state time-averaged shape and electric current distribution. A momentum source due to the Lorentz force and an energy source due to Ohmic heating, within the plasma arc, were implemented by user defined functions. The Discrete Ordinate model was employed for the radiation field in the reactor, and a novel method for obtaining average absorption coefficients from published net emission coefficients is presented. The reactor gas is considered single-component and single-phase, and no chemical reactions or phase transitions were considered.

A sensitivity study was performed to evaluate the importance of various key parameters with respect to temperature. It was seen that the main factor affecting the temperature field in general was the choice of process gas (Argon vs. Helium). In addition, the vertical position of the substrate and the gas inlet velocity have significant effects on the temperature at the substrate holder base.

Keywords: CFD, Gas, Source-Domain, Thermal plasma .

NOMENCLATURE

Greek Symbols

ε_N	Net emission coefficient, $[W/m^3 sr]$.
κ	Absorption coefficient, $[1/m]$.
μ_0	Magnetic permeability of free space, $[4\pi \cdot 10^{-7} N/A^2]$.
ν	Radiation frequency, $[Hz]$.
φ	Azimuthal coordinate, $[rad]$.
σ	Electric conductivity, $[S/m]$.
σ_{SB}	Stefan-Boltzmann constant, $[5.67 \cdot 10^{-8} W/m\ K^4]$.

Latin Symbols

B	Magnetic field, $[T]$.
C	Integration constant .
F_L	Lorentz force, $[N]$.
H	Distance between cathode tip and anode top, $[m]$.
$I_{b,\nu}$	Isotropic, spectral black body radiation intensity, $[W/m^2\ sr\ Hz]$.
I_ν	Spectral radiation intensity, $[W/m^2\ sr\ Hz]$.
J	Total electric current, $[A]$.
j	Electric current density, $[A/m^2]$.
k	Heat conductivity, $[W/m\ K]$.
k_B	Boltzmann's constant, $[1.3806488 \cdot 10^{-23} J/K]$.
P	Power density, $[W/m^3]$.
q_e	Elementary charge, $[1.602176565 \cdot 10^{-19} C]$.
R	Radius, $[m]$.
r	Radial coordinate, $[m]$.
$\mathbf{r}$	Position vector.
$\mathbf{s}$	Direction vector.
T	Temperature, $[K]$.
z	Axial (vertical) coordinate, $[m]$.

Sub/superscripts

a	Anode .
c	Cathode .
i	Inner .
o	Outer .

INTRODUCTION

This paper reports from a CFD study of the PPM (Plasma Production of Materials) reactor developed at SINTEF in project no. 242368, managed by Ola Raaness (2002-2005), and reported in SINTEF Report no. STF80MK F05388 (Kleveland, 2006). Originally, the PPM reactor was developed for production of carbon nano-tubes, but the current project aims at assessing the PPM reactor's suitability for production of other materials. The aim of the current CFD study was to estimate flow conditions, wall temperatures and heat transport under various experimental parameters in the PPM reactor, to provide input for the design of modifications to the reactor set-up.

The reactor consists of a cylindrical vessel with a central cathode and a cylindrically shaped anode positioned below the cathode. Process gas is introduced through a cathode sheath and through three retractable lances protruding from the top of the vessel. At the bottom of the vessel there is a substrate where the product deposits. The vertical position of the substrate is adjustable, and as materials are growing on the substrate, the substrate may be lowered to maintain a constant position of the material surface. Gas and entrained solids may exit the vessel by flowing past the substrate holder. The vertical cross-section of the reactor is shown in Figure 1, and in Figure 2 a 3-dimensional representation of the reactor chamber is shown.

The plasma arc forms because the electrical potential difference between the cathode and the anode is large enough to

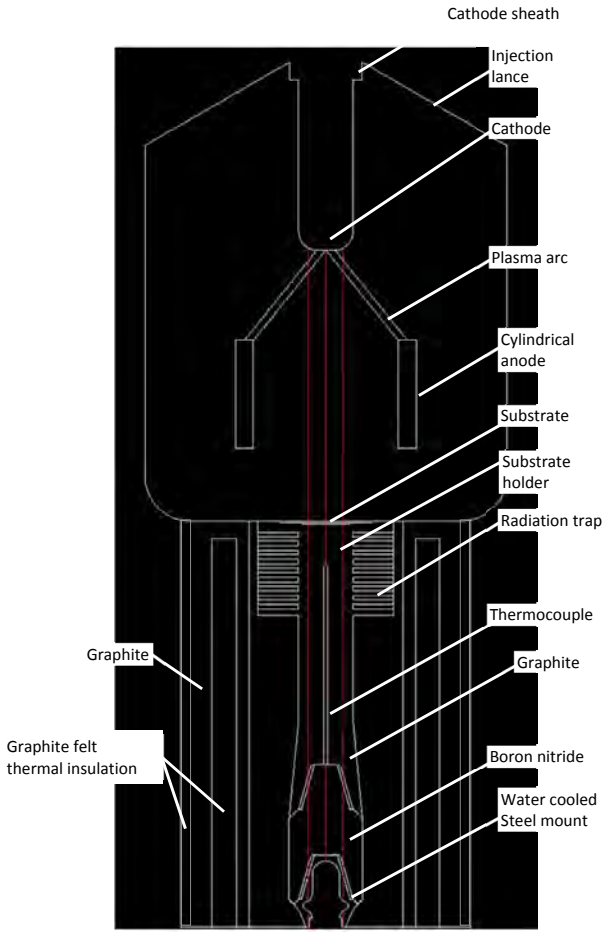

Figure 1: Vertical cross-section of the CFD model geometry.

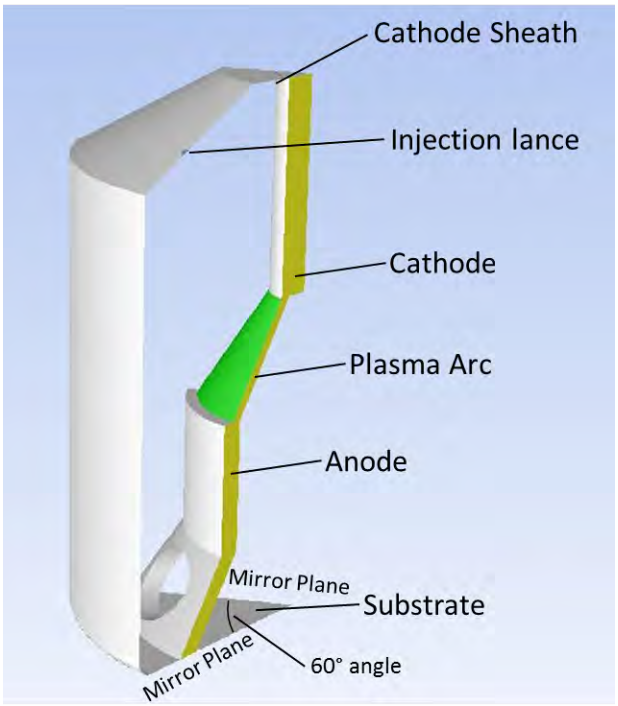

Figure 2: 3-dimensional representation of a 60° sector of the reactor chamber above the substrate.

cause electrical discharge. Due to the high electrical resistivity of gas, the electrical current generates high-temperature ionized gas inside the plasma arc. The high temperatures and ionization of process gas that are obtained in the plasma arc enable chemical reactions that require high activation energy. External magnetic fields are employed to control and rotate the plasma arc about the cylindrical anode, to increase the gas volume affected.

Table 1: Overview of material properties implemented in the CFD model.

Material	Property	Implementation	Value	Units
All	Scattering coefficient	const.	0	$1/m$
	Scattering phase function	isotropic	-	
	Refractive index	const.	1	
(Solids)	Absorption coefficient	const.	0	$1/m$
	Solid-solid contact resistance	N/A		m^2K/W
Boron Nitride (solid)	Thermal conductivity	const.	100	W/mK
Graphite felt (solid)	Thermal conductivity	udf	f(T)	W/mK
Graphite (solid)	Thermal conductivity	udf	f(T)	W/mK
Steel (solid)	Thermal conductivity	const.	16	W/mK
Process gas (fluid)	Mass density	udf	f(T)	kg/m^3
	Specific heat	udf	f(T)	$J/kg\,K$
	Thermal conductivity	udf	f(T)	W/mK
	Viscosity	udf	f(T)	$kg/m\,s$
	Absorption coefficient	udf	f(T)	$1/m$
	Speed of Sound	none	-	m/s

MODEL DESCRIPTION

The model of the PPM reactor was implemented in the commercial CFD software ANSYS Fluent 13. User defined functions (UDFs) were established to model the plasma arc, the interaction between the plasma arc and the process gas, and the temperature-dependent material properties of the process gas and solids.

The CFD model described in this paper is based on the concept known as Source Domain modeling, suggested by Ravary (1997) and later employed by e.g. Westermoen and Ravary (2003) and Westermoen (2007b). The modeling concept is based on the assumption that the dynamics of the plasma arc are extremely fast compared to other dynamics in the model. Thus, the SD model allows for treating the rotating plasma arc as a stationary (time averaged) hollow cone-shaped source of momentum and energy. The SD model has been shown to produce good results for simple axisymmetric geometries (Westermoen *et al.*, 2005).

Materials

Due to the wide range of temperatures encountered in the plasma reactor, temperature-dependent material properties are required for the process gas in particular.An overview of solid and fluid material properties employed in the CFD simulations, are given in Table 1.

The reactor is mainly built from graphite and boron nitride components to be able to withstand high temperatures and to be electrically insulating. For the modeling, it was assumed that the substrate was made of graphite. Since the process is assumed to be stationary, only parameters affecting the stationary heat transfer are important with regards to the solid modeling. Mass density and heat capacity is only relevant in the transient case. The thermal conductivities of graphite and graphite felt were obtained from the manufacturer and were modeled as

$$k_{graphite} = 0.1343 \cdot \exp\left[8.781 \cdot 10^{-4} T\right] , \qquad (1)$$

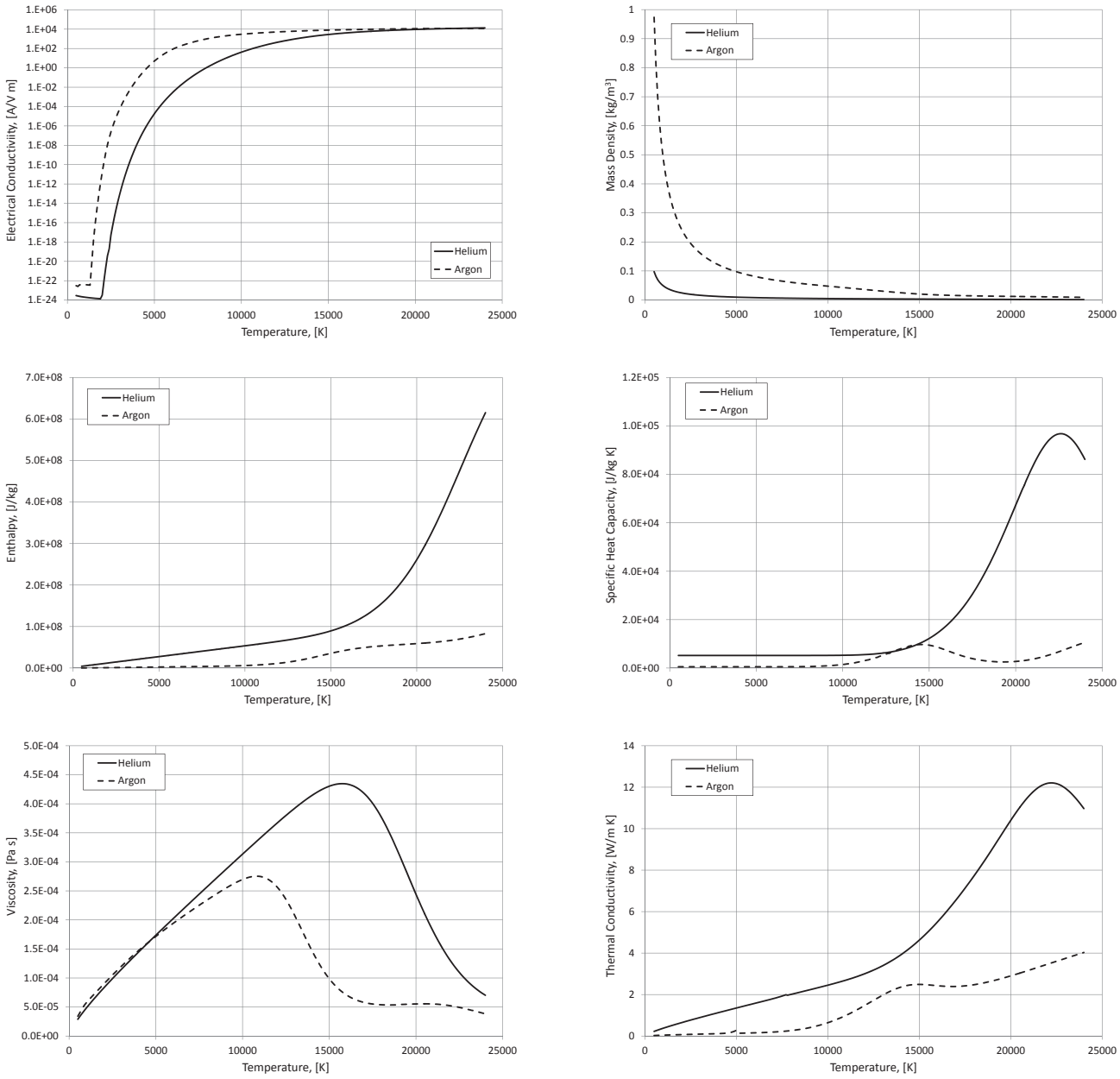

Figure 3: Temperature-dependent material properties for Argon and Helium (Boulos *et al.*, 1994), at 1 atm.

and

$$k_{graphfelt} = 0.20863 \cdot \exp\left[5.7121 \cdot 10^{-4} T\right] , \qquad (2)$$

respectively. Other solid material properties were assumed constant.

For simplicity, it was assumed that the process gas was single-component Argon (or Helium). The required temperature-dependent properties for Argon and Helium were taken from Boulos *et al.* (1994). These include electrical conductivity, mass density, sensible enthalpy, specific heat capacity, viscosity, and thermal conductivity (Figure 3). Although the plasma in reality consists of three phases (neutral process gas, positive ion gas and electron gas), the plasma and process gas are treated as the same phase. Furthermore, any solid or liquid generation in the reactor was disregarded in the CFD study.

Plasma Arc Geometry

In reality, the plasma arc is fluctuating and highly unstable. Due to the short time-scale of the plasma arc compared to other dynamics in the PPM reactor, a time-average of the plasma arc is considered. This reduces the cathode-anode-plasma arc geometry to 2D axisymmetry about the z-axis. In Figure 4 a sketch of the plasma arc geometry is shown. The plasma arc is represented by a hollow cone of height H, inner radius $r_i(z)$, and outer radius $r_o(z)$. The top of the cone is cut off to match the cathode spot radius R_c. It is assumed that the plasma arc hits the anode such that $r_i(z=H) = R_{ai}$, and $r_o(z=H) = R_{ao}$, where R_{ai} is the anode inner radius and R_{ao} is chosen to estimate the plasma arc width.

Current Density

The plasma arc conducts a total electric current of J. The current flux density is in general a function of position and is expressed as a vector function of vertical, radial and azimuthal positions (cylinder coordinates), $\mathbf{j}(z,r,\varphi)$. Due to the axisymmetry about the z-axis, $j_z(z,r,\varphi) \equiv j_z(z,r)$, and by making the coarse assumption that the axial current density inside the arc is independent of the radial position, $j_z(z,r) \equiv j_z(z)$, the relationship between the axial current density and the to-

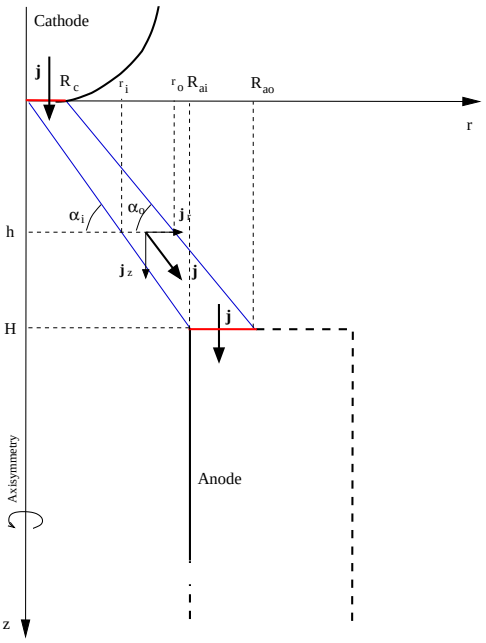

Figure 4: Sketch of Plasma arc geometry and parameters.

tal current is readily obtained;

$$J = \int_0^{2\pi}\int_{r_i}^{r_o} j_z(z,r,\varphi)d\varphi dr = \int_{r_i}^{r_o} 2\pi r\cdot j_z(z)dr = \pi j_z(z)\left(r_o^2 - r_i^2\right)$$

$$\Rightarrow j_z(z) = \frac{J}{\pi\left(r_o^2 - r_i^2\right)}\ , \tag{3}$$

where

$$r_o \equiv r_o(z) = R_c + \left(\frac{R_{ao}-R_c}{H}\right)\cdot z\ , \tag{4}$$

and

$$r_i \equiv r_i(z) = \left(\frac{R_{ai}}{H}\right)\cdot z\ . \tag{5}$$

Utilizing the continuity equation for the current density, an expression for the radial current density is obtained;

$$\nabla\mathbf{j} = 0\ \Rightarrow \frac{1}{r}\frac{\partial\left(r\cdot j_r\right)}{\partial r} = -\frac{\partial j_z}{\partial z}\ \Rightarrow$$

$$j_r(z,r) = \frac{J\left[r_o\left(R_{ao}-R_c\right) - r_i R_{ai}\right]}{\pi H\left(r_o^2 - r_i^2\right)^2}\frac{\left(r^2+C\right)}{r}\ . \tag{6}$$

Employing the boundary condition $j_r(z=0, r=R_c)=0$, the radial current density is given by

$$j_r(z,r) = j_z(z)\cdot\frac{\left[r_o\left(R_{ao}-R_c\right) - r_i R_{ai}\right]}{H\left(r_o^2 - r_i^2\right)}\cdot\frac{\left(r^2 - R_c^2\right)}{r}\ . \tag{7}$$

Magnetic Field

The radial and axial components of the magnetic field, **B**, are assumed to be negligible, and the azimuthal component is obtained by integrating the axial component of Ampere's law,

$$\mu_0\mathbf{j} = (\nabla\times\mathbf{B})\ \Rightarrow \mu_0 j_z = \frac{1}{r}\frac{\partial\left(rB_\varphi\right)}{\partial r}\ \Rightarrow$$

$$B_\varphi(z,r) = \begin{cases} C_i/r\ \text{ for } r\le r_i \\ 0.5 j_z\mu_0\left(r^2 + C_a\right)/r\ \text{ for } r_i < r \le r_o \\ C_o/r\ \text{ for } r_o < r \end{cases} \tag{8}$$

Requiring that the magnetic field vanishes at $r=0$, $C_i\equiv 0$, continuity of the magnetic field gives $C_a = -r_i^2$, and $C_o = J\mu_0/2\pi$, and the azimuthal magnetic field for $0<z<H$ finally becomes

$$B_\varphi(z,r) = 0.5 j_z\mu_0\left(r^2 - r_i^2\right)/r\ \text{ for } r_i < r \le r_o \tag{9}$$

In the regions where the electric current is zero we simply disregard the magnetic field.

The Lorentz Force

The Lorentz force acts on an electrically conducting media subject to a magnetic field, **B**, and is expressed as

$$\mathbf{F}_L = \mathbf{j}\times\mathbf{B}\ . \tag{10}$$

The previously mentioned assumptions and calculations give the axial and radial components of the Lorentz force

$$F_{L,z} = j_r B_\varphi\ , \tag{11}$$

and

$$F_{L,r} = -j_z B_\varphi\ . \tag{12}$$

The Lorentz force components enter into the CFD model as momentum equation source terms, implemented as UDFs. The calculated Lorentz force is in reality only acting on the electrically charged phases in the plasma, but for simplicity, since we only consider one single phase, the Lorentz force acts on the process gas itself, as it passes through the predefined plasma arc source domain.

Ohmic Heating

The local energy production due to Ohmic (resistive) heating is given by

$$P_{Ohmic} = \mathbf{j}^2/\sigma\ , \tag{13}$$

where σ is the temperature dependent electrical conductivity, and P_{Ohmic} is given in terms of Watts per m^3. The Ohmic heating enters into the CFD model as an energy equation source term.

Radiation Heat-Transfer

To handle the effect of thermal radiation on the plasma, process gas and wall temperatures, the built-in Discrete Ordinate (DO) radiation model of ANSYS Fluent was employed. The DO model is well suited for all optical thicknesses and comes at a reasonable computational cost. In addition it also allows for the possibility of including the effect of radiation scattering and non-grey radiation which could be a future add-on to the model.

The governing equation for the DO model is the radiative transfer equation (RTE). For a non-scattering medium the RTE for the spectral intensity field, $I_\nu \equiv I_\nu(\mathbf{r},\mathbf{s})$, is given by

$$(\nabla I_\nu)\cdot\mathbf{s} = \kappa_\nu\left[I_{b,\nu} - I_\nu\right]\ , \tag{14}$$

where **r** is the spatial position vector, **s** is the direction vector of the radiation, $I_{b,\nu}\equiv I_{b,\nu}(\mathbf{r})$ is the local isotropic blackbody intensity, and ν is the radiation frequency (Siegel and Howell, 2002). Because local thermal equilibrium is assumed, the spectral absorption and emission coefficients are equal and denoted κ_ν. The directional dependency was modeled by using an angular division of 3 in both azimuthal and polar directions, for each octant, giving a total of 72 additional equations to account for radiative heat transfer.

Absorption/emission coefficients for Argon were derived from (Aubrecht *et al.*, 2009). Aubrecht et al. measured

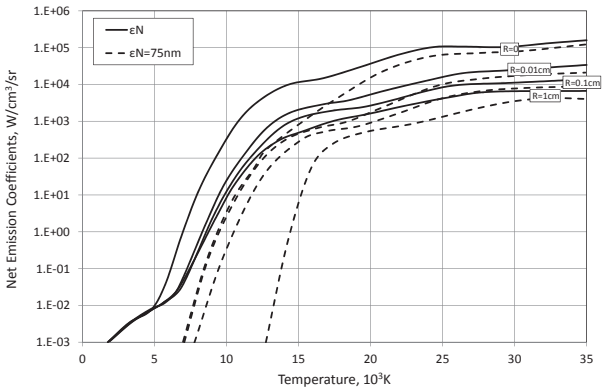

Figure 5: Temperature dependent Argon net emission coefficients at 1 atm (Aubrecht *et al.*, 2009).

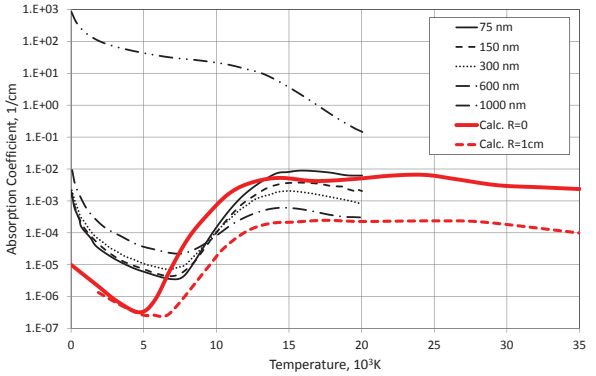

Figure 6: Argon wave-length and temperature dependent absorption coefficients (Aubrecht *et al.*, 2009) along with calculated average absorption coefficients.

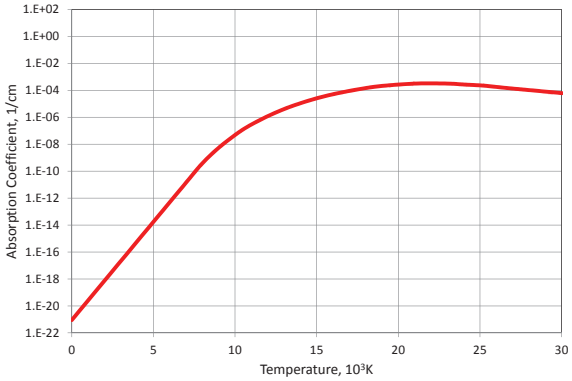

Figure 7: Calculated Helium absorption coefficients based on net emission coefficients from Cressault *et al.* (2010).

the wave-length dependent absorption coefficients for Argon plasma and calculated the net spectral emission rates, ε_N, from the formula

$$\varepsilon_N = \int_{\nu_1}^{\nu_2} I_{b,\nu}\,\kappa_\nu \exp\left(-\kappa_\nu R\right) d\nu \;, \qquad (15)$$

where R is a measure of the thickness of the plasma arc. The temperature dependent net emission coefficients for various plasma radii R are reproduced in Figure 5.
By employing the Stefan-Boltzmann law, $\int I_{b,\nu} d\nu = \sigma_{SB} T^4/4\pi$, where σ_{SB} is the Stefan-Boltzmann constant, and introducing the average, spectral-independent, but temperature dependent absorption coefficient, $\bar{\kappa}$, we obtain

$$4\pi\varepsilon_N = \sigma_{SB} T^4 \bar{\kappa} \exp\left(-\bar{\kappa} R\right) \;. \qquad (16)$$

For $R = 0$, $\bar{\kappa}$ is easily obtained from Eq.16, and for non-zero R it can be found by numerical methods. Outside the plasma, the gas was considered as transparent with $\bar{\kappa} = 0$. In Figure 6, the calculated over-all absorption coefficients for $R = 0$ and $R = 1\ cm$ are compared to the frequency-dependent absorption coefficients reported by Aubrecht *et al.* (2009). The radiation absorption effect reflected in choosing $R > 0$ is handled implicitly by the CFD model. Thus $R = 0$ was chosen in the current CFD calculations.
Temperature dependent absorption coefficients for pure Helium gas were obtained in the same manner by employing Eq.16 on net emission coefficients reported by Cressault *et al.* (2010). The calculated absorption coefficients are shown in Figure 7.

CFD Model Implementation

The steady-state, 2-dimensional axisymmetric model of the PPM reactor was implemented in the commercial CFD software ANSYS Fluent 13. The standard $k-\varepsilon$ turbulence model was employed, with the *enhanced wall treatment* option activated. The geometry was produced in Gambit 2.4.6.

Geometry

Three different geometries were evaluated in this study. The base-case geometry is shown in Figure 8a. In addition two more geometries were employed to study the effect of lowering (Figure 8b) or raising (Figure 8c) the substrate holder. The mesh consisted of approximately a hundred thousand quad-cells of size $1-2mm$ and refined boundary layer mesh along the solid surfaces ($y^+_{wall} < 10$). A grid refinement study showed that mesh-related inaccuracy was negligible.

Model Parameters

Figure 8d gives an overview of the boundary conditions for the CFD model, in relation to the physical lab reactor:

- The reactor top is well insulated such that zero heat flux is found appropriate for this boundary.
- Reactor side wall has been given a constant temperature of $2273K$, based on available measurements.
- The lower, insulated part of the reactor was given a constant temperature of $300K$ and a wall thickness of $0.3m$ to represent insulation layers not included in the geometry.
- The process is assumed to be axisymmetric. This gives zero normal gradients along the axis.
- Due to the axisymmetry, the three separate injection lances are represented by an annular inlet in the model. The inlet velocity was chosen to reproduce the mass in-flow of the lab reactor.
- The air gaps in the radiation trap on the substrate holder are modeled as a solid with heat conductivity $1^W/_{m\,K}$. This avoids unnecessary computational efforts in solving the fluid equations in these narrow gaps, and at the same time reduces the thermal conductivity in the substrate holder to a realistic figure.

Sensitivity Study

The aim of the CFD study was to assess the effect of varying experimental parameters on the substrate temperature, since optimizing the temperature is crucial for growing high-quality crystals on the substrate. Thus, a sensitivity study was performed in the CFD model to assess the temperature

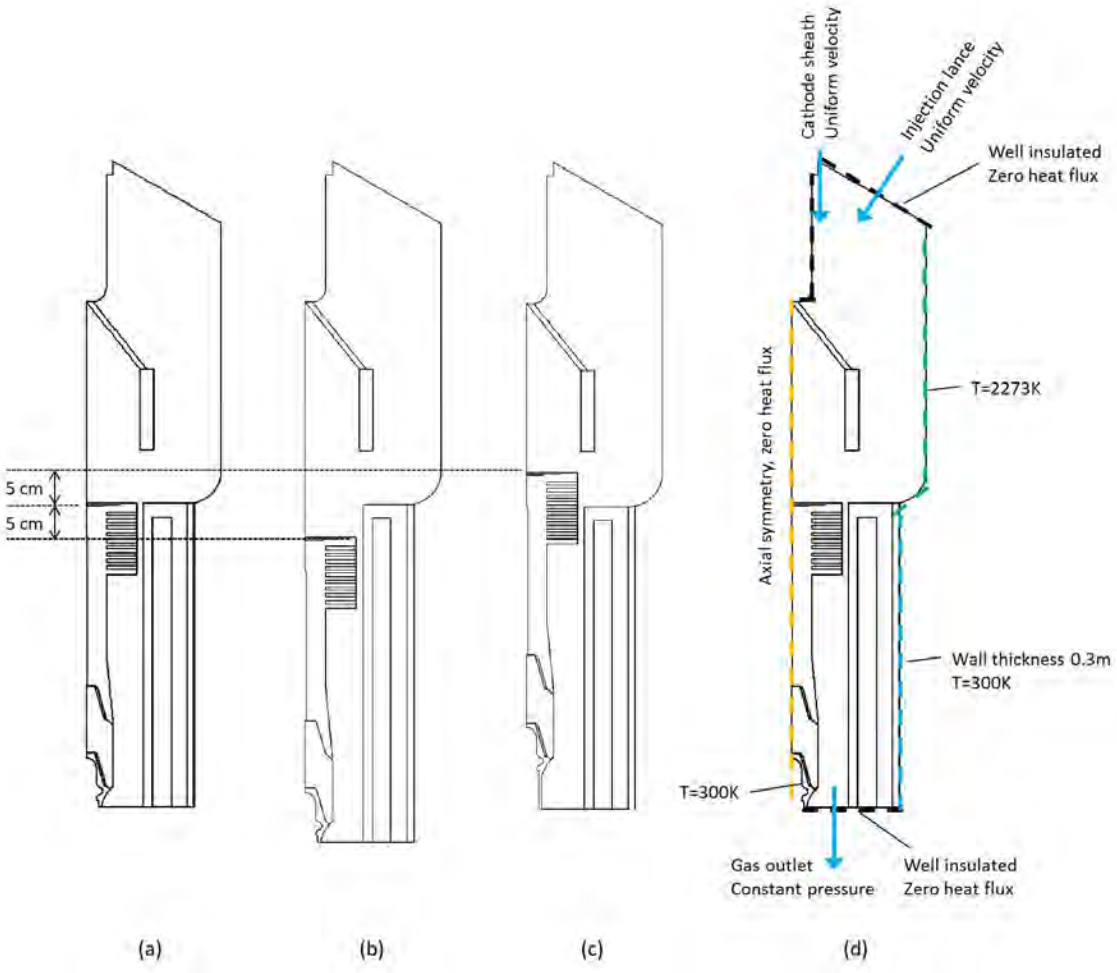

Figure 8: PPM reactor geometries; a) base-case; b) low and c) high substrate holder positions; and d) CFD Boundary conditions.

field dependency on a range of key parameters. The sensitivity parameters and values are summarized in Table 2. In the sensitivity study, all parameters were kept identical to the base-case value except for the parameter being studied. Results from the sensitivity study are reported below.

RESULTS AND DISCUSSION

The main goal of the CFD study was to assess the effect of varying experimental parameters on the substrate temperature. Additionally, it was of interest to evaluate the temperatures in the substrate holder, and especially at the base where the steel mount attaches to the boron nitride column, since the steel will lose its properties if the temperature becomes too high.

A sensitivity study was performed to assess the reactor temperature field when key experimental parameters were varied one at a time. In Figure 9, base-case temperature, incident radiation and velocity magnitude contour-plots are shown along with a stream-line plot. The results from the sensitivity study are presented in graphical form as temperature vs. position along the center-axis and 2cm outside the center-axis, as indicated by the red lines in Figure 1, in Figure 10. The substrate holder is located $0.3m$ from the cathode, and the water-cooled steel mount at the base of the substrate holder is located $0.67m$ away from the cathode. Due to the thermocouple cavity in the center of the substrate holder, temperature data are missing for the symmetry axis-line in the interval between $0.35m$ and $0.57m$ away from the cathode.

The substrate surface temperature is quite insensitive to the variations in the sensitivity parameters. The only significant effect is seen by switching from Argon to Helium process gas, which increases the temperature everywhere in the reactor. This is due to radiation being the dominant mechanism for heat transfer in the reactor chamber.

For the steel mount at the base of the substrate holder, however, the picture is more complex. It is seen that the temperature is affected by the choice of process gas, the substrate holder position and the lance inlet velocity. Helium gives a higher temperature than Argon, and the temperature increases with the lance inlet rate. For the substrate position,

Table 2: Sensitivity parameters and values.

Parameter		Low value	Base-case	High value
Plasma Gas		He	Ar	
Substratholder vertical pos.		$-5\ cm$	0	$+5\ cm$
Tot. current	$500\ A$	$750\ A$	$1000\ A$	$1250\ A$
Cathode inlet rate			$10\ l/min$	
Lance inlet rate		$30\ l/min$	$50\ l/min$	$100\ l/min$

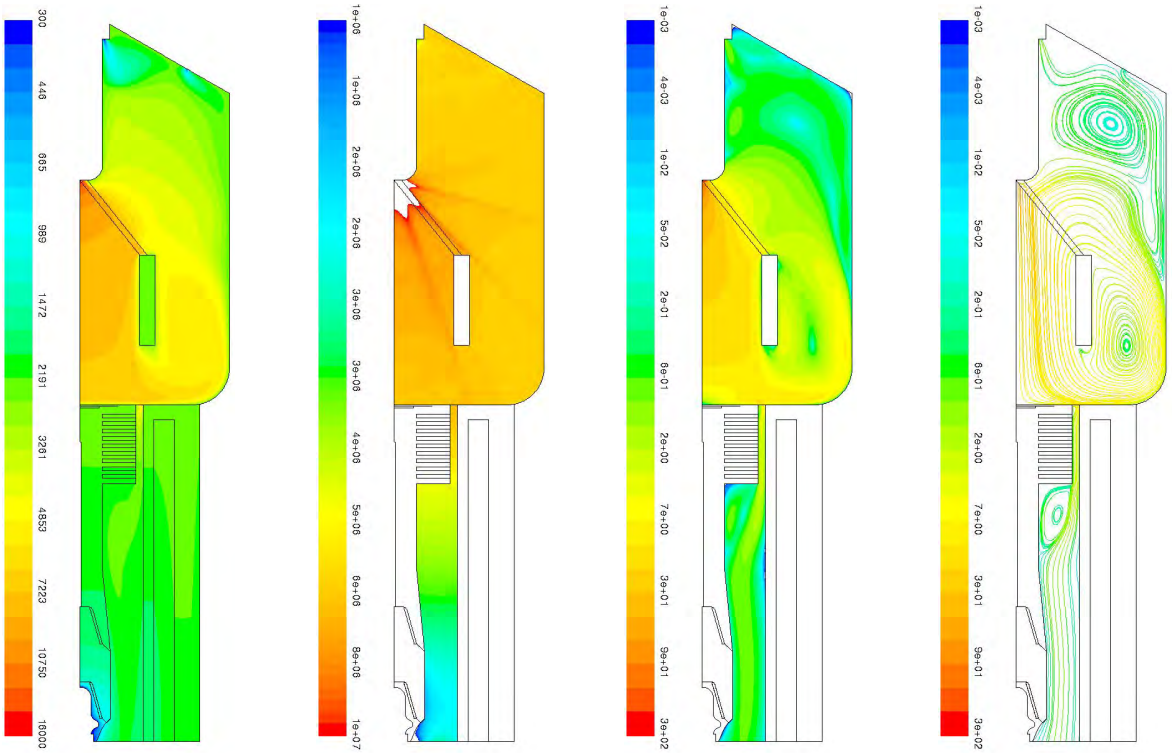

(a) Temperature Field, K (b) Incident radiation, W/m^2 (c) Velocity magnitude, m/s (d) Pathlines colored by velocity magnitude, m/s

Figure 9: Base-Case simulation results.

however, the relationship is non-monotonous. That is, the base-case gives the highest temperature while both the lowered and raised substrate positions results in reduced steel surface temperature. Close to the outlet, the radiation intensity is relatively low, as can be seen in Figure 9b, and the temperature at the base of the substrate holder is affected by convective heat transfer. By reducing the lance inlet rate, the flow velocity decreases at the outlet, reducing the convective heat transfer to the base of the substrate holder, which results in reduced temperature at the steel-boron nitride contact. The opposite effect takes place if the lance inlet rate is increased. When the substrate is raised or lowered, less radiation enters the narrow gap between the substrate holder and the reactor wall, and the radiation intensity at the substrate holder base is dramatically reduced. The result is that both raising and lowering the substrate give less radiative heating of the substrate holder.

The reactor and plasma models are based on previously developed simplified models by Andreas Westermoen and others. Main simplifications include 2D axisymmetry, steady-state, and treating the plasma arc as a momentum/energy source domain of predefined shape and current density.

The axisymmetric approach introduces a slight deviation from the lab reactor, but it is expected that the deviation has only a limited effect on the simulation results. The reactor chamber possesses an angular symmetry, as shown in Figure 2, where the sector is bounded by two mirror planes 60° apart. The gas injection lances are in reality three separate inlets, but in the CFD model they are modeled as an annular inlet. This leads to a mismatch between gas flow rate and velocity magnitude between the lab reactor and the CFD model. However, the gas from the lance inlets diffuses quickly in both cases, unless inlet velocity is very high, and is not expected to have a significant impact on the results. In the CFD model, the inlet velocity was given to reproduce the mass inflow in the physical reactor. This has also been discussed by e.g. Westermoen (2007a). The recirculation zone in the upper part of the reactor depends on the lance inlet velocity and lance position. The sensitivity to the lance position was not considered in this work, but the lance inlet velocity had little effect on the substrate surface temperature. The lance throughput may, however, have a significant impact on gas residence time in the reactor and may thus affect the material production. At the base of the anode, there is a discrepancy between the modeled geometry and the lab reactor. In reality, the anode is put on top of a conical base with three large holes through which the gas may pass. This leads to a mismatch between the model and lab reactor gas flow pattern below the anode and may also affect the heat transport away from the anode. The temperature contour plot in Figure 10a indicates that the temperature of the anode and the wall where the base is attached are of similar magnitude, so the conductive heat transport through the base would be negligible. Finally, the model gas outlet at the base of the substrate holder deviates somewhat from the lab reactor gas outlet, but it is not expected that this deviation will be important.

There is some uncertainty associated with high-temperature material properties due to lack of experimental data, but this is a general issue in high-temperature physics. Moreover, the reactor gas is considered single-component and single-phase, and no chemical reactions or precipitation/dissolution are considered. In the actual process, however, the gas would be a mixture of gases to obtain the required chemical reactions, and the composition of the process gas may affect the temperature dependent gas properties significantly.

Furthermore, any solid or liquid generation in the reactor was disregarded in the CFD study. It should be kept in mind that such constituents may affect the radiation and thus temperature field in the reactor considerably. E.g. solid particles will scatter the radiation much more effectively than pure gas.

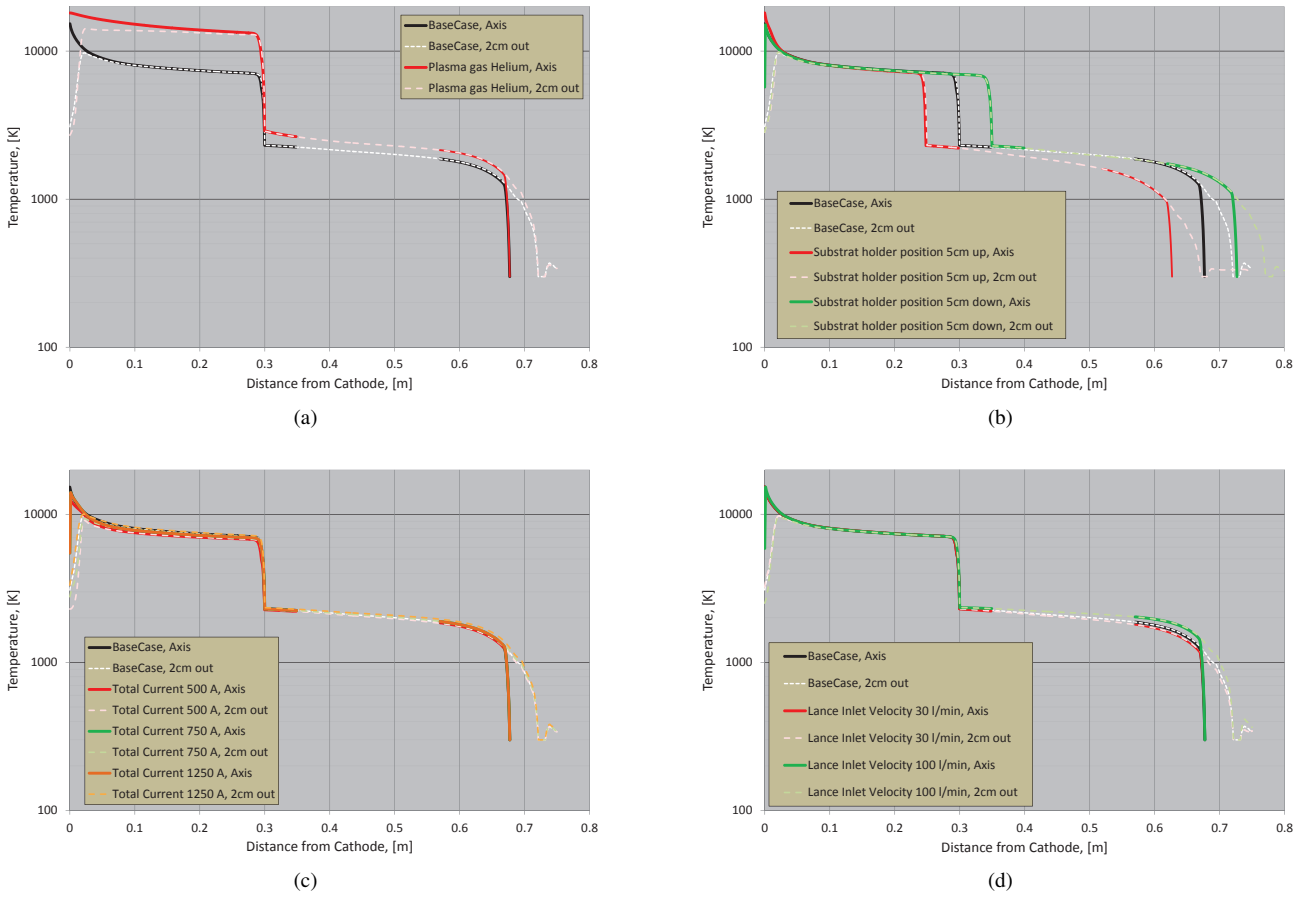

Figure 10: Temperature profile's sensitivity to the a) plasma gas (Helium vs. Argon); b) substrate holder position (see Figure 8); c) total electric current; and d) gas inlet velocity at the injection lance.

Deposition of solids and or liquid droplets may also affect how radiation is absorbed and reflected at walls. In previous experiments in the PPM reactor it was seen that deposition of solids on the inside of the cylindrical anode made the anode surface mirror-like, reflecting radiation from the plasma arc down onto the substrate, giving a higher substrate surface temperature than expected.

CONCLUSION

A CFD model based on sound simplifications and best-available data was established and a first impression of the flow-, temperature- and radiation-fields in the Plasma Production of Materials reactor has been established. The simulations give a solid foundation for further design studies of the reactor, but further CFD studies with increased complexity may be required to investigate e.g. the discrepancy between the simplified 2D-model and a full 3D model, or the effects of chemical reactions. Furthermore, it is paramount that these simulation results are seen in connection with experimental results to validate the model.

ACKNOWLEDGMENTS

This work was financed by SINTEF Materials and Chemistry, Norway. In particular, our colleagues Mari Juel and Roar Jensen have been of invaluable assistance in the project.

REFERENCES

AUBRECHT, V. *et al.* (2009). "Radiation properties of argon thermal plasma in various spectral regions". 29th International Conference on Phenomena in Ionized Gases, 12-17 July 2009, Cancun, Mexico.

BOULOS, M.I. *et al.* (1994). *Thermal Plasmas - Fundamentals and Applications*, vol. 1. Plenum Press, New York, USA.

CRESSAULT, Y. *et al.* (2010). "Net emission of Ar-H_2-He thermal plasmas at atmospheric pressure". *Journal of Physics D: Applied Physics*, **43(33)**.

KLEVELAND, K. (2006). "Final technical report (2002-2005) for the PPM (Plasma Production of Materials) project". Tech. Rep. STF80MK F05388, SINTEF Materials and Chemistry, Trondheim, Norway.

RAVARY, B. (1997). *Modelisation Thermique et Hydrodynamique d'un Reacteur Plasma Triphase...* Ph.D. thesis, Ecole des Mines de Paris, Paris, France.

SIEGEL, R. and HOWELL, J. (2002). *Thermal Radiation Heat Transfer*. 4th ed. Taylor & Francis, New York, USA.

WESTERMOEN, A. (2007a). "Modeling of gas and particle flow for different outlet geometries in the PPM reactor." Tech. Rep. F2485, SINTEF Materials and Chemistry, Trondheim, Norway.

WESTERMOEN, A. (2007b). *Modelling of Dynamic Arc Behaviour in a Plasma Reactor*. Ph.D. thesis, Norwegian University of Science and Technology, NTNU.

WESTERMOEN, A. and RAVARY, B. (2003). "Simulations of gas flow in the PPM-reactor". Tech. Rep. STF24 F03545, SINTEF Materials and Chemistry, Trondheim, Norway.

WESTERMOEN, A. *et al.* (2005). "A comparison of the source domain and the magneto-fluiddynamical models to characterize a DC plasma reactor". 17th International Symposium of Plasma Chemistry, 7-12 August 2005, Toronto, Canada.

NUMERICAL INVESTIGATION OF SYNGAS COMBUSTION IN A HITAG SYSTEM USING CFD TECHNIQUES

M. SAFFARI POUR[1]*, P. MELLIN[1], W. YANG[1], W. BLASIAK[1]

[1] Division of Energy and Furnace Technology, KTH Royal Institute of Technology, Brinellvägen 23 SE 100 44, Stockholm, Sweden

* E-mail: mohsensp@kth.se

ABSTRACT

Utilization of gasified biomass in the case of combustion could introduce a prominent way to high energy efficiency, pollutant emissions reduction, and heat recovery purposes. In this paper, secondary syngas combustion chamber of high temperature agent gasification (HiTAG) system is modelled with computational fluid dynamics (CFD) techniques. The numerical data in terms of temperature distribution and flue gas concentrations are compared with experimental measurements through the whole volume of such chamber. In order to reduce the pollutant emissions, and more efficient volumetric combustion, a low NO_X burner is used in the secondary chamber. The validation of numerical results with experimental measurements shows a good consistency through the entire chamber. It is concluded that the NO_X emission due to secondary air injection, and low NO_X burner decreased significantly prior to spread in atmosphere. Moreover, the concentration of oxygen and carbon monoxide at the combustion exhaust reveals a reliable combustion system.

Keywords: HiTAG, CFD, Combustion, Syngas, pollutant emission, NO_X

NOMENCLATURE

Latin Symbols

p	Pressure, [Pa]
$\mathbf{u}$	Velocity, [m/s]
b	body forces
t	Time [s]

Greek Symbols

ρ	Density, [kg/m^3]
μ	Dynamic viscosity, [kg/m.s]

Subscripts

f	Fluid flow

INTRODUCTION

In general, global warming is a critical issue that governments face due to residential and industrial activities. Environmental concerns lead engineering efforts to improve the thermal efficiency in a close relation with safety issues in combustion facilities [1, 2]. It means that, in all ignition systems, a reasonable balance should exist between thermal efficiencies, safety matters, and environmental concerns.

Researchers in all over the world contribute lots of effort to reduce the pollutant emissions from combustion instruments. So, they offered several solutions such as different methods of combustion, burner design, and fuel switching to cover the mentioned concerns [3]. Although, this applied and advanced topic of research attracts the attention of scientist, and laboratories to improve the performance of their systems, but the lack of ideal instruments is still obvious, so it needs much more attention in the following years [4].

Traditional fossil fuels such as coal, oil, and coke due to their heavy hydrocarbon, sulphur, and nitrogen bonds in compare with biofuels produce huge amounts of pollutants, and particulate matters during their operation in heat and power generation plants [5].

Generally, there are several facilities that operate with solid biomass such as gasifiers, combustors and boilers. All of the above systems must be individually re-design for different types of solid biomass to maximize the attainable thermal efficiencies. In order to produce syngas, gasification appears to be the most economically promising way of thermal treatment of the solid biomass [6, 7].

The quality of product gas from gasified biomass is totally different, based on variety of solid biomass, and also methods of biomass production [8]. The result gas after partial combustion (gasification) with air/steam as the gasifying medium is the mixture of carbon monoxide (CO), hydrogen (H_2), methane (CH_4), carbon dioxide (CO_2), water (H_2O) and nitrogen (N_2).

The objective of this research is to investigate the performance of syngas combustion in a secondary combustion chamber of experimental lab scale HiTAG facilities. The numerical and experimental results are compared in terms of temperature distribution, O_2, CO_2, CO concentrations, and NO_X emissions.

In this paper, we look at pollutant emissions reduction which is provided by combustion of syngas fuel with a low NO_X burner. First the experimental setup with

HiTAG facilities is given, then numerical methodology, and finally the results are presented.

EXPERIMENTAL FACILITIES

The experimental equipment was rebuilt and modified during several years in order to accomplish coal combustion and then changing to biomass gasification. These lab scale facilities are designed for capacity of 0.5 MW power. Figure 1 shows the entire experimental facilities which are consisted of preheater, fixed bed gasifier and secondary combustion chamber. The secondary combustion chamber was constructed to use heat recovery processes, and also NO_X emission reduction from the whole HiTAG system. Secondary burner as it is shown in Figure 1 is a natural gas burner which works with methane (CH_4) fuel. This burner is designed base on the pilot fuel injection trough a nozzle enclosed by pilot air which is injected in a shell around of it.

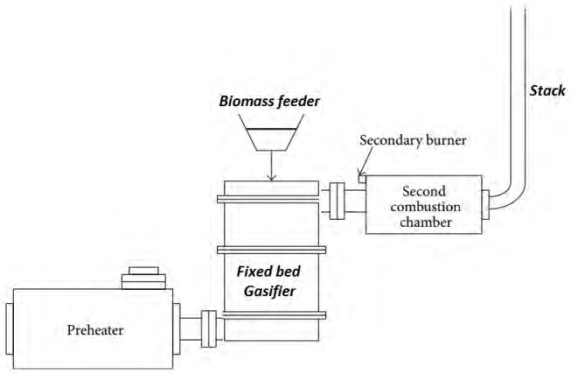

Figure 1: Schematic of HiTAG facilities

In order to model the syngas chamber the experimental data from initial pilot burner, syngas composition and mass flow rates are needed. Therefore, tables 1 to 3 show the syngas composition analysis, pilot fuel characteristics, and reactant flow rates respectively which are in focus of computational calculations for the combustion chamber.

Table 1: Syngas properties

Syngas composition (Mole %)	
CH_4	3.29%
CO_2	6.52%
N_2	51.20%
C_3H_8	0.38%
CO	30.10%
H_2	8.51%

Table 2: Pilot fuel properties

Pilot fuel composition (Mole %)	
CH_4	92%
N_2	2%
C_2H_6	2%
C_3H_8	4%

Table 3: Reactants flow rates

Mass flow rate [m^3/h]	Injection point
315.5769231	Pilot fuel + pilot air
168.25	Syngas fuel
470.68	Secondary air

NUMERICAL METHODOLOGY

The generated geometry, and meshes for secondary combustion chamber are shown in Figures 2 and 3 respectively. The optimum computational domain is created for 0.45 m^3 with 258510 tetrahedral meshes. The mesh density is tested for several fluid flow cases to ensure the independency of grid sizes to the numerical results accuracy.

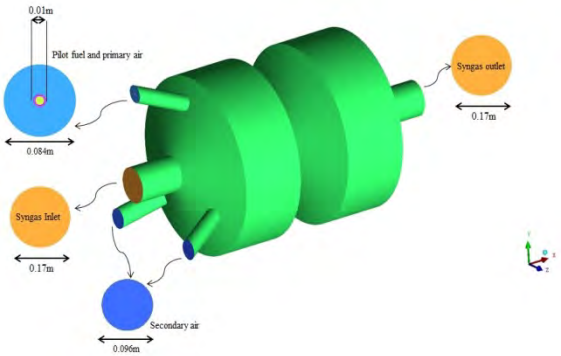

Figure 2: Schematic of combustion geometry

Figure 3: Schematic of generated mesh

The numerical calculations are obtained by using CFD techniques, for mass, momentum, energy and species transport. In this study, fluid flow is calculated with the commercial ANSYS FLUENT 14.0 [9] software by using user defined function (UDF) for species properties, and chemical reactions. The species transport model is used for combustion and chemical reactions inside the computational domain. The 3D fluid flow is simulated with Reynolds-Averaged Navier Stokes (RANS) equation together with RNG $K-\varepsilon$ turbulence model. In order to calculate the NO_X emission the entire involved mechanisms such as, prompt, fuel, and thermal NO_X are considered simultaneously as post-processing approach. However, the optical thickness of flame was not distinguishable; the discrete ordinate (DO) method

was applied to cover variety ranges of optical thicknesses.

There are several mathematical equations for computational domain. For instance, the governing equations for syngas flow inside the chamber are briefly presented as the following equations [9]:

Continuity equation:

$$\frac{\partial \rho_f}{\partial t} + \nabla \cdot \left(\rho_f \mathbf{u}\right) = 0 \quad (1)$$

Momentum equation:

$$\frac{\partial \rho \mathbf{u}}{\partial t} + \nabla \cdot \left(\rho \mathbf{u}\mathbf{u}\right) = -\nabla p + \nabla . \mu \nabla \mathbf{u} + b \quad (2)$$

A six-step reduced mechanism for syngas combustion is used in this combustion system [10]. The following reactions are listed as a sample of numerous reactions due to syngas combustion:

$$CH_4 + 0.5O_2 \rightarrow CO + 2H_2 \quad (3)$$
$$CO + 0.5O_2 \rightarrow CO_2 \quad (4)$$
$$H + O_2 \rightarrow OH + O \quad (5)$$
$$H_2 + O \rightarrow OH + H \quad (6)$$
$$CO + OH \rightarrow CO_2 + H \quad (7)$$
$$CO + HO_2 \rightarrow CO_2 + OH \quad (8)$$

Furthermore, Activation energy E_a, pre-exponential factor A and temperature exponent β is listed in table 4

Table 4: optimized kinetics of reactions

Reaction	A	E_a(J/kmol)	β
(3)	1.398762e10	1.16712e8	-0.062
(4)	7.381123e11	7.65969e7	0.215

$$RR_1 = f_1(\varphi) A_1 T^{\beta_1} e^{\frac{-E_{a1}}{RT}} [CH_4]^{0.5} [O_2]^{1.066} \quad (9)$$
$$RR_2 = f_2(\varphi) A_2 T^{\beta_2} e^{\frac{-E_{a2}}{RT}} [CO_2]^2 [O_2]^1 \quad (10)$$

Where R is the gas constant, f_1 and f_2 some correction factors based on [11].

RESULTS AND DISCUSSIONS

The numerical results are prepared based on temperature distribution, and flue gas concentration along the syngas chamber. Figure 4 presents the computational temperature in compare with experimental data. The temperature validation was done by thermocouples data which are located at the top of the gasifier close to syngas inlet, middle of syngas chamber, and outlet flue gases respectively. Temperature variations along the centreline of this chamber show a reliable consistency with experimental measurements. The maximum peak points of this figure reveal the maximum temperature in the middle of combustion throat in which the maximum velocity and turbulent mixtures could take place.

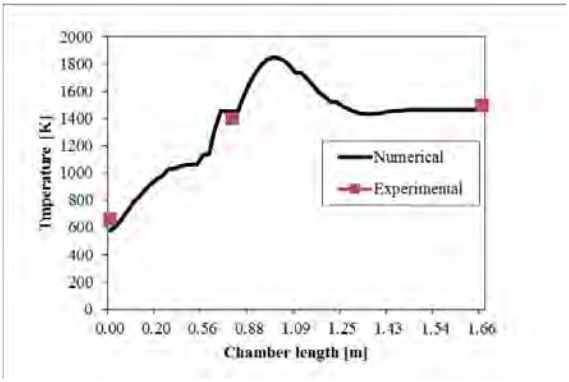

Figure 4: Temperature distribution inside chamber

Figure 5 shows the oxygen distribution inside the chamber. The maximum existence peak is related to the excess air injection through the secondary tube in order to reduce pollutant emission and more volumetric combustion. The high concentration of oxygen in flue gases reveals air infiltration due to gas sampling probe because of high negative pressure of exhaust fan.

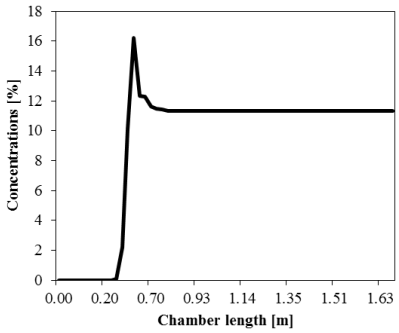

Figure 5: Oxygen distribution along the chamber

Figure 6 shows the distribution of one of the most important combustion products. From this Figure, it is visible that CO_2 increased by increasing the temperature according to plotted graph in Figure 4. It is significant to notice that syngas is introduced as a released gas from gasifier simultaneously with secondary air injection in the whole volume of chamber. Additionally, a pilot burner with CH_4 as fuel is needed to give enough activation energy as primary fuel to combust the whole gases inside the chamber. Otherwise, due to low calorific value (LCV) of syngas, such products would not be able to combust alone. It means that, in order to have a chamber with syngas as the primary fuel we need to improve the calorific values somehow. It is visible in both Figures 6 and 7 the concentration of CO and CO_2 start from some initial values because of syngas composition as reported in table 1. Figure 7 particularly shows CO distribution inside chamber. In this figure, due to syngas flow inside the chamber, the increasing trend is observed before combustion, and then due to excess air injection decreasing trend to reach an eventual rate at outlet was observed.

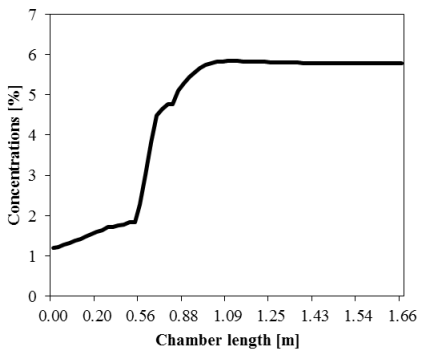

Figure 6: CO_2 distribution along the chamber

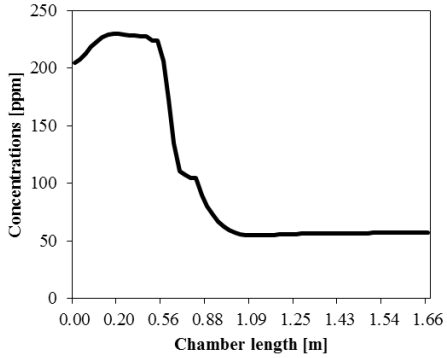

Figure 7: CO distribution along the chamber

Figure 8 shows the distribution of pollutant NO along the centreline of combustion chamber volume. The whole involved mechanisms of NO_X (fuel, prompt, and thermal) considered in the calculations. The peak points in this graph reveal the maximum temperature in which the thermal NO play a dominant role. In other regions fuel NO play the dominant role in computational domain due to high concentration of N_2 in syngas flue as well as secondary air, and pilot air.

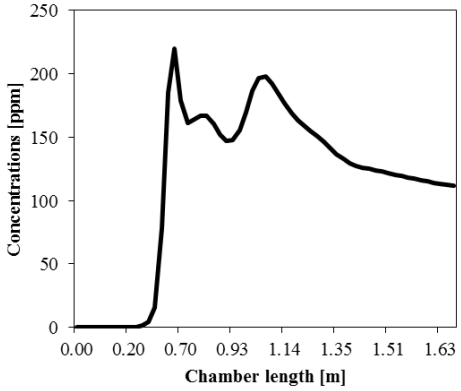

Figure 8: Pollutant NO along the chamber

CONCLUSION

In this research the performance of syngas combustion as a low calorific value gas by using a low NO_X burner from a HiTAG system is numerically and experimentally investigated and the following statements concluded:

1. During the numerical modeling it is observed that by increasing the secondary air injection to a certain amount the pollutant emission decreased significantly in the outlet flue gases.
2. The special design of low NO_X burner aid to increases the flame volume to form more mixture of combustible materials to reach a desirable temperature distribution inside the chamber.
3. The special design of chamber, improve the fuel/air turbulent mixture together with increasing the velocity at exhaust to evacuate the flue gases from combustion volume.
4. However, injection of more excess air inside chamber leads less amounts of CO emissions but it can also decrease the combustion efficiency.
5. It is important to keep a reasonable balance for air injection rates. For instance, high excess air due to introducing more nitrogen in addition to oxygen leads more temperature and also increasing the NO_X emissions which is not desirable for the combustion system.
6. Due to LCV of syngas, the operation of syngas chamber is highly depending on a pilot fuel to increase the reactivity of syngas components.
7. High concentration of oxygen (~10%) in flue gases shows air infiltration during the sampling process due to high back pressure at the exhaust line.

ACKNOWLEDGMENTS

The authors would like to gratefully acknowledge Dr. Jan Chmielewski for experimental measurements setup and guidance. Moreover, special thanks to experimental colleagues for their kindly supports through measurements.

REFERENCES

[1] IEA 2012 annual report. www.iea.org.

[2] IPCC, 2005. In: Metz, B., Davidson, O., de Coninck, H., Loos, M., Meyer, L. (Eds.), IPCC Special Report on Carbon Dioxide Capture and Storage. Cambridge University Press, New York.

[3] Gharebaghi M, Irons RMA, Ma L, Pourkashanian M, Pranzitelli A. Large eddy simulation of oxy-coal combustion in an industrial combustion test facility. Int J Greenhouse Gas Control 2011;5:S100–10.

[4] Ma L, Jones JM, Pourkashanian M, Williams A. Modelling the combustion of pulverized biomass in an industrial combustion test furnace. Fuel 2007;86: 1959–65.

[5] Mohsen Saffari Pour and Yang Weihong, Performance of Pulverized Coal Combustion under High Temperature Air Diluted by Steam, ISRN Mechanical Engineering, vol. 2014, Article ID 217574, 10 pages, 2014. doi:10.1155/2014/217574.

[6] D.L. Klass, Biomass for Renewable Energy, Fuels, and Chemicals, Academic Press, 1998.

[7] C. Higman, M. van der Burgt, Gasification, 2nd ed., Gulf Professional Publishing, 2008.

[8] Wender I. Reactions of synthesis gas. Fuel processing technology, vol. 48; 1996. p. 189–207.

[9] ANSYS FLUENT 14.0 Theory guide, 2011.

[10] SIGFRID, I., WHIDDON, R., COLLIN, R. & KLINGMANN, J. 2011a Experimental investigation of lean stability limit of an prototype syngas burner for low calorific value gases. ASME Turbo Power Expo, Power for land, Sea and Air, GT2011-45694.

[11] FRANZELLI, B., RIBER, E., SANJOSE, M. & POINSOT, T. 2010 A two-step chemical scheme for kerosene-air flames. Combustion and Flame 175, 1364-1373.

CFD SIMULATION OF A BURNER HEAD IN A SECONDARY REFORMER FOR AMMONIA SYNTHESIS

Jakub BUJALSKI[1]* , Justas DAUPARAS[2]

[1] Yara International ASA, CCC Process Technology, Hydrovegen 67, 3936 Porsgrunn, NORWAY

[2] Department of Applied Mathematics and Theoretical Physics, University of Cambridge Wilberforce Road, CB3 0WA, UK

* E-mail: Jakub.Bujalski@yara.com

ABSTRACT

In Chemical process industry Computational Fluid Dynamics (CFD) is gaining an acceptance as an investigation tool to gain insight to determine the root cause of unscheduled plant shutdowns and abnormal plant operation. As an example of such an investigation this paper presents the CFD simulations that were carried out to examine root cause of an unscheduled ammonia plant shutdown caused by a damage to a burner head of a secondary reformer.

To accurately model the reactor the CFD simulations included reactions, heat transfer and radiation in the full production scale. The simulations showed that under normal operation there is no problem with excessive temperatures and damage that was found during the reactor shutdown inspection. Investigating of the potential scenarios that could lead to the observed damage, showed that slight changes in the geometry could lead to the equipment damage that was found during the post incident inspection. The root cause of the damage to the reactor was found and solution to this problem was proposed for implementation.

Keywords: reaction, ammonia synthesis, material damage, geometry modification

NOMENCLATURE

Greek Symbols

ρ Mass density, [kg/m^3].

μ Dynamic viscosity, [kg/m.s].

Latin Symbols

Cp Specific Heat, [J/kg K].

k Thermal conductivity, [W/(m K)].

INTRODUCTION

Yara Ammonia Plant located in Pilbara, Australia experienced increase in pressure drop in the Secondary Reformer reactor. The reactor is of a KBR Inc. (previously M.W. Kellogg) design (see Fig. 1), which is very similar as in operation in as in Yara Ammonia Plant NII in Porsgrunn, Norway.

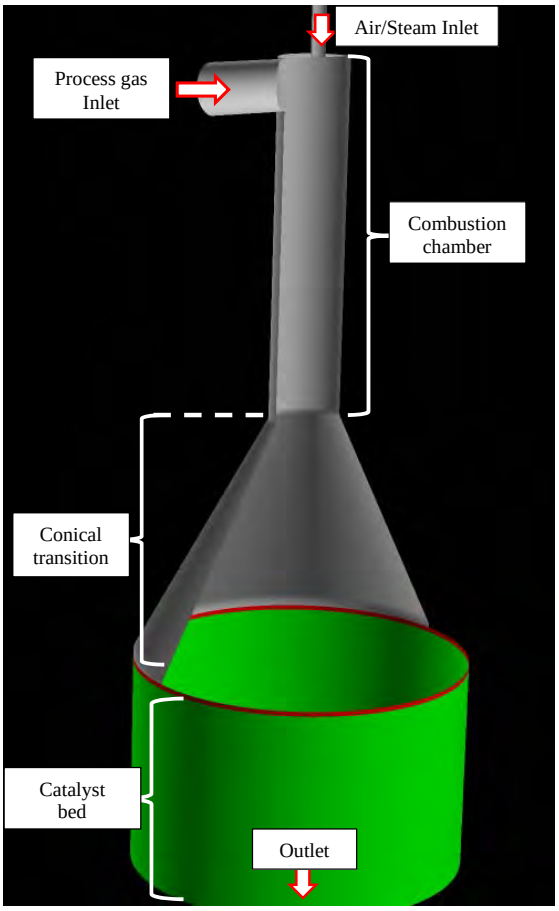

Figure 1: Secondary reformer reactor geometry used in CFD simulations

Due to increase in pressure drop the plant was stopped and the secondary reformer was inspected. The inspection found that the protecting tiles above the catalyst bed had been dislodged exposing the catalyst to the higher temperatures from the burner. At the bottom of the catalyst the metal plate which is part of the burner

head was found. The damage to the catalyst bed is similar to the damage reported in the literature (Brightling and Roberts, 2005) for slightly different burners (the burner head is closer to the catalyst bed). In this case the fuel to air ratio was not maintained, leading to stoichiometric combustion ratio and melting of catalyst in the centre as the temperatures exceeded 2100 °C. From the geometry point of view, the burner head in this design is much further away so this should not occur and the gas velocities are lower (NITROGEN, 1995).

Damage was found on the surface of the burner head, the protective metal plate was not in its place and the white insulation material was missing, see Fig. 2. Original construction is shown in Fig.A1.

Figure 2: Pilbara Air/steam burner head with missing protection plate

Due to the extreme damage found during the inspection, the flow pattern and operating conditions inside the reactor could be the cause during normal operation. CFD simulation were done to model the burner design in the secondary reformer. This reactor design has been reported previously in the literature (Blanchard and Le Blank,1994) giving good agreement to experimental work. This work is not to validate fully the CFD results that have been done previously, but focused on simulating the reactor operating at abnormal operating conditions to pinpoint the root cause of the observed damage.

MODEL DESCRIPTION

The simulations were run in ANSYS Fluent 14.5.

Geometry

The geometries were used in the simulations; full Secondary reformer geometry and Burner head.

Secondary reformer

The geometry of the reactor was created using ANSYS DesignModeler. The mesh was tetrahedral and with around 0.9 million mesh cells and was generated using ANSYS Mesh with a refined mesh generated around the air and process gas injection inlet pipe as it entered the conical transition towards the catalyst.

Two different geometries were simulated:
CASE 1: The base case geometry which is installed in the factory (see Fig. 1)
CASE 2: The case where the metal plate is damaged and dislodged at a 45° angle to the process gas stream (see, Fig. 3).

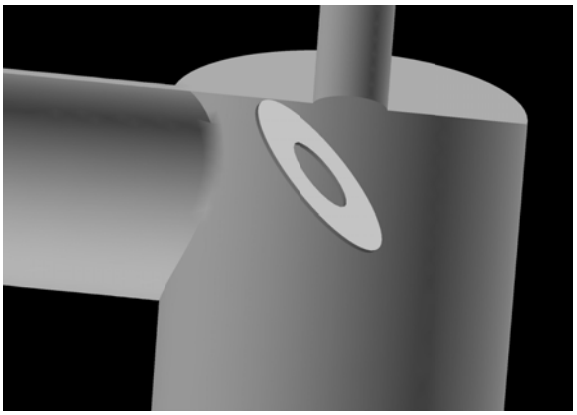

Figure 3: Pilbara Air/Steam burner head with missing protection plate

Figure 1 shows the whole simulated geometry. The grey zones are the normal insulated walls and the green zone is the location of the catalyst bed. The red zone is the position of the tiles located on the top surface of the catalyst bed. The Cases 2 is set up in exactly the same way with the only difference of the addition of the broken metal ring see Fig. 3

The burner head

Two different designs of the burner head designs have been modelled. The difference was the location and the shape of the weld between the air/steam pipe and the metal plate. Figure 4 shows the Pilbara design and highlighted in red is weld location. A bypass of part of the air was modelled by adding a second air inlet at the outer edge of the plate (orange).

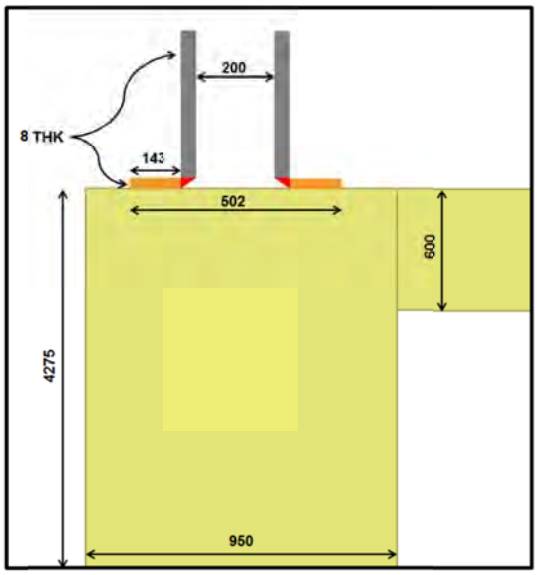

Figure 4: Diagram of the location of the protection plate on the burner head in Pilbara

In Fig. 5 is the construction design that has been installed in Porsgrunn NII (Fig. A2). The weld is in the different location and is protected by the air/steam pipe.

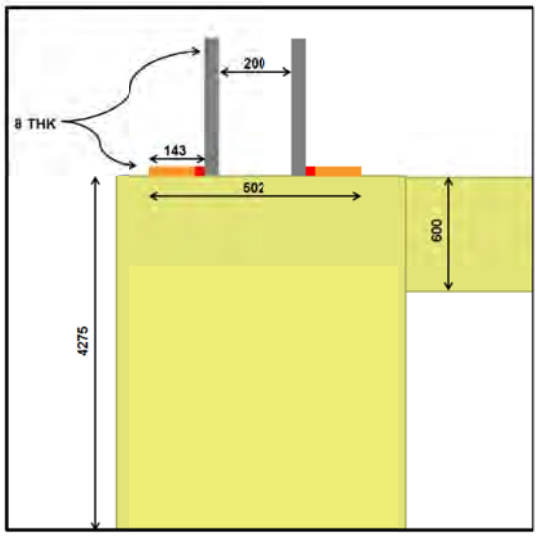

Figure 5: Diagram of the location of the protection plate on the burner head in NII

The meshed using ANSYS Mesh with the high mesh resolution on the weld. The tetrahedron mesh was converted to the polyhedral one of the size of 2.8 million.

Boundary conditions

The outlet was a pressure boundary. The inlets were set up as mass flow boundaries with gas composition based on 2405 tonnes per day, see Table 1.

Table 1: Inlet flow composition and temperature

	Air Steam Inlet	Process Gas Inlet
Mass flow [ton/h]	159.8	153.9
Mass flow [kg/s]	44.4	42.77
Mole fraction O_2 [-]	0.1982	0.0
Mole fraction CH_4 [-]	0.0	0.13581
Mole fraction N_2 [-]	0.7476	0.06741
Mole fraction H_2 [-]	0.0	0.31823
Mole fraction CO [-]	0.0	0.0002
Mole fraction CO_2 [-]	0.0003	0.033
Mole fraction H_2O [-]	0.0539	0.44534
Temperature [^oC]	501	734
Viscosity μ [kg/m s]	1.8×10^{-5}	1.8×10^{-5}

The catalyst bed pressure drop was used from the plant data and modelled as porous media with different resistance coefficients as given in Table 2.

Table 2: Aluminium oxide used properties

Porous media	Porosity [-]	X direction [m^{-2}]	Y direction [m^{-2}]	Z direction [m^{-2}]
Catalyst bed	0.5	$1.0x10^{+9}$	$1.0x10^{+9}$	$1.0x10^{+9}$
Normal tiles	0.45	$1.0x10^{+7}$	$1.0x10^{+11}$	$1.0x10^{+11}$

Pipe walls and the protective metal plate were modelled using steel as material (FLUENT database, ANSYS FLUENT manual, 2012) and aluminium oxide was used for insulation parts (Table 3).

Table 3: Aluminium oxide properties

Density (ρ) [kg/m^3]	2719
Specific Heat, (Cp) [J/kg K]	850
Thermal conductivity (k) [W/(m K)]	28
Refractive index [-]	0.5

Turbulence

The macro flow rate turbulence was modelled using the standard steady state k-epsilon turbulence model using the standard modelling constants. An RSM turbulence model was tested but there was no major difference in the obtained results. This was simulated under steady state conditions.

Combustion modelling

To model the combustion is based on the non-Premixed combustion model (turbulence modelling) and the mixing distribution of the chemical species was based on the beta probability distribution generated in Fluent for the temperature range from 500 K to 2300 K. For completion the model includes the addition of the simple radiation model know as P-1. See ANSYS FLUENT manual, for more details.

Non-Premixed combustion model

Combustion modelling is complex system. ANSYS Fluent has a number of different models to simulate combustion in sub-supersonic flames. The model used in this work is the non-premixed combustion model which uses an approach that solves the transport equations for one or two mixture fractions (scalars). On top of them the multiple species concentrations was derived from the predicted mixture fraction distribution.

Beta probability density function

Property data for the species is accessed through the chemical database. The turbulence chemistry interaction is modelled using a pre generated Beta-function for the Probability Density Function of the reacting species. This generates a chemical species look-up table to determine the mean species mass fractions, density and temperature from the values of mean mixture fraction and mixture fraction variance when calculating the combustion flow in ANSYS FLUENT (ANSYS FLUENT manual, 2012).

Solution Procedure

The model did not include modelling of the reformer reaction occurring in the catalyst therefore there was no temperature drop in the catalyst bed due to the lack of the endothermic reaction. This simplification was considered as being appropriate as it would not give more information on the catalyst damage and would just extend the simulation time.

The simulations were run with the second order scheme for scalars and energy equations whilst pressure was in the PRESTO! scheme and double precision was used as standard. The convergence was aimed for 10^{-3}. To achieve this the under-relaxation factors had to be reduced form the standard settings by around 10%. To achieve this the simulations had to run for 3000 iterations.

RESULTS

The velocity vectors for the CASE 1 are shown in Fig. 6. The flow is dominated by the air flow at 90 m/s which agrees well with the design data of up to 100 m/s for air (red) and 15 m/s (light blue) for process gas stream (Farnell, 1994) as shown in Fig. 6.

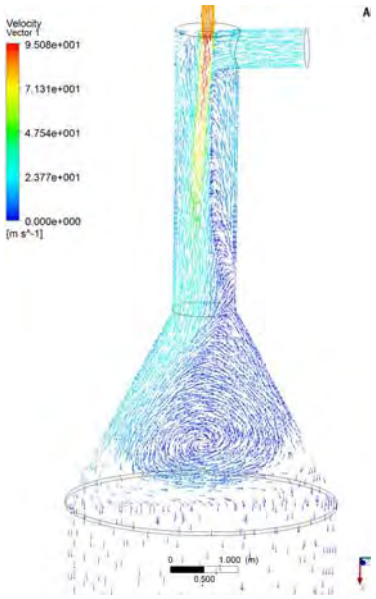

Figure 6: Velocity flow pattern and magnitude in CASE 1

Figure 6 shows that in the cone the gas will oscillate, so a model generates a rotating vortex instead. The calculated maximum velocities on the surface of the catalyst are only around 5 m/s which are in the acceptable range in this operation and should not lead to the observed material damage.

Thermal temp

Figure 7 shows the cross section of the temperature profile for the two cases. The predicted temperatures of the flame in CASE 1 is in line with the results reported by Blanchard and Le Blank (1994) where the flame temperature was designed for 1326°C. The maximum flame core temperature should develop far away from the metal insert. The only problem that could occur, if the edge flame, on the outside of the air jet can get hotter and interact with the metal around the air injector.

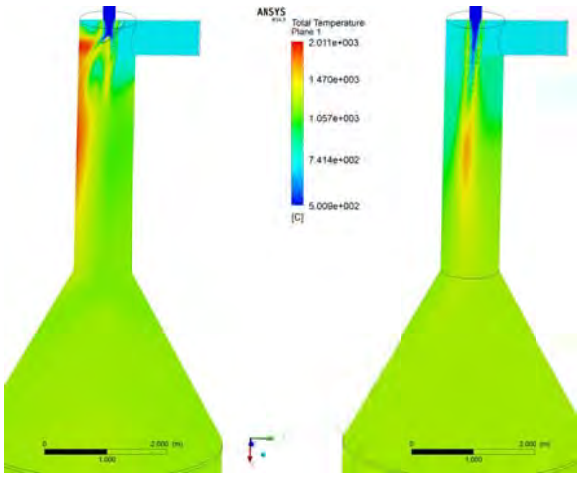

Figure 7: Gas temperature profile CASE 2 (left) and CASE 1 (right)

The 45° bent plate CASE 2 changes drastically the flow pattern in the burner head. It splits the air flow into two flows and it deflects part of it on to the opposite wall. Also it dampens the velocity magnitude of the air jet leading to a much slower air flow at around 47 m/s after the process gas injection.

This change in the gas flow velocity leads to a flame temperature of around 2000°C as shown in Fig. 7. This is an increase in the temperature compared to the 1400°C found under normal operation (CASE 1).

Oxygen in combusting chamber

The literature from the designer, KBR Inc (NITROGEN, 1995), states that "all the oxygen is consumed at about one-third of the length of the combustion chamber". The normalised concentration plot in Fig. 8 shows that there is a complete use up of the Oxygen half way down the burner zone (at 2 meters) –note the Logarithmic scale of the oxygen concentration.

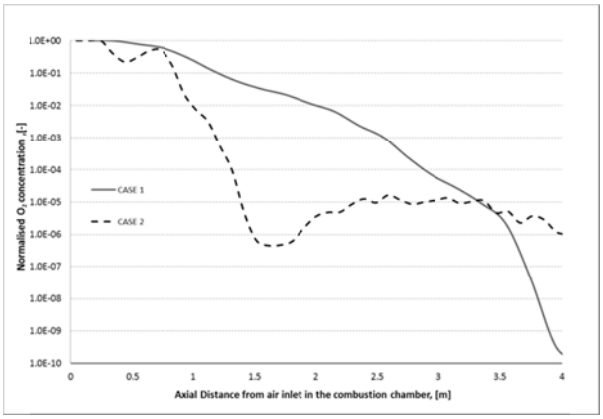

Figure 8: Axial profile of normalised O_2 concentration in the combustion chamber for CASE 1 and CASE 2

Figure 8 indicates that the dislodged plate does not allow for full mixing of the air and causes a bypass of the air causing additional mixing further downstream in the burner. This causes additional reaction and very fast depletion of the oxygen from 0.7 m to 1.5 m. In the CASE 1 the depletion of oxygen is smooth and is reduced completely at the end of the combustion chamber.

Simulation of the burner head

The question is why the plate dislodged from the burner head. The same design of the burner as in Pilbara (Fig. A1) is installed in Porsgrunn NII (Fig. A2). The burner head design difference is in the welding of the top plate to the air inlet pipe as shown in Fig. 3 for Pilbara and Fig. 4 for NII.

Figure 9 shows an example of the velocity filed from the simulations where the maximum air jet velocity was 85 m/s. The steady state simulation shows the strong gas vortex structure interaction between the air jet and the tangential process gas stream.

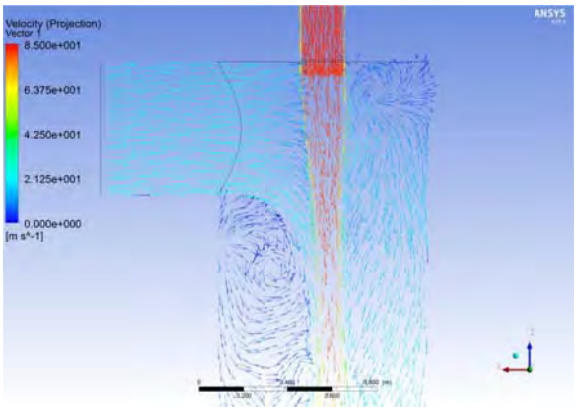

Figure 9: Gas velocity at the gas mixing point Pilbara

Figure 10 and 11 show the gas temperature in the combustion chamber for the two inlet designs. The process gas temperatures for both are similar for the both designs.

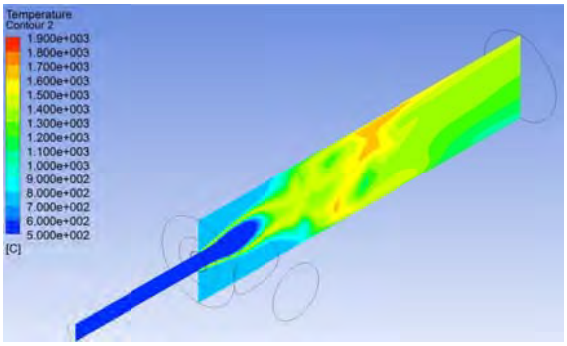

Figure 10: Temperature plot in the Fig. 4 design

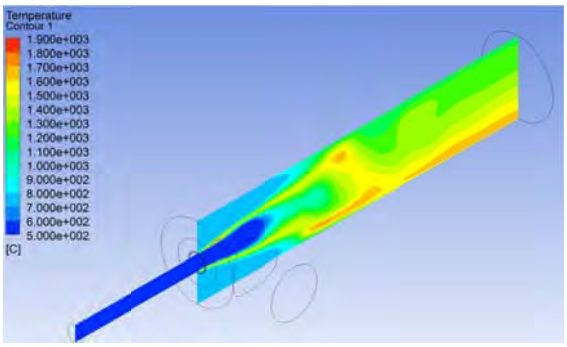

Figure 11: Temperature plot in the Fig. 5 design

Both show cold zones of around 700°C around the burner air inlet with a high temperature generated further down the combustion chamber

Burner head surface temperature

The surface temperature of the Pilbara design is shown in Fig. 12. The design shows high temperate hot spots of around 1400°C around the location of the weld.

The same surface temperature plot in the NII reactor is shown in in Fig. 13. The difference is the lack of any temperature hot spots near the metal plate and the welds. The temperatures around on the weld are 800°C. Figure 13 has a maximum colour scale less than 200°C compared to Fig.12 but still there is no visible hot spots.

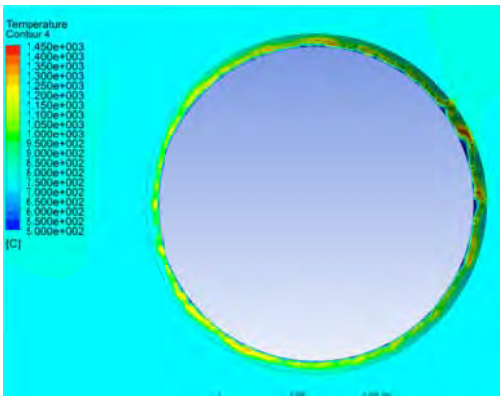

Figure 12: Schematic diagram of Fig. 4 geometry

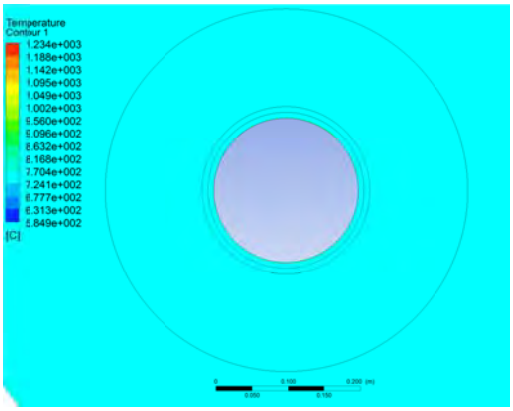

Figure 13: Schematic diagram of Fig. 5 geometry

The shape and construction of the burner will affect the local surface temperatures and generate the damage to the burner head.

Air inlet bypass

In Figure 2 additional damage to the burner was found on the edge of the plate and similar damage was found on the NII burner. This should not be a cause of installation and not the actual design of the burner. To test this, the burner geometry was modified to allow for air bypass around the metal burner head and the insulation. Figure 14 and 15 show the effect of this air gap on the temperature field.

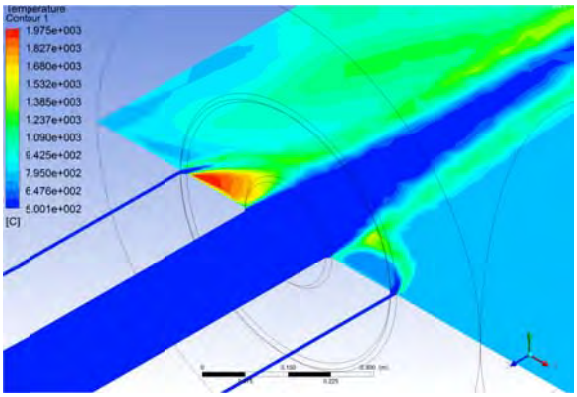

Figure 14: The effect of air bypass on the gas temperature (horizontal plot)

The simulations show that this set up would generate local gas temperatures of over 1900°C near the burner plate.

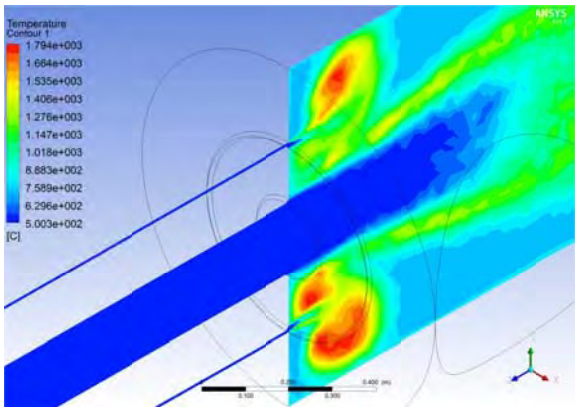

Figure 15: The effect of air bypass on the gas temperature (vertical plot)

The air bypass will generate secondary flames which will hold high temperatures on the burner metal plate. The simulations show that any bypassing air entering the burner will generate a thermal hotspot on top of the plate as can be shown by the high temperature zone in Fig. 16.

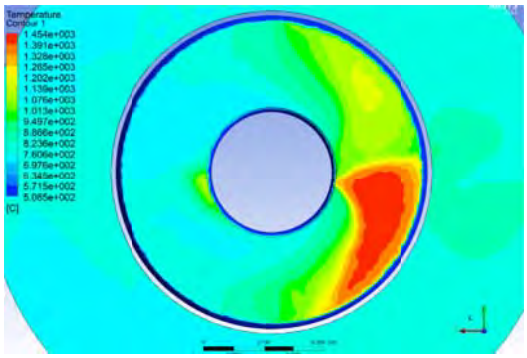

Figure 16: Plot of temperature on the burner metal plate in Pilbara design with air bypass

Air flowing through the gap will cause the combustion just near the protective metal plate and lead to the damage. Figure17 shows the blistered burner plate recovered from the bottom of the reactor in Pilbara, the damage of the plate is almost the same as the location of the high temperature zone in Fig. 16.

Figure 17: The metal plate found in a the bottom of Secondary Reformer (Pilbara)

CONCLUSION

The conclusions are:

1. There is very little effect of the plate if it is not interacting the air flow inlet.
2. If the plate detaches and interacts with the air inlet flow there is a significant increase in the flame temperature from around 1350°C to 1900°C in the combustion zone.
3. The location of the weld between the plate and the air/steam inlet pipe is the cause of the burner plate detachment and damage to the reactor.
4. Air bypass will generate a secondary flame which will increase temperature of the burner metal plate, leading to its damage and possible detachment.

REFERENCES

ANSYS Fluent 14.5, (2012), "User manual" Chapter 16.1.3.

BLANCHARD, K.L. and Le BLANK, J.R., (1994), "Application of combustion chambers in secondary reformers", *AIChE Ammonia Safety Symposium*, Vancouver, B.C. Canada, October 3-6, 195-204.

BRIGHTLING J. ROBERTS M., (2005), "Catalyst Catastrophes 11" *Ammonia technical manual*, 136-147.

CHRISTY CATALITICS, (2010), "Custom crafted™ hexagonal target tile" *Product Brochure*.

COTTON, B., (2003), "Secondary Reformers - Opportunities for Process & Mechanical Improvements" *Synetix Nitrogen seminar*, Warsaw.

FARNELL, P:W. (1993) “Secondary Reforming: Theory and Application” *AIChE Ammonia Safety Symposium*, Orlando, Florida, USA, September 3-16, 24-37.

NITROGEN, (1995), "Advances in modelling improve designs" NITROGEN, *Syngas production*, September-October, 26-31.

APPENDIX A

The burner head in different Ammonia Plants before installation.

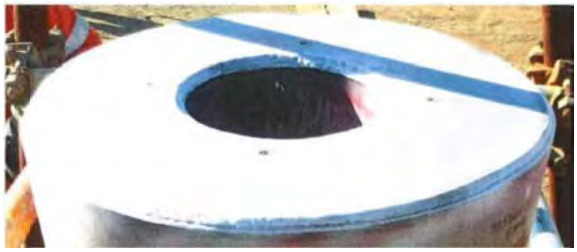

Figure A1: Pilbara burner head – brand new

Figure A2: Porsgrunn NII burner head – brand new

NUMERICAL INVESTIGATION OF THE VERTICAL PLUNGING FORCE OF A SPHERICAL INTRUDER INTO A PREFLUIDIZED GRANULAR BED

Y.(Yupeng) XU[1*], J.T.(Johan) PADDING[1†], M.A.(Martin) VAN DER HOEF[2‡], J.A.M.(Hans) KUIPERS[1§]

[1]Department of Chemical Engineering and Chemistry, Eindhoven University of Technology, 5600 MB, Eindhoven, The Netherlands

[2]Department of Science and Technology, University of Twente, 7500 AE, Enschede, The Netherlands

[*] E-mail: y.xu@tue.nl
[†] E-mail: j.t.padding@tue.nl
[‡] E-mail: m.a.vanderhoef@utwente.nl
[§] E-mail: j.a.m.kuipers@tue.nl

ABSTRACT

The plunging of a large sphere into a prefluidized granular bed with various constant velocities is investigated using a state-of-the-art hybrid Discrete Particle and Immersed Boundary Method (DP-IBM), with which both the gas-induced drag force and the contact force exerted on the intruder can be investigated separately. Our simulation method has been validated by comparison with the existing experimental results. Current simulation results show a concave-to-convex plunging force as a function of depth and in the concave region the force fits to a power-law with exponent around 1.3, which is in good agreement with existing experimental observations.

Keywords: prefluidized granular bed, plunging force, moving internals, Immersed Boundary Method.

NOMENCLATURE

Greek Symbols

ε	Gas volume fraction, $[-]$
η	Dynamic viscosity, $[Pa \cdot s]$
μ	Friction coefficient, $[-]$
ρ	Mass density, $[kg/m^3]$
τ	Viscous stress tensor, $[Pa]$
ω	Angular velocity, $[rad/s]$

Latin Symbols

d	Granular particle diameter, $[m]$
D	Intruder particle diameter, $[m]$
$\mathbf{F}$	Force, $[N]$.
I	Moment of inertia, $[kg \cdot m^2]$.
m	Mass, $[kg]$.
$\mathbf{r}$	Coordinate, $[m]$.
R	Particle radius, $[-]$
$\mathbf{s}$	Force density, $[N/m^3]$
$\mathbf{T}$	Torque, $[N \cdot m]$.
u	Gas velocity, $[m/s]$
v	Particle velocity, $[m/s]$
z	Depth from surface, $[m]$.

Sub/superscripts

a	Particle index a.
b	Particle index b.
c	Contact.
d	Drag.
g	Gas or gravity.
m	Marker-point index.
n	Normal direction.
p	Pressure.
t	Tangential direction.

INTRODUCTION

The plunging of a high-speed intruder into a dense granular bed occurs in many different cases, such as meteor impacts and footprints on sand. Many studies have tried to find the macroscopic force law exerted on the intruder and different variations of the force law were found.

Experimental results (Hou *et al.*, 2005; Katsuragi and Durian, 2007) of a vertically free falling object impacting onto a horizontal bed of granular particles with relatively large initial contact velocities show that the macroscopic force law contains a term scaling as kz, where z is the depth from the surface. In (Hou *et al.*, 2005), hollow cenospheres (diameter $\approx$ 74 - 100 μm) of density 0.693 g/cm^3 are used. Particles are first poured into the bed and then loosed by slowly pulling a sieve (mesh size=0.4 mm) which was initially buried at the bottom. The volume fraction of the bed produced by this procedure consistently gives a value of about 0.54. In (Katsuragi and Durian, 2007), spherical glass beads (diameter range 250-350 μm, density ρ_g = 1.52 g cm^{-3} and friction coefficient $\mu = 0.45$) were used as granular medium. The medium was fluidized, and gradually defluidized by a uniform upflow of N_2 gas. The volume fraction occupied by the beads was 0.590 ± 0.004 after fluidization. A steel sphere of diameter $D = 2.54$ cm was used as a projectile. Also, investigations done by Lohse et al. (Lohse *et al.*, 2004) showed that for freely falling projectiles with zero impact velocity (v_0=0), the macroscopic force law can be described simply by the term kz, where the parameter k characterizes the increase in force with increasing depth z.

Completely different results are obtained for intruders moving with constant but relatively small vertical velocities. Stone et al. pushed a flat plate vertically into a granular medium (Stone *et al.*, 2004a,b), and found that the penetration force increases with increasing depth nearly linearly in an initial regime, then followed by a depth-independent regime. When the plate was pushed near the bottom of the container, the penetration force showed an exponential increase. The authors deem that the initial linear regime is due to hydrostatics while the depth-independent regime is a Janssen-like regime, which is due to side wall support. Hill

et al.(Hill *et al.*, 2007) measured the drag force of an intruder plunging into and withdrawing from a shallow granular bed (about 100 mm), and found that both the plunging and the withdrawing forces had power-law dependence on the immersion depth with exponents greater than unity, i.e., 1.3 for plunging and 1.8 for withdrawing. Peng et al. (Peng *et al.*, 2009) found that the plunging force curves of fully immersed intruders have a concave-to-convex transition and the depth dependence of the force turns from supralinear to sublinear. They found that the plunging force at the inflection point is proportional to the intruder's volume and the inflection point occurs when the intruder is fully buried to a level of around twice its diameter. Within the shallow regime, i.e. before reaching the inflection point, the plunging force fits exhibits a power-law dependence for all spherical intruders, with an exponent of 1.3 ± 0.02.

Clearly, the form of the force experienced by an impacting intruder is still not unified, and understanding of this problem remains limited. At the same time, we are also interested in the details of this plunging process, such as the reorganization of the granular particles around the large intruder. Simulations are an effective alternative way to investigate this problem. In our former work, a state-of-the-art discrete particle method (DPM) combined with an immersed boundary (IB) method was introduced to investigate the kinematics of an intruder freely dropping on a prefluidized granular bed. We showed that our simulations results are in good agreement with the experimental observations, thus offers another powerful tool to investigate the gas-induced and contact forces directly and independently (Xu *et al.*, 2013).

According to former experimental results, the granular plunging process is influenced by many parameters, such as the intruder diameter D, plunging depth z, and intruder velocity v. Thus, a very straightforward idea would be to vary one parameter whilst keeping the other parameters constant. In this paper, we use our simulation method to further investigate the force on an intruder moving with a constant velocity through a prefluidized bed. The relation between the force F and the intruder penetration depth z, intruder diameter D, and intruder velocity v are investigated. Moreover, the re-arrangement of the granular particles in the bed is investigated by using a layer colored bed.

MODEL DESCRIPTION

The DPM-IBM model used in this work has been detailed in another work (Xu *et al.*, 2013) and the applicability of the model has been verified by a good agreement between the our simulation results and existing experimental work. Our model consists of two major sub-models, the discrete particle (DP) and immersed boundary (IB) model. The DP model deals with the motion of suspended small (granular) particles, taking into account the action of gravity, gas-solid drag forces, as well as particle-particle and particle-wall collisions. In this model, the gas phase is solved on a computational mesh with a length scale larger than the size of the small particles and the gas-particle coupling is treated by empirical drag relations (Van der Hoef *et al.*, 2006). The IB method deals with the motion of the large intruder through the continuous phase (consisting of gas and suspended solid particles).

We now give a brief technical description of the DP model and the IB method. A schematic representation of the DP model and IB method is shown in figure 1.

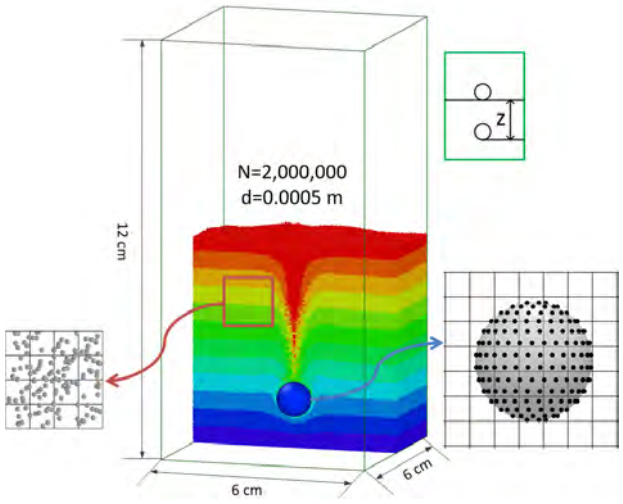

Figure 1: Schematic representation of the DP and IB methods. In the DP model the motion of the small particles is solved, taking into account detailed contact forces, as well as drag forces caused by motion relative to the interstitial gas. The particles are smaller than the grid on which the gas phase equations are solved (left), requiring empirical drag relations. The intruder is much larger than the gas grid and coupled to the gas phase through the IB method, which enforces no-slip boundary conditions by a distribution of force points across the surface of the intruder (right). Schematic representation of (half) the bed geometry is also shown (center); particles are colour coded according to their initial position in z direction. Visualization was carried out using OVITO (Stukowski, 2009).

Equations of motion for the small particles

The motion of a spherical granular particle a with mass m_a, moment of inertia I_a and coordinate $\mathbf{r}_a$ is described by Newton's equations for rigid body motion:

$$m_a \frac{\mathrm{d}^2 \mathbf{r}_a}{\mathrm{d}t^2} = \mathbf{F}_{\mathrm{g},a} + \mathbf{F}_{\mathrm{d},a} + \mathbf{F}_{\mathrm{p},a} + \mathbf{F}_{\mathrm{c},a} \qquad (1)$$

$$I_a \frac{\mathrm{d}\boldsymbol{\omega}_a}{\mathrm{d}t} = \mathbf{T}_a \qquad (2)$$

The four terms on the right-hand side of Eq 1 account for the gravitational force, the gas drag force, the force due to pressure gradients in the gas phase, and the sum of the individual contact forces exerted by all other particles in contact with particle a. In Eq 2 , $\boldsymbol{\omega}_a$ is the angular velocity and $\mathbf{T}_a$ is the torque around the centre-of-mass of particle a. Regarding the contact model, two types of collision models are widely used, namely the hard sphere model and the soft sphere model. In our simulation, the soft sphere model is used since the hard sphere model is not suited for systems where quasi static particle configurations exist. More detailed information can be found in (Van der Hoef *et al.*, 2006; Alder and Wainwright, 1957).

For the calculation of $\mathbf{F}_{\mathrm{c},a}$, a three-dimensional linear spring and dashpot type soft sphere collision model along the lines of Cundall and Strack is used (Cundall and Strack, 1979; van Sint Annaland *et al.*, 2005; Xiong *et al.*, 2011). In this model, the total contact force on particle a of radius R_a is given by a

sum of normal and tangential pair forces with neighbouring particles,

$$\mathbf{F}_{\mathrm{c},a} = \sum_{b \in \text{contactlist}} (\mathbf{F}_{n,ab} + \mathbf{F}_{t,ab}) \tag{3}$$

where the normal forces $\mathbf{F}_{n,ab}$ depend linearly on the overlap $\delta = R_a + R_b - |\mathbf{r}_a - \mathbf{r}_b|$ and the relative normal velocity $\mathbf{v}_{n,ab} = ((\mathbf{v}_a - \mathbf{v}_b) \cdot \mathbf{n}_{ab})\,\mathbf{n}_{ab}$, with $\mathbf{n}_{ab}$ the unit vector pointing from the centre of b to the centre of a. Similarly, the tangential forces $\mathbf{F}_{t,ab}$ depend linearly on the tangential overlap δ_t, defined as the integral of the relative tangential velocity from the time of first contact, and the relative tangential velocity $\mathbf{v}_{t,ab} = (\mathbf{v}_a - \mathbf{v}_b) - \mathbf{v}_{n,ab}$ itself. The tangential forces also lead to a torque on the particles:

$$\mathbf{T}_a = \sum_{b \in \text{contactlist}} (R_a \mathbf{n}_{ab} \times \mathbf{F}_{t,ab}) \tag{4}$$

Governing equations for the gas phase

The gas flow is governed by the conservation equations for mass and momentum:

$$\frac{\partial(\varepsilon\rho_g)}{\partial t} + \bigtriangledown \cdot \varepsilon\rho_g \mathbf{u} = 0 \tag{5}$$

$$\frac{\partial(\varepsilon\rho_g \mathbf{u})}{\partial t} + \bigtriangledown \cdot \varepsilon\rho_g \mathbf{u}\mathbf{u} = -\varepsilon \bigtriangledown p - \bigtriangledown \cdot \varepsilon\tau + \varepsilon\rho_g \mathbf{g} \tag{6}$$

$$+\mathbf{s}_p + \mathbf{s}_{\mathrm{ibm}}, \tag{7}$$

where ε is the local gas voidage (gas volume fraction), ρ_g is the gas phase density, $\mathbf{u}$ the gas velocity, p the gas pressure, τ the viscous stress tensor, $\mathbf{g}$ the gravitational acceleration, $\mathbf{s}_{\mathrm{ibm}}$ the source term for the momentum exchange with large bodies such as an intruder, and $\mathbf{s}_p$ a source term which describes the momentum exchange with the small solid particles:

$$\mathbf{s}_p = \sum_{a=1}^{N_{\mathrm{part}}} \mathbf{F}_{\mathrm{d},a}\,\delta(\mathbf{r} - \mathbf{r}_a) \tag{8}$$

where the summation is performed over all particles and the drag force $\mathbf{F}_{\mathrm{d},a}$ is identical to what is used in the equation of motion of the particles. For the momentum exchange with small solid particles which are smaller than the Eulerian grid, it is necessary to introduce empirical drag correlations to take the gas-particle interaction into account:

$$\mathbf{F}_{\mathrm{d},a} = 6\pi\eta_g R_a (\mathbf{u} - \mathbf{v}_a) \cdot \mathrm{F}(\mathrm{Re}, \varepsilon) \tag{9}$$

where η_g is the dynamic gas viscosity. For $\mathrm{F}(\mathrm{Re}, \varepsilon)$ the Ergun (Ergun, 1952) and Wen&Yu (Wen and Yu, 1966) correlations are used:

$$\mathrm{F}(\mathrm{Re}, \varepsilon) = \begin{cases} \varepsilon^{-2.65}(1 + 0.15\mathrm{Re}^{0.687}) & \text{for} \quad \varepsilon > 0.8 \\ \dfrac{150}{18}\dfrac{1-\varepsilon}{\varepsilon} + \dfrac{1.75}{18}\dfrac{\mathrm{Re}}{\varepsilon} & \text{for} \quad \varepsilon < 0.8 \end{cases} \tag{10}$$

here $\mathrm{Re} = 2R_a\rho_g\varepsilon|\mathbf{u} - \mathbf{v}_a|/\eta_g$ is the particle Reynolds number.

Immersed boundary method

The interaction of the gas phase with an intruder larger than the size of the CFD cells is modelled with the immersed boundary method (IBM) where Lagrangian marker points are situated on the boundary of the large particle. Each marker exerts a force on the gas phase such that the local velocity of the gas is equal to the velocity of that marker. IBM has been widely used to study fluid-structure interaction and was pioneered by Peskin to investigate cardiac flow problems (Peskin, 2002). Subsequently, the method has been extended to flow around rigid bodies. The implementation that we adopt is along the lines of Uhlmann (Uhlmann, 2005). The IBM source term $\mathbf{s}_{\mathrm{ibm}}$ at the grid cell faces is calculated by summing the contribution of all Lagrangian force points:

$$\mathbf{s}_{\mathrm{ibm}} = \sum_{m=1}^{N_{\mathrm{langr}}} \mathbf{F}_m\,\delta(\mathbf{r} - \mathbf{r}_m), \tag{11}$$

where in our discretised simulations $\mathbf{F}_m$ is constructed such that the forcing results in a zero slip velocity at the surface of the sphere and $\delta(\mathbf{r} - \mathbf{r}_m)$ is a volume weighing delta function which distributes the forces to the surrounding grid cell faces. For detailed implementation of this method we refer to (Deen *et al.*, 2004; Gerner, 2009; Kriebitzsch, 2011).

Table 1: Parameters used in the simulations

Gravity z-direction	$\mathrm{m/s^2}$	9.81
Intruder diameter	m	0.01
Intruder density	$\mathrm{kg/m^3}$	2500
Particle diameter	m	5×10^{-4}
Particle density	$\mathrm{kg/m^3}$	2500
Restitution coefficient (normal)	–	0.97
Restitution coefficient (tangential)	–	0.33
Friction coefficient	–	0.10
Normal spring stiffness	N/m	100
Tangential spring stiffness	N/m	32.13
Contact time step	s	7.2×10^{-5}
Gas viscosity	kg/(ms)	1.8×10^{-5}
Computation domain		
x-direction	m	0.06
y-direction	m	0.06
z-direction	m	0.12
Number of grid cells		
x-direction	–	30
y-direction	–	30
z-direction	–	60

SIMULATION SETTINGS

In the simulation, we use a container with dimensions $6 \times 6 \times 12$ $\mathrm{cm^3}$ (width, depth, height). It contains one large intruder and 2,000,000 granular particles. The intruder has a diameter of 1 cm, while the granular particles are of average diameter 0.5 mm, with a Gaussian size distribution ($\sigma = 0.02$ mm) to avoid excessive ordering of the bed. According to the experimental results shown in (Nelson *et al.*, 2008) and (Seguin *et al.*, 2008), the ratio between size of the container and the intruder in our simulation ($L_{box}/D = 6$) is large enough so that the surrounding walls have negligible effect on the dynamics of the intruder. A schematic representation of the bed geometry is shown in figure 1. A summary of the simulation parameters is given in table 1.

In all simulations the coefficient of restitution is set to 0.97 for the normal direction, and to 0.33 for the tangential direction. For the particle-wall interaction the same collision parameters are used as for the particle-particle interaction. The friction coefficient is set to 0.1. All these values are typical for glass spheres/walls. We note that the normal spring stiffness k_n is in principle related to Young's modulus and the

Poisson ratio of the solid material; however, in practice its value must be chosen much smaller to prevent the use of impractically small integration time steps. Therefore the spring stiffness is chosen as low as possible while ensuring that the lowered spring stiffness does not have a significant influence on the phenomena observed. We investigated the influence of varying the spring stiffness between $k_n = 100, 200, 400$ and 800 N/m with an intruder initially located at z = 0.11 m and initial velocity equal to 2 m/s. The results showed that the lower normal stiffnesses do not significantly influence the collision kinematics (not shown). Thus, to enhance the computational efficiency, $k_n = 100$ N/m was used in all subsequent simulations. The granular particles are fluidized by a uniform up-flowing gas, which was gradually turned off with the goal to make a homogeneous particle bed with a flat surface. The depth of the resulting static bed is about 5.84 cm with a solids volume fraction of about 0.62. For most simulations reported here, we let the intruder move constantly downwards from a height of 11 cm, which is about 5 cm above the bed and stop near the bottom. The only exception is the validation of the model reported in the next section, where we apply a constant external gravitational force on the intruder.

VALIDATION

The validation of our simulations is done by comparing our simulation results with the experimental work by Katsuragi and Durian (Katsuragi and Durian, 2007). Unfortunately, a full one-to-one comparison is not possible due to limitations in computing capacity. That is, our granular particles are about two times larger while the intruder is 2.5 times smaller than the experimental ones.

The complete data sets for the position $z(t)$, velocity $v(t)$, and acceleration $a(t) + g$ of the intruder are shown in figure 2. The time origin is *defined* as the time of initial impact, and the position is measured upwards from the granular surface, opposite to the gravitational direction. The curves are colour-coded according to the initial impact speed of the intruder, v_0, which ranges from 0 to 400 cm/s, similar to the values used by Katsuragi and Durian (Katsuragi and Durian, 2007). Although a quantitative agreement is not expected because of the different particle diameters, the observed time evolution of the intruder dynamics is in good qualitative agreement with the experimental results, which are repeated here also for clarity. More details can be found in our previous work (Xu *et al.*, 2013) which shows that also other measurements, such as oscillatory terminal behaviour and the dependence of the final penetration depth on impact velocity, are in good agreement with experimental observations.

RESULTS

In these new simulations, the intruder is moved at constant velocity through the granular bed. Because the time step needs to be small in order to successfully capture the details of the collision processes, the simulation time for extremely small intruder velocities would become prohibitively long. Thus in the current simulations, the lowest intruder velocity was limited to 0.01 m/s. According to Albert et al. (Albert *et al.*, 1999), when the velocity of the intruder is less than $v < \sqrt{2gd}/10 \approx 0.01$ m/s, the system is in the so-called low velocity regime where the force exerted on the intruder is independent of the plunging velocity. On the other hand, due to the limited size of the system, boundary effects are expected to become important at very large velocities. Also by checking the animation, we found that for larger intruder velocities, a long channel following the intruder will form and will take more time to be refilled by granular particles. We therefore limited our intruder velocity to a maximum of 0.40 m/s.

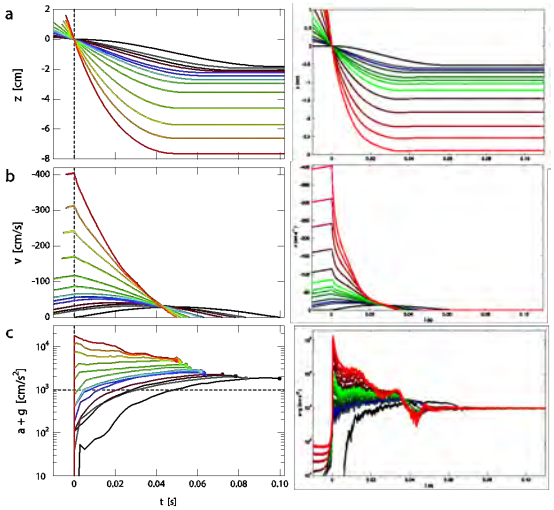

Figure 2: Detailed comparison between literature results (left) and our simulation results (right) for (a) the intruder depth, (b) intruder speed and, (c) net acceleration versus time for an intruder driven by gravity. Reproduced with permission from (Katsuragi and Durian, 2007). Note that the granular particle size is about two times smaller and the intruder 2.5 times larger than in our simulations. Curves are colour-coded according to the initial impact speed of the intruder, v_0, which can be read from panel (b) at $t = 0$.

Figure 3 shows snapshots of the bed configuration at the time when a $D = 10$ mm spherical intruder has moved one diameter ($z = D$) since initial contact, at four different impact velocities of $v_0 = 0.1$, 0.2, 0.3 and 0.4 m/s. Note how the granular particles are perturbed much more at higher velocities, leading to formation of a granular crater. Investigation of the force experienced by an intruder moving at constant velocity is very helpful to understand the dynamics of granular cratering and the factors that determine its severity. Because both the plunging velocity and the intruder size are important parameters, we investigate them separately.

Figure 4 shows the force experienced by the 10 mm spherical intruder under different impact velocities. At the low-

Figure 3: Bed structure under different impact velocities of a 10 mm spherical intruder at the time when the intruder has moved one diameter since initial contact. Granular particles are colour coded according to their velocities.

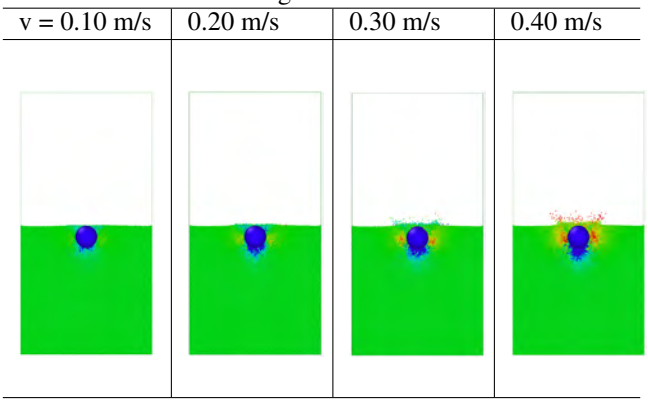

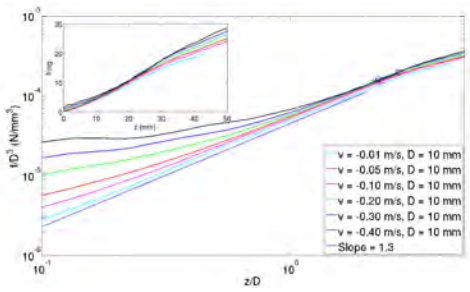

Figure 4: Plunging force f of a 10 mm intruder with different intruding velocities as a function of penetration depth z. The inset shows the measured force on the intruder, nondimensionalised by its weight, on a linear scale. The main plot shows the measured force on a double-logarithmic scale, emphasizing its power-law dependence. The inflection point is indicated by a square on each curve.

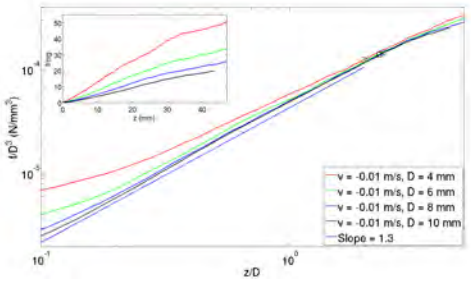

Figure 5: Plunging force f of intruders with different size under an impact velocity of 0.1 m/s as a function of penetration depth z. The inset shows the measured force on the intruder, nondimensionalised by its weight, on a linear scale. The main plot shows the measured force nondimensionalised by the intruder volume D^3 versus penetration depth nondimensionalised by the intruder diameter D, both on a logarithmic scale. The inflection point is indicated by a square on each curve.

est intruder velocity of 0.01 m/s, we find a good agreement with a total force scaling as a power-law with exponent 1.3, up to a depth of slightly more than twice the intruder diameter D. For higher intruder velocities, the initial force is slightly larger, but converges to the same power-law behaviour beyond a depth of approximately one intruder diameter. Moreover, a concave-to-convex transition it observed at all intruder velocities. These results are very similar to the former experimental results in (Peng *et al.*, 2009; Hill *et al.*, 2007). It was found that, in the experiments, the inflection point occurs when the intruder is fully buried to a level of 2.4 times the intruder diameter. In our simulations, the inflection point occurs similarly at a depth ranging from 2.0 to 2.7 times the intruder diameter, as shown in figures 4 and 5. Note that for high intruder velocities the impact is relatively violent and the forces exerted on the intruder are quite noisy. Thus for velocities larger than 0.10 m/s, forces have been averaged over different runs. Further smoothing using an averaging window of 2.5 mm was applied for all velocities.

Figure 5 shows the force experienced by spherical intruders of different size, ranging from $D = 4$ mm to 10 mm, at an impact velocity of 0.1 m/s. When we scale the penetration depth z by the intruder diameter D, and scale the force f by D^3, as conducted in (Peng *et al.*, 2009), all the data collapses for depths beyond approximately D. A slight offset is observed for different intruder diameters, which is related to different velocity-dependent drag forces experienced by the intruders. This is the topic of ongoing work which will be reported in a future paper.

CONCLUSION

A state-of-the-art DPM-IBM model has been extended to study the vertical plunging force of a spherical intruder into a granular bed. Our simulation method has been validated by our former work (Xu *et al.*, 2013) on gravity-driven intruder dynamics. In the current work we used it to investigate the force on the intruder when it is inserted into the granular bed at constant velocity. Our method successfully captures the experimentally observed concave-to-convex plunging force behaviour. In the initial regime, we find that the force fits to a power-law with an exponent of 1.3, which is also in good agreement with existing experimental observations. Finally, the plunging force for different intruder diameters is observed to approach a master curve when the force is scaled with the intruder volume and the pentration depth is scaled with the intruder diameter. The deviations are mainly a consequence of differences in the drag force experienced by the intruder, which is a topic of future work.

ACKNOWLEDGEMENTS

This work is part of the research program of the Foundation for Fundamental Research on Matter (FOM), which is part of the Netherlands Organization for Scientific Research (NWO).

REFERENCES

ALBERT, R. *et al.* (1999). "Slow drag in a granular medium". *Physical review letters*, **82(1)**, 205–208.

ALDER, B. and WAINWRIGHT, T. (1957). "Phase transition for a hard sphere system". *The Journal of Chemical Physics*, **27(5)**, 1208–1209.

CUNDALL, P.A. and STRACK, O.D. (1979). "A discrete numerical model for granular assemblies". *Geotechnique*, **29(1)**, 47–65.

DEEN, N.G. *et al.* (2004). "Multi-scale modeling of dispersed gas–liquid two-phase flow". *Chemical Engineering Science*, **59(8)**, 1853–1861.

ERGUN, S. (1952). "Fluid flow through packed columns". *Chem. Eng. Prog.*, **48**, 89–94.

GERNER, H.J. (2009). *Newton vs Stokes: Competing Forces in Granular Matter*. University of Twente.

HILL, G. *et al.* (2007). "Scaling vertical drag forces in granular media". *EPL (Europhysics Letters)*, **72(1)**, 137.

HOU, M. *et al.* (2005). "Projectile impact and penetration in loose granular bed". *Science and Technology of Advanced Materials*, **6(7)**, 855–859.

KATSURAGI, H. and DURIAN, D. (2007). "Unified force law for granular impact cratering". *Nature Physics*, **3(6)**, 420–423.

KRIEBITZSCH, S.H. (2011). *Direct Numerical Simulation of Dense Gas-Solid Flows*. Eindhoven University of Technology.

LOHSE, D. *et al.* (2004). "Granular physics: creating a dry variety of quicksand". *Nature*, **432(7018)**, 689–690.

NELSON, E.L. *et al.* (2008). "Projectile interactions in granular impact cratering". *Phys. Rev. Lett.*, **101**, 068001.

PENG, Z. *et al.* (2009). "Depth dependence of verti-

cal plunging force in granular medium". *Phys. Rev. E*, **80**, 021301.

PESKIN, C.S. (2002). "The immersed boundary method". *Acta numerica*, **11(0)**, 479–517.

SEGUIN, A. *et al.* (2008). "Influence of confinement on granular penetration by impact". *Phys. Rev. E*, **78**, 010301.

STONE, M.B. *et al.* (2004b). "Local jamming via penetration of a granular medium". *Phys. Rev. E*, **70**, 041301.

STONE, M.B. *et al.* (2004a). "Stress propagation: Getting to the bottom of a granular medium". *Nature*, **427(6974)**, 503–504.

STUKOWSKI, A. (2009). "Visualization and analysis of atomistic simulation data with ovito–the open visualization tool". *Modelling and Simulation in Materials Science and Engineering*, **18(1)**, 015012.

UHLMANN, M. (2005). "An immersed boundary method with direct forcing for the simulation of particulate flows". *Journal of Computational Physics*, **209(2)**, 448–476.

VAN DER HOEF, M. *et al.* (2006). "Multiscale modeling of gas-fluidized beds". *Advances in chemical engineering*, **31**, 65–149.

VAN SINT ANNALAND, M. *et al.* (2005). "Numerical simulation of gas–liquid–solid flows using a combined front tracking and discrete particle method". *Chemical engineering science*, **60(22)**, 6188–6198.

WEN, C. and YU, Y. (1966). "Mechanics of fluidization". *Chem. Eng. Prog. Symp. Ser.*, vol. 62, 100.

XIONG, Q. *et al.* (2011). "Large-scale dns of gas-solid flows on< i> mole-8.5</i>". *Chemical Engineering Science*.

XU, Y. *et al.* (2013). "Detailed numerical simulation of an intruder impacting on a granular bed using a hybrid discrete particle and immersed boundary (dp-ib) method". *Chemical Engineering Science*, **104**, 201–207.

10th International Conference on CFD in Oil & Gas, Metallurgical and Process Industries
SINTEF, Trondheim, Norway *CFD 2014*
17-19 June 2014

OPERATING EXPERIENCE WITH A HIGH-TEMPERATURE PSEUDO-2D FLUIDIZED BED REACTOR DESIGNED ESPECIALLY FOR DETAILED LOCAL DATA COLLECTION

Abdelghafour ZAABOUT[1*], Schalk CLOETE[2], Stein Tore JOHANSEN[1] & Shahriar AMINI[1]

[1]Department of Flow Technology, SINTEF Materials and Chemistry, Norway

[2]Department of Energy and Process Engineering, Norwegian University of Science and Technology (NTNU), Norway

*E-mail: abdelghafour.zaabout@sintef.no

ABSTRACT

This paper reports practical experience from the high-temperature operation of a pseudo-2D fluidized bed reactor running redox reactions typically occurring in a Chemical Looping Combustion process. The reactor was designed for the primary purpose of providing detailed local data for the validation of reactive multiphase flow models. For this purpose, the pseudo-2D bed was equipped with multiple measurement ports which allowed for the simultaneous measurement of temperature, pressure and gas composition at various positions within the bed. Multiple unforeseen challenges were encountered and solved (within practical limits) during this first-of-a-kind experimental campaign. Extensive recommendations are given to guide future experimental campaigns aiming to build on this work. In spite of these challenges, initial comparisons between experiments and simulations show reasonable agreement.

Keywords: Fluidized bed reactor, validation, experiments, Two Fluid Model.

INTRODUCTION

Fluidized bed reactors find application in a wide range of process industries where efficient gas-solid reactions, heat transfer and/or mass transfer, is desired. The very large exposed surface area and excellent mixing displayed by these reactors makes them ideal for this purpose. However, fluidized bed reactors typically display very complex hydrodynamics which directly influences the mass and heat transfer occurring within the bed. This complexity makes design, scale-up and operation challenging.

Due to the continued exponential increase in computational power and availability, fluidized bed reactor modelling using the Kinetic Theory of Granular Flows (Jenkins and Savage, 1983, Lun et al., 1984, Gidaspow et al., 1992, Syamlal et al., 1993) is now becoming a viable strategy for improving the understanding of the complex multiphase flow in fluidized bed reactors and thereby accelerating the design and scale-up of these processes. The traditional Two Fluid Model approach to fluidized bed flow modelling has been under development for a number of decades now and has been proven to result in reliable hydrodynamic predictions (Taghipour et al., 2005, Ellis et al., 2011, Cloete et al., 2013), but such validation studies are largely absent for reactive systems. This absence is of significant concern because such reactive validation campaigns are crucial to the development and widespread acceptance of reactive multiphase flow modelling as a tool for accelerating the development and scale-up of fluidized bed reactors.

There are good reasons for the absence of such work to date. Reactive validation studies are much more difficult to perform because of the high temperatures which are typically involved. The detailed local flow measurements necessary to properly evaluate model performance are also much more challenging to collect from such high-temperature systems. It is therefore to be expected that reactive validation campaigns involve a much greater risk of unexpected additional complexities, costs and unforeseen problems with data collection.

In recognition of these challenges, the work reported in this paper aims to greatly reduce these resistances to dedicated validation campaigns for reactive multiphase flow modelling by presenting a detailed account of the operating experiences in such a campaign. The purpose of this work is

therefore to guide future experimental campaigns dedicated to the collection of reactive data for the purpose of model validation, thereby greatly accelerating the development of reactive multiphase flow modelling of fluidized bed reactors.

EXPERIMENTAL SET UP AND METHODOLOGY

The experimental setup (Figure 1) consisted of a pseudo-2D vertical column with a height of 1.5 m, a width of 0.3 m and a depth of 0.015 m (identical dimensions to a cold-flow unit operated previously (Cloete et al., 2013)). The reactor column was made from Inconel 600 in order to withstand the harsh conditions created by the high temperature (up to 1000°C) and reacting gas-solid flows. A ceramic porous plate with a 40 micron average pore size and 7 mm thickness was used as the gas distributor.

Four electrical heaters were installed on the back of the reactor in order to maintain the target temperature along the reactor height. Each of these heaters was controlled separately allowing for good control over the heat supply to different regions in the reactor. Temperature control was carried out using data from thermocouples positioned on the external wall of the reactor.

A particulate insulation material (vermiculate) was selected for the bulk of the insulation layer. The heaters and the reactor body were first covered by 5 cm of blanket insulations before being placed in a metallic box filled with vermiculate to result in an additional 20 cm of insulation.

Three mass flow controllers are used for feeding gases to the reactor. A cooler was positioned at the outlet of the reactor to cool down the stream of hot

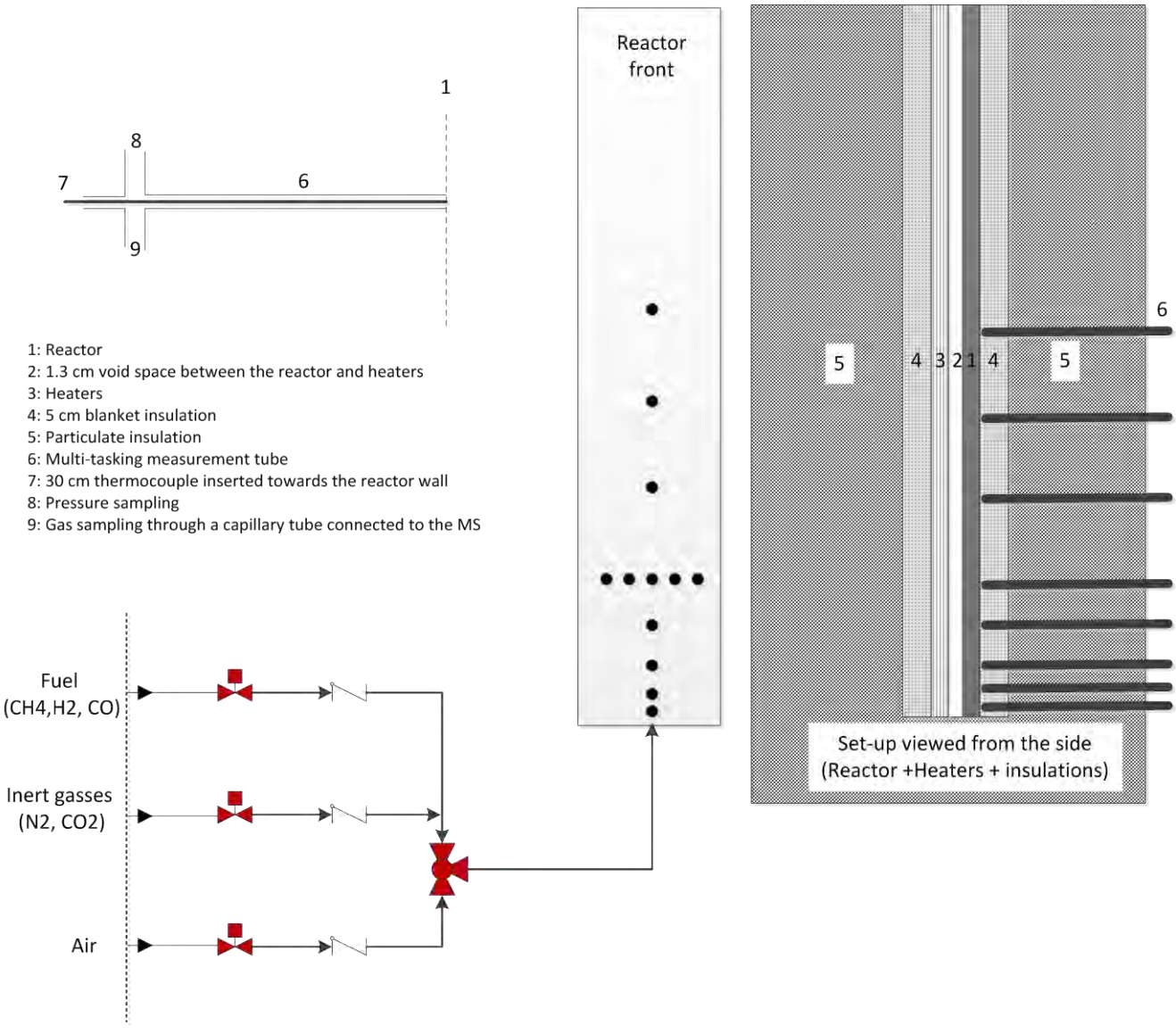

Figure 1: Schematic representation of the experimental set up.

gases before it is sent to the vent.

Data acquisition ports were positioned on the front side of the reactor along the central axial axis and laterally at a height of 0.3 m above the gas distributor. Since larger gradients are expected close to the distributor, ports were positioned closer together in this region.

A multi-purpose tube, of 0.3 m in length and 0.001 m in diameter, was connected to each data acquisition port to allow for simultaneous measurements of pressure, temperature and gas composition at each position. A fine stainless mesh (40 μm spacing) was fixed tightly at the entrance of each tube to prevent infiltration of fine particles from the reactor into the tube. The outer end of the tube was connected to a Swagelok tee where a thermocouple (0.3 m length) was mounted and inserted through the central axis of the tube to measure the temperature exactly at the internal wall of the reactor. Pressure was measured through transducers capable of withstanding a maximum temperature of 250°C. In order to ensure that hot gasses from the reactor are cooled down sufficiently before reaching the pressure transducer, a 0.25 m non-insulated tube was placed between the pressure transducer and the multi-purpose measurement tube. The influence of the multi-purpose measurement tube on the average pressure has been tested by measuring the pressure with and without this whole measurement system at ambient temperature. This test confirmed that the measurement system had no influence on the average pressure measurement. The known weight of particles inside the reactor was also used to double-check the accuracy of the pressure measurements.

Gas composition was measured through a capillary tube connected to the second exit of the Swagelok tee. Under experimentation, sampled gases were sent continuously to a Mass Spectrometer from MKS Instruments Inc. for analysis. Temperature was measured continuously in each port along the entire front of the reactor using thermocouples of type K.

REACTOR OPERATION AND TROUBLESHOOTING

The reactions studied in this work are those occurring in the Chemical Looping Combustion (CLC) process (Hossain and de Lasa, 2008). CLC is a promising technology for cost effective power generation with integrated CO_2 capture, but development is being hampered by the substantial funding challenges faced by CO_2 capture technology. Despite this challenge, however, it is very important that CLC technology reaches the commercial scale by the time that a consistent CO_2 price is finally implemented so that widespread deployment can commence without further delay. Fundamental flow modelling has a very important role to play in this rapid and economical scale-up process.

The experimental setup reported in this study will simulate the two reactors usually employed in CLC (For oxidation and reduction of the oxygen carrier) by alternatively exposing a fixed mass of oxygen carrier material to fuel and air feeds.

Nickel oxide particles supported on Al_2O_3 (NiO/Al_2O_3 ratio is 65/35) were used as the oxygen carrier. The particle size cut-off D50 was determined to be 161.7 μm (Zaabout et al., 2013).

Heating strategy

CLC redox reactions usually occur above 600°C and it is therefore desired that the reactor can be heated to a target temperature beyond 600°C as quickly as possible. The first heating experience showed, however, that rapid heating from the back of the reactor caused the reactor body to bend due to different rates of thermal expansion of the front and back plates of the reactor – a situation which could cause severe damages to the reactor. In order to avoid excessive bending of the reactor body, the temperature difference between the front and back plates of the reactor had to be kept within tolerable limits. This could be achieved by lowering the rate of heating from the back and by increasing the rate of heat transfer from the back plate to the front plate. The following strategy was followed to achieve this purpose: i) Two thermocouples were installed on the front plate of the reactor in order to inspect the transient temperature evolution on this plate as the reactor was heated up. ii) The bed was fluidized at a relatively high fluidization velocity of 0.4 m/s to create a large amount of mixing and improve heat transfer from the back to the front of the reactor. iii) Incremental heating was carried out from the back of the reactor based on the measured temperature difference between the back and the front plates.

Gas residence time in the multi-purpose measurement tube

Pressure, temperature and gas composition data can be collected simultaneously using the custom-designed multi-purpose tube. It was always possible to get accurate measurements of pressure and temperature, but species measurements through the multi-purpose measurement tube led to extensive signal delay and diffusion due to the large inner space of the 30 cm tube (10 mm ID) where the sample gases have to go through before reaching the capillary tube.

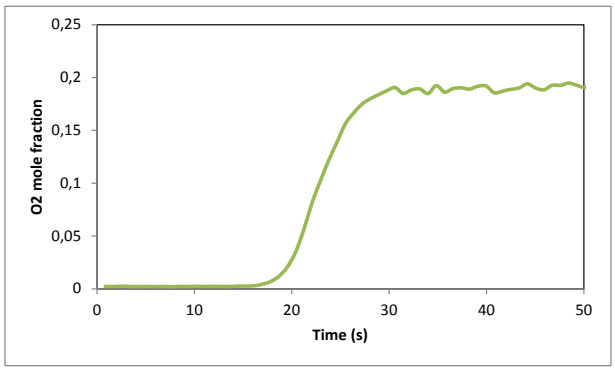

Figure 2: The transient mole fraction of O2 measured at 0.7 m above the distributor following a step change in the feed gas from pure N2 to air.

To overcome this issue, the design of the multi-purpose tube was modified so that the capillary tube is inserted together with the thermocouple through the centreline of the tube to reach the reactor internal wall (as showed in Figure 1). In this case, the gas sampling occurs exactly at the internal wall, effectively removing the delay and diffusion caused by the 30 cm multi-purpose tube (4 minutes delay). The transient oxygen evolution measured with the modified multi-purpose tube shows that only 30 s of delay time is required for the step change to be fully registered by the MS (Figure 2). Based on this result, the first 40 seconds was omitted in all gas composition measurements.

Choice of the reducing gas

The use of fuels which generate steam upon combustion (CH_4 for example) should be avoided because the steam condenses in the capillary tube leading to the MS. When this happens, the MS shows a high water content in the sampling port for several hours, implying that the port is saturated with water and it can't be used for the sampling until the accumulated water is completely removed. The gasses extracted from the reactor could theoretically be dried or sent to a cooler to trap before being sent to the MS, but this would increase the signal delay and diffusion shown in Figure 2. The second issue arising from the use of methane as fuel in this application is the side reactions which occur when CH_4 reacts with Ni-based oxygen carriers. This created additional uncertainty regarding the gas composition measurements. In addition, the CFD modelling will require more complex reaction kinetics to be implemented for the side reactions. This added complexity introduces unwanted uncertainty regarding the comparison between simulation and experiment. For these reasons, CO was used as the fuel gas. The reaction of CO with the Ni-based oxygen carrier produced only CO_2 from a single reaction ($CO + NiO \rightarrow Ni + CO_2$), thereby simplifying the reaction mechanism and solving the issue of capillary tube blockage. However, the use of CO introduced another problem with carbon deposition. The Boudouard carbon deposition reaction ($2CO \rightarrow CO_2 + C$) can occur on the Ni-based oxygen carrier employed in this study, especially when the oxygen carrier becomes highly reduced (Cho et al., 2005). In this case, some of the CO is deposited on the oxygen carrier particles as carbon instead of reducing NiO to form Ni and CO_2.

For this study, the primary problem is the added modelling complexity created by the Boudouard reaction which would be very difficult to model accurately. For the sake of reliable validation data, it is therefore very important to reduce this phenomenon to the point where it can be safely neglected in the modelling.

There are two options for reducing the degree of carbon deposition: preventing the oxygen carrier from becoming highly reduced (pure nickel catalyses the Boudouard reaction) and adding CO_2 (to influence the reaction equilibrium of the Boudouard reaction). Five experiments have been designed and carried out in order to quantify the carbon deposition sensitivity to the oxygen carrier reduction degree and dilution of CO with CO_2. As shown in Table 1, the amount of carbon deposition was not large, but still significant. Increasing the degree of reduction of the oxygen carrier up to 60% did not appear to have a clearly distinguishable effect on the carbon deposition. However, when CO_2 was fed to the reactor together with CO, the amount of carbon deposition dropped to below 1%.

Such a small amount of carbon deposition can be safely neglected in the simulations.

Table 1: Changes in the amount of carbon deposition with changes in the degree of oxygen carrier reduction and the dilution of the CO fuel gas with CO_2.

Experiment	Reduction time (s) [Degree of reduction]	CO_2 in fuel gas (%)	CO_2/CO (%)
1	383 [20%]	0	2.41
2	766 [40%]	0	3.07
3	1150 [60%]	0	1.94
4	1437 [60%]	36	0.73
5	1916 [60%]	60	0.87

REACTOR BEHAVIOUR

Axial temperature gradient

A uniform temperature distribution is important for CFD validation because it would remove the uncertainty created by various unexplained temperature gradients. In this reactor, it was assumed that the good mixing achieved would ensure a relatively uniform temperature distribution even though cold gas is being fed from the bottom of the reactor. It is therefore important to assess the degree of temperature non-uniformity in the bed.

As indicated in Figure 3, however, experimental results show a significant difference between the temperatures recorded at the bottom and the top of the bed. This temperature difference increases both with a decrease in fluidization velocity and an increase in the overall reactor temperature. The reduction in the axial temperature gradient as the fluidization velocity was increased is a direct result of the improved axial mixing taking place with more vigorous fluidization. However, larger feed rates of cold gas would also lead to a higher rate of heat removal from the solids residing in the bottom of the reactor, thereby countering this effect to some degree. Since the curves in Figure 3 tend to flatten out towards higher fluidization velocities, it appears as if these two effects would balance each other out while a significant temperature difference still exists. A previous hydrodynamics study (Cloete et al., 2013) has also shown that the large friction imposed by the front and back walls of the pseudo-2D bed impedes the formation of a strong re-circulatory flow pattern, thereby reducing axial mixing. It is therefore highly likely that the axial temperature gradient would be much smaller in a standard cylindrical bed.

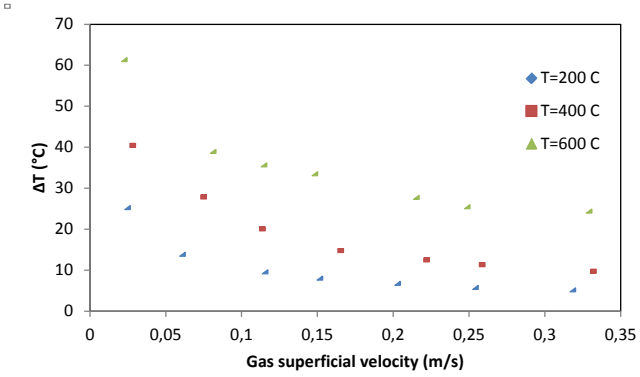

Figure 3: The temperature difference between two axial locations in the reactor (0.3 m and 0.02 m) as a function of fluidization velocity and reactor temperature.

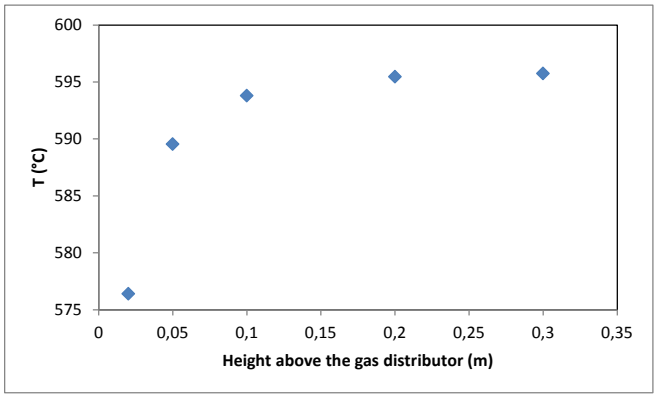

Figure 4: Axial temperature distribution for a fluidization velocity of 0.33 m/s and a reactor temperature of 600°C.

From a modelling point of view, the resulting axial temperature gradient might be too large to safely ignore. In that case, it would be necessary to impose a fixed axial temperature profile in the simulation similar to that measured in the experiments (e.g. Figure 4) so that the temperature effect on the kinetic rate would be correctly captured.

Gas species measurements: the problem of complete conversion

When collecting species data for model validation, it is important that incomplete reactant conversion is achieved. Without a certain degree of fuel gas

slippage, there is essentially nothing to use as a comparison between simulation and experiment. In addition, it is important that incomplete conversion occurs over a range of flow conditions so that model generality can be properly evaluated. Generality is the ultimate aim of any fundamental predictive model. If the model is used to meet aims such as prototyping, design, optimization and scale-up, adequate generality is implicitly assumed since the model will inevitably be used to simulate conditions far removed from those under which it was validated.

Experience showed that these requirements imposed large restrictions on the experimental planning. The Ni-based oxygen carrier used in this study was highly reactive and resulted in complete conversion for normal CLC operating temperatures (>600°C) for the maximum velocity that could be afforded before significant particle elutriation occurred. For this reason, significantly lower temperatures had to be used in order to achieve a satisfactory degree of fuel slippage. Figure 5 displays trends of incomplete CO conversion for different low temperatures at the highest fluidization velocity that could be afforded before elutriation (0.4 m/s). A 20/80 CO/CO_2 ratio was selected based on the findings in the previous section.

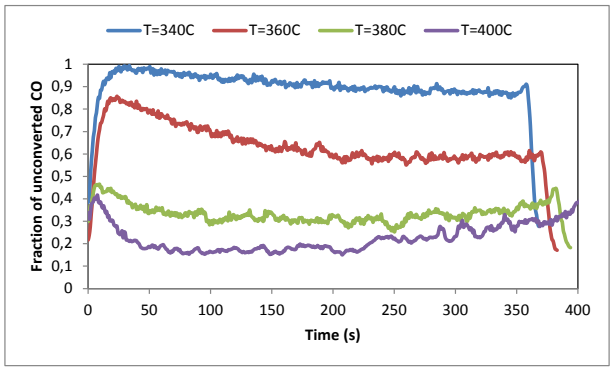

Figure 5: Transient CO mole fraction profiles measured at a height of 0.7 m above the distributor during reduction with CO (diluted with 80% CO2) for several operating temperatures. The gas fluidization velocity was 0.4 m/s.

From a modelling point of view, the slow kinetics at such low temperatures also reduces the value of experimental data. If reaction kinetics become very slow, the overall reactor performance (degree of conversion achieved) is controlled primarily by the kinetic rate implemented in the simulation (usually derived from TGA experiments). Correct prediction of the bubble-to-emulsion mass transfer achieved in the reactor (which is determined by the reactor hydrodynamics) is therefore of lesser importance. This results in a situation where the hydrodynamics resolved by the flow simulation has only a small impact on the overall reactor performance, implying that model performance is not rigorously evaluated. For faster kinetics, however, the bubble-to-emulsion mass transfer becomes highly limiting and the correct resolution of the hydrodynamics becomes very important as discovered in a previous reactive validation study (Cloete et al., 2012). Experiments with such fast kinetics will be required to properly evaluate model performance.

INITIAL COMPARISON

Some initial comparisons have already been made to evaluate the ability of the standard Two Fluid Model (TFM) approach (the equation system can be viewed in (Cloete et al., 2011)) to predict reactor performance over a range of fluidization velocities and reactor temperatures. The reactor was operated with periodic gas switching to alternatively reduce and oxidize the oxygen carrier. Only the reduction stage was studied for the purpose of model validation because the oxygen carrier had to be maintained in a highly oxidized state in order to prevent carbon deposition. This meant that oxidation could not be started from a fully reduced particle in order to ensure reliable data collection.

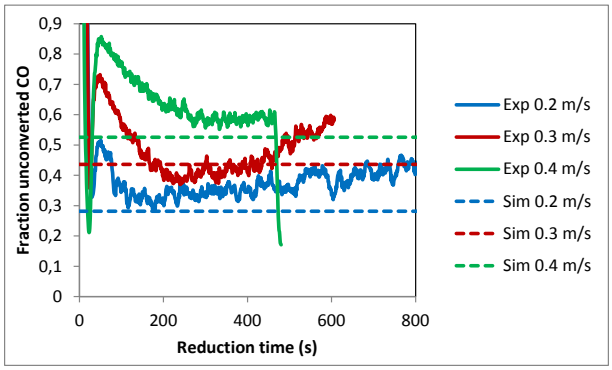

Figure 6: Comparison between experimental and simulation results for three fluidization velocities at a reactor temperature of 360°C.

The resulting comparison is shown in Figure 6 and Figure 7. It is clear that the experimental trends in the amount of CO exiting the bed without reacting generally trend downwards and then upwards again. The initial downwards trend is due to a temporary activation phase that the oxygen carrier experiences at the start of each reduction stage. TGA studies confirmed this behaviour at the low temperatures

considered here. The subsequent upward trend is expected to be due to the oxygen carrier becoming more reduced and therefore less reactive as time goes by. Experiments were stopped after the time it would take the oxygen carrier to be 20% reduced if 100% CO conversion was achieved after which the oxygen carrier was fully oxidized in preparation for the next experiment.

For comparison, simulations were run for only 30 seconds of real time steady state operation at the reaction rate displayed by a highly oxidized and fully activated powder. The dashed lines in Figure 6 and Figure 7 represent the time-averaged reactor performance over the simulation period. It is clear that both figures show a satisfactory match between simulation and the part of the experimental curve following the initial activation time even for the simple 2D TFM approach. In general, the simulation slightly over-predicted reactor performance (under-predicted the amount of unconverted CO exiting the reactor), but captured the trend with changing temperatures and fluidization velocities quite successfully.

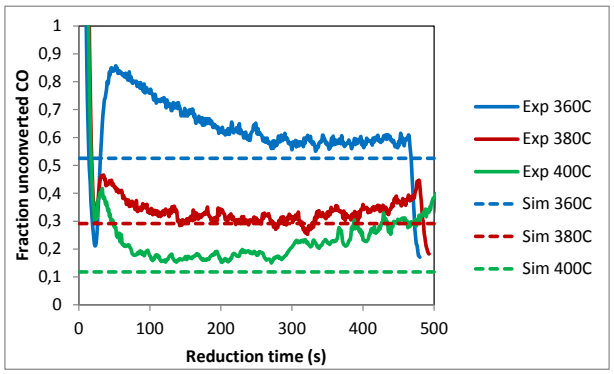

Figure 7: Comparison between experimental and 2D TFM simulation results for three reactor temperatures at a fluidization velocity of 0.4 m/s.

Part of the reason for the good simulation performance even with the simple 2D TFM approach is the fact that the reaction rate was quite slow at these low temperatures, implying that the overall reactor performance was mostly limited by the kinetics and not as much by the bubble-to-emulsion mass transfer.

This is a very important point to consider in future fluidized bed reactor validation experiments because the ability of the model to predict the bubble-to-emulsion mass transfer is the most crucial aspect to be validated. For this purpose, fast reaction kinetics is required so that mass transfer becomes the limiting factor. However, in bubbling fluidized bed reactors, such fast kinetics would result in complete reactant conversion only a short distance above the distributor plate, making the collection of meaningful validation data impossible.

CONCLUSIONS AND RECOMMENDATIONS

This study presented a wide range of operating experiences with a first-of-a-kind pseudo-2D fluidized bed reactor designed especially for the purpose of detailed reactive multiphase flow model validation. Chemical Looping Combustion (CLC) reactions using a Ni-based oxygen carrier material were carried out in the reactor while custom-designed multi-purpose measurement tubes were used to extract local data from various locations inside the bed.

Due to the novelty of this endeavour, many unforeseen problems were encountered and solved within practical limits. The experience gained with this first reactor operation will be used to guide future model validation campaigns both with this reactor and with future improved reactor designs. Overall, the following recommendations can be made for future work:

Two important factors should be ensured in the temperature control strategy: relatively fast heating and good performance of the insulation material even after long periods of operation. For start-up from ambient temperature, a burner can be used to supply hot gas which can heat up the reactor in a uniform manner within a relatively short timeframe.

Local gas species concentrations must be sampled as close to the bed material as at all possible in order to prevent an excessively long time delay in signal transmission and the resulting uncertainties caused by the gas diffusion. It is also advisable to choose reactions which do not result in wet product gasses and, if this is unavoidable, special measures must be taken to dry the gas before analysis. This will probably not be possible for online local measurements where a large signal delay cannot be afforded.

Reactants with known carbon deposition issues (such as CO with NiO) should be avoided, but, if this is unavoidable, carbon deposition can be minimized by feeding a significant amount of CO_2 with the CO feed. In order to improve the accuracy of the data for model validation and reduce modelling complexities, reactants with complex

side reactions (such as CH_4 with NiO) should be avoided.

Effective model validation also requires that measures be taken to prevent complete reactant conversion. This can be done in three ways: 1) reducing the kinetic rate (operating at lower temperatures or using a less reactive material), 2) increasing the fluidization velocity (within the bounds imposed by particle elutriation) or 3) by increasing the mass transfer resistance (by injecting the reactant in a highly concentrated manner).

An initial comparison between standard Two Fluid Model predictions and experimental results collected according to Option 1 above showed good agreement over different temperatures and fluidization velocities. This is only an initial indication of good model performance, however, because the low reaction rates used will not properly test the ability of the CFD model to accurately predict the bubble-to-emulsion mass transfer.

ACKNOWLEGMENTS

The authors would like to acknowledge the funding received from the Research Council of Norway which enabled the completion of this work. Joost Kors is also acknowledged for constructing and maintaining the experimental setup.

REFERENCES

CHO, P., MATTISSON, T. and LYNGFELT, A., (2005), "Carbon Formation on Nickel and Iron Oxide-Containing Oxygen Carriers for Chemical-Looping Combustion", *Industrial & Engineering Chemistry Research*, **44**(4), 668-676.

CLOETE, S., AMINI, S. and JOHANSEN, S. T., (2011), "On the effect of cluster resolution in riser flows on momentum and reaction kinetic interaction", *Powder Technology*, **210**(1), 6-17.

CLOETE, S., JOHANSEN, S. T. and AMINI, S., (2012), "An assessment of the ability of computational fluid dynamic models to predict reactive gas–solid flows in a fluidized bed", *Powder Technology*, **215-216**(0), 15-25.

CLOETE, S., ZAABOUT, A., JOHANSEN, S. T., ANNALAND, M. V., GALLUCCI, F. and AMINI, S., (2013), "The generality of the standard 2D TFM approach in predicting bubbling fluidized bed hydrodynamics", *Powder Technology*, **235**, 735-746.

ELLIS, N., XU, M., LIM, C. J., CLOETE, S. and AMINI, S., (2011), "Effect of Change in Fluidizing Gas on Riser Hydrodynamics and Evaluation of Scaling Laws", *Industrial & Engineering Chemistry Research*, **50**(8), 4697-4706.

GIDASPOW, D., BEZBURUAH, R. and DING, J., (1992), "Hydrodynamics of Circulating Fluidized Beds, Kinetic Theory Approach", *7th Engineering Foundation Conference on Fluidization* 75-82.

HOSSAIN, M. M. and DE LASA, H. I., (2008), "Chemical-looping combustion (CLC) for inherent CO2 separations-a review", *Chemical Engineering Science*, **63**(18), 4433-4451.

JENKINS, J. T. and SAVAGE, S. B., (1983), "Theory for the rapid flow of identical, smooth, nearly elastic, spherical particles", *Journal of Fluid Mechanics*, **130**, 187-202.

LUN, C. K. K., SAVAGE, S. B., JEFFREY, D. J. and CHEPURNIY, N., (1984), "Kinetic Theories for Granular Flow: Inelastic Particles in Couette Flow and Slightly Inelastic Particles in a General Flow Field", *Journal of Fluid Mechanics*, **140**, 223-256.

SYAMLAL, M., ROGERS, W. and O'BRIEN, T. J. (1993). MFIX Documentation: Volume 1, Theory Guide. Springfield, National Technical Information Service.

TAGHIPOUR, F., ELLIS, N. and WONG, C., (2005), "Experimental and computational study of gas–solid fluidized bed hydrodynamics", *Chemical Engineering Science*, **60**(24), 6857-6867.

ZAABOUT, A., CLOETE, S., JOHANSEN, S. T., ANNALAND, M. V. S., GALLUCCI, F. and AMINI, S., (2013), "Experimental Demonstration of a Novel Gas Switching Combustion Reactor for Power Production with Integrated CO2 Capture", *Industrial & Engineering Chemistry Research*, **52**(39), 14241-14250.

HEAT TRANSFER IN GAS-SOLID FLUIDIZED BED THROUGH AN INTEGRETED DIA/PIV/IR TECHNIQUE

Amit PATIL[1*], **Elias A.J.F.PETERS**[1†], **Johannes A.M.KUIPERS**[1‡]

[1]TU Eindhoven Department of Chemical Engineering, 5600MB Eindhoven, THE NETHERLANDS

[*] E-mail: a.v.patil@tue.nl
[†] E-mail: e.a.j.f.peters@tue.nl
[‡] E-mail: j.a.m.kuipers@tue.nl

ABSTRACT

A new combined IR (infrared)/PIV (particle image velocimetry)/DIA (digital image analysis) measuring technique for studying heat transfer in gas-solid fluidized bed is presented. The infrared images are coupled with visual images that are recorded simultaneously using an external trigger system. This gives instantaneous thermal and hydrodynamic data of a pseudo 2D fluidized bed that can be used to validate simulations of heat transfer in such a bed. The well-established technique of DIA/ PIV (van Buijtenen *et al.*, 2011; de Jong *et al.*, 2012) can be applied on visual images to get hydrodynamic information and its combination with IR images gives the thermal dynamics. Since the visual and infrared images were recorded with different cameras with different image sizes, mapping of the images is needed to obtain a good superposition. It will be shown that the used method results in a good superposition and synchronization of hydrodynamic and thermal data. The combined technique was used to get insightful information into issues like the mean temperature of particles as function of time, spatial temperature distributions as function of: particle sizes, bed aspect ratio and background gas velocity. The measured data from the technique can also be used to obtain heat fluxes inside the bed alongside with the solids mass flux. These experimental results can be used to validate CFD models on heat transfer in gas-solid fluidized beds.

Keywords: multiphase flow, particle image velocimetry, digital image analysis, infrared thermography, fluidized beds, heat transfer
.

A complete list of symbols used, with dimensions, is required.

NOMENCLATURE

Greek Symbols

ρ	Mass density, $[kg/m^3]$
T	Temperature, $[K]$
Cp	Heat capacity, $[J/kgK]$
k	Thermal conductivity, $[W/mK]$
ε	particle fraction, $[-]$
h	heat transfer coefficient, $[W/(m^2K)]$
E	Young's modulus', $[GPa]$
ν	Poisson's ratio', $[-]$

Sub/superscripts

g	Gas.
i	Index grid interrogation cell in x direction i.
j	Index grid interrogation cell in z direction j.
p	Particle.
w	Wall.
ext	external environment.
c	contact.
rel	relative.

INTRODUCTION

Fluidized beds are encountered in a variety of industries because of their favorable mass and heat transfer characteristics. Some of the prominent processing applications include coating, granulation, drying, and synthesis of fuels, base chemicals and polymers. Many of the important applications of fluidized beds involve highly exothermic or endothermic reactions which give rise to a high rate of heat removal or supply to the system. Fluidized catalytic cracking, fluidized bed coal combustion and polymerization for production of polyethylene (UNIPOL) are some of the well known processes. Under such conditions formation of hot spots or zones is a phenomenon which can severely effect the overall performance of the reactor. Hence in depth knowledge of the heat transfer processes in fluidized beds is highly relevant.

In recent years several, infrared (IR) techniques for measuring temperature in fluidized beds have been developed (Tsuji *et al.*, 2010; Brown and Lattimer, 2013). Tsuji *et al.* (2010) proposed an idea of combining IR with PIV to study heat transfer in fluidized beds. Infrared thermography has been used frequently in process engineering research for heat transfer measurements and studies (Findlay *et al.*, 2005; Astarita and Carlomagno, 2012; Vollmer and Mollmann, 2011; Kaplan, 2007). This measuring technique is quite well known to be reliable for non-insitu measurements. Recent work by Dang *et al.* (2013) demonstrated the suitability of an infrared camera (fitted with spectral filters) for CO_2 concentration measurement in gas voids using in pseudo 2D fluidized beds. This work builds on the measuring method proposed by Tsuji *et al.* (2010) using improved experimental and post processing techniques.

Earlier a visual processing method known as digital image analysis/particle image velocimetry (DIA/PIV) method was developed (de Jong *et al.*, 2012; van Buijtenen *et al.*, 2011). In this method DIA provides the 3D particle fraction and PIV provides the velocity field of the particles in a pseudo-2D fluidized bed. Both combined provided the solids mass flux.

Here we couple this method with infrared (IR) solids thermography to give the integrated DIA/PIV/IR method where by accommodating temperature field it gives particulate heat fluxes.

Besides introducing the measurement techniques in this paper we will also show results on the effects of particle size and background gas velocity on the heat transfer characteristics in fluidized beds. The data generated in these studies can be used for validating CFD models. Further a typical validation of a DEM is shown where comparisons have been made between experimental and computational results. In order to be able to make good comparison the wall heat loss was taken into account in the DEM.

EXPERIMENTAL TECHNIQUE

Fluidized Bed and Procedure

The experimental study is carried out on a small pseudo 2D fluidized bed. A schematic view of the set up is shown in Fig 1. The fluidized bed is 8 cm wide, 20 cm high and 1.5 cm in depth. The front wall of the fluidized bed is made up of sapphire glass specifically chosen to give a high transmittance to the infrared light.

The back and side walls consist of aluminum coated from the inside with matt finish black paint to reduce reflection. The aluminum frame was anodized to give the material better adhesion for paints and glue used to attach the sapphire mirror and other accessories to the frame. It also provides corrosion and wear resistance to the whole frame and helps to reduce charging of the particles. The back aluminum frame was fitted with thermocouples to measure its temperature at two different heights.

The polished aluminum has a low emissivity of 0.09. This helps in reducing any interference that may arise due to heating of the frame. The emissivity of anodized aluminum is 0.77. The internal walls of the fluidized beds as can be seen is anodized aluminum and hence helps in reducing any reflection of radiation from hot particles in the system. This gives a good contrast and clarity in observing the particles during fluidization which can be observed in the instantaneous infrared images shown in Fig. 2.

The control of the setup is done using Labview. In the presented set of experiments nitrogen at room temperature is supplied at the bottom through a porous plate gas distributor. The mass flow controller was calibrated to adjust the flow rate to a predefined value.

The fluidization experiments are performed with glass particles of sizes 0.5 mm and 1 mm. The particle properties are provided in Table 1. Hot particles heated in an oven at 120 °C are charged into the empty bed at room temperature, after which a constant gas stream at 20 °C is supplied through the bottom plate.

Along with fluidization the cold gas flow causes cooling of the hot particles in the bed with time which is recorded by the two cameras. The recording of the cameras is started before charging of the particles and is continued for about 2-3 minutes. This is approximately the time required by the fluidizing gas to cool the particles in the system. We choose to cool the particles instead of heating them up, because in this case the contrast between hot particles and cold background is large initially. It was observed that the background effects could be easily filtered and a high quality measurements of particulate temperature was possible.

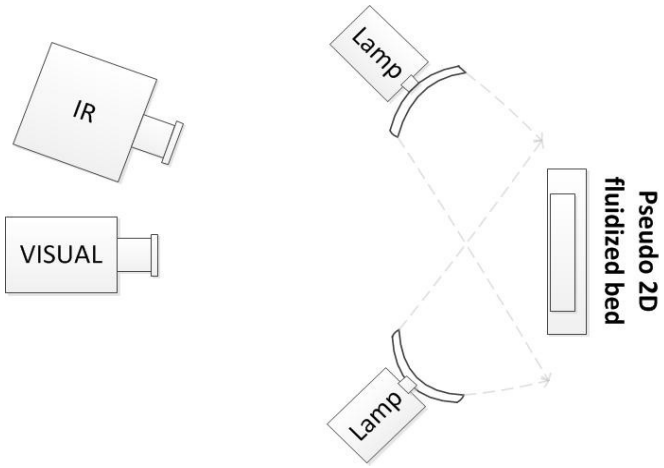

Figure 1: Top view of the experimental setup illustrating the arrangement of the visual and infrared camera with respect to the pseudo 2D fluidized bed.

Table 1: Particle properties and settings used in the experiments.

Particle material	Glass
Particle density ρ_p	2500 kg/m^3
Norm. coeff. of restit.	0.97
Tang. coeff. of restit.	0.33
Particle heat capacity $C_{p,p}$	840 J/(kgK)
Fluid heat capacity $C_{p,f}$	1010 J/(kgK)

d_p (mm)	Geldart type	u_{bg} (m/s)	Bed mass (g)
0.5	B	0.51	75
0.5	B	0.86	75
1.0	D	1.20	75 & 125
1.0	D	1.54	75 & 125
1.0	D	1.71	75 & 125

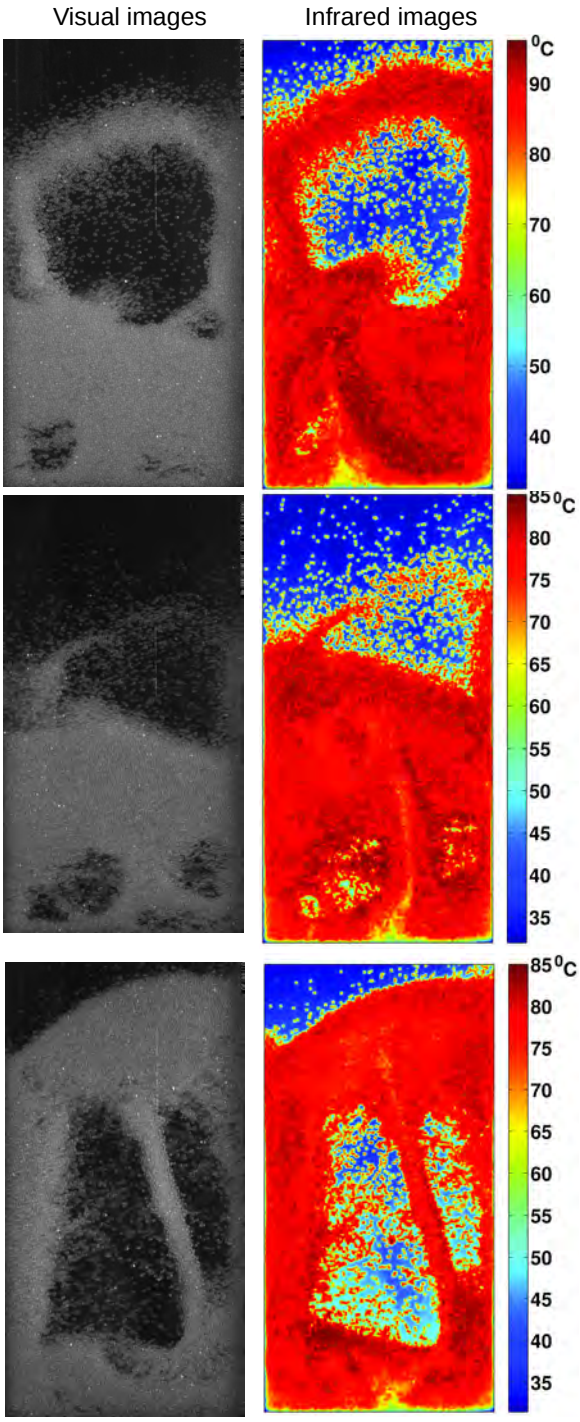

Figure 2: Paired infrared and visual images recorded by the trigger mechanism

Imaging Method

The fluidization is recorded by a high speed visual camera (La Vision ImagePro, 560×1280 resolution) and an infrared camera (FLIR SC7600, 250×512 resolution). The IR camera is sensitive in the 1.5 - 5.1 μm spectral range. The cameras are placed on a tripod in front of the fluidized bed. To minimize the difference in views the cameras are placed as close as possible. The set up is illuminated using a pair of white LED lamps. White LED have blue and yellow peaks in the spectrum, but have very low intensity in the infrared band. Therefore the lights do not interfere with the IR thermography. The lamps are placed at an angle of 45° with respect to the normal of the fluidized bed. This reduces effects like reflection and shining on the fluidized bed. See Fig. 1 for details.

The visual camera has an exact front view of the sapphire window, but the IR camera is placed at a small angle. The visual and infrared cameras are connected to the computer system via a trigger box system. During the high signal the cameras are in capture mode. The trigger box sends simultaneous (or with a small preset delay) pulses to both the visual camera and the IR camera, which ensures that the two cameras record images at the same instant in time. In this way we can map the thermographic data (heat transfer) on the hydrodynamic data and perform a completely coupled study of heat transfer and concurrent gas-solid flow. Examples of the paired frames captured is shown in Fig. 2.

The images are recorded at 10 Hz frequency, so the time for one cycle is 100 ms. In one cycle the signal sent to the infrared camera is high during 600 μs and low for the remaining 99.4 ms. Simultaneously with the high signal sent to the IR camera also a high signal of 700 μs is sent to the visual camera. Because we want to perform PIV measurements we need to record two close consecutive images with the visual camera. Therefore, the first high signal is followed by a 200 μs low signal and then a second 700 μs high pulse. This second pulse causes the second PIV frame to be captured. After this second pulse, the signal sent to the visual camera is low for the remaining 98.4 ms.

For this calibration a glass particle was fitted at the tip of a thermocouple probe. This particle was placed inside a fixed bed of particles in the fluidized bed near to the sapphire glass such that it is visible to the infrared camera. The thermographic radiation recorded by camera from this exact position was calibrated against the temperature reading shown by the thermocouple. The output of this calibration procedure is shown in Fig. 3. The digital level (DL) signal from the FLIR camera is a 14-bit number (so the maximum is 16383). It is important for the accuracy of the measurements to use most of the available range, but avoid saturation at high temperatures. By using an integration time of 600 μs the range of 30 - 100 °C is well represented. The shown solid curve is a third order polynomial fit with a least square error of 0.46 °C. This calibration curve is used in all subsequent data processing to convert DL to temperatures.

DIA/PIV/IR coupling

The background of PIV and DIA is fairly standard and will not be discussed here (de Jong *et al.*, 2012; van Buijtenen *et al.*, 2011). The visual image has a size of 560×1280 pixels. The PIV performed here uses a multi-pass algorithm using an interrogation window of 32×32 with 50 % overlap for computing the cross correlations. This is performed using the Davis software. This results in a post processed velocity

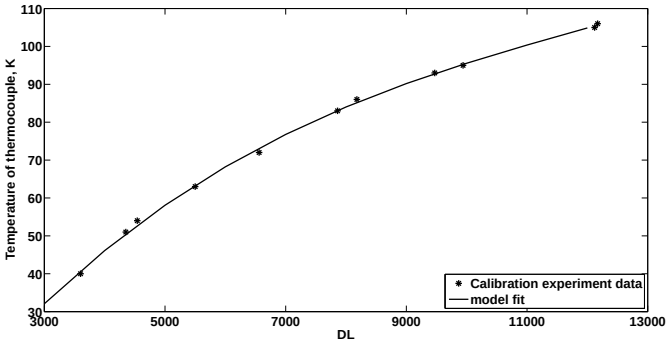

Figure 3: Calibration curve of IR camera. The digital level (DL) is plotted against the temperature of the thermocouple. The fitted curve is used to translate DL into temperature in all presented results.

field on a 80×35 grid for the pseudo 2D bed. vides the 3D particle fraction from the 2D visu process of this translation was adopted from (2012). Fig. 4a shows a typical 3D particle f bution obtained from DIA processing the firs shown in fig. 2. Coupling the PIV results w mass flux field which has been shown in fig. 4

The processing of the IR images involves filt ground and then particle temperature pixel av interrogation area. This processing will not b detail here. Instead we directly show the fi temperature distribution data (interrogation are 4b. This image was obtained by processing image in fig. 2. With the IR integration we stantaneous particulate heat flux shown in fig. complete integration established we can move cuss the various forms of data analysis and re obtained with the technique.

Data Analysis

The IR image gives the temperature distribut main. While calculating the mean temperatu this temperature field should be weighted with the solids volume fraction to obtain the correct mean temperature of particles in the system. So the solids-volume-fraction weighted average is computed as

$$\langle T_p \rangle_\varepsilon = \frac{\sum_{i,j} \varepsilon_p(i,j)\, T_p(i,j)}{\sum_{i,j} \varepsilon_p(i,j)} \qquad (1)$$

Here i and j represent the given interrogation area of the processed DIA and IR images. The infrared image observations that were made during a sample run are shown in fig 5. Fig 5 also shows a set of temperature distribution plots for various stages of the cooling process. These distributions have a well defined single peak. It can be observed that the distribution spread becomes narrower as the cooling proceeds. This is expected because at higher particle temperatures the difference between particles and inlet gas is larger which causes the temperature differences between mixing particles to be also larger.

The mean of the particle Image temperature distribution was calculated using equation 1 and its standard deviation was calculated using eq. 2.

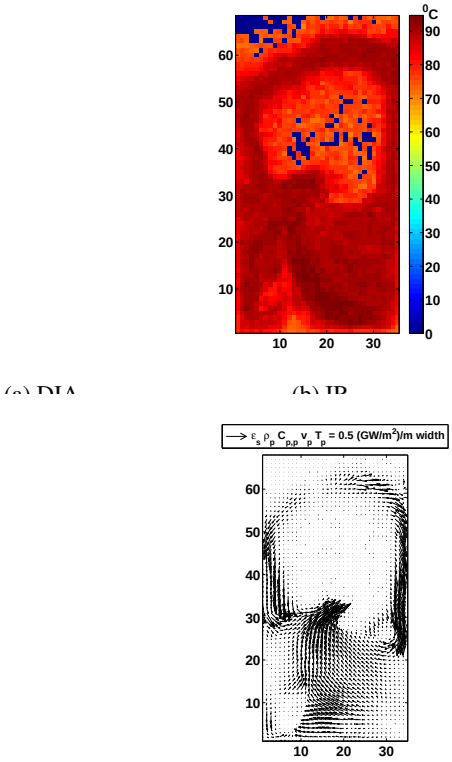

Figure 4: Instantaneous DIA, PIV and IR processed results giving the particle fraction field, temperature field, mass flux field and heat flux field. This data is for an instantaneous image from a fluidized bed run of particle size 1 mm, background gas velocity 1.2 m/s and bed mass 125 g.

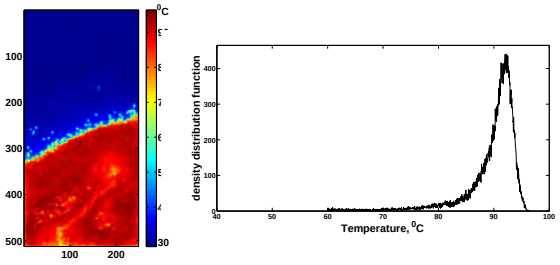

(a) t = 0s

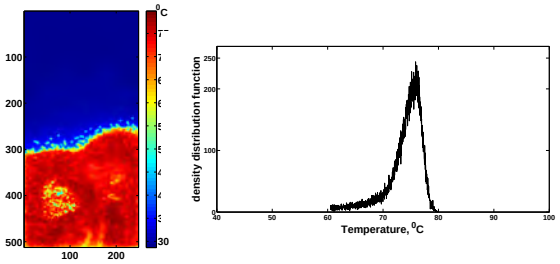

(b) t = 5s

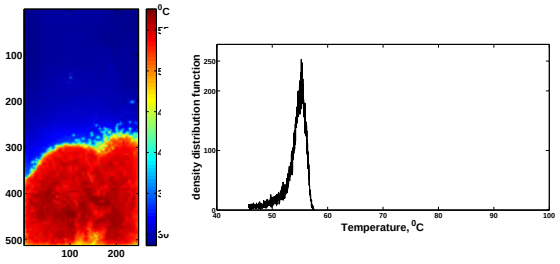

(c) t = 14.3s

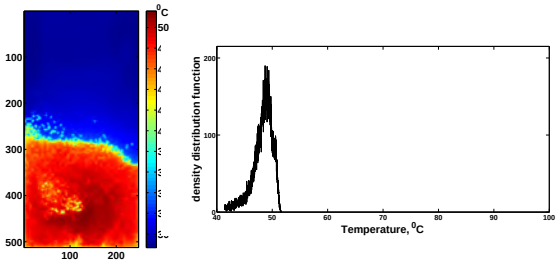

(d) t = 16.5s

Figure 5: Raw IR images and their corresponding temperature distribution of a cooling bed with particle size 1 mm, background gas velocity 1.2 m/s and bed mass 75 g.

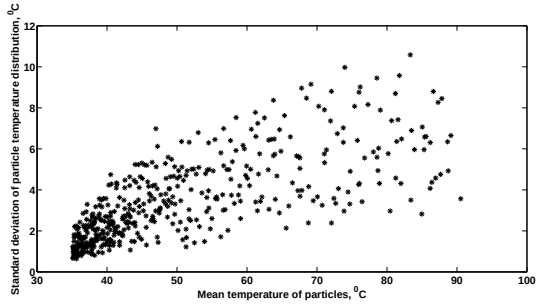

(a) Spatial standard deviation of the particle temperature.

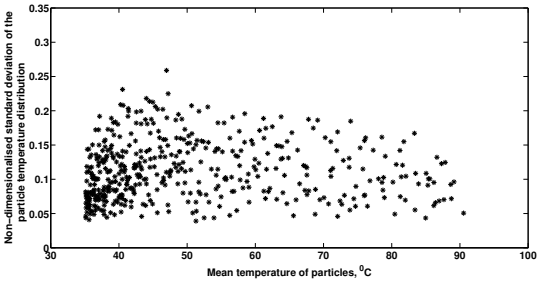

(b) Non-dimensionalised standard deviation for the same data points as shown in (a).

Figure 6: The standard deviation of the instantaneous temperature as function of the instantaneous volume averaged particle temperature. The bed parameters are: bed mass 75 g, particle size 1 mm and background gas velocity 1.2 m/s.

$$\sigma_p^2 = \left\langle \left(T_p - \langle T_p \rangle_\varepsilon\right)^2 \right\rangle_\varepsilon = \frac{\sum_{i,j} \varepsilon_p(i,j)\,(T_p(i,j) - \langle T_p \rangle_\varepsilon)^2}{\sum_{i,j} \varepsilon_p(i,j)} \tag{2}$$

To obtain an impression of the relation between the bed temperature and the width of the temperature distribution σ_p was plotted against the mean particle temperature in Fig. 6a in an absolute and a relative way. These plots clearly demonstrate the decreasing standard deviation as the bed cools down.

In the relative plot the standard deviation is normalized by the thermal 'driving force' for the cooling process: $\langle T_p \rangle_\varepsilon - T_{g,\text{in}}$. Fig. 6b shows that this normalized standard deviation is more or less constant. However, we also observe a quite large variation in the standard deviation of the temperature distribution. This is due to the fact that in bubbling fluidization there are inherently large fluctuations in time even on the scale of the entire bed.

Since the bed is cooling down it does not make much sense to time-average the temperature. The analysis of the standard deviation in the previous section suggests that the thermal driving, $\langle T_p \rangle - T_{g,\text{in}}$, is a good quantifier for the internal temperature differences. It therefore makes sense to look at temperature differences that are made dimensionless using this thermal driving force. This leads to the definition of a time-averaged dimensionless temperature difference,

$$\overline{\Gamma_p(i,j)} = \frac{1}{\sum_t \varepsilon_p(t,i,j)} \sum_t \varepsilon_p(t,i,j)\, \frac{T_p(t,i,j) - \langle T_p(t) \rangle_\varepsilon}{\langle T_p(t) \rangle_\varepsilon - T_{g,\text{in}}(t)} \tag{3}$$

This quantity is analyzed for runs of varying particle sizes, background velocity and bed mass in the next section.

This Eq. is used for runs with varying background velocity which will be discussed in the section (Time-averaged data results). The time averaged data of mass fraction and mass

flux is calculated using the same equations reported in literature (de Jong *et al.*, 2012; van Buijtenen *et al.*, 2011).

DEM MODEL DESCRIPTION

The modeling of hydrodynamics and heat transfer using DEM is quite well known. The details of the model implementation can be found in literature (Patil *et al.*, 2014). The hydrodynamics and energy modeling of gas-solid flow is done by treating the gas phase as a continuum (Eulerian) and particulate phase as discrete (Lagrangian). Through two-way-coupling the continuum and particulate phase exchange momentum and heat with each other. The momentum exchange between particles is modeled through the soft sphere model first proposed by (Cundall and Strack, 1979).
Besides gas-particle heat exchange also other forms of heat exchange have also been introduced in the DEM in order to be able to match the experimental results better. The extra mechanisms are particle-particle direct contact conduction, particle-wall direct contact conduction and gas-wall heat transfer coefficients. These individual transfer mechanisms and their implementation in DEM discussed here. Fig 7 shows a schematic view diagram of how these mechanisms contribute to the loss of heat from the fluidized bed to the surroundings.

Particle-Particle and Particle-Wall Direct Conduction Heat Transfer

This form of heat transfer takes place through the contact area when the two particles or a particle and a wall come in direct contact. Since these contacts last for a very short time ($10^{-6}s$) the amount of heat transferred during a single collision is very small. However thousands of such collisions take place for each of the individual particles during particulate flow. Thus over longer time scales the amount of heat transferred becomes significant.
An implementation for accounting for this type of heat transfer is introduced which is slightly different from some of the previous works (Zhou *et al.*, 2009, 2010; Hou *et al.*, 2012). The DEM implementation of (Zhou *et al.*, 2009) uses the Hertzian model for collision dynamics whereas in our case (Cundall and Strack, 1979) model is used.
In the soft sphere model of DEM the simulation spring stiffness is much less than real spring stiffness of real particles, so that longer DEM time steps can be taken for simulations, keeping the overlap in check. The overlap is kept under 0.1% of particle diameter for a particle relative velocity equal to twice the fluidization velocity. Due to the reduced spring stiffness the contact area calculated in simulation is higher than the contact area caused by real collision leading to an exaggerated heat transfer between particles. Thus in the proposal made by (Zhou *et al.*, 2009, 2010; Hou *et al.*, 2012) a correction factor was used to get the corrected contact area and hence a corrected heat transfer calculation for each of the DEM time steps. This correction is based on the theoretical calculation of contact area proposed by (Sun and Chen, 1988; Zhang and Whiten, 1998).
In our modeling methodology for particle mechanics we use a simpler method. Instead of a correction we calculate the correct total heat transfer energy during one collision and directly transfer it as a packet of energy at the beginning of the collision. This calculation is based on (Sun and Chen, 1988) model where the integral of energy transferred during collision has been theoretically derived and presented. This integral is calculated from the contacting particle properties, relative velocity, etc as primary parameters. These primary

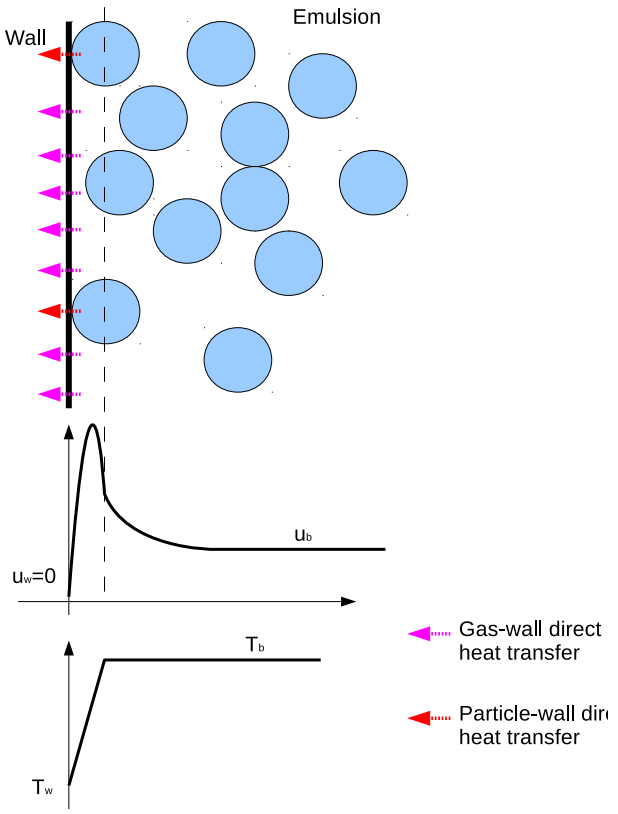

Figure 7: A schematic view diagram showing the mechanisms by which the fluidized bed looses heat to the surrounding walls.

parameters also give the generated maximum contact area, and contact time which are also accounted for in the energy integral given below in

$$q_c = \frac{0.87(T_{p1} - T_{p2})A_c t_c^{1/2}}{(\rho_{p1}C_{pp1}k_{p1})^{(-1/2)} + (\rho_{p2}C_{pp2}k_{p2})^{(-1/2)}} \quad (4)$$

Where, A_c the maximum contact area is given by;

$$A_c = \pi r_c^2 = \pi(\frac{5mR^2}{4E})^{\frac{2}{5}} v^{4/5} \quad (5)$$

The total contact duration is given by;

$$t_c = 2.94(\frac{5m}{4E})^{\frac{2}{5}}(Rv_{p,rel})^{-1/5} \quad (6)$$

For 2 particles undergoing collision the parameters in above equation are given by R $= \frac{R_1R_2}{R_1+R_2}$ and m $= \frac{m_1m_2}{m_1+m_2}$
E is Young's (elastic) modulus for the colliding particles which is a function of Young's modulus of particle 1 and 2 (E_1 and E_2) and Poisson's ratio (ν_1 and ν_2) given by;

$$E = \frac{\frac{4}{3}}{\frac{1-\nu_1^2}{E_1} + \frac{1-\nu_1^2}{E_1}} \quad (7)$$

A similar expression to Eq. 4 has been developed for a particle wall collision theoretical heat transfer. This equation is given by,

$$q_c = \frac{5.36(m/E)^{3/5}(Rv)^{7/10}(T_{p1} - T_w)}{(\rho_{p1}C_{pp1}k_{p1})^{(-1/2)} + (\rho_{p2}C_{pp2}k_{p2})^{(-1/2)}} \quad (8)$$

Table 2: Material properties in the simulations

Properties ()	Glass	Aluminum	Sapphire glass
Poisson ratio $(-)$	0.22	0.34	0.25
Young's modulus (GPa)	60	69	35
Thermal conductivity (W/mK)	1.4	30	30
Heat capacity $(J/(KgK))$	840	2700	3980

Here the temperature of the wall T_w is the bulk wall temperature which is 20 ^0C available from the experiments. Relevant wall properties are tabulated in table 2.

Gas-wall heat transfer coefficient

The wall heat loss estimation is accounted for in the DEM via a boundary condition imposed on the gas phase thermal energy equation. The external temperature or the temperature deep in the boundary wall is assumed to be the environment temperature that is $T_{ext} = 20^0$C. The boundary cells are shown in Fig 8 where temperature being a scalar quantity is defined cell centered in a staggered grid system. The heat loss through the wall is given by;

$$-k_g^{\text{eff}}\frac{(dT_g)}{dx} = h_w(T_{ext} - T_{x\to 0}) \tag{9}$$

Discretization and rearrangement leads to Eq. 10. The relevant temperatures are in fig. 8. In eq. 10 h_w represents the pure gas-wall heat transfer coefficient. It should be noted that this heat transfer coefficient does not accommodate direct particle-wall contact heat transfer.

$$T_0 = \frac{2k_f^{\text{eff}} - h_w dx}{2k_f^{\text{eff}} + h_w dx}T_1 + \frac{2h_w dx T_{ext}}{2k_f^{\text{eff}} + h_w dx} \tag{10}$$

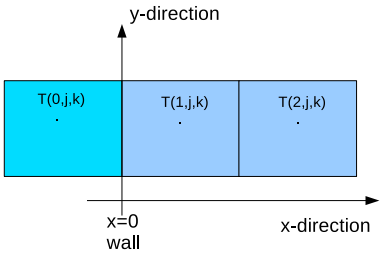

Figure 8: Eulerian grid and relevant temperatures for the treatment of the boundary condition.

RESULTS

Time-averaged data results

The temperature distribution of particles in the fluidized bed depends on the solidity density distribution and the flow pattern that exists in the beds. Figs. 9 shows time-averaged fields of the solids-volume fractions, mass flux and dimensionless temperature. Fig. 9 is for a bed mass of 75 g with particle size of 1 mm, which corresponds to a bed aspect ratio of 0.5

The DIA analysis provides the time-averaged particle density distribution of the bed. These data are given in Figs. 9a - c for background gas velocities 1.2 m/s, 1.54 m/s and 1.71 m/s respectively.

The DIA/PIV coupling provides solids mass fluxes that are plotted in Figs. 9d - f for the same three gas velocities. The influence of the background gas velocity is noticeable in the circulation pattern of the particulate phase. The increase in the background gas velocity causes a more pronounced circulation and back mixing of particles in the bed. This can be observed more closely in the Fig. 10 that shows the cross-sectional profile of the solids mass flux given for these three background gas velocities at a height of 2.3 mm above the bottom plate.

Typical instantaneous IR images were shown earlier in Fig. 2. Here one sees a small jet of cold particles issuing into the bed from the bottom-centre of the bed. This is a typical narrow cold zone created along the axial direction from the bottom that tends to diminish as it propagates into the bed. This narrow cold zone ("jet") of particles is created due to the circulation pattern of the particles which moves from the sides of the bed to centre from the bottom. During this process the particles come into contact with fresh cold gas and exchange more heat before movement from the centre. During fluidization runs, the jet oscillates in the bed with a relatively stable base.

It was observed that at the lower background gas velocity of 1.2 m/s the narrow cold zone is more stable compared to higher background gas velocity. Thus when a time-average of the dimensionless temperature distribution is computed, using Eq. (3), we obtain a distribution as shown in Fig. 9g. In this figure at the centre bottom the narrow cold zone leaves its mark. This causes relatively hotter zones to appear on the sides of the bed.

At higher background gas velocities the narrow cold zone tends to oscillate more as well as move around the bottom of the bed. Thus when a time-average is performed the resulting field is more uniform. This can be observed for background gas velocities 1.54 and 1.71 m/s in Fig. 9h and Fig. 9i, respectively. Also the hotter zones forming at the sides of the pseudo 2D bed tend to diminish at higher background gas velocity.

Position averaged data results

The post-processing of images was performed for all the experiments that are listed in table. 1. The mean particle temperature was calculated as function of time and plotted together for comparison. Fig. 11a shows a plot of the mean particle temperature variation with respect to time for the bed mass of 75 g and particle sizes 1 mm and 0.5 mm. There are two important observations that can be made from this plot. For constant particle size of 1 mm and 0.5 mm as the background gas velocity is increased the cooling rate of the bed increases. Furthermore, as the particle size decreases the cooling rate of the bed increases. The background gas velocities for 1 mm particle are 1.2 m/s, 1.54 m/s and 1.71 m/s which are 2.06, 2.66 and 2.95 times minimum fluidization velocity ($u_{\mathbf{mf}} = 0.58$ m/s). Similarly the background gas velocity for 0.5 mm particles is 0.51 m/s and 0.86 m/s which are 2.83 and 4.78 times minimum fluidization velocity ($u_{\text{mf}} = 0.18$ m/s).

All curves in Fig. 11a are for the same bed mass of 75 g. In Fig. 11b we present a comparison between the cooling rate for two bed masses, namely, 75 g and 125 g with otherwise the same 1 mm particle size and two background velocities. The higher bed mass gives a slower rate of cooling of the bed as expected.

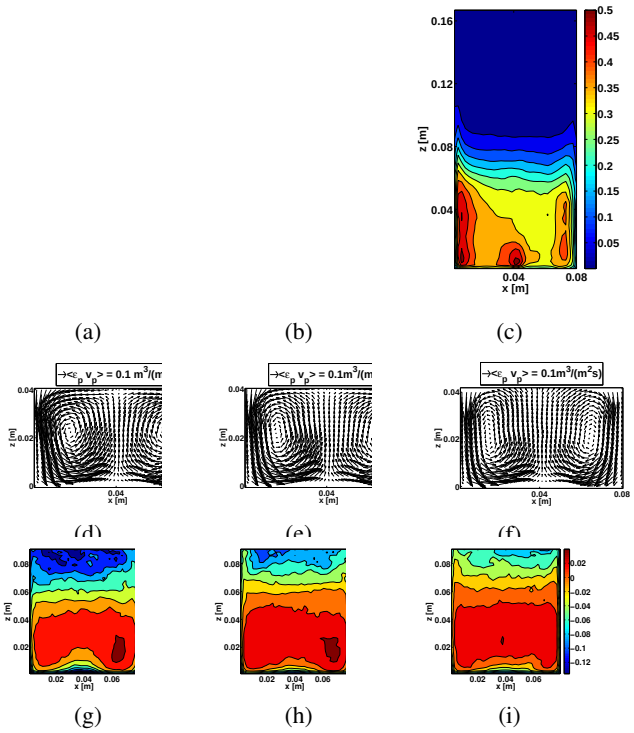

Figure 9: Time-averaged fields for particle size $d_p = 1$ mm and bed mass 75 g. The three columns present data for different background gas velocities, namely, $u_{bg} = 1.2$ m/s, 1.54 m/s and 1.74 m/s. The first row of plots, a-c, shows the solids volume fraction in the bed obtained from DIA. The second row shows solids mass flux fields obtained by DIA/PIV coupling. The third row shows the time-averaged dimensionless particle temperature, Eq.(3), obtained by DIA/IR coupling.

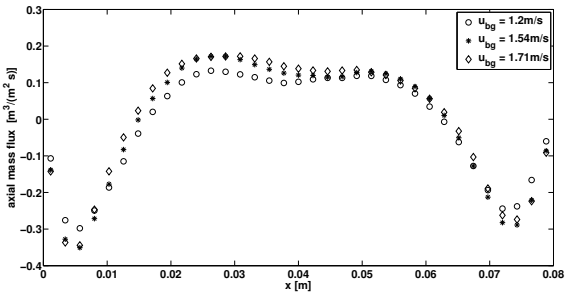

Figure 10: The axial component of the mass flux at height 2.3 mm above the bottom of the fluidized bed with 1 mm particles.

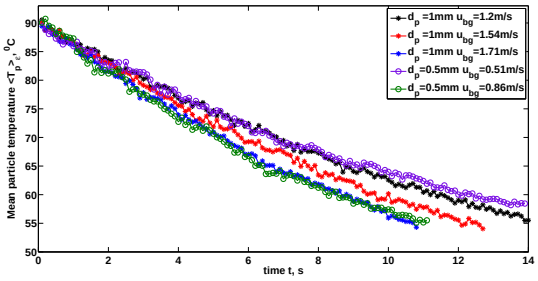

(a) Mean temperature of particles plot against time in a cooling bed for different background gas velocity and particle sizes at a bed mass of 75 g.

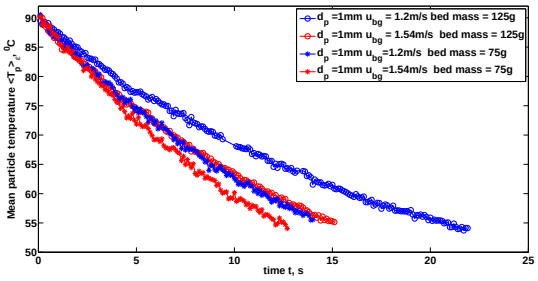

(b) Mean temperature of particles plotted against time for a particle size of 1 mm and two bed masses: 75 g and 125 g, respectively.

Figure 11: Mean particle temperature against time for varying background gas velocity, particle size and bed mass

These plots accurately give the rate of heat loss of the particles. This heat loss is the sum of heat exchange between particles and gas due to multiphase flow, heat radiating from the particles to the surrounding and heat exchange between the gas phase and surrounding walls by means of heat conduction.

Comparison with DEM

Fluidized bed DEM simulations with the glass particle properties tabled in 1 and wall boundary properties tabled in 2 were used. Here only a sample simulation comparison is shown where the background gas velocity is 1.2 m/s and bed mass is 75g. In these simulations the gas-particle drag of Beetstra *et al.* (2007) and the gas-particle heat transfer coefficient from Gunn (1978)'s empirical correlation are used. According to Kunii and Levenspiel (1991) the wall heat transfer coefficient h_w discussed earlier in section (DEM Model De-

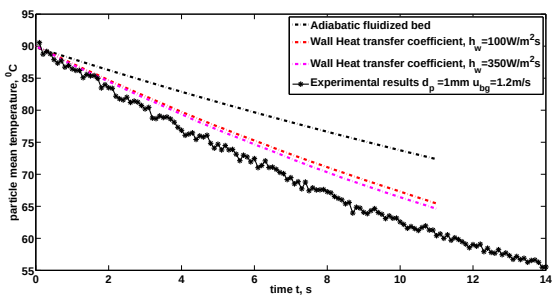

Figure 12: Experimental and DEM simulation results for mean temperature of particles plotted against time for a particle size 1 mm and bed mass 75g. DEM simulations are shown for adiabatic walls, wall heat transfer coefficients.

scription) is in the range of 25-350W/m^2K. Since their accurate correlations are not readily available we used different values in these ranges for DEM simulations. In fig 12 results with heat transfer coefficient h_w values of 0 W/m^2K (adiabatic wall), 100 W/m^2K and 350 W/m^2K are given. This comparison clearly shows that the cooling rate is lower compared to experiments. This indicates that some other factors causing wall heat loss have not been considered in the model which is currently under study.

CONCLUSION

A measuring technique involving the use of visual and infrared images has been developed. The visual and IR recordings were successfully synchronized and coupled with image mapping. With these plots the varying exchange rate between particles and gas can be recorded. Time averaged temperature distribution field of the fluidized bed were calculated and presented for various configurations.

With this work measurements of four important synchronized parameters of multiphase flow in non-isothermal pseudo 2D fluidized beds are made available, namely, solids volume fractions, temperature fields and mass- and heat-flux fields. This has produced detailed data sets that can be used to analyze the heat transfer mechanisms inside a fluidized bed in more detail, e.g., by comparison with CFD computations.

Complex mechanisms of heat transfer from a fluidized bed to wall were introduced in the heat transfer DEM model. A sample comparison between experimental and simulation was made by using the gas-wall heat transfer coefficient h_w as fitting parameter with the reasonable range provided in literature. It was observed that with the current implemented mechanisms of heat transfer the DEM simulations under predict the cooling rate of the fluidized bed with respect to experiments.

ACKNOWLEDGMENTS

The authors would like to thank the European Research Council for its financial support, under its Advanced Investigator Grant scheme, contract number 247298 (Multiscale Flows). The authors would also like to acknowledge the Dutch polymer institute (DPI) which had supported the building of the set up. The technicians Lee McAlpine and Paul Aendenroomer (TNO) are specially thanked for constructing and maintaining the set up. The author would also like to thank T.Y.N. Dang and Y.M. Lau for helping out with image processing. Acknowledgment also goes to Mariet Slagter, Stijn Smits, Tom Kolkman and Rohit Rewagad for providing help and suggestions at various levels during the development of the set up and measurement method.

REFERENCES

ASTARITA, T. and CARLOMAGNO, G. (2012). *Infrared Thermography for Thermo-Fluid-Dynamics*. Experimental fluid mechanics. Springer.

BEETSTRA, R. *et al.* (2007). "Drag force of intermediate reynolds number flow past mono- and bidisperse arrays of spheres". *AIChE Journal*, **53(2)**, 489–501.

BROWN, S.L. and LATTIMER, B.Y. (2013). "Transient gas-to-particle heat transfer measurements in a spouted bed". *Experimental Thermal and Fluid Science*, **44(0)**, 883 – 892.

CUNDALL, P. and STRACK, O. (1979). "A discrete numerical model for granular assemblies". *Geotechnique*, **29(1)**, 47–65.

DANG, T. *et al.* (2013). "Development of a novel infrared technique for instantaneous, whole-field, non invasive gas concentration measurements in gas-solid fluidized beds". *Chemical Engineering Journal*, **219(0)**, 545 – 557.

DE JONG, J. *et al.* (2012). "Development and validation of a novel digital image analysis method for fluidized bed particle image velocimetry". *Powder Technology*, **230(0)**, 193 – 202.

FINDLAY, P. *et al.* (2005). "Determination of fluidized bed granulation end point using near-infrared spectroscopy and phenomenological analysis". *J. Pharm. Sci.*, **94(28)**, 604–612.

GUNN, D. (1978). "Transfer of heat or mass to particles in fixed and fluidised beds". *Int. J. Heat and Mass Transfer*, **21**, 467–476.

HOU, Q.F. *et al.* (2012). "Computational study of heat transfer in a bubbling fluidized bed with a horizontal tube". *AIChE Journal*, **58(5)**, 1422–1434.

KAPLAN, H. (2007). *Practical Applications of Infrared Thermal Sensing and Imaging Equipment*. Tutorial Text Series. Society of Photo Optical.

KUNII, D. and LEVENSPIEL, O. (1991). *Fluidization engineering*. Butterworth-Heinemann series in chemical engineering. Butterworth-Heinemann Limited.

PATIL, A.V. *et al.* (2014). "Modeling bubble heat transfer in gas solid fluidized beds using dem". *Chemical Engineering Science*, **105(0)**, 121 – 131.

SUN, J. and CHEN, M. (1988). "A theoretical analysis of heat transfer due to particle impact". *Int. J. Heat Mass Transfer*, **31(5)**, 969–975.

TSUJI, T. *et al.* (2010). "Simultaneous measurement of particle motion and temperature in two-dimensional fluidized bed with heat transfer". *Kona Powder and Particle Journal*, **(28)**, 167–179.

VAN BUIJTENEN, M.S. *et al.* (2011). "An experimental study of the effect of collision properties on spout fluidized bed dynamics". *Powder Technology*, **206(1?2)**, 139 – 148.

VOLLMER, M. and MOLLMANN, K. (2011). *Infrared Thermal Imaging: Fundamentals, Research and Applications*. Wiley.

ZHANG, D. and WHITEN, W. (1998). "An efficient calculation method for particle motion in discrete element simulation". *Powder technology*, **98**, 223–230.

ZHOU, Z.Y. *et al.* (2009). "Particle scale study of heat transfer in packed and bubbling fluidized beds". *AIChE Journal*, **55(4)**, 868–884.

ZHOU, Z. *et al.* (2010). "A new computational method for studying heat transfer in fluid bed reactors". *Powder technology*, **197**, 102–110.

HYBRID EULERIAN-LAGRANGIAN MODELLING OF BI-DISPERSE FLUIDIZED BEDS

Simon SCHNEIDERBAUER[1], Stefan PUTTINGER[1], Stefan PIRKER[1*]

[1] Dep. Particulate Flow Modelling, Johannes Kepler Univ., 4040 Linz, AUSTRIA

Corresponding author's e-mail: stefan.pirker@jku.at

ABSTRACT

Most industrial applications of fluidized bed reactors include poly-disperse materials. Thus, it is important to understand the mixing and segregation of particles classes in the reactor to evaluate its efficiency. Since the total number of particles involved in most practically relevant fluidized beds is extremely large, it may be impractical to solve the equations of motion for each particle. It is, therefore, common to investigate particulate flows in large process units using averaged equations of motion, i.e. two-fluid models (TFM), which include the inter-particle collisions statistically by kinetic theory based closures of the particle stresses. However, in poly-disperse flows each particle class requires additional momentum and continuity equations, leading to high computational costs which might be prohibitive for pragmatic industrial simulations.

In this paper, we, therefore, present a hybrid model for the numerical assessment of poly-disperse gas-solid fluidized beds. The main idea of such a modelling strategy is to use a combination of a Lagrangian discrete phase model (DPM) and an Eulerian kinetic theory based TFM to take advantage of the benefits of those two different formulations. On the one hand, the local distribution of the different particle diameters, which is required for the gas-solid drag force, can be obtained by tracking statistically representative particle trajectories for each particle diameter class. On the other hand, the contribution from the inter-particle stresses, i.e. inter-particle collisions, can be deduced from the TFM solution. These then appear as additional body force in the force balance of the DPM. Note that in a first step we solely consider diameter averaged solids stresses since the drag force is at least on order of magnitude higher than the solids stresses in fluidized beds.

Finally, the numerical model is applied to a fluidized bed of a bi-disperse mixture of glass particles (0.5 mm and 2.5 mm particles) and with a cross-section of 0.15 m x 0.02 m. The results are then analysed with respect to experimental data of Puttinger et al (2014). This comparison demonstrates that the computed bed hydrodynamics (including bed expansion, segregation and channelling) is in fairly good agreement with the experiment. However, the results also suggest that sub-grid drag and sub-grid stress corrections (Schneiderbauer et al., 2013; Schneiderbauer et al., 2014) for poly-disperse fluidized beds are required to make the numerical investigation of industrial scale fluidized bed units accessible.

Keywords: CFD Fundamentals and Methodology, Fluidized Beds, Eulerian Two-Fluid Model, Lagrangian Particle Model, Poly-disperse Materials.

NOMENCLATURE

Greek Symbols

β	Drag coefficient, [kg m^{-3} s^{-1}].
ε	Volume fraction, [-].
ε_s^{max}	Maximum packing ratio, [-].
μ	Dynamic viscosity, [kg m^{-1} s^{-1}].
$\bar{\mu}_s$	Filtered solids shear viscosity , [kg m^{-1} s^{-1}].
ρ	Mass density, [kg m^{-3}].

Latin Symbols

a	Characteristic length, [m].
$\mathbf{D}$	Rate of deformation tensor, [s^{-1}].
d	Particle diameter, [m].
Fr	Particle Froude number, [-].
g	Gravitational constant, [m s^2].
H_D	Heterogeneity index, [-].
L	Characteristic length scale of sub-filter heterogeneous structures, [m].
l	Width of the fluidized bed, [m].
p	Pressure, [Pa].
$\bar{p}_s$	Filtered solids pressure, [N m^{-2}].
Re_s	Particle Reynolds number, [-].
$\mathbf{S}$	Deviatoric part of the rate of deformation tensor, [s^{-1}].
$\mathbf{T}_g$	Shear stress tensor of gas phase, [-].
$\mathbf{u}$	Velocity, [m/s].
u_{gs}	Gas-particle slip velocity, [m s^{-1}].
u_t	Terminal settling velocity, [m s^{-1}].
W_g	Vertical superficial gas velocity, [m s^{-1}].
Δ	Grid spacing, [m].
Δ_f	Filter length, [m].

Sub/superscripts

b	Bed.
G	Gas phase.
s	Solid phase.

INTRODUCTION

During the last decades the analysis of the hydrodynamics or the efficiency of fluidized beds through numerical simulations has become increasingly common. Since the total number of particles involved in most practically relevant fluidized beds is extremely large, it may be impractical to solve the equations of

motion for each particle. It is, therefore, common to investigate particulate flows in large process units using averaged equations of motion (Anderson and Jackson, 1967; Ishii, 1975). These two-fluid model (TFM) equations take account of the behavior of the particles by considering a huge ensemble of particles and, thus, closures are required for the solids stresses arising from particle-particle contacts.

However, the TFM approach requires considerably fine grids since the minimum stable sizes of clusters and shear bands are around ten particle diameters (Andrews, Loezos and Sundaresan, 2005). Thus, due to computational limitations a fully resolved simulation of industrial scale reactors is still unfeasible. It is, therefore, common to use coarse grids to reduce the demand on computational resources. However, such a procedure inevitably neglects small (unresolved) scales, which leads, for example, to a considerable overestimation of the bed expansion in the case of fine particles. Many sub-grid drag modifications have, therefore, been put forth by academic researchers to account for the effect of small unresolved scales on the resolved meso-scales in this case (Hong et al., 2012; Igci and Sundaresan, 2011; Milioli et al., 2013; Parmentier, Simonin and Delsart, 2012; Schneiderbauer and Pirker, 2014; Schneiderbauer, Puttinger and Pirker, 2013; Wang et al., 2010).

In this paper, we verify the filtered constitutive relations for the unresolved parts of the drag and the solids stresses presented in our previous study (Schneiderbauer and Pirker, 2014). The numerical results are analyzed on the one hand, with respect to fine grid simulations presented in (Schneiderbauer et al., 2013). This comparison includes the evaluation of the bed expansion, the time averaged filtered solids phase distribution and the bubble rise velocity. On the other hand, we compare the numerical results with experimental data of the time average solids volume fraction in case of an industrial scale turbulent bed. Furthermore, we present a hybrid modelling concept by adding poly-disperse tracer particles to a TFM with a heterogeneous diameter distribution. Finally, results of this hybrid TFM are compared to segregation results obtained by bi-disperse fluidized beds (Puttinger et al 2014).

FILTERED SUB-GRID CORRECTIONS

In the case of coarse grids it is common to use balance equations for the filtered counterparts of the local-average volume fraction ε_q of phase q and the local-average velocity $\mathbf{u}_q$ of phase q. These equations can be obtained by applying a spatial filter (Schneiderbauer et al., 2013) to the microscopic TFM equations (Schneiderbauer, Aigner and Pirker, 2012)

$$\frac{\partial}{\partial t}\overline{\varepsilon}_q\rho_q + \nabla\cdot(\overline{\varepsilon}_q\rho_q\,\tilde{\mathbf{u}}_q) = 0, \tag{1}$$

$$\begin{aligned}&\frac{\partial}{\partial t}(\overline{\varepsilon}_g\rho_g\,\tilde{\mathbf{u}}_g) + \nabla\cdot(\overline{\varepsilon}_g\rho_g\,\tilde{\mathbf{u}}_g\,\tilde{\mathbf{u}}_g) = \\ &\quad -\overline{\varepsilon}_g\nabla\overline{p} + \nabla\cdot\varepsilon_g\overline{\mathbf{T}}_g - \beta^{eff}(\tilde{\mathbf{u}}_g - \tilde{\mathbf{u}}_s) + \overline{\varepsilon}_g\rho_g\mathbf{g},\end{aligned} \tag{2}$$

$$\begin{aligned}&\frac{\partial}{\partial t}(\overline{\varepsilon}_s\rho_s\,\tilde{\mathbf{u}}_s) + \nabla\cdot(\overline{\varepsilon}_s\rho_s\,\tilde{\mathbf{u}}_s\,\tilde{\mathbf{u}}_s) = \\ &\quad -\overline{\varepsilon}_s\nabla\overline{p} - \nabla\cdot\overline{\Sigma}_s + \beta^{eff}(\tilde{\mathbf{u}}_g - \tilde{\mathbf{u}}_s) + \overline{\varepsilon}_s\rho_s\mathbf{g}.\end{aligned} \tag{3}$$

Here we distinguish between filtered $\overline{\varepsilon}_s$ and Favre averaged variables $\tilde{\mathbf{u}}_s$. The gas shear stress tensor is given by $\overline{\mathbf{T}}_g = 2\mu_g\overline{\mathbf{S}}_g$ with $\overline{\mathbf{S}}_q = \overline{\mathbf{D}}_q - \frac{1}{3}\mathbf{tr}(\overline{\mathbf{D}}_q)$ and $\overline{\mathbf{D}}_q = \frac{1}{2}\left(\nabla\tilde{\mathbf{u}}_q + (\nabla\tilde{\mathbf{u}}_q)^t\right)$. Note a complete explanation of the notation is given at the beginning of the paper.

In the literature it is common to model the effective drag, which includes the formation of sub-grid heterogeneities, as follows (Milioli et al., 2013; Schneiderbauer and Pirker, 2014)

$$\begin{aligned}\beta^{eff} &= \left(1 - h_\varepsilon(\overline{\varepsilon}_s)h_\Delta(\hat{\Delta}_f)\right)H_u(\overline{\varepsilon}_s,\hat{\Delta}_f,\tilde{u}_{gs})\tilde{\beta} \\ &\equiv H_D\tilde{\beta},\end{aligned} \tag{4}$$

where H_D is usually referred to as heterogeneity index (Hong et al., 2012) and $\tilde{\beta}$ denotes the microscopic drag of Wen and Yu (Wen and Yu, 1966) evaluated using filtered variables:

$$\begin{aligned}&\tilde{\beta} = \frac{3}{4}\tilde{C}_d\frac{\overline{\varepsilon}_g\overline{\varepsilon}_s\rho_g\left\|\tilde{\mathbf{u}}_g - \tilde{\mathbf{u}}_s\right\|}{d_s}\overline{\varepsilon}_g^{-2.65}, \\ &\tilde{C}_d = \begin{cases}\frac{24}{\mathrm{Re}_s}\left(1 + 0.15\mathrm{Re}_s^{0.687}\right) & \mathrm{Re}_s < 10^3 \\ 0.44 & \mathrm{Re}_s \geq 10^3\end{cases}, \\ &\mathrm{Re}_s = \frac{\overline{\varepsilon}_g\rho_g\left\|\tilde{\mathbf{u}}_g - \tilde{\mathbf{u}}_s\right\|d_s}{\mu_g}.\end{aligned} \tag{5}$$

In our previous study (Schneiderbauer and Pirker, 2014) we derived constitutive relations for the functions $h_\varepsilon(\overline{\varepsilon}_s)$, $h_\Delta(\hat{\Delta}_f)$ and $H_u(\overline{\varepsilon}_s,\hat{\Delta}_f,\tilde{u}_{gs})$ from a highly resolved simulation of a bubbling fluidized bed. These relations read

$$\begin{aligned}h_\varepsilon(x = \overline{\varepsilon}_s/\overline{\varepsilon}_s^{\max}) &= \frac{-6.743x^2 + 6.728x}{x^3 - 7.247x^2 + 6.289x + 0.384} \\ h_\Delta(\hat{\Delta}_f) &= \frac{\hat{\Delta}_f^{2.664}}{\hat{\Delta}_f^{2.664} + 25.89} \\ H_u(\overline{\varepsilon}_s,\hat{\Delta}_f,\tilde{u}_{gs}) &= \left(\frac{\tilde{u}_{gs}}{u_t}\right)^{-9\overline{\varepsilon}_s(\overline{\varepsilon}_s^{\max}-\overline{\varepsilon}_s)\hat{\Delta}_f^5/(\hat{\Delta}_f^5+1024)}\end{aligned} \tag{6}$$

where $\tilde{u}_{gs} = \left\|\tilde{\mathbf{u}}_g - \tilde{\mathbf{u}}_s\right\|$. Furthermore, $\hat{\Delta}_f = \Delta_f/L$ denotes the dimensionless filter size and L is a characteristic length scale $L = u_t^2/g\ \mathrm{Fr}^{-2/3}$. Here, Fr is the particle based Froude number, which can be calculated from $\mathrm{Fr} = u_t^2/d_s g$.

In Figure 1 the heterogeneity index H_D is plotted as a function of the filtered gas volume fraction. It is observed that on the one hand, the effective drag shows

a considerable dependence on $\overline{\varepsilon}_g$ and approaches the microscopic drag relation for very dilute and very dense conditions, i.e. no heterogeneous sub-grid structures form in these situations. On the other hand, the effective drag decreases with increasing filtered slip velocity $\tilde{u}_{gs}$ and increasing filter length $\hat{\Delta}_f$. Note that our previous study (Schneiderbauer and Pirker, 2014) clearly shows that the heterogeneity index reveals an asymptotic behavior for large filter length and large slip velocities, which is in agreement with other filtered constitutive relations for the drag coefficient (Milioli et al., 2013; Parmentier et al., 2012).

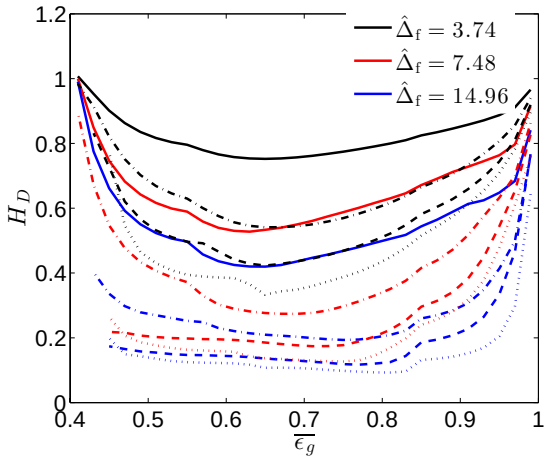

Figure 1: Variation of H_D with the filtered void fraction for different filter sizes Δ_f and slip velocities u_{gs}: — u_{gs} = 0.25 m s^{-1}; - · - u_{gs} = 0.75 m s^{-1}; - - - u_{gs} = 1.25 m s^{-1}; · · · u_{gs} = 1.75 m s^{-1} (redrawn from our previous study Schneiderbauer and Pirker, 2014).

Compared to the magnitude of drag force the magnitude of the particle stresses is much smaller. However, neglecting their unresolved contribution produces quantitative changes in the predicted results (Igci and Sundaresan, 2011). Especially, in this case the rise velocity of bubbles is considerably overestimated (Schneiderbauer et al., 2013). In our previous study (Schneiderbauer and Pirker, 2014) it has been shown that the filtered solids stress tensor can be written as

$$\overline{\Sigma}_s = \overline{p}_s \mathbf{I} - 2\overline{\mu}_s \overline{\mathbf{S}}_s \tag{7}$$

where the filtered normal stresses are given by

$$\frac{\overline{p}_s}{\rho_s u_t^2} = 4 C_p \mathrm{Fr}^{-31/21} \hat{\Delta}_f^{16/7} \left\| \overline{\mathbf{S}}_s u_t / g \right\|^2$$
$$C_p = 0.17\overline{\varepsilon}_s + \frac{0.0235\overline{\varepsilon}_s}{\varepsilon_s^{\max}(\varepsilon_s^{\max} - \overline{\varepsilon}_s)^{3/4}} \tag{8}$$

The filtered shear viscosity reads

$$\frac{\overline{\mu}_s g}{\rho_s u_t^3} = 4 C_\mu \mathrm{Fr}^{-4/3} \hat{\Delta}_f^2 \left\| \overline{\mathbf{S}}_s u_t / g \right\|$$
$$C_\mu = 0.105\overline{\varepsilon}_s + \frac{0.001\overline{\varepsilon}_s}{\varepsilon_s^{\max}(\varepsilon_s^{\max} - \overline{\varepsilon}_s)} \tag{9}$$

Note that the last terms in equations (8) and (9) account for the frictional stresses close to the maximum packing conditions. Plots of equations (8) and (9) as a function of the filtered gas volume fraction can be found in our previous study (Schneiderbauer and Pirker, 2014).

VERIFICATION OF FILTERED SUB-GRID CORRECTIONS

To verify the presented filtered constitutive relations we computed the gas-solid in bubbling fluidized beds of Geldart B particles using a coarse grid and compare the results with highly resolved simulation presented in our previous study (Schneiderbauer et al., 2013). The material properties and simulation parameters are given in Table 1.

Table 1: Gas and solid properties and parameters used in simulations.

	(Schneiderbauer et al., 2013)	(Werther and Wein, 1994)
d_s (m)	$1.5 \cdot 10^{-4}$	$2.4 \cdot 10^{-4}$
ρ_s (kg m^{-3})	2500	2600
μ_g (Pa s)	$1.8 \cdot 10^{-5}$	$1.8 \cdot 10^{-5}$
u_t (m/s)	0.96	1.92
$\varepsilon_s^{\mathrm{mf}}$	0.55	0.55
h_{mf} (m)	0.5	0.62
Δ (d_s)	64	100
A (m × m)	0.15 × 0.04	0.5 × 0.5

We obtained a time-dependent solution using a grid spacing $\Delta = 64 d_s$ ($\Delta = 32 d_s$) for two different superficial gas velocities $W_g^{in} = 0.21 \mathrm{ms}^{-1}$ and $W_g^{in} = 0.63 \mathrm{ms}^{-1}$. In (Schneiderbauer et al., 2013) it has been shown that neglecting sub-grid inhomogeneities leads to a significant over-prediction of the bed expansion using a coarse grid. In fact, the bed expansion is overestimated by about 80% compared to the fully resolved reference simulation.

Figure 2 reveals that the axial profiles of the time averaged filtered solids volume fraction are in fairly good agreement with the highly resolved simulations for both superficial gas velocities. On the one hand, the coarse grid simulations using the presented filtered constitutive relations for gas-solid drag and solids stresses yield appropriate measures of the bed expansion. On the other hand, the presented sub-grid modifications predict the axial time-averaged profiles of the solids volume fraction appropriately, which is characterized by higher particle concentrations in the gas-inflow area and lower particle concentrations at lower hydrostatic pressure $z / h_0 > 0.5$.

Following the methodology of (Busciglio et al., 2008; Schneiderbauer et al., 2013) we additionally evaluate the bubble rise velocities. In our previous studies (Schneiderbauer and Pirker, 2014; Schneiderbauer et al., 2013) it was demonstrated that neglecting the unresolved part of the frictional stresses yields to a considerable overestimation of the bubble rise velocity (by about 50%). However, Figure 3 clearly shows that using the presented constitutive relations for the filtered solids stresses reveals the correct bubble rise velocities for both superficial gas velocities. Finally, it has to be emphasized that the presented sub-grid modifications appear to be insensitive to the grid resolution.

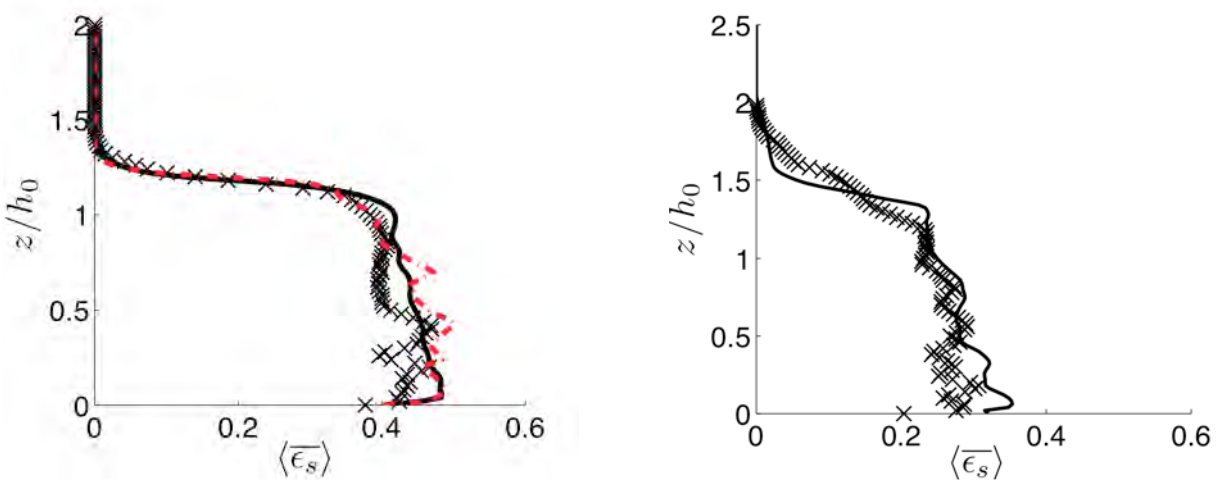

Figure 2: Axial profiles of the time averaged solids volume fraction (h_0 = 0.5 m).): —— filtered model using a grid spacing of $64d_s$; – · – filtered model using a grid spacing of $32d_s$; × highly resolved simulation (Schneiderbauer et al., 2013); a) W_g^{in} = 0.21 ms^{-1}; b) W_g^{in} = 0.63 ms^{-1}. The averaging time is 10s.

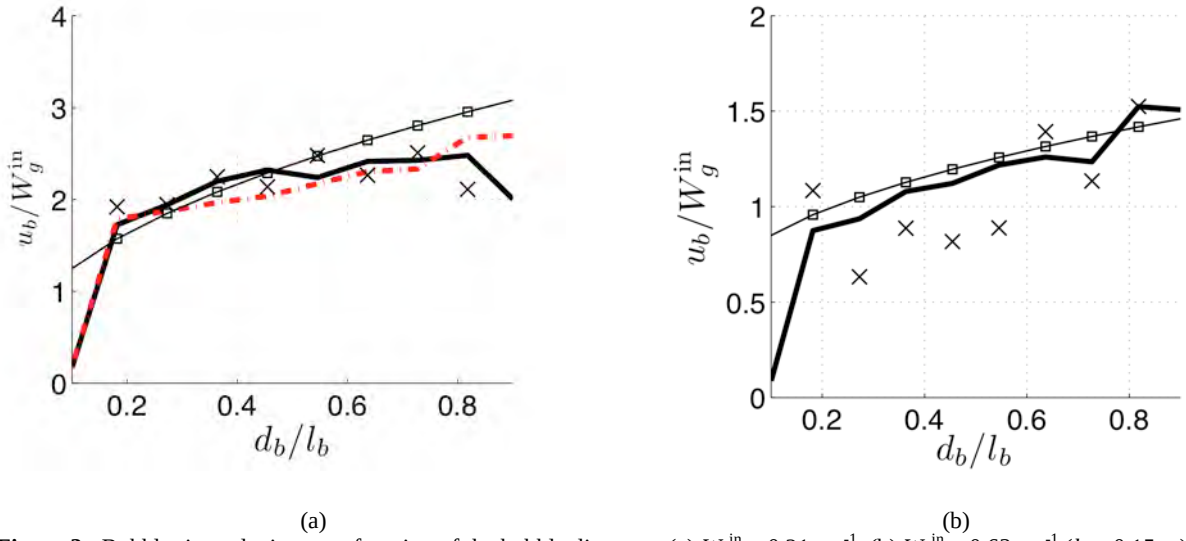

Figure 3: Bubble rise velocity u_b as function of the bubble diameter: (a) W_g^{in} = 0.21 ms^{-1}; (b) W_g^{in} = 0.63 ms^{-1} (l_b = 0.15 m); — filtered model ($64d_s$); – · – filtered model ($32d_s$); × highly resolved simulation (Schneiderbauer et al., 2013); - - Experimental correlation of Werther (1978). Further details on the experimental correlation are given in Schneiderbauer et al. (2013)

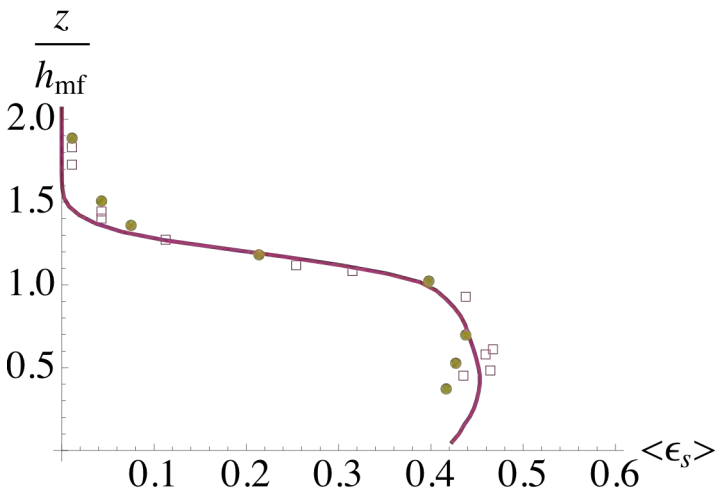

Figure 4: Axial profile of the time averaged filtered solids volume fraction: —— filtered model; Capacitance probe measurements, ● X-ray absorption measurements (Werther and Wein, 1994); The averaging time is 20 s.

VALIDATION OF FILTERED SUB-GRID CORRECTIONS

In this section, we show that coarse grid simulations using the presented sub-grid modifications can predict the bed expansion characteristics of industrial-scale turbulent fluidized beds reasonably well. Details of the gas and solid properties are summarized in Table 1. We use a grid spacing between of $100\,d_s$ in order to prove that our modifications also apply to coarser grids than used in the previous section.

In Figure 4 a comparison of the axial solid volume fraction distribution obtained from numerical simulations with those obtained from the experimental measurement of Werther and Wein (Werther and Wein, 1994) for $U_g / U_{\mathrm{mf}} = 3.8$ is shown. The figure clearly reveals that the axial solids volume fraction distribution is in fairly good agreement with measurements in the case of β^{eff} (equation (4)). Wang et al. (2010) demonstrated that without consideration for the contribution from the sub-grid heterogeneities to the drag force, i.e. using the microscopic drag law of Wen and Yu (1966) the bed expansion is over-predicted considerably (by about 40%) in this case.

MODELLING OF POLY-DISPERSE GAS-SOLID FLOWS

Most industrial applications of fluidized bed reactors include poly-disperse materials. Thus, it is important to understand the mixing and segregation of the particles in the reactor to evaluate its efficiency. One of the most straight forward numerical methods to account for poly-disperse mixtures is DEM (discrete element method). However, since the total number of particles involved in most practically relevant fluidized beds is extremely large, it may be impractical to solve the equations of motion for each particle. It is, therefore, common to investigate particulate flows in large process units using averaged equations of motion, i.e. two-fluid models (TFM), which include the inter-particle collisions statistically by kinetic theory based closures of the particle stresses. Even though each representative particle diameter requires an additional momentum and continuity equation, which considerably raises the computational demand with increasing number of particle diameters.

In this paper, we therefore present a hybrid model for the numerical assessment of poly-disperse gas-solid fluidized beds. The main idea of such a modeling strategy is to use a combination of a Lagrangian discrete phase model (DPM) and a coarse-grained TFM to take advantage of the benefits of those two different formulations.

On the one hand, the local distribution of the different particle diameters, which is required for the gas-solid drag force, can be obtained by tracking statistically representative particle trajectories for each particle diameter class along the solids flow obtained from the coarse-grained TFM. The momentum balance for such a "tracer" trajectory therefore reads

$$\frac{\partial \mathbf{u}_{p,i}}{\partial t} = -\frac{1}{\tau_{c,i}}(\mathbf{u}_{p,i} - \mathbf{u}_s) + \mathbf{F}_{poly,i}\,, \qquad (10)$$

where $\mathbf{u}_{p,i}$ denotes the velocity of the Lagrangian tracer of particle diameter class i, $\mathbf{u}_s$ the solids velocity and τ_c is a collisional time scale required to accelerate a single particle to the average solids velocity $\mathbf{u}_s$ (Schellander et al., 2013). Since the tracers are allowed to have different physical properties (e.g. particle diameter) $\mathbf{F}_{poly,i}$ accounts for the difference of the drag force on a single particle to the drag force on the local ensemble of particles. In our previous study we have shown that such an approach reduces the computational cost considerably compared to multi-fluid models, where each particle diameter class is represented by its own phase (Schellander et al., 2013).

Following Beetstra et al. (2007) the drag force per unit volume exerted on a poly-disperse mixture of spherical particle can be written as follows

$$\mathbf{F}_d = \beta_{\langle d\rangle}\beta_{poly}(\mathbf{u}_g - \mathbf{u}_s)\,, \qquad (11)$$

where

$$\beta_{\langle d\rangle} = 18\mu_g\varepsilon_s\varepsilon_s^2 F_{\langle d\rangle}(\varepsilon_g, \varepsilon_s, \mathrm{Re}_{\langle d\rangle}),$$

$$\beta_{poly} = \sum_{i=1}^{N_{sp}} \frac{x_i F_i}{d_{p,i}^2}\,.$$

For the exact definitions of $F_{\langle d\rangle}$ and F_i can be found in Beetstra et al. (2007). Here, $\mathbf{u}_g$ denotes the gas-velocity, Re the particle Reynolds number and N_{sp} the number of particle classes. Above equation reveals that the drag force can be split into a part $\beta_{\langle d\rangle}$, which solely depends on the local solids volume fraction and the Sauter mean diameter $\langle d\rangle$ of the poly-disperse mixture and into a part β_{poly}, which accounts for effect of the different diameters with volume fraction $\varepsilon_{s,i} = x_i\varepsilon_s$. Thus, we find

$$\mathbf{F}_{poly,i} = \frac{1}{\varepsilon_s\rho_s}\beta_{\langle d\rangle}\left(\frac{F_i}{d_{s,i}^2} - \beta_{poly}\right)(\mathbf{u}_g - \mathbf{u}_s)\,, \qquad (12)$$

Finally, the average diameter used in the TFM simulation is computed from

$$\langle d\rangle_{TFM} = \left(\sum_{i=1}^{N_{sp}} \frac{x_i}{d_{p,i}}\right)^{-1}\,, \qquad (13)$$

where the x_i's are determined from the distribution of the Lagragian tracer particles based on the Eulerian grid used for the TFM part. Note that in the case where no tracer particle is in a specific numerical cell we apply a diffusive smoothening approach to the exchange fields locally (Pirker et al., 2011).

On the other hand, the contribution from the inter-particle stresses, i.e. inter-particle collisions, can be deduced from the coarse-grained TFM solution. These then determine the collisional time scale τ_c appearing in the momentum balances of the tracer particles. Note that in a first step we solely consider diameter averaged solids stresses since the drag force is at least on order of magnitude higher than the solids stresses in fluidized beds.

For the numerical simulation we use the commercial CFD-solver FLUENT (version 14), whereby we implemented the poly-disperse drag force (Beetstra et

al., 2007) and the coarse grained solid stresses of Schneiderbauer et al. (2013) and Schneiderbauer and Pirker (2014) by using user defined functions. For the discretization of all convective terms a second-order upwind scheme is used. The derivatives appearing in the diffusion terms in are computed by a least squares method, and the pressure–velocity coupling is achieved by the SIMPLE algorithm, whereas the face pressures are computed as the average of the pressure values in the adjacent cells (linear interpolation). For further details the reader is referred to our previous work (Schneiderbauer et al., 2012, Schneiderbauer et al., 2013).

Finally, we use a grid resolution equal to three times the diameter of the largest particle fraction. However, such a coarse grid resolution inevitably neglects the small scale flow structures, i.e. sub-grid heterogeneities of the fine particles. Thus, we apply sub-grid modifications for the gas-solid drag force and the solids stresses to account for the effect of those small unresolved scales (Schneiderbauer et al., 2013; Schneiderbauer and Pirker, 2014; Schneiderbauer and Pirker, 2014a).

A correct numerical model should therefore be able to produce inhomogeneous bed segregation and a similar channel-building behaviour when initialized by a local inhomogeneity in the particle mixture similar to the experiment.

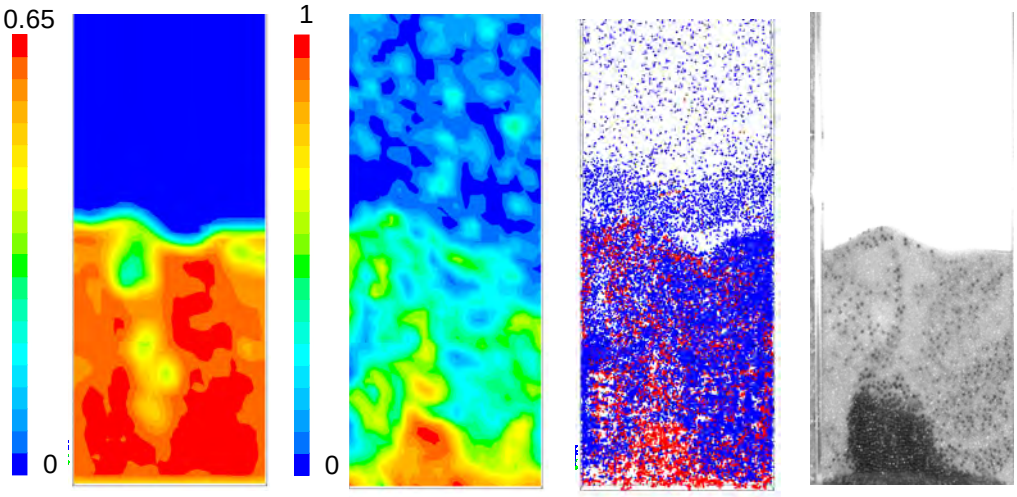

Figure 5: Validation example – Partial de-fluidization in a bi-disperse fluidized bed due to de-mixing of two particle classes: Large (black) particles form a non-uniform packed bed just above the distributor plate; process gas channels to the upper part of the bubbling fluidized bed of small (gray) particles. Our hybrid simulation model is able to reproduce this critical behaviour: (from left to right) solid-phase volume fraction, fraction of large particles, tracer particles colored by their size, experimental observation

RESULTS OF POLY-DISPERSE GAS-SOLID FLOW SIMULATIONS

The numerical hybrid model is applied to a fluidized bed of a bi-disperse mixture of glass particles (0.5 mm and 2.5 mm particles) and with a cross-section of 0.15 m x 0.02 m. The initial mass fraction of the 0.5 mm particle was set homogenously to $x_i = 60\%$. To break symmetry we initialised a small area above the distributor blade with a partially smaller mass fraction of the 0.5 mm particles. Finally, the initial bed height was given by 0.2 m and the superficial gas velocity was 0.44 m/s. Note that one single tracer trajectory represents on the one hand a parcel of 64 0.5 mm particles and on the other hand, a parcel of 2 2.6 mm particles. In this case

In Figure 5 a comparison of numerical and experimental results (Puttinger et al., 2014) is shown. The results show that during settlement of the bed segregation occurs for this combination of particle sizes. Due to the initial inhomogeneity above the distributor plate, an area of large particles is formed right above this region.

The experimental data (Puttinger et al., 2014) further shows that this effect is reproducible for particle mixtures in the range x_i=40..60% and superficial velocities in the range 0.4 to 0.5m/s. The small particle fraction is fluidized at this gas rate (minimum fluidization velocity 0.32m/s) while the large particles are not (1.6m/s). Therefore the large particles do not move anymore as soon as they have settled in a certain place.

The comparison further demonstrates that the hybrid model yields (including bed expansion, segregation and channelling) fairly good agreement with experiments. Especially, the formation of the "dead man", which manifests a stationary accumulation of large particles in the centre, is predicted appropriately. The formation of this stationary zone leads to a partial de-fluidization. Only the small particles above the dead man remain fluidized.

CONCLUSIONS

In this paper we have verified the constitutive relations for the filtered drag and the filtered particle stresses presented in our previous study (Schneiderbauer and Pirker, 2014). The results show that the model is able to predict the hydrodynamics of bubbling and turbulent gas-solid fluidized beds appropriately using coarse grids. In particular, applying the presented sub-grid modifications yields a fairly good estimate of the rise velocity of bubbles. Hence, a sub-grid stress modification for the frictional stresses is indispensable

to estimate the bubble rise velocity in bubbling fluidized beds precisely. Furthermore, we presented a new hybrid Two Fluid Model (TFM) by additionally considering poly-disperse tracer particles.

To conclude, the sub-grid heterogeneity based TFM is applicable to mono-disperse industrial-scale fluidized beds yielding a reasonable agreement of the bed expansion with experiments. In addition, the hybrid TFM is able to picture poly-disperse gas-solid flows and segregation phenomena.

REFERENCES

ANDERSON, T.B., JACKSON, R., (1967), "Fluid mechanical description of fluidized beds. Equations of motion", *Industrial & Engineering Chemistry Fundamentals*, **6**(4), 527-539.

ANDREWS, A.T., LOEZOS, P.N., SUNDARESAN, S., (2005), "Coarse-grid simulation of gas-particle flows in vertical risers", *Industrial & Engineering Chemistry Research*, **44**(16), 6022-6037.

BEETSTRA, R., VAN DER HOEF, M.A., KUIPERS, J.A.M., (2007), "Drag force of intermediate Reynolds number flow past mono- and bidisperse arrays of spheres", *AIChE J.*, **53**, 489–501.

BUSCIGLIO, A., VELLA, G., MICALE, G., RIZZUTI, L., (2008), "Analysis of the bubbling behaviour of 2D gas solid fluidized beds Part I. Digital image analysis technique", *Chem. Eng. J.*, **140**(1-3), 398-413

HOLLOWAY, W. & SUNDARESAN, S. (2014), "Filtered models for bidisperse gas-particle flows", *Chem. Eng. Sci.*, **108**, 67–86.

HONG, K., WANG, W., ZHOU, Q., WANG, J., LI, J., (2012), "An EMMS-based multi-fluid model (EFM) for heterogeneous gas-solid riser flows: Part I. Formulation of structure dependent conservation equations", *Chem. Eng. Sci.*, **75**, 376-389.

IGCI, Y., SUNDARESAN, S., (2011), "Constitutive models for filtered two-fluid models of fluidized gas-particle flows", *Industrial & Engineering Chemistry Research*, **50**(23), 13190-13201.

ISHII, M., (1975), "Thermo-fluid dynamic theory of two-phase flow", *Collection de la Direction des études et recherches d'Électricité de France*, **22**, Paris: Eyrolles.

MILIOLI, C.C., MILIOLI, F.E., HOLLOWAY, W., AGRAWAL, K., SUNDARESAN, S., (2013), "Filtered two-fluid models of fluidized gas-particle flows: new constitutive relations", *AIChE J.*, **59**(9), 3265-3275.

PARMENTIER, J.-F., SIMONIN, O., DELSART, O., (2012), "A functional subgrid drift velocity model for filtered drag prediction in dense fluidized bed", *AIChE J.*, **58**(4), 1084-1098.

PIRKER, S., KAHRIMANIVIC, D., GONIVA, C. (2011), "Improving the applicability of discrete phase simulations by smoothening their exchange fields", *Appl. Math. Modelling*, **35**(5), 2479 – 2488.

PUTTINGER, S., SCHNEIDERBAUER, S., VON BERG, L. AND PIRKER, S., (2014), "Inhomogeneous segregation of binary mixtures in fluidized beds", *Proc. of the WCPT7*, Beijing, China.

SCHELLANDER, D., SCHNEIDERBAUER, S. & PIRKER, S., (2013), "Numerical study of dilute and dense poly-dispersed gas-solid two-phase flows using an Eulerian and Lagrangian hybrid model", *Chem. Eng. Sci.*, **95**, 107–118.

SCHNEIDERBAUER, S., AIGNER, A., PIRKER, S., (2012), "A comprehensive frictional-kinetic model for gas-particle flows: analysis of fluidized and moving bed regimes", *Chem. Eng. Sci.*, **80**, 279–292.

SCHNEIDERBAUER, S. AND PIRKER, S., (2014a), "A coarse-grained two-fluid model for gas-solid fluidized beds", *J. Comput. Multiph. Flows*, **6**, 29–47.

SCHNEIDERBAUER, S., PIRKER, S., (2014), "Filtered and heterogeneity based sub-grid modifications for gas-solid drag and solids stresses in bubbling fluidized beds", *AIChE J.*, **60**(3), 839–854.

SCHNEIDERBAUER, S., PUTTINGER, S., PIRKER, S., (2013), "Comparative analysis of subgrid drag modifications for dense gas-particle flows in bubbling fluidized beds", *AIChE J.*, **59**(11), 4077–4099.

WANG, J, VAN DER HOEF, M.A., KUIPERS, J.A.M., (2010), "Coarse grid simulation of bed expansion characteristics of industrial-scale gas-solid bubbling fluidized beds", *Chem. Eng. Sci.*, **65**(6), 2125-2131.

WEN, C. Y., YU, Y. H. (1966)." Mechanics of fluidization", *Chemical Engineering Progress Symposium Series* **62**, 100.

WERTHER, J., (1978). "Effect of gas distributor on the hydrodynamics of gas fluidized beds", *German Chemical Engineering*, **1**, 166–174.

WERTHER, J., WEIN, J., (1994), "Expansion behavior of gas fluidized bed in turbulent regime", *AIChE J. Symposium Series*, **90**(301), 31-44.

COMPARING EULER-EULER AND EULER-LAGRANGE BASED MODELLING APPROACHES FOR GAS-PARTICLE FLOWS

Markus BRAUN[1], Markus LAMBERT[1], Shailesh OZARKAR[2]*, Jay SANYAL[2]

[1] ANSYS Germany GmbH, Birkenweg 14a, D-64295 Darmstadt, Germany

[2] ANSYS Inc., 275 Technology Drive, Canonsburg, PA, 15317, US

* E-mail: shailesh.ozarkar@ansys.com

ABSTRACT

Comparative assessment of Euler-Euler and Euler-Lagrange modelling approaches for gas-particle flows is performed by comparing their predictions against experimental data of two fluidization challenge problems put forth by National Energy Technology Laboratory (NETL), Morgantown, WV, USA. The first fluidization challenge problem is based on laboratory scale fluidized bed while second fluidization challenge problem is based on pilot scale circulating fluidized bed. It is found that the both models predict comparable results and those results are in qualitative agreement with the experimental data.

Keywords: Euler-Euler, Euler-Lagrange, Gas-Particle flows, Fluidized bed.

NOMENCLATURE

Greek Symbols

ϕ	Volume fraction of particles.
δ	Normal overlap, [m].
γ	Damping coefficient, [kg/s].
μ	Coefficient of friction.
η	Coefficient of restitution.

Latin Symbols

$\vec{u}_p$	Velocity of a particle p, [m/s].
$\vec{F}$	Various forces acting on a particle, [N].
$\vec{F}_1$	Normal contact force acting on particle 1, [N].
Re_m	Mean flow Reynolds number.
d_p	Diameter of a particle, [m].
m_i	Mass of a particle i, [kg].
m_{12}	Reduced mass, [kg].
K	Normal spring constant, [N/m].
$\vec{e}_{12}$	Unit vector defined from particle 1 to particle 2.
$\vec{v}_{12}$	Relative velocity, [m/s].
t_{coll}	Time scale of collision, [s].

INTRODUCTION

Simulations of gas-particle flows in commercial scale devices such as fluidized beds are of interest to many industries including chemical processing, oil and gas, and energy. For these simulations, traditional Euler-Euler models based on kinetic theory of granular flow (KTGF) along with classical or refined form of gas-particle drag law[1-6] have being used for a long time. With recent advances in computing power and computational algorithms, there is a growing interest in using Euler-Lagrange models since these models are well suited for accounting for particle size distributions in comparison to Euler-Euler KTGF models.

In this computational study, a comparative assessment of Euler-Euler KTGF and Euler-Lagrange models is performed using small (laboratory) scale fluidized bed (SSFB) and pilot scale circulating fluidized bed (CFB) challenge problems designed for validation. Both problems are particularly suited for modelling using Euler-Euler KTGF and Euler-Lagrange models and for their comparative assessment since the particles considered in both problems are nearly mono disperse (Geldart Group D in SSFB and Group B based cases in CFB). The advantage with mono disperse particle system based comparative assessment of models is that the system remains free of size or density based segregation effects and poly disperse gas-particle drag force related effects. Furthermore, for gas-particle systems, drag force is the most dominant interaction force and it can easily be accounted in an equivalent manner in both models. In SSFB, inventory of particles corresponds to about 93000 particles. Therefore, Euler-Lagrange simulations with Discrete Element Method (DEM) to resolve collisions based on individual particles can be performed in affordable manner. In CFB problem, time-averaged inventory of particles in main riser section is such that the Euler-Lagrange with DEM simulations can only be performed by tracking trajectories and collisions of group of particles or parcels.

This paper is organized as follows. We begin with a brief description of experimental facilities, flow conditions and experimental measurements. Next, we give an overview of models along with geometry simplification, grid resolutions and boundary conditions considered in simulations. After that, results from SSFB and CFB simulations are presented with the conclusion in the end.

EXPERIMENTAL FACILITY

On NETL website both challenge problems (NETL CFB 2010, NETL SSFB 2013) are well documented including information on test units, geometrical dimensions, instrumentation, and experimental measurements. Here we provide only brief description.

NETL Small Scale Fluidized Bed

A schematic of the rectangular fluidized bed test unit is shown in Figure 1. Physical properties of gas (air) and particles (Geldart Group D) are given in Table 1. Experimental flow conditions are given in Table 2. Gas entering the test unit at the bottom first gets distributed by bottom distributor and then gets redistributed by top distributor above which fluidized bed particles are present. The diameter of each orifice on the top distributor is slightly smaller than the diameter of a particle.

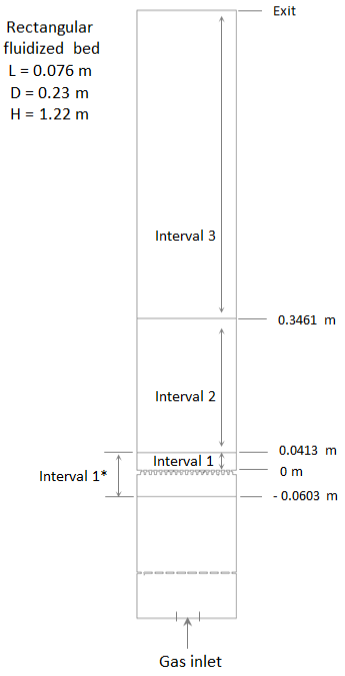

Figure 1: Schematic of small scale fluidized bed test unit.

Table 1: Physical properties of gas and particles

Particle diameter	3.256×10^{-3} m
Particle density	1131 kg/m^3
Gas density	1.2 kg/m^3
Gas viscosity	1.8×10^{-5} kg/m s

Experimental data have been reported in the form of mean and standard deviation of differential pressure (DP) across Interval 1*, Interval 2 and Interval 3; mean and additional statistical quantities of vertical and horizontal velocities of the particles; and granular temperature. The DP across Interval 1* includes DP across distributor and DP across interval 0 m to 0.0413 m which henceforth referred to as Interval 1. Since DP data across Interval 1 are not provided in the experimental data set, we extracted DP data across this interval by subtracting DPs across Intervals 2 and 3 from DP estimated based on total inventory of particles. Such extracted DP data across Interval 1 were used for comparison with simulation predictions.

Table 2: Flow conditions

Case	Solid Weight (Kg)	Gas Superficial Velocity (m/s)
1	1.9	2.19
2	1.9	3.28
3	1.9	4.38

NETL Circulating Fluidized Bed

The NETL circulating fluidized bed test unit is shown in Figure 2. Gas (air) enters the test unit from axial inlet located at the bottom of riser and solids returning from standpipe are recirculated back into the riser from a side inlet. The CFB was operated at five different flow conditions out of which only Case 3 is considered in this study. Case 3 corresponds to Group B particles with mean diameter $748\,\mu$m and density $863.3\,\mathrm{kg/m^3}$. Superficial velocity of gas and solids circulation rate are $5.71\,\mathrm{m/s}$ and $5.54\,\mathrm{kg/s}$, respectively.

MODEL DESCRIPTION

Simulations of both SSFB and CFB were performed using Euler-Euler KTGF model and Euler-Lagrange model with DEM to account for particle or parcel collisions.

Euler-Euler KTGF model

In this modelling approach, gas and particle phases are treated in an Eulerian frame and a set of conservation equations is solved for each phase. The governing equations of this model are well documented (Crowe et al. 1998) and hence will not be repeated here. Gas-particle drag force that couples the motion of phases is the most dominant interaction force for gas-particle system since the Stokes number based on particle is typically large. In this computational study, we explored two drag force formulations.

First one is the widely used Gidaspow drag force formulation (Gidaspow et al., 1992). Second one is the drag force formulation put forth by Tenneti et al. (2011)

based on DNS study of flow past fixed random assemblies of monodisperse spheres with finite fluid inertia using immersed boundary method. This drag

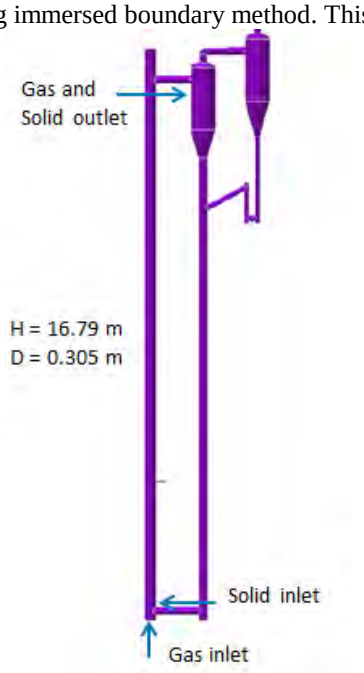

Figure 2: Pilot scale circulating fluidized bed test unit.

force formulation is given as a function of particle volume fraction $\phi\ (0.1 \le \phi \le 0.5)$, and mean flow Reynolds number $\mathrm{Re}_m\ (0.01 \le \mathrm{Re}_m \le 300)$ which is calculated based on particle diameter and magnitude of slip velocity between two phases. In that study, it is shown that the values obtained from Gidaspow drag force formulation begin to differ quite significantly from DNS results in the limits of higher volume fraction $(\phi > 0.2)$ and mean flow Reynolds number. Since both limits are being satisfied in the SSFB problem, for its simulation the use of second drag force formulation is essential. In the CFB problem, average volume fraction of particles remains below 0.2 where Gidaspow drag force formulation does not differ significantly from DNS results over the range of Re_m and thus usage of Gidaspow drag force formulation is adequate.

Euler-Lagrange model

In this modelling approach, the gas phase is treated in Eulerian frame and for the solution of its conservation equations particle volume fraction and velocity information is needed at the centre of each cell in fixed Eulerian grid. This information is provided by averaging over particle field data and then mapping it to Eulerian grid. The particle phase is treated in Lagrangian frame by tracking discrete particles or groups of particles or parcels with their trajectories described by

$$m_p \frac{d\vec{u}_p}{dt} = \vec{F}_d + \vec{F}_p + \vec{F}_{vm} + \vec{F}_g + \vec{F}_{other} + \vec{F}_{contact} \qquad (1)$$

In this equation, terms on right hand side represent drag force, pressure force, virtual mass force, gravitational force, any other forces acting on particle, and particle-particle contact force. The last term is calculated using Discrete Element Method (DEM) based on work of Cundall and Strack (1979). Briefly, the normal contact force on particle 1 which is in contact with particle 2 is calculated using a spring-dashpot model:

$$\vec{F}_1 = \left(K\delta + \gamma(\vec{v}_{12} \cdot \vec{e}_{12})\right)\vec{e}_{12} \qquad (2)$$

In tangential direction only sliding contact between particles is considered in this study and tangential contact force is calculated using the equation for Coulomb friction:

$$\vec{F}_{friction} = \mu \vec{F}_{normal} \qquad (3)$$

In simulations involving parcels, the contact force is calculated based on parcel mass and its diameter. The parcel mass is calculated as sum of mass of all particles in a parcel and the parcel diameter is calculated from mass of a parcel and density assumed to be the same as the particle density.

SIMULATIONS

In this computational study, all simulations were carried out using ANSYS Fluent 15.0.

SSFB simulations

First, a set of Euler-Euler KTGF model based simulations of Case 1 (considered as a test-bed) were performed to check the effects of drag force formulations and gas-inlet configurations. After these simulations, simulations of Case 2 and Case 3 were performed with one selected gas-inlet configuration and without making any changes to the model. For Case 1 simulations, we considered three different types of gas-inlet configurations. In first type of configuration, only a portion of geometry above top distributor was considered, and without resolving nozzles in geometry, gas mass flow rate corresponding to the superficial velocity given in Table 2 was specified on the whole inlet surface. This configuration is referred to as Uniform Inlet. In the second type of configuration referred to as Distributor Inlet, we kept the geometry as in first configuration but resolved all of the nozzles on the top distributor. In the third type of configuration referred to as Complete Geometry, we considered the whole geometry shown in Figure 1. In all of the configurations, the cell size in the main part of the fluidized bed (above inlet regions) was kept approximately as 3.9 times particle diameter. Total number of cells in the grids with Uniform Inlet, Distributor Inlet and Complete Geometry were 10000, 48000 and 244000, respectively. For both gas and particle phases, wall boundary condition was set to no-slip.

Euler-Lagrange model simulations require the cell size in the grid to be bigger than the size of particle or parcel. The grid with Uniform Inlet configuration can easily satisfy this requirement but the grids with Distributor Inlet and Complete Geometry configurations

cannot. Therefore for these simulations, instead of accurately resolving nozzles, we considered simplified rectangular shaped nozzles as shown in Figure 3 and generated a grid with cell size of about 3.5 times particle diameter. For particle-particle and particle-wall collision calculations, spring constant, coefficient of restitution and coefficient of friction were arbitrarily set to 500 N/m, 0.9 and 0.1, respectively. Particle time step was set to $t_{coll}/5$ where t_{coll} is the collisional time scale that is given by

$$t_{coll} = \left(\frac{m_{12}}{K} \left(\pi^2 + (\ln \eta)^2 \right) \right)^{\frac{1}{2}} \quad (4)$$

where, reduced mass is calculated from masses of particle 1 and 2: $m_{12} = (m_1 m_2 / (m_1 + m_2))$. All simulations of SSFB were run up to at least 15 sec of flow time calculations and next 10 sec of flow time data were used for time-averaging. Data gathering frequency was set to 1000 Hz.

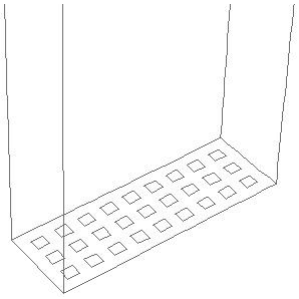

Figure 3: Gas-inlet configuration considered for Euler-Lagrange model based simulations.

CFB simulations

Agrawal et al. (2001) showed that for realistic predictions of gas-particle flows, grid resolution must be of the order of few particle diameters in order to resolve fine scale structures (clusters and streamers) that are shown to further reduce gas-particle drag. For understanding the change in simulation predictions with successive grid refinements and for comparative assessment study, we performed CFB simulations using Euler-Euler KTGF model with three different grid resolutions – coarse, intermediate and refined grids consisting of 65000, 1.67 million and 3 million cells, respectively. The various parameters of these grids are shown in Table 3.

Recently we started CFB simulations using Euler-Lagrange model. Since it is nearly impractical to perform individual particles based simulations, for CFB study, we took parcel based approach. Here we present results from a preliminary simulation run that was performed using 96000 hexahedral cells and 0.47 million parcels with 1826 particles per parcel. Parcel-Parcel collisions were accounted using DEM with spring constant, coefficient of restitution and friction coefficient arbitrarily set to 1000 N/m, 0.7 and 0.25, respectively. Subsequent simulations with lesser number of particles per parcel will need to be performed to understand its effect on simulation predictions. All CFB simulations were run for sufficiently longer time to allow cases to reach statistical steady state before gathering data for time-averaging.

Table 3: The various parameters of grids considered in CFB simulations using Euler-Euler KTGF model.

	Approximate cell lengths			
	Along circumference	Across diameter	Along axis	Grid Size
Coarse	90* d_p	31*d_p	40*d_p	65000
Intermediate	22* d_p	10*d_p	10*d_p	1.67M
Fine	10* d_p	10*d_p	10*d_p	3 M

RESULTS AND DISCUSSIONS

SSFB simulation results

Mean DP values across Interval 2 from experiments and simulations of Case 1 are given in Table 4. Several points emerge from this table after we compare these values. Overall, simulations slightly over predict mean DP values compared to experiments. As expected, the values obtained from simulations using Tenneti et al. drag law are lower compared to those obtained using Gidaspow drag law and closer to experimental data. By comparing the values for three different gas-inlet configurations obtained from Euler-Euler KTGF simulations with Gidaspow or Tenneti et al. drag law, we see that Uniform Inlet always leads to higher solids hold up in that interval compared to other two gas-inlet configurations which give almost same mean DP values. Mean DP values predicted by Euler-Lagrange model with Tenneti et al. drag law for two different gas-inlet configurations do not differ much indicating that assumed size of each rectangular shaped nozzle in Distributor Inlet configuration is too coarse and overall gas-particle flow distribution is same with both inlet configurations. By comparing mean DP values from Euler-Lagrange and Euler-Euler KTGF models, it can be said that predictions from both models are comparable.

Figure 4 shows snapshots of volume fraction of particle-phase obtained from simulations using Euler-Euler KTGF model with Tenneti et al. drag law for three different inlet configurations. In case of Uniform Inlet, we see constant presence of thin uniform layer consisting of lower volume fraction of particle-phase next to inlet surface. This forces more particles into Interval 2 and hence leads to higher hold up predictions in that interval. With other two inlet configurations, gas streams emerging from nozzles merge together and periodically generate bubbles that rise upward and eventually burst into free board region. We see that the particles flow upward in centre region and downward adjacent to walls. Since there is no significant difference

between Distributor Inlet and Complete Geometry results, we performed simulations of Case 2 and Case 3 using Distributor Inlet configuration and Tenneti et al. drag law with Euler-Euler KTGF as well as Euler-Lagrange model. In simulations of Case 2 and 3, fluidization behaviour looked significantly different from Case 1. At higher superficial velocities both models predict vigorous fluidization as opposed to periodic generation of bubbles seen in Case 1.

Table 4: Mean DP across Interval 2 from experiments and simulations of Case 1.

Case 1	Mean DP across Interval 2 (kPa)
Experiments	0.686
Euler-Euler KTGF model with Gidaspow drag law	
Uniform Inlet	0.916
Distributor Inlet	0.862
Complete Geometry	0.857
Euler-Euler KTGF model with drag law proposed by Tenneti et al.	
Uniform Inlet	0.844
Distributor Inlet	0.783
Complete Geometry	0.794
Euler-Lagrange model with drag law proposed by Tenneti et al.	
Uniform Inlet	0.856
Distributor Inlet - Square nozzles	0.873

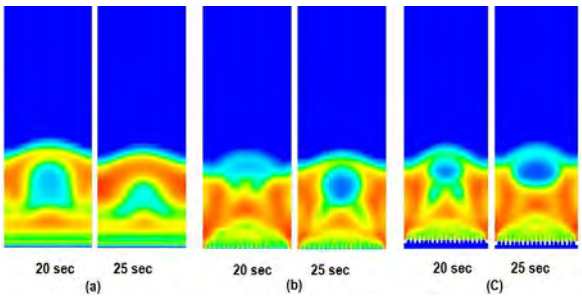

Figure 4: Snapshots of particle-phase volume fraction at 20 and 25 sec of flow time from simulations using Euler-Euler KTGF model with Tenneti et al. drag law. (a) Uniform Inlet. (b) Distributor Inlet. (c) Complete Geometry (bottom portion not shown).

Figure 5 shows comparison of mean DP predictions obtained from Euler-Euler KTGF model based simulations of three cases (listed in Table 2) with the experimental data. In this figure, filled symbols represent experimental data and open symbols with lines represent simulations. Circles are for mean DP across Interval 1, squares are for Interval 2 and triangles are for Interval 3. In experiments, with increase in superficial velocity, mean DP increases across Intervals 1 and 3, and decreases across Interval 2. Euler-Euler KTGF model qualitatively captures the trends for the Intervals 1 and 3 but does not predict significant decrease in mean DP across Interval 2 as seen with experimental data.

Figure 6 shows predictions from Euler-Lagrange model simulations. These simulations do predict decrease in mean DP across Interval 2 with the increase in superficial velocity. From last two figures, we see that both Euler-Euler KTGF and Euler-Lagrange models predict comparable mean DP values for all three intervals but when compared with experimental data, quantitative

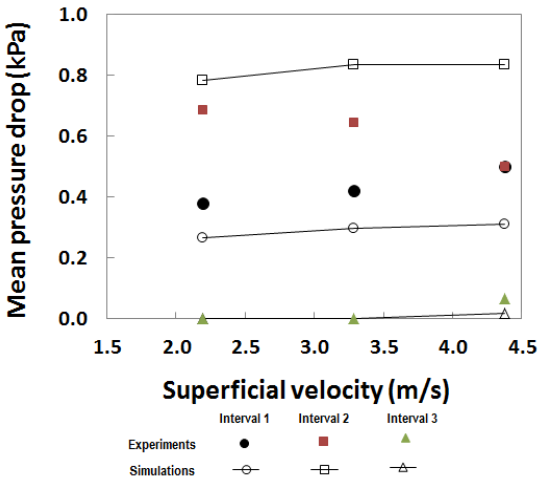

Figure 5: Effect of superficial velocity on mean DP across three intervals. Simulation predictions are from Euler-Euler KTGF model.

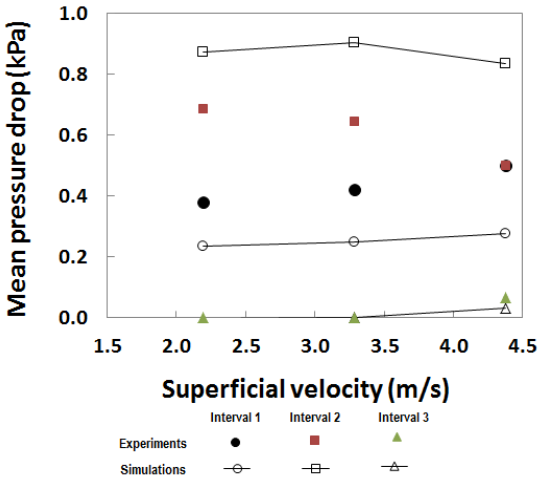

Figure 6: Effect of superficial velocity on mean DP across three intervals. Simulation predictions are from Euler-Lagrange model.

differences are clearly visible. We have not yet explored the effect of wall boundary conditions as well as Euler-Euler KTGF model parameters such as coefficient of restitution, which might play some role in the model predictions. Similar study with Euler-Lagrange approach is also needed.

Figure 7 shows comparison of standard deviation of DP across Interval 2 obtained from Euler-Euler KTGF and Euler-Lagrange models with experimental data. Predictions from both models are in good agreement

with experimental data at smallest and largest superficial velocities but not at intermediate superficial velocity.

We now compare time-averaged particle-phase vertical velocity predictions obtained from Euler-Euler KTGF and Euler-Lagrange models with the experimental data. In experiments, particle-phase velocity measurements were performed using high speed PIV that traced particles appearing in cells (0.0457 m X 0.0457 m X 0.003 m)

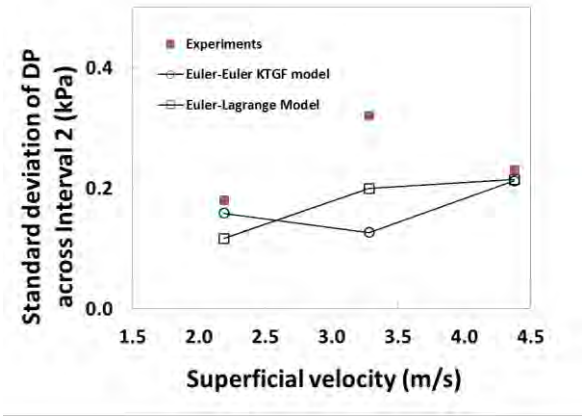

Figure 7: Effect of superficial velocity on standard deviation of DP across Interval 2.

located adjacent to the wall and at the mid-point elevation of 0.0762 m measured from top distributor. Since these measurements were performed within a particle diameter distance from the wall, the measurements were expected to be strongly influenced by particle-wall interactions.

Figure 8 shows comparison of time-averaged particle-phase vertical velocity profiles obtained from Euler-Euler KTGF model based simulations with the experimental data. Since these profiles are from near wall regions and in simulations we used no-slip boundary condition for both phases, as expected, we see under prediction of velocities at all lateral locations. Since in Euler-Lagrange simulations particles were allowed to slip with specified particle-wall collision parameters, we see visible improvements in velocity predictions in Figure 9. Slight asymmetry in velocity profiles indicates that the considered time interval for simulation data gathering was not long enough.

CFB simulation results

To understand the change in simulation predictions with successive grid refinements and for comparative assessment of the models, we performed a set of simulations using Euler-Euler KTGF model with coarse, intermediate and refined grids consisting of 65000, 1.67 million and 3 million cells, respectively. Figure 10 shows time-averaged gas-phase axial pressure gradient profiles obtained from these simulations. In this figure, experimental data is also shown for comparison. With successive global grid refinements we see improvements in pressure gradient predictions, however even with refined grid where cell size is about ten times particle diameter, the model under predicts the hold up.

Predictions from Euler-Lagrange model are also given in Figure 10. The Euler-Lagrange simulations were performed on a coarse grid consisting of 96000 cells and

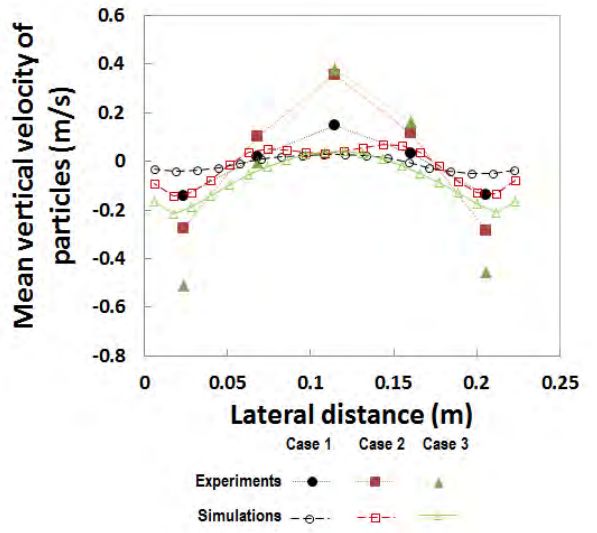

Figure 8: Comparison of time-averaged particle-phase vertical velocity profiles obtained from Euler-Euler KTGF simulations with experimental data. Profiles are from regions adjacent to the wall.

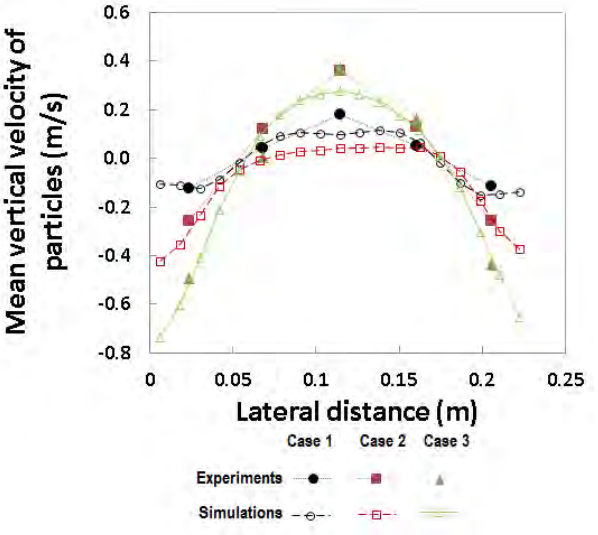

Figure 9: Comparison of time-averaged particle-phase vertical velocity profiles obtained from Euler-Lagrange simulations with experimental data. Profiles are from regions adjacent to the wall.

0.47 million parcels. We see that the predictions from Euler-Lagrange model are comparable to those obtained from Euler-Euler KTGF model using coarse grid. Comparison of time-averaged particle-phase axial velocity profiles obtained at 8.88 m elevation is shown in Figure 11. These preliminary results indicate that further studies with Euler-Lagrange model are also needed to understand the effects of grid and boundary layer resolution along with the number of parcels on model predictions.

SUMMARY

Euler-Euler KTGF and Euler-Lagrange models gave similar results for gas-particle flows in small scale fluidized bed (SSFB) and pilot scale circulating fluidized bed (CFB). In SSFB study, the results were found to be in qualitative agreement with the experimental data. Resolving nozzles on gas distributor and using DNS based drag law proposed by Tenneti et al. (2011) led to further improvement in results. In CFB study, both models gave similar results with coarse grid resolution. Euler-Euler KTGF model predictions improved with successive global grid refinements; however additional elaborate study is needed to understand the effects of various parameters including resolution of boundary layer cells. Similar CFB study with Euler-Lagrange model is needed to understand the effects of grid and boundary layer resolution, number of parcels, and parameters used in DEM calculations.

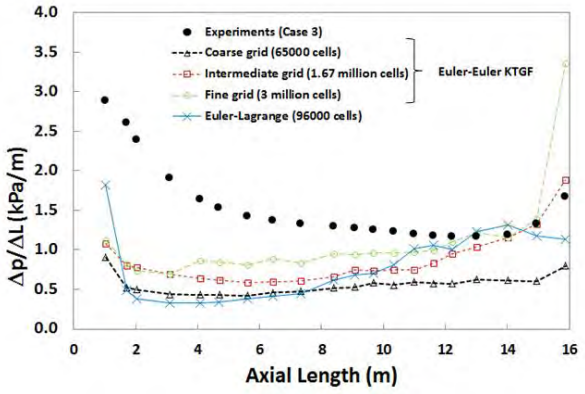

Figure 10: Predictions of time-averaged gas-phase axial pressure gradient from Euler-Euler KTGF and Euler-Lagrange simulations. Experimental data is also shown for comparison.

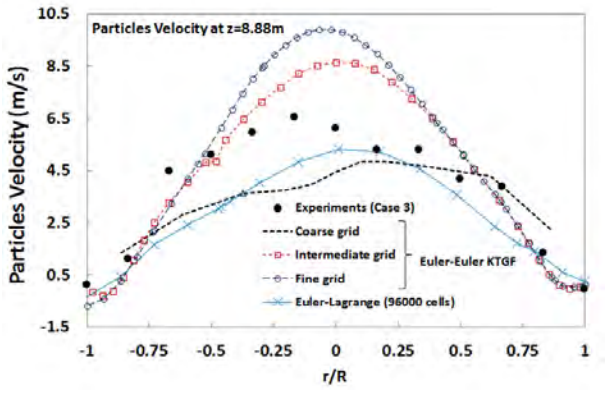

Figure 11: Predictions of time-averaged particle-phase axial velocity from Euler-Euler KTGF and Euler-Lagrange simulations. Experimental data is also shown for comparison.

REFERENCES

1. Wen, C.-Y. and Yu, Y. H., (1966), "Mechanics of fluidization", *Chem. Eng. Prog. Symp. Series.*, **62**, 100–111.

2. Gidaspow, D., Bezburuah, R. and Ding, J., (1992), "Hydrodynamics of circulating fluidized beds, kinetic theory approach", *In Fluidization VII, Proceedings of the 7th Engineering Foundation Conference on Fluidization*, 75–82.

3. Li, J. and Kwauk, M., (1994), "Particle-Fluid two-phase flow: Energy-Minimization Multiscale Method", Beijing, P. R. China, Metallurgical Industry Press.

4. Parmentier, J-F., Simonin, O. and Delsartk, O., (2012), "A functional subgrid drift velocity model for filtered drag prediction in dense fluidized bed", *AIChE J.*, **58**, 1084-1098.

5. Igci, Y. and Sundaresan, S.,(2011), "Constitutive models for filtered two-fluid models of fluidized gas-particle flows", *Ind Eng Chem Res.*, **50,** 13190-13201.

6. Milioli, C., Milioli, F., Holloway, W., Agrawal, K. and Sundaresan, S., (2013), "Filtered two-fluid models of fluidized gas-particle flows: New constitutive relations", *AIChE J.*, **59,** 3265-3275.

7. NETL CFB 2010 challenge problem https://mfix.netl.doe.gov/challenge/index_2010.php

8. NETL SSFB 2013 challenge problem https://mfix.netl.doe.gov/challenge/index.php

9. Crowe, C., Sommerfeld, M. and Tsuji, Y., (1998), "Multiphase Flows with Droplets and Particles", CRC Press.

10. Tenneti, S., Garg, R. and Subramaniam, S., (2011), "Drag law for monodisperse gas-solid systems using particle-resolved direct numerical simulation of flow past fixed assemblies of spheres", *Int. J. Multiphase Flow*, **37,** 1072-1092.

11. Cundall, P.A. and Strack, O.D.L., (1979), "A discrete numerical model for granular assemblies. *Geo-technique*, **29,** 47-65.

12. Agrawal, K., Loezos, P. N., Syamlal, M. and Sundaresan, S., (2001), "The role of mesoscale structures in rapid gas-solid flows", *J. Fluid Mech.*, **445,** 151-185.

AGGLOMERATION STUDY IN THE INLET SECTION OF A LARGE SCALE SPRAY DRYER USING STOCHASTIC EULER-LAGRANGE MODELLING

Sandip K. PAWAR[1], Johan T. PADDING[1]*, Niels G. DEEN[1], Alfred JONGSMA[2], Fredrik INNINGS[2], J.A.M. (Hans) KUIPERS[1]

[1]Multiphase Reactors Group, Department of Chemical Engineering and Chemistry,
Eindhoven University of Technology , P.O. Box 513, 5600 MB Eindhoven, THE NETHERLANDS

[2]Tetra Pak CPS, Heerenveen, THE NETHERLANDS

* E-mail: J.T.Padding@tue.nl; Tel: (+31) 40 247 3674

ABSTRACT

Spray drying is an essential unit operation for the production of powders from liquid slurry. Main events occurring inside the spray dryer are droplet drying and interactions between droplets and fine particles, leading to bouncing collisions, coalescence, agglomeration, and satellite droplet formation. In recent years, there has been growing interest to use computational fluid dynamics (CFD) for exploring such phenomena inside spray dryer systems. Researchers have extensively investigated single droplet-droplet and single particle-particle interactions using numerical and experimental methods. However, the literature on droplet-particle interactions with a quantitative description of agglomeration in spray drying is scarce, and mainly qualitative.

In this paper, we explore the development of an Euler-Lagrange model with a stochastic approach for the prediction of collision, coalescence and agglomeration of partially wet particles in a spray dryer. In this approach, the dynamics of the gas phase is solved by an Eulerian equation as a continuum and the dynamics of the solid phase is solved by a Lagrangian equation as a dispersed phase, with conventional gas-solid coupling. Inside the spray chamber, the turbulent gas flow has an effect on the particle interactions. In a spray dryer, the number density of droplets is usually more than 10^{11} per cubic meter, effectively ruling out a deterministic approach in which each particle is individually tracked. We introduce a stochastic Direct Simulation Monte Carlo (DSMC) approach in which each particle searches randomly, in a local and spherical searching scope, for another particle to collide with during a particle time step. In a spray dryer, different outcomes can occur when a pair of particles collide. We use elementary models for collision, coalescence, break-up, drying and agglomeration, validated by experimental results from the literature and industrial data. In this paper we present details of the modelling approach using sub-models and preliminary simulation results. The ultimate aim of this project is to develop a simulation tool that can provide the particle size, velocity and flux distribution for a section of a large-scale spray dryer. These results ought to be used as boundary conditions for even coarser simulations, which will be used to design more efficient spray dryers that can produce higher throughputs.

Keywords: Agglomeration, Break-up, Spray Drying, Stochastic Modelling.

NOMENCLATURE

Greek Symbols

ρ_d	Droplet density, [kg/m^3].
μ	Dynamic viscosity, [kg/m.s].
β_i	Drag coefficient, [kg/(s.m^3)].

Latin Symbols

p	Pressure, [N/m^2].
$\mathbf{u}_g$	Gas velocity, [m/s].
V_{cell}	Volume of the cell, [m^3].
$\mathbf{v}_i$	Velocity of particle (parcel) i, [m/s].
V_i	Volume of particle, [m^3].
d_i	Diameter of particle, [m].
m_i	Mass of particle,[kg].
$\mathbf{F}_{g,i}$	Gravity force, [N].
$\mathbf{F}_{d,i}$	Drag force, [N].
$\mathbf{F}_{p,i}$	Pressure force, [N].
S_p	Source term that couples the gas to the dispersed phase, [N/m^3].
X	Moisture content per solid mass, [kg/kg].
T_g	Glass transition temperature, [K].

Sub/superscripts

g	Gas.
i	Index *i*.
j	Index *j*.

INTRODUCTION

Spray drying is an important unit operation in many industrial processes such as chemical, pharmaceutical, food, and dairy processing for making powders from liquid slurry. A spray dryer unit generally appears at the end of the processing line, as it is an important step to control the final product quality. A better understanding of the underlying phenomena in spray dryers can help in optimal design, operation and scale-up of these processes. The liquid feed contain solid fraction in insoluble or dissolved state and is atomized in the spray chamber. The resulting droplets are mixed with hot

air/gas flow to transform into dry particles in a single step operation. The sprayed liquid feed can be a slurry, paste or solution. Granules, agglomerates and powder represent the resulting dried product.

Agglomerated powders are produced to give improved physical properties such as flow ability, dispersibility and decreased bulk density. They can be obtained by improving wettability and through size enlargement using agglomeration (Williams, 2007). Agglomeration is achieved by returning fines to the top of the spray drier and contacting them with concentrate droplets, followed by evaporative drying. This allows small particles to combine and form large, porous, open structures (Figure 1).

Graham (1997) distinguished two types of agglomeration processes, called primary and secondary. Primary agglomeration involves collisions between atomized droplets. Secondary agglomeration involves collisions between droplets and dry particles, and can be forced agglomeration or spontaneous agglomeration. Spontaneous agglomeration refers to fine particles being dragged into the agglomeration zone by aerodynamic recirculation. Forced agglomeration refers to the spraying of atomized droplets on to a fines recycle stream that enters the top of the drier. The appearance of agglomerates has been described as onion, raspberry or grape-like (Williams, 2007). An onion is created when small droplets of high moisture (i.e. low viscosity) contact the fine particles and spread over the surface. A raspberry is formed when large droplets of high moisture collide with a large amount of fines. The fines adhere to the outer surface but do not penetrate the droplets. When dried, raspberry and onion structures may have high mechanical strength but are often difficult to dissolve. A grape is created by the collision of the droplets and fine particles.

Agglomeration takes place when two sticky particles collide and form a (viscoelastic) liquid bridge that is strong enough to resist mechanical deformations, while the integrity of the particles is maintained. The major material properties influencing the collision behavior of droplets are surface tension, effective density, and dynamic viscosity. Various researchers have calculated the critical viscosity for sticking during contact times of a few seconds by applying various models. As a result, the critical viscosity appears to be in the range of 106-10^8 Pa.s. This value has been confirmed experimentally by various investigators (Wallack *et al.* 1988). At much lower viscosities the particles will coalesce upon collision, while at higher viscosities the particles will not stick together but bounce.

Only little information is available in the literature concerning the modeling of the agglomeration processes of colliding droplets and particles during spray drying. Roos (2002) pointed out the importance of glass transition temperature for the sticking behavior of amorphous materials as they occur in lactose containing foods. The boundary between viscous droplets and dry particles is determined with help of the sticky point temperature, which was found to be around 20 K above the glass transition temperature of the lactose containing surface of the particle. If the particle temperature exceeds the sticky point temperature, the particle surface will become viscous and the particle is classified as a viscous droplet. Below the sticky point temperature the particle is considered as dry.

Ho and Sommerfeld (2002) described a stochastic collision model to mimic particle agglomeration in turbulent flows. They considered a collision propensity based on the relative inertia of the particles and an agglomeration efficiency based on the van der Waals interaction. Sommerfeld and Stübing (2010) extended this approach to agglomerate structure also in the frame of the Lagrangian point-particle approach the collision and agglomeration model for storing the additional information of the agglomerates.

Verdurmen *et al.* (2004) have reported an attempt to simulate the entire agglomeration process. However, a better understanding of particle agglomeration is needed to translate this to industrial operating guidelines. In the literature, little existing work is available that spatially addresses the agglomeration in a spray dryer.

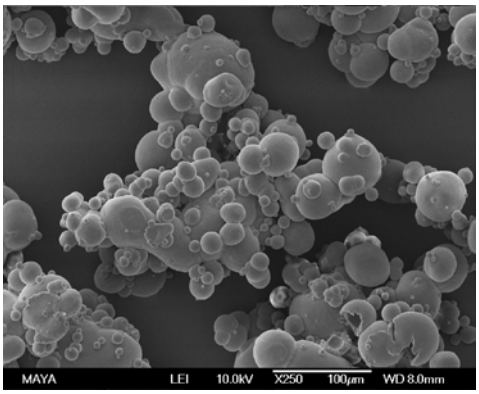

Figure 1: Agglomeration of milk particles to form milk powder (from Tetra Pak).

The main objective of this research is to develop a simulation tool that can provide the particle size, velocity and flux distribution for a highly turbulent gas flow section of a large-scale spray dryer. These results ought to be used as boundary conditions for coarse-grained simulations. For this purpose, we will use an Eulerian-Langrangian approach, while considering the various phenomena of collisions, coalescence and agglomeration between droplet-droplet, droplet-particle and particle-particle combinations in a highly turbulence gas flow at the top section (near the nozzle) of a spray dryer.

THE SPRAY DRYING MODEL

Computational Fluid Dynamics (CFD) is a very powerful and versatile tool, which has been increasingly employed to study the optimal design, operation and scale-up of industrial processes. However, the complex transport phenomena that occur in a spray dryer cannot yet be modeled with high accuracy. The main objective of our research is to develop a simulation tool that can provide the particle size, velocity and flux distribution

for a highly turbulent section of a large-scale spray dryer. These results ought to be used as boundary conditions for more coarse-grained simulations. In this study, we focus at the top section of the spray dryer where most of the events such as collision, coalescence, breakup, drying and agglomeration occur. To systematically build up this model, we split the modelling process into four different steps, including gas and particle flow modeling, collision detection modeling, collision outcome modeling, and drying kinetics modeling, as shown schematically in Figure 2. We will describe the essential features of each component.

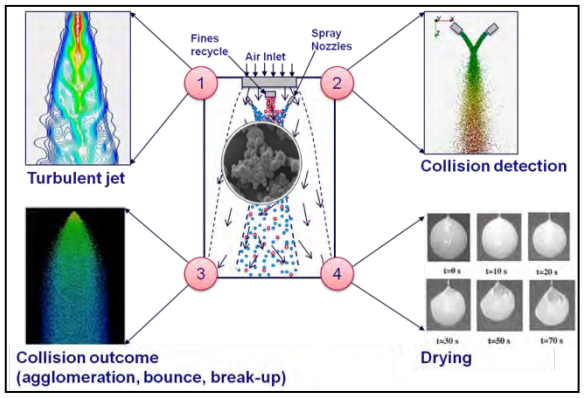

Figure 2: Spray drying model development stages, including (1) turbulent flow modeling, (2) collision detection, (3) collision outcome modeling, and (4) drying kinetics modeling.

Gas and Particle Flow Modeling

The liquid feed is atomized in the cylindrical chamber where hot air enters at the top as a swirling or non-swirling flow and the resulting droplets are mixed with hot air/gas flow to transform into dry particles in a single step operation. One of the challenges faced by designers and operators is to understand the complexity of the particle/air mixing in spray chambers. Improper gas flow patterns inside the chamber can cause roof and wall fouling and the quality of the final product can deteriorate.

Accurate measurement of the gas flow inside an industrial scale spray dryer is difficult to achieve experimentally, leading to a growing interest in the use of Computational Fluid Dynamics. In this study, we use a sub-grid scale (SGS) model, proposed by Vreman (2004), for the investigation of highly turbulent gas flow effects on the droplet/particle trajectories. One of the main advantages of this model that it is more accurate than the Smagorinsky model and as good as the standard dynamics model. The SGS model is able to adequately handle not only turbulent but also transitional flow. Moreover, the Smagorinsky model is known for a poor turbulence modelling close to walls. The Vreman model is expected to correct for this effect. Still, there may be an over prediction of the shear. The turbulent statistics can enlighten these effects. We have validated our turbulent flow model using experimental literature data for different Reynolds numbers (Pawar *et al.* 2014b).

In more detail, we compute the Navier-Stokes equations for the gas phase and Newtonian equations for the motion of the individual droplets/particles, which are possibly represented by a lower number of representative droplets, with conventional two-way coupling for the momentum exchange between the gas and discrete phase. For the gas phase, we write the equation of conservation of mass and momentum:

$$\frac{\partial}{\partial t}(\rho_g \varepsilon_g) + \nabla \cdot (\rho_g \varepsilon_g \mathbf{u}_g) = 0 \qquad (1)$$

$$\frac{\partial}{\partial t}(\rho_g \varepsilon_g \mathbf{u}_g) + \nabla \cdot (\rho_g \varepsilon_g \mathbf{u}_g \mathbf{u}_g) = -\varepsilon_g \nabla p - \nabla \cdot (\varepsilon_g \bar{\boldsymbol{\tau}}_g) - \mathbf{S}_p + \rho_g \varepsilon_g \mathbf{g} \qquad (2)$$

where $\mathbf{u}_g$, ρ_g and p are the gas velocity, density and pressure, respectively, $\boldsymbol{g}$ and is the acceleration due to gravity. $\boldsymbol{\tau}_g$ is the viscous stress tensor, in which the turbulent eddy viscosity is calculated from the sub-grid scale stress model, as described in (Vreman *et al.* 2004). $\mathbf{S}_p$ is a source term that couples the gas to the dispersed phase. It is defined as:

$$\mathbf{S}_p = \frac{1}{V_{cell}} \int \sum_{i=1}^{Ndrop} \frac{n_i \beta V_i}{1-\varepsilon_g} (\mathbf{u}_g - \mathbf{v}_i) \delta(\mathbf{r} - \mathbf{r}_i) dV \qquad (3)$$

Here $\mathbf{v}_i$ is the velocity of a representative droplet with index i, V_i is its volume, n_i the number of real droplets it represents, and V_{cell} the volume of the Eulerian grid cell. The distribution-function δ distributes the reaction force of the droplets acting on the gas phase to the velocity nodes on the (staggered) grid. To calculate the inter-phase momentum transfer coefficient β, for this investigation we employed the drag model of Beetstra *et al.* (2006), which is valid for monodisperse and polydisperse systems.

For the spray dryer simulations, the motion of droplets and particles (in between collisions) is described by Newton's second law:

$$m_i \frac{d\mathbf{v}_i}{dt} = \mathbf{F}_{p,i} + \mathbf{F}_{d,i} + \mathbf{F}_{g,i} \qquad (4)$$

where m_i represents the mass of droplet or particle i and the forces acting on that droplets include gravity, drag and pressure forces. Collisions between droplets and particles significantly affect their trajectories, complicate the calculations of particle tracks, and extend the computational time needed for the simulations. Nevertheless, it is essential to model droplet and particle interactions that influence the quality of final product. With the purpose of keeping the model simple, in the present model we neglect rotational motion of the droplets.

Collision Detection - DSMC

In our model, droplet collisions are treated separately and stochastically because the large number of droplets present in a spray make a deterministic treatment of all droplets trajectories and all droplet collision events

unfeasible. Our approach for detecting droplet collisions is based on the Direct Simulation Monte Carlo (DSMC) method, first proposed by Bird (1976) for simulation of dilute molecular gases. The method is very popular for the investigation of large numbers of particles, because real particles can be represented by a lower number of representative particles, and the trajectories of only these representative particles are calculated. In this way, computer memory and computation time can be reduced significantly (Tsuji *et al.* 1998). O'Rourke (1981) has described application of the DSMC method to granular particle collisions. In this approach, the path of each representative particle is updated sequentially during a large time step. After each update, a collision partner for a particle is sought within the same rectangular cell as the particle in question. Unfortunately, this leads to a lack of communication across cell boundaries, as well as anisotropic (rectangular) bias in the distribution of colliding particles. To avoid such lattice artifacts, the approach was later modified to a stochastic model in which the collision probability and the search for collision partners are based on a spherical region generated from the local particle parameters (Du *et al.* 2011). In some situations, the latter method yields inconsistent results, especially when the particle time step is limited by external factors such as a flow solver. We have recently shown how to amend the method to yield consistent results which are in quantitative agreement with detailed deterministic discrete particle simulations. The modified method automatically and self-consistently increases its searching scope until it contains a minimum number of neighbouring particles to ensure a statistically accurate and unbiased estimate of the average collision frequency. The major advantage of the stochastic-DSMC model is its capability to handle many millions of particles for simulation in a reasonable computation time. We also extensively described the limitations of the stochastic-DSMC model. The stochastic-DSMC model was verified by an extensive comparison with the results obtained from more detailed DPM simulations of two colliding streams of elastic as well as inelastic monodisperse spheres. More details are given in Pawar *et al*. (2014a).

Collision Outcome

Introduction

Accurate measurements of collision events at the nozzle exit and inside of the spray are difficult to obtain in very dense spray. As droplets are drying, their collision properties will change in time. Moreover, in industrial practice dried fine particles are usually returned to the spray dryer. The interactions between droplets and fine particles lead to a rich spectrum of bouncing collisions, coalescence, agglomeration, and satellite droplet formation. Researchers have extensively investigated droplet-droplet and particle-particle interactions using numerical and experimental methods. However, the literature on droplet-particle interactions leading to agglomeration in spray drying is scarce, and mainly qualitative. In this work, the outcome of a collision is first and foremost determined by the surface glass transition temperature of the particle, which depends on the relative amount of solids and liquid in the surface. If the particle temperature is between 10-30 degrees above the glass transition temperature, the particles are sticky and will agglomerate.

For example, during the production of milk powder, collisions and adhesion between milk droplets and recycled fines take place, leading to complex macro particles, which are agglomerates of several primary particles. The primary particles can be dry particles, or droplets. A number of primary particles contribute to the formation of an agglomerate, with each primary particle having its own diameter d (assuming a spherical particle) and its wetness *w* (a variable between 0 and 1, 0 for recycled dry fines and 1 for water droplets). We keep track of these variables in our simulations, giving us the possibility to keep track of the drying of the moisture content inside the agglomerates. The outcome of a collision between two agglomerates depends on the stickiness, viscosity and surface tension, which we will discuss now.

Stickiness

For powders with a high carbohydrate content, the phenomenon of stickiness is related to the physical state of the carbohydrate components, i.e. normally an amorphous glassy state. In the course of drying, viscosity and surface tension become extremely high around a critical water activity level which is dependent on composition and temperature (Adhikari *et al.* 2007). The high viscosity/high surface tension state is sometimes referred to as a rubbery state (Roos and Karel, 1992). Further drying leads to a solid glassy state which is non-sticky (Foster *et al.* 2006). There is a region roughly between the rubbery and non-sticky states known as a glass transition region (Brostow et al. 2008, Bhandari and Howes, 1999). In other words, powders become prone to stickiness in a range of temperatures above the T_g level. Note that during drying the water content and water activity are changing, leading to a changing T_g (Abiad *et al.* 2009). It is therefore essential to model the dependence of the glass transition temperature on the surface moisture content of the particle.

Water activity and moisture isotherm

The level of interaction of water with dry matter is expressed by the water activity, defined as the ratio between the water vapour pressure at the droplet surface and the saturated vapour pressure of pure water at the considered temperature:

$$a_{w,s} = \frac{P_{v,s}}{P_{v,sat}} \qquad (5)$$

The surface vapour pressure is determined using Raoult's law (Patel and Chen 2008).

The equilibrium is characterized by the sorption isotherms, which represent the a_w variation as a function of water content X of the product for a given temperature (each point representing an equilibrium state) (Mathlouthi and Roge, 2003). Sorption isotherms depend on temperature, but slightly for the range of temperatures considered here (20 - 40 °C). They are usually established by water sorption on the dry product, where hysteresis exists between absorption and desorption.

The surface moisture content is calculated using the relevant isotherm model of the specific material. For droplets, the equilibrium moisture isotherm was presented using the popular Guggenheim-Anderson-deBoer (GAB) model (Adhikari *et al.* 2004). The surface moisture content of droplets X_s (kg/kg, dry basis) during drying can be estimated using the following isotherm model:

$$X_s = \frac{m_0 CKa_{w,s}}{(1-Ka_{w,s})(1-Ka_{w,s}+Cka_{w,s})} \qquad (6)$$

where m_0, C and K are constants. For droplets m_0, C and K were reported to be 0.04290, 8.78 and 0.909 at 52 ^oC, respectively (Lin et al, 2006).

Glass Transition Temperature (T_g)

The glass-transition temperature (T_g) of the droplets containing solids is the moisture concentration dependent property of the material. The Gordon-Taylor equation has widely used in the literature to estimate T_g of the droplet containing solid of single or multiple solutes (Adhikari et al, 2004). Since we are interested in estimating the surface glass-transition temperature ($T_{g,s}$), the Gordon-Taylor equation is expressed as:

$$T_{g,sur} = \frac{\omega_s T_{g,s} + K_G \omega_w T_{g,w}}{\omega_s + K_G \omega_w} \qquad (7)$$

where K_G is a constant, $T_{g,s}$ and $T_{g,\mathrm{w}}$ are glass transition temperatures of solids and water, and ω_s and ω_w are mass fractions of solids and water, respectively, at the surface of the particle:

$$\omega_w = \frac{X_s}{1+X_s}, \omega_s = \frac{1}{1+X_s} \qquad (8)$$

Surface viscosity

Williams *et al.* (1955) found that the viscosity of amorphous glucose above its glass transition was similar to the viscosity of other inorganic and organic glass-forming compounds. The viscosity was related to material relaxation times, valid above Tg, and followed an empirical relationship known as the William-Landel-Ferry (WLF) (1955) equation, which was derived from the viscosity data for a number of compounds:

$$\log \frac{\mu_{sur}}{\mu_g} = \frac{C_1 T_d - T_{g,\mathrm{sur}})}{C_2 + (T_d - T_{g,\mathrm{sur}})} \qquad (9)$$

Here μ_g is the viscosity at T_g (estimated as 10^{12} Pa.s), and C_1 and C_2 are empirical coefficients. The values C_1 = 51.6, C_2 = -17.4 are valid for most polymer materials.

Various researchers have calculated the critical viscosity for sticking during contact times of a few seconds by applying various models. As a result the critical viscosity appears to be in the range of 10^6 - 10^8 Pa.s (leading to the quoted range of temperatures within which particles are sticky). This value has been confirmed experimentally by various investigators (Wallack *et al.* 1988; Downton *et al.* 1982). At lower viscosities the particles exhibit more droplet-like behaviour, while at higher viscosities the particles will not stick together.

However, to have a generally applicable model, we must realise that the empirical WLF correlation is only valid for relatively dry (lower moisture content) droplets. Therefore, for higher average moisture content, the agglomerate viscosity was calculated using an empirical correlation for the viscosity of a dispersion of solid particles in liquids (Mooney, 1950):

$$\mu_{agglo} = \mu_l \exp\left[\frac{2.5\varepsilon_s}{1-K\varepsilon_s}\right] \qquad (10)$$

Here μ_l is the pure liquid (i.e. water) viscosity and ε_s is the average solids volume fraction. The constant K is chosen such that the viscosity diverges near a maximum solids volume fraction of 65%. In the transition region, the minimum of eqs. (9) and (10) is assumed to be the true viscosity.

Binary collision outcome

The outcome of a binary collision is summarized in Table 1. If the temperature of either particles is between 10 - 30 ^oC above the glass transition temperature, the particles are sticky and will agglomerate. If the temperature of both particles is less than 10 ^oC above the glass transition temperature, the particles are assumed to be solid and bounce. Droplets (and particles) with a temperature more than 30 ^oC above the surface glass transition temperature are treated separately.

Table 1: Collision outcome rules used in this work for partially wetted particles, droplets and agglomerates.

T-$T_{g,sur}$	< 10 ^oC	10 - 30 ^oC	> 30 ^oC
< 10 ^oC	Bounce	Stick	**
10 - 30 ^oC	Stick	Stick	**
> 30 ^oC	**	**	**

**	Oh_1 < 1.0	Oh_1 > 1.0
Oh_2 < 1.0	Coalesce / Bounce / Stretching / Reflexive	Coalesce
Oh_2 > 1.0	Coalesce	Bounce

For low viscosity droplets, which are dominated by surface tension (both droplets have an Ohnesorge number < 1), the outcome of a collision depends on the values of the Weber number and impact angle. Four different types of collision outcomes can be distinguished. When two droplets strike each other, the gas between them is trapped and the pressure increases inside this gap. If the relative velocity of droplets is not enough to overcome the pressure force, two droplets do not intermix and simply bounce. For higher relative velocities, depending on the impact angle, one droplet may merge with another droplet directly and coalescence takes place. At very high relative velocities, again depending on the impact angle, the kinetic energy

of impact is so high that the droplet breaks up again, leading to stretching or reflexive separation, including the formation of new satellite droplets. The model by Ko and Ryou (2005) improves the widely used model for droplet-droplet collisions developed by O'Rourke (1981) by considering the collision-induced break up process in more detail. The post-collisional diameters and velocities of the droplets, including possible formation of satellite droplets, are determined based on momentum and energy conservation equations. The formation of satellites costs surface energy. Therefore, for stretching or reflexive separation at higher Weber numbers (and depending on the impact parameter) the additional kinetic energy can be used to generate an increasing amount of satellite droplets. We have implemented this model in our simulations. For details the reader is referred to Ko and Ryou (2005).

Finally, when one of the droplets has a very high viscosity (but not high enough to be sticky), i.e. when the Ohnesorge number larger than 1, the outcome of a collision is assumed to be coalescence (one droplet is highly viscous but the other is not) or bouncing (when both droplet are highly viscous).

We note that this part of the model is least certain, and can be improved in future work using correlations from detailed experiments and direct numerical simulations. For example, experimental data of a hollow-cone pressure swirl nozzle spray, obtained by Phase Doppler Anemometry (PDA) at different inlet pressure and liquids, can be used to validate the resulting evolution of the droplet/particle size distribution. More details are given in Pawar *et al*. (2012).

Drying

One of the key component of the simulation tool is the modelling of the drying characteristics of droplets containing solids. A drying model of a droplet containing solids using a reaction engineering approach (REA) was introduced. The model was validated with experimental literature data for the drying of a single droplet of whole milk and skim milk containing 20% solid at different conditions and different correlation for the determination of heat and mass transfer coefficients. The effect of drying on the droplets in the top section of a large scale spray dryer was studied by coupling this drying model to the developed Euler-DSMC approach. For technical details the reader is referred to Pawar et al. (2014c).

SIMULATION PARAMETERS

We model two droplets sprays and one dry particle (returned fines) spray. We choose droplets from a Rosin-Rammler distribution and introduce them in the domain at 0.2m from the top boundary, using 0.2 m distance between the two nozzles. In between the two droplets sprays, we introduce the dry particle spray. All sprays have an initial volume fraction of O(0.1). For the simulation, we used a domain of 0.6 x 0.6 square meters and a height of 0.7 meters, using a cartesian grid with 50 cells in x, y direction and 60 cells in the z-direction. Additional simulation parameters are given in Table 2.

Table 2: Simulation case parameters

Parameters	Values	Unit
Density of dry particles (ρ_p)	1300	kg/m^3
Injected dry particle diameter (d_p)	6.0 x 10^{-5}	m
Particle nozzle diameter	0.01	m
Dry mass flow rate	1.25	kg/s
Dry particle parcel size	10	
Injected dry particle velocity	80	m/s
Density of droplet (ρ_d)	1000	kg/m^3
Surface tension of droplet	0.073	Pa.s
Viscosity of droplet	0.001	kg / m.s
Injected droplet diameter (d_d)	2.5 x 10^{-5}	m
Droplet nozzle diameter	0.00464	m
Liquid mass flow rate	0.275	kg/s
Droplet parcel size	1000	
Injected droplet velocity	140	m/s
Spray angle	52	degree
Gas temperature	100	^{o}C
Geometry dimensions (W x D x H)	0.6 x 0.6 x 0.7	m
No. gas cells (NX x NY x NZ)	50 x 50 x 60	
Gas time step	2.5x 10^{-6}	s

RESULTS

Figure 3 shows the wetness distribution of droplets, particles and agglomerates in the spray. The particle-droplet interactions start from the middle of the domain where the different streams meet.

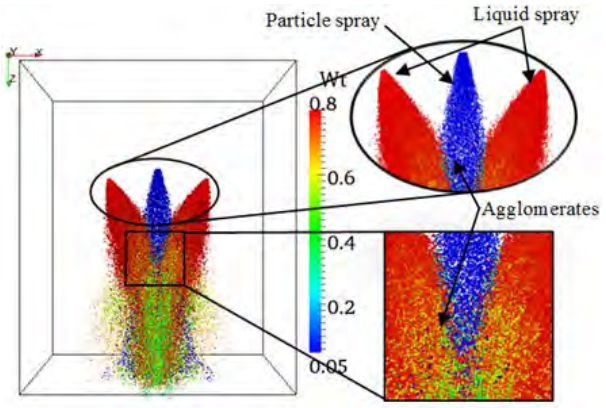

Figure 3: Two droplets spray and one primary particle spray meeting at the center. Colour denotes the wetness of the agglomerates. Blue colour means dry particles. Red colour means pure liquid droplets. Green particles are partially wet.

The effect of the drying model can be seen in Figure 4a, where the droplet/particle temperature is observed to increase with increasing axial distance. Droplets and particle velocities at different locations are shown in Figure 4b. Figure 4c shows the glass transition temperature of the droplet/particle surfaces in the simulation domain. Different sizes of the droplets are introduced through the nozzle (from a Rosin-Rammler distribution) and when the droplets and particles interact, their size decreases (due to break-up) or increases (due to coalescence and agglomeration). Figure 4d is showing the radius of the droplets or particles or agglomerates.

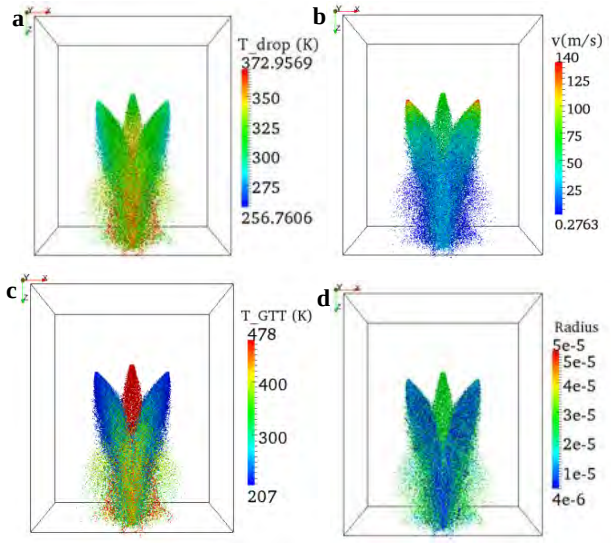

Figure 4: Different parameters of the droplets / particles in the simulation domain: a) droplet/particle temperature, b) velocity of the droplets/particles, c) surface glass transition temperature of the droplets/particles, and d) radius of the droplets/particles/agglomerates.

Figure 5(a-d) shows the frequency of droplet-droplet collision events (per second per cell) occurring on the cutting plane along the axial and radial direction in the simulation domain. As expected, most events take place in the densest droplet regions (near the spray nozzles).

Figure 6a shows the overall particle-particle bouncing frequency (per second per cell) on the same cutting plane. Particles are not only bouncing off each other in the dry particle stream, but also when small droplets have coalesced with dry particles and subsequently dried. Figure 6b shows the agglomeration frequency. As could be expected, most agglomeration is occurring when the dry and wet sprays are colliding with each other. Our simulation model is now also able to quantify this process.

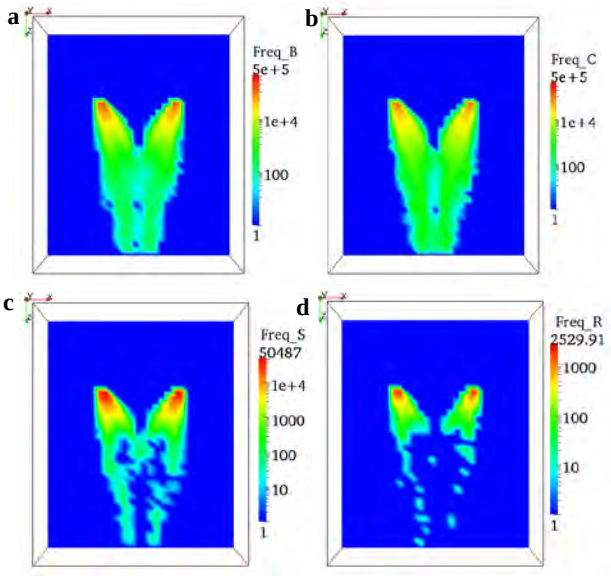

Figure 5: Frequency of droplet-droplet events occurring in the spray: a) bouncing, b) coalescence, c) stretching, d) reflexive separation.

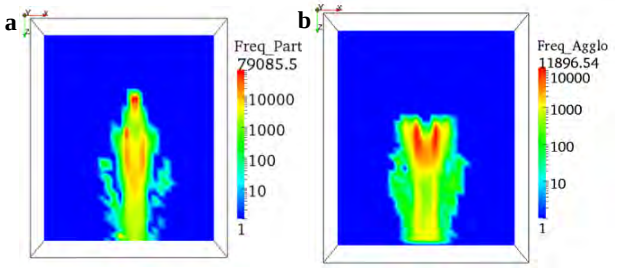

Figure 6: Frequency of particle-particle events occurring in the spray: a) particle bouncing, b) particle agglomeration.

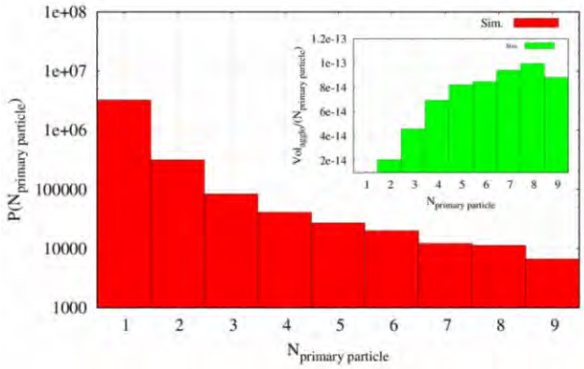

Figure 7: Main figure: histogram of the number of primary particles per agglomerate (note the logarithmic scale). Inset: average volume per primary particle as a function of the number of primary particles in an agglomerate. Sample taken at 0.48 m below the nozzle exit.

Figure 7 shows a histogram of the number of primary particles per agglomerate at 0.48 m below the nozzle exit. We observe an exponential distribution for higher numbers of primary particles per agglomerate. The inset of Figure 7 shows a histogram of the average volume per primary particle as a function of the number of primary particles per agglomerate. This shows and quantifies how agglomerates with more primary particles also tend to contain larger primary particles.

CONCLUSION

In the present work, we explore the development of an Euler-Lagrange model with a stochastic approach for the prediction of collision, coalescence, break-up, drying and agglomeration of partially wet particles in a spray dryer. We present details of the modeling approach using elementary models for collision, coalescence, break-up, drying and agglomeration. and preliminary simulation results we described. The results of the simulation cases shows droplet/particle wetness, temperature, surface glass transition temperature, velocity and radius. We also measured the frequencies of different collision events. Because the model stores the primary particle history of the agglomerates, we are able to show how larger primary particles also tend to form agglomerates with a larger number of primary particles. These results should be viewed as preliminary, especially because we have not yet validated the agglomeration model at this stage. However, our simulation model already predicts reasonable results which are in qualitative agreement with experimental observations. In our future work we will further refine and validate the model.

REFERENCES

ABIAD, M. G., (2009), "Thermal properties of food and pharmaceutical powders" PhD Dissertation. Purdue University, West Lafayette, IN.

ADHIKARI, B., HOWES, T., BHANDARI, B. R., TROUNG, V., (2007), "Surface Stickiness of Drops of Carbohydrate and Organic Acid Solutions During Convective Drying: Experiments and Modeling", Drying Technology: An International Journal, **21**(5), 839-873.

ADHIKARI, B., HOWES, T., BHANDARI, B.R. AND TROUNG, V., (2004), "Effect of addition of maltodextrin on drying kinetics and stickiness of sugar and acid-rich foods during convective drying: experiments and modelling", Journal of Food Engineering, Vol. **62**(1), pp. 53-68.

BEETSTRA, R., VAN DER HOEF, M.A., KUIPERS, J.A.M., (2006), "Drag force from lattice Boltzmann simulations of intermediate Reynolds number flow past mono- and bidisperse arrays of spheres", Manuscript-AIChE J.

BHANDARI, B.R., HOWES, T., (1999), "Implication of glass transition for the drying and stability of dried foods", Journal of Food Engineering, **40**, 71-79.

BIRD, A., (1976), "Molecular Gas Dynamics and Direct Simulation of Gas Flow", Clarendon, Oxford.

BROSTOW, W., CHIU, R., KALOGERAS, I.M., VASSILIKOU-DOVA, A., (2008), "Prediction of glass transition temperatures: binary blends and copolymers", Mater Lett **62**,3152-3155

DOWNTON, G.E., FLORES-LUNA, J.L., KING, C.J., (1982), "Mechanisms of Stickiness in Hygroscopic, Amorphous Powders", Ind. Eng. Chem. Fundamental. **21** (4), 447-451.

DU, M., ZHAO, C., ZHAO, B., GUO, H., HAO Y., (2011), "A modified DSMC method for simulating gas-particle two-phase impinging streams" Chemical Engineering Science. **66**, 4922-4931.

FOSTER, K. D., BRONLUND, J.E., PATERSON, A., (2006), "Glass transition related cohesion of amorphous sugar powders", J Food Engg **77**, 997-1006.

GRAHAM, B. A., (1997), "Recent advance in agglomeration during spray drying", Food Australia. **49** (4), 184-185.

HO, C.A., SOMMERFELD, M., (2002), "Modelling of micro-particle agglomeration in turbulent flow", Chemical Engineering Science, **57**, 3073-3084.

KO, G.H., RYOU, H.S., (2005), "Modeling of droplet collision-induced breakup process" International Journal of Multiphase Flow, **31**, 723-738.

LIN S. X. Q. and CHEN X. D., (2006), "A Model for Drying of an Aqueous Lactose Droplet using the Reaction Engineering Approach", Drying Technology **24**, 1329-1334,.

MATHLOUTHI., AND ROGÉ B., (2003), "Water Vapour Sorption Isotherms and the Caking of Food Powders", Food Chemistry,82, 61 - 71.

MOONEY, M., (1950), "The viscosity of a concentrated suspension of spherical particles", General Laboratories of the United States Rubber Company, Passaic, New Jersey.

O'ROURKE, P. J., (1981), "Collective drop effect on vaporizing liquid sprays" Ph. D. thesis, Mechanical and Aerospace Engineering. Princeton University, USA.

PATEL, K.C. AND CHEN, X.D., (2008), "The reaction engineering approach to estimate surface properties of aqueous droplets during convective drying", 16th International Drying Symposium (IDS 2008), Hyderabad, India 9-12.

PAWAR, S.K., PADDING, J.T., DEEN, N.G., JONGSMA, A., INNINGS, F., KUIPERS, J.A.M., (2014a), "Lagrangian modelling of dilute granular flow-modified stochastic DSMC versus deterministic DPM" Chemical Engineering Science, **105**, 132-142.

PAWAR, S.K., PADDING, J.T., DEEN, N.G., JONGSMA, A., INNINGS, F., KUIPERS, J.A.M., (2014b), "Numerical and Experimental Investigation of the Droplet-Droplet Interaction in a Spray Nozzle" Manuscript-International Journal of Multiphase Flow.

PAWAR, S.K., PADDING, J.T., DEEN, N.G., JONGSMA, A., INNINGS, F., KUIPERS, J.A.M., (2014c), "Drying kinetics of droplets containing solids using reaction engineering approach.", 19th International Drying Symposium, Lyon, France.

PAWAR, S.K., PADDING, J.T., DEEN, N.G., KUIPERS, J.A.M., JONGSMA, A., INNINGS, F., (2012), "Eulerian-Lagrangian modeling with stochastic approach for droplet-droplet collisions. CSIRO, 10-12 December 2012, Melbourne Australia.

ROOS, Y., KAREL, M., (1992), "Crystallization of amorphous lactose", J. Food Sci. **57**, 775–777.

ROOS, Y.H., (2002), "Importance of glass transition and water activity to spray drying and stability of dairy powders", Le Lait, **82** (4), 475-484.

SOMMERFELD, M. and STÜBING, S., (2012), Lagrangian modelling of agglomeration for applications to spray drying", 9th International ERCOFTAC Symposium on Engineering Turbulence Modeling and Measurements (ETMM 9), Thessaloniki, Greece, 6.

TSUJI, Y. T., TANAKA, T. S., YONEMURA S., (1998), "Cluster patterns in circulating fluidized beds predicted by numerical simulation (discrete particle model versus two-fluid model)", Powder Technol., **95**.

VERDURMEN, R.E.M., MENN, P., RITZERT, J., BLEI, S. , NHUMAIO, G.C.S., SONNE SØRENSEN, T., GUNSING, M., STRAATSMA, J., VERSCHUEREN, M., SIBEIJN, M., SCHULTE, G., FRITSCHING, U., BAUCKHAGE, K., TROPEA, C., SOMMERFELD, M., WATKINS, A. P., YULE A. J., SCHØNFELDT, H., (2004), "Simulation of Agglomeration in Spray Drying Installations: The EDECAD Project", Drying Technology, **22** (6), 1403.

VREMAN, A.W., (2004), "An eddy- viscosity sub grid-scale model for turbulence shear flow: algebraic theory and application", Physics of fluid 16, 3670-3681.

WALLACK, D.A. and KING, C.J., (1988), "Sticking and agglomeration of hygroscopic", amorphous carbohydrate and food powders Biotechnology Progress, **4** (1), 31-35.

WILLIAMS, A.M., (2007), "Instant Milk Powder Production: determining the extent of agglomeration", PhD Thesis, Massey University, Palmerston North, New Zealand.

WILLIAMS, M.L., LANDEL, R.F., FERRY, J.D., (1955), "Temperature Dependence of Relaxation Mechanisms in Amorphous Polymers and Other Glass-Forming Liquids", J. Am. Chem. Soc. **77**, 3701-3707.

STATE OF THE ART IN MAPPING SCHEMES FOR DILUTE AND DENSE EULER-LAGRANGE SIMULATIONS

Stefan RADL,[1*] Begona C. GONZALES,[1] Christoph GONIVA,[2,3] Stefan PIRKER[3]

[1] Institute of Process and Particle Engineering, TU Graz, AUSTRIA

[2] DCS Computing GmbH, Linz, AUSTRIA

[3] Department of Particulate Flow Modelling, JKU Linz, AUSTRIA

* E-mail: radl@tugraz.at

ABSTRACT

Euler-Lagrange (EL) simulations are an extremely important tool for academia and industry to better understand gas-particle flows. We present simulation results for various gas-particle flow configurations using a variety of Lagrangian-to-Euler coupling schemes. Specifically, we have combined the idea of smoothing the exchange fields (as proposed by Pirker et al. (2011), as well as Capecelatro and Desjardins (2013)) to design a new generation of robust mapping schemes that allow implicit, explicit or a hybrid implicit/explicit time marching. Our schemes enable EL simulations of highly loaded gas-particle flows in which particles have a broad size distribution. We demonstrate the performance of our mapping schemes for the case of (i) a bubbling bi-disperse fluidized bed, (ii) a freely sedimenting suspensions, as well as (iii) particle injection in turbulent cross flow configurations.

Keywords: Euler-Lagrange, numerical schemes, gas-particle flow.

NOMENCLATURE

Greek Symbols

β	Friction coefficient, [kg/m³/s].
ϕ	Mass density, [kg/m^3].
γ	Transported quantity (scalar or vectorial).
κ	Indicator function.
η	Dynamic viscosity, [Pa.s].
μ	Mass loading, [kg/kg].
μ_{pp}	Inter-particle friction coefficient.
ρ	Mass density, [kg/m^3].
τ	Characteristic time scale, [s].
$\boldsymbol{\tau}$	Stress, [Pa].
$\boldsymbol{\Phi}$	Volumetric coupling force, [N/m³]

Latin Symbols

$\mathbf{a}$	Acceleration, [m/s²].
d	Diameter, [m].
e	Coefficient of restitution.
$\mathbf{f}$	Force, [N].
$\mathbf{g}$	Gravity, [m/s²].
l	Length, [m].
m	Mass flow rate, [kg/s].
p	Pressure, [Pa].
t	Time, [s].
$\mathbf{u}$	Fluid velocity, [m/s].
$\mathbf{v}$	Particle velocity, [m/s].
w	Weighting function.
x,y,z	Cartesian coordinate, [m].
CG	Coarse graining ratio, ($CG = d_{parcel}/d_p$).
Co	Courant number.
D	Diffusion coefficient, [m²/s].
L,H,W	Channel length, height, width, [m].
N	Number of particles.
S	Source term (scalar or vectorial).
U	Characteristic velocity, [m/s].
V	Volume, [m³].
X,Y,Z	Overall extension of simulation domain, [m].

Sub/superscripts

*	Dimensionless quantity.
$\langle\rangle$	Domain-averaged quantity.
c	Cell centred value.
d	Drag.
f	Fluid.
i	Particle index.
$inlet$	At the inlet.
j	Fluid cell index.
jet	Jet property.
m	Sub-time stepping index.
n	Time index.
p	Particle (primary).
$parcel$	Parcel (computational).
s	Superficial.
t	Terminal.
$slip$	Relative between the two phases.
$orig$	Original (unsmoothed) variable.

INTRODUCTION

EL simulations are of key importance to simulate the flow in (i) gas-particle separation devices, (ii) reactive fluidized beds with changing particle properties (e.g., size, porosity, or chemical composition), or (iii) particle

classification equipment. In case the particle population is polydisperse and particles are non-spherical, EL (or hybrid EL-Euler) simulations are currently the only reliable tool to investigate cluster formation, mixing or segregation effects. However, EL simulations are computationally expensive, and this work aims on providing some guidance for selecting appropriate numerical schemes that alleviate challenges associated with the maximum allowable computation time.

One important class of numerical schemes used in EL simulations is the coupling scheme that is used to transfer information from the particle phase to the Eulerian phase (i.e., "two-way" or "back-coupling"). For the coupling scheme a variety of strategies are available in literature. For example, the group of Sommerfeld (Lain and Sommerfeld, 2008; Sommerfeld and Lain, 2012) used an under-relaxation technique in which particle-phase properties are pre-averaged before the back-coupling is performed. Despite the great success of this technique in predicting experimental data, this approach cannot be used for a time-resolved simulation, and also cannot strictly guarantee Newton's Third Law (i.e., "action et reactio") in an instantaneous sense. Another approach (called "EUgran+poly") has been chosen by the group around Pirker (Schellander et al., 2013), in which a transient simulation (based on an Euler-Euler approach and a mean particle diameter of the particle cloud) is performed first. Then, tracer particles are used to predict individual particle trajectories in a polydisperse particulate flow. Finally, the mean particle diameter of the granular (Euler) phase is updated, and the transient Euler-Euler simulation is continued. While both strategies have proven to be very efficient in terms of computation time, they are not fully transient in the sense that both phases are updated in a time-resolved fashion. Furthermore, these two approaches are limited to moderately dense flows, because their collision models rely on closures from kinetic theory.

In this work we focus on a fully transient approach, which is based on the classical CFD-DEM (Zhou et al., 2010). This approach allows simulations of fluid-particulate flows from the dilute to very dense regimes (i.e., near or above the close-packing limit), which is its key advantage. Specifically, we have chosen the implementation CFDEMcoupling (www.cfdem.com) as the basis of our work, which relies on a parallel implementation of a finite-volume fluid solver (N.N., 2013), and the DEM (Kloss et al., 2012).

In the next chapter we briefly explain the underlying model equations, and the coupling algorithms we have implemented in CFDEMcoupling. We then analyse the time-step restrictions immanent to phase coupling, and finally consider a variety of test cases in order to benchmark the coupling algorithms. By considering a wide range of numerical parameters, we highlight the effect of these parameters on the predictions and the implications in terms of the computation time step required to ensure a stable integration. This allows us to give recommendations for numerical parameters that yield predictions with acceptable accuracy at a minimal computational cost.

MODEL DESCRIPTION

CFD-DEM Approach

The well-known CFD-DEM approach (Zhou et al., 2010) relies on the solution of the filtered Navier-Stokes equations, i.e.,

$$\frac{\partial\left(\rho_f \phi_f\right)}{\partial t} + \nabla\cdot\left(\rho_f \phi_f \mathbf{u}\right) = 0\,, \qquad (1)$$

$$\frac{\partial\left(\rho_f \phi_f \mathbf{u}\right)}{\partial t} + \nabla\cdot\left(\rho_f \phi_f \mathbf{u}\mathbf{u}\right) = -\phi_f \nabla p_f - \phi_f \nabla\cdot\boldsymbol{\tau}_f + \boldsymbol{\Phi}_d + \rho_f \phi_f \mathbf{g}\,, \qquad (2)$$

and the integration of Newton's equation of (translational and rotational) motion for each individual particle. Here $\boldsymbol{\Phi}_d$ is a volumetric coupling force (excluding buoyancy effects), i.e., the force exerted by the particle phase on the fluid phase per unit volume of the gas-particle mixture.

Assuming a fixed particle mass, Newton's equation of translational motion yields an equation for the acceleration of each individual particle. Taking into account (i) contact, (ii) drag, (iii) fluid-stress, and (iv) gravitational forces, this equation is:

$$\mathbf{a}_i = \frac{\mathbf{f}_{cont,i}}{\rho_p V_{p,i}} + \frac{\beta_{p,i}}{\rho_p}\left(\mathbf{u}_i - \mathbf{v}_i\right) - \frac{1}{\rho_p}\nabla\cdot\boldsymbol{\tau}_f + \mathbf{g}\cdot \qquad (3)$$

The integration of the above equations is straight forward once each force component has been computed based on particle and fluid data at the time t^m and t^n, respectively. Note, that in this work we have considered only contact forces to integrate the equations of rotational motion, and have neglected hydrodynamic torque.

The above equation requires closures for the contact forces, the fluid-particle friction coefficient, and the fluid stress. We use a standard linear spring-dashpot model for the contact forces, the model proposed by Beetstra et al. (2010) for the friction coefficient, and a laminar fluid stress model.

CFD-DPM Approach

In order to simulate systems of industrial scale, the CFD-DEM approach cannot be used because of the excessively large number of (physical) particles. Instead, various flavours of "parcel methods", in which computational parcels are used represents multiple physical particles, have been documented in literature during the last fifteen years. In CFDEMcoupling, both the MP-PIC method introduced by Snider (2001), as well as the DPM approach by Patankar and Joseph (2001) is available. While the MP-PIC approach does not require direct tracking of (parcel) collisions, DPM relies on a detection of collisions of spheres that represent a typical collision volume of each parcel. In parcel-based approaches, fluid-particle interaction forces are based on the physical diameter of the particles that are represented by each parcel. In such a way, fluid-particle momentum transfer can be modelled correctly.

We find that for situations involving dense granular flows the DPM results in much more robust simulation compared to the MP-PIC method. Consequently, we have used the DPM approach in all the simulations presented in this paper.

Coupling Algorithm

The overall flow chart for the coupling algorithm implemented in CFDEMcoupling is illustrated in Figure 1. Starting with the known fluid and particle velocities, fluid quantities (e.g., the fluid velocity, or the voidage) are interpolated at the particle location to allow the computation of forces acting on each particle. Particle properties (i.e., velocity and position) are then updated with sub-time stepping (index m), either in an implicit or an explicit way. Note, that for implicit time marching of the particles the fluid velocity at the particle position and the drag coefficient must be known. In this work, we have used explicit time marching for the particle phase.
The update of the fluid properties is more involved, and is detailed in the following paragraphs.

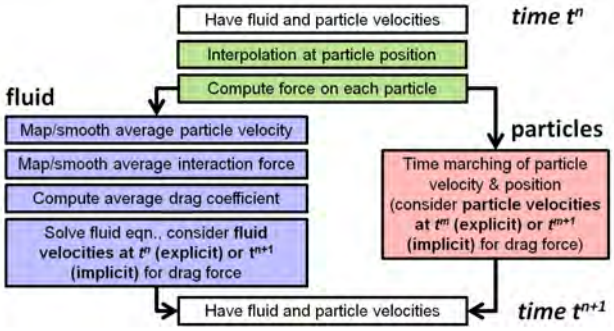

Figure 1: Flow chart of the coupling algorithm.

Mapping Algorithm

A mapping algorithm is used to determine the weights w_{ij} that determine the contribution of the properties of particle i to cell j. The algorithm used in this work is based on a simple search algorithm that uses 29 satellite points (located inside the particle or parcel volume) to determine w_{ij}. Specifically, w_{ij} is determined by the number of satellite points of particle i that are located in cell j, divided by the total number of satellite points (of particle i) that are located in the fluid domain. This simple algorithm is very robust, conserves particle properties, can be used for any polyhedral mesh, and naturally handles situations in which particles are located near walls. Note that each particle (or parcel) only contributes to cells which are physically overlapping with the particle. This situation is unsatisfactory in case the typical size of a fluid cell is in the order of, or smaller than the particle (or parcel) diameter. In the following, we discuss an approach to overcome this limitation.

Smoothing

After the mapping algorithm has been executed, filtered Eulerian quantities (with a filter length equal to the grid spacing Δx) of the particle properties are available at the fluid grid. These quantities can now be smoothed over a length l_{smooth}. The physical meaning of this smoothing length is that each particle (or parcel in case of the DPM) will influence the fluid around it over a certain distance. Naturally, this distance will be some multiple of the particle (or parcel) radius. Typically, we have chosen $l_{smooth} = 3d_p$ in this work. Note that such a smoothing procedure is only relevant for small $\Delta x/d_p$ ratios. In case this ratio is large, however, the smoothing inherent to the mapping algorithm already yields smooth exchange fields, and smoothing has no effect.
The smoothing operation is realized by (implicit) solution of a diffusion equation for each transferred quantity γ:

$$\frac{\partial \gamma}{\partial t} = D\nabla^2\gamma \cdot \qquad (4)$$

Here the diffusion coefficient is computed as $D = l_{smooth}^2/\Delta t$. Note that this smoothing operation is conservative, and has been already used in previous work (Capecelatro and Desjardins, 2013; Pirker et al., 2011).
In case an implicit time marching for the fluid phase is used (see next section), a smoothed mean particle velocity field must be available. In this case the mean particle velocity field must be fixed in cells where particles are present ("filled cells"), and smoothing must be applied only to neighbour cells (of these filled cells). This can be realized by adding a source term S in the diffusion equation, i.e.,

$$S_\alpha = \frac{\kappa}{\Delta t}\left(\gamma_{orig} - \gamma\right), \text{ with}$$
$$\kappa = \begin{cases} 10^5 \ \textit{if} \ \gamma_{orig} \neq 0 \\ 0 \quad \textit{otherwise} \end{cases}, \qquad (5)$$

that forces the original values (γ_{orig}) in filled cells to remain unchanged during the smoothing operation (Pirker et al., 2011).

Implicit/Explicit Time Marching for the Fluid Phase

At this point it is important to note that the volumetric coupling force $\mathbf{\Phi}$ can dominate Eqn. 2 in dense gas-particle flows involving small (i.e., $d_p <$ ca. 100 µm) particles. In such a situation, this term is balanced (to a first approximation) with the pressure gradient term (i.e., the first term on the right hand side of Eqn. 2). Consequently, an implicit treatment of the coupling force $\mathbf{\Phi}$ would be desirable when updating the fluid's velocity and pressure field, because it would improve the stability of the integration. Indeed, we find that an implicit handling allows us to take 5 to 15 times larger fluid time steps, critically reducing the computation time in situations in which the load from the fluid solver is substantial compared to the particle solver.
In most gas-particulate flows, the drag force is the key force component, and hence $\mathbf{\Phi}_d$ is a function of the local fluid and particle velocity, as well as the fluid-particle friction coefficient experienced by each individual particle. Thus, the total coupling force (before updating the fluid velocity) available at the new time t^{n+1} is:

$$\mathbf{\Phi}_{d,j}{}^{n+1} = -\frac{1}{V_j}\sum_i w_{ij} V_{p,i} \beta_{p,i} \left(\mathbf{u}_i{}^n - \mathbf{v}_i{}^{n+1}\right) \qquad (6)$$

Note that it is not possible to consider the new fluid velocity $\mathbf{u}_i{}^{n+1}$ in the calculation of the total coupling force, since the particle velocities are advanced with sub-time stepping. To realize an implicit coupling, i.e., consider the new fluid velocity $\mathbf{u}_c{}^{n+1}$ located at the cell centres, it is necessary to recast the coupling force in an expression that involves an average fluid-particle friction coefficient, as well as an average relative particle velocity. Thus,

$$\mathbf{\Phi}_{d,j}^{n+1} = -\frac{\left\langle w_{ij} V_{p,i} \beta_{p,i} \right\rangle}{V_j} \left(\mathbf{u}_c^{\,n} - \left\langle \mathbf{v}_i^{\,n+1} \right\rangle \right), \qquad (7)$$

and one can easily calculate the average friction coefficient $\langle w_{ij} V_{p,i} \beta_{p,i} \rangle$ from this relationship. In case an implicit handling of the coupling force is performed, the new fluid velocity appears in the expression of the latter, i.e.,

$$\mathbf{\Phi}_{d,j}^{n+1'} = -\frac{\left\langle w_{ij} V_{p,i} \beta_{p,i} \right\rangle}{V_j} \left(\mathbf{u}_c^{\,n+1} - \left\langle \mathbf{v}_i^{\,n+1} \right\rangle \right). \qquad (8)$$

Thus, an implicit handling of the coupling force has two important consequences: (i) Newton's Third Law is not strictly enforced, and (ii) the effect of particle velocity fluctuations (which might affect $\beta_{p,i}$) is not accounted for. While the latter is thought to be of minor importance for typical gas-particle flows involving particles with d_p < 100 µm, the former is of concern in case an exact conservation of the system's momentum is required. We will discuss this point in our results for the freely sedimenting suspensions.

The interested reader might have observed another subtle difference between Eqn. 6 and 7: particle-based quantities (index *i*) need to be replaced by cell-based quantities (index *c*) when solving the fluid's governing equations. We have previously proposed a force splitting scheme (see Radl et al., 2012) that accounts for this discrepancy by splitting-off an explicit force component. Tests show that in dense flows (e.g., packed beds) this splitting increases the stability of the fluid solver (data not shown). We have indicated results obtained by such an improved method by "split impl./expl." in the current work. Furthermore, we have considered a variant of the coupling algorithm in which we treat the coupling force in cells that are void of particles (and hence no average particle velocity can be estimated) explicitly. In the remaining fluid cells the coupling force was treated implicitly. Such an approach avoids the need for smoothing the particle velocity field, which might be problematic in regions with high particle velocity gradients.

THEORETICAL CONSIDERATIONS

Relaxation Times

A key physical time scale in a gas-particle flow is the particle relaxation time τ_p defined as (for simplicity we assume Stokes drag law):

$$\tau_p = \frac{\boldsymbol{d_p}^2 \rho_p}{18 \eta_f}. \qquad (9)$$

This time scale sets an upper bound for the numerical integration of the particles' equation of motion (note that the particle-particle interaction force model might impose an additional limitation on the time step). Physically, this time scale can be interpreted as the time needed to accelerate the particle to a certain fluid velocity *U* by means of drag forces. The time step used for the integration of the particle equations must be smaller than the particle relaxation time in order to ensure an accurate and stable (in case of a simple forward Euler integration) numerical simulation.

Similarly, one can define a fluid relaxation time τ_f defined as:

$$\tau_f = \frac{\boldsymbol{U}}{\boldsymbol{a_f}} = \frac{\tau_p}{\mu} = \frac{\boldsymbol{d_p}^2 \rho_f}{18 \eta_f} \frac{1-\phi_p}{\phi_p}. \qquad (10)$$

Here a_f is a typical acceleration of the fluid due to drag forces. This time scale can be interpreted as the time it takes for the fluid to accelerate to a certain particle velocity *U* under the action of drag forces. This time scale sets an upper bound for the numerical integration of the equations that govern fluid flow. Clearly, the time step used for the integration of the Navier-Stokes equations must be smaller than the fluid relaxation time. In typical gas-particle flows with moderately small to large particle volume fractions and particles in the µm size-range, this fluid relaxation time is $O(10^{-5})$ seconds or smaller, depending on the mass loading.

Time Step Restrictions

In addition to the above characteristic relaxation times, the Courant number *Co* must be kept sufficiently low (typically less than 0.5) in order to ensure a stable numerical solution. Thus, the characteristic time scale

$$\tau_{Co} = \frac{\Delta \boldsymbol{x}}{\boldsymbol{U}} \boldsymbol{Co} \qquad (11)$$

limits the fluid time step. The time step restrictions for integrating the Navier-Stokes equations are summarized in Figure 2 for a freely sedimenting gas-particle suspension. Note that in this figure the particle and fluid relaxation time for dense suspensions at non-zero Reynolds numbers have been computed using the drag model of Beetstra et al. (2010). As can be seen, for a dilute suspension (i.e., ϕ_p = 0.001), the particle relaxation time becomes the limiting time scale in case particles are smaller than ca. 15 µm. However, for moderately dense suspensions (i.e., ϕ_p = 0.001) the largest possible time step is set by the fluid relaxation time for particle diameters smaller than ca. 200 µm. For particles with a diameter of ca. 20 µm or smaller, the largest possible time step is of $O(10^{-6})$ seconds or smaller. Thus, an integration of the Navier-Stokes equations for these systems requires very small time steps, or a robust (implicit) coupling algorithm, such as the one we have outlined above.

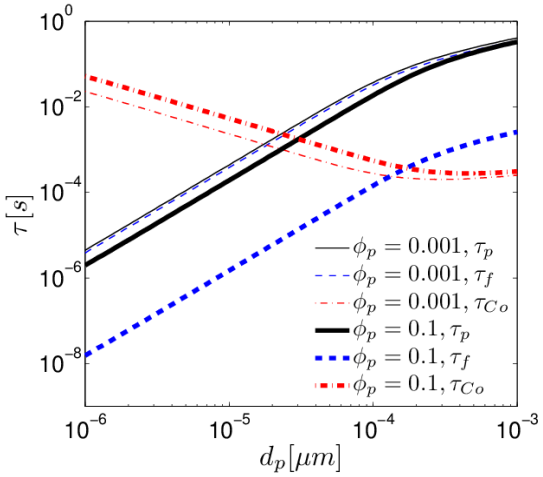

Figure 2: Characteristic time scales relevant for the simulation of a freely-sedimenting gas-particle suspension (ρ_p = 1500 [kg/m³], $\eta_f = 1.8 \cdot 10^{-5}$ [Pa·s], ρ_f = 1.3 [kg/m³], Beetstra et al. drag law).

RESULTS

Bi-Disperse Bubbling Fluidized Bed (CFD-DEM)

To illustrate that the proposed methodology can handle systems near close packing, we have simulated the bubbling fluidized originally studied by Goldschmidt et al. (2003), and simulated recently by Capecelatro and Desjardins (2013). Key system parameters are summarized in Table 1. In these simulations an implicit time marching for the fluid phase was performed, and no smoothing of exchange fields was performed.

Predictions both from the current work and from literature are summarized in Figure 3. As can be seen, there is reasonable agreement in the predicted particle distribution. However, the shape of the interface between the two particle species is different, especially for longer simulation times. A possible explanation of this difference is the different drag law used in the simulations. Specifically, the comparison in might hint to differences in the particle flow pattern caused by bubbling. Unfortunately, we could not find reference results for the particle flow pattern in literature. Hence, we can only speculate about the effect of bubbling, and have included snapshots of the particle velocity distribution in .

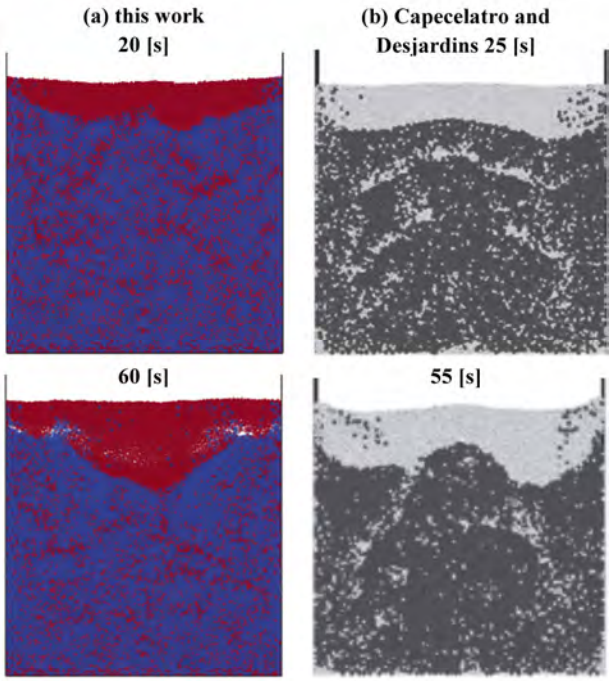

Figure 3: Snapshots of the spatial distribution of particles in a bubbling fluidized bed (a: this work, small particles are colored red and large particles are colored blue; b: literature data from Capecelatro and Desjardins, 2013, using the Tenneti et al., 2011, drag model).

Our results indicate that there is noticeable particle motion only near the free interface of the particle bed, and distinct bubbles do not form. Also, we found that even for moderate diameter ratios (i.e., 1.67 as in the current presentation), the drag formulation had a significant impact on the predicted bed expansion (i.e., bubbles occurred for other drag models) and segregation profile. Surprisingly, we found that the standard (i.e., mono-disperse) formulation of the drag model provided by Beetstra et al. (2010) gave the best agreement with the experimental data of Goldschmidt et al. (2003). Interestingly, also Capecelatro and Desjardins (2013) used a drag law that has been designed for mono-disperse particle beds. Thus, more research is needed to explain why a mono-disperse drag formulation gives better predictions for bi-disperse bubbling bed compared to more elaborate drag models.

Table 1: Physical parameters of the bubbling fluidized bed test case.

Parameter	*Value*
Domain (X x Y x Z)	0.15 x 0.015 x 0.45 [m]
Particle density (ρ_p)	2525 [kg/m³]
Particle diameter (d_p)	1.5 … 2.5 [mm]
Gas density (ρ_f)	1.13 [kg/m³]
Gas dynamic viscosity (η_f)	$1.77 \cdot 10^{-5}$ [Pa.s]
$N_{p,1}$ / $N_{p,2}$	17,940 / 27,720
U_s	1.3 [m/s]
e_p / μ_{pp}	0.9 / 0.1

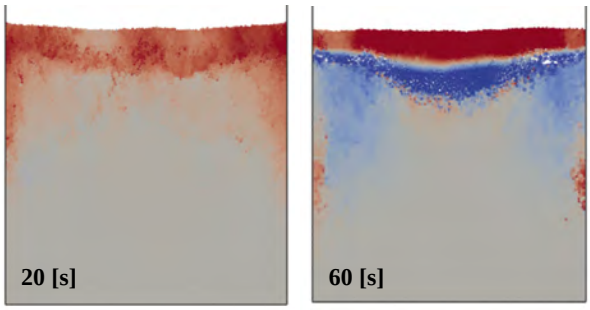

Figure 4: Snapshots of the vertical (i.e., z-) particle velocity in a bubbling fluidized bed (colors indicate velocities between -0.06 and +0.06 [m/s], t = 60 [s]).

Freely Sedimenting Suspension (CFD-DPM)

A critical test for an EL code is its ability to predict the fluid-particle slip velocity during the sedimentation in a fully periodic box. In such a configuration no external forces act on the fluid-particle system (the weight of the system must be balanced by pressure gradient, though), and hence the total momentum of the system should remain unchanged. We have performed simulations of a sedimenting gas-particle mixture (d_p = 150 µm, ρ_p = 1500 kg/m³, $\langle\phi_p\rangle$ = 0.10, the gas phase was air at ambient conditions) using implicit and explicit time marching for the fluid phase. Results for the domain-averaged slip velocity (i.e., the difference between the momentum-averaged velocity of the two phases) for a number of dimensionless fluid time steps $\Delta t^* = \Delta t/t_f$ are summarized in Figure 5. The simulations using an explicit time marching were performed with a time step of Δt^*=0.025 - larger simulations were impossible due to stability reasons. As can be seen, the results of the implicit time marching are in good agreement with the results for the explicit procedure (fluid grid size effects are typically larger, see blue and black symbols in Figure 5; note that these fluid grid size effects arise naturally due to non-resolved fluid velocity fluctuations, see Radl et al., 2012). The advantage of the implicit

procedure is that it allows a time step up to 17.5 times larger than the one used for an explicit procedure.

As mentioned in the previous chapter, an implicit procedure does not perfectly enforce Newton's Third Law, and hence leads to a drift of the system's momentum. In order to control the drift velocity, it is necessary to add a correction force that is in the order of 5 to 15% of the total system weight (the correction in case of the explicit procedure is much smaller, i.e., 0.4%; splitting the coupling force into an implicit and explicit part reduces the necessary correction force to ca. 1% of the system weight). This correction force reflects the integral error due to the violation of Newton's Third Law. Furthermore, we find that the correction force depends on the fluid grid size (smaller grid size lead to a smaller correction), i.e., the correction is proportional to the number of particles per fluid grid cell. In summary, one should carefully evaluate whether implicit time marching yields accurate results, especially in case comparably coarse fluid grid cells are used. Our simulation results indicate that this is typically the case for moderately dense to dense gas-particle suspensions. In dilute flows (for which τ_f is close to, or larger than τ_p), we suggest using an explicit procedure, or an algorithm based on implicit/explicit force splitting because of a more satisfactory conservation of the system's momentum.

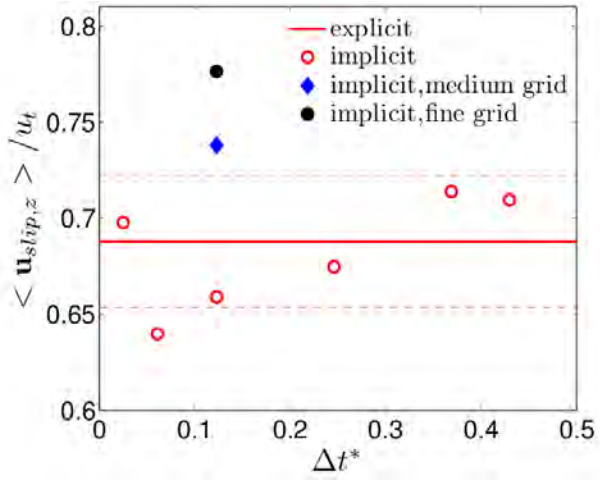

Figure 5: Predicted slip velocity of a freely-sedimenting gas-particle suspension for various dimensionless fluid time steps (the red dashed lines indicate ± 5% of the results using the explicit coupling procedure).

2D Bi-Disperse Jet in Cross Flow (CFD-DPM)

Setup

To investigate the performance of the mapping and smoothing schemes to model comparably dilute flows, we consider the injection of a particle jet in a turbulent cross flow (JICF). Specifically, we consider a synthetic configuration, in which a bi-disperse particle population is injected into a (pseudo) two-dimensional fluid flow field (i.e., air at ambient conditions). The physical parameters of the JICF configuration are summarized in Table 2. The fluid mesh resolution was Δx = 0.01 [m], and the time resolution of the base case was $\Delta t = 10^{-5}$ [s] to advance the fluid's governing equations.

Table 2: Physical parameters of the 2D JICF test case.

Parameter	*Value*
Domain (X x Y x Z)	1.8 x 0.7 x 0.002 [m]
Particle density (ρ_p)	2500 [kg/m³]
Particle diameter (d_p)	5 … 20 [µm]
Gas density (ρ_f)	1.1 [kg/m³]
Gas dynamic viscosity (η_f)	$1.91 \cdot 10^{-5}$ [Pa.s]
Mass loading ($\mu = m_p/m_f$)	0.5
Rel. particle injection velocity ($\mathbf{v}_y/\mathbf{u}_{inlet,x}$)	0.591
Crossflow velocity ($\mathbf{u}_{inlet,x}$)	25.4 [m/s]

Particle Penetration

Maps of the time-averaged magnitude of the gas velocity, as well as the particle positions are shown in Figure 6. Again, we have attempted to assess the effect of an implicit vs. an explicit time marching procedure on key flow features. As can be seen, explicit time marching leads to a more pronounced particle penetration into the cross flow compared to the implicit procedure (cp. Figure 6a and b). However, the recirculation behind the injection point has a similar extension in the main flow direction whether the implicit or the explicit procedure is employed. The advantage of implicit time marching is that we were able to use a substantially (i.e., 4.9 times) larger time step. Such a large time step could not be realized with explicit time marching, highlighting the robustness of the implicit procedure. Furthermore, we show results for the implicit/explicit coupling force splitting in Figure 6c (in Figure 7 the splitting of the coupling force is illustrated). As we will show in the next paragraph, this force splitting approach yields results that are practically indistinguishable from that obtained with an explicit procedure, but require less computational resources.

Velocity Profiles

A more quantitative comparison of the 2D JICF results is provided in Figure 8, where we have plotted profiles of the time-averaged streamwise (i.e., x-) fluid velocity component. As can be seen, the results for various flavours of the implicit time marching are essentially indistinguishable from each other. Same as for the particle penetration illustrated in Figure 6, the explicit procedure leads almost identical predictions for the velocity distribution when compared to the implicit/explicit mapping approaches. For the time being, we need to accept our result obtained with the explicit and implicit/explicit mapping approach as the most accurate prediction (in these simulations Newton's third law is satisfied with an error of less than 1%; experimental validation was addressed to future work). In contrast, and as can be seen in Figure 8, an implicit procedure leads to an underprediction of the fluid velocity, especially near the bottom wall. Inspection of the error due to the implicit handling of the coupling force indicates that this error indeed can be substantial (data not shown). This is especially true for the

uppermost layer of particles that experiences the highest acceleration, and hence also exerts the largest force onto the fluid.

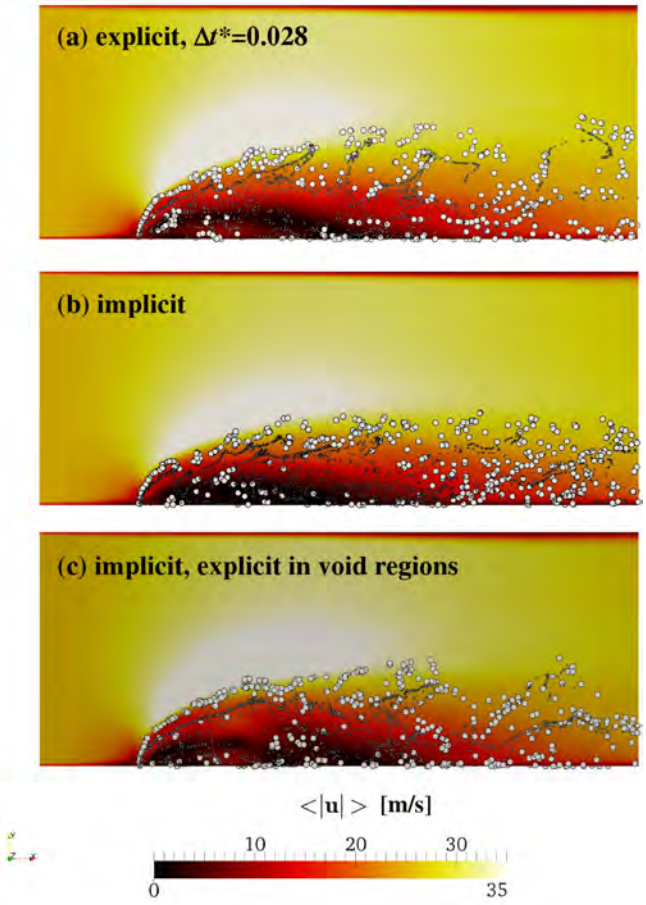

Figure 6: Time-averaged magnitude of the fluid velocity (contours), and particle distribution in the 2D JICF test case (Δt^*=0.138; the simulations in panel c employed impl./expl. force splitting based on fluctuating velocities; smoothing based on the local particle diameter was applied; particles are scaled according their primary particle diameter).

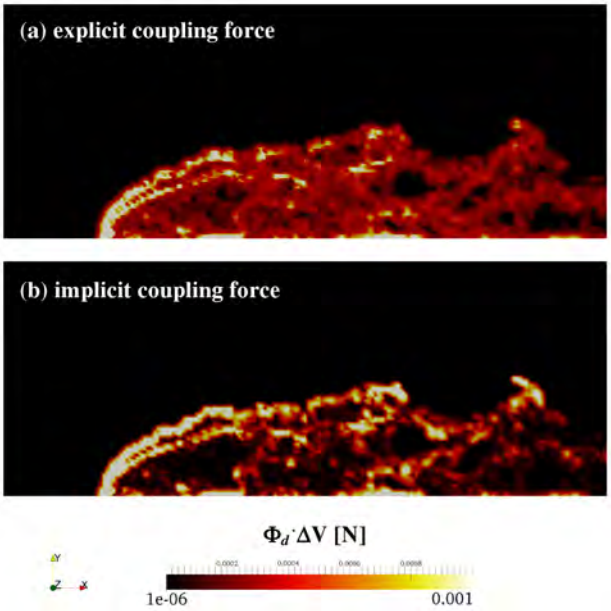

Figure 7: Local coupling force obtained from simulations with implicit force coupling in dense regions, and explicit force treatment in regions void of particles (data from Figure 6c; impl./expl. force splitting was performed).

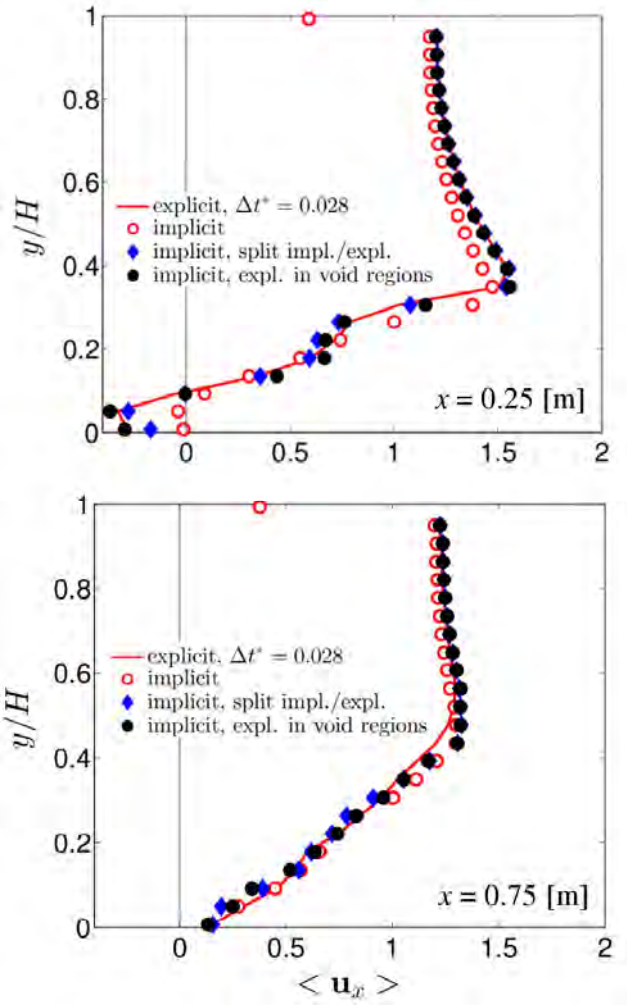

Figure 8: Sensitivity of the fluid velocity profiles in the JICF configuration to the coupling procedure and the fluid time step.

Finally, we note that whether smoothing is employed or not results in minimal differences in the predicted flow pattern. This is because of the comparably large fluid grid to parcel diameter ratio that results in a sufficient smoothing inherent to the grid size.

The Salzman 3D JICF Configuration (CFD-DPM)

To investigate whether the developed coupling algorithm can give results independent of parcel size and fluid grid resolution, the (three-dimensional) JICF configuration of Salzman and Schwarz was simulated. The physical parameters are summarized in Table 3, and the geometrical details are shown in Figure 9.

The Salzman configuration has been analysed numerically by Li and Lin (2010), as well as Han and Chung (1992). Only a limited amount of reliable reference data is available for this setup. Therefore, in this work we have used a highly-resolved CFD-DPM simulation with approximately 12.7 Mio. fluid cells to provide reference data for the subsequent analysis. A sub-grid-scale stress model for unresolved fluid velocity fluctuations has been used in this reference simulation. Analysis of the resolved and sub-grid-scale velocity fluctuations indicate that the former are roughly three times larger than the latter downstream of the injection point. Thus, we conclude that sub-grid scale (fluid)

velocity do not play an essential role for this reference simulation.

Table 3: Physical parameters of the Salzman JICF test case.

Parameter	*Value*
Jet Diameter (d_{jet})	4.62 [mm]
Particle density (ρ_p)	2638 [kg/m³]
Particle diameter (d_p)	15 [µm]
Gas density (ρ_f)	1.1 [kg/m³]
Gas dynamic viscosity (η_f)	$1.91 \cdot 10^{-5}$ [Pa.s]
Jet mass loading ($m_p/m_{f,jet}$)	20.8
Rel. particle injection velocity $(\mathbf{v}_y/\mathbf{u}_y)_{jet}$	1
Rel. jet velocity ($\mathbf{u}_y/\ \mathbf{u}_{inlet,x}$)	1.57
Crossflow velocity ($\mathbf{u}_{inlet,x}$)	16.8 [m/s]

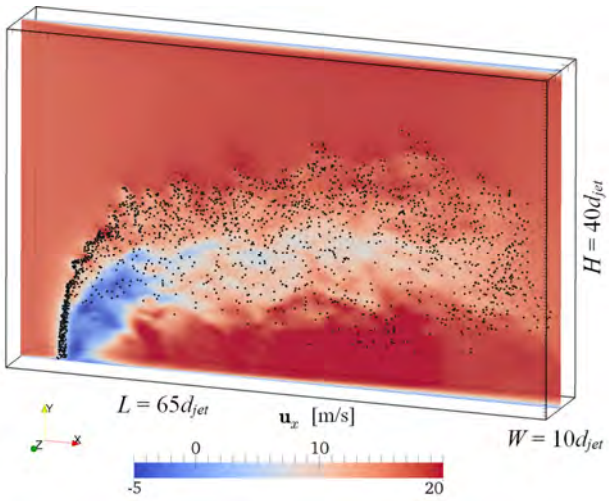

Figure 9: Instantaneous *x*-component of the fluid velocity (contours are shown in a central cut plane), and particle distribution (black dots) in the Salzman JICF configuration.

Particle Penetration

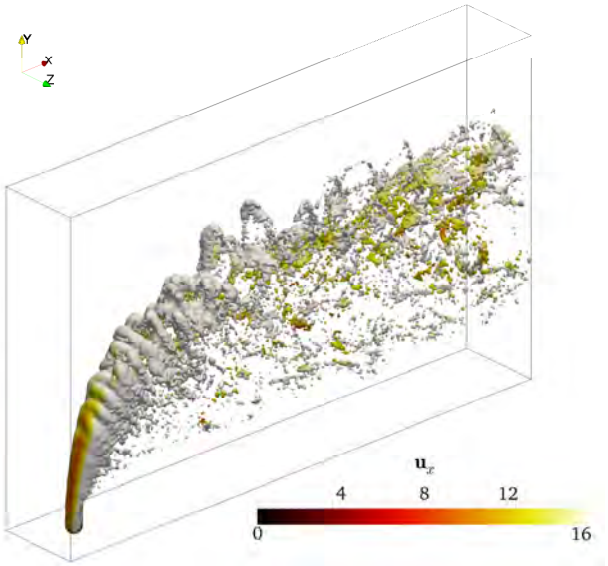

Figure 10: Instantaneous fluid velocity distribution (in [m/s]) on an iso-surface of the particle volume fraction ($\phi_p = 3.5.10^{-4}$) for the Salzman JICF configuration (reference simulation with *CG* = 5, 510 x 314 x 79 grid cells).

and Figure 11 summarize the results for the particle dispersion pattern, as well as the effect of the fluid grid resolution and the coarse graining ratio (*CG*) on our predictions. The reference simulation (see Figure 10) highlights that a complex three-dimensional flow structure develops downstream of the particle injection point. The particle concentration is highest in a U-shaped region that becomes more and more diffuse in the streamwise (i.e., *x*-) direction. Interestingly, the reference simulation predicts a region of comparably low fluid velocity inside this U-shaped region.

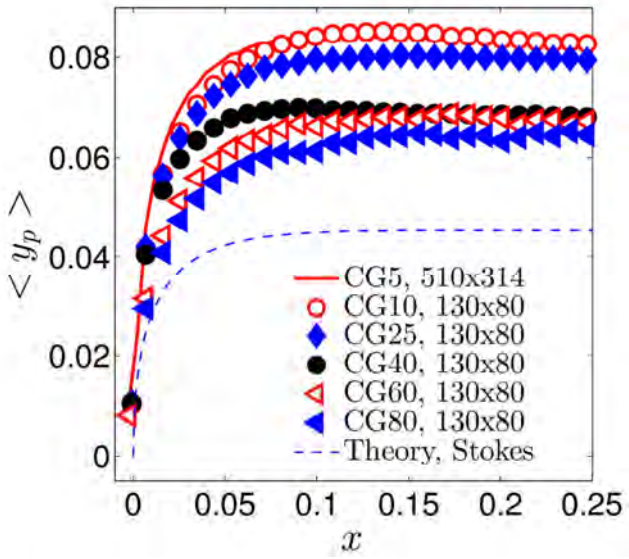

Figure 11: Mean vertical particle position as a function of the streamwise (i.e., *x*-) position to quantify the penetration of the particle jet into the cross flow (dimensions in [m]; all simulations used the smoothing algorithm).

By computing the centre of mass position of the particle population as a function of the streamwise position, we quantify the effect of various numerical settings on the predicted gas-particle flow. As can be seen, all results with *CG* = 25 (or smaller), show reasonable agreement with the reference results. For these simulations the smoothing procedure as well as the details of the coupling algorithm had a comparably small effect on the particles' mean trajectory. Results with *CG* = 40 (or larger) give less satisfactory results, and not employing the smoothing algorithm for *CG* = 40 (or larger) gave the worst predictions (data not shown). Also, we find that increasing the smoothing length does not improve the predictions for *CG* = 40 or larger (data not shown). The physical reason for this limitation is the inability to resolve particle and fluid velocity fluctuations when employing extremely large CG ratios. This indicates that (for large parcel sizes) the introduction of a smoothing step can improve the quality of predictions, however, the predictive capabilities are limited by clustering effects not accounted for by the models used by us.

We also would like to note that smoothing introduces only an incremental computational cost. Specifically, our simulations indicate that smoothing introduces an additional computational overhead of ca. 18%, but improves the predictions substantially as discussed above.

In summary, we observe that for excessively large CG ratios the jet penetration is underestimated, i.e. a too small disturbance of the flow is predicted. In Figure 11 (blue dashed line) we have also included the theoretical trajectory of an injected particle under the assumption of (i) an undisturbed background flow, as well as (ii) the validity of Stokes' drag relation. As can be seen, all our simulations predict a penetration of the particle jet into the cross flow that is ca. 1.5 to 2 times larger than this theoretical result.

CONCLUSION

We have presented details of numerical schemes implemented in the open-source package CFDEMcoupling, which are relevant for the robust simulation of gas-particle flows involving broad particle size distributions. We made an attempt to estimate relevant time scales that limit the time step in these simulations. We then critically analysed the effect of an implicit time marching procedure for various test cases. Based on our results for a freely sedimenting gas-particle suspension, we conclude that the proposed implicit integration procedure is not strictly conservative, and gives an error between 5% and 15 % depending on the number of particles per computational cell. An improved coupling algorithm that splits the force into an explicit and implicit contribution can alleviate this problem. Clearly, an implicit procedure is essential for a robust simulation in case very small particles need to be modelled. Typically a time step ca. 15 times larger than that required for an explicit procedure can be used in case an implicit or hybrid implicit/explicit procedure is employed.

From our results of the jet-in-cross flow configuration, we conclude that:

1. The implicit integration procedure leads to less particle penetration into the cross flow compared to an explicit procedure. An improved algorithm that splits the coupling force into an implicit and explicit part improves the situation.
2. Smoothing is key for the correct prediction of particle penetration into the cross flow for the 3D JICF configuration in case large CG ratios must be used. Thus, smoothing becomes essential for CG > 40, which is typically required to simulate industrial-scale problems.
3. A coarse graining ratio of 25 still gives accurate results for the 3D gas-particle JICF configuration with 15 µm primary particles.

Future work might focus on the experimental validation of our JICF simulations to confirm our conclusions.

ACKNOWLEDGEMENTS

The help of Stefan Darmann (TU Graz) in setting up the 2D JICF configuration is greatly acknowledged.

REFERENCES

BEETSTRA, R., VAN DER HOEF, M.A., and KUIPERS, J.A.M., (2010), "Drag Force of Intermediate Reynolds Number Flow Past Mono- and Bidisperse Arrays of Spheres", *AIChE J.*, **53,** 489-501.

CAPECELATRO, J., and DESJARDINS, O., (2013), "An Euler–Lagrange Strategy for Simulating Particle-Laden Flows", *J. Comput. Phys.*, **238,** 1-31.

GOLDMISCHDT, M.J.V., LINK, J.M., MELLEMA, S., and KUIPERS, J.A.M., (2003), "Digital image analysis measurements of bed expansion and segregation dynamics in dense gas-fluidised beds", *Powder Technol.*, **138,** 135-159.

HAN, K.S., and CHUNG, M.K., (1992), "Numerical Simulation of Two-Phase Gas-Particle Jet in a Crossflow", *Aerosol Sci. Technol.*, **16**, 126-139.

KLOSS, C., GONIVA, C., HAGER, A., AMBERGER, S., and PIRKER, S., (2012), "Models, Algorithms and Validation for OpenSource DEM and CFD-DEM", *Progr. Comput. Fluid Dyn.*, **12,** 140-152.

LAIN, S. and SOMMERFELD, M., (2008), "Euler/Lagrange computations of pneumatic conveying in a horizontal channel with different wall roughness", *Powder Technol.*, **184,** 76-88.

LI, G., and LIN, J., (2010), "Characteristics of Particle Dispersion in a Jet in Cross-Flow Based on Computational Fluid Dynamics", in: *Asia-Pacific Power and Energy Engineering Conference*.

N.N., (2010), "OpenFOAM 2.2.1 User Manual", www.opencfd.co.uk .

PATANKAR, N.A., and JOSEPH, D.D., (2001), "Modeling and numerical simulation of particulate flows by the Eulerian-Lagrangian approach", *Int. J. Multiphase Flow*, **27**, 1659-1684.

PIRKER, S., KAHRIMANOVIC, D., and GONIVA, C., (2011), "Improving the applicability of discrete phase simulations by smoothening their exchange fields", *Appl. Math. Mod.*, **35,** 2479-2488.

RADL, S., GIRARDI, M. and SUNDARESAN, S., (2012), "Effective Drag Law for Parcel-Based Approaches - What Can We Learn from CFD-DEM?", in: *ECCOMAS 2012*.

SCHELLANDER, D., SCHNEIDERBAUER, S., and PIRKER, S., (2013), "Numerical study of dilute and dense poly-dispersed gas-solid two-phase flows using an Eulerian and Lagrangian hybrid model", *Chem. Eng. Sci.*, **95,** 107-118.

SNIDER, D.M., (2001), "An incompressible three-dimensional multiphase particle-in-cell model for dense particle flows", *J. Comput. Phys.*, **170,** 523-549.

SOMMERFELD, M., and LAIN, S., (2012), "Analysis of dilute phase pneumatic conveying through pipe systems by the Euler/Lagrange approach", in: *Ninth International Conference on CFD in the Minerals and Process Industries*.

TENNETI, S., GARG, R., and SUBRAMANIAM, S., (2011), "Drag law for monodisperse gas – solid systems using particle-resolved direct numerical simulation of flow past fixed assemblies of spheres", *J. Multiphase Flow*, **37,** 1072-1092.

ZHOU, Z.Y., KUANG, S.B., CHU, K.W., and YU, A.B., (2010), "Discrete particle simulation of particle–fluid flow: model formulations and their applicability", *J. Fluid Mech.*, **661,** 482-510.

Numerical Simulation of Ice Accretion on Vessels and Structures due to Sea Spray

MIHAELA POPESCU[1]* AND STEIN TORE JOHANSEN[1,2]

[1] SINTEF Materials and Chemistry, 7465 Trondheim, NORWAY

[2] Department of Energy and Process Engineering, Norwegian University of Science and Technology, 7491 Trondheim, Norway

* E-mail: mihaela.popescu@sintef.no

ABSTRACT

In the Arctic area, wave impacts against vessel hulls and solid structures result in sea sprays. At low ambient temperatures the spray droplets may deposit on surfaces and solidify, which can lead to hazardous ice accumulation. As ice accretion on vessels and off-shore structures may cause severe stability problems, predictive models are critical for safe operations in the Arctic.

We simulate the transport of the droplets, caused by the wave impacts. Effects of the droplet size and wind characteristic (speed and direction) is studied using two phase flow theory - using the Euler-Lagrangian method to simulate the flow and deposition of the droplets. The sea spray is simulated as a discrete mass and momentum source of droplets, localized in given volumes close to the hull of the vessel. The accumulation rate of the droplets which drive the ice accretion is simulated based on the idea that ice accretion only takes place if the velocity is below some critical limit. If the droplet impact velocity is very high, the contact time with the surface is short and main parts of the droplets will rebound and will not contribute to ice accretion.

The present study is done using a fixed mass and mass flow rate of the wave induced spray source. The spray droplet size distribution is mono-disperse in order to be able to investigate the direct effect of droplet drop size, and the wind on the ice accumulation. The result shows that droplets smaller than 1.0 mm have the greatest contribution to the ice accretion. The wind velocity has a direct effect on accumulation of the ice on the vessel superstructures: larger wind speed create a larger ice accumulation on the superstructures, not on the entire ship.

Keywords: CFD, marine icing, two phase flow, droplets

NOMENCLATURE

Greek Symbols

ρ	=	Mass density, [kg/m^3].
μ	=	Dynamic viscosity, [kg/m.s].

Latin Symbols

d	=	droplet diameter [mm]
p	=	pressure [Pa]
t	=	time [s]
x,z	=	horizontal axes
y	=	vertical axis
u	=	velocity [m/s]
ε	=	turbulent dissipation [m^2/s^3]

INTRODUCTION

The prediction of vessel icing is very important for marine operations in the Arctic. Physical processes associated with the ice accretion are numerous and complex and no simple or precise rules can be formulated in spite of many studies that were conducted during the past decades. Sur et al (2006) studied the hydrodynamics of the flow around naval combatant ships, and found that the overall flow has a direct impact on the bow spray. Karev et al (2003), Kreeger et al (2005), Overland (1989), Dai et al (1997), Dommermuth et al (2006) and Fu et al (2005) contributed with further understanding of the icing and its dependency on the formation of the spray. Cao et al (2008) studied icing using numerical simulations based on an Eulerian method.

Sea spray icing may appear during marine operations when the temperature is between minus 2^{0}C and minus 17^{0}C, together with strong wind. Many ships and lives have been lost when ships sank, or became disabled because of the ice accretion on decks and superstructures. In the latter case, the ship stability is lost due to large amount of ice that changes the vessel's center of mass. (Overland (1990), Fett and Kozo (1992) and Fett et al (1992)).

In general, ice accretion is investigated by three means: experiments, engineering methods and numerical simulations. Experiments can give insightful information about ice accumulation, but they are very

expensive. Engineering methods employ empirical formulae, extracted from representative experimental data, to investigate the ice accretions (Wilder (1977)). Numerical simulations deals with detailed flows and geometries and they can give a more physics based analysis. It is well known that the actual icing potential is a characteristic of each individual vessel, depending on the design of the ship. Hence, the only feasible manner to determine the icing potential of a vessel will be by numerical simulations. The results from the numerical simulations can be used to extend and improve the engineering models.

As a first step in this direction we wish to support the forecast of ice accretion by predicting how some wave splash parameters and wind speed impact the droplet deposition on a given vessel. We investigate the droplet flow responsible for ice accretion by studying the flow of droplets, originating from a splash source, and how the deposition of droplets is impacted by the vessel design and wind conditions. The Euler-Lagrangian method is used to simulate the behavior of the spray droplets.

First we present the modelling concept. By investigating the effects of the droplet size on droplet accumulation to determine which droplet size contributes most. Next, the contribution of the wind is examined. In the last chapter we present the conclusion.

MODEL DESCRIPTION

Computational set up

To simplify the study, the vessel is modelled only above the water line. The computational domain is a rectangular parallelepiped (see Figure 1) in which the spray generated by the ship/wave interaction is simulated by a droplet mass source that presents a certain mass flow rate. The wave impacts is an intermittent process which here it is assumed to be regular, with a given time between wave impact, and where the sea spray is active in a fraction of this period. The mass flux of the spray from one splash event is thereby given by the total mass flow rate of the droplet source, representing the sea spray, and the duration of the spray event.

The sea sprays is here represented as a cyclical droplet jets, and we simulate the result of the wave induced spray during on single wave period.

The difficulty in the dynamic and thermodynamic evolution of the droplet spray is further simplified, as we assume that temperature equilibrium is obtained when the droplets impinge on the vessel.

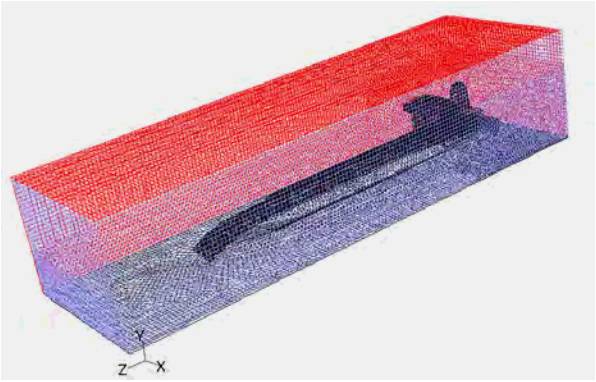

Figure 1. Computational domain.

The computations were done for a temperature range which assures maxim accretion. Hence, the simulations are done for air temperatures lower than -2^0 C (28^0 F), but higher than -17^0C (1^0 F). For temperatures lower than -17^0 C, the wind-induced spray is less dangerous since most droplets freeze before they reach the surface of the vessel. Such "snow" particles do not adhere easily to the vessel and is also easily re-dispersed. The complete ice accretion phenomenon is depending on the thermal droplet state (speed, number density and temperature) at impact, as well as the fate of the droplet after adhering to the surface ice. However, since we focus our study on the temperature and wind speed range where maxim accretion is expected, we do not include thermal calculations in our simulation.

As a result of above limitations and simplification, our ice accretion model is basically a result of the droplet deposition rate in which we take into consideration that high speed droplet will not contribute to ice accretion.

The present unsteady computation flow was done using the k-ε turbulent model, as implemented in ANSYS Fluent 12.1. The Lagrangian model used was the DPM (Discrete Particle Model), and the accretion model was added by applying a User Defined Function (UDF). The UDF was used to determine if a droplet will contribute to the accretion or not (rebound) and to compute the mass deposition rate. The droplet deposition rate depends on the volume fraction and wall normal velocity of the droplet. The accretion rate is defined by:

$$R_{accretion} = \sum_{p=1}^{N} \frac{\dot{m}_p}{A_{face}} \qquad (1)$$

where $\dot{m}_p$ is the mass flow rate of the particle stream, and A_{face} is the area of the wall face where the particle strikes the boundary.

In order to solve the governing equation for the air flow, the boundary conditions were set up as follows:

- At the upwind sides of the computational domain a velocity inlet boundary condition was applied.
- Solid walls: Standard wall functions are used for momentum, turbulent energy k and dissipation rate ε.
- Sea surface was modelled as solid walls, but the impact of waves are simulated by applying wall

roughness (wave roughness)

- Outflow boundary condition: all variable satisfy the condition $\partial Q/\partial \mathbf{n} = 0$, where Q denotes any of the variables $\boldsymbol{u}$, p, k, ε.

Figure 2. The mesh: the simplified model of the membrane ship.

The computation is done for a membrane-type ship, with a length of 47 m and 8 m wide. The model does not take into consideration all the geometrical details of the ship (see **Figure 2**). The grid size is 0.5 m and we use a structured grid away from ship while an unstructured grid is used at the surface of and close to the ship (see **Figure 3**). The total number of grid nodes is 1.4 million, which assure that the computation can be done in an affordable time when we use parallel computation, and at the same time to grid is not too coarse to compromise accuracy. The study of mesh convergence is not done in this work, but will be done in future work.

Figure 3. Mesh in a transversal section of the ship.

Droplet predictions and model assumptions

The configuration of the droplet spray is highly influenced by the states of the wind, the interaction between the sea and the vessel, as well as the vessel geometry. In this work, we have made the simplifying assumption that the wave hits the bow and sides of the ship simultaneously. The spray source is in the present study quite evenly distributed along the port and starboard side of the ship, but with a larger fraction of the spray originating from the bow. The total mass of water ejected in on spray event was 495 kg.

When the spray is produced a certain distribution of different sized droplets appears. However, in the present study we assume all droplets to be of the same size in one simulation. In this manner we can learn more about the effects of droplet size.

The surface of the sea water is modelled like a rough wall through which the droplets escape.

The fluid phase is treated as a continuum by solving the time-averaged Navier-Stokes equations, while the dispersed phase is solved by tracking a large number of droplets through the calculated flow field.

FLUENT predicts the trajectory of a droplet integrating the force balance on the particle, which is written in a Lagrangian reference frame. According to Newton's second law we can write:

$$\frac{d\vec{u}_d}{dt} = F_D\left(\vec{u} - \vec{u}_d\right) + \frac{\vec{g}\left(\rho - \rho_d\right)}{\rho_d} + \vec{F}_{other} \qquad (2)$$

Where F_{other} represent non-drag forces (force/ unit particle mass), and $F_D(\vec{u} - \vec{u}_d)$ is the drag force per unit droplet mass, $\vec{u}_d$ is droplet velocity, $\vec{u}$ is fluid flow velocity, ρ fluid flow density and ρ_d is droplet density.

Prediction of the turbulence induced droplet dispersion is based on the replacing the instantaneous fluid velocity in equation (2) with

$$u_i = \langle u_i \rangle + \varsigma_i(rnd)\sqrt{\frac{2}{3}k} \qquad (3)$$

Here $\langle u_i \rangle$ is the ensemble averaged fluid velocity and $\varsigma_i(rnd)$ is a random generated function of Gaussian shape, having a zero average and a standard deviation of 1.0, and k is the specific turbulent energy. The droplets are exposed to a turbulent structure with velocity given in (3), having a duration which is represented by the interaction time between the fluid and the droplet. The interaction time is a composite of the Lagrangian timescale for the turbulent flow and the time needed for a droplet to traverse a turbulent structure (crossing trajectory effect). When a droplet is leaving a turbulent structure, or the Lagrangian timescale is elapsed, new fluid velocities are updated according to equation (3). This drives the simulated turbulent dispersion of the droplets.

Furthermore, the flow of the air is also influenced by the presence of the droplets. This is simulated by using Newton's third law, where the force from the droplets on the fluid (here drag force) is identical in magnitude to the force acting on the air from the droplets. The droplet trajectories are now computed as a result of a full two way coupled momentum exchange between the air flow and the droplets.

The following assumptions are used in this study:

- Water droplets are spherical
- Droplets do not break up
- Evaporation of the droplets is negligible
- Turbulence is allowed to impact droplet motion
- Flow is incompressible
- Droplet Knudsen numbers are large
- Droplets with impact velocity over a certain critical value do not lead to deposition because due to short contact time to freeze before re-dispersion.

RESULTS AND DISCUSSION

In Figure 4 we see the results (snap shot) of a simulated sea spray event.

The study was done using the source of the droplet that is situated around the ship. The source: i) is situated 1 m away from ship; ii) is distributed in 23 points around the ship; iii) has 10 m/s upward velocity and lasts 1.6 - 2 s; iv) the splash source start first in the front of the ship, and later starts gradually along the sides of the ship, following the propagation of a large wave.

For interpretation of the results the term "ice accretion density" is introduced. Ice accretion density is the mass of water droplets, which will form surface ice, deposited on a surface during a single splash event. The unit for the "ice accretion density" will be mass per area.

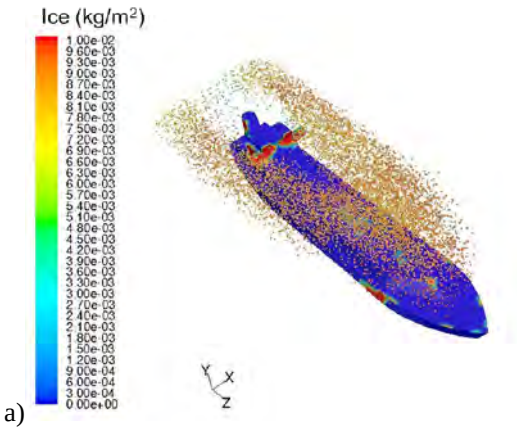

a)

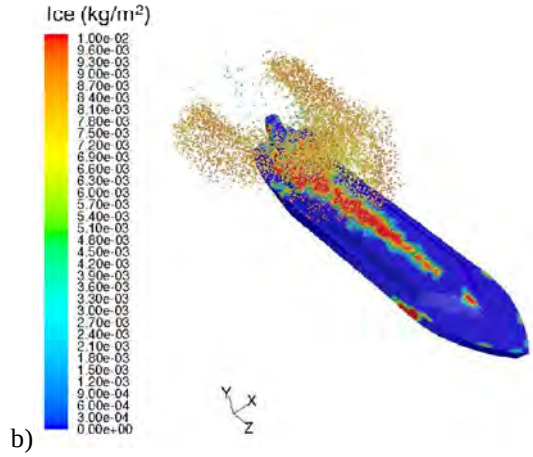

b)

Figure 4. Droplet spray and "ice accretion density" (kg/m^2) on structures. The speed of the wind is 10 m/s, with direction of 0^0 with the axis of the ship. The "ice accretion density" is from a single splash: a) t = 1 s; b) t = 3 s after the splash hits the ship.

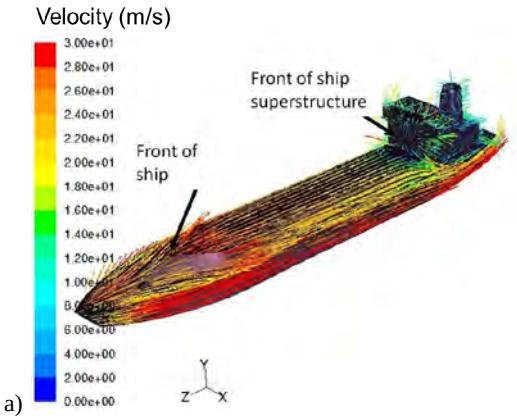

a)

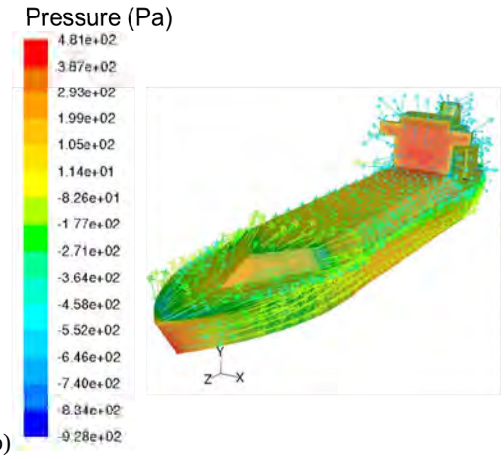

b)

Figure 5. a) The predicted air velocity vectors around the ship b) the air velocity vector and pressure distribution on ship surface; all for wind velocity u_{wind}=25 m/s and time t = 10s.

Flow around the ship

Figure 5 shows the velocity vectors of air around the ship, as well as the pressure distribution on the surfaces of the ship. The air hits the ship powerfully in the bow as well as on its superstructure (see distribution of the pressure on the ship). The trajectories of the droplets are influenced by the air velocity distribution, the droplets size and mass, as well as the ship design.

Figure **5**b shows a zone of the front of the ship superstructure where the pressure is high and the wind is strongly deflected. Here the wind hits the superstructure wall powerfully; hence the accumulation of ice in that zone can be slow as the droplet momentum at contact is high, and they may be quickly redirected.

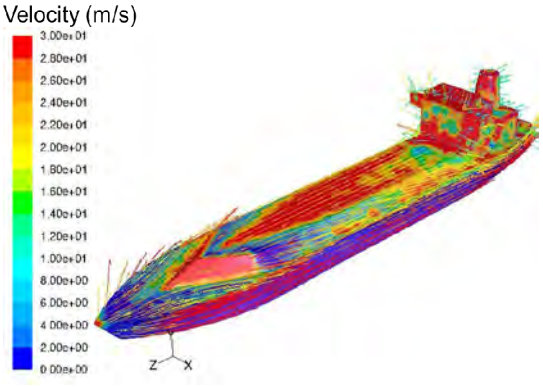

a)

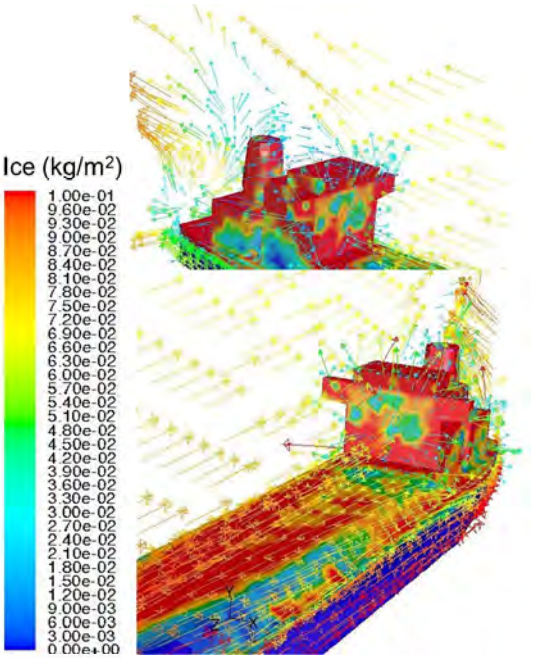

b)

Figure 6. Details of the air velocity vectors (m/s) around the ship and "ice accretion density" (kg/m^2) on the surface of ship. Wind velocity is u_{wind}=25 m/s; t = 10s, $d_{droplet}$ = 0.1 mm: a) complete ship; b) close up

In Figure 6 one can observe the distribution of the wind and the "ice accretion density" for small droplets ($d_{droplet}$= 0.1 mm). It should be noted that the ice-density scale only goes up to 0.1 kg/m^2, even if the maximum ice accumulation ("ice accretion density") may be as high as 6 kg/m^2. We use such a low scale because the surface with high "ice accretion density" has small area, and we wish to clearly notice surfaces where accretion is present. The front part of the ship is exposed to a relative high "ice accretion density" because of the high volume of droplets that hit this zone of the vessel.

The presence of high air vorticity and low velocity behind the superstructure can clearly be observed (see Figure 6b). The droplets deposit easily here, and contribute to the ice accretion. In this case, with 0.1 mm diameter droplets, we find a relatively high "ice accretion density" behind the first superstructure.

Drop size study

When the spray is produced, a distribution of droplets sizes appears. The droplet size determines the efficiency of the ice accretion. After deposition, the droplet induced brine film will cool and freeze as a function of the contact time as the heat exchange does not happen instantaneously. If the droplet speed at impact with a surface is too high the droplets may get atomized and are re-dispersed.

A theoretical evaluation is performed to ascertain the contribution of the different droplet diameters to the ice accretion. The study is based on splashes containing sea sprays with mono sized droplets. Simulations are performed with drop sizes ranging from 100 μm to 10 mm.

The investigations were done using the same mass flow rate and wind speed for all cases - wind direction is opposite vessel heading.. In this way the accumulation of ice depends only on the droplet size

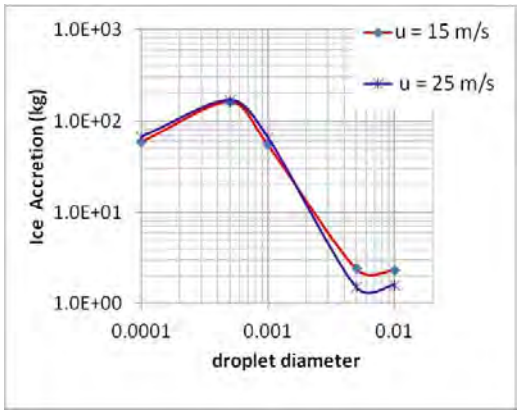

Figure 7. Ice accretion at ship surface as function of the drop size [m], caused by a single splash spray event.

We can see from Figure 7, the integral accumulation of ice, caused by a single splash event, is larger for smaller diameters and lower for higher diameters. The maximum accretion rate is found for a droplet diameter of approximately 0.5 mm. The droplets with 0.5 mm diameter have momentum and hydrodynamic drag that allow them to have the highest probability to contribute to the ice accretion on the ship. When the particle size is very small (well below 100 microns) the reduced droplet inertia will reduce the probability of deposition, since these droplets are dispersed easily by the wind. In general, the droplets with diameter between 0.1 and 1.0 mm show an overall high contribution to the ice accretion (see Figure 7).

As we can see from Figure 8 a) 0.1 mm droplets deposit frequently on the upper horizontal surfaces of the ship, but much less frequent on the front of the ship. The deposition on the front of the ship will increase with increasing droplet diameter, until the diameter is so large that they will fall down directly into the ocean, before they hit the ship. In fact large diameter droplets have a large weight, and their trajectories will mainly depend on their initial velocity and diameter (weight). For the investigated vessel configuration we find a very lower ice accretion for the large drops compared to the smaller sizes. This is seen also in Figure 8b), where the large droplets (5 mm diameter) deposit on the broadside of the hull and at some extremities of the superstructure. The large droplets appear when waves splash against an object in the water, such as the ship hull. Nevertheless their number and total mass is much smaller than that of small droplets (Borinsekov (1974), Wu (1979)).

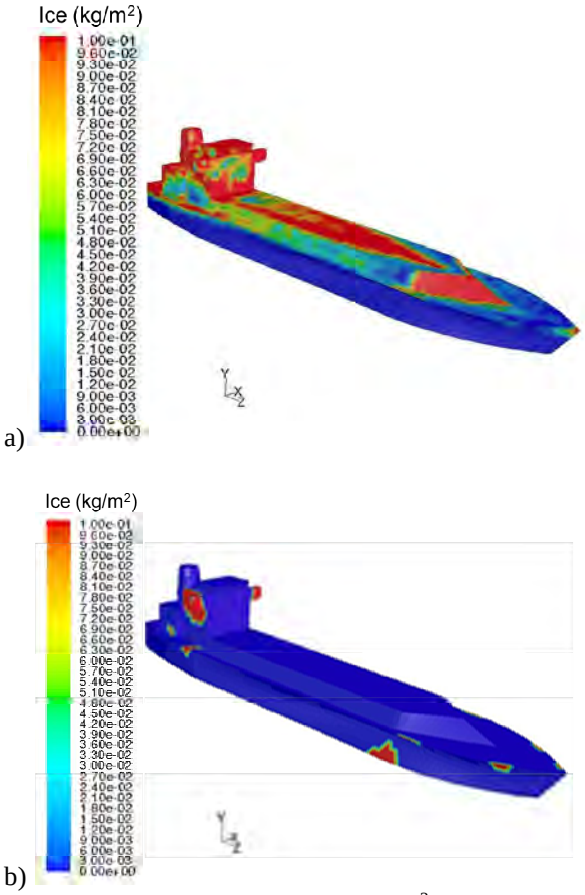

Figure 8. "Ice accretion density" (kg/m^2) for wind speed = 25 m/s: a) droplet diameter = 0.1 mm; b) droplet diameter = 10 mm

Wind speed

To study the influence of the wind speed on the ice accretion we take into consideration wind velocities ranging from 10 m/s to 30 m/s. The study was done for 1.0 mm and 0.1 mm droplet diameters. We chose values around 1mm for the diameter, because this value is close to the mean value of the droplet diameter in a freezing sea spray, which is 2.4 mm (Borinsekov et al 1974)**.**

The simulations show that the wind speed had a direct effect on the accretion as seen in Figure 9. The solutions are obtained for a vessel heading opposite of the wind direction. This is a result of the mixture between the air flow field, the droplets inertia and the design of the vessel. As the spray source configuration is constant in the various simulations, the differences in the outcome are a pure result of the wind speed variation.

Higher wind speed spreads out a higher number of droplets on the ship surface and modifies the droplet momentum, thus determining accretion. However, if the speed is too high, the probability that droplets contribute to the accretion may be lower because high velocity leads to: i) droplet fragmentation and rebound; ii) wind induce a longer trajectory of the droplets that determine that the droplets miss the vessel.

Due to the changes in air flow patterns and the effects of droplet inertia, the wind speed can increase or decrease the accretion, and the results of these two tendencies can be seen in Figure 9.

We can see in Figure 9 that ice accretion decreases when wind speed increases for small diameter droplets (d = 0.1 mm). For larger droplets (d = 1.0 mm) the ice accretion is increasing by increasing wind speed for velocities between 15 m/s and 25 m/s. For low wind velocities (less than 15 m/s relative to the ship) the ice accretion is decreasing as wind speed increases.

We wish to emphasize that all the computations are done for a single event – a single splash, with the same splash mass flux in all simulations. As a result, the above study does not exclude the idea that a stronger wind may lead to a relatively higher accretion, because of the increased frequency of the sea sprays and larger splash mass flux.

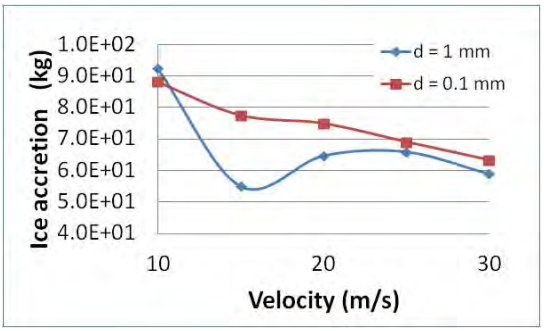

Figure 9. Ice accretion on the ship surface (kg/m^2), as function of the wind speed. The vessel heads in the opposite wind direction.

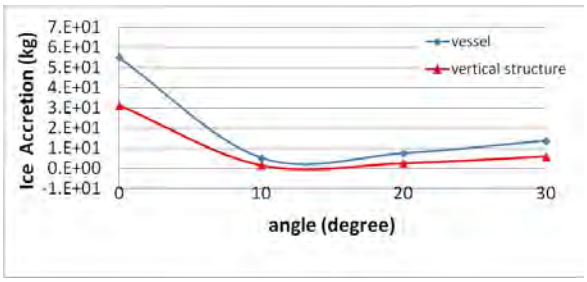

Figure 10. Ice accretion on the ship surface when the wind speed makes an angle with the vessel axis. Wind speed=15 m/s

The wind does not influence the ice accretion only through its magnitude, but also through its direction. How the wind inclination angle influences the ice accumulation is determinate by the design of the vessel superstructure: more than 60% of the accumulated ice is found on the vessel superstructures (see Figure 10 and Figure 11)

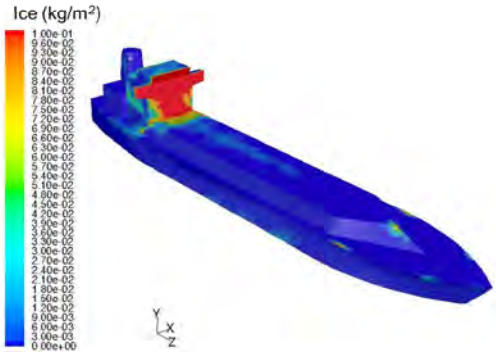

Figure 11. "Ice accretion density" (kg/m^2), for wind speed = 20 m/s and droplet diameter = 1mm. vessel heading opposite of the wind direction.

CONCLUSION

In this paper we have studied how droplets from sea spray result in ice accretion on a given vessel in cold weather. The flow of air and droplets were simulated using the Eulerian-Lagrangian method.

The ice accumulation as function of the droplet size was simulated for diameters ranging from 0.1 mm to 10 mm. The computations show that the size of the droplets has a significant impact on the ice accretion. The largest contribution to the ice accretion is caused by small droplets (diameter less than 1 mm). It is known that the average diameter of the spray cloud is around 2.4 mm (Borinsekov et al 1974). Hence a significant percentage of the spray droplets can contribute to the ice accretion. As a consequence, for a given sea spray, accurate knowledge about the vertical distribution of the droplet concentration, velocity and size is very important in order to determine the ice accretion accurately.

The wind speed is another important factor that contributes to the ice accretion. The study of the icing due to a single sea spray event indicates that, for a vessel heading in the opposite of wind direction, the larger contribution comes from wind at relatively low speed (less than 15 m/s for this ship). A lower contribution to the ice accretion is obtained for a wind with a very high velocity. As the sea spray event frequency and mass flow increases with wind speed, the effect on the effective ice accretion will need further investigations. In all the cases studied, more than 50% of the ice accumulated is on the superstructure of the vessel. Consequently, an optimal vessel design is critical in order to reduce ice accumulation and loss of stability.

ACKNOWLEDGEMENTS

The work was supported by SINTEF Materials and Chemistry. Special thanks go to Jon Samseth and Ernst Meese for their support.

REFERENCES

Guest, *P.," Photographs of Vessel Icing",* Courtesy of James Overland, National Oceanic and Atmospheric Administration's *(NOAA) Pacific Marine Environmental Laboratory (PMEL).,*

Funk, C., James Royce, J., (2012), "Freezing Spray and Ice Accretion on Vessels: A Comprehensive Summary", *Proceedings of the National Conference on Undergraduate Research (NCUR) 2012,* Weber State University, Ogden UT, 2012

URL:h*ttp://www.weather.nps.navy.mil/~psguest/polarmet/vessel/ves_photos.html*

Sur, T.W and Chevalier, K. (2006) "Semi-Empirical Bow Spray Modeling*", 26th Symposium on Naval Hydrodynamics*, Rome, ITALY, 17–22 September 2006

Karev, A.R. , Farzaneh, M , Lozowski, , E.P. (2003), "Character and stability of a wind-driven supercooled water film on an icing surface—I. Laminar heat transfer", *International Journal of Thermal Sciences,* No.42, pp. 481–498

Kreeger, R. E., Wright, W. B., (2005), "The Influence of Viscous Effects on Ice Accretion Prediction and Airfoil Performance Predictions", *43rd Aerospace Sciences Meeting and Exhibit sponsored by the American Institute of Aeronautics and Astronautics Reno*, Nevada, January 10–13

Overland, J.E., (1989), "Prediction of the icing for near-freezing sea temperature", *Weather and Forecasting*, vol.5, 1989, pp.62-77

Dai, Z., Hsiang, L.-P., and Faeth, G., (1997), "Spray Formation at the Free Surface of Turbulent Bow Sheets," *Proceedings of the Twenty-First Symposium on Naval Hydrodynamics, Office of Naval Research*, pp. 490–505.

Dommermuth, D.G., O'Shea, T.T., Wyatt, D.C., Sussman, M., Weymouth, G.D., and Yue, D.K.P., (2006), "The Numerical Simulation of Ship Waves using Cartesian Grid and Volume-of-Fluid Methods," *Proceedings of the Twenty-Sixth Symposium on Naval Hydrodynamic*s, Office of Naval Research.

Fu, T.C., Karion, A., Walker, D., Rice, J. and Ratcliffe, T., (2005), "Bow Wave Measurements of the R/V Athena I: 2004," *NSWCCD-50-TR-2005/035, Naval Surface Warfare Center Carderock Division*, West Bethesda, MD.

Cao, Y, Zhang, Q., and Sheridan, J., (2008), "Numerical simulation of rime ice accretions on an aerofoil using an Eulerian method", *The Aeronautical Journal*, No.3230, pp.243-247.

Overland, J.E., (1990) "Prediction of vessel icing for near-freezing sea temperatures", *Weather and Climate*, 5, pp.62-77.

Fett, R.W., and T.L. Kozo, (1992), "*Navy Tactical Applications Guide"*, Volume 8, Part 2, Arctic - East Siberian/Chukchi/Beaufort Seas Weather Analysis and Forecast Applications, NRL/PU/7541--92-0005, Naval Research Laboratory, Monterey, California, pp. 388

Fett, R.W., R.E. Englebretson and D.C. Perryman, (1993), "*Forecasters handbook for the Bering Sea, Aleutian Islands and Gulf of Alaska"*, NRL/PU/7541--93-0006, Naval Research Laboratory, Monterey, California, pp.302

Furey, D., Fu, T.C., Karion, A., Sur, T.W., Rice, J.R., and Walker, D.C., (2003), "Experimental Study of the Wave Field Produced by a Submerged Hydrofoil," *Proceedings of the Eighth International Conference on Numerical Ship Hydrodynamics*, Busnan, Korea.

Bowden, D.T., Gensemer, A.G. and Sheen, C.A., (1963), "Engineering summary of airframe icing thnical data", *FAA Technical Report ADS-4.*

Wilder, R.W, (1977), "A theoretical and experimental means to predict ice accretion shapes for evaluation aircraft handling and performance characteristics", *Paper5, AGARD Advisory Report ADS-4*

Borinsekov, E.P. and Panov, V.V., (1974), "Basic results and prospects of research of hydrodynamical condition on

shipboard", *Investigation of the physical Nature of Ship Icing"*, USA Cold Regions Research and Engineering Laboratory, Draft Translation 411, ADA003215, pp. 1-30

Wu, J., (1979), "Spray in the atmospheric surface layer: Review and analysis of laboratory and ocean results", *Journal of Geophysical Research*, 84 (C4) , pp.1693-1704

MULTI-SCALE MODELLING OF TURBULENT FLOWS BY EMBEDDED LATTICE-BOLTZMANN CO-SIMULATION

Stefan PIRKER[1*] , Stefan PUTTINGER[1], Philippe SEIL[1], Simon SCHNEIDERBAUER[1]
[1] Dep. Particulate Flow Modelling, Johannes Kepler Univ., 4040 Linz, AUSTRIA

Corresponding author's e-mail: stefan.pirker@jku.at

ABSTRACT

Turbulent flows are of crucial importance for many industrial processes. However, in an industrial context it is often not possible to resolve three-dimensional turbulent structures due to limited computational resources.

In this paper we nestle a finely resolved lattice-Boltzmann simulation into a global finite volume simulation. While in the global simulation turbulence is addressed by Reynolds averaged turbulence models, the embedded lattice-Boltzmann co-simulation actually resolves coherent turbulent structures by a Large Eddy Simulation (LES) at smaller length and time scales. At regular communication interrupts this detailed information on turbulent structures is transferred back to the global simulation by a fortified Navier Stokes approach.

We have implemented this two-way coupled modelling approach into the commercial software ANSYS/Fluent by adding an in-house lattice-Boltzmann code by the way of user defined functions (udf's).

After validation by focusing on turbulent flow over a wall mounted cube and turbulent structures of a round jet, we apply this concept to submerged entry nozzles in continuous casting of steel. Summarizing we can state that this concept delivers accurate results of turbulent flows at very low computational costs.

Keywords: CFD Fundamentals and Methodology, Multilevel/Multi-scale, Pragmatic Industrial Modelling, Finite Volume Simulation, Lattice-Boltzmann Simulation.

INTRODUCTION

Flow simulations can be either based on the Boltzmann equation, which describes the probability of movement of fluid particles, or on the Navier-Stokes equations, which comprise mass and momentum balances of a continuum.

Neither of the governing flow equations can be solved easily. In both cases the partial differential equations have to be discretised in time and space; in case of the Boltzmann equation also in velocity space. As the most prominent discretisation concepts the lattice-Boltzmann (LB) method and the finite volume (FV) method have been established for the Boltzmann and the Navier-Stokes equation, respectively.

In engineering applications most flows can be characterized as turbulent. Accurately resolving large scale turbulent structures by numerical simulations is of crucial importance in many flow situations such as detaching flow in aerodynamics, flow in mixing devices, reacting or thermal flows. Although in principle the turbulent flow pattern can be described by the governing flow equations without any further modelling these Direct Numerical Simulations (DNS) are restricted to simple cases only due to excess computational resources. In typical engineering applications the simulation of turbulent flows relies on turbulence modelling.

The vast range of turbulence models which have been proposed in the last decades can be organized roughly into Reynolds Averaged Navier Stokes (RANS) models and scale resolving Large Eddy Simulation (LES) models. While the first set of models is motivated by a velocity decomposition concept the latter is based on spatial filtering of the governing flow equations.

In literature turbulence models have been introduced based on both governing flow equations – Boltzmann and Navier-Stokes – and they have been implemented into the framework of the corresponding discretisation schemes. Especially, in case of the LES model lattice Boltzmann simulations have been reported to significantly speed up simulation times compared to FV based LES with the same spatial and temporal resolution (e.g. Dersken, 2000). At the same time simulation results obtained from these turbulent LB simulations agree with measurements and FV based LES (e.g. Geller et al., 2006, Gronald, 2011).

An obvious advantage of the lattice Boltzmann based LES is its simplicity. The underlying mathematical algorithm can be solved very efficiently with respect to computational times and storage consumption. On the other hand standard LB simulations are based on an under-lying equidistant lattice. While it is possible to locally refine lattice resolution by doubling the lattice points in each direction even dynamically it is not possible to apply LB simulations on arbitrary grids without impairing efficiency (e.g. He et al., 1996). This drawback becomes crucial if lattice Boltzmann

simulations are applied to flow situations where an interesting turbulent free shear layer occupies only a small region of the computational domain.
An obvious advantage of finite volume based turbulence models is their flexibility. Firstly, finite volume methods can be applied to arbitrary grids without restrictions to cell size or the cell's polyhedral form. Secondly, a vast amount of dedicated turbulence models exists for distinct flow situations. Nevertheless, as a major drawback especially scale resolving FV based turbulence models are limited by computational resources. In engineering applications FV based LES are often prohibited by excess costs.
In this paper a hybrid – lattice Boltzmann and finite volume based – turbulence model is introduced. In this concept a finely resolved lattice Boltzmann based LES is embedded into a region of interest of a coarse grid finite volume simulation (either RANS or coarse grid LES). In the course of coupled simulations the embedded lattice Boltzmann simulation receives information from the finite volume simulation by an unsteady corona boundary condition. On the other hand the flow pattern in the Finite Volume simulation is locally influenced by the underlying lattice Boltzmann simulation by a direct forcing method.
In the next section the modelling concept is shortly reviewed before in Section 3 several applications are presented.

MODEL DESCRIPTION

The hybrid turbulence model has been presented in detail in a previous publication (Pirker et al. 2013). For sake of completeness in this place an abbreviated version of this presentation is given.

Finite Volume Simulations

The incompressible Navier-Stokes equations comprise mass balance

$$\nabla \cdot \boldsymbol{u}_{FV} = 0, \qquad (1)$$

with the macroscopic velocity $\boldsymbol{u}_{FV}$ and momentum balance

$$\frac{\partial \boldsymbol{u}_{FV}}{\partial t} + \nabla \cdot \boldsymbol{u}_{FV}\boldsymbol{u}_{FV} = -\frac{1}{\rho}\nabla p + \nabla \cdot \boldsymbol{\tau} + \boldsymbol{b}_{FV}, \qquad (2)$$

with t, ρ and p denoting time, fluid density and fluid pressure. The subscript $_{FV}$ indicates that this flow field is resolved by Finite Volume simulations. The stress tensor can be expressed as

$$\boldsymbol{\tau} = \frac{\mu_m}{\rho}\left(\nabla \boldsymbol{u}_{FV} + \nabla \boldsymbol{u}_{FV}{}^{T}\right), \qquad (3)$$

where μ_m is the dynamic viscosity. Finally, $\mathbf{b}$ denotes a specific acceleration which will be described later. Based on Reynolds velocity decomposition Reynolds Averaged Navier Stokes (RANS) turbulence models can be deduced, which add either an additional turbulent viscosity or expressions for the Reynolds stresses (e.g. Pope, 2000).

Lattice Boltzmann Simulations

In contrast to the Navier-Stokes equations the Boltzmann equation considers the behaviour of fluid particles rather than the behaviour of a continuum. Motivated by Newton's second law the Boltzmann equation reads

$$\frac{\partial f}{\partial t} + \boldsymbol{u}_{LB} \cdot \nabla f + \boldsymbol{b}_{LB} \cdot \nabla_{\boldsymbol{u}} f = \dot{f}_{coll}, \qquad (4)$$

where $f = f(\boldsymbol{x}, \boldsymbol{c}, t)$ denotes the particle distribution function, and $\mathbf{u}$ and $\mathbf{b}$ are velocity and body forces. The collision operator $\dot{f}_{coll}$ relates the changes of the particle distribution function to interparticle collisions. The most popular model for $\dot{f}_{coll}$ is the BGK approximation (Bhatnagar et al., 1954), which assumes that relaxation towards a local equilibrium happens on a single timescale τ by

$$\dot{f}_{coll} = -\frac{1}{\tau_c}\left(f - f^{eq}\right) \qquad (5)$$

with f^{eq} denoting the Maxwellian equilibrium state. The relaxation parameter τ can be directly linked to fluid viscosity by $\tau_c = 3\mu/\rho + 1/2$.
In the lattice Boltzmann version of LES the strain rate tensor can be related to the distance of the actual thermodynamic state from the equilibrium state by

$$S_{ij} = -\frac{1}{2\rho_0 c_s^2 \tau}\sum_{\alpha} \varepsilon_{\alpha i}\varepsilon_{\alpha j}\left[f_\alpha - f_\alpha^{eq}\right] \qquad (6)$$

with $c_s = \sqrt{1/3}$ denoting the speed of sound on an equidistant lattice and $\varepsilon_{\alpha i}$ as the α^{th} component of the lattice velocity $\boldsymbol{e}_i$. Based on Smagorinky's model (1963) this leads to a subgrid relaxation parameter

$$\tau_{c,m}^2 = 4\sqrt{2}\left(C_S\Delta_x\right)^2\left(c_s^2\delta_t\right)^{-1} S\,\tau_{c,eff}^{n-1},$$
$$\tau_{c,SG}^n = \frac{1}{2}\left(\sqrt{\tau_{c,0}^2 + \tau_{c,m}^2} - \tau_{c,0}\right), \qquad (7)$$

with $\tau_{c,eff}^{n-1} = \tau_{c,0} + \tau_{c,SG}^{n-1}$ taken from the last time-step. Finally, $\tau_{c,eff}^{n} = \tau_{c,0} + \tau_{c,SG}^{n}$ is used for the current time-step relaxation. Further information of lattice Boltzmann based LES can be found in Yu et al. (2005).

Embedded Lattice Boltzmann Simulations

Throughout this study the local lattice Boltzmann region is assumed as an equidistant lattice which extends over a distinct hexahedral sub-region of the computational domain. In order to guarantee mass conservation the outermost lattice points are defined as bounce back points representing a wall. As a consequence the amount of fluid particles inside the lattice Boltzmann domain remains constant which reflects the situation of incompressible flow. Next, a corona region is defined which reaches from the outermost bounce back hull a distance of three lattice points into the inner lattice Boltzmann region.
In a communication step each Finite Volume cell checks, if its cell midpoint is inside the lattice Boltzmann corona region. If this is the case the particle distribution functions of the closest lattice point are set to the corresponding equilibrium functions which are obtained by the finite volume based velocity by parameter

$$f_{a,cor}^{eq} = w_a \rho_0 \left[1 + 3\frac{\boldsymbol{e}_a \cdot \boldsymbol{u}_{FV}}{c^2} + \frac{9}{2}\frac{\left(\boldsymbol{e}_a \cdot \boldsymbol{u}_{FV}\right)^2}{c^4} - \frac{3}{2}\frac{\boldsymbol{u}_{FV}^2}{c^2} \right] \qquad (8)$$

where w_a are weighting factors, c is the lattice speed and $\boldsymbol{e}_a$ are the unit direction vectors. Note, that this corona condition allows transfer of mass and momentum into the inner region of the lattice Boltzmann patch, although the outermost lattice points are defined as bounce back.

Within the embedded lattice Boltzmann region the turbulent viscosity of the finite volume simulation is set to zero. Next, the locally averaged lattice Boltzmann velocity influences the coarse grid Finite Volume simulation by a direct forcing method (Shirgaonkar et al., 2009). Thereby, the actual velocity pattern which has been obtained from the underlying lattice Boltzmann calculation is transferred into a force field by

$$\boldsymbol{b}_{FV} = \frac{\left(\overline{\boldsymbol{u}}_{LB} - \boldsymbol{u}_{FV}\right)}{\Delta t_{FV}} \qquad (9)$$

with the overbar denoting time averaging. In the framework of this hybrid turbulence model passive Lagrangian particle tracking can be realised by substituting the local fluid velocity by $\mathbf{u}_f = \mathbf{u}_{LB}$ in the region of the embedded lattice Boltzmann simulation and by $\mathbf{u}_f = \mathbf{u}_{FV}$ elsewhere.

MODELLING SETUP

In creating an environment of embedded LB simulations special attention has been laid on user friendly applicability. Based on the commercial finite volume solver ANSYS/Fluent (2014) a dedicated LB code has been realised by user defined functions (udf's). After specifying the region of interest, the embedded LB simulation is automatically set-up based on a set of pre-defined simulation parameters (like the maximum lattice speed or the global lattice size).

After a finite volume simulation step flow the corona boundary is set for the embedded LB simulation. Subsequently, a series of LB sub iterations is performed depending on the global time-step size and the lattice spacing. Finally, the direct forcing field is returned to the finite volume simulation (Fig. 1).

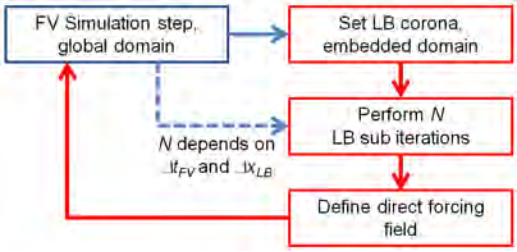

Figure 2: Flow sheet of embedded LB simulations; after one global finite volume simulation step a series of *N* lattice Boltzmann sub iterations are performed to update the direct forcing field of the subsequent next finite volume simulation step.

Because of its explicit formulation LB simulations are well accessible for parallelisation, motivating the development of a hybrid parallelisation concept. While the finite volume domain is subdivided by an arbitrary partitioning algorithm (e.g. by the Metris algorithm), the embedded sub-domain is partitioned into regular slices in Cartesian x-direction (see Fig. 2). Communication between those parallelization concepts is realised by many to many parallelisation in a way that a finite volume cell of processor *i* can exchange data with LB lattice points of different processors (e.g. *j* and *k*).

RESULTS

In this section the hybrid turbulence model is applied to two prominent flow situations for the purpose of validation before it is applied to an industrial application of continuous casting.

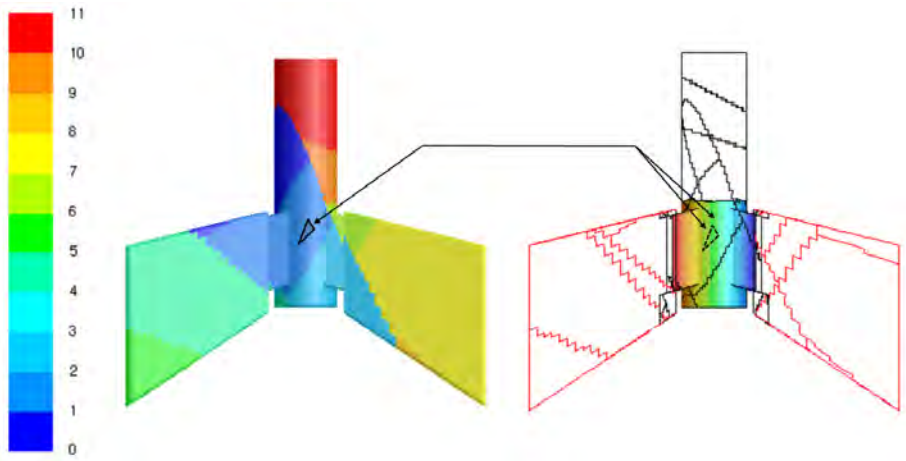

Figure 1: Communication between finite volume simulation and lattice Boltzmann simulation by many to many parallelisation; finite volume parallelisation with 12 processors (left) and LB parallelisation of an embedded domain (right); a finite volume cell of processor *i* exchanges data with LB lattice points of processors *j* and *k*.

Validation – Wall Mounted Cylinder

The example comprises a wall mounted cylinder of finite height which is exposed to a wall parallel flow. In the wake of the cylinder eventually a complex three-dimensional system of detached vortices establishes. Furthermore, in case of a sufficiently high cylinder this wake pattern evolves into periodically unsteady vortex shedding.

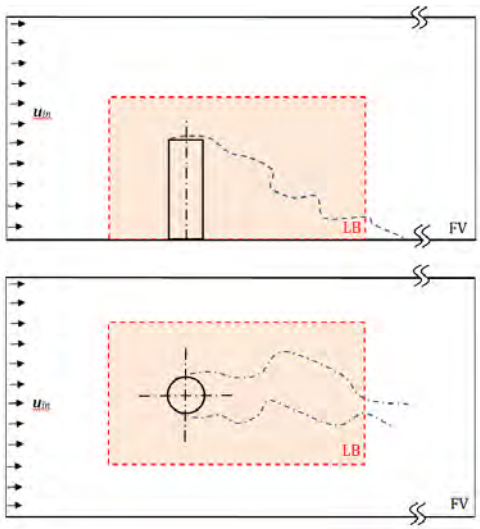

Figure 3: Sketch of the computational domain for the FV simulation of the wall mounted cylinder; the embedded LB domain is depicted by the dashed line.

Not surprisingly, a Reynolds averaged based turbulence model applied on a very coarse grid results in no unsteady vortex shedding behind the cylinder (Fig. 4). The corresponding mean drag coefficient $C_{D,RANS} = 0.26$ of the cylinder is only about a third of the value of $C_D = 0.88$ which is suggested by finely resolved finite volume based LES of Fröhlich and Rodi (2004) and by experimental data cited therein.

Figure 4: Iso-surface of helicity magnitude, $H = \left|\mathbf{u} \cdot (\nabla \times \mathbf{u})\right|$ as result of conventional finite volume based URANS simulation (top) and embedded LB simulations (bottom); in the latter case unsteady vortex shedding is observed.

In contrast to coarse grid Finite Volume based RANS simulations the hybrid model exhibits a dominantly unsteady wake behaviour. Obviously, the underlying lattice Boltzmann simulation introduces a periodical vortex shedding to the global Finite Volume based simulation. The resulting drag coefficient of $C_{D,Hybrid} = 0.83$ is by far more realistic than in pure finite volume based RANS simulations.

These improvements are obtained at very low computational costs. In Table 1 the computational time in relation to the coarse grid simulation $\Delta t / \Delta t_{coarse}$ is given. In relation to a 9.5 million cell finite volume based LES with a similar wake resolution the hybrid turbulence model is at least by one order of magnitude faster.

Table 1: Wall clock time span for simulation of 1 ms physical time; computational times are given in relation to the time required for the coarsest grid simulation.

FV 150k	FV 9.5m	FV 150k LB 750k	FV 150k LB 2.6m
1	129.3	2.3	12.3

Validation – Round Jet

A turbulent round jet which emits from a nozzle into a slower co-flow represents one of the most prominent and well examined examples of turbulent flows. In this study we focus on a setting proposed by Wang et al. (2008). Numerical results are further compared to findings of Wynanski and Fiedler (1996).

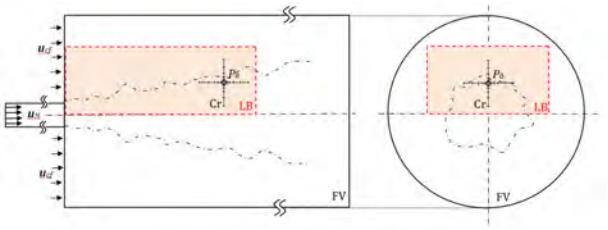

Figure 5: Sketch of the computational domain for the FV simulation of the wall mounted cylinder; the embedded LB domain is depicted by the dashed line.

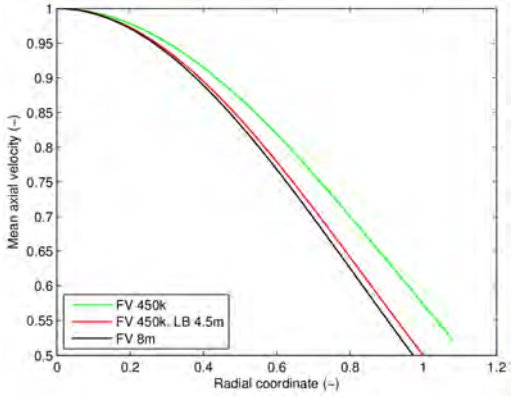

Figure 6: Profiles of mean axial jet velocity over radial coordinate ten nozzle diameters downstream the nozzle exit; the 'lattice Boltzmann magnification lens' improves coarse grid prediction of jet dispersion.

In a first test jet spreading is investigated by plotting the radial profile of axial velocity at a distance of ten nozzle diameters (Fig. 6). Obviously, a conventional coarse grid finite volume simulation over predicts jet spreading if compared to a finely resolved simulation. If, however, this coarse grid simulation is augmented by an embedded LB simulation, jet dispersion agrees well with

the reference solution. Interestingly, these results can be obtained by a factor of 15 less computational time.

In order to evaluate the directional information on turbulent fluctuations obtained with the hybrid model we concentrate on spatial two point correlations of velocity fluctuations. Axial and radial two-point correlations are defined as

$$R_{11}(s)=\frac{\overline{u'_{x,F}\left(x+½s,r,\theta\right)u'_{x,F}\left(x-½s,r,\theta\right)}}{\left(\overline{u'_{x,F}\left(x+½s,r,\theta\right)^2}\cdot\overline{u'_{x,F}\left(x-½s,r,\theta\right)^2}\right)^{1/2}} \qquad (10)$$

with x, r and θ as cylindrical coordinates (e.g. Pope 2000).

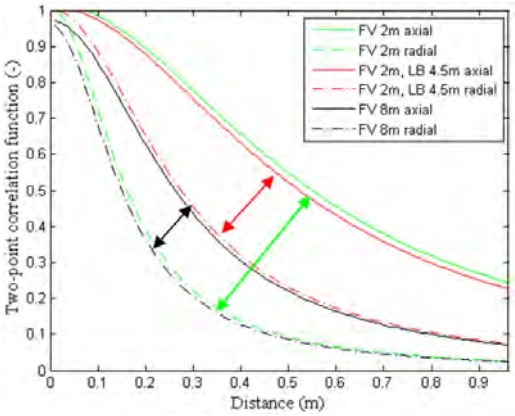

Figure 7: Axial and radial two-pint correlation functions of axial velocity fluctuations evaluated within the boundary layer of a round turbulent jet.

In Fig. 7 the axial and radial two-point correlation functions of the axial velocity fluctuation is given. First, it can be seen that for all simulations the axial two point correlation curve is well above the radial one. Next, the correlation curves for the fine grid are lower than that for the medium and coarse grid.

Finally, the spreading between the axial and the radial correlation function is in the same range for the fine grid finite volume simulation but is significantly increased in case of the two million grid finite volume simulation. In the latter case the grid has been composed of axially stretched cells.

Obviously, this unfavourable cell aspect ratio of this grid deteriorates the resulting three-dimensional structure of the turbulent flow pattern. These findings are further underlined by the evaluation of the integral turbulent length scales. In case of the two million grid a high value of the turbulent length scale ratio, $L_{11}/L_{22}=3.8$, coincides with the high cell aspect ratio.

The hybrid turbulence model compensates the unfavourable cell aspect ratio of the global finite volume grid. In this case the ratio between axial and radial turbulent length scale accounts to $L_{11}/L_{22}=1.9$, which agrees well with measurements. Obviously, by embedding an equidistant lattice Boltzmann simulation, the global finite volume based simulation becomes independent of its grid cell aspect ratio.

Application – Submerged Entry Nozzle in Continuous Casting of Steel

Submerged Entry Nozzles (SEN) are a key component of Continuous Casting (CC) machines. In two-port SEN the liquid steel is guided from the tundish into the mould where this down-pouring liquid stream is re-directed to the two opposing ports, defining the origin of two confined jets. More precisely, the SEN geometry, i.e. the realisation of this re-direction determines the macroscopic flow conditions inside the mould, which, in turn, are responsible for smooth CC operation and finally product quality.

During operation small non-metallic inclusions can hit the inner walls of a SEN and due to the non-wetting surface conditions between SEN and liquid steel, they can easily build up dominant accretions. This process, called clogging, favourably occurs at flow deflections and recirculation areas. In two-port SEN clogging is known to occur at the lowest submerged section, directly in the region of flow deflection. This clogging phenomenon is of major concern for steel producers, since (i) it constricts the effective port opening, leading to asymmetric jets of higher initial momentum, which changes the global flow pattern and (ii) it might deteriorate steel quality, if junks of accreted material are washed into the mould. In CC operation it is therefore necessary to replace the SEN, if clogging starts to become dominant.

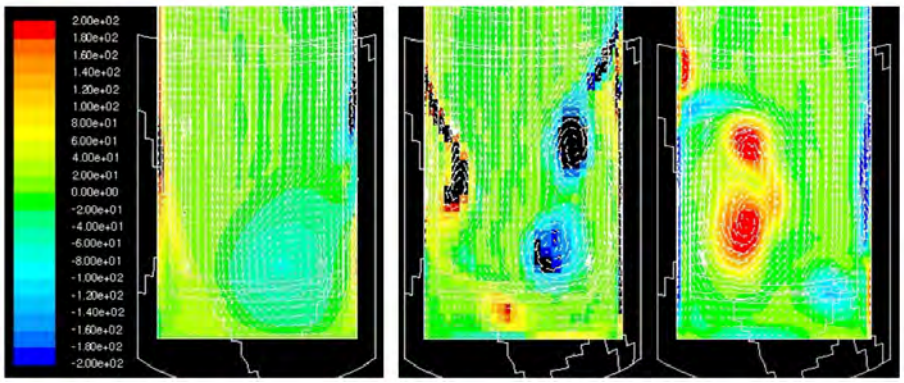

Figure 8: Contour plots of vorticity magnitude normal to the port openings picturing secondary vortex formation in case of URANS simulations (left) and embedded LB simulations (two snap-shots, right), in case of URANS simulations the secondary vortex remains stationary.

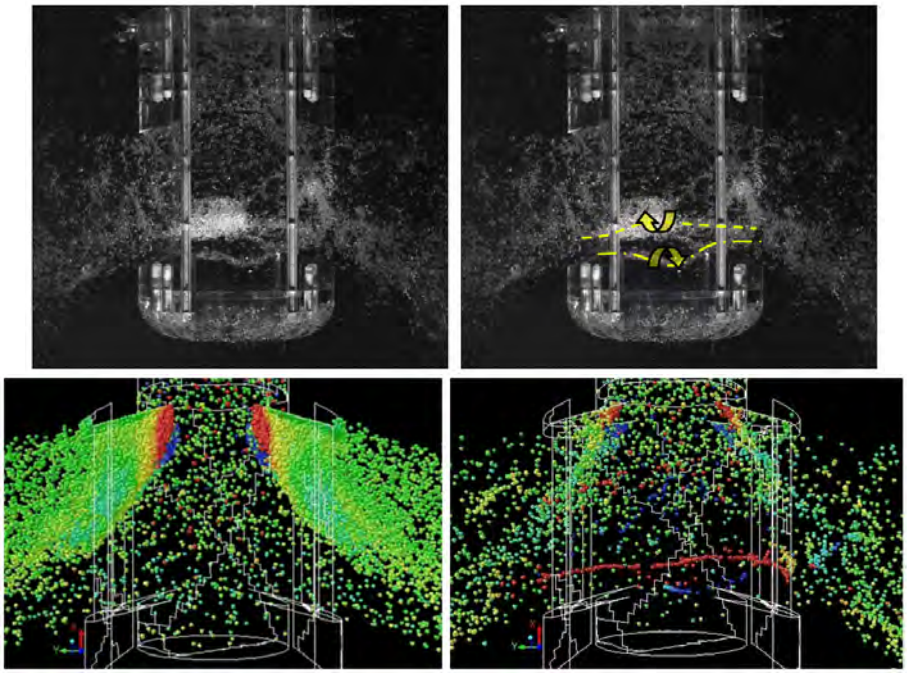

Figure 9: Bubble distribution during a SEN water experiment; snap shot of a high speed video (top left) and additional sketch of vortex axis and vortex orientation as obtained by visual observation of the video (top right); Bubble distribution as result of conventional finite volume based URANS simulations (left) and embedded LB simulations (right); bubbles are coloured by local fluid vorticity (± 100 1/s).

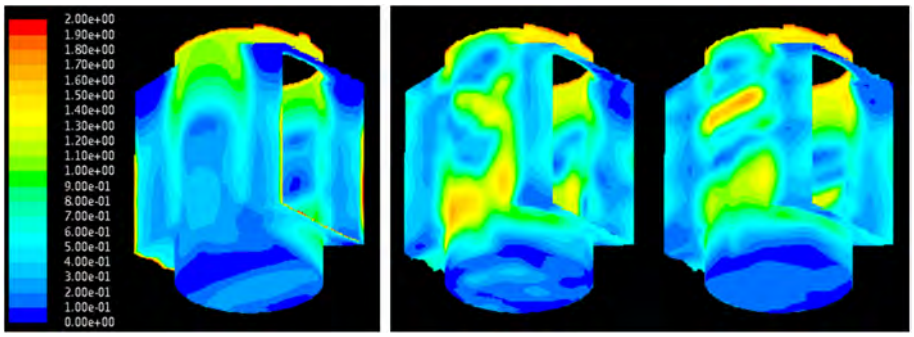

Figure 10: Contour plots of vorticity magnitude normal to the port openings picturing secondary vortex formation in case of URANS simulations (left) and embedded LB simulations (two snap-shots, right), in case of URANS simulations the secondary vortex remains stationary.

In this purely numerical study the flow deflection inside a two-port SEN is focused by conventional finite volume simulations and newly developed embedded lattice Boltzmann (LB) simulations. In the latter case a multi-scale approach is realised with the embedded LB simulation acting as a magnification lens, which is considered in addition to a global finite volume simulation. Although this investigation does not include dedicated experimental validation, numerical results are substantiated by experimental evidence obtained by previous studies.

Since no direct experimental validation is available for this study we concentrate on phenomenological results rather than on quantitative evidence. In a first presentation of results we investigate the occurrence and dynamical behaviour of secondary vortices. Water experiments show that in single-phase flows horizontal secondary vortices irregularly establish and decay with changing orientation of rotation at high alternation rates (Pirker et al. 2014).

However, classical finite volume simulations based on URANS turbulence models cannot recover this phenomenon (Fig. 8a). Instead of highly unsteady secondary vortex pairs those simulations result in a single secondary vortex with persisting position and orientation. Even very expensive finite volume bases LES do not result in the highly unsteady secondary vortex pair interaction, which is reported from experiments.

In contrast to that, embedded LB simulations immediately result in highly unsteady interaction of secondary vortices of alternating orientations, which from a phenomenological point of view agrees well with experimental observations. Interestingly, these results come along with only eight percent of additional computational time. Fig. 8b and 8c show two snap shots of the vorticity field in the SEN's mid plane (facing the port openings in normal direction), exhibiting the detailed formation, movement and decay of these secondary vortices.

While it is very difficult to observe these secondary vortices by classical experimental methods like Particle Image Velocimetry (PIV) due to their high dynamics and restricted optical accessibility inside the SEN, it is easy to visualize them by adding a small amount of stopper gas injection. Small gas bubbles tend to be captured in the cores of secondary vortices forming characteristic bubble threads, which can be recorded by high speed camera. Fig. 9 shows a snap shot of a corresponding video with the dashed lines indicating the bubble threads and the arrows hinting to vortex orientation.

In case of low gas injection it is reasonable to assume only two-way momentum coupling between (point) bubbles and the surrounding liquid. If this simplified bubble tracking is added to a conventional finite volume based URANS simulation, no bubble threads can be observed (Fig. 9a). Obviously, in this case the simulated secondary vortex is too weak to capture bubbles. Instead a multitude of bubbles is collected in the upper region of the port opening, locally violating the assumption of independent bubble tracking. In contrast to this, embedded LB simulations render a completely different picture. In this case gas bubbles are more dispersed in the lower part of the SEN and they are obviously captured by the secondary vortices, forming characteristic bubble threads. Once again, from a phenomenological point of view this simulation results agrees well with corresponding experimental observations.

From a metallurgical point of view these results are only of limited relevance at first glance. However, the unsteady flow field of the secondary vortices governs the local wall shear pattern which controls the stability of wall attached particle aggregates (i.e. clogging). In Fig. 10 the wall shear pattern are in line with the previous results. While classical finite volume simulations based on URANS turbulence models predict a low and homogeneous wall shear distribution, the embedded LB simulation exhibits a heterogeneous and unsteady wall shear pattern. It seems to be reasonable to assume, that those highly unsteady secondary vortices and their subsequent impact on local wall shear might be favourable for a delayed onset of clogging.

CONCLUSION

In this study a hybrid simulation concept has been presented which combines a classical finite volume based simulation of turbulent flow with an embedded lattice Boltzmann (LB) based simulation. In this concept the embedded LB co-simulation serves as a magnification lens, identifying coherent turbulent structures which are subsequently handed over to the coarse finite volume simulation by direct forcing.

The main findings can be summarized as follows:

1. Since the embedded LB concept has been realised in the framework of a commercial solver, setting up such hybrid simulations is straight forward.
2. Both finite volume simulation and LB co-simulation work fully parallel using many to many MPI parallelisation.
3. The embedded LB simulation concept works numerically stable and produces reasonable results at very low computation costs.
4. The embedded LB simulation concept can be applied to industrial flow configurations.

In the future we will focus on multiphase capabilities of embedded LB co-simulations.

REFERENCES

ANSYS Fluent, http://www.ansys.com (retrieved 3/2014).

BHATNAGAR P., GROSS E.P. and KROOK M.K. (1954) A model for collision processes in gases, *Phys. Rev.*, **94**, 511-525.

DERKSEN J.J. and VAN DEN AKKER H.E.A. (2000) Simulation of vortex core precision in a reverse-flow cyclone, *AIChE J.*, **46**, 1317-31.

FRÖHLICH J. and RODI W. (2004), LES of the flow around a circular cylinder of finite height, *Int. J. Heat and Fluid Flow*, **25**, 537-48.

GELLER S., KRAFCZYK M., TÖLKE J., TUREK S. and HRON J. (2006), Benchmark computations based on lattice-Boltzmann, finite element and finite volume methods for laminar flows, *Comp. & Fluid*, **35**, 888-897.

GRONALD D. and DERKSEN J.J. (2011), Simulating turbulent swirling flow in a gas cyclone: A comparison of various modeling approaches, *Powder Techn.*, **205**, 160-171.

HE X., LUO L.-S. and DEMBO M. (1996) Some Progress in Lattice Boltzmann Method. Part I. Nonuniform Mesh Grids, *J. Comp. Physics*, **129**, 357-363.

PIRKER S., GONIVA C., KLOSS C., PUTTINGER S., HOUBEN J. and SCHNEIDERBAUER S. (2013) Application of a hybrid – Lattice Boltzmann and Finite Volume – turbulence model to cyclone short-cut flow, *Powder Techn.*, **235**, 572–580.

PIRKER S. and THUMFART M. (2014) Numerical Simulation of Secondary Flow Instabilities in Submerged Entry Nozzle (SEN) Flow, *ECCC 2014 conf. Proc.*, Graz, Austria.

POPE S.B. (2000) Turbulent Flows, Cambridge Univ. Press, ISBN 10-05-2159886-9.

SHIRGAONKAR A.A., MACIVER M.A. and PATANKAR N.A. (2009), A new mathematical formulation and fast algorithm for fully resolved simulation of self-propulsion, *J. Comp. Physics*, **228**, 2366-90.

SMAGORINSKY J. (1963) General Circulation Experiments with the Primitive Equations: The Basic Experiment. *Month. Weather Rev.*, Vol.164, pp. 91-99.

YU H., GIRIMAJI S.S. and LUO L.-S. (2005), DNS and LES of decaying isotropic turbulence with and without rotation using lattice Boltzmann method, *J. Comp. Physics*, **209**, 599-616.

WANG P., FRÖHLICH J., MICHELASSI V. and RODI W. (2008), Large-eddy simulation of variable-density turbulent axisymmetric jets, *Int. J. Heat and Fluid Flow*, **29**, 654-664.

WYGNANSKI I and FIEDLER H. (1969), Some measurements in the self-preserving jet, *J. Fluid Mech.*, **38**, 577-612.

MODELING OF POST COMBUSTION INSIDE THE OFF-GAS DUCT SYSTEM OF THE OVAKO ELECTRIC ARC FURNACE

Niloofar ARZPEYMA[1*], Mikael ERSSON[1] , Pär JÖNSSON[1]

[1] Department of Materials Science and Engineering, Royal Institute of Technology (KTH), 100 44, Stockholm, SWEDEN

* E-mail: arzpeyma@kth.se

ABSTRACT

In order to study the post combustion (PC) inside the duct system of an electric arc furnace (EAF), a three-dimensional computational fluid-dynamics (CFD) model was developed. The reactions between the off gas species (oxygen and hydrogen) and oxygen which leaked into the duct, through the air gap, was considered. The off-gas composition, the off – gas velocity and the outlet pressure were considered as parameters affecting the PC. The results showed that there was a considerable amount of the uncombusted CO to be captured. The highest CO concentration was found at the central part of the duct. The results also showed that a higher off-gas mass flow rate and a higher power of the outlet fan led to a higher combustion of CO and H_2. An off-gas analysis probe was then installed after the air gap, where the tip of the probe was placed according to the predicted high CO concentration area found in the simulations. Thereafter, the measured off-gas composition was used to predict the off-gas composition at the outlet of the EAF.
.

Keywords: CFD, electric arc furnace, duct system, off - gas.

NOMENCLATURE

A complete list of symbols used, with dimensions, is required.

Greek Symbols

η'	Exponent rate for reactant.
η''	Exponent rate for product.
ε	Turbulence dissipation rate, [m^2/s^3].

Latin Symbols

p	Pressure, [Pa].
v	Velocity, [m/s].
ρ	Density, [kg/m^3].
C	Molar concentration [kg mole/m^3].
k	Rate constant [m^3/gmol-s].
R_k	Kinetic rate, [kgmol/m^3-s].
R_e	Turbulence rate, [kgmol/m^3-s].
Y	Mass fraction.
A_r	Pre – exponential factor[m^3/gmol-s].
mf	Mole fraction.
M	Molecular weight, [kg/kgmol].
R	Gas law constant [J/kgmol-k].
N	Nnumber of species.
ν	Stoichiometric coefficient.
k	Turbulent kinetic energy, [m^2/s^2].

Sub/superscripts

r	Reaction.
f	Forward.
j	Species.
P	Product.
R	Reactant.

INTRODUCTION

The off – gas which leaves the EAF contains CO and H_2, so it can be an important source of energy. This energy,in turn, can be reused to preheat scrap to be used in the EAF. However, in many EAFs, this energy is lost. Thus, an online measurement of the off – gas contributes to estimate this wasted amount of energy. In order to get an accurate off gas extraction, an off – gas analysis probe should be positioned before a location where the off gas is exposed to the air leaking from the air gap at the EAF elbow. In the current EAF (Ovako EAF located in Hofors, Sweden), the only technically possible place to install the probe was after the air gap between the furnace elbow and the duct system. It was approximately 1.5 m from the air gap as shown in Figure 1 (b). Thus, first, the combustion inside the duct was modeled using computational fluid dynamics (CFD) to estimate the amount of the off – gas dilution due to the air leakage into the off- gas stream. Second, after installation of the probe, the off – gas composition at the probe position was used to estimate the off – gas composition at the outlet of the furnace using different fan powers. These results were then further used as an outlet boundary condition in the whole model of the EAF.

Off – gas modeling in duct systems using CFD

Off- gas flows in steelmaking furnaces have previously been modelled using CFD. For example, Tang et al. [1] modeled the exhaust gas system in an argon oxygen decarburization (AOD) converter. They showed that at an optimal low rate of blowing argon, the air is infiltrated into the converter.

Tang et al [2] studied the post combustion in a horizontal duct system using CFD. In their model, the reaction rate of CO and H_2 combustion was controlled by temperature and turbulence. Their results showed that an increased ratio of the air to the off –gas volume flow led to a lower post combustion of CO and H_2 in the off – gas. That was due to the entrance of cold oxygen into the duct.

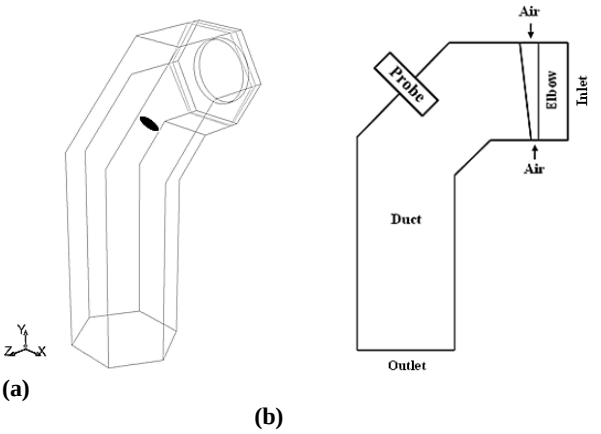

(a) **(b)**

Figure 1: (a) The computational domain of the duct showing the air gap and the area where the concentration of CO and O_2 are computed; (b) the cross sectional view of the domain, showing the boundary conditions and the probe position.

Also, Karbowniczek et al. [3] used CFD to study temperature distribution in a duct system of an EAF. The model showed a drop of 900 K due to the ingress of air at the gap into the duct.

As mentioned earlier, CFD is used in this study to investigate the dilution of the off – gas due to an air leakage and also to predict the gas composition at the EAF outlet before the air gap.

MODEL DESCRIPTION

Computational domain

A three dimensional gas flow is modeled in an EAF duct system. The off gas emerges from the inlet defined at the furnace elbow, and the air is infiltrated through the air gap. The air gap width at the lower part and upper part of the gap is 5 cm and 15 cm respectively. Thus, the computational domain consists of the duct system, part of the elbow and the air gap between the duct and the elbow. The sketch of the geometry is shown in Figure 1 (a).

Reactions and governing equations

A steady state gas flow is modeled by solving the mass, momentum, energy and species conservation equations. The following reactions are considered for CO and H_2 combustion inside the duct for the first part of the study:

$$CO + 0.5\,O_2 \rightarrow CO_2 \qquad (1)$$

$$H_2 + 0.5\,O_2 \rightarrow H_2O \qquad (2)$$

For the second part only the first reaction is considered since the analyzed off –gas by the probe does not contain water.

The species source term in species conservation equation is determined using the kinetic rate (R_k) and turbulence mixing rate (R_e). Both are computed, and the lower value is used as the limiting rate of reaction. The molar kinetic rate of reaction is calculated as follows:

$$R_{j,k} = \left(v_{j,r}^{''} - v_{j,r}^{'}\right) k_{f,r} \prod_{j=1}^{N_R} C_{j,r}^{\eta_{j,r}^{'}+\eta_{j,r}^{''}} \qquad (3)$$

where $C_{j,r}$ is the molar concentration of species j (kgmol/m^3) in reaction r, $\eta_{j,r}^{'}$ is the exponent rate for reactant species j in reaction r, N_R is the number of reactions and $\eta_{j,r}^{''}$ is the exponent rate for product species j in reaction r, $v_{j,r}^{''}$ is the stoichiometric coefficient of products, $v_{j,r}^{'}$ is the stoichiometric coefficient of reactants and k_f is the forward rate constant. The latter is a function of the temperature, according to the Arrhenius expression, which is defined as:

$$k_{f,r} = A_r T^{\beta} \exp\left(-\frac{E_r}{RT}\right) \qquad (4)$$

where β is the temperature exponent and A_r is the pre – exponential factor, and E is the activation energy (J/kgmol) for the reactions, shown in Table 1 [4].

The reactions are considered irreversible. The values for the rate exponent of the reactants are shown in Table 1[4].

Table 1: The constants used in calculation of kinetic reaction rate .

Reaction	(1)	(2)
A_r	2.239×10^{12}	9.87×10^{8}
E	1.7×10^{8}	3.1×10^{7}
$\eta_{O2}^{'}$	0.25	1
$\eta_{CO}^{'}$	1	-
$\eta_{H2}^{'}$	-	1

The turbulence rate is calculated from the following expressions for the rate of combustion.

$$R_{j,e} = v_j^{'} A M_{w,j} \rho \frac{\varepsilon}{k} \min_R \left(\frac{Y_R}{v_R^{'} M_{w,R}}\right)$$

$$R_{j,e} = v_j^{'} M_{w,j} AB \frac{\varepsilon}{k} \frac{\sum_P Y_P}{\sum_j^N v_j^{''} M_{w,j}}$$

where Y_R and Y_P are the mass fractions of product species P and reactant species R respectively, k is the turbulent kinetic energy, ε is the turbulence dissipation rate, N is the number of species and $M_{w,j}$ is the molecular weight of species j. A is constant for reactant equal to 4 and B is product constant equal to 0.5. The lower value determines the rate of reaction [5].

Boundary conditions

The model consists of two inlets for the off-gas and air. The pressure outlet was applied to the outlet boundary. Variations of off gas composition, velocity and pressure, which represents the fan power, were applied to the inlet and outlet. The boundary conditions applied to the off-gas at the inlet are presented in Table 2. The applied velocity inlet is obtained from the output data from the CFD modeling of the whole furnace [6]. The model includes the area above the bath surface, three virtual lance burners and the elbow. The flow rate of CO arising from the bottom surface was around 1 kg/s.

Table 2: Boundary conditions used in the duct model.

Case	Off-gas composition	V (m/s)	P (Pa)
1	0.25 CO-0.15 CO_2	19	-200
2	0.25 CO-0.15 CO_2	25	-200
3	0.25 CO-0.15 CO_2	22	-300
4	0.25 CO-0.15 CO_2	22	-250
5	0.25 CO-0.15 CO_2	22	-200
6	0.25 CO-0.15 CO_2	22	-150
7	0.25 CO-0.15 CO_2	22	-100
8	0.25 CO-0.15 CO_2	22	-50

An atmosphere pressure and a temperature of 300 K were set to the air gap. The inlet temperature was set to 1800 K.

Calculation procedure

ANSYS FLUENT 13.0.0 [7] was used to create the geometry, to generate the mesh and to solve the conservation equations. First, a tetrahedral mesh was generated using ANSYS Meshing, and then the tetrahedral cells were converted to polyhedral ones in FLUENT. The mesh independency of the results was investigated. The standard k-ε model was applied to describe the turbulent flow. In addition, the Finite Rate/Eddy Dissipation model in FLUENT was used to model the reactions. The SIMPLE algorithm and Standard scheme were applied for the pressure – velocity coupling and pressure discretization, respectively.

RESULTS AND DISCUSSION

1. Modeling of the off – gas composition after the air gap

The CO distributions given in mole fraction for different cases are shown for the central cross section of the duct in Figure 2 and Figure 3. In Figure 2 (a) and (b), the effect of velocity inlet on CO distribution is shown. For case 1, in which the velocity is equal to 19 m/s, the CO concentration is lower than for case 2 with an inlet velocity of 25 m/s. In lower velocity of 19 m/s, the air ingress into the duct is higher, and the combustion of CO starts in the regions closer to the inlet. The CO concentration has its highest value at the center of the duct. A velocity of 22 m/s is chosen to study the effect of the fan power on the flow [6].

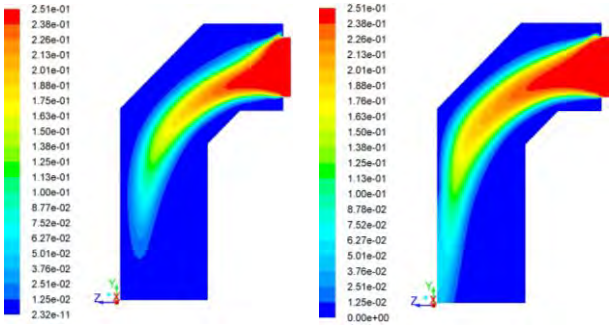

(a) **(b)**

Figure 2: CO distribution in the cross sectional plane of the duct in mole fraction for (a) case 1 with an inlet velocity of 19 m/s and (b) case 2 with an inlet velocity of 25 m/s.

Figure 3 shows CO and CO_2 distribution for case 3, case 5 and case 7 which have pressure outlet values of -300 -200 and -100 Pa respectively.

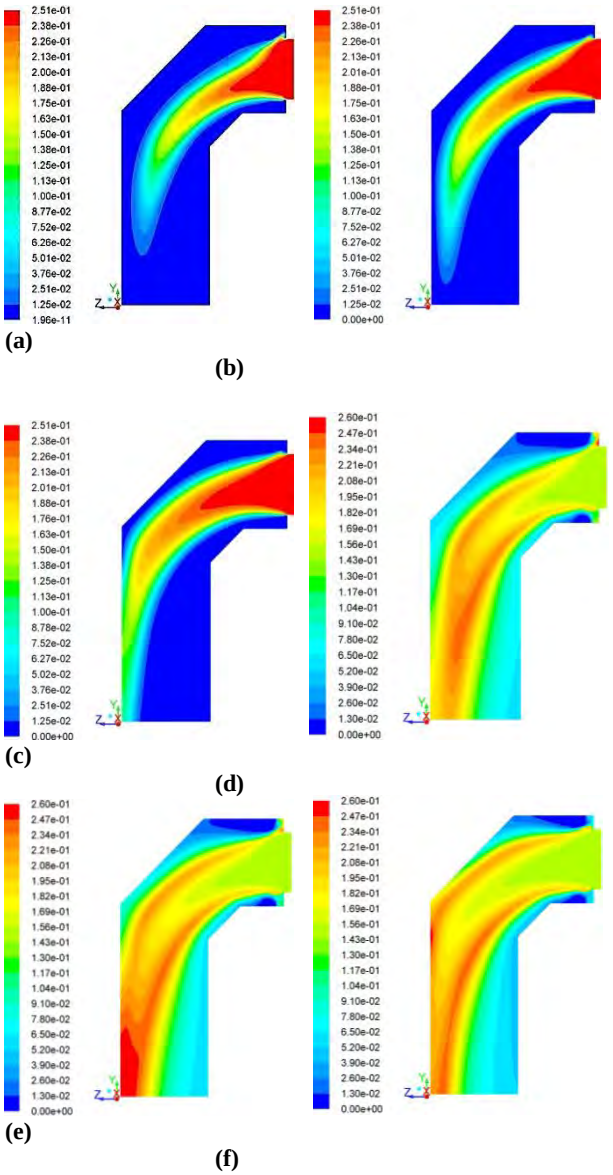

(a) **(b)** **(c)** **(d)** **(e)** **(f)**

Figure 3: CO distribution in mole fraction (a) case 3, (b) case 5, (c) case 7 and the CO_2 distribution in mole fraction for (d) case 3, (e) case 5 and (f) case 7, in the cross sectional plane of the duct.

The CO concentration is lower at the center of the plane for the case with the highest gauge pressure of -300 Pa. The CO_2 distribution shows that when the pressure increases, the combustion of CO air into CO_2 occurs at a closer distance to the duct inlet. This indicates that more air is sucked into the duct at higher absolute gauge pressures.

The results of the CO concentration due to the outlet pressure variation are shown in Figure 4. They show that the CO amount has the maximum value at the center of the plane. The maximum CO concentration at high pressures (case 3 and case 4) has its maximum value at the lower part of the plane. This is due to the less air leakage from the lower part of gap. At lower pressures, case 7 and case 8, the maximum CO concentration is located close to the center of the plane.

It was expected that with higher fan pressure, less air would be sucked into the duct from the gap. However, the results in Figure 3 and Figure 4 show that by decreasing the absolute gauge pressure from 300 Pa to 50 Pa, Figure 4 (a) – (f), the amount of the uncombusted CO at the probe position is increased. The average value of CO and O_2 at the small surface, shown in Figure 1 (a), has also been calculated. The results are shown in Table 3. It can be seen that by increasing the absolute gauge pressure (subtraction of the operating pressure from the absolute pressure), the concentrations of CO and O_2 decreases and increases respectively.

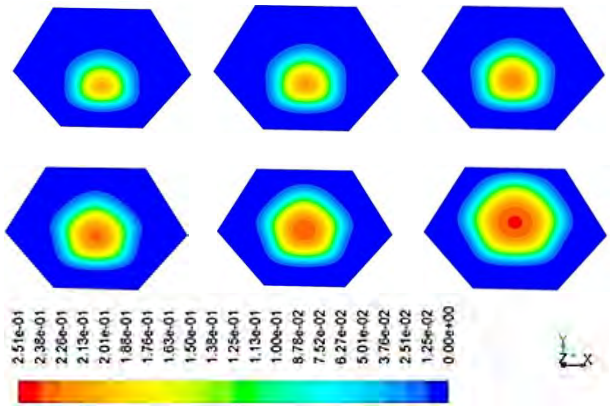

Figure 4: CO distribution in mole fraction in the plane at the probe direction (a) case 3, (b) case 4, (c) case 5, (d) case 6, (e) case 7 and (f) case 8.

It is suggested that the tip of the probe should be at the center of the duct where the CO concentration has its highest value, as shown in Figure 4.

Table 3: Average concentration of CO and O_2 at the area shown in Figure 1 (a).

Case	P_{outlet} (Pa)	CO (mf)	O_2 (mf)
3	-300	0.14	0.01
4	-250	0.17	0.006
5	-200	0.19	0.003
6	-150	0.21	0.0019
7	-100	0.22	0.001
8	-50	0.22	0.0009

Backward modeling of the off – gas flow to predict the gas composition at the outlet

Figure 5 and 6 show the measured off- gas composition in volume fraction (%) at the probe position for the first charge of two operations (case A and case B). Typically, the furnace is loaded by two heats in each operation. The probe is located after the air gap. The off gas composition at the outlet of the furnace before the air gap is calculated by backward modeling.

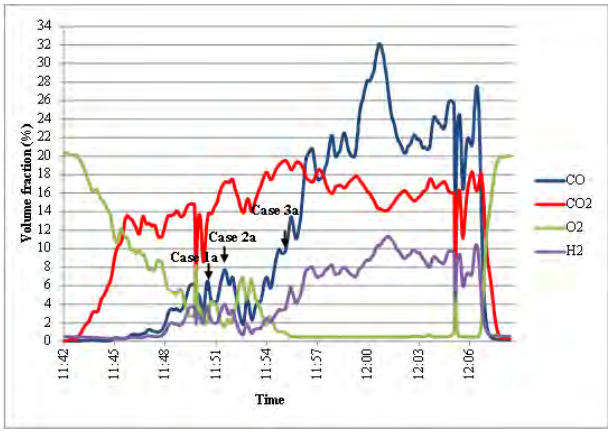

Figure 5: Off-gas composition versus time for the charge A.

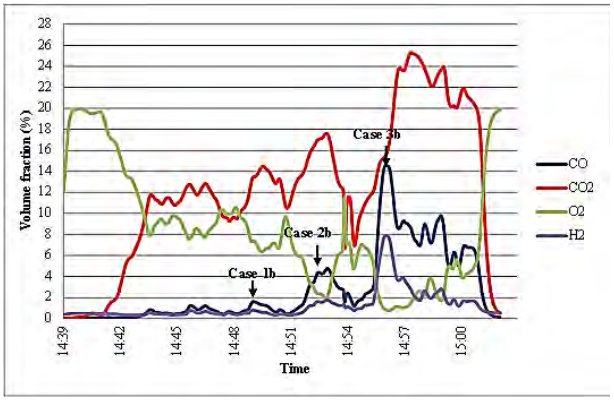

Figure 6: Off-gas composition versus time for the charge B.

Three cases are considered for each case A and B during the furnace operation where the focus is to study the CO peaks. These correspond to 6%, 8% and 10 % for case A, as it is shown in Figure 5. Furthermore, they correspond to 2 %, 5% and 15 % CO for case B respectively, as it is shown in Figure 6.

The final results of the off gas composition in mole fraction (equivalent to volume fraction for an ideal gas mixture) at the duct inlet, which meets the composition at the probe spot, are shown in Table 4 and Table 5.

The rest of the predicted duct inlet concentrations is around 54 % to 67 % and contain nitrogen, nitrogen oxide and water. These results will be used to estimate the off gas composition at the outlet in the furnace model in a further work. The combined model is shown in Figure 7.

Table 4: The predicted composition at the duct inlet for the heat A in mole fraction.

Case	Composition at the duct inlet			Composition at the Probe		
	CO	CO_2	O_2	CO	CO_2	O_2
1a	0.14	0.14	1e-4	0.06	0.168	0.017
2a	0.2	0.16	1e-4	0.082	0.18	0.022
3a	0.2	0.14	1e-4	0.11	0.176	0.01

Table 5: The predicted composition at the duct inlet for the heat B in mole fraction.

Case	Composition at the duct inlet			Composition at the Probe		
	CO	CO_2	O_2	CO	CO_2	O_2
1b	0.1	0.12	0.08	0.015	0.18	0.062
2b	0.13	0.15	1e-4	0.053	0.173	0.019
3b	0.25	0.12	1e-5	0.155	0.161	0.007

The results predict a low mole fraction of CO, lower than 0.15, at the outlet of the furnace during the melting process. When combining these results with the mass flow rate of gas from the furnace, it can be concluded that the amount of the chemical energy which leaves the furnace is low.

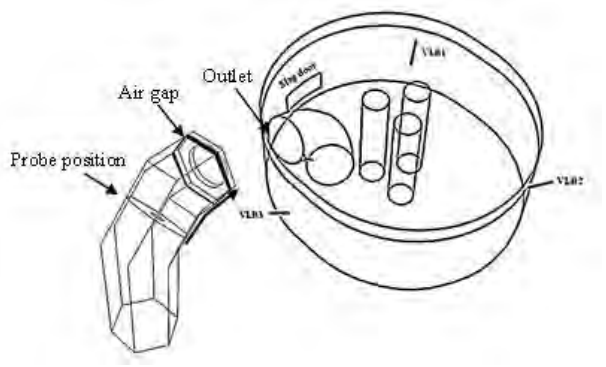

Figure 7: The combined model of duct system and EAF model used in backward modeling of the EAF outlet off-gas composition using the off-gas composition at the probe.

CONCLUSION

The flow inside the duct system of an EAF was modelled to investigate the gas dilution due to an air leakage and to study the effect of the fan power on the air leakage into the duct. The results show that the gas at the installed probe position, after the air gap at a distance of the 1 meter from the furnace outlet indicate that a considerable amount of CO is present. This CO concentration may be measured by the probe. The results also showed that the amount of air ingress into the duct is dependent on the outlet pressure and the flow rate and composition of the off-gas leaving the EAF which changes during the melting and refining stages.
The off – gas analysis measurement at the probe position were used to predict the gas composition at the furnace outlet. These results can be applicable as boundary condition to the EAF model.

REFERENCES

[1] TANG, Y., FABRITIUS, T. and Härkki, J., (2005), "Mathematical modelling of the argon oxygen decarburization converter exhaust gas system at the reduction stage", Applied Mathematical.

[2] TANG, X., KIRSCHEN, M., ABEL, M. and PFEIFER, H., (2003), "Modelling of EAF off-gas post combustion in dedusting systems using CFD methods", Steel Research International, 74, 201 -210.

[3] KARBOWNICZEK, M., KAWAKOWSKI, M., (2007), "The electric arc furncae off-gasses modeling using CFD", 16th IAS Steelmaking Conference, Argentina.

[4] MILEWSKI, J. ŚWIRSKI, K., SANTARELLI, M., Leone, P., (2011), Advanced Methods of Solid Oxide Fuel Cell Modeling, Green energy and technology.

[5] MAGNUSSEN, B. F., HJERTAGER B. H., (1976), "On mathematical models of turbulent combustion with special emphasis on soot formation and combustion", 16th Symp. On Combustion, The Combustion Institute.

[6] ARZPEYMA, N., ERSSON, M., JÖNSSON P., (2014), "Mätteknik för optimering av efterbränning", manuscript.

[7] ANSYS FLUENT Theory and User's Guide, Release 13.0.0, 2010.

ACKNOWLEDGEMENTS

This project was supported by the Swedish Energy Agency (Energimyndigheten). The authors wish to thank Patrik Undvall from Ovako Hofors AB, Erik Sandberg from Swerea MEFOS AB and Robert Vikman from Jernkontoret (The Swedish Steel Producers' Association), who contributed to this project.

MODELLING OF THE FERROSILICON FURNACE: EFFECT OF BOUNDARY CONDITIONS AND SIO BURST

Balram PANJWANI [1*], **Jan Erik OLSEN**[1†]

[1]SINTEF Materials and Chemistry, 7465 Trondheim, NORWAY

[*] E-mail: balram.panjwani@sintef.no
[†] E-mail: jan.e.olsen@sintef.no

ABSTRACT

A by-product from the ferrosilicon process is process gas which escapes into the furnace hood were it reacts with air. The process gas mainly consists of CO with some SiO and moisture. Modeling the gas behavior inside the furnace hood is very challenging due to the complex interaction between flow, reactions, radiation and turbulence. Another challenge is the selection of proper boundary conditions, especially, the boundary condition used for the charge surface through which the process gas is released, which is neither a wall surface nor a mass flux boundary. Traditionally, this boundary condition is modeled as a mass flux boundary, without considering the effect of roughness due to uneven distribution of charge material. A rough wall condition is compared with the traditional mass inlet boundary condition. It is observed that process gas is frequently released in local bursts typically with a high concentration of SiO. This is believed to promote local hot spots which favor NOx formation. Bursts of SiO are modeled and results show that both the strength of the burst and its location play a significant role in the NOx production.

Keywords: Ferrosilicon, Blowing, burst, SiO_2 dust, Combustion, Charge surface.

INTRODUCTION

Ferrosilicon is produced in submerged arc furnaces (SAF) where ore (silica) and carbon (coke, coal, etc.) are mixed inside a furnace. Both ore and carbon react when high voltage electric energy is supplied through electrodes, and this process is known as a reduction process. The reduction process produces alloys and an energy rich off-gas inside the reduction zone, which is beneath the charge surface and close to the electrode tip. The alloys, which is in liquid phase, sink to the bottom and this molten metal is collected through a tapping hole. The energy rich process gas rises upward from reduction zone and escape through the charge surface into a furnace hood. Simultaneously air is sucked into the hood through various open areas on the furnace walls due to the pressure drop. The air and process gas reacts inside the furnace hood and produces an off-gas potentially containing harmful substances. In a ferrosilicon furnace the process gas emerging from the charge surface mainly consists of CO with some SiO, water vapor, and volatiles. Reaction taking place between process gas and air in the furnace hood creates high temperature zones sufficient enough for formation of thermal NOx.

Release of process gas from the charge surface is non-uniform not only due to the transient and inhomogeneous reduction process but also due to inhomogeneous porosity distribution of charge material beneath the charge surface. Occasionally, the process gas (CO and SiO) bursts through the charge surface. Mainly these bursts consist of high concentration of SiO. The reaction of SiO is highly exothermic resulting in local hot pockets inside the furnace hood which subsequently leads to the formation of NOx. From industrial experience the strength of the jets or bursts and the amount of NOx formation are strongly correlated to each other. The high temperature bursts are triggered by avalanches in the charge. The charge avalanches causes outburst of large quantities of combustible gases, like CO/SiO, that rise from pockets of poorly carbonized charge material (Grådahl *et al.*, 2007). Blowing is another extreme situation, where SiO rich gas from around the electrode tip is released through a gas channel in the charge. Then large quantities of SiO are burnt in air to silica dust (SiO2). The observed correlation between NOx and silica is also valid under blowing: blowing results in both high NOx and silica formation. Compared to the avalanche phenomenon, which is always short in duration, the blowing phenomenon can last much longer as long as channels are left open between the cavity below the electrodes (also called crater). A boundary condition accounting for SiO bursts have been developed and further studied to establish the impacts of SiO jets on NOx.

Another challenge when modeling of furnace hoods is choice of type of boundary condition for the charge surface due to the non-uniform distribution of charge material (ore and carbon) on the surface. Traditionally, the charge surface is modeled as a mass flux boundary condition with no roughness effects accounted for. Alternatively the charge surface can be modeled as a wall with roughness. However, a wall has no inherent inflow of fluid which is required for the charge surface. While modeling the charge surface as a wall boundary condition, a model that is valid for the range from smooth to fully rough walls is required. However, with the standard turbulence model to describe the near wall zone is not accurate and therefore special treatment is required closer to the inner wall regime. One of the common approaches is to use a wall function proposed by Launder and Spalding (Launder and Spalding, 1974). In this approach the continuity and momentum equations along with the turbulence model equations are only solved in the outer region of the boundary layer. The inner region of the boundary layer is resolved with a predefined wall function. There have been many studies in the

development of the wall function applicable for both smooth and rough walls (Jiménez, 2004). In this paper, a law of wall suitable for rough-wall surfaces is reviewed. While modeling the charge surface as a wall boundary condition the release of process gas from the charge surface need to be done explicitly. A most appropriate approach is to use source term for the mass, momentum, species and energy equations. These source terms will ensure that the correct amount of process gas with correct momentum and energy is released from the charge surface.

Metal industries in Norway are committed toward the improvement of furnace operation and their aim is to lower NOx levels and other pollutants, and to achieve this a better understanding of the flow phenomena inside the furnace hood and specially close to the charge surface is needed. Major aim of the present study is to gain more understanding of the flow phenomena taking place inside the furnace hood using CFD. A steady state CFD model is developed using the commercial software ANSYS FLUENT (ANSYS, 2011). The major objectives of the present research work is to address

1. How the surface roughness of the charge surface affects the flow distribution?
2. How does SiO burst affects the temperature and NOx formation?
3. Does the location of burst have impact on the NOx formation?

CFD MODEL AND BOUNDARY CONDITIONS

A steady state CFD model solving for continuity, momentum, energy, species transport and radiation equations is developed using a general purpose CFD tool ANSYS FLUENT (ANSYS, 2011). The Radiation is modeled through Discrete Ordinance (DO) model and the turbulence is modeled through RNG k-ε turbulence model and standard wall functions. For rough walls appropriate roughness height and roughness constant are chosen. The process gas with a certain magnitude of velocity and temperature is escaped through the charge surface. It is rather easy to set the flow parameters of process gas at the charge surface using mass flux boundary condition, however, setting the process gas flow parameters at the charge surface with wall boundary condition is not very straightforward. FLUENT specific user defined functions (UDF) are used to model the flow phenomena close to the charge surface. UDF were incorporated for the source term in the continuity, momentum, energy and species transport equations. The value of the source term was non-zero at the first grid cell of charge surface and zero for the rest of computational domain.

The spatial discretization scheme was second order accurate. The pressure interpolation scheme was standard and the pressure gradient term was discretized using Green-Gauss cell based approach. The pressure velocity coupling was based on the SIMPLE algorithm.

Combustion Model and Reaction Mechanism

In present study Eddy Dissipation Concept (EDC) model was used for turbulence chemistry interaction (Magnussen and Hjertager, 1977). The EDC model is derived from turbulent energy cascade theory, where turbulent kinetic energy cascades from the larger eddies to smaller eddies. The cascading process continues until eddies are sufficiently small and they can't transfer energy further down. The EDC model assumes that the chemical reaction occurs on these smaller dissipative eddies, whose length and time scales are of the same order as the Kolmogorov length scale. Reaction within the fine eddies is assumed to occur as a constant pressure Perfectly Stirred Reactor (PSR) (GRAN and MAGNUSSEN, 1996a,b), where reactions proceed over the time scale, governed by the Arrhenius rates of Equation.

Table 1: Reduced reaction scheme with kinetic parameters in Kelvin, cal/mol, cm3

Reaction	Ar	N	Er
$2CO + O_2 \rightarrow 2CO_2$	2.24E+18	0.00	4776
$2SiO + O_2 \rightarrow 2SiO_2$	1.00E+18	0.00	0.24

The gas species accounted in the CFD model is CO, SiO and H_2O originating from the furnace crater, O_2 and N_2 from surrounding air and CO_2 and SiO_2 which are products of the reactions. Generally, there is an extensive reaction scheme governing the combustion process, accounting detailed kinetics lead to the larger CPU cost. Therefore, a simplified or reduced scheme shown in the Table 1 has been investigated. NOx formation is estimated using post processing approach available with FLUENT (ANSYS, 2011) but without considering the fluctuation in temperature and species.

Furnace Geometry and Computational Domain

The modeled geometry is the pilot scale furnace designed and developed at SINTEF/NTNU. The pilot furnace is a kind of scaled version of the actual ferroalloys furnace, however there are some noticeable differences. The pilot furnace has one electrode in the middle but the actual furnace consist of three electrodes. Furthermore, the height to diameter ratio of the pilot furnace is more than the actual furnace. Despite these difference, the processes such as reduction of ore and resulting process gas formation inside the pilot furnace are exactly similar to the actual furnace. The pilot furnace can be operated with both AC and DC power supply. The furnace hood is connected to an off gas system, and equipment for monitoring composition and temperature of the gas is installed at the exhaust. A sketch of the furnace is shown in 1. The original pilot furnace is asymmetric due to an offset in the exhaust, which makes impossible to investigate this geometry through 2D axis-symmetric approach, and therefore the geometry has to be modeled in 3D which results in higher CPU cost. 3D CFD validation of the pilot furnace have been performed under varies condition in previous work (Panjwani and Olsen, 2013). In the present study, a modified pilot furnace, which is devised from original pilot furnace is proposed by modifying the exhaust pipe as shown in Figure 2. This modification will allow 2D CFD simulations of the pilot furnace while preserving the underline physics of the ferrosilicon furnace.

The furnace computational domain is divided into two domains, furnace domain (see Figure 2) and surrounding domain. The surrounding domain is a cylindrical volume around the furnace hood and it is a part of the computational domain. The surrounding domain is provided for an appropriate distribution of air through different openings on the furnace.

Most of the boundary conditions used for furnace modeling are difficult to measure, and are thus subject for qualified estimation based on experience. An important boundary condition is the amount of process gas going through the charge surface into the furnace hood. The metallurgical process below the charge surface are responsible for process gas

formation. These process are not considered in the model. Therefore the amount of process gas is a priori unknown to the model. The only known parameters are the mass flow through the off-gas channel, offgas temperature and its composition. The mass flow of process gas and its temperature escaping through the charge surface is thus estimated by tuning these values such that the measured mass flow and temperature in the off-gas channel is matched. It is possible to measure the composition of off-gas and temperature at the off-gas channel. For calculating the gas composition at the charge surface an elemental mass balance is performed. The composition of the process gas escaping through the charge surface is estimated from the measured composition in the off-gas channel and the composition of air from the surrounding. Since molecules containing C and Si are introduced by the process gas, the measured amounts of CO, CO2 and SiO2 in the off-gas will give the amount of CO and SiO in the process gas. Generally, a mass flux boundary is used at the charge surface. The distribution of the process gas is non-uniform through the charge surface. Therefore the charge surface have been divided into seven zones (see Figure 3), which make easier to set different input values at different zones. The electrode is modeled as solid zone with a fixed power supply. On the wall boundaries depending on the type of the wall a suitable boundary condition either convective or adiabatic is applied. The amount of air and its temperature being sucked into the furnace hood is supplied at the surrounding exterior surface through mass flux boundary condition. The mass flow rate through the surrounding was 1 kg/s and total amount of process gas was 0.08 kg/s. At the offgas outlet a pressure outlet boundary condition is employed. The specified outlet gauge pressure was 0 Pascal. The solid zones such as refractory, concrete and steel etc shown in Figure 2 are modeled explicitly.

CFD simulations were continued until all the residuals were below pre-specified values. In addition to that area averaged temperature at the offgas outlet surface was monitored. Our observation shows that even though the residuals for the governing equations were bellow the predefined value but the averaged temperature at outlet was not constant. Therefore all the simulation were continued until both criterion were satisfied.

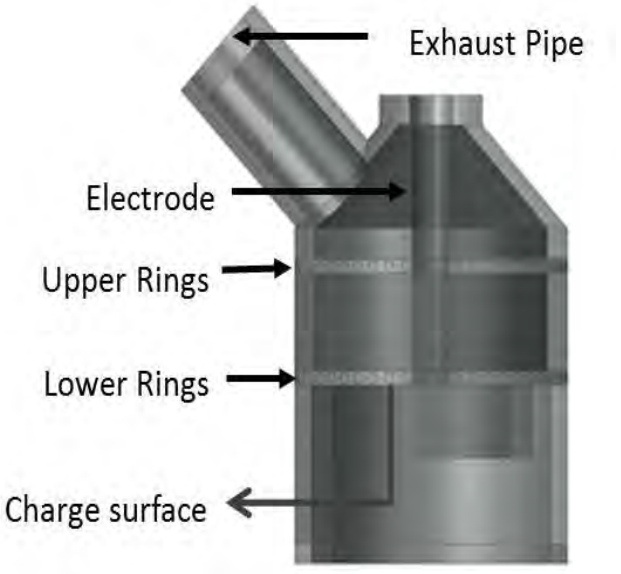

Figure 1: 3D schematic of the geometry

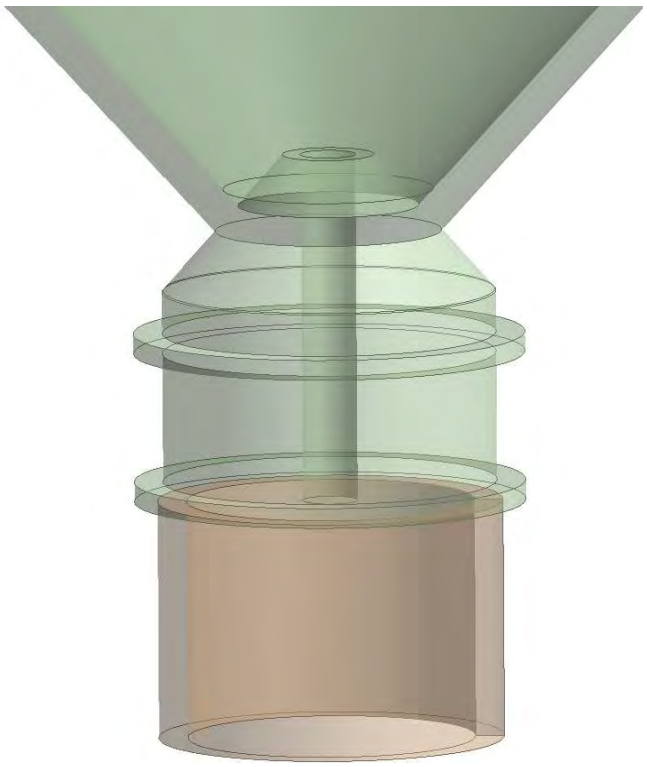

Figure 2: Schematic of the modified axis-symmetric geometry

Roughness Modeling

The near-wall region consists of three main regimes: the laminar layer or linear sublayer, the buffer layer and the logarithmic layer. The laminar law holds in the linear sublayer,

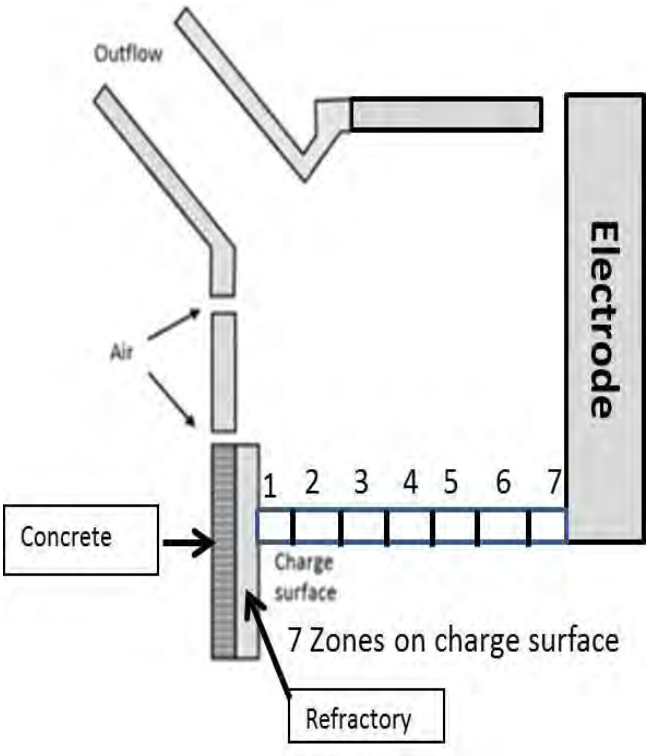

Figure 3: Schematic of the Furnace geometry with different zones and solid material

which is valid upto y^+=5. The logarithmic law holds in the log layer and it is valid from y^+=30 to y^+=500 - 1000. The modification of the log law for rough surfaces was proposed by Nikuradse (Nikuradse, 1933) through extensive experiments on flow inside the rough pipe. According to Nikuradse (Nikuradse, 1933) the mean velocity distribution near rough walls has the same slope ($1/\kappa$) as smooth pipe but a different intercept. The law-of-the-wall for mean velocity modified for roughness has the form (Cebeci and Bradshaw, 1977; Nikuradse, 1933):

$$\frac{U}{u^*} = \frac{1}{\kappa}\ln(\frac{\rho u^* y}{\mu}) + B - \Delta B \quad (1)$$

ΔB depends, in general, on the type (uniform sand, rivets, threads, ribs, mesh-wire, etc.) and size of the roughness. For the fully rough regime, Cebeci and Bradshaw (Cebeci and Bradshaw, 1977) reported the following analytic fit to the sand-grain roughness data of Nikuradse (Nikuradse, 1933).

$$\Delta B = \frac{1}{\kappa}\ln f_r \quad (2)$$

where f_r is a roughness function that quantifies the shift of the intercept due to roughness effects. There is no universal roughness function valid for all types of roughness. The roughness function is a function of $K_s^+ = \rho K_s u^*/\mu$, but takes different forms depending on the K_s^+ value. Where K_s is the physical roughness height and $u^* = C_\mu^{1/4} k^{1/2}$. Based on the measurements three distinct regimes have been identified hydro-dynamically smooth ($K_s^+ \leq 2.25$), transitional ($2.25 < K_s^+ \leq 90$) and fully rough ($K_s^+ > 90$) According to the data, roughness effects are negligible in the hydrodynamically smooth regime, but become increasingly important in the transitional regime, and take full effect in the fully rough regime. In FLUENT, the whole roughness regime is subdivided into the three regimes, and the formulas proposed by Cebeci and Bradshaw (Cebeci and Bradshaw, 1977) based on Nikuradse's (Nikuradse, 1933) data are adopted to compute ΔB for each regime. For instance, in the fully rough regime ($K_s^+ > 90$) the value of $\Delta B = \frac{1}{\kappa}\ln(1 + C_s K_s^+)$. Where C_s is the roughness constant.

RESULTS AND DISCUSSIONS

In total eight steady state simulations were performed to understand the effect of burst on temperature and NOx, appropriateness of boundary condition for charge surface, and how roughness affects the mixing and reaction rate closer to the charge surface. Before going into the further discussions on the effect of burst and boundary condition, we would like to discuss about velocity distribution obtained from the pilot furnace simulation. The velocity distribution is very similar for all the simulations therefore only one velocity vector is plotted for discussion. The velocity vector plot colored with O_2 concentration for the pilot furnace is shown in Figure 4. It can be seen from vector plot that the air from the surrounding domain enters into the furnace through upper and lower rings/openings. The respective amount of air entering through different openings on furnace depends mainly on the air mass flow rate through surroundings and the complex processes taking place inside the furnace hood. The air entering through the lower ring/opening is parallel to the charge surface and it interacts with the process gas escaping through the charge surface. The rate of mixing depends on the air velocity magnitude and direction and roughness of the charge surface. The flow around the roughness height resembles as flow around the bluff bodies, where turbulence behind the bluff body depends on the bluff body heights and incoming velocity and direction. Similarly, surface with higher roughness height will create large turbulence leading to the more mixing. It can also be seen that the direction of air changes from horizontal to the vertical due to the offgas location and buoyancy. The air is not able to penetrate in the middle of the furnace hood.

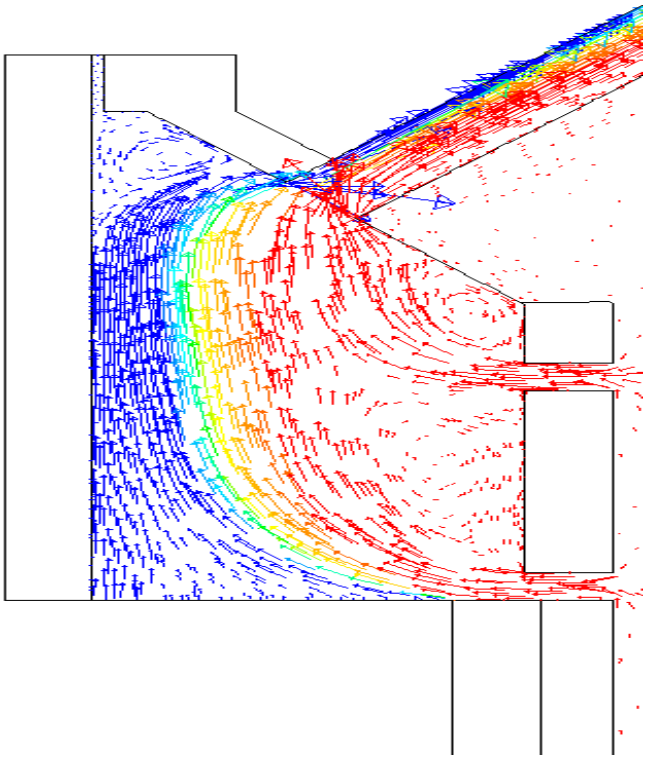

Figure 4: Vector plots for velocity distribution colored with O_2 mass fraction

Process gas from Burst

Occurrence of SiO burst have been observed in the real operation of ferro silicon furnace. The burst causes a sudden release of SiO/CO jets through the charge surface. Influence of SiO burst on the temperature, SiO_2 dust particles and NOx formation is depicted through two CFD simulation. In Case-1, SiO was released uniformly throughout the charge surface and in Case-2, the same amount of SiO was released far from the electrode in the localize area on the charge surface. Formation rate of SiO_2 dust particles is much faster than the CO_2 gas formation rate due to the higher reaction rate of SiO with O_2 compare to the CO reaction rate with O_2. Figure 5 and 6 show the SiO_2 distribution of Case-1 and Case-2 respectively. A large amount of SiO_2 concentration is clearly visible at some locations when SiO is released in a concentrated way at the localized area (see Figure 6) compared to uniform release (see Figure 5). All the contour plots for SiO_2 distribution have been plotted on the same color bar and this color bar is shown with Figure 5. A common color bar for temperature which is applicable for all the temperature contour plots is shown with Figure 7. Similarly, a common color bar for NOx density which is applicable for all the NOx density contour plots is shown with Figure 9.

The SiO reaction with O_2 is highly exothermic leading to the formation of higher temperature zones responsible for thermal NOx. The temperature distribution for both the cases,

Case-1 and Case-2, is shown in Figure 7 and 8 respectively. High temperature zones are clearly visible in a case with concentrated SiO release (see Figure 8).
Distribution of NO density for Case-1 and Case-2 is shown in Figure 9 and 10 respectively. Total amount of NOx was 2.16 kg/hr when SiO was released uniformly from the charge surface, whereas the amount of NOx was 2.7 kg/hr when SiO was released locally. It can be concluded from this study is that the formation of burst leads to the higher NOx formation even though the average SiO_2 dust particles formation is same in both the operation. Normally, the formation of burst will be very irregular and it is very difficult to predict the location of the burst. However, the most likely location of the burst formation is close to the electrodes.

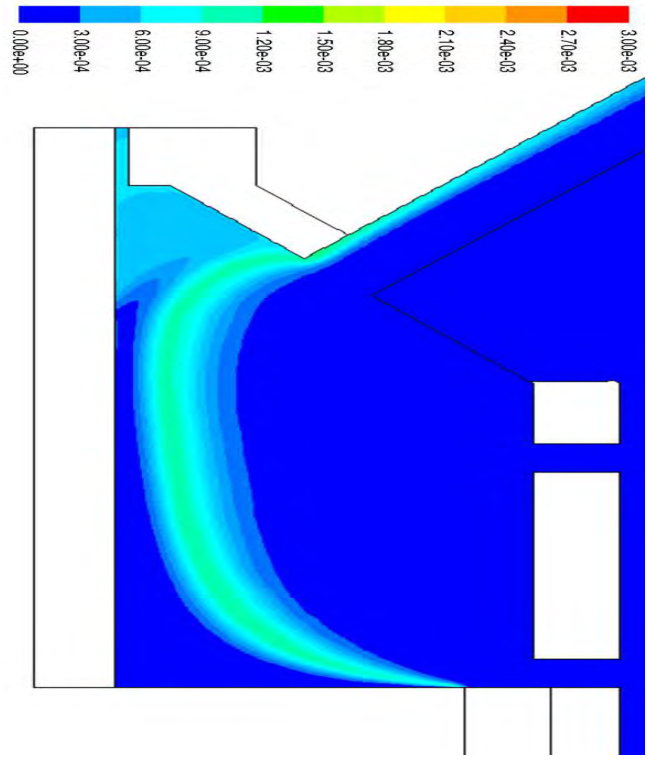

Figure 5: Case-1:Contour plot of SiO_2 mass fraction

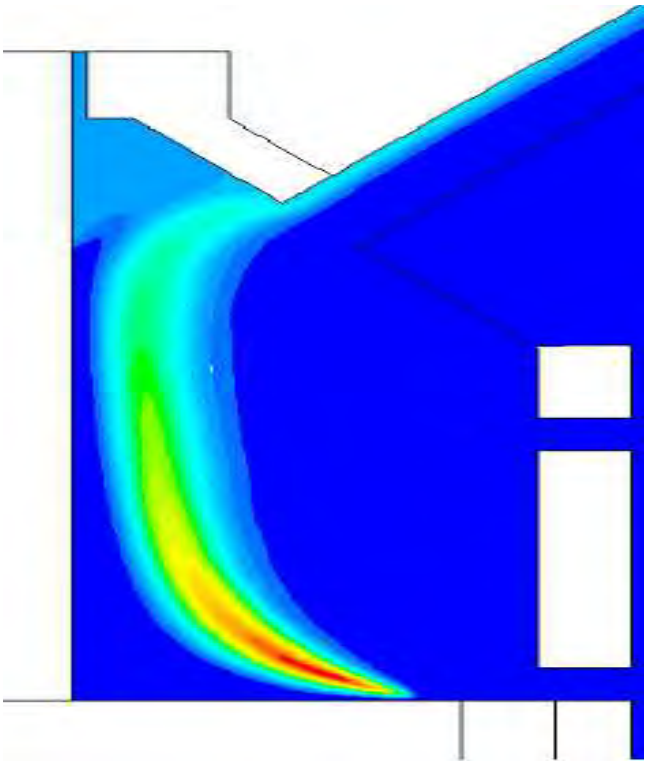

Figure 6: Case-2:Contour plot of SiO_2 mass fraction

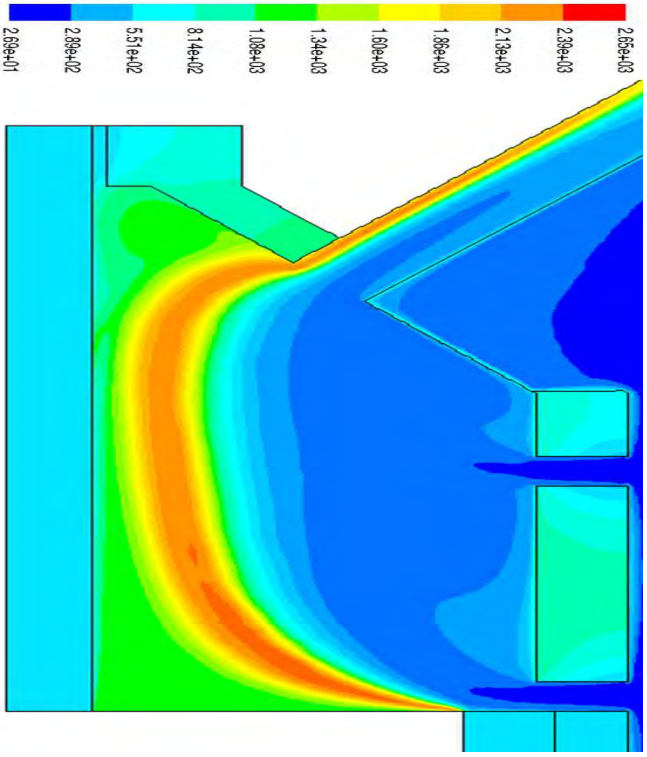

Figure 7: Case-1:Contour plot of Temperature distribution °C

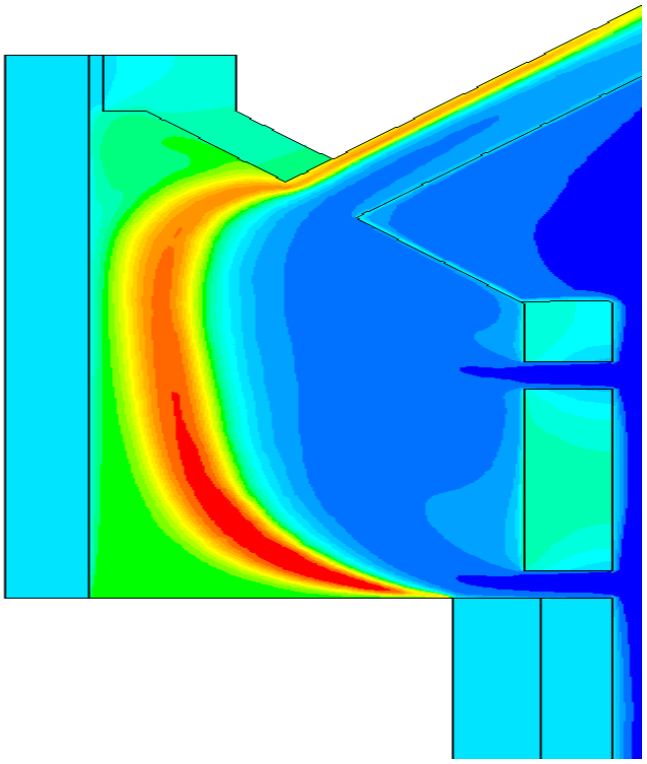

Figure 8: Case-2:Contour plot of Temperature distribution °C

One more CFD simulation, Case-3, was performed to understand the effect of location of SiO burst on flow behavior. In Case-3, it was assumed that the SiO burst occur close to the electrode. It has been observed from velocity vector plot the air does not penetrate in the middle of furnace hood (see Figure 4) and there is not enough air supply close to the electrode. Therefore, in limited amount of air supply there is less possibility of the SiO reaction in the middle of the furnace specially closer to the charge surface. In this situation most of the SiO reacts above the charge surface and close to the exhaust pipe, where concentration of air is higher (see Figure 11).

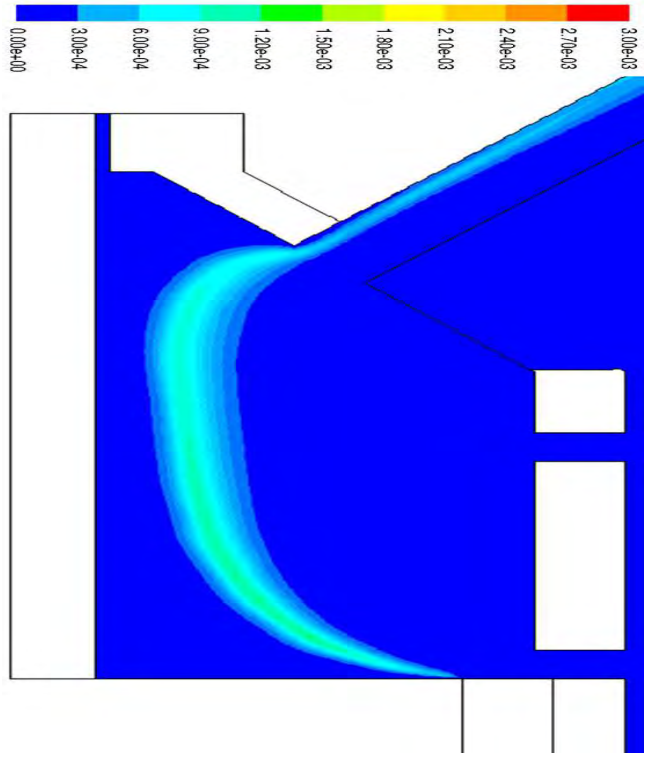

Figure 9: Case-1:Contour plot of NO density (kg/m^3)

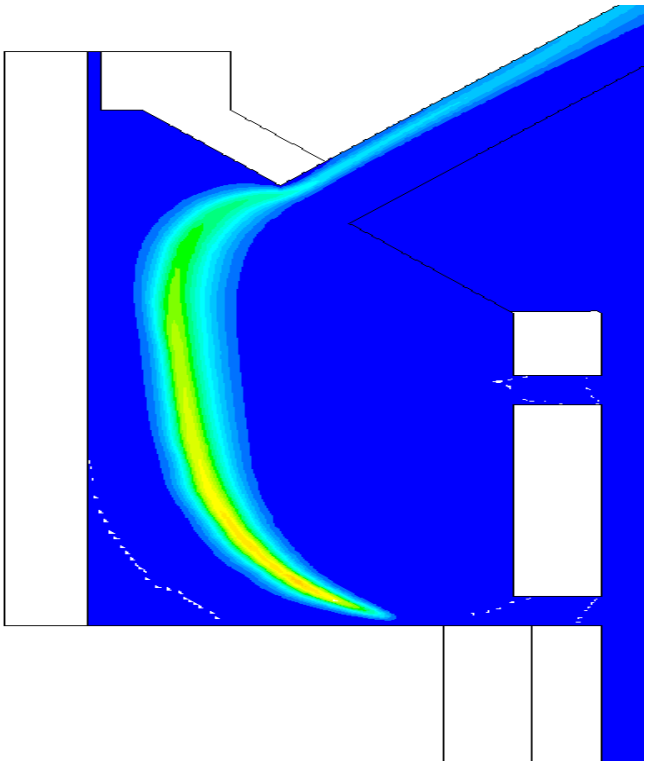

Figure 10: Case-2:Contour plot of NO density (kg/m^3)

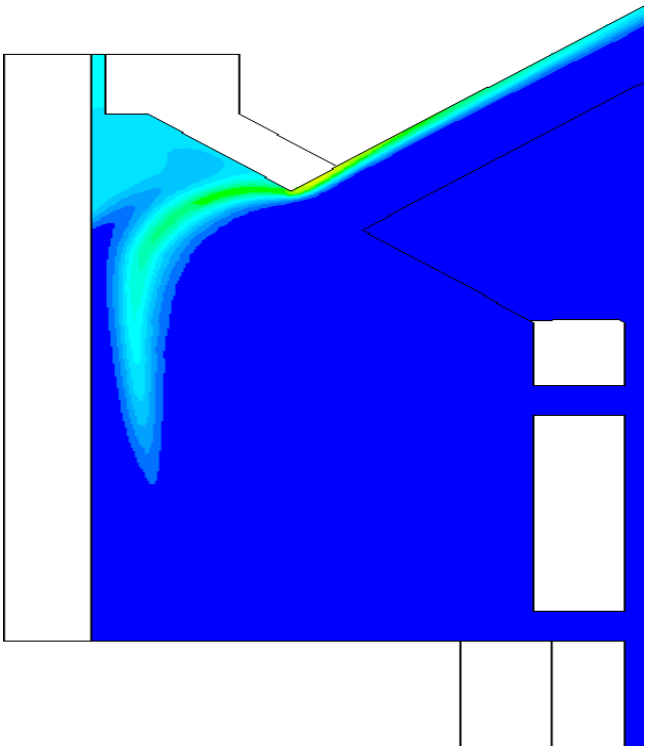

Figure 11: Case-3:Contour plot of SiO_2 mass fraction

It can be concluded from the results obtained from Case-2 and Case-3 that the not only the location of burst but also the availability of air affects the NOx formation. In present study only the reaction of SiO with O_2 is considered. It is not very clear whether SiO reacts with other species such as H_2O, CO and CO_2.

Previous measurements have shown that the SiO_2 dust particles concentration correlate well with the NOx formation. Increase in the SiO_2 concentration leads to increase in the NOx. In order to understand this effect one more CFD simulation, Case-4, is carried out. The Case-4 is similar to the Case-2, except the amount of SiO released is five times from the same location on the charge surface as in Case-2. The simulation parameters of Case-4 were the same as Case-2. Figure 12 shows the SiO_2 mass fraction of Case-4, it can be seen that an increase in SiO concentration leads to the increased concentration of dust particles. This increase in SiO_2 concentration also leads to the increase in temperature and subsequent NOx formation as shown in Figure 13. The studies shows that total amount of NOx increases upto 11.5 kg/hr from 6.5 kg/hr by increasing the SiO mass fraction by five times.

Effect of boundary condition

Two CFD simulations: Case-5 and Case-6 were carried out. Case-5 corresponds to the situation where mass flux boundary condition was applied on the charge surface, whereas Case-6 refers to the situation where wall boundary condition was applied on the charge surface. Otherwise, all other boundary conditions, chosen models and numerical schemes are same in both the cases. In Case-6, the roughness effects is not considered because objectives from this simu-

lation (Case-6) was to find the appropriateness of the wall boundary condition for the charge surface in a place of mass flux boundary condition.

Figure 14 and 15 shows the SiO_2 mass fraction of Case-5 and Case-6 respectively. It can be seen that there is not any significant difference between SiO_2 distribution obtained from both simulations. Although, the results obtained from both the boundary conditions are similar, applicability of the wall boundary condition posses a challenge. And one of the biggest challenges is to calculate the source terms for momentum and energy equation from the species mass source. one of the biggest advantage offered by mass flux boundary is that all the flow variables of the charge surface can be set very conveniently. As it is mentioned that a main purpose of using wall boundary condition is to account for the surface roughness on the charge surface. The wall roughness influences

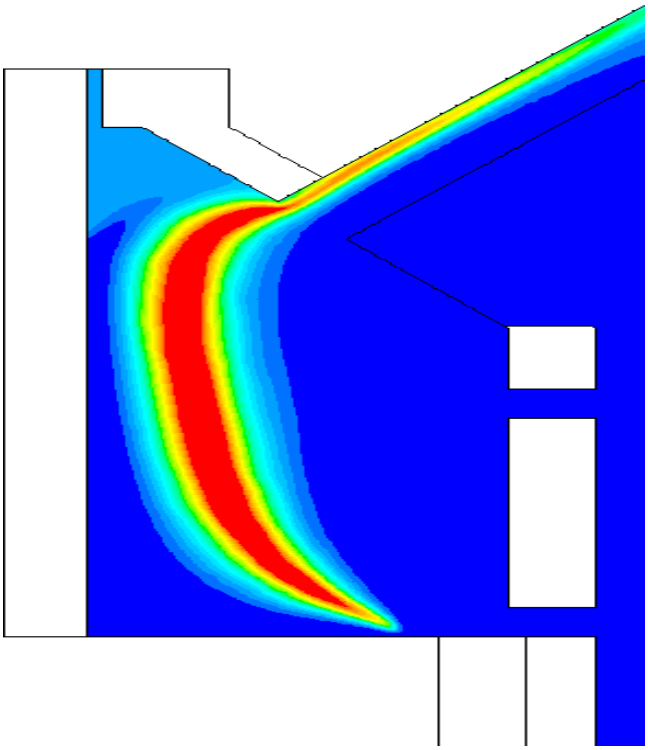

Figure 12: Case-4:Contour plot of SiO_2 mass fraction

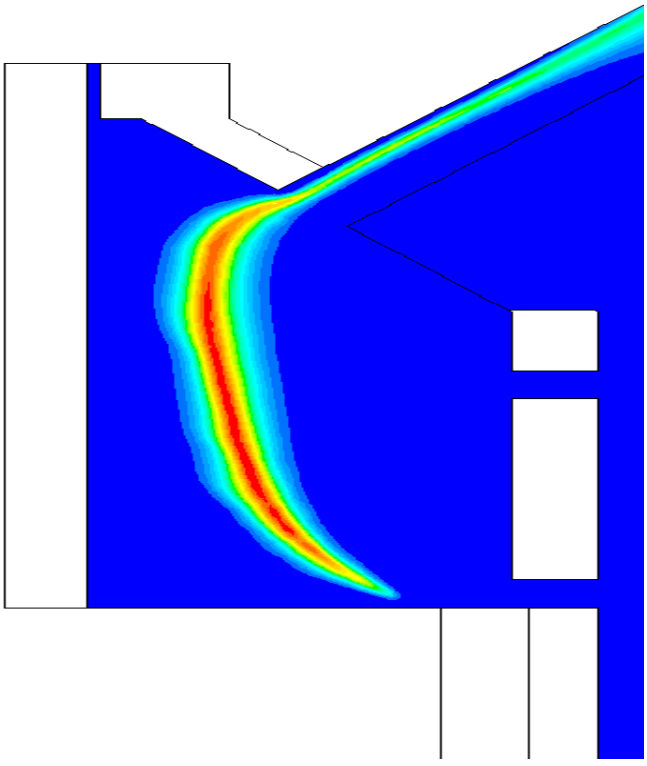

Figure 13: Case-4:Contour plot of NO density (kg/m^3)

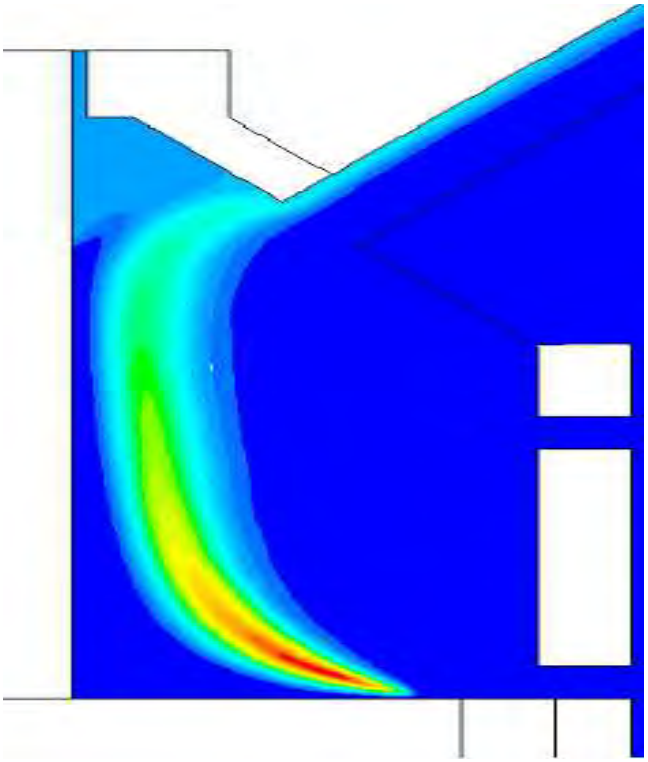

Figure 14: Case-5:Contour plot of SiO_2 mass fraction

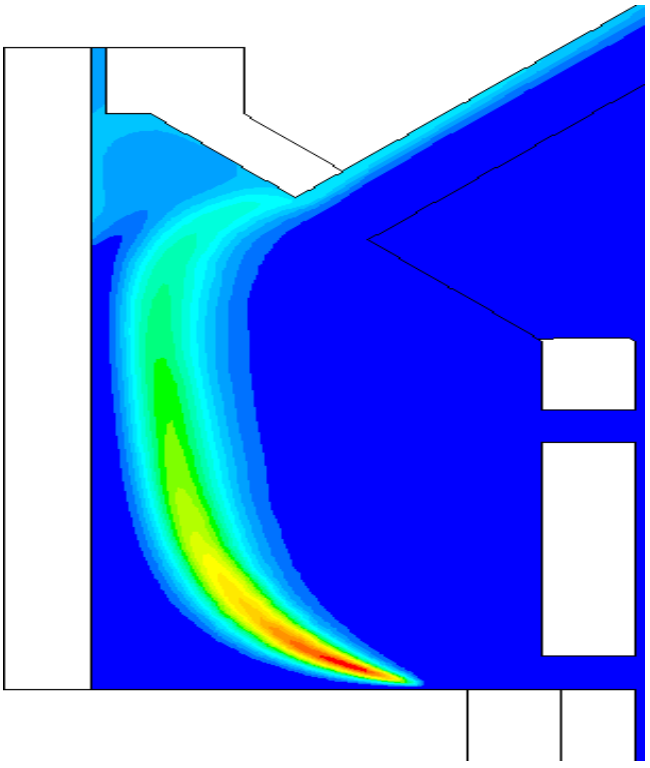

Figure 15: Case-6:Contour plot of SiO_2 mass fraction

the mixing between process gas emerging from the charge surface and incoming air flow from lower opening. In ferrosilicon furnace, at what extent roughness affects the mixing is not very clear. Now, there is an open question whether accounting roughness, which improves physics close to the wall but introduces complexity in modeling the charge surface, overweight the simplification offered by the mass flux boundary condition. To answer this question two more CFD simulation namely Case-7 and Case-8 are performed.

Effect of Wall Roughness

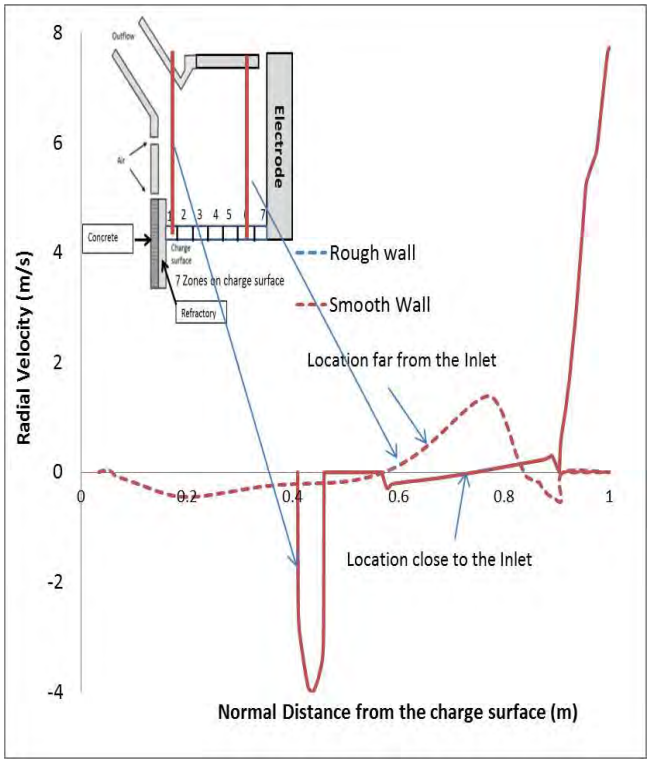

Figure 16: Radial Velocity profiles for smooth and rough pipes

Roughness wall model implemented in the FLUENT was mainly developed for the flow without any lateral pressure gradients and normally the dominate flow direction is assumed to be along the wall. However, the present case is slightly different where flow is subjected to the lateral pressure gradient due to the off-gas channel location. In industrial furnace a fan is installed at the off-gas channel which maintains a pressure gradient throughout the furnace. Furthermore, a continuous supply of the process gas normal to the charge surface posses challenges with respect to roughness modeling as implemented in FLUENT. Despite wall roughness model restriction a CFD study using FLUENT roughness model was carried out and in this case charge surface was assumed as a rough wall. The roughness height K_s was 4 mm and roughness constant C_s was 0.5. Present study showed that there was not any significant differences between the flow field of smooth and rough charge surface cases while examining the contour plots for both the cases. To illustrate this a radial velocity distribution for both the cases is plotted and shown in Figure 16. Difference in velocity can hardly be noticed in the radial velocity profiles. A similar behavior was also observed in the axial velocity profile (not shown here). To illustrate the effect of the roughness on skin friction, the skin frication coefficients of the charge surface wall is plotted for both rough and smooth cases(see Figure 17). A noticeable difference in the skin friction coefficient can be seen at the location close to the inlet, however far from the inlet the skin friction coefficient is negligible. The reason for this behavior can be understood by carefully examining the velocity vectors (see Figure 4). It can be seen that the incoming air from the surrounding is parallel to the charge surface and therefore higher value of skin frication coefficient at the location close to the inlet (far from the electrode), however due to the lateral pressure gradients inside the furnace the direction of flow becomes normal to the charge surface at a location close to the electrode and this leads to reduction in skin friction coefficient. From present study it is very difficult to identify the role of charge surface roughness on turbulent mixing and reaction. Furthermore, applicability of the wall roughness models is questionable under strong lateral pressure gradient cases. The impact of wall roughness on mixing and subsequent reaction can by well understood through an explicit modeling of charge surface roughness.

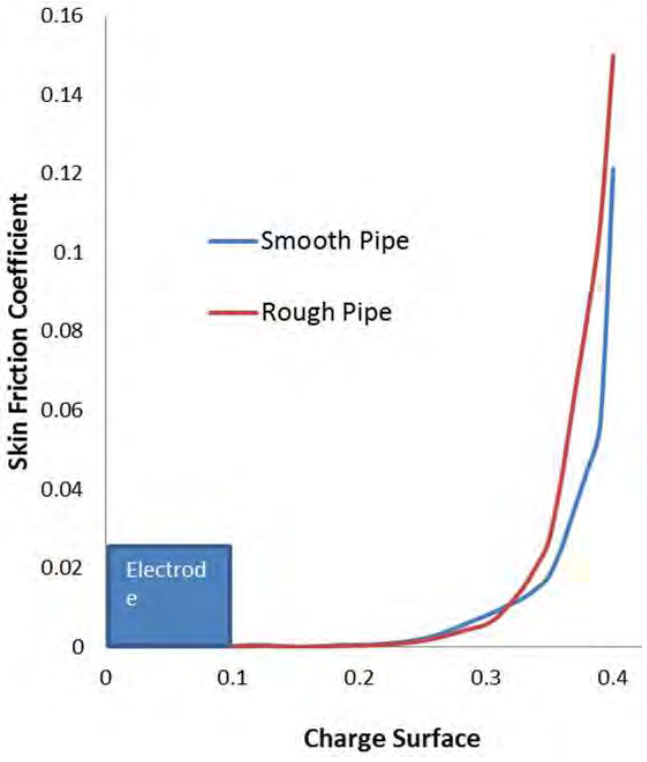

Figure 17: Skin friction coefficients for smooth and rough pipes

CONCLUSIONS

A steady state CFD model solving for governing equation is developed using ANSYS FLUENT. Two approaches: wall boundary condition and mass flux boundary condition for modeling the charge surface is presented. Studies showed that both the approaches gives a similar result but using a wall boundary condition is a challenge. Furthermore, a simplified approach for modeling the SiO jets have been discussed in this study. Study showed that the concentrated SiO generates local zones of higher temperature which are responsible for NOx formation. In addition to that, location of the SiO jets and local distribution of air supply play a major role in the NOx formation.

REFERENCES

ANSYS (2011). *ANSYS FLUENT Theory Guide*.

CEBECI, T. and BRADSHAW, P. (1977). *Momentum Transfer in Boundary Layers*. Hemisphere/McGraw-Hill, New York.

GRAN, I.R. and MAGNUSSEN, B.F. (1996a). "A numerical study of a bluff-body stabilized diffusion flame. part 1. influence of turbulence modeling and boundary conditions". *Combustion Science and Technology*, **119(1-6)**, 171–190.

GRAN, I.R. and MAGNUSSEN, B.F. (1996b). "A numerical study of a bluff-body stabilized diffusion flame. part 2. influence of combustion modeling and finite-rate chemistry". *Combustion Science and Technology*, **119(1-6)**, 191–217.

GRåDAHL, S. *et al.* (2007). "Reduction of emissions from ferroalloy furnaces". *INFACON XI*.

JIMéNEZ, J. (2004). "Turbulent flows over rough walls". *Annual Review of Fluid Mechanics*, **36(1)**, 173–196.

LAUNDER, B. and SPALDING, D. (1974). "The numerical computation of turbulent flows". *Computer Methods in Applied Mechanics and Engineering*, **3(2)**, 269 – 289.

MAGNUSSEN, B. and HJERTAGER, B. (1977). "On mathematical modeling of turbulent combustion with special emphasis on soot formation and combustion". *Symposium (International) on Combustion*, **16(1)**, 719 – 729.

NIKURADSE, J. (1933). "Laws of flow in rough pipes". Tech. Rep. TECHNICAL MEMORANDUM 1292/Forschung Arb. Ing.-Wes. No. 361.

PANJWANI, B. and OLSEN, J.E. (2013). "Combustion and mechanisms for nox formation in ferrosilicon electric arc furnaces". *European Combustion Meeting, ECM*.

A STUDY OF BREAKAGE BY SINGLE DROP EXPERIMENTS

Jannike SOLSVIK[1*], **Hugo A. JAKOBSEN**[1†]

[1]Department of Chemical Engineering, NTNU, Trondheim, NORWAY

[*] E-mail: jannike.solsvik@chemeng.ntnu.no
[†] E-mail: jakobsen@nt.ntnu.no

ABSTRACT

The population balance equation (PBE) is a modeling approach which is often used to describe the evolution of the size distribution in dispersed systems. In order to develop predictive PBE models, detailed experimental investigations of the breakage and coalescence mechanisms are required. This work focus on the breakup process. Data has been collected from single drop breakage experiments in a stirred tank. The breakage time and number of daughter drops are quantitatively determined using high-speed imaging. Multiple breakup was the most likely outcome in the experiments. This observation contradicts the binary breakup assumption frequently used in PBE modeling. The models proposed in the literature for the breakage time are contradictory. The present experimental observations support the observation of some researchers that the breakage time increases with increasing mother drop diameter.

Keywords: population balance equation, breakage time, oil-in-water, stirred tank, number of daughters, dispersed flow.

NOMENCLATURE

Greek Symbols

$\overline{\varepsilon}$	Average energy dissipation rate, $[\mathrm{m^2/s^3}]$.
ε	Local energy dissipation rate, $[\mathrm{m^2/s^3}]$.
$\varepsilon_{\mathrm{loc,max}}$	Highest local energy dissipation rate, $[\mathrm{m^2/s^3}]$.
ξ	Internal coordinate, diameter, [m].
ξ_{KH}	Maximum stable diameter, [m].
ζ	Internal coordinate, diameter, [m].
ν	Number of daughter drops per breakage, $[-]$.
$\overline{\nu}$	Average number of daughter drops per breakage, $[-]$.
ω	Impeller rotation speed, $[1/\mathrm{s}]$.
ρ	Density, $[\mathrm{kg/m^3}]$.
μ	Dynamic viscosity, $[\mathrm{Pa \cdot s}]$.
σ_I	Interfacial tension, $[\mathrm{N/m}]$.

Latin Symbols

D	Diameter, [m].
c	Empirical parameter.
b	Breakage frequency, $[1/\mathrm{s}]$.
f	Number density function, $[1/\mathrm{m^3 \cdot m}]$.
$\mathbf{r}$	Space coordinate, vector, [m].
t	Time, [s].
t_b	Breakage time, [s].
v	Velocity, $[\mathrm{m/s}]$.
$\mathbf{v}$	Velocity vector, $[\mathrm{m/s}]$.
B_D	Breakage death term in the PBE, $[1/\mathrm{m^3 \cdot m \cdot s}]$.
B_B	Breakage birth term in the PBE, $[1/\mathrm{m^3 \cdot m \cdot s}]$.
C_B	Coalescence birth term in the PBE, $[1/\mathrm{m^3 \cdot m \cdot s}]$.
C_D	Coalescence death term in the PBE, $[1/\mathrm{m^3 \cdot m \cdot s}]$.
P	Daughter size distribution function, $[1/\mathrm{m}]$.
N_p	Impeller power number, $[-]$.
N	Total number of drops, $[-]$.
V_l	Liquid volume in tank, $[\mathrm{m^3}]$.
T	Temperature, [K].
E	Energy, [J].

Sub/superscripts

ξ	Internal coordinate.
$\mathbf{r}$	External coordinate.
B	Birth.
D	Death.
I	Impeller.
l	Liquid.
d	Dispersed phase (oil).
T	Tank.

INTRODUCTION

In stirred tanks with liquid–liquid systems, the interphase mass and heat fluxes do not only depend on the dynamics of the motion between the two immiscible liquids, but also on the drop size distribution. The PBE (Ramkrishna, 2000; Sporleder *et al.*, 2012; Jakobsen, 2008; Solsvik and Jakobsen, 2014) can be use to describe the evolution of a statistical density function representing the behavior of a population of entities such as drops dispersed in a continuous liquid phase. The statistical density function is defined in a phase space that comprises the the spatial coordinates and one or more properties of the dispersed drops. If the property space relates to the size of the drops, the density function provides information on the evolution of the drop size distribution. The PBE is given as

$$\begin{aligned}&\frac{\partial f(\xi,\mathbf{r},t)}{\partial t}+\nabla_{\mathbf{r}}\cdot[\mathbf{v}_{\mathbf{r}}(\mathbf{r},\xi,t)f(\xi,\mathbf{r},t)]\\&+\nabla_{\xi}\cdot[v_{\xi}(\mathbf{r},\xi,t)f(\xi,\mathbf{r},t)]=\\&-B_D(\xi,\mathbf{r},t)+B_B(\xi,\mathbf{r},t)-C_D(\xi,\mathbf{r},t)+C_B(\xi,\mathbf{r},t)\end{aligned}\tag{1}$$

The LHS of Eq. (1) holds the transient term and the convection terms in the physical and property spaces. The RHS of Eq. (1) holds the birth and death terms due to breakage and coalescence. This work focus on the breakage phenomena,

hence the breakage terms of the PBE (1) are relevant:

$$B_D(\xi,\mathbf{r},t) = b(\xi) f(\xi,\mathbf{r},t) \tag{2}$$

$$B_B(\xi,\mathbf{r},t) = \int_{\xi}^{\xi_{\max}} vP(\xi,\zeta) b(\zeta) f(\zeta,\mathbf{r},t)\,\mathrm{d}\zeta \tag{3}$$

Here, b denotes the breakage frequency, v is the number of daughter drops generated in a breakage event, and P holds information on the size distribution of the daughter drops generated in a break-up.

Experimental studies of drop size distributions (i.e. the density function in the PBE) of breakage dominated oil-in-water systems have recently been performed by, e.g., Becker *et al.* (2011, 2013). Such data can be used to identify empirical parameters in the breakage models (Solsvik *et al.*, 2014b). As different criteria are proposed in the literature for drop breakage (Solsvik *et al.*, 2013; Liao and Lucas, 2009), the drop breakage models give contradictory predictions (Solsvik *et al.*, 2013). To advance the development of theoretical drop breakage models, it is necessary to experimentally investigate drop break-up in detail. Experimental investigations at the level of the single drop have been performed by, e.g., Andersson and Andersson (2006), Maaß *et al.* (2007), and Maaß and Kraume (2012).

Andersson and Andersson (2006) performed single drop experiments for dodecane-in-water and octanol-in-water systems with average energy dissipation rates 1.13–8.54 $\mathrm{m}^2/\mathrm{s}^3$. The particular construction of the flow system by Andersson and Andersson (2006) aimed to provide turbulence which was much more homogeneous than in a stirred tank. However, the experiments showed that multiple fragmentation occurs with higher probability than binary breakup. The probability for binary breakup was less than 40% whereas the probability for three or more fragments was larger than 60%. Further, small drops and drops with high viscosity may become highly deformed before they eventually break up into a number of fragments.

By use of high speed camera (650 frames per second), Maaß *et al.* (2007) investigated single drop breakage (petroleum oil-in-water) in a stirred (Rushton turbine) tank. The number of daughter drops was recorded for mother drops in the size range of 0.3–2 mm. The maximum number of daughter drops observed was 97 for a 2 mm mother drop. With increased mother drop size the average number of daughter drops generated in a breakage increased. Furthermore, for a given mother size the probability of binary breakage increased with decreased flow velocity (i.e. power input). The measurements were recorded in a region close to the impeller blades where the average energy dissipation may rate differ significantly from the local energy dissipation rate. For the average energy dissipation rates $\bar{\varepsilon} = [0.3, 0.8, 1.8]\ \mathrm{m}^2/\mathrm{s}^3$, Maaß *et al.* (2007) estimated the maximum local energy dissipation rates from CFD: $\varepsilon_{\mathrm{loc,max}} = [3.4, 26.1, 88.0]\ \mathrm{m}^2/\mathrm{s}^3$.

The aim of the study by Maaß and Kraume (2012) was to validate breakage frequency models used for simulation of drop size distributions in stirred tanks with anisotropic turbulence. The experimental set-up tended to give turbulence conditions comparable to those in a stirred tank. Moreover, a high-speed camera with 822 frames per second were used to record 750 breakup events for each parameter combination. The mother drop sizes were in the range of 0.5–3.5 mm. Two oil-in-water systems were investigated: toluene and petroleum oils. The breakage frequency models by Coulaloglou and Tavlarides (1977), Alopaeus *et al.* (1999), Chen *et al.* (1998), Vankova *et al.* (2007b), and Raikar *et al.* (2009) were investigated.

The aim of the present study is to investigate single drop breakup in details by single drop experiments. In particular, the objective is to quantify the number of daughter drops and the breakage time in a stirred liquid tank. The measurements will be compared with the results of previous single drop experiments. Furthermore, breakage time models given in the literature will be examined. A motivation for investigation of the breakage time is the contrary behavior in the literature (Solsvik *et al.*, 2013). Furthermore, the motivation for the investigation of the mean number of daughter drops is the frequently used assumption of binary breakage in PBE modeling.

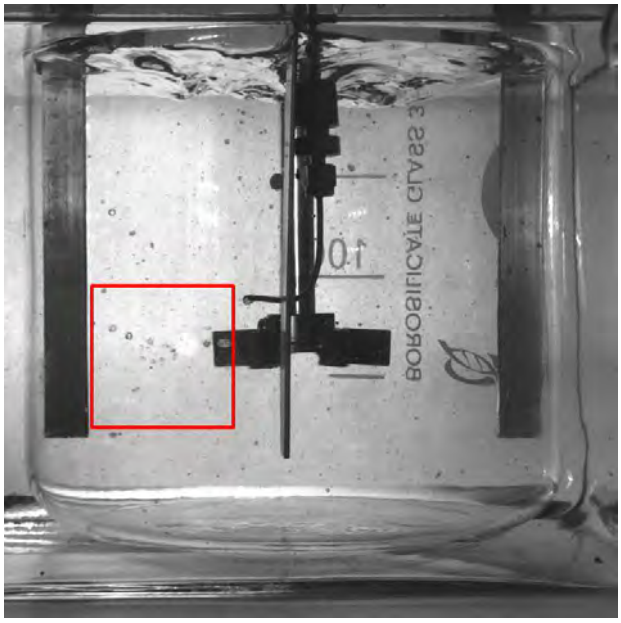

Figure 1: The stirred liquid tank. The location with highest probability of breakage is indicated.

Table 1: Description of the experimental system.

ω	[rpm]	620
N_p	[-]	5.75
T	[K]	293
D_I	[m]	0.05
V_l	[dm^3]	2
$\bar{\varepsilon}$	[$\mathrm{m}^2/\mathrm{s}^3$]	1
ρ_d	[kg/m^3]	866.7
μ_d	[mPa·s]	0.6
σ_I	[mN/m]	33
number of impeller blades	[-]	6
impeller location (from bottom)	[m]	0.04
number of baffles	[-]	4
D_T	[m]	0.143

SINGLE DROP BREAKAGE EXPERIMENTS

The single drop breakage experiments were carried out in a stirred tank. A Rushton turbine was used to generate turbulent flow in the tank with an average energy dissipation rate of 1.0 $\mathrm{m}^2/\mathrm{s}^3$. The average energy dissipation rate of the stirred tank system can be estimated from the power number

equation (Becker *et al.*, 2011):

$$\bar{\varepsilon} = \frac{N_p \omega^3 D_I^5}{V_l} \tag{4}$$

A syringe pump (model KDS-100) was used to introduce the mother oil drops (toluene) into the stirred liquid (distilled water) tank. The experimental measurements must be done with sufficient spatial and temporal resolution because the breakup process occurs on very small scales. A high speed camera was used (Photron Fastcam 1024PCI model 100K with software PFV v3.18) with resolution of 1024×1024 pixels and a record rate of 1000 frames per second. The toluene oil was blended with a non-water soluble black dye (Sudan Black powder), which increases the optical evaluation possibilities. Halogen projector lamps were used to improve the quality of the image analyzes. Also, a light diffuser paper was used to avoid light reflection. The mother drop size was measured using the software KLONK Image Measurements.
Details of the experimental system is given in Tab. 1. Fig. 1 shows a frame of the tank as taken by the high-speed camera.

BREAKAGE FREQUENCY MODELS

Coulaloglou and Tavlarides (1977) defined the breakage frequency of a drop of size ξ as

$$\begin{aligned} b(\xi) &= \left(\frac{1}{\text{breakage time}}\right) \times \left(\text{fraction of drops breaking}\right) \\ &= \frac{1}{t_b}\frac{\Delta N(\xi)}{N(\xi)} \end{aligned} \tag{5}$$

where $N(\xi)$ is the total number of drops of size ξ. The breakage time was given as

$$t_b = c_1 \xi^{2/3} \varepsilon^{-1/3} \tag{6}$$

and the probability of breakage was given as

$$\frac{\Delta N(\xi)}{N(\xi)} = \exp\left(-\frac{\bar{E}_{\text{crit}}}{E}\right) = \exp\left(-\frac{c_2 \sigma_I}{\rho_d \varepsilon^{2/3} \xi^{5/3}}\right) \tag{7}$$

The breakage criterion used in this model derivation is that an oscillating deformed drop will break if the drop kinetic energy $\bar{E}$, transmitted to the drop by turbulent eddies through eddy–drop interactions, exceeds the drop surface energy $\bar{E}_{\text{crit}}$. In particular, Coulaloglou and Tavlarides (1977) used

$$\bar{E}_{\text{crit}} = c' \sigma_I \xi^2 \tag{8}$$

$$\bar{E} = c'' \rho_d \xi^3 \overline{\delta v^2(\xi)} = c''' \rho_d \xi^{11/3} \varepsilon^{2/3} \tag{9}$$

Chen *et al.* (1998) employed the modeling framework (5) by Coulaloglou and Tavlarides (1977) and proposed a new representation of the breakage time and introduced the dispersed phase viscosity into the formulation of the breakage probability. Contrary to the work by Coulaloglou and Tavlarides (1977), Chen *et al.* (1998) used a constant breakage time, i.e. $1/t_b = c_3$. Furthermore, Chen *et al.* (1998) considered that the disruptive external turbulent stresses; due to the flow of the continuous fluid, was balanced by the stabilizing stresses constituting the interfacial tension and the viscous stresses. The breakage frequency function suggested by Chen *et al.* was given as

$$b(\xi) = c_3 \exp\left(-\frac{c_4 \sigma_I}{\rho_d \varepsilon^{2/3} \xi^{5/3}} - \frac{c_5 \mu_d}{\rho_d \varepsilon^{1/3} \xi^{4/3}}\right) \tag{10}$$

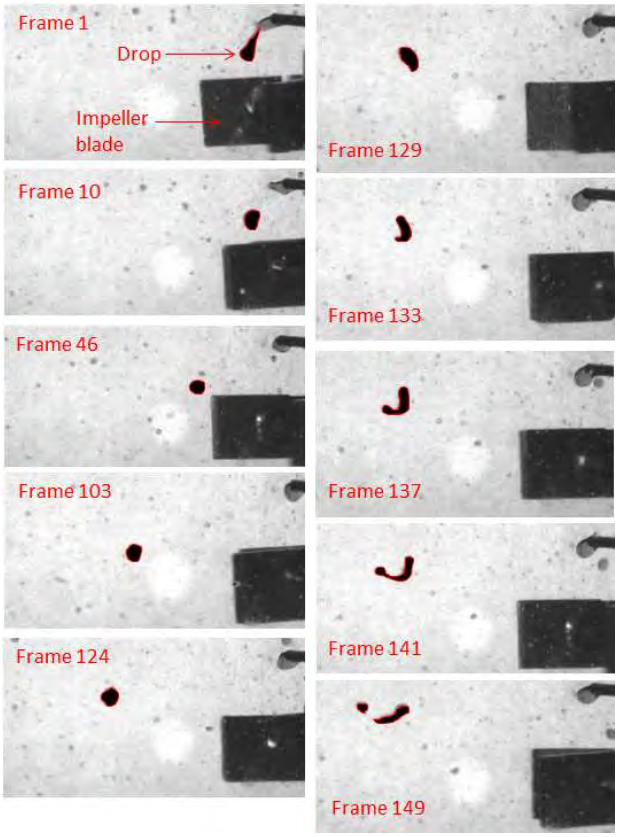

Figure 2: Time series of a drop breakup starting from the injection of the drop (image processing). Toluene-in-water. Binary breakup.

The extension of the Coulaloglou and Tavlarides (1977) theory proposed by Chen *et al.* (1998) ensures that the breakage frequency model constitutes a monotonously growing function with increasing mother drop diameter. It is noticed that c_3 in Eq. (10) is not dimensionless. In dimensional analysis (Buckingham π theorem) standard practice in engineering is to work with dimensionless groups and dimensionless proportionality coefficients or parameters. A model parameter having units might indicate that the parameter is a function of system properties etc. and thus not being of general nature.
Reviews of numerous breakage frequency models are provided by Solsvik *et al.* (2013), Liao and Lucas (2009), Sajjadi *et al.* (2013), among others.

RESULTS AND DISCUSSION

Fig. 2 presents a time series starting from the injection of a mother drop and ends with the drop breakage. At some point after the injection, the mother drop starts to deform and finally breaks into two daughter drops. Multiple breakup may also occur, as shown in Fig. 3.
In the present study, 120 single drop events such as shown in Figs. 2 and 3 have been analyzed. However, drop breakage events caused by collision with the impeller blade or baffles are not considered. Also, breakup in the very vicinity of the impeller blades are not evaluated. Drops which are transported into this region usually smash into a large number of small fragments due to high shear and dissipation rates.
Drops may get energy in the vicinity of the impeller and deforms while they are transported with the continuous fluid phase and eventually breaks into two or more fragments some distance away from the impeller blades. The local en-

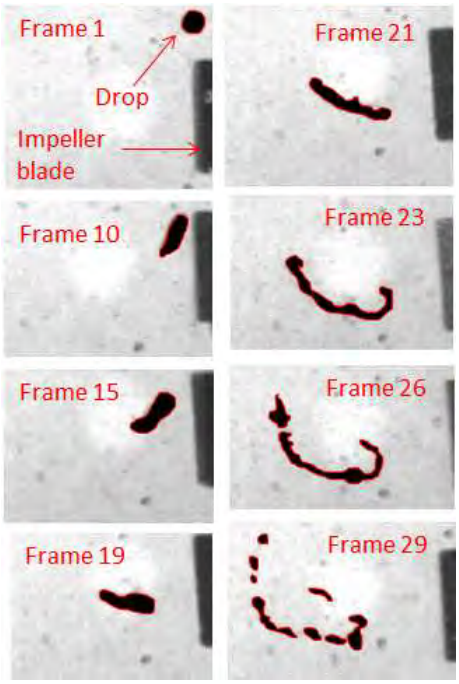

Figure 3: Time series of a drop breakup (image processing). Toluene-in-water. Multiple daughter drops.

ergy dissipation rate is significantly larger in the impeller region than the average energy dissipation rate (Maaß *et al.*, 2007; Roudsari *et al.*, 2012). The stirred liquid tank is turbulent but anisotropic and inhomogeneous. Thus the breakup process is spatially dependent. The location in which most of the breakup events took place is indicated by a frame in Fig. 1. This region is related to the flow pattern generated with Rushton turbines (see Fig. 4). However, not all drops break into smaller daughter drops. In the present system, the critical mother drop size for breakage was around 1 mm. That is, breakup of mother drops of this size and smaller were seldom observed. The smallest observed and measured mother drop which deformed and broke was 0.95 mm. A higher power input, i.e. increased stirring rate, will likely give also breakup of smaller mother drop sizes. According to the Kolmogorov–Hinze theory of emulsification in inertial turbulent regime (Kolmogorov, 1949; Hinze, 1955), for drops with viscosity comparable to that of water, the maximum stable drop diameter can be estimated as (Vankova *et al.*, 2007a)

$$\xi_{\mathrm{KH}} = c_6 \varepsilon^{-2/5} \sigma_I^{3/5} \rho_c^{-3/5} \tag{11}$$

where c_6 is a constant of proportionality of the order of unity (Vankova *et al.*, 2007a). According to this formula, the maximum stable mother drop diameter of the present system is 2 mm for $\varepsilon = 1\,\mathrm{m}^2/\mathrm{s}^3$ and 0.44 mm for $\varepsilon = 44\,\mathrm{m}^2/\mathrm{s}^3$. As previously discussed, the local energy dissipation rate may change significantly through the stirred liquid tank (Maaß *et al.*, 2007).

Number of daughter drops

For mother drop sizes in the range 1–3 mm, Fig. 5 shows that it is most likely that the mother drop undergo multiple breakup. There is approximately 37% probability for binary breakage and 63% probability for multiple breakage. The higher probability for multiple breakup event observed in the present study is supported by the previous studies by Maaß *et al.* (2007) and Andersson and Andersson (2006).

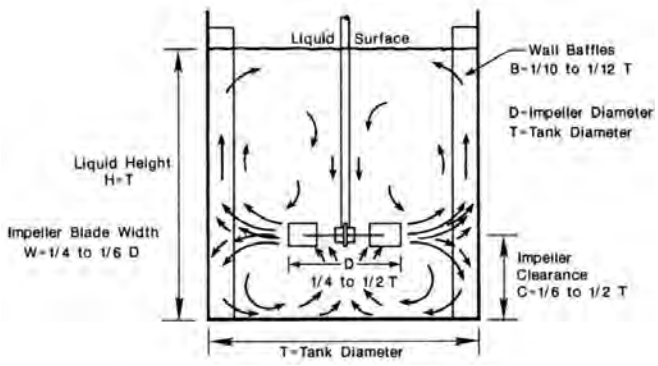

Figure 4: Flow pattern in a stirred liquid tank using a radial impeller (Rushton turbine) (Tatterson, 1991).

Fig. 6 holds the probability of different numbers of daughter drops. Binary breakup has the largest probability, approximately 37%, followed by ternary and quaternary with probabilities of approximately 26% and 17%, respectively. Higher order breakage is predicted to occur with a probability lower than approximately 5%. The largest number of daughter drops observed in the present study was 10.
The average number of daughter drops generated in a breakage event can be computed as

$$\bar{\nu} = \frac{\sum_{i=1}^{N_b} \nu_i}{N_b} \tag{12}$$

where N_b denotes the total number of breakup events and ν_i is the number of daughter drops in an event i. Based on the present study, the average number of daughter drops generated from breakup of mother drops in the range 1–3 mm was estimated to $\bar{\nu} = 3.5$.
It should be noticed that small fragments of a breakup is hard to observe due to the image and temporal resolution of the camera. Also, the two-dimensional view of the breakup process limits the observation. Thus, in some breakup events, it is likely that number of daughter drops is higher than those observed and accounted for in the image analyzes.

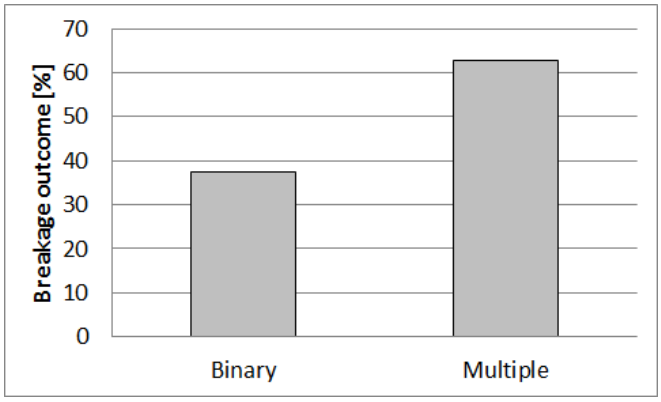

Figure 5: Relative occurrence of binary and multiple breakage.

Daughter drop size distribution

A number of daughter size distribution functions (denoted as $P(\xi, \zeta)$ in the PBE (1)–(3)) is given in the literature (Solsvik *et al.*, 2013; Liao and Lucas, 2009; Sajjadi *et al.*, 2013). Many of these are based on the assumption of equal-size breakup. The qualitative observation of the daughter

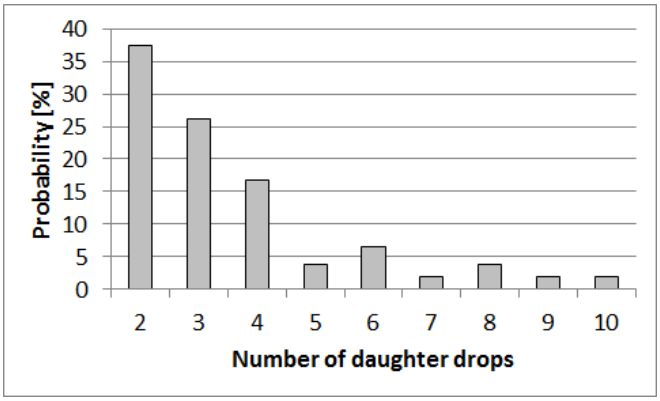

Figure 6: Probability of different number of daughter drops.

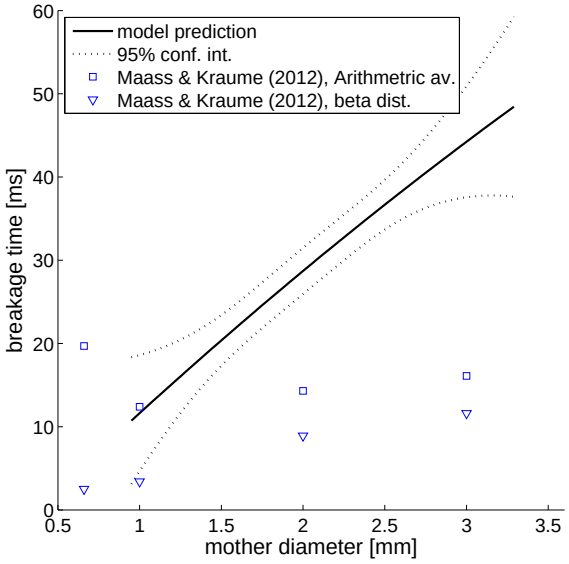

Figure 7: Breakage time. Experimental data of toluene-in-water.

drop size distribution in the present study contradicts the equal-size breakup assumption.

Breakage time

The breakage time is estimated as the number of frames taken from the deformation of the mother drop started to the breakage event is completed. It should also be noticed that local flow variations are important for the breakup process.

Fig. 7 compares the present experimental data (trend line) of the breakage time with the work by Maaß and Kraume (2012). The present experimental data shows an increase in the breakage time with increasing mother drop diameter. Two interpretations of the experimental breakage time measurements were given byMaaß and Kraume (2012); arithmetic average and the peak of the beta-distribution. The two presentations of the experimental data by Maaß and Kraume (2012) differ significantly, in particularly for the smallest mother drop diameters. Independent of the statistical presentation of the experimental data by Maaß and Kraume (2012), the present data and the data by Maaß and Kraume (2012) contradict each other. A much higher breakage time is observed in the present study compared to that of Maaß and Kraume (2012). The contradiction in the experimental data can be explained from the fact that the experiments were performed in different equipments under different operation conditions, etc. This makes direct comparison of the results very difficult, if not impossible.

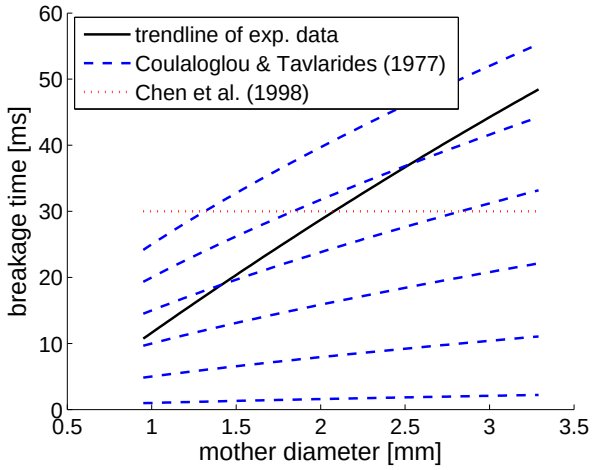

Figure 8: Comparison of breakage time models (Chen *et al.*, 1998; Coulaloglou and Tavlarides, 1977) with experimental data. c_1 is in the range 1–25.

The broad examination of the drop breakage mechanisms have lead to several contradicting models. For example, the Coulaloglou and Tavlarides (1977) breakage frequency model has been criticized because the predicted function profile has a maximum value for a certain parent drop diameter. The critic anticipated that a physically realistic relation should rather predict a monotonically rising breakage frequency function with increasing mother drop diameters such as, e.g. the Chen *et al.* (1998) model (Solsvik *et al.*, 2013, 2014a).

The comparison of experimental and theoretical breakage times is given in Fig. 8. The present breakage time data clearly shows an increasing trend with increasing mother drop size. This contradicts the assumption of constant breakage time as proposed in the model by Chen *et al.* (1998). Fig. 8 also reveals that the present experimental breakage time data as a function of mother drop size gives a steeper slope than the Coulaloglou and Tavlarides (1977) breakage time model. However, $\varepsilon = 1\,\mathrm{m}^2/\mathrm{s}^3$ were used in the breakage time model by Coulaloglou and Tavlarides (1977). Although the average energy dissipation rate, $\bar{\varepsilon}$, were estimated to unity, significant local variation of the energy dissipation rate existed in the stirred liquid tank.

Experimental set-up

There are some issues of the experimental set-up that influence on the experimental results as well on the analyses of the data, and should be noticed:

- Drop breakage process is significantly influence by local flow variations. Large variation in the local energy dissipation rate which is not reflected well by the value of the average energy dissipation rate.
- The smallest fragments generated in a breakup are difficult to recorded due to temporal and spatial resolutions.
- Two-dimensional view limits the observation of the breakup process.
- Manually analysis of the images is time consuming. Six seconds of record gives 6000 frames to be analyzed. A

high number of single drop breakup observations is required for a statistical meaningful results.

- The breakage time is estimated from the initiation of the drop deformation until daughter drops are formed. Temporal and spatial resolution, as well as two-dimensional view only, give rise to error in the determination of the breakage time.

- The mother drop size is determined using the software KLONK Image Measurements. An sphere is added to the liquid tank and used for calibration. The position of the reference sphere in the liquid tank relative to the breaking mother drop, as well as spatial resolution, are sources of error for determining the mother drop size.

- Too high stirring velocity gives air bubbles in the liquid phase. The present experimental apparatus is thus limited to low values of the average energy dissipation rate. Further improvements with the experimental setup must be performed in order to operate under higher energy dissipation rates.

Further work

A number of 120 single drop breakage events has been analyzed in the present study. For statistically meaningful results the present number of breakup observations should be extended. However, the single drop breakage experiments are time consuming as both the number of daughter drops and the breakage time must be determined manually. No high-accurate software is available for the particular complexity of the experiments.

The present data was collected with turbulent conditions corresponding to an average energy dissipation rate of $1.0\,m^2/s^3$. Further work should investigate the sensitivity to the power input in the tank on the number of daughter drops formed in the breakage events as well as on the breakage time.

Toluene oil-in-water was the present chemical system investigated in this study. The experimental matrix should be extended evaluating other oils with different physical properties, e.g. viscosity and surface tension.

CONCLUSION

In the present, study detailed experiments have been performed for the investigation of single drop breakup in turbulent flow. Devices are used that allow the breakup process to be studied by high spatial and temporal resolution. In particular, data are collected for determination of the breakage time and the average number of daughter drops, as applied in PBE modeling.

There is a larger probability for multiple breakup than binary breakup. Hence, the commonly applied assumption of binary breakup in PBE modeling is not appropriate for dispersed liquid–liquid systems. Moreover, unequal-breakage is most likely.

The trend of the single drop experiments shows an increase of the breakage time with increasing mother drop size. In the literature, some model approaches for the breakage time do not coincide with the the trend in the experimental data.

Further experimental investigation is required. The data set must be enlarged for statistical meaningful results. Moreover, different systems and operation conditions should be investigated, e.g. energy dissipation rate, interfacial tension, oil viscosity, etc.

REFERENCES

ALOPAEUS, V. *et al.* (1999). "Simulation of the population balances for liquid-liquid systems in a non-ideal stirred tank. Part 1: Description and qualitative validation of the model". *Chem Eng Sci*, **54**, 5887–5899.

ANDERSSON, R. and ANDERSSON, B. (2006). "On the breakup of fluid particles in turbulent flows". *AIChE J*, **52**, 2020–2030.

BECKER, P.J. *et al.* (2011). "Investigation of discrete population balance models and breakage kernels for dilute emulsification systems". *Ind Eng Chem Res*, **50**, 11358–11374.

BECKER, P.J. *et al.* (2013). "Monitoring silicone oil droplets during emulsifiction in stirred vessel: Effect of dispersed phase concentration and viscosity". *Can J Chem Eng*, **92**, 296–306.

CHEN, Z. *et al.* (1998). "A population balance model for disperse systems: Drop size distribution in emulsion". *Chem Eng Sci*, **53**, 1059–1066.

COULALOGLOU, C.A. and TAVLARIDES, L.L. (1977). "Description of interaction processes in agitated liquid–liquid dispersions". *Chem Eng Sci*, **32**, 1289–1297.

HINZE, J.O. (1955). "Fundamentals of the hydrodynamic mechanism of splitting in dispersion processes". *AIChE*, **1**, 289–295.

JAKOBSEN, H.A. (2008). *Chemical reactor modeling: Multiphase reactive flows*. Springer: Berlin.

KOLMOGOROV, A.N. (1949). "On the breakage of drops in a turbulent flow". *Compt Rend Acad Sci URSS*, **66**, 825–828.

LIAO, Y. and LUCAS, D. (2009). "A literature review of theoretical models for drop and bubble breakup in turbulent dispersions". *Chem Eng Sci*, **64**, 3389–3406.

MAASS, S. and KRAUME, M. (2012). "Determination of breakage rates using single drop experiments". *Chem Eng Sci*, **70**, 146–164.

MAASS, S. *et al.* (2007). "Experimental investigations and modelling of breakage phenomena in stirred liquid/liquid systems". *Chem Eng Research and Design*, **85**, 703–709.

RAIKAR, N.B. *et al.* (2009). "Experimental studies and population balance equation models for breakage prediction of emulsion drop size distributions". *Chem Eng Sci*, **64**, 2433–2447.

RAMKRISHNA, D. (2000). *Population balance: Theory and applications to particulate systems in engineering*. Academic Press: San Diego.

ROUDSARI, S.F. *et al.* (2012). "CFD modeling of the mixing of water in oil emulsions". *Comp & Chem Eng*, **45**, 124–136.

SAJJADI, B. *et al.* (2013). "Review on applicable breakup/coalescence models in turbulent liquid–liquid flows". *Rev Chem Eng*, **29**, 131–158.

SOLSVIK, J. and JAKOBSEN, H.A. (2014). "The foundation of the population balance equation – A review". Journal of Dispersion Science and Technology, DOI:10.1080/01932691.2014.909318.

SOLSVIK, J. *et al.* (2013). "On the constitutive equations for fluid particle breakage". *Rev Chem Eng*, **29**, 241–356.

SOLSVIK, J. *et al.* (2014a). "Evaluation of breakage kernels for liquid–liquid systems: Solution of the population balance equation by the least-squares method". *Can J Chem Eng*, **92**, 234–249.

SOLSVIK, J. *et al.* (2014b). "Population balance model: Breakage kernel parameter estimation to emulsification data". *Can J Chem Eng*, **92**, 1082–1099.

SPORLEDER, F. *et al.* (2012). "On the population balance equation". *Rev Chem Eng*, **28**, 149–169.

TATTERSON, G.B. (1991). *Fluid mixing and gas dispersion in agitated tanks*. McGraw-Hill, New-York.

VANKOVA, N. *et al.* (2007a). "Emulsification in turbulent flow 1. Mean and maximum drop diameters in inertial and viscous regimes". *J Colloid Interface Sci*, **312**, 363–380.

VANKOVA, N. *et al.* (2007b). "Emulsification in turbulent flow 2. Breakage rate constants". *J Colloid Interface Sci*, **313**, 612–629.

MODELLING OF BUBBLE SIZE DISTRIBUTION BY USING HOMOGENEOUS AND INHOMOGENEOUS POPULATION BALANCE APPROACHES

Lilunnahar DEJU[1], Sherman C. P. CHEUNG[1], Guan H. YEOH[2,3] and Jiyuan TU[1*]

[1] School of Aerospace, Mechanical and Manufacturing Engineering, RMIT University, VIC 3083, AUSTRALIA

[2] Australian Nuclear Science and Technology Organization (ANSTO), NSW 2234, AUSTRALIA

[3] School of Mechanical and Manufacturing Engineering, UNSW, NSW 2052, AUSTRALIA

*E-mail: Jiyuan.Tu@rmit.edu.au

ABSTRACT

To account the coalescence and breakup phenomenon of gas-liquid bubbly flows, the population balance equation (PBE) has to be solved along with the continuity and momentum equations within the two fluid modelling frameworks. A previous study by Deju et al. (2013) has been carried out to assess the performance of different population balance approaches in tracking the changes of gas void fraction and bubble size distribution under complex flow conditions. This reveals that the behaviour of breakup and coalescence kernels has dominant effect on the solution of PBE.

Nonetheless, the study assumes all bubbles travel in one single velocity field which may not valid in practical systems. In this paper, the *inhomogeneous* MUSIG approach has been applied to obtain a deeper understanding of the flow structure in the bubble column reactor that helps to describe the breakup and coalescence of bubbles and the evolution of the bubble size distribution. The *inhomogeneous* MUSIG model enables consideration of different velocity fields for bubbles with different sizes. Meanwhile, the bubble breakup and coalescence phenomenon can also be modelled to capture the bubble interactions and their impact on the bubble size distribution. Two breakage kernels were chosen; the widely adopted breakage kernel by Luo and Svendsen (1996) along with a more recent one by Wang et al. (2003). The coalescence kernel by Prince and Blanch (1990) was applied. The results from *homogeneous* and *inhomogeneous* MUSIG models were compared against experimental data from the TOPFLOW test facility at HZDR (Lucas et al. 2010). Furthermore, the performance of different breakage and coalescence kernels and their coupling effects with multiple velocity fields were also assessed.

Numerical results have shown that the modelled lateral separation of small and large bubbles is in well agreement with the experimental measurements. The evolution of the bubble size and its associated bubble migration due to lift forces is well described by the *inhomogeneous* MUSIG approach.

Keywords: Bubble column, Homogeneous MUSIG, Inhomogeneous MUSIG, Bubble breakup, Bubble coalescence.

NOMENCLATURE

a	Coalescence rate
a_{if}	Interfacial area concentration
C_f	Coefficient of surface area
C_L	Lift coefficient
D_H	Maximum bubble horizontal dimension
d_{ij}	Equivalent diameter
D_s	Sauter mean bubble diameter
$e(\lambda)$	Kinetic energy of eddy with size λ
Eo	Eötvos number
Eo_d	Modified Eötvos number
f	Size fraction
f_{BV}	Break-up volume fraction
F^{lg}	Total interfacial force
h_o	Initial film thickness
h_f	Critical film thickness
$h\ (M_i, M_j)$	Collision frequency in terms of mass
j	Superficial velocity
k	Turbulent kinetic energy
M	Mass scale of gas phase (bubble)
n_w	Outward vector normal to the wall
n	Average bubble number density
P	Pressure
P_b	Breakage probability
$P_e(e(\lambda))$	Energy distribution function
r	Breakage rate
Re_b	Bubble Reynolds number
t	Physical time
t_{ij}	Time for two bubbles to coalesce
$\mathbf{u}$	Velocity vector
u_t	Turbulent velocity
v	Volume of bubble
We	Webber number
We_{cr}	Critical Webber number
y_w	Distance from the wall boundary

Greek Symbols

α	Void fraction
$\beta(f_{BV}, 1)$	Daughter bubble size distribution
ε	Dissipation of turbulent kinetic energy
λ	Size of eddy in inertia sub-range
$\lambda\ (M_i, M_j)$	Coalescence efficiency
μ	Viscosity
ρ	Density
σ	Surface tension
ξ	Internal space vector

Sub/Superscripts

g	Gas phase
l	Liquid phase
i,j,k	Bubble class
T	Turbulence

INTRODUCTION

The complexity of two-phase flow structure can lead the flow evolution dynamically and thereby it can evolve into different flow regimes. So reliable simulation is a necessity for the phenomenological understanding of interfacial area concentration and bubble dispersion behaviour. In the bulk liquid flow, bubbles undergo significant coalescence and breakage; results in changes to the bubble size distribution. The interfacial momentum transfer is another crucial part in modelling

the gas-liquid flow that poses significant influence on bubble size distribution. The total interfacial force consists of viscous drag force and other non-drag forces (such as: lift force, wall lubrication force, turbulent dispersion force etc.). The bubbles influenced by lift force that cause lateral migration of bubbles in the perpendicular direction to the main flow of a vertical pipe. Depending on the bubble size the lift force coefficient changes its sign (Tomiyama 1998, Bothe et al. 2006), and consequently separates the larger bubbles that migrate towards the pipe centre, from the smaller bubbles flowing along the pipe wall.

To account for the coalescence and breakage phenomenon, population balance equation (PBE) needs to be solved in the two-fluid model framework along with mass and momentum conservation equations. Different approach to solve the PBE can be found in the literature (Cheung et al. 2009, Yeoh et al. 2012). Among these models, *homogeneous* MUSIG is frequently employed to predict the non-uniform bubble size distribution by solving a range of bubble classes. This model assumes that all the bubbles travel in a same velocity. Later introduced by Lucas et al. (2001) and implemented by Krepper et al. (2005), it has been found that it is worthwhile to consider different velocity fields for bubbles of different sizes.

Moreover, the understanding and modelling of bubble coalescence and breakage mechanisms have significant importance in the theoretical and experimental area. Investigation and understanding the physical mechanisms of these models is necessary to assess their applicability.

In the current work, *inhomogeneous* MUSIG results are compared with *homogeneous* predictions for different selected coalescence and breakage model. The widely adopted breakage model by Luo and Svendsen (1996) is selected along with a more recent one by Wang et al. (2003). On the other hand, coalescence model by Prince and Blanch (1990) has been chosen. Numerical predictions are then validated against experimental data by Lucas et al. (2010) for large vertical pipe (diameter 195.3 mm).

MATHEMATICAL MODEL

Population balance equations (PBEs) have been applied in many diverse applications which involve particulate systems. These equations are particularly useful for situations where particulates continually lose their identities, e.g. in crystallizers, liquid-liquid and gas-liquid contactors, microbial fermentors, fluidized beds and polymer reactors (Ramkrishna 1985). In accordance with Fleischer et al. (1996), the particle (bubble) size distribution is calculated according to the population balance equation that is generally expressed in an integro-differential form:

$$\frac{\partial f(x,\xi,t)}{\partial t} + \nabla \cdot \left(\boldsymbol{u}(x,\xi,t) f(x,\xi,t)\right) = S(x,\xi,t) \quad (1)$$

where $f(x,\xi,t)$ is the particle (bubble) number density distribution per unit mixture and particle (bubble) volume, $\boldsymbol{u}(x,\xi,t)$ is velocity vector in external space dependent on the external variables x for a given time t and the internal space ξ whose components could be characteristic dimensions such as volume, mass etc. On the right hand side, the term $S(x,\xi,t)$ contains the particle (bubble) source/sink rates per unit mixture volume due to the particle (bubble) interactions such as coalescence, break-up and phase change.

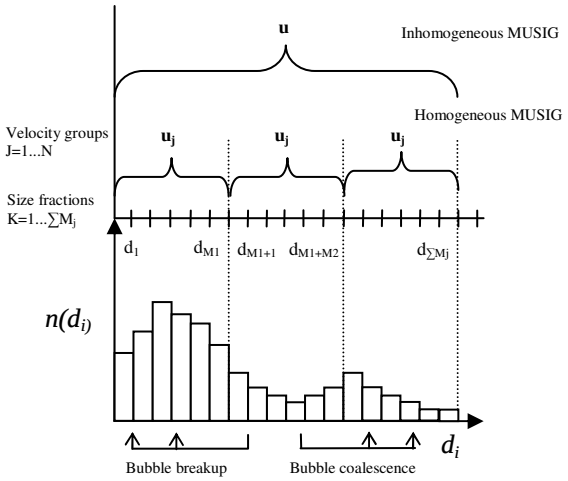

Figure 1: Graphical illustration of *homogeneous* and *inhomogeneous* MUSIG model.

Homogeneous MUSIG which was first introduced by Lo (1996), represents the most commonly used technique for solving PBE. According to this approach, the disperse phase is divided into M bubble size groups of size fractions of f_i. To describe the mass conservation of size fractions the population balance method is applied and inter-fraction mass transfer results from bubble coalescence and breakage. This model assumes that all the bubble size groups are travelling with the same velocity field. On the other hand, the *inhomogeneous MUSIG* model divides the gaseous phase into N number of velocity groups (or phases) and characterized by its own velocity field (Shi et al. 2004, Krepper et al. 2008). Figure 1 graphically illustrates the difference between inhomogeneous and homogeneous MUSIG model. Each velocity group is further divided into a number of sub-size fractions in terms of bubble diameter range and PBM is applied to the sub size groups considering bubble coalescence and breakage. Therefore, conservation of mass is ensured between the size fractions of dispersed phase across different velocity field. The bubble number density equation for the inhomogeneous MUSIG model can be re-expressed in terms of the volume fraction and size fraction of the bubble size class (Cheung et al. 2008), can be written as:

$$\frac{\partial \rho_{g,j} \alpha_{g,j} f_i}{\partial t} + \nabla \cdot \left(\boldsymbol{u_g} \rho_{g,j} \alpha_{g,j} f_i\right) = S_i \quad (2)$$

The momentum equation for and gaseous and liquid phase has the form:

$$\frac{\partial(\rho_g \alpha_g \boldsymbol{u_g})}{\partial t} + \nabla.(\rho_g \alpha_g \boldsymbol{u_g u_g}) = -\alpha_g \nabla P + \alpha_g \rho_g + \nabla.\left[\alpha_g \mu_e \left(\nabla \boldsymbol{u_g} + (\nabla \boldsymbol{u_g})^T\right)\right] + F_{lg} + S_{Mj} \quad (3)$$

$$\frac{\partial(\rho_l \alpha_l \boldsymbol{u_l})}{\partial t} + \nabla.(\rho_l \alpha_l \boldsymbol{u_l u_l}) = -\alpha_l \nabla P + \alpha_l \rho_l \boldsymbol{g} + \nabla.\left[\alpha_l \mu_e \left(\nabla \boldsymbol{u_l} + (\nabla \boldsymbol{u_l})^T\right)\right] + F_{lg} + S_{Mj} \quad (4)$$

In the above equations, S_{Mj} represents the momentum transfer between different velocity groups. The total interfacial force, F_{lg}, is given by the drag, lift, wall lubrication and turbulent dispersion forces,

$$F_{lg} = F_{lg}^{drag} + F_{lg}^{lift} + F_{lg}^{wall\ lubrication} + F_{lg}^{turbulent\ dispersion} \quad (5)$$

Lift force in terms of the slip velocity and the curl of the liquid phase velocity can be described according to:

$$F_{lg}^{lift} = C_L \alpha_g \rho_l (\nabla \times \boldsymbol{u_l}) \times (\boldsymbol{u_g} - \boldsymbol{u_l}) \quad (6)$$

In equation (6), the constant C_L has been correlated according to Tomiyama (1998) – a relationship that is expressed as a function of the Eotvos number (Eo) which allows positive and negative lift coefficients depending on the bubble size and accounts for the effects of bubble deformation and asymmetric wake of the bubble. It can be expressed by:

$$C_L = min[0.288 \tanh(0.121\, Re_b), f(Eo_d)]\ , Eo < 4$$

$$C_L = f(Eo_d) = 0.00105 Eo_d^3 - 0.0159 Eo_d^2 - 0.0204 Eo_d + 0.474, \quad 4 \le Eo \le 10 \quad (7)$$

$$C_L = -0.29, Eo > 10$$

Wall lubrication force, which is in the normal direction away and decays with distance from the wall, is expressed by:

$$F_{lg}^{wall\ lubrication} = \frac{\alpha_g \rho_l \left[(\boldsymbol{u_g} - \boldsymbol{u_l}) - (\boldsymbol{u_g} - \boldsymbol{u_l}) \cdot \boldsymbol{n_w}\right]^2}{D_s} \left(C_{w1} + C_{w2} \frac{D_s}{x_w}\right) \boldsymbol{n_w} \quad (8)$$

Where, D_s is the mean Sauter bubble diameter. Turbulence induced dispersion based on the consistency of Favre-averaging developed by Burns et al. (2004) is applied. It is given as:

$$F_{lg}^{turbulent\ dispersion} = -C_{TD}\left[\frac{1}{8} C_D a_{if} \rho_l |\boldsymbol{u_g} - \boldsymbol{u_l}|\right] \times \frac{\mu_g^t}{\rho_g Sc_b}\left(\frac{\nabla \alpha_g}{\alpha_g} - \frac{\nabla \alpha_l}{\alpha_l}\right) \quad (9)$$

The interfacial momentum force models development can be found out in more details from the literature.(Tomiyama 2004, Hibiki and Ishii 2007, Lucas et al. 2007)

In equation (2), S_i represents the net change in the number density distribution due to coalescence and breakage processes. The interaction term $S_i (= B_C + B_B - D_C - D_B)$ contains the source rates of B_C, B_B, D_C and D_B, which are the birth rates due to coalescence B_C and breakage B_B and the death rates to coalescence D_C and breakage D_B of bubbles respectively. On the basis of the discrete approximation given in equation (2) the birth and death rates can be formulated according to:

$$B_C = \left(\rho_j^g \alpha_j^g\right)^2 \frac{1}{2} \sum_k \sum_l f_k f_l \frac{M_k + M_l}{M_k M_l} a(M_k, M_l) \quad (10)$$

$$D_C = \left(\rho_j^g \alpha_j^g\right)^2 \sum_k f_i f_k \frac{1}{M_k} a(M_i, M_k) \quad (11)$$

$$B_B = \rho_j^g \alpha_j^g \sum_k r(M_k, M_i) f_k \quad (12)$$

$$D_B = \rho_j^g \alpha_j^g f_i \sum_k r(M_i, M_k) \quad (13)$$

In the current study, the coalescence model by Prince and Blanch (1990) and breakage model by Luo and Svendsen (1996) and Wang et al. (2003) are selected. In Table 1 the model combinations are listed out as Kernel combination 1 and 2 respectively.

Table 1: Coalescence and breakage model Combinations.

Kernel Combination	Coalescence Model	Breakage Model
1	Prince and Blanch (1990)	Luo and Svendsen (1996)
2	Prince and Blanch (1990)	Wang et al. (2003)

Coalescence and Breakage Model

Coalescence model by Prince and Blanch (1990)

Turbulent random collision is considered for the bubble coalescence by Prince and Blanch (1990). In their paper, coalescence process in turbulent flows has been described in three steps. Firstly, the bubbles trap small amount of liquid between them. Then the liquid drains out until the liquid film thickness reaches a critical thickness. Finally, the bubbles rupture and coalesce together. Coalescence rate of bubbles has been proposed based on the collision rate of bubbles and the probability at which collision will result in coalescence.

$$h(M_i, M_j) = C_3(d_i + d_j)^2 \left(d_i^{2/3} + d_j^{2/3}\right)^{1/2} \varepsilon^{1/3} \quad (14)$$

The constant value C_3 can vary between the ranges of 0.28 to 1.11.

The coalescence efficiency for deformable particle with mobile surfaces has been given by Prince and Blanch (1990) as following.

$$\lambda(M_i, M_j) = exp\left(-\frac{t_{ij}}{\tau_{ij}}\right) \quad (15)$$

Here τ_{ij} is the contact time for two bubbles and t_{ij} is the time required for two bubbles to coalesce having diameters d_i and d_j.

The contact time and coalescence time is given by the following equations.

$$\tau_{ij} = \frac{\left(\frac{d_{ij}}{2}\right)^{2/3}}{\varepsilon^{1/3}} \quad (16)$$

$$t_{ij} = \left[\frac{\left(\frac{d_{ij}}{2}\right)^3 \rho_f}{16\sigma}\right]^{1/2} ln\left(\frac{h_0}{h_f}\right) \quad (17)$$

The equivalent diameter d_{ij} is calculated based on the proposal by Chesters and Hofman (1982): $d_{ij}=(2/d_i+2/d_j)^{-1}$. The initial film thickness $h_o = 1\times10^{-4}$ m and critical film thickness $h_f = 1\times10^{-8}$ m at which rupture occurs for air-water systems have been employed.

Finally the total coalescence rate by Prince and Blanch (1990) is calculated as following,

$$a(M_i, M_j) = C_3(d_i + d_j)^2 \left(d_i^{2/3} + d_j^{2/3}\right)^{1/2} \varepsilon^{1/3} \lambda(M_i, M_j) exp\left(-\frac{t_{ij}}{\tau_{ij}}\right) \quad (18)$$

Breakage model by Luo and Svendsen (1996)

Bubble break-up rate by Luo and Svendsen (1996) is based on the assumption of bubble binary break-up under isotropic turbulence situation. Breakup event is determined by the energy level of arriving eddy with smaller or equal length scale compared to the bubble diameter to induce the oscillation. The daughter size distribution is accounted using a stochastic break-up volume fraction f_{BV}. Denoting the increase coefficient of surface area as c_f = [$f_{BV}^{2/3}$ +(1- f_{BV})$^{2/3}$-1], the breakage rate in terms of mass can be obtained as:

$$r(M_i, M_j) = 0.923(1 - \alpha_g) n \left(\frac{\varepsilon}{d_j}\right)^{1/3} \int_{\xi_{min}}^{1} \frac{(1+\xi)^2}{\xi^{11/3}} \mathrm{P_b}(f_{BV}|d_j, \lambda) d\xi \quad (19)$$

The breakage probability, $\mathrm{P_b}(f_{BV}|d_j, \lambda)$ calculated by using the energy distribution of turbulent eddies. Angelidou et al. (1979) developed an energy distribution function for fluid particles in liquid, which was used by Luo and Svendsen (1996). The energy distribution of eddies with size λ is as follows:

$$P_e(e(\lambda)) = \frac{1}{\bar{e}(\lambda)} exp\left(-\frac{e(\lambda)}{\bar{e}(\lambda)}\right) \quad (20)$$

$\bar{e}(\lambda)$ is the mean kinetic energy of an eddy with size λ. Finally the breakage rate becomes,

$$r(M_i, M_j) = 0.923(1 - \alpha_g) n \left(\frac{\varepsilon}{d_j}\right)^{1/3} \int_{\xi_{min}}^{1} \frac{(1+\xi)^2}{\xi^{11/3}} exp\left(-\frac{12 c_f \sigma}{\beta \rho_f \varepsilon^{2/3} d_j^{5/3} \xi^{11/3}}\right) d\xi \quad (21)$$

where $\xi = \lambda / d_j$ is the size ratio between an eddy and a bubble in the inertial sub-range and consequently $\xi_{\min} = \lambda_{\min} / d_j$ and $\beta = 2.0$ are determined from fundamental consideration of the break-up of drops or bubbles in turbulent dispersion systems. Equation (21) can either be calculated analytically via incomplete gamma functions suggested by Selma et al. (1991) or determined numerically via Boole's rule (4th order approximation). The latter has been adopted in the current study.

For binary breakage, the value of the dimensionless variable describing breakage volume fraction should between 0 and 1 ($0<f_{BV}<1$). $f_{BV} = 0.5$ refers to equal breakage and $f_{BV} = 0\ or\ 1$ would refer to no breakage. From equation (21), $r(M_i, M_j)$ represents the breakage rate of bubble with mass of M_i into fraction of f_{BV} and $f_{BV} + df_{BV}$ for a continuous f_{BV} function. The total breakage rate of bubbles can be obtained by integrating the partial breakage over the whole interval of 0 to 1. Total breakage rate can be expressed as,

$$r(M_i) = \frac{1}{2}\int_0^1 r(M_i, M_j)\, df_{BV} \quad (22)$$

The advantage of this model is that it provides the partial breakage rate, $r(M_i, M_j)$ directly. Then the daughter bubble size distribution for mother bubbles with size fraction of f_{BV} can be derived by normalizing the partial breakup rate, $r(M_i, M_j)$ by the total breakup rate, $r(M_i)$.

$$\beta(f_{BV},1)=\frac{r(M_i,M_j)}{r(M_i)} = \frac{2\int_{\xi_{min}}^{1}\frac{(1+\xi)^2}{\xi^{11/3}}\exp\left(-\frac{12C_f\sigma}{\beta\rho_f\varepsilon^{2/3}d_i^{5/3}\xi^{11/3}}\right)d\xi}{\int_0^1\int_{\xi_{min}}^{1}\frac{(1+\xi)^2}{\xi^{11/3}}\exp\left(-\frac{12C_f\sigma}{\beta\rho_f\varepsilon^{2/3}d_i^{5/3}\xi^{11/3}}\right)d\xi\,df_{BV}} \quad (23)$$

Breakage model by Wang et al. (2003)

While Luo and Svendsen (1996) only considered the energy constraint, Wang et al. (2003) extended the model by adding the capillary constraint to calculate the breakage. According to this model, the dynamic pressure of the turbulent eddy must be larger than the capillary pressure resulting in minimum breakup fraction. On the other hand, eddy kinetic energy must be larger than the increase of the surface energy resulting in maximum breakup. The advantage of this model is having no adjustable parameter and providing the daughter size distribution directly by normalizing the partial breakup frequency by the total frequency.

$$r(M_i,M_j) = 0.923(1-\alpha_d)n\epsilon^{1/3}\int_{\lambda_{min}}^{d_i}P_b\left(f_{BV}|d_i,\lambda\right)\frac{(\lambda+d)^2}{\lambda^{11/3}}d\lambda \quad (24)$$

The minimum eddy size, λ_{min} is taken between 11.4 and 31.4 times the Kolmogorov length scale (Tennekes and Lumley 1972). The probability density for bubble of size d_i breaking into breakup fraction of f_{BV} is calculated by

$$P_b(f_{BV}|d_i,\lambda) = \int_0^{\infty}\frac{1}{f_{BV,max}-f_{BV,min}}P_e\left(e(\lambda)\right)de(\lambda) \quad (25)$$

$P_e\left(e(\lambda)\right)$ is calculated similarly as Luo and Svendsen (1996).

The total breakup rate can be calculated by,

$$r(M_i)=\int_0^{0.5}r(M_i,M_j)\,df_{BV} \quad (26)$$

The daughter bubble size distribution can be expressed similarly as (Luo and Svendsen 1996).

According to this model, breakup of bubbles will occur only when the dynamic pressure of approaching turbulent eddy exceeds the capillary pressure of bubbles. Thus the daughter size distribution function would vanish as the breakup fraction, f_{BV} approaches zero. This is due to the fact that, a smaller bubble with radius of curvature tends to zero characterized by higher capillary pressure and therefore it is unlikely to break a very small bubble. Wang et al. (2003) have also mentioned that a local minimum probability exists for equal breakup as it requires more energy than a binary unequal breakup.

NUMERICAL AND EXPERIMENTAL DETAILS

Numerical predictions from all simulation cases were validated and assessed against the TOPFLOW experimental data measured in the HZRD facility. In TOPFLOW experimental facility, a large size vertical cylindrical pipe with height 9000 mm and inner diameter of 195.3 mm inner diameter was adopted. Water was circulated from the bottom to the top with a constant temperature of 30ºC, maintained by a heat exchanger installed in the water reservoir. A variable gas injection system was constructed by equipping with gas injection units at 18 different axial positions from L/D = 1.1-39.9; between the individual gas injections and the first measurement plane of the wire mesh sensor located in direction of flow. Starting from the location L/D=1.1 is used as boundary condition for CFD simulation and simulated results are verified for fully developed flow at location L/D=39.9. The inlet flow condition is tabulated in Table 2. Details of experimental setup, measuring techniques and the variable gas injection unit with a list of vertical measuring location can be found out from literature (Lucas et al. 2010).

Numerical calculations were achieved through the use of the generic computational fluid dynamics code ANSYS-CFX12.1. Transport equation with appropriate source and sink terms describing the coalescence and break-up rate of bubble was implemented through the CFX Command Language (CCL). Computational geometry was simplified through consideration of a 60^0 radial sector of the pipe with symmetry boundary conditions being imposed at both vertical sides of the computational domain.

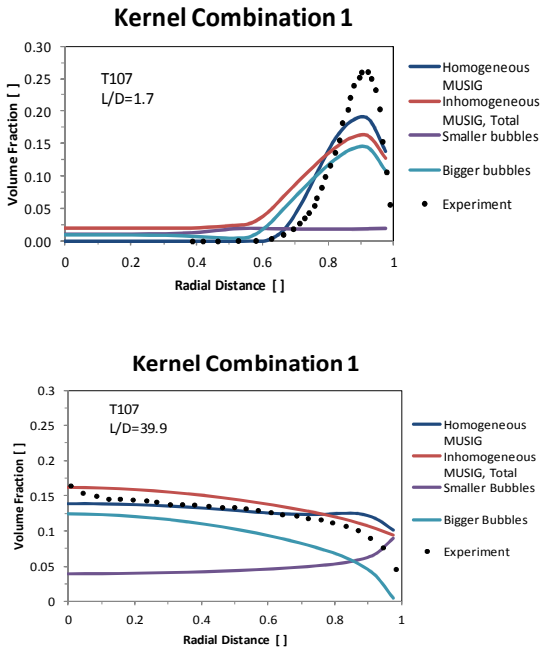

Figure 2: Void fraction distribution along radial distance for kernel combination 1.

RESULTS AND DISCUSSION

The simulated results are compared with the experimental data for two different vertical distances; L/D=1.7 corresponds to the location close to the inlet of the pipe (injection distance is 335 mm) and L/D=39.9 corresponds to the location close to the pipe outlet (injection distance is 7802 mm). Figure 2 shows the comparison of measured and predicted radial gas void fraction distribution for different population balance

method considering the kernel combination 1. The *inhomogeneous* MUSIG predictions are compared with the *homogeneous* MUSIG as well as with the experimental data. For Inhomogeneous MUSIG model, bubble size range boundaries are selected based on the lift coefficient dependent on the bubble size. As found in literature (Tomiyama, 1998), lift force has a vital impact on the lateral movement of bubbles. Moreover experimental observation reveals that bubbles of less than 5.8 mm diameter have a tendency to travel to the near wall region due to positive lift force. On the other hand larger bubbles move towards the center of the pipe due to negative lift force.

Table 2: Flow condition

TOPFLOW Experiment (T107)	
$\langle j_g \rangle\|_{L/D=0}$	1.107 m/s
$\langle j_l \rangle\|_{L/D=0}$	0.140 m/s
$\alpha_g\|_{L/D=0}$	12.1 %
$D_S\|_{L/D=0.0}$	20.18 mm

Based on the dependency on bubble sizes, the disperse gas phase has been divided into two bubble size classes. The first dispersed phase had 2 sub-size classes and the second disperse phase consisted of 13 sub-size classes; all the classes have equal size step of 3 mm.

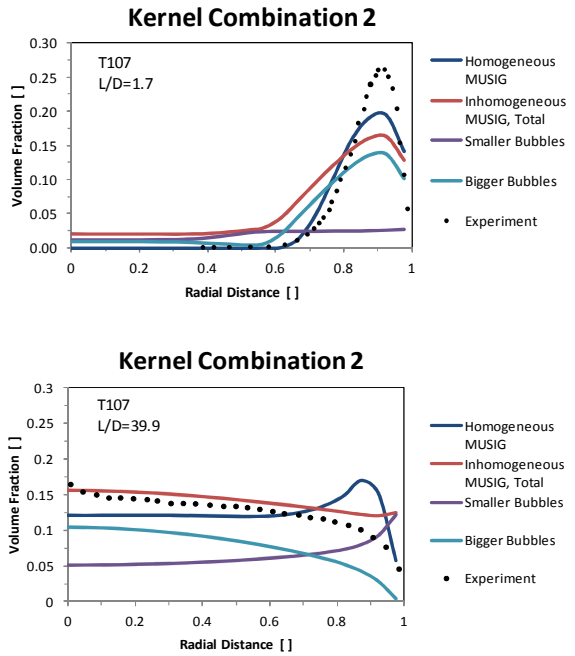

Figure 3: Void fraction distribution along radial distance for kernel combination 2.

For both kernel combination, the disperse phase with smaller bubbles group showed a wall peak and the group containing larger bubbles found to have a core peak (see Figure 2 and 3). Moreover, the comparison for total gas volume fraction profiles demonstrates that *inhomogeneous* MUSIG gives better predictions compared to the *homogeneous* one. For kernel combination 2 in particular, the *inhomogeneous* MUSIG gives noticeable improvement in the core peak profile near the outlet of the pipe; whereas *homogeneous* MUSIG predicted a large wall peak (Figure 3). The error in void fraction prediction by *homogeneous* MUSIG at the near wall region reaches almost 55%. On the other hand, the *inhomogeneous* MUSIG model predicts with only around 10% of error. Similarly, *homogeneous* MUSIG under predicts the void fraction by 30% at the centre of the pipe, whereas *inhomogeneous* MUSIG was able to capture the core peak reasonably (less than 5% error).

Figure 4 and 5 illustrate the cross sectional bubble size distribution at two different axial location of L/D= 1.7 and 39.9 for experimental case T107. In general, both *homogeneous* and *inhomogeneous* MISIG gave similar prediction.

Bi-modal distribution was captured near the vicinity of the injection unit and predictions from the model were compared well with experimental data. This bi-modal distribution eventually transformed into single-modal distribution at the downstream axial location L/D=39.9.

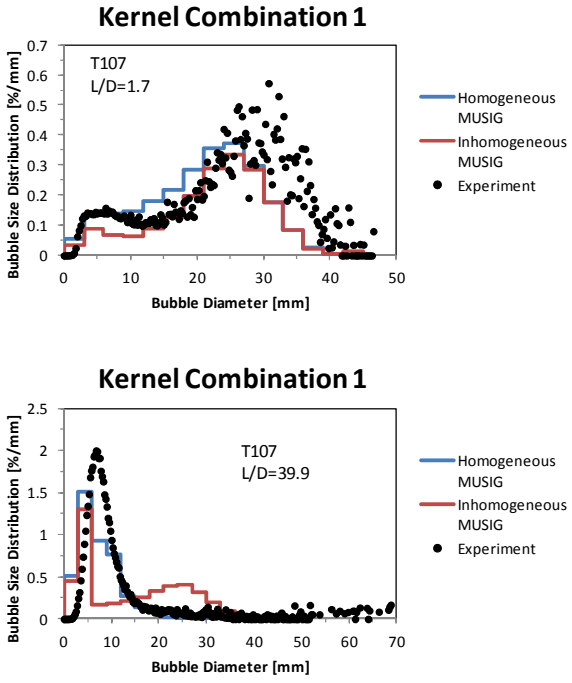

Figure 4: Bubble size distribution along radial distance for kernel combination 1.

Nonetheless, *inhomogeneous* MUSIG model predicted slightly higher fraction of larger bubbles at the downstream (Z/D=39.9). Possibility of this discrepancy could be resulted from the division of dispersed phase only into two groups. Further classification of larger bubbles into more groups travelling in different velocity field might improve the prediction.

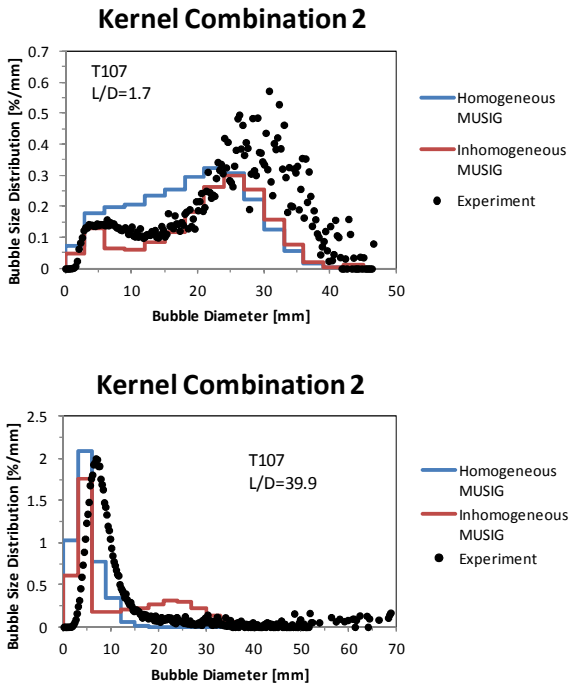

Figure 5: Bubble size distribution along radial distance for kernel combination 2.

Figure 6 depicts the breakage frequency for Homogeneous and Inhomogeneous MUSIG model at the axial location L/D=39.9 for kernel combination 1 and 2 for flow condition T107. In case for Homogeneous MUSIG the breakage frequency for group 2 bubbles showed a wall peak characteristic.

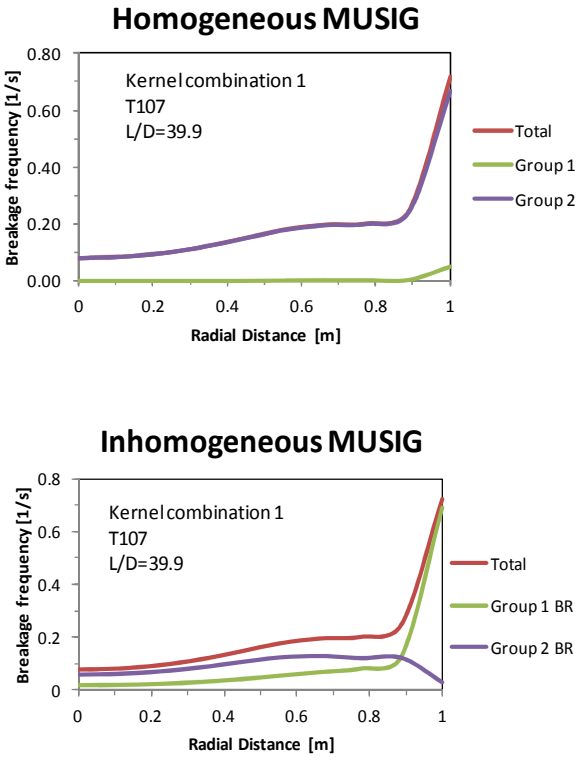

Figure 6: Comparison of *homogeneous* and *inhomogeneous* model breakage frequency along radial distance for kernel combination 1.

But as discussed earlier, the bubbles greater than 6 mm diameter have a tendency to move towards the center of the pipe. So breakage frequency should also follow the similar trend for bigger bubbles as these bubble are residing in the center of the pipe. *inhomogeneous* MUSIG model on the other hand, was able to capture this phenomenon. It was able to successfully predict the wall peak breakage rate for smaller bubbles and a core peak for bigger bubbles.

ACKNOWLEDMENT

The financial support provided by the Australian Research Council (ARC project ID DP130100819) is gratefully acknowledged.

CONCLUSION

A numerical comparison has been done for *homogeneous* and *inhomogeneous* MUSIG model with different coalescence and breakage model implementation. The population balance model was coupled with the Eulerian-Eulerian two fluid model to handle the bubbly flow under isothermal condition is presented in this paper. Different interfacial forces such as, drag, lift, wall lubrication and turbulent dispersion force were accommodated through interfacial momentum transfer. In general, better predictions were observed in case for *inhomogeneous* compared to *homogeneous* MUSIG to predict the gas volume fraction. However, prediction from *inhomogeneous* MUSIG for bubble size distribution was found to over-predict the larger bubble. Nevertheless, radial separations of large and small bubbles are well captured by *inhomogeneous* approach. In examining the effect of different breakage model, Wang et al. (2003) found to have a sharp wall peak in the void fraction distribution for *homogeneous* MUSIG compared to Luo and Svendsen (1996). The results from *inhomogeneous* MUSIG found to overcome the discrepancies. Nonetheless, other mechanisms such as, wake entrainment, surface instability or shearing off should be considered in order to apply a proper closure model for coalescence and breakage.

REFERENCES

Angelidou, Christina, M. Psimopoulos and G. J. Jameson (1979). "Size distribution functions of dispersions." Chemical Engineering Science **34**(5): 671-676.

Bothe, D., M. Schmidtke and H. J. Warnecke (2006). "VOF-simulation of the lift force for single bubbles in a simple shear flow." Chemical Engineering & Technology **29**(9): 1048-1053.

Burns, A.D., T. Frank, I. Hamill and J. Shi (2004). The Farve averaged drag model for turbulent dispersion in Eulerian Mulit-phase flows. Proceeding of the Fifth International Conference on Multiphase flow.

Chesters, A. K. and G. Hofman (1982). "Bubble Coalescence in Pure Liquids." Applied Scientific Research **38**: 353-361.

Cheung, S. C. P., G. H. Yeoh and J. Y. Tu (2008). "Population balance modeling of bubbly flows considering the

hydrodynamics and thermomechanical processes." AIChE Journal **54**(7): 1689-1710.

Cheung, Sherman, Guan Heng Yeoh and Jiyuan Tu (2009). "A Review of Population Balance Modelling for Isothermal Bubbly Flows." The Journal of Computational Multiphase Flows **1**(2): 161-199.

Doubliez, L. (1991). "The drainage and rupture of a non-foaming liquid film formed upon bubble impact with a free surface." International Journal of Multiphase Flow **17**: 783-803.

Fleischer, Claus, Stefan Becker and Gerhart Eigenberger (1996). "Detailed modeling of the chemisorption of CO2 into NaOH in a bubble column." Chemical Engineering Science **51**(10): 1715-1724.

Hibiki, T. and M. Ishii (2007). "Lift force in bubbly flow systems." Chemical Engineering Science **62**(22): 6457-6474.

Krepper, E., D. Lucas, T. Frank, H. M. Prasser and P. J. Zwart (2008). "The inhomogeneous MUSIG model for the simulation of polydispersed flows." Nuclear Engineering and Design **238**(7): 1690-1702.

Krepper, E., D. Lucas and H. M. Prasser (2005). "On the modelling of bubbly flow in vertical pipes." Nuclear Engineering and Design **235**(5): 597-611.

Lo, S.M. (1996). "Application of Population Balance to CFD Modelling of Bubbly Flow via the MUSIG model." AEA Technology, AEAT-1096.

Lucas, D., M. Beyer, L. Szalinski and P. Schutz (2010). "A new database on the evolution of air-water flows along a large vertical pipe." International Journal of Thermal Sciences **49**(4): 664-674.

Lucas, D., E. Krepper and H. M. Prasser (2007). "Use of models for lift, wall and turbulent dispersion forces acting on bubbles for poly-disperse flows." Chemical Engineering Science **62**(15): 4146-4157.

Lucas, Dirk, Eckhard Krepper and Horst-Michael Prasser (2001). "Prediction of radial gas profiles in vertical pipe flow on the basis of bubble size distribution." International Journal of Thermal Sciences **40**(3): 217-225.

Luo, H. and H. F. Svendsen (1996). "Theoretical model for drop and bubble breakup in turbulent dispersions." AIChE Journal **42**(5): 1225-1233.

Prince, M. J. and H. W. Blanch (1990). "Bubble Coalescence and Break-up in Air-Sparged Bubble-Columns." AIChE Journal **36**(10): 1485-1499.

Ramkrishna, D. (1985). The Status of Population Balances. Reviews in Chemical Engineering. **3:** 49.

Shi, J.M., P.J. Zwart, T. Frank, U. Rohde and H.M. Prasser (2004). Development of a multiple velocity multiple size group model for poly-dispersed multiphase flows. *Annual Report of Institute of Safety Research*. Germany, Forschungszentrum Rossendorf.

Tennekes, H. and J.L. Lumley (1972). A First Course in Turbulence, MIT Press.

Tomiyama, A. (1998). Struggle with computational bubble dynamics. Third International Conference on Multiphase Flow. Lyon, France 157.

Tomiyama, A. (2004). Drag, lift and vitrual mass forces acting on a single bubble. 3rd International Symposium on two-phase flow modelling and experimentation. Pisa**:** 22-24.

Wang, T. F., J. F. Wang and Y. Jin (2003). "A novel theoretical breakup kernel function for bubbles/droplets in a turbulent flow." Chemical Engineering Science **58**(20): 4629-4637.

Yeoh, G., Sherman Cheung and J. Tu (2012). "On the Prediction of Bubble Size Distribution and Void Fraction in Vertical Gas-Liquid Flows." The Journal of Computational Multiphase Flows **4**(1): 1-22.

SIMULATION OF POLYDISPERSE GAS-LIQUID SYSTEMS WITH QBMM: MODEL VALIDATION WITH THREE DIFFERENT TEST CASES

Antonio BUFFO[1*], **Daniele L. MARCHISIO**[1], **Marco VANNI**[1], **Julia HOFINGER**[2], **Peter RENZE**[2]

[1]Department of Applied Science and Technology, Politecnico di Torino, 10129 Torino, ITALY

[2]Department for Chemical and Process Engineering, BASF SE, Ludwigshafen, GERMANY

[*] E-mail: antonio.buffo@polito.it

ABSTRACT

Different industrial scale dispersed gas-liquid systems can be successfully described by considering that gas bubbles are polydisperse, namely the gas phase is characterized by a distribution of bubbles with different velocity, size and composition. Phase coupling issues can be properly overcome by considering the evolution in space and time of such bubble distribution, which is dictated by the so-called Generalized Population Balance Equation (GPBE) (Marchisio and Fox, 2013), with the inclusion of specific mesoscale models for taking into account momentum, heat and mass exchange with the liquid phase, as well as bubble coalescence and breakage. The choice of these mesoscale models is of crucial importance for the prediction of the relevant properties of a gas-liquid system. A computationally efficient approach for solving the GPBE is the quadrature-based moments methods, where the evolution of the entire bubble population is recovered by tracking some specific moments of the distribution and a quadrature approximation is used to solve the "closure problem" typical of moment-based methods. Among these methods, the Conditional Quadrature Method of Moments (CQMOM), is particularly interesting. As pointed out in our previous works on this topic (Buffo *et al.*, 2013b; Buffo and Marchisio, 2014), the development of a very general and fully predictive methodology, useful for simulating different gas-liquid equipments, is the final aim of this work. However, only with reliable mesoscale models for the different interfacial forces, this goal can be achieved. In this work, the focus will be on the relationship for the drag force coefficient, with particular attention to the effect of microscale turbulence and bubble swarm. The proposed methodology is here adopted for the simulation of very different gas-liquid systems, mainly rectangular and circular bubble columns, as well as aerated stirred tank reactors (Laakkonen *et al.*, 2006; Kulkarni *et al.*, 2007; Diaz *et al.*, 2008) and simulation results are eventually compared with the available experimental data.

Keywords: population balance modelling, gas-liquid systems, quadrature-based moment methods .

NOMENCLATURE

Greek Symbols

ε	Turbulent dissipation rate, $[m^2/s^3]$
μ	Dynamic viscosity, $[kg/ms]$
ρ	Mass density, $[kg/m^3]$
σ	Surface tension, $[kg/s^2]$
ϕ	Bubble composition, $[mol]$
$\dot{\phi}$	Bubble composition change rate, $[mol/s]$

Latin Symbols

C_A	Constant parameter, $[-]$.
C_B	Constant parameter, $[-]$.
C_D	Drag coefficient, $[-]$.
C_μ	Constant parameter of $k-\varepsilon$ model, $[-]$.
d	Diameter, $[m]$.
Eo	Eötvos number, $[-]$.
g	Gravitational acceleration magnitude, $[m/s^2]$.
G	Bubble growth/shrink rate, $[m/s]$.
h	Source term of PBE, $[1/m^4 mols]$.
k	Turbulent kinetic energy, $[m^2/s^2]$.
L	Bubble size, $[m]$.
$M_{k,l}$	Generic order moment of NDF, $[m^{k+1}mol^{l+1}/m^4 mol]$.
n	Number Density Function, $[/m^4 mol]$.
N	Total number of quadrature nodes, $[-]$.
N_1	Number of quadrature nodes with respect to bubble size, $[-]$.
N_2	Number of quadrature nodes with respect to bubble composition, $[-]$.
Re	Reynolds number, $[-]$.
$\mathbf{U}$	Velocity vector, $[m/s]$.
U_T	Bubble terminal velocity, $[m/s]$.
$\mathbf{x}$	Position vector, $[m]$.
w_{i_1}	Weight of quadrature, $[1/m^3]$.
w_{i_1,i_2}	Conditional weight of quadrature, $[-]$.

Sub/superscripts

b	Disperse bubbly phase.
c	Continuous liquid phase.
eff	Effective.
i_1	Index i_1 with respect to N_1.
i_2	Index i_2 with respect to N_2.

Abbreviations

CFD	computational fluid dynamics.
CFL	Courant-Friedrichs-Lewy.
CQMOM	conditional quadrature method of moments.
DQMOM	direct quadrature method of moments.
GPBE	generalized population balance equation.
NDF	number density function.
PBE	population balance equation.
PBM	population balance model.
PBM	probability density function.
QBMM	quadrature-based moment method.

QMOM quadrature method of moments.

INTRODUCTION

Gas-liquid systems are encountered in many processes of the process industry. Stirred tanks, bubble columns, air loop columns are very common types of gas-liquid contactors, in which many important chemical reactions are usually carried out (e.g., oxidations, hydrogenations, etc.). These kinds of reactors usually work under turbulent conditions, in order to enhance the mass and energy transfer rates, allowing for the reduction of the overall costs of the process. The simulation of turbulent gas-liquid systems is of crucial importance, due to the increasing important role played during scale-up and optimization. In fact, the design of such equipment is too often limited by the use of empirical correlations, valid only for a specific geometry working under a subset of operating conditions.

These systems have been widely investigated in the past with computational fluid dynamics (CFD), leading to the development of different computational models. Among them, the most popular and the only feasible approach to describe industrial scale systems with realistic global gas volume fractions is based on the idea of solving equations for some characteristic macro-scale properties of the gas-liquid systems, such as gas and liquid volume fractions, as well as gas and liquid mean velocities. This resulting model is often referred to as multi-fluid approach, or Eulerian-Eulerian approach (van Wachem and Almstedt, 2003). It can be shown that these macro-scale properties are moments of a number density function (NDF) that completely defines the gas-liquid system, whose evolution is in turn defined by the GPBE (for details see Buffo and Marchisio, 2014) .

Basically with the multi-fluid model every phase presents in the system shares a portion of the available space, through the definition of volume fractions, and interacts with each other through phase coupling. As a consequence, the proper modeling of the phase-coupling terms is essential for a sound prediction of the behavior of these systems. These terms represent how the gas and the liquid phases exchange mass, momentum and energy: the formulation of these terms is based on bubble-liquid and bubble-bubble interactions at the meso-scale level and usually depends on the size of the disperse bubbles in the continuous phase. The majority of such models formulated in the past years refers to simplified systems, in which the continuous phase is stagnant and the local gas volume fraction is quite low (i.e. dilute limit), and their application is usually extended to turbulent systems at high gas volume fractions, without any correction for turbulence and bubble swarm effects. This fact constitutes a limit for the CFD simulations, because it often brings to results far from the reality, when comparisons with experimental data are performed both in terms of local and global properties (such as velocity profiles and global gas-hold up), leading the modeler to treat the bubble size not as a variable but as a tuning parameter of the simulation.

However, in gas-liquid systems, the size (and shape) of the disperse bubbles are dynamical variables, varying from point to point into the vessel according to the shear experienced by the bubbles moving in the liquid phase. It is intuitive to think that the bubble population is unlikely monodisperse, in fact their characteristic properties (such as size, temperature, chemical composition) are usually distributed over different values. The distribution of the so-called internal coordinates of the bubble population can be theoretically described by means of the population balance model (PBM) approach: a NDF is opportunely defined to represent the local bubble population and its evolution in space and time is predicted by the so-called GPBE, where the relevant physical phenomena are accounted for. For systems in which gas bubbles are dispersed in a continuous liquid phase, bubble coalescence and breakage due to bubble collisions, bubble growth and shrink due to molecular processes and the different interfacial forces acting on bubbles are the common physical phenomena that determine the system dynamics.

The efficient coupling of CFD simulation with PBM in order to obtain a fully predictive methodology was the subject of our latest works: QBMM introduced by Marchisio *et al.* (2003) and Marchisio and Fox (2005) were implemented in a commercial CFD code and used to simulate the behavior of an aerated stirred tank reactor (Petitti *et al.*, 2009, 2010). Then, the solution methods were extended to consider both size and composition distribution in order to properly describe the mass transfer process: DQMOM and CQMOM were both implemented and compared, showing that CQMOM is more suitable for gas-liquid systems (Buffo *et al.*, 2012, 2013a). More recently, QMOM and CQMOM were implemented in the opensource CFD code OpenFOAM to predict the behavior of a pseudo 2D bubble column and the results given by the model were validated through the comparison with the experimental data (Buffo *et al.*, 2013b).

This contribution follows the latest works and focuses on the validation of the CFD-PBM methodology for gas-liquid systems through the comparison with experimental data available in the literature for very different gas-liquid systems, both in terms of geometry and operating conditions. In fact, in this way we are able to assess the reliability of such methodology; moreover the importance of the corrections for turbulence and swarm effects for the drag relation will be pointed out in order to properly describe gas-liquid systems under practical conditions.

MODEL DESCRIPTION

Multi-fluid model

The Eulerian-Eulerian multi-fluid approach is here adopted to model the behavior of a gas-liquid system, considering both phases as incompressible. The $k-\varepsilon$ model for multiphase system proposed by Kataoka and Serizawa (1989) is used for describe the turbulence since it represents a good trade-off between accuracy and computational cost. For more details on the governing equations and the relationship with the PBM, readers should refer to the works of Marchisio and Fox (2013); Buffo *et al.* (2013b); Buffo and Marchisio (2014). Since the motion of the bubbles in the physical space is determined by the sum of interfacial forces acting on them, it is crucial to model these terms appearing in the momentum balance equations in a proper way. It is well-know that buoyancy, gravity and drag forces play an important role in the description of gas-liquid systems, followed in order of importance by lift, virtual mass, turbulent dispersion and Basset forces (Scargiali *et al.*, 2007; Montante *et al.*, 2007; Diaz *et al.*, 2008; Petitti *et al.*, 2010). In this work, we decided to neglect the latter four forces at the moment; this aspect may be in contrast with some works presented in literature, especially concerning the importance of the lift force in the prediction the local variable profiles. It is important to remark that most of the models available for such interfacial forces in literature are formulated from experimental or theoretical works in which a single bubble moves in a simplified flow field: therefore, the use of such relations for turbulent

systems with high local gas volume fraction represents an approximation. For more details on the different interfacial forces for gas-liquid system, readers may refer to the work of Buffo and Marchisio (2014). Moreover, we will see here that it is possible to obtain good results neglecting such additional forces, but taking into account the effect of turbulence and bubble swarm on drag force. However, this aspect of gas-liquid simulations is currently under investigation and it will be the subject of our future communications.

As far as the drag coefficient is concerned, through a simple force balance acting on a single bubble in a quiescent fluid (considering only buoyancy, gravity and drag forces), the very popular drag coefficient relationship in terms of the bubble terminal velocity U_T (Clift *et al.*, 1978), can be written:

$$C_\mathrm{D} = \frac{4}{3}\frac{\rho_\mathrm{c}-\rho_\mathrm{b}}{\rho_\mathrm{c}}\frac{d_\mathrm{b} g}{U_\mathrm{T}^2}. \qquad (1)$$

The bubble terminal velocity can be in turn estimated through correlations based on fluid properties and bubble diameter, derived from extensive experimental campaigns. An example of such approach is the wave analogy of Mendelson (1967) or the correlation reported in Clift *et al.* (1978), as a function of the important dimensionless numbers, notably Morton, Eötvos and Reynolds. These correlations combined with Eq. (1) provide an empirical expression for the drag coefficient, that when the bubbles reach equilibrium, results in the desired (e.g. experimentally observed) terminal velocity. Another popular expression was proposed by Tomiyama *et al.* (2002), obtained from experiments on air-tap water system:

$$C_\mathrm{D} = \max\left[\frac{24}{\mathrm{Re}_\mathrm{b}}(1+0.15\mathrm{Re}_\mathrm{b}^{0.687}), \frac{8}{3}\frac{\mathrm{Eo}}{\mathrm{Eo}+4}\right], \qquad (2)$$

where the Eötvos number is defined as: $\mathrm{Eo} = g(\rho_\mathrm{c}-\rho_\mathrm{b})d_\mathrm{b}^2/\sigma$ and the Reynolds number as: $\mathrm{Re}_\mathrm{b} = \rho_\mathrm{c} d_\mathrm{b}|\mathbf{U}_\mathrm{c}-\mathbf{U}_\mathrm{b}|/\mu_\mathrm{c}$.

As previously mentioned, these correlations for the drag coefficient are typically derived for single bubbles (i.e. under the dilute regime, $\alpha_\mathrm{c} \to 1$) and under laminar flow conditions; therefore corrections to standard drag relationships must be applied in order to account for deviations from ideal conditions. In our previous works, we adopted two different strategies (Buffo *et al.*, 2013b; Buffo and Marchisio, 2014): a global correction, based on the fact that all bubbles have the same terminal velocity, which is a reasonable assumption when the investigated bubble size range lies between 2 and 10 mm (Clift *et al.*, 1978), and a more rigorous local correction, based on local values of gas volume fraction and turbulent quantities. In the former case, the estimation of the drag coefficient is carried out through the Eq. (1) with U_T assumed constant and equal to a value slightly smaller than that measured in a single bubble experiment, to account for the presence of the other bubbles and for microscale turbulence. However, although this method can be very effective as demonstrated by Petitti *et al.* (2009) for stirred tanks and by Buffo *et al.* (2013b) for bubble columns, the choice of a proper value for U_T is still subjected to empiricism, since it depends on the system geometry (i.e., it varies from 20 cm/s for bubble columns in homogenous regime, to 12 cm/s for stirred tanks with low gas hold-up). Otherwise, with the latter approach, it is possible to modify Eq. (2) in the following way:

$$C_\mathrm{D} = (1-\alpha_\mathrm{b})^{C_\mathrm{A}} \max\left[\frac{24}{\mathrm{Re}_\mathrm{eff}}\left(1+0.15\mathrm{Re}_\mathrm{eff}^{0.687}\right), \frac{8}{3}\frac{\mathrm{Eo}}{\mathrm{Eo}+4}\right], \qquad (3)$$

where the first part of the expression is formulated in analogy with the correlation of Wen and Yu (1966) for fluidized beds, in order to account for the presence of other bubbles and where the Reynolds number is modified for considering the effect of microscale turbulence as proposed by Bakker and Van den Akker (1994):

$$\mathrm{Re}_\mathrm{eff} = \frac{d_\mathrm{b}\rho_\mathrm{c}|\mathbf{U}_\mathrm{c}-\mathbf{U}_\mathrm{b}|}{\mu_\mathrm{eff}}, \quad \mu_\mathrm{eff} = \mu_\mathrm{c} + C_\mathrm{B}\rho_\mathrm{c}\frac{k^2}{\varepsilon}. \qquad (4)$$

As already reported in our previous works (Buffo *et al.*, 2013b; Buffo and Marchisio, 2014), this latter approach should be intended as a sort of semi-empirical adjustment of the Tomiyama correlation. The range of these two constants should not be different from the one indicated by the corresponding theories: C_A is usually taken between -3.0 and -1.0 according to the work of Wen and Yu (1966) and it usually depends on the Reynolds number (i.e., it increases to -1.0 at high Re number; here it is assumed constant on a first approximation), while C_B should be smaller than $C_\mu = 0.09$ of the $k-\varepsilon$ model, since only the eddies smaller than the bubble size are responsible for microscale turbulence and for the bubble terminal velocity reduction. In a preliminary work, the two model parameters were found by a simple trial and error procedure through a comparison for different gas superficial velocities between the simulation results obtained with a couple of values with the experimental data for the case of Diaz *et al.* (2008): the final result of this procedure was $C_\mathrm{A} = -1.3$ and $C_\mathrm{B} = 0.005$. In this work, these values are used for simulating both bubble columns and stirred tanks, with the aim of demonstrating the ability of the approach to be fully-predictive.

Population balance model

As mentioned, the overall gas-liquid system is defined by a general NDF. By applying the moment transform to this NDF equations for volume fractions and gas and liquid velocities are obtained, constituting the basis of the multi-fluid model. As often done in physics and engineering, some degrees of freedom are integrated out (or coarse-grained), and the problem is reduced down to a simpler problem (or in order words characterized by smaller dimensionality). In this work, the bubble population is described through a "marginal" NDF (or simply NDF in the reminder of the paper), defined in such a way that the following quantity

$$n(L,\phi;\mathbf{x},t)\,\mathrm{d}L\,\mathrm{d}\phi$$

represents the expected number of bubbles per unit volume $\mathrm{d}\mathbf{x}$ centered at the position $\mathbf{x}$ and time t with size L ranging between L and $L+\mathrm{d}L$ and chemical composition ranging between ϕ and $\phi+\mathrm{d}\phi$.

In this work, an isothermal air-water is considered, with the chemical composition described in terms of absolute number of moles of one single chemical component (i.e., oxygen). Moreover all bubbles are assumed to locally move with the same velocity: this means that bubble velocity is not an internal coordinate of the NDF and the local interfacial forces are estimated with an average bubble diameter (i.e., the mean Sauter diameter d_{32}); this approach can be considered accurate when the range of bubble sizes is between 2-10 mm, when the terminal velocity reached is more or less the same for all the bubbles (Clift *et al.*, 1978). However, this fact does not imply that the C_D is constant and fixed during the simulation: since the bubble size distribution is here calculated with

the PBM, the interfacial forces may vary from point to point into the geometry.

The continuity statement of the NDF is the so-called PBE (which is a coarse-grained version of the GPBE) and it can be written as follows (omitting for brevity the dependencies on internal coordinates as well as space and time):

$$\frac{\partial n}{\partial t} + \nabla \cdot (\mathbf{U}n) + \frac{\partial}{\partial L}(Gn) + \frac{\partial}{\partial \phi}(\dot{\phi} n) = h \qquad (5)$$

where $\mathbf{U}$ represents the velocity of the bubbles (calculated through the well-known momentum balance equation for the gas phase of the multi-fluid model), G represents the rate of change of bubble size due to continuous processes (i.e. molecular processes, such as mass transfer and chemical reaction), $\dot{\phi}$ is the rate of change of bubble chemical composition due to continuous processes and h is the term accounting for collisional events, such as bubble coalescence and breakage.

It is important to remark that sub-models are needed to close Eq. (5). In fact, as mentioned this is obtained after integrating out (or coarse-graining) some degrees of freedom and the details regarding these sub-models can be found in our previous works (Buffo *et al.*, 2013a,b; Buffo and Marchisio, 2014). All of them are function of the local value of the turbulent dissipation rate, estimated here through the solution of the multiphase $k-\varepsilon$ model. The mass transfer rate is calculated using the penetration theory, considering the eddy renewal time equal to the Kolmogorov time-scale (Lamont and Scott, 1970). Bubble coalescence and break-up can be caused by different mechanisms but in turbulent systems (as the ones we want to consider) bubble collisions are mainly due to turbulent fluctuations: the coalescence efficiency is estimated as the ratio between the contact and drainage time-scales, whereas bubble breakage results in two bubbles of different sizes (prescribed by a $\beta-$PDF daughter distribution function) and same bubble concentration. The expression of these terms can be found in our previous works (Buffo *et al.*, 2013a,b; Buffo and Marchisio, 2014). It is worth mentioning that the effect of bubble composition on such kernels is here neglected; this essentially due to a lack of knowledge regarding the kernel formulation under the conditions in which composition effects on coalescence and breakage are important. As shown in our previous work (Buffo *et al.*, 2013a), the methodology can be efficiently used also with composition-dependent kernels.

The solution of Eq. (5) is challenging since the unknown is a multidimensional functional: many numerical methods have been developed in the past with different degrees of accuracy and correspondent computational costs. As shown by Marchisio and Fox (2013), a particularly convenient class of methods is represented by the so-called Quadrature-Based Moments Methods (QBMM), in which the evolution of some lower order moments of the distribution is tracked by solving their corresponding equations, obtained in turn by applying the moment transform to Eq. (5) (Buffo *et al.*, 2013a). In some simple cases the moment equations can be written as a function of the moments themselves, but in most cases (of practical interest) this is not possible. This is the so-called closure problem initially pointed out by Hulburt and Katz (1964) and generally solved by assuming a specific functional form of the NDF. With the QBMM, the NDF is written of a summation of basis functions, often Dirac delta functions, in turn centered on the nodes of a Gaussian quadrature. In the case of a bivariate distribution (as in this case, considering bubble size and composition) the quadrature approximation can be expressed as:

$$n(L,\phi) = \sum_{i_1=1}^{N_1} \sum_{i_2=1}^{N_2} w_{i_1} w_{i_1,i_2} \delta(L - L_{i_1}) \delta(\phi - \phi_{i_1,i_2}) \qquad (6)$$

where the N_1 weights w_{i_1}, the $N = N_1 N_2$ conditional weights w_{i_1,i_2} and the N nodes of quadrature $[L_{i_1}; \phi_{i_1,i_2}]$ are calculated from a specific set of mixed order moments through the so-called CQMOM algorithm (for details see Marchisio and Fox, 2013; Buffo *et al.*, 2013a). The number of nodes determines the degree of accuracy; in general a number of nodes between two and four is desirable for the bubble size, while for the chemical composition one is usually enough for describing mass transfer problems. In this latter case, when $N_2 = 1$, it follows that $N = N_1$ and therefore Eq. (6) can be rewritten as:

$$n(L,\phi) = \sum_{i=1}^{N} w_i \delta(L - L_i) \delta(\phi - \phi_i) \qquad (7)$$

namely the entire bubble population is divided in N subgroups, each one characterized by a number density w_i and characteristic values of size L_i and composition ϕ_i. An example is represented by the case of $N_1 = 4$ and $N_2 = 1$, eight pure moments (i.e., $M_{0,0}, M_{1,0}, M_{2,0}, M_{3,0}, M_{4,0}, M_{5,0}, M_{6,0}, M_{7,0}$) with respect to size are tracked in order to calculate the four weights (w_1, w_2, w_3, w_4) and the four nodes (L_1, L_2, L_3, L_4), while another four mixed-order moments are needed to calculate the nodes with respect to composition $(\phi_1, \phi_2, \phi_3, \phi_4)$ (i.e., $M_{0,1}, M_{1,1}, M_{2,1}, M_{3,1}$).

It is important to notice that, although this methodology was developed for treating mass transfer problems, the CQMOM methods can be used also for simulate case without mass transfer. In this specific case, CQMOM reduces to QMOM since only a monovariate distribution is described, namely only the transport equations for the moments with respect to bubble size are solved.

TEST CASE AND NUMERICAL DETAILS

In this work, three different geometries are simulated: a rectangular bubble column experimentally investigated by Diaz *et al.* (2008), a cylindrical bubble column investigated by Kulkarni *et al.* (2007) and an aerated stirred tank investigated by Laakkonen *et al.* (2006, 2007). In the first case, the simulated experimental equipment consists of a 0.2 m wide, 1.8 m high and 0.04 m deep partially aerated bubble column, filled with tap water up to 0.45 m from the bottom at room temperature and atmospheric pressure, while the air is fed through a sparger composed of eight centered holes of 1 mm of diameter and 6 mm pitch. The second case is a partially aerated cylindrical bubble column of 0.15 m diameter with two different spargers (a 3.17 mm centered single hole sparger and a multi-point sparger composed by fifteen holes of 1.96 mm) filled with water up to 0.9 m from the bottom, and the latter case considered is a 1.96-liter four baffled reactor, agitated by a six-blade Rushton turbine and with a circular metal porous sparger with diameter of 3.3 cm and mean pore size of 15 μm, located 10.5 cm below the impeller. For such systems, numerous experimental data are available, although none of these contains the good mix of local and global measurements useful to fully validate a numerical simulation; here only the significant comparisons with simulation are shown for the sake of brevity.

Table 1: Numerical schemes and boundary conditions adopted in the simulations

Variable	Scheme	Inlet	Outlet	Wall
Gas vol. frac.	Lim. 2nd ord. upwind	0.5	Zero grad.	Zero grad.
Gas velocity	Lim. 2nd ord. upwind	Depends on flow rate	Zero grad. with backflow	Free-slip
Liquid velocity	Lim. 2nd ord. upwind	0.0 m/s	Zero grad.	No-slip
Pressure	1st ord. upwind	Zero grad.	1 bar	Zero grad.
k	Lim. 2nd ord. upwind	Based on Turbulence Intensity equal to 5% and Length Scale equal to the hole diameter	$10^{-4}\,\mathrm{m^2/s^2}$ (backflow only)	Std. wall func
ε	Lim. 2nd ord. upwind		$10^{-5}\,\mathrm{m^2/s^3}$ (backflow only)	Std. wall func.
Moments	1st ord. upwind	Log-normal distrib.	Zero grad.	Zero grad.

The OpenFOAM time-dependent solver based on the two-fluid Eulerian-Eulerian equations for compressible systems (i.e. `compressibleTwoPhaseEulerFoam`) was partially modified in order to include the PBM via CQMOM, as described by Buffo *et al.* (2013b). As already mentioned, the main element of novelty here is that the overall modeling approach is validated (with the same value for all the constant parameters) in three different test cases, without any further fitting or fine tuning. In particular, all the simulations were run with the same values of the drag force parameters $C_A = -1.3$ and $C_B = 0.005$ of Eq. 3.

In all the cases, the system investigated was constited by air as disperse phase and tap water as continuous phase and standard physical properties were used. The spatial discretization schemes and boundary conditions are summarized in Table 1. The time integration was carried out according to a first-order backward scheme, with an adaptive selection of the time step according to the CFL condition: this choice ensures the stability of the simulation even at higher superficial gas velocities. The inlet condition for the gas phase, especially for the moment of the bubble population, was discussed in detail in our previous works (see Buffo *et al.*, 2012, 2013b). In all cases, the process of bubble formation and detachment from the sparger was not simulated, but modeled through the use of velocity-inlet surfaces with total area equal to the total area enclosed by the sparger. Since there are significant differences between porous and holed spargers in terms of resulting bubble diameters, two different correlations are used to estimate the inlet mean bubble size: in the former case the correlation of Kazakis *et al.* (2008) was used, while in the latter case the correlation formulated by Geary and Rice (1991) was adopted.

DISCUSSION AND RESULTS

Let us start the discussion of the results with the cylindrical bubble column of Kulkarni *et al.* (2007) with the multi-point sparger with a gas superficial velocity equal to 20 mm/s. In Fig. 1 model predictions for the time-averaged axial liquid velocity along the radial direction are compared with experiments at four different heights of the bubble column. As it is possible to see from the figure, the model is capable of predicting quite well the fluid dynamics behavior of the system: the liquid rises in the central part and it descends along the walls of the column as viewed in the experiments. This is a remarkable result since the drag coefficient, which it strongly influences both gas and liquid flow fields, is calculated with a drag correlation, function of local values of bubble mean Sauter diameter, calculated as the ratio between $M_{3,0}$ and $M_{2,0}$, and of turbulent quantities such as k and ε.

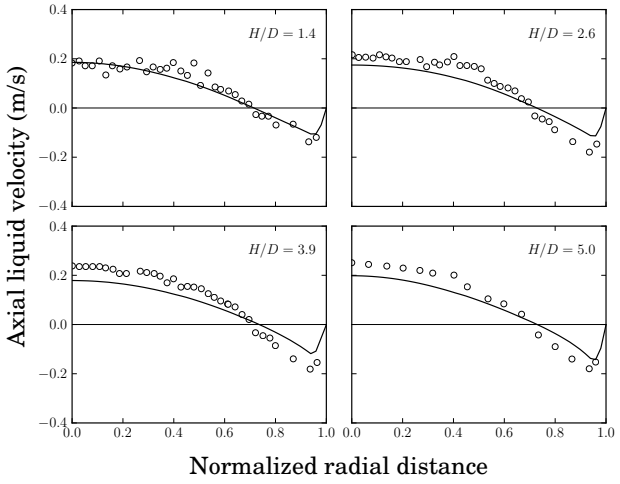

Figure 1: Comparison with experimental (open circles) and predicted time-average vertical liquid velocity profiles (continous line) at four different heights of the multi-point sparger cylindrical column of Kulkarni *et al.* (2007).

Another interesting result is reported in Fig. 2 where the comparison of the predicted and experimentally measured turbulent energy dissipation rate along the radial distance for four column heights is shown. As it can be clearly seen, the numerical results have the same order of magnitude of the experimental data. This is indeed a very good results, given the employed model approximations and the measurement uncertainties. This means that not only good predictions can be obtained by using an approximate turbulence model, but also that the local value of ε used in all the sub-model (i.e., coalescence and breakage kernels, mass transfer model, drag relationship) is not so far from the physical reality. Unfortunately, no experimental measurements of bubble size distribution are available for this test case. The only information reported about the gas phase is represented by the local gas hold-up profiles, whose comparison is shown in Figure 3.

In this case, the predicted gas hold-up radial profiles present a deviation from the experimental data, especially for measurement points close to the free liquid surface. However, in the absence of measurements of global gas hold-up and of a detailed description of the sparger section, it is impossible to draw definitive conclusions. The comparison between some experimental correlations and simulation results is reported in Table 2. Although these correlations are formulated for taller columns with larger diameters and different sparger geometries, the predicted global gas hold-up seems realistic.

The importance of the sparger configuration can be pointed out through the comparison of local gas volume fraction profiles for the single-point sparger at the same gas superficial velocity for the same bubble column shown in Fig. 4. In this case, the experimental profiles are different from the multi-point sparger case, even far from the sparger section, however the agreement between predictions and experiments is satisfactory.

This is the quantitative demonstration that multi-point sparg-

ers are capable of better dispersing the bubbles in the column, in comparison with single-point spargers. Also the simulated global gas hold-up, reported in Table 2, is significantly lower than those of the multi-point sparger. As it is possible to see in Fig. 4, the model agreement with the experiments is good at all measurement levels: in this case, there are no uncertainties regarding the inlet section modeling and the comparison is therefore better than the multi-point sparger case.

In Fig. 5 the comparison between predicted and experimentally measured axial liquid velocity profiles for the single-point sparger is reported. In this case, the agreement between simulation and experiments is slightly worse than for the multi-point case, since the liquid velocity in the rising and re-circulation zones is under predicted. However, the experimental trend at every measurement height is correctly reproduced; moreover, since the fluid dynamic behavior of the gas and liquid phases is strongly coupled, it is important to consider the overall comparison between simulations and experiments, considering both Figs 4 and 5, which is quite good despite all the uncertainties.

The lack of global gas hold-up and other superficial gas velocity measurements for the test case of Kulkarni *et al.* (2007) led us to consider other test cases for which such data is available, as for example the rectangular bubble column of Diaz *et al.* (2008). In Fig. 6 the measured global gas hold-up values at different superficial gas velocity for this bubble column are compared with the simulation results. As it can be seen, the agreement is very good both in terms of trend and absolute values. A similar agreement proves that the choice of the drag model here used is appropriate, at least for these operating conditions and this fluid dynamic regime (i.e., homogeneous regime). It is important to notice that the bubble size diameter is no longer used as a model fitting parameter but it is calculated through the PBM; moreover the reduction of the bubble terminal velocity due to swam effect and local turbulence dissipation rate is properly described also in terms

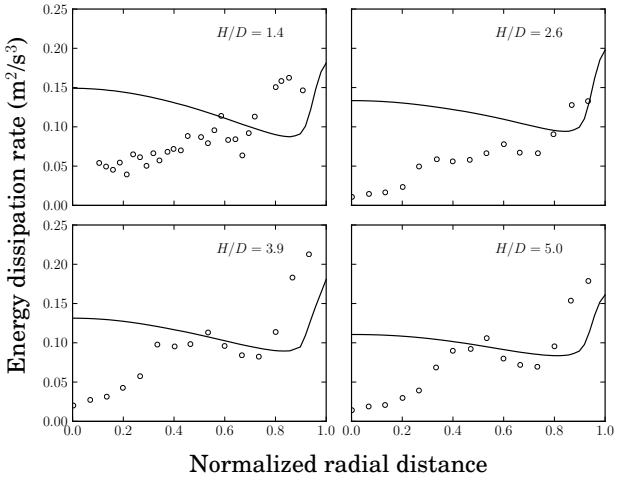

Figure 2: Comparison with experimental (open circles) and predicted time-average local turbulent dissipation rate profiles (continous line) at four different heights of the multi-point sparger cylindrical column of Kulkarni *et al.* (2007).

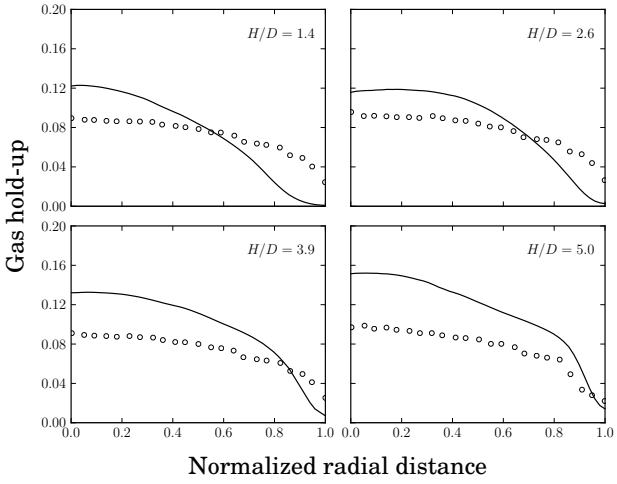

Figure 3: Comparison with experimental (open circles) and predicted time-average local hold-up profiles (continous line) at four different heights of the multi-point sparger cylindrical column of Kulkarni *et al.* (2007).

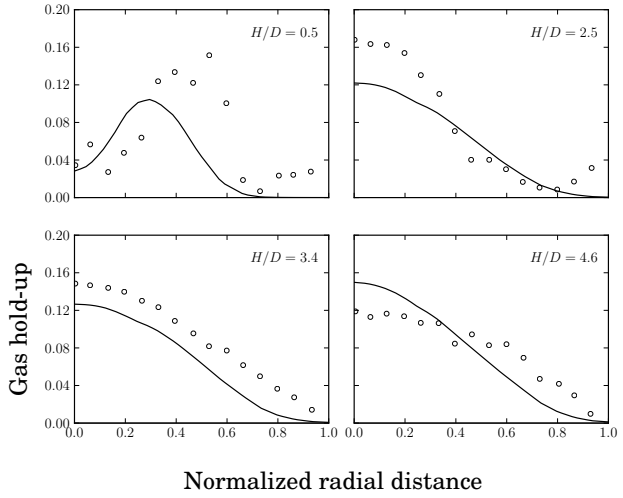

Figure 4: Comparison with experimental (open circles) and predicted time-average local hold-up profiles (continous line) at four different heights of the single-point sparger cylindrical column of Kulkarni *et al.* (2007).

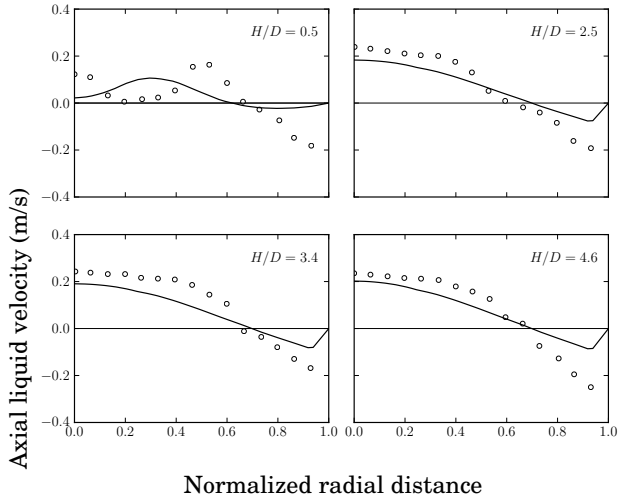

Figure 5: Comparison with experimental (open circles) and predicted time-average vertical liquid velocity profiles (continous line) at four different heights of the single-point sparger cylindrical column of Kulkarni *et al.* (2007).

Table 2: Comparison between predicted from experimental correlations and simulated global gas hold-up for the cylindrical bubble column of Kulkarni *et al.* (2007).

Hughmark (1967)	5.17 %
Akita and Yoshida (1973)	5.41 %
Hikita et al. (1980)	6.32 %
Multi-point simulation	7.47 %
Single-point simulation	3.65 %

of global quantities.
Figure 7 shows the comparison between the predicted and the experimentally measured mean Sauter diameter d_{32} at different gas superficial velocities. Since the exact position of the measurement point is not reported in the experimental work, the comparison should be intended as a qualitative feedback for the PBM. If the simulation results are compared with the

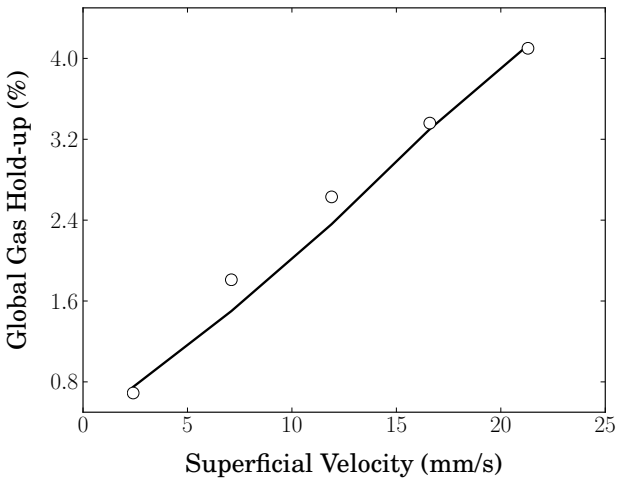

Figure 6: Comparison between experimental (open circles) and predicted (continuous line) global gas hold-up at different gas superficial velocity for the pseudo 2D bubble column of Diaz *et al.* (2008).

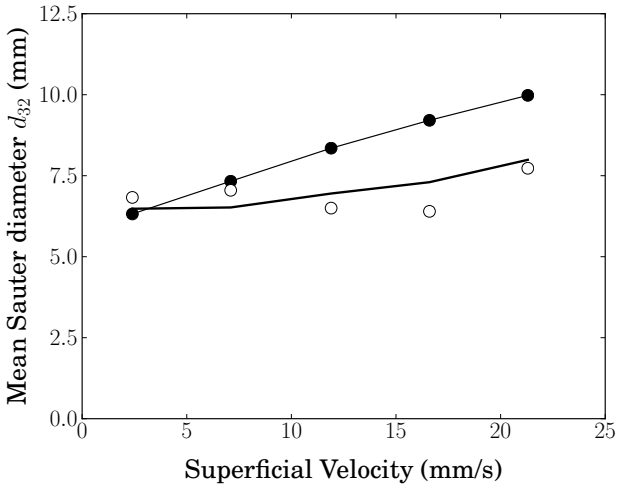

Figure 7: Comparison between experimental (open circles) and predicted (continuous line) mean sauter diameter (mm) at the center of the column and at the inlet (filled circles) calculated with the correlation of Geary and Rice (1991) at different gas superficial velocity for the pseudo 2D bubble column of Diaz *et al.* (2008).

Table 3: Experimental and simulated mean Sauter diameter d_{32} (mm) in five different point of the stirred tank of Laakkonen *et al.* (2006). Operating condition: 250 rpm 0.052vvm.

	R2	**R4**	**R6**	**R8**	**R12**
Exp.	2.74	2.93	2.17	2.01	3.18
Sim	2.20	2.69	2.43	2.17	2.89

values imposed at the inlet through the Geary and Rice correlation, an interesting trend is highlighted: the mean bubble size at the center of the column increases much less with the gas flow rate than the bubble size at the inlet, pointing out that bubble breakage prevails over coalescence with the increasing of the gas flow rate. This fact is due to the enhancement of turbulent induced collisions of bubbles at higher gas superficial velocities.

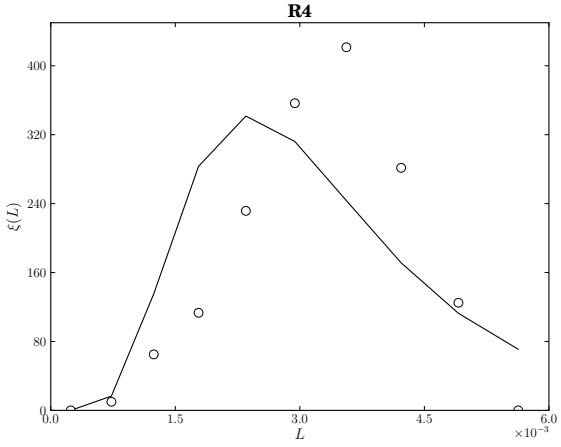

Figure 8: Comparison between the local bubble size distribution reconstructed from the moments (continuous line) with the experimental one (white circles) in one measurement point of the stirred tank of Laakkonen *et al.* (2006). Distributions are expressed in terms of the volume density function $\xi(L)$.

Other experimental data useful to validate the model are the local measurements of bubble size distribution, not present in the case of Kulkarni *et al.* (2007) and Diaz *et al.* (2008). For this reason, the aerated stirred tank, experimentally investigated by Laakkonen *et al.* (2006, 2007) was here simulated. Moreover this case represents a good test in terms of reliability of the whole CFD-PBM approach for gas-liquid systems, since this aerated stirred tank is simulated with the very same models for coalescence and breakage, as well as for the interfacial forces, of the previous bubble column test cases. Unfortunately, the measurements of global properties such as gas hold-up and power consumption are not present for this specific case, therefore this can not be considered a definitive validation of the model. However, the comparison with the available data is still useful to assess the reliability of the methodology.
A preliminary result is reported in Table 3, where predictions and experiments are compared in terms of the mean Sauter diameter in five different points of the aerated stirred tank of Laakkonen *et al.* (2006). Although only one operating condition is not sufficient to draw a general conclusion, it is important to notice that not only the predictions are very close to experiments, but more importantly the experimental trend is also correctly reproduced.

Figures 8 and 9 show the comparison between experiments and simulations of the local bubble size distribution for two different measurement points of the aerated stirred tank. It is important to remark that the reconstruction of the predicted distribution is a complex mathematical problem here solved by assuming a specific functional form (i.e. log-normal), since this information is lost by tracking the moments of NDF (for details on distribution reconstruction see Buffo and Marchisio, 2014). As it is possible to see from Figures 8 and 9, the agreement with the experimental data is acceptable, especially if we consider that the actual shape of the predicted bubble size distribution may not be log-normal as assumed.

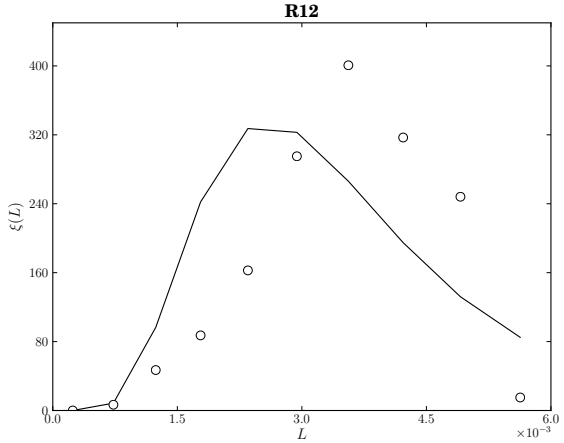

Figure 9: Comparison between the local bubble size distribution reconstructed from the moments (continuous line) with the experimental one (white circles) in one measurement point of the stirred tank of Laakkonen *et al.* (2006). Distributions are expressed in terms of the volume density function $\xi(L)$.

CONCLUSIONS

In this work, a CQMOM implementation in the open source CFD code OpenFOAM is used to simulate three different gas-liquid systems: the cylindrical bubble column of Kulkarni *et al.* (2007), the rectangular bubble column of Diaz *et al.* (2008) and the aerated stirred tank of Laakkonen *et al.* (2006). The comparison with the experimental data shows in general a good agreement for both local and global properties. However the results for the stirred tank are preliminary and further investigations are needed. The results show also that the proposed modification for the Tomiyama drag relationship, for taking into account the effect of turbulence and bubble swarms, can be successfully used to predict the behavior of such systems. This fact represents an important improvement in gas-liquid system modeling, since in this way the entire CFD-PBM approach does not contain any model parameter depending on the system geometry.

In absence of the perfect test case with a numerous measurements of global and local properties, the validation procedure will continue in the future with the simulation of other geometries and operating conditions.

REFERENCES

BAKKER, A. and VAN DEN AKKER, H.E.A. (1994). "Gas-liquid contacting with axial flow impellers". *Chemical Engineering Research and Design*, **72**, 573–582.

BUFFO, A. and MARCHISIO, D.L. (2014). "Modeling and simulation of turbulent polydisperse gas-liquid systems via the generalized population balance equation". *Reviews in Chemical Engineering*, **30**, 73–126.

BUFFO, A. *et al.* (2012). "Multidimensional population balance model for the simulation of turbulent gas-liquid systems in stirred tank reactors". *Chemical Engineering Science*, **70**, 31–44.

BUFFO, A. *et al.* (2013a). "Multivariate quadrature-based moments methods for turbulent polydisperse gas-liquid systems". *International Journal of Multiphase Flow*, **50**, 41–57.

BUFFO, A. *et al.* (2013b). "Simulation of polydisperse multiphase systems using population balances and example application to bubbly flows". *Chemical Engineering Research and Design*, **91**, 1859–1875.

CLIFT, R. *et al.* (1978). *Bubbles, Drops, and Particles*. Dover Publications.

DIAZ, M.E. *et al.* (2008). "Numerical simulation of the gas-liquid flow in a laboratory scale bubble column influence of bubble size distribution and non-drag forces". *Chemical Engineering Journal*, **139**, 363–379.

GEARY, N.W. and RICE, R.G. (1991). "Bubble size prediction for rigid and flexible spargers". *AIChE Journal*, **37**, 161–168.

HULBURT, H.M. and KATZ, S. (1964). "Some problems in particle technology: A statistical mechanical formulation". *Chemical Engineering Science*, **19**, 555–574.

KATAOKA, I. and SERIZAWA, A. (1989). "Basic equations of turbulence in gas-liquid two-phase flow". *International Journal of Multiphase Flow*, **15**, 843–855.

KAZAKIS, N.A. *et al.* (2008). "Experimental study of bubble formation at metal porous spargers: Effect of liquid properties and sparger characteristics on the initial bubble size distribution". *Chemical Engineering Journal*, **137**, 265–281.

KULKARNI, A.A. *et al.* (2007). "On the development of flow pattern in a bubble column reactor: Experiments and CFD". *Chemical Engineering Science*, **62**, 1049–1072.

LAAKKONEN, M. *et al.* (2006). "Validation of bubble breakage, coalescence and mass transfer models for gas-liquid dispersion in agitated vessel". *Chemical Engineering Science*, **61**, 218–228.

LAAKKONEN, M. *et al.* (2007). "Modelling local bubble size distributions in agitated vessels". *Chemical Engineering Science*, **62**, 721–740.

LAMONT, J.C. and SCOTT, D.S. (1970). "An eddy cell model of mass transfer into the surface of a turbulent liquid". *AIChE Journal*, **16**, 513–519.

MARCHISIO, D.L. and FOX, R.O. (2005). "Solution of population balance equations using the direct quadrature method of moments". *Journal of Aerosol Science*, **36**, 43–73.

MARCHISIO, D.L. and FOX, R.O. (2013). *Computational Models for Polydisperse Particulate and Multiphase Systems*. Cambridge Series in Chemical Engineering. Cambridge University Press, Cambridge, UK.

MARCHISIO, D.L. *et al.* (2003). "Quadrature method of moments for aggregation-breakage processes". *Journal of Colloid and Interface Science*, **258**, 322–334.

MENDELSON, H.D. (1967). "The prediction of bubble terminal velocities from the wave theory". *AIChE Journal*, **13**, 250–253.

MONTANTE, G. *et al.* (2007). "Experimental analysis and computational modelling of gas - liquid stirred vessels". *Chemical Engineering Research and Design*, **85**, 647–653.

PETITTI, M. *et al.* (2009). "Effect of drag modeling on the

prediction of critical regime transitions in agitated gas-liquid reactors with bubble size distribution modeling". *Multiphase Science and Technology*, **21**, 95–106.

PETITTI, M. *et al.* (2010). "Bubble size distribution modeling in stirred gas-liquid reactors with QMOM augmented by a new correction algorithm". *AIChE Journal*, **56**, 36–53.

SCARGIALI, F. *et al.* (2007). "Modelling and simulation of gas - liquid hydrodynamics in mechanically stirred tanks". *Chemical Engineering Research and Design*, **85**, 637–646.

TOMIYAMA, A. *et al.* (2002). "Terminal velocity of single bubbles in surface tension force dominant regime". *International Journal of Multiphase Flow*, **28**, 1497–1519.

VAN WACHEM, B.G.M. and ALMSTEDT, A.E. (2003). "Methods for multiphase computational fluid dynamics". *Chemical Engineering Journal*, **96**, 81–98.

WEN, C.Y. and YU, Y.H. (1966). "Mechanics of fluidization". *Chemical Engineering Progress Symposium Series*, **62**, 100–111.

CFD simulations of a Wankel pump with moving and static grids

Jason LEONG Yu Chuan[1], BA Te[1], Stephen WAN Yee Ming[1], ZHAO Yuqiao[2], KANG Chang Wei[1], LOH Wai Lam[2], Arthur LIM Teck Bin[1*]

[1] IHPC Fluid Dynamics, 138632 SINGAPORE

[2]NUS Department of Mechanical Engineering, 117576 SINGAPORE

* E-mail: limtba@ihpc.a-star.edu.sg

ABSTRACT

This paper presents the numerical analysis of a Wankel pump using 3 different CFD techniques. The Wankel pump is a positive displacement pump which consists of an eccentrically rotating rotor in a housing that can be described by an epitrochoid and has not been well investigated numerically. Considering the use of this design as an internal combustion engine, the Wankel pump, as with most positive displacement pumps, is expected to perform well for multiphase flow condition, even at high gas volume fractions. This would be a marked advantage over centrifugal pumps which tend to gas lock when exposed to highly gassy flows.

Conventional CFD technique using Moving Reference Frame (MRF) approach for turbomachinery simulations cannot be used to simulate typical Wankel pump design due to the tight clearances between the rotor and casing coupled with the unconventional rotor trajectory. To explore other CFD techniques, three different approaches were attempted here to compare their use for simulation analysis on Wankel pump performance. The dynamic meshing capabilities in FLUENT were used to morph the mesh according to the topological changes with respect to the rotation of the rotor. The immersed solid method was used in CFX. This technique used two overlapping grids to identify the location of the solid rotor. Finally, in FLOW3D, the Eulerian gridding technique was used where the geometry building and grid generation are independent operations.

In this paper the pump performance, measured by torque and flow rate, was compared for the three CFD approaches while varying the clearance between the pump housing and rotor, rotor speed and pressure differential between the pump inlets and outlets. It was found that all three approaches were able to capture the main features of the flow and should be considered as viable methods to study the Wankel pump. This study will serve as the foundation for subsequent multiphase flow performance analysis in the Wankel pump in future work.

Keywords: Positive displacement pump, Computational fluid dynamics, Downhole equipment, Hydraulic performance.

NOMENCLATURE

A complete list of symbols used, with dimensions, is required.

Greek Symbols

μ Dynamic viscosity, [kg/m.s].
ρ Mass density, [kg/m^3].
ω Shaft angular speed, [s^{-1}].

Latin Symbols

A Area, [m^2].
p Fluid pressure, [kg/m.s^2].
$\boldsymbol{u}$ Fluid velocity, [m/s].
e Eccentricity, [m].
F VOF function, [-].
R Rotor centre-to-tip distance, [m].
S Source term, [kg/m^2.s^2].
t time, [s].
V Volume fraction, [-].

Sub/superscripts

F Fluid.
m Momentum
x X-direction.
y Y-direction.
z Z-direction.

INTRODUCTION

Pumps are devices with important domestic and industrial applications. Primarily used to move fluids, pumps can be classified into two major categories by mode of action: velocity and positive displacement. Pumps are typically operated by reciprocating or rotary mechanism, and the driving mechanism in most cases, determines the performance envelope and installation setup.

In the oil and gas industry, pumps are used mainly for production and transportation. In the past decade, multiphase production has emerged as a viable production method of crude oil and gas. Multiphase pumps are the key to long-distance transportation and have been proven to be a cost-effective, easy to operate and a reliable alternative in the development of marginal fields or remote wells.

Twin screw, progressive cavity, piston and diaphragm pumps are popular positive displacement pumps for multiphase production. Alternatively, helico-axial and multi-stage centrifugal (electrical submersible type) pumps are the common velocity type pumps. Positive displacement pumps are more tolerant of high gas content and can even operate in pure gas conditions as encountered in slug flow. Therefore, the common multiphase problems for pumps, such as gas lock and oil-water emulsion can be tolerated.

In order to explore possible solutions for slug flow, some devices and mechanisms, which are designed to handle pure gas, have been studied. Reciprocating piston pumps seems to be an option. However, reciprocating motion often causes vibration and requires more energy to operate, which makes it unsuitable for high flow rate applications. Piston pumps are also generally not compact hence making this design unsuited for offshore applications with spatial constraints. Conventional centrifugal pumps, conversely, have very limited tolerance to the presence of gas in the produced fluid. Rotary mechanism with positive displacement action seems to be a potential solution which is both compact and tolerant of high gas volume fractions.

A possible candidate is the Wankel engine design. This spark ignition engine design would be able to handle high gas volume fractions of up to 100% and with a positive displacement mechanism of action. This preliminary study will investigate the efficacy of a Wankel pump in single phase operation.

The numerical study is complicated by the unconventional trajectory and design of the Wankel geometry as well as the tight clearances between the rotor and pump housing. As the rotor does not rotate about a fixed axis, it is not possible to use sliding mesh techniques. The highly transient nature of the flow would mean that the multiple rotating reference frame technique is not suitable. Because of this, there have been limited numerical studies (Zhao et al., 2011) on the Wankel pump.

The methods explored can be broadly classified into two different categories: methods utilising static grids and moving grids available in the three commercial codes, FLUENT, CFX and FLOW3D. The codes are used to predict the pump performance under different operating conditions. This will include varying the pressure difference across the pump inlets and outlets and varying the clearance between the rotor and pump housing. The findings from this study will serve as a guide for computational fluid dynamicists planning to use commercial CFD codes to analyse Wankel type compressors or pumps.

GEOMETRY AND BOUNDARY CONDITIONS

In light of the preliminary nature of this work and limitations on computational resources, this comparative study will only be carried out in a 2 dimensional geometric model of the Wankel pump.

The operational elements of the rotary pump, the rotor and pump housing, are shown in Figure 1 together with a pair of inlets and outlets. The pump housing is defined by the mathematical shape known as a trochoid or epitrochoid. Conversely, the rotor resembles an equilateral triangle with circular arc flanks, which is the enclosed area formed by the innermost envelopes of the troichoid curve.

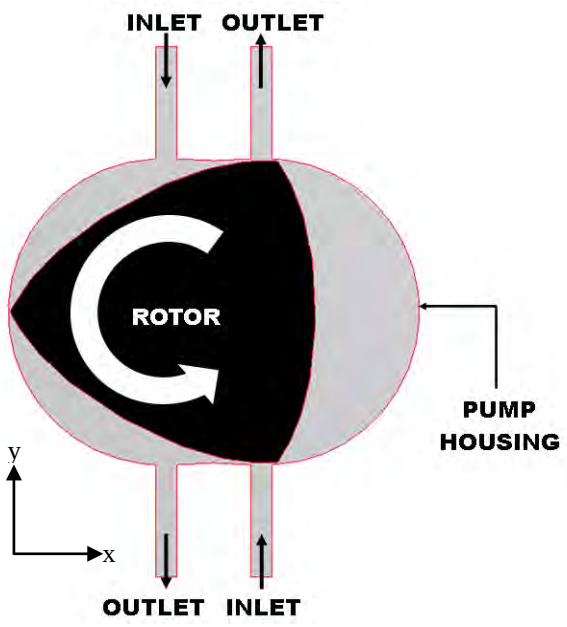

Figure 1: Schematic diagram of Wankel pump.

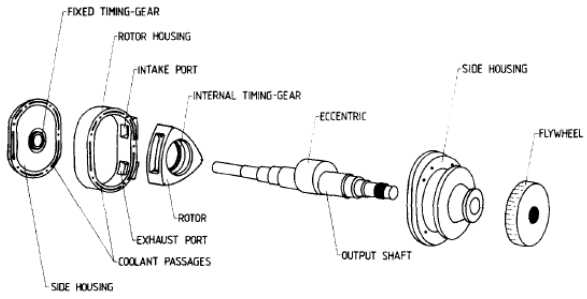

Figure 2: Exploded view of Wankel engine. Note eccentric element on output shaft (Badr et al., 1991).

The shaft runs through the rotor and coincides with the axis of the pump housing. However, the rotor is mounted and rotates on an eccentric element on the shaft which allows the rotor to rotate with the eccentric element. A similar assembly is present in the Wankel engine and illustrated in Figure 2.

The rotor tip coordinates can be defined by the following set of equations (Weston, 1992):

$$x = e.\cos(\omega t) + R.\cos\left(\frac{\omega t}{3}\right) \quad (1)$$

$$y = e.\sin(\omega t) + R.\sin\left(\frac{\omega t}{3}\right) \quad (2)$$

It should be noted that the trajectory of the rotor tips also define the pump housing shape. The eccentricity in the preceding equations is defined as the distance between the housing axis and the rotor centroid defined by the edges of the rotor. In this study, e = 0.015 m and R = 0.10622 m. This produces a Wankel pump with a major axis length of 0.24 m and a minor axis length of 0.18 m. In all three CFD codes, the rotor is defined as a rigid body with a prescribed motion defined with respect to the centre of mass of the rotor.

The working fluid used in the Wankel pump is oil with a density of 889 kg/m^3 and a viscosity of 0.2 Pa.s. A shaft angular speed of 90, 180 and 360 rpm will be considered in this study. In addition, a pressure difference of 0 and 90 kPa will be applied across the outlet and inlet. Finally, three clearance sizes between the rotor and pump housing will be considered. These are 1.44, 0.96 and 0.48 mm. However, it should be noted that FLOW3D and CFX allow for a completely flush configuration between the rotor and housing.

GOVERNING EQUATIONS

The fluid flow is governed by the unsteady incompressible Navier-Stokes equations for a Newtonian fluid of continuity and momentum as listed below:

Continuity equation

$$\nabla.\mathbf{u} = 0 \quad (3)$$

Momentum equation

$$\rho\left(\frac{\partial \mathbf{u}}{\partial t} + \mathbf{u}.\nabla\mathbf{u}\right) = -\nabla p + \mu\nabla^2\mathbf{u} \quad (4)$$

NUMERICAL PROCEDURES

As discussed earlier, three commercial CFD codes are used to study the flow within the Wankel pump during operation. These will be discussed in greater detail in the following subsections.

FLUENT

The mesh requirements in FLUENT are more stringent because of the dynamic nature of the mesh in the subsequent simulations. Great care was taken in producing a fine triangular mesh especially in the proximity of the rotor walls and pump housing walls as shown in Figure 3. In the FLUENT model, only the fluid volume mesh is needed as the dynamic mesh functionality in FLUENT is able to deform and remesh the initial mesh in accordance to the rotor movements. In performing a grid sensitivity analysis, it was found that the grid density in the clearance region between the rotor and pump housing was critical to accurately capture the torque and pressure. It was found that 12-15 cells in the clearance region were sufficient for this purpose. A mesh interval size of 1.0 × 10^{-4} m was used.

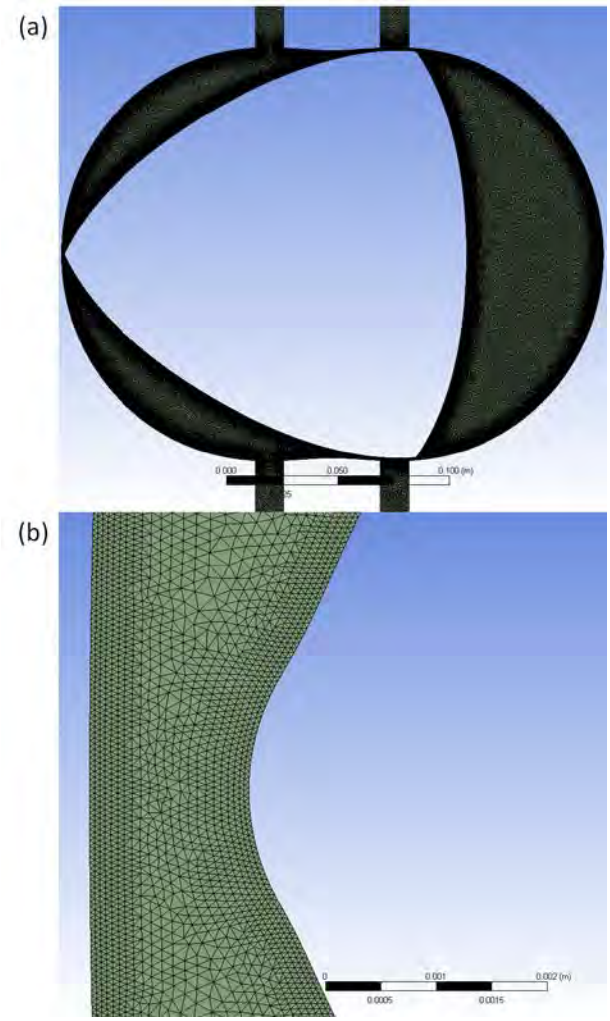

Figure 3: (a) Initial mesh for FLUENT model. Only the fluid volume is meshed in FLUENT. (b) Illustration of the fine mesh at the left most rotor tip. The distance between the rotor tip and the pump housing in (b) is 1.44 mm.

FLUENT is a CFD code based on the finite volume method. In the FLUENT model, dynamic meshing is utilised to account for the topological changes as the rotor rotates within the pump housing. A user defined function (UDF) is used to define the movement of the rotor within the pump cavity. The UDF defines the movement of the Wankel pump rotor as a rigid body with x, y and rotational components of velocity.

Two main dynamic mesh functionalities are enabled when performing the simulation. The first is diffusion based mesh smoothing which allows the deformation of the mesh when there are changes in the location of the boundary surfaces. Next, dynamic remeshing was enabled to ensure that the mesh quality, as measured by the skewness, could be maintained as the solution progresses. It also allowed the mesh growth rate from

the wall boundaries to be maintained even after the mesh is deformed.

The non-iterative time advancement (NITA) solver available in FLUENT was used in the simulations to shorten simulation time. The NITA solver solves only one outer iteration per time-step. Although this method introduces several sub-iterations due to the segregation of the constitutive equations, there is still a net decrease in time over the iterative methods while maintaining overall time accuracy. In addition, the PISO pressure-velocity coupling method was used. The PRESTO! pressure interpolation scheme was used with the second order upwind scheme for momentum discretisation. Temporal discretisation was performed using the second order scheme. It should be noted that this scheme has only recently been implemented in FLUENT 15.0 to be used with dynamic meshing.

A time step of 1/100000th of the period of one shaft revolution was used for all simulations. This small time step was needed because of the fine mesh at the clearance regions.

There were some limitations in the FLUENT model. It should be noted that it is not possible to specify a case where the rotor was flush (zero clearance) with the pump housing. Next, the dynamic meshing requires a fine mesh in the clearance areas which slows the simulation significantly. The remeshing of the fluid volume in these areas leads to a fluctuating number of computational cells. To illustrate, the 1.44 mm case produces a cell count of between 700000 to 750000.

CFX

The immersed solid technique, implemented within the finite volume code of CFX, treats the presence of a solid object by applying a source term, S_m, to the momentum equation, in the fluid volume geometrically occupied by the solid object in the fluid domain. Therefore, an additional term appears in the momentum equation:

$$\rho\left(\frac{\partial \mathbf{u}}{\partial t}+\mathbf{u}.\nabla\mathbf{u}\right)=-\nabla p+\mu\nabla^2\mathbf{u}+\boldsymbol{S_m} \qquad (5)$$

To track the movement of the immersed solid, the solver updates the mesh positions of the immersed solid at the beginning of each time step, and applies the immersed solid sources, S_m, to the fluid nodes that lie within the immersed solid in attempting to match the fluid velocity with the immersed solid velocity.

For all the simulations both the rotor (immersed solid) and the pump cavity (enveloping fluid domain) were meshed with a cell size of 0.003 m. In addition the cavity wall boundaries were inflated with 5 prismatic layers; the thickness of each layer growing at rate of 1.3, the first layer being 0.0005 m thick. The meshes used for the pump cavity and rotor are illustrated in Figure 4 and Figure 5 respectively. The meshing parameters discussed resulted in a cell count of 6514 for the rotor and 32874 for the pump cavity.

A first order upwind scheme was used to discretise the convective terms. Temporal discretisation was performed with the first order backward Euler scheme performing 10 outward iterations per time step with a residual target of 10^{-4} RMS. The coupled solver in CFX was used to couple the pressure and velocity terms.

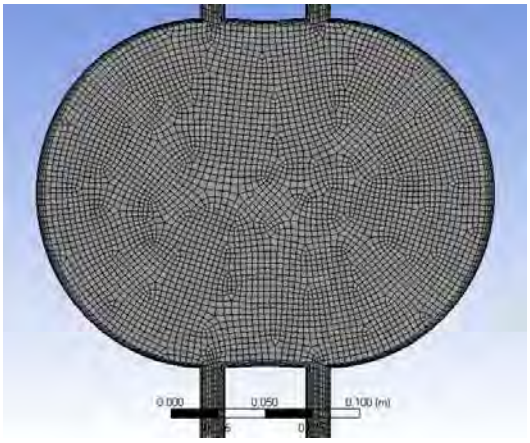

Figure 4: Mesh of Wankel pump housing for simulations performed in CFX. In this simulation, the pump housing is the enveloping fluid domain.

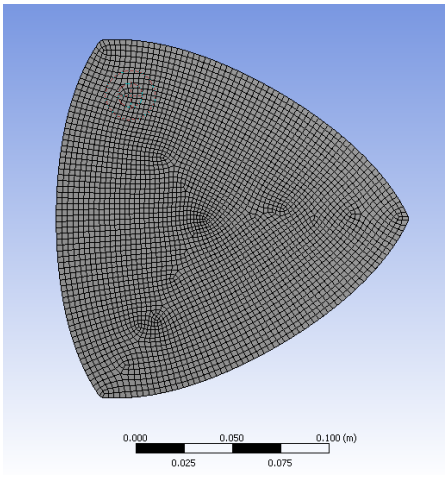

Figure 5: Mesh of Wankel pump rotor for simulations performed in CFX. In this simulation, the rotor is the 'immersed solid'.

For all simulations, the time step was chosen to be 1/500th of the period of one rotor shaft revolution. For example, given a shaft speed of 90 RPM, the time step used was 0.001333 s.

FLOW3D

The Eulerian gridding technique is employed in FLOW3D. In this method, fixed rectangular mesh grids are created in two-dimensional space with a cell size of 0.001 m in both x and y directions resulting in a mesh size of 343200 cells. In order to create separate boundary conditions for the inlets and outlets, two mesh

blocks (indicated as BLK1 and BLK2), as shown in the Figure 6, with the same sizes are created with an inter-block boundary in-between. This multi-block meshing strategy also allows for the control of mesh grid density and setup of multiple boundary conditions. The rotor motion is modelled using the general moving object (GMO) model in FLOW3D. At each time step, the area and volume fractions of the solid boundary cells are updated in the fixed grids in accordance with the moving object's prescribed motion. It has advantages over the deforming and moving mesh methods because the motion and shape of the objects are not restricted by the complexity of the meshing procedure.

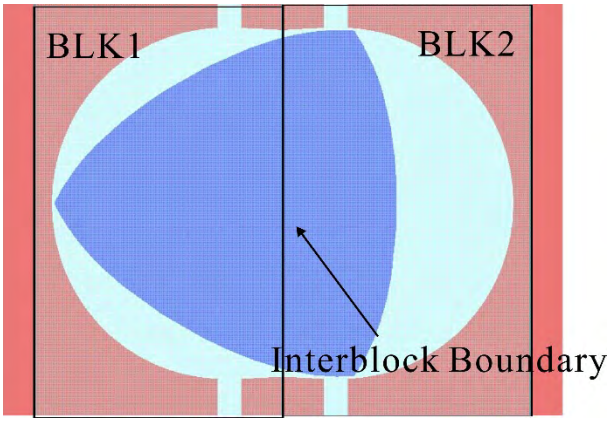

Figure 6: Mesh of Wankel pump by the Eulerian gridding technique in FLOW3D.

FLOW3D essentially solves the fluid interface using the Volume-of-Fluid (VOF) method and the fluid-solid interface using the FAVOR (Fractional Area/Volume Obstacle Representation Method) technique. The continuity equation is modified to include the fraction parameters:

$$V_F \frac{\partial \rho}{\partial t} + \frac{\partial}{\partial x}(\rho u_x A_x) + \frac{\partial}{\partial y}(\rho u_y A_y) = 0 \qquad (6)$$

where V_F is the volume fraction open to the flow and A_x and A_y are the area fraction open to the flow in the respective Cartesian directions. The VOF function F satisfies the equation:

$$\frac{\partial F}{\partial t} + \frac{1}{V_F}\left[\frac{\partial}{\partial x}(F A_x u_x) + \frac{\partial}{\partial y}(F A_y u_y)\right] = 0 \qquad (7)$$

First order accurate schemes were utilised for both spatial and temporal discretisation in a finite difference framework. In addition, the explicit time integration scheme was used in this work.

The time step is dynamically varied during the solution and has a minimum value of 1×10^{-5} s. This small value is required because of the minute spatial scales involved in the vicinity of the rotor tip.

RESULTS AND DISCUSSION

A comparison of the average net flow rate with respect to shaft speed for varying clearance sizes is presented in Figure 7. It can be seen that the flow rate is found to respond linearly to shaft speed. This behaviour is observed for cases simulated with any of the CFD codes used.

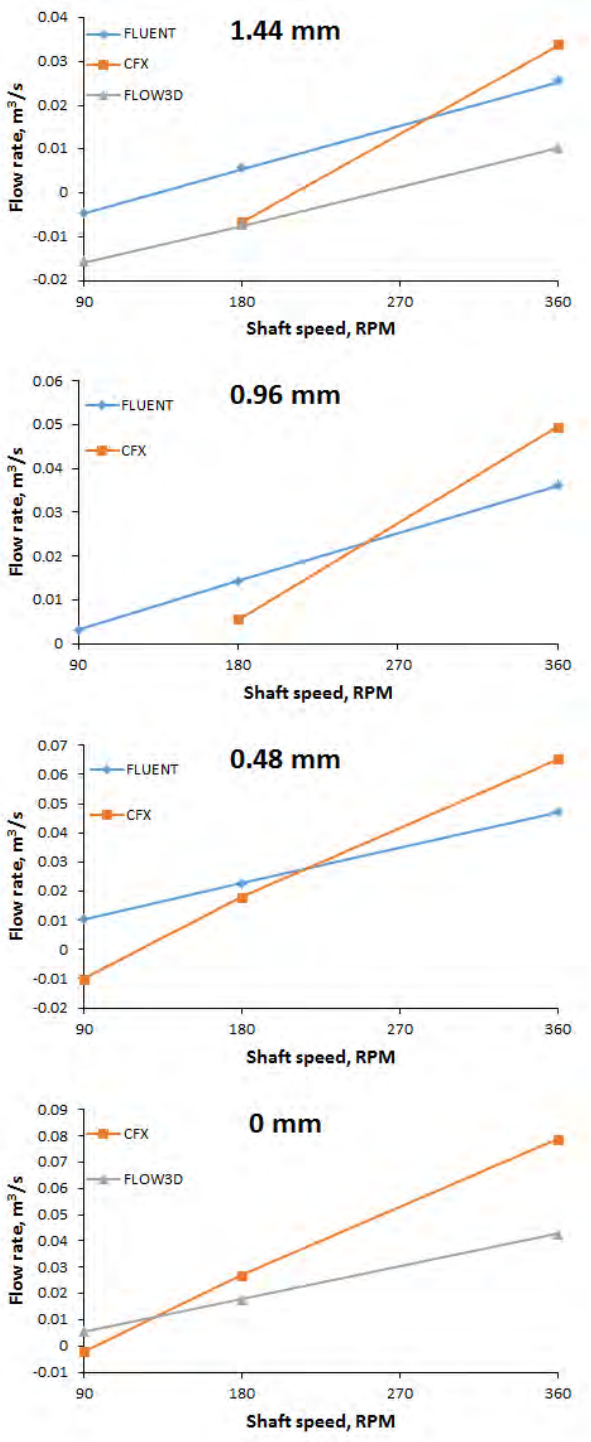

Figure 7: Average flow rate with respect to shaft speed for different clearance sizes in different CFD codes. Simulations performed with a pressure difference of 90 kPa between the inlet and outlet boundaries.

There however seems to be some differences in the magnitudes of the predicted flow rates from the 3 different codes. The CFX and FLOW3D models seem to predict an earlier onset of backflow compared to the FLUENT model. In the CFX simulations, this has led to unstable flow for the lowest shaft speed of 90 RPM when clearance sizes of 1.44 mm and 0.96 mm was used. This may be an indication of the limitations of the static grid methods as a finer grid could not be

employed at the rotor surfaces unless a uniformly finer mesh is used in the pump housing fluid volume. FLUENT consistently predicts higher flow rates for all cases.

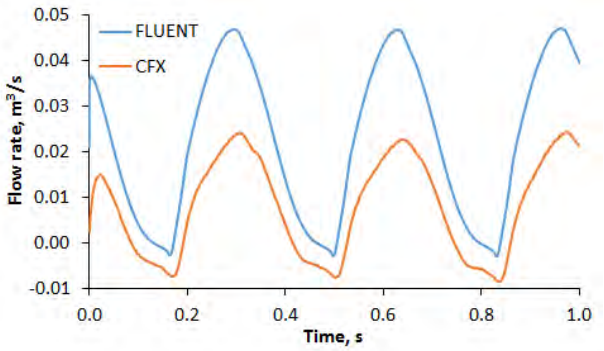

Figure 8: Instantaneous outlet flow rate comparison for CFX and FLUENT with respect to time. Simulations performed for a shaft speed of 180 RPM, a clearance size of 0.48 mm and a pressure difference of 90 kPa at the inlet and outlet boundaries.

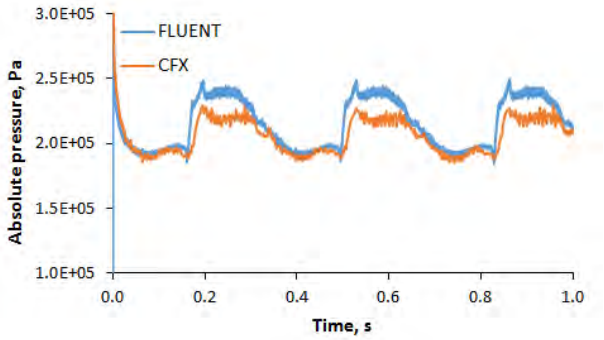

Figure 9: Instantaneous outlet pressure comparison for simulations performed with CFX and FLUENT. Simulations performed for a shaft speed of 180 RPM, a clearance size of 0.48 mm and a pressure difference of 90 kPa at the inlet and outlet boundaries.

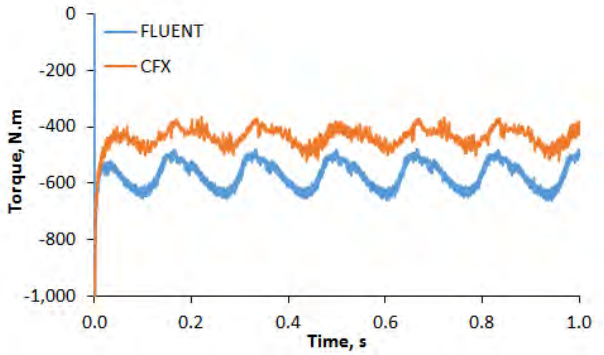

Figure 10: Torque measured about shaft performed with CFX and FLUENT. Simulations performed for a shaft speed of 180 RPM, a clearance size of 0.48 mm and a pressure difference of 90 kPa at the inlet and outlet boundaries.

A selected instantaneous flow rate comparison is illustrated in Figure 8. The flow rate illustrated in Figure 8 was recorded at every time step and is not the time averaged flow rate in Figure 7 and Figure 11. In this case, the transient flow rate predicted by FLUENT was consistently higher compared to CFX. This is congruent with the average flow rate results. This trend was also observed in the outlet pressure and shaft torque illustrated in Figure 9 and Figure 10 respectively.

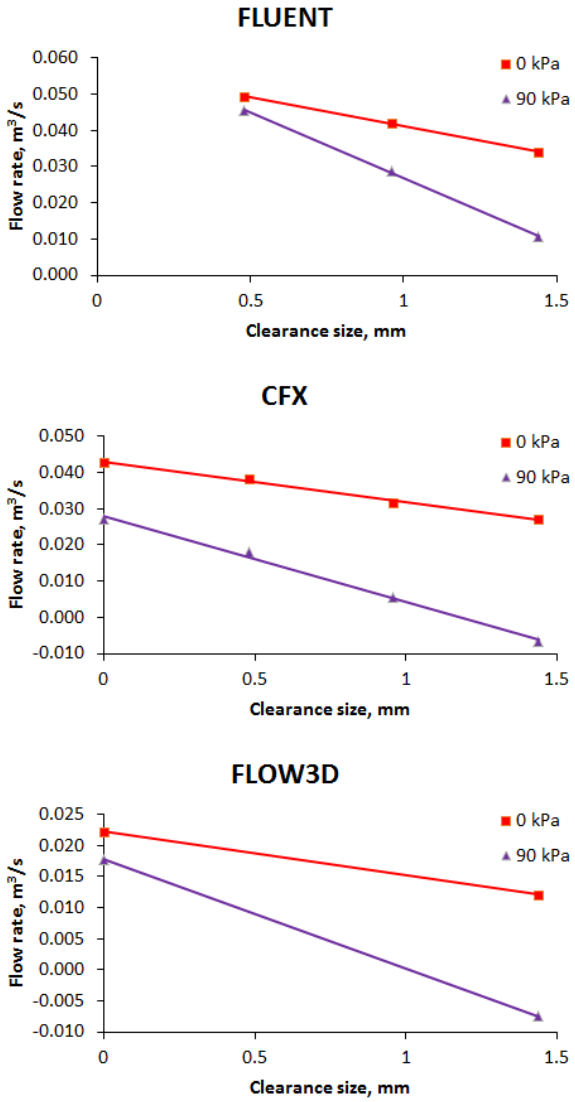

Figure 11: Flow rate with respect to clearance size for varying pressure differences of 0 and 90 kPa. Results generated by (a) FLUENT, (b) CFX and (c) FLOW3D. Simulations performed for a shaft speed of 180 RPM.

The flow rate was observed to vary linearly with the clearance size for the models simulated with FLUENT and CFX as illustrated in Figure 11 (only two data points were available for the FLOW3D model). In light of this observation, the simulations in FLOW3D were restricted to only the maximum (1.44 mm) and minimum (0 mm) clearance sizes. Simulating the intermediate clearance sizes of 0.48 and 0.96 mm was not feasible as FLOW3D only supports Cartesian grids with no inflation layers at the boundaries. This trend was maintained even when the pressure difference was varied from 90 kPa to 0 kPa. Therefore, to accurately simulate the intermediate clearance sizes would be very expensive. As mentioned earlier, it is not possible to simulate a rotor with no clearance between the rotor and pump housing in the FLUENT model. Although both the 0 and 90 kPa cases exhibit a linear relationship between flow rate and clearance size, it is not likely that this trend will maintain when the rotor is flush with the pump

housing surface, i.e. no gap. By observation, these lines will intersect between 0 and 0.48 mm which would result in the counter-intuitive observation of a higher flow rate in the 90 kPa case. Therefore, it is possible that there is some asymptotic behaviour as the clearance size approaches 0 mm. This was not observed in the CFX model perhaps due to the coarser mesh on the rotor surface.

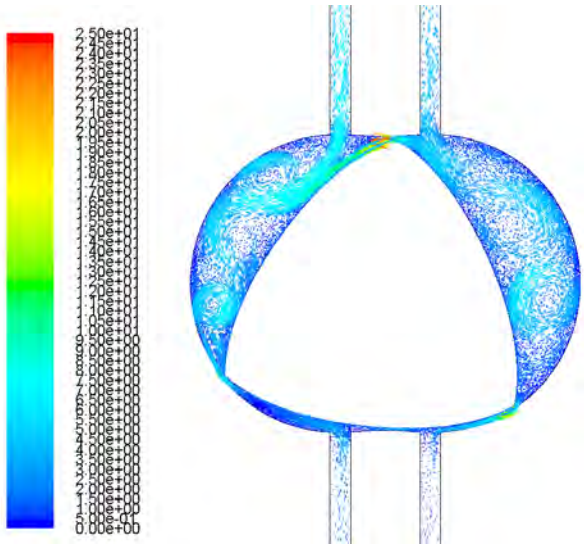

Figure 12: Velocity vectors within the Wankel pump fluid volume in FLUENT model. Simulation performed for a shaft speed of 360 RPM, a clearance size of 1.44 mm and a pressure difference of 90 kPa at the inlet and outlet boundaries. Observation performed at t = 0.2 s.

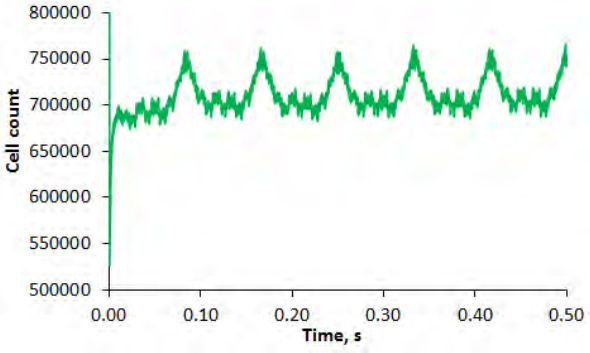

Figure 13: Cell count with respect to simulation time for FLUENT case simulated at a shaft speed of 360 RPM, a clearance size of 1.44 mm and a pressure difference of 90 kPa.

The velocity vectors in Figure 12 illustrates that the highest fluid velocities are encountered in the clearance area. This is consistent with the rotor action which constricts and expands the volume of the fluid chambers separated by the rotor volume. This action motivates the fluid to squeeze through the clearance gap and is the reason for the high velocities observed in the clearance region. Therefore, the fluid simulations would benefit from the fine mesh assigned to the rotor walls and pump housing walls. In addition, there were large vortices observed within the pump housing chamber as the rotor draws fluid into the pump housing.

It was important to ensure a stable cell count evolution with simulation time in the dynamic meshing used in FLUENT. As illustrated in Figure 13, it was found that although there were some changes in the cell count, it was ultimately periodic in nature and dependent on the mesh requirements of a given rotor position. For a clearance size of 1.44 mm, it was found that the mesh cell count fluctuated between 700000 and 750000 cells.

Table 1: Summary of computational requirements for different CFD codes in this study. Note that FLOW3D utilises a variable time step method and FLUENT uses a dynamic mesh method. Therefore, the number of timesteps in FLOW3D and the mesh size in FLUENT are approximate values.

	FLUENT	CFX	FLOW3D
# CPU cores	8	1	8
Timesteps/rev.	100000	500	52000
Time/rev. (hrs.)	182	1	16
Mesh size	700-750k	40k	343k

Table 1 summarises the computational requirements for each of the CFD codes used in this study. Clearly, there is a huge disparity between the dynamic meshing method in FLUENT and the static grid methods in CFX and FLOW3D in terms of temporal requirements. This large difference is attributed to the high computational effort expended by the mesh solver between time steps which is compounded by the extremely fine mesh in the clearance region. It should be noted that although the dynamic mesh method should be able to accurately resolve the flow field in the vicinity of the rotor and pump housing walls due to the much finer mesh, it cannot simulate a case when there is no clearance between the rotor and pump housing walls.

CONCLUSION

The three codes utilised in this study were able to capture the main features of the flow field with varying clearance size, rotational speed and pressure difference. Therefore, all three methods employed: dynamic meshing, immersed solid method and Eulerian gridding technique, are all viable tools to study the flow characteristics of the Wankel pump. However, the limitations of each method discussed earlier should be carefully considered. Although the dynamic meshing technique in FLUENT was able to morph the fine mesh in the vicinity of the pump housing and rotor walls, it is generally slower because of the additional computational requirements by the mesh solver. In addition, the dynamic meshing technique in FLUENT cannot be used when there is no clearance between the rotor and the pump housing. The static grid methods in CFX and FLOW3D would need a uniformly fine mesh as it is not possible, by definition, to refine the mesh with respect to the wall boundary locations.

The accuracy of the codes could not be commented on as there were no experimental results to benchmark against. However, as there are some discrepancies in the results from the three codes, some form of experimental validation will be performed in the near future. Next, the simulations were only conducted in two dimensions which prohibits any observations of any three dimensional behaviour. Any wall effects which would manifest in the extruded two dimensional geometry of

the Wankel pump presented in this work would also benefit from the three dimensional simulation. It is expected that the additional computational effort in the dynamic mesh method would result in much slower computational times in the three dimensional simulations as compared to the static grid methods. Finally, as there is an intention to explore the use of the Wankel pump as a multiphase artificial lift device, the work presented in this study will be extended to multiphase flow.

REFERENCES

BADR, O., NAIK, S., O'CALLAGHAN, P. W. and PROBERT, S. D., (1991), "Rotary Wankel engines as expansion devices in steam Rankine-cycle engines", *Appl. Energ.*, **39**, 59-76.

CFX, (2013), "ANSYS CFX Reference Guide", ANSYS, Inc., Southpointe, 275 Technology Drive, Canonsburg, PA 15317, October 2012.

FLUENT, (2013), "ANSYS FLUENT User's Guide", ANSYS, Inc., Southpointe, 275 Technology Drive, Canonsburg, PA 15317, October 2012.

FLOW3D, (2012), "FLOW-3D User Manual",Harkle Road Suite A 683, Santa Fe, NM87505, 2012.

HIRT, C. W. and SICILIAN, J. M., (1985), "A porosity technique for the definition of obstacles in rectangular cell meshes", *Proc. Fourth Int. Conf. Ship Hydrodynamics*, National Academy of Science, Washington D. C., September.

WESTON, K. C., (1992), "Energy Conversion", West Publishing Company.

ZHAO Y., LOH W. L. and LEE T. S., (2011), "2D CFD simulation of a pump with Wankel engine geometry", *The 11th Asian Int. Conf. on Fluid Machinery*, IIT Madras, Chennai, India, November 21-23.

10th International Conference on CFD in Oil & Gas, Metallurgical and Process Industries
SINTEF, Trondheim, Norway
17-19 June 2014 *CFD 2014*

CFD STUDY OF THE INFLUENCE OF PRE-ROTATION OF MULTIPHASE FLOW ON PUMP PERFORMANCE

Mikhail P. STRONGIN
Xylem Inc. AWS, Morton Grove, IL 60053, USA
mikhail.strongin@xyleminc.com

ABSTRACT

This work studied the influence of pre-rotation flow on pump performance for multiphase flows.
Two stages of vertical mixed flow pump were modeled. The mixer multiphase model was chosen for the mixture model. The SST k-ω model for turbulence was selected. The gravity was taken into account. A multi-reference frame approach was used for rotation domains. The volume fraction of solid particles in the mixture ranged from 0.5% to 10%. The swirl number on the pump inlet was 1.
The pump heads displayed a difference of approximately 1%. The efficiency of the pump with high solid phase load was much lower than the efficiency of the pump with pure water with the same flow rate. An obvious difference in the volume fraction distribution can be seen on the stage 1 and stage 2 outlets for the all mixture flow rates.
The difference in efficiency was more than 10 percentage points in the cases where volume fraction of solid particles in the mixture is 10%.

Keywords: Pump, pre-rotation, multiphase, separation.

INTRODUCTION

Pre-rotation is a common phenomenon in industrial applications of pumps. It may have a significant influence on pump performance [1]. Even though the number of CFD works was done for liquid only with pre-rotation, such as [2], a CFD study of behavior of liquid-solid mixture with pre-rotation in the pump is practically non-existent.
An extensive literature exists regarding the use of CFD to predict water flow through a centrifugal pump. There are a significant number of publications about gas – liquid mixing in the pump. They are connected with cavitation [3] or aeration [4]. However, the CFD simulations for the mixing processes of two fluids or liquid-solid in a pump are not frequently used.
The mixing process of two fluids was investigated in [5]. The results showed a significant change in the mixing uniformity coefficient γ, which depended on the injected secondary fluid location on the inlet.
The evaluation of the influence of particles density, particles diameter, and particles injector location on the pump inlet on the particles distribution at the outlet was done in [6]. In this work the influence of the solid phase on the pump performance was assumed negligible.
It is important to estimate the influence of the amount of solid phase in the solid-liquid mixture on the pump performance parameters for relatively high solid particles load (up to 10% of volume fraction of solid particles in the mixture). In addition, the estimation of different fluid flow rates on the pump performance parameters should also be done.
The importance of CFD for understanding of pump multiphase performance is emphasized by the high level of complexity of the experimental study of this phenomenon in rotomachinery [7].
The goal of the current work was to reveal the mechanisms of impact of solid phase with mixture pre-rotation on the pump performance. Therefore, the local behavior of mixture was also in the focus of the study. The local solid phase distribution inside a pump is important for understanding not only of pump performance, but also of the erosion of pump parts.
Hence, in this work, the behavior of liquid-solid mixing with pre-rotation in the pump was studied.

NOMENCLATURE

D_s Solid particles diameter, [m]
eff Efficiency for mixture case, [dimensionless]
eff_w Efficiency for pure water cases, [dimensionless]
H Total dynamic head for mixture, [m]
H_w Total dynamic head for pure water, [m]
k Kinetic energy of turbulence, [m^2/s^2]
n Impeller rotation speed, [rpm]
n Specific speed – $n*(Q^v_w)^{1/2}/H^{3/4}$
Q Mixture mass flow rate, (kg/s)

Q_s Solid phase mass flow rate, [kg/s]
Q_w Liquid phase mass flow rate, [kg/s]
Q^v_w Liquid phase volume flow rate, [m^3/h]
Y^+ First node dimensionless wall distance
ρ Liquid density, [kg/m^3]
ρ_s Solid particles density, [kg/m^3]
ω Specific dissipation rate, [1/s]

Sub/superscripts
s Solid phase
v Volume
w Liquid phase

MODEL

Two stages of vertical mixed flow pump were modeled. The pump model consists the impeller and discharge (bowl) parts for each stage, which were studied as a single entity. This setup makes it possible to analyze the effects of non-uniformity of velocity and particles distribution on the pump domain.
Due to absence of symmetry on the pump, full geometry is considered (see Figure 1). In the given geometry diameters of inlet and outlet were the same and they were equal to 0.098m.

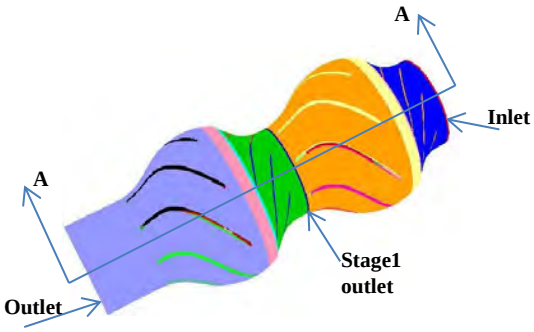

Figure 1. Pump Geometry

The FLUENT 14.5.7 commercial code was used for simulations. The mixer multiphase model was chosen for the mixture model. Here the different phases are treated mathematically as interpenetrating continua.
Since the volume of a phase cannot be occupied by the other phases, the volume equations for the secondary phases, and algebraic expressions for the relative velocities were used for this model. In this case the phases move at different velocities, but assume local equilibrium over short spatial length scales. This model allows taking into account the slip velocity between phases. It permits to model the separation phenomenon. Since the local concentration of the particles may exceed the concentration of the particles on the pump inlet the granular approach was used for secondary phases of the mixture. It allowed preventing the increase of the volume of fraction of the solid phase the value 0.5.
Coupled scheme was used for pressure – velocity coupling.
The drag force used as Schiller-Naumann formulation with Manninen slip velocity approach [8].
Due to very low friction heat between phases and isothermal conditions on the inlet, the temperature of mixture was assumed to be constant.
Lun model [9] was used for solid phase's pressure calculations.
The SST k-ω model for turbulence was used. The gravity was taken into account.
A multi-reference frame approach was used for rotation domains. It permitted to use steady state approach for calculations. The angular velocity for the rotation domain was 185.35rad/s.
The total number of mesh cells was 9 million**.** The solution was grid-independent in this case.
The test calculation was done for a finer mesh with 13 million cells. The difference in the results was less than 0.5%.
Due to slow convergence, the total number of iterations was up to 30,000.
Y^+ for calculated cases lies between 20 and 200.
The fluid was water under normal conditions with ρ = 998.2 kg/m^3.The secondary (solid) phases were represented by silicon spherical particles with diameters 0.2 mm.
The volume fraction of solid particles in the mixture ranged from 0.5% to 10%.
Specific speed per stage **n** was ~ 2500.
Three different solid phase mass flow rates were considered. They are listed in Table 1:

Table 1. Mass flow rates on the pump inlet.

Case#	1	2	3	4	5	6
Q_s (kg/s)	2	20	40	0	0	0
Q (kg/s)	198	198	198	196	178	158
Q_w (kg/s)	196	178	158	196	178	158

Mass flow inlet boundary condition (BC) was used on the inlet; pressure outlet BC was used on the outlet. Swirl number S was determined as the ratio of mass-weighted average tangential velocity to mass-weighted average axial velocity; S on the inlet was 1.

RESULTS AND DISCUSSION

The contours of volume fraction of solid phases with particles on the sections locations AA, inlet, outlet, and stage 1 outlet of the pump for cases 1 – 3 are shown on the Figures 2 – 10 .

The contours of volume fraction distribution of solid phase on the pump inlet are shown on the figures 2 – 4. The distribution is absolutely uniform.

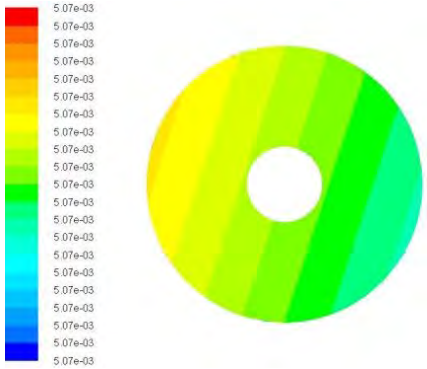

Figure 2. Contours of volume fraction of solid phase on the inlet, case 1

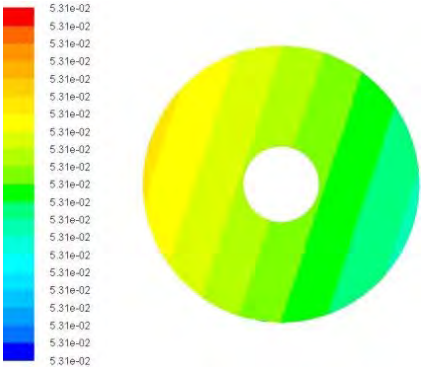

Figure 3. Contours of volume fraction of solid phase on the inlet, case 2

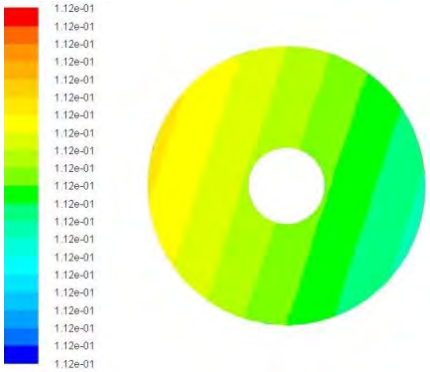

Figure 4. Contours of volume fraction of solid phase on the inlet, case 3

The local relative solid fraction distribution is defined as a local volume fraction distribution of solid phase distribution to the distribution on the inlet.

In this case it is clear from figures 5 – 10 that relative volume fraction distribution for the same location on the pump is close together.

As it was previously mentioned, the relative volume fraction distribution on the pump is close for different loads on the same location.

A visible difference in the volume fraction distribution on the stage 1 and stage 2 outlets for the all mixture flow rates could be observed. That difference is illustrated by figures 5 – 10 with the contours of phase volume fraction on the first stage outlet and the pump outlet.

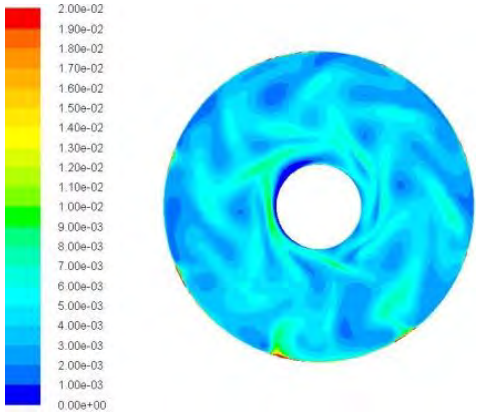

Figure 5. Contours of volume fraction of solid phase on the outlet, case 1

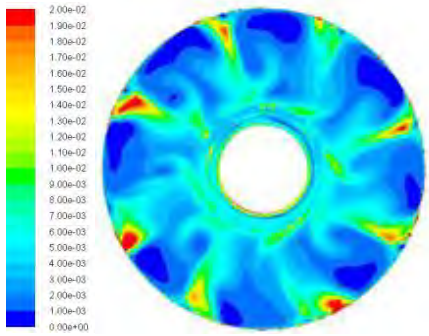

Figure 6. Contours of volume fraction of solid phase on the stage 1 outlet, case 1

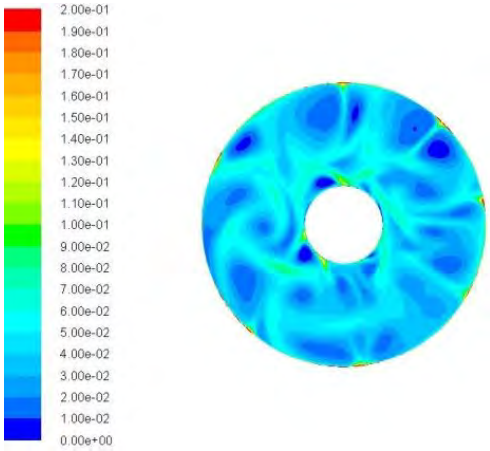

Figure 7. Contours of volume fraction of solid phase on the outlet, case 2

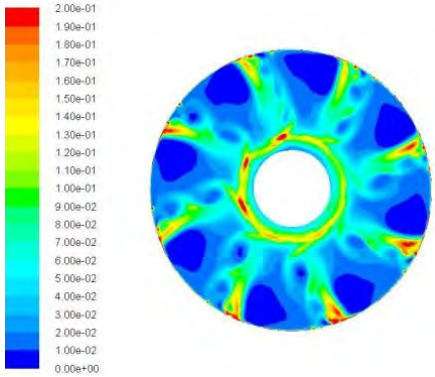

Figure 8. Contours of volume fraction of solid phase on the stage 1 outlet, case 2

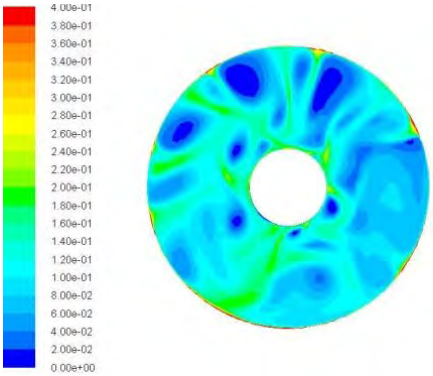

Figure 9. Contours of volume fraction of solid phase on the outlet, case 3

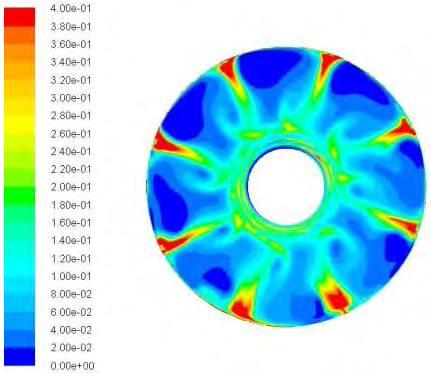

Figure 10. Contours of volume fraction of solid phase on the stage 1 outlet, case 3

It is easy to see that the volume fraction distribution on these surfaces is smoother for the pump outlet. Furthermore it should be noted that a large part of the solid particles is located near the outer wall of the pump, due to centrifugal effect.

Comparison of the pump head for mixture and for pure water with the same water flow rate is shown on the figure 11. It demonstrates that the results for head are close within ~1.5% difference.

Note that the pump head is determined by the liquid phase. In contrary, the efficiency of the pump with high solid phase load was much lower in comparison with the same flow rate of water for pure water case (see figure 12).

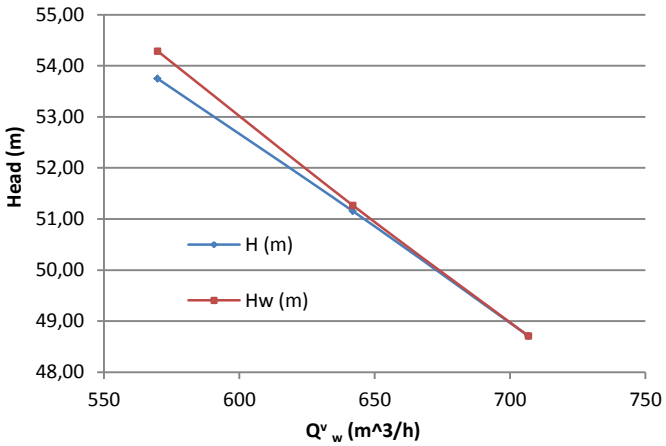

Figure 11. The pump head for mixture and the pump head for pure water.

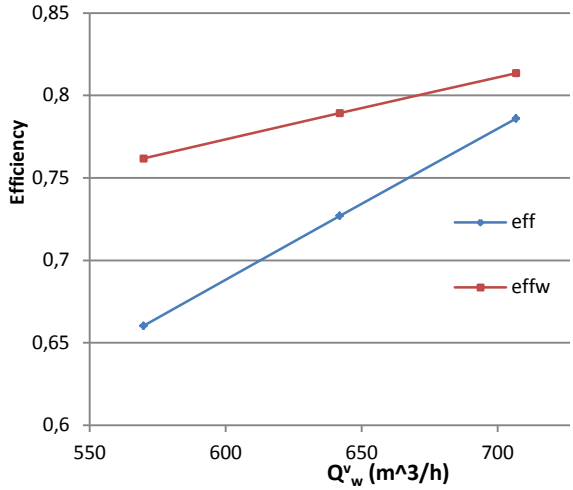

Figure 12. The pump efficiency for mixture and the pump efficiency for pure water.

Figures 13 and 14 shows streamlines on the part of the section AA for case 3 and case 6 respectively. From this figure it is easy to see that a large change of the load of solid phases visibly changes the flow field in spite of the fact that the maximum volume fraction for solid part of mixture on the inlet was only 5%. Changes have applied not only to the streamlines form, but to maximum velocity value.

Figure 13. Streamlines on the section AA, case 3, liquid phase

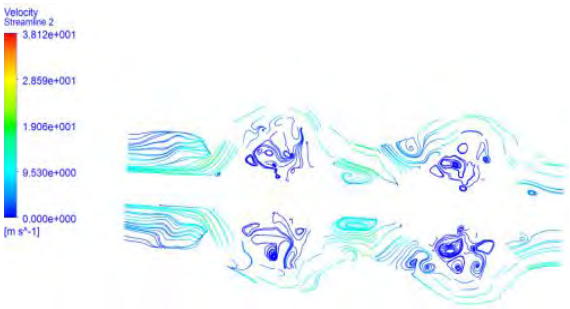

Figure 14. Streamlines on the section AA, case 6, liquid phase

The pump head for the mixture and the pump head for pure water with the same water flow rate demonstrate close results within ~1% difference.

On the other hand the results for efficiency of the pump for mixture with a relatively high solid phase load showed much lower efficiency in comparison with the same flow rate of water for pure water case.

To explain the results, a number of things must be taken into consideration. Note that all calculating cases have the same mixture flow rate (see Table1).

The power added from the pump to the mixture is the deferens between mixture power on the pump outlet and inlet. By definition, the efficiency is determined by the following ratio: the power added to the mixture from the pump to the total power consumed by the pump. The power added from the pump to the mixture has two parts:

1. The power added to the liquid phase, which is determined as a head.
2. The power added to the solid phase. In our case this was less than 1% of head power even for the highest solid phase load, which explains the analysis results.

The contribution of solid phases of the mixture to the total power consumption in the pump is very complex. Roughly speaking, impeller inputs power into liquid and solid parts of the mixture proportionally to their flow rates. The power can be transformed from velocity to pressure for the liquid phase. However, in our case, this transformation for the solid phase is negligible. Here, power losses due to slip velocities between liquid and solid phases could be considered as the most important mechanism for the solid phase power dissipation.

Additional losses in the pump performance may take place as a result of the change of the flow field due to the influence of solid phases (see figures 12 – 13). This may change the turbulent viscosity and velocity near the wall. Hence, it may influence dissipation of energy.

Due to the large re-distribution of solid phase down to the pump, the high volume fraction of solid phase may be concentrated in some local areas of the pump. The examples of this may be seen on the figures 5 – 10. In these locations the volume fraction of solid phase could increase the volume fraction of solid phase on the pump inlet in order of magnitude. It may have an influence on an erosion process in the pump parts, especially on the parts that rotate.

CONCLUSIONS

It is well known that the pre-rotation affects the pump head, but it may have a relatively low influence on the pump efficiency. The result of the current work revealed the influence of solid phase on the pump performance with pre rotation.

CFD simulations can help to identify spots with high particle concentration. It could give an idea of how to change design, which, in turn, could help avoid substantial damage to the pump.

The results presented in this work can help in a pump design for pumping of pre rotating liquid – solid mixture.

REFERENCES

1. Stepanoff A. J., (1957), "Centrifugal and Axial Flow Pumps: Theory, Design, and Application", New York: Wiley, 462 pages.

2. Mewis F., (2009), "A Novel Power-Saving Device for Full-Form Vessels", *First International Symposium on Marine Propulsors SMP'09,* Trondheim, Norway.

3. Sung-Eun Kim (2009), "Multiphase CFD Simulation of Turbulent Cavitating Flows in and Around Marine Propuslors", *Open Source CFD International Conference 2009*, Barcelona, Spain

4. Som Dutta; Yovanni Catano; Xiaofeng; and Marcelo H. Garcia (2010), "Computational Fluid Dynamics (CFD) Modeling of Flow into the Aerated Grit Chamber of the MWRD's North Side Water Reclamation Plant", *World Environmental and Water Resources Congress 2010*, Providence, Rhode Island, United States, May 16-20, 2010

5. Mikhail Strongin (2009), "Pump Mixing Process Calculations", *Sixth International Symposium on Pumping Machinery, FEDSM2009-78395*

6. Mikhail Strongin (2013), "CFD simulation of water flow mixing with discrete phase in a pump", *Proceedings of the ASME 2013 Fluids Engineering Summer Meeting, FEDSM2013-16184*

7. Tan, D.Y., Miorini, R.L., Keller, J., Katz, J. (2012), "Flow Visualization using Cavitation within the Rotor and Stator Blade Passages of an Axial Waterjet Pump Rotor at and Below Best Efficiency Point", *29th Symposium in Naval Hydrodynamics*.

8. Manninen M., Talvassalo V., Kallio S. (1996), "On the mixture model for multiphase flow", *VVT Publications 288,* Technical Research Centre of Finland.

9. C. K. K. Lun, S. B. Savage, D. J. Jeffrey, and N. Chepurniy. (1984), "Kinetic Theories for Granular Flow: Inelastic Particles in Couette Flow and Slightly Inelastic Particles in a General Flow Field". *J. Fluid Mech*. 140. 223–256.

FORECASTING TURBULENT DRAG REDUCTION IN A PIPELINE FLOW ON THE BASIS OF TAYLOR-COUETTE DEVICE EXPERIMENTAL DATA

Dmitry ESKIN

SCHLUMBERGER DBR Technology Center, 9450-17 Ave., Edmonton, AB T6N 1M9, CANADA

E-mail: deskin@slb.com

ABSTRACT

A model of drag reduction in a pipe flow, based on a boundary layer concept, is developed. An approach of Yang and Dou (2010) for modelling a stress deficit in the laminar boundary sublayer, caused by drag reducing additives, is employed. In this case, the laminar sublayer thickness is calculated by an empirical equation as a function of the so-called drag reduction parameter. Use of a simple Prandtl Mixing-Length model of turbulence for derivation of model equations allows us to formulate the drag reduction model as a modified Prandtl-Karman correlation for the Fanning friction factor. The model developed contains only one parameter that must be identified from experiments. This parameter is a function of the drag additive type and concentration. The model predictions are in good agreement with the results obtained by a more complicated model of Yang and Dou (2010) that was verified experimentally. Note that only a couple of experiments at different Reynolds numbers are required for identification of the mentioned model parameter.

Application of a wide-gap Taylor-Couette device instead of flow loop for drag reducer performance studies is suggested. A turbulent drag reduction model is developed for a device, in which an inner cylinder rotates and an outer one is immobile. The basic principles of both the developed drag reduction model in a pipe and an engineering model of a turbulent Taylor-Couette flow (Eskin, 2010) are employed for deriving a model of drag reduction in a Taylor-Couette device. We suggest identifying the drag reduction model parameter for a certain chemical additive from laboratory-scale experiments in a Taylor-Couette device and further using this parameter for drag reduction forecasting in industrial-scale pipe flows for a wide range of Reynolds numbers.

Keywords: Couette device, Drag reduction, Polymer additive, Pragmatic industrial modelling, Pipeline Flows, Turbulence

NOMENCLATURE

Greek symbols

α_* parameter that is a function of the polymer type and its concentration.
ΔB increment of the velocity in the turbulent. boundary layer due to drag reduction, m/s.
δ laminar sublayer thickness.
γ dimensionless function of a and λ.
η radius ratio r_0/R.
κ von Karman constant.
λ dimensionless velocity at the top of the layer of the thickness b.
ν kinematic fluid viscosity, [m^2/s].
ν_{eff} effective kinematic viscosity, [m^2/s].
ρ fluid density, [kg/m^3].
ω inner cylinder angular velocity, [*rad/s*].
u' stream-wise component of the fluctuation velocity, [m/s] .
v' transversal component of the fluctuation velocity, [m/s].
ξ dimensionless parameter of the Couette flow model.

Latin symbols

a laminar boundary layer thickness parameter.
b total dimensionless thickness of the buffer and the boundary layer.
D_* drag reduction (DR) parameter.
f Fanning friction factor.
G non-dimensional torque.
H width of a Couette device gap , [m].
m laminar boundary layer thickness parameter.
R the outer Couette device radius , [m].
R_m centerline radius of a Couette device gap, [m].
r radial coordinate, [m].
r_0 inner Couette device radius, [m].
Re pipe Reynolds number.
Re_c Couette device Reynolds number.
T torque, [N.m].
U mean flow velocity in a pipe, [m/s].
U_i circumferential velocity of the inner Couette device cylinder, [m/s].
u circumferential flow velocity, [m/s].
u_* friction velocity, [m/s].
y distance from the wall, [m].

Sub/ Superscripts

0 related to the outer wall.
a asymptote.
i related to the inner wall.
$+$ dimensionless variable in terms of laminar sublayer parameters.

INTRODUCTION

According to the literature, an addition of a small amount of high-weight polymer to fluids may reduce the pressure gradient up to 80 % (Benzi et al., 2004, L'vov et al., 2004).

In industry, testing of polymer additives is associated with expensive and time-consuming experiments in flow loops for regimes, closely imitating field conditions. A purpose of this work is developing a technique of characterization of drag reduction in pipelines operating under field conditions by experimental data obtained in a laboratory Couette device. A reliable model of a flow accompanied by drag reduction for both devices is needed for this purpose.
This work focuses on forecasting of the pressure gradient in hydraulically smooth pipelines that is important for application of drag reducing additives.

In engineering applications a pipeline flow is modelled on the basis of a boundary layer approach. In the absence of drag reduction agent, the velocity profile across a pipe can be approximately expressed as (Schlichting and Gersten, 2000):

$$u^+ = y^+, \qquad y^+ \le 11.6 \tag{1}$$

$$u^+ = 2.5 ln\, y^+ + 5.5, \quad y^+ > 11.6 \tag{2}$$

where $u^+ = u/u_*$, $y^+ = u_* y/\nu$, y is the distance from the wall, u is the streamwise velocity, $u_* = (\tau_w/\rho)^{0.5}$ is the friction velocity, ν is the fluid kinematic viscosity, τ_w is the shear stress at the wall and ρ is the fluid density.

Based on this velocity distribution, one can derive the Prantl-Karman equation, determining the friction factor for a pipe flow as (e.g., Schlichting and Gersten, 2000):

$$\frac{1}{f^{0.5}} = 4 log_{10}\left(Re\, f^{0.5}\right) - 0.4 \tag{3}$$

where $f = 2u_*^2/U^2$ is the Fanning friction factor, U is the mean flow velocity through a pipe, $Re = UD/\nu$ is the pipe Reynolds number and D is the pipe diameter.
Note that Eq.3 is the most accurate for high *Re* number flows ($Re > 10^5$).

Turbulent flows in a Couette device (see Fig.1) have been studied in a number of papers (e.g., Lathrop et al., 1992, Lewis and Swinney, 1999). However, there is no widely accepted engineering model of such flows. The model of Eskin (2010) is a basis for modelling a Couette flow in this work. Eskin (2010) simulated a device, in which the inner cylinder rotates and the outer one is immobile. His model establishes an analytical relation between the dimensionless torque, applied to the rotor, and the Reynolds number.

Different investigators (e.g., Rudd, 1972, Reischman and Tiederman, 1975, Luchik and Tiederman, 1988, Willmarth et al., 1987) studied the boundary layer structure by laser-Doppler anemometry (LDA) and particle image velocimetry (PIV) in dilute polymer solution flows. Experiments showed that adding a polymer leads to an increase in the laminar boundary layer thickness, most probably caused by a local increase in a fluid viscosity, and in reducing the Reynolds shear stress in the buffer layer due to a decrease in the normal fluctuation velocity. The decrease in the Reynolds shear stress leads to the drag reduction.

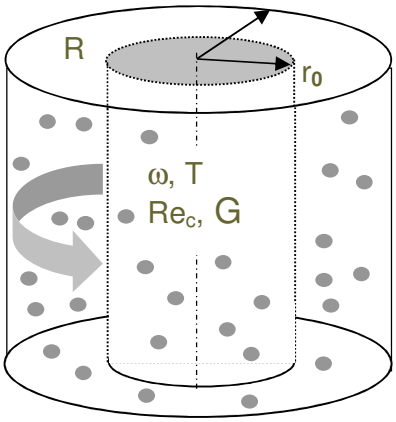

Figure 1: Taylor-Couette device diagram.

One of the important steps to drag reduction modelling was an approach of Virk (1971[b]), who suggested a semi-empirical drag reduction model, based on the well-known three-layer representation of the boundary layer structure (e.g., Schlichting and Gersten, 2000). According to Virk (1971[b]), the drag reduction caused by a polymer additive occurs due to a change in the velocity distribution across the buffer layer, while the velocity distributions across the laminar sublayer and the turbulent boundary layer are not affected by the additive. Virk (1971[b]) assumed that the dimensionless velocity distribution across the buffer layer ("elastic sublayer" according to the Virk terminology) is:

$$u^+ = 11.7 ln\, y^+ - 17 \tag{4}$$

This distribution was derived based on the empirical equation for the maximum drag reduction asymptote; i.e., the minimum friction factor achievable (Virk, 1971[a]). The maximum drag reduction occurs when the elastic sublayer is extended from the laminar sublayer boundary to the pipe center. Thus, according to Virk (1971[b]), the velocity distribution in the laminar sublayer is described by Eq.1, in the buffer layer by Eq.4, and in the turbulent boundary layer by an equation reminding Eq.2 but in which the second parameter is different from 5.5 and determined as a function of a position of the boundary between the buffer and the turbulent boundary layers. However, this position depends on a polymer type and concentration and has to be determined experimentally. Moreover, Reischman and Tiederman

(1975) measured the velocity distribution in the elastic sublayer and found it to be different from the Virk's distribution (Eq.4).

Let us now briefly describe an approach of Yang and Dou, which was employed as a basis for our model of turbulent drag reduction. These authors published a number of papers, where they presented a technique allowing rather accurate modelling of drag reduction in both smooth (Yang and Dou, 2005, 2008) and rough (Yang and Dou, 2010) pipes. This technique is based on experimental observations (e.g., Willmarth et al., 1987, and Gyr and Tsinober, 1997), which revealed that the total shear stress in a drag reduction flow is higher than the sum of the viscous shear stress and the Reynolds shear stress if Newtonian fluid rheology is assumed. Gyr and Tsinober (1997) defined this stress deficit in a pipe flow as:

$$G(y)=\tau-\left(\mu\frac{\partial u}{\partial y}+(-\rho\overline{u'v'})\right) \tag{5}$$

where ρ is the fluid density, $\tau=\rho u_*^2(1-y/R)$ is the total shear stress, *R* is the channel radius, $-\rho\overline{u'v'}$ is the Reynolds shear stress, $\mu\partial u/\partial y$ is the viscous shear stress.

The stress deficit effect is caused by a Non-Newtonian viscoelastic rheology of a polymer additive. To take the stress deficit into account Gyr and Tsinober (1997) represented it as follows:

$$G(y)=\rho\nu_{eff}\frac{du}{dy} \tag{6}$$

where ν_{eff} is the effective viscosity.

Yang and Dou (2005) suggested calculating the effective viscosity by analogy with the Boussinesq's expression for the eddy viscosity (e.g., Schlichting and Gersten 2000), i.e. as:

$$\nu_{eff}=\alpha_* u_* R \tag{7}$$

where α_* is the parameter that is a function of the polymer type and its concentration.

Accounting for Eqs.6, 7 one can write Eq.5 in the following form (Yang and Dou, 2008):

$$\begin{aligned}u_*^2\left(1-\frac{y}{R}\right)&=(\nu+\nu_{eff})\frac{du}{dy}-\overline{u'v'}\\&=\nu D_*\frac{du}{dy}-\overline{u'v'}\end{aligned} \tag{8}$$

where D_* is the drag reduction (DR) parameter that is calculated as:

$$D_*=1+\alpha_*\frac{u_*R}{\nu}=1+\alpha_* R^+ \tag{9}$$

$R^+=0.5\ Re\sqrt{f/2}$ is the dimensionless pipe radius equal to the Reynolds number based on the friction velocity.

In the dimensionless form Eq.8 can be written as:

$$\left(1-\frac{y^+}{R^+}\right)=D_*\frac{du^+}{dy^+}-\overline{u'^+v'^+} \tag{10}$$

The boundary condition for Eq.10 is zero velocity at the wall: $u^+(0)=0$.

Using the stochastic theory of turbulence Yang and Dou (2008) modelled the Reynolds shear stress. Substituting this stress into Eq.10 they obtained the equation for the dimensionless velocity distribution $u^+(y^+)$ as:

$$\begin{aligned}u^+=&\frac{1}{\kappa}ln\left(1+\frac{\kappa y^+}{2D_*}\right)+\frac{1}{2}\left(\frac{\delta^+}{D_*}+\frac{1}{\kappa}\right)\left(\frac{\kappa y^+}{2D_*+\kappa y^+}\right)^2\\&+\frac{1}{\kappa}\frac{\kappa y^+}{2D_*+\kappa y^+}\end{aligned} \tag{11}$$

where $\kappa=0.4$ is the von Karman constant, δ^+ is the dimensionless viscous sub-layer thickness.

The key element of the Yang and Dou (2008) model is the dimensionless viscous sub-layer thickness that is calculated by the experimental correlation (Yang and Dou, 2005):

$$\delta^+=11.6\ D_*^3 \tag{12}$$

Based on the velocity distribution, the friction factor is determined straightforwardly. The dimensionless mean flow velocity is calculated by averaging the velocity u^+ over the pipe cross-section as:

$$\frac{U}{u_*}=\sqrt{\frac{2}{f}}=\frac{1}{\pi R^{+2}}\int_0^R u^+ 2\pi R^+\left(R^+-y^+\right)dy^+ \tag{13}$$

After integration of Eq.13 and further simplifications, Yang and Dou (2010) obtained the equation for the friction factor that they recommended to use for engineering calculations. The final form of this equation is (Yang and Dou, 2010):

$$\sqrt{\frac{2}{f}}=2.5ln\frac{R^+}{D_*}-6.69\left(\frac{R^+}{D_*^{3.5}}\right)^{-0.72}+5.8D_*^2-4 \tag{14}$$

It was demonstrated (Yang and Dou, 2010) by comparing the calculation results with the experimental data of Virk (1971[a]) that Eq.14 accurately predicts the friction factor if the empirical coefficient α_* defining D_* is identified correctly. For practical purposes, Eq.14 can be applied as follows. For a given additive type and concentration a couple of experiments are performed with an experimental flow loop. Each experiment is carried out at a different flow rate. Then, the coefficient α_* is identified to provide the best fit of the computed pressure gradients to the experimental data.

Thus, in contrast to the approach of Virk (1971[b]), the described technique assumes that the drag reduction is caused by the Non-Newtonian behavior of the laminar boundary layer. The thickness of this layer rapidly increases with the polymer additive concentration that leads to a reduction in the Reynolds shear stress in the turbulent boundary layer (Yang and Dou, 2010).

MODELLING OF DRAG REDUCTION IN A PIPE FLOW

Initially, our idea was to directly use an approach of Yang and Dou for modelling a Couette flow. However, their turbulent viscosity model (Yang and Dou, 2008) cannot be applied to a Couette flow straightforwardly. That model gives zero turbulent viscosity in the pipe center that contradicts experimental observations (e.g., Schlichting and Gersten, 2000). Thus, although the Yang and Dou model provides rather accurate velocity

profiles in a pipe flow, it cannot be applied to a Couette flow that is characterized by high turbulence intensity at the gap centerline.

Because Virk (1971[a]) found out experimentally that in the turbulent core of a polymer solution pipe flow the velocity distribution can be described by the same equation as that used for a Newtonian flow (see Eqs.1, 2) but with some velocity increment, ΔB, we can use this fact in our model. We will look for the dimensionless velocity profile in a pipe in the following form (Virk 1971[a]):

$$u^+ = 2.5 ln\, y^+ + 5.5 + \Delta B \qquad (15)$$

Let us employ the known modelling approach (Eqs.1, 2) assuming the two-layer structure of the boundary layer. According to it, the viscous sub-layer, characterized by a linear velocity distribution is extended (up to $\delta^+ = 11.6$ for a Newtonian flow), while the buffer layer is ignored. For description of the laminar sub-layer we will use the approach of Yang and Dou, described above.

The momentum equation for the viscous sub-layer follows from Eq.8 and takes the following form:

$$D_* \frac{du^+}{dy^+} = 1 \qquad (16)$$

Then the velocity distribution across this sub-layer is:

$$u^+ = \frac{y^+}{D_*},\ y^+ \le \delta^+ \qquad (17)$$

The thickness of the viscous sub-layer for a polymer solution flow is calculated by Eq.12. Then, the velocity at the boundary separating the viscous sub-layer and the turbulent boundary layer is:

$$u^+(\delta^+) = \frac{\delta^+}{D_*} = \frac{11.6 D_*^3}{D_*} = 11.6 D_*^2 \qquad (18)$$

Equating the velocity expressed by Eq.18 to that determined by Eq.15 we obtain the equation for the velocity increment ΔB as:

$$\Delta B = 11.6(D_*^2 - 1) - 7.5 \ln D_* \qquad (19)$$

Then, the velocity distribution across the turbulent boundary layer is:

$$u^+ = 2.5 ln\, y^+ + 11.6 D_*^2 - 7.5 \ln D_* - 6.1 \qquad (20)$$

The equation for the Fanning friction factor is derived by averaging this distribution over the pipe cross-section (see Eq.13). As a result we obtain the Prandtl-Karman equation, modified for polymer solutions, as follows:

$$\frac{1}{f^{0.5}} = 4 log_{10}(Re\, f^{0.5}) + 8.2 D_*^2 - 8.6 - 12.2 log_{10} D_* \qquad (21)$$

As one can see, this equation is reduced to the regular Prandtl-Karman equation (Eq.3) if the DR parameter D_* is 1. Since Eq.21 is based on the same turbulence model as Eq.3, we expect that Eq.21 provides highest accuracy at high Reynolds numbers ($Re > 10^5$).

To validate the model developed we compared it with the model of Yang and Dou (Eq. 14). The authors (Yang and Dou, 2010) demonstrated a very good agreement of their calculation results with the experimental data of Virk (1971[a]). In Fig. 2 one can see the curves $1/f^{0.5}$ vs. $Re\, f^{0.5} = 2\sqrt{2}\, R^+$, calculated for the different polymer solutions in water, obtained by both the models. The polymer type and its corresponding concentration for each curve are shown in Fig.2. The solid lines correspond to Eq.21, the dash-point lines to Eq.14. Yang and Dou (2010) identified the coefficients α_* from the experimental data of Virk (1971[a]). We identified the coefficients for our model (α_{*_o}) to provide the best fit of our results to the curves, calculated by Eq.14. Both the coefficients α_* and α_{*_o} are also given in Fig.2. One can see that the agreement between the results obtained by the different models is reasonably good. The differences between the curves practically disappear at relatively high Reynolds numbers. This observation is in line with our expectations of the highest accuracy of the modified Prandtl-Karman equation (Eq.21) for high *Re* numbers. Note also that the coefficients α_* and α_{*_o} employed by the compared models are noticeably different.

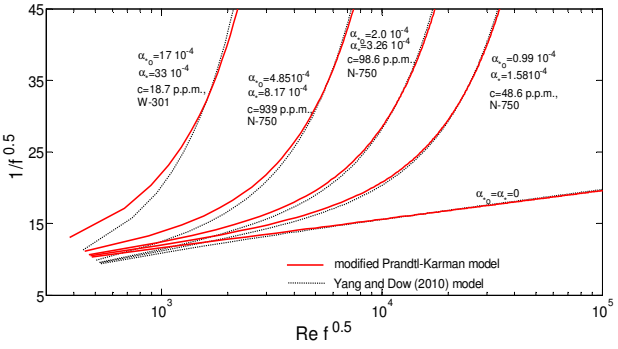

Figure 2: Comparison of the drag reduction effect in a pipe flow, estimated by the model of Yang and Dow (2010), with the effect obtained by the modified Prandtl-Karman model.

The comparison of our model with the model of Yang and Dou (2010) showed that the model developed can be employed for modelling turbulent drag reduction in pipelines of industrial scales, which are usually characterized by high Reynolds numbers. The successful modelling of the turbulent drag reduction in a pipe flow by using the modified Prandtl-Karman model shows the suitability of the Yang and Dou approach to modelling a Taylor-Couette flow. This is because the Prandtl mixing length turbulence model that is the basis of the Prandtl-Karman model is suitable for description of a Taylor-Couette flow (Schlichting and Gersten, 2000, Eskin, 2010).

TAYLOR-COUETTE DEVICE

We will consider a Couette device where the inner cylinder rotates while the outer one is immobile (see Fig.1). It is convenient to study a flow in such a device in terms of the dimensionless torque and the Reynolds number. The dimensionless torque is defined as follows:

$$G = \frac{T}{\rho \nu^2 L} \qquad (22)$$

where L is the Couette device height.

The Reynolds number for a Couette flow is calculated as:

$$Re_c = \frac{\omega r_0 (R - r_0)}{\nu} \tag{23}$$

where R is the outer cylinder radius, r_0 is the inner cylinder radius, $T = \tau_w 2\pi R^2 L$, ω is the rotor angular velocity.

As it was already mentioned in Introduction, Eskin (2010) developed a model of a flow in a Couette device. He employed an empirical velocity distribution across both the viscous and the buffer boundary layers (Schlichting and Gersten, 2000) and the Prandtl mixing length turbulence model for a turbulent core flow. Because the Couette flow model needed to be applicable for a wide gap Couette device, the streamline curvature was taken into account within the turbulence model. The author (Eskin, 2010) derived an analytical equation linking the dimensionless torque and the Couette device Reynolds number as:

$$\varsigma(\eta)\frac{Re_c}{\sqrt{G}} = ln\sqrt{G} + \phi(\eta) + \xi \tag{24}$$

where $\eta = r_0/R$, $\varsigma(\eta) = \frac{\kappa}{(1/\eta + \eta)}\frac{\sqrt{2\pi}}{(1-\eta)}$, $\phi = \frac{2}{1/\eta + \eta} - ln\left(\frac{1+\eta}{1-\eta}\right)$, $\kappa = 0.44$ is the von-Karman constant for a Couette flow (Lewis and Swinney, 1999) and ξ is the parameter.

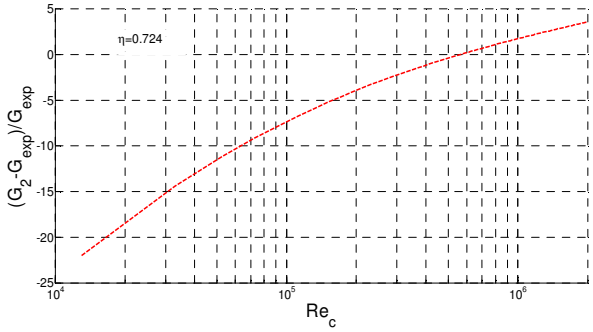

Figure 3: Relative deviation of the dimensionless torque computed by the model developed from the experimental data vs. Reynolds number.

The parameter ξ is a function of the boundary (initial in this case) condition for a flow domain, for which the Prandtl mixing length model is applied. This parameter depends on the total laminar and buffer boundary layer thickness and the velocity distribution across this thickness and calculated as (Eskin, 2010):

$$\xi = \kappa\lambda - (1 + ln(b)) - ln\sqrt{2\pi} \tag{25}$$

where $b = \delta_{tot}^+$ is the total dimensionless thickness of the buffer and the boundary layer, $\lambda = u^+(b)$ is the dimensionless velocity at the top of the layer of the thickness b.

Based on the experimental dimensionless velocity distribution across the buffer layer of a Couette flow, Eskin (2010) using the data of Schlichting and Gersten (2000) assumed $b = 70$ that provides $\lambda = 14.94$, and then Eq.23 gives $\xi = 0.406$.

Note that Eq.24 was derived by assuming that the total thickness of the viscous and the buffer boundary layers, *b*, is negligibly small, compared to the wall radius. Equation 24 demonstrated a reasonably good accuracy for relatively high Reynolds numbers $(Re_c > 13000)$, at which an effect of Taylor vortexes on a turbulent flow structure is negligibly small (Lewis and Swinney, 1999).

Flow Model

To model the turbulent drag reduction effect in a Couette device by using the same approach as for modelling a pipe flow, we need to modify the Couette flow model by applying the two sub-layers approach to flow field description. Also, because our estimations made for a pipe flow show that for a polymer solution case the viscous sub-layer thickness may reach relatively high values, we discarded the assumption about smallness of the viscous sub-layer thickness in comparison to the wall radius.

The velocity distribution across the viscous sub-layer in a Couette flow is also linear:

$$u^+ = y^+, y^+ \le \delta^+ \tag{26}$$

By analogy with the pipe flow, the thickness of the viscous sub-layer can be determined at the intersection of the linear velocity profile within the viscous sub-layer and the velocity profile in the turbulent core.

The velocity distribution across the turbulent region, confined by the outer boundary of the viscous sub-layer at the outer wall and the gap centerline, is described by the ordinary differential equation as (Eskin, 2010):

$$\frac{d}{dr}\frac{u}{r} = -\frac{u_{0*}R}{\kappa(R-r)r^2} \tag{27}$$

The initial condition for this equation is the velocity at the viscous sub-layer surface $u^+(\delta_0^+) = \lambda$.

The analytical solution of this equation is:

$$\frac{u(r)}{u_{0*}} = \frac{1}{\kappa}\left(1 + \frac{r}{R}ln\left(\frac{R}{r} - 1\right)\right) + \gamma\frac{r}{R}, \tag{28}$$

where

$$\gamma = \frac{\lambda - \frac{1}{\kappa}\left(1 + (1-a)ln\left(\frac{a}{1-a}\right)\right)}{1-a} \tag{29}$$

and $a = \delta_0^+/R^+$, $\delta_0^+ = \delta_0/(\nu/u_{0*})$ is the dimensionless viscous sub-layer thickness at the outer wall.

The dimensionless outer Couette device radius R^+ is expressed through the dimensionless torque *G* as:

$$R^+ = \sqrt{\frac{G}{2\pi}} \tag{30}$$

The momentum conservation equation for the turbulent flow area between the centerline and the outer surface of the viscous sub-layer at the inner cylinder is (Eskin, 2010):

$$\frac{d}{dr}\frac{u}{r} = -\frac{u_{0*}R}{\kappa(r-r_0)r^2} \tag{31}$$

The initial condition for this equation is the velocity at the gap centerline that is calculated using Eq.28 as:

$$\frac{u(R_m)}{u_{0*}} = \frac{1}{\kappa}\left(1+\frac{1+\eta}{2}ln\left(\frac{1-\eta}{1+\eta}\right)\right)+\gamma\frac{1+\eta}{2} \qquad (32)$$

where $R_m = 0.5(r_0 + R)$.

Then, the analytical solution of Eq.31 is (Eskin, 2010):

$$\frac{u(r)}{u_{0*}} = \frac{u(R_m)}{u_{0*}}\frac{r}{R_m}+\frac{1}{\kappa}\frac{R}{r_0}\left(-1+\frac{r}{R_m}+\frac{r}{r_0}ln\left(\frac{1-\frac{r_0}{R_m}}{1-\frac{r_0}{r}}\right)\right) \qquad (33)$$

The circumferential velocity of the inner cylinder is calculated as (Eskin, 2010):

$$U_i = u(r_0+\delta_i)+\lambda u_{i*} \qquad (34)$$

where u_{i*} is the friction velocity at the inner wall, δ_i is the viscous sub-layer thickness at the inner wall.

One can easily express the parameters of the boundary layer at the inner cylinder through those at the outer cylinder (see Eskin et al., 2010) and rewrite Eq.34 as follows:

$$\frac{U_i}{u_{0*}} = \frac{u(r_0+\delta_i)}{u_{0*}}+\frac{\lambda}{\eta} \qquad (35)$$

Expressing the left-hand side of this equation through the dimensionless torque and the Reynolds number we obtain:

$$\frac{(2\pi)^{0.5}}{1-\eta}\frac{Re_c}{G^{0.5}} = \frac{u(r_0+\delta_i)}{u_{0*}}+\frac{\lambda}{\eta} \qquad (36)$$

The velocity $u(r_0+\delta_i) = u(r_0+\delta_0\eta)$ is calculated by Eq.33, and after performing a routine math takes the form:

$$\frac{u(r_0+\delta_i)}{u_{0*}} = \frac{u(R_m)}{u_{0*}}\frac{2\eta}{1+\eta}(1+a)+ \frac{1}{\kappa}\left(-\frac{1}{\eta}+\frac{2(1+a)}{1+\eta}+\frac{1+a}{\eta}ln\frac{(1-\eta)}{(1+\eta)}\frac{(1+a)}{a}\right) \qquad (37)$$

The set of Eqs. 32, 36 and 37 allows calculating the dimensionless torque applied to the Couette device rotor. Note that we employed the von-Karman constant $\kappa = 0.44$, identified by Lewis and Swinney (1999) from the Couette flow experimental data, and considering similarity of the near-wall boundary layer in a Couette flow to that in a pipe flow, assumed $\delta_0^+ = 11.6$. Following the two-layer approach to modelling the boundary layer, employed for a pipe flow, we consider $b = \delta_0^+ = 11.6$ and, therefore, the velocity at the viscous sub-layer boundary is determined by Eq.26 as $u^+(11.6) = \lambda = 11.6$. We also checked how the simplified model (Eq.24) that neglects the boundary layer thickness in comparison with the Couette device radius performs against the model developed. It turned out that the solutions obtained by the developed and the simplified models are practically identical for $Re_c > 13000$. This result was expected, because in the case of a pure fluid (free of a drag reducer) the laminar sublayer thickness is negligibly small in comparison with the Couette device radii.

In Fig.3 we showed the relative deviations of the dimensionless torque calculated by Eq.36 from the data of Lewis and Swinney (1999), who accurately approximated their experimental results by the following correlation:

$$log_{10}G = -0.00636\,(log_{10}Re_c)^3 + 0.1349\,(log_{10}Re_c)^2 + 0.885\,(log_{10}Re_c) + 1.61 \qquad (38)$$

One can see that the agreement is very good in the wide range of Re numbers, except the relatively low Re values. The accuracy is excellent for $Re > 10^5$. For such high Re numbers the deviations of the computed results from the measured data do not exceed 7%.

Drag Reduction Model

Application of the approach, proposed for modelling of turbulent drag reduction in a pipe, to that in a Couette device is straightforward.

The drag reduction parameters are different for the outer and the inner cylinders and calculated as:

$$D_{0*} = 1+\alpha_*\frac{u_{0*}H}{2\nu} \qquad (39)$$

$$D_{i*} = 1+\alpha_*\frac{u_{i*}H}{2\nu} \qquad (40)$$

where H is the Couette device gap width.

By taking into account Eq.36, one can rewrite Eqs.39 and 40 as follows:

$$D_{0*} = 1+\alpha_*\frac{Re_c}{2}\frac{u_{0*}}{U_i} = 1+\frac{\alpha_*}{2}(1-\eta)\sqrt{\frac{G}{2\pi}} \qquad (41)$$

$$D_{i*} = 1+\alpha_*\frac{Re_c}{2}\frac{u_{i*}}{U_i} = 1+\frac{\alpha_*}{2}\frac{(1-\eta)}{\eta}\sqrt{\frac{G}{2\pi}} \qquad (42)$$

By analogy with a pipe flow, the laminar sub-layer thicknesses at the outer and the inner surfaces of a Couette device are:

$$\delta_0^+ = 11.6\ D_{0*}^3 \qquad (43)$$

$$\delta_i^+ = 11.6\ D_{i*}^3 \qquad (44)$$

Then the corresponding flow velocities at the top of the laminar sub-layers, needed for application of the Couette flow model, are:

$$\lambda_0 = \frac{\delta_0^+}{D_{0*}} = 11.6D_{0*}^2 \qquad (45)$$

$$\lambda_i = \frac{\delta_i^+}{D_{i*}} = 11.6D_{i*}^2 \qquad (46)$$

Let us briefly formulate a computational algorithm of a polymer solution flow in a Couette device. Equation 36 is the major model equation that has to be solved by iterations over the Re number. The dimensionless velocity $\lambda = \lambda_i$ is determined by Eq.46. The flow velocity at the inner viscous sub-layer surface is calculated by the equation derived on the basis of Eq.33 and takes the following form:

$$\frac{u(r_0+\delta_i)}{u_{0*}} = \frac{u(R_m)}{u_{0*}}\frac{2\eta}{1+\eta}(1+m)+ \frac{1}{\kappa}\left(-\frac{1}{\eta}+\frac{2(1+m)}{1+\eta}+\frac{1+m}{\eta}ln\frac{(1-\eta)}{(1+\eta)}\frac{(1+m)}{m}\right) \qquad (47)$$

where $m = \delta_i^+ / r_0^+$, $r_0^+ = R^+$ (R^+ is calculated by Eq.30).

The dimensionless velocity at the gap centerline $u(R_m)/u_{0*}$ is computed by Eq.32. The parameter γ is

calculated by Eq.29. The parameters a and $\lambda = \lambda_0$, needed for using this equation, are determined for the outer cylinder by Eqs.41, 43 and 45.

Computational Examples and Discussion of the Drag Reduction model in a Couette Device

Because the Couette device Reynolds number is based on the rotor circumferential velocity, we will employ flow parameters at the inner cylinder surface for further analysis. The shear stress at the inner cylinder wall can be calculated as:

$$\tau_{wi} = \frac{\rho f U_i^2}{2} \tag{48}$$

where f is the Fanning friction factor for a rotating wall. From Eqs.23-30 and 48 we obtained the equation for calculating the factor f in the following form:

$$\frac{1}{f^{0.5}} = \frac{Re_c}{(1/\eta - 1)\sqrt{G/\pi}} \tag{49}$$

We would like to emphasize that it is important to clearly determine an applicability of the model developed for practical calculations. As it was mentioned in Introduction, Virk (1971[b]) using experimental data assumed that the maximum drag reduction effect in a pipe flow is achieved when the elastic sublayer (buffer layer, affected by a drag reducer) is extended from the laminar sublayer boundary to the pipe center. Since the developed model of a Couette flow is based on the same principles as that of a pipe flow, we can confidently assume the same mechanism of obtaining the drag reduction asymptote in a Couette device. The Couette device gap half-width plays a role of the pipe diameter in this case. Because the drag reduction modelling concept employed in our work is based on the two-layer representation, it does not contain the elastic layer thickness explicitly and, therefore, the model developed cannot be directly used in the calculation of the maximum drag reduction effect. However, it is possible to employ for this purpose an empirical correlation of Virk (1971[b]), derived for calculation of the minimum achievable friction factor for a pipe flow, which has the following form:

$$\frac{1}{f_a^{0.5}} = 19 \log_{10}\left(Re\, f^{0.5}\right) - 32.4 \tag{50}$$

where f_a is the minimum drag reduction factor for a certain Re number.

From Eqs.41-44, one can easily figure out that because the drag reduction parameter D_{i^*} is larger than D_{0^*}, the dimensionless thickness of the laminar sub-layer at the inner cylinder is larger than that at the outer wall. Thus, the model developed indirectly assumes that the drag reduction effect, caused by an increase in the Couette device spindle rotation speed, reaches its maximum when the total boundary layer thickness at the inner cylinder wall becomes equal to the gap half-width. Therefore, the Reynolds number Re_c based on the circumferential velocity of the inner cylinder, has to be substituted in Eq.50 for calculation of the drag reduction asymptote in a Couette device. Then the asymptotic dimensionless torque can be calculated based on equating Eqs.49 and 50. As a result, we obtain the drag reduction asymptote for the dimensionless torque as follows:

$$G_a = \pi \left(\frac{Re_c \sqrt{f_a}}{1/\eta - 1} \right)^2 \tag{51}$$

where G_a is the minimum dimensionless torque achievable due turbulent drag reduction.

To demonstrate the model performance we performed the two sets of Couette flow calculations for the two different radius ratios $\eta = 0.5$ and 0.75. The computations were carried out for the same range of Re numbers and for the same parameters (except the highest $\alpha_{*_o} = 17\ 10^{-4}$), which were employed for illustration of drag reduction in a pipe flow (see Fig.2). The drag reduction asymptotes for both the radius ratios have also been calculated. The computed dependences of the dimensionless torque on the Couette device Reynolds number are shown in Fig.4. From this figure one can also see how the parameter α_{*_o} affects the dimensionless torque and how the latter increases with an increase in the radius ratio. However, the most important practical result demonstrated by this figure is identification of an applicability range of the Couette device for testing drag reducing chemicals. Flow regimes, providing torque values that are lower than those predicted by the drag reduction asymptote equation (Eq.51), are not realistic and, therefore, cannot be used for testing drag reducers. Reduction in the radius ratio η allows widening the Couette device applicability range. For example, Fig.4 clearly shows that the drag reducing additive characterized by the parameter $\alpha_{0^*} = 4.85\ 10^{-4}$ cannot be tested in a device with the radius ratio $\eta = 0.75$, whereas testing the same drag reducer in a device with the smaller radius ratio $\eta = 0.5$ is possible for a relatively wide Reynolds number range. Thus, an efficient testing of drag reducing chemicals requires using a Couette device with a relatively low radius ratio η.

We would like to emphasize that in the present work we developed the drag reduction models for pipe and Couette flows, which can be useful tools for scaling the drag reduction effect from a Couette device to an industrial pipeline. Although, no experimental data on drag reduction in a Couette flow are available yet, there are strong indirect proofs of validity of the modelling approach developed. Both the models are based on the same assumptions, and the employed turbulence model is proven to be valid (Schlichting and Gersten, 2000, and Eskin, 2010) for both the flow types. The drag reduction modelling has been mainly reduced to description of the viscous sub-layer flow affected by a polymer additive. Because the viscous sub-layer is relatively thin, the sub-layer flow patterns for a pipe and a Couette device are nearly identical. Therefore, because validity of the drag reduction model for a pipe flow has been confirmed by the experimental data (see Fig.2), the same modelling approach is certainly applicable to a Taylor-Couette flow.

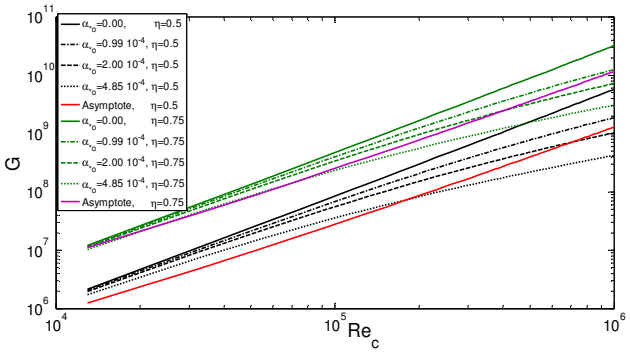

Figure 4: Dimensionless torque, applied to the inner Couette device cylinder, vs. Reynolds number at different drag reducing additives and for different radius ratios.

CONCLUSIONS

An engineering model of turbulent drag reduction in a pipe has been developed. An approach of Yang and Dou (2010) to modelling the drag reduction effect, as that caused by a Non-Newtonian rheology of a laminar sublayer flow, is employed. The modified Prandtl-Karman equation for calculation of the friction factor in a pipe flow of a dilute polymer solution has been obtained. The derived equation contains the only empirical parameter that is a function of a polymer type and concentration. The results computed by using the model developed are in a good agreement with those, calculated by the Yang and Dou model (2010) verified against experimental data.

An engineering model of a turbulent dilute polymer solution flow in a Couette device has also been developed. The same approach to modelling drag reduction as that in a pipe flow was applied. The model developed allows to compute the dimensionless torque applied to the Coutte device rotor as a function of the rotation speed for a given polymer type and concentration.

It was also shown that the empirical drag reduction asymptote, known for a pipe flow, can be used for a Couette flow Also, the calculations showed that the Couette device with a lower inner to outer radius ratio η is preferable for drag reducer testing because allows operating in regimes, which are further from drag reduction asymptote than in the case of a higher η. The results of the work conducted allow us to recommend employing a small-scale laboratory Couette device for identifying the empirical parameter that characterizes the drag reduction effect. The parameter identified can be applied for forecasting drag reducing effect in industrial-scale pipeline flows.

ACKNOWLEDGMENT

The author is thankful to Prof. J.R.A. Pearson (Schlumberger Gould Research Center) for the constructive discussion of this work.

REFERENCES

BENZI, R., CHING, E.S.C., HORESH, N. and PROCACCIA, I., (2004), "Theory of Concentration Dependence in Drag Reduction by Polymers and the Maximum Drag Reduction Assymptote", *Phys. Rev. Lett.*, **92**, 078302.

ESKIN, D., (2010), "An engineering model of a developed turbulent flow in a Couette device", *Chem. Eng. Proc.*, **49**, 219–224.

GYR, A., TSINOBER, A., (1997), "On the rheological nature of drag reduction phenomena," *J. Non-Newtonian Fluid Mech.,* **73**, 153-162.

LATHROP, D.P., FINEBERG, J., SWINNEY, H.L., (1992), "Transition to shear-driven turbulence in Couette–Taylor flow", *Phys. Rev. A,* **46**, 6390–6405.

LEWIS, G.S., SWINNEY, H.L., (1999), "Velocity structure functions, scaling and transitions in high-Reynolds-number Couette–Taylor flow", *Physical Review E*, **59**, 5457–5467.

LUCHIK, T.S., TIDERMAN, W.G., (1988), "Turbulent structure in low-concentration drag-reducing channel flows", *J. Fluid Mech.,* **190**, 241-263.

L'VOV, V. S., POMYALOV, A., PROCACCIA, I., TIBERKEVICH, V., (2004), "Drag reduction by polymers in wall-bounded turbulence", *Phys. Rev. Lett.,* **92**, 244503.

PROCACCIA, I., L'VOV, V. S., (2008), "Colloquium: Theory of drag reduction by polymers in wall-bounded turbulence", *Rev. Mod. Phys.*, **80**, 225–247.

REISCHMAN, M., TIEDERMAN, W.G., (1975), "Laser-Doppler anemometer measurements in drag-reducing channel flows", *J. Fluid Mech.,* **70**, part 2, 369-392.

RUDD, M. J., (1972), "Velocity measurements made with a laser Doppler meter on the turbulent pipe flow of a dilute polymer solution", *J. Fluid Mech.,* **51**, 673-685.

SCHLICHTING, H., GERSTEN, K., (2000), "Boundary-Layer Theory", Springer-Verlag, Berlin, Heidelberg, New York.

TOMS, B. A., (1948), *Proc. 1st Int. Congress on Rheology*, North Holland.

VIRK, P. S., (1971[a]), "Drag reduction in rough pipes", *J. Fluid Mech.,* **45**, 225–246.

VIRK, P. S., (1971[b]), "An elastic sublayer model for drag reduction by dilute solutions of linear macromolecules", *J. Fluid. Mech.,* **45**, 417–440.

WILLMARTH, W.W., WEI, T., LEE, C.O., (1987), "Laser anemometer measurements of Reynolds stress in a turbulent channel flow with drag reducing polymer additives", *Phys. Fluids*, **30**, 933-935.

YANG, S.-Q. , DOU, G., (2010), "Turbulent drag reduction with polymer additive in rough pipes", *J. Fluid Mechanics*, **642**, 279-294.

YANG, S.-Q. , DOU, G., (2008), "Modelling of viscoelastic turbulent flow in channel and pipe", *Phys. Fluids*, **20**, 065105.

YANG, S.-Q. , DOU, G., (2005), "Drag reduction in a flat-plate boundary layer flow by polymer additives", *Phys. Fluids,* **17**, 065104.

CFD MODELLING OF GAS ENTRAINMENT AT A PROPAGATING SLUG FRONT

Jinsong HUA[1]*, Jørgen NORDBØ [2] and Martin FOSS [1]

[1] Institute for Energy Technology, PO Box 40, NO-2027 Kjeller, NORWAY

[2] NTNU Department of Chemical Engineering, 7491 Trondheim, NORWAY

* E-mail: jinsong.hua@ife.no

ABSTRACT

Slug flow is encountered frequently during multiphase fluid transport in pipes. The gas entrainment process at a slug front significantly affects the hydrodynamic behaviour of slug flows. Due to the complexity of the flow physics and the dynamic coupling of the affecting factors, the mechanism by which these factors contribute to the gas entrainment process is not clearly understood. Typical factors affecting the gas entrainment are pipe inclination, Taylor bubble propagation and liquid film. Current experiments are not able to clarify the effect of these factors on the flow characteristics of slugs. Hence, a computational fluid dynamics based numerical method is applied in this paper to simulate the gas entrainment process at the slug front. The objective is to investigate the factors affecting the gas entrainment. A 2D numerical model is created using a commercial CFD package Star-CCM+. To capture the dynamic behaviour of liquid-gas interface at the slug front, the volume of fluid (VOF) model with relatively fine mesh and small time step is used. The simulation results show that the turbulent kinetic energy at the slug front is closely related to the gas entrainment rate. The effects of pipe inclination, Taylor bubble propagation and liquid film flow parameters on the turbulent kinetic energy generation and gas entrainment process at the slug front are also discussed.

Keywords: CFD, slug flow, gas entrainment, two-phase flow, VOF method.

NOMENCLATURE

Greek Symbols

α Gas volume fraction, [-].
ε Dissipation rate of turbulent kinetic energy, [m^2/s^3].
θ Pipe inclination, [degree].
κ Interface curvature, [1/m].
μ Dynamic viscosity, [kg/m/s].
ρ Mass density, [kg/m^3].
σ Surface tension coefficient, [N/m].
Φ Gas shedding flux, [m/s].

Latin Symbols

C_μ, C_1 and C_2 Turbulence model constants, [-].
C_0 Velocity distribution coefficient, [-].
D Pipe diameter, [m].
$\boldsymbol{F}_{ST}$ Surface tension force distributed in volume, [N/m^3].
g Gravity acceleration, [m/s^2].
G_k Turbulent kinetic energy production term, [m/s^2].
k Turbulent kinetic energy, [m^2/s^2].
$\mathbf{n}$ Interface unit normal vector, [-].
p Pressure, [Pa].
R_{LC} Liquid recirculating rate in bubble wake zone, [-].
t time, [s].
$\mathbf{u}$ Velocity, [m/s].
U_m Mixture velocity, [m/s].
U_d Drift velocity, [m/s].

Sub/superscripts

b Taylor bubble.
f Liquid film.
G Gas phase.
L Liquid Phase.
R Moving reference frame.
s slug front or slug body.
t Turbulence.
w Pipe wall or Taylor bubble wake.

INTRODUCTION

Gas-liquid slug flow is encountered frequently in long distance pipelines over a wide range of gas and liquid flow rates and pipe inclinations. The two-phase slug flow is described by alternating elongated large bubbles (also known as Taylor bubbles) moving above liquid films and liquid slugs containing small bubbles. The small gas bubbles in the liquid slugs originate from the gas entrainment process occurring on the dynamic gas-liquid interface between the tail of the elongated gas bubble and the front of liquid slug. Propagation and dispersion of small bubbles into the liquid slug change the hydrodynamic characteristics (e.g. pressure drop) of the aerated liquid slug significantly. The accuracy of pressure drop predictions in long pipelines depends strongly upon accuracy in estimating the small gas bubble concentration (or the liquid holdup) in the liquid slug. Slug liquid holdup is required for the closure of most slug flow models, including those of Kokal and Stanislav (1989) and Taitel and Barnea (1990). A slug

liquid holdup model, empirical or mechanic, is thus an essential part of any slug flow model. The development of an improved liquid holdup model should therefore be based on a detailed understanding of the gas entrainment process at the slug front.

The flow complexity of the gas entrainment process at the propagating slug introduces significant challenges and difficulties for accurate measurement in experiments. This hinders the exploration of flow physics and quantification of the flow parameters. First of all, the gas entrainment process involves dynamic interaction between the elongated bubble tail and the propagating slug front. It is challenging for the current multiphase flow measurement techniques to track and measure the fluid flow parameters close to the dynamic liquid-gas interface. It is also challenging to track the volume changes of the elongated bubble with an irregular tail and the gas content in the liquid slug. Secondly, the fluid flow at the slug front is highly turbulent. The turbulence eddy at the slug front interacts with the liquid-gas interface, creating waves and perturbations on the interface. Thirdly, multi-scale sized bubbles are involved in the gas entrainment process. The elongated bubble has the largest scale of the bubbles involved. Due to the shear flow between the liquid film and the slug front, the rolling waves are formed on the liquid-gas interface, and the tail of the elongated bubble is broken up into medium sized bubbles. They are shed into the slug front or the wake region of the elongated bubble. In this region the bubbles are broken up into smaller bubbles due to the strong turbulence eddies. The presence of gas bubbles also modifies the turbulence structure at the slug front. Some of the smaller bubbles are dispersed further into the downstream liquid slug body. In spite of these challenges, research efforts have been put on experimental studies of the gas entrainment process. The experimental results have been used to develop some fundamental mechanistic models or empirical formulations for predicting gas entrainment rate and void fraction in liquid slug.

The early research efforts on the gas entrainment process focused on the development of purely empirical correlations for predicting slug liquid holdup based on experimental statistical data. Gregory et al. (1978) proposed a simple correlation to predict slug liquid holdup as a function of mixture velocity only. The correlation was based on experimental data obtained from two horizontal 0.0258 m and 0.0512 m pipe diameter flow loops using air/oil system. Since the correlation neglected the effect of fluid properties and pipe geometric parameters such as pipe inclination, the correlation gave inaccurate predictions compared to data from other flow loops under different conditions. The correlation was improved by Malnes (1982) taking into account the physical properties of fluid such as surface tension and liquid density. The correlation of Gregory et al. is widely used due to its simplicity and reasonable accuracy.

Andreussi and Bendiksen (1989) investigated the effects of pipe diameter, inclination angle and fluid physical properties on slug liquid holdup for air/water flows in horizontal and near horizontal pipes. A semi-correlation was proposed to account for the effects of these parameters. Experimental data by Nydal and Andreussi (1991) showed that the gas entrainment is approximately proportional to the relative velocity between the slug front and the liquid film and to the interfacial width. Further statistical study of Nydal et al. (1992) revealed that slug liquid holdup is a weak function of liquid superficial velocity and pipe diameter in horizontal pipes. The liquid viscosity effect on slug liquid holdup was investigated experimentally by Nadler and Mewes (1995) using three different fluid systems, air/light oil, air/heavy oil and air/water. The experimental results showed that the slug liquid holdup increases significantly with increasing liquid viscosity, which indicates a reduced gas entrainment rate at the slug front. It was also observed that the slug liquid holdup differs significantly between the air/oil system and air/water system. This is attributed to the difference in surface tension and liquid density.

Based on the available experimental data over a wide range of two-phase slug flow conditions, improved correlations were developed taking into account better understanding of the slug flow physics. Gomez et al. (2000) developed a correlation to predict the void fraction in liquid slugs in pipes from horizontal to vertical. The experimental data they used included 283 data points collected from six different slug flow studies covering a wide range of pipe diameters, fluid properties and inclination angels. The correlation treats the liquid slug holdup as a function of the inclination angle and the slug Reynolds number. The slug Reynolds number lumps the effect of mixture velocity, liquid viscosity, pipe diameter. Abdul-Majeed (2000) proposed another correlation for estimating slug liquid holdup in horizontal and slightly inclined pipes. It was based on a large data bank consisting of 423 data point from different laboratories. The correlation performed satisfactorily when validated against the horizontal data. However, it performed poorly when validated against the data for inclined pipes.

The exercise on developing empirical correlations indicated that the validity of correlations depends strongly on the range of experimental data set used. The correlations cannot be extended to new flow conditions, which is a strong limitation of the empirical correlations as a predictive tool. Another approach for predicting the gas entrainment and liquid holdup in slugs is to develop a unified mechanistic model, which includes the gas entrainment mechanism. Based on the unit cell model proposed by Dukler and Hubbard (1975), Taitel and Barnea (1990, 1998) developed a slug tracking flow model predicting the evolution of slugs in a pipeline. Brauner and Ullmann (2004) proposed a unified approach to predict slug void fraction in horizontal, inclined and vertical slug flows. Slug aeration is attributed to a recurrent bubble entrainment from the Taylor bubble tail. The gas entrainment rate is determined based on an energy balance between the rate of turbulence kinetic energy production and the rate of bubble surface energy production. The gas entrainment

model of Brauner and Ullmann (2004) was incorporated into the slug flow model of Issa et al. (2006) that improves the slug void fraction prediction at moderate and high mixture velocity.

Zhang et al. (2003) developed a unified mechanistic model to predict slug liquid holdup based on the balance between turbulent kinetic energy of the liquid phase and surface free energy of dispersed, spherical gas bubbles. The turbulent kinetic energy is estimated using the shear stress at the pipe wall and the momentum exchange between the liquid slug and the liquid film in a slug unit. Al-Safran (2009) proposed a new correlation for predicting slug liquid holdup in horizontal pipes using an independent, mechanistic, dimensionless variable. The variable is the momentum transfer rate between the slug body and the liquid film. The correlation was developed using 410 horizontal experimental data points with a wide range of fluid physical properties, pipe size scale, operational and geometrical conditions. It was claimed that the performance of this correlation is much better than other correlations.

As indicated in the development of the mechanistic models (Taitel and Barnea 1998; Zhang et al. 2003; Brauner and Ullmann 2004) and the one-dimensional two-fluid model (Issa et al. 2006) for slug flows, many assumptions, simplifications and empirical correlations are required for closure of the governing equations. This affects the model accuracy and model extension to other flow conditions. The first principal numerical simulation based on computational fluid dynamics provides another approach to simulate slug flows using constitutive correlations that are less empirical. Yan and Che (2011) investigated hydrodynamic characteristics like velocity field, volume fraction distribution of dispersed small bubbles, wall shear stress and mass transfer coefficient in the gas-liquid upward slug flow in a vertical pipe. Hua et al. (2012) reported the validation study of using VOF method to simulate the propagation of a single elongated bubble in inclined pipes. The numerical predictions agree well with experiments.

In this paper, a CFD modelling approach based on the volume of fluid (VOF) method was applied to simulate the gas entrainment process at a propagating slug front. To capture the dynamic liquid-gas interface, a fine resolution mesh and a small time step size are required. Due to the high requirement of computational resources, a 2D model is used in this study. A moving reference attached to the gas bubble is implemented to allow the slug front to be located near the centre of the computational domain during the long simulation time. This was done to incorporate the propagation of slug front and elongated bubble. The focus of this study is on understanding the mechanism of gas entrainment at slug front and influencing factors. They include Taylor bubble traveling speed, pipe inclination and liquid film velocity and thickness. The gas entrainment process can also be affected by other factors such as surface tension and fluid properties. Since the CFD simulations are computationally expensive and the simulation time is long, this limited the number of numerical tests. The simulations provide new insights about the flow physics of gas entrainment process, which may enable development of better correlations and mechanistic models.

NUMERICAL MODEL DESCRIPTION

Problem Description

A schematic diagram of a slug unit of gas-liquid slug flow in an inclined pipe is shown in Figure 1. The diameter of pipe is set to D, and the inclination angle to horizontal is set to θ. The gas and liquid mixture flow upwards along the pipe with superficial velocities of U_{SG} and U_{SL} for the liquid and gas phases respectively. The mixture velocity for the slug flow is $U_m = U_{SL} + U_{SG}$. The propagating speed of the elongated bubble along the pipe is U_b. The liquid film under the Taylor bubble has a liquid holdup of H_f, and an upward flowing speed of U_f. The liquid slug front velocity is U_s. Normally, the slug front velocity is faster than the liquid film velocity ($U_s > U_f$), the highly turbulent flow at the liquid-gas interface may break the Taylor bubble tail into small bubbles. The bubbles are entrained into the slug front at a flux of Φ_{Ge}. Some of the relatively large bubbles in the Taylor bubble wake can be carried back to the liquid-gas interface by the recirculating liquid flow and merge with the Taylor bubble. The flux for this process is Φ_{Gb}.

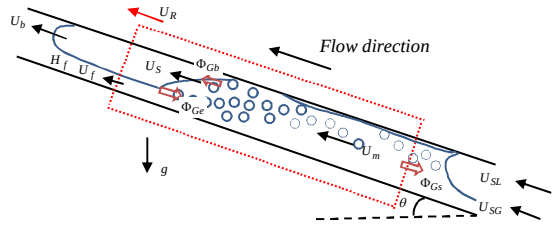

Figure 1: Schematic diagram of a slug unit propagating upward an in inclined pipe.

If the slug flow reaches its fully developed status, the Taylor bubble may reach a quasi-steady state. This means that there is no significant change in the Taylor bubble size. Under this situation the net gas volume shedding rate from the Taylor bubble tail to the slug front ($\Phi_{Ge} - \Phi_{Gb}$) is approximately equal to the gas flux entering into the nose of the tailing Taylor bubble (Φ_{Gs}). The traveling speeds of the Taylor bubble and the slug front are approximately equal ($U_b \approx U_s$).

CFD Model

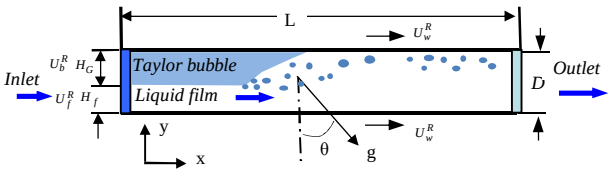

Figure 2: Schematic diagram of the CFD model for gas entrainment process at propagating slug front.

A CFD model partially covering the Taylor bubble, the liquid film and the slug body, as indicated by the dot-lines in Figure 1, is built for studying the gas entrainment process. To achieve a better focus on the

dynamic gas-liquid interface between the Taylor bubble and the slug, a moving reference frame with the same moving speed with the Taylor bubble ($U_R = U_b$) along the pipe is applied. The schematic diagram of the CFD model is shown in Figure 2. The diameter of pipe is set $D = 0.1\,m$. The ratio of pipe length to diameter is L/D=20. An air-water fluid system is set in the model.

The pipe wall is moving in the opposite direction of the Taylor bubble travelling velocity: $U_w^R = U_b$. No-slip condition is applied on the pipe wall. Flow inlet boundary condition is specified on the left end of the pipe, and outflow boundary condition on the right end of the pipe where the reference pressure is set to zero. The inlet velocity of the liquid film layer is assumed to be $U_f^R = U_b - U_f$ in the moving reference frame. Liquid holdup for the Taylor bubble section is assumed to be H_f. The corresponding liquid film thickness is $(H_f \cdot D)$ for the flow inlet boundary. Since the reference frame is moving with the Taylor bubble, the inlet velocity for the gas phase layer is set zero ($U_G^R = 0$). The pipe inclination angle (θ) is set by specifying the direction of the gravitational acceleration inside the computational domain.

Mathematical Formulations

The dynamics of the gas-liquid interface inside the computational domain is tracked using a volume of fluid method. A phase volume fraction function (α) is used to identify the liquid phase ($\alpha = 0$) and gas phase ($\alpha = 1$). The two-phase fluid system is treated as a fluid mixture with variable properties (density ρ and viscosity μ), which is weighted by the fluid properties of each phase and its volume fraction,

$$\rho = \rho_G \cdot \alpha + \rho_L \cdot (1-\alpha) \quad (1)$$

$$\mu = \mu_G \cdot \alpha + \mu_L \cdot (1-\alpha) \quad (2)$$

It is reasonable to assume both the gas and liquid phases are incompressible under the specified flow conditions in the present study. The Navier-Stokes equations for single phase flow can be extended for the fluid mixture of two-phase flow.

The continuity equation the fluid mixture reads

$$\nabla \cdot (\mathbf{u}) = 0 \quad (3)$$

And the momentum equation can be expressed as

$$\frac{\partial \rho \mathbf{u}}{\partial t} + \nabla \cdot (\rho \mathbf{u}\mathbf{u}) = -\nabla p + \nabla \cdot (\mu_e \nabla \mathbf{u}) + \mathbf{F}_{ST} + (\rho - \rho_L)\mathbf{g} \quad (4)$$

where μ_e is the effective viscosity, consisting of laminar mixture viscosity and turbulent viscosity $\mu_e = \mu + \mu_t$. $\boldsymbol{F}_{ST}$ stands for the surface tension force, which can be calculated as

$$\boldsymbol{F}_{ST} = \sigma \cdot \kappa \cdot \nabla \alpha \,. \quad (5)$$

Here, σ is the surface tension coefficient, and κ is the interface curvature, which is calculated by the divergence of the interface normal ($\boldsymbol{n}$),

$$\kappa = \nabla \cdot \boldsymbol{n} \text{ and } \boldsymbol{n} = \frac{\nabla \alpha}{|\nabla \alpha|} \quad (6)$$

The dynamic evolution of the volume fraction function is governed by the conservation of gas phase,

$$\frac{\partial \alpha}{\partial t} + \nabla \cdot (\boldsymbol{u}\alpha) = 0 \,. \quad (7)$$

To close the above governing equations, turbulent viscosity (μ_t) is required for the momentum equation. Hence, a standard k-ε turbulence model is solved. Two governing equations for turbulent kinetic energy (k) and dissipation rate (ε) are expressed as

$$\frac{\partial \rho k}{\partial t} + \nabla \cdot (\rho \boldsymbol{u} k) = \nabla \cdot \left[\frac{\mu + \mu_t}{\sigma_k} (\nabla k) \right] + (G_k - \rho\varepsilon) \quad (8)$$

$$\frac{\partial \rho \varepsilon}{\partial t} + \nabla \cdot (\rho \boldsymbol{u} \varepsilon) = \nabla \cdot \left[\frac{\mu + \mu_t}{\sigma_\varepsilon} (\nabla \varepsilon) \right] + \frac{\varepsilon}{k} (C_1 G_k - C_2 \rho\varepsilon) \quad (9)$$

where G_k is the turbulent kinetic energy production term. σ_k and σ_ε are the turbulent Prandtl numbers for turbulent kinetic energy and dissipation. C_1 and C_2 are the model constants. The turbulent viscosity (μ_t) can be calculated as

$$\mu_t = \rho C_\mu k^2 / \varepsilon \,. \quad (10)$$

The turbulent kinetic energy production can be estimated as

$$G_k = 2\mu_t S_{ij} S_{ij} \text{ and } S_{ij} = \frac{1}{2}\left(\frac{\partial u_j}{\partial x_i} + \frac{\partial u_i}{\partial x_j} \right) \quad (11)$$

Model Implementation

The commercial CFD package Star-CCM+ is used as the base numerical tool for implementing the proposed CFD model and solving the governing equations. A uniform square mesh is applied to the CFD model. After some numerical tests on the model sensitivity to mesh grid size and time step size, it is found both of them should be small enough to capture the dynamic liquid-gas interface with acceptable phase volume conservation. The mesh with 100 grids along the diameter and 2000 grids along the axis is a suitable choice for the present study. Therefore, the grid size is at the order of one millimetre. Such fine mesh makes the CFD model capture the sharp interface of the Taylor bubbles reasonably well, but it is still not fine enough to capture the interface for the small dispersed bubbles. A constant time-step size is set to 1.0×10^{-4} s in the simulations, and a second order temporal discretization scheme is applied. The initial Taylor bubble is assumed to be rectangular shape with length of $(5 \cdot D)$ and width of $[(1 - h_f) \cdot D]$ located in the upper left part of the model.

RESULTS AND DISCUSSION

In the proposed CFD model, an air-water system with constant densities and viscosities ($\rho_G = 1.18\,kg/m^3$, $\rho_L = 997\,kg/m^3$, $\mu_G = 1.85 \times 10^{-5}\,Pa\,s$, $\mu_L = 0.88 \times 10^{-3}\,Pa\,s$) and the interfacial tension coefficient ($\sigma = 0.074\,N/m$) is applied. The pipe diameter is set as $D = 0.1\,m$. The simulation can then be specified by the remaining four flowing parameters; (1) pipe wall velocity (U_w^R) that reflects the Taylor bubble travelling speed in the lab reference frame; (2) liquid holdup (H_f) for the section of the Taylor bubble, and it reflects the liquid film thickness; (3) liquid film velocity (U_f^R); (4) pipe inclination (θ). These four flow parameters are varied one by one to study their effects on the gas entrainment process at the slug front by comparing the simulation results to that of a base reference case.

Base Reference Simulation Case

The flow condition for the base reference case is defined by the following settings:

$U_w^R = 1.5\,m/s$; $U_f^R = 1.0\,m/s$; $H_f = 0.4$; $\theta = 10°$

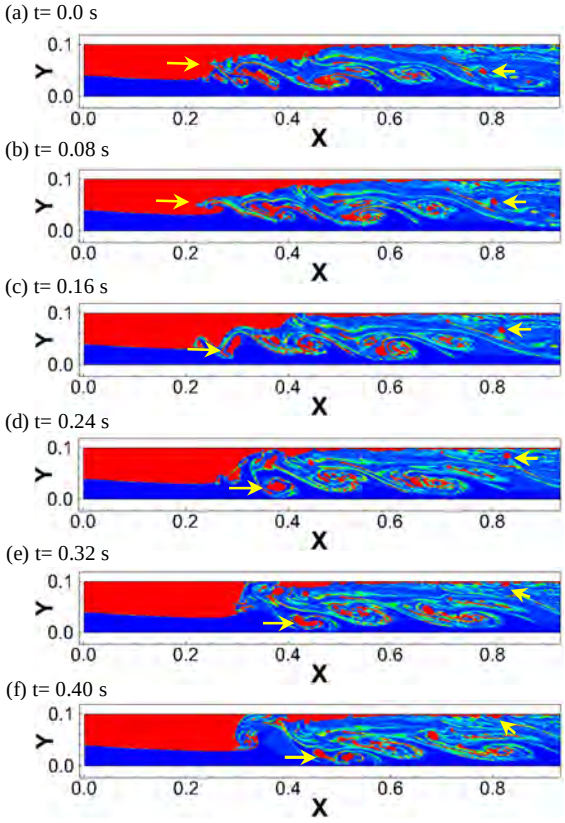

Figure 3: Temporal variation of phase distribution predicted by the CFD model during the gas entrainment process.

Figure 3 and Figure 4 shows the temporal variation of void fraction and velocity field at every 0.08 s over a short period of 0.4 s. The red colour represents the gas phase with void fraction higher than 0.2, while the blue colour stands for liquid phase with void fraction of zero. As highlighted by the long yellow arrows shown in Figures 3 and 4, the fragmentation process of a large gas bubble from the Taylor bubble tail and its entrainment into the slug is highlighted. As shown in Figure 4(a), a liquid jet is initiated from the liquid-gas interface due to the interaction between the liquid film and the recirculating liquid flow at the slug front. The liquid jet protrudes into the Taylor bubble as shown in Figures 3(b) and 4(b). Due to gravity, the liquid jet tip moves downward and impinges on the liquid film under the Taylor bubble. A small amount of gas is trapped between the protruded liquid jet and the liquid film as shown in Figure 3(c), and a new strong circulating vortex is formed at slug front due to the shearing flow between the liquid film and slug front as shown in Figure 4(c). Under the effect of the circulating vortex, the entrained gas bubble is shed into the lower part of pipe as shown in Figures 4(d), and small bubbles are pinched off around the large bubble as shown in Figure 3(d). The large entrained bubble is stretched further by the vortex as shown in Figure 3(e) and finally it is broken up into two smaller bubbles as shown in Figures 3(f) and 4(f). These small bubbles will be dispersed further into the slug body.

As shown in Figure 4, there are about four vortexes between the slug front and the developed slug body. The region from the slug front to the developed slug body is also known as the Taylor bubble wake zone. It has been reported from experiments that the wake zone length is about four to seven pipe diameters.

As the flow develops further into the slug body, the strength of the circulating vortices becomes weaker. Some of the dispersed bubbles in the wake zone with relatively large size start to rise upward due to buoyancy as indicated by the short yellow arrows in Figures 3 and 4. Finally they will reach the top pipe wall, forming a thin gas layer, which is also known as Taylor bubble tail. Due to the effect of circulating vortexes, the gas layer moves toward the Taylor bubble or slug front. Hence, the characteristics of the dynamic Taylor bubble tail is determined by the balance of the decaying rate of circulating vortexes in the wake zone and the dispersed bubble size. After the wake zone, the small bubbles are dispersed further into the slug body together with the liquid flow.

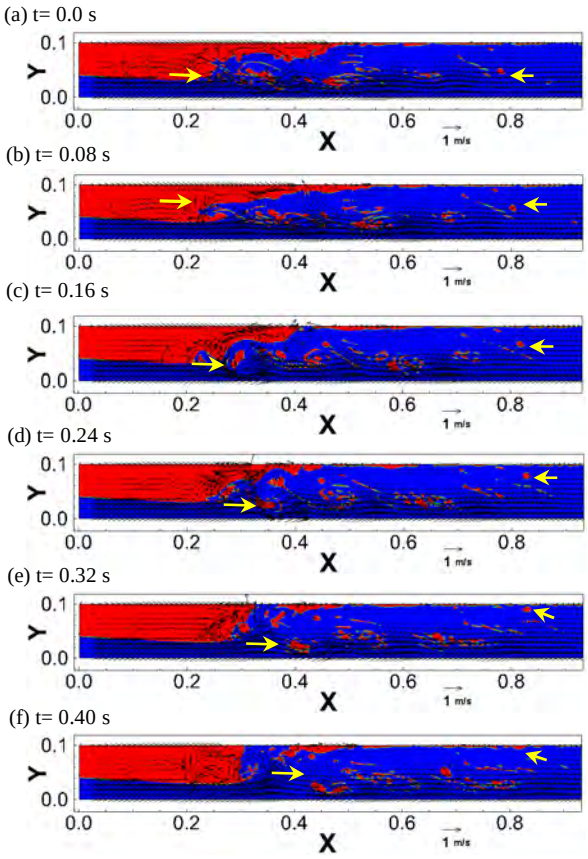

Figure 4: Temporal variation of velocity field predicted by the CFD model during the gas entrainment process.

To estimate the gas entrainment rate, it is important to measure the dynamic change of the Taylor bubble volume and the shedding rate of gas phase out of the slug body. This is shown in Figure 5. As the simulation is conducted in a 2D CFD model, the area covered by gas phase in the model is used to indicate the physical gas volume. The total gas volume decreases steadily with time at a shedding rate of $\dot{V}_G = -1.14 \times 10^{-3}\,m^2/s$. As suggested in (Nydal and Andreussi 1991), it is better to express the gas phase shedding flux using the shedding velocity $\Phi_{Gs} = \frac{-\dot{V}_G}{D} = 1.14 \times 10^{-2}\,m/s$. Due to the complex dynamic behaviour at

the slug front, the Taylor bubble volume fluctuates significantly due to gas entrainment, breakup and coalescence with the tailing small bubbles. In a time averaging view, the Taylor volume also decreases with time at a rate of $\dot{V}_b = -1.33 \times 10^{-3}\, m^2/s$. The corresponding gas entrainment velocity is expressed as $\Phi_{Ge} = \frac{-\dot{V}_b}{D} = 1.33 \times 10^{-2}\, m/s$. A mean gas shedding flux $\Phi_G = (\Phi_{Ge} + \Phi_{Gs})/2$ is used to quantify the gas entrainment rate in this study.

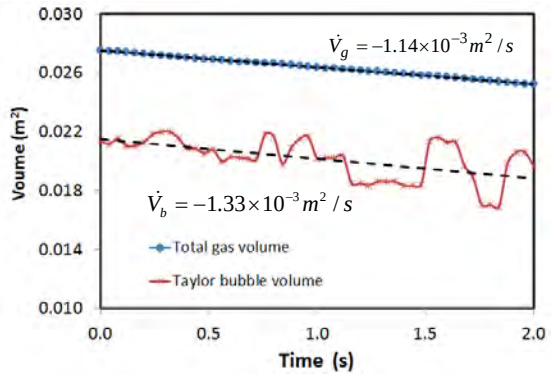

Figure 5: Temporal variation of total gas phase volume and Taylor bubble volume predicted by the 2D CFD model.

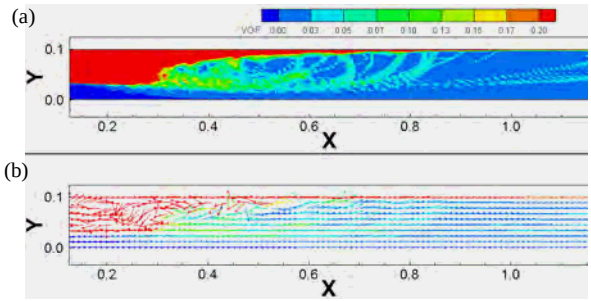

Figure 6: Time averaged variable field of (a) gas volume fraction and (b) fluid flow direction.

Due to the highly dynamic features of liquid-gas interface at the slug front, it is difficult to extract useful and quantified information from the temporal fields of phase distribution and velocity. Instead, we average the temporal variable fields over a longer period of time, about 2 s. Figure 6(a) shows the time averaged field of gas volume fraction. The region of red colour shows the time–averaged Taylor bubble shape. The region with medium gas volume fraction stands for the bubble wake zone. The developed slug body is shown by the blue region. The time averaged velocity field shown in Figure 6(b) illustrates the direction vector of fluid flow, which is coloured by the gas volume fraction. It clearly shows that the fluids near the gas-liquid interface front flows towards the Taylor bubble. This is a result of the strong circulating vortexes at the slug front and wake zone. Hence, the definition of liquid circulation rate proposed by Hua et al. (2012) is used to quantify the strength of circulating flow, $R_L = (U_{LD} - U_L)/U_{LD}$, where U_L is the net liquid flux and U_{LD} is the flux of liquid flowing towards the downstream.

The variation of liquid circulation rate along the pipe axis is shown in Figure 7. The liquid circulation rate is nonzero at the slug front and wake zone. The highest peak of recirculation rate corresponds to the slug front, where the gas is entrained by a strong circulating vortex. The region with nonzero circulation rate in the downstream of the slug front corresponds to the wake zone. The liquid circulation rates of the liquid film under the Taylor bubble and the developed slug body are approximately zero. Hence, the distribution of liquid circulation rate can be used as an indicator for different flow regions in slug flow.

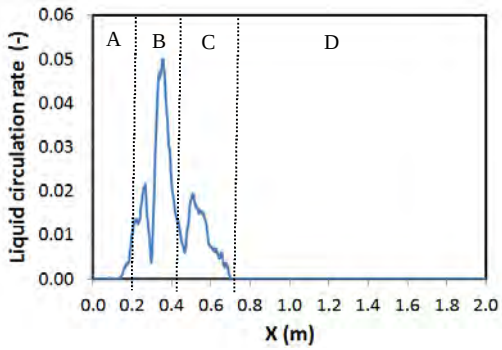

Figure 7: Variation of liquid circulation rate along the pipe axis and the corresponding regions: A for liquid film; B for slug front; C for wake zone; and D for developed slug body.

As illustrated in the simulation results, the gas entrainment process is related to the instability of liquid-gas interfaces and flow velocity fluctuation. Actually, the flow velocity fluctuation can be characterised by the turbulent kinetic energy. Figure 8 shows the variation of sectional averaged turbulent kinetic energy along the pipe axis. The turbulent kinetic energy is increasing in the liquid film, and reaches the highest value at the slug front. The turbulent kinetic energy decays downstream the slug front, and reaches a medium steady value at the wake zone. After the wake zone, the turbulent kinetic energy decays in the developed slug body.

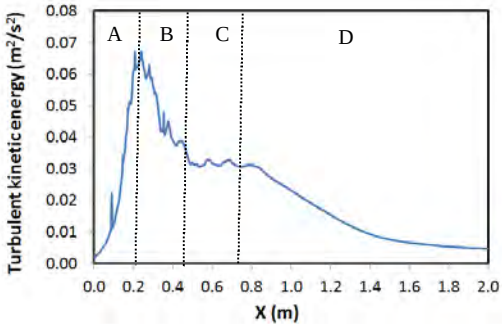

Figure 8: Variation of sectional averaged turbulent kinetic energy along pipe axis for different zones: A for liquid film; B for slug front; C for wake zone; and D for developed slug body.

The pressure drop along the pipe axis due to flow friction is shown in Figure 9. The effect of hydrostatic pressure is subtracted from the static pressure calculated in the CFD simulation. A low pressure region is formed after the Taylor bubble, which is travelling faster than the liquid. This low pressure induces significant acceleration of the slug front, which generates liquid jets. The interaction of liquid jets and liquid film is a mechanism for gas entrainment.

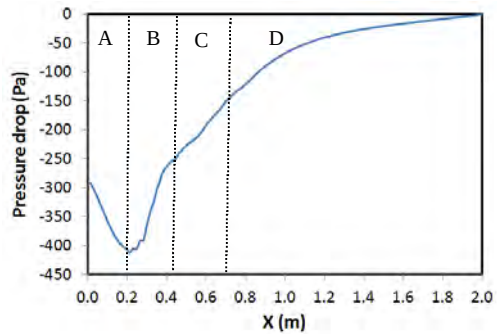

Figure 9: Variation of pressure drop along pipe axis for different zones: A for liquid film; B for slug front; C for wake zone; and D for developed slug body.

From the results of the base reference simulation case, it can be concluded that the gas entrainment process is caused by the interaction between the turbulent slug front and the liquid film. The fluid acceleration at the slug front is attributed to the pressure gradient caused by the low pressure zone created by the travelling Taylor bubble. Hence, the gas entrainment rate is affected by the turbulent kinetic energy at the slug front and the pressure drop. As we know, both the turbulent kinetic energy and the pressure drop along the pipe can be affected by flow conditions such as pipe inclination, Taylor bubble travelling speed, liquid film thickness and liquid film velocity.

Effect of Pipe Inclination (θ)

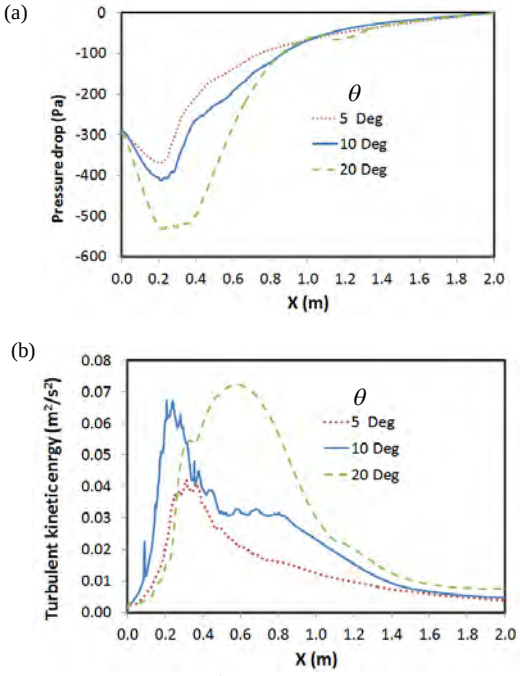

Figure 10: Variation of (a) pressure drop and (b) turbulent kinetic energy along pipe axis under different pipe inclination angle of 5º, 10º and 20º.

The effect of pipe inclination on the distribution of pressure drop and turbulent kinetic energy along the pipe axis is shown in Figure 10. Here, only pipe inclination angle is changed, while other parameters are kept constant. As shown in Figure 10(a), the overall pressure drop due to friction is not significantly affected by varying the pipe inclination. However, the pressure jump over the slug front increases significantly with inclination angle. The turbulent kinetic energy distribution along the pipe shown in Figure 10(b) indicates that the turbulent kinetic energy at slug front increases with the pipe inclination. The gas shedding velocity (Φ_G), void fractions in the wake zone (α_w) and developed slug body (α_s) for different pipe inclinations are listed in Table 1. The gas entrainment rate increases with the pipe inclination.

Table 1: Variation of gas shedding velocity and void fractions under different pipe inclinations.

θ	5º	10°	20º
Φ_G (m/s)	7.50E-3	1.24E-3	1.28E-2
α_w	1.40E-1	1.12E-1	9.59E-2
α_s	2.09E-2	2.57E-2	3.79E-2

Effect of Taylor Bubble Propagating Speed

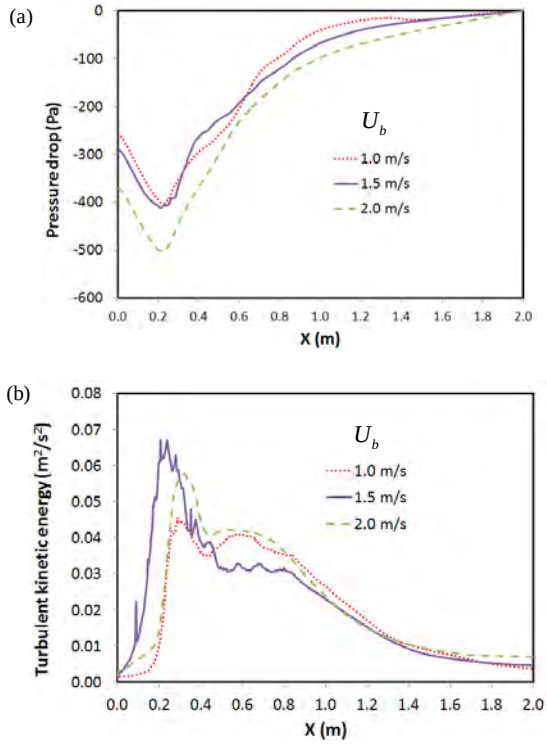

Figure 11: Variation of (a) pressure drop and (b) turbulent kinetic energy along pipe axis under different Taylor bubble travelling speed of 1.0 m/s, 1.5 m/s and 2.0 m/s.

The Taylor bubble propagating speed is used to set the pipe wall velocity in the CFD model with moving reference frame. As shown in Figure 11(a), the overall pressure drop due to friction increases with the Taylor bubble travelling speed. However, the local pressure gradient at the slug front is related to the local turbulent kinetic energy. The data shows that the highest turbulent kinetic energy at the slug front is seen when the Taylor bubble velocity is 1.5 m/s, as shown in Figure 11(b).

Table 2: Variation of gas shedding velocity and void fractions under different Taylor bubble travelling speeds.

U_b (m/s)	1.0	1.5	2.0
Φ_G (m/s)	8.46E-3	1.24E-2	1.35E-2
α_w	1.66E-1	1.12E-1	2.16E-1
α_s	3.44E-2	2.57E-2	2.71E-2

The gas shedding velocity (Φ_G), void fractions in the wake zone (α_w) and developed slug body (α_s) for different Taylor bubble travelling speeds are listed in Table 2. The gas entrainment rate increases with the Taylor bubble travelling speed.

Effect of Liquid Film Thickness (h_f)

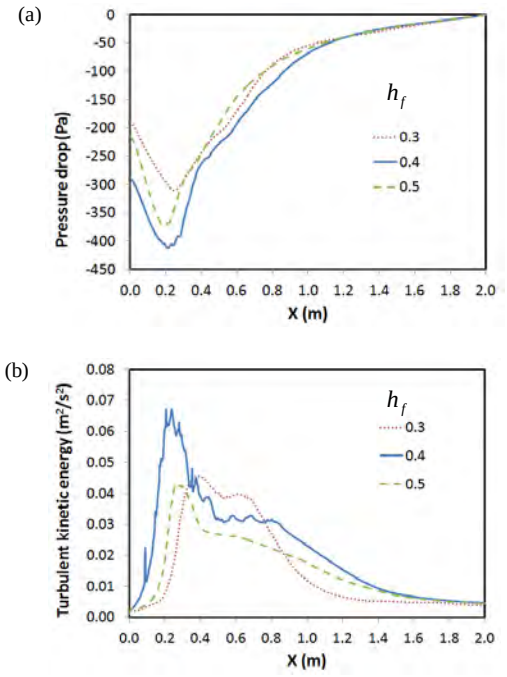

Figure 12: Variation of (a) pressure drop and (b) turbulent kinetic energy along pipe axis under different liquid film thickness.

The effects of liquid film thickness (i.e. liquid holdup under Taylor bubble) on the distribution of pressure drop and turbulent kinetic energy along the pipe axis are shown in Figure 12. When the liquid film has a medium liquid holdup, the interaction between the slug front and the liquid film is at its highest. A high turbulent kinetic energy at the slug front is seen for this situation as shown in Figure 12(b). When the liquid film is thinner, it has less momentum to interact with slug front. On the other hand, when the liquid film is thicker, the liquid slug front does not have enough momentum to affect the flow status in liquid film. The momentum exchange between the liquid film and slug front is higher when their individual momentums are similar. This creates strong disorder in the flow and generates high turbulent kinetic energy. The pressure drop shown in Figure 12(a) also shows that the liquid film with a medium thickness has the highest overall pressure drop.

Table 3: Variation of gas shedding velocity and void fraction under different liquid film thicknesses.

h_f	0.3	0.4	0.5
Φ_G (m/s)	5.08E-3	1.24E-2	1.12E-2
α_w	2.00E-1	1.12E-1	1.89E-1
α_s	2.23E-2	2.57E-2	2.31E-2

The gas shedding velocity (Φ_G), void fractions in the wake zone (α_w) and developed slug body (α_s) for different liquid film thicknesses (or liquid holdup) are listed in Table 3. The case with a medium liquid film has the highest gas entrainment rate.

Effect of Liquid Film Velocity

The effect of liquid film velocity on the gas entrainment process is also illustrated by the variation in pressure drop and turbulent kinetic energy at the slug front as shown in Figure 13. Clearly, the shearing between liquid film and slug front increases with increasing liquid film velocity. The high shearing rate at the slug front will lead to higher turbulent mixing and produce higher turbulent kinetic energy as shown in Figure 13(b). The highly turbulent flow at the slug front induces extra friction from the pipe wall, and increases the pressure drop at slug front. This is shown in Figure 13(a).

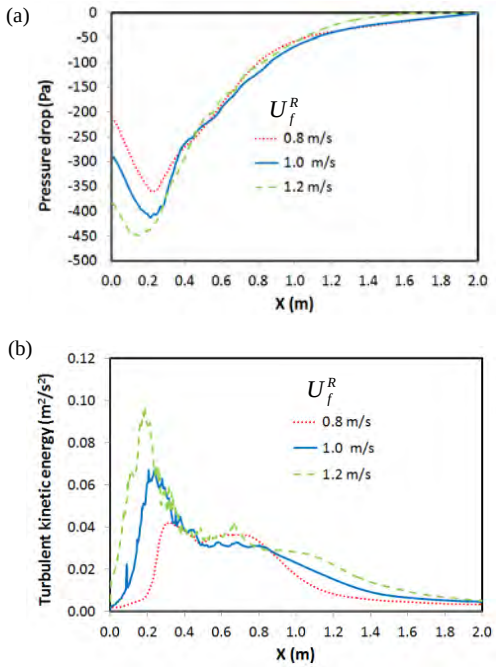

Figure 13: Variation of (a) pressure drop and (b) turbulent kinetic energy along pipe axis under different liquid film velocity.

Table 4: Variation of gas shedding velocity and void fraction under different liquid film velocities.

U_f^R (m/s)	0.8	1.0	1.2
Φ_G (m/s)	6.11E-3	1.24E-2	1.27E-2
α_w	1.74E-1	1.12E-1	2.18E-1
α_s	2.10E-2	2.57E-2	3.28E-2

The gas shedding velocity (Φ_G), void fractions in the wake zone (α_w) and developed slug body (α_s) for different liquid film velocities are listed in Table 4. The gas entrainment rate increases with the liquid film velocity.

CONCLUSION

A CFD model has been applied to simulate the gas entrainment process at a propagating slug front. To capture the dynamic gas-liquid interface, a 2D VOF CFD model with fine mesh (about $1\,mm$) and small

time step size (about $1.0 \times 10^{-4}\ s$) is implemented using the commercial CFD package Star-CCM+. In addition, to simulate the propagating slug front, the numerical model is implemented using a moving reference frame attached the Taylor bubble. The gas entrainment rate is obtained by monitoring the decrease of total gas volume or the shrinkage of Taylor bubble volume.

From the flow field and phase volume fraction distribution results, it can be concluded that the amount of gas entrained is determined by the interaction between the liquid film under Taylor bubble and the circulating vortex flow at the slug front. The interaction strength can be characterised by the turbulent kinetic energy at the slug front. This can be affected by many factors such as pipe inclination, Taylor bubble travelling speed, liquid film thickness and liquid film velocity. The parameter sensitivity studies outline the mechanism of action by these factors on the gas entrainment process. High pipe inclination will cause high pressure drop at the slug front and higher liquid acceleration. High Taylor bubble travelling speed will result in lower pressure in the bubble wake zone, which leads to higher pressure drop at the slug front. A medium liquid film thickness has the highest momentum exchange rate between the liquid film and the slug front. High or low liquid film thickness reduces the momentum exchange. Increasing the liquid film velocity will result in high shearing at slug front, which induce high momentum exchange. In general, highly turbulent fluctuations at the slug front will lead to high gas entrainment.

A limited number of simulations have been finished to study the gas entrainment at a propagating slug under different flow conditions. The gas entrainment process can be affected by other factors (e.g. surface tension coefficient, fluid properties) which are not considered in this paper. This can be included in future research tasks. The simulation results describes gas entrainment process reasonably well, and provide new insight for developing and improving the mechanistic model for gas entrainment in slug flows.

ACKNOWLEDGEMENT

The authors would like to thank the support from the FACE center - a research cooperation between IFE, NTNU and SINTEF, funded by The Research Council of Norway, and by the following industrial partners: Statoil ASA, GE Oil&Gas, Schlumberger, FMC technologies, CD-adapco, and Shell Technology Norway AS.

REFERENCES

ABDUL-MAJEED, G.H., (2000), "Liquid slug holdup in horizontal and slightly inclined two-phase slug flow". *J. Petr. Sci. Eng.*, **27**, 27-32.

AL-SAFRAN, E., (2009), "Prediction of slug liquid holdup in horizontal pipes", *J. Energy Resour. Technol.*, **131**, 023001-1 - 023001-8.

ANDREUSSI, P. and BENDIKSEN, K., (1989), "An investigation of void fraction in slugs for horizontal and inclined gas-liquid slug flow", *Int. J. Multiphase Flow*, **15**, 937-946.

BRAUNER, N., and ULLMANN, A., (2004), "Modelling of gas entrainment from Taylor bubbles. Part A: Slug flow", Int. J. Multiphase Flow, **30**, 239-272.

DUKLER, A. and HUBBARD, M., (1975), "A model for gas-liquid slug flow in horizontal and near horizontal tubes", *Ind. Eng. Chem. Fundam.*, **14**, 337-347.

GOMEZ, L.E., SHOHAM, O. and TAITEL, Y., (2000), "Prediction of slug liquid holdup horizontal to upward vertical flow", *Int. J. Multiphase Flow*, **26**, 517-521.

GREGORY, G., NICHOLSON, M. and AZIZ, K. (1978), "Correlation of the liquid volume fraction in the slug for horizontal gas-liquid slug flow", *Int. J. Multiphase Flow*, **4**, 33-39.

HUA, J., LANGSHOLT, M. and LAWRENCE, C., (2012) "Numerical simulation of single elongated bubble propagation in inclined pipes", *Prog. in Comput. Fluid Dynamics*, **12**, 131–139.

ISSA, R.I., BONIZZI, M. and BARBEAU S., (2006), "Improved closure models for gas entrainment and interfacial shear for slug flow modelling in horizontal pipes", *Int. J. Multiphase Flow*, **32**, 1287-1293.

KOKAL, S. and STANISLAV, J., (1989), "An experimental study of two-phase flow in slightly inclined pipes-II: liquid holdup and pressure drop", *Chem. Eng. Sci.*, **56**, 681-693.

MALNES, D., (1982), "Slug flow in vertical, horizontal and inclined pipes", Institute for Energy Technology, Kjeller Norway, Report No. IFE/KR/E-83-002 V.

NADLER, M., and MEWES, D., (1995), "Effect of the liquid viscosity on phase distribution in horizontal gas-liquid slug flows", *Int. J. Multiphase Flow*, **21**, 253-266.

NYDAL, O. and ANDREUSSI, P., (1991), "Gas entrainment in long liquid slug advancing in a near horizontal pipe", *Int. J. Multiphase Flow*, **17**, 179-189.

NYDAL, O., PINTUS, S. and ANDREUSSI, P., (1992), "Statistical characterization of slug flow in horizontal pipes", *Int. J. Multiphase Flow*, **18**, 439-453.

TAITEL, Y. and BARNEA, D., (1990), "Two-phase slug flow", *Adv. Heat Transfer*, **20,** 83-132.

TAITEL, Y. and BARNEA, D., (1998), "Effect of gas compressibility on a gas slug tracking model", *Chem. Eng. Sci.*, **53**, 2089-2097.

YAN, K. and CHE, D., (2011), "Hydrodynamic and mass transfer characteristics of slug flow in a vertical pipe with and without dispersed small bubbles". *Int. J. Multiphase Flow*, **37**, 299–325.

ZHANG, H.Q., WANG, Q., SARICA, C., BRILL, J.P., (2003). "A unified mechanistic model for slug liquid holdup and transition between slug and dispersed bubble flows", *Int. J. Multiphase Flow*, **29**, 97–107.

10th International Conference on CFD in the Minerals and Process Industries
SINTEF / NTNU Trondheim, Norway
17-19 June 2014

COMPUTATIONAL MODELLING OF SUBSEA HYDRATES FORMATION AND ASSOCIATED RISKS AND IMPACT ON FLOW ASSURANCE

M. Labois, N. Pagan, D. Lakehal, C. Narayanan*

ASCOMP GmbH, Zurich, SWITZERLAND
*Corresponding author, E-mail address: chidu@ascomp.ch

ABSTRACT

Deep sea oil spills are a great concern today given the proliferation of oil production from wells at great depth. In the event of a spill, contingency plans including capping and collection have to be developed and validated. In particular, collection systems consisting of a simple dome and riser system can be critical in containing the environmental impact until a permanent solution such as a capping stack is operational. The current proof-of-concept study presents a full model to simulate the installation process of a dome over a spill with active mitigation, including accounting for hydrates formation and dissociation and hydrate adhesion. Active hydrates mitigation using methanol or hot water injection has been added to the modelling portfolio.

INTRODUCTION

Subsea hydrate formation may cause blockages in oil production lines, and as such it remains today one of the main concerns to deep-sea field developments. Current mitigations strategies of operators consists in the deployment of prevention methods that aim at producing outside the hydrate domain, via pipeline insulation (for oil systems) or by means of chemical injection (for gas systems). Another strategy is to produce still inside the hydrate domain by transporting the hydrate phase as slurry of hydrate particles dispersed in the oil phase.

But the context in which hydrates mitigation is vital relates to deep-sea oil spills, which become a great concern today given the proliferation of oil production from wells at great depth (1500-3000m below sea level). In the event of a spill, contingency plans including both capping and collection system have to be developed and validated. In particular, collection systems consisting of a simple dome and riser system can be critical in containing the environmental impact until a permanent solution such as a capping stack is ready for installation. The use of a collection system in deep sea is complicated by the thermodynamic conditions of high pressure and low temperature, which results in rapid conversion of gaseous hydrocarbons to hydrates within a very short distance resulting in complete plugging of the dome.

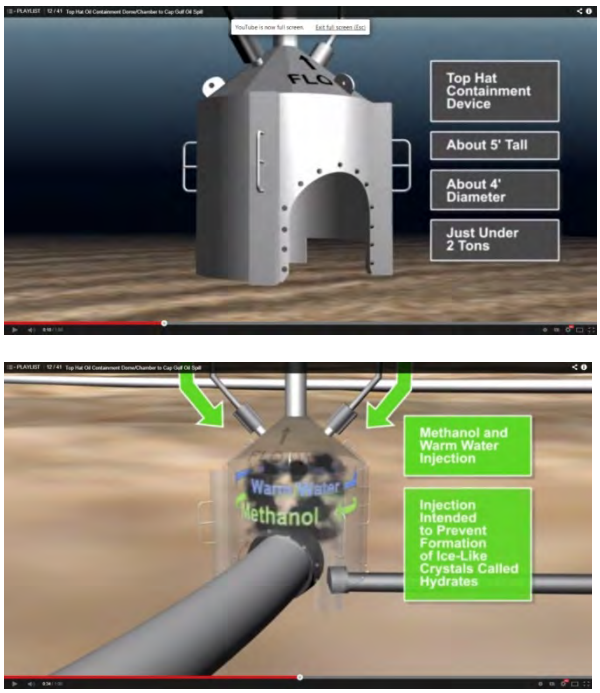

Figure 1: The top-hat solution used by BP to contain the Deepwater horizon spill (BP, 2010).

The containment effort of BP for the Deepwater Horizon oil spill was unsuccessful due to severe hydrates plugging. Such a containment response was first attempted using the cofferdam solution (BBC News, 2010). The cofferdam is a large dome that was lowered on to the well head, however, hydrates formed in large quantities inside during the descent of the cofferdam thereby rendering it ineffective. After this attempt a more sophisticated system was deployed, referred to as the top-hat solution. The top-hat solution has integrated injection of hot water and methanol inside the dome to prevent hydrates plugging (Figure 1). Although installed successfully, its collection effectiveness was low as reported in The New York Times (2010). The article reports that oil continued to blow out from under the top-hat and through the four open vents on top of the device, which the engineers were unable to close as originally planned. A better design was thus required to take into account the complex multiphase flow created by the spill jet along with thermodynamics related to hydrates formation.

Advanced CFD/CMFD models can really help design strategies to ensure restarting after a long shutdown due to hydrate blockage, or help design better capping domes for oil spills. The current study is in this spirit. We introduce in this paper the hydrate physics module built into our code TransAT, coupled to the N-phase multiphase flow model. The hydrates module includes models for hydrate formation and dissociation kinetics, formation enthalpy, hydrates rheology including effect of agglomeration and hydrates adhesion. The modelling was recently extended to include the possibility to model the mixing and dissolution of miscible liquids such as methanol and hot water as active mitigations mechanisms.

MATHEMATICAL MODELLING

At large depths thermodynamic conditions are very favourable for hydrate formation given the high pressures, low temperatures and availability of water. Several factors can affect the risk of plugging such as the depth of spill defining the ambient pressure and temperature, the composition of the reservoir fluid, the amount of free gas at the ambient pressure, the temperature of the spill and the mass-flow rate of the spill. In order to access the risk of hydrates plugging, knowledge of the physical phenomenon that govern the formation and transport of hydrates is essential. Briefly, the thermodynamics of hydrates formation and dissociation, the jet flow path and water entrainment, the temperature evolution inside the top-hat, and the adhesion behaviour of hydrates to the upper surface of the top-hat should be modelled.

Multiphase Flow Modelling Context

The multiphase mixture model with algebraic slip (Manninen and Taivassalo, 1996) between the phases has been employed to simulate this problem. Here the transport equations are solved for the mixture quantities (subscript *m*) rather than for the phase-specific quantities (subscripts *G* and *L*):

$$\boldsymbol{u}_m = \sum_{k=G,L} \alpha_k \rho_k \boldsymbol{u}_k / \rho_m \,;\; \rho_m = \sum_{k=G,L} \alpha_k \rho_k$$
$$Y_k = \alpha_k \rho_k / \rho_m \,;\; \boldsymbol{u}_D = \mathbf{u}_G - \boldsymbol{u}_m \qquad (1)$$

where $\mathbf{u}$, ρ, α, Y and $\mathbf{u}_D$ are the velocity, density, volume fraction, mass fraction and slip velocity. The mixture momentum equation is solved for the entire system, reducing the number of equations to be solved in comparison to the 2-fluid model:

$$\partial_t \rho_m + \nabla \cdot \left(\rho_m \boldsymbol{u}_m\right) = 0 \qquad (1)$$

$$\partial_t \left(\rho_G \boldsymbol{\alpha}_G\right) + \nabla \cdot \left(\rho_G \boldsymbol{\alpha}_G \left(\boldsymbol{u}_m + \boldsymbol{u}_D\right)\right) = 0 \qquad (2)$$

$$\partial_t (\rho_m \boldsymbol{u}_m) + \nabla \cdot \rho_m \left(\boldsymbol{u}_m \boldsymbol{u}_m + \frac{Y_G}{Y_L} \overline{\boldsymbol{u}_D \boldsymbol{u}_D} - \Pi_m\right) = \nabla \cdot \left[2\alpha_G \mu_G \boldsymbol{\sigma}_G^D + 2\alpha_L \mu_L \boldsymbol{\sigma}_L^D\right] + \rho_m \boldsymbol{g} \qquad (3)$$

$$\rho^m C_p^m \partial_t T + \rho^m C_p^m V_j^m \nabla T = \nabla \cdot \left(\left(\frac{\mu^m}{Pr} + \frac{\mu_T^m}{Pr_T}\right) \nabla T\right) + \sum_p \dot{m}_p \mathcal{L}_p \qquad (5)$$

where, index p sums over the number of phasic reactions (for example for hydrate formation and dissociation) and $\dot{m}_p$ and $\mathcal{L}_p$ are the corresponding rates of mass transfer and latent heats. Closure models are required for the slip velocity and associated stresses.

Since the reservoir fluid contains oil and gas phases based on thermodynamic equilibrium at the average temperature between the spill and the ambient water, it is necessary to model a minimum of four phases including oil, gas, water and hydrates; plus Methanol or another mitigation fluid if needed. This led to the use of the N-Phase approach invoked in situations involving more than two phases. In the N-phase framework, the above transport equations (2-3) become now:

$$\partial_t \left(\rho_G \boldsymbol{\alpha}_G\right) + \nabla \cdot \left(\rho_G \boldsymbol{\alpha}_G \left(\boldsymbol{u}_m + \boldsymbol{u}_k^D\right)\right) = 0 \qquad (6)$$

$$\partial_t (\rho_m \boldsymbol{u}_m) + \nabla \cdot \rho_m \left(\boldsymbol{u}_m \boldsymbol{u}_m + \sum_k Y_k \overline{\boldsymbol{u}_k^D \boldsymbol{u}_k^D} - \Pi_m\right) = \nabla \cdot \left(\sum_k 2\alpha_k \mu_k \boldsymbol{\sigma}_k^D\right) + \rho_m \boldsymbol{g} \qquad (7)$$

In summary, the mass conservation equation is solved for each phase including mass exchange due to hydrates formation. Only the mixture momentum and mixture temperature are solved for along with the drift velocity of each phase with respect to the mixture. The drift velocity accounts for the relative motion between phases due to buoyancy, drag and turbulent dispersion.

Turbulence Modelling

The jet issuing from the spill is unsteady and turbulent, with the small scales in the flow causing rapid mixing between the jet fluid and the surrounding water. The best approach to model turbulence here is the Very-Large Eddy Simulation (V-LES) approach (Labois and Lakehal, 2010), also known as filter-based approach. The idea is based on the concept of filtering a larger part of turbulent fluctuations as compared to LES; only the turbulent scales below a certain grid-independent filter scale are modelled. In TransAT, the V-LES is based on the k−ε model for the sub-scales. For multiphase flow, only the turbulence of the mixture is solved for.

Hydrates Modelling

In TransAT, hydrates are split into two phases: non-adhesive hydrates denoted by subscript ^{na} and adhesive hydrates, denoted by subscript ^{a}. The non-adhesive hydrates never stick to the walls and are assumed to be mixed in the flow and form in the bulk away from the walls. The adhesive hydrates form

closer than a prescribed distance from the wall (or existing adhered hydrate structure), and stick to the wall (or existing hydrate structure) immediately on formation. The equations for these phases read,

$$\frac{\partial}{\partial t}\alpha_{na}\rho_{na} + \frac{\partial}{\partial x_j}\alpha_{na}\rho_{na}u_{j,na} = \dot{m}^{f} - \dot{m}^{d}_{na} - \dot{m}^{na-a} \quad (8)$$

$$\frac{\partial}{\partial t}\alpha_{a}\rho_{a} + \frac{\partial}{\partial x_j}\alpha_{a}\rho_{a}u_{j,a} = -\dot{m}^{d}_{a} - \dot{m}^{na-a} \quad (9)$$

where $\dot{m}^{f}$ and $\dot{m}^{f}$ denote the hydrate formation and dissociation rates, and $\dot{m}^{na-a}$ is the fraction of sticking hydrates forming at a given location, and is set to zero away from the wall and one otherwise. While only non-adhesive hydrates are formed from hydrocarbon phase, both adhesive and non-adhesive hydrates can dissociate to hydrocarbon and water under appropriate thermodynamics conditions.

Further, hydrates formation from methane is based on a single-step exothermic reaction given as,

$$CH_4 + nH_2O \rightarrow (CH_4 nH_2O) \quad (10)$$

where n=5.75 is the hydration number of methane. The finite-rate kinetics model of Vysniauskas and Bishnoi (1983) is used. The heat of formation for methane hydrates is 54.2kJ/mol. Hydrates dissociation is considered to be as instantaneous. The hydrate equilibrium temperature as a function of pressure and methanol fraction in water should be provided as a model input.

Hydrates suspended in the flow behave like a slurry where the mixture behaves like a shear-thinning fluid (Colombel et al., 2009). The viscosity of the slurry (μ_s) is then calculated using a multiplier to the viscosity of the continuous phases (μ_c), based on the effective volume fraction (α_e) of hydrates.

$$\mu_s = \mu_c \left[\frac{1-\alpha_e}{\left(1-\frac{\alpha_e}{\alpha_{max}}\right)^2} \right] \quad (11)$$

where $\alpha_e=\alpha_h(\tau/\tau_0)b$ accounts for the agglomeration of hydrates under low shear conditions. τ represents the local shear stress, b is a constant, τ_0 is the critical shear stress set to 250Pa and α_{max} is the volume fraction at close packing. The adhesion of hydrates to solid walls is a complex phenomenon about which not much is still known. Therefore, in order to have a conservative estimate hydrates coming in contact with walls are assumed to adhere to the walls and hydrates coming into contact to an existing adhered structure will adhere to this layer.

VALIDATION/APPLICATIONS

Miscible phases

The mixing and dissolution of miscible phases such as methanol and water was simply modelled by turbulent mixing. The slip velocity between the miscible phases was explicitly set to zero so that once the phases mix they would not be able to separate out. This simple model was shown to be adequate by comparison to experiments (Debacq et al., 2003).

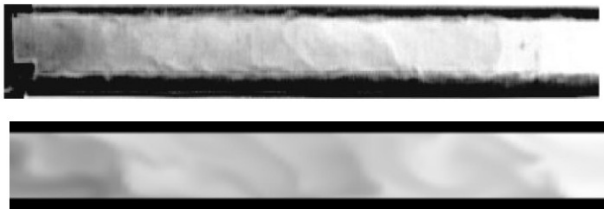

Figure 2: Comparison of density contours between experiment (top) and simulation (bottom).

The experiments measure the diffusion of miscible liquids into each other in a vertical pipe starting with the heavier fluid at the top and the lighter one at the bottom. The mixing is initiated through the Rayleigh-Taylor instability and driven by turbulent diffusion. The density contours obtained from the simulations are qualitatively comparable to the experimental results (Fig. 2). Quantitative comparison is presented in Table 1 where the simulations predict the diffusion coefficients with reasonable accuracy.

Case	**D** (mm)	**ν** (m^2/s)	D (m^2/s)	D_{exp} (m^2/s)
1	44	1.10^{-6}	$2{,}3.10^{-3}$	$1{,}7.10^{-3}$
2	20	1.10^{-6}	$8{,}69.10^{-4}$	$5{,}6.10^{-4}$
3	20	2.10^{-6}	$1{,}08.10^{-3}$	8.10^{-4}

Table 1: Comparison of prediction of diffusion coefficient between miscible liquids

Plugging of a deepwater riser with hydrates

Prior to using the model for hydrate plugging of subsea caps, for example, as employed by BP to cap the Macondo well, it was first employed to predict the plugging of a vertical riser flow initially filled with oil and water and methane. The 50m long, 10cm diameter riser is hypothetically placed at 1500m below sea level, where the pressure is 150 bars and water temperature is 4 deg. C. The rise is assumed to contain a hydrocarbon mixture flowing at a speed of 0.5/s, equivalent to Re=17.000. The density and viscosity of the mixture is 850 kg/m3 and $2.5e^{-3}$ Pa.s, respectively. The density of oil is 650 kg/m^3 oil and that of methane as 130 kg/m^3. At the pipe inflow, the composition of the mixture is modelled as follows: 50% water, 45 % oil (37% of heavy components and 8% of light components), and 5% methane. The hydrate form instantaneously; no kinetics is employed. The flow regime is considered to be bubbly, with bubble diameters of 10mm.

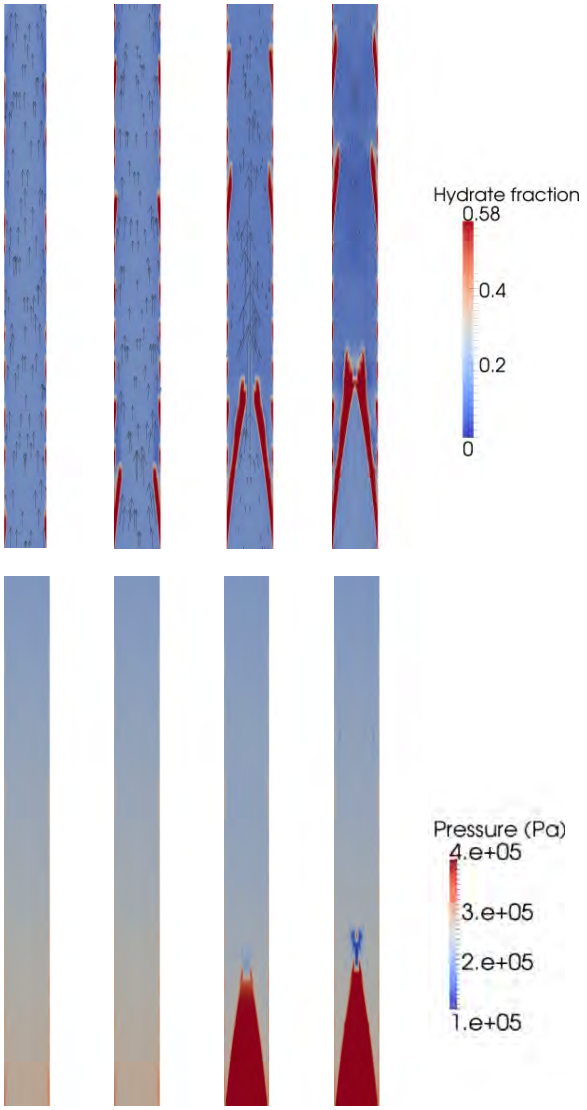

Figure 3: Hydrate formation and corresponding pressure in the pipe, at different instances.

The 2D-axisymmetric simulations have run in transient mode using a second-order time marching scheme. Turbulence was modelled using the V-LES approach described above, with a prescribed filter width of 1/10th the pipe diameter. Figure 3 clearly shows the gradual formation of the hydrates from the wall, from an initial hydrates-to-wall-adhesion mechanism. The last two sequences shown indicate that the rise has been literally plugged, as is well suggested by the pressure contours shown below. Note that the structures of hydrates tend to transform the flow regime into slug, with a succession of oil/water plugs, a mechanism out of reach of the mixture model employed here. The volume fraction of the water, which was initially constant –prior to hydrates formation- varies between 0.35 and 0.55, translating the consumption of water by the hydrates along the pipe. The pictures don't show gas contours since the only 5% of methane have already been consumed in the formation of hydrates.

Plugging of a vertical pipe with hydrates

This additional application test-case presented here is meant to predict the plugging by hydrates in a complex tubing system of 32m long and 20cm diameter. The hydrocarbon mixture containing 95% water and 5% of methane is injected from the lower port at a speed of 2 m/s. The same model ingredients fluid properties as in the previous case were used as well. The absence of oil in this configuration reduces the number of equations to be solved in the N-phase approach, and reduces the phase-change (hydrates formation) only to the contact of water and methane.

Figure 4 below shows the contours of pressure, viscosity and hydrates at two instances of the simulation (19.3 and 20.7s). As the hydrates form - also from a wall-adhesion mechanism- the viscosity of the mixture increases, which, in turn, affects the pressure of the system, leading eventually to plugging.

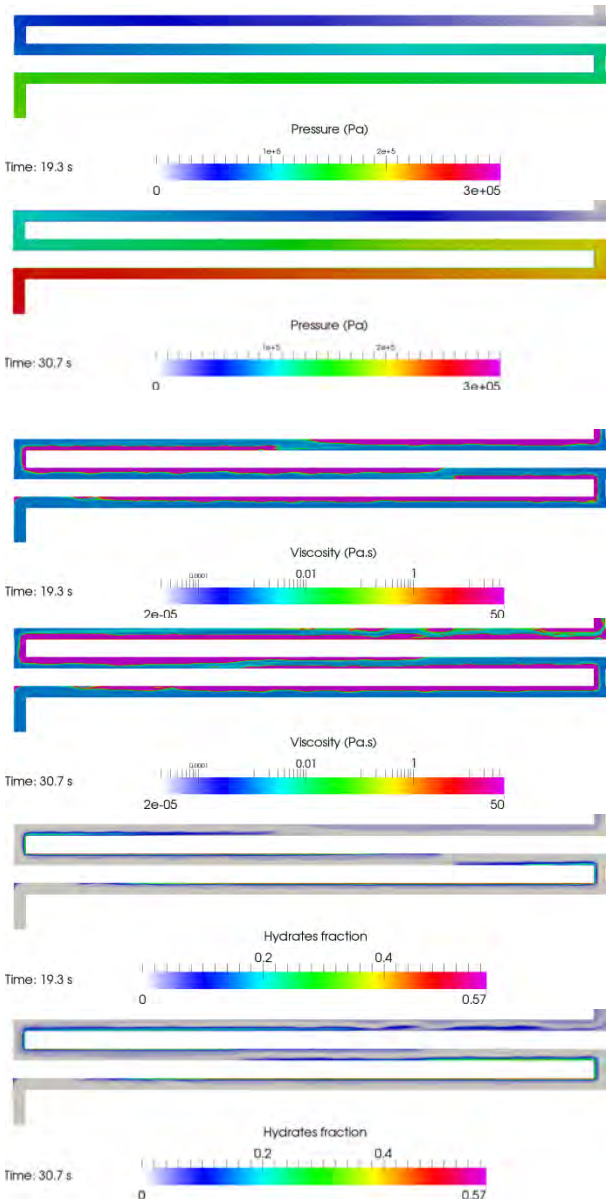

Figure 4: Hydrate formation and corresponding pressure and viscosity in the tubing system.

HYDRATES IN THE BP CAPPING DOME

Problem setup

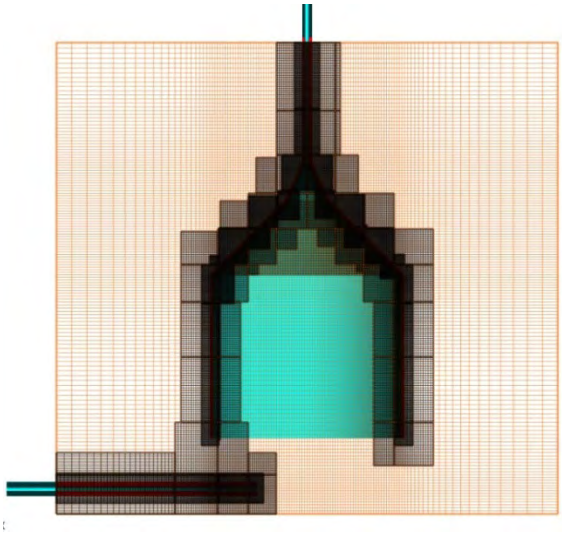

Figure 5: IST meshing of the cofferdam placed by BP to seal the Macondo well (from CAD file available in the DOE website relating to the spill).

The containment of the Deepwater Horizon oil spill -the cofferdam solution- by BP was unsuccessful due to severe hydrates plugging, as discussed in the introduction. Our objective here was to test the hydrates model of TransAT to predict a real scenario. The CAD file representing the cofferdam was first used to mesh the computational domain around the spill (Fig. 5). Here we have employed the IST meshing technique proper to TransAT, where the solid represented by a solid level set function re-produced from a CAD file is immersed in a Cartesian grid. Use was made of the complete model to simulate the flow along with hydrate formation inside the dome. The ambient condition of water corresponds to a depth of 1500m with a temperature of 4° C. The density of water was set as 1035kg/m^3, those of the oil and gas phases were 781kg/m^3 and 124kg/m^3, respectively. The hydrate equilibrium temperature of 20.5° C was used. These data are now available in the media.

Results and discussions

Figure 6(a) shows a snapshot of the flow featuring only oil (coloured) and water (blue), before activating the complete hydrate module, including formation, adhesion and melting. The result suggests that the flow escapes partially from the canopy. These first results have indicated that the jet flow features strong unsteadiness and could only be well predicted using a time dependent approach; steady-state simulations are simply meaningless in this context. Since use of LES is prohibitive for similar problems, we have extended the model to couple the N-phase with hydrate module with V-LES described above; URANS was useless as well in the sense that various scales were smeared out.

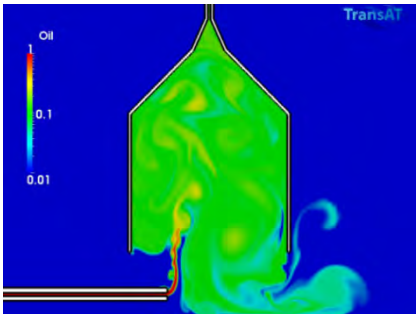

(a) Only oil and water (black oil assumption)

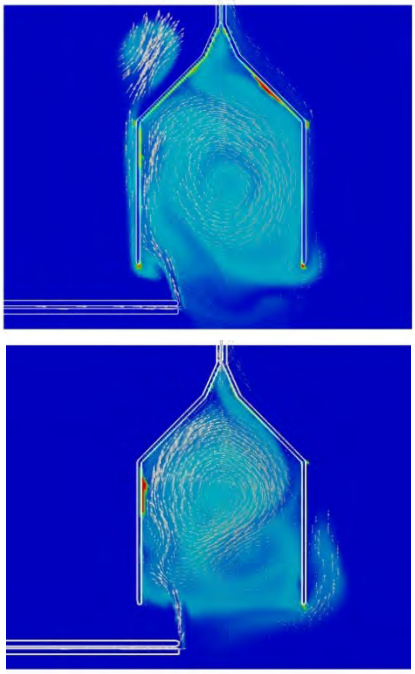

(b) No methanol 80 s (c) With methanol 80 s

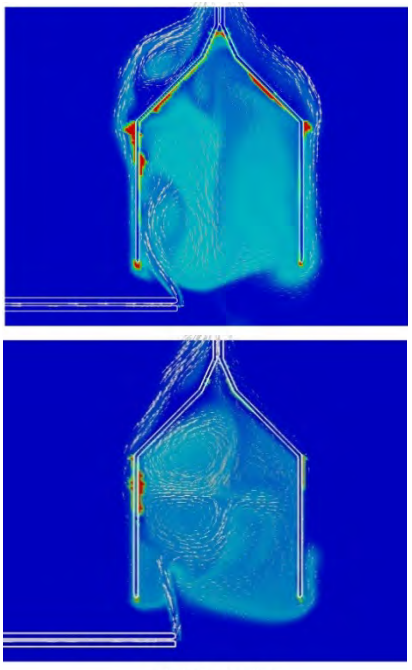

(d) No methanol 120 s (e) With methanol 120 s

Figure 6: Simulation of the BP top-hat canopy.

The results illustrated in Fig. 6 suggest that the stability model employed in connection with the rheology model (Eq. 11) renders well the adherence of the hydrates on the canopy internals, leading to a blockage of the flowlines that evacuate the oil via the riser. The figures show the sequence beyond blockage, when oil starts escaping from the canopy. To try and prevent blockage, it was proposed to inject methanol from various small nozzles inside the canopy (details not shown here) - the effect of methanol is to locally lower the critical temperature of hydrate formation. In the presented case, although some hydrates still adhere to the walls, the riser does not get blocked and almost no oil escapes the canopy (Fig. 6, c and d panels). Clearly, detailed CMFD provides an invaluable prediction tool for this problem.

Coupling with OLGA (1D)

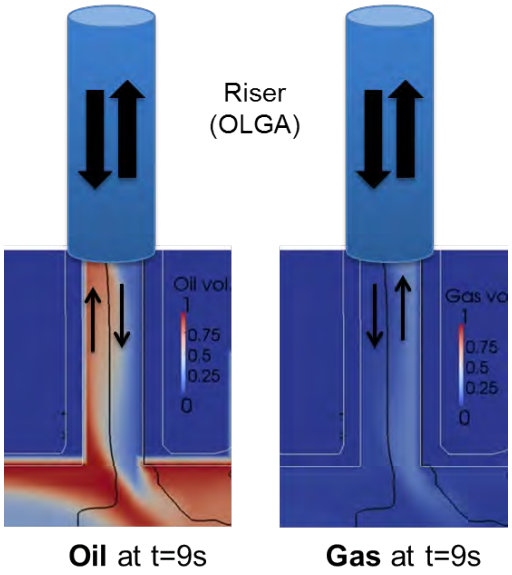

Figure 7: Coupled solution at the OLGA/TransAT interface showing oil and gas iso-contours at t=9s

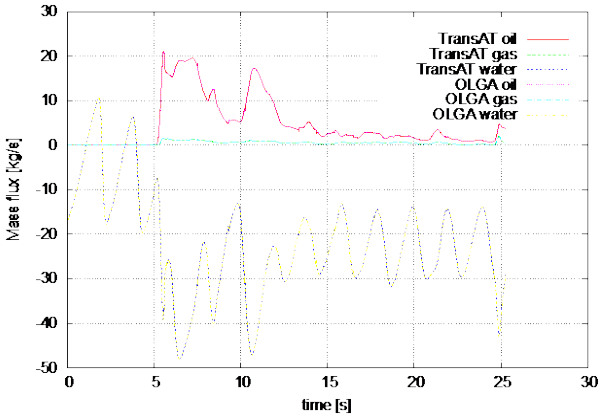

Figure 8: Mass flux at the OLGA/TransAT interface

For more realistic flow conditions at the riser's exit, however, this 2D simulation (or 3D) should be coupled with a 1D code to simulate the entire process: from oil collection near the source to the collector vessels at the surface. This seems to be needed in particular to account for potential flow reversal at the port. This has now been accomplished by coupling TransAT with OLGA (thanks to SPT's crew help); the results of which are shown in Figs. 7 and 8. Now since OLGA cannot yet account for the presence of hydrates at any pipe inflow, we have considered the case without hydrates; results shown in panel (a) of Fig. 6. Briefly, since this is not the scope of this paper OLGA/TransAT coupling has been implemented in a rigorous flux-conserving context, under implicit, transient conditions. Figure 7 shows actually that the flow exhibits reversal at the exit port; both gas and oil could re-enter the dome from the exit pipe. Figure 8 shows that the mass fluxes at the coupling interface are well conserved, mimicking the flow reversal.

Conclusions

A proof-of-concept study is presented based on complex C*M*FD simulation of hydrocarbon multiphase flows under deep sea conditions to address hydrate risk for the containment design of leaking wells and associated flow assurance. A modelling methodology such as the one presented can be a useful tool to arrive at a better design for top-hat concepts, remedying the issues faced by BP in installing the containment system of Macondo. This temporary collection method should be a critical part of spill response since typically the final solution of capping the well usually takes several months resulting in irreparable damage to the environment and correspondingly large losses to the operators. It is obvious that a more quantitative evaluation of the ability of the present model to predict real-life scenarios is needed.

REFERENCES

BBC News 2010 Plan to cap gulf of mexico oil leak with dome delayed. http://news.bbc.co.uk/

British Petroleum 2010 Top hat oil containment dome-chamber to cap gulf oil spill. https://www.youtube.com/watch?v=wkgaiacjota.

Colombel, E., Gateau, P., Barre, L., Gruy, F. & Palermo, T. 2009 Discussion of agglomeration mechanisms between hydrate particles in water in oil emulsions. Oil & Gas Sce. and Tech. 64, 629–636.

Debacq, M., Hulin, J.-P., Salin, D., & Hinch, E. J. 2003 Buoyant mixing of miscible fluids of varying viscosities in vertical tubes. Phys. Fluids 15, 3846.

Manninen, M. & Taivassalo, V. 1996 On the mixture model for multiphase flow, , vol. 288. Espoo, Finland: VTT Publications.

The New York Times 2010 Methods that have been tried to stop the leaking oil. http://www.nytimes.com

TRANSAT, (2012), TransAT: *ASCOMP GmbH, Zürich, Switzerland*, www.ascomp.ch/transat/.

Vysniauskas, A. & Bishnoi, P. R. 1983 A kinetic study of methane hydrate formation. Chemical Engineering Science 38 (7), 1061{1072.

CFD SIMULATIONS OF FLOW IN RANDOM PACKED BEDS OF SPHERES AND CYLINDERS: ANALYSIS OF THE VELOCITY FIELD

Ferdaous DORAI[1*], Matthieu ROLLAND[1], Anthony WACHS[1], Manuel MARCOUX[2], Eric CLIMENT[2]

[1] IFPEN, Rond-Point de l'Échangeur de Solaize, 69390 Solaize, France

[2] IMFT, 1 Allée du Professeur Camille Soula, 31400 Toulouse, France

* E-mail: ferdaous.dorai@ifpen.fr

ABSTRACT

In this work, we aim to better understand the flow patterns in a random arrangement of particles that might affect local mass transfer and effective reactor performance.
Using the DEM code Grains3D, spherical or cylindrical particles are randomly inserted inside a horizontally bi-periodic container and fall under gravity. Hydrodynamic simulations are performed with PeliGRIFF, a Fictitious Domain/Finite Volume numerical model. Simulations parameters are the bed height and particulate Reynolds number. Effect of random packing on the flow field is analysed in terms of the probability distribution function (PDF) of the normalized vertical velocity.
A higher Reynolds number makes more backward flow zones and changes the PDF curves that we interpret as thinner boundary layers.
Unexpectedly, internal variability is independent of bed height. We propose that the probability of occurrence of random structures increases with bed volume in opposition with volume averaging effects.
Internal and external variability are similar for beds of spheres and cylinders of aspect ratio (< 2). However, for longer cylinders (higher aspect ratio), subdomains with same thickness are statistically different from one bed to another. We propose that the subdomain thickness required to average out sources of variability increases with high particle aspect ratio.

Keywords: Chemical Reactors, packed beds, velocity distribution, probability density function.

NOMENCLATURE

Greek Symbols

ρ Fluid density, [kg/m^3].
μ Dynamic viscosity, [kg/m.s].
ε Porosity (void fraction)

Latin Symbols

a Aspect ratio of a cylinder (length /diameter of cylinder)
d Particle equivalent diameter, [m].
l Cylinder length, [m].
P Pressure, [Pa].
U Velocity, [m/s].

Subscripts

c relative to a cylinder
s relative to a sphere
ls liquid, superficial
z vertical direction

INTRODUCTION

In this study, we are interested in small size fixed bed reactors which contain spherical or cylindrical catalysts with a characteristic size of 2-3 mm. These reactors are used to test small amounts of catalyst and are *a priori* more prone to random effects than industrial reactors.
Reactive testing performed inside these reactors involves complex mass transfer interactions between the fluid flow and reaction in the particles. In this paper, we are interested in the flow patterns in random packed beds. In literature, flow distributions are obtained using either an experimental approach (PIV (Particle Image Velocimetry), NMR (Nuclear Magnetic Resonance imaging), MRI (Magnetic Resonance Imaging) ...) or a numerical one. Concerning numerical works in random packing, Maier (1998) performed Lattice-Boltzmann simulations to study viscous fluid flow in a column of glass beads. He found that the velocity distribution is affected by bed porosity and Reynolds number. Rong (2013) performed also Lattice-Boltzmann simulations inside periodic randomly beds of mono-disperse spheres with porosity ranging from 0.37 to 0.8. However, the aforementioned studies do not study and quantify the local variability inside the bed.

The purpose of this work is to give a quantitative information of local velocity field and to link this information to internal and external structural variabilities. Internal variability is defined as variability within a bed, whereas external variability is defined as the difference arising between two random beds.
Numerical simulations for packed beds of spheres and cylinders are performed. We study the effect of Reynolds number, packed bed heights, and local random structure (repeatability) on velocity distributions.

SIMULATIONS DESCRIPTION

In order to examine the flow through packed beds of catalysts, simulations of packed beds of mono-disperse spheres and cylinders were performed in single phase flow in laminar regime (Re<15). The packing is created using the DEM (Discrete Element Method) code Grains3D (Wachs et al. (2012)). Particles are randomly inserted inside a container. They fall from the top under gravity and collide with each other and the bottom of the reactor. The boundary conditions used are periodic in the horizontal directions. Hydrodynamics simulations are performed with PeliGRIFF (Wachs (2010)), using the packing created with Grain3D. The meshing of the fluid domain is based on a cartesian structured grid with a constant grid size in the 3 directions. The CFD boundary conditions are: periodic boundary conditions in the same directions as the DEM simulations, uniform vertical upward velocity in the inlet (bottom wall of the domain) and uniform pressure in the outlet of the domain (top wall of the domain).
The simulations performed for spheres and cylinders are summarised in Table 1.

Table 1: Simulated cases for spheres and cylinders packed beds

Case Label	Particle size (mm)	Reynolds Number	Particles number	Number of repetitions of packing
S1-0.07	$d_s = 3$	0.07	540	1
S1-0.7	$d_s = 3$	0.7	540	1
S1-7	$d_s = 3$	7	540	10
S1-14	$d_s = 3$	14	540	1
S2	$d_s = 3$	7	1000	1
S3	$d_s = 3$	7	1500	1
S4	$d_s = 3$	7	2000	1
C2	$l_c = 2$ $d_c = 1.6$	0.37	380	3
C3	$l_c = 3$ $d_c = 1.6$	0.43	250	3
C4	$l_c = 4$ $d_c = 1.6$	0.47	180	3

Particulate Reynolds number is based on the equivalent diameter (diameter of a sphere of the same volume). It is defined as follows:

$$\mathrm{Re} = \frac{\rho \boldsymbol{U}_{ls} d}{\mu} \qquad (1)$$

In Figure 1-a and b, bed S1 is presented showing the CFD boundary conditions and the mesh used. For S1, the computational domain dimensions are $6d_s$*$6d_s$*$17d_s$ (which corresponds to 18 mm*18 mm*51 mm) with entry and exit zones. The spatial resolution used (20 points / particle diameter) gives a computational domain composed of about 5 millions of cells. This resolution has been set after a convergence study toward exact analytic solutions of pressure loss in various packed beds.

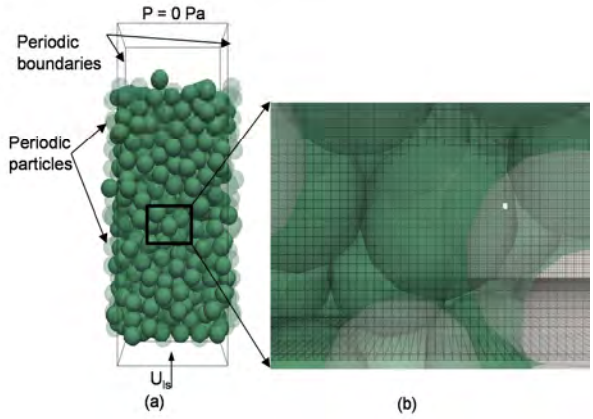

Figure 1: (a) Simulated packed bed of monodisperse spheres (S1) and (b) mesh of the geometry

For packed beds of cylinders, we considered 3 classes of cylinders with the same diameter d_c = 1.6 mm and an increasing length: 2 mm, 3 mm and 4 mm (Table 1). Each case was repeated three times. The bed height is approximately 40mm in all the cases (Figure 2). Particulate Reynolds number is below 0.5. The computational domain dimensions are 8 mm*8 mm*49 mm with entry and exit zones (below and above). The spatial resolution used (32 points / particle diameter) results in a computational domain composed of about 25 millions of cells. It has been chosen after a convergence study that showed that convergence was slower than for spheres Dorai et al. (2014).

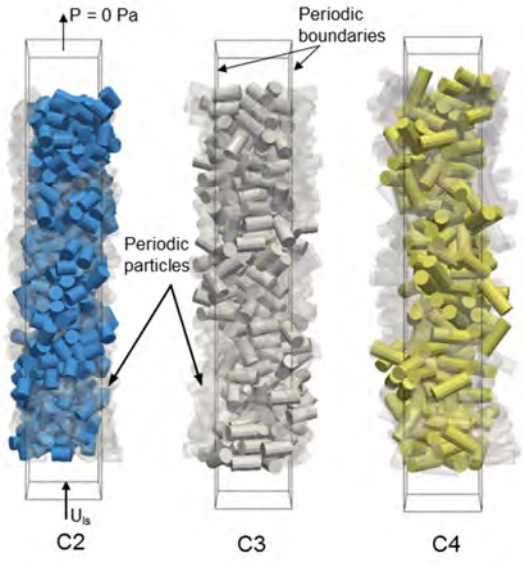

Figure 2: Simulated packed beds of monodisperse cylinders

ANALYSIS METHODOLOGY

Construction of PDF curves

The objective of this work is to compare the spatial velocity distributions for various cases and derive quantitative information for velocity fields in the case of random packed beds with low porosities (around 0.4). The analysis of the results is performed by considering the velocity field as the occurrence of a random variable such as described in Cedenese (1996), Rong (2013). Results are thus presented in the form probability

density functions (PDF) of the normalized vertical velocity (P (U_z / U_{ls})).
The PDF is constructed by first defining velocity classes, then, by counting the number of fluid cells whose velocity belongs to each class. At this step, we obtain a histogram that is converted to a PDF by normalizing the vertical velocity so that it satisfies equation (2).
As we use a large number of velocity classes (400), the information is better presented as a curve.

$$\int P(U_z / U_{ls})dU = 1 \qquad (2)$$

All PDF curves present the same general features (Figure 3): (i) in the left side, the proportion of negative velocity is negligible (about 1% of all occurrences), (ii) sharp peak near U_z /U_{ls}= 0, (iii) gradual decrease for velocities U_z /U_{ls} > 1 (the curve becomes flatter). These observations were also reported by Maier (1998) and Rong et al., (2013) for packed structures (ε~0.36). Rong observed bimodal shapes for loose structures and high Reynolds number.

Effect of entrance and exit regions

By dividing the bed in non-overlapping sub-domains of equal thickness in the vertical direction (= 2*d_s), it is possible to compare the velocity fields within a bed. The PDFs obtained by dividing S1-7 in 7 zones are plotted in Figure 3. Zone 7 (outlet, top of the bed) and the lower extent zone 1 (inlet) have distinct PDF shapes. In zone 7, porosity is much higher as there are some vacancies in the lattice due to lower densification by lack of impacting particles. In zone 1, the rigid flat bottom constraints the packing that is not as random as in the other subdomains. This has been reported and discussed elsewhere (Dorai, 2012). From here on, we will exclude from analysis all subdomains near the top and bottom of the packed beds (excluded zone thickness = 2*d_s for spheres and 2*d_c for cylinders).

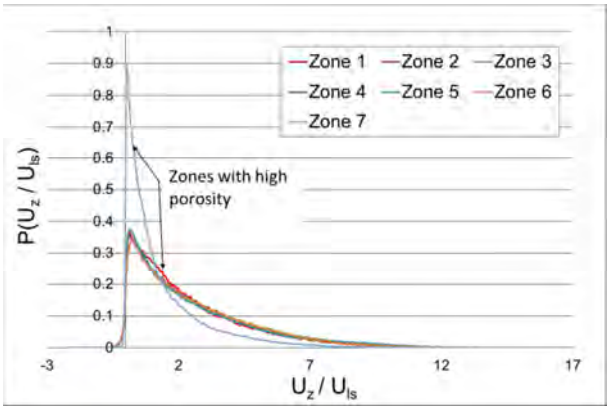

Figure 3: Effect of entrance and exit regions on PDF curves (bed S1-7)

PDFs comparison

Comparison of PDF curves has been performed with two methods: subtraction and statistical. Both methods require to have the same velocity classes for PDF curves. In the subtraction method, we compute the class to class difference between PDFs which is referred to as "PDF deviation" in the rest of the text. If the number of PDFs to compare is larger than 2, it is more convenient to subtract a common reference that should be chosen so as to represent some asymptotic or average case. When studying internal variability, the reference is the PDF of the whole bed (inlet and outlet excluded). If the focus is on external variability, the reference is chosen as the longest bed for length comparison or average of all PDF bed for repeatability. When comparing many PDF curves, after subtracting the reference, we calculate the "Maximum deviation function" that is constructed by choosing for each class the maximum deviation (absolute values) from the reference among all PDFs. Deviation functions are an indicator of the maximum variability within the domain studied. They do not respect equation (2).

Another way to compare PDF functions is to use the statistical "variance test" (Fischer test) that tests the hypothesis H_0 "PDF is identical for all domains". The statistical test is run for each velocity class. The variance test has been used to determine whether domains extracted from different beds present significant differences or not. In other words, can we distinguish a sub domain from another when they do not belong to the same bed.

RESULTS

Simulations with different Reynolds numbers

In this section, the effect of Reynolds number is studied in the same packed bed of spheres in laminar regime (S1, ε = 0.39). PDF curves are presented in Figure 4.

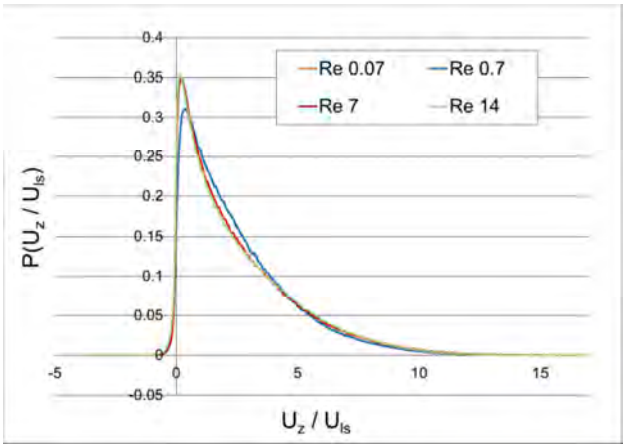

Figure 4: PDFs for different Reynolds numbers, bed S1

At very low Reynolds numbers 0.07 and 0.7 (creeping flow), curves are identical. The peak near 0 is more important for higher Reynolds number, which has also been reported in Rong et al. for ε = 0.5. In all cases, highest velocity can exceed 8*U_{ls}. At higher Reynolds number (7 and 14), there are more fluid cells with important velocity U_z / U_{ls} > 7 and less cells with small velocity (U_z / U_{ls} between 1 and 4) (Figure 5). We propose that increasing the Reynolds number leads to thinner boundary layers and increased number of fluid cells with high velocities.

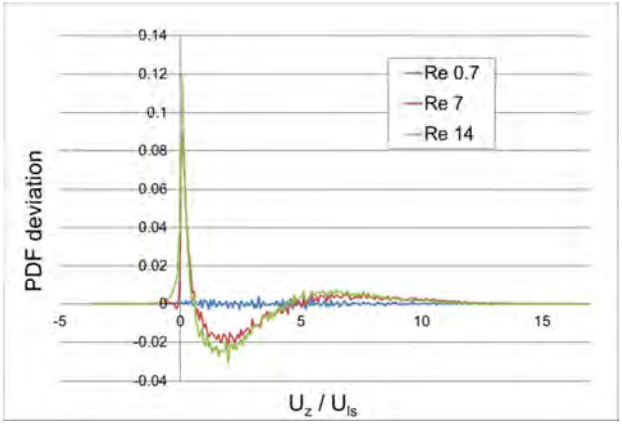

Figure 5: PDFs deviations calculated to PDF of lowest Reynolds number (0.07)

The proportion of negative vertical velocity (backward flow) is higher for higher Reynolds number (Figure 5 and Figure 6). This increase in proportion is more due to an increase in the number of backward flow zones rather than an increase in their size. For S1-14, the backward flow zones are homogeneously distributed in all domains.

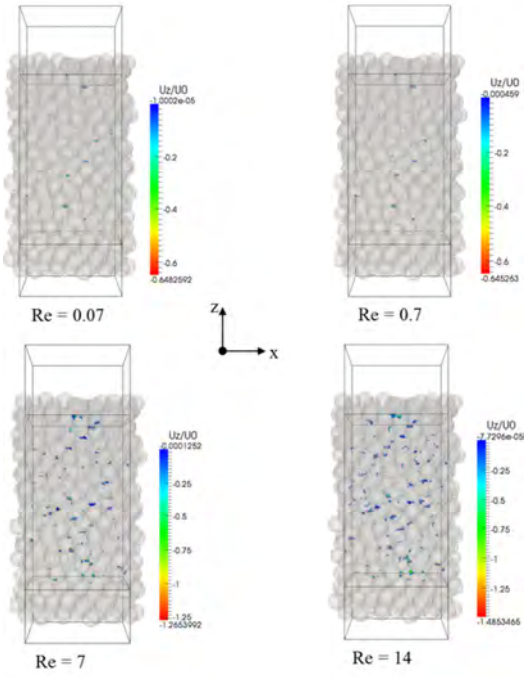

Figure 6: Zones with negative vertical velocity

Comparison of beds with different heights

Four packed beds of spheres (S1, S2, S3 and S4) are divided into regions with equal thickness ($2*d_s$). We calculated the deviation of PDFs in every region to the PDFs of longest packed bed (S4). We expected that maximum PDF variations would be higher for the shortest packed bed and that a longer bed would provide more averaging, which is not the case (Figure 7).
Moreover, the shortest bed (S1) presents less internal variability than the others. An explanation could be that increasing bed length increases the probability of occurrence of sources of variability, may-be from average random structures (tightly packed or loosely packed for example). In conclusion, bi-periodic long beds present the same internal variability as short ones.

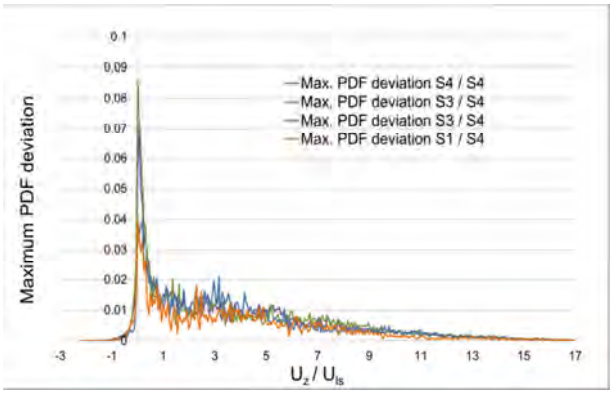

Figure 7: Maximum deviation functions calculated for S1, S2, S3 and S4 to mean PDFs of S4

External and internal variability for spheres

In this section, we want to know if there are any differences in flow structure in random packed beds composed of the same number of spheres (repetition of packing), and if these variations can be compared to the variations inside a given packed bed.
To answer the first question, we performed CFD simulation on 10 randomly packed beds with the same number of spheres; each bed has a different structure from the other. PDF deviation to the average PDF of all repeated cases indicate that some variability between beds is visible (Figure 8), for example “repeat5” bed present less “low velocity” cells and more “high velocity” cells than the average. Except near 0, deviation of all beds remains within a value of 0.003. It would be interesting to compare this value to the internal PDF variations (inside a single packed bed).

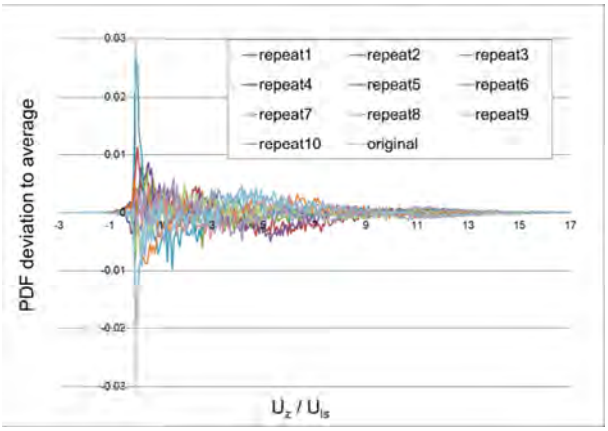

Figure 8: PDFs deviation to the average PDF of all repeated cases

To examine variability inside a bed, S1-7 is divided into domains of equal thickness ($2*d_S$) and PDFs deviations are calculated using the PDF of S1-7 as reference (Figure 9). In this case, except near 0, deviations are within a value of less than 0.01. Before comparing with the variations induced by repetitions (Figure 8), it is worth mentioning that the deviation to the average tends

to decrease linearly with the number of sub-domains used. For example, if we would use two sub-domains instead of five to produce Figure 9, then the deviation would be 2.5 times lower. As the external variability value of 0.003 has been obtained on domains of thickness $10*d_S$, and internal variability value of 0.01 has been estimated of domains of $2*d_S$, the external variability value on 10*ds subdomains in the order of 0.003*5, which is quite similar to the internal variability. We conclude that internal and external variabilities are very similar.

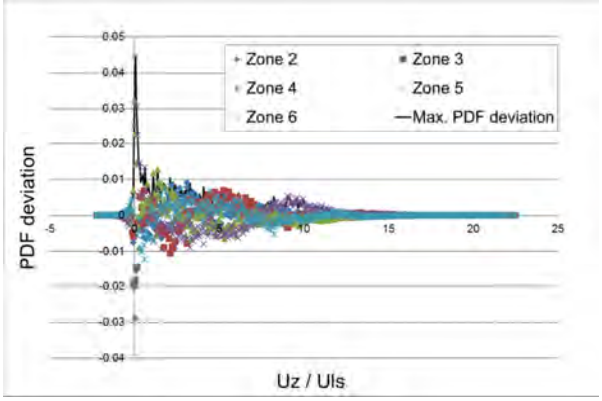

Figure 9: PDFs deviation calculated to the average PDF of all regions in S1

This conclusion is coherent with a variance analysis test performed on 5 sub-domains of S1-7 and 5 sub-domains of S1-7-repeat1. The analysis shows that for 99.5% of classes there is no statistical difference (at 5% risk) between S1-7 and S1-7-repeat1 sub-domains based on flow patterns.

External and internal variability for cylinders

Identical methodology has been applied to packed beds of cylinders with 3 repetitions on each cylinder length case. Variability between repeated beds is similar to that of spheres (Figure 10). Variability inside one bed is also of the same order of magnitude.

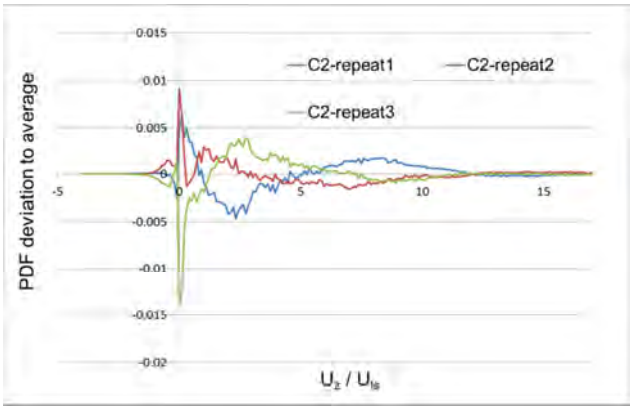

Figure 10: PDF deviation calculated to average PDF of repeated simulations of C2

The variance analysis gives a slightly more precise information. More classes are found to present difference between repetitions: 12.5 % of classes for C4 (a = 2.5), compared to 1.25 % and 0.25 % for C2 (a = 1.25) and C3 (a = 1.875) respectively. C2 and C3 appear to behave like packed beds of spheres: for aspect ratio up to 1.875, subdomains of thickness of $2*d_c$ present the same variability regardless of their origin (any location in any bed). On the opposite, for the highest aspect ratio case, subdomains of the same thickness are statistically different from one bed to another. It may be that higher particle anisotropy increases the minimum volume required to average out the sources of variability, also called Representative Elementary Volume (REV).

CONCLUSION

Simulations of fluid flow in bi-periodic packed beds of mono-disperse spheres and cylinders have been performed using a Fictitious Domain/Finite Volume numerical model. The simulations provide detailed information on the hydrodynamics and local velocity fields. Effect of random packing on the flow field is analysed by considering the velocity field as the occurrence of a random variable characterized by its probability distribution function (PDF).

- Top and bottom part of the packing are excluded from the analysis as they do not present the same flow patterns, due to lack of densification (top) and due to the presence of a flat surface (bottom) that prevents random positioning of particles on a layer of about two particle diameters.
- PDF curves for packed beds of spheres and cylinders have the same overall shape.
- A higher Reynolds number results in the presence of more backward flow zones and change in the PDF curves that we interpret as thinner boundary layers.
- Unexpectedly, internal variability is independent of bed height. We propose that the probability of occurrence of random structures increases with bed volume in opposition with volume averaging effects.
- Internal and external variability are similar for beds of spheres and cylinders of aspect ratio lower than 2. However, for longer cylinders (higher aspect ratio), sub-domains of the same thickness ($2*d_c$) are statistically different from one bed to another. We propose that the subdomain thickness required to average out sources of variability increases with high particles aspect ratio.

Perspectives are: to explore the link between shape and Representative Elementary Volume dimensions, to focus on how the presence of walls may change the results presented in this work and to perform simulations of reactive transport and study the link between structure, flow and reactivity variations in random packed beds.

REFERENCES

CENEDESE A., VIOTTI P., (1996), "Lagrangian analysis of nonreactive pollutant dispersion in porous

media by means of the particle image velocimetry technique", *Water Resources Research*, **32** (8), 2329-2349.

DORAI F., ROLLAND M., WACHS A., MARCOUX M., CLIMENT E., (2012), "Packing Fixed Bed Reactors with Cylinders: Influence of Particle Length Distribution", *Procedia Engineering*, **42**, 1335-1345.

DORAI F., DE MOURA T. C., ROLLAND M., CLIMENT E., MARCOUX M., WACHS A., (2014), "Fully-resolved simulations of the flow through a packed bed of cylinders: effects of size distribution", *under submission in Oil & Gas Science and Technology*.

GUNJAL P.R., RANADE V.V., CHAUDHARI R.V., (2005),"Computational Study of a Single-Phase Flow in Packed Beds of Spheres", *AICHE Journal*, **51** (2), 365-378.

MAIER R.S., KROLL D.M., KUTSOVSKY Y.E., DAVIS, H.T. BERNARD R.S., (1998), "Simulation of flow through bead packs using the lattice Boltzmann method", *Phys. Fluids*, **10** (1), 60-74.

RONG, L.W., DONG, K.J., YU, A.B., (2013), "Lattice Boltzmann simulation of fluid flow through packed beds of uniform spheres: Effect of porosity", *Chemical Engineering Science*, **99**, 44-58.

WACHS A., GIROLAMI L., VINAY G., FERRER G., (2012), "Grains3D, a flexible DEM approach for particles of arbitrary convex shape - Part I: numerical model and validations", Powder *Technology*, **224**, 374-389.

WACHS A., (2010), "PeliGRIFF, a parallel DEM-DLM/FD direct numerical simulation tool for 3D particulate flows", *Journal of Engineering Mathematics*, **71**, 131-155.

PORE-SCALE SIMULATION OF FLUID FLOW IN PACKED-BED REACTORS VIA RIGID-BODY SIMULATIONS AND CFD

Gianluca BOCCARDO[1]*, **Luigi DEL PLATO**[1], **Daniele MARCHISIO**[1], **Frederic AUGIER**[2], **Yacine HAROUN**[2], **Daniel FERRE**[2], **Matteo ICARDI**[3]

[1]DISAT - Politecnico di Torino, Torino, ITALY

[2]IFP Energies nouvelles, Rond point de l'échangeur de Solaize, BP3, 69360 Solaize, France

[3]CEMSE - KAUST, Thuwal, Saudi Arabia

* E-mail: gianluca.boccardo@polito.it

ABSTRACT

The problem of fluid flow in porous media is of paramount importance in the process, oil and metallurgical industries, since it is involved in the extraction of minerals and oil, in aquifer dynamics, as well as chemical reactions carried out in fixed bed catalytic reactors. Its CFD simulation is particularly interesting, as it offers the possibility of reducing the extent of costly experimental investigations, but presents a number of technical challenges. One of the main issues is the generation of a geometrical model that realistically represents the porous medium/particle packing. Its derivation from experiments (i.e. micro-computer tomography) is complicated and packing codes are often limited to simple convex (mainly spherical) objects. In this work a computational tool developed in computer graphics, and integrated with the Bullet Physic Library, is used to generate realistic packings of polydisperse catalytic spheres and trilobes. The geometrical model is then meshed with SnappyHexMesh and then simulated with Ansys Fluent. Results show excellent agreement with experiments, demonstrating the great potentiality of the approach.

Keywords: Porous media, fixed bed catalytic reactor, Blender, Fluent, CFD, fluid dynamics, Ergun law.

NOMENCLATURE

Greek Symbols

ρ	Mass density, $[kg/m^3]$
μ	Dynamic viscosity, $[kg/ms]$
ν	Kinematic viscosity, $[m^2/s]$
ε	Porosity, $[-]$
ε_m	Geometric model porosity, $[-]$
ε_g	Meshed model porosity, $[-]$

Latin Symbols

V_s	Superficial velocity, $[m/s]$.
P	Pressure, $[Kg/ms^2]$.
D_t	Circumscribing trilobe diameter, $[m]$.
D_g	Grain diameter, $[m]$.
D_g^*	Effective grain diameter, $[m]$.
L	Domain length, $[m]$.

INTRODUCTION

In chemical engineering many processes involve fixed bed (mainly catalytic) reactors and as such, the study of the hydrodynamics and transport phenomena inside these systems are of great interest, and fundamental to their design. Usually, parameters of interest (such as mass transfer or dispersion coefficients) are obtained from the corresponding experimentally validated correlations, or from new experimental investigations. However, due to the geometrical features proper of these reactors, these studies are not at all straightforward: many small-scale complexities may arise, which have a great impact on the overall system behavior, both in the fluid flow and in transport processes. This makes the preparation of comprehensive bench-scale experiments difficult, and results in a challenging scale-up of the results obtained at the small-scale to the larger industrial scale of interest. Moreover, it is very difficult to explore the whole range of variation of the properties of interest, as for example the packed bed porosity, the size distribution of the catalyst particles and their shape. These issues are in fact shared by the larger field of study of flow and transport in random porous media. In this respect, an interesting alternative to experimental investigation is represented by computer simulations via computational fluid dynamics (CFD), which can help in limiting the number of experiments to be conducted and allowing for wider exploration of packing characteristics and operating conditions. Moreover, complex small-scale phenomena can be more deeply investigated, in a way usually not attainable with the use of experiments only. Many works have already demonstrated the effectiveness of this approach in the study of packed bed reactors (Augier *et al.*, 2010b,a).

In order to perform a reliable CFD simulation, the starting point is in the choice of an accurate geometric model representing the actual system, and it being as realistic as possible. Two ways of doing this are available. The first lies in using actual experimental data, be it via SEM imaging of the catalytic particles, micro-computer tomography scans of a portion of the packed bed loading, or other such methods. While these procedures have a merit in the precision with which the description of the medium at the pore-scale is obtained, they suffer from a great difficulty in the post-processing of these scans, in order to extract a suitable mesh for the CFD code, and in the high cost of the equipment needed for the experiment itself. The second possibility, and the one chosen in this work, is to rely on a *in-silico* algorithmic reconstruction of a geometrical model, which faithfully represents the real system in all of its features: the first advantage is the extremely lower cost of such an approach with respect to using the more sophisticated experimental techniques mentioned, coupled with the easiness of generating and testing a

very high number of loading realizations, with varying particle shapes and particle size distributions. Obviously, great care must be given as to ensure that the reconstructed model is accurate both as a purely geometrical description and, perhaps more importantly, in showing the same fluid dynamic behaviour of the real system under investigation.
The objective of this work is therefore to demonstrate the validity of the procedure just described, in both these aspects. First, a procedure for the replication of the catalyst loading process, via computer graphics and ballistic physics simulation, was developed and tested for a number of different catalyst shapes. A validation of the viability of the resulting geometries was performed, involving the comparison of the models void fractions with experimental results. In this way, a number of models representing different packed bed configurations were obtained. Also, a great deal of attention was given to the meshing process. Meshes with different levels of refinement were generated, and results concerning the evaluation of the critical cell size necessary to obtain both a good discretization of the grains surface and a precise description of the contact points between them, are shown. Finally, CFD simulations were performed on these systems: fluid flow was described by solving the continuity and Navier-Stokes equations. The results, especially regarding pressure drop in the bed, were compared to empirical models of pressure drop in porous media.

THEORETICAL BACKGROUND

Obtaining the geometric model

As mentioned, the first part of this work dealt with the development of a robust tool for effectively simulating the stacking of particles in a packed bed, with particular attention to catalytic particles and catalytic reactors. In order to do that the software `Blender` (Van Gumster, 2009) was used, which itself avails of the Bullet Physics Library, which is a large collection of codes used to manage the dynamics of rigid bodies and, most importantly, to detect and calculate the outcome of the collisions between these bodies. This library provides for a number of iterative methods combining accuracy, speed and robustness, enabling for the simulations of a very large number of elements, as it will be shown further on; moreover, a clear advantage of using this code with respect to many other algorithms used to recreate granular media models lies in the possibility to manage any particle shape, even complex non-convex ones, which are the ones of most difficult treatment in rigid body simulations. The choice of the code Blender was also made due to its extensive scripting functionality. A tool was then developed (in the language Python3) and plugged into the main rigid body simulation code, with the purpose of quickly setting up different simulation cases, with several particle shapes, particle size distributions, total numbers, and containers in which the particles settle. The shapes considered were spheres and trilobe extrudates, while the containers tested were cubes and cylinders. An example of two cylindrical loadings, one of spheres and one of trilobes, can be found in Fig. 1
Since the purpose is to mimic the loading of the catalyst beads into the reactor in a realistic manner, the particles are initially placed on top of the container, with gravity causing their deposition into it, with the end state of the simulation provided by a stable solution of the balance of the forces acting on them, namely gravity and the interaction forces. The choice of the initial placement of the grains in the setup of the rigid body simulation is a step worth mentioning. As mentioned, the purpose is to replicate the process of physically filling the reactor with catalyst particles as accurately as possible: to that end, different ways of funneling the particles in the system have been devised and tested, and they are shown in Fig. 2.
In short, the first way is the simplest to implement but the less realistic one, with every particles falling in the container through a single straight line, while the other two represent the actual process quite well, with the random "grid" placement giving the best results. The difference in the latter lies in the additional step of allowing for a certain distance between the grids, resulting in more time for each set of particle to settle and thus in a more stable simulation. When items which do not possess spherical symmetry are considered, such as trilobes, a randomization is also added to their original orientation during their placement in the grid.
Two other very important points in the setup of the physical simulation concern the geometric description of the particles during the resolution of the collision events and the mechanical parameters governing their behavior. All particle shapes are represented in Blender with a "watertight" (closed) external mesh, constituted of triangular or quadrangular elements. Hence, the representation of a sphere (for example) will depend on the definition with which the surface is discretized: its refinement level. The higher this refinement level is, the better the model will be but also obviously the heavier the computational cost for calculating the rigid body dynamics and collision events will be. For example, a sphere with refinement level equal to 1 is an icosahedron, with each further refinement level splitting each triangular face into four triangles, resulting in a smoother surface. In the results section the choice for a suitable trade-off in this matter will be presented and justified. Moreover and even more importantly, a choice has to be made of the collision model of the particle. Many times in fact it may not be necessary to use an object surface mesh: in the simple case of a sphere for example, only a two-parameter description (its center and its radius) is necessary to perfectly describe its position and behavior in the physical simulation. The savings in both memory requirements and computational cost with respect to the use of the full surface mesh is evident. There are of course scales of increasing complexity: for an highly non-spherical convex

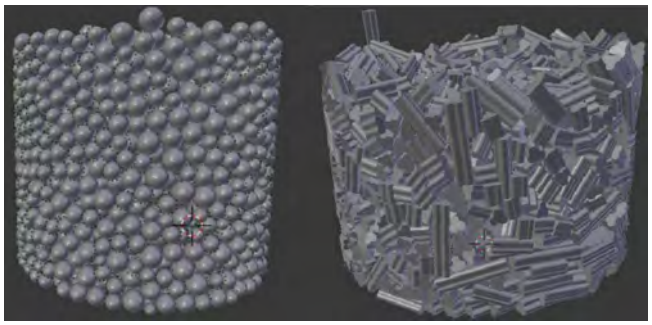

Figure 1: Packing of spheres and trilobes in cylindrical containers.

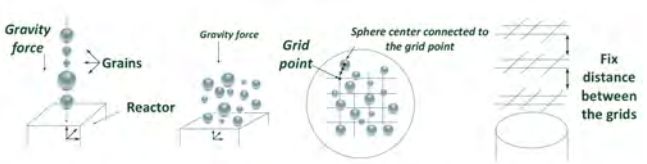

Figure 2: Three different types of initial particle placement.

shape the computation of the nearest-approximating convex hull will be needed, and the most complex case is that of a non-convex shape, and the trilobes considered in this work pertain to this category. In this last case, the whole surface mesh will be needed during the rigid body dynamics computation, leading in a more expensive simulation with respect to the case of spheres.

Lastly, the parameters governing the calculation of interactions between the objects have to be considered: these are the friction factor and the coefficient of restitution. Both of these parameters can be modified, greatly influencing the outcome of the physical simulation. In almost all cases, these settings have been specified in order to replicate the real physical characteristics of the materials involved, but in some cases this was not the most desirable course of action. For the case of trilobes, using the true values for these parameters led to an unrealistic geometric model, showing an excessive packing anisotropy and porosity. In this case, these two parameters were then tuned (reducing the friction factor and increasing the restitution coefficient) in order for the geometrical characteristics of the resulting model to match corresponding validated experimental data. The rationale in this case was to give priority to obtain a realistic and precise simulation result over trying to describe accurately the intermediate deposition and settling steps: the same methodology was followed in (Augier *et al.*, 2010b), where a DEM (Discrete Elements Method) approach was used, in order to improve the density of the loading. Results pertaining this effect and our solution for it will be presented in the next section.

Mesh Generation

After having obtained the geometric models with Blender and having validated them, the analysis of the pressure drop through the identified granular beds was conducted. In this work, fluid flow results pertaining to two different geometric models will be presented. The first one is a rectangular cuboid sample of a packing of Gaussian distributed spheres with average diameter equal to 1.99 mm and standard deviation equal to 0.29, with square faces 9 mm in size and 24 mm long in the direction parallel to fluid flow. The second model share the same bounding volume of the first one but the packing is constituted by trilobes, with circumscribing diameter $D_t = 1.8$ mm (and equivalent diameter $D_g = 1.44$ mm), with a Gaussian distribution in length with average length equal to 4.77 mm and standard deviation equal to 1.8.

A mesh was thus created for these two cases, to be used in the finite volume CFD code. The mesh utility `snappyHexMesh`, included in the open-source package `OpenFOAM` (OpenCFD, 2013), was used. The first step in the meshing process is the creation of a structured, cartesian grid in the entirety of the bounding volume of the system considered. Next, the volume pertaining to the geometric model is subtracted, leaving a cartesian grid in the fluid portion approximating the particles surface with a stair-step description. Finally, the mesh is further modified by moving each boundary vertex, relocating them closer to the original model surface, resulting in a body fitted mesh. The mesh generation process is critical to both obtaining grid independent results during the fluid flow simulation, and for ensuring that the CFD model constitutes a faithful representation of the original geometry. In all the simulations presented in this work, the cell layer next to the surface of the particles underwent an additional refinement step, to account for the sharper momentum boundary layer near the walls and thus adequately describing it. Moreover, a certain level of refinement near the surface of the particles is necessary to give a satisfactory definition of the contact points, which can be wrongly approximated as larger contact solid volumes if too coarse a mesh is employed. An example of this phenomenon is given in Fig. 3.

Figure 3: Grain surface definition at three increasing mesh refinement levels.

Moreover, the mesh porosity strictly depends on the dimension of the cells around the grains: an adequate number of cells is needed for the discretized model in the mesh to adequately represent the original model. Again, Fig. 3 visually clarifies this phenomenon. In order to quantify the number of cells needed in a mesh a study was conducted, by analyzing a 7 mm sized sample in a larger packing, constituted of a Gaussian distribution of spheres of average diameter equal to 1.99 mm. The porosity of the actual model, result of the `Blender` simulation, is 0.344. Then, several meshes with different cell dimensions were created, and the ratio between the porosity of the meshed sample and the original geometry, $\varepsilon_m/\varepsilon_g$, is calculated. The results are presented in Fig. 4.

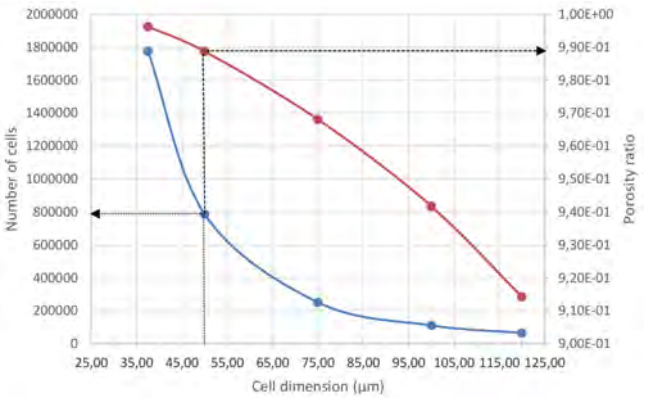

Figure 4: Porosity ratio and number of cells versus cell dimension for a spheres packing

As it can be seen, very coarse meshes can result in a very low $\varepsilon_m/\varepsilon_g$ ratio, down to $\varepsilon_m/\varepsilon_g = 0.9$, while a grid with mesh cell size of 50 μm (corresponding to 800,000 cells in this sample geometry) led to $\varepsilon_m/\varepsilon_g = 0.989$, which corresponds to a faithful representation of the original model. The acceptable cell dimension obviously depends on the average particle diameter: this result shows that an analysis of this type is a necessary step during the mesh generation process.

Finally, a further modification has been made to the final meshes, in which premixing and postmixing zones were added to the mesh (of size equal to approximately 2 grain diameters), respectively before the inlet and after the outlet. This was done with the purpose of obtaining a well developed velocity profile at the surface bordering the granular volume, and reduce flow anomalies (backflow, recirculation) due to the complex nature of the packing. This procedure was already employed in another work studying pore-scale flow in complex geometries, with good results (Boccardo *et al.*,

2014): the result of this operation and the final mesh can be seen in Fig. 5 and Fig. 6. The final meshes for the spheres and the trilobe packing are approximately of the same size, with around 5 million cells, with cells 50 μm in size next to the grains surface and 100 μm in size in the fluid bulk. The first packing contains about 200 spheres, with a resulting porosity of 0.355, while the other one contains about 100 trilobes, with a resulting porosity of 0.388.

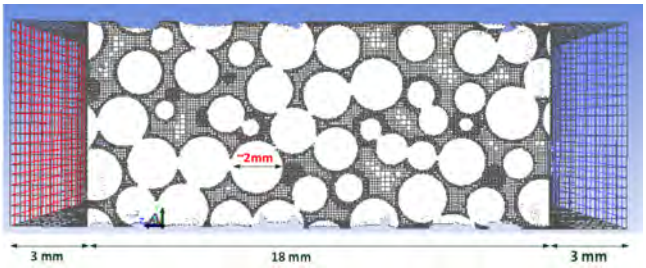

Figure 5: Final mesh, packing of spheres

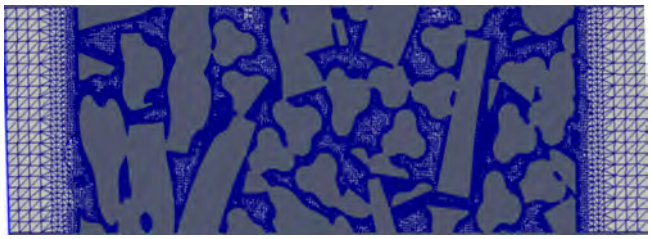

Figure 6: Final mesh, packing of trilobes

Pore-scale CFD simulations

Using the meshes obtained as described in the previous part, fluid dynamic simulations are performed using the CFD code `Ansys Fluent 15`. The fluid velocity field was determined by solving the continuity and Navier-Stokes equations, A no-slip boundary condition was applied on the grain surface. An inlet zone was set on one side of the geometry (one of the two smallest faces of the rectangular cuboid), with fluid entering the domain at a fixed velocity, and an outlet zone at the opposite face, with a condition of zero relative pressure. No additional forces (like gravity), were considered. On the remaining sides a condition of symmetry was set, implying no fluid flow across these surfaces. The fluid considered was air, with density $\rho = 1.225$ kg m^{-3} and dynamic viscosity $\mu = 1.789 \times 10^{-5}$ kg m^{-1}s^{-1}. The range of superficial velocities, V_s, explored went from 0.01 to 0.1 m s^{-1} ($0.3 < \mathrm{Re} < 30$). The system was solved for in laminar conditions and under steady-state, with density and viscosity considered constant. The energy equation was not solved.

The most important result of these simulations was the calculation of pressure drop, which was simply calculated as the difference between values of static pressure at the start and at the end of the actual granular bed. To clarify: the pressure drop was calculated in the inner zone where the packing was present, ignoring the conditions in the outer pre- and post-mixing "buffer" zones.

These results were then compared with the predictions from Ergun law, usually employed to describe flow in packed filter beds:

$$\frac{\Delta P \rho}{G_0^2}\frac{D_g}{L}\frac{\varepsilon^3}{(1-\varepsilon^3)} = 150\frac{1-\varepsilon}{(D_g G_0)/\mu} + 1.75\,, \tag{1}$$

where G_0 is the mass flux ($G_0 = \rho V_s$) ε is the porosity. D_g is the grain size: in the case of spheres it is the corresponding Sauter diameter, while for the trilobes it is the calculated equivalent diameter. This value is obtained following the findings of (Boyer *et al.*, 2007), where the empirical correlation $D_g = C\,D_t$ was found to provide the best agreement between the experimental data and Ergun law. The empirical factor C depends on the trilobe size, and is equal to 0.8 in this case.

Grid independence of the CFD results also needed to be ensured: the parameter used to assess this is the equivalent diameter D_g^*. Following a methodology used and described in greater detail in a previous work (Boccardo *et al.*, 2014), each different mesh refinement level is characterized by an effective diameter D_g^*, which is used as a fitting parameter comparing the pressure drop results from steady-state flow simulations at different fluid velocities to the predictions of the Ergun law for that operating conditions. Variations of D_g^* versus cell dimension can then be analyzed, and the mesh ensuring grid independent result identified. Results for the case of a packing of Gaussian distributed spheres with an average diameter of 2 mm can be found in Fig. 7. In this case, a cell dimension of 50 μm will result in a satisfactory discretization of the momentum boundary layer.

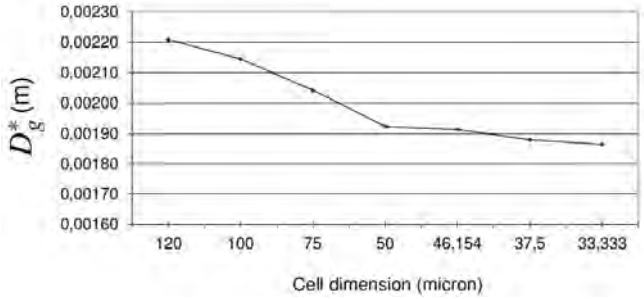

Figure 7: Effective grain size, D_g^*, with varying cell dimension

RESULTS

Geometrical Models Validation

The first test done had the purpose of identifying a suitable "size" of the simulation (regarding the total number of grains), in order to identify the smallest representative elementary volume (REV) for the system under investigation. A cubic container, 2.3 cm in size, was filled with 1772 spherical particles, distributed along a Gaussian distribution with an average diameter of 1.99 cm. Cubic samples of different dimensions were taken inside the system, all centered in the center of gravity of the domain, and the corresponding porosity was computed: the results are shown in Fig. 8. Three different packings, with spheres of different refinement level, are analyzed.

At smaller dimensions, very high porosities are reported: this is expected as for sample sizes of the order of the grains diameter a disproportionately high fraction of a pore or a grain could end up in the sample. At 5 mm and for bigger sizes, the reported porosities reach a stationary value around 0.355, showing another instability arising only with sample sizes of the order of the container size, where wall effects come into

play (Zou, 1995). Finding this behavior for this kind of analysis is very satisfactory and equivalent results can be found in other examples in the literature (Bear, 1988). Moreover, this offers an indication for the choice of a refinement level for the particles description: as it can be seen, there are not substantial differences between the three cases except for small sample sizes. What is indicated as refinement level 3 is the most suitable for these applications, as it combines a good representation of the actual shape with an acceptable computational cost during the packing simulation.
Cylindrical containers were also tested, as they resemble the actual reactor shape; moreover, lab-scale experiments are also usually carried out in cylindrical test containers. A polydisperse Gaussian distribution of 4000 particles, with an average diameter equal to 1.99 mm, is loaded with the random grid technique in a series of different containers, as specified in Tab. 1. As expected, since the same particle distribution is used in all cases, the results are very close at around $\varepsilon = 0.36$; this result is also in line with data (pertaining to the same particle size) coming from a large experimental campaign dealing with the study of flow conditions in trickle bed reactions (Boyer *et al.*, 2007).

Case	Container		Samples		ε
	Diameter (cm)	Height (cm)	Diameter (cm)	Height (cm)	(-)
P1	3	3	2.9	2.9	0.362
P2	3.5	3	3.35	2.27	0.358
P3	3.7	2.8	3.5	2.2	0.359
P4	4	2.4	3.9	2	0.359

Table 1: Porosity for spherical particle loadings in four different containers, with the corresponding sample dimensions.

For each geometry the porosity has been calculated both via averaging a series of 50 cylindrical samples randomly placed in the container (with diameter and height both equal to 5 mm), and via calculating the global packing porosity: the latter is reported in Tab. 1. It has to be noted that the dimension of the global sample is slightly lower than that of the container itself: again, this is a necessary precaution in order to avoid the effect of the presence of the walls on this sampling operation, which would markedly affect the porosity reported, with increases of up to one percent.
This wall effect has also been more deeply investigated by examining the packing P3 (as referred to in Tab. 1). In this case a different sampling strategy has been adopted: 200 annular samples, with height equal to 2 cm, were taken. Each of these was placed at the center of the container, and each had

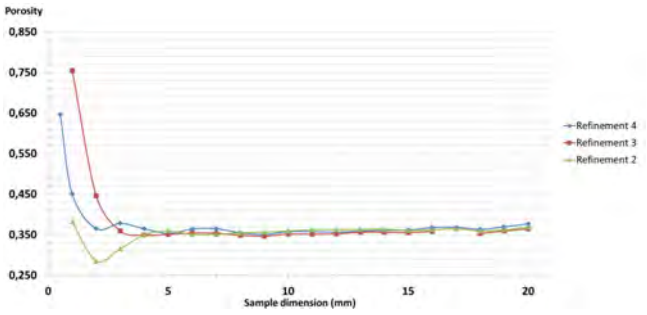

Figure 8: Porosity for increasingly large cubic samples, for three different spheres refinement levels

a fixed volume but an increasing diameter, effectively calculating the local porosity value along the radial direction from the center of the packing. The results are shown in Fig. 9

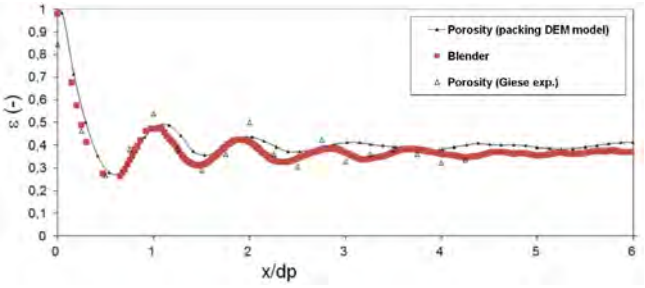

Figure 9: Comparison of local porosity values: old packing model (black symbols), current work packing model (red symbols) and experimental data (white triangles).

In the same figure, these results are compared with two other analyses of the same type: one conducted on an earlier study of an algorithmically generated packing (Augier *et al.*, 2010b), and the other one being actual experimental data (Giese *et al.*, 1998). The accordance between the results obtained in this work and the experimental data is satisfactory, as it confirms that the physical simulation replicates the characteristics of a real packing consistently.
Lastly, tests were conducted with trilobe packings in cylindrical containers: a Gaussian distribution in length of 3000 trilobes with an average length of 4.77 mm and a circumscribing diameter $D_t = 1.8$ mm (and equivalent diameter $D_g = 1.44$ mm) and standard deviation equal to 1.8 was considered, in a container with diameter and height respectively equal to 3.5 cm and 3 cm.
As mentioned before, the setup of the physical simulation in the case of the trilobe shape is of the utmost importance, as the resulting loading porosity will vary widely depending on the choice of the bounding volume and of the particular friction factor and coefficient of restitution used. Three simulations comparing different settings of these two parameters were performed, and both the global bed porosity and the porosity distribution inside the bed (using a number of randomly placed samples) were calculated. The results are shown in Tab. 2.

Cases	Restitution coefficient	Friction factor	Total ε (-)	Sampled ε (-)
T1	0	0.5	0.415	0.411
T2	0.7	0.325	0.39	0.377
T3	0.85	0.325	0.378	0.364

Table 2: Restitution coefficient and friction factor used in three different packing simulations of trilobes, with the resulting total and sampled porosity.

The data shown in this table show how strongly these two physical parameters influence the mixing effect mentioned earlier, and hence the resulting bed porosity. Once again it has to be noted that the total bed porosity is higher than the average porosity calculated through sample averaging, due to the presence of the walls. The difficulties in treating the dynamics of rigid body interactions in the case of such a complex particle shape notwithstanding, it stands to notice that when the right set of collision parameters is used (cases T2 and T3) a remarkable accordance to experimental data was found (Boyer *et al.*, 2007).

Fluid Flow Results

Packing of spheres

The first interesting result can be found in Fig. 10, where the pressure profile (for Re = 3.47) for the first geometry (packing of spheres) is shown in comparison with the predictions of Ergun law. The fact that the system shows a linear pressure profile is a good indicator of the validity of the simulated sample chosen, and that can be considered a representative volume for the granular system investigated in this case. The first and last points in the graph, apparent outliers, refer to points in the fluid buffer zone, and are not thus considered.

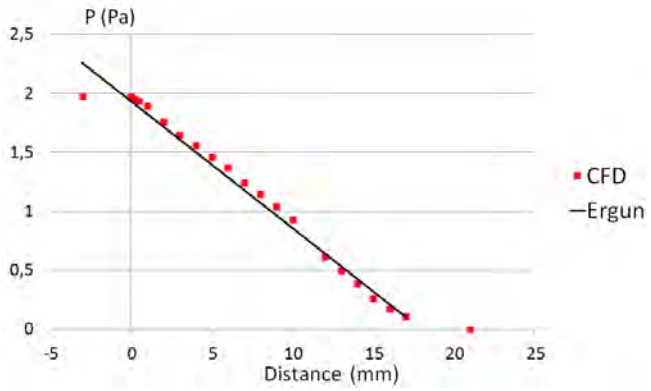

Figure 10: Pressure profile inside the granular medium for the packing of spheres, Re = 3.47

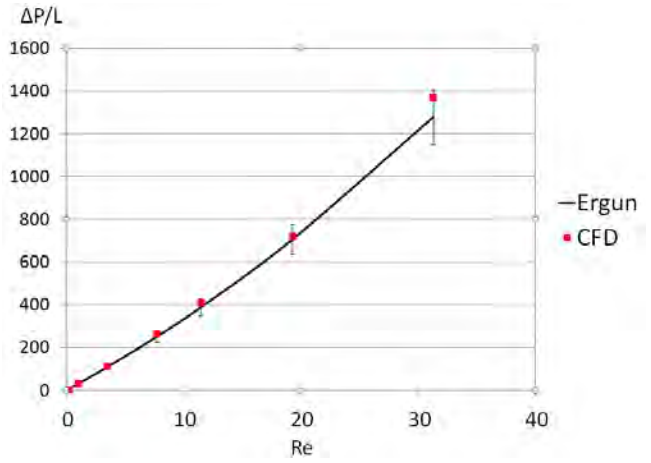

Figure 11: Pressure drop versus Re, CFD results (red squares) and Ergun law predictions (continuous line) for the packing of spheres

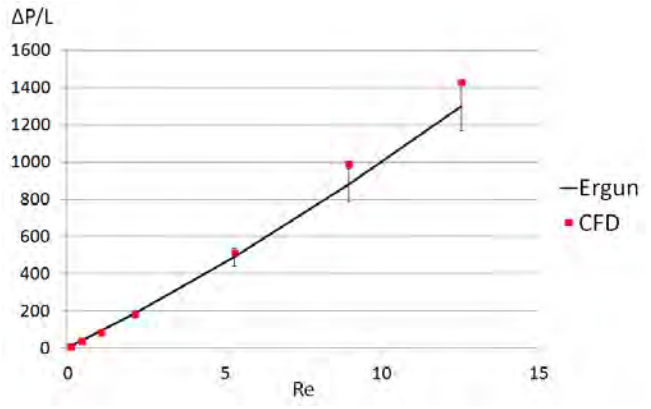

Figure 12: Pressure drop versus Re, CFD results (red squares) and Ergun law predictions (continuous line) for the packing of trilobes

The aggregate results for all the superficial velocities considered can be found in Fig. 11, again compared to Ergun law. As it is shown, the CFD results follow the predictions of the theoretical law within a 10% error margin, as evidenced by the error bars.

Packing of trilobes

The same results were obtained for the other geometric model, the packing of trilobes. Again, the pressure profile along the granular medium was linear, exhibiting the same behavior shown in Fig. 10. Moreover, Fig. 12 shows that even for this complex catalyst shape, the results of the CFD simulations matched the predictions of Ergun law to a good degree, again showing a disparity less than 10% in value. It is worth mentioning here that the mean grain size used in the Ergun law, reported in Eq. (1), was derived in a previous internal study carried out at IFP Energies nouvelles, based on a very large number of experiments. Therefore the agreement between CFD simulations and the Ergun law in this context should be considered as an equivalent validation with experiments.

CONCLUSION

In this work a computational tool developed in computer graphics, `Blender`, integrated with the Bullet Physics Library, is used to generate realistic packings of (catalyst) particles of different shapes. The main advantage of this approach (versus other alternatives) stands in the possibility of simulating packings constituted by particles with complex shapes (e.g. non-convex objects such as trilobes).

Results show that attention should be paid to the strategy with which particles are inserted into the container, as well as to the meshing procedure, carried out here with `snappyHexMesh`. The mesh has to be fine enough to describe well the geometrical details of the pores within the packing, as well as the momentum boundary layer around each particle. The validation with experimental data demonstrate that the generated packings realistically describe the behaviour of catalytic fixed bed reactors. In particular, when working with polydisperse spherical particles, the well known radial porosity profiles are obtained, with an accuracy superior to other similar tools. Moreover, pressure drop simulations, carried out with `Ansys Fluent` showed very good agreement with the predictions of the Ergun law (considered "exact" in this context). When working with polydisperse trilobes very good results are also obtained, especially considering that these complex non-convex objects are very difficult to treat. Also in this case comparison between simulated pressure drops and those predicted with the Ergun law (by using a grain size in turn obtained from corresponding experiments) showed excellent agreement. These results show that the approach developed in this work can be used to more deeply study the effect that the shape, size and length distribution of catalyst particles have on the fluid flow in fixed bed reactors, and improve existing models for pressure drop predictions.

In the next steps of our work chemical reactions and heat transfer will also be considered.

Acknowledgments

The authors would like to acknowledge the help and useful suggestions of Rajandrea Sethi and Tiziana Tosco.

REFERENCES

AUGIER, F. *et al.* (2010a). "Numerical approach to predict wetting and catalyst efficiencies inside trickle bed reactors". *Chemical Engineering Science*, **65(1)**, 255 – 260. 20th International Symposium in Chemical Reaction Engineering-Green Chemical Reaction Engineering for a Sustainable Future.

AUGIER, F. *et al.* (2010b). "Numerical simulations of transfer and transport properties inside packed beds of spherical particles". *Chemical Engineering Science*, **65(3)**, 1055 – 1064.

BEAR, J. (1988). *Dynamics of fluids in porous media*. Dover.

BOCCARDO, G. *et al.* (2014). "Microscale simulation of particle deposition in porous media". *Journal of Colloid and Interface Science*, **417**, 227–237.

BOYER, C. *et al.* (2007). "Hydrodynamics of trickle bed reactors at high pressure: Two-phase flow model for pressure drop and liquid holdup, formulation and experimental validation". *Chemical Engineering Science*, **62(24)**, 7026 – 7032. 8th International Conference on Gas-Liquid and Gas-Liquid-Solid Reactor Engineering.

GIESE, M. *et al.* (1998). "Measured and modeled superficial flow profiles in packed beds with liquid flow". *AIChE Journal*, **44(2)**, 484–490.

OPENCFD (2013). *The Open Source CFD Toolbox, User Guide*. OpenCFD (ESI).

VAN GUMSTER, J. (2009). *Blender For Dummies*. Wiley.

ZOU, R. (1995). "The packing of spheres in a cylindrical container: the thickness effect". *Chemical Engineering Science*, **50(9)**, 1504–1507.

AUTOMATED WORKFLOW FOR SPATIALLY RESOLVED PACKED BED REACTORS WITH SPHERICAL AND NON-SPHERICAL PARTICLES

Thomas EPPINGER[1]*, **Nico JURTZ**[1]†, **Ravindra AGLAVE**[2]‡

[1]CD-adapco, Nordostpark 3-5, 90411 Nuremberg, Germany

[2]CD-adapco, 11000 Richmond Avenue, Houston, TX, 77042, United States

* E-mail: thomas.eppinger@cd-adapco.com
† E-mail: nico.jurtz@cd-adapco.com
‡ E-mail: ravindra.aglave@cd-adapco.com

ABSTRACT

Packed bed reactors are widely used in the chemical and process industry amongst others for highly exothermic or endothermic catalytic surface reactions. Such reactors are characterized by a small tube to particle diameter ratio D/d to ensure a safe thermal management. For the design of such apparatuses the well-known correlations for packed bed reactors cannot be used, because these reactors are dominated by the influence of the confining wall, which affects the porosity and the velocity field and as a result also the species and temperature distribution within the bed.

For spatially resolved simulations of packed bed reactors a randomly packed bed has to be generated and meshed. Special attention has to be paid on the mesh at the particle-particle and particle-wall contact points. We developed a method, which flattens the particles locally in the vicinity of the contact points and we could show, that this method does not affect significantly the bed properties and the fluid dynamics in terms of bed porosity, radial porosity distribution and pressure drop.

Based on this published work we developed a workflow and a tool which allows an automated simulation: generation of a packed bed with DEM (discrete element method), meshing and solving the transport equations with a finite volume code. The whole workflow is done within the software package STAR-CCM+ by CD-adapco. The simulation time could be reduced significantly and depends on the number of particles (typically 1-2 days for 1500 particles).

Further we used the built-in DEM capability to generate random packings of non-spherical particles like cylinders and Raschig rings, which are more often used in the chemical industry, as a composition of spherical particles. For the meshing and the CFD calculation these approximated shapes are replaced by their original exact shape.

With the described workflow we have investigated spherical as well as non-spherical packings with D/d between 2 and 10 and packing heights between 10d and 40d. The results are validated in terms of bed porosity, radial porosity and velocity distribution and temperature profiles with experimental results from literature.

Based on these results the interplay between the flow field, the temperature, the species distribution and the chemical reaction in packed bed reactors can be investigated in detail.

Keywords: DEM, packed beds, chemical reactors, process industry, CFD, hydrodynamics .

NOMENCLATURE

Greek Symbols

δ	Identity matrix, $[-]$.
λ	Thermal conductivity, $[W/m^2K]$.
μ	Dynamic viscosity, $[Pas]$.
ν	Poisson coefficient, $[-]$.
ξ	Friction coefficient, $[-]$.
ρ	Mass density, $[kg/m^3]$.
τ	Stress tensor, $[Pa]$.
Θ	Dimensionless temperature, $[-]$.

Latin Symbols

c	Heat capacity, $[J/kgK]$.
d	Particle diameter, $[m]$.
e	Coefficient of restitution, $[-]$.
$\mathbf{g}$	Gravity vector, $[m/s^2]$.
h	Particle height, $[m]$.
p	Pressure, $[Pa]$.
r	Particle radius, $[m]$.
$\mathbf{v}$	Velocity vector, $[m/s]$.
v_{mag}	Velocity magnitude, $[m/s]$.
A	Area, $[m^2]$.
D	Tube diameter, $[m]$.
E	Young's modulus, $[Pa]$.
H	Total Enthalpy, $[J]$.
R	Tube radius, $[m]$.
T	Temperature, $[K]$.
$\dot{\mathbf{Q}}$	Heat flow, $[W]$.
$\dot{\mathbf{q}}$	Heat flux, $[W/m^2]$.

Sub/superscripts

eff	Effective.
sl	Sliding.
r	Rolling.
t	Turbulent.
$solid$	Solid phase.
$fluid$	Fluid phase.
N	Normal.
T	Tangential.

INTRODUCTION

Packed bed reactors are widely used in the chemical and process industry amongst others for catalyzed heterogeneous reactions, adsorption processes, heat storage or filter applications. They consist of a container - mostly a tube - which

is filled with particles. Although a broad variety of industrially manufactured particle shapes exist most applications are using spherical or cylindrical shaped particles.

Based on the particle to diameter ratio D/d different numerical approaches can be used to describe fluid flow, heat and mass transfer. For large D/d (D/d > 10-20) a pseudo-homogeneous model approach can be used. In its simplest form a plug-flow velocity profile corrected with the bed porosity is assumed and physical properties like thermal conductivity are averaged based on the volume fraction of the solid and fluid phase. This model was extended in the past by several research groups to describe packed bed reactors more accurately.

Packed bed reactors with small D/d (D/d < 10-20) are often used for highly exothermic or endothermic catalytic reactions. These reactors are dominated by the wall effect: Due to the confining wall the particles are only in point contact with the wall which leads to a high porosity in the near wall region and as a result to a high volumetric flow which acts like an isolating film and hinders the heat transport to or from the wall. For the design of these kind of reactors the pseudo-homogeneous approach fails because they are dominated by local effects and an exact description of the flow, temperature and species distribution is needed.

Due to the increasing computational power in the last years it is now possible to simulate such reactors in a spatially resolved way. First CFD simulations of packed beds with spherical particles were published in the end of the 1990s and in the last years a huge amount of research work was published.

For a spatially resolved simulation two main challenges have to be managed: Firstly an accurate description of the randomly packed bed is needed and secondly the meshing at the contact points between particles and between the particles and the wall has to be handled to avoid either highly skewed cells or a large number of cells due to local refinement in the vicinity of the contact points.

There are several ways to obtain a description of the packing for the CFD calculation. For ordered packings the position of each particle can easily be calculated analytically, which can then be used to create a CAD description. Such a description can also be derived based on experimental MRT measurement of an existing packing. But there are also numerical methods to generate a random packing. The Monte-Carlo method basically positions particles randomly within the domain and if this position fulfills a certain stability criteria the particle is kept, otherwise the particle is removed. This is repeated until the final packing height is reached. A second numerical method is based on the discrete element method (DEM) which was first described by (Cundall, 1979). In this model the particles are injected into the domain and Newton's law of motion is solved for each particle with consideration of all relevant forces acting on the particles. The DEM method has several advantages: It is inexpensive compared to the experimental methods, computationally more efficient than the Monte-Carlo method and the physical process of filling is approximated, which can include obstacles or special features like macroscopic wall structures which can influence the local void fraction distribution.

Also for the second issue, the mesh generation in the vicinity of the contact points, several methods are known from literature which are depicted in Figure 1. Shrinking the particles a certain amount, mostly in the range of 0.5-1 % of the particle diameter d, is a widely used technique (see e.g. (Nijemeisland and Dixon, 2004) or (Bai *et al.*, 2009)). As a result the contact points disappear and cells can be generated in the gap. On the other hand the solid fraction and therefore the porosity of the packed bed is reduced, which influences the pressure drop significantly. A similar method is suggested by (Guardo *et al.*, 2005), but instead of shrinking he suggested to inflate the particles a certain amount. The contact points become contact lines or areas and the cell quality in that region can be increased. But analogous to the shrinking method the porosity is influenced significantly and a subsequent correction is needed. (Ookawara *et al.*, 2007) have presented a method where the particles are bridged with a small cylinder while (Eppinger *et al.*, 2011) use a local flattening technique: the particle surface is modified as soon as the normal distance between the surfaces of two particles fall below a prescribed value in such a way that a small gap is created which can then be filled with a small number of cells with a reasonable quality. The method by Ookawara as well as the method by Eppinger has a reduced influence on the porosity and on the pressure drop because the packing is only modified locally. Another advantage of the local flattening method is, that it can be easily adapted to any kind of particle shapes and contact type like e.g. the contact line of cylindrical particles which are in contact at their lateral surface.

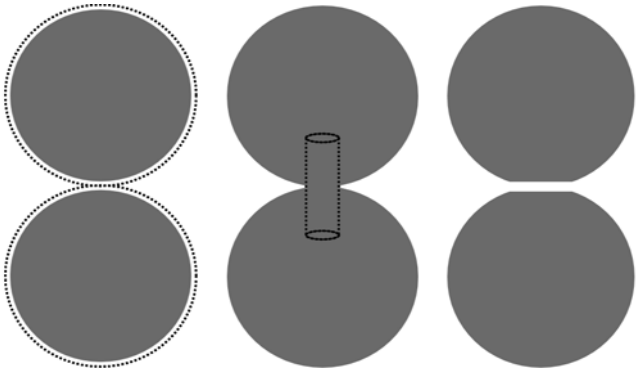

Figure 1: Schematic overview of the different contact point treatment methods. Left: Shrinking the particles, middle: bridging the gap with a cylinder, right: local flattening of the particles.

If heat transport in the packed bed is considered the heat conduction between the solid particles has to be treated carefully. Generally the heat flow Q between two solids which are in contact at an area A can be described with following equation

$$\dot{Q} = \dot{q} * A = -\lambda \Delta T * A \tag{1}$$

where λ is the thermal conductivity, $\dot{q}$ is the heat flux and T is the temperature. It is obvious that the amount of heat which can be transferred by conduction depends on the used contact point meshing method. For the shrinking and the local flattening method the heat transfer by conduction will be zero because there is no contact area while for the inflating and the bridging method the heat transport by conduction will be overpredicted. A more detailed discussion on this topic follows.

In this study an automated workflow for the simulation of packed bed reactors is presented. The workflow consists mainly of a DEM simulation to create a random packing, a conversion step to create a CAD description out of the DEM data, an automated mesh generation based on the CAD description and the solver run including post-processing. All steps are controlled by a script to ensure convergence and

short calculation times. Some results of this workflow are presented and validated with experimental data.

MODEL DESCRIPTION

For the investigation of spatially resolved 3 dimensional packed bed reactors we have developed an automated and fully numerical workflow based on CD-adapco's finite volume code STAR-CCM+. For the generation of a random packing we used DEM and for the contact point treatment the local flattening method as described in detail in (Eppinger *et al.*, 2011). A short summary and validation is given in the next subsection. All single steps are concatenated with a java-macro, which on the one hand reduces the number of possible user errors and on the other hand reduces the simulation time not only by reducing the idle time but also by adjusting the stopping criteria based on the given parameters.

Generation of a random packing

The generation of the random packing is done with the implemented DEM in STAR-CCM+. Monodisperse spherical particles are initialized randomly at the top of the tube and fall because of gravity to the bottom of the tube. For each of these particles Newton's law of motion is solved which takes the gravity and the interaction between the particles and between the particles and the tube wall into account. Drag force resulting from the interaction with the gas phase in the tube is neglected so that the following equations have to be solved:

$$m_i \frac{dv_i}{dt} = F_g + \sum_{np} F_c + \sum_{nb} F_c \tag{2}$$

and

$$\frac{dI_i \omega_i}{dt} = \sum_{np} T_c + \sum_{nb} T_c \tag{3}$$

where m_i, v_i, I_i and ω_i are the mass, velocity, mass moment of inertia and angular velocity of particle i, respectively. F_g is the gravitational force acting on particle i. F_c and T_c are, respectively, the contact force and the contact torque acting on particle i due to its neighbor particles np or neighbor boundaries nb which are in contact with particle i. The contact forces and torques are calculated using a spring-dashpot model. For these simulations the non-linear Hertz-Mindlin model was used, where the forces and torques are calculated as a function of the parameters stated in Table 1.

Table 1: Particle properties used for the DEM simulation

Property	Symbol	Unit	Value
Density	ρ	kg/m^3	2500
Norm. coeff. of restitution	e_N	-	0.9
Tang. coeff. of restitution	e_T	-	0.5
Poisson coefficient	ν	-	0.235
Young's modulus	E	Pa	78.5e9
Sliding friction coefficient	ξ_{sl}	-	0.2
Rolling friction coefficient	ξ_r	-	0.002

The DEM simulation is stopped when all particles are in a final stable position. This is assumed when the velocity of all particles is below a given value (mostly a value of $v_{mag} < 10^{-4} m/s$ was used).

For the generation of packings with non-spherical particles the composite particle model is used: Non-spherical particles are approximated by a certain number of spheres, which are fixed together and do not separate during the DEM simulation. The composite particle model treats the individual spheres as separate entities only for contact detection while for the rest of the simulation it is a single object and forces and torque are calculated with respect to the center of mass. An example for a cylindrical particle is shown in Figure 2. The simulation itself is conducted in the same way as for spherical particles.

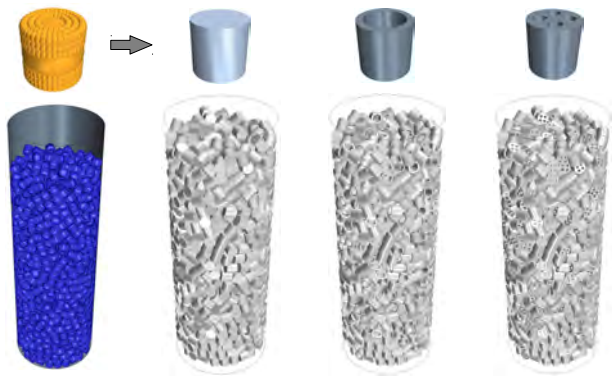

Figure 2: Example for packings with non-spherical particles: Left: Composite particle for the DEM simulation made of 330 spheres and resulting randomly packed bed. Right: CAD description of packed beds with different particle shapes (left to right: full cylinders, Raschig-rings and 4-hole cylinders) based on the same DEM result.

Generation of a CAD description and meshing

The mesh generation process can be divided into two steps. Firstly the position and diameter of the centroid of the spheres of the randomly packed bed from the DEM simulation is extracted and in a subsequent step a CAD description based on these data is generated. The whole tube can be divided in three sections, the upstream region, the region with the packed bed, and a downstream region. The upstream part is needed for the development of the flow profile while the downstream part is mainly to avoid backflow at the outlet boundary. To avoid the meshing problems at the contact points the local flattening method by (Eppinger *et al.*, 2011) is used with the parameters given in table 2. All parameters are set relative to a given base size which gives a constant polyhedral mesh quality for different sizes of the particles by changing only one parameter.

Table 2: Settings for the meshing parameters

Property	Value
Base size (bs)	d
Surface edge size (ses) on spheres	0.04-0.10 d
Surface grow rate	1.3
Number of prism layers	2
Thickness of the prism layers	0.03 d
Minimum distance between two surfaces	0.12 ses

In principle the mesh generation for non-spherical particles is done in a similar same way but some additional steps has to be included: Firstly the orientation of the non-spherical particles in the packed bed is important and has to be exported

from the DEM simulation too. Secondly for the DEM simulation the shape of the non-spherical particle is approximated by a certain number of spheres and therefore it is not an exact description. But for the CAD description the approximated DEM shapes can be replaced with the exact shape. This is done by generating one non-spherical CAD-part which is then cloned and positioned according to the exported DEM data. The resulting packed bed for different particle shapes is depicted in Figure 2.

Simulation setup

For the steady state flow and heat transfer simulation in this study the following governing equations for mass, momentum and energy are solved.
Conservation of mass:

$$\nabla \rho \mathbf{v} = 0 \tag{4}$$

where ρ is the mass density and $\mathbf{v}$ is the velocity vector.
Conservation of momentum:

$$\nabla \rho \mathbf{v}\mathbf{v} = -\nabla p + \nabla \tau + \rho \mathbf{g} \tag{5}$$

with pressure p, gravity vector $\mathbf{g}$ and the stress tensor τ

$$\tau = \mu_{eff}[\nabla \mathbf{v} + \nabla \mathbf{v}^T - \frac{2}{3}(\nabla \cdot \mathbf{v})\delta] \tag{6}$$

where δ is the identity matrix and the effective viscosity μ_{eff} can be expressed as $\mu_{eff} = \mu + \mu_t$, the laminar and turbulent viscosity, respectively.
Conservation of energy:

$$\nabla(\rho H \mathbf{v}) = -\nabla \dot{\mathbf{q}} + \nabla \cdot (\tau \cdot \mathbf{v}) \tag{7}$$

with total enthalpy H and heat flux $\dot{\mathbf{q}}$.
A schematic reactor overview is given in Figure 3. All CFD simulations are conducted in steady state with air as an ideal gas with constant physical properties according to the relevant tables in the following subsections. Turbulence is modeled with the realizable k-ε turbulence model using 'All y+-wall treatment'. If the heat transport in the solid phase was taken into account a conformal mesh at the solid-fluid interface was created. At the inlet a constant plug flow profile with a constant temperature is assumed. At the outlet a constant absolute pressure of 1.013 bar was specified. A constant temperature was set at the heated wall.

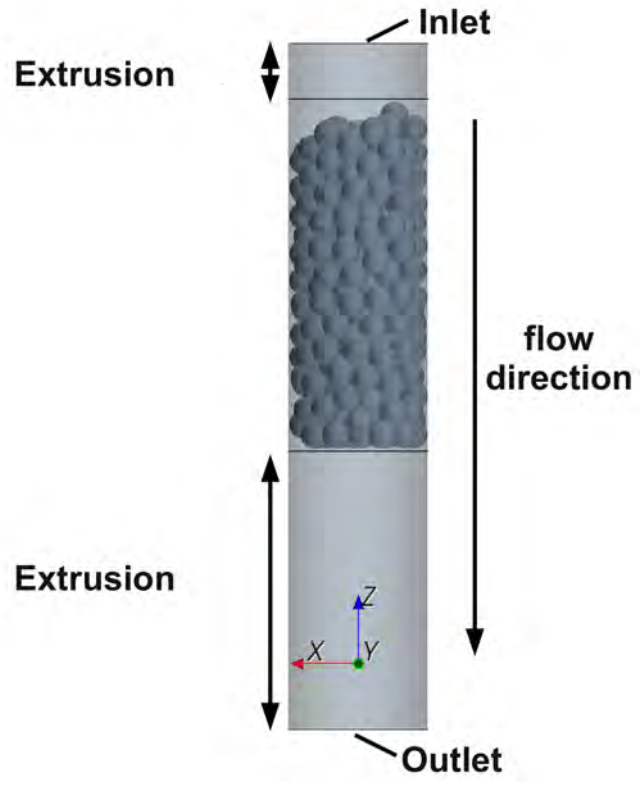

Figure 3: Schematic reactor overview.

Process automation

To decrease the total simulation time by reducing the idle time and to avoid user mistakes during the simulation setup the whole process consisting of the previously described single steps is automated with a java-script. A summary about the workflow described above for spherical as well as for non-spherical particles is given in Figure 4, where the additional steps for non-spherical particles are highlighted in red. A GUI collects all relevant parameters and settings for the DEM, the mesh and the CFD calculation. Based on these data two scripts are generated. The first one generated the packing geometry using DEM. The second script which starts automatically after the first one has terminated, generates the CAD geometry, the mesh and all numerical and physical settings for the CFD simulation. Several parameters are calculated based on literature data, e.g. the expected packing height, so that the particles are injected closely above this value to ensure all particles can be injected and the distance which the particles have to travel are not needlessly long. Also some standard post processing routines are added like an automated area based calculation of the radial and axial porosity profiles and pressure drop.

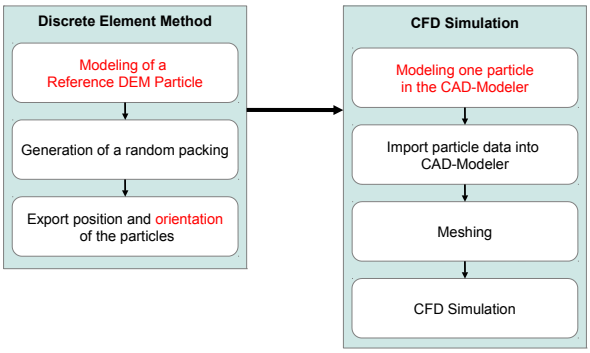

Figure 4: Workflow for the whole process. The additional steps for non-spherical particles are highlighted in red.

RESULTS

In this section some results are presented with a focus on non-spherical particles and heat transport. A detailed presentation and validation against correlations on bed porosity, radial porosity distribution, pressure drop and velocity profiles for packed beds with spherical particles can be found in (Eppinger *et al.*, 2011) and (Zobel *et al.*, 2012). For that reason only a few results for spherical particles are presented in this paper.

Validation of bed porosity and local porosity distribution

(Mueller, 1992) investigated packed beds of monodisperse spheres made of plexiglas in a cylindrical tube with D/d ranging from 2.02 to 7.99. The radial porosity profile was derived by analysing a large number of radial annular layers of equal thickness and the local porosity of each layer is calculated as ratio of the solid volume and the total volume of the layer. We reproduced this work numerically and found an excellent agreement between the numerical and the experimental results for all investigated D/d-ratios as depicted exemplarily in Figure 5 for D/d = 3.96.

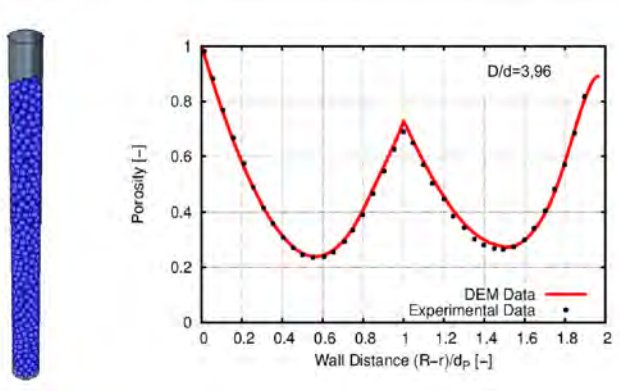

Figure 5: Comparison of the radial porosity profile for a monodisperse packed bed with D/d = 3.96. Experimental data are taken from (Mueller, 1992).

A validation of the bed porosity, which is defined as ratio of the volume of the void in the packing and the volume of that region when no particles are present, and local radial porosity distribution for packed beds made of cylinders, Raschig rings and 4-hole cylinders was conducted against correlations by (Dixon, 1988) and (Foumeny and Benyahia, 1991). The generated packed beds are depicted in Figure 2. The tube diameter is $D = 0.22m$, the cylindrical particle diameter d and the height h is $d = h = 0.025m$, which gives a D/d of 8.8. The total bed height is approximately $H = 0.55m$. The bed porosity for all three particles shapes is shown in Figure 6. For all three particle shapes the numerical results are between the values of both correlations.

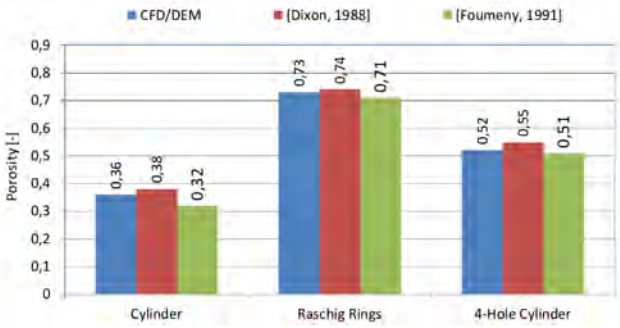

Figure 6: Comparison of the bed porosity of packed bed with different particle shapes.

A more detailed validation is shown in Figure 7 and 8 where the axial and circumferential averaged radial porosity profile for cylinders and Raschig rings is depicted. The numerical results are compared with experimental results by (Roshani, 1990) and (Giese *et al.*, 1998), respectively and with numerical results by (Caulkin *et al.*, 2012). Generally the agreement between experimental and the numerical data is quite high. For cylindrical particles this is especially given in the near wall region up to a distance of approximately one particle diameter, while with increasing distance to the confining tube wall the randomness of the packed bed gets more important and slight shifts in the amplitude and the frequency of the decaying profile can be found. Also the results for Raschig rings agree well with the experimental data, the typical decrease in porosity directly at the wall and at one, two and three particle diameters away from the wall are predicted correctly.

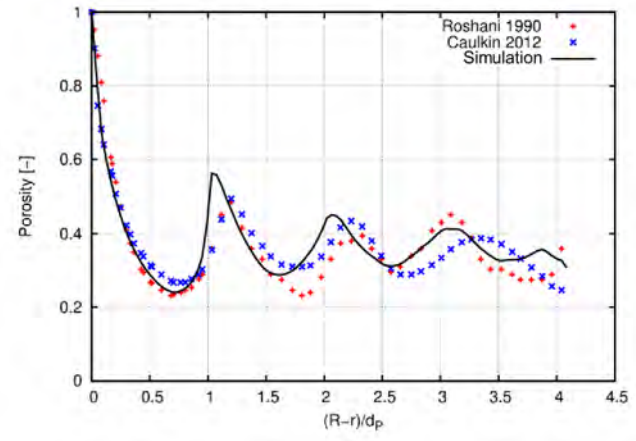

Figure 7: Comparison of the radial porosity distribution of a packed bed with cylindrical particles.

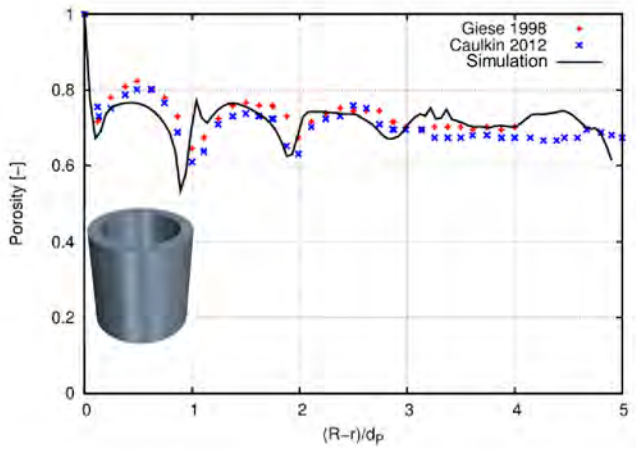

Figure 8: Comparison of the radial porosity distribution of a packed bed with Raschig rings.

Validation of heat transport

One critical point of the simulation of packed bed reactors is the accurate calculation of the temperature profile. Especially the heat transport via conduction between the particles and between the particles and the wall has to be examined because the choice how the contact points are treated may influence the result as already mentioned in the introduction. To judge the influence detailed experimental temperature data from within the packed bed is needed. Getting these data is not an easy task because of the accessibility for measurement devices or techniques. The research group of Anthony

Dixon has published several papers over the last years which we used to validate our simulation results. The experimental setup is a single packed tube with a steam-heated wall. An air flow enters the tube and in a first unheated zone of the packed bed the flow profile should develop while in the second zone the air is heated through the wall with a constant temperature. Temperature is measured with a thermocouple cross at the outlet of the packed bed. To obtain temperature profiles within the packed bed different bed heights were used. More detailed information can be found in (Nijemeisland, 2000), (Nijemeisland and Dixon, 2001) and (Dixon *et al.*, 2012).
A first validation is done against experimental data from (Nijemeisland, 2000) and (Nijemeisland and Dixon, 2001) where a packing of 44 nylon spheres with a diameter of $d = 25.4mm$ were placed in a regular arrangement in a tube with diameter $D = 50,8mm$ (D/d = 2) resulting in a packing height of approximately $H \approx 400mm$ like depicted in Figure 9. The inlet velocity was varied in such a way that particle Reynolds numbers in the range of $Re = 373$ upto $Re = 1922$ were covered. For the simulation three different geometries based on the contact point treatment were generated. The first geometry is based on the global shrinking method (1% of the diameter) and parameters are used according to (Nijemeisland and Dixon, 2001), therefore it is named in the following 'Nijemeisland'. The second geometry is based on the bridging method with a bridging tube diameter of 10 % of the sphere diameter d and is named 'Ookawara'. And the third geometry is based on the local flattening method according to the description above and is named 'Eppinger'. The boundary layer resolution is varied between two layers and 'All y+ treatment' and seven layers and a 'Low Reynolds model'. The resulting polyhedral mesh contains approximately 700 000 cells for the model with two layers and 1.5 million cells for the model with seven layers. The physical properties are set according to Table 3.

Table 3: Settings for the validation simulation according to (Nijemeisland and Dixon, 2001).

property	value
λ_{fluid}	0.026 W/(m·K)
λ_{solid}	0.242 W/(m·K)
ρ_{fluid}	1.225 kg /m^3
ρ_{solid}	1300 kg /m^3
$c_{p,fluid}$	1003.6 J/(kg·K)
$c_{p,solid}$	1000 J/(kg·K)
T_{inlet}	298 K
T_{wall}	383 K

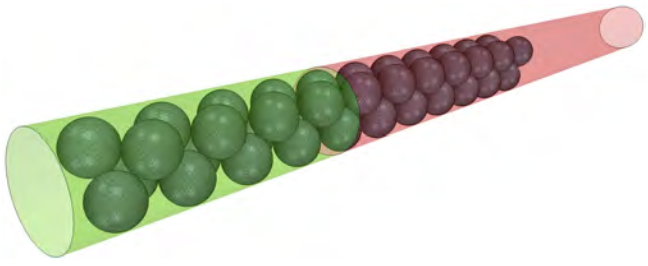

Figure 9: Sketch of the experimental and numerical setup. The heating zone starts behind the light green zone.

In Figure 10 detailed results of the dimensionless temperature $\Theta = (T - T_{inlet})/(T_{wall} - T_{inlet})$ for Re = 986 is shown.

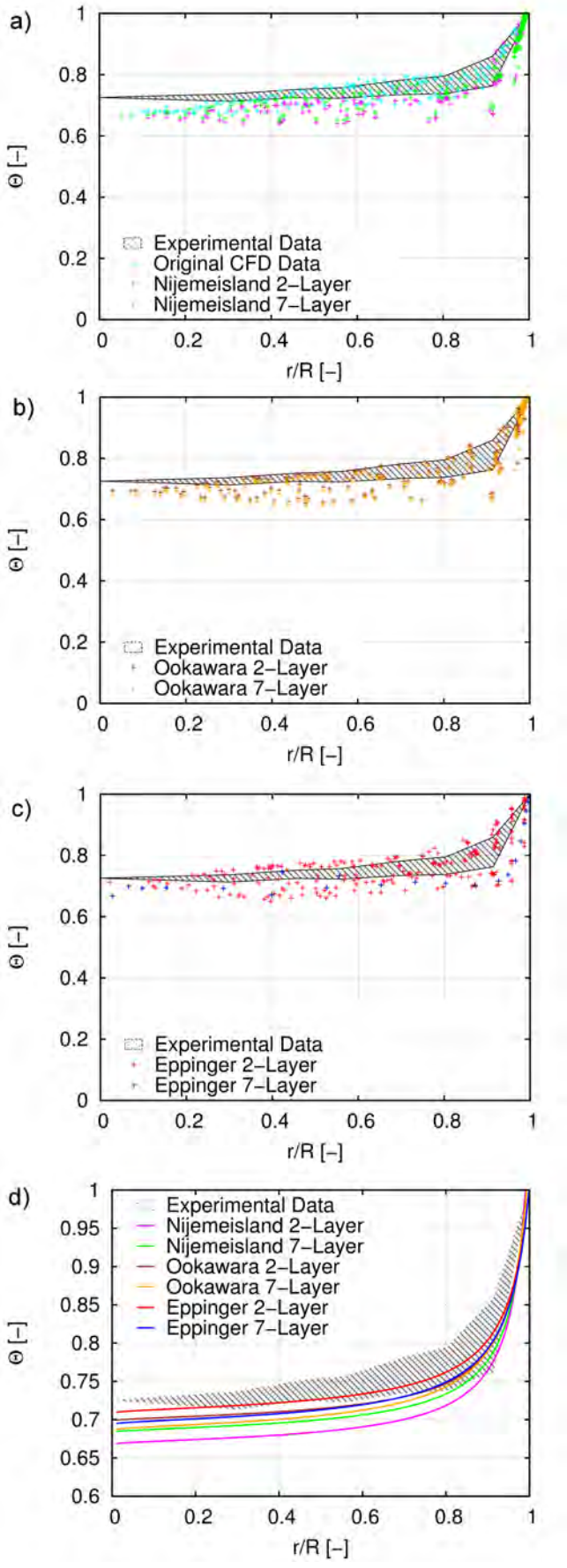

Figure 10: (a)-(c) Comparison of temperature data at the outlet of the packed bed for different contact point methods and experimental data for Re = 986. (d) Best-fit curves based on the results from (a)-(c).

Each dot in Figure 10(a)-(c) represents a temperature value approximately 5 mm above the top layer. The numerical results show for all three methods a quit good agreement with a slight spread around the experimental range of data. The contact point treatment according to Nijemeisland or Ookawara slightly underpredicts the temperature profile, especially towards the center of the tube. This can not be seen when the local flattening method is used. Similar results are found for Re = 373, 1724 and 1922, which are not depicted in this paper. For an easier comparison of the different simulations a least square best-fit curve for Θ is used with

$$\Theta = \frac{A}{log(\frac{B}{r/R})} + C \tag{8}$$

and fitting parameters A, B and C. In 10(d) it can be seen that all models predict the temperature profile in the near wall region quit accurately. Towards the center of the tube all models underpredict the temperature with the largest deviation for the global shrinking method while the local flattening with two layers gives the most accurate result. Similar results are also found for Re = 373, 1724 and 1922, respectively which are depicted in Figure 11, 12 and 13. The

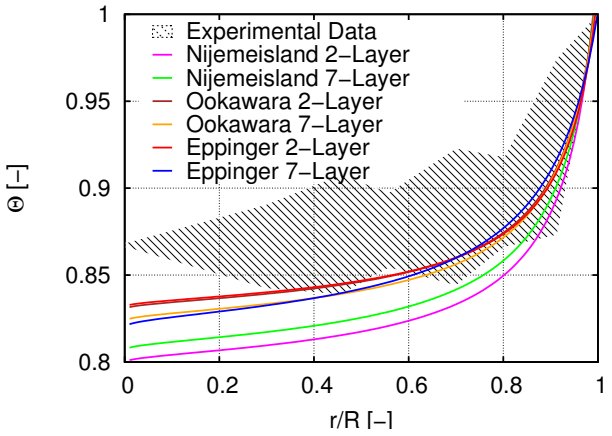

Figure 11: Best-fit curves based on the simulation results for Re = 373.

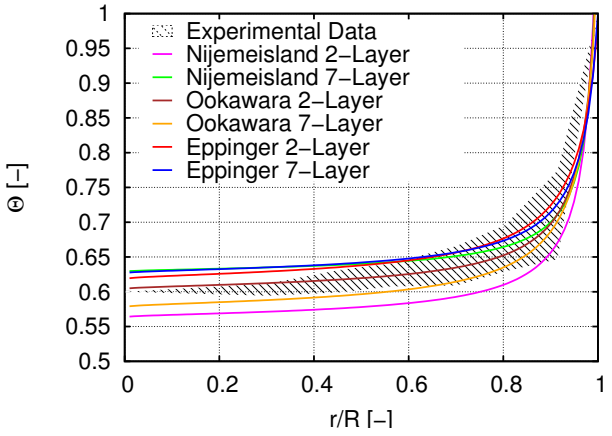

Figure 12: Best-fit curves based on the simulation results for Re = 1724.

global shrinking method always underpredicts the temperature profile, while the local flattening method gives a slight overprediction for high Re numbers. For high Re numbers the bridging method gives the most accurate results although the particles are bridged with a cylinder with a relatively large diameter which increases the particle heat conduction. It can be concluded that for high Re number the heat transport by conduction does not play a significant role, at least in this case, where the conductivity of the solid phase (nylon) is not very high.

A second validation was done against a similar investigation, but with D/d = 5.45 and a randomly packed bed made of monodisperse spherical particles. The remaining setup is the same as in the previous one. For details see (Dixon *et al.*, 2012) and Table 4. The numerical results in (Dixon *et al.*, 2012) are derived by two different approaches for the contact point treatment. One is the global shrinking method and the other is a mixed approach consisting of the bridging method in the near wall region and the local shrinking in the rest of the bed. When the particles are bridged an effective thermal conductivity for the solid phase is used to compensate the enhanced heat conduction due to the increased contact by an additional heat transport resistance.

Table 4: Solid settings for the validation simulation according to (Dixon *et al.*, 2012).

property	value
λ_{solid}	0.25 W/(m·K)
ρ_{solid}	1140 kg /m^3
$c_{p,solid}$	1700 J/(kg·K)
T_{inlet}	298 K
T_{wall}	373 K

In Figure 14 a comparison of the experimental and numerical results taken from the paper with simulation results with the local flattening method and different mesh sizes is shown. It has to be noted that an increase in base size or in minimum surface size leads directly to a mesh with fewer cells but also to a larger gap between the particles. The larger gap influences the velocity field, especially a velocity increase can be detected in the gap and as a result the heat transport is affected. With a finer mesh and a smaller gap the experimental results can be reproduced quite well with almost the same accuracy as the published numerical data. The deviation in the near wall region between the numerical and the experimental results are attributed by the authors of the paper to either a cold backflow or problems with the thermocouples. It can be concluded based on these simulations that with the local flattening method without further modifications like an

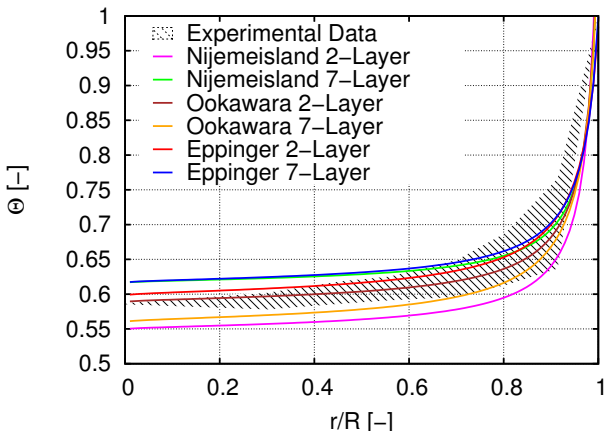

Figure 13: Best-fit curves based on the simulation results for Re = 1922.

adjustment of the effective thermal conductivity the experimental results can be reproduced.

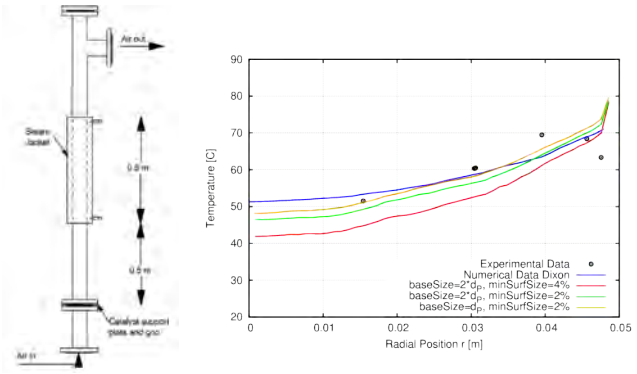

Figure 14: Radial temperature profile for a packed bed with D/d = 5.45 at a bed height of z = 0.48m.

Simulation time

Beside the accuracy of the results the calculation time for the simulation is also of high interest, especially if such simulation should be used as a standard tool or method for the design of packed bed reactors. The calculation time depends on the mesh size and on the complexity of the physics; therefore it is difficult to give exact numbers for the calculation time. E.g. the mesh could be much coarser if only the pressure drop is of interest compared to a mesh for an accurate prediction of the heat transport. Furthermore the calculation time of the packing generation depends not only on the physical properties but also on the DEM time step size which depends heavily on the Young's modulus and the particle size. But to give some rough ideas on the needed calculation time some numbers are presented. The DEM generation of a randomly packed bed with 1500 cylindrical composite particles ($h = d = 1cm$) made of 330 spheres each needs around 1 hour for particles made of rubber (Young's modulus = 0.5 MPa) and around 24h for particles made of glass (Young's modulus = 75800 MPa). Simulation was done using one CPU. The mesh size can be roughly estimated with 10000 volume cells per particle. This leads in the example above to a total mesh size of 15 million cells. The generation of such a mesh takes approximately 7 hours on a single CPU. The CFD calculation itself with the physical assumptions mentioned above and including heat transfer needs around 3 hours on 64 CPUs. All in all such a simulation can be conducted within 24 hours.

CONCLUSION

In this contribution we have shown and validated a completely numerical and automated workflow for the simulation of three dimensional and spatially resolved packed beds of spherical and non-spherical particles. The workflow is hidden behind a GUI which collects all relevant parameter and generates a set of macros to control the process. This approach is validated against

- bed porosity,
- radial porosity distribution,
- pressure drop,
- radial velocity profile and
- heat transport.

Additionally the automation leads to a reduced simulation time by avoiding user mistakes during the setup and by controlling and terminating the simulations when necessary or desired and therefore by reducing the idle time.
With simulation times in the range of one to a few days 3 dimensional and spatially resolved simulations are starting to be feasible for design studies and optimization of catalytic packed bed reactors.

REFERENCES

BAI, H. *et al.* (2009). "A coupled dem and cfd simulation of flow field and pressure drop in fixed bed reactor with randomly packed catalyst particles". *Industrial & Engineering Chemistry Research*, **48(8)**, 4060–4074.

CAULKIN, R. *et al.* (2012). "Predictions of porosity and fluid distribution through nonspherical-packed columns". *AIChE Journal*, **58(5)**, 1503–1512.

CUNDALL, P.; STRACK, O. (1979). "a discrete numerical model for granular assemblies". *Géotechnique*, **29**, 47–65.

DIXON, A.G. (1988). "Correlations for wall and particle shape effects on fixed bed bulk voidage". *Can. J. Chem. Eng.*, **66(5)**, 705–708.

DIXON, A.G. *et al.* (2012). "Experimental validation of high reynolds number cfd simulations of heat transfer in a pilot-scale fixed bed tube". *Chemical Engineering Journal*, **200(0)**, 344 – 356.

EPPINGER, T. *et al.* (2011). "Dem-cfd simulations of fixed bed reactors with small tube to particle diameter ratios". *Chemical Engineering Journal*, **166(1)**, 324 – 331.

FOUMENY, E. and BENYAHIA, F. (1991). "Predictive characterization of mean voidage in packed beds". *Heat Recovery Systems and CHP*, **11(2-3)**, 127–130.

GIESE, M. *et al.* (1998). "Measured and modeled superficial flow profiles in packed beds with liquid flow". *AIChE J.*, **44(2)**, 484–490.

GUARDO, A. *et al.* (2005). "Influence of the turbulence model in cfd modeling of wall-to-fluid heat transfer in packed beds". *Chemical Engineering Science*, **60(6)**, 1733 – 1742.

MUELLER, G.E. (1992). "Radial void fraction distributions in randomly packed fixed beds of uniformly sized spheres in cylindrical containers". *Powder Technology*, **72(3)**, 269 – 275.

NIJEMEISLAND, M. (2000). *Verification Studies of Computational Fluid Dynamics in Fixed Bed Heat Transfer*. Master's thesis, Worcester Polytechnic Institute.

NIJEMEISLAND, M. and DIXON, A.G. (2001). "Comparison of cfd simulations to experiment for convective heat transfer in a gas-solid fixed bed". *Chemical Engineering Journal*, **82(1-3)**, 231 – 246.

NIJEMEISLAND, M. and DIXON, A.G. (2004). "Cfd study of fluid flow and wall heat transfer in a fixed bed of spheres". *AIChE J.*, **50(5)**, 906–921.

OOKAWARA, S. *et al.* (2007). "High-fidelity dem-cfd modeling of packed bed reactors for process intensification". *Proceedings of European Congress of Chemical Engineering (ECCE-6), Copenhagen*.

ROSHANI, S. (1990). *Elucidation of local and global structural properties of packed bed configurations*. Ph.D. thesis, University of Leeds.

ZOBEL, N. *et al.* (2012). "Influence of the wall structure on the void fraction distribution in packed beds". *Chemical Engineering Science*, **71(0)**, 212 – 219.

NUMERICAL MODEL FOR FLOW IN ROCKS COMPOSED OF MATERIALS OF DIFFERENT PERMEABILITY

Ruru LI[2], Sam YANG[3],Jinxiao PAN[2], Gerald G PEREIRA[1*] ,John A. TAYLOR[4], Ben CLENNELL[5], Caineng ZOU[6]

[1] CSIRO Computational Informatics, Clayton 3169, AUSTRALIA

[2] North University of China, School of Information and Communication Engineering, Shanxi, 030051, CHINA

[3]CSIRO Materials Science and Engineering, Clayton, 3166, AUSTRALIA

[4]CSIRO eResearch & Computational & Simulation Sciences, Canberra, 2601, AUSTRALIA

[5]CSIRO Earth Science and Resource Engineering, Bentley, 6102, AUSTRALIA

[6]Research Institute of Petroleum Exploration and Development (RIPED), PetroChina, Beijing, CHINA

* E-mail: Gerald.Pereira@csiro.au

ABSTRACT

In the oil and gas industry permeability measurements on rock samples give an indication of the capacity to produce the output. Permeability on small samples can be derived from x-ray Computed Tomography (CT) scans which yields a three-dimensional (binary) digital image of the sample. Then using suitable numerical tools, one can use this digital data to compute a velocity field and hence the permeability of the sample. Up to now, this has been done on the assumption that fluid can only flow in pores (with no flow in solid regions). However, if the sample is made up of different materials, each material can have a different permeability to fluid flow. Hence, here we consider numerical modelling of flow through such a material. We use the Lattice Boltzmann method to model this flow, but need to change the usual streaming and collision steps to account for the partial permeability of voxels. We first implement this new algorithm on some well known test cases, with excellent agreement with analytic results and then use our algorithm on some real CT digital data. Our results clearly show the effect of increasing the local fraction of a high permeability material within a sample on the global permeability.

Keywords: Lattice Boltzmann, Computed tomography scan, digital data, partial permeability.

NOMENCLATURE

Greek Symbols

ρ LB particle density, [dimensionless].
μ LB dynamic viscosity, [dimensionless].
ν LB kinematic viscosity, [dimensionless].

Latin Symbols

n_s Solid fraction, [dimensionless].
p_f Percolating fraction, [dimensionless].
P LB Pressure, [dimensionless].
f LB particle distribution function, [dimensionless].
$\mathbf{u}$ LB Velocity, [dimensionless].
c_s LB speed of sound, [dimensionless].
K LB Permeability [dimensionless].

Sub/superscripts

α LB velocity direction.
x Index x – Cartesian axis.
y Index y – Cartesian axis.
z Index z – Cartesian axis.

INTRODUCTION

Fluid flow in porous media is widely encountered in oil and gas development and production, in addition to various other physical and chemical processes. The Lattice Boltzmann model (LBM) has recently attracted considerable attention in fluid flow simulations in porous media. However, LBM simulations often require an explicit and discrete description of the underlying pore-space geometry. For some applications, such as with unconventional oil and gas reservoirs, the pore sizes encompassing length scales from the nm to mm are relevant. It is technically unfeasible to characterize the pores across such multiple length scales, and computationally unpractical to simulate fluid flow on them with the traditional LBM. As an alternative approach, a partial-bounce-back LBM was suggested by Dardis and McCloskey (1998a, 1998b), which is a meso-scale LBM approach that incorporates the permeability of the medium as a model parameter. Multiple neighboring voxels could be grouped together to form nodes. The LBM simulations were performed on a lattice consisting of such nodes. Rather than a lattice comprising nodes that are either solid or fluid, this is a probabilistic model, where lattice node properties are varied to reflect the local permeability of the material. Their model was inspired by earlier work with lattice gases in which variable permeability materials were simulated by introducing random scatters into the lattice (Balasubramanian *et al.*, 1987; Gao and Sharma, 1994). However, Dardis and McCloskey's (1992a, 1992b) Lattice Boltzmann approach avoided the statistical noise that is inherent in lattice gas models. To date, several different possible models have been proposed for formulating partial-bounce-back LBM approach,

described in (Thorne and Sukop, 2004; Walsh *et al.*, 2009; Zhu and Ma, 2013). In all these models, a key parameter n_s referred to as solid fraction is used. It is worth noting that the solid fraction should be regarded as an internal model parameter related to the permeability, rather than a reflection of the actual proportion of solid material at each node. An analytic expression that relates the permeability to solid fraction was derived by Walsh *et al.* (2009). As will be discussed in the next section, an effective percolating fraction p_f (equivalent to 1-n_s) would be a more appropriate notation. We introduce the effective percolating rather than using a solid fraction because, as we shall see in the section on real rocks, the percolating fraction can encompass effects in addition to just the porosity (e.g., voxel permeability, material composition etc).

For the existing partial-bounce-back LBM approach, it is required to determine n_s at every lattice node. The discrete internal structure of a node may be characterized approximately using X-ray CT together with an image segmentation method Desrues *et al* (2006). The permeability of the node is calculated based on its internal structure. When the local permeability of a node was known, and it was homogeneous and isotropic, n_s for the node could be estimated using the equation given in Walsh *et al* (2009). A procedure for estimating the model parameter n_s is proposed in Zhu and Ma (2013). However, a typical sample may contain too many lattice nodes for this to work in practice. Even if the local permeability is estimated at a limited set of selected locations only, it is a non-trivial task to extrapolate them to other locations to obtain all the required n_s values.

It is worth noting that the existing LBM approaches are modeled on binary voxels. That is, a voxel is occupied by either solid or void. If a voxel is partial solid or void, the existing LBM is not applicable. Recently, a data-constrained modeling (DCM) approach has been developed which can generate microscopic partial volume distributions of materials and pores, therefore incorporating the effects of the fine length scale below X-ray CT resolution (Yang *et al*, 2007, Yang *et al*, 2008). In the model, each voxel was represented by partial volumes of various different materials rather than the binary value of only one material present in traditional image segmentation.

In this paper, the partial-bounce-back LBM approach is combined with the DCM partial volume model to simulate fluid flow in porous materials. The partial-bounce-back LBM is extended to incorporate such partial volume voxels at the microscopic length scale on a regular lattice. This enables more accurate permeability simulations for macroscopic samples with fine structures below voxel resolution. The effective percolating fraction p_f introduced in the advanced partial-bounce-back LBM is non-constant through porous medium which can be estimated using the volume fractions of the voxels. The advanced approach has been applied to simulate flow between parallel walls and in a rectangle duct flow in 2D and 3D respectively. The permeability of two real world sandstone samples are also calculated with the presented method.

Note that we use a single relaxation time (SRT) implementation of the LBM method in this study. However, it is well known (Pereira *et al.*, 2012) that the permeability obtained from an SRT scheme is viscosity dependent. As such, to obtain viscosity independent results, one should use a multi-relaxation time (MRT) scheme. Since we are only demonstrating the feasibility of a new partial bounce-back approach, we implement the simpler SRT scheme in this paper and leave a full MRT scheme to future work.

MODEL DESCRIPTION

Partial-bounce-back Lattice Boltzmann model

The Lattice Boltzmann model is a numerical technique for modeling fluid dynamics. The fluid is represented by discrete fluid particles, with a given mass and velocity, which propagate on a lattice. At each time-step in traditional LBM method, the fluid particles undergo a two-step process:

(1) Streaming step: In this step, the fluid particles are propagated between neighboring nodes. Streaming should be treated as an intermediate step. The result after streaming is denoted by f^*_α:

$$f^*_\alpha(\mathbf{x}+\mathbf{e}_\alpha\Delta t,t) = f_\alpha(\mathbf{x},t), \qquad (1)$$

where, $f_\alpha(\mathbf{x},t)$ is the particle distribution function in the direction α, $\mathbf{x}$ is the centre coordinate of a lattice node and t is time while Δt is the time increment. $\mathbf{e}_\alpha$ is the unit velocity vector in direction α. In this study, the two-dimensional 9-velocity (D2Q9) and three-dimensional 19-velocity (D3Q19) lattice Boltzmann models were used. That is, the direction α takes 9 and 19 discrete *values* respectively (which include the null vector).

(2) Collision step: In this step, the fluid particles, converging on individual nodes, are redistributed according to a set of predefined rules. Which rule is applied in the collision step depends on whether the node is part of the fluid domain or part of the solid-fluid boundary.

(I) If the node represents part of the fluid domain, then the evolution equation is

$$f_\alpha(\mathbf{x},t+\Delta t) = f^*_\alpha(\mathbf{x},t) + [f^{eq}_\alpha(\mathbf{x},t) - f^*_\alpha(\mathbf{x},t)]/\tau, \qquad (2)$$

where, τ is the dimensionless relaxation time. In this study τ is taken to be one. $f^{eq}_\alpha(\mathbf{x},t)$ are the equilibrium distribution functions and selected according to a Maxwell distribution.

(II) If a lattice node is part of a solid-fluid boundary with no-slip conditions, then the fluid particles undergo a bounce-back boundary condition. As the name suggests, at these nodes, the incoming fluid particles are reflected in the opposite direction during the collision step, α' is the opposite direction of α:

$$f_\alpha(\mathbf{x},t+\Delta t) = f^*_{\alpha'}(\mathbf{x},t)\ . \qquad (3)$$

For porous media, the collision step (I) would be considered as a second intermediate step after streaming, and the partial-bounce-back method and collision step (II) were both incorporated into the third

process, referred to as porous media step. Denoting f_α^{**} as the result of the collision step (I), at each time-step the fluid particles undergo a three-step process:

(1) streaming step:

$$f_\alpha^{*}(\mathbf{x}+\mathbf{e}_\alpha\Delta t,t)=f_\alpha(\mathbf{x},t)\ , \qquad (4)$$

(2) collision step:

$$f_\alpha^{**}(\mathbf{x},t+\Delta t)=f_\alpha^{*}(\mathbf{x},t)+[\,f_\alpha^{eq}(\mathbf{x},t)-f_\alpha^{*}(\mathbf{x},t)]/\tau\ , \qquad (5)$$

(3) porous media step:

$$f_\alpha(\mathbf{x},t+\Delta t)=f_\alpha^{**}(\mathbf{x},t+\Delta t)+n_s\cdot\Delta f\ , \qquad (6)$$

where, $n_s(\mathbf{x})$ is the solid fraction mentioned previously per lattice node $\mathbf{x}$. The density per node ρ and the macroscopic flow velocity $\boldsymbol{u}$ are defined in terms of the particle distribution function by (the D2Q9 model)

$$\sum_{\alpha=0}^{8} f_\alpha=\rho\ ,\ \sum_{\alpha=0}^{8} f_\alpha\,\mathbf{e}_\alpha=\rho\mathbf{u}\ , \qquad (7)$$

where the pressure is given by $P = c_s^2\rho$, and c_s is the speed of sound with $c_s^2=1/3$.

According to different partially bounce-back models, the term Δf has various forms. The following are three common forms:

(I) first form:

$$\Delta f = f_{\alpha'}(\mathbf{x},t)-f_\alpha(\mathbf{x}-\mathbf{e}_\alpha\Delta t,t)\ . \qquad (8)$$

This form was proposed by Dardis and McCloskey (1998).

(II) second form:

$$\Delta f = f_{\alpha'}^{**}(\mathbf{x}+\mathbf{e}_\alpha\Delta t,t+\Delta t)-f_\alpha^{**}(\mathbf{x},t+\Delta t)\ . \qquad (9)$$

This form was proposed by Thorne and Sukop (2004).

(III) third form:

$$\Delta f = f_{\alpha'}^{*}(\mathbf{x},t)-f_\alpha^{**}(\mathbf{x},t+\Delta t)\ . \qquad (10)$$

This form is proposed by Walsh *et al* (2009). It was demonstrated in this paper that only the third form can conserve mass in heterogeneous media.

Partially percolating Lattice Boltzmann model

In order to incorporate the partial volume effect into the traditional partial-bounce-back LBM, an effective percolating fraction p_f for each voxel is introduced to replace the solid fraction n_s. In the above, the first and second forms both use data from the neighbouring nodes to calculate the term Δf. This would create complications for parallel computation implementation. Significant data exchange and synchronization would be required between processors at each time-step. The third model has the advantage that the collision and porous media step are performed simultaneously without referring to neighbouring nodes. In the following, the third form was used which was named as partially-percolating Lattice Boltzmann model (PP-LBM).

Similar to the LBM approach for porous media, at each time-step in PP-LBM the fluid particles undergo a three-step process: streaming, collision, and porous media steps. The third step could be expressed as:

$$f_\alpha(\mathbf{x},t+\Delta t)=f_\alpha^{**}(\mathbf{x},t+\Delta t)+\left[1-p_f(\mathbf{x})\right]\cdot[\,f_{\alpha'}^{*}(\mathbf{x},t)-f_\alpha^{**}(\mathbf{x},t+\Delta t)]\ . \qquad (11)$$

SIMULATIONS IN REGULAR GEOMETRIES

Flow between parallel walls

With an incompressible fluid, Poiseuille flow is created between stationary parallel walls (which forms a channel) when a constant pressure difference ΔP is applied between the two openings at the end of the walls. The velocity distribution can be solved analytically. It is parabolic and is given by

$$u(y)=\frac{G\cdot(L-y)\cdot y}{2\mu}\ , \qquad (12)$$

where G is a constant pressure gradient, μ is the dynamic viscosity, L is the perpendicular separation between the two parallel walls so that fluid flows in the channel between $0\le y\le L$.

In order to evaluate the accuracy of the PP-LBM approach as described in Equations (4), (5) and (11), the flow is simulated numerically on a 51×101 square lattice with a D2Q9 model, where $0\le x\le 50$, $0\le y\le 100$, using pressure boundary conditions at the inlet and outlet. To model the impermeable walls, where we have a no slip boundary condition, we simply use p_f = 0. The lattice sites between the two walls were assigned the value p_f = 1. That is, it is fully void between the walls. For numerical convenience, the simulations were carried out using LBM units where the fluid density is ρ = 1, and the dynamic viscosity μ = 1/6. The flow was driven by a constant pressure difference between the inlet and outlet of the flow region, which is generated using a pressure boundary condition in 2D (Zou and He, 1997, Hecht and Harting, 2010). The pressure difference is expressed as $\Delta P=c_s^2(\rho_{in}-\rho_{out})$, ρ_{in} is the density of nodes at the inlet with ρ_{in} =1.00001 and ρ_{out} is the density of nodes at the outlet with ρ_{out} = 0.99999. The value of the pressure difference is ΔP = 0.67 x 10^{-5}. A relationship between Reynolds number and pressure difference $\mathrm{Re}=\sqrt{(\Delta P/\Delta x)\cdot L^3\cdot\rho}/\mu$ is used to relate the LBM units to physical units. For a fluid with a density ρ = 10^3 kg/m^3 and a dynamic viscosity μ = $10^{-3}\,\mathrm{kg/m\cdot s}$, the value of constant pressure difference is ΔP = 1.5 x 10^{-5} Pa, for a voxel size (with edge length) 40 microns. When the flow reaches a steady-state, the fluid speed depends only on y. The simulation results and the analytic solution are shown in Figure 1. The figure shows an excellent agreement between the analytical solution and the PP-PBM numerical results.

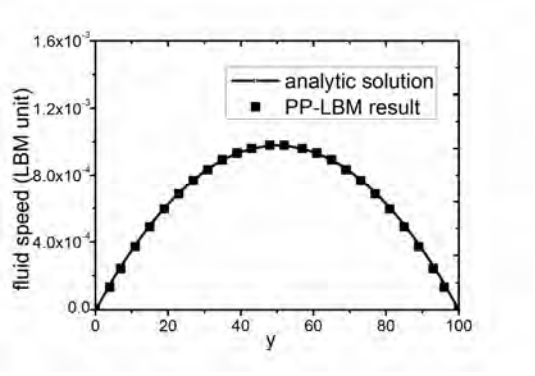

Figure 1. PP-LBM simulation of flow between parallel walls. Analytical solution from Eq. (12) is shown as solid lines and the PP-LBM numerical results at *x*=25 are shown as circles.

When pixels between the two non-percolating walls are partially percolating with $p_f < 1$, the fluid velocity distribution is quite different. This problem can also be solved analytically (Balasubramanian, 1987). The solution is expressed as

$$u(y) = -\frac{G}{\varphi\rho}[1-\frac{\cosh[r(y-L/2)]}{\cosh(r\cdot L/2)}] \ , \qquad (13)$$

where φ is a damping coefficient proportional to 1-p_f. φ and r are related through $r=\sqrt{\varphi/\nu}$, $\nu=\mu/\rho$ is the kinematic viscosity. As $\varphi \to 0$ the solution (13) returns to the standard Poiseuille equation. As additional verifications of the PP-LBM approach, various uniform values of the effective percolating fraction p_f between the non-percolating walls have been simulated from 0.01 to 0.9. Again, the steady-state flow speed depends only on *y*. The simulated speed distributions (symbols) for various uniform values p_f as a function of *y* are shown in Figure 2. The analytic results (continuous curves) are also included in Figure 2. Excellent agreement has been obtained between the PP-LBM numerical simulations and analytic solutions. In addition, our numerical results show no abnormal behaviour for all values of p_f in (0, 1). In contrast, the model by Dardis and McCloskey has produced obvious errors near the boundaries for $p_f < 0.7$ (Chen and Zhu, 2008).

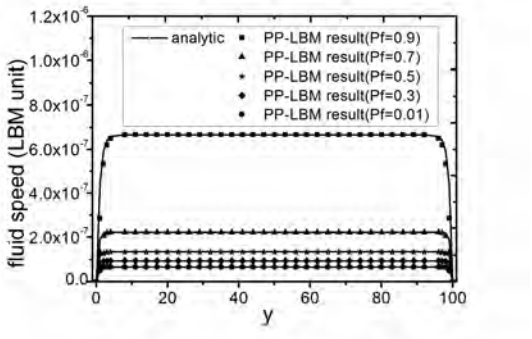

Figure 2. Simulation results when the percolating fraction changed. Analytical solutions from Eq. (13) are shown as solid lines and the PP-LBM numerical results at x=25 are shown as markers.

Flow in a rectangular duct

For a duct with a rectangular cross section, the same pressure difference ΔP creates a quasi-parabolic velocity distribution when the effective percolating fraction is p_f = 1. It can be calculated that the product of the friction coefficient f (a dimensionless variable which quantifies the overall viscous drag) and the Reynolds number Re is a constant. This quantity is given by (Tao and Xu, 2001)

$$f\cdot \mathrm{Re} = \frac{2\cdot\Delta P\cdot de^2}{\mu\cdot L_z\cdot\bar{u}}, \qquad de = \frac{4\cdot L_x\cdot L_y}{2(L_x+L_y)} \ , \ (14)$$

where L_z is the duct length along the *z* axis in the flowing direction, L_x and L_y are the duct widths in the *x* and *y* directions respectively, $\bar{u}$ is the average velocity of a cross section.

As another validation of the PP-LBM approach, a numerical simulation was implemented on a 101 x 101 x 51 simple cubic lattice with a D3Q19 model, where $0 \le x \le 100$, $0 \le y \le 100$, $0 \le z \le 50$. To model the four impermeable walls, where we have a no-slip boundary condition, we simply use p_f = 0. The lattice sites in the rectangular flow region were assigned the value p_f = 1. The flow is driven by the same pressure difference as the 2D simulation along the *z* axis direction and is generated using the pressure boundary condition in 3D (Zou and He, 1997). All other parameters are the same as given in the previous section. The simulation results are shown in Figure 3. The average velocity $\bar{u} = 2.76\times10^{-4}$ was calculated using the velocity profile displayed in Figure 3. Substitution of the simulated average velocity into Equation (14) gives a value of *f*. Re = 56.82. This is in good agreement with the experimentally measured value of 57 (Tao and Xu, 2001).

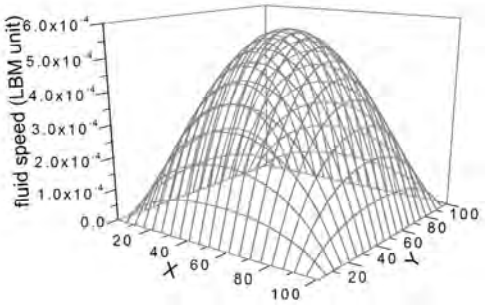

Figure 3. Fluid velocity profile of a cross section at *z*=25 in a rectangular duct.

A number of simulations have also been carried out by sub-dividing the flow region into multiple sub-regions. Different sub-regions have been assigned different constant values of p_f. The model is robust since it does not show any numerical abnormalities.

SIMULATIONS IN REAL ROCKS

The present PP-LBM model is now applied to a real world tight-sandstone sample which consists of quartz, albite, calcite and pyrite. The cylindrical sample has a diameter and height of 3mm and 20mm respectively, which was drilled from Yaodian area of Yan'an in Erdors Basin, China. The 3D microscopic distribution of mineral phases in the sample is generated with the in-

house DCM software in a cubic region of 600 x 600 x 700 voxels (Li *et al.*, 2013). Each voxel represents a size of 3.7 x 3.7 x 3.7 μm^3. An arbitrary sub-domain of 200 x 200 x 50 voxels was selected for the following PP-LBM simulations.

In the sample, pyrite, quartz and albite particles are not permeable. Fluid can flow through void and the partially permeable calcite. Denoting the effective percolating fraction of calcite as p^c_f, the effective percolating fraction of a voxel is approximated as

$$p_f = v_o + p_f^c \cdot v_c \quad , \qquad (15)$$

where v_o and v_c denotes the volume fractions for pore and calcite in the voxel respectively.

The flow is driven by the same pressure difference as the rectangular duct simulation along the z axis direction. The pressure difference is implemented numerically in the same way which has been discussed in the previous section. All other parameters are the same as given in the previous section. Various values of p^c_f from 0.0 to 0.2 have been used in the simulation. The typical velocity distributions in the simulated sample region are shown in Figure 4. As shown in Figure 4(a), the high-speed flow occurs only in small regions in the tight sandstone. By comparing Figure 4(b) with 4(c), it was found that just a small proportion of pores participated in the flow. Some pores effectively are not part of the flow path, as has been highlighted by the boxed regions in the figure. Most of flowing path is occupied by calcite with a low flow speed. There are isolated relatively high-speed regions in the calcite. This indicates the existence of fine flow paths in these regions.

The same method is applied to a CIPS (Calcite In situ Preciptation System) core sandstone sample which consists of quartz and calcite. The 3D microscopic distribution of these mineral phases in this sample is generated with the DCM software in a cubic region of 1450 x 1470 x 340 voxels (Yang *et al*, 2012). Each voxel represents a size of 3.7 x 3.7 x 3.7 μm^3. An arbitrary sub-domain of 200 x 200 x 50 voxels is selected for the following PP-LBM simulations. The flow is driven by the same constant pressure difference as the tight-sandstone in the z axis direction and all the other parameters are the same as well. The same method as defined in Equation (15) is used to determine the effective percolating fractions. We do not show the corresponding plots due to space and file size restrictions for this article.

In the LBM simulations, once flow is deemed to have reached steady state, the bulk permeability of the medium can be calculated based on the generated velocity datasets using Darcy's law as follows:

$$K = \frac{\mu \cdot < p_f \cdot u >}{\nabla P} \quad , \qquad (16)$$

where K is the bulk permeability, ∇P is the pressure gradient in a particular direction, μ is dynamic viscosity of the fluid, p_f is the percolating fraction and u is the component of the velocity in the same direction as the pressure gradient. The quantity $< p_f \cdot u >$ is the average velocity over all the flow voxels.

The simulation is terminated once the following criterion has been reached:

$$\sum_t \frac{\|K(t) - K(t-1)\|}{\|K(t)\|} < 10^{-5} \quad . \qquad (17)$$

The convergence curves of the two samples are shown in Figure 5. The permeability of sandstone converges faster than tight sandstone. For sandstone, it requires 24000 time-steps to reach steady state, while it would need 162000 time-steps for tight sandstone. The code uses OpenMP to implement parallel computation to increase the calculating speed in C++ programs.

The calculated bulk permeability is shown in Figure 6. As anticipated, the bulk permeability increases with the effective percolating fractions of calcite. The bulk permeability of the tight-sandstone is more sensitive to the effective percolating fraction of calcite than for sandstone. That is, fine flow paths in calcite are more important for tight-sandstone than for sandstone. Flow in calcite phase in sandstone makes an insignificant contribution to the bulk permeability. The sandstone has

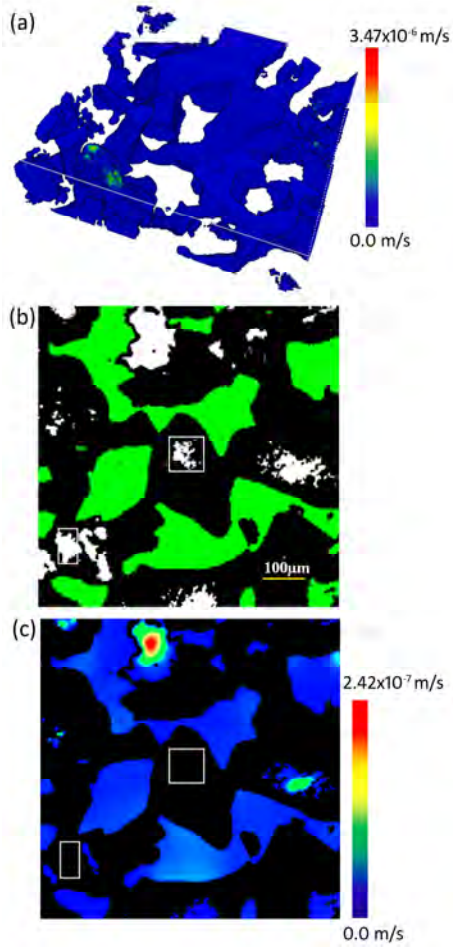

Figure 4. Velocity distribution of tight sandstone sample where the non-percolating regions voxels are displayed as white and the percolating fraction of calcite is 0.2. (a) 3D velocity distribution image. The high flow speed region is small so it is not visible clearly on the figure. (b) Microstructure composition distribution at slice 15 with pore, calcite and mixture of quartz, albite and pyrite represented by white, green and black. (c) Velocity distribution at slice 15.

a permeability value up to two orders of magnitude greater than the tight sandstone.

In relation to bulk permeability, flow in the calcite phase is essential for tight-sandstone, whereas it could be neglected for sandstone.

CONCLUSIONS

A partially percolating lattice Boltzmann model (PP-LBM) defined on partial volume voxels rather than binary voxels is developed. An effective percolating fraction is introduced on each voxel to incorporate the partial volume effect into the partial-bounce-back LBM model. The partial volume effect is related to the fine structures which are smaller than the voxel size which can be characterized using DCM. The effective percolating fractions of voxels were estimated using the DCM generated volume factions. The PP-LBM is implemented numerically on the square lattice in 2D with square pixels and on the simple cubic lattice in 3D with cubic voxels. In relation to fluid flow, each voxel (pixel) is defined by an effective percolating fraction p_f which is related to the voxel (pixel) permeability, compositional volume fractions and sub-voxel (sub-pixel) fine structures. Fluid flows on regular geometries in 2- and 3-dimentions have been simulated. The numerical results agree with known analytic solutions.

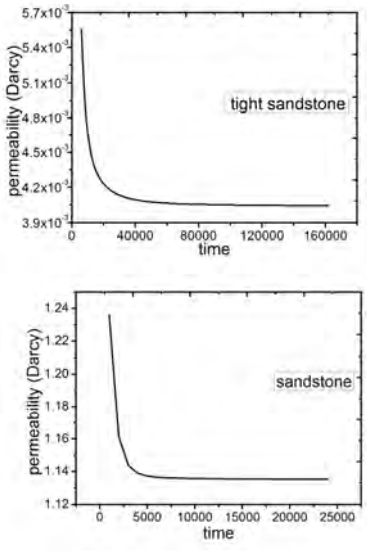

Figure 5. Convergence lines of permeability for tight sandstone and sandstone. The percolating fraction of calcite is 0.0.

The PP-LBM approach has been used to simulate flow in two real-world rock samples – a tight-sandstone and a CIPS sandstone. With the CIPS sandstone, the bulk permeability is insensitive to flow in the calcite phase. Therefore, the conventional LBM flow simulations on image-segmented X-ray CT images would be adequate. However, with the tight-sandstone, the numerical results indicate that the fine flow paths in the calcite phase play a critical role. When the flow paths in the calcite phase are neglected, the sample is essentially non-permeable. That is, the conventional LBM simulation on image-segmented X-ray CT images would produce misleading results. The tight oil & gas resources are going to play an increasingly important role for sustainable energy supply in the world. The PP-LBM and DCM would be useful tools for characterization and modeling of the tight reservoirs.

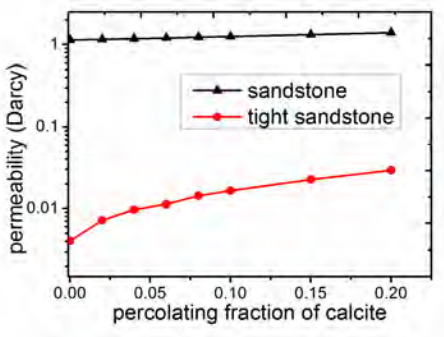

Figure 6. Effect of different percolating fractions of calcite on bulk permeability.

The PP-LBM approach is generic and should be applicable to other types of unconventional reservoirs and advanced materials. Work along this line is in progress.

REFERENCES

BALASUBRAMANIAM, K., HAYOT, F. and SAAM,W.F., (1987) “Darcy’s law from lattice- gas hydrodynamics”, *Phys. Rev. A*, **36**, 2248–2253.

CHEN, Y. and ZHU, K., (2008) “A study of the upper limit of solid scatters density for gray Lattice Boltzmann Method”, *Acta Mech. Sin.*, **24**, 515–522.

DARDIS, O. and McCLOSKEY, J., (1998a) “Lattice Boltzmann scheme with real numbered solid density for the simulation of flow in porous media”, *Phys. Rev. E*, **57**, 4834–4837.

DARDIS, O. and McCLOSKEY, J., (1998b) “Permeability porosity relationships from numerical simulations of fluid flow”, *Geophys. Res. Letts.*, **25**, 1471–1474.

DESRUES, J., VIGGIANI, G. and BESEUELLE, P. (eds) (2006) “Advances in X-Ray Tomography for Geomaterials”, (London: ISTE)

GAO, Y. and SHARMA, M.M., (1994) “A LGA model for fluid flow in heterogeneous porous media”, *Transp. in Por. Media*, **17**, 1–17.

HECHT, M. and HARTING, J., (2010), “Implementation of on-site velocity boundary conditions for D3Q19 lattice Boltzmann simulations, J. of Stat. Mech.: Theory and Exp. (http://iopscience.iop.org/1742-5468/2010/01/P01018)

LI, R.R., KONG, H., YANG, S., MAYO, S., ZHU, R., BAI, B., PAN, J. and WANG, H., (2013) *CSIRO Data Collection: Erdors Basin Yanchang Formation Tight Sandstone 3D Microstructures*

PEREIRA, G.G., DUPUY, P.M., CLEARY, P.W., DELANEY, G.W., (2012), “Comparison of permeability of model porous media”, *Prog. in Comput. Fluid Dyn.*, **12**, 176-186.

TAO, J., and XU, J., (2001), “The fluid flow rule at laminar flow in rectangle shape channel”, *Journal of Huainan Institute of Technology*, **2**,1-10.

THORNE, D. and SUKOP, M., (2004) "Lattice Boltzmann model for the Elder problem" In: Proceedings of the XVth International Conference on Computational Methods in Water Resources (CMWR XV), Chapel Hill, NC, USA, June 13–17. Elsevier, Amsterdam, 2004, pp. 1549–1557

WALSH, S.D.C., BURWINKLE, H. and SAAR, M.O., (2009) "A new partial-bounce back lattice-Boltzmann method for fluid flow through heterogeneous media", *Computers & Geosciences*, **35**, 1186–1193.

YANG, Y.S., TULLOH, A., COLE, I., FURMAN, S. and HUGHES, A., (2007) "A data-constrained computational model for morphology structures", *J. Aust. Ceram. Soc.*, **43**, 159–164.

YANG, Y.S, FURMAN, S and TULLOH, A. "A data-constrained 3D Model for material compositional microstructures", *Adv. Mat. Res.*, **32**, 267-270.

YANG, S, LIU, K, MAYO, S, and TULLOH, A, (2012) *CSIRO Data Collection: CIPS sandstone microstructure*

ZHU, J. and MA, J.S., (2013) "An improved gray lattice Boltzmann model for simulating fluid flow in multi-scale porous media", Adv. in Water Res., **56**, 61–76.

ZOU, Q and HE, H., (1997) "On pressure and velocity boundary conditions for the lattice Boltzmann BGK model", *Phys. Fluids*, **9**, 1591-1598.

MODELLING THERMAL EFFECTS IN THE MOLTEN IRON BATH OF THE HISMELT REDUCTION VESSEL

Peter J. WITT[1*], Yuqing FENG[1] and Mark P. DAVIS[2]

[1] CSIRO Computational Informatics, Melbourne 3169, AUSTRALIA

[2] HIsmelt Corporation Pty Ltd, Kwinana 6966, AUSTRALIA

* E-mail: peter.witt@csiro.au

ABSTRACT

Over a thirty year period the HIsmelt process has been developed as an alternative to the traditional blast furnace for the production of pig iron. This process involves the injection of fine iron ore and non-coking coal particles into a molten iron bath though a number of wall lances. These jets induce substantial mixing and splashing of molten droplets into the top space of the vessel due to the substantial volume of gas generated within the bath. Control of heat transfer, reactions and the complex multiphase fluid dynamics is critical to successful operation of the process. Since inception computational fluid dynamics has played an important role in scale-up and process optimisation (Davis *et al.* 2003, Davis and Dry, 2012).

A "Bath model" has been developed which focuses on the smelt-reduction processes occurring within the bath volume of the HIsmelt vessel (Stephens *et al.* 2011). As this model is a transient multi-component Eulerian-Eulerian model with Lagrangian particle tracking for the coal and ore particles, it requires a substantial computational effort. For this reason (and due to the large thermal inertia of the liquid bath) earlier versions of the model have been isothermal.

Particles enter the molten iron bath at close to ambient temperature. Heating of both the particles and gas stream by the bath will require a finite time and cause local cooling around the particle jet. To investigate this effect the bath model has been extended to include convective heat transfer between the bath, gas and particles, and radiation within the gas cavity.

This paper reports on the incorporation of thermal effects into the model and presents results showing their impact.

Keywords: CFD, Multiphase heat and mass transfer, Process metallurgy, HIsmelt process, Iron Making, Thermal Radiation.

NOMENCLATURE

Greek Symbols

α volume fraction.
ε energy dissipation rate, [m^2 s^{-3}].
λ thermal conductivity, [W m^{-1}].
ρ mass density, [kg m^{-3}].
ϕ_p particle diameter, [m].
τ stress tensor, [Pa].
μ viscosity, [kg m^{-1} s^{-1}].

Latin Symbols

A interfacial area [m^2].
Cp specific heat, [J kg^{-1} K^{-1}].
g gravitational acceleration, [m s^{-2}].
F_D, F_B particle drag and buoyancy force, [N].
h static enthalpy, [J kg^{-1}].
k turbulence kinetic energy, [m^2 s^{-2}].
m_p particle mass, [kg].
$M_{F,r}$ inter-phase drag force, [N m^{-3}].
p pressure, [Pa].
Q_C, $Q_{M,}$, Q_R particle convective, mass transfer and radiation heat sources, [W].
Sc Schmidt number.
T temperature [K].
u_D, u_S drift and slip velocity, [m s^{-1}].
$\mathbf{u}$ velocity, [m s^{-1}].
$\mathbf{v}$ particle velocity, [m s^{-1}].
V_P particle volume [m^3].
$\mathbf{x}$ particle position, [m].
Y species mass fraction.

Sub/superscripts

g gas phase.
i chemical species index.
l liquid bath phase.
p particle phase.
r phase index.

INTRODUCTION

HIsmelt is a direct smelting technology for converting iron ore fines into pig iron. The process has been developed over a number of years and is slowly building into a serious challenge to the blast furnace. It offers the advantages of lower capital and operating costs, and greater raw material flexibility, whilst maintaining a high-quality metal product.

Development of the process has moved through a number of pilot plant designs to a commercial-scale facility of 0.8 Mt/a in Kwinana, Western Australia (2002-2008). All of these plant designs have been aided by the use of physical and CFD models. The plant is

currently being moved to Shandong in China to continue its development.

Scale up of any metallurgical process is problematic due to the increasing scales over which turbulent flow processes operate. Understanding the fluid dynamics involved and the associated heat and mass transfer has been critical to understanding and predicting the behaviour of the process and enabling the progression to larger smelting vessels.

CFD modelling of the HIsmelt Bath has been undertaken at the CSIRO for a number of years and has culminated in the development of the ANSYS/CFX thermal model presented in this paper.

MODEL DESCRIPTION

The domain for the CFD bath model includes the entire volume of the Smelt Reduction Vessel (SRV), illustrated in Figure 1, but the main focus is on ore reduction within the metal bath, coal devolatilisation and dissolution (into the metal), and the mass of liquid splashed into the gas space above the bath. Distinct gas, liquid and solid-particle phases are present in the computational domain and are critical to the smelting process and fluid dynamics behaviour. Each phase is comprised of a number of different components as summarised in Table 1 and Figure 2. There are large regions of continuous gas and similar volumes of continuous liquid; making the multi-fluid Eulerian-Eulerian approach the most appropriate way to model both the liquid bath and gas phases.

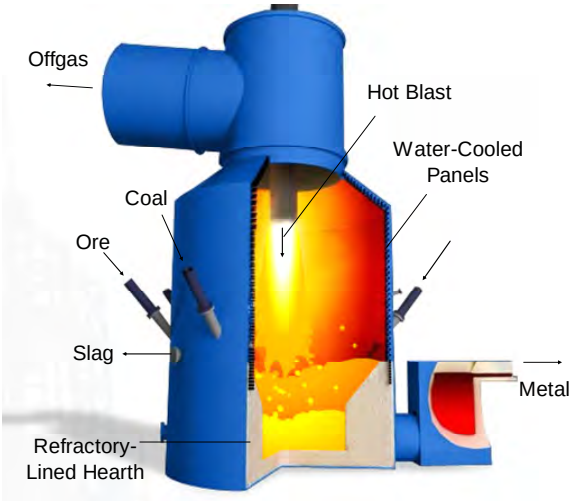

Figure 1: The HIsmelt Smelt Reduction Vessel.

The Eulerian-Eulerian model must simulate both the gas-continuous regions in which the liquid bath phase is assumed to be in dispersed form (splashes of droplets, fingers, sheets, etc in the upper regions of the SRV), as well as the liquid-continuous regions of the bath-proper in which the gas is assumed to be in the form of dispersed bubbles.

Within the gas phase a variable composition mixture is used to account for nitrogen (used as a carrier gas to inject the particles), carbon monoxide (evolved from ore reduction reactions) and hydrogen (evolved from coal devolatilisation). The liquid bath consists of two components, slag and metal. The slag is treated as a constant composition component, while the metal is considered to be a variable composition mixture of iron and carbon. An Algebraic Slip Model (or mixture model in CFX terminology) is used to account for the relative motion of slag and metal (Fe/C melt), as first demonstrated in models of gas injection into a slag/metal bath by Schwarz and Taylor (1998).

Table 1: Phases and their compositions

Phase	Type	Components
Gas	Eulerian	N_2, CO, H_2
Liquid Bath	Eulerian	Fe, Carbon, Slag
Ore particles	Lagrangian	Fe_2O_3, H_2O
Coal particles	Lagrangian	Coal fixed component, and Coal volatile component.

Iron ore and coal particles are modelled using the Lagrangian particle tracking approach. Iron ore particles are considered to be composed of hematite (Fe_2O_3) and moisture (H_2O). Coal particles are a variable composition mixture of fixed carbon and volatile carbon.

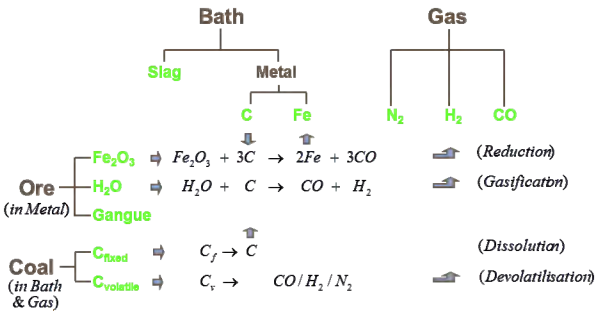

Figure 2: Schematic of the phase and component descriptions and associated reactions

The reduction process is described by a series of idealised chemical reactions representing coal dissolution (into the molten iron):

$$C_{coal(sol)} \Rightarrow C_{metal} \quad (1)$$

coal devolatilisation (evolution of gaseous volatiles):

$$C_{vol(sol)} \Rightarrow CO + N_2 + H_2 \quad (2)$$

iron ore reduction (by dissolved carbon in the bath to form molten iron and carbon monoxide gas):

$$Fe_2O_{3\,ore} + 3C_{metal} \Rightarrow 2Fe_{metal} + 3CO \quad (3)$$

and gasification (water vapour in the ore particles reacts with dissolved carbon in the metal, generating hydrogen and carbon monoxide gas):

$$C_{metal} + H_2O_{ore} \Rightarrow H_2 + CO \quad (4)$$

Model Equations

For each Eulerian phase (gas and liquid-bath) continuity and momentum equations are solved to calculate the phase velocity, volume fraction and turbulence level. These transport equations can be written as:

Continuity equation with mass transfer

$$\frac{\partial}{\partial t}(\alpha_r \rho_r) + \nabla \cdot (\alpha_r \rho_r \mathbf{u}_r) = S_r \quad (5)$$

Here, the phases *r* are liquid bath phase (*r*=*l*) and gas phase (*r*=*g*). The term S_r is the net mass transfer to phase *r* from other interacting phases due to various reactions (described in detail in sections below).

Momentum equation

$$\frac{\partial}{\partial t}\left(\rho_r \alpha_r \mathbf{u}_r\right) + \nabla \cdot \left(\rho_r \alpha_r \mathbf{u}_r \mathbf{u}_r\right) = -\nabla \cdot \left(\alpha_r \tau_{ij,r}\right) - \alpha_r \nabla P + \alpha_r \rho_r g + M_{F,r} + MS_r' \quad (6)$$

$$\sum \alpha_r = 1 \quad (7)$$

The terms on the right hand side of the momentum equation, (equation 6), represent respectively the stress, pressure gradient, gravity, momentum exchange between the phases due to interfacial forces (only the drag force is considered here) and the net momentum transfer to phase *r* by other phases due to net mass transfer (MS_r'). Pressure is shared by both the phases. The stress term for phase *r* is described as follows:

$$\tau_{ij,r} = -\mu_{eff,r}\left(\nabla \mathbf{u}_r + (\nabla \mathbf{u}_r)^T - \frac{2}{3} I(\nabla \mathbf{u}_r)\right) \quad (8)$$

The effective viscosity for each phase, $\mu_{eff,r}$ is composed of two contributions: the molecular viscosity and the turbulent viscosity. The turbulent eddy viscosity is formulated using the *k*-*ε* turbulence model and turbulence is considered homogeneous across both phases (*k* and *ε* values are the same for each phase):

$$\mu_{T,r} = \rho_r C_\mu \frac{k^2}{\varepsilon} \quad (9)$$

The turbulence kinetic energy (*k*) and its energy dissipation rate (*ε*) are calculated from their governing transport equations (equations 10 and 11 respectively). The term τ_m in these equations (as computed by equation 14) takes into account the phasic turbulent viscosity (equation 9) and the molecular viscosity of each phase.

$$\frac{\partial \rho_m k}{\partial t} + \nabla \cdot \left(\rho_m \mathrm{u}_m k\right) = -\nabla \cdot (\Gamma_m \nabla k) + (G_m - \rho_m \varepsilon) \quad (10)$$

$$\frac{\partial \rho_m \varepsilon}{\partial t} + \nabla \cdot \left(\rho_m \mathrm{u}_m \varepsilon\right) = -\nabla \cdot (\Gamma_m \nabla \varepsilon) + \frac{\varepsilon}{k}(C_{\varepsilon 1} G_m - C_{\varepsilon 2} \rho_m \varepsilon) \quad (11)$$

where

$$\rho_m = \rho_l \alpha_l + \rho_g \alpha_g \quad (12)$$

$$u_m = u_l \alpha_l + u_g \alpha_g \quad (13)$$

$$\tau_m = \tau_l \alpha_l + \tau_g \alpha_g \quad (14)$$

The model constants used are the standard values, viz. C_μ =0.09; σ_k=1.00; σ_ε=1.00; $C_{\varepsilon 1}$=1.44, $C_{\varepsilon 2}$=1.92. The term *G* in above equation is the production of turbulence kinetic energy and described by:

$$G = \tau_m : \nabla u_m \quad (15)$$

Thermal Energy Transport

Conservation of thermal energy in the gas and liquid phases is calculated by solving for the phase static enthalpy, h_r :

$$\frac{\partial}{\partial t}(\alpha_r \rho_r h_r) + \nabla \cdot (\alpha_r \rho_r \mathbf{u}_r h_r) = \nabla \cdot (\alpha_r (\lambda_r + \lambda_r^t) \nabla T_r) + S_{h,r} + SH_{p,r} + SH_{m,r} + S_{rad,r} \quad (16)$$

where $\lambda_r + \lambda_r^t$ are the molecular and turbulent thermal conductivities, T_r is the temperature for phase *r* and source terms $S_{h,r}$, $SH_{p,r}$, $SH_{m,r}$, $S_{rad,r}$ are for energy transfer between phases, to and from particles, particle mass transfers and thermal radiation. Static enthalpy and temperature are related through the phase specific heat, Cp_r, by:

$$h_r = Cp_r \, T_r \quad (17)$$

Thermal radiation transport is calculated using the Discrete Transfer model of Shah (1979) and provides source terms for the phase-enthalpy and particle transport equations. A high value for the absorption coefficient is set for the liquid phase such that radiation transport only effectively occurs within the gas only volumes and from the liquid surfaces.

Species Transport

Mass fractions of individual components (CO, N_2) in the multi-component gas phase are computed by solving each component's transport equation (equation 18) with relevant source/sink terms, while the mass fraction of H_2 in the gas phase is determined using constraint equation 19.

$$\frac{\partial \alpha_g \rho_g Y_{gi}}{\partial t} + \nabla \cdot \left(\alpha_g \rho_g \mathrm{u}_g Y_{gi}\right) = \nabla \cdot \Gamma_{gi} \alpha_g \nabla Y_{gi} + S_{gi} \quad (18)$$

$$\sum Y_{gi} = 1 \quad (19)$$

where *Y* is the mass fraction of species *i* in the *r* phase. Similarly, the mass fraction of individual components (Fe, C and slag) in the multi-component liquid phase is obtained by applying the algebraic slip model (ASM, equation 20 and 21). This is done in order to enable the separation of slag from metal. The slag is considered to be continuous in the liquid bath and its fraction is computed using constraint equation 22. The ASM enables computation of a slip velocity between metal (Fe/C) and slag, and the drift velocity of Fe/C. The drift velocity of a component is taken relative to the mixture (i.e. the liquid bath) velocity, whereas the slip velocity of a component is taken relative to the velocity of continuous medium in the mixture (i.e. slag velocity in this case).

$$\frac{\partial \alpha_l \rho_l Y_{li}}{\partial t} + \nabla \cdot \left(\alpha_l \rho_l (\mathrm{u}_l + u_{Di}) Y_{li}\right) = \nabla \cdot (\Gamma_{li} + \frac{\mu_t}{\mathrm{Sc}_t}) \alpha_l \nabla Y_{li} + S_{li} \quad (20)$$

where, u_{Di} is the drift velocity of species *i*, and is related to the slip velocity u_{Si} by equation 21.

$$u_{Di} = u_{Sig} - \sum_i u_{Sig} Y_{gi} \quad (21)$$

$$\sum Y_{li} = 1 \quad (22)$$

Lagrangian particle tracking of ore and coal

The velocities, trajectories and temperatures of representative ore and coal particles are computed using the Lagrangian tracking approach, originally developed by Crowe *et al.* (1977), which involves solving the momentum equations based on Newton's second law (equations 23 to 25) and a particle temperature equation 26. Ore and coal particles are treated as separate phases. The interaction between the carrier fluid and particles has been treated using two-way coupling. The carrier fluid for particles can be the Eulerian gas phase or the Eulerian liquid bath phase, the appropriate phase being decided based on a critical volume fraction of these phases at the location of the particle. Particle drag and heat transfer switches from gas to liquid at this critical voidage. Equations 23 and 24 compute the particle displacement using forward Euler integration of particle velocity over the time-step. In forward integration, the particle velocity is calculated at the start of the time step and is assumed to prevail over the entire time step. At the end of the time step, the new particle velocity is computed using the particle momentum equation 25. Momentum is transferred between fluid and particles only through the inter-phase forces. In general these forces would be drag force, added mass force, pressure force, buoyancy force and Basset force. In this work, only drag and buoyancy has been considered, as they are the dominant forces.

$$\frac{dx_i}{dt} = v_i \tag{23}$$

$$x_i^n = x_i^0 + v_i^0 \partial t \tag{24}$$

$$\frac{d(m_p v_i)}{dt} = F_D + F_B \tag{25}$$

$$\frac{d(m_p C_p T_p)}{dt} = Q_C + Q_M + Q_R \tag{26}$$

The effect of turbulent dispersion on particle motion has been included for the gas phase but not the liquid phase as particle motion in the latter is dominated by the drag force. The mass, momentum and energy sources transferred by the particles to the phase in contact (gas or bath) is determined by the reactions occurring (ore reduction, coal devolatilisation and coal dissolution). Similarly, energy sources between particle and the phase in contact are computed using the Ranz Marshall model for convective heat transfer, Q_C, and the Discrete Transfer model calculates the radiation sources, Q_R. These particle sources are applied in the control volume in which the particle is located during the time step. These sources are then applied each time the fluid coefficients are calculated.

Interfacial mass, momentum and energy exchange

The following phase-pairs interact during the simulations and exchange mass, momentum and energy:

Bath-Gas, Ore-Gas, Ore-Bath, Coal-Gas and Coal-Bath

The drag force, $M_{F,r}$, between the liquid bath and gas is computed using a user-defined drag function derived from experimental models (Schwarz, 1996). Heat transfer between the gas and bath is calculated using the model of Tomiyama (1998).

For ore–gas phase and ore-liquid phase interaction, the drag force coefficient is computed using the Schiller-Naumann drag model.

For a coal particle that undergoes devolatilisation or dissolution, coal particle porosity is computed and used in a modified Schiller-Naumann model in which the particle diameter remains constant (i.e. there is no swelling of the coal particle).

Mass transfer that arises due to particle reactions produces source terms in the continuity equation, S_r, (equation 5) momentum equation, MS_r (equation 6) and the energy equation, $SH_{m,r}$ (equation 16) The mass transferred is dependent upon the rate of reaction of each reaction. These reactions are now discussed in more detail.

Coal devolatilisation reaction

$$\begin{array}{lll} \mathrm{Coal_{(s)}} \rightarrow & \mathrm{Volatiles_{(g)}} & + \quad \mathrm{Char_{(s)}} \\ & \{\mathrm{CH_4}, \mathrm{H_2O}, \text{etc}\} & \{\mathrm{C} + \text{ash}\} \end{array} \tag{27}$$

This reaction is simplified to:

$$\begin{array}{l} \mathrm{Coal_{(s)}} \rightarrow \mathrm{aCH_{4(g)}} + \mathrm{bC_{(s)}} \\ \{\text{cracking}\} \\ \rightarrow \qquad \mathrm{xC_{(s)}}\{\text{soot}\} + \mathrm{yH_{2(g)}} + \mathrm{zC_{(s)}} \end{array} \tag{28}$$

Although soot will behave differently from char, it is assumed that within the bath the soot will react with oxygen to form CO. This has been assumed to also occur within the gas phase, although in reality some soot will escape with the gas into the topspace.

$$Coal_{(s)} \Rightarrow aC_{(s)} + bCO + cH_2 \tag{29}$$

The main aim of including devolatilisation in the bath model is to allow for the generation of large volumes of volatiles gas within the bath and to simulate the spatial distribution of this generation. Data from the literature have been used to give a simple representation of the way coal particles devolatilise. A simplified linear fit to the Oeters and Orsten (1989) results was implemented in previous CFD models (Schwarz, 1994, Stephens *et al.* 2011).

With the inclusion of thermal effects into the model, combined with the endothermic nature of coal devolatilisation and the low heat capacity of the gas, it is possible that cooling of the particles could occur as volatiles are released. If the reaction is too fast then the particle temperature can drop to unphysical values. The model of Oeters assumes that the particle is injected directly into the liquid bath and that it heats up to close to the bath temperature before evolving volatiles. Once volatiles are released they form a gas bubble in which the particle is located. Hence the heat transfer and mass transfer to and from the particle are through gas in the bubble surrounding the particle. This would suggest that the reaction rate from Stephens *et al.* (2011) is the maximum rate and would also apply in a turbulent gas stream that was at the bath temperature.

However at lower temperatures the reaction rate would reduce. Assuming that the model from Stephens *et al.* (2011) gives the maximum rate then a reduction factor

could be applied to that rate depending on particle temperature. Using an Arrhenius model and arbitrarily assuming that no reaction occurs below 500°C and the maximum rate is achieve at 1200°C, the reduction function is:

$$f(T_p) = 60e^{\frac{-6000}{T_p}} \quad (30)$$

where T_p is the particle temperature [K]. This function is plotted in Figure 3.

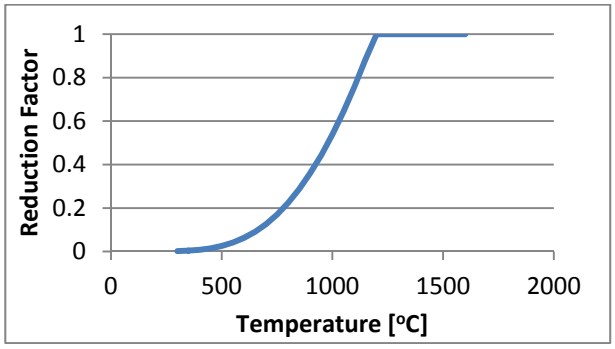

Figure 3: Reduction function, $f(T_p)$.

The overall rate of the devolatilisation reaction for each track is then given by:

$$Rate = \frac{dm}{dt} = 60e^{\frac{-6000}{T_p}} \frac{C_{coalvolatile}\, V_p\, \rho_p}{0.35\times 1.05(\emptyset_p)^{1.5}} \quad (31)$$

where V_p is the initial volume of the particle in the track.

Coal Dissolution

Coal dissolution (equation 1) is only allowed to occur between coal particles and metal. Furthermore it is assumed that it only occurs after devolatilisation is complete. In reality, some of the coal will not contact metal, but will rather react in the slag. The metal volume fraction is used to weight the reaction rate, R_{coal}, which is given by:

$$\frac{dR_{coal}}{dt} = A_{p,coal}\rho_l \chi (C_{carbon,sat} - C_{carbon}) Y_{metal} \quad (32)$$

where $A_{p,coal}$ is the coal particle interfacial area, ρ_l is the liquid density, χ is the mass transfer coefficient for liquid side transport, $C_{carbon,sat}$ is the saturation carbon concentration in the bath, C_{carbon} is the carbon concentration in the vicinity of the particle and Y_{metal} is the metal mass fraction in the vicinity of the particle. The particles shrink as they dissolve, so the interfacial area is:

$$A_{p,coal} = \pi \emptyset_{p,coal}^2 \quad (33)$$

Ore Dissolution

Equation 3 describes the ore reduction and dissolution process. Here, we simplify by assuming that all the iron (Fe) produced reports to the metal phase. In reality, some ore will melt as FeOx in slag. The equation for the mass reaction rate, R_{ore} is:

$$\frac{dR_{ore}}{dt} = A_{p,ore}\rho_l \chi C_{carbon} Y_{metal} \frac{196}{36} \quad (34)$$

where $A_{P,ore}$ is the ore particle interfacial area. The particles shrink as they dissolve, so the interfacial area is again given by:

$$A_{p,ore} = \pi \emptyset_{p,ore}^2 \quad (35)$$

The stoichiometric mass coefficients in equation 3 are:

$$MC_{Fe_2O_3} = \frac{160}{196};\ MC_C = \frac{36}{196};\ MC_{Fe} = \frac{112}{196};\ MC_{CO} = \frac{84}{196}.$$

The mass transfer coefficient, χ, is estimated based on reported reaction rates measured for ore reduction by Nagasaka and Banya (1992). Table 2 summarizes the discussions above.

Table 2: Reaction physics summary.

Material	Reaction	Location	Depends on
Coal	Devolatilisation	Bath and Gas	Temperature and particle diameter. Particle diameter remains constant.
	Dissolution	Bath (Slag and Metal)	Carbon concentration in the Bath. Liquid side mass transfer control. Particle diameter reduces.
Ore	Reduction	Metal	Carbon concentration in the bath. Liquid side mass transfer control. Particle diameter reduces.

Numerical Model

The commercial code ANSYS/CFX (ANSYS, 2010) is used to solve the equations and physical models described above. ANSYS/CFX 13 uses a finite volume method to iteratively solve the above equations on an unstructured grid. Coupling between pressure, velocity and phases is handled implicitly by the CFX coupled volume fraction solver. The second order accurate "Compressive Scheme" was used to discretise advection terms in the equations to improve solution accuracy.

A second order backward Euler implicit time integration scheme was used to advance transient terms in the equations. An initial time step of 0.0005 seconds was used to advance the solution in time for the first few time steps. Due to the highly transient nature of the flow with splashing and gas evolution an adaptive time stepping strategy was used to minimise computational time and ensure convergence at each time step. After the initial start up transient the typical time step was 0.001 seconds with on average 6 coefficient loops required at each time step to reduce the residuals below 2 x 10^{-4} RMS and to achieve the conservation target.

Density for the gas phase is calculated based on the perfect gas law and is a function of composition, pressure and temperature. The liquid bath was assumed incompressible. At wall boundaries scalable turbulent wall functions were used to capture near wall effects.

The simulations were run on quad core dual CPU, 3.6GHz Intel Westmere processors installed in CSIRO's CFD cluster. The model was run for 10 seconds of simulated time on 16 parallel partitions. Total wall time for the simulation was approximately 8 days. Further details of the numerical approach and implementation are described in ANSYS (2010).

GEOMETRY, BOUNDARY AND INITIAL CONDITIONS

The model described above was applied to the HIsmelt Research and Development Facility (HRDF) pilot plant reactor. Internal diameter of the reactor is 2.7 m in the hearth and 5.1 m in the top space with a height of roughly 6 m. To reduce the model size and run time a vertical symmetry plane is used through the centre of the lances. Model geometry is shown in Figure 4. Coal and ore particles are injected through the base of the lances with a nitrogen carrier gas at a temperature of 30°C and velocity of 80.4 ms^{-1}. The particle size distribution is accounted for using a Rosin-Rammler distribution with the coal mean diameter being 294 µm and an ore mean diameter of 1112 µm. Particles are uniformly injected from the lance exits at a rate proportional to their mass flow rate. Gas can leave the domain through a pressure boundary at the offgas outlet.

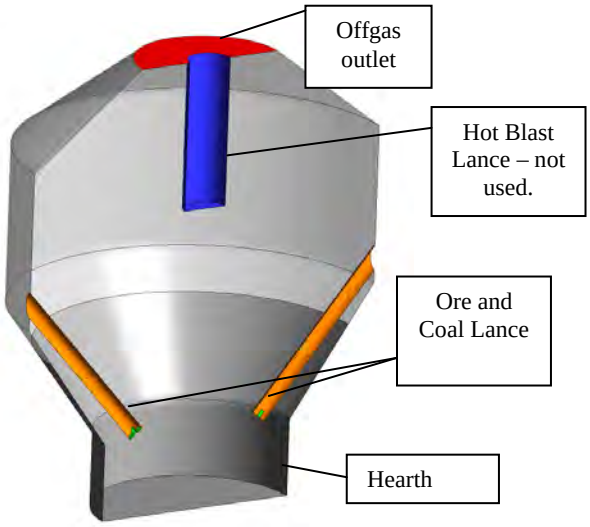

Figure 4: HIsmelt SRV geometry.

The mesh for the domain consists of over 45,000 nodes and 255,000 tetrahedral elements. An indication of the mesh resolution is shown in Figure 5 for the symmetry plane and shows the refinement used to capture the steep gradients at the lance exits.

Initial conditions for the simulation are that the gas and bath temperatures at 1437°C, the metal height is 530 mm and slag depth above the metal is 1189 mm. The bath is assumed quiescent with no gas bubbles or cavities and contains no particles.

RESULTS

The model described above was run for 10 seconds of real time and the predicted gas distributions at four time instants are plotted in Figure 6. Gas injection and more significantly gas generation from the particles induces complex flow behaviour such as splashing and formation of a fountain in the top space of the vessel. Such behaviour is consistent with previous iso-thermal model results such as Stephens *et al.* (2011).

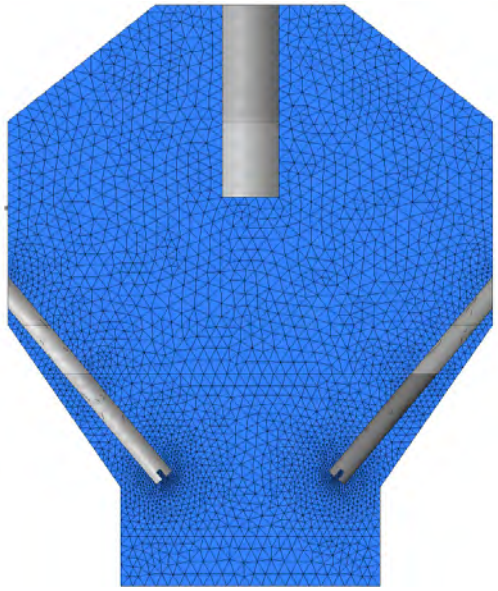

Figure 5: Symmetry plane mesh.

In this work we have extended the previous work by including heat transfer and predicted gas temperature distributions at the same times are plotted in Figure 7. Black contour lines for a gas volume fraction of 0.8 are superimposed over the temperature plots. Particles and carrier gas enter the vessel at 30 °C and gas is heated rapidly to the bath temperature. However cavities with gas temperatures below 500 °C occur directly above the lances and a cool jet below 100 °C is predicted for a couple of lance diameters downstream of the lance tips. As shown by the liquid bath temperature plots in Figure 8, bath temperature remains nearly constant with only drops entrained into the gas cavities near the lance and in the top space experiencing some cooling.

Temperature of typical coal particles is plotted in Figure 9 up to a time of 9.14 seconds. Figure 9a shows how coal particles larger than 200 µm in the gas phase penetrate a significant distance into the bath and generally do not experience a rapid rise in temperature. Smaller coal particles, in Figure 9b, only partially penetrate the bath; with many being entrained by gas plumes into the top space where they undergoing heating. Many particles contact the bath and in the model are reborn into the liquid phase. Temperatures for coal particles in the liquid are shown in Figure 9(c) and (d), note the different temperature scales used for particle in the gas and liquid phases. It is also apparent that once particles contact the liquid bath they undergo rapid heating; this is for both small and large particles.

Temperatures of the larger diameter ore particles are plotted in Figure 10. With a mean diameter of 1112 µm ore particles do not experience a large temperature rise until they enter the bath. They also penetrate into the liquid bath without being entrained into the top space with the gas.

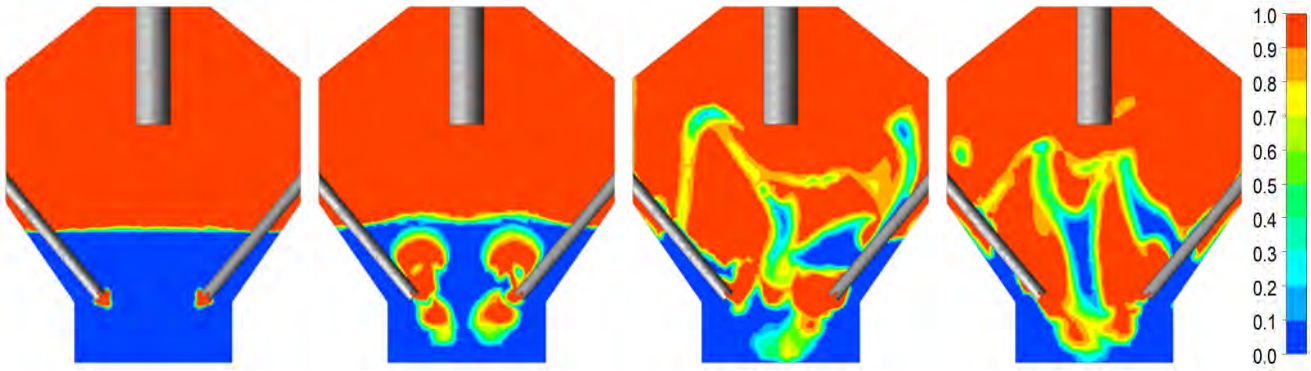

t= 0.046 [s] t =0.47 [s] t = 2.4 [s] t = 9.14 [s]

Figure 6: Gas volume fraction at various times.

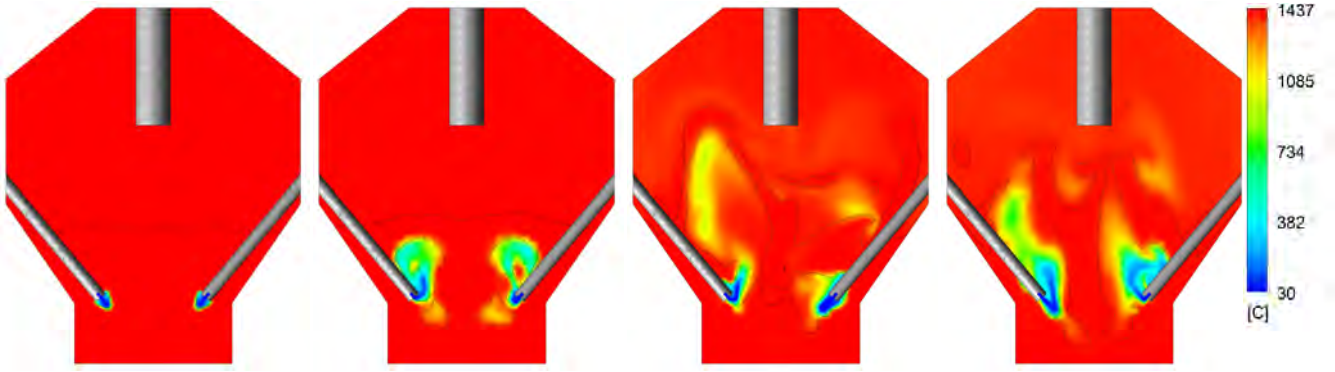

t = 0.046 [s] t =0.47 [s] t = 2.4 [s] t = 9.14 [s]

Figure 7: Gas temperature at various times.

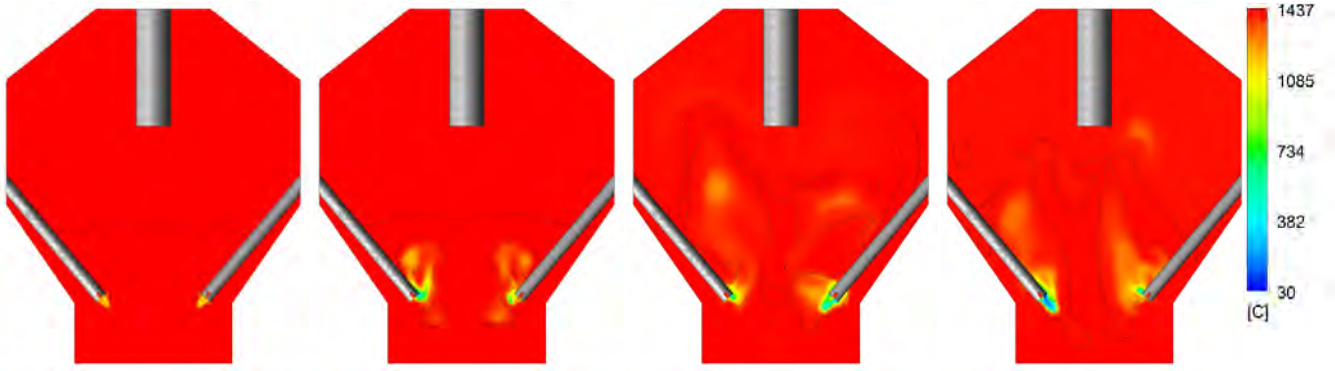

t = 0.046 [s] t =0.47 [s] t = 2.4 [s] t = 9.14 [s]

Figure 8: Bath temperature at various times.

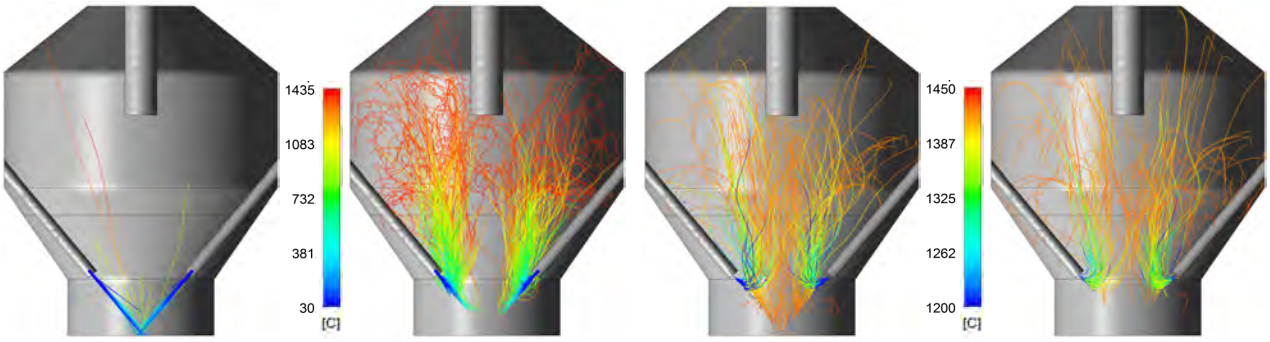

(a) >200 µm in gas (b) ≤200 µm in gas (c) >200 µm in bath (d) ≤200 µm in bath

Figure 9: Coal particle temperatures up to a time of 9.14 [s].

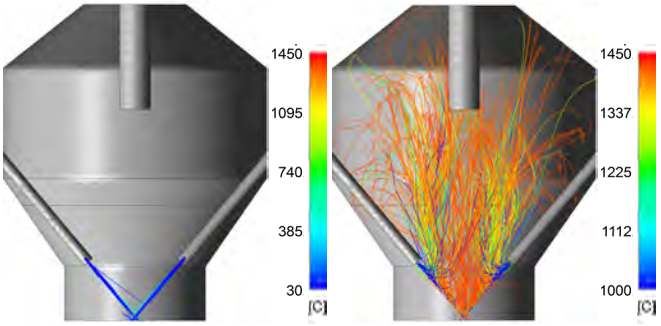

(a) Ore in gas (b) Ore in bath

Figure 10: Ore particle temperatures to a time of 9.14 [s].

Heating of the coal particles results in devolatilisation and the release of volatiles; the change in coal volatile mass fraction is plotted in Figure 11 for the same particle groups shown in Figure 9. Large particles in the gas phase undergo little volatile release due to the slow heating rate, see Figure 11a; but once they enter the bath, as shown in Figure 11c, they rapidly evolve their volatiles. Smaller particles in the gas phase undergo devolatilisation more rapidly than the larger particles in the gas, as shown in Figure 11b, but not as fast as large particles in the bath phase. When small particles contact and enter the bath they undergo rapid devolatilisation, Figure 11d, with most of the volatiles being released near the lance tip.

Rapid devolatilisation of the coal produces large gas source terms that are primarily carbon monoxide and hydrogen. Plots of the CO and H_2 mass fractions in the gas phase are shown in Figures 12 and 13. In Figure 6 at 0.47 seconds a gas cavity has formed below the lance with a region of liquid between the cavity and lance tip. An analysis of results at 25 ms intervals shows the cavity is formed by coal particles penetrating the liquid and devolatilising within the liquid. This can also be seen by the high CO and H_2 concentrations in Figures 12 and 13 at 0.47 seconds.

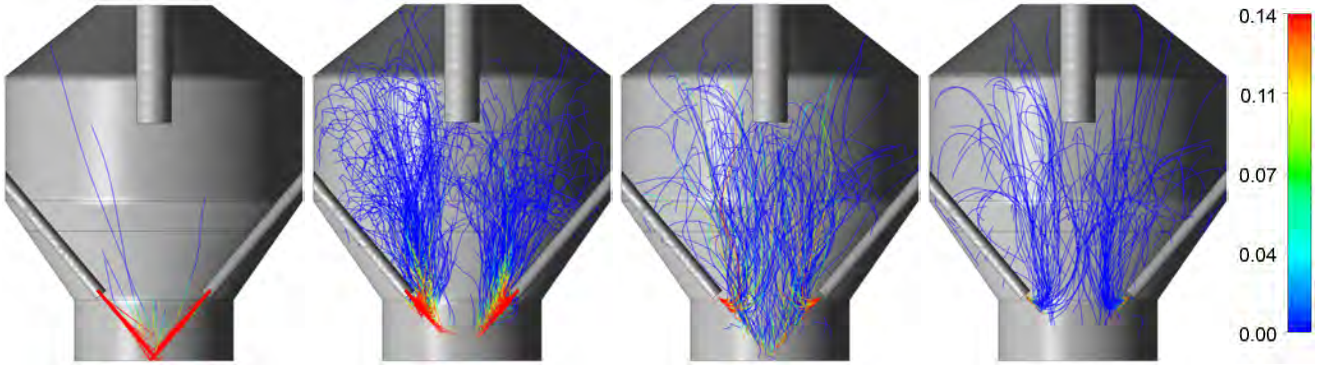

(a) >200 µm in gas (b) ≤200 µm in gas (c) >200 µm in bath (d) ≤200 µm in bath

Figure 11: Coal particle volatile mass fraction to a time of 9.14 [s].

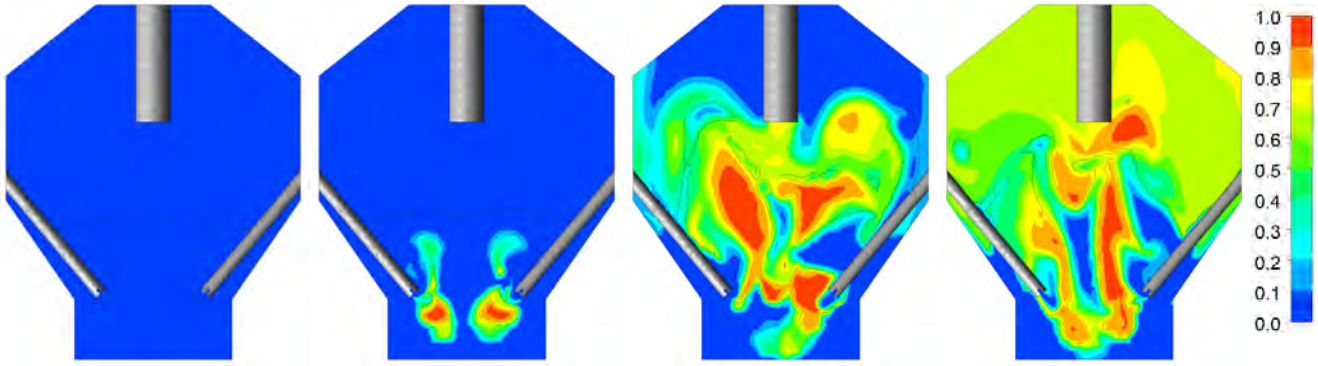

t = 0.046 [s] t =0.47 [s] t = 2.4 [s] t = 9.14 [s]

Figure 12: Carbon monoxide mass fraction at various times.

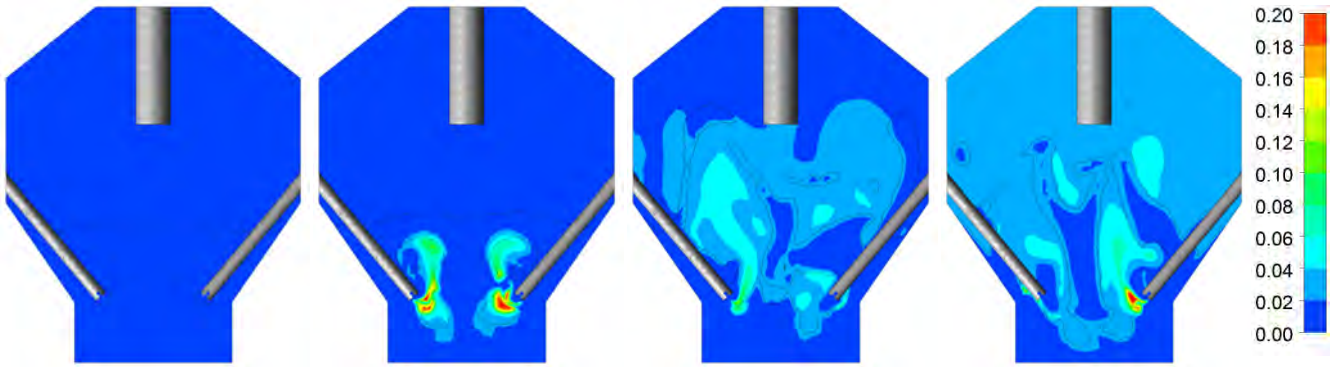

t = 0.046 [s] t =0.47 [s] t = 2.4 [s] t = 9.14 [s]

Figure 13: Hydrogen mass fraction at various times.

CONCLUSION

Multiphase fluid dynamics and heat transfer within the HIsmelt vessel are critical to plant operation and performance. Understanding these processes is critical to scale-up and further development of the HIsmelt process. A previously developed isothermal model of the bath has been extended to include heat transfer processes for both convection and radiation so as to allow the prediction of temperature distributions and particle heating rates.

Model results show that bath temperature is relatively constant and that cooler gas cavities exist near and above the lance tips. Coal particles undergo rapid heating once they enter the liquid bath, which causes rapid devolatilisation leading to the formation of gas cavities below the liquid surface. Particles in the gas smaller than 200 µm in diameter were found to increase in temperature and undergo devolatilisation. Larger coal particles tended to only devolatilise once they contracted the liquid bath. This work indicates that, while adding to computational cost, inclusion of thermal effects can be important for particle heating rates and gas generation within the bath and subsequent bath dynamics.

ACKNOWLEDGMENTS

The authors would like to thank HIsmelt Corporation for permission to publish this work, and in particular Dr Rod Dry for his long-standing support and technical inputs to the modelling effort.

REFERENCES

ANSYS Workbench / Fluent 13.0, ANSYS Inc., USA. 2010.

CROWE, C. T., SHARMA, M. P. and STOCK, D. E., (1977), "The Particle-Source-in-Cell (PSI-CELL) Model for Gas-Droplet Flows", *J. Fluids Eng.*, **99**, 325-332.

DAVIS, M., and DRY, R., (2012), "CFD modelling in the development and scale-up of the HIsmelt process", 9th *Int. Conference on CFD in the Mineral and Process Industries*, CSIRO, Melbourne, Australia, 10-12 Dec.

DAVIS, M., DRY, R., and SCHWARZ, M.P., (2003), "Flow Simulation of the HIsmelt Process", *3rd Int. Conference on CFD in the Mineral and Process Industries*, CSIRO, Melbourne, Australia, 10-12 Dec.

NAGASAKA, T. and BANYA, S., (1992), "Rate of Reduction of Liquid Iron Oxide", *Tetsu-to-Hagane*, **78**, 1753-1767.

OETERS F., and ORSTEN S., (1989), "Degassing of coal particles injected into iron melts", *Steel Research*, **60**, 145-150.

SCHWARZ, M.P., (1994), "The role of Computational Fluid Dynamics in process modeling", *Proc. of 6th AusIMM Extractive Metallurgy Conference*, pages 31-36, Aus.IMM, 1994.

SCHWARZ, M.P., (1996), "Simulation of Gas Injection into Liquid Melts", *Applied Mathematical Modelling*, **20**, 1996, 41-51.

SCHWARZ, M.P. and TAYLOR, I. F., (1998), "CFD and Physical Modelling of Slag-Metal Contacting in a Smelter", *4th World Conference on Applied Fluid Mechanics*, Freiburg, Germany: WUA-CFD, 4:1-4:15.

SHAH, N.G., (1979), "A New Method of Computation of Radiant Heat Transfer in Combustion Chambers", *PhD thesis*, (Imperial College of Science and Technology, London).

STEPHENS, D., TABIB, M., DAVIS, M., and SCHWARZ, M.P., (2011), "CFD Simulation of Bath Dynamics in the HIsmelt Smelt Reduction Vessel for Iron Production", *8th Int. Conference on CFD in Oil & Gas, Metallurgical and Process Industries*, SINTEF/NTNU, Trondheim, Norway, 21-23 June.

TOMIYAMA, A., (1998), "Struggle with computational bubble dynamics". Third International Conference on Multiphase Flow, Lyon, France. June 8-12.

DESIGN OPTIMIZATION OF A METAL TAPPING ROOM FOR MINIMIZED DUST EMISSION

Balram PANJWANI [1]*, **Bernd WITTGENS**[1†], **Stein T. JOHANSEN**[1‡], **Benjamin RAVARY**[2§]

[1]SINTEF Materials and Chemistry, 7465 Trondheim, NORWAY

[2]Research and Development Manager, Eramet Norway, 7037 Trondheim, NORWAY

* E-mail: balram.panjwani@sintef.no
† E-mail: bernd.wittgens@sintef.no
‡ E-mail: stein.t.johansen@sintef.no
§ E-mail: benjamin.ravary@erametgroup.com

ABSTRACT

In the metal tapping room, metal flows from a tapping hole through a shute and pours into a ladle. Dust is formed due to the oxidation of the metal. The dust is spread into the working area, and this dust needs to be collected due to health and environmental issues. Currently, in the tapping room, a suction system and air curtain are provided to capture the dust. The observed flow pattern and the accompanying dust distribution in the tapping area is unsteady and very complex, reducing the efficiency of dust collection. If the suction systems are not mounted at a proper location, the dust will be diluted with air and the capturing efficiency of the suction system is reduced considerably provided a given volume is extracted. The main objective of the present study is to assess the effect of an installed air curtain system and improve the suction system in the tapping room of Eramet Sauda using a CFD-modeling approach. First, a 3D simulation of the tapping room has been performed to validate the existing system and verify that boundary conditions for the model are properly chosen and observed effects are modeled correctly. For validating the model, some visual experiments are performed. Simulation in 3D is computationally expensive, thus for parametric studies, a 2D simulation approach is proposed. The results from the 2D simulation are used to identify promising candidates for an optimized suction system. Based on the combined 2D and 3D simulation approach the design of tapping room is suggested for achieving the maximum capturing of the dust.

Keywords: CFD, Tapping room, Ventilation, Dust distribution .

INTRODUCTION

The objective behind designing an air curtain is to control the heat and mass leakage from a compartment, while preserving an easy access to the compartment. The air curtain unit (ACU) consists of single or multiple plane jets installed on the entrance of a compartment either vertically (upwards or downwards) or horizontally. The most common applications of ACU are sealing of the access sections of furnaces for thermo-chemical treatments; preservation of refrigerated or frozen food products; control of thermal comfort and air quality in specific zones (e.g., non-smoking) of public and commercial buildings; etc. The increase demands for internal comfort and walls free operation have triggered the usage of the air curtains. Although, the operation of the air curtain is very simple, physics associated with air curtain is rather complex. Major complexities in ACU operation is caused by the unsteady air curtain jets and its interaction with surrounding medium and activities such as transport of objects etc.

Over the decades ACU have been studied experimentally, empirically and numerically (Hayes and Stoecker, 1969a,b; Hetsroni *et al.*, 1963). Probably, a research work from Hayes and Stoecker (Hayes and Stoecker, 1969a,b) is one of a highly referred studies and it is a basis for the design handbook of the air curtain (Hayes and Stoecker, 1969a). As per recommendation from Hayes and Stoecker, in ACU the jet should be oriented toward the warm side with an angle of 15-20 degree to the vertical (normal to the air curtain inlet) and the minimum values of the jet momentum should be sufficient enough to ensure a continuous air curtain sheet to the ground. There have been few studies, where empirical approach have been developed for designing the air curtains. For instance, Sirén (Sirén, 2003a,b) devised an approach for the technical dimensioning of the air curtain considering a fluid dynamic and heat flux approach. Later on an improved semi-analytical methods fine tuned with CFD and experiments have been proposed by Giráldez et al. (Giráldez *et al.*, 2013), which was based on the study from Siren (Sirén, 2003a,b). These semi-analytical models usually predicts the development of the air jet produced by an ACU assuming that the jet is bi-dimensional (Sirén, 2003a,b).

CFD models have been used for designing an air curtain to estimate the sealing efficiency of the air curtain for a given installation and analyzing the jet behavior of the air curtain during operation. Influence of the different dynamic and geometrical parameters on the sealing efficiency of a downward-blowing air curtain device have been studied by Costa et al. (Costa *et al.*, 2006). Jaramillo et al. (Jaramillo *et al.*, 2011) carried out a detailed study of the plenum of an ACU by means of Reynolds Average Navier Stokes equations (RANS) techniques, and they conclude that the quality of the produced air jet is strongly affected by the geometry of the plenum and the turbulence at the discharge nozzle. Foster et al. (Foster *et al.*, 2003) performed an experimental verification of analytical and CFD model predictions of infiltration through cold store entrances. They concluded that the CFD models were more accurate than the fundamental analytical models but less accurate than those based on a semi-empirical approach. If the conditions were such that the infiltration rate changed with time or if door protection devices (e.g. air curtains) were used, CFD would become much more advantageous in predicting infiltration. A combination of CFD and experimental techniques was presented by Foster et al. (Foster *et al.*, 2007). The aim of their study was to

compare the measured effectiveness of a commercially available air curtain at different jet velocities against a 3-D CFD model.

Most of the studies dedicated so far on the ACU are limited to a situation when flow inside the compartment is not very complex in nature such as metal tapping operation. In the tapping room, a suction system for capturing the dust introduces a strong pressure gradients and in addition there is a strong buoyancy force due to very hot surfaces such as ladles. Furthermore, during the tapping operation, dust is formed due to the oxidation of the metal. This dust particles will rise up to the ceiling due to buoyancy and infiltrate in the working area at the door. Confining such a complex flow and dust particles within a compartment through air curtains will be a challenge. Therefore, for modeling such a complex flow phenomena with the semi-analytical model (Giráldez *et al.*, 2013) is questionable.

Metal industries in Norway are committed toward the improvement of working environment, and to achieve this they have taken appropriate measures. One of the common measures is to use a mechanical suction system to capture the dust. The present study is focused on an industrial plant owned by Eramet, the plant is located at Sauda, Norway. In this plant, both a suction system and air curtain are being used to capture the dust formed during the tapping operation. However, the dust capturing efficiency of a suction system depends on the suction capacity and its nozzle locations. If the suction systems are not mounted at proper locations, the fumes which is being sucked through a suction hood will be diluted with air due to long residence time inside the tapping room. This will have substantial impact on the dust capturing efficiency of the suction system. Inspired from the applicability of air curtain as a protection device against the infiltration, an air curtain at the Sauda plant was installed to confine the dust within the tapping room. Although, the air curtain principle seems to be intuitive and easy to implement, in reality it introduces a very complex flow pattern due to a pressure and temperature gradient across the air curtain. To the best of author knowledge, there are not many studies for understanding the air curtain performance under tapping operation. Present work would like to shed some light on the applicability of the air curtain for such operations.

In the present study a CFD model is developed in ANSYS FLUENT (ANSYS, 2012) Objectives of the present research work is to find out

1. Whether an air curtain is effective?
2. What is the ideal location of the suction system?
3. What will be a combined effect of air curtain and suction system?

METHODOLOGY: CFD MODEL SETUP AND BOUNDARY CONDITIONS

Model Setup

A steady state CFD model solving for continuity, momentum, energy and radiation equations is developed using a general purpose CFD tool ANSYS FLUENT. The Radiation is modeled through Discrete Ordinance (DO) model and the turbulence is modeled through RNG k-ε turbulence model, and the near wall treatment is achieved through standard wall functions. Discrete Phase Model (DPM) available with FLUENT was used for tracking the dust particles. The steady state DPM model was solved, once the governing equations for the flow were converged. In DPM one way coupling was considered, where fluid phase influences particulate phase via drag and turbulence. Particle turbulent dispersion was handled using the stochastic Discrete Random Walk (DRW) model (ANSYS, 2012). The chosen particles were inert type with density of 1500 kg/m^3 and diameter of 1μm. "Trap" DPM boundary condition on all walls and "escape" DPM boundary condition on the inlets and outlets were used. The particle injection type was "surface", where dust particles were released from the ladle top surface. In addition to the DPM model for understanding the dust distribution, a transport equation for inert species was solved. FLUENT specific user defined functions (UDF) for the source terms to account for the dust generation were incorporated in the continuity, momentum, energy and species transport equation. The value of the source term was non-zero at the ladle top surface and zero for the rest of computational domain. The spatial discretization scheme was based on second order upwind scheme (ANSYS, 2012). The pressure interpolation scheme was standard and the pressure gradient term was discretized using Green-Gauss cell based approach. The pressure velocity coupling was based on the SIMPLE algorithm (ANSYS, 2012).

In the present study both 2D and 3D CFD simulations are performed. A main purpose behind performing 3D simulations is to quantitatively validate the CFD model and also to verify the chosen boundary condition, selected computational domain and other models such as radiation and turbulence. Whereas, 2D simulations are carried out for parameter studies of the air curtain installation and for simultaneously optimization of suction system location. The knowledge gained from the 2D simulations is finally used for designing the suction system.

Computational Domain and Boundary conditions

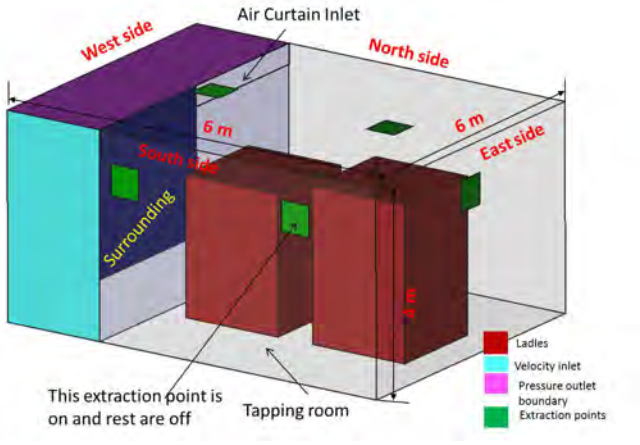

Figure 1: Schematic diagram of geometry : CFD model setup

Flow inside the metal tapping compartment interacts with its surrounding in two ways. Fresh air from the surrounding area enters into the compartment and gas filled with dust from the compartment escape into the surroundings. CFD modeling of the tapping room along with surroundings area requires a larger computational domain, which could be computationally demanding in terms of CPU. However, it is still possible to perform a CFD simulation with a smaller computational domain, which indeed will reduce the computational time. This is achieved by creating a smaller computational box adjacent to the front opening and then adjusting the boundary conditions of the surrounding area. The boundary conditions

of the smaller computational domain have been adjusted to mimic the similarity of a larger computational domain. Although, the approach is not very accurate, it is good enough for qualitative assessment of flow pattern due to suction and air curtain interaction.

Figure 1 shows the tapping compartment geometry along with surrounding area and the associated boundary conditions. The dimensions of tapping room are 6 m in depth, 6 m in width and 4 m in height. The model consists of two box-shaped ladles; in real practice the ladles have a conical shape. The CFD model of the metal tapping room has been de signed with five different possibilities of installing the suction system, two on the South side wall , two on the roof just above the ladles and one on the east side wall. However, only one suction system will be in operation at any time. This dynamic CFD model gives us an opportunity to assess the effectiveness of the suction system with respect to the location of the extraction point. The air curtain is installed on the front side of the tapping room. Width of the air curtain inlet is 20 mm, length is 6 m, whereas the height of the front opening is approximately 4 m. The air curtain is installed horizontally on the front opening and blowing the air in downward direction with 20 degree inclination toward the ladles side. Geometry and mesh of the computational domain have been created using ANSYS Design modeler and ANSYS mesh.

The computational box/surrounding is on the left side of the front opening, and on the South side of the computational box/surrounding, a velocity boundary condition with a specified velocity is used. The specified velocity have been obtained from the previous 3D simulation of Sauda building but without tapping operation (Panjwani *et al.*, 2013). On the North side of surrounding and top side of the computational domain a pressure boundary condition with a specified pressure is applied. At the suction/extraction area of the tapping room, a pressure outlet boundary condition with specified pressure was employed. A velocity inlet boundary condition was employed at the air curtain inlet. The rest of boundaries are wall boundary condition, in which a constant wall temperature boundary condition was used on the ladle outer and top surface. The ladles top surface was maintained at 1400 °C and the ladle side surfaces were maintained at 1000 °C. Applied value of the temperature on ladles surfaces are based on the experiences and internal discussions.

RESULTS: VALIDATION AND DISCUSSIONS

Figure 2: Smoke bomb experiments during Scenario-1

CFD model validations are performed against the measurements (Midtdal and Panjwani, 2013), and all the validations are of qualitative type. The CFD model have been validated for three scenarios. In the first scenario (see Figure 2 and Figure 3) the tapping operation was not performed and the suction system (capturing of the dust) was switched off. In this scenario only the air curtain was switched on. A jet development consists of three regime 1) initial development regime, 2) transitional regime and 3) breakdown regime. The first regime is more streamlined, therefore less entrainment from the surrounding. However, the last regime, responsible for mixing and convection across air curtain, is mostly dominated by turbulent eddies resulting in more entrainment from the surroundings. The length of the initial development regime can be increased by increasing the air curtain jet inlet momentum and also by lowering the initial turbulence. . In

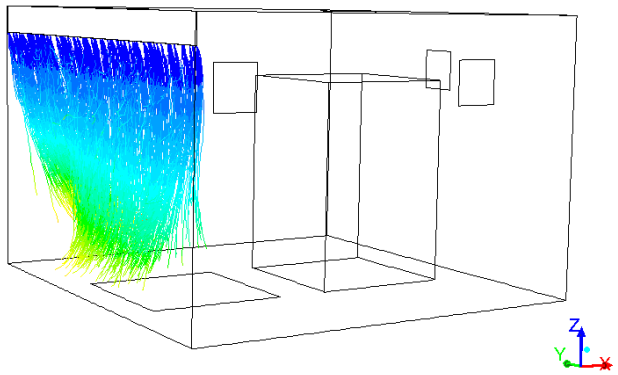

Figure 3: Particle released from air curtain inlet: Scenario-1

Figure 4: Distribution of Dust during Scenario-2 : Measurement Campaign

the measurements campaign, smoke bombs were employed to visualize and improve the understanding of the flow pattern around the air curtain jet. The smoke was released in one height just below the air curtain nozzle on the side towards the tapping room as shown in Figure 2. It can be seen that even though the smoke bomb is just outside the air curtain flow direction, a considerable amount of smoke mixes with air curtain jet stream and is distributed to both sides. The smoke is pushed downwards and close to the ground the stream splits into two directions, one part of the smoke goes into the tapping room and the remaining part is going into the surrounding room. The breakdown regime dominated with turbulent eddies is also visible.

A CFD study of Scenario-1 is carried out. In the DPM model, the dust particles were released from the air curtain inlet and the corresponding distribution of dust particles is shown in Figure 3. In the measurement campaign smoke was released just below the air curtain and instantaneous photograph of this process was taken and shown in Figure 2. The observed smoke distribution from the measurements (see Figure 2) and particle distribution from CFD (see Figure 3) are not exactly the same, but are in good agreement. For instance, spreading of the air curtain jet and splitting of the jet closer to the ground is predicted in the CFD model. It is obvious from Figure 3 and Figure 2 that the flow from the air curtain is very turbulent, and therefore protection against infiltration of the dust particles from tapping room into the surrounding is not very effective.

In the second scenario the air curtain was switched off whereas a tapping operation was performed and suction hood for collecting the dust was also at maximum capacity (27 500 Nm^3/h). A CFD simulation of Scenario-2 was carried out. The dust distribution predicted by the CFD-simulation is compared against the dust distribution from a measurement campaign (see Figures 4 and 5). The CFD estimated dust distribution is in good agreement with the measurement (see Figures 4 and 5), the dust particles from the ladles top surface are rising up to the ceiling due to buoyancy. These dust particles are eventually escaping into the surroundings.

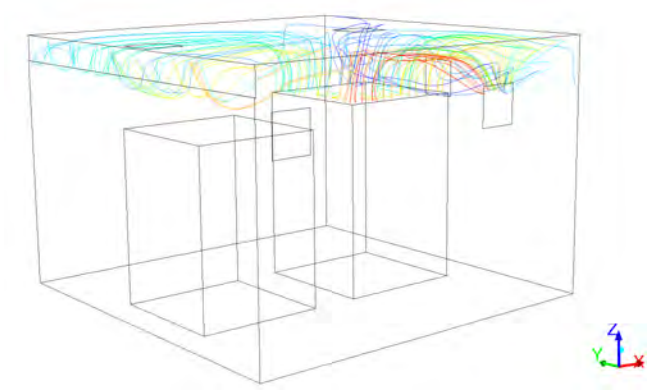

Figure 5: Distribution of Dust during Scenario-2 : CFD Studies

Figure 6: Distribution of Dust during Scenario-3 : Measurement Campaign

In the final scenario, the tapping of the metal is undergoing and the air curtain is in operation, further the suction system for collecting the dust is switched on. The dust distribution obtained from the CFD is compared against the measurements (see Figures 6 and 7). The estimated dust distribution from CFD is similar to the measurements. However, there are some differences in the dust distribution especially towards the opposite side of the extraction point/North side (see Figure 7). Measurement shows that the dust on the opposite side of the extraction point (North part of the tapping room) goes in the upward direction; however this behavior is not very clear from the CFD model. The reason for this discrepancy could be due to the boundary conditions used in the simplified CFD model.

In Scenario-3, the dust suction system is located on South side of the tapping room as shown in Figure 7. The asymmetric location of dust suction system introduces an asymmetric flow pattern inside the metal tapping room. Some part of the dust is being extracted toward the suction system, however, the remaining part of the dust is being escaped into the surrounding from the North side of the tapping room as shown in the Figures 6 and 7.

In addition to the DPM approach for tracking of the dust particles, an approach where a transport equation for an inert species along with basic governing equation was solved for

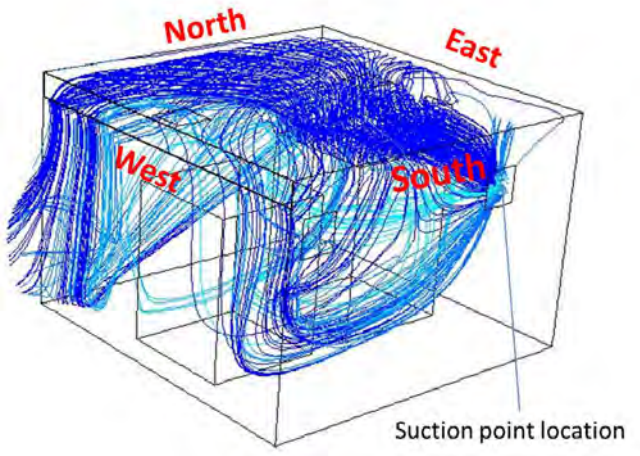

Figure 7: Distribution of Dust during Scenario-3 : CFD Studies

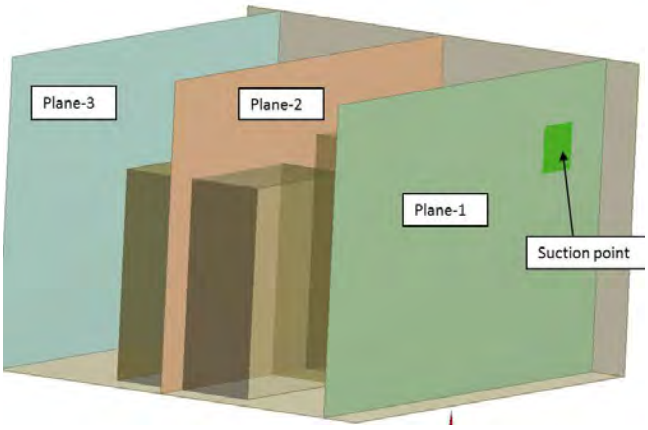

Figure 8: Position of three different planes inside the metal tapping room

understanding the dust distribution. A contour plot of the distribution of inert species is plotted at three different planes and position of these planes inside the tapping room is shown in Figure 8. Plane-1 is located close to the suction system (side wall), plane-2 is located in the middle of the tapping room and plane-3 is located at the North side of the tapping room and far away from the suction side. It is observed that less dust particles escape into the surrounding at a location corresponding to the plane-1 (see Figure 9) compared to the locations corresponding to the plane-2 (see Figure 10) and plane-3 (see Figure 11). At the opposite side of the suction side (see Figure 11), a large amount of dust particles are being escaped into the surrounding. This result clearly indicates that the location of the suction system affects the dust distribution inside the tapping room and that dilution of the dust due to long residence time decreases the suction system capturing efficiency. The simulation results and the measurement campaign performed shows that the air curtain is not as effective as planned during the installation at the Sauda plant. The air curtain should have stopped the dust particles from escaping into the surrounding (see Figures 10 and 11).

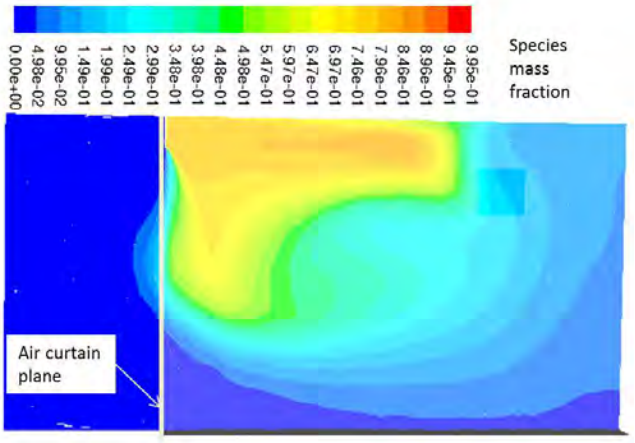

Figure 9: Mass fraction of inert species at Plane-1 during Scenario-3

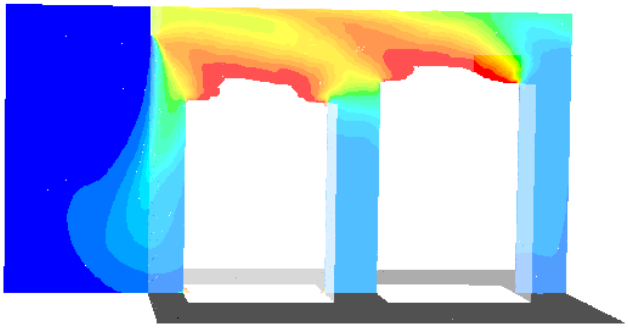

Figure 10: Mass fraction of inert species at Plane-2 during Scenario-3

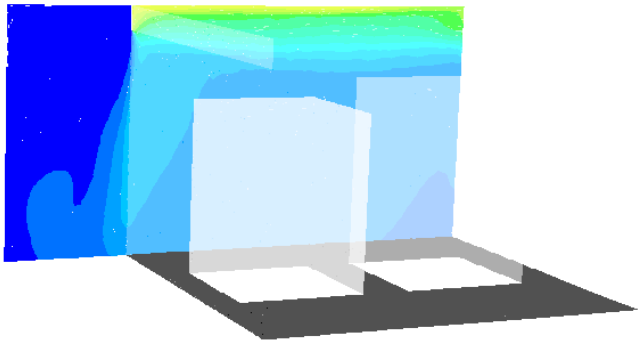

Figure 11: Mass fraction of inert species at Plane-3 during Scenario-3

2D Parametric model studies

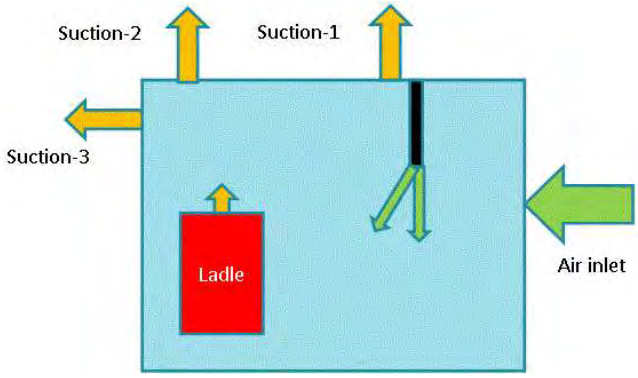

Figure 12: CFD model setup for Case

Sealing efficiency of an air curtain depends on many parameters i.e. capacity, air curtain sealing depth, initial turbulence at air curtain inlet, the pressure difference across the air curtain, inclination angle, blowing direction(upward/downward, horizontally/vertically) and the location of the suction system relative to the air curtain. The main reasons for the pressure difference between compartment and surrounding are the taping operation and balance between the suction system and an air curtain. Normally, the pressure inside the tapping room will be lower than the surroundings and the pressure difference across the air curtain affects it performance substantially.

The capacity, initial turbulence levels and height of the air curtain are fixed. For the present parametric study only the inclination angle of the air curtain and the location of the suction system are varied. A 2D CFD model is developed using ANSYS Design Modeler and ANSYS Mesh. A schematic of 2D geometry along with suction system locations is shown in Figure 12. In real practice the ladles are 3D and therefore the gas filled with dust will flow around the ladles. To mimic a similar behavior, a 2D geometry was simplified (see Figure 12) by providing a gap underneath the ladle. The underneath gap will mimic the 3D flow effects by allowing dust particles to pass through underneath the ladles. As per boundary conditions, a constant heat flux boundary condition at the ladle top surface, a constant velocity boundary condition at air curtain inlet (see Table 1), and pressure outlet boundary condition with a specified pressure at the suction point was used. In total five 2D simulations were carried out, and in all five simulation the dust particles were released from the ladle top surface. The DPM model was used for the dust particle studies. The matrix of these simulations is given in Table 1.

In Case-1 air curtain was switched off and in Case-2 air curtain was switched on. In both the cases suction was located close to the air curtain. One of the major objectives was to identify the role of the air curtain and also to find out whether the air curtain is effective in itself for the current application? The particle distributions for both the cases (Case-1 and Case-2) are shown in Figures 13 and 14, respectively.

Table 1: Modelling conditions.

CFD Run	Air curtain	velocity	angle	Location of suction point
Case-1	OFF	0 (m/s)	0°	Close to air curtain
Case-2	ON	15 (m/s)	0°	Close to air curtain
Case-3	ON	15 (m/s)	20°	Close to air curtain
Case-4	ON	15 (m/s)	20°	Above the ladle
Case-5	ON	15 (m/s)	20°	On the end wall

All the particle contour plots are colored with particle residence time. In the absence of the air curtain (Case-1), the particles are less disturbed and most of the particles are captured through the suction system (see Figure 13). However, in the presence of an air curtain (Case-2) a strong recirculation zone is created between the air curtain and ladles as shown in Figure 14. Particles will be trapped inside the recirculation zone (see Figure 14), which will lead to an increase of the particle residence time and subsequent dilution. The simulation indicates that the case without air curtain is more effective compare to the case with air curtain. It can be concluded that introducing the air curtain is not always beneficial; specially under conditions with strong pressure gradients. Therefore, while designing the air curtain for the metal tapping operation one has to be cautious since the suction system and hot ladles introduce a strong pressure gradient across the air curtain, which significantly affects the air curtain performance. Another important parameter is the inclination of the air curtain. Based on recommendations from Hayes et al. (Hayes and Stoecker, 1969a,b) the air curtain should be inclined 15-20 degree toward the warm side. A CFD study was performed with an air curtain inclination of 20 degree and this case is referred as Case-3, with the remaining settings as identical to Case-2. The particle distribution for Case-3 is shown in Figure 15. It can be observed that the inclined air curtain does not interact strongly with the dust (see Figures 14 and 15). There is less dilution of the gases being sucked into the suction system in close proximity to the air curtain. It can be concluded that the air curtain inclination

Figure 13: Case-1: Particle distribution without air curtain

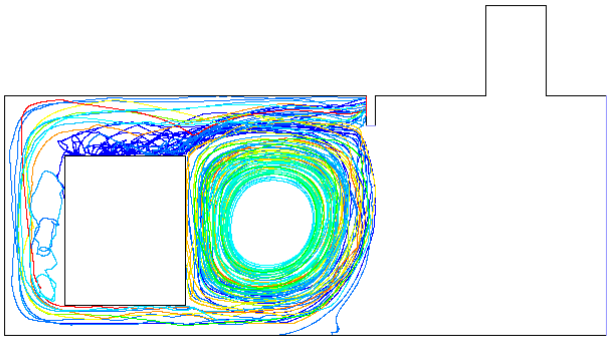

Figure 14: Case-2: Particle distribution with air curtain located close to the front opening

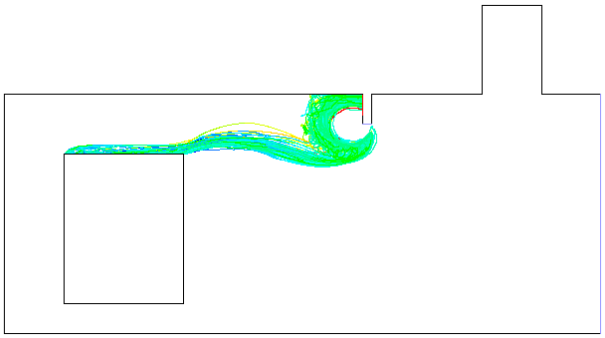

Figure 15: Case-3: Particle distribution with air curtain, 20° inclination, suction system close to the air curtain/front opening

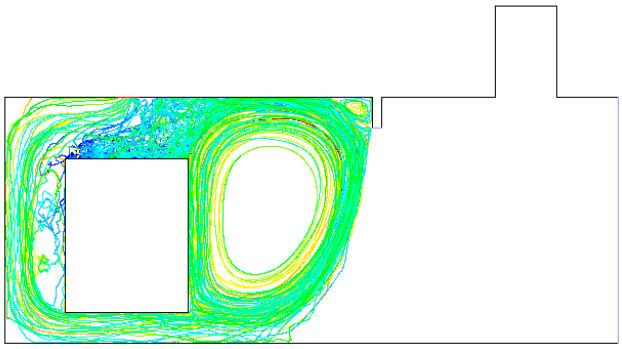

Figure 16: Case-4: Particle distribution with air curtain, 20° inclination, suction system on top of the ladles

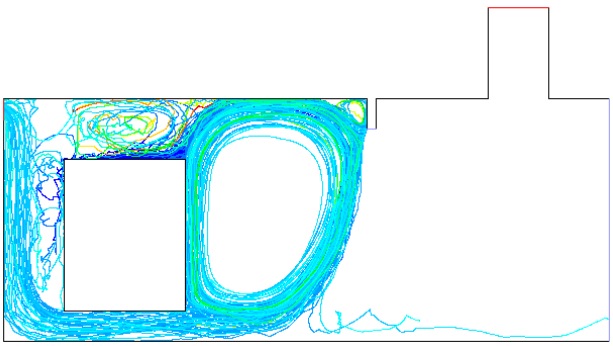

Figure 17: Case-5: Particle distribution with air curtain, 20° inclination, suction system on the end wall

might be effective, but it needs to be verified with more studies.

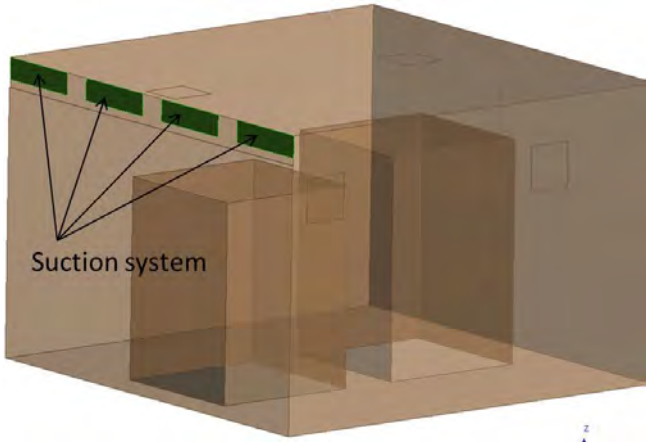

Figure 18: Proposed Design Recommendation

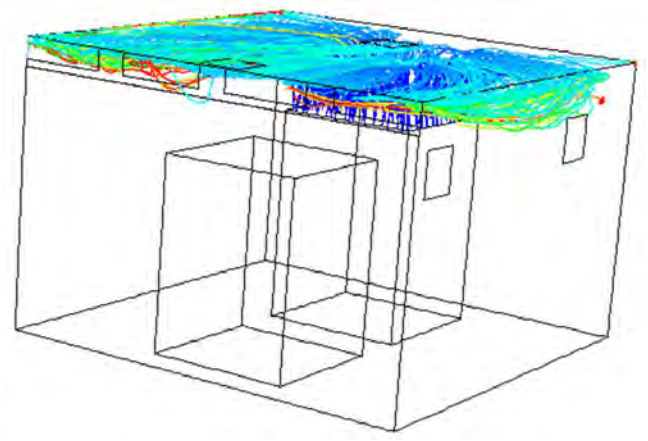

Figure 19: Particle distribution of the proposed design

A final parametric study regarding the suction system location was carried out. Two CFD simulations were performed, namely Case-4 and Case-5. In Case-4 the suction system was located just above the ladle surface and in Case-5 the suction system was located at the end wall. The particle distribution for Case-4 and Case-5 is shown in Figures 16 and 17, respectively. Effect of the suction system location on the dust distribution inside the tapping room can be understood by carefully comparing Figures 15, 16 and 17. It is obvious that the escaping of the dust particle from the compartment depends on the suction point location. The suction system located just above the ladle surface is not very effective for capturing the dust. The explanation of this behavior could be understood from the transport of dust particles under strong buoyancy force. Naturally, the emitting dust from the ladles surface has some vertical momentum, and this dust loses its vertical momentum when it touches the ceiling of the tapping room. The vertical component of the momentum of the dust particles converts into other momentum component, and this dust spreads in all direction underneath the roof. A suction system located just above the ladles will capture dust depending on the opening area. The results shows that a suction system located on the sidewall will be better than the suction system located above the ladle surface. Nevertheless, overall results shows that the best location for the suction system is closer to the air curtain inlet/front opening. Naturally dust follows the roof and try to escape out at the front opening, and therefore providing a suction system at the front opening will ensure a better capturing of the dust particles.

Design Suggestion

2D parametric studies suggest that the suction system located close to the air curtain/front opening is most efficient. A 3D design of the tapping room with this modification is proposed and shown in Figure 18. The suction systems are located close to the front opening, and there are four suction points of equal dimension and equal capacity; an curtain was not installed in this design modification. The given total capacity of the whole suction system is 27 500 Nm^3/h. CFD simulation of this design was carried out using ANSYS FLUENT. The boundary conditions and other setup have been described in the previous section. For assessing the dust capturing efficiency, a DPM study was performed. The particles were released from the ladle surface and resulting dust distribution inside the tapping room is shown in Figure 19. It can be observed that the particles rises up due to buoyancy and follows the tapping room ceilings, and most of the particles will eventually be captured through the design suction system.

CONCLUSION

A CFD model have been developed to assess the effectiveness of an installed air curtain and simultaneously investigating the proper location of a suction system in the tapping room at Eramet, Sauda plant. Measurements have been conducted using smoke bombs. In addition to that photographs of the ongoing tapping operation and resulting dust distribution have been taken. A simplified 3D-CFD model has been proposed and it has been qualitatively validated through observations. Simulation in 3D is computationally expensive, thus for parametric studies, a 2D simulation approach is proposed. The study clearly shows that the air curtain is not very effective especially under strong pressure gradient across the air curtain. Furthermore, the air curtain inclination towards the warm side might be beneficial, but it has to be verified with more studies. A major conclusion from this study is that a symmetrical suction system located close to the front opening is more effective for this operation:

1. Air curtain is not effective under strong pressure gradients and complex flow interaction.

2. The ideal location of the suction system is close to the front opening.

3. Study of each individual case is necessary to design a cost-efficient system.

ACKNOWLEDGMENTS

Present work is a part of ongoing project:FUME-Fugitive Emission in the Ferroalloys Industry. The financial support from Norwegian Research Council and the Norwegian Ferroalloy Producers Research Association (FFF) is gratefully acknowledged.

REFERENCES

ANSYS (2012). “Ansys fluent theory guide”.

COSTA, J. *et al.* (2006). “Energy savings by aerodynamic sealing with a downward-blowing plane air curtainŮa numerical approach”. *Energy and Buildings*, **38(10)**, 1182 – 1193.

FOSTER, A. *et al.* (2003). "Experimental verification of analytical and cfd predictions of infiltration through cold store entrances". *International Journal of Refrigeration*, **26(8)**, 918–925.

FOSTER, A. *et al.* (2007). "Three-dimensional effects of an air curtain used to restrict cold room infiltration". *Applied Mathematical Modelling*, **31(6)**, 1109 – 1123.

GIRáLDEZ, H. *et al.* (2013). "Improved semi-analytical method for air curtains prediction". *Energy and Buildings*, **66(0)**, 258 – 266.

HAYES, F. and STOECKER, W. (1969a). "Design data for air curtains". *ASHRAE Transactions*, **(2)**, 168–180.

HAYES, F. and STOECKER, W. (1969b). "Heat transfer characteristics of the air curtain". *ASHRAE Transactions*, **(2)**, 153Ű167.

HETSRONI, G. *et al.* (1963). "Heat transfer properties of an air curtain". *Trans. of the ASAE*, **(4)**, 328–334.

JARAMILLO, J. *et al.* (2011). "Detailed analysis of turbulent flows in air curtains". *Progress in Computational Fluid Dynamics*, **11(6)**, 350–362.

MIDTDAL, H. and PANJWANI, B. (2013). "Study of an air curtain to improve the collection of fumes". research report Report/Project Number: 102001794, SINTEF, Material and Chemistry, Trondheim, Norway. Under review.

PANJWANI, B. *et al.* (2013). "Development of a cfd model for improvement of an interior environment in metallurgical industries: Modeling". *The Thirteen International Ferroalloys Congress Efficient Technologies in Ferroalloy Industry, INFACON XIII*, 999–1008. Almaty, Kazakhstan.

SIRéN, K. (2003a). "Technical dimensioning of a vertically upwards blowing air curtain - part i". *Energy and Buildings*, **35(7)**, 681–695.

SIRéN, K. (2003b). "Technical dimensioning of a vertically upwards-blowing air curtain - part ii". *Energy and Buildings*, **35(7)**, 697–705.

HEAP LEACHING SIMULATION: BEYOND SHRINKING CORE MODELS

Liping CAI[1,2*], Richard J. FERRIER[2,1†], Qingyang LIN[1], Peyman MOSTAGHIMI[1,2], Gerard J. GORMAN[2], Stephen J. NEETHLING[1,2‡]

[1]Rio Tinto Centre for Advanced Mineral Recovery, Department of Earth Science and Engineering, Imperial College London, London SW7 2AZ, UNITED KINGDOM

[2]Applied Modelling and Computation Group, Department of Earth Science and Engineering, Imperial College London, SW7 2AZ, UNITED KINGDOM

[*] E-mail: liping.cai11@imperial.ac.uk
[†] E-mail: r.ferrier@imperial.ac.uk
[‡] E-mail: s.neethling@imperial.ac.uk

ABSTRACT

Heap leaching is an established method for extracting metals from low grade ore. It is important to be able to model the leaching process accurately for both design and control purposes. The shrinking core model(SCM) has been the standard approach for coupling the solute transport to various physico-chemical reactions. At heap scale the accuracy of the SCM is sensitive to variables such as the ore size distribution and shape, and the mineral grain distribution within the rocks. In this paper a novel semi-empirical model is proposed. As with the classical SCM, the dependency of reaction rate on the chemical conditions and current leaching state of the ore particles are regarded as separable from one another. However, in the present work this separation is extended to larger scales under certain assumptions, so that the difficult-to-model dependency on rock properties is simply represented as a function that is calibrated from experiments. The model has been implemented for the leaching of chalcopyrite and validated against 1-D column leaching experiments. This favourable result motivates us to further test and extend the model in future work.

Keywords: CFD in heap leaching, reactive transport, chalcopyrite leaching .

NOMENCLATURE

Greek Symbols

θ	Hold-up of the fluid
ϕ	Porosity of porous heap
ρ	Mass density, $[kg/m^3]$.
κ	The rate equation of surface reaction.
ρ_m	Molar density, $[mole/m^3]$.
μ	Dynamic viscosity, $[kg/ms]$.
ε	The extracted fraction of a rock.

Latin Symbols

C	Concertration $[mole/m^3]$.
$\mathbf{D}$	Dispersion coefficient, $[m^2/s]$.
Ea	Activation energy, $[KJ/mol]$.
R	Gas constant $[J/kmol]$.
S	Saturation
T	Temperature $[k]$.
t	Time $[s]$.
p	Pressure, $[Pa]$.
N	The amount of mineral substance, $[mole]$.
r	Radius, $[m]$.
n	Number of rocks per volume of heap $[1/m^3]$.
N_p	Total amount of the minerals per rock $[mole]$.
$\mathbf{u}$	Darcy velocity, $[m/s]$.
k	Reaction rate constant based on experiment.
$\mathbf{K}$	Effective permeability.
$\mathbf{g}$	Gravitational acceleration, $[m/s^2]$.
$\mathbf{X}$	The radius rock, $[m]$.
V	Volume, $[m^3]$.
v_{jrt}	Jarosite precipitation rate, $[mol/m^3 s]$.
DO	Molal concentration of dissolved oxygen, $[mol/kg]$.

Sub/superscripts

b	bulk.
c	capillary.
w	wetting.
nw	non-wetting.
G	Gas.
i	Index of mineral grains in the rock.
j	Phase of fluid.
l	Species of reactant.

INTRODUCTION

Heap leaching is a method for extracting a wide range of metals from low grade ore. Crushed ore is piled into large heaps, and leaching solution is then applied to the top of the heaps. The solution percolates through the rocks, dissolving metals. Valuable metals are recovered from the collected pregnant solutions (McBride *et al.*, 2012). Heap leaching is most commonly used for copper oxides and secondary sulphides, but as chalcopyrite is the most abundant copper mineral (Leahy and Schwarz, 2009), it is attracting increasing interest as a leaching target and is the specific focus of this paper. The methodology outlined is more generally applicable though.

CFD modelling offers a fast, effective way of testing and optimizing the heap leaching process compared with performing physical experiments. However, the leaching process involves both multiphase flow and physico-chemical reactions. The coupling between the mass transport of species in different phases and the various chemical reactions raise difficulties in formulating an accurate reactive transport model for leaching. The shrinking core model (SCM) is the most widely used approach for approximating the fluid-solid reactions of particles in metal leaching simulations. Chae et al (1989) developed the large-scale one-dimensional leaching model for copper oxides with isothermal reactions, which uses the pseudo-steady state

SCM to approximate the kinetics for the ore particles within the bed. Gao et al (1983) modelled the in situ leaching of copper, including the heat and oxygen balances, while the dissolution rates of the particles were approximated by a modified SCM. Bennett et al (2012) developed a model suitable for large-scale leaching, in which the simple SCM model was applied separately to the kinetics of each mineral in each characteristic particle size. Leahy et al (2005) used a SCM similar to Neuburg et al (1991) to model the bioleaching of chalcocite to examine the temperature dependence.

Although the SCM of mixed control can take into account the effects of both the diffusion and reaction rates, the model itself is assumed to be linearly dependent on the bulk concentration of a single species and therefore diffusion and reaction act in series (Levenspiel, 2006). However, the empirical rate laws for oxidative leaching of chalcopyrite by Fe(III) (Kimball *et al.*, 2010) suggests that the reaction rate might be non-linearly dependent on multiple species. This non-linear dependence cannot be represented in the mixed control SCM. The non-linear rate equations can only be applied directly if the diffusion terms were excluded, but this might be an oversimplification.

In this paper, a new model for the CFD simulation of chalcopyrite leaching will be presented and validated against 1-D isothermal column leaching data. The model is semi-empirical, being based on results developed from column leaching experiments. The key assumption of the proposed model is that the effects of the bulk concentration and temperature are mathematically separable from that of the current state of the particles when predicting leaching rates. The justification for this assumption and its limitations are discussed within the paper.

While the present model and the classical SCM share the same key assumption, the present model is flexible enough to include non-linear reaction rate laws which, being based on experimental results, should lead to more accurate results. On the other hand, the model must be calibrated for each class of ore using experiments conducted for a family of rock sizes. In this paper only validation of the model against experiments on one size of rock is presented.

The CFD simulation is implemented within the Fluidity framework(Modelling and Group, 2010), an open source CFD code that allows for transient simulations in any number of dimensions, and has the advantageous feature of dynamic remeshing. The present model is implemented with the control volume finite element method (CVFEM) which, unlike the conventional FEM, is conservative. Conservation is important when fluid flow, mass transport and heat transfer are strongly coupled.

FLUID FLOW MASS TRANSPORT MODEL

Multiphase flow

The simulation is implemented using the same multiphase flow simulator presented by Mostaghimi et al (2014) . The superficial velocity for phase j inside a porous medium is defined by Darcy's law (Bear, 1972):

$$\mathbf{u}_j = -\frac{K_j}{\mu_j}(\nabla p_j - \rho_j \mathbf{g}) \tag{1}$$

where K_j, μ_j and ρ_j are the effective permeability, dynamic viscosity and density of the phase, and $\mathbf{g}$ is acceleration due to gravity. The mass conservation equation is:

$$\frac{\partial \phi S_j \rho_j}{\partial t} + \nabla \cdot (\rho_j \mathbf{u}_j) = 0 \tag{2}$$

where ϕ is porosity of the heap and S_j is phase saturation. Additional constraints include saturation continuity,

$$\sum_j S_j = 1 \tag{3}$$

and a pressure jump across the phase interfaces defined by capillary pressure p_c.

$$p_{nw} - p_w = p_c(S_w) \tag{4}$$

Superscripts nw and w denote the non-wetting and wetting phases, respectively.

Using the constraint from Equation 3 and assuming incompressible flow, Equation 2 is summed over the phases to give a global continuity equation

$$\nabla \cdot \left[\sum_j \frac{K_j}{\mu_j} (\nabla p_j - \rho_j \mathbf{g}) \right] = 0 \tag{5}$$

The effective permeability K is calculated using the Brooks and Corey correlation (Brooks and Corey, 1964), which is a function of saturations and absolute permeability.

The heap leaching models have been implemented within the Fluidity framework. A major advantage of using Fluidity is that it includes dynamic remeshing. This is important in heap leaching where small scale effects associated with, for instance, the initial wetting and final drying of the heap need to be resolved, but where efficient long term simulation is also required. Figure 1 shows dynamic mesh adaptivity for the simulation of transient flow with initial wetting, the mesh is refined at the front of the flow where saturations rapidly varies (Mostaghimi *et al.*, 2014).

Mass transport in porous heap

The continuity equation for convective-dispersive transport of species l in a porous heap is defined as (Bennett *et al.*, 2006),

$$\frac{\partial (\theta_j C_{lb})}{\partial t} - \nabla \cdot (\theta_j \mathbf{D_l} \nabla C_{lb}) + \nabla \cdot (\mathbf{u_j} C_{lb}) = R_l \tag{6}$$

Where C_{lb} is the bulk concentration of species l, D_l is the species dispersion coefficient, θ_j is the holdup of phase j defined by the equation:

$$\theta_j = \phi S_j \tag{7}$$

The generations and consumptions of the species l by chemical reactions are included in the source term R_l, with the sources from the dissolution of chalcopyrite and pyrite minerals being calculated using the semi-empirical models developed in the following section.

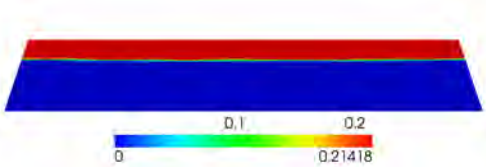

(a) The calculated saturation distribution

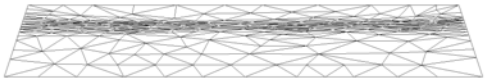

(b)The dynamic remeshing

Figure 1: The dynamic remeshing during simulation of initial wetting (Mostaghimi *et al.*, 2014)

CHEMISTRY BASIS

Reactions of Chalcopyrite leaching

The leaching of chalcopyrite involves both dissolution reactions and solution phase reactions:

Dissolution reactions

$$CuFeS_2 + 3Fe^{3+} \rightarrow Cu^{2+} + 5Fe^{2+} + 2S^0 \quad (8)$$

$$2S^0 + 3O_2 + 2H_2O \rightarrow 4H^+ + 2SO_4^{2-} \quad (9)$$

$$FeS_2 + 14Fe^{3+} + 8H_2O \rightarrow 15Fe^{2+} + 2SO_4^{2-} + 16H^+ \quad (10)$$

Solution phase reactions

$$4Fe^{2+} + O_2 + 4H^+ \rightarrow 4Fe^{3+} + 2H_2O \quad (11)$$

$$3Fe^{3+} + 2SO_4^{2-} + 6H_2O + M^+ \rightarrow MFe_3(SO_4)_2(OH)_6 + 6H^+ \quad (12)$$

We assume all the elemental sulphur generated from oxidation of Chalcopyrite (Equation 8) is dissolved by Equation 9 so that no elemental sulphur accumulates, and we excluded bacterial actions which may exist in the chalcopyrite leaching. These factors will be reconsidered in future work.

All the empirical reaction rates equations are listed in Table 1. These rate equations are applied for the dissolution of Chalcopyrite (Equation 8) and pyrite (Equation 10), ferrous oxidation (11), jarosite precipitations (Equation 12) and the function for oxygen solubility. The dissolution of Chalcopyrite and pyrite are nonlinear functions of concentrations on the mineral surface, and k is the rate constant based on experiment. Jarosite precipitation is a switching function which sets the jarosite precipitation rate to be a constant if the concentration of Fe^{3+} is higher than a log–linear relationship with pH. The equilibrium function for the molal concentration of dissolved oxygen, DO, is also listed in Table 1, which is thermodynamics-based.

A new semi-empirical model for leaching

Conventionally the dissolution reactions within heap leaching are modelled using shrinking core or related models (Neuburg *et al.*, 1991; Bennett *et al.*, 2012; Leahy and Schwarz, 2009). These models are often hard to calibrate to experimental results due to the assumptions inherent in the model. Real ores contain a range of particle sizes each with a range of grain sizes within them, properties which are hard to capture within shrinking core type models. In this paper we will present a framework for directly using laboratory scale experimental data to predict the heap scale performance in a computationally efficient manner.

The key assumption of this modelling approach is that the effect of the bulk fluid conditions (concentrations, temperatures, pH etc.) and the current state of the particles (characterised in this paper by the current extent of extraction, ε) on the leaching rate are mathematically separable, an assumption shared with the shrinking core models. This means that leaching rate of a particular mineral species at a particular location in the heap can be expressed as follows:

$$\frac{d\varepsilon}{dt} = \kappa(C_{1b}, C_{2b}, T, etc) f(\varepsilon) \quad (13)$$

Where κ is the function that comes from Table 1, subscript b refers to the bulk concentrations. These concentrations, as well as the extents of reaction of each of the mineral types, will be a function of time and position within the heap.

To demonstrate that the assumption that the behaviour is separable is reasonable, we need to consider what is happening at three different scales:

Grain scale

If a single grain within the rock is considered, then we can write out the kinetics of dissolution of that grain, i, in terms of its surface reaction kinetics:

$$\rho_m \frac{dV_i}{dt} = -f(r_i) k e^{-Ea/RT} C_1^{m1} C_2^{m2} \quad (14)$$

Where the concentrations are those within the rock at the surface of grain, ρ_m is the molar density of the grain, Ea is the activation energy and $f(r_i)$ is the surface area of the grain.

In a more generic form this can thus be written as:

$$\frac{dV_i}{dt} = -f(r_i)\kappa(C_1, C_2, T, etc) \quad (15)$$

At the scale of a single grain the behaviour is thus mathematically separable. If we now consider all the mineral grains within a small volume of the rock, these will all experience the same chemical conditions, but will have different sizes and surface areas. The overall leaching rate of all these grains can thus be expressed as follows:

$$\frac{dV}{dt} = -\kappa(C_1, C_2, T, etc) \sum_{i=0}^{N} f(r_i) \quad (16)$$

The behaviour is thus still separable for a collection of different sized grains all experiencing the same chemical conditions, where V is the sum of the volume of the mineral grains.

Rock scale

Within a single rock the chemical conditions can be a function of position due to the competing effects of surface reaction and diffusion. If the position within the particle is characterised using the vector, $\mathbf{X}$, then the overall behaviour

Table 1: Empirically derived rates of chemical reaction. All concentrations, denoted by square brackets, have units $\mathrm{mol}/\mathrm{m}^3$. P_{O_2} is the partial pressure of oxygen, and DO is the molal concentration of dissolved oxygen.

Source	Model	Ea (kJ/mol)
Dissolution reactions		
Kimball et al (2010)	$\mathrm{d}[\mathrm{CuFeS_2}]/\mathrm{d}t = 4\pi r^2 k \mathrm{e}^{-Ea/RT}[\mathrm{H^+}]^{0.8}[\mathrm{Fe^{3+}}]^{0.42}$	48
Williamson and Rimstidt (1994)	$\mathrm{d}[\mathrm{FeS_2}]/\mathrm{d}t = 4\pi r^2 k \mathrm{e}^{-Ea/RT}[\mathrm{Fe^{3+}}]^{0.93}[\mathrm{Fe^{2+}}]^{-0.4}$	50
Solution phase and precipitate reactions		
Lowson (1982)	$\mathrm{d}[\mathrm{Fe^{2+}}]/\mathrm{d}t = 4\pi r^2 k \mathrm{e}^{-Ea/RT}[\mathrm{Fe^{2+}}]^2 P_{O_2}[\mathrm{H^+}]^{-0.25}$	74
Leahy and Schwarz (2009)	$v_{\mathrm{jrt}} = 5.7\times10^{-5}[\mathrm{Fe^{3+}}]$ if $\log_{10}(0.056[\mathrm{Fe^{3+}}]) > -1.43\,\mathrm{pH} + 0.87$	—
Tromans (1998)	$\mathrm{DO} = P_{O_2}\exp\left[\frac{T}{8.3144}\left(0.046T^2 + 203.35T\ln(T/298) - (299.378+0.092T)(T-298) - 20.591\times10^3\right)\right]$	—

of the individual rock will be separable if the 'driving force', κ, can itself be expressed in a separable form:

$$\kappa(\mathbf{X}) = \kappa(C_{1b}, C_{2b}, T, etc)g(\mathbf{X}) \tag{17}$$

Where,

$$\kappa(\mathbf{X}) = \kappa(C_1, C_2, T, etc) \tag{18}$$

Importantly, $g(\mathbf{X})$ is not a function of κ.

This is actually an assumption and will not be universally true. It is true, though, if the concentrations are at pseudo-steady state (a reasonable assumption given the slow kinetics of most heap leaching systems) and that the behaviour is either reaction limited or the surface reactions are linear or the system is diffusion limited in terms of one of the reagents (though this will change the form of κ). In non-linear systems which are neither reaction nor diffusion limited this assumption will not be completely true, but the effect of this assumption is still likely to be a smaller effect than that of, for instance, the grain size and particle size distributions and is thus worth making. Given enough experimental or small scale simulation data this assumption can be relaxed by making use of a family of curves rather than a single curve.

Bulk scale

If the behaviour of a single rock particle is separable in terms of the effect of bulk chemistry and its current state of leaching on its leaching rate, then the behaviour of a collection of these particles will also be separable for very similar reasons to why the overall behaviour of a group of different sized mineral grains experiencing the same chemical conditions are separable.

CALIBRATING THE MODEL

Base Experiment

From small scale leaching tests, the volumetric change of the mineral grains during leaching was captured by the micro-CT scanning, which is illustrated in Figure 2. The leaching column was scanned at various time points over the entire leaching period. After image processing, the total volume of the grains left in the ore particle, and then the extraction, was calculated. The extraction of the rock was calculated by averaging over a certain number of rocks with the same sizes; thus the semi-empirical function developed from this experiment is expected to represent a specific class of ore with a certain size.

We can get the extraction as a function of time from the small scale leaching tests (Figure 3 shows copper extraction as a function of time). This type of data is often used to calibrate heap scale models, but in this paper we will make use of this data directly. We can rewrite Equation 13 as follows:

$$\frac{\mathrm{d}\varepsilon}{\mathrm{d}t}\frac{1}{\kappa} = f(\varepsilon) \tag{19}$$

We assume in this work that the form of κ is the same as that for the surface reactions listed in Table 1, though this could be obtained experimentally as well. As this is a small column, it is reasonable to assume that the concentrations at the outlet are representative of those within the column and thus κ is known as a function of time for the experiment. The left hand side of Equation 19 can thus be plotted by numerically differentiating the curve in Figure 3. (see Figure 4). If Figure 3 had been noisy either smoothing or curve fitting would need to be used as Figure 4 will inherently be noisier than Figure 3. This graph thus represents Equation 19 and is used within the simulation as a lookup table with interpolation between the points.

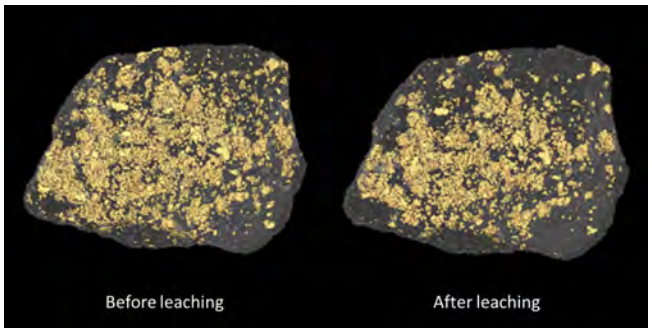

Figure 2: Micro-CT scan of a single rock within the rock, showing the change of extraction of the mineral grains.

Numerical Implementation of the simulations

The implicit pressure, explicit saturation algorithm (IMPES) is used to solve for the multiphase flow. Equation 5 is discretised and solved implicitly for pressure at time t by using the

explicit saturation, then the solved pressure is used to solve the Equation 2 for saturation; thus saturation and pressure are decoupled in the system (Mostaghimi *et al.*, 2014). The spatial discretization is based on the continuous finite element basis for pressure, and a discontinuous node centred control volume method for saturation and concentration, so that the mass transport is conservative.

Concentration is solved implicitly while the source term R_l is calculated explicitly. The reaction of chalcopyrite, pyrite and ferrous oxidation are regarded as reacting simultaneously with the same values of concentrations, while the equilibrium of the oxygen dissolution and jarosite precipitations are calculated when all other reactions have completed and the concentrations have been updated.

For the reaction of chalcopyrite and pyrite, the rate of extraction, $\mathrm{d}\varepsilon/\mathrm{d}t$, is calculated explicitly by passing simulated values for the concentrations and extracted fractions into the semi-empirical model based on Equation 19. Then the source term in Equation 6 due to the dissolution of the chalcopyrite and pyrite will be:

$$R_l = N_p\, n \frac{d\varepsilon}{dt} \tag{20}$$

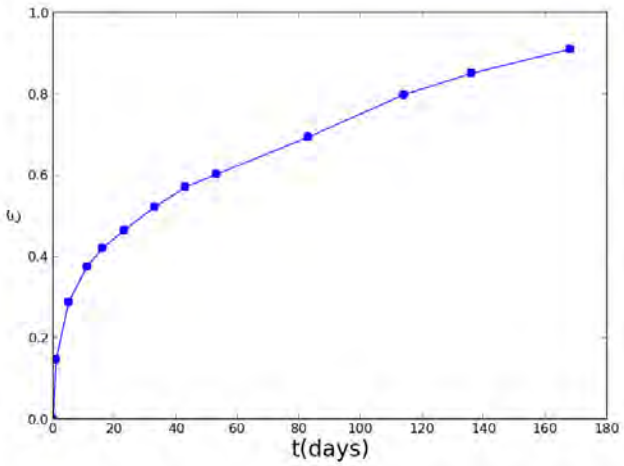

Figure 3: The extraction of copper against time from column leaching experiment

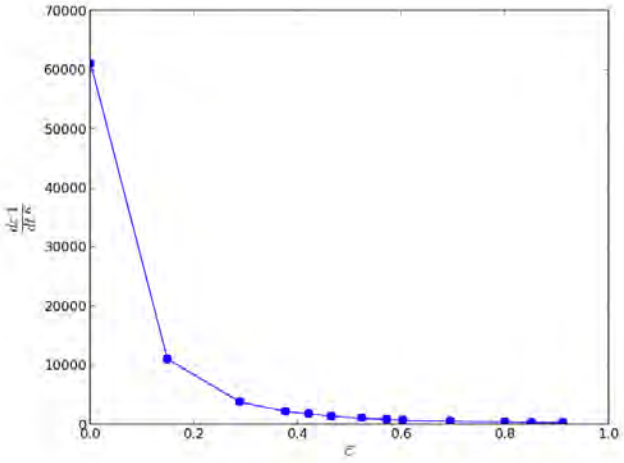

Figure 4: The semi-empirical curve, ε Versus $\frac{\varepsilon}{dt}\frac{1}{\kappa}$, of copper

Where N_p is the total molar amount of the mineral per rock, and n is the number of rocks per unit volume of the heap. The coupling between the species are related by the the stoichiometric factors from the chemistry equations, and the corresponding sources are added into the transport equations accordingly.

Simulation model

An 1-D isothermal CFD simulation was implemented to validate the model against the 1-D column experiments. The parameters for the column and rocks used in the simulation were the same as those used in the experiment. They are listed in Table 2.

It was assumed that $CuFeS_2$ was the only copper-bearing mineral in the rocks, which is reasonable since secondary sulphides and oxides account for less than 5% of the copper in this ore. The various reaction rates of different copper bearing minerals is actually captured in the semi-empirical model fitted from experiment. As the column is small, the saturation and liquid velocity achieved steady state very rapidly compared with the overall leaching time.

The simulation was implemented with a constant darcy velocity $u_w = 7.8mm/hour$ from the top of column, which results in an average water saturation at steady state of $S_w = 0.08226$. The air inside the column is set to be at hydrostatic equilibrium. Since the size of the column is small and the leaching very slow, to ensure the CFL stability with respect to the interstitial velocity at a large time step, we carried out the simulation on a coarse mesh with a time step $dt = 300s$ to validate the model. Given the larger scale, this is not a serious restriction when simulating full scale heaps.

The simulation parameters and the initial and boundary conditions for the transport equation are listed in Table 3.

Table 2: Parameters of the model

Parameter	value
Column	
Hight (m)	0.19
Diameter (m)	0.028
Porosity ϕ	0.4
Absolute permeability ($\frac{m^2}{s}$)	2.3×10^{-9}
Saturation of Solutes	0.08226
Temperature (°C)	60
Rock	
Mean diameter (m)	0.01
Amount of $CuFeS_2$ per rock (mole)	0.000128
Amount of FeS_2 per rock (mole)	0.000969

RESULTS

The results of CFD simulation is compared with the column experiments over 168 days. The extraction of $CuFeS_2$ and the amount of Cu^{2+} extracted is illustrated in Figure 5. The concentrations of Fe^{2+} and Fe^{3+}, and Cu^{2+} in the leachate are shown in Figure 6 and 7, respectively.

Most of the leachate concentrations approach steady state after about 20 days. The concentration of copper and ferrous in the leachate initially decreased rapidly followed by a

Table 3: Modeling condtions for mass transport

C($\frac{mol}{m^3}$)	I.C.	B.C. (Top/bottom)	D ($\frac{m^2}{s}$)
Cu^{2+}	0	Dirichlet: 0 / Neumann: 0	9.3×10^{-6}
H^{+}	63.1	Dirichlet: 63.1 / Neumann: 0	8.2×10^{-5}
Fe^{3+}	0	Dirichlet: 89.3 / Neumann: 0	6.9×10^{-5}
Fe^{2+}	0	Dirichlet: 0 / Neumann:0	6.7×10^{-5}
DO	0.22	Dirichlet: 0.22 / Neumann: 0	5.5×10^{-5}

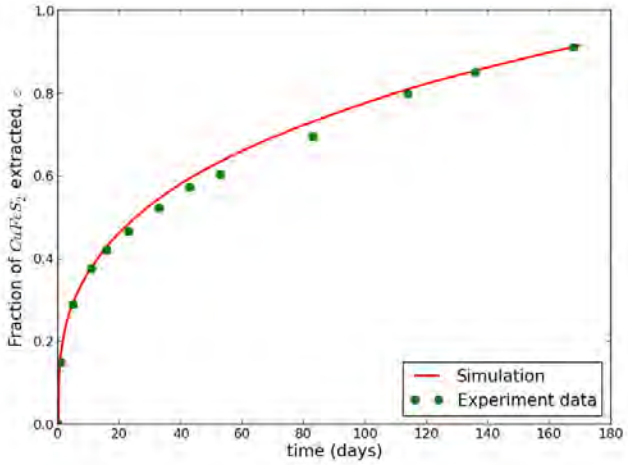

(a) The extracted fraction of $CuFeS_2$

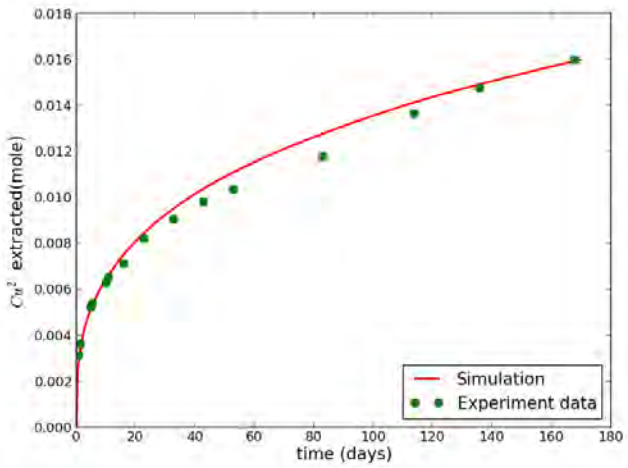

(b)The amount of Cu^{2+} extracted (mole)

Figure 5: The extraction of $CuFeS_2$ and Cu^{2+}

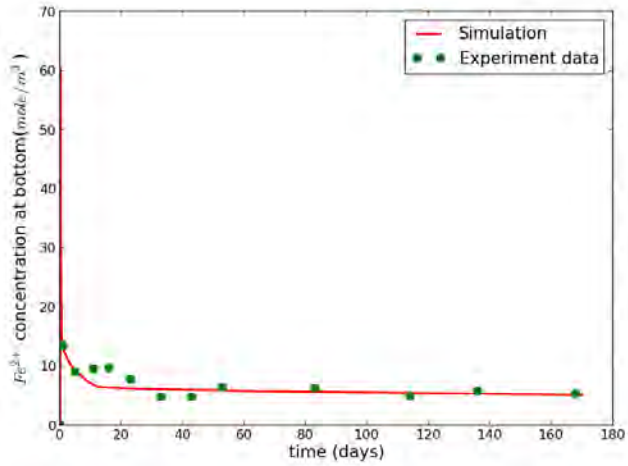

(a) Concentration of Fe^{2+} at bottom of column ($\frac{mol}{m^3}$)

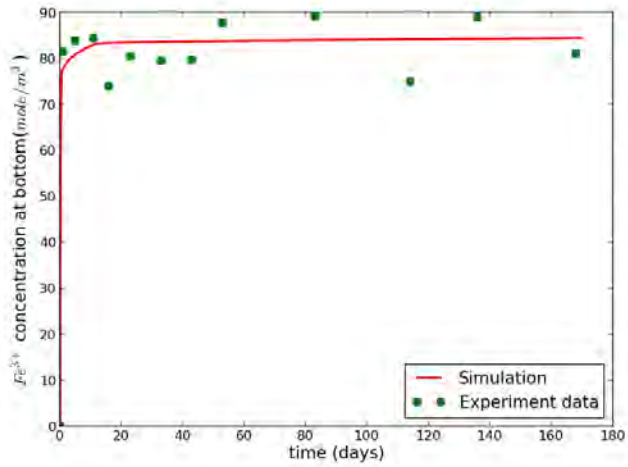

(b) Concentration of Fe^{3+} at bottom of column ($\frac{mol}{m^3}$)

Figure 6: Concentration of Fe^{3+} and Fe^{2+} at bottom of column ($mole/m^3$)

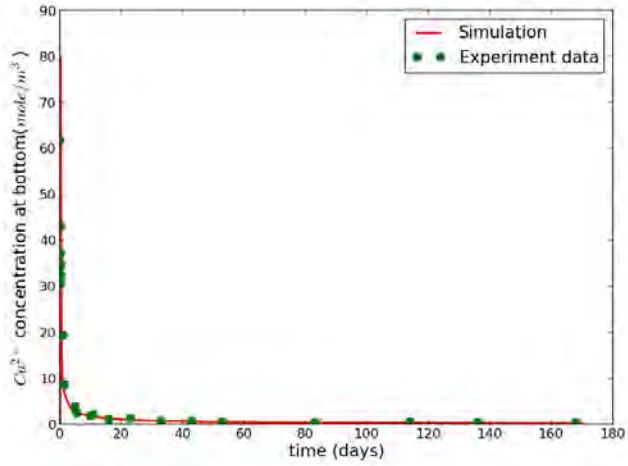

Figure 7: Concentration of Cu^{2+} at bottom of column ($mole/m^3$)

slow decrease. The simulation results of concentration and extractions fit the experiment results well. This suggests that the semi-empirical model is valid, and, by combining this model with the reactive transport simulation, can generate accurate results.

CONCLUSION

A new semi-empirical model, which is based on the data from experiments, is developed in this paper. This new model suggests that the rate of extraction of the rock is a function of the current extraction along with the bulk concentrations for a specific class and size of ore. This CFD simulation of a 1-D isothermal leaching of a chalcopyrite ore is implemented. This simulation has included the coupling reactions and, by employing this new model, the results fit the experiment data well. In the future work, the simulation will be refined by including bacteria actions, and the the heat transport effects.

REFERENCES

BEAR, J. (1972). *Dynamics of fluids in porous media*. Dover Civil and Mechanical Engineering Series. DOVER PUBN Incorporated.

BENNETT, C. *et al.* (2006). "Simulation technology to support base metal ore heap leaching". *Mineral Processing and Extractive Metallurgy*, **115(1)**, 41–48.

BENNETT, C. *et al.* (2012). "A comprehensive model for copper sulphide heap leaching: Part 1 basic formulation and validation through column test simulation". *Hydrometallurgy*, **127-128(0)**, 150–161.

BROOKS, R. and COREY, A. (1964). *Hydraulic Properties of Porous Media*. Colorado State University Hydrology Papers. Colorado State University.

CHAE, D. and WADSWORTH, M. (1989). "In situ recovery of minerals". *Engineering Foundation, New York, NY*, 1–21.

GAO, H. *et al.* (1983a). "A mathematical model for the solution mining of primary copper ore: Part I. leaching by oxygen-saturated solution containing no gas bubbles". *Metallurgical Transactions B*, **14(4)**, 541–551.

GAO, H. *et al.* (1983b). "A mathematical model for the solution mining of primary copper ore: Part II. leaching by solution containing oxygen bubbles". *Metallurgical Transactions B*, **14(4)**, 553–558.

KIMBALL, B.E. *et al.* (2010). "Chalcopyrite dissolution rate laws". *Applied Geochemistry*, **25(7)**, 972–983.

LEAHY, M.J. and SCHWARZ, M.P. (2009). "Modelling jarosite precipitation in isothermal chalcopyrite bioleaching columns". *Hydrometallurgy*, **98(1–2)**, 181–191.

LEAHY, M. *et al.* (2005). "A model for heap bioleaching of chalcocite with heat balance: Bacterial temperature dependence". *Minerals Engineering*, **18(13–14)**, 1239–1252.

LEVENSPIEL, O. (2006). *CHEMICAL REACTION ENGINEERING, 3RD ED*. Wiley India Pvt. Limited.

MCBRIDE, D. *et al.* (2012). "Heap leach modeling employing CFD technology: A 'process' heap model". *Minerals Engineering*, **33(0)**, 72–79.

MODELLING, A. and GROUP, C. (2010). *Fluidity Manual*. Applied Modelling and Computation Group, Department of Earth Science and Engineering, Imperial College London, version 4.0-release ed.

MOSTAGHIMI, P. *et al.* (2014). "A control volume finite element method for adaptive mesh simulation of flow in heap leaching". *Journal of Engineering Mathematics*, 1–11.

NEUBURG, H.J. *et al.* (1991). "A model for the bacterial leaching of copper sulfide ores in pilot-scale columns". *International Journal of Mineral Processing*, **31(3–4)**, 247–264.

TROMANS, D. (1998). "Oxygen solubility modeling in inorganic solutions: concentration, temperature and pressure effects". *Hydrometallurgy*, **50(3)**, 279–296.

WILLIAMSON, M.A. and RIMSTIDT, J. (1994). "The kinetics and electrochemical rate-determining step of aqueous pyrite oxidation". *Geochimica et Cosmochimica Acta*, **58(24)**, 5443–5454.

DESIGN AND IMPROVEMENT OF AN INDUSTRIAL AIRLIFT REACTOR USING COMPUTATIONAL FLUID DYNAMICS

Tao SONG[1, 2]*, Kaixi JIANG[2], Junwu ZHOU[2], Deyu WANG[3], Ning XU[2], Yuqing FENG[4]

[1] School of Materials and Metallurgy, Northeastern University, Shenyang 110819, CHINA

[2] BGRIMM, Beijing General Research Institute of Mining and Metallurgy, 100160 Beijing, CHINA

[3] Shandong Gold Group, 250100 Jinan, CHINA

[4] CSIRO Computational Informatics, Clayton VIC 3168, AUSTRALIA

* E-mail: songtao@bgrimm.com

ABSTRACT

The performance of an airlift reactor in cyanide leaching relies on the good mixing between solid particles and reagents. As the increase of tank sizes, the design of efficient large scale reactors turns to be difficult. An Eulerian multi-fluid model with extra user defined subroutines has been developed and validated to provide insights into a big size airlift reactor used in gold leaching plants. The CFD model enables the efficiency of the investigation of the likely effect of several main design and/or operating parameters, including gas inlet designs and different gas flow rates. The developed CFD model has been run under a wide range of reactor designs and process conditions, and the relative performance has been compared in terms of the circulation velocities, gas holdup in the tank and bubble residence time distribution. In particular, a patented BGRIMM designed air nozzle which can produce high speed gas jet flow was evaluated in an industrial airlift reactor. CFD simulations demonstrated that the BGRIMM design shows a better performance than the original reactor design. The BGRIMM design has been applied in a full-scale airlift reactor at a Shandong Gold Group leaching plant in Laizhou China. Consistent with the CFD findings, the industrial operations showed that the new designs bring improvements in slurry circulation and bubble distribution.

Keywords: gas liquid flow, airlift reactor, air inlet design, CFD simulation.

NOMENCLATURE

Subscripts

c	liquid phase
d	gas phase
D	drag force
L	lift force
TD	turbulent dispersion force
WL	wall lubrication force
α	phase number
β	phase number

Greek Symbols

ε	turbulent eddy dissipation [s^{-1}]
ρ	density [kg m^{-3}]
μ	viscosity [N s m^{-2}]

Latin Symbols

C	viscosity coefficient [dimensionless]
F	interfacial force [N m^{-3}]
g	gravity vector [m s^{-2}]
k	turbulent kinetic energy [m^2 s^{-2}]
p	pressure [Pa]
r	volume fraction [dimensionless]
S	source
t	time [s]
$\mathbf{U}$	velocity vector [m s^{-1}]

INTRODUCTION

Air currents for agitation of fluid contents of a tank have been used in industry for a long time. These airlift reactor vessels are widely used in the chemical and hydrometallurgical industries. Agitation in airlift reactors is based on a density difference, generated by the rising gas bubbles, between the riser and downcomer zone. This creates simultaneously circulation of the liquid and solid phases through both zones. The circulation results in efficient suspension of heavy sediments in the liquid and therefore intensive mixing and mass transfer of all three phases throughout the reactor.

Pachuca tanks are air agitated slurry reactors used as leaching vessels in hydrometallurgical industries for extraction of nonferrous metals and the bacterial oxidation of pyrite. They are cylindrical in cross section with a conical bottom and may be equipped with concentric draft tubes. The performance of industrial Pachuca leaching usually depends on some process parameters like the flow regimes, bubble size distributions, coalescence characteristics, gas holdup, gas liquid interfacial area and critical solid holdup. Several investigations have been carried out in laboratory scale bubble columns to determine the effect of design and operating parameters, such as superficial gas velocity, draft tube diameter/height, tank height, cross-section area of riser/downcomer, physical properties of liquid/slurry, on the process parameters described above (Koide *et al.*, 1985; Shekhar and Evans, 1989; Roy *et al.*, 1998; Roy *et al.*, 2000). Correlations

and guidelines have also been provided for optimum design and operation of these reactors. However, Pachuca tanks used in various applications in different industries vary widely both in dimension and operating conditions. The tank scales are usually much larger than the facilities used in laboratory. Therefore, extrapolations of results from these reactors to industrial Pachuca tanks may not be justified. A new design of large scale Pachuca tank still needs experimental and numerical evaluations.

This paper is focused on numerical study of two phase hydrodynamics in an industrial large scale Pachuca tank which has been implemented at a Shandong Gold Group leaching plant in Laizhou China. The CFD model was firstly used to evaluate the performance of the original design. Thereafter, the CFD model was setup and run under a range of reactor gas inlet nozzle designs and gas flow rates. Their effect on reactor performance has been compared in terms of the circulation velocities, gas holdup in the tank and bubble residence time distribution in order to obtain an optimal design and operating condition. The industrial implementation of the optimal designs had shown improvements in slurry circulation and bubble distribution.

MODEL DESCRIPTION

Modelling of the gas-liquid flow in the Pachuca tanks has been carried out using an Eulerian two-fluid model, where the phases are treated as interpenetrating continua and conservation equations are solved for each phase (Koh *et al.*, 2003; Lane *et al.*, 2005). The continuity equations and momentum equations take the following form (where α = c for liquid, α = d for gas):

$$\frac{\partial(r_\alpha \rho_\alpha)}{\partial t} + \nabla \cdot (r_\alpha \rho_\alpha U_\alpha) = S_\alpha \quad (1)$$

$$\frac{\partial(r_\alpha \rho_\alpha U_\alpha)}{\partial t} + \nabla \cdot (r_\alpha (\rho_\alpha U_\alpha \otimes U_\alpha)) = -r_\alpha \nabla p_\alpha + \nabla \cdot \left(r_\alpha \mu_\alpha \left(\nabla U_\alpha + (\nabla U_\alpha)^T\right)\right) + F_\alpha + r_\alpha \rho_\alpha g + S_{M\alpha} \quad (2)$$

$$F_\alpha = F_{\alpha,D} + F_{\alpha,L} + F_{\alpha,WL} + F_{\alpha,TD} \quad (3)$$

Here r_α is the phase volume fraction, ρ_α is the density, t is time, U_α is the mean velocity vector for each phase, p_α is pressure and μ_α is effective viscosity. F_α is the sum of interfacial momentum transfer forces between phases such as drag force $F_{\alpha,D}$, lift force $F_{\alpha,L}$, wall lubrication force $F_{\alpha,WL}$, inter-phase turbulent dispersion force $F_{\alpha,TD}$. The source terms S_α and $S_{M\alpha}$ represent the transfer of gaseous phase mass and momentum between different velocity groups due to bubble break-up and coalescence processes leading to bubbles of certain size belonging to a different velocity group. Consequently these terms are zero for the liquid phase transport equations.

The effective viscosity is sum of the molecular and turbulent viscosities:

$$\mu_\alpha = \mu_0 + \mu_t \quad (4)$$

Phase dependent turbulence models have been used in this work: the dispersed phase zero equation model for the gas phase and *k-ε* two-equation model for the liquid phase. The turbulence eddy viscosity is calculated as:

$$\mu_{tc} = C_\mu \rho_c \frac{k_c^2}{\varepsilon_c} \quad (5)$$

for the liquid phase, and:

$$\mu_{td} = \frac{\rho_d}{\rho_c} \frac{\mu_{tc}}{P_r} \quad (6)$$

for the gas phase.

The parameter P_r is the turbulent Prandtl number relating the dispersed phase kinematic eddy viscosity to the continuous phase kinematic eddy viscosity. C_μ is the *k-ε* turbulent model constant (default value is 0.09). k and ε are the turbulence kinetic energy and turbulence dissipation rate respectively.

The drag force can be the most important factor for determining gas holdup and distribution, since in the absence of acceleration a balance between drag and buoyancy forces determines the bubble slip velocity. It is common to describe the drag force F_D in the following form:

$$F_D = -\frac{1}{2} C_D \rho_c \pi \frac{d_d^2}{4} |U_d - U_c| (U_c - U_d) \quad (7)$$

d_d is the bubble diameter, and C_D is the drag coefficient. The drag coefficient strongly depends on fluid properties, bubble equivalent diameter, gravity and the degree of contamination on the gas-liquid interface (Clift *et al.*, 1978). In this paper Ishii & Zuber model (Ishii and Zuber, 1979) was used for the drag force calculation.

Turbulent dispersion forces result in additional dispersion of phases from high volume fraction regions to low volume fraction regions duo to turbulent fluctuations. Burns *et al.* (2004) presented a general framework for modelling of turbulent dispersion in Eulerian multiphase flows. They derived an expression for Favre Averaged Drag (FAD) model for dispersed two-phase flow:

$$F_{c,TD} = -F_{d,TD} = -C_{TD} C_{CD} \frac{\nu_{tc}}{\sigma_{tc}} \left(\frac{\nabla r_d}{r_d} - \frac{\nabla r_c}{r_c} \right) \quad (8)$$

Here, C_{CD} is the momentum transfer for the interphase drag force, and σ_{tc} is the turbulent Schmidt number for continuous phase volume fraction, currently set to be 0.9. C_{TD} is taken to be 1.

The lift force describes the interaction of the bubble with the shear field of the liquid. This results in net force acting perpendicular to the motion of the bubble relative to the liquid on the bubble (Lucas *et al.*, 2007). The lift force related on the unit volume is calculated as:

$$F_{c,L} = -F_{d,L} = r_d \rho_c C_L (U_d - U_c) \times curl U_c \quad (10)$$

C_L is lift force coefficient. Tomiyama lift force model (Tomiyama, 1998) was used here.

Wall lubrication force tends to push the dispersed phase away from the wall. Generally, the wall lubrication force can be written as:

$$F_{WL} = -C_{WL} r_d \rho_c |U_c - U_d|^2 n_W \quad (9)$$

where C_{WL} is the wall lubrication force coefficient, and n_w is the unit normal pointing away from the wall. Frank wall lubrication force model (Frank *et al.*, 2008) was

put into simulation to describe the bubble distribution near tank wall area in the reactor.

A commercial CFD code ANSYS CFX14.5 has been used to obtain a solution of the above equations, and subroutines were implemented to calculate the interfacial forces. A gas outlet boundary condition has been used on the top surface of the Pachuca tank through which gas leaves the tank at the rate it arrives from below (an option called "degassing condition" in CFX). Wall solid boundaries were set as no slip for water and free slip for air.

RESULTS AND DISCUSSION

The industrial large scale Pachuca tank equipped at a Shandong Gold Group leaching plant in Laizhou China was different from common Pachuca tank design. The main feature of the new design lies in that the three draft tubes were located in the center of the tank. The height of the draft tubes was 11 m, and the inner diameter was 1.1 m. The 4 mm slot-shaped gas inlet was set above the bottom of the draft tube. The height of the tank was 16 m, and the diameter of the tank was 5.5 m. The total volume of the reactor was 340 m^3. The cone angle was 30 degrees. There was a slurry inlet located near tank wall above the circulation tubes. The slurry outlet was 0.7 m above the slurry inlet. The diameters of them were all 0.3 m.

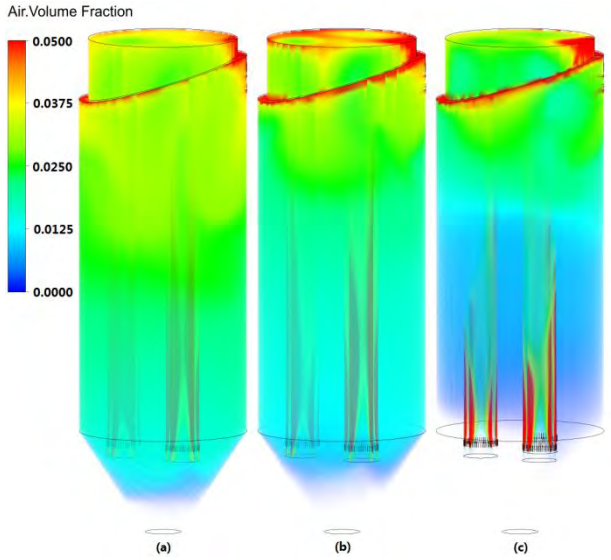

Figure 1: Gas volume fraction in the middle slice plane for the gas flow rate of 6 m^3/min: (a) 1 mm bubble nozzle; (b) 2 mm bubble nozzle; (c) 4 mm bubble nozzle.

To evaluate the industrial performance, the CFD model has been setup using the geometry of a full-scale Pachuca tank. The structural grid was 663,458 cells. As 95% of the particle sizes in the leaching tank were under 37 μm, a user defined slurry material was used as the liquid phase to present the mixture of water, mineral particles and the reagent. The density of the slurry phase was 1428 kg/m^3. Gas flow rates in the riser were 2 m^3/min, 4 m^3/min and 6 m^3/min for different operation conditions. The net slurry flow through the slurry inlet was 0.25 m/s, and the same value was used for the slurry output velocity. Three kinds of gas inlet nozzle were investigated here. One was the original 4 mm slot-shape gas inlet. The other two were patented BGRIMM designed gas inlet nozzles, which can produce high speed gas jet flow. The diameters of the two high speed nozzles were 2 mm and 1 mm respectively.

Due to the absence of some detailed information, the model was setup with several assumptions. The slurry viscosity was set as 60 cP. The average bubble diameter generated by 4 mm bubble nozzle was assumed to be 8 mm. The average bubble sizes of 2 mm bubble nozzle and 1 mm bubble nozzle were set as 3 mm and 1.5 mm respectively. These two values were from the observation of laboratory experiments in a water environment.

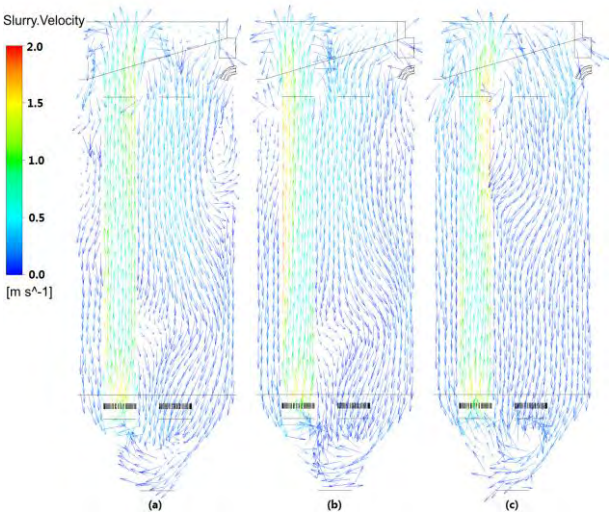

Figure 2: Slurry velocity vectors in the middle slice plane for the gas flow rate of 6 m^3/min: (a) 1 mm bubble nozzle; (b) 2 mm bubble nozzle; (c) 4 mm bubble nozzle.

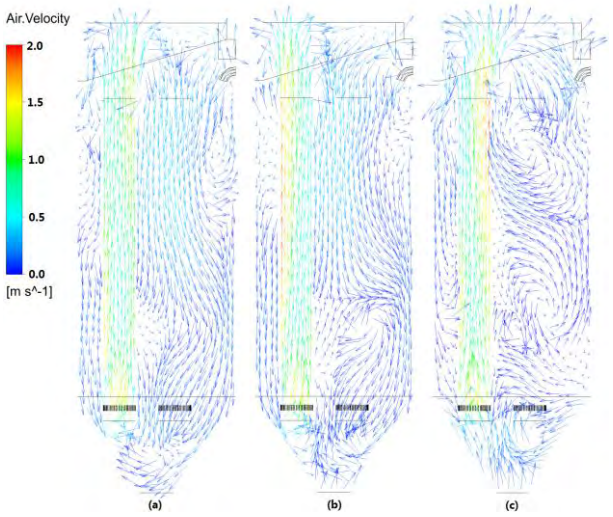

Figure 3: Gas velocity vectors in the middle slice plane for the gas flow rate of 6 m^3/min: (a) 1 mm bubble nozzle; (b) 2 mm bubble nozzle; (c) 4 mm bubble nozzle.

The extraction reaction needs oxygen as reactant. Good mixing of dissolved oxygen, cyanide reagent and particles carrying gold can vastly improve the recovery of gold. So oxygen mass transfer and particle suspension turn to be two very important considerations in cyanide leaching of gold. Thus, process parameters, such as gas/liquid circulation regime and gas bubble distribution, are the key points to be assessed.

Figure 1 shows the simulation results of gas volume fraction distributions in the middle slice plane for the

gas flow rate of 6 m^3/min. In the original design condition, bubbles mainly concentrated at the riser area and the top of the tank. When the gas inlet nozzles were changed to be the new designs and small bubbles were generated, the gas phase reached the bottom of the draft tubes. The contact area between bubble surface and slurry increased to a higher level and the oxygen mass transfer rate should also be increased. Consequently, more gold should be extracted from solid particle into liquid phase.

The suspension of particles can be decided by the circulation flow in the reactor. If the gas rise can generate a good circulation flow regime between riser and downcomer, the solid particles will be carried by the flow and seldom sink to the tank bottom. Figure 2 and Figure 3 show the simulation results of slurry and gas velocity vectors in the middle slice planes for the gas flow rate of 6 m^3/min. The Pachuca tank with three draft tubes basically could generate a circulation flow regime. The solid particles moved with the flow both in riser and downcomer, and the particles had more chance to contact with oxygen and cyanide reagent. The small bubble from 1 mm and 2 mm bubble nozzle mostly followed the slurry flow. However, bigger bubbles from original 4 mm bubble nozzle did not move in a regular flow pattern, but in several big swirls. That might be one of the reasons why bubbles nearby did not reach the bottom half area of the tank.

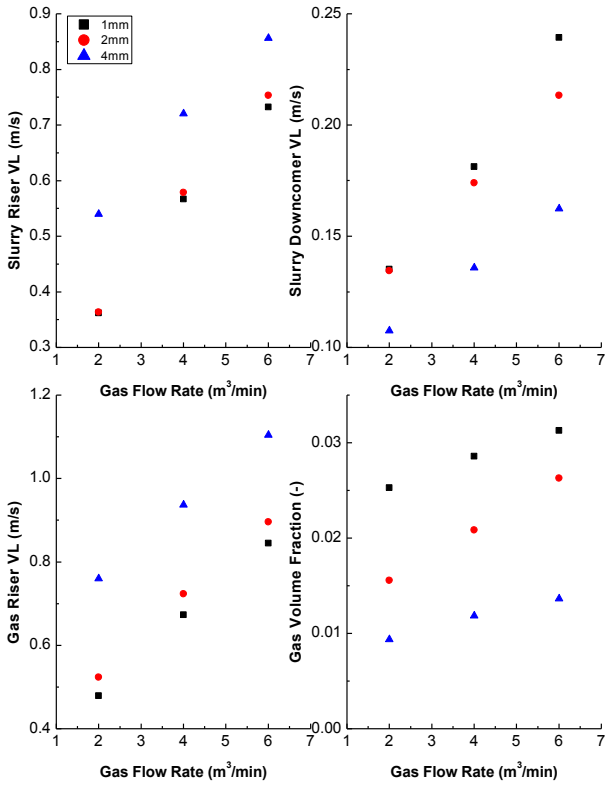

Figure 4: Comparisons between different nuzzle settings under three gas flow rates: (a) slurry average velocities in riser; (b) slurry average velocities in downcomer; (c) gas average velocities in riser; (d) gas volume fraction in the whole reactor.

Figure 4 compares the effect of different nuzzle settings on the reactor performance under gas flow rates of 2 m^3/min, 4 m^3/min and 6 m^3/min. The slurry velocity increases with the increase of gas flow rate and the bubble average diameters both in the riser and downcomer sections. The bigger sized bubbles, which had higher terminal velocities, mostly moved up to the top of the tank in the riser. So the average density difference between riser and downcomer was smaller. The slurry flow with the high speed gas flow also moved faster and the downcomer slurry velocity driven by the pressure difference was lower. The gas holdup in the whole tank was also increased with the increase of the gas flow rates. Because the tank diameter is large, the downcomer cross-section area is nearly 7 times larger than the riser cross-section area. Therefore, more gas bubbles in the downcomer will be helpful for improving the extraction reaction performance.

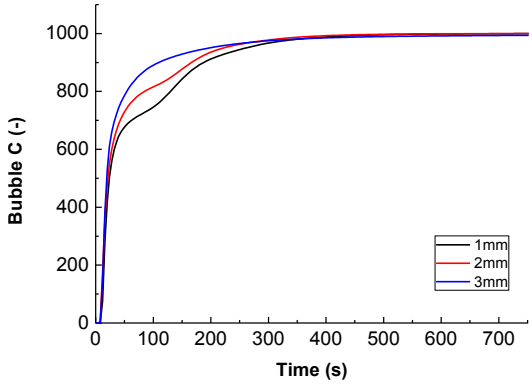

Figure 5: Outlet concentration for the step input bubble tracer under different bubble nuzzle settings.

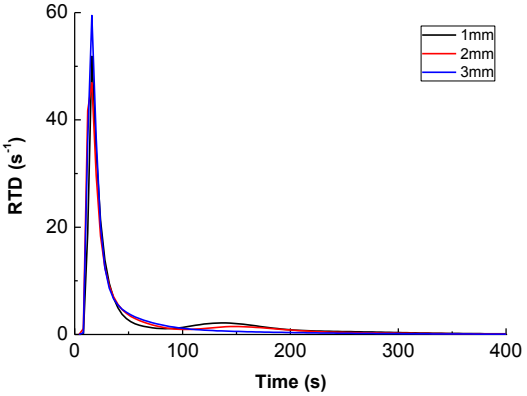

Figure 6: Residence time distribution (RTD) for step input bubble tracer under different bubble nozzle settings.

Simulations of the full-scale Pachuca tank allow the analysis of the effect of different gas inlet nozzle designs, based on the same inlet gas flow rate of 6 m^3/min. Three kinds of step input bubble tracers, which represent the new 1 mm bubble nozzle, 2 mm bubble nozzle and the original 4 mm bubble nozzle settings, were put into the reactor at the gas inlet from initial time of transient simulations. The concentrations of the bubble tracers were all set 1000. Figure 5 plots the outlet concentration curves for the step input bubble tracers. The results showed that big sized bubbles stay less time in tank than smaller bubbles, but not too much. After 400 s from initial time, all kinds of bubble tracers have gone out of the tank. Figure 6 showed the residence time distribution (RTD) curves for step input bubble tracers. Apparently, the same results were given by the RTD curves. New designs of gas inlet nozzle had a little larger residence time for gas in the riser. The 1 mm bubble nozzle and 2 mm bubble nozzle basically has the similar performance in terms of bubble RTD.

The water tracer was injected from the slurry inlet of the tank as a pulse input. The initial concentration was 1000 in the whole injection area. Because of the large size of the Pachuca tank, the mixing time was much longer than that in the laboratory reactors. In our 3,000 s transient simulations, the full mixing of the water tracer was not achieved. However, based on the intermediate results, it shows that the average water tracer concentration in the draft tube bottom area was larger when using the new designed bubble nozzle.

Through the CFD simulations of the industrial Pachuca tank under different nozzle designs and three gas flow rates, the smaller sized bubbles generated by the new bubble nozzles made the process parameters more suitable for the high performance of gold leaching. The higher air supply for single Pachuca tank also made the leaching environment better. Taking the consideration of the air supply ability at the leaching plant, the 2 mm bubble nozzle was chosen to be installed in one Pachuca tank at Shandong Gold Group leaching plant in Laizhou China in December 2013. Several pressure sensors were put into the tank to monitor the variation of slurry density and the flow pressure. One dissolved oxygen concentration sensor was set in the tank too. Because of the tough environment, no detailed measurement have been made. However, through overall experimental observation, the new design showed an improvement in slurry circulation and bubble distribution. From the sample analysis, the recovery of gold in the experiment Pachuca tank increased from 88% to 90% on average.

CONCLUSION

CFD modelling offers enormous capability for optimization of airlift reactor design. In this paper, CFD modelling has been used to provide insight and understanding of many features required of a large-scale Pachuca tank gas inlet nozzle and the whole tank performance under varying gas flow rates. The CFD model predicted the circulation velocities, gas holdup in the tank and bubble residence time distribution. The simulation results enable the efficiency of the functions of several gas inlet designs and different gas flow rates. The patented BGRIMM designed air nozzle which can produce high speed gas jet flow was evaluated in the industrial airlift reactor. Under the new settings, CFD simulations demonstrated a better performance than the original reactor design. Based on these new understandings and concepts, the 2 mm bubble nozzle was installed at Shandong Gold Group leaching plant. The improved Pachuca tank showed a better performance in present industrial trials.

ACKNOWLEDGEMENTS

The simulation work is financially supported by Beijing General Research Institute of Mining and Metallurgy, CSIRO and National High Technology Research and Development Program of China (No. 2011AA060202). The Pachuca tank design and industrial experimental spot are supported by Shandong Gold Group leaching plant in Laizhou China.

REFERENCES

KOIDE K., HORIBE K., KAWABATA H., ITO S., (1985), "Gas holdup and volumetric liquid-phase mass transfer coefficient in solid-suspended bubble column with draught tube", *Journal of Chemical Engineering of Japan*, **18(3),** 248-254.

SHEKHAR R. and EVANS J.W., (1989), "Fluid flow in Pachuca (air-agitated) tanks: Part I. Laboratory-scale experimental measurements", *Metallurgical Transactions B*, **20(6),** 781-791.

ROY G.G., SHEKHAR R., MEHROTRA S.P., (1998), "Particle suspension in (air-agitated) Pachuca tanks", *Metallurgical and Materials Transactions B*, **29(2),** 339-349.

ROY G.G., BERA A., MANKAR J.H., (2000), "Effect of design and operating parameters on gas hold-up in Pachuca (air-agitated) tanks", *Mineral Processing and Extractive Metallurgy*, **109(2),** 90-96.

KOH P.T.L., SCHWARZ M.P., ZHU Y., BOURKE P., PEAKER R., FRANZIDIS J.P., (2003), "Development of CFD Models of Mineral Flotation Cells", *Third International Conference on CFD in the Minerals and Process Industries*, Melbourne, Australia, December 10-12.

LANE G.L., SCHWARZ M.P., G.M. EVANS, (2005), "Numerical Modelling of Gas-Liquid Flow in Stirred Tanks", *Chemical Engineering Science*, **60(8-9)**, 2203-2214.

CLIFT R., GRACE J.R., WEBER M.E, (1978), *Bubbles, Drops, and Particles*, Academic Press, New York.

ISHII M., ZUBER N., (1979), "Drag coefficient and relative velocity in bubbly, droplet or particulate flows", *AIChE Journal*, **25(5)**, 843-855.

BURNS A.D., FRANK T., HAMILL I., SHI J.-M., (2004), "The Favre averaged drag model for turbulence dispersion in Eulerian multi-phase flows", *Proc. 5th International Conference on Multiphase Flow*, *ICMF2004*, Yokohama, Japan.

LUCAS D., KREPPER E., PRASSER H.-M., (2007), "Use of models for lift, wall and turbulent dispersion forces acting on bubbles for poly-disperse flows", *Chemical Engineering Science*, **62(15)**, 4146-4157.

TOMIYAMA, A., (1998), "Struggle with computational bubble dynamics", *Multiphase Science and Technology*, **10(4)**, 369-405.

FRANK T., ZWART P.J., KREPPER E., PRASSER H.-M., LUCAS D., (2008), "Validation of CFD models for mono- and polydisperse air-water two-phase flows in pipes", *Nuclear Engineering and Design*, **238(3)**, 647-659.

A CRITICAL COMPARISON OF SURFACE TENSION MODELS FOR THE VOLUME OF FLUID METHOD

Maike W. BALTUSSEN[1]*, **J. A.M. KUIPERS**[1]†, **Niels G. DEEN**[1]‡

[1]Eindhoven University of Technology, Postbus 513, 5600 MB Eindhoven, THE NETHERLANDS

* E-mail: m.w.baltussen@tue.nl
† E-mail: j.a.m.kuipers@tue.nl
‡ E-mail: n.g.deen@tue.nl

ABSTRACT

Flows involving two immiscible fluids are frequently encountered in industrial processes. These flows can be described using a multi-scale computational fluid dynamics approach. The smallest scale model in this approach corresponds to Direct Numerical Simulation (DNS). In this study, we adopt the Volume of Fluid method. The advantage of this method is that the model inherently conserves mass. However, it is difficult to accurately account for surface tension in this method. In this paper, three different surface tension models are compared: the commonly used continuum surface force model, the height function model and the new tensile force method. Both the height function model and the tensile force method produce better results in verification tests. Furthermore, the height function model can generally be used to simulate bubbles with Eo ≤ 10 and the tensile force method for bubbles with Eo ≥ 1. The effect of the Morton number on the applicability of the surface tension models is small.

Keywords: Bubble and droplet dynamics, Multi-scale modeling, Direct Numerical Simulation, Volume of Fluid, Surface tension modeling .

NOMENCLATURE

Greek Symbols

Δz	Grid size in z direction, $[m]$.
κ	Curvature, $[1/m]$.
μ	Dynamic viscosity, $[kg/ms]$.
ρ	Mass density, $[kg/m^3]$.
σ	Surface tension coefficient, $[N/m]$.
τ	Stress tensor, $[Pa]$.

Latin Symbols

CFD	Computational Fluid Dynamics.
DNS	Direct Numerical Simulations.
Eo	Eötvös number.
F	Phase fraction.
$\mathbf{F}$	Force, $[N]$.
FT	Front Tracking.
$\mathbf{g}$	Gravitational acceleration, $[m/s^2]$.
h	Height, $[m]$.
Mo	Morton number.
$\mathbf{n}$	Normal.
PLIC	Piecewise Linear Interface Calculation.
p	Pressure, $[Pa]$.
t	Time, $[s]$.
$\mathbf{t}$	Tangent, $[m]$.
$\mathbf{u}$	Velocity, $[m/s]$.
VOF	Volume of Fluid.

Sub/superscripts

σ	Surface tension.
CSF	Continuum surface force model.
HF	Height function model.
i	Index i.
j	Index j.
k	Index k.
m	Index m.
TF	Tensile force method.

INTRODUCTION

Bubbly two phase flows are frequently encountered in industrial practice and natural phenomena (Scardovelli and Zaleski, 1999). Due to the large variation of time and length scales in e.g. industrial size bubble columns, a multi-scale modeling approach is used to account for the complex hydrodynamics in such complex systems. In the multi-scale modeling approach, the larger scale models use closure correlations, e.g. the drag correlation, obtained from the smaller scale models (Yang *et al.*, 2007; Roghair *et al.*, 2011).

In this paper, the smallest scale model of the multi-scale modeling approach, Direct Numerical Simulation (DNS), will be used. In DNS, the Navier-Stokes equations are solved without strong assumptions. However, in DNS, only O(10^2) bubbles can be treated due to the high computational costs (Roghair *et al.*, 2011; Baltussen *et al.*, 2014).

DNS methods can be divided into two main groups: moving grid methods and fixed grid methods. In the first method, a body-fitted mesh is used, which accurately represents the phase boundary, while in fixed grid methods a fixed Eulerian grid is used for solving the Navier-Stokes equations. In this paper a fixed grid method is used, because these models are able to handle the pronounced topological changes which will occur for highly deformed bubbles (Scardovelli and Zaleski, 1999; van Sint Annaland *et al.*, 2005; Roghair *et al.*, 2011).

Here, the VOF method will be used to simulate the gas bubble behavior, because this model offers inherent mass conservation which is not ensured in the other main fixed grid methods (Front Tracking and Level-Set). The VOF method tracks the interface using a color function, i.e. the phase fraction.

Using this color function, the interface can be reconstructed and advected according to equation 1.

$$\frac{DF}{Dt} = \frac{\partial F}{\partial t} + \mathbf{u} \cdot \nabla F = 0 \tag{1}$$

Although the reconstruction of the interface ensures mass conservation, the reconstruction of the surface also leads to problems with the connectivity of the surface, which will lead to difficulties in calculating the interface properties, like the surface tension (Lafaurie *et al.*, 1994; Jafari *et al.*, 2007). Therefore, many different methods have been devised to represent the surface tension.

In the continuum surface stress method, the surface tension is introduced as a capillary pressure tensor. However, this implementation as a stress tensor is less accurate than introducing the surface tension as a body force (Lafaurie *et al.*, 1994; Renardy and Renardy, 2002; Meier *et al.*, 2002; Jafari *et al.*, 2007; Albert *et al.*, 2012).

The most common method to implement the surface tension is as a body force: the continuum surface force (CSF) method of Brackbill *et al.* (1992). In this method, the body force is calculated from the surface tension coefficient, σ, the curvature, κ, and the normal, $\mathbf{n}$, by equation 2.

$$\mathbf{F}_\sigma = \sigma \kappa \mathbf{n} \tag{2}$$

To calculate the normal and the curvature of the interface, the first and second order spatial derivative of the color function should be determined, respectively. Because the color function is a step function over the surface, the color function is smoothed around the interface to enable the calculation of these surface properties. However, this operation leads to smearing of the surface (Renardy and Renardy, 2002; van Sint Annaland *et al.*, 2005; Gerlach *et al.*, 2006).

The main problem in the CSF method is the calculation of the curvature (Afkhami and Bussmann, 2009). Therefore, several methods have been developed to improve the CSF model. First of all, the interface representation can be improved to ensure by better reconsruction techniques (Rider and Kothe, 1998; Renardy and Renardy, 2002; Pilliod Jr. and Puckett, 2004). Nevertheless, these improvements of the interface reconstruction techniques will considerably reduce the speed of the simulations (Son, 2003; Gerlach *et al.*, 2006).

Another option is to combine the VOF model with the Level-Set model. In this approach the smooth Level-Set function, which tracks the interface, can be used to accurately determine the surface properties. However, to ensure mass conservation, the Level-Set function has to be reinitialized. This reinitialization can be done with the color function of the VOF, but this implies that the surface reconstruction has to be accurate for both the color function advection and the reinitialization (Son, 2003; Gerlach *et al.*, 2006; Albadawi *et al.*, 2013).

In addition, the curvature estimation can also be improved using the height function model. In this model, the curvature in one direction is neglected. Summing the phase fractions in this direction will provide the height, which represents the surface. The curvature can be determined by taking the spatial derivative of the height in all the directions. The main advantage of this method is that the implementation of the height function eliminates the need of smoothing, improves the accuracy and reduces spurious currents (Gerrits, 2001; Cummins *et al.*, 2005; Francois *et al.*, 2006; Popinet, 2009).

Finally, a totally different approach can be taken to calculate the surface tension inspired by the approach taken in Front Tracking (FT). In FT model, the tensile force method has been used to determine the surface tension. In this method, the tensile forces of all neighboring interface segments are summed (Tryggvason *et al.*, 2001; Shin and Juric, 2002; Dijkhuizen *et al.*, 2010b). A similar approach can be used for the Piecewise Linear Interface Calculation (PLIC) interfaces in the VOF method (Baltussen *et al.*, 2014).

In this paper, three different surface tension methods for the VOF model will be compared for the simulation of single bubbles: the CSF method, the height function model and the tensile force method. In the next section, the details of the VOF method and the surface tension models will be discussed. Following, 33 different cases of single bubbles will be simulated and compared with the experimental data of Grace *et al.* (1976) and Tomiyama (1998). Finally, this paper will conclude with the operating windows of the different models.

MODEL

For this paper, the Volume of Fluid method of Baltussen *et al.* (2014) will be used and only the main characteristics of the method will be discussed in this paper.

Governing equations

In the Volume of Fluid method, the incompressible Navier-Stokes equation and continuity equation are solved, respectively equation 3 and 4.

$$\rho \frac{\partial \mathbf{u}}{\partial t} = -\nabla p - \rho \nabla \cdot (\mathbf{u}\mathbf{u}) + \nabla \cdot \boldsymbol{\tau} + \rho \mathbf{g} + \mathbf{F}_\sigma \tag{3}$$

$$\nabla \cdot \mathbf{u} = 0 \tag{4}$$

Because the velocity field is continuous even across the interface, the one-fluid formulation can be used. However, the effects of the surface tension should be taken into account using the extra body force, $\mathbf{F}_\sigma$. In this paper, we will determine the effect of different implementations of this force, which will be explained in the next section.

The velocity field is solved on a staggered grid using a projection-correction method. This method calculates an estimate of the new velocity profile using the Navier-Stokes equations. In this calculation, all terms in equation 3 are determined explicitly with the exception of the diffusion term which is treated semi-implicit. The division between the explicit part and the implicit part of the diffusion term is done ensuring that the implicit part of the velocity can be solved separately in the different directions. The convective part of the Navier-Stokes equation is discretized using a second order flux-delimited Barton scheme, wheres a second order central differencing scheme is used for the diffusion term. Subsequently, the obtained velocity profile is corrected to satisfy the continuity equation. Both the implicit part of the projection step and the implicit correction step are solved using an ICCG matrix solver.

Using the obtained velocity profile, the new phase fraction, F, can be determined in each cell using geometrical advection of the phase fraction. This advection is performed with a Piecewise Linear Interface Calculation (PLIC) algorithm of Youngs (1982). In this method, the interface is represented by five different types of linear planes. Although there are 64 linear planes possible in the PLIC algorithm, the number of planes can be reduced to five by changing the co-ordinate directions, interchanging the co-ordinate directions and interchanging the phases. When the interface is known, the interface is advected using equation 1.

When the phase fraction in each cell is known, the new density, ρ, and viscosity, μ, in each cell can be determined using linear weighing and harmonic weighing respectively.

Surface tension models

In this paper, three different surface tension models will be used to model the different single bubbles.

Continuum surface force (CSF) model

The most often used surface tension model in the VOF model is the Continuum surface force (CSF) model of Brackbill *et al.* (1992), equation 2. In this model, the extra body force is calculated using equation 5, where the phase fraction is used as the color function.

$$\mathbf{F}_{\sigma,CSF} = 2F\sigma\kappa\mathbf{n} \tag{5}$$

The curvature of the bubble and the normal can be determined as the second and first order derivative of the phase fraction, as shown in equation 6 and 7.

$$\kappa = -(\nabla\cdot\mathbf{n}) \tag{6}$$

$$\mathbf{n} = \frac{\nabla F}{|\nabla F|} \tag{7}$$

To enable the calculation of the normal using the phase fraction, the phase fraction is smoothed using the polynomial expression of Deen *et al.* (2004). The chosen smoothing width is two grid cells, which effectively means that the interface has a width of three grid cells (Renardy and Renardy, 2002; van Sint Annaland *et al.*, 2005).

Height function (HF) model

The main problem in the CSF model is the calculation of the curvature. Therefore, the main difference between the CSF and the height function model is the calculation of the curvature; the normal and the surface tension can thus still be calculated using equation 7 and 2, respectively. However, the calculation of the normal uses the non-smoothed phase fraction instead of the smoothed phase fraction (Gerrits, 2001; Cummins *et al.*, 2005; Francois *et al.*, 2006).
The curvature is calculated using the height, which is the summation of the phase fraction in the direction of the largest normal. The phase fraction is summed over 7 cells in the direction of the largest normal. Assuming the largest normal is in the z-direction, the height in cell (i,j,k) is calculated with equation 8.

$$h(i,j,k) = \sum_{k-3}^{k+3} F(i,j,k)\Delta z \tag{8}$$

Assuming that there is no curvature in the direction of the largest normal, the curvature can be calculated with equation 9.

$$\kappa = \frac{\partial}{\partial x}\left(\frac{\frac{\partial h}{\partial x}}{\sqrt{1+(\frac{\partial h}{\partial x})^2+(\frac{\partial h}{\partial y})^2}}\right) + \frac{\partial}{\partial y}\left(\frac{\frac{\partial h}{\partial y}}{\sqrt{1+(\frac{\partial h}{\partial x})^2+(\frac{\partial h}{\partial y})^2}}\right) \tag{9}$$

The resulting force cannot directly be used in the Navier-Stokes equation, because these equations require force densities while the calculated surface tension is the force per square meter interface. Therefore, the surface tension body force resulting from equation 2 and 9 has to be multiplied by the surface per volume of the cell.

The implementation of the height function model increases the accuracy of the VOF, eliminates the need of smoothing and diminishes spurious currents. Equation 8 and 9 show that the calculation of curvature using the height function model is based on a $7x3x3$ stencil, which suggest that two interfaces should be more than three grid cells apart. However, this does not have to be the case for wobbling, spherical cap, skirted and dimpled bubbles.

Tensile force (TF) method

The last surface tension method uses a different approach. The tensile force method calculates the surface tension from the tensile forces exerted on each interface element. Every neighboring element, i, exerts a tensile force on the interface element, m, that can be calculated with equation 10 (Dijkhuizen *et al.*, 2010a; Tryggvason *et al.*, 2001).

$$\mathbf{F}_{\sigma,i\to m} = \sigma(\mathbf{t}_{i,m}\times\mathbf{n}_i) \tag{10}$$

The tangent can be determined from the PLIC-reconstruction of the surface, according to the right hand-rule. While the normal to the interface is again determined from the phase fraction using equation 7. The total force on the interface element can be determined by summing the contributions of all the neighbors. However, the sum of all the force on an enclosed surface is 0. Therefore, the total surface tension can be calculated using the following equation (Dijkhuizen *et al.*, 2010a; Tryggvason *et al.*, 2001):

$$\mathbf{F}_{\sigma,TF} = \frac{1}{2}\sum_i(\mathbf{F}_{\sigma,i\to m}) \tag{11}$$

This surface tension model is based on connectivity between the different interface elements. In the VOF model, there is the possibility that a cell neighboring an edge does not contain any phase fraction. The tensile force of this edge will then be set to zero.

Verification

The model was verified for surface tension implementation, interface advection and the interchange between the surface tension modeling and the momentum equations. The results show that both the height function model and the tensile force method improve the accuracy of the VOF method. However, these tests did not show decisive results on the best surface tension model for the VOF method (Baltussen *et al.*, 2014).

RESULTS AND DISCUSSION

Because the verification of the model did not give conclusive results on the best model to use for the VOF, 33 different single bubble simulations were performed. The results of these simulations are compared with the experimental data available in the Grace diagram (Grace, 1973; Grace *et al.*, 1976). Because the correlations used to construct the Grace diagram are only partly known, Tomiyama (1998) developed new correlations to describe the bubble velocity in an infinite liquid. However, these correlations deviate from the graphical Grace diagram in the spherical and dimpled regime.
The simulation settings used for all the single bubble simulations are shown in table 1. The different cases with their Eötvös (Eo) and Morton (Mo) numbers are indicated in figure 1 by numbers. In all simulations, the bubbles and the liquid were started at rest. The boundary conditions are set to free slip boundary conditions. To overcome the bubble moving out of the domain, all simulations were started with

Table 1: Simulation settings for the single bubble simulations, which are also shown in figure 1 by the numbers

Bubble diameter (mm)	1.0 ... 5.5
Bubble diameter (grid cells)	30
Initial bubble shape	spherical
Domain size (grid cells)	$(150, 150, 150)$
Initial bubble position (grid cells)	$(75, 75, 100)$
Grid size Δx, Δy & Δz (mm)	0.033 ... 0.18
Time step (s)	$1 \cdot 10^{-7}$ ... $1 \cdot 10^{-5}$
Eo	0.1 ... 40
log Mo	-11 ... 1

window shifting, which ensures that the bubble remains in the same position with respect to the domain.

Figure 1 also shows the visualization of PLIC interfaces of seven cases (case 6, 16, 21, 25, 28, 30 and 33). The visualization of these bubbles show some differences between the models.

For the wobbling bubbles three snapshots are chosen at arbitrary uncorrelated moments. Furthermore, the results were taken when the bubble was in steady wobbling state, except for the CSF model because this model did not even reach this wobbling state. Comparing the different snapshots of bubble 16, only the tensile force method shows a wobbling motion of the surface, while the shape of the bubble using the CSF model and the height function model are constant. Therefore, the tensile force method will most accurately describe the deformations of the surface of the wobbling bubble.

Furthermore, the spherical cap bubbles (case 25) also show a difference between the three models. Both the CSF and the height function model show a very thin skirt and this skirt is shedding. This will lead to a decrease in bubble size. Only the tensile force method is able to simulate the spherical cap as reported by Grace *et al.* (1976). Hence the CSF model and the height function model cannot be used to simulate bubbles in the spherical cap regime, while the tensile force method is able to simulate the correct bubble shape in the spherical cap regime. The authors expect that an increase in the grid resolution will lead to a slightly better representation of the shape of the bubble, but the increase in resolution will not affect the bubble rise velocity.

Finally, there is also some difference between the models in the spherical regime. Comparing case 6 and 21, the representation of the bubble surface is the same in the CSF and the height function model. However, the tensile force method shows a different representation for case 21. The different PLIC interfaces of this bubble do not show connectivity. This behavior was observed for all bubbles with a Eo < 1. This can be explained looking at the stationary bubble test of simulation case 26 and 31, which have similar Reynolds numbers and different Eo numbers (Eo $= 0.2$ and Eo $= 4$, respectively). It was expected that the obtained error in the pressure jump of these bubbles would be similar, however the error in case 26 was 10 times higher than for case 31. Furthermore, the spurious currents increased from 10^{-12}m/s (case 31) to 10^{-4}m/s for case 26. These differences can deteriorate the connectivity in cases with low Eo. However, this also means that the surface tension force is not accurate in these cases.

Besides the shape of the bubbles, the terminal rise velocity of the bubbles was also compared with the experimental results of the Grace diagram and the correlations of Tomiyama (1998), when these are applicable. The CSF model shows a quite good comparison with respect to the Reynolds numbers of Grace diagram. However, simulation 32 shows a very large deviation from the expected results. Furthermore, the visualization shows that the model is not able to predict the shape of the bubbles in the wobbling, the spherical cap and the skirted regime. Therefore the CSF model can only be used for spherical, slightly wobbling, ellipsoidal and dimpled ellipsoidal-cap bubbles.

The Reynolds number determined for the simulations using the height function model do not deviate much from the experimental results of Grace *et al.* (1976) and the correlations of Tomiyama (1998) for all the cases. However, from the previous discussion on the shape of the bubbles, it can be concluded that the model cannot be used for spherical cap, wobbling bubbles and skirted bubbles. However, for wobbling bubbles with a low Eo (case 1 and 2) the obtained Reynolds numbers of the height function are in better agreement than the other methods.

The tensile force method also shows a good comparison between the experimental results. However, for bubbles with Eo < 1 the velocity prediction deviates largely from the experimental results, as expected from the lack of connectivity as discussed before. Therefore the tensile force method cannot be used for single bubbles with Eo < 1. At $log(\text{Mo}) = -11$ and $log(\text{Mo}) = -10$, these problems are also found at slightly higher Eo(Eo ≤ 2 and Eo ≤ 1, respectively).

The regions in which the height function model and the tensile force method can be used are shown in figure 1 as the stripped red and the green area, respectively. The region of applicability of the CSF model is overlapping either one or both the regions indicated in figure 1. Furthermore, the verification results show a better prediction of the pressure jump and a decrease in spurious currents when the height function model or the tensile force method is used instead of the CSF model (Baltussen *et al.*, 2014). As a consequence, the use of the CSF model for modeling single bubbles is not advised, whereas the height function model can generally be used to simulate bubbles with Eo ≤ 10 and the tensile force method for bubbles with Eo ≥ 1. For $log(\text{Mo}) < -7$ the applicability of the height function and the tensile force method decreases to Eo ≤ 2 and Eo ≥ 2, respectively. Furthermore, at $log(\text{Mo}) \geq 1$ the height function model can also be used for bubbles with Eo > 10.

CONCLUSION

In this paper, three different surface tension models for the VOF model were compared for their performance on single bubble simulations. The region in which CSF model accurately predicts the terminal rise velocity and the shape of the bubbles overlaps with the regions of the other models. Furthermore, the verification showed that the CSF model was the least accurate in predicting the pressure jump and had the largest spurious currents. Therefore, the use of the CSF model for simulating single bubbles is not recommended. The use of the height function model is generally advised for bubbles with Eo ≤ 10, except for simulations with $log(\text{Mo}) < -7$ and $log(\text{Mo}) \geq 1$ where the height function can be used for simulations with Eo ≤ 2 and Eo ≤ 40, respectively. Finally, the tensile force method can be used for simulating bubbles with Eo ≥ 1, except at $log(\text{Mo}) < -7$ where the tensile force method can only be used when Eo ≥ 2.

ACKNOWLEDGMENT

The authors would like to thank the European Research Council for its financial support, under its Starting Investi-

gator Grant scheme, contract number 259521 (CuttingBubbles).

REFERENCES

AFKHAMI, S. and BUSSMANN, M. (2009). "Height functions for applying contact angles to 3d vof simulations". *International Journal for Numerical Methods in Fluids*, **61(8)**, 827–847.

ALBADAWI, A. *et al.* (2013). "On the analysis of bubble growth and detachment at low capillary and bond numbers using volume of fluid and level set methods". *Chemical Engineering Science*, **90**, 77 – 91.

ALBERT, C. *et al.* (2012). "Influence of surface tension models on the hydrodynamics of wavy laminar falling films in volume of fluid-simulations". *International Journal of Multiphase Flow*, **43**, 66 – 71.

BALTUSSEN, M.W. *et al.* (2014). "A critical comparison of surface tension models for the volume of fluid method". *Chemical Engineering Science*, **109**, 65–74.

BRACKBILL, J.U. *et al.* (1992). "A continuum method for modeling surface tension". *Journal of Computational Physics*, **100(2)**, 335 – 354.

CUMMINS, S.J. *et al.* (2005). "Estimating curvature from volume fractions". *Computers & Structures*, **83(6-7)**, 425 – 434.

DEEN, N.G. *et al.* (2004). "Multi-scale modeling of dispersed gas-liquid two-phase flow". *Chemical Engineering Science*, **59(8-9)**, 1853–1861.

DIJKHUIZEN, W. *et al.* (2010a). "DNS of gas bubbles behaviour using an improved 3D front tracking model, model development". *Chemical Engineering Science*, **65(4)**, 1427–1437.

DIJKHUIZEN, W. *et al.* (2010b). "DNS of gas bubbles behaviour using an improved 3D front tracking model âĂŤ model development". *Chemical Engineering Science*, **65(4)**, 1427–1437.

FRANCOIS, M.M. *et al.* (2006). "A balanced-force algorithm for continuous and sharp interfacial surface tension models within a volume tracking framework". *Journal of Computational Physics*, **213(1)**, 141–173.

GERLACH, D. *et al.* (2006). "Comparison of volume-of-fluid methods for surface tension-dominant two-phase flows". *International Journal of Heat and Mass Transfer*, **49(3âĂŞ4)**, 740 – 754.

GERRITS, J. (2001). *Dynamics of liquid-filled spacecraft*. Ph.D. thesis, University of Groningen.

GRACE, J.R. (1973). "Shapes and velocities of bubbles rising in infinite liquids". *Trans. Inst. Chem. Eng.*, **51**, 116–120.

GRACE, J.R. *et al.* (1976). "Shapes and velocities of single drops and bubbles moving freely through immiscible liquids". *Transactions of the Institution of Chemical Engineers*, **54**, 167–173.

JAFARI, A. *et al.* (2007). "An improved three-dimensional model for interface pressure calculations in free-surface flows". *International Journal of Computational Fluid Dynamics*, **21(2)**, 87–97.

LAFAURIE, B. *et al.* (1994). "Modelling merging and fragmentation in multiphase flows with {SURFER}". *Journal of Computational Physics*, **113(1)**, 134 – 147.

MEIER, M. *et al.* (2002). "A novel technique for including surface tension in plic-vof methods". *European Journal of Mechanics - B/Fluids*, **21(1)**, 61 – 73.

Pilliod Jr., J.E. and PUCKETT, E.G. (2004). "Second-order accurate volume-of-fluid algorithms for tracking material interfaces". *Journal of Computational Physics*, **199(2)**, 465 – 502.

POPINET, S. (2009). "An accurate adaptive solver for surface-tension-driven interfacial flows". *Journal of Computational Physics*, **228(16)**, 5838 – 5866.

RENARDY, Y. and RENARDY, M. (2002). "Prost: A parabolic reconstruction of surface tension for the volume-of-fluid method". *Journal of Computational Physics*, **183(2)**, 400–421.

RIDER, W.J. and KOTHE, D.B. (1998). "Reconstructing volume tracking". *Journal of Computational Physics*, **141**, 112.

ROGHAIR, I. *et al.* (2011). "On the drag force of bubbles in bubble swarms at intermediate and high reynolds numbers". *Chemical Engineering Science*, **66**, 3204–3211.

SCARDOVELLI, R. and ZALESKI, S. (1999). "Direct numerical simulation of free-surface and interfacial flow". *Annual Review of Fluid Mechanics*, **31**, 567.

SHIN, S. and JURIC, D. (2002). "Modeling three-dimensional multiphase flow using a level contour reconstruction method for front tracking without connectivity". *Journal of Computational Physics*, **180**, 427–470.

SON, G. (2003). "Efficient implementation of a coupled level-set and volume-of-fluid method for three-dimensional incompressible two-phase flows". *Numerical Heat Transfer, Part B: Fundamentals*, **43(6)**, 549–565.

TOMIYAMA, A. (1998). "Struggle with computational bubble dynamics". *Third International Conference on Multiphase Flow*, 369–405.

TRYGGVASON, G. *et al.* (2001). "A front-tracking method for the computations of multiphase flow". *Journal of Computational Physics*, **169(2)**, 708 – 759.

VAN SINT ANNALAND, M. *et al.* (2005). "Numerical simulation of gas bubbles behaviour using a three-dimensional volume of fluid method". *Chemical Engineering Science*, **60(11)**, 2999 – 3011.

YANG, G.Q. *et al.* (2007). "Bubble formation and dynamics in gas-liquid-solid fluidization-a review". *Chemical Engineering Science*, **62(1-2)**, 2–27.

YOUNGS, D.L. (1982). *Numerical Methods for Fluid Dynamics*, chap. Time-dependent multi-material flow with large fluid distortion., 273–285. Academic Press, New York (edited by K.W. Morton and M.J. Bianes).

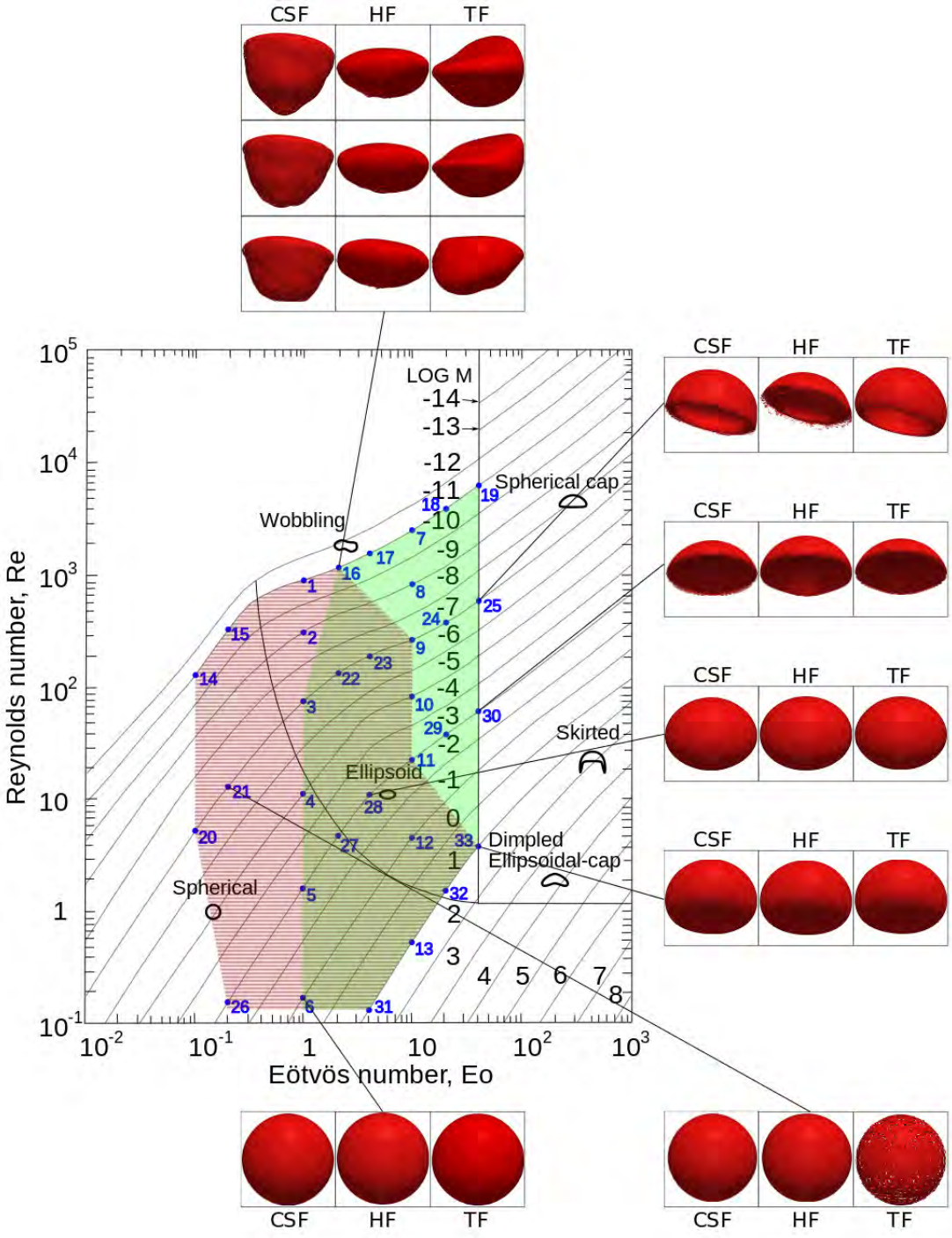

Figure 1: The performed single bubble simulations for several physical properties and bubble sizes. The figure also shows the shapes of the bubbles for various cases for all surface tension models. The striped red area in graph shows the region in which the height function model is within 10% accuracy or the best performing model. While the green area shows the region in which the tensile force method is the best performing model. Reproduced with premission from Baltussen *et al.* (2014). Copyright Elsevier 2014.

10th International Conference on CFD in Oil & Gas, Metallurgical and Process Industries
SINTEF, Trondheim, Norway *CFD 2014-0034*
17-19 June 2014

NUMERICAL SIMULATION OF THE INFLUENCE OF BUBBLE BURSTING ON A MOLTEN IRON SURFACE

Yonggui XU*, Mikael ERSSON, Pär JÖNSSON
Division of Applied Process Metallurgy, Royal Institute of Technology
(KTH), Brinellvägen 23, SE-100 44 Stockholm, Sweden

E-mail: yonggui@kth.se

ABSTRACT

The transport of an argon bubble through a molten iron bath and across its free surface was investigated by CFD simulations. The Volume-of-Fluid (VOF) model was used to track the interface between argon and liquid iron as well as the free surface of the liquid iron. The bubbling dynamics inside the liquid phase was studied in terms of the bubble's rising velocity and shape. For a bubble with a specific size, two groups of small metal droplets can be formed due to the bubble bursting at the liquid iron free surface. One group is the "film droplets" which are formed by the rupture of the liquid film when a bubble comes to rest and protrudes at the liquid surface. Another group is the "jet droplets", which are formed due to the collapse of the remains after the bursting of a bubble cap. Simulations of both droplet types were qualitatively compared to experimental data and the agreement was found to be good. The influences of bubble size and liquid surface tension on the droplets were investigated systematically.

Keywords: CFD, VOF, bubble bursting, surface, molten iron.

NOMENCLATURE

Greek Symbols

α Volume fraction.
ρ Density, [kg/m^3].
μ Dynamic viscosity, [kg/m.s].
σ Surface tension, [N/m].

Latin Symbols

d Diameter, [mm].
p Pressure, [Pa].
t time, [s].

$\mathbf{F_s}$ surface tension force, [kg/m^{2}s^2]
g Gravitational acceleration, [m/s^2].
u Velocity, [m/s].

Sub/superscripts

g Gas.
l Liquid.
b Bubble.

INTRODUCTION

Bubbles play an important role in process metallurgy. They are often generated by gas injection in metallurgical processes such as ladle treatment, RH degasing, and continuous casting (CC) (Zhang et al. 2006). It is well known that the injected gas increases the thermal and chemical homogenization of the melts as well as helps to remove inclusions.

For a relative low gas injection rate, bubbles are generated separately. The analysis of single bubble behaviour has been carried out by a large number of researchers (Clift et al. 1978). An imaging technique using a high-speed camera is often used in water-air systems. X-ray attenuation techniques (Shevchenko et al. 2013) have also been used to investigate liquid metal two-phase flows. When a gas bubble leaves the molten metal surface, metal droplets will be dispersed into the surrounding atmosphere. This is called a bubble bursting phenomenon or a liquid entrainment process. It represents a significant step for the accomplishment of equilibrium between multi-phases. Particularly, a critical bubble size (Han and Holappa, 2003) has been found in an argon/iron system, which corresponds to a maximum injection rate. During vacuum treatment, it has been estimated that the decarburization from the ejected droplets could be as much as one third of the total removed carbon (Lin et al. 2010). Also, dust formation due to the bursting of CO bubbles in the Electric Arc Furnace (EAF) operation is the source for as much as 60% (Guézennec et al. 2004) of the final EAF dust.

Gas bubbles also have important applications in other areas such as in cell damage processes, in transfer of mass and various contaminants for chemical and nuclear industries and in the geophysical field (Chakraborty et al. 2013).

The development of CFD technology has provided a convenient, effective and inexpensive tool to study multiphase flows in process metallurgy. This represents a complement to experimental measurements. Several numerical methods (Boundary element method, Marker-chain method, Coupled LS-VOF) have been used to

study the bubble bursting at a free surface in an air-water or similar flow system (Duchemin et al. 2002; Georgescu et al. 2002; Chakraborty et al. 2013). However, there are few simulation results in a molten metal system focusing on the bubble bursting phenomenon.

Our aim is to show the bubble bursting phenomenon in an argon/iron system numerically. The critical bubble size was investigated, and the effect of surface tension was studied. At last the bubble shape and terminal velocity were studied.

NUMERICAL ASSUMPTIONS

The following assumptions were made when developing the mathematical model:

A. Argon and iron are incompressible Newtonian fluids;
B. The physical properties are constant;
C. No chemical reactions take place;
D. The temperature is constant in the bath;
E. The flow is considered to be laminar.

MODEL DESCRIPTION

The mass and momentum conservation equations for the incompressible Newtonian fluids can be written as follows:

Continuity equation

$$\nabla \cdot \mathbf{u} = \mathbf{0} \tag{1}$$

Momentum equation

$$\frac{\partial}{\partial t}(\rho \mathbf{u}) + \nabla \cdot (\rho \mathbf{u}\mathbf{u}) = -\nabla p + \nabla \cdot \left[\mu\left(\nabla \mathbf{u} + \nabla \mathbf{u}^T\right)\right] + \rho \mathbf{g} + \mathbf{F}_s \tag{2}$$

where $\mathbf{u}$ is the velocity vector, ρ and μ are the fluid density and dynamic viscosity, respectively. p and $\mathbf{g}$ are the pressure and gravitational acceleration, respectively. $\mathbf{F}_s$ represents the surface tension force.

Volume fraction equation

In the VOF model, the method of tracking the interface between different phases is achieved by solving a volume fraction continuity equation for one phase. For the gas phase, the volume fraction equation is:

$$\frac{\partial \alpha_g}{\partial t} + \mathbf{u} \cdot \nabla \alpha_g = 0 \tag{3}$$

The liquid-phase volume fraction is computed based on the following constraint:

$$\alpha_g + \alpha_l = 1 \tag{4}$$

where α_g is 0 for the full liquid cell and 1 for the full gas cell. For a cell involves interface, α_g should be between 0 and 1.

The calculating method of density and viscosity of a mixed fluid in a computational cell is as follows:

$$\rho = \alpha_g \rho_g + \left(1 - \alpha_g\right)\rho_l \tag{5}$$

$$\mu = \alpha_g \mu_g + \left(1 - \alpha_g\right)\mu_l \tag{6}$$

Continuum surface force model

In Eq. (2), the surface tension force term is considered by using the continuum surface force (CSF) model (Brackbill et al. 1992). The expression for a two-phase system is given by:

$$\mathbf{F}_s = \sigma \frac{\rho \kappa \nabla \alpha_l}{0.5(\rho_g + \rho_l)} \tag{7}$$

where $\kappa = \nabla \cdot \hat{\mathbf{n}}$, $\hat{\mathbf{n}} = \frac{\mathbf{n}}{|\mathbf{n}|}$, $\mathbf{n} = \nabla \alpha_g$.

BOUNDARY CONDITIONS AND NUMERICAL SIMULATION STRATEGIES

The geometry of the gas (argon)–liquid (molten iron) system was a cylindrical bath. An axisymmetric computational domain (R=15mm, H=50mm) with cylindrical coordinates (r, z) is shown in Figure 1. An argon bubble was located 1mm below the iron surface. The mass of iron was 150g for all simulation cases initially. The top atmosphere above the iron surface was considered as argon as well. The physical properties of the fluids are summarized in Table 1.

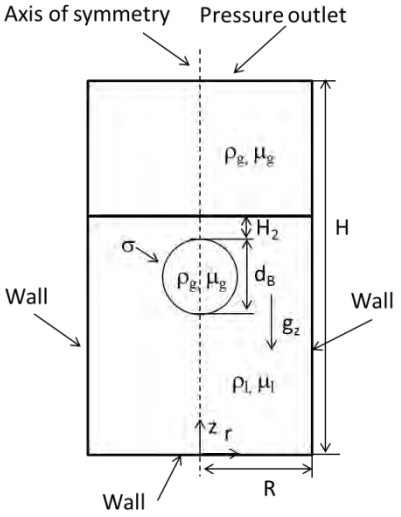

Figure 1: Computational domain for a single bubble bursting phenomena at the free surface on a (r, z) plane.

Table 1: Parameters used in the simulation

ρ_{argon} (kg/m^3)	ρ_{iron}(kg/m^3)	μ_{argon} (kg/m·s)	μ_{iron} (kg/m·s)
1.6228	7100	2.125×10^{-5}	0.006

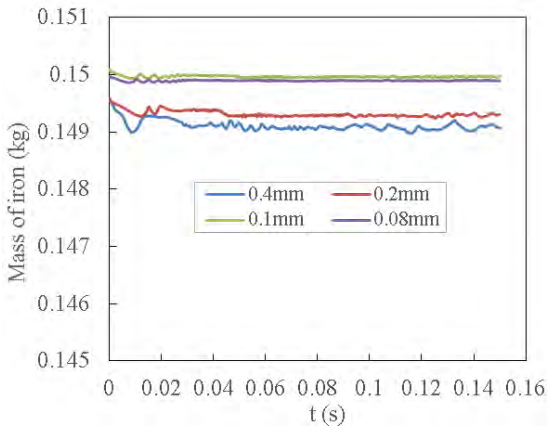

Figure 2: Simulation results of iron mass with different computational meshes.

The governing equations were solved using the commercial CFD package ANSYS Fluent 14.5®, which uses a finite-volume method. No-slip boundary conditions were used at the walls. Also, axisymmetric boundary condition was applied at the axis of symmetry. A pressure outlet condition was employed at the outflow. In addition, the uncoupling arithmetic method was used to separate and solve model equations; the pressure–velocity coupling was solved using the pressure-implicit with splitting of operators (PISO) method. A geometric reconstruction scheme was

applied to track the free surface shape between the gas and the liquid. The convergence criteria were set to 1×10^{-3} for the residual of all dependent variables. A constant time step of 5×10^{-5} s was used in the present simulations.

The mesh was done by using ANSYS Workbench 14.5®. The grid independence was checked by monitoring the variation of iron mass versus time, as shown in Figure 2. The investigated grid sizes were 0.4mm, 0.2mm, 0.1mm, and 0.08mm, respectively. Furthermore, the corresponding numbers of grid points were 4750, 18750, 75000, and 117500, respectively. The mass of the iron should be constant unless droplets are formed that escapes from the computational domain. All cases show an oscillation at the very beginning; this may be caused by a numerical problem. In addition, the mass with 0.4mm and 0.2mm grid sizes are lower than the supposed value (150g), probably due to that the coarse square mesh loses information of the circle shaped bubble due to the low resolution. The grid sizes 0.1mm and 0.8mm, agree well with the supposed value and this conserve the mass satisfactorily. By considering the computational cost together with the calculation accuracy, it was decided to use a 0.1mm grid size in the present simulations.

RESULTS AND DISCUSSIONS

Bubble bursting process

The iron droplet formation from a bubble bursting on the free iron surface has been observed by an X-ray imaging experiment (Han and Holappa, 2003). Here, we are using a CFD simulation method to investigate such phenomena. To simplification, the bubble rising process was ignored. A 9.3mm bubble was assumed initially located 1mm below the molten iron surface (for all cases unless noted otherwise). Figure 3 shows the evolution of the bubble bursting.

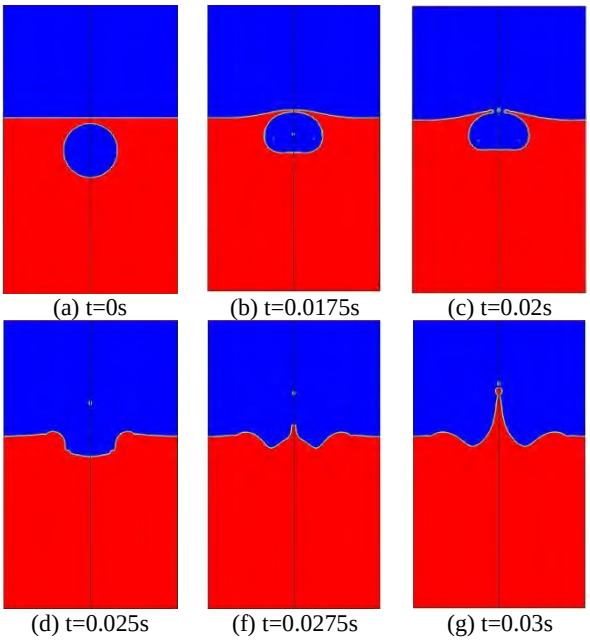

(a) t=0s (b) t=0.0175s (c) t=0.02s

(d) t=0.025s (f) t=0.0275s (g) t=0.03s

Figure 3: Simulation results of bubble bursting when d_B=9.3mm, σ=1.8N/m.

From Figure 3 (a) to (b), the bubble is moving upwards. As the upper surface of the bubble is approaching the interface and a thin layer appears between them. Figure 3 (c) illustrates that the thin layer is broken while the bubble continuous to rise. At the same time, the film droplet is formed. The rest of the bubble cap begins to collapse in Figure 3 (d), followed by a jet emerging from the central line. The jet continues to grow from Figure 3(f) to Figure 3(g). At t=0.03s, the first jet droplet is produced. Both the film droplets and the jet droplets rise up with a certain velocity. In this case, the velocity is large enough to carry the droplets out from the domain. This is similar with Han's experiment (Han and Holappa, 2003) where a ceramic plate was used to collect droplets on the top of the bath. In the next section, the simulated ejections and the collected ejections by experiment are compared.

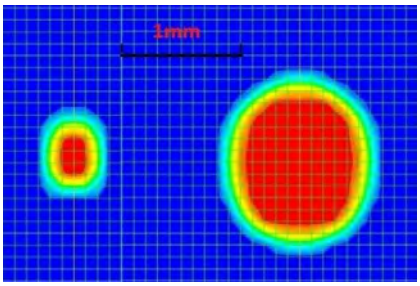

Figure 4: The size of film droplet (left) and jet droplet (right) when d_B=9.3mm, σ=1.8N/m.

The enlarged droplets are shown in Figure 4. The film droplet size is of 0.4mm, while the jet droplet is 1.2mm. In the experimental observation (Han and Holappa, 2003), the film droplet was found to have a size between a few microns to 0.5mm in diameter; while the jet droplet was several millimetres in diameter. Obviously, the simulation results are all in accordance with the experimental observations.

The effect of bubble size on droplet

With a certain surface tension, the amount of ejections is controlled by the bubble size. It has been found that a critical bubble size exists which produces a maximum amount of ejections. Figure 5 shows the mass of ejection produced by bubble bursting versus the bubble diameter; for a surface tension value of 1.4N/m. The amount of escaped ejections is calculated based on the size of the droplets. Here, the value of the amount by simulation is expanded one hundred times to match the experiment results. Because in Han's experiment, they collected droplets after 100 argon bubbles had been injected (Han and Holappa, 2003).

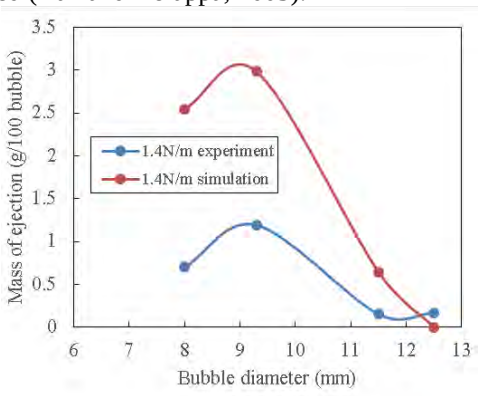

Figure 5: Effect of bubble size on the mass of ejections when the surface tension is 1.4N/m (Han and Holappa, 2003).

Obviously, there is a maximum value in Figure 5 for both the experiments (Han and Holappa, 2003) and the simulations when the bubble diameter is 9.3mm. However, overall the simulation values are higher than the experimental data.

The effect of surface tension on droplet

It has been reported that the surface tension of the liquid phase has a strong influence on the bubble bursting (Han and Holappa, 2003). In the molten iron system, the surface tension can be modified by changing the oxygen content. Han et al (Han and Holappa, 2003) carried out bubble bursting experiments. Specifically, 1.2 N/m, 1.4 N/m and 1.8 N/m surface tension values were obtained for the corresponding oxygen contents [O]~10ppm, [O]~200ppm and [O]~500ppm, respectively. In the present simulation, the same surface tension values were used in order to compare the simulation and experimental results.

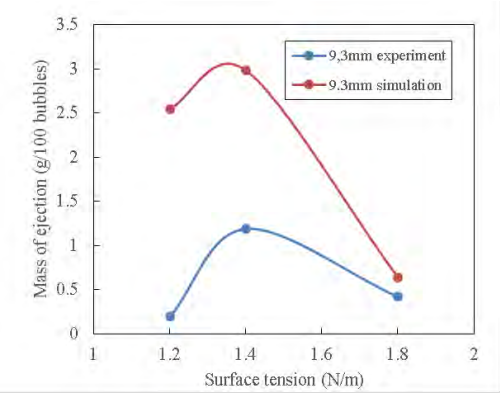

(a)

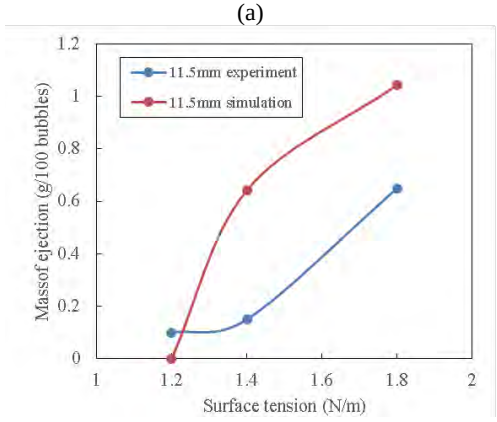

(b)

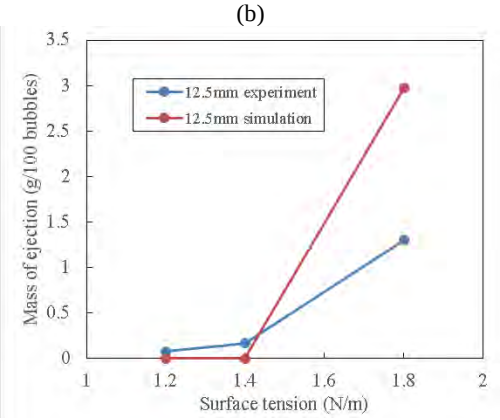

(c)

Figure 6: Effect of surface tension of molten iron on the mass of ejection produced from bubble bursting (Han and Holappa, 2003) where (a) d_B=9.3mm, (b) d_B=11.5mm, (c) d_B=12.5mm.

When the bubble size is 9.3mm, the effect of surface tension on droplet is summarized in Figure 6(a) together with the experimental results (Han and Holappa, 2003). From Figure 6(a) we can see that the simulation values are higher than the experimental data. However, the variation trends are almost the same where a maximum value exists for both methods. As mentioned in the previous section, when the surface tension is 1.4N/m, the critical bubble size is 9.3mm. It implies that the bubble droplet decreases with a critical bubble size at higher surface tension.

In Figure 6(b) and (c), the effects of a surface tension value on the droplet mass are studied for an 11.5mm and 12.5mm bubble respectively. Both cases show an increasing trend for the mass of the ejection with an increased surface tension value. A critical bubble size cannot be observed in Figure 6(b) and (c). In this case, a higher surface tension value leads to a higher injection. Here, the experimental data are still lower than the simulation results, except for a couple of non-ejection locations. The non-ejection locations in the simulation represent those cases where the droplets are too small to be captured by the current mesh resolution.

In the experiment, the mass of the molten iron decreases after one bubble bursting. Thereafter, the coming bubble experiences a different environment. Also, the transient motion of molten iron in the bath is likely to affect the results of the subsequent bubbles. However in the simulation, we assume that each bubble experiences the same environment. This causes the simulation values to be higher than the experimental data.

Bubble rising velocity and shape

When a spherical bubble initially is located just under the interface (1mm below), we have simulated the bubble bursting phenomenon in the iron-argon system successfully. However, bubbles are usually generated from nozzles located at a vessel bottom and they experience a rising process. During the movement, a bubble may reach a terminal velocity and a change of its original shape. In this case, the bubble bursting becomes more complex. In this section, the bubble rising velocity and shape are studied instead of the bubble bursting.

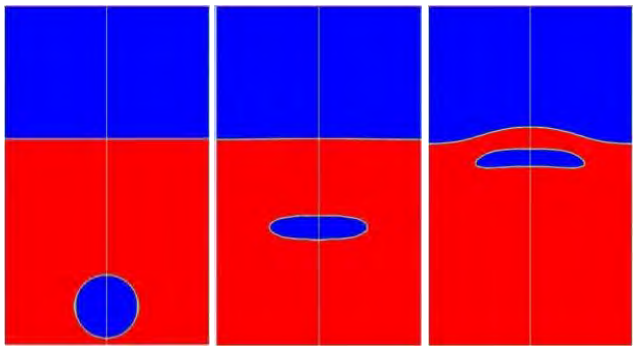

(a) t=0s (b) t=0.06s (c) t=0.1s

Figure 7: The bubble rising process when d_B=9.3mm, σ=1.4N/m.

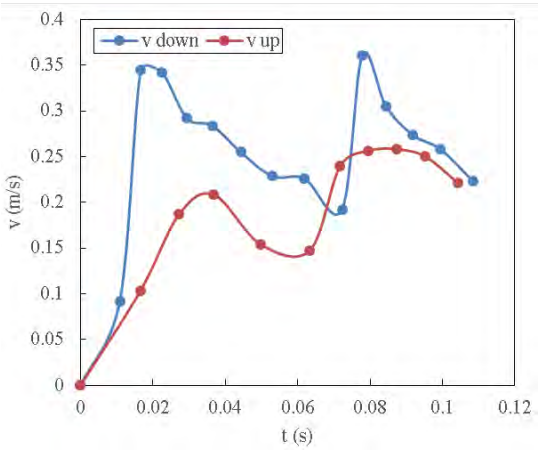

Figure 8: The bubble rising velocity versus time when d_B=9.3mm, σ=1.4N/m.

In Figure 7, a 9.3mm spherical bubble is located 1mm above the bottom with an initial surface tension value of 1.4N/m. Thereafter, it starts to rise upwards. During its movement, the bubble changes from a spherical to an elliptical shape. Furthermore, the bubble rising velocity is summarized in Figure 8 by monitoring the upper and lower surface of the bubble, respectively. During the first 0.065s, the lower surface rises faster than the upper surface. That is the reason for the deformation of the bubble shape. This is followed by a slight fluctuation of both velocities around 0.25m/s, which represents the terminal velocity for this particular case.

CONCLUSION

The bubble bursting phenomena in the argon-iron two-phase system was investigated by using mathematical simulations. Both film droplets and jet droplets were captured. Their sizes were found to be of the same magnitude as the experimental measurements. When the surface tension is 1.4N/m, the critical bubble size is 9.3mm. Also, the ejection was found to increase with an increased surface tension value, unless a critical bubble size is reached. A 9.3mm bubble is changed to an elliptical shape while rising in the bath and its terminal velocity is about 0.25m/s for the current conditions. The further research will be focused on the bubble bursting with bubble rising.

Acknowledgments

Yonggui Xu would like to extend his sincere grateful to the CSC (China Scholarship Council) for financial support of his PhD study in KTH-Royal Institute of Technology, Sweden.

REFERENCES

BRACKBILL, J.U., KOTHE, D.B. and ZEMACH, C., (1992), "A continuum method for modeling surface tension", *Journal of Computational Physics*, **100**(2), 335-354.

CHAKRABORTY, I., BISWAS, G. and GHOSHDASTIDAR, P.S., (2013), "A coupled level-set and volume-of-fluid method for the buoyant rise of gas bubbles in liquids", *International Journal of Heat and Mass Transfer*, **58**(1–2), 240-259.

CLIFT, R., GRACE, J.R. and WEBER, M.E., (1978), "Bubbles, Drops, and Particles", *Academic Press*: New York.

DUCHEMIN, L., POPINET, S., JOSSERAND, C. and ZALESKI, S., (2002), "Jet formation in bubbles bursting at a free surface", *Physics of fluids*, **14**, 3000.

GEORGESCU, S.C., ACHARD, J.L. and CANOT, É., (2002), "Jet drops ejection in bursting gas bubble processes", *European Journal of Mechanics B/Fluids*, **21**(2), 265-280.

GUÉZENNEC, A.G., HUBER, J.C., PATISSIECQ, P., BIRAT, J.P., (2004), "Dust formation by bubble-burst phenomenon at the surface of a liquid steel bath", *Isij International*, **44**(8), 1328-1333.

HAN, Z. and HOLAPPA, L., (2003), "Bubble bursting phenomenon in gas/metal/slag systems", *Metallurgical and Materials Transactions B*, **34**(5), 525-532.

LIN, P., WANG, F.L., LIU, L. and HE, Q., (2010), "Characteristics of Iron Droplet Ejection Caused by Gas Bubble Bursting Under Reduced Pressure", *Journal of Iron and Steel Research, International*, **17**(1), 7-11, 17.

SHEVCHENKO, N., BODEN, S., ECKERT, S., BORIN, D., HERNZE, M. and ODENBACH, S., (2013), "Application of X-ray radioscopic methods for characterization of two-phase phenomena and solidification processes in metallic melts", *The European Physical Journal Special Topics*, **220**(1), 63-77.

ZHANG, L., AOKI, J. and THOMAS, B.G., (2006), "Inclusion removal by bubble flotation in a continuous casting mold", *Metallurgical and Materials Transactions B*, **37**(3), 361-379.

AN ENHANCED FRONT TRACKING METHOD FEATURING VOLUME CONSERVATIVE REMESHING AND MASS TRANSFER

Ivo ROGHAIR[1]*, **Martin VAN SINT ANNALAND**[1]†, **Hans KUIPERS**[2]‡

[1]Chemical Process Intensification, Multiphase Reactors Group, Eindhoven University of Technology, The Netherlands

[2]Multiscale Modeling of Multiphase Flows, Multiphase Reactors Group, Eindhoven University of Technology, The Netherlands

* E-mail: i.roghair@tue.nl
† E-mail: m.v.sintannaland@tue.nl
‡ E-mail: j.a.m.kuipers@tue.nl

ABSTRACT

A chemical species transport model is developed and coupled to an improved Front-Tracking model, enabling dynamic simulation of gas-liquid mass transfer processes in dense bubbly flows. Front-Tracking (FT) is a multiphase computational fluid dynamics technique where the location of a fluid-fluid interface is tracked via the advection of interface marker points, which make up a triangular mesh. A common drawback of FT implementations is that the volume enclosed by a mesh is not conservative during transient simulations. A remeshing technique is adopted to counteract these volume defects while keeping all physical undulations unharmed. The new remeshing procedures have been verified by comparison with results from the literature.

Species transport is modelled by a convection-diffusion equation which is discretized on a Eulerian grid, superimposed and possibly refined with respect to the grid used for the solution of the fluid flow equations. The velocity components have been interpolated to the refined grid using a higher-order solenoidal method. Enforcement of the Dirichlet condition for the concentration at the gas-liquid interface is achieved with an immersed boundary method, enabling the description of gas to liquid mass transfer. Careful validation of the newly implemented model, using synthetic benchmarks (exact solutions) and a comparison with correlations from the literature, has shown satisfactory results.

The model is used for a variety of hydrodynamic studies. In particular, the model is very suited to simulate (dense) bubbly flows due to the absence of artificial coalescence. A number of results, such as a closure of the drag force for bubbles rising in a bubble swarm and simulations of the bubble-induced turbulent energy spectra will be outlined.

The liquid side mass transfer coefficient in dense bubble swarms, with gas fractions between 4% and 40%, has been investigated using the new model. The simulations have been performed in a 3D domain with periodic boundaries, mimicking an infinite swarm of bubbles. To prevent the liquid phase to become saturated with chemical species (with the consequence of a vanishing chemical species flux due to saturation of the liquid bulk), simulations have been performed using either artificial fresh liquid inflow, or a first order chemical reaction in the liquid phase. The results indicate that the liquid-side mass transfer coefficient rises slightly with increasing gas fraction.

Keywords: CFD, hydrodynamics, bubbly flows, turbulence, mass transfer .

NOMENCLATURE

Greek Symbols

α	Gas hold-up, [-].
Γ	Solution grid, [-].
ϕ	Volume fraction, [-].
ρ	Mass density, [kg/m^3].
μ	Dynamic viscosity, [Pa s].
σ	Surface tension, [N/m].
χ	Aspect ratio, [-].

Latin Symbols

A,S	Surface, [m^2].
$\mathbf{c}$	Centroid, [m].
c	Concentration, [mol/L].
C_D	Drag coefficient, [-].
d	Diameter, [m].
$\mathscr{D}$	Diffusion coefficient, [m^2/s].
Eo	Eötvös numer Eo $= \frac{gd^2\rho}{\sigma}$, [-].
F	Force, [N].
g	Gravity constant, [m/s^2].
H	Henry's constant, [-].
k_L	Mass transfer coefficient, [m/s].
p	Pressure, [Pa].
Pe	Péclet number Pe $= \frac{v_\infty d}{\mathscr{D}}$, [-].
Re	Reynolds number Re $= \frac{\rho\|\mathbf{u}\|d}{\mu}$, [-].
Sh	Sherwood number Sh $= \frac{k_L d}{\mathscr{D}}$, [-].
$\mathbf{n}$	Normal, [-].
$\mathbf{t}$	Tangent, [-].
t	Time, [s].
$\mathbf{u}$	Velocity, [m/s].
V	Volume, [m^3].

Sub/superscripts

a,b,c,i,m	Marker indicator.
h,s	Hydrodynamic/Species mesh.
b	Bubble.
$n,*,n+1$	Previous, intermediate, next (time step).
∞	Single rising bubble in a quiescent liquid.

INTRODUCTION

In the chemical industry, many processes involve the exchange between (possibly reacting) components between a gas and liquid phase, for instance in oxidation or hydrogenation processes (Deen *et al.*, 2010). Such processes are typ-

ically performed in bubble column (slurry) reactors, a column filled with liquid (and possibly a solid catalyst) in which gaseous reactants are introduced at the bottom or via immersed spargers. The gas flow rate is usually large so that dense bubble swarms rise through the liquid.

In order to understand and optimize these processes, it is important to gain insight in the the hydrodynamic and mass transfer characteristics of bubbles rising in a swarm. In recent work, we have used direct numerical simulations (DNS) to study the drag acting on bubbles rising in a swarm (Roghair *et al.*, 2011b), and the resulting closure relations have successfully been applied in a (larger scale) discrete bubble model (Lau *et al.*, 2011). The use of DNS, as opposed to detailed experiments, has advantages, as it provides full insight in the dynamics of the flow, including the deformation of the interface and the micro-structure of the flow field. Besides studying the drag acting on rising bubbles, the method can be used to describe bubble clustering and bubble induced turbulence, but when a suitable extension with mass transfer equations is provided, it can be used to study the overall mass transfer coefficient k_L in dense bubble swarms.

The current work presents a number of hydrodynamic studies that have been performed with the Front Tracking model as well as our recent achievements to obtain the gas-to-liquid mass transfer coefficient for bubbles rising in a swarm. We outline the implementation of the numerical model (hydrodynamics and mass transfer), provide validation of the implementation and evaluate the results.

MODEL DESCRIPTION

The front tracking model used in this work has been in development in our group for about 9 years. The hydrodynamics discretisation and implementation using the Finite Volume Method is also described in detail in Dijkhuizen *et al.* (2010b). In the sections below, the basic routines of the algorithm are described. We want to highlight the renewed remeshing procedures and the incorporation of the mass transfer module.

Hydrodynamics modeling

The governing equations of the fluid flow field are given by the incompressible Navier-Stokes equation and the continuity equation, discretized on a Cartesian coordinate system using a one-fluid formulation:

$$\rho\frac{\partial \mathbf{u}}{\partial t}+\rho\nabla\cdot(\mathbf{uu})=-\nabla p+\rho\mathbf{g}+\nabla\cdot\mu\left[\nabla\mathbf{u}+(\nabla\mathbf{u})^T\right]+\mathbf{F}_\sigma \tag{1a}$$

$$\nabla\cdot\mathbf{u}=0 \tag{1b}$$

where $\mathbf{u}$ is the fluid velocity and $\mathbf{F}_\sigma$ representing a singular source-term for the surface tension force at the interface. The velocity field is continuous even across interfaces, so a one-fluid formulation has been used. The equations are solved with a finite volume technique using a staggered discretisation (see Figure 1). The flow field is solved using a two-stage projection-correction method. After solving the momentum balance for each velocity component separately, a pressure-correction step is taken to satisfy the continuity equation. These steps use an incomplete Cholesky conjugate gradient (ICCG) method to solve the linearized equations. The boundary conditions can be adjusted between free-slip, no-slip and periodic, but only the latter is used in this work.

Surface mesh

The interface is parameterized by Lagrangian tracking (control) points. The connectivity of the points build up a mesh with triangular cells, called markers (Figure 1). The positions of the control points are updated each time step. After the fluid flow has been calculated, the Lagrangian control points are moved with the interpolated velocity to their new locations (a cubic spline method is used for interpolation). The actual movement is performed using a 4$^{\text{th}}$ order Runge-Kutta time stepping scheme.

Surface tension force and pressure jump

In Eq. 1a, $\mathbf{F}_\sigma$ represents the surface tension force, a vector quantity that can be directly calculated from the positions of the interface markers. The individual pull-force of neighbouring marker i acting on marker m can be computed from their normal vectors and joint tangent as illustrated in Figure 2:

$$\mathbf{F}_{\sigma,i\to m}=\sigma\left(\mathbf{t}_{mi}\times\mathbf{n}_{mi}\right) \tag{2a}$$

The shared tangent $\mathbf{t}_{mi}$ is known from the control point locations, and the shared normal vector $\mathbf{n}_{mi}$ is obtained by averaging, from which we can discard one term due to orthogonality:

$$\mathbf{t}_{mi}\times\mathbf{n}_{mi}=\frac{1}{2}\left(\underbrace{(\mathbf{t}_{mi}\times\mathbf{n}_m)}_{=0}+(\mathbf{t}_{mi}\times\mathbf{n}_i)\right) \tag{2b}$$

Hence, the total surface tension force on a marker m is obtained by summing Eq. 2a for all three neighbouring markers:

$$\mathbf{F}_{\sigma,m}=\tfrac{1}{2}\sigma\sum_{i=a,b,c}(\mathbf{t}_{mi}\times\mathbf{n}_i)=\tfrac{1}{2}\sum_{i=a,b,c}\mathbf{F}_{\sigma,i\to m} \tag{2c}$$

As a result, three pull forces on each marker are defined which yield a net force inward, opposing the pressure jump.

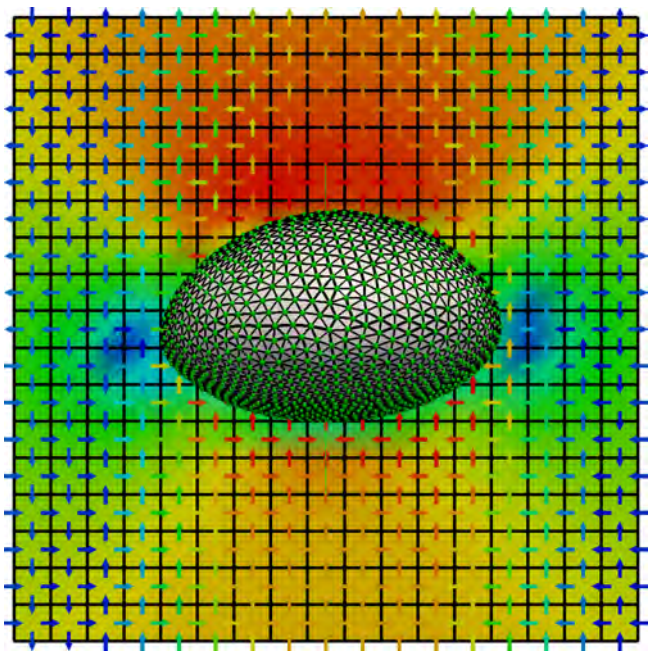

Figure 1: A zoomed snapshot of a rising FT bubble (at a very low resolution for illustration purposes), showing the tracking points and surface mesh, and the background grid with staggered velocity vectors. The colors of the background grid indicate the pressure profile, and the colors of the velocity vectors represent the magnitude.

For a closed surface, the net surface tension force on the entire object will be zero. This force $\mathbf{F}_\sigma$ is then mapped to the Eulerian cells closest to marker m using mass-weighing (Deen *et al.*, 2004) (regularized Dirac function). An important aspect of DNS involving small bubbles (e.g. $d_b \leq 1.0$ mm air bubbles in water) is the large pressure jump at the gas-liquid interface, which may cause parasitic currents that may affect the final solution significantly. While these artificial currents are decreased by the mass weighing implementation (explained above), Popinet and Zaleski (1999) demonstrated that the coupling between the surface forces and the pressure jump is crucial to further minimize them. Our approach is outlined in Dijkhuizen *et al.* (2010b). The Front-Tracking model uses a method similar to Renardy and Renardy (2002) and Francois *et al.* (2006), where the pressure forces will be extracted from the surface forces at the interface, only mapping the resulting net force.

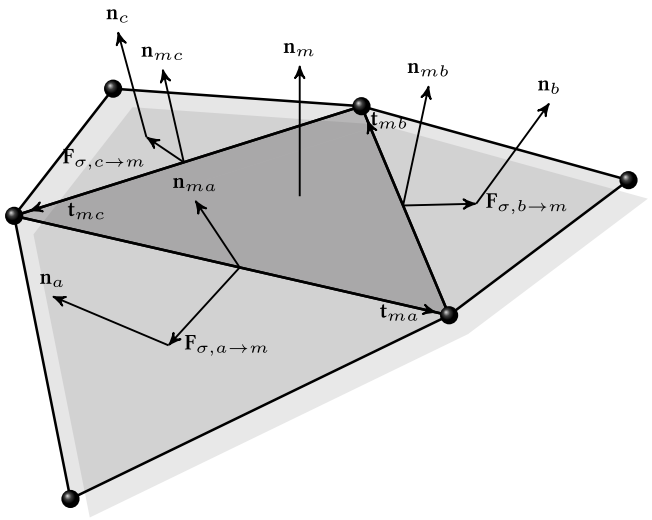

Figure 2: The surface tension calculation on marker involves the calculation of three pull-forces using the tangent and normal vectors shared with the neighbouring marker.

First note that the partial pressure drop (i.e. the pressure jump $[p]$ resulting from the surface tension force on a single marker), can be calculated using Eq. 3, if the shear stress in the normal direction is neglected.

$$\int_{\partial S} [p]\, dS = \int_{\partial S} \mathbf{F}_\sigma \cdot \mathbf{n}$$
$$[p] = \frac{\int_{\partial S} \mathbf{F}_\sigma \cdot \mathbf{n}}{\int_{\partial S} dS} = \frac{\sum_m \mathbf{F}_{\sigma,m} \cdot \mathbf{n}_m}{\sum_m S_m} \tag{3}$$

The sum of the surface forces of all markers yields the pressure jump of the bubble as a whole. By distributing the total pressure jump equally back to the Eulerian mesh, the pressure jump is incorporated in the right-hand side of the momentum equations. For interfaces with a constant curvature (i.e. a sphere), the pressure jump and surface tension cancel each other out exactly, and if the curvature varies over the interface, only a relatively small nett force will be transmitted to the Euler grid.

Phase fraction and physical properties

Since the marker positions are exactly known, the phase fraction ϕ in each Eulerian cell can be computed exactly using geometric analysis. With the phase fraction, the density of each Eulerian cell is calculated by weighted averaging. The viscosity is obtained by harmonic averaging of the kinematic viscosities (Prosperetti, 2002):

$$\rho(\mathbf{x}) = \sum_{p=0}^{n_{\text{phase}}-1} \phi_p(\mathbf{x})\, \rho_p \tag{4a}$$

$$\frac{\rho(\mathbf{x})}{\mu(\mathbf{x})} = \sum_{p=0}^{n_{\text{phase}}-1} \phi_p(\mathbf{x})\, \frac{\rho_p}{\mu_p} \tag{4b}$$

The bubble properties *viz.* total surface area, volume and centroid position, can be efficiently obtained by summing over all triangular markers of an interface n_m. A scale factor s_m is defined, equal to twice the surface area of a marker obtained by the magnitude of the cross product of two marker edges $\mathbf{t}_{ma}$ and $\mathbf{t}_{mb}$:

$$s_m = |\mathbf{t}_{ma} \times \mathbf{t}_{mb}| \tag{5}$$

The total surface area of bubble b is computed with:

$$A_b = \frac{1}{2} \sum_{m=1}^{n_m} s_m \tag{6}$$

The volume of a bubble is obtained using:

$$V_b = \frac{1}{6} \sum_{m=1}^{n_m} s_m (\mathbf{c}_m \cdot \mathbf{n}_m) \tag{7}$$

with $\mathbf{c}_m$ the geometric centre of the marker and $\mathbf{n}_m$ the unit normal vector of the marker. Finally, the bubble centroid follows directly from the centroids of the triangular markers weighted with the surface area:

$$\mathbf{c}_b = \frac{\sum_{m=1}^{n_m} s_m \mathbf{c}_m}{\sum_{m=1}^{n_m} s_m} \tag{8}$$

The bubble velocity is computed from the displacement of the bubble centroid. Also, the bubble diameter along the Cartesian directions can be obtained from the minimum and maximum location of the marker points.

Remeshing

The remeshing procedure is an essential part of the Front-Tracking technique. Due to interface advection, velocity gradients induce surface grid distortion and marker elements become too large or too small, leading to a poor grid quality and in its turn decreased accuracy in the surface tension force computation. To overcome this, the remeshing procedure takes care of local relocation of the points and marker connectivity (topology changes), without "ironing out" physical undulations.

Volume changes

In the Front-Tracking method, the volume enclosed by an interface mesh may change. Although the volume changes per time step are very small, these volume changes may accumulate significantly during a simulation due to the very large number of time steps required (Figure 3) and hence must be prevented (Pivello *et al.*, 2013). Especially for the simulation of bubble swarms, where simulations should last for a longer time than for single rising bubbles, it is essential to prevent such effects. The change in volume can be caused by remeshing operations, such as edge splitting, collapsing, smoothing and swapping and due to the advection of the interface.
Bunner and Tryggvason (2002) have proposed to solve this problem by displacing the points with respect to the bubble centroid every 100 time steps in such a way that the volume

of the bubble is identical to the original bubble volume. This might cause problems when the centroid lies outside the actual enclosed volume (*viz.* skirted bubbles). In this work, a remeshing technique was implemented to prevent bubble volume changes, with a minimal impact on the bubble shape.

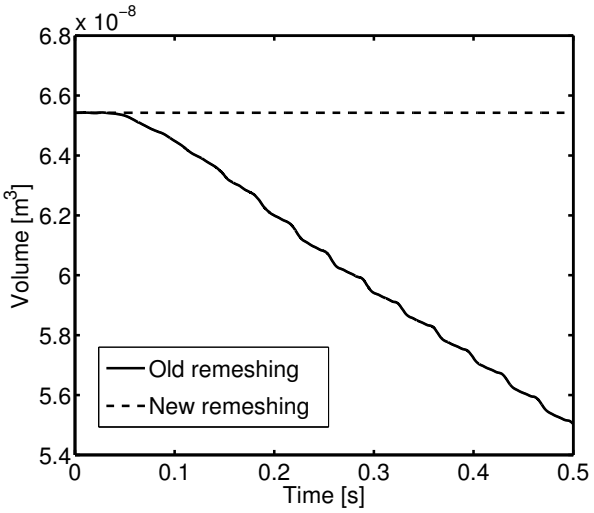

Figure 3: Volume changes may accumulate significantly during a simulation, due to advection of the interface and by using traditional, non volume-conservative remeshing methods. Using a volume-conservative remeshing technique, these effects can be prevented. The figure shows a volume vs time plot of a $d_b = 5.0$ mm air bubble in water, using both the old and new remeshing techniques.

Elementary remeshing operations

The traditional remeshing approach involves edge splitting, collapsing and swapping. In the remeshing technique presented here, these common procedures have been extended with volume conservative smoothing (regularization of the interface markers) as discussed below. Additionally, procedures are required to prevent the occurrence of rare but catastrophic mesh configurations, such as pyramids (tetraeders connected to the mesh by only a single point) or double folded marker cells.

Edge splitting and collapsing An edge is splitted (node addition) or collapsed (node removal) based on the edge length criterium which relates the edge length ℓ_m to the Eulerian cell size h according to $\frac{1}{5}h \leq \ell_m \leq \frac{1}{2}h$. In order to obtain a higher resolution in more deformed regions of the mesh, the local mesh roughness (defined as the minimum dot product of any two adjacent normals of markers connected to a node) is used to shift the balance in this algorithm towards node addition or removal.

Edge swapping In some cases, it is preferable to swap an edge rather than deleting or adding a node to the mesh. Whether or not an edge needs to be swapped depends on the number of connections of the nodes involved. This procedure ensures that equilateral marker cells are preferred.

Smoothing By distributing the control points over the interface, the grid quality can be enhanced and the required frequency of applying the other remeshing algorithms can be strongly decreased. In our algorithm, we have opted for edge-relaxation as explained by (Kuprat *et al.*, 2001).

Volume restoring/conservation

We have implemented a volume restoration/conservation method as described by Kuprat *et al.* (2001) in the Front-Tracking model. Here we present the general idea of the algorithm, the referred work provides more details on its implementation.

Whenever a node is displaced, a volume defect can be obtained by considering the volume for the situation before and after remeshing. The volume is obtained by selecting all marker cells that are connected to that node, and creating several tetrahedra using the three nodes of each marker and the bubble centroid using a scalar triple product. This volume defect can be corrected by shifting edges such that the original volume is restored, while the impact on the actual geometry of the mesh is minimized.

While this technique resolves volume changes due to prescribed point removal, edge swapping or smoothing, any volume changes that may have occurred during mesh advection, however, still need to be restored. Therefore, after the mesh restructuring, the algorithm sweeps over an entire interface mesh at once, distributing any additional volume corrections over the entire interface. This may cause the interfaces of different dispersed elements in very close proximity to cross each other, hence yield non-physical results. If such a situation occurs, the points crossing another interface are moved back and the volume difference is again distributed over all nodes of the interface, excluding those that have been moved back. We use a k-dimensional tree (kdtree, Tsiombikas (2009)) to efficiently find any points that may overlap with another interface.

Performance of the new remeshing technique

The complete revision of a cornerstone element such as the remeshing must be thoroughly validated before the code can be used for production runs. We have simulated a $d_b = 4.0$ mm air bubble in water using the old and new technique and compared the interface mesh (Figure 4) and the rise velocity profile as a function of time (Figure 5).

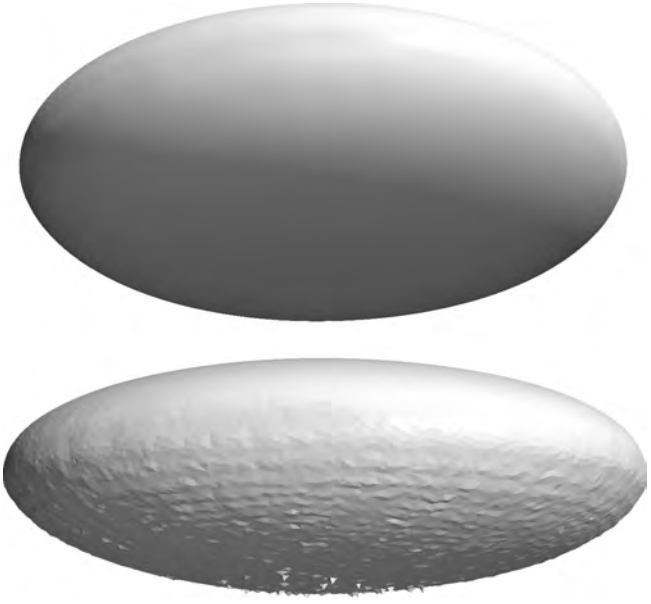

Figure 4: The mesh structure compared for the old and new remeshing techniques. It can be seen that the bubble interface using the old remeshing technique shows profound undulations and artefacts.

The interface mesh is, as expected, much smoother compared to the old remeshing technique. The rise velocity shows a slightly different profile; although both techniques show the onset of the velocity oscillations at the same time (due to the wobbling behaviour of the bubble), the velocity profiles are out of phase. The new remeshing makes the bubble rise velocity oscillate with a slightly larger amplitude (due to stronger shape deformations), resulting in a slightly lower frequency. Partly, this is due to the volume conservative properties of the new remeshing method, but also the enhanced mesh topology may be of importance. The time-averaged rise velocities do not differ significantly after discarding the transient period of the first 0.2 s, the new remeshing yields 2.82 m/s, whereas the old remeshing gives 2.88 m/s.

The Front-Tracking model with the traditional remeshing technique was used to derive a drag closure for single rising bubbles in an infinite quiescent liquid (Dijkhuizen *et al.*, 2010a). These results were validated against experimental data, and therefore these results provide a good benchmark to assess the performance of the new remeshing implementation. The drag closure that was derived combines a Reynolds dependent part and an Eötvös dependent part:

$$C_D = \sqrt{C_D(\mathrm{Re})^2 + C_D(\mathrm{Eo})^2} \tag{9a}$$

using an empirically derived correlation for the Eötvös dependent part, and the correlation by Mei *et al.* (1994) for the Reynolds dependent part:

$$C_D(\mathrm{Eo}) = \frac{4\mathrm{Eo}}{\mathrm{Eo}+9.5} \tag{9b}$$

$$C_D(\mathrm{Re}) = \frac{16}{\mathrm{Re}}\left(1+\frac{2}{1+\frac{16}{\mathrm{Re}}+\frac{3.315}{\sqrt{\mathrm{Re}}}}\right) \tag{9c}$$

Further details are omitted here, since they are discussed in more detail in Dijkhuizen *et al.* (2010a). The new remeshing technique has also been used to perform simulations using air bubbles in water, and air bubbles in a viscous liquid ($\mu_l = 0.1$ Pa s), using bubble diameters varying from $d_b = 0.1$ mm and 7.0 mm. The extracted drag coefficients for all these cases have been checked to match very well with the previously derived correlation.

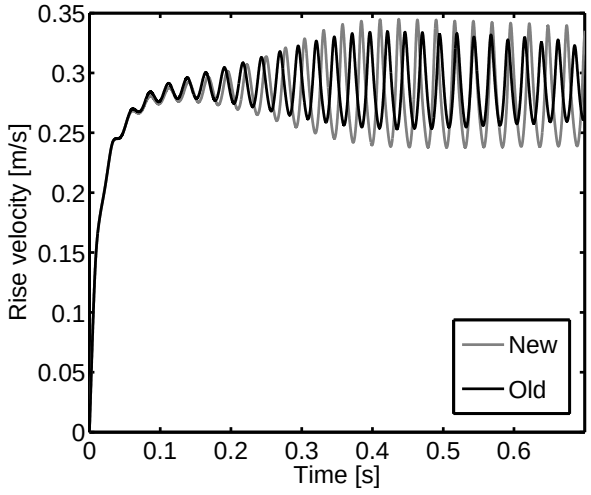

Figure 5: Comparison of the bubble rise velocity vs. time for a 4 mm bubble. While the average rise velocity is consistent in both techniques, the oscillations of the bubble occur at a slightly different frequency.

Mass transfer

In order to investigate the mass exchange between the gas and liquid phase in a bubble swarm in full detail, a mass transport model was implemented and coupled to the flow field of the Front-Tracking model. The mass transfer model accounts for convection, diffusion, species transfer from the gas to the liquid through the interface, and first-order chemical reaction. This section describes the implementation of the species transport equations into the Front-Tracking framework.

Convection-diffusion equation and boundary conditions

The mass transport equations are solved on a regular Cartesian grid, Γ_s, which is a possibly refined Eulerian mesh directly superimposed onto and aligned with the hydrodynamics grid Γ_h. A refinement factor $\mathscr{R} \in \mathbb{N}$ is used to set the relative mesh size, hence a "parent" hydrodynamics cell contains $\mathscr{R}^3$ "daughter" cells in 3D for solving the mass transfer equations. This technique allows a detailed calculation of the species balance, while keeping the computational time required for the flow solver (especially the expensive pressure-Poisson equation) within limits. Due to the deforming bubble interface and changing flow field properties emerging from the hydrodynamics part of the model, the mass transfer equations must be solved at every time step. The mass balance is given by the convection-diffusion equation on Γ_s as:

$$\frac{\partial c}{\partial t} + \nabla\cdot(\mathbf{u}c) = \mathscr{D}\nabla^2 c - k_1 c + F_s \tag{10}$$

Here c denotes the concentration in mol/L, $\mathbf{u}$ the velocity, $\mathscr{D}$ the diffusion coefficient in m^2/s, and F_s the source term to enforce the boundary condition at the interface. The diffusion and first order chemical reaction terms are treated implicitly, while the other terms are treated explicitly. The convection term is discretized using the Van Leer scheme.

The solution method uses a projection-correction algorithm to accurately enforce the interface condition, i.e. $c_{\text{interface}} = c_{\text{saturation}}$. First, the equations are solved without a source term F_s^* (Eq. 11) to obtain an intermediate concentration field c^*. The appropriate forcing term can then be calculated after which the correction step follows (Eq. 12).

$$\frac{c^* - c^n}{\Delta t} = -\nabla\cdot(\mathbf{u}^n c^n) + \mathscr{D}\nabla^2(c^*) - k_1 c^* \tag{11}$$

$$\frac{c^{n+1} - c^*}{\Delta t} = -\nabla\cdot(\mathbf{u}^n c^n) + \mathscr{D}\nabla^2\left(c^{n+1}\right) - k_1 c^{n+1} + F_s^* \tag{12}$$

The ICCG matrix solver used to solve the momentum and pressure-Poisson equations in the hydrodynamics part of the code, was also employed here.

Immersed boundary method

An immersed boundary method (IBM) is employed to enfore the interface condition. The species volumetric forcing term F_s^* is determined by calculating the forcing terms for a cell i using the intermediate solution:

$$f_i^* = \frac{Hc_0 - c_i^*}{\Delta t} \tag{13}$$

where H is Henry's constant (dimensionless) and c_0 is the concentration inside the bubble. The forcing term should

only be accounted for near the interface. The regularization of the forcing term is achieved by using a weighing factor (Eq. 14) from a mapping function (Eq 15), typically using volume weighing (Deen *et al.*, 2004).

$$F^*_{s,i} = w_i \cdot f^*_i \tag{14}$$

$$w_i = \sum_m D\left(\bar{x}_i - \bar{x}_m\right) \frac{V_m}{V_{\text{cell}}} \tag{15}$$

where V_m is the volume associated with a marker m, defined as the marker area A_m multiplied with the characteristic grid cell size:

$$V_m = A_m \sqrt[3]{V_{\text{cell}}} \tag{16}$$

Velocity interpolation

The velocity, required to calculate the convective fluxes of the species, is only known on Γ_h. For $\mathscr{R} > 1$, however, the velocity is required on the refined mesh as well, and an interpolation method is required. It is important to make sure that the resulting velocity field on Γ_s is also divergence free (solenoidal), to prevent local sources or sinks for the concentration and assure that the overall mass balance is intrinsically conserved. Two interpolation techniques that have this property have been implemented:

Piecewise linear interpolation This method, where each direction is interpolated individually, is based on the work of (Rudman, 1998), who initially described it to perform advection of a colour function on a refined grid. For mass transfer, the method has already been applied in the work of (Darmana, 2006).

Higher order solenoidal interpolation This method also takes into account the orthogonal translation of the velocity components on the interpolated mesh, describing the velocities on refined cell faces using multiple (one for each direction) second-order polynomials. Details are found in the work of (Balsara, 2001).

For both methods it has been verified that the initial divergence-free velocity field on Γ_h can be interpolated to Γ_s while maintaining the divergence-free criterium. The latter method shows somewhat smaller errors in our evaluation using synthetic benchmarks, and it will be used as the default interpolation technique.

Initial conditions and boundary conditions

The initial concentration is typically set to zero for cells that contain only liquid, while the concentration inside the bubble is set to the saturation concentration (gas concentration c_0 multiplied by the dimensionless Henry's constant.) To account for cells containing partially gas, the following condition is applied:

$$c_g = c^* = \begin{cases} Hc_0 & \text{if } \phi_{g,i} \geq 0.99 \\ 0 & \text{if } \phi_{g,i} < 0.99 \end{cases} \tag{17}$$

where $i \in \Gamma_s$ denotes the cell on the species grid and $\phi_{g,i}$ the gas fraction in that cell.
Robin (mixed) boundary conditions have been implemented fully implicitly, which can be tuned by setting (α, β, γ) to appropriate values:

$$\alpha c_{\text{wall}} + \beta \left.\frac{\partial c}{\partial x}\right|_{\text{wall}} = \gamma \tag{18}$$

Mass transfer coefficients

The mass transfer between the phases is quantified by calculating the mass transfer coefficient k_L, which can be defined in two different ways;

- Global mass transfer coefficient, integrated over the entire domain. This mass transfer coefficient is calculated using the change of species concentration in the domain before and after the forcing step:

$$k_{L,\text{domain}} = \frac{V_{\text{cell}}}{A_{\text{total}} \Delta t \left(Hc_0 - \langle c \rangle\right)} \sum_{i=0}^{i=n_{\text{cells}}} \left(c_i^{n+1} - c_i^n\right) \tag{19}$$

- Bubble wise, by summing the mass forcing for each marker on a bubble ($F^*_{s,i}$, see Eq. 14), followed by summing the mass transfer for all bubbles. The advantage of this approach is that the mass forcing can be plotted per-marker (for visualisation purposes), and for bubbles rising in swarms, the mass transfer for each bubble can be inspected separately. For a given bubble i, this mass transfer coefficient is given by:

$$k_{L,\text{bubble}} = \frac{V_{\text{cell}}}{A_b \Delta t \left(Hc_0 - \langle c \rangle\right)} F^*_{s,i} \tag{20}$$

Note that the average liquid concentration, $\langle c \rangle$, vanishes for single bubbles rising in a clean, "infinite" liquid. It has been varified that the average of $k_{L,\text{bubble}}$ over all bubbles yields $k_{L,\text{domain}}$.

Validation

Simulations of mass transfer of single rising bubbles have been performed to allow for comparison with correlations from the literature. Many correlations to predict the Sherwood number Sh for single rising bubbles can be found in literature, which are often applicable to a specific regime. An experimentally derived correlation was proposed by Takemura and Yabe (1998) for spherical gas bubbles with a Reynolds number less than 100, and Péclet numbers $\text{Pe} > 1$:

$$\text{Sh} = \frac{2}{\sqrt{\pi}} \left(1 - \tfrac{2}{3} \frac{1}{\left(1 + 0.09\text{Re}^{\frac{2}{3}}\right)^{\frac{3}{4}}}\right)^{\frac{1}{2}} \left(2.5 + \sqrt{\text{Pe}}\right) \tag{21}$$

Lochiel and Calderbank (1964) present Eq 22a to account for the Sherwood number of oblate spheroidal bubbles:

$$\text{Sh} = \frac{2}{\sqrt{\pi}} \sqrt{\text{Pe}} \left\{ \frac{2}{3} \left(1 + - \left(\frac{e\chi^2 - \chi \sin^{-1} e}{e - \chi \sin^{-1} e}\right)\right)\right\}^{1/2} \times \frac{2\chi^{1/3} \left(\chi^2 - 1\right)^{1/2}}{\chi \left(\chi^2 - 1\right)^{1/2} + \ln\left[\chi + \sqrt{\chi^2 - 1}\right]} \tag{22a}$$

where $\chi = \frac{\text{major axis}}{\text{minor axis}}$ is the bubble aspect ratio and e the corresponding eccentricity given by:

$$e = \sqrt{(1 - \chi^2)} \tag{22b}$$

Simulations of a single rising bubble in an infinite liquid, including mass transfer from the gas to the liquid phase, have been performed. The performance of all aspects of the mass

transfer model (diffusion, convection, immersed boundary method) have been verified.
The comparison of these results with the correlations is presented in Figure 6. We have determined that the simulations describe the results within 12% of the literature values.

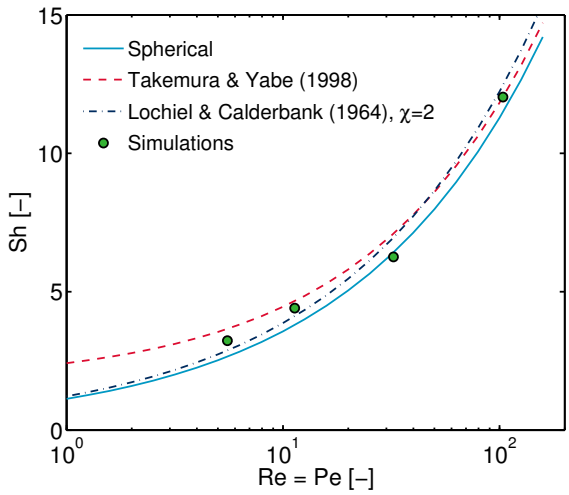

Figure 6: The Sherwood number of a single rising bubble in an infinite, initially quiescent liquid is compared to the exact correlation for flow around a sphere (potential flow) and the correlations of Takemura and Yabe (1998) and Lochiel and Calderbank (1964), the latter plotted for $\chi = 2$

RESULTS

Drag correlation

Simulations have been performed to derive a drag correlation for bubbles rising in a swarm as a function of the gas hold-up (Roghair *et al.*, 2011b).

Simulation settings

The simulation settings (physical parameters) to derive the drag closure are given in this section. Initially, the bubbles are placed randomly throughout the periodic domain. The physical properties of the gas and liquid phases are, for the base case, set up using the values for air bubbles in water. These properties have been varied to investigate the influence of the Eötvös and Morton number. These properties and the resulting Morton and Eötvös numbers are shown in Table 1. For each case, multiple simulations were performed to account for different gas fractions, varying between 5 and 45%. The cases 1–5 were selected to study the influence of the Eötvös number, whilst keeping the Morton number constant. Cases 6–8 are used to study the influence of the Morton number, so we have chosen a set of three Eötvös numbers to which we should compare the results of these cases. For all cases described, the bubble Reynolds number is typically between 150 and 1200.
Although it depends on the exact conditions (viscosity of the liquid phase, bubble diameter, gas fraction), the simulation time is typically about 1.0 s, using a time step of $1 \cdot 10^{-5}$ s. The time-averaged slip-velocity (excluding the initial 0.2 seconds to omit start-up effects) has been used to derive the drag coefficient for each bubble, which is then again averaged to deliver a single drag coefficient.

A drag correlation for bubbles rising in swarms

The relative drag coefficient resulting from the simulations were sorted into series with identical Eötvös numbers. Plotting the drag coefficients, normalised with the drag coefficient on a single rising bubble (Eq. 9a, $C_{D,\infty}$), vs the gas fraction reveals a linear relation with the gas fraction, which starts at $C_D/C_{D,\infty} = 1$ for single rising bubbles, i.e. $\alpha = 0$. The slope of the linear relation varies significantly with the Eötvös number, as shown in Figure 7. A correlation that predicts the drag coefficient of a bubble in a swarm taking into account the Eötvös number and the gas hold-up α can be written as Eq. 23, where the function g incorporating Eo determines the slope of the drag coefficient vs. α.

$$\frac{C_D}{C_{D,\infty}(1-\alpha)} = f(\alpha) = 1 + g(\mathrm{Eo})\alpha \tag{23}$$

A least squares fit has yielded:

$$\frac{C_D}{C_{D,\infty}(1-\alpha)} = 1 + \left(\frac{18}{\mathrm{Eo}}\right)\alpha \tag{24}$$

In the range of $1 \leq \mathrm{Eo} \leq 5$ the correlation performs particularly well, describing the drag coefficient found in the simulations within, on average, 1.5% accuracy, while the maximum deviation was found to be 21%. Note that the limit of $\mathrm{Eo} \to 0$ yields an infinitely large drag coefficient, however, it can be expected that at such low Eötvös numbers, a Reynolds number dependency will be found rather than an Eötvös number dependency.

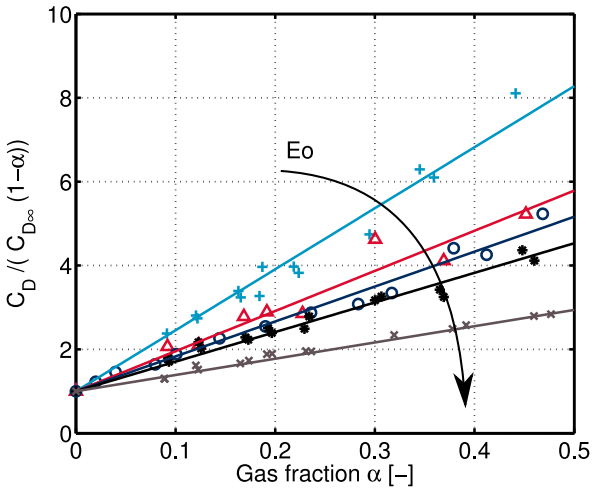

Figure 7: The drag coefficient of a bubble in a swarm, normalized with the drag on a single rising bubbles as a function of the gas fraction, for series of different Eötvös numbers. Legend: +: Eo = 1.21; △: Eo = 1.92; ○: Eo = 2.15; ∗: Eo = 2.58; ×: Eo = 4.83

The simulation results shown in Figure 7 have been lumped into data series with identical Eötvös numbers, disregarding the fact that they may have different Morton numbers.
The cases that are lumped together are (see Table 1): 1 with 8 (Eo = 1.21), 4 with 6 (Eo = 2.58) and 5 with 7 (Eo = 4.83). It can be observed in Figure 7, that for all cases, no different trends or otherwise distinctive features due to differences in the Morton numbers can be discerned. In the relatively small range of Morton numbers used in the simulations (between $\mathrm{Mo} = 2 \cdot 10^{-9}$ and $\mathrm{Mo} = 4 \cdot 10^{-12}$), the Morton number does not affect the drag coefficient.

Table 1: Physical properties for the air-water (base case) simulations.

Case	d_b [mm]	μ_l [Pa s]	ρ_l [kg/m^3]	σ [N/m]	-log(Mo)	Eo	Comment
1	3.0	$1.0 \cdot 10^{-3}$	1000	0.073	10.6	1.21	Air-water
2	6.0	$1.5 \cdot 10^{-3}$	750	0.138	10.6	1.92	
3	4.0	$1.0 \cdot 10^{-3}$	1000	0.073	10.6	2.15	Air-water
4	6.0	$2.0 \cdot 10^{-3}$	1250	0.171	10.6	2.58	
5	6.0	$1.0 \cdot 10^{-3}$	1000	0.073	10.6	4.83	Air-water
6	4.5	$1.5 \cdot 10^{-3}$	950	0.073	9.87	2.58	
7	4.5	$2.0 \cdot 10^{-3}$	1025	0.042	8.67	4.83	
8	4.5	$1.0 \cdot 10^{-3}$	840	0.138	11.35	1.21	

The derived drag closure, Eq. 24, has been implemented in a discrete bubble model and its performance has been evaluated in Lau *et al.* (2011). The proposed correlation was found to significantly improve the description of the hydrodynamics of bubble columns in comparison to drag coefficients that have been derived using single rising bubbles only. Especially the description of the velocity profiles in the centre part of the column in higher regions has improved with the newly derived correlation.

Bubble induced turbulence

Apart from bubble rise velocities and hence drag coefficients, the front tracking model can also yield information on the liquid characteristics. As bubbles rise, they induce liquid fluctuations which are referred to as pseudo-turbulence. A correct understanding of the pseudo-turbulence is critical for the simulation of bubbly flows, since it influences momentum, heat, and mass transfer rates. The Front Tracking model has been used to study these turbulent fluctuations (Roghair *et al.*, 2011a).

The characteristics of these turbulent fluctuations in the liquid are reflected in the energy spectrum. It has been shown that the energy cascade of pseudo-turbulence behaves differently from homogeneous single-phase turbulence, and hence deserves special attention in large-scale models. (Lance and Bataille, 1991) studied bubbles rising through an imposed turbulent flow. They measured the energy spectrum of the fluctuations and found a power law scaling with a slope of about $-8/3$, in contrast to the classical $-5/3$ for homogeneous single-phase turbulence.

In the numerical work on pseudo-turbulence by (Mazzitelli and Lohse, 2009) a slope of $-5/3$ of the energy spectrum was observed. However, in those simulations bubbles were approximated as point-like particles, thus disregarding finite-size effects and capillary phenomena. As (Mazzitelli and Lohse, 2009) mentioned in their paper, the "wrong" $-5/3$ scaling cannot be the signature of real (experimental) bubble columns.

Indeed, the experimental work of (Martínez Mercado *et al.*, 2010) found a scaling of the energy spectrum close to -3 for various gas fractions in the very dilute regime. These results were obtained by single-point measurements in flows with gas fractions ranging from $\alpha = 0.8$ to 2.2%, using a phase-sensitive constant-temperature anemometry (CTA) probe.

Simulation settings

Analogue to the experiments due to (Martínez Mercado *et al.*, 2010), simulations have been performed with the Front Tracking model, hence using finite size bubbles in contrast to the numerics due to (Mazzitelli and Lohse, 2009). A number of $N_b = 16$ air bubbles in water have been simulated in a fully periodic domain. The bubble Reynolds number is of order O(1000), and the Eötvös number is 2.15.

The simulation time is 4.0 s and we use a time step of $5 \cdot 10^{-5}$ s. Similar to the previous section, transient effects of the initially quiescent liquid and bubbles are excluded by discarding the interval of 0.0—0.2 s for the analysis. Numerical probes have been implemented to record the liquid velocity at different points in the simulation domain. These probes register the phase fraction and the fluid velocity vector in a computational cell at each time step, providing a signal very similar to the signal from the experiments. Hence, these probes are the numerical equivalent to the experimental phase sensitive CTA probe. An array of $3 \times 3 \times 3$ probes has been set up throughout the computational domain.

Turbulent energy spectrum

For the calculation of the energy spectra of liquid fluctuations we follow the method described in (Martínez Mercado *et al.*, 2010). Since the liquid velocity can only be used if the probe resides in a liquid-filled cell, the velocity signal becomes segmented in time due to passing bubbles. For each probe we calculate the power spectrum density of the segments larger than 256 data points and average over all segments. Finally, an ensemble average over all the 27 probes is done to obtain the final power spectrum.

Figure 8 shows the averaged spectrum of all 27 numerical probes of an $\alpha = 5\%$ simulation together with the experimental data by (Martínez Mercado *et al.*, 2010). The simulation shows a good agreement, having a slope close to -3 in the frequency range of 20—200 Hz. The scaling frequency range for the simulations is shorter as compared to the experimental case due to the difference in simulation and measurement time. (Risso and Ellingsen, 2002) pointed out that the power spectra are not influenced by α, based on their experimental findings. In spite of a shorter simulation time and the above discussed convergence problems, in figure 8 we also show the spectra for a case with $\alpha = 15\%$. Due to the smaller signal segments, caused by the smaller distance between the bubbles at higher gas loadings, the -3 scaling range decreases to less than a decade.

Our finding gives additional support to the idea that this particular power law scaling in pseudo-turbulence is related to the wake of the finite-size bubbles. Whether the actual mechanism is dissipiation or transfer should be further investigated. This conclusion lies in line with experiments by (Roig

and de Tournemine, 2007; Risso *et al.*, 2008), and theoretical arguments by (Lance and Bataille, 1991; Risso, 2011), who have also indicated the importance of bubbles' wake phenomena.

Mass transfer in bubble swarms

In this section, mass transfer from the gas phase to the liquid phase in a rising bubble swarm is studied using direct numerical simulations. We focus on the industrially relevant case of wobbling air bubbles rising in water. The chemical species that is dissolving has a dimensionless Henry constant of $H = 0.8371$ and a diffusion coefficient of $\mathscr{D} = 10^{-6}$ m/s^2.

Preventing solute accumulation

To prevent the accumulation of species in the domain, and hence to allow for simulation of an indefinite time, the top and bottom boundaries of Γ_s are treated such that the concentration of any inflowing liquid is set to zero, whereas the concentration gradient in the normal direction is gradient free for outflowing fluid. Note that the hydrodynamic equations will still be solved in a regular periodic domain. This way,the domain can be considered as a continuously stirred tank reactor (CSTR), from which the mass transfer coefficient $k_{L,\mathrm{CSTR}}$ can be determined:

$$k_{L,\mathrm{CSTR}} = \frac{\phi_v c_{\mathrm{out}}}{A_{\mathrm{lg}}\left(c^* - c_{\mathrm{out}}\right)} = \frac{\phi_v \langle c \rangle}{A_{\mathrm{lg}}\left(c^* - \langle c \rangle\right)} \tag{25}$$

Another method of limiting the liquid concentration below the saturation concentration is to incorporate a reaction term into the species balance, so mass transfer to the liquid phase will eventually balance the chemical consumption. In contrast to the method described above, the boundaries are fully periodic, hence there is no inflow or outflow to be considered. When it is assumed that the domain can be represented as a well stirred tank, the domain can be described as an integral mass balance for a batch reactor with mass transfer and reaction in steady state, and the mass transfer coefficient can be determined after rearranging the integral balance:

$$k_{L,\mathrm{batch}} = \frac{k_1 \langle c \rangle}{A_{\mathrm{lg}}\left(c^* - \langle c \rangle\right)} \tag{26}$$

Snapshots of the simulations at $\alpha = 8\%$ and $\alpha = 30\%$, using the CSTR approach and fast and slow chemical reactions, have been provided in the appendix, Figures 11 and 12.

Determining the mass transfer coefficient

The two methods described above have been used to determine the evolution of the mass transfer coefficient for bubbles rising in a swarm as a function of the gas hold-up. For the CSTR case, the time averaged mass transfer coefficient $k_{L,\mathrm{CSTR}}$ as a function of the gas hold-up is given in Figure 9. It is calculated using the forcing terms acting on the interface markers, and using Eq. 25 using both $\langle c \rangle$ and c_{out}. A marginal increase of $k_{L,\mathrm{CSTR}}$ can be discerned when increasing the gas hold-up from 4% to 40%. Extrapolating the trend towards $\alpha = 0.0$ approaches $k_L = 0.016$ m/s, the result for a single rising bubble in an infinite, quiescent liquid. The accuracy of the results strongly decreases for lower gas hold-up ($\alpha < 0.1$), since the number of bubbles, and thus statistics, is limited.

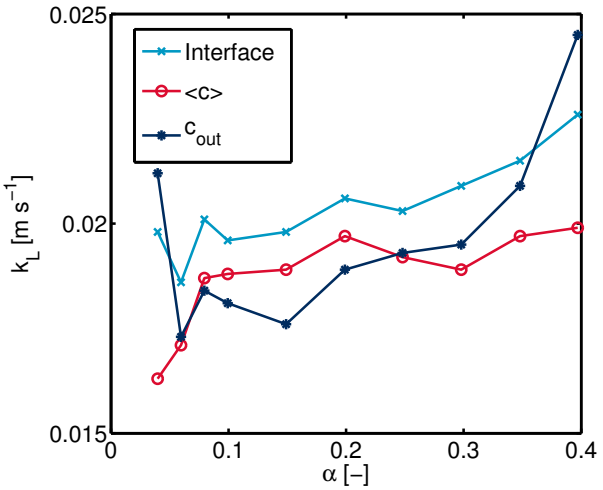

Figure 9: The mass transfer coefficient k_L of bubbles rising in a swarm plotted as a function of the gas hold-up α, determined using fresh inflow boundaries on the top and bottom walls.

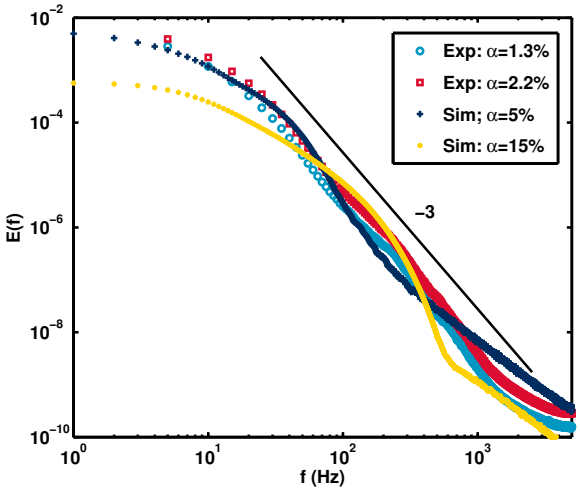

Figure 8: The energy spectra of the simulation is compared to experimental results. For the simulation with $\alpha = 5\%$, a power law close to -3 is observed for nearly one decade starting for frequencies of about 20 Hz till 200 Hz. We also show the simulation case with $\alpha = 15\%$ and with 2 s simulation time, which is not yet fully converged.

The difference between the interface derived mass transfer coefficient and that using the integral balance, is explained by the large fluctuations in the concentration throughout the domain; a closer examination of the liquid concentration in the domain revealed that the standard deviation is of the same order of magnitude as the average concentration. Hence, despite the thorough mixing induced by the bubbles, high and low concentration zones exist throughout the domain, whereas the integral balance assumes a uniform bulk concentration. Rising bubbles encounter both high concentration zones, in the wakes of preceding bubbles, and low concentration zones due to the fresh inflow. The largest portion of the mass transferred through the interface, originates from the top of the bubble. If this part is surrounded by a high concentration wake of another bubble, the mass transfer rate suddenly decreases.
For the batch reactor approach, two reaction rates have been selected; $k_1 = 50$ s^{-1} and $k_1 = 5$ s^{-1}. The mass transfer

coefficient for both cases is shown in Figure 10, using both the integral mass balance (Eq. 26) and the interface forcing terms.

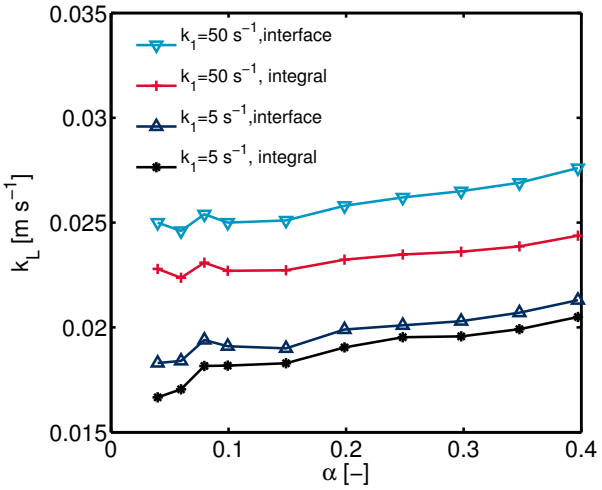

Figure 10: The mass transfer coefficient k_L of bubbles rising in a swarm plotted as a function of the gas hold-up α, determined using a first-order chemical reaction in the liquid phase.

It is observed that the mass transfer coefficient derived from the interface forcing terms is slightly higher than the mass transfer coefficient from the integral balance. The reason for this is similar to that given in the previous section; the concentration field that a bubble actually surrounds, may be quite different from the domain average concentration.

CONCLUDING REMARKS

This work has outlined the implementation of a volume-conserving remeshing technique for the Front Tracking method, and the incorporation of chemical species transport equations. The versatility of the model has been shown by studies focusing on the drag coefficient, bubble induced turbulence and mass transfer for bubbles rising in a swarm.

REFERENCES

BALSARA, D. (2001). "Divergence-free adaptive mesh refinement for magneto-hydrodynamics". *J. Comp. Phys.*, **174**, 614–648.

BUNNER, B. and TRYGGVASON, G. (2002). "Dynamics of homogeneous bubbly flows part . rise velocity and microstructure of the bubbles". *J. Fluid Mech.*, **466**, 17–52.

DARMANA, D. (2006). *On the multiscale modelling of hydrodynamics, mass transfer and chemical reactions in bubble columns*. Ph.D. thesis, University of Twente.

DEEN, N. *et al.* (2004). "Multi-scale modeling of dispersed gas-liquid two-phase flow". *Chem. Eng. Sci.*, **59(8-9)**, 1853–1861.

DEEN, N. *et al.* (2010). *Ullmann's Encyclopedia of Industrial Chemistry*, chap. Bubble Columns. Wiley-VCH Verlag GmbH & Co. KGaA, Weinheim.

DIJKHUIZEN, W. *et al.* (2010a). "DNS of gas bubbles behaviour using an improved 3D front tracking model–drag force on isolated bubbles and comparison with experiments". *Chem. Eng. Sci.*, **65(4)**, 1415–1426.

DIJKHUIZEN, W. *et al.* (2010b). "DNS of gas bubbles behaviour using an improved 3D front tracking model–model development". *Chem. Eng. Sci.*, **65(4)**, 1427–1437.

FRANCOIS, M. *et al.* (2006). "A balanced-force algorithm for continuous and sharp interfacial surface tension models within a volume tracking framework". *J. Comp. Phys.*, **213(1)**, 141–173.

KUPRAT, A. *et al.* (2001). "Volume conserving smoothing for piecewise linear curves, surfaces, and triple lines". *J. Comp. Phys.*, **172**, 99–118.

LANCE, M. and BATAILLE, J. (1991). "Turbulence in the liquid phase of a uniform bubbly air–water flow". *J. Fluid Mech.*, **222**, 95–118.

LAU, Y. *et al.* (2011). "Numerical investigation of the drag closure for bubbles in bubble swarms". *Chem. Eng. Sci.*, **66**, 3309–3316.

LOCHIEL, A. and CALDERBANK, P. (1964). "Mass transfer in the continuous phase around axisymmetric bodies of revolution". *Chem. Eng. Sci.*, **19**, 471–484.

MARTÍNEZ MERCADO, J. *et al.* (2010). "On bubble clustering and energy spectra in pseudo-turbulence". *J. Fluid Mech.*, **650**, 287–306.

MAZZITELLI, I. and LOHSE, D. (2009). "Evolution of energy in flow driven by rising bubbles". *Phys. Rev. E*, **79(6)**, 066317.

MEI, R. *et al.* (1994). "A note on the history force on a spherical bubble at finite Reynolds number". *Phys. Fluids*, **6**, 418–420.

PIVELLO, M. *et al.* (2013). "A fully adaptive front tracking method for the simulation of two phase flows". *International Journal of Multiphase Flow*.

POPINET, S. and ZALESKI, S. (1999). "A front-tracking algorithm for the accurate representation of surface tension". *Int. J. Numer. Meth. Fluids*, **30**, 775–793.

PROSPERETTI, A. (2002). "Navier-stokes numerical algorithms for free-surface flow computations: an overview". *Drop-surface interaction*, **237**.

RENARDY, Y. and RENARDY, M. (2002). "Prost: A parabolic reconstruction of surface tension for the volume-of-fluid method". *J. Comp. Phys.*, **183(2)**, 400–421.

RISSO, F. (2011). "Theoretical model for k^{-3} spectra in dispersed multiphase flows". *Phys. Fluids*.

RISSO, F. and ELLINGSEN, K. (2002). "Velocity fluctuations in a homogeneous dilute dispersion of high-Reynolds-number rising bubbles". *J. Fluid Mech.*, **453**, 395–410.

RISSO, F. *et al.* (2008). "Wake attenuation in large Reynolds number dispersed two-phase flows". *Phil. Trans. R. Soc. A*, **366**, 2177–2190.

ROGHAIR, I. *et al.* (2011a). "Energy spectra and bubble velocity distributions in pseudo-turbulence: Numerical simulations vs. experiments". *Int. J. Multiphase Flow*, **37(9)**, 1093–1098.

ROGHAIR, I. *et al.* (2011b). "On the drag force of bubbles in bubble swarms at intermediate and high Reynolds numbers". *Chem. Eng. Sci.*, **66**, 3204–3211.

ROIG, V. and DE TOURNEMINE, L. (2007). "Measurement of interstitial velocity of homogeneous bubbly flows at low to moderate void fraction". *J. Fluid Mech.*, **572**, 87–110.

RUDMAN, M. (1998). "A volume-tracking method for incompressible multifluid flows with large density variations". *Int. J. Numer. Meth. Fl.*, **28(2)**, 357–378.

TAKEMURA, F. and YABE, A. (1998). "Gas dissolution process of spherical rising gas bubbles". *Chem. Eng. Sci.*, **53(15)**, 2691–2699.

TSIOMBIKAS, J. (2009). "kdtree: A simple C library for working with KD-trees `http://code.google.com/p/kdtree/`".

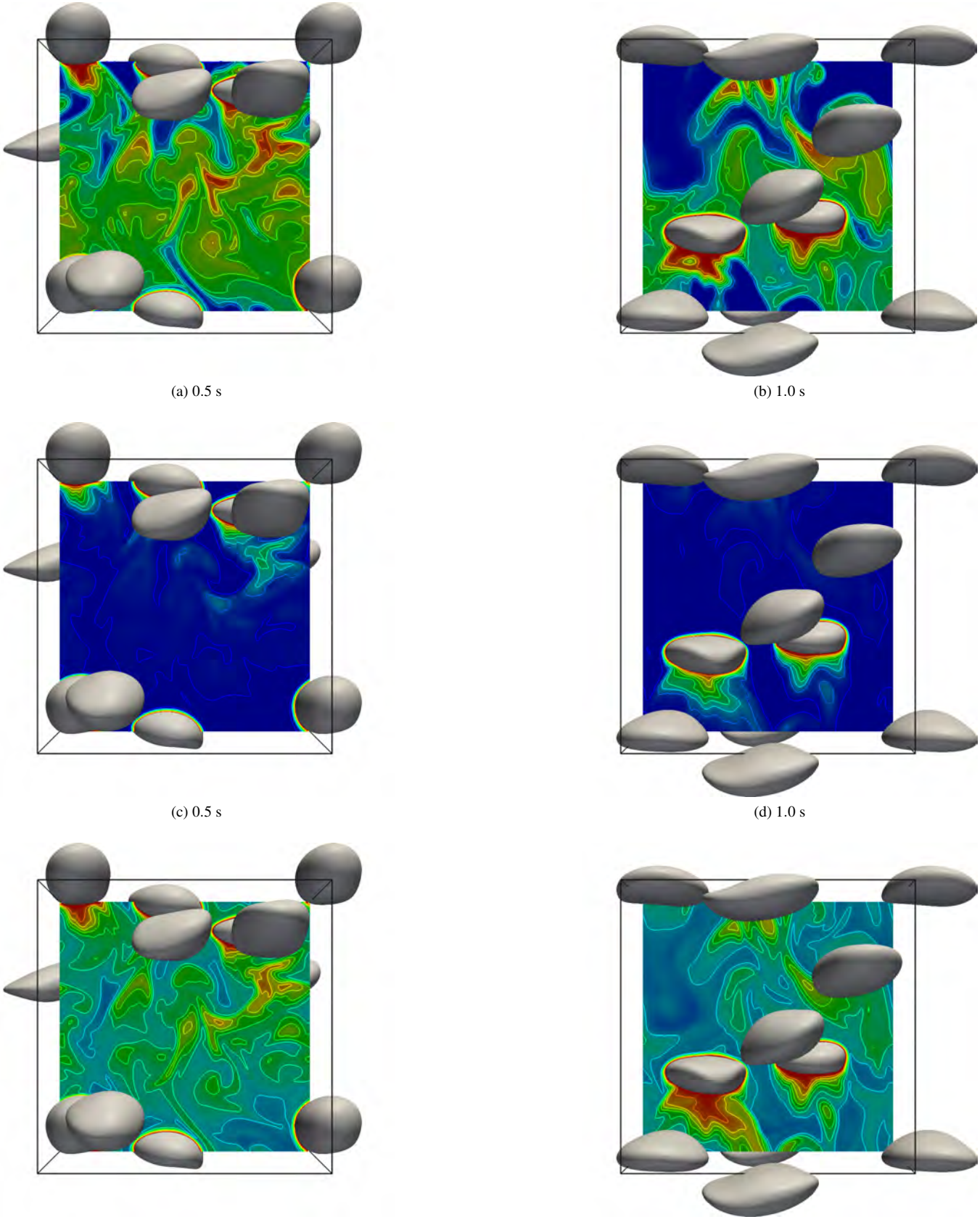

(a) 0.5 s

(b) 1.0 s

(c) 0.5 s

(d) 1.0 s

(e) 0.5 s

(f) 1.0 s

Figure 11: Snapshots of the $\alpha \approx 0.08$ simulations showing the concentration profile in a bubble swarm. From top to bottom, the CSTR approximation, fast reaction and slow reaction are displayed at 0.5 sand 1.0 s. Bubbles on the foreground have been removed for visibility reasons.

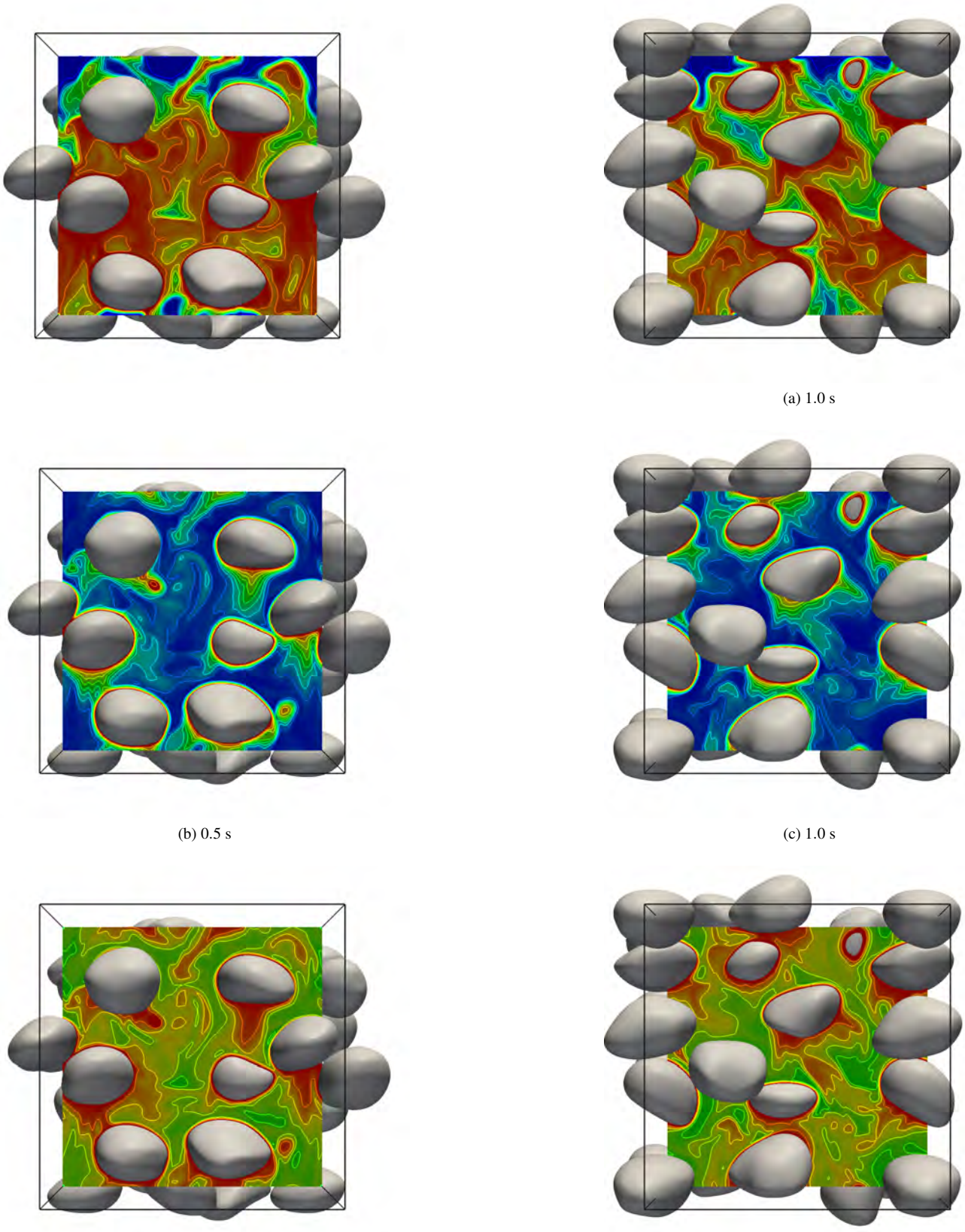

(a) 1.0 s

(b) 0.5 s

(c) 1.0 s

(d) 0.5 s

(e) 1.0 s

Figure 12: Snapshots of the $\alpha \approx 0.30$ simulations showing the concentration profile in a bubble swarm. From top to bottom, the CSTR approximation, fast reaction and slow reaction are displayed at 0.5 sand 1.0 s. Bubbles on the foreground have been removed for visibility reasons.

DROP BREAKUP MODELLING IN TURBULENT FLOWS

Benjamin LALANNE[1,4*], Sébastien TANGUY[2,4], Jiří VEJRAZKA[3], Olivier MASBERNAT[1,4], Frédéric RISSO[2,4]

[1] Laboratoire de Génie Chimique, TOULOUSE

[2] Institut de Mécanique des Fluides de TOULOUSE

[3] Institute of Chemical Process Fundamentals, PRAGUE

[4] Fédération de recherche FERMAT, TOULOUSE

* E-mail: Benjamin.Lalanne@ensiacet.fr

ABSTRACT

This paper deals with drop and bubble break-up modelling in turbulent flows. The deformation of a drop is caused by continuous interactions with turbulent vortices; the drop responds to these interactions by performing shape-oscillations and breaks up when its deformation reaches a critical value. Thus, a model of forced oscillator that describes the dynamic deformation of the drop in the flow is used to predict break-up probability, but requires a characterization of the shape-oscillation dynamics of the drop. As this dynamics is known theoretically only under restrictive conditions (without gravity, surfactants), CFD two-phase flow simulations, based on the *Level-Set* and *Ghost Fluid* methods, are used to determine the interface dynamics in more complex situations: deformation of a drop in the presence of gravity, bubble-vortex interactions. Results are compared with experimental data.
With a perspective to apply this model to breakup occurring during emulsification in turbulent flows, we propose to account for the presence of surfactants. We also discuss how to extend the model to predict daughter-drop-size distribution.

Keywords: Bubble and droplet dynamics, DNS, breakup modelling, turbulent flows, emulsions.

NOMENCLATURE

Greek Symbols

ρ Mass density, [kg/m^3].
μ Dynamic viscosity, [Pa.s].
$\hat{\rho}$ Ratio of densities: $\hat{\rho} = {\rho_d}/{\rho_c}$, [-].
$\hat{\mu}$ Ratio of densities: $\hat{\mu} = {\mu_d}/{\mu_c}$, [-].
ω Frequency of oscillation, [rad/s]
β Damping rate of the oscillations, [s^{-1}].
∂u Fluctuation of velocity, [m/s].
σ Surface tension, [N/m].
ϕ Level-Set function, [m].
θ Colatitude angle of spherical coordinates, [rad].
κ Interface curvature, [m^{-1}].

Latin Symbols

d Diameter of the drop or bubble, [m].
D Pipe diameter, [m].
R Radius of the drop or bubble, [m].
t Time, [s].
$\tilde{t}$ Normalized time, [-].
r Radial position in spherical coordinates, [m].
K Constant of the model, [-].
P Pressure, [Pa].
$\boldsymbol{U}$ Velocity, [m/s].
$\boldsymbol{g}$ Acceleration of gravity, [m/s²].
$\boldsymbol{D}$ Rates of deformation tensor, [s^{-1}].
a_2 Amplitude of deformation (harmonic 2), [m].
$\widetilde{a_2}$ Normalized amplitude$\widetilde{a_2} = a_2/d$, [-].
We Weber number, [-].
Re Reynolds number, [-].
Bo Bond number, [-].
F Non-dimensional function, [-].
G Non-dimensional function, [-].
P Legendre polynomial.
V_v Vortex velocity, [m/s].
a Length of large axis of an ellipsoid, [m].
b Length of mean axis of an ellipsoid, [m].
c Length of short axis of an ellipsoid, [m].
d_0 Initial distance, [m].

Sub/superscripts

$\overline{\ }$ Mean value.
c Continuous phase.
d Dispersed phase.
l Number of a mode of oscillation.
$crit$ Critical value that indicates breakup.
th Values predicted by the theory.
$_{ASC}$ Used to characterise rising motion.
$_{OSC}$ Used to characterise oscillating motion.
∞ Used to characterise a value in steady state.
[ ] Jump notation at the interface.

INTRODUCTION

In industrial chemical processes, turbulent flows with dispersed deformable media (drops, bubbles) are commonly encountered and a better control of the size of the drops is desired for transport and/or separation issues, and maximization of interfacial area. Examples include oil industry with problems of separation of oil and water, health and food industry with the need to produce emulsions of very fine droplets in high-pressure homogenizers, nuclear energy industry with pulsed extraction columns for treatment of irradiated nuclear fuel or chemical industry for enhancement of mass transfers in gas-liquid reactors.

In CFD Eulerian codes, population-balance approaches are often used to calculate the drop (or bubble) size distribution. These approaches require models for coalescence and breakup phenomena, which contribute to reconfigure dispersions.

The present study focuses on breakup phenomena occurring in turbulent flows. A recent review by Liao and Lucas (2009) has shown that several models exist to describe breakup and predict breakup probability, breakup frequency, daughter-drop size distribution. Most of these existing models use a breakup criterion based on a critical Weber number We_{crit} able to cause breakup: it is a static force balance between hydrodynamic forces responsible for deformation (turbulent stresses at the scale of the drop) and surface tension that resists to shape deformations. Performing a comparison of these models, Liao and Lucas have shown that they can predict very different breakup frequencies or daughter drop size distributions when applied to a process that is not the one for which they have been calibrated. The conclusion of their paper is that physical improvements are needed in these models.

We are currently developing of new approach to consider breakup. The concept consists in modelling the deformation process of a drop in a turbulent flow using a scalar parameter $\widetilde{a_2}$ that describes its deformation. In such an approach, breakup criterion is based on a critical deformation $\widetilde{a_2}_{crit}$. This new model calculates the dynamic response of drops that are excited by turbulent fluctuations of the continuous phase. As shown in Galinat et al. (2007) or in Maniero et al. (2012), it gives better predictions of breakup probability than models based on a We_{crit} when compared to experimental breakup statistics.

Section 1 of this article presents our new approach and the physics on which it is based. Then, predictions of breakup probability with our new model are compared with experimental statistics for heptane drops in a turbulent pipe flow after a restriction. This section will show that our model requires a description of the drop interface dynamics, which lies on two parameters: the frequency of oscillation ω_2 and their damping rate β_2. Nevertheless, these parameters are known only in limited configurations: for deformations of low amplitudes, in the absence of gravity effects and without surfactants adsorbed at the interfaces.

The objective of the present paper is to show how Direct Numerical Simulations can be used to calculate ω_2 and β_2 in situations of practical interest. To achieve this goal, two-phase flow simulations using the *Level-Set* method are performed. Section 2 describes the numerical methods.

Then, after validation of the code, two examples of interface dynamics are emphasized in section 3: (a) the study of influence of gravity on ω_2 and β_2 , and (b) the study of the interaction between a rising bubble and a single strong vortex.

Finally, the conclusion will introduce the perspectives of development of this model.

DROP DEFORMATION MODEL DESCRIPTION

As example of turbulent flow, let us consider a water pipe flow downstream of a restriction at a Reynolds number of 2100 (based on the orifice diameter) like in Galinat et al. (2007). Fig. 1 shows experimental pictures of a colored heptane drop travelling through this flow. The velocity field has been measured by PIV. From the results, we define a turbulent Weber number We based on the square of the fluctuating velocity $\partial u^2(d)$ between two points distant of the drop diameter d (we take the maximum of the difference between vertical, transversal and diagonal directions): $We = \frac{\rho\, \partial u^2(d) d}{\sigma}$. Averaging $\partial u^2(d)$ in time, we obtain a map of the mean turbulent Weber number $\overline{We} = \frac{\rho\, \overline{\partial u^2(d)} d}{\sigma}$, shown in fig. 1. It is observed that breakup locations correspond to the maximum values of $\overline{We}$, indicating that turbulent fluctuations cause drop breakup. In turbulent flows, the deformation of a drop is due to its interaction with turbulent vortices, which occurs continuously and randomly.

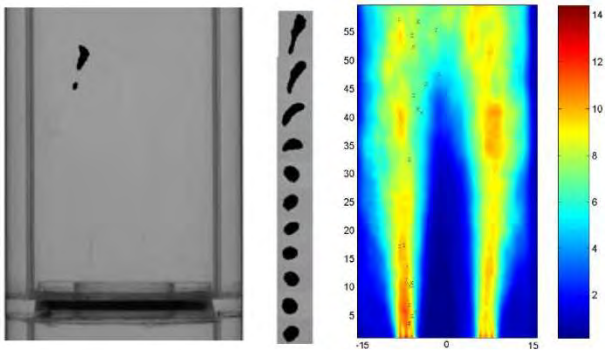

Figure 1: Experiment of breakup of a heptane drop in the flow downstream of a restriction: deformation of the drop and map of $\overline{We}$ (with crosses indicating breakup locations). From Galinat et al. (2007) and Galinat (2005).

Fig. 1 illustrates also the deformation process of the drop that leads to breakup. As mentioned by Risso and Fabre (1998), the time evolution of the surface area of the drop shows the existence of a characteristic angular frequency ω_2 of oscillation of the shape. The time scale $t_2 = \frac{2\pi}{\omega_2}$ is that of the response of an interface submitted to perturbations of its shape, in a similar way than what occurs in turbulent flows. The oscillations of a drop submitted to low-amplitude shape deformations constitute a problem mathematically studied by Lamb

(1932), Miller and Scriven (1968) or Prosperetti (1980). They have theoretically calculated the modes of oscillation, which are described by the spherical harmonics of order *l*, and a frequency ω_l and a damping rate β_l (due to the dissipation of energy ensured by viscous effects) associated to each mode. The mode *l=2* is generally enough to describe the shape of the drop in first approximation, so their theoretical expressions for ω_2^{th} and β_2^{th} can be also used to characterize the oscillations of a drop or a bubble observed in a turbulent flow.

Thus, we propose to model the drop as an oscillator, forced by the turbulent fluctuations from the continuous phase. ω_2 and β_2 are the time scales of this oscillator. Consequently, if the residence time t_r of the drop is short compare to its response time t_2, breakup can occur only if the turbulent fluctuations are intense enough, as predicted by a critical Weber number method. Nevertheless, if t_r is of same order or larger than t_2, the dynamic response of the drop cannot be ignored to describe deformation and breakup; in this case, an approach limited to the determination of a critical Weber number will not be sufficient to predict breakup, since turbulent fluctuations are filtered by the drop dynamics at its natural frequency ω_2.
Following these observations, in order to model the temporal deformation of the drop, we define a scalar parameter $\widetilde{a_2}$ corresponding to the amplitude of the deformation normalized by *d*, as the solution of the following forced oscillator:

$$\frac{d^2\widetilde{a_2}}{d\tilde{t}^2} + 2\frac{\beta_2}{\omega_2}\frac{d\widetilde{a_2}}{d\tilde{t}} + \widetilde{a_2} = K\,We \qquad (1)$$

($\tilde{t} = t/t_2$, and *K* is a constant parameter of the model that can be identified from experimental data). Breakup will occur when $\widetilde{a_2}$ will be larger than a critical value $\widetilde{a_2}_{crit}$. Experiments show that the maximum length of a drop before breakup is about twice its diameter, giving $\widetilde{a_2}_{crit} \cong 1/2$.
The 1D model of eq. (1) needs to know (i) the time evolution of the turbulent fluctuations $We(\tilde{t})$ experienced by the drop along its trajectory and (ii) the time scales of oscillation of the drop ω_2 and β_2. Note that $We(\tilde{t})$ can be obtained either by PIV measurements of the continuous-phase flow or by DNS of the single phase carrier flow like in Maniero et al. (2012).

Fig. 2 presents the computation of the response of the drop $\widetilde{a_2}$ to a turbulent signal We obtained from the experiment of fig. 1. On this illustrative example, $\widetilde{a_2}$ overheads its critical value after 3 periods of oscillation: breakup does not result from the instantaneous interaction of the drop with one strong vortex but from a resonant interaction between the drop and several moderate vortices that allow the drop to accumulate energy of deformation in time. Thus, a model based on a critical Weber number is not accurate to predict this breakup event. To confirm this conclusion, fig. 3 compares the predictions of breakup given by either an approach based on a critical deformation or a model assuming a critical Weber number approach with the experimental breakup probability.

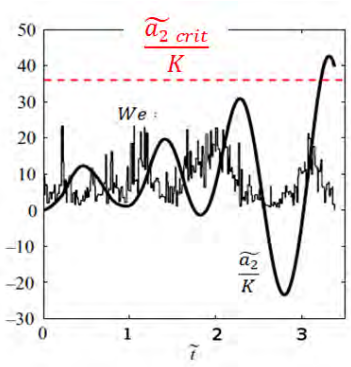

Figure 2: Computation of the deformation of the drop from model (1) knowing time evolution of the turbulence at the scale of the drop We. From Galinat et al. (2007)

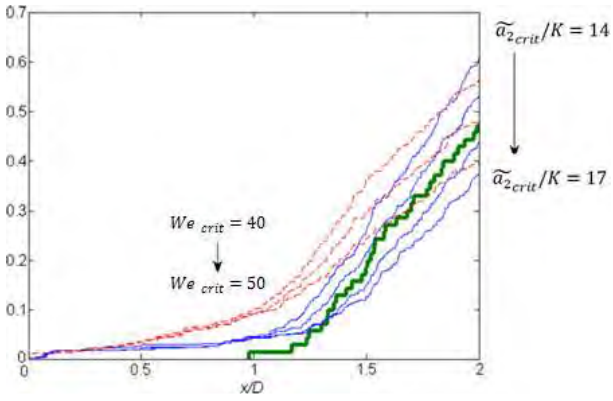

Figure 3: Breakup probability versus the distance from the orifice in the pipe. Thick continuous line: experiment. Thin continuous lines: prediction of model (1) assuming different values of $\widetilde{a_2}_{crit}$. Dotted lines: predictions of model (1) assuming different We_{crit}. From Maniero et al. (2012).

It is observed that an approach based on We_{crit} overestimates the breakup probability in the interval $0.5 < x/D < 1.5$ whereas our model based on $\widetilde{a_2}_{crit}$ reproduces well the experimental data, the best criteria being $\widetilde{a_2}_{crit}/K = 16$ for this experiment. This validation against experimental data validates the coupling between local turbulent forcing and drop deformation dynamics to describe accurately physics of fragmentation.

To apply this model, one needs to be able to know the interface dynamics time scales corresponding to ω_2 and β_2. As already mentioned, theoretical expressions ω_2^{th} and β_2^{th} for these parameters have been derived by various authors; for example, Miller and Scriven (1968) gave

$$\omega_2^{th} = \omega_2^* - \frac{\mu_d}{\rho_d R^2} F\sqrt{Re_d} \qquad (2)$$

$$\beta_2^{th} = \frac{\mu_d}{\rho_d R^2}\left[-2F^2 + G + F\sqrt{Re_d}\right] \qquad (3)$$

with $\omega_2^* = \sqrt{\frac{24\,\sigma}{(3\rho_d + 2\rho_c)\,R^3}}$, $Re_d = \frac{\rho_d \omega_2^* R^2}{\mu_d}$, *F* and *G* being two functions of the ratios of density and viscosity given in appendix A. Expressions (2) and (3) are valid in the linear regime of oscillations, do not take into account neither effect of gravity nor that of surfactants

adsorbed at the interfaces. Thus, we need to describe the interface dynamics in more complex configurations to deal with applications: drops in emulsions, concentrated media, flows with rising bubbles for example. One way to reach this goal is to perform Direct Numerical Simulations in order to study the different effects separately.
Next section describes the numerical methods used in our CFD code.

To conclude this presentation of our new 1D model, note that a similar approach that describes oscillating and distorting droplets, known as the TAB model (Taylor Analogy Breakup), exists, is implemented in industrial codes like *Fluent*, and is commonly used by engineers to calculate breakup in low Weber number sprays (cf O'Rourke and Amsden (1987)).

NUMERICAL METHODS FOR TWO-PHASE FLOW SIMULATIONS

Configurations which are studied in the context of interface dynamics include axisymmetric and three-dimensional simulations of shape-oscillations of rising drops or bubbles, interaction between a bubble and a vortex, breakup of drops in turbulent flows. Direct Numerical Simulations based on the *Level-Set* and *Ghost-Fluid* methods to solve the two-phase flows are performed, their outlines are briefly described in this section.

The interface is numerically represented by the zero-level curve of a continuous function ϕ which is defined as the algebraic distance to the interface. Its displacement in a velocity field $\boldsymbol{U}$ is computed by solving an advection equation:

$$\frac{\partial \phi}{\partial t} + \boldsymbol{U}.\boldsymbol{\nabla}\phi = 0 \qquad (4)$$

The droplet motion is calculated by solving the incompressible Navier-Stokes equations by means of a projection method:

$$\begin{cases} \nabla.\boldsymbol{U} = 0 \\ \dfrac{\partial \boldsymbol{U}}{\partial t} + (\boldsymbol{U}.\nabla)\boldsymbol{U} + \dfrac{\nabla P}{\rho(\phi)} = \dfrac{\nabla.(2\mu(\phi)\boldsymbol{D})}{\rho(\phi)} + \boldsymbol{g} \end{cases} \qquad (5)$$

where P is the pressure, μ the dynamic viscosity, ρ the density, $\boldsymbol{g}$ the acceleration of the gravity and $\boldsymbol{D}$ the tensor of rates of deformation.
In these equations, ρ, μ and P are discontinuous across the interface. The normal stress balance at the interface assumes that

$$[P] = \sigma\kappa + 2\left[\mu\frac{\partial U_n}{\partial n}\right], \qquad (6)$$

where U_n is the velocity normal to the interface, n is the coordinate in the direction normal to the interface, σ the surface tension and κ the interface curvature.

To handle the discontinuity of the pressure at the interface and calculate accurately its derivatives, a *Ghost Fluid method* has been implemented: the jump condition is extrapolated in one ghost cell on each side of the interface. The numerical formulation for the viscous term and the pressure jump at the interface follows the method detailed in Sussman et al. (2007).
An algorithm of redistanciation is used to ensure that ϕ remains a distance function at each time step, as described in Tanguy and Berlemont (2005).

These partial differential equations are discretized using the finite volume technique on staggered grids. Spatial derivatives are estimated with a second order central scheme while a fifth order *WENO* scheme is used for the convective terms, which ensures that solution is robust. Temporal derivatives are approximated with a second-order Runge-Kutta scheme.

DNS OF INTERFACE DYNAMICS

This section illustrates how CFD is used to calculate interface dynamics in several configurations. First, the shape-oscillations of drops and bubbles are calculated and results compared with both theory and experiments for validation of the numerical code. Then, linear shape-oscillation of rising drops are simulated in order to assess the influence of gravity on the oscillations and to extend the theoretical results in that case. Thirdly, another configuration of interaction between a rising bubble and a single vortex is studied in order to characterise the interface dynamics for non-linear deformations as those occurring in a turbulent flow.

Validation of the code for interface dynamics

The numerical methods previously presented are used to calculate the shape-oscillations of deformed drops and bubbles.
For the case of the drop, the initial amplitude of deformation is chosen low enough to compare the results with the linear theory of oscillation.
For the case of the bubble, the numerical results are validated against an experiment.

Comparison with theory and mesh convergence

Axisymmetric simulations of the shape-oscillations of an initially deformed drop in the absence of gravity are performed. The imposed deformation corresponds to the mode l=2 of oscillation with an initial amplitude ${a_2(0)}/{R} = 0.1$. In order to characterize the oscillations, we define a Reynolds number of oscillation, that compares the inertial effects of deformation over the viscous damping: $Re_{OSC} = \dfrac{\rho_C\sqrt{{\sigma}/{\rho R^3}}R^2}{\mu_C}$. Three values of Re_{OSC} investigated are: 50, 100, 200. Calculations are performed on a regular mesh of 16, 32 and 64 grid points per drop radius so as to study mesh convergence of the results.

Thanks to the Level-Set function, the drop contour in spherical coordinates, $r(\theta,t)$ is extracted from the simulation at each time step and the interface is decomposed into spherical harmonics so as to recover the amplitude of oscillation of mode 2:

$$r(\theta,t) = R + a_2(t)\,P_2(\cos\theta), \qquad (7)$$

P_2 being the Legendre polynomial of order *l*=2.

From the time evolution of a_2, the frequency ω_2 and damping rate β_2 of the oscillations can be obtained and compared against the predictions of the linear theory ω_2^{th} and β_2^{th}:

$$a_2(t) = a_2(0)\,\cos(\omega_2\,t)\,e^{-\beta_2\,t}. \qquad (8)$$

	Mesh : N grid points on R	Re_{OSC} = 50	Re_{OSC} = 100	Re_{OSC} = 200
Error on ω_2^{th}	16	-0.07%	-0.51%	-0.43%
	32	0.06%	0.07%	-0.27%
	64	0.19%	0.01%	-0.09%
Error on β_2^{th}	16	0.18%	0.91%	5.67%
	32	-0.68%	-0.45%	-0.07%
	64	-1.15%	-1.07%	-0.76%

Table 1: Validation of the axisymmetric calculation of the shape-oscillations of non-rising drops.

Relative errors are reported in table 1 for the three Re_{OSC}. Results show that the numerical code gives very accurate results on both frequency and damping rates in this range of Re_{OSC}, for grids containing 32 or 64 points in a radius. Spatial convergence of the simulations is also proved by the tests reported in the table.

Thus, these results provide a strong validation of our axisymmetric numerical code to deal with interface dynamics problems. In order to validate also the Cartesian version of the code, a 3D simulation of the shape-oscillations of a bubble is carried out at $Re_{OSC} = 50$ on a grid containing 16 cells in a radius. Results obtained are superimposed on fig. 4 with the curves given by the axisymmetric version of the code with 8, 16, 32 and 64 grid points in a radius.

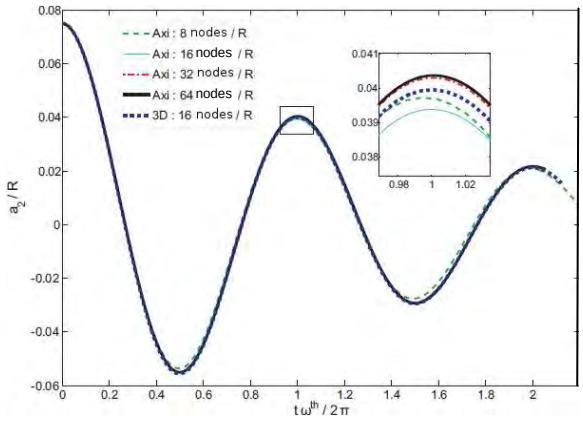

Figure 4: Validation of the 3D and axisymmetric calculation of the shape-oscillations of a non-rising bubble at $Re_{OSC} = 50$.

Fig. 4 proves again the mesh convergence of the numerical simulations for the axisymmetric calculations, and shows that oscillations calculated by the 3D Cartesian version of the code have an accuracy comparable to the axisymmetric calculation with the same number of grid points. Thus, we conclude that a calculation with 16 points in a radius of the bubble at $Re_{OSC} = 50$, either in an axisymmetric cylindrical calculation or in a 3D Cartesian simulation, gives very accurate results in accordance with the theory.

Comparison with an experiment

Then, the code is validated by comparison with an experiment that records the shape-oscillations of a bubble. In the experiment, the bubble is initially attached to a capillary; its translation causes the detachment of the bubble that rises in water performing shape-oscillations. The experiment is conducted in ultra-pure conditions to avoid contamination due to surfactants. The oscillations, characterized by $Re_{OSC} = 164$, are described by several modes and the initial amplitudes, obtained from the experimental shape at the instant of detachment, are larger than in the previous case ($a_2(0)/R = 0.18$). The Bond number $Bo = \frac{(\rho_c-\rho_d)gd^2}{\sigma}$ is very low ($Bo = 0.08$) to ensure that gravity has negligible effects on both the oscillations and the mean shape of the bubble (which remains spherical during its rising motion).

The shape of the interface is decomposed in spherical harmonics (until order 10):

$$r(\theta,t) = \sum_{l=0}^{10} a_l(t)\,P_l(\cos\theta). \qquad (9)$$

Fig. 5 compares the time evolution of a_2, a_3 and a_4 between the experiment and a simulation on a mesh with 32 nodes in R.

Results show an excellent agreement between the numerical simulations and the experiment for the different modes of oscillation, with a very good precision until amplitudes less than 0.005R.

They validate again the use of our DNS code to capture the interface dynamics in the bubble case.

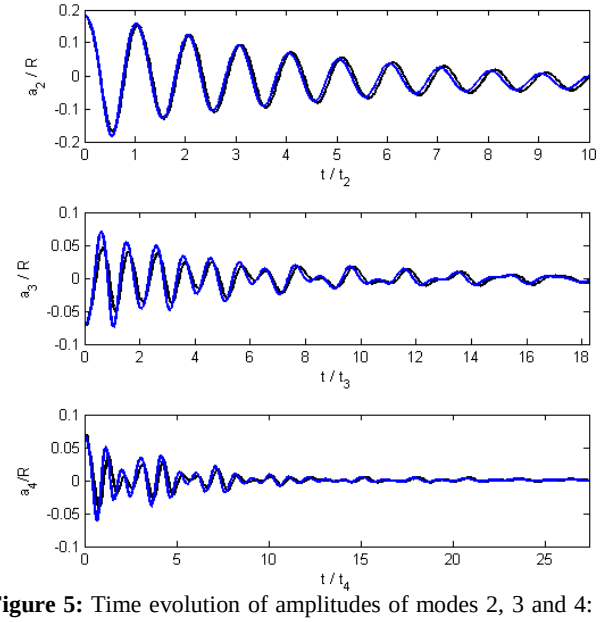

Figure 5: Time evolution of amplitudes of modes 2, 3 and 4: comparison between experiments (black lines) and simulations (blue lines).

Shape-oscillations of rising drops

We carry out axisymmetric simulations of an ascending drop, its shape being initially slightly elongated in the vertical direction. Thus, the drop performs linear shape-oscillations.
The objective is to determine the effect of the rising motion on these oscillations and to compare frequency and damping rates with the values ω_2^{th} and β_2^{th} predicted by the linear theory in the absence of gravity.

This problem is described by four non-dimensional numbers: ratios of density and viscosity $\hat{\rho}$ and $\hat{\mu}$, a Reynolds number of translation $Re_\infty = \frac{\rho_C V_\infty d}{\mu_C}$ based on the rising drop velocity V_∞, and a Reynolds number of oscillation Re_{OSC} based on the oscillating velocity. For these simulations, $\hat{\rho}$=0.99 and $\hat{\mu} = 1$ (liquid-liquid configuration), Re_{OSC} is varied between 50 and 200, and Re_∞ ranges from 60 to 600.
The initial deformation of the drop is set to ${a_2}/{R} = 0.1$.
The regular grid used for the simulation is composed of 32 nodes in a drop radius.

Let us examine the shape-oscillations of this rising drop. At $Re_{OSC} = 100$, fig. 6 presents the time evolution of the Reynolds number of rising $Re_{ASC} = \frac{\rho_C V(t) d}{\mu_C}$ for four different Re_∞ and fig. 7 displays the corresponding time evolution of the amplitude of harmonic 2.

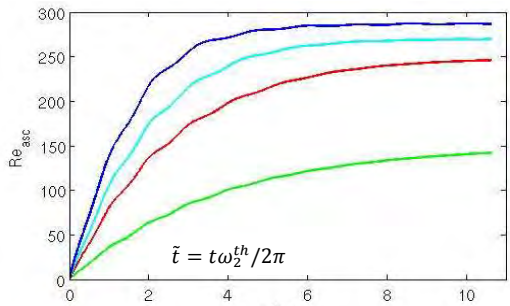

Figure 6: Time evolution of Reynolds number of rising for four drops at Re_∞ = 150, 200, 270, 290 and $Re_{OSC} = 100$. Figure from Lalanne (2012).

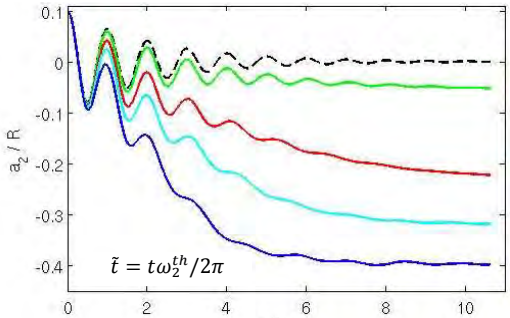

Figure 7: Time evolution of amplitude of harmonic 2 for four rising drops at Re_∞ = 150, 200, 270, 290 and $Re_{OSC} = 100$. Dotted line: calculation for a non-rising drop. Figure from Lalanne (2012).

For each drop, the rising velocity increases until the steady state is reached. Translational velocity is not much affected by the presence of the shape-oscillations, which are damped in time. The evolution of the shape of the drop shows that during its acceleration stage, it flattens, which corresponds to a global diminution of a_2. Shape-oscillations due to the initial perturbation of the drop are also visible. In order to analyse them and see the effect of the rising motion, we apply a high-pass filter at frequency ω_2^{th} to the time evolution of a_2 in order to separate the evolution of the mean shape of the drop which flattens in time from the oscillations. Then, we measure frequency and damping rate of the oscillations on the filtered signal. We observe that the frequency of oscillation is maximum for the non-rising drop and decreases slightly (-10%) when the rising velocity increases. At the contrary, we note a strong damping (+250%) of the oscillations for high values of Re_∞. In both cases, it is interesting to note that ω_2 and β_2 do not have constant values at a given Re_∞ but values evolving monotonically in time. These observations are valid for the three Re_{OSC} investigated.

Consequently, we propose to relate the decrease of frequency and the increase of damping rate with the drop instantaneous velocity. Fig. 8 and 9 display the results for drops at Re_{OSC}=50, 100, 200 and several Re_∞: ω_2 and β_2 are presented as a function of an instantaneous Weber number $We(t) = {1}/{2}\left({Re_{ASC}}/{Re_{OSC}}\right)^2$ that compares the magnitudes of rising and oscillatory motions. Thus, the evolutions of both frequency and damping gather around master curves. Despite a certain scattering of the results that indicates that other factors may play a role on the oscillations (drop acceleration for example), these figures prove that the deviation from the theory are mainly controlled by the instantaneous velocity.

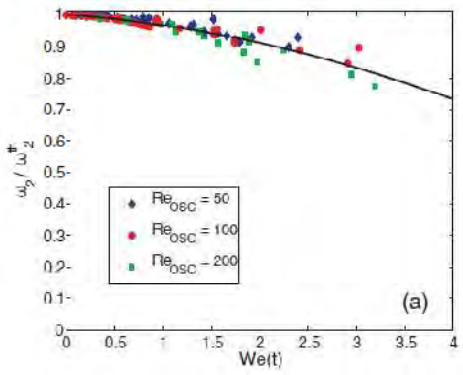

Figure 8: Frequency of oscillation of a rising drop normalized by the theoretical frequency for a non-rising drop, versus $We(t)$. From Lalanne et al. (2013).

The main effect of the rising motion on the shape-oscillations of drops is thus to increase the rate of dissipation of the energy of oscillation, provided the rising velocity is large enough compared to the oscillating velocity.
For non-rising drops, the linear theory of oscillation shows that the dissipation takes place in boundary layers of oscillation located in both sides of the interface, as

illustrated by fig. 10, which represents the vorticity field of a shape-oscillating drop in the absence of gravity.

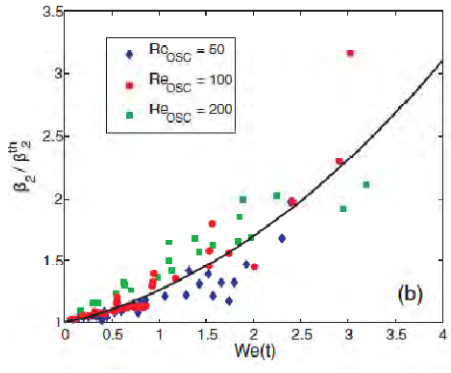

Figure 9: Damping rate of oscillation of a rising drop normalized by the theoretical damping rate for a non-rising drop, versus $We(t)$. From Lalanne et al. (2013).

From our numerical simulations, we are able to examine the vorticity of rising drops. For slow-rising and oscillating drops, i.e when the damping rate of the oscillations is not really affected by the rising motion, we observe that the vorticity of the flow is the sum of the vorticity involved in the motion of the same slow-rising drop which does not oscillate (called "flow of pure rising") and of the vorticity involved in the motion of the same oscillating drop that does not rise (called "flow of pure oscillation"). Thus, flow of pure rising and flow of pure oscillation do not interact in case of a slow-rising and oscillating drop, what explains why β_2 remains close to β_2^{th}. Nevertheless, for rapidly rising and oscillating drops, this is not the case: we observe that vorticity of rising and of oscillatory motion interact, what results in an increase of the dissipation of the energy of oscillation.

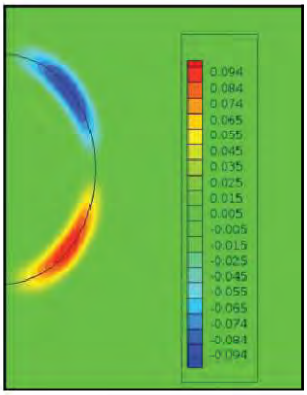

Figure 10: Vorticity field (normalized by ω_2^{th}) of an oscillating and non-rising drop at $Re_{OSC} = 100$. From Lalanne et al. (2013).

Consequently, the effect of the rising motion on the damping rate of oscillation can be explained by looking at the vorticity of the drops.
Nevertheless, for micrometer or millimeter-sized drops that are commonly involved in many industrial flows, the Weber number based on the rising velocity can hardly be larger than unity. Therefore, the present results show that the predictions of the linear theory of oscillation, which do not include the effect of gravity, provide good estimations of ω_2 and β_2 (less than 5% of discrepancy for ω_2 and less than 30% of discrepancy for β_2).

Let us consider now the experimental investigation of an oscillating heptane drop which is rising in water, carried out by Abi Chebel and al (2012). For two drops of contrasted sizes, the authors have measured the damping rates of the oscillations. Results are displayed in table 2. Using our numerical results of fig. 9, we are able to predict what should be the damping rate of the oscillations for pure fluids and clean interfaces. Experimental measurements show that β_2 is twice the predicted value. Thus, another mechanism is involved: the strong increase of β_2 can be related to the presence of contaminants adsorbed at the liquid-liquid interface. Indeed, it is extremely difficult to carry out experiments with pure fluids in liquid-liquid dispersions and the contamination is proved by calculating the experimental drag coefficient of the drops, which is found to match that of a solid sphere and not that of a drop with clean interface. Table 2 shows that the effects of the surface-active contaminants alter significantly shape-oscillations dynamics.

d (mm)	Re_{OSC}	Re_∞	We	Measured β_2 / β_2^{th}	Prediction of β_2 / β_2^{th} based on fig. 7
0.59	120	17	0.01	2.0	1.0
3.52	293	480	1.34	2.7	1.4

Table 2: Experimental results for oscillating and rising drops of heptane in water. From Abi Chebel et al. (2012).

Further studies are required to characterise completely the interface dynamics of drops in the presence of surfactants.

Bubble-vortex interaction

In turbulent flows, the key mechanism responsible for bubble (or drop) deformation is the interaction with a vortex. An experiment of breakup of a rising bubble in a turbulent flow, carried out by Ravelet et al. (2011), has shown that larges deformations caused by turbulence are quickly damped and the authors have not observed shape-oscillations of the bubbles in their turbulent flow, contrary to what is observed in microgravity conditions (cf Risso and Fabre (1998)).
In order to investigate this open question, a three-dimensional simulation of the interaction between a rising bubble and a vortex has been carried out. The objective of the simulation was to study the response of the bubble to large deformations of its shape.

The non-dimensional parameters that describe the rising bubble are: the ratio of density $\hat{\rho}$=0.001, the ratio of viscosity $\hat{\mu} = 0.016$, the Reynolds number of oscillation Re_{OSC}=50, the Reynolds number of rising Re_∞= 89 or

142. A Hill's vortex of same dimension than the diameter of the bubble has been chosen in order to provoke bubble deformations at large scales. Indeed, it is admitted since Hinze and Kolmogorov pioneering works that vortices of same size as the bubble are the more efficient for breakup.
The initial condition of the calculation is as illustrated by fig. 11. It is the superimposition of the velocity field induced by an Hill's vortex (which is known analytically and involves a potential flow at characteristic velocity V_{v0} which is the initial velocity of an Hill's vortex, cf the analytical solution in Benteboula (2006)) and the flow corresponding to a rising bubble at terminal velocity characterized by Re_∞ (calculated through a preliminary simulation). To avoid singular conditions, the vortex and the bubble are off-centered from a distance $d_0 = {\sqrt{2}}/{2}\, R$. The mesh is Cartesian but non uniform far from the bubble. The bubble dynamics is captured thanks to the use of 16 grid points in a radius.

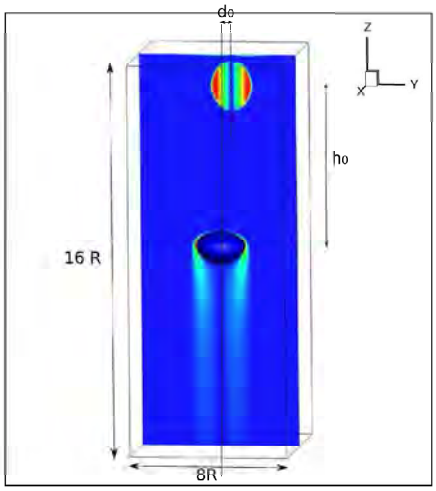

Figure 11: Initial condition (vorticity field) for a 3D-calculation of the interaction of a rising bubble and a Hill's vortex.

The intensity of the interaction between the vortex and the bubble is characterized by a Weber number based on the velocity V_v of the vortex at the instant it encounters the bubble: $We_v = \frac{\rho_C {V_v}^2 d}{\sigma}$.

Fig. 12 displays pictures of the simulation in the case of a very intense interaction: $We_v = 16.5$ and $Re_\infty = 142$. Before the interaction, the bubble is flattened with an aspect ratio of 1.84 because of its rising motion. During the interaction, bubble breakup is not observed but large and non-axisymmetric bubble deformations are observed. To obtain an accurate description of the global shape of the bubble, we calculate the equivalent ellipsoid, defined as the ellipsoid of same inertia matrix as the bubble. In the following, we note a the length of the major semi-axis of the ellipsoid, b the length of the intermediate semi-axis, and c the length of the shorter semi-axis. Fig. 13 displays the evolution of a, b and c in the simulation that corresponds to fig. 12.
The bubble shape is initially symmetric around a vertical axis (see picture 1 of fig. 12) and its rising motion is steady. When the vortex arrives at the bubble location, it causes a large elongation of the bubble and consequently a strong increase of its major axis. In the same time, its medium axis is sligthy reduced, leading to a shape close to a cylinder with a large major axis and two small other axes. The maximum deformation is that of picture 3 in fig. 12. It is remarkable that the symmetry of the bubble has changed from an axisymmetric oblate shape before the interaction with the vortex to an axisymmetric prolate shape at the maximum of deformation. Finally, the vortex leaves the bubble, which relaxes towards its equilibrium shape. Its rising motion is now unsteady and follows a *zig-zag* path. It can be observed in fig. 13 that the major part of the large perturbation induced by the vortex is quickly attenuated. The residual departure to the initial shape leads to slowly damped shape oscillations.

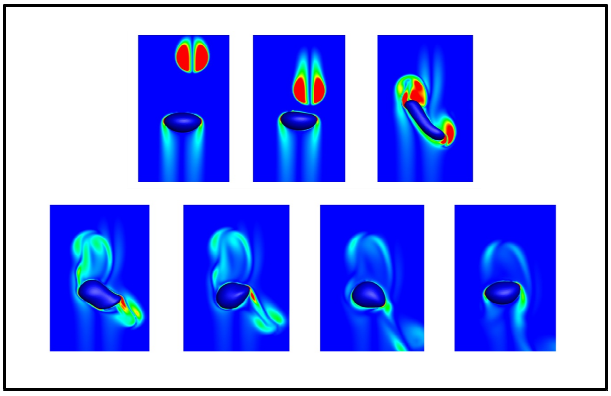

Figure 12: Bubble-vortex interaction at $We_v = 16.5$ and $Re_\infty = 142$. Colors correspond to vorticity levels. Times increases from left to right and from top to bottom.

Consequently, the bubble-vortex interaction can be described in two phases: the first one corresponds to a large deformation of the bubble, which is quickly damped; the second one corresponds to the relaxation of the bubble through linear oscillations.

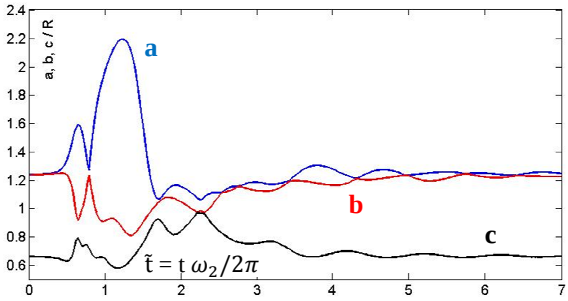

Figure 13: Time evolution of bubble semi-axes during its deformation by a vortex at $We_v = 16.5$ and $Re_\infty = 142$.

Various simulations have been carried out from different sets of parameters (rising bubble velocity and vortex intensity). The decomposition of the interaction into two phases is relevant for every case.
During the first phase of large deformation, it is observed that the length of the major axis of the bubble is proportional to We_v. Fig. 14 shows the time evolution of the length of the major axis for different cases, the time being normalized by the frequency of oscillation of

the bubble given by the theory of Meiron (1989) for a rising bubbles. The duration of the large deformation of the bubble is found to be very close to one period of oscillation.
These conclusions are in agreement with the experimental observations of Ravelet et al. (2011), who have also noticed that: (1) large deformations correspond to prolate bubbles, (2) the duration of the large deformation is equal to one period of oscillation, and (3) large bubble deformations are proportional to large turbulent fluctuations.
Consequently, in situations where the turbulent intensity is weak, the bubble can be considered as a strongly damped oscillator, breakup is rare and occurs during the interaction with a strong vortex characterized by a large We_v.
In the simulations, breakup is observed when the bubble elongation (compare to its initial length) is about one diameter.

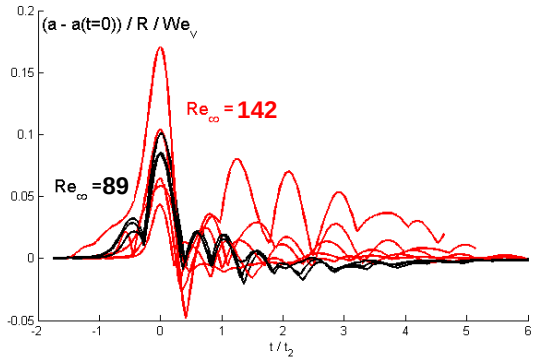

Figure 14: Time evolution the bubble elongation defined as $(a - a(t{=}0))/R$ and normalized by We_v, for several bubble-vortex interactions at Re_∞= 89 or 142 , and 1.5 $\leq We_v \leq$16.5.

CONCLUSION

A new dynamic 1D approach to make predictions of breakup probability of drops or bubbles in turbulent flows has been presented. This approach uses a scalar to describe the dynamics of deformation of a bubble or a drop in a turbulent flow and predicts breakup occurrences on the basis of a critical value of deformation, contrary to most of the other approaches that consider a critical Weber number. The dynamics of deformation of a drop or a bubble is modelled as a linear oscillator forced by the turbulent fluctuations experienced by the particle along its trajectory in the flow. Two time scales are used to characterize the drop-oscillator: its frequency of oscillation and its damping rate.
These parameters are theoretically known in limited cases: in the absence of gravity, for low-amplitude oscillations and in the absence of surfactants. The purpose of this paper was to show how CFD simulations (but also complementary experiments) can be used to determine these parameters which are characteristics of the interface dynamics. In this way, we have studied the influence of gravity on ω_2 and β_2 . For liquid-liquid flows, this influence is generally low due to low density differences. Nevertheless, for gas-liquid flows, buoyancy effects should be taken into account. Hence, simulations of the interaction between a rising bubble and a Hill's vortex reveals overdamped oscillations. This configuration is a first step in the understanding of the complexity of breakup phenomenology in turbulent flows.

In order to be able to handle practical situations like those involved in chemical processes, other effects have to be considered, like those related to the presence of surfactants adsorbed at the interfaces, which give them properties of elasticity and viscosity. Thanks to comparisons between experimental and numerical damping rates of oscillating drops, it has been shown that the presence of contaminants can modify drastically the interface dynamics. Further studies, combining experimental and numerical tools, are required to understand the effect of surfactants on the frequency and the damping rate of the shape-oscillations. Moreover, to deal with concentrated emulsions, we should also be able to determine how drop interactions alter the drop dynamics with respect to an isolated drop, like in the work of Galinat et al (2007) who have considered cases until volume fractions of 20%.

Presently, our 1D model is able to predict the breakup probability of one drop (with clean interface) travelling in a turbulent inhomogeneous flow. One perspective is to extend this 1D model to more complex flows after numerical and experimental elementary studies of the interface dynamics in such configurations: turbulent flows of multiplum bubbles, emulsions with surfactants. Another perspective is to benefit from the data calculated by the model, i.e the amplitude of deformation of a drop at the instant of breakup, in order to quantify its excess surface energy and to use it to predict the number and size of daughter drops that will be formed after breakup. We are currently focusing on the validation of such an approach to predict daughter-drop size distribution against experimental data, including cases of binary breakup and breakage into several droplets.
Then, this 1D dynamic model could be used to design new breakup kernels for balance population equations in CFD Eulerian codes.

REFERENCES

ABI CHEBEL N., VEJRAZKA J., MASBERNAT O., RISSO F. (2012). Shape oscillation of an oil drop rising in water: Effect of surface contamination. *Journal of Fluid Mechanics*, **702**, 533-542.

BENTEBOULA S. (2006) Résolution des équations de Navier-Stokes à faible nombre de Mach : Application à l'étude de l'anneau de vorticité à masse volumique variable. *Thèse Université de Marne-la-Vallée*, Laboratoire d'Etude des Transferts d'Energie et de Matière.

GALINAT S. (2005). Etude expérimentale de la rupture de gouttes en écoulement turbulent. *Thèse INPT*, Laboratoire de Génie Chimique.

GALINAT S., RISSO F., MASBERNAT O., GUIRAUD P. (2007). Dynamics of drop breakup in inhomogeneous turbulence at various volume fractions. *Journal of Fluid Mechanics*, **578**, 85–94.

LALANNE B. (2012) Simulation numérique directe des oscillations, de la déformation et de la rupture d'une bulle en ascension dans un écoulement instationnaire. *Thèse INPT*, Institut de Mécanique des Fluides de Toulouse.

LALANNE B., TANGUY S., RISSO F. (2013). Effect of rising motion on the damped shape oscillations of drops and bubbles. *Physics of Fluids*, **25**, 112107.

LAMB (1932). *Hydrodynamics*. Cambridge University Press.

LIAO, Y., LUCAS, D. (2009). A literature review of theoretical models for drop and bubble breakup in turbulent dispersions. *Chemical Engineering Science*, **64**, 3389-3406.

MANIERO R., MASBERNAT O., CLIMENT E., RISSO F. (2012).Modelling and simulation of inertial drop break-up in a turbulent pipe flow downstream of a restriction. *International Journal of Multiphase Flow*, **42**, 1-8.

MEIRON D.I. (1989). On the stability of gas bubbles rising in an inviscid fluid, *Journal of Fluid Mechanics*, **198**, *101-114.*

MILLER C.A., SCRIVN L.E. (1968). The oscillations of a fluid droplet immersed in another fluid, *Journal of Fluid Mechanics*, **32**, 417-435.

O'ROURKEP. J., AMSDEN A. A. (1987). The TAB method for numerical calculation of spray droplet, SAE Technical Paper, **218**, 872089.

PROSPERETTI A. (1980). Normal mode analysis for the oscillations of a viscous liquid drop in an immiscible liquid. *Journal de Mécanique*, 19, 149-182.

RAVELET F., COLIN C., RISSO F. (2011). On the dynamics and breakup of a bubble immersed in a turbulent flow. *Physics of Fluids*, **23**, 103301.

RISSO F., FABRE J. (1998). Oscillations and breakup of a bubble immersed in a turbulent field. *Journal of Fluid Mechanics*, **372**, 323-355.

SUSSMAN M., SMITH K.M., HUSSAINI M.Y., OHTA M., ZHI-WEI R. (2007) A sharp interface method for incompressible two-phase flows, Journal of Computational Physics, **221**, 469-505.

TANGUY S., BERLEMONT A. (2005). Application of a Level-Set method for simulation of droplet collisions. *International Journal of Multiphase Flow*, **31**, 1015-1035.

APPENDIX A

We give here the *F* and *G* functions corresponding to the theoretical calculation of Miller and Scriven (1968) for frequency and damping of the axisymmetric shape-oscillations of mode *l*= 2, valid for a drop or a bubble in zero-gravity conditions and without surfactants:

$$F = \frac{25\ (\hat{\rho}\hat{\mu})^{1/2}}{2\sqrt{2}(2\hat{\rho}+3)(1+\ (\hat{\rho}\hat{\mu})^{1/2})}$$

$$G = \frac{5\ (\ 6+4\hat{\mu}-\hat{\rho}\hat{\mu}+\ 16\ \hat{\rho}\hat{\mu}^2\ )}{2\ (2\hat{\rho}+3)(1+\ (\hat{\rho}\hat{\mu})^{1/2})}.$$

10th International Conference on CFD in Oil & Gas, Metallurgical and Process Industries
SINTEF, Trondheim, Norway *CFD 2014*
17-19 June 2014

The parametric sensitivity of fluidized bed reactor simulations carried out in different flow regimes

Schalk CLOETE*, Jan H. CLOETE, Stein Tore JOHANSEN & Shahriar AMINI
[1] SINTEF Materials and Chemistry, 7465 Trondheim, NORWAY

* E-mail: schalk.cloete@sintef.no

ABSTRACT

Fluidized bed simulations carried out within the Kinetic Theory of Granular Flows framework utilize a number of model coefficients which are highly case dependent and difficult to determine accurately. The most important of these are the specularity coefficient (the degree of friction at the wall) and the particle-particle restitution coefficient (inelasticity of inter-particle collisions). This paper demonstrated that modification of these coefficients can trigger a regime change in very narrow and fast risers, thereby introducing a great amount of uncertainty. For situations sufficiently far from the dilute transport regime, however, sudden regime changes are not observed and the influence of these unknown parameters is more systematic. In the case of wide bubbling beds, the effect of these unknown model coefficients can become completely negligible, making these reactors highly attractive for simulation studies. Faster and narrower geometries, on the other hand, exhibit greater sensitivity to changes in the specularity coefficient and particle-particle restitution coefficient, thereby introducing ever-increasing quantities of uncertainty stemming from these unknown model coefficients.

Keywords: Fluidized bed reactors, Two Fluid Model, Kinetic Theory of Granular Flows, Specularity coefficient, Restitution coefficient.

NOMENCLATURE

α	Volume fraction
ϕ	Damping of fluctuating motions [kg/(m.s^2)]
γ_{Θ_s}	Collisional dissipation rate [kg/(m.s^2)]
Θ	Granular temperature [m^2/s^2]
ρ	Density [kg/m^3]
$\bar{\bar{\tau}}$	Stress tensor [kg/(m.s^2)]
$\vec{\upsilon}$	Velocity vector [m/s]
∇	Gradient or Del operator [1/m]
C	Species concentration [mol/m^3]
d	Diameter [m]
$\vec{g}$	Gravity vector [m/s^2]
$\bar{\bar{I}}$	Identity tensor
K	Momentum exchange coefficient [kg/(m^3.s)]
k	Reaction rate constant
k_{Θ_s}	Granular temperature conductivity [kg/(m.s)]
p	Pressure [Pa]
Q	Volumetric flow rate [m^3/s]
R	Universal gas constant [kcal/(K.mol)]
R^H	Heterogeneous reaction rate [mol/(m^{3}s)]
S	Source term
T	Temperature [K]
t	Time [s]
V	Volume [m^3]
w	Solids weight [kg]
x	Mass fraction
Y	Species mass fraction

Sub/superscripts

$\vec{\upsilon}$	Momentum
g	Gas
i	Species index
sg	Inter-phase
s	Solids

INTRODUCTION

Fluidized bed reactors find application in a wide range of process industries, primarily due to their excellent gas-solid mass transfer and mixing characteristics. Despite these very attractive advantages, however, these reactors are difficult to design and scale up due to the complex hydrodynamics of fluidization. Almost all types of fluidization are characterized by the formation of transient clusters of particles which dominate all transport phenomena inside the reactor. The behaviour of these clusters depends on a wide range of parameters and must be understood to ensure effective reactor design and scale-up.

With the continued exponential increase in computational power and availability, fundamental flow modelling has emerged as a very promising method for improving the understanding of the complex behaviour exhibited by fluidized bed reactors. The foremost of

these modelling frameworks, the Two Fluid Model (TFM) closed by the Kinetic Theory of Granular Flows (KTGF) (Jenkins and Savage, 1983, Lun et al., 1984, Gidaspow et al., 1992, Syamlal et al., 1993), has progressed to a high level of maturity over the past three decades of development and can already offer reliable predictions of fluidized bed behaviour (Taghipour et al., 2005, Ellis et al., 2011, Cloete et al., 2013). It therefore holds great potential to support the design and accelerate the scale-up of fluidized bed reactor technology.

The primary challenge facing the TFM is the fine grids required to accurately resolve all of the small scale particle clusters. These fine grids make simulations very computationally expensive and often restrict the TFM to small scale 2D simulations. Alternative modelling approaches such as the Dense Discrete Phase Model (Popoff and Braun, 2007) and the filtered Two Fluid Model (Igci et al., 2008) are currently under development to also allow for the simulation of cases with fine powders and fast kinetics, but the standard TFM is likely to form the foundation of fluidized bed reactor modelling for many years into the future.

Just like the grid dependence behaviour of the TFM depends greatly on the flow conditions simulated, practical experience has shown the type of flow conditions being simulated to also have a major influence on simulation behaviour. This is an important observation because fluidized bed reactors can be designed to operate in a wide range of different flow regimes depending on the characteristics of the solid material and the desired reaction. For example, the classic work of Bi and Grace (Bi and Grace, 1995) distinguishes between batch operation (typical bubbling or turbulent fluidization) and vertical transport (typical for the riser of a circulating fluidized bed), also identifying different flow regimes within each of these two categories.

TFM simulations of the carbonator in a potassium looping process for post combustion CO_2 capture (more information about this process can be found in (Samanta et al., 2011)) will be employed to illustrate one flow regime where simulations are very sensitive to mostly unknown model coefficients (the wall friction and particle restitution coefficient). This will henceforth be termed the "example study". Subsequently, a more generic study of the impact of these two model coefficients under different flow conditions will be made. This will be termed the "generic study".

MODEL DESCRIPTION

The standard TFM equation set is employed with different drag closure laws for the example study (potassium looping) and the generic study (broad study across different flow regimes).

Conservation equations

In all cases, the fundamental conservation equations for mass, momentum and species were solved. Mass was conserved as follows:

$$\frac{\partial}{\partial t}\left(\alpha_g \rho_g\right)+\nabla\cdot\left(\alpha_g \rho_g \vec{v}_g\right)=\alpha_g S_g \qquad (1)$$

$$\frac{\partial}{\partial t}\left(\alpha_s \rho_s\right)+\nabla\cdot\left(\alpha_s \rho_s \vec{v}_s\right)=0 \qquad (2)$$

The source term for the gas phase equation (right hand term in (**1**) is included to account for mass transfer due to the heterogeneous reaction. Mass changes in the solids phase are neglected because these changes would be insignificant relative to the total mass of the solids.

Momentum conservation for the gas phase is written as

$$\frac{\partial}{\partial t}\left(\alpha_g \rho_g \vec{v}_g\right)+\nabla\cdot\left(\alpha_g \rho_g \vec{v}_g \vec{v}_g\right)=-\alpha_g \nabla p+\nabla\cdot\bar{\bar{\tau}}_g+\alpha_g \rho_g \vec{g}+K_{sg}\left(\vec{v}_s-\vec{v}_g\right)+S_g^v \qquad (3)$$

and for the solids as

$$\frac{\partial}{\partial t}\left(\alpha_s \rho_s \vec{v}_s\right)+\nabla\cdot\left(\alpha_s \rho_s \vec{v}_s \vec{v}_s\right)=-\alpha_s \nabla p-\nabla p_s+\nabla\cdot\bar{\bar{\tau}}_s+\alpha_s \rho_s \vec{g}+K_{gs}\left(\vec{v}_g-\vec{v}_s\right) \qquad (4)$$

Species are also conserved for the gas phase.

$$\frac{\partial}{\partial t}\left(\alpha_g \rho_g Y_{g,i}\right)+\nabla\cdot\left(\alpha_g \rho_g \vec{v}_g Y_{g,i}\right)=\nabla\cdot\alpha_g \vec{J}_{g,i}+\alpha_g S_{g,i} \qquad (5)$$

No energy conservation was considered under the assumption of isothermal reactor operation.

Closure relations

The conservation equations need to be closed by additional modelling.

Interphase momentum exchange

The drag laws governing the interphase momentum exchange ($K_{gs}=K_{sg}$ in (**3**) and (**4**)) were different for the two studies considered. For the example study, the correlation from Wen and Yu (Wen and Yu, 1966) was used, while the more generic Syamlal and O'Brien drag law (Syamlal et al., 1993) was implemented for the generic study. These are fairly standard selections in the literature.

Solids stresses

Solids stresses were modelled using the well documented kinetic theory of granular flows (KTGF) (Jenkins and Savage, 1983, Lun et al., 1984, Gidaspow et al., 1992, Syamlal et al., 1993). In the KTGF analogy, the random motion of granular particles is likened to the vibration of gas molecules where the kinetic theory of gasses is applied. This analogy allows the determination of fluid properties for the particulate phase by accounting for the inelasticity of the particles. The granular temperature is a measure of the energy contained in these random particle motions and is conserved as follows:

$$\frac{3}{2}\left[\frac{\partial}{\partial t}\left(\alpha_s \rho_s \Theta_s\right)+\nabla\cdot\left(\alpha_s \rho_s \vec{v}_s \Theta_s\right)\right]=\left(-p_s \bar{\bar{I}}+\bar{\bar{\tau}}_s\right):\nabla\vec{v}_s+\nabla\cdot\left(k_{\Theta_s}\nabla\Theta_s\right)-\gamma_{\Theta_s}+\phi_{gs} \qquad (6)$$

On the right hand side of the equation, the terms represent the generation of granular temperature via the solids stress tensor, granular temperature conductivity (Gidaspow et al., 1992), dissipation of energy due to inelastic collisions (Lun et al., 1984) and the energy exchange between the gas phase and the random motions of the particles (Gidaspow et al., 1992).

The granular temperature is subsequently used to calculate values of the solids viscosity which is used in the solids stress tensor. Bulk viscosity (Lun et al., 1984) and the three components of shear viscosity, collisional (Gidaspow et al., 1992, Syamlal et al., 1993), kinetic

(Gidaspow et al., 1992) and frictional (Schaeffer, 1987), were considered in the calculations.

Normal stresses modelled according to the solids pressure are calculated according to (Lun et al., 1984). The radial distribution function which is a measure of the average distance between particles is a central concept in the KTGF and is calculated according to (Ogawa et al., 1980).

Reaction kinetics description

Due to the novelty of the potassium looping CO_2 capture process simulated in the example study, a sufficiently generic description of reaction kinetics specifically formulated for implementation into numerical models is not yet available from a single source. Therefore, the approach used in this paper uses insights from different works studying the kinetics of the carbonation reaction:

$$CO_2 + H_2O + K_2CO_3 \rightarrow 2KHCO_3$$

A simple reaction kinetics description where the rate is dependent only on the CO_2 concentration and the volume fraction of solids was used by (Chalermsinsuwan et al., 2010).

$$R^H = k_1 \alpha_s C_{CO_2} \tag{7}$$

This formulation is very easy to implement in the code, but the reaction rate constant (taken as $k_1 = 1.95\ s^{-1}$ in this case) was derived from a parallel plate reactor (not the real fluidized bed application studied here) and it was not expressed as a function of temperature.

Another research group studied the kinetics of the carbonation reaction by collecting CO_2 breakthrough data from a packed reactor and fit a deactivation model to this data (Park et al., 2006). The deactivation model produced a good fit and described how the catalyst was deactivated over time due to the diffusion resistance from a dense product layer forming on its outside. This deactivation process occurred on a rather long timescale (~1h in the experiments conducted) and will therefore not be significant in real applications where the particle residence time is in the order of seconds or minutes. The deactivation model used was also derived in terms of variables like the gas-solid contact time and the feed rate to the packed bed which is not suitable for implementation into a CFD model.

Therefore, it was assumed that the deactivation caused by the product layer formation is not significant and the rate is exclusively controlled by the kinetics. The aforementioned work (Park et al., 2006) determined a reaction rate constant as a function of time, but it was expressed in rather unconventional units (m^6/(kg.kmol.min)) as follows:

$$k_b = 1.191 \times 10^5 \exp\left(\frac{-7.544}{RT}\right) \tag{8}$$

Here, R is the universal gas constant expressed in kcal/(K.mol) and T is the temperature in Kelvin. In order to be useful for numerical modelling, however, this reaction rate constant has to be converted to a more standard form with the units of s^{-1}. This was done as follows:

In the experimental work (Park et al., 2006), this reaction rate constant was used in a 1D species conservation equation through the packed bed:

$$-Q_g \frac{dC_{CO_2}}{dw} = k_b C_{H_2O} C_{CO_2} \tag{9}$$

Here, Q_g is the volumetric flow rate of the feed gas and w is the weight of solids in the bed. In order to be useful for implementation into the CFD model, however, this equation has to be written in a dC_{CO_2}/dt form. This can be done through manipulation using the chain rule:

$$-Q_g \frac{dC_{CO_2}}{dw} = -Q_g \frac{dC_{CO_2}}{dt}\frac{dt}{dw} = -Q_g \frac{dC_{CO_2}}{dt}\frac{dt}{dV}\frac{dV}{dw} = -Q_g \frac{dC_{CO_2}}{dt}\frac{\alpha_g}{Q_g}\frac{1}{\alpha_s \rho_s} \tag{10}$$

(9) can now be rewritten in the desired form:

$$-\frac{dC_{CO_2}}{dt} = \left(\frac{k_b C_{H_2O} \rho_s}{\alpha_g}\right) \alpha_s C_{CO_2} \tag{11}$$

Here, the bracketed term represents the rate constant in the correct form with the units of s^{-1} as written in (7). (7) therefore implicitly assumes that the reaction rate is independent of the water vapour concentration, but this was proven not to be the case in (Park et al., 2006) where a first order dependency was observed. This work will therefore use a rate equation dependent on both the water vapour and CO_2 molar concentrations.

In addition, another work (Sharonov et al., 2004) also observed an inverse proportionality between the reaction rate and the particle diameter. This is a well-known relationship implying that the reaction occurs on the surface of each particle and that smaller particles would present a larger combined surface area per unit volume than larger particles according the ratio between particle surface area and volume $(6/d_s)$.

The final rate equation will therefore be written in the form:

$$-\frac{dC_{CO_2}}{dt} = \frac{6}{d_p} \alpha_s k C_{H_2O} C_{CO_2} \tag{12}$$

In order to arrive at the correct expression for the reaction rate constant, the particle density and particle surface area per volume ratio have to be taken into account:

$$k = \frac{k_b \rho_s d_p}{6\alpha_g} \tag{13}$$

Taking into account that the particle density was 2394 kg/m^3, the particle diameter was 401.67 µm and the bed void fraction was 0.475 in the experiments, (13) can be rewritten as follows where the reaction rate constant has the units of (m^3/kmol).(m/s):

$$k = 669.75 \exp\left(\frac{-7.544}{RT}\right) \tag{14}$$

For the generic study, the very simple hypothetical reaction rate description given below was used in order to convert species A into species B with a 1:1 stoichiometric ratio. Species A and B had the same material properties in order to ensure that the reaction would not have any influence on the hydrodynamics.

$$-\frac{dC_A}{dt} = 0.25 \alpha_s x_A \tag{15}$$

Geometry and meshing

The riser in the example study was modelled according to the specifications provided in (Yi et al., 2007). The total length of the riser was 6 m with an inner diameter of 2.5 cm. The lower 0.45 m of the riser was a mixing zone with a wider inner diameter of 3.5 cm which narrowed to 2.5 cm at a height of 0.6 m. 2.5 mm cubical cells were used in the mesh, resulting in a cell size roughly 25 times the particle size. A limited number of computationally very expensive simulations were also performed on a mesh with 1.25 mm cells which resulted in 1.7 million cells in the domain.

Simulations for the generic study were carried out on a simple 2D planar geometry meshed with 2.5 mm cells which were also about 13 times the particle size. Five different geometries were studied both under batch (Table 1) and vertical transport (Table 2) operation where the total volume of the domain, the total gas flow through the domain and the total amount of solids within the domain was kept constant between runs as the aspect ratio was varied over a large range.

Table 1: Dimensions and fluidization velocity of the batch operation cases in the generic study.

Width (m)	Height (m)	Fluidization velocity (m/s)
2.4	0.3	0.1
1.2	0.6	0.2
0.6	1.2	0.4
0.3	2.4	0.8
0.15	4.8	1.6

Table 2: Dimensions and fluidization velocity of the vertical transport cases in the generic study.

Width (m)	Height (m)	Fluidization velocity (m/s)
0.600	1.200	1.600
0.424	1.697	2.263
0.300	2.400	3.200
0.212	3.394	4.525
0.150	4.800	6.400

Boundary conditions

The lower face of the geometry in the example study was specified as a velocity inlet, injecting gas at a velocity of 1.02 m/s and solids at a velocity of 0.0209 m/s and a volume fraction of 0.2. The gas stream consisted of 9.72% CO_2, 19% H_2O and the balance N_2 (on a molar basis). These specifications resulted in a gas superficial velocity of 2 m/s in the 2.5 cm body of the riser and a solids flux of 15 kg/m^{2}s. These were the conditions reported for the 11-17 hour operational period in (Yi et al., 2007).

For the generic study, the lower face of the geometry was also specified as a velocity inlet, injecting gas at the velocity specified in Table 1. The bed was initialized in such a way that the average solids volume fraction over the entire bed was 0.1. For the vertical transport cases in the generic study (Table 2), solids were also continuously injected over the velocity inlet at a volume fraction of 0.1 and a velocity which was 10% of the gas injection velocity.

The outlets of both geometries were specified as pressure outlets at atmospheric pressure. No-slip wall boundary conditions were specified for the gas phase, while partial slip boundary conditions (Johnson and Jackson, 1987) were specified for the solids phase. The specularity coefficient (ς in (16) and (17)) and the particle-wall restitution coefficient (e_{sw} in (17)) were varied between the different simulations carried out in this work.

$$\vec{\tau}_s = -\frac{\pi}{6}\sqrt{3}\varsigma\frac{\alpha_s}{\alpha_{s,\max}}\rho_s g_{0,ss}\sqrt{\Theta_s}\vec{U}_{s,\|} \tag{16}$$

$$q_s = \frac{\pi}{6}\sqrt{3}\varsigma\frac{\alpha_s}{\alpha_{s,\max}}\rho_s g_{0,ss}\sqrt{\Theta_s}\vec{U}_{s,\|}\cdot\vec{U}_{s,\|} - \frac{\pi}{4}\sqrt{3}\frac{\alpha_s}{\alpha_{s,\max}}\left(1-e_{sw}^2\right)\rho_s g_{0,ss}\Theta_s^{3/2} \tag{17}$$

For the example study, the temperature was fixed as a function of the reactor height in order to reproduce the temperature measurements taken in the experiments (Yi et al., 2007). The temperature (T) was fixed as a function of the height (h) through the following fourth-order polynomial:

$$T = -0.2073h^4 + 4.4354h^3 - 26.619h^2 + 45.941h + 353.15$$

No energy conservation was included in the bubbling fluidized bed simulations.

Material properties

Material properties for the gas and solids phases are given in Table 3 and Table 4. For the example study, the solids density was calculated from the given bulk density of 1100 kg/m^3 (Yi et al., 2007) assuming a solids volume fraction of 0.6 under packing.

Table 3: Material properties for the example study.

Gas density:	Ideal gas law
CO_2 viscosity:	$4.68\text{E-}8T + 1.00\text{E-}6$ kg/(m.s)
H_2O viscosity:	$3.42\text{E-}8T - 3.75\text{E-}7$ kg/(m.s)
N_2 viscosity:	$4.32\text{E-}8T + 4.94\text{E-}6$ kg/(m.s)
Solids density:	1833 kg/m^3
Particle size:	98 μm

Table 4: Material properties for the generic study.

Gas density:	0.3 kg/m^3 (species A & B)
Gas viscosity:	4E-5 kg/(m.s) (species A & B)
Solids density:	2500 kg/m^3
Particle size:	200 μm

RESULTS AND DISCUSSION

This section will be divided in two parts discussing results from the example and generic studies.

Example study

The sensitivity of this narrow riser simulation to unknown model coefficients; the specularity coefficient, the particle-wall restitution coefficient and the particle-particle restitution coefficient, was evaluated by means of a central composite design (Montgomery, 2001). This is a form of experimental design (also applicable to simulation experiments) where the response of specific dependent variables to changes in various independent

variables can be easily assessed, accurately quantified and visualized. The three aforementioned model coefficients were taken as the independent variables and simulation behaviour was quantified by means of two dependent variables: the overall pressure drop and the overall degree of CO_2 absorption.

The central composite design consisted of 16 simulation experiments, filling the three dimensional parameter space with the reactor performance resulting from each specific set of model coefficients. Results will be displayed in two ways: an analysis of variance (ANOVA) and response surfaces of dependent variables to changes in various independent variables. The ANOVA will be used to quantify the significance of the independent variables (i.e. identify the model coefficients which had a statistically significant influence on the simulation behaviour).

The significance of factors will be defined by the p-value which is an indication of the probability of the observed effect to result purely by random chance. If this value becomes small $(p < 0.05)$, the effect is said to be significant because the probability of it arising from pure chance is fairly small. A value of $p < 0.01$ is generally regarded as highly significant. The p-value is calculated from the F-test which weighs the amount of explained variance in the design against the amount of unexplained variance (experimental error, rounding error, averaging error, data not fitting the second order model etc.). This ratio can then be evaluated as a p-value to decide whether the variance is caused by a significant effect or is simply random.

Table 5: ANOVA table summarizing the response of the total pressure drop and the degree of CO_2 absorption to changes in the three unknown model coefficients under investigation: the specularity coefficient (S), the particle-particle restitution coefficient (PP) and the particle-wall restitution coefficient (PW). Significant factors are shown in bold, while highly significant factors are shown in bold italics. The factors are denoted by S (specularity coefficient), H (particle-wall restitution coefficient) and d (particle-particle restitution coefficient). Different effects are indicated by L (linear), Q (quadratic) and by (interaction).

Effect	Residence time		Mass transfer	
	SS (%)	p-value	SS (%)	p-value
S(L)	***36.12***	***0.0006***	***37.38***	***0.0032***
S(Q)	**5.16**	**0.0453**	3.02	0.2271
PP(L)	***32.29***	***0.0007***	***31.63***	***0.0048***
PP(Q)	4.54	0.0561	2.78	0.2442
PW(L)	4.20	0.0635	6.22	0.1016
PW(Q)	1.26	0.2605	1.71	0.3501
S(L) by PP(L)	***15.56***	***0.0047***	**10.74**	**0.0441**
S(L) by PW(L)	0.11	0.7222	0.00	0.9936
PP(L) by PW(L)	0.13	0.7009	0.02	0.9083
Error	4.88		10.00	
Total	100.00		100.00	

The relative variance explained by each factor will also be given as the percentage of the total sum of squares (SS). The total sum of squares is the sum of all the squared distances between the various data points and the mean. A larger total sum of squares implies that the data are scattered wide around the mean and there is a lot of variance in the design. This measure will give an indication of the importance of significant effects relative to each other. The ANOVA results for the riser simulation are given in Table 5.

It is clear from the data in Table 5 that changes in the specularity coefficient and the particle-particle restitution coefficient had the greatest impact on the results, while the effect of particle-wall restitution coefficient was not statistically significant. This is in line with results from an earlier study on the parametric sensitivity of riser simulations (Cloete et al., 2011).

However, the most important result from this central composite design is the magnitude of the variations in overall pressure drop and CO_2 absorption caused by changes in the unknown model coefficients. This large variation is shown in Figure 1.

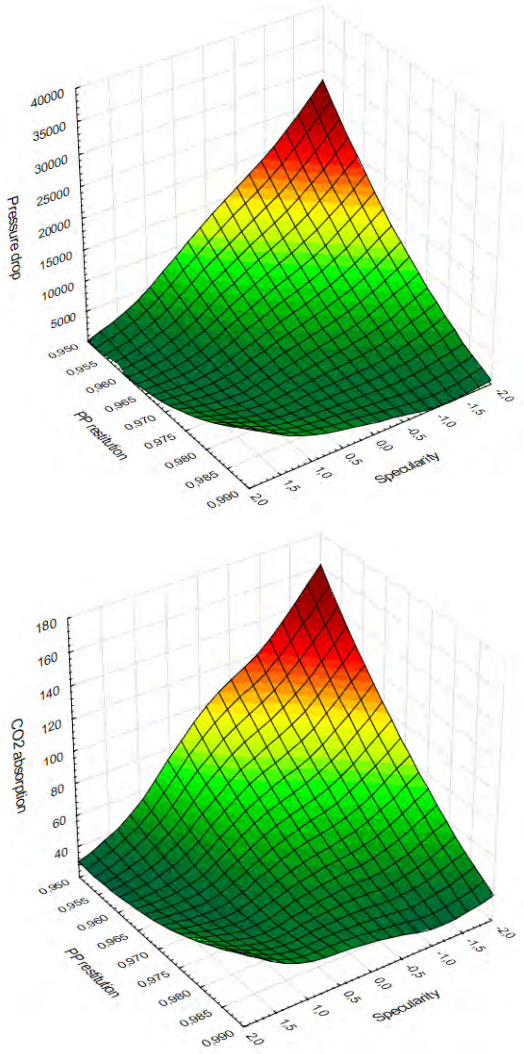

Figure 1: Response of the total pressure drop (Pa) and the CO2 absorption (%) in response to changes in the specularity coefficient and the particle-particle restitution coefficient. Note that the specularity coefficient is given in coded variables (c) where the actual specularity coefficient is given by: $\varsigma = 0.002 \times 2^c$ **.**

Firstly, it must be pointed out that the maximum values in Figure 1 (at the lowest values of the specularity and particle-particle restitution coefficients) can be misleading because it is an extrapolation of a very sharp gradient. For example, the CO_2 absorption cannot be more than 100%, but the extrapolated value projects an absorption of 160% at the lowest specularity and particle-particle restitution coefficients observed in the simulation.

When looking at results from the simulations, a specularity coefficient of 0.001 (coded variable of -1) and a particle-particle restitution coefficient of 0.96 returned a pressure drop of 12.5 kPa and 89.2% CO_2 absorption, while a specularity coefficient of 0.004 (coded variable of 1) and a particle-particle restitution coefficient of 0.98 returned a pressure drop of 1.3 kPa and 34.7% CO_2 absorption. It is therefore clear that this relatively small variation in model coefficients caused almost an order of magnitude difference in the solids holdup in the riser.

The reason for this very large influence is the non-linear influences that cluster formation has on riser performance. Cluster formation can be a self-reinforcing phenomenon since the presence of clusters creates the large velocity gradients necessary to separate free particles from streamlines so that they join into the bulk of the cluster. This non-linear nature of clustering causes the very large difference in riser hydrodynamics shown in Figure 2.

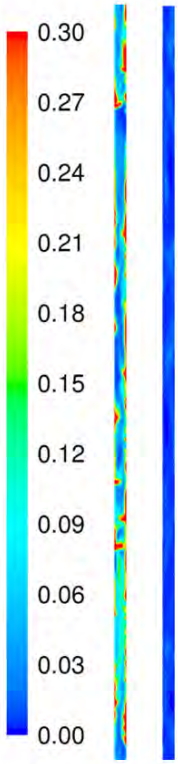

Figure 2: (On the left) Instantaneous volume fraction profiles in identical locations in the riser for the case with a specularity coefficient of 0.001 and a particle-particle restitution coefficient of 0.96 (left) and the case with a specularity coefficient of 0.004 and a particle-particle restitution coefficient of 0.96 (right).

Lower particle-particle restitution coefficients are beneficial to clustering due to the increased dissipation of granular temperature (and the associated reduction in granular pressure) in denser regions. Lower specularity coefficients are beneficial to clustering due to the free slip of denser clusters across smoother walls without being broken up by excessive shear forces. It appears evident that cluster formation is triggered over a very small range of these unknown model coefficients and causes very large differences in riser behaviour after being triggered.

In order to assess the influence of the grid size on these phenomena, three very computationally expensive simulations were completed on a mesh which was refined via hanging node adaption. Interestingly, the clustering was triggered at significantly lower specularity and particle-particle restitution coefficients than on the coarse mesh. This is counter-intuitive because finer meshes are normally more conducive to clustering. Finer meshes can resolve the high flow gradients around clusters, allowing free-flowing particles to deviate from the streamlines and join in the bulk of the cluster. It is expected that this trend is caused by the larger flow gradients resolved at the walls which can break up clusters more efficiently than on the coarser grid.

The three fine grid simulations were therefore carried out using a particle-particle restitution coefficient of 0.9 and specularity coefficients varying over a wide range of 0.01, 0.001 and 0.0001. The resulting match to pressure drop data from the experiment is given in Figure 3.

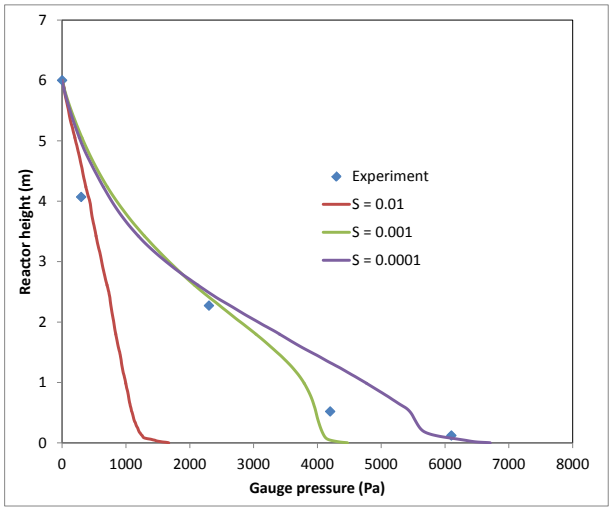

Figure 3: Model comparisons to axial pressure measurements (Yi et al., 2007) using different specularity coefficients (S) and a particle-particle restitution coefficient of 0.9.

It is shown that the simulations with a low specularity coefficient matched the experimental results well, but a higher specularity coefficient caused a situation where very little cluster formation was simulated and the solids holdup in the reactor was greatly under-predicted.

For the low specularity coefficient cases, a comparison was also made to species measurements at the outlet of the reactor. The simulation returned values around 70% CO2 capture at the outlet while the experimental measurements returned about 50% CO2 capture. This implies that the reaction rate constant in (14) is too high and will need refinement through dedicated experiments.

Generic study

The discussion will be split between the batch operation cases (Table 1) and the vertical transport cases (Table 2).

Batch operation cases

It can be expected that the very large influence of unknown model coefficients on important model outputs observed in the previous section for the riser will be significantly reduced for dense fluidization. There are two main reasons for this observation.

Firstly, dense fluidized beds generally have larger diameters due to the fact that they have to employ smaller fluidization velocities. A larger diameter implies a smaller walls/volume ratio and therefore a smaller wall

influence. In addition, the slower fluidization in dense beds will result in smaller wall shear forces and therefore less of an influence on the overall reactor behaviour.

Secondly, dense fluidized beds, if solved on a sufficiently fine grid, will always display clustering. The sudden transition from a situation of no clustering to a situation of significant clustering illustrated in Figure 2 can therefore not happen in dense fluidized beds.

As a result of these two factors, it is reasoned that dense fluidization can be simulated with a much larger degree of confidence than riser flow. This assumption was tested via the five cases outlined in Table 1.

Two main variables will be extracted to describe the macroscopic behaviour of the reactor: the pressure drop over the bottom 25% of each domain (an area filled with solids in all cases) and the reactor performance defined as the negative logarithm of the reactant mole fraction exiting the reactor unreacted.

The aim of using the $-\log(x_A)$ measure is to linearize the performance achieved by the reactor running a first order reaction. For example, if all other variables were kept constant, a reactor running a first order reaction would require twice the amount of residence time to achieve 99% conversion than to achieve 90% conversion. Hence, the reactor performance of a reactor achieving 99% conversion is $-\log(0.01)=2$ while the reactor performance of a reactor achieving 90% conversion is $-\log(0.1)=1$.

Firstly, the grid dependency behaviour of the dense fluidized bed cases must be evaluated. As shown in Figure 4 and Figure 5, the influence of different grid sizes on the reactor behaviour was fairly small, especially with regard to the pressure drop. For engineering applications, results derived from the 5 mm grid would be adequate, but the 2.5 mm grid was used in the remainder of this study.

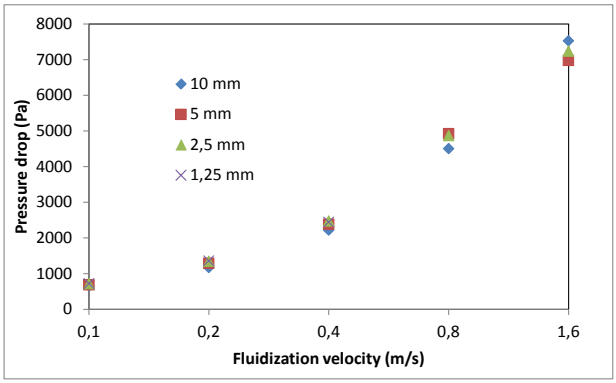

Figure 4: Pressure drop in the lower 25% of the reactor for the five different cases in Table 1 calculated using different cell sizes.

The grid dependency effects displayed in Figure 4 and Figure 5 are small in comparison to that observed in the riser case where one refinement could cause a transition from fast fluidization to pneumatic transport, thereby completely changing the behaviour of the reactor.

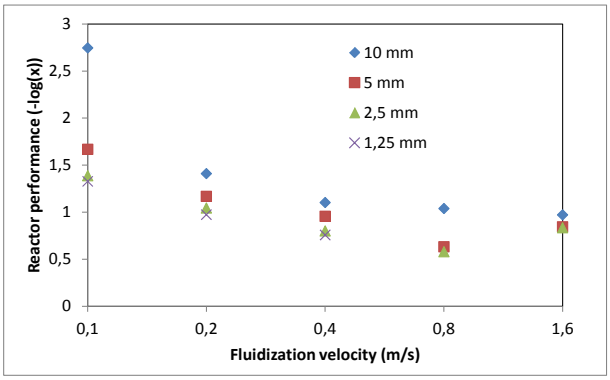

Figure 5: Reactor performance for the five different cases in Table 1 using different cell sizes.

Secondly, the effect of specularity coefficient was assessed with results presented in Figure 6 and Figure 7.

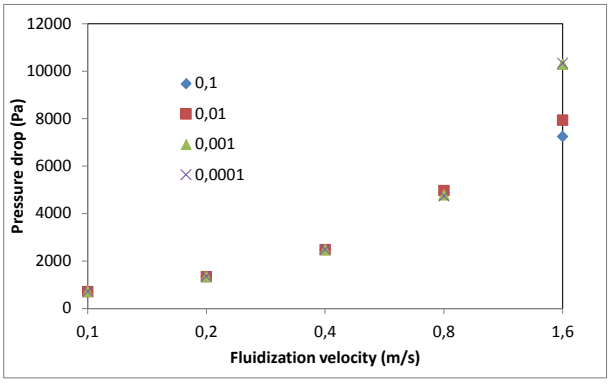

Figure 6: Pressure drop in the lower 25% of the reactor for the five different cases in Table 1 calculated using different specularity coefficients.

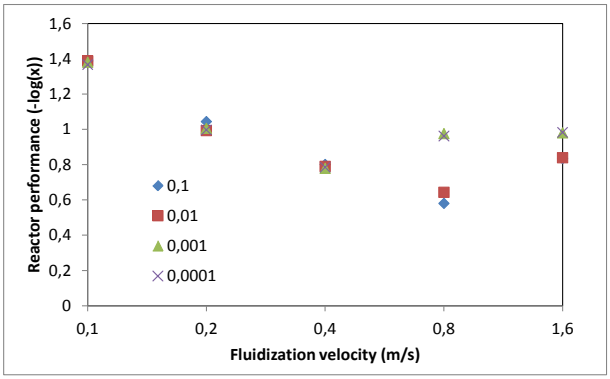

Figure 7: Reactor performance for the five different cases in Table 1 using different specularity coefficients.

It is clear that large changes in the specularity coefficient had no discernible impact on the model results for the cases with a fluidization velocity of 0.4 m/s and below. For the cases with a fluidization velocity of 0.8 m/s and 1.6 m/s, however, a significant difference in rector performance can be observed when transitioning from a specularity coefficient of 0.01 to a specularity coefficient of 0.001.

These geometries were only 30 and 15 cm in diameter respectively and therefore were subject to a significant degree of influence from the walls. As shown in Figure 8, this influence had a significant impact on the nature of the cluster formation in the fluidized bed.

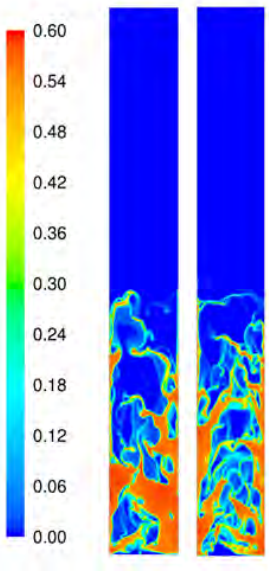

Figure 8: (On the left) Instantaneous volume fraction profiles for the case with a fluidization velocity of 0.8 m/s. The left-hand image is for a specularity coefficient of 0.01 and the right hand image is for a specularity coefficient of 0.001.

The difference in hydrodynamics created by a change in the specularity coefficient from 0.01 to 0.001 is evident from Figure 8. When the specularity coefficient is lowered, falling solids near the wall create higher shear forces, leading to finer and more chaotic flow structures. When looking at Figure 7, it is clear that these finer flow structures led to increased gas-solid contact and improved reactor performance (greater conversion).

Figure 6 shows, however, that this improved gas-solid contact was cancelled out to a certain degree in the 1.6 m/s fluidization velocity case by a more compacted bed in the lower reactor regions. This more compact bed reduced the quality of contact between gas and solid in this region thereby countered the improved mass transfer effect of the finer flow structures to a certain degree. This is the reason why the specularity coefficient appears to have a larger influence on the reactor performance in the case with 0.8 m/s fluidization velocity than in the case with 1.6 m/s fluidization velocity.

Thirdly, the sensitivity of the dense fluidized bed simulations to changes in the particle-particle restitution coefficient was assessed. As shown in Figure 9 and Figure 10, the impact is again moderate at higher fluidization velocities and negligible at lower fluidization velocities.

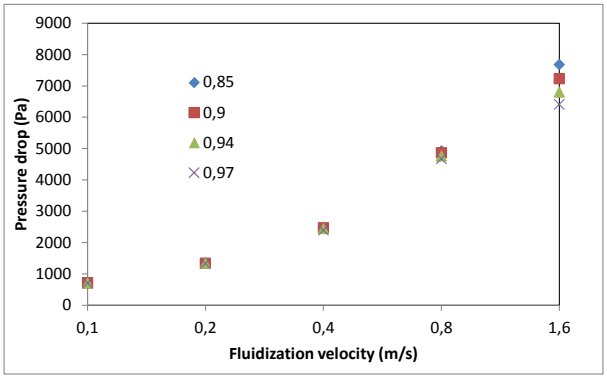

Figure 9: Pressure drop in the lower 25% of the reactor for the five different cases in Table 1 calculated using different particle-particle restitution coefficients.

For the reactor performance (Figure 10) all cases show a discernible impact of the highest particle-particle restitution coefficient (0.97). At this value, cluster formation was sufficiently suppressed to enhance gas-solid contact and thereby increase reactor performance. However, for particle-particle restitution coefficients around values that are usually employed (~0.9), the impact seems to be very small.

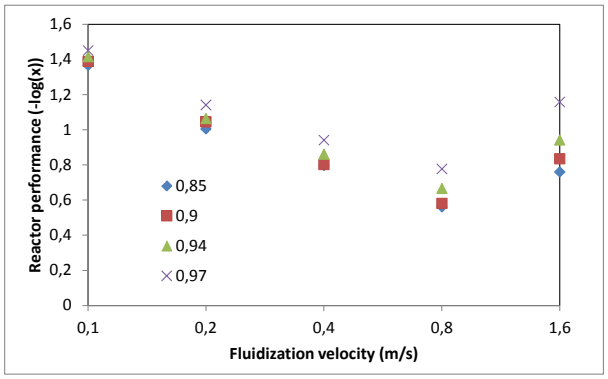

Figure 10: Reactor performance for the five different cases in Table 1 using different particle-particle restitution coefficients.

It is therefore clear that the sensitivity of dense fluidized bed simulations to changes in the two most important unknown model coefficients is much smaller than for the narrow riser case shown in Figure 1.

Vertical transport cases

For the vertical transport simulations in Table 2, $-\log(x_A)$ was also used to evaluate the amount of conversion that takes place. However, the average volume fraction of the solids phase within the entire geometry was used as the hydrodynamic performance measure.

When varying the specularity coefficient it is observed (Figure 11) that there is a small effect on solid holdup at all velocities. The overall effect appeared to be too small to distinguish a clear trend on how the specularity coefficient influences the amount of solids in the riser. On the other hand, when evaluating the reactor performance (Figure 12), the effect of the specularity coefficient is highly significant at lower fluidization velocities, but almost disappears for the highest two velocities investigated.

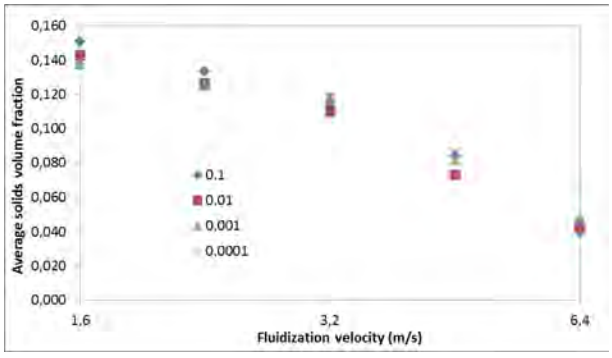

Figure 11: Average solid holdup for five different cases in Table 2 using different specularity coefficients.

Plots of the instantaneous solids volume fraction for different specularity coefficients aid in explaining these trends. Figure 13 shows such plots for the case with a fluidization velocity of 2.26 m/s, where the largest changes in reactor performance were observed. It is shown that at lower specularity coefficients there are streaks of falling solids near the walls. This is similar to

what occurred in the dense fluidized bed and the resulting shear stresses cause finer flow structures to form. With an increase in the specularity coefficient, the amount of falling solids decrease and more distinct solids clusters form.

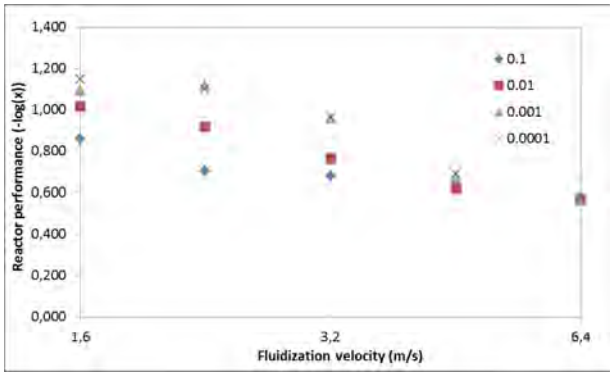

Figure 12: Reactor performance for five different cases in Table 2 using different specularity coefficients.

There are therefore two effects that influence the solid holdup as the specularity coefficient is decreased. Firstly, an increase in falling solids near the walls will tend to keep the solids in the riser column. On the other hand, the finer solid structures will be more easily transported from the column by the gas flow. The relatively small change in solid holdup with specularity coefficient observed in Figure 11 therefore shows that these two effects balance each other out over all fluidization velocities considered.

No sudden regime transitions as seen in the example study were observed. The complete lack of sensitivity of the faster cases to changes in the specularity coefficient is especially surprising considering the large influence of the wall in these cases. This result illustrates that the two effects described above effectively cancel each other out in narrow geometries and that a step change can only be expected when approaching the dilute transport regime where a sudden transition between smooth and clustered flow can be triggered.

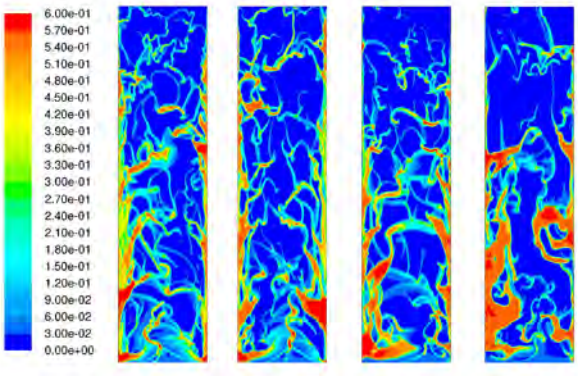

Figure 13: Instantaneous volume fraction profiles for the case with a fluidization velocity of 2.26 m/s. From left to right the specularity coefficients used are: 0.0001, 0,001, 0.01 and 0.1.

In the case of reactor performance, the finer flow structures at low specularity coefficients lead to better gas-solid contact, which explains the increase in conversion with a decrease in specularity coefficient observed in Figure 12.

Analyses of the solid holdup at different particle-particle restitution coefficients shows a clear trend of increased solids holdup with a decrease in the particle-particle restitution coefficient. This effect changes from moderate (13% increase) at low fluidization velocity to severe (113% increase) at high fluidization velocities. Clusters will form more readily at lower particle-particle restitution coefficients and there will be fewer fine solid structures that can easily be transported from the column.

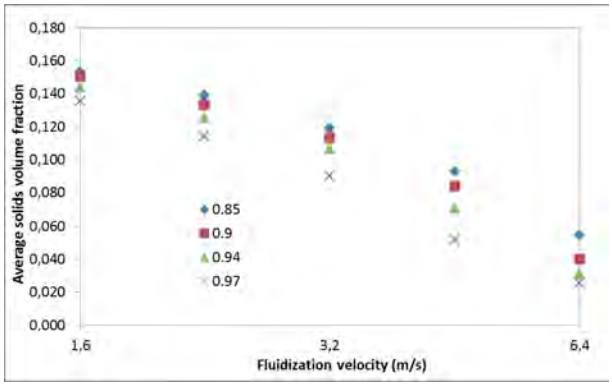

Figure 14: Average solid holdup for five different cases in Table 2 using different particle-particle restitution coefficients.

When assessing the effect on reactor performance (Figure 15), it is seen that, for lower fluidization velocities, the reactor performance increases at higher particle-particle restitution coefficients. This is due to better gas/solid contact in the finer flow structures that form. However, at faster fluidization velocities, the amount of solids present in the riser column decreases significantly at increased particle-particle restitution coefficients, which limits the conversion in the gas phase. Therefore, at fluidization velocities of 4.53 m/s and 6.4 m/s the effect on the reaction rate of increases in solid-gas contact and decreases in the amount of solids present cancel each other almost exactly. This explains why changes in the particle-particle restitution coefficient have a negligible impact at faster fluidization velocities.

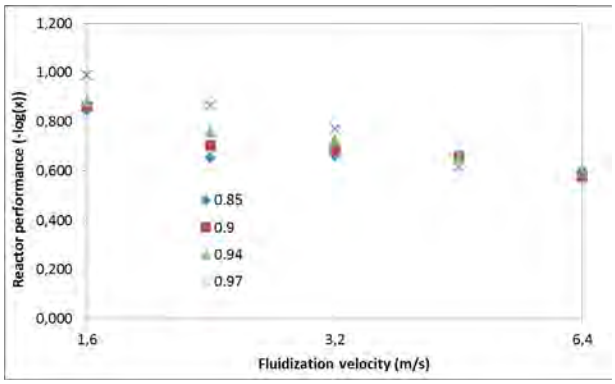

Figure 15: Reactor performance for five different cases in Table 2 using different particle-particle restitution coefficients.

CONCLUSION

The kinetic theory of granular flows commonly used in granular flow simulations involves a number of relatively unknown model coefficients which are often used as tuning coefficients. These coefficients introduce a significant amount of uncertainty to fluidized bed simulations and can potentially have a very large impact on model results.

This study investigated three such model coefficients: the specularity coefficient, the particle-wall restitution coefficient and the particle-particle restitution coefficient. Of these coefficients, the specularity and particle-particle restitution coefficient were shown to have the greatest impact on model results.

The impact of these unknown model coefficients on simulation results depends strongly on the flow regime under which the simulations were carried out. A very narrow riser case showed very large non-linear responses to changes in the specularity and particle-particle restitution coefficients as these coefficients triggered a regime change in the reactor. On the other hand, for bubbling, turbulent and fast fluidization where cluster formation is always present, such rapid regime changes were not observed.

For bubbling fluidization in wide reactors, the effect of these unknown coefficients can become completely negligible. This, combined with the fact that bubbling beds generally use larger particle sizes and slower reaction rates, makes such reactors much simpler to simulate than faster riser reactors. Even though rapid step changes were not observed for clustered flows in narrower geometries under faster fluidization, the influence of the unknown model coefficients did become increasingly significant, thereby introducing significant amounts of uncertainty into the simulation results.

ACKNOWLEDGEMENTS

The authors gratefully acknowledge the research funding received from the Research Council of Norway as well as the Notur supercomputing facilities used to carry out the very expensive riser simulations in this paper.

REFERENCES

BI, H. T. and GRACE, J. R., (1995), "Flow regime diagrams for gas-solid fluidization and upward transport", *International Journal of Multiphase Flow*, **21**(6), 1229-1236.

CHALERMSINSUWAN, B., PIUMSOMBOON, P. and GIDASPOW, D., (2010), "A computational fluid dynamics design of a carbon dioxide sorption circulating fluidized bed", *AIChE Journal*, **56**(11), 2805-2824.

CLOETE, S., AMINI, S. and JOHANSEN, S. T., (2011), "A fine resolution parametric study on the numerical simulation of gas-solid flows in a periodic riser section", *Powder Technology*, **205**(1-3), 103-111.

CLOETE, S., ZAABOUT, A., JOHANSEN, S. T., VAN SINT ANNALAND, M., GALLUCCI, F. and AMINI, S., (2013), "The effect of frictional pressure, geometry and wall friction on the modelling of a pseudo-2D bubbling fluidized bed reactor", *Powder Technology*, **With co-authors**.

ELLIS, N., XU, M., LIM, C. J., CLOETE, S. and AMINI, S., (2011), "Effect of Change in Fluidizing Gas on Riser Hydrodynamics and Evaluation of Scaling Laws", *Industrial & Engineering Chemistry Research*, **50**(8), 4697-4706.

GIDASPOW, D., BEZBURUAH, R. and DING, J., (1992), "Hydrodynamics of Circulating Fluidized Beds, Kinetic Theory Approach", *7th Engineering Foundation Conference on Fluidization* 75-82.

IGCI, Y., ANDREWS, A. T., SUNDARESAN, S., PANNALA, S. and O'BRIEN, T., (2008), "Filtered two-fluid models for fluidized gas-particle suspensions", *AIChE Journal*, **54**(6), 1431-1448.

JENKINS, J. T. and SAVAGE, S. B., (1983), "Theory for the rapid flow of identical, smooth, nearly elastic, spherical particles", *Journal of Fluid Mechanics*, **130**, 187-202.

JOHNSON, P. C. and JACKSON, R., (1987), "Frictional-Collisional Constitutive Relations for Granular Materials, with Application to Plane Shearing", *Journal of Fluid Mechanics*, **176**, 67-93.

LUN, C. K. K., SAVAGE, S. B., JEFFREY, D. J. and CHEPURNIY, N., (1984), "Kinetic Theories for Granular Flow: Inelastic Particles in Couette Flow and Slightly Inelastic Particles in a General Flow Field", *Journal of Fluid Mechanics*, **140**, 223-256.

MONTGOMERY, D. (2001). Design and Analysis of Experiments. New York, John Wiley and Sons.

OGAWA, S., UNEMURA, A. and OSHIMA, N., (1980), "On the Equation of Fully Fluidized Granular Materials", *Journal of Applied Mathematics and Physics*, **31**, 483.

PARK, S.-W., SUNG, D.-H., CHOI, B.-S., LEE, J.-W. and KUMAZAWA, H., (2006), "Carbonation kinetics of potassium carbonate by carbon dioxide", *Journal of industrial and engineering chemistry*, **12**(4), 522-530.

POPOFF, B. and BRAUN, M., (2007), "A Lagrangian Approach to Dense Particulate Flows", *6th International Conference on Multiphase Flow*, Leipzig, Germany.

SAMANTA, A., ZHAO, A., SHIMIZU, G. K. H., SARKAR, P. and GUPTA, R., (2011), "Post-Combustion CO2 Capture Using Solid Sorbents: A Review", *Industrial & Engineering Chemistry Research*, **51**(4), 1438-1463.

SCHAEFFER, D. G., (1987), "Instability in the Evolution Equations Describing Incompressible Granular Flow", *Journal of Differential Equations*, **66**, 19-50.

SHARONOV, V., OKUNEV, A. and ARISTOV, Y., (2004), "Kinetics of carbon dioxide sorption by the composite material K2CO3 in Al2O3", *Reaction Kinetics and Catalysis Letters*, **82**(2), 363-369.

SYAMLAL, M., ROGERS, W. and O'BRIEN, T. J. (1993). MFIX Documentation: Volume 1, Theory Guide. Springfield, National Technical Information Service.

TAGHIPOUR, F., ELLIS, N. and WONG, C., (2005), "Experimental and computational study of gas-solid fluidized bed hydrodynamics", *Chemical Engineering Science*, **60**(24), 6857-6867.

WEN, C. Y. and YU, Y. H., (1966), "Mechanics of Fluidization", *Chemical Engineering Progress Symposium Series*, **62**, 100-111.

YI, C.-K., JO, S.-H., SEO, Y., LEE, J.-B. and RYU, C.-K., (2007), "Continuous operation of the potassium-based dry sorbent CO2 capture process with two fluidized-bed reactors", *International Journal of Greenhouse Gas Control*, **1**(1), 31-36.

BED EXPANSION AND PRESSURE DROP IN A BUBBLING FLUIDIZED BED

Kevin J. MANDICH and Robert J. CATTOLICA*
University of California, San Diego, 9500 Gilman Drive, La Jolla, CA 92093
* E-mail: rjcat@ucsd.edu

ABSTRACT

A series of computational fluid dynamics (CFD) simulations were used to model a laboratory scale gas-fluidized bed as a function of gas velocity. The work was performed as part of an effort to construct a validation platform for future applications and simulations. A parameter of interest is the particle restitution coefficient, along with its effect on bed height, pressure drop, and minimum fluidization velocity. The simulations, based on a multi-phase particle-in-cell method, were compared with results obtained from experiment. Qualitative and quantitative agreement was found between both methods. Simulations with particles of greater elasticity yielded higher bed heights and lower normalized pressure drops over the bed.

Keywords: CFD, fluidization, validation

NOMENCLATURE

Greek Symbols

δ	Bed expansion
ε_{mf}	Voidage at minimum fluidization
ρ	Mass density [kg-m^{-3}]
μ	Dynamic viscosity, [kg-m^{-1}-s^{-1}]
φ	Solid-phase volume fraction
φ_s	Sphericity of particles

Latin Symbols

d	Particle diameter [m]
e_p	Particle restitution coefficient
l	Length of cell [m]
h	Bed height [m]
n	Number of cells
p	Gas-phase pressure [Pa]
U	Superficial gas velocity [cm-s^{-1}]
U_{mf}	Minimum fluidization velocity [cm-s^{-1}]

Sub/superscripts

g	Gas
i	Index in x-direction
j	Index in y-direction
k	Index in z-direction
o	Denotes an at-rest quantity
s	Solid
x	Denotes x-direction
y	Denotes y-direction
z	Denotes z-direction

INTRODUCTION

Validation through experiment is a critical element in producing reliable computational fluid dynamics models. Plais (2012) studied the effect of changing the drag law, fluidization velocity, and the initial bed height on the jet penetration into a fixed bed. Abbasi et al. (2012) obtained axial and transverse velocity distributions of a pilot-scale downer reactor via computation. Parker et al. (2013) carried out a series of computational experiments to select operating parameters for scale-up of a fluidized bed system as a function of bed geometry, material characteristics, and inlet flow rate. Qualitative and quantitative data were compared with that obtained from experiment. The aforementioned studies all employed Barracuda (2014) CFD software as a central tool in their validation studies.

The present study explores the effect of a single material parameter, the restitution coefficient, on the expansion of the bed for different fluidization velocities. Reuge et al. (2008) carried out a similar analysis, although the particle phase was assumed to be a continuum (Eulerian-Eulerian model). Currently, CFD simulations employing a hybrid Eulerian-Lagrangian model were carried out on a gas-fluidized bed and compared with the results obtained from a lab-scale experiment. The three quantitative measurements of interest were the time-averaged pressure drop over the bed, the time-averaged bed expansion, and the minimum fluidization velocity estimated from the prior quantities. Computational data was obtained for fluidization velocities ranging from U_s/U_{mf} = 0.1 to 2.1, for two values of the particle restitution coefficient: e_p*=0.9* and e_p*=1.0*.

A lab-scale experiment was performed to produce bed height and pressure drop data with which to compare the computational results. A comparison of the simulations and experiments was carried out to validate the computational method on a simple non-reacting, cold-flow, gas-fluidized bed before more complex systems are investigated. In addition, the present research sets a framework by which the parameters of the simulation can be investigated to determine their effect on matching the phenomena observed in experiment.

MODEL DESCRIPTION

Barracuda (2014) software, employing the multiphase particle-in-cell method (Andrews & O'Rourke, 1996), was employed to run the simulations. In this method, the particles are treated as discrete computational particles and as a continuum. At each time step, the particles are mapped to the Eulerian grid through linear interpolation functions. Here, vector properties are interpolated to the cell faces while the scalar properties are interpolated to the center of the cells. The continuum derivative terms are obtained by solving the incompressible fluid phase transport equations. Finally, the particle properties are mapped back to the Lagrangian particles. Particle properties – volume fraction, velocity, density – are determined by integrating probability distribution functions for the respective property. The particle and fluid phases are coupled through the particle acceleration term, which incorporates the drag model and the interparticle stress model. The current computations employed the Wen-Yu (1966) drag correlation, and the interparticle stress model is an explicit function of the particle restitution coefficient e_p.

The domain matches that used in the experiment, with the flow field consisting of a cylindrical tube, vertically-oriented, with diameter 3.5" (8.89 cm) and height 50" (127.0 cm). The domain is discretized into a Cartesian grid, with the boundary cells being truncated to match the shape of the bounding walls. A grid sensitivity analysis was carried out to determine the largest cell size which captured the important features of the flow, as well as the value at which no significant qualitative differences in the pressure drop and bed height were realized when reducing the cell size further.

The initial condition of the gas phase consists of motionless, atmospheric air at STP throughout the domain. That of the particle phase consists of a distribution of particles at the bottom 20" (50.8 cm) of the cylinder with mean volume fraction 0.60. Close packing is defined as φ = 0.62. The particle phase boundary conditions consist of partial slip and no penetration at the walls. With this, the particle mass of the bed remains constant throughout the computation. Boundary conditions for the gas phase include: no penetration of the side walls; no slip at the side walls; an atmospheric pressure boundary condition for the gas phase at the top of the bed; and a uniform, normal flow at the bottom face.

The particle phase is modelled from the CarboHSP proppant ceramic particle with mean diameter 430.0 µm and density 3560 kg-m^{-3}, corresponding to the Geldart B (1973) classification. The particle distribution is modelled as Gaussian with the standard deviation of 62.6 µm determined via optical microscope from a sample of 670 particles. The distribution is separated into bins of diameter range 30 µm.

The pressure drop over the bed is determined by averaging the fluid-phase pressure over the cells adjacent to the bottom edge of the domain. Calculation of the bed height is found by summing the bed mass until 95% of the mass is obtained. Starting at the "first" cell (i=1, j=1, k=1), the running total of the bed mass is increased by adding the value of the particle volume fraction φ per cell multiplied by the particle density ρ_s. The cells are looped through in the following order when adding mass: i, j, k. This is continued until the running total reaches a certain fraction of the initial bed mass – in the current work, a fraction of 0.95 is used. The bed height is then calculated using the following interpolation formula:

$$h = \sum_{m}^{t-1} l_{z,m} + l_{z,t} \frac{(r+s)}{(n_x+n_y)} \qquad (1)$$

Here, r, s, and t are the i, j, and k values at which the mass criteria was met. Since the bed height of the bubbling bed varies in time, the bed height h was determined every 0.1 seconds for the 30 second duration of each simulation. The mean bed height was obtained by averaging these values. The volume fraction is determined in a similar manner:

$$\phi = \sum_{a}^{r} \sum_{b}^{s} \sum_{c}^{t} \phi_{a,b,c} \qquad (2)$$

Values of φ are averaged over time to obtain the mean volume fraction of the bed.

EXPERIMENT

A schematic of the experiment is shown in Figure 1. The dimensions of the bed and the particle characteristics are the same as described in the computation. Non-intrusive pressure taps were bored into the side walls, with pressure transducers connected via flexible tubing. The amplified signal was captured and analysed using LabVIEW software.

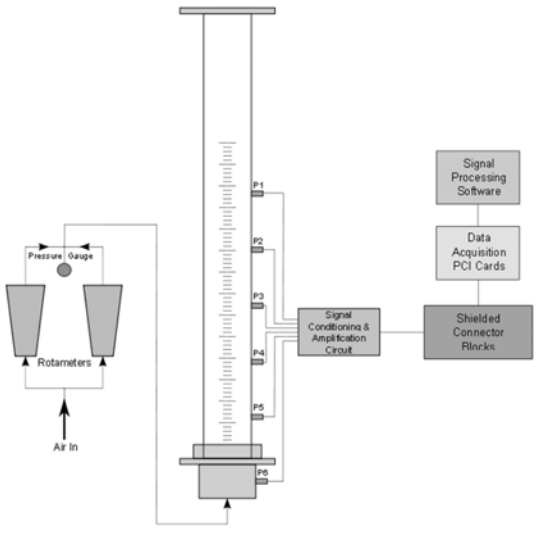

Figure 1: Schematic of experimental set-up.

Pressure and height measurements are averaged over four separate experiments. In the first two, the fluidization velocity is increased from zero to the maximum, while

the other two had the opposite progression. The latter series of measurements were taken to alleviate the effect of particle packing on the quantities of interest when the bed is at rest. Each run averages 30 seconds of pressure signals sampled at 120Hz.

Time-averaged height measurements are obtained by video recording over the course of the experimental run. Notches marked every 0.25" (0.635 cm) on the wall are used to estimate the bed height every 3 frames (0.1 seconds). Bed height measurements are used to compute the bed expansion, given by:

$$\bar{\delta}(h) = \frac{\bar{h} - h_o}{h_o} \qquad (3)$$

Once known, the mean bed height may be used to compute the mean volume fraction, given the bed height and volume fraction at rest, h_o and φ_o.

The minimum fluidization velocity was computed using the following methods. The experimentally-determined, time-averaged pressure drop over the bed is plotted as a function of the superficial gas velocity. The measured minimum fluidization velocity is defined as the point at which this pressure drop reaches its maximum. Time-averaged pressure drop data from the simulations was used in the same fashion to determine the minimum fluidization velocity from computation. Values of U_{mf} computed in each way were compared with the theoretical value determined by evaluating the following force balance (Kunii 1992):

$$U_{mf} = \frac{d^2(\rho_s - \rho_g)g}{150\mu_g} \frac{\varepsilon_{mf}^3 \phi_s^2}{1 - \varepsilon_{mf}} \qquad (4)$$

RESULTS

In Figure 2 the bed expansion is plotted against the number of grid cells in the diameter direction. The error bars are equal in the top and bottom and display the error used when determining the bed height, using the interpolation formula (1). This was performed to determine the number of grid cells used in the simulation. The data in this figure was obtained for the model running with e_p=*1.0* and U_s=*46.0 cm-s*$^{-1}$. A value if n_d=*20* was determined to give the optimal balance between accuracy and computational cost.

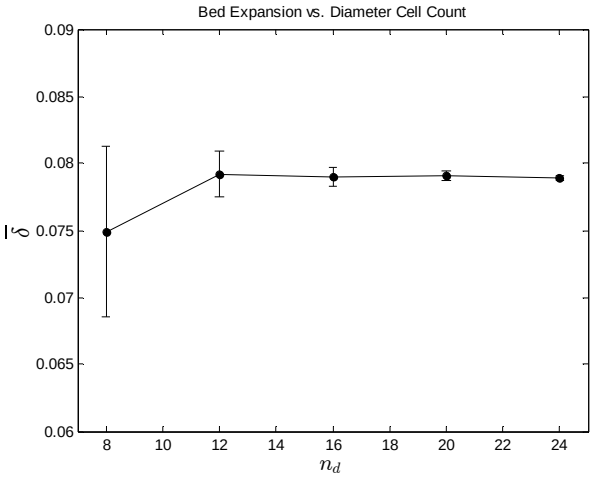

Figure 2: Bed expansion as a function of the number of cells in the diameter direction for the case when e_p=*1.0* and U_s=*46.0 cm-s*$^{-1}$.

In Figure 3 the cross-section of the computational grid is shown with the number of cells in the diameter direction used in the sensitivity study in Figure 2. This view shows the cells before the grid is created. Figure 4 shows the computed grid for the case of n_d=*20*.

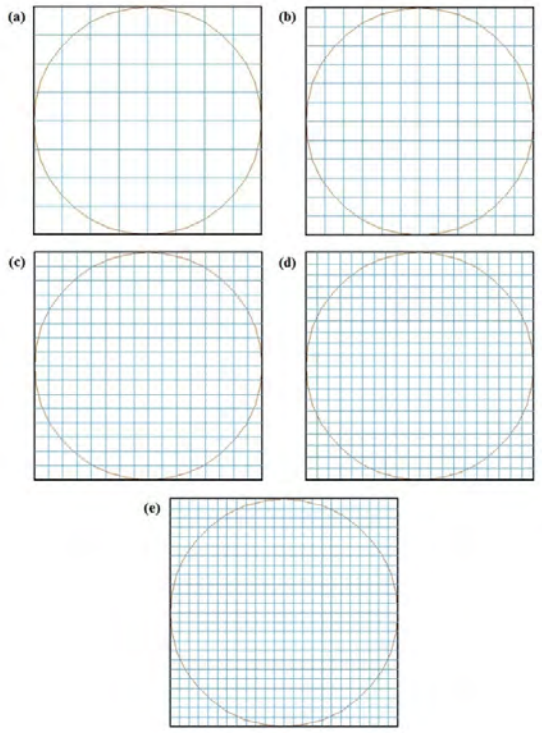

Figure 3: Horizontal cross-sections of the computational domain showing the number of cells in the diameter direction: (a) n_d=*8*; (b) n_d=*12*; (c) n_d=*16*; (d) n_d=*20*; (e) n_d=*24*.

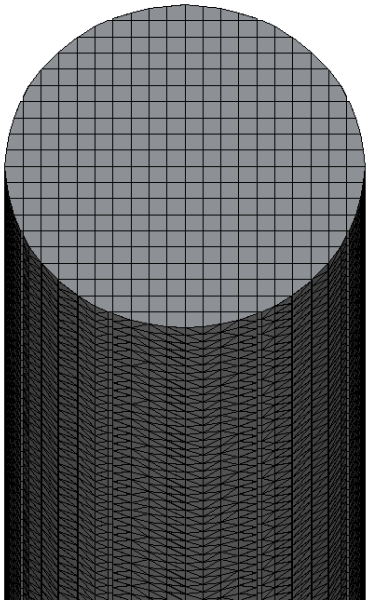

Figure 4: The top end of the domain with edges truncated, shown with 20 cells in the diameter direction and 250 cells in the lengthwise direction.

The solid-phase volume fraction for two sample simulations with varying fluidization velocity are shown in Figures 5 and 6. At a superficial gas velocity of U_s=41.6 cm-s^{-1}, the bed is in the bubbling regime of fluidization. Visible at the bottom are volume fraction disturbances which evolve into bubbles as they traverse the bed. The bubbling becomes more vigorous and the bed height becomes increases significantly when the fluidization velocity is increased to U_s=60.4 cm-s^{-1}

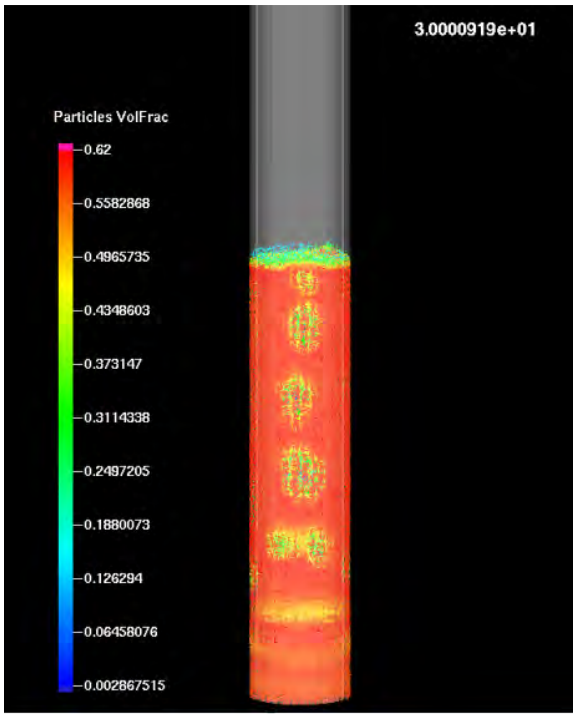

Figure 5: Solid-phase volume fraction for e_p=1.0, U_s=41.6 cm s^{-1}.

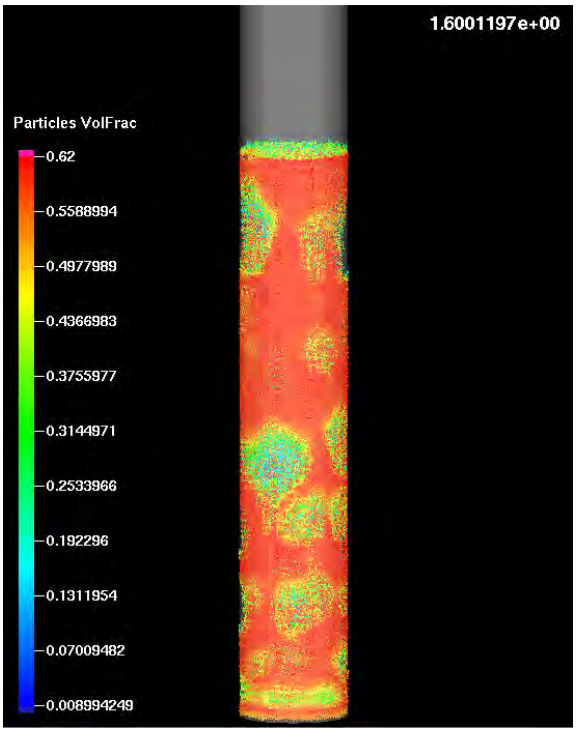

Figure 6: Solid-phase volume fraction for e_p=1.0, U_s=60.4 cm s^{-1}.

The mean pressure drop values for the experiment and for the computations with two values of the particle restitution are presented as a function of the superficial gas velocity in Figure 7.

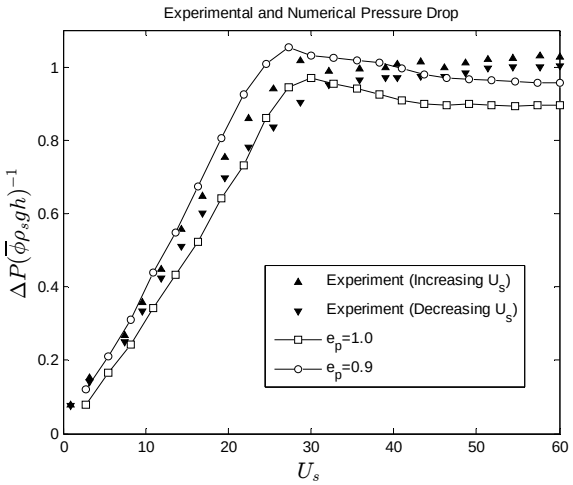

Figure 7: Time-averaged pressure drop for the experiment and for simulations with e_p=0.9 and e_p=1.0.

Mean pressure data for the four separate experimental data points are represented by the triangle symbols. The upward-facing triangles represent the mean pressure for the two experiments in which the fluidization velocity was increased from zero, while the downward-facing triangles represent the mean pressure for the two experiments in which the fluidization velocity was decreased from the maximum. The effect of packing is noticeable in the trace of the upward triangles, in which the bed height is lower, and the normalized pressure

higher, than the downward triangles. This occurs because, at rest, the bed has had a chance to settle, whereas this does not occur when decreasing the velocity from an already fluidized state.

There are a few notable differences between the experimental and the computational data. The point at which the maximum pressure drop is obtained, defining the minimum fluidization velocity, is much sharper in the simulations than for the mean experimental data. Possible reasons for this difference include: vertical settling of the particles in the experiment, the bin size used when modelling the normal distribution of particle diameters, and the fluid-solid drag model employed.

Further, the computational model shows a decrease in the normalized pressure drop after the point of minimum fluidization. This is generally expected since the dimensional pressure drop generally remains constant after minimum fluidization while the mean bed height keeps increasing. The experimental data exhibits a region of secondary, albeit minor, increase in the normalized pressure drop after minimum fluidization. This could be the result of the error involved in estimating the experimental bed height, especially at the higher fluidization velocities.

The normalized pressure drop is higher for the simulations run with $e_p=1.0$ than those with $e_p=0.9$ for all fluidization velocities encountered. This discrepancy is largest around the point of minimum fluidization and is a manifestation of the kinetic energy lost due to inelastic particle collisions. At low fluidization velocities, particles move at slow velocities and the bed is tightly packed, so this mechanism of bed expansion is small. In the region before and after minimum fluidization, particle velocities are higher and the mean volume fraction of the solid phase is lower. As the fluidization velocity is increased further, the decreased amount of particle collisions due to greater particle scarcity is evident.

Minimum fluidization velocities for the experiment, the two simulation runs, and that obtained from equation (4) are shown in Table 1.

Table 1: Comparison of the minimum fluidization velocity determined from three methods

	U_{mf} [cm s^{-1}]
Experiment	**35.5**
Computation: $e_p=0.9$	**29.9**
Computation: $e_p=1.0$	**27.0**
Theory (Kunii 1991)	**32.1**

The superficial gas velocity at minimum fluidization determined from the experiments is higher than that obtained from the analytical mono-disperse theory, and significantly higher than that obtained from the simulations. The higher minimum fluidization velocity U_{mf} from the experiments is likely a result of the runs in which the gas velocity was increased with the bed at rest. In these cases, an amount of settling took place in the bed, delaying fluidization to a higher velocity. This is not realized in the simulations due to the model employed. Notable is the higher value of U_{mf} for the computation with a restitution coefficient of 0.9.

Bed height data for the three data sets are displayed in Figure 8 as a function of the fluidization velocity, normalized by the respective values given in Table 1. The experimental data are plotted in the same manner as in Figure 7.

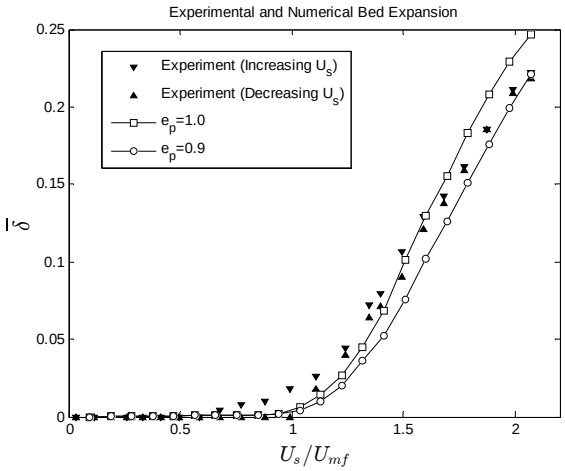

Figure 8: Time-averaged bed expansion from the experiment and from simulations with $e_p=0.9$ and $e_p=1.0$.

In the simulations the elastic particles (e_p=1.0) yield a taller bed. At low values of U_s/U_{mf}, the bed height for the experiment is greater than those of each simulation. At higher velocities ($U_s/U_{mf}>1.5$) the experimental bed height data is bounded by the simulations.

The experimental data in Figure 8 also reveals the effect of decreasing the fluidization velocity from maximum to minimum: at $U_s/U_{mf}=1.0$, there is a rapid increase in the bed height which would not be the case when increasing from minimum to maximum. This coincides with the computational data, which reflect the fact that solid-state packing is not captured by the simulation.

CONCLUSION

Pressure drop and bed height values obtained from CFD simulations were compared with data acquired from a lab-scale, gas-fluidized bed experiment. The work was performed to validate the performance of the simulation for a parametric study of gas-fluidized beds.

The pressure drop and bed height dependencies on the superficial gas velocity for experiment and simulation realized qualitative and quantitative similarities. The effect on these quantities was significant when changing the particle restitution coefficient. In particular, the bed height was observed to increase significantly when the restitution coefficient was increased, especially in the region of fluidization velocity surrounding that of minimum fluidization. As a result, the normalized

pressure drop was lower for beds with greater particle elasticity at all fluidization velocities tested. The mechanism responsible for this discrepancy is the kinetic energy lost due to inelastic particle collision.

ACKNOWLEDGEMENT

This research was supported by the University of California Discovery Program Grant 2012-0489 in collaboration with West Biofuels, Inc.

REFERENCES

PARKER, J., LAMARCHE, K., CHEN, W., WILLIAMS, K., STAMATO, H., and THIBAULT, S., (2013), *Powder Technology* **235**, 115-120.

ABBASI, A., ISLAM, M., Ege, P., and DE LASA, H., (2012), *AiChE* **59** (5), 1635-1647.

PLAIS, C., (2012), *Ninth International Conference on CFD in the Minerals and Process Industries*, CSIRO, Melbourne, Australia.

REUGE, N., CADORET, L., COUFORT-SAUDEJAUD, C., PANNALA, S., SYAMLAL, M., and CAUSSAT, B., (2008) *Chemical Engineering Science* **63**, 5540-5551.

Barracuda Documentation (2014), http://www.cpfd-software.com.

ANDREWS, M., and O'ROURKE, P., (1996), *International Journal of Multiphase Flow*, **22** (2), 379-402.

WEN, C., and YU, Y., (1966) *Chem. Eng. Progr. Symp. Ser.* **62** 100-110.

KUNII, D. and LEVENSPIEL, O., (1991), *Fluidization Engineering (2nd ed.)*, Butterworth-Heinemann.

GELDART, D., (1973), *Powder Technology* **7** (5), 285-292.

VALIDATION OF A CFD MODEL FOR 3D CYLINDRICAL GAS-SOLID FLUIDIZED BEDS

Vikrant VERMA, Johan T. PADDING*, Niels G. DEEN, J.A.M. KUIPERS

Eindhoven University of Technology; Dept. of Chemical Engineering and Chemistry
PO Box 513, 5600MB Eindhoven, The Netherlands
* E-mail: J.T.Padding@tue.nl

ABSTRACT

An efficient CFD two-fluid model (TFM) using Kinetic Theory of Granular Flow is used to perform 3D simulations of gas-solid fluidized beds. Simulation results are compared with experimental results from the literature. The TFM can predict the bubble and solids flow characteristics in close agreement with experimental observations. The equivalent bubble size obtained from simulations shows a fair agreement with X-ray tomographic measurements. The particle circulation patterns are in fair agreement with the experimental work of Laverman et al. (2012). Simulated bubble sizes in a 1.0 meter diameter bed show good agreement with the Darton et al. (1977) correlation. For fluidization at high pressure, the simulation results are consistent with the experimental work of Godlieb et al. (2012), where the bubble size is observed to decrease with increasing pressure. Homogeneous fluidization takes place at very high pressures. We conclude that the TFM can successfully predict the hydrodynamics of very large fluidized beds under different operating conditions.

Keywords: Two-fluid model, hydrodynamics, fluidized bed, bubbles, solids.

NOMENCLATURE

Greek Symbols

β Interphase momentum transfer coefficient, [kg/m^{3}s]
γ Dissipation, inelastic particles collisions, [kg/m s^3]
ε Volume fraction, [-]
Θ Pseudo particles temperature, [m^2/s^2]
τ Stress tensor, [Pa]
ρ Mass density, [kg/m^3]
μ Dynamic viscosity, [kg/m s]

Latin Symbols

C Fluctuation particle velocity, [m/s]
g Gravitational constant, [m/s^2]
H Height from the bottom, [m]
p Pressure, [Pa]
q Kinetic fluctuation energy, [kg/s]
r radial position, [m]
Re Reynolds number, [-]
t Time, [s]
u Velocity [m/s]

Sub/superscripts

s Solid phase
g Gas phase

INTRODUCTION

Gas-solid fluidized beds (FBs) are extensively used in process industries because of their impressive capabilities as a reactor, mixer and possibility of continuous operation. Understanding the dynamics of FBs is a key issue in improving efficiency and rational scale-up to a commercial scale. The performance of a FB is majorly governed by the formation of gas bubbles and their distribution, facilitating rapid solids motion and high heat transfer rates to immersed surfaces. The bubbles grow while moving through the bed, mainly because of coalescence. The gas-solid hydrodynamics is very complex in these reactors, particularly when it comes to real three-dimensional (3D) systems. Traditionally, two-dimensional (2D) or pseudo-2D CFD simulations are used to study the hydrodynamics of FBs on larger scales. Numerical integration using very small time-steps and longer periods of time is still a challenge for full 3D fluidized beds, due to the high computational cost. Fortunately, with increasing computational power, numerical simulations have become possible to predict the dynamics of dense gas-solids flows, even in large 3D FBs. The advantage of a numerical approach is that it can provide much detailed information on the hydrodynamics and subsequently contribute to an efficient design and scale-up of fluidization process equipment. However, validation of the computational models is indispensable, specifically for 3D geometries. Experimental studies of 3D fluidized beds, available in the literature, provide details on bubble and solid flow

characteristics at various operating conditions, and can be used to validate 3D numerical models.

In this work, we present the results of two-fluid model (TFM) simulations of bubbling fluidization in 3D cylindrical beds. The model is validated by comparing our results with experimental work, reported in the literature, on bubble characteristics and solids motion. We also test our model for high-pressure fluidization, typical for industrial operating conditions, and compare with experimental results.
This paper is organised as follows, first we give a short description of TFM with Kinetic Theory of Granular Flow (KTGF) closures. Results for different simulation settings are discussed, starting with a comparison of the predicted bubble size with experimental results of Verma et al. (2014), and followed by simulation results for a 1.0 m diameter bed. Then we compare the predicted solids motion with experimental work of Laverman et al. (2012). Finally we compare fluidization at elevated pressure. We end with our conclusions.

MODEL DESCRIPTION

The TFM describes both the gas phase and the solids phase as fully interpenetrating continua using a generalized form of the Navier-Stokes equations for interacting continua.

Continuity equations:

$$\frac{\partial(\varepsilon_g \rho_g)}{\partial t} + \nabla \cdot \left(\varepsilon_g \rho_g \bar{u}_g \right) = 0 \tag{1}$$

$$\frac{\partial(\varepsilon_s \rho_s)}{\partial t} + \nabla \cdot \left(\varepsilon_s \rho_s \bar{u}_s \right) = 0 \tag{2}$$

Momentum equations:

$$\frac{\partial(\varepsilon_g \rho_g \bar{u}_g)}{\partial t} + \nabla \cdot \left(\varepsilon_g \rho_g \bar{u}_g \bar{u}_g \right) = -\varepsilon_g \nabla p_g - \nabla \cdot \left(\varepsilon_g \bar{\bar{\tau}}_g \right) - \beta \left(\bar{u}_g - \bar{u}_s \right) + \varepsilon_g \rho_g \bar{g} \tag{3}$$

$$\frac{\partial(\varepsilon_s \rho_s \bar{u}_s)}{\partial t} + \nabla \cdot \left(\varepsilon_s \rho_s \bar{u}_s \bar{u}_s \right) = -\varepsilon_s \nabla p_g - \nabla p_s - \nabla \cdot \left(\varepsilon_s \bar{\bar{\tau}}_s \right) + \beta \left(\bar{u}_g - \bar{u}_s \right) + \varepsilon_s \rho_s \bar{g} \tag{4}$$

The gas and solid phases are coupled through the inter-phase momentum transfer coefficient β appearing in the momentum equations. The mechanism and formulation of these inter-phase interaction forces have been presented in detail by Van der Hoef et al. (2005). In short, a local drag force is caused by a local velocity difference between the phases. Drag relations derived from Lattice Boltzmann simulations are often presented as a dimensionless drag force F, by dividing the measured drag force by the theoretical drag force on a single particle in the creeping flow limit. The momentum exchange coefficient β can then be expressed in terms of this dimensionless drag force as:

$$\beta = 18 \left(1 - \varepsilon_g \right) \varepsilon_g \mu \frac{F}{d^2} \tag{5}$$

In this work drag force correlation, *F* from van der Hoef et al. (2005) is used, given by equation 6.

$$F = F_0 \left(\varepsilon_s \right) + F_1 \left(\varepsilon_s \right) \mathrm{Re} \tag{6}$$

where

$$F_0 \left(\varepsilon_s \right) = 10 \frac{\varepsilon_s}{\left(1 - \varepsilon_s \right)^2} + \left(1 - \varepsilon_s \right)^2 \left(1 + 1.5 \sqrt{\varepsilon_s} \right)$$

$$F_1 \left(\varepsilon_s \right) = \frac{0.48 + 1.9 \varepsilon_s}{18 \left(1 - \varepsilon_s \right)^2}$$

To describe the particle-particle interactions the KTGF is used, which expresses the isotropic and deviatoric parts of the solids stress tensor (i.e. the solids pressure and solids viscosities) as a function of the granular temperature, defined as the mean square solids velocity fluctuations:

$$\Theta = \frac{1}{3} < \bar{C}_s \cdot \bar{C}_s > \tag{7}$$

In this work, the constitutive equations by Nieuwland (1995) have been used. The granular temperature evolves according to:

$$\frac{3}{2} \left[\frac{\partial}{\partial t} \left(\varepsilon_s \rho_s \Theta \right) + \nabla \cdot \left(\varepsilon_s \rho_s \Theta \bar{u}_s \right) \right] = -\left(p_s \bar{\bar{I}} + \varepsilon_s \bar{\bar{\tau}}_s \right) : \nabla \bar{u}_s - \nabla \cdot \left(\varepsilon_s q_s \right) - 3 \beta \Theta - \gamma \tag{8}$$

To gain stability and speed of the model, we obtain solution to the governing equations implicitly as much as possible, including deferred correction, solution with a two-step projection method, *P-ε* algorithm, and parallel implementation of ICCG matrix solver. Details of the two-fluid model used in this work, as well as the approach to efficient numerical solution in cylindrical coordinates, have been reported in Verma et al. (2013).

Computational domain

The governing equations are discretised on a cylindrical grid structure as shown in Figure 1. The motivation for using a curvilinear/cylindrical grid structure is that it simplifies simulation of cylindrical bed geometries commonly used in the industry. Using such a grid structure introduces different grid cell aspect ratios when moving from the central axis to the side wall. Therefore, an optimum number of cells in the radial, azimuthal and axial direction is required to maintain a well-defined distribution of flow structure throughout the domain. Details on the effect of grid cell size are given in Verma et al. (2013). To precisely understand the effect of grid structure on the distribution of the flow structure, a comparison between a cylindrical and a Cartesian grid structure, in combination with a cut-cell method to simulate a cylindrical bed, should be performed. This comparison is beyond the scope of this work, and is open for further research.

A gas inlet is located at the bottom and a prescribe pressure boundary condition at the top. No-slip and partial slip boundary conditions are imposed for the gas and solids, respectively, at the walls. The central axis must be treated carefully to ensure conservation of momentum around the axis, as presented in Verma et al.

(2013). The initial (unfluidized) solids fraction in the domain of interest is set to o.6.

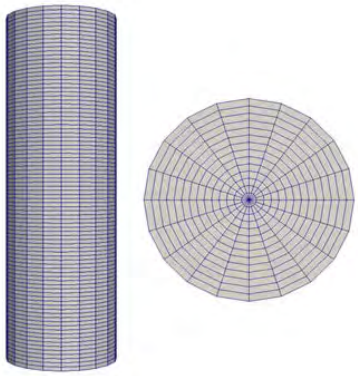

Figure 1: Schematic diagram of 3D computational geometry, front and top view.

RESULTS

The bubble characteristics and solids motion are validated with experimental work available in the literature. The predicted bubble size is compared with X-ray tomographic (XRT) measurements by Verma et al. (2014). The solids motion is compared with measurement of positron emission particle tracking (PEPT) by Laverman et al. (2012). To test the hydrodynamics in a large scale bed, the bubble size and solids motion in a 1.0 m diameter bed is simulated and compared with experimental correlations. Fluidization behaviour at elevated pressure is compared with the experimental work of Godlieb et al. (2012). All these simulations and experiments have in common that they were carried out for linear low density polyethylene (LLDPE) particles in the bubbling regime.

Validation of bubble properties

Simulation settings corresponding to XRT experiments, described in Verma et al. (2014), are given in Table 1. The TFM simulations provide gas and solids volume fractions in each computational cell. Cells with a gas fraction greater than 0.70 are classified as bubble cells. The equivalent bubble diameter can be obtained from the area of a bubble, as shown in Figure 2.

Table 1: Simulation setting for bubble size validation

Properties	Values
Particle type	LLDPE
Particle density	800 kg/m^3
Particle diameter	1.1 mm
Coefficient of restitution	0.69
Minimum fluidizing velocity	0.26 m/s
Superficial velocity	2.0U_{mf}
Bed radius (grid size)	0.05 m (1.5625)
Particle bed height (grid size)	0.20 m (1.5625)
Gas-particle drag	van der Hoef et. al. (2005)
Frictional stress model	Srivastava et al, (2003)

Figure 3 shows the evolution of the bubble size with height. The bubble size increases from the bottom to the top of the bed because of coalescence of bubbles, as well as continuous extraction of gas by the bubbles from the emulsion phase. The equivalent bubble size obtained from the simulations shows a fair agreement with XRT measurements and with correlations of Werther (1975). The XRT measurements show slightly larger bubble diameters because very small bubbles in the vicinity of larger bubbles are not resolved in the processing of the tomographic images, as discussed in Verma et al. (2014). Furthermore, the reliable Darton et al. (1977) correlation (Karimipour et al. 2011) predicts a larger bubble size in the upper section of the bed. We attribute this difference to the fact that the bubble size is not calculated from a real 3D bubble volume: tomographic images can only provide bubble information in a horizontal cross-sectional plane.

A detailed validation for different granular materials has been presented in Verma et al. (2014). They showed that the bubble rise velocity predicted from simulations is in good agreement with experimental results for different granular materials, and that the Hilligardt and Werther (1986) correlation can accurately predict bubble rise velocity for nearly ideal particles, such as glass, but deviates significantly for inelastic particles, such as LLDPE.

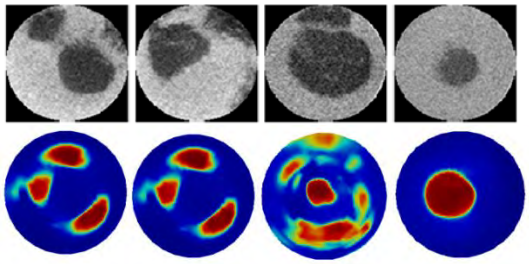

Figure 2: Bubble shape in a horizontal cross-sectional plane: (top) X-ray imaging, (bottom) TFM simulations.

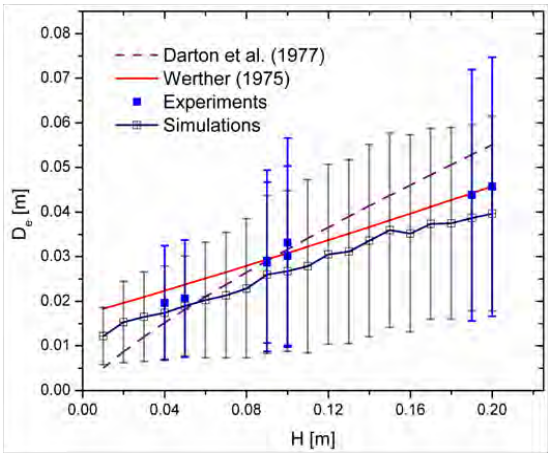

Figure 3: Equivalent bubble size as a function of height from the bottom. Comparing simulations with experiments (Verma et al., 2014) and literature correlations.

Validation of solids motion

The solids motion in the fluidized bed is compared with the experimental work of Laverman et al. (2012). To study the effect of different granular materials at different superficial gas velocities, they performed experiments using positron emission particle tracking on a 0.306 m diameter bed. We compare the solids motion of LLDPE particles for this bed size using an inlet gas velocity of 2.5U_{mf}. Details on the simulation settings are

given in Table 2. To test grid size independence, simulations were performed on a grid size of 3.4 and 5.0 mm (same grid size in both radial and axial directions).

Figure 4 shows the average axial solids velocity as a function of lateral position at three different heights. The simulation results are in good agreement with experimental observations for the grid size of 3.4 mm. This shows that refined grid simulations should be preferred to obtain accurate solutions. Figure 5 shows the azimuthally and time-averaged solids circulation patterns, comparing experiment and simulation. The results are in close agreement with experimental findings, with a small difference in the lower vortex configuration, which is very clear in the simulation and diminished in the experiment. Such small differences in simulation and experimental results are attributed to the particle size distribution in the experiments.

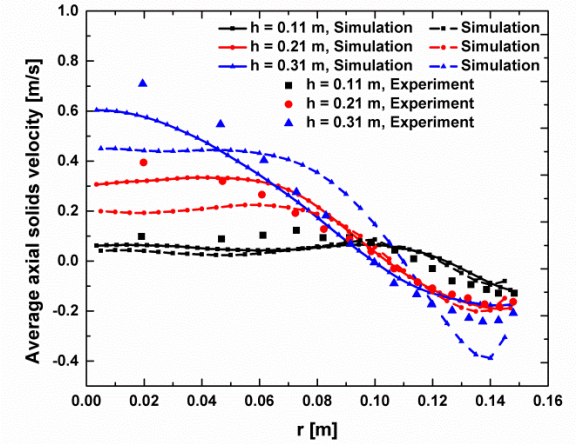

Figure 4: Azimuthally and time-averaged axial solids velocity at three different height, comparing experiments and simulations. Solid and dashed lines represent simulations on a grid size of 3.4 mm and 5.0 mm, respectively.

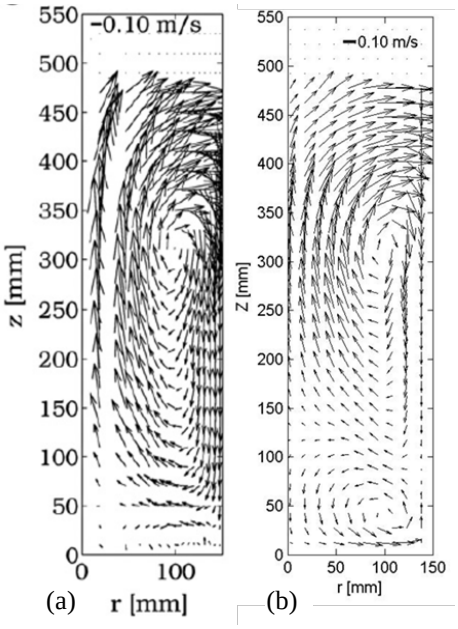

Figure 5: Azimuthally and time-averaged solids circulation in a bed of diameter 0.30 m, obtained from (a) experiment (Laverman et al., 2012) and (b) simulation. For clarity, only every third vector in radial and axial direction is shown.

Table 2: Simulation setting for solids motion validation

Properties	Values
Particle type	LLDPE
Particle density	800 kg/m^3
Particle diameter	1.1 mm
Coefficient of restitution	0.69
Minimum fluidizing velocity	0.26 m/s
Superficial velocity	2.5U$_{mf}$
Bed radius (grid size)	0.15 m (3.4 mm/5.0 mm)
Particle bed height (grid size)	0.30 m (3.4 mm/5.0 mm)
Gas-particle drag	van der Hoef et. al. (2005)
Frictional stress model	Srivastava et al, (2003)

Simulation of a large bed

To test our CFD model for industrial applications, a simulation of a 1.0 m diameter bed is performed, with an initial particle bed height of 1.0 m. A grid size of 5.0 mm in the radial and axial directions was used. The number of grid cells in the azimuthal direction was equal to 30. Other simulation settings are as reported in Table 2. The 3D bubble contours in Figure 6(a) show that bubbles are initiated near the wall and move towards the center of the bed, caused by the lower hydrodynamic resistance experienced in the center. This is also clear from the solids circulation shown in Figure 6(b). The pattern is similar to that observed in Figure 5, but with an important difference in elongation of the upper vortices. The elongated vortices, almost equal to the bed height, are due to gulf stream circulations mentioned by Merry and Davidsons (1973). These type of gulf streams prevail in industrial scale reactors, promoting bubbles to rise faster and carry a larger amount of solids from bottom to top. This phenomenon is clearly captured by our CFD simulations. Figure 7 shows how the bubble size increases with increasing height. The results are compared with correlations of Werther (1975) and Darton et al. (1977). It is interesting to see that in a small bed of 0.10 m the bubble size closely follows the correlation of Werther (Figure 3), while in a bed of 1.0 m the bubble size follows the correlation of Darton et al. (Figure 7). We attribute this to the appearance of regularly shaped bubbles in small beds, and chaotic and randomly shaped bubbles in large beds. Furthermore, note that in Figure 3 the bubble size is calculated from the horizontal cross-sectional area, whereas for the larger bed (Figure 7) the full 3D bubble volume was taken into account to calculate the equivalent bubble size. This shows not only that bubbles can have different behaviour in small and large scale fluidized beds, but also that caution should be taken when measuring the size of bubbles. Finally, the bubble rise velocity in Figure 8 shows close agreement with the Hilligardt and Werther (1986) correlation. Overall, our results show that the TFM model can successfully predict the hydrodynamics for large scale fluidized beds.

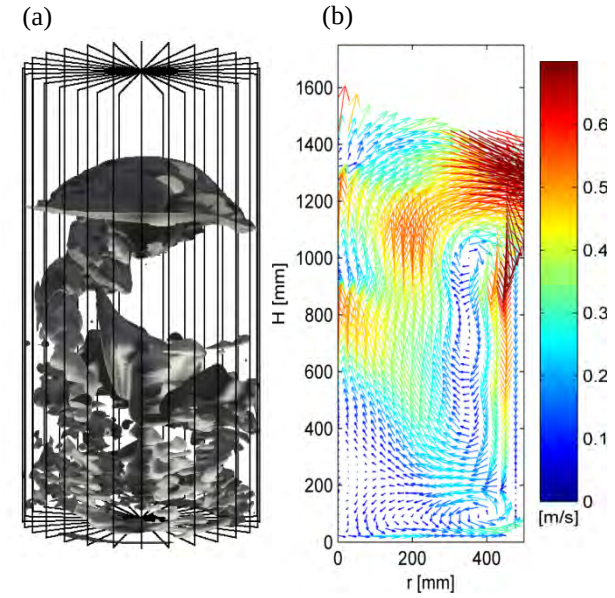

Figure 6: (a) Instantaneous 3D bubble contours in a 1.0 m diameter bed. (b) Azimuthally and time-averaged solids circulation in the 1.0 m diameter bed. The colour bar represents the magnitude of the axial solids velocity.

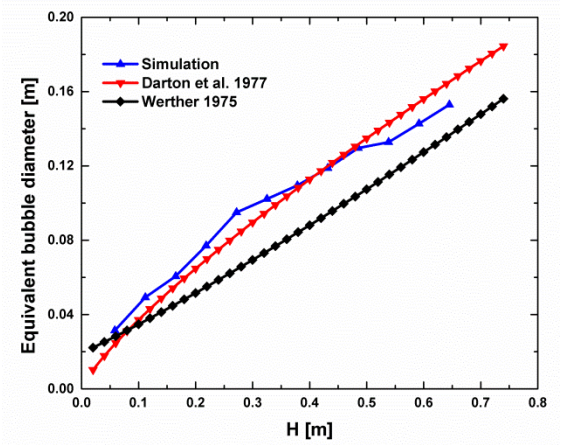

Figure 7: The equivalent bubble diameter predicted from simulation, assuming spherical bubble volume, compared with two literature correlations.

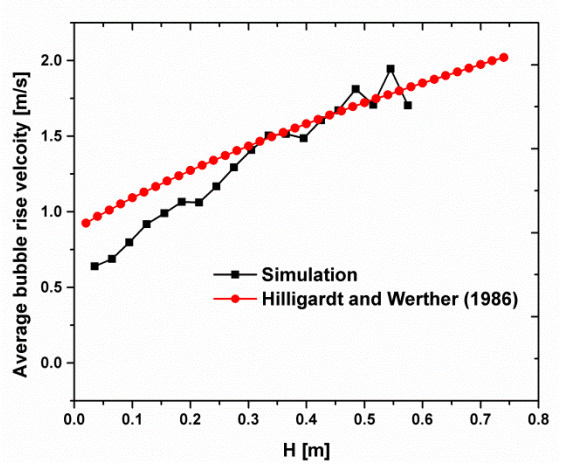

Figure 8: The average bubble rise velocity predicted from simulation, compared with Hilligardt and Werther correlation.

High pressure fluidization

Most industrial fluidized beds operate at critical operating condition such as high pressure and high temperature, e.g. during polymerization reactions. Experimental measurements are difficult to perform under such conditions. Nevertheless, researchers have succeeded to investigate the hydrodynamics in fluidized beds at such critical operating conditions. Godlieb et al. (2012) performed experiments at elevated pressures up to 20 bar using electrical capacitance tomography. They found completely different hydrodynamics at different pressure. To obtain a detailed insight in the pressure effect, we performed simulations at elevated pressures in a bed with a diameter of 0.30 m. The minimum fluidization velocity decreases with increase in pressure. Therefore, to maintain a constant total bubble volume, a constant excess gas velocity is used for comparison. The same value of U_{mf} and excess gas velocity (equal to U_{mf} at 1 bar) is used as reported by Godlieb et al. (2012). Figure 9 shows instantaneous porosity plots at elevated pressure. At higher pressure, more and smaller bubbles are created, with more random shapes, compared to bubbles at low pressure. The porosity distribution function plot in Figure 10 reveals the more homogenous porosity distribution with increase in pressure. These predictions from our simulations are consistent with the experimental results of Goblieb et al. (2012). This shows that TFM with KTGF can also successfully predict high pressure fluidization behaviour.

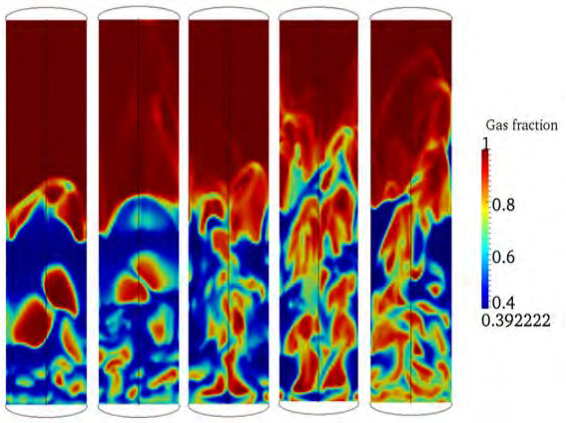

Figure 9: Instantaneous porosity plots at elevated pressures of (left to right) 1,2,4,8,16, and 20 bar.

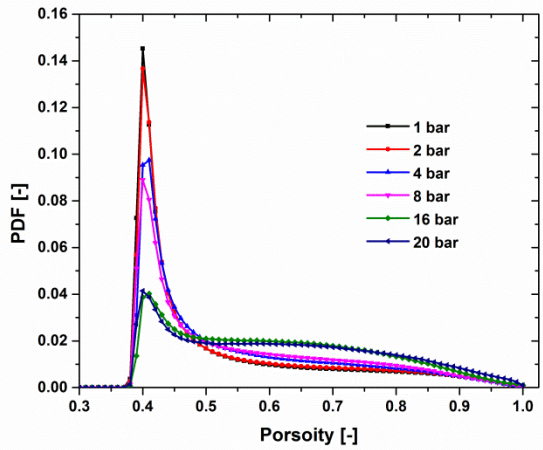

Figure 10: Porosity distribution function, measured at a height of 10 to 15 cm from the bottom.

CONCLUSION

In this work we have validated a CFD Two-fluid model based on Kinetic Theory of Granular Flow for fluidized

beds. The predicted bubble and solids flow characteristics are in good agreement with experimental observations. The bubble size increases with increasing height from the bottom. The equivalent bubble size obtained from simulations shows a fair agreement with X-ray tomographic measurements. The solids circulation patterns are in fair agreement with the experimental work of Laverman et al. (2012). The time-averaged solid velocities at different heights in the bed are comparable with experimental results, where the solution is most accurate on fine grids. Simulation results for a bed diameter of 1.0 m show good agreement with the Darton correlation for bubble size and reasonable agreement with the Hilligardt and Werther correlation for bubble rise velocity. The solid circulation in this large diameter bed shows the appearance of a gulf stream, with vortices almost equal to the bed height. This gulf stream, dominant in industrial scale reactors, promotes bubbles to rise faster. When comparing fluidization at high pressure, the simulation results are consistent with the experimental work of Godlieb et al. (2012), where the bubble size is observed to decrease with increase in pressure. Homogeneous fluidization takes place at very high pressures. Overall, this work shows that TFM can successfully predict the flow behaviour in a 3D gas-solids fluidized bed under different operating conditions. TFM can be used to study the hydrodynamics for even larger scale fluidized beds, which can help in a rational scale-up of such reactors.

ACKNOWLEDGMENT

The authors thank the European Research Council for its financial support, under its Advanced Investigator Grant scheme, contract number 247298 (MultiscaleFlows).

REFERENCES

DARTON, R.C., LA NAUEZA, R.D., (1977), "Davidson JF, Harrison D. Bubble growth due to coalescence in fluidized beds", *Trans. Inst. Chem. Eng*, **55**, 274–280.

GODLIEB, W., GORTER, S., DEEN N.G., KUIPERS, J.A.M., (2012), "Experimental study of large scale fluidized beds at elevated pressure", *Ind. Eng. Chem. Res*, **51**, 1962-1969.

HILLIGARDT, K., WERTHER, J., (1986), "Local bubble gas hold-up and expansion of gas/solid fluidized beds", *Ger. Chem. Eng*, **9**, 215-221.

KARIMIPOUR, S., PUGSLEY, T., (2011), "A critical evaluation of literature correlations for predicting bubble size and velocity in gas–solid fluidized beds", *Powder Technology*, **205**, 1–14.

LAVERMAN, J.A., FAN, X., INGRAM, A., VAN SINT ANNALAND, m., PARKER, D.J., SEVILLE, J.P.K., KUIPERS, J.A.M., (2012), "Experimental study on the influence of bed material on the scaling of solids circulation patterns in 3D bubbling gas-solid fluidized beds of glass and polyethylene using positron emission particle tracking", *Powder Technology*, **224**, 297-305.

MERRY, J.M.D., DAVIDSON, J.F., (1973), "Gulf-stream circulation in shallow fluidized-beds", *Trans. Instn. Chem. Engrs*, **8**1, 361-368.

NIEUWLAND, J.J., (1995), "Hydrodynamic modelling of gas-solid two-phase flows", *Ph.D. Thesis*, Twente University, Enschede, The Netherlands.

SRIVASTAVA, A., SUNDARESAN, S., (2003), "Analysis of a frictional-kinetic model for gas-particle flow", *Powder Technology*, **129,** 72-85.

Van der HOEF, M.A., BEETSTRA, R., KUIPERS, J.A.M., (2005), "Lattice-Boltzmann simulations of low-Reynolds number flow past mono- and bidisperse arrays of spheres: results for the permeability and drag force", *J. Fluid Mech.*, **528**, 233–254.

VERMA, V., DEEN, N.G., PADDING, J.T., KUIPERS, J.A.M., (2013), "Two-fluid modeling of three-dimensional cylindrical gas–solid fluidized beds using the kinetic theory of granular flow", *Chemical Engineering Science*, **102**, 227–245.

VERMA, V., PADDING, J.T., DEEN, N.G., KUIPERS, J.A.M., BIEBERLE, M., BARTHEL, F., WAGNER, M., HAMPEL, U., (2014) "Bubble dynamics in a 3-D gas–solid fluidized bed using ultrafast electron beam X-ray tomography and two-fluid model", *AIChE J.*, DOI 10.1002/aic.14393.

WERTHER, J., (1975), "Bubble growth in a large diameter fluidized beds", Int. Fluidization conference, Pacific Grove, USA, in: D.L, Keairns (Ed.), *Fluidization Technology*, Hemisphere Publ. Co., Washington DC, 1976, pp. 215-235.

PROCEDURAL METHOD FOR SIMULATING AN INDUSTRIAL UREA GRANULATION PROCESS

Philipp LAU[1], Matthias KIND[1]*

[1] Department of Thermal Process Engineering, Karlsruhe Institute of Technology, 76131 Karlsruhe, GERMANY

*E-mail: matthias.kind@kit.edu

ABSTRACT

The process of fluidized bed spray granulation unites the steps of solid formation and product formulation in one apparatus and is used for the continuous industrial urea granulation process.
In this connection, the granulator is build up by connecting several granulation chambers in series using dividing walls and multiple nozzles in each chamber.
Thereby, the hot urea melt is atomized with nozzles and sprayed into the fluidized bed which contains granulate particles of the same material. The droplets deposit on the particles near the spray zone and form a film which solidifies to a crystalline layer in the cold fluidization air. Step-by-step, a raspberry-like product is formed. Besides drop deposition, there are two more important mechanisms which influence the particle growth: attrition due to particle-particle collisions and dust integration on wet surfaces.
The tailored product size distribution can be obtained by a downstream screening-crushing process. Granules larger than the product size desired are crushed in a mill and fed back to the granulator together with small particles.
The aim of this development is to minimize the recirculation of particles behind the screen deck. Therefore, it is necessary to get information about the growth and attrition rates of the granules to solve the population balance equation to predict the development of the particle size distribution during the process. Hence, a 3D-multiphase model is developed to extract data which are not available in experimental research, e.g. particle exchange streams, particle size-dependent growth rates and particle residence times. Due to the large number of nozzles and the large dimension of such a device, a granulator cannot be described completely using a numerical simulation tool.
The fluid dynamics, granulation mechanisms (implemented with user-defined functions) and energy equations are solved in a representative domain in each chamber using a two-fluid model (TFM) and two periodic boundary conditions. The interactions between particles and air can be described with the model of Gidaspow (1994). The particle-particle momentum exchanges are modelled with the equations of Syamlal and O'Brien (1987). The population balance can finally be solved by obtaining important information of CFD simulation and coupling the granulation chambers with exchange streams.
In this research, a 3D-multiphase model is developed to generate growth and attrition rates of the granules to predict the particle size distribution in the large-scale granulator. With this information, it is possible to optimize process parameters and minimize recirculation. This investigation is still in progress, so that only first approaches and results are provided here.

Keywords: Fluidized/packed beds, granular flow, multiphase heat and mass transfer, process industries, stirred tanks.

NOMENCLATURE

Greek Symbols

α	Volume fraction, [-].
ε	Porosity of fluidized bed, [-].
η	Deposition efficiency of droplets, [-].
λ	Bulk viscosity, [Pa.s].
λ_{air}	Thermal conductivity of air, [W/m/K].
μ_{air}	Dynamic shear viscosity of air, [kg/m/s].
ρ	Mass density, [kg/m^3].
τ	Strain stress, [N/m²].
φ	Impingement efficiency, [-].

Latin Symbols

a	Parameter for drop deposition model, [-].
b	Parameter for drop deposition model, [-].
C	Coefficient of friction between two phases, [-].
c	Particle concentration, [#/m³].
c_p	Isobaric specific heat capacity, [kJ/kg/K].
d	Particle diameter, [m].
d_{32}	Sauter diameter of droplets, [m].
e	Restitution coefficient, [-].
F	External force, [N].
G	Elasticity modulus, [N/m²].
g	Acceleration of gravity, [m/s²].
g_0	Radial distribution coefficient, [-].
H	Height of considered volume, [m].
h	Adhesion probability, [-].
K	Momentum exchange coefficient, [-].
$\dot{m}$	Mass flow, [kg/s].
N	Number of CSTR units, [-].
n	Total number of phases, [-].
p	Pressure, [Pa].
P	Solids pressure, [Pa].
q	Phase name, [-].
R	Interaction force, [N].
t	Time, [s].
v	Velocity, [m/s].

Sub/superscripts

q	Phase q
p	Phase p
pq	From phase p to phase q
qp	From phase q to phase p
s	Solid
g	Gas
I	Identity matrix
fr	Friction

Dimensionless number

Re_s	Reynolds number
We	Weber number
St	Stokes number
C_D	Drag coefficient

INTRODUCTION

Granules are used in a wide range of industries (e.g. fertilizer production, food processing technology, chemical and pharmaceutical industry) depending on the product properties, manageability and safety. Fertilizer, for example, must be easy to dose, free-flowing and dust-free to guarantee a uniform distribution on the field and trouble-free filling without risk of dust explosion.
One of the methods of producing fertilizer granules is continuous fluidized bed spray granulation, which unites the steps of solid formation and product formulation in one apparatus. Figure 1 shows the simplified schematic diagram of an industrial urea fertilizer melt granulation process.
Particles move and grow in the large-scale granulator. The particle size distribution of the product can be obtained by a downstream screening-crushing process, classifying the urea granules in a screen with two screen decks. Particles with the product size desired are discharged. The recycle stream, which contains particles which are too small (fines) and crushed oversize, is conveyed back into the granulator to serve as seed material in the bed.

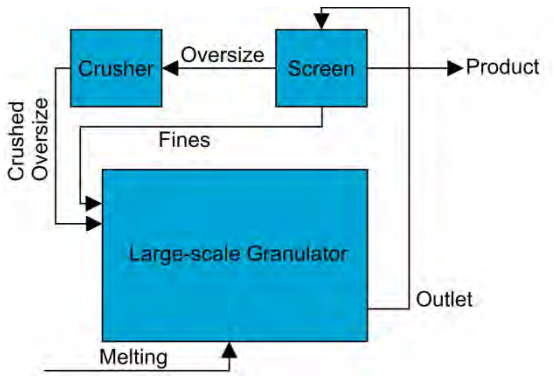

Figure 1: Simplified schematic diagram of the urea fertilizer cycle in a large-scale granulation process.

Besides experimental research, numerical methods have become more and more important to optimize the processes economically. Hence, the aim of this development is to minimize the reflux after the screening and optimize other process parameters, e.g. the geometrical dimensions of the granulation chambers.
Firstly, a detailed understanding of the melt spray granulation process followed by a complete numerical description of this process are very important for successful development.
This investigation is still in progress, so the procedural method of this work, first approaches and results regarding fluid dynamics, drop deposition and experimental validation of particle exchange streams are provided here.

MODEL DESCRIPTION

In Figure 2, a simplified description (e.g. particles are assumed as ideally spherical shaped) of the physical mechanisms occurring during the melting granulation process are considered in more detail.
A packed bed is fluidized with fluidization air which enters the granulation chamber over a perforated plate on the bottom. It has been shown that the fluid dynamics in a granulation chamber play a crucial role in the correct description of granulation mechanisms.

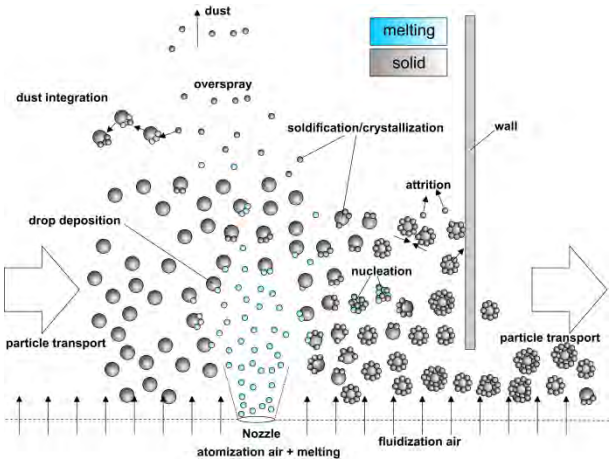

Figure 2: Simplified diagram of typical physical mechanisms during the fertilizer granulation process.

Urea melting is atomized with atomization air and sprayed into the granulation chamber through nozzles. The nozzles can be used in a top spray or bottom spray configuration. Drops can coat fluidized particles of the same material (drop deposition). In addition to drop deposition, other process-relevant mechanisms, such as dust formation caused by attrition and overspray, lead to dust integration on wet particle surfaces, which also influences the particle growth during the process. Through attrition and overspray (less than 100% of drop mass is deposited on the particle surface), dust leaves the granulation chamber with the exhaust air.

A large-scale granulator is build up by connecting N granulation chambers in series using dividing walls and multiple nozzles in each chamber. With the assumption that each chamber is perfectly mixed, the granulator can be considered as a series connection of continuous stirred-tank reactors (CSTR) (see Figure 3). Depending on the capacity of the process, the number of CSTR units N and the number of nozzles can differ. Particle size and time-dependent mass exchange streams in flow

and counter current flow directions exist between directly connected units.
It is impossible to take all chambers and nozzles into account for CFD simulation. Therefore, a method has been developed to simulate the complete process with acceptable effort.

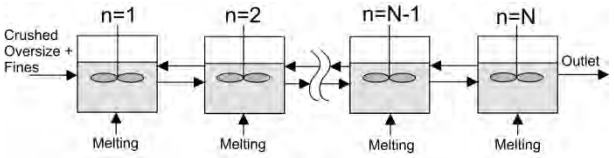

Figure 3: Series connection of continuous stirred-tank reactors to model a large-scale granulator.

A representative domain in each chamber is simulated with CFD using the Euler-Euler multiphase model, which is also known as the two-fluid model (TFM). It has been shown that this is a possible method to consider a gas/solid suspension with a large number of particles (Gidaspow, 1994). In this method, the gas phase and particle phase are treated as penetrated continua. Considering volume fraction α_q, we obtain the conservation equations for mass and momentum (for phase q):

Continuity equation for phase q:

$$\frac{\partial}{\partial t}(\alpha_q \rho_q) + \nabla \cdot \left(\alpha_q \rho_q \vec{v}_q\right) = \sum_{p=1}^{n} (\dot{m}_{pq} - \dot{m}_{qp}) \tag{1}$$

Momentum equation for phase q:

$$\frac{\partial}{\partial t}(\alpha_q \rho_q \vec{v}_q) + \nabla \cdot \left(\alpha_q \rho_q \vec{v}_q \vec{v}_q\right) = -\alpha_q \nabla p + \nabla \cdot \bar{\bar{\tau}}_q + \alpha_q \rho_q \vec{g} + \sum_{p=1}^{n} (\vec{R}_{pq} + \dot{m}_{pq}\vec{v}_{pq} - \dot{m}_{qp}\vec{v}_{qp}) + \vec{F}_q \tag{2}$$

It should be mentioned that the continuity equation is written down without considering any external source terms. $\dot{m}_{pq}$ and $\dot{m}_{qp}$ characterize the mass transfer from phase p to q and phase q to p, respectively. The phase stress-strain tensor in the momentum equation is defined as follows:

$$\bar{\bar{\tau}}_q = \alpha_q \mu_q (\nabla \vec{v}_q + \nabla \vec{v}_q^T) + \alpha_q (\lambda_q - \frac{2}{3}\mu_q) \nabla \cdot \vec{v}_q \bar{\bar{I}} \tag{3}$$

Hereby, μ_q and λ_q are the shear and bulk viscosity, respectively, of phase q. The term $\vec{R}_{pq}$ in Eq. 2 describes the interaction force between phases and is defined as follows, where K_{pq} is the interphase momentum exchange coefficient:

$$\sum_{p=1}^{n} \vec{R}_{pq} = \sum_{p=1}^{n} K_{pq} (\vec{v}_p - \vec{v}_q) \tag{4}$$

Depending on the physical condition of the phases, there are different models to characterize the momentum exchange between phases. The interaction between particles (s) and air (g) for fluidized beds can be described with the model of Gidaspow (1994). He combined the models of Ergun (1952) and Wen and Yu (1966):
For $\alpha_g < 0.8$

$$K_{sg} = \frac{3}{4} C_D \frac{\alpha_s \alpha_g \rho_g \left|\vec{v}_s - \vec{v}_g\right|}{d_s} \alpha_g^{-2,65} \tag{5}$$

For $\alpha_g > 0.8$

$$K_{sg} = 150 \frac{\alpha_s (1-\alpha_g)\mu_g}{\alpha_g d_s^2} + 1{,}75 \frac{\rho_g a_s \left|\vec{v}_s - \vec{v}_g\right|}{d_s} \tag{6}$$

The drag coefficient C_D can be calculated with different equations as follows, depending on the Reynolds number:
For $Re_s < 1000$

$$C_D = \frac{24}{Re_s}\left[1 + 0.15 \cdot Re_s^{0.687}\right] \tag{7}$$

For $Re_s > 1000$

$$C_D = 0.44 \tag{8}$$

Where the dimensionless relative Reynolds number is then defined as:

$$Re_s = \frac{\alpha_g \rho_g d_s \left|\vec{v}_s - \vec{v}_g\right|}{\mu_g} \tag{9}$$

In the case of the existence of more than one particle phase, the interactions between particles (phase s and p) are modelled with the equation of Syamlal and O'Brien (1987):

$$K_{sp} = \frac{3(1+e_{sp})(\frac{\pi}{2} + C_{fr,sp}\frac{\pi^2}{8})\alpha_s \rho_s \alpha_p \rho_p (d_s + d_p)^2 g_{o,sp}}{2\pi(\rho_s d_s^3 + \rho_p d_p^3)} \left|\vec{v}_s - \vec{v}_p\right| \tag{10}$$

The momentum exchange coefficients for granular flows include physical quantities which have to be modelled, e.g. coefficient of restitution and radial distribution function. These model parameters are important to describe the kinetic theory of granular flows. We refer to Gidaspow (1994), Lun & Savage (1984) and Syamlal et al. (1993) for further information concerning this.

Modelling of representative domain

The representative chamber unit consists of a small volume element which contains one nozzle in the centre. Due to periodic boundary conditions in the x and y direction, particles in this volume feel like they are in a chamber with infinite dimensions. Due to the large dimensions of such a granulator chamber, the particle-wall interaction is negligible in comparison to particle-particle interactions, so the periodic boundary conditions are justified. Figure 4 shows an example of a chamber unit which is used to simulate granulation mechanisms and fluid dynamics representing the whole chamber.

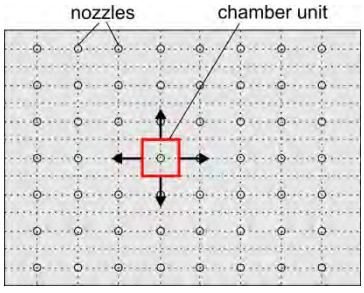

Figure 4: Method for simulation a large-scale granulator using a representative domain in each chamber.

The fluid dynamics in this small domain seem to be different, because bubbles which have larger dimensions than those in the chamber unit cannot be

modelled. With the assumption that the granulation takes place near the nozzle, the bubble movement and coalescence (which occur in the upper region of the bed) have only a small influence on the granulation.
A boundary condition for the nozzle is used to decrease the grid cells in the domain in order to solve the fluid dynamics of the multiphase flow, energy equations and implemented granulation mechanisms in less time. Therefore, a high-resolution 3D simulation of a two-component jet is carried out to extract a 3D fluid flow profile which is used as a boundary condition for further simulations of the granulation chamber.
The case set-up takes place using an ANSYS workbench platform. The geometry there was built using the top-down method and the meshing takes place using the structured cut-cell method. It is important to get two identical boundary zones in each case to obtain a periodic boundary condition through this.
There are at least three phases used for simulating the fluid dynamics in the chamber unit: the air, which fluidizes the particles and atomizes the melt behind the nozzle, and two phases of granules.
The basic settings for the simulation model are summarized in Table 1. Settings for modelling the characteristics of the kinetic theory of granular flows can be followed in Table 2.

Table 1: General Settings for numerical set-up.

Number of grid cells	120000
Mode of calculation	Transient
Particle sizes	$d_{p1} = 2\,\text{mm}$, $d_{p2} = 3\,\text{mm}$
Height of fixed-bed	1.2 m
Time step	0.00001 – 0.001 s
Energy equation	yes
Multiphase model	Euler implicit
Turbulence model	k-epsilon dispersed
Discretization	First-Order-Upwind
Computation of pressure	SIMPLE algorithm
Gravity acceleration	-9.81 m/s²
Modelling of air density	compressible fluid $c_p = c_p(\rho,T)$ $\lambda_{air} = \lambda_{air}(\rho,T)$ $\mu_{air} = \mu_{air}(\rho,T)$

Table 2: Models used to simulate granular flows.

Characteristic of granular phase	**Computational model**
Granular viscosity	Gidaspow (1994)
Granular bulk viscosity	Lun et al. (1984)
Frictional viscosity	Neglected
Granular temperature	Algebraic
Solids pressure	Lun et al. (1984)
Radial distribution	Lun et al. (1984)
Elasticity modulus	$G = \frac{\partial P_s}{\partial \alpha_s}, G > 0$
Packing limit	0.63; constant
Restitution coefficient	0.9; constant

Drop deposition

Drop deposition is one of the important mechanisms for particle growth during granulation. Therefore, the drop deposition in this investigation is modelled by using the model of Löffler (1988). Löffler describes the change of particle concentration in a monodisperse packed bed with the equation as follows:

$$-\frac{dc}{c} = 1.5\frac{1-\varepsilon}{\varepsilon}\frac{\eta}{d_s}dH \tag{11}$$

To solve equation (11), we have to find a term for the deposition efficiency η. Löffler describes the deposition efficiency with two parts, namely the impingement efficiency φ and the adhesion probability h.

$$\eta = \varphi \cdot h \tag{12}$$

The impingement efficiency defines the possibility of a droplet hitting the surface of a particle. According to Löffler, the impingement efficiency is a function of the Stokes number and of parameters “a” and “b”, where “a” is also a function of the Reynolds number:

$$\varphi = \left(\frac{St}{St+b}\right)^a \tag{13}$$

We refer to Löffler (1988) for further information. The adhesion probability defines the probability of a droplet sticking to the particle surface. Bai et al. (2002) defined four different cases where a droplet can interact with the particle surface: A droplet can stick to the surface without deformation, or it can reflect, atomize or spread. The adhesion probability depends on the Weber number, and the different cases are limited with critical Weber numbers. One can see that only the cases “stick” and “spread” lead to an adhesion probability above zero. We refer to Panao and Moreira (2004) for further information.

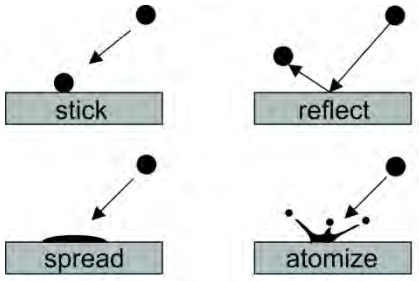

Figure 5: Bai et al. (2002) describe four different cases for obtaining the adhesion probability.

Experimental validation of exchange streams

Considering Figure 3, particle exchange streams occur between different CSTR units, which are very important for calculating the whole granulation process. Exchange streams in a counter-current flow direction can cause a change of particle residence time which dramatically influences the product properties. An experimental set-up is used to validate the fluid dynamics in the chambers and the exchange streams (see Figure 6). The 3D experimental test station consists of two parts which are separated by a horizontal perforated plate. In the lower part, the fluidization air is conveyed by a radial ventilator. The air flows through the perforated plate and fluidizes the particles in the chamber. Beneath the perforated plate there is a fixed net which prevents that small particles fall into the lower part. It is possible to

separate the fluidized bed into two regions by means of a movable wall.

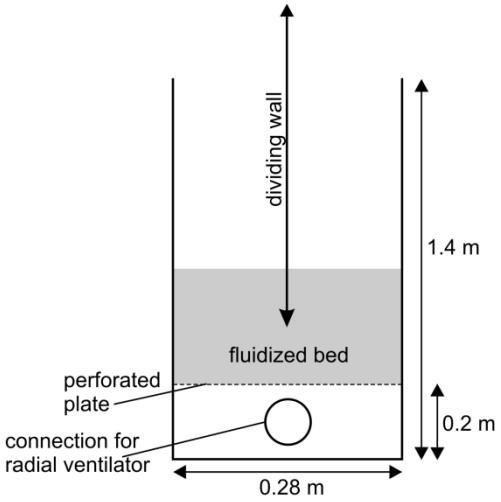

Figure 6: Experimental set-up for validating fluid dynamics and exchange streams in two connected fluidized beds.

It is difficult to measure the flux streams below the dividing wall in a 3D set-up because visual measuring methods cannot be used. Hence, the unsteady start-up behavior of particles of different sizes (to distinguish them) is used to measure the exchange behavior indirectly. The procedure of measuring is shown in Figure 7.

The glass particles of different sizes are placed in the left (FB1) and right chambers (FB2), respectively, with the dividing wall closed. The particle size distributions can be measured with the Camsizer particle analyser (Retsch Technology). Particles are selected so that both particle size distributions do not overlap. This guarantees an ideal separation of these two fractions. After placing the particles into FB1 and FB2, the fan is switched on and the particles fluidize in each chamber. The dividing wall is then lifted, producing a slot at a defined height. The fluidized beds cause particles to move and exchange between chambers.

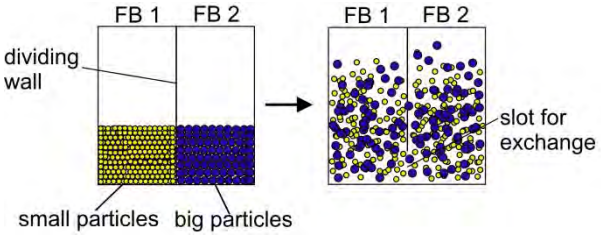

Figure 7: Procedural method for measuring the exchange behavior of particles of different sizes in two connected fluidized beds.

The slot is closed again after a defined period of time. The particle mass of each chamber (FB1 and FB2) is screened and weighed afterwards. Because of the different particle diameters, it is possible to have an ideal separation due to the screening process. This procedure is repeated for different periods of time.

Fluidization air velocity can be measured and controlled with a hot-wire anemometer above the bed. The properties of the glass beads used and the general settings for the experiment discussed are shown in Tables 3 and 4. The minimum fluidization velocities are calculated with the equations described in VDI-Wärmeatlas (2002).

Table 3: Properties of glass beads used for measuring the exchange streams in two connected fluidized beds.

	Small particles	Big particles
Volumetric mean diameter $d_{50,3}$	0.932 mm	2.161 mm
Density	2500 kg/m³	2500 kg/m³
Bulk density	1500 kg/m³	1530 kg/m³
Minimal fluidization velocity	0.726 m/s	1.262 m/s

Table 4: General Settings for experimental set-up.

Slot for exchange	50 mm
Particle bed mass in each chamber	10.53 kg
Static bed height in each chamber	100 mm
Process temperature	25°C
Starting bed mass (for each chamber)	10.53 kg
Diameter of perforated plate holes	2 mm
Point in time for measuring mass in each chamber	0, 5, 10, 20, and 40 s
Fluidization air velocity	2.58 m/s

RESULTS

Representative domain

The fluid dynamics in a representative domain can be modelled using the settings from Tables 1 and 2. Firstly, particles are patched into the domain. The bottom air velocity and the atomization air velocity are increased slowly during the simulation to get stability.

The atomization air from the nozzle has big impact on the fluid dynamics in the chamber. A snapshot contour plot of the volume fraction of particles with a diameter of 2 mm and air is shown in Figure 8. Particles fluidize in the chamber and the volume fraction of air above the nozzle is very high.

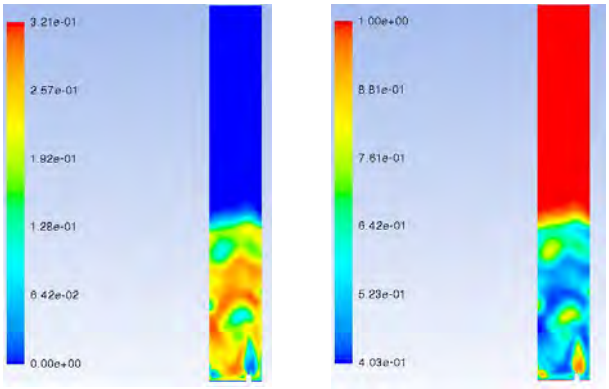

Figure 8: Volume fraction of particles with diameter of 2 mm (left) and volume fraction of air (right).

It should be mentioned that Figure 8 shows a multiphase simulation with three phases (1x air, 2x granules). It is necessary to include more phases, e.g. a liquid phase for the coating droplets, to simulate several granulation mechanisms. We refer to the next section for further information.

Drop deposition

The granulation mechanisms are implemented in the ANSYS Fluent code with user-defined functions. These functions can be dynamically loaded to enhance the standard features of ANSYS Fluent.
After simulating fluid dynamics, the model can be extended with a fourth phase which represents the droplets of the melt. Due to the complexity of the atomization process, a mean droplet diameter (Sauter diameter) is calculated with the model of Walzel (1990). We refer to the Appendix for further information. This model is adjusted to the nozzle configuration used. These droplets enter the representative domain fully atomized, with the assumption that the momentum ratio between air and melting is at least more than 100. Consequentially, the main contribution for fluid dynamics delivers the atomization air due to the high velocities near the orifice, so the momentum of the liquid phase is neglected.
Figure 9 shows the rate of droplets deposited referring to the total particle surface of each particle class. Considering the fact that, by filling up the chamber with the same mass of small and large particles, small particles provide a bigger surface for droplet deposition, thus the total mass of droplets deposited is higher on the surface of the small particles. Regarding the specific surface of each particle phase, Figure 9 shows that large particles "collect" more droplets per m². This is because large particles usually exist in the lower part of the chamber, while small particles are located in the upper part.
Through this segregation phenomenon in the fluidized bed, droplets which exist near the nozzles have better access to larger particles, so that the specific drop deposition rate (per m² particle surface) is higher.

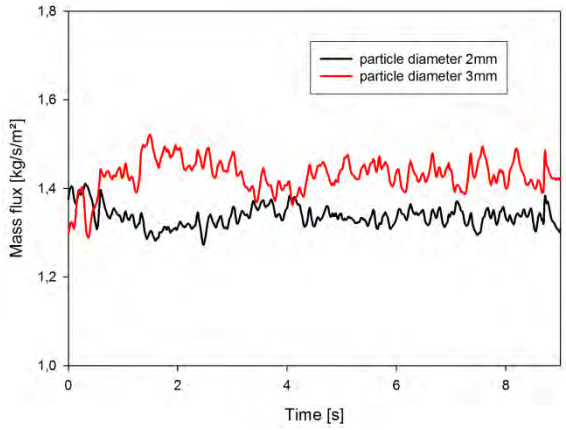

Figure 9: Mass flux of droplets deposited referring to total provided particle surface of urea particles with a diameter of 2 mm and 3 mm.

Internal process parameters are time-dependent quantities due to the unsteady behavior of a fluidized bed. Figure 9 shows that there are two kinds of deviations in the bed. The small deviations result from small bubbles which have a minor influence on the droplet deposition. On the other hand, there are bigger deviations which occur due to larger bubbles and high internal particle mass flow rates, which have a major effect on drop deposition.

It should be mentioned that the case discussed only occurs at very high bed heights so the droplets deposit to 100% on the particle surface. In this case no overspray (droplets crystallizing in the cold fluidization air) is considered.

Experimental validation of exchange streams

The characterization of exchange streams described above is very important to simulate the development of the particle size distribution in the chambers.
The set-up for validation of the numerical simulation is quite similar to the settings given in Tables 2, 3 and 4 (only the bed height changes). The dimensions for the numerical geometry are extracted from the experimental test station. In addition to the volumetric mean diameters measured, the packing limit and an input for the simulation are obtained. Figure 10 shows the experimental and numerical results of unsteady particle mass exchange in two connected fluidized beds. Therefore, the particle mass of each fraction is plotted against the process time.

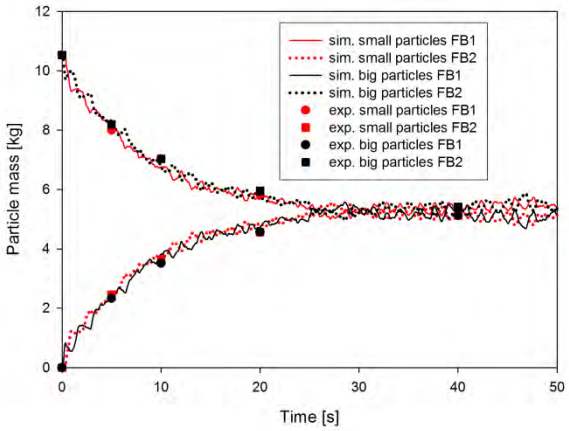

Figure 10: Unsteady particle mass exchange in two connected fluidized beds with a bed height of 100 mm and a slot height of 50 mm at a fluidization air velocity of 2.58 m/s.

Considering that particles of different sizes are ideally separated at the beginning of the experiment, one can see that particles move to the other chamber after lifting the dividing wall (t = 0 s) until the total mass of each particle fraction is equal in both chambers. This steady-state is achieved after 25 seconds in this case, and depends on different process parameters, e.g. slot height, particle bed height and fluidization air velocity. Comparing the results of experimental research (indicated as dots) and numerical simulation (indicated as continuous lines) in Figure 10, it becomes clear that the data fit very well. This shows that the models used for the hydrodynamics of gas and particles give a good description of the physics of granular flow in fluidized bed processes.

CONCLUSION

The aim of this work is to describe the development of particle size distribution in the industrial granulation process to minimize recirculation (shown in Figure 1) and optimize process parameters, e.g. slot height of the divided wall.

Therefore, a procedural method for simulating an industrial urea granulation process is developed in this investigation and first approaches and results are introduced.

Because of the large dimensions of the granulator accompanied by a huge numerical effort, a representative unit in each granulation chamber is used to simulate the multiphase fluid dynamics and granulation mechanisms (drop deposition, overspray, attrition, dust integration, crystallization, and nucleation) to extract important data, such as particle size-dependent growth, attrition rates and particle exchange streams between chambers. These kinetics are obtained with CFD simulation and used afterwards to solve population balance equations for the holistic process.

Using the TFM for fluid dynamics together with different approaches for modelling the interaction and behavior of granular flow, a representative domain with two periodic boundary conditions can be solved. The most important mechanism for particle growth is called drop deposition, which is introduced with the model of Löffler (1988). Therefore, the CFD model is extended with one more phase, which describes the liquid droplet phase. First results show that more droplets deposit on smaller particles, caused by the higher surface area provided. Referring to the total particle surface of each phase, large particles receive more droplets, caused by their better location near the nozzle due to segregation in the bed.

Exchange streams are used to connect the chambers of the granulator to get an overall description of the process. For this reason, an experimental set-up is provided here where it is possible to measure the unsteady mass exchange behavior of particles of different sizes. Results of experimental research and numerical simulation fit very well. This leads to the statement that the models used (to describe particle flow in fluidized beds) can deliver physically meaningful results. Other process parameters are varied, e.g. particle bed height, slot height in dividing wall and fluidization velocity, for further validation.

As a future perspective, the CFD model is extended using more user-defined functions to describe all relevant granulation mechanisms in each chamber. The population balance equation can be solved using the direct quadrature method of moments by extracting the kinetics and mass exchange streams. The development of particle size distributions are compared with results from an industrial urea granulation process. After successful validation, the process parameters can be changed to optimize the reflux ratio behind the screen deck and further process parameters.

REFERENCES

BAI, C., RUSCHE, H. and GOSMAN A.D., (2002), "Modeling of gasoline spray impingement", *Atomization Sprays*, **12**,1-27.

ERGUN, S. and ORNING, A.A., (1952), "Fluid flow through packed columns", *Chem. Eng. Prog.*, **48**, 89-94.

GIDASPOW, D., (1994), "Multiphase Flow and Fluidization: Continuum and Kinetic Theory Description", Academic Press, New York.

LÖFFLER, F., (1988), "Staubabscheiden", Georg Thieme Verlag, New York.

LUN, C. and SAVAGE, S., (1984), "Kinetic Theories for Granular Flow: Inelastic Particles in Couette Flow and Slightly Inelastic Particles in a General Flow Field", Cambridge University Press: Cambridge.

PANAO, M.R.O. and MOREIRA, A.L.N., (2004), "Experimental study of the flow regimes resulting from the impact of an intermittent gasoline spray", *Exp. Fluids*, **37**, 834-855.

SYAMLAL, M., (1987), "The Particle-Particle Drag Term in a Multiparticle Model of Fluidization", National Technical Information Service, Springfield, VA, DOE/MC/21353-2373.

SYAMLAL, M., ROGERS, W. and O'BRIEN, T.J., (1993), "MFIX Documentation, Theory Guide", U.S., Department of Energy, West Virginia.

VEREIN DEUTSCHER INGENIEURE-Gesellschaft Verfahrenstechnik und Chemieingenieurwesen (GVC), (2002), "VDI-Wärmeatlas, 9. bearbeitete und erweiterte Auflage", Springer, New York.

WALZEL, P., (1990), "Zerstäuben von Flüssigkeiten", *Chem.-Ing. Tech.*, **62**, 983-994.

WEN, Y. and YU, Y., (1966), "Mechanics of fluidization", *Chem. Eng. Prog. Symp. Series*, **62**, 100-111.

APPENDIX

Walzel (1990) introduced the following equation for obtaining the Sauter diameter of a spray for externally mixed two-component jets:

$$\frac{d_{32}}{d_D} = C_3 \left[\frac{\Delta p_G^*}{(1+\mu_p)^2} \right]^m (1 + C_4 Oh^j) \tag{14}$$

Thereby, the Ohnesorge number is defined as the quotient of the square root of the Weber number divided by the Reynolds number. This term depends only on the material properties (η_L: dynamic viscosity of liquid, ρ_L: mass density of liquid, σ_L: surface tension of liquid) and nozzle geometry (d_D: diameter of orifice for liquid):

$$Oh = \frac{\sqrt{We}}{Re} = \frac{\eta_L}{\sqrt{\rho_L \sigma_L d_D}} \tag{15}$$

The dimensionless pressure drop and the liquid-to-air ratio are defined as

$$\Delta p_G^* = \frac{\Delta p_G d_D}{\sigma_L} \tag{16}$$

$$\mu_p = \frac{\dot{m}_L}{\dot{m}_G} = \frac{1}{ALR} \tag{17}$$

Eq. 14 is a function of the material properties, nozzle geometry and four coefficients, namely C_3, C_4, j, and m. It is possible to obtain the coefficients which only depend on nozzle geometry by measuring the droplet sizes with a laser-doppler anemometer for an easy two component system, e.g. water-air.

With known coefficients, it is possible to calculate a new Sauter droplet diameter for an unknown spray experiment of a two-component system (where the material properties are known) to pretend a characteristic droplet diameter for a numerical simulation.

COOL DOWN SIMULATIONS OF SUBSEA EQUIPMENT

Atle JENSEN[12*], Stig GRAFSRØNNINGEN[1]
[1] FMC Technologies, 1386 Asker, NORWAY
[2] UiO Department of Mathematics, 0316 Oslo, NORWAY
* E-mail: atle.jensen@fmcti.com

ABSTRACT

Experiments and numerical conjugate heat transfer simulations are performed on a simple T-pipe geometry. The T-pipe geometry is partially insulated and mimics subsea equipment which are subjected to cool down after a production shut-down. During flowing conditions the flow is turbulent before closing down and cool down starts. After some time after shut-down the flow becomes near stagnant in parts of the geometry whereas it remains turbulent in the vertical section for a long time after shut-down due to large buoyant forces. Velocities were measured with PIV, whereas temperature was measured using RTD's and thermocouples. A particular focus is on the effect of using RANS turbulence models on a buoyant flow which is laminar, transitional and turbulent within a single fluid domain.

Keywords: CFD, turbulence, natural convection, PIV.

NOMENCLATURE

Greek Symbols
ρ Mass density, [kg/m^3].
μ Dynamic viscosity, [kg/ms].
ν Kinematic viscosity, [m²/s].
β Coefficient of thermal expansion, [1/K].
α Thermal diffusivity, [m²/s].
σ Stefan-Boltzmann constant, [W/m²K^4].
ε Emissivity, [-].
ε Turbulent dissipation rate, [m²/s³].
δ Kronceker Delta, [-].
ω Turbulence eddy frequency, [1/s].

Latin Symbols
L Characteristic length, [m].
p Pressure, [Pa].
u Velocity, [m/s].
g Gravity [m/s²].
h Heat transfer coefficient [W/m²K].
k Thermal conductivity, [W/mK].
k Turbulent kinetic energy [m²/s²].
T Temperature, [°C].

Sub/superscripts
G Gas.
i Index *i.*
j Index *j*.
s Surface.
∞ Ambient.
t Turbulent.

INTRODUCTION

In subsea oil and gas industry, thermal insulation of equipment is often used as a method to slow down cool down, and to facilitate shut-down procedures. Great effort is spent on predicting the thermal behaviour of hydrocarbon production systems in order to identify and prevent hydrate formation in the production fluid during normal production, and during planned or unplanned shut downs.

Subsea equipment generally cannot be fully insulated for different reasons; avoid overheating of electronic components, facilitate ROV access, clearance, and various other reasons. The uninsulated parts of the subsea equipment create cold-spots which may have a severe effect on the thermal performance. Detailed thermal analyses are required to assess the effect of these cold-spots and to make sure the equipment is adequately insulated. An increasingly larger fraction of the detailed thermal analyses within the subsea industry nowadays are conjugate heat transfer CFD simulations.

Engineering flows are generally turbulent and laminar flows are seldom encountered. One exception is natural convection, i.e. buoyancy driven flow. During cool down of subsea equipment laminar, transitional and turbulent flow may occur simultaneously within the same domain. RANS-turbulence models, which is the only feasible level of turbulence treatment in CFD for engineering purposes on full scale equipment, are developed for high Reynolds number flow and are generally unable to predict the correct solution if the actual flow is laminar or transitional.

CFD simulations are often used in the design process of the insulation on subsea equipment in the subsea industry. However, the accuracy and uncertainty of the simulations are seldom reported, nor are the results verified against experimental data. The use of mainstay engineering CFD approaches introduces an uncertainty

due to the inadequacy of the RANS-models to capture laminar to turbulent transitions and relaminarizations.

An assessment of the effect of using turbulence models on such flow has been performed in order to shed some light on the uncertainty of thermal CFD cool down simulations.

Only a few papers have investigated the thermal performance of straight vertical or horizontal dead legs in order to understand the convective behavior of the fluid. Habib et al. (2005) conducted an experimental and numerical study of the effect of dead leg geometry and average flow velocity on oil/water separation in dead legs. The length of the dead leg was varied and a fluid mix of 90% oil and 10% water were considered. They concluded that the size of the stagnant fluid region increased with increased length to diameter ratio and decreased with increased inlet velocity. Asteriadou et al. (2009) presents several CFD models of a flow in a T-piece configuration. The computational models were validated by experiments. The flows varied from laminar to turbulent. The authors report that finer mesh and enhanced wall functions application with mesh refinement did not seem to have a positive impact on the solution.

A handful of papers were found on cool-down, numerical modelling and experiments. Taxy and Lebreton (2004) conducted CFD simulations and full scale insulation tests. They concluded that numerical simulations helped to understand the phenomenology observed during different tests and were the key element to determine the correct action to implement in the insulation design. In Moe et al. (2005) the temperature development in two simple geometries and one gate valve were tested in a laboratory and analyzed with CFD. They found excellent agreement in some of the cases and concluded that CFD is a suitable tool for cool-down simulations. Furthermore, they also claimed that CFD would provide valuable input to FEA simulations to correct for the convective heat transfer. A full scale cool-down test of an X-Tree was used to verify the design and numerical models in Aarnes et al. (2005). CFD and FEA agreed very well with the test results in the main part of the X-Tree system.

Mme et al. (2008) presented results from both experiments and numerical modeling of a cool-down in a pipe with a cold spot. The inclination of the pipe was varied and it was found that the heat transfer was most efficient when the inclination was close to horizontal. CFD with a k-ε model was used to simulate the cool-down. The heat flow by the simulations was reported to be under-predicted up to 25%. In a recent paper by Lu et al. (2011) CFD and FEA were validated against controlled experiments. A coated 24 inch steel pipe was welded onto a production tree and elbow. The test assembly was placed in fresh water and temperatures were measured with thermocouples. Measurements were conducted in steady-state and during cool-down. The discrepancy was 5% between CFD and experiments for both cases. FEA gave similar results compared to the experiments.

This article presents results from conjugate heat transfer cool down CFD simulations with comparison against cool down tests with a particular focus on the effect of using RANS turbulence-models on a buoyant flow which is laminar, transitional, and turbulent, within a single fluid domain.

EXPERIMENTS

Experiments were conducted at the Hydrodynamics laboratory, University of Oslo for validation of the CFD model. An idealized geometry in transparent material (Plexiglass) was chosen to give access to optical measurement techniques but also the possibility for more quantitative analysis, e.g. observations.

Experimental setup and techniques

A large diameter (ID 6") horizontal pipe (3m long header) with a vertical branch (1m) mounted together was used in the experiments (shown in Figures 1 and 2). The vertical dead-leg must be long to be able to generate flow with Rayleigh numbers ($Ra = \frac{g\beta\Delta TL^3}{\nu\alpha}$) encountered in subsea equipment. The characteristic length scale used in the Rayleigh number is the free vertical length, i.e. the length of the dead-leg in the dead-leg, and the diameter in the header region.

Water was used as test media and circulated until the required temperature was met and steady state conditions were reached (stage 1 - steady state). The flow rate was 1300 kg/h with an accuracy of +/- 0.5%. The inlet temperature was 45°C and the ambient temperature was 21°C.

A set of valves were mounted on each side of the test rig to be able to enclose the flow (state 2 - cool down). The header was insulated with Glava (40mm) and installed horizontally on a table covered with Styrofoam to avoid heat transfer to and from the table.

Fluid velocities and external/internal temperatures were measured with high accuracy using Particle Image Velocimetry (PIV), flow meters, PT100 RTD sensors and thermocouples. PIV has seen a rapid growth over the last two decades, much caused by the developments in camera and laser technology. This method is using pattern matching techniques to be able to track the motion of passive particles which are added to the flow. A sequence of images is used in the post-processing to find the temporal variation of the velocity in a flow. Kinematics and dynamics can be found using various processing techniques. The PT100 sensors were measuring the water temperature, whereas the thermocouples were measuring the wall temperature at different positions in the interior and exterior. The accuracy of PIV is very high if the experiments are carefully executed, the error is expected to be around 1%.

The vertical pipe (dead-leg) is not insulated, thus, from a modeling point of view, the external boundary

conditions between the pipe geometry and the air (a heat transfer coefficient in conjunction with an ambient temperature and the radiative heat loss) is very important. Contradictory to for fully insulated equipment the value of the heat transfer coefficient will potentially influence the results to a great extent. However, the header is insulated to be able to simulate more realistic subsea conditions, i.e. equipment which is partially insulated.

During stage 2 (cool down) the internal and external temperatures were measured together with velocity fields. The temperatures were sampled continuously, but the velocity fields were acquired every five minutes. The velocity field results presented herein is the average of several experiments.

Water temperature was measured at 7 different locations using RTD's inserted 50 mm into the header and dead-leg. The locations of the sensor locations/measuring points are listed in Table 1. The location of the RTD's can also be seen in Figure 1 and a different view with coordinate system in Figure 2.

Table 1: Internal sensor locations.

Sensor name	Location		
	X [m]	Y [m]	Z [m]
PT1	0	0.0225	-0.977
PT2	0	0.0225	-0.377
PT3	0	0.0225	0.396
PT4	0	0.0225	0.996
PT5	0	0.397	0.023
PT6	0	0.797	0.023
PT7	-0.059	0.950	0

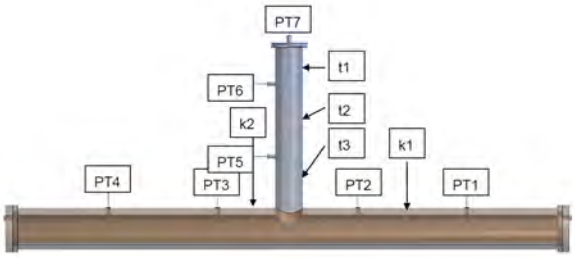

Figure 1: Side view of CFD-model with insulation and sensor locations.

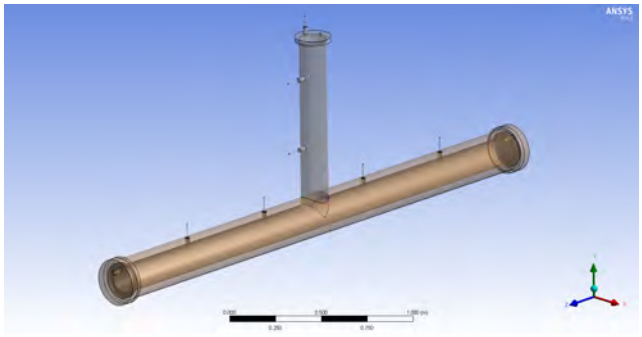

Figure 2: Perspective view showing the orientation of the coordinate system.

Type-t and type-k thermocouples were used to measure the external temperature of the test-geometry. For redundancy three sensors were used to measure the external temperatures at each location. The results from these sensors are not presented.

CFD SIMULATIONS

A side view of a CFD-model of the experimental setup is shown in Figure 1. The model contains the Plexiglas geometry, the insulation, and sensors. The RTD's used to measure the internal fluid temperatures are large and intrusive and may influence the results if not accounted for. Hence, a simplified version of the sensor was included in the CFD-model. The simulations were run using ANSYS CFX v.14.5.

The CFD-simulations were run in two stages; the first to mimic the production phase in a subsea system, i.e. flow through the geometry before a planned or unplanned shut-down. The second stage emulates the shut-down phase, i.e. from the initial valve closure and the subsequent cool-down. The second stage uses the results from the first stage as an initial condition.

The heat transfer from the test geometry to the ambient air is governed by radiation and convection. The radiative heat transfer was modeled assuming black body radiation, i.e. the heat loss due to radiation is modeled as

$$q_{rad} = \epsilon\sigma({T_s}^4 - {T_\infty}^4) \quad (1)$$

where ε is the emissivity of the body, σ is the Stefan-Boltzmann constant, T_s is the surface temperature, and T_∞ is the ambient temperature. The external Nusselt number ($Nu = \frac{hL}{k}$) due to convective heat transfer on the dead-leg was computed using the following empirical correlation

$$\overline{Nu} = [0.825 + \frac{0.387Ra^{1/6}}{[1+(\frac{0.492}{\mathrm{Pr}})^{9/16}]^{8/27}}]^2 \quad (2)$$

This equation is valid for vertical walls, and vertical cylinders under certain conditions. A similar correlation (other constants) was used to compute the Nusselt number for the header, see Incropera (2007).

During stage 1 the flow in the geometry is a combination of forced, mixed and natural convection. The flow in the header is dominated by forced convection, whereas both forced and natural convection is of importance in the lower part of the dead-leg. In the upper part of the dead-leg natural convection is of sole importance. Similar effects are expected for actual subsea equipment as well.

During stage 2, after the circulation has stopped and the isolation valves are closed, a convective pattern inside the geometry develops due to the thermal differences in the system. The level of mixing in the header during stage 1 and stage 2 depends on the flow pattern. If the

flow is turbulent, the mixing between the header and dead-leg regions is large whereas it is limited if the flow is laminar. Whether a flow is laminar or turbulent is given by local conditions.

Turbulence is generated by mean velocity shear and coupled turbulent velocity and temperature fluctuations, whereas it is suppressed by thermal stratifications and turbulent shear. Mean shear dominates production of turbulent kinetic energy, hence for a vertical pipe, given that the Rayleigh number is large enough, the turbulence will be generated in the shear region close to the wall. For intermediate Rayleigh numbers such a configuration may lead to intermittent flow, where intermittent alludes to a flow which spatially and temporally is turbulent.

Simulations with different turbulence models were conducted to determine the effect of the various RANS turbulence models;

- *k-ω*
  - Two-equation model – first moment closure model
- *SST*
  - Two-equation model – first moment closure model
- *RSM-ω*
  - Reynolds Stress model – second moment closure model
- *k-ε*
  - Two-equation model – first moment closure model

Historically the *k-ε* model has been the mainstay turbulence model within engineering, and still is within some communities. Turbulence models are generally developed based on assumptions of high Reynolds number flow, which does not fit the nature of turbulent natural convection flow very well.
The near wall mesh in turbulent simulations is generally very important to accurately calculate the wall shear and heat fluxes. RANS-models often use wall functions to predict the near wall physics as the near wall mesh requirements may become prohibitively stringent for high Reynolds number flow. The wall functions use models to account for the near wall physics without having to resolve the innermost region of the boundary layer with the computational grid. Wall functions are based on functions which describe the viscous sub-layer and the buffer layer found in high Reynolds number flow. However, the near wall physics found in turbulent natural convection does not resemble that of the forced flow; hence wall functions cannot be used to accurately predict turbulent natural convection.

Some of the turbulence models available in CFX (*ω*-based models, both single moment and second moment closures) and other CFD-packages use a low-Reynolds number formulation in innermost part of the boundary layer. In order to exploit the low-Reynolds number formulation a near wall mesh resolution of $y^+ < 1$ is required to avoid the use of wall functions.

The *ε*-based turbulence models, both first moment closures and second moment closures generally rely on wall functions even though the near wall mesh is $y^+ < 1$. It should be noted that it is generally recommended to avoid very fine near wall mesh resolutions ($y^+ > 30$) when using the *k-ε* model as this combination is known to produce strange results. A $y^+ > 30$ cannot be guaranteed even for rather coarse near wall meshes for such geometries due to near stagnant flow in some regions. The *ε*-based turbulence models do not switch to a low-Reynolds number formulation close to walls for fine meshes. This makes the *ε*-based turbulence models unsuited for turbulent natural convection flows. A simulation using the widely used *k-ε* model is included to assess the effect of using this model even though it is anticipated that the results are poor. The results observed herein for the *k-ε* model may to a certain extent be attributed to a too fine near wall mesh.

Barakos and Mitsoulis (1994) investigated natural convection in a square cavity for a wide range of Rayleigh numbers numerically using turbulence models with and without wall functions. Their results show that the predicted Nusselt number deviates significantly from the experimental data when wall functions are used. The predicted Nusselt number is twice that of the experimental data for large Rayleigh numbers, whereas results from simulations without wall functions compare well with the experimental data.

The *k-ω* turbulence model is known to produce good results for natural convection in enclosures and lid-driven cavities. However, all the single moment closures use a single scalar to describe the turbulence which leads to the inherent assumption that the turbulence is isotropic, which for buoyant turbulent flows is not the case. Furthermore, the single moment closures rely on the Boussinesq-approximation to relate Reynolds stresses to the mean shear $-\overline{u_i u_j} = 2\nu_t S_{ij} - 2/3k\delta_{ij}$. Here $\overline{u_i u_j}$ is Reynolds stresses, ν_t is turbulent eddy viscosity, S_{ij} is the rate of strain tensor, and k is turbulent kinetic energy. This assumption leads further to an inherent equilibrium between the Reynolds stresses and mean shear, which is generally not valid for buoyant turbulent flows. Nevertheless, even though single moment closures does not have the best prerequisites to accurately model this type of flow, simulations using single moment closure models are included here to see if they are able to produce adequate results or not.

Simulations with three different meshes using the *k-ω* model were conducted to determine which mesh level that was required to obtain mesh independent results. All meshes were made of a combination of tetrahedrons, hexagons and prisms. Conformal mesh was used for nearly the entire model. On curved interphases such as for the inner pipe wall it is important to use a conformal mesh. If a non-conformal mesh is used it is vital that the mesh resolution is fine enough so that the surface area on both sides of the interphase is accurately predicted. On the interphase the heat flux is conserved, if the surface area on each side of the interphase is different,

the heat flux will not be conserved. A non-conformal coarse surface (interphase) mesh may significantly influence the results in a conjugate heat transfer simulation. Sweep mesh was used on the piping where possible. The mesh in a part of the geometry is shown in Figure 3 below.

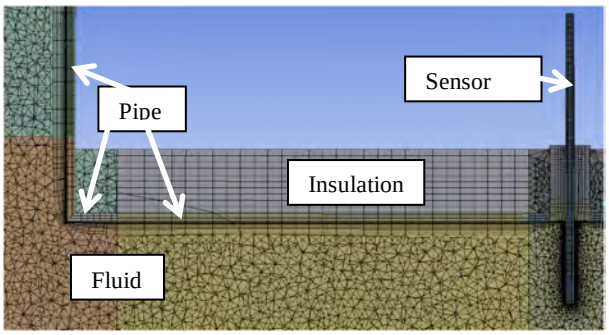

Figure 3: Fine mesh - note that the domains have been decomposed to ease the meshing process, hence the same domain may have different colors in this figure.

Key mesh sizes for the coarse, intermediate, and fine mesh are listed in Table 2 below.

Table 2: Mesh sizes

	Coarse	Intermediate	Fine
Total number of nodes	0.42M	1.10M	1.54M
Radial cell count insulation	2	6	10
Radial cell count uninsulated piping	2	5	8
Radial cell count insulated piping	2	3	5
Circumferential cell count on piping	40	40	60
First layer height piping	2e-3 [m]	2e-4 [m]	2e-4 [m]
Number of layers piping	7	12	12
Body sizing on piping (where applicable)	5e-3 [m]	5e-3 [m]	4e-3 [m]
Body sizing on insulation (where applicable)	1e-2 [m]	5e-3 [m]	5e-3 [m]
Body sizing on fluid	1.5e-2 [m]	7e-3 [m]	7e-3 [m]

The mesh convergence tests showed that the intermediate and fine mesh produced near identical results, but that there were minor differences, hence the fine mesh was used for the rest of the simulations. Results from the mesh convergence test are shown in Figure 4 and Figure 5 below. Note that the difference in internal temperature between the intermediate and fine mesh hardly is discernible here. The differences in internal wall temperatures were larger. The wall temperatures in the dead-leg (both internally and externally) for the intermediate and fine mesh differed to some extent, hence it is concluded that the fine mesh is required (results not shown here).

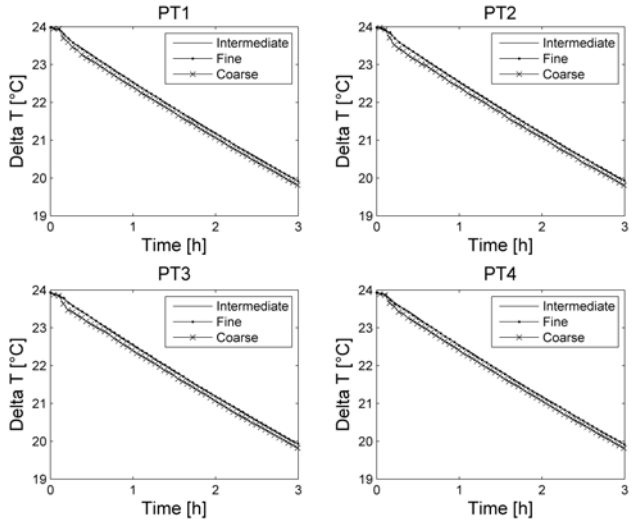

Figure 4: Mesh convergence - temperature data during cool down

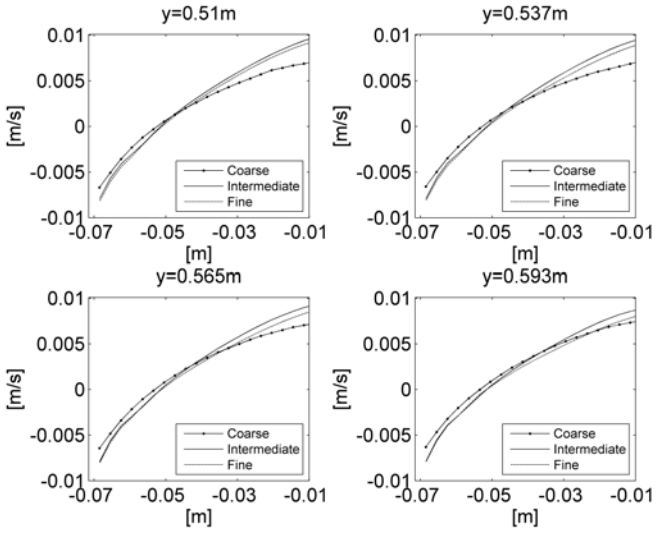

Figure 5: Mesh convergence - velocity profiles after 45 minutes cool down

The CFD simulations were run with a time step of maximum 1 s or a RMS CFL-number of 5, whichever was the most stringent.

RESULTS

The temperature excess ΔT is shown in Figure 6 and Figure 7 for all internal temperature sensors during three hours of cool down. The comparisons show good agreement between the simulations (using the fine mesh) and experiments. Here the results from simulations with the *k-ω* model are shown together the simulation without any turbulence model and the experimental data. The results show that there is good agreement between the CFD simulations and the experimental data, but that the CFD simulations generally over estimates the temperature in the dead-leg region during both steady-state and cool down.

The *k-ω* model was chosen for the comparison here because there is virtually no difference between the *k-ω*, SST, and RSM-*ω* models. See Figure 11 and Figure 12

for a comparison of results from simulations with different turbulence models.

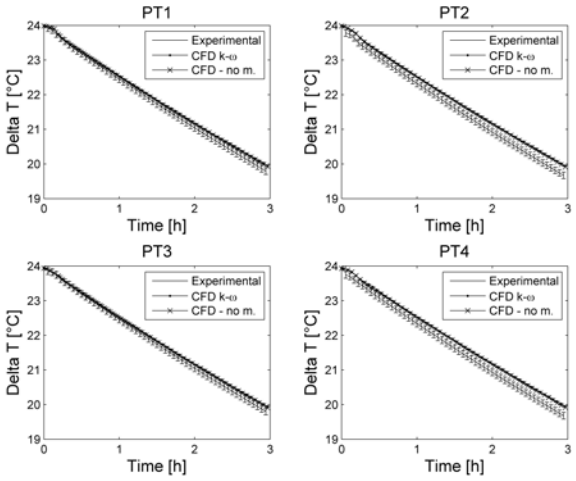

Figure 6: Experimental vs. CFD; PT1 - PT4 (internal sensors in the header)

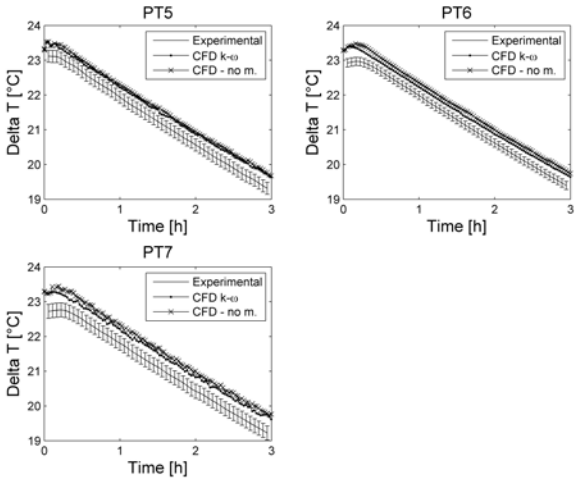

Figure 7: Experimental vs. CFD; PT5 - PT7 (internal sensors in the dead-leg)

A comparison between velocity profiles from CFD for the fine mesh and experiments are given in Figure 8 to Figure 10. Close to the wall in the dead-leg the production of turbulent kinetic energy is large, thus the flow is most likely fully turbulent here during the first part of the cool down period. In the middle of the dead-leg, there is less mean shear; hence there is less production of turbulent kinetic energy. Turbulent kinetic energy is to some extent transported from the shear region to middle of the pipe, but due to the limited amount of production the turbulence level in this region is smaller. As the insulated geometry cools down the driving force for the buoyant flow, the temperature excess ΔT, is smaller, hence the velocities also slow down. These two effects lead to a state where the flow close to the wall is turbulent, whereas the flow in the middle of the dead-leg is laminar. As mentioned earlier, this is a type of flow RANS-models cannot be expected to predict accurately.

After approximately two hours, see Figure 10, the production of turbulence in the shear zone is reduced and a laminar model is describing the velocity profiles better.

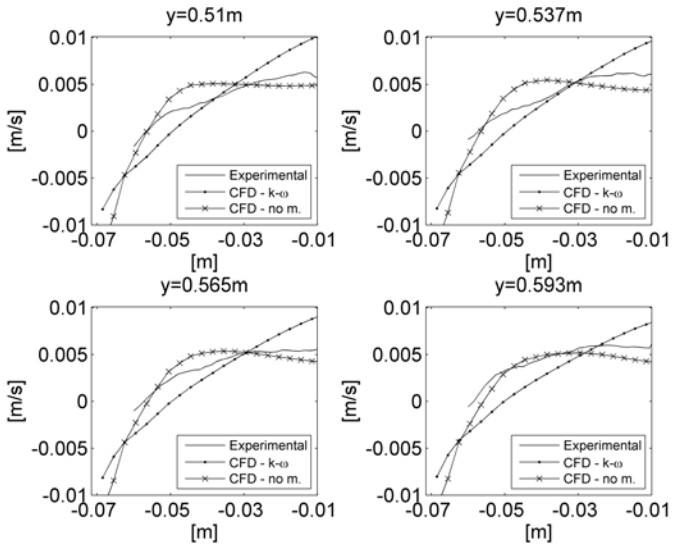

Figure 8: Mean velocity CFD vs. exp - 15 min.

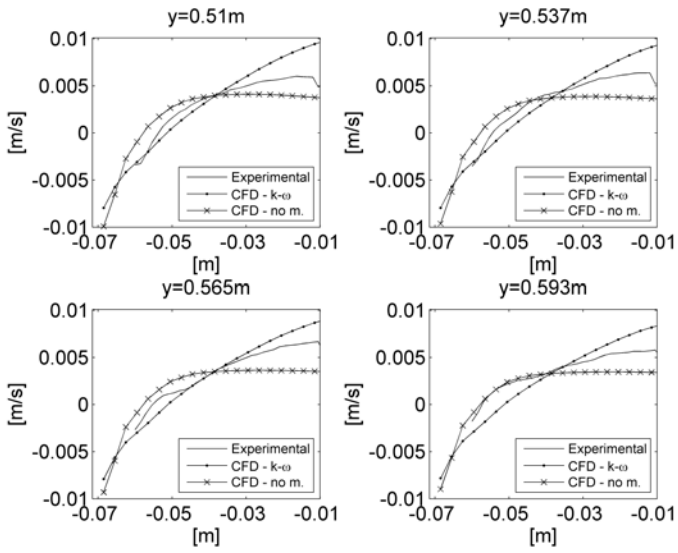

Figure 9: Mean velocity CFD vs. exp - 60 min.

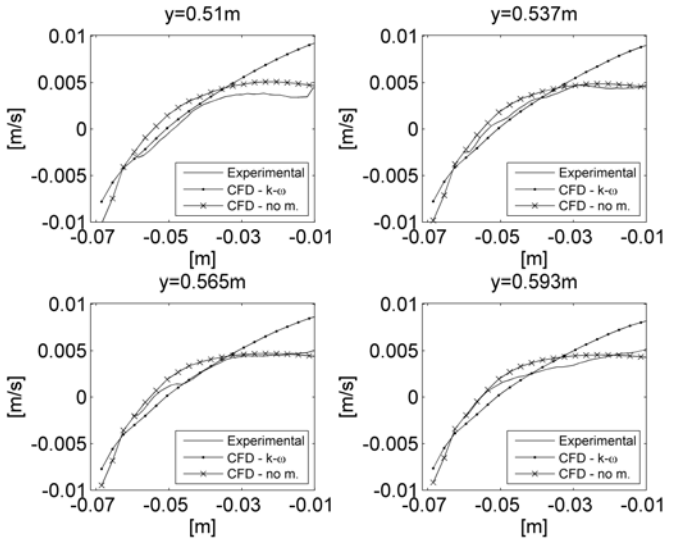

Figure 10: Mean velocity CFD vs. exp - 135 min.

Results from simulations with various turbulence models are shown in Figure 11 and Figure 12. The fine mesh was chosen and from the figures it is clear that the choice of model is important for accurate prediction of the velocity. The results show that the, and as already mentioned, there is virtually no difference between the *k-ω*, SST, and RSM-*ω* models in this case. Even though the RSM-*ω* model includes more physics compared to the two other models, it does not predict the velocity field better than the simpler two-equation models.

As previous shown, the *k-ω* model compares satisfactory with the tests for the first 100 minutes of the cool down close to the wall. However, when the flow is laminar the *k-ω* fails in reproducing the velocity profiles. Then, a laminar model can be used. It can be seen from the results that the *k-ε* fails at all times. The reason for this is because this model uses wall functions, and then the near wall physics is not resolved nor accurately predicted. A RANS turbulence model that are able to simulate accurately the whole time period is not available. In this case, more sophisticated methods of treating turbulence are required, such as Direct Numerical Simulations (DNS) or Large Eddy Simulation (LES). LES with dynamic models such as the dynamic Smagorinsky-model have the prerequisite to predict this type of flow better than RANS-models. However, LES come with a highly elevated computational cost compared to the RANS-simulations.

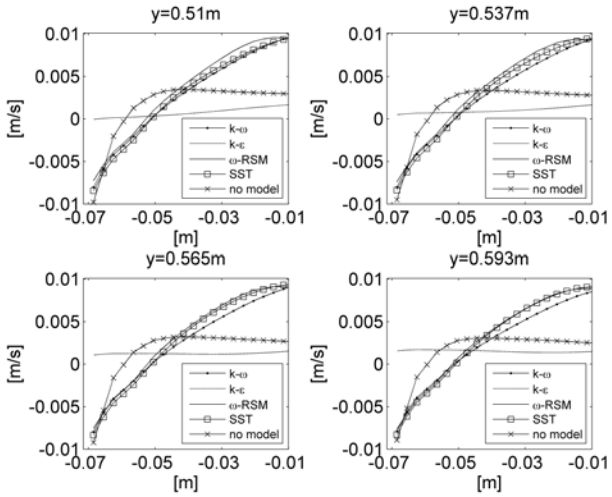

Figure 11: Mean velocity at different vertical locations for different numerical models. The x-axis denotes the horizontal position in the dead-leg - 30min.

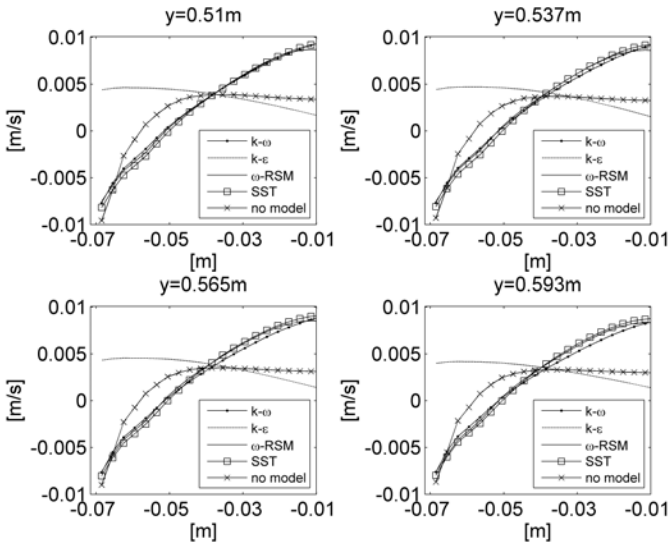

Figure 12: Mean velocity at different vertical locations for different numerical models. The x-axis denotes the horizontal position in the dead-leg - 120min.

CONCLUSION

A thorough comparison between results from CFD simulations and experimental tests of a simplified geometry resembling actual subsea equipment cool down is conducted.

The choice of turbulence models and mesh refinement is discussed.

There are large discrepancies between results from the different turbulence models and also when the mesh size is varied. However, the results of the velocity profiles from *k-ω*, *ω-RSM* and *SST* are almost identical. The results clearly show the inadequacy of the often used standard of *k-ε* model for such problems. The reason for this is that the standard *k-ε* model uses wall functions that approximate the near wall physics which again is used to compute the wall shear and wall heat flux.

Even though the turbulence generated by buoyancy is anisotropic the results show that for this type of simulations an isotropic turbulence model can be used, e.g. the *k-ω* turbulence model. The anisotropy is weak compared to other effects. Furthermore the results show that in this case the Boussinesq-approximation may be used, the enforced equilibrium between Reynolds stresses and mean shear does not introduce any additional errors.

A mesh convergence test was carried out to determine the mesh level required for such type of geometries. The velocity fields proved rather insensitive to the mesh test, but the effect was clearly seen on the temperature field, particularly on the wall temperatures. It is concluded that when CFD-cool down simulations are carried out, it is more important to conduct simulations on a proper mesh compared to choosing sophisticated turbulence models. (This is contradictory to what often is done in engineering, it is quicker and easier to change turbulence model rather than to re-mesh the model).

For this case the overall goal is to be able to estimate the temperature during cool down. The choice of turbulence

model is less important, but the quality and size of the mesh should get most of the attention.

Based on visual observations and a comparison between the CFD and experimental data it is concluded that the flow field after about 60 minutes is laminar, particularly in the middle of the dead-leg. Hence, no turbulence model should be used to predict the flow. However, in real life, for design simulations of thermal insulation on subsea equipment the actual flow field inside the geometries during a cool down is unknown. One may make an estimate based on the expected Rayleigh number, but in practice, it is very difficult to accurately determine the type of flow. The CFD simulations have shown that the thermal field is generally insensitive to choice of turbulence models vs. no-model for this type of geometry. Hence, if it is uncertain whether the flow is turbulent or laminar, a turbulent simulation using the k-ω model will most likely produce adequate results for insulated equipment.

The results presented in this report are performed for the given pipe dimensions and flow rates. These results are not easily scalable, but methodology and mesh strategy are valid and carefully investigated and may be used for simulations of subsea equipment.

REFERENCES

K.A. Aarnes, J. Lesgent and J.C. Hübert (2005), "Thermal Design of a Dalia SPS Deepwater Christmas Tree – Verified by Use of Full-Scale Testing and Numerical Simulations", *Offshore Technology Conference*

K. Asteriadou, A. P. M. Hasting, M. R. Bird and J. Melrose (2009), "Exploring CFD Solutions for Coexisting Flow Regimes in a T-Piece", *Chem. Eng. Technol,*, Vol 32, pp 948-955

M. A. Habib, H. M. Badr, S. A. M. Said, E. M. A. Mokheimer, I. Hussaini and M. Al-Sanaa, (2005) "Characteristics of flow field and water concentration in a horizontal deadleg", *Heat and Mass Transfer*, Vol 41, pp 315-326

G. Barakos and E. Mitsoulis, (1994) "Natural convection flow in a square cavity Revisited: laminar and turbulent models with Wall functions", *International Journal for Numerical Methods in Fluids*, Vol. 18, 695-719

F. P. Incropera, D. P. Dewitt,T.L. Bergman and A. S. Lavine, (2007), *Fundamentals of Heat and Mass Transfer* (6th ed.). Hoboken: John Wiley & Sons

Y. Lu, E. Marotta and B. Skeels (2011), "CFD Thermal Analysis of Subsea Equipment and Experimental Validation ", *Offshore Technology Conference*

U. Mme, S. T. Johansen, S. Sarkar, R. Moe, A. Goldszal and Y. Ladam (2008), "Flow and heat transfer in pipe caused by localised cold spot", *Progress in Computational Fluid Dynamics*

R. Moe, S. Sørbye, K. Skogen and C. Lofseik (2005), "A comparison of experimental data and CFD predicted cool down in subsea equipment", *Fourth International Conference on CFD in the Oil and Gas, Metallurgical & Process Industries*

S. Taxy and E. Lebreton (2004), "Use of Computational Fluid Dynamics to Investigate the Impact of Cold Spots on Subsea Insulation Performance", *Offshore Technology Conference*

PREDICTING EMULSION PRESSURE DROP IN PIPES THROUGH CFD MULTIPHASE RHEOLOGY MODELS

Nathanael J. INKSON[1]*, **Jose PLASENCIA**[2†], **Simon LO**[1‡]

[1]CD-adapco, Trident House, Trident Park, Basil Hill Road, Didcot, Oxfordshire, OX11 7HJ, UNITED KINGDOM

[2]GE Oil & Gas, Eyvind Lyches vei 10, 1338 Sandvika, NORWAY

* E-mail: nathanael.inkson@cd-adapco.com
† E-mail: jose.plasencia@ge.com
‡ E-mail: simon.lo@cd-adapco.com

ABSTRACT

A CFD model has been developed that fits laminar data of both suspensions and stabilized water-in-oil emulsions using a relative viscosity model combined with a model for the stress of particles in a suspension. An analysis of rheology data for both suspensions and emulsions revealed that they share similar physics. We follow the approach that an emulsion can be treated as a suspension that does not reach maximum packing of particles, but rather undergoes a phase inversion at a critical dispersed volume fraction. By combining the rheology with a model of suspension stress in the context of Eulerian multiphase flow in a commercial CFD code STAR-CCM+, it has been possible to quantitatively model the pressure drop of salt water in crude oil emulsions during pipe flow with minimal fitting. A suspension model with negative normal stresses and one without were used to correctly fit the curve of pressure drop against volume fraction once the highest pressure drop was calibrated to the maximum packing of the relative viscosity model as well as the inversion point of the emulsion. The shear relative viscosity was an important quantity to estimate the pressure drop and for suspensions the strength of normal stresses controlled the migration of particles. These are attributes of the materials that could be determined in a lab via a rheometer for the prediction of emulsion behaviour in a scaled-up simulation.

Keywords: Bubble and droplet dynamics, Rheology, Emulsion physics, Surfactants and interfaces, Multiphase pipeline transport, Mixing, Oil & Gas .

NOMENCLATURE

Greek Symbols

α	Volume fraction.
ρ	Mass density, $[kg/m^3]$.
μ	Newtonian dynamic viscosity, $[kg/ms]$.
η	Mixture shear viscosity $[kg/ms]$.
$[\eta]$	Intrinsic viscosity.
η_r	Dimensionless shear relative viscosity.
η_n	Dimensionless normal relative viscosity.
$\dot{\gamma}$	Shear strain-rate, $[1/s]$
ϕ	Dispersed phase volume fraction.
ϕ_m	Dispersed phase maximum packing volume fraction.
ϕ_i	Emulsion inversion point volume fraction.
$\mathbf{\Sigma}_p$	Total mixture particle stress, $[kg/ms^2]$.
$\boldsymbol{\tau}$	Phase extra stress, $[kg/ms^2]$.

Latin Symbols

a'''	Symmetric interaction area density, $[1/m]$.
d	Particle diameter, $[m]$.
$\boldsymbol{D}$	Rate of deformation tensor, $[1/s]$.
$\boldsymbol{F}_D$	Inter-phase drag force, $[kgm/s^2]$.
$\boldsymbol{g}$	Gravitational acceleration, $[m/s^2]$.
K_n	Normal contact contribution.
K_s	Shear contact contribution.
p	Pressure, $[Pa]$.
$\boldsymbol{S}$	Momentum source terms $[kgm/s]$.
$\boldsymbol{Q}$	Dimensionless suspension anisotropy tensor.
$\mathbf{u}$	Fluid velocity, $[m/s]$.

Sub/superscripts

c	Continuous phase.
d	Dispersed phase.
p	Particle phase.
k	kth-phase.

INTRODUCTION

We have identified candidate models to improve the mathematical modelling of the rheology of emulsions in CFD. The driving force was that the standard formulations of Eulerian multiphase (EMP) flow in STAR-CCM+ was known to under-predict the pressure drop for salt water in crude oil emulsions as seen in the laminar pipe experiments performed by Jose Plasencia within the FACE project (Plasencia *et al.*, 2013). A review of the literature regarding emulsions was performed, although little published data was found on rheology. However, it was discovered that extensive work had been performed on suspension rheology and that substantial experimental and theoretical progress had been made. A combination of numerical simulation and experiments had produced advanced models for the diffusion of suspension particles in mainly a "single phase" formulation for the mixture. From studying the theoretical developments for suspensions in the literature it was found that many Brownian Dynamics simulations and experiments had been performed for colloids and suspensions of larger particles (Mewis and Wagner, 2012). It was discovered that several models for the diffusion of particles in flow had been developed which we shall discuss further. There are two main models in the literature for particle migration of suspensions in low Reynolds number (Re) flows. The simplest is the "Diffusion flux model" of Phillips et. al. (Phillips *et al.*, 1991) and a later formulation is the "Suspension balance model"

of Nott and Brady (Nott and Brady, 1994). The diffusion flux model has a simple form although it has a draw-back of having a discontinuity in volume fraction where the shear-rate is zero, although there are subsequent modifications to solve this problem (Ahmad *et al.*, 2010). It has been shown that the suspension balance model reduces to the diffusion flux model in simple pipe flows. Later work by Morris and Boulay (Morris and Boulay, 1999) showed that a formulation of the stress tensor as a combination of shear relative viscosity and normal relative viscosity reproduces the physics of suspension particle migration of the Diffusion flux model and suspension balance models. When implemented into the source code of STAR-CCM+ it was found that these suspension models were indeed able to predict the experimental pressure drop of emulsions with minimal fitting.

SUSPENSION MODELS

We implemented a generic form of the Morris and Boulay Model that combines a mathematical description of the shear relative viscosity and a normal relative viscosity.

Suspension Stress

(Morris and Boulay, 1999) proposed a tensorial stress model for suspensions that they demonstrated gave the same results as the suspension balance model. They discovered that by defining a negative normal relative viscosity the desired particle migration is observed. The total particle stress tensor for the mixture is given by

$$\boldsymbol{\Sigma}_p = -\mu_c \eta_n(\phi)\dot{\gamma}\boldsymbol{Q} + 2\mu_c \eta_r(\phi)\boldsymbol{D}, \tag{1}$$

where ϕ is the dispersed particle volume fraction, μ_c is the continuous liquid viscosity, $\dot{\gamma}$ is the shear strain-rate, $\eta_n(\phi)$ is the normal relative viscosity and $\boldsymbol{Q}$ is the anisotropy tensor

$$\boldsymbol{Q} = \begin{pmatrix} 1 & 0 & 0 \\ 0 & \lambda_1 & 0 \\ 0 & 0 & \lambda_2 \end{pmatrix}, \tag{2}$$

$\lambda_1 = 0.8$ and $\lambda_2 = 0.5$ are the anisotropy parameters. Note that this was derived for flow sheared in the $x-$direction. $\boldsymbol{D}$ is the rate-of-deformation tensor of the mixture

$$\boldsymbol{D} = \frac{1}{2}(\boldsymbol{\nabla u} + \boldsymbol{\nabla u}^T). \tag{3}$$

Relative Viscosities

In emulsion and suspension rheology the dimensionless relative viscosity is required to describe the numerics of the mixture viscosity which tends to infinity as the dispersed phase reaches the limit of maximum packing. The relative viscosity is defined as

$$\eta_r = \frac{\eta}{\mu_c}, \tag{4}$$

where η is the mixture viscosity and μ_c is the continuous phase (Newtonian) viscosity.
There are many models with a similar form. One of the earliest from the study of suspensions is the Krieger-Dougherty model (Krieger and Dougherty, 1959)

$$\eta_r(\phi) = \left(1 - \frac{\phi}{\phi_m}\right)^{-[\eta]\phi_m}, \tag{5}$$

where $[\eta]$ is the intrinsic viscosity. $[\eta] = 2.5$ for spherical particles and ϕ_m is the maximum critical packing fraction for which ($\phi_m = 0.645$) for mono-disperse hard spheres.
In the Morris and Boulay model the relative viscosity is defined

$$\eta_r(\phi) = 1 + 2.5\phi\left(1 - \frac{\phi}{\phi_m}\right)^{-1} + K_s\left(\frac{\phi}{\phi_m}\right)^2\left(1 - \frac{\phi}{\phi_m}\right)^{-2}, \tag{6}$$

and the normal relative viscosity by

$$\eta_n(\phi) = K_n\left(\frac{\phi}{\phi_m}\right)^2\left(1 - \frac{\phi}{\phi_m}\right)^{-2}. \tag{7}$$

K_s and K_n are the shear and normal contact strengths and were found to be approximately 0.1 and 0.75 respectively by comparing with experiment.

Eulerian multiphase CFD

The original models for suspensions are usually derived from a "single phase" perspective, with the modelling of the volume fraction of particles as an extra transport equation. However we felt that we would attempt to generalise the model into a fully multi-fluid model by following Lhuiller (Lhuillier, 2009) who formulated the most complete two-fluid model version for suspensions which emphasises how the particle stresses are linked with hydrodynamic stresses.
The Eulerian multiphase formulation in STAR-CCM+ uses the Euler-Euler approach where phases are assumed as inter-penetrating continua coexisting in the domain. Each phase has its own distinct velocity, temperature and physical properties. Conservation equations are solved for each phase with additional closure laws to model the interactions between the phases. The SIMPLE algorithm is used to control the overall solution. (CD-adapco, 2014) Star-CCM+ solves the continuity and momentum equation for each phase, k. The conservation equations for mass and momentum take the following form,

$$\frac{\partial}{\partial t}(\alpha_k \rho_k) + \boldsymbol{\nabla}.(\alpha_k \rho_k \boldsymbol{u}_k) = \boldsymbol{0}$$

$$\frac{\partial}{\partial t}(\alpha_k \rho_k \boldsymbol{u}_k) + \boldsymbol{\nabla}.(\alpha_k \rho_k \boldsymbol{u}_k \boldsymbol{u}_k) = -\alpha_k \boldsymbol{\nabla} p + \alpha_k \rho_k \boldsymbol{g} + \boldsymbol{\nabla}.(\alpha_k(\boldsymbol{\tau}_k + \boldsymbol{\tau}_k^t)) + \boldsymbol{F}_k + \boldsymbol{S}_k, \tag{8}$$

where $\boldsymbol{F}_k$ are the interaction forces between the phases and are comprised of contributions from drag force, lift force, virtual mass force, and wall lubrication force. In this work we only considered the effect of drag force. $\boldsymbol{S}_k$ are additional source terms added to the momentum equation. For laminar flows the turbulent stress is zero, $\boldsymbol{\tau}^t = \boldsymbol{0}$ and the Newtonian stress tensor is

$$\boldsymbol{\tau}_k = 2\mu_k \alpha_k \boldsymbol{D}_k - \frac{2}{3}(\boldsymbol{\nabla}.\boldsymbol{v})\boldsymbol{I}. \tag{9}$$

For suspensions and emulsions we have an additional stress tensor similar to the Morris and Boulay equation (1) which has separate equations for the dispersed particle and continuous fluid phases. The mixture shear stress is

$$\boldsymbol{\Sigma}_{shear} = 2\mu_c \eta_r(\alpha_d)\boldsymbol{D}. \tag{10}$$

In order to split this stress between the phases, we consider the relation of the volume averaged mixture velocity to the inter-penetrating velocities of each phase

$$\boldsymbol{u} = \alpha_c \boldsymbol{u}_c + \alpha_d \boldsymbol{u}_d, \tag{11}$$

substituting into equation 3 and expanding with the chain rule gives the mixture average deformation rate tensor in terms of the phases

$$\boldsymbol{D} = \alpha_c \boldsymbol{D}_c + \alpha_d \boldsymbol{D}_d + \boldsymbol{u}_c \nabla \alpha_c + \boldsymbol{u}_d \nabla \alpha_d + (\boldsymbol{u}_c \nabla \alpha_c)^T + (\boldsymbol{u}_d \nabla \alpha_d)^T. \tag{12}$$

In this work we have made the assumption that the gradients of volume fraction are small (which is true for a homogeneous mixture) and neglected latter terms. However a preliminary investigation found these terms made the flow unstable and did not lead to physical results, although we may investigate the validity of this assumption further in later work. The approximate deformation rate tensor is now split by volume-weighted averaging by the respective volume fractions of the two phases

$$\boldsymbol{D} \approx \alpha_c \boldsymbol{D}_c + \alpha_d \boldsymbol{D}_d. \tag{13}$$

Substituting this into the total shear stress equation (10) gives

$$\boldsymbol{\Sigma}_{shear} = 2\mu_c \eta_r(\alpha_d)(\alpha_c \boldsymbol{D}_c + \alpha_d \boldsymbol{D}_d). \tag{14}$$

However as we already account for the viscous stress of the continuous phase in the Newtonian stress

$$\boldsymbol{\tau}_{c,Newtonian} = 2\mu_c \alpha_c \boldsymbol{D}_c, \tag{15}$$

we subtract one from the relative viscosity to give only the extra-stress due to the presence of the particles in the mixture. This gives the continuous phase an additional shear stress contribution from the presence of the particles as

$$\boldsymbol{\tau}_{c,extra} = 2\alpha_c \mu_c (\eta_r(\alpha_d) - 1)\boldsymbol{D}_c. \tag{16}$$

The total stress for the continuous phase is

$$\boldsymbol{\tau}_{c,total} = \boldsymbol{\tau}_{c,Newtonian} + \boldsymbol{\tau}_{c,extra} \tag{17}$$

The dispersed phase has a similar treatment for the shear term and the particle stress (the normal stress due to particle collisions) entirely goes into the dispersed phase,

$$\boldsymbol{\tau}_{d,extra} = 2\alpha_d \mu_c (\eta_r(\alpha_d) - 1)\boldsymbol{D}_d - \mu_c \eta_n(\alpha_d)\dot{\gamma}_d \boldsymbol{Q}. \tag{18}$$

This completes the formulation of the stress tensors. The only term remaining in the momentum equations is the interphase drag. We choose a drag force defined

$$\boldsymbol{F}_D = A_D |\Delta \boldsymbol{v}|. \tag{19}$$

where $|\Delta \boldsymbol{v}|$ is the slip between phases and the linearised drag, A_D is given by

$$A_D = \frac{a'''}{8} \rho_c |\Delta \boldsymbol{v}| C_D. \tag{20}$$

where a''' is the symmetric interaction area density and is defined as

$$a''' = \frac{6\alpha_c \alpha_d}{d} \tag{21}$$

where d is the droplet diameter. The drag coefficient, C_D is a Schiller-Naumann drag for particles

$$C_D = \frac{24}{Re}(1 + Re^{0.681}). \tag{22}$$

We modify the drag to tend to infinity as maximum packing is approached to prevent slip between the phases due to the network structure of particles.

Experiments

A comparative study of the pipe flow of water-in-crude oil emulsions was performed and reported in (Plasencia *et al.*, 2013). The pipe flow of emulsions were based on six different crude oils (viscosities from 4.8 to 23.5 mPa s) and salt water were investigated experimentally using a small scale flow loop. The formation of the emulsions was induced by the flow shear itself by circulating the oil and water mixture in a closed loop system (pipe internal diameter 2.2 cm). We study the crude oils "A" and "B" from the paper at several average flow velocities and cover the full range of volume fractions (water cuts) to capture the full extent of the pressure drop data.

Simulation

All simulations were performed using the development version of the commercial computational fluid dynamics package STAR-CCM+ (version 9.03), they were ran as transient simulations with time-steps between 0.0001 and 0.01 s and run until steady state is achieved. The suspension was modelled in an axisymmetric pipe of radius $1.27cm$ and length $3.048m$ with 15000 cells. The fine mesh was necessary to correctly capture the particle migration along the radial direction. The water-in-oil emulsions were simulated using the Eulerian Multiphase model with no additional forces other than drag and the addition of the relative viscosities detailed above. We make the assumption that a stabilised emulsion is a suspension of liquid particles and as such we use the same models that were used for the modelling of suspension flow. However emulsions are known to undergo a phase inversion where the dispersed phase switches to the continuous phase and vice versa. It is not possible to predict this inversion point so we have to input this into the script, at which dispersed volume fraction the phase inversion occurs. The emulsion simulations were performed unsing two geometries: a 3D pipe and an axisymmetric pipe. The axisymetric geometry was used to generate all the results of this paper and was validated using the 3D geometry with one vertical plane of symmetry. The effects of gravity were compared and it was found to have a negligible effect on pressure drop. The 3D pipe was modelled as a pipe of 2.2 cm diameter and 4.5 m length with 43800 cells and a reflection symmetry axis down the centre of the pipe. The axisymmetric pipe was of radius 1.1 cm and 3.4 m length consisting of 2500 cells. The results were generated using a mixture of perl and java scripts to control STAR-CCM+.

RESULTS

Suspension model

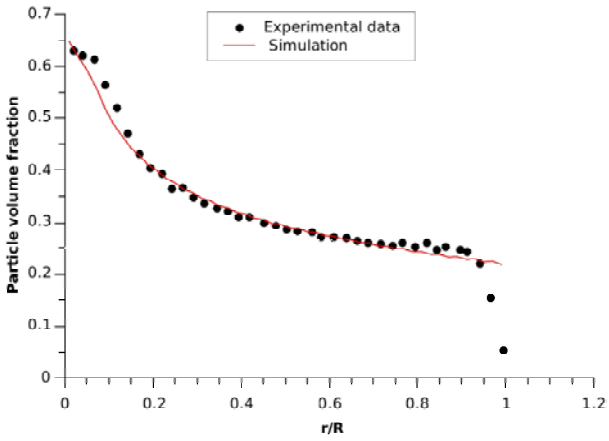

Figure 1: Volume fraction of particles across the pipe radius close to the outlet

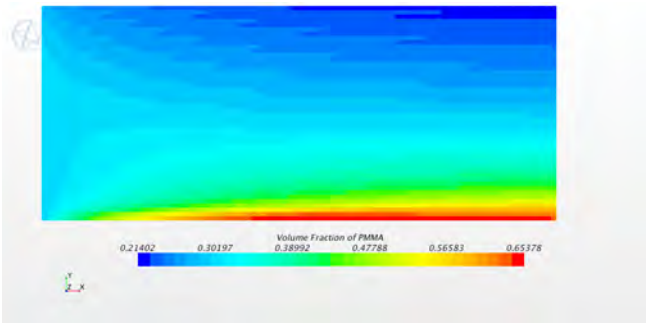

Figure 2: Volume fraction of particles across the pipe, $y-$axis is expanded by a factor of 100.

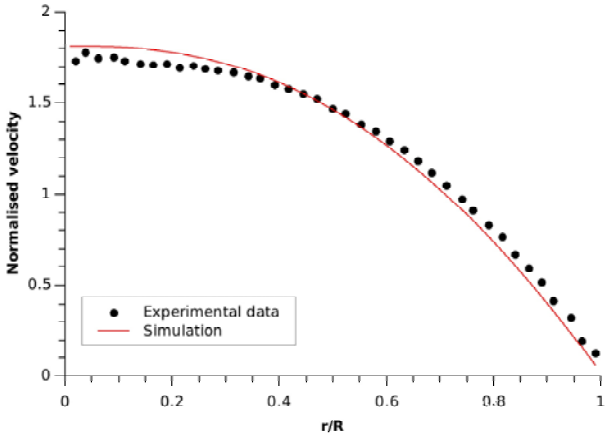

Figure 3: Normalised particle velocity profile compared to experiment

The suspension model was validated using the NMR data of a suspension of PMMA particles in a pipe performed by Hampton et. al. (Hampton *et al.*, 1997) for particles of size $650\mu m$ where the particles are neutrally buoyant with the suspending oil. The oil was modelled with density $1180.7 kgm^{-3}$, viscosity $2.1 Pa.s$. The simulations were run using the Morris and Boulay model until steady state was achieved. Figure 1 shows particle volume fraction for the case when the overall particle volume fraction = 0.3 and input velocity was $0.1 ms^{-1}$. This initial result is a very good agreement to the experimental data with minimal fitting: The normal stress contact parameter K_n was increased to 3.2 from the original value of 0.75 in order to promote the migration of particles and the desired volume fraction at the centre of the pipe. It can be seen in the experimental data that the particles are pushed away from the wall of the pipe, we do not capture this effect in our current model. Figure 2 shows the volume fraction throughout the pipe showing that the concentration is dependent on the position along the pipe (at steady state) with the $y-$axis expanded by a factor of 100. The velocity profiles in Fig. 3 are good, but not exact, however this is expected as we have no shear-thinning in this model which is expected to give a blunter profile than predicted. Only the particle velocity is shown but it is equal to the carrier fluid velocity showing that we have no slip between the phases. This is an excellent result that gives encouragement in the combination of the Morris and Boulay model with the EMP framework for modelling suspension flow.

Emulsion model

Table 1: Krieger-Dougherty and Morris-Boulay Model parameters.

Dispersed phase	ϕ_m^{KD}	ϕ_m^{MB}	K_n^{MB}	ϕ_i
particle suspension	-	0.7	3.2	-
Oil A	1.05	0.71	0.75	0.45
Oil B	0.88	0.7	0.75	0.57

We applied the Krieger-Dougherty and Morris and Boulay relative viscosity models (with the standard values of $K_s = 0.1$ and $K_n = 0.75$) to water-in-oil emulsions in pipe flow and compared with the pressure drop data performed within the FACE Project by Jose Plasencia (Plasencia *et al.*, 2013). We found that the maximum packing gave the most variation in pressure drop and changing K_s and K_n add little effect in comparison. Several simulations were performed in STAR-CCM+ at varying volume fractions. We find that the pressure drop for crude oil A and seawater emulsion in horizontal pipe of diameter $2.21 cm$ and at a velocity of $0.44 m/s$ in the laminar regime can be matched very well with both models. The sea water had density $1009 kgm^{-3}$ and a viscosity of $0.509 mPa.s$. Oil A was modelled with density $865 kgm^{-3}$, viscosity $7.5 mPa.s$, the mean diameter of the drops was $40\mu m$. The droplet diameters were estimated using a second order polynomial (Boxall *et al.*, 2010) based on the measured chord length by Focused Beam Reflectance(Plasencia *et al.*, 2013). In Figure 4 we see that both models are capable of describing the pressure drop at various volume fractions. Note that the point of inversion is decided by the engineer and is not predicted by the modelling approach. For oil A the inversion point is 0.45 water volume fraction. The set of experiments was also modelled with the standard Eulerian multiphase treatment with the emulsion rheology model switched off. In can be seen that the pressure drop stays roughly constant and no increase is seen. The set of parameters used to generate this plot was the Krieger-Dougherty maximum packing $\phi_m = 1.05$ and the Morris and Boulay maximum packing $\phi_m = 0.71$, It is of note that these values are so different, so clearly the meaning of "maximum

packing" is actually model dependent and perhaps weaker for emulsions than suspensions, for emulsions the surface of the liquid drop is expected to deform therefore changing the value of the intrinsic viscosity $[\eta]$ in the Krieger-Dougherty model. Also note that any variation in polydispersity of the droplet size distribution will also act to increase the maximum packing in the model, which may explain why our values are larger than the expected value. Furthermore the Morris and Boulay has a normal relative viscosity contribution that reduces the stress in the mixture, as this is zero in the Krieger and Dougherty model we see that they have competing effects. This is something we shall look into a greater depth in later work. The experimental data was fitted by matching the highest pressure drop point, and the other values simply followed through simulation. It can be seen that there is some deviation with the data at large volume fractions. This could be explained by the inverted emulsion perhaps having a different value of maximum packing after the inversion. Or there may be a physical reason, in that Plasencia et. al. observed some formation of oil-in-water-in-oil droplets that adds complexity beyond our simplistic model. The last point for the pure water may be effected by turbulence as the mixture viscosity becomes low.

We modelled the Oil A emulsion at a higher average velocity of 0.60 ms^{-1} and the pressure drop is shown in Figure 5. Using the same parameter set also gave very good agreement with the experimental data. Oil B was modelled with density $847kgm^{-3}$, viscosity $4.8mPa.s$ and mean droplet diameter $167\mu m$. The set of parameters used to generate this plot was the Krieger-Dougherty maximum packing $\phi_m = 0.88$, the Morris and Boulay maximum packing $\phi_m = 0.7$, and the inversion point dispersed volume fraction was at $\phi_i = 0.57$. Whilst both the models can fit the pressure drop nicely, the Morris and Boulay model scatters the disperse particles and changes the volume fraction profile of the emulsions. It is not clear if this actually happens in experiment. So we can conclude that perhaps the Krieger-Dougherty model is the preferred model for emulsion rheology. Note that all the parameters of the modelling are collated in table 1. Whilst both models can result in the same pressure drop curve, we found that the shear relative viscosity curves were different, indicating that the pressure drop is also sensitive to the normal stresses. Variation of the drag also had little effect on the pressure drop as this is primarily determined by the forces at the wall.

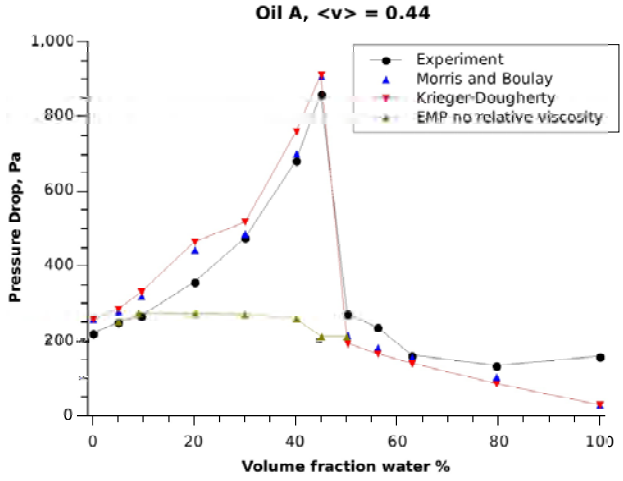

Figure 4: Pressure Drop for sea water-in-oil A emulsion at average velocity 0.44 ms^{-1}.

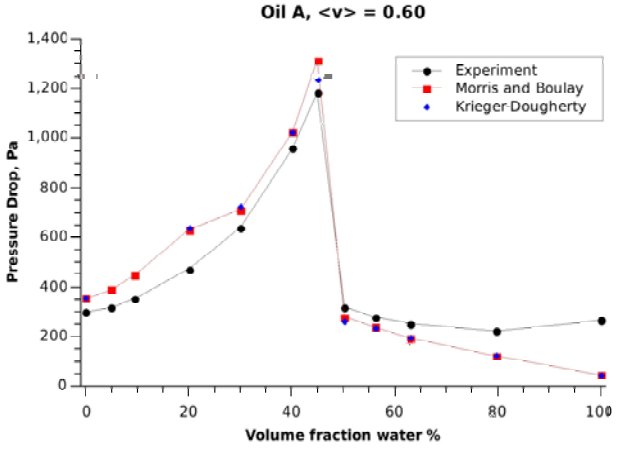

Figure 5: Pressure Drop for sea water-in-oil A emulsion at average velocity 0.60 ms^{-1}.

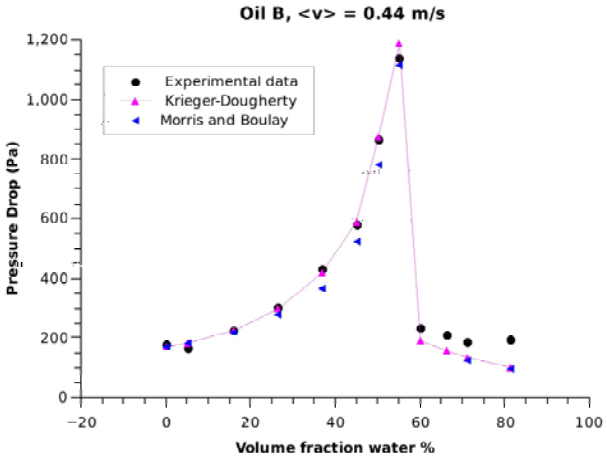

Figure 6: Pressure Drop for sea water-in-oil B emulsion at average velocity 0.44 ms^{-1}.

CONCLUSION

Following an extensive literature review we have identified the necessary models for suspension and emulsion rheology and implemented them into the commercial CFD software STAR-CCM+ written by CD-adapco. We have shown that the combination of the full stress tensor model of Morris and Boulay applied with the multi-fluid Eulerian model can successfully model particle migration of a suspension of particles. Using an assumption that we can also model an emulsion like a suspension of fluid particles using the same relative viscosity formulation, we are able to predict the increased pressure drop effect due to the presence of fluid particles at high volume fraction in an emulsion. This modelling approach is suitable to emulsions with small surfactant-stabilised droplets (in the micrometer to submillimetre range), and also if the droplets have higher viscosity than the carrier fluid. However, for emulsions with larger droplets or for ones that are not stabilised with surfactants we would expect the droplet size distribution to be in an equilibrium between droplet breakup and coalescence. Breakup and coalescence is something to be investigated with these models in future work. We would also expect heavy droplet

distortion and the formation of bi-continuous morphologies before phase inversion that has been predicted recently by direct numerical simulation (Skartlien *et al.*, 2012) to be a cause of deviation for our simple model. The experimental data was fitted by matching the highest pressure drop point along with the known inversion point, and the other values simply followed through simulation. However, it could be envisaged that fitting the relative viscosity models in a lab rheometer along with the determination of the inversion point would enable successful CFD prediction of pressure drop for scale up in an industrial setting. The author would like to thank Mohit Tandon and Andrew Splawski (both of CD-adapco) for advice in code design. We would also like to thank the other members of the FACE group (The Multiphase Flow Assurance Innovation Centre) who have shared their experimental data to make this work possible. FACE is a research cooperation between IFE, NTNU and SINTEF. The centre is funded by The Research Council of Norway and by the following industrial partners: Statoil ASA, GE Oil & Gas, SPT Group, FMC Technologies, CD-adapco and Shell Technology Norway.

REFERENCES

AHMAD, Y. *et al.* (2010). "CFD simulation of shear induced particle migration". *ICMF2010, 30 May-4 June 2010, Tampa, Florida, USA*.

BOXALL, J.A. *et al.* (2010). "Measurement and calibration of droplet size distributions in water-in-oil emulsions by particle video microscope and a focused beam reflectance method". *Ind. Eng. Chem. Res.*, **49**, 1412–1418.

CD-ADAPCO (2014). *STAR-CCM+ documentation*.

HAMPTON, R.E. *et al.* (1997). "Migration of particles undergoing pressure-driven flow in a circular conduit". *Journal of Rheology*, **41**, 621.

KRIEGER, I.M. and DOUGHERTY, T.J. (1959). "A mechanism for non-Newtonian flow in suspensions of rigid spheres". *Transactions of the Society of Rheology*, **3**, 137–152.

LHUILLIER, D. (2009). "Migration of rigid particles in non-brownian viscous suspensions". *Phys. Fluids*, **21(2)**, 023302.

MEWIS, J. and WAGNER, N.J. (2012). *Colloidal Suspension Rheology*. Cambridge University Press.

MORRIS, J.F. and BOULAY, F. (1999). "Curvilinear flows of noncolloidal suspensions: The role of normal stresses". *J. Rheol.*, **43**, 1213.

NOTT, P.R. and BRADY, J.F. (1994). "Pressure-driven flow of suspensions: simulation and theory". *J. Fluid Mech.*, **275**, 157–199.

PHILLIPS, R.J. *et al.* (1991). "A constitutive equation for concentrated suspensions that accounts for shear-particle migration". *Phys. Fluids. A*, **4**, 30.

PLASENCIA, J. *et al.* (2013). "Pipe flow of water-in-crude oil emulsions: Effective viscosity, inversion point and droplet size distribution". *Journal of Petroleum Science and Engineering*, **101**, 35–43.

SKARTLIEN, R. *et al.* (2012). "Direct numerical simulation of surfactant-stabilized emulsions: Morphology and shear viscosity in starting shear flowsedimentation and fluidisation: part i". *Rheol Acta*, **51(7)**, 649–673.

TRANSIENT MODELLING OF RELIEF LINES FOR SURFACE TESTING APPLICATION

Barbara ZIELINSKA* , Francis ALLOUCHE, Laurence FRASER, Naveed ZAFAR

Etudes et Productions Schlumberger, 1, rue Becquerel, BP 202
92142 Clamart CEDEX, FRANCE

* E-mail: zielinska@slb.com

ABSTRACT

Severe pressure and velocity transient effects occur when the pressure safety valves open suddenly during a well testing operation. High-pressure gas discharges into a relief line, creating highly transient reaction forces.

Here we present an axisymmetric computational fluid dynamics (CFD) model for predicting transient reaction forces acting on the conduit in the case of sudden valve opening. We propose a method to calculate transient reaction forces from CFD data and apply the method to a simple relief line geometry.

We show that the reaction force is equivalent to the force acting on solid walls of the conduit and compare transient and steady-state values for subsonic and supersonic flows.

Keywords: Oil & Gas, surface well testing, relief line, safety valves, reaction force, transient CFD

NOMENCLATURE

Greek Symbols

ρ Mass density, [kg/m^3]
γ Specific heat ratio

Latin Symbols

a Speed of sound, [m/s]
P Pressure, [Pa]
u Velocity, [m/s]
T Temperature, [K]
M Mach number
A Surface, [m2]
F Force, [N]

INTRODUCTION

As gas usage is expected to grow three times as fast as that of oil and coal through 2030, the global demand for natural gas is projected to increase 2% per year. This significant increase in demand triggers the need for the operators to continue to explore and drill gas prospects and to test these reservoirs to be able to prove reservoir potential, certify reserves with accuracy, and make investment decisions with full certainty.

Well testing in a gas environment is much more complex and challenging when it comes to the risks associated with the operation's safety and well integrity. This is even more applicable to surface well testing because the personnel involved in the operations are directly exposed to such risks. Today the industry has all the necessary standards and tools in the form of processes and technologies that allow careful assessment and handling of the risks. However, there is significant room to continue developing a deeper understanding of the specific challenges and risks and to apply scientific knowhow to ensure continuous improvement toward operations safety.

The pressure of gas arriving at the rig surface must be carefully controlled by flow valves. Relief line and safety valves are mandatory on all pressure vessels (such as separators or surge tanks) used in surface well testing. They preserve the equipment integrity in case of overpressure due to unexpected events. Severe transient effects occur when the pressure safety valves open suddenly. These effects, which are typically very short in duration, produce substantial reaction forces and can tear off the line, creating dramatic events.

Reaction forces on pipes due to the fluid flow can be calculated using existing industry practices (Duxbury, 1979, Grossel, 1988). These practices express reaction force in terms of gas pressure, velocity, and density, which are not easy to predict. Moreover, the transient effects due to reflection of shock fronts from piping elements, such as open ends or changes in cross section, can modify the pressure field. Because of the high pressure and size of a well testing installation, there are relatively few full-scale test data available. Also, because of the emergency nature of this equipment, field experience is scarce.

Advances in modern computers allow routine use of CFD methods to model transient flows. Here we present a CFD model for predicting transient reaction forces acting on the conduit in the case of sudden valve opening. Commercially available software with density-based solver and explicit time stepping is used for modelling. The model is axisymmetric and is validated with data from a shock tube classic experiment.

We study a model of a simple relief line geometry and propose a method to calculate transient reaction forces from CFD data (BAGANOFF, D, 1965). We show that the reaction force is equal to force exerted by the fluid on solid walls of the conduit. This force varies strongly in time due to shock wave reflections from obstacles such as pipe openings, nozzle walls, etc. We show that, in some cases, reaction force transients can be substantially higher than the steady-state value.

After validation of the transient CFD model with shock tube data, we present four different cases of a simple relief line consisting of a high-pressure reservoir, a nozzle, and a portion of straight pipe. First, we present a case of compressible subsonic flow and show the effect of reflected pressure waves on the reaction force. Following that, we present a case with a stationary shock front downstream of the nozzle and subsonic flow at the pipe end (with and without an intermediate change in pipe diameter). Finally, we present a case in which the flow downstream of the nozzle and at pipe end is supersonic.

TRANSIENT MODEL DESCRIPTION AND VALIDATION

The model was built and run with ANSYS Fluent v.14.0 modelling software program with finite volume solver. This software was successfully used to simulate shock tube experiments in a recent thesis project (Lamnaouer, 2010).

For transient compressible flows with traveling shocks, the density-based explicit solver with explicit time stepping is the most efficient option (Vasilev, Danilchuck, 1994). We applied default spatial discretization. A two-equation, k-ω shear stress transport (SST) turbulence model with compressibility effects was used. The fluid was modelled as an ideal gas.

High- and low-pressure areas were initiated at their respective values at initial time $t = 0$. The flow was allowed to develop for $t > 0$. A constant high-pressure value was imposed on the inlet, and a constant low-pressure value was imposed on the outlet.

A fully structured mesh with boundary layers was constructed. Typically, at least 40 mesh cells were created in the valve radius. Dynamic mesh refinement based on velocity gradient was used. Only axisymmetric (two-dimensional) cases were considered.

The shock tube consists of a long tube of constant area in which a diaphragm initially separates two bodies of gas at different pressures (see Figure 1).The shorter section of the tube is at a higher pressure. The remaining, longer part of the tube is at a lower pressure. When the diaphragm is removed rapidly, for example by bursting it, a flow of short duration is established in the tube. A shock (compression) wave travels into the low-pressure driven section while a train of rarefaction (expansion) waves travels into the high-pressure driver section (Figure 1). The flow regions induced between these waves are separated by a discontinuity interface, across which the pressure and velocity are equal but the density and temperature are quite different. In general, the shock propagation speed u_s is larger than the flow velocity u_2 behind the shock front.

The Mach number of the advancing shock wave is defined as

$$M_s = \frac{u_s}{a_1}. \quad (1)$$

Here u_s is the shock wave velocity, and $a_1 = (\gamma P_1 / \rho_1)^{0.5}$ is the speed of sound in the undisturbed region.

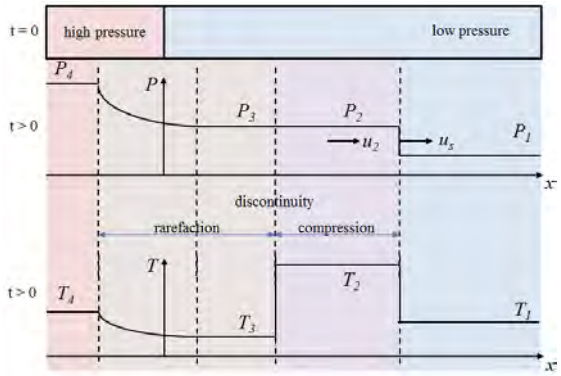

Figure 1: Pressure and temperature dependence in shock tube experiment.

For an ideal gas, the flow properties in a shock tube can be described by the following set of equations (see, for example, Anderson, 2002):

$$\frac{u_2}{a_1} = \frac{2(M_s^2 - 1)}{(\gamma + 1)M_s} \quad (2)$$

$$\frac{P_4}{P_1} = \frac{P_2}{P_1}\left[1 - \frac{(\gamma - 1)(P_2 / P_1 - 1)}{\sqrt{2\gamma(2\gamma + (\gamma + 1)(P_2 / P_1 - 1))}}\right]^{-2\gamma/(\gamma - 1)} \quad (3)$$

$$\frac{T_2}{T_1} = \left(1 + \frac{\gamma - 1}{2} M_s^2\right)\left(\frac{2\gamma}{\gamma - 1} M_s^2 - 1\right)\frac{2(\gamma - 1)}{M_s^2(\gamma + 1)^2} \quad (4)$$

$$M_s = \left(\frac{\gamma + 1}{2\gamma}\left(\frac{P_2}{P_1} - 1\right) + 1\right)^{0.5}. \quad (5)$$

The CFD model of a shock tube was run with air considered as an ideal gas and with $P_4 = 10$ bar, $P_1 = 1$ bar, and the initial temperature $T = 300$ K. At $t = 0$, the boundary between the high- and low-pressure region was at $x = 1$ m.

Figure 2 shows the results of the simulation on the symmetry axis at 2 ms. Using the value of $P_4 / P_1 = 10$ and $\gamma = 1.4$, one can calculate P_2 / P_1 from Equation (3) to be 2.84, very close to $P_2 = 2.85$ bar, the value found in simulation.

By measuring the distance the shock wave has travelled after 2 ms, we obtain $u_s = 560$ m/s. Calculating the speed of sound in the undisturbed region and using Equation (1), we obtain $M_s = 1.61$. Equation (2) offers an independent means of calculating M_s if u_2 is known. Using the u_2 value from Figure 2, we obtain again $M_s = 1.61$. Using Equation (5) with $P_2 / P_1 = 2.84$, we find again $M_s = 1.61$.

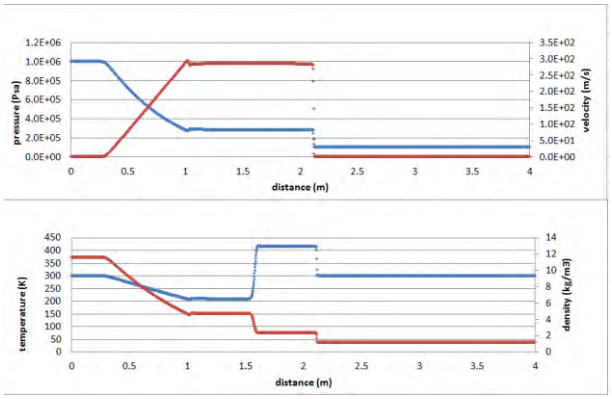

Figure 2: Results of the CFD model of the flow tube at t = 2 ms.

Equation (4) predicts T_2 / T_1 = 1.39, with M_s = 1.61. Using the values from Figure 2, we equally obtain 1.39. Therefore, we can conclude that the CFD model correctly predicts the flow behavior in the shock tube experiment.

CALCULATION OF THE REACTION FORCE

To calculate the transient reaction force acting on the walls of a relief line, we use the momentum conservation equation, which states that the rate of change of the momentum of a system is equal to the sum of all external forces acting on this system.

$$\frac{D}{Dt}\iiint_{system} \rho \vec{u}\, dV = \sum F_{system} \,. \qquad (6)$$

Developing the total derivative on the left side of Equation (6) and applying momentum conservation to the control volume *cv* shown in Figure 3, we obtain

$$\frac{\partial}{\partial t}\iiint_{cv} \rho \vec{u} dV + \oiint_{cv} \rho \vec{u}(\vec{u}\cdot\vec{n}) dA = \sum F_{cv} \,, \qquad (7)$$

where the first integral in Equation (7) is taken over the control volume delimited by a dashed line in Figure 3, and the second integral is taken over this control volume surface ($\vec{n}$ is the unit vector normal to the control volume surface).

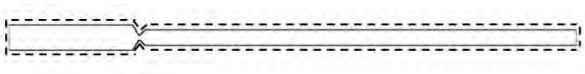

Figure 3: Simple relief line and control volume (delimited by dashed line) used in Equation (7).

On the other hand, the sum of forces acting on the control volume shown in Figure 3 can be written as a sum of forces at the boundaries:

$$\sum F_{cv} = (p_{in} - p_{ref})A_{in} - (p_{out} - p_{ref})A_{out} + F_{rf} \,, \qquad (8)$$

where p_{in}, p_{out}, p_{ref} are the inlet, outlet, and reference (taken to be 1 bar here) pressure, respectively; A_{in} is the inlet surface; A_{out} is the outlet surface; and F_{rf} is the reaction force acting on the device. A CFD model provides all the information needed to calculate the reaction force F_{rf} from Equations (7) and (8).

PRESSURE RELIEF LINE MODEL—SUBSONIC FLOW

Simple nozzle relief line

A simple relief-line model (Figure 4) shows, from left to right, the high-pressure reservoir, the safety valve nozzle, and a conduit discharging into a large reservoir set to the reference pressure. The model is axisymmetric. The relief line consists of a nozzle with diameter of 0.0766 m and a 7-m-long pipe section with 0.254-m diameter. The nozzle opens to the straight pipe with a 45° angle. Pressure of 1.3 bar is imposed at the inlet, and 1-bar pressure is imposed at the outlet. The working fluid is methane treated as an ideal gas. At t = 0, the region upstream of the nozzle is initiated with 1.3-bar pressure, and the region downstream of the nozzle is initiated with 1-bar pressure. This initial state is allowed to develop for t > 0. These boundary conditions result in subsonic flow, with maximum Mach number M = 0.9 at the nozzle throat. Because the flow is subsonic, it is relatively easy to interpret. Supersonic flow will be studied in the next section.

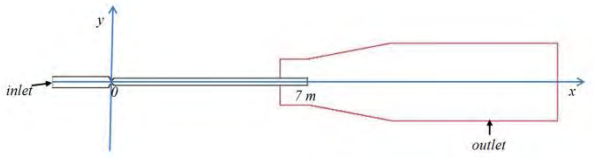

Figure 4: Model of a simple relief line consisting of high-pressure reservoir, valve nozzle, and a piece of straight pipe.

Sum of the forces on the relief line $\sum F_{cv}$ is calculated independently using Equation (7) and Equation (8) to prove the consistency of the model. In this approach, we substitute the axial component of the force acting on the solid walls as the reaction force. The result is shown in Figure 5. We can see that indeed both equations give essentially the same total force value. Therefore, we can conclude that, in the case of a straight relief line, the reaction force is equal to the axial component of the force on all solid walls. This approach can be generalized to a more complex 3D geometry, such as a pipe bend.

In most cases, we are interested in the reaction force applied to the low-pressure part of the relief line, because the high-pressure part is mechanically fixed to the ground. In a CFD model, it is straightforward to calculate these forces separately. The reaction force on the low-pressure wall is shown in Figure 6. We can see that this force attains –200 N very quickly, but changes sign and reaches about 550 N after 45 ms and drops again to nearly zero after 85 ms. To understand this behaviour, we studied transient pressure profiles along the symmetry axis.

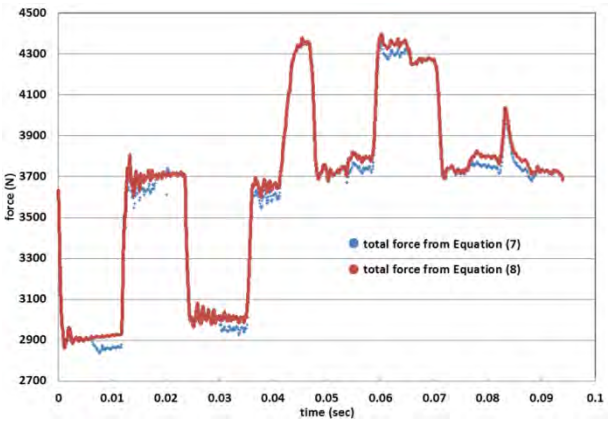

Figure 5: Transient reaction force calculated using Equations (7) and (8).

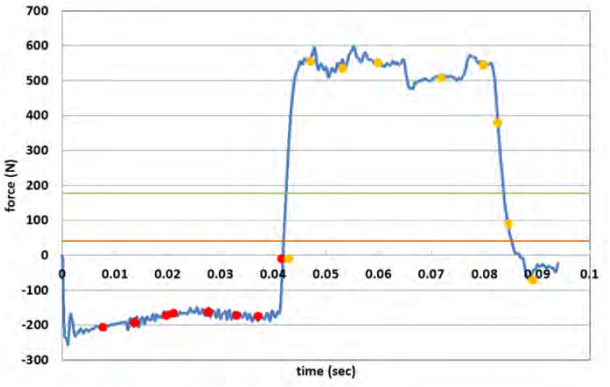

Figure 6: Transient reaction force on the low-pressure wall of the relief line shown in Figure 4. Red and yellow dots correspond to time instances in Figures 7 and 8, respectively. The green line corresponds to the calculated steady-state force, and the orange line corresponds to the result of Equation (9).

In Figure 7, pressure profiles along the symmetry axis are shown. The point x = 0 corresponds to the nozzle throat, and point x = 7 m corresponds to the pipe outlet (see Figure 4). The first three profiles (time instances of 8, 12, and 20 ms) represent the initial propagating shock front. This front reaches the pipe outlet after about 20 ms and gets reflected. The reflected shock wave reaches the nozzle after about 42 ms. We can see in Figure 7 that the pressure field directly downstream of the nozzle (which will determine the force on the wall) does not change during this time. The average pressure is above the reference pressure of 1 bar, and the resulting force is negative (with respect to the x axis direction). However, at 42 ms, the pressure downstream of the nozzle has diminished significantly due to the arrival of the reflected wave. Average pressure is now close to the reference value, and the reaction force is close to zero.

Figure 8 shows the progress of the shock wave for later time instances (shown as yellow dots in Figure 6). We can see that the shock wave is again reflected at the nozzle, causing strong reduction of pressure and, consequently, strong positive force at the wall. It travels back to the pipe exit and reflects again, arriving at the nozzle at about 80 ms, causing pressure to increase and producing slightly negative force.

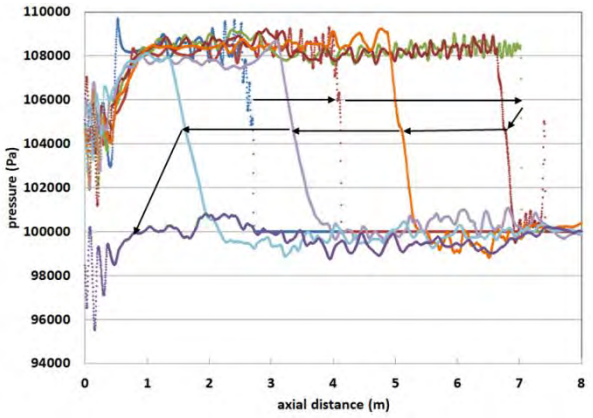

Figure 7: Pressure profiles along the symmetry axis for time instances corresponding to red dots in Figure 6. Arrows indicate the time sequence.

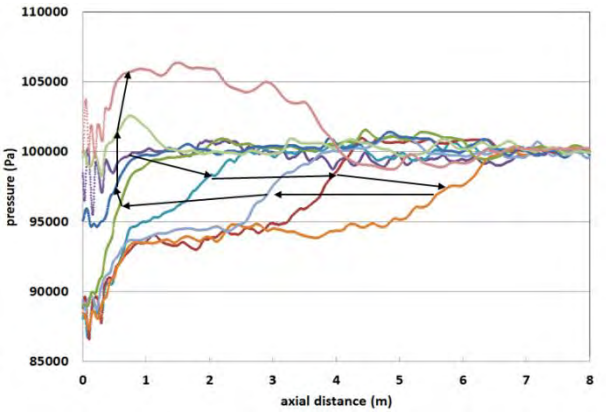

Figure 8: Pressure profiles along the symmetry axis for time instances corresponding to yellow dots in Figure 6. Arrows indicate the time sequence.

Inspecting Figures 7 and 8, we can see that the pressure gradient of the wave diminishes significantly with every reflection. Therefore, it can be concluded that, after a number of reflections, the force on the wall will settle at a steady-state value. This value, calculated with a steady-state CFD model, is shown as a green line in Figure 6. We can see that it is significantly lower than the transient force.

Another way of calculating the reaction force, is derived from an analogy with thrust engines (Grossel, 1988 and Perbal, 1993):

$$F / A = p + \rho u^2, \qquad (9)$$

where A is the pipe outlet area, p is the corresponding relative pressure, ρ is average outlet density, and u is average outlet flow velocity. Formula (9) is not easy to apply since it presupposes the knowledge of pressure, density, and velocity field. In Perbal (1993), pressure was measured and density and velocity were calculated from the Fanno flow formula. Inserting data from the CFD model at the pipe exit into Equation (9), we obtain a value of 33 N force (see orange line in Figure 6), which is again much lower than the steady-state wall reaction force predicted by CFD modelling.

Relief line with varying cross section

A realistic pressure relief line is much more complex that the simple model presented in Figure 4 (Fokeev, V. P. and Gvozdeva, L. G., 1990). To study the effect of pipe diameter change, a model of a relief line shown in Figure 9 was studied. The dimensions of the high-pressure region and nozzle diameter are the same as in the previous model. The nozzle opens into a pipe with a diameter of 0.203 m and, after a distance of 4 m, the pipe diameter changes to 0.254 m.

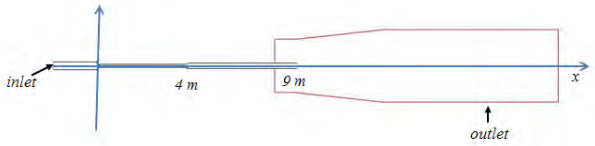

Figure 9: Model of a relief line with variable pipe cross section.

Transient reaction force on the low-pressure wall section is shown in Figure 10. A comparison with Figure 6 for a relief line with constant cross section shows a supplementary negative force at about 11 ms. This supplementary force is caused by the arrival of the initial high-pressure wave at the diameter change. Sudden cross section change leads to formation of a jet, and gas decompression and the force diminishes at around 22 ms. In Figure 11, pressure profiles along the symmetry axis are shown. The point $x = 0$ corresponds to the nozzle throat, and $x = 4$ m corresponds to the cross section change. The first three profiles (time instances of 3, 5, and 11 ms) represent the initial propagating shock front. This front reaches the cross section change ($x = 4$ m) after about 11 ms and gets partially reflected. The next two instances in Figure 11 (at 13 and 18 ms) show the reflected and time-forward pressure front. These fronts will reflect from the nozzle and pipe end and further interact with each other and geometry obstacles, giving the rather complicated force profile seen in later instances in Figure 10. Note again that the reaction force value obtained from steady-state calculation is significantly lower than the transient value and somewhat lower that the steady-state value for the case of a simple pipe.

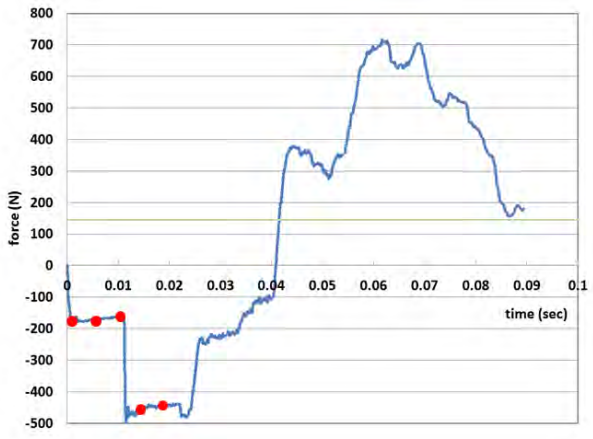

Figure 10: Transient reaction force on the low-pressure wall of the relief line shown in Figure 9. Red dots correspond to time instances in Figure 11. Green line corresponds to the calculated steady-state force.

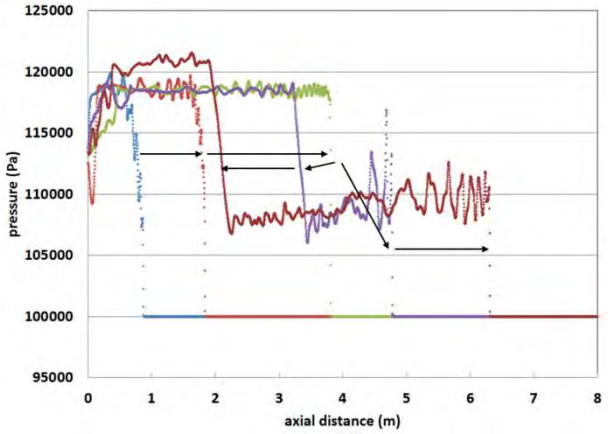

Figure 11: Pressure profiles along symmetry axis for time instances corresponding to red dots in Figure 10. Arrows indicate the time sequence.

We can conclude that a relief line with a cross section that opens progressively in two steps has a lower steady-state reaction force but higher transient reaction forces.

PRESSURE RELIEF LINE MODEL—SUPERSONIC FLOW

Simple nozzle relief line

The simple nozzle relief line shown in Figure 4 was initialized with 10 bar in the high-pressure region. The resulting flow is supersonic, with a maximum Mach number of $M = 4.5$. The underexpanded nozzle flow causes a strong barrel shock wave, ending with a Mach disc (see Figure 12). The flow at the outlet of the pipe is subsonic. The reaction force on the low-pressure wall is shown in Figure 13. We can see that, except during a very short period of initial time, this force is positive with respect to the direction of the x axis. The steady-state value of the reaction force is shown in green. At around 50 ms, the force increases considerably. Similar to the subsonic case, the shock wave is reflected from the pipe end, as it can be seen in Figure 14. In contrast to the subsonic case, however, there is no evidence of a pressure wave reflected from the stationary shock front.

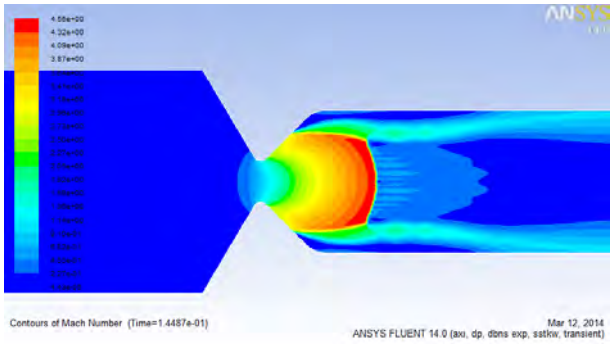

Figure 12: Mach number for 10-bar inlet pressure. Barrel-shape shock front and Mach disc are clearly visible in simulation results.

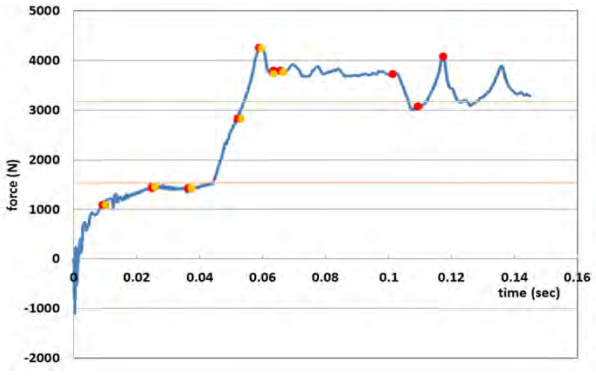

Figure 13: Transient reaction force on the low-pressure wall of the relief line shown in Figure 4. Red and yellow dots correspond to time instances in Figures 14 and 15, respectively. Green line corresponds to force from steady-state simulation, and orange line corresponds to force obtained from Equation (9) using steady-state CFD data.

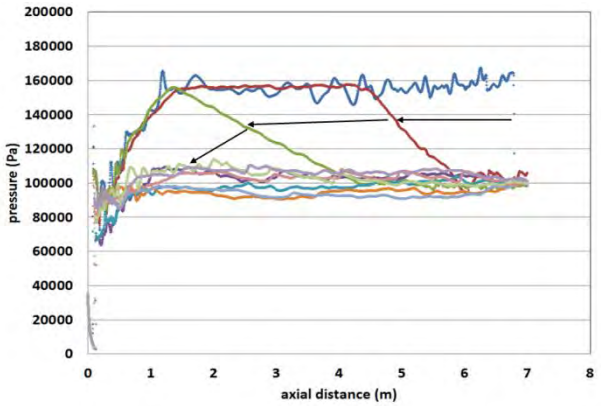

Figure 14: Pressure profiles along symmetry axis for time instances corresponding to red dots in Figure 13. Arrows indicate the time sequence.

This is why the force in Figure 13 stays at a nearly constant level, close to its steady-state value, for later time instances. To understand further this phenomenon, the pressure profiles within the first 20 cm after the nozzle (corresponding to the stationary shock front) are shown in Figure 15.

We can see that the shock front was stationary during the first three instances (14, 16, and 38 ms) corresponding to the backward-travelling, reflected pressure front. The arrival of the reflected shock front (instances of 53 and 58 ms) has moved the stationary shock front further downstream. Some of the absorbed energy was released at instances 64 and 66 ms, and the shock front has partially moved upstream.

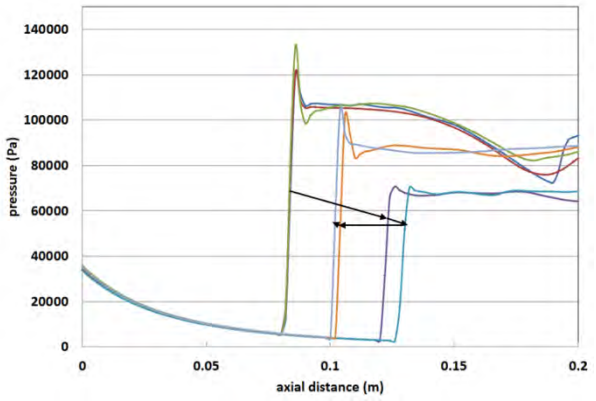

Figure 15: Pressure profiles along symmetry axis for time instances corresponding to yellow dots in Figure 13. Arrows indicate the time sequence.

Relief line with modified nozzle shape

Because of the high pressure and size of a well testing installation, there are relatively few full-scale test data available. One example of full-scale data can be found in Perbal (1993). We studied a model corresponding to the ”small-scale experiment” in this reference (shown in Figures 16 and 17). The diameter of the downstream pipe is 0.041 m, and the ratio of the diameter of the pipe to that of the nozzle is 3. The nozzle expands at an angle of 30°. A reducer with an angle of 8° relative to the axis is placed between the high-pressure region and the nozzle.

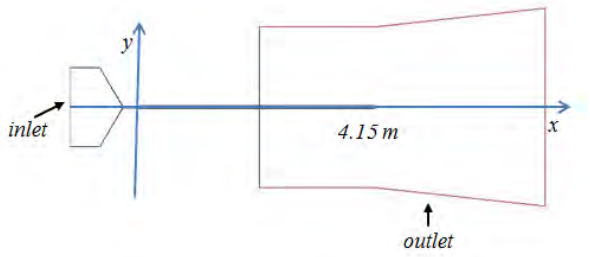

Figure 16: Model of a relief line in “small-scale experiment” in Perbal (1993).

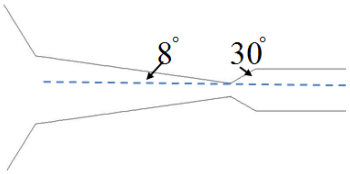

Figure 17: Details of the nozzle section in “small-scale experiment” model from Perbal (1993).

Following the experimental conditions in Perbal (1993), the high-pressure section was initialized at 34 bar. The working fluid is nitrogen discharging into air at 1 bar. We can see in Figure 18 that a complex jet structure develops in these conditions, with a supersonic jet attached to the pipe wall and ending in secondary shock wave fronts. Maximum Mach number is $M = 5.7$.

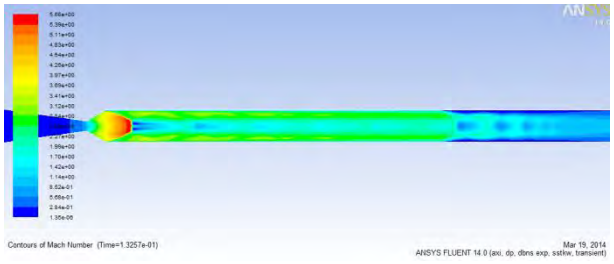

Figure 18: Mach number at 132 ms for "small-scale experiment' conditions from Perbal (1993).

Another supersonic underexpanded jet with $M = 2.5$ is created at the outlet of the flow pipe, as shown in Figure 19.

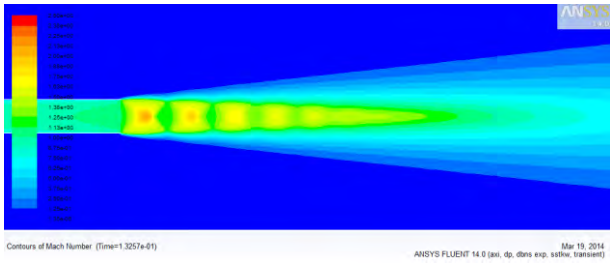

Figure 19: Mach number at the pipe outlet at 132 ms for "small-scale experiment" conditions from Perbal (1993).

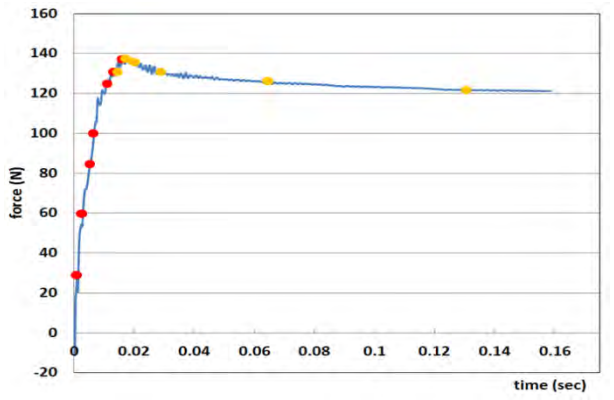

Figure 20: Transient reaction force on the low-pressure wall of the relief line shown in Figures 16 and 17. Red and yellow dots correspond, respectively, to time instances in Figures 21 and 22.

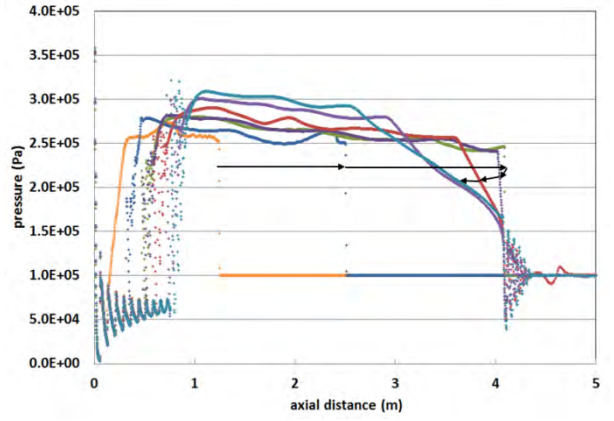

Figure 21: Pressure profiles along symmetry axis for time instances corresponding to red dots in Figure 20. Arrows indicate the time sequence.

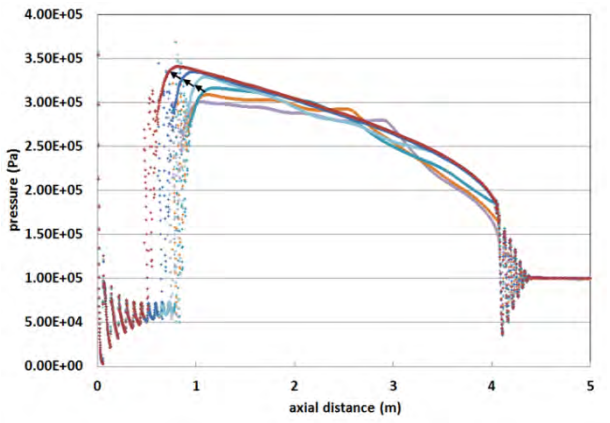

Figure 22: Pressure profiles along symmetry axis for time instances corresponding to yellow dots in Figure 20. Arrows indicate the time sequence.

The reaction force on the low-pressure wall is shown in Figure 20. We can see that, contrary to Figure 13, there is no second increase in reaction force due to a pressure wave reflected from the pipe end. To verify this, pressure profiles for instances 2.4, 5, 8, 8.2, 11, 15, and 18 ms (corresponding to red dots in Figure 20) are shown in Figure 21. The initial pressure shock wave arrives at the pipe end after 8 ms. After initial propagation, the reflected pressure wave becomes nearly stationary at 18 ms. This is further confirmed in Figure 22 (time instances corresponding to yellow dots in Figure 20). Slow decay in the reaction force for later instances correlates with length reduction of the jet downstream of the nozzle (as shown by arrows shown in Fig. 22).

Therefore, we can conclude that because of supersonic flow at the pipe exit, only a weak pressure wave is reflected from the pipe end; this modifies the structure of the primary jet downstream of the nozzle but does not produce substantial change in reaction force on the wall. Contrary to subsonic flow, where pressure forces dominate, viscous forces dominate for supersonic flows.

The reaction force for this case was calculated by Perbal (1993) using Equation (9). Pressure was measured and velocity was estimated from the Fanno formula. This resulted in about 330 N of reaction force, which is much higher than shown in Figure 20. We were not able to obtain steady-state solution in this case. Applying CFD results from transient simulations (at 158 ms) to Equation (9), we obtain 430 N. Equation (9) strongly overestimates reaction forces compared to CFD results when the flow is choked at the pipe outlet.

CONCLUSIONS

Using a CFD model, we can calculate the transient reaction force from the momentum conservation equation and show that this force is equal to the force on the walls of the flow line.

Transient reaction forces vary rapidly because of reflections of traveling shock waves from obstacles like open pipe ends or solid walls. These reflected pressure waves have a strong impact on wall forces for subsonic flows, but only moderately impact supersonic flows.

A simple equation for reaction force, derived analogous to that of thrust engines, gives correct prediction of the reaction force in the case of a single supersonic nozzle front (see Figure 13) but does not account for the contribution of the reflected pressure front. Such a reflected pressure front is present in the case of subsonic flow at the pipe outlet and a supersonic shock wave front at the valve nozzle. The returning reflected shock wave interacts with the stationary shock wave at the exit of the nozzle and results in a much higher reaction force.

In the case of two stationary supersonic fronts (at nozzle and at pipe exit), the analogy with thrust engines is not correct and the simple Equation (9) overpredicts the reaction force.

We conclude that reaction force calculated from steady-state conditions or from simple equations is substantially lower than the transient force for subsonic flows but substantially higher than the transient forces in supersonic flows.

The approach presented here can be generalized to three-dimensional models, where the effect of more complex piping elements on the reaction force can be calculated.

REFERENCES

ANDERSON, J.D., (2002), *Modern Compressible Flow: With Historical Perspective*, New York, NY, McGraw-Hill Science/Engineering/Math.

BAGANOFF, D. *"Experiments on the Wall Pressure History in Shock-Reflection Processes,"* 1965, J. Fluid Mech, **23**, pp. 209-228.

DUXBURY, H. A., *Relief line sizing for gases*, The Chemical Engineer, pp. 783-787/851-857 (1979).

FOKEEV, V. P. and GVOZDEVA, L. G. "Study of Bifurcation of Reflected Shock Waves in Channels of Various Cross-Sections,". [book auth.] Y. (ed.) Kim. *Current Topics in Shock Waves. Proceedings of the 17th International Symposium of Shock Waves and Shock Tubes.* New York : AIP, 1990, pp. 862-866.

GROSSEL, S. S., *Containment, disposal, and mechanical design*, DIERS AIChE (1988).

LAMNAOUER, M., (2010), "Numerical modeling of the shock tube flow fields before and during ignition delay time experiments at practical conditions", PhD thesis, University of Central Florida. http://gradworks.umi.com/3415064.pdf.

PERBAL, R., (1993), "Transient flow phenomena and reaction forces during blowdown of gas at high pressures through relief lines behind rupture discs", *Process Safety Progress*, **12**, (4), 232–239.

VASILEV, E. I. and DANILCHUCK, E. V. *"Numerical Solution of the Problem of Shock Tube Flow Development with Transverse Diaphragm Withdrawal,"* 1994, Fluid Dynamics, **29**, No2, pp. 270-276.

TOWARDS A MECHANISTIC MODEL FOR SUBCOOLED FLOW BOILING AT LOW-PRESSURE

Sara VAHAJI[1] , Sherman Chi Pok CHEUNG[1], Guan Heng YEOH[2,3], JiYuan TU[1*]

[1] School of Aerospace, Mechanical and Manufacturing Engineering, RMIT University, Victoria 3083, Australia

[2] Australian Nuclear Science and Technology Organisation, Locked Bag 2001, Kirrawee DC, NSW 2232, Australia

[3] School of Mechanical and Manufacturing Engineering, UNSW, Sydney, NSW 2052, Australia

* E-mail: jiyuan.tu@rmit.edu.au

ABSTRACT

For the modeling of subcooled flow boiling at low pressures in upward vertical channels, special consideration needs to be done on the dynamic behavior of two-phase flow and bubbles experiencing breakup, coalescence, and condensation in the bulk subcooled liquid as well as on the characterisation of the heat transfer occurring in the near-wall region. In terms of demonstrating the latter physics, several empirical models have been proposed for predicting the heat flux partitioning in subcooled flow boiling (Tu and Yeoh (2002)).

In this paper, a more mechanistic model is proposed for computing the active nucleation site density, bubble sliding and lift-off diameters, and bubble frequency and is implemented in the two-fluid model along with the population balance equation to solve governing equations. The first parameter is determined through the fractal hypothesis (Xiao and Yu (2007)) and the rest are calculated through the force balance model (Yeoh, Cheung, Tu and Ho (2008)). In this model, the additional heat flux at the heated wall caused by surface quenching of sliding bubbles is included. For the sake of better understanding and more comprehensive study, this model along with a set of selected empirical correlations is compared against experimental measurements of the axial and local distributions of void fraction and bubble Sauter mean diameter. The selected experiments (Zeitoun and Shoukri (1996); Lee, Park and Lee (2002)) cover a wide range of different inlet subcooling temperatures and heat and mass fluxes for water as the working fluid.

The results show that not one single combination of empirical correlations can acceptably predict all the assessed axial and local conditions. Also, the proposed mechanistic model clearly demonstrates the impact of subcooling temperature on the activation of the nucleation sites at the heated wall. The calculated wall superheat temperature is constantly under-estimated by the selected combinations of empirical correlations while predictions by the current model are in satisfying agreement with experiments. It has been found out that the bubble sliding along the heated wall has a high influence on heat partitioning and surface quenching during the process of subcooled flow boiling.

Keywords: Multiphase heat and mass transfer, subcooled boiling flow, wall heat partitioning.

NOMENCLATURE

Greek Symbols

δ	Thermal boundary layer thickness, [m].
η	Thermal diffusivity, [m^2/s].
μ	Viscosity, [Pa.s].
φ	Bubble contact angle, [rad].
ρ	Density, [kg/m^3].
σ	Surface tension, [N/m].

Latin Symbols

A_{tc}	Fraction of heater area occupied by stationary bubbles.
A_{tcsl}	Fraction of heater area occupied by sliding bubbles.
C_1	Constant defined in Eqs. (13,14,19).
C_2	Constant defined in Eq. (19).
C_3	Constant defined in Eqs. (13,14).
C_p	Specific heat [J/kg.K].
d_f	Fractal dimension.
D	Average bubble diameter [m].
D_c	Active cavity diameter [m].
$D_{c,max}$	Largest active cavity diameter [m].
$D_{c,min}$	Smallest active cavity diameter [m].
$\overline{D}_{c,max}$	Averaged value over all the maximum active cavities.
D_d	Bubble departure diameter [m].
D_{sl}	Bubble sliding diameter [m].
D_l	Bubble lift-off diameter [m].
D_s	Sauter mean bubble diameter [m].
f	Bubble frequency [Hz].
F_b	Buoyancy force [N].
F_{cp}	Contact pressure force [N].
F_h	Force due to the hydrodynamic pressure [N].
F_{du}	Unsteady drag force due to asymmetrical growth of the bubble [N].
F_{qs}	Quasi steady-drag force [N].
F_s	Surface tension force [N].
F_{sL}	Shear lift force [N].
F_x	Forces along the x-direction [N].
F_y	Forces along the y-direction [N].
g	Gravitational constant [m/s^2].
h_{fg}	Latent heat of vaporization [J/kg].
h_l	Single-phase heat transfer coefficient for forced convection [W/m^2.K].
H	Enthalpy [J/kg].

Ja	Jakob number [-].
k	Thermal conductivity [W/m^2.K] or turbulent kinetic energy [m^2.s^{-2}].
K	Projected area of bubble [m^2].
l_s	Sliding distance [m].
N_a	Active nucleation site density [m^2].
Q_w	Wall heat flux [W/m^2].
Q_c	Heat transfer due to forced convection [W/m^2].
Q_e	Heat transfer due to evaporation [W/m^2].
Q_{tc}	Heat transfer (transient conduction) due to stationary bubble [W/m^2].
Q_{tcsl}	Heat transfer (transient conduction) due to sliding bubble [W/m^2].
r_c	Cavity radius at heated surface [m].
r_r	Curvature radius of the bubble at heated surface [m].
Re	Bubble Reynolds number [-].
R_f	Ratio of the actual number of bubbles lifting off to the number of active nucleation sites.
R_i	Radius of inner heated wall [m].
R_o	Radius of outer unheated wall [m].
s	Spacing between nucleation sites [m].
St	Stanton number [-].
t	Time [s].
t_g	Bubble growth period [s].
t_w	Bubble waiting period [s].
T	Temperature [K].
T_b	Bubble internal temperature [K].
T_{sub}	Liquid subcooling temperature [K] equal to $T_{sat} - T_l$.
T_{sup}	Wall superheat temperature [K] equal to $T_w - T_{sat}$.
T_w	Wall surface temperature [K].
ΔT	Difference in temperature [K].
P	Pressure [N/m^2].
u	Velocity [m/s].
ΔU	Relative velocity [m/s].
x	Cartesian coordinate along x
y	Cartesian coordinate along y

Sub/superscripts

$axial$	Axial distribution
g	Vapor
$inlet$	Channel entrance
l	Liquid
$local$	Local distribution
s	Surface heater
sat	Saturation
sub	Subcooled
sup	Superheated
tot	Total
w	Wall

INTRODUCTION

It is a great challenging task to model two-phase flows involved in boiling that crucially happen in a few engineering systems. Specifically, subcooled flow boiling could be utilised in a variety of systems for energy conversion due to its high efficiency mode of heat transfer. It is also substantially important in the design, operation and thermal-hydraulic safety analysis of a nuclear reactor. Similar to other boiling processes, subcooled flow boiling is an unsteady one which is thermodynamically non-equilibrium between liquid and vapor phases. Usually, near the heated wall is a high-temperature two-phase region while away from the heated wall is a low-temperature single-phase liquid flow. Bubbles start to nucleate within the small cavities labelled as nucleation sites. When the temperature of the surface goes above the saturation temperature of the liquid at the local pressure, these nucleation sites get activated. However, the liquid far from the wall is subcooled due to its temperature that remains below saturation.

Mainly two regions should be considered for the modeling of subcooled flow boiling at low pressures (Yeoh and Tu (2004); Yeoh and Tu (2005)): (1) Wall heat flux partitioning and heat transfer during subcooled flow boiling at the heated wall and (2) Two-phase flow and bubble behaviours in the bulk subcooled liquid far from the heated wall. The application of two-fluid model coupled with a population balance model or an interfacial area transport equation could predict the flow characteristics for the category (2). The partitioning of the wall heat flux into surface quenching or transient conduction, evaporation and single-phase turbulent convection could model the heat transfer rate during subcooled flow boiling for the category (1). For the wall heat flux partition model, it is required to determine three parameters: active nucleation site density (N_a), bubble departure/lift-off diameter (D_d or D_l) and bubble departure frequency (f). The heat flux partitioning model was originally developed by Kurul and Podowski (1990) that has been implemented by many researchers. However, there are a few shortcomings on this model. Immediate release of the bubbles into the bulk subcooled liquid is assumed in the original heat flux partitioning model. This notion could be valid for some horizontal cases; however, Klausner, Mei, Bernhard and Zeng (1993) and Ahmadi, Ueno and Okawa (2012) experimentally demonstrated the influence of sliding bubbles on thermodynamic non-equilibrium between liquid and vapor phases. Yeoh, Cheung, Tu and Ho (2008) improved the heat partitioning model by considering the sliding bubbles.

Several empirical correlations have been proposed for the evaluation of aforementioned parameters (active nucleation site density, bubble size and bubble frequency). Each of which is only applicable to a restricted range of experimental conditions. This limitation has encouraged the researchers to reconsidering the fundamental physics governing the boiling process to overcome the problem. The improvements have also been made in Yeoh, Cheung, Tu and Ho (2008) to mechanistically determine the bubble frequency and bubble lift-off diameters through the force balance approach developed in Yeoh and Tu (2006). Nonetheless, the use of empirical correlation, for example, for the active nucleation site density in the heat flux partitioning model is one of the drawbacks of this model that cannot have a satisfactory prediction of important phasic parameters for particular subcooled flow conditions.

Yeoh, Cheung, Tu and Ho (2011) carried out a preliminary study on the application of the fractal model by Xiao and Yu (2007) for a particular vertical subcooled flow boiling configuration. In principle, the

fractal method not only considers the wall superheat temperature, but also takes into account the other flow parameters including the liquid subcooling, fractal dimension, minimum and maximum active cavity sizes contact and bulk velocity and physical properties of the adjacent fluid. This model has revealed a high potential in prediction of active nucleation site density on the heated wall. The main focus of this paper is to introduce a method that could lead towards a more systematic way to resolve the underlying physics. Therefore, the performance of the proposed model coupled with two-fluid model and population balance approach is assessed against an axial and a local experiment. The results show that it could be a possible direction for future work.

HEAT FLUX PARTITIONING MODEL

There has been copious research in the development of useful empirical correlations based on experimental data for active nucleation site density, bubble departure diameter and bubble departure frequency. Some selected correlations are further described in the preceding sections.

Active Nucleation Site Density- Empirical Approach

At the heated wall, only some of the nucleation sites will be activated as the temperature of the surface exceeds the saturation liquid temperature at the local pressure. The active nucleation site density depends on the distributions of cavities on the wall surface, heater and liquid properties, and contact angle between liquid and the wall. As aforementioned, active nucleation site density plays an important role towards the evaluation of one of the heat flux components of the wall heat flux partition model. Basu, Warrier and Dhir (2002) and Lemmert and Chawla (1977) empirically correlated the active nucleation site density.

Lemmert and Chawla (1977) investigated the nucleation site density for experiments on pool boiling of saturated water. They observed that the nucleation site density is dependent on local wall superheat by assuming that vapour is trapped in conical cavities that exist on the surface of the heated wall before any nucleation could occur. The proposed equation is in the form of

$$N_a = \left[nT_{sup}\right]^m \qquad (1)$$

Končar, Kljenak and Mavko (2004) proposed to adopt values of n and m as 185 and 1.805, respectively. Kurul and Podowski (1990) suggested the value of n as 210; these values are thus employed in the current study.

Basu, Warrier and Dhir (2002) conducted subcooled flow boiling experiments using a nine-rod (zircalloy-4) bundle and a flat plate with a copper surface to correlate the partitioning of the heat flux supplied at the wall. They also needed to quantify the active nucleation site density to calculate the energy that is carried away by bubbles from the heated wall. They obtained pictures using a CCD camera and manually counted the individual sites. The active nucleation site density takes the form of:

$$\begin{aligned} N_a &= 0.34e4(1-\cos\varphi)\,T_{sup}^2 && \Delta T_{ONB}<T_{sup}<15\ K \\ N_a &= 0.34(1-\cos\varphi)\,T_{sup}^{5.3} && 15\ K<T_{sup} \end{aligned} \qquad (2)$$

Bubble Departure Diameter – Empirical Approach

There has been a considerable amount of research and experiment investigating the bubble departure diameter in subcooled liquid boiling including Kocamustafaogullari and Ishii (1983), Fritz (1935) and Ünal (1976). Most of the empirical correlations have been defined as a function of bubble contact angle, Jacob number, or other thermo-hydraulic parameters.

Fritz (1935), considered the static equilibrium between adhesive force and buoyancy to predict the bubble departure diameter, which is given by

$$D_{dF} = 0.0208\varphi\left[\frac{\sigma}{g(\rho_l-\rho_g)}\right]^{0.5} \qquad (3)$$

where φ is the contact angle in degrees and according to Rogers and Li (1994) is set to 80°.

Ünal (1976) investigated different sets of experiments to find empirical correlations for bubble growth rate, maximum bubble diameter and maximum bubble growth time of subcooled boiling water. For calculating bubble departure diameter, he used the superposition method of Rohsenow (1953) to determine the subcooled nucleate flow boiling heat transfer. Then he applied a method to calculate the heat transfer coefficient. His studies show that the proposed equation for bubble departure diameter has a good agreement with most of the experiments within ±30% uncertainty. The proposed equation by Ünal (1976) for the bubble departure diameter can be written as

$$D_d = \frac{2.42\times10^{-5}p^{0.709}a}{\sqrt{b\phi}} \qquad (4)$$

where

$$a = \frac{(Q_w - h_l T_{sub})^{1/3}k_l}{2C^{1/3}h_{fg}\sqrt{\pi k_l/\rho_l c_{pl}\rho_g}}\sqrt{\frac{k_w\rho_w c_w}{k_l\rho_l c_{pl}}},$$

$$C = \frac{h_{fg}\mu_l\left[c_{pl}/\left(0.013h_{fg}Pr^{1.7}\right)\right]^3}{\left[\sigma/(\rho_l-\rho_g)g\right]^{0.5}},$$

$$b = T_{sub}/2\left(1-\rho_g/\rho_l\right),$$

$$\phi = \begin{cases} \left(\frac{u_l}{0.61}\right)^{0.47} & for\ u_l \geq 0.61\ m/s \\ 1.0 & for\ u_l < 0.61\ m/s \end{cases}$$

The experimental range for this correlation is:

Pressure	P = 0.1-17.7 MN/m^2
Wall heat flux	Q_w = 0.47-10.64 MW/m^2
Liquid velocity	u_l = 0.08-9.15 m/s
Liquid Subcooling	T_{sub} = 3-86 K
Bubble diameter	D_{bW} = 0.08-1.24 mm.

The bubble departure diameter correlation based on Kocamustafaogullari and Ishii (1983) has been formulated in boiling systems which has shown good agreement with their experimental water data around atmospheric pressure. This equation has been modified for higher pressures in accordance with

$$D_d = 0.0012\left(\frac{\rho_l-\rho_g}{\rho_l}\right)^{0.9}D_{dF} \qquad (5)$$

where D_{dF} is the bubble diameter expression provided by Eq. (3).

Bubble Departure Frequency – Empirical Approach

Several investigations have been performed on the bubble departure frequency. Cole (1960) investigated the boiling phenomena in the vicinity of the critical heat

flux through a photographic study. Based on the basic assumption that when successive bubbles leave the surface, touch and coalesce, and critical heat flux happens, the bubble frequency multiply by the bubble diameter at break-off can be taken to be equal to the rate that bubbles leave the surface. The bubble departure frequency is calculated according to

$$f = \left[\frac{4g(\rho_l - \rho_g)}{3D_d\rho_l}\right]^{0.5} \quad (6)$$

Heat Flux Partitioning

The unsteady nature of the physics of subcooled flow boiling is accounted for in the heat flux partitioning model. At an active nucleation site, a vapour bubble nucleates and will grow to its maximum size at the heated wall. This particular heat transfer rate is referred as microlayer evaporation (Q_e). As the bubble lifts off from the wall, colder liquid rushes in to occupy that area previously occupied by the nucleating bubble. The heat transfer rate to this colder fluid is different from the purely single-phase turbulent convection (Q_c) to a relatively warmer fluid and is accounted for by the surface quenching or transient conduction (Q_{tc}).

The wall heat flux component due to evaporation which occurs at the nucleate boiling region can be ascertained from

$$Q_e = N_a f\left(\frac{\pi D_d^3}{6}\right)\rho_g h_{fg} \quad (7)$$

where N_a, f, D_d and h_{fg} are the active nucleation site density, the bubble frequency, departing bubble diameter and the latent heat, respectively.

The wall heat flux component contributed by surface quenching is formulated accordingly. As liquid comes in contact with the hot surface, the heat is transferred to liquid mainly based on transient conduction which can be determined from

$$Q_{tc} = \left(\frac{2}{\sqrt{\pi}}\sqrt{k_l\rho_l C_{pl}}\sqrt{f}\right)A_{tc}(T_w - T_l) \quad (8)$$

where A_{tc} denotes the fraction of the wall area that is in contact with the fresh liquid and is cooled down by transient conduction. This area is calculated from

$$A_{tc} = N_a\left(K\frac{\pi D_d^2}{4}\right) \quad (9)$$

Heat transfer due to turbulent convection can be defined based on local Stanton number as

$$Q_c = St\rho_l C_{pl} u_l(1 - A_{tc})(T_w - T_l) \quad (10)$$

where u_l is adjacent liquid velocity and St is the Stanton number.

IMPROVED HEAT FLUX PARTITIONING MODEL

Active Nucleation Site Density- Fractal Model

The active nucleation site density for subcooled flow boiling in vertical channels at low pressures could be determined based on the fractal distribution of the nucleation sites on heated surfaces. According to Xiao and Yu (2007) the generated active cavities on the heated surface can be taken to be similar to the existence of pores in porous media. Thus, the cumulative number of active cavities with diameters equal to and greater than a particular active cavity diameter, D_c, can be described by

$$N_{a(D\geq D_c)} = \left(\frac{D_{c,\max}}{D_c}\right)^{d_f} \quad (11)$$

The total number of active nucleation sites per unit area (sites/cm^2) from the smallest to the largest active cavity diameter can be obtained from the above equation as

$$N_{a,\text{tot}} = \left(\frac{D_{c,\max}}{D_{c,\min}}\right)^{d_f} \qquad D_{c,\min} \leq D_c \leq D_{c,\max} \quad (12)$$

where $D_{c,\min}$ and $D_{c,\max}$ are smallest and largest active cavity diameters, respectively, and d_f is the fractal dimension.

The smallest and largest active cavity diameters for nucleation site distribution are evaluated based on Hsu (1962),*viz.*,

$$D_{c,\min} = 2\frac{\delta}{C_1(T_{sup} + T_{sub})}\left\{T_{sup} - \sqrt{T_{sup}^2 - \frac{4\zeta C_3}{\delta}(T_{sup} + T_{sub})}\right\} \quad (13)$$

$$D_{c,\max} = 2\frac{\delta}{C_1(T_{sup} + T_{sub})}\left\{T_{sup} + \sqrt{T_{sup}^2 - \frac{4\zeta C_3}{\delta}(T_{sup} + T_{sub})}\right\} \quad (14)$$

where $\zeta = 2\sigma T_{sat}/\rho_g h_{fg}$, $C_1 = (1 + \cos\theta)/\sin\theta$, $C_3 = 1 + \cos\theta$, T_{sup} is the wall superheat (T_w-T_{sat}), T_{sub} is the temperature of subcooled liquid adjacent to the heated wall (T_{sat}-T_{liq}) and δ is the thickness of the thermal boundary layer which can be expressed as $\delta = k_l/h_l$ where h_l is the single-phase heat transfer coefficient for forced convection and can be evaluated from the local Stanton number St for turbulent convection.

The fractal dimension d_f of nucleation sites for a boiling system can be derived from Yu and Cheng (2002) as

$$d_f = \frac{\ln\left[\frac{1}{2}\left(\frac{\overline{D}_{c,\max}}{D_{c,\min}}\right)^2\right]}{\ln\left(\frac{D_{c,\max}}{D_{c,\min}}\right)} \quad (15)$$

where $\overline{D}_{c,\max}$ is the averaged value over all the maximum active cavities, which is determined based on Xiao and Yu (2007) as

$$\overline{D}_{c,\max} = \frac{1}{T_{sup}}\int_{T_{sat}}^{T_w} D_{c,max_{(T_w)}}\,dT_w = \frac{1}{T_{sup}}\sum_{i=1}^{n} D_{c,max_{(T_{w,i})}}\,\delta T_w = (1/n)\sum_{i=1}^{n} D_{c,max_{(T_{w,i})}} \quad (16)$$

where δT_w is assumed as a constant (for example, $\delta T_w = 0.1$); $T_{w,i} = T_{sat} + i(\delta T_w)$ with i =1, 2, …, n; and $n = T_{sup}/\delta T_w$.

Bubble Lift-off Diameter – Force Balance Approach

The growth of a bubble is influenced by different forces acting on parallel and normal directions to a vertical heating surface. Figure 1 illustrates a description of growth, sliding and lift-off of a typical bubble at the

heated surface of the wall. For vertical subcooled flow boiling, forces acting on the bubble in the *y* direction influence on bubble sliding diameter as it could slide on the heated wall while it is still attached to it; whereas, the ones acting on *x* direction determine the bubble lift-off diameter. These forces are formulated based on the studies of Klausner, Mei, Bernhard and Zeng (1993) as:

$$\sum F_x = F_{sx} + F_{dux} + F_{sL} + F_h + F_{cp} \qquad (17)$$

$$\sum F_y = F_{sy} + F_{duy} + F_{qs} + F_b \qquad (18)$$

where F_s is the surface tension force, F_{du} is the unsteady drag due to asymmetrical growth of the bubble and the dynamic effect of the unsteady liquid such as the history force and the added mass force, F_{sL} is the shear lift force, F_h is the force due to the hydrodynamic pressure, F_{cp} is the contact pressure force accounting for the bubble being in contact with a solid rather than being surrounded by liquid, F_{qs} is the quasi steady-drag in the flow direction, and F_b is the buoyancy force. Details of calculation of these forces could be found in Yeoh, Cheung, Tu and Ho (2008).

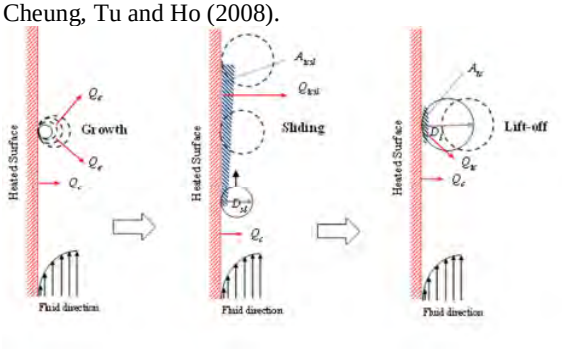

Figure 1: A schematic illustration of the different heat flux components of the improved heat flux partitioning model.

When the sum of the parallel forces (*y*-direction) equals to zero, a bubble could begin sliding while it is still attached to the wall. Therefore, by solving $\Sigma F_y = 0$, the bubble sliding diameter (D_{sl}) is evaluated. Similarly, for a bubble ready to lift-off and detach from the wall, the sum of the normal forces (*x*-direction) is equivalent to zero. Hence, by solving $\Sigma F_x = 0$, the bubble lift-off diameter (D_l) is calculated.

Bubble Frequency – A Mechanistic Model

A mechanistic approach is adopted to determine the bubble frequency based on the description of an ebullition cycle in nucleate boiling where the waiting time t_w and the growth time of the bubbles t_g play role in determining the frequency of bubble departure Basu, Warrier and Dhir (2002).

The period between the times when one bubble leaves the nucleation site (begins to slide or lifts off) and when the next bubble is generated, is called waiting time. It is estimated as

$$t_w = \frac{1}{\pi\eta}\left[\frac{(T_{sup}+T_{sub})C_1 r_c}{(T_{sup})+2\sigma T_{sat}/C_2\rho_g h_{fg} r_c}\right]^2 \qquad (19)$$

where T_{sup} is the wall superheat (T_w-T_{sat}), T_{sub} is subcooled temperature of the liquid replacing the bubbles (T_{sat}-T_{liq}), C_1 and C_2 are $C_1 = (1+\cos\theta)/\sin\theta$ and $C_2 = 1/\sin\theta$, and r_c is the cavity radius which is given by

$$r_c = F\left[\frac{2\sigma T_{sat} k_l}{\rho_g h_{fg} Q_w}\right]^{1/2} \qquad (20)$$

where Q_w is the wall heat flux and F is the degree of flooding of the available cavity size and the wettability of the surface. F is estimated by $F = \left(\frac{1}{C_1 C_2}\right)^{1/2} = \left(\frac{\sin^2\theta}{1+\cos\theta}\right)^{1/2}$. For more details, refer to Yeoh, Cheung, Tu and Ho (2008).

The growth time t_g can be determined by

$$t_g = \frac{1}{16}\frac{\pi}{\eta}\frac{D_d^2}{b^2 Ja^2} \qquad (21)$$

The lift-off period t_l can also be similarly calculated based on the bubble lift-off diameter. The sliding time t_{sl} is therefore evaluated as the difference between the bubble lift-off period and the bubble grow period ($t_{sl} = t_l - t_g$). Subsequently, the sliding distance could be estimated as $l_s = (2/3)C_v t_{sl}^{3/2}$ where C_v is an acceleration coefficient which reflects the rise of the bubble velocity in time after it starts to slide away from a nucleation site. It is determined by $C_v = 3.2u_l + 1$ where u_l is the tangential liquid velocity adjacent to the heated surface.

The frequency of the bubble departure is thus evaluated as

$$f = \frac{1}{t_w + t_g} \qquad (22)$$

Modified Heat Flux Partitioning Model

A fractal model for the wall heat partition model is derived based on the concept that the nucleation site size distribution follows the fractal power law such as described in equation (12). By differentiating equation (12), the number of active cavities for the sizes of cavities between D_c and D_c+dD_c can be obtained as $-\mathrm{d}N_a = d_f\left(D_{c,\max}^{d_f}/D_c^{d_f+1}\right)\mathrm{d}D_c$ where $\mathrm{d}D_c > 0$ and $-\mathrm{d}N_a > 0$. The different heat flux components for the modified heat flux partitioning model are derived in the following.

Surface quenching

The process of surface quenching or transient conduction occurs in regions that are swept by sliding bubbles, Q_{tcsl}, or in regions at the point of inception, Q_{tc} (refer to Figure 1). The transient conduction heat flux for a stationary bubble is given in Yeoh, Cheung, Tu and Ho (2008)Yeoh, Cheung, Tu and Ho (2008)Yeoh, Cheung, Tu and Ho (2008). Here, a fractal model for the heat flux from the smallest site $D_{c,\min}$ to the largest site $D_{c,\max}$ is given by

$$\begin{aligned} Q_{tc} &= \int_{D_{c,\min}}^{D_{c,\max}} 2\sqrt{\frac{k_l\rho_l C_{pl}}{\pi(t_w+t_{sl})}}(T_{sup}+T_{sub})R_f\left(K\frac{\pi D_{sl}^2}{4}\right)t_w f(-\mathrm{d}N_a) \\ &+ \int_{D_{c,\min}}^{D_{c,\max}} 2\sqrt{\frac{k_l\rho_l C_{pl}}{\pi(t_w+t_{sl})}}(T_{sup}+T_{sub})R_f\left(\frac{\pi D_{sl}^2}{4}\right)(1-t_w f)(-\mathrm{d}N_a) \end{aligned} \qquad (23)$$

The transient conduction that takes place during the sliding phase and the area occupied by the sliding

bubble at any instant of time from the smallest site $D_{c,\min}$ to the largest site $D_{c,\max}$ is nonetheless given by the fractal model for the heat flux as

$$\begin{aligned} Q_{tcsl} &= \int_{D_{c,\min}}^{D_{c,\max}} 2\sqrt{\frac{k_l\rho_l C_{pl}}{\pi(t_w+t_{sl})}}\left(T_{sup}+T_{sub}\right)R_f l_s K D t_w f(-\mathrm{d}N_a) \\ &+ \int_{D_{c,\min}}^{D_{c,\max}} 2\sqrt{\frac{k_l\rho_l C_{pl}}{\pi(t_w+t_{sl})}}\left(T_{sup}+T_{sub}\right)R_f f t_{sl}\left(\frac{\pi D^2}{4}\right)(1-t_w f)(-\mathrm{d}N_a) \end{aligned} \quad (24)$$

where D is the average bubble diameter given by $D = (D_{sl} + D_l)/2$; K is the ratio of the *area of influence* (the area from where the liquid is drawn in when the bubble leaves the heater surface) to the projected area of the bubble (Judd and Hwang (1976)Judd and Hwang (1976)Judd and Hwang (1976)); and R_f is the reduction factor. R_f is the ratio of the actual number of bubbles lifting off per unit area of the heater surface to the number of active nucleation sites per unit area which is given by

$$\begin{aligned} R_f &= 1/(l_s/s) & l_s \geq s \\ R_f &= 1 & l_s < s \end{aligned} \quad (25)$$

where s is the spacing between nucleation sites which can be estimated from $s = 1/\sqrt{N_{a,\mathrm{tot}}}$.

Evaporation

The heat flux due to vapour generation occurs at the nucleate boiling region which is calculated by the energy carried away by the bubbles lifting off from the heated surface. A fractal model for this heat flux from the smallest site $D_{c,\min}$ to the largest site $D_{c,\max}$ is given by

$$Q_e = \int_{D_{c,\min}}^{D_{c,\max}} R_f f\left(\frac{\pi D_l^3}{6}\right)\rho_g h_{fg}(-\mathrm{d}N_a) \quad (26)$$

Turbulent convection

Based on fractal characteristics, there is an expression that could relate the pore volume fraction to fractal dimension, minimum and maximum pore size in porous media. This expression is given by $\psi = \left(D_{c,\min}/D_{c,\max}\right)^{d-d_f}$ where d = 2 in a two-dimensional space. The forced convection will always prevail at all times in areas of the heater surface that are not influenced by the stationary and sliding bubbles. This heat flux can be obtained as

$$Q_c = St\rho_l C_{pl} u_l (1 - K\psi)\left(T_{sup} + T_{sub}\right) \quad (27)$$

where u_l is the adjacent liquid velocity.

The total wall heat flux Q_w is thus obtained as sum of the aforementioned heat flux components: $Q_w = Q_{tc} + Q_{tcsl} + Q_e + Q_c$. Numerical integration is performed via the Simpson's rule to obtain the respective heat flux components during the calculations

Two-fluid and Population Balance Models

Ensemble-averaged of mass, momentum and energy transport equations are considered for each phase which is based on the interpenetrating media approach. Two sets of conservations (one conservation equation for mass, momentum and energy of the liquid phase as well as vapour phase) can be written in terms of phase-averaged properties. These equations can be written as:

Continuity equation of liquid phase

$$\frac{\partial \rho_l \alpha_l}{\partial t} + \nabla.(\rho_l \alpha_l \vec{u}_l) = \Gamma_{lg} \quad (28)$$

Continuity equation of vapor phase

$$\frac{\partial \rho_g \alpha_g f_i}{\partial t} + \nabla.\left(\rho_g \alpha_g \vec{u}_g\right) = S_i - f_i \Gamma_{lg} \quad (29)$$

Momentum equation of liquid phase

$$\begin{aligned} &\frac{\partial \rho_l \alpha_l \vec{u}_l}{\partial t} + \nabla.(\rho_l \alpha_l \vec{u}_l \vec{u}_l) \\ &= -\alpha_l \nabla P + \alpha_l \rho_l \vec{g} + \nabla[\alpha_l \mu_l^e(\nabla \vec{u}_l + (\nabla \vec{u}_l)^T)] \\ &\quad + \left(\Gamma_{lg}\vec{u}_g - \Gamma_{gl}\vec{u}_l\right) + F_{lg} \end{aligned} \quad (30)$$

Momentum equation of vapor phase

$$\begin{aligned} &\frac{\partial \rho_g \alpha_g \vec{u}_g}{\partial t} + \nabla.\left(\rho_g \alpha_g \vec{u}_g \vec{u}_g\right) \\ &= -\alpha_g \nabla P + \alpha_g \rho_g \vec{g} \\ &\quad + \nabla\left[\alpha_g \mu_g^e\left(\nabla \vec{u}_g + \left(\nabla \vec{u}_g\right)^T\right)\right] \\ &\quad + \left(\Gamma_{gl}\vec{u}_l - \Gamma_{lg}\vec{u}_g\right) + F_{gl} \end{aligned} \quad (31)$$

Energy equation of liquid phase

$$\begin{aligned} &\frac{\partial \rho_l \alpha_l H_l}{\partial t} + \nabla.(\rho_l \alpha_l \vec{u}_l H_l) \\ &\quad = \nabla[\alpha_l \lambda_l^e(\nabla T_l)] \\ &\quad + \left(\Gamma_{gl} H_l - \Gamma_{lg} H_g\right) \end{aligned} \quad (32)$$

Energy equation of vapor phase

$$\begin{aligned} &\frac{\partial \rho_g \alpha_g H_g}{\partial t} + \nabla.\left(\rho_g \alpha_g \vec{u}_g H_g\right) \\ &\quad = \nabla\left[\alpha_g \lambda_g^e(\nabla T_g)\right] \\ &\quad + \left(\Gamma_{lg} H_l - \Gamma_{gl} H_g\right) \end{aligned} \quad (33)$$

The interaction between the two phases in this so-called two-fluid model can now be fully described by the constitutive relationships governing the inter-phase mass, momentum and energy exchange terms acting on each phase.

The inter-phase exchange mass term accounts for the condensation in the bulk subcooled liquid. In the continuity equation of the vapour phase, additional source terms due to coalescence and breakup for the range of bubble classes are also included. Sub-forces influencing on the interface between liquid and vapour phases are considered in the inter-phase exchange momentum term. These comprise the drag and non-drag forces. The non-drag forces acting on the vapour in subcooled flow boiling are to lift, wall lubrication and turbulent dispersion.

The Multiple Size Group (MUSIG) boiling model is employed as the population balance model for subcooled flow boiling. Mechanisms formulated by Prince and Blanch (1990) for bubble coalescence and Luo and Svendsen (1996) for bubble breakup are adopted. More detailed descriptions of the two-fluid and population balance models can be found in Yeoh, Cheung, Tu and Ho (2008).

EXPERIMENTAL DETAILS

Two different experiments are investigated for the assessment of vapour distribution in both axial and

radial directions. Experimental conditions for the local and axial data are presented in Table 1.

Table 1: Modelling conditions.

Case	P_{inlet} (MPa)	T_{inlet} (°C)	$T_{sub@inlet}$ (°C)	Q_w (kW/m^2)	G (kg/m^{2}s)
Axial	0.150	94.6	16.6	508.0	264.3
Local	0.143	96.9	13.4	152.9	474.0

The test section for axial experiment performed by Zeitoun and Shoukri (1996) consisted of a vertical concentric annulus. The inner tube had an outside diameter of 12.7 mm and a length of 30.6 cm. This wall was made of stainless-steel with 0.25 mm thickness. The outer tube had an inside diameter of 25.4 mm. The working fluid was distilled-degassed water. Measurements for bubble size distributions along the subcooled boiling region were performed via analysing high speed video information obtained from digital image processing technique. The uncertainties in the measurements of bubble size, void fraction, flow rate, temperature and pressure are estimated to be within ±0.05 mm, ±4.0%, ±2.0%, ±0.2°C and ±1 kPa, respectively.

Local experiment performed by Yun, Park, Song and Chung (1997) comprised a vertical concentric annulus with an outer diameter of 19 mm of the inner heating rod as the test section. The heated section was a 1.67 m. The outer wall was made of two stainless-steel tube with an inner diameter of 37.5 mm. Radial measurements of phasic parameters was located at 1.61 m downstream of the beginning of the heated section. Demineralized water was used as the working fluid. A two-conductivity probe method was employed to measure local gas phase parameters such as local void fraction, bubble frequency and bubble velocity. The bubble Sauter mean diameters (assuming spherical bubbles) were determined through the interfacial area concentration (IAC), calculated using the measured bubble velocity spectrum and bubble frequency. The uncertainties in the measurement of local void fraction, velocity, volumetric flow rate, temperature, heat flux and pressure are estimated to be within ±3.0%, ±3.3%, ±1.9%, ±0.2°C, ±1.7% and ±0.0005 MPa, respectively.

RESULTS

The conservation equations for mass, momentum and energy for each phase are solved using the finite volume method for a two-dimensional domain. In order to accommodate coalescence, break-up and condensation of bubbles, a total number of 15 bubble classes has been adopted for the dispersed phase which represented an additional set of 15 transport equations to be solved and coupled with the flow equations during the simulations (Yeoh, Cheung, Tu and Ho (2008)). Since uniform heat flux is applied, only one quarter of the annulus is modelled as the domain for both axial and local cases. Grid independence is examined; further grid refinement did not result in any significant changes to the mean values of the two-phase flow parameters. Six different combinations of empirical correlations for active nucleation site density by Lemmert and Chawla (1977) and Basu, Warrier and Dhir (2002), bubble departure diameter by Ünal (1976), Fritz (1935) and Kocamustafaogullari and Ishii (1983) and bubble frequency by Cole (1960) are assessed against axial and local radial experimental data for the subcooled flow boiling at low pressure. The improved heat flux partitioning model is also assessed against the same experimental conditions for the axial data and local radial data.

Void Fraction

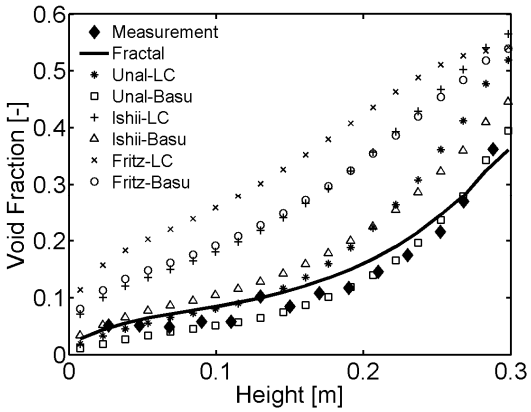

Figure 2: Predicted axial void fraction profiles and experimental data of axial experiment.

The predicted and measured axial profile of void fraction for experiment of Zeitoun and Shoukri (1996) – named as "axial experiment" from now on in this paper – along the heated section is presented in Figure 2. Bubbles have a tendency to rise in the channel which causes the void fraction to be higher close to the exit as compared to the entrance of the channel. As depicted in Figure 4, this phenomenon is captured by all empirical correlations. It could be seen that the combination of Unal-Lemmert and Chawla correlations gives a more accurate prediction in the axial case. At the same time, Basu's correlation compared to Lemmert and Chawla's correlation under-predicts the void fraction. This is most probably attributed to the lower prediction of nucleation site density by Basu's correlation, which will be further discussed in detail later. On the whole, the improved heat flux partitioning model based on the fractal approach shows a closer agreement to the measurements when compared to all of the combined empirical correlations.

Figure 3 presents the predicted and measured local profiles of void fraction for experiment of Yun, Park, Song and Chung (1997) and Lee, Park and Lee (2002) – named as "local experiment" from now on in this paper– in the radial direction at the measuring plane 1.61 m downstream of the beginning of the heated section. Note that in all figures related to the local experiment, the dimensionless parameter (r-Ri)/(Ro-Ri) equal to 1 and 0 which indicates the inner surface of the unheated flow wall and the surface of the heating rod in the annulus respectively. Bubbles are generated at the heated wall and then as they are exposed to the subcooled liquid, they condense further away until there is no significant void fraction near the outer wall at the measuring plane. This phenomenon is captured by all empirical correlations. Predictions of combinations of Unal-Basu and Unal-Lemmert and Chawla correlations are relatively lower in all local cases. This can be attributed to the conditions under which the empirical

correlation for bubble departure diameter has been formulated. The results indicate that the combination of Fritz-Basu correlations gives more accurate predictions for the local case. The improved heat flux partitioning model based on the fractal approach successfully predicts the increasing void fraction near the heated wall. Paradoxically, the use of Fritz's and Ishii's correlations in determining the bubble lift-off diameter, which over predicts the axial profile of void fraction by a significant margin, agree rather well with the local profile of void fraction while the use of Unal's correlation severely under predicts the local profile for this Case.

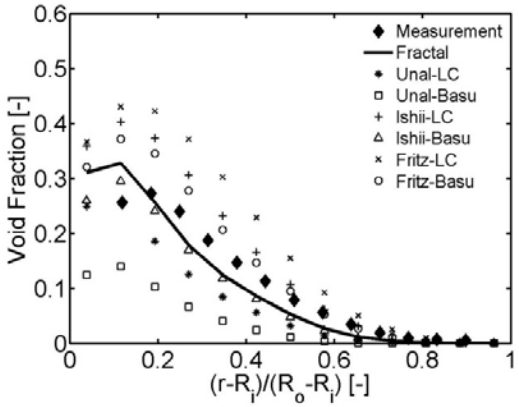

Figure 3: Predicted local void fraction profiles and experimental data of the local experiment at the measuring plane.

According to the predictions of void fraction profile for both axial and local cases, the least error combinations of empirical correlations are presented in Table 2. Hence, following figures compare the selected combinations of empirical correlations against the improved heat flux partitioning model for different parameters.

Table 2: Modelling conditions.

Case	Least error combination
Axial	Unal-Basu, Unal-LC
Local	Ishii-LC, Fritz-Basu

Nucleation Site Density

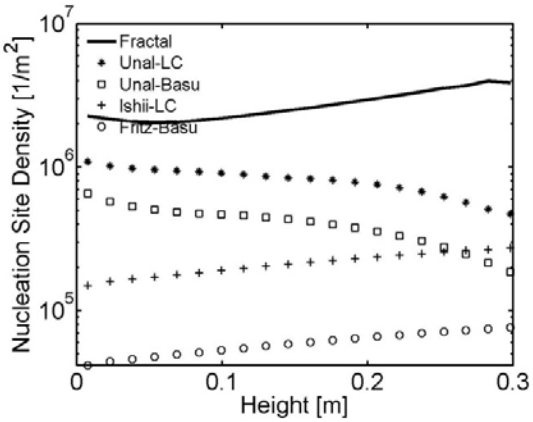

Figure 4: Predicted nucleation site density profiles for the axial experiment.

The active nucleation site density plays an important role in the determination of the wall nucleation rate which subsequently affects the void fraction distribution in the two-phase flow boiling. Predictions of active nucleation site density along the heated section in the vertical annulus for axial and local experiments are depicted in Figures 4 and 5. In general, the improved heat flux partitioning model based on the fractal approach predicts higher values of active nucleation site density when compared to the combinations of empirical correlations being applied. Both Basu's and Lemmert and Chawla's active nucleation site density correlations are based primarily on the superheat temperature at the wall. Basu's correlation considers the contact angle as well, but neither of these correlations considers the subcooling effect of the liquid. It can be seen that the combinations of Unal-Lemmert and Chawla and Unal-Basu correlations predict decreasing values of active nucleation site density along the height of the annulus which clearly contradict the actual flow boiling phenomena. This could be explained by the decreasing wall superheat temperatures being predicted through the numerical calculations based on Lemmert and Chawla's and Basu's correlations where the active nucleation site density is expressed as a functions of the wall superheat temperatures only. It can also be seen that Basu's correlation of active nucleation site density yield values that are much lower than Lemmert and Chawla's correlation of active nucleation site density as well as the fractal model.

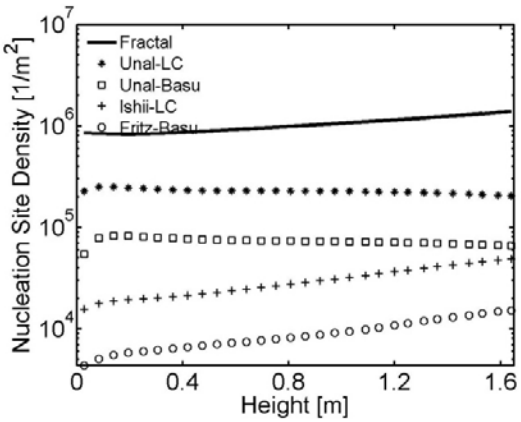

Figure 5: Predicted nucleation site density profiles for the local experiment.

Bubble Departure Frequency

Figures 6 and 7 present the profiles of bubble departure frequency at the heated wall for axial and local experiments along the channel height. It can be seen that the bubble departure frequency of Fritz-Basu and Ishii-Lemmert and Chawla correlations are constant whereas the bubble departure frequency of Unal-Basu and Unal-Lemmert and Chawla correlations are decreasing along the height of the annulus. In Cole's empirical correlation, the only changing parameter is the bubble lift-off diameter. By definition, Fritz's and Ishii's empirical correlations result in constant bubble lift-off diameters being imposed at the heated wall; the bubble departure frequency is thus a constant. Nevertheless, Unal's correlation, which has considered thermal and hydrodynamic effects of the fluid on the bubble lift-off

diameter, leads to increasing diameter along the height of the annulus. As a result, the frequency decreases.

Nevertheless, the improved heat flux partitioning model based on the fractal approach predicts much lower bubble departure frequency when compared to the combined empirical correlations. This is mostly attributed to the fact that all empirical models have been determined based on Cole's correlation in the absence of any bubble sliding being prevalent at the heated wall. In the force balance model of the improved heat flux partitioning model, the influence of sliding is considered. As a result, the time before the bubble lifts off increases; the predicted frequency is thus lower. A closer inspection on the waiting time and growth time of the model reveals that the waiting time decreases along the pipe which results in increasing the frequency along the pipe while the growth time does not exert much influence on the bubble departure frequency. One plausible explanation is that since the waiting time is dependent on the difference between the wall and bulk liquid temperatures, i.e. $(T_w\text{-}T_l)$, the waiting time decreases due to decreasing of the subcooling temperature. This model prediction is probably closer to the flow boiling physics due to the fact that as the liquid is warming up it needs less time before the bubble lifts off.

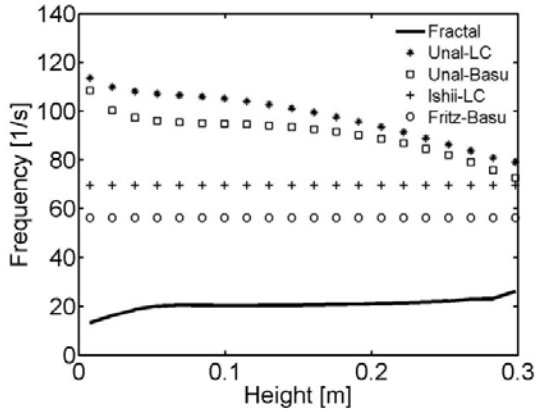

Figure 6: Predicted bubble departure frequency profiles for the axial experiment.

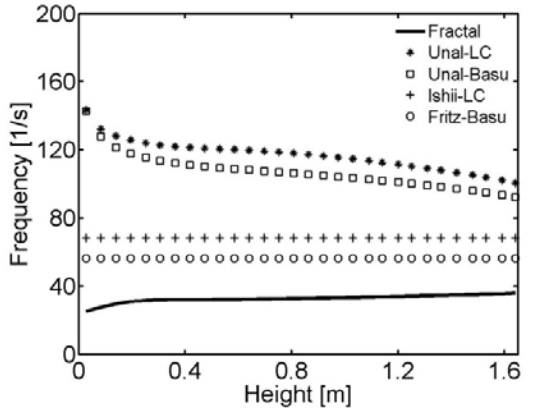

Figure 7: Predicted bubble departure frequency profiles for the local experiment along the vertical direction.

Wall Heat Flux Components

The percentage of quenching heat component of the wall heat flux along the vertical direction is depicted in Figures 8 and 9 for axial and local experiments, respectively. The quenching effect as a result of the use of the combined empirical correlations decreases for the axial Case but increases for the local Case along the height of the annulus. The latter contradicts the vertical flow boiling physics which should exhibit the same characteristics as the former. This directly points to the use of empirical correlations that are void of any flow physics due to bubble sliding as well as the effects of liquid subcooling, minimum and maximum active cavity sizes contact and bulk velocity and physical properties of the adjacent fluid being accounted for in the multi-dimensional model. However, the improved heat flux partitioning model based on the fractal approach demonstrates consistent flow boiling physics in both the axial and local Cases.

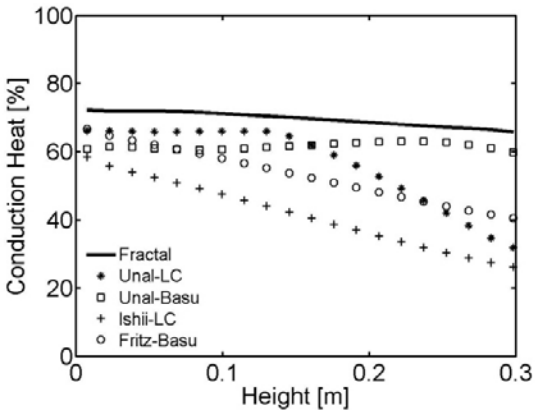

Figure 8: Predicted profiles of quenching heat percentage for the axial experiment

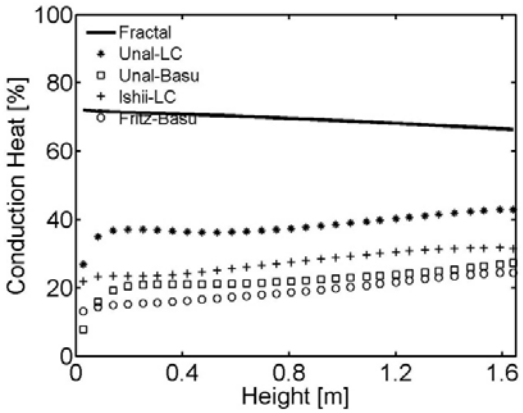

Figure 9: Predicted profiles of quenching heat percentage for the local experiment along the vertical direction.

CONCLUSION

In this paper, the heat flux partitioning model along with the improved heat flux partitioning model are coupled with the two-fluid and MUSIG models and have been assessed against axial and local experiments for subcooled boiling flow at low pressure for water as the medium. For the former model, some empirical correlations for active nucleation site density, the bubble departure diameter and bubble departure frequency are selected as closure; whereas, for the latter model, a more mechanistic approach is applied for the prediction of active nucleation site density – introduced as fractal

method in this paper. Also, the bubble departure diameter and frequency are predicted through the force balance method, and the effect of sliding bubbles is also taken into account.

The predicted void fraction distributions from the fractal method show good agreement with measured data for both axial and local experiments. Some combinations of empirical correlations yield reasonably well predictions for the void fraction distribution in axial condition; whereas, the predictions of other combinations were found to provide a better agreement with the local measured data predictions. Also, predictions for the bubble departure frequency of selected empirical correlations have been found to be in contradiction with what is expected from physical mechanisms. Numerical results have also discovered the importance of considering bubble sliding along the wall surface and its influence on the heat partitioning and surface quenching heat flux.

Nevertheless, a more detail inspection on a wider range of heat flux and inlet subcooling temperature is required to investigate the functionality of the proposed method.

ACKNOWLEDGEMENT

The financial support provided by the Australian Research Council, Australia (ARC project ID DP130100819) is gratefully acknowledged.

REFERENCES

TU, J. Y. and YEOH, G. H., (2002), "On numerical modelling of low-pressure subcooled boiling flows", *International Journal of Heat and Mass Transfer*, **45**(6), 1197-1209.

XIAO, B. and YU, B., (2007), "A fractal analysis of subcooled flow boiling heat transfer", *International Journal of Multiphase Flow*, **33**(10), 1126-1139.

YEOH, G. H., CHEUNG, S. C. P., TU, J. Y. and HO, M. K. M., (2008), "Fundamental consideration of wall heat partition of vertical subcooled boiling flows", *International Journal of Heat and Mass Transfer*, **51**(15–16), 3840-3853.

ZEITOUN, O. and SHOUKRI, M., (1996), "Bubble behavior and mean diameter in subcooled flow boiling", *Journal of Heat Transfer*, **118**(1), 110-116.

LEE, T. H., PARK, G. C. and LEE, D. J., (2002), "Local flow characteristics of subcooled boiling flow of water in a vertical concentric annulus", *International Journal of Multiphase Flow*, **28**(8), 1351-1368.

YEOH, G. H. and TU, J. Y., (2004), "Population balance modelling for bubbly flows with heat and mass transfer", *Chemical Engineering Science*, **59**(15), 3125-3139.

YEOH, G. H. and TU, J. Y., (2005), "Thermal-hydrodynamic modeling of bubbly flows with heat and mass transfer", *Aiche Journal*, **51**(1), 8-27.

KURUL, N. and PODOWSKI, M. Z., (1990), "Multi-dimensional effects in forced convection sub-cooled boiling", *Proc. Ninth Heat Transfer Conference*. Jerusalem, Israel: Hemisphere Publishing Corporation.

KLAUSNER, J. F., MEI, R., BERNHARD, D. M. and ZENG, L. Z., (1993), "Vapor bubble departure in forced convection boiling", *International Journal of Heat and Mass Transfer*, **36**(3), 651-662.

AHMADI, R., UENO, T. and OKAWA, T., (2012), "Experimental identification of the phenomenon triggering the net vapor generation in upward subcooled flow boiling of water at low pressure", *International Journal of Heat and Mass Transfer*, **55**(21–22), 6067-6076.

YEOH, G. H. and TU, J. Y., (2006), "Numerical modelling of bubbly flows with and without heat and mass transfer", *Applied Mathematical Modelling*, **30**(10), 1067-1095.

YEOH, G. H., CHEUNG, S. C. P., TU, J. Y. and HO, M. K. M., (2011), "Modeling Vertical Subcooled Boiling Flows at Low Pressures", *ASTM International*, **8**(4), 1-20.

BASU, N., WARRIER, G. R. and DHIR, V. K., (2002), "Onset of Nucleate Boiling and Active Nucleation Site Density During Subcooled Flow Boiling", *Journal of Heat Transfer*, **124**(4), 717-728.

LEMMERT, M. and CHAWLA, J., (1977), "Influence of flow velocity on surface boiling heat transfer coefficient", *Heat Transfer in Boiling*, **237**, 247.

KONČAR, B., KLJENAK, I. and MAVKO, B., (2004), "Modelling of local two-phase flow parameters in upward subcooled flow boiling at low pressure", *International Journal of Heat and Mass Transfer*, **47**(6–7), 1499-1513.

KOCAMUSTAFAOGULLARI, G. and ISHII, M., (1983), "Interfacial area and nucleation site density in boiling systems", *International Journal of Heat and Mass Transfer*, **26**(9), 1377-1387.

FRITZ, W., (1935), "Maximum volume of vapor bubbles", *Physik Zeitschr*, **36**(11), 379-384.

ÜNAL, H. C., (1976), "Maximum bubble diameter, maximum bubble-growth time and bubble-growth rate during the subcooled nucleate flow boiling of water up to 17.7 MN/m2", *International Journal of Heat and Mass Transfer*, **19**(6), 643-649.

ROGERS, J. T. and LI, J.-H., (1994), "Prediction of the Onset of Significant Void in Flow Boiling of Water", *Journal of Heat Transfer*, **116**(4), 1049-1053.

ROHSENOW, W. M., (1953), "Heat transfer with evaporation", *Proc. Proceedings of Heat Transfer—A Symposium Held at the University of Michigan During the Summer of 1952*.

COLE, R., (1960), "A Photographic study of pool boiling in the region of the critical heat flux", *Aiche Journal*, **6**(4), 533-538.

HSU, Y., (1962), "On the size range of active nucleation cavities on a heating surface", *Journal of Heat Transfer (US)*, **84**.

YU, B. M. and CHENG, P., (2002), "Fractal models for the effective thermal conductivity of bidispersed porous media", *Journal of Thermophysics and Heat Transfer*, **16**(1), 22-29.

JUDD, R. and HWANG, K., (1976), "Comprehensive model for nucleate pool boiling heat transfer including microlayer evaporation", *J. Heat Transfer;(United States)*, **98**(4).

PRINCE, M. J. and BLANCH, H. W., (1990), "Bubble coalescence and break-up in air-sparged bubble columns", *Aiche Journal*, **36**(10), 1485-1499.

LUO, H. and SVENDSEN, H. F., (1996), "Theoretical model for drop and bubble breakup in turbulent dispersions", *Aiche Journal*, **42**(5), 1225-1233.

YUN, B. J., PARK, G., SONG, C. and CHUNG, M., (1997), "Measurements of local two-phase flow parameters in a boiling flow channel", *Proc. Proceedings of the OECD/CSNI specialist meeting on advanced instrumentation and measurement techniques*.

ENABLING CFD CODES TO PERFORM SYSTEMATIC PARAMETER CONTINUATION AND STABILITY ANALYSIS FOR REALISTIC APPLICATIONS

N. Cheimarios [1], E.D. Koronaki[1*], H. Laux[2], A. G. Boudouvis[1]

[1] School of Chemical Engineering, National Technical University of Athens, 15780, GREECE
[2]OSRAM Opto Semiconductors GmbH, 493055, Regensburg, GERMANY

*E-mail: ekor@mail.ntua.gr

ABSTRACT

A computational framework is presented for enabling commercial, "black-box" Computational Fluid Dynamics codes to perform certain nonlinear analysis tasks that contribute significantly to the understanding of the studied physical problem. Among those tasks are parameter continuation along entire solution branches and stability analysis. The former, is important for the identification of ranges of operating parameters where multiple solutions exist. The stability of each solution is determined as a by-product of the method. When among the multiple solutions there are periodic orbits, the main idea is adjusted to compute the frequency and amplitude of the oscillation. The additional tasks do not require any alteration of the CFD model or intervention on the solver. The illustrative example here is that of a flow around a cylinder, where for varying Re numbers a branch of periodic solutions emanates from a branch of stationary ones. Stable and unstable, stationary and periodic states are computed for the same parameter values.

Keywords: Nonlinear phenomena, CFD software, solution multiplicity, periodic solutions

NOMENCLATURE

Greek Symbols

ρ	Mass density, [kg/m^3].
ν	Kinematic viscosity, [m^2/s].
λ	physical parameter
$\boldsymbol{\varphi}$	function of initial value, period T

Latin Symbols

r	Cylinder radius [m]
d	Cylinder diameter [m]
U	Velocity far from cylinder [m/s]
ps	Pressure, [Pa].
u	Velocity field, [m/s].
Re	Reynolds number
t	time [s]
$\mathbf{U}^n$	Solution vector at iteration n
F	time-stepper function
P	invariant subspace of dominant eigenvalues
Q	orthogonal complement of **P**
P	projector of $\mathbf{R}^N$ on **P**
Q	projector of $\mathbf{R}^N$ on **Q**
p	projection of **F** on **P**
q	projection of **F** on **Q**
N	dimension of the problem
Z	basis of **P**
I	identity matrix
H	reduced jacobian matrix
n_{max}	maximum number of iterations n
N	arc-length condition
s	solution branch arc-length
T	period of oscillation
x	solution of dynamic system
s_p	phase condition
M	monodromy matrix
y	eigenvectors of full problem
$\mathbf{y_Z}$	eigenvectors of **H**
St	Strouhal number
f	frequency

Sub/superscripts

n	iteration index
l_Z	dimension of basis **Z**

INTRODUCTION

In the past several years Computational Fluid Dynamics (CFD) codes have established themselves as valuable tools both for industrial and academic use. This is due to the combined effect of the advances in the numerical methods that contribute to fast and efficient solvers, the specialization of commercial CFD codes in a wide range of subjects and finally the availability of low-cost computational resources. It is now feasible and economical to tackle realistic, complex problems with a commercial CFD code.

In dealing with realistic physical problems, both in an experimental and a computational setting, their nonlinear nature has to be accounted for. Nonlinearity "hints" at phenomena such as the existence of multiple solutions for the same operating conditions (solution multiplicity) and their respective stability and also the existence of non-stationary solutions, periodic or even chaotic.

Systematic parameter continuation unravels entire solution branches that possibly contain more than one stable solution for the same parameter values. Stand-alone CFD codes are not able to perform this task because they cannot convergence on unstable states which oftentimes connect different branches of stable solutions. Most works in the past (Henderson, 1997; van Santen et al., 2001; Thompson et al., 1996; Kushnir et al., 2014), where nonlinear phenomena were analysed in CFD applications, have used home-made codes where continuation algorithms and eigenvalue analysis of the available matrices was used to provide the desired information. More recently a new idea was presented for a computational module that wraps around commercial CFD codes and enables systematic continuation and stability analysis. The concept is applied on a model of a Chemical Vapor Deposition (CVD) reactor (Cheimarios et al., 2011; 2012) where the competition of free convection, due to the temperature differences and forced convection, due to the velocity of the incoming gas feed, leads to solution multiplicity. Over a range of parameter values, a branch of buoyancy dominated stable states co-exists with a branch of forced convection dominated stable states. The two branches are connected with a branch of unstable solutions upon which the stand-alone CFD code cannot converge. In the region of multiplicity, the stand-alone code may converge on either stable branch at random.

In this work, we take this idea a step further and expand the methodology to cases where stationary solutions co-exist with periodic ones. The illustrative example is that of a flow around an infinite length cylinder (Henderson, 1997). Experimental and numerical studies have indicated the transition from a stationary flow at low Re numbers to a periodic regime, in two dimensions for Re ≈ 46 ((Jackson, 1987; Mathis et al., 1987). At even higher Re numbers two additional critical parameter points are identified at Re ≈ 190 and Re ≈ 260 where the flow loses stability when subjected to three-dimensional perturbations.

The module-enhanced CFD model is able to converge upon the stationary solution branch even when the solutions lose stability. The eigenvalue analysis that is a by-product of the method, is able to determine the critical parameter value with accuracy without further analysis or computational effort. The module is adjusted appropriately by adding an extra constraint in order to compute the stable periodic solutions that branch out from the stationary solution branch.

The paper is structured as follows: a brief presentation of the physical problem is followed by an overview of the Recursive Projection Method which is the basis or the proposed module. Two variations of the method are presented, one for arc-length continuation and one for the computation of the period of the orbit. The results of the implementation are presented and prove in excellent agreement with the literature.

MODEL DESCRIPTION

Application: flow around a cylinder

The benchmark application for the proposed methodology is circular cylinder of radius r=1, with its cross-section on the (x,y) plane, exposed to the uniform flow of a fluid with density, ρ=1, and kinematic viscosity, ν = 1. Given that the velocity of the fluid far away from the cylinder is uniform, U, the Reynolds number is equal to Re= U d/ν; d here is the diameter of the cross-section.

The velocity and pressure fields, **u** and **ps** respectively are given by the Navier-Stokes equations,

$$\frac{\partial \mathbf{u}}{\partial t} + (\mathbf{u}\cdot\nabla)\mathbf{u} - \frac{1}{\mathrm{Re}}\nabla^2\mathbf{u} + \nabla\mathbf{ps} = 0; \qquad \nabla\cdot\mathbf{u} = 0, \tag{1}$$

along with the no-slip boundary condition on the surface of the cylinder and the assumption of uniform fluid velocity, U=1m/s far away from it.

The set of governing equations and boundary conditions are discretized with the finite volume method and solved with the commercial CFD code ANSYS/Fluent (henceforth Fluent) (www.ansys.com, FLUENT, 2014).

For the purposes of this work, in order to apply the proposed computational module, it is convenient to think of Fluent in terms of a time-stepper of the general form:

$$\mathbf{U}^{n+1} = \mathbf{F}(\mathbf{U}^n, \mathrm{Re}), \quad \mathbf{U}\in \mathrm{R}^N \tag{2}$$

Fluent is viewed as a function, **F**, of the solution vector at the n-th iteration, $\mathbf{U}^n$, for a particular value of the Re number that yields the solution at the next iteration, $\mathbf{U}^{n+1}$. In practice, Fluent has to deliver to the external module the vector $\mathbf{U}^n$ after a predefined number of time-steps. Also, Fluent must be able to read the solution vector provided by the computational module and initialize the subsequent iterations with the new value of **U**. This exchange of information is possible through a user defined function (UDF), programmed in C.

The computational module: Recursive projection method (RPM)

In this section, a brief discussion of the recursive projection method is offered. The method is described in detail by Shroff and Keller (1993) and in its implementation in (Cheimarios et al., 2011). The RPM was initially proposed for the stabilization of fixed point iterative procedures such (2). Henceforth in this paragraph, the dependence on the parameter Re is implied but not explicitly written.

Consider the invariant subspace **P** that corresponds to the, usually few, eigendirections in which the linearized map, **F**, is slowly contracting or even slowly expanding. Let **Q** be its orthogonal complement. By *P* and *Q* we denote the orthogonal projectors of $\mathbf{R}^N$ on **P** and **Q** respectively. The solution **U** is decomposed into **p** and **q** such that **U** = **p** + **q**, where **p** and **q** are the projections of **F**(**U**) onto *P* and *Q* , respectively:

$$\mathbf{p} = P\mathbf{F}(\mathbf{p}+\mathbf{q})$$
$$\mathbf{q} = Q\mathbf{F}(\mathbf{p}+\mathbf{q}) \quad (3)$$

Under certain assumptions, the RPM stabilizes fixed-point iterative procedures such as Eqn. (1) by first computing an approximation of **P** and consequently of **Q**. The projection **p** is then computed by performing a Newton's method step on *P*; **q** is determined by the projection of **F**(**U**) on *Q*. Subsequently, the Picard iteration acts on the sum, **U** = **p** + **q**. The fixed-point iteration (1) is stable when all the eigenvalues of the matrix $\mathbf{F_U}(\mathbf{U}) \equiv \partial\,\mathbf{F}/\partial\mathbf{U} \in \mathbf{R}^{N\times N}$ lie in the unit disk.

Let $l_\mathbf{Z}$ be the number of the usually few eigenvalues of $\mathbf{F_U}$ (typically O(10)) close to the unit circle and the dimension of **P** and $\mathbf{Z} \in \mathbf{R}^{N\times l_Z}$ an orthonormal basis of the invariant subspace **P.** Then the matrix

$$\mathbf{H} = \mathbf{Z}^T\mathbf{F_U}\mathbf{Z} \in \mathbf{R}^{l_Z\times l_Z} \quad (4)$$

is the projection of $\mathbf{F_U}$ on the invariant subspace.

The projectors *P* and *Q* can be expressed in terms of the basis $\mathbf{Z} \in \mathbf{R}^{N\times l_Z}$ which is built and updated in the course of continuation every n_{max} iterations: $P = \mathbf{Z}\mathbf{Z}^\mathbf{T}$, $Q = \mathbf{I} - \mathbf{Z}\mathbf{Z}^\mathbf{T}$, $\mathbf{Z}^\mathbf{T}\mathbf{Z} = \mathbf{I}_{lz}$. Using these projections on low dimensional subspaces, the Newton step described above is performed using small Jacobian matrices and minimal computational cost.

The complete algorithm implementing RPM around Fluent is summarized below:

Algorithm 1.
(i) initialization, define $\mathbf{U}^0$; **Z**= **0**; **H**= **0**; define tol; define n_{max}; n= 0; $l_Z = 0$
(ii) Fluent: evaluate **F**← **F**($\mathbf{U}^0$)
while($\|\mathbf{U}-\mathbf{F}\|_2 > tol$)
(iii) **z**← $\mathbf{Z}^\mathbf{T}$ **U**; **ζ**← $\mathbf{Z}^\mathbf{T}$**F**; **q**←**U**− **Zz**
(iv) **z**←**z**+($\mathbf{I}_{lZ}$− **H**)$^{-1}$(**ζ**− **z**); **q**← **F**− **Zζ**
(v) **U**← **Zz**+**q**
(vi) Fluent: **F**←**F**(**U**)
(vii) n←n+1
if (n = n_{max}) then
(viii) increasel_Z; update basis **Z**; compute **H**← $\mathbf{Z}^\mathbf{T}$[$\mathbf{F_U}$ **Z**]
(ix) n←0
endif
endwhile

where n is a counter used which is nullified each time **Z** is updated. In this procedure, the iteration **F**(**U**) is the result of time-integration over a predetermined time-interval performed by Fluent with initial solution **U**.

RPM for arc-length continuation and computation of periodic solutions

The Newton iteration performed on the low dimensional subspace **P**, step (iv) of algorithm 1 can be augmented with additional constrains according to the particularities of the underlying physical problem. One such constraint is the arc-length equation that changes the parametrization from the physical parameter to the arc-length of the solution curve. This enables convergence along solution branches with multiplicity (Keller, 1977; Koronaki et al. 2003). Another constraint is a so-called pinning-condition, for the computation of periodic solutions (Lust et al. 1998). These two additions are presented in the following paragraphs.

Pseudo arc-length continuation

The iteration presented in Algorithm 1 fails to converge when the matrix ($\mathbf{I}_{lz}$ − **H**) becomes singular, i.e. when eigenvalues cross the limit of the unit disk. This happens at singular points which correspond to turning points or bifurcation points. The arc-length constraint introduces the new parameter s and in the new parametrization the turning point does not exist because arc-length increases monotonically along the branch. The original coupled iteration is augmented by a new scalar constraint:

$$\mathrm{N}(\mathbf{p},\lambda_p,s) \equiv \dot{\mathbf{p}}^\mathrm{T}(\mathbf{p}-\mathbf{p}_0) + \dot{\lambda}_p(\lambda_p-\lambda_{p0}) - (s-s_0) = 0 \quad (5)$$

Notice that N depends only on **p** since the matrix ($\mathbf{I}_{lZ}$ − **H**) that becomes singular is the projection of (**I** − $\mathbf{F_U}$) on the low dimensional subspace **P**. Here $\mathbf{p_0}$ and λ_{p0} are the values of **p** and λ_p at a given initial value of the parameter s_0; $\dot{\mathbf{p}}$ and $\dot{\lambda}_p$ are tangents along the solution path and in practice they are replaced by the approximations:

$$\dot{\mathbf{p}} \approx \frac{(\mathbf{p}-\mathbf{p}_0)}{(s-s_0)} \qquad \dot{\lambda} \approx \frac{(\lambda_p-\lambda_{p0})}{(s-s_0)} \quad (6)$$

Given initial estimates for **u** and λ_p at s, the resulting augmented coupled iteration reads:

$$\text{(i)}\ \begin{pmatrix}\mathbf{p}^{n+1}\\ \lambda_p{}^{n+1}\end{pmatrix} = \begin{pmatrix}\mathbf{p}^{n}\\ \lambda_p{}^{n}\end{pmatrix} - \begin{bmatrix}\mathbf{I}-\mathbf{f_p} & -\mathbf{f}_{\lambda_p}\\ \dot{\mathbf{p}}^\mathrm{T} & \dot{\lambda}_p\end{bmatrix}^{-1}\begin{pmatrix}\mathbf{p}^n-\mathbf{f}^n\\ \mathrm{N}^n\end{pmatrix}$$

$$\text{(ii)}\ \mathbf{q}^{n+1} = Q\mathbf{F}^n + Q\mathbf{F}_{\lambda_p}{}^n\Delta\lambda_p{}^n$$

A more detailed presentation of the Algorithm and its implementation can be found in (Cheimarios et al., 2012).

Computation of Periodic Solutions

The RPM is a specific implementation of the so-called Newton-Picard methods for the computation and determination of stability of periodic solutions of a parameter-dependent autonomous dynamical system:

$$\frac{d\mathbf{x}}{dt} = \mathbf{h}(\mathbf{x},\lambda_p), \mathbf{x}\in\mathbf{R}^N, \lambda_p \in \mathbf{R} \quad (7)$$

For fixed parameter λ_p, a periodic solution is determined by N+1 unknowns, i.e. the initial condition $\mathbf{x(0)} \in \mathbf{R}^N$ and the period T. To find these unknowns the following system must be solved:

$$\begin{aligned}&\mathbf{x}(T) - \mathbf{x(0)} = \mathbf{0}\\ &s_p(\mathbf{x(0)}, T) = 0\end{aligned} \quad (8)$$

The second equation is a phase condition required in order to eliminate the invariance of periodic solutions of autonomous dynamical systems under time translation. What this means is that if T is the period of a solution, so is nT with n=1,2,3,4,…∞. This phase condition limits the computed period to T. In the computations discussed bellow, s_p is a linear phase condition:

$$s_p(\mathbf{x(0)}, T, \lambda_p) := \mathbf{h}(\mathbf{x(0)}^{(0)}, \lambda_p)^\mathrm{T}(\mathbf{x(0)} - \mathbf{x(0)}^{(0)}) = 0 \quad (9)$$

where $\mathbf{x(0)}^{(0)}$ is the starting value of the iterations. In practice it is the solution in a previous but close parameter value.

Let $\boldsymbol{\varphi}(\mathbf{x(0)},\mathrm{T},\lambda_p)$ denote the outcome of (7) at t=T with initial condition **x(0)**, then (8) is written as:

$$\begin{bmatrix} \boldsymbol{\varphi}(\mathbf{x(0)},\mathrm{T},\lambda_p)-\mathbf{x(0)} \\ s_p(\mathbf{x(0)},\mathrm{T},\lambda_p) \end{bmatrix}=\mathbf{0} \qquad (10)$$

and its solution is denoted by $(\mathbf{x(0)}^*,\mathrm{T}^*,\lambda_p)$. The functions $\boldsymbol{\varphi}$ and s_p are considered to be twice differentiable with respect to **x(0)**, T and λ_p.

The matrix $\mathbf{M}^*$ given by

$$\mathbf{M}^* := \left.\frac{\partial \boldsymbol{\varphi}}{\partial \mathbf{x}}\right|_{(\mathbf{x(0)}^*,\mathrm{T}^*,\lambda_p)} \qquad (11)$$

is the monodromy matrix. Its eigenvalues, μ_i with i=1,2,…,N, (called Floquet multipliers) determine the stability of the periodic orbit. The orbit is linearly stable if $|\mu_i|<1$ for all I, otherwise is orbit is considered unstable.

The system of nonlinear equations (10) can be solved with Newton's method. Each Newton step requires the solution of the linear system:

$$\begin{bmatrix} \frac{\partial \boldsymbol{\varphi}}{\partial \mathbf{x(0)}}-\mathrm{I} & \frac{\partial \boldsymbol{\varphi}}{\partial \mathrm{T}} \\ \frac{\partial s_p}{\partial \mathbf{x(0)}} & \frac{\partial s_p}{\partial \mathrm{T}} \end{bmatrix}\begin{bmatrix} \Delta\mathbf{x(0)} \\ \Delta\mathrm{T} \end{bmatrix}=-\begin{bmatrix} \boldsymbol{\varphi}(\mathbf{x(0)},\mathrm{T},\lambda_p)-\mathbf{x(0)} \\ s_p(\mathbf{x(0)},\mathrm{T},\lambda_p) \end{bmatrix}$$

When N is large this is not feasible or practical because the jacobian $\frac{\partial \boldsymbol{\varphi}}{\partial \mathbf{x(0)}}$ must be calculated using finite differences, with each function evaluation requiring the solution of an initial value problem. Newton-Picard methods such as the RPM seek to reduce the computational cost of the Newton iteration assuming that there are "a few", for example m, eigenvalues μ of $\mathbf{M}:=\partial\boldsymbol{\varphi}/\partial\mathbf{x(0)}$ whose magnitude is close to 1 whereas the remaining N-m eigenvalues have magnitude close to zero.I accordance to the case for the arc-length parametrization, the new augmented system is:

i) $$\begin{bmatrix} \mathbf{p}^{n+1} \\ \mathrm{T}^{n+1} \end{bmatrix}=\begin{bmatrix} \mathbf{p}^{n} \\ \mathrm{T}^{n} \end{bmatrix}+\begin{bmatrix} \mathbf{f}_p-\mathbf{I} & \mathbf{f}_T \\ \partial s_p/\partial \mathbf{p} & s_T \end{bmatrix}^{-1}\begin{bmatrix} \mathbf{p}^{n}-\mathbf{f}^{n} \\ s_p{}^{n} \end{bmatrix}$$

ii) $$Q\mathbf{F}^{n+1}=Q\mathbf{F}^{n}+Q\mathbf{F}_T{}^{n}\Delta\mathrm{T}^{n}$$

The algorithm for the Newton-Picard iteration is as follows:

Algorithm 2.

Initialization: **Z= 0;** define tol; define n_{max}; n=0; ds; $(\mathbf{x(0)}^*,\mathrm{T}^*,\lambda_{p0})$; step size = dγ; $\mathbf{x(0)_{ref}}=\mathbf{x(0)}^*$

while ($\gamma<\gamma_{max}$)

(i) evaluate $\boldsymbol{\varphi}^0=\boldsymbol{\varphi}(\mathbf{x(0)}^*,\mathrm{T}^*,\lambda_p)$;

(ii) define $h_{init}=\mathbf{h}(\mathbf{x(0)}^{(0)},\mathrm{T}^{(0)},\lambda_p)$;

(iii) Fluent: evaluate $\boldsymbol{\varphi}^1\leftarrow\boldsymbol{\varphi}(\mathbf{x(0)}^{(0)},\mathrm{T}^{(0)},\lambda_p)$; $\mathbf{r}=\boldsymbol{\varphi}^1-\boldsymbol{\varphi}^0$

(iv) Evaluate $\boldsymbol{\varphi}_T:=\partial\boldsymbol{\varphi}/\partial\mathrm{T}$

ν = 0; m = 0

while ($\|\mathbf{r}\|_2>tol$)

(v) $\mathbf{z}\leftarrow\mathbf{Z}^T\boldsymbol{\varphi}^0$; $\boldsymbol{\zeta}\leftarrow\mathbf{Z}^T\boldsymbol{\varphi}^1$; $\mathbf{q}\leftarrow\boldsymbol{\varphi}(\mathbf{x(0)}^{(0)},\mathrm{T},\lambda_p)-\mathbf{Zz}$;
$\mathbf{q}\leftarrow\boldsymbol{\varphi}^1-\mathbf{Z}\boldsymbol{\zeta}$; $s_p\leftarrow\mathbf{h}_{init}(\boldsymbol{\varphi}^1-\mathbf{x(0)_{ref}})$;

(vi) evaluate derivative $[\boldsymbol{\varphi}_x\mathbf{Z}]$; $\mathbf{H}\leftarrow\mathbf{Z}^T[\boldsymbol{\varphi}_x\mathbf{Z}]$;

(vii) $$\begin{pmatrix}\delta\mathbf{z}\\ \delta\mathrm{T}\end{pmatrix}\leftarrow\begin{bmatrix}\mathbf{I}_m-\mathbf{H} & -\mathbf{Z}^T\boldsymbol{\varphi}_T \\ \mathbf{h}^T{}_{init}\,\mathbf{Z} & \mathbf{h}^T{}_{init}\,\boldsymbol{\varphi}_T\end{bmatrix}^{-1}\begin{pmatrix}\boldsymbol{\zeta}-\mathbf{z}\\ -s_p\end{pmatrix}$$

(viii) $\mathbf{z}=\mathbf{z}+\delta\mathbf{z}$; $\mathbf{q}\leftarrow\boldsymbol{\varphi}^0-\mathbf{Z}\boldsymbol{\zeta}+(\boldsymbol{\varphi}_T-\mathbf{Z}(\mathbf{Z}^T\boldsymbol{\varphi}_T)\,\delta\mathrm{T}$;
$\mathbf{x(0)}\leftarrow\mathbf{Zz}+\mathbf{q}$; $\mathrm{T}\leftarrow\mathrm{T}+\delta\mathrm{T}$;

(ix) Evaluate: $\varphi(\mathbf{x(0)},\mathrm{T},\lambda_p)$; $\mathbf{r}=\varphi^1-\varphi(\mathbf{x(0)},\mathrm{T},\lambda_p)$;
$\varphi^0=\varphi^1$;

(x) n←n +1

if ($n=n_{max}$) then

(xi) increase m; update basis **Z**; compute $\mathbf{H}\leftarrow\mathbf{Z}^T[\boldsymbol{\varphi}_x\mathbf{Z}]$

(xii) n←0

endif

endwhile

$\lambda_p=\lambda_p+\delta\lambda_p$;

endwhile

Implementation details

For the implementation of the computational module, information must be exchanged with Fluent in every outer iteration, i.e. each time Fluent is executed. First of all, the solution vector has to be delivered by the module in the beginning of CFD iterations and it must be read back by the RPM once the predefined number of inner, or CFD iterations, is reached.

It is also possible to have the CFD code read the time-step of the iteration from a file. This is useful for initial testing, but it is not something that has to be altered once a suitable value is determined. The number of time steps that the CFD code will perform and the number of iterations per time step are set in the script that is executed every time that Fluent is called by the module. In addition, for the arc-length module, the value of the physical parameter that is updated by the method must be provided to the CFD code each time it is executed. For the periodic module, it is the period that is altered at each iteration and information about the number of time-steps must be given to the code.

Results

Stationary Solutions

The first task is to trace the stationary solution branch and identify critical parameter values. Each time Fluent is called, time-integration advances over 15 time-steps with size dt=1 sec. At each time-step, a maximum of 400 iterations is allowed even though in most cases Fluent reaches the predetermined tolerance, i.e.1.e-7, in far less iterations (ranging typically from 10 to 50). The starting point for every continuation algorithm is a couple of solutions on the branch, here for Re=10 and Re=12. These solutions are used in order to compute an estimate for the solution in the next parameter value with some

accuracy. In the course of branch tracing, the RPM-basis, **Z**, built in the initial parameter values is maintained for the subsequent ones, adding to the economy of the method.

The implementation of the arc-length continuation method imposes convergence on the stationary solution branch for Re values well passed the critical value. By monitoring the eigenvalues of the reduced jacobian matrix **H**, defined in (4) it is possible to determine the critical parameter value. This is achieved with minimal extra cost since the size of **H** does not get larger than 6 x 6. Here a Hopf point is found at $\mathrm{Re} \approx 44$ which is considered in good agreement with other findings taking into account the various values found in the literature, i.e. at $\mathrm{Re} \approx 46.5$ (Henderson 1997). A typical stable, stationary flow (Re = 41) is shown in Figure 1a, whereas a typical unstable stationary flow (Re = 157) is shown in Figure 1b.

At the Hopf point a pair of conjugate complex eigenvalues cross the limit of stability, the unit circle. The spectrum of **H** just before and just past the critical parameter value are shown in Figure 2 showing this transition.

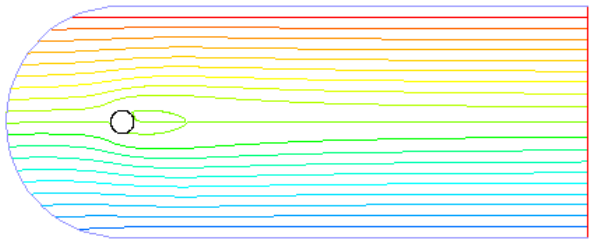

(a)

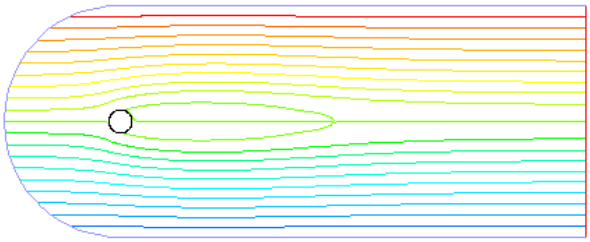

(b)

Figure 1: Typical stream functions of stationary flows (a) stable flow; Re=41, (b) unstable flow; Re=157.

An interesting by-product of the method, is the dominant eigenvector of the problem at the Hopf point that can be reconstructed from the eigenvectors of the reduced jacobian **H**. If $\mathbf{y_Z} \in \mathbf{R}^{l_Z \times l_Z}$ contains the l_Z eigenvectors of **H** then the eigenvectors of the full-sized problem a given simply by $\mathbf{y}=\mathbf{Z}\,\mathbf{y_Z}$. The eigenvector corresponding to the y-velocity component is shown in Figure 3.

These reconstructed eigenvectors correspond to the critical perturbation that leads the solution to transition to time-periodic states in two dimensions. In the case of stand-alone CFD codes, the stationary solution perturbed with the reconstructed eigenvector can be used to initialize the iterations so that the periodic state may be reached.

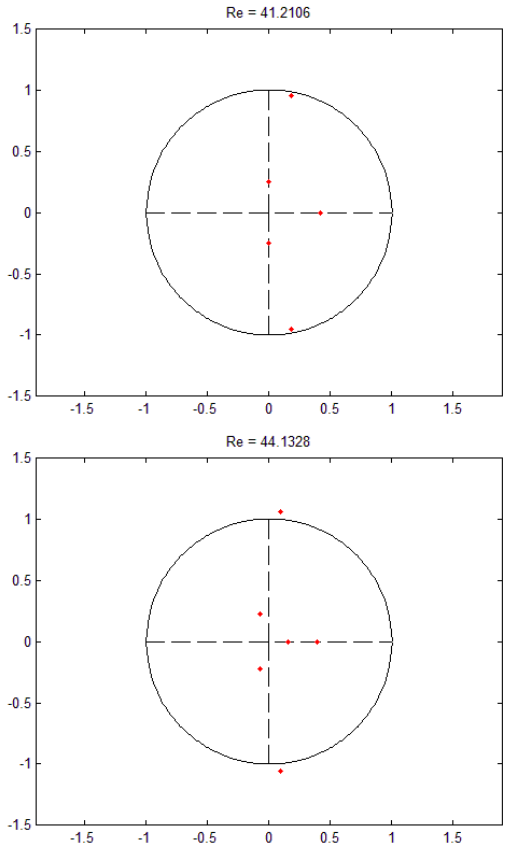

Figure 2: Spectrum of the RPM-derived matrix **H** at Re = 41.2106 (just before the Hopf point) and Re = 44.138 (just past the Hopf point).

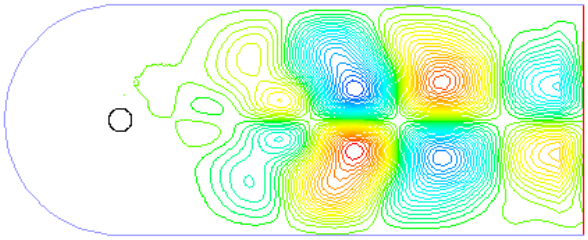

Figure 3: Reconstructed eigenvector of **H** at the Hopf point (y-velocity component); this is the critical disturbance that leads to periodic states.

Periodic States

Periodic states with the stand-alone Fluent code can be approximately defined with the help of phase portraits that can provide a very rough estimate of the period at a particular parameter value. This is useful as a first step for the application of the proposed computational module. It is easier to start with a point further away from the Hopf bifurcation, here at Re=113 and move-in toward it.

A typical phase portrait for the solution at his parameter value, shown in Figure 4, is formed by plotting the y-velocity component, v_y, at a random point in the geometry, v_2, against its value at another one, v_1, at each

time step. The inset is a blow up of the starting point and the ending point of the periodic oscillation that coincide forming a limit cycle.

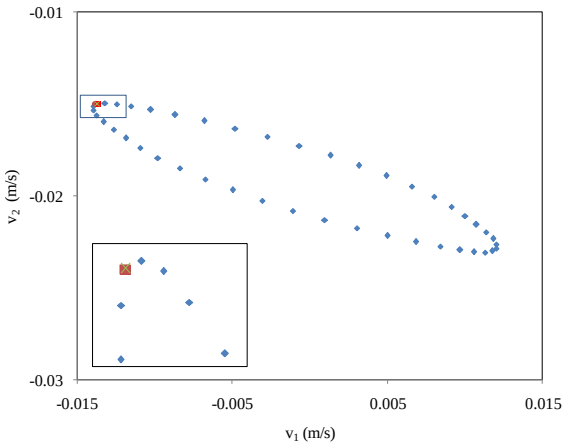

Figure 4: Phase portrait, Re=113. The inset shows the starting and end points of the limit cycle.

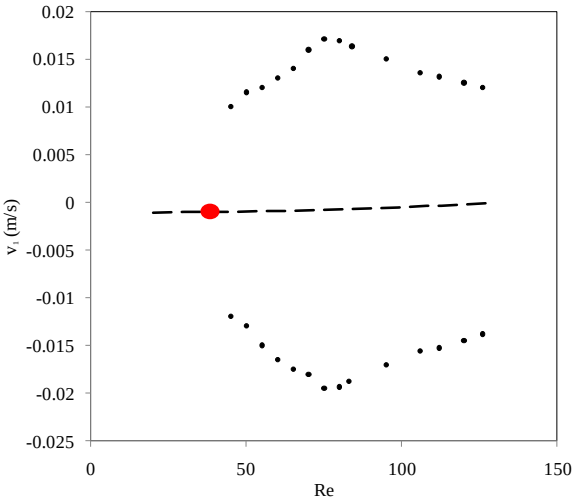

Figure 5: Multiple solution branches: Stable steady states (solid line), Unstable steady states (dashed line), minimum and maximum value of v1 (circles). Hopf bifurcation (red circle) at Re ≈ 44.

The time-step set in Fluent has to be properly adjusted for the computations to be economical - in terms of computational time - without sacrificing the accuracy of the results. Here the time-step is set to 0.13, roughly 15 % of the period that was approximately computed in the initial step.

Solution multiplicity is shown clearly in Figure 5 where a value, v_1, of the y-velocity component in a random point in the discretization is plotted over Re. The branch of stationary solutions (cf. Figure 5, solid line) loses stability past the Hopf bifurcation at Re ≈ 44 (cf. Figure 5, dashed line). A branch of stable periodic solutions emerges at the Hopf. The black circles in Figure 5 represent the minimum and maximum values of v_1 in the time-span of one period. The stable periodic solution and the unstable stationary solution for Re=103 are shown in Figure 6.

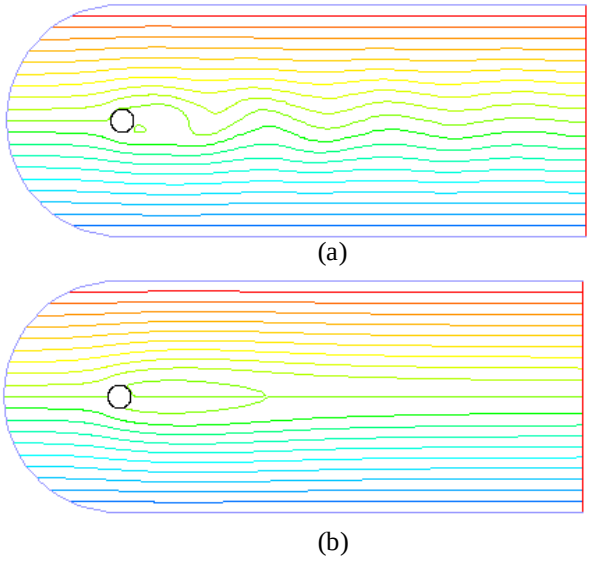

Figure 6: Streamlines of stable periodic solution (a) and unstable stationary solution (b) at Re=103.

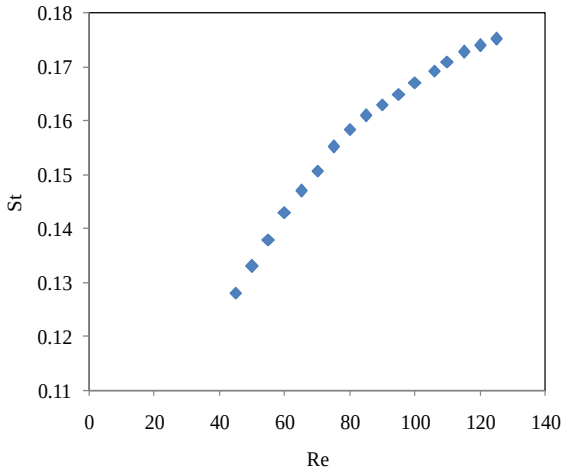

Figure 7: Evolution of the frequency of periodic oscillations: St vs Re.

In non-dimensional form the frequency of oscillations is given by the Strouhal number St = d f/U, f being the frequency. The typical Reynolds-Strouhal number relationship that characterises the flow around a cylinder is reproduced here with accuracy (Figure 7).

CONCLUSIONS

The proposed computational module broadens the capabilities of commercial CFD software with minimal extra computational cost. Codes such as Fluent can be used for tracing efficiently entire solution branches even past critical parameter values where the states are unstable. Stability is determined by solving very small eigenvalue problems (typically O(10)) as a by-product of the method. Making nonlinear analysis available without having to resort to home-made codes is

important for the understanding of complex physical phenomena. The existence of multiple states for a range of physical parameters is correlates to the different mechanisms that dominate each state. Therefore the end result of the process may present significant differences for the same parameter values.

REFERENCES

HENDERSON R. (1997), "Nonlinear dynamics and pattern formation in turbulent wake transition ", *J. Fluid Mech.*, **352**, 65-112.

VAN SANTEN H., KLEIJN C.R., VAN DER AKKER H.E.A (2001), "On multiple stability of mixed-convection flows in a chemical vapor deposition reactor", *Int J. Heat Mass Tranf.*, **44**, 659-672.

THOMPSON M., HOURIGAN K., SHERIDAN J. (1996), "Three-dimensional instabilities in the wake of a circular cylinder", *Exp. Therm. Fluid Sci.*, **12**, 190-196.

KUSHNIR R., SEGAL V., ULLMANN A., BRAUNER N. (2014) , "Inclined two-layered stratified channel flows: Long wave stability analysis of multiple solution regions", *Int. J. Mult. Flow,* **62** ,17-29.

CHEIMARIOS N., KORONAKI E. D. and BOUDOUVIS A. G. (2011), "Enabling a commercial computational fluid dynamics code to perform certain nonlinear analysis tasks", *Comput. & Chem. Eng.*, **35**, 2632-2645.

CHEIMARIOS N., KORONAKI E. D. and BOUDOUVIS A. G. (2012), "Illuminating nonlinear dependence of film deposition rate in a CVD reactor on operating conditions", *Chem. Eng. J.*, **181-182**, 516-523.

JACKSON C. P. (1987), "A finite-element study of the onset of vortex shedding in flow past variously shaped bodies", *J. Fluid Mech.*, **182**, 23-45.

MATHIS C., PROVANSAL M., BOYER L. (1987), "Bénard-von Kármán instability: Transient and forced regimes", *J. Fluid Mech.*, **182**, 1-22.

www.ansys.com, FLUENT, 2014.

SHROFF G., KELLER H.B. (1993), "Stabilization of unstable procedures – the recursive projection method", *SIAM J. Numer. Anal.*, **30,** 1099–1120.

KELLER H. B. (1977) Numerical Treatment of Bifurcation Problems by Adaptive Condensation, Academic Press, New York, 1977.

KORONAKI E. D., BOUDOUVIS A.G., KEVREKIDIS I.G. (2003), "Enabling stability analysis of tubular reactor models using PDE/PDAE integrators", *Comp.& Chem. Eng.*, **27**, 951-964.

LUST K., ROOSE D., SPENCE A. and CHAMPNEYS A. (1998), "An adaptive Newton-Picard algorithm with subspace iteration for computing periodic solutions", *J. Sci. Comput.*, **18**, 1188-1209.

EXTENDING A SERIAL 3D TWO-PHASE CFD CODE TO PARALLEL EXECUTION OVER MPI BY USING THE PETSC LIBRARY FOR DOMAIN DECOMPOSITION

Åsmund ERVIK[1*], **Svend Tollak MUNKEJORD**[2†], **Bernhard MÜLLER**[1‡]

[1]NTNU Department of Energy and Process Engineering, NO-7491 Trondheim, NORWAY

[2]SINTEF Energy Research, P.O. Box 4761 Sluppen, NO-7465 Trondheim, NORWAY

* E-mail: asmund.ervik@ntnu.no
† E-mail: svend.t.munkejord@sintef.no
‡ E-mail: bernhard.muller@ntnu.no

ABSTRACT

To leverage the last two decades' transition in High-Performance Computing (HPC) towards clusters of compute nodes bound together with fast interconnects, a modern scalable CFD code must be able to efficiently distribute work amongst several nodes using the Message Passing Interface (MPI). MPI can enable very large simulations running on very large clusters, but it is necessary that the bulk of the CFD code be written with MPI in mind, an obstacle to parallelizing an existing serial code.

In this work we present the results of extending an existing two-phase 3D Navier-Stokes solver, which was completely serial, to a parallel execution model using MPI. The 3D Navier-Stokes equations for two immiscible incompressible fluids are solved by the continuum surface force method, while the location of the interface is determined by the level-set method.

We employ the Portable Extensible Toolkit for Scientific Computing (PETSc) for domain decomposition (DD) in a framework where only a fraction of the code needs to be altered. We study the strong and weak scaling of the resulting code. Cases are studied that are relevant to the fundamental understanding of oil/water separation in electrocoalescers.

Keywords: Parallelization, Oil/water separation, Surfactants and interfaces, Bubble and droplet dynamics .

NOMENCLATURE

μ	Dynamic viscosity of a fluid.	Pa·s
ν	Kinematic viscosity of a fluid.	m^2/s
ρ	Density of a fluid.	kg/m^3
$\mathbf{f}$	External acceleration.	m/s^2
$\mathbf{u}(\mathbf{x})$	Velocity field of a fluid.	m/s
$p(\mathbf{x})$	Pressure of a fluid.	Pa
κ	Curvature of the interface.	1/m
σ	Coefficient of surface tension.	N/m
n	Time step index.	
Re	Reynolds number.	

INTRODUCTION

In 1965 Gordon Moore famously predicted that transistor density (and hence computing power for a given chip) would double each year in the foreseeable future (Moore, 1965). Dubbed Moore's law, this trend continued to hold for roughly 40 years and meant that life was easy for people needing greater and greater computational power. While serious High-Performance Computing (HPC) was dominated in most of this period by vector machines like the seminal Cray 1, by the mid-1990s clusters of many interconnected scalar CPUs had become a cheaper solution, leading to the industry-wide adoption of distributed memory architectures.

Around 2005 Moore's law finally started hitting a barrier when the high heat production of chips and, somewhat later, the diffraction limits for photolitography began forcing chip makers to alter their ways. Two complementary solutions were introduced, namely shared-memory architectures (multi-core CPUs) and vector instruction sets (SSE, AVX, FMA)[1]. Both solutions were adopted in HPC, leading to hybrid shared-memory/distributed-memory systems. In the last five years accelerator technologies (GPGPU, MIC)[2] have furthered the return to vector processing, so HPC has in a sense come full circle. All in all this gives a very heterogeneous environment for HPC where the onus is on the application programmer to ensure that his/her code can make the most of the available resources.

In contemporary numerical codes, omitting here the use of accelerators, the two main programming paradigms for leveraging parallelism are OpenMP and MPI. OpenMP takes advantage of shared-memory architectures, while MPI can use distributed-memory architectures. On current systems, OpenMP can scale from 1 to 32 cores, while MPI can scale to thousands and even millions of cores. This means that MPI is the paradigm of choice for HPC, possibly in combination with OpenMP used by each MPI process.

We will use the following nomenclature when discussing parallelism: a "process" is one MPI rank which is executing code. A CPU has several "cores", each of which may execute a process. The CPUs are located on "nodes", e.g. a desktop computer or a blade in a cluster. Typical cluster nodes have 2 (or more) CPUs, each having a separate "socket" connecting the CPU to

[1]SSE: Streaming SIMD Extensions. AVX: Advanced Vector Extensions. FMA: Fused Multiply-Add.

[2]GPGPU: General-Purpose Graphics Processing Unit. MIC: Many Integrated Core.

the memory (RAM). Each socket has one communication channel to memory shared by all cores on this socket. Many nodes can communicate over the "interconnect", which should preferrably be very fast and have very low latency.

This paper will focus on the use of MPI to port an existing serial implementation of a 2D/3D incompressible Navier-Stokes solver. This code can simulate two-phase flows relevant e.g. for the fundamental understanding of oil/water separation, but for 3D cases the runtime is very long (weeks and months). The majority of this runtime is due to the solution of a Poisson equation for the pressure, and state of the art algorithms for this problem are bound by the memory bandwidth rather than CPU speed. This makes OpenMP a poor solution in this case and leaves MPI as the necessary paradigm for parallelism. We will employ the PETSc library, specifically the DMDA component, to do domain decomposition. The solution of the Poisson equation is also done using PETSc routines. We establish a framework in Fortran where it is possible to reuse the existing serial code.

The rest of this paper is organized as follows: in the next section, the basic equations are established, after which the numerical methods are presented. Then we describe the framework and the specific changes that were needed to port the serial code. Computations performed with the resulting code are discussed and we study the strong and weak scaling on several architectures. Finally some closing remarks are given.

MODEL DESCRIPTION

The equations that govern the two-phase flow system under consideration are the incompressible Navier-Stokes equations:

$$\boldsymbol{\nabla} \cdot \mathbf{u} = 0 \tag{1}$$

$$\frac{\partial \mathbf{u}}{\partial t} + (\mathbf{u} \cdot \boldsymbol{\nabla})\mathbf{u} = -\frac{\boldsymbol{\nabla} p}{\rho} + \frac{\mu}{\rho}\boldsymbol{\nabla}^2 \mathbf{u} + \mathbf{f} \tag{2}$$

These equations are valid for single-phase flow. To extend this formulation to two-phase flow we keep these equations in each of the two phases, where the densities and viscosities are constant in each phase. We will restrict ourselves to laminar flow, as we are interested in situations with Reynolds numbers $\mathrm{Re} \sim \mathcal{O}(1)$.

Across the interface between the fluids, a jump in the normal component of the traction vector will arise due to the surface tension σ, and this jump together with effects of the jump in density and viscosity must be added to our equations. We introduce these effects using the continuum surface force method (CSF) (Brackbill *et al.*, 1992). The location of the interface is captured using the level-set method (LSM) (Osher and Sethian, 1988; Osher and Fedkiw, 2001), see Ervik *et al.* (2014) for a detailed description, we provide only a short outline here.

The level-set method is a method for capturing the location of an interface. It is widely used not just for multi-phase fluid flow but also in other contexts where an interface separates two regions. The interface is represented by a level-set function $\phi(\mathbf{x})$ which is equal to the signed distance to the interface. In other words, the interface is given by the zero level set $\{\mathbf{x} \,|\, \phi(\mathbf{x}) = 0\}$, hence the name. Rather than advecting the interface location, one advects the function $\phi(\mathbf{x})$ directly according to the transport equation

$$\frac{\partial \phi}{\partial t} = -\mathbf{u} \cdot \boldsymbol{\nabla} \phi \tag{3}$$

giving an implicit formulation that automatically handles changes in interface topology.

The level-set method can be visualized as in Fig. 1 for a 2D fluid flow with a drop next to a film, seen on the right-hand side in this figure as gray shapes. The distance is shown as isocontour lines superimposed on these shapes. On the left-hand side the level-set function is shown visualized in 3D as surfaces where the height above water corresponds to the signed distance. The analogy to a map describing an island rising out of the water is quite striking, except that the roles of "reality" and "tool for description" have been reversed.

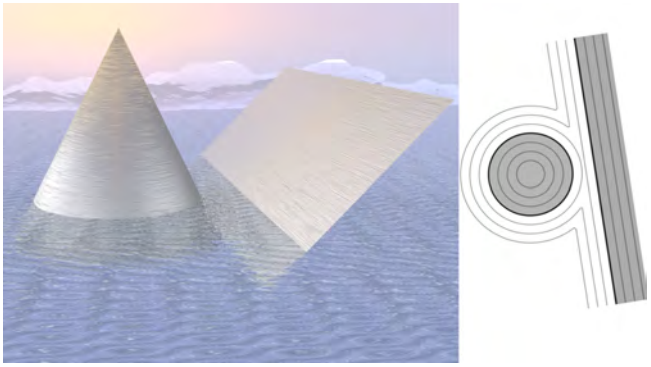

Figure 1: Illustration of the level-set method. Right: in 2D, a fluid drop (dark gray) seen next to a fluid film (dark gray), both immersed in a different fluid (white). Left: the signed-distance function representing these two fluid bodies, the drop and the film.

When the location of the interface is known, the curvature κ can be calculated from ϕ, and together with σ this gives the surface tension force. In the CSF method this force is incorporated as a volume-force term which is non-zero only in a thin band around the interface. This thin band is produced by smearing out the delta function, making the force term continuous For such a smeared-out delta function, we can compute the volume-force term at a point $\mathbf{x}$ close to the interface as

$$\mathbf{f}_\mathrm{s}(\mathbf{x}, t) = \int_\Gamma \mathbf{f}_\mathrm{sfd}(\mathbf{s}, t)\delta(\mathbf{x} - \mathbf{x}_I(s))d\mathbf{s}, \tag{4}$$

where $\mathbf{f}_\mathrm{sfd}$ is a surface-force density and $\mathbf{x}_I(s)$ is a parametrization of the interface. The surface-force density is such that the integral of $\mathbf{f}_\mathrm{s}(\mathbf{x}, t)$ across the (smeared-out) interface approximates the surface tension force, see Brackbill *et al.* (1992) for details. Note that in the level-set context it is not necessary to parametrize the interface since $\phi(\mathbf{x})$ stores the distance to the interface, so we have $\mathbf{x} - \mathbf{x}_I(s) = \phi(\mathbf{x})$ as long as $\phi(\mathbf{x})$ is a signed distance function. There are several ways to smear out the delta function, we follow Osher

and Fedkiw (2003, Eq. 1.23),

$$\delta(x) = \begin{cases} 0 & \text{if } |\phi| > \epsilon \\ \frac{1}{2\epsilon}\left(1 + \cos\left(\frac{\pi\phi}{\epsilon}\right)\right) & \text{else} \end{cases} \tag{5}$$

where $\epsilon = 1.5\Delta x$ is employed. This one-dimensional delta function is composed into the three-dimensional version by taking $\delta(\mathbf{x}) = \delta(x)\delta(y)\delta(z)$.

This formulation leads to a source term which incorporates the effects of surface tension. It is also necessary to smear out the viscosity and density differences across the interface in order to be consistent with the above formulation. A smeared-out Heaviside function $H(\mathbf{x})$ is used to accomplish this, given by Osher and Fedkiw (2003, Eq. 1.22) as

$$H(x) = \begin{cases} 0 & \text{if } \phi < -\epsilon \\ \frac{1}{2}\left(1 + \frac{\phi}{\epsilon} + \frac{1}{\pi}\sin\left(\frac{\pi\phi}{\epsilon}\right)\right) & \text{if } -\epsilon < \phi < \epsilon \\ 1 & \text{if } \phi > \epsilon \end{cases} \tag{6}$$

NUMERICAL METHODS

To discretize the Navier-Stokes equations and the equations for the level-set method we employ finite difference methods, specifically WENO (Liu *et al.*, 1994) for the convective terms and central differences for the viscous terms in Eq. (2), and WENO also for Eq. (3). The time integration is done with an explicit second-order Runge-Kutta method (SSPRK (2,2) in the terminology of Gottlieb *et al.* (2009)) for both Eq. (2) and Eq. (3).

The grid is a structured rectangular uniform staggered grid. A staggered grid is employed to avoid checkerboarding of the pressure field; this means that the pressure and other scalars "live" at cell centers, while the velocities "live" at the cell faces. To be more precise, if we have a pressure at one point $p_{i,j,k}$, the velocities (u, v, w) around this point are $u_{i\pm1/2,j,k}, v_{i,j\pm1/2,k}, w_{i,j,k\pm1/2}$ located at the 6 cell faces. In the actual code we store the velocity values for $u_{i+1/2,j,k}$, $v_{i,j+1/2,k}$, $w_{i,j,k+1/2}$ at the index `(i,j,k)` even though these values are not physically colocated.

The major problem when solving Eqs. (1) and (2) is that this is not a set of PDEs, it is a differential-algebraic equation (DAE) with a Hessenberg index of two. In other words, even though we have four equations (Eq. (2) is three equations) and four unknowns (u, v, w, p), Eq. (1) cannot be used directly to find p. The first solution to this conundrum was presented by Chorin (1968). This method can be understood as calculating an approximate velocity field $\mathbf{u}^*$ which does not satisfy Eq. (1), and subsequently projecting this velocity field onto the manifold of vector fields satisfying Eq. (1). For this reason, the method is often called Chorin's projection method or simply *the* projection method. It consists of these three steps, where we calculate three quantities successively, namely $\mathbf{u}^*, p_{n+1}, \mathbf{u}_{n+1}$:

$$\frac{\mathbf{u}^* - \mathbf{u}_n}{\Delta t} = -\left(\mathbf{u}_n \cdot \boldsymbol{\nabla}\right)\mathbf{u}_n + \nu\boldsymbol{\nabla}^2\mathbf{u}_n \tag{7}$$

$$\boldsymbol{\nabla}^2 p_{n+1} = \frac{\rho}{\Delta t}\boldsymbol{\nabla}\cdot\mathbf{u}^* \tag{8}$$

$$\mathbf{u}_{n+1} = \mathbf{u}^* - \frac{\Delta t}{\rho}\boldsymbol{\nabla}p_{n+1} \tag{9}$$

The pressure Poisson equation (8) that arises here is elliptic, so the numerical solution is very time consuming and a vast amount of research has gone into developing fast solvers. For two-phase flows with high density differences, the condition number of the matrix that results when Eq. (8) is discretized will make matters even worse than for the single-phase problem (Duffy *et al.*, 2002). This matrix is very large even in sparse storage formats, for a 256^3 grid it has 117 million non-zero elements. The current state-of-the-art consists in combining a (geometric or algebraic) multigrid preconditioner with a conjugate gradient method (often BiCGStab) for solving the resulting sparse linear system. Our experience with 2D axisymmetric simulations suggests that the Bi-Conjugate Gradient Stabilized method (van der Vorst, 1992) with the BoomerAMG preconditioner (Henson and Yang, 2000) is an optimal choice. For the simulations performed here, however, the straigth-forward successive over-relaxation (SOR) preconditioner turned out to be faster than BoomerAMG. This has not been investigated in greater detail. We employ the PETSc and Hypre libraries for these methods (Balay *et al.*, 2014; *hypre* , 2014).

We note also that the boundary conditions for Eq. (8) are of pure Neumann type (unless e.g. an outlet pressure is specified), which results in a singular matrix. These boundary conditions arise from the projection method and are not physical. The common "engineering" approach of fixing the singularity, simply fixing the pressure at some point in the domain, is not a very good approach as it may pollute the spectrum of the preconditioner. Instead, projecting the discretized singular equation into the orthogonal complement of the null space of the singular matrix seems to be a good solution (Zhuang and Sun, 2001). In other words, for $Ax = b$, we construct the Krylov operator $K = (\mathbb{I} - \mathbb{N})P^{-1}A$ such that $b, Kb, K^2b, ...$ is orthogonal to the null space $\mathbb{N}$. Here $\mathbb{I}$ is the identity matrix, so $(\mathbb{I} - \mathbb{N})P^{-1}$ is the desired projection. In the PETSc library that we employ here (Balay *et al.*, 2014), this is achieved using the `KSPSetNullSpace()` routine.

PARALLELIZATION

The starting point for the parallelization was an in-house code consisting of a 2D/3D Navier-Stokes solver and a multi-physics framework that enables the simulation of two-phase flows with the possibility of applying electric fields, and/or adding surface-active agents to the interface. The interface between the two phases is captured using a level-set method, so interfaces with changing topology such as two merging drops can be simulated. The code has been successfully applied to the study of both liquid-liquid (Teigen and Munkejord,

2010) and liquid-gas systems (Ervik *et al.*, 2014), but the long runtime has restricted its use to 2D axisymmetric cases so far.

The PETSc DMDA framework for domain decomposition was chosen as the main methodology for parallelizing the code. Domain decomposition consists in splitting the whole domain into subdomains which are each distributed to one MPI node. Each node then has a computational domain with some internal cells where the flow is computed, and some ghost cells which represent either boundary conditions or values that belong to neighbouring domains. This means that regular communication between the nodes is necessary such that all ghost cells have correct values. Such a splitting is shown in Fig. 2 below. Neglecting for a moment the pressure Poisson equation, this approach can scale well to millions of CPU cores, see e.g. Rossinelli *et al.* (2013) for an example in compressible flow.

By using the PETSc DMDA framework we can avoid the gritty details of domain decomposition and MPI programming. At the initialization of the code, some routines are called to set up three DMDAs which are objects that manage the decomposition. Using these objects we input how large our computational domain should be in terms of grid points, and the library decides an optimal decomposition *at runtime* depending on the number of MPI processes the code is run with. We also specify the physical dimensions of our uniform grid, and the library returns the physical dimensions for each subdomain.

This framework is very convenient, but one enhancement was made to further facilitate the reuse of the serial code. In the standard PETSc framework, the local work arrays that represent the solution on a given subdomain and the values in the ghost cells are indexed using the global indices. The existing code naturally expects indices that go from 1 to the maximum value `imax`. In Fortran, the bounds of an array may be re-mapped when the array is passed to a subroutine, and this feature was used to ensure that each local work array had bounds as expected by the serial code. Thus we will use `imax` as the final `i` index *on each subdomain* in the following.

With this enhancement, the only thing that had to be re-written in the original code was the handling of the staggered grid for the velocity. In the formulation used here, we have one less point for e.g. u in the x direction, since these values are located at the cell faces. In the serial code this is handled by not solving for u at the point `imax`. In the parallel version, u at the point `imax` should however be solved for on those processes that are not at the actual boundary but where there is a neighbouring process in the positive x-direction.

Furthermore, this means that a communication step is also necessary in the projection method. After the pressure has been calculated from the Poisson equation, we calculate e.g. the x-component of $\boldsymbol{\nabla} p$ at the cell face corresponding to u at `imax`. Numerically this is `(p(imax+1) - p(imax))/dx`, so the ghost value at `imax+1` must be updated before this calculation for those subdomains where `p(imax+1)` represents a pressure value on another subdomain and not a boundary condition.

Returning to the pressure Poisson equation Eq. (8), the elliptic nature of this equation means that, in some sense, all nodes must communicate during the solution. A further reduction in speedup potential is due to the fact that the solvers for this equation are mostly bound by memory bandwidth, which is shared amongst all cores on a modern CPU. These limits imply that we must lower our expectations somewhat in comparison with the impressive results mentioned earlier for compressible flows.

In the DMDA framework, the Poisson equation is set up such that each process computes its own portion of the matrix and right-hand side vector. This is the only scalable way of solving it, even when sparse storage formats are used.

RESULTS

Manufactured solution case

After the code had been parallelized it was tested using a manufactured solution (Roache, 2002) inspired by that used in John *et al.* (2006). The debugging tool Valgrind (Nethercote and Seward, 2007; Nethercote *et al.*, 2014) was used in the memory checking mode to ensure that the code does not e.g. make use of uninitialized values, a common programming error. When all such errors were fixed, the code was used to solve the single-phase Navier-Stokes equations with the following exact solution used as an initial – boundary value problem on a (1.0 m)^3 domain, where the origin is in the lower left front corner (cf. Fig. 2).

$$\begin{aligned} u &= t^3 yz \\ v &= t^2 xz \\ w &= txy \\ p &= x + y + z - 1.5 \end{aligned} \tag{10}$$

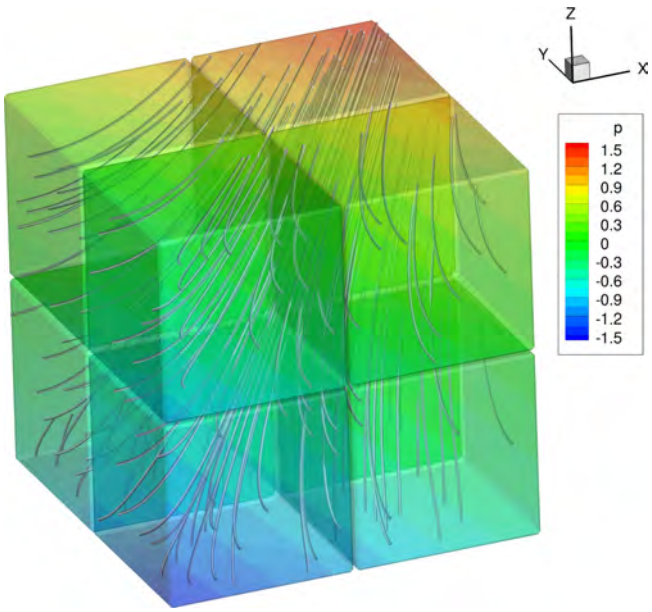

Figure 2: The computed solution after 0.031 s (100 time steps) on a 128^3 grid run on 8 processors. The blocks show the decomposition of the domain, the pressure field is shown superimposed on these blocks, and the streamlines illustrate the flow.

Insertion into Eq. (1) confirms that this solution is divergence free, and the resulting body force can be computed by inserting Eq. (10) in Eq. (2). In order to minimize the risk of human error, this was done symbolically using Maple, the resulting expression was copied into the Fortran code and regular expressions were used to convert Maple syntax into Fortran. A plot of the computed solution is shown in Fig. 2. Here the velocity streamlines are shown together with the pressure field which has been superimposed on blocks representing the parallel decomposition.

Convergence

Using the manufactured solution in Eq. (10), the convergence under grid- and time step refinement, as well as the strong and weak scaling, was tested on the Kongull cluster at NTNU. This cluster has dual-socket nodes with Intel Xeon E5-2670 8-core CPUs and a 1 Gb/s Ethernet interconnect. The STREAM benchmark (McCalpin, 2014, 1995) was run on one core and gave an effective memory bandwidth of 9800 MB/s for the Triad test[3].

To test the grid- and time step refinement, a base case was selected with a 256^3 grid, giving a grid spacing `dx` of $3.91 \cdot 10^{-3}$ m, the CFL condition following Kang *et al.* (2000) with a CFL number of 0.5 then giving a time step of $1.28 \cdot 10^{-4}$ s. This case was solved for 100 time steps, as were solutions on coarser grids 128^3 and 64^3 computed with the same time step. All simulations were run on 32 processes (8 nodes with 4 processes each). Subsequently, the same cases were run but with $1/2$, $1/4$ and $1/8$ the time step using 200, 400 and 800 time steps, respectively. The results are shown in Fig. 3.

It is seen that the convergence behaviour is as expected. First of all, the temporal order is 1 (not 2) due to an irreducible splitting error from the projection method. This can be overcome e.g. by using the incremental pressure form (see Guermond *et al.* (2006) for a review of projection methods), but has not been considered in this work. Second, the grid refinement does not influence the error. This is due to the fact that the velocity field is linear in space, so the error is completely dominated by the temporal order.

Strong scaling

To test the strong scaling of our code, i.e. how simulating a given case speeds up when more processes are used, a 128^3 grid was used giving a grid spacing `dx` of $7.81 \cdot 10^{-3}$ m, the CFL condition giving a time step of $3.10 \cdot 10^{-4}$ s. The solution was computed for 100 time steps. Since the Poisson solver performance should be bound by memory bandwidth, the test was made using 2 processes per node (one per socket) and several nodes. The resulting speedup relative to one process is shown in Fig. 4. In this figure, the black points indicate the speedup compared to running on one process. The scaling seen is quite good, but as expected lower than the theoretical linear scaling. It is seen that the peak memory usage (orange) increases slightly with more processes.

[3]The Triad test consists of repeated computations of the operation `a(i)=b(i)+q*c(i)` where `q` is constant and `i` is incremented.

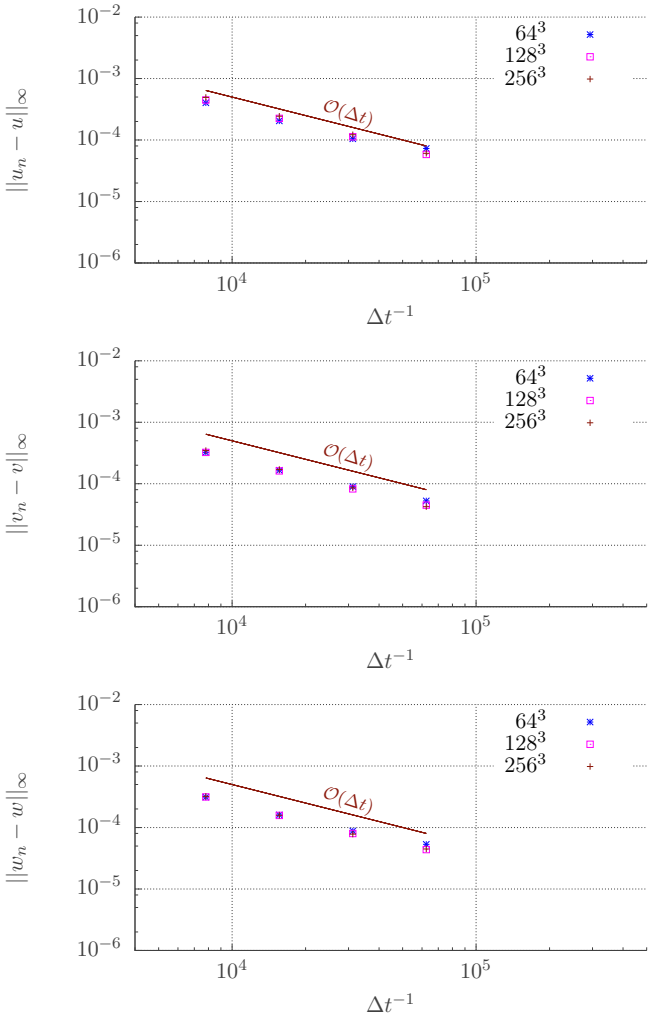

Figure 3: Time step and grid refinement on 32 processes. Top to bottom: u, v and w velocities. The maximum error of the solution, e.g. $||u_n - u||_\infty$ is plotted against the inverse of the time step. Here u_n denotes the numerical solution at time step n while u denotes the exact solution at this time.

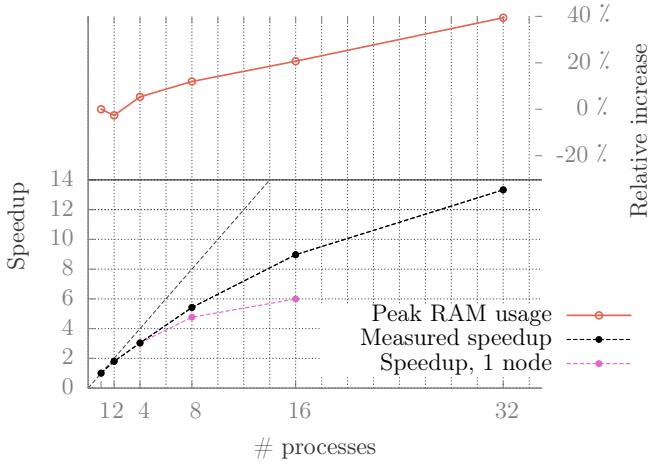

Figure 4: Strong scaling: with the left-hand-side y-axis, measured (black and magenta) and the optimal (dotted gray) speedup plotted against the number of processes. With the right-hand-side y-axis, increase in memory use.

To investigate the hypothesis that using only 2 processes per node and several nodes is better than using many processes on one node, we also tried running with 8 and 16 processes on one node. These results are plotted in magenta in Fig. 4 and confirm the hypothesis. We can conclude that even on this particular cluster with a slow (by HPC standards) interconnect, the added memory bandwidth afforded by using more nodes (thus more sockets) outweighs the penalty of increased communication between nodes. This also indicates that the results for 2 processes per node are bound by the interconnect speed, such that the speedup would be closer to the optimal (linear) scaling when run on a more tightly-coupled cluster.

Weak scaling

The weak scaling of the code was also studied. The base case was the same manufactured solution on a $(0.5\text{ m})^3$ domain resolved with a 64^3 grid, run on one process. Then a $(0.5\text{ m})^2 \times (1.0\text{ m})$ domain with a $64^2 \times 128$ grid was solved with two processes, a $(0.5\text{ m}) \times (1.0\text{ m})^2$ domain with a 64×128^2 grid was solved on 4 processes, etc. In this way, the number of grid points and the number of processes are both increased proportionally. The equations were solved for 50 time steps, and the results are shown in Fig. 5.

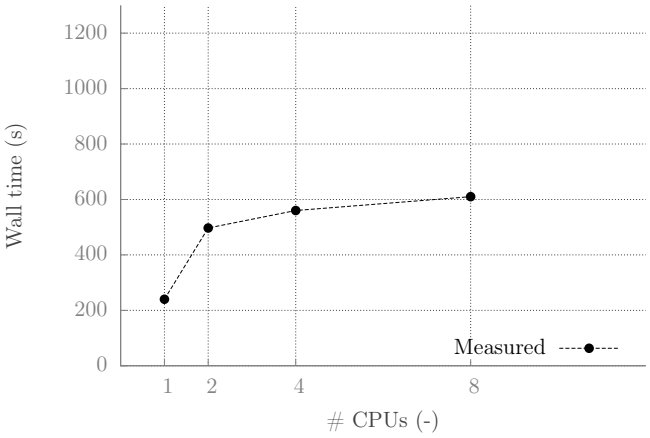

Figure 5: The weak scaling of the code as the number of processes and the number of grid points are both increased proportionally.

As is seen in this figure, there is obviously a performance hit initially; the perfect behaviour would be a flat line. This is as expected. When going from 1 to 2 processes, we go from no communication to overhead from communication. Furthermore, when going from 2 to 4 processes, there is the added overhead of intra-node communication, as opposed to the case with 2 processes where the communication is not over the network but over the CPU bus. The weak scaling seen here is quite decent. One should also be aware that it is more difficult to ensure that cases are "equivalently hard" for weak scaling than for strong scaling (Aagaard *et al.*, 2013).

Two-phase results

As an initial test of the two-phase capabilities of the parallelized code, the CSF method was employed to simulate a 2 cm diameter drop with properties $\rho_1 = 2\text{ kg/m}^3$, $\mu_1 = 0.01$ Pa s falling through a bulk fluid with properties $\rho_2 = 1\text{ kg/m}^3$, $\mu_2 = 0.05$ Pa s. The interfacial tension was set to $\sigma = 0.01\text{ N/m}$. The domain was $(10\text{ cm})^3$ resolved by a $(128)^3$ grid, the simulation was run on 8 processes for 33900 time steps up to $t = 0.01\text{ s}$. The drop has not yet achieved a substantial falling velocity, so the spurious currents are quite visible. The result is shown in Fig. 6, where the drop is shown with the pressure superimposed on the surface, streamlines indicating the flow. A plane is shown intersecting the centre of the drop, on this plane the pressure field, velocity field and level-set function contour lines are shown. A reference vector is shown on the right.

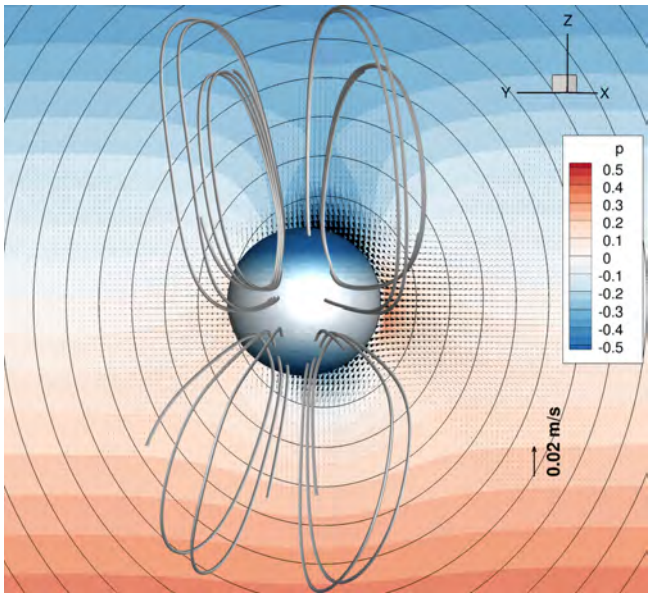

Figure 6: The falling drop after a short time (0.01 s). The pressure field is shown superimposed on the surface, and on the plane behind the drop. On this plane the velocity field and the level-set isocontours are also shown. Streamlines indicate the velocity field.

Spurious currents is a well-known challenge with the CSF method, and experience with the 2D serial code has led us to prefer the ghost-fluid method (GFM) (Kang *et al.*, 2000), which is somewhat more complicated to implement. This was not done within the scope of this paper. Nevertheless, this demonstrates that the parallel code is capable of two-phase fluid simulations with both density- and viscosity-jumps.

CONCLUSIONS

In this paper we have discussed the parallelization of an existing serial 3D incompressible Navier-Stokes solver for two-phase flow. The PETSc DMDA domain decomposition framework has been leveraged to apply MPI parallelism, enabling the code to make use of modern HPC facilites. We have discussed the alterations that were necessary for the serial code and established a framework where these were as few as possible.

Based on this code, we have reported the strong and weak scalings for a manufactured-solution case on a cluster with dual-socket nodes and 1 Gb/s Ethernet interconnect. It is seen that the code scales rather

well, but that one should take care to maximize the number of sockets used, since the Poisson solver is bound by memory bandwidth. If this code is run on a cluster simultaneously with CPU-bound parallell codes (e.g. using Monte Carlo methods), sensible resource allocation would benefit from taking the available memory bandwidth into account. Then it would not be optimal to allocate all cores on N nodes to this code, but rather e.g. 50% of the cores on $2N$ nodes, while a CPU-bound code could effectively utilize the remaining 50% of the cores.

The speedup seen in the strong scaling test (13x faster on 32 processes) is sub-linear but does not level-off. Together with the possibility of running on more tightly-coupled clusters where the behaviour should be closer to linear, and using more than 32 cores, this will give a substantial speedup and reduce the runtimes of weeks and months for the serial code to something more managable, i.e. a few days or less.

Initial tests demonstrate that the code is able simulate two-phase flow, but the ghost-fluid method (GFM) should be used instead of the CSF method currently employed, in order to minimize the spurious currents.

This effort has left us with a code that scales quite well and a framework where the remaining multi-physics components can easily be introduced. In the end this will enable future simulations of full 3D cases relevant for the fundamental understanding of electrocoalescence.

ACKNOWLEDGEMENT

We would like to thank Matthew Knepley, Barry Smith and Jed Brown of the PETSc project for useful discussions around the framework employed here.

This work was funded by the project *Fundamental understanding of electrocoalescence in heavy crude oils* coordinated by SINTEF Energy Research. The authors acknowledge the support from the Petromaks programme of the Research Council of Norway (206976), Petrobras, Statoil and Wärtsilä Oil & Gas Systems.

REFERENCES

AAGAARD, B.T. *et al.* (2013). "A domain decomposition approach to implementing fault slip in finite-element models of quasi-static and dynamic crustal deformation". *J. Geophys. Res.: Solid Earth*, **118(6)**, 3059–3079.

BALAY, S. *et al.* (2014). "PETSc Web page". `http://www.mcs.anl.gov/petsc`.

BRACKBILL, J. *et al.* (1992). "A continuum method for modeling surface tension". *J. Comput. Phys.*, **100(2)**, 335–354.

CHORIN, A.J. (1968). "Numerical solution of the Navier-Stokes equations". *Math. Comput.*, **22(104)**, 745–762.

DUFFY, A. *et al.* (2002). "An improved variable density pressure projection solver for adaptive meshes". Unpublished. See `http://www.math.fsu.edu/~sussman/MGAMR.pdf`.

ERVIK, Å. *et al.* (2014). "A robust method for calculating interface curvature and normal vectors using an extracted local level set". *J. Comput. Phys.*, **257**, 259–277.

GOTTLIEB, S. *et al.* (2009). "High order strong stability preserving time discretizations". *J. Sci. Comput.*, **38(3)**, 251–289.

GUERMOND, J. *et al.* (2006). "An overview of projection methods for incompressible flows". *Comp. Meth. Appl. Mech. Eng.*, **195(44)**, 6011–6045.

HENSON, V.E. and YANG, U.M. (2000). "BoomerAMG: a parallel algebraic multigrid solver and preconditioner". *Appl. Numer. Math.*, **41**, 155–177.

hypre (2014). *High Performance Preconditioners*. Lawrence Livermore National Laboratory. `http://www.llnl.gov/CASC/hypre/`.

JOHN, V. *et al.* (2006). "A comparison of time-discretization/linearization approaches for the incompressible Navier–Stokes equations". *Comput. Meth. Appl. Mech. Eng.*, **195(44)**, 5995–6010.

KANG, M. *et al.* (2000). "A boundary condition capturing method for multiphase incompressible flow". *J. Sci. Comput.*, **15(3)**, 323–360.

LIU, X.D. *et al.* (1994). "Weighted essentially non-oscillatory schemes". *J. Comput. Phys.*, **115(1)**, 200–212.

MCCALPIN, J.D. (1995). "Memory bandwidth and machine balance in current high performance computers". *IEEE Computer Society Technical Committee on Computer Architecture (TCCA) Newsletter*, 19–25.

MCCALPIN, J.D. (2014). "STREAM web site". `http://www.cs.virginia.edu/stream/`.

MOORE, G. (1965). "Cramming more components onto integrated circuits". *Electronics*, **38(8)**.

NETHERCOTE, N. and SEWARD, J. (2007). "Valgrind: a framework for heavyweight dynamic binary instrumentation". *ACM Sigplan Notices*, vol. 42, 89–100.

NETHERCOTE, N. *et al.* (2014). "Valgrind Web page". `http://valgrind.org/`.

OSHER, S. and FEDKIW, R.P. (2001). "Level set methods: An overview and some recent results". *J. Comput. Phys.*, **169(2)**, 463 – 502.

OSHER, S. and FEDKIW, R.P. (2003). *Level Set Methods and Dynamic Implicit Surfaces*. Springer, Berlin.

OSHER, S. and SETHIAN, J.A. (1988). "Fronts propagating with curvature-dependent speed: Algorithms based on Hamilton-Jacobi formulations". *J. Comput. Phys.*, **79(1)**, 12 – 49.

ROACHE, P.J. (2002). "Code verification™ by the method of manufactured solutions". *ASME J. Fluids Eng.*, **124(1)**, 4–10.

ROSSINELLI, D. *et al.* (2013). "11 PFLOP/s simulations of cloud cavitation collapse". *SC*, 3.

TEIGEN, K.E. and MUNKEJORD, S.T. (2010). "Influence of surfactant on drop deformation in an electric field". *Phys. Fluids*, **22(11)**. Article 112104.

VAN DER VORST, H. (1992). "Bi-CGSTAB: A fast and smoothly converging variant of Bi-CG for the solution of nonsymmetric linear systems". *SIAM J. Sci. Comput.*, **13(2)**, 631–644.

ZHUANG, Y. and SUN, X.H. (2001). "A high-order fast direct solver for singular Poisson equations". *J. Comput. Phys.*, **171(1)**, 79 – 94.

10th International Conference on CFD in Oil & Gas, Metallurgical and Process Industries
SINTEF, Trondheim, NORWAY *CFD 2014*
17-19th June 2014

SPACE-TIME HP-ADAPTIVE DG-FEM SCHEME FOR ONE-DIMENSIONAL MULTIPHASE FLOW MODELS

Joost S.B. VAN ZWIETEN[1*], Ruud A.W.M. HENKES[23], Duncan R. VAN DER HEUL[1], Patricio I. ROSEN ESQUIVEL[3], Benjamin SANDERSE[3], C. (Kees) VUIK[1]

[1]Delft Institute of Applied Mathematics, TU Delft, Delft, THE NETHERLANDS

[2]Department of Process and Energy, TU Delft, Delft, THE NETHERLANDS

[3]Pipelines, Flow Assurance and Subsea Systems, P&T, Shell, Amsterdam, THE NETHERLANDS

[*] E-mail: j.s.b.vanzwieten@tudelft.nl

ABSTRACT

We present an adaptive *hp*-refinement procedure for non-conservative hyperbolic systems discretised with a space-time DG-FEM scheme. For every time slab a solution is computed on a coarse mesh with constant *hp*. Based on a smoothness indicator the mesh is refined and a solution on the refined mesh is computed. When measured in number of degrees of freedom the adaptive refinement procedure gives an improvement in efficiency compared to constant *hp* schemes. Measured in time, the efficiency of our implementation of the adaptive scheme is comparable to constant *hp* schemes.

Keywords: multiphase flow, one-dimensional, implicit time integration, space-time DG-FEM, hp-adaptive, shock capturing .

NOMENCLATURE

Greek Symbols

Γ	Edge of an element, $\Gamma \subset \Omega$.
Ω	Domain, $\Omega \subset \mathbb{R}^K$.
α	Volume fraction, [].
λ	Lebesgue measure.
μ	DLM-measure.
ρ	Mass density, [kg m^{-3}].
τ	Integration variable.
ϕ	Integration path.
ξ	Position in space-time, $\xi \in \Omega$.

Latin Symbols

$\mathscr{B}$	Basis.
$\mathscr{E}$	Set of elements, a partition of Ω.
$\mathscr{E}_m$	Time slab, $\mathscr{E}_m \subset \mathscr{E}, m \in \{1,2,\dots\}$.
$\mathscr{S}_{\text{ext}}$	Set of element boundaries shared with the domain boundary, paired with outward normals.
$\mathscr{S}_{\text{int}}$	Set of element boundaries shared with other element boundarues, paired with normals.
E	DG-FEM element, $E \subset \Omega$.
F	Flux in non-conservative form, $F : \mathbb{R}^J \to \mathbb{R}^{K\times I\times J}$.
F^{nc}	Non-conservative part of F, $F^{\text{nc}} : \mathbb{R}^J \to \mathbb{R}^{K\times I\times J}$.
H	$K-1$-dimensional Hausdorff measure.
I	Number of equations.
J	Number of unknowns.
K	Number of space-time dimensions.
P	Pressure, [Pa].
c	Function mapping unknowns to conserved quantities, $c : \mathbb{R}^J \to \mathbb{R}^I$.
f^{c}	Conservative part of F in conservative form, $f^{\text{c}} : \mathbb{R}^J \to \mathbb{R}^{K\times I}$.
g	Gravitational acceleration, [m s^{-2}].
n	Unit normal, $n \in \mathbb{R}^K$.
n_{dofs}	Number of degrees of freedom.
p	Number of basis functions per dimension for one element.
q	Vector of unknowns, $q : \Omega \to \mathbb{R}^J$.
t_{solver}	Time required to solve a discrete system.
u	Velocity, [m s^{-1}].
v	Test function, $v \in \mathscr{B}^I$.

Sub/superscripts

β	Phase index, $\beta \in \{\text{L},\text{G}\}$.
L	Liquid phase.
G	Gas phase.
i	Index over equations, $i \in \{1,2,\dots,I\}$.
j	Index over unknowns, $j \in \{1,2,\dots,J\}$.
k	Index over dimensions, $k \in \{1,2,\dots,K\}$.
t	Time dimension.
x	Space dimension.

INTRODUCTION

Multiphase flow plays an important role in many industrial processes, such as oil and gas recovery, chemical processing, power generation and various civil applications. For the design of very long multiphase pipeline systems, the industry relies on time-dependent one-dimensional hyperbolic models. Earlier attempts to solve these models numerically, based on finite difference and finite volume schemes and a conservative drift flux model for the interaction between the phases (Romate, 1998), often fail to accurately predict the onset and propagation of unstable flow, such as terrain slugs and hydrodynamic slugs. To improve the accuracy *slug capturing* models have been developed (see for example Issa and Kempf (2003)). When solved using a first order Finite Volume Method a relatively fine mesh is required, which is computationally expensive for long pipelines. In this study we investigate whether we can improve the time to solve these models by using an *hp*-adaptive space-time DG-FEM scheme.

DG-FEM differs from traditional FEM in that solutions in the former are discontinuous at element edges. At the edges an FVM-like numerical flux needs to be applied. DG-FEM allows a mesh to be refined locally and allows the order of

the basis functions to vary per element. Using high order basis functions and coarse elements in regions where the solution to the Partial Differential Equations is smooth and a fine mesh and low order basis functions in regions where discontinuities appear, may yield a considerable reduction of the number of coefficients needed to achieve a certain accuracy compared to a structured mesh with constant order of the basis functions.

Compressible twofluid models have very large eigenvalues, corresponding to fast travelling pressure waves. These waves cause the time step restriction for an explicit time integration method to be very small. For our application the pressure waves are less important, hence we use an implicit time integration method, allowing us to use much larger time steps, at the cost of less accurately resolving the pressure waves. We use the space-time DG-FEM method (Rhebergen *et al.*, 2008), which is implicit in time and which simultaneously discretises space and time. This method allows us to refine the mesh and the order of the basis functions in space and time simultaneously, in a unified way. The discrete system in space and time is not solved at once. The time dimension is subdivided in time slabs, each time slab consisting of a group of space-time elements. The time slabs are solved one by one using a Newton solver for non-linear systems with a direct solver for the Jacobian.

We apply an adaptive procedure to obtain a discrete solution. For each time slab:

- a solution on a coarse mesh with high-order basis functions is computed with low accuracy,
- elements where discontinuities are detected are refined and
- the solution is computed again on the fine mesh, with high accuracy, also if no elements are refined.

Then we proceed with the next time slab and repeat the procedure.

One-dimensional multiphase flow models often contain non-conservative products in the phase momentum balance equations which represent momentum transfer between phases. For a discussion on these models and the source of the non-conservative product, see for example Van Zwieten (2013). The non-conservative products require special attention in the derivation of the weak formulation. We use the technique developed by Dal Maso *et al.* (1995) and adopted for DG-FEM by Rhebergen *et al.* (2008).

This article is organised as follows. We start with deriving a space-time DG-FEM weak formulation for a general, non-conservative, hyperbolic system of PDE's. Then we describe the *hp*-refinement procedure, which uses a smoothness indicator to decide where to refine. The DG-FEM scheme with *hp*-refinement is applied to two test problems: the inviscid Burgers' equation with a sine wave as initial condition and the water faucet test problem using the twofluid model.

WEAK FORMULATION

Let $\Omega \subset \mathbb{R}^K$ be a domain in space-time where K is the number of dimensions (including time). We are concerned with the discretisation of a hyperbolic system of PDE's on Ω with non-conservative products:

$$\sum_{j,k} F_{kij}\left(q\left(\xi\right)\right) \frac{\partial q_j\left(\xi\right)}{\partial \xi_k} = s_i\left(q\left(\xi\right)\right). \tag{1}$$

where $\xi \in \Omega$ denotes a position in space time, $q := \Omega \rightarrow \mathbb{R}^J$ is a vector of unknowns with J the number of unknowns and $j \in \{1,2,\ldots,J\}$, F_{kij} is the flux matrix in direction $k \in \{1,2,\ldots,K\}$, s_i the source term, I is the number of equations and $i \in \{1,2,\ldots,I\}$.

Before we state the weak formulation we need the following definition and theorem.

Definition 1 (Integration paths, (Dal Maso *et al.*, 1995))**.** *A Lipschitz continuous path $\phi : [0,1] \times \mathbb{R}^J \times \mathbb{R}^J \rightarrow \mathbb{R}^J$ is called an integration path if it satisfies the following properties:*

$$\phi_j\left(0;q^-,q^+\right) = q_j^- \text{ and } \phi_j\left(1;q^-,q^+\right) = q_j^+ \quad \forall j, \forall q^-, q^+ \in \mathbb{R}^J, \tag{H1}$$

$$\phi_j\left(\tau;q,q\right) = q_j \; \forall j, \forall q \in \mathbb{R}^J, \tau \in [0,1], \tag{H2}$$

For every bounded set $\mathscr{U}$ of $\mathbb{R}^J$, there exists $k \geq 1$ such that

$$\left| \frac{\partial \phi\left(\tau;q^-,q^+\right)}{\partial \tau} - \frac{\partial \phi\left(\tau;w^-,w^+\right)}{\partial \tau} \right| \leq k \left| \left(q^- - w^-\right) - \left(q^+ - w^+\right) \right| \quad \forall q^-, q^+, w^-, w^+ \in \mathscr{U}, \tau \text{ a.e.} \in [0,1]. \tag{H3}$$

$$\phi_j\left(\tau;q^-,q^+\right) = \phi_j\left(1-\tau;q^+,q^-\right) \quad \forall q^-, q^+ \in \mathbb{R}^J, \; \tau \in [0,1] \tag{H4}$$

Theorem 1 (DLM measure, (Dal Maso *et al.*, 1995))**.** *Let ϕ be a family of Lipschitz paths in $\mathbb{R}^I$, which satisfies (H1)–(H4). Let $q : \Omega \rightarrow \mathbb{R}^J$ be a bounded function of bounded variation and $F : \mathbb{R}^J \rightarrow \mathbb{R}^{K \times I \times J}$ be a locally bounded Borel function. We subdivide Ω in Ω_q, the set of points of approximate continuity of q, Γ_q, the set of points of approximate jump and I_q, the set of irregular points of q. Then there exists a unique family of real-valued bounded Borel measures μ_i on Ω, $i \in \{1,2,\ldots,I\}$, characterised by the three properties:*

1. *if B is a Borel subset of Ω_q then*

$$\mu_i(B) = \int_B \sum_{j,k} F_{kij}\left(q\left(\xi\right)\right) \frac{\partial q_j\left(\xi\right)}{\partial \xi_k} d\lambda\left(\xi\right), \forall i, \tag{2}$$

   where λ is the Lebesgue measure,

2. *if B is a Borel subset of Γ_q then*

$$\mu_i(B) = \int_{B \cap \Gamma_q} \int_0^1 \sum_{j,k} F_{kij}\left(\phi\right) \frac{\partial \phi_j}{\partial \tau} n_k\left(\xi\right) d\tau d\lambda\left(\xi\right), \forall i, \tag{3}$$

   where $\phi = \phi\left(\tau; \langle\langle q;-n \rangle\rangle\left(\xi\right), \langle\langle q;n \rangle\rangle\left(\xi\right)\right)$,

3. *if B is a Borel subset of I_q then*

$$\mu_i(B) = 0. \tag{4}$$

Let $\mathscr{E}$ be a set of non-overlapping, non-empty, connected, open subsets of Ω such that

$$\bigcup_{E \in \mathscr{E}} \overline{E} = \overline{\Omega}. \tag{5}$$

Let $\mathscr{S}_{\text{ext}}$ be the set of all edges of elements of $\mathscr{E}$ which overlap with the domain boundary $\partial\Omega$ paired with the unit outward normal:

$$\mathscr{S}_{\text{ext}} := \left\{ \left(\partial E \cap \partial\Omega, n^{\partial E} \right) : E \in \mathscr{E}, \partial E \cap \partial\Omega \neq \emptyset \right\}. \quad (6)$$

Similarly, we introduce a set of 'internal' element boundaries, i.e. all boundaries of elements which are also a boundary of another element. We pair these boundaries with the outward unit normal of one of both elements. Which one is unimportant: the weak formulation derived below is invariant with respect to the sign of the normal in the set $\mathscr{S}_{\text{int}}$. To make this formal, let $\mathscr{E}_{\text{sorted}}$ be any sequence of the elements of $\mathscr{E}$. Then, we define the set of internal element boundaries $\mathscr{S}_{\text{int}}$ as

$$\mathscr{S}_{\text{int}} := \left\{ \left(\partial A \cap \partial B, n^{\partial A} \right) : A, B \in \mathscr{E}_{\text{sorted}}, A < B \right\}, \quad (7)$$

where $A < B$ means 'A occurs before B in the sequence $\mathscr{E}_{\text{sorted}}$.'

Let $\mathscr{B}$ be a subset of all functions $\xi \to \mathbb{R}$ which are continuous on all elements $E \in \mathscr{E}$. The functions may jump at element edges. If $q_j \in \mathscr{B}$ then Ω_q of Theorem 1 corresponds to the union of all elements, $\bigcup_{E\in\mathscr{E}}$, and Γ_q to the union of all internal element edges, $\{\partial A \cap \partial B : A, B \in \mathscr{E}\}$.

We use the following definitions to obtain a one-sided value or jump of some function $f \in \mathscr{B}$ at an element boundary. The side operator takes the value of f at the side of a boundary defined by the normal $n \in \mathbb{R}^K$,

$$\langle\langle f; n \rangle\rangle (\xi) := \lim_{\varepsilon \to 0^+} f(\xi + \varepsilon n). \quad (8)$$

and the average operator yields the average value of f at both sides,

$$\{\{ f; n \}\} (\xi) := \frac{\langle\langle f, +n \rangle\rangle (\xi) + \langle\langle f; -n \rangle\rangle (\xi)}{2}. \quad (9)$$

The jump operator gives the difference of f at both sides as a vector in direction n:

$$[\![f; n]\!]_k (\xi) := (\langle\langle f; +n \rangle\rangle (\xi) - \langle\langle f; -n \rangle\rangle (\xi)) n_k. \quad (10)$$

The average and jump operators are invariant to the sign of n: $\{\{f;n\}\} = \{\{f;-n\}\}$ and $[\![f;n]\!] = [\![f;-n]\!]$.

The weak formulation of the non-conservative hyperbolic system of PDE's (1) is given by (Rhebergen *et al.*, 2008):

Definition 2 (Weak formulation, initial version)**.** *Find $q_j \in \mathscr{B}$ such that $\forall v_i \in \mathscr{B}$:*

$$0 = \sum_i \int_\Omega v_i(\xi)\, d\mu_i(\xi) - \sum_i \int_\Omega v_i(\xi)\, s_i(q(\xi))\, d\lambda(\xi) + \sum_i W_i^{stab}. \quad (11)$$

The stabilisation term W_i^{stab} is defined below.

In the following we apply a series of transformations to the weak formulation. We split the flux matrix F in a conservative and non-conservative part and apply integration by parts to the conservative part.

We expand the first integral of Equation (11) using the definition of the DLM-measure for smooth regions (2), i.e. the elements, and discontinuous regions (3), i.e. the element edges:

$$\sum_i \int_\Omega v_i(\xi)\, d\mu_i(\xi) = \sum_{\substack{E\in\mathscr{E} \\ i,j,k}} \int_E v_i(\xi) F_{kij}(q(\xi)) \frac{\partial q_j(\xi)}{\partial \xi_k} d\lambda(\xi) + \sum_{\substack{(\Gamma,n)\in\mathscr{S}_{\text{int}} \\ i,j,k}} \int_\Gamma v_i(\xi) \int_0^1 F_{kij}(\phi) \frac{\partial \phi_j}{\partial \tau} n_k(\xi)\, d\tau dH(\xi), \quad (12)$$

where $\phi = \phi(\tau; \langle\langle q; -n \rangle\rangle(\xi), \langle\langle q, n \rangle\rangle(\xi))$. Since v_i is undefined on element boundaries, we replace v_i in the boundary integral by the average of v_i, $\{\{v_i; n^{\partial E}\}\}$ (see Rhebergen *et al.* (2008)).

We split the matrix F in a non-conservative and conservative part,

$$F_{kij}(q) = F^{\text{nc}}_{kij} + \frac{\partial f^{\text{c}}_{ki}(q)}{\partial q_j}, \quad (13)$$

and write the conservative part of the first term of the left hand side of Equation (12) as

$$\begin{aligned} &\sum_{\substack{E\in\mathscr{E} \\ i,j,k}} \int_E v_i(\xi) \frac{\partial f^{\text{c}}_{ki}(q(\xi))}{\partial q_j} \frac{\partial q_j(\xi)}{\partial \xi_k} d\lambda(\xi) \\ &= \sum_{\substack{E\in\mathscr{E} \\ i,k}} \int_E v_i(\xi) \frac{\partial f^{\text{c}}_{ki}(q(\xi))}{\partial \xi_k} d\lambda(\xi) \\ &= -\sum_{\substack{E\in\mathscr{E} \\ i,k}} \int_E \frac{\partial v_i(\xi)}{\partial \xi_k} f^{\text{c}}_{ki}(q(\xi))\, d\lambda(\xi) \\ &+ \sum_{\substack{E\in\mathscr{E} \\ i,k}} \int_{\partial E} \left\langle\left\langle v_i(\cdot) f^{\text{c}}_{ki}(q(\cdot)); -n^{\partial E} \right\rangle\right\rangle (\xi) n_k^{\partial E}(\xi)\, dH(\xi). \end{aligned} \quad (14)$$

Because v and q are possibly multi-valued at the element edges, the last term uses the side operator to select the value at the inner side of the boundary. In the last term of the right hand side we change the summation from elements to internal and external edges,

$$\begin{aligned} &\sum_{\substack{E\in\mathscr{E} \\ i,k}} \int_{\partial E} \left\langle\left\langle v_i(\cdot) f^{\text{c}}_{ki}(q(\cdot)); -n^{\partial E} \right\rangle\right\rangle (\xi) n_k^{\partial E}(\xi)\, d\lambda(\xi) \\ &= \sum_{\substack{(\Gamma,n)\in\mathscr{S}_{\text{int}} \\ i,k}} \int_\Gamma - [\![v_i(\cdot) f^{\text{c}}_{ki}(q(\cdot)); n]\!]_k (\xi)\, dH(\xi) \\ &+ \sum_{\substack{(\Gamma,n)\in\mathscr{S}_{\text{ext}} \\ i,k}} \int_\Gamma v_i(\xi) f^{\text{c}}_{ki}(q(\xi)) n_k dH(\xi). \end{aligned} \quad (15)$$

Using

$$[\![ab]\!] = [\![a]\!] \{\{ b \}\} + \{\{ a \}\} [\![b]\!], \quad (16)$$

the first term on the right hand side of (15) can also be written as

$$\begin{aligned} &\int_\Gamma - [\![v_i(\cdot) f^{\text{c}}_{ki}(q(\cdot)); n]\!]_k (\xi)\, dH(\xi) \\ &= \int_\Gamma - [\![v_i; n]\!]_k (\xi) \{\{ f^{\text{c}}_{ki}(q(\cdot)); n \}\} (\xi)\, dH(\xi) \\ &+ \int_\Gamma - \{\{ v_i; n \}\} (\xi) [\![f^{\text{c}}_{ki}(q(\cdot)); n]\!]_k (\xi)\, dH(\xi). \end{aligned} \quad (17)$$

The last term on the right hand side is equal to the conservative part of the path integral in Equation (12):

$$\begin{aligned}&\int_\Gamma -\{\!\{v_i;n\}\!\}(\xi)\,[\![f^c_{ki}(q(\cdot));n]\!]_k(\xi)\,dH(\xi)\\&=\sum_j\int_\Gamma -\{\!\{v_i;n\}\!\}(\xi)\int_0^1\frac{\partial f^c_{ki}(\phi)}{\partial\phi_j}\frac{\partial\phi_j}{\partial\tau}d\tau n_k(\xi)\,dH(\xi),\end{aligned}\tag{18}$$

where $\phi=\phi(\tau;\langle\!\langle q;-n\rangle\!\rangle(\xi),\langle\!\langle q,n\rangle\!\rangle(\xi))$.
Substituting Equations (12)–(18) in Equation (11) gives the final form of the weak formulation:

Definition 3 (Weak formulation)**.** *Find $q_j\in\mathscr{B}$ such that $\forall v_i\in\mathscr{B}$:*

$$\begin{aligned}0=&\sum_{\substack{E\in\mathscr{E}\\i,j,k}}\int_E v_i(\xi)F^{nc}_{kij}(q(\xi))\frac{\partial q_j(\xi)}{\partial\xi_k}d\lambda(\xi)\\&-\sum_{\substack{E\in\mathscr{E}\\i,k}}\int_E\frac{\partial v_i(\xi)}{\partial\xi_k}f^c_{ki}(q(\xi))\,d\lambda(\xi)\\&+\sum_{\substack{(\Gamma,n)\in\mathscr{S}_{ext}\\i,k}}\int_\Gamma v_i(\xi)\,f^c_{ki}(q(\xi))\,n_k(\xi)\,dH(\xi)\\&-\sum_{\substack{(\Gamma,n)\in\mathscr{S}_{int}\\i,k}}\int_\Gamma[\![v_i;n]\!]_k(\xi)\,\{\!\{f^c_{ki};n\}\!\}(\xi)\\&+\sum_{\substack{(\Gamma,n)\in\mathscr{S}_{int}\\i,j,k}}\int_\Gamma\{\!\{v_i;n\}\!\}(\xi)\int_0^1F^{nc}_{kij}(\phi)\frac{\partial\phi_j}{\partial\tau}d\tau n(\xi)\,dH(\xi),\\&+W^{stab}_i-\sum_{\substack{E\in\mathscr{E}\\i}}\int_E s_i(q(\xi))\,d\lambda(\xi),\end{aligned}\tag{19}$$

where $\phi=\phi(\tau;\langle\!\langle q;-n\rangle\!\rangle(\xi),\langle\!\langle q,n\rangle\!\rangle(\xi))$.

STABILISATION

We use the Local Lax-Friedrichs or Rusanov stabilisation (Castro *et al.*, 2010), given by

$$W^{\text{stab}}_i=\sum_{\substack{(\Gamma,n)\in\mathscr{S}_{\text{int}}\\i,k}}\int_\Gamma\frac{C_k(q)}{2}[\![v_i;n]\!]_k\,[\![f^c_{ti}(q(\cdot));n]\!]_k\,dH,\tag{20}$$

where q and both jump operators are functions of the integration variable ξ. The function C controls the amount of diffusion added to the system and should be chosen not smaller than the largest (in magnitude) eigenvalue of the flux matrix. In the time dimension the eigenvalues are usually one, hence we let $C_t=1$. This corresponds to an upwind scheme.

INTEGRATION PATH

We assume a straight path connecting the left and right states, q^- and q^+ respectively:

$$\phi_j\left(\tau;q^-,q^+\right):=a_j(1-\tau)+b_j\tau.\tag{21}$$

The choice of the integration path affects the solution to the discrete system, however, this is outside the scope of this study. For a discussion on integration paths see Alouges and Merlet (2004) and Chalmers and Lorin (2009).

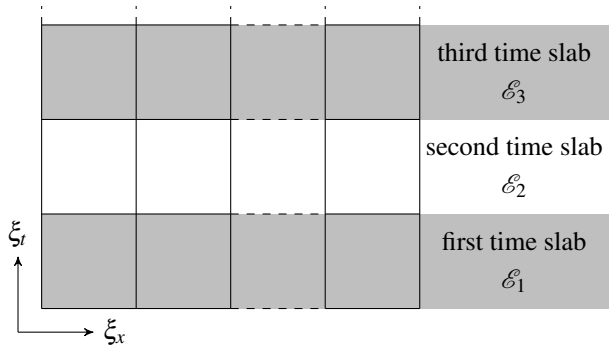

Figure 1: Time slabs

MESH AND BASIS

We assume the space-time domain Ω to be an orthotope — in a two-dimensional space this is a rectangle — i.e. we can write Ω as a tensor product of one-dimensional intervals. One-dimensional models with time-invariant spatial domains satisfy this assumption. An orthotope can be partitioned with elements which are orthotopes as well.
For some element $E\in\mathscr{E}$ we define a set of basis functions which has support only on this element E. We use a tensor product of Legendre polynomials, zero-extended outside E. The basis for the total domain Ω is the union of all element bases. Instead of a tensor product of Legendre polynomials, we could also use a tensor product of different polynomials. As long as the space spanned by the basis remains the same, the solution to the discrete system will be the same. However, the choice of the basis functions might affect the performance and stability of the numerical solver used to solve the discrete system.

TIME-SLABS

Given a space-time mesh $\mathscr{E}$ and basis, solving the complete discrete system at once is in general too expensive and unnecessary. We create a possibly finite sequence $\{\mathscr{E}_1,\mathscr{E}_2,\mathscr{E}_3,\dots\}$ of subsets of $\mathscr{E}$, such that the sequence is a partition of $\mathscr{E}$. We impose the extra condition that each *time slab* $\mathscr{E}_m$ depends only on previous time slabs $\mathscr{E}_{m'},m'<m$. The following is a sufficient condition: on all boundaries of $\Gamma\subset\partial\mathscr{E}_m$ which are common with boundaries of higher time slabs, we require the eigenvalues of the matrix $\sum_k F_{kij}(\phi(\tau))n_k$, i denoting the rows and j the columns and n the unit outward normal of $\mathscr{E}_m$, to be positive for all $\tau\in[0,1]$. In practice information is not flowing back in time, hence choosing 'pure' time intervals as time slabs is safe. See for an example Figure 1. Given a sequence of time slabs, we can solve each time slab one after another.

HP-REFINEMENT

Hyperbolic systems may develop shocks, even when the initial condition is smooth. Projecting a discontinuous function onto a space spanned by a finite set of polynomials gives an oscillatory result, the *Gibbs phenomenon*. Increasing the order of the polynomials does not attenuate the oscillation. There are several techniques to prevent the DG-FEM scheme to generate oscillatory solutions. Cockburn and Shu (2001) use a slope limiter which modifies the solution locally to ensure that the total variation of a solution is bounded. Limiters allow shocks to be represented within an element, however, the limiter may destroy the accuracy in smooth regions. (Persson and Peraire, 2006) add variable diffusion terms to

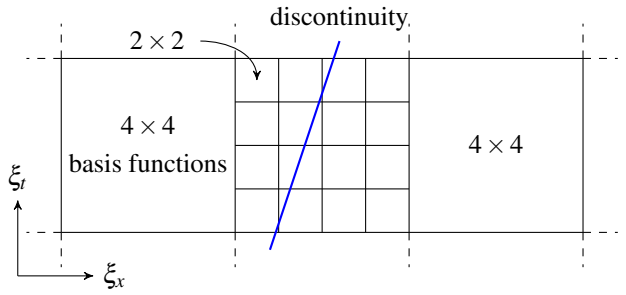

Figure 2: Example *hp*-refinement near a discontinuity

the partial differential equations. The amount of diffusion added depends on the smoothness of the solution locally.
We apply *hp*-refinement to reduce oscillatory solutions and represent discontinuities sharply. In the neighbourhood of discontinuities we want a higher density of elements than in smooth regions and a reduced set of basis functions, with lower order. The refinement procedure is as follows. For each time slab $\mathscr{E}_m, m \in \{1,2,3,\dots\}$:

R1 Solve, with low accuracy, the discrete system on the subset (coarse mesh) $\mathscr{E}_m$ with (high-order) basis $\mathscr{B}_m$.

R2 Locate elements which may contain discontinuities.

R3 Refine those elements by subdividing the elements in $n_{\text{subdivs.}}$ equal parts per dimension, this gives a new set of elements $\mathscr{E}_m^{\text{r}}$, and reduce the order of the basis functions, this gives the basis $\mathscr{B}_m^{\text{r}}$.

R4 Project the solution of step R1 onto the refined basis $\mathscr{B}_m^{\text{r}}$.

R5 Solve, with high accuracy, the discrete system using $\mathscr{E}_m^{\text{r}}$ and $\mathscr{B}_m^{\text{r}}$ and using the projected solution of step R4 as initial guess.

Some remarks:

- At step R1 we compute the solution using a few iterations of the non-linear solver. This turns out to be enough to locate discontinuities.
- Even when the mesh is not refined, i.e. at step R2 we have not found any discontinuity, we still proceed with step R5.
- At step R1 we deliberately do not use the refined mesh from the previous time slab. This would complicate the refinement procedure, as we would need to coarsen the mesh in regions where the solution is smooth enough. Furthermore, reuse of the refined mesh is of limited use in case of fast moving shocks.

Figure 2 shows an example mesh and indication of the number of basis functions for a time slab with refinement near a discontinuity.

SMOOTHNESS INDICATOR

This leaves the detection for discontinuities to be defined. The solution to the discrete system when using the coarse mesh and high order basis, step R1, will be oscillatory or non-smooth near discontinuities. We measure smoothness of the discrete solution q in some element $E \in \mathscr{E}$ using the following smoothness indicator (Persson and Peraire, 2006):

$$S_v(q,E) = \frac{\int_E \left| v(q(\xi)) - v\left(q^{\text{low}}(\xi)\right)\right|^2 d\lambda(\xi)}{\int_E |v(q(\xi))|^2 d\lambda(\xi)}. \qquad (22)$$

Here, q^{low} is the discrete solution restricted to a lower order basis and v is a functional of which we determine the smoothness. The difference of $v(q)$ and $v(q^{\text{low}})$ represents the high frequency part of the solution. If the smoothness indicator S is above a threshold S_v^{th} we will apply refinement.
The smoothness indicator is not invariant to scaling and translation: let v_1 be some functional of q and $v_2(q) := av_1(q) + b$ for some constants $a, b \in \mathbb{R}$, then $S_{v_1} \neq S_{v_2}$. Choosing a 'good' functional v and threshold S_v^{th} requires prior knowledge about the range of solution values q.

NUMERICAL RESULTS

We test the DG-FEM scheme with and without adaptive *hp*-refinement using two test problems. The numerical scheme is implemented in C++ (computationally expensive parts) and Python. All results are obtained on a laptop with an Intel Core 2 Duo Processor P8700 using one thread.

Burgers' sine test problem

First, we consider the inviscid Burgers' equation on a 2π-periodic spatial domain,

$$\frac{\partial u(\xi)}{\partial \xi_t} + \frac{1}{2}\frac{\partial u^2(\xi)}{\partial \xi_x} = 0, \qquad (23)$$

with initial condition

$$u(\xi) = \frac{2 + \sin(\xi_x)}{2}, \quad \forall \xi : \xi_t = 0. \qquad (24)$$

The smooth sine wave will develop into a sawtooth-like wave, travelling with dimensionless velocity 1 and with a discontinuity at $\xi_x = \pi + 2m\pi + \xi_t$, $m \in \mathbb{Z}$.
We apply the DG-FEM scheme defined above to PDE (23) and initial condition (24). The conservative part of the flux is given by

$$f_k^{\text{c}}(q) = \begin{cases} q & \text{if } k = k_t, \\ \frac{1}{2}q^2 & \text{if } k = k_x. \end{cases} \qquad (25)$$

the non-conservative part of the flux and the source are zero, $F_k^{\text{nc}}(q) = 0$, $s(q) = 0$.
Figure 3 shows the discrete solution in the first column and the pointwise error in the second column. All results in this figure are based on a structured (coarse) mesh with 32 elements in x-dimension. The ratio of the element size in x and t is fixed. In the first row we used two basis functions per dimension per element, without *hp*-refinement. The error is large in a wide band around the discontinuity. Increasing the number of basis functions per element to three gives the results as shown in the second row. The pointwise error is improved mainly in the smooth regions. The third row shows the result of enabling *hp*-refinement. Elements where the smoothness indicator, shown in the third column, is above a threshold are refined, with eight subdivisions and two basis functions per dimension per element. Compared with the former two solutions, the *hp*-refined solution has a very sharp discontinuity, and the large error bandwidth is reduced substantially. It must be noted that, while the *hp*-refined solution

is much more accurate, also the number of degrees of freedom and the time to solve the discrete system are larger than for the other two simulations.
Figure 4 shows the L_1-error versus the number of degrees of freedom (left) and the time to solve (right) the system for an increasing number of elements at the coarse mesh for various numbers of basis functions p. If hp-refinement is applied, the number of subdivisions is indicated by $n_{\text{subdivs.}}$ and the number of basis functions in refined elements is two. The convergence rate for $p = 1$ and $p = 2$ is one half with respect to the number of degrees of freedom, hence one with respect to the number of elements in x. See, e.g., Hesthaven and Warburton (2008) for a discussion on the rate of convergence near discontinuities. Using two basis functions per dimension per element yields a much more efficient scheme, measured both in n_{dofs} as in time to solve the discrete system t_{solver}. Increasing the number of basis functions to three further increases the efficiency measured in n_{dofs}. Measured in t_{solver}, however, there is only a small improvement over $p = 2$ when using four subdivisions. Using eight subdivisions takes more time to solve than a scheme with constant h and $p = 2$. Our implementation of the DG-FEM scheme is not designed or optimised for hp-refinement. An implementation specifically designed for hp-refinement might give different results for the error plot with respect to t_{solver}.
All schemes, with and without hp-refinement, tend to a convergence rate of one half with respect to n_{dofs}. Instead of increasing the number of elements in the coarse mesh, it might be more efficient to apply multiple levels of refinement, gradually increasing the number of elements and reducing the number of basis functions towards the discontinuity. We did not yet explore this idea.

Water faucet test problem

The second test that we consider is the *water faucet problem* (see for example Evje and Flåtten (2003) and the references therein). The *water faucet test problem* consists of a vertical pipe, 12 m long, filled with a mixture of water (volume fraction of 0.8) and air. Water flows initially with 10 m s^{-1} downwards, the air is at rest. At the top of the pipe the conditions are the same as the initial conditions. The bottom of the pipe is at a constant pressure of 10^5 Pa.
We use the same twofluid model as Evje and Flåtten (2003). For each phase $\beta \in \{\text{L},\text{G}\}$ there is a mass balance equation,

$$\frac{\partial \alpha_\beta \rho_\beta}{\partial \xi_t} + \frac{\partial \alpha_\beta \rho_\beta u_\beta}{\partial \xi_x} = 0, \tag{26}$$

and a momentum balance equation,

$$\frac{\partial \alpha_\beta P_\beta}{\partial \xi_t} + \frac{\partial \alpha_\beta \rho_\beta u_\beta}{\partial \xi_x} + \frac{\partial \alpha_\beta P}{\partial \xi_x} - (P - P_{\text{hc}}) \frac{\partial \alpha_\beta}{\partial \xi_x} = \alpha_\beta \rho_\beta g. \tag{27}$$

Here, α_β (dimensionless) denotes the volume fraction of phase β, ρ_β [kg m^{-3}] the mass density, u_β [m s^{-1}] the phase velocity, P [Pa] the pressure, P_{hc} [Pa] a hyperbolic correction term and g [m s^{-2}] the gravitational acceleration. The volume fractions of the phases sum to one,

$$\sum_{\beta \in \{\text{L},\text{G}\}} \alpha_\beta = 1. \tag{28}$$

The twofluid model with $P_{\text{hc}} = 0$ is conditionally hyperbolic. The following value for the pressure correction term P_{hc} makes the twofluid model unconditionally hyperbolic,

$$P_{\text{hc}} = 1.2 \frac{\alpha_\text{G} \alpha_\text{L} \rho_\text{G} \rho_\text{L}}{\rho_\text{G} \alpha_\text{L} + \rho_\text{L} \alpha_\text{G}} (u_\text{G} - u_\text{L})^2. \tag{29}$$

Test case: assume phase L is water-like:

$$\rho_\text{L} = 1000 + 10^{-6} \left(P - 10^5 \right) \tag{30}$$

and phase G is air-like

$$\rho_\text{G} = 10^{-5} P \tag{31}$$

The Equations (26)–(31) can be written in the form of the general non-conservative system (1) as follows. We define the vector of unknowns q_j as

$$q_j = \begin{cases} \alpha_\text{L} & \text{if } j = j_{\alpha_\text{L}}, \\ P & \text{if } j = j_P, \\ u_\text{L} & \text{if } j = j_{u_\text{L}}, \\ u_\text{G} & \text{if } j = j_{y_\text{G}}, \end{cases} \tag{32}$$

and the vector of conserved quantities as

$$c_i(q) := \begin{cases} \alpha_\text{L} \rho_\text{L}(P) & \text{if } i = i_{\text{massL}}, \\ (1 - \alpha_\text{L}) \rho_\text{G}(P) & \text{if } i = i_{\text{massG}}, \\ \alpha_\text{L} \rho_\text{L}(P) u_\text{L} & \text{if } i = i_{\text{momL}}, \\ (1 - \alpha_\text{L}) \rho_\text{G}(P) u_\text{G} & \text{if } i = i_{\text{momG}}. \end{cases} \tag{33}$$

We introduce a generalised velocity in space-time:

$$\tilde{u}_{ki}(q) := \begin{cases} 1 & \text{if } k = k_t, \\ u_\text{L} & \text{if } k = k_x, i \in \{i_{\text{massL}}, i_{\text{momL}}\}, \\ u_\text{G} & \text{if } k = k_x, i \in \{i_{\text{massG}}, i_{\text{momG}}\}. \end{cases} \tag{34}$$

Then, the conservative part of the flux is given by

$$f^\text{c}_{ki}(q) = \tilde{u}_{ki}(q) c_i(q) + \begin{cases} \alpha_\text{L} P & \text{if } i = i_{\text{momL}}, \\ (1 - \alpha_\text{L}) P & \text{if } i = i_{\text{momG}}, \\ 0 & \text{otherwise}, \end{cases} \tag{35}$$

the non-conservative part by

$$F^{\text{nc}}_{kij}(q) = \begin{cases} P - P_{\text{hc}} & \text{if } k = k_x, i = i_{\text{momL}}, j = j_{\alpha_\text{L}}, \\ P_{\text{hc}} - P & \text{if } k = k_x, i = i_{\text{momG}}, j = j_{\alpha_\text{L}}, \\ 0 & \text{otherwise}, \end{cases} \tag{36}$$

and the source term by

$$s_i(q) = \begin{cases} \alpha_\text{L} \rho_\text{L}(P) g & \text{if } i = i_{\text{momL}}, \\ (1 - \alpha_\text{L}) \rho_\text{G}(P) g & \text{if } i = i_{\text{momG}}, \\ 0 & \text{otherwise}. \end{cases} \tag{37}$$

Since there is no exact solution for this test problem with compressible water and liquid phases, we computed a reference solution using the DG-FEM scheme described above with 8192 elements in x-dimension and two basis functions per dimension per element. Figure 5 shows this reference solution. The water jet initially present in the pipe accelerates with roughly constant rate under influence of gravity, see the bottom left subplot of Figure 5, and maintains its initial shape, see the liquid volume fraction in the top left subplot. New water enters the pipe with constant velocity and mass

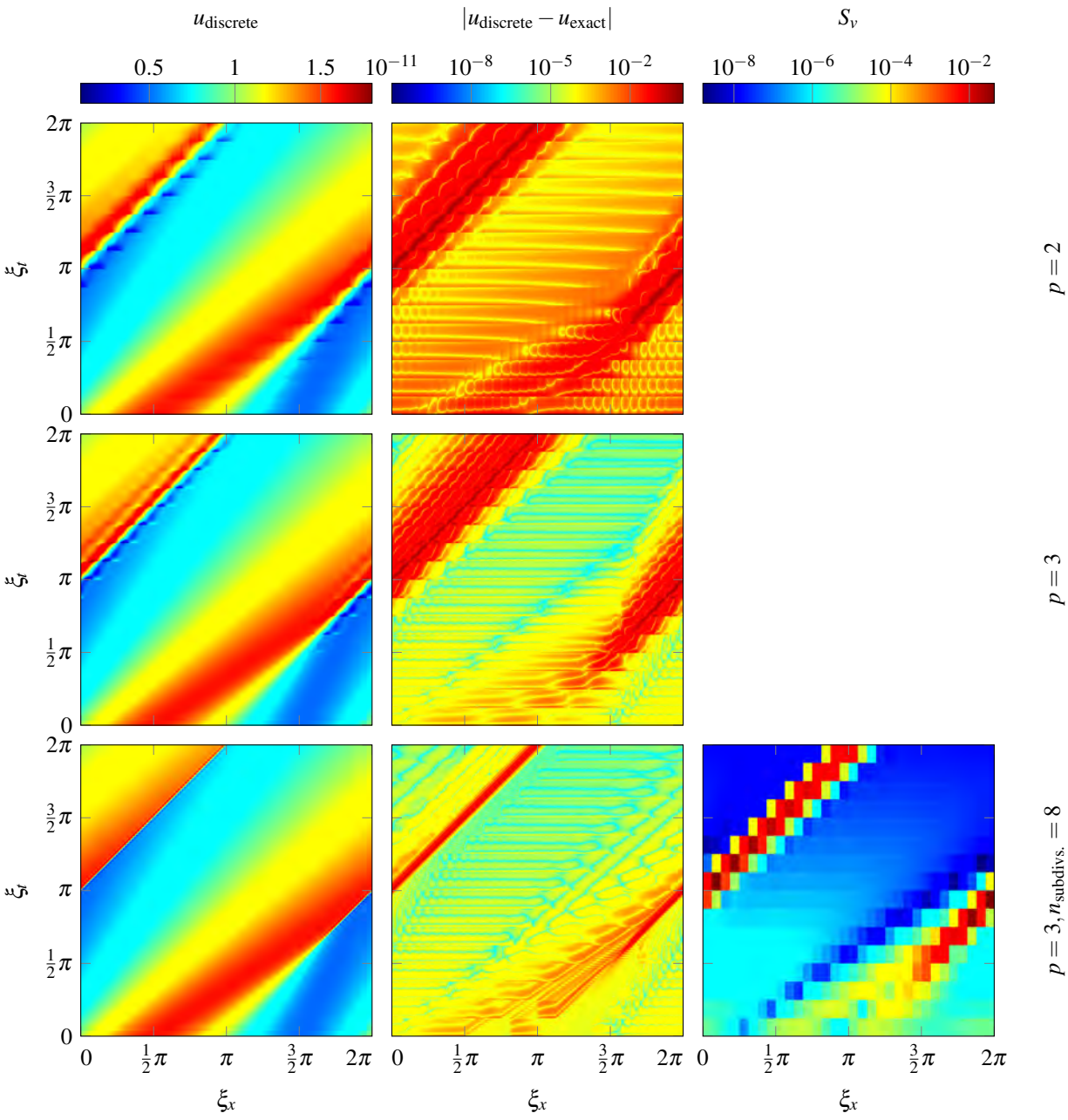

Figure 3: Solution and pointwise error for Burgers' test problem

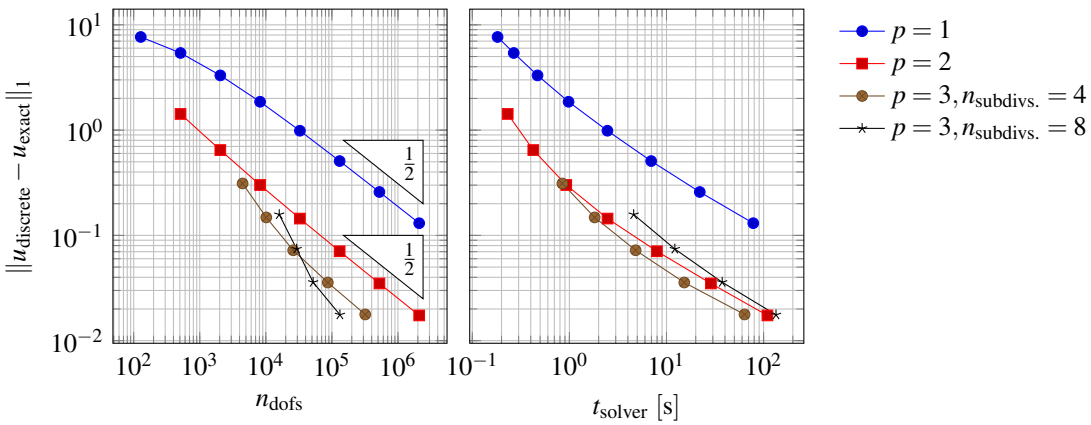

Figure 4: L_1-error versus number of degrees of freedom (n_{dofs}, left) and time to solve (t_{solver}, right) for Burgers' test problem

flow rate, and gradually accelerates along x due to gravity, causing the water jet to contract. At the junction between new and old water the liquid volume fraction jumps.

We analyse the DG-FEM scheme with and without hp-refinement in the same way as for Burgers' equation sine test problem. Figure 6 shows the discrete liquid volume fraction in the first column and the pointwise error for the liquid volume fraction in the second column. In this figure all results are obtained using a mesh with 64 elements in dimension x. In the first row we used two basis functions per dimension per element, without hp-refinement. Similar to the Burgers' test problem, the pointwise error is large in a wide band around the discontinuity. Increasing the number of basis functions to three gives the results as shown in the second row. Contrary to the Burgers' test problem, the large error band around the discontinuity is somewhat reduced. Applying hp-refinement, see the plots in the third row with smoothness indicator in the last column, reduces the error in the neighbourhood of the discontinuity even further.

Figure 4 shows the L_1-error versus number of degrees of freedom (left) and the time to solve (right) the system for increasing number of elements for various numbers of basis functions p. In absence of an exact solution, we define the error as the L_1-norm of the difference between the discrete and the reference solution, which is computed with respect to the reference solution obtained using 8192 elements in dimension x and $p = 2$. If hp-refinement is applied, the number of subdivisions is indicated by $n_{\text{subdivs.}}$ and the number of basis functions in refined elements is two. The DG-FEM scheme with $p = 2$ is significantly more efficient than $p = 1$, both measured in number of degrees of freedom n_{dofs} and in time to solve the discrete system t_{solver}. The convergence rate for $p = 2$ with respect to n_{dofs} is slightly higher than the theoretical maximum. This might be caused by the use of a reference solution instead of the exact solution: the error (w.r.t. the reference solution) goes to zero since the reference solution is computed using the same DG-FEM scheme and basis. Using three basis functions per dimension per element and enabling hp-refinement is more efficient when measured in n_{dofs}. It takes, however, more time to solve the discrete system. As noted earlier, our implementation of the DG-FEM scheme is not designed or optimised for hp-refinement.

CONCLUSIONS

We have examined the efficiency gain when using adaptive hp-refinement over constant hp in combination with a space-time DG-FEM scheme suitable for hyperbolic differential equations with non-conservative products. Such equations appear when describing the multiphase flow in pipelines with a one-dimensional twofluid model. The numerical examples, all involving discontinuities, show that adaptive hp-refinement improves the ratio L_1-error versus the number of degrees of freedom, up to a factor ten. The asymptotic rates of convergence under coarse mesh refinement for the ordinary and the adaptive DG-FEM scheme are roughly the same. This is caused by unnecessary refinement in smooth regions, increasing the number of degrees of freedom but not significantly reducing the error. We recommend multiple levels of refinement to improve the rate of convergence.

When measuring efficiency in terms of the time required to obtain a discrete solution with a certain L_1-error, the results are mixed. In some cases hp-refinement gives a minor improvement compared to a mesh with constant hp, in other cases a constant mesh is faster. Our implementation of the adaptive DG-FEM scheme, however, is not optimised for hp-refinement. We strongly believe that a DG-FEM implementation designed for hp-refinement can significantly improve the efficiency in time.

REFERENCES

ALOUGES, F. and MERLET, B. (2004). "Approximate shock curves for non-conservative hyperbolic systems in one space dimension". *Journal of Hyperbolic Differential Equations*, **1(4)**, 769–788.

CASTRO, M. *et al.* (2010). "On some fast well-balanced first order solvers for nonconservative systems". *Mathematics of Computation*, **79(271)**, 1427–1472.

CHALMERS, N. and LORIN, E. (2009). "Approximation of nonconservative hyperbolic systems based on different nonconservative product definitions". *Canadian Applied Mathematics Quarterly*, **17(3)**.

COCKBURN, B. and SHU, C. (2001). "Runge-Kutta Discontinuous Galerkin methods for convection-dominated problems". *Journal of Scientific Computing*, **16(3)**, 173–261.

DAL MASO, G. *et al.* (1995). "Definition and weak stability of nonconservative products". *Journal de Mathématiques Pures et Appliquées*, **74(6)**, 483–548.

EVJE, S. and FLÅTTEN, T. (2003). "Hybrid flux-splitting schemes for a common two-fluid model". *Journal of Computational Physics*, **192(1)**, 175–210.

HESTHAVEN, J. and WARBURTON, T. (2008). *Nodal Discontinuous Galerkin Methods*. No. 54 in Texts in Applied Mathematics. Springer New York.

ISSA, R. and KEMPF, M. (2003). "Simulation of slug flow in horizontal and nearly horizontal pipes with the two-fluid model". *International Journal of Multiphase Flow*, **29(1)**, 69–95.

PERSSON, P. and PERAIRE, J. (2006). "Sub-cell shock capturing for Discontinuous Galerkin methods". *Proceedings of the 44th AIAA Aerospace Sciences Meeting and Exhibit*. American Institute of Aeronautics and Astronautics.

RHEBERGEN, S. *et al.* (2008). "Discontinuous Galerkin finite element methods for hyperbolic nonconservative partial differential equations". *Journal of Computational Physics*, **227(3)**, 1887–1922.

ROMATE, J. (1998). "An approximate Riemann solver for a two-phase flow model with numerically given slip relation". *Computers and Fluids*, **27(6)**, 455–477.

VAN ZWIETEN, J. (2013). "Towards advanced one-dimensional numerical models for multiphase flow in pipelines". Tech. Rep. 13-06, Delft Institute of Applied Mathematics.

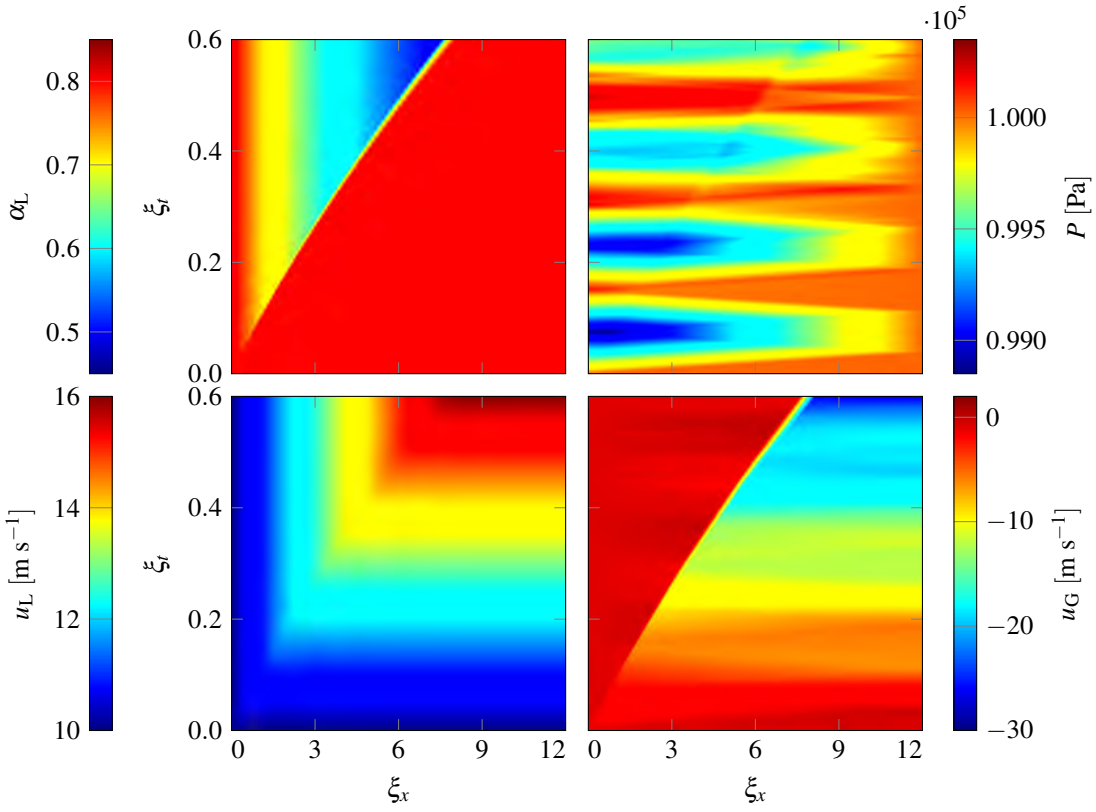

Figure 5: Reference solution of the water faucet test problem, computed using the DG-FEM scheme with 8192 elements in x and two basis functions per dimension per element, without *hp*-refinement

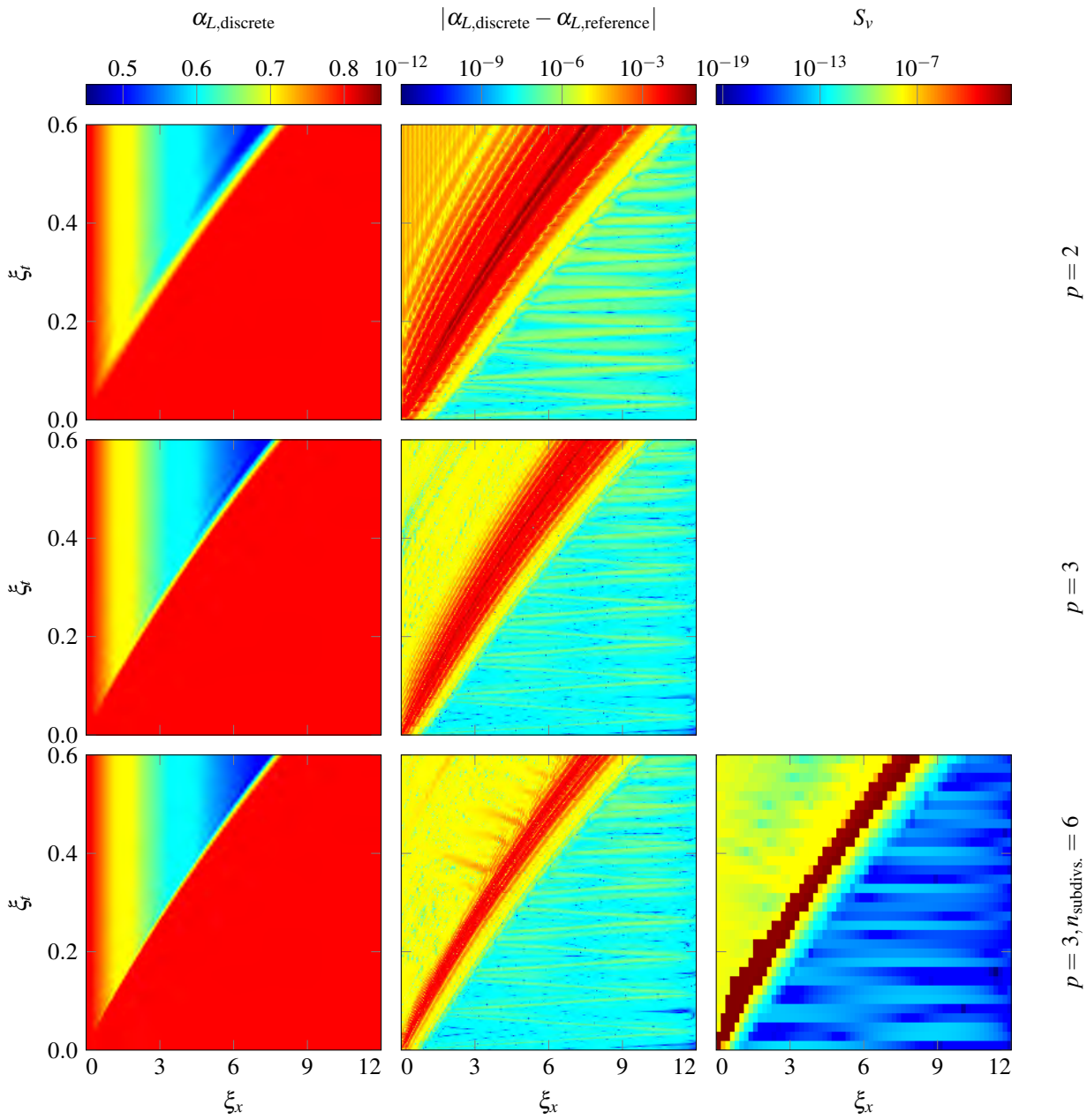

Figure 6: Solution and pointwise error for the water faucet test problem

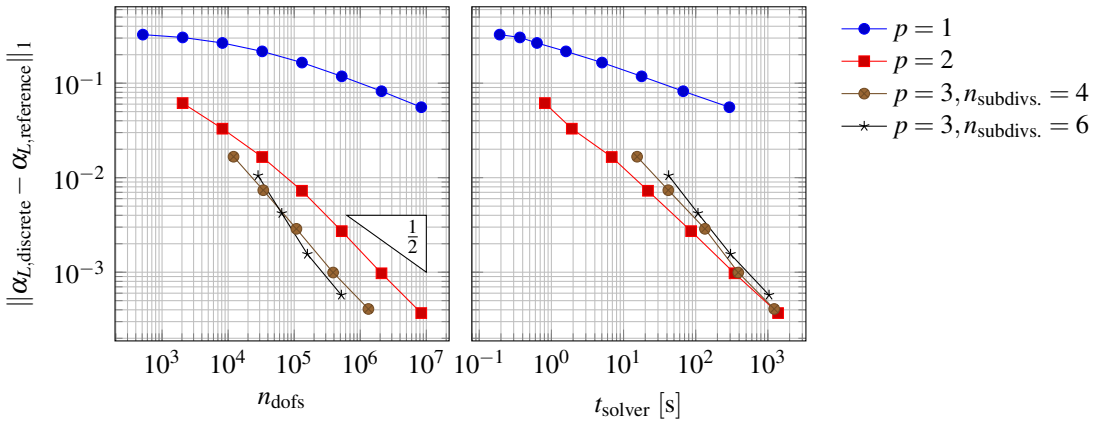

Figure 7: L_1-error versus number of degrees of freedom (n_{dofs}, left) and time to solve (t_{solver}, right) for the water faucet test problem

DEM DEVELOPMENT OF HEAT AND MASS TRANSFER IN A SPOUT FLUIDIZED BED WITH LIQUID INJECTION

Vinayak S. SUTKAR [1*], Stefan C. TAALMAN [1], Niels G. DEEN [1], Vitalij SALIKOV [2], Sergiy ANTONYUK [2], Stefan HEINRICH [2], J.A.M. KUIPERS [1]

[1] Multiphase Reactors Group, Department of Chemical Engineering and Chemistry,

Eindhoven University of Technology, P.O. Box 513, 5600 MB Eindhoven, THE NETHERLANDS

[2] Institute of Solids Process Engineering and Particle Technology, Hamburg University of Technology, 21071 Hamburg, GERMANY

* E-mail: V.S.Sutkar@TUe.nl; Tel.: +31 40 2478028; Fax: +31 40 2475833

ABSTRACT

Spout fluidized beds with liquid injection are often utilized in the pharmaceutical, food and chemical industries for granulation, coating and polymerization operations involving physical and/or chemical transformations with simultaneous heat and mass transfer. This is because these beds combine advantages of both spouted and fluidized beds. During these operations a small change in the operating conditions like particle temperature, liquid injection rate may significantly alter the overall bed performance.

In this work, systematic model development and its validation is presented to study the heat and mass transfer phenomena in a spout fluidized bed using the DEM/CFD framework. In this approach both particles and droplets were treated as discrete elements. Further, the effect of liquid injection with simultaneous heat and mass transfer on dynamics of a flat-bottom pseudo-2D spout fluidized bed with and without draft plates were studied by atomizing water droplets via bed bottom spray.

Keywords: spout fluidized bed, liquid atomization, wet restitution coefficient, DEM/CFD, heat and mass transfer, evaporation.

NOMENCLATURE

Greek Symbols		
$\varepsilon_g, \varepsilon_p$	Porosity of gas and particle	[--]
ρ_g, ρ_p	Density of gas and particle	[kg/m^3]
δ	Distribution function	[--]
$\boldsymbol{\tau}_g$	Stress tensor	[Pa]
Latin Symbols		
A_p	Particle area	[m^2]
Bi	Biot number	[--]
C_p	Specific heat capacity	[J/kg K]
D	Bed depth	[m]
$D_{eff,g}$ $D_{e,g}$	Effective and molecular diffusivity	[m^2/s]
e_{wet}	Wet restitution coefficient	[--]
e_{dry}	Dry restitution coefficient	[--]
$\mathbf{F}$	Force	[N]
H	Bed height	[m]
h_g	Convective heat transfer coefficient	[W/m^2 K]
H_g	Gas enthalpy	[J/kg]
ΔH_r	Heat of evaporation	[J/kg]
h_l	liquid layer thickness	[μm]
k_{eff}	Effective thermal conductivity	[W/m K]
k_f	Thermal conductivity	[W/m K]
k_m	Mass transfer coefficient	[m/s]
m_p, m_d	Mass of the particle and droplet	[kg]
Nu	Nusselt number	[--]
$\mathbf{q}_h$	Heat flux due to conduction	[W/m^2]
Re_p	Particle Reynolds number	[--]
S_p, S_h, S_m	Source term for momentum, heat and mass transfer	[--]
Sh	Sherwood number	[--]
St_c	Critical Stokes number	[--]
T_g, T_p	Temperature of gas and particle	[K]
$\mathbf{u}_g$	Gas velocity	[m/s]
$\mathbf{v}_p, \mathbf{v}_d$	Velocity of the particle and droplet	[m/s]
$v_{p,i}$	Particle impact velocity	[m/s]
V_p	Volume of particle	[m^3]
$w_{a,g}$	Concentration of liquid in gas	[kg/kg]
$w^*_{a,g}$	Saturated concentration of liquid	[kg/kg]
W	Bed width	[m]
Sub/superscripts		
c	Critical	
eff	Effective	
g	Gas phase	
dt	Draft tube	
h	Heat transfer	
m	Mass transfer	
p	Solid/particle phase	

INTRODUCTION

Gas-solid spout fluidized beds with liquid injection are commonly used in a number of applications comprising physical and chemical transformations. This is because these beds combine features from both the spouted and fluidized beds with intense gas-solid mixing, and efficient heat and mass transfer. Detailed discussions and other distinguishing features of the spout fluidized beds can be found in Epstein and Grace, (2011) and Sutkar et al., (2013a). Since the development of the spout fluidized bed (Chatterjee, (1970)) a series of modifications were suggested to improve the bed performance like: various geometrical configurations (rectangular, conical bottom, slotted rectangular, multiple and elevated spout) and insertion of a draft tube inside the bed. The insertion of a draft tube in a spout fluidized bed comprises an additional flexibility to control the particle velocity, bed porosity and gas residence time by adjusting the operating parameters and the geometrical configurations, e.g. the entrainment height and the draft tube dimension. Chemical processes that use gas-solid spout fluidized beds with draft plates with liquid injection (either from top, bottom or side) through a two-fluid nozzle include particle granulation and coating, and olefins polymerization: In the former a liquid binder (suspensions, solutions and melts) mixed with a solvent solution is atomized on the fluidizing particles. After fast drying of the wet particle (to prevent unnecessary liquid absorption inside the particle), the particle surface start evaporating the solvent and the binder sticks to the particle to form a layer-wise progressive particle growth. This layering of the liquid usually results in a uniform dried liquid layer around the particle to form bigger granules (Teunou and Poncelet 2002). In olefins polymerization the catalyst particles (anionic, cationic, free-radical, Ziegler-Natta etc.) are fluidized under reactive operating conditions using a monomer gas (olefins, polar vinyl, acetylene etc.). The exothermic reaction heat can be removed by injecting a liquid solvent, because the latent heat of liquid evaporation has a substantially larger heat removal capacity.

However, during these process a small change in the operating conditions often leads to a heat and mass imbalance between rate of liquid injection and evaporation rate. This eventually contribute to a poor bed performance due the local de-fluidization and enhanced agglomerations/particle-lumps. In addition, an intense evaporation often leads in accumulation of a thick vapour layer around the particle, which may inhibit the direct particle-droplet contact i.e. non-wetting contact or Leidenfrost regime (Yang and Fan (2007)). Under these conditions, the heat flux near the contact area significantly decreases, despite of the high temperature gradient across the vapour layer. Further, wet particles often collide with dry or partial wet particles to form agglomerates, leading to a significant variation in the physical properties and appearance. This may lead to bigger agglomerates with a higher weight and size, which makes fluidization difficult. Additionally, the local process conditions and moisture distribution also strongly influence the overall drying rate and agglomeration kinetics.

A detailed understanding of complex multi-phase and multi-scale interactions together with particulate flow transitions, heat and mass transfer are of primary importance for the process design and scale-up. This can be either achieved by performing experiments or numerical simulations. Often, it is troublesome to perform experiments on an industrial scale, because it is difficult to access the relevant areas experimentally. Numerical simulations can offer a platform that can be used to obtain better insight in the particle-droplet interaction.

In this work, a discrete element model (DEM) with heat and mass transfer was developed, used to simulate the bed dynamics. The gas phase dynamics were treated by solving momentum, energy and species balance equations whereas the motion of individual spherical particles were described by Newton's law of motion with a soft sphere collision model. The heat and mass transfer from the fluid to the particle were determined using overall energy and species balance equations. The convective heat and mass transfer coefficients were evaluated using empirical Nusselt and Sherwood correlations. Additionally, various test cases were simulated to verify the heat and mass transfer implementation by comparing the obtained results with analytical solutions. Further, the dynamics of a flat-bottom pseudo-2D spout fluidized bed with glass particles ($d_p = 1\text{mm}$ and $\rho_p = 2526$ kg/m^3) were investigated with water droplet injection (with mean size of $d_d = 60\ \mu m$).

Note that in this work, simulations were carried out using DEM/CFD because it resolves the particulate flow at an individual particle level and can provide information about various forces acting on the particles and droplets. In reality, the droplets impacting on the particles undergo various stages like spreading, stretching, recoiling and rebounding, which are difficult to re-reproduce in DEM/CFD. So, the net effect arising due to the various forces (gravitational, surface tension, buoyancy, drag, contact between the particle and the wall, viscous and capillary) with liquid injection were lumped by estimating the wet restitution coefficient using a model/correlation based on experiments (as reported by Davis et al. 2002). Also, in this study detailed information about droplet spreading has been neglected due to the lower droplet to particle diameter ratio.

In addition, the energy dissipation during the wet collisions through various forces (gravitational, surface tension, buoyancy, drag, contact between the particle and the wall, viscous and capillary) is more important than the actual collision behaviour.

MODEL DESCRIPTION

In this study the simulations were carried out by extending our previous DEM/CFD. A detailed description about the governing equations, motion of

the droplets, particle-particle-droplet interactions, and the inter-particle collisions can be obtained in van Buijtenen et al., (2009). The collisions of the particles with draft plates were explained in Sutkar et al., (2013b).

Momentum transfer and collision treatments of discrete elements

Gas phase

The gas-phase dynamics were determined by solving the volume-averaged Navier-Stokes equations accounting for the local porosity and the drag force exerted by the particles and the droplets.

Particle motion

The motion of each individual particle is calculated using Newton's laws of motion:

$$m_p \frac{d\mathbf{v}_p}{dt} = \sum_{\text{contact list}} \underbrace{(\mathbf{F}_{ab,n} + \mathbf{F}_{ab,t})}_{\text{contact forces}} + \underbrace{\mathbf{F}_{drag,a} + \mathbf{F}_{gravitational,a}}_{\text{external forces}} \quad (1)$$

Droplet motion

The motion of each individual droplet was evaluated on a similar basis (see Eq. (2)). However, collisional forces in the normal and tangential directions were neglected due to the small size. The inter-phase momentum transfer coefficiewent was determined by considering two-way coupling.

$$m_d \frac{d\mathbf{v}_d}{dt} = \underbrace{\mathbf{F}_{drag,a} + \mathbf{F}_{gravitational,a}}_{\text{external forces}} \quad (2)$$

where m_d and $\mathbf{v}_d$ is the droplet mass and velocity.

Dry particle-particle interaction

Dry particle-particle interactions were estimated using a linear soft-sphere approach (Cundall and Strack (1979)). In this approach, the particles are assumed to overlap/deform during the contact and the contact forces were calculated using a mechanical analogy consisting of a spring (for particle overlap), dash-pot (for viscous dissipation), and slider (for friction between the particles). This arrangement provides a flexibility to estimate the energy dissipation due to the non-ideal particle collisions using input parameters as spring stiffness, damping coefficient, restitution coefficient (in normal and tangential directions), and the friction coefficient.

Particle-droplet interaction

The particle-droplet collisions were treated in a similar manner as described by van Buijtenen et al. (2009); Goldschmidt et al. (2003). In this, the colliding droplets always transfer their mass and momentum to the particle. This leads to an increase in the particle mass and associated momentum, given by:

$$m_p^{'} = m_p + m_d \quad (3)$$

$$m_p^{'}\mathbf{v}_p^{'} = m_p\mathbf{v}_p + m_d\mathbf{v}_d \quad (4)$$

where $m_p^{'}$ and $\mathbf{v}_p^{'}$ is the new particle mass and velocity after the droplet interaction. Further, break-up of the droplets after the impacting on the particle is neglected and after the impact the droplets are removed from the simulation domain. This assumption is reliable due to small droplet to particle diameter ratio. Upon a droplet-particle impact, the position of the particle remains the same and the droplet will form a uniform liquid layer around the particle without changing the particle shape (i.e. the particle remains spherical) as shown in Figure 1.

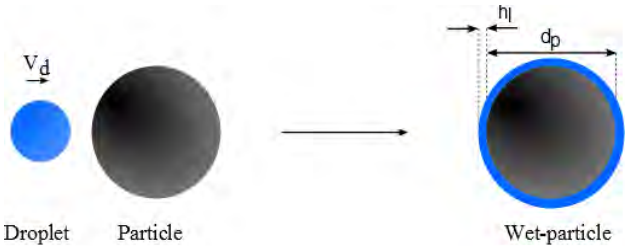

Figure 1. Collision of the droplet with the particle, assuming a uniform liquid layer thickness.

Wet-wet, wet-dry particle interactions

For a wet system the particle properties significantly alter due to additional moisture, which lead to variation in the collisional energy dissipation during wet particle-particle interaction as compared with dry particle-particle interactions. This effect can be accounted for by using a variable restitution coefficient as function of moisture content, physical properties of the liquid and impact velocity. There are numerous experimental and numerical studies dealing with quantification of the restitution coefficient. Recently, van Buijtenen et al. (2009) performed simulations for a wet system with a variable restitution coefficient as a function of only moisture. In reality, at low velocities and/or high viscosity particles will stick together to form agglomerates with zero restitution coefficient. However, in their simulations the restitution coefficient never becomes zero, which is unrealistic. In this work a simplified model proposed by Davis et al. (2002) has been used to quantify the wet restitution coefficient as:

$$\begin{aligned} e_{wet} &= e_{dry}\left(1 - \frac{St_c}{St}\right) && St > St_c \\ e_{wet} &= 0 && St < St_c \end{aligned} \quad (5)$$

Where e_{dry} is the dry restitution coefficient and St is the Stokes number. Eq. (5) is valid for $St > St_c$. No particle rebound was observed at $St_c > St$ due to significant loss of particle kinetic energy in the liquid (viscous dissipation). The limiting value of the critical Stokes number (St_c) depends on the physical properties of liquid and solid, particle impact velocity ($v_{p,i}$), and liquid layer thickness (h_l).

The effective restitution coefficient ($e_{eff,a,b}$) of the two colliding particles a and b (which may be either dry or wet with different restitution coefficients) was determined using a harmonic averaging as:

$$\frac{1}{e_{eff,a,b}} = \frac{1}{2}\left(\frac{1}{e_a} + \frac{1}{e_b}\right) \tag{6}$$

Heat and mass transfer

The related equations used to solve heat and mass balances for the gas and particle phases are summarized in Table 1 and Table 2.

Gas phase

The gas phase dynamics were treated by solving Navier-Stokes equations for energy (Eq.7). S_h represents the source term from interphase energy transfer. The convective heat transfer coefficient (h_g) was evaluated using the empirical Nusselt correlation given by Gunn (1978) (see Eq. 10).

Particle and droplet phase

The convective heat transfer from the particle and droplets to the gas phase and vice-versa was estimated by solving Eq. 13. Note that, this equation is only valid for low Biot numbers; i.e. we assume an uniform internal particle temperature.

The saturated mass concentration of liquid ($w^*_{a,g}$) at the liquid-solid interface was determined using the Clapeyron equation (Eq. 13), which is a function of interface particle temperature, partial pressure and heat of evaporation (ΔH_r). The interface parameters are illustrated in figure 2.

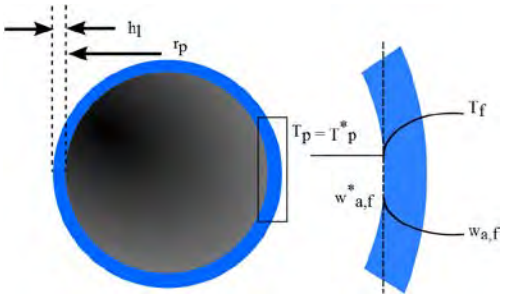

Figure 2. Schematic representation of the determination of the interface parameters on the wet particle with liquid layer.

Table 1. Heat transfer equations used for numerical simulations of a spout fluidized bed with liquid injection.

Heat balance equation

$$\frac{\partial}{\partial t}(\varepsilon_g \rho_g H_g) + \nabla\cdot\left(\varepsilon_g \rho_g \mathbf{u}_g H_g\right) = -\nabla\cdot\left(\varepsilon_g \mathbf{q}_h\right) + S_h \tag{7}$$

$$H_g = C_{p,g} T_g ; \mathbf{q}_h = -k_{eff}\nabla T_g ; \quad k_{eff} = \frac{1-\sqrt{1-\varepsilon_g}}{\varepsilon_g} k_f \tag{8}$$

Source term

$$S_h = \frac{1}{V_{cell}} \sum_{N_p} \delta(\mathbf{r}-\mathbf{r}_p)\, h_g A_p \left(T_p - T_g\right) \tag{9}$$

Gunn correlation for heat transfer

$$Nu_p = \left(7 - 10\varepsilon_g + 5\varepsilon_g^2\right)\left[1 + 0.7\,\mathrm{Re}_p^{0.2}\,\mathrm{Pr}^{0.33}\right] + \left(1.33 - 2.4\varepsilon_g + 1.2\varepsilon_g^2\right)\mathrm{Re}_p^{0.7}\,\mathrm{Pr}^{0.33} \tag{10}$$

$$Nu_p = \frac{h_g d_p}{k_g}; \quad \mathrm{Re}_p = \frac{\varepsilon_g \rho_g \left|\mathbf{u}_g - \mathbf{v}_g\right| d_p}{\mu_g}; \quad \mathrm{Pr} = \frac{\mu_g C_{p,g}}{k_f} \tag{11}$$

Particle heat transfer ($Bi << 1$)

$$V_p \rho_p C_{p,p} \frac{dT_p}{dt} = h_g A_p \left(T_p - T_g\right) \tag{12}$$

Clapeyron equation

$$\left(\frac{dP}{dT}\right)_{eq} = \frac{\Delta H_r}{R \Delta T} \tag{13}$$

Table 2. Model equations used for numerical investigations of a spout fluidized bed with species balance.

Species balance equation

$$\frac{\partial}{\partial t}(\varepsilon_g \rho_g w_{a,g}) + \nabla\cdot\left(\varepsilon_g \rho_g \mathbf{u}_g w_{a,g}\right) = -\nabla\cdot\left(\varepsilon_g \rho_g \mathbf{q}_m\right) + S_m \tag{14}$$

Source term

$$S_m = \frac{1}{V_{cell}} \sum_{N_p} \delta(\mathbf{r}-\mathbf{r}_p)\, k_m A_p \left(w^*_{a,g} - w_{a,g}\right) \tag{15}$$

$$\mathbf{q}_m = -D_{eff,g}\nabla w_{a,g} ; D_{eff,g} = \frac{1-\sqrt{1-\varepsilon_g}}{\varepsilon_g} D_{e,g}$$

Gunn correlation for mass transfer

$$Sh_p = \left(7 - 10\varepsilon_g + 5\varepsilon_g^2\right)\left[1 + 0.7\,\mathrm{Re}_p^{0.2}\,Sc^{0.33}\right] + \left(1.33 - 2.4\varepsilon_g + 1.2\varepsilon_g^2\right)\mathrm{Re}_p^{0.7}\,Sc^{0.33} \tag{16}$$

$$Sh_p = \frac{k_m d_p}{D_{e,g}}; \mathrm{Re}_p = \frac{\varepsilon_g \rho_g \left|\mathbf{u}_g - \mathbf{v}_g\right| d_p}{\mu_g}; \quad Sc = \frac{\mu_g \rho_g}{D_{e,g}}$$

Particle mass transfer

$$\frac{dm_d}{dt} = k_m A_p \left(w^*_{a,g} - w_{a,g}\right) \tag{17}$$

RESULTS

In this section various test cases were simulated to verify the heat and mass transfer implementation and obtained results were compared with analytical solutions. Subsequently, the effect of liquid injection on overall bed dynamics with and without draft plates will be discussed.

Verification test cases

Gas-particle heat transfer coupling

To test the implementation of the heat balances, initially a fixed bed test without heat transfer was

considered by passing a gas at a certain velocity through a fixed bed of stationary particles (see Table 3 for simulations settings) and the obtained pressure drop was measured and compared with Ergun equation. More details about the boundary conditions and analytical equation can be found in van Sint Annaland et al. (2005). The simulation results show 2.8% over-predication in a pressure per unit length as compared with the value obtained from the Ergun equation (200 Pa/m).

Table 3. Simulations setting used during fixed bed test without heat transfer.

Property	Value	Unit
Gas density	1.29	[kg/m^3]
Gas viscosity	1.8 x 10^{-5}	[kg/(ms)]
Domain dimensions	0.02x0.02x0.06	[m^3]
Number of grids	8 x 8 x 24	[--]
Particle configuration	18 x 18 x 27	[--]
Particle diameter	1 x 10^{-3}	[m]
Gas velocity	0.1	[m/s]

Additionally a similar fixed bed test was performed with heat transfer, in which a fixed bed of cold particles and cold fluid (at 300K) was heated by injecting a hot fluid (400 K) through the bottom at 0.25 m/s inflow velocity. During this, the cold particles and fluid in the domain heat up with time leading to a heat front moving through the bed. The simulations settings are shown in Table 4.

Table 4. Simulations setting used during fixed bed test with heat transfer.

Property	Value	Unit
Gas density	74.84	[kg/m^3]
Gas viscosity	1 x 10^{-5}	[kg/(ms)]
Gas heat capacity	1670	[J/kg K]
Gas thermal conductivity	0.0209	[W/mK]
Gas velocity	0.25	[m/s]
Domain dimensions	0.02x0.02x0.2	[m^3]
Number of grids	8 x 8 x 80	[--]
Particle configuration	18 x 18 x 180	[--]
Particle diameter	1 x 10^{-3}	[m]
Particle density	2526	[kg/m^3]
Particle heat capacity	1670	[J/kg K]
Initial bed temperature	300	[K]
Inlet temperature	400	[K]

The verification of the simulated results was done using a 1D-convection equation, which takes into account heat-exchange between the fluid and the particle. The axial dispersion of the heat due to the conduction in the radial direction is neglected due to high Péclet number Pe = 24,996. The energy balance equations for the gas and particle phase are given by:

$$\varepsilon_g \rho_g C_{p,g} \frac{\partial T_g}{\partial t} + \varepsilon_g \rho_g C_{p,g} u \frac{\partial T_g}{\partial z} = -h_g a_p \left(T_g - T_p\right) \quad (18)$$

$$\left(1-\varepsilon_g\right)\left(1-\rho_g\right) C_{p,p} \frac{\partial T_p}{\partial t} = h_g a_p \left(T_g - T_p\right) \quad (19)$$

Where $a_p = 6(1-\varepsilon_g)/d_p$ is the specific surface area of particle. The analytical solution for the given system can be obtained by integrating Eqs. (18) and (19) using Bessel functions in Matlab. Details of the solution methodology can be found in Patil et al. (2014). The comparison of the temperature along height with time is shown in figure 3, which illustrates a good agreement.

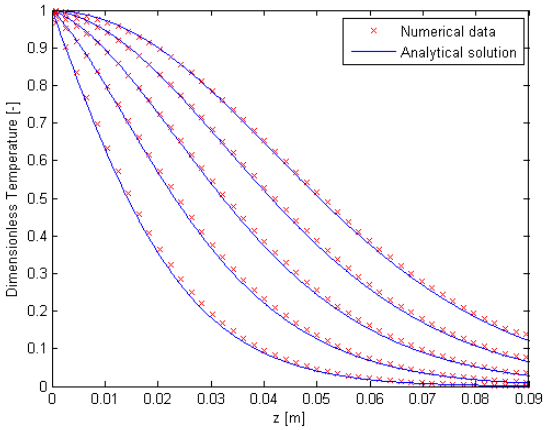

Figure 3. Fixed bed test with heat transfer results: comparison of the simulated dimensionless temperature with an analytical solution with time.

Coupled heat and mass transfer

Verification of the coupled convective heat and mass transfer was done by passing a fluid through a fixed bed of stationary particles detained at a certain temperature (349 K) with an initial mass fraction i.e. 100 times lower than the inlet mass fraction (0.5 kg of air/kg of water). A test simulation was performed with almost similar simulations settings as mentioned in Table 4. The other additional settings are shown in Table 5.

Table 5. Simulations setting used during gas-particle heat and mass transfer test.

Property	Value	Unit
Gas velocity	0.25-1	[m/s]
Initial mass fraction	0.005	[kg/kg]
Initial bed temperature	349	[K]
Inlet mass fraction	0.5	[kg/kg]
Diffusion coefficient	2.11 x 10^{-5}	[m^2/s]

The simulated results were compared with an analytical solution obtained from a 1D-heterogeneous plug flow model:

$$\left\langle w_{a,g} \right\rangle = \left\langle w_{a,0} \right\rangle e^{-\left[\frac{k_m a_p z}{u_z}\right]} \quad (20)$$

In this model axial dispersion of the species is neglected and mass transfer coefficient (k_m) was estimated form an analogous empirical Sherwood number correlation based on Gunn (1978), see Eq. (a3).

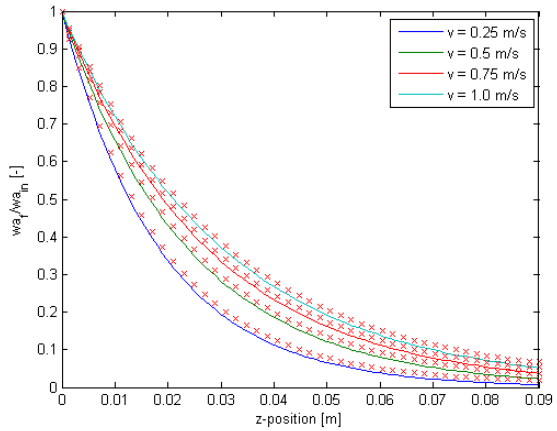

Figure 4. Gas-particle heat and mass transfer test: comparison of simulated fluid concentration with the analytical solution obtained from a 1D-heterogeneous plug flow model (cross symbol indicate simulation results).

A comparison between the steady-state axial profiles of the fluid concentration and the analytical solution obtained from a 1D-heterogeneous plug flow model is shown in figure 4.

Spout fluidized bed simulations

Simulations were carried out for a pseudo-2D spout fluidized bed geometry (as shown in figure 5) of the dimensions W x D x H = 8 x 1.5 x 18 cm^3 with the spout of W_{sp} x D_{sp} = 0.06 x 1.5 cm^2.

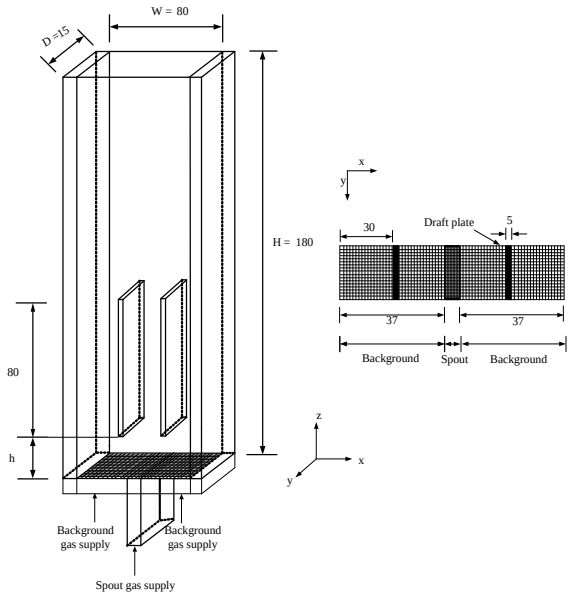

Figure 5. Simulated geometry of spout fluidized bed with draft plates (all dimension in mm).

Two symmetrical draft plates each of dimension W_{dt} x D_{dt} x H_{dt} = 0.05 x 1.5 x 8 cm^3 were positioned inside the bed at a distance of 3 cm from the side walls and at an entrainment height h = 1.5 cm from the bottom. The bed was initially filled to a height H_0 = 6 cm. The physical properties of the particles and gas, and numerical settings used in the CFD/DPM simulations are listed in Table 6.

Table 6. Physical properties of gas and particles and numerical settings.

Property	Value	Unit
Gas phase		
Background gas velocity	0.8	[m/s]
Spout gas velocity	25.4	[m/s]
Gas viscosity	1.8×10^{-5}	[kg/(ms)]
Molecular weight	0.028	[kg/mol]
Gas thermal conductivity	0.0257	[W/mK]
Gas specific heat at constant pressure	1250	[J/kg K]
Gas inflow temperature	293	[K]
Initial mass fraction	0.005	[--]
Particle phase		
Particle diameter	1×10^{-3}	[m]
Particle density	2526	[kg/m^3]
Number of particles	82,505	[--]
Gas specific heat at constant pressure	840	[J/kg K]
Dry restitution coefficient	0.97	[--]
Poisson ratio	0.28	[--]
Young's modulus	1.4×10^{10}	[--]
Droplet		
Mean drop diameter	60×10^{-6}	[m]
Injection frequency	2526	[kg/m^3]
Initial temperature	293	[K]
Molecular weight	0.018	[kg/mol]
Liquid density	997	[kg/m^3]
Liquid heat of evaporation	-40.68×10^3	[J/mol]
Liquid viscosity	1×10^{-3}	[kg/(ms)]
Domain and simulation settings		
Domain dimensions	8 x 1.5 x 18	[cm^3]
Number of grids	80 x 18 x 140	[--]
Gas time step	2×10^{-5}	[s]
Particle time step	1×10^{-6}	[s]
Neighbour list time step	1×10^{-5}	[s]

Figure 6 (a-b), illustrate snapshots of the particulate flow pattern with and without draft plates.

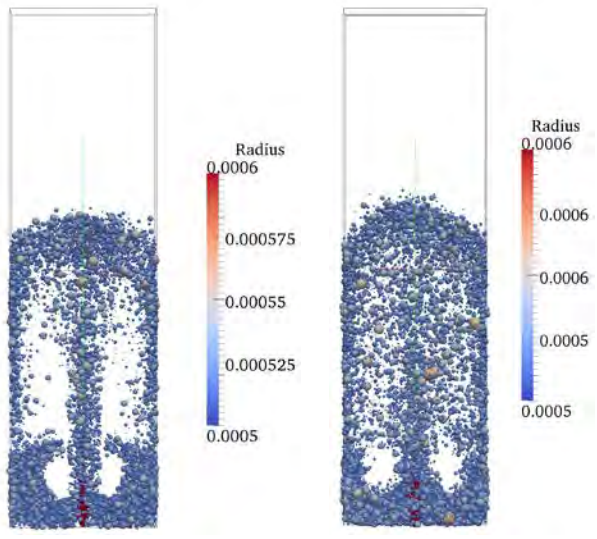

(a) (b)

Figure 6. Snapshots of the particulate configurations at t = 2.04 s in spouted fluidized bed with (a) and without (b) draft plates, with liquid injection (wet particle with higher diameter are indicated by colour and droplets by dark red colour).

In the spout fluidized bed with draft plates (figure 6 (a)), at a high spout velocity, a stable spout is observed, in which the particles are continuously transported upwards through the draft plates. After reaching the zones above the draft plates, particles lose their momentum and fall down through the annulus forming systematic flow characteristics with a fountain like structure. Additionally, insertion of draft plates lead to efficient particle-droplet interactions in the entrainment height, which can illustrated a high number of wet particle in the spout, the region above the draft plates. Figure 6 (b) also shows the particles are elevated to a certain height with enhanced random particle mixing between spout and annulus without any clear distinction between the spout and annulus. Additionally, spout fluidized bed without draft plates shows random distribution of the bigger wet particles.

The distribution of the gas temperature and mass fraction in the spout fluidized bed with and without draft plates has been shown in figures 7 and 8. The system without draft plates shows formation of the cold spots (low temperature and high mass concentration zones) near the bottom (see figures 7 (b), 8 (b) and 9 (b)). Whereas, system with draft plates shows a uniform temperature and mass concentration distributions in the annulus with high mass concentration zones a certain distance from the distribution plate (see figures 7 (a) and 8 (a)). This may be due to the creation of distinct wetting and drying regions. Moreover in system with draft plates, the wetted particles are often transported vertically without any random motion and falling into the annulus. This results in an enhanced liquid evaporation in the spout, leading to a higher mass fraction in the gas phase. Additionally, the presence of a large number of wet particles also leads to uniform temperature distributions in the annulus.

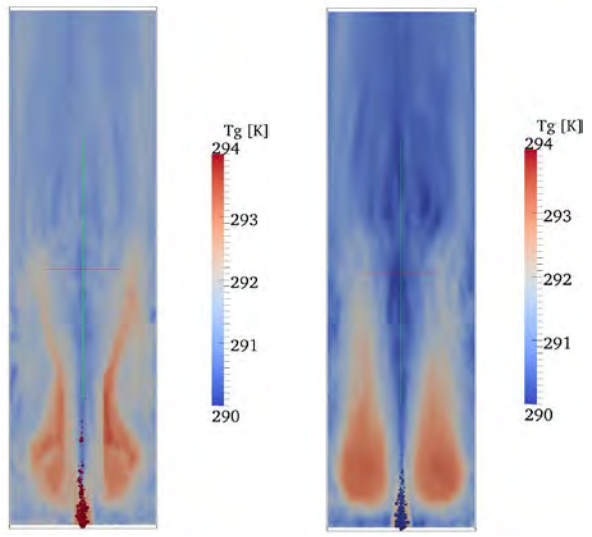

Figure 7. Snapshots of the gas temperature at t = 2.04 s in spouted fluidized bed with (a) and without (b) draft plates, with liquid injection.

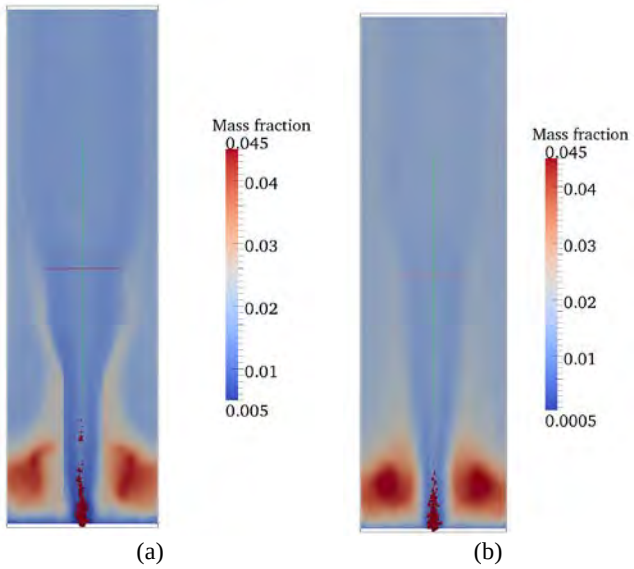

Figure 8. Snapshots showing distribution of the mass fraction t = 2.04 s in spouted fluidized bed with (a) and without (b) draft plates with liquid injection.

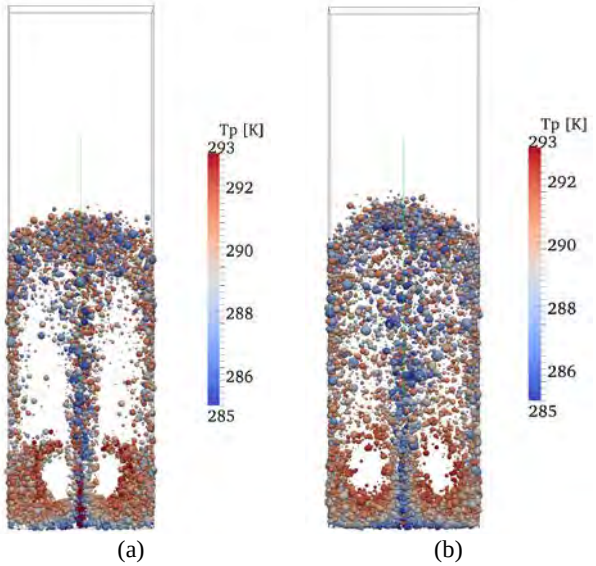

Figure 9. Snapshots showing distribution of the particle temperature t = 2.04 s in spouted fluidized bed with (a) and without (b) draft plates with liquid injection.

CONCLUSIONS

In this work, DEM/CFD model has been extended for heat and mass transfer with liquid injection. The implementation of the heat transfer was verified by simulating various test cases and obtained results were compared with analytical solutions, showing a good agreement. Hence, the heat and mass transfer effects were successfully implemented. Further, simulations were carried out to analyse the heat and mass transfer effects in a spouted fluidized bed with and without draft plates with liquid injection. At high spout velocity, systematic flow characteristics with fountain like structure was observed with insertion of the draft plates. Additionally, a uniform temperature and mass concentration distributions was observed in the annulus without any cold spot near the distribution plate.

ACKNOWLEDGEMENTS

This research is supported by the Dutch Technology Foundation STW, applied science division of NWO and the Technology Program of the Ministry of Economic Affairs in The Netherlands, as well as by the DFG (German Research Foundation) in Germany.

REFERENCES

CHATTERJEE, A., (1970) “Spout-fluid bed technique”, Industrial and engineering chemistry process design and development, 9, 340-341.

CUNDALL, P. A. and STRACK, O. D. L., (1979) “A discrete numerical model for granular assemblies”, Geotechnique, 29, 47-65.

DAVIS, R. H., RAGERD, D. A., GOOD, B.T., (2002) “Elastohydrodynamic rebound of spheres from coated surfaces”, Journal of fluid mechanics, 468, 107-119.

EPSTEIN, N., GRACE, J.R., (2011) “Spouted and Spout fluid beds”, Cambridge university press, 29-54.

GOLDSCHMIDT, M.J.V., WEIJERS, G.G.C., BOEREFIJN, R., KUIPERS, J.A.M., (2003) “Discrete element modelling of fluidised bed spray granulation”, Powder technology, 138, 39-45.

GUNN, D.J., (1978), “Transfer of mass and heat to particles in fixed and fluidized beds”, International journal of heat and mass transfer, 21, 467-476.

PATIL, A. V., PETERS, E.A.J.F., KOLKMAN, T., KUIPERS, J.A.M., (2014) “Modelling bubble heat transfer in gas-solid fluidized beds using DEM”, Chemical engineering science, 105, 121-131.

SUTKAR, V. S., DEEN, N. G., KUIPERS J.A.M., (2013a), “Spout fluidized beds: recent advances in experimental and numerical studies”, Chemical engineering science, 86, 124-136.

SUTKAR, V. S., DEEN, N. G., MOHAN, B., SALIKOV, V., ANTONYUK, S., HEINRICH, S., KUIPERS, J.A.M., (2013b) “Numerical investigations of a pseudo-2D spout fluidized bed with draft plates using a scaled discrete particle model”, Chemical engineering science, 104, 790-807.

TEUNOU, E. and PONCELET, D. (2002), “Batch and continuous fluid bed coating-review and state of the art”, Journal of food engineering 53, 325-340.

VAN BUIJTENEN, M. S., DEEN, N. G., HEINRICH, S., ANTONYUK, S., KUIPERS, J. A. M, (2009) “A discrete element study of wet particle-particle interaction during granulation in a spout fluidized bed”, The Canadian journal of chemical engineering, 87, 308-317.

VAN SINT ANNALAND, M. DEEN, N.G., KUIPERS, J.A.M., (2005) “Numerical simulation of gas-liquid-solid flows using a combined front tracking and discrete particle method”, Chemical engineering science, 60, 6188-6198.

YANG, G. E., and FAN, L. S., (2007) “Droplet-particle collision mechanics with film-boiling evaporation”, Journal of fluid mechanic, 573, 311-337.

SIMULATION OF RECTANGULAR FLUIDIZED BED WITH GELDART D PARTICLES

Mohit P. TANDON[1*] , Aditya U. KARNIK[1]

[1] CD-adapco, 4th Floor, Parakh House, Boat Club Road, Pune - 411001, INDIA

* E-mail: mohit.tandon@cd-adapco.com

ABSTRACT

In this study, simulations are carried out using the Euler-Euler granular model in STAR-CCM+ for a gas-solid flow in a rectangular bubbling fluidized bed. The problem studied was announced as Small Scale Challenge Problem (SSCP-I) in 2013. Experiments for this problem were conducted by The Department of Energy's (DOE) National Energy Technology Laboratory (NETL). The objective of this numerical study is to evaluate the reliability of the kinetic theory based granular model (KTGF) in predicting the hydrodynamics of gas-solid flows.

The experimental measurements of the bubbling fluidized bed investigated in this numerical study are 3"x9"x48". The bed material for the experiment is Geldart group D particles of uniform size and high sphericity. Simulations were performed for all the three gas superficial velocities (U = 2.19, 3.28 and 4.38 m/s) for which experiments were conducted. Results from numerical simulations are validated for vertical component of particle velocity, horizontal component of particle velocity, granular temperature and the mean axial pressure gradient. The effect of the treatment at wall boundaries and coefficient of restitution (particle-particle interactions) is studied on the results.

Keywords: Fluidization, Bubbling fluidized bed, Geldart D particle, Kinetic theory of granular flow

NOMENCLATURE

Greek Symbols

α	Volume fraction.
ρ	Density, [kg/m^3].
τ	Stress Tensor, [kg/ (m.s^2)].
μ	Viscosity, [kg/(m.s)].
θ	Granular temperature [m^2/s^2].
γ_s	Collisional dissipation rate, [kg/ (m.s^2)].
φ	Specularity coefficient.

Latin Symbols

$\boldsymbol{U}$	Superficial velocity, [m/s].
p	Pressure, [Pa].
$\boldsymbol{u}$	Velocity, [m/s].
$\boldsymbol{g}$	Gravity, [m/s^2].
F	Force, [N].
d	Particle diameter, [m].
Re	Reynolds Number.
$\boldsymbol{c}$	Fluctuating velocity, [m/s].
e	Coefficient of restitution.
k	Granular conductivity, [kg/(m.s)].
J	Work done by fluctuating force, [kg/ (m.s^2)].
g_o	Radial Distribution Function.
A	Interphase momentum coefficient [kg/ (m^3.s)].
n	normal [m].
z	height measured from the inlet [m].

Sub/superscripts

mf	minimum fluidization.
i	i-th phase.
g	gas phase.
s	solid phase.
int	interaction.
b	bulk.
k	kinetic.
max	maximum packing limit.
$slip$	slip.
w	wall.

INTRODUCTION

Fluidized beds are widely used in many plant operations in chemical, energy production, oil & gas, mineral and agricultural industries. They are used widely because of their good mixing characteristics and high contact surface area between gas and solid phases.

The complex flow patterns associated with them make flow modelling of these systems a challenging task. The fundamental problem arises due to complex motion of phases where interface is unknown and transient, and interaction is understood only for limited range of conditions (Gilbertson *et al.*, 1996). Gas velocity and coefficient of restitution have significant impact on the hydrodynamic behaviour of the fluidized beds. CFD has emerged as an effective tool for modelling hydrodynamics of a fluidized bed. Mainly two approaches have been used to model gas – solid fluidized beds: Lagrangian approach, which tracks discrete particles and Euler-Euler approach where both phases are treated as interpenetrating continua. Gera *et al.* (1988) compared both these approaches.

In the Lagrangian approach, equations of motions are solved for each discrete particle and collisions between

particles are modelled via hard-sphere (Gera *et al*., 1988, Hoomans *et al*., 1996) or soft-sphere approach (Tsuji *et al*., 1993, Kobayashi *et al*., 2000). But this approach is computationally very expensive and hence its usage is limited to problems with smaller number of particles. This makes Euler-Euler approach being more widely used to simulate gas – solid fluidized beds.

In Euler-Euler approach, particles are treated as a continuous medium. Governing equations are solved for each phase to ensure conservation of their continuity, momentum and energy. The interactions between the gas and solid phases appear as additional source terms in the conservation equations. The interphase momentum transfer between gas and solid phase is accounted for by the drag force. In fluidized beds, drag is affected by the presence of other particles. Many researchers, Wen *et al.* (1966), Syamlal *et al.* (1987), Arastoopour *et al.* (1990) and Di Felice, (1994) have proposed correlations for modelling drag for gas – solid flows.

The particle phase momentum equations require closure laws for additional terms that represent the rheology of the fluidized particles. Kinetic theory of granular flow was developed by Lun *et al.* (1984), Ahmadi *et al.* (1986) and Ding *et al.* (1990) to model the motion of a dense collection of spherical particles. This theory is based on the assumption that the motion of particles is analogous to random motion of molecules in a gas. Kinetic theory introduces a concept of granular temperature which represents the specific energy associated with fluctuations in velocity of particle about the mean. In gas-solid flows, fluctuations in the velocity result in collisions between particles which are being carried along by the mean flow.

In this study we focus on the Eulerian approach and investigate the impact of coefficient of restitution on the hydrodynamics of fluidized bed. Coefficient of restitution quantifies the elasticity of particle collisions. It takes value of one for fully elastic collisions and zero for fully inelastic collisions. Jenkins *et al.* (1983) were the first to account for loss of energy due to collision of particles. A number of studies have shown the effect of coefficient of restitution on the hydrodynamics of gas - solid flows (Goldschmidt *et al*., 2001, Taghipour *et al*., 2005 and Zimmermann *et al*., 2005).

The objective of this study is to investigate the effect of coefficient of restitution and wall boundary treatment of particle phase on the hydrodynamics of a bubbling fluidized bed.

EXPERIMENT DETAILS

The bubbling fluidized bed system investigated in this study was declared as a challenge problem, Small Scale Problem – I (SSCP-I) by NETL in 2013 (Gopalan *et al*., 2013). This system is a rectangular (pseudo 2-D) fluidized bed (3"x9"x48") using Geldart D type particles (Nylon beads). Experiments were performed at three different gas superficial velocities, $\mathbf{U}_g$ = 2.19, 3.28 and 4.38 m/s. The minimum fluidization velocity of the system, $\mathbf{U}_{mf}$ is 1.05 m/s. The mean particle size is 3.256 mm.

The data was collected for pressure drop across the bed, vertical and horizontal particle phase velocities and the granular temperature at 5 locations across the radius at 0.076 m distance downstream of the inlet. Additional details of the experiments can be found at Gopalan *et al*. (2013).

MODEL DESCRIPTION

In Euler-Euler model, each phase has its own distinct velocity, temperature and physical properties. Conservation equations are solved for each phases, but additional closure laws are required to model the interactions between the phases.

STAR-CCM+ solves the continuity and momentum equation for each phase, i. The conservation equations for mass and momentum take the following form,

Continuity:

$$\frac{\partial}{\partial t}\alpha_i\rho_i + \nabla\cdot\alpha_i\rho_i\boldsymbol{u_i} = 0 \tag{1}$$

Momentum equation for gas phase:

$$\frac{\partial}{\partial t}\alpha_g\rho_g\boldsymbol{u_g} + \nabla\cdot\alpha_g\rho_g\boldsymbol{u_g}\boldsymbol{u_g} = -\alpha_g\nabla p + \alpha_g\rho_g\boldsymbol{g} + \nabla\cdot\tau_{g+F_{int,gs}} \tag{2}$$

Momentum equation for solid phase:

$$\frac{\partial}{\partial t}\alpha_s\rho_s\boldsymbol{u_s} + \nabla\cdot\alpha_s\rho_s\boldsymbol{u_s}\boldsymbol{u_s} = -\alpha_s\nabla p + \alpha_s\rho_s\boldsymbol{g} + \nabla\cdot\tau_{s-F_{int,gs}} \tag{3}$$

τ_g is modelled as,

$$\tau_g = \alpha_g\mu_g\left(\nabla\boldsymbol{u_g} + \left(\nabla\boldsymbol{u_g}\right)^T - \frac{2}{3}\nabla\cdot\boldsymbol{u_g}\right) \tag{4}$$

In this study, the interphase momentum transfer, $F_{int,gs}$, is modelled using the drag correlation proposed by Arastoopour *et al.* (1990).

$$F_{int,gs} = \left(\frac{17.3}{Re_s} + 0.336\right)\frac{\rho_s}{d_s}\left|\boldsymbol{u_s} - \boldsymbol{u_g}\right|\alpha_s\alpha_g^{-2.8}\left(\boldsymbol{u_s} - \boldsymbol{u_g}\right) \tag{5}$$

Granular stress, τ_s, is modelled as,

$$\tau_s = -p_s + \mu_s\left(\nabla\boldsymbol{u_s} + (\nabla\boldsymbol{u_s})^T + \left(\mu_{b,s} - \frac{2}{3}\right)\nabla\cdot\boldsymbol{u_s}\right) \tag{6}$$

Granular Stress Model

Solid stress is modelled using the KTGF theory. This theory enables us to determine the fluid properties of the particle phase by accounting of the inelasticity of the particles. It assumes the solid viscosity and stress to be function of granular temperature. Granular temperature,

θ_s, is defined based on fluctuations in solid phase velocity, $\boldsymbol{c_s}$ as:

$$\theta_s = \frac{1}{3} < \boldsymbol{c_s c_s} > \tag{7}$$

KTGF introduces a transport equation for granular temperature which is given as,

$$\frac{3}{2}\left[\frac{\partial}{\partial t}\alpha_s\rho_s\theta_s + \nabla\cdot\alpha_s\rho_s\theta_s\boldsymbol{u_s}\right] = \nabla\cdot k_s\nabla\theta_s + \tau_{s,k}:\nabla u_s - \gamma_s - J_s \tag{8}$$

First term on the right hand side of this equation is diffusion of fluctuating energy along gradients in granular temperature. The second term on the right hand side is generation of fluctuating energy due to shear in the particle phase. Third term, γ_s, represents the dissipation due to inelastic collisions and the fourth term, J_s, represents the dissipation or creation of fluctuating energy because of the work done by the fluctuating force exerted by gas through the fluctuating velocity of the particles.

Granular temperature is used to estimate solid pressure, P_s, which represents the normal force due to interactions between the particles and prevents the particle phase from exceeding maximum packing limit of solids. It is modelled as given by Lun *et al.* (1984),

$$P_s = \alpha_s\rho_s\theta_s(1 + 2(1+e)\alpha_s g_o) \tag{9}$$

The solid bulk viscosity describes the resistance of the particle phase against compression. It is again modelled using the expression given by Lun *et al.* (1984),

$$\mu_{b,s} = \frac{4}{3}\alpha_s^2\rho_s g_o d_s(1+e)\sqrt{\frac{\theta_s}{\pi}} \tag{10}$$

Soild shear viscosity, μ_s, is used to calculate the tangential forces due to translational and collisional interaction of particles. In this study we use the form given by Syamlal *et al.* (1993),

$$\mu_s = \frac{4}{5}\alpha_s^2\rho_s g_o d_s(1+e)\sqrt{\frac{\theta_s}{\pi}} + \frac{\alpha_s\rho_s d_s\sqrt{\pi\theta_s}}{6(3-e)}\begin{bmatrix}1+\frac{2}{5}\alpha_s\\(1+e)(3e-1)g_o\end{bmatrix} \tag{11}$$

Similarly, the solid thermal conductivity, k_s, consists of a kinetic contribution and a collisional component. The form used in this study was proposed by Syamlal *et al.* (1993),

$$k_s = \frac{15\alpha_s\rho_s d_s\sqrt{\pi\theta_s}}{4(41-33e)}\begin{bmatrix}1+\frac{12}{5}\alpha_s e^2(4e-3)g_o +\\ \frac{16}{15\pi}\alpha_s e(41-33e)g_o\end{bmatrix} \tag{12}$$

The dissipation of granular energy (fluctuating energy), γ_s, due to inelastic particle - particle collisions is modelled in this study as in Lun *et al.* (1984). Their work omitted the term accounting for $\nabla\cdot\boldsymbol{u_s}$ which was included in the form proposed by Jenkins *et al.* (1983).

$$\gamma_s = 12(1-e^2)\frac{\alpha_s^2\rho_s g_o}{d_s\sqrt{\pi}}\theta_s^{3/2} \tag{13}$$

The production or dissipation of granular energy, J_s, due to fluctuating force exerted by gas has two terms: first one due to correlation between particle velocity fluctuations and second due to correlation between particle and gas velocity fluctuations. Gidaspow (1994) proposes it to be modelled as, $3A_{int,gs}\theta_s$. The second term is modelled using the form proposed by Louge *et al.* (1991). The originally proposed form is divided by the radial distributional function to ensure it tends to zero as particle volume fraction approaches the maximum solid packing.

$$J_s = A_{int,gs}\left[3\theta_s - \frac{A_{int,gs}d_s(\boldsymbol{u_g}-\boldsymbol{u_s})^2}{4\alpha_s\rho_s g_o\sqrt{\pi\theta_s}}\right] \tag{14}$$

Radial distribution function, g_o, is an estimate of particle pair density at a distance equivalent to the particle diameter. It increases with increasing particle volume fraction. In this study, we used the expression by Ding *et al.* (1990),

$$g_o = \frac{3}{5}\left[(1-\alpha_s/\alpha_{s,max})^{1/3}\right]^{-1} \tag{15}$$

The radial distribution function is written as a Taylor series approximation at high volume fractions close to maximum packing. The expression in equation 15 was numerically blended with Taylor series expression to avoid convergence difficulties.

COMPUTATIONAL INVESTIGATION

The simulations in this work are carried out using STAR-CCM+ from CD-adapco. The code uses PC-SIMPLE (Vasquez *et al*., 2000) for pressure – velocity coupling. In this algorithm, velocity components are solved together for phases in a segregated fashion. The pressure correction equation is based on total volume continuity. To avoid decoupling between the pressure – velocity fields, STAR-CCM+ uses Rhie-Chow algorithm (Rhie *et al*., 1983) as demonstrated by Tandon (2008).

In this study, simulations were performed for all three gas superficial velocities for which experiments were performed (Case 1: 2.19 m/s, Case 2: 3.28 m/s and Case 3: 4.38 m/s). A 2-D computational domain with 44100 cells (90 X 490) was used. Uniform grid spacing was used in both the directions. Figure 1 shows the schematic of bed geometry.

All the simulations use second order convection scheme for volume fraction, velocity and granular temperature. Time step of 5 X 10^{-4} s was used for all the simulations. All the simulations were run for 50 s. The time averaged distributions of flow variables were computed for period of 20 – 50 s. The start time of 20 s ensures that the time averaging is performed only after the bed has reached quasi-steady state.

In this study we investigate the impact of the coefficient of restitution for particle – particle interactions, e, on

the bed hydrodynamics. We used three values for e: 0.8, 0.84 and 0.9 in this study. The coefficient of restitution for particle – particle interactions reported in experiments ranged between 0.77 and 0.91.

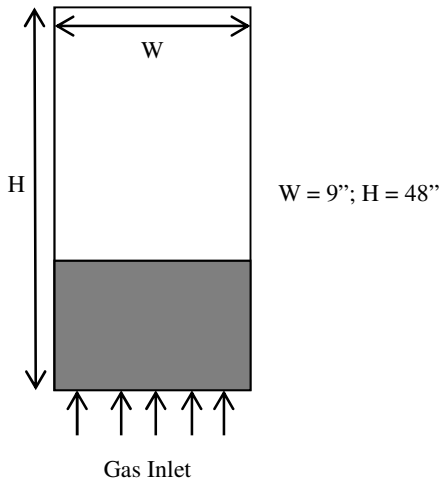

Figure 1: Schematic representation of the bed.

Boundary Conditions

Dirichlet boundary condition was used for gas phase at the inlet of the bed. Pressure outlet boundary condition was used for the top boundary. The pressure is specified as atmospheric. At the side walls, no-slip boundary condition was specified for the gas phase but it is commonly accepted in literature that it is an unrealistic condition for the particle phase in bubbling fluidized beds (Li *et al.*, 2010, Li *et al.*, 2013). In this study, we investigated both free-slip boundary conditions and the partial-slip boundary conditions proposed by Johnson *et al.* (1987) for particle phase. The equation for boundary conditions proposed by Johnson – Jackson are given by,

$$u_{s,w} = -\frac{6\alpha_s\mu_s}{\sqrt{3\theta_s}\pi\varphi\rho_s\alpha_s g_o}\frac{\partial u_{s,w}}{\partial n}, \qquad (16)$$

$$\theta_{s,w} = -\frac{k\theta_s}{\gamma_w}\frac{\partial\theta_{s,w}}{\partial n} + \frac{\sqrt{3}\pi\varphi\rho_s\alpha_s u_{s,slip}^2 g_o\theta_s^{3/2}}{6\alpha_{s,max}\gamma_w}, \qquad (17)$$

where, γ_w, is expressed in term of particle - wall restitution coefficient, e_w, as

$$\gamma_w = \frac{\sqrt{3}\pi(1-e_w^2)\alpha_s\rho_s g_o\theta_s^{3/2}}{4\alpha_{s,max}} \qquad (18)$$

The equation 17 represents the granular energy conducted to the wall after accounting for the generation of granular energy due to particle slip at the wall and the dissipation of granular energy due to inelastic collisions between the particles and the wall.

In this study, we investigate the impact of two specularity values: 0.01 and 0.05. It should be noted that free-slip condition represents specularity equal to zero.

The main parameters used in the simulations can be found in Table 1.

Parameter	Value
Gas density	1.2 kg/ m^3
Gas viscosity	1.9 X 10^{-5} Pa-s
Particle density	1131 kg/m^3
Particle diameter	3.256 mm
Particle-wall coefficient of restitution	0.92
Particle-particle coefficient of restitution	0.8, 0.84 and 0.9
Maximum packing limit	0.624
Initial bed voidage	0.424
Minimum Fluidization Velocity	1.05 m/s

Table 1: Parameters used in the numerical simulations.

RESULTS AND DISCUSSION

This section is divided into two parts, one discussing the effect of the coefficient of restitution between particle – particle collisions and second discussing the effect of the specularity coefficient.

To investigate the effect of coefficient of restitution between particle – particle collisions, simulations were performed for three values of coefficient of restitution (0.8, 0.84 and 0.9). Free-slip boundary condition was used for the particle phase at the wall in the first part.

In all the simulations it was observed that pressure dropped significantly at the inception of fluidization. The pressure drop stabilized around the mean value in all the simulations after approximately 3 seconds. The fluctuations in the pressure drop are attributed to continuous breakage and coalescence of bubbles in the fluidized bed (Taghipour *et al.*, 2005). Steady state pressure drop was measured in the experiments between z = 0.0413 m and z = 0.3048 m. It can be seen in the Figure 2 that there is no significant difference between the computationally predicted mean pressure drop for the different coefficients of restitution investigated in this study. The qualitative trend for variation in the mean pressure drop with the gas superficial velocity is in good agreement with the experiments. It is also observed that the agreement improves with an increase in the gas superficial velocity.

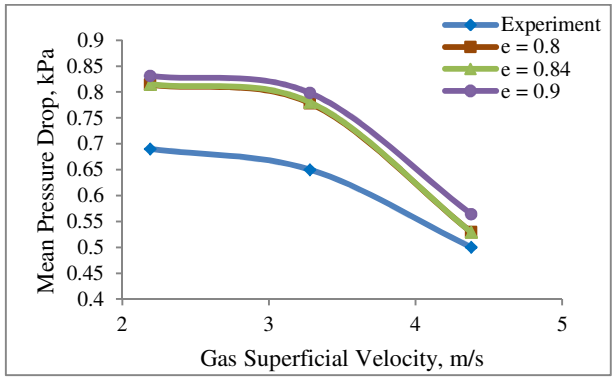

Figure 2: Comparison of the experimental and predicted mean pressure drop for three different coefficients of restitution.

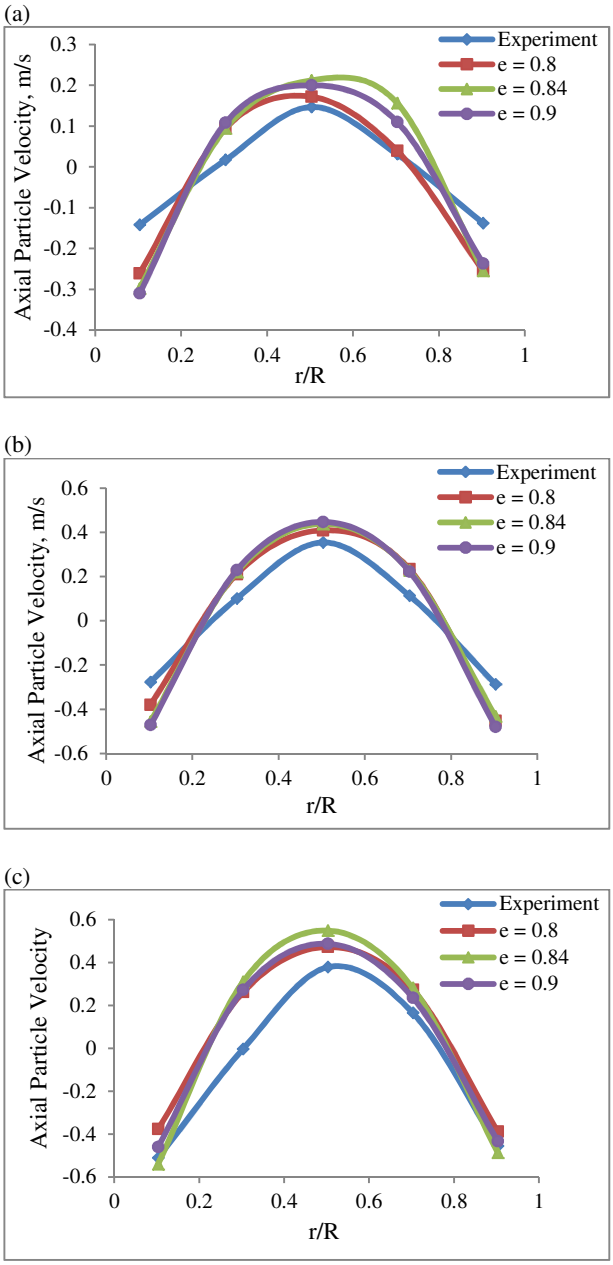

Figure 3: Axial particle velocity comparison with experimental data for three coefficients of restitution: (a) Case 1 (b) Case 2 (c) Case 3.

Particle phase velocity is one of the most important parameters in the flow pattern of a fluidized bed. Its importance is highlighted by the significance of accuracy in its prediction when investigating several phenomena such as heat and mass transfer.

The experimental measurements for the velocity profile were performed at z = 0.0762 m. The experimental time – averaged axial particle velocity is compared with the predicted simulation results for different coefficients of restitution in Figures 3 (a), (b) and (c) for $\mathbf{U}_g$ = 2.19, 3.28 and 4.38 m/s respectively. It is observed that there is good agreement between simulation results and corresponding experimental data for the axial particle velocity. It is also seen that there is no significant impact of the coefficient of restitution on the axial particle velocity for all three cases. From Figure 3, it can be deduced that for all three gas superficial velocities, particle phase rises in the centre of the bed and falls down close to the wall indicating core – annular flow pattern of the particle phase for all cases. It is observed that with increase in rising particle velocity in the centre of the bed, downward particle velocity near the wall also increases.

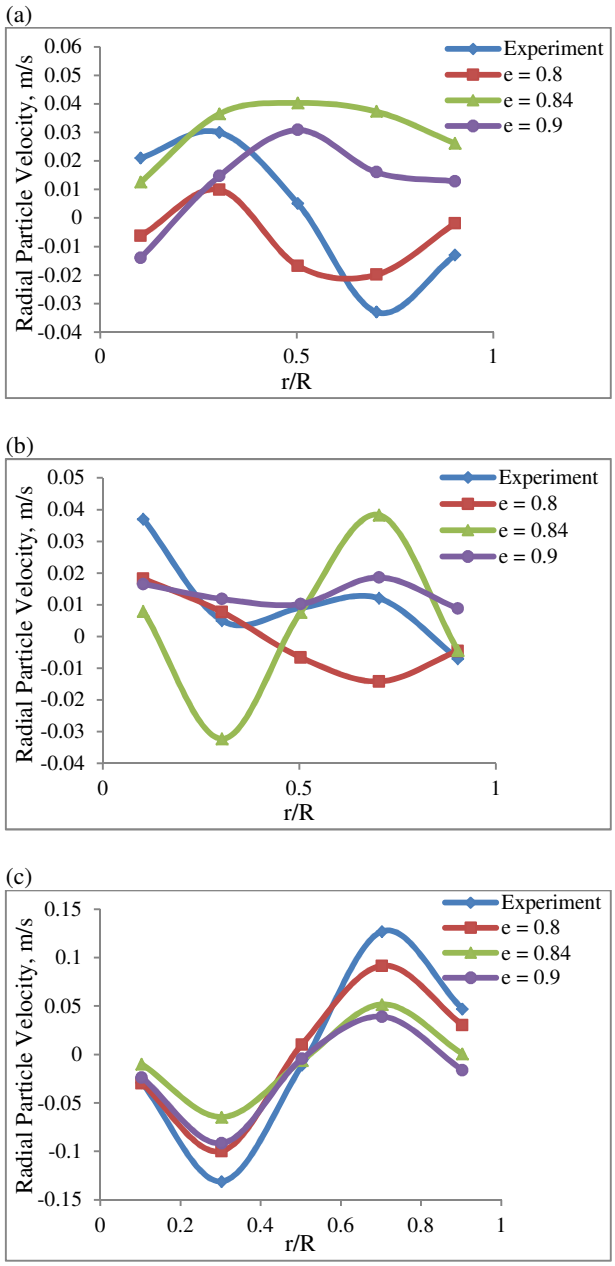

Figure 4: Radial particle velocity comparison with experimental data for three coefficients of restitution: (a) Case 1 (b) Case 2 (c) Case 3.

Comparison between results from the simulations and the experiments for the time – averaged radial particle velocity for different coefficients of restitution can be seen in Figures 4 (a), (b) and (c) for $\mathbf{U}_g$ = 2.19, 3.28 and 4.38 m/s respectively. It is observed that agreement for radial particle velocity is satisfactory for the case 3 (highest gas superficial velocity). For cases 1 and 2 radial particle velocity comparisons are less satisfactory. It can be deduced from the experimental results that solid particles are moving towards the core of the bed for case 1 and 2 at z = 0.076 m, but moving towards the

wall for case 3 at z = 0.076 m. It is felt that discrepancy in cases 1 and 2 could be because of not being able to correctly capture the wall – particle interactions. So, in the second part of this study the effect of specularity coefficient is investigated by employing equations from Johnson *et al.* (1987) at walls.

Specularity coefficient is indicative of the fraction of collisions which transfer momentum to the wall. It varies between zero for free-slip boundary condition and unity for perfectly diffuse collisions (no-slip boundary condition). It was first introduced by Hui *et al.* (1984). Li *et al.* (2011) demonstrated that it is closely related to local flow dynamics near the wall and the large-scale roughness of the surface.

In this study three values of specularity coefficient (0, 0.01 and 0.05) were used to investigate the effect of specularity coefficient on all the three cases. For this study we fixed the coefficient of restitution for particle – particle collisions at 0.84 and the coefficient of restitution for particle – wall collisions at 0.92. The coefficient of restitution for wall – particle interactions reported in experiments ranged between 0.90 and 0.94

It can be seen in Figure 5 that the qualitative trend for variation in the mean pressure drop with the gas superficial velocity is in good agreement with the experiments for all three values of specularity coefficient used in this study. The quantitative predictions for the mean pressure drop are similar for all the three specularity values for $\mathbf{U}_g$ = 2.19 and 3.28 m/s. The best agreement for $\mathbf{U}_g$ = 4.38 m/s is seen with the perfectly specular boundary assumption.

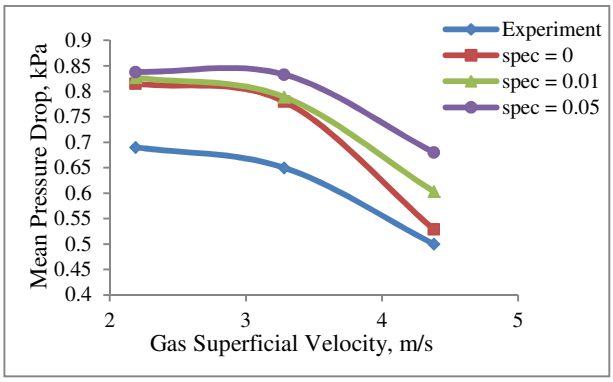

Figure 5: Comparison of the experimental and predicted mean pressure drop for three different specularity coefficients.

Comparison between results from the simulations and the experiments for the time – averaged axial particle velocity for different specularity coefficients can be seen in Figures 6 (a), (b) and (c) for $\mathbf{U}_g$ = 2.19, 3.28 and 4.38 m/s respectively. In general there is good agreement between simulation results and corresponding experimental data for all the three values of specularity coefficients. There is a moderate variation in the simulation results for the axial particle velocity with the specularity coefficient. The core – annular flow pattern of the particle phase is seen for all the cases. It is observed that rising particle velocity in the centre of the bed decreases with the increase in the specularity coefficient coupled with the decrease in the downward particle velocity near the wall.

The experimental time – averaged radial particle velocity is compared with the predicted simulation results for different specularity coefficients in Figures 7 (a), (b) and (c) for $\mathbf{U}_g$ = 2.19, 3.28 and 4.38 m/s respectively. It is observed in Figure 7(a) that satisfactory agreement is seen for radial particle velocity with the experimental results for specularity coefficient values of 0.01 and 0.05 for $\mathbf{U}_g$ = 2.19 m/s. The better agreement is seen with the value of 0.01. It is seen in Figure 7(c) that perfect specular assumption (specularity equal to zero) gives best agreement for $\mathbf{U}_g$ = 4.38 m/s. However, the comparisons for radial particle velocity for $\mathbf{U}_g$ = 3.28 m/s are less satisfactory with only moderate qualitative agreement seen with specularity coefficient value of zero.

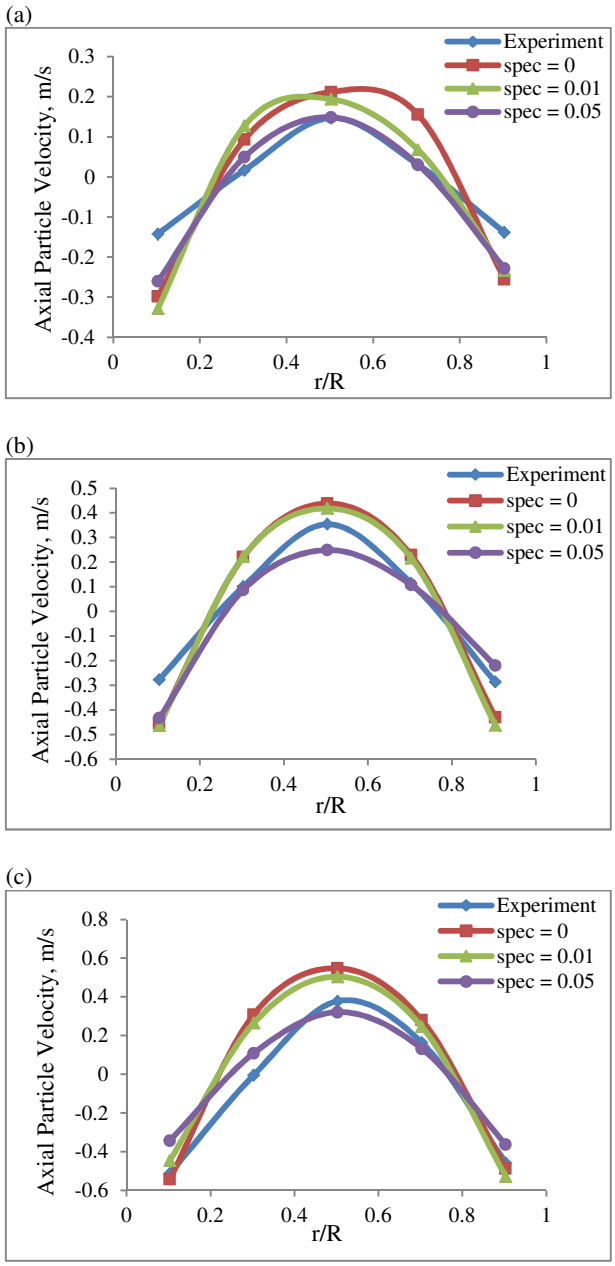

Figure 6: Axial particle velocity comparison with experimental data for three specularity coefficients: (a) Case 1 (b) Case 2 (c) Case 3.

(a)

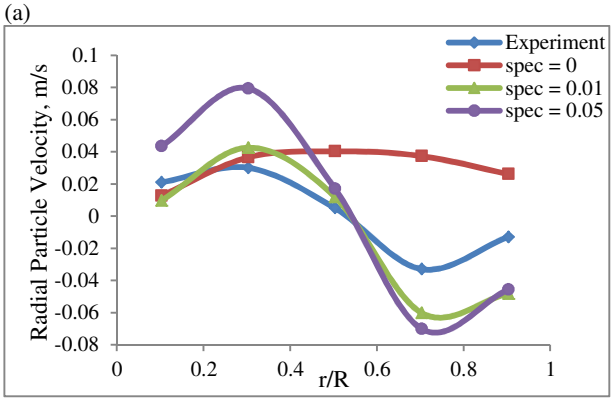

(b)

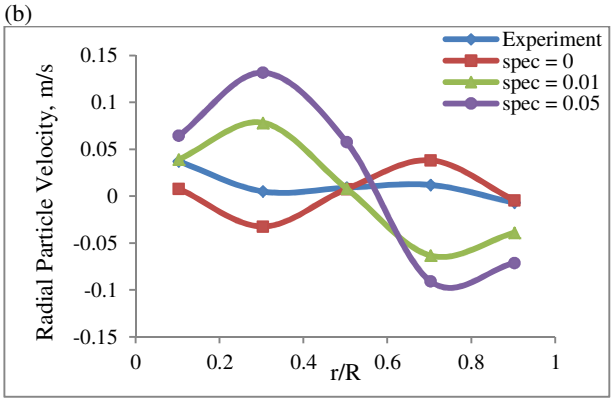

(c)

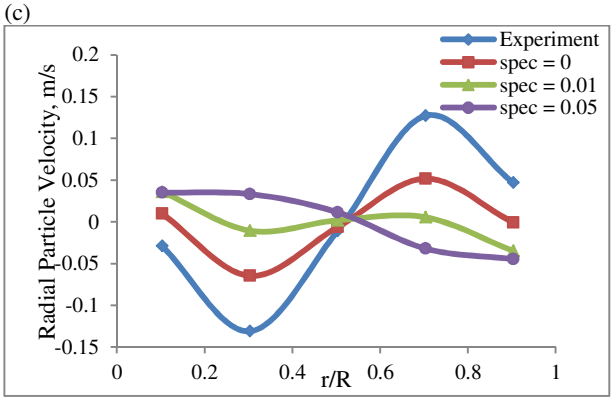

Figure 7: Radial particle velocity comparison with experimental data for three specularity coefficients: (a) Case 1 (b) Case 2 (c) Case 3.

It can be seen from the Figure 7(a) that simulations correctly predict the particle motion towards the core of the bed for case 1 at z = 0.076 m for specularity values of 0.01 and 0.05 while Figure 7(c) shows that the simulations using specularity value of zero correctly predict the particle motion towards the wall for case 3 at z = 0.076 m. This observation is also supported by the vector plot of the time – averaged particle velocity seen in Figure 8.

The observations from Figure 7 and 8 demonstrate that the flow field (specifically radial particle velocity) is very sensitive to the choice of specularity coefficient. This indicates that specularity coefficient will also influence the particle distribution along the radial direction. It is also observed that the gas superficial velocity affects the specularity coefficient and that specularity coefficient decreases with increase in gas superficial velocity. This observation is consistent with the findings from other studies (Li *et al.*, 2010, Li *et al.*, 2013).

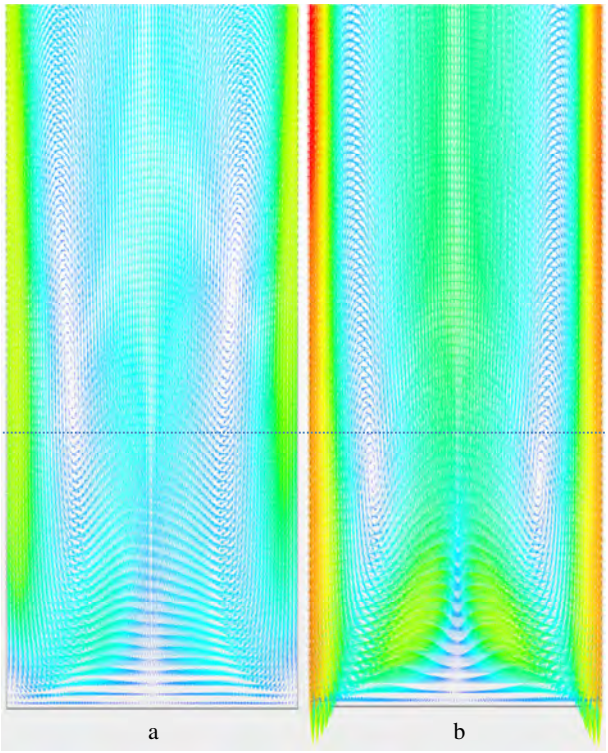

Figure 8: Vector plot of time – averaged particle velocity. (a) Case 1 (coefficient of restitution = 0.84, specularity = 0.01) (b) Case 3 (coefficient of restitution = 0.84, specularity = 0). Dotted line represents z = 0.076 m, height at which experimental velocity measurements were made.

CONCLUSIONS

Euler – Euler granular model in STAR-CCM+ based on KTGF theory was used successfully in this study to simulate the hydrodynamics of a bubbling fluidized bed using Geldart D particles. It was successful in predicting the core – annular flow pattern for solid as reported in the experiments. This study investigated two unknown model coefficients in KTGF theory: particle – particle coefficient of restitution and specularity coefficient. It was observed that the impact of the particle – particle coefficient of restitution on the hydrodynamics of the bed is not significant. However, it is shown that the specularity coefficient for particle – wall interaction has strong impact on the flow field in the bubbling fluidized bed investigated in this study. The study also demonstrates that specularity coefficient is strongly affected by the gas superficial velocity. It is felt that it will be useful to evaluate the correlation proposed for specularity coefficient by Li *et al.* (2011) for interaction between a rapid granular and a flat, frictional surface.

ACKNOWLEDGEMENTS

Authors would like to thank Balaji Gopalan (formerly from National Energy Technology Laboratory) for sharing the experimental data to make this work possible.

REFERENCES

AHMADI, G. and MA, D.N., (1986), "A kinetic model for granular flows of nearly elastic particles in grain-inertia regime," *International Journal of Bulk Solid Storage Soils*, **2**, 8–16.

ARASTOOPOUR, H., PAKDEL, P. and ADEWUMI, M., (1990), "Hydrodynamic analysis of dilute gas–solids flow in a vertical pipe," *Powder Technology*, 62, 163–170.

DI FELICE, R., (1994), "The voidage functions for fluid – particle interaction system," *International Journal of Multiphase Flow*, **20**(1), 153-159.

DING, J. and GIDASPOW, D., (1990). "A bubbling fluidization model using kinetic theory of granular flow," *AIChE Journal*, **36**, 523–538.

GERA D., GAUTAM M., TSUJI, Y., KAWAGUCHI, T. and Tanaka T., (1988), "Computer simulation of bubbles in large fluidized beds," *Powder Technology*, **98**, 38-47.

GIDASPOW, D., (1994), "Multiphase flow and fluidization," Academic Press, San Diego.

GILBERTSON, M.A. and YATES, J.G., (1996), "The motion of particles near a bubble in gas-solid fluidized bed," *Journal of Fluid Mechanics*, **323**, 377-385.

GOLDSCHMIDT, M.J.V., KUIPERS, J.A.M. and VAN SWAAIJ, W.P.M., (2001), "Hydrodynamic modelling of dense gas – solid beds using the kinetic theory of granular flow: effect of coefficient of restitution on bed dynamics," *Chemical Engineering Science*, **56**, 571-578.

GOPALAN, B., and JONATHAN, T., (2013), https://mfix.netl.doe.gov/challenge

HOOMANS, B.P.B., KUIPERS J.A.M., BRIELS, W.J. and Van Swaaij, W.P.M., (1996), "Discrete particle simulation of bubble and slug formation in a two - dimensional gas-solid fluidized bed: A hard sphere approach," *Chemical Engineering Science*, **51**, 99-118.

HUI, K., HAFF, P.K. and UNGAR, J.E., (1984), "Boundary conditions for high – shear grain flows," *Journal of Fluid Mechanics*, **145**, 223-233.

JENKINS, J.T. and SAVAGE, S.B., (1983), "A theory for the rapid flow of identical, smooth, nearly elastic, spherical particles," *Journal of Fluid Mechanics*, **130**, 187-202.

JOHNSON, P.C. and JACKSON, R., (1987), "Frictional-collisional constitutive relations for granular materials, with application to plane shearing", *Journal of Fluid Mechanics*, **176**, 67-93.

KOBAYASHI, N., YAMAZAKI, R. and MORI, S., (2000), "A study on the behaviour of bubbles and solids in bubbling fluidized beds," *Powder Technology*, **113**, 327-344.

LI, T., GRACE, J.R., and BI, X., (2010), "Study of wall boundary condition in numerical simulations of 2D bubbling fluidized beds," *Powder Technology*, 203, 447-457.

LI, T. and BENYAHIA, S., (2011), "Revisiting Johnson and Jackson boundary conditions for granular flows," *AIChE Journal*, **58**, 2058-2068.

LI, T. and BENYAHIA, S., (2013), "Evaluation of wall boundary condition parameters for gas – solid fluidized bed simulations," *AIChE Journal*, **59**, 3624-3632.

LOUGE, M.Y., MASTORAKOS, E. and JENKINS, J.T., (1991), "The role of particle collisions in pneumatic transport," *Journal of Fluid Mechanics*, **231**, 345-359.

LUN C.K., SAVAGE S.B., JEFFREY D.J. and CHEPURNIY N., (1984), "Kinetic theories for granular flow: inelastic particles in Couette flow and slightly inelastic particles in a general flow field," *Journal of Fluid Mechanics*, **140**, 223–256.

RHIE, C.M. and CHOW, W.L., (1983), "Numerical study of the turbulent flow past an airfoil with trailing edge separation," *AIAA Journal*, **21**, 1525-1532.

SYAMLAL, M. and O'BRIEN, T.J., (1987), "Derivation of a drag coefficient form velocity-voidage correlation," Technical Note, U.S. Department of Energy, Office of Fossil Energy, National Energy Technology Laboratory, Morgantown, WV.

SYAMLAL, M., ROGERS, W. and O'BRIEN, T.J., (1993), "Mfix documentation theory guide," Technical Note, U.S. Department of Energy, Office of Fossil Energy, National Energy Technology Laboratory, Morgantown, WV.

TAGHIPOUR, F., ELLIS, N. and CLAYTON, C., (2005), "Experimental and computational study of gas – solid fluidized bed hydrodynamics," *Chemical Engineering Science*, **60**, 6857-6867.

TANDON, M., (2008), "Structured Adaptive Mesh Refinement (SAMR) Simulation Study of the Buoyant Plumes", PhD Dissertation, University of Utah.

TSUJI, Y., KAWAGUCHI, T. and TANAKA T., (1993), "Discrete particle simulation of two – dimensional fluidized bed," *Powder Technology*, **77**, 79-87.

VASQUEZ, S.A. and IVANOV, V.A, (2000), "A phase coupled method for solving multiphase problems on unstructured meshes," *Proceedings of ASME 2000 Fluids Engineering Division Summer Meeting*, ASME Press, New York.

WEN, C.Y. and HU, Y.H., (1966), "Mechanics of Fluidization," *Chemical Engineering Progress Symposium Series*, **62**(2), 100 – 111.

ZIMMERMANN, S. and TAGHIPOUR, F., (2005), "CFD modelling of the hydrodynamics and reaction kinetics of FCC fluidized bed reactors," *Industrial & Engineering Chemistry Research*, **44**, 9818-9827.

HYDRODYNAMIC INVESTIGATION INTO A NOVEL IC-CLC REACTOR CONCEPT FOR POWER PRODUCTION WITH INTEGRATED CO_2 CAPTURE

Abdelghafour Zaabout*, Schalk Cloete, Shahriar Amini
SINTEF Materials and Chemistry, Flow Technology Department, 7034 Trondheim, NORWAY
* E-mail: Abdelghafour.zaabout@sintef.no

ABSTRACT

This paper presents an investigation of the hydrodynamics of a new Chemical Looping Combustion (CLC) reactor concept for power generation with integrated CO_2 capture. This concept consists of an internal circulating fluidized bed (IC-CLC) where a single reactor is divided into two separate sections in a way that oxidation and reduction of the oxygen carrier take place separately. Such a reactor configuration would significantly reduce the costs and solids handling challenges currently hampering the scale-up of CLC technology.

Fundamental multiphase flow models (based on the Kinetic Theory of Granular Flow or KTGF) have been used to investigate the hydrodynamics in different reactor designs in order to identify the most optimized one which maintains minimized leakage between the two reactor sections. The performance of each design has been evaluated through a quantified parameter which is the volumetric gas/solid leakage ratio between the two reactor sections. Reactor designs with narrow connecting ports proved to be the most reliable in minimizing the gas leakage and therefore would maintain high CO_2 purity and CO_2 capture efficiency.

The most optimized reactor design has then been selected for further investigation through a statistical method (central composite design) where the reactor performance response to the change in the bed loading and the air fluidization velocity has been evaluated. Values close to 1 were found for the fuel/solid leakage ratio parameter implying that high CO_2 capture efficiency can be achieved through the chosen design in a wide range of bed loadings and fluidization velocities. In general, the reactor proved to perform best under conditions with high static bed heights and/or high fluidization velocities.

Keywords: Fluidized bed; Chemical Looping Combustion; Simulation-Based Reactor Design.

INTRODUCTION

Carbon capture and storage (CCS) is increasingly seen as a potential environmentally sustainable way for fulfilling world energy needs while minimizing the environmental impact of fossil fuel combustion (Butt, Giddings et al. 2012; IEA 2012). Chemical-looping combustion (CLC) has arisen as a promising technology to carry out CO_2 capture at low energy penalty compared to CO_2 capture technologies, such as pre- and post-combustion technologies (Ekström, Schwendig et al. 2009). CLC is a combustion process which integrates power generation and CO_2 capture. It consists of two interconnected reactors, an air and a fuel reactor. A solid oxygen carrier circulating between them, thereby playing the role of oxygen transporter which transfers the oxygen required for fuel combustion from the air to the fuel. Consequently, any contact between the fuel and the air is inherently avoided in this process, and therefore a pure CO_2 stream, ready for compression and sequestration is produced (Ishida, Zheng et al. 1987).

In addition to development and selection of suitable oxygen carriers materials (Abad, Adanez et al. 2007; Hossain and de Lasa 2008; Adanez, Abad et al. 2012), research on CLC has so far been focused predominantly on the use of dual Circulating Fluidized Beds (CFBs) configuration for the recirculation of the oxygen carrier between the air and the fuel reactors (Abad, Garcia-Labiano et al. 2007; Ekström, Schwendig et al. 2009). Although this configuration has been demonstrated experimentally at lab and pilot scales (Kronberger, Johansson et al. 2004; Linderholm, Abad et al. 2008; Ding, Wang et al. 2012), the dual CFB-based CLC process is still facing many technical and operational complexities which arise mainly from the interconnected reactors configuration. Aside from the design and operational complexity created by the need to manage the solids exchange so that mass and heat balances within the closed loop are fulfilled, the exchange of solids itself brings additional costs and complexity. This circulation between the two reactors requires efficient and costly particles separation system such as a cyclone. This particle separation is particularly difficult due to the extremely harsh reactive and high temperature conditions.

Attempts have followed in recent years to address these issues where reactor concepts with no external solid circulation have been proposed (Noorman, van Sint Annaland et al. 2007; Hamers, Gallucci et al. 2013; Zaabout, Cloete et al. 2013). Following this philosophy, this paper will present a new CLC reactor concept with no external solids circulation. The proposed IC-CLC concept consists of a single reactor divided into two sections, the air and fuel sections, with an oxygen carrier circulating internally between them. This concept is expected to bring large benefits in terms of process simplification through avoiding external solids circulation and process intensification by direct heat integration and ability of operation under pressurized conditions. A large flexibility in the solids circulation rate is also granted due to the ability to operate the air section in a wide range of gas velocities between the bubbling and fast fluidization regime. The fuel section is operated under bubbling regime conditions.

All of these advantages make the IC-CLC concept the most practical solution by which the most important advantages of the interconnected configuration can be

maintained, while alleviating the most important challenges encountered in this configuration.
This paper will use fundamental flow modelling approach for a virtual proof of concept. Fundamental CFD modelling is ideal for this kind of virtual prototyping application because it can be used to quickly and economically evaluate a range of new process ideas and reactor configurations before any expensive and time-consuming physical experiments are conducted. This paper presents a numerical investigation of the hydrodynamics in different reactor designs of the IC-CLC concept. The most optimized design is selected for further hydrodynamic investigation with a dedicated central composite design.

NEW CONCEPT

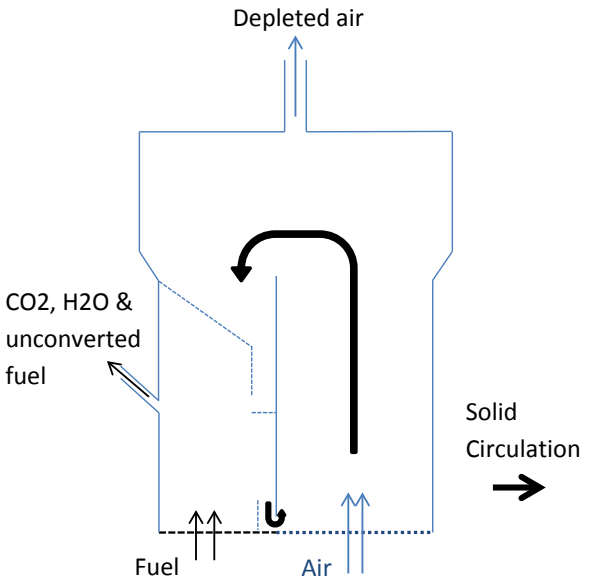

Figure 1: Internal circulating CLC concept IC-CLC

The proposed IC-CLC concept consists of a single reactor with internal physical partitions creating two reactor sections as shown in Figure 1. Air is injected in one section of the reactor (the fast region) for oxidation of the oxygen carrier while a gaseous fuel is injected to the second reactor section (the slow region) where oxygen carrier reduction takes place. An expanding freeboard region is added where the depleted air transporting oxygen carriers slows down before it leaves the reactor from the outlet at the top while the oxygen carriers fall down into the fuel region. To complete the cycle the oxygen carriers flow back to the air region through the opening at the bottom of the reactor. Reduction gases products leave the reactor from the fuel section outlet on the side of the reactor (Figure 1).
The two reactor sections are connected to each other without any physical separation or seals. This will certainly allow for gas leakage between the two sections in both sides. The viability of this concept will therefore be proved only when the gas leakage between the two sections can be minimized to tolerable quantities.
In order to calculate the amount of gas leakage that will occur, it can be assumed that the gas will leak from one reactor section to the other at a rate proportional to the solids circulation rate. Hence, a new variable for the volumetric ratio of gas to solids transferred from one reactor section to the next can be defined: the gas/solids leakage ratio. At a fixed gas/solids leakage ratio, the gas leakage will therefore be proportional to the solids circulation rate required to react with a given gas stream. If the rate of solids recirculation is very small in relation to the gas feed streams and the gas/solids leakage ratio is kept small by good reactor design, it is possible that gas leakages can become very small.
As an example, the gas/solids leakage ratio can be calculated for a CLC system using a NiO oxygen carrier and methane as fuel. The reaction occurring in the fuel reactor section is as follows (assuming full oxidation of methane):

Equation 1 :

$$4NiO + CH_4 \rightarrow 4Ni + CO_2 + 2H_2O$$

When assuming a solids circulation rate $\left(\dot{m}_{solids}\right)$ of 1 kg/s, a desired degree of solids conversion $\left(c_{NiO}\right)$ of 50% and an active material content in the oxygen carrier $\left(x_{NiO}\right)$ of 40%, the molar flowrate of NiO $\left(\dot{n}_{NiO}\right)$ to be reacted coming into the fuel reactor can be calculated as:

Equation 2:

$$\dot{n}_{NiO} = \frac{\dot{m}_{solids} c_{NiO} x_{NiO}}{M_{NiO}} = \frac{1 \cdot 0.5 \cdot 0.4}{0.0747} = 2.677 \text{ mol/s}$$

According to the stoichiometric ratio of reactants, 0.669 mol/s of methane would be required to achieve 50% conversion of the solids being fed at 1 kg/s. Assuming 99.9% fuel conversion and no side-reactions, the outlet stream of the fuel reactor section would consist of 0.669 mol/s CO_2, 0.00067 mol/s of unreacted CH_4, 1.337 mol/s of H_2O (which will be easily condensed out before compression, transport and storage) and a certain amount of depleted air which leaked from the air reactor.
For an oxygen carrier material density $\left(\rho_{solids}\right)$ of 3400 kg/m^3, a reactor temperature $\left(T\right)$ of 1200 K and atmospheric pressure $\left(P\right)$, the molar flowrate of gas leakage between reactor sections $\left(\dot{n}_{leak}\right)$ can be calculated as a function of the gas/solids leakage ratio $\left(X\right)$.

Equation 3:

$$\dot{n}_{leak} = \frac{\dot{V}_{leak} P}{RT} = \frac{X \frac{\dot{m}_{solids}}{\rho_{solids}} P}{RT} = X \frac{\frac{1}{3400} 101325}{8.314 \cdot 1200} = 0.00299 \cdot X \text{ mol/s}$$

Assuming that the gas leaking from the fuel reactor to the air reactor is fully converted (consisting only of CO_2 and H_2O in a 1:2 molar ratio), the rate of CO_2 leakage to the air reactor will be one third of that calculated in Eq. 3. Using this information, the purity of the CO_2 (after water condensation) from the fuel reactor and the CO_2 capture efficiency (determined by the CO_2 which leaked

to the air reactor) can be plotted as a function of the gas/solids leakage ratio. For this particular example, this plot is given in Figure 2.

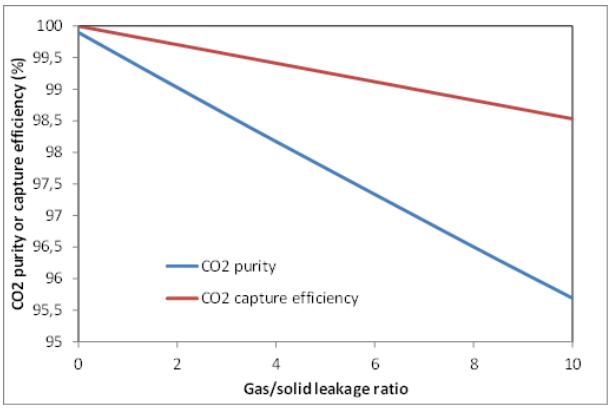

Figure 2: CO_2 purity and CO_2 capture efficiency as a function of gas/solid leakage ratio.

It can be seen that both the CO_2 purity and CO_2 capture efficiency remain high even at high gas/solid leakage ratios. This is a result of the very small volumetric flowrate of solids that is required to react with a given volumetric flowrate of gas and shows that the IC-CLC concept holds great promise for this particular process.
The potential for practically controlling the gas/solids leakage ratio will be further investigated in this work through CFD simulations. This paper will explore options of reactor and connection ports design and operating conditions which would result in minimized gas leakage between the two reactor sections. It is important that the gas leakage is minimized in a way to result in high CO_2 capture efficiency and CO_2 purity. The effect of reducing the contact areas between the two reactor sections by adding physical separation walls (as show the dashed lines in figure 1) close to the connecting opening at the top and the bottom will be investigated using CFD simulations.

SIMULATIONS

Simulations were carried out the well-established two fluid model (TFM) closed by the kinetic theory of granular flows (KTGF).

Model equations

Conservation equations are solved for each of the two phases present in the simulation. The continuity equations for the gas and solids phases phase are given below:

Equation 4:

$$\frac{\partial}{\partial t}\left(\alpha_g \rho_g\right)+\nabla\cdot\left(\alpha_g \rho_g \vec{\upsilon}_g\right)=0$$

$$\frac{\partial}{\partial t}\left(\alpha_s \rho_s\right)+\nabla\cdot\left(\alpha_s \rho_s \vec{\upsilon}_s\right)=0$$

Momentum conservation for the gas phase is written as

Equation 5:

$$\frac{\partial}{\partial t}\left(\alpha_g \rho_g \vec{\upsilon}_g\right)+\nabla\cdot\left(\alpha_g \rho_g \vec{\upsilon}_g \vec{\upsilon}_g\right)=-\alpha_g \nabla p+\nabla\cdot\bar{\bar{\tau}}_g+\alpha_g \rho_g \vec{g}+K_{sg}\left(\vec{\upsilon}_s-\vec{\upsilon}_g\right)$$

And for the solids as

$$\frac{\partial}{\partial t}\left(\alpha_s \rho_s \vec{\upsilon}_s\right)+\nabla\cdot\left(\alpha_s \rho_s \vec{\upsilon}_s \vec{\upsilon}_s\right)=-\alpha_s \nabla p-\nabla p_s+\nabla\cdot\bar{\bar{\tau}}_s+\alpha_s \rho_s \vec{g}+K_{gs}\left(\vec{\upsilon}_g-\vec{\upsilon}_s\right)$$

The inter-phase momentum exchange coefficient $\left(K_{gs}=K_{sg}\right)$ was modelled according to the formulation of Syamlal and O'Brian (Syamlal, Rogers et al. 1993).
Solids phase stresses were determined according to the KTGF analogy. The conservation equation for granular temperature is given below:

Equation 6:

$$\frac{3}{2}\left[\frac{\partial}{\partial t}\left(\alpha_s \rho_s \Theta_s\right)+\nabla\cdot\left(\alpha_s \rho_s \vec{\upsilon}_s \Theta_s\right)\right]=\left(-p_s \bar{\bar{I}}+\bar{\bar{\tau}}_s\right):\nabla\vec{\upsilon}_s+\nabla\cdot\left(k_{\Theta_s}\nabla\Theta_s\right)-\gamma_{\Theta_s}+\phi_{gs}$$

This partial differential equation was simplified to an algebraic equation by neglecting the convection and diffusion terms (Van Wachem, Schouten et al. 2001). The two final terms in Eq. 6 are the collisional dissipation of energy (Lun, Savage et al. 1984) and the interphase exchange between the particle fluctuations and the gas phase (Gidaspow, Bezburuah et al. 1992). Solids stresses are calculated according to shear and bulk (Lun, Savage et al. 1984) viscosities. The shear viscosity consists of three parts: collisional (Gidaspow, Bezburuah et al. 1992; Syamlal, Rogers et al. 1993), kinetic (Syamlal, Rogers et al. 1993) and frictional (Schaeffer 1987). The solids pressure formulation by Lun et al. (Lun, Savage et al. 1984) was enhanced by the frictional pressure formulation by Johnson and Jackson (Johnson and Jackson 1987). The radial distribution function of Ogawa and Oshima (Ogawa, Unemura et al. 1980) was employed.

Boundary conditions

A simple no-slip wall boundary condition was set for the gas phase. The Johnson and Jackson (Johnson and Jackson 1987) boundary condition was used for the granular phase with a specularity coefficient of 0.25.

Equation 7:

$$\vec{\tau}_s=-\frac{\pi}{6}\sqrt{3}\varsigma\frac{\alpha_s}{\alpha_{s,\max}}\rho_s g_{0,ss}\sqrt{\Theta_s}\vec{U}_{s,\|}$$

The inlet condition was specified as a velocity inlet injecting air at a flow rate of 0.6 m/s. CO_2 was injected through a velocity inlet on the back wall to mimic the experiment. In the 2D simulation, CO_2 was injected via a source term. The outlet was designated as a pressure outlet at atmospheric pressure.

Flow solver and solver settings

The commercial software package, FLUENT 13.0 was used as the flow solver. The phase coupled SIMPLE scheme (Patankar 1980) was used for pressure-velocity coupling and the higher order QUICK scheme (Leonard and Mokhtari 1990) for the spatial discretization of all remaining equations. First order implicit temporal discretization was used (Cloete, Amini et al. 2011). Unsteady state simulations have been performed with a time step of 0.001s. A restitution coefficient of 0.9 has been used. Further model setting can be found in (Cloete, Zaabout et al. 2013)

RESULTS AND DISCUSSIONS

The IC-CLC concept allows for large flexibility in terms of designing the partitions and connections between the

fuel and the air zones. The resulting reactor design has a direct impact on the reactor performance. A reliable reactor design should be able to maintain minimized leakage between the two reactor sections to ensure high CO2 purity and CO2 capture efficiency. Hence, to reduce the risk, it is highly recommended to use an efficient and quick numerical tool to assess the different reactor design before any expensive and time-consuming experimental demonstration is done. The well-known Two Fluid Model ((TFM) approach closed by the Kinetic Theory of Granular Flows (KTGF)) was used for this purpose as will be shown below.

Reactor design

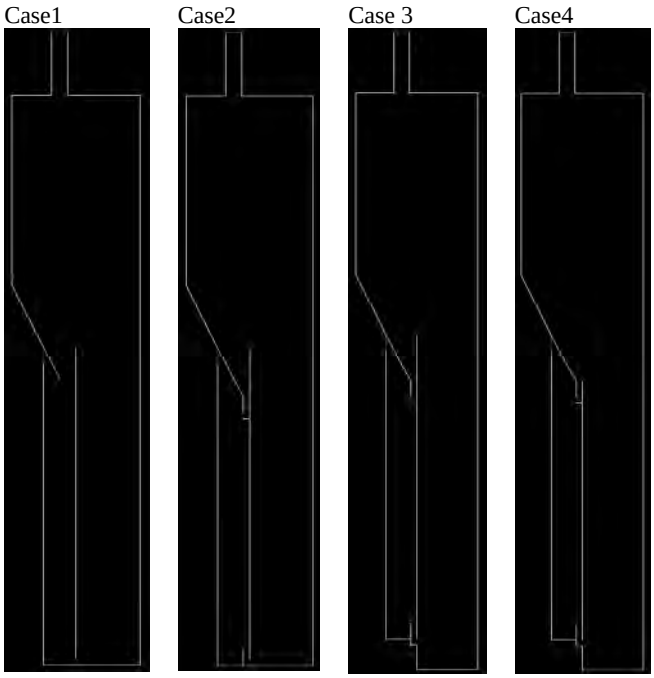

Figure 3: IC-CLC concept: investigated reactor configurations.

Several reactor configurations have been investigated as shown in Figure 3 where the emphasis was put on changing the extent of the connection areas between the two reactor sections (the high of the unit is 2 m in total; the reactor zone is 1 m height and the freeboard region is 1 m. The fuel section width is 0.1 m and the air section width is 0.2 m). Case 1, for example, exhibits large contact areas between the two reactor sections while, for the three other configurations, the contact areas were narrowed to 2 cm width connecting ports; one at the bottom and the other at top. Parameters such as solids circulation rate, air leakage to the fuel section and fuel leakage to the air section have been quantified for each reactor configuration and the performances of each configuration were compared through the previously discussed gas/solid leakage ratio parameter which describes the ratio between the volumetric gas leakage through the port and the volumetric solids circulation rate. Gas feeds to both reactor sections and the static bed height were kept the same for the four reactor configurations during this comparative study: air was used as a feed gas to the air section with 1 m/s fluidization velocity, U, and methane was used as a feed gas to the fuel section with a fluidization velocity of 0.3 m/s. The initial static bed height, H_s, was 0.5 m. Glass beads of 200 µm mean diameter and 2500 kg/m^3 density were used as a bed to be fluidized (The minimum fluidization velocity is 0.0451 m/s).

As shown in Table 1, results from case 1 show high air and fuel leakages through the two connections with a very low solid circulation rate between the two reactor sections. With large connecting areas between the two reactor sections in case 1, gases in both reactor sections find less resistance to flow freely in both sides, causing therefore a large amount of leakage. The resulting air/solid and fuel/solid ratios are very high, implying that this reactor design fails to deliver high CO_2 purity and CO_2 capture efficiency.

Table 1: Effect of reactor design: simulations results. Data have been averaged over 30s real process time.

	Case 1	Case 2	Case 3	Case 4
Air flow rate-bot (m3/s)	0.00189	2.02E-05	0.00037	1.24 E-5
Air flow rate -top (m3/s)	0.00857	0.00692	0.00604	0.00541
Fuel flow rate-bot (m3/s)	0.00837	0.00531	0.00432	0.00781
Fuel flow rate -top (m3/s)	0.01299	0.00043	0.00092	0.00032
Total-solid flow rate (m3/s)	0.00022	0.00386	0.00337	0.00530
Fuel flow rate /solid ratio	93.9225	1.4865	1.55856	1.53449
Air flow rate /solid ratio	46.0169	1.795499	1.90612	1.02368

For the three other cases where the connections between the two regions are narrowed, high solids circulation rates were observed. Case 2 and 3 showed comparable values of solids circulation rate although the extension of the air region at the bottom for case 3. Case 4 however showed a 25 % increase in the solids circulation rate compared to case 2 and 3; by shortening the bar separating the two regions in case 4 to the level of the narrow port at the top it becomes easier for more entrained solids to the freeboard to reach the side and fall into the port to circulate to the fuel section. As for the gas leakage between the two reactor sections, the fuel was found to leak mainly through the port at the bottom while the air leaks through the port at the top. It naturally follows the solids circulation path.

The reactor performance with respect to gas leakage was quantified in the form of fuel/solid and air/solids leakage ratio parameters. The three reactor designs with narrow connection ports show values lower than 2 for both fuel/solid and air/solid leakage ratios implying that the three of them have the potential to maintain high CO_2 capture efficiency and CO_2 purity. The port design is therefore the most influential parameter in the gas leakage between the two reactor sections; narrow connection port creates conditions with solids flowing close to maximum packing which make them play the role of a physical plug that restricts the gas freedom to flow through the port.

In the light of the results presented above, the reactor configuration depicted in Figure 4 was selected for further investigation. The top part of the unit was

expanded in both the right and left sides for allowing for larger air flow rate while preventing solids elutriation. Instantaneous solids holdup in the unit shows denser bed conditions in the fuel section due to low gas feed and dilute bed conditions in the air section due to the high fluidization velocity in that region.

Continuous solids circulation between the two reactor sections is established due the difference in the gas feed velocities in each section: solids are first entrained by air to the freeboard then fall into the connecting port at the top, and thereafter flow down to the fuel section. Accumulation of solids in the fuel section leads to hydrostatic pressure build up which drives the solids to flow back to the air section through the connecting port at the bottom.

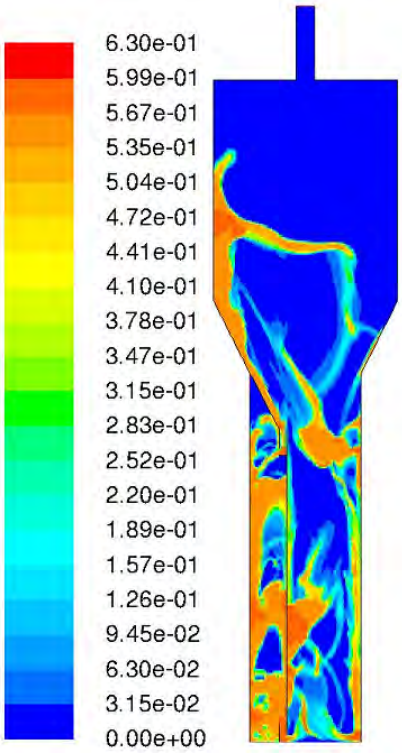

Figure 4: Instantaneous solid holdup in the rig; Hs= 0.6 m and U= 1.25 m/s.

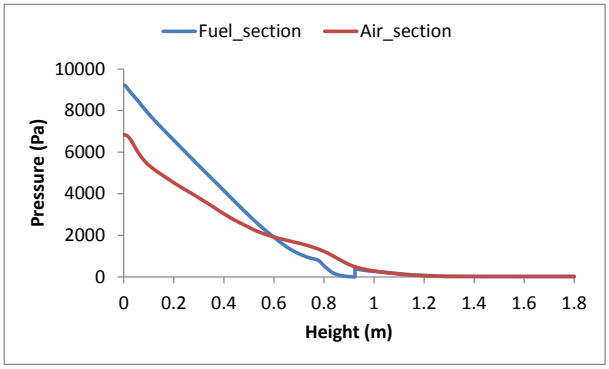

Figure 5: Mean axial pressure plotted along the two reactor sections; Hs= 0.6 m and U= 1.25 m/s.

The axial pressure plotted along the height of the reactor in both the fuel and the air sections (Figure 5) illustrates this solids circulation mechanism where it shows the pressure build up in the fuel section. At the bottom part of the reactor the pressure in the fuel section is higher than in the air section. This forces the solids to flow to the air region through the port at the bottom. At the top part of the reactor the situation is inversed: the pressure in the air section becomes higher than in the fuel one. This pressure difference drives the solids to flow to the fuel section through the port in the top.

More detailed investigation of the reactor configuration

In the light of this good gas leakage performance, the chosen reactor configuration was further investigated by means of a central composite design. A central composite design is a statistical method which allows for the fitting of a second order model through a set of data collected from well-defined experiments (simulation experiments in this case). The relative importance of the different effects in relation to each other can be quantified, together with the accuracy by which the model fits the data. In this case, however, only the response surface is required to gain a better understanding of the performance of this concept as two independent variables were varied:

- The first independent variable was the static bed height (solids loading inside the reactor). Since the mass transfer between reactor sections is driven by hydrostatic pressure differences, the height of the beds in the respective sections are expected to have an influence on the solids recirculation rate and the gas leakage. This factor is expressed as the static bed height with which the simulation was initialized (the initial solids volume fraction was 0.6).
- The velocity at which the air bed section was fluidized was the second factor. A greater difference between the fluidization velocities in the two reactor sections is expected to increase the solids recirculation rate. This factor was expressed as the ratio between the fluidization velocity in the fast section and that in the slow section which was kept constant at 0.3 m/s. As can be seen in **Error! Reference source not found.**, the section at the right was taken as the fast section (air section) and the left section as the slow one (fuel section).

Table 2: Central composite design with varying the fluidization velocity in the air section and the static bed height.

	U (m/s)	H (m)
1	0.8965	0.2586
2	0.8965	0.5414
3	1.6036	0.2586
4	1.6036	0.5414
5	0.7500	0.4000
6	1.7500	0.4000
7	1.2500	0.2000
8	1.2500	0.6000
9 (C)	1.2500	0.4000
10 (C)	1.2500	0.4000

Ten simulations were completed at different values of these two independent variables as specified in Table 2. The same particles as in the previous section are used

for this central composite design study. The response of the following three dependent variables was recorded:

- The solids recirculation rate (m^3/s) quantified as the average volumetric flowrate of the solids through the two connection ports.
- The gas/solid leakage ratio from the air reactor section into the fuel reactor section.
- The gas/solid leakage ratio from the fuel reactor section into the air reactor section.

Reactor performance within the central composite design

As expected, both the fluidization velocity in the air section and the static bed height play a major role in driving solids circulation between the two reactor sections. As can be seen in Figure 6, solid flow rate increases with both the initial static bed height and the fluidization velocity in the air section, although it tends to plateau for higher values. Naturally by increasing either the static bed height or the fluidization velocity larger amount of solids is entrained to the freeboard and falls into the fuel region. Greater solids accumulation in the fuel section leads to greater hydrostatic pressure which builds up and thereby forces a greater amount of solids to circulate back to the air region through the port at the bottom.

This is actually true as along as the port in the top is not completely full of solids. The form of the plateau shown by the response surface is due to the restriction imposed by the size of the connections ports on the solids flow; at high solids entrainment the connections ports get completely filled with solids and therefore restrict further increase in the solids circulation rate. At high static bed heights the unit can also face a loss of solids through the outlet in the fuel section. This explains the decrease in the solids circulation rate shown by the response surface at high static bed heights combined with high fluidization velocity in the air section.

Through this kind of surface response it is also easy to identify the operating conditions under which no solids circulation takes place making it therefore clearer to identify where the process would fail.

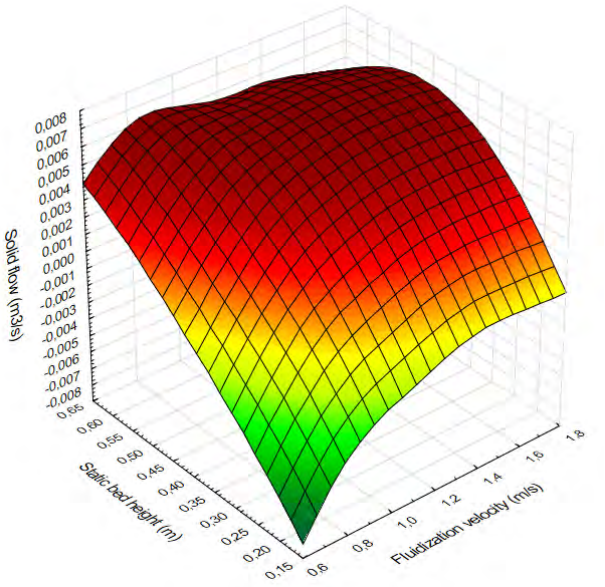

Figure 6: Volumetric solid flow rate response to the change in the fluidization velocity in the air section and the initial static bed height

As for the gas leakage it was found that fuel leakage takes place mainly through the port at the bottom while the air leakage takes place through the port at the top.

The fuel/solid leakage ratio response to the change in the fluidization velocity and the static bed height showed similar shape to that found for the solids flow rate (Figure 7); it increases with the increase in the fluidization velocity and static bed height and then plateaus. As explained previously the plateau forms due to the maximum solids packing conditions which take place in the port during high solids entrainment from the air section. In these conditions any further increase in the solids circulation rate and gas leakage is restricted by the port size.

Values close to 1 were found for the fuel/solid leakage ratio for all operating conditions within the central composite design (the negative values at very low static bed heights and fluidization velocities are simply the result of extrapolation). This means that the chosen reactor configuration is able to maintain very high CO_2 capture efficiency.

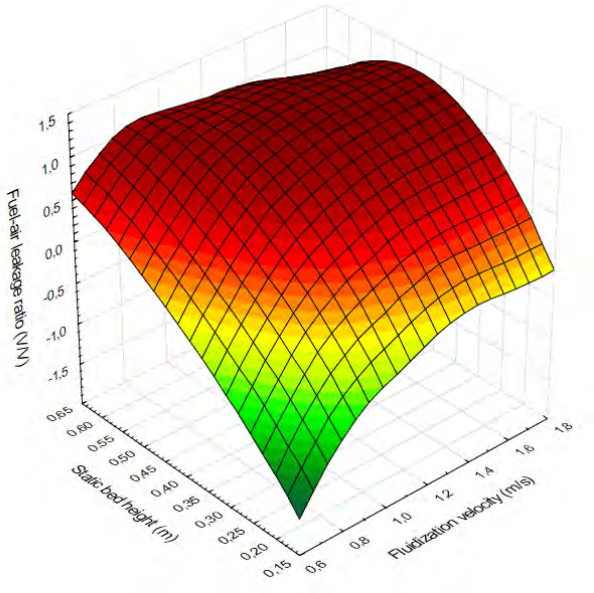

Figure 7: Fuel/solid leakage ratio response to the change in the fluidization velocity in the air section and the initial static bed height

The air/solid leakage ratio responds differently to the change in the air fluidization velocity and the static bed height. Values close to one were found for large fluidization velocities and static bed heights proving the ability of this reactor configuration to maintain very high CO_2 purity within these conditions. However, regions of poor performance were identified where operation of the concept should be avoided; combining low air fluidization velocities with low static bed heights results in very high air/solids leakage ratio and thereby very low CO_2 purity according to the discussion in section 2. The high values of the air/leakage ratio are consequences of the low solids circulation rate between the two reactor sections (Figure 8). As shown earlier, high solids circulation rates are required to create

conditions close to maximum solids packing in the port at the top (from where most of the air leakage takes place), to reduce the freedom of air to leak to the fuel section.

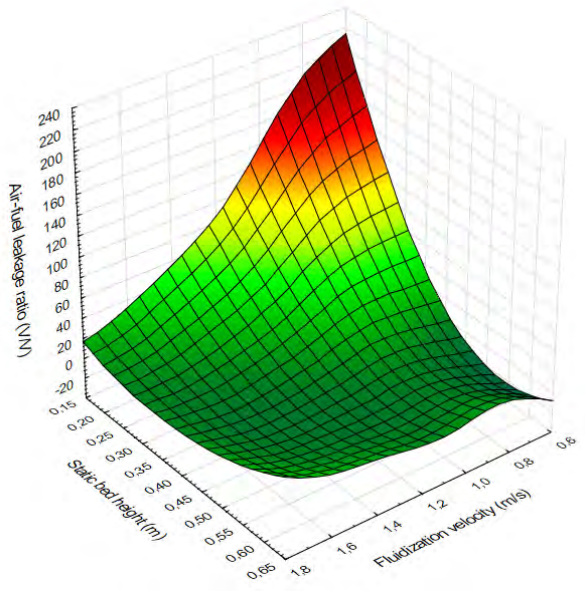

Figure 8: Air/solid leakage ratio response to the change in the fluidization velocity in the air section and the initial static bed height

Experimental unit

In the light of the promising results showed by simulations, a pseudo 2D (1.5 cm depth) experimental unit was constructed and operated in order to study the hydrodynamics of the IC-CLC concept. The bottom part of the unit is 1m height and the freeboard is 80 cm. Narrow connections ports of 2 cm width have been made (Figure 9). First tests of the unit with glass particles of 200 µm showed stable operation with continuous solids circulation between the two unit sections. Conditions where solids flow close to maximum packing in the connection ports were also observed (Figure 9); no blockage of the ports have been observed to take place in these conditions.

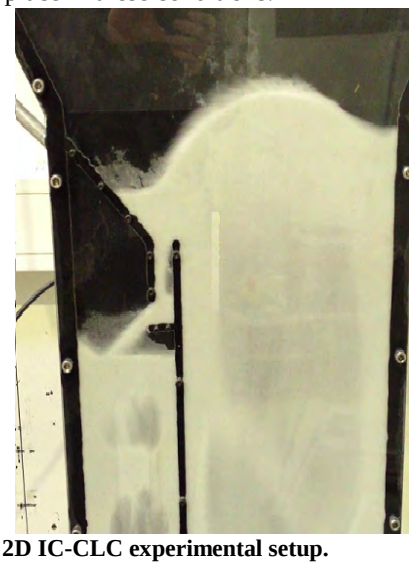

Figure 9: Pseudo 2D IC-CLC experimental setup.

Further testing on this unit is still required to prove experimentally the potential of this concept to maintain minimized leakage between the two unit sections. Parameters such as the solids circulation rate and gas leakages between the two unit sections will be quantified within a wide range of operating conditions.

CONCLUSION

A hydrodynamic investigation of an innovative CLC concept based on internal circulating fluidized bed (IC-CLC) has been carried out. The new concept consists of a single reactor with a physical separation inside dividing it into two sections; the fuel and the air sections. Oxygen carriers circulate between the two sections through two connecting ports, one at the bottom and one at the top. These connections allows for gas leakage in both sides which reduces the concept ability to capture CO_2 and generate high purity CO2. Good reactor design is therefore the key for the IC-CLC concept to succeed in maintaining high CO_2 purity and high CO_2 capture efficiency.

Fundamental multiphase flow models (based on the Kinetic Theory of Granular Flow KTGF) have then been used in this study to investigate the hydrodynamics in different reactor designs in order to identify the most optimized one before any expensive experimental demonstration is made. Reactor designs with narrow connection ports have resulted in the best leakage performance; small port size creates solids packing conditions which play the role of a physical plug that restricts the gas freedom to flow through the ports. The most optimized design has been further investigated in a framework of a central composite design where the bed loading and gas fluidization velocity in the air section are varied. Values close to 1 have been found for the fuel/solid ratio parameter implying that high CO_2 capture efficiency can be achieved through this design in a wide range of operating conditions. Regions of poor performance were also identified where the design would fail to maintain high CO_2 purity. In particular, low bed loadings and low fluidization velocities in the air section should be avoided as they results in high values of the air/solid ratio.

In the light of the promising results found in simulations, an experimental unit designed with narrow connection ports was constructed. The first tests already showed that low gas/solid leakage ratio can be achieved by this design.

REFERENCES

ABAD, A., ADANEZ, J., et al. (2007). "Mapping of the range of operational conditions for Cu-, Fe-, and Ni-based oxygen carriers in chemical-looping combustion." Chemical Engineering Science **62**(1-2): 533-549.

ABAD, A., GARCIA-LABIANO, F., et al. (2007). "Reduction kinetics of Cu-, Ni-, and Fe-based oxygen carriers using syngas (CO + H-2) for chemical-looping combustion." Energy & Fuels **21**(4): 1843-1853.

ADANEZ, J., ABAD, A., et al. (2012). "Progress in Chemical-Looping Combustion and Reforming technologies." Progress in Energy and Combustion Science **38**(2): 215-282.

BUTT, T. E., GIDDINGS, R. D., et al. (2012). "Environmental sustainability and climate change mitigation-CCS technology, better having it than not having it at all!" Environmental Progress & Sustainable Energy **31**(4): 642-649.

CLOETE, S., AMINI, S., et al. (2011). "On the effect of cluster resolution in riser flows on momentum and reaction kinetic interaction." Powder Technology **210**(1): 6-17.

CLOETE, S., ZAABOUT, A., et al. (2013). "The generality of the standard 2D TFM approach in predicting bubbling fluidized bed hydrodynamics." Powder Technology **235**: 735-746.

DING, N., WANG, W. R., et al. (2012). "Development and Testing of an Interconnected Fluidized-Bed System for Chemical Looping Combustion." Chemical Engineering & Technology **35**(3): 532-538.

EKSTRÖM, C., SCHWENDIG, F., et al. (2009). "Techno-Economic Evaluations and Benchmarking of Pre-combustion CO2 Capture and Oxy-fuel Processes Developed in the European ENCAP Project." Energy Procedia **1**(1): 4233-4240.

GIDASPOW, D., BEZBURUAH, R., et al. (1992). Hydrodynamics of Circulating Fluidized Beds, Kinetic Theory Approach. 7th Engineering Foundation Conference on Fluidization 75-82.

HAMERS, H. P., GALLUCCI, F., et al. (2013). "A novel reactor configuration for packed bed chemical-looping combustion of syngas." International Journal of Greenhouse Gas Control **16**(0): 1-12.

HOSSAIN, M. M. and DE LASA, H. I. (2008). "Chemical-looping combustion (CLC) for inherent CO2 separations-a review." Chemical Engineering Science **63**(18): 4433-4451.

IEA (2012). World Energy Outlook 2012, International Energy Agency.

ISHIDA, M., ZHENG, D., et al. (1987). "Evaluation of a chemical-looping-combustion power-generation system by graphic exergy analysis." Energy **12**(2): 147-154.

JOHNSON, P. C. and JACKSON, R. (1987). "Frictional-Collisional Constitutive Relations for Granular Materials, with Application to Plane Shearing." Journal of Fluid Mechanics **176**: 67-93.

KRONBERGER, B., JOHANSSON, E., et al. (2004). "A two-compartment fluidized bed reactor for CO2 capture by chemical-looping combustion." Chemical Engineering & Technology **27**(12): 1318-1326.

LEONARD, B. P. and MOKHTARI, S. (1990). ULTRA-SHARP Nonoscillatory Convection Schemes for High-Speed Steady Multidimensional Flow. NASA TM 1-2568 (ICOMP-90-12), NASA Lewis Research Center.

LINDERHOLM, C., ABAD, A., et al. (2008). "160 h of chemical-looping combustion in a 10 kW reactor system with a NiO-based oxygen carrier." International Journal of Greenhouse Gas Control **2**(4): 520-530.

LUN, C. K. K., SAVAGE, S. B., et al. (1984). "Kinetic Theories for Granular Flow: Inelastic Particles in Couette Flow and Slightly Inelastic Particles in a General Flow Field." Journal of Fluid Mechanics **140**: 223-256.

NOORMAN, S., VAN SINT ANNALAND, M., et al. (2007). "Packed Bed Reactor Technology for Chemical-Looping Combustion." Industrial & Engineering Chemistry Research **46**(12): 4212-4220.

OGAWA, S., UNEMURA, A., et al. (1980). "On the Equation of Fully Fluidized Granular Materials." Journal of Applied Mathematics and Physics **31**: 483.

PATANKAR, S. (1980). Numerical Heat Transfer and Fluid Flow, Hemisphere Publishing Corporation.

SCHAEFFER, D. G. (1987). "Instability in the Evolution Equations Describing Incompressible Granular Flow." Journal of Differential Equations **66**: 19-50.

SYAMLAL, M., ROGERS, W., et al. (1993). MFIX Documentation: Volume 1, Theory Guide. Springfield, National Technical Information Service.

VAN WACHEM, B. G. M., SCHOUTEN, J. C., et al. (2001). "Comparative analysis of CFD models of dense gas-solid systems." AIChE Journal **47**(5): 1035-1051.

ZAABOUT, A., CLOETE, S., et al. (2013). "Experimental Demonstration of a Novel Gas Switching Combustion Reactor for Power Production with Integrated CO2 Capture." Industrial & Engineering Chemistry Research **52**(39): 14241-14250.

CFD MODELLING OF HEAT SUPPLY IN FLUIDIZED BED FAST PYROLYSIS OF BIOMASS

Pelle MELLIN[1]* , Yueshi WU[1], Efthymios KANTARELIS[1] , Weihong YANG[1]

[1] KTH Royal Institute of Technology, Division of Energy and Furnace Technology, Brinellvägen 23, 10044 Stockholm, SWEDEN

* E-mail: pmellin@kth.se

ABSTRACT

This paper investigates the heat supply to the fast pyrolysis process, by addition of oxygen in the fluidizing gas. Since the technology will be further developed, a solution for the heat supply in a large-scale reactor must be conceived, which is one option to achieve the primary target: to operate with as little extra heat as possible.

Corrections for the granular bed material and the biomass particles are implemented in the simulation. User Defined Functions (UDF) is extensively used to describe interactions of heat and momentum between the phases and a chemistry model is employed to describe the chemical reactions after pyrolysis.

The results are preliminary; however, the oxygen clearly reacts to provide heat. Primarily the secondary tar reacts and a loss of about 30% organic liquid yield is the result in this simulation, at an equivalence ratio of 0.026.

If heat only can be recovered from the bed zone, through the bed material, then a higher equivalence ratio than what was investigated in this paper would be needed.

If heat can be recovered from the whole reactor then a slight injection of oxygen would result in an autothermal system; which means the necessary heat to generate and pre-heat steam would be available.

Temperature instability in the freeboard prevented investigation of higher equivalence ratios, which should be pursued in further work.

Keywords: CFD, fast pyrolysis, pyrolysis oil.

INTRODUCTION

Fast pyrolysis of biomass implies pyrolysis with conditions maximized for production of liquids. The liquids are in vapour form in the process but when condensed outside the reactor they will typically form a dark, viscous, liquid called pyrolysis oil. A common reactor is the fluidized bed, which either is circulating or bubbling.

The main idea of our previous work is to use steam, as fluidizing agent that according to (Kantarelis et al. 2013) will produce deoxygenated oil, which in turn improves stability, acidity and calorific value. Dilution by water is a matter to be resolved; however, different separation methods exist by which chemicals can be extracted.

This process has the potential to convert large amounts of woody biomass to various fuels or chemicals, if upgraded in-situ or ex-situ. The concept, which we investigated previously, involves a fluidized bed with sand as the bed material and steam as the fluidizing gas (Kantarelis et al. 2013). The use of catalytic bed material in combination with steam was introduced in two prior publications (Kantarelis et al. 2014, Kantarelis et al. 2014). The catalyst contributes to a much higher quality of the liquid product, requiring less post treatment.

Constructing an industrial scale fluidized bed reactor for fast pyrolysis (or catalytic fast pyrolysis) of biomass requires consideration for sufficient heat supply. The fast pyrolysis can only be accomplished if high temperature in the bed material can be maintained; in this paper, we try to solve this by introducing oxygen mixed with the fluidizing gas. However, other solutions can be found in literature, these include:

- Heat supplied by pre-heated fluidizing gases
- Heat supplied by the reactor walls, through convection and radiation
- Pipes or channels inside the fluidized bed, which supplies heat from a secondary reactor where pyrolysis char or gas is combusted

Fluidized beds can also be used for heat exchange applications, meaning that the bed is a heat sink or heat source. This is typical in boilers where water-filled pipes generate high-pressure steam, with aid of the bed as a heat source.

Heat by an oxidizer is another method, which could provide benefits of uniform heating and flexibility in operation. The temperature drop by using a moist feedstock could be counteracted with an extra oxygen supply, as an example.

In order to the investigate potential, a model which takes into account the fluid flow of the reactor is needed. Hence, this paper uses CFD coupled with a pyrolysis-oxidation model, to estimate the heat generation due to oxygen in the fluidizing gas and what pyrolysis products that primarily react with oxygen. With this information, the effect on product composition can be estimated.

In previous modelling work (Mellin et al. 2013, Mellin et al. 2014), nitrogen was used as a fluidizing agent.

In this work, we have utilized steam but nearly the same results should be obtained using any other inert fluidizing agent with the same molar flow rate.

(Li et al. 2014) have investigated the influence of the Equivalence Ratio (ER) in a previous paper.

Autothermal operation was achieved at an equivalence ratio of about 0.05, which consumed about 22% of pyrolysis oil (at 500°C).
The purpose of this paper is to investigate the operation for our conditions, to see which reactions that primarily is responsible for heat release as well as the distribution. The equivalence ratios used for this paper is given in Table 1, the molar flow rate of the fluidizing gas is kept constant at 55.55 mol/h. The feeding rate of biomass was 5.7 kg/h, with a moisture content of 9.8 %wt.

Table 1: Parametric study of oxygen addition as ER.

ER [-]	O_2 [mol/h]	H_2O [mol/h]	[$g_{O2}/g_{dry\ biomass}$]
0	0.000	55.554	0.000
0.0088	1.946	53.604	0.004
0.0175	3.892	51.658	0.008
0.0263	5.838	49.712	0.012

Preferably, the exothermic and the endothermic reactions should balance each other at the same location in order to ensure temperature uniformity. In fact, uniformity in the bed is an important aspect when scaling up the technology.
In the next section, the model is described together with the pyrolysis-oxidation model. Then results are shown for the four cases shown in Table 1.

MODEL DESCRIPTION

The model is based on an Euler-Euler multiphase framework. ANSYS Fluent 14.5 is used for the simulations, using the Ferlin cluster through the Swedish National Infrastructure for Computing (SNIC). A heterogeneous kinetically controlled sub model describes the chemistry.
The main interest in this work is the oxygen, reacting with components in the gas phase. As a result, a simplified approach is considered adequate. Therefore, sand and biomass is modelled as one phase eulerian phase, which is a simplification introduced in a previous paper (Mellin et al. 2013).
We have also developed another more comprehensive model with three phases to take better into account the solids flow (Mellin et al. 2014). The comprehensive model is more demanding in computational resources, which is prohibitive for parametric studies.
Conservation equations are solved for each phase, the mixture phase and each specie at each iteration in every time step. The mass conservation equation for any phase is given in (1). The source term in the equation is due to reactions or any inlet.

Mass equation

$$\frac{\partial}{\partial t}(\alpha_i \rho_i) + \nabla \cdot (\alpha_i \rho_i \vec{u}_i) = \dot{m}_i + S_i \qquad (1)$$

The momentum (2) equation for the fluid phase is written in similar way. The stress tensor for the fluid phase and the granular phase is given in (4) and (5) respectively. The bulk viscosity of the granular phase is given in (6). The shear viscosity is given in (7), where the kinetic viscosity is assumed zero while collisional and kinetic viscosity is defined in (8) and (9) respectively.

This momentum equation also considers the interaction between the phases, which is expressed by (10); following the work by (Syamlal and O'Brien, 1993). The u_{mf} is estimated to 0.08 m/s at room temperature for this bed material, see Figure 1.

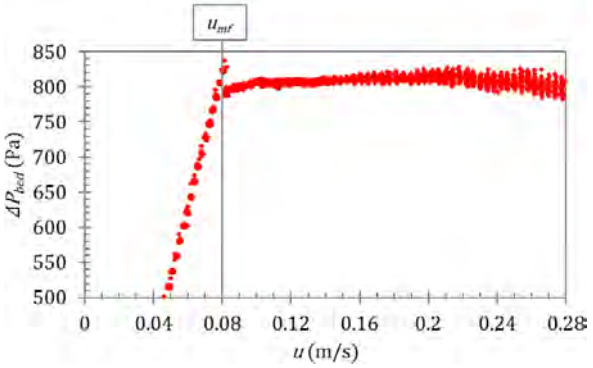

Figure 1: Pressure drop and fluidization velocity. (Mellin et al. 2013)

The drag force is computed using coefficients defined in (11) and (12), tuning of the coefficients C_1 and C_2 has been done according to the measured minimum fluidization velocity, u_{mf}, and thus being set to 9.19 and 0.28 respectively.

Momentum equation for fluid phase

$$\frac{\partial}{\partial t}(\alpha_f \rho_f \vec{v}_f) + \nabla \cdot (\alpha_f \rho_f Y_f \vec{v}_f \vec{v}_f) = -\alpha_f \nabla p + \nabla \bar{\bar{\tau}}_f + \alpha_f \rho_f \vec{g} + K_{fs}(\vec{v}_f - \vec{v}_s) + \dot{m}_{fs} \vec{v}_f \qquad (2)$$

Momentum equation for granular phase

$$\frac{\partial}{\partial t}(\alpha_f \rho_f \vec{v}_f) + \nabla \cdot (\alpha_f \rho_f Y_f \vec{v}_f \vec{v}_f) = -\alpha_f \nabla p + \nabla \bar{\bar{\tau}}_f + \alpha_f \rho_f \vec{g} + K_{fs}(\vec{v}_f - \vec{v}_s) + \dot{m}_{fs} \vec{v}_f \qquad (3)$$

Stress tensor equation for fluid phase

$$\bar{\bar{\tau}}_f = \mu_f \left[(\nabla \vec{v}_f + \nabla \vec{v}_f) - \frac{2}{3} \nabla \cdot \vec{v}_f I \right] \qquad (4)$$

Stress tensor equation for granular phase

$$\bar{\bar{\tau}}_s = \mu_s (\nabla \vec{v}_f + \nabla \vec{v}_f) + \left(\lambda_s - \frac{2}{3} \mu_s \right) \nabla \cdot \vec{v}_f I \qquad (5)$$

Equation for bulk viscosity in the granular phase

$$\lambda_s = \frac{4}{3} \alpha_s \rho_s d_s g_{0,ss} (1 + e_{ss}) \left(\frac{\theta_s}{\pi} \right)^{1/2} \qquad (6)$$

Equation for solid shear viscosity

$$\mu_s = \mu_{s,col} + \mu_{s,kin} + \mu_{s,fr} \qquad (7)$$

Collisional and kinetic viscosity respectively

$$\mu_{s,col} = \frac{4}{5} \alpha \rho d_s g_{0,ss} (1 + e_{ss}) \left(\frac{\theta_s}{\pi} \right)^{1/2} \alpha_s \qquad (8)$$

$$\mu_{s,kin} = \frac{\alpha d \rho \sqrt{\theta_s \pi}}{6(3 - e_{ss})} \left[1 + \frac{2}{5} (1 + e_{ss})(3e_{ss} - 1) \alpha_s g_{0,ss} \right] \qquad (9)$$

Moment interaction coefficient between the phases

$$K_{fs} = \frac{3 \alpha_s \alpha l \rho_f}{4 v_{r,s}^2 d_s} C_D \left(\frac{Re_s}{v_{r,s}} \right) \left| \vec{v}_s - \vec{v}_f \right| \qquad (10)$$

Minimum fluidization velocity

$$v_{r,s} = 0.5 \left(A - 0.06 Re_s + \sqrt{(0.06 Re_s)^2 + 0.12 Re_s (2B - A) + A^2} \right) \qquad (11)$$

$$A = \alpha_f^{4.14} \quad B = \begin{cases} \alpha_f^{C_1}, \ \alpha > 0.85 \\ C_2 \alpha_f^{1.28}, \ \alpha \le 0.85 \end{cases} \qquad (12)$$

Equation (13) gives the energy conservation equation for the fluid phase; here another interaction term is used. The interaction term corresponds to the work (Gunn, 1978); see (14) and (15).

Energy equation

$$\frac{\delta}{\delta t}\left(\alpha_f \rho_f h_f\right)+\nabla\cdot\left(\alpha_f \rho_f Y_f \vec{v}_f h_f\right)=-\alpha_f \frac{\partial p}{\partial t}+\bar{\bar{\tau}}_f:\nabla\vec{v}_f-\nabla\vec{q}_f+S+Q+\dot{m}_k h_k \qquad (13)$$

Energy interaction coefficient between the phases

$$h_{sf}=\frac{6k_f\alpha_s\alpha_f Nu_s}{d_s^2} \qquad (14)$$

$$Nu_s=\left(7-10\alpha_f+5\alpha_f^2\right)\left(1+0.7Re_s^{0.2}Pr^{1/3}\right)+\left(1.33-2.4\alpha_f+1.2\alpha_f^2\right)Re_s^{0.7}Pr^{1/3} \qquad (15)$$

Equations are also solved for each specie (16), here taking into account creation and destruction due to reactions. A diffusivity of 2.88×10^{-5} m^2/s is assumed for the gas phase and 1×10^{-10} m^2/s for the solid phase. The species involved in this simulation is given in Table 3.

Specie equation

$$\frac{\partial}{\partial t}\left(\alpha_f \rho_f Y_i\right)+\nabla\cdot\left(\alpha_f \rho_f Y_f \vec{v}_f\right)=\dot{m}_f+S_f \qquad (16)$$

The reactions used in this work are shown in Table 2, alongside the reference to mechanism and kinetic data. Stoichiometric coefficients are given in Table 3.

Table 2: Reactions employed in this work.

No.	Reaction	Mechanism
1	Water gas shift	(Zhang et al. 2011)
2	Primary pyrolysis to gas and char	(Mellin et al 2013)
3	Primary pyrolysis to p.tar	(Mellin et al 2013)
4	Secondary pyrolysis to s.tar and gas	(Mellin et al 2013)
5	Drying of biomass	(Mellin et al 2013)
6	Steam gasification of char	(Zhang et al. 2011)
7	Volatile activation	(Mellin et al 2013)
8	Oxidation of CO	(Wu et al. 2013)
9	Oxidation of H2	(Wu et al. 2013)
10	Oxidation of p.tar	(Wu et al. 2013)
11	Oxidation of s.tar	(Wu et al. 2013)
12	Oxidation of CH4	(Wu et al. 2013)
13	Oxidation of char to CO(CO2)	(Wu et al. 2013)
14	Gasification of char	(Wu et al. 2013)

Table 3: Stoichiometric coefficients for the reactions.

No.	CO	CO_2	H_2O	H_2	C_2H_4	C	CH_4	Tar1	Tar3	O_2
1	-1	1	-1	1						
2	0.32	0.19	2.65	0.02	0.08	6.14	0.15			
3								1		
4	2.90	0.36		1.25			0.80	-1	0.41	
5			1							
6	1		-1	1		-1				
7										
8	-1	1								0.5
9			1	-1						0.5
10		5.54	0.33					-1		3.3
11		6	3						-1	7.5
12	1		1				-1			0.5
13	2	(1)				-2(1)				-1
14	2	-1				-1				

Reactor geometry, mesh and time step

The reactor is cylindrical with an initial bed height of 12 cm, as the simulation progresses the fluidization results in a bed height of about 14 cm. In total, the bed material consists of 0.5 kg of SiO_2. The geometry is shown in Figure 2. The walls are adiabatic in this model, while in previous work a fixed temperature was used. The mesh size is large, in order to enable parametric studies. Total cell number is 31,141 with a maximum cell volume of 2.3×10^{-7}, equivalent to side length of about 6 mm.

The time step was kept at a fixed value of 7.5×10^{-4} s though during the starting seconds a lower value of 1×10^{-4} s to 5×10^{-4} s was used. Until about 0.5 s, a Stiff Chemistry Solver was utilized to aid in the convergence of the simulation.

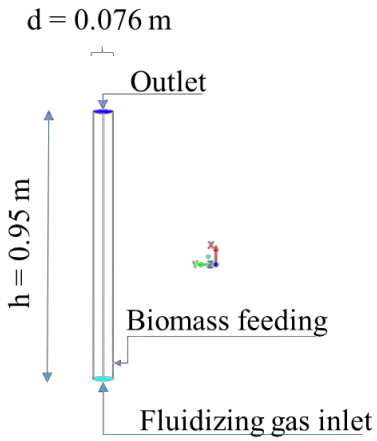

Figure 2: Reactor geometry, inlet and outlet.

RESULTS

20 seconds of physical time was computed in total for all cases. The initial temperature in all cases was 500 °C. At the end of the simulation, the average bed temperature was 455, 461, 463 and 464 °C respectively; this indicates that temperature so far only has a small effect on the reactions employed in this simulation. However, it will change as the conditions slowly stabilize. Figure 3 shows the mass fraction of O2 in the reactor, most reacts in the lower part.

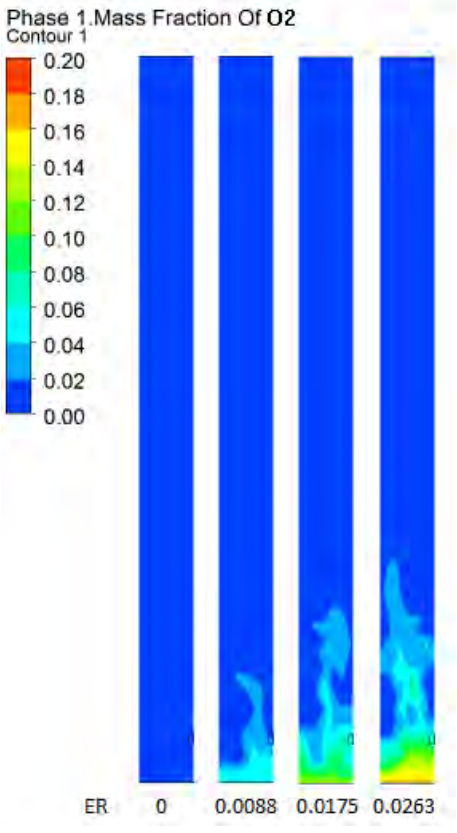

Figure 3: Mass fraction of O_2 in cross section (Z = 0), at 20 s.

Table 4: Reaction rate in the reactor for different ER.

No.	Reaction rate			
	ER = 0	ER = 0.0088	ER = 0.0175	ER = 0.0263
1	1.63E-08	2.16E-08	2.26E-08	2.20E-08
2	4.94E-06	4.94E-06	4.95E-06	4.95E-06
3	4.96E-06	4.95E-06	4.96E-06	4.95E-06
4	1.34E-06	2.39E-06	2.54E-06	2.60E-06
5	8.81E-06	8.61E-06	8.74E-06	8.81E-06
6	1.01E-09	1.24E-09	1.67E-09	1.65E-09
7	9.89E-06	9.88E-06	9.88E-06	9.89E-06
8	0.00E+00	1.34E-07	2.45E-07	4.23E-07
9	0.00E+00	2.78E-07	3.44E-07	4.27E-07
10	0.00E+00	2.67E-11	8.99E-11	2.22E-10
11	0.00E+00	4.74E-08	8.62E-08	1.26E-07
12	0.00E+00	7.89E-12	2.77E-11	7.08E-11
13	0.00E+00	7.33E-14	1.50E-13	2.35E-13
14	6.58E-19	8.23E-19	9.37E-19	9.99E-19

The simulation results were evaluated based on the reaction rates in the whole reactor, which are given in are given in Table 4. The temperature field at the top maintained a high temperature; a limit was put on temperature not to exceed 850 K, as to have realistic yields.

The oxidizing reactions, 8-13, increase steadily with higher ER. The reactions were used to determine what oxygen prefers to react with; Figure 4 shows the fractionation of oxidizing reactions, secondary tar is quickly consumed, after that H_2 and then CO. A deeper investigation into the kinetics data should be made to determine why.

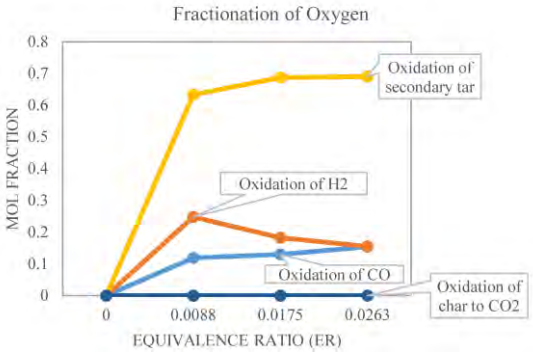

Figure 4: The fraction of O_2 towards different reactions.

Figure 5 shows the resulting product distribution of the different cases, at the outlet of the reactor (except for char which was evaluated based on formation rate). The liquid yield decreases, which is a trade-off for an authothermal process. The gas yield is comparatively low for the first case; however, it quickly increases as with higher oxygen additions and increasing temperature.

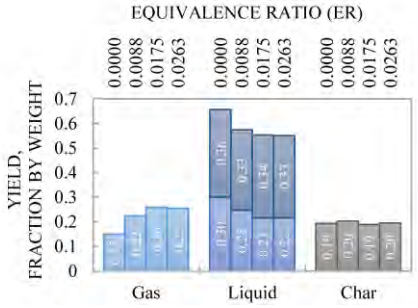

Figure 5: The pyrolysis products as function of ER.

The higher gas yield with higher temperature is due to secondary tar cracking. See the temperature field in Figure 6. The water yield remains similar in all cases, the difference of a few 2-3 % may be attributed to temporary fluctuations in each case.

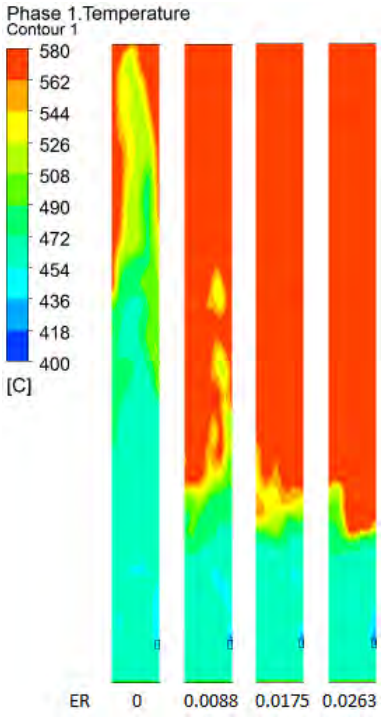

Figure 6: Gas temperature in cross section (Z = 0), at 20 s.

The momentous heat provided by the reactions is given in Figure 7. At this slightly elevated temperature, the organic liquid cracks and produce heat, which results in the first case having a positive net reaction heat. However, most of this heat is generated in the upper part of the reactor. Only a small net heat gain is evident in the lower part of the reactor.

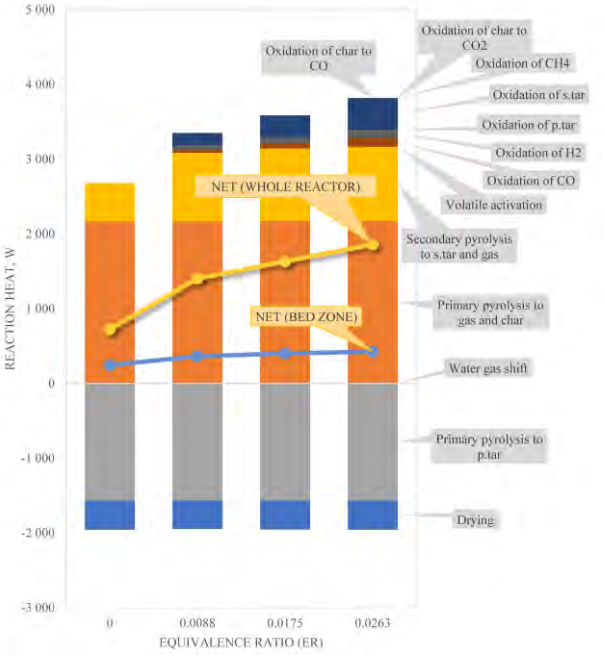

Figure 7: The heat generated by different reactions as function of ER, also net heat generation for the bed zone and the whole reactor.

The pre-heated gas provides, in all cases about 240 W of sensible heat and 628, 606, 584 and 562 W of latent heat; in the case of ER = 0, 0.0088, 0.0175 and 0.0263 respectively. Thus to generate the same amount of preheated steam, the requirement is high, which is shown in Figure 8. The process could be autothermal if the heat were recovered from the whole reactor, with a very small amount of oxygen. If heat only can be recovered from the bed zone, then a higher equivalence ratio than what has been investigated in this paper of would be needed.

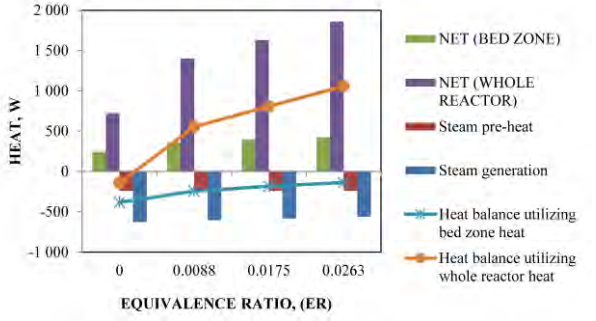

Figure 8: The pyrolysis products as function of ER.

These numbers are preliminary and higher ER should be investigated as well. Temperature stability could be a bigger problem in that case; as such, the model should be further investigated and developed to understand this complex phenomenon better.

The char generated in the process could be used as well to generate heat for the process. This char is not a part of the estimates in this paper and should be investigated further. A secondary reactor with a separate heat balance would be needed to utilize this heat, which requires further considerations.

Regarding the other reactions participating in the fast pyrolysis, it is interesting to note that the Water gas shift reaction is not so active. Neither is the steam gasification, which commonly results in high gasification efficiency. However, temperature is likely too low in this case, which makes the reactions occur very slowly.

CONCLUSION

The conclusions are:

1. The results are preliminary; however, the oxygen clearly reacts to provide heat. Primarily the secondary tar reacts and a loss of about 30% organic liquid yield is the result in this simulation, at an equivalence ratio of 0.026.
2. If heat only can be recovered from the bed zone, through the bed material, then a higher equivalence ratio than what was investigated in this paper would be needed.
3. If heat can be recovered from the whole reactor then a slight injection of oxygen would result in an autothermal system; which means the necessary heat to generate and pre-heat steam would be available.
4. Temperature instability in the freeboard prevented investigation of higher equivalence ratios, which should be pursued in further work.

REFERENCES

GUNN, D. (1978), "Transfer of heat or mass to particles in fixed and fluidised beds", *International Journal of Heat and Mass Transfer*, **21**, 467-476.

KANTARELIS, E., YANG, W., BLASIAK, W., (2013), "Production of liquid feedstock from biomass via steam pyrolysis in a fluidised bed reactor", *Energy & Fuels*, **27**, 4748-4759.

KANTARELIS, E., YANG, W., BLASIAK, W., (2014), "Effect of zeolite to binder ratio on product yields and composition during catalytic steam pyrolysis of biomass over transition metal modified HZSM5", *Fuel*, **122**, 119-125.

KANTARELIS, E., YANG, W., BLASIAK, W., (2014), "Effects of Silica-Supported Nickel and Vanadium on Liquid Products of Catalytic Steam Pyrolysis of Biomass", *Energy & Fuels*, **28**, 591-599.

LI, D., BERRUTI, F., BRIENS, C., (2014), "Autothermal fast pyrolysis of birch bark with partial oxidation in as fluidized bed", *Fuel*, **121**, 27-38.

MELLIN, T., ZHANG, Q., KANTARELIS, E., YANG, W., (2013), "An euler-euler approach to modeling biomass fast pyrolysis in fluidized-bed reactors – focusing on the gas phase", *Applied Thermal Engineering*, **24**, 344-353.

MELLIN, T., KANTARELIS, E., YANG, W., (2014), "Computational fluid dynamics modeling of biomass fast pyrolysis in a fluidized bed reactor, using a comprehensive chemistry scheme", *Fuel*, **117**, 704-715.

SYAMLAL, M., ROGERS, W., O'BRIEN, T. J. (1993) "MFIX Documentation: Theory Guide", U.S. Department of Energy: Morgantown, WV.

WU, Y., ZHANG, Q., YANG, W., BLASIAK, W., (2013), "Two-Dimensional Computational Fluid Dynamics Simulation of Biomass Gasification in a Downdraft Fixed-Bed Gasifier with Highly Preheated Air and Steam", *Energy & Fuels*, **25**, 4129-4137.

ZHANG, Q., DOR, L., YANG, W., BLASIAK, W., (2011), "An eularian model for municipal solid waste gasification in a fixed bed plasma gasification melting reactor", *Energy & Fuels*, **25**, 4129-4137.

ACKNOWLEDGEMENTS

The authors wish to acknowledge funding from The Swedish Energy Agency (contract no. 33284-1). This work was supported by the Swedish National Infrastructure for Computing (SNIC 001-11-26) via PDC.

LATTICE BOLTZMANN SIMULATIONS APPLIED TO UNDERSTANDING THE STABILITY OF MULTIPHASE FLUID INTERFACES

Gerald G. PEREIRA

CSIRO, Computational Informatics, Clayton, 3169, AUSTRALIA

E-mail: gerald.pereira@csiro.au

ABSTRACT

Multiphase flow occurs in a multitude of industrial and technological situations ranging from oil and minerals recovery to microfluidics and nanofluidics. In these cases we are interested in modelling the flow of two immiscible phases through a complex geometrical domain. In the past few years, the Lattice Boltzmann method has been developed to model fluid flow both for single phase flow and two (or more) phases. In this study we consider the flow of a less viscous phase into a more viscous fluid (say water into oil) and focus on the stability of the interface. In particular it is known the interface becomes unstable leading to fingers of the less viscous phase jetting through the more viscous phase which has deleterious effects on oil recovery. We use the LB method to model this flow for a variety of fluid geometries.

Keywords: Multiphase, interface stability, oil and gas .

NOMENCLATURE

Greek Symbols

ρ	LB density, [*dimensionless*]
ν	LB kinematic viscosity, [*dimensionless*]
τ	LB relaxation time, [*dimensionless*]
γ	LB surface tension, [*dimensionless*]

Latin Symbols

f	LB distribution function, [*dimensionless*].
P	LB Pressure, [*dimensionless*].
$\mathbf{r}$	LB lattice position, [*dimensionless*].
$\mathbf{u}$	LB Velocity, [*dimensionless*].
$\mathbf{e}$	LB discrete velocity vectors, [*dimensionless*].
$\mathbf{F}$	LB force, [*dimensionless*].
g	LB interaction potential, [*dimensionless*].
w	LB weights, [*dimensionless*].
c_s	LB speed of sound, [*dimensionless*].

Sub/superscripts

k	Multiphase component
i	LB velocity direction.

INTRODUCTION

Undertanding immiscible multiphase flow is vital in a vast array of industries such as oil recovery, mining, and technologies such as micro or nanofluidics. In our work we have been most interested in applications in the oil and gas industries where initially the rock or *porous medium* is filled with a wetting (oil phase). A second, non-wetting phase (i.e. water) is then injected to displace the wetting phase. Since the two phases are immiscible a well defined interface exists between the two phases.

One of the most important quantities to determine the capacity of a porous medium to produce oil is the permeability. When there are two (or more) phases present relative permeability curves are determined. In this case, as the second phase is injected instabilities in the interface between the two fluids can cause trapping of the initial phase by the injected phase. As such the relative permeability of the initial phase falls rapidly, even though there may be a large amount of that phase still present in the porous medium.

Although relative permeabilities can be measured experimentally this can be quite difficult and time and/or money consuming. Alternatively , if one can obtain a digital model (such as from computed tomography X-ray scans or CT scans) of the rock at the pore level then this data may be imported into suitable numerical solvers so as to solve for the transport properties in the porous medium. There are a number of numerical methods which may, in principal, solve for the flow field in a real porous media. For example, in the past network models (Blunt, 2001; Pereira, 1999) have been used to determine relative permeability curves. In this case the complex topology of the porous medium is approximated by an equivalent network of interconnected pores and throats. The pores hold most of the fluid while the throats are where most of the pressure drops occur. Pores are approximated as spheres (or some similar regular geometry) while the throats are approximated by long, thin cylinders. Although relative permeability curves can be calculated with this method, the biggest problem is to accurately represent the complex topological microstructure with much simpler network models. Invariably, this leads to over-simplifications of the porous medium which then lead to results which are not representative of the real medium.

Alternatively, one can directly apply the numerical CFD solver to the CT data and solve for the (steady-state) flow field. Using techniques such as the finite element method one requires a suitable boundary mesh between the void space and solid domain of the porous medium. Because this is a highly irregular surface, this is typically very difficult. A relatively recent CFD method that overcomes many of the problems with the methods mentioned above is the Lattice Boltz-

mann (LB) method (Succi, 2001). This method is based on the Boltzmann transport equation which considers the microscopic motion of distributions of particles. In the LB method the velocity space is discretised (and limited) to a small subset of possibilities, which enables a solution on a suitable simplified lattice. However, the exact pore space that is present in the digital data is modelled, i.e. the resolution of the numerical model is at the same scale as the digital data with no approximations.

The LB method is now quite commonly used to compute flow fields for single phase flow (C.X. Pan and Miller, 2006). However, its application to immiscible multiphase flow is much more in its infancy. The main question to address is how to capture the effect of surface tension which causes the separation of the two phases? There have been a number of different attempts at representing the effect of surface tension. These include a colour gradient model (Gunstensen and Rothmann, 1992), a thermodynamic, free energy model (M.R. Swift and Yoemans, 1995), a mean-field theory model (X. He and Doolen, 1998) and a microscopic interaction model based on attractive and/or repulsive potentials between neigbouring particles (Shan and Chen, 1993). The methods by (M.R. Swift and Yoemans, 1995) and (X. He and Doolen, 1998) were developed to naturally model a change of phase whereas the other two methods are isothermal and so specifically model the two-phase (immiscible) region of phase space. In this study we adopt the so called *Shan-Chen model* (Shan and Chen, 1993) to model surface tension. In the next section we introduce this model and extract macroscopic parameters such as surface tension and contact angles from it. We then apply it to a sample porous medium so as to determine two-phase relative permability curves.

MODEL DESCRIPTION

The LB model is mesoscopic method to study incompressible fluid dynmaics. Its main advantages over more conventional CFD techniques (which directly solve the Navier-Stokes equations) are its programming simplicity, computational efficiency and inherent parallelism due to a large amount of local computations. In addition, as mentioned in the Introduction, it naturally deals with complex porous media if suitable digital information is provided. Details of this method, applied to single phase flow, are available (Succi, 2001; Chen and Doolen, 1998) and thus we shall only focus here on the LB method applied to immiscible, multiphase flow.

In the LB method distributions of fluid particles are propagated on a discrete lattice. At each time-step the fluid particles undergo a two-step process where particles are propagated to adjacent lattice nodes (called "*streaming*") and then collided with other particles which converge on a specific node (called "*collision*"). Solid boundaries are treated in the streaming step whereby a bounce-back boundary condition is implemented (i.e. any fluid particles which stream into a solid site are simply reversed). More complex and accurate boundary conditions such as half-way bounce-back or linear interpolation boundary conditions are also possible. In the collision step particle distributions relax towards a given equilibium distribution – a Maxwellian distribution. Then macroscopic properties such as fluid density, fluid velocity and the stress tensor can be derived from the particle distributions. If we are dealing with only a single fluid one set of particle distributions is defined, i.e. $f(\mathbf{r},\mathbf{u},t)$ which denotes the distribution of particles travelling with a particlular velocity $\mathbf{u}$ at time t at lattice node $\mathbf{r}$. We will only consider a three dimensional model in this paper so that we implement the common D3Q19 model which indicates that there are 18 possible vectors, $\mathbf{e}_i$, in which particles may move in addition to the null vector. These 18 possibilities are the vectors ($\pm$ 1, 0, 0), (0,$\pm$1,0), (0,0,$\pm$1), ($\pm$1,$\pm$1,0), ($\pm$1,0,$\pm$1), (0,$\pm$1,$\pm$1).

For n phases we now define n sets of distributions functions, which represent each immiscible phase - $f^1(\mathbf{r},\mathbf{u},t)...f^n(\mathbf{r},\mathbf{u},t)$. For each phase we solve the LB equation at node i. So for the k^{th} phase (where $k \in 1,...n$) we need to solve the LB equation:

$$f_i^k(\mathbf{r}+\mathbf{e}_i\Delta t, t+\Delta t) - f_i^k(\mathbf{r},t) = -\frac{1}{\tau_k}\left[f_i^k(\mathbf{r},t) - f_i^{k,eq}(\mathbf{r},t)\right]. \quad (1)$$

The term $f_i^{k,eq}$ is the equlibrium Maxwell distribution given by

$$f_i^{k,eq} = w_i\rho_k\left[1+\frac{\mathbf{e}_i\cdot\mathbf{u}_k^{eq}}{c_s^2}+\frac{(\mathbf{e}_i\cdot\mathbf{u}_k^{eq})^2}{2c_s^4}-\frac{\mathbf{u}_k^{eq}\cdot\mathbf{u}_k^{eq}}{2c_s^2}\right], \quad (2)$$

where w_i are weights which are defined for the given D3Q19 model. In Eq.(1), τ_k represents a relaxation time for phase k and it can be shown to be related to kinematic viscosity via $\nu_k = c_s^2(\tau_k - 1/2)$, where c_s is the sound speed and equal to $1/\sqrt{3}$.

The relationship to macroscopic parameters such as density and velocity of the k^{th} phase are given by

$$\rho_k = \sum_i f_i^k \qquad \text{and} \qquad \rho_k\mathbf{u}_k = \sum_i f_i^k\mathbf{e}_i. \quad (3)$$

The Shan-Chen model (Shan and Chen, 1993) (also referred to sometimes as the *pseudo-potential* model) imploys nearest neighbour inter-particle potentials to model the interactions between components. In a sense this follows physical reality at the microscopic level where molecules interact via short-range Lennard-Jones type potentials. In the Shan-Chen model lattice nodes which have a separation of less than or equal to $\sqrt{2}$ units are coupled together. More recent models (based on pseudo-potentials) such as the one by (M.L. Porter and Carey, 2012) extend this range of interaction up to $\sqrt{10}$ lattice units. They have shown by including these additional interactions the so-called *spurious currents* which are due to numerical artifacts and lead to unrealistically large velocities near the interface between fluid components can be reduced significantly. While this implementation is useful for multiphase flow in the bulk or even near smooth and regular solid boundaries it becomes problematic for more irregular or random solid boundaries such as in porous media. Essentially for longer ranges, it must be ascertained that the straight line path between two fluid components is not impeded by a solid phase. This extra degree of complication makes implementation of the longer range potentials more problematic for real porous media. As such we implement the Shan-Chen model with only a maximum separation of $\sqrt{2}$ units between lattice nodes.

In the Shan-Chen model, the interaction potential between components is accommodated via a force, $\mathbf{F}_k$ which is introduced through the velocity $\mathbf{u}_k^{eq}$ in Eq.(1). This velocity is defined as (Shan and Chen, 1993)

$$\rho_k\mathbf{u}_k^{eq} = \rho_k\mathbf{u}' + \tau_k\mathbf{F}_k. \quad (4)$$

In this equation $\mathbf{u}'$ is a combined velocity and to satisfy momentum conservation must be

$$\mathbf{u}' = \frac{\sum_k \tau_k^{-1}\rho_k \mathbf{u}_k}{\sum_k \tau_k^{-1}\rho_k}. \quad (5)$$

The fluid-fluid interaction for phase k at lattice node $\mathbf{r}$ is then given

$$\mathbf{F}_k(\mathbf{r}) = \rho_k(\mathbf{r})c_s^2 \sum_{k'\neq k} g_{kk'} \sum_i w(|\mathbf{e}_i|^2)\rho_{k'}(\mathbf{r}+\mathbf{e}_i)\mathbf{e}_i, \quad (6)$$

where $g_{kk'}$ is the interaction potential (or coupling parameter) between dissimilar components. The weights w depend on the separation between interating nodes with $w(1) = 1/6$ and $w(2) = 1/12$. Note, we assume the coupling is zero for similar components. The pressure in this model is given by the equation of state $P = c_s^2 \sum_k \rho_k + 3\sum_{kk'} g_{kk'}\rho_k\rho_{k'}$.

Relationship to macroscopic surface tension

The Shan-Chen model yields an interface between two immiscible phases via microscopic parameters g_{12}, g_{s1} and g_{s2}. (The subscript s refers to a solid surface so that g_{s1} is the interaction between solid surface and phase 1.) They need to be related to macroscopic surface tension and contact angle measurements. To do this we use the Young-Laplace equation

$$\Delta P = \frac{\gamma}{R}, \quad (7)$$

where γ is the macroscopic surface tension and R is a droplet radius. To obtain γ we begin with a number of different sized cubical droplets. These quickly relax to spheres of different radius (see Fig. 1a) and then we measure the pressure difference between the interior and exterior of the droplet. This plot is shown in Fig. 2 and the surface tension is extracted from the gradient. To convert this surface tension to physical (SI) units we need to suitably scale it with physical values of mass and time. Properties such as length and mass can be easily related to physical case of interest. However, time is more difficult. A time scale can be extracted by relating the physical viscosity and LB viscosity.

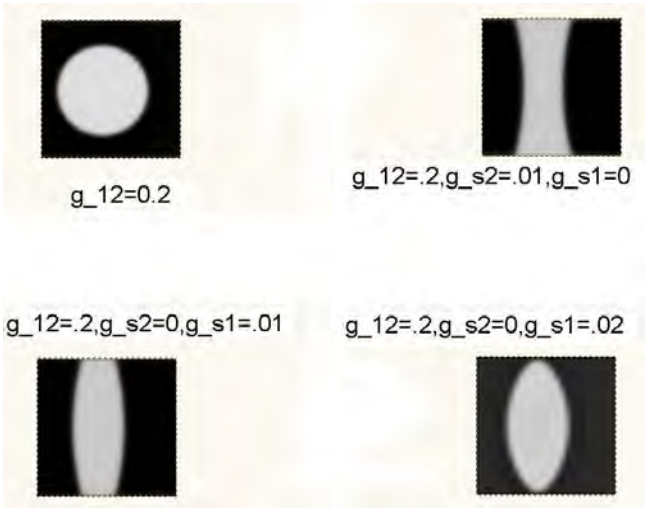

Figure 1: Droplets created using the Shan-Chen model (a) In the bulk, (b) wetting droplet (light shade) between two hard, flat surfaces (c) non-wetting droplet between surfaces and (d) different contact angle non-wetting drop between two surface.

We can also model different contact angles of droplets on hard surfaces as shown in Fig. 1b, c and d. This is done by varying the surface-droplet parameters g_{s1} and g_{s2}. In Fig. 1a these parameters are set to $g_{s1} = 0.01$ and $g_{s2} = 0.0$ resulting in a wetting droplet (the light shade corresponds to the droplet). In Fig 1c and d we change these parameters to $g_{s1} = 0.0$ and $g_{s2} = 0.01$ (for c) and $g_{s1} = 0.0$ and $g_{s2} = 0.02$ (for d) resulting in different non-wetting contact angles.
It is well know that the Shan-Chen model gives surface tensions which can depend on the viscosity ratio between fluids. The model, based on Shan-Chen, but with a larger range of potential and modified force law by (M.L. Porter and Carey, 2012) overcomes this drawback. It is also leads to smaller spurious currents near the interface (by an order of magnitude or two) which leads to greater numerical stability.

IMMISCIBLE FLUID DISPLACEMENT

We next apply the LB model to flow in a square capillary or tube. The tube is initially filled with a wetting fluid and a second non-wetting fluid is injected to displace the wettign fluid. This can be acheived in one of two ways - either with an inlet and outlet pressure difference or with a body force (such as gravity) on the whole fluid. The pressure boundary conditions are implemented by prescribing densities (via the distribution functions) on the inlet and outlet (Zou and He, 1997). Body forces can be included by adding them to the force in Eq.(4).

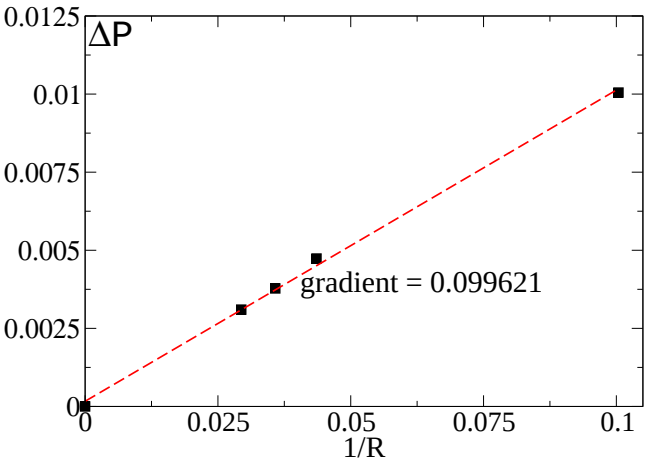

Figure 2: Young-Laplace law for $g_{12} = 0.2$. We plot the pressure difference between the interior and exterior of the droplet versus the inverse radius of the droplet. Black squares represent the LB results while the dashed line is a best fit line which passes through the origin and the squares.

Capillary pressure

When a non-wetting fluid displaces a wetting fluid in a capillary tube it must overcome the capillary pressure given by $2\gamma/D$ where D is the tube cross-sectional diameter. So for a given pressure difference between the inlet and outlet the non-wetting fluid will only enter the tube with a diameter greater than $2\gamma/\Delta P$. To test that the model captures this correctly we ran a number of simulations with a narrow, rectangular throat joining the inlet and outlet reservoirs. (The inlet is at the bottom edge of Fig. 3 and outlet is at the top edge of this figure. The invading fluid is the A-phase which is blue.) For each simulation the pressure gradient is kept the same but the throat radius is succesively decreased. In Figs. 3-6

we show the results for throats of diameters 11, 7, 5, and 3 LB units respectively.

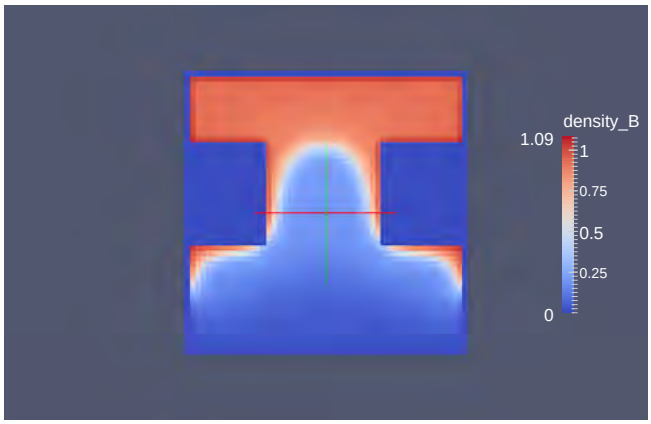

Figure 3: Meniscus in a rectangular pore throat which is 11 LB units wide.

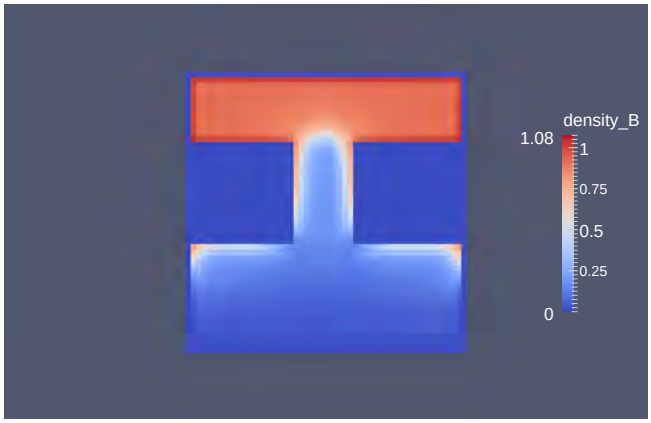

Figure 4: Meniscus in a rectangular pore throat which is 7 LB units wide.

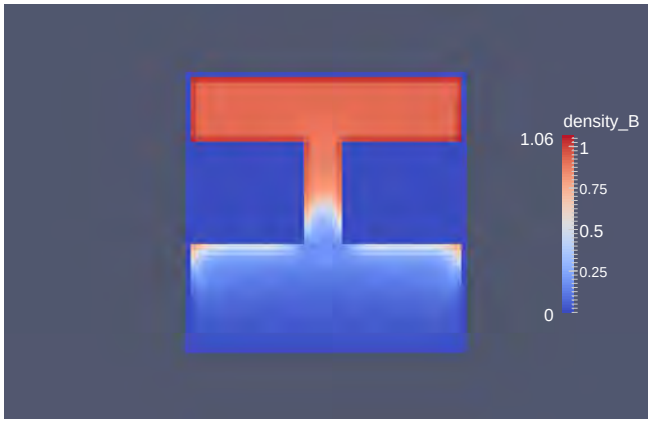

Figure 5: Meniscus in a rectangular pore throat which is 5 LB units wide.

In Fig.3 note that the meniscus in the bottom (inlet) reservoir cannot fill the corners as the pressure in the A-phase (blue region) is not large enough. Thus even though the A-phase can enter and fill the joining throat, this capillary pressure is not sufficiently large to fill the corner regions of the inlet reservoir. By Fig.4, where the joining throat diameter has decreased to 7 LB units, the A-phase has not only been able to enter the narrow throat but has gone much further into the corner regions of the inlet reservoir. It is the increased capillary pressure which has allowed this to occur. By Fig.5 the A-phase has just entered the narrower throat (diameter of 5 LB units) and also almost completely filled the corners of the inlet reservoir. However, in Fig.6, where the narrow throat diameter is only three LB units even though the the capillary pressure is sufficiently large for the A-phase to fill the corners of the inlet reservoir it is not large enough to exceed the threshold pressure to enter the narrow throat. In this case, even though we ran the simulation for as long as possible, the A-phase never filled the narrow throat.

Porous media

The aim of this work is to be able to model multiphase flow in a real porous medium. Previously we have done this for single phase flow in carbonate rocks using CT scan digital data (J. Liu and Regenauer-Leib, 2014). Multiphase flow poses a much larger numerical problem due to surface tension which causes the two phase to remain demixed. Applying the present model directly to CT data is a serious problem for a number of reasons. Firstly, the complex and irregular pore space can lead to extremely narrow throats and hence extremly high pressures. The multiphase LB algorithm becomes numerically unstable very quickly and the solution cannot be acheived. Secondly, the multiphase method requires to solve for up to n distribution functions which can mean an exorbitantly large amount of compute time and memory. Thirdly the complex three-dimensional topology of real porous media makes it extremly difficult to visualize and (hence) understand the flow transport paths.

For the reasons just mentioned in this study we implement a much simpler porous medium. These are pseudo three-dimensional models. We previously (Pereira, 1999) used these types of model to understand the rules for three-phase displacement (i.e., displacement of oil and water by a third phase such as gas). Although they are an over-simplification of a real porous medium, they are extremely useful in developing new numerical models since they allow us to follow the pore-scale fluid flow.

The sample porous medium we use is a rectangular domain (in the x and y directions) with a small thickness (in the third direction, z). The length of the sample in the y direction is greater than in the x direction. Solid spheres are placed in a two-dimensional, hexagonal pattern in the rectangular domain. The spheres have a variable diameter selected from a uniform distribution. Figure 7 shows the sample porous

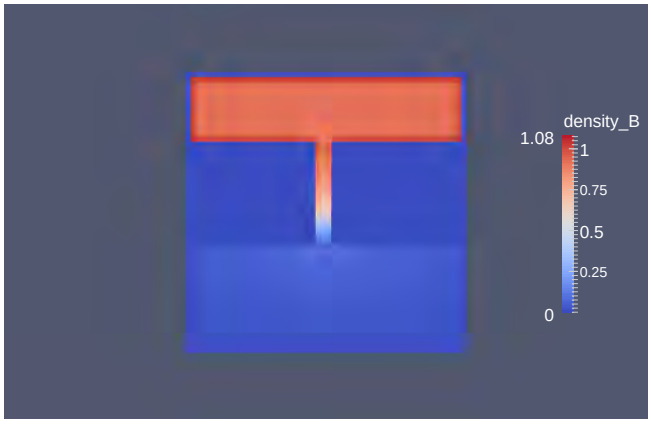

Figure 6: Meniscus in a rectangular pore throat which is 3 LB units wide.

medium with the inlet placed along the bottom edge and the outlet along the top edge. Along these edges we have density/pressure boundary conditions to drive the invading fluid from the inlet to the outlet. Solid boundary conditions are imposed on the left-hand and right-hand side-walls. The x dimension is 120 LB units and the y dimension is 60 LB units. The z direction thickness is only 6 LB units but we have periodic boundary conditions in this direction.

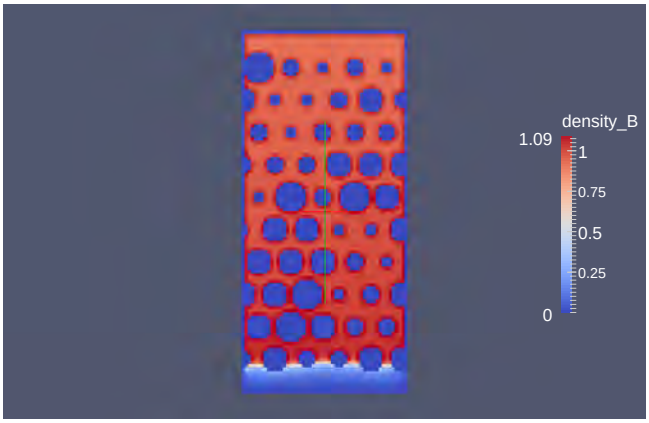

Figure 7: Initial configuration in two-phase immiscible displacement. A slice in the $x-y$ plane is shown. The A-phase (blue) is the non-wetting/invading fluid while the B-phase (red) is the wetting/defending fluid. A-phase is injected from the bottom edge using pressure boundary conditions.

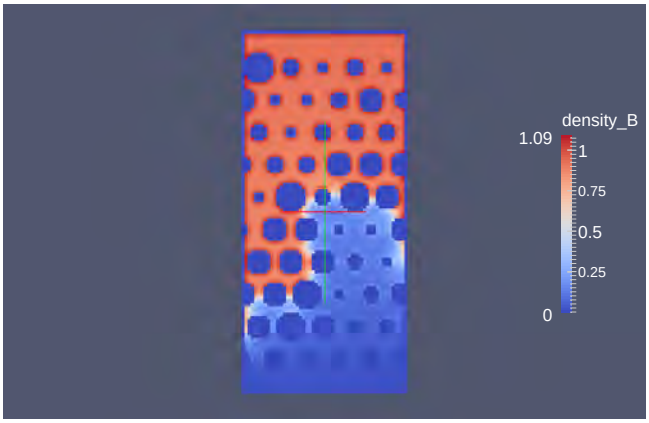

Figure 8: Intermediate configuration in two-phase immiscible displacement. Non-wetting fluid preferentially moves up the right hand side of the domain.

Figure 8 displays the flow at an intermediate time during the primary drainage flood. In the bottom left corner (near the inlet) there exists a cluster of relatively large spheres. Thus the gap between these spheres is quite small and hence the capillary pressure required to invade this region is large. As a result the invading fluid preferably floods the right hand side of the domain. As the flood proceeds (by the time the invading fluid front has reached the centre of the domain, Fig. 9) the largest channels now exist in the central region and as a result the invading phase fingers through the porous medium, leaving behind unexplored regions of the B-phase (red), before reaching the outlet.
In principal, we can calculate relative permeability curves for this primary drainage flood using a single phase, multiple-relaxation time, LB method as we have previously done (J. Liu and Regenauer-Leib, 2014). At various stages during the flood, the configuration of each phase is input into the single phase code and permeabilities are calculated. In a realistic (three-dimensional) domain, one obtains non-zero permeabilities for each phase during the flood. However, in this simplified scenario, as soon the invading phase spans the width of the sample porous medium (see Fig.8) the defending phase permeability drops to zero. So the relative permeability curves become almost trivial. As such we do not display them for this case.

CONCLUSION

The present work is an initial attempt to model the complex process of multiphase flow in porous media. While we have focussed on applications in oil recovery, where the porous medium can have a highly irregular, random topology we also would like to apply this to other technological applications such as in micro or nanofluidics.
However, there are a number of issues/problems that remain to be addressed in this work before a complete working three-dimensional, multiphase numerical model can be applied to realistic rocks. These are:

1. Implementation of a more (numerically) stable LB multiphase method, e.g. by including a larger range for the interaction potential.

2. Capability to deal with much larger three-dimensional domains, so as to model a real porous medium.

We shall address these issues before the CFD2014 conference and present results on multiphase flow in realistic three dimensional rocks.

REFERENCES

BLUNT, M. (2001). “Flow in porous media - pore netowrk models and multiphase flow”. *Curr. Opin. Coll. Int Sci.*, **6**, 197–207.

CHEN, S. and DOOLEN, G. (1998). “LB method for fluid flows”. *Ann. Rev. Fluid Mech.*, **30**, 329–364.

GUNSTENSEN, A. and ROTHMANN, D. (1992). “LB studies of immiscible two phase flow through porous media”. *J. Geophys. Res.*, **98**, 6431–6441.

HE, X., S.C. and DOOLEN, G. (1998). “A novel thermal model for the lattice Boltzmann method in the incompressible limit”. *J. Comput. Phys.*, **146**, 282–300.

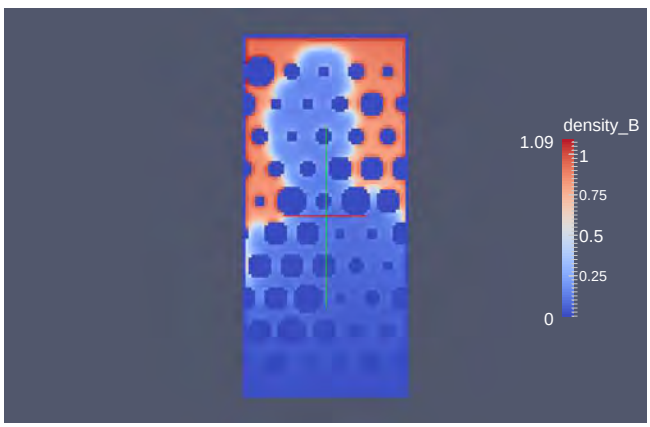

Figure 9: Breakthrough configuration in two-phase immiscible displacement. Non-wetting fluid fingers through the center of the domain.

LIU, J., PEREIRA, G.G. and REGENAUER-LEIB, K. (2014). "From characterisation of pore structures to simulations of pore-scale fluid flow and the upscaling of permeability using microtomography: A case study of heterogeneous carbonates". *J. Geochem. Exp.*, **140**, DOI: 10.1016/j.gexplo.2014.01.021.

PAN, C.X., L.L. and MILLER, C. (2006). "An evaluation of lb schemes for porous medium flow simulation". *Comp. and Fluids*, **35**, 898–909.

PEREIRA, G.G (1999). "Numerical pore-scale modelling of three-phase fluid flow: Comparison between simulation and experiment". *Phys. Rev. E*, **59**, 4229–4238.

PORTER, M.L., E.T. COON, Q.K.J.M. and CAREY, J. (2012). "Multicomponent inter-particle potential lb model for fluids with large viscosity ratios". *Phys. Rev. E*, **86**, 036701(1–8).

SHAN, X. and CHEN, H. (1993). "LB model for simulating multiple phases and components". *Phys. Rev. E*, **47**, 1815–1819.

SUCCI, S. (2001). *The Lattice Boltzmann Equation for Fluid Dynamics and Beyond*. Oxford, UK.

SWIFT, M.R., W.O. and YOEMANS, J. (1995). "LB simulation of non-ideal fluids". *Phys. Rev. Lett.*, **75**, 830–833.

ZOU, Q. and HE, X. (1997). "On pressure and velocity boundary conditions for the lattice boltzmann bgk model". *Phys. Fluids*, **9**, 1591–1598.

ORR-SOMMERFELD STABILITY ANALYSIS OF TWO-FLUID COUETTE FLOW WITH SURFACTANT USING CHEBYSHEV COLLOCATION METHOD

V.P.T.N.C.Srikanth BOJJA[1*], **Maria FERNANDINO**[1†]

[1]NTNU Department of Energy and Process Engineering, 7491 Trondheim, NORWAY

[*] E-mail: srikanth.bojja@ntnu.no
[†] E-mail: maria.fernandino@ntnu.no

ABSTRACT

In the present work, the surfactant induced instability of a sheared two fluid system is examined. The linear stability analysis of two-fluid Couette system with an amphiphilic surfactant is carried out by developing Orr-Sommerfeld type stability equations along with surfactant transport equation and the system of ordinary differential equations was solved by Chebyshev collocation method (Weideman and Reddy, 2000)(Canuto, 1988). Linear stability analysis reveals that the surfactant either induces Marangoni instability or significantly reduces the rate at which small perturbations decay (Halpern and Frenkel, 2003)(Blyth and Pozrikidis, 2004a).

Keywords: Lagrangian method, Linear stability, Orr-Sommerfeld, Marangoni mode, Surfactants and interphases, Oil transport .

NOMENCLATURE

Greek Symbols

Ω	Growth rate
Γ	Surfactant concentration
ρ	Mass density, $[kg/m^3]$
μ	Dynamic viscosity, $[kg/ms]$
η	Dimensionless height of perturbed inteface
σ	Surface tension
α	Wave number
ϕ,ψ	Stream functions

Latin Symbols

Ca	Capillary number
Ma	Marangoni number
N	Number of Collocation pints
Re	Reynolds number
U	Plate/Wall velocity
c	Complex wave spped
d	Width of fluid layer
f	Amplitude of Pressure disturbance
g	Amplitude of surfactant concentration disturbance
h	Amplitude of interface perturbation
m	Viscosity ratio
n	Depth ratio
s	Shear of basic velocity
$\mathbf{u}$	Dimensionless velocity

Sub/superscripts

i	Index i.
j	Index j.
$\tilde{}$	Perturbed quantities
0	Base state quantities
$-$	Dimensionless base state quantities

INTRODUCTION

Two layer channel flows and flows with and without surfactants have been given considerable importance because of its numerous industrial applications. Oil recovery (Slattery, 1974), lubricated pipelining (Joseph and Renardy, 1993), liquid coating processes (Severtson and Aidun, 1996) are typical industrial situations where two-layer channel flows are often seen. Surfactants also have wide range of industrial applications for example in enhanced oil recovery (Banat, 1995).

Using perturbation analysis, the primary instability of the two-layer plane Couette-Poiseuille flow was studied by Yih (Yih, 1967).Using analytical solution by asymptotic analysis, his studies revealed that even at small Reynolds numbers, the interface is susceptible to long-wave instability associated with viscosity stratification. Yiantsios & Higgins (Yiantsios and Higgins, 1988) later extended this study for small to large values of wave number and confirmed the existence of the shear mode instability. Boomkamp & Miesen (Boomkamp and Miesen, 1996) came up with the method of an energy budget for studying instabilities in parallel two-layer flows, where energy is supplied from the primary flow to the perturbed flow and instability appears at sufficiently long wave numbers through the increase of kinetic energy of an infinitesimal disturbance with time. In the presence of surfactant at the sheared interface, Frenkel & Halpern (Halpern and Frenkel, 2003)(Frenkel and Halpern, 2002) discovered that even in the Stoke's flow limit, the interface is unstable as the surfactant induces Marangoni instability, which was later confirmed by Blyth & Pozrikidis (Blyth and Pozrikidis, 2004b). In the case of Stoke's flow, they identified two normal modes, the Yih mode due to viscosity stratification inducing a jump in the interfacial shear, and the Marangoni mode associated with the presence of the surfactant. In contrast, at finite Reynolds numbers, infinite number of normal modes are possible and by parameter continuation with respect to the Reynolds number the most dangerous Yih and Marangoni modes can be identified.

In this article, the effect of an insoluble surfactant on the stability of two-layer couette channel flow is studied in detail for

low to moderate values of the Reynolds number. To isolate the Marangoni effect, gravity was suppressed in this problem and this was done by considering equal density fluids. Linear stability analysis was carried out by formulating Orr-Sommerfeld boundary value problem, which was solved numerically using Chebyshev collocation method (Weideman and Reddy, 2000)(Canuto, 1988) for all wave numbers. Both Marangoni mode and shear mode are detected and utmost focus is given to Marangoni mode as shear mode is always stable at moderate to long wave numbers under the influence of inertia.

The rest of the paper is organized as follows. In §Model Description, the governing equations for the system in question are laid out, normal mode analysis of the physical system is carried out and Orr-Sommerfeld boundary value problem is formulated. General description of Chebyshev collocation method and detailed description of numerical simulation of Orr-Sommerfeld boundary value problem by Chebyshev collocation method is given in §Numerical method .Validation of the numerical method with literature data is given in §Validation of the code. Detailed discussion of results done in §Results and Discussions. The concluding remarks and outlook for further-work in §Conclusions. Finally acknowledgements in §Acknowledgements.

MODEL DESCRIPTION

Consider two super-imposed immiscible liquid layers between two infinite parallel plates located at $y=-d_1,d_2$, as in Fig.1. Let the basic flow be driven only by steady motion of plates. It is well known that the basic "Couette" velocity profiles are steady and vary only in the span-wise direction and in the basic state, the unperturbed interface between the liquids is flat and is located at $y=0$. The gravity is suppressed in this problem by considering equal densities in order to investigate the effects of surfactant and inertia on the stability of the system under consideration. The subscripts 1 and 2 refer to the lower or upper fluids respectively and channel walls move in the horizontal direction, x, with velocities $-U_1$ and U_2. The interface is occupied by an insoluble surfactant with surface concentration Γ which is only convected and diffused over the interface, but not into the bulk of the fluids thus locally changing the surface tension σ.

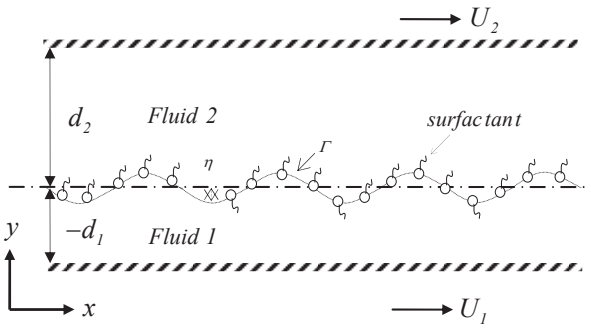

Figure 1: Schematic sketch of Couette-Poiseuille flow with surfactant laden interface. The perturbed interface $y=\eta(x,t)$ is shown as sinusoidal curve. Γ is the concentration of insoluble surfactant.

Governing equations

The mass and momentum conservation equations governing the two-layer system are

$$\nabla.\mathbf{u}_j=0\ ,\ \rho(\frac{\partial \mathbf{u}_j}{\partial t}+\mathbf{u}_j.\nabla\mathbf{u}_j)=-\nabla p_j+\mu_j\nabla^2\mathbf{u}_j \quad (1)$$

Where subscript $j=1,2$ represents lower and upper liquid layers respectively. Here
$\nabla=(\partial/\partial x,\partial/\partial y)$,$\mathbf{u_j}=(u_j(x,y,t),v_j(x,y,t))$
The associated boundary conditions for the system are no slip and no penetration boundary conditions at the walls.
$u_1=-U_1$,$v_1=0$ at $y=-d_1$ and
$u_2=U_2$, $v_2=0$ at $y=-d_2$
The associated interface conditions are continuity of velocity, tangential stress and normal stress.
Continuity of velocity at the interface
$u_1=u_2$ at $y=0+\eta(x,t)$
The tangential and normal stress conditions at the interface are given by

$$(T1-T2)=\sigma(\nabla.n)n-(1/H)\sigma_x t \quad (2)$$

Where T_1,T_2 are stress tensors, n is unit normal, t is unit tangent, η is dimensionless height of perturbed interface and $H=\sqrt{1+(\eta_x)^2}$
Kinematic interfacial condition is
$\eta_t=v_1-u_1\eta_x$
The surfactant transport equation (Stone, 1990) at the interface is given by

$$\partial_t(\Gamma H)+\partial_x(u_1H)=D_s\partial_x\{(1/H)\partial_x\Gamma\} \quad (3)$$

Where D_s is surface molecular diffusivity of surfactant. D_s is usually negligible and neglected in this case.
We introduce dimensionless variables as follows:
$(x,y)=(x^*,y^*)/d_1$, $t=t^*/(d_1\mu_1/\sigma_0)$
$(u,v)=(u^*,v^*)/(\sigma_0/\mu_1)$, $\Gamma=\Gamma^*/\Gamma_0$, $\sigma=\sigma^*/\sigma_0$
The dimensionless variables in base state for the Couette flow with flat interface $\eta=0$ and uniform surfactant concentration $\bar{\Gamma}=1$ are given by
$\bar{u}_1(y)=sy$,$\bar{v}_1(y)=0$ $(-1\le y\le 0)$ and
$\bar{v}_2(y)=0$, $\bar{u}_2(y)=sy/m$ $(0\le y\le n)$
Where $m=\mu_2/\mu_1$, $n=d_2/d_1$, s is shear of basic velocity at interface and is given by $s=d\bar{u}_1(0)/dy$,
We consider the perturbed state with small deviation from the base state:
$\eta=0+\tilde{\eta}$, $u_j=\bar{u}_j+\tilde{u}_j$, $v_j=0+\tilde{v}_j$, $p_j=\tilde{p}_j$, $\Gamma=\bar{\Gamma}+\tilde{\Gamma}$
Now we represent disturbance velocity in disturbance stream-functions $\tilde{\phi}$ and $\tilde{\psi}$ such that $\tilde{u}_1=\tilde{\phi}_y$, $\tilde{v}_1=-\tilde{\phi}_x$, $\tilde{u}_2=\tilde{\psi}_y$, $\tilde{v}_2=\tilde{\psi}_x$
Performing normal mode analysis by substituting $(\tilde{\eta},\tilde{\phi},\tilde{\psi},\tilde{p}_j,\tilde{\Gamma})=[h,\phi(y),\psi(y),f_j(y)g]\,e^{i\alpha(x-ct)}$
Where α is wave number of the disturbance, g and h are constants and $c=c_r+c_i$ is the complex wave speed.
Linearizing the kinematic boundary condition yields
$h=\phi(0)/c=\psi(0)/c$.
Linerarizing the dimensionless x and y-components of Navier-Stokes equation (2) followed by subtraction from the corresponding base state equations and elimination of pressure terms, yields two 4th order Orr-Sommerfield ODEs in stream-functions, one for each fluid.

$$\left(D^2-\alpha^2\right)^2\phi=\tfrac{\mathrm{Re}}{Ca}\left[(\bar{u}_1-c)\left(D^2-k^2\right)\phi-\phi\tfrac{d^2\bar{u}_1}{dy^2}\right] \quad (4)$$

$$m\left(D^2-\alpha^2\right)^2\psi = ik\frac{\mathrm{Re}}{Ca}\left[(\bar{u}_2-c)\left(D^2-k^2\right)\psi - \psi\frac{d^2\bar{u}_2}{dy^2}\right] \tag{5}$$

Where $Re = \rho V d_1/\mu_1$ is the Reynolds number and $Ca = \mu_1 V/\sigma_0$. (when $U_2 > U_1$, $Ca = s$)
Boundary conditions at wall in terms of stream-functions are

$$\phi(-1) = \phi^{'}(-1) = 0, \tag{6}$$

$$\psi(n) = \psi^{'}(n) = 0 \tag{7}$$

Continuity of velocity at interface gives

$$\phi(0) = \psi(0)\ ,\ \phi^{'}(0) - \psi^{'}(0) = \frac{1-m}{m}\frac{s}{c}\phi(0) \tag{8}$$

Linearization of normal stress condition gives

$$m\psi^{'''}(0) - \phi^{'''}(0) - 3\alpha^2[m\psi^{'}(0) - \phi^{'}(0)] = -i\frac{\alpha^3}{c}\psi(0) \tag{9}$$

Linearization of surfactant transport equation gives

$$g = (1/c)\phi^{'}(0) + (s/c)\phi(0) \tag{10}$$

Linearization of tangential stress balance condition gives

$$m\psi^{''}(0) - \phi^{''}(0) + \alpha^2[m\psi(0) - \phi(0)] = iMa\alpha g \tag{11}$$

Where $Ma = E\Gamma_0/\sigma_0$ is the Marangoni number.
By substituting the value of g from linearized surfactant transport equation (10) in linearized tangential stress balance condition (11) gives

$$\begin{aligned} m\psi^{''}(0) - \phi^{''}(0) + \alpha^2[m\psi(0) - \phi(0)] \\ = iMa\alpha[(1/c)\phi^{'}(0) + (s/c)\phi(0)] \end{aligned} \tag{12}$$

For each value of α, Eqs.(4)-(12) forms a eigen value problem, which was numerically solved using Chebyshev collocation method (Weideman and Reddy, 2000)(Canuto, 1988) and QZ algorithm for determining the complex phase velocity c.

Numerical method

The two Orr-Sommerfeld equations Eqs.(4) and (5) along with eight boundary conditions Eqs.(6)-(9) and (12) are solved numerically using Pseudo-spectral Chebyshev collocation method (Weideman and Reddy, 2000)(Canuto, 1988). To implement the Chebyshev method, we transformed each of the two fluid domains into standard Chebyshev domain $0 \le x \le n$ that is Fluid 1 domain $-1 \le y \le 0$ is mapped to $-1 \le z_1 \le 1$ and Fluid 2 domain $0 \le y \le n$ is mapped to $1 \ge z_2 \ge -1$ by substituting $z_1 = 2y+1$ and $z_2 = -\frac{2}{n}y+1$ respectively.
Next, we represent each stream function as truncated summation of orthogonal Chebyshev polynomials by setting

$$\phi(z_1) = \sum_{k=0}^{N} a_{1k}T_k(z_1)\ and\ \psi(z_2) = \sum_{k=0}^{N} a_{2k}T_k(z_2) \tag{13}$$

Where a_{1k} and a_{2k} are unknown Chebyshev coefficients and N is the number of Cheyshev collation points in each domain.

Upon substituting Eq.(13) in Eqs.(4) and (5) and projecting them on to arbitrary orthogonal functions $T_m(z_1)$ and $T_m(z_2)$ respectively by taking the Chebyshev inner product,

$$\langle T_m(z_1), \phi(z_1)\rangle = \int_{-1}^{1} \frac{1}{\sqrt{1-{z_1}^2}} T_m(z_1)\phi(z_1)dz_1,$$

$$\langle T_m(z_2), \psi(z_2)\rangle = \int_{-1}^{1} \frac{1}{\sqrt{1-{z_2}^2}} T_m(z_2)\psi(z_2)dz_2$$

these two Chebyshev inner products forms $N-3$ equations each summing up to $2N-6$ equations and $N+1$ coefficients in a_{1k} and $N+1$ coefficients a_{2k}. $2N-6$ equations along with 8 boundary conditions obtained by substituting Eq.(13) in Eqs.(6)-(9)&(12) and $2N+2$ coefficients forms a linear system
$A.\mathbf{x} = cB.\mathbf{x}$
Where, $\mathbf{x} = (a_{10}, a_{11}, ..., a_{1N}, a_{20}, a_{21}, ..., a_{2N})$ and A,B are square matrices of size $2N+2$.
This generalized eigen value problem was solved by QZ algorithm to obtain and c subsequently growth rate, $\Omega = kc_i$.We used,$N = 40$ above which the eigen values are independent of number of collocation points.

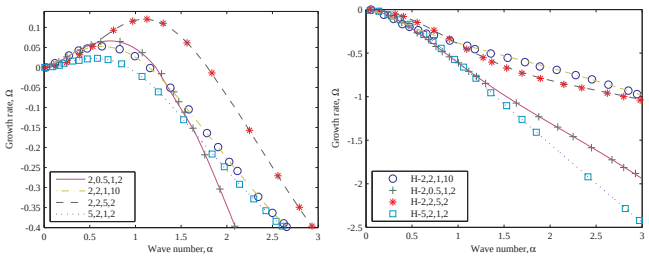

(a) Unstable (b) Stable

Figure 2: Dispersion curves for the most (a)Unstable (b)Stable modes. Lines represent this work and Markers represent Halpern's (Halpern and Frenkel, 2003) work

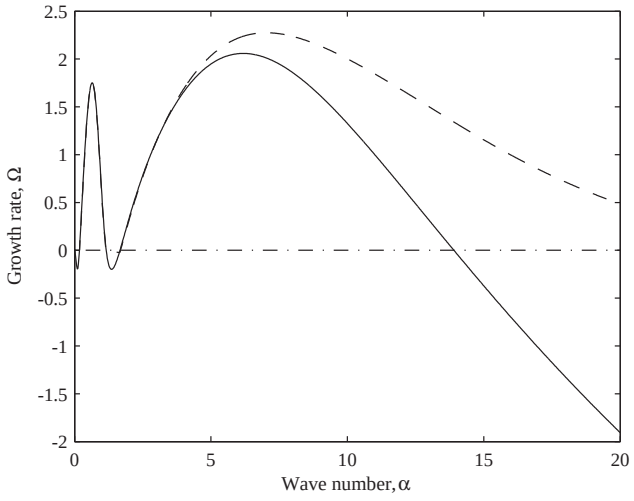

Figure 3: Dispersion curve for the $Ma = 0$ (solid line),$Ma = 1.0$ (dashed line) at $Re = 20.0$, $m = 0.5$, $n = 2.0$, $s = 2.0$

VALIDATION OF THE CODE

The accuracy of the numerical method was checked by comparing current results with published literature (Halpern and Frenkel, 2003) for the two layer Couette flow with an insoluble surfactant in Stoke's flow limit and (Blyth and Pozrikidis,

2004a) for arbitrary Reynolds numbers and wave numbers. To make comparison with Hapern's findings, growth rates are calculated by muting the inertial terms by setting $Re = 0$ in the code and with same parameters as in Halpern's (Halpern and Frenkel, 2003) Fig.(2a) and Fig.(2b), where growth rates are predicted by long-wave evolution equation. Fig.2 shows excellent agreement between the two numerical procedures.
Blyth and Pozrikidis (Blyth and Pozrikidis, 2004b) observed that in the Stoke's flow limit, there exists two modes that govern the stability of a two-layer Couette flow system with surfactant: the Marangoni mode and the Yih mode associated with surfactant and the clean liquid-liquid interface respectively. But on the other hand, in flows with inertia, there exists more than two normal modes. From Fig.3, the broken line corresponding to $Ma = 0.1$ is above the solid line, which corresponds to $Ma = 0$, shows excellent match to Blyth's Fig.3 (Blyth and Pozrikidis, 2004a). This reconfirms the fact that the surfactant in the presence of inertia significantly reduces the rate at which small perturbations decay. Earlier stability analysis (Blyth and Pozrikidis, 2004b) for Stoke's flow in presence of surfactant opens up a range of unstable wave numbers extending from zero up to the

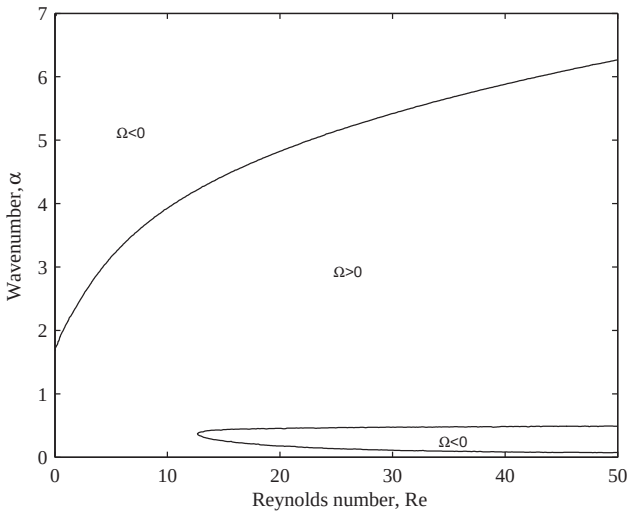

Figure 4: Neutral stability curves for $Ma = 1.0$, $n = 2.0$, $s = 2.0$, $Ca = 2.0$ and $m = 0.5$

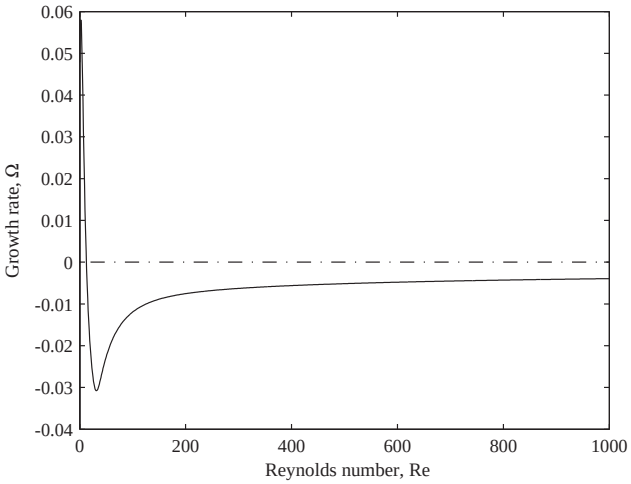

Figure 5: Growth rate vs. Reynolds number for the Marangoni mode for $Ma = 1.0$, $m = 0.5$, $n = 2.0$, $s = 2.0$, $Ca = 2.0$ and $\alpha = 0.37$

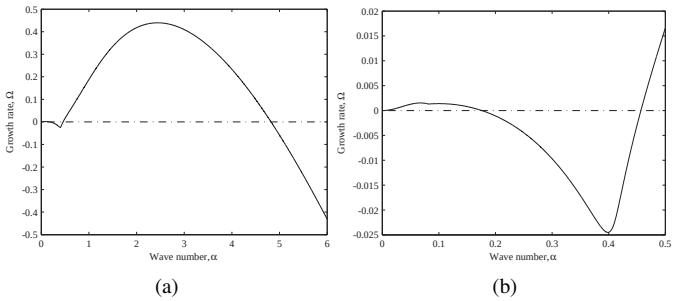

Figure 6: Dispersion curve for the Marangoni mode (solid line) for $Re = 20.0$, $Ma = 1.0$, $m = 0.5$, $n = 2.0$, $s = 2.0$, $Ca = 2.0$ (b) Zoom-in of (a) around $\alpha = 0$

critical wave number $\alpha_{cr} = 1.65$.The neutral stability curve Fig.4 for values ($Ma = 1.0$, $n = 2.0$, $s = 2.0$, $Ca = 2.0$ and $m = 0.5$) is in accordance with Fig.4 of Blyth (Blyth and Pozrikidis, 2004a) and in addition Fig.4 confirms the findings of Blyth (Blyth and Pozrikidis, 2004a), that at $Re_{cr} = 12.63$, a second small window of stable wave numbers appears to form an island of stable modes, with the island tip located at $(Re_{cr}, \alpha_{cr}) = (12.63, 0.37)$. In Fig.5 we plot the growth rate of the Marangoni mode against the Reynolds number, up to and beyond Re_{cr}, for $\alpha = 0.37$, corresponding to the stable island tip. At $Re = 0$, linear stability for Stoke's flow predicts the growth rate $\Omega = 0.0479$, for the Marangoni mode. The present results confirms that the Marangoni mode (Blyth and Pozrikidis, 2004a) at $Re = 12.63$ marks the inauguration of the lower stable loop.
In Fig.6 for a fixed Reynolds number $Re = 20$, we investigate the dependence of the growth rates of the Marangoni mode on the wave number. The close-up near $\alpha = 0$, presented in Fig.6(b), shows that the Marangoni mode has negative growth rate for small band of wave numbers ranging from $\alpha = 0.18\ to\ 0.46$ and has positive growth rate thereafter up-to $\alpha = 5$, beyond which the Marangoni mode is stable again. These results are in excellent match with Fig.6 of Blyth (Blyth and Pozrikidis, 2004a) and reconfirms the crucial role of the surfactant, which either provokes instability or significantly lowers the rate of decay of infinitesimal perturbations.
Blyth (Blyth and Pozrikidis, 2004a) suggested that on changing the viscosity ratio, keeping other parameters at ($Ma = 1.0$,$n = 2.0$, $s = 2.0$ and $Ca = 2.0$), has significant impact on the topology of the neutral stability curve. By increasing m, the upper neutral stability curve shrinks towards low wave numbers and bulges outwards close to $Re = 0$, while the lower island of stable modes moves to the left Fig.7(a)-7(b) confims this, until they meet point as shown in Fig.7(c). Blyth also stated that upon on further raising m, the two curves split leaving small island of unstable modes close to the origin and even bigger island of unstable mode to its upper right, Fig.7(d) reconfirms the Blyth's findings. The small island of unstable modes around the origin shrinks and finally disappears at $m = 4 \simeq n^2$ Fig.7(e) and this confirms the findings of Halpern (Halpern and Frenkel, 2003) and Blyth (Blyth and Pozrikidis, 2004a) at creeping flow limit.

RESULTS AND DISCUSSIONS

We also noticed that a further increase in m does not change the topology of neutral stability, but the thumb shaped unstable region moves in the direction of increasing Re as shown in Fig.7(f).

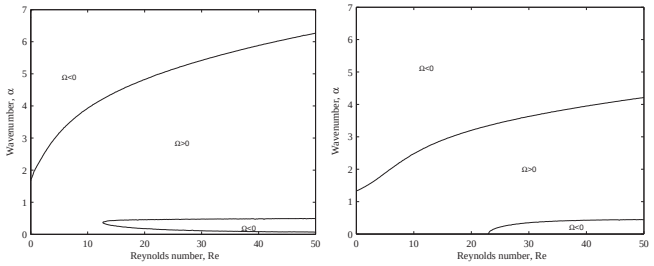

(a) $m = 0.5$ (b) $m = 2.0$

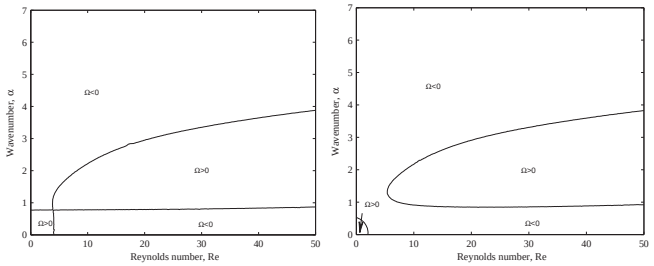

(c) $m = 3.158$ (d) $m = 3.5$

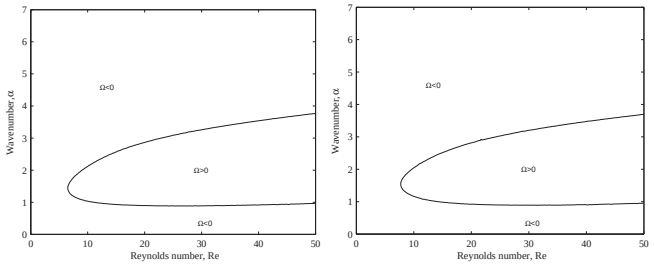

(e) $m = 4.0$ (f) $m = 5.0$

Figure 7: Neutral stability curves for $Ma = 1.0$, $n = 2.0$, $s = 2.0$, $Ca = 2.0$

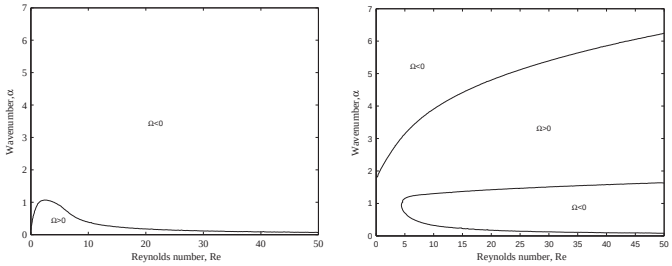

(a) $Ma = 0$ (b) $Ma = 0.2$

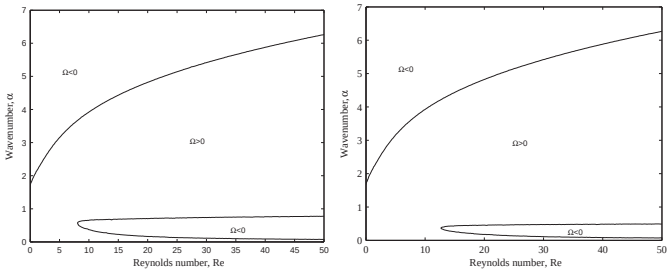

(c) $Ma = 0.6$ (d) $Ma = 1.0$

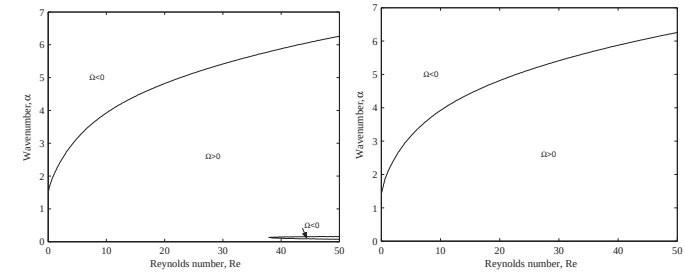

(e) $Ma = 3.0$ (f) $Ma = 5.0$

Figure 8: Neutral stability curves for $m = 0.5$, $n = 2.0$ and $Ca = 2.0$, $s = 2.0$

Further, we investigated the effect of Marangoni number on the stability of the system under consideration via Fig.8(a) and this shows that in the devoid of surfactant (that is at $Ma = 0$), there is very small band of wave numbers where the system is unstable for any Reynolds number. Moreover around $Re = 0$, the band of unstable wave numbers is slightly larger than at any arbitrary Re. In presence of surfactant, $Ma > 0$ Fig.8(b)-8(e) a second small window of stable wave numbers appears to form an island of stable modes. By further increasing the Marangoni number, the upper curve doesn't change but the island of secondary stable modes gets thinner and eventually disappears at around $Ma = 5$ Fig.8(f), leaving space for more unstable modes and thus making system more unstable.

CONCLUSION

Early studies of Yih (Yih, 1967) revealed that even at small Reynolds numbers, the interface is susceptible to long-wave instability. Blyth et al. (Blyth and Pozrikidis, 2004a) found that with both inertia and surfactant present, the surfactant can either induce Marangoni instability or significantly reduce the rate at which small perturbations decay. The influence of surfactant on stability of two-layer Couette flow was investigated. By normal mode analysis, Orr-Sommerfeld equations were formulated and growth rate was computed for different values of parameters using Pseudo-spectral Chebyshev collocation method. The results obtained for small wave numbers in Stoke's flow limit agrees with those reported by Halpern et al. (Halpern and Frenkel, 2003). Neutral stability curves are plotted and critical values of Reynolds number and Wave numbers are found and our results reconfirmed Blyth's findings, that beyond the critical Reynolds number a small island of stables modes are found and also a band of wave numbers with positive growth rates for Reynolds number less than critical value are found. By increasing the viscosity ratio, Blyth's studies revealed formation of multiple regions of stable and unstable modes and on further increasing viscosity ratio, the small island of unstable regions around the origin shrinks and finally disappears leaving large region of unstable modes and our results with Chebyshev collocation method are in accordance with the Blyth's findings. We observed that and further increase in viscosity ratio, shrinks the large regions of unstable modes in the direction of increasing Reynolds number.The influence of Marangoni number on stability was investigated and we found that by increasing the Marangoni number, the small island of stable modes shrink in the direction of increasing Reynolds number and eventually disappear making system more unstable.

For the future work, it would be interesting to compare results of the linear stability analysis with numerical simulation of two-layer flow in presence of surfactant using our Lattice Boltzmann based flow simulator for arbitrary density ratios, depth ratios, viscosity ratios, Reynolds numbers and wave

numbers.

ACKNOWLEDGEMENT

We acknowledge the financial support from The Multiphase Flow Assurance Innovation Centre (FACE). FACE is a research cooperation between IFE, NTNU and SINTEF. The centre is funded by The Research Council of Norway and by the following industrial partners: Statoil ASA, GE Oil & Gas, SPT Group, FMC Technologies, CD-adapco, Shell Technology Norway.
We would also like to thank Prof. Sahu for providing early insights on linear stability analysis.

REFERENCES

BANAT, I. (1995). "Biosurfactants production and possible uses in microbial enhanced oil recovery and oil pollution remediation: A review". *Bioresour. Technol.*, **51**, 01–12.

BLYTH, M. and POZRIKIDIS, C. (2004a). "Effect of inertia on the marangoni instability of two-layer channel flow, part ii: normal-mode analysis,". *J. Eng. Math.*, **50**, 329–341.

BLYTH, M. and POZRIKIDIS, C. (2004b). "Effect of surfactant on the stability of film flow down an inclined plane". *J. Fluid Mech.*, **521**, 241–250.

BOOMKAMP, P. and MIESEN, R. (1996). "Classification of instabilities in parallel two-phase flow". *Int. J. Multiph. Flow*, **22**, 67–88.

CANUTO, C. (1988). *Spectral Methods in Fluid Dynamics*. Springer-Verlag.

FRENKEL, A. and HALPERN, D. (2002). "Stokes-flow instability due to interfacial surfactant". *Phys. Fluids 1994-Present*, **14**, L45–L48.

HALPERN, D. and FRENKEL, A. (2003). "Destabilization of a creeping flow by interfacial surfactant: linear theory extended to all wavenumbers". *J. Fluid Mech.*, **485**, 191–220.

JOSEPH, D. and RENARDY, Y. (1993). "Fundamentals of two-fluid dynamics. pt. ii: Lubricated transport, drops and miscible liquids, in: Fundam. two-fluid dyn. pt ii lubr. transp. drops miscible liq." *Interdiscip. Appl. Math.*, **4**, 459.

SEVERTSON, Y. and AIDUN, C. (1996). "Stability of two-layer stratified flow in inclined channels: applications to air entrainment in coating systems". *J. Fluid Mech.*, **312**, 173–200.

SLATTERY, J. (1974). "Interfacial effects in the entrapment and displacement of residual oil". *AIChE J.*, **20**, 1145–1154.

STONE, H. (1990). "A simple derivation of the time-dependent convective-diffusion equation for surfactant transport along a deforming interface". *Phys. Fluids Fluid Dyn. 1989-1993*, **2**, 111–112.

WEIDEMAN, J. and REDDY, S. (2000). "A matlab differentiation matrix suite". *ACM Trans Math Softw.*, **26**, 465–519.

YIANTSIOS, S. and HIGGINS, B. (1988). "Linear stability of plane poiseuille flow of two superposed fluids". *Phys. Fluids 1958-1988*, **31**, 3225–3238.

YIH, C. (1967). "Instability due to viscosity stratification". *J. Fluid Mech.*, **27**, 337–352.

EFFECT OF COMPRESSIBILITY IN CFD SIMULATIONS OF AN OSCILLATING WATER COLUMN DEVICE

Arun KAMATH[1*], **Hans BIHS**[1†], **Jan Erik OLSEN**[2‡], **Øivind A. ARNTSEN**[1§]

[1]NTNU Department of Civil and Transport Engineering, 7491, Trondheim, NORWAY

[2]SINTEF Materials and Chemistry, 7465 Trondheim NORWAY

[*] E-mail: arun.kamath@ntnu.no
[†] E-mail: hans.bihs@ntnu.no
[‡] E-mail: jan.e.olsen@sintef.no
[§] E-mail: oivind.arntsen@ntnu.no

ABSTRACT

An Oscillating Water Column (OWC) device is a wave energy converter that has a chamber with an air column above a water column. The water column in the device is excited by the incident waves and it transfers kinetic energy to the air column. The air is then alternatively driven out and sucked in to the chamber. This motion of the air drives a turbine to generate electrical energy. The hydrodynamics of an OWC device can be studied in detail using CFD simulations as it provides a large amount of detail regarding the flow field in and around the device. This is essential in order to understand the hydrodynamics of the device and produce an efficient and stable design. Water is generally modeled as an incompressible fluid in CFD simulations relating to coastal and marine civil engineering problems. In the case of an OWC device, the compressibility of air could have an influence on the efficiency of the device. CFD simulations with compressible air and incompressible water are carried out in a two-phase model to investigate the influence of air compressibility. This is compared with simulations with air modeled as an incompressible fluid. The ratio of the air column height and the water depth is also varied to identify the condition at which modeling air compressibility becomes an important factor in the simulations. The results show that the effect of air compressibility on the free surface and pressure variation in the chamber of the device at the scales tested in this study is negligible.

Keywords: CFD, oscillating water column, OWC, compressibility .

NOMENCLATURE

Greek Symbols

ρ	Fluid density, $[kg/m^3]$
ν	Kinematic viscosity, $[m^2/s]$
ν_t	Eddy viscosity, $[m^2/s]$
ω	Specific turbulent dissipation rate, $[1/s]$
$\phi(\vec{x},t)$	Level set function, $[m]$
λ	Wavelength, $[m]$

Latin Symbols

U	time-averaged velocity, $[m/s]$.
P	Pressure, $[Pa]$.
g	Acceleration due to gravity, $[m^2/s]$.
k	Turbulent kinetic energy, $[m^2/s^2]$
R	Gas Constant, $[J/kgK]$.
T	Temperature, $[K]$.
H	Wave height, $[m]$.

Sub/superscripts

i	Index i.
j	Index j.

INTRODUCTION

An Oscillating Water Column (OWC) is a renewable energy device used to convert wave energy into electrical energy. It consists of a chamber partially submerged in water so that it encloses an air column over the water column. The water column in the chamber is excited by the incident waves and the motion of the water column is transferred to the air column. The air is inhaled into and exhaled out of the chamber. This drives a turbine that converts the kinetic energy from the motion of the air column into electrical energy. The ability of the device to transfer the incident wave energy to the air column is measured using the hydrodynamic efficiency. An illustration of an OWC device with its various parts is presented in Figure 1.

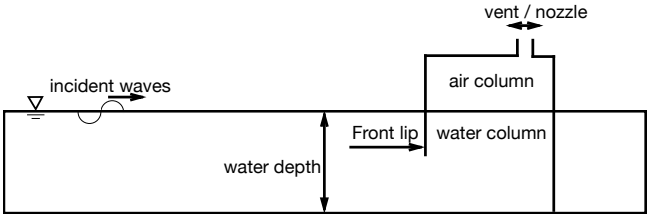

Figure 1: Illustration of an OWC device.

Several authors have analysed OWC devices and presented a mathematical description of the oscillation of the water column. Evans (1978) analytically calculated the efficiency of a wave energy converter device modeled as a pair of parallel vertical plates with a float connected to a spring-dashpot on the free surface as the wave energy absorber and showed that the maximum efficiency in this setup is about 50%. The oscillating water column was treated to be a massless piston in this analysis. Evans (1982) and Sarmento and Falcão (1985) analyzed an OWC device in two dimensions considering the spatial variation of the free surface of the water column. In these studies, the hydrodynamic efficiency of the device is measured as the work done by the air column under the pressure developed in the chamber due to the turbine over the air column. Sarmento and Falcão (1985) also found through their analysis that air compressibility could be a factor for

smaller values of relative water depth. Experimental campaigns have been carried out by several authors to obtain a better understanding of the OWC device. Sarmento (1992) carried out wave flume experiments on an OWC device and studied linear and non-linear power take off (PTO) mechanisms using filters and orifice plates respectively. They found that the difference in the efficiency using a non-linear PTO mechanism is slightly lower than that obtained using a linear PTO mechanism. Thiruvenkatasamy and Neelamani (1997) studied the effect of nozzle area on the efficiency of an OWC device through wave flume experiments. They reported that for nozzle areas greater than 0.81% of the free surface area, there was a dramatic drop in the efficiency of the OWC device due to very low pressures developed in the chamber. Morris-Thomas *et al.* (2007) carried out experiments to determine the hydrodynamic efficiency of an OWC device and the influence of the front wall shape, draught and thickness over various wavelengths. Several numerical studies have also been carried out to simulate the working of the OWC device. Hong *et al.* (2007) used a boundary integral equation to numerically study the effects of air duct width, chamber length, skirt thickness and variation of bottom slope and compared it with experiments. They concluded that the dominance of pneumatic damping reduces for larger chamber volumes. Koo and Kim (2010) used the boundary element method to simulate an OWC device using viscous damping terms in the model and showed that the highest work done by the pneumatic pressure in the chamber occurred at resonance. Computational Fluid Dynamics (CFD) modeling has been utilized to investigate the hydrodynamics of the OWC device, studying the two phase flow of air and water. Senturk and Ozdamar (2011) analyzed a simplified scaled model of an OWC prototype device and reported a deviation of up to 30% between the analytical solution and the numerical result for nozzle velocity. Zhang *et al.* (2012) numerically replicated the experiments of Morris-Thomas *et al.* (2007) and reported over prediction of the efficiency due to complex pressure changes in the chamber around resonance. Various studies so far have dealt with the working of the OWC device and calculated the efficiency of the device under various configurations. The hydrodynamic efficiency of the device in these studies is based on the pressure developed in the chamber due to the damping provided by the turbine and the velocity of the free surface. These parameters quantify the work done by the air column. So far, the various studies on the OWC device using numerical modeling have assumed air to be an incompressible fluid. Compressibility of the air phase affects the volume of air in the chamber and consequently can influence the pressure developed in the chamber and the oscillation and the velocity of the free surface. The importance of compressibility on the working of the device can be investigated using a two-phase numerical model that treats air as a compressible phase and water as an incompressible phase.

In this study, a CFD model is used to simulate an OWC device in a two-dimensional wave flume. Simulations are carried out to study the difference between the free surface oscillation and the variation of pressure in the device chamber with air as a compressible phase and as an incompressible phase. The variation of the free surface and the pressure in the device chamber in the two scenarios are compared for different geometries of the device. The influence of the height of the air column in the chamber is studied by varying the chamber height while keeping the water depth and the depth of immersion of the front wall a constant. In order to study the influence of air compressibility at larger scales, a simulation is carried out by scaling up the setup by three times and the behavior of the free surface and pressure in the chamber is studied.

NUMERICAL MODEL

Governing Equations

The numerical model uses the Reynolds-averaged Navier Stokes (RANS) equations along with the continuity equation to solve the two-phase fluid flow problem:

$$\frac{\partial U_i}{\partial x_i} = 0 \tag{1}$$

$$\frac{\partial U_i}{\partial t} + U_j \frac{\partial U_i}{\partial x_j} = -\frac{1}{\rho}\frac{\partial P}{\partial x_i} + \frac{\partial}{\partial x_j}\left[(\nu + \nu_t)\left(\frac{\partial U_i}{\partial x_j} + \frac{\partial U_j}{\partial x_i}\right)\right] + g_i \tag{2}$$

The projection method by Chorin (1968) is used to determine the pressure and the Poisson pressure equation is solved using a preconditioned BiCGStab iterative solver developed by van der Vorst (1992). Turbulence modeling is handled using the two equation k-ω model proposed by Wilcox (1994). The strain due to waves in the numerical wave tank leads to an unphysical over production of turbulence. This is avoided using eddy viscosity limiters as shown by Durbin (2009). In a two-phase model with air and water, there is a large difference at the interface which leads to an overproduction of turbulence at the interface. This is reduced by introducing free surface turbulence damping with a limiter around the interface for the source terms as shown by Egorov (2004).

Free Surface

The free surface is determined using the level set method by Osher and Sethian (1988). In this method, the zero level set of a signed distance function, $\phi(\vec{x},t)$, represents the interface between water and air as shown in Equation 3:

$$\phi(\vec{x},t)\begin{cases} > 0 & if\ \vec{x}\ is\ in\ phase\ 1 \\ = 0 & if\ \vec{x}\ is\ at\ the\ interface \\ < 0 & if\ \vec{x}\ is\ in\ phase\ 2 \end{cases} \tag{3}$$

For the rest of the domain, the level set function gives the closest distance to the interface and the sign distinguishes between the two fluids across the interface. The level set function is continuous across the interface and provides a sharp representation of the free surface. The signed distance property of the level set function is restored after convection using a partial differential equation based reinitialisation procedure presented by Peng *et al.* (1999) after every time step as shown in Equation 4:

$$\frac{\partial \phi}{\partial t} + S(\phi)\left(\left|\frac{\partial \phi}{\partial x_j}\right| - 1\right) = 0 \tag{4}$$

where S(ϕ) is the smooth signed function:

$$S(\phi) = \frac{\phi}{\sqrt{\phi^2 + \left|\frac{\partial \phi}{\partial x_j}\right|^2 (\Delta x)^2}} \tag{5}$$

Discretization Schemes

The fifth-order conservative finite difference Weighted Essentially Non-Oscillatory (WENO) scheme proposed by Jiang and Shu (1996) is used for discretization of convective terms of the RANS equations. The level set function,

turbulent kinetic energy k and the specific turbulent dissipation rate ω are discretized using the Hamilton-Jacobi formulation of the WENO scheme shown by Jiang and Peng (2000). The WENO scheme provides the accuracy required to model complex free surface flows and has numerical stability from its non-oscillatory property. The scheme considers the local smoothness of the stencils and can handle large gradients and provides a minimum of third-order accuracy. A TVD third order Runge-Kutta explicit time scheme developed by Shu and Osher (1988) is employed for time advancement of the level set function and the reinitialisation equation. The time step size in the simulation is determined using an adaptive time stepping method. The maximum velocities in the domain during the current time step are used to evaluate the next time step size to satisfy the CFL criterion. The time treatment for turbulent kinetic energy and dissipation are handled by a first-order implicit scheme as they have lower influence from the convective terms. Explicit handling of the terms in the turbulence model can lead to very small time steps due to the large source terms involved. Due to the use of an implicit scheme to handle these terms and the diffusion, the CFL criterion is satisfied using only the maximum velocities in the domain. The model uses a Cartesian grid for spatial discretization. This facilitates a straight forward implementation of the finite difference schemes. The boundary conditions for complex geometries are handled using an adaptation of the Immersed Boundary Method (IBM), a method initially proposed for elastic boundaries by Peskin (1972). This was further developed by Tseng and Ferziger (2003) to a ghost cell IBM, where the values from the fluid region are extrapolated along the orthogonal to the boundary into the solid region using cells called ghost cells. In order to extend the solution smoothly in the same direction as the discretization for which it would be used, a local directional ghost cell approach was adopted by Berthelsen and Faltinsen (2008). In the current study, a multiple ghost cell IBM (MGCIBM) implemented by Bihs (2011) using object oriented programming techniques is used, where the ghost cell values can be updated from multiple directions. The code is run as a fully parallel program to increase the computational efficiency by using MPI (Message Passing Interface). The domain is decomposed into smaller pieces and a processor is assigned to each part to carry out the computations in parallel.

Numerical Wave Tank

Wave generation and wave absorption in the numerical wave tank is carried out using the relaxation method (Larsen and Dancy, 1983). In this method, the analytical solution from wave theory is used to moderate the computationally generated waves in the wave tank. In the wave generation zone, the computational values of velocity and free surface are taken from zero to the analytical values expected by wave theory. The wave theory used to moderate the values is chosen based on the water depth and wave steepness in the simulation. At the numerical beach, the computational values for the velocity and free surface are brought to zero and all the energy is smoothly removed from the wave tank. The relaxation functions shown by Jacobsen *et al.* (2011) are implemented in the numerical model.

This method of wave generation and absorption requires some part of the computational domain to be reserved for the relaxation zones. The relaxation zone at wave generation is one wavelength long and two times the generated wavelength at the beach. This takes up a length of about three wavelengths in the wave tank, but the process is carried out without additional computation and in a clean manner without spurious waves polluting the result in the wave tank. The relaxation function in the generation zone also absorbs the waves reflected from the objects in the wave tank so that the wave generation is not affected. This simulates an environment of wave generator with absorption.

Treatment of Compressibility

The effect of compressibility of air in the OWC chamber is represented in the numerical model using the ideal gas law. It is implemented by linking the density of air with the pressure as follows:

$$\rho_{air} = \frac{P}{RT} \tag{6}$$

The pressure for every point in the domain at any given time step is available from the solution to the Poisson equation. The density of the air phase is then re-evaluated at every time step according to Equation 3. As the pressure in the OWC device chamber increases, the compressibility of air leads to an increase in the density of air. The new value of the density of air is used to solve the RANS equations in the next time step. In this way, the compressibility of air in the OWC chamber is accounted for and its influence on the flow problem can be studied.

RESULTS

The OWC device simulated in this study has the same dimensions as in the experimental campaign by Morris-Thomas *et al.* (2007). The front wall thickness is 0.04m with a draught of 0.15m in a water depth of 0.92m. The total height of the device chamber is 1.275m, with a 0.355m high air column and the length of the chamber is 0.64m. The nozzle at the top of the device which provides damping is 0.05m wide. Porous media flow relation is used to provide a damping equivalent to that from a 0.005m nozzle that is used in the experiments. This configuration of the device is referred to as the standard configuration of the device. A schematic diagram of the geometry of the device is provided in Figure 2. The OWC device is placed in a two-dimensional numerical wave tank of length 20m and height 2.20m. A grid size of 0.025m is used and linear waves with wave height H = 0.06m and wavelength λ = 3.54m are generated in the wave tank. The OWC device in the numerical wave tank during the process of exhalation of air from the chamber is shown in Figure 3. It is learnt from the experimental campaign by Morris-Thomas *et al.* (2007) that the selected wave excites a resonant response from this configuration of the OWC device. The variation of the pressure and free surface in the chamber are maximum at resonance. So, the effect of compressibility at resonance is investigated for various configurations of the device chamber to identify the conditions under which air compressibility has a major influence on the

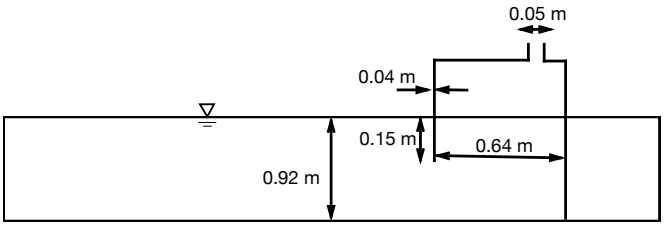

Figure 2: Schematic diagram of device geometry.

working of the device. The various configurations used in the study are listed in Table 1. A simulation considering air compressibility and a simulation assuming incompressible air are carried out for each of the listed configurations.
At first, the standard configuration of the device is simulated

Table 1: Chamber configuration in the simulations.

Simulation	Chamber vent	Chamber height (m)
Validation: 1	open	standard - 1.275
2	open	standard - 1.275
3	closed	standard - 1.275
4	open	reduced - 1.175
5	open	increased - 1.575
6	open	large scale - 3.825

with incompressible air. The variation of the free surface at the center of the chamber and the pressure in the chamber is calculated. The numerical model is validated by comparing the results from the simulation to the experimental data from Morris-Thomas *et al.* (2007) for this scenario. The numerical results are found to match the experimental observations in Figures 4 and 5. The simulation is then repeated with compressible air. The variation of the free surface at the center of the chamber for this setup with compressible and incompressible air is observed to be similar in Figure 6. The variation of the pressure in the chamber is also the same as seen in Figure 7. Thus, it can be concluded that the results from the numerical model with both compressible and incompressible air match the experimental observations. This means that the effect of compressibility for this configuration is negligible.

In the next simulation, the chamber of the device is closed by removing the vent at the roof of the chamber. In this configuration, the external damping on the chamber can be considered to be infinite. The variation of the free surface at the center of the closed chamber with compressible and incompressible air is found to be the same in Figure 8. The variation of the chamber pressure in the incompressible case obtains slightly higher peaks than when air is considered compressible in Figure 9. This is justified by the fact that a part of the energy from the chamber is used up to compress the air. It is observed that the difference in the pressures in the two cases is very small. The absolute values of the pressures in this case are also small due to infinite damping on the chamber when it is closed. A large difference is seen in the values of pressure when the chamber is closed compared to the chamber pressure when the vent is opened and a finite external damping is provided. This is because when the chamber is closed, the damping on the device chamber is

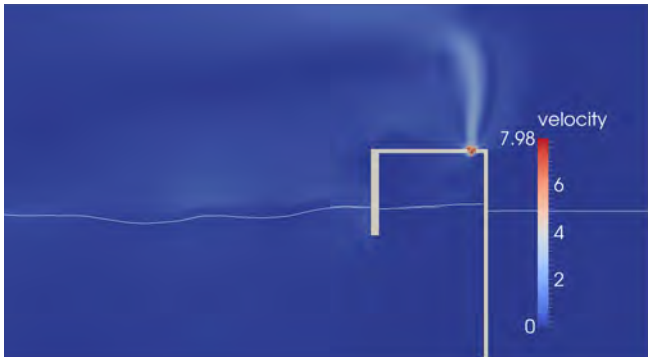

Figure 3: OWC device in the numerical wave tank during exhalation.

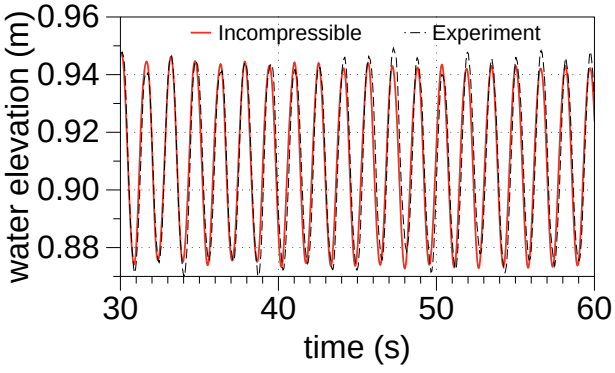

Figure 4: Validation: Free surface with standard chamber

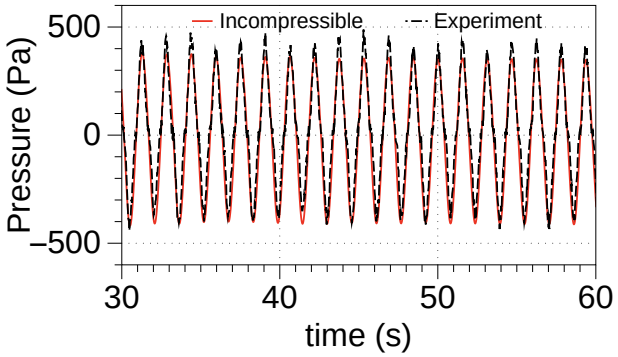

Figure 5: Validation: Chamber pressure with standard chamberr

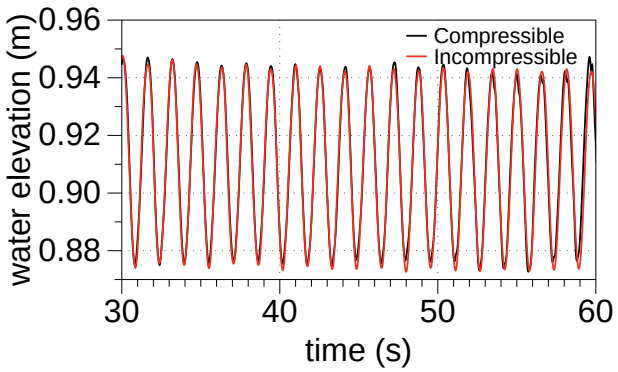

Figure 6: Free surface variation: standard chamber

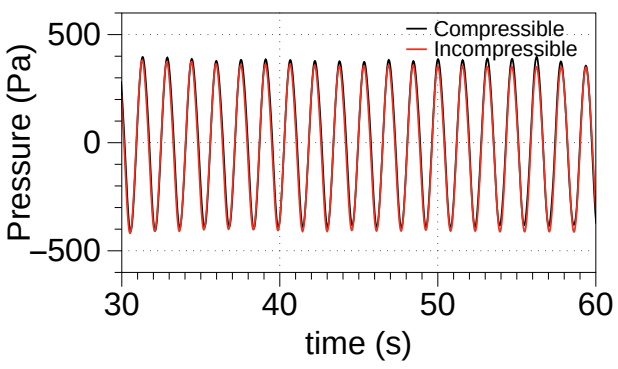

Figure 7: Pressure variation: standard chamber

infinite and the device does not absorb most of the incoming wave energy. This scenario represents the state of the device where the OWC device is turned off for power generation.

The influence of compressibility on reducing the height of the air column is studied by changing the chamber height to 1.175m resulting in an air column height of 0.255m. The variation of the free surface with compressible and incompressible air is presented in Figure 10 and found to be the same in both the cases. The pressure variation in the chamber in Figure 11 is also the same with compressible and incompressible treatment of air.

In the next simulation, the influence of compressibility on increasing the height of the air column is studied by changing the chamber height to 1.575 resulting in an air column of height 0.655m. The variation of the free surface at the center of the chamber in simulations with compressible and incompressible treatment of air is found to be the same in Figure 12. The pressure variation in the chamber is also found to be the same for both the cases as seen in Figure 13.

It is observed that no differences are found in the oscillations of the free surface and the pressure in the chamber with compressible and incompressible treatment of the air in the chamber in the various configurations simulated above. So, it can be concluded that the compressibility of air does not have a major influence on the device chamber at this scale for various air column lengths.

In order to investigate the scale effect of compressibility, a large scale simulation is carried out by increasing the chamber length, chamber height and the water depth to three times their original values. The front wall thickness of the device is maintained at 0.04m. The draught of the front wall is increased to 0.45m in a water depth of 2.76m. The total height

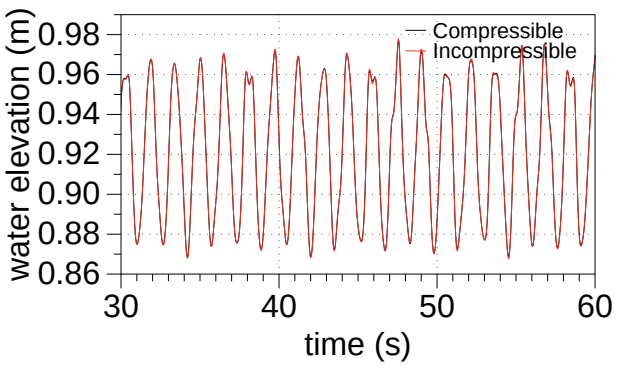

Figure 8: Free surface variation: closed chamber

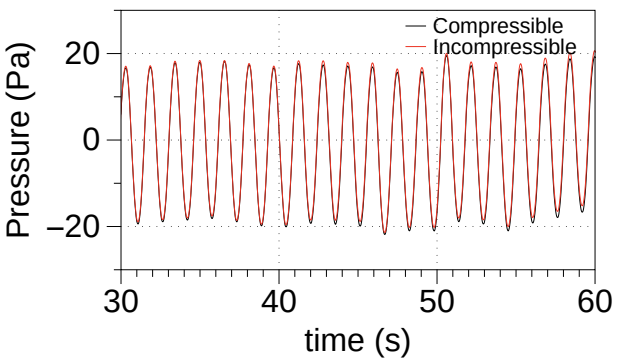

Figure 9: Pressure variation: closed chamber

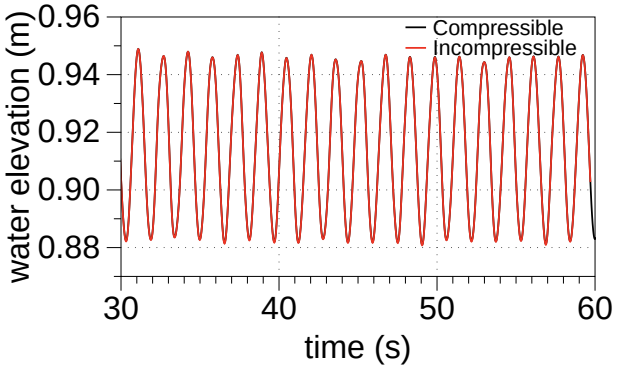

Figure 10: Free surface variation: smaller chamber

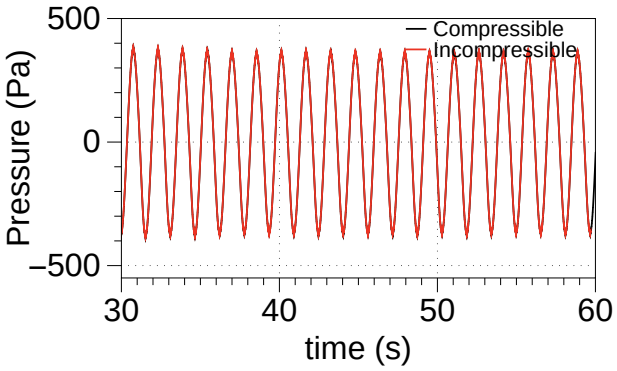

Figure 11: Pressure variation: smaller chamber

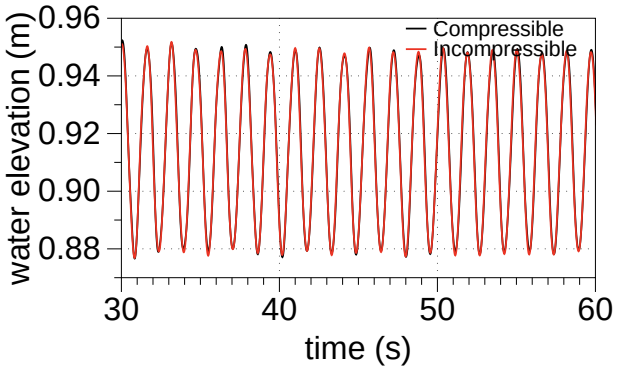

Figure 12: Free surface variation: larger chamber

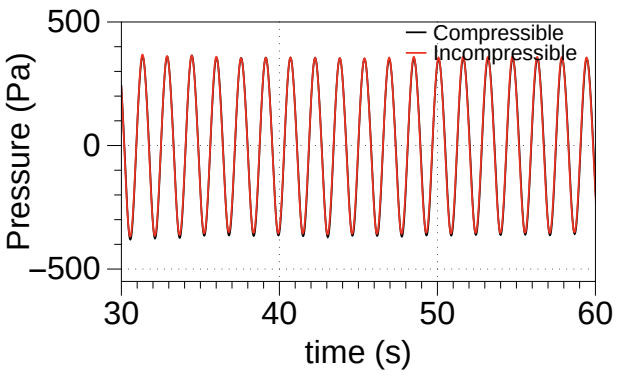

Figure 13: Pressure variation: larger chamber

of the device chamber is 3.825m, with a 1.065m high air column and the length of the chamber is increased to 1.92m. The nozzle at the top of the device which provides damping is 0.15m wide. The external damping on the device is maintained the same as in the previous cases using the porous media flow relation. The numerical wave tank is 60m long and 6.0m high for this simulation. A grid size of 0.025m is used and linear waves with wave height H= 0.1m and wavelength $\lambda = 10.62$m are generated in the wave tank.
This configuration is simulated with compressible and incompressible treatment of air in the chamber of the device. The variation of the free surface in both the cases is observed to be the same in Figure 14. The variation of the pressure in the chamber in both the cases is also observed to be the same with both compressible and incompressible treatment of air in the numerical model.

From the simulations carried out above, no major difference is seen between the simulation with compressible air and the simulation with incompressible air. The free surface and pressure oscillations in the device chamber remain the same in compressible and incompressible cases on increasing and reducing the height of the air column in the device. There was no influence of air compressibility in a simulation carried out at a larger scale as well.

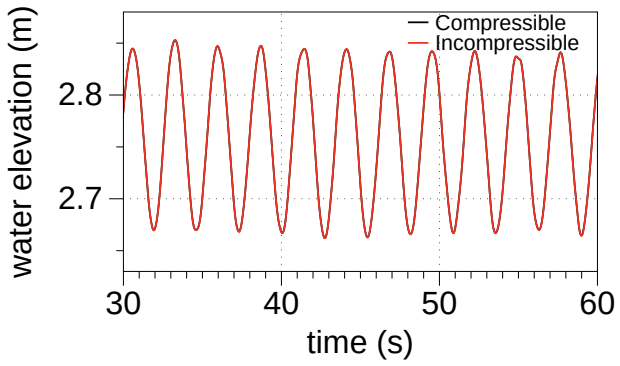

Figure 14: Free surface variation: large scale simulation

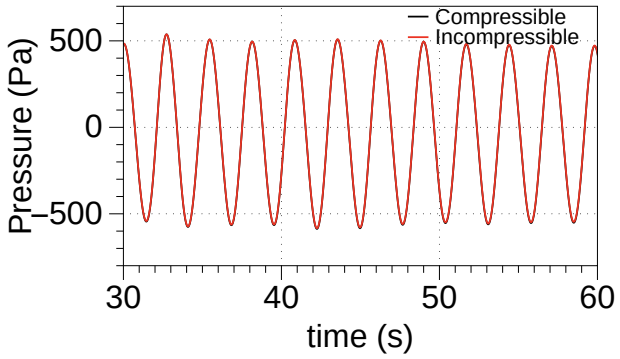

Figure 15: Pressure variation: large scale simulation

From the various simulations carried out in this study, the effect of compressibility of air on the pressure and free surface is found to be negligible. This is because the density of air varies linearly with the pressure. Considering constant temperature in Equation 6 and with gas constant $R = 286.9$ J/kg K, the density of air changes as $0.0035P$, where P is the pressure in the chamber. The maximum pressure observed in the simulation is of the order of 500Pa. The change in density due to this pressure is very small and thus the effect of compressibility in these simulations is negligible. The effect of compressibility will be apparent only when the external damping from the PTO device is large enough to cause an appreciable change in the density of air. Thus, at the model scales used to investigate the hydrodynamics of the OWC device, a simulation considering incompressible air provides a good representation of the physics involved.

CONCLUSION

1. The numerical model simulated an OWC device considering air compressibility in the device chamber and compared the free surface oscillation and pressure in the chamber with a simulation assuming air to be incompressible in the OWC chamber.

2. A small difference in the pressure oscillation in the device chamber was observed when the chamber vent was closed representing infinite damping on the device. The small reduction in amplitude of the pressure in the simulation with compressible air may be due to the energy spent in compressing the air in the chamber.

3. The amplitude of the free surface and the pressure in the chamber were found to be the same for different heights of the air column in the device chamber. Air compressibility did not affect the results in the simulations with external damping from a power takeoff device.

4. A large scale simulation was carried out to study the scale effect on air compressibility by simulating a device with three times the dimensions used in the other simulations. The amplitude of oscillation of the free surface oscillation and the pressure in the device chamber were found to be the same with both compressible and incompressible treatment of air in the numerical model.

5. The influence of air compressibility in the device chamber for the OWC device simulated in this study is negligible and did not have any major consequence on the working of the OWC device.

ACKNOWLEDGEMENTS

This research was carried out as a part of the OWCBC project (No. 217622/E20) and the authors are grateful for the grants obtained from the Research Council of Norway.

REFERENCES

BERTHELSEN, P.A. and FALTINSEN, O.M. (2008). “A local directional ghost cell approach for incompressible viscous flow problems with irregular boundaries”. *Journal of Computational Physics*, **227**, 4354–4397.

BIHS, H. (2011). “Three-dimensional numerical modeling of local scouring in open channel flow”. PhD thesis No. 127, Department of Hydraulic and Environmental Engineering, Norwegian University of Science and Technology, Trondheim, Norway.

CHORIN, A. (1968). “Numerical solution of the Navier Stokes equations”. *Mathematics of Computation*, **22**, 745–762.

DURBIN, P.A. (2009). “Limiters and wall treatments in applied turbulence modeling”. *Fluid Dynamics Research*, **41**, 1–18.

EGOROV, Y. (2004). “Validation of CFD codes with PTS-relevant test cases”. Tech. Rep. 5th Euratom Framework Programme ECORA project, EVOL-ECORA âĂŞD07.

EVANS, D.V. (1978). "Oscillating water column wave energy convertors". *IMA Journal of Applied Mathematics*, **22**, 423–433.

EVANS, D.V. (1982). "Wave power absorption by systems of oscillating surface pressure distributions". *Journal of Fluid Mechanics*, **114**, 481–499.

HONG, K. *et al.* (2007). "Effects of shape parameters of owc chamber in wave energy absorption". *Proc.,* 17*th International Offshore and Polar Engineering Conference, Lisbon*.

JACOBSEN, N.G. *et al.* (2011). "A wave generation toolbox for the open-source CFD library: OpenFOAM". *International Journal for Numerical Methods in Fluids*, **70(9)**, 1073–1088.

JIANG, G.S. and PENG, D. (2000). "Weighted eno schemes for Hamilton-Jacobi equations". *SIAM Journal on Scientific Computing*, **21**, 2126–2143.

JIANG, G.S. and SHU, C.W. (1996). "Efficient implementation of weighted ENO schemes". *Journal of Computational Physics*, **126**, 202–228.

KOO, W. and KIM, M.H. (2010). "Nonlinear nwt simulation for oscillating water column wave energy convertor". *Proc.,* 29*th International Conference on Ocean, Offshore and Arctic Engineering, Shanghai*.

LARSEN, J. and DANCY, H. (1983). "Open boundaries in short wave simulations - a new approach". *Coastal Engineering*, **7**, 285–297.

MORRIS-THOMAS, M.T. *et al.* (2007). "An investigation into the hydrodynamic efficiency of an oscillating water column". *Journal of Offshore Mechanics and Arctic Engineering*, **129**, 273–278.

OSHER, S. and SETHIAN, J.A. (1988). "Fronts propagating with curvature- dependent speed: Algorithms based on hamilton-jacobi formulations". *Journal of Computational Physics*, **79**, 12–49.

PENG, D. *et al.* (1999). "A PDE-based fast local level set method". *Journal of Computational Physics*, **155**, 410–438.

PESKIN, C.S. (1972). "Flow patterns around the heart valves". *Journal of Computational Physics*, **10**, 252–271.

SARMENTO, A.J.N.A. (1992). "Wave flume experiments on two-dimensional oscillating water column wave energy devices". *Experiments in Fluids*, **12**, 286–292.

SARMENTO, A.J.N.A. and FALCÃO (1985). "Wave generation by an oscillating surface pressure and its application in wave energy extraction". *Journal of Fluid Mechanics*, **150**, 467–485.

SENTURK, U. and OZDAMAR, A. (2011). "Modelling the interaction between water waves and the oscillating water column wave energy device". *Mathematical and Computational Applications*, **16(3)**, 630–640.

SHU, C.W. and OSHER, S. (1988). "Efficient implementation of essentially non-oscillatory shock capturing schemes". *Journal of Computational Physics*, **77**, 439–471.

THIRUVENKATASAMY, K. and NEELAMANI, S. (1997). "On the efficiency of wave energy caissons in array". *Applied Ocean Research*, **19**, 61–72.

TSENG, Y.H. and FERZIGER, J.H. (2003). "A ghost-cell immersed boundary method for flow in complex geometry". *Journal of Computational Physics*, **192**, 593–623.

VAN DER VORST, H. (1992). "BiCGStab: A fast and smoothly converging variant of Bi-CG for the solution of nonsymmetric linear systems". *SIAM Journal on Scientific and Statistical Computing*, **13**, 631–644.

WILCOX, D.C. (1994). *Turbulence Modeling for CFD*. DCW Industries Inc., La Canada, California.

ZHANG, Y. *et al.* (2012). "Air-water two phase flow modelling of hydrodynamic performance of an oscillating water column device". *Renewable Energy*, **41**, 159–170.

CFD MULTIPHASE SIMULATION OF TWO-FLUID SLOSHING WITH FREE SURFACE MOTION USING THE LEVEL SET METHOD

Hans BIHS[1]*, **Arun KAMATH**[1], **Øivind A. ARNTSEN**[1]

[1]Department of Civil and Transport Engineering, NTNU Trondheim

* E-mail: hans.bihs@ntnu.no

ABSTRACT

A numerical model is used to calculate sloshing of two immiscible fluids in a rectangular tank with free surface, resulting in three-phase flow. The numerical results are compared with experimental data. In the experiments the rectangular tank rotates around the horizontal axis, generating the sloshing of the fluids. Measurements of the interface motion between the lighter and heavier fluid and between the lighter fluid and air exist. The numerical model uses the level set method for the prediction of the interfaces between the different phases. A numerical approach is presented, how two level set functions can uniquely identify the three different phases. The comparison between numerical and experimental data shows good agreement.

Keywords: Multiphase Flow, Sloshing, Three-Phase Flow, Level Set Method .

INTRODUCTION

In many engineering disciplines, fluid flow problems with more than one phase are quite common. Predicting the correct location of the interface between different fluids or gases is important for many applications, such as for example sloshing dynamics. The numerical computation of such a flow case is challenging in many ways. The numerical procedure is required to be stable, fast and accurate. Qualities which are harder to obtain for multiphase flow systems, as discontinuities in the material properties i.e. the density and the viscosity occur. In addition, numerical discretization schemes need to be of high-order of accuracy in order to preserve the sharp division between the phases.

Different approaches to the numerical solution of the interface capturing exist. One of the earliest is the Marker-and-Cell (MAC) scheme (Harlow and Welch, 1965). Here massless marker particles are used to represent the phases. The distribution of the particles determines the location of the interface, which must be reconstructed explicitly. The computing effort is rather large because the grid needs to be refined along interface in order to avoid smeared solutions. In the Volume of Fluid method (VOF) (Hirt and Nichols, 1981) the marker particles are replaced by a scalar field, which describes the volume fraction of one fluid for each discretization cell. A convection equation is solved in order to move the scalar field along with the external velocity field. For the extraction of the geometrical interface from the fraction function, a reconstruction algorithm needs to be used. In the accurate reconstruction of the interface lies the main difficulty of this method, and it negatively affects mass conservation. In addition, an effect known as foaming, the smearing of the interface can be a problem, due to the numerical diffusion resulting from the discretization of the fraction function.

In the present paper the level set method is used (Osher and Sethian, 1988). The main idea behind this method is that the location of interface is represented implicitly by the zero level set of the smooth signed distance function. In contrast to the VOF method the level set function varies continuously across the interface. The location of the interface is readily available and does not require any reconstruction procedure. Since mass conservation is not enforced directly by the level set method, it is supplemented with a particle correction algorithm. The numerical model is used to simulate three-phase sloshing in a rectangular tank. A numerical approach is presented on how multiple level set functions can be used to model multiple fluid interfaces.

NUMERICAL MODEL

Equations of Motion

For the investigations in the present paper the three-dimensional numerical model REEF3D is used (Bihs, 2011). The governing equations for the mass and momentum conservation are the continuity and the incompressible Reynolds-averaged Navier-Stokes (RANS) equations:

$$\frac{\partial U_i}{\partial x_i} = 0 \tag{1}$$

$$\frac{\partial U_i}{\partial t} + U_j \frac{\partial U_i}{\partial x_j} = -\frac{1}{\rho}\frac{\partial P}{\partial x_i} + \frac{\partial}{\partial x_j}\left[(\nu + \nu_t)\left(\frac{\partial U_i}{\partial x_j} + \frac{\partial U_j}{\partial x_i}\right)\right] + g_i \tag{2}$$

U is the velocity averaged over the time t, x the spatial geometrical scale, ρ the water density, ν the kinematic viscosity, ν_t the eddy viscosity , P the pressure and g is the gravity.

Turbulence Model

The eddy viscosity ν_t in the RANS-equations is determined through the two-equation k-ω model (Wilcox, 1994), with the equations for turbulent kinetic energy k and the specific turbulent dissipation ω as follows:

$$\frac{\partial k}{\partial t}+U_j\frac{\partial k}{\partial x_j}=\frac{\partial}{\partial x_j}\left[\left(\nu+\frac{\nu_t}{\sigma_k}\right)\frac{\partial k}{\partial x_j}\right]+P_k-\beta_k k\omega \quad (3)$$

$$\frac{\partial \omega}{\partial t}+U_j\frac{\partial \omega}{\partial x_j}=\frac{\partial}{\partial x_j}\left[\left(\nu+\frac{\nu_t}{\sigma_\omega}\right)\frac{\partial \omega}{\partial x_j}\right]+\frac{\omega}{k}\alpha P_k-\beta\omega^2 \quad (4)$$

P_k is the turbulent production rate, the coefficients have the values α=$\frac{5}{9}$, $\beta_k=\frac{9}{100}$and β=$\frac{3}{40}$.
In order to avoid overproduction of turbulence in highly strained flow outside the boundary layer, the turbulent eddy viscosity ν_t is bounded through the following limited formulation (Durbin, 2009):

$$\nu_t=\min\left(\frac{k}{\omega},\sqrt{\frac{2}{3}}\frac{k}{|\mathbf{S}|}\right) \quad (5)$$

Pressure

The pressure gradient term in the RANS-equations is modeled with Chorin's projection method (Chorin, 1968) for incompressible flow. Here the pressure gradient is removed form the momentum equations. Instead the updated velocity after each Euler step of the time discretization is the intermediate velocity U_i^*. Then the Poisson equation for pressures is formed by calculating the divergence of the intermediate velocity field.

$$\frac{\partial}{\partial x_i}\left(\frac{1}{\rho\left(\phi^n\right)}\frac{\partial P}{\partial x_i}\right)=-\frac{1}{\Delta t}\frac{\partial U_i^*}{\partial x_i} \quad (6)$$

The Poisson equation is solved using the fully parallelized Jacobi-preconditioned BiCGStab algorithm (van der Vorst H., 1992). The pressure is then used to correct the velocity field, making it divergence free.

Discretization of the Convective Terms

The convective terms of the RANS equations are discretized with the fifth-order WENO (weighted essentially non-oscillatory) scheme by Jiang and Shu (Jiang and Shu, 1996) in the conservative finite-difference framework. The convection term is approximated in x-direction as follows:

$$U\frac{\partial U}{\partial x}\approx\frac{1}{\Delta x}\left(\tilde{U}_{i+1/2}U_{i+1/2}-\tilde{U}_{i-1/2}U_{i-1/2}\right) \quad (7)$$

Here $\tilde{U}$ is the convection velocity, which is obtained at the cell faces through simple interpolation. For the cell face $i+1/2$, $U_{i+1/2}$ is reconstructed with the WENO procedure:

$$U_{i+1/2}^{\pm}=\omega_1^{\pm}U_{i+1/2}^{1\pm}+\omega_2^{\pm}U_{i+1/2}^{2\pm}+\omega_3^{\pm}U_{i+1/2}^{3\pm} \quad (8)$$

The $\pm$ sign indicates the upwind direction. U^1, U^2 and U^3 represent the three possible ENO stencils. For upwind direction in the positive i-direction, they are:

$$\begin{aligned}U_{i+1/2}^{1-}&=\frac{1}{3}U_{i-2}-\frac{7}{6}U_{i-1}+\frac{11}{6}U_i,\\ U_{i+1/2}^{2-}&=-\frac{1}{6}U_{i-1}+\frac{5}{6}U_i+\frac{1}{3}U_{i+1},\\ U_{i+1/2}^{3-}&=\frac{1}{3}U_i+\frac{5}{6}U_{i+1}-\frac{1}{6}U_{i+2}\end{aligned} \quad (9)$$

The nonlinear weights ω_n are determined for each ENO stencil and calculated based on the smoothness indicators IS. Large smoothness indicators indicate a non-smooth solution in the particular ENO stencil. Accordingly, the non linear weights ω_n for this stencil will be small. By assigning them the largest weights ω_n, the WENO scheme favors stencils with a smooth solution. As a result the scheme can handle large gradients right up to the shock very accurately. In the worst-case situation, where large gradients are present in all three stencils, the WENO scheme will achieve a third-order of accuracy. In the areas where the solution is smooth, it will deliver 5th-order accurate results. In comparison to popular high resolution schemes such as MUSCL (van Leer B., 1979) or TVD (Harten, 1983) schemes, the WENO scheme does not smear out the solution. Instead it maintains the sharpness of the extrema. The conservative WENO scheme is used to treat the convective terms for the velocities U_i, while the Jacobi-Hamilton version is used for the variables of the free surface and turbulence algorithms.

Time Advancement Scheme

For the time treatment a third-order accurate TVD Runge-Kutta scheme is employed, consisting of three Euler steps (Shu and Osher, 1988).

$$\begin{aligned}\phi^{(1)}&=\phi^n+\Delta tL(\phi^n)\\ \phi^{(2)}&=\frac{3}{4}\phi^n+\frac{1}{4}\phi^{(1)}+\frac{1}{4}\Delta L\left(\phi^{(1)}\right)\\ \phi^{n+1}&=\frac{1}{3}\phi^n+\frac{2}{3}\phi^{(2)}+\frac{2}{3}\Delta L\left(\phi^{(2)}\right)\end{aligned} \quad (10)$$

This scheme provides a high-order of temporal accuracy, and for Courant - Friedrichs - Lewy (CFL) numbers below 1 it shows very good numerical stability through its Total Variation Diminishing (TVD) properties. Adaptive time stepping is used in order to control the CFL number. The CFL coefficient is determined by the maximum ratios for the velocity $U_{\max}/dx$, diffusion $\Gamma_{\max}/dx^2$ and the maximum values of the source terms. For a RANS model, where the turbulence magnitude is expressed through the eddy viscosity, the diffusion criterion can become prohibitively restrictive. As a solution, the diffusion part of the RANS equation is treated implicitly, thus removing it from the CFL criterion. The third-order accurate TVD Runge-Kutta is used for all transport equations in the numerical model with the exception of the turbulence model. A special characteristic of two-equation turbulence models is that they are mostly source term driven. In comparison, the convective and diffusive terms play only a minor role. For explicit time discretization of the k and ω equations, the large source terms result in a significantly smaller time step than for the velocities due to the CFL criterion. Instead of letting the turbulence model determine the time step, its equations are discretized with a first-order implicit Euler scheme.

The Numerical Grid

All model equations are discretized on a Cartesian grid with a staggered arrangement of the variables. The velocity variables are defined on the center of the cell faces, while all others such as the level set function, the pressure or the variables of the turbulence model on the cell centers. This way oscillations due to velocity-pressure decoupling are avoided. At the solid boundaries of the fluid domain a ghost cell immersed boundary method is employed. In this method the solution is analytically continued through the solid boundary by updating the fictitious ghost cell in the solid region by extrapolation. That way the numerical discretization does not need to account for the boundary conditions explicitly, instead they are enforced implicitly. The algorithm is

based upon the local directional approach by Berthelsen and Faltinsen (Berthelsen and Faltinsen, 2008) which was implemented in 2D. In the current implementation the extrapolation scheme is decomposed into the components of the three-dimensional coordinate system. Because the computational domain in the present paper consists of rectangular cuboids, no cut cells are present.
The ghost cell approach has several advantages: Grid generation becomes trivial, the numerical stability and order of the overall scheme is not affected. In addition the method integrates well into the domain decomposition strategy for the parallelization of the model. Here ghost cells are used to update the values from the neighboring processors via MPI.

Level Set Method

The level set method was first presented by Osher and Sethian (Osher and Sethian, 1988). It was devised for computing and analyzing the motion of an interface Γ between two phases in two or three dimensions. The location of interface is represented implicitly by the zero level set of the smooth signed distance function $\phi(\vec{x},t)$. In every point of the modeling domain the level set function gives the closest distance to the interface and the phases are distinguished by the change of the sign. This results in the following properties:

$$\phi(\vec{x},t)\begin{cases} >0 \; if \; \vec{x} \in phase\ 1 \\ =0 \; if \; \vec{x} \in \Gamma \\ <0 \; if \; \vec{x} \in phase\ 2 \end{cases} \tag{11}$$

Also the Eikonal equation $|\nabla\phi| = 1$ is valid. When the interface Γ is moved under an externally generated velocity field $\vec{v}$, a convection equation for the level set function is obtained:

$$\frac{\partial\phi}{\partial t} + U_j \frac{\partial\phi}{\partial x_j} = 0 \tag{12}$$

When the interface evolves, the level set function looses its signed distance property. In order to maintain this property and to ensure mass conservation the level set function is initialized after each time tep. In the present paper a PDE based reinitialization equation is solved (Sussman *et al.*, 1994):

$$\frac{\partial\phi}{\partial t} + S(\phi)\left(\left|\frac{\partial\phi}{\partial x_j}\right| - 1\right) = 0 \tag{13}$$

$S(\phi)$ is the smoothed sign function by Peng et al. (Peng *et al.*, 1999).

$$S(\phi) = \frac{\phi}{\sqrt{\phi^2 + \left|\frac{\partial\phi}{\partial x_j}\right|^2 (\Delta x)^2}} \tag{14}$$

With this numerical setup it is possible to define the interface between two immiscible fluids. Without special treatment there is a jump in the density ρ and the viscosity ν across the interface which can lead to numerical stability problems. The solution is to define the interface with the constant thickness 2ε. In that region smoothing is carried out with a regularized Heavyside function $H(\phi)$. The thickness ε is proportional to the grid spacing, in the present paper it was chosen to be $\varepsilon = 1.6\Delta x$.

$$H(\phi) = \begin{cases} 0 & if\ \phi < -\varepsilon \\ \frac{1}{2}\left(1 + \frac{\phi}{\varepsilon} + \frac{1}{\Pi} sin\left(\frac{\Pi\phi}{\varepsilon}\right)\right) & if\ |\phi| < \varepsilon \\ 1 & if\ \phi > \varepsilon \end{cases} \tag{15}$$

In the current study, the aim is to model three different fluids. For the sloshing scenario, only two different types of interfaces exist: water-oil and oil-air. In the more general scenario, an additional interface water-air is possible. So in a generic three-phase flow, three different interfaces exist and the goal is to account for them numerically with two separate level set functions ϕ_1 and ϕ_2. This can be achieved with the following logic:

$$\begin{aligned} \textbf{water} \quad & if\,(\ \phi_1 > 0\ \&\&\ (\phi_2 > 0\ ||\ \phi_2 < 0)) \\ \textbf{oil} \quad & if\,(\ \phi_1 < 0\ \&\&\ \phi_2 > 0) \\ \textbf{air} \quad & if\,(\ \phi_1 < 0\ \&\&\ \phi_2 < 0) \end{aligned} \tag{16}$$

Next, the material properties need to be assigned to each of the three phases. H_1, H_2 and H_3 are defined in such a way, that the different combinations of the signs of the level set functions give a unique identification of the three phases. H_1, H_2 and H_3 also incorporate the smoothing of the generic Heavyside function.

$$\begin{aligned} \rho(\phi_1,\phi_2) &= \rho_1 H_1(\phi_1,\phi_2) + \rho_2 H_2(\phi_1,\phi_2) + \rho_3 H_3(\phi_1,\phi_2) \\ \nu(\phi_1,\phi_2) &= \nu_1 H_1(\phi_1,\phi_2) + \nu_2 H_2(\phi_1,\phi_2) + \nu_3 H_3(\phi_1,\phi_2) \end{aligned} \tag{17}$$

RESULTS

The setup for the three phase sloshing case has been taken from the experiments performed by La Rocca *et al.* (2005). The experimental data is used to compare with the numerical results. A plexiglass tank with the extension $0.5m \times 0.5m \times 0.3m$ $(x \times y \times z)$ can rotate parallel to the y-axis. The numerical simulations are performed in 2D, assuming symmetry plane boundary conditions in y-direction. The oscillations of the tank are described by the amplitude of the roll angle θ_0 and the frequency f. For relatively small amplitudes the motion of the tank can be defined as follows:

$$\theta = \theta_0 \sin\omega t \tag{18}$$

Here ω is the angular frequency and is defined as $\omega = 2\pi f$. The acceleration of the sloshing tank is implemented through sources terms in the RANS eqations in the x an z direction (Armenio and La Rocca, 1996):

$$\begin{aligned} S_x &= \ddot{\theta}(z - z_m) + \dot{\theta}^2(x - x_m) - g\sin\theta \\ S_y &= -\ddot{\theta}(x - x_m) + \dot{\theta}^2(z - z_m) - g\cos\theta \end{aligned} \tag{19}$$

Here $\dot{\theta}$ and $\ddot{\theta}$ are the first and second derivative of the roll angle θ over time. In the current study, the amplitude of the roll angle is $\theta_0 = 3^\circ$ and the frequency is $f = 0.7Hz$. The variables x_m and z_m are the coordinates of the center of the rotation.
For the present simulations, the tank is filled with water up to the height $H_1 = 0.08m$. On top of the water a layer of vaseline oil with the thickness $H_2 = 0.06$ is inserted. For the water a density of $\rho = 998.2kg/m^3$ and a kinematic viscosity $\nu = 1.004 \times 10^{-6} m^2/s$ is used, for the vaseline oil a density of $\rho = 840.0kg/m^3$ and a kinematic viscosity $\nu = 3.0 \times 10^{-4} m^2/s$.
Fig.1 shows the fluid interfaces water-oil (bottom) and oil-air (top) over time at the location $x = 0.125m$. At first a grid convergence study is performed (Fig. 1a), comparing the results

for the interfaces from three different uniform mesh spacings ($dx = 0.01m$, $dx = 0.005m$, $dx = 0.0025m$). For the coarsest grid, the interface motion is dampened out, especially for the interface oil-air. With $dx = 0.005m$ the peaks in the interface waves become much more pronounced. As the difference in results between $dx = 0.005m$ and the finest mesh with $dx = 0.0025m$ becomes very small, grid convergence is assumed. In Fig. 1b, the comparison between the interfaces recorded in the experiments (La Rocca *et al.*, 2005) and the numerical model results from the finest grid are depicted. The numerical model predicts slightly higher peaks for the interface water-oil than the experiment, but for the interface oil-air the wave height agrees very well. For both interfaces, a slight phase lag occurs. For the interface water-oil, this occurs in the later stage of the experiment, while for the interface oil-air it happens towards the beginning. All in all, a good agreement between numerically predicted and experimentally measured interface locations exists.
It can be seen, that a phase shift occurs for the sloshing motion for the two interfaces in Fig. 1. This becomes more obvious in Fig. 2, where the interface locations are shown for different stages of the tank rotation. Fig. 3 shows the velocity magnitude and velocity vectors during a full tank rotation. At $t/T = 0.25$ and $t/T = 0.75$ the tank changes the rotation direction and as a result, the lowest velocities are observed. The velocities are maximum for $t/T = 0.0$ and $t/T = 0.5$, and the flow pattern is uniformly circular. During the stages $t/T = 0.375$ and $t/T = 0.875$, an additional smaller recirculation pattern forms, which has a direct impact on the shape of the interface water-oil in its vicinity.

CONCLUSION

In the current paper, the implementation of multiple level set functions for the calculation of three-phase flow is presented. The numerical model is applied to predict the interfaces water-oil and oil-air in a rotating rectangular tank. The numerical model shows reasonably good agreement with experimentally recorded interface locations. The approach of multiple level set methods shows good promise for the treatment of multiphase flows. For future research three-phase sloshing can be further investigated by modeling different roll angle amplitudes and frequencies. The presented numerical approach has also a large potential for other types of multiphase applications.

REFERENCES

ARMENIO, V. and LA ROCCA, M. (1996). "On the analysis of sloshing of water in rectangular containers: numerical study and experimental validation". *Ocean Engineering*, **23(8)**, 705–739.

BERTHELSEN, P.A. and FALTINSEN, O.M. (2008). "A local directional ghost cell approach for incompressible viscous flow problems with irregular boundaries". *Journal of Computational Physics*, **227**, 4354–4397.

BIHS, H. (2011). "Three-dimensional numerical modeling of local scouring in open channel flow". PhD thesis.

CHORIN, A. (1968). "Numerical solution of the navier stokes equations". *Math. Comput.*, **22**, 745–762.

DURBIN, P.A. (2009). "Limiters and wall treatments in applied turbulence modeling". *Fluid Dynamics Research*, **41**, 1–18.

HARLOW, F. and WELCH, J. (1965). "Numerical calculation of time dependent viscous incompressible flow of fluid with a free surface". *Physics of Fluids*, **8**, 2182–2189.

HARTEN, A. (1983). "High resolution schemes for hyperbolic conservation laws". *Journal of Computational Physics*, **49**, 357–393.

HIRT, C. and NICHOLS, B. (1981). "Volume of fluid vof method for the dynamics of free boundaries". *Journal of Computational Physics*, **39**, 201–225.

JIANG, G.S. and SHU, C.W. (1996). "Efficient implementation of weighted eno schemes". *Journal of Computational Physics*, **126**, 202–228.

LA ROCCA, M. *et al.* (2005). "Experimental and theoretical investigations on the sloshing of a two-liquid system with free surface". *Physics of Fluids*, **17**, 62–101.

OSHER, S. and SETHIAN, J.A. (1988). "Fronts propagating with curvature- dependent speed: Algorithms based on hamilton-jacobi formulations". *Journal of Computational Physics*, **79**, 12–49.

PENG, D. *et al.* (1999). "A PDE-based fast local level set method". *Journal of Computational Physics*, **155**, 410–438.

SHU, C.W. and OSHER, S. (1988). "Efficient implementation of essentially non-oscillatory shock capturing schemes". *Journal of Computational Physics*, **77**, 439–471.

SUSSMAN, M. *et al.* (1994). "A level set approach for computing solutions to incompressible two-phase flow". *Journal of Computational Physics*, **114**, 146–159.

VAN DER VORST H. (1992). "BiCGStab: A fast and smoothly converging variant of Bi-CG for the solution of nonsymmetric linear systems". *SIAM J. Sci. Stat. Comput.*, **13**, 631–644.

VAN LEER B. (1979). "Towards the ultimate conservative difference scheme V. A second order sequel to Godunovs method". *Journal of Computational Physics*, **32**, 101–136.

WILCOX, D.C. (1994). *Turbulence Modeling for CFD*. DCW Industries Inc., La Canada, California.

APPENDIX A

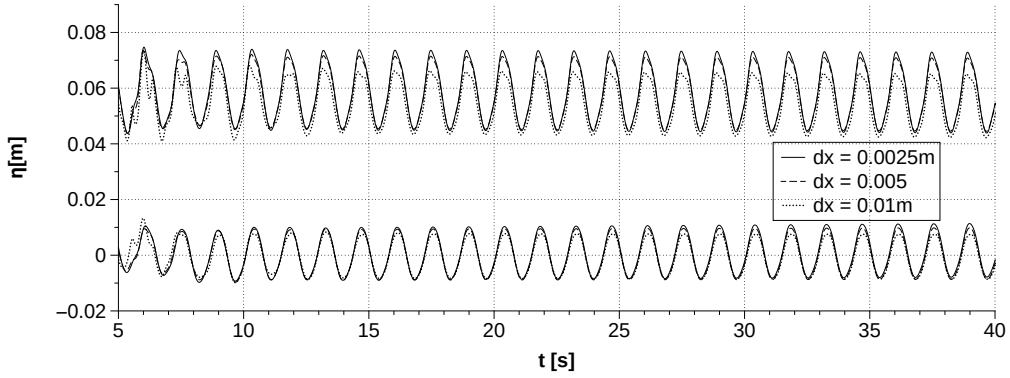

a) Grid Convergence

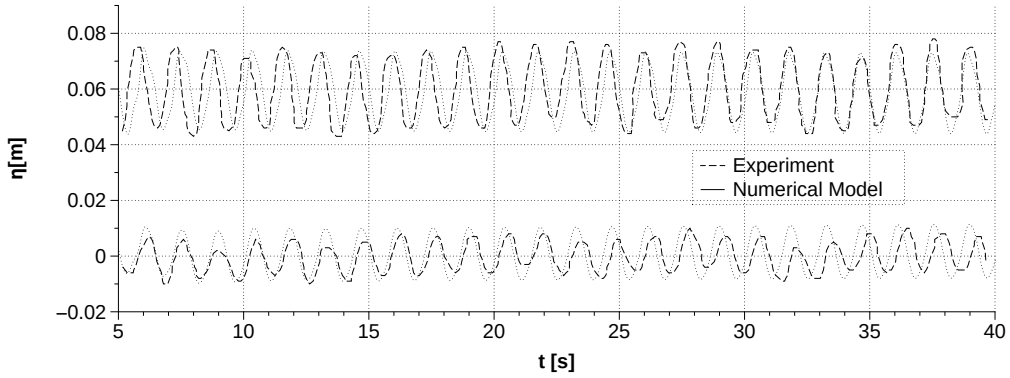

b) Experiment and Numerical Model

Fig. 1: Fluid interfaces at $x = 0.125m$ for $\theta_0 = 3^\circ$ and $f = 0.7Hz$

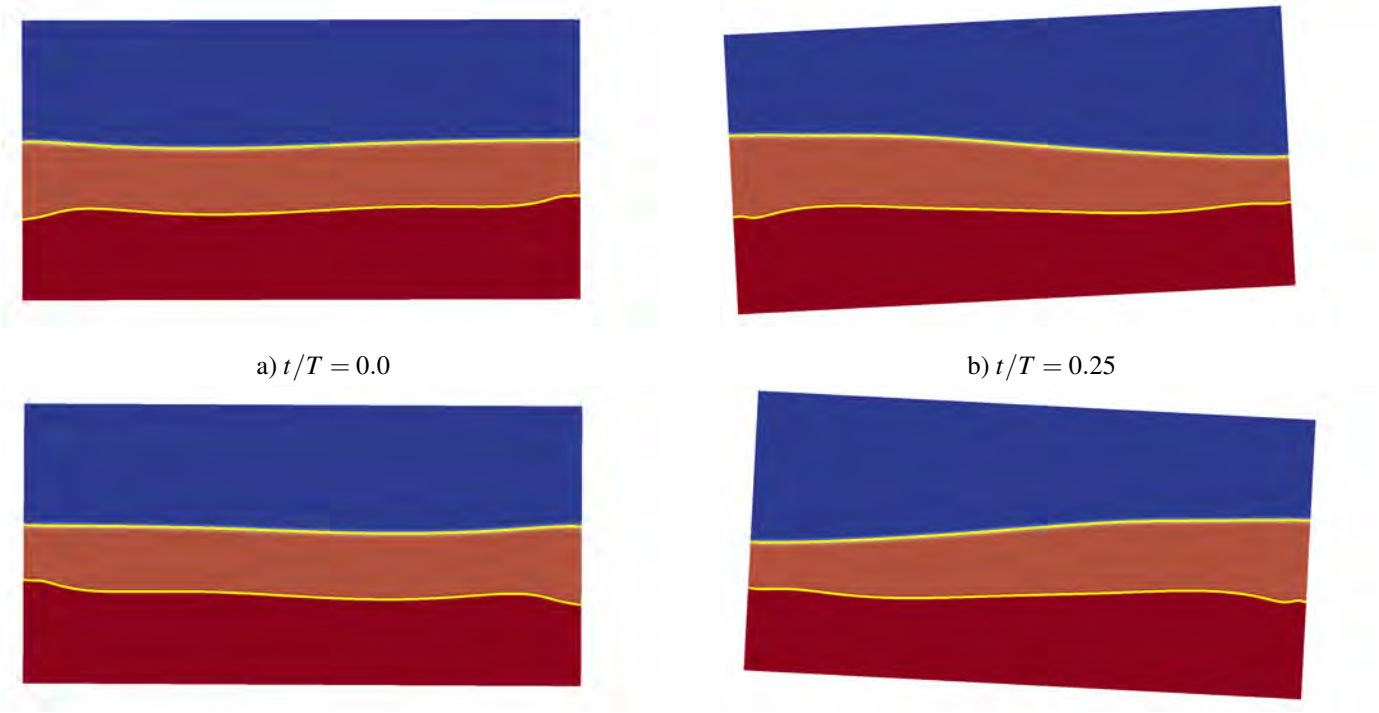

a) $t/T = 0.0$

b) $t/T = 0.25$

c) $t/T = 0.5$

d) $t/T = 0.75$

Fig. 2: Sloshing tank with water, oil and air; fluid interfaces for $\theta_0 = 3^\circ$ and $f = 0.7Hz$

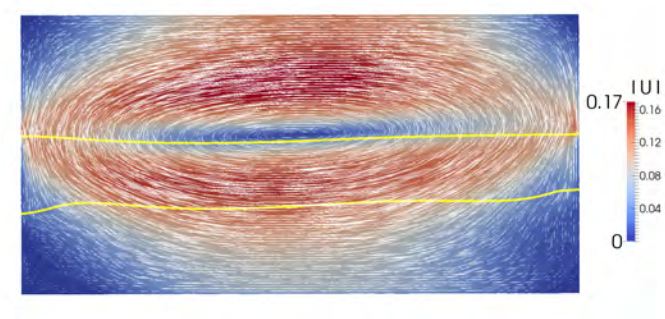

a) $t/T = 0.0$

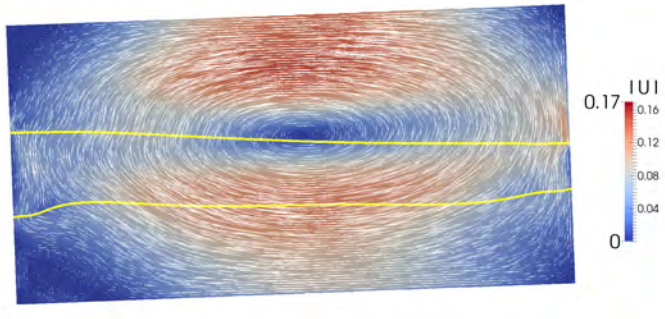

b) $t/T = 0.125$

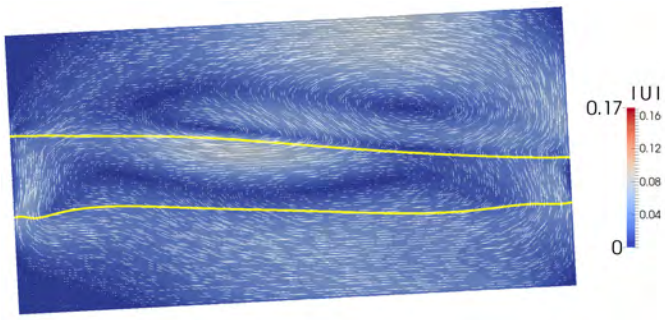

c) $t/T = 0.25$

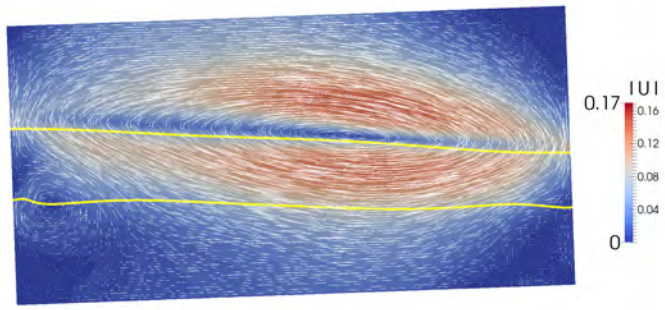

d) $t/T = 0.375$

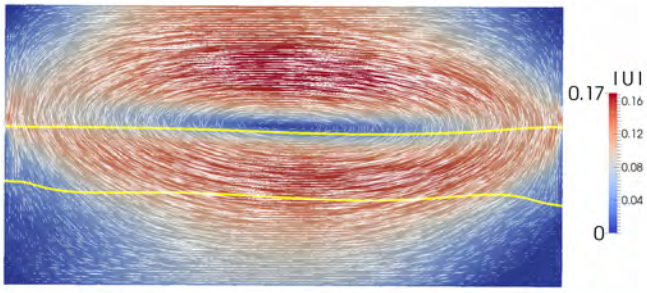

e) $t/T = 0.5$

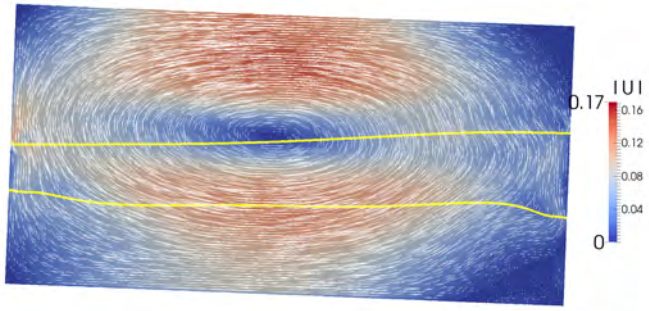

f) $t/T = 0.625$

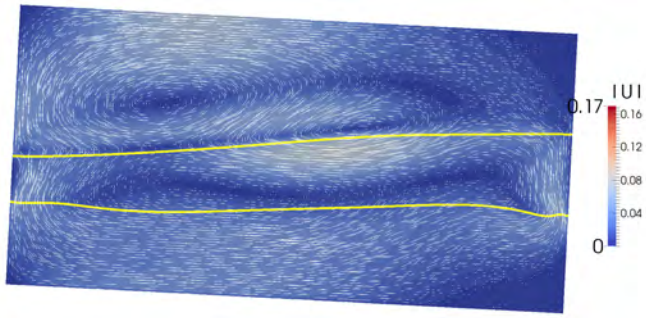

g) $t/T = 0.75$

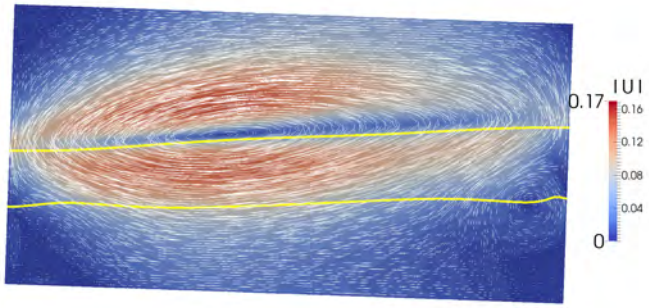

h) $t/T = 0.875$

Fig. 3: Sloshing tank with fluid interfaces, velocity magnitudes and velocity vectors for $\theta_0 = 3^\circ$ and $f = 0.7Hz$

,

CFD SIMULATION OF THE TWO-PHASE FLOW OF DIFFERENT MIXTURES IN A CLOSED SYSTEM FLOW WHEEL

José F. ROCA R.[1*], **João N.E. CARNEIRO**[1], **José E.S. OLIVEIRA**[1], **Sjur MO**[2], **Martin FOSSEN**[3], **Stein T. JOHANSEN**[2]

[1]Instituto SINTEF do Brasil, 22251-050 Rio de Janeiro, BRAZIL

[2]SINTEF Materials and Chemistry, 7465 Trondheim, NORWAY

[3]SINTEF Petroleum Research, 7465 Trondheim, NORWAY

[*] E-mail: jose.roca@sintefbrasil.org.br

ABSTRACT

The objective of this work is to study the behaviour of mixtures involving air/water and oil/water at low pressures and oil/ high CO_2-content gas at high pressures in a closed system 'Wheel Flow Loop'. Such apparatus has been used in different contexts before, e.g. to evaluate the mixture apparent viscosity of different emulsions or the hydrate behaviour under realistic conditions of pressure and temperature. Typically, torque and velocity measurements are used to estimate the overall wall shear stresses. In a few cases, there exists the possibility to visualize the interface between phases through a (sapphire) window. Furthermore, secondary flow present in such curved configurations may have an effect on pressure loss depending on ratio of pipe diameter and curvature radius and flow regime. Consequently, more detailed information on the flow and phase distribution in the wheel is very relevant to understand the underlying physics in the wheel and aid data interpretation.

In this paper, two-phase flow in the Wheel Flow Loop geometry is simulated numerically, by means of a classic Volume of Fluid (VOF) approach and a kind of coupled "VOF" / Eulerian-Eulerian approach. Numerical results have been compared with experimental data obtained in the SINTEF Multiphase Flow Laboratory at Tiller in Norway for different mixtures showing reasonable agreement. Torque/velocity output data has received special attention.

Experiments have evidenced hysteretic behaviour when an increasing-decreasing stepwise rotation velocity is imposed to the wheel. Both this phenomenon and the carry-over starting point have been successfully reproduced by the CFD calculations. Finally, 3D calculations of the flow using the commercial tool ANSYS FLUENT have been critically compared with a Quasi-3D (Q3D) approach.

Keywords: Wheel flow loop, CO_2-rich mixture, two-phase flow, Quasi-3D.

NOMENCLATURE

Greek Symbols

ℓ	Turbulent length scale, [m]
λ	Friction factor, $[-]$
μ	Dynamic viscosity, $[\mathrm{Pa}\cdot\mathrm{s}]$
ρ	Mass density, $[\mathrm{kg/m^3}]$
θ	Polar coordinate (angle), $[^\circ]$
τ^{wall}	Wall shear stress, [Pa]

Latin Symbols

a	Pipe radius, [m]
A^{wall}	Wall area, $[\mathrm{m}^2]$
d	Pipe diameter, [m]
De	Dean number ($\mathrm{De} = \mathrm{Re}\sqrt{\frac{a}{R}}$), $[-]$
GOR	Gas-oil ratio, $[\mathrm{m^3/m^3}]$
k	Turbulent kinetic energy, $[\mathrm{m^2/s^2}]$
LSI	Large Scale Interface
N_X	Number of x-cells, $[-]$
N_Y	Number of y-cells, $[-]$
$Q3D$	Quasi-3D
r	Polar coordinate (radius), [m]
R	Wheel radius, [m]
Re	Reynolds number ($\mathrm{Re} = \frac{\rho U_0^{\mathrm{wall}} d}{\mu}$), $[-]$
$\mathrm{Re_c}$	Critical Reynolds number, $[-]$
t	Time, [s]
T	Torque, $[\mathrm{N}\cdot\mathrm{m}]$
U^{wall}	Wall velocity of the wheel, $[\mathrm{m/s}]$
x	Streamwise coordinate, [m]
y	Transversal coordinate, [m]

Sub/superscripts

i	x-index (streamwise)
j	y-index (transversal)

INTRODUCTION

During oil production gas, oil and water may flow simultaneously in pipes, forming complex mixtures which are often difficult to characterize under realistic conditions. A closed system wheel flow loop has been used by different authors (e.g. Johnsen et al., 2001) as an approach to estimate the apparent viscosity of mixtures under different water cuts and realistic pressure - temperature conditions. The idea behind such setting is that the wheel may, in some respect, resemble a pressurized infinite loop. Recently, mixtures with high CO_2 content have received special attention due to current pre-salt scenarios in Brazil (Almeida et al., 2010). The presence of CO_2 in unusual amounts may compromise mechanical integrity due to pipeline corrosion while influencing other issues related to flow assurance such as excessive Joule - Thomson cooling, wax deposition, inorganic scaling, among others. Experiments for such mixtures in flowing systems are very expensive and rarely found. Thus, the wheel setup has been also evaluated here for systems containing significant CO_2 content.

In the work of Urdahl et al. (1996) a closed wheel flow loop is used to evaluate the effective viscosity of live oil. The imposed rotation produces a relative velocity between fluid and pipe wall. This resembles transportation of the fluid in a pipe. They found that at constant temperature viscosity increases with higher velocities. This happens when mixing between oil- and water phase takes place.

Johnsen et al. (2001) used also a rotating wheel to calculate the apparent viscosity of emulsion through measurements of torque at a wide range of velocities ranging from 0.7 m/s to 3.0 m/s. They compared the results with results obtained from viscometers and traditional flow loops, finding reasonable agreement with emulsion of $50\% - 60\%$ water cut.

On the other hand, Mori and Nakayama (1964) studied the effect of secondary flows in curved pipes. Over a wide range of laminar- and turbulent regimes, they noted that fluid is driven to the outer wall by centrifugal forces creating vortices in the cross section as shown in Figure 1. In addition, they noticed that secondary flows create an extra flow resistance which depends on the ratio of the wheel to the pipe radii R/a affecting pressure drop for different regimes. Figure 2 depicts the friction factor λ as function of a wide range of Reynolds numbers Re. It was observed that the curvature effects is higher at laminar regimes than for turbulent flow. In fact, the diminution of curvature effect is even more evident at higher $\mathrm{Re} \sim 10^4$. Furthermore, the critical Reynolds number Re_c, at which transition to turbulent flow occurs, increases as radii ratio R/a diminishes, i.e. when curvature effect augments.

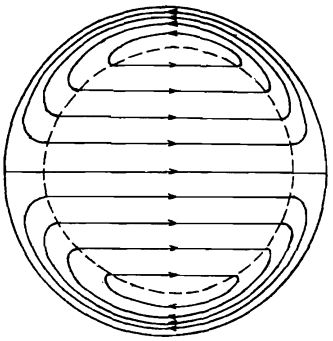

Figure 1: Secondary flow at large Dean numbe
$\mathrm{Re}\sqrt{\frac{a}{R}}$), Mori and Nakayama (1964).

During the last decade SINTEF, ConocoPhillips, a
have developed LedaFlow, a multiphase numerica
order to predict multiphase flow phenomena in p
This tool has been extended to handle the rotati
geometry using the quasi-3D (Q3D) approach. T
approach compromises speed and accuracy by aver
flow over transversal slices and is described in mo
below.

MODEL DESCRIPTION

Quasi-3D model (Q3D)

The model and numerical method, together with soi
cations have been described previously in Laux et a
2008b; 2008a), Ashrafian et al. (2011) and Mo et a

The model is based on a multi-field concept where mass and momentum equations are formed for all fields in question. This means that for 3-phase flows we normally deal with 9 fields and for 2-phase flow with 4 fields. In our case the mass and momentum equations for each phase are obtained by merging all the fields of a phase into a common transport equation. This process introduces simplifications of the physics but also reduces the solver requirements since the number of equations is reduced. The turbulence is modeled using a $k - \ell$ model where k is the turbulent kinetic energy and ℓ is a turbulent length scale (Laux et al. 2007). Transport equations for turbulent kinetic energy is solved for each phase while the turbulent length scales are solved by a Poisson equation, using a length scale boundary condition at the walls and the large scale interfaces. The sizes of the dispersed fields (bubbles and droplets) are represented by evolution equations for the Sauter mean diameter. The large scale interfaces (LSIs) are reconstructed from the predicted phase volume fractions without solving an own transport equation for fraction functions. At each side of the LSI the model behaves as an Euler-Euler model with a continuous phase containing possible dispersed phases. At the LSI the momentum exchange between the continuous fluids (phases) is computed from standard wall functions for rough walls, see e.g. Ashrafian and Johansen (2007). The roughness of the large scale interface is computed by a Charnock model (1955). The same type of wall functions are used to represent the wall boundary conditions (wall friction).

Finally, the model is simplified by assuming small variation over the slices. This allows slice averaging the equations over the transversal dimension (z) of the pipe, as illustrated in Figure 3, thereby reducing the spatial dimensionality. This is important in order to reduce computational time significantly without sacrificing too much of the physics. In addition the model allows for vertical pipe bends. The bends are composed of bend segments with constant radius of curvature. This approach is therefore very well adapted to handle the wheel geometry. In each of the bent segments we use local spherical coordinates, which after the slice averaging is reduced to 2D polar coordinates. The numerical methods applied in this work have been explained previously

importance in engineering applications is found, are excluded.

The bend of a curve indicating the transition from laminar to turbulent flow is written according to the Ito's empirical formula for critical Reynolds numbers in R/a,

$$Re_{cr} = 2 \times 10^4 \, (a/R)^{0.32}. \qquad (42)$$

The Reynolds number at which λ_{c4} comes to exceed λ_{c1} increases, as R/a decreases. This fact seems to imply the same inclination of Re_{cr} as shown in equation (42).

Similar criterion are written for the Reynolds

found that $Re'_s \doteqdot 5{\cdot}0 \times 10^4$. Since $Re' > Re'_s$, equation (43) is not available for R/a larger than 170. For such large R/a, it is recommended to use Re'_s as the lower limit for λ_{c5}. However,

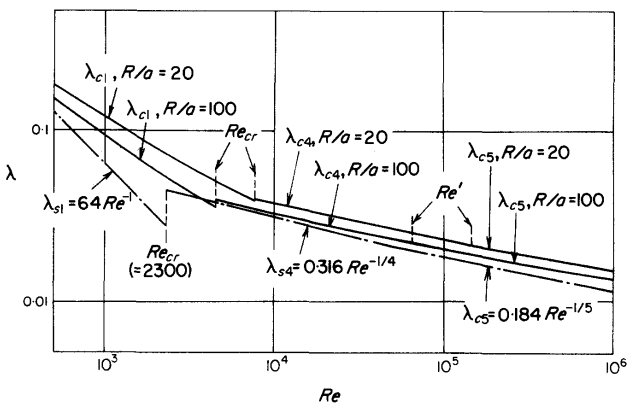

FIG. 4. λ–Re diagram.

because of little difference between λ_{c4} and λ_{c5} in the slope of the curves against Re, the availability of λ_{c4} would fail distinctly at Reynolds numbers far larger than Re' given by equation (43). Usually, it is difficult to make Reynolds number so large in curved pipes. Owing to this reason the experimental data obtained up to the present by many investigators are in good agreement with λ Therefore, equation

Figure 2: Friction factor as a function of Reynolds number, $\mathrm{Re}\sqrt{R/a}$, Mori and Nakayama (1965).

Wheel

The simulation domain is sketched in Figure 4. The geometry has the shape of a wheel with radius $R = 1$ m with $d = 5$ cm pipe diameter. For our cases the wheel is filled with two fluids. The wheel and fluids are initially at rest. When the simulation is started the wall velocity is either ramped up or set instantaneously to a given rotation velocity $U^{\text{wall}}(r) = (r/R)U_0^{\text{wall}}$. During the simulations the wall shear stress is directly calculated. The torque is then given by:

$$T = \int dA^{\text{wall}} \tau^{\text{wall}}(r,\theta) r \tag{1}$$

where $dA^{wall} = dA^{\text{wall}}(r,\theta)$ is the differential wall area. For Q3D the total torque at a given time is then calculated based on the wall shear stress for each slice as:

$$T = \sum_{i=1}^{N_X} \sum_{j=1}^{N_Y} \tau_{j,i}^{\text{wall}} A_{j,i}^{\text{wall}} (R - a + y_j) \tag{2}$$

where (j,i) is cell index across and along the pipe respectively and N_Y, N_X is the number of cells in the given directions. Also $\tau_{j,i}^{\text{wall}}$ is the shear stress and $A_{j,i}^{wall}$ is the slice wall area (two sides) for the given Q3D slice.
If the wheel radius R is large compared to the pipe radius a the following approximation can be used:

$$T \approx 2\pi a R^2 \int_0^{2\pi} \tau_{\text{1D}}^{\text{wall}}(\theta) d\theta \tag{3}$$

Using 1D-collapsed Q3D variables (cross-sectionally averaged) we get:

$$T \approx R \sum_{i=1}^{N_X} \tau_{\text{1D},i}^{\text{wall}} A_{\text{1D},i}^{\text{wall}} \tag{4}$$

where $\tau_{\text{1D},i}^{\text{wall}}$ is the 1D collapsed wall shear stress in 1D-cell i and $A_{\text{1D},i}^{\text{wall}}$ is the wall area for this 1D-cell.

Fluent models (3D)

Fluent 14.5 was used to simulate the full 3D wheel geometry. We employed the compressive volume of fluid method (VOF) to simulate the two-phase flow phenomena. The VOF method uses a color function, F, to capture the fluid volume and identify the free surface position. The color function is defined as a step function which represents the volume fraction of one of the fluids within each cell. When F is equal to 0 or 1 the cell is away from the interface and the cell is fully filled with one phase, while for values between 0 and 1 the cell is filled with both phases and therefore the cell contains a free surface. VOF belongs to the so called one-fluid family of methods, where a single momentum equation is solved for the domain and the resulting velocity field is shared among the phases. Due to Re $\sim 10^4$ in several cases, the turbulence needs to be considered, and modeled by means of the Reynolds Averaged Navier-Stokes equation and the realizable k-ε model. The latter solves two additional transport equations for the turbulent kinetic energy and the dissipation rate. A complete description of the method and the governing equations can be found in Fluent Theory Guide by ANSYS, Inc (2013).

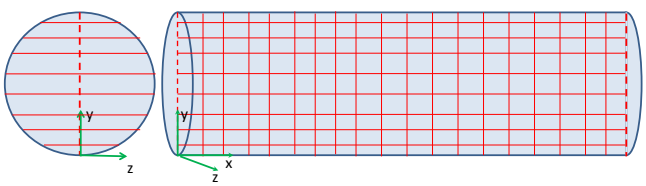

Figure 3: Grid layout of a pipe. The model equations and predicted field quantities are averaged over the slices seen in left part of the figure.

Experimental setup

The Wheel Flow Loop consists of a 5.25 cm inner diameter stainless steel pipe bent into a 1 m radius wheel shaped loop which gives a total volume of 13.4 *litres*. The wheel used in the current tests can be operated at 250 bar of pressure and is placed inside a climate chamber for temperature control from -5 to $+60$ °C. Furthermore, the wheel has a shorter section consisting of a sapphire pipe for visual observations of phenomena inside the wheel. There is a video camera attached to the wheel which follows it during rotation and thus can capture videos from all positions.

The wheel is instrumented with temperature sensor PT100, pressure sensor and a Shaft Type Reaction Torque Transducer from Sensotec with a range up to 135 N.m. Additionally, filling of the wheel is done by high pressure pumps outside the wheel chamber and all components, liquids and gases, are filled by weight with a accuracy of the weight being ± 5 g. For CO_2 cases, the amounts filled of each composition is given in Table 1.

Table 1: Mass composition of CO_2 experiment

Compound	Amount [g]	Mass fraction [%]
CO_2	676	8%
CH_4	965	12%
Oil	6479	80%

At 60 °C this gave a pressure of 250 bar. The wheel was ro-

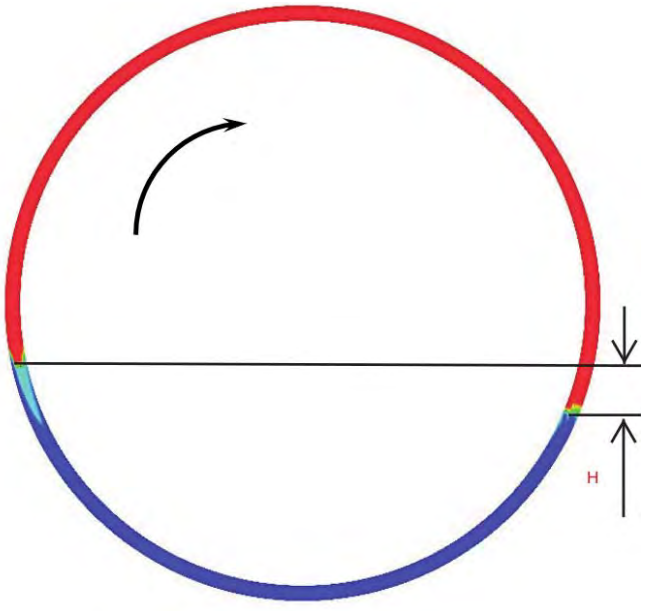

Figure 4: Sketch of a $R = 1$ m radius wheel made of $d = 5$ cm diameter pipe. Here the wheel is filled with approximately $(40\%, 60\%)$ of 'blue' and 'red' phase respectively.

tated at various velocities ranging from 0.05 m/s to 2 m/s as for the 3D and Q3D simulations. Experiments were performed at temperatures ranging from 25 °C to 55 °C with steps of 10 °C between.

RESULTS

In this work three different mixtures have been selected for comparison of experimental data with numerical results obtained by Fluent and our Q3D approach. The properties of some fluids are listed in Table 2. Additionally, different meshes of our wheel were generated for Fluent and Q3D simulations.

Table 2: Fluid properties at $P = 1$ bar and $T \approx 20$ °C

	Air	Water	Oil
Density [kg/m^3]	1.2	1000	800
Viscosity [Pa.s]	1.9E-5	1.0E-3	3.2E-3

Some numerical simulations using Fluent were performed with two different meshes. The coarse mesh is composed of $\approx$ 80000 cells while the refined mesh has a total of $\approx$ 230000 cells. The difference in the calculated torque on the two meshes was less than 2%. The coarse mesh provides sufficient accurate results with less computational effort; therefore the coarse mesh was adopted for the subsequent simulations. The Q3D approach used less cells, approximately 5000.

As seen in Figure 5, the steady-state is reached for both simulations ($t > 12$ s) even though initial conditions are quite different. For instance, at the beginning Fluent imposes *instantaneously* full velocity generating a high torque to spin the wheel.

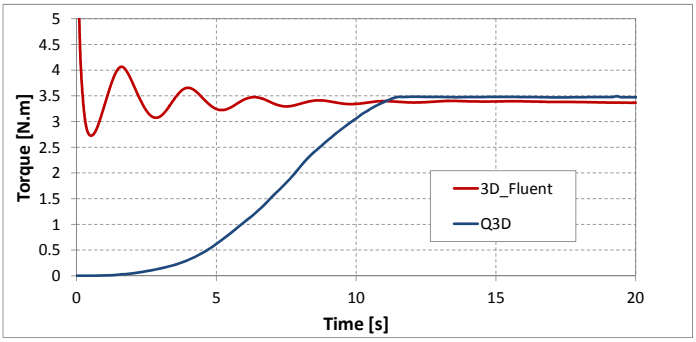

Figure 5: Transient evolution of torque for Fluent and Q3D.

In Q3D the wall velocity was slowly increased in order to help convergence, unlike Fluent which did not evidence any problem related to convergence when using a step velocity.

It should be noted that, for calibration purposes, a constant offset was applied to ensure that experimental torque vanishes at zero velocity for all mixtures. For instance, an offset 0.49 N.m was applied in air/water mixture, while 0.37 N.m in oil/water mixture. Furthermore, due to uncertainties and current limited understanding of experimental torque oscillations, we try to focus on the comparison of qualitative flow behaviour in the Wheel. As further work, improvement of raw data treatment, as well as Wheel balancing, will be assessed, since in some cases standard deviation can reach up to 1.75 N.m.

Air and water mixture $\alpha_W = 40\%$

The first mixture is composed of 60% air and 40% water. Here different velocities are imposed and torque measured for each velocity. For none of the cases, carry-over was predicted and main contribution of torque is due to water phase. Figure 6 shows that numerical results are below experimental data with a maximum difference around 1.2 N.m at 2 m/s. Furthermore, Fluent and Q3D presented very similar results, evidencing the prediction capabilities of both tools, although Q3D uses significantly less cells. Regarding simulation time, Fluent took 4.5 hours over 6 cores, while Q3D spent approximately 2 hours over 2 cores to simulate 20 seconds.

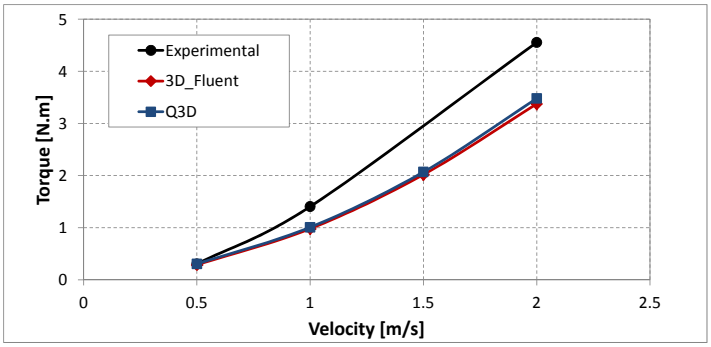

Figure 6: Torque versus velocity for air-water mixture.

In addition, the height H shown in Figure 4 will balance the torque needed to rotate the wheel and is correlated to wall shear stress. Visual comparison between Q3D and Fluent showed that values are very similar, i.e. $H = 0.16$ m at 1.5 m/s.

Oil and water mixture $\alpha_W = 50\%$

Oil and water composes the second mixture, filling the wheel evenly. Due to small difference between densities, one phase carries the other, generating emulsions when velocity is above 1 m/s. Most of the simulations faced few problems with convergence.

According to Figure 7, torque also increases with velocity and is still underestimated with 0.7 N.m as the difference between experimental and Q3D at 1 m/s.

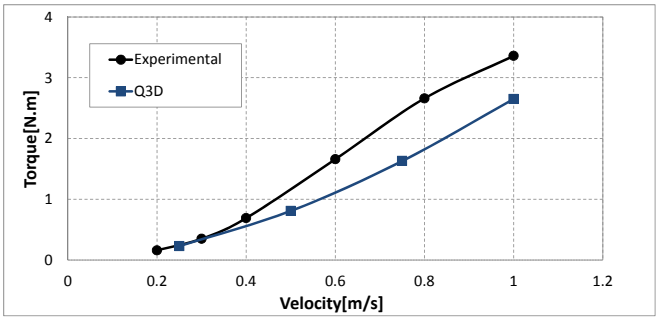

Figure 7: Torque versus velocity for oil-water mixture.

CO_2 mixtures $\alpha_{CO_2} = 22.2\%$

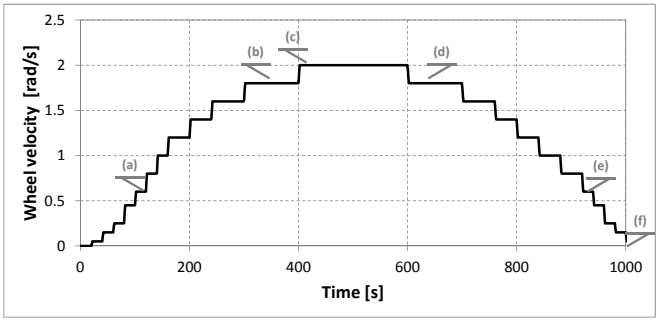

Figure 8: Stepwise velocity imposed to the wheel.

The molar composition of the third mixture is 15.3% CO_2, 61.3% CH_4 among others components (similar to mixture detailed in Table 1), with $GOR = 220\ \mathrm{m^3/m^3}$. An increasing-decreasing stepwise rotation velocity is imposed to the wheel at different pressure-temperature conditions as seen in Figure 8. Comparison between lab data and numerical results of torque versus wheel velocity is presented in Figures 9 and 10. Notice that error bars represent the standard deviation around the mean torque value indicating a transient effect due to changes in the velocity, evidencing oscillations in torque for some points. However, points with small deviation do not show bars.

Experimentally, it is observed that torque increases with velocity until a certain velocity is reached and liquid starts to be carried over, causing a sudden drop in torque. When deceleration begins, lower torque values are measured and hysteresis is clearly evidenced.

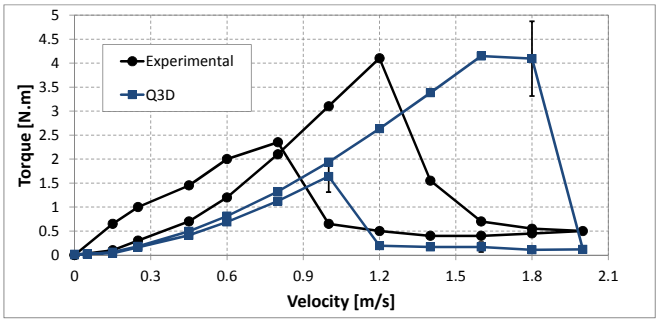

Figure 9: Torque versus velocity for CO_2 mixture at $P = 182.4$ bar and $T = 15.3\ ^\circ$C.

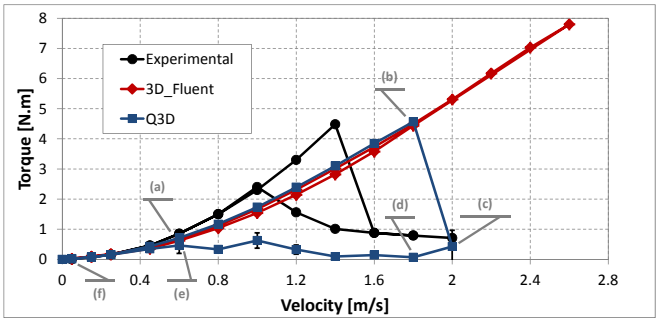

Figure 10: Torque versus velocity for CO_2 mixture at $P = 250$ bar and $T = 60\ ^\circ$C.

Q3D results showed that hysteretic behaviour is predicted qualitatively when the particle size equation is solved and coalescence time is increased to delay formation of larger bubbles which separate out of the liquid phase. Moreover, Figure 9 shows in detail that the predicted velocity needed to cause torque drop differs in 0.6 m/s from experimental, whereas in Figure 10, the difference is 0.4 m/s. Thus, the numerical model underestimates the torque needed for a given velocity and carry over starts at higher velocity than observed in experiments.

On the other hand, as expected the results obtained with Fluent VOF did not present the abrupt drop in torque and hysteretic behaviour, because the dynamics of particle size is not modelled in VOF.

Figure 11 shows the mixture at different times. Notice that each snapshot is related to Figures 8 and 10 showing how the wheel velocity evolves and the associated average torque for each velocity. When the wheel accelerates, break-up process of the large bubble starts and dispersed phase is progressively formed. After $t = 402$ s the interface completely vanished (the gas phase is fully dispersed in the liquid) causing a torque drop as shown at $t = 650$ s. Then, as wheel velocity decreases, bubbles start to coalesce restoring gas phase cap again, generating a small torque recovery.

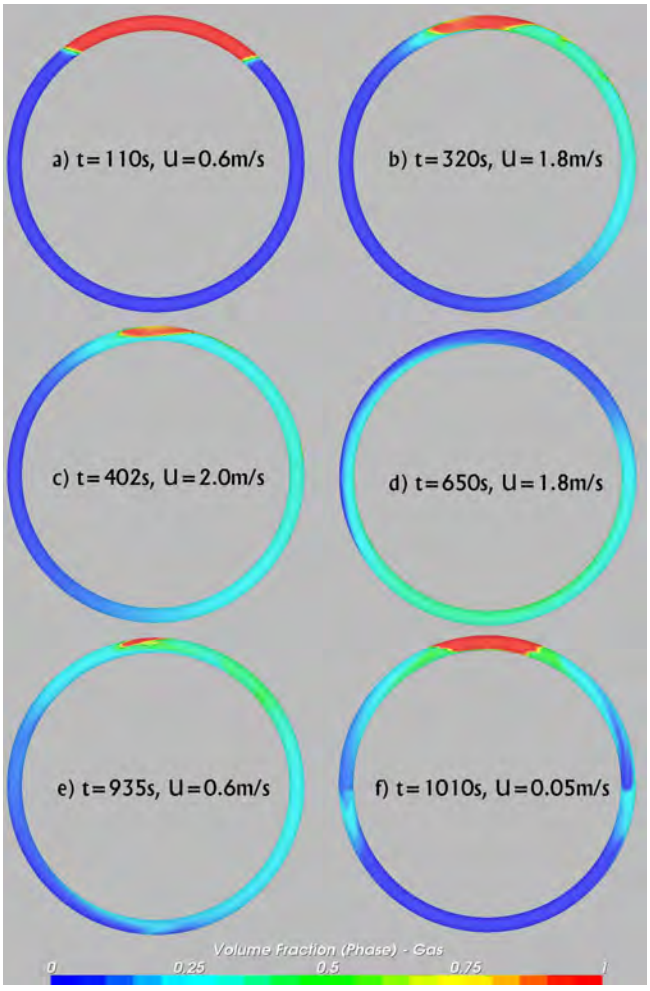

Figure 11: CO_2 mixture at different velocities ($P = 250$ bar and $T = 60\ ^\circ$C).

CONCLUSION

The conclusions are:

1. Numerical results using Q3D approach and Fluent were compared with lab data for three different mixtures. Predictions are generally below experimental data in all cases. Qualitatively, both Fluent and Q3D are able to reproduce the torque dependence on different parameters such as velocity and especially phase viscosities. However, only Q3D is able to predict the drop in torque for high velocities.

2. Relative error between Fluent 3D and Q3D is below 4% and may be considered insignificant when taking into account that Q3D simulations were faster and used less cells. The minor importance of secondary flow (3D effect associated) for this ratio $R/a = 40$ and flow regime may explain the close agreement.

3. Dynamic treatment of particle size in dispersed phase is a critical element to reproduce the hysteresis on torque.

Current work is focused on mitigating the difference between experimental and numerical results. In particular, the large oscillations in torque measurements need to be further understood. Finally, a coupled VOF-Multi Fluid approach in Fluent will be compared to the Q3D results.

ACKNOWLEDGEMENT

The financial support to the Leda Project, the long-time contributions from the Leda Technical Advisory Committee, as well as permission to publish, by Total, ConocoPhillips, and SINTEF are all gratefully acknowledged. Our colleagues Ernst Meese, Runar Holdahl, and Jørn Kjølås (SINTEF), Wouter Dijkhuizen and Dadan Darmana (Kongsberg Oil & Gas Technologies), Harald Laux (OSRAM Opto Semiconductors GmbH, Regensburg), and Alain Line (INSA, Toulouse) are acknowledged for their contributions to the development.

REFERENCES

ALMEIDA, A.S. *et al.* (2010). "CCGS opportunities in the Santos basin pre-salt development". Society of Petroleum Engineers, Rio de Janeiro, Brazil.

ANSYS (2013). "14.5 Fluent Theory Guide". *ANSYS, Inc*.

ASHRAFIAN, A. and JOHANSEN, S. (2007). "Wall boundary conditions for rough walls". *Progress in Computational Fluid Dynamics*, **7(2-4)**, 230–236.

ASHRAFIAN, A. *et al.* (2011). "Multidimensional modeling of stratified wavy three-phase flows". *Rio Pipeline Conference & Exposition, Sep. 20-22*.

CHARNOCK, H. (1955). "Wind stress on a water surface". *Quart. J. Roy. Meteor. Soc*, **81**, 639–640.

JOHNSEN, E.E. *et al.* (2001). "A simplified experimental approach for measuring viscosity for water-in-crude-oil emulsions under flowing conditions". *J. Dispersion Science and Technology*, **22**, 33–39.

LAUX, H. *et al.* (2007). "Simulation of multiphase flows composed of large scale interfaces and dispersed fields". *Proc. Int. Conf. Multiphase Flows, Leipzig, July 9-13th*.

LAUX, H. *et al.* (2008a). "Multi-dimensional simulations of slug and slug-like flows in inclined pipes and channels". *6th North American BHRG Conference on Multiphase Technology*. Banff, Canada.

LAUX, H. *et al.* (2008b). "Multidimensional simulations of multiphase flow for improved design and management of production and processing operation". *2008 Offshore Technology Conference*. Houston, Texas, U.S.A. OTC-19434.

MEESE, E.A. (1998). *Finite volume methods for the incompressible Navier–Stokes equations on unstructured grids*. Ph.D. thesis, NTNU.

MO, S. *et al.* (2014). "Quasi-3d modelling of two-phase slug flow in pipes". *The Journal of Computational Multiphase Flows*, **6**, 1–12.

MORI, Y. and NAKAYAMA, W. (1964). "Study on forced convective heat transfer in curved pipes (1st report, laminar region)". *Int. J. Heat Mass Transfer*, **8**, 67–82.

MORI, Y. and NAKAYAMA, W. (1966). "Study on forced convective heat transfer in curved pipes (2nd report, turbulent region)". *Int. J. Heat Mass Transfer*, **10**, 37–59.

URDAHL, O. *et al.* (1996). "Viscosity measurements of water-in-crude-oil emulsions under flowing conditions: A theoretical and practical approach". *Colloids and Surface A: Physicochemical and Engineering Aspects*, **123**.

10th International Conference on CFD in the Minerals and Process Industries
SINTEF / NTNU Trondheim, Norway
17-19 June 2014

MODELLING OF PARTICLE TRANSPORT AND BED-FORMATION IN PIPELINES

C. Narayanan*, S. Gupta, D. Lakehal

ASCOMP GmbH, Zurich, SWITZERLAND
*Corresponding author, E-mail address: chidu@ascomp.ch

Keywords: Two-phase flow, Eulerian-Lagrangian method, black powder, four-way coupling, VLES, LES

ABSTRACT

Particle transport and bed formation in gas and condensate pipelines could occur under various flow regimes, from dilute flows to high mass-loading conditions, to conditions where particle beds form in the pipeline. Proper modelling requires therefore a comprehensive approach that can handle all the different regimes. A range of complex phenomena have first to be accounted for, including turbulence of the carrier phase, particle-turbulence and particle-wall interactions, surface roughness effects, particle-particle interactions, particle agglomeration, deposition, saltation and re-suspension. We present here recent results of TransAT's particle transport predictions to conditions of one-way, two-way and four-way particle-flow coupling, spanning the three flow regimes evoked: (i) dilute suspensions, (ii) high mass-loading conditions, and (iii) particle beds in the pipeline.

INTRODUCTION

In dense-particle beds systems, the flow behaves in a very subtle way, with very complex physical mechanisms taking place near the wall, where the particles accumulate. A number of simplified analytical solutions to determine the conditions of particle-bed removal in pipes and channels have indeed been proposed, but with limited success due the simplifications implied. Today intensive research is devoted to understand the conditions for dense particle-bed formation and removal, in hydrocarbon and in many other related areas, but the difficulties encountered in measurements and flow visualization have hindered this progress.

In particle-laden pipelines, the particles tend to be transported through the pipeline by gas flow under specific conditions. The velocity required to move the particles could in some cases be estimated, made based on pipeline diameter, gas pressure, and particle size and density (Tsochatzidis and Maroulis, 2007; Smart, 2007). Deposition of black powder will occur if there are solids in the pipeline fluid and the velocity is not high enough to drag the particles along by viscous flow forces. Sediment deposits can lead to blockage of the line, especially during pigging, while flowing powder can damage compressors, plug filters and damage user equipment. In some extreme cases, the piping could be half full of black powder, causing shutdown of the compressor and up to 60 tons of black powder could subsequently be removed from the piping. Similarly, promising oil extraction techniques such as hydraulic fracturing involve transporting a proppant, such as sand, into rock fractures to keep them open and facilitate oil flow.

There are various incentives to explore the use of advanced prediction methods for this class of flows, featuring Lagrangian particle tracking spanning one to four-way particle-flow coupling, instead of average Euler-Euler formulations, Large-Eddy Simulation (LES) instead of RANS, and transient rather than steady-state simulations. The current study which falls in this spirit presents a hierarchical modelling framework for the particle transport regimes mentioned above including validation and application of the model to select practical figures-of-merit (pressure drop in particle laden flows in pipes, and particle bed-formation and prediction of critical velocity of transport in pipes).

The modelling focuses on the statistical representation of particle-particle interactions close to the close-packing limit (collision stress) and particle-wall interactions, including the effect of statistical roughness. In terms of turbulence modelling, unsteady simulations will be used given the limitations of the RANS approach; Large eddy simulation (LES) and Very Large Eddy Simulation (VLES) methods will be emphasized, which have the ability to provide sufficient flow unsteadiness needed to lift up the particles and move the deposited bed. The results were obtained with the CMFD code TransAT. The main issues and limitations will be discussed in the paper.

THE PHYSICAL MODEL IN Trans*AT*

The Numerical Approach

The CMFD code TransAT© is a multi-physics, finite-volume solver for the multi-fluid, Navier-Stokes equations. It uses structured multi-block meshes, and uses both the BFC and IST techniques for mesh generation; IST is a sort of force-based Immersed Boundary Method (not a penalty approach). The solver is pressure based corrected for low-Mach number compressible flows. High-order schemes can be employed; up to 3rd-order Monotone schemes in space and 5th order Runge-Kutta scheme in time. Multiphase flows with or without phase change can be

tackled using interface tracking for both laminar and turbulent flows (Level Set, VOF, and Phase Field), the phase averaged mixture model, and the Lagrangian particle tracking, including with heat transfer).

Turbulence Simulation (LES vs. V-LES)

The basic idea of V-LES (or filter based as referred to by Johansen et al. 2004) is to combine RANS and LES for a specific flow, where the size of the most important scales can be identified. Here the flow is decomposed into resolved and subscale part, the latter being independent from the grid (in contrast to the sub-grid scale modelling in LES), but is dependent on the flow, and thus the flow characteristic length scale. Larger scales than this cut-off scale are resolved, while the rest is modelled, though with more refined statistical turbulence models than zero-equation ones, because turbulence sub-scales are neither isotropic nor independent of the boundary conditions, as speculated in LES. The approach assumes that the Kolmogorov equilibrium spectrum applies to the sub-filter.

Lagrangian modelling for dilute systems

In this formulation, individual particles are tracked in a Lagrangian way within an Eulerian flow field. One-way coupling refers to particles cloud not affecting the carrier phase, because the field is dilute, in contrast to the two-way coupling, where the flow and turbulence are affected by the presence of particles (mildly charged but still in the dilute regime). In the one- and two-way coupling cases, the carrier phase is solved in the Eulerian way, i.e. solving for the continuity and momentum equations:

$$\nabla \cdot \boldsymbol{u} = 0 \tag{1}$$

$$\partial_t(\rho \boldsymbol{u}) + \nabla \cdot (\rho \boldsymbol{u}\boldsymbol{u}) - \nabla \cdot \boldsymbol{\tau} = -\nabla p + \boldsymbol{F}_b + \boldsymbol{F}_{fp} \tag{2}$$

This set of transport equations is then combined with the Lagrangian particle equation of motion:

$$d_t(v_{p_i}) = -f_d \frac{9\mu}{2\rho_p d_p^2}\left(u_{p_i} - u_i[x_p(t)]\right) \qquad f_d = 1 + 0.15Re_p^{2/3} \tag{3}$$

where $\boldsymbol{u}$ is the velocity of the carrier phase, $\boldsymbol{u}_{p_i}$ is the velocity of the carrier phase at the particle location $\boldsymbol{x}_{p_i}$, $\boldsymbol{v}_{p_i}$ is the particle velocity, $\boldsymbol{\tau}$ is the viscous stress and p the pressure. The source terms in (2) denote body forces, $\boldsymbol{F}_b$, and the rate of momentum exchange per volume between the fluid and particle phases, $\boldsymbol{F}_{fp}$. The coupling between the fluid and the particles is achieved by projecting the force acting on each particle onto the flow grid:

$$F_{fp} = \sum_{i=1}^{N_p} \frac{\rho_p V_p}{\rho_m V_m} R_{rc} f_i W(x_i, x_m) \tag{4}$$

where *i* stands for the particle index, N_p for the total number of particles in the flow, f_i for the force acting on a single particle centered at $\boldsymbol{x}_i$, R_{rc} for the ratio between the actual number of particles in the flow and the number of computational particles, and W for the projection weight of the force onto the grid node $\boldsymbol{x}_m$, which is calculated based on the distance of the particle from those nodes to which the particle force is attributed. V_m is the fluid volume surrounding each grid node, and V_p is the volume of a single particle (Narayanan and Lakehal, 2006).

Lagrangian modelling for dense systems

The Eulerian-Lagrangian formulation for dense particle systems featuring mild-to-high volume fractions (α > 5%) in incompressible flow conditions is implemented in TransAT as follows (Eulerian mass and momentum conservation equations for the fluid phase and Lagrangian particle equation of motion):

$$\partial_t(\alpha_f \rho) + \nabla \cdot (\alpha_f \rho \boldsymbol{u}) = 0 \tag{5}$$

$$\partial_t(\alpha_f \rho \boldsymbol{u}) + \nabla \cdot (\alpha_f \rho \boldsymbol{u}\boldsymbol{u}) = -\nabla p + \nabla \cdot \boldsymbol{\tau} + \boldsymbol{F}_b + \boldsymbol{F}_{fp} - \boldsymbol{F}_{coll} \tag{6}$$

where α is the in-cell volume of fluid ($\alpha + \alpha_p = 1$), $\boldsymbol{u}$ is the velocity of the carrier phase, $\boldsymbol{u}_\mathrm{p}$ is the velocity of the carrier phase at the particle location, v_p is the particle velocity, Π is the sum of viscous stress σ and pressure p, τ is the turbulent stress tensor (depending whether RANS, V-LES or LES is employed).

In this dense-particle context, the Lagrangian particle equation of motion (3) should have an additional source term $\boldsymbol{F}_{coll}$ denoting the inter-particle stress force. The interphase drag model in (3) is set according to Gidaspow (1986). The particle volume fraction is defined from the particle distribution function (ϕ) as

$$\alpha_p = \iiint \phi V_p dV_p d\rho_p du_p \tag{7}$$

The inter-phase momentum transfer function per volume in the fluid momentum equation (2) is

$$F_p = \iiint \phi V_p [A] dV_p d\rho_p du_p; \tag{8}$$

with A standing for the particle acceleration due to aerodynamic drag (1st term in the RHS of Eq. 3), i.e. excluding body forces and interparticle stress forces (2nd and 3rd terms, respectively). The pressure gradient induced force perceived by the solids is not accounted for. The fluid-independent force $\boldsymbol{F}_{coll}$ is made dependent on the gradient of the so-called interparticle stress, π, using

$$\boldsymbol{F}_{coll} = \nabla \pi / \rho_p \alpha_p \tag{9}$$

Collisions between particles are estimated by the isotropic part of the inter-particle stress (its off-diagonal elements are neglected.) In most of the models available in the literature π is modelled as a continuum stress (Harris & Crighton, 1994), viz.

$$\boldsymbol{\pi} = \frac{P_s \alpha_p^{\beta(=2-5)}}{max[\alpha_{cp} - \alpha_p; \varepsilon(1-\alpha_p)]} \qquad (10)$$

In TransAT, the particle field is predicted in a Lagrangian way first, which enables defining the particle volume fraction (7) and interphase momentum transfer function (8), then high-order accurate interpolations are resorted to map the Eulerian field (to estimate π), then back again to the Lagrangian system to determine $\boldsymbol{F}_{coll}$). The constant Ps has units of pressure, and α_{cp} is the particle volume fraction at close packing, and constant β is set according to Auzerais *et al.* (1988). The original expression by Harris & Crighton (1994) was modified to remove the singularity at close pack by adding the expression in the denominator (Snider, 2001). The ε is a small number on the order of 10^{-7}. The particle stress is unaffected by the modification except when the volume fraction approaches or exceeds close pack limit, which is arbitrary and depends on the size, shape, and ordering of the particles. This limit can actually be physically reached or even slightly exceeded.

ONE-WAY COUPLING: DROPLET DEPOSITION IN A PIPE

Problem setup and modeling

The example discussed here was simulated using TransAT in the context of analyzing pipeline transport of natural gas and condensates. The objective is to predict the situation illustrated in Figure 1 (Brown et al., 2008), where liquid can be entrained under strong interfacial shearing conditions in the form of droplets from the liquid layer sitting at the bottom of the pipe. These should ultimately deposit on to the walls of the tube forming a film or redeposit back onto the pool itself. The core region consists of a mixture of gas and entrained liquid droplets. In the present study, it is assumed that entrainment of liquid droplets from the film on the upper surface of the pipe is negligible; an assumption consistent with experimental observations in relatively large diameter pipes (Brown et al., 2008).

A 3D body-fitted grid was generated containing 500.000 cells well clustered near the pipe wall. Two turbulence prediction strategies were employed: URANS and LES. The reason for this comparison is to identify the predictive performance of the models in reproducing the interaction between turbulence and the particles. The Lagrangian approach (1-3) under one-way conditions were employed to track the particles together with a particle-wall interaction model. The Langevin model for particle dispersion was used for RANS (Lakehal, 2002). In the LES, periodic boundary conditions along the pipe were employed to sustain turbulence; of course the pipe was shortened in length compared to RANS ($L = 2\pi D$).

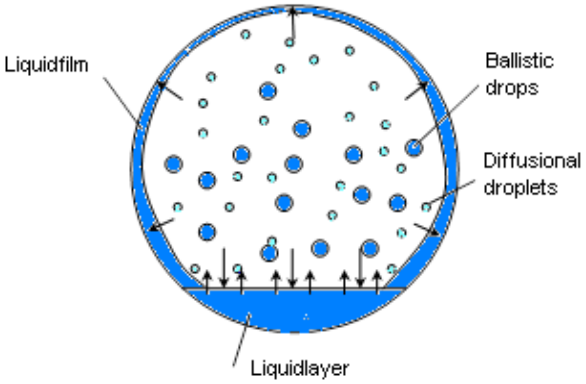

Figure 1: Schematic of the droplet entrainment model (extracted from Brown et al., 2008).

The WALE sub-grid scale model has been used for the unresolved flow scales only (not for particles). About 3.000 droplets were injected, with a Gaussian size distribution around a 500μ mean particle diameter, including: Range 1 :10 < D^p < 48μm; Range 2 : 49 < D^p < 85μm ; Range 3 : 86 < D^p < 123μm; Range 4 : 124 < D^p < 161 μm ; Range 5 : 162 < D^p < 200μm . Simulations run on a 64 Proc. parallel cluster using MPI protocol.

Discussion of the results

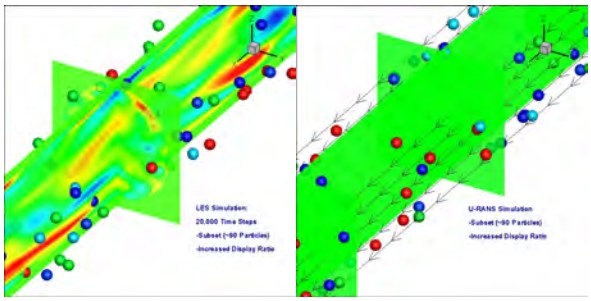

Figure 2: Snapshots of the flow in a gas pipe showing particle interaction with turbulence: left (LES); right (RANS).

The results depicted in Fig. 2 shows a clear difference between URANS and LES. While the LES (left panel) depicts a clear turbulence dispersive effect on the particles, drifting some to the wall region, the URANS results (right panel) deliver a steady path of the particles with the mean flow. This is an important result, suggesting that albeit detailed 3D simulations, the results are sensitive to turbulence modeling.

The droplets population remaining in the gas core has been thoroughly studied by Lecoeur et al. (2013), and plotted as a function of two parameters (axial distance travelled in the pipe and the size of the droplets) for both RANS and LES. The results obtained show important discrepancies between the two approaches: (i) the droplet size has a more important effect in LES than in RANS: while in LES larger droplets tend to deposit faster than the smaller ones due to their ballistic nature (free-flight mechanism), in RANS, however, it seems that the smallest droplets do deposit faster than the large ones.

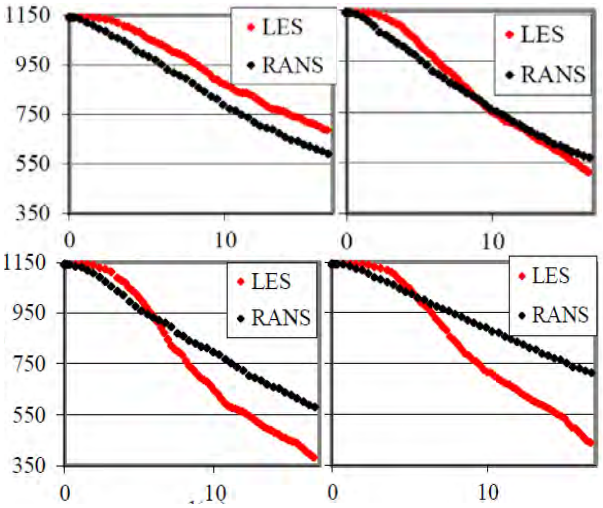

Figure 3: Cumulative number of droplets remaining in the pipe core for selected ranges of droplet sizes. (upper panels) Range 1 ($10< D <48\ \mu m$) and 2 ($49< D <85\ \mu m$). (lower panels): Range 3 ($86< D <123\ \mu m$) and 5 ($162< D <200\ \mu m$).

It was also found that the RANS-predicted deposition rate of droplets is rather monotone (see Fig. 4, black lines) and almost at equal rate or speed in the range 10-160 μm; differences start to be perceived for heavier droplets of diameter larger than 160 μm (see Fig. 3, black line in the 4th panel). The variation in the rate of droplet deposition is better depicted using LES, since particles of different sizes react differently to the various resolved eddies.

Looking closely at Figure 3 reveals more details about to the rate of droplet deposition in the pipe. The number of droplets remaining in the gas core is shown there as a function of the axial distance travelled in the pipe, for for all droplet-size ranges (10-48μ; 49-85μ; 86-123μ and 162-200μ). Smaller droplets (Range 1) tend to deposit faster in RANS than in LES; a tendency that changes gradually to Range 2 droplets that deposit equally be it with RANS or LES, to the extreme situation where ballistic droplets (Range 3 & 4) deposit way faster in LES than in RANS. Simply, LES is capable to distinguish between diffusional and free-flight deposition mechanisms (Botto et al., 2003).

TWO-WAY COUPLING: HEAVY-LOADED PARTICULATE FLOW IN A PIPE

Problem setup and modeling

The distribution of particles in a highly-loaded rough-wall channel was validated against experiments of Laín et al. (2002). The setup is a 2D channel of height 3.5cm and length 6m. The particles have a diameter of 130µm and a density of 2450 kg/m^3. The void fraction of the inflow fluid is set to a very-small number (~0.001) so as to turn on the two-way coupling module. The mean inflow velocity was set to 20m/s in the x-direction with a standard deviation of 1.6m/s in x and y directions. The initial angular velocity of the particles is set to 1000 s^{-1}. A grid size of 125x34 was used. The simulations were run using the two-way coupling model and a Langevin forcing to account for the effects of turbulence on the particles. Further, since the pressure-drop in the channel is strongly affected by wall roughness, its effect on particles should be modelled, too. We use for the purpose the model proposed by Sommerfeld and Huber (1999), which assumes that the particle impact angle is composed of the trajectory angle with respect to the wall and a stochastic component to account for wall roughness, $\alpha' = \alpha + \gamma\xi$, where ξ is a Gaussian random variable with zero mean and a standard deviation of one, and γ is a model constant. The particle wall restitution and friction coefficients are calculated using Laín and Sommerfeld's (2008) expressions.

Discussion of the results

Figure 4: Particle dispersion in the channel showing re-suspension after a tendency for settling (two parts of the channel).

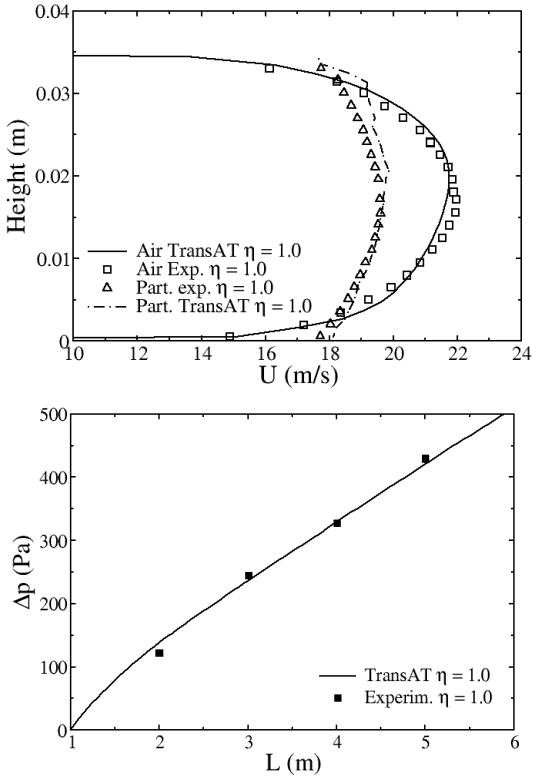

Figure 5: (upper panel) velocity profiles, and (lower panel) pressure drop in the pipe with wall roughness gradient of 1.5°, for a mass-loading of 1.0. : Exp. vs. TransAT

As seen in figure 4, as the simulation proceeds in time a particle tend to move towards the bottom of the channel before re-suspension occurs thanks to the roughness model. The results in Fig. 5 (upper panel) show excellent agreement between the fluid and particle velocity profiles measured experimentally and that simulated by TransAT. The symmetry of the particle profile (like the fluid one) reflects the perfect dispersion of the particles in the channel, due to their systematic re-suspension cuased by wall roughness. The lower panel of Fig. 5 shows that the simulation accurately predicts the pressure drop along the channel (the results are shown for a wall roughness gradient of 1.5 and a mass loading of 1).

FOUR-WAY COUPLING

Validation: Particle suspension sedimentation

This 3D problem was first proposed by Snider (2001) to validate his model. A well-mixed suspension of sand particles and air are left to settle to close pack by sole effect of gravity. The calculation parameters are given below. Particles are initially motionless and are uniformly, randomly distributed. The initial fluctuation in volume fraction is about the average 0.3 volume fractions, as shown in Fig. 10. The heavy, large-size particles fall by the action of gravity in a 0.3m deep container filled with in a lighter fluid (density ratio of 1/1000). The problem has an analytical solution to the evolution of the upper mixture interface between suspended particles and clarified fluid: $h = gt^2/2$.

Particle radius	300μm
Particle density	2500 kg/m^3
Fluid density	1.093 kg/m^3
Fluid viscosity	1.95e^{-5} kg/ms
Initial particle volume fraction	0.3
Size of container	13.8^{2}x30 cm
Comp. Grid	15x15x41

Table 1. Fluid flow conditions and parameters

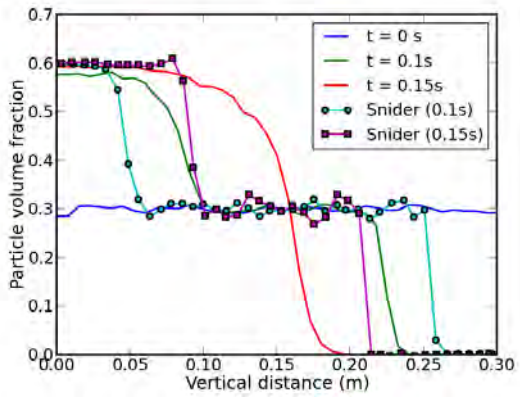

Figure 6: Volume fraction at times during sedimentation

Figure 6 shows the particle volume fractions, including comparison with the original data of Snider (2001). While the interface between clarified fluid and mixture at 0.1s matches well with Snider's (2001) data and with the analytical value of 0.25m from the bottom, our results are better for 0.15s at which the particle-interface reaches 0.19m from the bottom (0.23m in Snider's results). Figure 7 shows that at 0.2s the entire particle mixture is close pack, and at 8s no further settling beyond close pack has occurred. Figure 8 shows the particle distributions during settling at four instants (1, 2, 15 and 18s). The present four-way coupling solution, with the particle normal stress model as presented here and as implemented in TransAT, gives a natural settling to close pack.

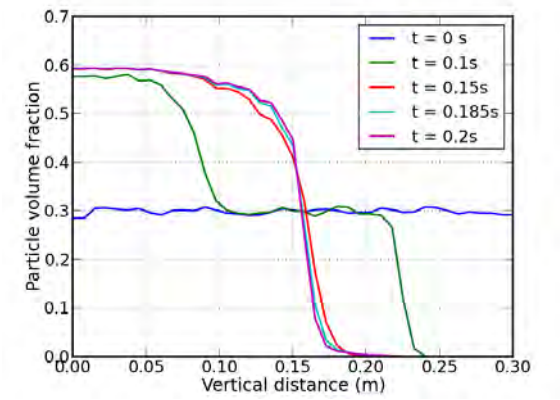

Figure 7: Volume fraction at times during sedimentation

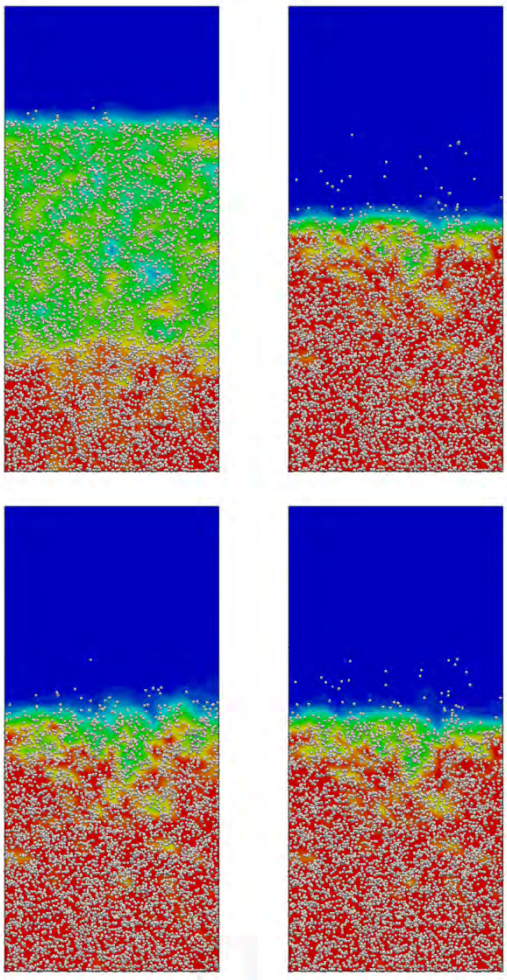

Figure 8: Particle volume-fraction distribution α^p (red=0.6; blue=0) at 0.1, 0.15, 0.185 and 0.2s.

Sand-particle transport in a pipeline

Danielson (2007) proposes a model to predict the critical velocity of bed formation for particle transport in pipes, based on the assumption that there is a critical slip velocity between the sand and the fluid that remains constant over a wide range of flow velocities. Sand transported in (near) horizontal pipes will drop out of the carrier flow and from a stable, stationary bed at below critical velocities. The bed height develops to an extent such that the velocity of the fluid above the bed equals the critical velocity. When the velocity reaches a critical value, sand is transported in a thin layer along the top of the bed. A

steady state is reached such that the sand eroded from the top of the bed is replaced by new sand from the upstream. At higher velocities, the sand bed breaks up into slow moving dunes and further increase in velocity results in sand transported as a moving bed at the bottom of the pipe. If the velocity is above the critical velocity, sand is entrained in the fluid flow:

$$\boldsymbol{Uc} = \mathrm{K}\ \vartheta^{-1/9}\, d^{-1/9}\, [gD(s-1)]^{5/9} \qquad (11)$$

where K is a model constant equal to 0.23 based on SINTEF data and ϑ is the fluid viscosity. The sand transport simulation is made here in two-dimensions with conditions given in Danielson (2007). Particles with diameter of 250, 350 and 450 μm are simulated for fluid velocities of 0.78, 1.2 and 1.6m/s. The particle volume fraction at the inlet is 0.1. The channel length is 0.3m and height is 0.01 m, and is covered by 12 cells in the cross flow direction.

Figure 9 shows a set of results at three instants; each set (or panel) gathers results of the cases with fluid velocities of 0.78, 1.2 and 1.6 m/s, respectively. As the simulation proceeds in time a particle bed starts to form at the bottom of the channel and the inelastic wall reflection results in a non-homogeneous particle distribution along the height of the channel. There is a slowdown of fluid in regions of higher particle volume fractions, bottom of the channel, and higher fluid velocity region in regions of lower particle volume fraction, top of the channel, and this is well captured due to the four-way coupling between particles and fluid momentum equations. The critical velocity predicted by (11) for a 3D pipe flow under these conditions is 4 m/s. For the simulation with inlet velocity of 0.78 m/s (first panel in each set), a stable bed is predicted with the fluid velocity at the top of the bed equilibrating to ~ 3m/s. Note that this is lower than the correlation most probably due to the fact that in the channel case, there is less wall friction (only at the bottom wall) than in a pipe. When the fluid velocity is increased (2nd and 3rd panels in each set), it can be seen through the images that the bed height indeed reduces such that the flow velocity at the top of the bed is again approximately 3m/s. Further validation of the model for 3D pipes are necessary.

Conclusions

The paper presents a simulation campaign of flows laden with solid particles of different size, under different flow conditions. Particle transport predictions were performed to conditions of one-way, two-way and four-way particle-flow coupling, spanning three flow regimes: (i) dilute suspensions, (ii) high mass-loading conditions, and (iii) suspension sedimentation and particle bed formation in pipelines.

REFERENCES

F.M. Auzerais, R. Jackson, W.B. Russel, The resolution of shocks and the effects of compressible sediments in transient settling, *J. Fluid Mech*. 195, 437 (1988).

L. Brown, G. Hewitt, B. Hu, C.P. Thomson, P. Verdin, Predictions of droplet distribution in low liquid loading, stratified flow in a large diameter pipeline, In Proc. BHR Conf. Cannes, France, May 2008.

T.J. Danielson, Sand transport in Multiphase pipelines, *OTC 18691*, Proc. Offshore Tech. Conf. Texas USA, 2007.

D. Gidaspow, Hydrodynamics of fluidization and heat transfer supercomputer modeling, *Appl. Mech. Rev.* 39, 1, (1986).

S.E. Harris, D.G. Crighton, Solutions, solitary waves and voidage disturbances in gas-fluidized beds, *J. Fluid Mech*. 266, 243 (1994).

S.T. Johansen, J. Wu, W. Shyy, 2004. Filtered-based unsteady RANS computations. *Int. Journal of Heat and Fluid Flow*, 25, 10-21, (2004).

C. Narayanan, D. Lakehal, Particle transport and flow modification in planar temporally evolving laminar mixingla yers. I.Particle transport under one-way coupling, *Physics of Fluids*, Part 1, 18: 9. 093302 (2006).

S. Lain, M. Sommerfeld, J. Kissin, Experimental studies and modelling of four-way coupling in particle-laden horizontal channel flow, *Int. Journal of Heat and Fluid Flow*, 23, 647-656, (2002).

N. Lecoeur, C. Narayanan and G. Hewitt, The role of turbulence modeling in the simulation of droplet transport in annular flow, Proc. ICMF 2013, Jeju, Korea, 2013.

M. Sommerfeld, N. Huber, Experimental analysis and modelling of particle–wall collision, *Int. J. Multiphase Flow, 25*, 1457–1489 (1999).

S. Lain, M. Sommerfeld, Euler/Lagrange computations of pneumatic conveying in a horizontal channel with different wall roughness, *Powder Technology*, 184, 76-88 (2008).

J. Smart, Determining the Velocity Required to Keep Solids Moving in Pipelines, *The Journal of Pipeline Engineering*, 6 No. 1 (2007).

D. M. Snider, An Incompressible Three-Dimensional Multiphase Particle-in-Cell Model for Dense Particle Flows, *JCP*, 170, 523–549, (2001).

TransAT User Manual, (2010). www.ascomp.ch/transat.

N.A. Tsochatzidis, K.E. Maroulis, Methods help remove black powder from gas pipelines, *Oil & Gas Journal*, 03 (2007).

L. Botto, C. Narayanan, M. Fulgosi, D. Lakehal, Effect of near-wall turbulence enhancement on the mechanisms of particledeposition, *International Journal Of Multiphase Flow*, 31:8. 940 (2005).

D. Lakehal, On the modelling of multiphase turbulent flows for environmental and hydrodynamic applications, International Journal of Multiphase Flow, 28:5. 823-863 (2002).

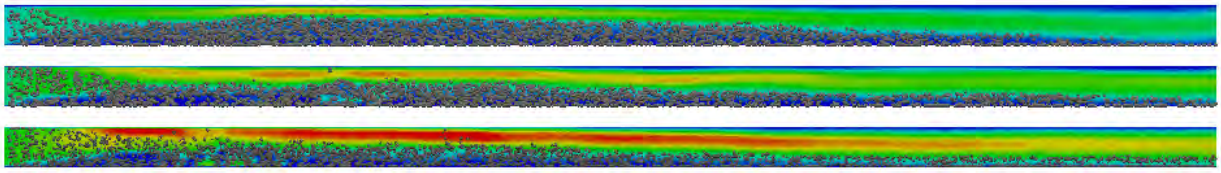

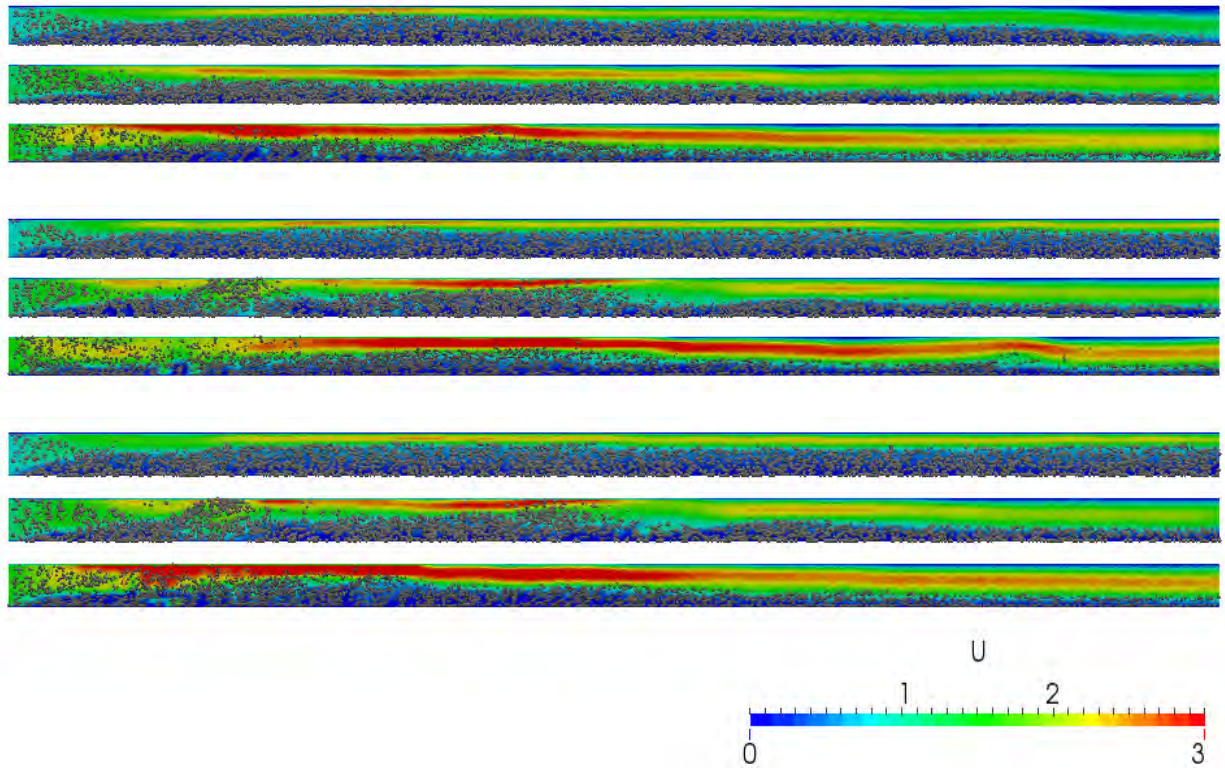

Figure 9: Particle distribution in the channel at 4 instants. Each set of panels refers to different inflow conditions (upper panel: 0.78m/s, middle panel: 1.2m/s, and lower panel: 1.6m/s).

QUASI-3D MODELLING OF TWO-PHASE FLOWS IN PIPES

Alexander VIKHANSKY
CD-adapco, Didcot, UK
E-mail: alexander.vichansky@cd-adapco.com

ABSTRACT

The paper demonstrated that the so-called quasi-3D (Q3D) pipe flow model can be implemented in a commercial CFD code with minimal modifications. We use a special meshing technique in order to create a two-dimensional block of control volumes stretched along the horizontal chord of the pipe so the code operating in the 3D mode effectively solves the Q3D chord-averaged Navier-Stokes equations. Turbulence is modelled by the $k-\varepsilon$ model with slightly modified coefficients.

Keywords: multiphase pipeline transport, free surface flow, pipe flow, quasi-3D .

NOMENCLATURE

Greek Symbols

α	Volume fraction.
ε	Turbulence dissipation rate, $[m^2/s^3]$.
κ	Relative roughness.
μ_T	Turbulent viscosity, $[kg/ms]$.
ρ	Mass density, $[kg/m^3]$.
τ	Reynolds stress, $[Pa]$.
τ_s	Particle relaxation time, $[s]$.

Latin Symbols

A	Cross section area, $[m^2]$.
C_D	Drag coefficient.
C_μ	Turbulent viscosity prefactor.
d_p	Particle diameter, $[m]$.
D_T	Turbulent dispersion coefficient, $[kg/ms]$.
F_{TD}	Turbulent dispersion force, $[kg/(ms)^2]$.
f	Friction factor.
$\mathbf{g}$	Acceleration of gravity, $[m/s^2]$.
$\mathbf{I}$	Identity matrix.
k	Turbulence kinetic energy, $[m^2/s^2]$.
p	Pressure, $[Pa]$.
Re	Reynolds number.
T_L	Lagrangian time scale, $[s]$.
$\mathbf{u}$	Velocity, $[m/s]$.
$\bar{\mathbf{u}}$	Mean velocity, $[m/s]$.
$\mathbf{u}'$	Deviation from the mean velocity, $[m/s]$.

Sub/superscripts

G	Gas.
L	Liquid.
S	Solid.
R	Relative.

INTRODUCTION

Traditionally the pipe flow simulators are based on 1D models, where the essential physics such as inter-phase drag and flow regimes are modelled using empirical correlations. Three decades or so of intensive R&D activity in the field imply that the 1D models reach maximum of their predictive capacity. On the other hand, the growing power of modern computers allows an engineer to perform more CPU time-consuming calculations either on his own computer or on a remote server. Although the full 3D modelling of a multiphase flow in an industrial pipeline belongs to a distant future, there is a growing interest to the Q3D models where parameters of the flow are either pre-integrated across the pipe (Biberg, 2007) or averaged along the horizontal chord of the pipe (Laux *et al.*, 2007). These models allow for (an approximate) resolution of the gas-liquid interface and therefore, the transition from the stratified to bubbly flow is computed rather than modelled.

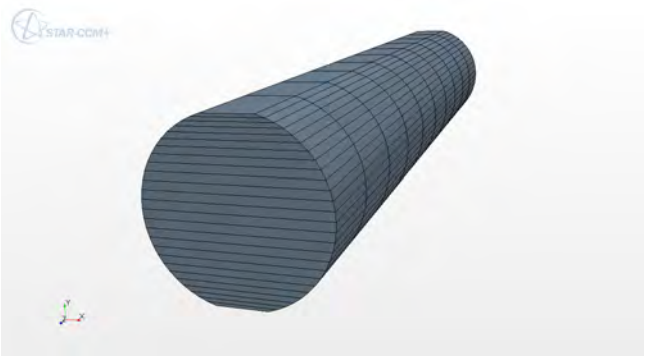

Figure 1: Q3D mesh.

Development of a dedicated Q3D software tool is an ambitious task; in the present work we demonstrate that an existing commercial 3D software can be used for the same purpose. The advantage of our approach is obvious: there are lot of physical models e.g., RANS turbulence, phase transition, VoF, which are already available for a general user. We show that the standard version of STAR-CCM+ enables one to perform transient two-phase Q3D simulations on a desktop PC within few days – an action, which would require weeks of a multiprocessor cluster if done in a full 3D mode.

MODEL DESCRIPTION

Although our aim is to model multiphase pipe flows, the essential elements of the approach can be illustrated on a

single-phase incompressible flow. The equations for the multiphase flows are familiar for an experienced reader and can be found elsewhere.

Pipe meshing

The Q3D mesh is shown in Figure 1. The initially circular shape of the pipe is slightly clipped from above and below in order to create a curvilinear rectangle with two horizontal edges. Then side edges are split into N_y segments and the Directed Mesh option of STAR-CCM+ is applied in order to create a two-dimensional block of prismatic cells.

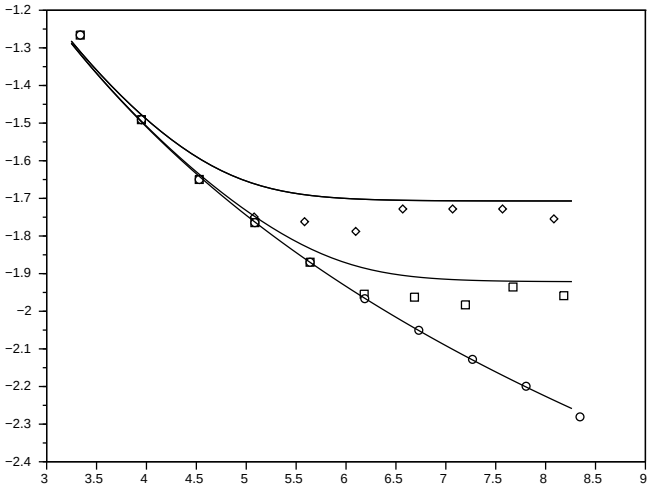

Figure 2: Moody chart ($\log f$ vs. $\log Re$) for different values of the relative roughness: $\kappa = 0$ (circles), $\kappa = 10^{-4}$ (squares), $\kappa = 10^{-3}$ (diamonds). The lines are calculated using the (Colebrook, 1939) equation; symbols correspond to the Q3D calculations with $C_\mu = 0.13$.

Flow modelling

The Reynolds-averaged Naiver-Stokes equations read:

$$\frac{\partial \rho \mathbf{u}}{\partial t} + \nabla \cdot (\rho \mathbf{u}\mathbf{u}) = -\nabla p - \nabla \cdot \tau, \tag{1}$$

where the Reynolds stress is modelled using the Boussinesq eddy viscosity assumption:

$$\tau = \mu_T \left(\nabla \mathbf{u} + (\nabla \mathbf{u})^T - \frac{2}{3} (\nabla \cdot \mathbf{u}) \mathbf{I} \right) - \frac{2}{3} \rho k \mathbf{I}. \tag{2}$$

Being averaged along the horizontal chord Eq. (1) yields:

$$\frac{\partial \rho \bar{\mathbf{u}}}{\partial t} + \nabla \cdot (\rho \bar{\mathbf{u}} \bar{\mathbf{u}}) = -\nabla \bar{p} - \nabla \cdot \bar{\tau} - \nabla \cdot \left(\rho \overline{\mathbf{u}'\mathbf{u}'} \right), \tag{3}$$

where $\mathbf{u}' = \mathbf{u} - \bar{\mathbf{u}}$ and the last term in Eq. (3) is an additional Reynolds stress due to the averaging. Following the Boussinesq approach we model the combined Reynolds stress $\bar{\tau} + \rho \overline{\mathbf{u}'\mathbf{u}'}$ by Eq. (2), where equation for the turbulent viscosity reads:

$$\mu_T = C_\mu \rho \frac{k^2}{\varepsilon}. \tag{4}$$

In the present work we use the $k - \varepsilon$ model in order to close Eqs. (3)-(4).
The standard version of the $k - \varepsilon$ model assumes that $C_\mu = 0.09$; due to the additional chord averaging C_μ for the Q3D model should be higher. In order to calibrate our model pressure drop in a pipe is been calculated with different values of C_μ. The results are presented in Figure 2. One can see that the Q3D model is in a good agreement with the Moody chart over the entire range of Reynolds numbers and relative roughnesses.

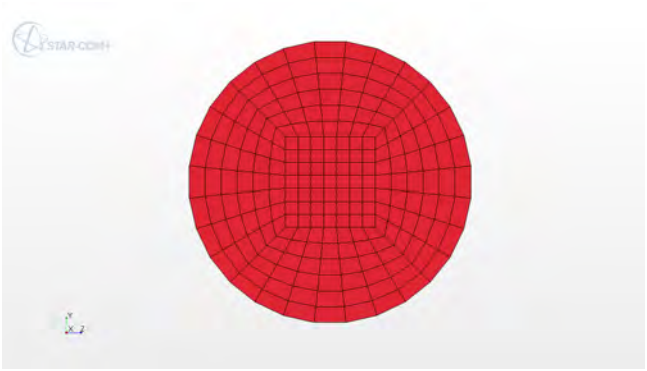

Figure 3: Fully 3D mesh.

RESULTS AND DISCUSSION

Hydrotransport

Transport of solids in horizontal pipelines is an important component of mineral processing industries (Karabelas, 1997; Eskin, 2012). The particles are suspended by the turbulent vortices against the gravity so the main force balance in the vertical direction is between the gravity force $(\rho_S - \rho_L)\mathbf{g}$ and the turbulent dispersion force (TDF) $\mathbf{F}_{TD}$. Several functional forms for the turbulent dispersion force have been proposed in the past; in the present work we adopt the model derived by (Burns *et al.*, 2004) via Favre averaging of the Navier-Stokes equations for a two-phase flow:

$$\mathbf{F}_{TD} = 3 D_T \frac{C_D}{d_p} |\mathbf{u}_R| \, \nabla (\ln \alpha_L - \ln \alpha_S). \tag{5}$$

Usually the turbulent dispersion coefficient is taken equal to the turbulent viscosity. This assumption is justified by the similarity between the turbulent mass and momentum transports. However, it was noted in the past that apparent diffusivity of the particles is higher than predicted. Taking the interphase slip into account (Eskin, 2012) proposed the following form for D_T:

$$D_T = \mu_T \left(1 + \frac{\tau_s}{T_L} \right). \tag{6}$$

The particle relaxation time is estimated as

$$\frac{1}{\tau_s} = 3 \frac{\rho_L}{\rho_S} \frac{C_D}{d_p} |\mathbf{u}_R| \tag{7}$$

and the Lagrangian time scale is given by the following formula:

$$T_L = C_\mu \frac{k}{\varepsilon}. \tag{8}$$

The calculations have been performed in Q3D and fully 3D modes. The 3D mesh is shown in Figure 3. Figure 4 shows distribution of $165 \mu m$ sand particles in water under a moderate mean volume fraction of particles ($\overline{\alpha_S} = 0.2$). The fully

3D calculations provide a justification for the chord averaging: as one can see, the level sets of α_S are nearly horizontal.

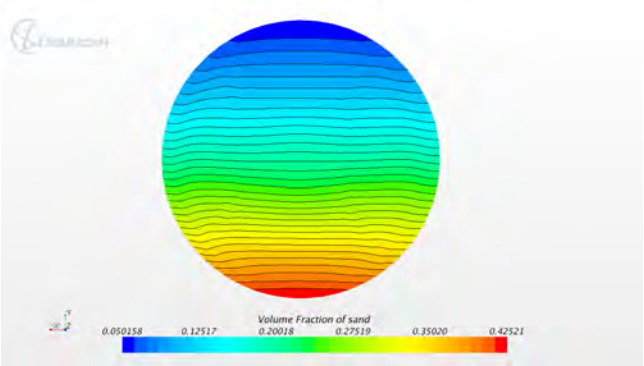

Figure 4: Volume fraction of sand in a horizontal pipeline; 3D mesh.

Distribution of the solid phase along the vertical centreline is shown in Fig. 5. Due to the TDF with the inertia correction (6) the results are in a good agreement with each other and with the experimental data (Karabelas, 1997).

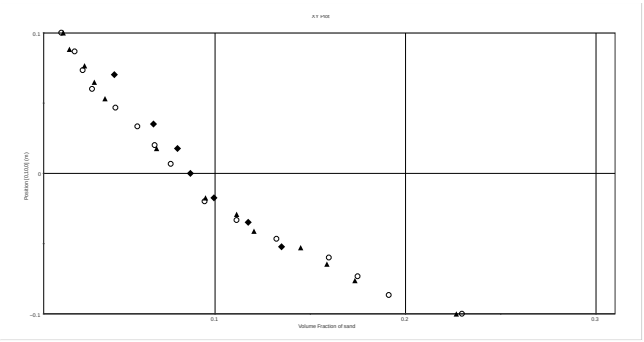

Figure 5: Distribution of sand (volume fraction vs. hight) along a the centreplane of a horizontal pipeline; 3D mesh (circles), Q3D mesh (triangles), experimental data (diamonds).

Slug flow

In order to assess the ability of the method to reproduce slug formation and evolution we performed a series of calculations under conditions described in (Ujang *et al.*, 2006). Gas-water flow in a horizontal $37m$-long pipe with internal diameter $7.8cm$ was modelled by the volume of fluid (VoF) method on 26×6200 Q3D mesh. Superficial gas velocity $\mathbf{u}_L$ varies from $0.22m/s$ to $0.61m/s$; superficial gas velocity $\mathbf{u}_G$ was set higher varying from $2.27m/s$ to $4.28m/s$.

The flow is initialised with corresponding superficial velocity for each phase and volume fractions as it is shown in Fig. 6. Due to the unphysical initial conditions the flat interface is destroyed quickly by the Kelvin-Helmholtz instability as shown in Fig. 7. After a transient time a more physically plausible structure of slug flow is established, namely, there is a slug left behind a low volume fraction of water As the gap between the wavy interface and the top of the pipe contracts, the gas accelerates and the slug overturns, so a typical slug captures some amount of gas as it is shown in Fig. 8. The obtained structure of the volume fraction is characterised by a large bubbles of the gas trapped by the water; it is an artefact of the VoF method used. In the future a more advanced Eulerian multiphase method allowing for modelling of dispersed bubbly flows of will be used.

In order to detect the slugs we monitor the volume fraction of water at different cross sections of the pipe (Fig. 9). The slugs are characterised by a high volume fraction ($\alpha_L \geq 0.8$). We manually count the number of peaks and the obtained slug frequency ($0.3s^{-1}$) is in a good agreement with the experimental data by (Ujang *et al.*, 2006).

A better indication of the slugs dynamics can be obtained from the pressure distribution along the pipe as it is shown in Fig. 10. The pressure jump is just at the slug. The slug can be considered as a body with variable mass: there is water entering with low velocity $\mathbf{u}_{in}$ (about $3m/s$) and water left behind with velocity of the slug $\mathbf{u}_{out}$ (about $6m/s$). The momentum balance is

$$A\Delta P = \rho Q(\mathbf{u}_{in} - \mathbf{u}_{out}), \tag{9}$$

where A is the cross section area, Q is the volumetric flux through the slug, Δp is the pressure drop, ρ_L is density of water. The volumetric flux can be estimated as

$$Q = cA(\mathbf{u}_{in} - \mathbf{u}_{out}), \tag{10}$$

where $c < 1$ is accounting for the fact that the water ahead of the slug occupies only a small (about $1/4$) portion of the cross section. Therefore

$$\Delta p \approx c\rho(\mathbf{u}_{in} - \mathbf{u}_{out})^2 \tag{11}$$

and the obtained estimate is in a good agreement with the numerical results.

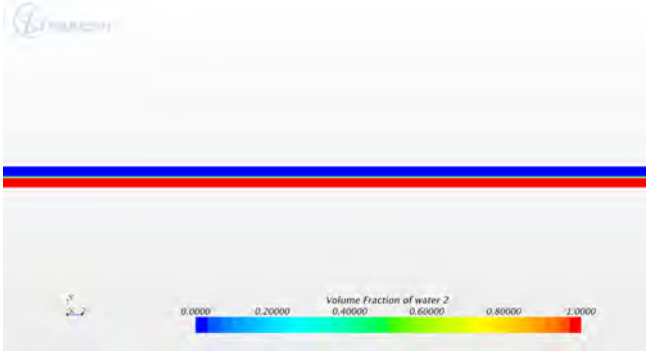

Figure 6: Slug flow: initial distribution of the volume fractions.

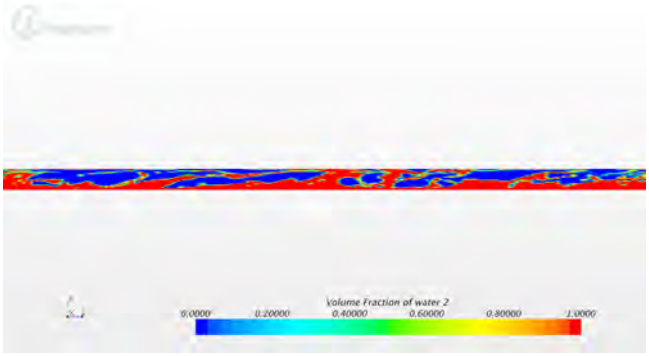

Figure 7: Slug flow: volume of fluid contour plot after $0.1s$.

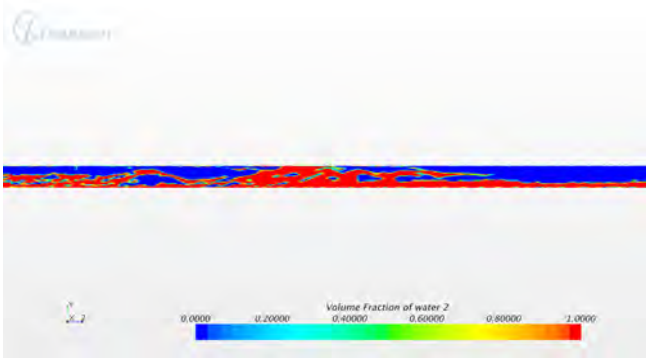

Figure 8: Slug profile after $100s$; $\mathbf{u}_G = 4.28m/s$, $\mathbf{u}_L = 0.8/s$.

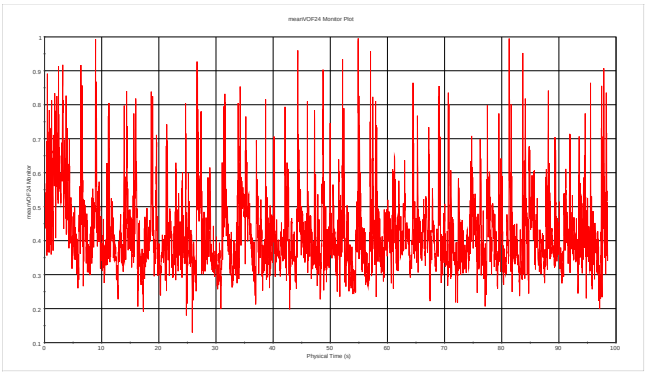

Figure 9: Cross-section averaged volume fraction as a function of time at $24m$ from the inlet; $\mathbf{u}_G = 4.28m/s$, $\mathbf{u}_L = 0.8/s$.

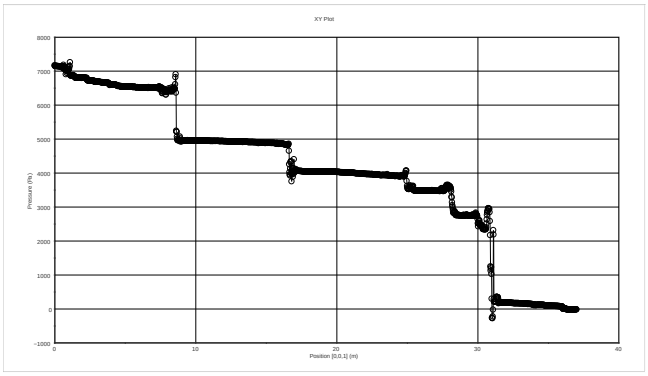

Figure 10: Pressure distribution along the pipe's centreline.

CONCLUSION

The Q3D modelling of single and two-phase pipe flows can be done using the standard version of STAR-CCM+ code with a minimum modification of the standard simulation practice. Due to the numerous physical models (e.g., phase change, heat and mass transfer) available to a general user, it constitute a valuable alternative to development of a dedicated Q3D code.

REFERENCES

BIBERG, D. (2007). "A mathematical model for two-phase stratified turbulent duct flow". *Journal of the ICE*, **11**, 1–48.

BURNS, A.D. *et al.* (2004). "The Favre averaged drag model for turbulent dispersion in Eulerian multi-phase flows". *5th International Conference on Multiphase Flows*. Yokohama, Japan.

COLEBROOK, C.F. (1939). "Turbulent flow in pipes". *Multiphase Sci. and Technology*, **19**, 133–156.

ESKIN, D. (2012). "A simple model of particle diffusivity in horizontal hydrotransport pipelines". *Chem. Eng. Sci.*, **12**, 84–94.

KARABELAS, A.J. (1997). "Vertical distribution of dilute suspensions in turbulent pipe flow". *AIChE Journal*, **23**, 426–434.

LAUX, H. *et al.* (2007). "Simulation of multiphase flows composed of large scale interfaces and dispersed fields". *6th International Conference on Multiphase Flows*. Leipzig, Germany.

UJANG, P.M. *et al.* (2006). "Slug initiation and evolution in two-phase horizontal flow". *International Journal of Multiphase Flow*, **32**, 527 – 552.

Simulation of two-phase viscous oil flow

Stein Tore JOHANSEN[1]*, Sjur MO[1], Jørn KJØLAAS[2], Christian BREKKEN[2] and Ivar ESKERUD SMITH[2]
[1]SINTEF Materials and Chemistry, 7465 Trondheim, NORWAY
[2]SINTEF Petroleum, 7465 Trondheim, NORWAY

* E-mail: Stein.T.Johansen@sintef.no

ABSTRACT

Multiphase flows of heavy oils and other fluids with high apparent viscosity is a particular industrial challenge. Main challenges here is that interfacial waves, atomization at the large scale gas–liquid interface as well as bubble entrainment and separation all are significantly modified by high fluid viscosity. In addition the viscous liquid may behave as laminar while gas and other low viscosity liquids show turbulent behaviour. Accordingly, correct modelling of the turbulence, including correct transitional behaviour between turbulent and laminar flow becomes of great importance.

In this paper we have investigated two phase flows of gas at a rather high density and viscous oil. Experiments have been performed at the SINTEF Multiphase Flow Laboratory at Tiller, Trondheim. The experimental section was horizontal, with a pipe inner diameter of 3". Pressure drop - and liquid hold-up time series, as well as video-documentation of the flow, were recorded

The experiments have been analysed and simulated by the Quasi-3D flow model which has been developed in the LedaFlow development project. The results show that flow regimes are well predicted, as well as liquid fractions (hold-up) and pressure drops. Furthermore, some cases have been identified where the Quasi-3D concept is challenged and where the full 3D effects need special attention and modelling.

In the paper we describe the experiments in more details, discuss the general challenges on viscous flow modelling, present the special features of our Quasi-3D flow model and compare predictions to the experimental results. Finally we discuss the perspectives of multidimensional modelling as a virtual laboratory for multiphase pipe flows comprising viscous liquids.

Keywords: Two phase pipe flow, viscous fluid, turbulence, laminar-turbulence transition, Quasi-3D modelling

NOMENCLATURE

Greek Symbols

α	Volume fraction	[#]
ε	Wall roughness	[m]
ε_m	Turbulent dissipation for phase m	[m^2/s^3]
κ	Von Karman Constant (≈ 0.4)	
μ_m	Molecular viscosity for phase m	[Pa·s]
μ_m^T	Turbulent viscosity for phase m	[Pa·s]
ρ_m	Density for phase m	[kg/m^3]
θ	Pipe inclination	[°]

Latin Symbols

D	Pipe diameter	[m]
Fr	Froude number ($Fr = v_{drift} \Big/ \sqrt{gD}$)	
v_{drift}	Drift velocity, $v_{drift} = U_g - U_o$	[m/s]
g	Gravity (9.81 m/s^2)	[m/s^2]
k_m	Turbulent kinetic energy for phase *m*	[m^2/s^2]
ℓ	Turbulent length scale	[m]
L	Pipe length	[m]
R	Pipe radius	[m]
Re_g	Gas Reynolds number ($\mathrm{Re}_g = \frac{\rho_g U_{sg} D}{\mu_g}$)	
Re_l	Liquid Reynolds number ($\mathrm{Re}_l = \frac{\rho_l U_{sl} D}{\mu_l}$)	
U_k	Stream wise velocity for phase k	[m/s]
U_{sk}	Stream wise superficial velocity for phase k ($U_{sk} = \alpha_k U_k$)	[m/s]
x	Axial distance	[m]
y	Transversal distance	[m]
$\Delta x, \Delta y$	Mesh spacing	[m]

Sub/superscripts

g gas.
l liquid
crit critical

INTRODUCTION

Multiphase flows containing viscous fluids appear in many oil and gas applications. Heavy oil contains large molecules and precipitates which result in a viscosity which is strongly temperature dependent and in some cases may lead to non-Newtonian behaviour. By heating

such fluids they may be transported easily as long as the temperature is kept high. However, in some cases heating and excessive insulation is very expensive and it is desirable to transport the fluids at approximately ambient temperature. Evaluation of the feasibility of such transport would rely on accurate flow models.
A special challenge here is that an oil phase at high viscosity may flow as laminar while the remaining phases (gas, water) may show turbulent behaviour. In addition, the interface structures, drainage of liquid wall films, entrainment processes and phase separation are all significantly modified by a high liquid viscosity.

Another challenge is that availability of high quality experimental data from multiphase flow in pipes larger than 2 inches is extremely scarce (Zhang et al., 2012). However, for pipe diameters less than 2 inches surface tension and wall wetting effects play a more significant role than in larger and industrial size pipes. Of the few experiments with somewhat larger pipe diameters we find Gokcal (Gokcal, 2005, Gokcal, 2008), who performed experiments in a 19 m long horizontal flow loop with inner diameter 50.8 mm. He used air and a viscous oil, where the oil viscosity varied from about 180 to 600 cP.

In a literature review (Zhang et al., 2012) it was commented that more experiments and physical models are needed in order to have appropriate understanding and good 1D model predictions. Improving the understanding of such gas/liquid flow is a major motivation of this paper.
In the paper we will discuss the capability of a multidimensional Quasi-3D model (Laux et al., 2007, Mo et al., 2012, Mo et al., 2013b, Mo et al., 2013a) in predicting this type of viscous two phase gas/liquid flows. Detailed experimental data, to be used to understand the physics and benchmark the model, has been recorded at the SINTEF Multiphase Flow facility at Tiller, outside Trondheim. This is further explained in the next section.

EXPERIMENTS

In the experiments we apply a horizontal pipe with 69 mm ID, and a test section which is 51.4 m. As the experimental loop is indoor, the fluid temperature was monitored and was kept quite constant, with less than 0.1 °C variations in temperature during one experiment.
The experimental setup is documented by (Eskerud Smith et al., 2011). In addition to the instrumentation (broad band gamma densitometers, pressure sensors) we have applied a traversing gamma densitometer. This instrument can record a statistically averaged liquid distribution across the pipe cross section.
From a larger set of two-phase experiments a subset was selected. These data is characterized by a gas/liquid density ratio of approximately 0.05 and a gas/liquid viscosity ratio of approximately 1.5e-4. The surface tension was measured to 0.02 N/m. The oil viscosity itself was in the range of 0.08 – 0.11 Pa·s, which is approximately 100 times more viscous than water. The experimental matrix with summarized overall experimental results is found in Table 1.

Table 1 Experimental matrix with measured liquid holdup and pressure drop.

Exp. ID	Re_liq	Re_gas	Liquid holdup [-]	Pressure gradient [Pa/m]
he10671	6.15E+02	1.03E+05	**0.82**	-506
he10643	6.12E+02	2.16E+05	**0.63**	-672
he11011	4.71E+02	4.32E+05	**0.63**	-746
he11013	4.92E+02	6.47E+05	**0.52**	-944
he10656	5.93E+02	8.64E+05	**0.44**	-1012
he10619	5.83E+02	1.08E+06	**0.39**	-1235
he10627	5.97E+02	1.30E+06	**0.30**	-1684
he11014	5.07E+02	1.51E+06	**0.29**	-1997
he11015	5.06E+02	1.73E+06	**0.24**	-2081
he11016	5.11E+02	1.94E+06	**0.20**	-2227

The Reynolds numbers in the table are based on the superficial velocity. We see that for an approximately constant superficial velocity based liquid Reynolds number (Re_l) the liquid fraction decreases significantly with increased gas Reynolds number (Re_g). As a consequence, the liquid phase velocity has increased by a factor of approximately 4 for the highest gas flow rate. Hence, as the gas Reynolds number increases the liquid will pass through the transition from laminar to turbulent liquid flow. This is a result of an increasing liquid Reynolds number based on the hydraulic diameter and phase velocity of the liquid phase. At the same time the pressure drop increases strongly with increasing gas flow rate.
More details about the experimental results are given in the result section, after introducing the flow model.

MODEL DESCRIPTION

Model basis

The flow model is based on a 3D and 3-phase formulation, where the equations are derived based on volume averaging and ensemble averaging of the Navier-Stokes equations. Conceptually, the model is based on the following elements (Laux et al., 2007). A multi-fluid Eulerian model allowing two types of dispersed fields[1] in each of the three continuous fluids.

i) The flow domain consists of several zones, each with a well-defined continuous fluid, separated by Large Scale Interfaces (LSIs)
ii) Between the zones local boundary conditions are applied (interface fluxes)
iii) A field based turbulence model with wall functions for LSIs and solid walls.
iv) Evolution models for droplet- and bubble sizes
v) By adding together the field-based equations for each phase, phase based mass-, momentum-, and turbulence equations are obtained

[1] Each phase can appear as different fields. For a 3-phase situation each phase may be continuous or dispersed in each of the other continuous phases.

At the LSIs we use the concept of wall functions, where the shear stresses from both sides of the interface are approximated by the wall functions for rough walls described by (Ashrafian and Johansen, 2007). The same wall functions are used to calculate the added turbulence production in LSI cells. The effect of non-resolved waves is modeled by a density corrected Charnock model (Charnock, 1955). The use of wall functions at the LSIs is supported by e.g. (Bye and Wolff, 2007) studying the air-sea interface.

The turbulence is modeled using a $k-\ell$ model where k is the turbulent kinetic energy and ℓ is a turbulent mixing length scale based on flow domain geometry. The length scale is solved from a Poisson equation where the length scale at solid walls and LSIs are related to roughness and given as boundary conditions:

$$\nabla^2 \ell = -\frac{\kappa}{R} \qquad (1)$$

Here κ is the von Karman constant and R is the pipe radius. The length scale in cells near walls and LSIs are given by algebraic relations. The turbulent kinetic energy equations are solved for each phase by applying wall laws at solid walls and the LSIs. The turbulent viscosity for phase m is given by:

$$\mu_m^T = \rho_m \ell \left(0.35 k_m\right)^{1/2} \qquad (2)$$

where ρ_m is density and k_m is turbulent kinetic energy for phase m. The turbulent dissipation rate for phase m is:

$$\varepsilon_m = \frac{\left(0.35 k_m\right)^{3/2}}{\ell} \qquad (3)$$

The resulting model gives the volume fractions and velocity (momentum) for the phases in the flow. In order to apply local boundary conditions inside the flow as described above we need to identify the LSIs. This is done based on an evaluation of the predicted phase volume fraction, based on the assumption that there is a critical volume fraction which controls phase inversion. In this work a phase is assumed continuous if the local volume fraction is above a critical volume fraction α_{crit} = 0.5. Based on a relatively simple reconstruction algorithm, the interface is reconstructed such that the local boundary conditions can be applied. Presently, the effects of surface tension on the motion of the LSI are not included. This simplification is valid as long as we use relatively coarse grids and do not want to resolve capillary waves.

This model framework has the capability to handle any 3D 3-phase (or less) multiphase flow as long as the flow can be described by 9 fields – 3 continuous fields with 2 dispersed fields in each. However, fields such as thin liquid wall films are not included. As this model is directed towards applications such as predictions of multiphase flows in pipelines the target is to simulate reasonably long sections of pipes for considerable flow-times. This restriction demands simplifications in order to be able to obtain results in a reasonable CPU time. Weeks or months of computer time on parallel machines would not be acceptable for most industrial applications. The simplification we have introduced is the Quasi-3D (Q3D) approximation. By slicing the pipe in one direction (usually the vertical direction), as demonstrated in Figure 1, the flow can be resolved on a 2-dimensional mesh, but still keeping important aspects from the 3D pipe geometry.

The full 3D model equations are then averaged over the transversal distance to create slice averaged model equations. In this process the 3D structures are homogenized and the flow becomes represented by slice averaged fields. One result is that the wall fluxes, such as shear stresses, becomes source terms in what we call Quasi-3D (Q3D) model equations (for details, see (Laux et al., 2007)). It should be noted that the length scale equation (1) is solved using the 2D Laplacian in the x-y plane (Figure 1).

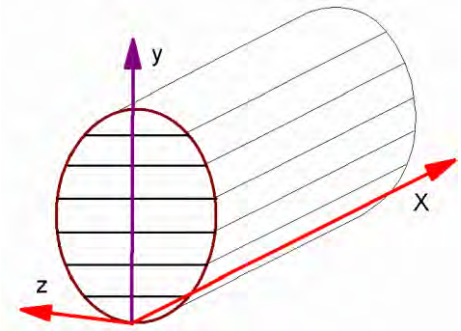

Figure 1 Quasi 3D grid cells, showing one axial (x-direction) and seven vertical cells (y-direction). The z-direction is averaged over to get Q3D equations.

The numerical solution is performed on a staggered Cartesian mesh, where the discrete mass, pressure and momentum equations are solved by an extended phase-coupled SIMPLE method (for details, see e.g. (Patankar, 1980)). The implicit solver uses first order-time discretization and up to third-order in space for convective terms (Laux et al., 2007).

The Quasi 3D model description is expected to perform well in horizontal stratified and hydrodynamic slug flows where the large scale interface is dominantly horizontal at a given axial position x, as seen in Figure 1 and demonstrated in previous papers (Laux et al., 2008a, Laux et al., 2008b, Laux et al., 2007).

The applicability of the Q3D approximation to horizontal gas liquid flows with high liquid viscosity will be discussed next. We note that the model has not included a field for the thin liquid film which is drained by gravity after passage of waves or slugs. Adding such a field with separate momentum- and mass conservation equations may be necessary in the case when the liquid is extremely viscous.

Simulations

Based on the 10 flow situations, represented by Table 1, 10 flow cases were defined. The length of the simulated domain was 20 meters, with diameter 69 mm. The

applied grid comprised 20 (transversal) x 1000 (axial) grid points. Thus, the grid aspect ratio is 5.8.
The simulations were run for 60 seconds real time, and data from the last 30 seconds were applied to calculate statistics from the simulations. The total simulation time spanned from approximately 4 to 30 times the fluid residence time in the flow domain. By further inspection of the data it was verified that the last 30 seconds should give a good representation of the capability of the model. At the flow inlet the flow was in all cases assumed stratified (liquid fraction of 0.4), with no dispersed droplets and bubbles. The inlet turbulent energy was 0.001 m^2/s^2. The model has several physical constants related to the bubble- and droplet transport models (Mo et al., 2013a), which are given in Table 2. Wave roughness is characterized by the Charnock constant (used default value of 10) and the dispersed phase concentrations at the Large Scale Interface are set to 0.3.

Table 2 Model constants for the size of dispersed fields (Mo et al., 2013a)

	C1	C2	C3	C4
Bubbles	10	0.1	1.00E-05	0.1
Droplets	0.02	0.002	1.00E-06	0.1

RESULTS

Pressure drop and liquid holdup

The time averaged pressure drop was calculated over the last 50% of the pipe length. The predicted and experimental pressure drops are compared in Figure 2. We see that for the lowest velocity the model and experiments compare well. With increased flow velocity we see a consistent under-prediction of the pressure drop, not exceeding 30%. The under-prediction is quite systematic with a good qualitative trend.

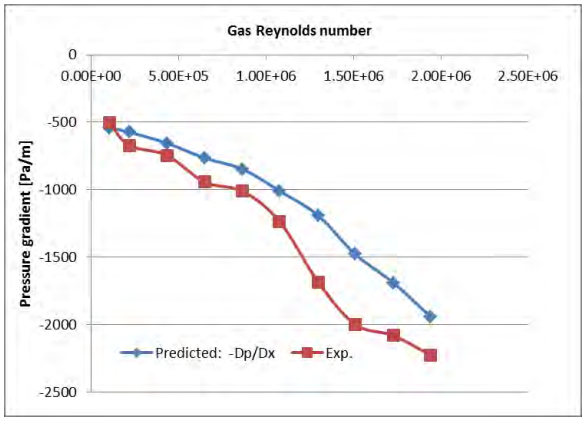

Figure 2 Predicted- and experimental pressure gradient versus gas Reynolds number.

One contribution to this discrepancy is the production of micro-bubbles which build up a significant population of small and rigid (surfactant effect) bubbles which in effect increases the apparent viscosity of the oil (Rønningsen, 2012). The contribution from these effects can only be sorted out by on-line measurements of the oil rheology.
The liquid holdup was calculated at a position 95% of the pipe length from the inlet. The results are shown in Figure 3, where we see that holdup is well reproduced for the entire velocity range. For the lowest gas Reynolds numbers we see some under-prediction of the liquid holdup. This can also be seen as an over-prediction of the gas velocity. The overall comparison is very good, both qualitative and quantitative.

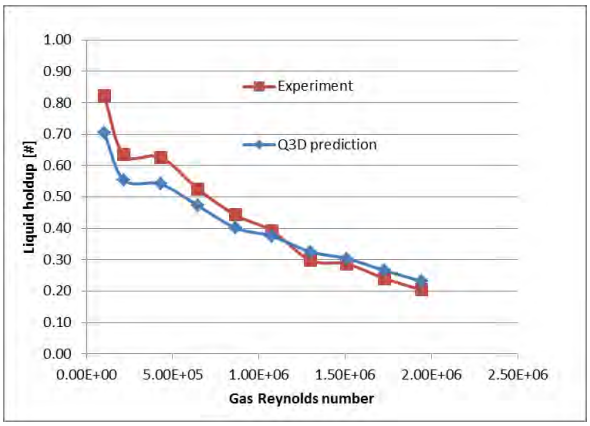

Figure 3 Predicted- and experimental liquid holdup versus gas Reynolds number.

Dynamic performance of the liquid holdup

The liquid holdup (fraction) was measured dynamically with a broad band gamma densitometer. In Figure 4 we see the comparison between the predicted- and experimental time traces of the liquid holdup, for all the cases, and where the ID codes refer to Table 1. We see that the two cases with lowest gas velocity have a typical slug type time trace. This is reproduced by the model, but the variations in the liquid fraction are larger in the predictions than in the experiments. In other words, the bubbles in the experiments are shallower than in the model.
With increasing gas velocities (moving upwards in the figure) the flow becomes more stratified, with lower amplitude oscillations in the liquid holdup. These trends are by large captured by the model. However, from the figure we have an indication that the Q3D model produces more large scale waves than observed in the experiment. We may note that for both experiments and simulations the data sampling interval is 0.1 sec. In the high gas velocity cases, such as he100671, the liquid velocity is approximately 5 m/s and only waves larger than 0.5 m are possible to resolve by the gamma densitometer (due to time averaging). However, the Q3D model reports the instantaneous results on the 20 mm grid. A better comparison would be to smooth the prediction results in the same manner as the gamma densitometer works. Then the simulation results would look smoother for the high flow rate cases.

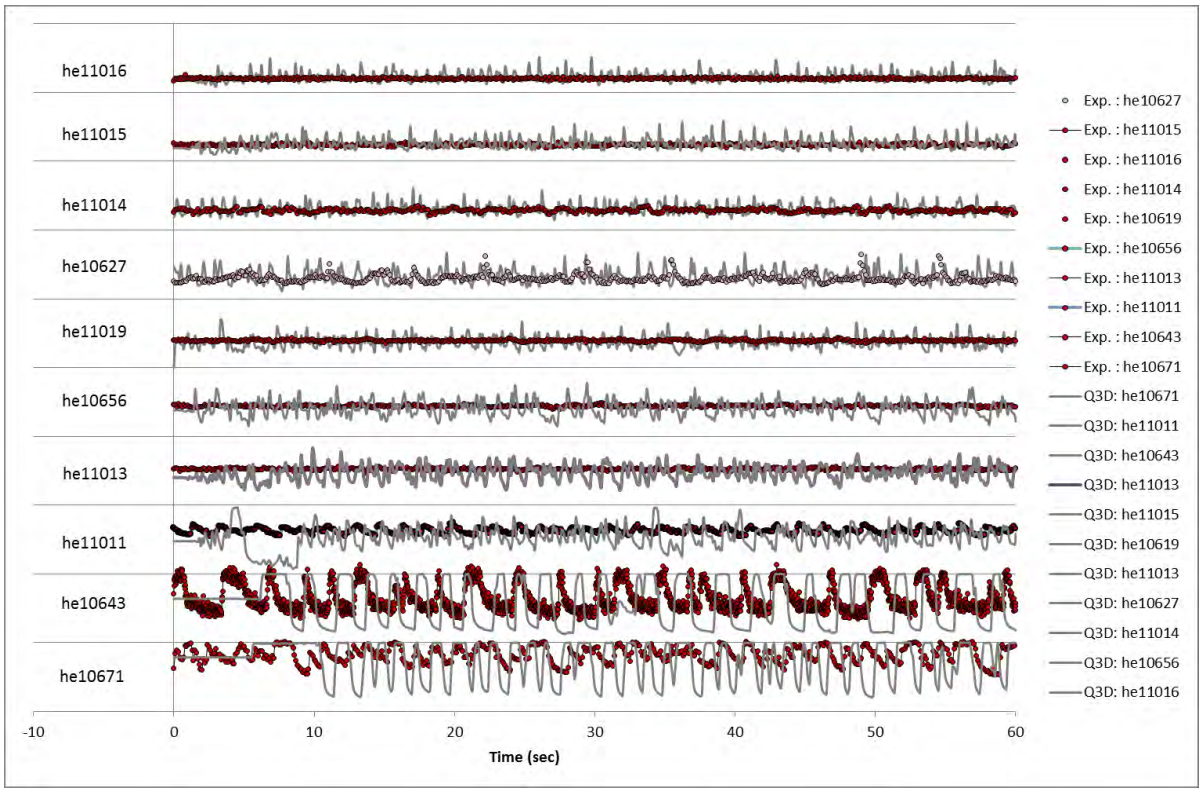

Figure 4 Predicted- versus experimental time traces of the liquid holdup for all 10 cases studied. The ID codes refer to Table 1. The gas velocity increases from bottom to top.

Flow structures and statistics

In Figure 5 to Figure 14 we show snap shots of the liquid distribution (red colour) for the different gas Reynolds numbers. Note that the diameter is increased by a factor four in the figures for visibility. Regions with yellow colour indicate high amounts (∼25%) of dispersed gas entrained into the liquid. Case IDs are defined in Table 1, and the gas velocity increases by increasing figure number. In addition the figures show the comparison between the experimental and predicted vertical distribution of the liquid. Note that for the experiments (blue lines) the scatter around the average liquid fraction is a combination of the variations on the physical volume fraction and the nature of the narrow band gamma instrument. The predicted profiles are extracted from position 95% of the pipe length (19 m).

What we see from the figures is that for the two lower gas flow rate cases (he10671 and he10643) the flow regime is slug flow. However, the predicted liquid profile does not agree well with the experimental liquid distribution in Figure 5, verifying that the predicted spreading of the large bubbles over the pipe cross section is not in accordance with the experiments. A main explanation for this is that our model is slice-averaged over the width of the pipe. The additional dispersion due to different velocities in the cross section is not included in the model. In turbulent flows this approximation is very good. However, in the present two cases the liquid is laminar and the reduced dispersion due to the dimension reduction has clearly some impact on the prediction. Still, both predicted pressure drop and holdup must be seen as acceptable.

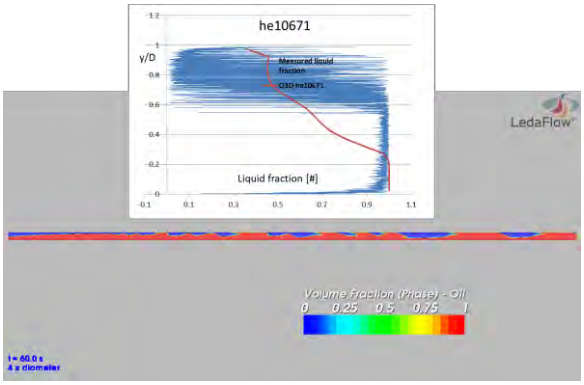

Figure 5 Case he10671: Snap shot of oil fraction. Insert shows predicted versus experimental ensemble averaged profile of vertical liquid holdup distribution.

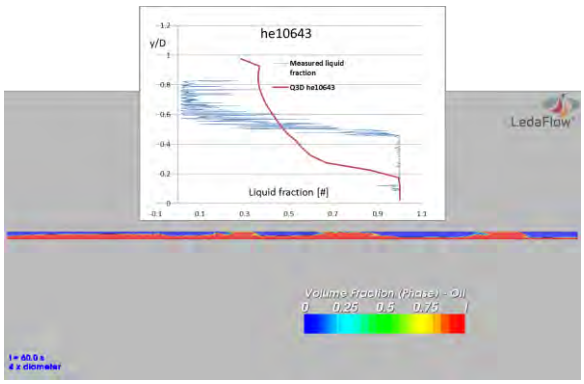

Figure 6 Case he10643: Snap shot of oil fraction. Insert shows predicted versus experimental ensemble averaged profile of vertical liquid holdup distribution.

For the cases he11011 to he10619 (Figure 7 to Figure 10) we see that our model is producing more waves than what can be supported from the traversing gamma holdup profiles. The reason for the relatively poor qualitative prediction of the liquid distribution seen in a case like he11013 is not clear. In an almost parallel experiment (he10648, not shown here) the predicted profile is much closer to the experiments. At the moment we do not have a good explanation why the experimental flow is much more stable than in the simulation. One possibility is that the effective friction at the Large Scale interface (LSI) is not accurate for this flow range, impacting the interface stability. At the same time the overall interface friction must be rather well reproduced due to the good prediction of liquid holdup. Understanding the combined role of droplet momentum exchange, wall and interface friction will need further investigations.

From case he10627 (Figure 11) and onwards (until Figure 12), we see that distribution of the liquid over the pipe cross section is rather well reproduced. For the three largest gas Reynolds numbers the comparison is very good. It is interesting to note that for these flow cases we have significant amounts of entrained bubbles (shown by the yellow regions).

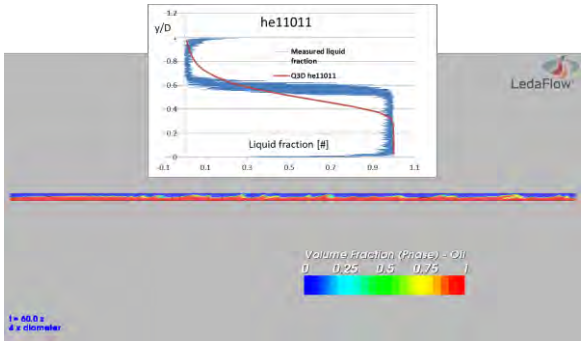

Figure 7 Case he11011: Snap shot of oil fraction. Insert shows predicted versus experimental ensemble averaged profile of vertical liquid holdup distribution.

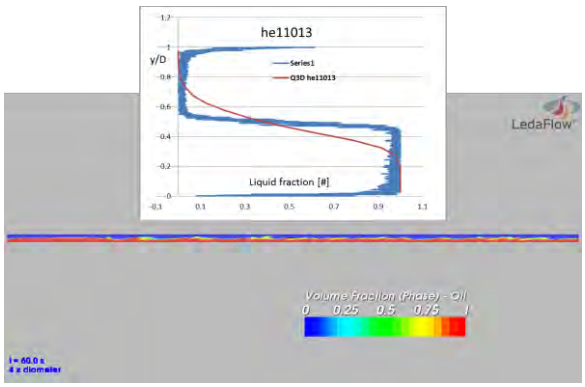

Figure 8 Case he11013: Snap shot of oil fraction. Insert shows predicted versus experimental ensemble averaged profile of vertical liquid holdup distribution.

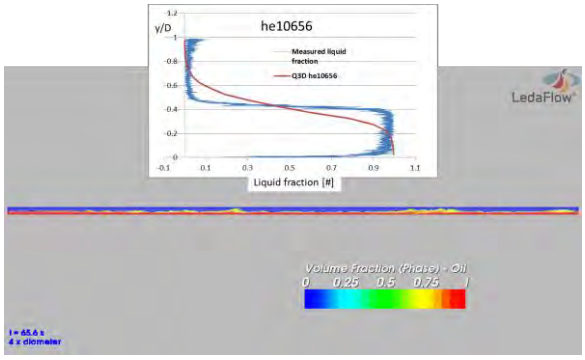

Figure 9 Case he10656: Snap shot of oil fraction. Insert shows predicted versus experimental ensemble averaged profile of vertical liquid holdup distribution.

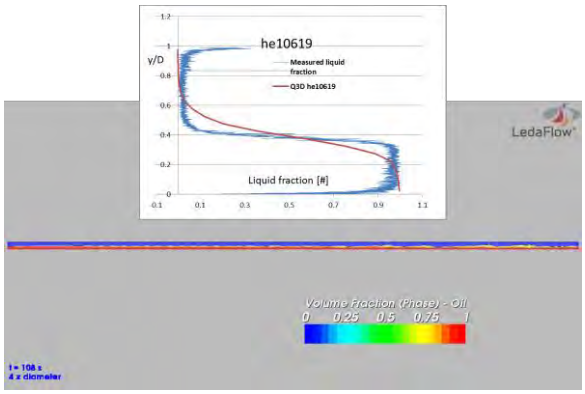

Figure 10 Case he10619: Snap shot of oil fraction. Insert shows predicted versus experimental ensemble averaged profile of vertical liquid holdup distribution.

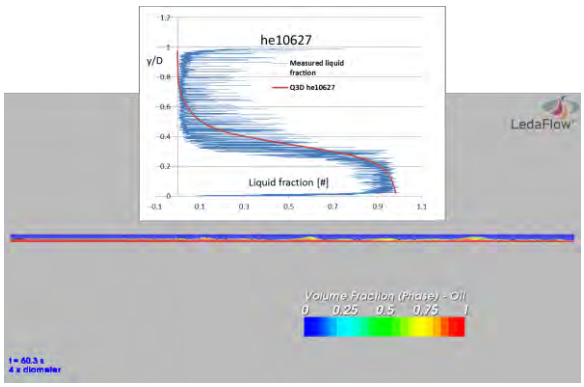

Figure 11 Case he10627: Snap shot of oil fraction. Insert shows predicted versus experimental ensemble averaged profile of vertical liquid holdup distribution.

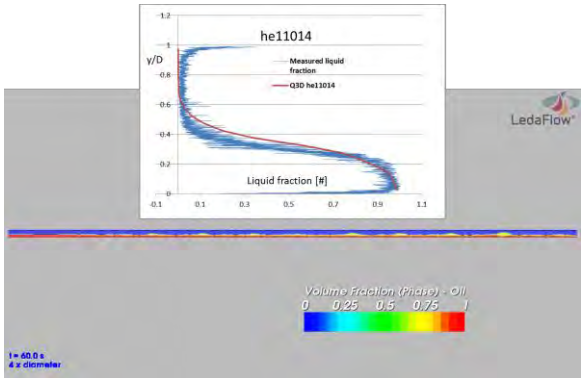

Figure 12 Case he11014: Snap shot of oil fraction. Insert shows predicted versus experimental ensemble averaged profile of vertical liquid holdup distribution.

Grid dependency

Introductory simulations with 15 and 20 grid points over the pipe cross section indicated that some improvements of the resolution of waves were achieved by going to 20 cells. The axial grid was tested at 500, 1000 and 2000 grid points. The 500 axial grid points led to suppression of waves. One case (he11014) was run using 2000 axial points. The predicted vertical profiles of the liquid holdup could not visually be distinguished from the case using 1000 point.

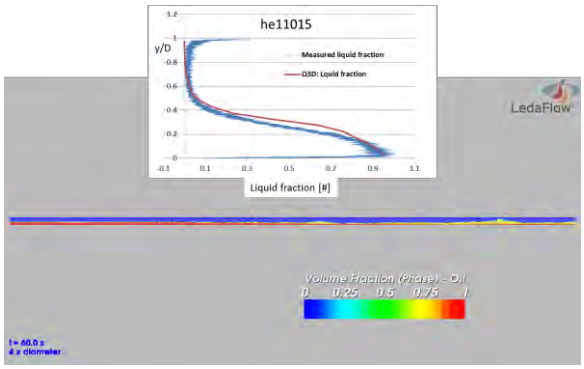

Figure 13 Case he11015: Snap shot of oil fraction. Insert shows predicted versus experimental ensemble averaged profile of vertical liquid holdup distribution.

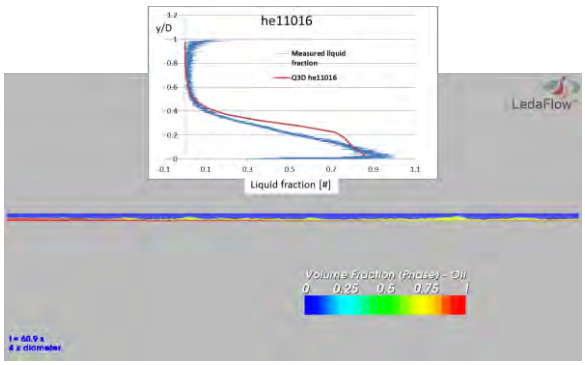

Figure 14 Case he11016: Snap shot of oil fraction. Insert shows predicted versus experimental ensemble averaged profile of vertical liquid holdup distribution.

Developed flow

The length needed to develop the flow depends on several physical phenomena, especially the entrainment and coalescence and separation of entrained bubbles. The development length will in general be longer at higher velocities since bubble coalescence time scales can be quite long. In general, the flow has been developed to a quite developed state, as seen in Figure 15. What we see here is representative for all the simulations. By doubling the length of the flow domain only marginal improvements can be expected.

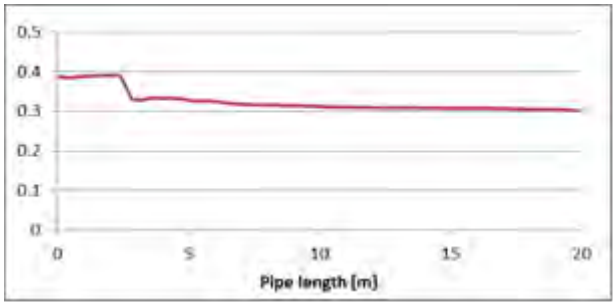

Figure 15 Time averaged liquid holdup versus length of simulated pipe (Case he11014).

CONCLUSIONS

Horizontal two-phase gas-liquid flow with a highly viscous liquid was simulated using a Quasi-3D flow model. Even if the model is reduced from 3D to 2D the prediction power of the model is good. The liquid holdup is very well predicted while the pressure drop shows a systematic under-prediction. Parts of this under-prediction may be due to an increased effective viscosity due to entrained micro-bubbles in the oil phase. Still the qualitative change in liquid holdup and pressure drop versus gas flow rate is very well reproduced, and the gas Reynolds number for transition between slug-flow and the stratified flow is predicted accurately.

From liquid holdup time traces and comparisons with the traversing gamma experiments it was found that during slug flow the bubble shape is not correctly reproduced by the model. This is a result of the

predominantly laminar flow in the liquid and strong variation in the liquid velocity within one computational cell (slice). In order to account for this effect a Taylor type dispersion mechanism must be included in the model. Even if the bubble propagation was not correctly predicted the quantitative prediction of pressure drop and liquid fraction was both better than $\pm 15\%$.

For the higher gas flow rates ($Re_g > 10^6$) it was found that the Q3D model predicts very well both the quantitative and qualitative flow behaviour.

It should be noted that the model was run without trying to improve on the model coefficients. With this in mind, it is clear that the Q3D model is capable of predicting viscous gas-liquid two-phase flows. Based on our findings we realize that the Q3D model has a significant potential to become a numerical laboratory for interpretation and extension of experimental data, and can in addition serve as a means to deduce closure laws for simplified 1D models.

A natural extension of this work is to investigate the performance of the Q3D model for inclined and vertical two-phase flows, and as a further step extend the investigation to three-phase flows. Already now we realize that access to high quality experiments including cross-sectional profiles will be crucial for such a development.

ACKNOWLEDGEMENTS

The financial support to the Leda Project, the long-time contributions from the Leda Technical Advisory Committee, as well as permission to publish, by Total, ConocoPhillips, and SINTEF are all gratefully acknowledged. Our colleagues Ernst Meese, and Runar Holdahl (SINTEF), Wouter Dijkhuizen and Dadan Darmana (Kongsberg Oil & Gas Technologies), Harald Laux (OSRAM Opto Semiconductors GmbH, Regensburg), and Alain Line (INSA, Toulouse) are acknowledged for their contributions to the development.

REFERENCES

ASHRAFIAN, A. & JOHANSEN, S. T. 2007. Wall boundary conditions for rough walls. *Progress in Computational Fluid Dynamics,* 7**,** 230-236.

BYE, J. A. T. & WOLFF, J.-O. 2007. Charnock dynamics: a model for the velocity structure in the wave boundary layer of the air-sea interface. *Ocean Dynamics,* 58**,** 31-42.

CHARNOCK, H. 1955. Wind stress on a water surface. *Quart J Roy Meteor Soc,* 81**,** 639-40.

ESKERUD SMITH, I., KRAMPA, F. N., FOSSEN, M., BREKKEN, C. & UNANDER , T. E. Year. Investigation of Horizontal Two-Phase Gas-Liquid Pipe Flow Using High Viscosity Oil: Comparison with Experiments Using Low Viscosity Oil and Simulations. *In:* 2011. BHR Group 2011 Multiphase 15, 2011 Cannes, France. BHR Group.

GOKCAL, B. 2005. *Effects of high oil viscosity on two-phase oil-gas flow*

behavior in horizontal pipes. Master of Science, University of Tulsa.

GOKCAL, B. 2008. *An experimental and theoretical investigation of slug*

flow for high oil viscosity in horizontal pipes. Ph.D. Dissertation,. PhD, The University of Tulsa.

LAUX, H., MEESE, E., JOHANSEN, S. T., LADAM, Y., BANSAL , K. A., DANIELSON, T. J., GOLDSZAL, A. & MONSEN, J. I. Year. Simulation of multiphase flows composed of large scale interfaces and dispersed fields. *In:* Int. Conf. Multiphase Flows, 2007 Leipzig.

LAUX, H., MEESE, E. A., MO, S., JOHANSEN, S. T., BANSAL, K. M., DANIELSON, T. J., GOLDSZAL, A. & MONSEN, J. I. Year. Multi-dimensional simulations of slug and slug-like flows in inclined pipes and channels. *In:* OTC 2008a Houston. 21-37.

LAUX, H., MEESE, E. A., MO, S., UNANDER, T. E., JOHANSEN, S. T., BANSAL, K. M., DANIELSON, T. J., GOLDSZAL, A. & MONSEN, J. I. 2008b. Multidimensional Simulations of Multiphase Flow for Improved Design and Management of Production and Processing Operation. *2008 Offshore Technology Conference.* Houston, Texas, U.S.A: SPE.

MO, S., ASHRAFIAN, A., BARBIER, J.-C. & JOHANSEN, S. T. Year. Quasi-3D modelling of two-phase slug flow in pipes. *In:* Ninth International Conference on CFD in the Minerals and Process Industries, CSIRO, 2012 Melbourne, Australia, 10-12 December

MO, S., ASHRAFIAN, A. & JOHANSEN, S. T. 2013a. Simulation of flow regime transitions in vertical pipe flow. *8th International Conference on Multiphase Flow, ICMF2013.* Jeju, Korea.

MO, S., ASHRAFIAN, A. & JOHANSEN, S. T. 2013b. Two phase flow prediction of fluid displacement operations. *8th International Conference on Multiphase Flow, ICMF 2013.* Jeju, Korea.

PATANKAR, S. V. 1980. *Numerical Heat Transfer and Fluid Flow,* New York, McGraw-Hill Book Company.

RØNNINGSEN, H. P. 2012. Rheology of petroleum fluids. *Annual Transactions of the Nordic Rheology Society,* 20**,** 11-18.

ZHANG, H.-Q., SARICA, C. & PEREYRA, E. 2012. Review of High-Viscosity Oil Multiphase Pipe Flow. *Energy & Fuels,* 26**,** 3979-3985.

ADDING ARGON INJECTION THROUGH THE DPM+VOF TECHNIQUE TO AN ADVANCED MULTI-PHYSICS AND MULTI-SCALE MODEL FOR CONTINUOUS CASTING OF STEEL

Pavel Ernesto RAMIREZ LOPEZ[1], Pooria Nazem JALALI[1], Ulf SJÖSTRÖM[1] and Christer NILSSON[2]

[1] Swerea MEFOS AB, Box 812, SE-971 25, Luleå, SWEDEN

[2] SSAB EMEA, SE-971 88, Luleå, SWEDEN

* E-mail: pavel.ramirez.lopez@swerea.se

ABSTRACT

An advanced numerical model able to predict transiently the multiphase flow, heat transfer and solidification in a Continuous Casting mould based on the Volume of Fluid Method (VOF) in combination with the tracking of bubble trajectories during argon injection through a Discrete Phase Model (DPM) is presented. This methodology allows studying the effect of Argon injection on process stability; particularly, it investigates the influence of the bubbles stream on steel/slag flow dynamics. Thus, different injection parameters such as bubble diameter and gas flow-rate were combined with specific casting practices to emulate industrial cases. As a result, the model makes possible the identification of stable or unstable flows within the mould under a variety of casting conditions (casting speed, nozzle submergence depth, etc.). Application to the industrial practice in a European Research Fund for Coal and Steel project is an ongoing task and preliminary results are illustrated. These results are fully applicable to explain the effect of gas injection on the behaviour of mould level fluctuations in the mould. Moreover, the predicted flow behaviour and bubble trajectories demonstrate good agreement with observed level changes, standing waves and gas departure positions observed on a physical model based on liquid metal and industrial observations. Ultimately, the increased process knowledge is used to optimize gas injection to provide a smooth distribution along the mould that benefits process stability. The robustness of the model combined with physical model observations make possible the description of phenomena difficult to observe in the caster, but critical for its performance and the quality of final products.

Keywords: Bubble dynamics, Argon injection, Discrete Phase Modelling, Volume of Fluid, Multiphase, Casting and solidification.

NOMENCLATURE

Greek Symbols

α Volume fraction
μ Dynamic viscosity
ρ Density
σ Surface tension

Latin Symbols

C Non dimensional coefficient
d Bubble diameter
g Gravity
Eo Eotvos Number
F Force
g Gravitational constant
p Pressure
T Temperature
u Velocity
V Volume

Sub/superscripts

b Bubble
D Drag
L Lift
VM Virtual mass

INTRODUCTION

Argon injection is used during continuous casting to improve the removal of inclusions, which are transported by the argon-bubbles stream to the slag bed; to be later assimilated in the liquid slag pool. A good deal of research has been done in this subject in the past 20 years, with mainly 2 numerical approaches to address the gas injection phenomena; namely Euler-Euler approach and Euler-Lagrangian approach (Cross, 2006; Díaz, 2008; Olmos, 2001). The Euler-Euler approach requires tracking of two different sets of equations, one for the *continuum phase* (i.e. steel) and one for the *dispersed phase* (i.e. argon). The phases are solved as non-interpenetrating, immiscible media with their own material properties (density, viscosity, thermal conductivity, etc.) (Zhang, 2006); thus, a complete set of flow equations (Navier-Stokes) is solved for each phase.

In contrast, in the Euler-Lagrangian approach; the fluid is treated as a continuum by solving the Navier-Stokes equations, while the dispersed phase is solved in a "superimposed" way by tracking the bubbles through the calculated flow field. The dispersed phase can exchange momentum, mass, and energy with the fluid phase; but the trajectories of bubbles or particles are computed individually at specific intervals (i.e. particle or flow time step) during the continuum phase calculation. Both methods have advantages and limitations. The Euler-Euler is very accurate and normally favoured for analyzing flow columns with high volumes of gas (i.e. slug or annular flows, where the calculation of individual bubbles cannot be resolved or is not of particular importance, Figure 1).

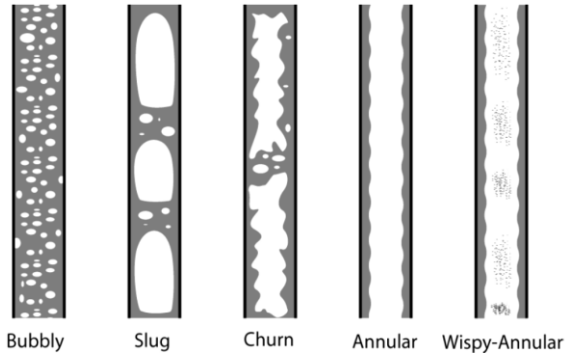

Figure 1: Different flow-gas regimes after Ghajar et al. (Ghajar, 2005).

On the negative side, the Euler-Euler method is already computationally expensive for 2 phases and becomes unrealistically time consuming for a multiphase system such as the continuous casting process where slag, metal and argon are present. In contrast, the Euler-Lagrange method allows individual tracking of the bubbles at lower gas fractions, but former versions of the model used to be inaccurate when the dispersed phase occupied a large volume fraction ($\propto_{gas} > 20\%$). However, improved versions of this approach are readily available in CFD codes such as FLUENT; which make possible to account for higher gas fractions. These are called Discrete Phase Model (DPM) and Dense DPM model(ANSYS-Inc., 2013). The DPM model allows more flexibility when coupled to other models such as turbulence, heat transfer and solidification. Moreover, DPM can be efficiently coupled to the Volume of Fluid (VOF) method to track the metal level (free surface) in a transient or steady mode. This VOF approach has been used successfully to track the evolution of the slag/metal interface on a model recently developed by the authors (Ramirez-Lopez, 2010; Ramirez Lopez, 2010). Nevertheless, the addition of a dispersed phase (argon) to the multiphase system (metal-slag) by DPM has not been tested before in CC modelling. Prior work has been done by Thomas et al. (Thomas, 1997) and Pfeifer et al. (Pfeiler, 2005) to use the DPM approach to simulate argon injection within the CC mould, but lacks the calculation of the free metal surface. Consequently, it was not possible to directly determine the effect of the gas on metal level stability or initial solidification at the meniscus. Recent application of the DPM technique combined with the VOF method to study metallurgical processes should be attributed to Cloete et al. (Cloete, 2009; Olsen, 2009) who applied the technique to analyze the stirring of steel ladles with argon. However, the slag phase is absent from the calculations. The use of the DPM+VOF technique in this work is based on such work, but has been extended to account for the slag phase. The fundamentals behind the DPM model can be found elsewhere and will not be reviewed in this manuscript. Instead, the present text is focused on the description of the modelling technique for adding argon injection to a multiphase-multiscale CC numerical model developed by the authors and validation of these predictions through experiments on a physical model with liquid metal and industrial observations.

BASE CONTINUOUS CASTING MODEL

The "base" CC model developed by the authors couples a multiphase steel-slag approach with heat transfer, mould oscillation and resultant solidification within the mould. The model uses the commercial code ANSYS-FLUENT v.14.5 to solve the Navier-Stokes equations together with the Volume of Fluid (VOF) method for calculation of the phase fractions (steel or slag) and the Continuum Surface Force (CSF) to account for surface tension effects in the meniscus (Brackbill, 1992; Liow, 2001). The κ-ε RNG turbulence model is used to capture flow turbulence, while heat transfer is solved through the Fourier equation. Heat extracted through the mould is calculated through a constant convection heat transfer coefficient based on the Nusselt number using typical water flow rates measured in the plants and a free stream temperature of 20°C. The heat flow through the slag bed is solved explicitly by addition of casting powder on top of the metal bulk and the calculation of the standard energy equation for a multiphase system on the VOF model. The boundary condition for powder feeding at the mould top depends on the industrial practice, being an air inlet if the slag bed does not fill the mould entirely; otherwise, a powder inlet is used. The slag-bed surface temperature measured with a thermal-camera is used as boundary condition at the mould top. Consequently, the thicknesses of the powdered, sinter and liquid slag layer are determined by the thermal conductivity of the slag as a function of temperature. Full details of the solution method have been published elsewhere (Ramirez-Lopez, 2010; Ramirez Lopez, 2010) and Figure 2 shows the boundary conditions used for the base model and argon injection. Predictions include the calculation of the metal flow pattern inside the mould, the metal level height (i.e. metal-slag interface) as well as the behaviour of slag in the bed. The withdrawal of the solidified shell drags liquid slag into the gap to produce a slag film (i.e. lubrication or infiltration). The interfacial resistance between the solid slag and the mould or contact resistance due to the slag film as described by Spitzer et al. (Spitzer, 1999) has been computed as a function of the powder's basicity (Ramirez Lopez, 2010). This process is affected by casting conditions such as mould oscillation, powder composition, mould level control, rim formation, etc. Metal flow pattern predictions are shown in Figure 2b. These reveal typical flow structures such as jet and rolls but also the formation of a standing wave at the meniscus resulting from the particular SEN design.

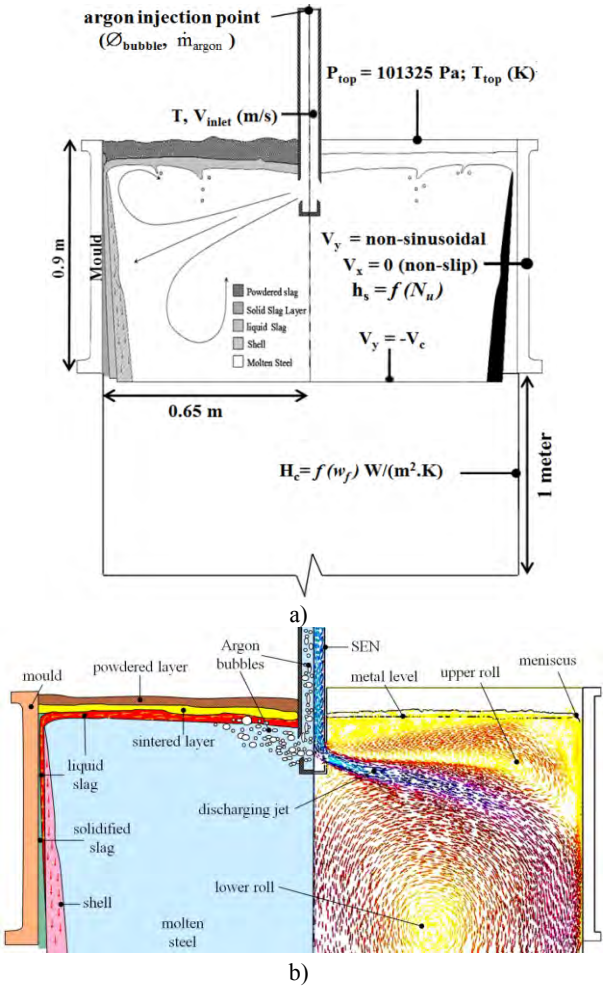

Figure 2: Numerical model for Continuous Casting, a) Boundary conditions used for base model and argon injection and b) Schematics of multiple phases present during casting (left) and typical metal flow predictions (right) after P.E. Ramirez Lopez et al. (Ramirez Lopez, 2013).

MODELLING ARGON INJECTION THROUGH THE DPM+VOF APPROACH

Although the fundamentals behind the DPM model can be found in the ANSYS-FLUENT v. 14 theory guide (ANSYS-Inc., 2013), some specific extra source terms (e.g. buoyancy, drag, lift, virtual mass and turbulent dispersion) were added as User Defined Functions (UDF's) (Cloete, 2009; Cloete, 2009; Olsen, 2009). Then, the momentum equation for the DPM model becomes:

$$\frac{du_b}{dt} = \frac{g(\rho_b - \rho)}{\rho_b} + F_D(u - u_b) + F_{VM} + F_L \qquad (1)$$

where u is the velocity in x, y or z axis; ρ and ρ_b are the density of the bulk flow and bubbles and F_D, F_{VM} and F_L are the source terms for drag, virtual mass and lift, respectively. The drag source term is defined as:

$$F_D = \frac{18\mu}{\rho_b d_b^2}\frac{C_D Re}{24} \qquad (2)$$

where $C_D = 0.666\sqrt{Eo/3}$, which is a function of the Eotvos number. The virtual mass and lift source terms are defined as:

$$F_{VM} = \frac{1}{2}\frac{\rho}{\rho_b}\left(\frac{\partial u}{\partial t} - \frac{\partial u_b}{\partial t}\right) \qquad (3)$$

$$F_L = C_D \rho_l V_b (u_l - u_g) \times (\nabla \times u_l) \qquad (4)$$

Different approaches have been used and a variety of experiments have been performed to determine the evolution of drag and lift for bubble columns and single bubbles (Tomiyama, 2004); however, such discussion is beyond the scope of this work. The present approach is based on a combination of coefficients as suggested by Olsen et al. (Olsen, 2009). Regarding turbulence, prior work has highlighted deficiencies on early κ-ε formulations for tracking bubbly flows since turbulence is scaled on mean flow gradients rather than bubble size (Johansen, 1988). The *random walk model* was used to address this issue. This approach is a type of "eddy lifetime" model that describes the effects of small-scale turbulent eddies on bubbly flows by using a Gaussian distribution for the turbulent fluctuating velocities and a characteristic timescale for the eddies (ANSYS-Inc., 2013). The bubble size is determined from experiments by Iguchi et al. (Iguchi, 1995), where diameter of gas bubbles in liquid iron was proven to depend on the inner diameter of the injection pipe for stagnant flow conditions. The robustness and accuracy of the DPM+VOF technique was validated by comparing to an experimental benchmark (Deen, 2001; Zhang, 2006). The benchmark consists of a quadrangular base column of water, where air is supplied at the bottom with a given velocity, mass flowrate, bubble size, etc. Details of the benchmark are presented on Figure 3.

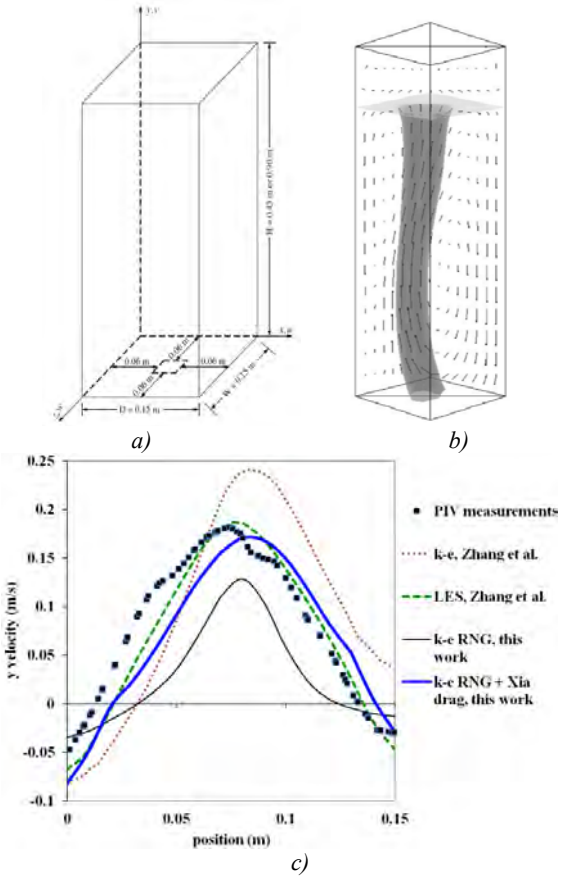

Figure 3: Bubble column experiment after (Deen, 2001; Zhang, 2006), a) Experiment dimensions, b) schematics of gas plume and c) Velocity comparison along a centreline at y=0.25 m for experiments and simulations by Zhang et al. (Zhang, 2006) and present model with DPM+VOF approach for different drag and turbulence conditions.

The main validation process consisted on predicting flow velocities along a transversal centreline (x axis) at different y positions (height positions); and compare them to the experimental benchmark. The DPM+VOF model showed good overall agreement at a transversal line; y=0.25m, when compared to PIV experiments in the benchmark, with a peak in positive $\boldsymbol{y}$ velocity (upwards) at the centre of the bubble column that decreases towards the exterior and switches to negative $\boldsymbol{y}$ velocity values (downwards) along the walls (Figure 3c). Furthermore, the standard spherical and non-spherical drag functions in FLUENT were compared to the VOF+DPM model with extra source terms added as UDF's (Figure 5). The spherical drag law provided closer results to experiments when compared to the non-spherical approach with 0.5 and 0.75 shape factor coefficients. However, native spherical and non-spherical laws still under predict the spreading of the bubble column (Figure 5a-left and centre). The addition of modified drag, lift and virtual mass forces provided a better agreement with the benchmark; with minor differences in velocity magnitude, but capturing satisfactorily the bubble column spread and overall intensity (Figure 5b). This is due to the fact that the built-in spherical and non-spherical produce a more closely packed column; whereas, the modified drag law provides a more realistic spreading of bubbles. Consequently, the combination of DPM+VOF with modified source terms was used as base to simulate argon injection within the mould during continuous casting.

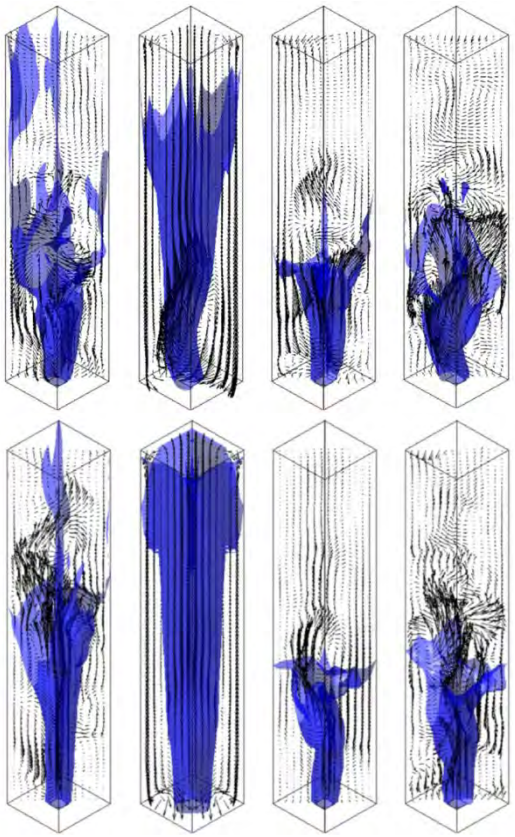

Figure 4: Comparison of bubble column spreading for different drag laws: a) Numerical simulations with several turbulence models after (Deen, 2001; Zhang, 2006).

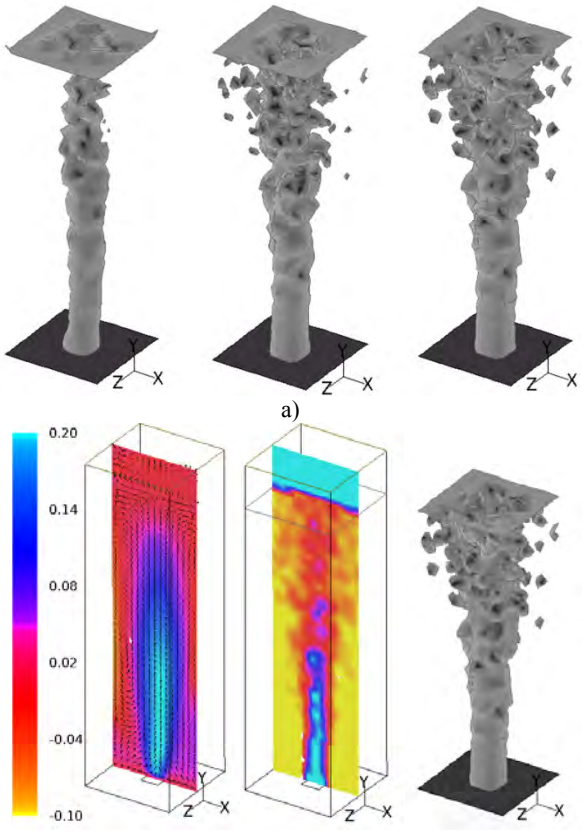

Figure 5: Comparison of bubble column spreading for different drag laws: This work with standard functions (from left to right): Non-spherical with shape factor=0.5, Spherical and Additional source term; b) Column velocities and spreading for additional terms case.

Once validated, the DPM technique was coupled to the "base" model developed previously by the authors. The model runs in transient mode until a stable flow is achieved (approximately 100-200 seconds after argon injection). This "stable period" is representative of the flow at a constant casting speed, fixed SEN immersion depth and constant cooling conditions (i.e. no casting speed ramping or SEN immersion depth changes). Boundary conditions for argon injection (DPM model) are as follows:

- Inlet: single point at the nozzle top-centre
- SEN walls and solid surfaces: reflection
- Mould top and outlet of numerical domain: escape
- Metal-slag interface and slag bed: not preconditioned (free transit between boundaries)

PRELIMINARY RESULTS AND VALIDATION

2D Simulations show that injected argon bubbles travel rapidly to reach the SEN ports (~2 s), while the bubble distribution along the SEN bore is considerably irregular along most of the nozzle height. However, before leaving the nozzle, the bubbles accumulate around the upper port and are dragged into the mould by the metal as it leaves the nozzle.

After leaving the port, the bubbles are entrained by the discharging jet for a distance clearly related to the bubble size and argon-flow rate. A variety of tests were carried out to compare FLUENT's built-in drag and numerical schemes (accuracy control, two-way turbulence coupling, tracking scheme selection, etc.), some of these predictions are shown in Figure 6.

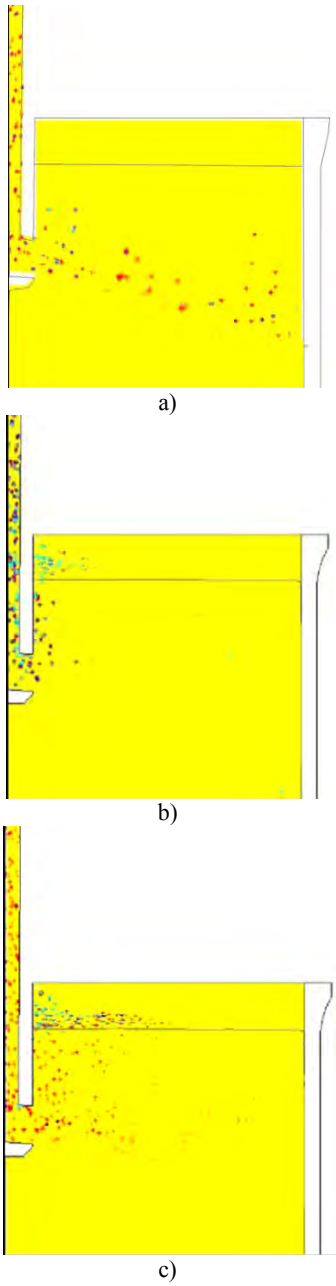

Figure 6: Fully developed bubble distribution for DPM+VOF model: a) DPM+VOF with Non-spherical-drag laws, bubble ∅=2000 µm, b) DPM+VOF with Spherical-drag laws, bubble ∅=2000 µm, and c) DPM+VOF with drag laws via UDFs', bubble ∅=2000 µm.

Results demonstrate clearly that the only approach producing a realistic spreading of bubbles is the DPM+VOF+additional UDF's approach (Figure 6c). In contrast, the non-spherical drag laws cause total entrainment of bubbles along the discharging jet (Figure 6a), whereas the spherical laws cause departure of most bubbles close to the nozzle (Figure 6b).

Simulations were performed to explore the influence of bubble size and different gas flow-rates in the calculations. For instance, Figure 7 shows the predicted velocity fields and bubble distribution for 4 and 5 lt/min at constant casting speed; which shows clear differences in bubble departure positions and flow behaviour. The 4 lt/min case produces a more even distribution of bubbles, which are entrained deeper into the melt by the discharging jet (Figure 7a). Thus, lower velocities close to the SEN are observed for the 4 lt/min case. In contrast, the 5 lt/min case leads to bubbles rising closer to the SEN due to coalescence and enhanced buoyancy and drag forces. Hence, bubbles leave "high velocity traces" when escaping the jet and reaching the surface. This creates higher departure velocities close to the SEN (e.g. dark red area adjacent to ports); and weakening of the discharging jet, which is also shorter and more distorted for the higher argon flow-rate (Figure 7b).

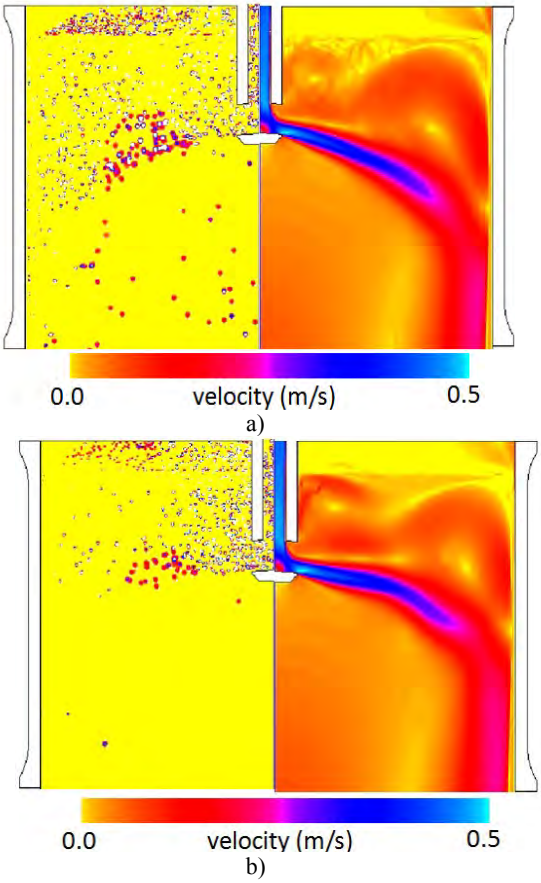

Figure 7: Simulated gas distributions and velocity fields for DPM+VOF model: a) Gas distribution for bubble ∅=4mm and 4 lt/min and b) Gas distribution for bubble ∅=4mm 5 lt/min.

This has deep implications when compared to the industrial praxis. Not incidentally, a transition from stable to unstable flow is detected when increasing the argon flow rate higher than 4.5 lt/min on industrial casters (which is the maximum gas flow rate employed by operators to avoid a "*boiling effect*" at the metal surface). Such *boiling effect* is known to be detrimental to mould level control due to unstable metal flows and produce more surface defects in the final product such as deep oscillation marks and cracks.

This effect is a limiting factor since higher argon flow rates are desirable to improve flotation of inclusions but not at the expense of process stability. A key point on the simulations is the use of slag as secondary phase for the VOF model with properties that make possible to distinguish between the liquid phase (slag pool), sintered layer and loose powder bed. The test runs with the improved model show that argon bubbles can reach the slag-metal interface, travel across it and exit the bed through the powdered layer with a corresponding change in bubble rising velocity through each of the slag layers due to viscosity changes (Figure 8).

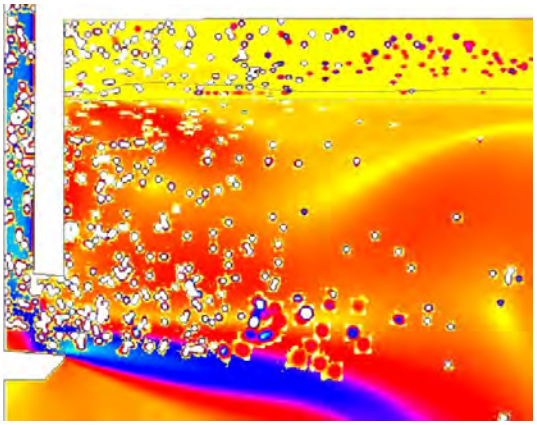

Figure 8: Argon bubble distribution and displacement through the slag-metal interface and through the slag with DPM+VOF embedded into existing CC model.

COMPARISONS WITH CASTING SIMULATOR (CCS-1)

Predictions of the average behaviour of the flow and bubbles once the flow stabilized were taken as basis for comparisons with a Continuous Casting Simulator (CCS-1) at Swerea MEFOS (Ramirez Lopez, 2012). Designed and built between 2004-2007 during a RFCS project (Higson, 2010), the model is equivalent to a continuous casting machine with tundish, stopper, Submerged Entry Nozzle (SEN) and mould. Hot metal is transported continuously from the tundish to the mould which is connected at the bottom to a heated tank/reservoir. A submerged pump sends the metal back from the tank to the tundish closing the flow loop (Figure **9**a). A low melting point alloy (58%Bi-42%Sn), is used as working media to simulate the steel flow. Such alloy was chosen due to its close resemblance on fluid properties to steel and its non-toxicity. Electrical properties of the alloy are also close to liquid steel, which make it an ideal candidate for testing Electro-Magnetic Stirring (EMS) or Electro-magnetic Breaking (EMBr) devices as well as Electromagnetic sensors. The alloy's melting point is approximately 135°C. Hence, temperature in the simulator is maintained within a few degrees to avoid solidification in the pump as well as ensuring a smooth flow control by a stopper, which is controlled through a laser system. The simulator can use replicas in stainless steel of the stopper/SEN or the actual ceramic versions used on real casters. Stable operation for casting speeds between 0.6 to 1.4 m/min for a mould 900 x 200 mm size can be achieved. Higher casting speeds (c.a. 1.5-1.8 m/min) are possible by scaling the mould. Argon is supplied through the stopper tip for testing injection up to 8 lt/min.

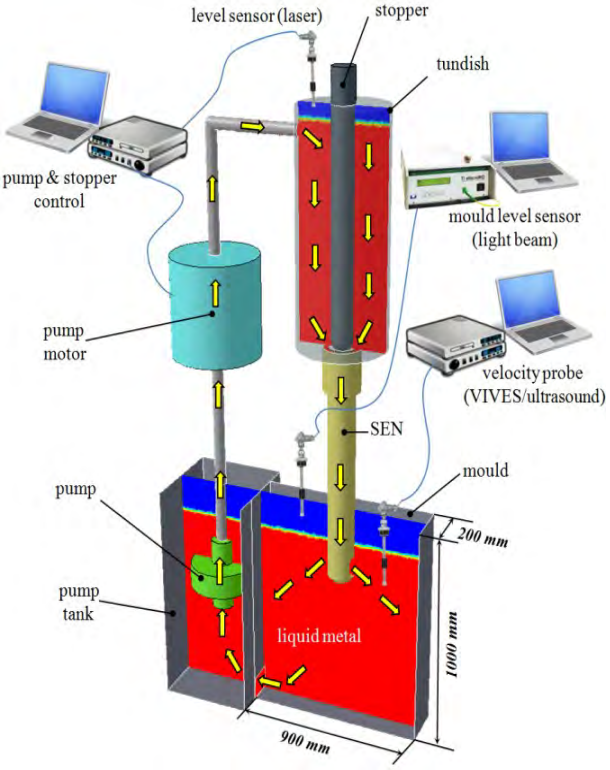

a)

b)

Figure 9: Continuous Casting Simulator CCS-1; a) Sensors and control schematics and b) Actual CCS-1 at Swerea MEFOS.

A variety of probes have been tested in order to find the most suitable tools to characterize the flow within the mould. Silicon oil was used to simulate the behaviour of

liquid slag on top of the melt, while argon was supplied through the stopper-SEN (Figure 10).

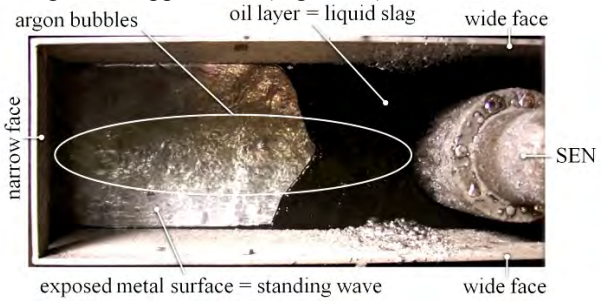

Figure 10: Top view of the metal level and oil simulating slag in CCS-1.

Observations of the metal level in CCS-1 at various flow-rates used typically during casting show that in all cases the bubbles have the following behaviour (Figure 10):

- Bubbles actually leave the metal bulk through the surface (opposite to results in Figure 6a).
- Bubbles are distributed along the whole metal surface (opposite to results in Figure 6b).
- Bubbles exit the metal surface along the whole mould width; with a higher amount bursting close to the SEN (in line with results on Figure 6c).

This demonstrates that the VOF+DPM approach with extra source terms is predicting realistically the behaviour of argon in the Casting Simulator and industrial practice. Furthermore, it is possible to deduct that the effect of higher argon flow-rates (e.g. from 4lt/min to 5lt/min) is an evident increase of instabilities in the mould due to bubble coalescence and augmented drag. In other words, the grouping of bubbles around the nozzle at higher argon loads would favour their collapse into larger bubbles, which offer a higher resistance to the discharging jet and reduce the number of smaller bubbles entrained deeper into the mould. This mechanism was observed by taking video sequences during tests in CCS-1 for the same argon flow rates: 4lt/min and 5 lt/min (Figures 11 and 12).

Figure 11: Video snapshots of the metal slag interface during argon injection tests at CCS-1 (taken every 10 seconds for a total time of 1 minute) for an argon mass flow rate=4 lt/min.

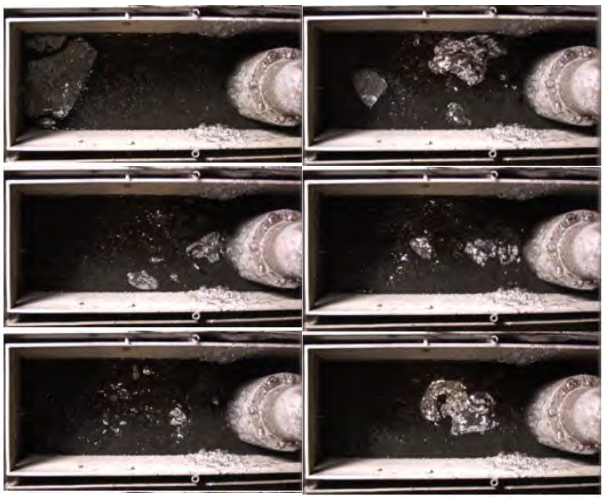

Figure 12: Video snapshots of the metal slag interface during argon injection tests at CCS-1 (taken every 10 seconds for a total time of 1 minute) for an argon mass flow rate=5 lt/min.

Differences in stability of the metal surface are easily noticeable by comparing the image-sequences. Lower argon flow rates produce a more stable flow pattern at the surface, with evidence of the well known "*double roll flow pattern*" (Ramirez-Lopez, 2005) (e.g. upper roll pushing constantly the oil layer towards the nozzle). In this case, argon bubbles depart uniformly along the mould width with smaller bubbles bursting closer to the narrow face; while slightly larger bubbles burst next to the SEN. In contrast, a higher argon flow rate produces an unstable metal surface (e.g. random oil distribution) with some medium size bubbles bursting at random positions and large bubbles exploding close to the SEN. Comparison between 2D numerical models and CCS-1 are only qualitative. Therefore, 3D runs were performed to analyse the bubble distribution along the metal surface in a full numerical model of CCS-1 (Figures 13 and 14).

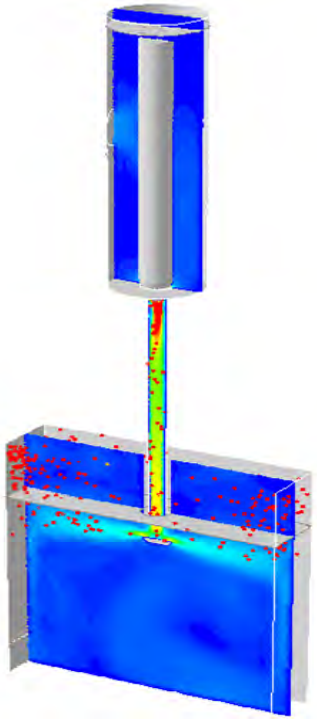

Figure 13: Numerical model of Continuous Casting simulator (CCS-1).

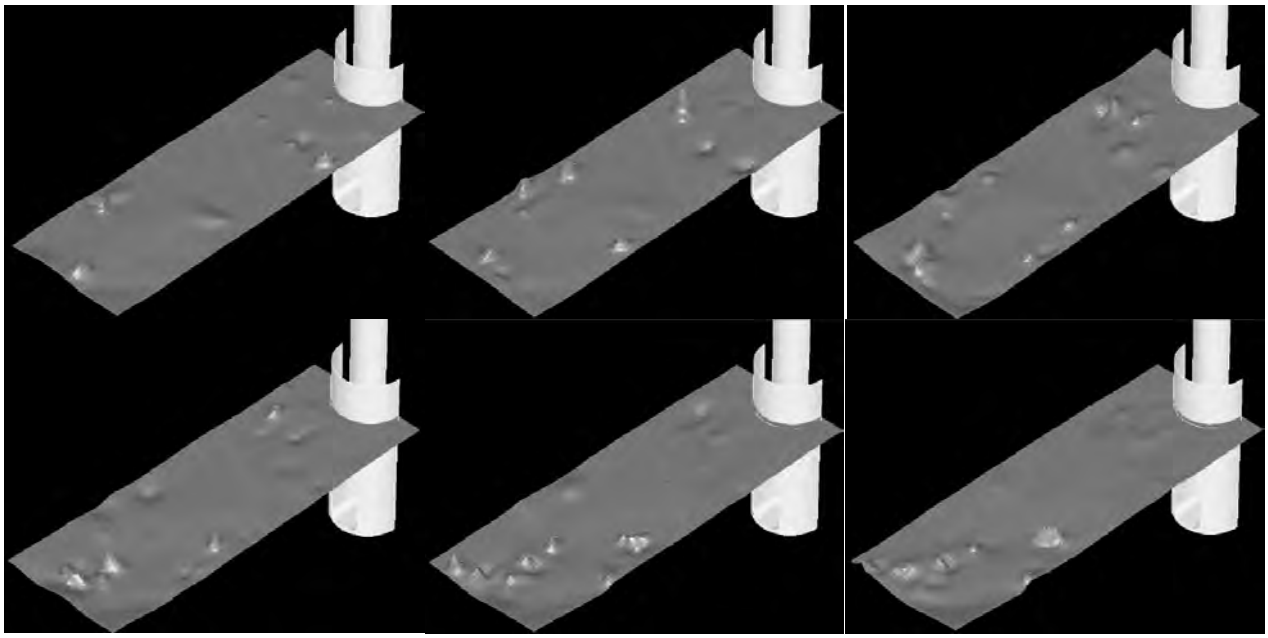

Figure 14: Snapshots every 0.5 s for a total of 3 s for 3D DPM+VOF model at 4lt/min and v_c=1.2 m/min.

Tracking of the bubbles bursting at the metal surface was performed by counting the number of bubbles departing at different positions along the mould thickness and width (Figure 14). Statistics after 100 seconds show that approximately 60% of the bubbles depart close to a central plane parallel to the wide faces; while the rest burst randomly closer to the mould walls. It was also observed than more than 50% of the bubbles depart burst close to the SEN. These observations are in line with experiments in CCS-1 and previous plant experiences. This demonstrates that the 2D model is not far from the 3D case as long as slight corrections to the argon flow rate and bubble frequency are performed. This has significant implications for nozzle design and finding optimal argon flow rates for improved process windows. Analysis of these effects are ongoing tasks by means of parametric studies, further tests in CCS-1 and plant trials in a EU funded project (Ramirez Lopez, 2013).

CONCLUSIONS

A numerical technique able to predict the multiphase (steel/slag) flow dynamics coupled with argon injection within the CC mould has been presented. The technique is based on the coupling of the DPM Lagrangian approach, which allows individual tracking of gas bubbles in a continuum phase; together with the Volume of Fluid method for calculation of free surfaces on multiphase flows. The model has been developed with the aim of analysing industrial practices (e.g. argon injection) by comparing results with physical modelling in a Continuous Casting Simulator (CCS-1) and industrial observations. The following conclusions can be drawn from the application of these models:

- The coupling of the DPM technique to an existing CC model based on the multiphase VOF method has proven possible. This includes predictions of the displacement of bubbles across the slag-metal interface and through the slag bed covering the melt.
- The modified DPM+VOF model with additional source terms is capable of describing realistically the distribution of bubbles as seen in the casting simulator and industrial practice.
- Both the numerical and physical models presented are capable of matching phenomena observed in the industrial practice such as the “boiling effect” at excessive argon flow rates and standing waves which are detrimental to process stability as well as the typical double roll pattern seen in most casters.

The combination of predictions with the model developed and observations in CCS-1 allow a deeper understanding of the mechanisms responsible for achieving stable or unstable flows during casting. Findings provide enough evidence to consider the DPM+VOF technique as reliable for analysis of argon injection in the Continuous Casting process.

ACKNOWLEDGEMENTS

PRL would like to thank operators at SSAB for fruitful discussions, Mr. Christer Olofsson for support during CCS-1 trials and Mrs. Pilvi Oksman at Aalto University for proof-reading the manuscript. PJ would like to thank Professor Pär Jonsson at KTH, Stockholm for continuing support during his M.Sc. and Doctoral studies. The research leading to these results has received funding from the European Union's Research Programme of the Research Fund for Coal and Steel (RFCS) under grant agreement n° [RFSR-CT-2011-00005].

REFERENCES

ANSYS-INC.: "ANSYS Fluent v.12 - User's Guide", *ANSYS Inc.*, (2013),

BRACKBILL, J.U., KOTHE, D.B.*, et al.*: "A continuum method for modeling surface tension", *J. Comput. Phys.*, **100** (1992), 335-54.

CLOETE, S., OLSEN, J.E.*, et al.*: "CFD modeling of plume and free surface behavior resulting from a sub-sea gas release", *Applied Ocean Research*, **31** (2009), 220-225.

CLOETE, S.W.P., EKSTEEN, J.J.*, et al.*: "A mathematical modelling study of fluid flow and mixing in full-scale gas-stirred ladles", *Progress in Computational Fluid Dynamics*, **9** (2009), 345-356.

CROSS, M., CROFT, T.N.*, et al.*: "Computational modelling of bubbles, droplets and particles in metals reduction and refining", *Applied mathematical modelling*, **30** (2006), 1445.

DEEN, N.G., SOLBERG, T.*, et al.*: "Large eddy simulation of the Gas–Liquid flow in a square cross-sectioned bubble column", *Chemical Engineering Science*, **56** (2001), 6341-6349.

DÍAZ, M.E., IRANZO, A.*, et al.*: "Numerical simulation of the gas–liquid flow in a laboratory scale bubble column: Influence of bubble size distribution and non-drag forces", *Chemical Engineering Journal*, **139** (2008), 363-379.

GHAJAR, A.J.: "Non-boiling heat transfer in gas-liquid flow in pipes: a tutorial", *Journal of the Brazilian Society of Mechanical Sciences and Engineering*, (2005),

HIGSON, S.R., DRAKE, P.*, et al.*: "FLOWVIS: measurement, prediction and control of steel flows in the casting nozzle and mould", **EUR 24205** (2010),

IGUCHI, M., CHIHARA, T.*, et al.*: "X-ray fluoroscopic observation of bubble characteristics in a molten iron bath", *ISIJ International*, **35** (1995), 1354-1361.

JOHANSEN, S.T., BOYSAN, F.*, et al.*: "Mathematical modelling of bubble driven flows in metallurgical processes", *Mathematical and Computer Modelling*, **10** (1988), 798.

LIOW, J.L., RUDMAN, M.*, et al.*: "A volume of fluid (VOF) method for the simulation of metallurgical flows", *ISIJ International*, **41** (2001), 225-233.

OLMOS, E., GENTRIC, C.*, et al.*: "Numerical simulation of multiphase flow in bubble column reactors. Influence of bubble coalescence and break-up", *Chemical engineering science*, **56** (2001), 6359.

OLSEN, J.E. and CLOETE, S.W.P.: "COUPLED DPM AND VOF MODEL FOR ANALYSES OF GAS STIRRED LADLES AT HIGHER GAS RATES", *Seventh International Conference on CFD in the Minerals and Process Industries,* (2009), Melbourne, Australia

PFEILER, C., WU, M.*, et al.*: "Influence of argon gas bubbles and non-metallic inclusions on the flow behavior in steel continuous casting", *Materials science & engineering. A, Structural materials*, **413-414** (2005), 115-120.

RAMIREZ-LOPEZ, P.E., LEE, P.D.*, et al.*: "A new approach for modelling slag infiltration and solidification in a continuous casting mould", *ISIJ International*, **50** (2010), 1797-1804.

RAMIREZ-LOPEZ, P.E., MORALES, R.D.*, et al.*: "Structure of turbulent flow in a slab mold", *Metall. Mater. Trans. B*, **36** (2005), 787-800.

RAMIREZ LOPEZ, P.E.: "Modelling Shell and Oscillation Mark Formation during Continuous Casting via Explicit Incorporation of Slag Infiltration", **PhD Thesis**, Imperial College London (2010), 170.

RAMIREZ LOPEZ, P.E., BJÖRKVALL, J.*, et al.*: "Development of a toolbox for direct defect prediction and reduction through the characterisation of the meniscus-slag bed behaviour and initial shell solidification in CC", European-Comission, **RFSR-CT-2011-00005** (2013),

RAMIREZ LOPEZ, P.E., BJÖRKVALL, J.*, et al.*: "Experimental Validation And Industrial Application Of A Novel Numerical Model For Continuous Casting Of Steel",*Ninth International Conference on CFD in the Minerals and Process Industries*, (2012), 1-6.Melbourne, Australia.

RAMIREZ LOPEZ, P.E., JALALI NAZEEM, J.*, et al.*: "Recent Developments of a Numerical Model for Continuous Casting of Steel: Validation and Industrial Application", *3rd International Symposium on Cutting Edge of Computer Simulation of Solidification, Casting and Refining (CSSCR2013). ,* (2013), Stockholm, SWEDEN and Helsinki, FINLAND.

RAMIREZ LOPEZ, P.E., LEE, P.D.*, et al.*: "Explicit modelling of Slag Infiltration and Shell Formation during Mould Oscillation in Continuous Casting", *ISIJ International*, **50** (2010), 425-434.

SPITZER, K., SCHWERDTFEGER, K.*, et al.*: "Laboratory study of heat transfer through thin layers of casting slag: Minimization of the slag/probe contact resistance", *Steel research*, **70** (1999), 430-436.

THOMAS, B.G., DENNISOV, A.*, et al.*: "Behavior of Argon Bubbles during Continuous Casting of Steel", *ISS 80th Steelmaking Conference,* (1997), Chicago, IL.

TOMIYAMA, A.: "Drag, lift and virtual mass forces acting on a single bubble", *Proc.Third Int. Symp.on Two-Phase Flow Modelling and Experimentation,* (2004), Pisa, Italy.

ZHANG, D., DEEN, N.G.*, et al.*: "Numerical simulation of the dynamic flow behavior in a bubble column: A study of closures for turbulence and interface forces", *Chemical Engineering Science*, **61** (2006), 7593-7608.

GOVERNING PHYSICS OF SHALLOW AND DEEP SUBSEA GAS RELEASE

Jan Erik OLSEN & Paal SKJETNE

SINTEF Materials and Chemistry, 7465 Trondheim, NORWAY

* E-mail: jan.e.olsen@sintef.no

ABSTRACT

A modelling concept for studying the resulting bubble plume from a subsea gas release is presented. Simulation results show good consistency with available experimental data. The modelling concept is applied to assess the importance of different physics and mechanisms assumed to influence the behaviour of the bubble plume. It is shown that buoyancy, drag, turbulent dispersion and gas dissolution are the governing mechanisms.

Keywords: subsea, gas release, Lagrangian, parcel, HSE, bubble plume, CFD

NOMENCLATURE

Greek Symbols

α Volume fraction [ ]
ρ Mass density [kg/m^3].
μ Dynamic viscosity [kg/m s]

Latin Symbols

C_D Drag coefficient[ ]
c Concentration [kg/m^3]
d Diameter [m]
$\boldsymbol{F}$ Force [N]
G Drag correction [ ]
k Mass transfer coefficient [m/s]
$\dot{m}$ Mass transfer rate [kg/s]
P Pressure, [Pa]
$\boldsymbol{u}$ Velocity, [m/s]

Sub/superscripts

B Buoyancy
b Bubbles
D Drag
i Species index
L Lift
l Liquid
PG Pressure gradient
sol Solubility
TD Turbuelent dispersion
VM Virtual mass

INTRODUCTION

Subsea gas release is caused by well blowouts, pipeline failures and other, and poses a threat to the safety of people and assets operating offshore. In order to perform risk assessments it is important to understand the quantitative impact of the gas release. Since realistic experiments are prohibitively expensive and potentially dangerous, quantitative models have been identified as interesting research tools.

Traditional integral methods (Fanneløp and Sjøen,1980) provide a good representation of the rising bubble plume if the model coefficients are tuned properly. However, the method yields limited results for the surface characteristics, which is a limitation since this is where the plume will interact with offshore structures, floating installations and ships. Multiphase computational fluid dynamics (CFD) provides greater generality since it is more fundamental and can, in principle, provide information on both the bubble plume and the surface behaviour. The computational cost of such models is significantly higher than the traditional integral models. However, it has been demonstrated that a 3D transient multiphase CFD model can be applied to the study of the ocean plume and the free surface behaviour (Cloete, *et al.*,2009).

A variety of forces and mechanisms influences the rising bubble plume. The significance of these mechanisms varies with gas rate and release depth. Some can be neglected and some must be accounted for. The study presented in this paper assesses the importance of the different mechanisms, and clarifies the governing physics of subsea gas release. Instinctively there is a suspicion that the governing physics might be different in a shallow and deep release. It is difficult to clearly define a shallow and deep release. Here it is linked to the length scales typical for offshore operations. We have chosen 30 meters to represent a *shallow* release and 300 meters to represent a *deep* release.

MODEL DESCRIPTION

An Eulerian-Lagrangian modelling concept has been developed to study subsea gas release. It is based on an Eulerian mixture model with interface tracking of the

ocean surface separating the ocean and atmosphere which constitutes two Eulerian phases, and Lagrangian tracking of the dispersed bubbles in the ocean. The Eulerian method with interface tracking is a VOF (volume of fluid) method, and the Lagrangian tracking method is a discrete phase model, i.e DPM. This is also known as a coupled DPM-VOF model (Cloete, et al.,2009).

The discrete phase model tracks the bubbles as parcels. Each parcel may consist of several bubbles. All bubbles within the same parcel share the same properties, i.e. equal density, diameter and more. This reduces the computational cost considerably since billions of bubbles can be represented by a reasonable amount of parcels. Without this feature, it would not have been feasible to study subsea gas release with Lagrangian bubble tracking. The bubble motion is governed by Newton's second law of motion stating that bubble acceleration equals the sum of all forces acting on the bubbles:

$$\frac{d\boldsymbol{u}_b}{dt} = \boldsymbol{F}_B + \boldsymbol{F}_D + \boldsymbol{F}_L + \boldsymbol{F}_{VM} + \boldsymbol{F}_{PG} + \boldsymbol{F}_{TD} \qquad (1)$$

Here we have listed contributions from buoyancy ($\boldsymbol{F}_B$), drag ($\boldsymbol{F}_D$), lift ($\boldsymbol{F}_L$), virtual mass ($\boldsymbol{F}_{VM}$), pressure gradient ($\boldsymbol{F}_{PG}$) and turbulent dispersion ($\boldsymbol{F}_{TD}$). These are the forces known to influence bubbles in a bubble plume. Note that these forces are normalized with bubble mass. In addition mass transfer due to dissolution of gas into the ocean is believed to have an important effect on the fate of bubbles resulting from the gas release. Gas dissolution is accounted for by the following expression for mass transfer rate

$$\dot{m}_i = -\pi\, d_b^2\, k_i \left(c_i^{sol} - c_i^l\right) \qquad (2)$$

where d_b is bubble diameter, k_i is mass transfer coefficient, c_i^{sol} is solubility concentration and c_i^l is bulk concentration of species *i*. We will limit this study to release of methane. The solubility data for methane of Lekvam & Bishnoi (1997) and the expression for mass transfer coefficient of Zhang & Zu (2003) are applied. The bubble size is modelled by a transport equation which is governed by turbulence (break-up and coalescence) (Cloete, *et al.*,2009).

The continuous phases , i.e. water and atmosphere, are mathematically described by the VOF model as mentioned above. Their motion is coupled to the bubble motion through the drag force which is implemented as an exchange term in the momentum equations. A standard k-ε model was initially assigned to the modelling concept (Cloete, *et al.*,2009). As in many implementations of the k-ε model the interphase between water and atmosphere is not recognized as boundary. In reality the ocean surface dampens turbulence since eddies can not be sustained over this interface. Due to this an enhanced implementation of the k-ε model has been developed. It includes a source term in the ε-equation which dampens turbulence at the surface and an additional source term in both equations due to the added buoyancy of density variations of a gas over large pressure variations (Pan, *et al.*,2013).

The modelling concept is implemented in the commercial software ANSYS/Fluent 14.5 via several user defined functions. The model has been compared against data from a series of controlled experiments where gas was released in a rectangular basin with a depth of 7 meters and a surface area of 6 x 9 meters (Engebretsen, *et al.*,1997). Air was released at the bottom at 3 different gas rates, of which the middle gas rate of 170 Nl/sec had the most complete set of results presented. Thus we have compared results from model simulations and experiments at this gas rate.

In Figure 1 we see the water velocity close to the water surface as a function of height above basin floor. Results from simulation performed with the standard and enhanced k-ε model are seen. Close to the surface the enhanced model has significantly better consistency with the experimental results than the standard model. Further down into the water, there is less discrepancy between the models. This is as expected since the enhancement primarily applies to the surface region. Figure 2 shows the velocity profiles at different elevations above the basin floor for both modelling and experimental results. Only data for the enhanced k-ε model are shown since the standard model produced almost equal results. We see a good agreement between model and experiments for the velocity profiles at the lower elevations (1.75 and 3.80 m). There is some discrepancy at the highest elevation (5.88 m). This is believed to be caused by an error in the flow measurements. Höntzsch turbine flow meters were applied. They are optimized for mono-directional flow, but for the bending flow close to the surface they will overpredict the flow velocity.

In these release scenarios gas dissolution has no effect due to the shallow depth and short residence time of the bubbles. The implemented model for mass transfer and gas dissolution have however been validated against experiments with good consistency in a separate study (Skjetne and Olsen,2012).

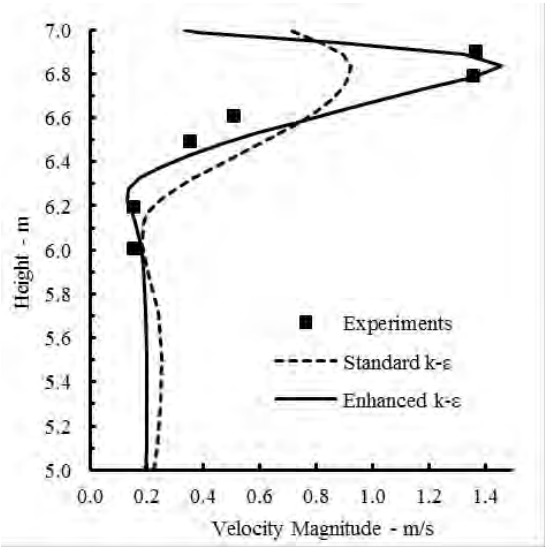

Figure 1**:** Velocity magnitudes near water surface for a gas rate of 170 Nl/s as a function of height above basin floor at a location 1.75 meters from plume centre. Models are compared with experiments.

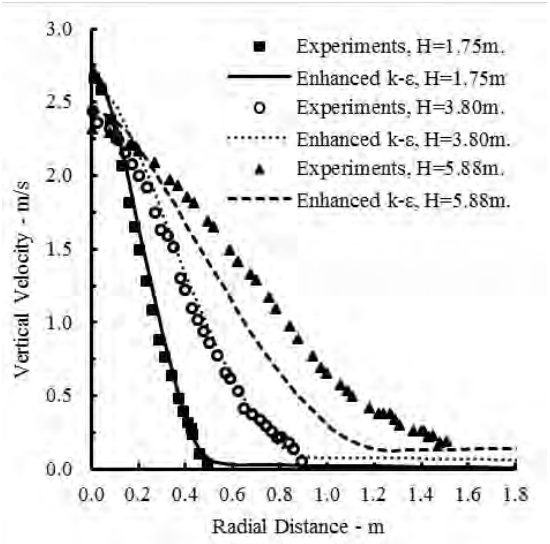

Figure 2**:** Plume velocity at 3 different elevations for a gas rate of 170 Nl/s. Model and experiments are compared.

SENSITIVITY ASSESSMENT

In the following we present results on sensitivity analyses on different physics assumed to affect the behaviour of a subsea gas release. Since buoyancy is the driving force of the plume, it always has to be accounted for. Drag forces are responsible for the coupling between the dispersed bubble phase and the continuous water phase and should thus not be neglected. The lift force has previously been shown to have a negligible effect on the bubble plumes associated with a subsea gas release (Olsen and Cloete,2009). Thus sensitivity to buoyancy, drag and lift will not be considered here. The effect of other forces and mechanisms are assessed in the following. In the assessment we will primarily focus on the vertical velocity along the centreline from ocean floor to ocean surface (i.e. plume axis).

Gas Expansion

Gas density is a function of pressure and temperature. The density increases with increasing pressure (i.e. depth). Thus the gas expands as the bubbles rise towards the surface. For low pressure this can be expressed by the ideal gas law, but the true density variation is more complex. Here we have applied the ideal gas law due its simplicity. In reality the true density deviates from the ideal gas laws at greater depths, but for a sensitivity analysis we assume that it is a valid assumption.

The effect of gas expansion can be assessed by comparing simulation results between expanding gas and gas with constant density. However, it is difficult to know which constant density to compare against. Here we have compared against bottom density (maximum), top density (minimum) and average density. In Figure 3 we see the effect of different density specifications on the vertical liquid velocity along the plume axis for a release from 30 meter at 10 kg/s. The results are taken after quasi steady state is reached. The height above the ocean floor (y-axis) is normalized with respect to ocean depth. This might exceed the value of 1 if the release is strong enough to sustain a fountain. We see that the velocity based on minimum and maximum densities deviate significantly from the velocity based on density from the ideal gas law. The average density is on average equivalent to the ideal gas law. However, it will give bad estimates of velocities close to the release zone. Note how the constant density approximations seem to decelerate the flow compared to an expanding gas. This tells us that gas expansion has an accelerating effect on the flow which is explained by the increasing buoyancy as gas density decreases during the ascent of the bubbles. In Figure 4 we see the same comparison for a release from 300 meter at 100 kg/s. The trend is the same as for the release from 30 meter, but not as pronounced. There are two reasons for a less pronounced effect of gas expansion. First there is significantly more gas dissolution at higher gas rates leaving less gas to expand. Secondly most gas expansion occurs close to the surface, and the surface region is less dominating in a deep release compared to a shallow release. Still the rise velocity is significantly affected by gas expansion. In addition other indicators such as total gas dissolution, plume spreading and more is affected when neglecting gas expansion (not shown here). Thus gas expansion needs to be accounted for.

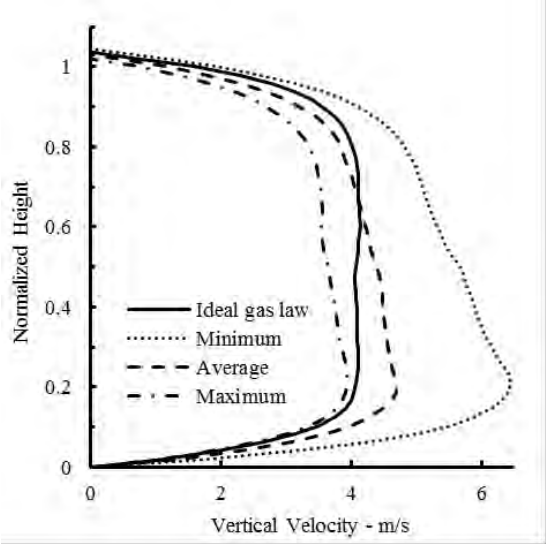

Figure 3: Effect of gas density on vertical velocity for a release from 30m at 10 kg/s.

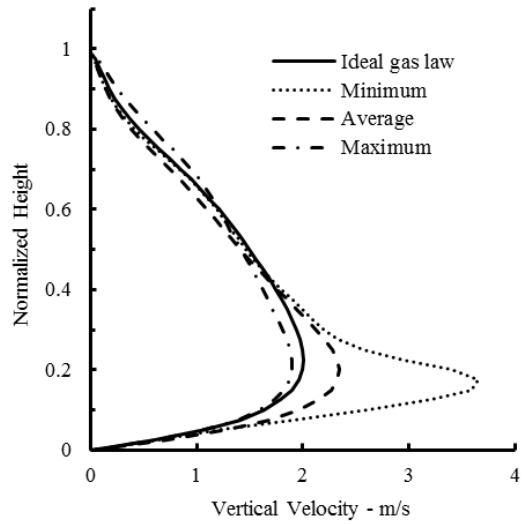

Figure 4: Effect of gas density on vertical velocity for a release from 300m at 100 kg/s.

Turbulent Dispersion

Turbulent dispersion is dispersion of bubbles, droplets and particles due to turbulence. In principle it is a drag force based on the fluctuating contribution to the instantaneous velocity. The standard drag force only accounts for the mean contribution, whereas the particle in reality is exposed to the instantaneous velocity. There are several models describing turbulent dispersion. We apply the random walk model (Gosman and Ioannides,1983) which is frequently used in Lagrangian tracking.

In Figure 5 we see how the vertical velocity varies from ocean floor to surface along the vertical centreline from the release point. Figure 5 shows results from simulations were turbulent dispersion has been neglected and accounted for. The results clearly demonstrate that there is a significant effect of the turbulent dispersion. Turbulent dispersion yields a lower vertical velocity due to lateral dispersion of bubbles. This is also illustrated in Figure 6 where we see that turbulent dispersion is responsible for the widening of the plume and hence the so-called *plume angle*. It is quite clear that turbulent dispersion can not be neglected.

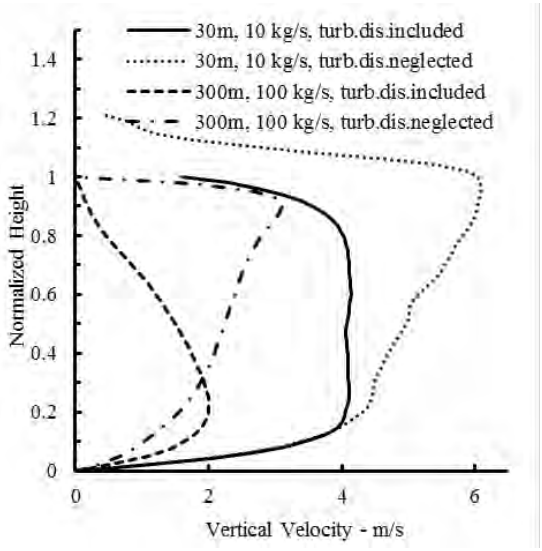

Figure 5: Effect of turbulent dispersion on vertical velocity.

Figure 6: Plume shape coloured by gas density for simulation with neglected (left) and included (right) turbulent dispersion.

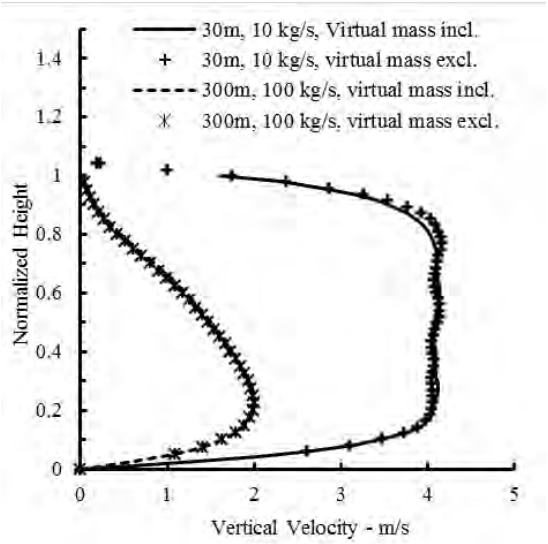

Figure 7: Effect of virtual mass on vertical velocity.

Virtual Mass

The virtual mass force is the force required to accelerate the fluid surrounding the particle. It is expressed by

$$\boldsymbol{F}_{VM} = \frac{1}{2}\frac{\rho_l}{\rho_b}\left(\frac{D\boldsymbol{u}_l}{Dt} - \frac{d\boldsymbol{u}_b}{dt}\right) \qquad (3)$$

Simulations including and neglecting the virtual mass force have been performed. The resulting vertical velocity along the plume axis is shown in Figure 7 for both shallow and deep release. We see that the virtual mass force has very little influence on the results, and it could be neglected.

Pressure Gradient Force

The pressure gradient force is the hydrodynamic force acting on the bubbles due to the pressure gradient in the surrounding liquid. Mathematically it is expressed by

$$\boldsymbol{F}_{PG} = \frac{\rho_l}{\rho_b}\boldsymbol{u}_b \nabla \boldsymbol{u}_l \qquad (4)$$

Results from simulations including and excluding the pressure gradient force are seen in Figure 8 and Figure 9. They show that the effect of the pressure gradient force can be neglected with respect to the vertical velocity along the plume centre axis.

The pressure gradient force could in principle have a more pronounced effect closer to surface as its nature typically affects a bending flow which is present at the surface. The horizontal velocity profile along the ocean surface was thus also assessed. The effect of the pressure gradient force was not detectable.

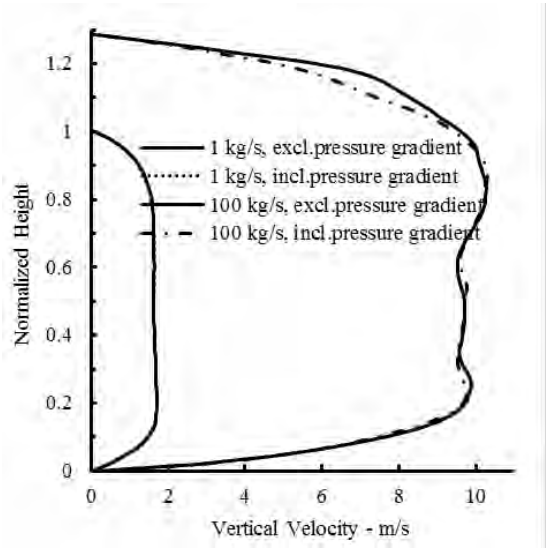

Figure 8: Effect of pressure gradient force on vertical velocity for release from 30 meter.

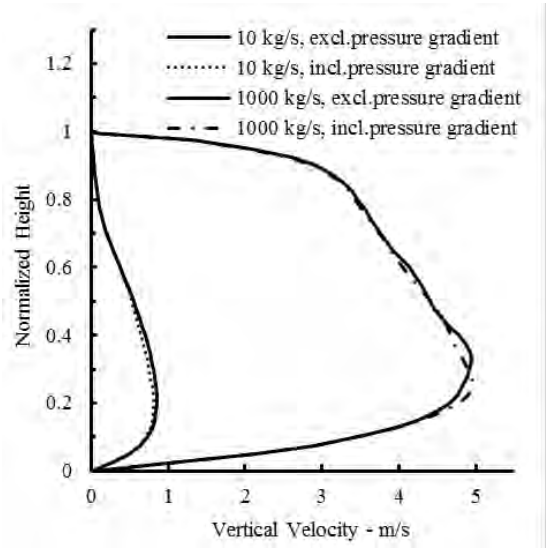

Figure 9: Effect of pressure gradient force on vertical velocity for release from 300 meter.

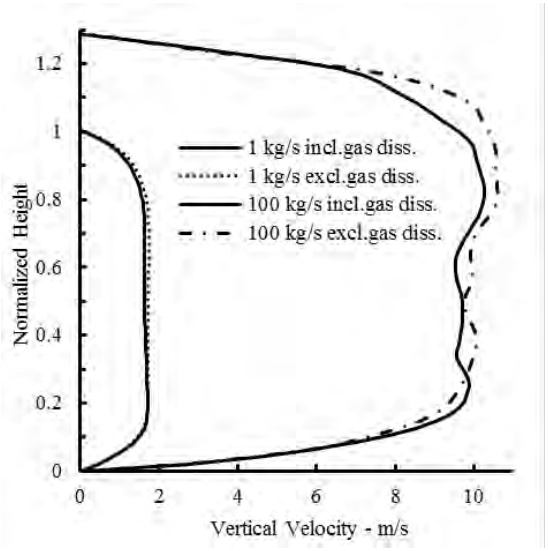

Figure 10: Effect of gas dissolution on vertical velocity for release from 30 meter.

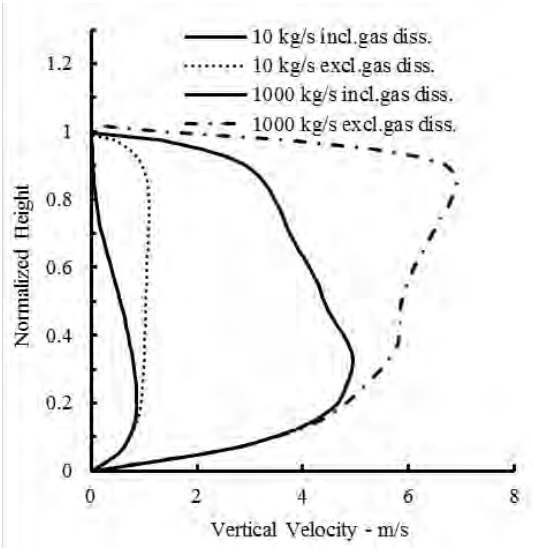

Figure 11: Effect of gas dissolution on vertical velocity for release from 300 meter.

Gas Dissolution

Gas dissolution transfers mass from bubbles to the ocean and reduces the buoyant potential of the bubble plume. Thus gas dissolution will decrease the amount of gas reaching the surface and reduce the vertical velocity. Gas dissolution increases with residence time and is thus expected to have a greater impact on a deep release than on a shallow release.

Simulations show that for a shallow release (depth of 30 meters) the effect of gas dissolution on the vertical velocity is practically negligible. This is seen in Figure 10 where vertical velocity is plotted along the plume centre axis for low and high gas rates with and without gas dissolution activated. For a release from 300 meter gas dissolution is significantly affecting the vertical velocity as shown in Figure 11. Gas dissolution results in a reduced vertical velocity. The trend is increasing towards the surface. This explained by the loss of buoyancy as gas is increasingly dissolved into the ocean as bubbles rises towards the surface. Thus gas dissolution decelerates the plume.

Based on the above it might be tempting to conclude that gas dissolution is insignificant for shallow releases. However, there are more aspects to the plume characteristics than the vertical velocity. The amount of surfacing gas is of even greater importance. When neglecting gas dissolution all released gas will reach the ocean surface. When accounting for gas dissolution, some gas is dissolved in the ocean. The amount of surfacing gas for the cases studied is seen in Table 1. We see that even for a shallow release, gas dissolution reduces the amount of surfacing gas. For some gas rates for a release from 300 meters, all gas is dissolved. The data in Table 1 supports that gas dissolution impact increases with depth and decreases with gas rates. This is explained by the fact that gas dissolution correlates strongly with residence times of bubbles in the ocean.

Table 1: Surfacing gas rates in kg/s with relative surfacing rate in parentheses.

Depth [m]	Release rate [kg/s]			
	1	10	100	1000
30	0.5 (50%)	7.45 (75%)	96.0 (96%)	-
300	-	0 (0%)	0 (0%)	195.6 (20%)

Drag Coefficient

Many correlations for the drag coefficient exist. A widely recognized set of correlations for bubbles was published by Tomiyama et.al. (1998). The drag coefficient varies with respect to Reynolds and Eotvos number and the correlations depend on whether the bubbles are rising in clean or contaminated water. Note that Tomiyama's correlations are only valid for dilute plumes. For denser bubble plumes the drag coefficient also depends on the void fraction α. This can be adjusted for by a correction factor as in

$$C_D = G(\alpha) C_{D0} \tag{5}$$

where C_{D0} is the drag coefficient for dilute flows and $G(\alpha)$ accounts for increased drag due to hindered settling and/or decreased drag due to acceleration of trailing bubbles. Roghair et.al. (2013) developed a correlation for bubbles neglecting coalescence and break up. This is related to hindered settling observed in particle flows. Tsuji et.al. (1982) published a correlation accounting for acceleration of trailing bubbles. These correction factors for high void fractions have opposite effects. This is shown in
Figure **12**. Roghair's correlation depends on bubble size (actually on Eotvos number), and plots for two bubble sizes are given. Based on this we expect lower slip velocities and higher rise time with the correlation of Roghair.

The effect of these correction factors have been assessed by numerical simulations. In Figure 13 and Figure 14 we see that the vertical velocity is not affected by the drag correction. Comparison of rise time and surfacing gas rates (not shown) also indicate that there is no significant effect of the drag correction factor. At lower gas rates the void fractions are low, and both corrections are small. At high gas rates, the slip velocity is small compared to the total velocity and thus the effect of void corrections is not significant. Note that Tsuji's correlation is used by default.

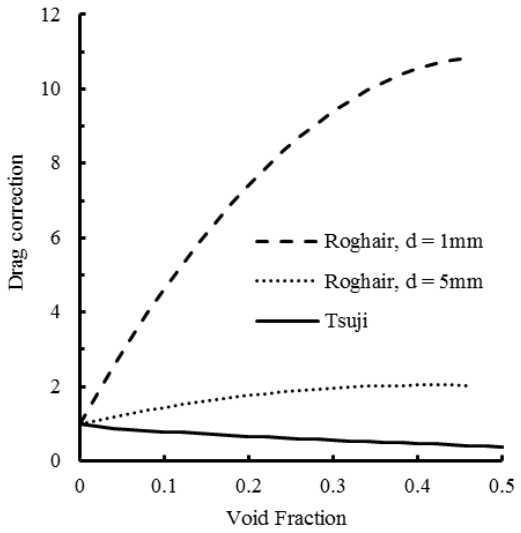

Figure 12: Drag correction *G* as function of void fraction for correlations of Roghair and Tsuji.

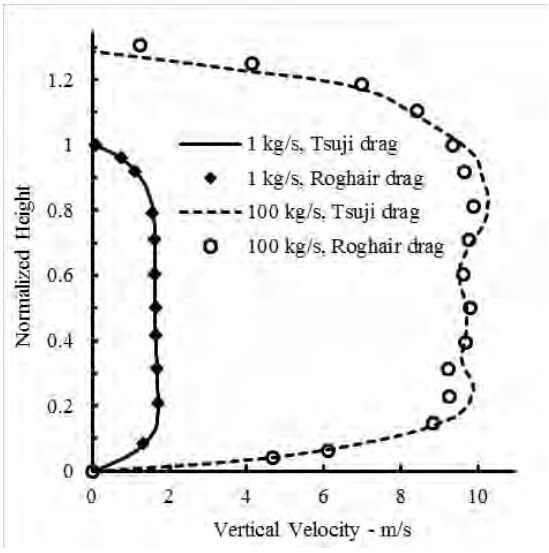

Figure 13: Effect of drag correction on vertical velocity for release from 30 meter.

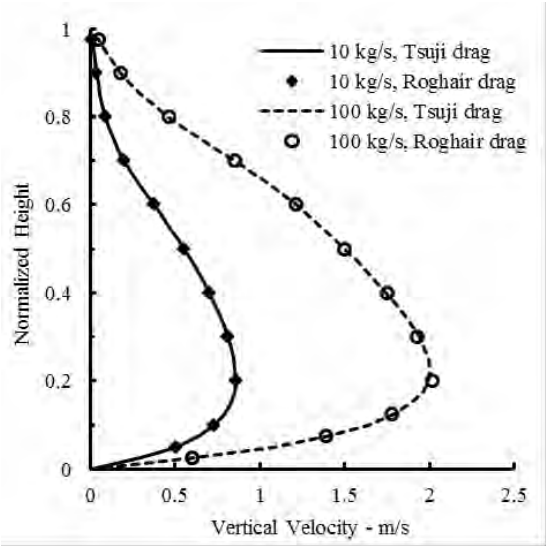

Figure 14: Effect of drag correction on vertical velocity for release from 300 meter.

Bubble Size

Bubble size is important for slip velocity and mass transfer rates. By default bubble size is governed by a bubble size model. However, to assess the sensitivity of the model with respect to bubble size the bubble size model was disabled and the bubble diameter was fixed at 1mm and 3mm for chosen release scenarios. The resulting vertical velocity along the plume axis is seen in Figure 15 and Figure 16. For releases from 30 meters there only seems to be an effect of bubble size close to the ocean surface. This is probably due to the effect of mass transfer which only becomes noticeable after a certain residence time of the bubbles. For the releases from 300 meters (Figure 16) we see a more pronounced effect. For the lower gas rate the smaller bubbles causes lower vertical velocity due to higher mass transfer and the resulting loss in buoyancy. At higher gas rates (1000 kg/s) there seems to be some kind of pulsations in the bubble plume which is not present when the default bubble size model is enabled. Reasons for this have not been investigated. Also here we see that on average the smaller bubbles give the lowest vertical velocity. The effect is significant.

In Table 2 we see the surfacing gas rate and the corresponding radius of the surfacing zone. The radius is defined by the area surrounding the zone releasing 98% of the gas. The trend is that smaller bubbles yield less surface gas and a narrower surfacing zone. However, the effect of bubble size on surfacing characteristics is not as pronounced as for vertical velocity. This is most likely due to counteracting mechanisms. Smaller bubble size gives higher total surface area for mass transfer, but it also gives lower slip velocity, mass transfer coefficient and residence time. It might be tempting to conclude that surface characteristics is not sensitive to bubble size, but due to the complexity in the interactions of different mechanisms more scenarios needs to be studied before a solid conclusion can be made.

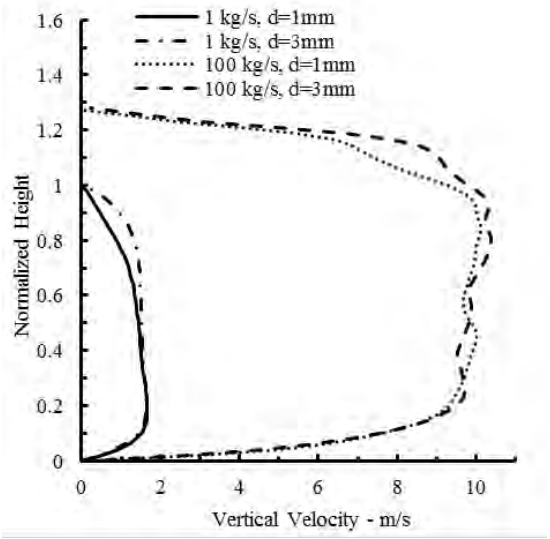

Figure 15: Effect of bubble size on vertical velocity for release from 30 meter.

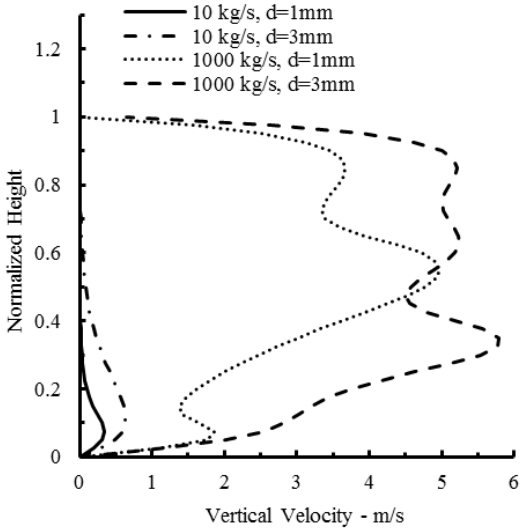

Figure 16: Effect of bubble size on vertical velocity for release from 300 meter.

Table 2: Resulting surface gas rate and surface radius for different bubble diameters and release scenarios.

Scenario	Surf. rate [kg/s]		Surf. radius [m]	
	1mm	3mm	1mm	3mm
30m., 1kg/s	0.01	0.66	12.4	16.0
30m., 100 kg/s	85.6	90.6	32	27.1
300m., 1000 kg/s	362.6	370.8	199.0	207.0

CONCLUSION

An assessment of relevant physics and mechanism governing the fate of shallow and deep subsea gas releases have been conducted by mathematical simulations with an Eulerian-Lagrangian transient 3D modelling concept as described above. Buoyancy is the driving force of the gas release, while drag is the interaction force between gas bubbles and water which sets the water in motion. Since these are governing mechanisms, they have to be accounted, and thus their importance has not been assessed in this assessment. The assessment was carried out on releases from 30 meters and 300 meters and it shows that gas expansion and turbulent dispersion are also of great importance. These effects can not be neglected. Exemptions can only be made for very shallow releases (depth < 2m) were gas expansion can be neglected and for releases with very low gas rates where turbulence and turbulent dispersion has no effect. The assessment shows that the pressure gradient force and virtual mass force are insignificant. Previous studies also show that lift forces have little effect.

Gas dissolution is important for bubbles residing sufficiently long in the water column. Residence time increases with release depth and decreases with gas rate. The assessment shows that gas dissolution has a greater impact on deep releases, but it should still not be

neglected for shallow releases. Here we have defined releases from 30 meters as a shallow release. However, there has to be limit at which gas dissolution can be neglected. This is governed by the residence time of bubbles in the ocean. Larger depths and smaller gas rates promote gas dissolution. In addition the effects of bubble size and drag correction due to high void fractions were assessed. Drag corrections for higher void fractions have very little impact on the plume behaviour. Bubble size has a small effect on shallow releases and somewhat large effect on deeper releases. This is directly coupled to gas dissolution. More cases should be considered before a solid conclusion can be made. However, the results consistently show that larger bubbles give less dissolution and more surface gas. Thus overestimating the bubble size is the conservative choice in a risk assessment.

The assessment shows that there is a difference in behaviour between deep and shallow releases. They are both driven by buoyancy which has an accelerating effect on the bubble plume for an expanding gas. Turbulent dispersion causes spreading of the plume and reduced centre velocity. This phenomenon is not affected by depth. The main difference between deep and shallow releases is their susceptibility to gas dissolution. A deeper release yields longer residence times for bubble and thus the importance of gas dissolution is more significant. However, a quantitative analysis of the behaviour of both shallow and deep releases needs to account for buoyancy, drag, turbulent dispersion and gas dissolution.

ACKNOWLEDGEMENT

This study was performed in the SURE joint industry project funded by BP, Gassco, Shell, Statoil, Total, DNV LG, Safetec, Wild Well Control and PSA (Petroleum Safety Authorities).

REFERENCES

CLOETE, S., OLSEN, J.E. & SKJETNE, P.(2009) CFD modeling of plume and free surface behavior resulting from a sub-sea gas release. *Appl Ocean Res* **31**, 220-225

ENGEBRETSEN, T., NORTHUG, T., SJØEN, K. & FANNELØP, T.K. (1997) Surface Flow and Gas Dispersion from a Subsea Release of Natural Gas.in *7th int. offshore and polar engineering conference*, Honolulu.

FANNELØP, T.K. & SJØEN, K.(1980) Hydrodynamics of Underwater Blowouts. *AIAA*

GOSMAN, A.D. & IOANNIDES, E.(1983) Aspects of computer simulation of liquid-fuelled combustors. *J.Energy* **7**, 482-490

LEKVAM, K. & BISHNOI, P.R.(1997) Dissolution of methane in water at low temperatures and intermediate pressures. *Fluid Phase Equilibr* **131**, 297-309

OLSEN, J.E. & CLOETE, S. (2009) Coupled DPM and VOF model for analyses of gas stirred ladles at higher gas rates.in *Seventh International Conference on CFD in the Minerals and Process Industries*, Melbourne.

PAN, Q.Q., JOHANSEN, S.T., SÆTRAN, L. & REED, M. (2013) An enhanced k-epsilon model for bubble plumes.in *8th International Conference on Multiphase Flow (ICMF)*, Jeju, Korea.

ROGHAIR, I., VAN SINT ANNALAND, M. & KUIPERS, J.A.M.(2013) Drag Force and Clustering in Bubble Swarms. *AiChE Journal* **59**, 1791-1800

SKJETNE, P. & OLSEN, J.E.(2012) A parcel based modelling concept for studying subsea gas release and the effect of gas dissolution. *Prog Comput Fluid Dy* **12**, 187-195

TOMIYAMA, A., KATAOKA, I., ZUN, I. & SAKAGUCHI, T.(1998) Drag coeffcients of single bubbles under normal and micro gravity conditions. *JSME International Journal, Series B* **41**, 472-479

TSUJI, Y., MORIKAWA, Y. & TERASHIMA, K.(1982) Fluid-dynamic interaction between two spheres. *Int.J.Multiphase Flow* **8**, 71-82

ZHANG, Y. & XU, Z.(2003) Kinetics of convective crystal dissolution and melting, with applications to methane hydrate dissolution and dissociation in seawater. *Earth and Planetary Science Letters* **213**, 133-148

MODELING OF BUBBLY FLOWS WITH FREE SURFACE USING A HYBRID VOLUME OF FLUID AND DISCRETE BUBBLE MODEL APPROACH

Deepak JAIN[1]*, **J. A. M. KUIPERS**[1]†, **Niels G. DEEN**[1]‡

[1]Eindhoven University of Technology, Department of Chemical Engineering and Chemistry, 5600 MB Eindhoven, NETHERLANDS

* E-mail: d.jain@tue.nl
† E-mail: j.a.m.kuipers@tue.nl
‡ E-mail: n.g.deen@tue.nl

ABSTRACT

Bubbly flows are quite prevalent in nature and are often accompanied with a free surface of the continuous (liquid) phase. Also in many processes in the chemical, biochemical and metallurgical industries, such flows have established their use. Therefore, to design and operate bubble column reactors, a thorough understanding of column hydrodynamics is needed. In this work, two well established CFD methods (VOF & DBM) are used to form a novel hybrid model. In this model a multi-phase system with three distinct phases, the gas phase, the liquid phase and the bubble phase, are considered. It should be noted here that, although the physical properties of gas and bubble phase are the same, the treatment in the model differs a lot. The gas and liquid phases are treated as continuous phases and are solved on a Eulerian grid. The surface between the gas and liquid phase is solved using a colour function which denotes the fractional amount of liquid in that particular grid cell. The bubbles are described in a Lagrangian framework using Newton's second law of motion. Four-way coupling is embedded to take care of bubble-bubble, bubble wall and bubble-liquid interactions. This new hybrid model is numerically verified and experimentally validated against the benchmark liquid PIV results reported by Deen *et al.* (2001). Results from free surface modelling can, for instance, be used to improve the ladle stirring in steel making process where slag formation on the top plays an important role.

Keywords: Bubble column reactor, discrete bubble model, volume of fluid method, free surface modeling, computational fluid dynamics .

NOMENCLATURE

Greek Symbols

ε	Volume fraction, $[-]$
μ	Dynamic viscosity, $[kg/ms]$
ρ	Mass density, $[kg/m^3]$
σ	Interfacial tension, $[N/m]$
$\boldsymbol{\tau}$	Stress tensor, $[N/m^2]$
Φ	Inter-phase transfer source term, $[N/m^3]$
δu^2	Mean square velocity difference, $[m^2/s^2]$
δt	Time step, $[s]$

Latin Symbols

C	coefficient, $[-]$.
CCF	coalescence calibration factor, $[-]$.
d	diameter, $[m]$.
$E\ddot{o}$	E$\ddot{o}$tvos number, $[-]$.
F	color function, $[-]$.
$\boldsymbol{f}$	force vector (Eulerian domain), $[N]$.
$\boldsymbol{F}$	force vector (Lagrangian domain), $[N]$.
$\boldsymbol{g}$	gravity acceleration, $[m/s^2]$.
h_o	initial film thickness, $[m]$.
h_f	final film thickness, $[m]$.
$\boldsymbol{f}$	force vector (Eulerian domain), $[N]$.
$\dot{M}$	interphase mass transfer term (liquid), $[kg/m^3s]$.
$\dot{m}$	interphase mass transfer term (bubble), $[kg/m^3s]$.
N	number of time steps, $[-]$.
p	pressure, $[N/m^2]$.
R	radius, $[m]$.
Re	Reynolds number, $[-]$.
t	time, $[s]$.
$\boldsymbol{u}$	Eulerian phase velocity vector, $[m/s]$.
$\bar{\boldsymbol{u}}$	mean velocity, $[m/s]$.
$\boldsymbol{u}'$	fluctuating velocity, $[m/s]$.
$\boldsymbol{v}$	Lagrangian phase velocity vector, $[m/s]$.
V	volume, $[m^3]$.
We	Weber number, $[-]$.

Sub/superscripts

b	Bubble.
D	Drag (swarm).
D,∞	Drag (single bubble).
eff	effective.
f	Fluid.
g	Gas.
G	Gravity.
l	Liquid.
L	Lift.
P	Pressure.
rel	relative.
VM	Virtual Mass.
W	Wall.
x,y,z	Co-ordinate dimensions.

INTRODUCTION

Bubbly flows are encountered in a variety of industrial applications. Often these flows contain some free surface, through which the bubbles leave the liquid. Experimental investigations of bubbly flows are difficult: the dynamic nature of the bubbly flow requires dynamic techniques that ideally do not disturb the flow. Moreover, for large systems one can either only measure macroscopic parameters like overall gas

holdup or one is practically limited to measurements at a finite number of sample points. For such circumstances, computational fluid dynamics (CFD) has proved to be useful to extend the understanding of these flows, and to provide detailed information, both in space and time.

Several types of CFD models, dedicated to all different length and time scales have been developed in the past few decades. Many authors adopt a multi-scale approach to understand and model large scale systems. Fully resolved simulations, also known as direct numerical simulation (DNS), are performed to obtain the micro-scale data. Through DNS studies, closures for various kinds of forces and coefficients are obtained, which can be used in coarse grained models like Euler-Lagrange model or two-fluid model (TFM). Usually, Euler-Lagrange models are employed for lab-scale simulations, while the TFM can be extended to industrial scale too. The advantage of using the former over TFM is to have a detailed outlook of bubble dynamics in these bubbly flows, e.g. bubble size distributions are a direct result of the simulation.

The Euler-Lagrange models usually treat the gas-liquid interface at the top of the column via some artificial boundary condition or a buffer zone technique. However, modeling of such systems is poorly understood in terms of evolution of the free surface. In this study, an attempt has been made to formulate a numerical model introducing the free surface at the top of the column in the Euler-Lagrange framework. The model presented here combines the volume of fluid (VOF) model of van Sint Annaland *et al.* (2005) and the discrete bubble model (DBM) of Darmana *et al.* (2005). The hybrid model uses DBM to study the bubble and fluid dynamics in the bubble column, and the volume of fluid method to create the free surface. Such a model formulation takes care of all the three phases, namely the liquid, the bubble and the gas phase. It is noted here that the bubbles are represented as dispersed elements, while the gas is treated as a continuous phase.

Volume of Fluid (VOF) methods (Hirt and Nichols (1981); Youngs (1982)) employ a color function F(x,y,z,t) that indicates the fractional amount of fluid present at a certain position (x,y,z) at time t. The evolution equation for F is usually solved using a geometrical advection scheme, in order to minimize numerical diffusion. In addition to the value of the color function, the interface orientation needs to be determined, which follows from the gradient of the color function. The VOF technique in this work uses the piecewise linear interface calculation (PLIC) method of Youngs (1982) to construct the interface.

In the discrete bubble model or Euler-Lagrange model, one phase (fluid) is solved on a Eulerian grid, while the other phase (bubbles, drops, particles etc.) is solved at Lagrangian marker points. The DBM accounts for bubble-liquid and bubble-bubble interaction using two way fluid-bubble coupling and a hard sphere collision model by Hoomans *et al.* (1996). In the current implementation, the bubbles are removed from the simulations domain as they reach the gas-liquid free surface.

Attempts have been made in the past to formulate models that combine interface tracking with bubble/particle/drop tracking. Tomiyama and Shimada (2001) have proposed a NP2 model, where they have combined the multi-fluid model with an interface tracking scheme. In the NP2 model, all the phases are solved in the Eulerian domain. Many authors have combined the discrete phase solved in Lagrangian domain, with the interface tracking, using CFD packages like Fluent and OpenFoam (Cloete *et al.* (2009); Mahrla and Hinrichsen (2012); van Vliet *et al.* (2013)). However, the basic disadvantage associated with these models is that the volume fraction of bubbles/particles is not considered while solving for the fluid-phase hydrodynamics. In dense bubbly flows, the volume fraction of bubbles has a large impact on the hydrodynamics. Therefore such models are valid only for dilute flows and should not be extended for studying the systems with high volume fractions of the discrete phase. The model presented here overcomes the aforementioned shortcoming and will allow us to study the dense-bubbly flows with a free surface.

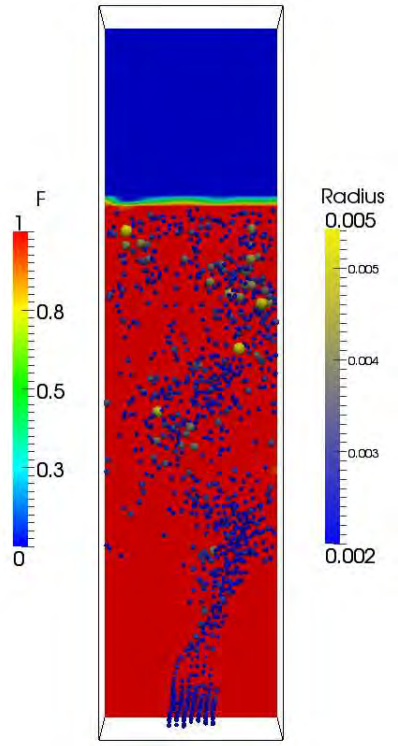

Figure 1: A three phase formulation with bubbles as discrete phase and gas (F=0) & liquid (F=1) in the continuous phase. In the interface cells, containing liquid and gas, 0<F<1.

The organisation of this paper is as follows: first the description of the model and the numerical solution method is given. Subsequently, the numerical verification and experimental validation of the method is provided, where the simulated test cases are examined against the experimental findings from Deen *et al.* (2001). Finally, the conclusions are presented.

MODEL DESCRIPTION

Our model consists of two main parts: one part deals with the presence of gas-liquid free surface (VOF model) whereas the other part accounts for the presence of the bubbles in liquid, taking into consideration, the possible collisions between the bubbles themselves and/or confining walls (DBM). First, the main conservation equations are presented along with the incorporation of surface tension and the advection of the deformable interfaces. The fluid-bubble coupling and the bubble dynamics are subsequently described.

Mass and momentum conservation

The mass conservation equation for the fluid phase is described through the continuity equation.

$$\frac{\partial \varepsilon_f}{\partial t} + \nabla.(\varepsilon_f \boldsymbol{u}_f) = 0 \tag{1}$$

where ε, and $\boldsymbol{u}$ represent the volume fraction and velocity, respectively. The subscript f represent the fluid phase. The fluid phase includes the liquid (l) and the gas (g) phases.
The momentum conservation can be described by a volume averaged Navier-Stokes equation.

$$\rho_f \left[\frac{\partial (\varepsilon_f \boldsymbol{u}_f)}{\partial t} + \nabla.(\varepsilon_f \boldsymbol{u}_f \boldsymbol{u}_f) \right] = - \varepsilon_f \nabla p - \nabla.(\varepsilon_f \boldsymbol{\tau}_f) + \rho_f \varepsilon_f \boldsymbol{g} - \boldsymbol{f}_\sigma - \boldsymbol{f}_{l \to b} \tag{2}$$

where $\boldsymbol{f}_\sigma$ is the surface tension term, and $\boldsymbol{f}_{l \to b}$ is the forcing term for bubble-liquid interactions. Here the subscript b represents the bubble phase. Note that when ε_f the single phase Navier-Stokes equations are retained.

Volume of fluid model

The volume of fluid approach uses the fractional amount of liquid present to determine the interface position and orientation in a given cell. This fractional amount of liquid is often called the color function and is denoted by F.

$$F = \frac{\varepsilon_l}{(\varepsilon_l + \varepsilon_g)} = \frac{\varepsilon_l}{\varepsilon_f} \tag{3}$$

The liquid and the continuous gas together are regarded as the fluid phase (ε_f), the motion of which is described with an advection equation.

$$\frac{DF}{Dt} = \frac{\partial F}{\partial t} + \boldsymbol{u}_f.\nabla F = 0 \tag{4}$$

The fluid phase density is defined as:

$$\rho_f = F\rho_l + (1-F)\rho_g \tag{5}$$

The local average fluid viscosity is calculated using a more fundamental approach proposed by Prosperetti (2002), via harmonic averaging of the kinematic viscosity of the involved phases according to the following expression:

$$\frac{\rho_f}{\mu_f} = F\frac{\rho_l}{\mu_l} + (1-F)\frac{\rho_g}{\mu_g} \tag{6}$$

Surface tension model

Among the surface tension models present, a recent publication by Baltussen *et al.* (2014) proposed a model for highly curved interfaces. It uses a height function to calculate the interface curvature. However, in our case the interface is rather flat because of the large cross sectional area of the column and therefore the simple continuum surface force (CSF) model (Brackbill *et al.* (1992)) has been used. For future studies, it is advised to introduce the height function model of Baltussen *et al.* (2014) for calculation of surface tension force in this model.

Interface reconstruction

The interface reconstruction is the most crucial part in the model and is carried out with the help of geometric advection. The interface normals are calculated using the gradient of color function in the particular cell. Then, with the help of series of transformations, five generic interface orientations are identified. Later the flux through these interfaces is computed with the help of a plane constant defined for the given cell. An elaborate description of the complete VOF model can be found in van Sint Annaland *et al.* (2005).

Discrete bubble model

The discrete bubble model accounts for the calculation of forces acting on bubbles and tracking of individual bubbles due to forces and collisions. The motion of the bubbles is solved by Newton's second law of motion.

Bubble tracking

The motion for each individual bubble is computed from Newton's second law while accounting for bubble-bubble and bubble-wall interactions via an encounter model of Hoomans *et al.* (1996). The liquid phase contributions are taken into account via the inter-phase mass transfer rate $\dot{m}$ and the net force experienced by each individual bubble. For an incompressible bubble, the equations can be written as:

$$\rho_b \frac{d(V_b)}{dt} = (\dot{m}_{l \to b} - \dot{m}_{b \to l}) \tag{7}$$

$$\rho_b V_b \frac{d(\boldsymbol{v})}{dt} = \boldsymbol{F}_G + \boldsymbol{F}_P + \boldsymbol{F}_D + \boldsymbol{F}_L + \boldsymbol{F}_{VM} + \boldsymbol{F}_W \tag{8}$$

where ρ_b, V_b, and $\boldsymbol{v}$, respectively are the density, volume and velocity of the bubble. The net force acting on each individual bubble is calculated by considering all the relevant forces. It is composed of separate, uncoupled contributions such as gravity, pressure, drag, lift, virtual mass and wall forces. Expressions for each of these forces can be found in Table 1. Detailed discussion about these forces can be found in Darmana *et al.* (2007). Note that the drag, lift and wall force closures used in the present study are obtained from Tomiyama *et al.* (1995, 2002). The drag coefficient used here does not take effects of contamination into account. A drag correlation correction for bubble swarms as proposed by Roghair *et al.* (2011) has been included in the model. These forces are calculated here at Lagrangian marker points and are mapped to the Eulerian grid using the polynomial mapping function from Deen *et al.* (2004).

Coalescence

In the model used used here, the collisions are resolved in a deterministic fashion using the hard sphere model of Hoomans *et al.* (1996). The bubble coalescence model proposed by Sommerfeld *et al.* (2003) is used later to determine

Table 1: Overview of forces acting on a bubble.

Forces	Closures
$F_G = \rho_b V_b g$	-
$F_P = -V_b \nabla P$	-
$F_D = -\frac{1}{2} C_D \rho_l \pi R_b^2 \lvert v-u \rvert (v-u)$	$C_{D,\infty} = max\left[min\left\{\frac{16}{Re}\left(1+0.15Re^{0.687}\right), \frac{48}{Re}\right\}, \frac{8}{3}\frac{E\ddot{o}}{E\ddot{o}+4}\right]$ $\frac{C_D}{C_{D,\infty}(1-\varepsilon_b)} = 1+\left(\frac{18}{E\ddot{o}}\right)\varepsilon_b$
$F_L = -C_L \rho_l V_b (v-u) \times \nabla \times u$	$C_L = \begin{cases} min\left[0.288tanh\left(0.121Re\right), f(E\ddot{o}_d)\right]; E\ddot{o}_d < 4 \\ f(E\ddot{o}_d); 4 \le E\ddot{o}_d < 10 \\ -0.29; E\ddot{o}_d \ge 10 \end{cases}$ $f(E\ddot{o}_d) = 0.00105E\ddot{o}_d^3 - 0.0159E\ddot{o}_d^2 - 0.0204E\ddot{o}_d + 0.474$ $E\ddot{o}_d = \frac{E\ddot{o}}{E^{2/3}}; E = \frac{1}{1+0.136E\ddot{o}^{0.757}}$
$F_{VM} = -C_{VM}\rho_l V_b \left(\frac{D_b v}{D_b t} - \frac{D_b u}{D_b t}\right)$	$C_{VM} = 0.5$
$F_W = -C_W R_b \rho_l \frac{1}{D_{bw}^2} \lvert u-v \rvert^2 . n$	$C_W = \begin{cases} e^{(-0.933E\ddot{o}+0.179)}; 1 \le E\ddot{o} < 5 \\ 0.0007E\ddot{o}+0.04; E\ddot{o} \ge 5 \end{cases}$

if the collision will result in coalescence or not. Bubble coalescence is incorporated by comparing the contact time with the film drainage time, which is calculated by the model of Prince and Blanch (1990). If the film drainage time is less than the bubble contact time, coalescence happens.

$$t_{drainage} = \sqrt{\frac{R_{eff}^3 \rho_l}{16\sigma}} ln\left(\frac{h_0}{h_f}\right) \tag{9}$$

$$t_{contact} = \frac{C_{ccf} R_{eff}}{|v_{rel}|} \tag{10}$$

where h_0 and h_f are the initial and final film thickness. R_{eff} is the equivalent bubble radius for the system and is the harmonic mean of the two interacting bubbles. The extent of coalescence can be controlled by C_{ccf}, the coalescence calibration factor (CCF). This CCF represents the ratio of deformation distance and the effective bubble radius. Such implementation of bubble coalescence has already been used earlier in the works of Darmana *et al.* (2006) and Lau *et al.* (2014).

Break-up

The bubble break-up model as proposed by Lau *et al.* (2010) is used here. To decide for the event of bubble break-up, the forces acting on an individual bubbles are compared. While the inertial forces acting on the bubble try to deform the bubble and increase the surface area, the surface tension does the opposite by keeping it in shape as one single bubble. A dimensionless number, the critical Weber number, represents the ratio of these forces:

$$We = \frac{\rho_l \delta u^2(d) d}{\sigma} \tag{11}$$

where $\delta u^2(d)$ is the mean square velocity difference over a distance equal to bubble diameter d. When the Weber number of a particular bubble is more than the critical Weber number We_{crit}, the break-up happens.

In literature, a wide range of critical Weber number as studied by various authors are presented. Sevik and Park (1973) have suggested a critical Weber number ~ 1 for air bubbles in turbulent fluid jets; while according to Kolev (2007), $We_{crit} = 12$ is the most frequently used value for hydrodynamic stability. In this work, a critical Weber number of 1 is taken as suggested by Lau *et al.* (2014). For a more extensive overview of critical Weber numbers, the above cited work is referred.

Bubble removal

In a real bubble column, bubbles disappear after leaving the gas-liquid interface to become part of the continuous gas phase. Therefore in simulations also, bubbles are removed once they reach the interface. However, due to smoothening of the volume fraction and forces when they are mapped from the Lagrangian to the Eulerian domain, volume conservation fails when bubbles get to close to the free surface. To solve this issue, bubbles are removed two cells below the interface. Although this does not reflect reality entirely, the consequences are small, because the cell size is quite small (in the range of the bubble diameter). Also this assumption has a negligible impact on the bubble and liquid hydrodynamics.

MODEL VERIFICATION AND VALIDATION

Mass conservation

The volume occupied by the bubble and the gas phase is not constant during the operation due to continuous addition and removal of bubbles in column. However the liquid volume in the column remains constant and mass conservation applies. There can be some numerical deviation in the total liquid volume owing to the volume truncation and addition in VOF method at very low phase fractions. Therefore the total liquid volume in the system is monitored for a duration of about 170 seconds. It is found that the error is quite low (~10^{-4} times liquid volume fraction). This error is in the range of the minimum threshold volume fraction truncated in VOF and hence the model is deemed to be numerically correct w.r.t. the mass conservation.

Experimental validation

For a qualitative validation of the simulation model, the benchmark case of Deen *et al.* (2001) for PIV in square bubble column is chosen. Experimental settings can be found in the work of Deen *et al.* (2001).

In the present study the time-averaged mean velocity and velocity fluctuations of the simulation are calculated for a duration of 150 s (from t=20 s to t=170 s). The mean velocity is calculated as follows:

$$\bar{u} = \frac{1}{N_t}\sum_{i=1}^{N_t} u_i \tag{12}$$

where N_t is the number of time steps used in the averaging. The large scale velocity fluctuation is calculated as:

$$u' = \sqrt{\frac{1}{N_t}\sum_{i=1}^{N_t}(u_i - \bar{u})^2} \tag{13}$$

The time averaged quantities are compared with the PIV measurements of Deen *et al.* (2001). Figure 3 shows the time averaged liquid velocity in the vertical direction while the liquid phase horizontal and vertical velocity fluctuations can

be seen in Figure 4 and 5. As seen in these figures, the simulation is in very good agreement with the experimental data. Hence it can be concluded that the model is able to simulate the column hydrodynamics correctly. Simulation snapshots in Figure 2 at various time steps show the movement of a bubble swarm and the evolution of gas-liquid interface in the column. Capturing this phenomenon in such detail is pretty difficult with existing experimental techniques.

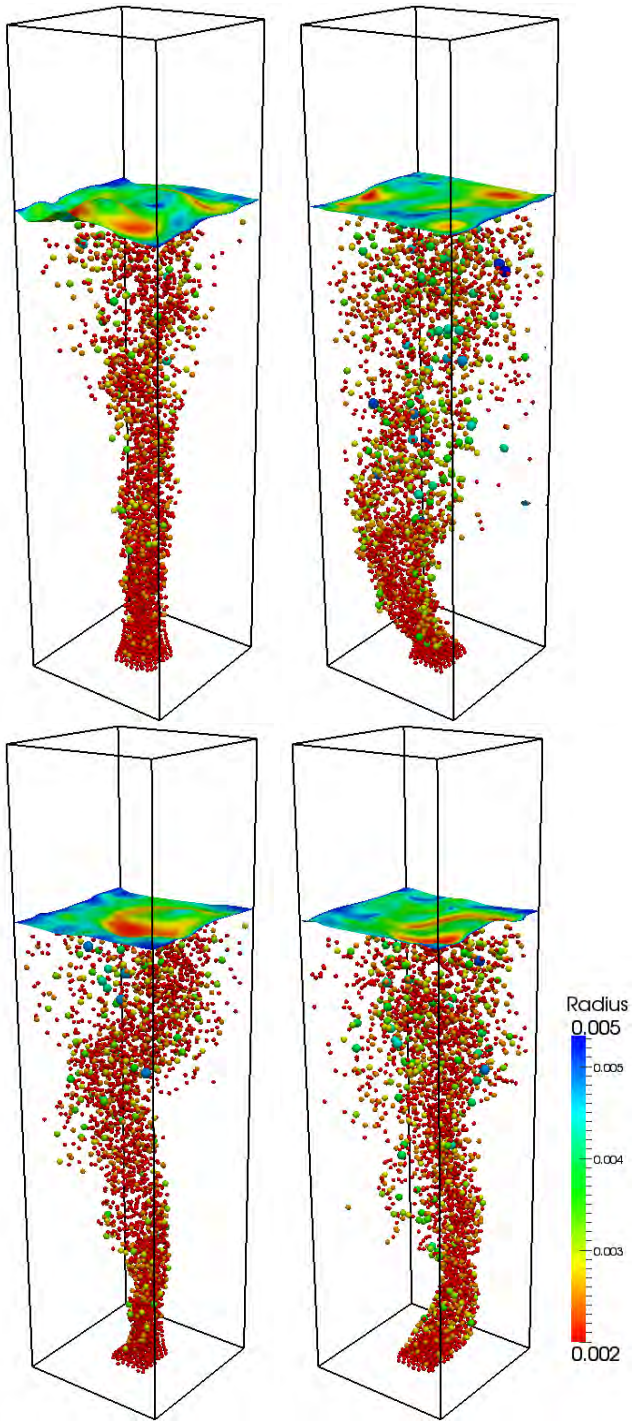

Figure 2: Snapshot of column showing the bubble swarm and evolution of gas-liquid interface at different time for the square bubble column.

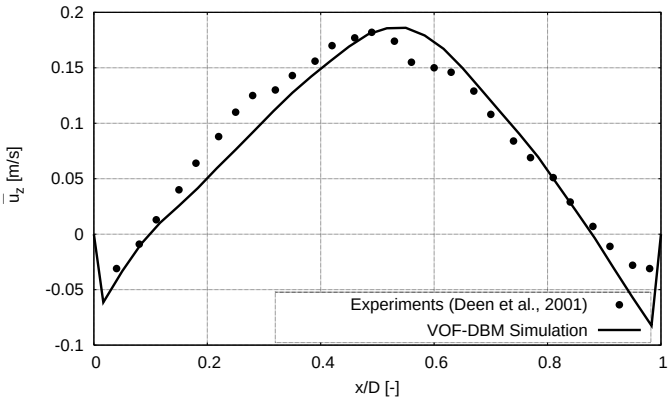

Figure 3: Comparison of simulated and experimental time averaged liquid vertical velocity profiles at a height of z/H=0.56 and a depth of y/W=0.5.

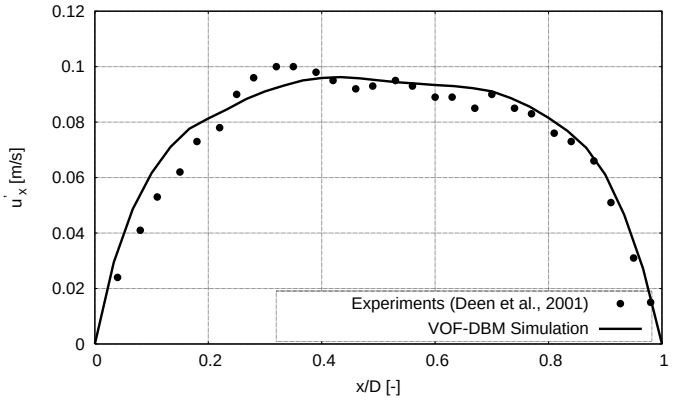

Figure 4: Comparison of simulated and experimental time averaged liquid velocity fluctuations in horizontal direction at a height of z/H=0.56 and a depth of y/W=0.5.

CONCLUSIONS

A new hybrid model based on combined volume of fluid and discrete bubble modeling has been proposed. The model is validated experimentally with the benchmark liquid PIV results of Deen *et al.* (2001). The dynamics of the free surface at gas liquid interface is also captured in the simulations. Bubble break-up and coalescence models are used to capture the dynamic bubble size distibution in the column. The evolution of the free surface at the interface between liquid and gas can be seen. The dynamics of the free surface are captured in great detail. Thus we can say that model is ready to be extended for more specific applications like gas-stirred laddles in steel-making industry.

ACKNOWLEDGEMENTS

The authors would like to thank the European Research Council for its financial support, under its Starting Investigator Grant scheme, contract number 259521 (CuttingBubbles).

REFERENCES

BALTUSSEN, M.W. *et al.* (2014). "A critical comparison of surface tension models for the volume of fluid method". *Chemical Engineering Science*.

BRACKBILL, J.U. *et al.* (1992). "A continuum method for modeling surface tension". *Journal of computational physics*, **100(2)**, 335–354.

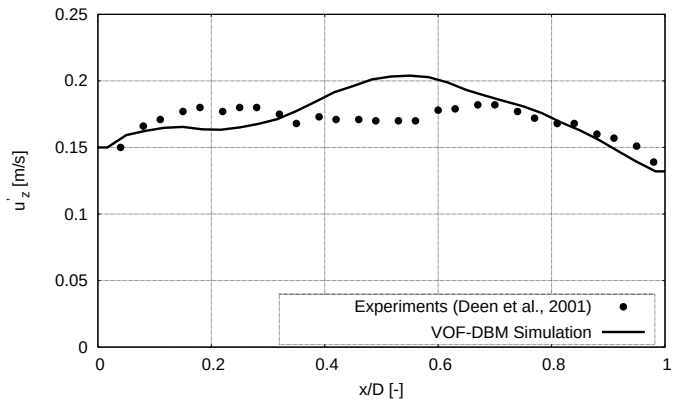

Figure 5: Comparison of simulated and experimental time averaged liquid velocity fluctuations in vertical direction at a height of z/H=0.56 and a depth of y/W=0.5.

CLOETE, S.W.P. *et al.* (2009). "A mathematical modelling study of fluid flow and mixing in full-scale gas-stirred ladles". *Progress in Computational Fluid Dynamics, An International Journal*, **9(6)**, 345–356.

DARMANA, D. *et al.* (2005). "Detailed modeling of hydrodynamics, mass transfer and chemical reactions in a bubble column using a discrete bubble model". *Chemical Engineering Science*, **60(12)**, 3383–3404.

DARMANA, D. *et al.* (2006). "Parallelization of an Euler–Lagrange model using mixed domain decomposition and a mirror domain technique: Application to dispersed gas–liquid two-phase flow". *Journal of Computational Physics*, **220(1)**, 216–248.

DARMANA, D. *et al.* (2007). "Detailed modelling of hydrodynamics, mass transfer and chemical reactions in a bubble column using a discrete bubble model: Chemisorption of CO2 into naoh solution, numerical and experimental study". *Chemical engineering science*, **62(9)**, 2556–2575.

DEEN, N.G. *et al.* (2004). "Multi-scale modeling of dispersed gas–liquid two-phase flow". *Chemical engineering science*, **59(8)**, 1853–1861.

DEEN, N.G. *et al.* (2001). "Large eddy simulation of the gas–liquid flow in a square cross-sectioned bubble column". *Chemical Engineering Science*, **56(21)**, 6341–6349.

HIRT, C.W. and NICHOLS, B.D. (1981). "Volume of fluid (vof) method for the dynamics of free boundaries". *Journal of computational physics*, **39(1)**, 201–225.

HOOMANS, B.P.B. *et al.* (1996). "Discrete particle simulation of bubble and slug formation in a two-dimensional gas-fluidised bed: a hard-sphere approach". *Chemical Engineering Science*, **51(1)**, 99–118.

KOLEV, N.I. (2007). "Multiphase flow dynamics, 1: Fundamentals".

LAU, Y.M. *et al.* (2010). "Bubble break-up in Euler-Lagrange simulations of bubbly flow". *International Conference on Multiphase Flow*.

LAU, Y.M. *et al.* (2013). "Experimental study of the bubble size distribution in a pseudo-2d bubble column". *Chemical Engineering Science*, **98**, 203–211.

LAU, Y.M. *et al.* (2014). "Numerical study of bubble break-up in bubbly flows using a deterministic euler–lagrange framework". *Chemical Engineering Science*, **108**, 9–22.

MAHRLA, A. and HINRICHSEN, O. (2012). "Cfd in gas-liquid-solid flow systems: From dpm to a coupled dpm-hires-tfm". *ISCRE 22 conference*.

PRINCE, M.J. and BLANCH, H.W. (1990). "Bubble coalescence and break-up in air-sparged bubble columns". *AIChE Journal*, **36(10)**, 1485–1499.

PROSPERETTI, A. (2002). "Navier-stokes numerical algorithms for free-surface flow computatios: An overview". *Courses and lectures-International centre for mechanical sciences*, 237–258.

ROGHAIR, I. *et al.* (2011). "On the drag force of bubbles in bubble swarms at intermediate and high reynolds numbers". *Chemical Engineering Science*.

SEVIK, M. and PARK, S.H. (1973). "The splitting of drops and bubbles by turbulent fluid flow". *Journal of Fluids Eng.*, **95**, 53–60.

SOMMERFELD, M. *et al.* (2003). "Euler/Lagrange calculations of bubbly flows with consideration of bubble coalescence". *The Canadian Journal of Chemical Engineering*, **81(3-4)**, 508–518.

TOMIYAMA, A. and SHIMADA, N. (2001). "(n+2)-field modeling for bubbly flow simulation". *Computational Fluid Dynamics J*, **9(4)**, 418–426.

TOMIYAMA, A. *et al.* (1995). "A simple numerical method for solving an incompressible two-fluid model in a general curvilinear coordinate system". *Advances in Multiphase Flow, Society of Petroleum Engineers Inc., Elsevier, Amsterdam*, 241–252.

TOMIYAMA, A. *et al.* (2002). "Transverse migration of single bubbles in simple shear flows". *Chemical Engineering Science*, **57(11)**, 1849–1858.

VAN SINT ANNALAND, M. *et al.* (2005). "Numerical simulation of gas bubbles behaviour using a three-dimensional volume of fluid method". *Chemical Engineering Science*, **60(11)**, 2999–3011.

VAN VLIET, E. *et al.* (2013). "Development and validation of a lagrangian-eulerian multi-phase model for simulating the argon stirred steel flow in a ladle with slag". *STEELSIM 2013 conference*.

YOUNGS, D.L. (1982). "Time-dependent multi-material flow with large fluid distortion". *Numerical methods for fluid dynamics*, **24**, 273–285.

ANALYSIS OF PARTICLE DEPOSITION FROM TURBULENT LIQUID-FLOW ONTO SMOOTH CHANNEL WALLS

Magali DUPUY[1*], Arunvady XAYASENH[1], Emmanuel WAZ[2], Pierre LE BRUN[2], Hervé DUVAL[1]

[1] Laboratory of Chemical Engineering and Materials, École Centrale Paris, 92295 Châtenay-Malabry, FRANCE

[2] Constellium, Voreppe Research Centre, CS 10027, 38341 Voreppe Cedex, FRANCE

* E-mail: magali.dupuy@ecp.fr

ABSTRACT

In this study, we analyse the motion of hydrosol particles in the near-wall shear layer of a turbulent channel flow. The liquid flow-field is described using the kinematic model proposed by Fan and Ahmadi (1995) combined with Lagrangian particle tracking. Numerical simulations were performed for friction velocity ranging from 1.5 mm.s^{-1} to 15 mm.s^{-1}, particle diameter from 5 to 50 µm, particle to liquid density ratio from 1 to 1.4 and wall roughness height from 0.1 to 1µm. The results show that the inertia effects are very weak. For nonbuoyant particles, direct interception is the main deposition mechanism and a law giving the deposition velocity as a function of the different parameters is proposed. For buoyant particles the deposition is controlled by sedimentation for the smallest values of friction velocity. When friction velocity increases, the direct interception contribution increases as well, and may prevail on sedimentation.

Keywords: Fouling/clogging, metal refining, turbulent deposition, Lagrangian methods, liquid aluminum.

NOMENCLATURE

Greek Symbols

δ Distance from particle surface to wall, [m].
ρ Mass density, [kg.m^{-3}].
τ_p Relaxation time, [s].
τ_p^+ Stokes number.
μ Dynamic viscosity, [kg.m^{-1}.s^{-1}].
ν Cinematic viscosity, [m^2.s^{-1}].
σ_w Shear stress at the wall, [kg.m^{-1}.s^{-2}].

Latin Symbols

C_0 Mean particle concentration, [m^{-3}].
D Domain length, [m].
d Diameter, [m].
e Shift in the velocity profile at the wall, [m].
f Friction coefficient.
F Force.
F_D Drag force.
F_L Lift force.
g Gravity, [m.s^{-2}].
J Particle mass transfer rate, [m^{-2}.s^{-1}].
k Roughness height, [m].
l^* Characteristic length scale at the solid wall, [m].
r_p Particle radius, [m].
t^* Characteristic time scale at the solid wall, [s].
u Velocity, [m.s^{-1}].
u^* Characteristic velocity at the solid wall, [m.s^{-1}].
V_d Deposition velocity, [m.s^{-1}].
V_s Sedimentation velocity, [m.s^{-1}].
y_c Capture distance, [m].
z_p Distance from particle center to wall, [m].

Suberscripts

d Deposition.
D Drag.
f Fluid.
l Limiting trajectory.
L Lift.
p Particle.
s Sedimentation.
w Wall.
$\parallel$ Parallel to the wall.
$\perp$ Perpendicular to the wall.

Superscripts

$+$ Dimensionless quantity.
$*$ Value at the solid wall.

INTRODUCTION

In aluminum industry, the elimination of inclusion is of great importance because the quality and properties of the aluminum products rely on it. Indeed, the presence of inclusions may lead to decohesion on forged products or tearoff during forming with high plastic deformation such as extrusion or rolling (Duval *et al.* 2009). It can also have a pernicious influence on fatigue properties, as many studies have shown (El-Soudani and Pelloux 1973, Jordon *et al.* 2010, Tijani *et al.* 2013, Tiryakioğlu 2009). That is why some processing operations are dedicated to removing inclusions from the liquid aluminum. Many studies have been conducted to estimate and improve the efficiency of such processes,

such as purification by flotation (Mirgaux *et al.* 2009), filtration with ceramic foam filters (Acosta and Castillejos 2000 I and II, Duval *et al.* 2009, Zhou *et al.* 2003), filtration with ceramic particle with active coatings (Zhou *et al.* 2003), or filtration with electromagnetic field (He *et al.* 2012, Natarajan and El-Kaddah 2002, Xu *et al.* 2007).

Metal processing often include transporting liquid metal from one apparatus to another thanks to a trough. This step might affect the inclusion content (advantageously or not) and is not yet accurately described. The present study attempts to give more insight about deposition of inclusions at the solid bottom wall of a trough carrying liquid aluminum. Even though deposition on solid walls has been widely studied for aerosol (Fan and Ahmadi 1993, Tian and Ahmadi 2007, Guha 1997, Lai 2005, Narayanan *et al.* 2003, Zhao and Wu 2006) it remains hardly ever investigated in the case of suspended particles in a liquid *i.e.* hydrosol. A hydrosol differs from an aerosol by its solid to fluid density ratio of the order of 1 whereas an aerosol is characterized by a large density ratio, *i.e.* about 10^3. Hydrosol turbulent deposition is addressed in this paper, by means of numerical simulations.

The following sections start with the description of the particle deposition model. Then the model is applied to the deposition of non-buoyant as well as buoyant inclusions. The influence on deposition of different parameters, such as the particle diameter or the inclusion to liquid density ratio for instance, is investigated. The main purposes of this paper are (i) to identify and quantify the deposition mechanisms, (ii) to establish the suitable kinetic laws for inclusion turbulent deposition in liquid aluminum.

MATHEMATICAL MODEL

The trough is modelled as an open rectangular channel. The present study focuses on the inclusion deposition on the horizontal solid bottom wall of the channel (figure 1). Inclusions can be transported by the turbulent liquid metal flow from the center of the channel to the bottom wall where they may be captured. Since we are interested in deposition, the turbulent flow field is not solved in the whole height of the channel but in a zone of interest close to the deposition wall (figure 1). Inside this zone of interest the flow field is described by the analytical sublayer model of Fan and Ahmadi (1995) and the inclusion trajectories are computed by Lagrangian particle tracking using an in-house CFD code.

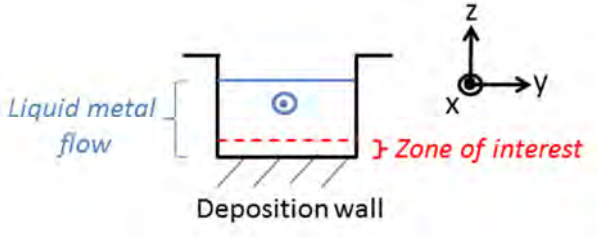

Figure 1: Configuration of liquid metal flow in a channel, with deposition at the channel bottom wall.

It is possible to determine a characteristic fluid velocity at the solid wall, called the friction velocity u^* and defined as

$$u^* = \sqrt{\frac{\sigma_w}{\rho_f}} \quad (1)$$

where $\sigma_w = \mu_f \, \partial u_{fx}/\partial z$ is the shear stress at the wall. Thanks to the characteristic velocity at the solid wall u^* it is possible to define characteristic time and length scales, t^* and l^* respectively, such as

$$t^* = \frac{\nu_f}{(u^*)^2} \quad (2)$$

$$l^* = \frac{\nu_f}{u^*} \quad (3)$$

These characteristic scales are used to make dimensionless the model parameters, which are then labeled with a $^+$ exponent.

Inclusion capture at the wall

As far as deposition is concerned, it is assumed that once there is a direct contact between the inclusion and the wall, the deposition process is completed with no rebound effect included. The solid wall is supposed to be smooth. Therefore the distance of capture y_c is defined as

$$y_c^+ = r_p^+ \quad (4)$$

Small wall roughness height k can be included in the model. The wall roughness modifies the capture height y_c^+ which becomes

$$y_c^+ = r_p^+ + k^+ - e^+ \quad (5)$$

with $k^+ = ku^*/\nu_f$ the dimensionless roughness height and e the shift in the velocity profile at the wall induced by the presence of the roughness. Its value is given by the model by Zhao and Wu (2006) such as

$$\frac{e^+}{k^+} = \begin{cases} 0 & \text{if } k^+ < 3 \text{ (hydraulically smooth)} \\ \left.\begin{array}{ll} 0.3219\ln(k^+) - 0.3456 & \text{if } 3 < k^+ < 30 \\ 0.0835\ln(k^+) - 0.4652 & \text{if } 30 < k^+ < 70 \end{array}\right\} & \text{(transition)} \\ 0.82 & \text{if } k^+ > 70 \text{ (completely rough)} \end{cases} \quad (6)$$

The configurations computed in the present study are hydraulically smooth.

Liquid metal turbulent flow

Many experimental and numerical studies have been carried out in order to investigate the flow field behavior in the turbulent boundary layer at a wall as well as the turbulent deposition at a solid wall (Cleaver and Yates 1975, Corino and Brodkey 1969, Kim *et al.* 1971, Kline *et al.* 1967, Smith and Metzler 1983). It has been found that the particles are conveyed to the wall by the fluid vortices close to the deposition wall. These eddies are organized with burst and sweep structures in the viscous sublayer ($z^+ < 10$) and the buffer layer ($10 \leq z^+ < 30$) (Kim *et al.* 1971). Fan and Ahmadi (1995) have proposed to model these structures by a frozen flow field, such as

$$u_f^+ = \begin{cases} u_{fx}^+ = \frac{1}{0.075}\tanh(0.075z^+) \\ u_{fy}^+ = \frac{11}{16}\left(\frac{2A}{\Lambda^+}\right)\left(\frac{2z^+}{\Lambda^+}\right)^{-5/16}\sin\left(\frac{2\pi z^+}{\Lambda^+}\right)\sin\left(\frac{2\pi y^+}{\Lambda^+}\right) \\ \quad + A\left(\frac{2\pi}{\Lambda^+}\right)\left(\frac{2z^+}{\Lambda^+}\right)^{11/16}\cos\left(\frac{2\pi z^+}{\Lambda^+}\right)\sin\left(\frac{2\pi y^+}{\Lambda^+}\right) \\ u_{fz}^+ = -A\left(\frac{2\pi}{\Lambda^+}\right)\left(\frac{2z^+}{\Lambda^+}\right)^{11/16}\sin\left(\frac{2\pi z^+}{\Lambda^+}\right)\cos\left(\frac{2\pi y^+}{\Lambda^+}\right) \end{cases} \quad (7)$$

where $\Lambda^+ = 100$ is the dimensionless mean distance between two bursts and $A = 34{,}7$ is a constant obtained by matching the downward velocity component u_{fy}^+ given by equation (7) to a characteristic downward velocity in turbulent boundary layer flow (Fan and Ahmadi 1995). The structure of the fluid velocity field obtained from equations (7) is depicted in figure 2.

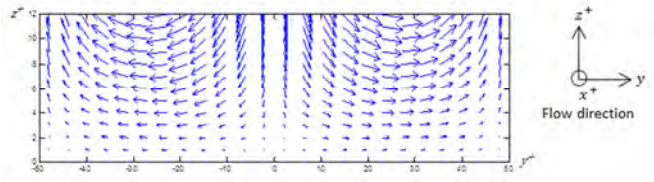

Figure 2: Fluid velocity vector field in the zone of interest (see fig.1) as given by the model of Fan and Ahmadi (1995).

Using the Fan and Ahmadi model to describe the fluid flow implies that the particles are carried out and captured at the wall thanks to the burst/sweep structures. It has been proven to be true for aerosol (Fan and Ahmadi 1995). In the present study it is assumed that it is true for hydrosol as well. On top of that, it is presumed that the burst/sweep structure has a longer lifetime than the particle trajectory.

It is expected that the main features of hydrosol deposition can be well-represented by this simplified fluid flow model of the near-wall turbulence structure.

Inclusion trajectory

Lagrangian particle tracking is considered under conditions of one-way coupling, that is to say that particle effects on flow as well as particle-particle interaction are not taken into account. This hypothesis is relevant as long as the particle volume fraction is lower than 10^{-6}. Particles are introduced in the domain at $z^+ = 12$ (figure 1) where the fluid flow reaches a maximum of turbulent kinetic energy production (Panton 2001). Therefore the particle concentration at $z^+ = 12$ is supposed to be homogeneous.

The dimensionless particle equation of motion is given as

$$\tau_p^+\frac{du_p^+}{dt^+} = \tau_p^+\left(1-\frac{\rho_f}{\rho_p}\right)\mathrm{g}^+ + \left(u_f^+ - u_p^+\right) + \tau_p^+\frac{\rho_f}{2\rho_p}\left(\frac{Du_f^+}{Dt^+} - \frac{du_p^+}{dt^+}\right) + \tau_p^+\frac{\rho_f}{\rho_p}\frac{Du_f^+}{Dt^+} + F_L^+ \quad (8)$$

where d_p is the particle diameter, μ_f the dynamic fluid viscosity, and ρ_p and ρ_f are, respectively, the particle density and the fluid density. Here g denotes the acceleration of gravity which is orientated towards the horizontal bottom wall, u_p is the particle velocity and u_f is the fluid velocity in the absence of the particle. $Du_f/Dt = \partial u_f/\partial t + u_f.\nabla u_f$ is the fluid acceleration at the instantaneous particle center. d/dt corresponds to the time derivative following the moving inclusion.

In Eq. (8), the left-hand side represents the particle inertial force. On the right-hand side, the terms are the gravitational force, the Stokes drag force (since the Reynolds particle number $Re_p = \rho_f\|u_p - u_f\|(d_p/2)/\mu_f$ is lower than 0.1), the added-mass force, the effects of pressure gradient of the undisturbed flow and the lift force. The expression of the lift force F_L is the "optimum" one given by Wang *et al.* (1997).

In Eq. (8), the Basset history term is neglected. Brownian diffusion is neglected as well since particle diameter is much larger than 1 µm.

When the particle is close to the deposition wall (*i.e.*, when the distance between the particle center and the wall is lower than about 10 d_p), it is possible to include the hydrodynamic interactions between the particle and the interface (*i.e.* lubrication effects) in the particle equation of motion. The lubrication effects are manifested in the drag force's deviation from the Stokes expression. Therefore they are taken into account through the introduction of the appropriate friction coefficients (Tien and Ramarao 2007) in the Stokes steady drag, such as

$$(F_D)_\parallel^+ = -\left[\left(u_p^+\right)_\parallel f_\parallel^t - \frac{1}{u^*}a^+ z_p^+ f_{1\parallel}^m - \frac{1}{u^*}b^+\left(z_p^+\right)^2 f_{2\parallel}^m\right]$$
$$(F_D)_\perp^+ = -\left[\left(u_p^+\right)_\perp f_\perp^t + \left(u_{f0}^+\right)_\perp f_{2\perp}^m\right] \quad (9)$$

where the subscript $\perp$ (resp. $\parallel$) is associated with the component perpendicular (resp. parallel) to the wall and z_p^+ is the dimensionless distance between the particle center and the solid wall. The values of the friction coefficients $f = f(\delta/d_p)$ depend on the separation distance δ between the particle and the solid wall made dimensionless by the particle diameter d_p as given by Tien and Ramarao (2007). The coefficients a and b are defined by (Tien and Ramarao 2007)

$$a^+ = -\frac{\partial\left(u_{f0}^+\right)_\parallel}{\partial z_p^+} + \frac{2\left(u_{f0}^+\right)_\parallel}{z_p^+}$$
$$b^+ = \frac{1}{z_p^+}\frac{\partial\left(u_{f0}^+\right)_\parallel}{\partial z_p^+} - \frac{\left(u_{f0}^+\right)_\parallel}{\left(z_p^+\right)^2} \quad (10)$$

It should be noted that $f \to 1$ when $\delta \to \infty$ and that the friction coefficient $f_\perp^t$ acting on the perpendicular component of the particle velocity, diverges as the reduced separation distance vanishes. Hence when lubrication effects are incorporated in the particle equation of motion, the solid wall roughness is included in the model as well. Consequently, the contact between the particle and the wall is achieved thanks to the roughness.

The particle equation of motion (8) is solved numerically using third-order Adams-Bashforth method.

The deposition velocity V_d is defined as

$$V_d = \frac{J}{C_0} \quad (11)$$

where J is the particle mass transfer rate at the wall and C_0 the mean particle concentration at $z^+ = 12$. The particle mass transfer rate J is evaluated thanks to the limiting trajectory. Indeed, there is a limiting value y_l

above which the inclusions introduced in the domain at the $z^+ = 12$ are transported outside the domain without ever reaching the solid wall. From the values of the limiting trajectory y_l, of u_{pl} the normal component of the inclusion velocity at $z^+ = 12$ and of D the domain length in the y^+ direction, the particle mass transfer rate can be estimated:

$$\mathrm{J} = \mathrm{C}_0 \left(\int_0^{y_l} \frac{u_{pl} \mathrm{dy}}{\mathrm{D}/2} \right) \quad (12)$$

In order to verify that the code is valid, it has been tested on a reference configuration for which experimental and numerous numerical data are available: simulations for the aerosol configuration of the experiment of Liu and Agarwal (1974) have been run. The deposition velocities computed were found to be in good agreement with the experimental results as well as the numerical models of Wood (1981) and Fan and Ahmadi (1993).
In the following, the numerical study actually consists of using the model of Fan and Ahmadi (1995) rethought in the case of a hydrosol.

Simulation parameters

The study focuses on the deposition of inclusions suspended in liquid aluminum. Numerical simulations have been run for different sets of parameters, with particle to liquid density ratio varying from 1 to 1.4, the particle diameter from 5 to 50 µm, the friction velocities from 1.5 to 15 mm.s^{-1}, and the wall roughness from 0.1 to 1 µm. The simulation parameters are summarized in table 1.

Table 1: Modelling conditions.

ρ_f	2360 kg. m^{-3}
ν_f	5.5085×10^{-7} m^2. s^{-1}
ρ_p/ρ_f	0.95 to 1.4
u^*	1.5 to 15 mm. s^{-1}
d_p	5 to 50 µm
k	0.1 to 1 µm

Some simulations are performed without inertia effects (resp. gravity): in this case, particle inertial force, added mass force, pressure gradient force and lift force (resp. gravitational force) are removed from Eq. (8). When inertia effects are taken into account, Faxen corrections are also included in the model. Indeed it has been found that even though not an inertia effect, Faxen corrections are of the same order of magnitude as the pressure gradient force (Maxey and Riley 1983).

RESULTS

As far as deposition on a horizontal wall is concerned sedimentation can overpower any other deposition mechanism. Thus, we have started by computing simulations without any gravity effect before including gravity in the model.

Simulations without gravity effect

As gravitational effect are not included in the results of figure 3, simulations run without inertia illustrate deposition by the direct interception mechanism (since inclusions are strictly moving along fluid flow streamlines) whereas simulations with inertia reveal the inertia impact mechanism. Figure 3 shows that the difference in deposition velocity, depending on whether inertia effects are included or not, remains small. Therefore, inertia is of no significant consequence in deposition and the only deposition mechanism is direct interception. This is consistent with the small values of the Stokes number τ_p^+ meaning that the particles have little inertia and react instantaneously to any modification of the fluid flow direction.

Results of figure 4 have been obtained without gravity nor inertia, thus depicting deposition by direct interception. It can be seen in figure 4 that the greater the friction velocity u^*, the more efficient the direct interception mechanism. These results actually reflect that the number of inclusion impact to the wall rises with the friction velocity. If the adhesion force between the inclusion and the wall is strong enough it will increase the deposition velocity. Nevertheless, in practice it can be suspected that if the greater the friction velocity, the more important the inclusion resuspension. Therefore, if this effect was taken into account in the present modelisation it could lessen the deposition velocity.
Figure 4 reveals that the roughness height has little effect on the deposition of the larger inclusions. On the other hand, it helps the deposition of the smallest particles. It can be concluded that the contact between the inclusion and the wall is more easily achieved when the roughness height represents a sufficient percentage of the inclusion diameter (typically when $k \geq 5\% d_p$).

The figure 5 shows that the numerical results for deposition by direct interception align well onto a curve. It is then possible to obtain a law giving the dimensionless deposition velocity by direct interception as a function of the particle diameter, the roughness height and the friction velocity as given by:

$$V_d^+ = 10^{-3} \left(\frac{d_p + 2k}{l^*} \right)^{1.7} \quad (13)$$

The effects of lubrication on direct interception have been investigated in figure 6. It is found that lubrication significantly reduces the deposition. Its effect is stronger as the roughness height is smaller. Indeed, roughness cuts off the lubrication effects which are stronger at short distance from the wall and can delay or even prevent the inclusion deposition. Nevertheless, for larger roughness height, such as those encountered in industrial processes (*i.e.* $k \gg 1$ µm), it can be expected that lubrication has no significant influence on deposition.

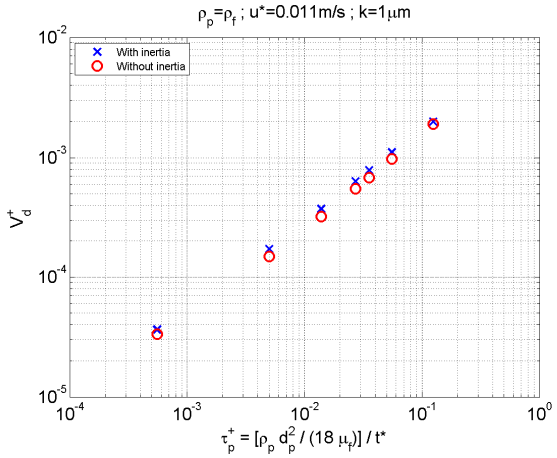

Figure 3: Dimensionless deposition velocity as a function of the inclusion Stokes number. Simulations without gravity.

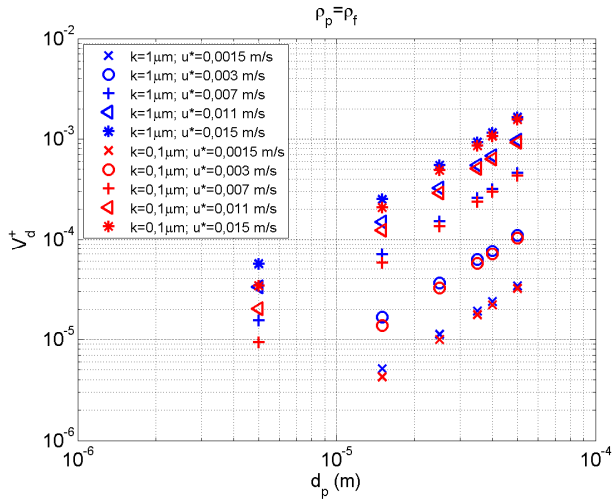

Figure 4: Dimensionless deposition velocity as a function of the inclusion diameter. Simulations without gravity nor inertia.

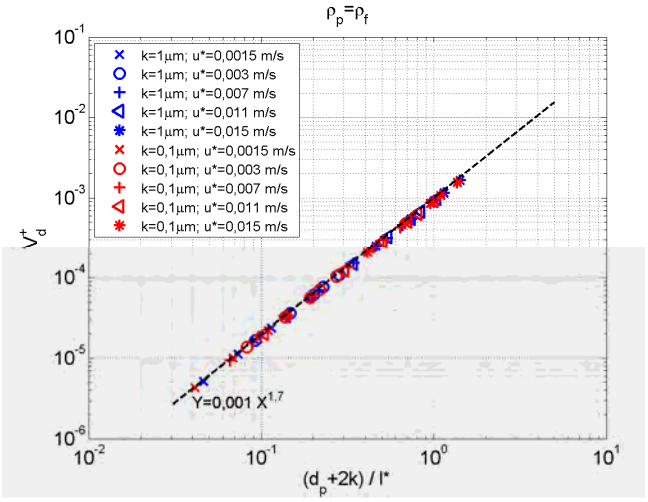

Figure 5: Dimensionless deposition velocity as a function of the inclusion diameter and the roughness height. Simulations without gravity nor inertia.

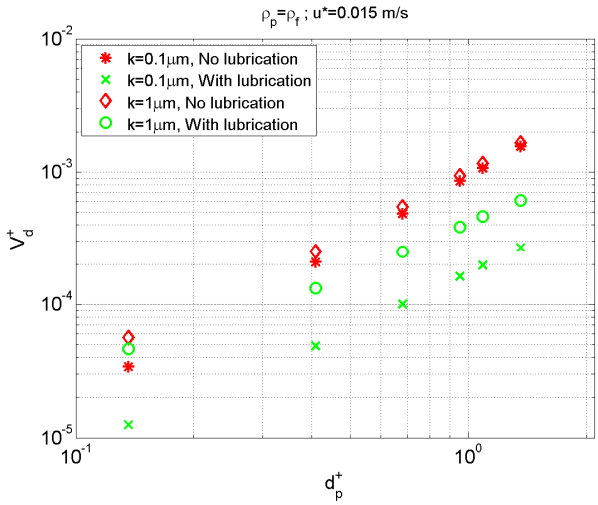

Figure 6: Dimensionless deposition velocity as a function of the dimensionless inclusion diameter. Simulations without gravity nor inertia.

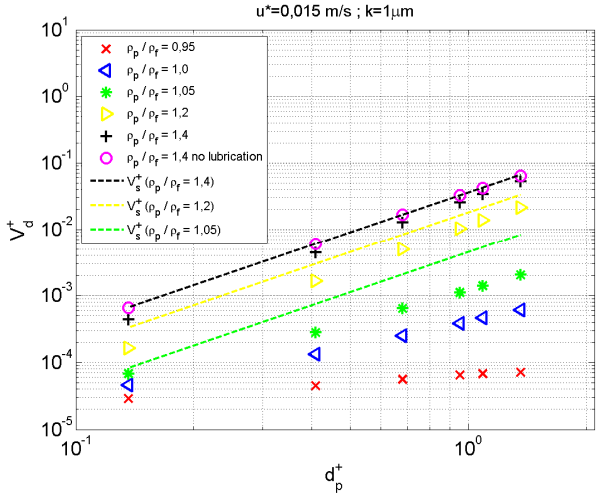

Figure 7: Dimensionless deposition velocity for different values of ρ_p/ρ_f. Simulations with lubrication.

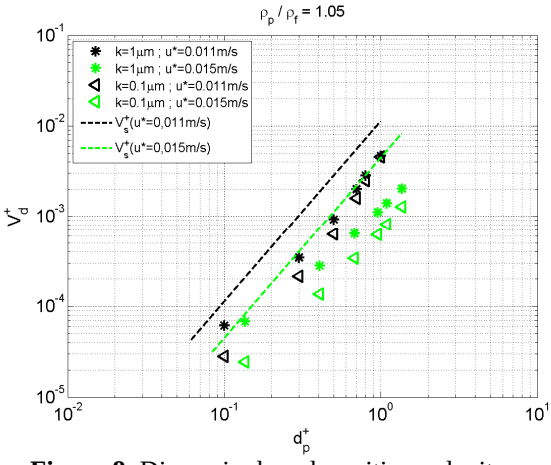

Figure 8: Dimensionless deposition velocity as a function of the dimensionless inclusion diameter. $\rho_p/\rho_f = 1.05$

Simulations with gravity effect

Configurations for which gravity is taken into account are investigated in figure 7 for different values of ρ_p/ρ_f. Figure 7 shows that for given values of friction velocity u^* and roughness height k, gravity goes against deposition for inclusion density smaller than the fluid one. On the other hand, gravity works in favour of the deposition if the inclusion density is greater than the fluid one. In that case, the greater the inclusion density compared to the fluid density, the closer to sedimentation velocity the deposition velocity. Hence it can be concluded that the sedimentation is the main deposition mechanism for inclusion dense enough compared to the fluid.
Figure 7 also shows that lubrication can reduce deposition compared to a configuration without lubrication. Nevertheless the reduction remains negligible, unlike for non-buoyant inclusions.

Unlike when $\rho_p/\rho_f > 1.2$, figures 7 and 8 show that for inclusions for which density is close to the fluid density (*i.e.* $0.95 \leq \rho_p/\rho_f \leq 1.2$), the deposition velocity significantly differs from the sedimentation velocity. It demonstrates that in that case sedimentation is not the main deposition mechanism. Figure 8 also points out that the difference between deposition velocity and sedimentation velocity grows bigger as u^* rises. Indeed, direct interception contribution on deposition increases with u^*. It can be concluded that for inclusion density larger than fluid density, sedimentation is cooperating with the direct interception mechanism and the balance between the two contributions depends on the value of ρ_p/ρ_f and u^*. As the two mechanisms react to lubrication and roughness height with different intensities as ρ_p/ρ_f and u^*vary, it becomes difficult to extract a general law that faithfully transposes the deposition velocity when $\rho_p/\rho_f \sim 1$.

CONCLUSION

Particle deposition onto a channel bottom smooth wall has been studied. Liquid aluminum flow has been obtained thanks to the sublayer model of Fan and Ahmadi (1995). Particle trajectories have been simulated by Lagrangian particle tracking under conditions of one-way coupling.
The inertia, lubrication, turbulence and wall roughness effects on deposition have been investigated.
For non-buoyant inclusions, inertia effects are not significant and the only deposition mechanism is direct interception. The higher the turbulence (*i.e.* the higher the value of u^*), the more efficient the direct interception. Wall roughness may help the deposition of the smallest inclusions. As far as direct interception is concerned, the simulated dimensionless deposition velocities (made dimensionless by the characteristic scales at the solid wall) align well onto a master curve which is a function of the particle diameter, the wall roughness and the friction velocity. On the smooth wall, lubrication has been found to significantly reduce the deposition by direct interception.

For buoyant inclusions, deposition is controlled by sedimentation for particles dense enough compared to the liquid metal. As the inclusion density gets closer to the fluid density, the sedimentation contribution on deposition decreases. On the other hand, direct interception mechanism contribution rises with $u^*$and may overcome sedimentation. As a consequence, the two mechanisms contribute to the deposition with different intensities, making it difficult to extract a general expression giving the deposition velocity for buoyant inclusions.

ACKNOWLEDGEMENTS

This research was supported by the Agence Nationale de la Recherche, as part of the PRINCIPIA project (PRocédés INdustriels de Coulée Innovants Pour l'Industrie Aéronautique, project ANR-2010-RMNP-007-01).

REFERENCES

ACOSTA G. F.A. and CASTILLEJOS E. A.H. (2000 I), "A mathematical model of aluminum depth filtration with ceramic foam filters: Part I. Validation for short-term filtration", *Metallurgical and Materials Transactions B*, **31B**, 492-502.

ACOSTA G. F.A. and CASTILLEJOS E. A.H. (2000 II), "A mathematical model of aluminum depth filtration with ceramic foam filters: Part II. Application to long-term filtration", *Metallurgical and Materials Transactions B*, **31B**, 503-514.

CLEAVER J.W. and YATES B. (1975), "A sublayer model for the deposition of particles from a turbulent flow", *Chemical Engineering Science*, **30,** 983-992.

CORINO E.R. and BRODKEY R.S.. (1969), "A visual investigation of the wall region in turbulent flow", *Journal of Fluid Mechanics*, **37,** 1-30.

DUVAL H., RIVIÈRE C., LAÉ É., LE BRUN P. and GUILLOT J.B. (2009), "Pilot-scale investigation of liquid aluminum filtration through ceramic foam filters: comparison between coulter counter measurements and metallographic analysis of spent filters", *Metallurgical and Materials Transactions B*, **40B**, 233-246.

EL-SOUDANI S.M. and PELLOUX R.M. (1973), "Influence of inclusion content on fatigue crack propagation in aluminum alloys", *Metallurgical Transactions*, **4**, 519-531.

FAN, F.G. and AHMADI, G., (1995), "Analysis of particle motion in the near-wall shear layer vortices – Application to the turbulent deposition process", *Journal of Colloid and Interface Science*, **172**, 263-277.

FAN, F.G. and AHMADI, G., (1993), "A sublayer model for turbulent deposition of particle in vertical ducts with smooth and rough surfaces", *Journal of Aerosol Science*, **24**(1), 45-64.

GUHA A. (1997), "A unified eulerian theory of turbulent deposition to smooth and rough surfaces", *Journal of Aerosol Science*, **28**(8), 1517-1537.

HE Y., LI Q. and LIU W. (2012), "Separating effect of a novel combined magnetic field on inclusions in molten aluminum alloy", *Metallurgical and Materials Transactions B*, **43B**, 1149-1155.

JORDON J.B., HORSTEMEYER M.F., YANG N., MAJOR J.F., GALL K.A., FAN. J. and McDOWELL D.L. (2010), "Microstructural inclusion influence on fatigue of a cast A356 aluminum alloy", *Metallurgical and Materials Transactions A*, **41A**, 356-363.

KIM H.T., KLINE S.J. and REYNOLDS W.C. (1971), "The production of turbulence near a smooth wall in a turbulent boundary layer", *Journal of Fluid Mechanics*, **50**, 133-160.

KLINE S.J., REYNOLDS W.C. and SCHRAUB F.A. (1967), "The structure of turbulent boundary layers", *Journal of Fluid Mechanics*, **30**, 741-773.

LAI A.C.K. (2005), "Modeling indoor coarse particle deposition onto smooth and rough vertical surfaces", *Atmospheric Environment*, **39**, 3823-3830.

MAXEY M.R. and RILEY J.J. (1983), "Equation of motion for a small rigid sphere in a nonuniform flow", *Phys. Fluids*, **26**(4), 883-889.

MIRGAUX O., ABLITZER D., WAZ E. and BELLOT J.P. (2009), "Mathematical modeling and computer simulation of molten aluminum purification by flotation in stirred reactor", *Metallurgical and Materials Transactions B*, **40B**, 363-375.

NARAYANAN C., LAKEHAL D., BOTTO, L. and SOLDATI A. (2003), "Mechanisms of particle deposition in a fully developed turbulent open channel flow", *Physics of Fluids*, **15**(3), 736-775.

NATARAJAN T.T. and El-KADDAH N. (2002), "A new method for three-dimensional numerical simulation of electromagnetic and fluid-flow phenomena in electromagnetic separation of inclusions from liquid metal", *Metallurgical and Materials Transactions B*, **33B**, 775-785.

PANTON R.L. (2001), "Overview of the self-sustaining mechanisms of wall turbulence", *Progress in Aerospace Sciences*, **37**, 341-383.

SMITH C.R. and METZLER S.P. (1983), "The characteristics of low-speed streaks in the near-wall region of a turbulent boundary layer", *Journal of Fluid Mechanics*, **129**, 27-54.

TIAN L. and AHMADI G. (2007), "Particle deposition in turbulent duct flows - Comparisons of different model predictions", *Journal of Aerosol Science*, **38**, 377-397.

TIEN C. and RAMARAO B.V. (2007), "Granular filtration of aerosols and hydrosols", *Elsevier Science & Technology Books.*

TIJANI Y., HEINRIETZ A., STETS W. and VOIGT P. (2013), "Detection and influence of shrinkage pores and non-metallic inclusions on fatigue life of cast aluminum alloys", *Metallurgical and Materials Transactions A*, **44A**, 5408-5415.

TIRYAKIOĞLU M. (2009), "Relationship between defect size and fatigue life distributions in Al-7 Pct Si-Mg Alloy castings", *Metallurgical and Materials Transactions A*, **40A**, 1623-1630.

WANG Q., SQUIRES K.D., CHEN M. and McLAUGHLIN J.B. (1997), "On the role of the lift force in turbulence simulations of particle deposition", *Int. J. Multiphase Flow*, **23**(4), 749-763.

WOOD N.B. (1981), "A simple method for the calculation of turbulent deposition to smooth and rough surfaces", *Journal of Aerosol Science*, **12**(3), 275-290.

XU Z., LI T. and ZHOU Y. (2007), "Continuous removal of non-metallic inclusions from aluminum melts by means of stationary electromagnetic field and DC current", *Metallurgical and Materials Transactions A*, **38A**, 1104-1110.

ZHAO B. and WU J. (2006), "Modeling particle deposition onto rough walls in ventilation duct", *Atmospheric Environment*, **40**, 6818-6927.

ZHOU M., SHU D., LI K., ZHANG W.Y., NI H.J., SUN B.D. and WANG J. (2003), "Deep filtration of molten aluminum using ceramic foam filters and ceramic particles with active coatings", *Metallurgical and Materials Transactions A*, **34A**, 1183-1191.

MODELLING PULVERISED FUEL TRANSPORT FOR INDUSTRIAL APPLICATIONS

Allan I.J. LOVE[1*], Donald GIDDINGS[1], Henry POWER[1]

[1] Energy and Sustainability Division, The University of Nottingham, Nottingham, UNITED KINGDOM

* E-mail: enxail@nottingham.ac.uk

ABSTRACT

The flow of pulverised fuel in a power plant is one example of gas-particle flows in the energy and process industries. Despite wide use, traditional CFD modelling approaches are often inadequate for solving industrial problems. An example is the concentration of particles within a coal burner's fuel feed due to particle inertia and inter-particle collisions. To address this a number of two-phase flow models have been investigated and their applicability and accuracy assessed by comparison with experiments in the literature for horizontal pipe sections and pipe bends (Huber and Sommerfeld,1994, Akilli et al.,2001) with a relatively high mass loading of the discrete phase. Models have been implemented in the commercial CFD software ANSYS FLUENT R14.5 for the Discrete Phase Model. The results indicate the key physics and the effects of scale on confined gas-particle flows. In addition, this paper discusses CFD model development for application to pulverised fuel flows and the gap between academic development and industrial adoption of advanced CFD models.

Keywords: Two-phase, industrial modelling, drag, particle, pneumatic conveying.

NOMENCLATURE

Greek Symbols

β Constant.
ε void fraction, [m^3/m^3].
μ Dynamic viscosity, [kg/m.s].
ν Frequency of collisions, [1/s].
ϕ Uniform random number.
ρ Density, [kg/m^3].
τ Shear stress, [Pa].
ω Effective drag coefficient.

Latin Symbols

C_D Drag coefficient.
D Diameter, [m].
d Particle diameter, [m].
f Friction factor.
F Force, [N].
N Number of particles.
P Pressure, [Pa].
p* Constant, [Pa].
Pr Probability.
Re Reynolds number.
t Time, [s].
$\mathbf{u}$ Velocity, [m/s].
U Superficial velocity [m/s]

Sub/superscripts

c Continuous phase.
cl Cluster.
col Collision.
D Drag.
den Dense phase.
dil Dilute phase.
p Discrete phase.
s Slip velocity.
0 Reference case.
i Index *i*.
j Index *j*.

INTRODUCTION

The flow of pulverised fuel in a power plant is one example of gas-particle flow in the energy and process industries. Typically coal is conveyed at a mass loading of 0.3-1kg/kg corresponding to a volume fraction, α, 0.0003-0.0008, while the volume fraction of biomass can be higher due a lower density. Therefore, assumptions based on dilute flow are often applied when modelling such systems. But this fails to account for the effects of plant geometry on the local concentration of the particles. The formation of particle 'ropes' downstream of pipe bends being the obvious example. In addition, environmental and cost pressures are necessitating the improved design of combustion systems, utilisation of new fuels (such as biomass or difficult coals) and potential adoption of dense phase conveying to lower energy requirements. All of these can be benefitted by accurate CFD modelling of the pulverised fuel flow beyond the traditional dilute limit (α=0.001).

The majority of experimental and modelling work in this area has been relatively small scale, for dilute flows and relatively large particle diameters. This has facilitated the use of non-intrusive measurement techniques (such as Laser and Phase Doppler Anemometry) and development of many particle force models, but thus far has neglected some of the realities of full scale plant. Huber and Sommerfeld (1994, 1998) investigated the flow of particles in a pneumatic conveying rig with different pipe diameters and wall materials both experimentally and numerically. They found that the effect of wall roughness was to re-suspend the particles and was paramount to obtaining the desired particle concentration profiles. In the

numerical model good agreement with experimental data was achieved for a standard deviation in the wall roughness angle of 17°. Giddings et al. (2004) performed experiments and modelling work, using a basic DPM approach, on a ¼ scale pneumatic conveying rig. Scaling was by dynamic similarity for Reynolds, Stokes and Froude numbers. Solid splits at the trifurcator are reported for mass loadings up to 0.4kg/kg and it was necessary to arbitrarily vary the normal and tangential restitution coefficients of particle wall collision to achieve agreement between the CFD model and experimental results. Likewise, Dodds et al. (2011) provides experimental and numerical results for a mill duct system featuring a trifurcator. The geometry investigated does not result in significant particle concentration or deviate significantly from a uniform distribution between each leg of the trifurcator and this is could have contributed to the apparent accuracy of the basic DPM approach used. In contrast, full scale plant is often characterised by non-ideal features such as tight bends, expansions and contractions prior to splitters which result in considerable concentration bias and transient effects.

The Euler/Lagrange approach is usually adopted for the discrete phase, known here as the Discrete Phase Model (DPM) (ANSYS, 2011). The trajectory of the particle is solved based on Newton's second law, accounting for gravity, drag forces and the coupling between the particle and the fluid at higher mass loadings. The approach has been extended to include the effects of wall roughness (Sommerfeld, 1999), lift force effects (Laín and Sommerfeld, 2008) and inter-particle collisions (Oesterle and Petitjean 1993). Stochastic inter-particle collision models are more efficient than the deterministic approach, but assume binary collisions dominate and thus may be limited in their applicability when it comes to moderately dense flows.

The fluidised bed is the traditional example of a dense particle flow. The high number and volume fractions of particles has necessitated the use of the Eulerian/Eulerian approach or Two Fluid Model (TFM), where inter-particle collisions are accounted for using the Kinetic Theory of Granular Flows and by modelling the solids shear stress. The applicability of this approach was extended by the Dense Discrete Phase Model, a hybrid model of the Lagrangian and Eulerian approaches for the discrete phase (Cloete et al. 2010).

The clustering of particles due to a combination of hydrodynamic effects, inelastic collisions and cohesive forces, has been shown to be significant in fluidised beds (Agrawal, 2001). Particle clustering lowers the drag force by a combination of drafting and a decrease in the air velocity within a cluster. This decreases the solids recirculation rate and increases the slip velocities of the particles. Even in pneumatic conveying the local concentration of particles due to inelastic collisions can lead to particle clustering (Wassen and Frank, 2001). Heynderickx et al. (2004) showed that particle clusters and their interphase momentum transfer effects can be resolved with high resolution grids (5-10d_p) using a TFM. However, such grids are impractical for industrial applications. Thus sub-grid scale models of the variation in discrete phase drag with local volume fraction have been developed, such as the correlation of Helland (2007) or the Energy Minimisation Multi-Scale methodology (EMMS) of Li and Kwauk (1994).

To investigate the ability of discrete phase modelling approaches to characterise high local particle concentration in pneumatic conveying we have investigated two cases reported in the literature for horizontal pipe sections and pipe bends (Huber and Sommerfeld (1994), Akilli et al. (2001)). Huber and Sommerfeld (1994) made measurements using Phase Doppler Anemometry (PDA) for glass spheres at various locations up and downstream of a horizontal to vertical bend. We use the 0.5kg/kg, U_c=14m/s, R/D=2.54 and steel pipe case for this work. Akilli et al. (2001) made measurements using an Optical Fibre Probe for coal particles at locations downstream of a vertical to horizontal bend. We use the 1.0kg/kg, U_c=30m/s and R/D=1.5 case for here. The number mean diameters of the particles are 58µm and 47µm in each case. Both cases (referred to as the Huber and Akilli cases respectively) combined provide an opportunity to compare the effects of physical scale, bend geometry and mass loading.

MODEL DESCRIPTION

Geometries and Mesh

The geometries for both the Huber and Akilli cases are shown in Figure 1. The Huber mesh consists of 340,000 cells and the Akilli case only 100,000. In both cases cell dimensions were ~150d_p in size. An o-grid was used and the cell aspect ratio was maintained throughout to ensure accurate particle collision statistics, rather than to reduce the cell count. Refining the meshes by 50% in each direction did not significantly alter the solutions.

Continuous Phase

Transient, isothermal simulations were performed using the commercial CFD package ANSYS FLUENT 14.5, which solves the Navier Stokes Equations using the finite volume method. The continuity and momentum equations for the continuous phase are:

$$\frac{\partial \rho_c}{\partial t} + \nabla \cdot (\rho_c \mathbf{u}) = 0 \qquad (1)$$

and

$$\frac{\partial \rho_c \mathbf{u}}{\partial t} + \nabla \cdot (\rho_c \mathbf{u}\mathbf{u}) = -\nabla P + \nabla . \mu \nabla \mathbf{u} + F_{other} \qquad (2)$$

where F_{other} is an external source due to the particles. Turbulence was modelled using the Realizable k-ε model. The pressure based solver with PISO algorithm was used for pressure correction. The convective and diffusion terms were represented using a second order upwind scheme. Time discretisation was achieved using the first order fully implicit scheme. The equation solver used was Algebraic Multigrid.

Transient solutions were initialized from the steady state case, but the final solutions were independent of these initial solutions. The time step was limited by the moment coupling between the two phases not the Courant number and is shown in Table 1. Gravity was

defined in the y-direction as $9.81 ms^{-2}$. Convergence was judged based on the global sum of the residuals for the main flow variables and equations, which were allowed to approach the accuracy for single precision. The mass balance between the inlet and outlet of the domain, pressure and particle concentration at key points were also monitored to ensure convergence.

Discrete Phase

The particle properties for each case are shown in Table 1. Rosin Rammler distributions based on the experimental particle size distributions were used in both cases. The discrete phase was modelled using the Lagrangian approach with FLUENT's Discrete Particle Model (DPM) (ANSYS, 2011). Here the Lagrangian tracking method is used to solve the individual trajectories of the theoretical particles by equating their inertia with external forces:

$$\frac{du_p}{dt} = F_D(u_p - u_c) + \frac{g(\rho_p - \rho_c)}{\rho_p} + F_{other} \qquad (3)$$

Two-way coupling, the exchange of momentum between the particles and fluid, was accounted for.

The spherical drag model of Morsi and Alexander (1972) has been used to model the particles. The effects of particle clustering and pipe diameter on the drag of an isolated particle have been modelled using a simple pressure balance model (Love et al. 2014) based on the EMMS model (Li and Kwauk, 1994). A reduction in the drag coefficient is attributed to a reduction in the air velocity within the dense cluster as the air chooses the path of least resistance around the cluster (illustrated in Figure 2). However, it has been shown that for small pipe diameters the friction on the pipe wall acts to maintain the air velocity within the cluster. The dimensions of the cluster in our cases are assumed to be a single 'plug' of particles, with diameter based on the local void fraction and overall mass loading. The pressure balance model can be summarised as follows:

$$N_{p,den}F_{D,den} = \frac{N_{cl}F_{D,cl}}{(1-\alpha_{cl})} + N_{p,dil}F_{D,dil} + \Delta P_{dil} \qquad (4)$$

Where N_p is the number of particles, F_D the drag force, subscripts *den*, *dil* and *cl* correspond to the dense phase, the dilute phase and the cluster respectively and ΔP_{dil} is the additional pressure drop associated with the pipe wall due to the dense phase:

$$\Delta P_{dil} = \frac{2 f \rho_g U_{dill}^2}{D_{pipe}} L - \Delta P_0 \qquad (5)$$

The drag forces for the particles in each phase and cluster were calculated using the formula of Flemmer and Banks (1996):

$$F_D = \frac{\pi d_p^2}{8} C_D \rho_g U_s^2 \qquad (6)$$

For $Re_p<1000$ the drag coefficient is

$$C_D = \frac{24}{\mathrm{Re}} + \frac{3.6}{\mathrm{Re}^{0.313}} \qquad (7)$$

Balancing Equation 4 for the dense phase air velocity results in the effect drag coefficient, ω, which is the ratio of the dense phase particle drag to the spherical particle drag. Figure 3 shows the variation of ω for each pipe diameter with void fraction, ε_s. The shapes of the curves agree well with the work of Zhang and Van der Hayden (2002) and are modelled using the linear functions shown in Figure 3. It can be seen that the pipe diameter has a large influence on the effective drag as a small pipe will result in greater influence of the wall and thus a higher pressure drop in the dilute phase which maintains the air velocity in a dense cluster. For the Huber case the structure dependant drag is likely to have a minimal effect on the solution, in contrast it is likely to play a key role in the Akilli case.

Where there is a significant reduction in the drag force this is associated with a reduction in the air velocity within a dense cluster. However in the DPM, reducing the drag coefficient will reduce the momentum coupling between the phases and the continuous phase will be ignorant of the presence of the cluster. To overcome this, a momentum source term proportional to the slip velocity between the fluid and the particle and the volume of air held by the cluster is applied within the continuous phase momentum equation when $\alpha>0.05$ in both cases.

Particle-particle collisions have been modelled using the Nanbu-Babovsky collision model (Gumprich, 2010). This is a stochastic collision model where the probability of a collision between particles is based on the volume of particles within a cell and their relative velocities, as follows:

$$P_{col} = \sum_{j=1}^{N_j} \{\frac{\pi}{4}(d_{p,i} + d_{p,j})^2 \,|\, u_{p,j} - u_{p,i} \,|\, n_{p,j}\} \Delta t_{col} \qquad (8)$$

The collision partner is determined at random from the other particles in the cell as:

$$j = \lfloor \phi N \rfloor + 1 \qquad (9)$$

where $\lfloor ... \rfloor$ is the integer part of the argument and ϕ is a random number between [0, 1]. The model requires a limit on the collision time step,

$$\Delta t_{col,\max} = \frac{2}{\max(\nu_{ij} N_p)} \qquad (10)$$

Where this limiting collision timestep is less than the particle time step, the collision loop is repeated until the sum of the collision timesteps is greater. The post collision velocities are calculated from the impulse equations derived by Crowe et al. (2012).

In addition, particle collisions can also be accounted for using a general collision force, F_{col}. These are typically used in the simulation of dense flows to ensure that the particle volume fraction does not exceed a close packing limit.

$$F_{col} = \frac{\nabla \tau_p}{\varepsilon_p \rho_p} \qquad (11)$$

The inter-particle stress, τ_p, is defined:

$$\tau_p = \frac{p^* \varepsilon_p^{\beta}}{\varepsilon_{\max} - \varepsilon_p} \qquad (12)$$

where p^* is 100Pa, ε_{max} = 0.6 and constant β=2 as defined by Snider (1998). It assumes the acceleration on the particle is independent of its size. This force is applied within the DPM by altering the particle's momentum with a random force vector perpendicular to the particle trajectory and a proportional deceleration

parallel to the particle trajectory. To facilitate application in the DPM, without resolving all the particle concentration gradients in the domain, the length scale of all concentration gradients was assumed to be $0.1D_{pipe}$. The direction of the vector perpendicular to the particles trajectory is under-relaxed based on the time for the particle to transit this distance and is reset upon a wall collision or upon entering a cell where $\alpha<0.03$.

The Magnus lift force is modelled according to approach of Laín and Sommerfeld (2008). The magnitudes of the Saffman lift force, and as will be shown the Magnus lift force (which is rendered insignificant by the torque from the fluid), are small in comparison to the drag force and so there contribution is minimal and not shown in this work. The virtual mass force is not accounted for due to the large density difference between the fluid and particle.

Boundary Conditions

The inflow condition was specified as a fully developed velocity profile parallel to the pipe axis. 14m/s and 30m/s were the mean air velocities for the Huber and Akilli cases respectively. A characteristic length based on the pipe diameter and an estimate of turbulence intensity was also defined. Particles were injected at random points on the inlet face with velocity 90% of the mean air velocity. Within 5D the flow had reached a steady velocity.

The no slip condition was used at the wall and the heights of the near wall cells were sufficient to accurately represent the boundary layer in each case. The Enhanced Wall Model has been used for the Huber case and the Standard Wall Function for the Akilli case due to the higher velocity. Particle wall collisions were accounted for using the wall roughness model of Sommerfeld (1999). The standard deviation of the wall roughness angle for steel was taken as 7.5 degrees, based on the mean particle diameter. The restitution and friction coefficients were modelled as:

$$e = MAX\left(1+\frac{1-e_H}{0-\varphi_e}\varphi, e_H\right) \qquad (13)$$

$$u_d = MAX\left(\mu_0+\frac{\mu_0-\mu_H}{0-\varphi_\mu}\varphi, \mu_H\right) \qquad (14)$$

RESULTS

Huber Case

In the experiment of Huber the particle flow first travels along a 5.5m horizontal pipe were it partially settles towards the bottom of the pipe, before going around the vertical to horizontal bend, concentrating into a particle rope and dispersing up the vertical pipe. The concentration profile for DPM model including the wall roughness (WR) and particle collisions (PCOL) models within the horizontal pipe at x=4500mm is shown in Figure 5 for a steel pipe. Reasonable agreement is obtained with the experimental results in the top ¾ of the pipe. The particle concentration in the bottom ¼ of the pipe is over predicted. Gravity pulls the particles towards the bottom of the pipe, but the action of the wall roughness and inter-particle collisions is to resuspend the particles away from the bottom wall. However, in this case there appears to be an under-prediction of this effect.

Figure 5 also shows the influence of the Magnus lift force (MAG) with and without the torque (T) on the particle. Although the Magnus lift force has the potential to be significant, for the small particle diameters in these cases the torque dominates and decreases the Magnus lift force to render it almost insignificant and so from a practical point of view it is just an expense to include it. It also does not have a significant effect on the over prediction of the discrete phase concentration at the bottom of the pipe.

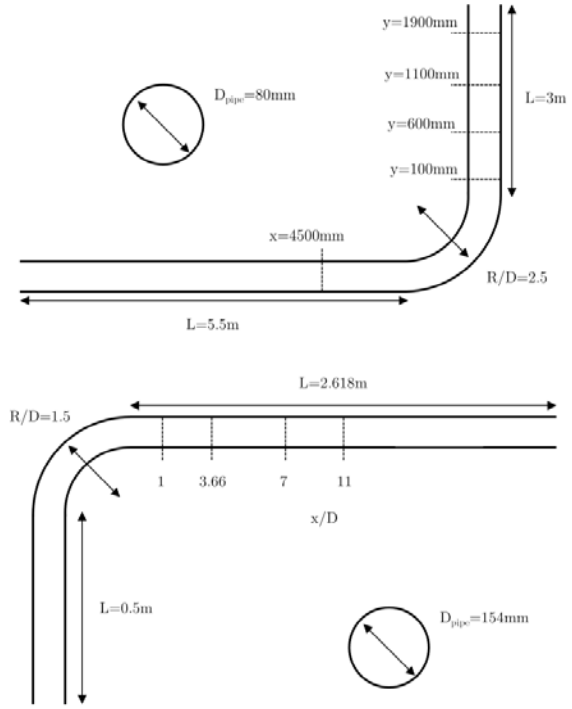

Figure 1: Schematic diagram of the geometries in the Huber (top) and Akilli (bottom) cases. [- - -] sample points.

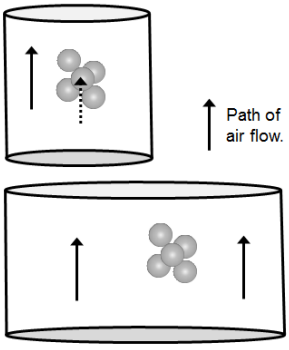

Figure 2: Schematic of cluster drag model. Air will flow around the cluster, or 'plug' of particles, in a larger pipe due to the decreasing significance of the wall.

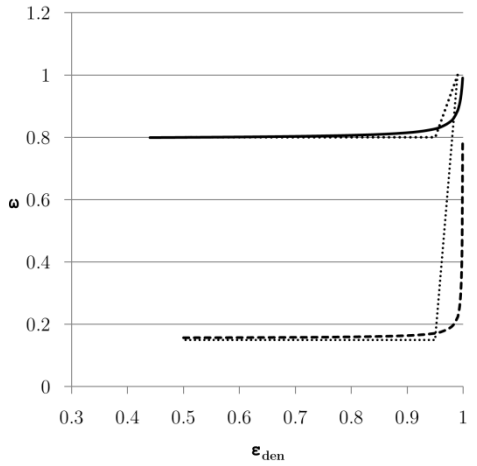

Figure 3: Variation in the effective drag coefficient, ω, with void fraction in the dense cluster, ε_{den}. [—] Huber, D_{pipe}=0.08m. [- - -] Akilli, D_{pipe}=0.154m. [….] Modelled linear function.

Table 1: Case parameters.

Case	Huber	Akilli
D_{pipe} [m]	0.08	0.154
d_p [μm]	47	58
ρ [kgm^{-3}]	2500	1680
No of particles/parcel	3,000	10,000
e	0.7	0.36
φ_e	22	21.3
μ_h	0.5	0.4
μ	0.15	0.15
φ_μ	20	60
e_{col}	0.9	0.36
$\Delta\gamma_{wall}$[degrees]	7.5	7.5
y^+	35	120
Δt	5x10^{-5}	2.5x10^{-5}

This over prediction of the particle concentration near the wall is also shown by the action of the pipe bend. Inertial effects and inter-particle collisions further concentrate the particles on the outside of the bend. Figure 6 shows the profiles of particle concentration in the vertical pipe at y=100, 600, 1100 and 1900mm for both the model and the experimental results of Huber in the steel pipe case. It can be seen that the particle concentration is substantially over predicted in the steel pipe case. This could be a consequence of the over prediction in the horizontal pipe section or due a similar reason for the over prediction in that section. Most likely it is a combination of both.

For steel an estimate of the standard deviation in the wall roughness angle was made based on profiles from a number of steel samples and the data of Sommerfeld (1999)(Figure 4). Huber and Sommerfeld (1998) used a value of 17°, over double our estimate in their numerical analysis and achieved good agreement with the experimental profiles. It will be shown for the Akilli case that such an increase in the wall roughness distribution angle cannot be regarded as universal fix. If we want to move towards a two-phase modelling methodology which is applicable across a wide range of cases competing explanations for this effect must be investigated. An under prediction in the effect of inter-particle collisions could also provide an explanation.

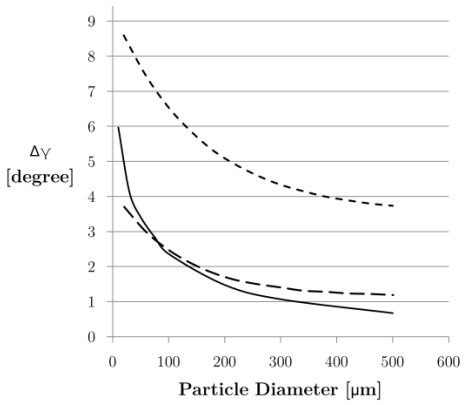

Figure 4: Variation in roughness angle distribution. [—] steel distribution from our work, [- - -] high and low roughness samples respectively of Sommerfeld (1999).

An under-prediction of the effect of inter-particle collisions would result in an over prediction in the particle concentration near the wall. The stochastic particle collision model assumes a collision frequency based on the volume of particles in a cell, however a collision event is resolved on a one to one basis for the number of particles in a parcel. A number of possible collision events between other particles in the parcels are not resolved, resulting in an under-prediction in the number of collisions. For the Huber and the Akilli cases the number of particles in a parcel for the mean particle diameter are 3,000 and 10,000 respectively. In an attempt to assess this under prediction two things can be done: increase the number of particles to reduce the number of particle per parcel; or simulate an increase in the number of collisions by reducing the restitution coefficient. Here we reduce the restitution coefficient. This effect was first highlighted in the work on riser flows of Benyahia and Glavin (2010), where an under predict in the number of particle collisions was associated with a lower granular temperature and incorrect particle velocity and concentration profiles. By lowering the restitution coefficient for inter-particle collisions in our model from 0.9 to 0.36 we indeed see a reduction in the particle concentration for both the horizontal and vertical pipe sections, shown in Figure 4 and Figure 5. This could indicate that the number of collisions is under-predicted by the particle parcel assumption or that in regions of high particle concentration the binary assumption of the stochastic collision model breaks down. The volume fraction on the outside of the bend in this case approaches 10%. Although this case alone does not clarify either of these two mechanisms, it will be shown in the next section, there is further evidence that it is the inter-particle collision effect which is key to the simulation of relatively dense gas-particle flows.

Akilli Case

In the experimental case of Akilli a dense coal rope forms on the outside of the bend before falling towards the centre of the pipe and dispersing with increasing downstream distance. The trajectory of the rope was found to vary with bend radius and velocity. The main differences between the Akilli and Huber case are the pipe diameter, mass loading, bend radius and velocity, all of which contribute to a higher particle concentration on the outside of the bend. Contours of concentration

for DPM models featuring combinations of the wall roughness (WR), particle collision (PCOL), solids pressure (PS) and drag modification (DM, CS) are shown in Figure 7. As was shown for the Huber case the effect of Magnus lift force is insignificant for this particle size. The contours in the preceding vertical section also indicate that the additional models do not influence the particle flow in dilute regions.

Figure 7a shows that the DPM model featuring wall roughness ($\Delta\gamma$=15°) and stochastic inter-particle collision model fails to capture the trajectory or dispersion of the rope. The predicted position of the rope remains at the top of the pipe. Akilli et al. (2001) performed numerical simulations using a basic DPM model for a bend radius of 3R/D and Z=0.333 kg/kg, good agreement between the experimental and model were obtained but it can be seen that this is probably due to the position of the rope rather than a model which accounts for an accurate representation of the physics. Likewise, Huber and Sommerfeld (1998) obtained good agreement by defining a standard deviation in the wall roughness angle double what has been obtained from experimental roughness profiles. We investigate that effect here by doubling the wall roughness angle to 15° but obtain no similar improvement in this case as the drag force on the particles dominates and the increase in pipe diameter reduces the influence of the pipe wall.

Figure 7b and 7c show the contribution of the structure dependent drag model and the solids pressure model. Both in isolation show a small improvement on the trajectory of the majority of particles immediately following the bend. In the case of the structure dependent drag model, the particles are sheltered from the air, lowering their velocity. In the case of the solids pressure model the particle velocities are lowered and the trajectories altered by the concentrated region in the outside of the bend. Though, as shown in Figure 7d, it is the combination of both which eventually leads to a substantially improved representation of the trajectory of the coal rope. This was further improved by turning off the discrete random walk model in FLUENT, which accounts for the effect of turbulence on the particles, and is shown in Figure 7e. The discrete random walk model has a significant effect on the dispersion of the particles within the rope.

The turbulence intensity contours are shown in

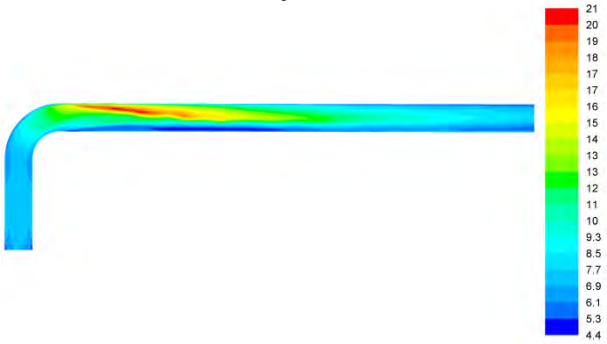

Figure 8. It can be see that the turbulence is very high within the rope. Particles can either augment or attenuate fluid turbulence depending on their size and the mass loading. It can be seen in this case that the fluctuation of the many particles in the simulated rope and the high local density and velocity gradient leads to the generation of turbulence. Based on the work of Tsuji et al. (1984) and Gore and Crowe (1989) an increase in the mass loading of the small particles in the Akilli case should lead to a dampening in the local turbulence intensity within the rope. In contrast, the turbulence intensity is likely to be high around the rope due to the high velocity gradients. These effects are not accounted for by the model described here. Therefore, the true solution is likely to lie between both models. However, it is shown that the model excluding stochastic tracking performs best in the region of the rope, indicating that the attenuation of turbulence by the particles is important to describing the dispersion of the rope.

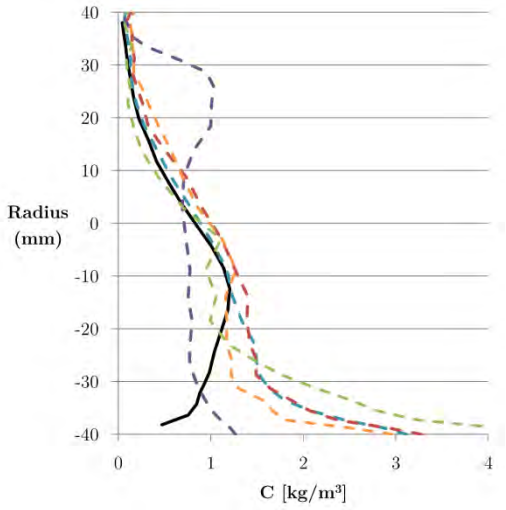

Figure 5: Concentration profiles in horizontal steel pipe at x=4500mm for Huber case. [—] Experimental. [●] WR, PCOL. [●] WR, PCOL, MAG. [●] WR, PCOL, MAG, T. [●] WR, PCOL e=0.36. [●] WR, PCOL, DM, CS.

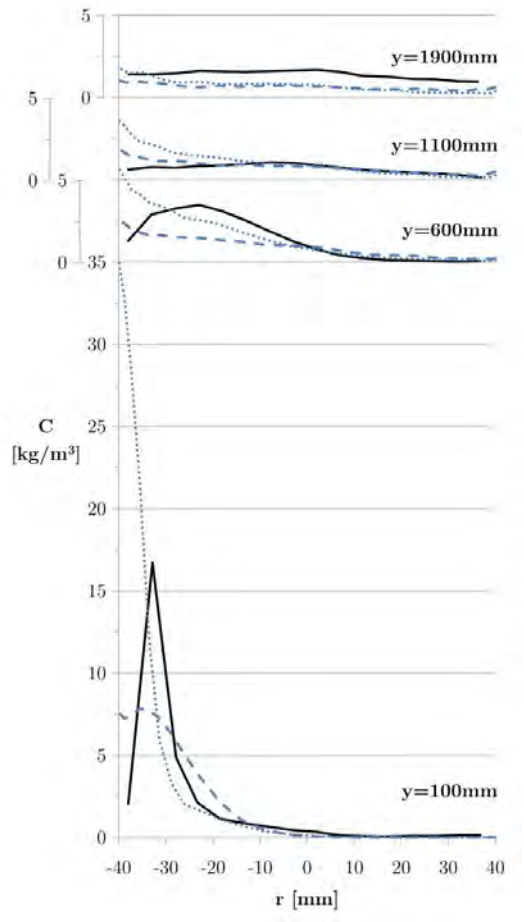

Figure 6: Concentration profiles in vertical pipe at for the Huber case. [—] Experimental. [….] WR, PCOL. [- - -] WR, PCOL e=0.36.

The concentration profiles of the DPM including WR PCOL DM CS PS are compared with experimental profiles in Figure 9. Reasonably good agreement for the position of the rope and peak concentration is obtained. As with the Huber case, the particle concentration on the outside of the bend is over predicted. In the basic DPM model there is nothing to stop the overlap of the theoretical particles, so a simplified implementation of the solids pressure was included to limit this effect. In the cases mentioned the peak concentration on the outside of the bend drops from ~350 kgm^{-3} to ~220kgm^{-3}. In our model, the particle first must move into a cell with a high particle concentration (usually isolated to 1 or 2 near wall cells on the outside of the bend) before it is subject to this additional collision force, which can push the particles apart. This does not stop an initial period of high concentration in the bend because we have not accounted for the particle concentration gradient directly. As we have shown by the doubling of the wall roughness angle distribution, this is likely to be an inter-particle collision effect.

CONCLUSIONS

Transient simulations of particles flows in steel pipes of two diameters have been investigated using the Discrete Particle Model featuring a number of additional particle force models in ANSYS FLUENT. These included wall roughness, inter-particle collision, Magnus lift and torque, an additional collision force and a structure dependent drag formulation. The main conclusions are:

1) An effective drag coefficient, based on particle clusters and accounting for the pipe wall pressure drop, shows a significant variation with pipe sizes. Application of this drag coefficient to the relatively large pipe of Akilli allowed the trajectory of the rope to be replicated.

2) The wall roughness distribution angle was defined based on roughness profile data. Increasing this value was found to have a minimal effect on the trajectory of the rope in the Akilli case.

3) A stochastic collision model has been applied within the DPM. An over prediction in the particle concentration near the wall in both cases could be due to an under-prediction in the number of particle collisions. The particle parcel assumption or the assumption of binary collisions could contribute. A reduction in the restitution coefficient, and an additional collision force model improved both the Huber and Akilli cases respectively. This indicates that traditional stochastic collision models may breakdown for large systems with high numbers of particles per parcel or for regions of high local concentration.

4) It has been confirmed that the effect of torque renders the Magnus lift force almost insignificant for this particle size.

5) The effects of scale and local concentration on the accuracy of the simulation are clear. There is both a physical scaling effect shown by the structure dependant drag force and a break down in the performance of stochastic collision models with increased mass loading.

Applications of industrial pneumatic transport are increasingly demanding improved accuracy of simulations and for application to challenging geometries. By improving our understanding of the fundamental physics and limitations of particle flow models we can develop models with greater applicability. This work is contributing to the characterisation of industrial pneumatic conveying systems. Future work will utilise a model which can represent the discrete phase concentration gradients directly and thus improve the prediction of the solids pressure and the effect of inter-particle collisions, such as FLUENT's Dense Discrete Phase Model.

ACKNOWLEDGEMENTS

The authors acknowledge the financial support of Research Councils UK, the Engineering and Physical Science Research Council and Doosan Power Systems Ltd.

REFERENCES

AGRAWAL, K., LOEZOS, P.N., SYAMLAL, M., and SUNDARESAN, S., (2001), "The role of meso-scale structures in rapid gas-solid flows", *Journal of Fluid Mechanics*, **445**, 151-185.

AKILLI, H., LEVY, E. K., and SAHIN, B., (2001), "Gas-solid flow behaviour in a horizontal pipe after a

90° vertical-to-horizontal elbow", *Powder Technology*, **116,** 43-52.

ANSYS (2011), "FLUENT Theory Guide", ANSYS, Inc. Release 14.0.

BENYAHIA, S. and GALVIN, J. E., (2010), "Estimation of numerical errors related to some basic assumptions in discrete particle methods", *Industrial Engineering and Chemical Research*, **49**, 10588-10605.

CLOETE, S., JOHANSEN, S., BRAUN, M., POPOFFM B. and AMINI, S., (2010), "Evaluation of a Lagrangian discrete phase modelling approach for resolving cluster formation in CFB risers", *7th International Conference on Multiphase Flow*, Tampa, Florida, USA

CROWE, C.T., SCHWARZKOPF, J.D., SOMMERFELD, M. and TSUJI, Y., (2012), "Multiphase Flows with Droplets and Particles", CRC Press, Taylor and Francis Group, Second Ed.

DODDS, D. NASER, J., STAPLES, J., BLACK, C., MARSHALL, L., and NIGHTINGALE, V., (2011), "Experimental and numerical study of the pulverised-fuel distribution in the mill-duct system of the Loy Yang B lignite fuelled power station", *Powder Technology*, **207**, 257-269.

GIDDINGS, D., AROUSSI, A., PICKERING, S.J., and MOZAFFARI, E., (2004), "A ¼ scale test facility for PF transport in power station pipelines", *Fuel*, **83**, 2195-2204.

GUMPRICH, W., CHRIGUI, M. BRAUN, M. and SADIKI, A. (2010), "Evaluation of collision models applied to varying dense particle jet flows", *7th International Conference on Multiphase Flow*, Tampa, Florida, USA

HELLAND, E., BOURNOT, H., OCCELLI, R. and TADRIST, L., (2007), "Drag reduction and cluster formation in a circulating fluidised bed", *Chemical Engineering Science*, **62**, 148-158.

HEYNDERICKX, G.J., DAS, A.K., DE WILDE, J. and MARTIN, G.B., (2004), "Effect of clustering on gas-solid drag in dilute two-phase flow", *Industrial and Engineering Chemistry and Research*, **43**, 4635-4646.

HUBER, N. and SOMMERFELD, M. (1994), "Characterization of the cross-sectional particle concentration distribution in pneumatic conveying systems", *Powder Technology*, **79**, 191-210.

HUBER, N. and SOMMERFELD, M. (1998), "Modelling and numerical calculation of dilute-phase pneumatic conveying in pipe systems", *Powder Technology*, **99**, 90-101.

LAÍN, S. and SOMMERFELD, M., (2008), "Euler/Lagrange computations of pneumatic conveying in a horizontal channel with different wall roughness", *Powder Technology*, **184**, 76-88.

LI, J., and KWAUK, M., (1994), "*Particle Fluid Two-phase Flow: The Energy-Minimization Multi-Scale Method*", Metallurgical Industry Press, China, Beijing.

MORSI, S.A. and ALEXANDER, A.J., (1972), "An investigation of particle trahectories in two-phase flow systems", *Journal of Fluid Mechanics*, **55**, 193-208.

OESTERLE, B. and PETITJEAN, A., (1993), "Simulation of particle-to-particle interactions in gas-solid flows", *International Journal of Multiphase Flow*, **19**, 199-211.

SCHADE, K., ERDMANN, H., HADRICH, T. SCHNEIDER, H. FRANK, T. and BERNET, K., (2002), "Experimental and numerical investigation of particle erosion caused by the pulverised fuel in channels and pipework of coal-fired power plant", *Powder Technology*, **125**, 242-250.

SNIDER, D.M., O'ROURKE, P.J., and ANDREW, M.J., (1998), "Sediment flow in inclined vessels calculated using a multiphase particle-in-cell model for dense particle flows", *International Journal of Multiphase Flow*, **24**, 1359-1382.

SOMMERFELD, M. and HUBER, N., (1999), "Experimental analysis and modelling of particle-wall collisions", *International Journal of Multiphase Flow*, **25**, 1457-1489.

SOMMERFELD, M., (2001), "Validation of a stochastic Lagrangian modelling approach for inter-particle collisions in homogeneous isotropic turbulence", *International Journal of Multiphase Flow*, **27**, 1829-1858.

WASSEN, E., and FRANK, T., (2001), "Simulation of cluster formation in gas-solid flow induced by particle-particle collisions", *International Journal of Multiphase Flow*, **27,** 243-458.

ZHANG, D.Z. and VADERHEYDEN, W.B., (2002), "The effects of mesoscale structures on the macroscopic momentum equations for two-phase flows", *International Journal of Multiphase Flow*, **28,** 805-822.

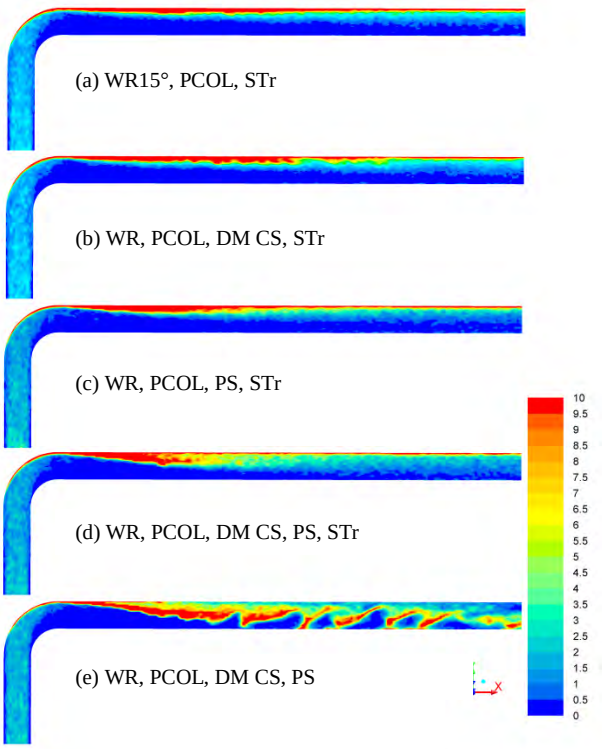

Figure 7: Contours of particle concentration (0-10 kg/m^3) for the Akilli case showing the position of the coal rope as predicted by each of the models.

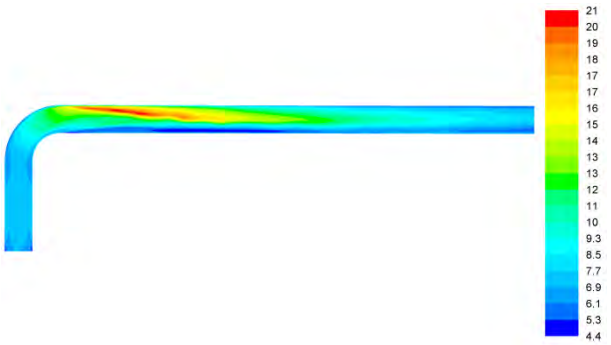

Figure 8: Contours of turbulence intensity for the DPM with WR, PCOL, DM CS, PS. Highest turbulence intensity is within the rope.

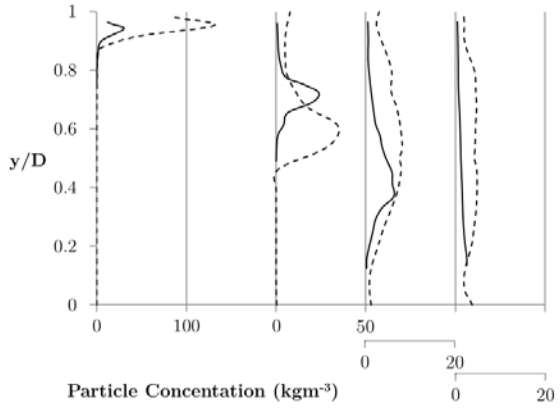

Figure 9: Experimental and particle concentration profiles for Akilli case for the DPM model including WR, PCOL, DM CS, PS.

NUMERICAL STUDY OF THE GAS-PARTICLE FLOW IN A CONVEYING LINE: ACCOUNTING FOR WALL-FRICTION AND WALL-ROUGHNESS

Afsaneh SOLEIMANI[1,2*], Simon SCHNEIDERBAUER[1,2], Stefan PIRKER[1,2]

[1] Christian Doppler Laboratory on Particulate Flow Modeling, Johannes Kepler University, Linz, Austria

[2] Department of particulate Flow Modelling, Johannes Kepler University, Linz, Austria

* E-mail: Afsaneh.Soleimani@jku.at

ABSTRACT

The Johnson-Jackson boundary conditions are included in the twoPhaseEulerFoam solver of OpenFOAM-2.2.x in order to consider the wall-friction effect on the movement of particles. A straight conveying line using Johnson-Jackson boundary conditions is simulated. The results show that the particles' velocity at the wall is in better agreement with the experimental results (Sommerfeld and Kussin, 2004), compared to the results of the original solver neglecting wall-friction. However, the model is valid only for a specific adjusted value of the specularity coefficient. Thus, Johnson-Jackson model is revisited based on the work of Li and Benyahia (2012). To improve the accuracy of the granular temperature contribution, a new boundary condition, which incorporates sliding and non-sliding collisions, proposed by Schneiderbauer et al. (2012), is included in the solver. The velocity profiles of the particles, using the latter boundary condition, are compared to that of the Johnson-Jackson cases as well as the experimental results. It appears that the boundary conditions of Schneiderbauer (Schneiderbauer et al., 2012) yield better agreement with experimental data since these are based on the physical properties and incorporate the coulomb limit to particle-wall collision. Furthermore, based on the experimental study of Sommerfeld (Sommerfeld and Kussin, 2004), wall-roughness appears to be an important factor for the transfer of tangential momentum in vertical direction. Accordingly, wall-roughness and shadow effect (Sommerfeld and Huber, 1999) are studied in order to propose a new model for including wall-roughness in TFM simulations. Finally, the proposed model is implemented in twoPhaseEulerFoam, and the effect of this phenomenon on the particle's velocity profile is studied. The results show that wall-roughness has a strong effect on rebound and redispersion of the particles and accordingly changes the particles' concentration in the section of conveying line significantly.

Keywords: Pneumatic conveying, gas-particle flow, wall-friction, wall-roughness, numerical modeling, boundary condition.

NOMENCLATURE

Greek Symbols

α Impact angle, [degree].
α_q Volume fraction of phase q.
β Interphase momentum exchange, [kg/m^3.s].
β_0 Tangential coefficient of restitution.
γ Virtual wall angle, [degree].
γ_θ Dissipation of energy by viscous damping, [kg/m.s^3].
Γ_s Production of energy, [kg/m.s^3].
μ Wall-friction factor.
ρ Density, [kg/m3].
σ Standard deviation of roughness, [degree].
ϕ Specularity coefficient.
ϕ' Effective specularity coefficient.
Θ Granular temperature, [m^2 /s^2].

Latin Symbols

D Dissipation of energy, [kg/s^3].
e Restitution coefficient.
g Gravity, [m/s^2]
g_0 Radial distribution function.
G Generation of energy, [kg/s^3].
J_v Dissipation term of energy, [kg/m.s^3].
N Normal stress, [kg/m.s^2].
p Pressure, [kg/m.s^2]
R Particle diameter, [m].
$\mathbf{u}$ Velocity, [m/s].
$\mathbf{q}$ Flux of pseudo thermal energy, [kg/s^3].
S Shear stress, [kg/m.s^2].

Sub/superscripts

g Gas phase.
n Normal component.
p Particle.
s Solid phase.
t Tangential component.
w Wall.
sl Sliding.

ave Average value over cross section

INTRODUCTION

In many industrial processes, powdery dust (like coal or cement) has to be conveyed from a feeding vessel towards its processing point. The associated gas-particle flow should be studied carefully in order to optimize the design and operation efficiency of such an industrial system. In these processes, the movement of the conveyed particles is strongly affected by the wall-friction and wall-roughness of the conveying line. Sommerfeld and Huber (1999) presented an experimental analysis and modelling of particle-wall collisions. A detailed experimental analysis was performed with special attention to the influence of wall-roughness. They also used this experimental data to validate a wall collision model in the frame of the Lagrangian approach. Following this work, several experimental and numerical studies were conducted using the same setup to study the contribution of boundary condition in gas-particle flow prediction. However, there are limited numerical studies concerning the effect of wall-friction and wall-roughness in the frame of two-fluid method (TFM).

In another work, Sommerfeld and Kussin (2004) experimentally studied the wall-roughness effects on pneumatic conveying of spherical particles in the same narrow channel. In this study, the significant effect of wall-roughness on particles' behaviour colliding with the wall is demonstrated. It was concluded that wall-roughness has a strong effect on rebound and redispersion of particles.

Benyahia et al. (2005) evaluated different boundary conditions for modelling a dilute, turbulent gas-solid flow in a pipe.

In this study, it was observed that the experimental data for solids velocity fall between the small-friction/all sliding and large-friction/no-sliding limits of Jenkins and Louge (1997). However, there was no obvious way to interpolate between the two limits and to get a good match with experiment. Therefore, Johnson-Jackson boundary condition with its adjustable specularity coefficient was considered as an alternative way of using the boundary condition of Jenkins and Louge (1997) (a high specularity coefficient for large-friction/no-sliding limit and a low specularity coefficient for small-friction/all-sliding limit).

Schneiderbauer et al. (2012) developed boundary conditions, which include sliding and non-sliding conditions in one expression with more accuracy in granular temperature prediction. This model delivered the same results as the calculation of Jenkins (1992) for large friction/no sliding and low friction/all sliding limits.

Considering the fact that wall boundary conditions for the solids wall shear stresses and the granular temperature, i.e. the transfer of momentum and energy, play an important role in the behavior of particles in a typical pneumatic conveying line, the present study is a preliminary step towards the improvement of boundary condition modeling in gas-particle flows, by considering the effect of wall-friction and wall-roughness, within kinetic theory, based TFM.

Different boundary conditions are implemented in the standard solver of OpenFOAM-2.2.x and evaluated based on the comparison with experimental data.

PRELIMINARY SIMULATIONS

In the present work, we simulate the gas-particle flow in a straight horizontal channel, using kinetic theory based TFM. Two-fluid model is a method originating from Eulerian representation of the dispersed phase, i.e. it is considered as a fluid.

Thus, the continuity equation reads:

$$\frac{\partial}{\partial t}\alpha_q\rho_q + \nabla.\left(\alpha_q\rho_q\mathbf{u}_q\right) = 0 \qquad (1)$$

where q denotes either gas (g) or solid (s) phase.

Momentum balance for gas phase is nearly the same as in case of single-phase flow. It is extended by an interphase exchange term $\beta\left(\mathbf{u}_g - \mathbf{u}_s\right)$ between the particle and the gas phase and the volume fraction α_g of the phase:

$$\begin{aligned}\frac{\partial}{\partial t}\left(\alpha_g\rho_g\mathbf{u}_g\right) + \nabla.\left(\alpha_g\rho_g\mathbf{u}_g\mathbf{u}_g\right) = \\ -\alpha_g\nabla p + \nabla.\alpha_g\mathbf{T}_g - \beta\left(\mathbf{u}_g - \mathbf{u}_s\right) + \alpha_g\rho_g\mathbf{g}\end{aligned} \qquad (2)$$

The interfacial momentum exchange term is computed by drag coefficient of Wen and Yu (Schneiderbauer et al., 2012).

where $\mathbf{T}_g$ denotes the shear stress tensor for the gas phase. The momentum balance for the solid phase is given by:

$$\begin{aligned}\frac{\partial}{\partial t}\left(\alpha_s\rho_s\mathbf{u}_s\right) + \nabla.\left(\alpha_s\rho_s\mathbf{u}_s\mathbf{u}_s\right) = \\ -\alpha_s\nabla p - \nabla.\left(\mathbf{S}_s^{kc} + \mathbf{S}_s^{fr}\right) + \beta\left(\mathbf{u}_g - \mathbf{u}_s\right) + \alpha_s\rho_s\mathbf{g}\end{aligned} \qquad (3)$$

where $\mathbf{S}_s^{kc}$ denotes the solids stress tensor arising from the kinetic and collisional contributions, $\mathbf{S}_s^{fr}$ the stress tensor from frictional contributions. For closures of $\mathbf{S}_s^{kc}$ and $\mathbf{S}_s^{fr}$ see Schneiderbauer et al. (2012).

Finally, the balance equation for granular temperature is given by:

$$\begin{aligned}\frac{3}{2}\left(\frac{\partial}{\partial t}\left(\alpha_s\rho_s\Theta\right) + \nabla.\left(\alpha_s\rho_s\mathbf{u}_s\Theta\right)\right) = \\ -\mathbf{S}_s^{kc} : \nabla\mathbf{u}_s - \nabla.\mathbf{q} - J_v - \gamma_\Theta + \Gamma_s\end{aligned} \qquad (4)$$

The first term on right hand side of the equation, denotes the generation of pseudo-thermal energy. The second term represents the diffusion of pseudo-thermal energy. J_v is the dissipation term, γ_Θ describes the dissipation of energy by viscous damping and Γ_s describes the production of energy by gas-particle slip between the

solid phase and the gas phase (Schneiderbauer et al., 2012).

In the present study, equations (1)-(4) are used to numerically model the gas-particle flow in a straight channel, studied experimentally by Sommerfeld and Kussin (2004). The dimensions of the channel are: length=6m, height= 35mm, wide=350mm. The computed domain contains 3428×20 uniform cells.

The particles diameter is equal to 195 μm and the density of particles is 2450 kg/m^3 with a loading ratio of 0.3 (dilute regime). the carrier gas is air with $\rho = 1.15\,\text{kg/m}^3$ and average velocity equal to 20 m/s.

In Figure 1 the vertical profiles of particle's velocity for different wall roughness resulted from Sommerfeld and Kussin's work at x=5.8m are plotted. The velocity profile obtained from twoPhaseEulerFoam solver (in which the wall friction is ignored), is illustrated in the black color. The figure shows that the predicted velocity profile is more asymmetric (lower velocities at the top of the channel) than the experimental data.

Furthermore, the experimental work of Sommerfeld shows that the wall-roughness introduces a transfer of horizontal momentum in vertical direction, originating from the effect of wall-roughness on the particles' rebound and redispersion, especially in a horizontal conveying line. Hence, in a narrow horizontal channel, where particle-wall collisions dominate the particle behavior, an increased wall roughness is expected to considerably change the vertical profile of particle velocity (Sommerfeld and Kussin, 2004).

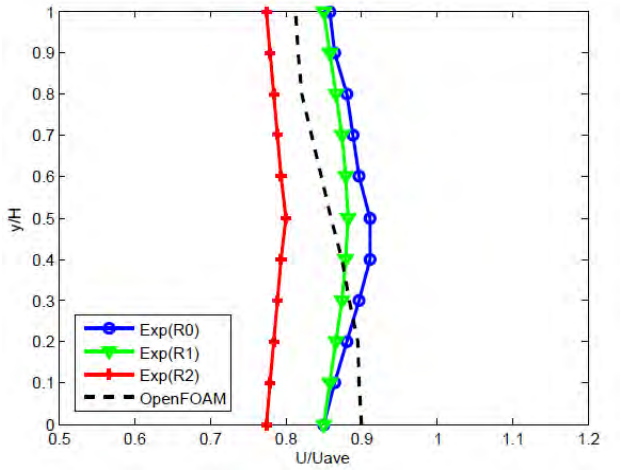

Figure 1: Measured velocity Profile for the 195- μm particles at a mass loading of 0.3 for different wall roughness (low roughness (R0), high roughness (R2))

Considering the fact that in the numerical analysis, wall friction and wall roughness are neglected, particles with high velocity are moving from the centre of the channel towards the lower wall (because of the effect of gravity), where they experience neither wall friction nor wall roughness. Therefore, there are fast-moving particles at the lower wall, without wall friction against their movement to decrease their velocity as observed in the experiment. These fast moving particles also do not face wall-roughness effect, which causes increased redispersion of particles. Accordingly, the model does not introduce any vertical momentum.

However, Sommerfeld's work reveals that increasing wall-roughness results in a decrease of horizontal momentum. In fact, increasing the wall-roughness leads to increasing particle's redispersion and thus, results additionally in a more symmetric profile.

Therefore, in order to reach more realistic results and better agreement with the experiment, in the present study, the wall-friction and wall-roughness are implemented in the standard TFM solver of OpenFOAM (twoPhaseEulerFoam).

In the next section, the equations derived by Johnson and Jackson (1987) for the boundary field and their implementation in OpenFOAM are presented. In the next step, the revisited Johnson-Jackson boundary conditions (Li and Benyahia, 2012) are studied and as a third step, more general boundary conditions, derived by Schneiderbauer (Schneiderbauer, et al., 2012), are implemented. Finally, a model for including wall-roughness effect in the solver based on the idea of using virtual wall angle model of Sommerfeld (1992) in comprehensive boundary conditions of Scneiderbauer is proposed.

Evaluating different boundary conditions demonstrates that Schneiderbauer boundary conditions are more comprehensive as they include both sliding (coulomb's law) and non-sliding conditions in one expression, and also, these are more accurate, computing the granular temperature, and leading to better agreement with the experiment.

Furthermore, including wall roughness using virtual wall model of Sommerfeld in general boundary conditions of Schneiderbauer yields reasonable trend of particle velocity profile and particle concentration profile according to the experiment, which validate the model for wall-roughness implementation.

INCLUDING WALL-FRICTION IN THE SOLVER

Johnson-Jackson Boundary Conditions

Johnson and Jackson (1987) developed boundary conditions that consider the tangential solids shear stress ($\mathbf{s}$) and the flux of fluctuation energy ($\mathbf{q}$) at a flat frictional wall.

$$\mathbf{S} = -\frac{\sqrt{3}\pi}{6}\phi\frac{\alpha_s\rho_s g_0}{\alpha_{s,\max}}\sqrt{\Theta}\mathbf{u}_s^{sl} \qquad (5)$$

$$-\mathbf{n}\cdot\mathbf{q} = -\mathbf{S}\cdot\mathbf{u}_s^{sl} + \frac{\sqrt{3}\pi}{4}\frac{\alpha_s\rho_s g_0}{\alpha_{s,\max}}\left(1-e^2\right)\Theta^{3/2} \qquad (6)$$

The specularity coefficient, ϕ, is a factor used in numerical modeling to specify the roughness or smoothness of the wall. The parameter changes between 0, for a smooth wall and 1, for a rough wall. Specularity coefficient depends on a number of factors including the material of the wall, the type of particles and the sloping/geometry of the walls (Johnson and Jackson, 2009). As a result, this factor increases the flexibility of Johnson-Jackson boundary condition according to the flow behaviour. In order to reach good agreement with the experiment, different specularity coefficient should be examined.

Equation (5) shows the shear stress used in boundary conditions of Johnson-Jackson and Equation (6) represents the flux of fluctuation energy for extracting granular temperature. Both of these equations are implemented in OpenFOAM through a mixed boundary condition.

Revisited Johnson-Jackson Boundary Conditions

As mentioned in the last section, in Johnson-Jackson boundary conditions, the momentum and energy transfer due to the colliding particles were characterized by a coefficient of specularity, which plays an important role in the prediction of solid flow.

Li and Benyahia (Li and Benyahia, 2012) revisited the Johnson and Jackson boundary conditions for granular flows and derived an equation for specularity coefficient. For this purpose, they considered the specularity coefficient as the average fraction of relative tangential momentum transferred in a particle-boundary collision. This model guarantees that shear stress is limited by coulomb's law. In their equation, specularity coefficient is a function of restitution coefficient, wall-friction factor and normalized sliding velocity. Bellow, the derived equations for specularity coefficient are presented (Li and Benyahia, 2011):

$$\phi = (1 - \frac{R}{2u_s}\frac{\partial u_s}{\partial n})\phi' , \tag{7}$$

where,

$$\phi' = \begin{cases} -\dfrac{7\sqrt{6\pi}(\phi_0')^2}{8k} r + \phi_0' & r \le \dfrac{4k}{7\sqrt{6\pi}\phi_0'} \\ \dfrac{2}{7}\dfrac{k}{r\sqrt{6\pi}} & otherwise \end{cases} \tag{8}$$

with

$$r = u / \sqrt{3\Theta}$$

$$\begin{aligned} \phi_0' = & -0.0012596 + 0.1064551k - 0.04281476k^2 \\ & + 0.0097594k^3 - 0.0012508258k^4 + \\ & 0.0000836983k^5 - 0.00000226955k^6 \end{aligned} \tag{9}$$

$$k = \frac{7}{2}\mu\ (1 + e_n)$$

Schneiderbauer Boundary Conditions

The revisited Johnson-Jackson boundary conditions only focus on the boundary traction. Hence, further analysis is still needed to improve its accuracy when applied to the boundary condition for granular temperature. For instance, the effect of wall-friction factor does not appear in dissipation term of granular temperature (second term of the right hand side of Equation 6).

Therefore, to improve the boundary field and accordingly the internal field, the boundary conditions of Schneiderbauer are implemented in the solver. These boundary conditions propose a theory connecting non-sliding and sliding collisions in one expression. Furthermore, the model is more accurate in calculating flux of fluctuation energy as the effect of wall-friction appears also in dissipation term of granular temperature.

The shear stress, derived by Schneiderbauer et al. (Schneiderbauer et al., 2012), which is used through a partial slip boundary condition in OpenFOAM is described as:

$$\mathbf{S} = -\frac{1}{2}(1+e)\mu\alpha_s\rho_s g_0 \Theta erf(\bar{u}_s)\frac{\mathbf{u_s^{sl}}}{\|u_s^{sl}\|} \tag{10}$$

$$erf(x) = \frac{2}{\sqrt{\pi}}\int_0^x \exp(-\xi^2)d\xi \tag{11}$$

Considering $\eta_w = \frac{1}{2}(1+e)$, flux of fluctuation energy is defined as:

$$\begin{aligned} \mathbf{n}\cdot\mathbf{q} = \mathbf{S}\cdot\mathbf{u_s^{sl}} - & \frac{\alpha_s\rho_s g_0 \eta_w \sqrt{\Theta}}{\sqrt{2}\mu_0^2\sqrt{\pi}} \exp(-\bar{u}_s^2) \\ & \Big\{ 2\mu^2 \|u_s^{sl}\|^2 (2\eta_w - \mu_0) + \Theta\mu \\ & (14\mu\eta_w - 4\mu_0(1+\mu\ ) \\ & - 6\mu\mu_0^2\eta_w) + \mu_0^2\sqrt{\Theta}\exp(\bar{u}_s^{sl\,2}) \\ & \left[\sqrt{\Theta}(4(\eta_w - 1) + 6\mu^2\eta_w)\right. \\ & \left. - \sqrt{2\pi}\mu\|\mathbf{u_s^{sl}}\| erf(\bar{u}_s)\right]\Big\} \end{aligned} \tag{12}$$

$$\mu_0 = \frac{7}{2}\frac{1+e}{1+\beta_0}\mu \tag{13}$$

Results of Including Wall-friction

The numerically predicted velocity profile of particles at the end of the channel (x=5.8), using different boundary conditions, are represented in this section.

In Figure 2, vertical profile of particles' velocity, using Johnson-Jackson boundary conditions, is compared to that of experimental work for different specularity coefficients.

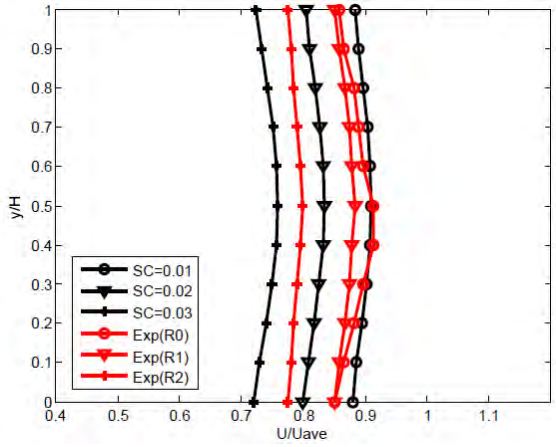

Figure 2: Normalized velocity profile of particles using Johnson-Jackson boundary conditions and comparison with experimental data (low roughness (R0), high roughness (R2)).

It has been illustrated that the flow field is very sensitive to the choice of specularity coefficient. Even very small changes in specularity coefficient make significant changes in the velocity profile of particles. Furthermore, in numerical study adjusting an appropriate specularity coefficient to fit the experimental data is a time-consuming process.

Figure 3 shows the normalized velocity profile in the same section of the channel using revisited Johnson-Jackson boundary conditions for different wall-friction factors.

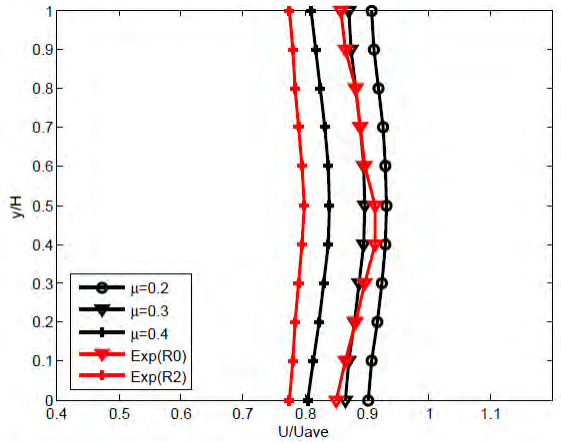

Figure 3: Normalized velocity profile of particles using revisited Johnson-Jackson boundary conditions and comparison with experimental data (low roughness (R0), high roughness (R2)).

As it is illustrated in Figure 3, using revisited Johnson-Jackson boundary conditions results in good agreement with experiment for lower wall-roughness (R0), but for higher wall-roughness (R2), even with wall-friction factor equal to 0.4 the agreement is not achieved.

According to the work of Sommerfeld (Sommerfeld and Huber, 1999), for low impact angle of particles, wall-friction factor depends on impact angle and changes linearly with it, while for high impact angles, it is a constant value. The maximum wall-friction factor for steel walls and glass particles, which are used in the experimental work of Sommerfeld, is about 0.4 and the minimum (constant value) is about 0.15. Therefore, considering the fact that in the present work Eulerian method (ensemble of particles) is used, an average value in between would be a reasonable value from physical point of view (material properties). Accordingly, the wall-friction factor more than 0.4 is rather far from physical consideration in this case. Figure 3 shows that the model does not satisfy the experiment even for maximum value of wall-friction.

In Figure 4 the particles' velocity profiles resulted from Schneiderbauer boundary conditions have been compared to those of Sommerfeld (experimental measurements).

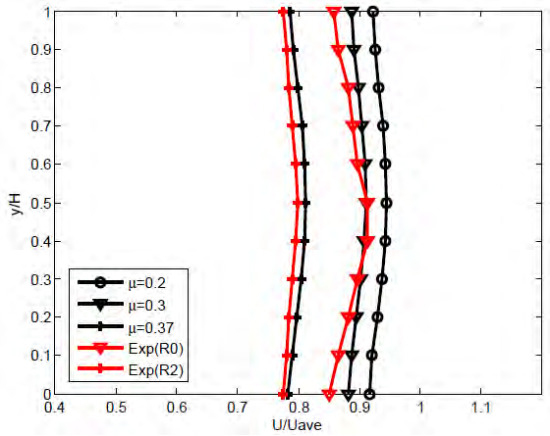

Figure 4: Normalized velocity profile of particles using Schneiderbauer boundary conditions and comparison with experimental data (low roughness (R0), high roughness (R2)).

Figure 4 demonstrates that with increasing the wall-friction factor, the velocity profile of particles moves toward the lower values, and the decrease of the momentum at the walls can be clearly seen. According to this figure, there is a good agreement of the simulated velocity using the latter boundary conditions with measurements of Sommerfeld for wall-friction factor equal to 0.3 and 0.37.

Note that in figures 3 and 4 the wall-friction factor is tuned to get agreement with the experimental results. While, the wall-friction factor is a material property, which can be measured by experiment, it is tuned to find the effective wall-friction factor. Considering the fact that the increase of wall-friction has the same effect of the increase of wall-roughness in experimental work of Sommerfeld, as it is shown in figures 3 and 4, it seems that the effect of wall-roughness may be included in the wall-friction factor.

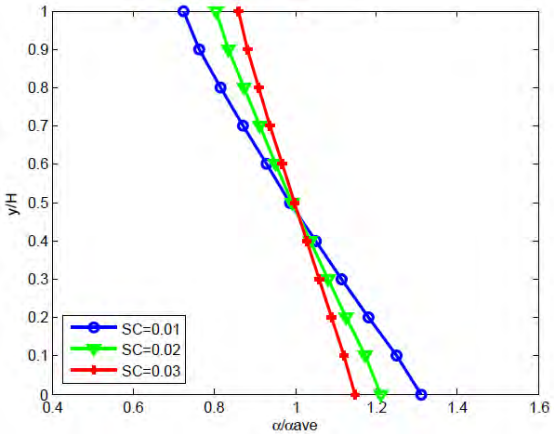

Figure 5: Normalized volume fraction of particles using Johnson-Jackson boundary conditions.

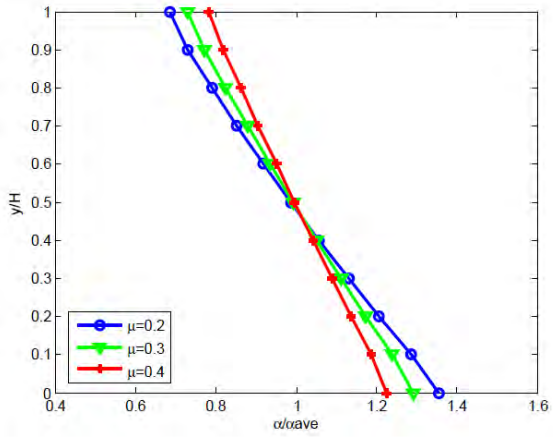

Figure 6: Normalized volume fraction of particles using revisited Johnson-Jackson boundary conditions.

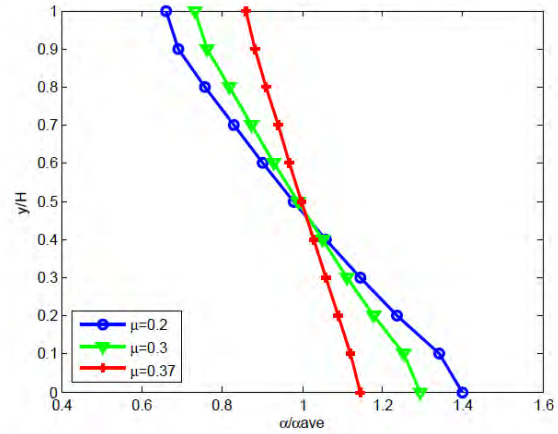

Figure 7: Normalized volume fraction of particles using Schneiderbauer boundary conditions.

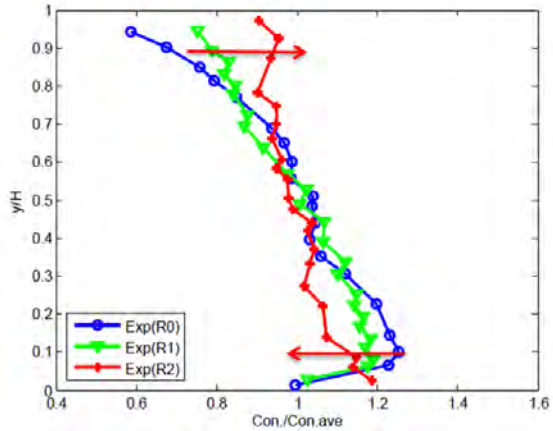

Figure 8: Normalized particles' concentration resulted from the experimental work of Sommerfeld (low roughness(R0), high roughness(R2))

Furthermore, the comparison of figure 5, 6 and 7 (the normalized volume fraction of particles in the cross section of the channel for Johnson-Jackson, revisited Johnson-Jackson and Schneiderbauer boundary conditions respectively) with the experimental concentration of particles in figure 8, reveals that the trends are remarkably similar. Thus, increasing wall-friction (or. spec. coeff.) yields a more constant (steeper) concentration profile (since the flux of fluctuation energy is increased and therefore the redispersion of the particles is enhanced). Increasing the wall-friction has therefore a similar effect as increasing the wall-roughness, as discussed before.

In order to be able to investigate the effect of wall-roughness as a phenomenon independent to the wall-friction factor, a model is required to include wall-roughness. Although, both Schneiderbauer and revisited Johnson-Jackson models have the authority in velocity part, however, as it was discussed, the Schneiderbauer model is more accurate in granular temperature part and furthermore, this model is more general (consists of the normal component of velocity and also normal stresses). Thus, Schneiderbauer et al.'s model is the appropriate one for including wall-roughness.

In the next step, the effect of wall-roughness has investigated in a constant value of wall-friction factor.

WALL-ROUGHNESS MODELLING AND IMPLEMENTATION IN OPENFOAM

To include wall roughness effect in the solver, the virtual wall angle model of Sommerfeld is implemented in general boundary conditions of Schneiderbauer (Schneiderbauer et al., 2012). Therefore, in this section, first, the virtual wall model of Sommerfeld is reviewed and then the idea of implementing virtual wall model in the general boundary conditions of Schneiderbauer is presented.

Virtual Wall Angle Model

The effect of wall roughness can be introduced into the boundary relations by means of the so-called ''virtual wall'' model of Sommerfeld (Sommerfeld, 1992). This model is based on the replacement of the actual wall, which in our case is a horizontal wall, by a virtual rotated wall (Figure 9).

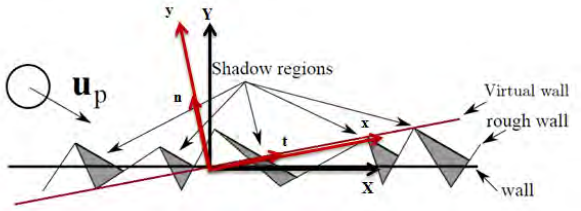

Figure 9: The virtual wall model and shadow effect.

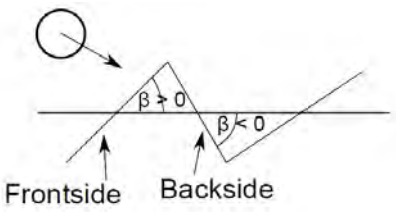

Figure 10: The particle can hit the front or backside of a wall triangle element.

The rotation angle of the wall (inclination of roughness) is defined based on a Gaussian distribution function ($f(\sigma,\beta)$) with a given standard deviation σ, which is characterized by the particle diameter and wall roughness measured by experiment, and a zero mean value.

For each characterized collision parameters, there are a large number of particles colliding with the wall. The

effective mean roughness angle seen by an ensemble of particles, can be calculated by computing the expectation value for β in $[-\alpha,\infty]$. Integrating from $-\alpha$ as the negative value of the impact angle ensures that the angles, in which particles collision with the wall is not possible physically, are disregarded (shadow effect) (Figure 10). Accordingly, this causes a shift of distribution function towards the positive values.

$$\gamma(\sigma,\alpha)=\frac{\int_{-\alpha}^{\infty}\beta.f(\sigma,\beta).d\beta}{\int_{-\alpha}^{\infty}f(\sigma,\beta).d\beta} \tag{14}$$

Evaluating Equation (14) yields:

$$\gamma(\sigma,\alpha)= \frac{-0.398942e^{-\frac{4050}{\sigma^2}}\sigma+0.398942e^{-\frac{0.5\alpha^2}{\sigma^2}}\sigma}{0.5erf\left(\frac{63.6396}{\sigma}\right)+0.5erf\left(\frac{0.707107\alpha}{\sigma}\right)} \tag{15}$$

Equation (15) represents the dependency of rotation angle to the impact angle of particles α and the standard deviation σ.
The velocity components in the virtual wall co-ordinate system are (Taniere, A., et al., 2004):

$$\mathbf{u}_{x,y}=\mathbf{P}\mathbf{u}_{X,Y} \tag{16}$$

$$P=\begin{bmatrix}\cos\gamma & \sin\gamma & 0\\ -\sin\gamma & \cos\gamma & 0\\ 0 & 0 & 1\end{bmatrix} \tag{17}$$

According to the equations (16) and (17), using the rotated coordinate system (x,y), results in an increase of the vertical component of velocity. The virtual wall model is implemented in the following section.

General Boundary Conditions of Schneiderbauer

Using virtual wall model leads to the generation of vertical component of velocity. As a result, in derivation of the shear stress, the vertical component of velocity cannot be neglected as done in equation (10). Therefore, the normal stress at the walls and its contribution to the generation of fluctuating energy should also be taken into consideration. These are satisfied in general boundary conditions of Schneiderbauer:

$$N=\frac{1}{2}(1+e)\rho_s\alpha_s g_0 \left((u_n^2+\Theta)erfc\left(\frac{u_n}{\sqrt{2\Theta}}\right)-\sqrt{\frac{2\Theta}{\pi}}u_n\exp\left(-\frac{u_n^2}{2\Theta}\right)\right) \tag{18}$$

$$erfc(x)=1-erf(x) \tag{19}$$

$$S=-\frac{1}{2\mu_0}\rho_s\alpha_s g_0(1+e)\mu \left\{ u_t u_n erfc(\bar{u}) +\sqrt{\frac{2\Theta}{\pi}}\left[\exp\left(-\frac{u_n^2}{2\Theta}\right)-\exp\left(-\bar{u}^2\right)\right]\mu_0 u_n +\left(u_n^2+\Theta\right)\mu_0\times\left[erf\left(\frac{u_n}{\sqrt{2\Theta}}\right)-erf(\bar{u})\right]\right\} \tag{20}$$

$$\bar{u}=\frac{u_t+\mu u_n}{\sqrt{2\Theta}\mu} \tag{21}$$

Equation (18) represents the normal stress and equation (20) shows the tangential stress at the wall.
Accordingly, the following equations show total flux of fluctuation energy:

$$q=G-D \tag{22}$$

$$G=-\boldsymbol{\tau}.\mathbf{u}=Su_t-Nu_n \tag{23}$$

In these equations, the first term G describes the generation of the fluctuation energy and D describes the dissipation of fluctuation energy. The equations derived for the dissipation term with non-zero vertical component of velocity, can be followed in the work of Schneiderbauer (Schneiderbauer et al., 2012), where the authors used Taylor series for its derivation.
Using the general form of stresses and the rotated velocity components leads to the transfer of the horizontal momentum in vertical direction. This is because of its contribution to the granular temperature and can be observed in the results provided in next section.

Results of Including Wall-roughness

Figure 11 shows how the velocity decreases with the increase of the standard deviation of the roughness angle and the comparison with the results of Sommerfeld's experiment.

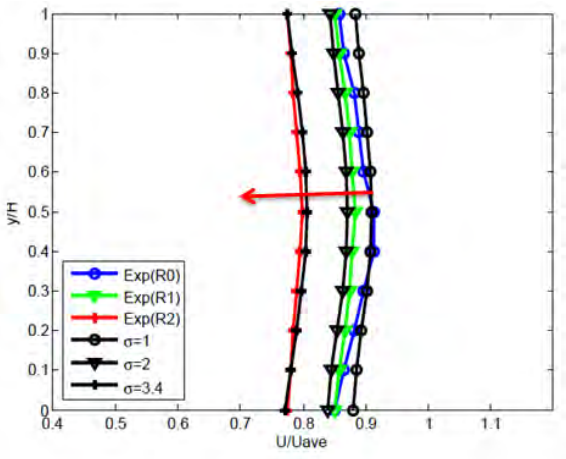

Figure 11: Normalized velocity profile of particles including wall-roughness and comparison with the experimental work of Sommerfeld (low roughness (R0), high roughness (R2)) with tuned standard deviations

In the experimental work of Sommerfeld, the roughness is described based on two length-scales (roughness in stream-wise direction and roughness in lateral direction), while in the present study it is modelled based on the wall-roughness angle (standard deviation) and the impact angle of particles. Accordingly, because of the lack of a correlation between these two wall-roughness descriptions, it is impractical to compare velocity diagrams directly. However, wall roughness characterization, using standard deviations for different material pairs, has been presented by, e.g., Sommerfeld and Huber (1999).

Figure 11 demonstrates the same trends of velocity decreasing with increasing wall-roughness, which is accounted for in the present simulations by an increasing standard deviation angle of virtual wall model.

It is also demonstrated in figure 11 that with tuning the standard deviation (σ) for the constant wall-friction factor equal to 0.2, the agreement with the experimental data can be achieved. However, it should be mentioned that σ can be measured by experiment (Sommerfeld and Huber, 1999).

Figure 12 represents normalized profile of particles' volume fraction in the cross section of the channel, predicted by the solver, including wall-roughness effect.

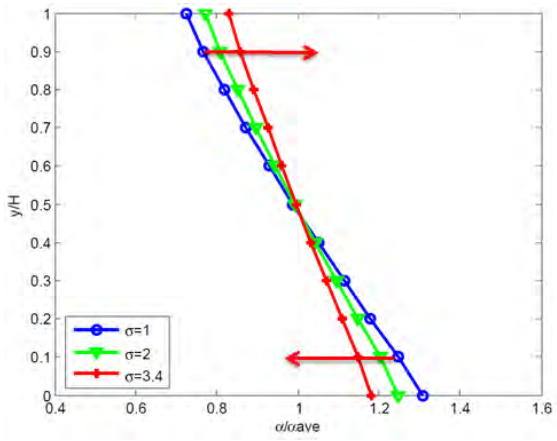

Figure 12: Normalized volum fraction of particles using Schneiderbauer boundary conditions including wall-roughness effect.

Comparing Figures 12 and 8 demonstrates that in both figures from low roughness to high roughness there is a rotating trend towards unification of particles concentration in the cross section of the channel.

The figures reveal that the increase of wall-roughness causes the increase of particles' rebound and redispersion, whereby the particles concentration profiles tend to uniform condition. In other words, rebound of particles leads to the enhancement of the particles' concentration at the upper wall and decrease at the lower wall.

The same trends of Figures 12 and 8 is another confirmation that the idea of using virtual wall model of Sommerfeld in combination with boundary conditions of Schneiderbauer reveals acceptable results.

However, the concentration of particles still needs more investigation when wall-roughness is included.

CONCLUSION

This paper presents a numerical simulation of particulate flow in a narrow horizontal channel with modification of a standard solver in OpenFOAM-2.2.x.

In modification of the solver as a first part, wall-friction effect is included in twoPhaseEulerFoam starting from Johnson-Jackson boundary conditions. However, these boundary conditions suffer from two main deficiencies:

First, these boundary conditions cannot distinguish between sliding and non-sliding conditions in particles' collision with the wall. Second, the specularity coefficient cannot be defined as material property and therefore cannot be measured by experiment.

As a second step in implementing wall-friction in the solver, revisited Johnson-Jackson boundary conditions are used. However, this model is missing the effect of wall-friction in dissipation term of fluctuation energy. Especially, at high wall-friction factors using these boundary conditions does not yield a further reduction of the horizontal solid phase velocity.

In the third step, the boundary conditions of Schneiderbauer are implemented in the solver. These boundary conditions include the effect of wall-friction in both boundary traction and granular temperature part.

These boundary conditions also include sliding and non-sliding condition in one expression.

Furthermore, these boundary conditions account for the local compression of the granular gas (non-zero normal velocities of the particle phase at the walls), which is required for the wall-roughness model.

Finally, the wall-roughness effect is implemented in twoPhaseEulerFoam based on the idea of using virtual wall model of Sommerfeld in general boundary conditions of Schneiderbauer.

The results show good agreement in trends with the experimental work of Sommerfeld.

In conclusion, the granular Eulerian solver, delivered with OpenFOAM (twoPhaseEulerFoam), was improved considerably by including wall-friction and wall-roughness effects. Nevertheless, the solver still needs additional improvement such as considering the turbulence effects in turbulent gas-particle flows. Furthermore, more investigations will be conducted in future work for validating the granular temperature of particles.

REFERENCES

BENYAHIA, S., et al., (2005), "Evaluation of boundary conditions used to model dilute, turbulent gas-solids flows in a pipe", *J. Powder Technology*, **156,** 62-72.

JENKINS, J.T., (1992), "boundary conditions for rapid granular flows: flat, frictional walls", *J. Appl. Mech.*, **59,** 120-127.

JENKINS, J.T. and LOUGE, M.Y., (1997), "On the flux of fluctuating energy in a collisional grain flow at a flat frictional wall", *J. Phys.Fluids*, **9 (10),** 2835–2840.

JOHNSON, P.C. and JACKSON, R., (1987), "Frictional-collisional constitutive relations for granular materials, with application to plane shearing", *J. Fluid Mechanics*, **176,** 67-93.

LI, T. and BENYAHIA, S., (2012), "Revisiting Johnson and Jackson Boundary Condition for Granular Flows", *J. AIChE*, **58, 7,** 2058-2068.

SCHNEIDERBAUER, S., et al., (2012), "Non-steady state boundary condition for collisional granular flows at flat frictional moving walls", *Int. J. Multiphase Flow*, **43,** 149-156.

SCHNEIDERBAUER, S., et al., (2012), "A comprehensive frictional-kinetic model for gas-particle flows: Analysis of fluidized and moving bed regimes", *Int. J. Chemical Engineering Science*, **80,** 279-292.

SOMMERFELD, M., (1992), "Modelling of particle-wall collision in confined gas-particle flows", *Int. J. Multiphase flow*, **18,** 905-926.

SOMMERFELD, M. and HUBER, N., (1999), "Experimental analysis and modeling of particle-wall collisions", *Int. J. Multiphase flow*, **25,** 1457-1489.

SOMMERFELD, M. and KUSSIN, J., (2004), "Wall roughness effects on pneumatic conveying of spherical particles in a narrow horizontal channel", *J.Powder Technology*, **142,** 180-192.

TANIERE, A., et al., (2004), "Focus on the dispersed phase boundary conditions at the wall for irregular particle bouncing", *Int. J. Multiphase flow*, **30,** 327-345.

10th International Conference on CFD in Oil & Gas, Metallurgical and Process Industries
SINTEF, Trondheim, Norway *CFD 2014-0046*
17-19 June 2014

A STUDY OF SIMULATION AND EXPERIMENT ON AIRBORNE WEAR PARTICLES FROM WHEEL-RAIL CONTACTS

Hailong LIU[1*] , Lage T. I. JONSSON[1] and Pär G. JÖNSSON[1]

[1] KTH-Royal Institute of Technology, Division of Applied Process Metallurgy, Department of Materials Science and Engineering, SE-100 44 Stockholm, Sweden.

* E-mail: hailongl@kth.se

ABSTRACT

The objective of this paper is to study if there is a correlation between experiments and simulations regarding the investigation of concentration and size distribution of airborne particles generated from wheel-rail contacts i.e. use simulation to find out the real size distribution and generation rate deviates from the measurements. The experimental part was performed on a pin-on-disc machine situated in a sealed box. The results show that particles are mostly smaller than 0.1 μm in diameter. A model was set up as the same size to the experimental apparatus. The calculations show that the flow field changes with varying revolution speed, and the particle transport varies as well. Moreover, the possibility that part of generated particles will stay in the box have been proved by an approximate estimation of particle loss rate and particle deposition velocity. Therefore, it can be deduced that the accuracy of experimental measurements could be affected.

Keywords: Airborne particles, concentration, deposition velocity, size distribution.

NOMENCLATURE

Greek Symbols

ρ Mass density, [kg/m^3].
μ Dynamic viscosity, [kg/m.].
μ_T Turbulent viscosity, [m^2/s].
ν Kinetic viscosity, [m^2/s].
ε Dissipation rate of kinetic turbulent energy, [m^2/s^3].
$\emptyset$ Scalar
τ Particle relaxation time, [s].
τ^+ Dimensionless particle relaxation time
ρ_p^0 Density of particulate material, [kg/m^3].
ρ_f Density of fluid, [kg/m^3].

Latin Symbols

C Mean particle concentration, [kg/m^3].
C_μ Eddy-viscosity coefficient
D_B Brownian diffusivity,[m^2/s].
D_B^+ Dimensionless Brownian diffusivity
D_T Temperature diffusivity, [m^2/s].
D_T^+ Dimensionless temperature diffusivity
J Particle mass transfer rate, [kg/m^2 s].
k Kinetic turbulent energy, [m^2 / s^2].
p Pressure, [Pa].
P_r Production term in the equation(4,5)
R_a Roughness, [m].
r Particle radius, [m].
$S_\emptyset$ Source
$\boldsymbol{u}_{i,j}$ Velocity, [m/s].
u_τ Friction velocity, [m/s].
v_d Deposition velocity, [m/s].
v_d^+ Dimensionless Deposition velocity
$\bar{V}_{py}^c$ Particle convective velocity in the y direction, [m/s].
$\bar{V}_{py}^{c^+}$ Dimensionless Particle convective velocity in the y direction
y^+ Dimensionless wall-normal distance

Sub/superscripts

$+$ Dimensionless dependent
B Brownian diffusion
d Deposition
f Fluid
i Index i
j Index j
p Particle
py Particle in the y direction
T Turbulent, temperature

INTRODUCTION

Recently, the air quality is a hot topic that people concerned about. Several researches have presented proofs of that the airborne particle distribution is one of the main criteria to evaluate when determining the air quality. Also, these particles are found to affect the respiratory tract dramatically. Generally, airborne particles are generated from several sources, such as fossil fuel combustion, an industrial gas emission, a variety of traffic and transportation vehicles. As the railway transport is developed rapidly all over the world, wheel-rail contact is deemed to be a new important contributor to generate airborne particles.

In the last decades, a number of experimental studies have been done using different measurement systems. A pin-on-disc machine is one efficient way of measuring generated particles from different contacts, for example, wheel-rail contacts, break systems and bearing-ball contacts. Several studies have been done by U.Olofsson (Olofsson, Olander et al. 2009; Wahlström, Söderberg et al. 2010) that implemented the pin-on-disc machine situated in a sealed box. The results show that size distribution and concentration of wear particles generated from contacts are quite different for different materials in brake discs and pans, wheel-rails and ball

bearings. In addition, the effects of different experimental conditions such as slide velocity, load and test time were investigated in these studies. However, all these particle measurements were done from samples taken at the outlet of pin-on-disc machine. Therefore, it is hard to figure out how many percent of total generated particles have been measured and what happened to the rest.

Therefore, a modelling study is needed to describe the picture of a particle transport in the sealed chamber. The theoretical background of particle a deposition model can be found in (Browne 1974; Fan and Ahmadi 1993; Guha 1997; K Lai and Nazaroff 2000). The main factors impacting the particle deposition velocity, v_d, is friction velocity, u_τ, particle density, particle size distribution and roughness of surface. Browne presented very early a prediction of the particle deposition on rough surfaces for a turbulent gas flow in a pipe. A stopping distance model was constructed by assuming that a particle will stop and remain until it reaches a distance from the wall that can touch the upper height of the wall surface roughness. In this model, the turbophoresis(the motion contributed to the interaction of particle inertia with the inhomogeneity of turbulence field) was not considered, while it was proved to have an essential effect of the particle deposition. Guha developed a simple, unified theory of deposition that includes the effects of thermophoresis, turbophoresis, electrostatic forces, gravity, lift force and surface roughness. The calculation results show that the surface roughness enhances the deposition especially for small particles. Also, thermophoresis, turbophoresis and roughness were found to play a key role for the deposition of particles of an intermediate size. Lai and Nazaroff derived a model based on the work of (Corner and Pendlebury 1951) to predict deposition onto smooth surfaces as a function of particle size and density. The effects of Brownian and turbulent diffusion and gravitational settlement were accounted for in this model. The simulation results showed a good agreement with the experimental data for a spherical cavity (Cheng 1997).

The purpose of this paper is to introduce a correlation between the experiments and simulations. Based on the experimental data, the mathematical model is set up as a pin-on-disc machine situated in a sealed box with the same real size, by using the commercial software PHOENICS. The numerical method, CFD (computational fluid dynamics) is used to simulate the turbulent flow and to predict particle loss rate, deposition rate in this model.

MODEL DESCRIPTION

Governing Equations

The continuity equation for the incompressible fluid is as follows,

$$\frac{\partial}{\partial x_j}(\rho \boldsymbol{u_i}) = 0 \qquad (1)$$

The conservation equation of momentum can be written,

$$\frac{\partial}{\partial t}\rho \boldsymbol{u_i} + \frac{\partial}{\partial x_j}\left(\rho \boldsymbol{u_i u_j}\right) = -\frac{\partial p}{\partial x_i} + \frac{\partial}{\partial x_j}\left[(\mu + \mu_T)\left(\frac{\partial \boldsymbol{u_i}}{\partial x_j} + \frac{\partial \boldsymbol{u_j}}{\partial x_i}\right)\right] \qquad (2)$$

The transport equation for scalar can be written as,

$$\frac{\partial}{\partial t}(\rho \emptyset) + div(\rho \boldsymbol{u} \emptyset) = div(\Gamma \operatorname{grad} \emptyset) + S_\emptyset \qquad (3)$$

Where $\emptyset$ denotes the instantaneous total value of the scalar, $S_\emptyset$ represents the source term.

Boundary Conditions and Assumptions

The following descriptions and assumptions are made in the mathematical model:

- The computational domain is shown in Figure 1. It is limited to a 3D sealed box with the dimensions of 660, 450, 360mm which represents the length, height and width respectively.
- In each case, the grid is Cartesian a quadrilateral shape in the computational domain.
- The surface roughness R_a is set to 70μm for all surfaces of the pin-on-disc machine and 6μm for all walls.
- Non-slip boundary condition and the standard logarithmic wall function are imposed for the air at all walls and surfaces of the objects.
- A pressure-inlet condition is set with an ambient pressure. The air flow is implemented at an inlet with a volume flow rate equal to 0.0021m^3/s. This is the same inlet condition which is used in the experiments. The pressure boundary condition is set to an outlet, as a prescribed value of P equals to zero.
- Four different revolution speeds are implemented on the disc 55r/min, 220r/min, 440r/min and 1000r/min, respectively.
- According to the results of experiments, particles with sizes below 0.1 μm in diameter. These particles are assumed to have the same transport behavior as the added source term (C1). The source is added at the object, PIN, and introduced with a fix value.
- The gravity and buoyancy forces are not considered in the model since the particle diameter is below 0.1 μm.

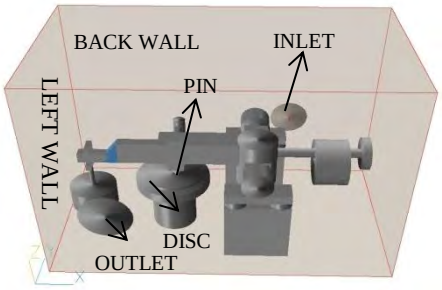

Figure 1: The geometry of computational domain.

Turbulence Model

As far as we know, the standard k-ε turbulence model is well-known and already applied in many research areas. However, some deficiencies emerged when the model performed in some specific cases. Typically, the form of two equation eddy-viscosity model which only employs a single time scale (k-ε) to characterize the various dynamic processes occurring in turbulent flows. Turbulence, however, comprises fluctuating motions with a spectrum of time scales. Thus, a single-scale approach is unlikely to be adequate under all circumstances because different turbulence interactions are associated with different parts of the spectrum.

In order to remedy this deficiency in the standard model, (Chen and Kim 1987) proposed a modification which improves the dynamic response of the ε equation by introducing an additional time scale, k/P_r. Here P_r is the volumetric production rate of k.

Turbulent transport equation

The equations for the turbulent kinetic energy and the dissipation rate of turbulent kinetic energy from the well-known k-ε model have been modified and written as below,

$$\rho\frac{\partial k}{\partial t} = \rho(P_r - \varepsilon) + \frac{\partial}{\partial x_j}\left(\frac{\mu_T}{\sigma_k}\frac{\partial k}{\partial x_j}\right) \quad (4)$$

$$\rho\frac{\partial \varepsilon}{\partial t} = (C_{\varepsilon 1}P_r - C_{\varepsilon 2}\varepsilon)\frac{\rho\varepsilon}{k} + \rho C_{\varepsilon 3}\frac{{P_r}^2}{k} + \frac{\partial}{\partial x_j}\left(\frac{\mu_T}{\sigma_\varepsilon}\frac{\partial \varepsilon}{\partial x_j}\right) \quad (5)$$

Where $\mu_T = \rho C_\mu \frac{k^2}{\varepsilon}, \nu_T = C_\mu \frac{k^2}{\varepsilon}$,
$C_\mu = 0.09,\ C_{\varepsilon 1} = 1.15,\ C_{\varepsilon 2} = 1.92,\ C_{\varepsilon 3} = 0.25,\ \sigma_K = 0.75\ and\ \sigma_\varepsilon = 1.15$
The third term, on the right side of ε-equation, which is the additional source term per unit volume, includes an extra timescale k/P_r .

PARTICLE DEPOSITION MODEL

Generally, the deposition velocity, v_d, is defined as the particle mass transfer rate to the wall, J, normalized by the mean concentration, C in the flow,

$$v_d = J/C \quad (6)$$

The particle relaxation time, τ , is a measure of particle inertia and denotes the time scale with which any slip velocity between the particles and the fluid is equilibrated

$$\tau = 2\rho_p^0 r^2/9\mu \quad (7)$$

Where ρ_p^0 represents the density of pure particulate material, r, the particle radius and μ , the dynamic viscosity of the fluid.
With the help of the fluid friction velocity, u_τ, the dimensionless of v_d and τ are derived as,

$$v_d^+ = v_d/u_\tau \quad (8)$$

$$\tau^+ = \frac{\tau u_\tau^2}{\nu} = \frac{2}{9}\left(\frac{\rho_p^0}{\rho_f}\right)\frac{r^2 u_\tau^2}{\nu^2} \quad (9)$$

For present study, the model from (NI, Jonsson et al. 2014) is used to predict the particle deposition. In this model, the flux of particles in the y direction (perpendicular to the wall) is calculated as

$$J = -(D_B + \varepsilon)\frac{\partial \bar{\rho}_p}{\partial y} - \bar{\rho}_p D_T \frac{\partial \ln T}{\partial y} + \bar{\rho}_p \bar{V}_{py}^c \quad (10)$$

Where D_B represents the Brownian diffusivity, $\bar{\rho}_p$, the particle concentration, D_T,the coefficient of temperature gradient dependent diffusion and $\bar{V}_{py}^c$, the particle convective velocity in the y direction.
The non-dimensional form of v_d^+ is derived as

$$v_d^+ = -\left(\frac{D_B}{\nu} + \frac{\varepsilon}{\nu}\right)\frac{\partial \rho_p^+}{\partial y^+} - \rho_p^+ D_T^+ \frac{\partial \ln T}{\partial y^+} + \rho_p^+ \bar{V}_{py}^{c+} \quad (11)$$

The details of mathematical derivation procedure can be found in (Guha 1997).

Friction Velocity

To describe the friction velocity on the surfaces of objects and walls, u_τ, is calculated as (Valentine and Smith 2005)

$$u_\tau = \sqrt{k\sqrt{C_\mu}} \quad (12)$$

Where k represents the turbulent kinetic energy close to the surface of objects and walls, $C_\mu = 0.09$.

Property

Air is treated as an incompressible fluid at the condition of a 20 degree temperature, a pressure of 1 atm, Also, $\rho\ is\ 1.189 kg/m^3\ and\ \nu\ is\ 1.544e-5\ m^2/s$ .All objects of the pin-on-disc machine are defined as a solid steel.

EXPERIMENT SET-UP

A pin-on-disc machine has been developed by (Olofsson, Olander et al. 2009) with a sealed chamber to control the cleanliness of the air, as shown in Fig. 2. In this set-up, air is sucked by the fan and passes a chamber via a filter, then comes to the outlet where particles measurement points are positioned. During the test, the filter can prevent some impurities in the air to enter the chamber. The pin sample was fastened on the arm of a pin-on-disc machine, which was loaded by a dead weight.

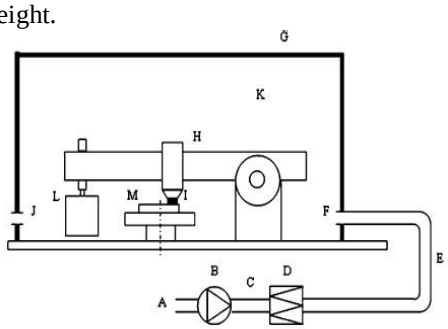

Figure 2: Schematic figure of the test equipment, (A) Room air; (B) fan;(C) flow rate measurement; (D) filter; (E) flexible tube; (F) inlet for clean air, measurement point; (G) closed chamber; (H) pin-on-disc machine; (I) pin sample; (J) air outlet, measurement points; (K) air inside chamber; (L): dead weight; (M) rotating disc sample (Olofsson, Olander et al. 2009).

Test Specimens

The discs and pins were made of a used R7 wheel and piece of a used UIC 60, 1100 rail with hardness of 270 and 280 HV, respectively.
The 110-mm-diameter discs and the 100-mm-high round-head pin(R=25mm) were cut from the materials using a water jet cutting machine. The quality of the machined surface, i.e., the $R_a$value, was 0.3-0.6μm for both materials. Before testing, all of the disc specimens were cleaned ultrasonically for 20 min with both heptane and methanol.

Test conditions

The load applied on the round-head pin was 2.5N. Four pins made of same materials were tested by various revolution speeds implemented for disc. The test conditions are illustrated in table 1.

Table 1: Four pins made of rail materials with different revolution speeds

Pin	Rpm r/min	Time/min	Load/N	Distance/m
#1	55	20	2.5	19
#2	220	5	2.5	17
#3	440	2	2.5	26
#4	1000	2	2.5	32

RESULTS AND DISCUSSION

Experimental Measurements

In the experimental tests, the results of particle measurement by FMPS are illustrated in Fig. 3. The horizontal axis represents the diameter of particles in the log scale based on 2. The vertical axis represents the frequency that each measured particle size occupies in relation to the total number of particles. As can be seen in the Fig. 3, the particles are mostly distributed (98% approximately) below the diameter of 0.1μm in all the tests. This distribution implies that the majority of generated particles is so small that these particles can be considered as source term with the properties of domain fluid in the simulation. Specifically, the particle size distribution is quite different between test1 and test 2, 3, 4. In test 1, the number of particles increases with the diameter bigger than 0.1 μm as a result of the slow slide velocity. The revolution speed is 55r/min which is giving a mean slide velocity 0.11m/s as computed from the distance between the wear track and the disc center. In addition, the peak in the frequency distribution in the fine particles (smaller than 0.1μm) around 0.01 μm can be found during test 1, while it is around 0.007 μm for the other 3 tests. The detail results of particles distribution will not affect simulation remarkably but would be very helpful for experimental analysis of the effect of revolution speed on the generated particles.

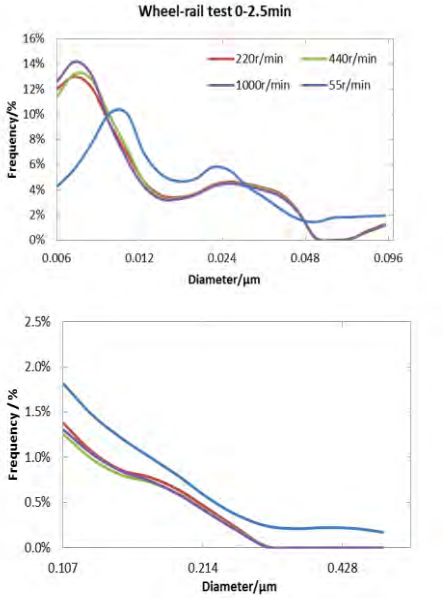

Figure 3: The size distribution of measured particles generated from wheel-rail contact during all tests in 0-2.5min.

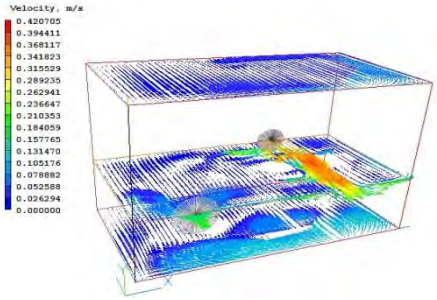

Figure 4: The vector pattern of flow velocity field at 3 positions (bottom, centerline of the inlet and top)on the Z plane (without revolution).

Flow Field

The turbulent flow field was calculated by the mathematical method, CFD, by using the turbulence model by (Chen and Kim 1987) with the commercial software, PHOENICS.

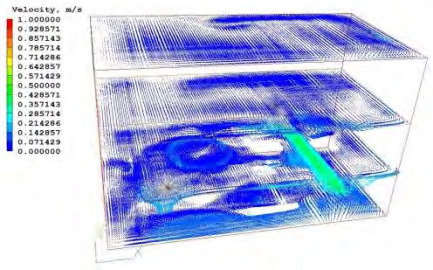

(a)

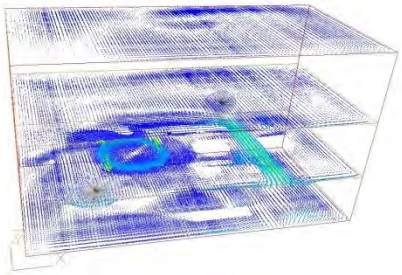

(b)

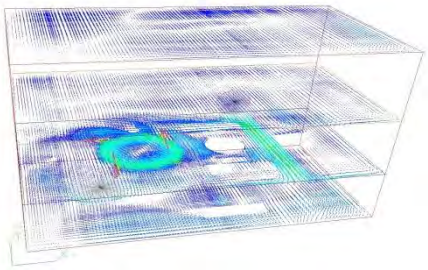

(c)

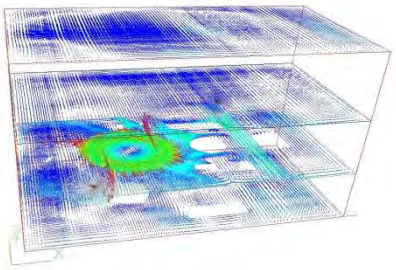

(d)

Figure 5: The vector pattern of flow velocity field at 4 positions (bottom, rotated disc plane, upper and top) on the Z plane with different revolution speeds, (a)55r/min, (b)220r/min, (c)440r/min, (d)1000r/min after 60 seconds calculation.

The flow field during the first 60 seconds without revolution is illustrated in the Figure 4. In order to show the flow field clearly, all of objects inside are hided in the figure.

The air change in the box was deduced to get close to one hundred percent from the unchanged velocity vector pattern. It shows a good agreement with the air change time (47 seconds) that was found in the experiments.

Furthermore, the flow fields with 4 different revolution speeds were calculated and can be found in Figure 5.
The contour box is not the specific one for each case, but modified to get an obvious comparison. The red vectors which represent the maximum value of velocity can be seen at the edge of the rotated disc in each case. The higher the revolution speed, the stronger the vortex being emerged around the disc. Consequently, the wider area with higher velocity was formed as well.
In addition, some vortices can be found in some certain areas close to the disc and around other objects. In terms of particle transport, these vortices will supply a remarkable driving force. On the other hand, it might make some particles lose their way and stay in the box.

Source Distribution

As can been found in the previous experimental results, the amount of generated particles are dominated by particles with diameters below $0.1\mu m$. Therefore, small particles can be treated as a source with a scalar variable (C1) in the model. This is due to the similar transport behavior can be expected between small particles and a scalar source in a stable flow field. The scalable variable C1 was added at the whole pin with a fix value, 1.0e-8 in each case. The physical meaning of the value is that 1.0e-8 kg of C1 is fed into the box per second. After 60 seconds of calculation, the patterns of C1 distribution at left wall, bottom wall, back wall and slice at the Z plane for each case were obtained. This can be found in Figure 6. It is clear that the C1 concentration spreads in a wider area with higher revolution speed. However, in these areas, the concentration of C1 differs for each case. In addition, C1 was driven by the flow field around the disc and inclined to diffuse to the corner region between the left wall, top wall and bottom wall. It seems to be that region where small particles prefer to deposit. The revolution speed influences the particle (C1) distribution dramatically, i.e. it will impact small particle transport. On the other hand, the turbulent diffusion can be considered as the dominant factor for the source transport to the walls.

Estimation of Loss Rate

In this model, a rough estimation of particle loss rate can be calculated by the ratio between the amount of added source and escape source from the outlet. The curve of particle loss rate can be found in the Figure 7.
At first, for the case of 55r/min, as the running time increases from 0 to 5 seconds, the rate seems to be almost constant while a slight raise can be found if this range is magnified. The reason can be that the majority of the source transport is found inside the box while fewer can escape from the outlet in such short time. In the following 10 seconds, the rate increases sharply, which is due to the source was constantly fed into the box. Meanwhile, an increasing number of the source starts to move out of the outlet as a result of the effect of flow field and transportation time. After 15 seconds, the rate continues to rise with a slow growth until be almost unchanged with a value, 67.5%.
For the other case, 1000 r/min, the tendency of loss rate is quite similar. The growth is faster than the case of 55r/min before 12 seconds and slower afterwards.

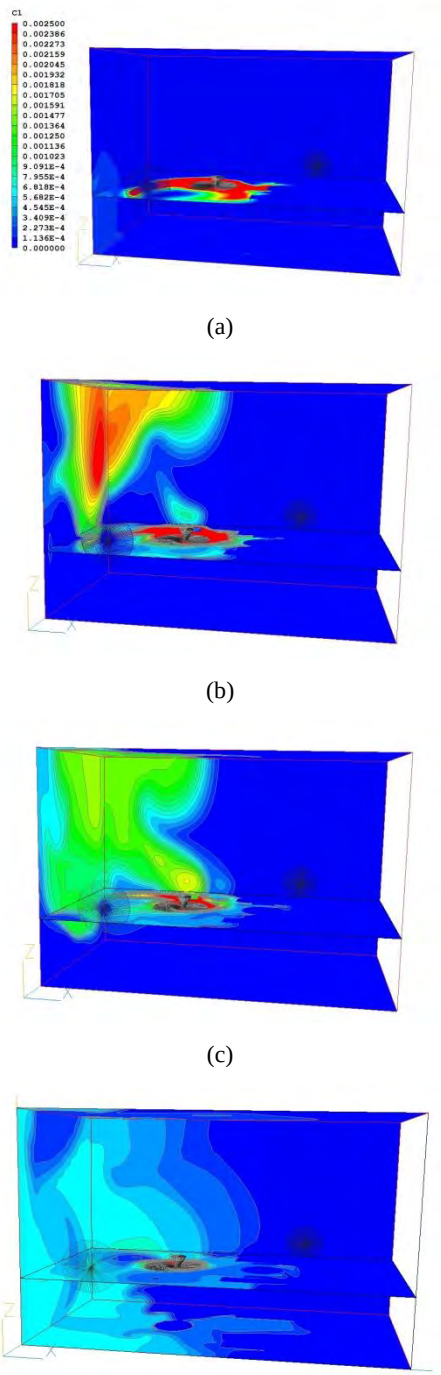

Figure 6: The distribution of source, C1, close to the top wall, bottom wall, left vertical wall and backward vertical wall after 60 seconds, (a)55r/min, (b)220r/min, (c)440r/min, (d)1000r/min.

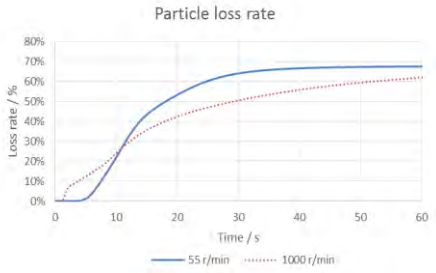

Figure 7: The particle loss rate varies with running time for two cases, 55 r/min and 1000 r/min.

The steady rate at least can be deemed to be a fact that approximate 30 percent of generated particles will stay in the sealed box during the first 60 seconds. It implies that the total number of generated particles in the experiments should be larger than the result of measurements with an approximate factor of 1.4 during first 60 seconds. Consequently, a long calculation time is needed to figure out the stable factor between the measured and the real generated particles.

Deposition Rate

The deposition model used in this paper is from Ni (2014) which is an enhanced model based on Guha's theory. It is certified by a good agreement with the experimental data from (Liu and Agarwal 1974). The only input parameters, the density of particle and the friction velocity, can be seen in the Table 2.

Table 2: The friction velocity, u_τ , for left vertical wall and backwards vertical wall and the density of particles.

Place	Revolution speed r/min	KE m^2/s^2	Friction velocity m/s
Left vertical wall	55	1.5e-4	5.5e-3
	1000	7.9e-4	1.4e-3
Backward vertical wall	55	2.0e-4	7.0e-3
	1000	5.6e-4	1.2e-2
Density of particles kg/m^3	7.0e3		

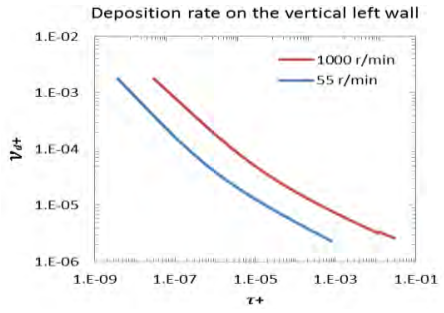

(a)

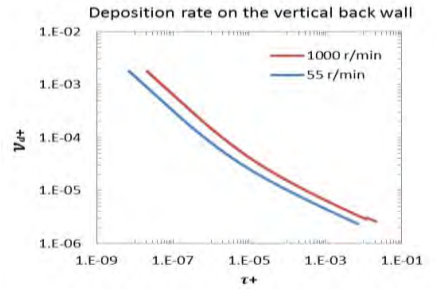

(b)

Figure 8: Deposition rate on (a) the vertical left wall and (b) back wall

The relation between dimensionless particle deposition velocity and particle relaxation time is shown in the Figure 8. As τ^+ increases, the deposition velocity decreases during the range of particle diameter $(10nm \leq d \leq 1\mu m)$. The curve agrees well with the typical plot of experimental results (the turbulent diffusion regime) that is mentioned in (Guha 1997). In this region, the transport of particles are dominated by the turbulent diffusion which is due to that particles are so small that they essentially follows the flow field. In terms of these two cases, the higher revolution velocity supplies more turbulent kinetic energy to the wall and results in a higher deposition velocity. On the other hand, the result of deposition velocity shows a very small value, i.e. few of particles with diameter smaller than 0.1 μm will deposit on these two vertical walls.

CONCLUSION

This paper presents experimental results and a mathematical model for airborne particles generated from wheel-rail contact in experiments.

For the experimental part, the total generated particles were dominated by small particles with a diameter below 0.1 μm.

In terms of flow field, particle transport, loss rate and deposition velocity, the model bridges the gap between particle generation and feasible measurements.

Firstly, the flow field was illustrated by the velocity vectors with four cases of different revolution speeds. The results clearly illustrate the flow field for each case in the sealed box during experiments. For these small particles it could be supposed to be the main driving force for the particle transport.

Secondly, a source represented by a scalar variable, C1, was added to study transport of small particles. The simulation results give a reasonable explanation to the transport process of small particles in the sealed box during the experiments performed. Further, different behaviors of source transport are found for each case during the first 60 seconds.

In addition, a rough estimation of particle loss rate during the first minute was given as the ratio between the amount of added source and source escape from the outlet. The results can be deduced that approximately 30 percent of generated particles will stay in the sealed box during the first 60 seconds, that is, only 70% of the particles can be counted by means of particle measurement instrumentation during the first minute test.

Lastly, the particle deposition velocity was predicted by the model from NI (NI, Jonsson et al. 2014). The results illustrate that a transport of small particles to vertical walls is dominated by the turbulent diffusion. Meanwhile, majority of small particles would not be deposited to the vertical walls since the deposition velocity is quite small.

For future study, a long time of calculation need to be done with the comparison of experimental measurement results. The transport of bigger particles will be studied. The effects between objects and particles will also be considered in the next step.

ACKNOWLEDGEMENTS

Thanks Chinese Scholarship Council for the financial support of my studies at KTH-Royal Institute of Technology, Stockholm, Sweden.

REFERENCES

BROWNE, L. (1974). "Deposition of particles on rough surfaces during turbulent gas-flow in a pipe." *Atmospheric Environment* (1967) **8**(8): 801-816.

CHEN, Y. S. and S. W. KIM (1987). "Computation of turbulent flows using an extended k-epsilon turbulence closure model." *NASA STI/Recon Technical Report* N **88**: 11969.

CHENG, Y. S. (1997). "Wall deposition of radon progeny and particles in a spherical chamber." *Aerosol science and technology* **27**(2): 131-146.

CORNER, J. and E. PENDLEBURY (1951). "The coagulation and deposition of a stirred aerosol." *Proceedings of the Physical Society. Section B* **64**(8): 645.

FAN, F. G. and G. AHMADI (1993). "A sublayer model for turbulent deposition of particles in vertical ducts with smooth and rough surfaces." *Journal of Aerosol Science* **24**(1): 45-64.

GUHA, A. (1997). "A unified Eulerian theory of turbulent deposition to smooth and rough surfaces." *Journal of Aerosol Science* **28**(8): 1517-1537.

K LAI, A. C. and W. W. NAZAROFF (2000). "Modeling indoor particle deposition from turbulent flow onto smooth surfaces." *Journal of Aerosol Science* **31**(4): 463-476.

LIU, B. Y. and J. K. GARWAL (1974). "Experimental observation of aerosol deposition in turbulent flow." *Journal of Aerosol Science* **5**(2): 145-155

NI, P., L. T. I. JONSSON, P.G. JONSSON. (2014). "On the Deposition of Particles in Liquid Metals onto Vertical Ceramic Walls." *International Journal of Multiphase Flow*.

OLOFSSON, U., L. OLANDER, A. JANSSON, (2009). "A study of airborne wear particles generated from a sliding contact." *Journal of tribology* **131**(4): 044503.

WAHLSTRÖM, J., A. SÖDERBERG, L. OLANDER, A. JANSSON, OLOFSSON, U.. (2010). "A pin-on-disc simulation of airborne wear particles from disc brakes." *Wear* **268**(5): 763-769.

FULLY COUPLED MULTIPHASE SIMULATION OF A BOTTOM-SPRAY WURSTER COATER USING A HYBRID CPU/GPU CFD/DEM APPROACH

Eva SIEGMANN[1*], Charles RADEKE[1], Johannes G. KHINAST[1,2]

[1] Research Center Pharmaceutical Engineering GmbH, Inffeldg. 13/2, 8010 Graz, AUSTRIA

[2] Institute for Process and Particle Engineering, Graz University of Technology, Inffeldg. 13/2, 8010 Graz, AUSTRIA

* E-mail: eva.siegmann@tugraz.at

ABSTRACT

Where most of the DEM simulations focus on dry material handling, some highly important applications involve liquid chemical sprays. Here, granular material is sprayed and coated.

Using an in-house DEM code, a lab-scale Wurster coater with one million particles was simulated for at least 60 seconds of processing time. The particles are coated continuously by a bottom spray nozzle and grow according to their residence time in the spray zone. The commercial code AVL FIRE® was used to simulate the liquid phase and our in-house GPU DEM code XPS was used for the modelling of the solid phase. By statistical means values like residence time distribution and size distribution of the particles were monitored.

Keywords: Discrete element modeling, CFD-DEM, Fluidized Bed, Multiphase, Coating.

NOMENCLATURE

Greek Symbols

β Inter-phase momentum transfer coefficient, [kg/(ms)].
δ Displacement, [m].
ε Volume fraction.
ρ Density, [kg/m^3].
τ Stress tensor.

Latin Symbols

d_p Particle diameter, [m]
$e_{n,p\to w}$ Normal restitution coefficient for particle-wall contact.
$e_{n,p\to p}$ Normal restitution coefficient for particle-particle contact.
$e_{t,p\to w}$ Tangential restitution coefficient for particle-wall contact.
$e_{t,p\to p}$ Tangential restitution coefficient for particle-particle contact.
$\mathbf{F}_{p\to p}$ Interaction forces due to colliding particles, [N].
$\mathbf{F}_{p\to w}$ Interaction forces due to collisions with walls, [N].
$\mathbf{g}$ Gravitational acceleration, [m/s^2].
k_n Normal spring stiffness, [N/m].
m Particle mass, [kg].
N_p Number of particles located in a DEM-cell.
$N_{p,total}$ Total number of particles.
N_w Number of particles colliding with walls.
N_x Number of DEM-cells in x-direction.
N_y Number of DEM-cells in y-direction.
N_z Number of DEM-cells in z-direction.
p Hydrodynamic pressure, [Pa].
$\mathbf{S}_p$ Inter-phase momentum transfer source term.
t Time, [s].
$\mathbf{u}$ Velocity, [m/s].
V Characteristic control volume of the gas-phase numerical model, [m^3].

Sub/superscripts

f Fluid.
n Normal.
p Particle.
t Tangential.
w Wall.

INTRODUCTION

Granular flows are important for many pharmaceutical and chemical processes. Simulations are a powerful tool to study this processes. The coupling of two different codes, one for the solid and one for the gas phase, makes it possible, to simulate these systems.

In our case a two way coupling of Discrete Element Model (DEM) and Computational Fluid Dynamics (CFD) was used. The DEM-code computes the motion of the individual particles by solving Newton's second law of motion. The CFD-code solves the volume-averaged Navier-Stokes equations to simulate the flow of a continuum fluid. The DEM part of the simulation is

executed on the Graphics Processing Unit (GPU) (Radeke et al. 2010) and the CFD part on the Central Processing Unit (CPU). In the presented work, our in-house DEM code XPS is coupled with the CFD code AVL FIRE®. Based on this approach a Wurster coater, which is used in manufacturing of powder granules in different areas, such as the food, chemical or pharmaceutical industry, was simulated for a process time of 70 sec.

The Wurster coater is a bottom spray granulator with a draft tube inside the bed. The tube creates a circulating flow pattern. Air flows into the granulator through a plate at the bottom, which consists of regions with different porosities. The plate has larger orifices below the Wurster tube, and therefore, the fluidization gas enters at higher velocity below the tube. Liquid suspension is sprayed continuously by a bottom spray nozzle, which is located inside the tube. The initial particles grow according to their residence time in the spray zone and get slightly polydisperse.

The spray is modelled by a ray tracing technique, which simulates a conical spray zone. When hitting a particle, particles add mass. Film thickness depends on the amount of time a particle spends on the spray zone.

Efficient simulations of coupled multiphase flow in the many-million particle range can be achieved using hybrid CPU/GPU running on a deskside workstation.

The advantage of our CFD-DEM hybrid CPD/GPU simulation method is that the code runs inside a single workstation but on separate computing platforms. Chemical or pharmaceutical engineering processes often last for several minutes to hours. The simulation of such processes is a challenge, in addition to the huge amount of particles. However, with our approach we were able to simulate a Wurster coater with one million particles for a process time of 70 sec in a reasonable computational time. Effectively, the optimization of a coating process demonstrates the strength of tailored simulation tools for chemical and pharmaceutical engineering.

MODEL DESCRIPTION

The simulation was realized using two coupled codes. The CFD code AVL FIRE®, running on CPU, simulates the gas-phase dynamics, which are described by the incompressible Navier-Stokes equation. Our in-house DEM code XPS, running on GPU, simulates the disperse phase (i.e., the particles), which is treated as a collection of individual particles, whose movement is described by applying Newton's second law. Our model is based on an Euler-Lagrange approach for a non-reactive flow. The two phases are coupled via the momentum exchange between gas phase and particles.

A detailed description of the models and the coupling can be found in Jajcevic et al. (2013). For completeness a short description of the different submodels is given here.

Modeling of the gas-phase

The gas phase is modelled by solving the volume-averaged Navier-Stokes equations. The variables are locally volume-averaged over the control volume V. The conservation of mass leads to

$$\frac{\partial}{\partial t}(\varepsilon_f \rho_f) + \nabla \cdot (\varepsilon_f \rho_f \mathbf{u}_f) = 0, \quad (1)$$

where ρ_f is the fluid density, ε_f the local fluid volume fraction, $\mathbf{u}_f$ the fluid velocity vector and t is the time. Similarly, the conservation of momentum can be written as

$$\frac{\partial}{\partial t}(\varepsilon_f \rho_f) + \nabla \cdot (\varepsilon_f \rho_f \mathbf{u}_f \mathbf{u}_f) = \quad (2)$$
$$-\varepsilon_f \nabla p - \nabla \cdot (\varepsilon_f \tau_f) + \varepsilon_f \rho_f \mathbf{g} - \mathbf{S}_p,$$

where p is the hydrodynamic pressure, τ_f is the stress tensor, $\mathbf{g}$ is gravitational acceleration and $\mathbf{S}_p$ is the inter-phase momentum transfer source term between particles and fluid.

Solid-phase and drag force modelling

The movement of the particles is described by Newton's equation of motion

$$m_p \frac{d\mathbf{u}_p}{dt} = \quad (3)$$
$$-V_i \nabla p + \beta(\mathbf{u}_f - \mathbf{u}_p) + \sum_{N_p} \mathbf{F}_{p\to p} + \sum_{N_w} \mathbf{F}_{p\to w} + m_p \mathbf{g}$$

where m_p is the mass of the particle, $\mathbf{u}_p$ is the particle velocity, $-V_i \nabla p$ is pressure gradient force, β is the inter-phase momentum transfer coefficient, $\mathbf{F}_{p\to p}$ are the interaction forces between colliding particles and $\mathbf{F}_{p\to w}$ are the interaction forces caused by wall-collisions.

In the literature, the drag-force model by Beetstra et al. (2007) is frequently used. Jajcevic et al. (2013) showed, that this drag-model gives good results for fluidized beds. This model is used in the present work.

Modeling of particle-particle and particle-wall interactions

In this work the soft-sphere approach is used to model particle-particle and particle-wall contacts, where a linear-spring and dashpot model is employed to calculate the contact forces. The overlap of two particles or of a particle and a wall results in a repulsive force. The force depends on the overlap δ, the relative velocity between the contact-partners $\mathbf{u}_{AB}$ and the material properties. The detailed model is shown in Jajcevic et al. (2013).

Modeling of particle-coating

The spray nozzle is modeled by defining a conical spray zone located inside the Wurster tube. In the spray nozzle, which is assumed to be a single point, many rays originate. The size of the resulting spray zone depends on the opening angle of the cone. Each of the rays detects intersecting particles. Particles hit by these rays increase their radii according to their residence time in the spray zone. The spraying is done in every single DEM-timestep.

CFD-DEM coupling

The DEM- and CFD-codes are coupled by exchanging the source term $\mathbf{S}_p$ and the gas volume fraction ε_f (Eq. (1) and (2)). In Figure 1 the scheme of the coupling between the CFD-code AVL FIRE® and the DEM-code XPS is shown. The details of the coupling are given in Jajcevic et al. (2013).

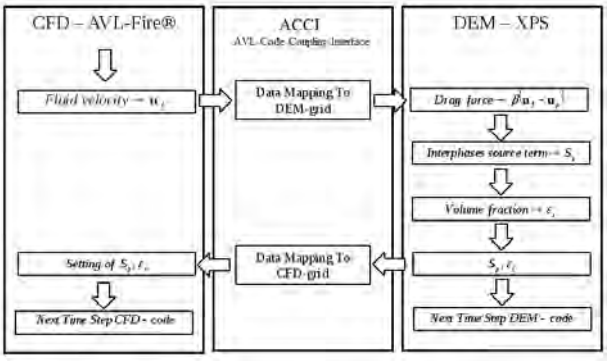

Figure 1: Sketch of CFD – DEM coupling method.

This method of coupling a CFD and a DEM simulation gives good results compared to experimental data. Using the example of different fluidized beds a good agreement with experiments (Van Buijtenen et al., 2011) was achieved (Jajcevic et al., 2013).

APPLICATION OF CFD-DEM SIMULATION

With this coupled CFD-DEM simulation a bottom spray Wurster Coater with 1 million particles was simulated for a process time of 70 seconds. For the simulation 8 CPUs and 1 GPU (Fermi class) were used. The computational speed was about 3 sec/day.

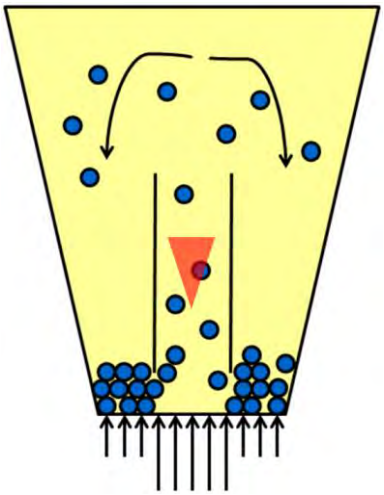

Figure 2: Sketch of a Wurster coater.

A Wurster coater consists of a cone in which the particles are fluidized due to incoming air entering through a distributor plate. Inside the Wurster coater is a tube, which creates a circulating flow pattern. Inside the tube is a spray nozzle which coats the particles. The operating mode of a Wurster coater is shown in Figure 2. The particles are fluidized through the incoming air and are coated in the spray zone inside the tube, which is marked red in Figure 2.

The distributor-plate at the bottom consists of three different regions with nozzles outlets of different sizes. This is demonstrated in Figure 3.

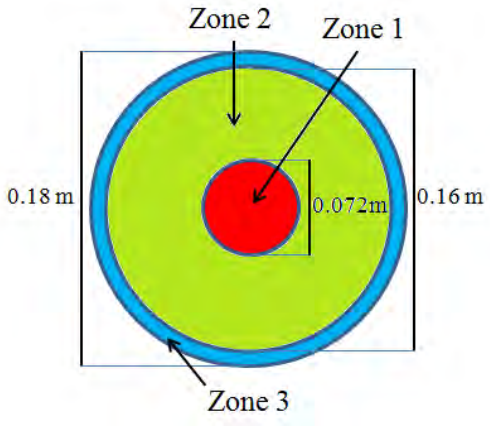

Figure 3: Sketch of the distributor plate.

The region under the Wurster tube (zone 1, marked red in Figure 3) has large nozzles, and therefore, the fluidization gas enters at higher velocity in this region. This leads to a circulation of the particles through the Wurster tube. In the annulus (zone 2), which is marked green in Figure 3, the porosity of the base-plate is much lower. And near the wall (zone 3, blue in Figure 3) the porosity (and thus the gas flow rate) of the distributor plate is slightly larger than in the annulus to avoid dead zones, where the particles are not moving. Due to the high air velocity directly under the Wurster tube the particles get fluidized, move up through the tube, are transported to the wall and recirculate downwards.

Table 1: DEM simulation-parameters and material properties.

Property	Value	Unit
$N_{p,total}$	1 000 000	-
N_x	149	-
N_y	163	-
N_z	149	-
d_p	0.001106	m
ρ_p	1500	kg/m³
k_n	500	N/m
$e_{n,p\rightarrow p}$	0.97	-
$e_{n,p\rightarrow w}$	0.8	-
$e_{t,p\rightarrow p}$	0.3	-
$e_{t,p\rightarrow w}$	0.3	-
DEM time step	10^{-5}	sec
Inital total particle-mass	1.06	kg
Spray rate	20	ml/min
Spray angle	20	Deg
Coating mass	0.02	kg
t_{end}	70	sec

Table 1 lists the relevant simulation- and material-parameters used in the DEM-simulation. d_p is the diameter of a particle before it is coated. During the simulation this value can increase due to the spraying which attaches liquid to the particles.

Table 2 lists the main simulation parameters used for the CFD-simulation. The mass flow increases during the process time of 60 sec linear from 0.04 to 0.05 kg/s due to the increasing mass of the coated particles.

Table 2: CFD simulation parameters.

Property	Value	Unit
Porosity in zone 1	0.5	-
Porosity in zone 2	0.1	-
Porosity in zone 2	0.15	-
Mass flow	0.04 – 0.05	kg/s
Number of CFD-cells	292 547	-
CFD time step	10^{-3}	sec

In the presented case the DEM-code XPS uses a time step size of 10^{-5} sec which, in this simulation, ensures that contacts between particles last for a certain number of time steps to resolve particle collisions. This avoids problems concerning energy conservation. For the CFD-code a bigger time step size of 10^{-3} sec can be used.

RESULTS & DISCUSSIONS

As stated above, a lab-scale Wurster coater was simulated for a process time of 70 sec. During the first 60 sec of the process the mass flow was increased due to the increasing weight of the coated particles. After 60 sec the air flow rate stops to let the particles settle. Figure 4 shows a screenshot of the simulation after a process time of 0.72 sec.

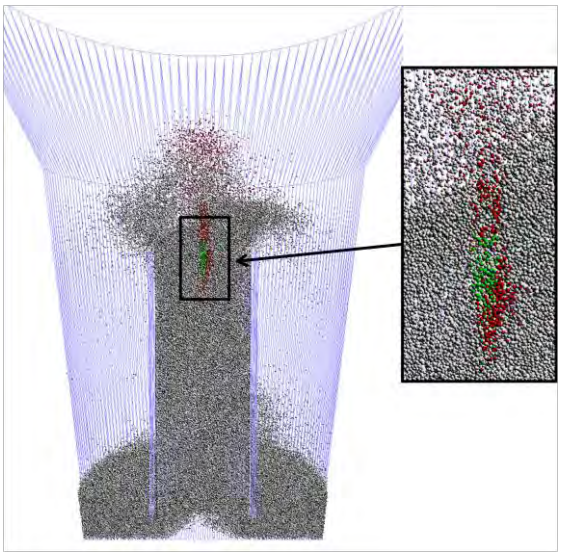

Figure 4: Screenshot of the simulation after a process time of 0.72 sec.

The figure shows a cut through the YZ-plane of the simulation to allow a better insight into the process. Here the particles, which have not yet been coated, are grey. The ones, which are currently in the spray zone of the spray nozzle, are green and those, which have already been coated, are red.

Statistical analysis by means of residence time distribution and size distribution of the particles was performed. In Figure 5 the development of the number of sprayed particles during the whole simulation time of 70 sec is shown. The increase of sprayed particles is nearly linear and after 60 sec no more particles pass the spray zone, as the air flow was stopped to let the particles settle at the bottom of the coater.

At the end of the simulation about $6.5 \cdot 10^5$ of the 10^6 particles are coated. Thus, 70 sec are not enough time to achieve homogeneity. To coat all the particles a longer process time would be needed.

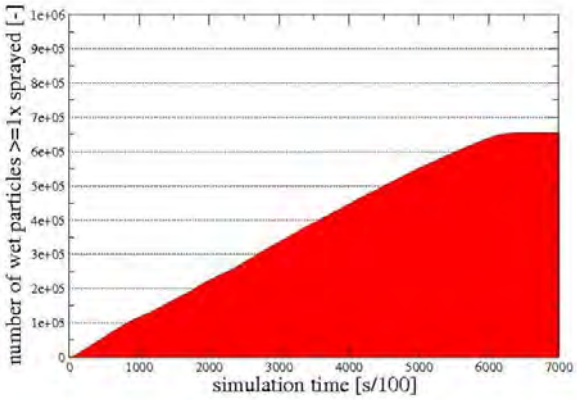

Figure 5: Increase of the number of sprayed particles during the whole process.

In Figure 6 the particles residence time distribution inside the draft tube is shown for 10 sec intervals. The longer the process runs, the more particles enter the Wurster tube. As the process lasts the curve shifts towards the right side, which means that more and more particles pass the tube more than once. But there is also a large amount of particles which have not been in the draft tube at all during the 70 sec. This could, for example, be due to the low porosity of the base plate in the regions adjacent to draft tube, leading to a reduced fluidization of particles near the wall and causing dead zones. Compared to the results of Fries et al. (2011) the results for the residence time distribution are different. This might be due to the different simulation parameters, like plate-porosities, gap distance between tube and bottom, particlesize or number of particles.

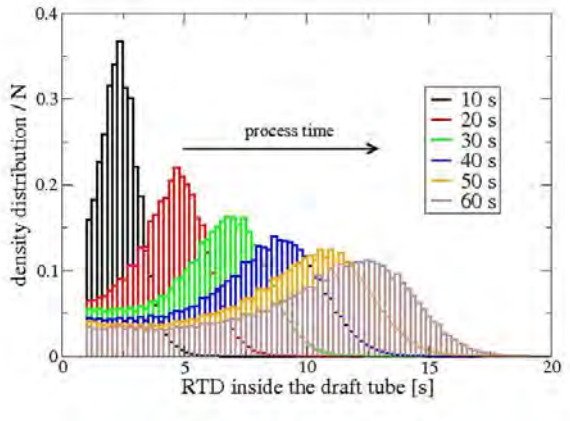

Figure 6: Particles residence time inside the draft tube for different process times (only particles at least ones inside the tube are considered).

Figure 7 shows the change in the amount of coating mass covering the particles during the process. At the beginning of the process most of the coated particles have only a very thin film of coating. As the process moves on, more and more particles obtain a thicker coating.

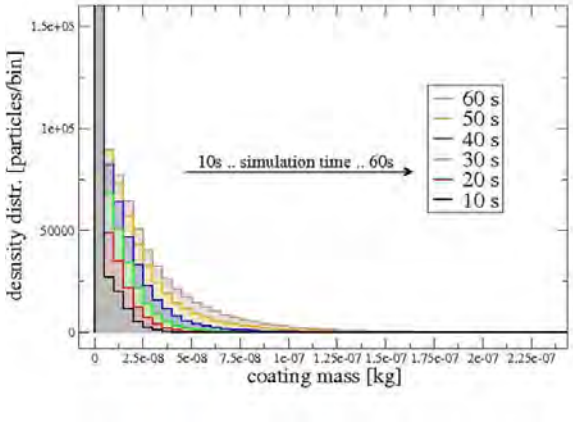

Figure 7: Coating mass attached to the particles for different process times.

A bigger spray zone would probably lead to more coated particles and to a thicker film of coating on the particles. However, this would not improve process homogeneity which is the ultimate goal of the coating process, i.e., particles should have approximately the same mass of coating. Adjusting the porosity of the distributor plate could help in improving the width of the distribution. A higher mass flow in the outer regions of the Wurster coater could avoid dead zones and could lead to a higher fluidization of the particles. Thus, the mobility of the particles would increase and the chance that they enter the draft tube is higher. Changing the gap height between Wurster tube and distributor plate could also lead to different results. This had been studied in Fries et al. (2011). Additionally a longer process time would lead to more coated particles.

CONCLUSION

An advantage of the presented simulation method, using a coupled CFD-DEM approach, is that a high number of particles can be simulated. An additional advantage is that the two codes (CFD and DEM) run on separate computing platforms, and therefore, do not affect each other's computing performance. These advantages made it possible to do a simulation of a lab-scale Wurster coater containing one million particles with inline spraying for a process time of 70 sec within a reasonable computational time.

Different values like number of sprayed particles, residence time inside the draft tube and coating mass were analyzed. The analysis states that the process does not lead to homogeneity of the coated particles. This is due to the fact that a huge amount of particles is not very agile and does not enter the draft tube and consequently the spray zone. The results are very different from those of Fries et al. (2011). Probably parameters like plate-porosities, mass flow, spray rate, size of spray zone or gap height play an important role. A further important point is, that we simulated one million particles where Fries et al. (2011) did their simulation with a number of 150,000 particles.

In summary a high-performance coupled CFD-DEM simulation was run for 70 sec with one million particles within a reasonable computational time. Thus, this highlights the capability of our code, as most currently published DEM-simulations are limited to smaller particle numbers and shorter process times.

ACKNOWLEDGEMENTS

This work was funded through the Austrian COMET Program by the Austrian Federal Ministry of Transport, Innovation and Technology (BMVIT), the Austrian Federal Ministry of Economy, Family and Youth (BMWFJ) and by the State of Styria (Styrian Funding Agency SFG).

We gratefully thank AVL LIST GMBH and Gebrüder Lödige Maschinenbau GmbH, partners in the project where this work was carried out, for their support and contribution.

REFERENCES

Beetstra, R., Van der Hoef, M., & Kuipers, J.A.M. (2007). "Numerical study of segregation using a new drag force correlation for polydisperse systems derived from Lattice-Boltzmann simulations". *Chemical Engineering Science 62* , pp. 246-255.

Fries, L., Antonyuk, S., Heinrich, S., & Palzer, S. (2011). "DEM-CFD modeling of a fluidized bed spray granulator". *Chemical Engineering Science 66*, pp. 2340-2355.

Jajcevic, D., Siegmann, E., Radeke, C., & Khinast, J.G. (2013). "Large-scale CFD-DEM simulations of fluidized granular systems". *Chemical Engineering Science 98* , pp. 298-310.

Radeke, C., Glasser, B., & Khinast, J.G. (2010). "Large-scale mixer simulations using massively parallel GPU architectures". *Chemical Engineering Science 65 (24)*, pp. 6435-6442.

Van Buijtenen, M.S., Van Dijk, W.J., Deen, G.N., Kuipers, J.A.M, Leadbeater, T. & Parker, D.J. (2011). "Numerical and experimental study on multi-spout fluidized beds". *Chemical Engineering Science 66*, pp. 2368-2376.

EFFECT OF THE WIND TURBINE WAKE IN LARGE OFFSHORE WIND FARMS

Mihaela Popescu[1], Balram Panjwani[1], Jon Samseth[1], Ernst Meese[1]

[1] SINTEF Materials and Chemistry, 7465 Trondheim, NORWAY
* E-mail: mihaela.popescu@sintef.no

ABSTRACT

The aim of this paper is to evaluate the wake effect on the performance of a wind farm using two approaches: CFD (OffWindSolver) and an engineering model (OffWindEng). The CFD solver is developed within the OpenFoam architecture. The unsteady PisoFoam solver is extended to account for wind turbines, where each turbine is modeled as a sink term in the momentum equation. Turbine modeling is based on actuator line concept derived from the SOWFA code, where each blade of the turbine is represented as a line of points. The second approach is a simplified explicit model of the wake (engineering model), which includes: the cumulative impact of multiple shadowing, the effects of wind direction, and the wind speed time delay. Results from the two approaches are applied to the Lillgrund wind turbine farm to illustrate the importance of wind turbine spacing. The maximum loss is 50% relative to the designed farm production, which occurs when the wind direction is 221.6^0 - when all turbines operating in the lee of other wind turbines experience total shading. The loss is relatively high, which is not surprising, for such a dense wind farm configuration as Lillgrund

Keywords: CFD, wind turbine, actuator line approach

NOMENCLATURE

Greek Symbols

α angle of attack
β twist angle
γ yaw angle
ρ mass density, [kg/m^3].
θ pitch angle
τ shear stress, [Pa]
ε parameter
η kernel

Latin Symbols

a induction coefficient
c chord length, [m]
d distance, [m]
e efficiency
f external force, [Pa/m]
f_a centrifugal force, [Pa/m]
f_{act} actuator line forces, [Pa/m]
f_c Coriolis force, [Pa/m]
p pressure, [Pa].
r radius, [m]
u, v, U Velocity, [m/s].
u_{rel} fluid velocity relative to the blade, [m/s]
w actuator width length, [m]
AL Actuator line
C_d drag coefficient
C_l lift coefficient
C_T thrust coefficient
D drag force, [N]
D_t diameter, [m]
L lift force, [N]
N-S Navier-Stokes equation
P power, [W]
S surface
WD wind direction

Sub/superscripts

i Index *i*.
j Index *j*.
n normal direction
t tangential direction
0 initial

INTRODUCTION

Norway is an advocate of climate change mitigation even it is the third-largest exporter of oil in the world. The country is taking climate policy very seriously and targets to reduce dramatically greenhouse emission. Norway joins the efforts of other countries to improve wind turbine technology (IEA, 2011).

A wind farm is a group of wind turbines, which are located at the same location and they are designed to extract energy from the wind to produce electricity power. These structures need to be positioned in places with certain wind characteristics (low turbulence and high wind speed) and in an area where they are socially accepted. Because of economical reasons, the distances between the wind turbines should be as small as possible.

Downstream of a wind turbine the wind has reduced speed, added turbulence, and vortex structures, which is called wake of wind turbine. A great problem from installing wind turbines in large arrays is the wake penalty that arises when a wind turbine operates in the lee of a previous one. The principal consequences of the

presence of the wake in the wind farm are: (i) reduction of the energy because of the reduction of the wind speed; (ii) increasing the dynamic loading because the presence of the turbulence. In consequence it is very important to investigate the effect of the wake when a wind farm is designed.

In the offshore environment, it is expected that wind turbine wakes to propagated over longer distance than over land because the offshore ambient turbulence is typically almost half of what is found for turbulence over land (Barthelmie, 2006): ambient offshore turbulence is typically between 6% and 8% at a height of about 50 m and inland turbulence is a minimum 10% – 12%. Hence, it is crucial for wind farm developers to estimate accurately the impact of wind turbine wakes because it has significant impact on wind farm power production.

Performing experiments for a wind farm is an expensive procedure; therefore numerical computational is required. Today, a considerable amount of resources are being utilized for research on harnessing the wind energy efficiently because of the complexity of the involved physics and the demands of a better prediction of the produced power in new wind turbine farms (Barthelmieetal., 2006, Menteretal., 2006; Potsdam and Mavriplis, 2009; Sørensenetal., 2002, Wu and Porté-Agel, 2011).

In the present work, the wake effect on wind farm performance is studied using CFD, actuator line model, and a simplified engineering model. CFD computations use the OpenFoam architecture with the actuator line (AL) model to represent the blades, and k-ε model for turbulence. The developed tool requires the same input as the established SOWFA framework (Churchfield 20012, Churchfield, January, 2012). The engineering model is the improved Advancement of Jensen (Park) wake model (Choi and Shan, 2013).

MATHEMATICAL MODELS

Turbine efficiency is a critical component of the overall economic justification for a potential wind farm; however the interaction of multiple wind turbines is more critical. Therefore the need for prediction methodologies that is capable of addressing the in-situ performance of multiple turbines is important.

CFD Approach (OffWindSolver): Actuator Line Model

The actuator Line method (ALM) was proposed by Sørensen and Shen (Sørensen and Shen, 2002; Sørensen, 2011). The method does not resolve the full geometry of the turbine blades, but rather models them as a set of points along each blade axis. In this way the body forces are distributed radially along the lines representing the blades of the wind turbine - each point represents a discrete section of the blade. In this way the flow field computation remains three dimensional. In this approach, the influence of a wind turbine rotating blades on the flow field is simulated by using the local angle of attack to determine local lift and drag forces: aerofoil tables are used to calculate local force, lift and drag.

2D Aerofoil Theory

The local flow velocity felt by a section of a blade consists in: axial velocity and tangential velocity as shown in **Figure 1**.

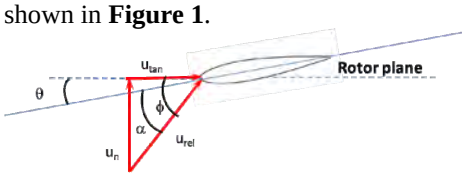

Figure 1. Velocity components at a section of the blade

All the 2D aerofoil geometry characteristics, including the type, pitch angle θ, twist, chord length and thickness, are tabulated data, that are used during the wind turbine flow computation to compute the local forces. The local angle of attack α is given by:

$$\alpha = \phi - \theta \tag{1}$$

Where ϕ is the angle between local velocity and rotor plane (see Figure 1).

Basic Equation

The ALM takes into consideration Navier-Socks (N-S) equation as follow.

$$\frac{\partial(\rho\bar{u})}{\partial t} + \nabla\cdot(\rho\bar{u}\bar{u}) = -\frac{1}{\rho}\nabla p + \nabla\cdot\bar{\bar{\tau}} + f \tag{2}$$

$$f = f_{act} + f_a + f_c$$

Where ρ is the density, u is the flow velocity, τ is the shear stress, p is pressure and f denotes the external body force and includes: the actuator line forces (f_{act}), centrifugal force (f_a) and Coriolis force (f_c).

Computation of the Actuator Line Forces

The actuator line model replaces the impact of the rotating blades by the body forces that are distributed in points along lines that stand up for wind turbine blades – each point represent a discrete section of the blade. In consequence a structured grid can be used around the wind turbine and much less grid points are necessary to capture the influence of the blades.

At a certain time step the local velocity at an element (see **Figure 2**) can be calculated from the solver. The flow produces local forces, Lift and Drag that are computed using tabulated data as chord, blade airfoil type, twist and local velocity in the center of each element of the blade:

$$L = \frac{1}{2}C_l(\alpha)\rho u_{rel}^2 cw \tag{3}$$

$$D = \frac{1}{2}Cd(\alpha)\rho u_{rel}^2 cw \tag{4}$$

Where C_l and C_d are lift and drag coefficient for 2D aerofoil respectively, c is the cord length, w is the actuator element width, α is angle of attack and u_{rel} is

the fluid velocity relative to the blade. The normal and tangential forces of each element of the blade are obtained by projecting lift and drag forces to the normal and tangential direction of the rotor. These forces are applied to the flow field thus coupling the effect of the wind turbine with the wind.

The fluid velocity relative to the blade is decomposed into a normal component U_n and a tangential component U_t, which are used together with twist angle (β) to compute the angle of attack (α).

$$\alpha = \tan^{-1}\left(\frac{U_n}{U_t}\right) - \beta \tag{5}$$

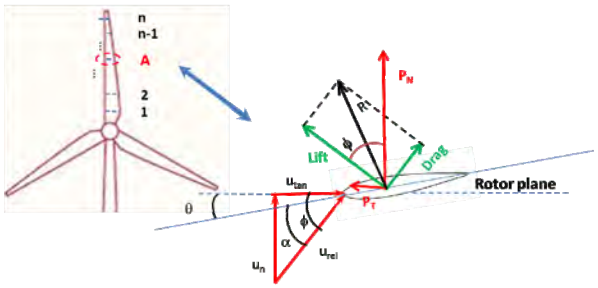

Figure 2. Computation of the actuator line force

If the actuator line forces are applied directly to the flow field, it causes a numerical singularity problem because the forces are defined in a single point. To avoid this problem the force is distributed smoothly on several mesh points (Gaussian distribution), which is implemented by taking the convolution between the force and the kernel:

$$f_\varepsilon = f \otimes \eta_\varepsilon \tag{6}$$
$$\eta_\varepsilon = \frac{1}{\varepsilon^2 \pi^2} \exp\left[-\left(\frac{d}{\varepsilon}\right)^2\right]$$

Where d is the distance between the considered point and the actuator line element, ε is a parameter that serves to adjust the concentration of the regularized load. The value of ε is connected to the airfoil chord length over which the lift and drag forces are computed.

Engineering model (OffWindEng)

The engineering model is the improved Jensen (Park) wake model idea (Choi and Shan, 2013). The model assumes linear expansion of the wake and the path taken by the wind that has passed through the turbine blades is represented by a cone. The radius of this cone, r, is calculated using the following expression (Choi and Shan, 2012; González-Longatt, 2012):

$$r = r_0 + kx \tag{1}$$

- The value of x indicates distance from the turbine.
- 'k' is a dimensionless scalar that determines how quickly the wake expands with distance. The value of 'k' depends on turbulent level. In this work k is not constant, but it depends on the turbulence level, which is ambient turbulence and wake turbulence, when a turbine is located in the lee of other turbine.

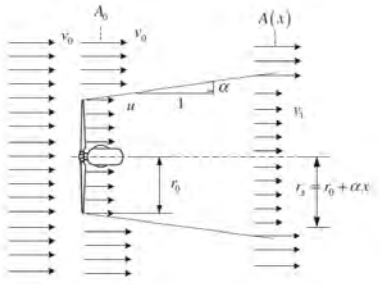

Figure 3. The wake model that assumes linear expansion of the wake cone (González-Longatt, 2012)

The velocity in the wake at a distance x from the wind turbine can be obtained by:

$$v_1 = v_0 + v_0\left(\sqrt{1-C_T} - 1\right)\left(\frac{r_0}{r}\right)^2 \tag{7}$$

A wind turbine is not aligned with the wind direction most of the operating time. Hence, it is important to take into consideration yaw misalignment. Hence thrust coefficient (C_T) depends on the γ and yaw angle in radians (Choi and Shan, 2012).

$$C_T = 4a\left(\cos\gamma - a\right) \tag{8}$$

In our work a is taken as a=cos (γ)/3, where γ is equal to zero.

It is known that the power is proportional to the cube and force to the square of velocity. Average wind speed for power and average wind speed for force are calculated differently in this approach. In this work we proposed that the wind speed for the power replaced the discrete summation by integral formula:

$$u_{i,power} = \sqrt[3]{\left(\frac{\int u_i^3}{\frac{S_{rotor}}{S_{rotor}}}\right)} \tag{9}$$

RESULTS

Test Case

The Lillgrund offshore wind power plant comprises 48 wind turbines, each rated at 2.3 MW, bringing the total wind farm capacity to 110 MW. The Lillgrund offshore wind power plant is located in a shallow area of Öresund, 7 km off the coast of Sweden and 7 km south from the Öresund Bridge connecting Sweden and Denmark. The wind turbine array distribution is shown in Figure 8.

The distance between the turbines in each row is $3.3xD_t$ (D_t = diameter of the turbines) and the distance between the rows is $4.3xD_t$. Note the opening in the center of the farm, due to shallow water at this location, which made turbine placement impossible because the vessels could not maneuver in that area (see VATTENFAL, (2008) – pilot project).

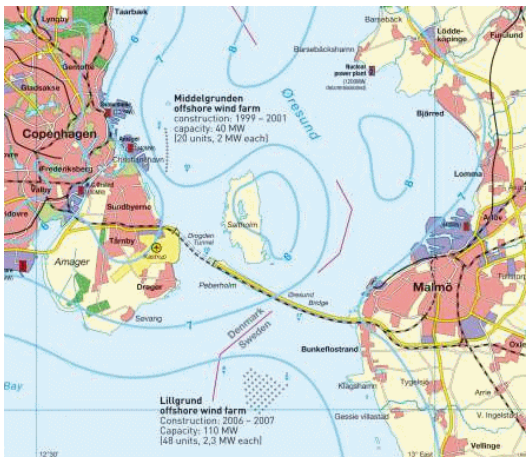

Figure 4. Location of the Lillgrund wind farm, showing wind turbine array -http://www.soziologie-etc.com/energien-erneuerbar/alle-zusammen/komb003-energy-turnaround-w-photos-ENGL.html.

Computational set up

The CFD computational domain is a box, where positive x direction corresponds to wind direction (from east to west). The y direction corresponds to normal direction to the wind (from south to north direction). The bottom of the domain corresponds to the sea level (see **Figure 5**).

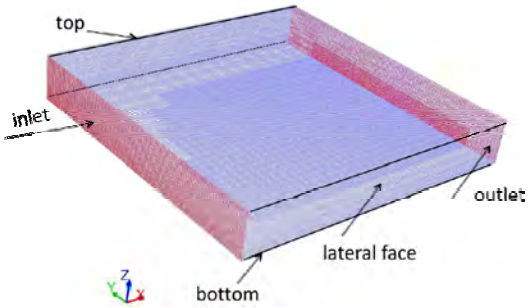

Figure 5. Computational domain.

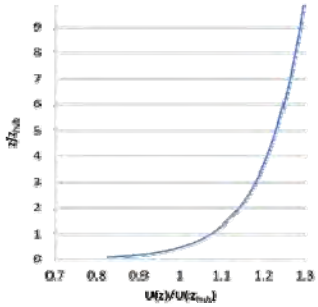

Figure 6: Vertical profiles of the marine atmospheric boundary layer (Panjwani et al (2014))

The sea surface waves are not modeled explicitly. The water surface is assumed as a flat surface. A no-slip boundary condition is used at the water surface. On the sides and top surfaces of the computational domain a free slip boundary condition is applied. At the exit of the computational domain a pressure outlet boundary condition is used. A logarithm velocity profile, shown in Figure 6 and given by Eq. 10, is used to approximate the marine atmospheric boundary layer (MABL),

$$U(z) = \frac{u_0}{k} \ln\left(\frac{z}{z_0}\right) \qquad (10)$$

where κ is the von Kármán constant, z is height, z_o is the aerodynamic roughness length and u_0 is the friction wind speed defined by $\sqrt{\tau/\rho}$; τ is the wind stress, and ρ is air density.

The turbulence model used for the study is the standard k-ε without modifying the dissipation rate equation (Churchfield et al (2012, 2012) and Kasmi (2008). The source term in the turbulence equation, which is due to rotation of the blades and also due to flow meandering (Churchfield et al (2012[2]), is not accounted in the present study.

In reality, turbulent kinetic energy and dissipation vary along the height. The variation in turbulent kinetic energy and dissipation depend on the atmospheric condition. However in present study a constant fixed value of turbulent kinetic energy and dissipation rate were used at the inlet of the domain. The inlet turbulent intensity was 0.15 and the turbulent viscosity ratio was 0.2. Furthermore standard wall functions were employed without correction for sea surface roughness (Blocken et al (2007)).

In present study neither the rigorous grid sensitivity studies nor the effect of model parameter associated with the ALM were performed. These parameters will strongly influence the turbulence and the velocity deficit behind the wind turbines. Nevertheless, some simulations with different meshes were performed until the power output of the turbines was independent of the mesh size.

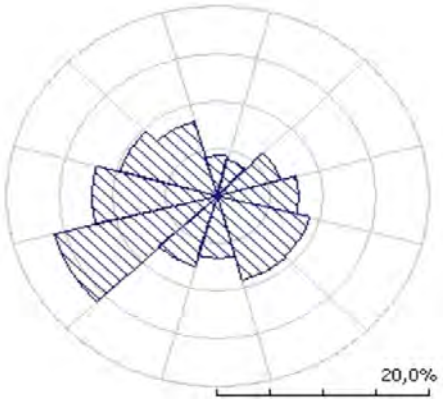

Figure 7. Measured wind rose at Lillgrund wind farm.

The CFD computation is done for 4 wind directions – the dominant wind direction of the wind in Lillgrund park (**Figure 7** and Figure 13). The computational domain is chosen so the wind direction to be always in the x direction. In consequence the computational domain does not have the same dimension for all 4 studied cases. The computational domain dimension will vary, but we impose that:

- The Distance from the first wind turbine (closest to the inlet) and inlet is 5.3 D_t (D_t=diameters of the turbine).

- The distance between last turbine (closest to the outlet) and outlet is $5D_t$.
- The distance from the top of the wind turbine to the top of the rotor is $6.3D_t$.

The grid size is around $0.12D_t$. The number of grid points is larger than 5 million grid points.

The reason for using the RANS k-ε turbulent model in this CFD work is to study how good results can be obtained with modest computing resources: course grid, 10 processors.

The engineering approach does not depend so much on the size grid, but the grid should have a minimum number of cells that assures a certain resolution of the presence of the wind turbines. The solution is much simpler than in case of CFD computations, hence the solution is obtained much faster. The results in this case are based on the some empirical parameters. The engineering model use 1000 grid points on the direction of wind propagation.

The distribution of wind turbines in the computation domain for all 4 studied cases can be seen in Figure 8. The position of the wind turbine is given in Jeppersson et al report (2008)

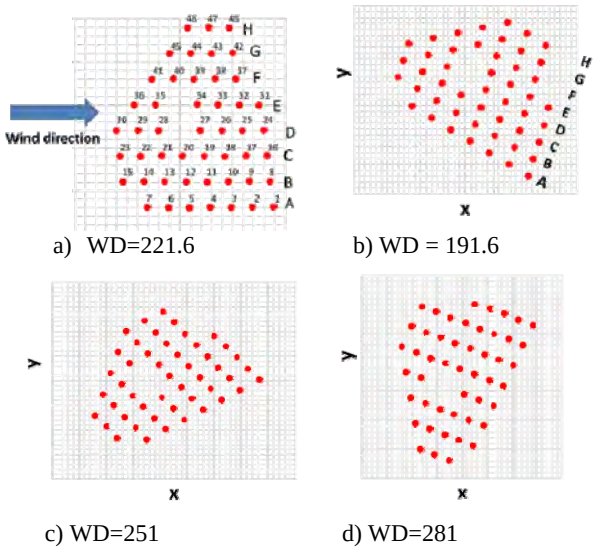

a) WD=221.6 b) WD = 191.6

c) WD=251 d) WD=281

Figure 8. Orientation of the wind farm relative to different wind velocities.

Power deficit as a consequence of the presence of the wake

The Lillgrund wind farm has a very dense configuration and it is used to investigate how shading effects (wake effects) will influence the production. We analyze the power output of the whole wind farm for different direction and wake effects. Shading effects are defined as the power ratio between the power outputs of one or more selected object turbines and the power levels of one or more reference turbines, located up front.

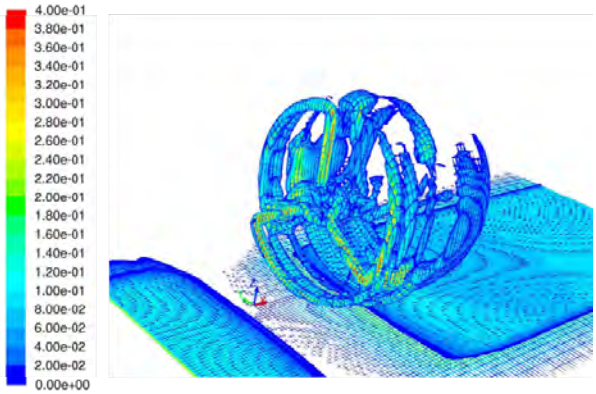

Figure 9. Contours of Vorticity behind the wind turbine – legend vorticity unit is 1/s.

Figure 9 shows the vortices behind a turbine. The near wake is dominated by counter-rotating helical vortex pairs. A counter-rotating helical vortex pair consists of a tip and root vortex shed from each blade. It can be observed that the rotating turbine induces the rotational component. A tip vortex forms at the blade tip due to the three-dimensional flow generated by the pressure difference between the 'pressure' and 'suction' sides of the blade. The vorticity sheds along the span of the blade then rolls up into the coherent tip vortices in a similar fashion to the fixed-wing case due to the induced flow of the tip vortex. The tip and root vortex path lines are helical in nature due to the rotating blades.

One of the targets of this study was to explore the ability of two methods to evaluate the power production of the wind turbines. First our simulations are compared to the production data (presented by Dahlberg, 2009) and LES simulation data (SOFA solver – Churchfield et al, 2012). So we can see in Figure 10 the engineering model can reproduce with a good accuracy the power level of the wind turbines in the farm. Sometimes the difference between experiment and engineering model results can be less than the difference between experiment and RANS results. The actual engineering model cannot reproduce the wind recovery because the dissipation is not accounted for in the engineering approach. In consequence, even though the engineering model sometimes gives better solution, it is overall less trustworthy because it cannot reproduce all relevant physics.

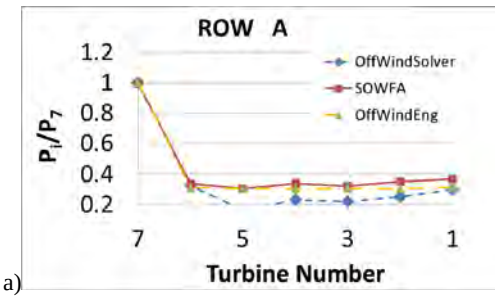

a)

b)

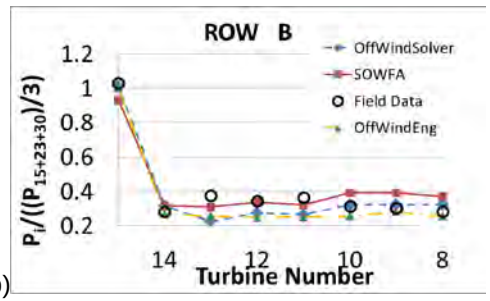

c)

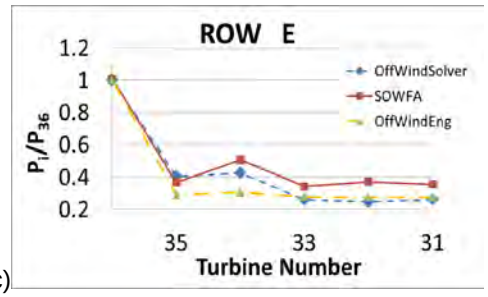

d)

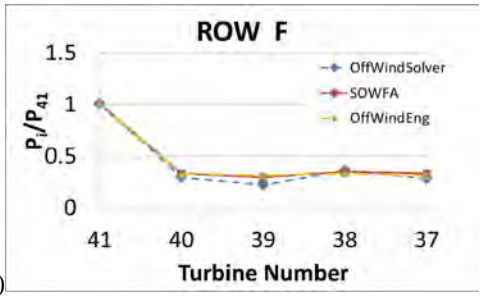

Figure 10. Simulation of the power produced by each turbine normalized by the average power of the first turbine in the row – WD = 221.6. Comparison among simulated data (SOFA, CFD and engineering model) and Lillgrund production data.

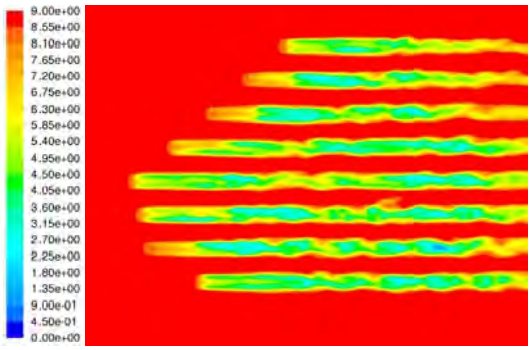

Figure 11: Contours taken in a horizontal plane at the rotor hub height of instantaneous velocity (legend velocity unit is m/s) – CFD computation.

Figure 11 depicts contours of streamwise velocity at the hub height - computed by using CFD approach. Near the center of the rotors there is a higher speed region of the flow. The reduced velocity from the upstream turbines reaches to the downstream turbine which subsequently reduces the power of downstream turbines.

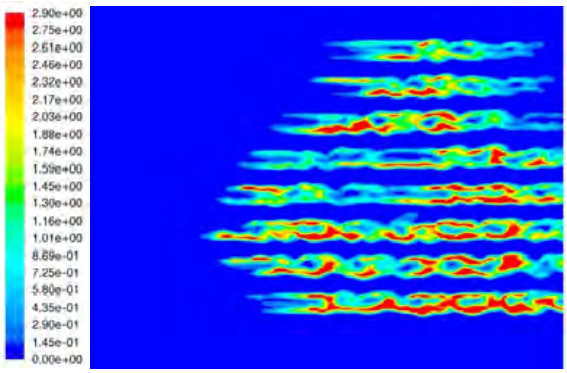

Figure 12. Contours taken in a horizontal plane at the rotor hub height of instantaneous turbulent kinetic energy (legend turbulent kinetic energy unit is m^2/s^2) – CFD computation

Figure 12 shows contour of turbulent kinetic energy at the hub-height that are computed using CFD approach. Turbulent kinetic energy is higher on the edges of wake because of higher velocity gradient in lateral direction. LES simulation [12] has showed that the greatest turbulent kinetic energy at the downstream turbines are due to the meandering of the downstream wakes (Smedman et al**,** 2009**)**. Meandering is not very visible here with the RANS based approach, but we still notice the greatest value of turbulent kinetic energy in the lines that present more wind turbines.

The power deficit for the wind farm for different directions of the wind is computed. Figure 13 shows that the dominant frequency wind direction are 180^0-210^0, 210^0-240^0, 240^0-270^0 and 270^0-300^0.

An attempt to estimate the power losses for the entire wind farm has also been made by dividing the wind farm in sectors and select different undisturbed turbines. These undisturbed turbines are located up front and used as reference turbines.

In this work we use the wind farm efficiency, *e*, defined as:

$$e = \sum_{r=1}^{7} \frac{1}{n_r} \sum_{t=1}^{n} \frac{P_{tr}}{P_{0r}} \qquad (11)$$

Where P_{tr} is the power of each turbine in the row *r*, P_{0r} is the power of the free stream turbine in the row *r* and n_r is the number of the turbine in the row *r*.

So we can see in Figure 14, the maximum power deficit for wind velocity equal to 9 m/s is obtained for a wind direction (WD) equal to 221.6^0, because in this case we deal with the total shading for the wind turbines situated in the lee of other turbine. In this case the power production of the wind farm is reduced with more than 50% relative to the designed wind farm power production.

The minimum power deficit is obtained for wind direction close to 281^0 because the shading of the wind turbines is low – in this case the wind farm loose around 20% relative to the designed wind farm power production.

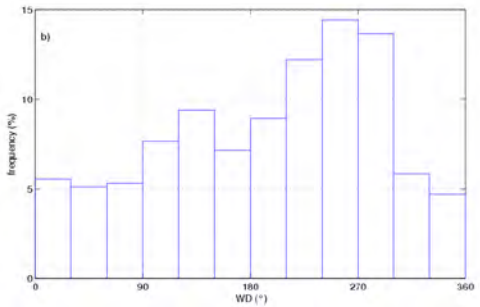

Figure 13. Wind directin frequencies at Lillgrund.

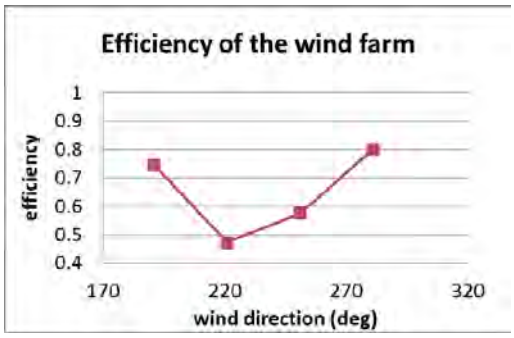

Figure 14. Relative power of the wind farm as function of the wind direction relative to the maxim power of the wind farm.

Significant wake effects occur when the wind is blowing along a row of turbines. The maximum peak loss occurs for the second turbine in the row when it is totally shaded and the loss is typically around 70% for Lillgrund farm – the loss is so big because the distance between turbines is small. To increases efficiency it is necessary to increase distance between wind turbines in the rows.

Figure 15 shows the computation of the wind power using the engineering model and CFD computation for wind direction equal to 281^0. It is notice that in this case the reduction of the power is much lower in vast majority wind turbine than in the case of wind direction equal to 221.6^0 - vast majority of them deal only with partial shadowing. Also we can remark that the difference between engineering and CFD computations is small. In other words engineering model can capture with a good approximation the power production in the wind farm.

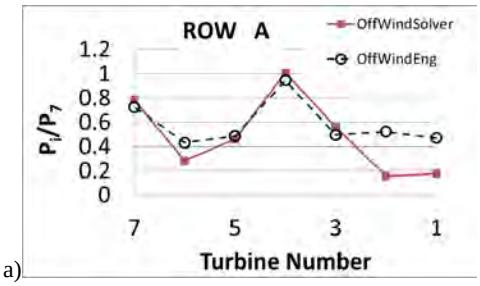

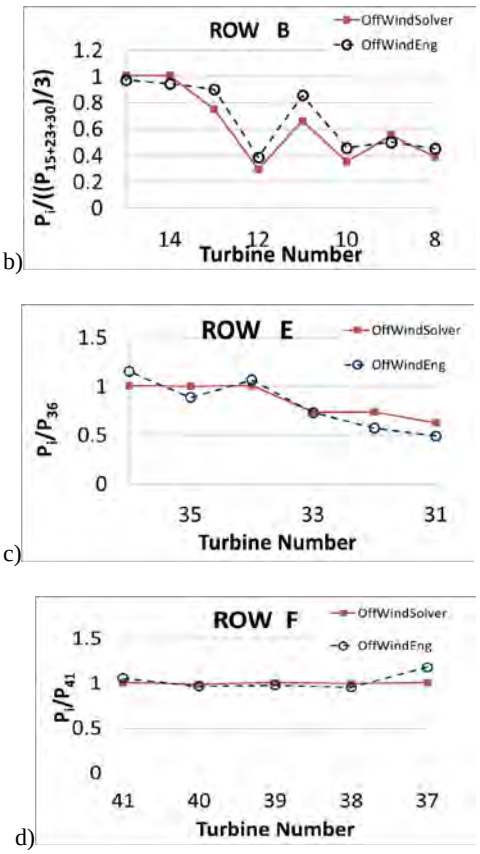

Figure 15. Simulation of the power produced by each turbine normalized by the average power of the first turbine in the row – WD = 281.6°.

CONCLUSION

Wake expansion and its effect on the power deficit were solved on two different levels of complexity:

i) CFD computation, within OpenFoam framework, which is developed for wind farm evaluation using the actuator line model and a k-ε turbulent model. The computation uses very modest resources and not a very fine grid. Even with these conditions the solutions capture the physics well.

ii) The engineering model (based on conservation on momentum) is based on the Jensen Wake model. The model was improved to approximate better the power deficit in the wind farm. The method can provide good results, but it needs some empirical coefficients, which may be computed based on CFD computation.

The CFD computation captures the physics better, but at a larger computational cost. The engineering approach takes less than 10 minutes on a single processor. It can give better solution than CFD, but it does not capture all the physics and some coefficients are based on CFD computation for calibration. In consequence the engineering model cannot be used independent of the CFD computations. The results for predicted power show good agreement with the experimental data for both approaches

The effect of wakes on power production is dramatic when we deal with total shadowing of the downstream turbines by the upstream turbines: the wind turbines affected by the upstream turbine wakes only have 30–

40% of the power of the first turbine in the row. In this case the total wind farm power is reduced to approximate 50% from designed wind farm power production. When the shadowing is partially the power can reduced much less – for example the wind farm power is reduced to approximate 80% from designed wind farm power production for the 281^0 wind direction.

More work remain to be done to improve the models, but both approaches (CFD – ALM and engineering model) used in this work are very promising.

REFERENCES

A.S. Smedman, U. Högström and E. Sahlee, (2009), "Obsrevation study of marine atmospheric boundary layer characteristics during swell", *J. Atmos. Sci*. 66, 2747-2763

Barthelmie, R.J., Larsen, G., Frandsen, S., Folkerts, L., Rados, K., Pryor, S., Lange, B., Schepers, G.,(2006), "Comparison of wake model simulations with off shore wind turbine wake profiles measured by sodar".*Journal of Atmospheric and Oceanic Technology* **23**,888–901.

Blocken, B., Stathopoulos, T. and Carmeliet, J. (2007) "CFD simulation of the atmospheric boundary layer: wall function problems", *Atmospheric Environment*, **vol. 41**, no. 2, pp. 238-252.

Choi, J. and Shan M., (2013), "Advancement of Jensen (Park) wake model", WEA Conference, Wien, Austria, February

Churchfield, M.J., Lee, S. and Moriarty, P.J., (2012),"A Large-Eddy Simulation of Wind-Plant Aerodynamics,", 50 *AIAA Aerospace Sciences Meeting*, Nasvhville, Tennessee, US.

Churchfield, M.J., Lee, S., Michalakes, and Moriarty, P.J., (2012), "A numerical study of the effects of atmospheric and wake turbulence on wind turbine dynamics," *Journal of Turbulence*, vol. 13, no. 14, pp. 1-32.

Dahlberg, J. Å., (2009), "Assessment of the Lillgrund Wind Farm: Power Performance Wake Effects,Vattenfall Vindkraft AB, 6_1 LG Pilot Report,"*Vattenfall Vindkraft AB, 6_1 LG Pilot Report*, Sept.2009.

González-Longatt, F., Wall, P., Terzija, V., (2012), "Wake effect in wind farm performance: Steady-state and dynamic behavior", *Renewable Energy*, **39**, pp.329-338.

International Energy Agemcy, "Energy Policies of IEA Country – Norway", 2011

Jeppsson, J., Larsen, P. E. and Larsson, Å. (2008). "*Vattenfall Vindkraft AB 2_1 LG Pilot Report",*

Kasmi, A.E. and Masson, C., (2008) "An extended k–e model for turbulent flow through horizontal-axis wind turbines," *Journal of Wind Engineering and Industrial Aerodynamics*, **96**, no. 1, pp. 103-122

Menter, F., Langtry,R. ,Völker, S., (2006), "Transition modelling for general purpose CFD codes".Flow,Turbulence and Combustion, **77**, 277–303.

Mo, J-O, Choudhry, A, Arjomandi, M, Kelso, R, Lee, Y-H, (2013) "Effects of wind speed changes on wake instability of a wind turbine in a virtual wind tunnel using large eddy simulation", *J. of Wind Eng. and Ind. Aerodyn*, 117, 38-56

Nielsen, P., (2003)"Offshore Wind Energy Projects Feasibility Study Guidelines SEAWIND,"*Altener Project* 4.1030/Z/01-103/2001

Panjwani, B., Popescu, M., Samseth, J. Ernst Meese and Jafar Mahmoudi, J., (2014)," OffWindSolver: Wind Farm Design Tool Based on Actuator Line/Actuator Disk Concept in OpenFoam architecture", *ITM Web of Conferences*, Vol.2, First Symposium on OpenFOAM® in Wind Energy

Potsdam, M.A., Mavriplis, D.J., (2009), "Unstructured mesh CFD aerodynamic analysis of the NREL Phase VI rotor". *AIAA Paper 2009-1221, AIAA Aerospace Sciences Meeting, Orlando, FL.*

Sørensen, J.N. and Shen, W.Z., (2002), "Numerical modeling of wind turbine wakes," *Journal of Fluids Engineering-Transactions of the Asme*, vol. 124, no. 2, pp. 393-399.

Sørensen, J.N., "Aerodynamic Aspects of Wind Energy Conversion," Annual Review of Fluid Mechanics, **43**, pp. 427-448, 2011.

Sørensen, N.N., Michelsen, J.A., Schreck, S., (2002), "Navier–Stokes predictions of the NREL phaseVI rotor in the NASA Ames 80ftx_120ft wind tunnel",*Wind Energy*, Vol.**5**, pp. 151–169.

VATTENFALL (2008), "Technical Description Lillgrund Wind Power Plant", *Pilot project*

Vermeer, L., Sørensen, J.N., Crespo,A., (2003) "Wind turbine wake aerodynamics". *Progress in Aerospace Sciences* Vol.39, pp.467–510.

Wu, Y.T., Porté-Agel, F., (2011), "Large-eddy simulation of wind-turbine wakes: evaluation of turbine parametrisations", *Boundary-Layer Meteorology*, **138**, 345–366.

ACKNOWLEDGMENTS

The work in this paper was supported by the Nordic Energy Research.

A MODELING STRATEGY FOR LARGE-SCALE MECHANICAL DRAUGHT AIR-COOLED SYSTEMS

Chris MEYER[1]*, **Albert ZAPKE**[2]†

[1]University of Stellenbosch, Department of Mechanical and Mechatronic Engineering, Stellenbosch, 7600, SOUTH AFRICA

[2]GEA Aircooled Systems (Pty) Ltd, Aberdein Street, Roodekop, Germiston 1401, SOUTH AFRICA

* E-mail: chris.meyer@ees-cfd.co.za
† E-mail: albert.zapke@gea.com

ABSTRACT

Large-scale mechanical draft air-cooled systems are used in arid regions where water for cooling purposes is unavailable. These systems can consist of as many as 384 axial flow fans with diameters in excess of 10 meters and are sensitive to a range of environmental and operating conditions with wind and cross-flows having the most detrimental effect on operation. The large size of these systems often limits or prohibits experimental investigation. A numerical analysis strategy, employing equivalent models for the operation of the axial flow fans and heat exchangers, is presented and validated. The models are implemented in OpenFOAM®and a strategy is introduced where the characteristics of the software is exploited to ensure parallel computation. The numerical strategy is subsequently employed to calculate the detailed flow and temperature fields of an air-cooled condenser (ACC) typically used at power stations.

Keywords: axial flow fan, heat exchanger, numerical model .

NOMENCLATURE

Greek Symbols

α	Blade element angle of attack, $[^\circ]$.
β	Flow angle, $[^\circ]$.
δ	Increment or element, $[-]$.
γ	Blade element stagger angle, $[^\circ]$.
ϕ	Generic variable, $[-]$.
π	Constant 3.14159, $[-]$.
ρ	Mass density, $[kg/m^3]$.
σ	Solidity ratio, $[-]$.
θ	Incidence angle, $[^\circ]$.

Latin Symbols

A	Area, $[m^2]$.
c	Blade chord, $[m]$.
c_p	Specific heat, $[J/kgK]$.
C	Coefficient, $[-]$.
$\mathbf{D}$	Drag force, $[N]$.
$\mathbf{F}$	Force, $[N]$.
h	Heat transfer coefficient, $[W/m^2K]$.
$\mathbf{L}$	Lift force, $[N]$.
$\dot{m}$	Mass flow rate, $[kg/s]$.
n	Number of fan blades, $[-]$.
$\dot{Q}$	Rate of heat transfer, $[W]$.
r	Radial coordinate, $[m]$.
$\mathbf{S}$	Source term, $[-]$.
t	Disc region axial thickness, $[m]$.
T	Temperature, $[K]$.
U	Total heat transfer coefficient, $[W/m^2K]$.
$\mathbf{U}$	Velocity vector field, $[m/s]$.
V	Volume, $[m^3]$.
$\mathbf{W}$	Velocity vector, $[m/s]$.
$\mathbf{x}$	Position vector, $[m]$.

Sub/superscripts

ϕ	Associated with generic variable.
a	Axial or air.
D	Drag.
i	Inlet.
L	Lift.
o	Outlet.
R	Relative.
s	Steam.
t	Tangential.

INTRODUCTION

Mechanical draft air-cooled systems do not only find widespread application in the process and petrochemical industries but also do duty as air-cooled condensers (ACCs) at power stations located in arid regions where water for cooling purposes is scarce or unavailable (Tawney *et al.*, 2005). At the time of commissioning the 6x650 MW Matimba power plant in South Africa utilized the worlds largest ACC, according to (Goldschagg, 1993), comprising of 288, 30 ft diameter axial flow fans. Currently, two additional dry-cooled power stations, Medupi (6x800 MW) and Kusile (6x900 MW), are under construction in South Africa.

A typical ACC consists of any number of horizontally mounted axial flow fans that force ambient air across arrays of delta-configured heat exchangers as schematically depicted in Figure 1.

Operational experience has demonstrated that ACCs are not only vulnerable to windy conditions but in systems comprising a large number of fans, the fans towards the interior of the ACC generate high flow velocities across the inlet of fans located at the periphery of the ACC with a subsequent reduction in performance of these fans.

In an experimental investigation (Salta and Kröger, 1995) showed that a reduction in platform height, and thus an increase in the cross-flow velocities at periphery fans, reduced the performance of periphery fans exponentially, a result that was confirmed by (Duvenhage *et al.*, 1996).

Deterioration of the performance of edge-fans is attributed to predominantly two effects: the formation of a region of recirculating air at the edge of the inlet bell-mouth and the addition of a cross-flow component at the face of the fan, (Meyer, 2005). The former creates a local region of low pressure air associated with severe flow distortions whilst the latter results in a velocity inlet field that deviates from that experienced under design or test conditions. (Stinnes and von Backström, 2002) and (Hotchkiss *et al.*, 2006) isolated the effect of the latter on fan performance characteristics as measured in a coded wind tunnel.

In addition to the aforementioned, ACCs are also susceptible to another performance deteriorating phenomenon: hot air recirculation, the result of the recirculation of the hot air plume issuing from the heat exchanger banks through the axial flow fans. (Duvenhage and Kröger, 1996) demonstrates that although hot air recirculation can occur without the presence of wind, a primary consequence of wind is an increase in hot air recirculation of especially the fans located on the down-wind side of the ACC.

Apart from the direct effect of wind on ACC performance, it stands to reason that the close proximity of structures typically associated with power stations (pipe racks, boiler- and turbine houses, smoke stacks etc.) will, based on their location with regards to the wind direction and ACC location, have a secondary effect on ACC performance. The shear size of most ACC installations and associated structures has lead many researchers to conclude that the use of computational fluid dynamics (CFD) remains the only viable option to analyse the effect of wind and other flow conditions on ACC performance. To this end a host of publications have seen the light.

(Duvenhage and Kröger, 1996) used a novel actuator disc (AD) model for the axial flow fans and a porous region (PR) with energy sources for the heat exchangers to investigate the effect of wind magnitude and direction on the fan and thermal performance of an air-cooled heat exchanger. (Meyer, 2005) used an AD fan model and a PR heat exchanger model to investigate cross-flow and flow separation effects at the inlet of axial flows fans. (Bredell *et al.*, 2005) used a so-called pressure jump (PJ) strategy to model axial flow fans in combination with a PR heat exchanger model to determine the effect of type of fan, platform height and walkway width on ACC performance. (van Rooyen and Kröger, 2008) considered the effect of wind on a larger ACC system using a AD model for the fans and a PR with energy sources for the heat exchangers and concludes that the primary effect of wind is the deterioration in performance of periphery fans with an increase in hot air recirculation playing only a secondary role.

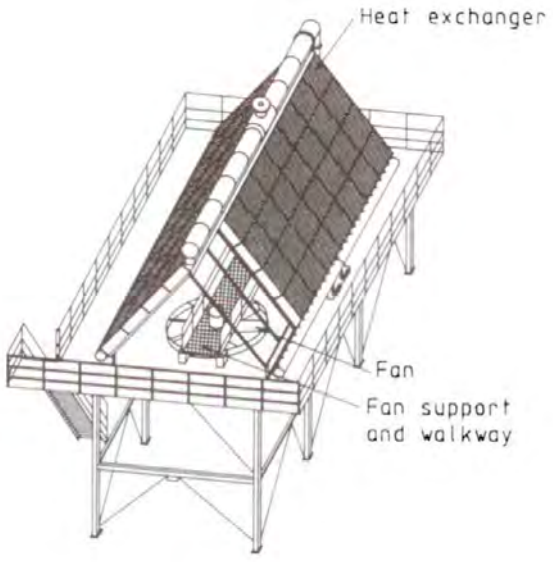

Figure 1: Schematic representation of a typical ACC (Kröger, 2004).

In an effort to determine the volumetric flow performance benefits of low noise fans in ACC applications, (van der Spuy *et al.*, 2009) used both an AD as well as a PJ fan model, individually as well as in combination and a PR heat exchanger model and concludes that axial flow fans with steeper pressure gradients offer distinct advantages in ACC applications under windy conditions.

With a growing interest in the combined effect of wind and wind interactions with associated power station structures on ACC performance, (Liu *et al.*, 2009) used a very simplified strategy to include the effect of axial flow fans and heat exchangers through the use of prescribed velocity boundary conditions. With similar intentions (Gao *et al.*, 2009) used a PJ fan modelling strategy in combination with a PR heat exchanger model with energy source terms to not only confirm the findings of previous authors with regards to the effect of wind on fan performance and hot air recirculation but also to demonstrate the dramatic effect that buildings can have on ACC performance. The investigation of (Yang *et al.*, 2010) used a similar modelling strategy to evaluate the effects of different strategies to mitigate the detrimental effect of wind on ACC performance. The investigation of (He *et al.*, 2013) follows a similar strategy.

(Yang *et al.*, 2011) used a computationally intensive strategy with regards to axial flow fan modelling in their work. The axial flow fan was modelled in detail using a rotating reference frame model calculating the detailed flow through the fan blade passages. This approach inevitably leads to very large mesh cell counts thus dramatically increasing the computational effort and limiting the scope of the simulation. A PR heat exchanger model with energy source terms was utilized.

The performance of a single fan-heat exchanger combination was considered by both (Zhang *et al.*, 2011) and (Meyer and Kröger, 2004) with the latter using an AD fan model in combination with a PR heat exchanger model and the former a rotating reference frame fan strategy with a PR heat exchanger model with energy source terms. In both investigations the complexity of the flow field within the enclosed region between the fan and heat exchanger, or plenum, is high-lighted as well as the effect on heat exchanger thermal performance due to the subsequent maldistribution of air.

A novel two-step approach was developed by (Owen and Kröger, 2011) and (Owen and Kröger, 2013) where a global or large-scale flow field with representative inner boundary conditions on the surfaces demarcating the boundary between the global flow field and an inner region containing the ACC and a detailed ACC flow field with representative boundary conditions for the global flow field are solved in succession to yield results that compare favourably with experimental measurements taken at an actual ACC installation. The method was developed to limit the computational expense of large-scale simulations and makes use of a PJ fan model and a PR heat exchanger model with energy source terms.

From the above it is evident that large-scale CFD simulations of ACCs have yielded results that are broadly consistent with observable phenomena. What is also clear is that simulations of this kind have, to a large degree, found acceptance within the industry. What is however not clear is what level of modelling presents the most sensible balance between the basic phenomenological requirements of the individual components of these systems and available or even affordable computational power. The primary modelling requirements are those demanded by the axial flow fans and heat exchangers. Given the wide range of modelling strategies listed above, especially for axial flow fans, the current body of work seeks to not only define the minimum requirement for models of this nature but attempts to present a strategy that fulfils these requirements.

AXIAL FLOW FAN MODEL

Modelling strategies for axial flow fans have varied from very simplistic models, where the fan is represented by some empirically developed velocity boundary condition to brute-force numerical resolution of the detailed flow within the fan blade passages. The importance of a properly constructed model is underlined by the finding that the reduction of fan performance is the primary factor in the deterioration of ACC thermal performance under windy conditions (Duvenhage and Kröger, 1996).

Although it is a well-established fact that fans in ACCs, particularly periphery fans, are subject to non-ideal inlet conditions, that is conditions that substantially deviate from those encountered in a fan test facility, it is also true that conditions at the fan outlet plane might exhibit a similar degree of deviation. Both (Goldschagg *et al.*, 1997) and (van Staden, 2000) note that under windy conditions flow reversal was observed through the axial flow fan. It is thus of vital importance that a fan model be able to respond to varying or non-ideal inlet and outlet flow conditions.

From the investigations of (Zhang *et al.*, 2011) and (Meyer and Kröger, 2004) it is clear that an accurate resolution of the plenum flow field is an important factor in predicting the thermal performance of the heat exchangers. The experimental study of (Meyer and Kröger, 1998) further demonstrates that different types of axial flow fans can have a marked effect on the plenum flow field and hence the losses associated with the plenum. In much the same way, heat exchanger inlet flow losses are extremely sensitive to the air angle of incidence at the heat exchanger inlet plane, (Meyer and Kröger, 2001a). It follows that the velocity field at the exit plane of the fan or then at the inlet plane to the plenum would play a significant role in the ACC flow and thermal performance.

Representing the fan through the specification of velocity boundary condition or using the PJ model exhibit severe restrictions in terms of the above requirements. The former relies completely on empirical information and is thus not responsive to either fan inlet or outlet conditions. The PJ model relies upon the fan pressure characteristics determined under ideal or test conditions which would most certainly not be a realistic expectation at periphery fans as demonstrated by the work of (Stinnes and von Backström, 2002) and (Hotchkiss *et al.*, 2006).

Furthermore, most implementations of the PJ model make no effort to account for the complex velocity field at the fan outlet. A notable exception is (Yang *et al.*, 2011) who furnish their model with a constant outlet swirl velocity field.

The above leads (van der Spuy *et al.*, 2009) to state that the PJ model is wholly inadequate to deal with flow conditions associated with periphery fans.

In an effort to better understand axial flow fan performance at low flow rates, (Louw *et al.*, 2014) uses CFD to resolve the detailed blade passage flow field of a single blade passage of a 1.542 m diameter axial flow fan. Grid independence was only achieved for a computational mesh of around 1 million cells and after a transient solution strategy was employed. Although other researchers have made an attempt to model large-scale fans using a similar, albeit steady-state strategy, (Zhang *et al.*, 2011) and (Yang *et al.*, 2011) it is doubtful that such a treatment presents a realistic approach for modelling of the periphery fans of large-scale systems.

According to (van der Spuy *et al.*, 2009) the AD model remains the only viable or computationally realistic methodology with which to model ACC fans in general and periphery fans in particular.

A number of authors including (Duvenhage and Kröger, 1996), (Meyer and Kröger, 2001b), (Meyer and Kröger, 2004), (Meyer, 2005), (Hotchkiss *et al.*, 2006), (Bredell *et al.*, 2005), (van Rooyen and Kröger, 2008), (van der Spuy *et al.*, 2009) and (Owen and Kröger, 2011) have demonstrated the ability of the AD model to submit to all of the above-mentioned requirements for an axial flow fan model.

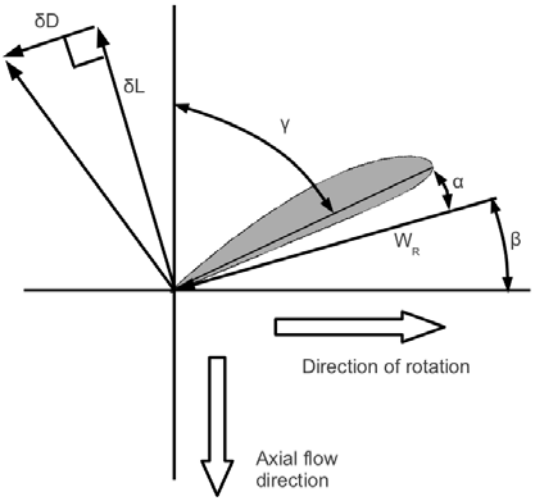

Figure 2: A schematic representation of a fan blade element.

In the AD model a momentum source term is specified in the computational cells within the disc-shaped region swept by the fan blades. The momentum source terms are developed using blade element theory.

Figure 2 shows a typical blade element where $\mathbf{W_R}$ is the relative velocity vector at the blade element, α the blade element angle of attack, β the angle between the relative velocity vector and the plane of rotation, or flow angle of the element and γ the blade element stagger angle.

The blade element lift and drag force, $\delta\mathbf{L}$ and $\delta\mathbf{D}$ can be calculated, respectively as

$$\delta\mathbf{L} = \frac{1}{2}\rho \mid \mathbf{W_R} \mid^2 C_L \times c \times \delta r \tag{1}$$

and

$$\delta\mathbf{D} = \frac{1}{2}\rho \mid \mathbf{W_R} \mid^2 C_D \times c \times \delta r \tag{2}$$

where C_L is the lift and C_D the drag coefficient of the blade element, c is the blade element chord length and δr is the radial thickness of the blade element.
The lift and drag forces can consequently be written as a force in the axial, $\delta\mathbf{F_a}$ and tangential, $\delta\mathbf{F_t}$, directions.

$$\delta\mathbf{F_a} = \delta\mathbf{L}\cdot\cos\beta - \delta\mathbf{D}\cdot\sin\beta \tag{3}$$

$$\delta\mathbf{F_t} = \delta\mathbf{L}\cdot\sin\beta + \delta\mathbf{D}\cdot\cos\beta \tag{4}$$

For inclusion in the Navier-Stokes equations it is necessary that the blade element axial and tangential forces be expressed on a per unit volume basis. It follows that

$$\frac{\delta\mathbf{F_a}}{\delta V} = \frac{n\cdot\delta\mathbf{F_a}}{2\pi r\cdot\delta r\cdot t} = \frac{\sigma\cdot\delta\mathbf{F_a}}{c\cdot\delta r\cdot t} \tag{5}$$

and

$$\frac{\delta\mathbf{F_t}}{\delta V} = \frac{n\cdot\delta\mathbf{F_t}}{2\pi r\cdot\delta r\cdot t} = \frac{\sigma\cdot\delta\mathbf{F_t}}{c\cdot\delta r\cdot t} \tag{6}$$

where r is the radial coordinate of the blade element, n the number of fan blades, t the thickness of the disc region in the axial direction and $\sigma = c\cdot n/2\pi r$ the solidity ratio of the fan.

HEAT EXCHANGER MODEL

In all but one of the studies listed earlier, the heat exchanger is modelled as a porous region. For the inclusion in a flow and thermal model of an ACC, the heat exchanger model should address both the fluid dynamic as well as heat transfer interactions between the air and heat exchanger. In terms of the flow field the heat exchanger not only redirects the air but a pressure drop is also experienced. In terms of the thermal field, heat or energy is added to the air stream.

Flow resistance

In the PR model, the porosity in the plane parallel to the heat exchanger inlet-outlet plane is adjusted to restrict the direction of air flow to a direction normal to the heat exchanger inlet-outlet plane. The porosity in the normal direction is again adjusted to ensure that the normal-flow pressure drop experienced by the air as it flows through the porous region is consistent with that measured across the heat exchanger under normal flow conditions.
In an experimental investigation of heat exchanger flow losses, (Meyer and Kröger, 2001a) demonstrate that for a certain inlet flow angle of incidence, θ, different heat exchangers not only exhibit differing inlet flow losses but that a change in the orientation of a single heat exchanger will also result in a different inlet flow loss for the same angle of incidence.
Figure 3 schematically demonstrates this concept where the flow is parallel to the finned surfaces in (a) but at an angle to the finned surfaces in (b). (Meyer and Kröger, 2001a) notes that this change in inlet flow losses due to a change in orientation is more pronounced for finned tubes that use a circular tube and less so for elliptical tubes, the latter acting as a flat plate more so than the former.
(Meyer, 2010) demonstrates that the use of a porous region to model oblique flow through a heat exchanger invokes a numerical inlet flow loss that reacts to a change in the air angle of incidence in much the same manner as that of actual heat exchangers but that the numerical inlet flow loss underestimates the inlet flow loss at acute angles of incidence.
The highly non-uniform nature of the flow within the ACC plenum indicates that heat exchanger oblique flow losses could be an important factor in accurately predicting the flow and thermal performance of an ACC.
Given the prohibitive nature of the alternative to a PR approach, modelling the finned tubes in detail, it is concluded that the shortcomings of the PR model is a necessary evil. In situation where ACCs with elliptical finned tubes are modelled these disadvantages are benign.

Heat transfer

(Duvenhage and Kröger, 1996) included the energy transfer from the heat exchanger to the air by calculating a heat exchanger outlet temperature and specifying the latter in the last row of cells at the heat exchanger outlet plane. This model was applied on a cell-by-cell basis and thus allows for the maldistribution of flow through the heat exchanger to be reflected in the heat exchanger outlet plane temperature distribution.
A similar method was followed by (van Rooyen and Kröger, 2008), (Gao *et al.*, 2009), (Yang *et al.*, 2010), (Owen and Kröger, 2011), (Owen and Kröger, 2013) and (He *et al.*, 2013) but instead of specifying an outlet temperature discreet heat sources in the region occupied by the heat exchanger were calculated.
According to (Duvenhage and Kröger, 1996) the air outlet temperature, T_{ao} for a given inlet temperature, T_{ai} can be calculated as

$$T_{ao} = T_s - (T_s - T_{ai})\exp -\frac{UA}{c_p\dot{m}_a} \tag{7}$$

where T_s is the steam temperature, c_p the specific heat of air, $\dot{m}_a$ the air mass flow rate and UA is defined as

$$UA = \left[\frac{1}{h_a A_a} + \frac{1}{h_s A_s}\right]^{-1} \tag{8}$$

with h_a and h_s the convection heat transfer coefficients of air and steam and A_a and A_s the total air and steam heat transfer areas respectively.
More often than not constant values are assumed for h_s and T_s whilst a heat exchanger-specific expression is used to calculate h_a.
In the current implementation energy source terms are calculated and specified in cells within the heat exchanger region where

$$\dot{Q} = \dot{m}_a c_p\,(T_{ao} - T_{ai}) \tag{9}$$

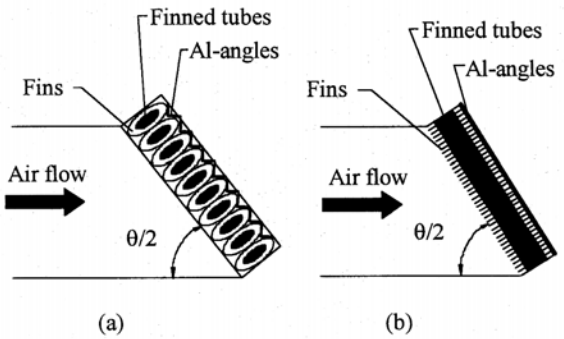

Figure 3: Orientation of the heat exchanger bundle (Meyer and Kröger, 2001a).

MODEL IMPLEMENTATION

The use of open source CFD software holds distinct advantages in terms of not only the ability to implement additional models and solution strategies but also in terms of cost reduction. The latter becomes particularly attractive when considering the large-scale modelling that is required for ACC systems and the subsequent necessity for the use of a parallel computational architecture.

Both the AD fan and PR heat exchanger models present challenges in terms of their CFD implementation, most notably the necessity for the non-transport transfer of information from one part of the computational domain to another.

A prime example of non-transport transfer of information is the calculation of the blade element relative velocity vector, $\mathbf{W_R}$ at cells located within the blade swept disc region of axial flow fans.

As stated earlier, $\mathbf{W_R}$ is an average velocity vector based on velocity vector values some distance up- and down stream of the disc cell under consideration. Although these velocities are calculated through the solution of the Navier-Stokes equations their transport to a different location or cell is not governed by the solution of a transport equation. This type of information transport requires a separate seek-and-identification process that would link the particular cell in the disc region with its up- and down stream counterparts. More often than not this can be accomplished with the construction of look-up tables.

The primary disadvantage of look-up tables is that their parallel implementation within a CFD code becomes problematic. Information might be located at a computational node different from the one at which the information is required. In the current body of work a novel technique is developed where a transport equation is used to transfer information across the calculation domain thus avoiding the use of look-up tables. The use of a transport equation implies that the native parallel environment of the open source software, OpenFOAM®, can be exploited to ensure that the information transfer occurs seamlessly across computational nodes.

A convection equation for a generic variable, ϕ is defined as follows

$$\frac{(\partial \phi \mathbf{U})}{\partial \mathbf{x}} + \mathbf{S}_\phi = 0 \tag{10}$$

where $\mathbf{U}$ is a velocity vector field that defines the path of information transfer and $\mathbf{S}_\phi$ is a source term.

The information or variable value that requires transport is defined as or placed within the source term of the convection equation and, provided that the velocity vector field is properly constructed, transported to the required location within the calculation domain through solution.

The heat exchanger inlet as well as outlet temperatures are transported across the heat exchanger region within the calculation domain using a similar strategy. This is required as the thermal properties of air used in the calculation of $\dot{Q}$ is calculated at the average heat exchanger air temperature, $(T_{ao}+T_{ai})/2$, which thus needs to be available to all cells within the heat exchanger region.

STRATEGY EVALUATION

The numerical strategy outlined above was implemented in the open source CFD library, OpenFOAM®. To demonstrate the computational efficiency of this strategy, a single-fan (diameter of 10 m) ACC system was modelled using a serial (single processor) strategy and the results compared to that obtained from the simulation of an 24-fan ACC installation consisting of 24 combined units of the single-fan ACC. For this system the fans were grouped in 4 rows of 6 fans each, yielding a 4 x 6 fan matrix. A parallel computational strategy was used in this instance, making use of a dual-processor, 6 core computer. The calculation domain was effectively divided into 12 regions.

The ACCs were not modelled in the free atmosphere, but rather in an elaborate-sized wind tunnel as shown in Figure 4 for the singe-fan system and Figure 5 for the 24-fan system. The primary motivation was that all cross-flow velocities could be eliminated and a direct comparison of the results for the single-fan system could be made with those of the individual units in the 24-fan system.

A velocity inlet boundary condition was used to specify the air mass flow rate into the domain whilst an outlet boundary condition was specified at the opposite parallel plane. These two boundaries formed the inlet and outlet, respectively of the wind tunnels. The sides of the wind tunnels were specified as symmetry planes.

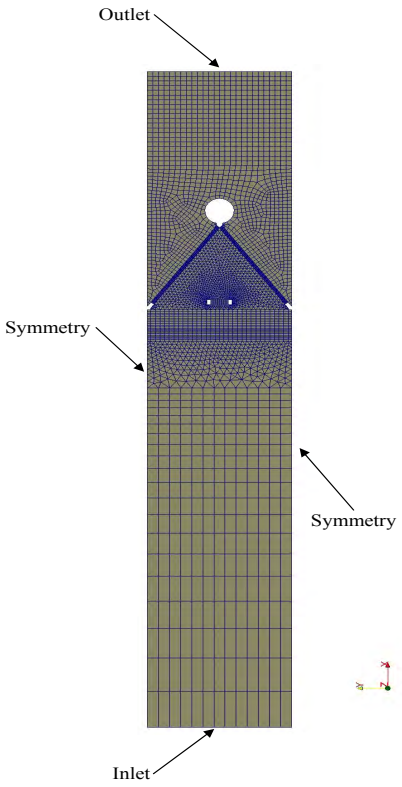

Figure 4: Wind tunnel configuration of single-fan ACC with boundary conditions.

In Figure 6 a stripped-down view of the 24-fan system geometry is displayed indicating the position of the fan hubs, steam pipes, fan bridge and fan inlet sections or bell mouths. One of the symmetry planes with computational mesh is also included to provide perspective. The computational mesh of the single-fan system consisted of around 500 000 and that of the 24-fan system of close to 12 million cells.

A comparison of the velocity magnitude and tangential velocity contours on a plane normal to the steam pipe and parallel to and located at the fan axis of the two ACC systems

are shown in Figures 7 and 8, respectively. The single-fan unit is at the top of the figures followed below by the 24-fan system. It is clear that the velocity fields are near-identical. The region of recirculating flow within the plenum chamber of the single-fan system is slightly more elongated than that for the 24-fan system. However, it should be remembered that the symmetry planes utilized as the side surfaces of the single-fan system are not entirely consistent with the planes between fan units of the 24-fan system as all of the fans rotate in the same direction. To ensure symmetry alternate fans should rotate in opposite directions.

The ACC temperature contours of the two systems are compared in Figure 9 using the same plane. The singe-fan unit is located, as before, at the top of the figure. The temperature fields are all but identical.

From the results of the numerical investigation it is quite obvious that the serial and parallel implementations of the solution strategy yields near-identical results and that the transport-equation methodology for information transfer across the domain works as well in series as it does in parallel. It should be noted that no additional software development was needed, apart from the implementation of the convection equation, to facilitate parallel implementation.

The numerical simulation furthermore demonstrates that the use of an AD fan model and PR heat exchanger model with source terms is a viable solution strategy for the simulation of large-scale ACC systems.

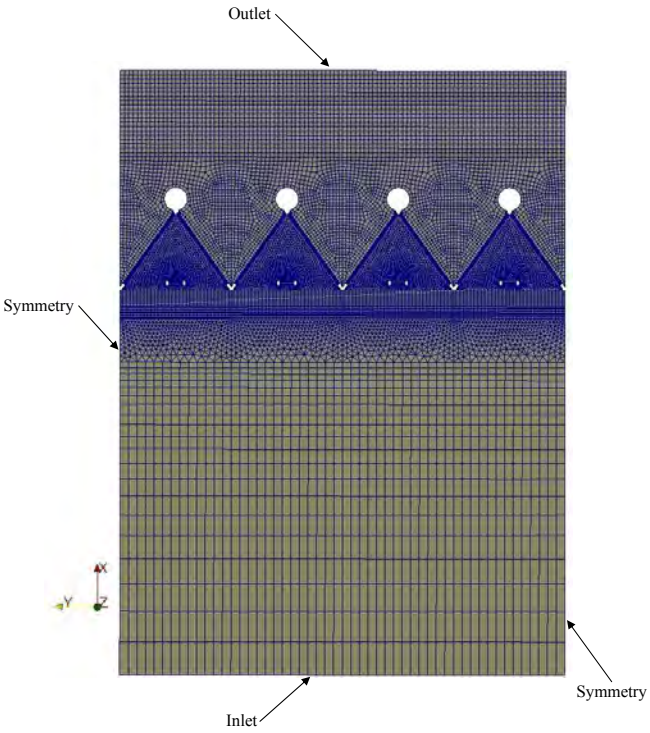

Figure 5: Wind tunnel configuration of 24-fan ACC with boundary conditions.

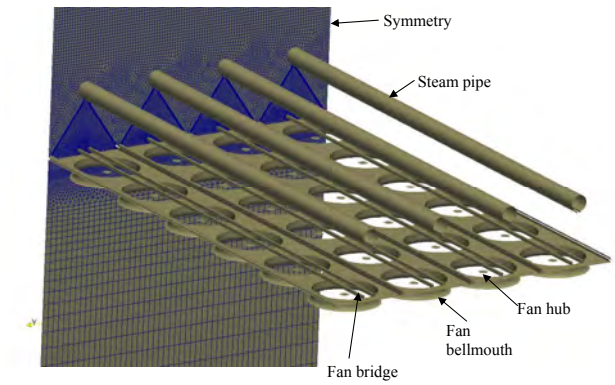

Figure 6: Detail of ACC system.

CONCLUSION

The text has demonstrated that the CFD simulation of large-scale ACC systems and associated structures have found application in the ACC industry and has provided results that are consistent with observations and even some experimental studies. Requirements for the inclusion of a fan and heat exchanger model have been identified.

For the fan model these are:

1. Sensitivity to flow conditions at both the fan inlet and outlet planes.

2. Accurate resolution or representation of the flow field at the fan outlet plane.

3. Realistic computational cost to deal with large number of fans.

For the heat exchanger:

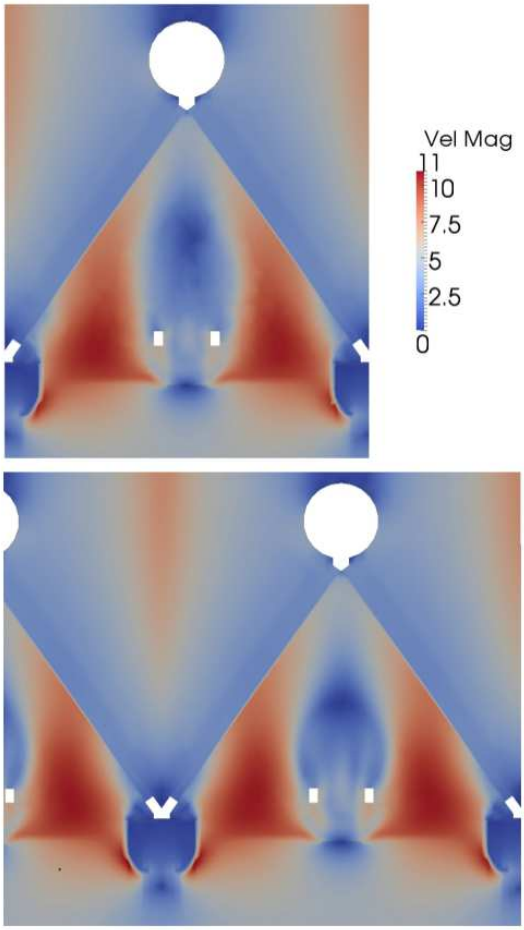

Figure 7: Comparison of ACC velocity magnitude (m/s) contours of a single fan- (top) and 24-fan ACC (bottom).

1. Accurate representation of the restriction on the direction of air flow and pressure drop through the heat exchanger.
2. Realistic inclusion of the additional resistance due to oblique flow conditions at the heat exchanger inlet plane.
3. Include an appropriate heat transfer model from steam to air within the heat exchanger region.
4. Realistic computational cost as heat exchangers occupy a relatively large volume of the computational domain.

It was demonstrated that an AD fan model and PR heat exchanger model with energy source terms are most likely to submit to all of the above requirements.
The subsequent numerical simulation has demonstrated that:

1. An AD fan model with a PR heat exchanger model can be used to simulate large-scale ACC systems at an acceptable level of computational cost.
2. The use of an additional convection equation for the transport of information across the calculation domain is a viable alternative to the use of look-up tables.

REFERENCES

BREDELL, J., KRÖGER, D. and THIART, G. (2005). "Numerical investigation of fan performance in a forced draught air-cooled steam condenser". *Applied Thermal Engineering*, **26**, 846–852.

DUVENHAGE, K. and KRÖGER, D. (1996). "The influence of wind on the performance of forced draught air-cooled heat exchangers". *Journal of Wind Engineering and Industrial Aerodynamics*, **62**, 259–277.

DUVENHAGE, K., VERMEULEN, J., MEYER, C. and KRÖGER, D. (1996). "Flow distortions at the fan inlet of forced-draught heat exchangers". *Heat Recovery Systems & CHP*, **16(8/9)**, 741–752.

GAO, X., ZHANG, C. and WEI, J. (2009). "Numerical simulation of heat transfer performance of an air-cooled steam condenser in a thermal power plant". *Heat and Mass Transfer*, **45**, 1423–1433.

GOLDSCHAGG, H., VOIGHT, F., DU TOIT, C., THIART, G. and KRÖGER, D. (1997). "Air-cooled steam condenser performance in the presence of cross-winds". *Proceedings: Cooling Tower Technology Conference, Electrical Power Research Institute*. Palo Alto, California, United States of America.

GOLDSCHAGG, H.B. (1993). "Lessons learned from the world's largest air cooled condenser". *EPRI proceedings, international symposium on improved technology for fossil power plants - new and retrofit applications*. Washington DC, United States of America.

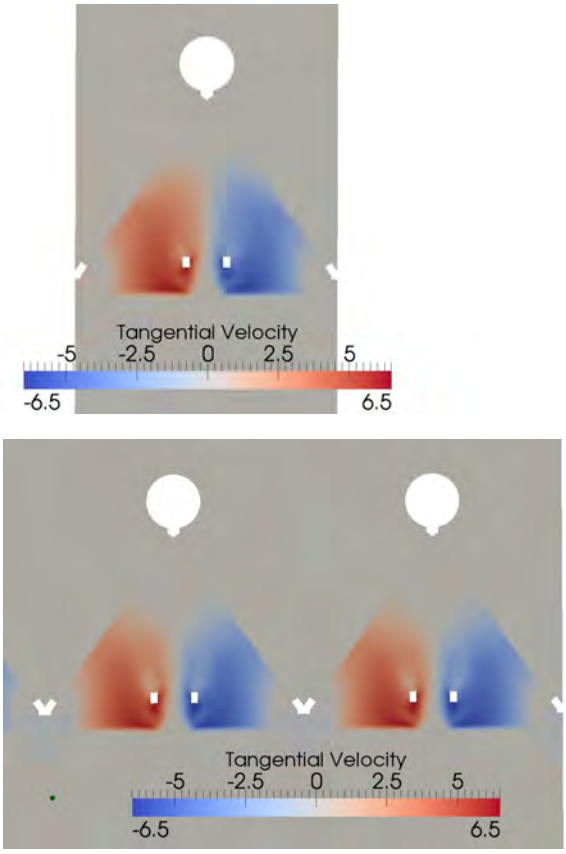

Figure 8: Comparison of ACC tangential velocity (m/s) contours of a single fan- (top) and 24-fan ACC (bottom).

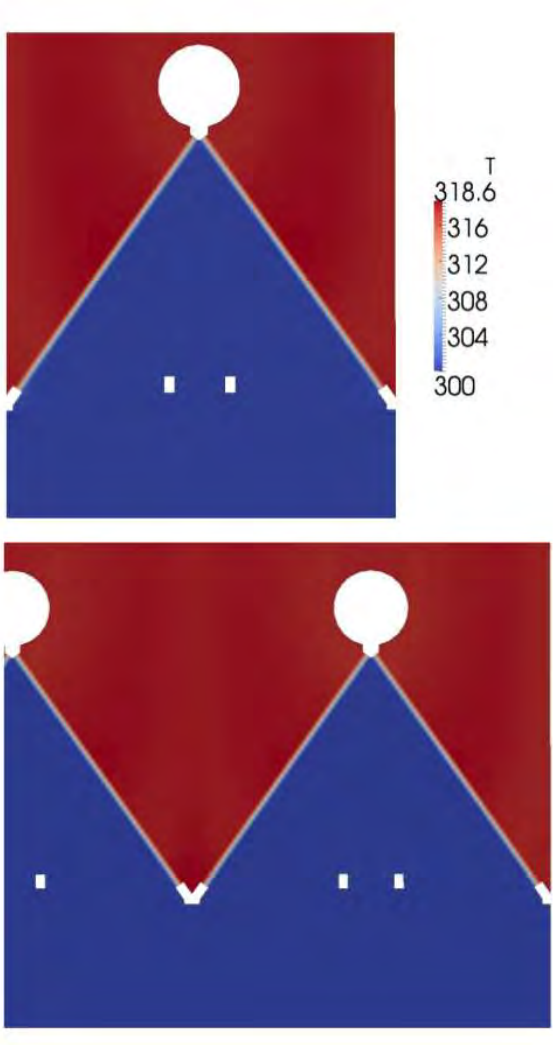

Figure 9: Comparison of ACC temperature (K) contours of a single fan- (top) and 24-fan ACC (bottom).

HE, W., DAI, Y., WANG, J., LI, M. and MA, Q. (2013). "Performance prediction of an air-cooled steam condenser using UDF method". *Applied Thermal Engineering*, **50**, 1339–1350.

HOTCHKISS, P., MEYER, C. and VON BACKSTRÖM, T. (2006). "Numerical investigation into the effect of cross-flow on the performance of axial flow fans in forced draught air-cooled heat exchangers". *Applied Thermal Engineering*, **26**, 200–2008.

KRÖGER, D. (2004). "Air-cooled heat exchangers and cooling towers". PenWell Corporation, Tulsa , United States of America.

LIU, P., DUAN, H. and ZHAO, W. (2009). "Numerical investigation of hot air recirculation of air-cooled condensers at a large power plant". *Applied Thermal Engineering*, **29**, 1927–1934.

LOUW, F., VON BACKSTRÖM, T. and VAN DER SPUY, S. (2014). "Modelling of the flow field in the vicinity of an axial flow fan, focusing on low flow rates". 9^{th} *South African Conference on Computational and Applied Mechanics*. Somerset West, Western Cape, South Africa.

MEYER, C. (2005). "Numerical investigation of the effect of inlet flow distortions on forced draught air-cooled heat exchanger performance". *Applied Thermal Engineering*, **25**, 1634–1649.

MEYER, C. (2010). "Numerical investigation of plenum chamber flow losses in mechanical draught air-cooled heat exchangers". *PhD thesis*. Department of Mechanical Engineering, University of Stellenbosch, South Africa.

MEYER, C. and KRÖGER, D. (1998). "Plenum chamber flow losses in forced draught air-cooled heat exchangers". *Applied Thermal Engineering*, **18**, 875–893.

MEYER, C. and KRÖGER, D. (2001a). "Air-cooled heat exchanger inlet flow losses". *Applied Thermal Engineering*, **21**, 771–786.

MEYER, C. and KRÖGER, D. (2001b). "Numerical simulation of the flow field in the vicinity of an axial flow fan". *International Journal for Numerical Methods in Fluids*, **36**, 947–969.

MEYER, C. and KRÖGER, D. (2004). "Numerical investigation of the effect of fan performance on forced draught air-cooled heat exchanger plenum chamber aerodynamic behaviour". *Applied Thermal Engineering*, **24**, 359–371.

OWEN, M. and KRÖGER, D. (2013). "Contributors to increased fan inlet temperature at an air-cooled steam condenser". *Applied Thermal Engineering*, **50**, 1149–1156.

OWEN, M. and KRÖGER, D. (2011). "Investigation of air-cooled steam condenser performance under windy conditions using computational fluid dynamics". *Journal of Engineering for Gas Turbines and Power*, **133**, 064502–1–064502–4.

SALTA, C. and KRÖGER, D. (1995). "Effect of inlet flow distortions on fan performance in forced draught air-cooled heat exchangers". *Heat Recovery Systems & CHP*, **15(6)**, 555–561.

STINNES, W. and VON BACKSTRÖM, T. (2002). "Effect of cross-flow on the performance of air-cooled heat exchanger fans". *Applied Thermal Engineering*, **22**, 1403–1415.

TAWNEY, R., KHAN, Z. and ZACHARY, J. (2005). "Economic and performance evaluation of heat sink options in combined cycle applications". *Journal for Engineering for Gas Turbines and Power*, **127(2)**, 397–403.

VAN DER SPUY, S., VON BACKSTRÖM, T. and KRÖGER, D. (2009). "Performance of low noise fans in power plant air-cooled steam condensers". *Noise Control Engineering Journal*, **57(4)**, 341–347.

VAN ROOYEN, J. and KRÖGER, D. (2008). "Performance trends of an air-cooled steam condenser under windy conditions". *Journal for Engineering for Gas Turbines and Power*, **130(2)**, 023006–1–023006–7.

VAN STADEN, M. (2000). "An integrated approach to transient simulation of large air-cooled condensers using computational fluid dynamics". *D. Eng thesis*. Department of Mechanical Engineering, Rand Afrikaans University, South Africa.

YANG, L., DU, X. and YANG, Y. (2010). "Measures against the adverse impact of natural wind on air-cooled condensers in power plant". *Science China Technological Sciences*, **53(5)**, 1320–1327.

YANG, L., DU, X., ZHANG, H. and YANG, Y. (2011). "Numerical investigation on the cluster effect of an array of axial flow fans for air-cooled condensers in a power plant". *Chinese Science Bulletin Engineering Thermophysics*, **56(21)**, 2272–2280.

ZHANG, W., YANG, L., DU, X. and YANG, Y. (2011). "Thermo-flow characteristics and air flow field leading of the air-cooled condenser cell in a power plant". *Science China Technoligical Sciences*, **54(9)**, 2475–2482.

A BASELINE MODEL FOR MONODISPERSE BUBBLY FLOWS

Roland Rzehak[1*] , Eckhard Krepper[1] , Thomas Ziegenhein[1] , Dirk Lucas[1]

[1] Helmholtz-Zentrum Dresden - Rossendorf, P.O. Box 510119, 01314 Dresden, Germany

* E-mail: r.rzehak@hzdr.de

ABSTRACT

For practical applications the Euler-Euler two-fluid model relies on suitable closure relations describing interfacial exchange processes. The quest for models with a broad range of applicability allowing predictive simulations is an ongoing venture. A set of closure relations for adiabatic bubbly flow has been collected that represents the best available knowledge and may serve as a baseline for further improvements and extensions. In order to allow predictive simulations the model must work for a certain range of applications without any adjustments. This is shown here for flows that allow to impose a fixed bubble size distribution which bypasses the need to model coalescence and breakup processes.

Keywords: Dispersed gas-liquid multiphase flow, Euler-Euler two-fluid model, closure relations, CFD simulation, model validation.

NOMENCLATURE

Greek Symbols

α	volume fraction [-]
ε	turbulent dissipation [$m^2\ s^{-3}$]
μ	viscosity [Pa s]
ρ	density [$kg\ m^{-3}$]
σ	surface tension [$N\ m^{-1}$]
τ	bubble-induced turbulence time scale [s]
ω	shear-induced turbulence time scale [s]

Latin Symbols

C	constant [-]
d	bubble diameter [m]
D	pipe / column diameter or width [m]
Eo	Eötvös number [-]
F	force [$N\ m^{-3}$]
g	gravitational constant [$m\ s^{-2}$]
J	superficial velocity [$m\ s^{-1}$]
k	turbulent kinetic energy [$m^2\ s^{-2}$]
ℓ	shear-induced turbulence length scale [m]
L	pipe / column length [m]
Mo	Morton number [-]
r	radial coordinate [m]
R	pipe / column radius or halfwidth [m]
Re	Reynolds number [-]
S	source term
u	axial component of mean velocity [$m\ s^{-1}$]
u'	axial component of fluctuating velocity [$m\ s^{-1}$]
y	coordinate normal to wall [m]

Sub/superscripts

B	bubble
eff	effective
G	gas
L	liquid
$turb$	turbulent
$\perp$	perpendicular to main motion

INTRODUCTION

CFD simulations of dispersed bubbly flow on the scale of technical equipment are feasible within the Eulerian two-fluid framework of interpenetrating continua. However, accurate numerical predictions rely on suitable closure models. A large body of work using different closure relations of varying degree of sophistication exists, but no complete, reliable, and robust formulation has been achieved so far.

An attempt has been made to collect the best available description for the aspects known to be relevant for adiabatic monodisperse bubbly flows (Rzehak and Krepper 2013), where closure is required for (i) the exchange of momentum between liquid and gas phases, and (ii) the effects of the dispersed bubbles on the turbulence of the liquid carrier phase. Apart from interest in its own right, results obtained for this restricted problem also provide a good starting point for the investigation of more complex situations including bubble coalescence and breakup, heat and mass transport, and possibly phase change or chemical reactions.

Predictive simulation requires a model that works without any adjustments within a certain domain of applicability. The purpose of the present contribution therefore is to validate this baseline model for a number of experimental data sets taken from the literature. These comprise flows in flat and round bubble columns as well as flows in vertical pipes of different diameter and length. A range of gas and liquid superficial velocities, gas volume fractions, and bubble sizes is covered. In all cases a fixed but not necessarily

monodisperse distribution of bubble sizes is assumed as taken from the measurements.

The results show that reasonable agreement is obtained for all different data with the exact same model. This demonstration is the main new achievement that goes beyond previous individual consideration of some of the tests (Rzehak and Krepper 2013, Rzehak et al. 2013, Ziegenhein et al. 2013).

Restriction to situations where a fixed distribution of bubble sizes may be imposed excludes the additional complexity of modelling bubble coalescence and breakup processes and thus facilitates a step-by-step validation procedure. Expanding the range of applicability as well as the achieved accuracy is a continuously ongoing development effort.

DATA

Four test cases have been selected for the present investigation as described below. A summary of the setups is given in Table 1.

Table 1: Experimental conditions.

name	D mm	J_L m/s	J_G m/s	$\langle d_B \rangle$ mm	$\langle \alpha_G \rangle$ %
bin Mohd Akbar et al. (2012): flat bubble column					
A1	240	-	0.003	4.3	1.4
A2	240	-	0.013	5.5	6.2
Mudde et al. (2009): round bubble column					
M1	150	-	0.015	4.02	6.1
M2	150	-	0.017	4.06	7.6
M3	150	-	0.025	4.25	11
M4	150	-	0.032	4.47	16
M5	150	-	0.039	4.53	20
M6	150	-	0.049	4.44	25
Liu (1998): round pipe					
L21B	57.2	1.0	0.14	3.03	10.6
L21C	57.2	1.0	0.13	4.22	9.6
L22A	57.2	1.0	0.22	3.89	15.7
L11A	57.2	0.5	0.12	2.94	15.2
TOPFLOW: round pipe					
TL12-041	195.3	1.017	0.0096	4.99	1.1

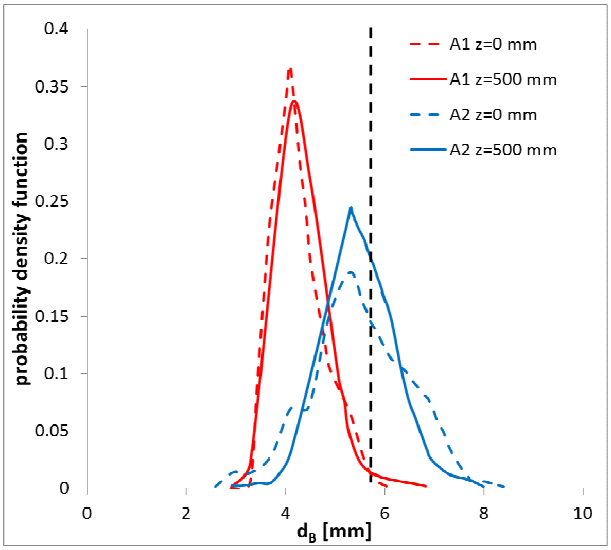

Figure 1: Measured bubble size distributions for tests A1 and A2.

Tests of bin Mohd Akbar et al. (2012)

The experiments of bin Mohd Akbar et al. (2012) were conducted in a flat bubble column of width D = 240 mm using air and water at ambient conditions. Without gas supply the water level was at 0.7 m. Profiles of gas volume fraction, axial liquid velocity, and axial turbulence intensity as well as the bubble size distribution were measured at a plane 0.5 m above the inlet. The bubble size distribution in addition was measured also near the inlet. As shown in Fig. 1 no significant change occurs over the column height. Two values of superficial gas velocities are available.

Tests of Mudde et al. (2009)

The setup of Mudde et al. (2009) consists of a round bubble column with diameter D = 150 mm again operated with air and water at ambient conditions. The ungassed fill-height was 1.3 m. Measurements of gas volume fraction and axial liquid velocity profiles were taken at different levels of which the one at 0.6 m above the inlet has been chosen for the comparison here. The sparger was designed specifically to provide highly uniform inlet conditions. Several values of the gas superficial velocity are available reaching rather large values of gas volume fraction. The mean bubble size and variation around it have been measured at two locations close to the inlet and close to the top water level. Since a slight increase is observed the average value of both measurements corresponding to the middle level has been used in the simulations.

Tests of Liu (1998)

The system studied by Liu (1998) is vertical upflow of water and air in a round pipe with inner diameter D = 57.2 mm, presumably at ambient conditions as well. The total length of the flow section was 3.43 m. A special gas injector was used that allowed to adjust the bubble size independently of liquid and gas superficial velocities. A variety of combinations of these three parameters are available. Radial profiles of void-fraction, mean bubble-size, axial liquid velocity, and axial liquid turbulence intensity were measured at an axial position $L / D = 60$ corresponding to fully developed conditions.

TOPFLOW tests

The TOPFLOW facility operated at HZDR has been specifically designed to obtain high quality data for the validation of CFD models. The tests used here (Lucas et al. 2010) have been run for cocurrent vertical upward flow of air and water in a round pipe with an inner diameter of D = 195.3 mm. Measurements were made by a wire mesh sensor at the top end of the pipe while gas injection occurs at different levels below. The operating conditions were set to a temperature of 30 °C and a pressure of 0.25 MPa at the location of the active gas injection. In this way the flow development can be studied as it would be observed for gas injection at a fixed position and measurements taken at different levels above. Distances L between the injection devices and the sensor are given in Table 2 for the different levels. The values of mean bubble size and average gas

Table 2: Length of test section for different levels of gas injection.

level		A	C	F	I	L	O	R
L	[mm]	221	335	608	1552	2595	4531	7802
L/D	[-]	1.1	1.7	3.1	7.9	13.3	23.2	39.9

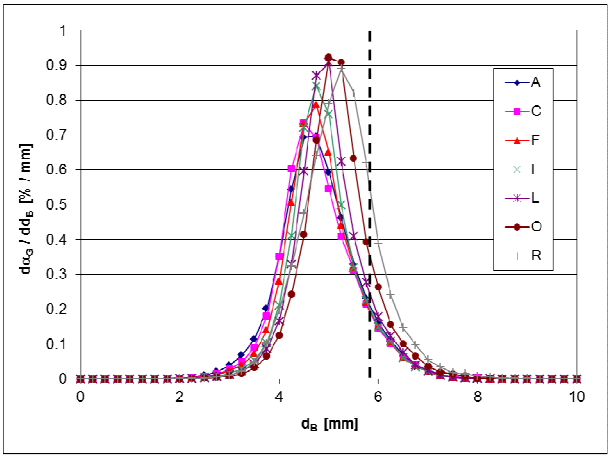

Figure 2: Distributions of bubble size for test TL12-041 at levels A to R.

volume fraction given in Table 1 correspond to the highest measurement level R.

Instrumentation with a wire mesh sensor allows collection of data on radial profiles of gas-fraction and gas-velocity as well as distributions of bubble size. A large range of liquid and gas superficial velocities was investigated in which all flow regimes from bubbly to annular occur. In the detailed report (Beyer et al. 2008) it has been noted that for bubbly flows the gas volume fluxes calculated from the measured profiles by integrating the product of volume fraction and velocity were systematically larger than those measured by the flow meter controlling the inlet. This deviation is likely to be caused by the distance between the sending and receiving wire planes, which leads to an increased value of void fraction, but a detailed explanation is not available yet. The ratio of the values calculated from the profiles (cf. Eq. (19)) to the values measured directly at the inlet has an approximately constant value of 1.2 over the bubbly flow regime (Beyer et al. 2008, Fig. 1-19). In the simulations the values measured by the flow meter will be used to set the inlet boundary condition. To get the same integral value of this conserved quantity for each cross-sectional plane, all measured void fractions are divided by 1.2 throughout this work.

A selection of tests in the bubbly flow regime has been made based on an examination of the measured bubble size distributions as shown in Fig. 2. It may be seen that a significant polydispersity is present as evidenced by a significant width of the measured bubble size distributions. The increase of average bubble size from level A to R is due to the decrease in hydrostatic pressure with height which in turn results in a proportionally decreasing gas density according to the ideal gas law. By transforming the distribution to the bubble mass as the independent variable this pressure effect may be eliminated. Apparently, for this test the opposing processes of bubble coalescence and -breakup are in a dynamic equilibrium where the net effect of both cancels. Therefore these processes need not be modeled explicitly but the measured bubble mass distribution may be imposed in the simulations.

MODELING

The conservation equations of the Euler-Euler two-fluid model have been discussed at length in a number of books (e.g. Drew and Passman 1998, Yeoh and Tu 2010, Ishii and Hibiki 2011), while the extension to treat multiple bubble size and velocity classes (inhomogeneous MUSIG model) have been presented in research papers (e.g. Krepper et al. 2008). A broad consensus has been reached, so this general framework will not be repeated here.

Closure relations required to complete the model, in contrast, are still subject to considerable variation between researchers. Therefore, the specific correlations used here are given following (Rzehak and Krepper 2013) with the inclusion of a virtual mass force.

Bubble Forces

Drag Force

The drag force reflects the resistance opposing bubble motion relative to the surrounding liquid. The corresponding gas-phase momentum source is given by

$$\mathbf{F}^{drag} = -\frac{3}{4d_B} C_D \rho_L \alpha_G \left|\mathbf{u}_G - \mathbf{u}_L\right| (\mathbf{u}_G - \mathbf{u}_L) \,. \quad (1)$$

The drag coefficient C_D depends strongly on the Reynolds number and for deformable bubbles also on the Eötvös number but turns out to be independent of Morton number. A correlation distinguishing different shape regimes has been suggested by Ishii and Zuber (1979), namely

$$C_D = \max\left(C_{D,sphere}, \min\left(C_{D,ellipse}, C_{D,cap}\right)\right), \quad (2)$$

where

$$\begin{aligned} C_{D,sphere} &= \frac{24}{\mathrm{Re}}\left(1 + 0.1\ \mathrm{Re}^{0.75}\right) \\ C_{D,ellipse} &= \frac{2}{3}\sqrt{\mathrm{Eo}} \\ C_{D,cap} &= \frac{8}{3} \end{aligned} \,. \quad (3)$$

This correlation was compared with an extensive data set on the terminal velocity of bubbles rising in quiescent liquids covering several orders of magnitude for each of *Re*, *Eo* and *Mo* in (Tomiyama et al. 1998) with good agreement except at high values of *Eo*.

Lift Force

A bubble moving in an unbounded shear flow experiences a force perpendicular to the direction of its motion. The momentum source corresponding to this shear lift force, often simply referred to as lift force, can be calculated as (Zun 1980):

$$\mathbf{F}^{lift} = -C_L \rho_L \alpha_G (\mathbf{u}_G - \mathbf{u}_L) \times rot(\mathbf{u}_L) \,. \quad (4)$$

For a spherical bubble the shear lift coefficient C_L is positive so that the lift force acts in the direction of decreasing liquid velocity, i.e. in case of co-current pipe flow in the direction towards the pipe wall. Experimental (Tomiyama et al. 2002) and numerical (Schmidtke 2008) investigations showed, that the direction of the lift force changes its sign if a substantial deformation of the bubble occurs. From the observation of the trajectories of single air bubbles rising in simple shear flow of a glycerol water solution the following correlation for the lift coefficient was derived:

$$C_L = \begin{cases} \min[0.288\tanh(0.121\mathrm{Re}), f(Eo_\perp)] & Eo_\perp < 4 \\ f(Eo_\perp) & for \quad 4 < Eo_\perp < 10 \\ -0.27 & 10 < Eo_\perp \end{cases}$$

with (5)

$$f(Eo_\perp) = 0.00105 Eo_\perp^3 - 0.0159 Eo_\perp^2 - 0.0204 Eo_\perp + 0.474 .$$

This coefficient depends on the modified Eötvös number given by

$$Eo_\perp = \frac{g(\rho_L - \rho_G) d_\perp^2}{\sigma} , \quad (6)$$

where $d_\perp$ is the maximum horizontal dimension of the bubble. It is calculated using an empirical correlation for the aspect ratio by Wellek et al. (1966) with the following equation:

$$d_\perp = d_B \sqrt[3]{1 + 0.163\ Eo^{0.757}} , \quad (7)$$

where *Eo* is the usual Eötvös number.

The experimental conditions on which Eq. (5) is based, were limited to the range $-5.5 \le log_{10} Mo \le -2.8$, $1.39 \le Eo \le 5.74$ and values of the Reynolds number based on bubble diameter and shear rate $0 \le Re \le 10$. The water-air system at normal conditions has a Morton number $Mo = 2.63e\text{-}11$ which is quite different, but good results have nevertheless been reported for this case (Lucas and Tomiyama 2011).

For the water-air system the sign change of C_L occurs at a bubble diameter of $d_B = 5.8$ *mm.*

Wall Force

A bubble translating next to a wall in an otherwise quiescent liquid also experiences a lift force. This wall lift force, often simply referred to as wall force, has the general form

$$\mathbf{F}^{wall} = \frac{2}{d_B} C_W \rho_L \alpha_G |\mathbf{u}_G - \mathbf{u}_L|^2 \hat{\mathbf{y}} , \quad (8)$$

where $\hat{\mathbf{y}}$ is the unit normal perpendicular to the wall pointing into the fluid. The dimensionless wall force coefficient C_W depends on the distance to the wall y and is expected to be positive so the bubble is driven away from the wall.

Based on the observation of single bubble trajectories in simple shear flow of a glycerol water solution Tomiyama et al. (1995) and later Hosokawa et al. (2002) concluded a different functional dependence

$$C_W(y) = f(Eo)\left(\frac{d_B}{2y}\right)^2 . \quad (9)$$

In the limit of small Morton number the correlation

$$f(Eo) = 0.0217\ \ Eo \quad (10)$$

can be derived from the data of Hosokawa et al. (2002). The experimental conditions on which Eq. (10) is based are $2.2 \le Eo \le 22$ and log10 Mo = -2.5 … -6.0 which is still different from the water-air system with Mo = 2.63e-11 but a recent investigation (Rzehak et al. 2012) has nonetheless shown that good predictions are obtained also for air bubbles in water.

Turbulent Dispersion Force

The turbulent dispersion force describes the effect of the turbulent fluctuations of liquid velocity on the bubbles. Burns et al. (2004) derived an explicit expression by Favre averaging the drag force as:

$$\mathbf{F}^{disp} = -\frac{3}{4} C_D \frac{\alpha_G}{d_B} |\mathbf{u}_G - \mathbf{u}_L| \frac{\mu_L^{turb}}{\sigma_{TD}} \left(\frac{1}{\alpha_L} + \frac{1}{\alpha_G}\right) \mathrm{grad}\,\alpha_G . \quad (11)$$

In analogy to molecular diffusion, σ_{TD} is referred to as a Schmidt number. In principle it should be possible to obtain its value from single bubble experiments also for this force by evaluating the statistics of bubble trajectories in well characterized turbulent flows but to our knowledge this has not been done yet. A value of $\sigma_{TD} = 0.9$ is typically used.

In the same work the expression for the so-called Favre averaged drag (FAD) model has also been compared with other suggestions from the literature and it was shown that all agree at least in the limit of low void fraction.

Virtual Mass Force

When a bubble is accelerated, a certain amount of liquid has to be set into motion as well. This may be expressed as a force acting on the bubble as

$$\mathbf{F}^{VM} = -C_{VM} \rho_L \alpha_G \left(\frac{D_G \mathbf{u}_G}{Dt} - \frac{D_L \mathbf{u}_L}{Dt}\right), \quad (12)$$

where D_G / Dt and D_L / Dt denote material derivatives with respect to the velocity of the indicated phase. For the virtual mass coefficient a value of 0.5 has been derived for isolated spherical bubbles in both inviscid and creeping flows by Auton et al. (1988) and Maxey and Riley (1983), respectively. Results of direct simulations of a single bubble by Magnaudet et al. (1995) suggest that this value also holds for intermediate values of *Re*. For steady parallel flows this force vanishes and can be excluded from the calculations**.**

Bubble-induced Turbulence

Due to the low density and small spatial scales of the dispersed gas it suffices to consider turbulence only in the continuous liquid phase. We adopt a two equation turbulence model for the liquid phase with additional source terms describing bubble induced turbulence. The formulation given is equally applicable to either k-ε, k-ω or SST model, but the latter (Menter 2009) will be used presently.

Concerning the source term describing bubble effects in the k-equation there is large agreement in the literature. A plausible approximation is provided by the

assumption that all energy lost by the bubble due to drag is converted to turbulent kinetic energy in the wake of the bubble. Hence, the k-source becomes

$$S_L^k = \mathbf{F}_L^{drag} \cdot (\mathbf{u}_G - \mathbf{u}_L). \quad (13)$$

For the ε-source a similar heuristic is used as for the single phase model, namely the k-source is divided by some time scale τ so that

$$S_L^\varepsilon = C_{\varepsilon B} \frac{S_L^k}{\tau}. \quad (14)$$

Further modeling then focuses on the time scale τ proceeding largely based on dimensional analysis. This follows the same line as the standard modeling of shear-induced turbulence in single phase flows (Wilcox 1998), where production terms in the ε-equation are obtained by multiplying corresponding terms in the k-equation by an appropriate time scale which represents the life-time of a turbulent eddy before it breaks up into smaller structures. In single phase turbulence the relevant variables are obviously k and ε from which only a single time scale $\tau = k_L/\varepsilon_L$ can be formed. For the bubble-induced turbulence in two-phase flows the situation is more complex. There are now two length and two velocity scales in the problem, where one of each is related to the bubble and the other to the turbulent eddies. From these a total of four different time scales can be formed. In the absence of theoretical arguments to decide which of these is the most relevant one, a comparison of all four alternatives (Rzehak and Krepper 2013, 2013a) has shown the best performance for the choice

$$\tau = \frac{d_B}{\sqrt{k_L}}. \quad (15)$$

For the coefficient $C_{\varepsilon B}$ a value of 1.0 to was found to give reasonable results.

For use with the SST model, the ε-source is transformed to an equivalent ω-source which gives

$$S_L^\omega = \frac{1}{C_\mu k_L} S_L^\varepsilon - \frac{\omega_L}{k_L} S_L^k \quad . \quad (16)$$

This ω-source is used independently of the blending function in the SST model since it should be effective throughout the fluid domain.

Since bubble-induced effects are included in k and ε / ω due to the respective source terms, the turbulent viscosity is evaluated from the standard formula

$$\mu_L^{turb} = C_\mu \rho_L \frac{k_L^2}{\varepsilon_L} \quad (17)$$

and the effective viscosity is simply

$$\mu_L^{eff} = \mu_L^{mol} + \mu_L^{turb}. \quad (18)$$

Boundary conditions on k and ε / ω are taken the same as for single phase flow, which is consistent with the view that the full wall shear stress is exerted by the liquid phase which contacts the full wall area. A single phase wall function is employed to avoid the need to resolve the viscous sublayer.

All turbulence model parameters take their usual single phase values.

RESULTS

Simulations were performed by a customized version of ANSYS CFX. Depending on the test under investigation different setups were used as listed in Table 3. The calculations were made either in stationary mode imposing plane / axisymmetric conditions by considering only a thin slice / sector of the domain together with symmetry conditions or in transient mode with subsequent averaging of the results and fully 3D on the same domain as the experiments. The reason to choose the stationary or quasi-2D approximation whenever applicable is that it drastically reduces the computation time. For the transient simulations the reported quantities are averages over the statistically steady state.

At the inlet a uniform distribution of gas throughout the cross-section was assumed or the injection nozzles or needles were modelled as CFX point sources. For the liquid, fully developed single phase velocity and turbulence profiles were assumed in the pipe flow cases.

At the top a pressure boundary condition was set for the pipe flow cases while the CFX degassing condition was employed for the bubble column cases. On the walls a no-slip condition was used for the liquid phase and a free-slip condition for the gas phase assuming that direct contacts between the bubbles and the walls are negligible. To avoid the need to resolve the viscous sublayer, the automatic wall function treatment of CFX was applied.

Concerning bubble size a monodisperse approximation was used whenever the bubbles are smaller than the critical diameter of 5.8 mm where the lift force changes its sign. In the other cases an inhomogeneous MUSIG model with two velocity groups groups corresponding to bubbles smaller and larger than 5.8 mm was applied.

Table 3: Simulation setup summary.

tests	domain	solution	MUSIG size groups	MUSIG velocity groups	inlet
bin Mohd Akbar et al. (2012): flat bubble column					
A1	3D	transient	1	1	needles
A2	3D	transient	2	2	needles
Mudde et al. (2009): round bubble column					
M1	3D	transient	1	1	uniform
M2	3D	transient	1	1	uniform
M3	3D	transient	1	1	uniform
M4	3D	transient	1	1	uniform
M5	3D	transient	1	1	uniform
M6	3D	transient	1	1	uniform
Liu (1998): round pipe					
L21B	2D sector	stationary	1	1	uniform
L21C	2D sector	stationary	1	1	uniform
L22A	2D sector	stationary	1	1	uniform
L11A	2D sector	stationary	1	1	uniform
TOPFLOW: round pipe					
TL12-041	3D	stationary	10	2	nozzles

If there is a significant variation of pressure within the domain, the gas density will change according to the ideal gas law and consequently the bubble size changes since mass is conserved. Yet the flow of both gas and liquid remains incompressible to a good approximation. To keep the computational advantage of treating both

gas and liquid as incompressible fluids with constant material properties in a fully developed flow, as discussed in Rzehak et al. (2012), the gas flux at the inlet is adjusted to the value obtained by evaluating

$$J_G = 2\pi \int_0^{D/2} \alpha_G(r)\, u_G(r)\, r\, dr \qquad (19)$$

using the data at the measurement location. In cases where only $\mathbf{u}_L$ but not $\mathbf{u}_G$ has been measured, an estimate of the latter may be obtained from the former and α_G based on the assumption of fully developed stationary flow. Where this procedure has been applied the adjusted values are given in Table 1.

Turbulence data frequently give the axial intensity of turbulent fluctuations while in the simulations based on two-equation models only the turbulent kinetic energy is available. For a comparison it has to be considered that wall-bounded turbulence is anisotropic with the axial component of fluctuating velocity being larger than those in radial and azimuthal directions. The ratio $\sqrt{k}$ / *u'* is bounded between $\sqrt{(1/2)} \approx 0.71$ and $\sqrt{(3/2)} \approx 1.22$ corresponding to unidirectional and isotropic limiting cases. Taking *u'* as an estimate for $\sqrt{k}$ thus provides an estimate that is accurate to within ~20%.

Tests of bin Mohd Akbar et al. (2012)

For the tests of bin Mohd Akbar et al. (2012) transient 3D simulations were performed using a gas inlet configuration that represents the experimental needle sparger. Due to the small column height the pressure effect is negligible. For the lower value of gas volume flux a monodisperse bubble size distribution was imposed, for the higher value two MUSIG size and velocity groups were used with diameters of 5.3 mm and 6.3 mm and relative amounts of 63 % and 37 %. For the evaluation of *k*, the axial component of the resolved transient fluctuations has been added to the unresolved part obtained from the turbulence model.

A comparison between simulation results and measured data is shown in Fig. 3. As may be seen the agreement between both is quite good for gas volume fraction and axial liquid velocity. Slight differences are that the predicted gas volume fraction profile is a little bit too peaked near the wall and there is a small dip in the predicted liquid velocity in the center of the column. The turbulent kinetic energy in the column center is somewhat underpredicted by the simulations and the peak in *k* near the wall is not reproduced by the simulations.

Tests of Mudde et al. (2009)

For the tests of Mudde et al. (2009), transient 3D simulations were performed assuming a uniform distribution of gas at the inlet. For the column height of 1.3 m the pressure effect is still small enough to be neglected. A monodisperse bubble size distribution corresponding to the measured values was used.

Measured and calculated values are compared in Fig. 4. Clearly the gas volume fractions are predicted within the experimental errors. The calculated liquid velocity profiles do not depend on the total gas hold-up. Since

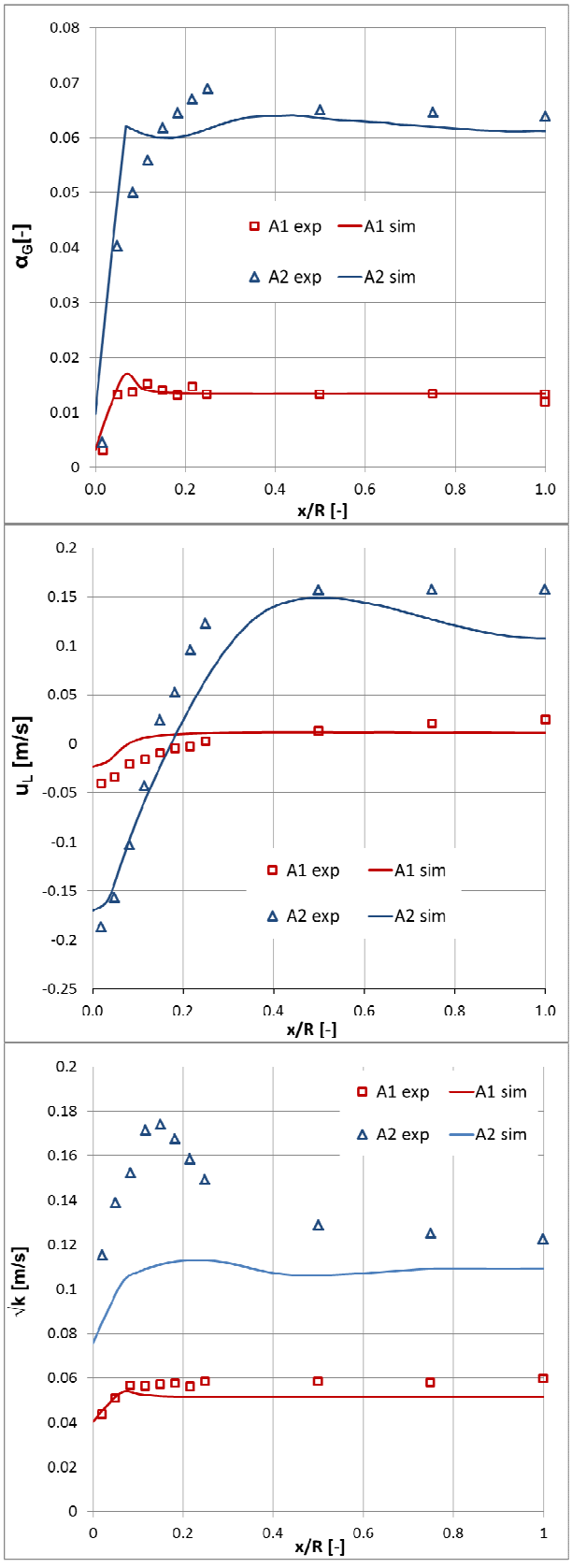

Figure 3: Gas volume fraction (top), axial liquid velocity (middle), and turbulent kinetic energy (bottom) for the tests of bin Mohd Akbar et al. (2012). Solid lines: simulation results, symbols: measured values. Only half of the column is shown.

the measured profiles do not show any systematic trend as a function of this variable, their variation is most likely an indication of the measurement errors.

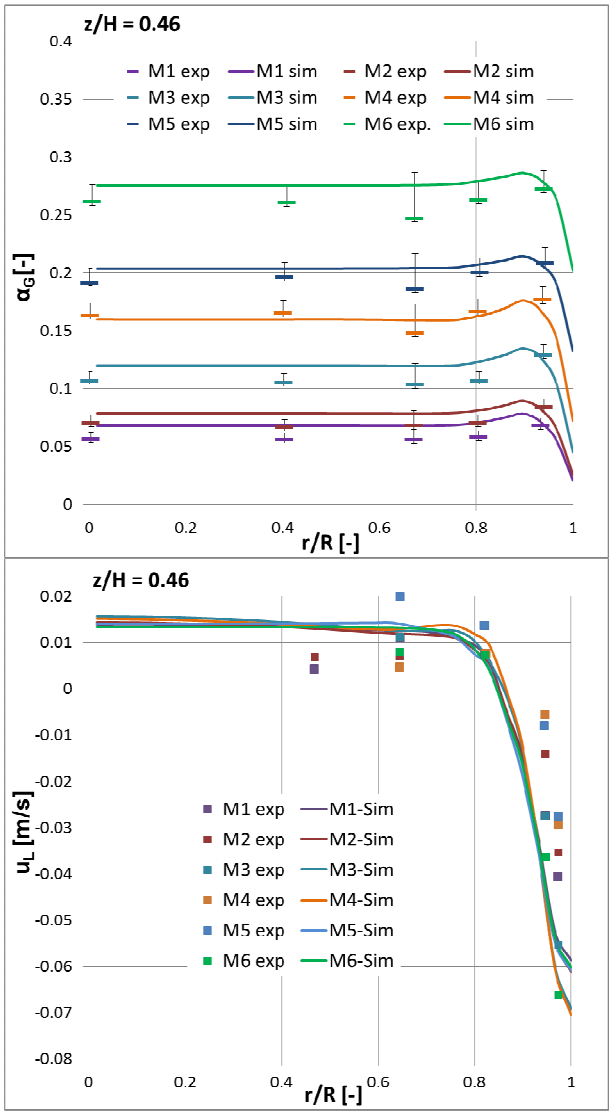

Figure 4: Gas volume fraction (top) and axial liquid velocity (bottom) for the tests of Mudde et al. (2009). Solid lines: simulation results, symbols: measured values.

Tests of Liu (1998)

For the tests of Liu (1998) stationary axisymmetric simulations were done assuming a uniform distribution of gas at the inlet. Since the pressure effect is significant for the 3.43 m long pipe, gas volume fluxes were adjusted to allow treating the gas as incompressible. A monodisperse bubble size distribution was imposed with the bubble size set equal to the average of the measured profiles.

The comparison of calculated and measured profiles in Fig. 5 shows reasonable agreement for the gas volume fraction and the axial liquid velocity. Notable deviations occur in the region close to the wall where the simulations predict the peak in the gas fraction too high and the gradient of the liquid velocity too steep. For the turbulent kinetic energy the agreement between simulation and measurement is not as good but possibly to a large extent due to the isotropic approximation.

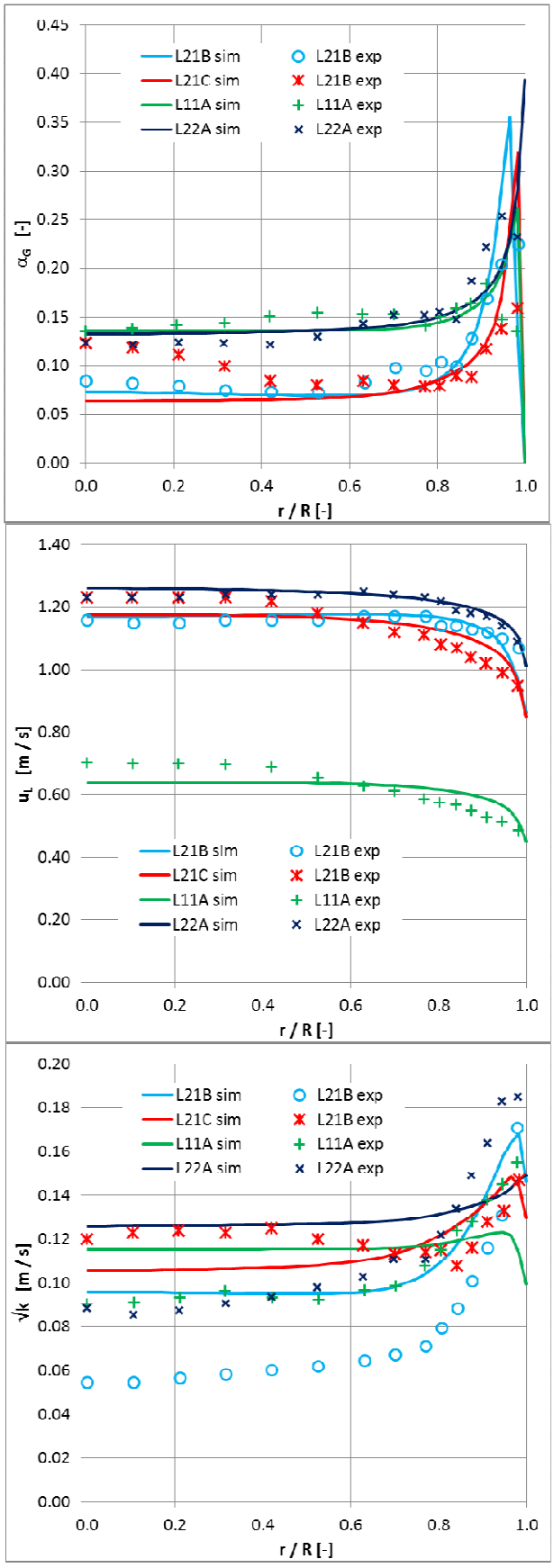

Figure 5: Gas volume fraction (top), axial liquid velocity (middle), and turbulent kinetic energy (bottom) for the tests of Liu (1998). Solid lines: simulation, symbols: experiment.

TOPFLOW tests

For the TOPFLOW test stationary axisymmetric simulations were done with the gas inlet modeled as individual nozzles. The pressure effect is included in the calculation using the MUSIG model since the implementation in CFX is based on classes of bubble mass and a transformation to / from bubble size occurs only as part of the pre- / post-processing. Two velocity groups were used as described above. For the size groups a width Δd_B = 1.0 mm was set and as many groups as needed to cover the range of the measured distributions from inlet to outlet were used.

Results for the development of gas volume fraction profiles are shown in Fig. 6. It can be seen that near the inlet the wall peak is underestimated by the simulation but at the higher levels it is overpredicted. Likewise the initial width of the peak comes out too broad in the simulations but the shoulder that develops subsequently has a narrower range than in the experiments.

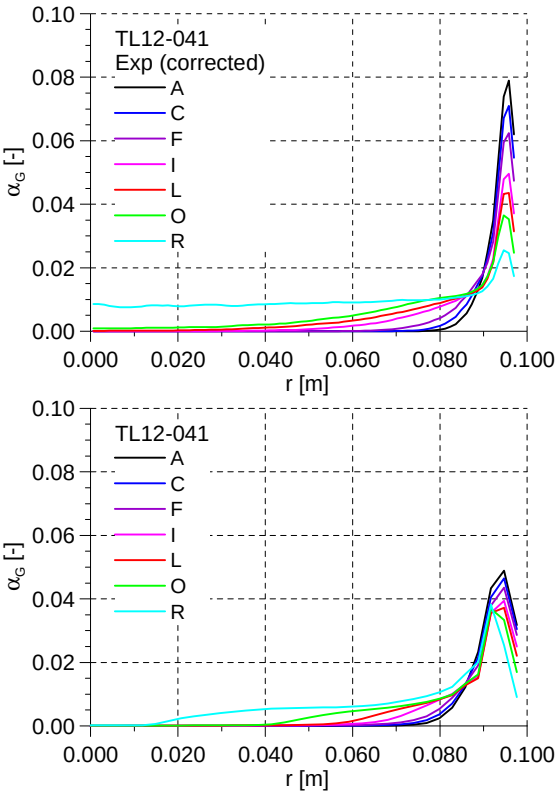

Figure 6: Gas volume fraction at different levels for the TOPFLOW test case TL12-041. Top: experimental data corrected as described in the text, bottom: simulation results.

CONCLUSION

A single model for bubbly two-phase flow has been applied to a range of diverse conditions. Reasonable agreement between data and simulations has been found for all investigated tests. Meaningful numbers quantifying the accuracy of the simulations are not readily given since experimental errors are rarely specified. As a rough guide it may be said that typical deviations between measured and simulated data are in the range of 15-20% for the void fraction and mean liquid velocity and 30-40% for the turbulent fluctuations. Maximum deviations tend to occur close to the wall where in the pipe flow cases the height of the void fraction peak is off by up to a factor of two whereas in the bubble column cases the point of zero liquid velocity is shifted which also results in a relative deviation up to a factor of two. This is encouraging for this first version of a baseline model although clearly there is still a need to expand its range of validated applicability as well as the quantitative agreement with the data.

To improve the model correlations for the bubble forces terms including effects of shear, turbulence and multiple bubbles should be derived from experiment of direct numerical simulations. The dependence of the turbulence source terms on additional dimensionless parameters like the ratio of bubble- and shear-induced length- and velocity scales could be obtained from direct numerical simulations as well.

REFERENCES

AUTON, T., HUNT, J. and PRUD'HOMME, M., (1988), "The force exerted on a body in inviscid unsteady non-uniform rotational flow", *J. Fluid Mech.,* **197**, 241.

BEYER, M., LUCAS, D., KUSIN, J. and SCHÜTZ, P., (2008), "Air-water experiments in a vertical DN200-pipe", *Helmholtz-Zentrum Dresden - Rossendorf* technical report FZD-505.

BURNS, A.D., FRANK, T., HAMILL, I. and SHI, J.-M., (2004), "The Favre averaged drag model for turbulence dispersion in Eulerian multi-phase flows", *5th Int. Conf. on Multiphase Flow*, ICMF2004, Yokohama, Japan.

DREW, D. A. and PASSMAN, S. L., (1998), "Theory of Multicomponent Fluids", *Springer*.

HOSOKAWA, S., TOMIYAMA, A., MISAKI, S. and HAMADA, T., (2002), "Lateral Migration of Single Bubbles Due to the Presence of Wall", *ASME Joint U.S.-European Fluids Engineering Division Conference*, FEDSM 2002, Montreal, Canada.

ISHII, M. and HIBIKI, T., (2011), "Thermo-fluid dynamics of two-phase flow", *Springer*, 2nd ed.

ISHII, M. and ZUBER, N., (1979), "Drag coefficient and relative velocity in bubbly, droplet or particulate flows", *AIChE J.,* **25**, 843.

KREPPER, E., LUCAS, D., FRANK, T., PRASSER, H.-M. and ZWART, P., (2008), "The inhomogeneous MUSIG model for the simulation of polydispersed flows", *Nucl. Eng. Des.,* **238**, 1690.

LIU, T. J., (1998), "The role of bubble size on liquid phase turbulent structure in two-phase bubbly flow", *3rd Int. Conf. on Multiphase Flow*, ICMF1998, Lyon, France.

LUCAS, D., BEYER, M., KUSSIN, J. and SCHÜTZ, P., (2010), "Benchmark database on the evolution of two-phase flows in a vertical pipe", *Nucl. Eng. Des.,* **240**, 2338.

LUCAS, D. and TOMIYAMA, A., (2011), "On the role of the lateral lift force in poly-dispersed bubbly flows", *Int. J. Multiphase Flow,* **37**, 1178.

MAGNAUDET, J., RIVERO, M. and FABRE, J., (1995), "Accelerated flows past a rigid sphere or a spherical bubble Part 1: Steady straining flow", *J. Fluid Mech.,* **284**, 97.

MAXEY, M. R. and RILEY, J. J., (1983), "Equation of motion for a small rigid sphere in a nonuniform flow", *Phys. Fluids,* **26**, 883.

MENTER, F.R. (2009). "Review of the shear-stress transport turbulence model experience from an industrial perspective", *Int. J. of Comput. Fluid Dyn.*, **23**, 305.

bin MOHD AKBAR, M.H., HAYASHI, K., HOSOKAWA, S. and TOMIYAMA, A., (2012), "Bubble tracking simulation of bubble-induced pseudo turbulence", *Multiphase Sci. Tech.*, **24**, 197.

MUDDE, R. F., HARTEVELD, W. K. and VAN DEN AKKER, H. E. A. (2009), "Uniform Flow in Bubble Columns", *Ind. Eng. Chem. Res.,* **48**, 148.

RZEHAK, R., KREPPER, E. and LIFANTE, C., (2012), "Comparative study of wall-force models for the simulation of bubbly flows", *Nucl. Eng. Des.,* **253**, 41.

RZEHAK, R. and KREPPER, E., (2013), "Closure Models for turbulent bubbly flows: A CFD study", *Nucl. Eng. Des.,* **265**, 701.

RZEHAK, R. and KREPPER, E., (2013a), "CFD modeling of bubble-induced turbulence", *Int. J. Multiphase Flow,* **55**, 138.

RZEHAK, R., LIAO, Y., LUCAS, D. and KREPPER, E., (2013), "Baseline model for CFD of dispersed bubbly flow", *15th International Topical Meeting on Nuclear Reactor Thermal-hydraulics*, NURETH-15, Pisa, Italy.

SCHMIDTKE, M., (2008), "Investigation of the dynamics of fluid particles using the Volume of Fluid Method", *University Paderborn*, PhD-Thesis (in German).

TOMIYAMA, A., SOU, A., ZUN, I., KANAMI, N. and SAKAGUCHI, (1995), "Effects of Eötvös number and dimensionless liquid volumetric flux on lateral motion of a bubble in a laminar duct flow", *2nd Int. Conf. on Multiphase Flow*, ICMF1995, Kyoto, Japan.

TOMIYAMA, A., KATAOKA, I., ZUN, I. and SAKAGUCHI, T., (1998), "Drag Coefficients of Single Bubbles under Normal and Micro Gravity Conditions", *JSME Int. J. B,* **41**, 472.

TOMIYAMA, A., TAMAI, H., ZUN, I. and HOSOKAWA, S., (2002), "Transverse migration of single bubbles in simple shear flows", *Chem. Eng. Sci.,* **57**, 1849.

WELLEK, R.M., AGRAWAL, A.K. and SKELLAND, A.H.P., (1966), "Shapes of liquid drops moving in liquid media", *AIChE J.,* **12**, 854.

WILCOX, D. C., (1998), "Turbulence Modeling for CFD", *DCW-Industries*.

YEOH, G. H. and TU, J. Y., (2010), "Computational Techniques for Multiphase Flows — Basics and Applications", *Butterworth-Heinemann*.

ZIEGENHEIN, T., LUCAS, D., RZEHAK, R. and KREPPER, E., (2013), "Closure relations for CFD simulation of bubble columns", *8th Int. Conf. on Multiphase Flow,* ICMF2013, Jeju, Korea.

ZUN, I., (1980), "The transverse migration of bubbles influenced by walls in vertical bubbly flow", *Int. J. Multiphase Flow,* **6**, 583.

MONODISPERSE BUBBLY FLOWS WITH ANSYS CFX AND OPENFOAM: A COMPARISON

Sebastian H.L. Kriebitzsch[1]*, Roland Rzehak[1] , Dirk Lucas[1]

[1] Helmholtz-Zentrum Dresden - Rossendorf, P.O. Box 510119, 01314 Dresden, Germany

* E-mail: s.kriebitzsch@hzdr.de

ABSTRACT

Within the framework of two-fluid modelling, the interfacial transfer processes need to be modelled by suitable closure relations. Based on previous simulations with ANSYS CFX (e.g Rzehak and Krepper, 2013) a set of closure relations applicable for adiabatic bubbly flow has been implemented in OpenFOAM. Great effort has been made to match all details of the models so that the same results may be expected.
In this work we compare simulation results for dispersed gas-liquid pipe flow with experimental data given by Liu (1998) as well as in-house data obtained with the MTLoop facility described in Lucas et al. (2005). Overall, the experimental data are reasonably well predicted and the predictions are comparable with the results computed with ANSYS CFX. However some differences can be observed, especially in the turbulent quantities in the near wall region. These differences presumably stem from unknown differences in the details of the implementation of the models in the region next to the wall, which arise from the different underlying numerical methods.

Keywords: Dispersed gas-liquid multiphase flow, two-fluid model, model validation, closure relations.

NOMENCLATURE

Greek Symbols

α	gas volume fraction, [-]
ρ	mass density, [kg/m^3]
μ	dynamic viscosity, [Pa·s]
σ	surface tension, [N/m]

Latin Symbols

C	constant, [-]
D	inner diameter of the pipe, [m]
d_B	diameter of the bubble, [m]
$\boldsymbol{F}$	force per unit volume, [N/m³]
H_m	measurement height, [m]
J	superficial velocity, [m/s]
k	turbulent kinetic energy, [m²/s²]
n	number of cells, [-]
p	pressure, [Pa]
$\boldsymbol{u}$	velocity, [m/s]
u	axial component of the velocity [m/s]
u'	axial component of the fluctuating velocity [m/s]
$\mathbf{T}$	stress tensor, [Pa]

Sub/superscripts

g	gas
l	liquid
eff	effective
turb	turb

INTRODUCTION

CFD simulations of the multiphase flow in technical equipment can provide a detailed insight into the local flow field and hence potentially be a valuable optimisation and design tool. Such simulations are feasible within the framework of interpenetrating continua, the so-called two-fluid modelling. Within this framework the details of the flow on the length scale of the disperse phase are unresolved and therefore the interfacial transfer processes need to be modelled by suitable closure relations, many of which have been provided in major commercial CFD codes for years. Recently there is an in increasing interest also in open source CFD packages and in particular OpenFOAM has become widely known.
To ensure that reliable and predictive results are obtained, the chosen set of closures has to be carefully validated for a broad number of different systems. As a safe starting point a baseline model applicable for adiabatic bubbly flows was defined and has successfully been validated for upward vertical pipe flow by Rzehak and Krepper (2013) and for fluid dynamics in bubble columns by Ziegenhein et al. (2013) using the commercial code ANSYS CFX.
The same model has now been implemented into OpenFOAM in version 2.2.x based on the existing twoPhaseEulerFOAM solver. Great care has been taken to match all known details with the ANSYS CFX physical modelling as much as possible so that the same results may be expected. Subsequently the OpenFOAM solver has been applied to compute the same vertical bubbly pipe flows that have previously been computed with ANSYS CFX: the tests given by Liu (1998) and the MTLoop tests (Prasser et al., 2003; Lucas et al., 2005).
We show that indeed comparable results are obtained with the different codes and that both codes reasonably well predict the experimental data. However some differences remain, especially in the near wall region. As, to our best knowledge, the same physical models were used, these residual discrepancies are presumably due to differences in the implementation of the models in the near wall region which are required because of the different underlying numerical methods.

DESCRIPTION OF THE EXPERIMENTAL DATA

Tests of Liu (1998)

The system studied by Liu (1998) is vertical upflow of water and air in a round pipe with inner diameter D = 57.2 mm. They performed experiments specifically designed to show the effects of bubble size by using a special gas injector that allows adjusting the bubble size independent of liquid and gas mass fluxes. All three parameters, average bubble size d_B, liquid volume flux J_L and gas volume flux J_L were varied in the investigation. Radial profiles of void-fraction α_G, bubble-size d_B, liquid velocity u_L and axial liquid turbulence intensity u_L' were measured at an axial position H_m/D = 60, so that fully developed flow conditions are realized. A change in the void fraction profile from wall to core peak with increasing bubble size was observed as well as turbulence suppression in the pipe centre for combinations of high liquid and low gas mass flux which correspond to the smallest bubble sizes. Lacking a precise specification, pressure and temperature presumably are at ambient conditions. An overview of the major characteristics of the test cases selected for the present work is given in table 1, where the letter "L" denotes the tests of Liu (1998).

name	D	$J_{L,nom}$	$J_{G,nom}$	$J_{G,adj}$	$<d_B>$	$<\alpha_G>$
	[mm]	[m/s]	[m/s]	[m/s]	[mm]	%
L21B	57.2	1.0	0.1	0.14	3.03	10.6
L21C	57.2	1.0	0.1	0.13	4.22	9.6
L11A	57.2	0.5	0.1	0.12	2.94	15.2
L22A	57.2	1.0	0.2	0.22	3.89	15.7
MT039	51.2	0.4050	0.0096	0.0111	4.50	1.89
MT041	51.2	1.0167	0.0096	0.0115	4.50	1.00
MT061	51.2	0.4050	0.0235	0.0309	4.50	5.03
MT063	51.2	1.0167	0.0235	0.0316	4.50	2.64

Table 1: Selected test cases. "L" denotes the tests of Liu (1998) and "MT" the MTLoop tests (Lucas et al., 2005). Nominal values are given in the references, however as discussed Rzehak and Krepper (2013), these had to be adjusted to match the simulations when incompressible gas is assumed.

MTLoop tests

The MTLoop facility was used to study upward vertical flow of air and water at a slightly elevated temperature of 30°C and atmospheric pressure, as described in detail in Prasser et al. (2003) and Lucas et al. (2005). The test section consists of a circular pipe with inner diameter D = 51.2 mm. The distance between the gas injector and the measurement location was varied between H_m = 0.03 m and H_m = 3.03 m, but in the present investigations only the measurements at the largest distance will be considered. This corresponds to a ratio H_m / D ≈ 60 so that again fully developed flow is observed. Radial profiles of gas volume fraction and gas velocity as well as distributions of bubble size were measured by a wire-mesh sensor. A large number of combinations of liquid and gas volumetric fluxes were investigated. For the present work a selection of tests has been made of cases showing a clear wall-peaked gas fraction profile. Under the conditions of the MTLoop experiments the gas volume fraction is rather low in all of these cases. The relevant parameters are summarized in table 1, where letters "MT" denote the MTLoop tests.

DESCRIPTION OF THE MODEL

In this work we use the Euler-Euler two-fluid model to describe disperse two-phase flow. The derivation of the conservation equations and the general framework of the two-fluid model have been discussed in many text books (e.g. Drew and Passman, 1999, Ishii and Hibiki, 2006, Yeoh and Tu, 2010) hence we will only give a short overview of the governing equations. Note that we show here the conservative form of the equations, which is used in ANSYS CFX (ANSYS, 2012), whereas the so-called phase-intensive form (Rusche, 2002) is used in the OpenFOAM solver.

Two-fluid equations

For adiabatic bubbly flows mass and momentum conservation have to be considered. Conservation of mass yields the following equation:

$$\frac{\partial}{\partial t}\rho_i\alpha_i + \nabla\cdot(\rho_i\alpha_i\,\boldsymbol{u}_i) = 0, \qquad (1)$$

and momentum conservation implies:

$$\frac{\partial}{\partial t}\rho_i\alpha_i\boldsymbol{u}_i + \nabla\cdot(\rho_i\alpha_i\,\boldsymbol{u}_i\boldsymbol{u}_i) = -\alpha_i\nabla p + \nabla\cdot(\alpha_i\boldsymbol{T}_i) + \alpha_i\rho_i\boldsymbol{g} + \boldsymbol{F}_i^{inter} \qquad (2)$$

ρ_i, α_i, $\mathbf{u}_i$ are the density, volume fraction and velocity of phase i, where i ∈ (L; G) denotes either the liquid or the gas phase. The stress tensor is

$$\boldsymbol{T}_i = \mu_i^{eff}(\nabla u_i + (\nabla u_i)^T) - \frac{2}{3}\rho_i k_i \boldsymbol{I} \qquad (3)$$

with the effective viscosity μ_i^{eff} and the turbulent kinetic energy k_i. Note that only turbulence in the liquid phase is considered, hence k_G=0 and $\mu_G^{eff} = \mu_G$. The interfacial force is modelled as the sum of drag, lift, wall and turbulent dispersion force:

$$\begin{aligned}\boldsymbol{F}_G^{inter} &= -\boldsymbol{F}_L^{inter} \\ &= \boldsymbol{F}^{drag} + \boldsymbol{F}^{lift} + \boldsymbol{F}^{wall} + \boldsymbol{F}^{disp}\end{aligned} \qquad (4)$$

Bubble forces

The drag force characterizes the resistance the bubbles experience due to the relative motion with the liquid phase. It is modelled using the standard ansatz:

$$\boldsymbol{F}^{drag} = -\frac{3}{4}C_D\frac{\rho_L\alpha_G}{d_B}|\boldsymbol{u}_G - \boldsymbol{u}_L|(\boldsymbol{u}_G - \boldsymbol{u}_L) \qquad (5)$$

and the drag coefficient C_D is computed using the correlation given by Ishii and Zuber (1979).

A bubble moving in unbounded shear flow experiences a force perpendicular to its direction of motion. This force is modelled by the lift force:

$$\boldsymbol{F}^{lift} = -C_L\rho_L\alpha_G(\boldsymbol{u}_G - \boldsymbol{u}_L)\times(\nabla\times\boldsymbol{u}_L) \qquad (6)$$

with the lift coefficient C_L. A correlation proposed by Tomiyama (2002) is used to estimate the lift coefficient C_L.

When a bubble moves parallel to a wall, it experiences an additional force, the so-called wall lift force or simply wall force. The general form is given as:

$$\boldsymbol{F}^{wall} = 2C_W\frac{\rho_L\alpha_G}{d_B}|\boldsymbol{u}_G - \boldsymbol{u}_L|^2\ \hat{\boldsymbol{y}} \qquad (7)$$

with the wall force coefficient C_W computed according to Hosokawa (2002).
Finally the turbulent dispersion forces accounts for the effect of the turbulent fluctuations of the liquid velocity on the bubbles. We employ the model proposed by Burns (2004):

$$\boldsymbol{F}^{disp} = -\frac{3}{4} C_D \frac{\rho_L \alpha_G}{d_B} |\boldsymbol{u}_G - \boldsymbol{u}_L| \cdot \frac{\mu_L^{turb}}{\sigma_{TD}} \left(\frac{1}{\alpha_L} + \frac{1}{\alpha_G}\right) \nabla \alpha_G \quad (8)$$

with the turbulent dispersion Schmidt number $\sigma_{TD.}$ Typically a value of σ_{TD}=0.9 is used.

Turbulence modelling

Due to the small spatial scales of the dispersed gas and its low density it suffices to model the turbulence of continuous liquid phase. We adopt the SST model of Menter (2009), however additional source terms were introduced to describe bubble-induced turbulence. A detailed description and comparison of different models for the bubble-induced turbulence can be found in Rzehak and Krepper (2013). In this work we use the model R1 proposed in that reference.

SIMULATION SETUP

Grid and boundary condtions

Within the Reynolds-averaged description, the flow statistically axisymmetric, therefore the simulations were performed in a quasi-2D cylindrical geometry. Only a narrow sector of 5° was used with symmetry boundary conditions applied on the side faces. In OpenFOAM a designated type of boundary condition termed “wedge” is available for this purpose and in CFX a generic symmetry boundary condition is selected.
At the bottom the liquid velocity profile is set to a typical single phase turbulent velocity profile. The gas velocity is set to the same profile however shifted such that the specified volumetric flow rate is obtained and the volume fraction is set to a uniform value. Turbulence intensity is set to 5% and the turbulent length scale is estimated as 10% of the pipe diameter to compute the inlet values for the turbulent kinetic energy and the turbulent frequency.
To ensure that the pressure boundary condition at the top of the computational domain does not influence the flow at the measurement height H_m, the length was chosen as L=1.1 H_m.
As wall boundary conditions we used no-slip for the liquid phase and free-slip for the gas phase. Turbulent wall functions are used to avoid the need to resolve the viscous sub-layer. We employ the “automatic wall treatment” (ANSYS, 2012; Esch et al., 2003), which blends the analytical solutions for the viscous sub-layer and the inertial sub-layer.
For the simulations of the tests of Liu (1998), we used a grid with n_z=649 cells in the axial direction. The CFX simulations were performed with a grid that had n_r=39 cells in the radial directions and was refined towards the wall by a factor of 0.5. In the OpenFOAM simulations a uniform grid with 57 cells in radial direction was used.
The MTLoop test simulations were performed with n_z=499 cells in the axial direction. In radial direction, n_r=37 cells were used in the CFX simulations, with a refinement factor of 0.5. Again in OpenFOAM a uniform grid with n_r=50 cells was used.
The material properties of air and water at atmospheric pressure and 25°C were used, which are given in table 2. Note that there is only little variation of the values of the material properties with temperature in the range 20°C to 30°C.

ρ_L	μ_L	ρ_G	μ_G	σ
[kg/m³]	[Pas]	[kg/m³]	[Pas]	[N/m]
997.0	$8.899 \cdot 10^{-4}$	1.185	$1.931 \cdot 10^{-5}$	0.072

Table 2: Material properties for the air-water system at atmospheric pressure and 25°C.

Differences Between OpenFOAM and CFX

The same physical models are used in the computations with the different codes, which however use different numerical methods for the discretisation of the governing equations. ANSYS-CFX uses an “element-based finite volume method” (ANSYS, 2012), whereas the OpenFOAM library uses “classical” finite volume discretisation (OpenFOAM Programmers Guide, ver. 2.2.2, 2013) The different approaches are illustrated in figure 1.

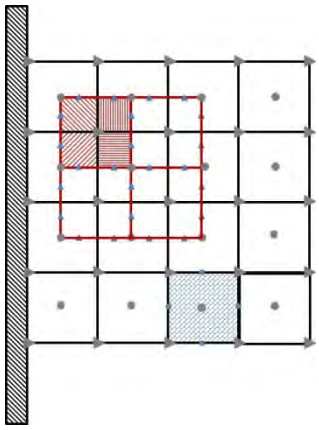

Figure 1: Illustration of the different discretisation and control volumes used in ANSYS-CFX and OpenFOAM. In ANSYS-CFX the variables are defined on the vertices, denoted by the grey triangles, whereas in OpenFOAM the variables are defined in the centres of the cells, denoted by the grey circles**.**

In ANSYS-CFX the variables are defined on the vertices of the grid and the finite volumes are constructed around each vertex using the so-called median dual. This means that in 2D the midpoints of the edges of the grid cell (element) are connected to the centroid of the cells, which are shown as the red squares in figure 1. Hence each control volume overlaps with several grid cells, in other words it consists of several sub-volumes which are used to evaluate the volume and surface integrals stemming from the finite volume discretisation. Finite-element shape functions are used to describe variation of the variables within each grid cell and thus allow to evaluate the values of variables or gradients needed in the approximation of the surface and volume integrals within each sub-volume. If for example the midpoint rule is used to approximate the surface integrals, values and gradients of variables are

needed at locations denoted by the blue triangles in figure 1.
In OpenFOAM the dependent variables and properties are stored at the centroids of the grid cells and the control volumes coincide with the grid, as depicted by the bluely shaded cell in figure 1. The midpoint rule is used to approximate the surface and volume integrals, therefore interpolation is necessary to evaluate the surface integrals, namely to compute the quantities required at the midpoints of the cell faces (the blue circles in figure 1).
Nonetheless a second-order-approximation to the integrals is used in both codes unless numerical stability requires (locally) a lower order discretisation.
The discretised governing equations are solved in a coupled manner within ANSYS-CFX whereas a segregated solution approach was implemented in our OpenFOAM solver.
Note that the different spatial discretisation procedures also imply some differences in the near-wall modelling because the first node in ANSYS-CFX is actually on the wall, whereas in the cell-based OpenFOAM code it is just inside the computational domain. The turbulent frequency is computed for the centroid in the near-wall cells in OpenFOAM whereas it is set to a fixed value on the wall in ANSYS-CFX using the distance to the first vertex inside the computational domain.

SIMULATION RESULTS

Tests of Liu (1998)

In figure 2 to figure 5 radial profiles of gas volume fraction, axial liquid velocity, turbulent kinetic energy and turbulent viscosity are plotted. The values obtained from the simulations with OpenFOAM and CFX and, if available, experimental data are shown.

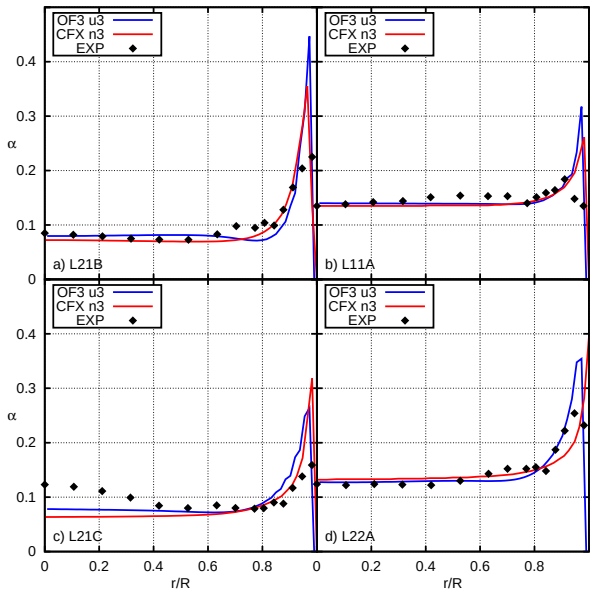

Figure 2: Comparison of the radial profiles of the volume fraction obtained using the baseline model in ANSYS-CFX and OpenFOAM with the experimental data of Liu (1998).

For the gas volume fraction shown in figure 2 similar profiles are obtained with both codes and both simulation results match the experimental data quite well. Larger differences can only be observed in the near wall region, where typically a too large wall peak is obtained from the simulations. Except for case L21C which also exhibits a centre-maximum, the flat volume fraction profile in the core of the pipe is well predicted.

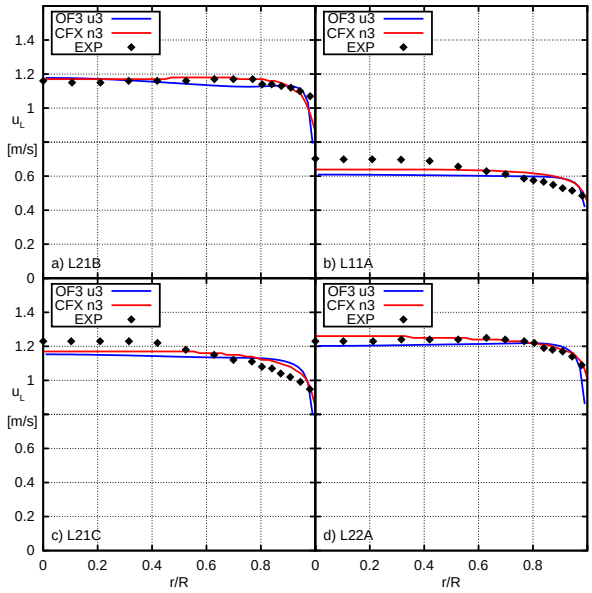

Figure 3: Comparison of the radial profiles of the liquid velocity obtained using the baseline model in ANSYS-CFX and OpenFOAM with the experimental data of Liu (1998).

The liquid velocity profiles are given in figure 3. Again similar agreement between simulation results and experimental data can be seen for profiles obtained with both codes. The OpenFOAM results are slightly lower in the pipe centre and a steeper gradient of the axial velocity can be seen near the wall.

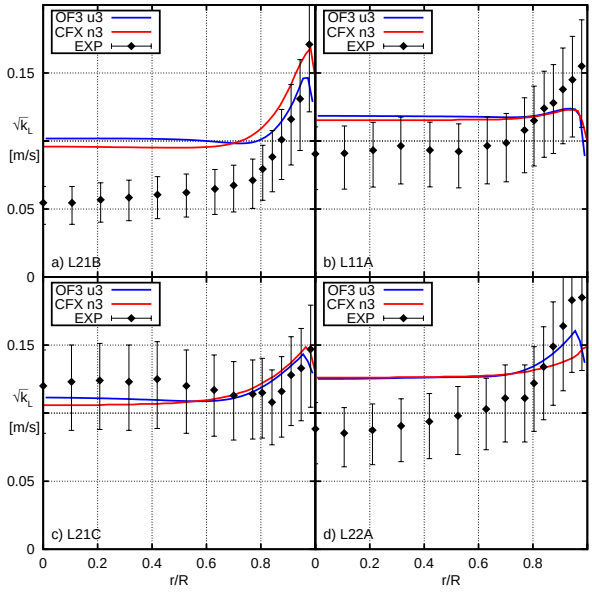

Figure 4: Comparison of the radial profiles of the liquid turbulent kinetic energy obtained using the baseline model in ANSYS-CFX and OpenFOAM with the experimental data of Liu (1998). The errorbars denote the estimates for k based on the assumption of isotropic or unidirectional turbulence, as only the fluctuations in axial direction were measured.

Profiles for the square root of the turbulent kinetic energy are given in figure 4. In the experiments only the fluctuating component in axial direction was measured,

therefore we plotted errorbars, which denote upper and lower bounds for k_L based on the assumption of isotropic turbulence and unidirectional turbulence, respectively. Larger differences in the simulation results obtained with the two codes can only be seen for cases L21B and L22A. For case L21B qualitatively similar profiles are obtained, only the near-wall peak is more pronounced in the CFX results. For case L22A a wall peak can only be seen in the OpenFOAM results whereas a monotonous increase of k towards the wall is visible in the results obtained with ANSYS CFX. Compared with the experimental data, rather large differences can be seen. Except for case L21C a too high value of the square root of the turbulent kinetic energy is predicted in the core of the pipe.
Similar profiles for the turbulent viscosity are obtained with both codes, as evident from figure 5. Slightly higher values are obtained with OpenFOAM in the centre region of the pipe, whereas higher values are obtained with CFX in the region next to the wall.

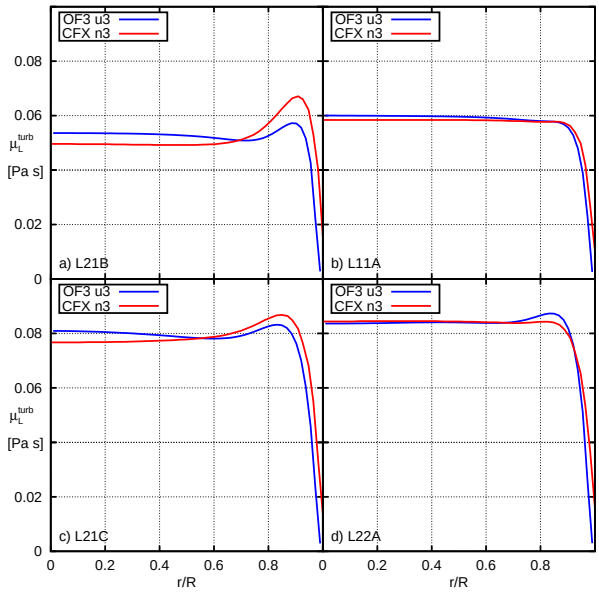

Figure 5: Comparison of the radial profiles of the turbulent viscosity obtained using the baseline model in ANSYS-CFX and OpenFOAM.

MTLoop tests

In figure 6 the profiles for the volume fraction at the measurement plane at 3.03 m from the inlet are given for the MTLoop tests. For the lower liquid fluxes (MT039, MT061) the simulation results from both codes reproduce the experimental data reasonably well and also the differences in the results obtained with both codes are small. A slightly larger peak near the wall and correspondingly slightly lower values in the pipe core are observed in the OpenFOAM profiles. Concerning the higher liquid fluxes (MT041, MT063), a larger deviation from the experiments is visible. A too high wall peak is computed in the simulations and almost no gas is left in the centre of the pipe. In this respect the CFX results are considerably closer to the experimental data than the profiles obtained with OpenFOAM. The over-prediction of the wall peak is much more pronounced in the OpenFOAM results and almost all gas is in the near-wall region.

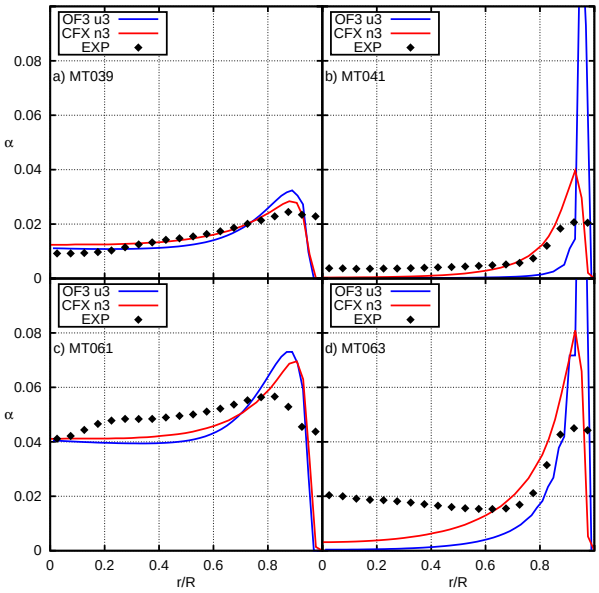

Figure 6: Comparison of the radial profiles of the volume fraction obtained using the baseline model in ANSYS-CFX and OpenFOAM with the experimental data from the MTLoop tests.

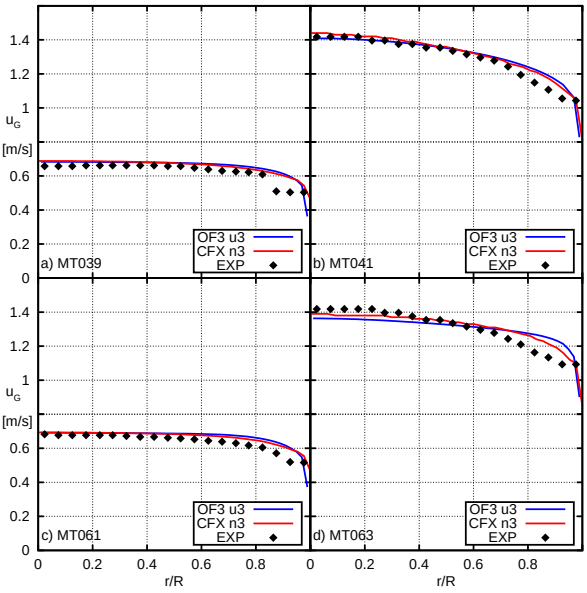

Figure 7: Comparison of the radial profiles of the gas velocity obtained using the baseline model in ANSYS-CFX and OpenFOAM with the experimental data from the MTLoop tests.

The gas velocity profiles are well predicted for all tests with both codes, as can be seen in figure 7. Slight differences can be observed for the higher liquid fluxes, where flatter profiles are computed in the simulations and consequently a steeper decrease of the gas velocity near the wall. Only minor disparities can be observed in the profiles obtained with the different codes.
In figure 8 we plot the profiles of the turbulent viscosity. Again quite similar results are obtained with both codes for the low liquid flux cases MT039 and MT061 and a higher turbulent viscosity near the wall can be seen in the CFX results.

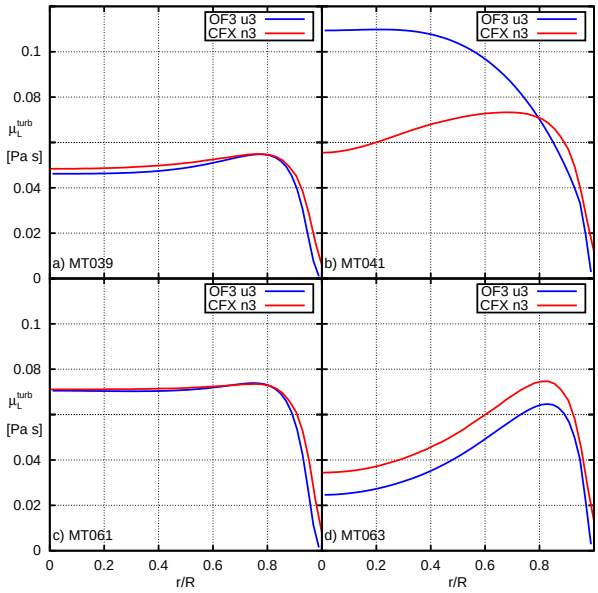

Figure 8: Comparison of the radial profiles of the turbulent viscosity obtained using the baseline model in ANSYS-CFX and OpenFOAM in simulations of the MTLoop tests.

Larger differences are evident for the higher liquid fluxes MT041 and MT063. Whereas the profiles for case for case MT063 are similar in shape with a near-wall peak and then decreasing towards the centre of the pipe but shifted by an almost constant amount, differently shaped profiles are obtained for case MT041, with no peak visible in the results obtained with OpenFOAM. These differences are consistent with the volume fraction profiles in figure 6 b) and d), where virtually all gas is in the region near the wall (r>0.8R) for MT041, whereas at least some gas remains in the core region of the pipe for MT063 and bubble-induced turbulence leads to a change of the turbulent viscosity profiles also in the OpenFOAM results.

Increased turbulent dispersion force

The results presented in the previous section show, that with OpenFOAM generally a larger peak in the void fraction is predicted and that the turbulent viscosity is lower in the near-wall region. An increased turbulent dispersion of the gas phase should reduce the near wall peak, therefore additional simulations were performed in which the turbulent dispersion force was increased by a factor of 2.

In figure 9 we present the results obtained for case L21B of Liu (1998) with OpenFOAM and CFX with the standard turbulent dispersion force and addtional results that have been computed with OpenFOAM with increased turbulent dispersion force. Differences are mainly visible in the peak region of the volume fraction profile. The peak is slightly reduced and more gas is pushed towards the centre of the pipe. Similar observations can be made for cases L21C, L11A and L22A, therefore the results are not shown here.

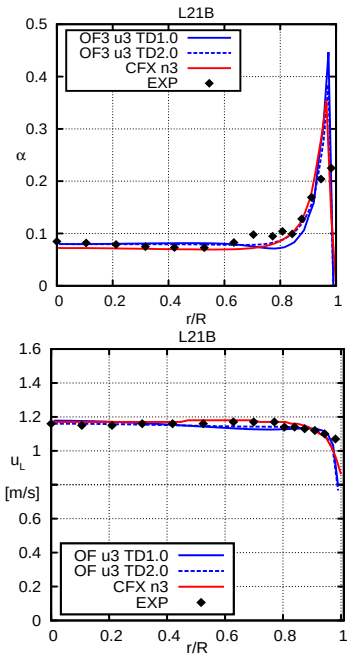

Figure 9: Turbulence dispersion increased by a factor of 2.0 in the OpenFOAM simulation. Comparison of results obtained with OpenFOAM and ANSYS-CFX for case L21B of the experimental data given by Liu (1998).

Figure 10 and figure 11 depict the profiles for the gas volume fraction and gas axial velocity for the MTLoop cases MT039, MT041, MT061 and MT063 as figures 6 and 7, however again additional profiles obtained from computations with OpenFOAM using an increased turbulent dispersion force are given.

For the low liquid fluxes a small but discernable influence of the increased turbulent dispersion force on the volume fraction profile can be seen. The OpenFOAM results with increased turbulent dispersion are closer to the experimental data and to the solution obtained with CFX.

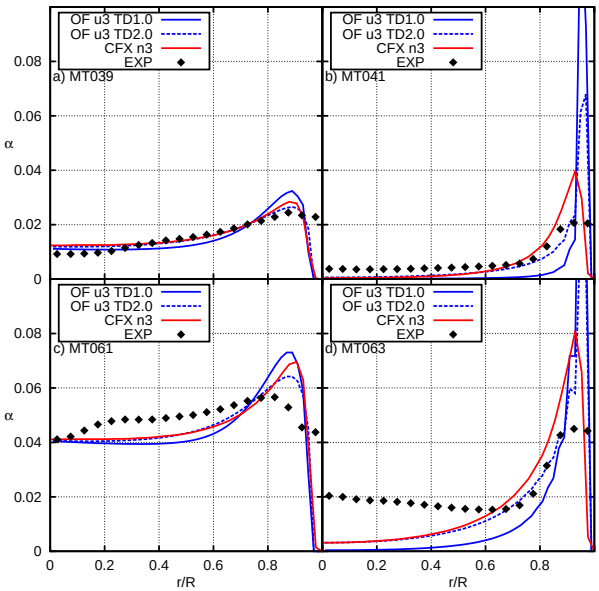

Figure 10: Same as in figure 6, however additional results are plotted, that were obtained with OpenFOAM using a turbulent dispersion force that was increased by a factor of 2.

A larger effect of the increased turbulent dispersion shows up in the volume fraction profiles for the higher

liquid fluxes MT041 and MT063. The high near-wall peak in the volume fraction profile is reduced by a factor of 2 and a non-zero gas volume fraction is obtained in the centre of the pipe.

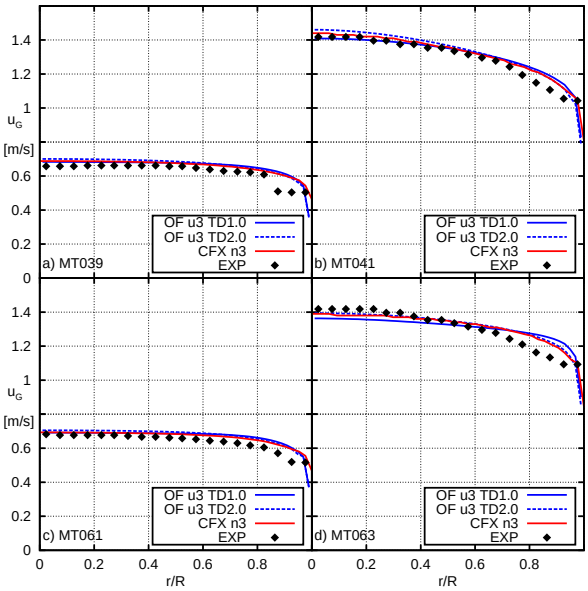

Figure 11: Same as in figure 7, however additional results are plotted, that were obtained with OpenFOAM using a turbulent dispersion force that was increased by a factor of 2.

The axial gas velocity profiles on the other hand are almost unaffected by the increased turbulent dispersion force as evident from figure 11.

Profiles for the turbulent viscosity are shown in figure 12. Only small differences due to the increased turbulent dispersion force can be observed for the low liquid flux cases MT039 and MT061. In contrast, the profile of the turbulent viscosity completely changes it shape for case MT041 with the increased turbulent dispersion, while its shape is preserved for case MT063 and only the value is increased in the centre of the pipe.

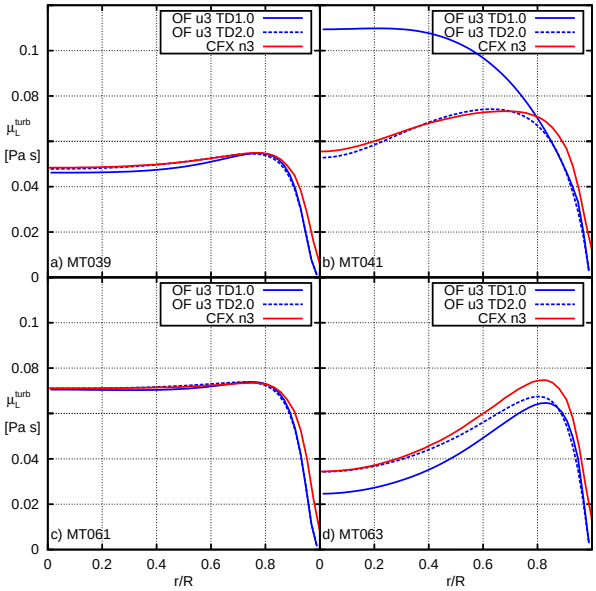

Figure 12: Same as in figure 8, however additional results are plotted, that were obtained with OpenFOAM using a turbulent dispersion force that was increased by a factor of 2.

The increased value of the turbulent viscosity of MT063 is easily understood: Due to the increased volume fraction in the core of the flow, the bubble-induced turbulence increases. Therefore both k_L and ω_L increase, however the relative increase of k_L compared to ω_L is stronger and the turbulent viscosity increases.

In case of MT041 on the other hand, the turbulent kinetic energy does not significantly change due to the increased turbulent dispersion, whereas the turbulent frequency ω_L does increase and hence the turbulent viscosity drops.

SUMMARY AND CONCLUSIONS

A baseline model for monodisperse bubbly flow was implemented in the OpenFOAM package and compared against experiments and reference solutions that have been obtained previously with ANSYS CFX (Rzehak and Krepper, 2013). In both codes the same physical models have been used, so that the same results were expected.

For the data of Liu (1998), with an average gas holdup of about 10% to 15%, qualitatively and except for the near-wall region also quantitatively similar results are obtained with both codes. The shape of the profiles of volume fraction and axial liquid velocity are reasonably well predicted with both codes. The wall-peak of the gas-volume fraction is generally over-predicted in the results of the computations and larger in the OpenFOAM results. Concerning the turbulent kinetic energy, larger differences with the experimental data are observed and again both codes give comparable results except for the near-wall region. Also for the turbulent viscosity the main differences are in the near-wall region and typically a higher turbulent viscosity can be observed in the CFX reference solution. Considering turbulent quantities like the turbulent kinetic energy and also turbulent viscosity are important for the modelling of additional physics such as coalescence and breakup, mass transfer or micro-mixing and chemical reactions, clearly additional work has to be done to identify the source of these discrepancies and to improve the modelling of multiphase turbulence.

The second dataset was measured on the MTLoop facility (Prasser et.al. 2003, Lucas et.al. 2005) which had comparable liquid fluxes as the data of Liu (1998) but lower gas fluxes were used and hence the average gas holdup was in the range of 1% to 5%. For cases MT039 and MT061 with a lower liquid flux of 0.4m/s, a similar picture as for the Liu data emerges. Both codes give comparable predictions and acceptable agreement of gas volume fraction and axial gas velocity profiles with the experimental data is observed. Also the wall peak in the gas volume fraction is more pronounced in the results obtained with OpenFOAM and a lower turbulent viscosity is visible near the wall in the OpenFOAM calculation compared to the CFX reference solution. At higher liquid fluxes of about 1m/s however, larger differences can be observed. The gas volume fraction in the core of the pipe is not well predicted and a too high wall-peak is obtained. Especially in the OpenFOAM results almost all gas is pushed towards the wall, giving a much too high peak. Interestingly though, the axial gas velocity profiles are still reasonably well predicted and the data obtained from the computations with the different codes are quite similar.

Based on the previous observations, additional simulations were done with the OpenFOAM package in which the turbulent dispersion force coefficient was increased by a factor of 2. The increased turbulent dispersion has only minor influence on the results of the simulation of the tests of Liu(1998), only the wall peak is slightly reduced and the gradient is less steep hence the agreement of simulation results and experimental data is slightly improved. Again similar observations can be made for simulations the MTloop experiments at low liquid flux. For the higher liquid fluxes a sensitivity to the increased turbulence dispersion force is seen. The wall peak is reduced by a factor of 2, however still larger than in the CFX results with the standard turbulent dispersion force, and a higher gas volume fraction is obtained in the core of the pipe, now comparable to the value obtained from the CFX simulations. The profiles of the axial velocity are still only barely affected by the increased turbulence dispersion force. The turbulent viscosity, in contrast is greatly changed in the centre region of the pipe due to the increased bubble-induced turbulence. For the MT041 case the shape of the profile is changed and the SST-model switches from from k-ω towards k-ε near the pipe centre.

Overall one can state that comparable results are obtained with both codes although some differences remain, in particular in the near wall region. Part of these differences can probably be attributed to some (unknown) discrepancies in the near-wall modelling of turbulence, in other words the details of the implementation of the turbulent wall functions arising from the different underlying numerical methods.

Also the prediction of the turbulent quantities should be termed at most satisfactorily, here a need for improved multiphase turbulence modelling is clearly identified. Further the near-wall peak is generally over-predicted, indicating that improved near-wall modelling of the bubble forces is desirable, which should reduce numerical problems due to the huge increase of the bubble forces when the mesh is refined near the wall.

REFERENCES

ANSYS (2012). *ANSYS CFX – Solver Theory Guide Release 14.5*. ANSYS Inc.

BURNS, A. *et al.* (2004). The Favre averaged drag model for turbulent dispersion in Eulerian multi-phase flows. *5th International Conference on Multiphase Flow, ICMF'04, Yokohama, Japan, May 30-June 4, 2004, Paper No. 392*.

DREW, D. and PASSMAN, S.L. (1999). *Theory of multicomponent fluids*, vol. 135 of *Applied mathematical sciences*. Springer, New York.

ESCH, T. *et al.* (2003). Heat transfer predictions based on two-equation turbulence models. *Proceedings of the 6th ASME-JSME Thermal Engineering Joint Conference*, TED-AJ03-542. Kohala Coast, Hawaii Island, Hawaii, USA.

HOSOKAWA, S. *et al.* (2002). Lateral migration of single bubbles due to the presence of wall. *Proc. ASME Joint U.S.-European Fluids Engineering Division Conference (FEDSM2002), Montreal, Quebec, Canada*, vol. ASME Conf. Proc. 2002 Vol. 1: Fora, Parts A and B / Advances in Free Surface and Interface Fluid Dynamics, 855.

ISHII, M. and HIBIKI, T. (2006). *Thermo-fluid dynamics of two-phase flow*. Springer Science+Business Media, Inc.

ISHII, M. and ZUBER, N. (1979). Drag coefficient and relative velocity in bubbly, droplet or particulate flows. *AlChE Journal*, **25**, 843.

LIU, T.J. (1998). The role of bubble size on liquid phase turbulent structure in two-phase bubbly flow. *Proc. Third International Congress on Multiphase Flow ICMF1998*. Lyon, France.

LUCAS, D. *et al.* (2005). Development of co-current air-water flow in a vertical pipe. *International Journal of Multiphase Flow*, **31**, 1304–1328.

MENTER, F.R. (2009). Review of the shear-stress transport turbulence model experience from an industrial perspective. *International Journal of Computational Fluid Dynamics*, **23**, 305.

MICHIYOSHI, I. and SERIZAWA, A. (1986). Turbulence in two-phase bubbly flow. *Nuclear Engineering and Design*, **95**, 253.

OPENFOAM (2013). *OpenFOAM Programmer's Guide Version 2.2.x*. OpenFOAM Foundation.

PRASSER, H.M. *et al.* (2003). Flow maps and models for transient two-phase flows. Tech. Rep. FZD-379, Forschungszentrum Dresden, FZR-379.

RUSCHE, H. (2002). *Computational Fluid Dynamics of Dispersed Two-Phase Flows at High Phase Fractions*. Ph.D. thesis, Imperial College of Science, Technology & Medicine Department of Mechanical Engineering.

RZEHAK, R. and KREPPER, E. (2013). Closure models for turbulent bubbly flows: A CFD study. *Nuclear Engineering and Design*, **265**, 701–711.

SHAWKAT, M. *et al.* (2008). Bubble and liquid turbulence characteristics of bubbly flow in a large diameter vertical pipe. *International Journal of Multiphase Flow*, **34**, 767.

TOMIYAMA, A. *et al.* (2002). Transverse migration of single bubbles in simple shear flows. *Chemical Engineering Science*, **57**, 1849–1858.

WANG, S.K. *et al.* (1987). 3-D turbulence structure and phase distribution measurements in bubbly two-phase flows. *International Journal of Multiphase Flow*, **13**, 327.

YEOH, G. and TU, J. (2010). *Computational Techniques for Multiphase Flows*. Butterworth Heinemann.

ZIEGENHEIN, T. *et al.* (2013). Closure relations for CFD simulation of bubble columns. *8th International Conference on Multiphase Flow ICMF2013, Jeju, Korea*.

EXPERIMENTAL STUDIES OF BUBBLY FLOW IN A MICRO-STRUCTURED BUBBLE COLUMN REACTOR USING DIGITAL IMAGE ANALYSIS

Krushnathej THIRUVALLUVAN SUJATHA[1*], **J.A.M. KUIPERS**[1†], **Niels G. DEEN**[1‡]

[1]Department of Chemical Engineering and Chemistry, Eindhoven University of Technology, P.O. Box 513, 5600MB Eindhoven, The Netherlands

[*] E-mail: k.thiruvalluv.sujatha@tue.nl
[†] E-mail: j.a.m.kuipers@tue.nl
[‡] E-mail: n.g.deen@tue.nl

ABSTRACT

Bubble columns are frequently encountered in the chemical industry for gas-liquid operations. In-spite of their widespread use, bubble columns possess some disadvantages which affect their performance. To overcome the problems of a conventional bubble column, a novel micro-structured bubble column (MSBC) reactor is proposed. Micro-structuring was realized by using a static mesh of thin wires. Wires serve the purpose of cutting the bubbles leading to a higher contact area and interface dynamics, which both depend upon the wire mesh geometry. The wire mesh can also be coated with a catalyst to perform heterogeneous catalyzed reactions. The MSBC reactor is suitable for fast reactions limited by gas-liquid mass transfer rates, as it enhances the interfacial area available for mass transfer and also reduces the liquid back- mixing leading to formation of compartments. Several experimental techniques are available to study gas-liquid flows: photographic imaging, particle image velocimetry, X-ray tomography, wire mesh sensors, etc.

The scope of this research is to gain a better understanding of the interactions between the bubbles and the wire-mesh (i.e. break-up/by-passing of bubbles). Bubble break-up is predominantly controlled by the geometry of the wire-mesh. The objective of the present work is to obtain a broad set of experimental data to understand the impact of wire-mesh on the hydrodynamics of two phase flow in an air-water system. These data will subsequently be used for the validation of a discrete bubble model (DBM) simulations. For more details on DBM, the reader is referred to the work of (Jain *et al.*, 2013).

Experiments are performed for different flow configurations, by varying gas superficial velocities and also for different wire-mesh lay-outs. The wire mesh is characterized by the mesh opening, pitch and wire diameter. Experiments are done with woven wire meshes with open area exceeding 60%. An advanced digital image analysis (DIA) technique developed by (Lau *et al.*, 2013a,b) is used to determine the bubble size distribution and the gas holdup in the column. The gas and liquid velocities are determined using Particle Image Velocimetry (PIV).

Keywords: Digital Image Analysis (DIA) , Micro-Structured Bubble Column(MSBC) , wire-mesh, bubble cutting .

NOMENCLATURE

Greek Symbols

ε	Gas holdup, $[-]$
μ	Dynamic viscosity, $[kg/ms]$

Latin Symbols

d	Diameter, $[m]$.
W	Width, $[m]$.
H	Height, $[m]$.
D	Depth, $[m]$.
A	Area, $[m^2]$.
h	height of liquid-gas dispersion, $[m^2]$.

Sub/superscripts

eq	Equivalent.
g	Gas.
k	Index k.
H	height expansion.
DIA	Digital Image Analysis.
f	Final.
0	Initial.

INTRODUCTION

Bubble columns are widely used as gas-liquid contactors in the chemical industry. The simple design involves a vertical cylinder with no internals, operated in the co-current or semi-batch mode. In the co-current operation both the gas and liquid are sparged using a distributor, whereas in the semi-batch mode the liquid is a batch phase with gas sparging. The key advantages of conventional columns are their simple design, relatively easy operation and good mixing characteristics. But, their undesirable characteristics at high flow-rates are considerable degree of back-mixing in the gas and liquid phase, low interfacial area due to high coalescence rates and short gas phase residence time. Several alternate configurations are proposed in literature(Shah *et al.*, 1982; Deckwer and Field, 1992; Deen *et al.*, 2000; Kantarci *et al.*, 2005), to avoid the undesirable effects for industrial operation. To overcome these drawbacks, a novel micro-structured bubble column (MSBC) reactor is proposed in this paper.

Structuring of the bubble column is preferred to reduce channeling and promote radial mixing. It is achieved by using sieve trays, hollow fibers, screens or foam packings. Meikap and his coworkers (Meikap *et al.*, 2001) used a multi-staged vertical cylindrical bubble column made of perspex fitted with a total of five disks with perforations (3 contraction disks and 2 expansion disks). The contraction disks caused large bubbles to breakup into irregular shaped bubbles accompanied by a swarm of smaller bubbles. Whereas in the expansion zone, the bubbles change in size due to coalescence, breakup and surface stretching or contraction. The

introduction of the hollow disks increases the mass transfer and gas holdup due to higher interfacial area(Meikap *et al.*, 2002, 2004) caused by bubble breakup and turbulence. Holler (Höller *et al.*, 2000) used a bubble column setup of hollow acrylic cylinders staged with structured fibrous catalytic layers. Their study concluded that the hydrodynamics parameters such as pressure drop and liquid circulation mainly depend on the distance between the threads. And the mass transfer coefficient in the bubble column with staged fibrous layers, was found to be 10 times higher than bubble column without internals(Höller *et al.*, 2001) . Krishna (Dreher and Krishna, 2001; Baten. and Krishna, 2003) performed residence time distribution (RTD) studies to study the effect of porous plate on the liquid back-mixing in a modified bubble column. Their experiments and simulations revealed that the introduction of sieve trays with small open area (18.6%) severely affects the liquid circulation between compartments and the liquid exchange velocity is practically independent of the column diameter. Yang et al.(Yang *et al.*, 2012) analyzed the interaction between the rising bubbles and the trays, to determine the bubble size distribution and the bubble breakup frequency. They reported that the main effect of the sieve tray is the added drag force and bubble breakup depending on the sieve pore size. Bubble breakup occurred when the sieve pore size was larger than the Sauter mean diameter, otherwise the bubbles were slowed down.

Chen et al.(Chen and Yang, 1989) conducted hydrodynamics and mass transfer experiments in a bubble column partitioned by 37 wire-mesh screen plates (6-mesh screen with fractional free area 0.64 and wire diameter of 0.58 mm) in columns with three different diameters (0.05, 0.075, 0.15 m). This configuration produced nearly identical bubbles of homogeneous size distribution, with small back-mixing of liquid phase, large gas holdup and large mass transfer coefficient. The mass transfer coefficient increased with increasing superficial gas and liquid velocities, and the effect of column diameter was negligible. However, they did not study the effect of wire diameter.

Ito et al. and several other researchers(Prasser *et al.*, 1998, 2001; Wangjiraniran *et al.*, 2003; Prasser *et al.*, 2005; Ito *et al.*, 2011) studied the intrusive effect of the wire mesh on the liquid flow. Bubble deformation, fragmentation, deceleration, hydraulic resistance, turbulence generation and disturbance of flow profile were the most important intrusive effects caused by the wires. They concluded that the dependency of bubble size on intrusiveness of the wire mesh needs further research.

In this work, a micro-structured bubble column(MSBC) is constructed by using a wire mesh in a bubble column reactor. The effect of wire mesh in two-phase bubbly flow is studied by using non intrusive experimental techniques such as Digital Image Analysis (DIA) and Particle Image Velocimetry (PIV). The effect of mesh opening and wire diameter are determined for several wire mesh layouts. Experiments are performed by varying the superficial gas velocities in the MSBC reactor from 5-30 mm/s. Visual observation is used for preliminary identification of different phenomena occurring in the MSBC reactor. Later, results of bubble size distribution, gas holdup and bubble velocity are used to analyze the impact of the wire mesh on bubble cutting and liquid circulation in the bubble column.

MATERIAL AND METHODS

A flat pseudo-2D bubble column reactor of dimensions (width W=0.2 m, depth D=0.03 m, height H=1.3 m) is chosen for experiments. The reactor walls are constructed out of transparent glass to enable visual observation by the eye or using a camera. The glass wall has a slit on the front and the back faces (slit dimensions are 200 mm$\times$15 mm.) at a height of 1 m from the bottom plate, to allow for the liquid to overflow to a storage vessel. A liquid pump is used to recirculate the liquid into the column at a set flowrate, through a liquid distributor plate. The liquid distributor plate has perforations of 3.2 mm diameter, arranged in a 60 degree staggered configuration with a distance of 4.5 mm between neighboring perforations. The gas is fed into the column via a group of fifteen (15) gas needles centrally arranged in the distributor plate. The needles have a length (L) = 50 mm, inner diameter (I.D.) = 1 mm and outer diameter (O.D.) = 1.5875 mm. The needles extend 10 mm above the bottom plate and are spaced with a center-to-center distance of 9 mm. An array of five needles is classified as a group, and each group of nozzle is connected to a mass flow controller. Subsequently, three mass flow controllers are used to control the gas flow rates in the column. Both the gas and liquid are fed into the reactor from the bottom by means of the distributor assembly. A schematic figure of the experimental setup is shown in Fig.1. Micro-structuring in the reactor is realized by means of thin wires of various dimensions arranged in a mesh structure. The wire mesh can be mounted onto the column by using the modular insert, designed for this purpose. The modular insert design allows full flexibility to attach one or more wire meshes at different locations of the insert. The dimensions of the column including the insert are as follows: width=0.14 m, depth=0.03 m, height=1.3 m. The location of the wire mesh was fixed for the experiments at a distance of 0.518 m from the bottom distributor plate.

Mesh #	diameter (mm)	opening (mm)	open area (%)
4	0.80	5.500	76
6	0.55	3.683	76
6	0.90	3.333	62
8	0.50	2.675	71
10	0.31	2.200	75
12	0.31	1.806	73
18	0.22	1.191	71

Table 1: Overview of different wire meshes used for experiments

Digital Image Analysis

Experiments are done in the MSBC for an air-water system, to determine the bubble sizes using Digital Image Analysis (DIA). The DIA technique (Lau *et al.*, 2013a,b) was developed to determine the mean diameter d_{eq}, bubble size distributions and gas holdup in pseudo-2D bubble column reactor. The image analysis algorithm has four main operations: a) Image filtering b) separation of bubbles into solitary and overlapping bubbles c) segmentation of overlapping bubbles using watershedding technique d) combination of solitary and overlapping bubble images. Image filtering involves using operations to obtain a desired image and removal of the inhomogeneous illumination using an Otsu filter(Otsu, 1975). Otsu filter determines the threshold for separating the bubbles from the background, by thresholding individual blocks of an image. The edges of the bubbles are detected by a canny edge detection algorithm. Objects with area smaller than 10 square pixels are filtered as noise, due to some improvements in DIA algorithm(100 square pixels in original

DIA of Lau et al. (Lau *et al.*, 2013b)). The images are separated into solitary bubbles and overlapping bubbles using roundness as a separation criteria. The images with solitary bubbles are segmented by marking the bubbles whereas the overlapping bubbles are segmented using the watershed algorithm proposed by Meyer (Meyer, 1994). Watershedding an image is analogous to flooding a catchment basin to determine the valley(minima) and contour peaks(maxima) in a topology. In the images, the center of the bubbles are the minima and the edges are the contours of the maxima. During watershed segmentation, the entire topology of the image is flooded by allowing water to rise from the points of minima to form catchment basins, creating watershed lines. The watershed lines are the divide lines between overlapping bubbles. The segmented images are used to determine the pixel area of each bubble object, and subsequently used to determine the average bubble diameter. In DIA technique, errors can occur due to different sources such as: imaging error, filtering errors, separation errors, segmentation error and computational error. For objects between 10-30 pixels, the maximum and minimum errors are estimated to be +2% and -6% respectively. For objects greater than 30 pixels, the error is estimated to be between +0.5% and -1.0%.
A CMOS camera with resolution of 2016 *pixel* $\times$ 2016 *pixel* is used to capture the images of two-phase bubbly flow by using back-lighting to obtain maximum contrast between the bubbles and the background. In this paper, the DIA technique has been extended to the MSBC. The MSBC is divided into five different sections for the purpose of imaging. Images from each section has a size of 0.21 m$\times$0.14 m and a small overlap of 0.05 m. The resolution of the image is 0.11 mm/pixel.

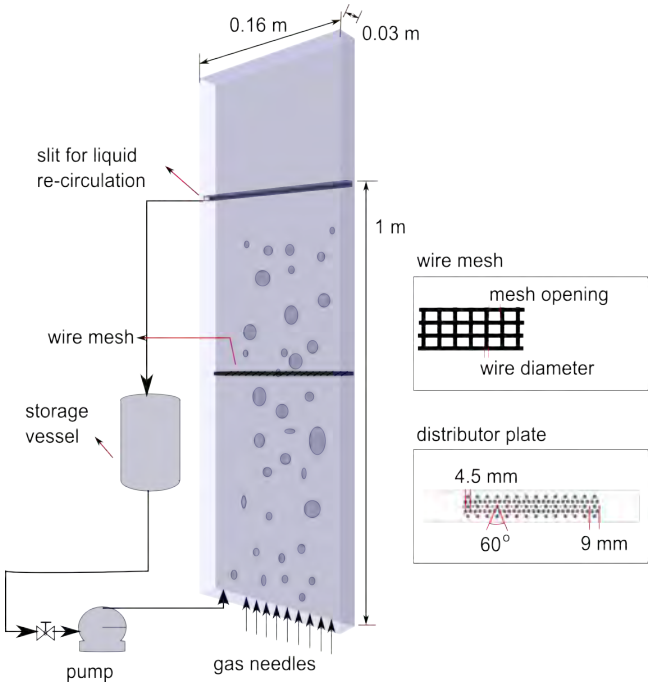

Figure 1: Schematic diagram of bubble column with wire mesh.

The equivalent diameter was determined from the bubble area as follows:

$$d_{eq} = \sqrt[2]{\frac{4A}{\pi}} \tag{1}$$

The Sauter mean diameter of an image is calculated from the equivalent diameter using the following equation:

$$d_{32} = \frac{\sum_{k=0}^{n} d_{eq,k}^3}{\sum_{k=0}^{n} d_{eq,k}^2} \tag{2}$$

The number density function (NDF) for a particular bubble diameter class is the ratio of number of bubbles in a particular diameter class(Δd_{eq}) to the sum of number of bubbles in all size classes. Therefore, the NDF of a particular size class(Δd_{eq}) is calculated from the number of bubbles and average bubble diameter as follows:

$$NDF_{\Delta d_{eq}} = \frac{N_{\Delta d_{eq}}}{\sum_{\Delta d_{eq,min}}^{\Delta d_{eq,max}} N_{\Delta d_{eq,k}}} \tag{3}$$

The gas holdup is determined for the air-water system by liquid expansion measurements. It is calculated by the following formula:

$$\varepsilon_{(g,H)} = \frac{h_f - h_0}{h_f} \tag{4}$$

where h_f is the height of the gas-liquid dispersion and h_0 is the initial height of the liquid. The integral gas holdup can bealso calculated from the DIA using the method used by Lau (Lau *et al.*, 2013b):

$$\varepsilon_{(g,DIA)} = \frac{\sum_{k=0}^{n} \frac{\pi d_{32,k}^3}{6}}{(W - 2d_{32})(H - 2d_{32})D} \tag{5}$$

Where $W \times D \times H$ are the dimensions of the field of view.

RESULTS

Visual observation

Images are obtained using the high-speed camera operated at 50 Hz, for a velocity of 5-30 mm/s for different wire meshes. Four different phenomena can be observed by varying superficial gas velocities and wire meshes: bubble cutting, bubble cutting and immediate re-coalescence, gas cap formation and gas by-passing.
It can be inferred from visual observation that the 3.3 mm wire mesh opening causes deceleration of the bubbles and bubble bypass. The 3.6 mm mesh causes some bubble cutting as shown in Fig.2. Finally, at a 5.5 mm mesh opening cutting and re-coalescence occurs (See Fig.3). When the mesh opening was smaller than 3.3 mm, the formation of a gas cap was observed as shown in Fig. 4. Fig. 3 shows a lamellar separation layer between the two bubbles after they are cut. As the bubbles rise in the column, the lamellae disappear and the bubbles re-coalesce to form a large bubble. At high velocities above 20 mm/s, there are distinct liquid circulation patterns observed below the wire mesh, thereby reducing the liquid back-mixing inside the reactor.

Bubble size and gas holdup using Digital Image Analysis (DIA)

Bubble size distributions for different wire meshes (3.3 mm, 3.6 mm and 5.5 mm mesh openings) are compared with the case without wire mesh, for section 3 (41-62 cm) as shown in Fig. 5. At low superficial gas velocities (5-15 mm/s), the bubble size distribution has one dominant peak that tends

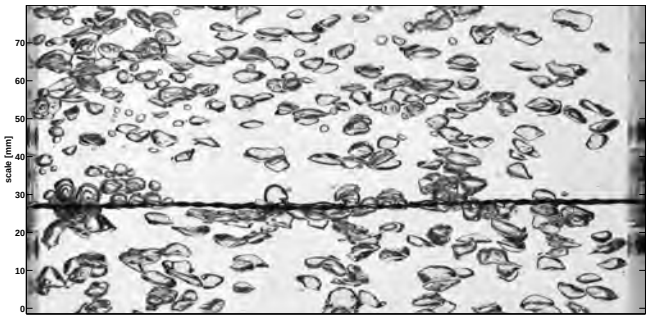

Figure 2: Bubble cutting with a 3.6 mm wire mesh at a superficial gas velocity of 15 mm/s. Small bubbles marked by red circles can be noticed above the wire mesh.

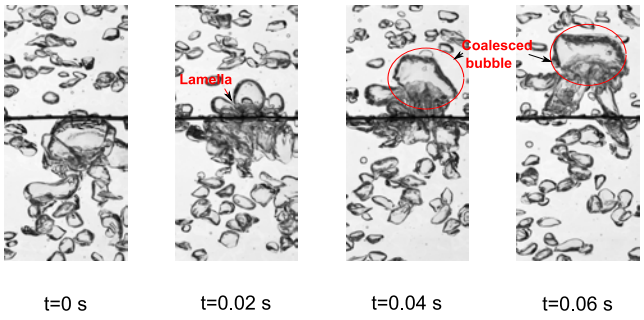

Figure 3: Bubble cutting with a 5.5 mm wire mesh at a superficial gas velocity of 15 mm/s. Lamella fomation and recoalescence of bubbles can be observed.

Figure 4: Bubble cutting with a 2.2 mm wire mesh at superficial gas velocity of 15 mm/s. Gas pocket formation can be noticed below the wire mesh.

to shift towards lower diameters in the presence of the wire mesh. At higher superficial gas velocities (20-30 mm/s), the wire mesh does not contribute favorably to bubble cutting.

The gas holdup is determined by height expansion measurements and DIA experiments. Fig. 6 shows the gas holdup vs superficial gas velocity for different cases with and without wire mesh. It can be observed from the DIA results that the gas holdup is higher for the 3.3 and 3.6 mm mesh openings than the case without wire mesh and 5.5 mm mesh opening. At high superficial gas velocity (30 mm/s) the gas holdup from DIA shows a large deviation from the gas holdup from expansion measurements, which is due to the limitation of the DIA algorithm to detect all bubbles at high gas holdups.

The bubble size distribution above and below the wire mesh are plotted in Fig.7. This figure clearly shows that above the wire mesh the bubble size distribution shifts towards small bubble diameters.

The presence of the wire mesh also affects the bubble plume and spreads the bubbles along the width of the column as shown in Fig. 8. This leads to a significant deceleration of the bubbles in the plume, thereby increasing the bubble residence time. The presence of the wire mesh generates microturbulence above the wire mesh and this will positively affect the mass transfer coefficient in cases with mass transfer and chemical reactions that are limited by gas-liquid mass transfer rates.

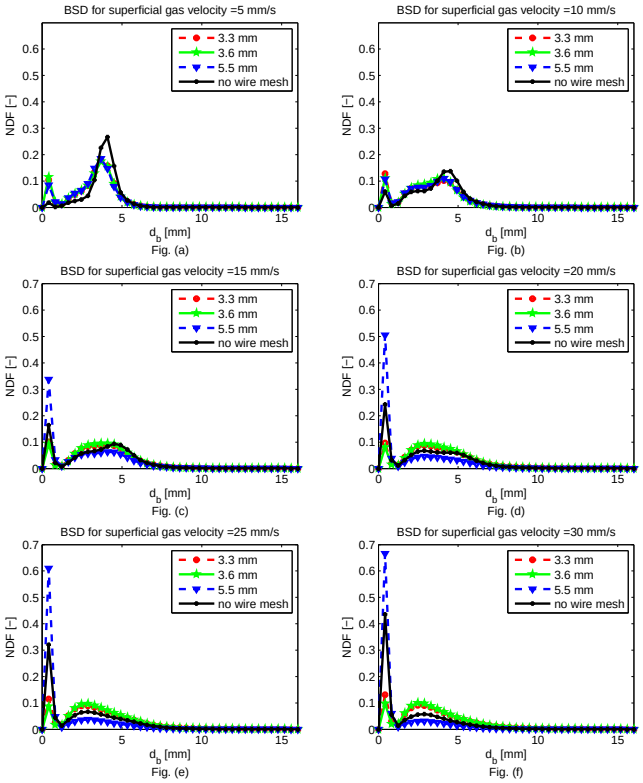

Figure 5: Evolution of bubble size distributions of section 3 (section with wire mesh placed in the middle) for increasing superficial gas velocities and with different wire mesh openings.

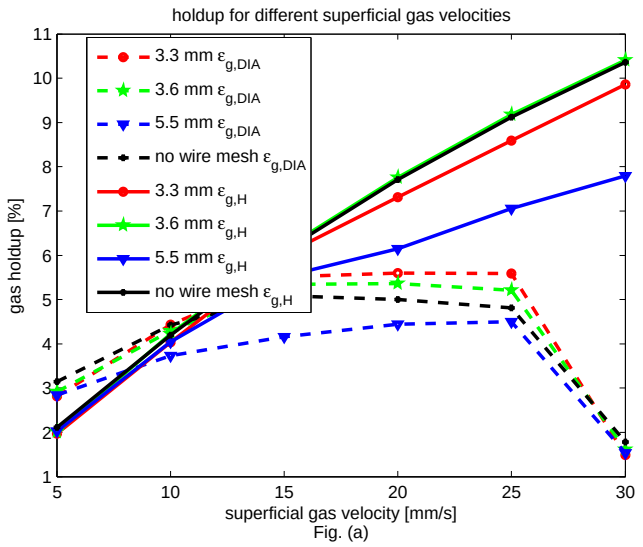

Figure 6: Evolution of the gas holdup depending on the superficial gas velocity for different wire mesh openings.

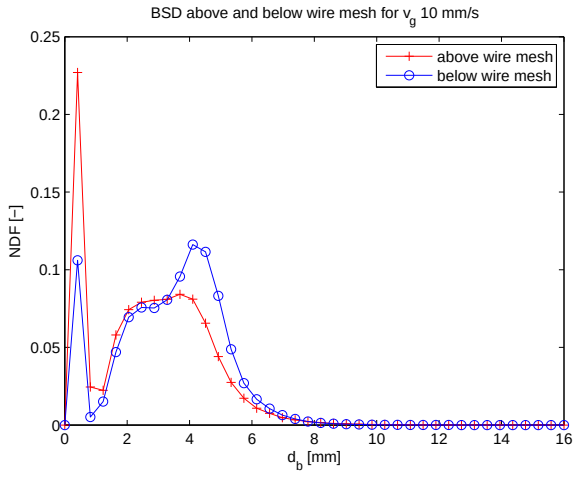

Figure 7: Evolution of the bubble size distribution above and below the wire mesh at a superficial gas velocity of 10 mm/s. The mesh opening is 3.6 mm.

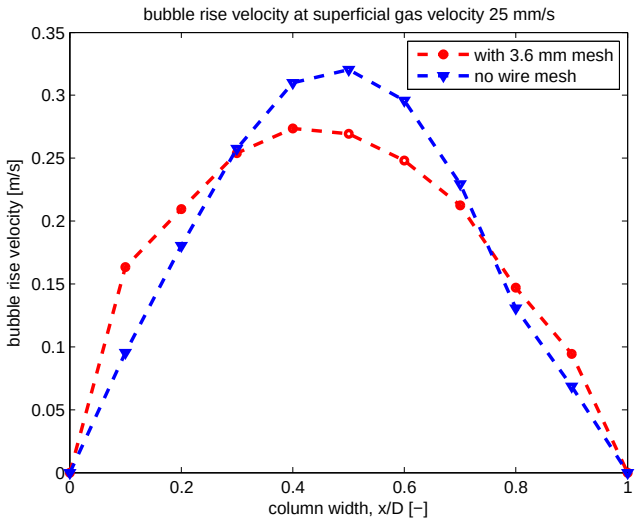

Figure 8: Bubble rise velocity at superficial gas velocity 25 mm/s to compare the cases with 3.6 mm wire mesh and without wire mesh.

CONCLUSIONS

A micro-structured bubble column (MSBC) has been designed and constructed, using wire meshes. The hydrodynamics of the MSBC reactor is studied using an advanced digital image analysis (DIA) technique. The DIA technique performs satisfactorily for gas velocities upto 25 mm/s. At higher superficial gas velocities, the bubble detection is impossible due to large gas holdup.

The bubble cutting was found to be a function of wire diameter, the mesh opening and also the superficial gas velocity. A small wire diameter and a mesh opening smaller than the average bubble size has good bubble cutting characteristics, in particular, the 3.6 mm mesh opening with 0.55 mm wire diameter. In case the mesh opening was smaller than 3.3 mm, the bubbles were slowed down by the wire mesh and the formation of a gas cap was noticed. In the 5.5 mm wire mesh opening, the bubbles bypass the wire mesh as the bubbles are smaller than the openings.

Bubble cutting was observed for superficial gas velocities from 5-15 mm/s and for higher gas velocities bubble cutting was insignificant. The presence of the wire mesh generates liquid circulation cells above and below the wire mesh, thereby reducing liquid back-mixing. The wire mesh also has an intrusive effect on the bubble plume and generates micro-turbulence above the wire mesh, that might favorably affect the mass transfer coefficient. The holdup in the MSBC was observed to be higher than in a conventional bubble column without any internals for mesh openings smaller than the average bubble diameter.

ACKNOWLEDGEMENTS

The authors would like to thank the European Research Council for its financial support, under its Starting Investigator Grant scheme, contract number 259521 (CuttingBubbles).

REFERENCES

BATEN., J.V. and KRISHNA, R. (2003). “Scale up studies on partitioned bubble column reactors with the aid of cfd simulations”. *Catalysis today*, **79**, 219–227.

CHEN, B. and YANG, N. (1989). “Characteristics of a cocurrent multistage bubble column”. *Industrial & engineering chemistry research*, **28(9)**, 1405–1410.

DECKWER, W. and FIELD, R. (1992). *Bubble column reactors*, vol. 200. Wiley Chichester.

DEEN, N. *et al.* (2000). *Bubble Columns*. Wiley-VCH Verlag GmbH & Co.

DREHER, A. and KRISHNA, R. (2001). “Liquid-phase backmixing in bubble columns. structured by introduction of partition plates”. *Catalysis today*, **69(1)**, 165–170.

HÖLLER, V. *et al.* (2000). “Fibrous structured catalytic beds for three-phase reaction engineering: Hydrodynamics study in staged bubble columns”. *Catalysis today*, **60(1)**, 51–56.

HÖLLER, V. *et al.* (2001). “Bubble columns staged with structured fibrous catalytic layers: residence time distribution and mass transfer”. *Industrial & engineering chemistry research*, **40(6)**, 1575–1579.

ITO, D. *et al.* (2011). “Uncertainty and intrusiveness of three-layer wire-mesh sensor”. *Flow Measurement and Instrumentation*, **22(4)**, 249–256.

JAIN, D. *et al.* (2013). “Discrete bubble modeling for a micro-structured bubble column”. *Chemical Engineering Science*.

KANTARCI, N. *et al.* (2005). “Bubble column reactors”. *Process Biochemistry*, **40(7)**, 2263–2283.

LAU, Y. *et al.* (2013a). “Development of an image measurement technique for size distribution in dense bubbly flows”. *Chemical Engineering Science*.

LAU, Y. *et al.* (2013b). “Experimental study of the bubble size distribution in a pseudo-2d bubble column”. *Chemical Engineering Science*.

MEIKAP, B. *et al.* (2001). “Prediction of the interfacial area of contact in a variable-area multistage bubble column”. *Industrial & engineering chemistry research*, **40(26)**, 6194–6200.

MEIKAP, B. *et al.* (2002). “Prediction of dispersed phase holdup in a modified multi-stage bubble column scrubber”. *The Canadian Journal of Chemical Engineering*, **80(2)**, 306–312.

MEIKAP, B. *et al.* (2004). “Mass transfer characteristics of a counter current multi-stage bubble column scrubber”. *Journal of chemical engineering of Japan*, **37(10)**, 1185–1193.

MEYER, F. (1994). “Topographic distance and watershed lines”. *Signal processing*, **38(1)**, 113–125.

OTSU, N. (1975). "A threshold selection method from gray-level histograms". *Automatica*, **11(285-296)**, 23–27.

PRASSER, H. *et al.* (1998). "A new electrode-mesh tomograph for gas–liquid flows". *Flow Measurement and Instrumentation*, **9(2)**, 111–119.

PRASSER, H. *et al.* (2001). "Bubble size measurement using wire-mesh sensors". *Flow measurement and Instrumentation*, **12(4)**, 299–312.

PRASSER, H. *et al.* (2005). "Comparison between wire-mesh sensor and ultra-fast x-ray tomograph for an air–water flow in a vertical pipe". *Flow measurement and instrumentation*, **16(2)**, 73–83.

SHAH, Y. *et al.* (1982). "Design parameters estimations for bubble column reactors". *AIChE Journal*, **28(3)**, 353–379.

WANGJIRANIRAN, W. *et al.* (2003). "Intrusive effect of wire mesh tomography on gas-liquid flow measurement". *Journal of Nuclear Science and Technology*, **40(11)**, 932–940.

YANG, J. *et al.* (2012). "Interaction between partitioning porous plate and rising bubbles in a trayed bubble column". *Chemical Engineering Research and Design*, **90(10)**, 1457–1466.

TWO DIMENSIONAL NUMERICAL SIMULATION OF BUBBLE DYNAMICS IN A VERTICAL HELE-SHAW CELL

Xue Wang[1]*, Bart Klaasen[1], Bart Blanpain[1], Frederik Verhaeghe[2]

[1] KU Leuven, Department of Materials Engineering, 3001 Leuven, BELGIUM

[2] Umicore Research & Development, 2250 Olen, BELGIUM

* E-mail: xue.wang@mtm.kuleuven.be

ABSTRACT

In the present paper, a volume of fluid (VOF) method is coupled with a continuum surface force (CSF) model and a wall friction model (porous media viscous resistance model) to investigate the bubble dynamics in a vertical Hele-Shaw cell. By adjusting the viscous resistance values, the effects of gap thickness on the bubble dynamics are simulated and compared with experimental results. It was found that in both simulation and experiment, with an increase of the gap thickness, *i.e.* from h = 0.5 mm to 0.7, 1.0 and 1.5 mm, the bubble shape gradually changes from oblate ellipsoid and spherical-cap to oblate ellipsoid, comma-shaped, bird flapping its wings and spherical-cap; the bubble path changes from only rectilinear to a combination of oscillating and rectilinear; the bubble terminal velocity also increases, which results in a higher bubble Reynolds number. From the simulation we also found that the increase of the gap thickness decreases the drag force, expands the streamlines and enlarges the vortices and wake structure.

Keywords: CFD, volume of fluid method, bubble dynamics, Hele-Shaw cell.

NOMENCLATURE

Greek Symbols

ρ	Mass density, [kg/m^3].
μ	Dynamic viscosity, [kg/m.s].
σ	Surface tension, [N/m].

Latin Symbols

α	Viscous resistance, [m^{-2}].
CFD	Computational Fluid Dynamics.
CSF	Continuum Surface Force.
d	Bubble diameter, [m].
Eo	Eötvös number.
f	Volume fraction, [dimensionless].
f	Force, [N].
g	Gravitational acceleration, [m^2/s].
h	Gap thickness, [m].
κ	Curvature, [m^{-1}].
p	Pressure, [Pa].
PLIC	Piecewise Linear Interface Calculation.
Re	Reynolds Number.
S	Area, [m^2].
SIMPLE	Semi-Implicit-Method for Pressure Linked Equations.
t	Time, [s].
u	Velocity, [m/s].
VOF	Volume of fluid.

Subscripts

g	Gas.
l	Liquid.
x	In the x-direction.
y	In the y-direction.
z	In the z-direction.
p	Porous media.

INTRODUCTION

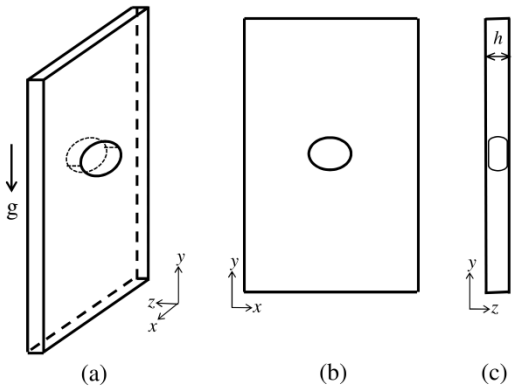

Figure 1: Illustration of a vertical Hele-Shaw cell. (a) isometric view; (b) front view; (c) side view.

A Hele-Shaw cell is a device that consists of two flat parallel plates separated by a small gap (Figure 1). A study of bubble dynamics in a Hele-Shaw cell is relevant to a wide range of applications as it contributes to a better understanding of bubble flow in porous media and confined media. Especially, the bubble dynamics in a vertical Hele-Shaw cell is the two dimensional counterpart of the bubble dynamics in unbounded media, studies on bubble behaviour in the vertical Hele-Shaw cell would help to clarify the complicated bubble dynamics in a real three dimensional system.

In a Hele-Shaw cell, various bubble Reynolds numbers ($Re = \rho ud/\mu$) can be obtained by tilting the angle of the cell and changing the fluid properties. Most of the earlier studies (before 1990s) focused on low Reynolds number bubble flow, *e.g.* analytically by Taylor and Saffman (1959), Tanveer (1986), Maruvada and Park (1996), and experimentally by Eck and Siekmann (1978), Maxworthy (1986), Kopf-Sill and Homsy (1988). Later, intermediate Reynolds number bubble flow was studied by Kelley and Wu (1997), Bush (1997), and Bush and Eames (1998). Recently, the Kawaguchi's group (Kawaguchi *et al*., 2006, Kozuka *et al*., 2009, Yamamoto and Kawaguchi, 2011) and Roig *et al*. (2012) expanded the studies to high Reynolds number bubble dynamics in a vertical Hele-Shaw cell. Kawaguchi *et al*. (2006) examined the steady-state bubble shape, trajectory, and peripheral length in water as a function of *Eo* ($Eo \leq 40$, $Re \leq 2 \times 10^3$, $Eo = \rho g d^2/\sigma$) and pointed out that *Eo* controls the path instability. This work was further extended to polymer solutions (Kozuka *et al*., 2009) and to transient states (Yamamoto and Kawaguchi, 2011). Roig *et al*. (2012) investigated the path and shape oscillation of bubbles in water in a wider *Re* range ($Eo \leq 140$, $Re \leq 1 \times 10^4$). In their experiments, *i.e.* both by Kawaguchi *et al.* and by Roig *et al.*, the same gap thickness was used ($h = 1.0$ mm), so their results are consistent. The shape oscillation and path instability are coupled in most of the *Re* range ($50 \leq Re \leq 5 \times 10^3$ in Roig *et al*. and $300 \leq Re \leq 1.5 \times 10^3$ in Kawaguchi *et al*.). In our previous study (Wang *et al.*, 2014), the gap thickness was decreased from $h = 1.0$ mm to $h = 0.5$ mm, and the unstable path and shape were not observed any more in the test with small gap thickness ($h = 0.5$ mm). The significant bubble behaviour differences brought us to the conclusion that the gap thickness plays an important role in determining the bubble dynamics in a vertical Hele-Shaw cell. However, to the knowledge of the authors, the relation between the gap thickness and the bubble dynamics has not yet been investigated elsewhere for high Reynolds number flow. In addition to the lack of experimental results on the effects of gap thickness on the bubble dynamics, simulations on high Reynolds number bubbles in a vertical Hele-Shaw cell are rare in the open literature, although numerical methods have been widely used for other media (see references in Ma *et al*, 2012). The objective of the present paper is to simulate high Reynolds number bubble dynamics, particularly to predict the effects of gap thickness on the bubble behaviour differences, and to investigate the role of the gap thickness on the bubble dynamics in a vertical Hele-Shaw cell.

MODEL DESCRIPTION

The main three simulation methods available for gas-liquid multiphase flow with sharp interface include the front tracking, the level-set and the volume of fluid (VOF) methods (van Sint Annaland *et al.*, 2005). The VOF method is used in the present study due to its simplicity, robustness and intrinsic mass conservation (Tryggvason *et al.*, 2011).

In the model, gas and liquid phases are considered as incompressible fluids, the flow is assumed to be laminar, surface tension σ is constant, the system is isothermal and constant fluid properties are applied. Particularly to the Hele-Shaw cell system, the thin liquid films formed between gas and the walls are neglected and the three dimensional effects caused by the curvature in the third dimension are not considered.

Governing equations

Based on the above assumptions, the bubble dynamics in a vertical Hele-Shaw cell can be numerically simulated by a gap-averaged two-dimensional multiphase model. In the VOF method, a single set of momentum and continuity equations for unsteady, incompressible, immiscible two-phase flow is applied to both phases. The tracking of the interfaces between the phases is accomplished by the solution of the continuity equation for the volume fraction of each fluid through the domain:

Continuity

$$\nabla \cdot \mathbf{u} = 0 \tag{1}$$

Volume fraction

$$\frac{\partial f}{\partial t} + \mathbf{u} \cdot \nabla f = 0 \tag{2}$$

Momentum

$$\rho \frac{\partial \mathbf{u}}{\partial t} + \rho \nabla (\mathbf{uu}) = -\nabla p + \nabla \cdot (\mu(\nabla \mathbf{u} + \nabla \mathbf{u}^T) + \rho \mathbf{g} + \mathbf{f}_\sigma + \mathbf{f}_w \tag{3}$$

where f is the volume fraction of the second fluid in the computational cell. When the cell is completely filled with liquid phase, f equals zero; and f equals one when the cell is completely filled with gas. For a cell containing the interface, f takes a value between 0 and 1. In our case, ρ and μ are constant in each fluid with a jump at the interface, they can be defined by

$$\rho = f\rho_g + (1-f)\rho_l \tag{4}$$

$$\mu = f\mu_g + (1-f)\mu_l \tag{5}$$

$\mathbf{f}_\sigma$ denotes an additional surface tension source term. The surface tension along the interface between gas bubble and water is described by the continuum surface force (CSF) model proposed by Brackbill (1991). The force at the surface can be expressed as a volume force using the divergence theorem, which is added to the momentum equation as a source term:

$$\mathbf{f}_\sigma = -\sigma \rho \kappa \nabla f / (0.5(\rho_g + \rho_l)) \tag{6}$$

where κ is defined in terms of the divergence of the unit normal:

$$\kappa = \nabla \cdot \left(\nabla f / |\nabla f| \right) \tag{7}$$

where ∇f is the gradient of the volume fraction f, $|\nabla f|$ the length of ∇f .

$\mathbf{f}_w$ is an additional in-gap wall friction source term, which can be described by Poiseuille's law:

$$\mathbf{f}_w = -12\mu\mathbf{u}/h^2 \tag{8}$$

It means the additional gap-averaged pressure drop in the Hele-Shaw cell has a linear relationship with the gap-averaged velocity. In the simulations, Darcy's law is used to calculate the in-gap wall friction due to the similarity of the Hele-Shaw cell wall resistance and porous media resistance. The equation of Darcy's law for porous media resistance is as follows:

$$\mathbf{f}_p = -\mu\mathbf{u}/\alpha \tag{9}$$

where α is the viscous resistance. By comparing the equation (8) with (9), the Hele-Shaw flow can be assumed as a two-dimensional flow in porous media, the viscous resistance α in the Hele-Shaw cell is equivalent to:

$$\alpha = 12/h^2 \tag{10}$$

By the equation (10), the bubble behaviour with different thicknesses can be simulated by adjusting the viscous resistance values. Four gap thicknesses are simulated, *i.e.*, h = 0.5, 0.7, 1.0 and 1.5 mm. In our previous paper (Wang *et al*., 2014), it was found when $d \geq 5$ mm, three-dimensional effects are less significant, so the simulation here is on the bubbles with $d \geq 5$ mm.

Solution domain and numerical schemes

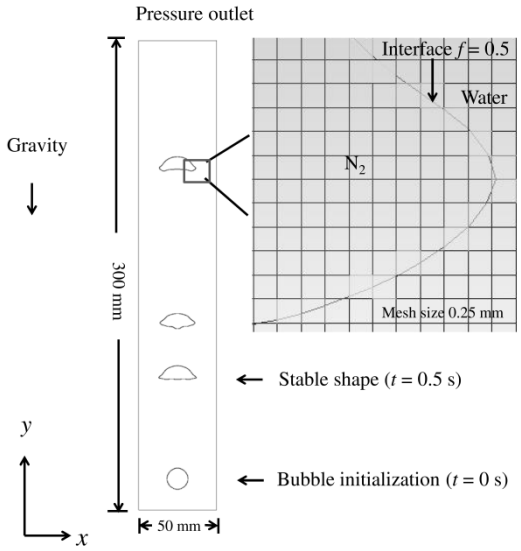

Figure 2: Computational domain and boundary conditions.

The commercial CFD software ANSYS Fluent 14.0 was used to simulate the motion of a single nitrogen gas bubble rising in a vertical Hele-Shaw cell filled with water. The computation domain consisted of a 50 mm in width by 300 mm in height rectangle, whose height was 200 mm less than the experimental conditions. No difference was found by decreasing the height due to the small hydrostatic pressure difference (less than 2%). The domain was filled with stationary water and a spherical nitrogen bubble was initialized in the centre at the bottom of the domain as shown in Figure 2. For the bubbles with large deformation (8 - 11 mm for h = 1.0 mm), spherical initial shape did not work well due to break-up. To solve the problem, left-right asymmetric initial bubble shapes such as semicircle were initialized. The operating pressure was 1 atm. No-slip boundary conditions were applied at the three walls (two side-walls and bottom wall). The initial bubble rise velocity was set to zero. The bubble was able to develop into a typical shape and to reach a terminal velocity within about 0.5 s and to rise to the liquid surface in 2.0 - 4.0 s depending on the terminal velocity. The steady-state data (1.0 - 2.0 s) was used for comparison. The volume fraction cut-off was 10^{-6}. The initial bubble size was assumed to be the simulated bubble size, where f equals 0.5 (Figure 2). The material properties were included in the Fluent database: the density of the water is 997 kg/m^3, the viscosity of the water is 0.894 kg/(m·s); the density of the nitrogen is 1.185 kg/m^3, the viscosity of the nitrogen is 1.663×10^{-5} kg/(m·s). The surface tension is 0.0729 N/m. Uniform quadrilateral meshing was used, each cell was 0.25 mm, which means 240,000 cells in total. Grid independence was proved by further reducing the cell size to 0.125 mm yielding only a 0.5% terminal velocity difference. A laminar model was chosen due to the small cell Reynolds number (characteristic length is gap thickness h).

During the calculation, the unsteady scalar (pressure, velocity components and volume fraction) transport equations were discretized to algebraic equations by a control-volume method. An explicit geometric reconstruction scheme that is based on the PLIC (Piecewise-Linear-Interface-Calculation) method of Young (1982) was used to solve the volume fraction equation. A second-order upwind scheme was used to discretize the convection terms of the velocity components. The diffusion terms were discretized using a second-order accurate central differencing scheme. The gradient of the scalars needed in the convection and diffusion discretization was calculated using the least squares cell-based method. The velocity-pressure coupling and overall solution procedure were based on the SIMPLE (Semi-Implicit-Method for Pressure Linked Equations) segregated algorithm. A first order implicit time-marching scheme was used for the integration of the transient term. A constant time step (0.0005 s) was used.

EXPERIMENTAL VALIDATION

Vertical Hele-Shaw cells with four different gap thicknesses (h = 0.5, 0.7, 1.0 and 1.5 mm) have been constructed, similar to Wang *et al*., 2014. The detailed introduction of the equipment is as described by Klaasen *et al*., 2014. The cell was made of soda-lime glass with a thickness of 10 mm. The glass plates were washed in advance with Piranha solution (3:1 mixture of 96% H_2SO_4 and 30% H_2O_2) to remove organic residues and hydroxylate surfaces, making the plates highly hydrophilic. A bubble was generated with a syringe needle (inner diameter range 0.3 - 0.8 mm) controlled by an electromagnetic micro valve (brand is Burker). By

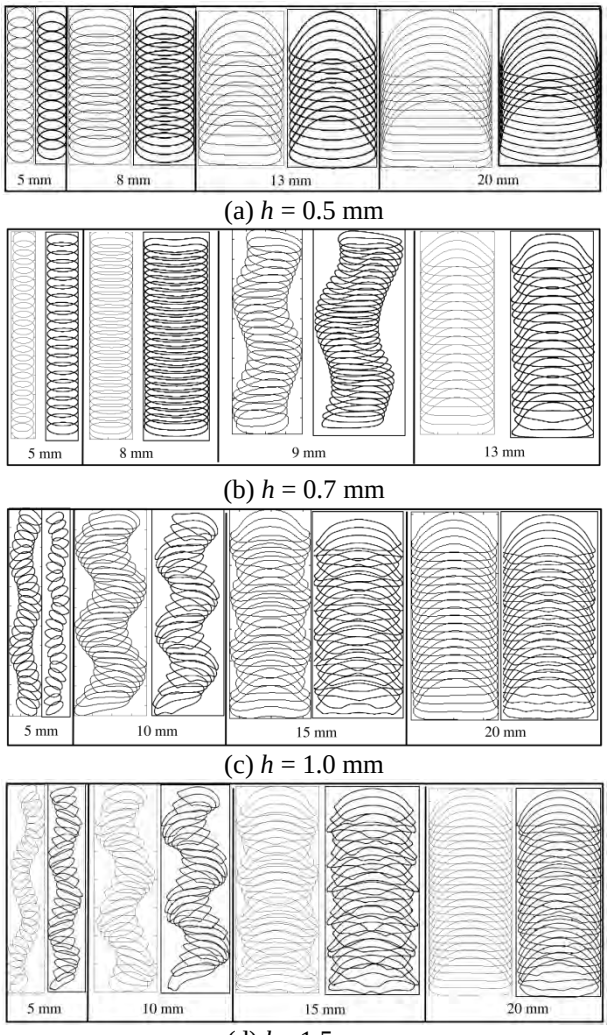

Figure 3: Comparison of bubble shape and path between experiment (left) and simulation (right): (a) h = 0.5 mm; (b) h = 0.7 mm, (c) h = 1.0 mm, (d) h = 1.5 mm. The successive contours are plotted at a time interval of 0.02 s.

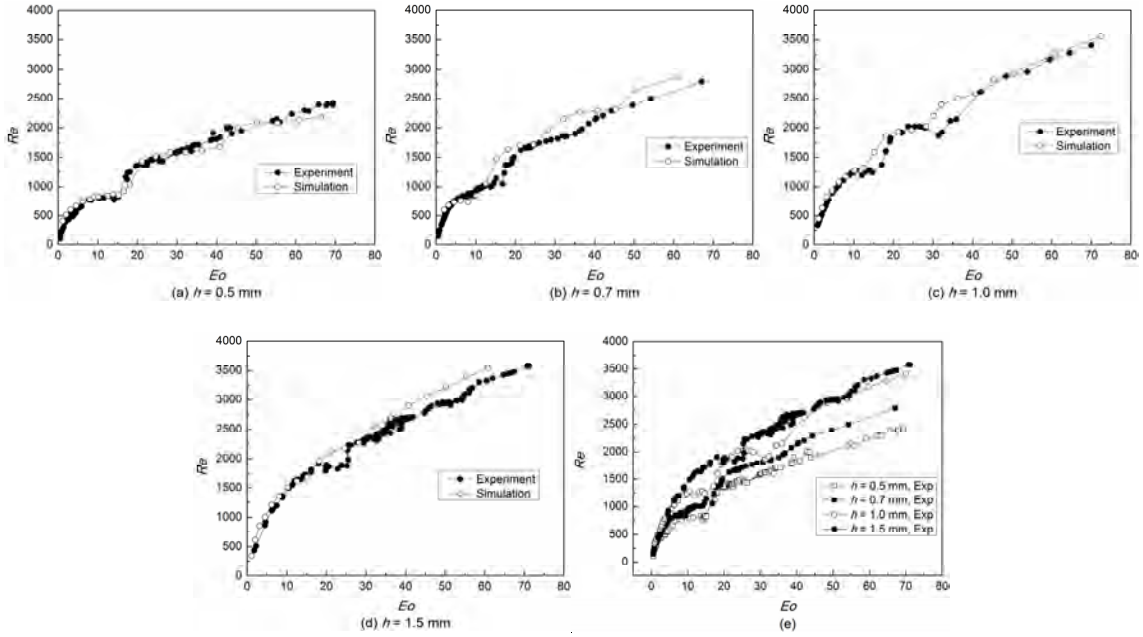

Figure 4: Comparison of *Re* as a function of *Eo*: (a) h = 0.5 mm, (b) h = 0.7 mm, (c) h = 1.0 mm, (d) h = 1.5 mm; (e) experimental results with different gap thicknesses.

varying the time step of the valve and the needle inner diameter, the initial bubble size was controlled. Technically pure nitrogen gas (99.9%) and ultrapure water (18.2 MΩcm resistivity at 25 ^{o}C produced by Millipore Direct-Q 3 UV ultrapure water system) were used to avoid the effect of surface active agents. Thin liquid films were formed between the gas bubble and the wall due to the total wetting of water on the washed glass cell. The images of the bubble were recorded with a Tesin Cyclocam high speed video camera at a frame rate of 250 fps (resolution 640×480 pixels). The shutter time in the experiment was 2 ms. The recorded image frames were sequentially analysed with a Matlab-based processing script. In each frame, the area S, and gravity centre (x, y) of the bubble were determined by mapping the bubble contour. The equivalent diameter d of the bubble was calculated as $d = 2(S/\pi)^{1/2}$; the terminal velocity u_y as $u_y = \Delta y/\Delta t$ and the horizontal velocity u_x as $u_x = \Delta x/\Delta t$, where Δt is the time step.

RESULTS

Bubble Shape and Path

The bubble shape and path at four different gap thicknesses are shown in Figure 3. For each gap thickness, four typical contours are selected and compared with experimental results.

When h = 0.5 mm, two stable bubble shapes can be seen: oblate ellipsoid and spherical-cap. All these bubbles have only rectilinear paths as shown in Figure 3(a). With the increase of h to 0.7 mm, the bubble shape becomes unstable when d = 9 mm and starts to vibrate (Figure 3(b)). Simultaneously, the bubble rising path deviates from the rectilinear path. However, the shape oscillation and path instability are still limited, and only happen for bubbles in the size range of d = 9 - 11 mm.

In Figure 3(c), *i.e.* h = 1.0 mm, the path evolution becomes quite different from the above two cases. Most of the bubbles are oscillating with a zigzag path except for very large bubbles (*e.g.* d = 20 mm in Figure 3(c)). The oscillation results in more complicated bubble shapes. Four bubble shapes are observed in both experiments and simulation: oblate ellipsoid bubbles, comma-shaped bubbles, bird flapping its wings bubbles and spherical-cap as described by Kozuka *et al.*, 2009. Figure 3(d) shows the bubble shape and path when h = 1.5 mm. The results are similar to that of h = 1.0 mm, *i.e.* small and medium bubbles have zigzag paths, while the large bubbles (*e.g.* d = 20 mm in Figure 3(d)) have straight paths. The further increase in gap thickness has limited influence on bubble shape and path behaviour.

Through the comparison of the predicted and measured bubble shape and path, we can conclude that the simulation predicts similar bubble shape and path in all cases. Main differences are detected for large bubbles of d = 20 mm when h = 1.0 mm and h = 1.5 mm. The lower surface of the bubbles in simulation is fluctuating, while it is not in the experiment.

Bubble Reynolds number

The bubble Reynolds number is the most important parameter that affects flow field. To further verify the simulation results, the predicted and observed bubble Reynolds number values are compared as a function of Eötvös number, as shown in Figure 4. In all the cases, *Re* increases with the increase of *Eo*. This arises from the terminal velocity change and bubble diameter increase. In all the cases, the obtained *Re* lies in the high Reynolds number range, and therefore results in high Reynolds number bubble motion. The absolute values of *Re*, however, strongly depend on the gap thickness. For the same *Eo* number, higher *Re* is obtained in the case of larger gap thickness (Figure 4(e)). It means the terminal velocity is higher for a same-size bubble when the gap thickness is larger. The increase of the terminal velocity slows down when h = 1.5 mm, therefore the curve overlaps with h = 1.0 mm in some points. The simulation results are close to the experimental values. The average deviation between experiments and simulation is around 10%. This deviation is probably due to the three-dimensional effects which are not considered in the present model.

Pressure field

To fully understand the bubble dynamics in a vertical Hele-Shaw cell, the pressure field and velocity field in the fluid have to be clarified. However, the relevant data is difficult to be obtained through experimental measurements. Since the present model successfully predicts similar bubble shape, path and Reynolds number, useful information on the pressure field and the velocity field are also expected to be obtained through simulation. The simulated pressure field is presented in Figure 5. The pressure here is static pressure, which is the gauge pressure relative to the operating pressure (1 atm in our case). Two typical bubble sizes are selected for comparison: one is d = 9 mm, whose vibration evolution as a function of gap thickness is observed; the other one is d = 20 mm, whose shape and path are stable in all four cases.

Figure 5(A) shows the results of d = 9 mm. The static pressure ranges from -80.3 Pa to 44.5 Pa. In all the four cases, the pressure distribution has something in common: higher pressure is observed in the liquid region just above the upper surface of the bubble, and the liquid region just below the lower surface of the bubble has lower pressure. Because the force on a fluid always points to the region with low pressure, we can easily conclude that for the liquid, the area below the bubble interface will be filled up with surrounding liquid, and the liquid above the bubble interface will flow away. That is to say, the liquid surrounding the bubble has a lift force. Since the fluid experiences a net upward force, the gas bubble experiences a net downward force, which is the drag force. By comparing the results of the four thicknesses in Figure 5(A), it is clear that with the increase of the gap thickness, the pressure above the

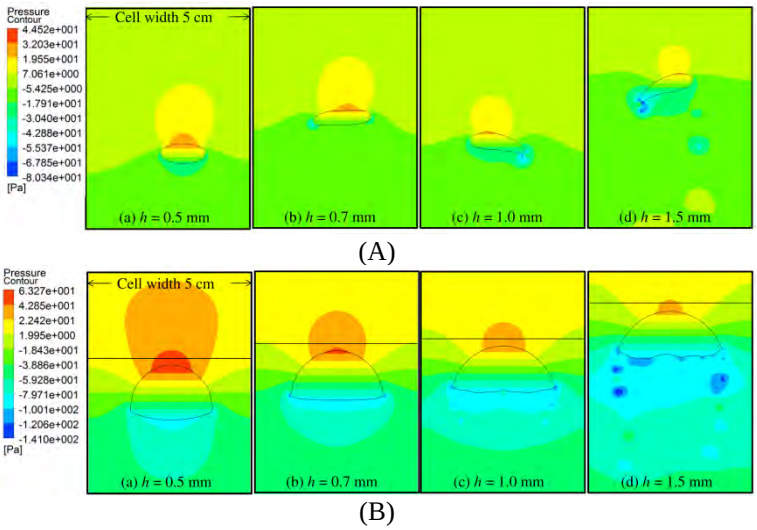

Figure 5: Simulated static pressure fields : (A) d = 9 mm; (B) d = 20 mm.

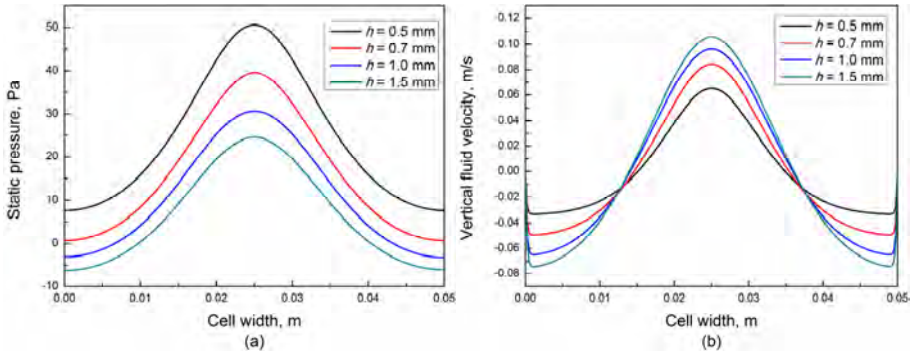

Figure 6: Static pressure and vertical fluid velocity as a function of cell width in Figure 5(B): (a) static pressure; (b) vertical velocity. The position was marked with black lines in Figure 5(B).

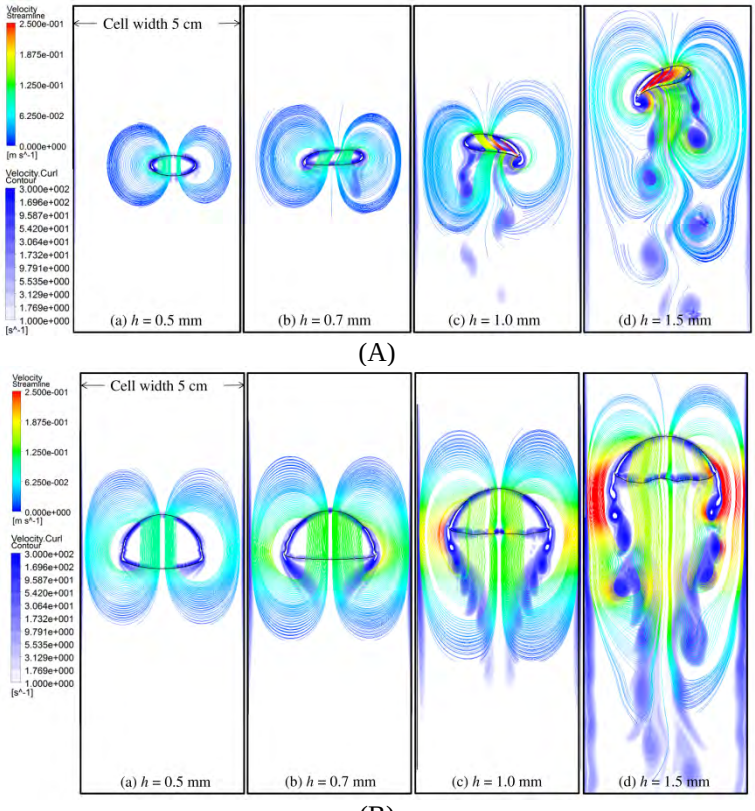

Figure 7: Streamlines and vortices in simulation : (A) d = 9 mm; (B) d = 20 mm.

upper surface of the bubble decreases, resulting in a decreased drag force. The same phenomena can also be observed when d = 20 mm in Figure 5(B). Through the comparison of Figure 5(A) and 5(B), it is found that for the same gap thickness, the increase of the bubble size also increases the pressure difference surrounding the bubble, which results in a higher flow resistance.

Since the bubble shape is similar, quantitative comparison is then possible. The comparison of the pressure distribution as a function of cell width located 2mm above the top surface of the bubbles is shown in Figure 6 together with the velocity distribution. From Figure 6(a), it is obvious that the static pressure decreases in increasing gap thickness. Correspondingly, the liquid velocity increases in increasing gap thickness, as can be seen in Figure 6(b).

Velocity field

To visualize the fluid flow in the Hele-Shaw cell, especially the bubble wake, the simulated streamlines are illustrated in Figure 7. Streamlines are instantaneously tangent to the velocity vector of the flow, showing the direction of travelling fluid at a given time. The velocity can vary in magnitude along a streamline. In the figure, the streamlines of velocity $u \geq$ 0.01 m/s are shown. Vorticity is twice the local angular velocity in the flow, its contours are shown together with the streamlines in Figure 7. Similarly, the results of two bubble sizes, *i.e.* d = 9 mm and d = 20 mm, are presented.

The streamlines in Figure 7(A) are well-formed closed lines attached to the bubble surface. They exactly show the liquid recirculation regions. As the gap thickness increases, the streamlines become wider, longer and unsteady. When h = 0.5 mm, symmetry of the streamline is evident. With the increase of h to 0.7 mm, vortices are formed along the streamlines. However, they are quite small, and closed streamlines are still visible. When h = 1.0 mm, the vortices are strong enough to form a vortex core. It detaches from the main streamlines and vortex shedding becomes evident. The magnitude of the vortices increases further when h = 1.5 mm. In all the cases, the velocity magnitude along the streamlines adjacent to the bubble interface also increases as the gap thickness increases. This means that a higher liquid velocity is obtained in a larger gap thickness.

For d = 20 mm, similar results are found: more liquid recirculation is observed in the case of larger gap thickness, which can be seen from the elongated streamlines. The magnitude of the velocity increases as the streamline approaches to the bubble interface. The velocity magnitude is much higher compared to that in case of d = 9 mm, especially when the region is very close to the bubble rim. It means that motion of large bubbles strongly depends on the boundary conditions at the side walls. Additionally, the symmetry of the streamlines are maintained except for h = 1.5 mm.

CONCLUSION

In this paper, a two dimensional VOF method coupled with a CSF model in porous media has been applied to simulate the bubble dynamics in a vertical Hele-Shaw cell. The simulation results are compared with experimental data. Based on the validation of bubble shape, bubble path and bubble Reynolds number, the effects of gap thickness on the bubble dynamics were quantified as follows:

(1) Two bubble shapes (oblate ellipsoid and spherical-cap) with a straight path are observed when h = 0.5 mm, three bubble shapes (oblate ellipsoid, spherical-cap and comma-shaped) with some vibrating paths (d = 9 – 11 mm) when h = 0.7 mm, while four shapes (oblate ellipsoid, comma-shaped, bird flapping its wings and spherical-cap) with strong path instability and shape oscillation when further increasing to h = 1.0 mm and h = 1.5 mm.

(2) The Reynolds number increases as the gap thickness increases, but the change is limited when $h \geq$ 1.5 mm.

(3) The pressure field is dependent on the gap thickness. With an increase of the gap thickness, the pressure above the bubble interface decreases, resulting in a lower drag force and higher liquid velocity.

(4) The streamlines and vortices also change with the gap thickness. Larger gap thickness results in larger streamline scale, more vortices and more unsteady bubble wake.

ACKNOWLEDGEMENTS

The work was supported by the Fund for Scientific Research-Flanders (FWO), project “Multiscale study of reactive gas injection in pyrometallurgical processses” G. 0433.10N.

REFERENCES

BRACKBILL J. U., KOTHE D. B., and ZEMACH C., (1991), “A continuum method for modeling surface tension,” *J. Comput. Phys.*, **100**, 335-354.

BUSH J. W. M., (1997), “The anomalous wake accompanying bubbles rising in a thin gap: a mechanically forced Marangoni flow,” *J. Fluid Mech.*, **352**: 283-303.

BUSH J. W. M., and EAMES I., (1998), “Fluid displacement by high Reynolds number bubble motion in a thin gap,” *Int. J. Multiphase Fluid*, **24**, 411-430.

ECK W., and SIEKMANN J., (1978), “Bubble motion in a Hele-Shaw cell, a possibility to study 2-phase flows under reduced gravity,” *Ing. Arch.*, **47**, 153-168.

KAWAGUCHI M., NIGA S., GOU N., and MIYAKE K., (2006), “Buoyancy-driven path instabilities of

bubble rising in simple and polymer solutions of Hele-Shaw cell," *J. Phys. So. Jpn.*, **75**, 124401.

KELLEY E., and WU M., (1997), "Path instabilities of rising air bubbles in a Hele-Shaw cell," *Phys. Rev. Lett.*, **79**, 1265-1268.

KLAASEN B., VERHAEGHE F., BLANPAIN B., and FRANSAER J., (2014), "A study of gas bubbles in liquid mercury in a vertical Hele-Shaw cell," *Exp. Fluids*, **55**, 1652.

KOPF-SILL A. R., and HOMSY G. M., (1988), "Bubble motion in a Hele-Shaw cell," *Phys. Fluids*, **31**, 18-26.

KOZUKA H., IKEDA Y., and KAWAGUCHI M., (2009), "Path instabilities of bubble rising in polymer solutions of Hele-Shaw cell," *J. Phys. Soc. Jpn.*, **78**, 114604.

MA D., LIU M., ZU Y., and TANG C, (2012), "Two dimensional volume of fluid simulation studies on single bubble formation and dynamics in bubble columns," *Chem. Eng. Sci.*, **72**, 61-77.

MARUVADA S. R. K., and PARK C. W., (1996), "Retarded motion of bubbles in Hele-Shaw cells," *Phys. Fluids*, **8**, 3229-3233.

MAXWORTHY T., (1986), "Bubble formation, motion and interaction in a Hele-Shaw cell," *J. Fluid Mech.*, **173**, 95-114.

ROIG V., ROUDET M., RISSO F., and BILLET A., (2012), "Dynamics of a high-Reynolds number bubble rising within a thin gap," *J. Fluid Mech.*, **707**, 444-466.

TANVEER S., (1986), "The effect of surface tension on the shape of a Hele-Shaw cell bubble," *Phys. Fluids*, **29**, 3537-3548.

TAYLOR G., and SAFFMAN P. G., (1959), "A note on the motion of bubbles in a Hele-Shaw cell and porous medium," *Quart. J. Mech. Appl. Math.*, **12**, 265-279.

TRYGGVASON G., SCARDOVELLI R., and ZALESKI S., (2011), *Direct numerical simulations of gas-liquid multiphase flows*. Cambridge University Press, 105.

VAN SINT ANNALAND M., DIJKHUIZEN W., DEEN N. G., and KUIPERS J. A. M., (2005), "Numerical simulation of behavior of gas bubbles using a 3-D Front-Tracking method," *AICHE*, **52**, 99-110.

WANG X., KLAASEN B., DEGRÈVE J., and BLANPAIN B., (2014), "Experimental and numerical study of buoyancy-driven single bubble flow in a vertical Hele-Shaw cell", submitted to *Phys. Fluids*.

YAMAMOTO M., and KAWAGUCHI M., (2011), "Differences in path instabilities between a bubble rising in water and in aqueous polymer solution in a Hele-Shaw cell in the transient and steady states," *J. Disper. Sci. Technol*, **32**, 1445-1451.

YOUNGS D. L., (1982), "Time dependent multimaterial flow with large fluid distribution, in :K. W. Morton, M. L. Norman (Eds.)," *Numer. Methods Fluid Dynam.*, **24**, 273-285.

CFD MODELING OF OIL-WATER SEPARATION EFFICIENCY IN THREE-PHASE SEPARATORS

Lanre OSHINOWO*, Ehab ELSAADAWY and Regis VILAGINES
Saudi Aramco Research and Development Center, Dhahran, SAUDI ARABIA
* E-mail: oshinoom@aramco.com

ABSTRACT

Variations in oil properties or the water content influence crude oil-water separation thereby posing challenges for separator operations when conditions change as the fields mature and in the design of new internals to improve separation efficiency. Computational fluid dynamics (CFD) is being used to predict separator vessel hydrodynamics and the studies of three-phase separators have characterized the dispersed phase with a single droplet size and constant phase properties. Modelling the evolving droplet size during separation is a critical requirement to developing a realistic separator model. Emulsion rheology is also an important phenomena typically overlooked in modelling oil-water separation. In this study, a transient Eulerian multiphase approach coupled with the population balance is used to predict the gas, oil and water separation behaviour in three-phase horizontal gas-oil-water gravity separators. Here, the secondary water phase is divided into multiple velocity groups and a number of bins describe the droplet distribution within each velocity group. By considering the dispersed phase fraction in the water-in-oil emulsion rheology and incorporating this into the interphase interaction, the high viscosity emulsion is formed at the interface between the oil and water phases, known as the dense packed layer or zone (DPZ). The resulting DPZ is shown to have an effect on oil-water separation efficiency. Experimental data was obtained from a high-pressure pilot scale three-phase separator rig and includes phase flow rates into and out of the vessel and vertical water fraction profiles at two locations in the separator. The data was compared to the CFD predictions of separation efficiency, phase distribution and DPZ thickness in the separator.

Keywords: Emulsion, gravity separation, three-phase, separator, oil, multiphase, population balance, CFD.

NOMENCLATURE

a Coalescence rate, [m^3/s].
b_1, b_2, b_3 Coalescence rate empirical constants, [-].
B Interfacial force constant, [N.m^2].
B Birth rate, [droplets/s].
C_D Droplet drag coefficient, [-].
d Droplet diameter, [m].
D Death rate, [droplets/s].
$\vec{f}$ Drag function, [-].
f_i Discrete bin fractions, [-].
$\vec{g}$ Gravitational acceleration, [m/s^2].
g Breakage frequency, [1/s].
h Collision frequency of droplets of volume V and V', [1/s].
$h_{w,l}$ Interface and liquid level, [m].
$\bar{\bar{I}}$ Unit tensor, [-].
k_B Boltzmann constant [J/K].
K_{ij} Mean interphase momentum exchange [kg/m^3.s].
m Mass transfer rate, [kg/s].
M Number of bins per phase/velocity group, [-].
n Droplet number, [droplets].
N Number of velocity groups, [-].
p Pressure, [Pa].
Pe Peclet number, [-].
Q Volumetric flow rate, [m^3/s].
Re Reynolds number, [-].
S population balance equation source term, [droplets/m^3].
T Temperature, [K].
u, v, w Components of velocity, [m/s].
V Droplet volume, [m^3].
x, y, z Coordinates, [m].

Greek Symbols
α Phase fraction, [-].
$\beta(V|V')$ probability density function of droplets breaking from volume V' to V.
λ Coalescence efficiency of a binary droplet pair, [-].
μ Viscosity, [kg/m.s].
ρ Mass density, [kg/m^3].
σ Interfacial tension, [N/m].
τ Particle relaxation time, [s].

Sub/superscripts
g, w, o Gas, Water, Oil.
l Liquid.
m Mixture.
c Continuous phase.
d Dispersed phase.
i, j, k Index i, j, k.

INTRODUCTION

The separation of gas, oil and water by gravity is found throughout oil and gas production operations. The multiphase separator is the first unit in the production line between the production manifold and the pipeline transport. In offshore production, the multiphase flow is separated into the requisite streams top-sides while onshore, the Gas-Oil Separation Plants (GOSP) handle the separation. Horizontal gravity separators are high-aspect ratio cylindrical vessels with a relatively short entrance region for disengagement of gas and liquid. To improve the efficiency of separation while reducing the overall vessel dimensions, various types of "internals" – plate, vane or cyclonic momentum breakers at the vessel inlet, coalescing plates, solid and perforated baffle plates, flow straighteners, foam breakers, weirs, mist eliminators,

electrocoalescers – are used to promote gas-liquid and liquid-liquid separation. Computational Fluid Dynamics (CFD) has long been recognized as a promising tool in design, size and retrofit studies of multiphase separators. In the CFD work by Hansen and co-workers, the three-phase separator was modelled by considering different two-phase regions of the separator: a freeboard region with dispersed liquid droplets in gas, and the liquid bath with water or oil droplets dispersed in oil or water (Hansen *et al*., 1991, Hansen and Rørtveit, 2005). The emulsion viscosity was modelled by changing the continuous phase oil viscosity with the local water volume fraction. Another approach has been to model the oil-water emulsion as a mixture using the volume of fluid model and determine the water separation efficiency by tracking a droplet distribution with an uncoupled Lagrangian dilute-phase particle tracking model (Laleh *et al*., 2012). The presumption of dilute flow may be valid for droplets dispersed in the gas phase but not in the liquid phase. The water phase accumulates and the dilute conditions become dense phase conditions in regions of the separator, making the dilute Lagrangian approach inappropriate for modelling the oil-water phase separation. The Eulerian multiphase modelling approach is the most appropriate to describe complex phase rheology, phase separation and inversion in oil-water emulsions that exist in continuous and batch separators (Hallanger *et al*., 1996). Phases are treated as interpenetrating continua in the Eulerian multiphase approach and phase volume fractions add up to one in each cell of the computational domain. A momentum transport equation is solved for each phase in addition to a continuity equation. Interphase interaction forces, like drag and lift, are modelled using momentum exchange coefficients. Several recent studies applied Eulerian multiphase models but the dispersed water phase was modelled with a constant droplet diameter (Vilagines and Akhras, 2010, Kharoua *et al*., 2012). While these studies and others have shown that CFD helps to elucidate the macroscopic parameters, such as, flow patterns, pressure drop, and phase residence time, CFD has been unable to predict separation performance accurately (Laleh *et al.*, 2012). The main reasons for these shortcomings have been a lack of a comprehensive treatment of the oil-water emulsion rheology and the poly-disperse nature of the multiple phases. It is widely recognized that the dispersed phase size distribution in liquid-liquid dispersions influences the separation kinetics in gravity separation (Henscke *et al*., 2002). The size distribution evolves with transport through the separation vessels due to varying shear, turbulence, and due to the effects of surface active agents naturally present or injected upstream of the GOSPs. In this study, a CFD methodology to model GOSPs is presented. The population balance model is used here to predict the evolving droplet size distribution in the oil emulsion and its viscosity varies with water content. Experimental data were obtained from a pilot-scale high-pressure, three-phase horizontal gravity separator, and compared to the CFD model results.

EXPERIMENTAL

The experimental data obtained for the CFD model study was obtained from a pilot scale, high-pressure, horizontal, three-phase gas-oil-water separator flow loop at the IFP Energies Nouvelles site in Solaize, France (Pagnier *et al.*, 2008). The closed flow loop, as illustrated in Figure 1, consists of feed tank for the oil and water and a gas compression system. The flow loop has instrumentation to quantify the flows in and out of the separator vessel. The mass flow rate, pressure and temperature for each phase are controlled. The temperature control is achieved using separate heat exchangers for cooling and for heating. The oil and water phases are mixed in a Y-branch followed by two static vane mixers, one upstream and the other downstream of the heat exchangers. The gas is introduced after the second liquid static mixer.

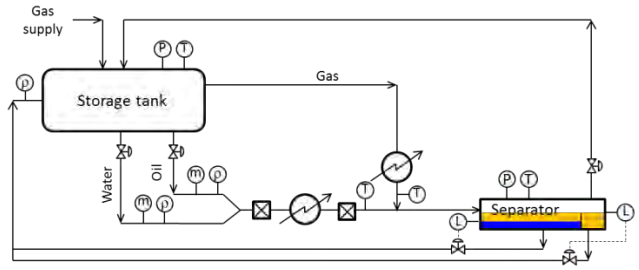

Figure 1. Pilot-scale, high-pressure, horizontal, three-phase gas-oil-water separator flow loop at the IFPEN (Pagnier, et al. 2008)

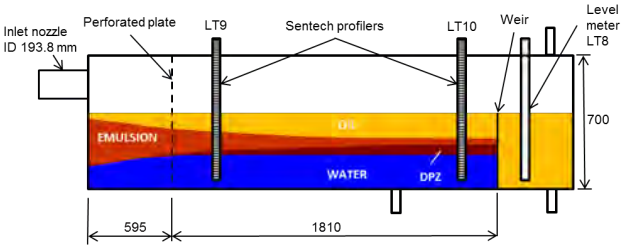

Figure 2: Schematic of the high-pressure, three-phase, pilot separator (ID 700mm, Length 3000mm).

The three-phase flow then travels approximately 15 m through a 3-inch (ID 73.66 mm) line to the multiphase separator vessel. The separator vessel is 700 mm in diameter and 3000 mm in length and is illustrated in Figure 2. The separator inlet is an 8-inch diameter nozzle (ID 193.8 mm) while 2-inch (ID 47.3 mm) nozzles are used for the gas, oil and water outlets. A perforated plate, located 595 mm from the inlet flange, separates the entry region from the settling zone in the vessel that extends 1810 mm to the weir. The perforated plate is 10 mm thick with 13 mm holes in a triangular pattern and a 54% open area. The weir is 400 mm from the vessel bottom. The evolution of the separating water phase is measured *in-situ* in the separator using two commercially-available electrical capacitance profilers (Schuller *et al.*, 2004). The two profilers, LT9 and LT10 (Figure 2), are mounted vertically just downstream of the perforated plate (750 mm from inlet flange) and upstream of the weir (2250 mm from inlet flange), respectively. The profilers determine the spatial distribution of the water phase and the interface boundaries between the water and emulsion, emulsion and oil, oil and gas. The profilers consist of a linear array of elements with each element having a single capacitance electrode. The elements are typically spaced every 10 mm and give a measurement related to permittivity that is calibrated to the water/brine volume fraction. It is then possible to ascertain the height of the water-emulsion and oil-gas interface from the maximum and minimum permittivity measurements. The dense packed zone (DPZ) forms in the emulsion layer above the water interface. In this zone, the water fraction typically exceeds the inlet water fraction. The height of the DPZ is interpreted from an inflexion in the water fraction profile, measured from the LT10 profiler as illustrated in Figure 3, typically corresponding to water fraction in excess of the inlet value. A water fraction of 0.1 defines the boundary between the emulsion and the oil layers. The oil/liquid level in the vessel is measured by the level transmitter LT8 and controlled by the valve on the oil outlet line. Alternatively, the liquid level is controlled by the weir. The water-emulsion interface level is controlled using the water outlet control valve, based on the interface level measurement from the LT10 profiler. The oil and water discharged from the separator are circulated back to the feed tank where the phases separate and return to the flow loop. The oil-water feed tank volume is 10 m^3 while the separator vessel has a capacity of approximately 1 m^3. The oil

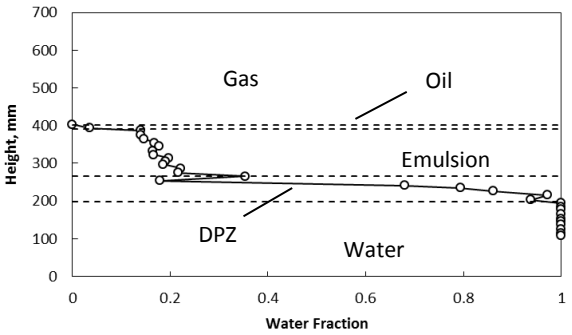

Figure 3. Measured water fraction obtained at the LT10 capacitance probe showing the dense packed emulsion zone.

used is a Saudi Arabian light crude oil with an API gravity of 35. The water is a brine mixture with 50 g/L NaCl. A demulsifier is added to the aqueous phase in a dosage of 50 ppm Clariant PT 4688. The gas phase is a mixture consisting of 97.8% methane, 1.1% nitrogen, 0.8% ethane, 0.2% propane, and 0.1% carbon dioxide. The operating temperature and pressure are 45°C and 24 bar, respectively. The experimental conditions selected for this paper are listed in Table 1.

Table 1. Experimental Conditions.

Oil Flowrate Q_o	m^3/h	3.40
Water Flowrate Q_w	m^3/h	1.50
Liquid Flow Q_l	m^3/h	4.9
Gas Flowrate Q_g	Am^3/h	13.95
Water Fraction Q_w/Q_l	-	0.27
Water Level h_w	mm	199
Liquid Level h_l	mm	405*

** Level controlled by weir.*

MODEL DESCRIPTION

An Eulerian-Eulerian multiphase method was used to model the characteristics of the multiphase dispersion encountered in gravity separators. The liquid-dispersions found in gravity separation can be characterized as dense with the volume fraction ranging from zero to 100%. With the dispersion of gas bubbles and water droplets in the continuous oil phase, the oil phase is considered in this work to be the primary phase while the gas and water phases are considered secondary phases. The poly-dispersity of the secondary droplet population is modelled with the population balance method.

Multi-fluid Multiphase Model

The conservation equations are derived by ensemble averaging the local instantaneous balance for each phase. The continuity equation for phase *j* is

$$\frac{\partial}{\partial t}(\alpha_j\rho_j) + \nabla\cdot(\alpha_j\rho_j\vec{v}_j) = \sum_{i=1}^{n}(\dot{m}_{ij} - \dot{m}_{ji}) \qquad (1)$$

where α_j, ρ_j and $\vec{v}_j$ are the phase volume fraction, density and velocity, and $\dot{m}$ is the mass transferred between phases. The momentum balance for phase *j* is

$$\frac{\partial}{\partial t}(\alpha_j\rho_j\vec{v}_j) + \nabla\cdot(\alpha_j\rho_j\vec{v}_j\vec{v}_j) = -\alpha_j\nabla p + \nabla\cdot \alpha_j\mu_j\left[\left(\nabla\vec{v}_j + \nabla\vec{v}_j^T\right) - \tfrac{2}{3}\nabla\cdot\vec{v}_j\bar{\bar{I}}\right] + \sum_{i=1}^{n}\left(K_{ij}(\vec{v}_i - \vec{v}_j) + \dot{m}_{ij}\vec{v}_{ij} - \dot{m}_{ji}\vec{v}_{ji}\right) + \alpha_j\rho_j\vec{g} \qquad (2)$$

where p is pressure, μ is viscosity, $\bar{\bar{I}}$ is the unit tensor, and $K_{ij}\left(=K_{ji}\right)$ is the mean interphase momentum exchange coefficient and can be written in general form as:

$$K_{ij} = \frac{\alpha_i\rho_j f}{\tau_j} \qquad (3)$$

The terms f and τ_i are the drag function and particle relaxation time, respectively, expressed as

$$f = \frac{C_D Re}{24} \qquad (4)$$

and,

$$\tau_i = \frac{\rho_j d_j^2}{18\mu_i} \qquad (5)$$

where d_j is the Sauter mean diameter coupling the momentum equations to the population balance equation. For settling or rising droplets, the drag originates from viscous surface shear and the pressure distribution, or form drag, around the droplet. For dilute dispersions, the droplets can settle or rise without interacting with neighbour droplets. For small droplets in the viscous regime, the Stokes law determines the terminal velocity in dilute or unhindered conditions. In the dense dispersions found in oil-water batch and continuous gravity separation, the drag function must include the influence of neighbour droplets and hindered settling. The Schiller-Naumann correlation for drag coefficient C_D is modified for dense suspensions using a mixture or emulsion Reynolds number Re_m based on the emulsion viscosity μ_m described later:

$$C_D = \frac{24}{Re_m}(1 + 0.15Re_m^{0.687}) \qquad (6)$$

$$Re_m = \frac{\rho_c|u_d - u_c|d_d}{\mu_m} \qquad (7)$$

The subscripts c and d refer to the continuous and dispersed phases, respectively. The drag force is the only contribution to the interphase interaction that was considered. Other forces including virtual mass force, transverse lift force, or wall lubrication force were not considered given droplet Reynolds numbers of the order 0.01 for water-in-oil dispersions relevant to crude oil separation. The turbulent dispersion force – that contributes to diffusion in dispersed flows – was not considered here. The mixture or emulsion viscosity depends on the viscosities of the dispersed and continuous phases, the concentration of the dispersed phase, the shear field, the droplet size distribution, temperature, and the emulsion stability. The interfacial stability is dependent on many non-hydrodynamic factors including the crude oil heavy fraction, solids, temperature, droplet size and distribution, pH, salinity, and composition (Kokal, 2005, Sanfeld and Steinchen, 2008). Brinkman derived the following equation for emulsion viscosity for suspensions of hard spheres (Brinkman, 1952):

$$\mu_m = \mu_c(1 - \alpha_d)^{-2.5} \qquad (8)$$

Krieger and Dougherty extended Brinkman's correlation by including the contribution of the maximum packing value (Krieger and Dougherty, 1959):

$$\mu_m = \mu_c\left(1 - \frac{\alpha_d}{\alpha_{max}}\right)^{-2.5\alpha_{max}} \qquad (9)$$

where α_{max} is the maximum packing value of 0.64 for hard spheres in non-equilibrium reaching the limit of 0.74 for a hexagonal close packed structure. With increased pressure, droplets can deform and the maximum packing value φ_{max} approaches unity. Ishii and Zuber extended the Krieger-Dougherty correlation by including a viscosity factor in the exponent (Ishii and Zuber, 1979):

$$\mu_m = \mu_c\left(1 - \frac{\alpha_d}{\alpha_{max}}\right)^{-2.5\alpha_{max}\mu_*} \qquad (10)$$

$$\mu_* = \left(\frac{\mu_d + 0.4\mu_c}{\mu_d + \mu_c}\right) \qquad (11)$$

Mills derived the following equation for the apparent shear viscosity of a concentrated suspension of hard spheres in a Newtonian fluid based on a free cell model (Mills, 1985):

$$\mu_m = \mu_c\frac{1 - \alpha_d}{(1 - \alpha_d/\alpha_{max})^2} \qquad (12)$$

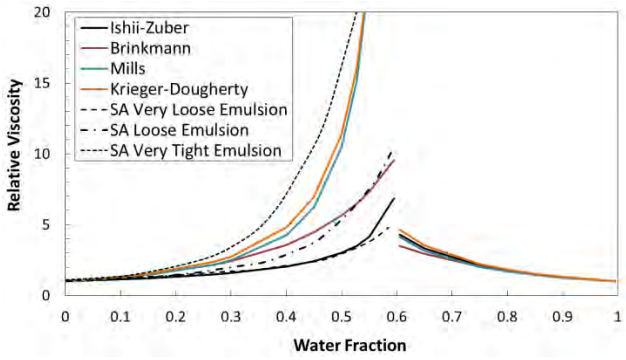

Figure 4. Emulsion viscosity correlations for Arab Light crude (API ~ 35) and brine (50 g/L) at 45°C. (Arabian crude emulsions from Kokal, 2005).

where α_{max} is 0.64. The emulsion viscosity equations are plotted in Figure 4 for a Saudi Arabian Light crude oil emulsion at 45°C. The relative viscosity increase in crude oil emulsions can be of the order 10 to 100 (Marsden and Mad, 1975). For comparison are the relative viscosity curves for very loose and very tight Arabian crude emulsions (Kokal, 2005). The terms "loose" and "tight" refer to the relative stability of the emulsion.

Population Balance Model

A population balance equation is coupled with the turbulent multiphase momentum equations conveniently describing the water droplet size distribution (Ramkrishna, 2000). The general population balance equation is written as a continuity statement of the droplet number density function:

$$\frac{\partial}{\partial t}[n(V,t)] + \nabla \cdot [\vec{v} n(V,t)] = S(V,t) \qquad (12)$$

The spatial location of the particle is an "external coordinate" in the particle state vector, while the droplet volume V is an "internal coordinate" of the population distribution. The source term $S(V,t)$ for breakage b and coalescence c due to birth (B) and death (D) rates is further expanded as:

$$S(V,t) = B_b(V,t) - D_b(V,t) + B_c(V,t) - D_c(V,t) \qquad (13)$$

The closure of Equation (12) requires a derivation of the source terms in Equation (13) above.

Breakage and Coalescence Kernels

The breakage rate kernel is the product of the breakage frequency $g(V')$ and the probability density function (PDF) $\beta(V|V')$ of droplets breaking from volume V' to V. The birth rate of droplets of volume V due to breakage is

$$B_b = \int_{\Omega_V} p\, g(V')\, \beta(V|V')\, n(V')\, dV' \qquad (14)$$

where $g(V')\, n(V')\, dV'$ droplets of volume V' break per unit time, producing for p child droplets, $p\, g(V')\, n(V')$ droplets of which a fraction $\beta(V|V')dV$ represents droplets of volume V (Luo and Svendsen, 1996). The breakage PDF $\beta(V|V')$ is also referred to as the daughter size distribution function where the fragments or daughter droplet mass must equal the original droplet mass. The death rate of droplets is

$$D_b = g(V)n(V) \qquad (15)$$

There are several different models for determining the breakage frequency and the breakage PDF to compute the breakage rate of the droplets. The coalescence kernel $a(V-V',V')$ is a product of the collision frequency $h(V-V',V')$ between droplets of volume V and V', and the coalescence efficiency $\lambda(V-V',V')$. The coalescence efficiency is the probability that droplets of volume V will coalesce with droplets of volume V'. The birth rate of droplets due to coalescence is

$$B_c = \frac{1}{2}\int_0^V a(V-V',V')\; n(V-V')n(V')\, dV' \qquad (16)$$

The death rate of droplets due to coalescence is

$$D_c = \frac{1}{2}\int_0^V a(V,V')\; n(V)n(V')\, dV' \qquad (17)$$

In the three-phase or two-phase separator settling zone, the complex oil-water emulsion evolves primarily due to droplet coalescence. Other phenomena including breakage, dissolution, aggregation, and flocculation occur to a lesser extent in the settling zone. Droplet breakage is more important at the separator entrance region where the multiphase flow is highly turbulent. Along with droplet breakage and mass transfer, coalescence influences the evolution of the droplet size distribution in liquid-liquid emulsions. Grimes (2012) developed a coalescence kernel in the context of batch gravity separation of oil-water emulsions. Droplet collisions are considered to depend on both Brownian and gravitational coalescence (Simons *et al.*, 1986). The collision frequency is (Grimes 2012):

$$h(d_k,d_j) = b_1 \frac{k_B T}{6\mu}\frac{(d_k+d_j)^2}{d_k d_j}\left[1 + Pe + 4.496 Pe^{\frac{1}{3}}\right] \qquad (18)$$

where Pe is the sphere pair Peclet number,

$$Pe = \frac{\pi}{12}\frac{(\rho_d-\rho_c)g}{k_B T}(1-\alpha)^{b_2} d_k d_j \left|d_k^2 - d_j^2\right| \qquad (19)$$

The coalescence is dependent on an interfacial force constant B, which can be related to the surfactant concentration (Grimes, 2012; Kralova *et al.*, 2011). The coalescence efficiency is expressed as the ratio of coalescence time and the contact time:

$$\lambda(d_k,d_j) = exp\left[-\frac{1.046}{b_3}\frac{\mu(\rho_d-\rho_c)g}{\sigma^{3/2}B^{1/2}}\left[\frac{d_k d_j}{2(d_k+d_j)}\right]^{9/2}\right] \qquad (20)$$

The empirical constant b_2 influences the hindered settling contribution to the collision frequency, based on the Richardson-Zaki hindered settling correlation, while b_3 is used to adjust the coalescence time. There are recognized weaknesses with coalescence kernels, including: the derivation of the collision frequency based on the kinetic theory of gases, the lack of history to capture the cumulative effects during the coalescence process, and other empiricism (Liao and Lucas, 2010). The kernels are relatively simplistic given the complexity of the system and the phenomena.

Population Balance Equation Solution Method

To model separation of the dispersed water phase from the oil phase, the solution to the population balance cannot be based on a shared velocity field since droplets of different sizes will rise or settle at different velocities. The droplet size distribution can range over two to three orders of magnitude or more, and the distribution can be mono- or multi-modal. Multivariate methods incorporating several velocity classes are required to model this tight coupling between the droplet size distribution and the secondary phase velocity distribution. There are a number of multivariate methods described in the literature but the Inhomogeneous Discrete Method (IDM) (Frank *et al.*, 2005, Sanyal *et al.*, 2013) will be used in this work. The population balance equation is written for the IDM in terms of volume fraction of particle or droplet size i and solved here for all discrete bin fractions f_i :

$$\frac{\partial}{\partial t}(\rho\alpha f_i) + \nabla\cdot(\rho\alpha f_i u_i) = \rho V_i\left(B_{c,i} - D_{c,i}\right) \qquad (21)$$

where ρ is the density of the secondary phase. The secondary phase is divided into N velocity groups or phases, each with M bins per phase for a total of $N \times M$ bins. The sum of

coalescence mass sources for all phases is zero, while each phase or bin could have a non-zero net mass source. Each bin is advected by phase velocity u_i and $\alpha f_i (= \alpha_i)$ is the volume fraction of bin i, defined for secondary phase 0 to $N-1$ as

$$\alpha_i = N_i V_i \tag{22}$$

$$N_i(t) = \int_{V_i}^{V_{i+1}} n(V,t)dV \tag{23}$$

The droplet coalescence birth and death rates are defined as

$$B_{c,i} = \sum_{k=1}^{N}\sum_{j=1}^{N} \alpha_{kj} N_k N_j \, x_{kj} \xi_{kj} \tag{24}$$

$$D_{c,i} = \sum_{j=1}^{N} \alpha_{ij} N_i N_j \tag{25}$$

where the coalescence rate $\alpha_{ij} = a(V_i, V_j)$ and

$$\xi_{kj} = \begin{cases} 1 & \text{for } V_i < V_c < V_{i+1}, \text{ where } i \le N-1 \\ 0 & \text{otherwise} \end{cases} \tag{26}$$

V_c is the particle volume resulting from the coalescence of droplets k and j defined as

$$V_c = \left[x_{kj} V_i + (1 - x_{kj}) V_{i+1}\right] \tag{27}$$

where

$$x_{kj} = \frac{V_c - V_{i+1}}{V_i - V_{i+1}} \tag{28}$$

Numerical Setup and Boundary Conditions

Model

A carefully constructed mesh consisting predominantly of hexahedral cells was built on a 180° symmetrical geometry using the cut-cell method. The resulting 1.4 million cells gives 8 mm cells in the bulk of the vessel and 4 mm cells in the outlet nozzles. Mesh refinement was applied at the walls.

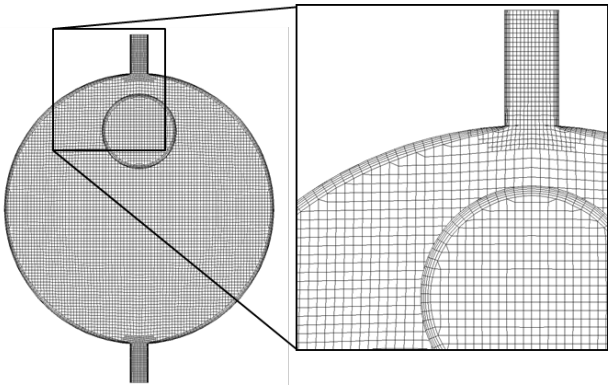

Figure 5. End-view of mesh showing details at the walls and the outlet nozzles.

Initial Droplet Size Distribution

In the pipe approaching the separator inlet, droplet size distribution evolves due to varying shear, and turbulence, the effects of surface-active agents naturally present, and the demulsifier. At the entrance to the separator, the complex oil-water emulsion continues to evolve due to breakage and coalescence. In the settling zone, coalescence processes are dominant and breakage, dissolution, aggregation, and flocculation occur to a lesser extent. In the absence of droplet size measurements at the separator inlet, the initial droplet diameter distribution is determined from the maximum stable droplet size. The maximum droplet size d_{max} is (Hinze, 1955)

$$d_{max} = \frac{0.725}{\left(\frac{\rho_l}{\sigma}\right)^{3/5} \epsilon^{2/5}} \tag{29}$$

where the mean turbulent energy dissipation per unit mass ϵ is

$$\epsilon = f \frac{u_m^3}{2D} \tag{30}$$

and the friction factor f is

$$f = F_2 + \frac{(F_1 - F_2)}{\left(1 + \left(Re_m/t\right)^c\right)^d} \tag{31}$$

where $F_1 = a_1 Re_m^{b_1}$ and $F_2 = a_2 Re_m^{b_2}$ (Garcia, et al. 2007). The minimum droplet size is determined from (Vielma, et al. 2008)

$$d_{min} = 8\frac{\sigma}{g\rho_l u_l^2} \tag{32}$$

The mean droplet diameter is

$$d_{mean} = 0.4 d_{max} \tag{33}$$

Using a 39- bin cumulative volume fraction distribution for water droplets dispersed in an Arabian Light crude oil (API > 35) with added demulsifier, each bin is assigned a droplet size based on a Rosin-Rammler distribution:

$$d_{i_0} = d_{mean}[-ln(1-\varphi_i)]^{1/n} \tag{34}$$

where φ_i is the $i-th$ bin fraction and the spread parameter n is 2. The droplet diameters are specified for each bin in the population balance model.

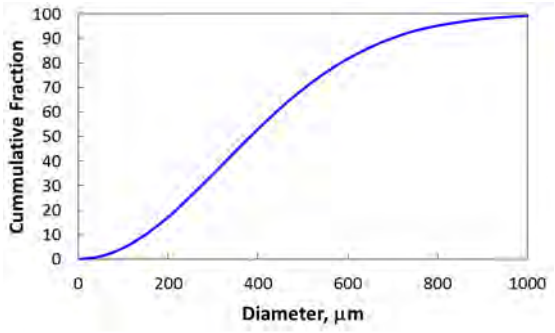

Figure 6. Cumulative droplet size distributions at the separator inlet.

Inlet Velocity Boundary Conditions

The inlet phase distributions are based on the incoming flow regime. For the experimental conditions modelled, the flow regime in the 3" pipe is stratified or intermittent elongated bubble based on three-phase gas-oil-water studies (Keskin *et al.*, 2007). The transition to the 8" nozzle will alter the flow regime to a separated or stratified flow regime. Though still developing through the reduction from the pipe to the nozzle, the larger cross-section will allow the gas to disengage and the flow regime will tend to stratified flow. A uniform velocity condition for each phase is assumed and the distribution of oil and water is considered fully mixed at the velocity inlet boundary. The inlet phase distribution is applied at the boundary using a user-defined function.

Perforated Plate

The perforated plate, described in the experimental section, is modelled as a porous cell zone. The inertial resistance of the porous media is based on the product of the loss coefficient and the local kinematic head and applied as a momentum source in the z-direction for the porous cell zone. The loss coefficient K is not constant but varies with the Reynolds number as shown in Figure 7. A user-defined function reads a table of $\log(K)$ as a function of the $\log(Re)$. The table is interpolated to return a value for K at the local Re determined from the local approach velocity. A high loss coefficient of 100,000 is applied in the transverse directions of the perforated plate cell zone.

Outlet Pressure Conditions

If the liquid outlet boundary pressure P_{outlet} is initially set assuming separated phases (A in Figure 8 below), the interface will drop until the steady-state distribution of water-in-oil (w/o) emulsion is reached (B). Since the w/o concentration distribution is unknown *a priori*, the outlet pressure (P_{outlet}) is initially estimated based on

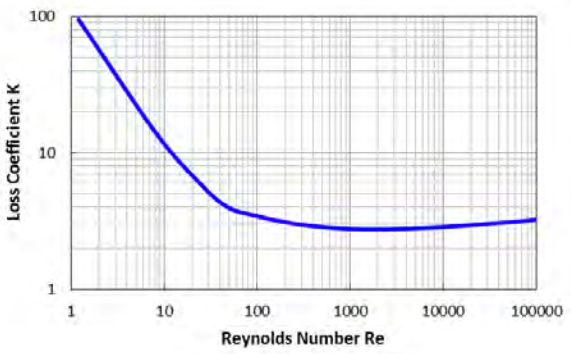

Figure 7. Perforated plate loss coefficient as a function of the perforation Reynolds number.

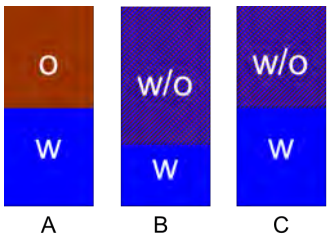

Figure 8. Illustration of the vertical column of oil (O), emulsion (w/o) and water (W) layers in the separator vessel.

$$P_{outlet} = \rho_{w/o} g h'_{w/o} + \rho_w g h_w \qquad (35)$$

and adjusted during the calculations in response to the interface level set point h_w. The interface level is determined from the average height (y-coordinate) of an iso-surface of water fraction of value 0.9 created at the intersection with a plane of constant z-coordinate at the LT9 and LT10 locations. The outlet pressure adjustment is executed manually or automatically. Here, an automatic interface level control is applied using a Proportional-Integral-Derivative (PID) controller algorithm to efficiently manage the simulation over long run-times. The outlet pressure is controlled to the set point of water-emulsion interface height.

Solution

The three-phase system was modelled with the Eulerian multiphase model in ANSYS FLUENT 14.5 (ANSYS Inc., 2012). A transient solution was obtained for each run with a fixed time-step of 0.5 seconds. The primary phase is the oil phase with water and gas as secondary phases. Dispersed gas bubbles have a constant diameter of 2 mm. The Inhomogeneous discrete model is used and three secondary phases discretise the water phase with two bins per phase. The droplet diameter range for each phase is determined from the droplet size distributions (Figure 6). An initial value for each of the six bin fractions is specified at the inlet boundary according to the droplet size distribution. The Grimes coalescence kernel described in is implemented in the population balance model through a user-defined function. From Figure 4, the Ishii-Zuber and Mills correlations are shown to bound the viscosity of the relevant emulsions. The application of the emulsion viscosity in the interphase momentum exchange term (Equation (3)) is applied through user-defined functions using the dilute mixture viscosity and relationships for the dense emulsion viscosity - Ishii-Zuber and Mills. The turbulence is modelled using the Realizable $k-\varepsilon$ mixture turbulence model. The solution methods are phase-coupled SIMPLE for pressure-velocity coupling, second-order upwind discretization for momentum and turbulence, QUICK discretization for the volume fraction equation. The solution is initialized with a zero velocity field and an idealized phase distribution – gas in the freeboard, inlet water fraction in the emulsion phase and clear water layer.

RESULTS

Flow Field

Figure 9 shows the liquid phase pathlines in the separator. The red pathlines are based on the oil phase velocity field, while the blue pathlines are computed from the secondary water phase with the largest diameters. All cases show the typical engineering assumption of a uniform plug flow in the separator is not achieved. The inlet section upstream of the perforated plate shows significant recirculation and mixing. At the lower emulsion viscosities (mixture and Ishii-Zuber) there is good segregation of the pathlines, while at the higher emulsion viscosity (Mills) there is intermingling of the pathlines throughout the settling section indicating poorer separation. The pathlines curve upwards approaching the weir. The higher viscosity emulsion layer thickness increases along the settling zone upstream of the weir, displacing the oil layer and increasing the water concentration towards the liquid level. Figure 10 plots the vertical profiles of the oil velocity w at the LT9 and LT10 locations shows the velocity field is significantly influenced by the emulsion rheology. The dense emulsion layer causes the oil to accelerate near the free surface.

Oil Distribution

Figure 11 shows the oil distribution in the mid-plane of the separator. The inlet region upstream of the perforated plate shows mixing of the oil-emulsion layer. In the settling zone between the perforated plate and the weir, there is a gradual vertical gradient of water. The mixture-averaged viscosity uses the Schiller-Naumann drag law, which assumes the droplets are settling in a quiescent environment. The interface

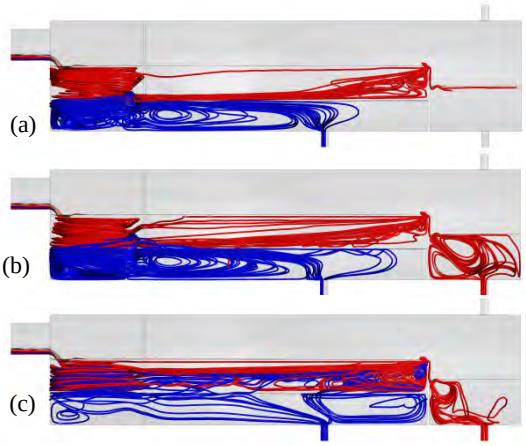

Figure 9. Pathlines of oil (red) and water (blue) on the time-averaged flow field: (a) Mixture-averaged viscosity, (b) Ishii-Zuber viscosity, (c) Mills viscosity.

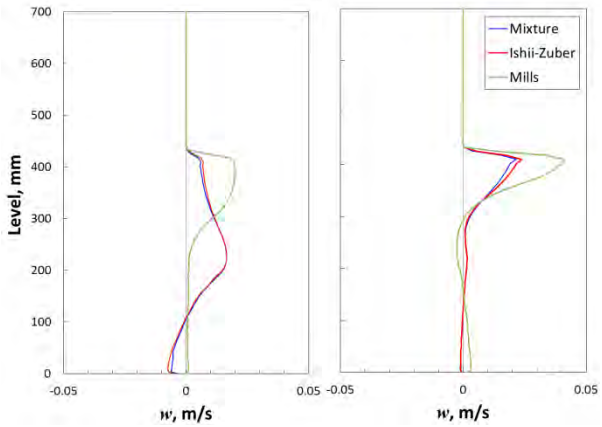

(a) w at LT9 (b) w at LT10

Figure 10. Oil velocity w profiles (time-averaged) at LT9 and LT10 for different emulsion viscosity correlations.

layer remains relatively constant throughout the vessel except around the perforated plate. With the higher emulsion viscosity of the Mills relationship (Figure 11(c)), there is a region of low oil and high water concentration above the water layer representative of a dense emulsion layer. The dense emulsion layer increases in thickness toward the end of the settling zone. As the relative viscosity of the emulsion increases, the settling rate slows relative to the coalescence rate allowing water to accumulate. Figure 12 shows the oil distribution in the vessel cross-section at two axial locations corresponding to the LT9 and LT10 level profilers.

Water Fraction

Figure 13 shows the water distribution in the mid-plane of the separator. The water phase gradually separates from the oil with the mixture viscosity and the Ishii-Zuber emulsion viscosity, while the Mills emulsion viscosity shows slow phase separation. Approaching the weir, the water fraction increases near the liquid level. Figure 14 shows the water distribution at the cross-section corresponding to the LT9 and LT10 profiler locations. Plotting the vertical water fraction distribution at the LT10 probe location in Figure 15 shows a distinct water-emulsion interface for each case. With the increased emulsion viscosity with the Mills relationship, a region of higher water fraction is established above the water interface. The water fraction is around 0.53 corresponding to the numerical limit on the relative viscosity of 20.

Relative Viscosity Distribution

Figure 16 shows the relative viscosity distribution in the

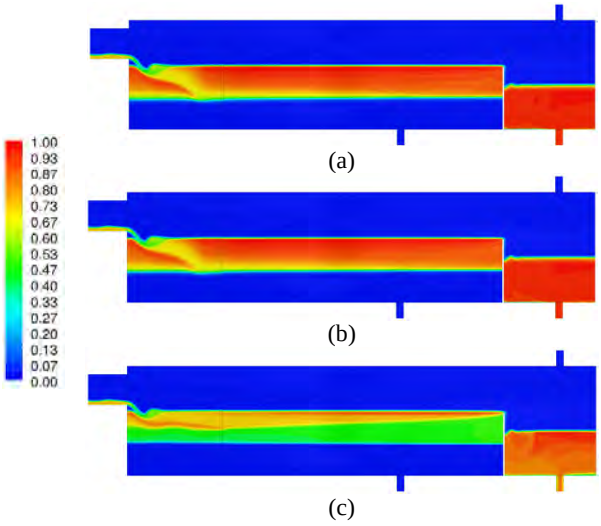

Figure 11. Time-averaged oil fraction distribution: (a) Mixture-averaged viscosity, (b) Ishii-Zuber viscosity, (c) Mills viscosity.

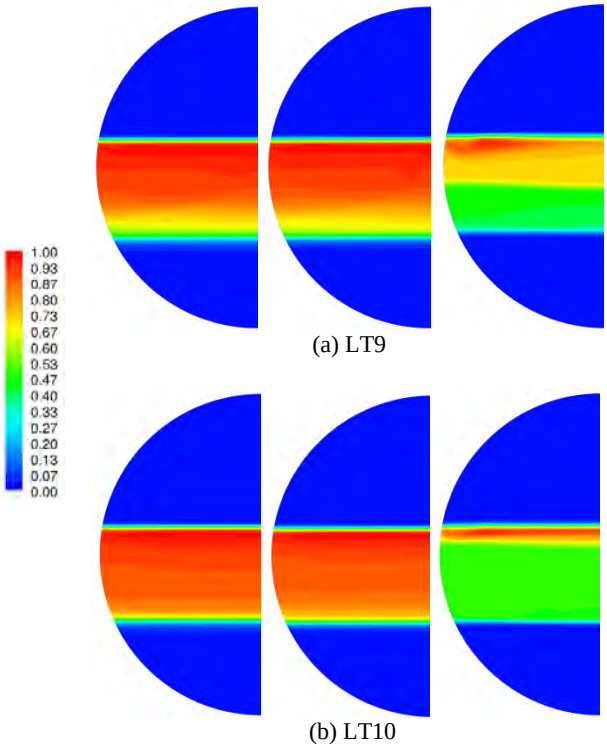

Figure 12. Time-averaged oil fraction distribution at cross-sections LT9 and LT10 (from left to right): Mixture-averaged viscosity, Ishii-Zuber viscosity, and Mills viscosity.

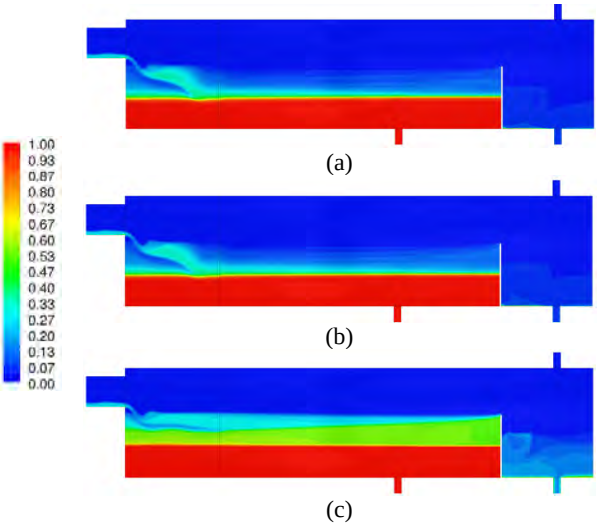

Figure 13. Time-averaged water fraction distribution: (a) Mixture-averaged viscosity, (b) Ishii-Zuber viscosity, (c) Mills viscosity.

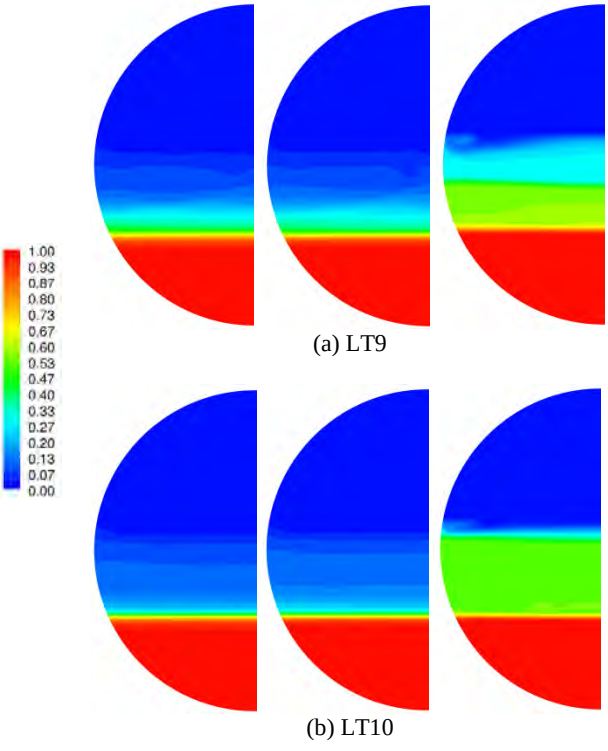

Figure 14. Time-averaged water fraction distribution at cross-sections LT9 and LT10 (from left to right): Mixture-averaged viscosity, Ishii-Zuber viscosity, and Mills viscosity.

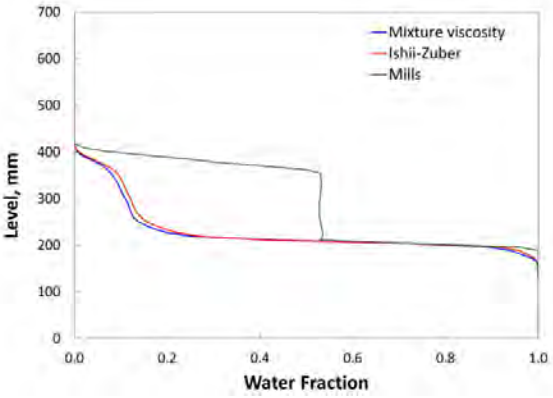

Figure 15. Time-averaged water fraction profiles at LT10 for different emulsion viscosity correlations.

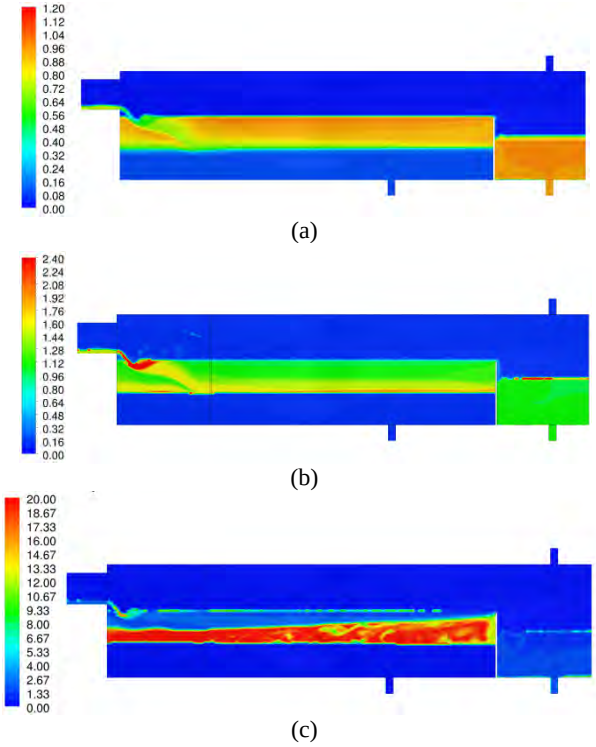

Figure 16. Time-averaged relative viscosity distribution: (a) Mixture-averaged viscosity, (b) Ishii-Zuber viscosity, (c) Mills viscosity.

separator mid-plane. There is an increase in the emulsion viscosity corresponding to the dense emulsion layer above the water interface when an emulsion viscosity relationship is used. The Ishii-Zuber emulsion viscosity is 1.5 times the oil viscosity at the inlet water fraction of 0.27. The Mills emulsion viscosity is 2.2 times at the same water fraction increasing rapidly with the water fraction approaching infinity at the close packing limit of 0.64. The emulsion viscosity relationships show the hindered settling behaviour of the destabilizing emulsion can be reproduced. For this case of an Arab Light crude emulsion with brine (50 g/L) at 45°C, the emulsion viscosity predicted by the Mills relationship is excessive. A rheological characterization is needed to determine the unique viscosity relationship for a specific oil-water emulsion.

Droplet Diameter Distribution

Figure 17 shows the average water droplet diameter of the three secondary water phases in the vessel cross-section at two axial locations corresponding to the LT9 and LT10 level profilers. As expected, the droplet diameter increases with retention time and water fraction. The larger droplets settle to the interface quickly resulting in a higher droplet diameter above the interface compared with the downstream LT10 location.

Emulsion Layer and Dense-Packed Zone

As the water droplets settle to the water interface in the settling zone, the droplets increase in diameter due to coalescence. The relative viscosity of the emulsion increases slowing separation as the droplets accumulate faster than they coalesce. The higher water concentration region above water interface is the dense packed zone or DPZ with a water fraction between the inlet emulsion and unity. Figure 18 compares the water, emulsion and oil layers at the LT9 capacitance profilers to the different CFD predictions with the different emulsion viscosity models. Figure 19 shows the water, emulsion, DPZ and oil layers at the LT10 profiler. While the comparison is qualitative based on how the interface boundaries are determined experimentally, the mixture and Ishii-Zuber reasonably reproduce the DPZ thickness while the Mills relationship significantly over-predicts the DPZ thickness. The emulsion layer thickness is significantly over-estimated by the three emulsion viscosity models suggesting that the water droplets are much larger either from higher coalescence rates or larger droplet sizes entering the separator. Larger droplets will increase the emulsion destabilization rates compared with the model predictions. The water fraction distribution in the separator is part of a more complete dataset required to validate the CFD predictions of droplet distribution and emulsion rheology.

Separation Efficiency

The efficiency of water separation from the oil is

$$Separation\ Efficiency, \% = \frac{Q_w|_{Inlet} - Q_w|_{Water\ Outlet}}{Q_w|_{Inlet}} \times 100\%$$

Figure 20 compares the experimentally determined separation efficiency to the different emulsion models. The separation efficiency decreased with the increase in emulsion viscosity showing that the DPZ retards emulsion destabilization. The mixture and Ishii-Zuber emulsion viscosity models under-

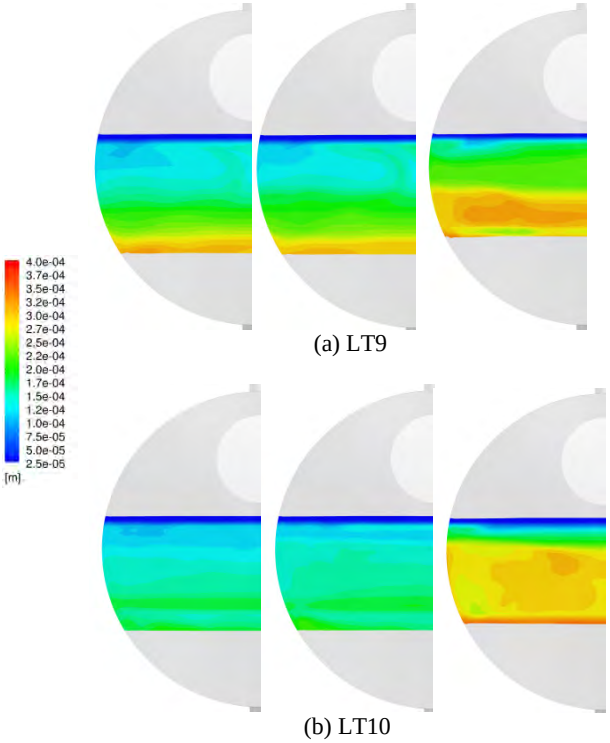

Figure 17. Time-averaged droplet diameter (in m) distribution at cross-sections LT9 and LT10 (from left to right): Mixture-averaged viscosity, Ishii-Zuber viscosity, and Mills viscosity.

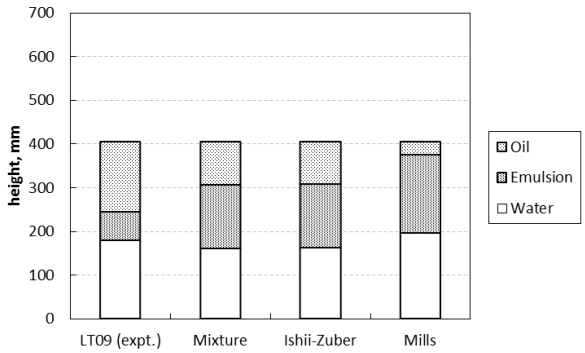

Figure 18. Oil, Emulsion and Water distribution at location LT9.

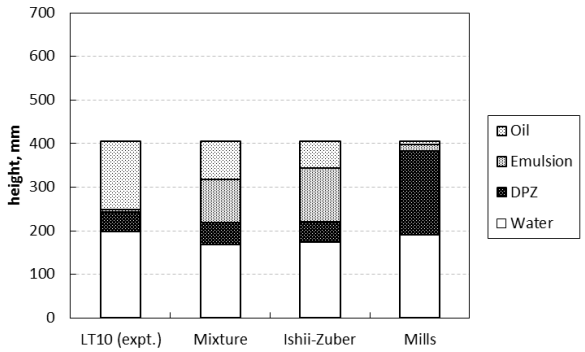

Figure 19. Oil, Emulsion, DPZ and Water distribution at location LT10.

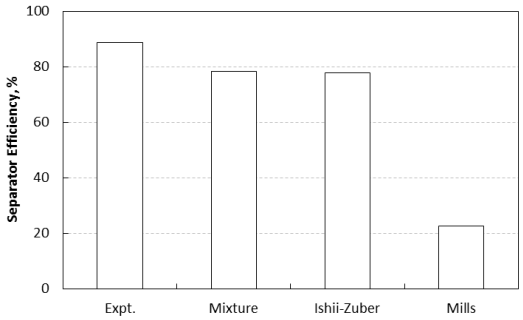

Figure 20. Comparison of experimental and predicted separation efficiency.

predict the separation efficiency. A number of model inputs including the inlet droplet size distribution, the emulsion viscosity relationship, the coalescence kernel parameters and others influence the predicted separation efficiency.

CONCLUSION

In this work, a detailed simulation of a pilot-scale high-pressure three-phase separator has been successfully carried out using the Eulerian multiphase model in ANSYS FLUENT to predict oil-water separation efficiency. The inhomogeneous population balance model was used to describe the evolving droplet size distribution in the polydisperse water phase. Simulations and experiments were performed within the domain of a separator vessel of diameter of 700 mm and length of 3000 mm. The treatment of the emulsion rheology was implemented through the inter-phase interaction terms between the oil phase and each of the secondary water phases. While there is uncertainty in the experimental water fraction, good agreement of the vertical distributions of the water phase is achieved at different locations in the separator. More detailed experimental data is required to validate the CFD models. The inlet multiphase flow must be adequately characterized for phase and size distribution. Droplet coalescence and breakage should be incorporated and be specifically defined for the horizontal multiphase separator configuration. The CFD methodology presented here is a step toward predicting the dense emulsion layer thickness above the water interface, the evolution of the droplets size distribution through the separator, and the oil-water separation efficiency. More study is needed to include a more accurate description of the emulsion rheology and the coalescence and breakage mechanisms, while taking in to consideration the complexity of crude oil inhomogeneity, pH, salinity, asphaltene content or impurities in the water, and the surface-active compounds added to the produced fluids.

ACKNOWLEDGEMENTS

The authors would like to acknowledge the Saudi Arabian Oil Company (Saudi Aramco) for supporting and granting permission to present and publish this article. The authors would also like to gratefully acknowledge IFPEN for conducting the experiments and to TOTAL for their role in coordinating the experimental test program. The authors would also like to acknowledge ANSYS for their support on the PID controller Scheme file and user-defined function.

REFERENCES

ANSYS Inc. *ANSYS FLUENT™ Theory Guide.* Canonsburg, PA: ANSYS Inc, 2012.

BRINKMAN, H.C. "The viscosity of concentrated suspensions and solutions." *J. Chem. Phys.* 20 (1952): 571.

FRANK, T., P.J. ZWART, J-M. SHI, E. KREPPER, D. LUCAS, and U. ROHDE. "Inhomogeneous MUSIG Model - a Population Balance Approach for Polydispersed Bubbly Flows." *International Conference on Nuclear Energy for New Europe, September 5-8.* Bled, Slovenia, 2005.

GARCIA, F., J.M. GARCIA, R. GARCIA, and D.D. JOSEPH. "Friction factor improved correlations for laminar and turbulent gas-liquid flow in horizontal pipelines." *International Journal of Multiphase Flow* 33 (2007): 1320-1336.

GRIMES, B.A. "Population Balance Model for Batch Gravity Separation of Crude Oil and Water Emulsions. Part I: Model Formulation." *Journal of Dispersion Science and Technology* 33 (2012): 578-590.

HALLANGER, A., F. SOENSTABOE, and T. KNUTSEN. "A Simulation Model for Three-Phase Gravity Separators (SPE 36644)." *SPE Annual Technical Conference and Exhibition, 6-9 October 1996.* Denver, Colorado, USA: Society of Petroleum Engineers, 1996. 695-706.

HANSEN, E.W.M., and G.J. RØRTVEIT. "Numerical Simulation of Fluid Mechanisms and Separation Behavior in Offshore Gravity Separators." Chap. 16 in *Emulsions and Emulsion Stability*, edited by J. Sjöblom, 593-605. CRC Press, 2005.

HANSEN, E.W.M., et al. "Fluid Flow Modeling of Gravity Separators." *5th International Conference on Multi-Phase Production.* Cannes, 1991.

HENSCKE, M., L.H. SCHLIEPER, and A. PFENNIG. "Determination of a Coalescence Parameter from batch-Settling Experiments." *Chemical Engineering Science* 85 (2002): 369-378.

HINZE, J.O. "Fundamentals of the hydrodynamic mechanism of splitting in dispersion processes." *AIChE J.* 1, no. 3 (1955): 289-295.

ISHII, M., and N. ZUBER. "Drag Coefficient and Relative Velocity in Bubbly, Droplet or Particulate Flows." *AIChE J.* 25 (1979): 843-855.

KESKIN, C., H.-Q. ZHANG, and C. SARICA. "Identification and Classification of New Three-Phase Gas/Oil/Water Flow Patterns." *SPE Annual Technical Conference and Exhibition, 11-14 November*. Anaheim, California, U.S.A.: Society of Petroleum Engineers, 2007.

KHAROUA, N., L. KHEZZAR, and H. SAADAWI. "Application of CFD to Debottleneck Production Separators in a Major Oil Field in the Middle East (SPE 158201)." *SPE Annual Technical Conference and Exhibition, 8-10 October*. San Antonio, Texas, USA: Society of Petroleum Engineers, 2012.

KOKAL, S. "Crude-Oil Emulsions: A State of the Art Review." *SPE Production & Facilities* (Society of Petroluem Engineers) 20, no. 1 (2005): 5-13.

KRIEGER, I.M., and I.M. DOUGHERTY. "A mechanism for non-Newtonian flow in suspensions of rigid spheres." *Trans. Soc. Rheol.* 3 (1959): 137.

LALEH, A.P., W.Y. SVRCEK, and W.D. MONNERY. "Design and CFD Studies of Multiphase Separators - A Review." *The Canadian Journal of Chemical Engineering* 90 (2012): 1547-1560.

LIAO, Y., and D. LUCAS. "A literature review on mechanisms and models for the coalescence process of fluid particles." *Chemical Engineering Science* 65 (2010): 2851-2864.

LUO, H., and H.F. SVENDSEN. "Theoretical Model for Drop and Bubble Breakage in Turbulent Dispersions." *AIChE J.* 42, no. 5 (1996): 1225-1233.

MARSDEN, S., and M. MAD. "Stability Of Concentrated Crude Oil-In-Water Emulsions As A Function Of Shear Rate, Temperature And Oil Concentration." *26th Annual Technical Meeting of the Petroleum Society of CIM, June 11-13*. Banff, Alberta, Canada: PETROLEUM SOCIETY OF CIM, 1975.

MILLS, P. "Non-Newtonian behaviour of flocculated suspensions." *J. Physique Lett.* 46 (1985): 301-309.

PAGNIER, P., C. NOIK, P. MAUREL, A. RICORDEAU, and J.-L. A. VOLLE. "Multiphase Loop Tests for Subsea Separation-Unit Development." *Paper SPE 115963 presented at SPE Annual Technical Conference and Exhibition.* Denver, Colorado, USA, 21-24 September: Society of Petroleum Engineers, 2008.

RAMKRISHNA, D. *Population Balances: theory and Applications to Particulate Systems in Engineering.* eBook: Academic Press, 2000.

SANFELD, A., and A. STEINCHEN. "Emulsion stability, from dilute to dense emulsions - Role of drops deformation." *Advances in Colloid and Interface Science* 140 (2008): 1-65.

SANYAL, J., S. OZARKAR, and F. LIU. "A Comprehensive CFD Strategy for the Simulation of Dense, Polydisperse Granular Flow in Fluidized Bed Reactors." *8th International Conference on Multiphase Flow (ICMF 2013), May 26 - 31*. Jeju, Korea, 2013.

SCHULLER, R.B., T. GUNDERSEN, M. HALLERAKER, and B. ENGEBRETSEN. "Measurement of water concentration in oil/water dispersions with a circular single-electrode capacitance probe." *Instrumentation and Measurement, IEEE Transactions* 53, no. 5 (2004): 1378-1383.

SIMONS, S., M.M.R. WILLIAMS, and J.S. CASSELL. "A kernel for combined Brownian and gravitational coagulation." *Journal of Aerosol Science* 17, no. 5 (1986): 789-793.

VIELMA, M., S. ATMACA, C. SARICA, and H. ZHANG. "Characterization of Oil/Water flows in horizontal pipes." *SPE Projects, Facilities & construction*, 2008: 1 - 21.

VILAGINES, R.D., and A.R. AKHRAS. "Three-phase Flows Simulation for Improving Design of Gravity Separation Vessels (134090)." *SPE Annual Technical Conference and Exhibition, 19-22 September 2010*. Florence, Italy: Society of Petroleum Engineers, 2010.

TOWARDS SIMULATING FLOTATION WITH OPENFOAM(R)

Gerhard HOLZINGER[1]*, **Gijsbert WIERINK**[1]†, **Stefan PIRKER**[1]‡

[1]JKU Department of Particulate Flow Modelling, 4040 Linz, AUSTRIA

* E-mail: gerhard.holzinger@jku.at
† E-mail: gijsbert.wierink@jku.at
‡ E-mail: stefan.pirker@jku.at

ABSTRACT

The process of flotation is widely used in many fields, e.g. mineral processing, or wastepaper deinking. The aim of this work is to implement a method for simulating the macroscopic flotation process within the CFD framework of OpenFOAM®while using established models known from literature.
A simple air-lift loop reactor is used as proof-of-concept simulation case. For validation, a cylindrical stirred tank is simulated. The stirred tank is equipped with a Rushton impeller due to the vast amount of available literature dealing with this set-up. The stirred tank simulation is validated against single-phase and two-phase results.
Including flotation modelling into a CFD code allows for studying the impact of the hydrodynamical processes inside a flotation apparatus on the flotation performance. This might provide a tool to improve the design of flotation machines.

Keywords: CFD, flotation, modelling, separation .

NOMENCLATURE

Dimensionless Groups

Bo	Bond number, [1].
Eo	Eotvos number, [1].
Fr	Froude number, [1].
Fl	Flow number, [1].
Re	Reynolds number, [1].
Po	Power number, [1].

Greek Symbols

α	Gas phase volume fraction, [1]
β	Bubble load factor, [1]
γ	Particle volume fraction, [1]
Γ	Diffusion constant, $[m^2/s]$.
δ	Bubble load factor, [1]
ε	Turbulent kineic energy dissipation, $[m^2/s^3]$
ϕ	Solids fraction, [1]
ρ	Mass density, $[kg/m^3]$
θ	Angle, $[rad]$
μ	Dynamic viscosity, $[kg/ms]$
ν	Kinematic viscosity, $[m^2/s]$
σ	Surface tension, $[N/m]$
ω	Angle, $[rad]$

Latin Symbols

d	Diameter, $[m]$.
D	Impeller Diameter, $[m]$.
E	Efficiency, [1].
f	Fractional number of particles, [1].
g	Gravity, $[m/s^2]$.
n	Number density, $[1/m^3]$.
N	Stirring speed, $[1/s]$.
p	Pressure, $[Pa]$.
P	Power, $[W]$.
S	Surface area ratio, [1].
T	Tank Diameter, $[m]$.
t	Time, $[s]$.
u	Velocity, $[m/s]$.
V	Volume, $[m^3]$.
Z	Bubble-particle collision frequency, $[m^3/s]$.
Z'	Bubble-particle detachment frequency, $[1/s]$.

Sub/superscripts

a	Attached.
eff	Effective.
f	Free.
i	Index i.
j	Index j.
max	Maximum.
A	Attachment.
B	Bubbles.
C	Collision.
G	Gas.
L	Liquid.
P	Particles.
S	Stability.

INTRODUCTION

Flotation is a process used to remove solid particles from a suspending liquid. The physical phenomenon utilized in flotation is a difference in hydrophobicity of the materials in use. In mineral flotation the target mineral is made hydrophobic whereas the gangue minerals are made less hydrophobic or even hydrophilic. If the valuable mineral is made hydrophilic and the gangue minerals are made hydrophobic the process is referred to as reverse flotation.
In a flotation apparatus the prepared slurry is aerated. Hydrophobic particles will attach themselves onto air bubbles once they are brought into contact. As particles of the more hydrophobic material have a higher probability to ascend with the bubbles to the surface, separation of materials based on their surface properties takes place.

Flotation is widely used in minerals processing to separate a valuable mineral of an ore from the gangue. This separation process is necessary to lower the costs or even to enable subsequent (extraction) processing steps. Another field of application of the flotation process is ink removal from recycled paper (deinking).

Batch flotation has been modelled as a kinetic process for decades (Sutherland, 1948). The flotation rate of the first order kinetic model is calculated using a number of detailed models for the relevant sub-processes of the flotation process. Bloom and Heindel (1997a,b) extended the kinetic model to include a forward and a reverse reaction (attachment and detachment). Such kinetic models describe the evolution of particle concentration within a flotation apparatus. Thus, the overall recovery of a flotation machine can be modelled over time. However, by using average flow properties the effects of local flow variations are neglected. Koh and Schwarz (2003) were the first to use CFD to study the flotation process in detail inside a flotation apparatus. This allows to look inside the flotation machine and take local flow properties into account.

The aim of this work is to implement flotation modelling within the framework of OpenFOAM®. This paper gives a brief overview of the model derivation and implementation. The model is applied to an air-lift reactor and a stirred tank. Furthermore, the flow within the stirred tank is validated with results from literature.

FLOTATION KINETICS

Flotation is widely modelled as a first order kinetic process. Eq. (1) shows the simplest possible model for flotation. This equation is expressed in the number density of the float-able particles n_P. In the case of a linear model it can also be expressed in absolute numbers or in concentrations.

$$\frac{\mathrm{d}n_P}{\mathrm{d}t} = -k n_B n_P \tag{1}$$

$$k = Z E_C E_A E_S \tag{2}$$

Bloom and Heindel (1997a,b, 2003) derived a kinetic model that considers particle-bubble attachment as well as detachment. Thus, the r.h.s. of Eq. (3) has two terms with different signs.

$$\frac{\mathrm{d}n_P}{\mathrm{d}t} = -k_1 n_B^f n_P + k_2 n_B^a \tag{3}$$

$$k_1 = Z E_C E_A E_S \tag{4}$$

$$k_2 = Z'(1 - E_S) \tag{5}$$

The rate constant of the kinetic model k respectively k_1 and k_2 subsume all the information provided by the various models for the sub-processes of flotation. The capturing of a particle by a bubble is represented by the superposition of bubble-particle collision, the formation of a three-phase bond and the stability of this bond.

Collision models

In this work the model of (Yoon and Luttrell, 1989) is used. This model is valid for intermediate flow conditions (Yoon and Luttrell, 1989; Miettinen *et al.*, 2010). This model calculates the probability E_C for a particle and a bubble to collide based on a potential stream function.

$$E_C = \left(1.5 + \frac{4}{15} Re_B^{0.72}\right) \left(\frac{d_P}{d_B}\right)^2 \tag{6}$$

Reviews on collision models can be found in (Miettinen *et al.*, 2010; Dai *et al.*, 2000).

Attachment models

The probability of attachment E_A depends on the time particles slide over the bubble's surface and the induction time. This is the time needed for the dis-joining liquid film to rupture. There is a specific collision angle – the attachment angle θ_A – at which the sliding time equals the induction time. All particles with a collision angle smaller than this attachment angle will attach to the bubble. The number of particles that have collided with the bubble can be related to the maximum collision angle θ_C.

The Dobby-Finch (Dobby and Finch, 1987) model is based on the ratio of the projected areas of the attachment angle and the maximum collision angle (Ralston *et al.*, 1999). The attachment angle θ_A is a function of the induction time t_{ind}, whereas the maximum collision angle θ_C is a function of only the bubble Reynolds number Re_B.

Eq. (8) shows the general form of the model for the induction time. Dai *et al.* (1999) reported that A is inversely to the particle diameter d_P and proposed $B = 0.6$. Koh and Schwarz (2006) proposed the following relation: $A = {}^{75}/_{\theta}$ with the contact angle θ.

$$E_A = \frac{\sin^2 \theta_A}{\sin^2 \theta_C} \tag{7}$$

$$t_{ind} = A\, d_P^B \tag{8}$$

A collection of attachment models can be found in (Miettinen *et al.*, 2010; Ralston *et al.*, 1999).

Stability models

The stability model proposed by Schulze is widely used in literature (Schulze, 1984; Miettinen *et al.*, 2010). This model balances the forces acting on a particle attached to a bubble. From a modified Bond number Bo', which is the ratio of detachment and attachment forces, the particle-bubble stability efficiency E_S is calculated.

$$E_S = 1 - \exp\left(A_S\left(1 - \frac{1}{Bo'}\right)\right) \tag{9}$$

$$Bo' = \frac{d_P^2(\Delta\rho g + \rho_P a_c) + 1.5 d_P f \sin^2(\omega)}{6\sigma \sin(\omega)\sin(\omega+\theta)} \tag{10}$$

$$\omega = \frac{\pi}{2} - \frac{\theta}{2} \tag{11}$$

$$f = \frac{4\sigma}{d_B} - d_B \rho_L g \tag{12}$$

$$a_c = 1.9 \varepsilon^{2/3} \left(\frac{d_B}{2} + \frac{d_P}{2}\right)^{-\frac{1}{3}} \tag{13}$$

The empirical constant A_S was introduced by (Bloom and Heindel, 2003) where a value of $A_S = 0.5$ was found. This empirical constant was used to fit the model to experimental results.

Collision frequency

The frequency at which particles collide with bubbles Z is computed with the model by (Schubert and Bischofberger, 1979). This model is derived for the case in which inertial effects have a strong influence (Schubert and Bischofberger, 1979; Koh and Schwarz, 2006; Schubert, 2008). The model of Schubert and Bischofberger computes the collision frequency from the root-mean-square value of the relative turbulent velocity fluctuations between the bubble or particle and the fluid (Schubert, 2008).

$$Z = 5\left(\frac{d_P + d_B}{2}\right)^2 \left(\overline{u_B'^2} + \overline{u_P'^2}\right)^{1/2} \tag{14}$$

$$\sqrt{\overline{u_i'^2}} = \frac{0.4\,\varepsilon^{4/9} d_i^{7/9}}{\nu_L^{1/3}} \left(\frac{\rho_i - \rho_L}{\rho_L}\right)^{2/3} \tag{15}$$

Detachment frequency

The bubble-particle detachment frequency Z' was derived in (Bloom and Heindel, 2002) from a model for floc disruption in turbulent flows. The value for the empirical constant $C_1 = 2$ was suggested by (Bloom and Heindel, 2003).

$$Z' = \frac{\sqrt{C_1}\varepsilon^{1/3}}{(d_B + d_P)^{2/3}} \tag{16}$$

Flotation model

In this work we derive a kinetic model for an arbitrary number of size classes of particles based on the model of Bloom and Heindel. First and foremost the underlying assumptions and limitations are listed.

The slurry is assumed to be Newtonian and the removal of ore particles does not change the properties of the slurry. In this work we consider mono-disperse gas bubbles. A potential non-sphericity of the bubbles is considered in the drag model of the two-phase flow equations. However, the models for the sub-processes in flotation all assume spherical bubbles.

Eq. (17) shows the kinetic equation for the i-th particle size class considering attachment and detachment. For attachment the number of free bubbles n_B is relevant. For detachment the number of bubble-particle aggregates with particles of the i-th size class $n^a_{B,i}$ is responsible.

$$\frac{\mathrm{d}n^f_{P,i}}{\mathrm{d}t} = -k_1 n^f_B n^f_{P,i} + k_2 n^a_{B,i} \tag{17}$$

Following (Koh and Schwarz, 2006), we introduce a bubble load factor β to express the number of free bubbles n^f_B and the number of bubble-particle aggregates n^a_B in terms of the total number of bubbles n_B. Furthermore, we need to introduce a fractional bubble load factor δ_i to determine the number of bubble-particle aggregates of the i-th size class $n^a_{B,i}$.

$$n^f_B = (1-\beta) n_B \tag{18}$$

$$n^a_{B,total} = \beta n_B \tag{19}$$

$$n^a_{B,i} = \delta_i n_B \tag{20}$$

$$\beta = \sum_i \delta_i \tag{21}$$

It is assumed that a bubble is fully loaded ($\beta = 1$) when half its surface is covered with particles. For mono-disperse particles this leads to Eq. (22). The maximum number a bubble can hold (S_{max}) is determined by half the ratio of bubble surface area and projected area of a single particle.

$$S_{max} = 2\left(\frac{d_B}{d_P}\right)^2 = \frac{n^a_P}{\beta n_B} \tag{22}$$

The calculation of S_{max} for poly-disperse particles follows the same idea. The ratio is computed with the bubble surface area and the weighted sum of projected areas. The number distribution f_i is used as weight factor.

$$S_{max} = 2\frac{d_B^2}{\sum_i f_i {d_{P,i}}^2} \tag{23}$$

$$\sum_i f_i = 1 \tag{24}$$

This model reflects the fact that – as various size classes float differently well – the particle size distribution change over time. In Eq. (23) the particle size distribution is considered in the model.

The flotation model computes the evolution of the free as well as the attached particles inside a flotation apparatus. Thus, the population balance equation needs to be solved for both particle families. Equations (25) and (26) show the population balance equations for the i-th size class. Both equations share the same r.h.s. with different signs. When particles are captured by a bubble, the particles change over from the population of free particles to the population of attached particles.

The attached particles travel with the air bubbles to the liquid surface at the top. Convection of attached particle over the top boundary is the way for particles to be removed from the simulation domain. The r.h.s. for the rate of change for the total number of particles – the sum of free and attached particles – vanishes.

$$\frac{\mathrm{d}n^f_{P,i}}{\mathrm{d}t} = -k_1(1-\beta) n_B n^f_{P,i} + k_2 \delta_i n_B \tag{25}$$

$$\frac{\mathrm{d}n^a_{P,i}}{\mathrm{d}t} = k_1(1-\beta) n_B n^f_{P,i} - k_2 \delta_i n_B \tag{26}$$

MODEL DESCRIPTION

Slurry properties

The flow within the flotation apparatus is considered a two-phase flow. Air bubbles are suspended in the liquid phase (slurry) which is a mixture of water and suspended solid particles. As the slurry contains a considerable amount of solids, up to 50 wt% (Bakker *et al.*, 2009), the effect of the solids on the slurry properties need to be taken into account. Depending on the nature of the suspended material and the involved flotation agents the slurry may even exhibit non-Newtonian behaviour (Bakker *et al.*, 2009).

In this work, the slurry is considered a Newtonian fluid for simplicity. However, density and viscosity are chosen according the volume fraction of the suspended solids using relations from literature.

The slurry density is calculated from the solids fraction ϕ and the densities of the constituents (water and solids).

$$\rho_{sus} = (1-\phi)\rho_{water} + \phi\rho_{solids} \tag{27}$$

Einstein (1905, 1911) was the first to derive a relation for the suspension viscosity (Eq. (28)) with respect to the fraction of suspended solids ϕ. Einstein's relation is, however, only valid for dilute suspensions ($\phi < 0.02$). For denser suspensions models of higher order exist. An example of the great number available models is the relation of Batchelor (Eq. (29)). A list of viscosity models for suspensions can be found in (Horri *et al.*, 2011)

$$\mu_{sus} = (1+2.5\phi)\mu_L \tag{28}$$

$$\mu_{sus} = (1+2.5\phi+6.2\phi^2)\mu_L \tag{29}$$

$$\mu_{sus} = \rho_{sus}\nu_{sus} \tag{30}$$

For the simulation of the flow two-phase Eulerian equations are solved as both phases are treated as interpenetrating continua. The two-phase fluid flow is described with a velocity field for each phase ($\mathbf{u}_G$ and $\mathbf{u}_L$), the gas phase volume fraction α and the pressure p common to both phases (Rusche, 2002). The effective viscosity of the liquid phase $\nu_{eff,L}$ is computed from the suspension viscosity ν_{sus} and the turbulent viscosity ν_t provided by the turbulence model. The gas phase is considered laminar ($\nu_{eff,G} = \nu_G$).

$$\frac{\partial \alpha_i}{\partial t} + \nabla\cdot(\alpha_i\mathbf{u}_i) = 0 \tag{31}$$

$$\frac{\partial \alpha_i\mathbf{u}_i}{\partial t} + \nabla\cdot(\alpha_i\mathbf{u}_i\mathbf{u}_i) - \nabla\cdot(\nu_{eff,i}\nabla\mathbf{u}_i) = -\alpha_i\frac{\nabla p}{\rho_i} + \alpha_i\mathbf{g} + \frac{\mathbf{M}_i}{\rho_i} \tag{32}$$

$$i \in \{G, L\}$$

Inter-facial momentum exchange is accounted for due to drag, lift and virtual mass.
Turbulence is considered by applying the $k-\varepsilon$ model to the liquid phase. This approach is known as dispersed turbulence modelling (ANSYS, Inc., 2011).

Derivation of governing equations

In order to include the flotation model into the CFD model two sets of scalar transport equations are solved. Eq. (33) shows the general form of a species transport equation in multiphase flows. The free particles, that are suspended in the liquid phase, and the attached particles, that are attached to air bubbles, are the two species under consideration.

$$\frac{\partial \alpha_j\gamma_i}{\partial t} + \nabla\cdot(\alpha_j\mathbf{u}_j\gamma_i) - \nabla\cdot(\alpha_j\Gamma_j\nabla\gamma_i) = \alpha_j S_i \tag{33}$$

When considering an arbitrary number of size classes, we need to solve two sets of transport equations in terms of particle volume fraction. One set of equations will be formulated for the free particles – one transport equation for each size class – and the other set is for the attached particles. The relation between number density and volume fraction is as follows:

$$\gamma_P = n_P V_P \tag{34}$$

Equations (35) to (39) repeat the governing equations of the flotation model.

$$\frac{\partial \alpha_L\gamma_i^f}{\partial t} + \nabla\cdot(\alpha_L\mathbf{u}_L\gamma_i^f) - \nabla\cdot(\alpha_L\Gamma_L\nabla\gamma_i^f) = \alpha_L S_i \tag{35}$$

$$\frac{\partial \alpha_G\gamma_i^a}{\partial t} + \nabla\cdot(\alpha_G\mathbf{u}_G\gamma_i^a) - \nabla\cdot(\alpha_G\Gamma_G\nabla\gamma_i^a) = -\alpha_G S_i \tag{36}$$

$$\alpha_G = \alpha \tag{37}$$

$$\alpha_L = 1-\alpha \tag{38}$$

$$S_i = -k_{1,i}(1-\beta)\frac{\alpha}{V_B}\gamma_i^f + k_{2,i}\frac{\gamma_i^a}{S_{max}} \tag{39}$$

NUMERICAL MODEL

For the numerical simulations the CFD framework OpenFOAM® has been used. OpenFOAM® is open source, i.e. the code is open for study and modification at any level. The standard two-phase Eulerian solver of OpenFOAM-2.2 has been extended with some models that are specifically designed for liquid-gas systems. OpenFOAM® is based on (Weller *et al.*, 1998) and the basics of the Eulerian two-phase solver are described in (Weller, 2005; Rusche, 2002; OpenFOAM Foundation, 2013).

Solver development

The flotation model is included into two solvers. The first solver solves only the scalar transport equations Equations (35) to (36). The flow properties in this case are held constant over time. This approach is valid for steady state flows and is sometimes referred to as *frozen flow* approach.
The second solver is the transient two-phase Eulerian solver with the extension of the flotation model. In every time step the flotation quantities are computed after the flow properties have been solved for.
In both cases the flotation solver used the same flotation model. The modular design of OpenFOAM® allows for an easy extension of a solver's capabilities (Weller *et al.*, 1998).

SIMULATION RESULTS

The flotation simulations are performed on an already established two-phase flow within the respective simulation domain. This reflects a somewhat unrealistic situation in which the flotation process kicks in at $t = 0\,\mathrm{s}$. However, this approach decouples the result of the flotation simulation from transient effects of the flow build-up. This approach seems justified for a continuous process in a flotation column or a batch process with a negligible time needed to establish the flow.

Air-lift reactor

The first test-case of the flotation solver is a simple air-lift loop reactor. This reactor has a very simple geometry. The cylindrical domain is divided by the draft tube into the central riser and the downcomer. At the bottom air is injected. The bubbles rise within the riser and entrain liquid as they ascend. As the air-lift reactor is merely a showcase to demonstrate the behaviour of the flotation model in a computationally cheap manner, the flow within the reactor is not validated.
For certain operational parameters the flow within the air-lift reactor reaches a steady state. This flow regime allows for the application of the frozen-flow approach as the flow properties do not change over time at a certain location. This provides a test case in which the flow equations do not need to be solved.
The simulation results of the steady state simulation as shown in Figs. 2a and 2b look very promising. The various size

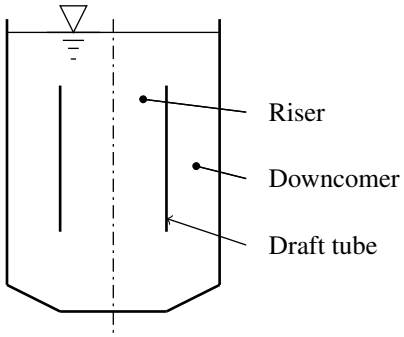

Figure 1: Schematic representation of the air lift reactor.

classes float differently well, this behaviour is widely known and was expected.

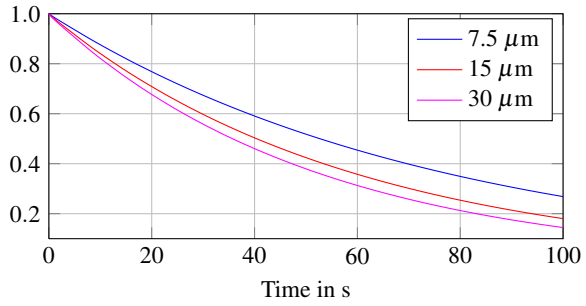

(a) Free particles, $\gamma_i^f / \gamma_{i,0}$

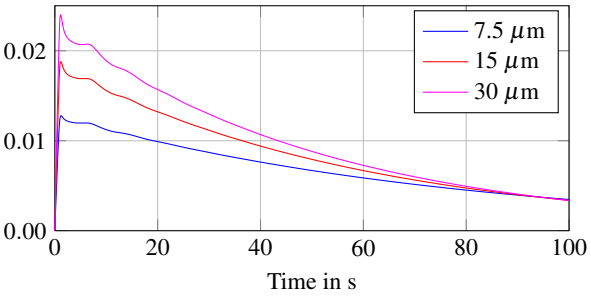

(b) Attached particles, $\gamma_i^a / \gamma_{i,0}$

Figure 2: Global volume fraction of particles of three different size classes within the air-lift loop reactor normalized with the initial volume fraction.

Stirred tank reactor

The second test case for the flotation model is a stirred tank. As stirred tanks are widely used in chemical engineering there exists a vast amount of literature with measurements and simulations. In contrast to the air-lift reactor – which is more of a show case – the stirred tank simulations are validated to some extent.

Geometry

For this simulations a cylindrical stirred tank with 4 baffles and a 6-bladed Rushton impeller was modelled. The numerical model made use of the MRF (multiple reference frames) approach.
The simulation domain is divided into two zones. The flow equations in the zone are solved in a rotating frame of reference. The velocity boundary condition on the rotor is corrected accordingly (ANSYS, Inc., 2011; Nilsson, 2013). This method has the advantage that it operates without any actual mesh motion. This saves computation cost compared to simulations with actual mesh motion (sliding mesh technique). The utilisation of the MRF approach is justified by the large clearance between rotor blades and baffles.
Figure 3 shows a schematic drawing of the stirred tank's geometry. It is common to relate all dimensions to the tank diameter T. Thus, for the description of a stirred tank only one dimension has to be stated in conjunction to several dimensionless ratios. Table 1 lists the parameters of the investigated stirred tank.

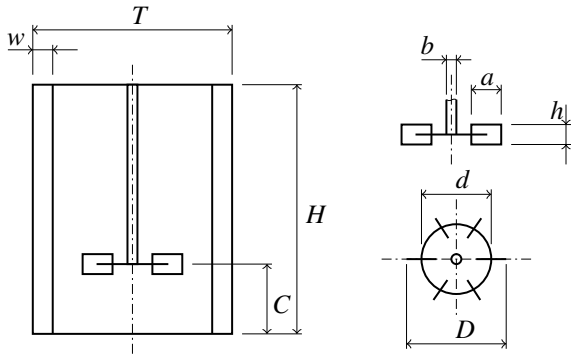

Figure 3: A schematic representation of the stirred tank's geometry with the relevant geometric parameters.

Table 1: The configuration of the stirred tank

T	H/T	C/T	w/T	D/T	d/D	a/D	h/D	b/D
0.195 m	1	1/3	1/10	1/3	3/4	1/3	1/5	3/20

Single phase simulations

At first the stirred tank was simulated with a standard single-phase solver of OpenFOAM®. This simulations provided normalized velocity profiles as well as the power number which were compared to measured data from (Rushton *et al.*, 1950; Wu and Patterson, 1989).

$$Po = \frac{P}{\rho N^3 D^5} \tag{40}$$

$$Re = \frac{ND^2}{\nu} \tag{41}$$

Figure 4 shows the power number Po over the impeller Reynolds number Re. The simulation results are compared to measurements from (Rushton *et al.*, 1950). The power number of the simulations obeys the asymptotes for the laminar and turbulent regime (Deglon and Meyer, 2006).
The normalized velocity profiles were also validated with LDA measurement data from (Wu and Patterson, 1989), see Figure 5. The velocity profiles were taken in a plane 45° from the baffles and normalised with the rotor tip velocity.
The validation of the single-phase simulations shows that the MRF approach provides a means of simulation with reasonable accuracy. This method is computationally cheaper than the sliding mesh approach as there is no actual mesh motion (Lane *et al.*, 2005).

Two-phase simulations

For the two-phase simulations, a ring-shaped aeration device is included into the domain below the impeller. The top sur-

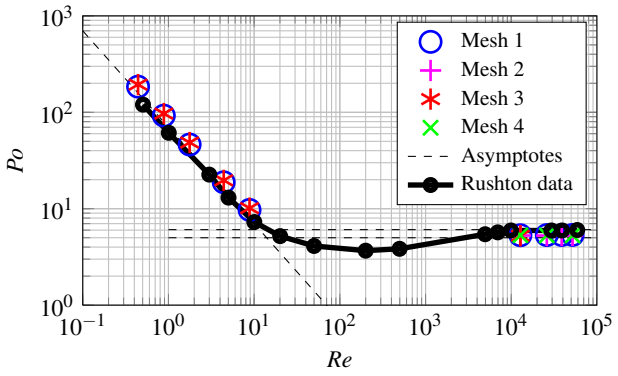

Figure 4: Power number for four meshes from 126k to 1.89M cells compared to measured data of (Rushton *et al.*, 1950).

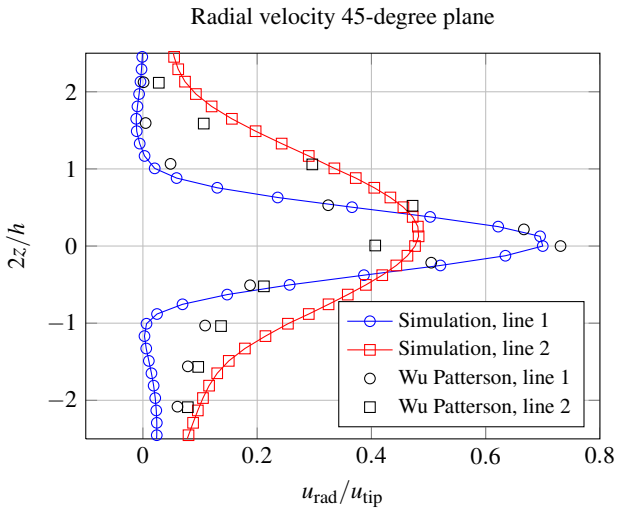

Figure 5: Normalized velocity profiles at $r/T = 0.185$ and $r/T = 0.285$ in the turbulent flow regime at $Re = 25983$. The vertical axis shows the vertical coordinate counted from the impeller disc and scaled with half the impeller blade height $h/2$.

face of the aerator is used as gas inlet. The two-phase simulation of the stirred tank has been set up according to parameters taken from (Koh and Schwarz, 2006).

The flow regime within an aerated stirred tank depends on gas flow rate as well as on stirring speed.

The flow in an aerated stirred tank can be characterized with two dimensionless numbers. The Froude number Fr as the ratio of the impeller driven acceleration and gravity and the aeration or flow number Fl as the ratio of gas flow rate and impeller driven flow rate.

$$Fr = \frac{N^2 D}{g} \tag{42}$$

$$Fl = \frac{Q_g}{N D^3} \tag{43}$$

Figure 6 shows the three main flow regimes and Figure 7 shows the characteristics (Eqs. (44) and (45)) for the flow regimes.

Transition from flooding to loading

$$Fl_F = 30\, Fr\, (T/D)^{-3.5} \tag{44}$$

Transition from loading to recirculating

$$Fl_L = 13\, Fr^2\, (T/D)^5 \tag{45}$$

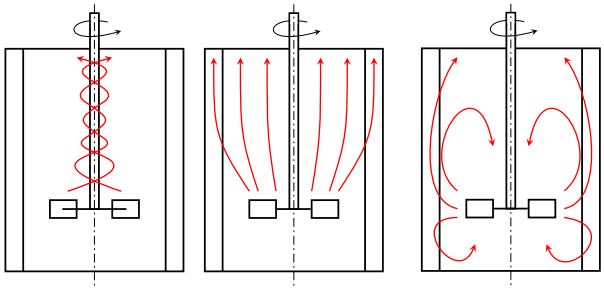

Figure 6: The three main flow regimes in an aerated stirred tank. Reproduced after (Mueller and Dudukovic, 2010). The red arrows schematically mark the trajectories of the air bubbles.

Figures 9 and 8 show simulations in the three main regimes. In Figure 7 the regime is predicted based on the operational parameters of these simulations. The flow regime of the CFD two-phase simulations corresponds well with the prediction for the flow regime based on the dimensionless numbers Fr and Fl.

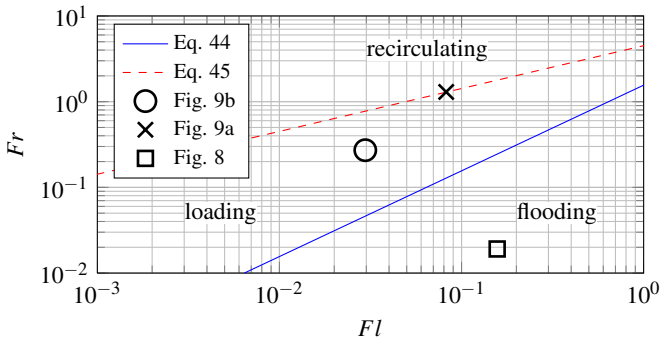

Figure 7: Regime map for a fully baffled aerated stirred tank. Transition limits according to Eqs. (44) and (45) and prediction for the conducted simulation, see Figs. 6, 9 and 8.

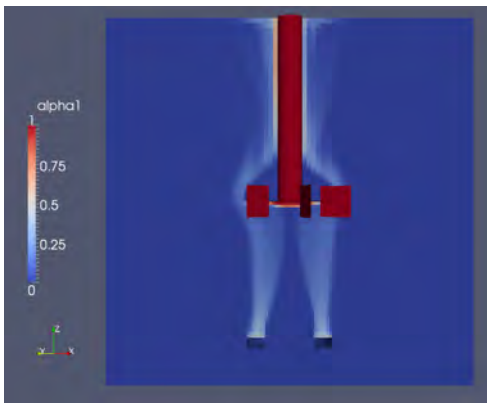

Figure 8: Aerated stirred tank with operating parameters in the flooding regime. Gas phase volume fraction: Field values in the 45° plane between stator baffles.

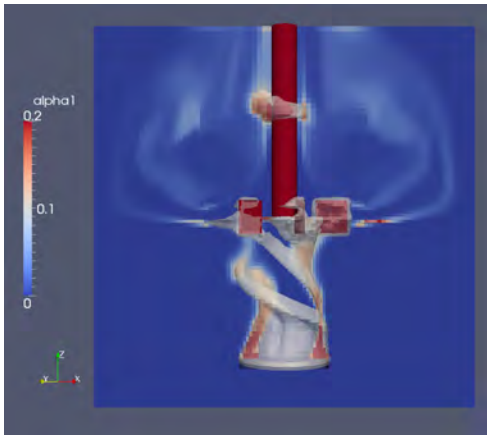

(a) Loading regime

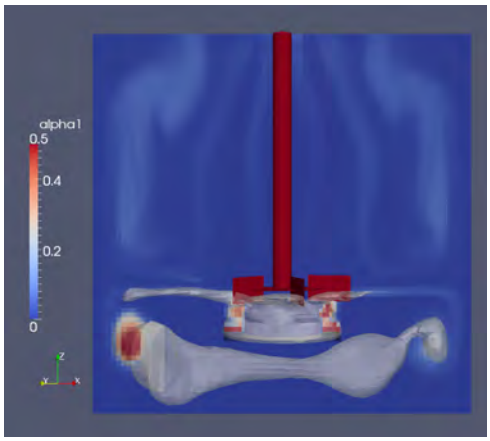

(b) Recirculating regime

Figure 9: Gas phase volume fraction: Field values in the 45° plane between stator baffles and iso-volume $\alpha < 0.1$ (grey shaded volume).

The simulations for the regime prediction has been conducted using two different geometries. The flotation simulations were conducted using the geometry shown in Figure 9b.
The flow within the investigated flotation cell lies in the fully recirculating regime, i.e. gas bubbles carried by the liquid flow throughout the whole domain. Gas bubbles accumulate in the centers of the two main vortex-structures within the tank.

Flotation simulations

The flotation simulation was set up based on (Koh and Schwarz, 2006). Geometric and fluid parameters are chosen accordingly. Koh and Schwarz (2006) simulated a flotation cell equipped with a Rushton impeller. Although, their paper presents the flotation behaviour of different size classes it is not clear whether the flotation of different size classes was simulated simultaneously or sequentially.
Figure 10 shows the volume fraction of the attached particles of the size class $d_P = 10\,\mu$m. The attached particles accumulate in the upper part of the stirred tank where the circulation pattern of the liquid flow causes air bubbles to accumulate, see Figure 9b.
Figures 11a and 11b show the time evolution of the average volume fraction of free and attached particles. The different size classes show a different flotation behaviour. The curves in Figure 11 are normalized with the initial volume fraction of their respective size class $\gamma_{i,0}$.

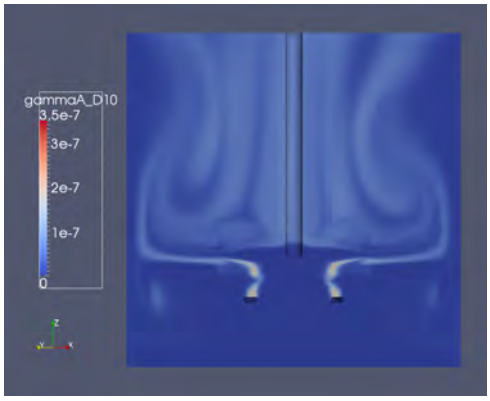

Figure 10: Particle volume fraction of attached particles with $d_P = 10\,\mu$m at $t = 2$ s.

Figure 11c shows the time evolution of the average volume fraction of all particles (free and attached). The decrease sets in after a certain time span. This is the time for the first captured particles to reach the top surface and leave the domain. Comparing Figures 11a and 11c illustrates that the total number of particles decreases slower than the number of free particles. Only attached particles that reach the liquid surface can be considered as recovered. Bubbles loaded with particles that recirculate within the flotation apparatus lower the number of free particles but do not contribute to recovery.

CONCLUSION

CFD modelling of the flotation process within the framework of an Eulerian two-phase simulation has been implemented in OpenFOAM®. The flotation model was demonstrated on two prominent test cases.
While a solver for steady state flow situations was used to demonstrate the model on an air-loop reactor, a transient solver was used to simulate flotation within a stirred tank. The set up of the latter case is resembling a mechanical flotation cell.
The model works numerically stable and produces reasonable and promising results. The flotation of different particle size classes was simulated simultaneously and those size classes strongly differed in recovery. The results show that the recovery of the smallest size fraction ($d_P = 10\,\mu$m) is significantly lower than the largest fraction ($d_P = 50\,\mu$m).
Further work is planned to validate the flotation model against experimental data of flotation experiments published in literature.

REFERENCES

ANSYS, Inc. (2011). *ANSYS FLUENT Theory Guide*, 14th ed.

BAKKER, C.W., MEYER, C.J. and DEGLON, D.A. (2009). "Numerical modelling of non-Newtonian slurry in a mechanical flotation cell". *Minerals Engineering*, **22**, 944–950.

BLOOM, F. and HEINDEL, T.J. (1997a). "Mathematical modelling of the flotation deinking process". *Mathl. Comput. Modelling*, **25**, 13–58.

BLOOM, F. and HEINDEL, T.J. (1997b). "A theoretical model of flotation deinking efficiency". *Journal of Colloid and Interface Science*, **190**, 182–197.

BLOOM, F. and HEINDEL, T.J. (2002). "On the structure of collision and detachment frequencies in flotation models". *Chemical Engineering Science*, **57**, 2467–2473.

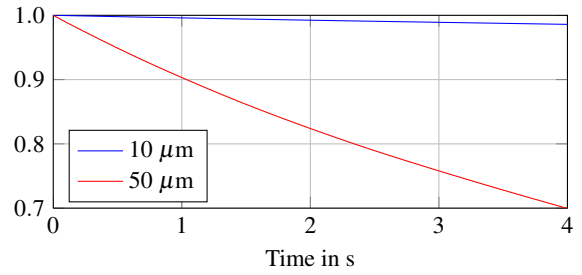

(a) Free particles, $\gamma_i^f/\gamma_{i,0}$

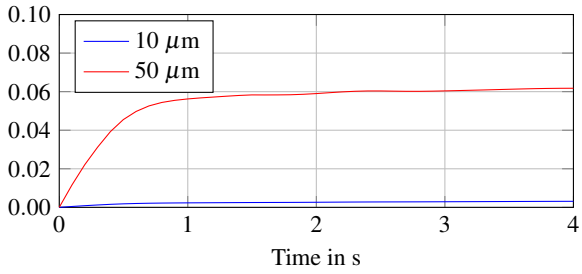

(b) Attached particles, $\gamma_i^a/\gamma_{i,0}$

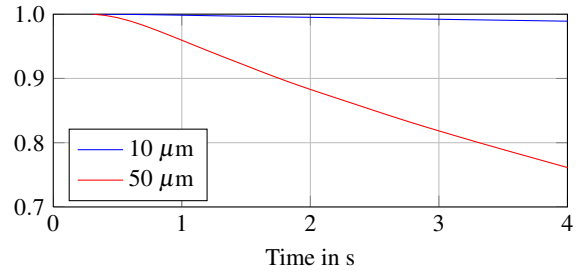

(c) Total particles, $(\gamma_i^f+\gamma_i^a)/\gamma_{i,0}$

Figure 11: Global volume fraction of particles of two different size classes within the stirred tank flotation cell normalized with the initial volume fraction.

BLOOM, F. and HEINDEL, T.J. (2003). "Modeling flotation separation in a semi-batch process". *Chemical Engineering Science*, **58**, 353–365.

DAI, Z., FORNASIERO, D. and RALSTON, J. (1999). "Particle-bubble attachment in mineral flotation". *Journal of Colloid and Interface Science*, **217**, 70–76.

DAI, Z., FORNASIERO, D. and RALSTON, J. (2000). "Particle-bubble collision models - a review". *Advances in Colloid and Interface Science*, **85**, 231–256.

DEGLON, D.A. and MEYER, C.J. (2006). "Cfd modelling of stirred tanks: numerical considerations". *Minerals Engineering*, **19**, 1059–1068.

DOBBY, G.S. and FINCH, J.A. (1987). "Particle size dependence in flotation derived from a fundamental model of the capture process". *Int. J. Mineral Processing*, **21**, 241–260.

EINSTEIN, A. (1911). "Berichtigung zu meiner arbeit: "eine neue bestimmung der moleküldimensionen"". *Annalen der Pysik*, **34**, 591–592.

EINSTEIN, A. (1905). *Eine neue Bestimmung der Moleküldimensionen*. Ph.D. thesis, Universität Zürich.

HORRI, B.A., RANGANATHAN, P., SELOMULYA, C. and WANG, H. (2011). "A new empirical viscosity model for ceramic suspensions". *Chemical Engineering Science*, **66**, 2798–2806.

KOH, P. and SCHWARZ, M. (2003). "Cfd modelling of bubble-particle collision rates and efficiencies in a flotation cell". *Minerals Engineering*, **16**, 1055–1059.

KOH, P. and SCHWARZ, M. (2006). "Cfd modelling of bubble-particle attachments in flotation cells". *Minerals Engineering*, **19**, 619–626.

LANE, G.L., SCHWARZ, M.P. and EVANS, G.M. (2005). "Numerical modelling of gas-liquid flow in stirred tanks". *Chemical Engineering Science*, **60**, 2203–2214.

MIETTINEN, T., RALSTON, J. and FORNASIERO, D. (2010). "The limits of fine particle flotation". *Minerals Engineering*, **23**, 420–437.

MUELLER, S.G. and DUDUKOVIC, M.P. (2010). "Gas holdup in gas-liquid stirred tanks". *Ind. Eng. Chem. Res.*, **49**, 10744–10750.

NILSSON, H. (2013). "Turbomachinery training at ofw8". Tech. rep., Chalmers University of Technology, Gothenburg, Sweden.

OpenFOAM Foundation (2013). *OpenFOAM - User Guide*, 2nd ed.

RALSTON, J., FORNASIERO, D. and HAYES, R. (1999). "Bubble-particle attachment and detachment in flotation". *Int. J. Mineral Processing*, **56**, 133–164.

RUSCHE, H. (2002). *Computational Fluid Dynamics of dispersed two-phase flows at high phase fractions*. Ph.D. thesis, Imperial College of Science, Technology & Medicine.

RUSHTON, J.H., COSTICH, E.W. and EVERETT, H.J. (1950). "Power characteristics of mixing impellers - Part II". *Chemical Engineering Progress*, **46**, 467–476.

SCHUBERT, H. (2008). "On the optimization of hydrodynamics in fine particle flotation". *Minerals Engineering*, **21**, 930–936.

SCHUBERT, H. and BISCHOFBERGER, C. (1979). "On the optimization of hydrodynamics in flotation processes". *Proceedings of the 13th International Mineral Processing Congress*, vol. 2, 1261–1285.

SCHULZE, H.J. (1984). *Physico-chemical Elementary Processes in Flotation: An Analysis from the Point of View of Colloid Science Including Process Engineering Considerations*. Elsevier, Amsterdam, New York.

SUTHERLAND, K.L. (1948). "Physical chemistry of flotation xi. kinetics of the flotation process". *Journal of Physical and Colloid Chemistry*, **52**, 394–425.

WELLER, H.G. (2005). "Derivation, modelling and solution of the conditionally averaged two-phase flow equations". Tech. rep., OpenCFD.

WELLER, H.G., TABOR, G., JASAK, H. and FUREBY, C. (1998). "A tensorial approach to computational continuum mechanics using object-oriented techniques". *Computers in Physics*, **12**, 620–631.

WU, H. and PATTERSON, G.K. (1989). "Laser-doppler measurements of turbulent-flow parameters in a stirred mixer". *Chemical Engineering Science*, **44**, 2207–2211.

YOON, R.H. and LUTTRELL, G.H. (1989). "The effect of bubble size on fine particle flotation". *Mineral Processing and Extractive Metallurgy Review*, **5**, 101–122.

LAGRANGIAN AND EULERIAN SIMULATIONS OF INCLUSION BEHAVIOUR IN LIQUID METAL PROCESSING

Jean-Pierre BELLOT[1], Vincent DESCOTES[1 2], Alain JARDY[1]

[1] Institut Jean Lamour, UMR 7198, CNRS ('LabEx DAMAS'), Université de Lorraine, 54011Nancy, France.

[2] Aperam Alloys Imphy, Centre de Recherche P. Chevenard, BP1, 58160 Imphy,France.

* E-mail: jean-pierre.bellot@univ-lorraine.fr

ABSTRACT

The control of metal cleanliness has always been an issue of great concern for the metallurgists since the inclusions directly influence the mechanical properties of the alloys. In most of the metallurgical routes a refining treatment of the molten alloy has been introduced in particular with the aim of improving the metal cleanliness, which means a better control of the particle amount (or the occurrence ratio for very rare exogenous inclusions), the particle size and morphology and finally their composition.

Three examples of numerical modelling of particle behaviour (transportation and growth in the metallic bath) achieved at Institut Jean Lamour are discussed. They illustrate the application of the Lagrangian technique (for isolated exogenous inclusion in titanium bath) and the Eulerian technique without or with aggregation process; applied to the precipitation and growth of inclusions at the solidification front of a Maraging steel, and to endogenous inclusions in molten steel bath of a gas-stirred ladle, respectively. The numerical techniques (modelling, equations and solving methods) are presented in the paper and useful references are reported. Examples of results of inclusion histories illustrate the possibility for effectively controlling inclusion number (or occurrence) and size.

Keywords: Metal Refining, Process Metallurgy, Lagrangian methods, Population balance methods.

NOMENCLATURE

Greek Symbols

ρ_i Density of solute i, [kg/m^3].
φ Mass flux density, [kg/m^2.s].
η Kolmogorov scale, [m].
ω Mass content, [-].

Latin Symbols

C_D Drag coefficient, [-].
d Diameter, [m].
D Diffusion coefficient, [m^2/s].
g_s Solid fraction, [-].
G Growing rate, [m/s].
H Collisional term in the PBE, [#/m^6.s].
k Mass transfer coefficient, [m/s].
M Number of classes, [-].
n Number density of inclusions, [#/m^6].
r Internal coordinate, [m].
t Time, [s].
$\mathbf{u}$ Velocity, [m/s].
x Space coordinate, [m].

Sub/superscripts

f Fluid.
p Particle.
i Class index.

INTRODUCTION

Since the beginning of the XXIst century the metal cleanliness is a new challenge for the metallurgists for two main reasons: on the one hand, the reduction of the weight of high performance materials together with the improvement of mechanical properties requires an improvement of the metal cleanliness. On the other hand, the increase of the recycling of used metal reinforces the role of molten metal refining.

But *exogenous* and *endogenous inclusions* must be distinguished as a function of industrial applications and metallic alloys. Otherwise the strong difference of occurrence and behaviour between these two categories of inclusions leads to two different methodologies of numerical modelling.

The *exogenous inclusions* have a very low occurrence and mainly concern reactive or refractory metals such as Ti, Zr, Nb… For economical and safety reasons a particular attention is paid on the elimination of this type of isolated inclusion which can grow or decrease in size by mass transfer with the liquid phase. Because the inclusions can then be considered as isolated particles, a Lagrangian approach for solving the fundamental dynamic equation emerged as an attractive alternative for tracking turbulent trajectories of inertial inclusions. As an illustration, the simulation of the behaviour of exogenous inclusions known as hard-alpha particles in titanium bath is presented.

The *endogenous inclusions* precipitate and grow in the liquid phase or during solidification with kinetics dependent on the supersaturation of the bath. The number density of this endogenous population reaches high values (up to 10^{12} #/m^3 for conventional steels) although the volume fraction remains lower than a few tens of ppm. The number of collisions occurring among the particles may have a predominant effect on the population distribution. Fig. 1 shows that the turbulent collision frequency increases with the square root of the stirring power, so that the treatment time applied in metallurgical reactors (several minutes) is large enough to encourage the aggregation process for inclusion phase concentration larger than 10 ppm.

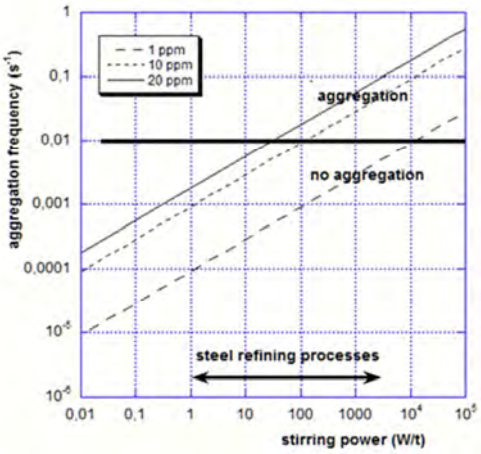

Figure 1: Frequency of the aggregation process as a function of the stirring power and the volume fraction of the inclusion phase.

The inclusion size distribution n(r,x,t) is the solution of the continuous population balance equations (PBE) where H is the collisional term modelled through the use of aggregation kernel (for weak inertia particles such as Saffman and Turner, 1956; for high inertia particles such as Abrahamson, 1975).

$$\frac{\partial n}{\partial t}+\frac{\partial nG}{\partial r}+\frac{\partial nu_p}{\partial x}=H \qquad (1)$$

The PBE is usually locally solved in the liquid bath assuming that the particles are transported by the mean liquid flow (u_p=u_f).

When aggregation can be neglected according to the Figure 1, the Eq. 1 without the right-hand side is more easily solved using Eulerian methods such as the finite volume method. An example is given with the precipitation and growing of inclusions at the solidification front of a maraging steel.

On the contrary when aggregation plays a major role, the solution of the PBE must be coupled to the CFD. Among the different techniques the class method (discretization of the number density distribution) combined with the fixed pivot technique (Kumar and Ramkrishna (1996)) solves the discrete formulation of Eq.1. As an illustration, the time evolution of a population of oxide inclusions in molten steel bath of a gas-stirred ladle is presented.

LAGRANGIEN TECHNIQUE: GROWTH AND REMOVAL OF EXOGENOUS INCLUSION

The industrial demand on premium-grade titanium processed by triple Vacuum Arc Remelting (VAR) has increased largely during the past few years. Extremely high quality is required for these products that compose the rotating parts of aircraft engines. A particular attention is paid on eliminating High Interstitial Defects (HIDs), also known as hard-α defects, which are nitrogen-enriched titanium particles. They are characterized by their high hardness and high melting point. Despite being rare (one inclusion in 500 tons (Bellot, 1997)), their presence in an engine component can lead to premature failure of titanium parts and fatal accidents. They represent one of the most deleterious anomalies encountered during the processing of titanium ingots.

The dissolution of an inclusion is governed (Bewlay and Gigliotti, 1997) by nitrogen transfer from the defect towards the liquid. This causes the formation of successive layers, in agreement with the Ti-N phase diagram. Therefore, a two-step model has been set up, which associates the computation of the nitrogen transfer and subsequent displacements of the interfaces to the simulation of a defect trajectory (Ghazal et al., 2010).

For each solid phase, the nitrogen diffusion equation is solved in a 1D geometry in spherical coordinates:

$$\frac{\partial \omega_N}{\partial t}=\frac{1}{r^2}\left(r^2 D_{N,i}\frac{\partial \omega_N}{\partial r}\right) \qquad (2)$$

where ω_N is the nitrogen mass fraction and $D_{N,i}$ the diffusivity in phase i. After solving the mass transport equation, the displacement of each interface is calculated from a mass balance. At the solid/liquid interface (liquid side), the calculation of the flux density towards the bulk is expressed by:

$$\phi = k\left(\rho_N^{\text{interface}}-\rho_N^{liq}\right) \qquad (3)$$

where $\rho_N^{\text{interface}}$ is the solute concentration of the liquid at the solid/liquid interface (obtained using the phase diagram given by Wriedt and Murray(1987)) and the concentration in the bulk, here equal to zero. The value of the mass transfer coefficient k depends mainly on the particle-liquid relative velocity and is computed using Ranz-Marshall correlation (Ranz and Marschall, 1952).

The trajectory model is a classical Lagrangian particle-tracking device. The movement of the defect is calculated by integrating Newton's law of motion (balance of forces) applied on a single spherical particle moving in a fluid media. The model accounts for all main forces acting on the particle, i.e. the gravity/buoyancy force, drag force, added mass effect and corrected Saffman lift force (Saffman, 1965; Mei, 1992). The hard-alpha defects can be considered as large inertia particles with a relatively high size ratio d_p/η. In consequence, the turbulent dispersion is neglected. However, the influence of turbulence is taken into account by modifying the drag coefficient through the correlation derived by Brucato (1998):

$$\frac{C_D - C_{D_0}}{C_{D_0}} = 8.67 \cdot 10^{-4} \left(\frac{d_P}{\eta} \right)^3 \qquad (4)$$

The trajectory model is implemented within the simulation software SOLAR (SOLidification during Arc Remelting), that describes the growth and solidification of the VAR ingot. At any time during the melting, SOLAR computes the velocity field in the liquid pool, intensity of flow turbulence, temperature and liquid fraction maps in the whole ingot (Quatravaux et al, 2004).

As already stated, the full modelling associates nitrogen transfer and trajectory calculations. An inclusion is assumed to fall from the electrode and is consequently introduced at the top of the ingot. The solution procedure consists on the following steps:

• At each time step, a dissolution computation is performed with updated values for the temperature and relative velocity. The nitrogen profile in the defect and the new particle size are calculated.

• Subsequently, the Lagrangian trajectory calculation gives the new position of the particle at the end of the time step. The new particle diameter, computed earlier, is used in the solution of Newton's law.

The procedure is repeated until the particle is totally dissolved or reaches the mushy zone. The model output consists in the 3D trajectory of the inclusion and the evolutions of the defect size and nitrogen profile. The calculation is reiterated for different initial locations and sizes of the particles leading to the assessment of the efficiency of the process to remove hard-alpha defects.

As an example, the successive trajectories of an inclusion (relative density 1.02, initial diameter 1 mm) during an actual triple VAR processing route were computed and are reported in Figure 2. As we can see, the model predicts that, in that case, the inclusion was eliminated during its residence in the third pool, where it was trapped in a 3D recirculation zone without escaping because of its small size at that moment.

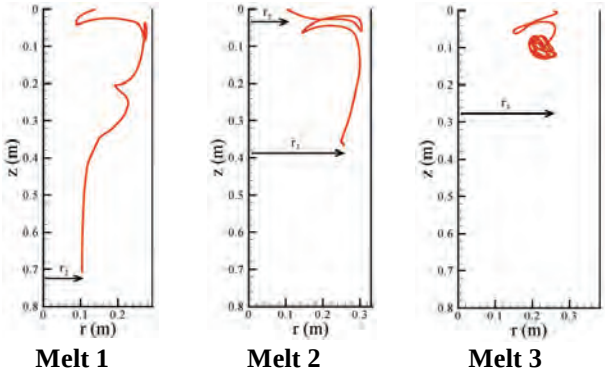

Figure 2: Top parts of the three successive ingots. Computed trajectories (projected in the (r,z) plane) of the inclusion in each of the ingots during triple VAR.

Figure 3 shows the overall evolution of the size of the α and β phases. In that case, the total dissolution time, around 200 s, was more or less equally distributed between the three successive melts.

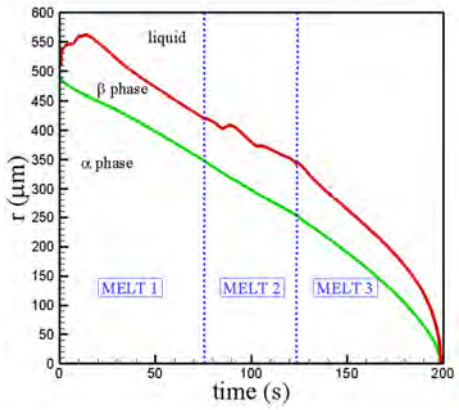

Figure 3: Computed evolution of the size of α and β phases of the hard-α particle.

This example highlights the effectiveness of combining a mass transfer model (for the particle dissolution rate) and a lagrangian particle-tracking calculation (for the particle trajectory).

NUCLEATION AND GROWTH OF INCLUSION AT THE SOLIDIFICATION FRONT

A maraging alloy is manufactured at APERAM and used in belts for CVT transmission in the automotive industry. This Fe-based alloy contains 18%Ni, 9%Co, 5%Mo and 0.45%Ti, and shows good fatigue properties. However, the Titanium combines itself with the small traces of Nitrogen present in the alloy to form endogenous inclusions of TiN. It leads to detrimental effect on the fatigue properties of the alloy by favouring the fatigue crack initiation and propagation.

Considering the very small amount of Nitrogen present in the liquid bath and the solubility product of TiN in liquid iron, it is thought that the TiN inclusions nucleate in the mushy zone during the ultimate remelting due to the segregation of solutes in the interdendritic liquid phase and to the reduction of the solubility of Nitrogen when temperature decreases.

A model has been developed to study the relationship between precipitation and segregation during solidification. An arbitrary volume of metal initially at liquidus temperature is considered, as sketched in Figure 4. This volume contains an imposed density of oxides spread into a log-normal distribution. The temperature is decreasing following an affine function of the final solidification time, which is an input parameter of the model. The solid fraction is directly related to temperature. The damping of the turbulence in the mushy zone and the cleanliness of this specialty steel make negligible the collision probability between TiN inclusions.

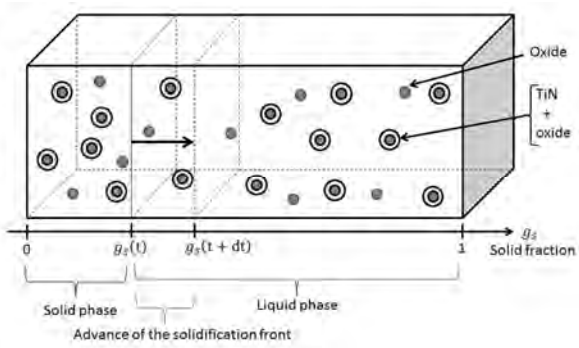

Figure 4: Sketch of the modeled system.

The model assumes that the nucleation can occur only on oxides if the supersaturation of the bath is at least higher than unity, the exact threshold depending on the size of the oxide nucleation site (Shibata et al, 1998). After nucleation, the growth of an inclusion is described by a first order kinetic law involving the distance to equilibrium.

An innovative part of this research relies in the treatment of the engulfment of inclusions during solidification coupled with the kinetics. The equations below describe this exchange (see Descotes, 2013):

$$\begin{aligned} d\left(g_s n^s_{TiN}(r,t)\right) &= +n^l_{TiN}(r,t)\,dg_s \\ d\left((1-g_s)n^l_{TiN}(r,t)\right) &= -n^l_{TiN}(r,t)\,dg_s \end{aligned} \qquad (5)$$

As stated in the introduction, the growth of a distribution of TiN is modelled by the PBE (Eq. 1) without right hand-side corresponding to the transport equation in the internal coordinate space (inclusion size):

$$\frac{\partial n^l_{TiN}(r,t)}{\partial t} = -G\,\frac{\partial n^l_{TiN}(r,t)}{\partial r} \qquad (6)$$

where G is the velocity of increase of the radius of a particle due to the reaction of precipitation ($m.s^{-1}$). The discretization of Eq. 6 in M classes was adopted and a Total Variational Diminishing (TVD) scheme (Leveque, 2008) was implemented to solve this none diffusive equation.

The calculation enables one to follow the evolution of the distributions of TiN in the liquid and solid phases. Figure 5 shows those two distributions after complete solidification as well as the oxide distribution which supports the TiN particles. It is seen that the oxide distribution and the TiN distribution in the last liquid volume have about the same shape. The difference is caused by some dispersion of the numerical scheme. Yet comparing with the resulting distribution of TiN in the solid phase, it clearly appears that the engulfment induces a radical change of distribution shape. The shape of this distribution is completely determined by the evolution of the growing speed of the inclusions in the liquid phase. In this case, the growing speed increases with time. The small TiN inclusions had therefore more time to be captured by the solidification front than the larger ones, resulting in a peak of density of small TiN in the solid phase.

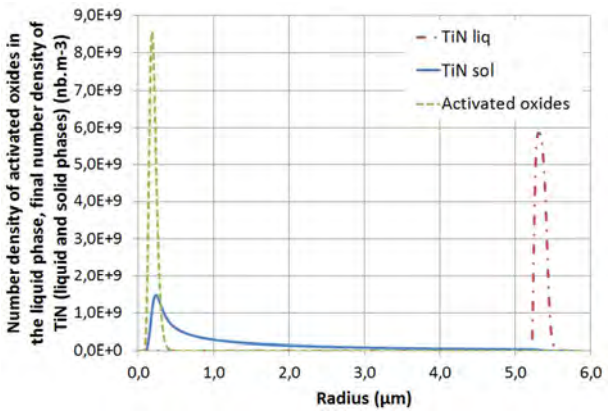

Figure 5: Initial oxide distribution in the liquid phase, and final TiN distributions in the liquid and solid phases.

Predicted maximal TiN sizes have been found to be qualitatively in accordance with industrial observations. The model reveals the important link between the solidification time and inclusion sizes, as well as the influence of the initial oxide density.

This inclusion model enables one to study the effect of several parameters of solidification on the inclusions growth: nitrogen content, oxide density, type of oxide, and solidification time. A coupling of this inclusion model with a process simulation at the ingot scale has been carried out and it improves the knowledge of our industrial partner regarding the effect of some process parameters on the inclusion behavior.

AGGLOMERATION AND REMOVAL OF ENDOGENOUS INCLUSIONS IN METALLURGICAL REACTOR

Gas-stirring ladle treatment of liquid steel has been pointed out for a long time as the processing stage mainly responsible for the inclusion population (Mazumdar and Guthrie, 1995; Söder et al, 2005), which are mainly composed of non-metallic oxide inclusions such as calcium aluminate inclusions. The injection of argon through one or more porous plugs at the bottom of the reactor provides both mixing of the liquid metal to achieve thermal and chemical homogeneity and the entrapment of the inclusions by the flotation mechanism. The large inclusion density (ω_p usually larger than 10 ppm) and the strong stirring power (1 to 1000 W/t) make the aggregation an important phenomenon (see figure 1), and the mechanisms involved are:

- the collisions between inclusions, which can lead to aggregation and the growth of aggregates,
- the collisions with bubbles, which lead to the mechanism of flotation,
- the entrapment at the interface between the liquid bath and slag coverage,
- the separation induced by gravity.

The approach adopted for reactor modelling is divided into two parts. The bubble plumes play an important role in metal bath mixing while, owing to their small weight fraction (<0.01%), the inclusions do not affect the flow. First, the two-phase flow turbulent bubble-liquid metal is simulated for the 3D geometry of the ladle and a strong coupling is achieved between the

liquid metal and the bubbles (Daoud et al, 2005). This resolution provides the velocity fields as well as the maps of local flow turbulence and retention rate (gas volume fraction in the mixture); these data define the conditions of inclusion interaction (aggregation, flotation, entrapment).
The discrete formulation of Eq. 1 is obtained by introducing N_i as:

$$N_i(x,t) = \int_{r_i}^{r_{i+1}} n(r,x,t)dr \qquad (7)$$

The transient solution to the Eq. 1 can be obtained by separating the transport and collision operators as proposed by Toro (1999). In the first step, the transport equation of the quantity N_i is solved using the Finite Volume Method:

$$\frac{\partial \mathbf{N_i}}{\partial \mathbf{t}} + \mathbf{div}(u_f \mathbf{N_i}) = 0 \qquad (8)$$

In the second step, the population balance (Eq. 9) is solved in each control volume applying the cell average technique (Kumar, 2006) which is a variant of the fixed pivot method of Kumar and Ramkrishna (1996) leading to a significant reduction in numerical diffusion:

$$\frac{\partial N_i}{\partial t} = H_i \qquad (9)$$

H_i is the sum of four terms corresponding to aggregation, flotation, settling and surface entrapment. The aggregation and flotation kernels are an issue of great development and the reader will find details of the physical phenomena and of the applied models in (Daoud et al, 2011; DeFelice, et al, 2012).
The solution to the system of Eq. (8 & 9) is based on the Fluent CFD code V13.0, where a large number of user defined functions (UDF) has been incorporated.

The numerical simulation is applied to a full scale 60 t steel ladle. Argon is injected through two porous plugs, located at the base of the ladle, and an example of gas-molten steel flow is given in Figure 6. We have used a log-normal distribution as an initial particle size distribution (psd) with a total mass content corresponding to 7.9 ppm of Total Oxygen (TO) content –considering a population of calcium aluminate inclusions. Unfortunately the log-normal law cut off the distribution for the inclusions larger than 30 µm; it does not fit with accurate cleanliness measurements which detect rare (but existing) large inclusions (>50 µm).

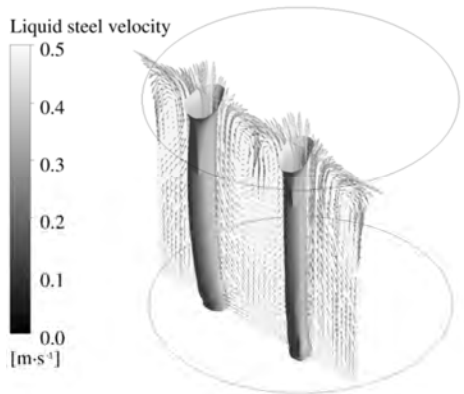

Figure 6: Predicted velocity of the liquid steel along with the argon plumes (isosurface of the 1% gas volume fraction).

The initial distribution is plotted in Figure 7 where the inclusion population is rendered discretely into twenty different sized classes. The computed distribution continuously evolves with time, as larger size particles appear due to the agglomeration of small size particles. Since the flotation and sedimentation mechanisms are strongly dependent of the particle size, the large size aggregates are preferentially removed. As a consequence the total mass of inclusions in the ladle diminishes and the associated rate of removal is not constant but slowly increases.

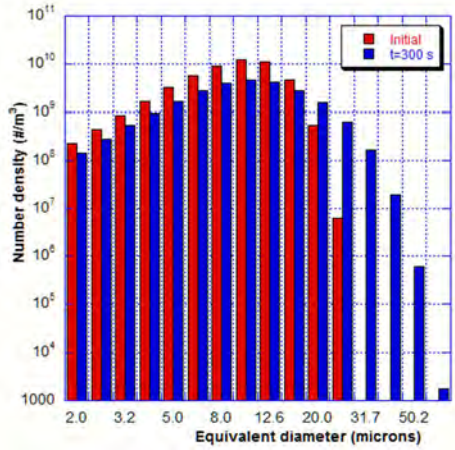

Figure 7: Initial psd and psd after 300 s of stirring

The numerical simulation allows us to compare the relative importance of the different mechanisms on the inclusion population. The frequencies of the four mechanisms (aggregation, flotation, settling and capture on the free surface) have been reported in Figure 8 (at time equal 300 s). The sign (-) or (+) indicates that the numerical density of a given class decreases or increases following the aggregation process. Of course the agglomeration mechanism modifies the distribution whereas the three other mechanisms remove the inclusions from the bath.

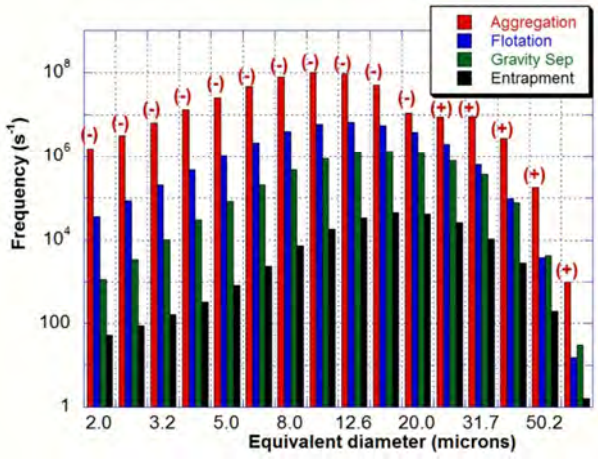

Figure 8: Frequency of mechanisms as a function of inclusion size at 300 s – (-): reduced (+): produced.

The Figure 8 clearly highlights that the major role is played by agglomeration, since the frequency of the flotation mechanism is two orders of magnitude lower than the agglomeration one. This is the main reason why the psd continuously evolves with time and does not reach the equilibrium in this example. This result readily explain the stirring practice proposed by Zhang

and Thomas (2003) consisting in a first vigorous stirring to give rise the production of large aggregates, followed by a weak stirring to facilitate the aggregate removal into the slag while minimizing the generation of larger inclusions via collisions.

CONCLUSION

This paper presents three modelling studies of inclusion behaviour in metallic bath involving dissolution or growing by mass transfer and aggregation. They illustrate the application of the Lagrangian technique (for isolated exogenous inclusion in titanium bath) and the Eulerian technique without or with aggregation process.

These numerical techniques are nowadays considered matures but still developing. In particular, accurate computation of the turbulent metal flow is of utmost importance, especially when physical mechanisms such as aggregation, coalescence or fragmentation of the particles have to be considered.

Finally the validation of these numerical simulations remains a tricky problem since dip sampling in liquid alloy at very high temperature is difficult to achieve.

ACKNOWLEDGEMENTS

The authors wish to acknowledge Ghassan Ghazal and Ismaël Daoud, formerly graduate students at IJL, for their implication in the works presented here. They also thank their partners in TIMET (A.F. Wilson, Y. Millet) and APERAM (V. Perrin-Guérin, S. Witzke) Companies. As a part of the CIREM (Behaviour of Inclusions in Metallurgical Reactors) Project, this work has been partly supported by the French National Research Agency (ANR06 MATPRO 0005).

REFERENCES

Abrahamson J., *Chem. Eng. Science*, 30, 1371 (1975).

Bellot J.P., Foster B., Hans S., Hess E., Ablitzer D. and Mitchell A., *Metall. Mater. Trans. B*, 1997, 28B, 1001 (1997).

Bewlay B.P. and Gigliotti M.F.X., *Acta Mater.*, 45, 357 (1997).

Brucato A., Grisafi F. and Montante G., *Chem. Eng. Sci.*, 53, 3295 (1998).

Daoud I.L.A. , Rimbert N., Jardy A., Oesterle B., Hans S. , Bellot J.P., *Advanced Engineering Materials*, 13, 543 (2011).

De Felice V., Daoud I.L.A, Dussoubs B., Jardy A., Bellot J.P., *ISIJ Int.*, 52, 1273 (2012).

Descotes V., Bellot J.P., Witzke S., Jardy A., International Symposium on Liquid Metal Processing and Casting LMPC 2013, september 2013, Austin (Texas, USA), *Proceedings edited by TMS*, pp..201-206

Ghazal G., Jardy A., Chapelle P. and Millet Y., *Metall. Mater. Trans. B*, 41B, 646 (2010).

Kumar J., Peglow M., Warnecke G., Heinrich S., Mörl L., *Chem. Eng. Sci.*, 61, 3327 (2006).

Kumar S., Ramkrishna D., *Chem. Eng. Sci.*, 51, 1311 (1996).

Leveque R., "Numerical Methods for Conservation Laws*". 2nd ed.; Birkhäuser Verlag* (2008).

Mazumdar D., Guthrie R.I.L., *ISIJ Int*., 35, 1 (1995).

Mei R., *Int. J. Multiphase Flow*, 18, 145 (1992).

Quatravaux T. , Ryberon S., Hans S., Jardy A., Lusson B., Richy P.E. and Ablitzer D., *J. Mater. Sci*., 39, 7183 (2004).

Ranz W.E. and Marshall W.R., *Chem. Eng Prog*., 48, 141 (Part I) and 173 (Part II) (1952).

Saffman P.G., Turner J.S., *J. Fluid Mech*.,1, 16 (1956).

Saffman P.G., *J. Fluid Mech*., 22, 385 (1965).

Söder M., Jönsson O., Jonsson L., Nzotta M., *Steel Research Int.*, 481 (2005).

Shibata H., Yin H., Yoshinaga S., Emi T., Suzuki M., *ISIJ International*, 38(2), 149 (1998).

Toro E.F., "Riemann solver and numerical methods for fluid dynamics: a pratical introduction", *Springer, Berlin*, (1999).

Wriedt H.A. and Murray J.L., "Phase diagrams of binary titanium alloys", J.L. Murray, ed., *ASM International*, 176 (1987).

Zhang L., Thomas B.G., *ISIJ Int*., 3, 271 (2003).